THE

PHILOSOPHICAL MAGAZINE

EDITOR
PROFESSOR N. F. MOTT, M.A., D.Sc., F.R.S.

EDITORIAL BOARD
SIR LAWRENCE BRAGG, O.B.E., M.C., M.A., D.Sc., F.R.S.
SIR GEORGE THOMSON, M.A., D.Sc., F.R.S.
PROFESSOR A. M. TYNDALL, C.B.E., D.Sc., F.R.S.

VOL. V.—EIGHTH SERIES

JANUARY—DECEMBER 1960

LONDON:
TAYLOR & FRANCIS LTD, RED LION COURT, FLEET STREET, E.C.4.

"Meditationis est perscrutari occulta; contemplationis est admirari perspicua.... Admiratio generat quæstionem, quæstio investigationem, investigatio inventionem."—*Hugo de S. Victore.*

——"Cur spirent venti, cur terra dehiscat,
Cur mare turgescat, pelago cur tantus amaror,
Cur caput obscura Phœbus furrugine condat,
Quid toties diros cogat flagrare cometas,
Quid pariat nubes, veniant cur fulmina cœlo,
Quo micet igne Iris, superos quis conciat orbes
Tam vario motu."

J. B. Pinelli ad Mazonium.

ALERE FLAMMAM.

CONTENTS OF VOL. V. Nos. (49–60)
(EIGHTH SERIES)

NUMBER 49—JANUARY

PAGE

Direct Observations of the Annealing of Prismatic Dislocation Loops and of Climb of Dislocations in Quenched Aluminium. By J. Silcox and M. J. Whelan, Crystallographic Laboratory, Cavendish Laboratory, Cambridge, England 1

On the Stability of the Dislocation Substructure in Quenched Aluminium. By R. Vandervoort and J. Washburn, Minerals Research Laboratory, University of California, Berkeley, California 24

Dislocation-locking by Carbon, Nitrogen and Boron in α-iron. By I. Codd and N. J. Petch, Metallurgy Department, University of Leeds 30

On Dislocation Formation by Vacancy Condensation. By G. Schoeck and W. A. Tiller, Westinghouse Research Laboratories, Beulah Road, Churchill Borough, Pittsburgh 35, Pennsylvania 43

An Approximate Correlation between the Electron Fermi Energy and Work Function of a Metal. By J. H. O. Varley, Atomic Energy Research Establishment, Harwell, Didcot, Berks. 64

The Density of States in Lead. By A. V. Gold, Division of Pure Physics, National Research Council, Ottawa, Canada 70

The Fine Structure of Films of Rubber and other Polymers. By M. Seal, Research Laboratory for the Physics and Chemistry of Solids, Department of Physics, University of Cambridge 78

The Thermal Conductivity of Germanium, Silicon and Indium Arsenide from 40°c to 425°c. By Audrey D. Stuckes, Metropolitan-Vickers Electrical Co. Ltd., Trafford Park, Manchester, 17 84

Correspondence:
- Hall Effect in Liquid and Solid Mercury. By P. W. Kendall and N. E. Cusack, Department of Physics, Birkbeck College, University of London 100
- The Effect of Electropolishing on the Retention of Vacancies During Quenching in Al and Al Alloys. By E. J. Freise, M. E. Fine and A. Kelly, Department of Materials Science, Northwestern University, Evanston, Illinois, U.S.A. 101

Reviews of Books 104

NUMBER 50—FEBRUARY

The de Haas–van Alphen Effect in Copper, Silver and Gold. By D. Shoenberg, Royal Society Mond Laboratory, Cambridge 105

Magnetoresistance of Copper, Silver and Gold. By M. G. Priestley, Royal Society Mond Laboratory, Cambridge 111

The g-factor and de Haas–van Alphen Effect of Electrons in Bismuth. By M. H. Cohen, Cavendish Laboratory, Cambridge and E. I. Blount, Westinghouse Research Laboratories, Pittsburgh, Pennsylvania 115

The Infra-red Absorption of Hot Semiconducting Diamonds. By C. D. Clark, P. Kemmey and E. W. J. Mitchell, Physics Research Laboratory, The University, Reading and B. W. Henvis, Naval Research Laboratory, Washington, D.C. 127

© = m13929
75
1 new

PAGE

The Effect of Internal Oxidation on the Damping Capacity of Copper–Silicon Alloys. By T. B. Gibbons and S. O'Hara, Royal College of Science and Technology, Glasgow, C.1 140

A 10 in. Diameter Liquid Hydrogen Bubble Chamber. By Margaret H. Alston, D. C. Cundy, W. H. Evans, R. W. Newport, and P. R. Williams, Nuclear Physics Research Laboratory, University of Liverpool 146

Systematic Track Distortion in a 10 in. Diameter Liquid Hydrogen Bubble Chamber. By D. C. Cundy, W. H. Evans, D. W. Hadley, P. Mason, R. W. Newport, J. R. Smith and P. R. Williams, Nuclear Physics Research Laboratory, University of Liverpool 154

The Angular Dislocation. By Elizabeth H. Yoffe, Cavendish Laboratory, Cambridge 161

The Kinetics of the Growth of Precipitates from Solid Solutions. By J. Burke, Department of Metallurgy, University of Liverpool 176

Correspondence:

- Density and Expansivity of Solid Krypton. By B. F. Figgins and B. L. Smith, Department of Physics, Queen Mary College (University of London), London, E.1 186
- An Anomaly in the Heat Capacity of Chromium at 38·5°c. By R. H. Beaumont, H. Chihara and J. A. Morrison, Division of Pure Chemistry, National Research Council, Ottawa, Canada 188
- Direct Observation of Dislocations in Magnesium Oxide. By J. Washburn, A. Kelly and G. K. Williamson, Department of Metallurgy, University of Cambridge 192

Reviews of Books 194

NUMBER 51—MARCH

Point Defects in Platinum. By G. R. Piercy, Atomic Energy of Canada Limited, Chalk River, Ontario 201

Study of Adsorbed Gas Films by Electron Diffraction. By L. H. Germer, E. J. Scheibner and C. D. Hartman, Bell Telephone Laboratories, Inc., Murray Hill, New Jersey 222

The Hardening of Lithium Fluoride by Electron Irradiation. By A. D. Whapham and M. J. Makin, Metallurgy Division, Atomic Energy Research Establishment, Harwell 237

The Electrical Resistivity of Stacking Faults. By A. Howie, Crystallographic Laboratory, Cavendish Laboratory, Cambridge 251

Infra-red Measurements of the Optical Constants of Liquid Silver. By J. N. Hodgson, University College of North Staffordshire, Keele, Staffordshire 272

The Damage and Recovery of Neutron Irradiated Tungsten. By M. W. Thompson, Atomic Energy Research Establishment, Harwell, Berks 278

Correspondence:

- A Possible Example of the Muon Radiative Decay with Internal Conversion of the γ-ray. By V. Mayes, H. H. Wills Physical Laboratory, University of Bristol 297
- Direct Electron Microscopy of Thin Foils of Internally Oxidized Dilute Copper Alloys. By M. F. Ashby and G. C. Smith, Department of Metallurgy, University of Cambridge 298

Reviews of Books 302

NUMBER 52—APRIL

PAGE

Observations on Extensive Air Showers. VIII. The Distribution in Declination and Curvature of the Shower Front. By E. F. Bradley and N. A. Porter, Atomic Energy Research Establishment, Harwell....... 305

The Relative Abundances of the Heavy Nuclei in the Primary Cosmic Radiation. By C. J. Waddington, H. H. Wills Physical Laboratory, University of Bristol.. 311

The Observation of Sharp Internal Friction Peaks in Beryllium. By E. W. Dickson, Tube Investments Research Laboratories, Hinxton Hall, Cambridge 325

Ferromagnetism in Pd-rich Palladium–Iron Alloys. By J. Crangle, Department of Physics, The University, Sheffield 10................... 335

Kinetics of Ordering in Fe_3Al. By R. Feder and R. W. Cahn, Department of Physical Metallurgy, University of Birmingham, England. 343

The Refractive Indices of Liquid and Solid Argon. By G. O. Jones and B. L. Smith, Department of Physics, Queen Mary College (University of London), London, E.1.. 355

Isotopic Spin Selection Rules. XIII. The 6·92 mev State of ^{16}O Revisited. By R. E. Pixley, J. V. Kane and D. H. Wilkinson, Brookhaven National Laboratory, Upton, N.Y., U.S.A. 359

Isotopic Spin Selection Rules. XIV. Transitions between Mirror States in ^{13}C and ^{13}N. By J. V. Kane, R. E. Pixley and D. H. Wilkinson, Brookhaven National Laboratory, Upton, N.Y., U.S.A................. 365

Microtwinning in Epitaxial Nickel–Iron Films. By R. D. Burbank and R. D. Heidenreich, Bell Telephone Laboratories, Incorporated, Murray Hill, New Jersey.. 373

Eutectic Compositions and Liquid Immiscibility in Certain Binary Alloys. By W. Hume-Rothery and E. Anderson, Department of Metallurgy, University of Oxford.................................. 383

Correspondence:

- An Observation of Crack Formation in MgO. By W. G. Johnston, General Electric Research Laboratory, Schenectady, N.Y......... 407
- Upper Limit to Anisotropy of Inertial Mass from Nuclear Resonance. By R. W. P. Drever, Department of Natural Philosophy, University of Glasgow... 409
- The Embrittlement of Molybdenum by Neutron Irradiation. By A. A. Johnson, Physical Metallurgy Department, Imperial College, London, S.W.7.. 413
- On Microcreep in Zinc Whiskers. By P. B. Price, Physics and Chemistry of Solids Laboratory, Cavendish Laboratory, Cambridge 417

Reviews of Books 421

NUMBER 53—MAY

Some Effects of Vibration on the Internal Friction of Sodium Chloride. By R. W. Whitworth, Department of Physical Metallurgy, University of Birmingham... 425

Reverse Bending of Crystals of Silver Chloride. By M. T. Sprackling, H. H. Wills Physics Laboratory, University of Bristol................. 441

The Generation of Dislocation Loops at the Surfaces of Crystals of Silver Bromide. By J. T. Bartlett and J. W. Mitchell, H. H. Wills Physics Laboratory, University of Bristol........................ 445

PAGE

The Electrical Resistance of Iron–Aluminium Alloys and its Dependence on Crystallographic Order. By R. W. Cahn and R. Feder, Department of Physical Metallurgy, University of Birmingham 451

Nuclear Magnetic Resonance in Lithium and Dilute Lithium–Magnesium Alloys. By D. G. Hughes, Division of Pure Physics, National Research Council, Ottawa 467

On the Growth of Cadmium Crystals from the Vapour. By P. B. Price, H. H. Wills Physical Laboratory, University of Bristol 473

The Dislocation Distribution, Flow Stress, and Stored Energy in Cold-worked Polycrystalline Silver. By J. E. Bailey and P. B. Hirsch, Crystallographic Laboratory, Cavendish Laboratory, Cambridge 485

Investigation of the Annealing of Nickel Deformed by Compression by X-ray and Stored Energy Measurements. By D. Michell and E. Lovegrove, Division of Tribophysics, Commonwealth Scientific and Industrial Research Organization, University of Melbourne, Australia 499

Calculation of Stored Energy from Broadening of X-ray Diffraction Lines. By E. A. Faulkner, Division of Tribophysics, Commonwealth Scientific and Industrial Research Organization, University of Melbourne 519

Correspondence:

Statistical Methods in Rock Magnetism. By S. K. Runcorn, King's College, Newcastle upon Tyne 523

The K Emission Spectrum of Metallic Lithium. By R. S. Crisp and S. E. Williams, University of Western Australia, Nedlands, Western Australia 525

Diamagnetic Shielding of Nuclei in Metals. By T. P. Das, Department of Chemistry, Columbia University, New York and E. H. Sondheimer, Department of Mathematics, Queen Mary College, London 529

Direct Evidence for the Presence of Quarter-dislocations in Talc Monocrystals. By S. Amelinckx and P. Delavignette, S.C.K. Mol-Donk, Belgium 533

NUMBER 54—JUNE

Nuclear Interactions of 5·7 Bev Protons in Photographic Emulsion. By V. Y. Rajopadhye, H. H. Wills Physical Laboratory, University of Bristol 537

A Statistical Theory of Ionospheric Drifts. By J. P. Dougherty, Cavendish Laboratory, Cambridge 553

Direct Observation of Defects in Evaporated Silver. By V. A. Phillips, General Electric Research Laboratory, Schenectady, New York 571

Atmospheric Temperature Effects on the Solar Daily Variation of Cosmic Ray Intensity. By J. J. Quenby and T. Thambyahpillai, Imperial College of Science and Technology, London 585

Cosmic-ray Intensity Variations and the Interplanetary Magnetic Field. By H. Elliot, Imperial College of Science and Technology, London 601

Electron-microscopic Observations on Radiation Damage in Graphite. By W. Bollmann, Batelle Memorial Institute, Geneva, Switzerland 621

Cross-tie Walls in Thin Permalloy Films. By M. Prutton, International Computers and Tabulators Ltd., Research and Design Division, Gunnels Wood Road, Stevenage, Herts 625

The Generation of Vacancies in Metals. By R. S. Barnes, Atomic Energy Research Establishment, Harwell, Berkshire 635

Reviews of Books 647

NUMBER 55—JULY

PAGE

Creep in Face-centred Metals and Solid Solutions with special reference to α-brasses. By P. FELTHAM and G. J. COPLEY, The University, Leeds 649

On Dislocations Formed by the Collapse of Vacancy Discs. By C. ELBAUM, Physics Department, Metals Research Laboratory, Brown University, Providence, Rhode Island 669

Palaeomagnetism of the British Carboniferous System. By C. W. F. EVERITT, Imperial College, London and J. C. BELSHÉ, Department of Geodesy and Geophysics, Cambridge.............................. 675

Recovery of Quenched-in Resistivity at High Temperatures in Gold. By M. MESHII and J. W. KAUFFMAN, Materials Science Department, Northwestern University Evanston, Illinois, U.S.A. 687

Localized Modes in Crystals and Sharp Details of the Optical Absorption Spectra. By ROBERT ENGLMAN, Department of Physics, Israel Institute of Technology, Haifa, Israel 691

Micro-cracks and their Relation to Flow and Fracture in Single Crystals of Magnesium Oxide. By F. J. P. CLARKE and R. A. J. SAMBELL, Atomic Energy Research Establishment, Harwell, Berks 697

Etching of Strained Aluminium. By G. A. BASSETT and C. EDELEANU, Tube Investments Research Laboratories, Cambridge 709

The Anhysteretic Remanence of Magnetic Recording Tapes. By E. P. WOHLFARTH, Department of Mathematics, Imperial College, London .. 717

An Electron Spin Resonance Investigation of Photographic Processes in Crystals of AgCl containing Traces of CuCl. By I. S. CICCARELLO, M. B. PALMA-VITTORELLI and M. U. PALMA, Istituto di Fisica dell'Università di Palermo 723

Dislocation Nets in Bismuth and Antimony Tellurides. By P. DELAVIGNETTE and S. AMELINCKX, Centre d'Etude de l'Energie Nucléaire, Mol-Donk, Belgium 729

Effect of Temperature on Yield and Flow Stress of B.C.C. Metals. By HANS CONRAD, Metallurgy Department, Westinghouse Research Laboratories, Pittsburgh 35, Pennsylvania 745

Correspondence:

On the Residual Resistance of Binary Alloys. By E. VERBOVEN, Instituut voor theoretische fysica der Rijksuniversiteit, Utrecht, Netherland 753

A Note on the Selection Rules for Optical Transitions in Alloys. By J. M. ZIMAN, Cavendish Laboratory, University of Cambridge ... 757

The Shear Component of Ductile Fracture. By K. E. PUTTICK, Davy Faraday Research Laboratory, The Royal Institution, 21 Albemarle Street, London, W.1 759

Reviews of Books.. 763

NUMBER 56—AUGUST

The Thermoelectric Power of Pure Copper. By A. V. GOLD, D. K. C. MACDONALD, W. B. PEARSON and I. M. TEMPLETON, Division of Pure Physics, National Research Council, Ottawa, Canada................ 765

Observations of the Decomposition of Crystals of Lead Iodide in the Electron Microscope. By A. J. FORTY, H. H. Wills Physics Laboratory University of Bristol.. 787

Dislocations with Burgers Vectors of $a\langle 100\rangle$ in Crystals of Silver Bromide. By J. T. BARTLETT and J. W. MITCHELL, H. H. Wills Physics Laboratory, University of Bristol.............................. 799

PAGE

The Atomic Diffusion of Platinum in Gold. By A. J. Mortlock, A. H. Rowe and A. D. Le Claire, Metallurgy Division, Atomic Energy Research Establishment, Harwell 803

Charged Dislocations in Lithium Fluoride. By R. L. Sproull, European Research Associates, Brussels, Belgium 815

Electron Microscope Observations on the Annealing Processes Occurring in Cold-worked Silver. By J. E. Bailey, Crystallographic Laboratory, Cavendish Laboratory, Cambridge 833

Strain-broadening of Nuclear Magnetic Resonance Lines in Copper. By E. A. Faulkner, Division of Tribophysics, Commonwealth Scientific and Industrial Research Organization, University of Melbourne, Australia 843

Observation of Interstitial Atoms in F.C.C. Metals. By A. Seeger, P. Schiller and H. Kronmüller, Max-Planck-Institut für Metallforschung, Stuttgart, and Institut für theoretische und angewandte Physik der Technischen Hochschule Stuttgart, Germany 853

Lattice Vibrations of Sodium Chloride: Experimental and Theoretical Heat Capacity Data. By J. R. Hardy, Department of Physics, University of Reading, Berkshire and A. M. Karo, Lawrence Radiation Laboratory, University of California, Livermore, California 859

Correspondence :

Measurements of Thermoelectricity below 1°K—IV. By D. K. C. MacDonald, W. B. Pearson and I. M. Templeton, Division of Pure Physics, National Research Council, Ottawa, Canada .. 867

Reviews of Books 871

NUMBER 57—SEPTEMBER

Pyramidal Glide and the Formation and Climb of Dislocation Loops in Nearly Perfect Zinc Crystals. By P. B. Price, Physics and Chemistry of Solids, Cavendish Laboratory, Cambridge 873

The Thermal Conductivity of Impure InAs at High Temperatures. By F. W. Sheard, Cavendish Laboratory, Cambridge 887

Nuclear Magnetic Resonance in β Brass. By G. W. West, Division of Tribophysics, Commonwealth Scientific and Industrial Research Organization, University of Melbourne, Australia 899

Some Magnetic Properties of the Ising Model. By D. M. Burley, Mathematics Department, The University, Glasgow, W.2 909

The Spacing of Prismatic Dislocation Loops. By R. Bullough and R. C. Newman, Research Laboratory, Associated Electrical Industries, Aldermaston Court, Aldermaston, Berkshire 921

Some Elastic and Thermal Properties of Zirconium and Tungsten. By A. Myers, Physics Department, the University, Leeds 927

The Mechanism of Quench-hardening and its Recovery in Gold. By M. Meshii and J. W. Kauffman, Materials Science Department, Northwestern University, Evanston, Illinois, U.S.A. 939

Unloading Effects in Aluminium and Aluminium–Zinc Single Crystals. By A. T. Thomas, Aluminium Laboratories Limited, Banbury, Oxon, England 947

Anomalous Electron Absorption Effects in Metal Foils. By H. Hashimoto, Metallurgy Department, Cambridge University and A. Howie and M. J. Whelan, Cavendish Laboratory, Cambridge 967

Reviews of Books 975

NUMBER 58—OCTOBER

PAGE

The Effects of Surface Condition on the Mechanical Properties of Lithium Fluoride Crystals. By A. R. C. Westwood, RIAS, 7212 Bellona Avenue, Baltimore 12, Maryland, U.S.A. 981

Electron Microscope Observations of Deformed Magnesium Oxide. By J. Washburn, G. W. Groves, A. Kelly and G. K. Williamson, Department of Metallurgy, University of Cambridge 991

Cyclotron Resonance in Lead. By J. E. Aubrey, The Royal Society Mond Laboratory, University of Cambridge 1001

The Anisotropy of Optical Absorption Induced in Sapphire by Neutron and Electron Irradiation. By E. W. J. Mitchell, J. D. Rigden and P. D. Townsend, Physics Department, The University, Reading 1013

Some Observations on the Stress-corrosion Cracking of α-brass and Similar Alloys. By C. Edeleanu, Tube Investments Research Laboratories, Hinxton Hall, nr. Cambridge and A. J. Forty, H. H. Wills Physics Laboratory, University of Bristol 1029

Thermal Aspects of the Growth of Thin Films by Vacuum Sublimation. By G. Gafner, National Physical Research Laboratory, P.O. Box 395, Pretoria, South Africa 1041

The Annealing of Electron Irradiation Damage in Graphite. By W. N. Reynolds and P. R. Goggin, Atomic Energy Research Establishment, Harwell, Berks. 1049

The Phonon Drag Component of the Thermoelectric Power of the Alkali Metals at Low Temperatures. By M. Bailyn, Northwestern University, Evanston, Illinois, U.S.A. 1059

Errata 1087

NUMBER 59—NOVEMBER

The Fermi Surface in White Tin. By A. V. Gold, Royal Society Mond Laboratory, University of Cambridge, and Division of Pure Physics, National Research Council, Ottawa, Canada and M. G. Priestley, Royal Society Mond Laboratory, University of Cambridge. 1089

The Determination of the Flux of Cosmic Ray Protons with Nuclear Emulsions. By C. J. Waddington, H. H. Wills Physical Laboratory, University of Bristol 1105

X-ray Evidence for Segregation of Solute to Stacking Faults in a Copper–Aluminium Alloy. By R. W. Cahn and R. G. Davies, Department of Physical Metallurgy, The University, Birmingham 15, England 1119

A Magnetic Study of Precipitation in a Gold–Cobalt Alloy. By P. Gaunt, Department of Physics, University of Sheffield, Sheffield, 10, 1127

Movement of Point Defects During Fatigue of Aluminium Crystals. By E. Roberts and R. W. K. Honeycombe, Department of Metallurgy, University of Sheffield 1147

The Variation with Time of the Flux and Energy Spectrum of Primary Cosmic Ray Alpha Particles. By P. J. Duke, H. H. Wills Physics Laboratory, University of Bristol 1151

Soft x-ray Emission from Potassium Metal in the 40–1000 Å Range. By R. S. Crisp, Department of Physics, University of Western Australia, Nedlands, W.A. 1161

The Influence of Solutes on Self-diffusion in Metals. By A. B. Lidiard, Physics Department, The University, Reading, Berkshire..... 1171

Optical Model Analysis of Nuclear Scattering. By B. Buck, R. N. Maddison and P. E. Hodgson, Clarendon Laboratory, Oxford........ 1181

Correspondence:

Giant Spin Density Fluctuations. By J. C. Phillips, Royal Society Mond Laboratory, Cambridge 1193

PAGE

The Etching of Sub-structures in Beryllium. By J. Sawkill and J. E. Meredith, Tube Investments Research Laboratories, Hinxton Hall, Cambridge 1195
Stress Concentrations at Crystal Surfaces and the Embrittlement of Sodium Chloride. By D. M. Marsh, Tube Investments Research Laboratory, Hinxton Hall, Saffron Walden, Essex 1197
Reviews of Books 1201
Book Notices 1202
Errata 1203

NUMBER 60—DECEMBER

The Soft x-ray Spectra of Lithium, Magnesium and Aluminium and their Alloys. By R. S. Crisp and S. E. Williams, Department of Physics, University of Western Australia........ 1205
Pitting of Aluminium at Grain Boundaries after Ageing. By G. A. Bassett and C. Edeleanu, Tube Investments Research Laboratories, Hinxton Hall, Essex........ 1217
Etch Pits and Dislocations in Ice Crystals. By G. W. Bryant and B. J. Mason, Imperial College, London........ 1221
Measurement of the Debye–Waller Temperature Factor for Silver and α-iron. By C. W. Haworth, Department of Metallurgy, Sheffield University; formerly Department of Metallurgy, Oxford University.... 1229
The Effect of Lattice Distortion Around Point Defects on the Scattering of Long Wavelength Neutrons. By D. G. Martin, Metallurgy Division, Atomic Energy Research Establishment, Harwell, Berks...... 1235
The Nature of Radiation-induced Point Defect Clusters. By R. S. Barnes and D. J. Mazey, Atomic Energy Research Establishment, Harwell, Didcot, Berks........ 1247
The Growth of Prismatic Dislocation Loops during Annealing. By C. A. Johnson, Materials Research Laboratory, University of California, Berkeley, California 1255
The Magnetic Susceptibility of Vanadium–Chromium Solid Solutions. By B. G. Childs, W. E. Gardner and J. Penfold, Atomic Energy Research Establishment, Harwell, Berks........ 1267
The Hyperfine Structure of ^{209}Bi. By R. S. Title and K. F. Smith, Cavendish Laboratory, Cambridge........ 1281
The Hyperfine Structure of ^{121}Sb and ^{123}Sb. By P. C. B. Fernando, G. K. Rochester, I. J. Spalding and K. F. Smith, Cavendish Laboratory, Cambridge........ 1291
Correspondence:
- On the Scattering of Phonons by Spins at Low Temperatures: Experimental. By H. M. Rosenberg and B. Sujak, The Clarendon Laboratory, Oxford........ 1299
- On the Scattering of Phonons by Spins at Low Temperatures: Theoretical. By R. Orbach, University of California, Department of Physics, Berkeley, California and Clarendon Laboratory, Oxford........ 1303
- The Spin of ^{124}Sb and the Spin and Moments of ^{122}Sb. By P. C. B. Fernando, G. K. Rochester and K. F. Smith, Cavendish Laboratory, Cambridge........ 1309
- Activation of Single Phonon Infra-red Lattice Absorption in Neutron Irradiated Diamond. By S. D. Smith and J. R. Hardy, J. J. Thomson, Physical Laboratory, University of Reading..... 1311

Reviews of Books........ 1315
Subject Index........ 1317
Index of Authors (with Titles)........ 1321
List of Contents........ iii
List of Plates........ xi

PLATES

1–5. Illustrative of J. Silcox and M. J. Whelan's Paper on Direct Observations of the Annealing of Prismatic Dislocation Loops and of Climb of Dislocations in Quenched Aluminium.
6–14. Illustrative of R. Vandervoort and J. Washburn's Paper on The Stability of the Dislocation Substructure in Quenched Aluminium.
15–18. Illustrative of M. Seal's Paper on the Fine Structure of Films of Rubber and other Polymers.
19–22. Illustrative of Margaret H. Alston *et al.*'s Paper on A 10 in. Diameter Liquid Hydrogen Bubble Chamber.
23–24. Illustrative of J. Washburn *et al.*'s Paper on Direct Observation of Dislocations in Magnesium Oxide.
25. Illustrative of G. R. Piercy's Paper on Point Defects in Platinum.
26–30. Illustrative of L. H. Germer *et al.*'s Paper on The Study of Adsorbed Gas Films by Electron Diffraction.
31–32. Illustrative of A. D. Whapham and M. J. Makin's Paper on the Hardening of Lithium Fluoride by Electron Irradiation.
33. Illustrative of V. Mayes' Paper on A Possible Example of the Muon Radiative Decay with Internal Conversion of the γ-ray
34. Illustrative of M. F. Ashby and G. C. Smith's Paper on Direct Electron Microscopy of Thin Foils of Internally Oxidized Dilute Copper Alloys.
35–40. Illustrative of R. D. Burbank and R. D. Heidenreich's Paper on Microtwinning in Epitaxial Nickel–Iron Films.
41. Illustrative of W. Hume-Rothery and E. Anderson's Paper on Eutectic Compositions and Liquid Immiscibility in Certain Binary Alloys.
42. Illustrative of A. A. Johnson's Paper on The Embrittlement of Molybdenum by Neutron Irradiation.
43. Illustrative of P. B. Price's Paper on Microcreep in Zinc Whiskers.
44. Illustrative of R. W. Whitworth's Paper on Some Effects of Vibration on the Internal Friction of Sodium Chloride.
45–47. Illustrative of M. T. Sprackling's Paper on Reverse Bending of Crystals of Silver Chloride.
48. Illustrative of J. T. Bartlett and J. W. Mitchell's Paper on The Generation Loops at the Surfaces of Crystals of Silver Bromide.
49–51. Illustrative of P. B. Price's Paper on the Growth of Cadmium Crystals from the Vapour.
52–53. Illustrative of J. E. Bailey and P. B. Hirsch's Paper on the Dislocation Distribution, Flow Stress, and Stored Energy in Cold-worked Poly-crystalline Silver.
54. Illustrative of D. Michell and E. Lovegrove's Paper on The Investigation of the Annealing of Nickel Deformed by Compression by x-ray and Stored Energy Measurements.
55–56. Illustrative of S. Amelinckx and P. Delavignette's Paper on Direct Evidence for the Presence of Quarter-dislocations in Talc Monocrystals.
57–66. Illustrative of V. A. Phillips' Paper on Direct Observation of Defects in Evaporated Silver.
67–70. Illustrative of W. Bollmann's Paper on Electron-microscopic Observations on Radiation Damage in Graphite.

71–76. Illustrative of R. S. Barnes' Paper on The Generation of Vacancies in Metals.

77–78. Illustrative of P. Feltham and G. J. Copley's Paper on Creep in Face-centred Metals and Solid Solutions with special reference to α-brasses

79–83. Illustrative of F. J. P. Clarke and R. A. J. Sambell's Paper on Micro-cracks and their Relation to Flow and Fracture in Single Crystals of Magnesium Oxide.

84–90. Illustrative of G. A. Bassett and C. Edeleanu's Paper on Etching of Strained Aluminium.

91–100. Illustrative of P. Delavignette and S. Amelinckx's Paper on Dislocation Nets in Bismuth and Antimony Tellurides.

101. Illustrative of K. E. Puttick's Paper on The Shear Component of Ductile Fracture.

102–108. Illustrative of A. J. Forty's Paper on Observations of the Decomposition of Crystals of Lead Iodide in the Electron Microscope.

109. Illustrative of J. T. Bartlett and J. W. Mitchell's Paper on Dislocations with Burgers Vectors of $a\langle 100\rangle$ Crystals of Silver Bromide.

110–117. Illustrative of J. E. Bailey's Paper on Electron Microscope Observations on the Annealing Processes Occurring in Cold-worked Silver.

118–128. Illustrative of P. B. Price's Paper on Pyramidal Glide and the Formation and Climb of Dislocation Loops in Nearly Perfect Crystals.

129–131. Illustrative of H. Hashimoto *et al.*'s Paper on Anomalous Electron Absorption Effects in Metal Foils.

132–134. Illustrative of A. R. C. Westwood's Paper on the Effects of Surface Condition on the Mechanical Properties of Lithium Fluoride Crystals.

135–140. Illustrative of J. Washburn *et al.*'s Paper on Electron Microscope Observations of Deformed Magnesium Oxide.

141–145. Illustrative of C. Edeleanu and A. J. Forty's Paper on Some Observations on the Stress-corrosion Cracking of α-brass and Similar Alloys.

146. Illustrative of E. Roberts and R. W. K. Honeycomb's Paper on Movement of Point Defects During Fatigue of Aluminium Crystals.

147–148. Illustrative of R. S. Crisp's Paper on Soft x-ray Emission from Potassium Metal in the 40–1000 Å Range.

149–150. Illustrative of J. Sawkill and J. E. Meredith's Paper on The Etching of Sub-structures in Beryllium.

151. Illustrative of D. M. Marsh's Paper on Stress Concentrations at Crystal Surfaces and the Embrittlement of Sodium Chloride.

152–155. Illustrative of R. S. Crisp and S. E. Williams' Paper on The Soft x-ray Spectra of Lithium, Magnesium and Aluminium and their Alloys.

156–158. Illustrative of G. A. Bassett and C. Edeleanu's Paper on Pitting of Aluminium at Grain Boundaries after Ageing.

159–160. Illustrative of G. W. Bryant and B. J. Mason's Paper on Etch Pits and Dislocations in Ice Crystals.

161–164. Illustrative of R. S. Barnes and D. J. Mazey's Paper on The Nature of Radiation-induced Point Defect Clusters.

165. Illustrative of B. G. Childs *et al.*'s Paper on The Magnetic Susceptibility of Vanadium–Chromium Solid Solutions.

THE

PHILOSOPHICAL MAGAZINE

A JOURNAL OF THEORETICAL, EXPERIMENTAL
AND APPLIED PHYSICS

First Published in 1798

[EIGHTH SERIES—VOL. 5]

Direct Observations of the Annealing of Prismatic Dislocation Loops and of Climb of Dislocations in Quenched Aluminium†

By J. Silcox and M. J. Whelan
Crystallographic Laboratory, Cavendish Laboratory,
Cambridge, England

[Received September 16, 1959]

Abstract

A high temperature stage fitted to a Siemens Elmiskop 1 electron microscope has been used to study directly the annealing of prismatic dislocation loops in thin foils prepared from quenched and aged bulk specimens of aluminium. In the temperature range 170–200°c the loops are observed to shrink and eventually to disappear. Observations on dislocations other than loops also present in the thin foils show that they become smoother while the loops are disappearing. The results are interpreted in terms of climb of dislocations by vacancy emission, and in the case of loops in thin foils, where vacancy supersaturation effects are thought to be negligible, the climb rate is governed by the line tension and curvature of the loops. The radius r of a loop as a function of time t is given by the theoretical expression $r=r_0[1-(t/\tau)]^{1/2}$ where τ is the lifetime of a loop of initial radius r_0. The temperature dependence is primarily $\tau=\tau_0 \exp(E/kT)$ where E is the activation energy of self diffusion. Comparison with experiment gives estimates of the activation energy in the range 1·2–1·3 ev.

Annealing experiments with bulk material have been carried out in parallel with the above experiments. They show that the loops anneal out in the same temperature range. The details are different however owing to vacancy supersaturation effects. Larger loops appear to grow at the expense of smaller ones. The theory gives a qualitative explanation of the annealing of electrical resistivity in quenched aluminium observed by other workers, although the shape of the isothermal annealing curve is difficult to predict quantitatively, owing to its dependence on the complex annealing behaviour of loops in bulk material. The experiments also suggest that the temperature rise of thin foils examined in the electron microscope due to heating by the electron beam is very small.

§ 1. Introduction

When a metal is rapidly cooled from high temperatures large numbers of vacant lattice sites in excess of the equilibrium concentration may be quenched-in. The changes in physical properties produced by quenching and the variation of these changes on subsequent annealing are therefore interpreted in terms of the properties and behaviour of vacancies (Maddin and Cottrell 1955, Bauerle and Koehler 1957, Koehler *et al.* 1957, Panseri and Federighi 1958, Federighi 1959, DeSorbo and Turnbull 1959, Kimura *et al.* 1959 a, b, Meshii and Kauffman 1959, for review see Cottrell 1957). An investigation of the annealing out of the increase in electrical resistivity of aluminium produced by quenching has recently been carried out by Panseri and Federighi (1958) and by Federighi (1959). These workers showed the presence of two stages in the isochronal annealing curves of specimens quenched from temperatures greater than ~400°C. The first stage took place in a few minutes at room temperature (Wintenberger 1957, Bradshaw and Pearson 1957, DeSorbo and Turnbull 1959) and was associated by Panseri and Federighi with the movement of vacancies to form clusters of some unspecified type. The second stage occurred at temperatures at which self-diffusion is important and was therefore associated with the dispersal of the clusters.

---

† Communicated by the Authors.

Recent observations (Hirsch, Silcox, Smallman and Westmacott 1958) using the transmission electron microscope technique, have revealed the presence of small prismatic dislocation loops in thin foils of aluminium prepared from quenched and aged bulk material. These are thought to be produced by the condensation of excess vacancies into disc-like cavities which subsequently collapse to form loops of whole dislocation line. However, as was pointed out by Federighi (1959), the identification of these loops with the clusters postulated by Panseri and Federighi was not unambiguous. Thus it was possible that while a fraction of the vacancies formed dislocation loops, another fraction formed clusters so small that they are not detected on transmission electron micrographs. Stage II of the resistivity annealing curves could then be associated with the annealing of small vacancy clusters and not necessarily with the disappearance of loops. It is therefore necessary to decide this point by experiment. Two types of experiment may be carried out using the transmission electron microscope. In the first a high temperature stage in the microscope is used to observe the annealing out phenomena directly in the thin foils. The behaviour of the loops on annealing can therefore be studied in detail. In the second, the annealing treatment is carried out on bulk material which is subsequently thinned and examined in the electron microscope. This paper describes the results of both types of experiment for aluminium and discusses their physical significance.

§ 2. EXPERIMENTAL TECHNIQUE

Aluminium of Johnson-Matthey 'specpure' quality, nominally 99·99% pure, and in the form of foil 0·003 in. thick, was quenched from about 600°C by dropping under gravity from a vertical tube furnace into iced brine. The foil was then allowed to age at room temperature for several hours. The foils were thinned by electropolishing in an 80% ethyl alcohol – 20% perchloric acid bath (Tomlinson 1958). Observations were recorded on photographic plates in the usual way, and also in some of the high-temperature stage experiments by direct ciné-photography of the fluorescent screen of the electron microscope using equipment described by Whelan *et al.* (1957). For the bulk material experiments a quenched and aged foil was cut into two parts. One part was thinned and examined directly to establish the existence of loops. The other part was annealed in an oil bath for six minutes prior to thinning and examination. Annealing temperatures of 100, 160, 170, 180, 190, 200, 210 and 220°c were employed.

Examination was carried out with a Siemens Elmiskop 1 electron microscope operating at 100 kv.

Figures 1 (*a*), (*b*) and (*c*) show the main details of the high temperature stage used for annealing the thin foils during observation. The specimen holder (fig. 1 (*a*) and (*b*)) is similar in shape to the conventional holder and is inserted through the airlock into the bore of the objective pole-piece in the usual manner. The specimen holder contains a two-pin socket E, insulated from the body of the holder and carrying a filament type specimen support AB. This support consists of two 0·4 mm diameter platinum legs B spot-welded to a 200 mesh stainless steel grid A and secured in the socket by two screws D. The grids are cut from RCA $\frac{1}{8}$ in. diameter stainless steel specimen supports. The spacing between the platinum legs at the grid is 1·5 mm, and the width of the grid is such that seven strands of wire conduct the heating current. Direct current is passed through the grid by means of a two-pin plug A at the end of a long rod inserted through the hole in the objective lens normally occupied by the stereo-drive (fig. 1 (*c*)). With this equipment therefore it is not possible to tilt the object during observation. The rod can move to follow the stage movement and can be withdrawn to an inoperative position when the specimen is removed. The instrument also requires a modified stage carriage (not shown) similar to the conventional carriage but without the stereo-mechanism. More complete details of this equipment have been reported by Whelan (1958).

The specimens are mounted by removing the end cap C in fig. 1 (*a*). The grid is dipped in a dilute solution of polybutene in xylol, which acts as an adhesive ; excess solution is blotted off and the specimen is placed in the centre of the grid as in fig. 1 (*b*).

The compact design of the stage prevents measurement of the temperature of the grid during observation. However grid temperature versus heating current curves have been determined by calibration of individual specimen supports in a high vacuum system. A Pt, Pt–13% Rh thermocouple of 48 s.w.g. (supplied by Johnson-Matthey) was placed as closely as possible to the centre of the grid. Millivolt readings were converted to degrees centigrade using Johnson-Matthey conversion tables. Measurements were reproducible to about ±2°c at 170°c. The current required to heat the centre of an average grid to 200°c was about 1·1 amp, the working temperature being attained a few seconds after switching on. The variation of temperature over the grid was not investigated. However, in a few cases a grid was recalibrated with a new thermocouple after use. The temperature usually differed slightly from the previous

Fig. 1

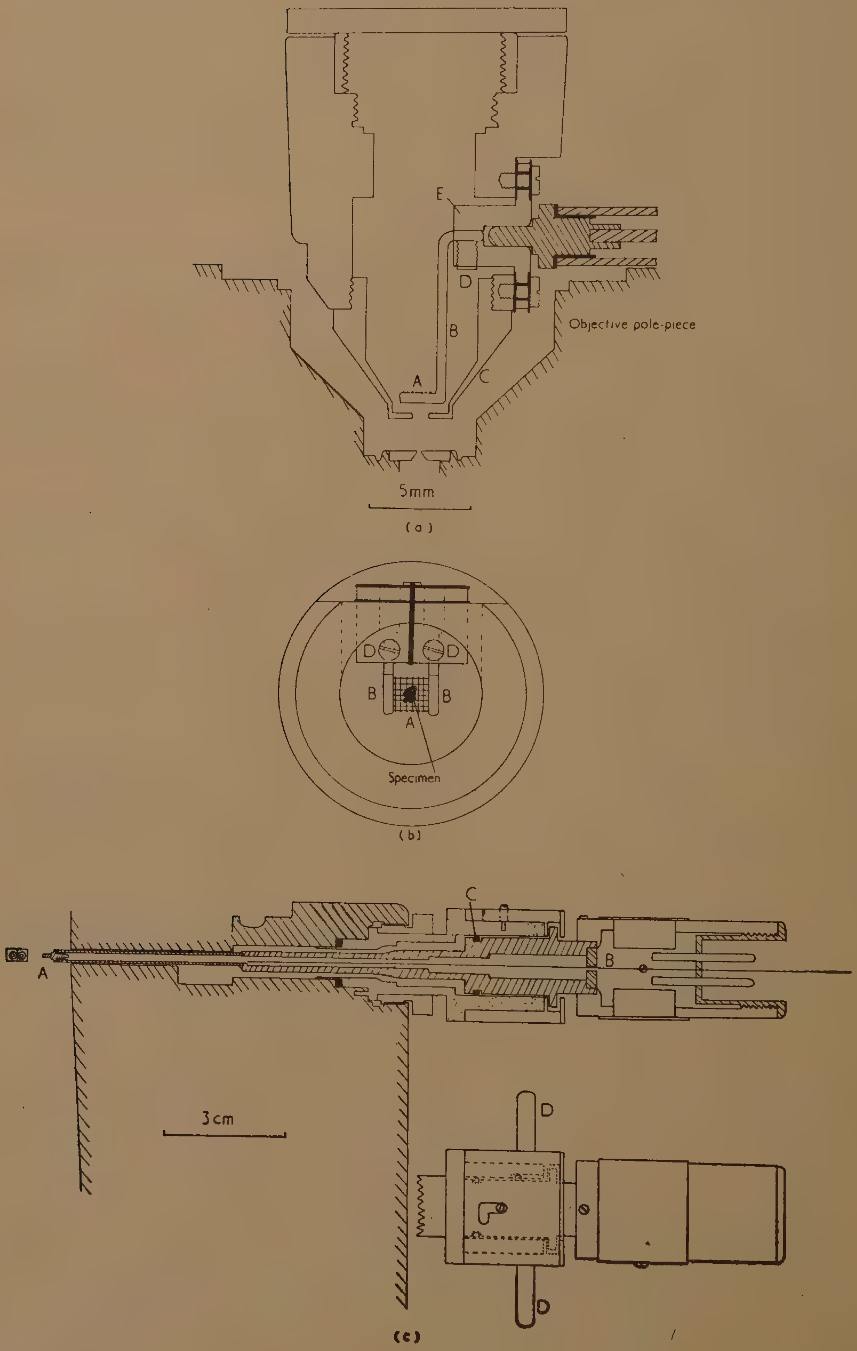
E
D
B
A
C
Objective pole-piece
5mm
(a)
D
D
B
B
A
Specimen
(b)
C
A
B
3cm
D
D
(c)

High temperature stage for the Elmiskop 1.

estimate. From such measurements the inaccuracy in stage temperature obtained from heating current in this way is very roughly estimated to be about ± 10°c. This does not include of course any rise of temperature of the thin foil due to heating by the electron beam. To minimize this last effect the double condenser was used with an illuminating spot about 10 μ diameter, with a 600 μ diameter aperture in condenser 2, and with a total beam current $\sim 15\ \mu$A.

§ 3. EXPERIMENTAL RESULTS

3.1. *High Temperature Stage Experiments*

When a specimen containing loops is heated in the electron microscope the loops are observed to shrink and eventually to disappear completely. The loops begin to shrink at a noticeable rate at a stage temperature of about 170°c; the rate of shrinking increases rapidly with increasing temperature. For example, timed sequences of micrographs and ciné-sequences have shown that the rates of decrease of radius of a loop about 250 Å radius are about 0·2, 1·5, and 33 Å sec^{-1} at temperatures $\sim$ 170, 200 and 220°c respectively. This shrinking is quite distinct from the process of prismatic slip observed by Hirsch, Silcox, Smallman and Westmacott (1958). Figure 2 (*a*), (*b*), (*c*) and (*d*) (Pl. 1) is a sequence of micrographs taken on photographic plates at an estimated stage temperature of 187°c. The time interval between successive micrographs was not recorded but is estimated to be about one minute. Most of the loops in fig. 2 (*a*) diminish in size and disappear during the sequence; loop A remains through the whole sequence although diminished in size. In general in the thin foils, loops which are originally round remain round as they shrink, i.e. there is no tendency to form angular shapes. Also all the loops (large and small) appear to shrink in the thin foils. There is no tendency for large loops to grow at the expense of small ones.

The rate at which a loop shrinks is not uniform but is a function of its radius. A small loop shrinks much faster than a large loop, i.e. the rate of shrinking of a loop is accelerated as it grows smaller. Figure 3 (Pl. 2) is a sequence of micrographs taken on photographic plates of a loop shrinking at a stage temperature of 197°c; the times in seconds at which these exposures were made are marked on each micrograph. The loop lies on an inclined plane, and the distance between the more steeply inclined and less visible parts of the loop (Hirsch, Howie and Whelan 1958, 1959) has been taken as a measure of the loop diameter. Figure 4 shows a plot of loop radius versus time. There is some uncertainty in the exact position of the centre of the dislocation line as judged from the contrast and this is indicated by the vertical spread in the points on fig. 4. However, the relative positions of the points are probably more accurate. With single exposures on photographic plates it is not possible to record the shrinking at very small radius owing to its rapidity. However using ciné-techniques the steep slope of the radius-time curve at small radius has been verified, although it is difficult to determine its functional form with accuracy.

The observations suggest that the loops are acting as vacancy sources, i.e. that the vacancies which condensed to form the loops after quenching are dispersing. Assuming that the only force acting to aid climb is that due to the line tension and curvature of the loop, the theory given in detail in § 4 suggests that the radius time curve of a shrinking loop should be approximately a parabola. Accordingly such a curve has been fitted to the experimental points of fig. 4 and the points are seen to be consistent with this curve. The dislocation loops are therefore climbing by vacancy diffusion in a sense to annihilate themselves. These results may be taken as direct proof of the hypothesis of climb of dislocations. Figure 5 (*a*), (*b*), (*c*) and (*d*) (Pl. 3) shows a sequence of micrographs from a region containing both loops and irregular dislocations (e.g. fig. 5 (*a*) at A). During the sequence, while the loops are disappearing, the irregular dislocations assume a noticeably smoother shape (e.g. at A). This effect has been observed a number of times and is thought to be due at least partly to climb.

Fig. 4

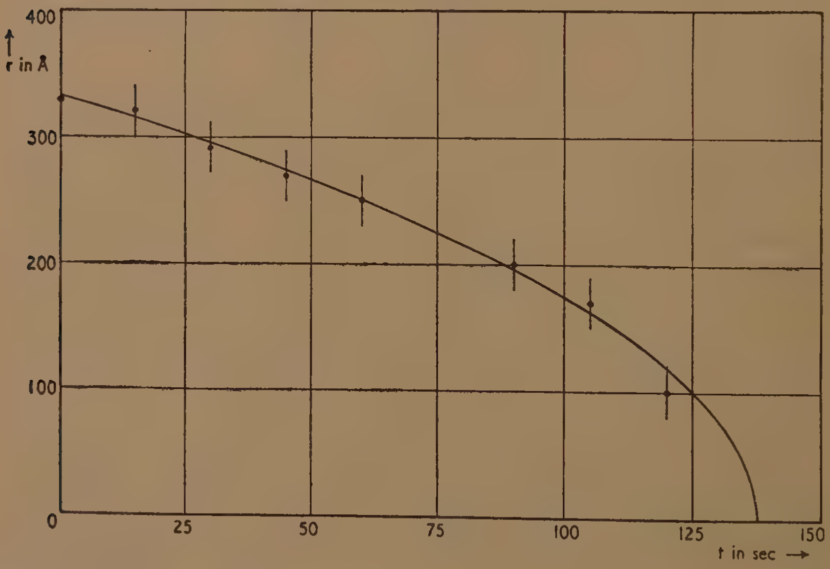

Radius versus time plot for the loop in fig. 3. A parabola has been fitted to the experimental points.

Relatively little slip of the loops has been observed. Occasionally however a loop has been observed to jump suddenly as a whole over a small distance, presumably along its slip cylinder, after it has shrunk to a very small size before it finally disappears. The explanation of this effect is not known with certainty; however prismatic slip is a very rapid way of transferring the last remaining vacancies as a whole to the surface as a nearby sink.

3.2. *Bulk Material Experiments*

The density of loops in the quenched and aged specimens is $\sim 6 \times 10^{14}$ cm^{-3} assuming a foil thickness of ~ 1000 Å. No noticeable change was observed in thin foils prepared from bulk material which had been annealed for six minutes at temperatures below 180°C. In specimens annealed at 180°C the density decreased slightly to $\sim 1{\cdot}3 \times 10^{14}$ cm^{-3}. A reduction in loop density was quite marked in foils annealed at 190°C and 200°C in which the densities were about 5×10^{13} and 5×10^{12} cm^{-3} respectively. These figures should be regarded as order of magnitude estimates only since variations were observed from specimen to specimen and from point to point on any one specimen. For reliable estimates of loop densities the foil thickness must be determined (for example from the projected width of a slip trace left by a dislocation moving on a $\{111\}$ plane). It has not always been possible to determine the foil thickness in this way, and an average thickness ~ 1000 Å has been assumed. Experience has shown that the foil-thickness in areas transparent to electrons is usually of this order. The change in number of loops on micrographs from as-quenched material and from material annealed at 190°C and 200°C is too large to be attributed to differences of foil thickness.

Figure 6 (*a*) (Pl. 4) shows a micrograph of a foil prior to annealing and fig. 6 (*b*) (Pl. 4) and fig. 6 (*c*) (Pl. 5) show micrographs of foils annealed at 190°C. Several large loops can be seen in these micrographs. This increase in size accompanying the decrease in loop density is also apparent in the micrograph of a foil annealed at 200°C shown in fig. 6 (*d*) (Pl. 5). In specimens annealed at 210°C and higher temperatures no loops were observed. The conclusion drawn from these results is that in bulk material large loops grow at the expense of smaller loops; eventually however they too either shrink and disappear or become large enough to be incorporated in the dislocation network of the crystal.

Sometimes the larger loops left in bulk material after annealing have angular shapes (e.g. figs. 6 (*b*) and (*c*) at A). Such loops may be parallelograms with edges in close packed directions although no experimental confirmation of this has been attempted. The shape of a large loop which has grown from a small one by vacancy absorption presumably depends on the detailed mechanism of growth of a loop (see § 4.1).

§ 4. THEORETICAL INTERPRETATION

4.1. *Climb of Dislocation Loops*

The observations leave little doubt that climb of the dislocation loops is occurring and it is therefore convenient to discuss the various factors which govern the climb of a prismatic loop. Friedel (1956) has considered the climb of a dislocation due to vacancy diffusion in terms of the movement of jogs. He gives the following expression for the velocity of a jog along the dislocation line:

$$v_{\mathrm{c}} = \frac{z\nu_{\mathrm{a}} b}{\sin\psi} \exp\left\{-\frac{(E_{\mathrm{f}}+E_{\mathrm{m}})}{kT}\right\}\left[\exp\left(\frac{F_{\mathrm{c}} b^2}{kT}\right) - \exp\left(\frac{F_{\mathrm{s}} b^2}{kT}\right)\right] \qquad (1)$$

where $z \sim 11$ (of the order of the atomic coordination number of the lattice), ν_{a} is an atomic frequency (of order 10^{13}); ψ is the angle between the Burgers vector **b** and the dislocation line; E_{f} is the formation energy and E_{m} the activation energy of movement of a vacancy; $E = E_{\mathrm{f}} + E_{\mathrm{m}}$ is the activation energy of self-diffusion; kT is the usual Boltzmann temperature factor; while F_{c} and F_{s} are forces per unit length acting on the dislocation line tending to make it climb out of its slip plane. F_{c} is a force due to an applied stress or due to the stress fields of other segments of dislocation. F_{s} is a chemical stress due to a deviation of the concentration of vacancies from the equilibrium value at temperature T. F_{s} is equal to

$$\frac{kT}{b^2} \log \frac{c}{c_0} \qquad . \ . \ . \ . \ . \ . \ . \ . \ . \ . \ . \qquad (2)$$

where c and c_0 are the actual and equilibrium concentrations of vacancies at temperature T.

Fig. 7

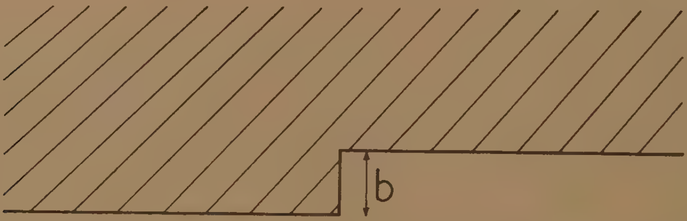

Climb of an edge dislocation by jog movement (following Friedel 1956).

Equation (1) may be given a simple physical interpretation. Consider an edge dislocation containing a jog in a simple cubic lattice as in fig. 7; the extra half plane of atoms is shown shaded. Under the action of a suitable force F_{c} tending to make the dislocation climb the jog will emit vacancies and will move to the right with an average velocity given by the left-hand term in the square brackets of eqn. (1) together with the factor outside the brackets. However vacancies will tend to recombine with the jog which will therefore move to the left, and this is taken into account by the right-hand term in the square brackets. The resultant velocity of the jog is the difference between these two terms. (The formula assumes that the force F_{c} does not affect the probability that a vacancy will combine with the jog, i.e. that the energy barrier to be surmounted when a vacancy combines with a jog is independent of the force F_{c}.) Clearly the rate of climb of the dislocation normal to its slip plane in fig. 7 is

$$v = v_{\mathrm{c}} b/x$$

where x is the average distance between jogs. b/x is called the concentration of jogs c_c by Friedel. c_c is a dimensionless quantity equal to unity for an edge dislocation in a simple cubic lattice running at 45° to its glide plane.

For a circular prismatic loop lying in a (111) plane in a face centred cubic metal such as aluminium the jog concentration will vary round the loop as shown schematically in fig. 8. c_c will be of the order of unity at the segments of the loop lying between close packed direction in the (111) plane (i.e. at the corners of the inscribed hexagon in fig. 8). The jogs on these segments will run along the loop in the directions indicated with arrows and will annihilate with jogs moving in opposite directions from the other joggy segments. Thus there is a tendency to produce a hexagonal loop lying inside the original circular loop as in fig. 8. However new jogs are expected to nucleate easily at the corners of the hexagon since this requires no additional line energy. The equilibrium form of the loop as it shrinks will be governed by the rate at which jogs are nucleated and the rate at which material is redistributed along the dislocation, i.e. on the rate of

Fig. 8

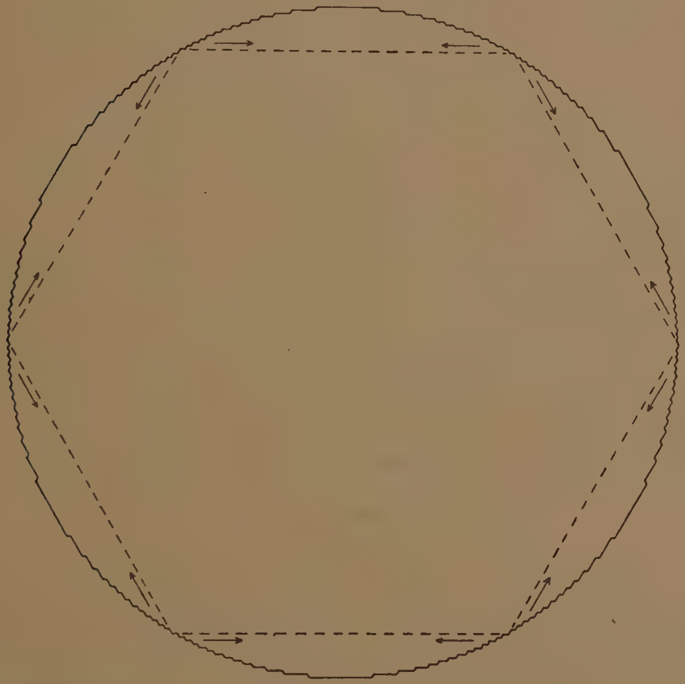

Circular dislocation loop in a (111) plane. The loop represents a disc of vacancies. The sides of the inscribed hexagon are parallel to close packed directions. The highest jog density occurs at the corners of the hexagon. Climb of the dislocation loops occurs by movement of jogs of opposite sign from adjacent corners and subsequent annihilation.

diffusion between jogs. This is a theoretical problem involving jog kinetics analogous to the type of problem discussed by Frank (1958) and Cabrera and Vermilyea (1958) for crystal growth kinetics. A similar theory could probably be applied to a shrinking loop, although the solution is not obvious. The experimental observations show however that as a circular loop shrinks it remains roughly circular, and this implies that jogs are nucleated and move at a rate sufficient to maintain a circular shape. It is worth noting here that in the converse process (i.e. when a small loop grows by absorption of vacancies as in the bulk material experiments) the details may be different, as a little consideration of fig. 8 suggests. In this case new jogs will ultimately have to be nucleated by condensation of vacancies. This will involve an increase in dislocation line energy and is therefore likely to be a difficult process. The dislocation loop will therefore tend to have a low concentration of jogs, i.e. to be angular with sides parallel to close packed directions. This is probably the explanation of the parallelogram shaped loops visible in figs. 6 (*b*) and (*c*).

Detailed considerations of fig. 8 show that for a loop in a (111) plane of a face centred cubic lattice the maximum rate of change of radius of the loop is $\frac{1}{2}v_c$, where v_c is measured along close packed directions, i.e. $c_c \sim \frac{1}{2}$. In this theory for simplicity it will be assumed that the loops are circular and lie in planes perpendicular to the axis of the glide cylinder (i.e. in (110) planes). Thus all segments of a loop are edge dislocations ($\sin\psi = 1$), and no dissociation into partial dislocations will occur. An average value of jog concentration $c_c \sim \frac{1}{2}$ will also be assumed to hold for all segments of a circular loop. For a loop lying in a (111) plane the situation is not expected to differ much from this provided dissociation into partial dislocations can be neglected. The rate of shrinkage of the loop will then be given by

$$\frac{dr}{dt} = -\frac{1}{2}v_c \quad . \quad . \quad . \quad . \quad . \quad . \quad . \quad . \quad . \quad (3)$$

where r is the radius of the loop at time t.

It should also be mentioned here that eqns. (1) and (3) give the climb rate of a dislocation assuming that vacancy emission (or absorption) is the rate determining process. This will be the case if vacancies diffuse rapidly to sinks (such as free surfaces, grain boundaries, or other dislocations). If the diffusion is not sufficiently rapid a local supersaturation will be set up at the dislocation which will suppress the emission. The rate of climb in this case will be determined by transport of vacancies away from the dislocation by diffusion (the ‘saturation’ case discussed by Friedel 1956). The solution of this problem is complicated and depends on the geometrical conditions in any particular case (i.e. on the nature and distribution of sinks). This point is discussed in § 4.4 and in the Appendix.

4.2. *The Effect of Up-quenching*

During the annealing process the climb rate of a loop will be determined by the factor in square brackets in eqn. (1). It is assumed that both in the bulk material and in the thin foil experiments the metal is not under any form of stress. In thin foils stresses may be produced by electron bombardment in the electron microscope; these however will be neglected since little prismatic slip was observed with low electron beam intensity. Neglecting forces between loops, the only elastic force acting on a segment of loop will be that due to its line tension and curvature. This force tends to contract the loop. As far as the chemical stresses are concerned the experiments can be visualized as follows. The foil containing loops is assumed to have a concentration of vacancies equal to the equilibrium value at room temperature. The foil is then up-quenched from room temperature to about 180°C. This gives rise to an undersaturation of vacancies. Consequently the initial chemical stress is not equal to zero and acts in a direction tending to shrink the loops. A simple calculation shows however that to restore equilibrium only about one vacancy per loop is required (assuming a loop concentration of $\sim 10^{14}\,\mathrm{cm}^{-3}$) and equilibrium is rapidly attained, i.e. $F_{\mathrm{s}}=0$.

Once vacancies are being produced by the dislocation loops it becomes necessary to consider the rate at which they are absorbed by sinks. There will now be a supersaturation of vacancies and a chemical stress will build up in opposition to the line tension stress, i.e. vacancies will tend to condense on the loops again. The discussion of this problem will be deferred to § 4.4 At present it will be assumed that vacancies are removed by sinks faster than they are produced by loops so that the chemical stress is small, i.e. the right-hand term in the square bracket of eqn. (1) is very nearly unity. This is thought to be the case in the thin foil annealing experiments where the foil surface is a very effective vacancy sink (see § 4.4 and Appendix).

4.3. *Climb of Loops in Thin Foils*

An approximate expression for the force F_{c} due to the line tension and curvature of a loop is (Frank 1950, Franz and Kröner 1955)

$$F_{\mathrm{c}}=\frac{Gb}{4\pi(1-\sigma)}\frac{\log\ (r/b)}{(r/b)} \quad . \quad . \quad . \quad . \quad . \quad . \quad . \quad . \qquad (4)$$

where the radius of the dislocation core is taken as b, G is the shear modulus and σ is Poisson's ratio. (The core energy of the dislocation is neglected in this expression.) Putting $F_{\mathrm{s}}=0$ in eqn. (1) the radius r of a loop as a function of time t is given by

$$\frac{dr}{dt}=-\tfrac{1}{2}z\nu_{\mathrm{a}}b\exp\left(-\frac{E}{kT}\right)\left[\exp\left(\frac{F_{\mathrm{c}}b^2}{kT}\right)-1\right]. \quad . \quad . \quad . \qquad (5)$$

With $G=2{\cdot}53\times10^{11}$ dynes cm^{-2} at 161°C, $b=2{\cdot}86$ Å, $\sigma=\frac{1}{3}$ and $k=0{\cdot}86\times10^{-4}$ ev degree C^{-1}, the reciprocal of the function in square brackets has been plotted as a function of r/b for temperatures of 161°C and 200°C in fig. 9. The curves approach infinity near $r/b=1$ but this corresponds to a range of r/b where the expression (4) is no longer valid. In the range of loop radius of interest therefore $[\exp(F_{\mathrm{c}}b^2/kT)-1]$ may be approximated by $\alpha b/r$ where $\alpha\sim72$ at 161°C and ~64 at 200°C. dr/dt is therefore only slightly dependent on temperature through the factor α and depends mainly on temperature through the term $\exp(-E/kT)$ in eqn. (5)†.

Fig. 9

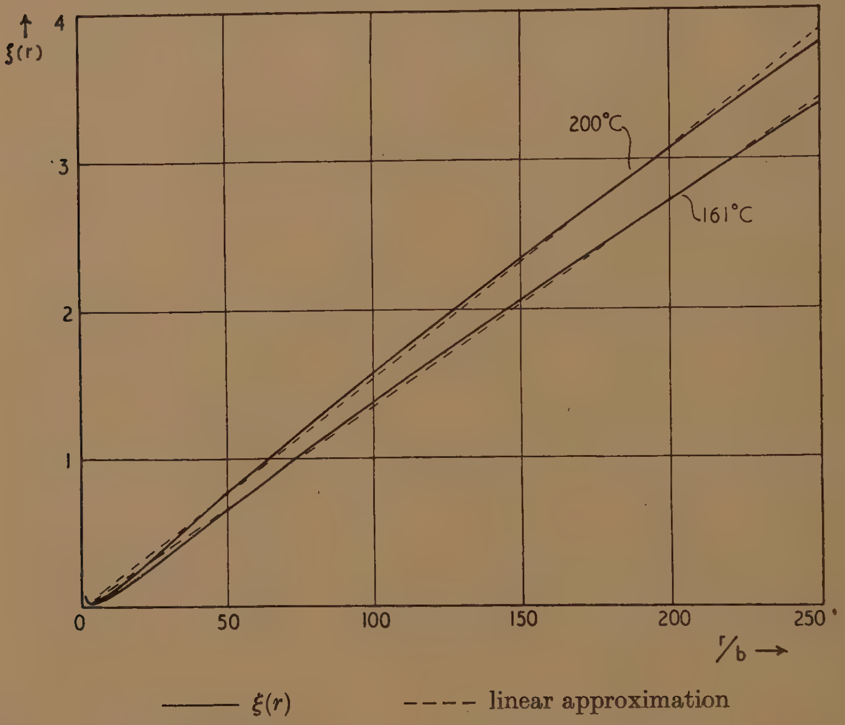

Plot of the function

$$\xi(r) = \left[\exp\left(\frac{Gb^3}{4\pi kT(1-\sigma)} \cdot \frac{\log(r/b)}{(r/b)}\right) - 1\right]^{-1}$$

as a function of r/b. Note that the function is approximately linear over the range of r/b of interest.

Then

$$\frac{dr}{dt} = -\tfrac{1}{2} z \nu_a b^2 \alpha \exp\left(-\frac{E}{kT}\right) \cdot \frac{1}{r} . \qquad (6)$$

Equation (6) can be integrated to give

$$r = r_0 (1 - t/\tau)^{1/2} \qquad (7)$$

where r_0 is the initial radius of the loop at $t=0$

$$\tau = \tau_0 \exp(E/kT) \qquad (8)$$

and where

$$\tau_0 = r_0^2 / (z \nu_a \mathbf{b}^2 \alpha). \qquad (9)$$

---

† *Note added in proof.*—Calculations show that an increase of the core radius of the dislocation has a similar effect on $\xi(r)$ as an increase of temperature, e g. at 161°c and 200°c changing the core radius to $2b$ causes α to decrease by about 10%.

Equation (7) shows that the radius–time curve of a shrinking loop should be parabolic as shown in the curve fitted to the experimental points of fig. 4. These points were obtained from the loop in fig. 3 climbing at ~197°C. In this case $r_0 \sim 330$ Å, $\tau \sim 138$ sec, $kT \sim 0{\cdot}0405$ ev. Substituting these figures in eqns. (8) and (9) with $z \sim 11$, $\nu_a \sim 10^{13}$, $\alpha \sim 64$, E is found to be 1·29 ev. The error in E due to 10°C error in temperature estimation is about 2%. The result also assumes the value of ν_a. The activation energy depends logarithmically on this factor and is relatively insensitive to it. Errors due to rises in temperature of the foil in the electron beam are not known but are thought to be small (see § 6). Other estimates of E from the rate of shrinkage of certain loops (for which complete radius–time curves were not obtained) gave values lying in the range 1·2 to 1·3 ev. Although these values of the activation energy cannot be claimed to be accurate owing to assumed factors and to uncertainty in the accuracy of the temperature, the values are consistent with those obtained by other workers: Bradshaw and Pearson (1957) give 1·2 ev; Federighi (1959) gives 1·33 ± 0·05 ev; DeSorbo and Turnbull (1959) give 1·31 ± 0·08 ev; while Spokas (reported by Federighi 1959) has obtained 1·4 ± 0·1 ev.

The rates of decrease of radius of a loop of radius 250 Å can now be calculated from eqn. (6). Assuming $\alpha \sim 70$ for all temperatures of interest, and taking $E = 1{\cdot}32$ ev (the average of the values quoted by Federighi and De Sorbo and Turnbull), the calculated rates are ~0·13, ~1·3, ~4 Å sec^{-1} at temperatures of 170, 200 and 220°C respectively. Considering the errors involved in estimating temperature and in assumed factors these rates are in good agreement with the observed rates mentioned in § 3.1.

The observations are therefore consistent with the theory of shrinking of loops by climb. The temperature dependence of the rates is best illustrated by considering the lifetimes τ obtained from eqn. (8) of a loop of radius ~140 Å. This is the average loop radius of the distribution shown in fig. 10, which is a histogram of loop sizes for a typical specimen quenched from 600°C (this histogram was obtained from fig. 1 of Hirsch, Silcox, Smallman and Westmacott (1958)). τ has the following values for several temperatures (α has been taken ~120 at 20°C and ~70 for all other temperatures):

T°C	20	160	170	180	190	200	210	220
τ	230 years	11·6 min	5·2 min	2·3 min	1·2 min	35 sec	17·5 sec	8·8 sec

It is seen that the loops will shrink at a noticeable rate for temperatures greater than ~170°C which is precisely the range in which the loops are observed to anneal out in the thin foils.

Equation (6) can be written as follows (the plane of the loop is perpendicular to the glide cylinder)

$$\frac{d}{dt}(\sqrt{2}\pi r^2 b^2) = -\sqrt{2}\pi z \nu_a \alpha \exp\left(-\frac{E}{kT}\right). \quad . \quad . \quad . \quad (10)$$

The left-hand side of (10) is the rate at which the number of vacancies forming the loop decreases (volume per vacancy $=b^3/\sqrt{2}$). The rate of emission of vacancies from the loop is then

$$\frac{dN}{dt}=\sqrt{2\pi z\nu_a\alpha}\exp\left(-\frac{E}{kT}\right) \quad . \quad . \quad . \quad . \quad . \quad (11)$$

and this is independent of loop size. It is seen therefore that at a fixed temperature the rate of change of area of a loop is constant.

Fig. 10

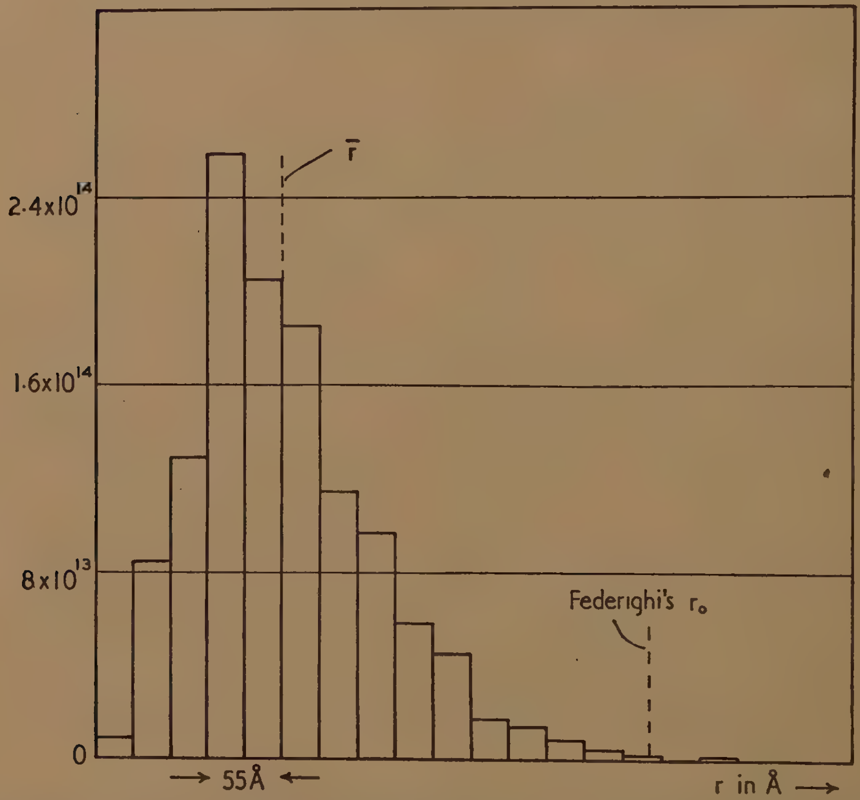

Histogram of loop sizes for the micrograph of fig. 1 of Hirsch, Silcox, Smallman and Westmacott (1958) taken from aluminium quenched from ~600°c. The average loop radius is 138 Å. The ordinate is loop density in number cm^{-3}, assuming a foil thickness of 1000 Å. See text for discussion of the radius r_0 derived from Federighi's results.

Attempts to verify the form of eqn. (7) are inaccurate for the following reasons. The dislocation core itself is not imaged in the electron microscope but its strain field gives rise to a diffraction image lying to one side of the core (Hirsch, Howie and Whelan 1958, 1959). There is therefore an inherent inaccuracy in the measurement of loop diameters owing to the uncertainty in position of the dislocation. In addition, during heating, the specimen may tilt, thus altering the contrast. The observations reported in figs. 3 and 4 are therefore considered to be in satisfactory agreement with theory.

4.4. *Annealing of Loops in the Bulk Material*

So far the chemical stress due to the vacancy supersaturation produced by vacancies released from loops has been neglected. In general it is not permissible to neglect this effect in experiments with the bulk material as the following considerations show. First consider the number of vacancies in equilibrium at various temperatures T in a cube of aluminium 1000 Å edge; this is approximately the volume occupied by a single loop in a region of typical loop density. Using the formula of Bradshaw and Pearson (1957) for vacancy concentration the following figures are obtained.

T°c	Equilibrium number of vacancies per cube 1000 Å edge
600	2×10^4
200	4
170	1·1
20	4×10^{-5}

The equilibrium number of vacancies near each loop in the annealing range (170–200°c) is therefore of order unity, so that even if only a few vacancies per loop remain in the vicinity of the loop (or of other loops) appreciable supersaturation occurs. The degree of supersaturation will be determined by several factors including the rate at which vacancies are produced by loops, the rate at which they move, and the nature and distribution of vacancy sinks (isolated dislocation lines, free surfaces and grain boundaries). The detailed solution of this problem is complicated. However some simple generalizations can be made. The number of jumps, n, made by a vacancy in time t is (Cottrell 1957)

$$n=z\nu_a t\exp\left(-\frac{E_m}{kT}\right)$$

and the mean square distance moved, assuming a random walk process, is

$$\overline{\Delta x^2}=b^2z\nu_a t\exp\left(-\frac{E_m}{kT}\right). \qquad (12)$$

Then the time taken for a vacancy to move to a sink at a distance l from the loop at which it originates is

$$t_l\sim(l^2/b^2z\nu_a)\exp\left(\frac{E_m}{kT}\right) \qquad (13)$$

Equation (11) also shows that if supersaturation effects are neglected the time interval t_s between emission of successive vacancies by a loop is on average

$$t_s\sim(\sqrt{2\pi z\nu_a\alpha})^{-1}\exp\left(\frac{E_m+E_f}{kT}\right). \qquad (14)$$

Then $$t_l/t_s \sim \sqrt{2\pi l^2 \alpha b^{-2}} \exp\left(-\frac{E_f}{kT}\right). \qquad (15)$$

Now for thin foils the surface is a very effective vacancy sink; l is then about the average distance of a loop from the surface, i.e. ~1000 Å. In bulk material however a vacancy may have to move about 1 to 10 μ before it encounters a sink such as a grain boundary or dislocation line (ignoring other loops which may act as sinks). The following are typical values of t_l/t_s for aluminium at various temperatures obtained from eqn. (15) assuming $\alpha \sim 70$, $E_f = 0{\cdot}76$ ev.

T°C	$l = 1000$ Å	$l = 1\,\mu$	$l = 10\,\mu$
170	$8{\cdot}7 \times 10^{-2}$	8·7	870
200	3×10^{-1}	30	3000
220	$6{\cdot}6 \times 10^{-1}$	66	6600

It can be seen that for thin foils ($l \sim 1000$ Å), a vacancy from a loop will on average reach the surface before the next vacancy is emitted by the same loop. The figures therefore suggest that the vacancy supersaturation will be small and that the chemical stress can be neglected in this case. The theory of the previous paragraph is therefore expected to hold for thin foils.

For loops in the interior of grains in bulk material however ($l \sim 10\,\mu$), t_l/t_s is large and increases with increasing annealing temperature. In this case supersaturation effects are expected to be important because vacancies are formed at loops at a rate greater than the rate at which they move to sinks. The effect of a vacancy supersaturation may be illustrated by using eqns. (1) and (2) to write eqn. (3) in the form

$$\frac{dr}{dt} = -\tfrac{1}{2} z\nu_a b \exp\left(-\frac{E}{kT}\right)\left[\frac{\alpha b}{r} - \frac{\Delta c}{c_0}\right] \qquad (16)$$

where $\Delta c = c - c_0$. The rate of change of radius of a loop will therefore depend on the local supersaturation of vacancies and it is readily seen that a loop of radius less than $r_c = \alpha c_0 b/\Delta c$ will shrink while a loop of radius greater than r_c will grow. The large loops therefore grow at the expense of the small loops which disappear giving rise to a lower concentration of larger loops. This conclusion is in agreement with the observations on bulk material annealed at 190°C and 200°C (fig. 6) where a definite difference in the diameter and density of the loops in the as-quenched and annealed specimens was detected.

In general local time-dependent inhomogeneities in vacancy concentration are to be expected. However the main physical features of the process as a whole can be illustrated in the following manner assuming a homogeneous supersaturation Δc. Consider first an idealized case of a metal containing no sinks for vacancies other than loops (e.g. a single crystal infinite in extent and perfect except for loops and vacancies). Let the metal contain a uniform density of loops of various sizes given by a distribution function $g(r)$ such that there are $g(r)\,dr$ loops per unit volume with radii between r and $r + dr$. Up-quench the metal to a temperature

$T \sim 200$°c. The rate of emission of vacancies now depends on loop size and vacancy concentration c. Since there are no vacancy sinks the following continuity equation holds:

$$\sqrt{2\pi z\nu_a}\exp\left(-\frac{E}{kT}\right)\int_0^\infty g(r)\left[\alpha-\frac{\Delta c}{c_0}\cdot\frac{r}{b}\right]dr=\frac{dc}{dt}. \qquad (17)$$

Now for small supersaturations once the initial c has been established, both c and dc/dt are expected to be small in comparison with the two integrals subtracted on the left hand side of eqn. (17) at temperatures ~ 170°c and 200°c, as substitution of typical figures suggests. With this assumption the right-hand side of eqn. (17) can be replaced by zero, giving

$$\Delta c/c_0=\frac{\alpha b\displaystyle\int_0^\infty g(r)\,dr}{\displaystyle\int_0^\infty rg(r)\,dr}=\alpha b/\bar{r} \quad . \quad . \quad . \quad . \quad . \quad . \quad . \qquad (18)$$

where $\bar{r}$ is the mean radius of the distribution $g(r)$. Electron micrographs suggest that $\bar{r} \sim 140$ Å in typical regions containing loops (see fig. 10). Putting $\alpha \sim 70$, c/c_0 is found to be $\sim 2{\cdot}4$ which confirms the assumption that c is small under near steady state conditions. For comparison the value of c/c_0 produced by quenching the metal from 600°c to room temperature is $\sim 10^9$.

Substitution of (18) in eqn. (16) gives

$$\frac{dr}{dt}=-\tfrac{1}{2}z\nu_a b^2\alpha\exp\left(-\frac{E}{kT}\right)\left[\frac{1}{r}-\frac{1}{\bar{r}}\right]. \quad . \quad . \quad . \quad . \quad . \qquad (19)$$

Equation (19) shows that the rate of shrinking of a loop now depends on $r-\bar{r}$, i.e. $r_c=\bar{r}$. Loops of above average radius will grow at the expense of those below average radius which will gradually disappear. Thus $g(r)$ will change with time in such a way that $\bar{r}$ increases, i.e. $\Delta c/c_0$ decreases. Ultimately only a few very large loops will remain.

In this idealized case the effects of grain boundaries and dislocations as vacancy sinks have been neglected. If these are taken into account even these large loops would shrink and vanish, provided they are not ultimately incorporated in a dislocation network. While therefore the final state produced by annealing bulk material for a sufficiently long time should be the same as that of the annealed thin foils (i.e. no loops), the detailed behaviour of loops as they anneal out will be different and is expected to depend markedly on their proximity to vacancy sinks. For example loops near grain boundaries would be expected to anneal out as in thin foils, while those in the interior of grains should behave as outlined. In this last case since large loops are involved the annealing out time is expected to be longer.

§ 5. DISCUSSION

The agreement between observations and the theory of the previous section leaves little doubt that the disappearance of loops is due to climb. The time and temperature dependences of the annealing rates in thin foils are as predicted theoretically and are consistent with an activation energy of self diffusion of about 1·3 ev. Bulk material experiments have shown results expected from the growth of large loops.

It is of interest to consider the results in relation to the resistivity experiments of Panseri and Federighi (1958) and of Federighi (1959) on quenched aluminium. The first stage of their isochronal annealing curves (see fig. 2 of Panseri and Federighi) can be interpreted in terms of the removal of vacancies at dislocation loops (and possibly at small clusters of unspecified shape), and at fixed sinks such as network dislocations and grain boundaries. Now the temperature range in which the loops are observed to disappear is exactly the same as that found for stage II annealing by Panseri and Federighi. Thus stage II includes the annealing of resistivity due to the dislocation loops. It is therefore tempting to identify stage II with the annealing out of loops. It is not known with certainty at present whether very small clusters (other than loops) would be detected on transmission electron micrographs. No effects which can be attributed to very small clusters are observed. Even loops ~50 Å diameter would be expected to produce contrast in the form of a dark spot about equal in diameter to the theoretical width of the image of a dislocation (~100 Å), and such dark spots have been observed (see fig. 1 of Hirsch, Silcox, Smallman and Westmacott 1958). However there is no evidence that these spots are due to anything other than loops. With these facts in mind stage II annealing in the quenched aluminium is tentatively considered to be due to the observed loops. Panseri and Federighi (1958) and Federighi (1959) have shown that the decrease in resistivity of aluminium during stage II annealing is $\sim 3\,\mathrm{m}\mu\,\Omega\,\mathrm{cm}$ after quenching from 600°c. If this is produced by loops of average radius ~140 Å and density $\sim 10^{15}\,\mathrm{cm}^{-3}$, the average resistivity of dislocations in loops is about $3\times10^{-19}\,\Omega\,\mathrm{cm}$ per centimetre length of dislocation. It is emphasized that this value is an order of magnitude estimate only. To make this type of estimate worthwhile electron microscope observations and resistivity measurements should be made on the same specimens. However it is worth noting that the value is comparable with estimates of dislocation resistivities in other metals. For example Seeger (1957) quotes figures leading to dislocation resistivities of $\sim 2{\cdot}5\times10^{-19}$ and $\sim 10^{-18}\,\Omega\,\mathrm{cm}$ per centimetre length for copper and nickel respectively.

Federighi (1959) has also studied the shape of the isothermal annealing curve of stage II resistivity in aluminium. He found (see fig. 4 of Federighi) that the fraction of resistivity remaining after annealing for time t at temperature T could be fitted very well for all except large t by the function.

$$f=1-\left(\frac{t}{\tau_\rho}\right)^m$$

where $m\approx0{\cdot}55$ and

$$\tau_\rho=\tau_{\rho 0}\exp\left(\frac{E}{kT}\right)$$

with $E=1{\cdot}32$ ev.

τ_ρ represents a decay time; more than 90% of the resistivity anneals out in time τ_ρ. $\tau_{\rho 0}$ was found to be $2{\cdot}6 \times 10^{-12}$ sec (see corrigendum to Federighi 1959).

Now if the resistivity of a loop is taken to be proportional to its perimeter (i.e. to its radius), the total resistivity of a distribution of loops $g(r, t)$ will be proportional to

$$\int_0^\infty rg(r,t)\,dr = \bar{r}(t)n(t),$$

where $\bar{r}(t)$ is the average radius of the distribution and $n(t)$ the total number of loops at time t. On this interpretation therefore the explanation of Federighi's empirical law should depend on the way in which the average radius and the total number of loops in the distribution changes with time. $g(r, t)$ will of course be determined by considerations such as those outlined in § 4.4 In the idealized case discussed there it is possible to formulate a differential-integral equation for $g(r, t)$; however the equation seems soluble only by numerical methods. In the absence of a complete solution it is only possible to speculate. It is thought that the initial rapid decrease in Federighi's annealing curve may be due to the initial rapid shrinking and disappearance of loops smaller than average radius and the growth of large ones. The subsequent slow decay would then be due to the slower shrinking of the large loops as vacancies are removed at network dislocations and grain boundaries at sinks. At present this problem is still unsolved and several other points are incompletely understood. It is not known for example what the contribution to the resistivity will be from heavily jogged dislocations. Furthermore examination of many specimens has shown that loops are not uniformly distributed over large regions. Loops tend to occur with high density in certain grains (usually free from isolated dislocations) and sometimes in patches in those grains. Other grains may show tangled networks of dislocation lines with lower loop density, e.g. fig. 5. These dislocations are probably produced by quenching stresses and are presumably heavily jogged by absorption of vacancies. During annealing these dislocations are observed to climb also; the jog density is thereby expected to decrease. This effect probably also contributes to resistivity although its magnitude is uncertain. Finally it must be pointed out that for small loops the contribution to electrical resistivity may not be proportional to r; for example it may be proportional to the loop area, i.e. *to* r^2. The shape of the isothermal annealing curve is therefore not determined by any simple considerations, but will depend on the complex annealing behaviour of loops in the bulk material.

However a plausible explanation of Federighi's τ_ρ and $\tau_{\rho 0}$ can be obtained by noting that τ_ρ depends on temperature in the same way as the theoretical quantity τ previously defined (eqns. (7), (8) and (9)), which refers to a loop of radius r_0 in a thin foil. Equating τ_0 and Federighi's value of $\tau_{\rho 0}$, it is found that $r_0 = 404$ Å. This is larger than the average loop size in material quenched from 600°c, as can be seen from the typical histogram of loop sizes in fig. 10. However this result is in accordance with the qualitative ideas of annealing of loops in bulk material, i.e. that loops of larger than average radius grow at the expense of smaller ones. The magnitude of the decay time of the resistivity is therefore expected to be determined by the simple theory of § 4.3 applied to a loop of larger than average radius. It must also be noted that τ_ρ is the time required for a large fraction of the resistivity to anneal out. It should therefore correspond to the lifetime of a large loop.

§ 6. CONCLUSIONS

Direct evidence for climb of dislocation loops has been obtained and the details confirm the theoretical predictions of the nature of the process, namely:

(*a*) The loops disappear by emitting vacancies.

(*b*) In thin foils the loops anneal out at an observable rate in the range of temperature $> \sim 170°\text{c}$ and at a rate consistent with an activation energy of about 1·3 ev. The rate has been followed and within experimental error is found to be as predicted by theory. Supersaturation effects are not important in thin foils owing to the very effective vacancy sinks provided by the surfaces.

(*c*) In bulk material experiments the loops anneal out in the same temperature range, but the details are dependent on vacancy supersaturation effects. Large loops are found to grow at the expense of smaller ones.

(*d*) The work has shown that the loops disappear in the temperature range in which certain electrical resistivity effects produced by quenching also anneal out. The loops are therefore tentatively identified as the main cause of the increase in resistivity, although at present other effects such as small clusters of vacancies (not observed in the electron microscope) and effects due to joggy dislocations cannot be completely ruled out.

As regards the technique it appears that useful information can be obtained by high temperature examination of crystalline materials in the electron microscope. Thus it has been possible to study directly for the first time the annealing kinetics of individual dislocations. Similar experiments on alloys may yield useful information on precipitation effects.

Finally the fact that the annealing effects occur in about the same measured temperature range both in thin foils and in bulk material, is fairly convincing proof that under the conditions of operation used in this work the temperature rise of the thin foil due to heating by the electron beam is small (probably less than 15°c). This is also confirmed by the fact that loops usually disappear simultaneously both for regions inside and well away from the area exposed to the electron beam.

ACKNOWLEDGMENTS

The authors are indebted to Professor N. F. Mott, F.R.S., and to Dr. W. H. Taylor for their interest and encouragement, and to Dr. P. B.

Hirsch for much valuable advice and criticism. Thanks are due to Drs. J. Friedel, T. Federighi and J. Weertman for fruitful discussions, and to Mr. F. Marks for excellent workmanship in the construction of the high temperature stage. Acknowledgments for financial support are due to the A.E.R.E., Harwell (J.S.), and to the Department of Scientific and Industrial Research and to Gonville and Caius College, Cambridge for Research Fellowships (M.J.W.)

REFERENCES

BAUERLE, J. E., and KOEHLER, J. S., 1957, *Phys. Rev.*, **107,** 1493.

BRADSHAW, F. J., and PEARSON, S., 1957, *Phil. Mag.*, **2,** 570.

CABRERA, N., and VERMILYEA, D., 1958, *Report of the Cooperstown Conference on Growth and Perfection of Crystals* (New York : Wiley Sons), p. 393.

COTTRELL, A. H., 1957, *Institute of Metals Monograph and Report Series*, N.23, p. 1.

DESORBO, W., and TURNBULL, D., 1959, *Acta Met.*, **7,** 83.

FEDERIGHI, T., 1959, *Phil. Mag.*, **4,** 502.

FRANK, F. C., 1950, *Plastic Deformation of Crystalline Solids*, Office of Naval Research, p. 89 ; 1958, *Report of the Cooperstown Conference on Growth and Perfection of Crystals* (New York : Wiley and Sons), p. 411.

FRANZ, H., and KRÖNER, E., 1955, *Z. Metallkde.*, **46,** 639.

FRIEDEL, J., 1956, *Les Dislocations* (Paris : Gauthier-Villars), p. 72.

HIRSCH, P. B., HOWIE, A., and WHELAN, M. J., 1958, *Report of the Fourth International Conference on Electron Microscopy, Berlin* (in the press); 1959, *Phil. Trans. roy. Soc.* (in the press).

HIRSCH, P. B., SILCOX, J., SMALLMAN, R. E., and WESTMACOTT, K. H., 1958, *Phil. Mag.*, **3,** 897.

KIMURA, H., MADDIN, R., and KUHLMANN-WILSDORF, D., 1959 a, *Acta Met.*, **7,** 145 ; 1959 b, *Ibid.*, **7,** 154.

KOEHLER, J. S., SEITZ, F., and BAUERLE, J. E., 1957, *Phys. Rev.*, **107,** 1499.

MADDIN, R., and COTTRELL, A. H., 1955, *Phil. Mag.*, **46,** 735.

MESHII, M., and KAUFMANN, J. W., 1959, *Acta Met.*, **7,** 180.

PANSERI, C., and FEDERIGHI, T., 1958, *Phil. Mag.*, **3,** 1223.

SEEGER, A., 1957, *Dislocations and Mechanical Properties of Crystals* (New York : Wiley and Sons), p. 347.

TOMLINSON, H., 1958, *Phil. Mag.*, **3,** 867.

WHELAN, M. J., 1958, *Report of the Fourth International Conference on Electron Microscopy, Berlin* (in the press).

WHELAN, M. J., HIRSCH, P. B., HORNE, R. W., and BOLLMANN, W., 1957, *Proc. roy. Soc.* A, **240,** 524.

WINTENBERGER, M., 1957, *C. R., Acad. Sci. Paris*, **244,** 2800.

APPENDIX

ON THE QUESTION OF EMISSION VERSUS TRANSPORT OF VACANCIES AS THE RATE DETERMINING PROCESS OF THE CLIMB OF LOOPS IN THIN FOILS

Friedel (private communication) has pointed out to the authors that under certain circumstances climb might be determined by transport of vacancies by diffusion even in thin foils. He has considered two simple models—(*a*) diffusion of vacancies along a cylinder, (*b*) diffusion from the centre of a sphere.

(*a*) *Diffusion Along a Cylinder*

Consider a loop of radius r at a distance l from both surfaces of the foil. Imagine the vacancies to be transported to the surfaces through cylinders of radius r and length l. Then the vacancy flux obtained from eqns. (1) and (2) (assuming $c=c_0$ at the loop, i.e. no supersaturation) is

$$\phi_1 = -\frac{2\pi r b}{V 2\pi r^2}\frac{dr}{dt} = \frac{z\nu_a b^2 \exp\left(-\dfrac{E}{kT}\right)}{Vr} c_c\left[\exp\left(\frac{F_c b^2}{kT}\right)-1\right]$$

$$= \frac{D}{Vr} c_c\left[\exp\left(\frac{F_c b^2}{kT}\right)-1\right] \quad . \quad . \quad . \quad . \quad . \quad . \quad (\mathrm{A}\,1)$$

where $V(=b^3/\sqrt{2})$ is the vacancy volume, and where

$$D = z\nu_a b^2 \exp(-E/kT)$$

is the self diffusion coefficient. However if emission occurs more rapidly than transport, $c=c_0 \exp(F_c b^2/kT)$ at the loop and $c=c_0$ at the surface. The vacancy flux due to diffusion would then be

$$\phi_2 = -\frac{D}{Vc_0}\,\mathrm{grad}\, c = \frac{D}{Vl}\left[\exp\left(\frac{F_c b^2}{kT}\right)-1\right]. \quad . \quad . \quad . \quad (\mathrm{A}\,2)$$

The climb rate is expected to be governed by transport of vacancies if $\phi_1 > \phi_2$, i.e. if $r/l < c_c$. Since $c_c \sim \frac{1}{2}$, r would have to be comparable with l for the climb to be determined by emission of vacancies.

(*b*) *Spherical Diffusion*

The above condition is however rather stringent and would be expected to apply to loops densely distributed in a plane at distance l from both surfaces. For randomly distributed loops in thin foils spherical diffusion is probably a closer approximation. In this case a loop of radius r is imagined to be at the centre of a sphere of radius $l(\gg r)$, i.e. for a very small loop in a thin foil. The vacancy flux at radius R for emission limited conditions (i.e. $c=c_0$ at the loop) is now

$$\phi_1 = \frac{Dr}{2VR^2} c_c\left[\exp\left(\frac{F_c b^2}{kT}\right)-1\right]. \quad . \quad . \quad . \quad . \quad (\mathrm{A}\,3)$$

However if $c=c_0 \exp(F_c b^2/kT)$ over a sphere of radius r at the loop and $c=c_0$ at $R=l$ (transport limited conditions) then

$$c = c_0 + c_0\left[\exp\left(\frac{F_c b^2}{kT}\right)-1\right]\frac{r}{R},$$

and the vacancy flux due to diffusion is

$$\phi_2 = -\frac{D}{Vc_0}\,\mathrm{grad}\, c = \frac{Dr}{VR^2}\left[\exp\left(\frac{F_c b^2}{kT}\right)-1\right]. \quad . \quad . \quad . \quad (\mathrm{A}\,4)$$

If the climb is determined by transport the condition $\phi_1 > \phi_2$ gives $c_c > 2$. In this case therefore vacancy emission from the loops appears to be the rate determining process since $c_c \sim \frac{1}{2}$. The actual case of loops in thin foils is expected to lie somewhere between these two cases but probably closer to case (*b*). Provided the loops are not too densely distributed and that the foil is not too thick, the approximation the authors have used in neglecting supersaturation effects in thin foils appears reasonable.

Finally, it must be remarked that the total flux of vacancies from the neighbourhood of the loop ($R \sim r$) under transport controlled conditions and assuming spherical symmetry is of the same order of magnitude as the total flux of vacancies emitted by the loop under emission controlled conditions. The form of eqns. (5) and (6) therefore remains similar. Essentially similar conclusions have been reached by Weertman (private communication) working on similar lines. It therefore appears that eqns. (5) and (6) are a valid description of the annealing process. However in the absence of more detailed observations on the rate of shrinking of loops it is not possible to decide by experiment whether the process is limited by emission or transport of vacancies. The considerations outlined above and in § 4.4 suggest that the rate would be determined by emission of vacancies.

On the Stability of the Dislocation Substructure in Quenched Aluminium†

By R. VANDERVOORT and J. WASHBURN
Minerals Research Laboratory, University of California, Berkeley, California

[Received August 14, 1959]

ABSTRACT

Dislocation loops formed by quenching thin aluminium specimens in iced brine were studied by the transmission electron microscope technique. As-quenched specimens contained loops 200 Å to 600 Å in diameter with a density of 10^{15} loops per cubic centimetre. Quenched-in loops were completely removed by heating to 200°c for ten minutes or by cold rolling to a 5% reduction in thickness. The disappearance of the loops was accompanied by an increase in the number of irregular kinked dislocation lines.

§ 1. INTRODUCTION

THE equilibrium concentration of vacant lattice sites in a crystal decreases with decreasing temperature according to the approximate relation:

$$C_v = \exp\left(-\frac{U_{fv}}{kT}\right)$$

where C_v is the fraction of the total number of lattice sites that are not occupied by an atom and U_{fv} is the energy of formation of a vacancy. Therefore, when a metal is cooled, vacant lattice sites must be eliminated. There are only three ways excess vacancies can be removed: (1) migration to an external surface, (2) precipitation on an edge dislocation line, or (3) clustering to form small voids or prismatic dislocation loops as proposed by Seitz 1950).

Resistivity measurements (Bauerle and Koehler 1957) suggest that when the cooling rate is rapid enough, the concentration of vacancies present at some higher temperature can be frozen in. As long as the temperature is then kept low enough to prevent migration no change in vacancy distribution can take place.

When an aluminium specimen which has been quenched from 600°c rapidly enough to retain the high temperature vacancy concentration is reheated to successively higher temperatures, the resistivity increment due to excess vacancies disappears in two distinct stages. The recent results of Panseri and Federighi (1958) are shown in fig. 1‡. The first stage of recovery which accounts for 80% of the total resistivity increment lies in the temperature range −80°c to just below room temperature. As pointed out by Panseri and Federighi it is probably due to disappearance of individual vacancies by formation of clusters. Direct electron microscope observations have shown that this thermal history does in fact produce vacancy clusters which collapse to form small dislocation loops 200 Å to 600 Å in diameter (Hirsch *et al.* 1958). A dislocation density as high as 10^{10} cm/cm^3 can be produced in this way. Therefore the resistivity increment remaining at room temperature may be due to the dislocations. The effect of the same thermal history on mechanical properties has been investigated by Maddin and Cottrell (1955). They observed a large increase in room temperature yield strength which must also be associated with the presence of prismatic dislocation loops.

---

† Communicated by the Authors.
‡ All figures except fig. 1 are as plates.

Fig. 1

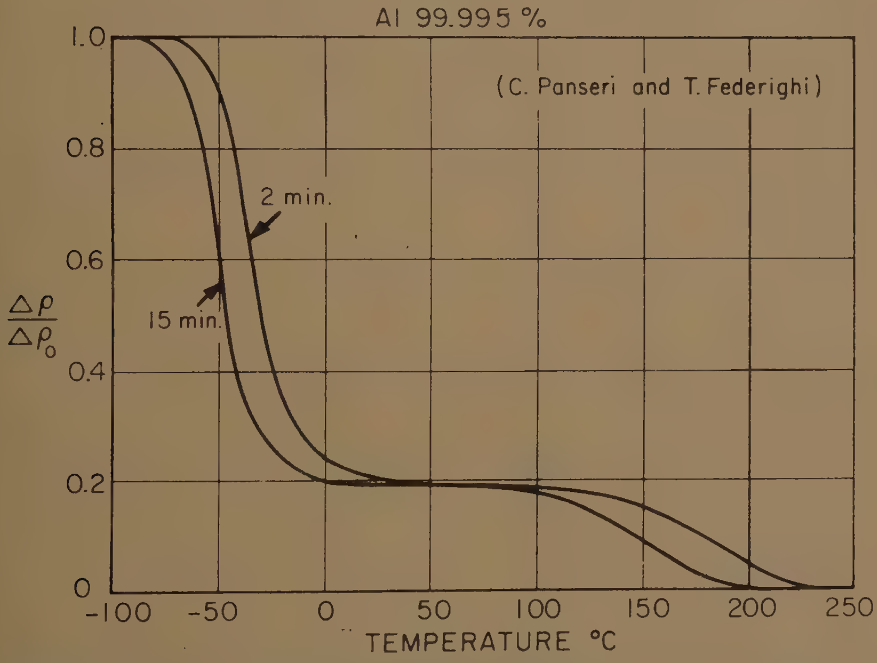

Resistivity decay for isochronal annealing of 2 or 15 min at each temperature after quenching from 600°c.

The second resistivity drop took place on heating into the temperature range between 100°c and 200°c. The activation energy for the process was found to be 1·33 ev (Federighi 1959). It seems likely that second-stage recovery may be associated with the disappearance of prismatic dislocation loops. Dislocation density could be greatly reduced by migration of vacant lattice sites from loops to other sinks or by growth of the largest loops at the expense of smaller ones. Small amounts of plastic deformation at room temperature also cause a decrease in resistivity

(Winterberger 1958). This suggests that loops can be swept out by moving dislocations even at room temperature. The present experiments were undertaken to obtain direct evidence concerning the mechanisms of this second stage resistivity decrease and of quench hardening. Changes in dislocation sub-structure in quenched aluminium specimens caused by reheating to successively higher temperatures or resulting from various amounts of cold work after quenching were observed by electron transmission microscopy.

§ 2. Experimental Procedure

Aluminium sheet specimens 0·005 cm thick of nominal purity 99·995% were quenched from 600°c into iced brine. The first series of specimens was then heated for ten minutes to either 100°c, 125°c, 150°c, 175°c, or 200°c. The second series was cold rolled at room temperature to $2\frac{1}{2}$%, 5%, 10%, 15%, or 45% reduction in thickness after quenching. A thicker specimen was cold rolled to 98% reduction in thickness. All specimens were then thinned by electropolishing in a solution of 20% perchloric acid 80% absolute alcohol to obtain fragments of about 1000 Å to 1500 Å in thickness. The thin foil fragments were examined in an RCA–2E electron microscope operating at 50 kv with either a 50 mil or a 25 mil aperture.

§ 3. Results and Discussion

As-quenched specimens which had not been heated above room temperature before electropolishing contained a dislocation sub-structure similar to that reported by Hirsch *et al.* (1958). Figure 2 shows a typical field. Nearly all areas of the foils that had convenient thickness for observation contained loops. They were absent only near occasional long dislocation lines or within about a micron from a grain boundary. Loops appeared to be nearly circular and apparently did not enclose a stacking fault. Therefore the Burgers vectors were probably of the type $(a/2)\langle 110\rangle$. The loops appeared to belong to four sets; those in each family being quite accurately parallel to each other. This was particularly noticeable in foils oriented such that two sets were approximately at right angles to the plane of the foil because half of the loops then appeared as short straight lines. Foil orientation could not be determined because the instrument did not permit a diffraction pattern to be obtained. However, the observations were consistent with the hypothesis that most loops lay approximately on {111} planes. Neighbouring loops lying on a given (111) plane often were revealed with vastly different contrast. This might be expected since the loops on any one plane should have three different Burgers vectors e.g. $(a/2)[110]$, $(a/2)[101]$, $(a/2)[011]$, on (111). A few appeared to have a dark centre and an approximately hexagonal shape. Whether this different appearance could be caused by a particular relationship between the Burgers vector, the crystallographic orientation of the foil, and the direction of the electron beam, could not be determined because there was no provision for slightly tilting the specimen while under observation. An alternative explanation might be the presence of some loops enclosing a stacking fault. Most loops had the appearance shown at A in fig. 3. Hexagonal loops with uniform darkening across the entire area are shown at B. A few were revealed in double contrast as at C. The double contrast effect has been explained by Hirsch *et al.* (1960).

Little or no change in the loops was produced by heating for ten minutes at 100°c. Figures 4, 5 and 6 show typical fields after heating to 125°c. As a result of a large number of observations, it was estimated that loops were absent in about one-third of the specimen volume. The number of irregular dislocation lines appeared to be greater and a few larger loops were found. Heating to 150°c decreased the proportion of specimen volume containing loops to about 50%. In the regions still containing loops their density was reduced and their average size increased compared to the as-quenched specimens as shown in fig. 7. Still fewer were present after heating to 175°c and essentially none remained after the 200°c heat treatment. Figure 8 shows a field still containing a few loops after 175°c heating.

The results clearly showed that prismatic loops were eliminated by dislocation climb. Vacant lattice sites migrated from the smaller loops to the larger ones, causing growth of some at the expense of others or from loops to long dislocation lines. During this process there was a definite increase in the number of irregular kinked dislocation lines. Further heating caused disappearance of all loops and a straightening of the irregular kinked dislocations. The observed decrease in dislocation density took place in exactly the same temperature range as the second-stage resistivity recovery reported by Panseri and Federighi (1958). This supports the hypothesis that the decrease in dislocation density accounts for the resistivity decrease. The kinetics of the process is complicated by microscopic inhomogeneity of the specimens. Even in as-quenched specimens the density of loops apparently varied from one part of the specimen to another. The disappearance of loops did not appear to take place primarily by a homogeneous coarsening process. Loops were eliminated in different parts of the same specimen at widely different temperatures. The higher the annealing temperature in the range between 125°c and 200°c the greater was the percentage of specimen volume that was free of loops. In those parts of the specimen where loops remained longest, growth of the larger ones at the expense of the smaller ones did take place. The rapid disappearance of loops in some regions suggests that they may have been eliminated during the heating by a combination of glide and short distance climb of nearby long dislocation lines. By combination of elements of the three dimensional dislocation network with vacancy loops the irregular kinked lines that were observed may have been produced. The regions that retained loops to the highest temperatures presumably were those farthest from network dislocations.

Further support for this general mechanism was provided by cold working after quenching. Dislocation loops combined at room temperatures with moving dislocations to form irregular kinked dislocation lines. All loops were swept out after only 5% reduction in thickness by cold rolling. A resistivity drop produced by room temperature deformation can therefore be associated with a decrease in total dislocation density. Figure 9 shows some loops remaining and irregular kinked dislocations after a plastic strain of 2½% in tension. Figures 10 to 15 show the gradual change from tangles of kinked dislocation lines to a system of well-defined sub-grains as the amount of cold work was increased.

The stress strain curve for quenched aluminium (Maddin and Cottrell 1955) can be qualitatively understood on the basis of these results. The yield stress was high, because the first dislocations to move appreciable distances became heavily jogged almost immediately by combination with loops. The resulting irregular dislocation lines were relatively immobile. At small strains the hardening effect due to formation of groups of tangled irregular dislocations was approximately compensated by the softening effect due to elimination of vacancy loops; therefore there was little strain hardening. Dislocation density decreased during the first few percent plastic strain. At higher strains the rate of hardening and the changes in dislocation sub-structure appeared to be the same in quenched as in furnace-cooled specimens except that the hardness and dislocation structure reached at 5% strain in the former was approximately equivalent to that produced by 10% strain in the latter.

§ 4. Conclusions

1. Dislocation loops formed by condensation of excess vacancies in quenched 99·995% aluminium began to disappear on heating for 10 min to 125°c and were completely eliminated by heating for 10 min to 200°c.

2. The process was not homogeneous throughout the specimen. Clear areas began to grow at about 125° and the proportion of specimen volume that was free of loops increased with increasing temperature of treatment.

3. In the regions still containing loops after heating into the upper part of the range coarsening took place by growth of the larger loops at the expense of the smaller ones.

4. Elimination of the high dislocation density associated with quenched-in loops probably explains the second-stage resistivity drop observed by Panseri and Federighi (1958).

5. Irregular kinked dislocation lines appeared during the disappearance of loops and then tended to straighten out and disappear again after the loops had been eliminated.

6. Moving dislocations combined readily with the loops at room temperature. Irregular kinked dislocation lines were produced. A plastic deformation of 5% reduction in thickness by rolling was sufficient to sweep out all the loops—resulting in a decrease in total dislocation density.

ACKNOWLEDGMENTS

The authors would like to thank the U.S. Atomic Energy Commission for support of this work. The continuous encouragement of Dr. R. R. Nash and Dr. D. K. Stevens has been greatly appreciated.

REFERENCES

BAUERLE, J. E., and KOEHLER, J. S., 1957, *Phys. Rev.*, **107,** 1493.
FEDERIGHI, T., 1959, *Phil. Mag.*, **4,** 502.
HIRSCH, P. B., SILCOX, J., SMALLMAN, R. E., and WESTMACOTT, K. H., 1958, *Phil. Mag.,* **3,** 897.
HIRSCH, P. B., HOWIE, A., and WHELAN, M. J., 1960, *Proc. roy. Soc.* (in the press).
MADDIN, R., and COTTRELL, A. H., 1955, *Phil. Mag.*, **46,** 735.
PANSERI, C., and FEDERIGHI, T., 1958, *Phil. Mag.*, **3,** 1223.
SEITZ, F., 1950, *Phys. Rev.*, **79,** 890.
WINTERBERGER, M. M., 1958, *Vacancies and Other Point Defects in Alloys* (The Institute of Metals), p. 201.

Dislocation-locking by Carbon, Nitrogen and Boron in α-Iron†

By I. Codd and N. J. Petch
Metallurgy Department, University of Leeds

[Received August 14, 1959]

Abstract

It is shown experimentally that nitrogen-locking is appreciably stronger than carbon-locking. This is contrary to the customary assumption and it is suggested that there may be chemical as well as elastic interaction with the dislocations. Boron is found to produce even stronger locking than nitrogen. These variations in the locking strength alter the ductile-brittle transition temperature. The stronger the locking, the higher the transition temperature.

§ 1. Locking by Boron

The locking of dislocations in α-iron by carbon and nitrogen due to relief of elastic strain energy is now well known (Cottrell 1948, Cottrell and Bilby 1949).

The present work began with an examination of the possibility of dislocation-locking by boron. Some doubt exists about the nature of the boron solution in α-iron. However, the observation of an internal friction peak at about room temperature and of a diffusion rate for boron in iron comparable to that of nitrogen and carbon suggests interstitial solution (Hasiguti and Kamoshita 1954, Thomas and Leak 1955, Samsonov and Tseitina 1955). Because of this and the fact that boron is a larger atom than either nitrogen or carbon, very strong dislocation-locking by boron seems possible.

The approach adopted to obtain information about this possibility involved an examination of the effect of boron on the lower yield point $\sigma_{\mathrm{l.y.p.}}$ of a steel at 18°c and −196°c over a wide range of grain diameter l. This permitted a study of the effect of boron on the constants σ_0 and k in the equation

$$\sigma_{\mathrm{l.y.p.}} = \sigma_0 + k l^{-1/2}. \qquad (1)$$

The form of this equation is consistent with the propagation of a Lüders band from grain to grain at the lower yield point by the concentrated shear stress generated ahead of a slip band where it is held up by a grain boundary. The constant k is taken to be a measure of the shear stress τ_d required ahead of the slip band to unlock a dislocation. In the expression given in the Appendix,

---

† Communicated by the Authors.

$$k \sim 4r^{1/2}\tau_d, \quad . \; . \; . \; . \; . \; . \; . \; . \quad (2)$$

where r is the distance of the dislocation from the end of the slip band. The other constant σ_0 in (1) is the stress opposing the motion of an unlocked dislocation along the slip plane. At room temperature, σ_0 is largely due to the interaction of the dislocations with fine precipitates, lattice defects and random impurity atoms, but at low temperatures another, very temperature-dependent contribution becomes dominant and this is apparently associated with the body-centred cubic structure (Cracknell and Petch 1955, Heslop and Petch 1956).

To study the effect of boron, three steels were used, representing the addition of molybdenum and of boron and molybdenum to a 0·13% carbon base material. The compositions are given in table 1 (A, B and C). This molybdenum–boron composition was chosen because it is representative of the principal boron steel used industrially.

Table 1. Analysis, Weight %

	C	Mn	Si	S	P	Mo	Al	N	0	' Acid-soluble ' B	' Acid-insol.' B
A	0·12	0·52	0·34	0·010	0·027	0·50	0·07	0·008	0·005	0·002	0·002
B	0·13	0·53	0·40	0·011	0·030	0·48	0·07	0·008	0·004	<0·0001	trace
C	0·13	0·47	0·30	0·010	0·031	0·11	0·08	0·008	0·005	<0·0001	trace
D	0·12	0·51	0·02	0·050	0·029	—	<0·01	0·008	—	<0·0001	nil
E	0·019	0·005	0·006	0·014	<0·002	<0·01	<0·005	0·007	—	nil	nil
F	0·045	0·47	0·02	0·035	0·018	—	0·01	0·006	—	nil	nil

Ni, Cr, V, Cu, Co, Ti and W were all <0·02%, except for 0·08% Ni and 0·05% Cr in D.

The general experimental procedure for the determination of the yield points followed that already described (Cracknell and Petch 1955). Specimens with 1 in. gauge length of 0·125 in. diameter were used and the strain rate was $2 \times 10^{-4}\,\mathrm{sec}^{-1}$. The specimens were machined, polished to 3/0 emery and, to vary the grain size, they were annealed *in vacuo* in the range 910°–1200°C, followed by cooling in the furnace at various rates. They were then tested. As commercially heat-treated, this boron steel is air-cooled and does not show a yield point probably because of the internal stresses arising from the low temperature of transformation from austenite. However, by using a cooling rate not exceeding $6^\circ\mathrm{C}\,\mathrm{min}^{-1}$, the yield point was retained.

The results of these measurements are shown in figs. 1 and 2, and the values of σ_0 and k obtained from them are in table 2. Throughout the present work, the least squares method was used for curve-fitting.

It is apparent that boron produces a substantial increase in the slope k both at 18° and −196°C. Thus, from (2), unless boron affects the distribution of the dislocations so that r alters, this increase in k must mean that boron increases τ_d, the dislocation-locking strength.

Fig. 1

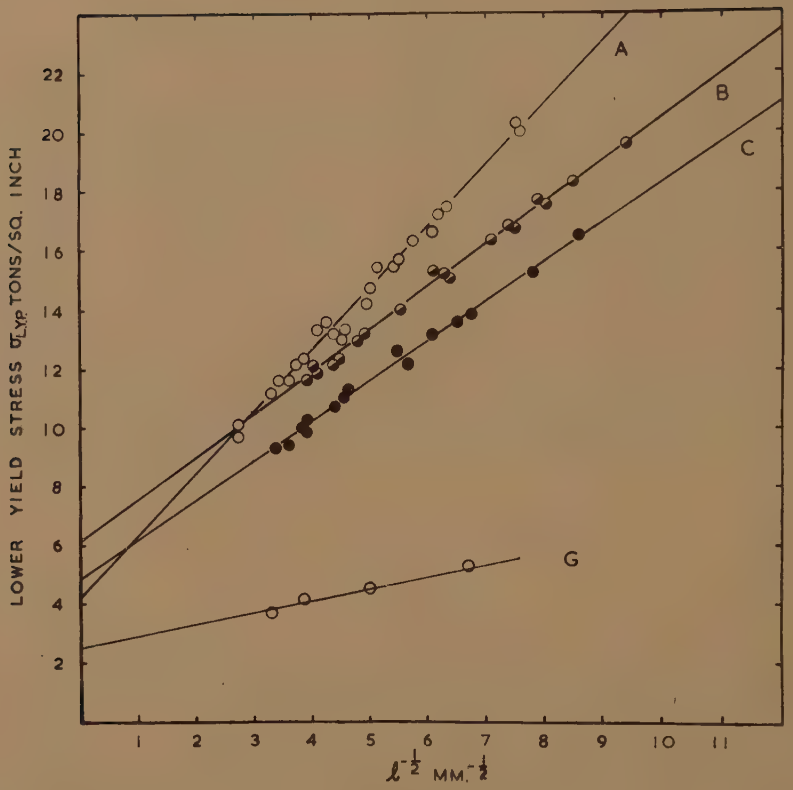

The lower yield point-grain size dependence at 18°c for steels A, B and C. G gives the limit of proportionality for the yield point-free material obtained from E.

Table 2. σ_0 and k Values

Steel	Temperature °c	σ_0 10^8 dynes cm^{-2}	k 10^8 cgs units
A (Mo–B)	18	6·5	1·02
B (Mo)	18	9·4	0·69
C (killed)	18	7·4	0·65
D (semi-killed)	18	7·1	0·74
A† (Mo–B)	18	6·6	0·66
A (Mo–B)	−196	40·1	1·94
B (Mo)	−196	45·0	1·28
C (killed)	−196	43·0	1·21
D (semi-killed)	−196	42·9	1·62
E′ (pure C)	−196	49·3	0·98
F′ (pure C)	−196	44·5	1·01
F″ (pure C–N)	−196	44·5	1·59

† Annealed 750–850°c.

Table 2 also shows that when the grain size range in the molybdenum–boron steel A was established by annealing at 750–850°c, instead of above 910°c, the effect of the boron on *k* disappeared. The solubility of boron in α-iron falls rapidly below 910°c to <0·0004% at 710°c (McBride *et al.* 1954), so it seems that the amount of boron retained in solution in this annealing range was too small to affect the dislocation-locking. On cooling from the higher annealing temperatures, equilibrium was presumably not established and the boron was retained in solution.

Fig. 2

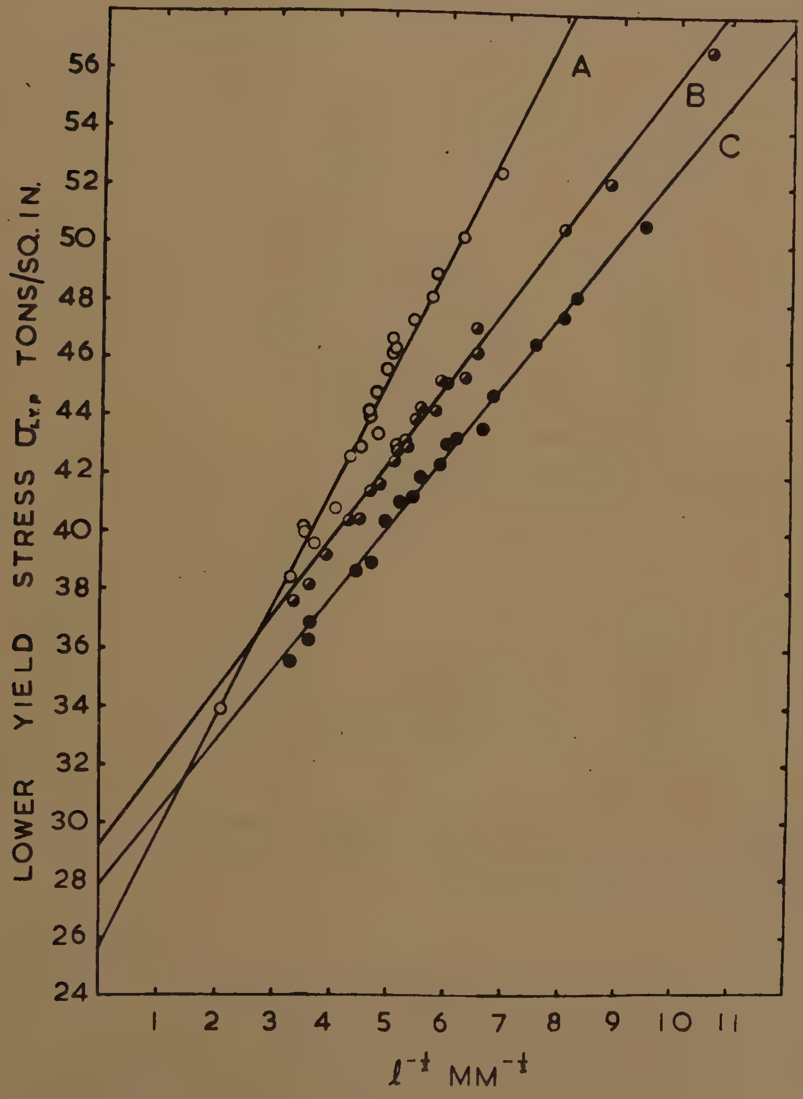

The lower yield point–grain size dependence at −196°c for steels A, B and C.

§ 2. Locking in Killed and Semi-killed Steels

The steels used in § 1 were fully killed (deoxidized) with Mn, Si and Al. Previously a semi-killed plain carbon steel had been examined (Cracknell and Petch 1955, Heslop and Petch 1956) and the σ_0 and k values for this steel D are included in table 2. The composition is in table 1. It is clear that the slope k is appreciably greater for the semi-killed D than for the fully-killed C, particularly at −196°c.

Fig. 3

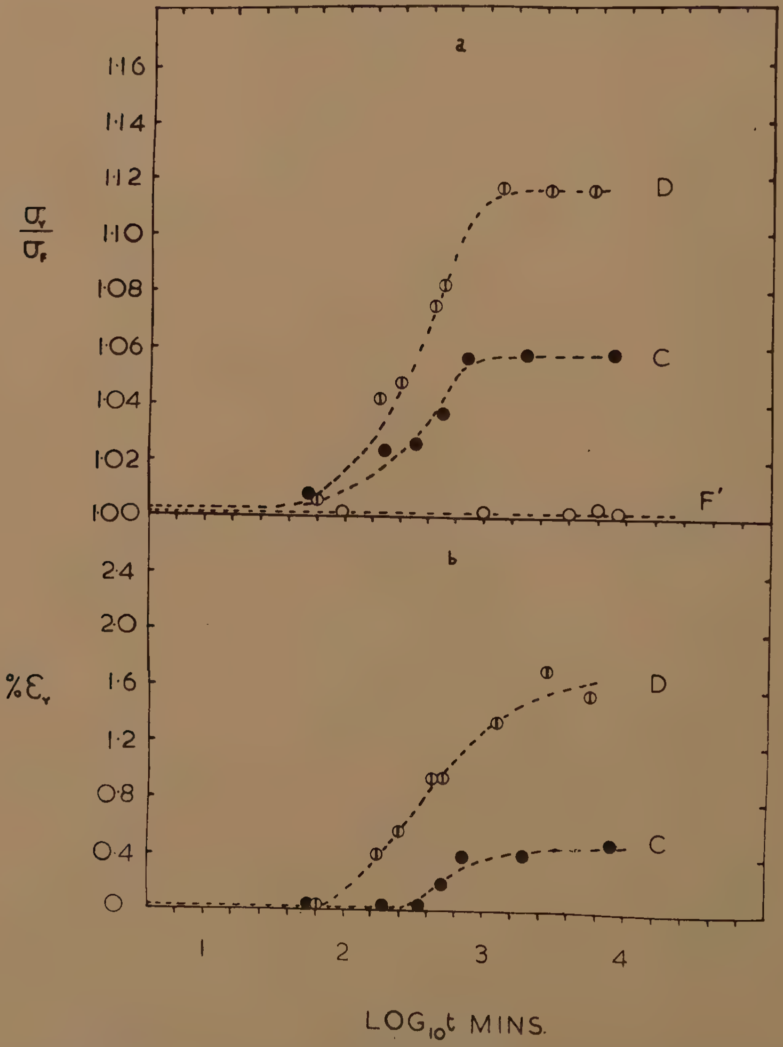

Strain-ageing at 35°c. Change with time of (*a*) the ratio of the yield point after ageing σ_Y to the flow stress σ_F at the end of the initial 4% strain, (*b*) the yield elongation.

In an annealed semi-killed steel there is much more nitrogen than carbon in solution in the ferrite at room temperature and available for dislocation-locking. Fully-killing a steel, however, not only deoxidizes it, but in addition largely precipitates the nitrogen as AlN. Thus, this reduction in the slope k observed with the fully-killed steel suggests that removal of nitrogen from solution has weakened the dislocation-locking.

To get some idea of the extent of the nitrogen removal in these steels, their strain-ageing was examined. This was carried out at 35°C, since the temperature is then too low for any ageing due to carbon. Specimens annealed to the same grain size were used. Figure 3 shows the measurements for the fully-killed C and the semi-killed D after 4% strain. Also included is a nitrogen-free, iron–carbon alloy F′, described later. From the rate of ageing, it appears that the content of uncombined nitrogen in the killed steel C is about one-third of that in the semi-killed D. Figure 3 also shows that the yield point elongation after ageing was shorter for the fully-killed steel. Since this elongation measures the strain required in one crystal to unlock a dislocation in the next, it seems that the nitrogen available in the fully-killed steel was insufficient for the development of full nitrogen-locking on ageing.

A similar effect to that of full-killing upon k has been observed with high manganese additions (1–2%) to a semi-killed steel (Heslop and Petch 1957) and, although there is no precipitation of a nitride in that case, there is a 0·2 ev attraction between the manganese and nitrogen atoms in solution that may interfere with the supply of nitrogen atoms to the dislocations.

§ 3. PURE CARBON-LOCKING AND PURE NITROGEN-LOCKING

To examine further this effect of the availability of nitrogen on the dislocation-locking strength, pure carbon-locking and pure nitrogen-locking were prepared.

Carbon and nitrogen were removed by wet hydrogen from specimens of a fairly pure Swedish iron and of a 0·47% Mn steel (E and F in table 1) until the yield point was suppressed†. Carbon alone was then replaced as described in § 6. This gave two nitrogen-free steels, one with 0·20–0·26% C, the other with 0·09–0·12% C, 0·47% Mn. Their lower yield points at −196°c are shown in fig. 4 and the k values are in table 2 (E′ and F′).

It is clear that the pure carbon-locking gives a value of k only about two-thirds that of the semi-killed steel D at −196°c. This carbon k is even lower than k for the fully-killed steels B and C, which still contain some free nitrogen, and is close to the value reached in a high manganese (1·9%) steel (Heslop and Petch 1957).

Replacement of the nitrogen to 0·008% in the carburized specimens returned k to the value for the semi-killed steel D (F″ in fig. 4 and table 2).

---

† The limit of proportionality for the yield point-free iron obtained from E is included at G in fig. 1.

Direct nitriding (0·013% N_2) of the yield point-free material gave the same result with $k = 1{\cdot}6 \times 10^8$ c.g.s. units at -196°c. (fig. 6).

Thus, it seems well established that carbon-locking is weaker than nitrogen-locking and that the locking in an annealed semi-killed steel is predominantly due to its nitrogen.

Fig. 4

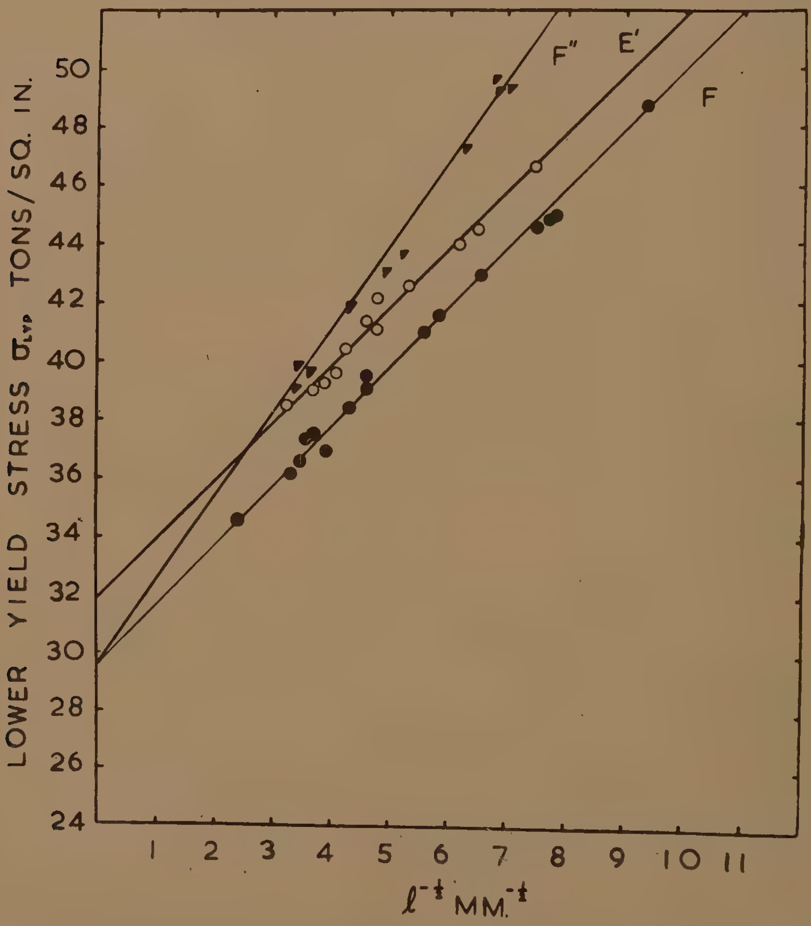

The lower yield point–grain size dependence at -196°c after treatment to give pure carbon-locking (E′ and F′) and after subsequent nitriding (F″).

Specimens of F treated to give pure boron-locking (0·004–0·006% 'soluble' B) have also been prepared (Codd, unpublished) and their k value at 18°c is very close to that for the molybdenum–boron steel A, so confirming that carbon–nitrogen-locking is replaced by boron-locking in this steel.

§ 4. THE RELATIVE STRENGTHS OF CARBON, NITROGEN AND BORON-LOCKING

In (2), a change in the slope k can arise from a change in the locking strength τ_d or from a change in the distance r between the end of the slip band and the dislocation that is unlocked in the propagation of yield from one grain to the next. Replacement of nitrogen-locking by carbon-locking changes not only k but also its temperature-dependence. An alteration in r would not have this effect. Also there seems no particular reason why r should change whenever the locking atoms change. On these grounds, the observed alterations in k have been interpreted as alterations in locking strength.

In the original Cottrell–Bilby theory, the dislocation-locking in α-iron was thought to be due to a condensed atmosphere consisting of a single line of carbon or nitrogen atoms at the dislocation. It now appears that the atmosphere is more extensive than this (Cottrell 1953 a, Dahl and Lücke 1954, Thompson 1958). Thus, one possible explanation of the greater strength of nitrogen-locking compared to carbon-locking is simply that the higher solubility of nitrogen in α-iron below about 580°C may give rise to a higher concentration of impurity atoms at the dislocations. Against this idea, there is the consideration that escape from a stronger-locking, more concentrated atmosphere would be expected to require a greater activation energy and this would make nitrogen-locking less temperature-dependent than carbon-locking, whereas the opposite is observed. Also, when the carbon-locked steel F′ was quenched from 650°C, its k value remained unchanged at the low value (F‴, fig. 5), and similarly on quenching the nitrogen-locked steel its k remained unchanged at the high value (fig. 6)†. Yet, in these treatments, the carbon concentration in the ferrite was greater than the nitrogen concentration. Thus, it does not seem possible to explain the difference between the carbon and nitrogen k values on the basis of a concentration effect.

It is now suggested that the observed difference in the k values shows that the interaction energy between a carbon atom and a dislocation is less than that between a nitrogen atom and a dislocation. This is, of course, contrary to the customary assumption based on the very nearly equal dilations produced by the two atoms and suggests that there must be some effect additional to the elastic interaction.

Recent theoretical work has emphasized the possible directional character of metallic bonding (Altman *et al.* 1957) and the observations of what may be an appreciable Peierls–Nabarro stress in α-iron also suggests directionality of bonding (Heslop and Petch 1957). Possibly, therefore, in the locking of a dislocation in α-iron, the important effect additional to the elastic interaction arises from a degree of residual chemical bonding at a dislocation to which the impurity atom becomes attached, as occurs in covalent silicon and germanium (Seitz 1952).

---

† There is an increase in the friction stress σ_0 on quenching the iron–carbon alloy (fig. 5) because of the increased concentration of carbon retained in solution in the ferrite, but there is little effect on σ_0 for the iron–nitrogen alloy (fig. 6) because most of the nitrogen is already in solution in the annealed specimens.

There is some evidence that such chemical bonding might be stronger for nitrogen than for carbon. The free energy of formation of the iron carbides and nitrides are about the same (Quill 1950) in spite of the greater stability of the bonding in elementary nitrogen (Pauling 1948), which suggests that the iron–nitrogen bond is stronger than the iron–carbon one.

Fig. 5

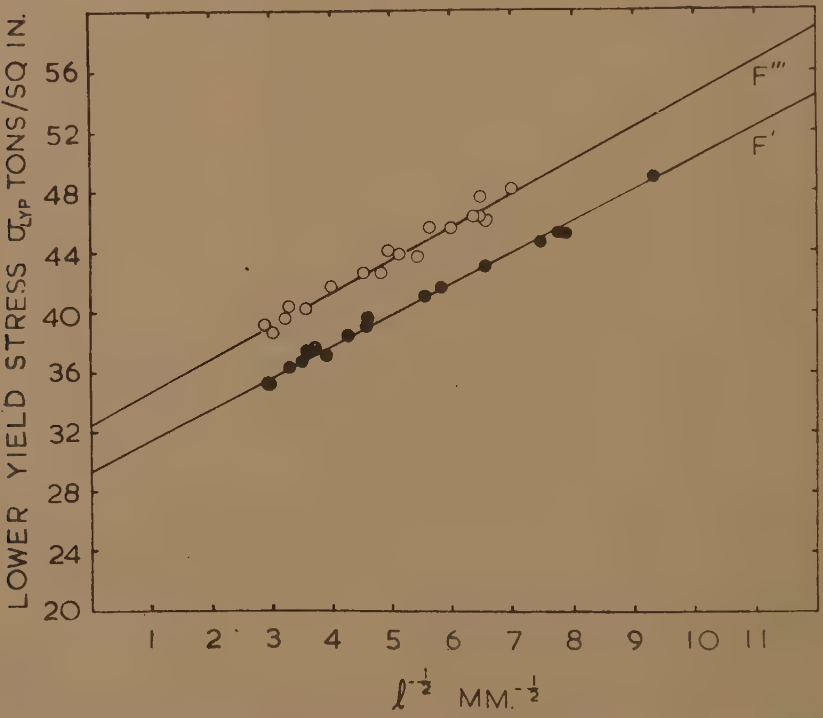

The effect of quenching from 650°c (F''') on the strength of the pure carbon-locking at −196°c.

Now consider the boron-locking. That it is the strongest is consistent with the atomic size of boron. The boron radius in α-iron is uncertain, but taking the value 0·94 Å from Fe_2B, the tetragonal strain in α-iron should be ~0·53 and in the transverse directions the strain should be ~0·08. Using the expression due to Cochardt *et al.* (1955), these figures make the interaction energy with an atom situated directly below an edge dislocation ~2·0 times as great for boron as for carbon. The observed ratio of k for boron and carbon is 2·0 at −196°c and ~1·7 at room temperature. This agreement is probably fortuitous since the boron radius is uncertain and chemical interaction is neglected.

Fig. 6

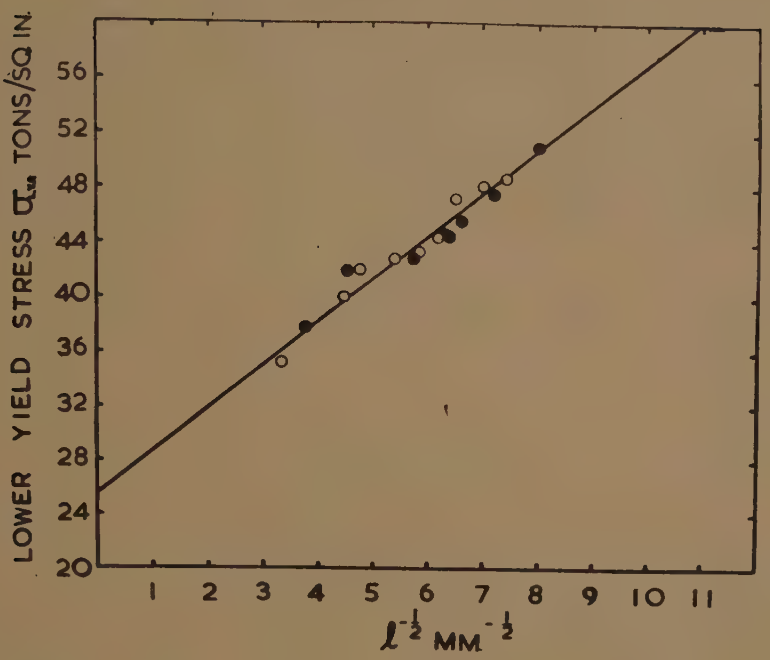

The lower yield point–grain size dependence at −196°c for pure nitrogen-locking; ○ annealed, ● quenched from 650°c.

§ 5. The Friction Stress and the Ductile–Brittle Transition

The value of σ_0 in (1) represents the friction opposing the movement of an unlocked dislocation along the slip plane. This is not a major concern in the present paper, so the observed values (table 2) will be discussed only briefly.

The friction σ_0 is due to the lattice itself and to interaction of the moving dislocation with precipitates, lattice defects and impurity atoms in solution. Between the semi-killed steel D and the fully-killed C there should be a fall in σ_0 due to the removal of nitrogen from solution, but this appears to be compensated for by the increased interaction with silicon. The addition of Mo in steel B makes a further contribution to σ_0. The subsequent fall on adding boron (steel A) presumably arises from further nitrogen fixation and possibly from some interaction of the boron and molybdenum atoms.

The variations in the dislocation-locking strength observed in the present measurements should be accompanied by variations in the ductile–brittle transition temperature (Heslop and Petch 1957, 1958, Cottrell 1958). The weaker the dislocation-locking, the easier is plastic deformation and the lower should be the transition temperature. This is confirmed for the present steels by fig. 7 in which the transition temperature is taken at

10 ft lb (~75% cleavage) for 5/16 in. V-notched specimens broken in a Charpy-type impact test.

The amount the transition temperature of the fully-killed C is below that of the semi-killed D agrees with previous measurements in which k was reduced by manganese (Heslop and Petch 1957).

The 1·3 ton in^{-2} increase in σ_0 between C and B (table 2) should give a 6°c rise in transition temperature (Heslop and Petch 1958).

Fig. 7

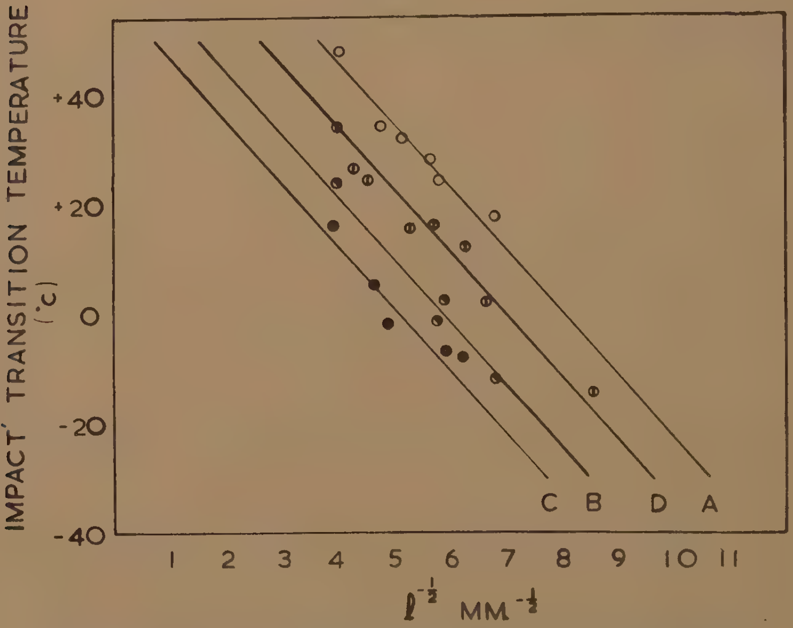

The ductile–brittle transition temperatures for boron-locked (A), killed (B and C) and semi-killed (D) steels.

§ 6. Exprimental Details

For the preparation of the pure carbon-locking, tensile specimens (1 in. gauge length of 0·125 in. diameter) were partly machined from the Swedish iron E and from a similar material F with 0·5% Mn added in the hope that it would help in the retention of a fine grain size. These specimens were heated in wet hydrogen at 850°c until samples showed that the carbon and nitrogen had been removed to such an extent that the yield point was suppressed (~600 hours). The treatment was continued for at least a further day and carbon only was then replaced by carburizing for a pre-determined time at 820°c in an atmosphere of purified hydrogen and hexane vapour.

To remove nitrogen and other gases from the hexane, it was previously refluxed at reduced pressure (2 mm) and temperature (0°c). After this treatment, the vacuum was released by purified hydrogen and, as an additional precaution, the hydrogen was bubbled slowly through the hexane for some time before passing the hydrogen–hexane mixture into the carburizing tube. Since there was very little carbon pick-up until the hexane decomposed at ~815°C, the hydrogen–hexane mixture was used to protect the specimens during heating and cooling and the time at 820°C gave a reasonable estimate of the carbon ingress. After homogenizing for eight days at 1050°C *in vacuo*, the specimens were machined to final size, polished and then heat-treated *in vacuo* to establish the desired grain size. Each specimen was analysed for carbon.

For the nitrogen-locking, nitriding was carried out at 580°C for ~100 hours in a stream of hydrogen bubbled through 3% ammonia in distilled water.

APPENDIX

CALCULATION OF THE SLOPE k

In Stroh's (1955) calculation, the distance r between the head of a slip band and the operated source (length s) in the next grain during the propagation of a Lüders band from one grain to the next at the lower yield point is taken to be at least equal to s. This is to allow sufficient room for the operation of the source. The shear stress ahead of a slip band depends upon $r^{-1/2}$, but the stress required for critical bowing of the source depends upon s^{-1}, so, with $s \sim r$ and no impurity-locking, the further the source is away from the slip band the longer it can be and the easier it is operated by the slip band. With a locked source, however, there will be a lower limit τ_d on the shear stress required for its working and the easiest source to bring into operation ahead of a slip band will then be the one for which the bowing stress and the locking stress are equal.

Stroh thus obtains

$$k \sim 2(2\tau_d \mu \mathbf{b})^{1/2}, \qquad \qquad (3)$$

where μ is the rigidity modulus and $\mathbf{b}$ is the Burgers vector.

This argument will however break down if the locking stress is greater than the bowing stress for all the sources present and it seems probable that this will be so in α-iron. At −196°C, τ_d is $\sim 1 \times 10^{10}$ dynes cm^{-2} and it is probably only a few times smaller at room temperature (Cottrell 1958). Thus, the locking stress is ~100 times greater than that required for the critical bowing of sources of the length (10^{-4} cm) normally expected in α-iron.

The argument for (3) in α-iron has been supported by showing that it gives the correct temperature-dependence of k from the temperature-dependence of τ_d. However, in this, τ_d was identified with the upper yield point, whereas it is now clear that the upper yield point is the stress required for the break-out of a plastic nucleus across the specimen (Cottrell 1953 b) and not the stress for unlocking a source. The upper yield point is influenced by the stress concentration ahead of slip bands in the plastic nucleus, so it depends on grain size in a similar way to the lower yield point (eqn. (1)). Thus the temperature-dependence of the upper yield point arises principally from the temperature-dependence of the friction stress σ_0 and it does not directly give the temperature-dependence of the locking strength τ_d in the way assumed in this support of (3).

In place of a value of r determined according to Stroh's suggestion, it may be that r is simply the average distance between the end of a slip band and the nearest source in the next grain. Then, from the equivalence of a crack and a slip band in the relaxation of shear stress

$$\tfrac{1}{2}(\sigma_{\text{l.y.p.}}-\sigma_0)(l/4r)^{1/2}=\tau_d,$$

or

$$k=4r^{1/2}\tau_d. \qquad (4)$$

At −196°c, with $\tau_d \sim 1\times10^{10}$ dynes cm^{-2} and $k=1{\cdot}6\times10^8$ c.g.s. units, r is $\sim$ $0{\cdot}2\times10^{-4}$ cm.

The main difficulty with (4) is that r has to be constant, independent of grain size. It may be that the width of the grain boundary stress field imposes such a constancy.

Another possibility is that instead of operating a source in the next grain, the yield is propagated by forcing a length of dislocation out from the grain boundary.

References

Altman, S. L., Coulson, C. A., and Hume-Rothery, W. 1957, *Proc. roy. Soc.* A, **240,** 145.

Cochardt, A. W., Schoek, G., and Wiedersich, H., 1955, *Acta Met.*, **3,** 533.

Cottrell, A. H., 1948, *Rept. Conf. Strength of Solids* (London: The Physical Society), p. 30; 1953 a, *Relation of Properties to Microstructure* (Amer. Soc. Metals), p. 131; 1953 b, *Dislocations and Plastic Flow in Crystals* (Oxford: University Press), p. 147; 1958, *Trans. Amer. Inst. min. (metall.) Engrs*, **212,** 192.

Cottrell, A. H., and Bilby, B. A., 1949, *Proc. phys. Soc. Lond.*, A, **62,** 49.

Cracknell, A., and Petch, N. J., 1955, *Acta Met.*, **1,** 186.

Dahl, W., and Lücke, K., 1954, *Arch. Eisenhüttenw.*, **25,** 241.

Hasiguti, R. R., and Kamoshita, G., 1954, *J. phys. Soc. Japan*, **9,** 646.

Heslop, J., and Petch, N. J., 1956, *Phil. Mag.*, **1,** 866; 1957, *Ibid.*, **2,** 649; 1958, *Ibid*, **3,** 1128.

McBride, C. C., Spretnak, J. W., and Speiser, R., 1954, *Trans. Amer. Soc. Met.*, **46,** 499.

Pauling, L., 1948, *The Nature of the Chemical Bond* (Cornell University Press), p. 177.

Quill, L. L., (Editor), 1950, *The Chemistry and Metallurgy of Miscellaneous Materials, Thermodynamics* (New York: McGraw-Hill), p. 13.

Samsonov, G. V., and Tseitina, N.Ya., 1955, *Fizika Metallov i. Metallovedenie*, **2,** 303.

Seitz, F., 1952, *Phys. Rev.*, **88,** 722.

Stroh, A. N., 1955, *Phil. Mag.*, **46,** 968.

Thomas, W. R., and Leak, G. M., 1955, *J. Iron St. Inst.*, **180,** 155.

Thompson, R., 1958, *Acta Met.*, **6,** 23.

On Dislocation Formation by Vacancy Condensation†

By G. Schoeck‡ and W. A. Tiller
Westinghouse Research Laboratories, Beulah Road, Churchill Borough,
Pittsburgh 35, Pennsylvania

[Received August 19, 1959]

Abstract

The mechanism of dislocation loop formation by vacancy condensation is examined in a quantitative manner. The critical vacancy supersaturation necessary for the growth of the loops and the climb rate of the dislocations are determined. It is shown that the mechanism proposed for lineage formation based upon loop growth (Frank, 1956 a) is inapplicable. The number of dislocation loops produced by collapsing vacancy discs is calculated as a function of the cooling rate, cooling range and dislocation density existing in the crystal before cooling.

§ 1. Introduction

Essentially five different mechanisms exist for the introduction of dislocations into freshly grown crystals: growth accidents (Frank 1950), vacancy condensation (Frank 1950, Seitz 1950, Kuhlmann-Wilsdorf 1958), segregation of solutes (Frank 1950, Friedel 1956, Goss *et al.* 1956, Tiller 1958), phase transformation and precipitation (Brooks 1952) and thermal and external stresses (Billig 1956, Wagner 1958). If one considers single phase crystals grown carefully from the melt so that both thermal and external stresses are absent we may neglect the last two mechanisms. In general, then, one needs to consider only the first three mechanisms in order to determine the total dislocation concentration either grown into the crystal at the solid–liquid interface or quenched-in during cooling of the crystal.

One would expect that not only the dislocation density but the dislocation arrangement in the crystal would differ depending on the mechanism by which they are introduced into the crystal. However, except in a few cases, little quantitative theoretical work has been carried out on the genesis of the original dislocations in metal crystals. Most theoretical investigations have been concerned with the somewhat simpler problem of the stable arrangements of dislocations either in two dimensional arrays (boundaries) or in three-dimensional networks.

Recently, Kuhlman-Wilsdorf (1958) has reconsidered the formation of dislocation rings from collapsed vacancy discs and proposed that these dislocation rings are actually the main sources for the multiplication of dislocations during plastic deformation. From the kinetics of the electrical resistivity recovery and from quench hardening, it has been concluded by Kimura *et al.* (1959) that the dislocation rings can be formed from vacancy aggregation provided the crystal is quenched over a sufficiently large temperature range. More recently Hirsch *et al.* (1958) have actually observed such dislocation loops in quenched Al (Hirsch *et al.* 1958), and defects related to dislocation loops in the noble metals (Hirsch and Silcox 1958).

---

† Communicated by the Authors.
‡ Now at CNEA, Av. Lib. Gen San Martin 8250, Buenos Aires, Argentina.

Fig. 1

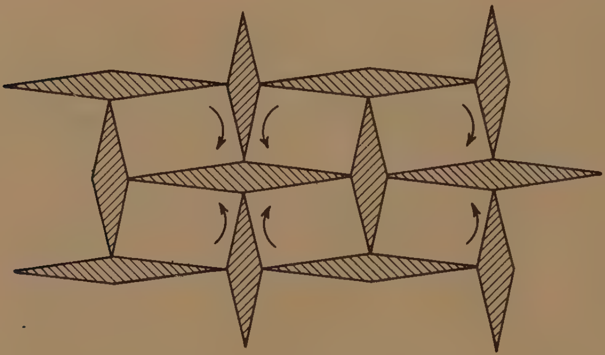

Striation-type dislocation array (after Frank).

The vacancy condensation model has also been used by Teghtsoonian and Chalmers (1951, 1952) and Atwater and Chalmers (1957) to account for a particular type of lineage structure called 'striations' observed to occur during the growth of crystals from the melt. This sub-structure consists of an assembly of low-angle grain boundaries which partitions the crystal into rod-like elements that are generally parallel to the crystal axis. The striations are often of the order of 1 sq. mm in cross-sectional area, the different rods being rotated with respect to each other about the growth axis by angles varying between a fraction of a degree and several degrees, as illustrated in fig. 1. In growing a single crystal without the use of a seed it is observed that the striations do not form immediately. They are observable only after a considerable length (approximately 1 cm) of solid has formed. After this incubation distance, the misorientations appear spontaneously and increase to a stable value with a little further solidification.

Frank (1956 a) has developed a detailed picture of the vacancy collapse mechanism to account for this 'striation' sub-structure giving a qualitative explanation of the origin, size and initial misorientation. It is very easy to show that the dislocations in the lineage array could not have been formed by the collapse of vacancy discs since the total vacancy concentration of the crystal is 2 to 3 orders of magnitude too small to provide the lineage size and misorientation. Therefore, Frank postulated the following.

The edge dislocation loops, formed by vacancy condensation at some distance behind the interface, grow in size to reduce the vacancy supersaturation. Those loops which lie in planes parallel to the growth axis will grow towards the interface and catch up to it. Once the dislocation has entered the interface it will contribute to the misorientation of the growing solid without further vacancy condensation. This is illustrated in fig. 2. He maintained that the elastic interaction between edge dislocations should cause them to assemble into parallel arrays as shown. A system of these arrays leads to the lineage type substructure (fig. 1). The ends of the loops in fig. 2 (*a*) are in an unstable position and are attracted into the interface with the liquid (fig. 2 (*b*)). The dislocations are then no longer effective for removing vacancies merely by lengthening and the vacancy excess will drive them apart. A new dislocation loop will then form preferentially in this central region (fig. 2 (*c*)) and the amount of rotation of the lineage boundaries will continually increase until the rate of production of new loops is balanced by the rate of annihilation of dislocations by the meeting of opposite pairs.

Fig. 2

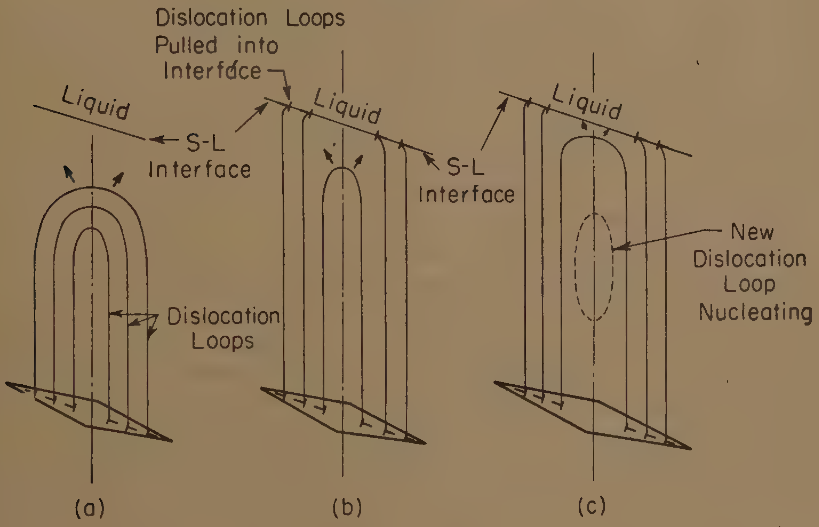
Dislocation Loops Pulled into Interface
Liquid
S-L Interface
Dislocation Loops
Liquid
S-L Interface
Liquid
New Dislocation Loop Nucleating
(a)
(b)
(c)

The climbing of dislocation loops into the solid–liquid interface.

The purpose of the present paper is to examine the vacancy condensation mechanism in a quantitative manner to determine (i) the critical vacancy supersaturation necessary for the formation and growth of dislocation loops by vacancy condensation and (ii) the climb rate of the dislocations as a function of the vacancy supersaturation. From these calculations and the experimental observations on striations it will be shown that Frank's model cannot account for the sub-structure. From the calculations it is also possible to determine the quenching rate and quenching range necessary for the formation of the dislocation loops by vacancy condensation. Finally, it is possible to estimate the density of dislocations introduced into the crystal by this mechanism during crystal growth.

§ 2. CONDENSATION OF VACANCIES

If the concentration of vacancies in a solid exceeds the thermal equilibrium value there is a tendency for the vacancies to anneal out by condensing into larger aggregates. The determination of the vacancy super-saturation necessary to nucleate this process is a very complex problem and has not yet been treated. It is very likely that the nucleation takes place heterogeneously in the neighbourhood of solute or impurity atoms rather than homogeneously, but it is not possible to state whether these aggregates will be preferentially pores or flat discs (Frank 1956 b). However, since we are interested in the formation of dislocations, we may assume that vacancy discs are formed which collapse into dislocation rings after they reach a critical size. After this has happened we can calculate the supersaturation necessary to keep the dislocation rings growing to a larger size by climbing. We thus know that the actual supersaturation must be at least this value. Since all dislocations formed by vacancy condensation must go through this early stage of growth we will obtain, in this way, a lower limit for the necessary vacancy supersaturation.

As has been discussed by various authors (Kuhlmann-Wilsdorf 1958, Kimura *et al.* 1959) the collapse of the disc will take place when the energy of the disc (which is essentially the surface energy) exceeds the energy of the dislocation ring (which is essentially strain energy). Usually the collapse of the disc will also form a stacking fault since the two lattice planes brought into contact with each other will generally have an incorrect stacking sequence. In very few cases the surface energy of this stacking fault is known. Since a coherency exists across the interface, the stacking-fault energy should be of the order of a coherent twin-boundary energy and it will not exceed, and in many cases be considerably less than, the energy of a large angle grain boundary. It seems therefore safe to assume that the stacking-fault energy γ_{st} is smaller than about $\frac{1}{3}$ or $\frac{1}{2}$ of the surface energy γ. To obtain an upper limit to the collapse radius in our calculations, we assume for numerical calculations $\gamma_{\mathrm{st}}=\frac{1}{2}\gamma$ in all cases where γ_{st} is unknown.

If r is the radius of the vacancy disc, the energy of the disc E_{d} for not too small values of r, will be

$$E_{\mathrm{d}} \approx 2\pi r^2 \gamma. \qquad (1)$$

The energy of a corresponding dislocation ring with the Burgers vector $\mathbf{b}$ perpendicular to the plane of the ring (Franz and Kroener 1955) and enclosing a stacking fault of surface energy γ_{st} will be

$$E_r=\frac{1}{2}\frac{G}{(1-\nu)}\mathbf{b}^2 r\left[\ln\frac{8r}{R_0}-1\right]+2\pi r\left[\pi\frac{R_0{}^2}{\mathbf{b}^2}L\right]+\pi r^2\gamma_{\mathrm{st}}, \qquad (2a)$$

where G is the rigidity modulus, ν is Poisson's ratio, R_0 is the radius of the dislocation core and L is the average strain energy per atom of this core. For numerical purposes we use $\nu=\frac{1}{3}$.

We may determine the minimum core radius by noting that the free energy of the core cannot be greater than the free energy of a cylinder of liquid of radius R_0. If one determines the core radius using such an energy balance including a term which incorporates the solid–liquid interfacial energy it is found that $R_0\sim\mathbf{b}/2$. However, for such a small cylinder of liquid the surface energy term should probably be excluded. If this term is neglected the core radius is given by

$$\frac{R_0}{\mathbf{b}}=\frac{1}{2\pi(1-\nu)}\left[\frac{G/\Delta H}{2\Delta T/T_{\mathrm{m}}}\right]^{1/2}\approx\left\{\frac{T_{\mathrm{m}}}{\Delta T}\right\}^{1/2}, \quad . \; . \; . \quad (2b)$$

where ΔH is the enthalpy difference between liquid and solid, T_{m} is the melting temperature and $\Delta T=T_{\mathrm{m}}-T$. For a typical value of

$$\Delta T/T_{\mathrm{m}}\sim 0{\cdot}25,\ R/\mathbf{b}=2$$

and eqn. $(2a)$ can be put in the form

$$E_r=\frac{1}{2}\frac{G}{(1-\nu)}\mathbf{b}^2 r\left[\ln\frac{r}{\mathbf{b}}+Z\right]+\pi r^2\gamma_{\mathrm{st}}. \quad . \; . \; . \; . \quad (2c)$$

For $R_0/\mathbf{b}=2$, 1 and 0·5, $Z=1{\cdot}98$, 1·48 and 1·96 respectively. We will choose the value of $Z=1{\cdot}8$ in our calculations as a representative value.

The condition for collapsing, $E_r=E_{\mathrm{d}}$, gives the critical radius r_{c} from the equation

$$\frac{\mathbf{b}}{r_{\mathrm{c}}}\left[\log\left(\frac{r}{\mathbf{b}}\right)+1{\cdot}8\right]=\frac{4\pi(2\gamma-\gamma_{\mathrm{st}})}{3G\mathbf{b}}. \quad . \; . \; . \; . \; . \; . \quad (3)$$

The critical radius r_{c} for several metals is given in table 1. In several cases r_{c} is astonishingly small and collapsing would occur according to eqn. (3) if the diameter of the disc is of the order of a few atomic distances. This estimate may not be quite realistic since the equation for the dislocation energy and the concept of surface energy may lose their significance for such small dimensions. Nevertheless it seems safe to assume that a disc with a radius of 10 atomic distances will have collapsed to form a dislocation ring. For some numerical estimates we will later assume that a vacancy disc exceeding a radius of 10 or 15 atomic distances will have formed a dislocation ring. Once the dislocation ring is formed, it is under the action of its own line tension and can grow or shrink by climbing. It will expand only if there is a sufficient supersaturation of vacancies. A vacancy condensing at the dislocation ring will increase its radius and hence its strain energy E_r. At the same time the free energy F_{v} of the crystal due to the vacancy supersaturation will decrease. If n is the number of vacancies, the critical supersaturation necessary to keep a dislocation ring of radius r from shrinking is obtained from the condition

$$\frac{\partial E_r}{\partial r} + \mu_V \frac{\partial n}{\partial r} \leqslant 0 . \qquad (5)$$

where μ_V is the chemical potential of a vacancy which is given by

$$\mu_V = \frac{\partial F_V}{\partial n} = kT \ln \frac{c}{c_0} . \qquad (6)$$

Here c is the actual vacancy concentration and c_0 the concentration of vacancies in thermal equilibrium at temperature T.

Table 1

	G 10^{11} dyne/cm²	b 10^{-8} cm	γ erg/cm²	γ_{st} erg/cm²	$\frac{4\pi(2\gamma-\gamma_{st})}{3Gb}$	$\frac{r_c}{b}$	Gb^3 ev
Sn	1·7	3·02	625†	$<\frac{1}{2}\gamma$	0·75	4·4	2·92
Pb	0·54	3·49	444†	$<\frac{1}{2}\gamma$	1·5	1·5	1·43
Zn	3·8	2·66	824	$<\frac{1}{2}\gamma$	0·52	7·5	4·5
Al	2·5	2·86	900	$\frac{2}{5}\gamma$(2)	0·83	3·75	3·66
Cu	4·1	2·55	1430‡	40(2)	1·1	2·5	4·25
Ag	2·6	2·88	1140‡	~40	1·2	2·1	3·86

† U.S. Atomic Energy Comm. Publ., (*Liquid Metals Handbook*, Wash. 1952).
‡ J. C. Fisher and C. G. Dunn, *Imperfections in Nearly Perfect Crystals* (John Wiley & Sons, Inc., New York 1950).

Since we want to obtain only a lower limit for the necessary supersaturation we are justified in neglecting the term in E_r in eqn. (2) which contains the energy γ_{st} of the stacking fault when we evaluate eqn. (5). The result then becomes somewhat simpler and we obtain from eqns. (2 c), (5) and (6)

$$\ln \frac{c}{c_0} = \frac{G\mathbf{b}^4}{4\pi(1-\nu)rkT}\left[\ln\left(\frac{r}{\mathbf{b}}\right) + 2\cdot 8\right] . \qquad (7)$$

In order to obtain an estimate of the temperature at which the dislocation ring will be stable we must know the actual concentration c of vacancies present. The concentration of vacancies in thermal equilibrium at temperature T is

$$c_0 = \beta \exp(-U_f/kT), \qquad (8)$$

where U_f is the energy of formation of a vacancy and the constant β which is of the order of unity may contain an entropy term. Let us now assume that the equilibrium concentration of vacancies at the melting point, T_{m}, is frozen in at the advancing liquid–solid interface. Since the mobility of vacancies at T_{m} is extremely large it is very unlikely that any in excess of this number are frozen-in. Only if no sinks are present will this number be retained in the interior of the solid during cooling to a temperature T and hence we obtain as an upper limit for c

$$c=\beta \exp(-U_{\mathrm{f}}/kT_{\mathrm{m}}). \qquad (9)$$

If we call $\Delta T=T_{\mathrm{m}}-T$ we obtain finally from eqn. (7) with eqns. (8) and (9)

$$\frac{\Delta T}{T_{\mathrm{m}}}=\frac{3G\mathbf{b}^3}{8\pi U_{\mathrm{f}}}\frac{\mathbf{b}}{r}\left[\ln\left(\frac{r}{\mathbf{b}}\right)+2\cdot 8\right]\dagger. \qquad (10)$$

(The entropy term β drops out if it is temperature independent.) Equation (10) gives the relative undercooling $\Delta T/T_{\mathrm{m}}$ necessary to keep a dislocation ring of radius r from shrinking. The magnitude of $\Delta T/T_{\mathrm{m}}$ depends on the parameter $\alpha=3G\mathbf{b}^3/8\pi U_{\mathrm{f}}$, which is listed in table 2 for various metals. When measurements of U_{f} were available the correct value was used whereas otherwise the value of U_{f} was assumed to be half the activation energy for self-diffusion. Equation (10) is plotted in fig. 3 as $\Delta T/T_{\mathrm{m}}$ *vs.* $r/\mathbf{b}$ for various values of α. The resulting supercooling for a dislocation loop radius of $r=10b$ and $r=15b$ is then also listed in table 2.

To obtain an estimate of the order of magnitude for $\Delta T/T_{\mathrm{m}}$ we may note that U_{f} is of the order (Friedel 1956 b)

$$U_{\mathrm{f}}\approx 5\,G\mathbf{b}^3. \qquad (11)$$

Using this estimate we obtain as a typical value, $\alpha=0\cdot 6$. For this value of α in fig. 3 we see that in order to keep a dislocation of radius $r=10b$ from shrinking, the relative temperature drop would have to be $\Delta T/T_{\mathrm{m}}\approx 0\cdot 35$. The corresponding value for a dislocation ring of radius $r=15b$ would be $\Delta T/T_{\mathrm{m}}\approx 0\cdot 21$. Assuming that a radius of $r=10b$ is realistic for a newly formed dislocation ring, the relative supercooling varies between 16% and 50% for the various metals (table 2). This means that the temperature at which these dislocation rings are stable is about 100°c to 400°c below the melting temperature if we are considering crystal growth or the temperature from which they are quenched if we are considering a quenching experiment. It must be remembered that these calculations assume the existence of no other vacancy sinks in the solid, otherwise the vacancy

---

† It has been pointed out by the referee that if the vacancies condense to form a ring of Frank sessile dislocation including a stacking fault, the Burgers vector of whole dislocations, $\mathbf{b}$, should not be used. Equation (10) and the tabulated values of $\Delta T/T_{\mathrm{m}}$ refer, therefore, to the case of no stacking fault. However, if one wishes to treat the stacking-fault case, the right-hand side of eqn. (10) must be multiplied by two-thirds to take account of the reduced Burgers vector and a term $\mathbf{b}^2\gamma_{\mathrm{st}}/U_{\mathrm{f}}$ added to take account of the stacking-fault energy. For rings of $r=10b-15b$ the two changes tend to cancel for reasonable γ_{st} leaving $\Delta T/T_{\mathrm{m}}$ negligibly changed.

Table 2

	U_d ev	D_0 cm²/sec	U_f ev	U_m ev	T_m °K	α $\left(\frac{3Gb^3}{8\pi U_f}\right)$	Radius of Ring r/b	$\frac{\Delta T}{T_m}$	ΔT_c °K	T_c °K	$\frac{c}{c_0}$	D cm²/sec.	$D\left(\frac{c}{c_0}-1\right)$ cm²/sec	V_0 cm/sec
Sn	1·11†	4·35†	$\frac{U_d}{2}$	$\frac{U_d}{2}$	505	0·63	10	0·33	166	339	10^2	10^{-15}	10^{-13}	$1{\cdot}6\times10^{-6}$
							15	0·20	101	404	11	3×10^{-13}	3×10^{-12}	5×10^{-5}
Pb	1·08	0·5	$\frac{U_d}{2}$	$\frac{U_d}{2}$	600	0·31	10	0·16	96	504	7·2	10^{-11}	$6{\cdot}2\times10^{-11}$	8×10^{-4}
							15	0·10	60	540	3·2	5×10^{-11}	$1{\cdot}6\times10^{-10}$	2×10^{-3}
Zn	1·00	0·4	$\frac{U_d}{2}$	$\frac{U_d}{2}$	692	1·07	10	0·57	394	298	6×10^4	4×10^{-18}	$2{\cdot}4\times10^{-14}$	$4{\cdot}5\times10^{-7}$
							15	0·35	252	450	90	10^{-11}	9×10^{-10}	$1{\cdot}2\times10^{-2}$
Al	1·34		0·76‡	0·58‡	933	0·57	10	0·29	270	663	2×10^3			
							15	0·18	168	765	6·1			
Cu	2·05	0·2	0·9	1·15	1356	0·56	10	0·29	394	962	23	$3{\cdot}8\times10^{-12}$	8×10^{-11}	$1{\cdot}6\times10^{-3}$
							15	0·18	244	1112	5·3	$1{\cdot}4\times10^{-10}$	6×10^{-10}	$1{\cdot}2\times10^{-2}$
Ag	2·00	0·4	0·8	1·2	1233	0·58	10	0·30	380	853	26	$6{\cdot}4\times10^{-13}$	$1{\cdot}7\times10^{-11}$	3×10^{-4}
							15	0·19	233	1000	5·7	4×10^{-11}	$2{\cdot}3\times10^{-14}$	4×10^{-3}

---

† J. D. Meakan and Klokholm, Cleveland Meeting AIJE (1958).
‡ C. Panseri and T. Federighi, *Phil. Mag.*, **3**, 1223 (1958).

supersaturation at any temperature will be lowered and the $(\Delta T/T_m)$ required to keep a loop from shrinking must be increased.

Fig. 3

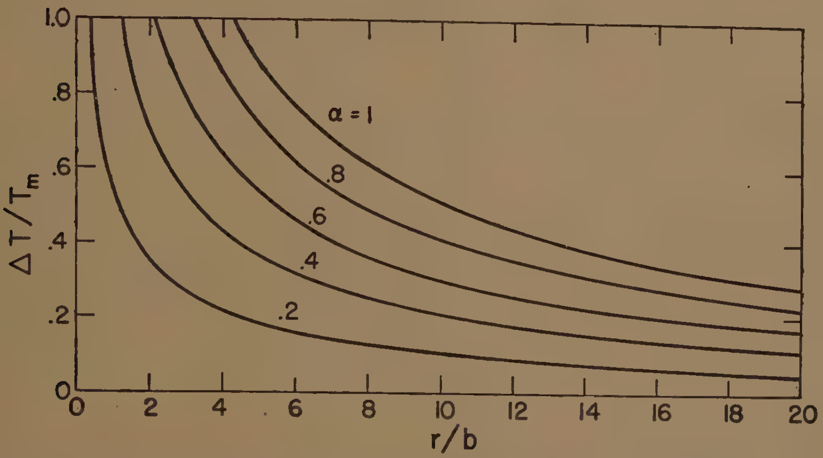

The relative undercooling, $\Delta T/T_m$, necessary to keep a dislocation ring of radius r atoms from shrinking (T_m = melting temperature).

§ 3. Rate of Dislocation Climbing

It was noted earlier that Frank's mechanism for striation formation (Frank 1956 a) requires that the dislocation loops, once formed behind the interface, must be able to climb towards the moving interface at such a rate that they can catch up with it. Therefore, we want now to consider the climb rate of the dislocations.

To simplify the problem we shall consider a crystal at a constant temperature, T, with a constant excess concentration, $c-c_0$, of vacancies present. In the crystal there may be a straight dislocation line which forms a perfect sink for vacancies. This last condition may perhaps not be satisfied for dislocations with high jog energies and hence a low concentration of thermal jogs. However, if the diffusion rate along the dislocation in its immediate neighbourhood is greatly enhanced, even a small number of jogs will be able to maintain the concentration of vacancies in thermal equilibrium all along the dislocation line. Furthermore, we are mainly interested in obtaining the fastest rate a dislocation could possibly climb; thus, we may neglect the problem of jog formation which could only slow down the climb process. We assume therefore that the concentration of vacancies at the dislocation will be kept in thermal equilibrium, c_0, and that the excess concentration will anneal out there. There are two reasons why vacancies diffuse to the dislocation line: (i) there is a chemical force due to the concentration gradient directed towards the line sink and (ii) the dislocation line attracts vacancies due to an elastic interaction (Friedel 1956 b). However, since the elastic interaction energy is proportional to

r^{-2}, the attractive force falls off rapidly with distance. As will be shown in Appendix I, in most cases the elastic interaction is too small to effect the steady-state climb rate.

From the formulation of the physical problem it is obvious that the dislocation will reach a steady state where it climbs with constant velocity. If we neglect the elastic attractive force an exact solution can be obtained (Jacob 1956) which is given in Appendix II. In order to gain a better understanding of how seriously our simplifying assumptions affect the final result we will derive the magnitude of this velocity by a simple physical argument, the result differing from the exact solution only by a numerical factor.

The dislocation will drain the surrounding region from its excess-vacancy concentration, $c-c_0$. After a radius r_0 has been drained, the number m of vacancies having arrived at the dislocation per atomic distance b are

$$m=\pi\frac{r_0^{\,2}}{\mathbf{b}^2}(c-c_0). \quad . \quad . \quad . \quad . \quad . \quad . \quad . \quad . \quad (12)$$

After m vacancies have arrived per atomic distance b on the dislocation line the distance it has climbed will be

$$l=m\mathbf{b}. \quad . \quad . \quad . \quad . \quad . \quad . \quad . \quad . \quad . \quad . \quad (13)$$

If $l=r_0$, the dislocation will essentially have climbed out of the region exhausted of vacancies and moved into a region which has not yet been drained. Hence from eqns. (12) and (13) we obtain as the radius of the drained region

$$r_0\approx\frac{\mathbf{b}}{\pi(c-c_0)}. \quad . \quad . \quad . \quad . \quad . \quad . \quad . \quad . \quad . \quad . \quad (14)$$

The steady state velocity of climbing v_0 will now essentially be determined by the time t_0 it takes to drain an area of radius r_0 and will be of the order of $v_0=r_0/t_0$. If the dislocation tends to move much faster insufficient vacancies diffuse to it to maintain the higher rate, and if it tends to move much slower the vacancies which arrive would push it ahead faster. Now, in the time t a vacancy can move over a distance $x=(D_{\mathrm{v}}t)^{1/2}$, where D_{v} is the diffusion coefficient for vacancies. Hence the radius r_0 which is effectively drained of vacancies will be smaller but of the order of magnitude $r_0\approx(D_{\mathrm{v}}t_0)^{1/2}$. By use of eqn. (14) we obtained then

$$v_0\approx\frac{r_0}{t_0}=\frac{\pi D_{\mathrm{v}}(c-c_0)}{\mathbf{b}}. \quad . \quad . \quad . \quad . \quad . \quad . \quad . \quad . \quad . \quad (15)$$

The exact solution in Appendix II shows that the right side of eqn. (15) must be multiplied by a numerical factor of $f=0{\cdot}2-0{\cdot}1$. If we further notice that the coefficient for self-diffusion is given by $D=c_0D_{\mathrm{v}}$ (assuming a vacancy mechanism for self-diffusion) we obtain finally

$$v_0\approx0{\cdot}5\frac{D}{\mathbf{b}}\left(\frac{c}{c_0}-1\right). \quad . \quad . \quad . \quad . \quad . \quad . \quad . \quad . \quad (16)$$

We must keep in mind that eqn. (16) has been derived for straight dislocation lines. It will therefore give a reliable result only if the radius of curvature of the dislocation line is larger than the radius r_0 of the drained region of eqn. (14). It can be shown that the climbing rate of a dislocation ring with radius r much smaller than r_0 will be smaller than v_0 if we neglect the action of the attractive potential. However, for much smaller r, the attraction of vacancies to the dislocation line becomes important, but we would not expect v_0 to be very different from that already calculated. An exact solution for an expanding ring would be very complicated and no attempt has been made to calculate the climbing rate in this case.

If we use eqn. (16), we see that a dislocation ring of 10 atoms radius is generally climbing, at its equilibrium temperature, towards the interface at a rate slower than a typical rate of advance of the interface (10^{-2}–10^{-3} cm/sec). However, a dislocation of 15 atoms radius is climbing, at its equilibrium temperature, at a rate which is equivalent to the rate of advance of the interface.

§ 4. Formation of Striations

1. A critical test of the origin of striations by vacancy collapse is to grow crystals under an ambient temperature so high that the critical supersaturation for the growth of dislocation rings is never reached. In this laboratory, crystals of Pb and Sn were grown in a horizontal crucible in an ambient temperature maintained at 20°c below the melting point. These crystals exhibited a fully developed striation type sub-structure. This sub-structure could be seen on the outer surfaces of etched crystals and on etched sections perpendicular to the growth axis. Since in these experiments $\Delta T/T_{\mathrm{m}} \leqslant 0{\cdot}04$, the radius of a ring which can expand by climbing would have to be at least $35\mathbf{b}$ in Pb and $85\mathbf{b}$ in Sn. It seems safe to say that rings of this size cannot be formed by spontaneous nucleation. Hence, we may conclude that collapsing vacancy discs are not responsible for striation formation.

Other objections to Frank's model (1956 a) can be made by considering the experiments of Teghtsoonian and Chalmers (1951, 1952). From the calculations of $\Delta T/T_{\mathrm{m}}$ necessary for a dislocation ring of 10 or 15 atoms radius to grow, we can see that the loops must nucleate several centimetres behind the solid–liquid interface. If we denote this value of $\Delta T/T_{\mathrm{m}}$ by $(\Delta T/T_{\mathrm{m}})_{\mathrm{c}}$ and the temperature gradient in the solid as G_{s}(°c/cm), then the distance, L, behind the interface at which the loops nucleate is given by $L \geqslant (\Delta T/T_{\mathrm{m}})_{\mathrm{c}}(T_{\mathrm{m}}/G_{\mathrm{s}})$. If we assume, for the moment, that Frank's (1956 a) model is correct and that all the vacancies collapse to form dislocations in lineage arrays, the angular misorientation, θ, between the striations at L cm from the beginning of the crystal (L is the incubation distance), is given by $tg\,\theta = c$. Thus, for reasonable values of $G_{\mathrm{s}} = 15$°c/cm and 30°c/cm for Pb and Cu respectively and for $c \approx 10^{-4}$ we see that the incubation distance for striation formation should be about 5–10 cm with a misorientation of about 10^{-2} degrees. However, the incubation distance is observed to be less than about 1 cm at high growth rates and the misorientation is observed to be about 1 degree.

2. We should now consider if a loop, once formed in the crystal, can catch up with the moving interface. As we see from table 2, a dislocation ring of 10 atoms radius will climb, at its equilibrium temperature, at a rate slower than the rate of advance of the interface and thus will be left behind.

However, a dislocation of 15 atoms radius is climbing at a rate which is equivalent to the rate of advance of the interface. If the initial loop size is 15 atoms radius there is some possibility that the loops will grow to a higher temperature if the interface is moving slowly. Whether it will climb close enough to the interface to be pulled into it by image forces must be decided.

If we write the diffusion coefficient in the form $D=D_0 \exp(-U_{\mathrm{d}}/Rt)$ the climbing velocity v_0 of eqn. (16) can be put in the form

$$v_0=\frac{0\cdot 5D_0}{\mathbf{b}}\exp\left(-\frac{U_{\mathrm{d}}}{RT}\right)\left[\exp\left(\frac{U_{\mathrm{f}}}{R}\left(\frac{1}{T_{\mathrm{m}}}-\frac{1}{T}\right)\right)-1\right] \quad . \quad . \quad (17)$$

and using the empirical relations $U_{\mathrm{d}} \approx 39T_{\mathrm{m}}$, $U_{\mathrm{f}} \approx \frac{1}{2}U_{\mathrm{d}}$ (Birchendal 1951), the reduced velocity $V=v_0\mathbf{b}/D_0$ is plotted *vs.* T_{m}/T in fig. 4. We see that there is a maximum in V at $\Delta T/T_{\mathrm{m}} \approx 0\cdot 1$. The climbing velocity vanishes for small T because there the vacancies become immobile and it also vanishes at the melting point, T_{m}, because there the supersaturation disappears. For $\Delta T/T_{\mathrm{m}} \lesssim 10^{-2}$ the velocity is practically linear with temperature.

Before a dislocation line can experience a significant influence of the image force at the solid–liquid interface it must move to, at least, a distance of 10^{-2} cm from the interface. Therefore, we are interested in v_0 at this point. With $G_{\mathrm{s}}=15$°c/cm and 30°c/cm for Pb and Cu respectively, $\Delta T/T_{\mathrm{m}}$ at this point is given by $\Delta T/T_{\mathrm{m}}=10^{-2}\,G_{\mathrm{s}}/T_{\mathrm{m}} \approx 2\cdot 5\times 10^{-4}$ for both these metals. Thus, at this point behind the interface the climb rate is of the order of 10^{-4}–10^{-5} cm sec and hence is about two orders of magnitude smaller than the conventional freezing rates. One must then conclude that the dislocations cannot catch up to the interface but can only trail behind it at a distance such that v_0 equals the freezing rate. From fig. 4, we see that this occurs at $\Delta T/T_{\mathrm{m}} \approx 10^{-2}$ which corresponds to a distance of about 0·5 cm from the interface. These calculations neglect any effect that thermal stresses may have upon the climb rate.

3. We have shown by various arguments that striations cannot be formed from collapsed vacancy discs. However, it is still possible that a number of independent dislocation loops may be produced by climb towards the interface in a manner similar to that suggested by Frank (1956 a). Let us consider this modified picture and calculate the upper limits to the number of dislocations introduced into the crystal in this manner. We will continue to assume that no other vacancy sinks are present in the crystal. Considering loops moving with the interface at a value of $\Delta T/T_{\mathrm{m}}=10^{-2}$, from eqn. (10) the minimum radius of the leading edge of the loop, r, may be determined to be about 10^4 atoms. From eqns. (8) and (9), the vacancy

excess is 10^{-5}; thus, the maximum number of elongated loops of width $2r$ in the crystal at the position corresponding to $\Delta T/T_m = 10^{-2}$, $\rho_{\max}$ is given by

$$\rho_{\max} = \frac{c - c_0}{2r\mathbf{b}} \quad . \ . \ . \ . \ . \ . \ . \ . \ . \quad (18)$$

Fig. 4

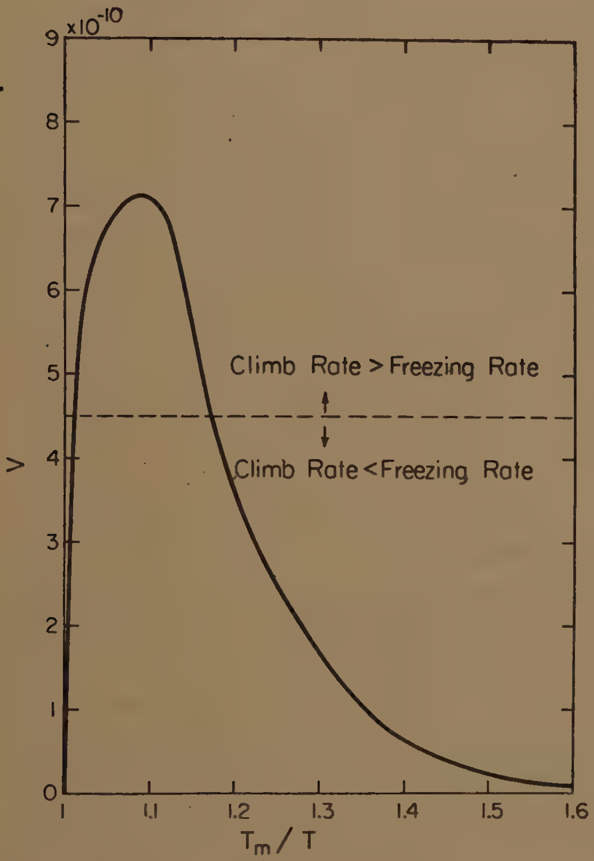

The reduced velocity of climb, V, as a function of $T_m/T(V = v_0\mathbf{b}/D_0$ where v_0 = climb rate, $\mathbf{b}$ = Burgers vector and D_0 = diffusion constant).

which gives $\rho_{\max} \approx 10^6\,\text{cm}^{-2}$. From this calculation we can see that, if no other vacancy sinks are present in the crystal and if the dislocation loops form at a value of $(\Delta T/T_m)_c$ where the climb rate is greater than the rate of interface advance, then a relatively large number of dislocation loops will form and trail the interface at a distance such that the climb rate is equal to the rate of interface advance. From Dash's (1958) work on dislocation-free Si crystals it would appear that $(\Delta T/T_m)_c$ is too large to allow the necessary climb rates.

4. It has been shown experimentally and theoretically that the 'vacancy disc mechanism' cannot account for the striation-type sub-structure, so the cause of striation formation is still unknown. It has been suggested that they most likely form from the dislocation lines grown into the crystal at microsegregation boundaries (Friedel 1956 a, Tiller 1958). The density of these dislocations is of the order of 10^5–10^8 lines/cm^2, which is sufficient to produce the striation arrays.

Evidence of these dislocation lines have been observed by etch pit techniques, in Zn (Bŏcek and Kratochvil 1959, Damiano private communication). Aggregation of these dislocations into micro-arrays occurs behind the solid–liquid interface, the arrays close to the interface being an order of magnitude smaller than striations and increase in size as the distance from the interface increases (Damiano, private communication).

A driving force for the growth of micro-arrays into striations is given by the strain energy of the system since the energy of the crystal containing a fixed number of dislocations arranged in small-angle cell boundaries decreases as the angle of the boundary increases. The limiting size of the striations would then be given by the distance a vacancy can diffuse to cause this rearrangement before the mobility drops to too low a value. This model gives the correct order of size for the striations (Frank 1956 a); however, a more detailed picture for striation formation is necessary before the model can be substantiated.

§ 5. THE INFLUENCE OF OTHER DISLOCATIONS

In the preceding sections we have always assumed that, except for the dislocations formed by vacancy condensation, there are no other sinks for vacancies. However, as just discussed, there will generally be other dislocations grown in either by growth accidents or by the micro-segregation of impurities. Since these dislocations will eat up part of the excess vacancy concentration, the number of vacancies frozen-in at the interface will never be available for dislocation ring formation. No attempt will be made to discuss the annealing of vacancies in general and its complicated kinetics (Kimura *et al.* 1959). We want only to estimate how many of the vacancies could possibly anneal out at the dislocations already present. For this purpose we assume again that a dislocation line forms a perfect sink for vacancies. This assumption may not be valid for metals in which the jog energy is high, i.e. in f.c.c. metals with low stacking fault energies. Specifically we wish to estimate how these grown-in dislocations affect the nucleation of dislocation rings in order to answer the following questions: (i) at what relative undercooling, $(\Delta T/T_{\mathrm{m}})_{\mathrm{c}}$, can dislocation rings grow as a function of the grown-in dislocation concentration and cooling rate, (ii) how many rings of a given area can be produced from the excess vacancies and what would be the resulting dislocation density from this source, (iii) if the rings should grow to form a network what would be the dislocation density?

It is possible to derive a differential equation for the actual vacancy concentration as a function of temperature, cooling rate, Q, and grown-in dislocation concentration, ρ_0, as parameters by considering the climb rate of these dislocations. However, if one wishes to study the solution as a function of these parameters, very tedious numerical integrations are necessary. Therefore, we calculate the excess vacancy concentration as a function of temperature by the following approximate method.

We consider the continuous cooling as being approximated by a series of sudden quenches over small temperature intervals, ΔT_i, with holding times of Δt_i at each temperature. The cooling rate will then be given by $Q=\Delta T_\mathrm{i}/\Delta t_\mathrm{i}$. In the time intervals Δt_i the area x_i^2 around a dislocation line drained of excess vacancies is of the order $x_\mathrm{i}^2=D_\mathrm{v}\Delta t_\mathrm{i}$. Let us now call the concentration of vacancies in thermal equilibrium after the ith quenching step c_i (c_i is identical with c_0 from eqn. 8) and the actual concentration p_i. Let us assume that the vacancies are uniformly distributed. If we have now ρ_0 grown-in dislocation lines/cm^2 they will drain an area $\rho_0 x_\mathrm{i}^2$ per unit area in the time Δt_i from the excess concentration $(p_\mathrm{i}-c_\mathrm{i})$. If we start with the equilibrium concentration c_0 at temperature T_0, then after the first quenching step the excess concentration will be

$$(p_1-c_1)=(c_0-c_1)(1-\rho_0 x_1^2) \quad . \; . \; . \qquad . \; . \quad (19)$$

and for each successive step it follows that

$$(p_\mathrm{i}-c_\mathrm{i})=(p_{\mathrm{i}-1}-c_\mathrm{i})(1-\rho_0 x_\mathrm{i}^2). \quad . \; . \; . \; . \; . \quad (20)$$

By using the abbreviations $\xi_1=(1-\psi D_\mathrm{v}\Delta T_\mathrm{i}/T_\mathrm{m})$, $\psi=\rho_0 T_\mathrm{m}/Q$ and $\Delta c_\mathrm{i}=c_{\mathrm{i}-1}-c_\mathrm{i}$ it can be easily shown with the aid of the recursion relation (20) that

$$p_n-c_n=\sum_{m=1}^{n}\Delta C_\mathrm{m}\left[\prod_{i=m}^{n}\xi_\mathrm{i}\right] \quad . \; . \; . \; . \; . \; . \; . \quad (21)$$

after the cooling interval $\Delta T=\sum_{i=1}^{n}\Delta T_\mathrm{i}$.

The equilibrium vacancy concentration, c_n, and the vacancy excess, p_n-c_n, are plotted in fig. 5 as a function of $\Delta T/T_\mathrm{m}$ with ψ as a parameter assuming the activation energies used for eqn. (17). From these curves we see that the final vacancy concentration, in the absence of disc formation, depends strongly on the parameter ψ.

With the aid of fig. 5 we can now discuss the previously proposed questions:

(i) The growth of vacancy discs will take place when the supersaturation p_n/c_n reaches a critical value Z given in table 3. The undercooling $(\Delta T/T_\mathrm{m})_\mathrm{c}$ is easily found in fig. 5 by noting that $\log p_n$ has to exceed $\log c_n$ by a fixed amount $\log Z$. As it is readily seen $(\Delta T/T_\mathrm{m})_\mathrm{c}$ depends very weakly on the magnitude of Z except for very small values of ψ. We take therefore as a typical value $Z=10$, and have listed the resulting $(\Delta T/T_\mathrm{m})_\mathrm{c}$ in table 3 for the case $T_\mathrm{m}=1000$°K, $Q=0{\cdot}1$°C/sec and various values of ρ_0. This cooling rate is representative for careful crystal growth so we see that the presence of 10^5–10^6 grown-in dislocation lines per cm^2 more than doubles the necessary undercooling $(\Delta T/T_{\mathrm{m}})_{\mathrm{c}}$ for dislocation loop growth compared with a dislocation free crystal.

(ii) The maximum number, N/cm^3 of dislocation loops of area, A, which can grow after the crystal has been cooled below the critical ratio $(\Delta T/T_{\mathrm{m}})_{\mathrm{c}}$ is given by

$$N=(p_n-c_n)/\mathbf{b}A \quad . \quad . \quad . \quad . \quad . \quad . \quad . \quad . \quad . \quad (22)$$

Fig. 5

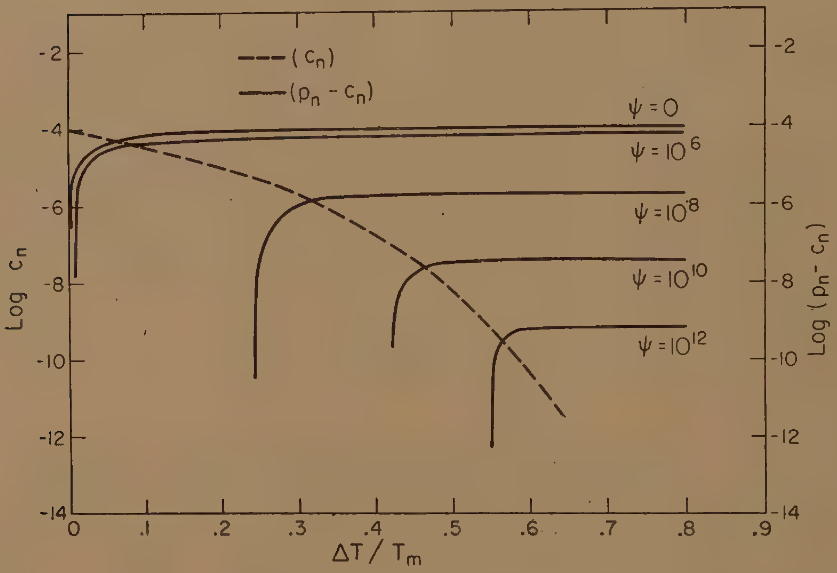

Plot used to determine the critical undercooling, $(\Delta T/T_{\mathrm{m}})_{\mathrm{c}}$ necessary to nucleate dislocation loops in the presence of ρ_0 grown-in dislocation lines/cm^2 as a function of the cooling rate, Q. (c_n = equilibrium vacancy concentration, p_n-c_n = vacancy excess, $\psi=\rho_0 T_{\mathrm{m}}/Q$.)

where $\mathbf{b}$ is the Burgers vector. In order for these loops to act as Frank–Read sources during plastic deformation, the loops should be of the order of 1 μ in diameter. The number of rings for this radius $r=1\,\mu$ and also for $r=10\,\mu$ have been listed in table 3 and we see that an appreciable number of such sources could be produced during crystal growth over a wide range of grown-in dislocation densities. The resulting dislocation density ρ, is given by

$$\rho \approx (p_n-c_n)/\mathbf{b}r \quad . \quad . \quad . \quad . \quad . \quad . \quad . \quad . \quad . \quad (23)$$

and is also listed in table 3 (total dislocation density, $\rho^T=\rho_0+\rho$). Loops of radius $r=1\,\mu$ cannot be detected by etch-pit techniques, and for $r=10\,\mu$, ρ must be about $10^6\,\mathrm{cm}^{-2}$ to appear uniformly distributed by etch-pit observation. Thus, if ρ_0 is 10^4–$10^6\,\mathrm{cm}^{-2}$ a uniformly distributed array of dislocation etch-pits could not be due to dislocation loops formed by vacancy condensation.

Table 3

$T_m = 1000°\text{K}$, $Q = 0{\cdot}1°\text{c/sec}$, $Z = 10$

ρ_0 cm^{-2}	$\left(\frac{\Delta T}{T_m}\right)_c$	$(\rho_n - c_n)$	N cm^{-3}		ρ_{net} cm^{-2}	ρ		$X = (D_v t)^{1/2}$		
			1 μ	10 μ		1 μ cm^{-2}	10 μ cm^{-2}	1 sec cm	10^2 sec cm	10^4 sec cm
0	0·20	10^{-4}	10^{11}	10^9	2×10^7	5×10^7	5×10^6	10^{-3}	10^{-2}	10^{-1}
10^2	0·22	8×10^{-5}	$6{\cdot}6 \times 10^{10}$	$6{\cdot}6 \times 10^8$	$1{\cdot}3 \times 10^7$	4×10^7	4×10^6	7×10^{-4}	7×10^{-3}	7×10^{-2}
10^4	0·40	$2{\cdot}5 \times 10^{-6}$	$2{\cdot}1 \times 10^9$	$2{\cdot}1 \times 10^7$	$1{\cdot}3 \times 10^4$	$1{\cdot}2 \times 10^6$	$1{\cdot}2 \times 10^5$	10^{-4}	10^{-3}	10^{-2}
10^6	0·52	5×10^{-8}	$4{\cdot}2 \times 10^7$	$4{\cdot}2 \times 10^5$	5	$2{\cdot}4 \times 10^4$	$2{\cdot}4 \times 10^3$	2×10^{-5}	2×10^{-4}	2×10^{-3}
10^8	0·60	8×10^{-10}	$6{\cdot}7 \times 10^5$	$6{\cdot}7 \times 10^3$	10^{-3}	$3{\cdot}8 \times 10^2$	38	$1{\cdot}7 \times 10^{-6}$	$1{\cdot}7 \times 10^{-5}$	$1{\cdot}7 \times 10^{-4}$

(iii) The loops can grow to a network, if their radius r grows to a size comparable with their spacing, i.e. if $N=1/r^3$. Thus the dislocation density, ρ_{net}, in a plane cut by the network is given by

$$\rho_{\text{net}} \approx \frac{1}{r^2} \approx (p_n - c_n)^2/\mathbf{b}^2. \qquad (24)$$

For the particular case of $T_{\mathrm{m}}=1000$°K and $Q=0{\cdot}1$°C/sec, ρ_{net} is also tabulated in table 3 for various ρ_0.

From these considerations it is not possible to tell whether the dislocations found in crystals are due to vacancy condensation or due to other mechanisms. The only conclusion that can be reached is that if in slowly grown crystals, a dislocation density $\rho_0 \geqslant 10^5\,\text{cm}^{-2}$ of grown-in dislocations exists, then there are not enough vacancies left to form an appreciable network. However, with fast quenching rates from high temperatures the crystal can contain a large number of dislocation loops formed by vacancy collapse even when the crystal contains appreciable numbers of grown-in dislocations.

Finally, we want to discuss very briefly some experiments on highly perfect Si crystals. Dash (1958) has postulated that dislocation climb in the solid behind the advancing solid–liquid interface allows the dislocations to move to the outer surface of his crystals; thus leaving them dislocation free. However, as we have already shown, the climb rate is extremely slow relative to the rate of advance of the interface at small distances from the interface. Thus, this mechanism does not seem very likely to have produced the dislocation free crystals. It is much more likely that the dislocations were removed from his crystals due to the shape of the solid–liquid interface during a portion of the crystal growth (interface convex to liquid).

APPENDIX I

Attraction of Vacancies to Dislocations due to Elastic Interaction

The interaction potential of vacancies with dislocations is (Friedel 1956 b)

$$U = W\frac{b^2}{r^2} \qquad (\text{A}\,1)$$

where W is the interaction constant, b the interatomic distance and r the distance from the dislocation line. Thus, the drift velocity v of vacancies towards the dislocation due to the interaction potential is

$$v = \frac{D}{kT}\frac{\partial U}{\partial r} = -\frac{2WDb^2}{kTr^3}. \qquad (\text{A}\,2)$$

The time t_0 it takes the vacancies within a radius r_0 to anneal out at the dislocation, due to the drift velocity in the energy gradient, is then easily shown to be

$$t_0 = \frac{kTr_0^{\,4}}{8WDb^2}. \qquad (\text{A}\,3)$$

From eqn. (14) we use $r_0 = b/\pi\Delta C$ as the radius of the region which can be drained by the dislocation before it moves out of the drained region.

By the same argument as used in the text we obtain then as the climbing velocity

$$v_0' = \frac{r_0}{t_0} = 8\pi^3 \frac{WD\Delta C^3}{bkT}. \qquad \text{(A 4)}$$

This velocity v_0' would be obtained if vacancies would move towards the dislocation exclusively due to the action of the elastic attraction potential. With typical values $W \leqslant 0{\cdot}5$ ev, $T \sim 1000$°K and $\Delta C \leqslant 10^{-3}$ this velocity is always several orders of magnitude smaller than the steady-state velocity obtained from eqn. (15) due to chemical diffusion.

That we can neglect the elastic attraction of vacancies in the climbing process can also be seen by the following argument: The average chemical potential gradient during the steady state climbing at temperature T is of the order of μ/r_0 where μ is the chemical potential of vacancies quenched-in at the temperature T_{m}. If the sample is cooled by a temperature interval ΔT we obtain

$$\frac{\mu}{r_0} = \frac{\pi U_{\mathrm{f}} \Delta T \Delta C}{bT_{\mathrm{m}}}. \qquad \text{(A 5)}$$

(U_{f} = energy of vacancy formation, ΔC = excess concentration over thermal equilibrium value, b = atomic distance). The elastic energy gradient is however from eqn. (A 1)

$$\frac{\partial U}{\partial r} = -\frac{2Wb^2}{r^3}. \qquad \text{(A 6)}$$

By equating (A 5) and (A 6) we obtain the radius r_1 at which both gradients have the same value. It can be shown that in all cases r_1 is less than a few percent of r_0. Hence the attraction potential can be neglected over the greatest part of the diffusion path. In typical quenching experiments r_1 is of the order of $10b$ or less. The presence of the elastic attraction can then be accounted for by replacing the dislocation by a sink of effective radius $r_1 \approx 10b$.

APPENDIX II

DISLOCATION CLIMB RATE

We assume a straight dislocation line lying in the z-axis of a cartesian system (x, y, z). It acts as a sink for vacancies and may move with constant velocity v_0 in the x direction. We also assume that a steady state is reached in the coordinate system (ξ, y, z) moving with the dislocation.

If r is the distance from the dislocation line, D_{v} is the diffusion coefficient for vacancies and c_{m} the concentration of vacancies at infinity, the concentration of vacancies at the point (r, ξ) is given by Rosenthal (1946) to be

$$c_{\mathrm{m}} - c = A \exp\left(-\frac{v_0 \xi}{2D}\right) K_0\left(\frac{v_0 r}{2D_{\mathrm{v}}}\right), \qquad \text{(A 7)}$$

where K_0 is the modified Bessel function of second kind, zero order.

The constant A will be determined as follows: As discussed in Appendix I, we use $r_s = 10b$ as sink radius for the dislocation. The velocity v_0 of the dislocation line is proportional to the flux of vacancies over a cylinder of radius r_s around the dislocation line, or

$$-2\pi D_V r_s \left(\frac{\partial c}{\partial r}\right)_{r=r_s} = v_0 b. \quad . \quad . \quad . \quad . \quad . \quad . \quad . \quad (A\,8)$$

If $r_s \ll D_V/v_0$ we obtain then

$$c_m - c = \frac{v_0 b}{2\pi D_V} \exp\left(-\frac{v_0 \xi}{2D_V}\right) K_0\left(\frac{v_0 r}{2D_V}\right). \quad . \quad . \quad . \quad . \quad (A\,9)$$

Now we have the additional condition that at $r = r_s$ the concentration c has its thermal equilibrium value c_0. From eqn. (A 9) we obtain, then, an equation to determine the velocity v_0 as a function of c_m and c_0 which leads, for $r_s \ll D_V/v_0$ to

$$v_0 = \frac{2\pi}{\ln(4D_V/\vartheta v_0 r_s)} \cdot \frac{D_V(c_m - c_0)}{b}. \quad . \quad . \quad . \quad . \quad . \quad (A\,10)$$

If we compare the exact result (A 10) with the velocity given by eqn. (15) we find that eqn. (15) must be multiplied by a factor $f = 2/\ln(4D_V/\vartheta v_0 r_s)$, where ϑ is Euler's constant ($\vartheta = 1{\cdot}78$). Since all variables in f give only a logarithmic dependence we may take average values for D_V and v_0 ($D_V \approx 10^{-5}$ cm^2/sec, $r_s \approx 3 \times 10^{-7}$, $v_0 = 10^{-3}$ cm/sec) and obtain $f \approx 0{\cdot}2$ to $0{\cdot}1$.

REFERENCES

Atwater, H., and Chalmers, B., 1957, *Canad. J. Phys.*, **35**, 208.

Billig, E., 1956, *Proc. roy. Soc.* A, **235**, 37.

Birchendal, C. E., 1951, *Atom Movements* (Cleveland: American Society of Metals).

Bŏcek, M., and Kratochvil, P., 1959, *Czech. J. Phys.* (to be published).

Brooks, H., 1952, *Metal Interfaces* (Cleveland: American Society of Metals).

Dash, W. C., 1958, *Growth and Perfection of Crystals* (New York: John Wiley and Sons, Inc.).

Frank, F. C., 1950, *Pittsburgh Symposium on the Plastic Deformation of Crystalline Solids* (O.N.R.), p. 150; 1956 a, *Deformation and Flow of Solids Madrid Conference* (Berlin: Springer-Verlag); 1956 b, *Dislocations and Mechanical Properties of Crystals* (New York: John Wiley and Sons, Inc.), p. 514.

Franz, H., and Kroener, E., 1955, *Z. Metallk.*, **46**, 639.

Friedel, J., 1956 a, *Les Dislocation* (Paris: Gautheir-Villars), p. 130; 1956 b, *Dislocations and Mechanical Properties of Crystals* (J. Fisher, editor) (New York: John Wiley and Sons, Inc.).

Goss, A. J., Benson, K. E., and Pfann, W. G., 1956, *Acta Met.*, **4**, 332.

Hirsch, P. B., Silcox, J., Smallman, R. E., and Westmacott, K. H., 1958, *Phil. Mag.*, **3**, 897.

Hirsch, P. B., and Silcox, J., 1958, *Growth and Perfection of Crystals* (New York: John Wiley and Sons, Inc.).

Jacob, M., 1956, *Heat Transfer*, **1** (New York: John Wiley and Sons, Inc.), p. 348.

KIMURA, H., MADDIN, R., and KUHLMANN-WILSDORF, D., 1959, *Acta Met.*, **7**, 154.

KUHLMANN-WILSDORF, D., 1958, *Phil. Mag.*, **3**, 125.

ROSENTHAL, D., 1946, *Trans. Amer. Soc. mech. Engrs*, **68**, 849.

SEITZ, F., 1950, *Phys. Rev.*, **79**, 890.

TEGHTSOONIAN, E., and CHALMERS, B., 1951, *Canad. J. Phys.*, **29**, 370; 1952, *Ibid.*, **30**, 388.

TILLER, W. A., 1958, *J. appl. Phys.*, **29**, 611.

WAGNER, R. S., 1958, *J. appl. Phys.*, **29**, 1679.

An Approximate Correlation between the Electron Fermi Energy and Work Function of a Metal†

By J. H. O. VARLEY
Atomic Energy Research Establishment, Harwell, Didcot, Berks.

[Received August 17, 1959]

ABSTRACT

The object of this paper is to estimate, semi-empirically, the Fermi energy of the free electrons in a metal and to indicate why a simple correlation may be expected between this quantity and the electronic work function. Such a straightforward correlation is found to hold approximately for most metals in Groups I to IV of the periodic table.

§ 1. INTRODUCTION

THE theoretical considerations of Wigner and Seitz (1933, 1934) on the cohesive energies of the alkali metals suggest that the energies of the electrons in the metal may be described to a fair approximation in the following manner. The valence electrons move under the influence of the periodic electrostatic field of the ion cores and also under their mutual interactions. In accordance with Fermi–Dirac statistics the electrons occupy a band of energy levels, based on a ground state energy, E_0, up to a maximum energy, $(E_0+\zeta_0)$, at absolute zero. E_0 is the lowest energy, potential plus minimum kinetic energy, which a valence electron can have in the field of a single positive ion core within the metal lattice, with the appropriate boundary conditions. ζ_0 is the *additional* kinetic energy of the most energetic electrons, since, by the requirement of Pauli's exclusion principle, all electrons cannot occupy the same quantum state. ζ_0 may be assumed to have the same value as for free electrons moving in a bounded region of constant potential V_0, outside which V is zero and within which the electron density is the same as in the metal under consideration.

In this wave mechanical treatment the mutual electron interactions give a further large positive contribution to the total energy not already accounted for in E_0. This is offset by a negative contribution arising from the exchange interactions between electrons with like spin and different wave numbers. Wigner and Seitz (1933, 1934) calculated the positive term on the assumption of a uniform distribution of negative charge and this was corrected to allow for the correlated motion of the electrons (Wigner 1934). The effect of this correlation and also of the exchange energy is to tend to keep the electrons away from each other and thus to reduce the mutual electrostatic interactions of a uniform electron distribution. The calculations indicate that together, for free electrons, these three contributions almost cancel one another, leaving only a small net interaction energy, Q_i, of the order of 10% of the average energy of an electron in the metal relative to an electron at rest in free space as the energy zero.

---

† Communicated by the Author.

The mean energy of an electron in the metal is thus approximately

$$E=E_0+\tfrac{3}{5}\zeta_0$$

where the factor $\frac{3}{5}$ is the averaging factor relating the mean additional kinetic energy of a free electron distribution to the maximum additional kinetic energy, ζ_0.

In the absence of any double layer at the metal surface least work is required to remove an electron from inside the metal to rest at infinity if an electron of maximum energy is ejected. This will require an amount of work of the order $-(E_0+\zeta_0)$ at absolute zero if there is no relaxation of the electronic charge distribution remaining within the metal. There will in fact be some relaxation of the electrons within the metal when one is ejected and therefore the energy required to remove one electron will be less than $-(E_0+\zeta_0)$ by the amount of this relaxation energy $(-\Delta Q_i)$ say.

Consider a ring of metal which is cut to create fresh surface. At the instant of separation of the two surfaces the electrons associated with the new surface ions have their potential energy increased (less negative) to approximately half the numerical value which was obtained before separation. This is because the electrons instantaneously associated with the surface ions are no longer completely surrounded by positive ions. The kinetic energy of the electrons in these surface states will, by the virial theorem, be reduced by a factor of approximately one half also, so that the numerical magnitude of the total mean energy of an electron in a surface state will be of the order of one half that of the mean energy of an electron in the interior of the metal. Similarly, the magnitudes of the maximum electron energies in the interior $(E_0+\zeta_0)$ and in the surface $(E_0+\zeta_0)_s$ will be in the approximate ratio of two to one.

Electrons will therefore move from the surface atomic cells towards the interior of the metal setting up a double layer of charge, with the positive layer on the outside. Equilibrium will be established when the work done to move an electron against the double layer field from the surface to the interior of the metal is equal and opposite to the decrease in energy $(E_0+\zeta_0)-(E_0+\zeta_0)_s$. The work, χ, required to remove an electron from anywhere in the system, interior or surface, to infinity is now the same. Thus to remove an electron from the interior requires an amount of work

$$\chi=-(E_0+\zeta_0)-4\pi ne^2x \quad . \quad . \quad . \quad . \quad . \quad . \quad . \quad . \quad (1)$$

where $4\pi ne^2x$ is the work gained in passing through the double layer of strength n electrons/sq. cm and thickness x. But

$$4\pi ne^2x+(E_0+\zeta_0)-(E_0+\zeta_0)_s=0. \quad . \quad . \quad . \quad . \quad . \quad . \quad (2)$$

Therefore χ in (1) also equals $(E_0+\zeta_0)_s$ which is the work required to remove an electron from the surface layer.

The work required to remove an electron at constant temperature and pressure from the system is a measure of the change in the free energy of the system per electron removed, which is the negative of the thermodynamic potential of the electrons. At equilibrium therefore the thermodynamic potential of the electrons in the metal is everywhere the same, as indeed it must be. For other and further discussions of electronic work functions reference may be made to the review article by Herring and Nichols (1949) and also the book by Seitz (1940).

The foregoing argument suggests that the work function χ should be of the order of $-\frac{1}{2}(E_0+\zeta_0)$, if the mutual interaction terms within the electron distribution of the metal can be neglected.

In the next section semi-empirical calculations of the Fermi energy $\zeta=(E_0+\zeta_0)$, are made using as many experimental facts as possible, and assuming that the resultant electron–electron interaction energy can in fact be neglected within the metal, but not between valence electrons in polyvalent atoms. The arguments used in computing ζ for elements with more than one valence electron have been set down before by the author (Varley 1954) but are reproduced here for completeness.

§ 2. EXPRESSIONS FOR THE FERMI ENERGY OF ELECTRONS IN METALS

2.1. *Monovalent Metals*

The average energy of an electron in the metal, relative to the energy zero of an electron at rest in free space, is taken to be $(E_0+\frac{3}{5}\zeta_0)$. The electrons within the metal can be brought to this zero energy state by vaporizing the solid and then ionizing the atoms. It follows that

$$E_0+\tfrac{3}{5}\zeta_0=-(\Lambda+I_1) \quad . \quad . \quad . \quad . \quad . \quad . \quad . \quad . \quad (3)$$

where Λ is the latent heat of vaporization per atom at absolute zero and I_1 is the first ionization energy of the free atom.

Thus $E_0=-(\Lambda+I_1+\frac{3}{5}\zeta_0)$,

$$\zeta_0=\frac{h^2}{8m}\left(\frac{3n}{\pi}\right)^{2/3},$$

where n is the number of free electrons per unit volume, h is Planck's constant and m is the electronic mass. The Fermi energy for monovalent metals is thus:

$$\zeta=(E_0+\zeta_0)=-\left[\Lambda+I_1-\frac{h^2}{20m}\left(\frac{3n}{\pi}\right)^{2/3}\right]. \quad . \quad . \quad . \quad (4)$$

2.2. *Polyvalent Metals of Groups II, III and IV*

In a polyvalent metal the exchange interactions between electrons of like spin approximately cancel out the repulsive, correlated Coulomb interactions. This effect of the exchange forces is lost when the metal is vaporized into free atoms and in the latter the repulsive electrostatic forces predominate. The exchange forces tend to keep electrons of like spin apart so that most of the exchange energy may be regarded as arising between electrons which are in different atomic cells. Therefore the energy per atom required to vaporize a polyvalent metal into free atoms may be considered to result from (*a*) changing the energy of the Z valency electrons associated with the ion core of each atom and (*b*) overcoming the exchange forces which produce an effective attraction between adjacent atomic cells.

The mean energy of an electron in the metal is $(E_0+\frac{3}{5}\zeta_0)$; its energy in the free atom is

$$-\frac{1}{Z}\sum_{i=1}^{Z} I_i$$

where I_i is the ionization energy of the ith valency electron and the sum is over the Z valency electrons. The change in energy on evaporation is thus:

$$-\frac{1}{Z}\sum_{i=1}^{Z} I_i-(E_0+\tfrac{3}{5}\zeta_0).$$

The exchange interaction energy between electrons of like spin in different atomic cells of the metal is approximately the difference between the total interaction energy per electron in the metal and that in the free atom. The total mutual interaction energy per electron in the metal is taken to be zero. That in the free atom is

$$\left\{I_Z-\frac{1}{Z}\sum_{i=1}^{Z} I_i-\frac{Z-2}{Z}I_T\right\},$$

where I_Z is the ionization potential of the last valence electron and I_T is the energy to promote an electron from the s to the p state in the ionization spectrum M^{Z+}. The last term only occurs in elements of valency greater than 2.

The energy of vaporization per electron is Λ/Z, where Λ is the experimental heat of vaporization per atom, and this is therefore equal to

$$I_Z-\frac{Z-2}{Z}I_T-\frac{2}{Z}\sum_{i=1}^{Z} I_i-(E_0+\tfrac{3}{5}\zeta_0). \quad . \; . \; . \; . \; . \quad (5)$$

It follows that

$$\zeta=(E_0+\zeta_0)=-\frac{2}{Z}\sum_{i=1}^{Z} I_i+I_Z-\frac{Z-2}{Z}I_T-\frac{\Lambda}{Z}+\frac{h^2}{20m}\left(\frac{3n}{\pi}\right)^{2/3} \qquad (6)$$

for an element with Z free electrons per atom.

§ 3. NUMERICAL COMPUTATIONS

Using data from standard references and published papers (*Handbook of Chemistry and Physics* 1957–8, Kubaschewski and Evans 1951) on ionization spectra and heats of vaporization, calculations of the Fermi energy, ζ, have been made for several metals in the first four groups of the periodic table. These calculated values, together with experimental values of the work function, χ (*Handbook of Chemistry and Physics* 1957–8) are set out in the table together with the ratio $(-\chi/\zeta)$ in the last column. It will be seen that in most cases this ratio is not too different from the value 0·5 suggested in the text.

Element	$-\zeta$	χ	$-\chi/\zeta$
Li	5·08	2·49	0·49
Na	5·01	2·28	0·46
K	4·45	2·24	0·50
Rb	4·34	2·09	0·48
Cs	4·06	1·81	0·45
Cu	8·38	4·5	0·54
Ag	8·33	4·73	0·57
Au	10·89	4·82	0·44
Be	6·88	3·9	0·57
Mg	5·50	3·68	0·67
Sr	5·78	2·74	0·47
Ba	5·72	2·5	0·44
Zn	6·22	4·0	0·64
Cd	6·54	4·07	0·62
Hg	7·85	4·5	0·57
Al	5·64	4·0	0·71
Ga	6·75	4·1	0·61
Tl	7·96	3·68	0·46
Ge	7·99	4·5	0·56
Sn	7·77	4·38	0·56
Pb	8·13	4·0	0·49

§ 4. CONCLUDING REMARKS

An exact ratio of 0·5 for $(-\chi/\zeta)$ is, of course, not to be expected for several reasons. There are many approximations in the calculations for the Fermi energy. For instance, it has been assumed that the energy to ionize an electron in a free monovalent atom gives a measure of the energy of that electron alone, whereas the electrons in the ion core will relax and their energies will be reduced when the valence electron leaves the atom.

Again, using the free electron value of ζ_0 is only approximately true, although soft x-ray spectra indicate that the true energy band widths are not very different from the free electron widths in several cases. However, differences are to be expected, especially in the case of the polyvalent elements in which the details of the energy bands are influenced by the periodic lattice potential (Brillouin zones) at the top of the Fermi distribution. Nevertheless, an approximate correlation between Fermi energy and work function seems to be indicated on the basis of these calculations and may possibly serve as a rough guide for other elements, such as the transition elements, in the periodic table.

REFERENCES

Handbook of Chemistry and Physics, 1957–8 (Ohio: Chemical Rubber Publishing Co.).

HERRING, C., and NICHOLS, M. H., 1949, *Rev. mod. Phys.*, **21,** 185.

KUBASCHEWSKI, O., and EVANS, E. Ll., 1951, *Metallurgical Thermochemistry* (London: Butterworth-Springer).

SEITZ, F., 1940, *The Modern Theory of Solids* (New York: McGraw-Hill Book Co. Inc.), p. 395.

VARLEY, J. H. O., 1954, *Phil. Mag.*, **45,** 887.

WIGNER, E., 1934, *Phys. Rev.*, **46,** 1002.

WIGNER, E., and SEITZ, F., 1933, *Phys. Rev.*, **43,** 804; 1934, *Ibid.*, **46,** 507.

The Density of States in Lead†

By A. V. Gold‡
Division of Pure Physics, National Research Council, Ottawa, Canada

[Received August 11, 1959]

Abstract

Refinements of the curve of density of states $n(E)$ in lead, as deduced from the de Haas–van Alphen effect, are inferred from existing superconductivity and transport data on pure lead and on Pb–Tl and Pb–Bi alloys when these data are interpreted in terms of a simple 'inverse transition metal' model. $n(E)$ is found to have a maximum just below the Fermi level. It is suggested that the maximum might be accounted for by supposing the multiply-connected portion of the Fermi surface to split up into separate portions as the electron concentration is reduced; however, this particular interpretation does not seem to be compatible with a model of rigid bands.

A highly schematic curve of density of electronic states $n(E)$ *versus* energy E for lead has been inferred recently from an interpretation of the de Haas–van Alphen effect (Gold 1958; hereinafter referred to as I) and is shown in fig. 1. Also shown are the contributions from the various Brillouin zones; the curves have been drawn in a more or less parabolic fashion from the computed values of $n(E_0)$ at the Fermi level such that their areas give the number of electronic states within the various parts of the Fermi surface. In order to obtain a more detailed $n(E)$ curve for pure lead we shall examine first of all the effects of varying the electron concentration as inferred from existing data on alloys of lead with thallium and bismuth. Since thallium and bismuth occur on either side of lead in the same row of the periodic table, alloying with these particular metals should produce the least distortions in the band structure of pure lead.

The variation of the density of states $n(E_0)$ at the Fermi level with decreasing electron concentration can be obtained from the superconducting critical-field curves of Pb–Tl alloys; no suitable data are available for the Pb–Bi system. $n(E_0)$ is related to the electronic specific heat constant γ_{el} by

$$n(E_0)=1{\cdot}59\times10^{-12}(a^3/4)(3/2\pi^2k^2)\gamma_{\mathrm{el}} \text{ per ev per atom} \qquad (1)$$

(cf. Mott and Jones 1936, p. 179), where a is the lattice constant in cm and γ_{el} is given by

$$\gamma_{\mathrm{el}}=1/2\pi(H_0/T_c)^2 \text{ erg cm}^{-3}\text{ deg}^{-2}, \quad . \quad . \quad . \quad . \quad (2)$$

---

† Communicated by the Author.
‡ National Research Laboratories Postdoctorate Fellow.

assuming the critical-field curves to be parabolic (Shoenberg 1952, Ch. III). The mean zero-field transition temperatures T_c have been interpolated from the results of Meissner *et al.* (1932) and the critical fields H_0 at the absolute zero have been extrapolated from the data of Schubnikow *et al.* (1936), taking the critical field to be the value at which magnetic flux begins to enter the specimen rapidly as the field is increased. The dependence of a on Tl concentration has been given by Tang and Pauling (1952) and the resulting variation of $n(E_0)$ deduced from (1) and (2) is shown in fig. 2 (a). Also shown is the value of $n(E_0)$ obtained by Decker *et al.* (1958) from the actual non-parabolic critical-field curve of pure lead; however, the data of Schubnikow *et al.* are insufficient to show up any significant departures from parabolicity for the alloys.

Fig. 1

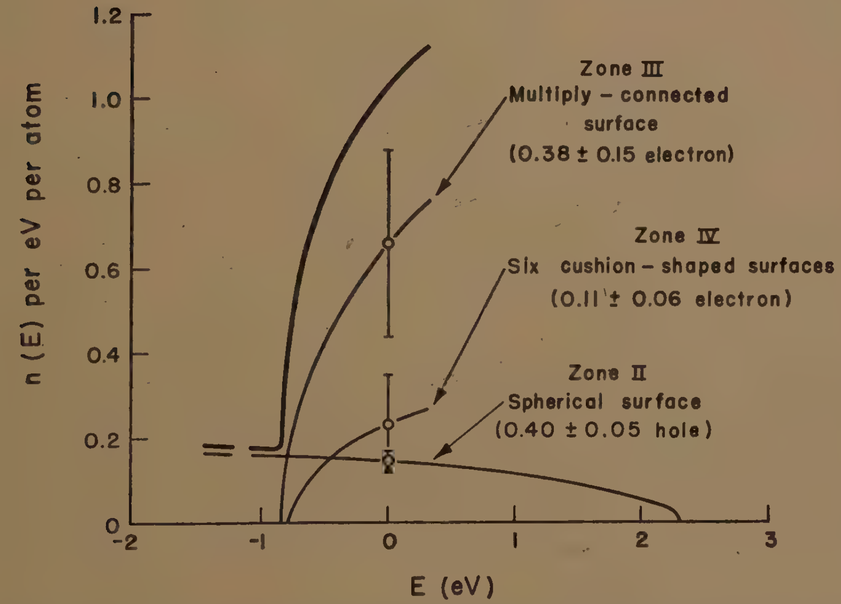

Schematic curve of density of states near the Fermi level as inferred from the de Haas–van Alphen effect (I). The energy is measured relative to the Fermi level.

While this interpretation of the superconductivity data is likely to be too naïve on account of the lack of a Meissner effect in the alloys, the curve of fig. 2 (a) nevertheless suggests that $n(E_0)$ drops rapidly from its value for pure lead, reaching some fairly constant value at about 15% Tl. It is worth noting that the γ_{el} values obtained by Stout and Guttman (1952) from the critical-field data on alloys of *tin* with up to 20% thallium show no such rapid variation, thus suggesting that the decrease found in the Pb–Tl system is indeed an electronic structure effect.

We can obtain further information about the variation of $n(E_0)$ on alloying from the temperature dependence of the resistivity, $\partial\rho/\partial T$, and from the absolute thermoelectric power S. In interpreting such data it is convenient to think of lead as a kind of 'inverse transition metal' since

Fig. 2

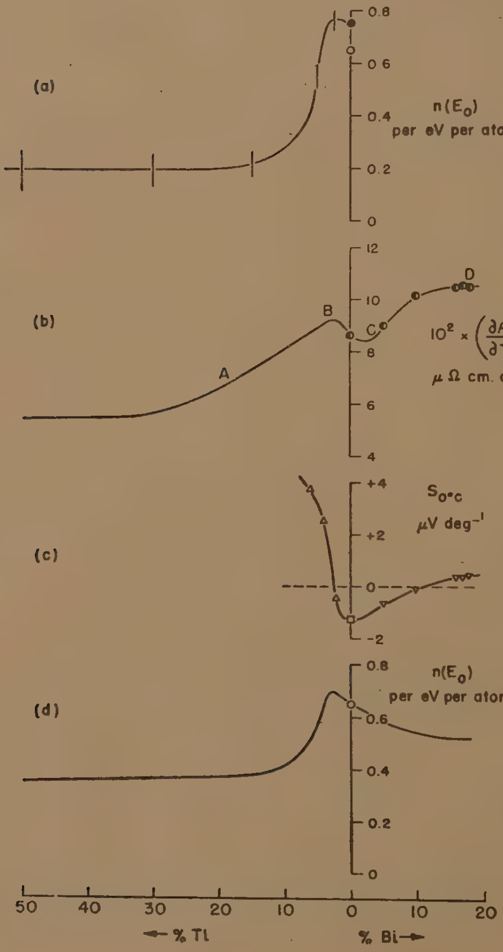

Variation with Tl and Bi concentration of (*a*) $n(E_0)$ from critical-field data, (*b*) $\partial\rho/\partial T$ at 0°c, (*c*) S at 0°c and (*d*) $n(E_0)$ as inferred from (*a*), (*b*) and (*c*). Curve (*a*) is from Meissner *et al.* (1932) and Schubnikow *et al.* (1936); the Pb–Tl portion of curve (*b*) is from Guertler and Schulze (1923) and Tammann and Rüdiger (1930) and is estimated to be reliable to about 2%. ●, Decker *et al.* (1958), assuming parabolic H_c vs. T curve; ○, Decker *et al.*, from actual non-parabolic H_c vs. T curve; ◐, ▽, Thomas and Evans (1933); △, Rolla (1915); □, Christian *et al.* (1958). The α-phase boundaries lie at 80% Tl and 18% Bi (cf. Hansen 1958), with ordering taking place at $PbTl_3$ (i.e. 75% Tl; Tang and Pauling 1952).

we see from fig. 1 that the rapidly varying contribution from the electrons to $n(E)$ is much greater than the slowly varying contribution from the holes. On the basis of such a model we should expect the major part of the conductivity to be due to the holes (cf. Mott and Jones 1936, p. 267); this has been confirmed experimentally by Borovik (1954) who has shown, on the basis of a two-band analysis of the galvanomagnetic effects, that the holes in fact account for between 85% and 90% of the total conductivity in pure lead. Thus, assuming the validity of the Mathiessen rule, we may write for the temperature dependence of resistivity (cf. Mott and Jones 1936, p. 301)

$$\frac{\partial\rho}{\partial T}=\frac{\partial\rho_T}{\partial T}=\frac{\partial}{\partial T}(m_{\mathrm{h}}^*/\mathcal{N}_{\mathrm{h}}e^2\tau_T)\propto\frac{n(E_0)}{\mathcal{N}_{\mathrm{h}}} \quad . \quad . \quad . \quad . \quad (3)$$

where $\mathcal{N}_{\mathrm{h}}$ is the number of holes per cc; we have taken $1/\tau_T \propto Tn(E_0)$ and have assumed that the effective mass of the holes is not appreciably altered on alloying ($m_{\mathrm{h}}^*(\mathrm{Pb})=1{\cdot}0m_0$ from I). Turning now to the thermoelectric power, we have rather generally

$$S=-\frac{\pi^2k^2T}{3e}\left\{\frac{\partial\log\rho(E)}{\partial E}\right\}_0; \quad . \quad . \quad . \quad . \quad . \quad (4)$$

for our model this reduces to (cf. Mott and Jones 1936, p. 313)

$$\begin{aligned}S&=-\frac{\pi^2k^2T}{3e}\frac{1}{n(E_0)}\left(\frac{\partial n(E)}{\partial E}\right)_0\\&=+2{\cdot}45T\frac{1}{n(E_0)}\left(\frac{\partial n(E)}{\partial E}\right)_0\mu\text{v deg}^{-1}, \quad . \quad . \quad . \quad (5)\end{aligned}$$

the energy being measured in ev.

The variation of $\partial\rho/\partial T$ at 0°c is given in fig. 2 (*b*); the Pb–Bi results are from Thomas and Evans (1933) while the Pb–Tl curve has been drawn from values of the temperature coefficient of resistance given by Guertler and Schulze (1923) and of the absolute resistivity given by Tammann and Rüdiger (1930) (the absolute resistivity measurements of Guertler and Schulze are fraught with systematic errors). As we move from left to right in fig. 2 (*b*) the number of holes in the second zone will be progressively reduced so that we should expect from (3) a smooth increase in $\partial\rho/\partial T$, modulated by $n(E_0)$. We therefore infer that $n(E_0)$ begins to increase from a roughly constant value near A, reaches a maximum near B and then falls through its value for pure lead, this decrease being offset near C by the effect of diminishing $\mathcal{N}_{\mathrm{h}}$; the flattening-off of the curve at D is probably due to an increasing contribution to the conductivity from the electrons so that (3) is no longer valid. Thus the behaviour of $\partial\rho/\partial T$ for the Pb–Tl series confirms qualitatively the scheme of fig. 2 (*a*) but it is difficult to draw any definite conclusions from the Pb–Bi results.

In fig. 2 (*c*) we show the variation of S at 0°c from Rolla (1915) and Thomas and Evans (1933), the relative values given by these authors having been converted into absolute values using the absolute value of S for pure lead given by Christian *et al.* (1958). Although the variation of

S with T for *pure* lead is approximately linear above about 100°K (Christian *et al.*), it is not exactly in accordance with (5) since the high-temperature results do not extrapolate to $S=0$ at $T=0$; this matter will be discussed later but for the present we shall take (5) to be approximately valid for our discussion of the alloys. While the effect of impurity scattering on S is not well understood we shall nevertheless suppose it to be small by comparison with the rapid rise in S with increasing Tl concentration. Assuming then a quasi rigid-band model for the alloys it seems reasonable from (5) to associate the large positive S at 6% Tl with a sharply rising $n(E_0)$ and the value $S=0$ at about 2·5% Tl with a maximum in $n(E_0)$; both inferences are in qualitative agreement with fig. 2 (*a*). The negative S near pure lead implies a falling $n(E_0)$ while the subsequent slow rise in S with increasing Bi concentration suggests that $n(E_0)$ begins to flatten-off somewhat; in view of the inapplicability of our model when the electronic contribution to the conductivity becomes appreciable, the rising $n(E_0)$ beyond 11% Bi as suggested by (4) must be viewed with some scepticism.

We are now in a position to give, in fig. 2 (*d*), an approximate curve of the variation of $n(E_0)$ with Tl and Bi concentration. For pure lead we have taken the value from Decker *et al.* as being the most reliable. Although the curve of fig. 2 (*a*) suggests a total drop in $n(E_0)$ of roughly 60% with the addition of about 15% Tl we shall take this drop to be nearer 30% as being more in keeping with the results of fig. 2 (*b*). Assuming then that any departures from the rigid-band model are not too large, so that changes in $n(E_0)$ on alloying can be related to the $n(E)$ curve for pure lead solely by a shift in the Fermi level, we give in fig. 3 a more realistic density of states curve for pure lead than that given in fig. 1, changes in area under the $n(E)$ curve being related to the corresponding changes in electron concentration in fig. 2 (*d*). The peak in the $n(E)$ curve is then found to lie at about 0·02 ev below the Fermi level. The contributions from the holes and overspill electrons are also indicated; as is required for a metal of even valency, these have been drawn in with equal area, this corresponding to a weighted mean of the number per atom of holes and electrons given in fig. 1, viz. $0{\cdot}41 \pm 0{\cdot}06$ per atom.

We shall now give a discussion of the temperature dependence of the thermoelectric power of pure lead (Christian *et al.* 1958) in relation to the $n(E)$ curve. The low-temperature values of S below about 6°K lie on a straight line with $S=0$ at $T=0$ (results of Steele; see fig. 3 of Christian *et al.*) and we have used these results and (5) to infer the slope of the $n(E)$ curve at the Fermi level (broken line in fig. 3); in this connection we note that the variation of S with addition of small amounts of impurities is in no sense 'anomalous' (Jan *et al.* 1958). As we have already mentioned, S also varies linearly with T above 100°K, but the variation is much slower than that below 6°K and, moreover, the high-temperature results do *not* extrapolate to $S=0$ at $T=0$ in accordance with (5). These features may be accounted for qualitatively in terms of the rapid change in $\partial n(E)/\partial E$

near the Fermi level from positive to negative values within an energy range comparable with kT. We can make a crude estimate of this effect by considering the $n(E)$ curve near the peak to consist of two intersecting straight lines and by supposing that we can replace $(\partial n(E)/\partial E)_0$ in (5) by a straightforward average of $\partial n(E)/\partial E$ over an energy range of $2kT$ on either side of the Fermi level. This results in the modification of (5) by the factor $((C+1)\epsilon/2kT-C+1)/2$, where C is the magnitude of the ratio of $\partial n(E)/\partial E$ below the peak to that above the peak and ϵ is the energy between the peak and the Fermi level ($2kT>\epsilon$). The modified linear expression for S can be fitted to the high-temperature results by choosing $C \sim 0{\cdot}8$ and $\epsilon \sim 0{\cdot}01$ ev. This crude argument thus suggests that the slopes of the $n(E)$ curve on either side of the peak are comparable in magnitude and the value of ϵ turns out to be comparable with that suggested by our rigid-band interpretation of the alloy results†.

Fig. 3

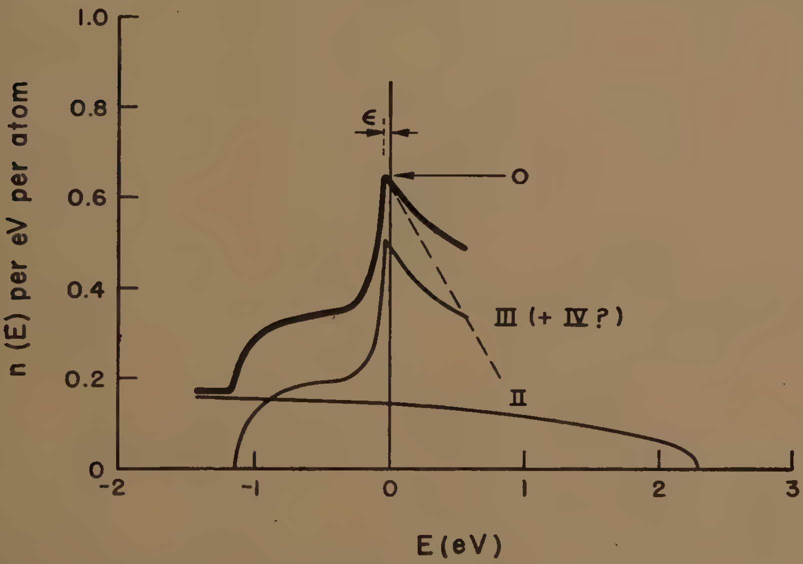

Proposed curve of density of states. The energy is measured relative to the Fermi level; – – –, slope at the Fermi level from absolute thermoelectric power below 6°K ; O, Decker *et al.* (1958).

It is tempting, at first sight, to account for the peak in the $n(E)$ curve at roughly 0·02 ev below the Fermi level in terms of the multiply-connected Fermi surface in the third Brillouin zone, a portion of which is illustrated diagrammatically in fig. 4 (*a*); a drawing showing the three-dimensional character of this surface is given in I. When the electron concentration has been sufficiently reduced (e.g. by alloying with Tl), this surface will break up into separate portions centred about either the zone corners W

---

† We should also expect the electronic contribution to the specific heat for $T > \sim 100$°K to be much less than that deduced from low-temperature measurements.

(fig. 4 (*b*)) or the mid-points K of the lines joining adjacent corners (fig. 4 (*c*)), depending on whether the energy is lowest at W or at K respectively. When the separate portions are nearly in contact, $\text{grad}_k E$ along zone lines will be particularly low, resulting in a peak in $n(E)$ when contact has just taken place. However, if this is the correct explanation, it is indeed surprising that the peak should lie so close to the Fermi level. The 'limbs' of the multiply-connected surface are, in fact, quite thick so that one would expect the breaking-up of the surface to occur at an energy comparable with that associated with complete disappearance of the surface, i.e. at roughly 1 ev below the Fermi level; thus the above interpretation of the peak does not seem to be compatible with a model of

Fig. 4

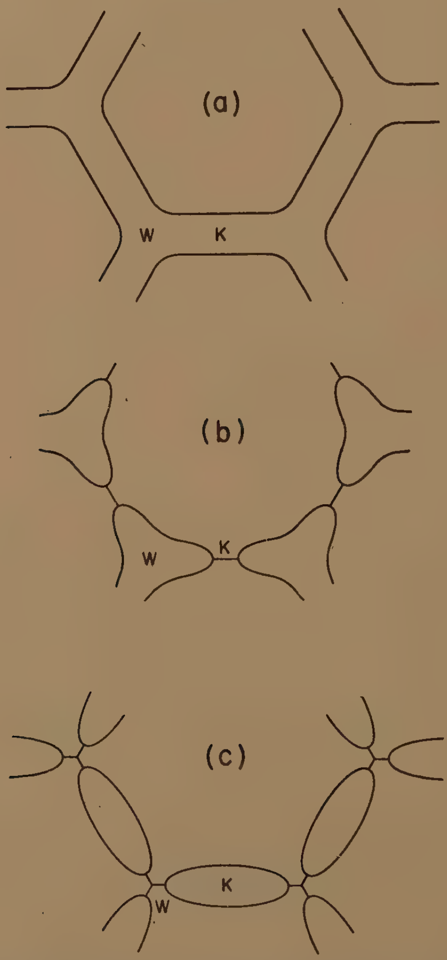

Diagrammatic illustration of the breaking-up of the multiply-connected third-zone Fermi surface.

rigid bands. In order to assess the extent of shifts in the band structure, low-temperature heat-capacity measurements on isoelectronic Pb–Tl–Bi alloys would be very desirable (cf. Guthrie 1959).

In conclusion we wish to point out that there is some doubt as to the existence of the cushion-shaped pieces of Fermi surface in the fourth zone. From the detailed reasoning given in I we can state that *either* there are electrons in this zone giving a reasonably large contribution, with the lowest energies in zones three and four being nearly equal (fig. 1), *or* the fourth zone is completely empty; the evidence from the de Haas–van Alphen effect alone is insufficient to distinguish unambiguously between these two possibilities. However, the values of the electronic specific heat and of the total area of the Fermi surface as deduced from the de Haas–van Alphen data can be brought into considerably better agreement with the results of other experiments by taking the fourth zone to be empty; this supposition also makes the numbers of electrons and holes more nearly equal. Since in drawing fig. 3 the data in fig. 1 for the holes have been more heavily weighted than that for the electrons, it makes little difference to the areas under the curves whether a contribution from the fourth zone is included or not.

ACKNOWLEDGMENTS

It is a pleasure to thank Drs. J. S. Dugdale, W. A. Harrison and D. K. C. MacDonald for helpful discussions and criticism.

REFERENCES

BOROVIK, E. S., 1954, *J. exp. theor. Phys.*, **27,** 355.

CHRISTIAN, J. W., JAN, J.-P., PEARSON, W. B., and TEMPLETON, I. M., 1958, *Proc. roy. Soc.* A, **245,** 213.

DECKER, D. L., MAPOTHER, D. E., and SHAW, R. W., 1958, *Phys. Rev.*, **112,** 1888.

GOLD, A. V., 1958, *Phil. Trans.* A, **251,** 85.

GUERTLER, W., and SCHULZE, A., 1923, *Z. phys. Chem.*, **104,** 269.

GUTHRIE, G. L., 1959, *Phys. Rev.*, **113,** 793.

HANSEN, M., 1958, *Constitution of Binary Alloys* (New York: McGraw-Hill Book Company).

JAN, J.-P., PEARSON, W. B., and TEMPLETON, I. M., 1958, *Canad. J. Phys.*, **36,** 627.

MEISSNER, W., FRANZ, H., and WESTERHOFF, H., 1932, *Ann. Phys., Lpz.*, **13,** 967.

MOTT, N. F., and JONES, H., 1936, *Theory of the Properties of Metals and Alloys* (Oxford: Clarendon Press).

ROLLA, L., 1915, *Gazz. chim. ital.*, **45,** 185.

SCHUBNIKOW, L. W., CHOTKEWITSCH, W. I., SCHEPELEW, J. D., and RJABININ, J. N., 1936, *Phys. Z. Sowjet.*, **10,** 165.

SHOENBERG, D., 1952, *Superconductivity* (Cambridge: University Press).

STOUT, J. W., and GUTTMAN, L., 1952, *Phys. Rev.*, **88,** 703.

TAMMANN, G., and RÜDIGER, H., 1930, *Z. anorg. Chem.*, **192,** 35.

TANG, Y.-C., and PAULING, L., 1952, *Acta Cryst.*, **5,** 39.

THOMAS, W. R., and EVANS, E. J., 1933, *Phil. Mag.*, **16,** 329.

The Fine Structure of Films of Rubber and other Polymers†

By M. SEAL
Research Laboratory for the Physics and Chemistry of Solids,
Department of Physics, University of Cambridge

[Received September 10, 1959]

ABSTRACT

High resolution electron microscopy has been used to examine thin films of natural rubber and other polymers. Dispersions of various materials (in particular neoprene and chlorinated natural rubber) in natural rubber have been studied. Structures which are believed to be the individual curled-up molecules of the dispersed polymer have been photographed. Stretched rubber films have also been examined and some information about the mode of deformation obtained.

§ 1. INTRODUCTION

FILMS of various plastic materials have been commonly employed in electron microscopy—for the most part as supports for other specimens and as replicas of solid surfaces from which they have been stripped. They have not, however, been used very much as specimens in their own right to provide information about the properties of the plastic material itself (a notable exception is the work of Agar *et al.* 1959, on polyethylene). In the present paper an account will be given of an electron microscope study of rubber films from which information about the rubber has been deduced. In particular, structures which are thought to be individual rubber molecules have been found.

§ 2. MATERIALS AND TECHNIQUE

2.1. *Materials*

Films of four materials were examined. These were natural rubber and three related polymers—neoprene, guttapercha, and Alloprene. Natural rubber is mainly cis-polyisoprene $(—CH_2—C.CH_3=CH—CH_2—)_n$, neoprene is polychloroprene $(—CH_2—C.Cl=CH—CH_2—)_n$, guttapercha is mainly trans-polyisoprene, and Alloprene is a chlorinated natural rubber made by Imperial Chemical Industries Limited (approximate composition $C_{10}H_{13}Cl_7$). A purified natural rubber was also used. This was rubber from which the small amounts of proteins, etc. which commonly occur in the natural product had been removed. None of these materials had been vulcanized. Thus, there was little cross-linking of the molecular chains and the polymers were soluble in suitable organic solvents. All the samples were obtained from the British Rubber Producers' Research Association.

---

† Communicated by Dr. F. P. Bowden, F.R.S.

2.2. *Specimen Preparation*

A solution in 'Analar' benzene of the material to be examined was made. A drop of this was allowed to fall on a clean water surface where it spread and, after evaporation of the benzene, left a floating film. Part of this was then picked up on a specimen grid and subsequently examined in the electron microscope—Siemens Elmiskop I. The film thickness was found to be critical. The concentration of the solution was therefore adjusted to give films of the correct thickness judged by the interference colour—low order white with veining of yellow. Such films (of the order of 1000 Å thick) were over most of their area too thick for high resolution electron microscopy, but they did show thin patches where the local thickness was probably less than 100 Å. These were the regions studied. Films of lower mean thickness could not be used since they formed networks of thin threads rather than continuous sheets.

Stretched rubber films were also examined. The technique of stretching them was as follows. The film while floating on the water surface was touched with two pieces of filter paper. Unvulcanized rubber being sticky, it adhered to them. The pieces of filter paper were then drawn apart and parts of the stretched film in between picked up on specimen grids. Once on a grid the film remained stretched since it adhered to the bars of the grid.

§ 3. RESULTS

3.1. *Changes Produced in Specimens by the Electron Beam*

Polymers suffer changes when irradiated with electrons (see, for example, Little 1954, Charlesby and Pinner 1959). Consequently, it was thought advisable to investigate the effect on a specimen of its irradiation during examination in the electron microscope. No visible changes occurred in rubber films as the electron beam intensity was increased from a low value, but a rubber film after examination in the electron microscope was found to be insoluble in benzene. This change was studied further by placing glass plates coated with a film of rubber in the camera of the electron microscope instead of the normal photographic plates, and exposing them to the much less intense beam of this part of the instrument. It was found that exposure for about 2 min to a fairly intense beam rendered the rubber insoluble in benzene. This suggested that, even if examined at low magnification (say 5000 ×) and low intensity, a rubber film in the normal specimen position would be rendered insoluble within a few milliseconds. Consequently, if a rubber specimen is examined in the electron microscope one cannot avoid altering it by the action of the electron beam.

However, sharp spotty diffraction patterns were obtained from crystalline polymers (polyethylene, guttapercha) provided that a reasonably low intensity beam was used. Thus the changes in these polymers caused by a weak electron beam were not too drastic. It seems likely that the first effect of the electron beam is a cross-linking of the molecular chains, followed after much greater irradiation by a complete disruption of the structure. The rubber specimens if examined at low intensity probably remained as rubber (albeit vulcanized rubber), but even if an intense beam was used the changes in structure produced no visible alteration of the specimen.

3.2. *Appearance of Rubber Films*

An electron micrograph of a purified natural rubber specimen is reproduced in fig. 1†. Such micrographs show little structure apart from gross features such as holes, wrinkles, thick and thin patches, etc. There is a granular structure on a scale of about 20 Å visible at high magnification, but this may well be due to electron-induced contamination. Films of ordinary natural rubber, neoprene, Alloprene, and guttapercha have a similar appearance.

Filled rubbers have also been examined and the dispersion of filler particles photographed (fig. 2). These are important since carbon black and other materials are commonly incorporated in rubber to improve its mechanical properties. A micrograph of a stretched filled rubber is shown in fig. 3. The thin patches (which occur sparsely in unstretched rubber) are more extensive and seem to have developed at the expense of the thicker regions. This would be expected for unvulcanized rubber will flow plastically but the sharpness of the boundary between thick and thin regions is perhaps surprising.

3.3. *Mixed Films*

The most interesting results were obtained from films made from a solution containing a mixture of polymers. Mixtures of purified natural rubber and neoprene, and purified natural rubber and Alloprene were used. The neoprene and Alloprene which contain a high percentage of chlorine might be expected to scatter electrons more strongly than the natural rubber which apart from impurities is entirely made up of carbon and hydrogen. Thus the neoprene or Alloprene should appear darker than the natural rubber in a bright field image. Films of natural rubber containing a few per cent of neoprene show numerous dark patches (fig. 4): these presumably are the neoprene. Furthermore films of neoprene containing a few per cent of natural rubber also have the expected appearance of light patches on a dark background (fig. 5), but it is difficult to distinguish these from the occasional thin patches which these films show.

A more detailed study was made of the Alloprene/natural rubber system. Figure 6 shows the appearance of a film containing equal parts by weight of the two materials. The contrast system is difficult to interpret, but the film is obviously not homogeneous. One would not expect it to be, for chemically different polymers are, in the absence of a solvent, generally immiscible or only slightly miscible (Dobry and Boyer-Kawenoki 1947, Scott 1949).

---

† With the exception of fig. 10, all figures are as plates.

Figure 7 was obtained from a film containing 20% of Alloprene. The dark spots presumably represent globules of the Alloprene. The profiles of these globules could be seen in regions where the edge of a film had curled over. They were thicker than the surrounding film and appeared to be flattened spheres. Thus at least part of the contrast is here due to the greater thickness of these globules. Again one would not expect miscibility of the polymers in these proportions. Similar pictures were obtained from films containing 10% of Alloprene. A micrograph of a stretched film having this composition is shown in fig. 8. It can be seen that the film has torn at the Alloprene globules indicating that the adhesion between the natural rubber and the Alloprene was weak.

When the proportion of Alloprene was reduced to about 5% it was found that the dark spots were smaller and of lower contrast (fig. 9). The proportions are similar to those of the neoprene/natural rubber system of fig. 4, and it may well be that in both cases the proportion of the minor constituent was sufficiently small to render the polymers completely miscible. In such a case the Alloprene or neoprene molecules would be randomly kinked and interwoven with the molecules of the natural rubber as are the molecules in the bulk of a pure rubber (see Treloar 1958). The contrast would then be due to the greater local concentration of chlorine and would be low, and the edges of the darker regions would be expected to be diffuse. Experimentally, it was found that the contrast was very low and that the darker patches which often had diffuse edges could only be seen in regions where the specimen was very thin. The contrast could be increased by operating the electron microscope at 40 kv instead of the usual 80 kv but was still low.

However, whether or not the polymers are miscible, there is one point of particular interest. The smaller dark patches are less than 100 Å in diameter and are of the order of size of the individual polymer molecules. It may well be that the smaller patches contain only one more or less tightly curled molecule. Information on this point was obtained by using a fractionated Alloprene, having a narrow range of molecular weights which was prepared for the author by the British Rubber Producers' Research Association. Films of purified natural rubber containing 5% of this material were prepared and examined and the size distribution of the dark spots measured. A histogram showing the size distribution of over 1000 spots is shown in fig. 10. Spots greater than 180 Å in diameter were not measured since they are outside the range of interest, nor were spots less than 40 Å in diameter since they become indistinguishable from the granular fine structure of the films. This fractionated Alloprene was stated to have a mean molecular weight of 70 000 ± 10 000 (determined by viscosity measurements). This would correspond to a sphere having the bulk density of Alloprene (1·6) of diameter 50 ± 10 Å. Thus the peak in the histogram at 80 Å probably corresponds to the diameter of a single molecule of the Alloprene, the slightly greater size being due either to it having a non-spherical envelope or to it being interwoven with the surrounding rubber molecules. The smaller spots presumably correspond to the tail of the molecular weight distribution.

Fig. 10

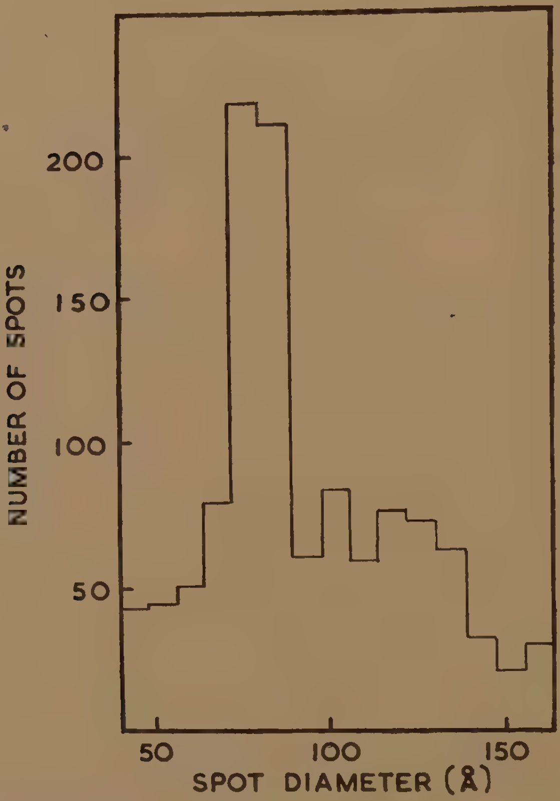

Histogram showing the distribution of spot size in natural rubber films containing about 5% Alloprene.

It would be interesting to study the appearance and distribution of the spots in stretched films and an attempt to do this has been made. Unfortunately the results were not reproducible. The film often stretched by thinning similar to that shown in fig. 3, but a few micrographs show evidence of the spots themselves. Figure 5 is an example. This film was not stretched deliberately but was deformed slightly by the stresses set up on drying and the spots appear elongated.

ACKNOWLEDGMENTS

The author thanks Dr. F. P. Bowden, F.R.S., for his interest and advice; Drs. L. C. Bateman, L. Mullins, and A. G. Thomas of the British Rubber Producers' Research Association for valuable discussions and for supplying the materials used in this work; and the British Rubber Producers' Research Association for a Fellowship.

REFERENCES

AGAR, A. W., FRANK, F. C., and KELLER, A., 1959, *Phil. Mag.*, **4,** 32.
CHARLESBY, A., and PINNER, S. H., 1959, *Proc. roy. Soc.* A, **249,** 367.
DOBRY, A., and BOYER-KAWENOKI, F., 1947, *J. polymer Sci.*, **2,** 90.
LITTLE, K., 1954, *Proc. 3rd International Conf. Electron Microscopy* (London: Royal Microscopical Society), p. 165.
SCOTT, R. L., 1949, *J. chem. Phys.*, **17,** 279.
TRELOAR, L. R. G., 1958, *The Physics of Rubber Elasticity*, 2nd edition (Oxford: The Clarendon Press).

The Thermal Conductivity of Germanium, Silicon and Indium Arsenide from 40°C to 425°C†

By Audrey D. Stuckes
Metropolitan-Vickers Electrical Co. Ltd., Trafford Park, Manchester, 17

[Received May 6, 1959 ; and in revised form August 24, 1959]

Abstract

Measurements have been made of the thermal conductivity of germanium, silicon, pure ($n=3\times10^{16}$) indium arsenide and impure ($n=10^{19}$) indium arsenide. In each case the electronic contribution κ_e to thermal conductivity has been calculated and the phonon contribution κ_L estimated by subtraction of κ_e from the experimental values. The thermal resistance of the lattice has not generally been found to be proportional to the absolute temperature as expected for three-phonon processes but the trend is towards a higher power relationship. The lattice resistance of heavily doped indium arsenide has been found to be greater than that of the pure material.

§ 1. Introduction

There have been few measurements of the thermal conductivity of semiconductors above room temperature. The possible application of semiconducting materials to the thermoelectric generation of electrical power makes thermal conductivity a factor of increasing importance. At the same time it is of interest theoretically since if one also has knowledge of the electrical properties of the semiconductor the lattice component of the thermal conductivity can be deduced near and above the Debye temperature.

§ 2. Method of Measurement

Earlier experiments on indium antimonide (Stuckes 1957) indicated the need for increased accuracy. Although the same comparative method (Stuckes and Chasmar 1956) has been used, certain modifications in thermometry and in thermal contacts have been found necessary to improve the accuracy to ±5% up to 450°c.

2.1. *Thermometry*

Many precautions must be taken to avoid errors in thermocouple measurements due to work hardening and temperature ageing effects.

---

† Communicated by the Author.

Continuous 0·005 in. diameter thermocouples of T_1-advance (nickel–chromium and copper–nickel alloys) have been found to give the least trouble amongst the more sensitive thermoelectric materials although it is necessary to have two sets of apparatus in use so that one can be kept for room temperature experiments only.

Temperature measurements in a vacuum furnace were found to be inconsistent when the thermocouple junctions were electrically insulated from the copper blocks because the presence of exchange gas was essential to bring the thermocouples into temperature equilibrium. Rather than discard the differential method of measurement (which necessitates electrical insulation between thermocouples) experiments were carried out in an inert atmosphere. Calculation of the sideways heat loss from the column was made assuming a uniform temperature surround. This was achieved by placing a cylindrical copper shield between the column and the cylindrical container; the temperature variation down the copper shield was found to be less than half a degree at 450°c.

2.2. *Thermal Contacts*

High accuracy in this method depends on there being virtually no contact resistance between any member of the stack and its thermocouple blocks. Since a good electrical contact is an indication of a good thermal contact, voltage probe measurements were taken along the column with a constant current flowing. A graph of voltage against distance should be a series of straight lines with sharp changes of slope at each contact—a step in the graph at the interface would indicate a high resistance at the contact. Precautions were necessary to eliminate thermoelectric e.m.f.'s when probing the surface of the semiconductor.

Indium–mercury and indium–gallium alloys, which are both liquid at room temperature, were found to be unsatisfactory as intermediate contact layers above 200°c. The stack was therefore assembled by a soldering technique using pure indium after copper or nickel plating the semiconductors. Very good permanent contacts between the standards and the copper blocks were made by a silver–copper eutectic alloying process.

2.3. *The Comparative Standards*

In all experiments FH stainless steel has been used as a standard. The material was supplied by the Brown–Firth Research Laboratory and had a composition and heat treatment very similar to that investigated by Powell in 1936 and his values of thermal conductivity have been used throughout.

As a subsidiary experiment the FH standards were compared with some Armco iron, which was part of a batch extensively measured by Powell (1934) and found to agree with Powell's results to ±3% up to 425°c.

§ 3. EXPERIMENTAL RESULTS

3.1. *Germanium*

Only one sample of germanium was available at the time of these experiments and this was n-type and had a resistivity of about 5 ohm cm at 300°K. Unfortunately, electrical probe measurements indicated that it was very inhomogeneous, having a high resistance or barrier region near the centre; this may not matter since the electronic component of thermal conductivity is found to be very small. The results of two sets of thermal measurements are given in fig. 1.

Fig. 1

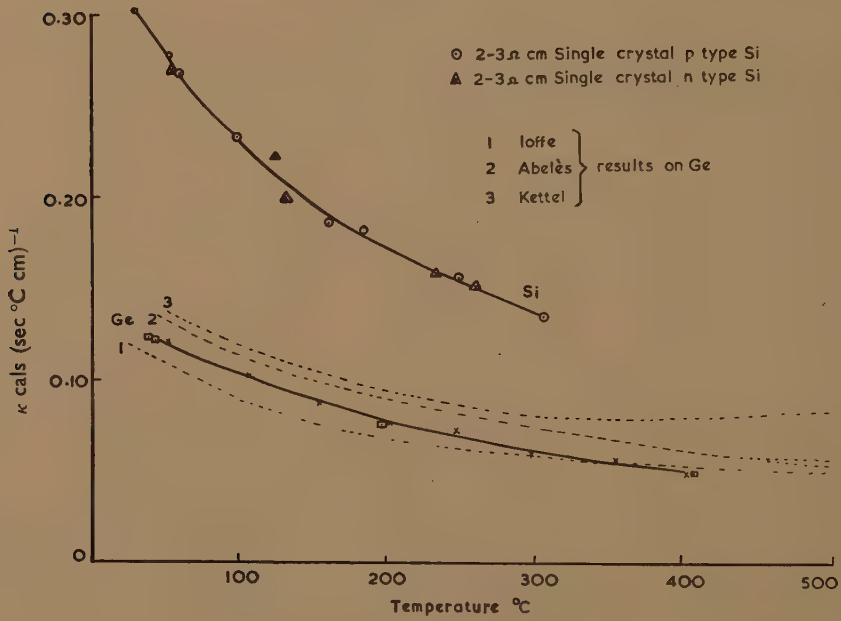

Thermal conductivity of germanium and silicon.

Four samples of germanium ranging in resistivity from 3 ohm cm to 0·001 ohm cm have been measured by Abelès (1958). Although there was a wide spread in his experimental points, up to 700°K, the thermal conductivity of all four samples can be represented by the line shown in fig. 1. Above 700°K the very impure sample deviates from the others and has a lower thermal conductivity. The results of Ioffe and Ioffe (1954) and those of Kettel (1959) are also shown in this figure.

3.2. *Silicon*

Two samples of single crystal silicon have been measured, one 'n' type and one 'p' type, both having a room temperature resistivity of about 3 ohm cm. Great difficulty was experienced in plating the silicon before soldering. A nickel layer was deposited by an electroless plating method (Sullivan and Eigler 1957); from this good ohmic contacts were obtained so long as great care was taken. The results of thermal measurements are given in fig. 1. As the contacts deteriorated rapidly above 300°c no useful measurements have been made above that temperature.

As far as it is known no other measurements on silicon at high temperature have been published. The value of 0·30 cals $(\text{cm}\,^\circ\text{c sec})^{-1}$ is in the middle of some rather divergent room temperature values. The *American Metals Handbook* (1948) quotes 0·20 cals $(\text{cm}\,^\circ\text{c sec})^{-1}$, Ioffe and Ioffe (1954) give 0·26 cals $(\text{cm}\,^\circ\text{c sec})^{-1}$ whilst 0·35 cals $(\text{cm}\,^\circ\text{c sec})^{-1}$ has recently been reported by Steele and Rosi (1958).

3.3. *Indium Arsenide*

One pure sample ($n \sim 3 \times 10^{16}$) and one sulphur-doped sample ($n \sim 10^{19}$) of polycrystalline indium arsenide have been measured. Electrical conductivity and Hall coefficient up to 500°c (fig. 2) were measured on a specimen from each ingot cut immediately adjacent to that used in the thermal measurements.

Fig. 2

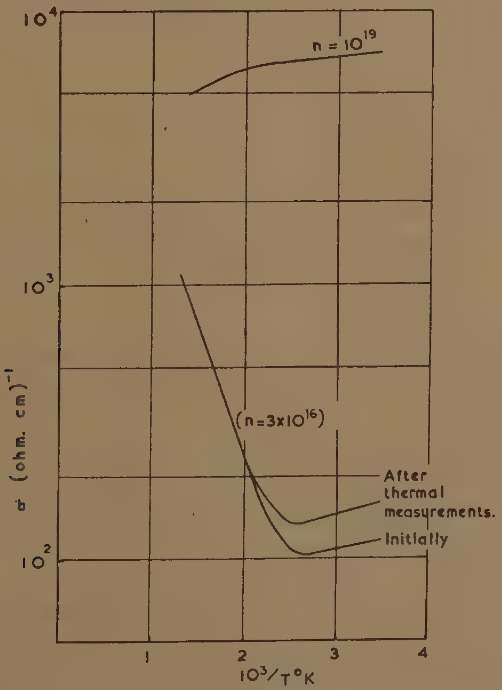

Electrical conductivity of two samples of indium arsenide.

From the ingot of pure material a piece 1·5 cm long was initially used (much larger than the usual samples). After one set of thermal measurements this specimen was cut into two further pieces 1 cm and 0·5 cm long and the experiment repeated on each. The results are given in fig. 3.

Only one sample of impure material was used but three sets of measurements, each on a freshly assembled stack, were made and the results shown in fig. 3.

Bowers *et al.* (1959) investigated two samples of indium arsenide, one similarly pure ($n \sim 5 \times 10^{16}$) and one rather less heavily doped ($n \sim 10^{18}$) than that measured in these experiments; their results are indicated in fig. 3.

Fig. 3

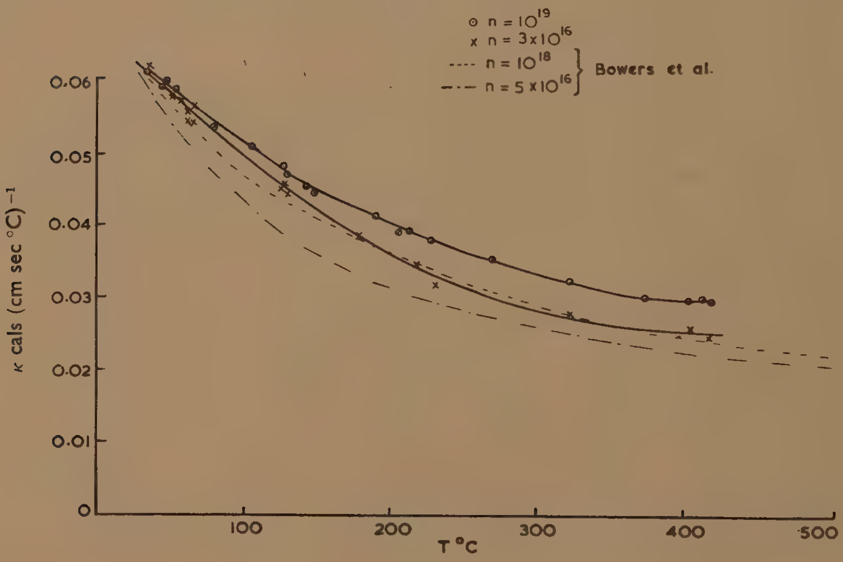

Thermal conductivity of pure ($n = 3 \times 10^{16}$) and impure ($n = 10^{19}$) indium arsenide.

§ 4. Electron Contribution to Thermal Conductivity

4.1. *Theoretical Discussion*

In the presence of a temperature gradient electrons and holes in a semiconductor will diffuse down the temperature gradient transporting kinetic energy from the hot to the cold end of the semiconductor. If on their way, an electron and a hole meet and recombine, they may give up their potential energy to the crystal lattice. This may be large compared to their kinetic energy and in some circumstances may be a very important mechanism of heat transfer; the terms 'ambipolar diffusion' or 'ionization energy transport' are sometimes applied to it. A further possible mechanism of heat conduction that has been postulated, but not so far definitely established, is exciton transport. An exciton is a related electron-hole pair with a weak binding energy; diffusing excitons could clearly carry thermal energy in a manner similar to free electron-hole pairs.

In addition to this electron contribution, heat is conducted through the semiconductor by vibrations of the crystal lattice (phonons) so that the thermal conductivity is given by

$$\kappa = \kappa_{\text{electronic}} + \kappa_{\text{lattice}}.$$

Neglecting any contribution from excitons, the electronic thermal conductivity κ_e may be expressed in the form

$$\kappa_e = \left(\frac{k}{e}\right)^2 T\sigma\Delta \quad . \ . \ . \ . \ . \ . \ . \ . \ . \quad (1)$$

where $\sigma = \sigma_n + \sigma_p$ is the electrical conductivity at temperature T°K and is the sum of the contributions from electrons and holes. The factor Δ may be expressed as a sum of terms

$$\Delta = \Delta_n + \Delta_p + \Delta_{np} \quad . \ . \ . \ . \ . \ . \ . \ . \ . \quad (2)$$

where the suffixes n, p and np refer to electrons, holes and electron-hole pairs respectively. The various terms involve Fermi–Dirac integrals whose form is related to the scattering mechanism in the semiconductor, while Δ_{np} also includes a term involving the energy gap.

This subject has been discussed by Price (1955), Ioffe (1956) and Madelung (1957).

In the particular case where the relaxation times for electron and hole scattering are given by $\tau \propto E^{\nu_n}$ and $\tau \propto E^{\nu_p}$ respectively, assuming that classical statistics apply, that the scattering is elastic and that the states distribution in valence and conduction bands is parabolic, it can be shown that

$$\Delta_n = (\nu_n + \tfrac{5}{2})\frac{\sigma_n}{\sigma}, \quad \Delta_p = (\nu_p + \tfrac{5}{2})\frac{\sigma_p}{\sigma}, \quad . \ . \ . \ . \ . \ . \quad (3)$$

$$\Delta_{np} = \frac{\sigma_n\sigma_p}{\sigma^2}\left\{\frac{E_g}{kT} + \delta_n + \delta_p\right\}^2. \quad . \ . \ . \ . \ . \ . \ . \ . \quad (4)$$

where $\delta_n = \nu_n + \tfrac{5}{2}, \quad \delta_p = \nu_p + \tfrac{5}{2};$

E_g is the forbidden gap width at T°K and

$$\sigma_n = n\mu_n e, \quad \sigma_p = p\mu_p e.$$

The value of ν depends on the particular mechanism of scattering of electrons; for example, it can range from $-\tfrac{1}{2}$ for acoustic scattering to $+\tfrac{1}{2}$ for polar scattering above the optical mode temperature and to $+\tfrac{3}{2}$ for either impurity scattering or electron-hole scattering.

The ambipolar contribution Δ_{np} will be most important when $\sigma_n \simeq \sigma_p$ that is for essentially intrinsic samples with comparable electron and hole mobilities. The value of E_g/kT is usually very much greater than $\nu_n + \nu_p + 5$ and is dominant in this term.

For partial degeneracy the Δ's may be evaluated in terms of Fermi–Dirac integrals (see Madelung). In the limit of complete degeneracy the results are again simple. For example, if the electron system is completely degenerate while the hole system is non-degenerate (classical) then for all forms of electron scattering

$$\Delta_n = \frac{\pi^2}{3}\frac{\sigma_n}{\sigma}, \quad \Delta_p = (\nu_p + \tfrac{5}{2})\frac{\sigma_p}{\sigma}, \quad . \; . \; . \; . \; . \; . \; . \; . \quad (5)$$

$$\Delta_{np} = \frac{\sigma_n \sigma_p}{\sigma^2}\left\{\frac{E_g}{kT} + \frac{\xi_n}{kT} + \nu_p + \tfrac{5}{2}\right\}^2 \quad . \; . \; . \; . \; . \; . \quad (6)$$

where ξ_n is the Fermi energy. In general, degeneracy tends to increase the term in brackets but the effect is small until the electrons become highly degenerate.

With sufficient knowledge of the electrical properties of a semiconductor κ_e can, therefore, be calculated. So long as κ_e is not too large compared to the measured value of thermal conductivity, the lattice component κ_L can then be deduced with reasonable accuracy.

4.2. κ_e *for Germanium and Silicon*

The germanium sample used in the experiments was fairly pure and by comparison with some results of Dunlap (1957) would be intrinsic by 500°K and the silicon by 600°K. Electrical data from Morin and Maita (1954 a, b) have, therefore, been used to calculate κ_e for intrinsic germanium and silicon. The ratio of electron to hole mobility has been taken from the extrapolated high temperature curves. The temperature dependence of mobility in germanium is found to be $T^{-1\cdot66}$ for electrons and $T^{-2\cdot33}$ for holes and in silicon is $T^{-2\cdot6}$ for electrons and $T^{-2\cdot3}$ for holes. Although acoustic mode scattering would lead to a $T^{-1\cdot5}$ dependence, nevertheless this has been assumed as a first approximation taking $\nu = -\frac{1}{2}$.

The results are given in fig. 4. Ambipolar diffusion is dominant in both materials there being virtually no kinetic energy transport in silicon up to 1000°K. By comparison with fig. 1 it can be seen that the electronic component in silicon is negligible and the experimental results represent the lattice conductivity.

The predominance of ambipolar diffusion in germanium is confirmed by the results of Abelès. He finds that the thermal conductivity of his pure sample starts to increase above 700°K (the temperature at which it becomes intrinsic) while that of his impure sample continues to decrease until about 900°K (where it becomes intrinsic). At this temperature κ for the pure material is 0·008 cals (cm°C sec)$^{-1}$ greater than that of the impure; this is equal to the calculated value for ambipolar diffusion in intrinsic germanium at 900°K.

Ioffe (1956) has also calculated the ambipolar contribution in germanium; he does not state what assumptions he has made but his results shown by the dotted line in fig. 4 seem somewhat high.

4.3. κ_e *for Indium Arsenide*

The calculation of κ_e in indium arsenide is extremely complex, for not only has it been shown to be weakly degenerate but it also has a non-parabolic conduction band so that the simple formulae given in § 4.1 do not apply. Moreover the scattering mechanism has not been established. Ehrenreich (1957) has considered the problem of electron scattering in the analogous compound InSb and finds that in the temperature range 200–500°K polar lattice scattering is predominant whereas at higher temperatures electron-hole scattering may become important.

Fig. 4

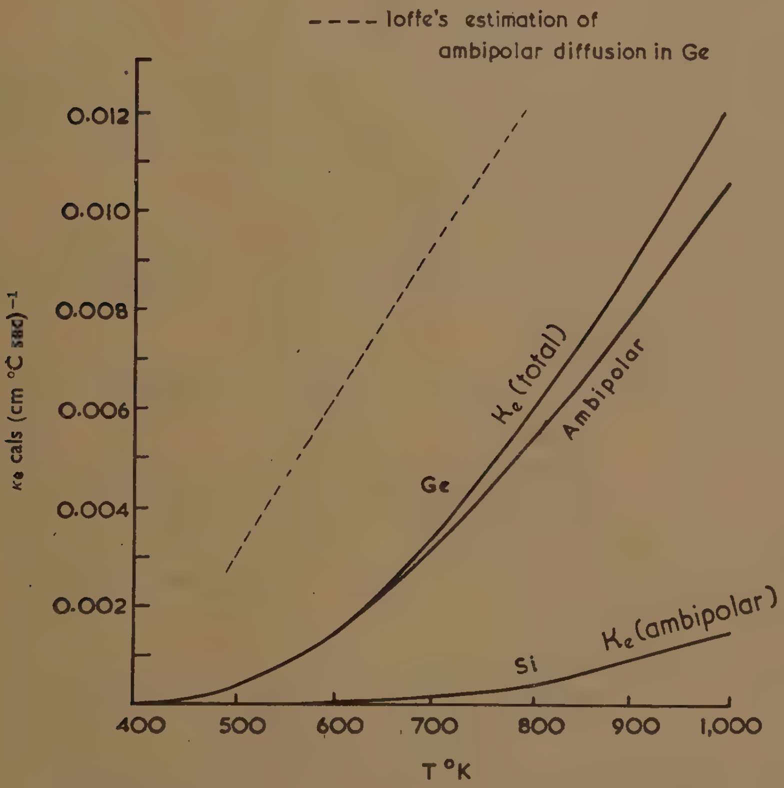

Calculated electronic component κ_e of thermal conductivity for intrinsic germanium and silicon.

In view of these facts no attempt has been made to use Ehrenreich's analysis for the ambipolar transport term (denoted as A by him). The simple formulae (§ 4.1) have been used, assuming classical statistics and polar scattering that is $\nu=\frac{1}{2}$.

In the calculation of Δ_{np} a value for the gap width E_g equal to $0{\cdot}5$ ev–$3{\cdot}5\times10^{-4}T$ has been used. The value of E_0 (E_g at 0°K) of 0·5 ev was obtained from thermoelectric measurements by Antell *et al.* (1956) while the temperature dependence was found from optical measurements by Oswald (1955). From a survey of the literature an average value for the ratio μ_p/μ_n of 1/64 at 300°K has been obtained, this being only slightly dependent upon impurity concentration. Owing to a lack of reliable information on the temperature variation of both electron and hole mobility the value of 1/64 has been taken as constant over the whole temperature range.

The kinetic energy and ambipolar contributions are shown in fig. 5 (*a*) while the total electronic component is given in fig. 5 (*b*). It can be seen that in indium arsenide the ambipolar diffusion is less than the kinetic energy transport.

An attempt has been made to estimate the effect of variations in the assumptions used in the above calculations. For example κ_e for two alternative scattering mechanisms is indicated by the dotted lines in fig. 5 (*b*). If, as seems likely by comparison with InSb, electron hole scattering dominates at the higher temperatures then κ_e will be increased to the values shown by the upper curve; should however, acoustic scattering predominate, κ_e would follow the lower curve.

From Oswald's optical measurements a value for the gap width $E_0 = 0{\cdot}43$ ev was obtained, surprisingly smaller than the value of 0·5 ev from thermoelectric measurements. This would lead to a reduction in κ_e of about 6%.

Components of κ_e for Various Scattering Mechanisms Allowing for Weak Degeneracy

Scattering mechanism	Kinetic energy transport $(\sigma/\sigma_n)\Delta_n$				Ambipolar transport δ_n			
	$\eta^* \to -\infty$	$\eta^*=0$	$\eta^*=1$	$\eta^*=2$	$\eta^* \to -\infty$	$\eta^*=0$	$\eta^*=1$	$\eta^*=2$
$\nu=-\frac{1}{2}$	2·0	2·17			2·0	2·37		
$\nu=\frac{1}{2}$	3·0		3·05		3·0		3·60	
$\nu=\frac{3}{2}$	4·0			3·73	4·0			4·81

It might be expected that the assumption of classical statistics in a material known to be weakly degenerate, would lead to an underestimate of κ_e. It has been shown by Antell *et al.* that for a similar sample measured over the same temperature range, the value of η^* (the Fermi energy in units of kT) will at no temperature exceed 0, 1 or 2, according to whether acoustic, polar or electron scattering predominates. Both components of κ_e (see table) have, therefore, been evaluated for these degrees of degeneracy using formulae given by Madelung (1957) in terms of Fermi–Dirac integrals, while the classical case ($\eta^* \to -\infty$) has been evaluated from equations 3 and 4.

From these figures, the maximum effect on the kinetic energy transport is an increase of about 8·5% which occurs for acoustic scattering. The effect on the ambipolar contribution is an increase of about 12% at 700°K where ξ_n/kT, E_g/kT and $\nu_p + \frac{5}{2}$ are all of the same order of magnitude—it will be less at lower temperatures and more at higher temperatures.

The assumption of a constant mobility ratio has almost certainly led to an overestimate of the ambipolar contribution, since this ratio probably decreases as the temperature increases. If the mobility is a function of temperature of the form $\mu \propto T^{-\alpha}$ then α (extrapolated from Folberth

Fig. 5

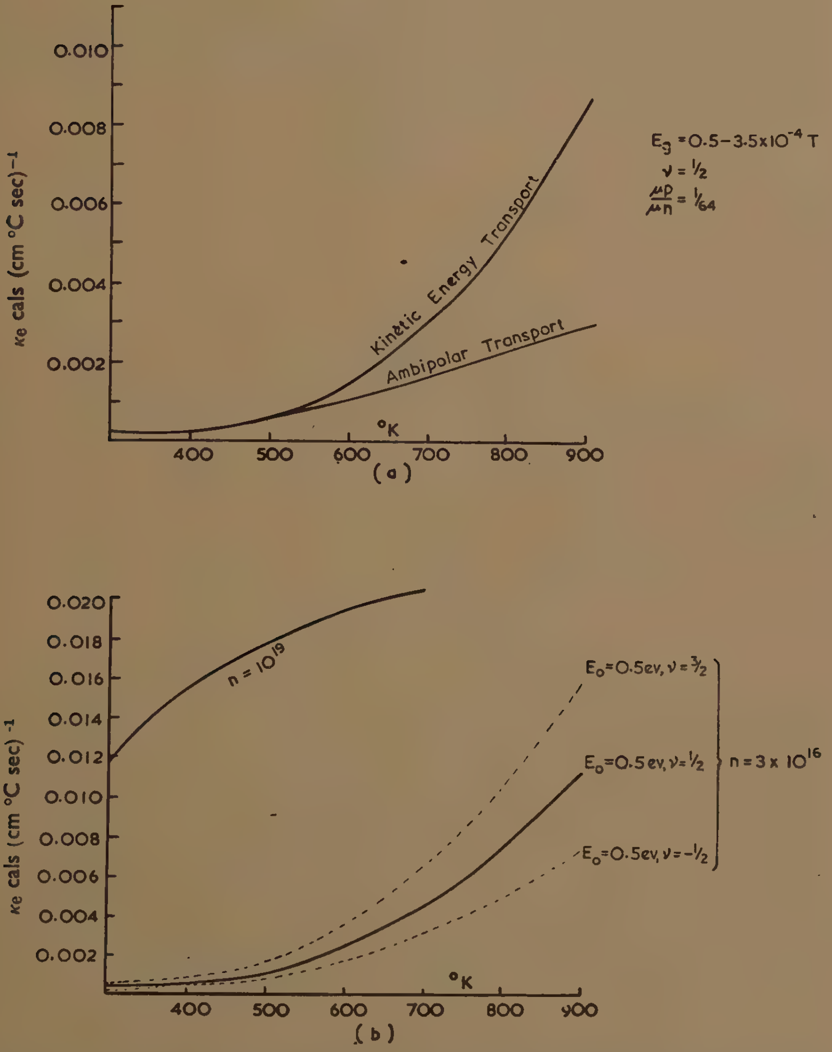

(*a*) Estimates of the kinetic energy and ambipolar transport in pure indium arsenide ($n = 3 \times 10^{16}$). (*b*) Estimated κ_e for pure ($n = 3 \times 10^{16}$) and impure ($n = 10^{19}$) indium arsenide.

et al. (1954) and Antell *et al.*) would be 2·3 for holes and between 1 and 1·5 for electrons, leading to a value for μ_p/μ_n at 750°K of about 40% of that at 300°K. Taking this into account and the effect of the lower value for the gap width, the lower estimate of the ambipolar diffusion would be about 10% of the kinetic energy contribution for all scattering mechanisms. This contrasts with the statement of Bowers *et al.* that up to 750°K the ambipolar term is less than 6% of the kinetic energy contribution. Unfortunately, they do not state what assumptions were made in their calculation.

Estimation of the electronic transport in the impure sample is less complex. The ambipolar contribution will be negligible owing to the small number of intrinsic holes. At the same time the electrons are highly degenerate so that the electronic component is given by

$$\kappa_e = \frac{\pi^2}{3}\left(\frac{k}{e}\right)^2 \sigma T.$$

The results are given in fig. 5 (*b*).

§ 5. Lattice Thermal Conductivity

5.1. *Theoretical*

The theory of lattice conduction is somewhat complex and has not yet been completely formulated (cf. Berman (1953), Peierls (1955), Klemens (1956)).

Above the Debye temperature Θ phonon–phonon U-processes predominate and the following laws should be obeyed

$$W_L \propto T \quad \text{three-phonon processes}$$

$$W_L \propto T^2 \quad \text{four-phonon processes}$$

where W_L $(1/\kappa_L)$ is the thermal resistance. The first equation applies where the major phonon interaction is one involving three phonons, either two phonons combine to form a third or one phonon splits up into two. The second equation holds where either one, two or three phonons interact to produce three, two or one phonon respectively.

Well below Θ, the resistance due to U-processes should decrease exponentially as the temperature is lowered until additional components of thermal resistance (such as phonon collisions with crystal imperfections, impurities, or crystal boundaries) swamp that due to interphonon collisions causing a rapid rise in W_L.

Even at high temperatures if there is a sufficiently large impurity concentration, there may be a contribution to the thermal resistance, due to phonon collisions with the impurities, which is comparable to the resistance arising from interphonon collisions. According to Peierls, above the Debye temperature, the impurities will contribute an additional thermal resistance which is independent of temperature: this depends on their number remaining constant and on their scattering cross section for a given phonon energy being constant, since ($T > \Theta$) the average phonon energy will be independent of temperature.

5.2. *Germanium and Silicon*

Since κ_e is found to be negligible in silicon up to 600°K the experimental results represent the lattice conductivity. κ_L has been deduced for germanium by subtraction of κ_e from the measured values. The lattice resistance for each material is shown in fig. 6. There is a linear relation between W_L and T up to 600°K for silicon (the full range of the experiment) but only up to 500°K for germanium. From 500°K to 700°K there is a marked increase in the temperature dependence. In neither case does the linear portion extrapolate through the origin.

Fig. 6

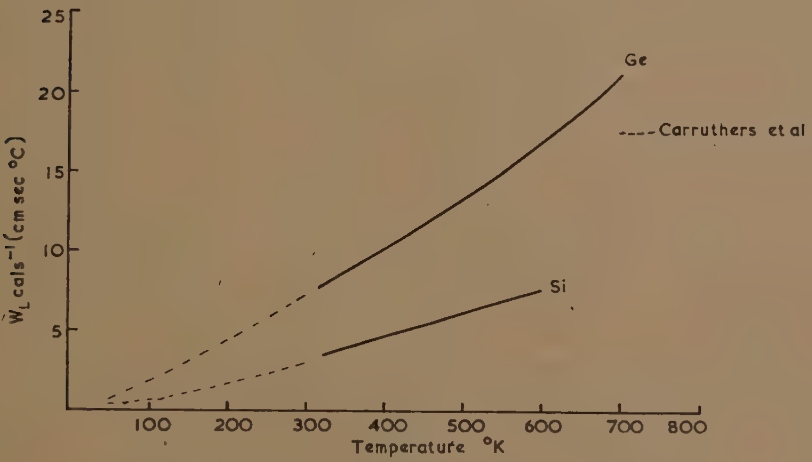

Estimated lattice resistance of germanium and silicon.

Low-temperature measurements by White and Woods (1956) and by Carruthers *et al.* (1957) have shown that the exponential dependence expected for U-process is not obtained in germanium or silicon but the thermal resistance in each case is approximately proportional to the temperature. This has been explained (cf. Berman *et al.* (1956)) by the presence of isotopes which scatter the phonons. As the temperature is increased the thermal resistance due to U-processes will increase and ultimately become dominant. It is not clear at what stage this will happen (Θ for germanium is 360°K and for silicon is 658°K) and it is perhaps not surprising that over the linear part W_L is found to be proportional to the absolute temperature minus a constant. The results of Carruthers up to 300°K, which agree closely with those of White and Woods, are shown by the dotted lines in fig. 6 where they can be seen to be mutually consistent with the high-temperature results: the merging of the two curves is particularly good in the case of germanium.

The logarithmic plot (fig. 9) indicates that as the temperature is increased, the thermal resistance in germanium is tending to the square law dependence expected for four phonon processes. Since κ_e is only 6% of the measured value at 700°K it seems unlikely that a false assumption in calculating it would account for the departure of W_L from linearity. Silicon does not show this effect; in this case measurements were not made above the Debye temperature.

5.3. *Indium Arsenide*

The lattice conductivity for both samples of indium arsenide has been deduced using values of κ_e calculated in § 4.3 and the results are given in fig. 7; the deduced values of Bowers are indicated by the dotted lines. The most striking feature is the much lower lattice conductivity of the impure sample ($n = 10^{19}$) compared to that of the pure sample ($n = 3 \times 10^{16}$), contrasting with the fairly close agreement obtained by Bowers for both his samples ($n = 5 \times 10^{16}$ and $n = 10^{18}$). However, the two impure samples are not identical and there may be increased scattering of the phonons by impurities in the more heavily doped material.

Fig. 7

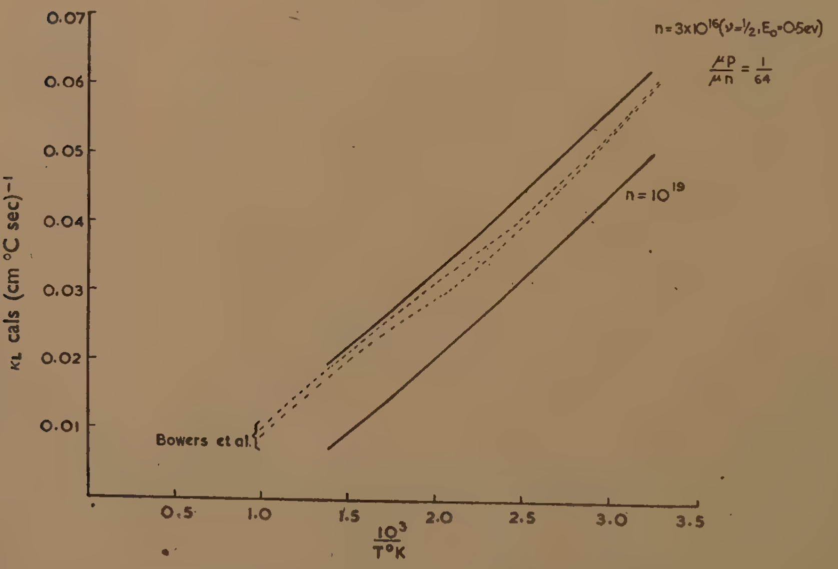

Estimated lattice conductivity of indium arsenide.

The full lines in fig. 8 represent the thermal resistance of the two samples assuming that the impure is completely degenerate and that for the pure material, classical statistics apply, polar scattering predominates and the mobility ratio is constant. The part shaded between the dotted lines on either side of the lower full line represents the range of values for W_L ($n = 3 \times 10^{16}$) taking into account the uncertainty of electrical properties discussed in § 4.3. The maximum values of W_L are obtained for electron-hole scattering, $E_0 = 0{\cdot}5$ ev, a constant mobility ratio and weak degeneracy. The minimum values correspond to $E_0 = 0{\cdot}43$ ev, a temperature dependent mobility ratio, acoustic scattering and no degeneracy.

The lattice resistance of the impure material could be reduced if κ_e has been overestimated by the assumption of complete degeneracy to the extent shown by the shaded curve, the lower limit representing acoustic scattering and classical statistics. This limit is extremely unlikely since even if there is only partial degeneracy, polar, electron-hole or impurity scattering is the more probable scattering mechanism to which the upper limit is a better approximation.

Fig. 8

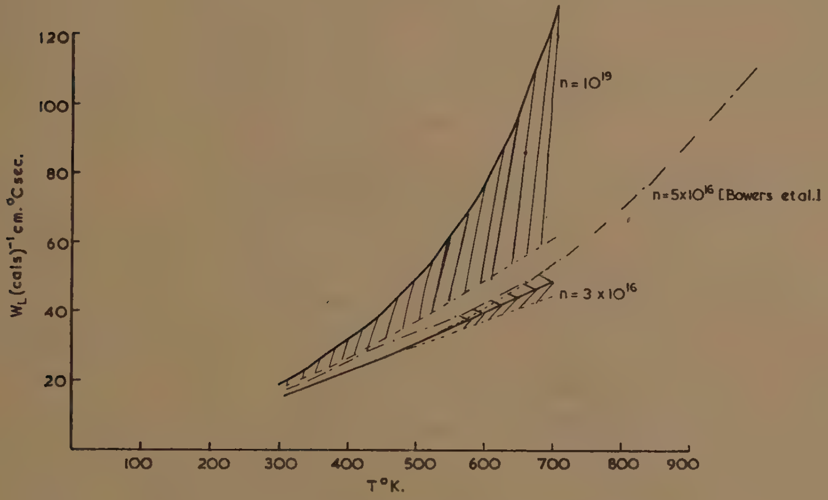

Estimated lattice resistance of indium arsenide.

It would, therefore, appear that the thermal resistance of the impure sample is greater than that of the pure and the additional component increases as the temperature increases.

Dr. J. M. Ziman and Mr. F. W. Sheard (private communication), however, have estimated that the sulphur-doped sample should have an additional component due to scattering of phonons by impurities of only about $0{\cdot}5$ cals^{-1} (cm °C sec) and this should be independent of temperature. They have suggested that the calculated value of κ_e may be too large (and hence too large a value for W_L) when there is scattering of electrons by optical modes instead of acoustic modes.

It is interesting to note that again the thermal resistance does not show a linear relationship with temperature over the whole range and the extrapolation of the lower part of the curves in neither case passes through the origin. Bowers' results between 700°K and 1000°K also indicate a more rapid dependence on temperature. From the logarithmic plot (fig. 9) the lattice resistance of the heavily doped sample can be seen to be approaching a square law dependence.

§ 6. Conclusions

Taking into account the accuracy obtained in measurements on stainless steel samples of known thermal conductivity and the reproducibility of repeated measurements on semiconductors the experimental accuracy of measurement using the techniques described here is estimated as ±5% up to 450°c.

Fig. 9

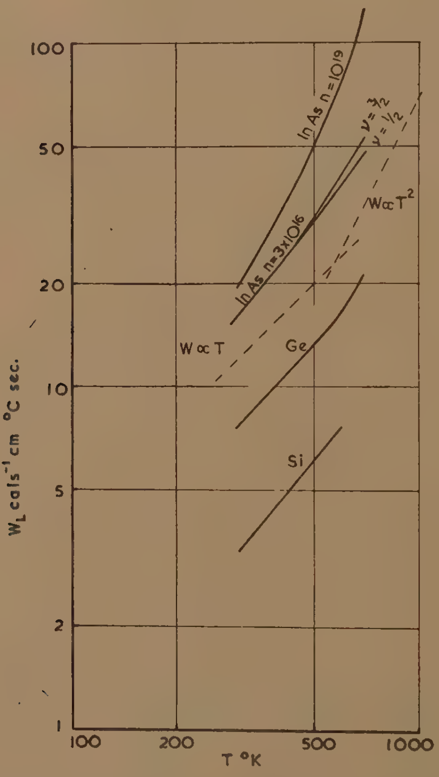

Lattice resistance against temperature for germanium, silicon and indium arsenide.

From fig. 9 it can be seen that in no case is the thermal resistance directly proportional to temperature over the whole range as expected for three-phonon processes, although germanium approximates to this at the lower temperatures. The trend in other materials is to a higher power relationship as found for indium antimonide (Stuckes 1957). Since a T^2 dependence would be expected for four-phonon processes it may be concluded that higher order phonon processes are operative in these materials.

An observation of particular interest is that the estimated lattice resistance of the highly impure InAs specimen is greater than that for the pure specimen, the difference being more marked at the higher temperatures. As a simple theoretical picture would suggest that impurity scattering should yield an additional thermal resistance independent of temperature, this result may be of both theoretical interest and also of practical importance in thermoelectric applications.

ACKNOWLEDGMENTS

The author wishes to thank the British Thomson-Houston Co. Ltd., the Brown Firth Research Laboratories and the National Physical Laboratory for providing some of the specimens used in this work. It is a pleasure to acknowledge the invaluable assistance in the measurements from Mrs. B. Brooks and the many helpful and stimulating discussions with Mr. R. P. Chasmar and Dr. R. Stratton. The author also wishes to thank Sir Willis Jackson, F.R.S., Director of Research and Education, Metropolitan-Vickers Electrical Company Limited, for permission to publish this paper.

REFERENCES

ABELÈS, B., 1958, *J. Phys. Chem. Solids*, **8**, 340.
Metals Handbook, 1948 (Cleveland : American Society for Metals).
ANTELL, G. R., CHASMAR, R. P., CHAMPNESS, C. H., and COHEN, E., 1956, *Report of the Meeting on Semiconductors* (London : The Physical Society), p. 99.
BERMAN, R., 1953, *Advanc. Phys.*, **2**, 103.
BERMAN, R., FOSTER, E. L., and ZIMAN, J. M., 1956, *Proc. roy. Soc.* A, **237**, 344.
BOWERS, R., URE, R. W., BAUERLE, J. E., and CORNISH, A. J., 1959, *J. appl. Phys.*, **30**, 930.
CARRUTHERS, J. A., GEBALLE, T. H., ROSENBERG, H. M., and ZIMAN, J. M., 1957, *Proc. roy. Soc.* A, **238**, 502.
DUNLAP, W. CRAWFORD, 1957, *An Introduction to Semiconductors* (New York : John Wiley and Sons), p. 230.
EHRENREICH, H., 1957, *J. Phys. Chem. Solids*, **2**, 21.
FOLBERTH, O. G., MADELUNG, O., and WEISS, H., 1954, *Z. Naturf.* A, **9**, 954.
IOFFE, A. F., 1956, *Canad. J. Phys.*, **34**, 1342.
IOFFE, A. V., and IOFFE, A. F., 1954, *Zhurn. Tekh. Fiz.*, **24**, 1910.
KETTEL, F., 1959, *J. Phys. Chem. Solids*, **10**, 52.
KLEMENS, P. G., 1956, *Handb. Phys.*, **14** (Berlin : Springer-Verlag), p. 198.
MADELUNG, O., 1957, *Encyclopaedia of Physics*, Vol. XX (Berlin : Springer-Verlag), p. 87.
MORIN, F. J., and MAITA, J. P., 1954 a, *Phys. Rev.*, **94**, 1525 ; 1954 b, *Ibid.*, **96**, 1528.
OSWALD, F., 1955, *Z. Naturf.* A, **10**, 927.
PEIERLS, R. E., 1955, *Quantum Theory of Solids* (Oxford: Clarendon Press), p. 52.
POWELL, R. W., 1934, *Proc. phys. Soc., Lond.*, **46**, 659 ; 1936, *Ibid.*, **48**, 351.
PRICE, P. J., 1955, *Phil. Mag.*, **46**, 1252.
STEELE, M. C., and ROSI, F. D., 1958, *J. appl. Phys.*, **29**, 1517.
STUCKES, A. D., 1957, *Phys. Rev.*, **107**, 427.
STUCKES, A. D., and CHASMAR, R. P., 1956, *Report of the Meeting on Semiconductors* (London : The Physical Society), p. 119.
SULLIVAN, M. V., and EIGLER, J. H., 1957, *J. electrochem. Soc.*, **104**, 226.
WHITE, G. K., and WOODS, S. B., 1956, *Phys. Rev*,, **103**, 569.

CORRESPONDENCE

Hall Effect in Liquid and Solid Mercury

By P. W. Kendall and N. E. Cusack
Department of Physics, Birkbeck College, University of London

[Received December 21, 1959]

Until about 1930 there was some doubt as to whether liquid metals showed Hall effects. In 1914, Fenninger failed to find Hall voltages in liquid Hg, but he also found a zero effect in solid Hg and the latter result has been contradicted in at least two subsequent experiments. In 1931, Kikoin and Fakidow showed that a liquid Na–K alloy possessed a Hall coefficient approximately equal to the free electron value of $-1/nec$, where n is the number of conduction electrons per unit volume. Nevertheless they too concluded that liquid Hg has zero Hall effect. Taken in conjunction with later results for solid Hg (e.g. those of Serduke and Fisher 1932), this would mean that the Hall coefficient, R, changes considerably on melting. It seemed desirable to check this result in the course of developing apparatus for investigating the Hall coefficient of liquid metals generally.

The measurement was by conventional d.c. techniques much as described by Lindberg (1952), the specimens being confined between flat glass plates whose separation was measured by an optical interference method. A Hall voltage, of the order 1 μv, was detected and was found to be proportional to the magnetic field for constant current through the specimen, and vice versa. The Hall coefficient was the same for three specimens of thicknesses 4·17, 2·03 and $5{\cdot}51\times10^{-3}$ cm. These facts indicate that a true Hall voltage was being measured, not seriously influenced by any magnetohydrodynamic effects. The mean of a large number of values of R was $-74{\cdot}6\times10^{-5}$ $\pm4\%$ e.m.u. and this was independent of temperature between room temperature and the M.P. ($-38{\cdot}9$°c).

The best way of describing electron states in liquid metals is not yet clear. Using the terminology normal in solid state theory, the conditions that R should have the free electron value are, according to Cooper and Raimes, (i) the Fermi surface should be spherical and (ii) the relaxation time should be isotropic. It seems plausible to assume that both these conditions should hold in a liquid devoid of long-range order. On this view the Hall coefficient of liquid mercury should be $-77{\cdot}4\times10^{-5}$ e.m.u. assuming two valence electrons per atom. This agrees quite well with the observed value. The results of Schulz (1957) on the optical properties of liquid Hg also fit very well with the free electron theory but the optical properties are not perfectly well established because the measurements of Hodgson (1959) do not confirm those of Schulz.

The values of R for solid Hg varied somewhat from specimen to specimen as did those of Serduke and Fisher (1932). It is possible that this is due to the different ways in which the mercury crystallized each time it was frozen, for the specimens may have contained fairly large oriented regions and the Hall coefficient is probably anisotropic. The values of R, which were independent of temperature between -39 and -71°c, ranged from -87 to -101×10^{-5} e.m.u.; those of Serduke and Fisher from -72 to -88×10^{-5} e.m.u. There is, of course, no reason to believe that either of Cooper and Raimes's conditions are fulfilled in the solid. It is interesting that R is negative in the solid Hg while it is positive in Zn and Cd. This is a possible point against Wallace's (1955) theory of bonding in these metals which treats them all on the same footing and entails the positive R in Zn and Cd.

The present results for liquid Hg disagree with those of Kikoin and Fakidow. If the value of R now reported is correct, then, other things being equal, the Hall voltage from Hg will be about 17% of that from the Na–K alloy used by Kikoin and Fakidow. Since the error reported in their value of R(Na–K) is ± 10%, it is possible that their method was not sensitive enough to detect reliably the effect with Hg. Nevertheless it would be desirable to repeat the measurement with an entirely different technique, as well as to extend it to other metals, and such work is in progress.

References

Cooper, J. R. A., and Raimes, S., 1959, *Phil. Mag.*, **4**, 145.
Fenninger, W. N., 1914, *Phil. Mag.*, **27**, 109.
Hodgson, J. N., 1959, *Phil. Mag.*, **4**, 183.
Kikoin, J., and Fakidow, I., 1931, *Z. Phys.*, **71**, 393.
Lindberg, O., 1952, *Proc. Inst. Radio Engrs, N.Y.*, **40**, 1414.
Schulz, L. G., 1957, *Advanc. Phys.*, **6**, 102.
Serduke, J. T., and Fisher, T. F., 1932, **39**, 831.
Wallace, W. E., 1955, *J. chem. Phys.*, **23**, 2281.

The Effect of Electropolishing on the Retention of Vacancies During Quenching in Al and Al Alloys†

By E. J. Freise‡, M. E. Fine and A. Kelly‡
Department of Materials Science,
Northwestern University, Evanston, Illinois, U.S.A.

[Received December 28, 1959]

Recently Smallman and Westmacott (1959) observed diffuse scattering of x-rays at small angles in quenched pure metal foils. They attributed the effect to double Bragg scattering caused by distortion due to dislocations formed by condensation of vacancies during quenching. Doherty

---

† This research was supported by the United States Air Force under Contract No. AF 49(638)–524 monitored by the A.F. Office of Scientific Research and Development Command.

‡ Present address: Department of Metallurgy, Cambridge University.

Fig. 1

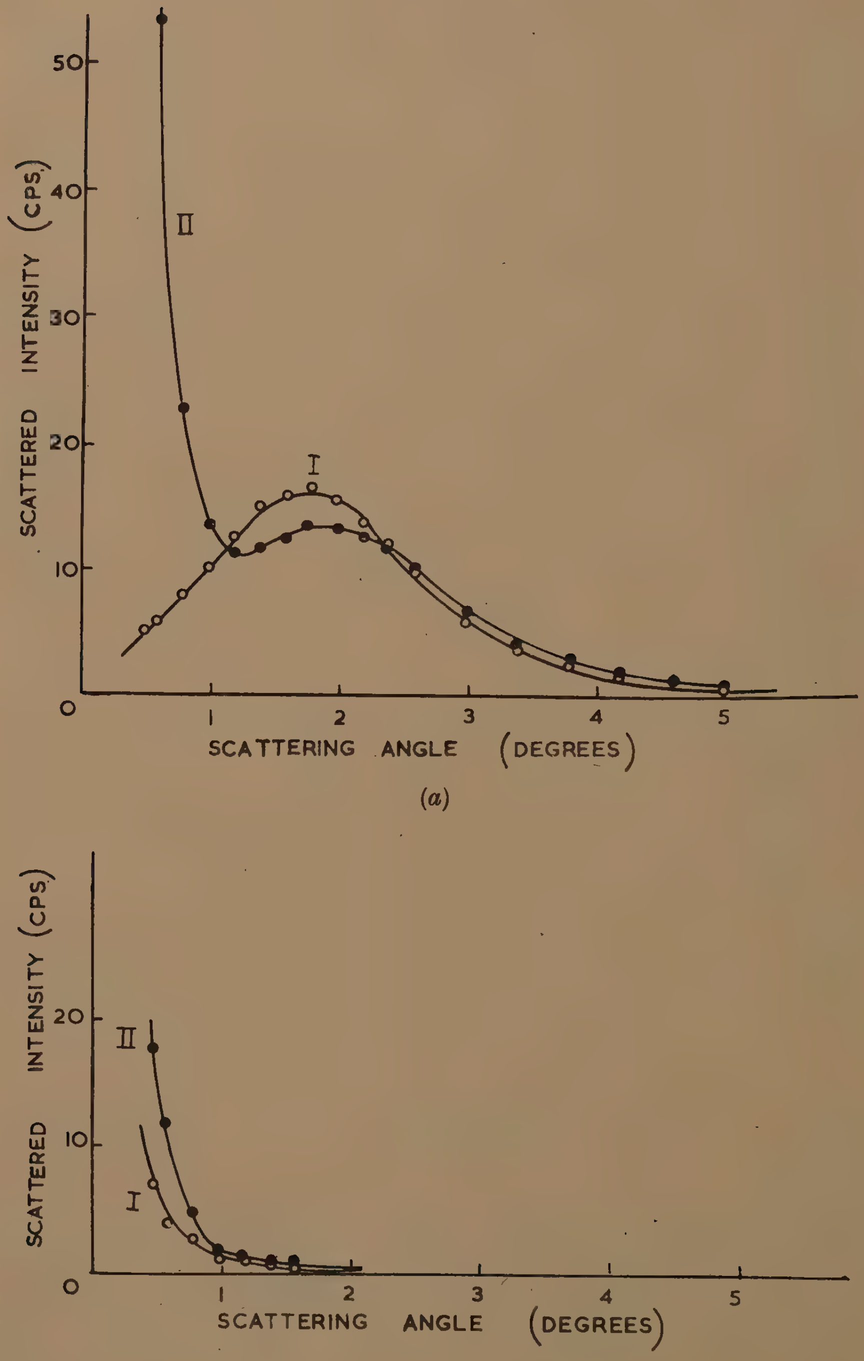

(*a*)

(*b*)

(*a*) Scattering curves for an Al–6 at. % Ag alloy : I—Electropolished and etched ; II—Electropolished only. (*b*) Scattering curves for pure aluminium : I—Electropolished and etched ; II—Electropolished only.

and Davis (1959) noted that surface oxide on aluminium prevented formation of surface pits which were due to condensation of vacancies. Herein are reported small angle scattering studies of foils (25 to 50 microns thick) of Al and an Al–6 at. % Ag alloy quenched from 540°c indicating that a surface film is effective in increasing the magnitude of the double Bragg scattering; escape of vacancies to the surface is reduced.

The small angle scattering was measured using a General Electric XRD–5 diffractometer using a balanced filter technique to isolate the scattering due to CuK_α radiation. The readings obtained were corrected for parasitic scattering. The foils were all capsulated in evacuated pyrex ampules (10^{-6} mm Hg pressure) and drop quenched in water from 540°c.

The figure gives the intensity of the small angle scattering for two conditions: I—Electropolished (in a bath of 817 cm^3 orthophosphoric acid, 40 cm^3 water, 156 g chromic acid, and 143 cm^3 sulphuric acid) and etched in hydrofluoric-nitric acid mixture; and II—Electropolished only. It is to be noted that the small angle scattering below 1° is considerably larger for the unetched samples. Sample foils of Al–6 at. % Ag with the as rolled surface gave curves essentially identical to fig. 1 (*a*)—I. In the case of the alloy the scattering peak between 1° and 2° is due to the presence of Guinier–Preston zones.

The following interpretation of the data in fig. 1 is suggested. In thin foils the surface is a very important sink for quenched-in vacancies. During electropolishing a surface film is presumed to form on the specimen, reducing escape of vacancies. The additional quenched-in vacancies then result in an additional number of dislocation loops or spirals. Etching removes the film and the effect is not observed.

REFERENCES

DOHERTY, P. E., and DAVIS, R. S., 1959, *Acta Met.*, **7**, 111.
SMALLMAN, R. E., and WESTMACOTT, K. H., 1959, *J. appl. Phys.*, **30**, 603.

REVIEWS OF BOOKS

Electrophoresis. Theory, Methods and Applications. Edited by MILAN BIER. (Academic Press Inc., 1959.) [Pp. 563.] 107*s*. 6*d*.

ELECTROPHORESIS has long played a major rôle in the study of colloidal systems and this volume sets out to give an account of the various forms of electrophoresis which have been employed and the systems which have been studied by this technique. The first three chapters are largely theoretical and are devoted to consideration of the distribution of electric potential at interfaces, acid-base equilibria of proteins and the theory of the moving boundary method of electrophoresis. Other chapters deal with the methods and applications of moving boundary, paper, zone and microscopic electrophoresis. The use of electrophoresis as a technique for the separation of mixtures and as a means of studying interacting systems is also discussed. The material, in general, appears to be soundly presented and well illustrated. The text is relatively free of typographical errors, but nomenclature, unfortunately, is not kept quite consistent from chapter to chapter. The emphasis of the book is very much in the direction of biological chemistry, a predominance not suggested by the title, and it is to be regretted that a little more space has not been devoted to the applications of electrophoresis to other large and important fields, such as, mineral dressing, hydrophobic sols, emulsions, and suspensions in non-aqueous media. This book does, however, make a useful and commendable contribution to the subject of electrophoresis.

R. H. O.

Semi-conductors. By R. A. SMITH. (Cambridge University Press, 1959.) [Pp. 494+xvii.] 65*s*.

THE output of work on solid state physics is now so great that the task of keeping up-to-date is an extremely difficult one. It is true that there are various series of summarizing reviews, but many of the articles are written before the subjects they deal with have been properly consolidated, and the student is often forced to read not only the reviews but the original papers as well. It is therefore a pleasure to find a book such as Dr. R. A. Smith's *Semi-conductors* which deals with a well-defined section of solid state physics in a workmanlike fashion.

The first part of the book gives an account of the fundamental principles of carrier concentrations in semi-conductors, of electron transport phenomena including the diffusion of electrons and positive holes, and of optical effects. The treatment is far from devoid of mathematics, but, since the various steps are spelled out in more detail than in most of the standard texts, it should be generally acceptable to physicists and engineers. The second part of the book deals with the methods of determining the characteristic properties of semi-conductors, followed by an account of the properties of elemental and compound semi-conductors and brief accounts of their more important applications. The chapters dealing with the properties of the individual semi-conductors are particularly valuable.

A. H. W.

[*The Editors do not hold themselves responsible for the views expressed by their correspondents.*]

Fig. 2

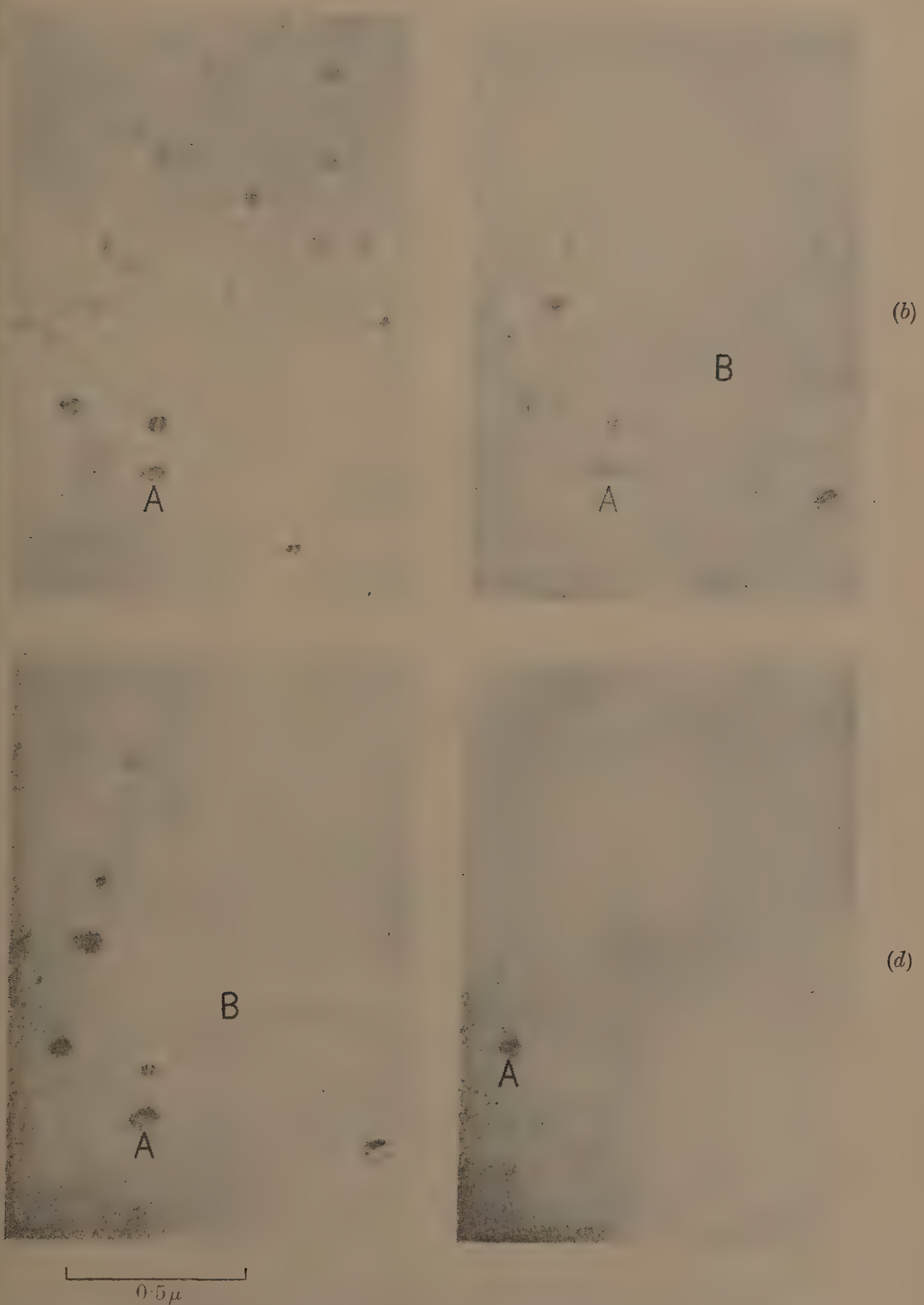

Sequence showing the annealing of loops in quenched aluminium. Stage temperature 187°c. The interval between exposures is ~1 min. Note the loop A which remains through the whole sequence. Note also the slip trace B left by a moving dislocation in (b) and (c). Mag. ×53 000.

Fig. 3

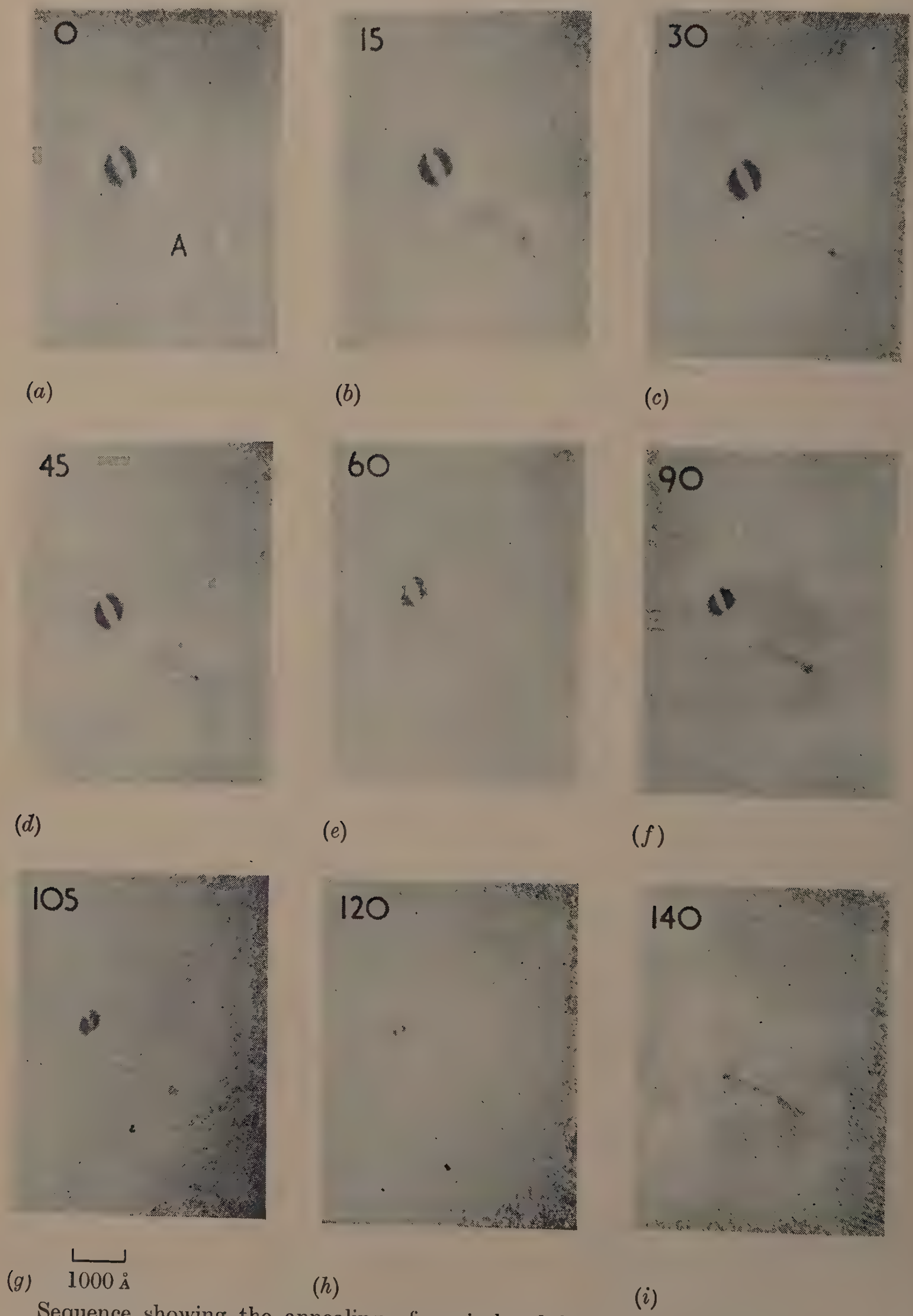

(a) (b) (c) (d) (e) (f) (g) (h) (i)

Sequence showing the annealing of an isolated loop near a dislocation A. Stage temperature 197°c. The numbers refer to the time in seconds at which exposures were made. The loop lies on an inclined plane and the more steeply inclined parts are less visible. Mag. ×82 500.

Fig. 5

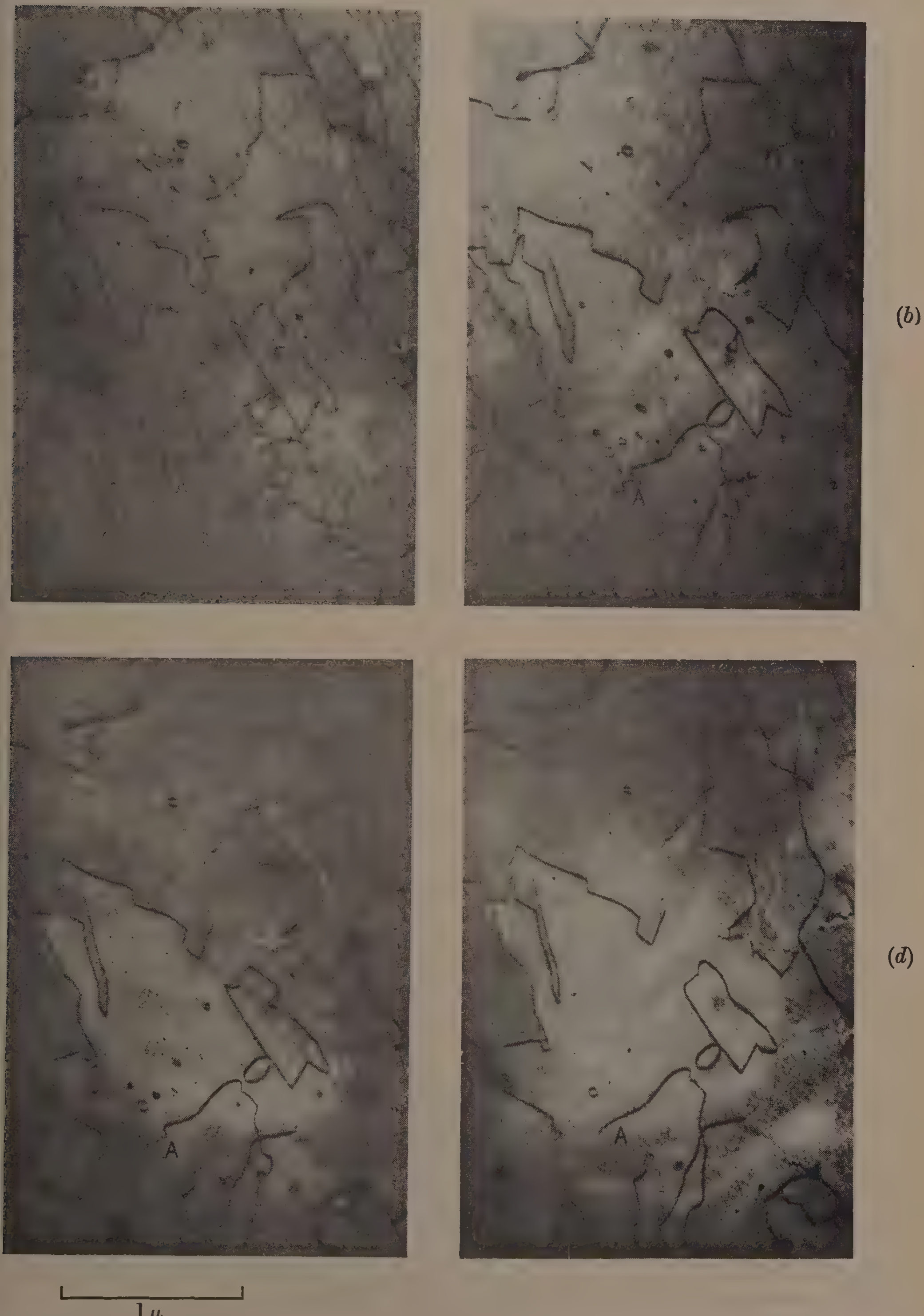

Sequence showing the annealing of loops near irregular dislocations. Stage temperature and time not recorded. As the loops anneal out the irregular dislocations become smoother. This effect is thought to be due at least partly to climb. Mag. ×28 000.

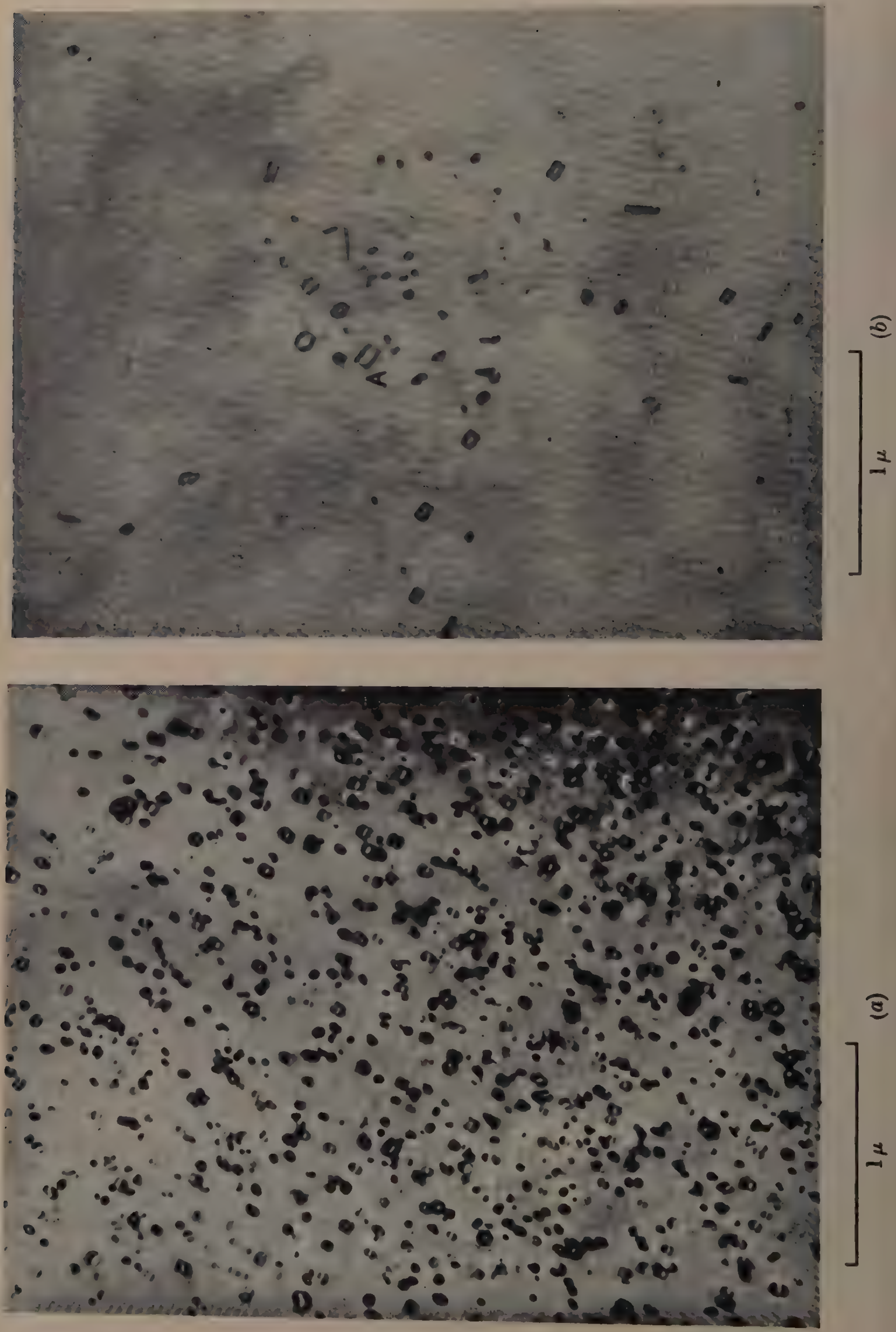

Fig. 6

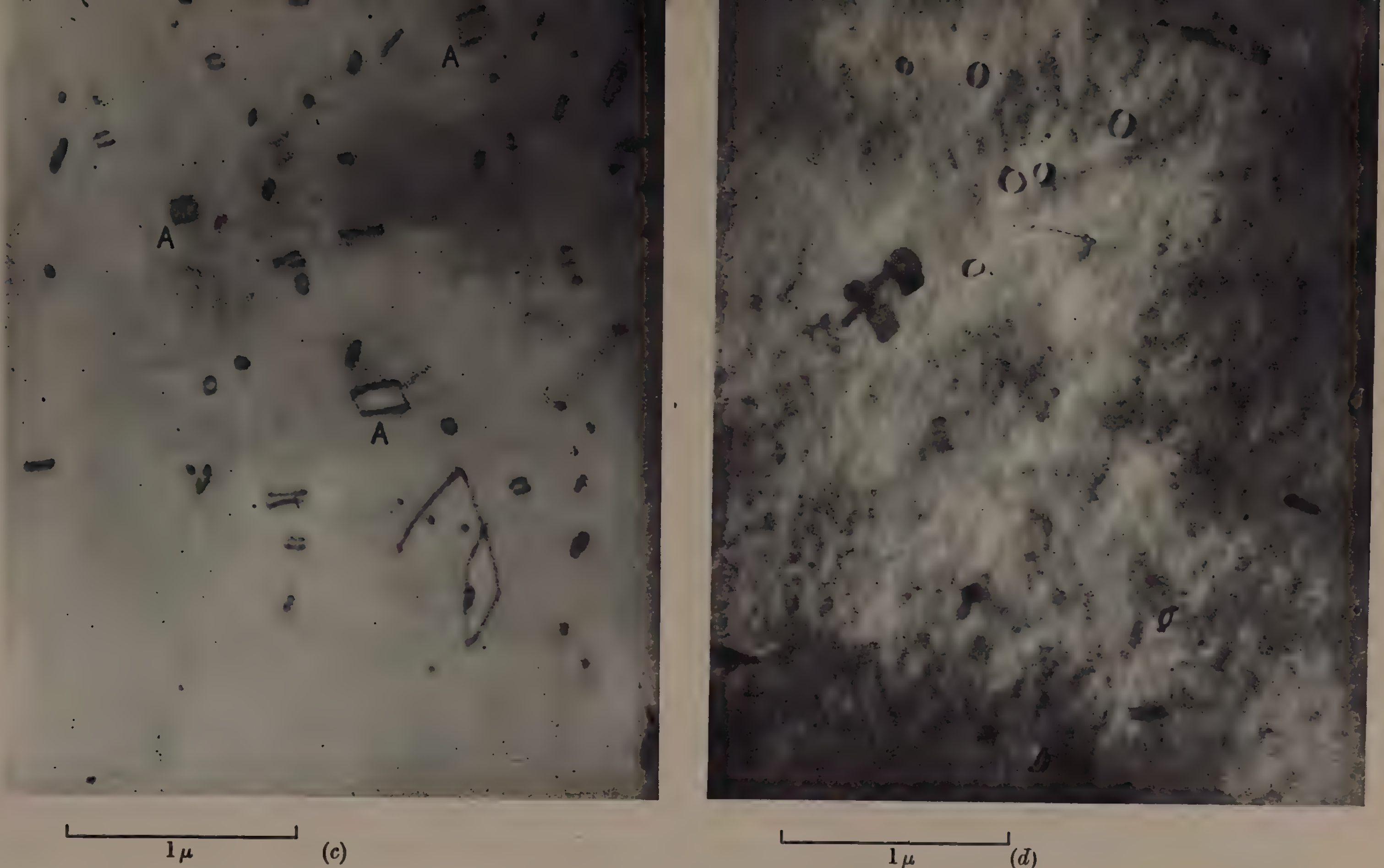

(c)

(d)

Typical micrographs showing the annealing of loops in bulk material.

(*a*) Typical micrograph of Al quenched from 600°c—no annealing. (*b*) and (*c*). Micrographs obtained after annealing the bulk material at 190°c for 6 minutes prior to thinning. Note the larger angular shaped loops at A. The small loops remaining are probably the remnants of larger loops which have almost disappeared during the 6-min. anneal. (*d*) Micrograph obtained after annealing the bulk material for 6 min at 200°c. Note the large loops. Mag. ×33 000.

Fig. 2

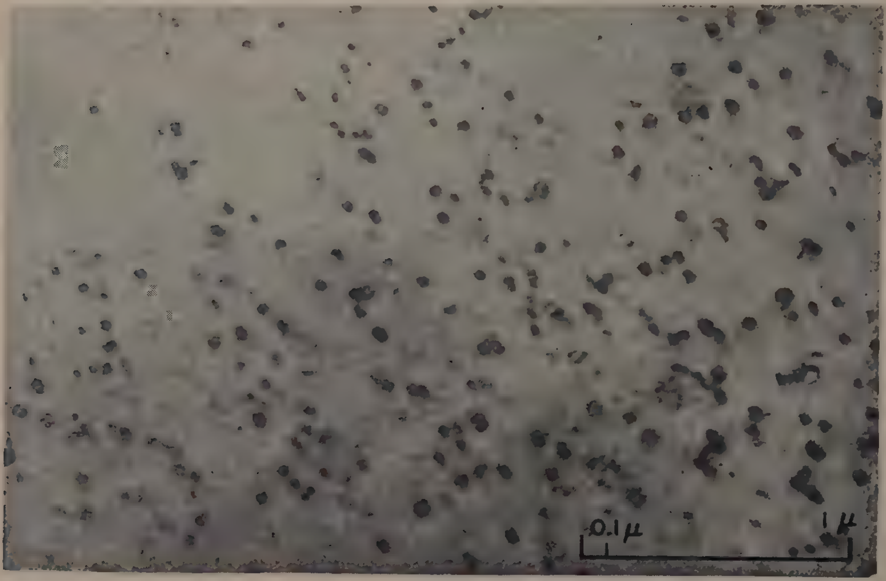

As-quenched dislocation loops.

Fig. 3

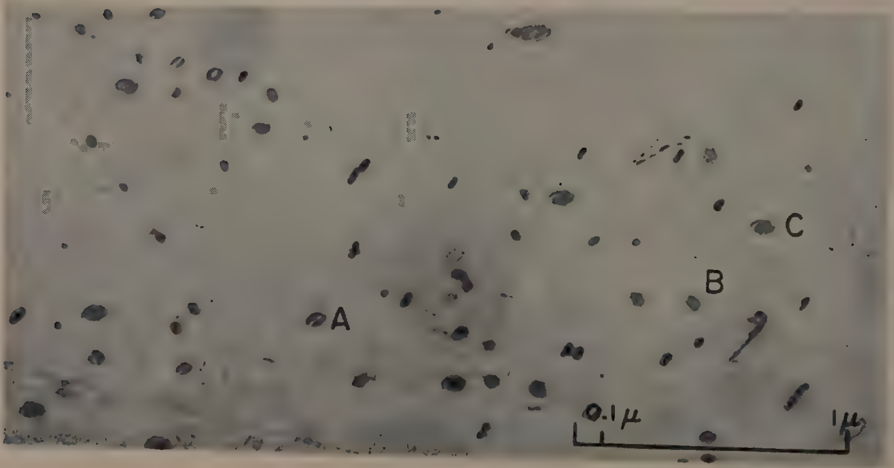

Three types of dislocation loops: (A) single loop, (B) hexagon, (C) double loop. (Note crystallographic alignment of the loops.)

Fig. 4

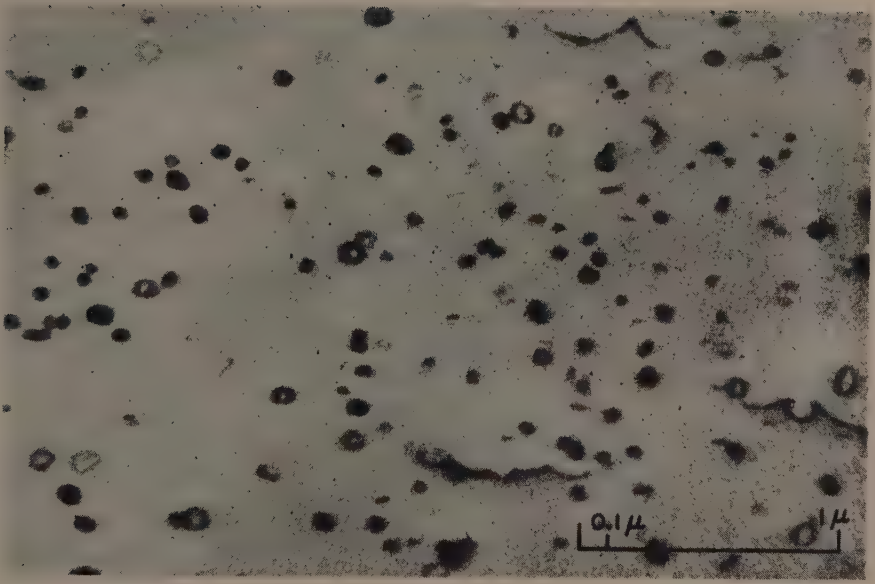

Annealed 10 min at 125°c after quenching.

Fig. 5

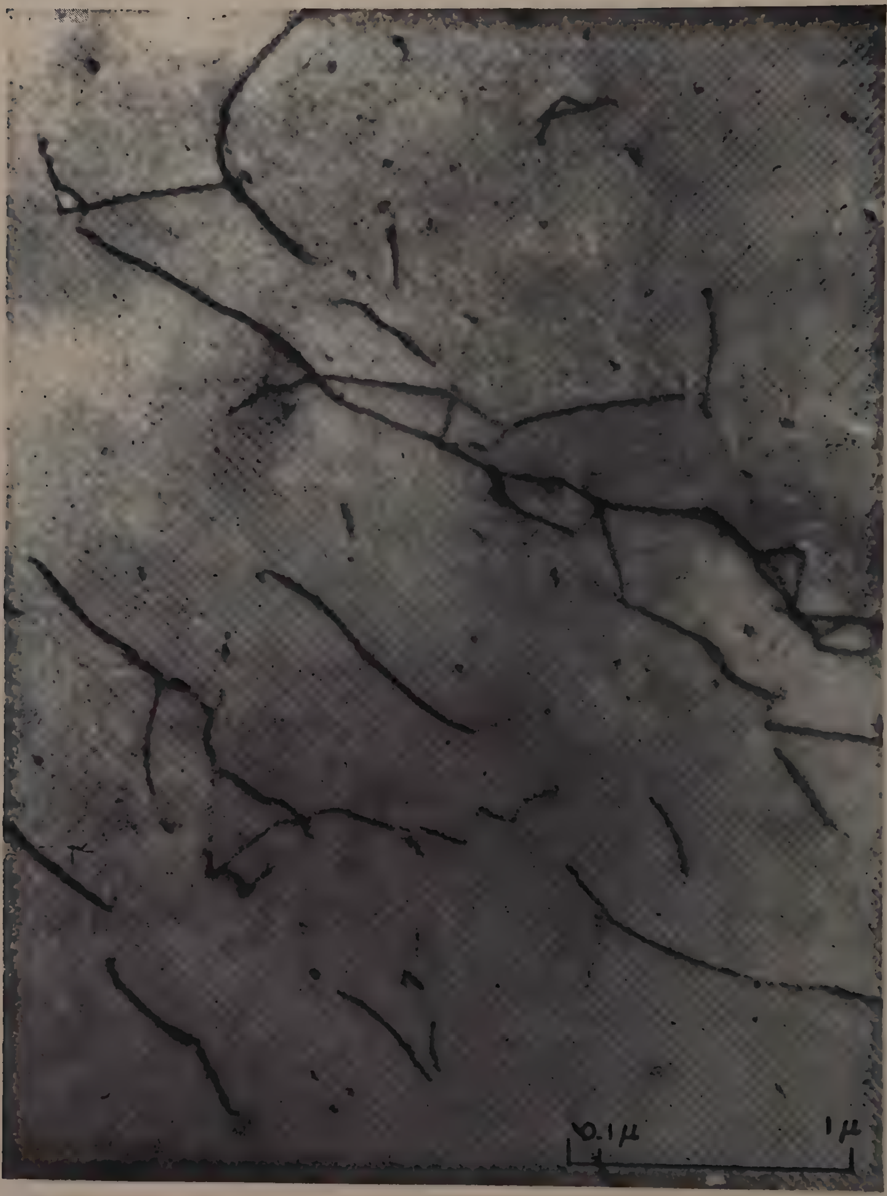

Annealed 10 min at 125°c after quenching.

Fig. 6

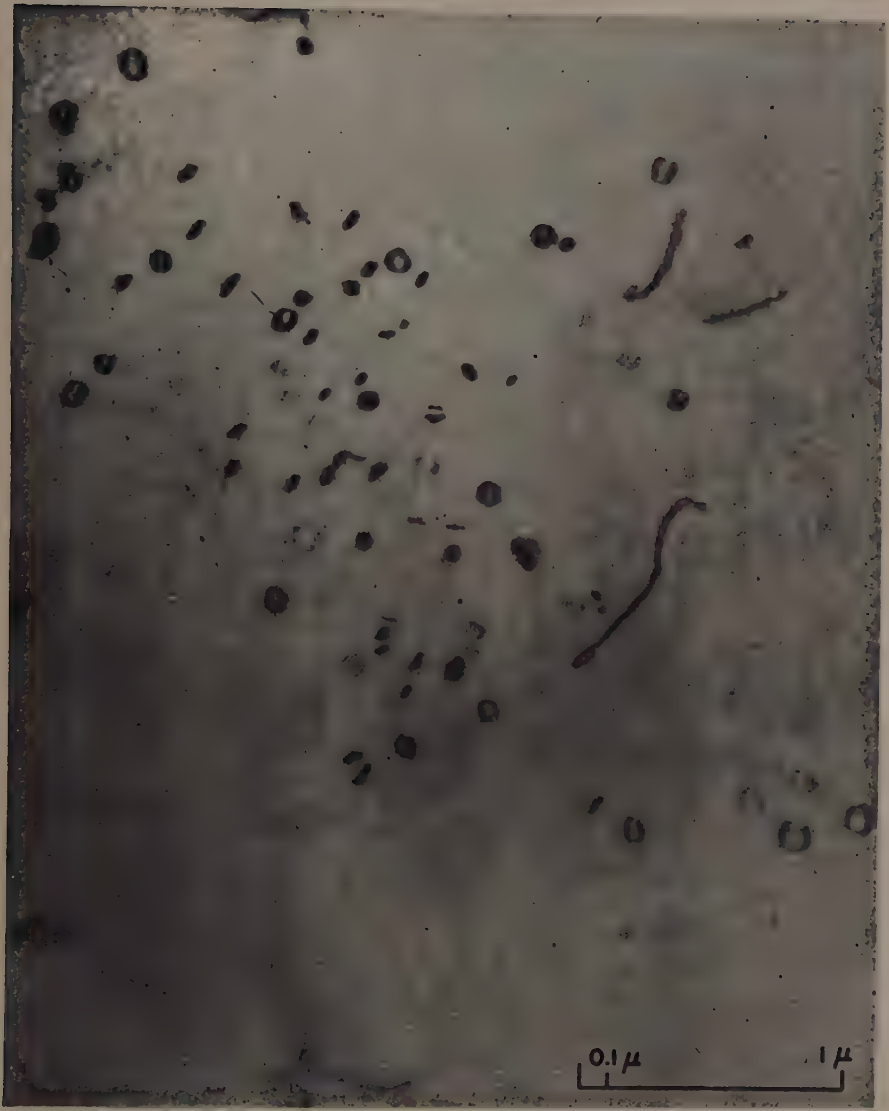

Annealed 10 min at 125°c after quenching.

R. VANDERVOORT and J. WASHBURN   Phil. Mag. Ser. 8, Vol. 5, Pl. 10.

Fig. 7

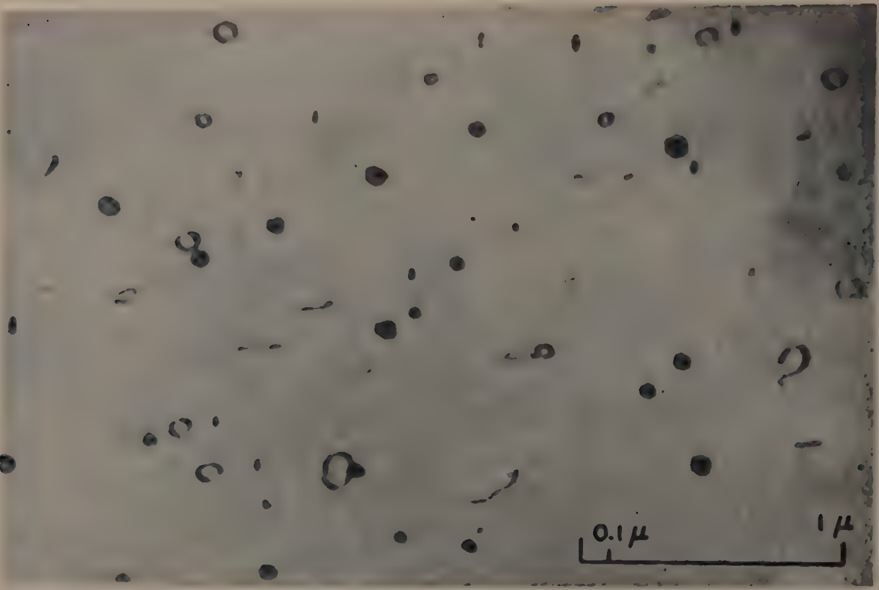

Annealed 10 min at 150°c after quenching.

Fig. 8

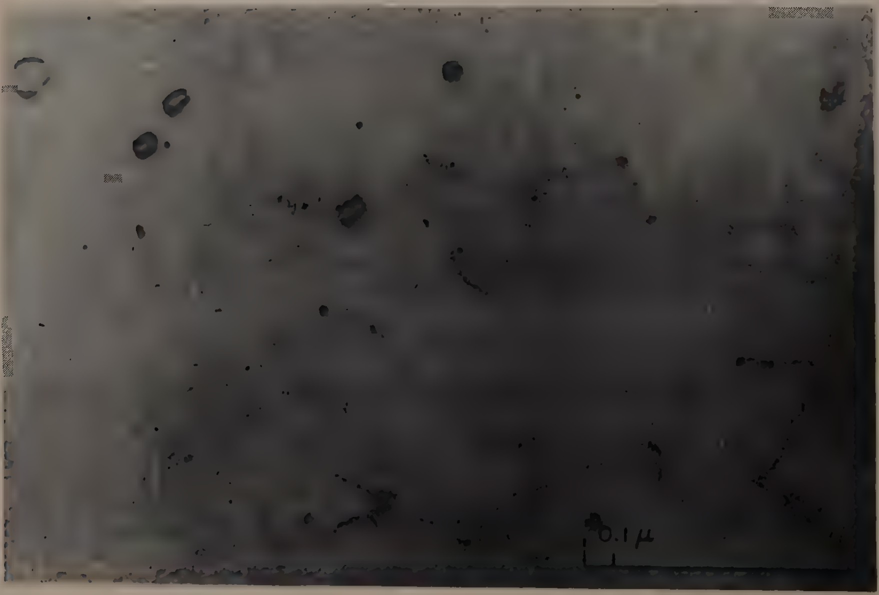

Annealed 10 min at 175°c after quenching.

Fig. 9

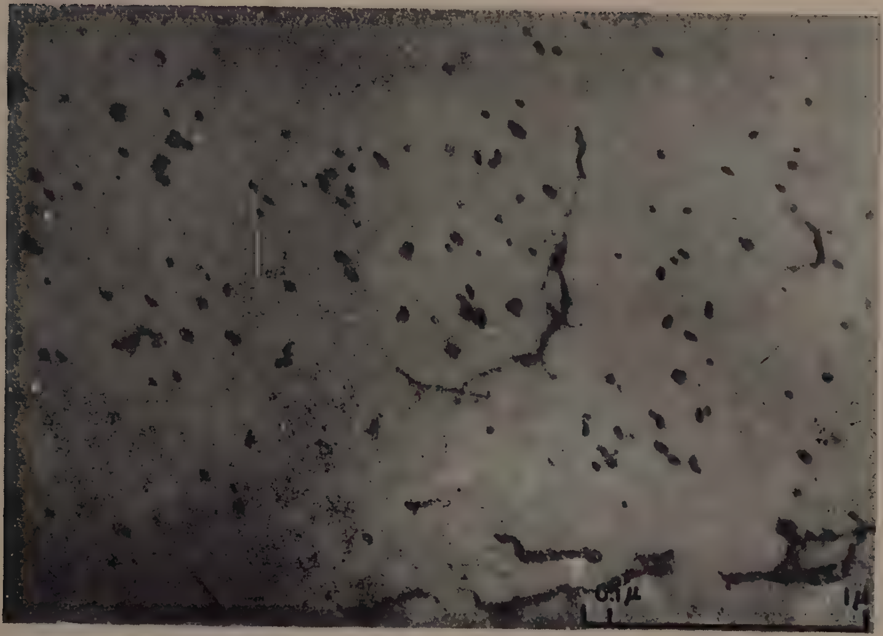

Extended $2\frac{1}{2}\%$ in tension after quenching.

Fig. 10

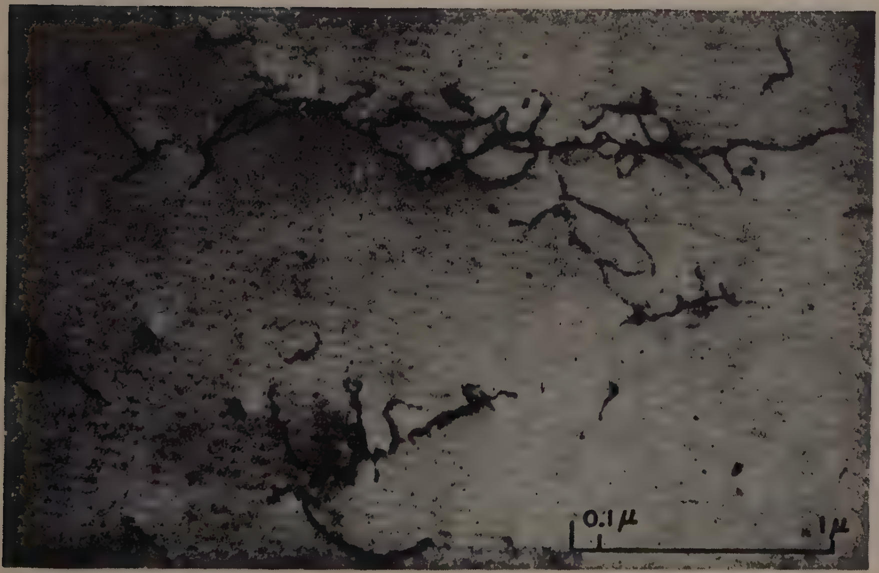

Cold rolled 5% after quenching.

Fig. 11

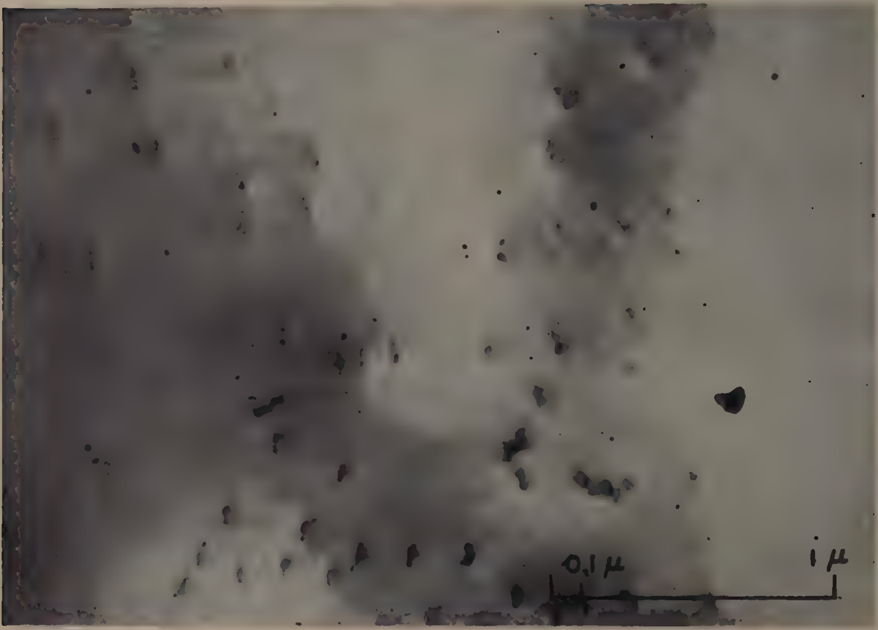

Cold rolled 5% after quenching.

Fig. 12

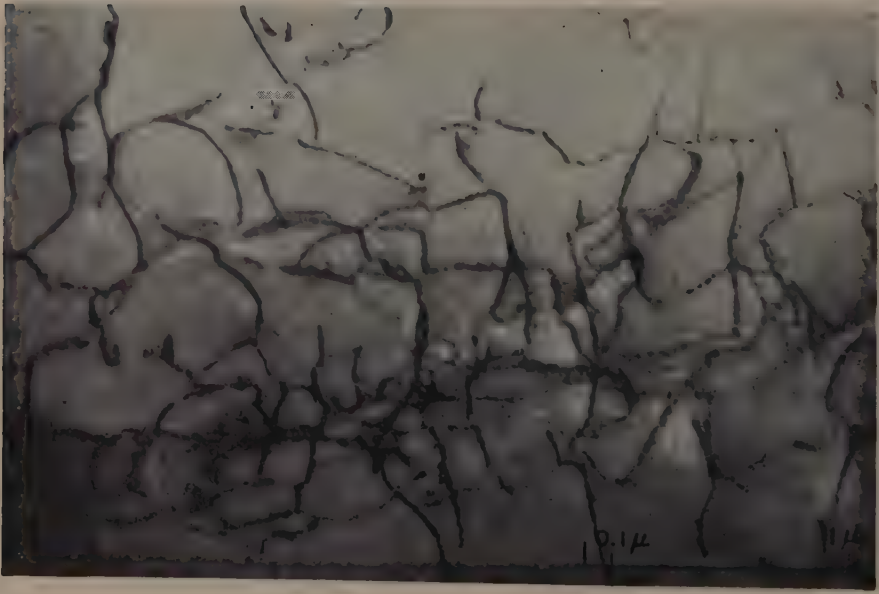

Cold rolled 15% after quenching.

Fig. 13

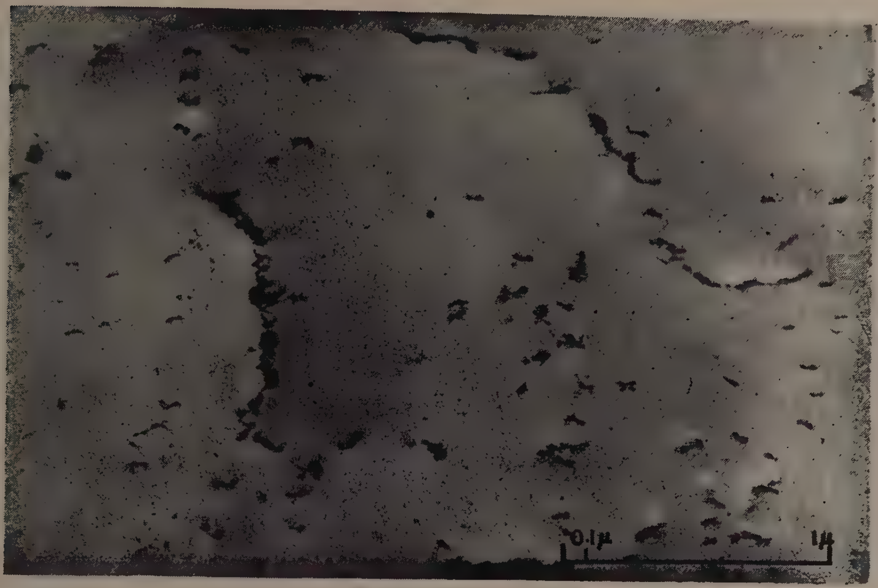

Cold rolled 15% after quenching.

Fig. 14

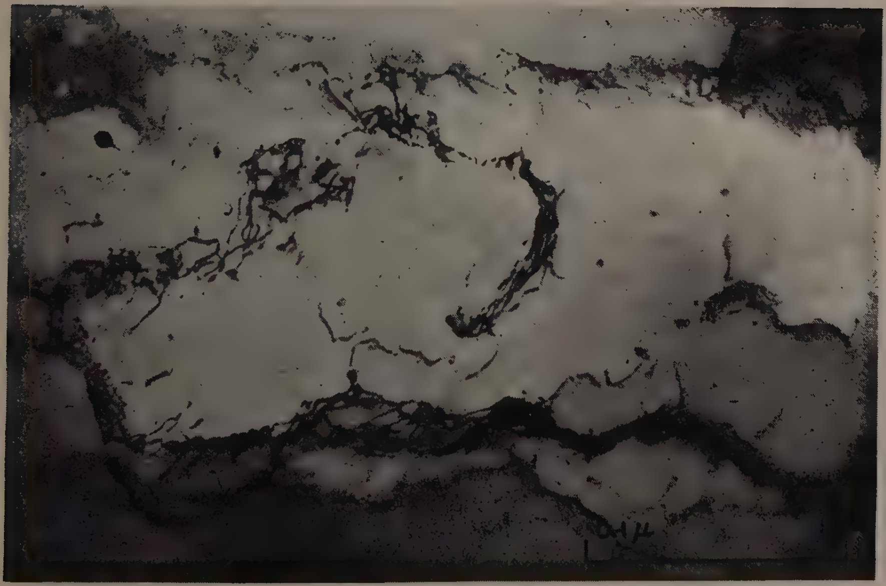

Cold rolled 45% after quenching.

Fig. 15

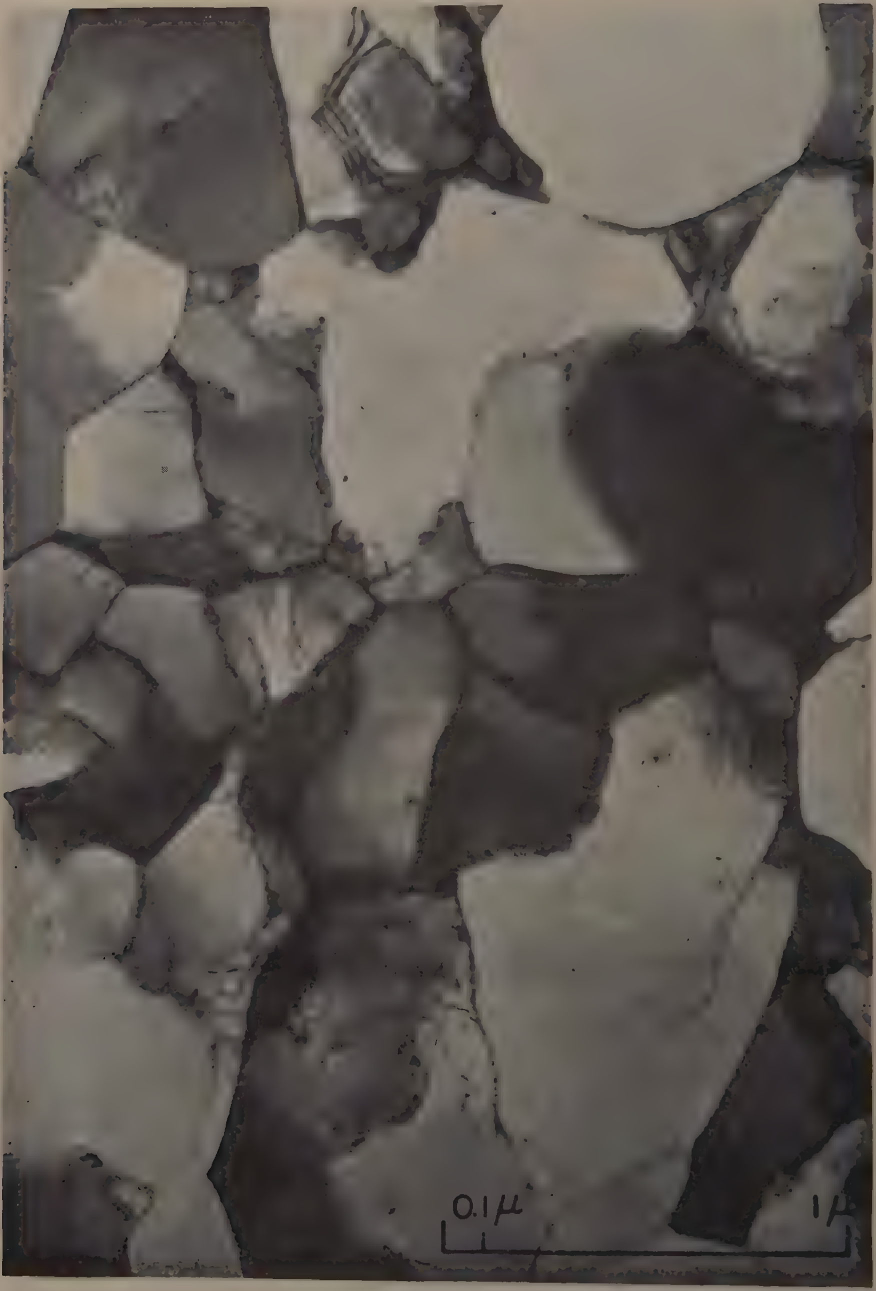

Cold rolled 98% after quenching.

Fig. 1

Natural rubber film. Very little structure is visible.

Fig. 2

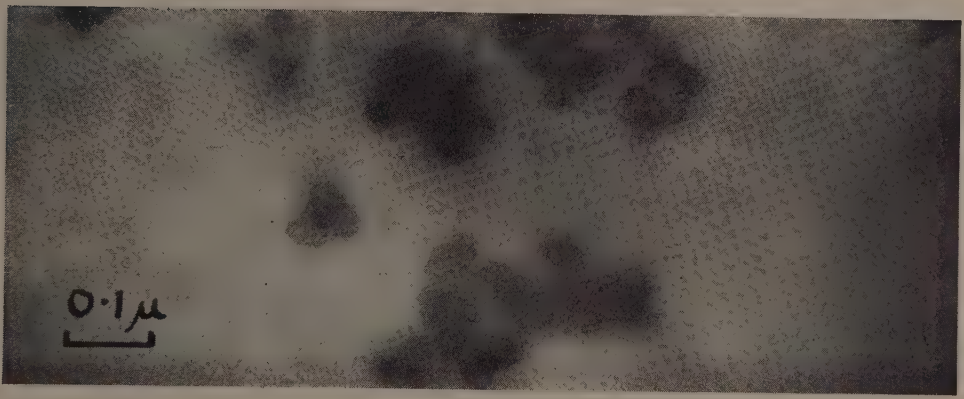

Film of natural rubber with 10% of carbon black (' MPC black ') filler.

Fig. 3

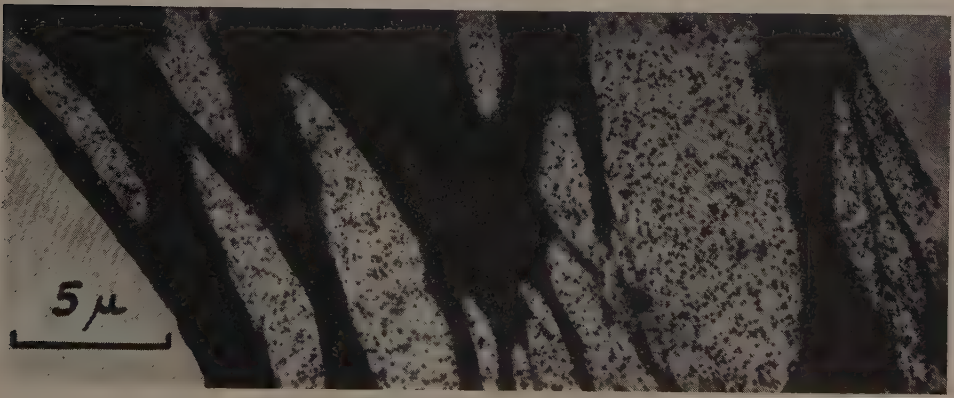

Film of natural rubber with 2% of carbon black (' MPC black ') filler, after being stretched. Numerous thin patches have developed in the film.

Fig. 4

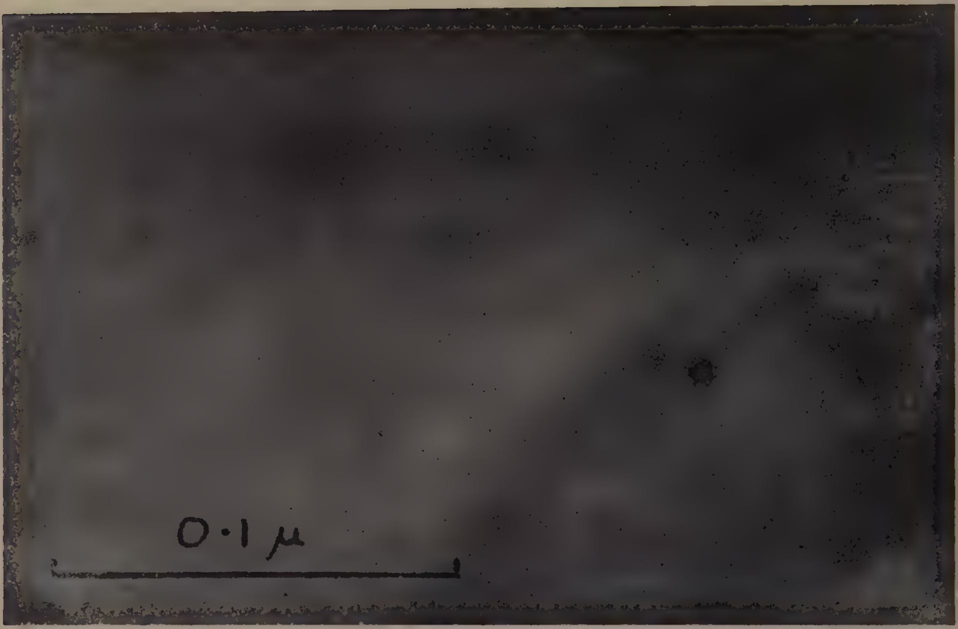

Film of natural rubber containing about 5% neoprene. The dark patches probably represent areas of neoprene, the smaller ones corresponding to individual molecules.

Fig. 5

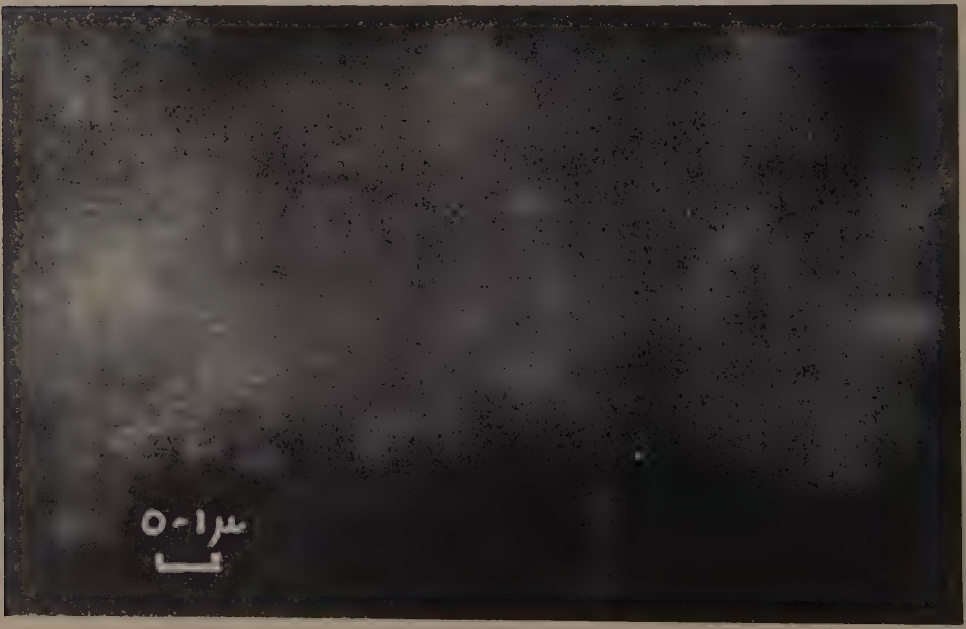

Film of neoprene containing about 5% natural rubber. This shows the expected appearance of light patches on a dark background.

Fig. 6

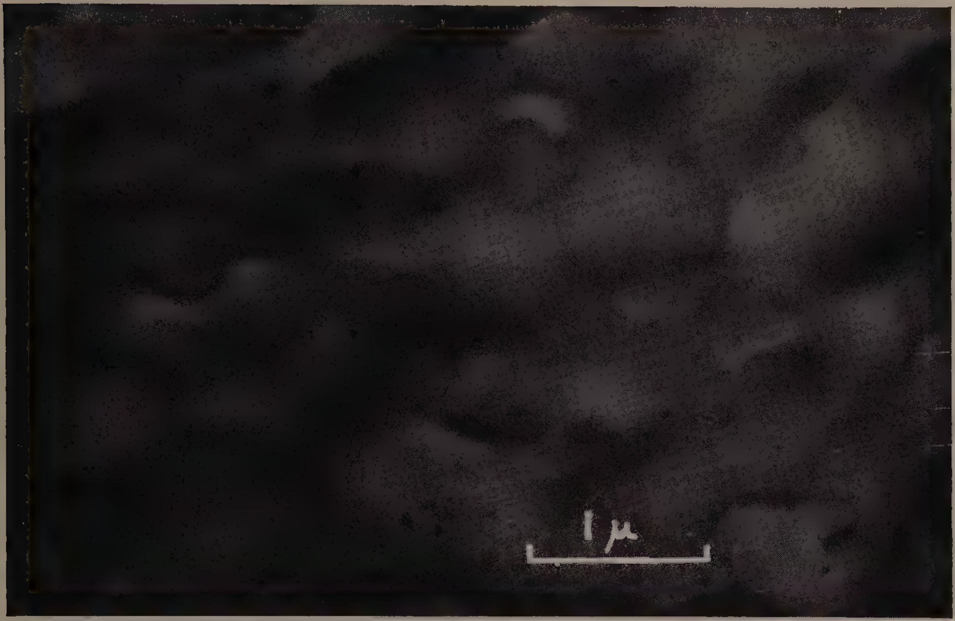

Film of 50% natural rubber, 50% Alloprene. The two polymers have not mixed and the film is inhomogeneous.

Fig. 7

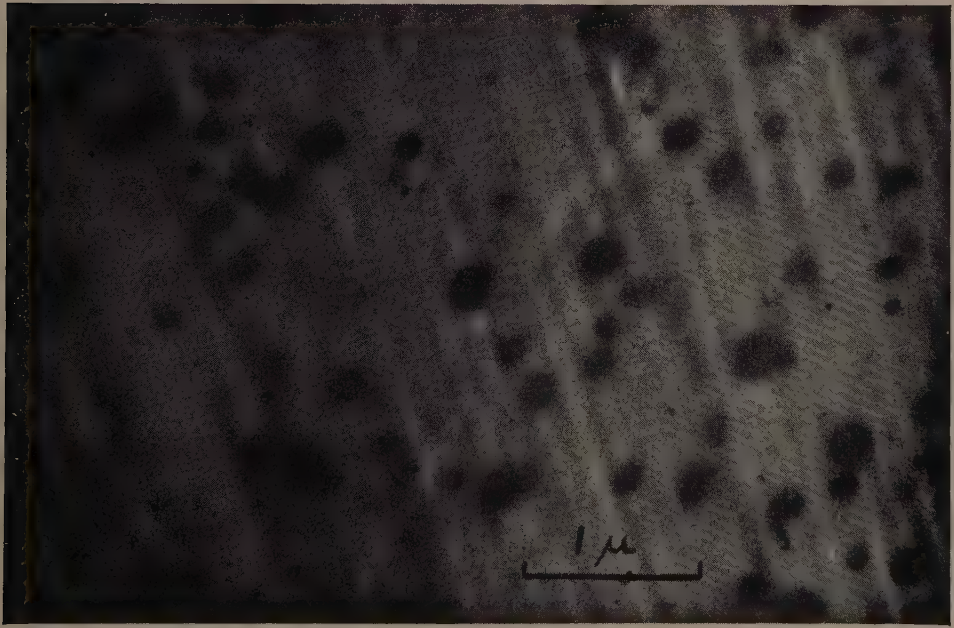

Film of 80% natural rubber, 20% Alloprene. The dark patches are thought to represent globules of Alloprene.

Fig. 8

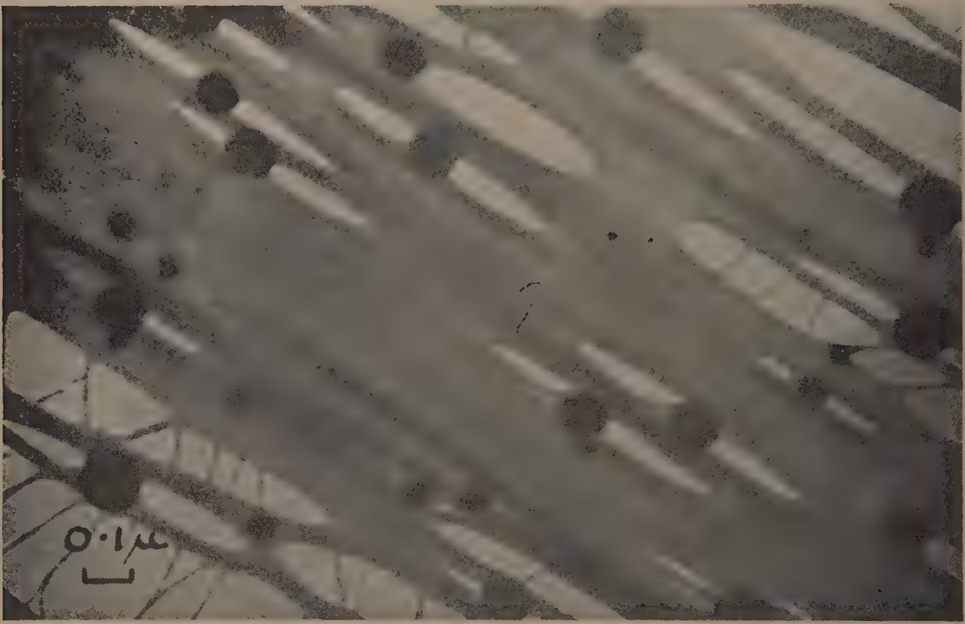

Film of 90% natural rubber, 10% Alloprene, after being stretched. The film has torn at the dark patches and this suggests that the adhesion between the two polymers was weak.

Fig. 9

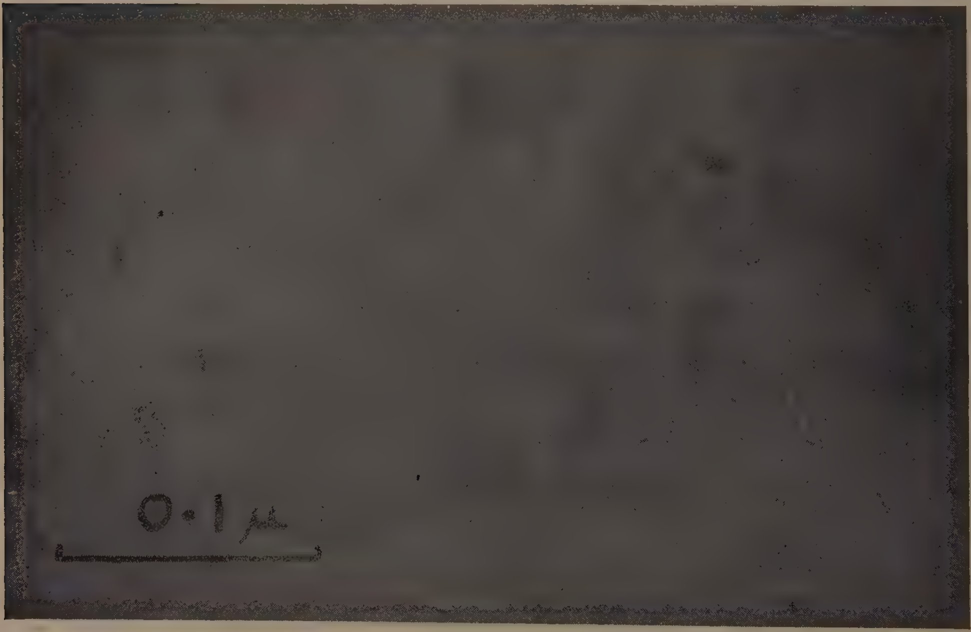

Film of 95% natural rubber, 5% Alloprene. Small dark patches—probably due to individual molecules of the Alloprene—are visible.

The de Haas–van Alphen Effect in Copper, Silver and Gold†

By D. Shoenberg
Royal Society Mond Laboratory, Cambridge

[Received January 5, 1960]

Abstract

Measurements of the de Haas–van Alphen effect in copper, silver and gold suggest strongly that the Fermi surfaces of these metals make contact with the hexagonal faces of the Brillouin zone. The areas of cross section of the main part of the Fermi surface and of the contact have been determined. Some provisional values of effective masses have also been obtained.

When the de Haas–van Alphen effect in copper was discovered a year ago by the impulsive field technique (Shoenberg 1959), the hope was expressed that this would open the way to a detailed study of the electronic structure of the monovalent metals. As far as copper, silver and gold are concerned this hope was been amply fulfilled and there is now little doubt that supplemented by guidance from studies by other methods, the de Haas–van Alphen effect will yield very detailed information about the Fermi surfaces of these metals. Since, however, it is clear that further progress will require certain improvements of experimental technique followed by systematic measurements which will inevitably take some time, it seems worth while giving a brief survey of the results obtained to date, even though many details are still incomplete.

The results strongly suggest that the Fermi surfaces for copper, silver and gold make contact with the eight [111] faces of the Brillouin zone (B.Z.). Thus the de Haas–van Alphen effect demonstrates that the general shape of Fermi surface proposed by Pippard (1957) for copper applies also to silver and gold. Except when the small departures from sphericity are of importance a convenient simplified model of this surface is a sphere (the 'belly') with eight short cylinders ('necks') protruding from it along the [111] directions to meet the hexagon faces of the B.Z. normally. The B.Z. can of course be thought of as the unit cell of an infinite lattice in which each cell contains a Fermi surface of the kind just described. We thus have a complicated multiply-connected surface and corresponding to any closed circuit of extremal area (which encloses either holes or electrons) produced by planes cutting the surface normally to the magnetic field direction, there should be de Haas–van Alphen oscillations of a period inversely proportional to the extremal area. It turns out that there is quite a variety of possible extremal circuits and the corresponding de Haas–van Alphen oscillations for some of these have been observed.

---

† Communicated by the Author.

The predominant period observed in most directions is that due to the belly and this period gives an area of cross section within a few per cent of that of the diametral section of a free electron sphere. Thus the belly periods vary between copper, silver and gold almost exactly as the two-thirds power of the atomic volumes, with a constant of proportionality appropriate to the assumption of one free electron per atom. In principle the multiple connectivity of the Fermi surface could be demonstrated by the absence of the belly period over certain restricted ranges of field directions for which no extremal closed circuit round the belly can exist. In fact some such ranges of field directions have been observed, and these are consistent with the hypothesis of multiple connectivity. However, no thorough study of these ' absent ' ranges has yet been made and in any case lack of observed oscillations is not in itself conclusive evidence, because amplitude may become small for a variety of reasons; more direct evidence for multiple connectivity is presented below.

The variation of the belly period with field direction is slight, because the area of cross section is evidently rather insensitive to even quite appreciable departures from sphericity. In order to study this slight variation of period two methods have been used which are rather more precise than the direct and absolute method of measuring the change of 1/H for a given number of periods. These are (*a*) measurement of the separation of the two resonant peaks which occur when the oscillations are amplified by a resonant circuit; because of the parabolic time variation of the field close to the maximum field this separation is directly proportional to the period and provides a rapid comparison method with a relative accuracy of order 1% in favourable conditions, (*b*) measurements of beats between the oscillations of two specimens of different orientations; in favourable conditions differences of period of 3% can be measured with an accuracy of 2 or 3% giving a relative accuracy of 0·1% or better. A summary of the results on belly periods is given in table 1; the most detailed results have been obtained for copper; those for silver and gold are based on far fewer experiments and should be regarded as somewhat provisional. The difference between the periods in [111] and [100], which has been determined rather precisely for copper, appears to be at variance with the prediction of Pippard's detailed model. The absolute values are also discrepant, but since absolute measurements of period are subject to many small corrections, it is not out of the question that some source of systematic error has been overlooked, which might yet change the absolute values by more than the errors suggested in table 1. The source of the discrepancy in the relative values is not yet clear, but it suggests that the detailed form of the departure from sphericity proposed by Pippard may not be unique in accounting for his anomalous skin effect data.

The general topological features of the Pippard model first received confirmation in a study of a gold crystal, which showed a long period, about 31 times that of the belly period, in a range of field directions around [111]. An obvious interpretation is to associate this long period with a cut through the neck in the [111] direction. The geometry of the B.Z. is such that the length of the neck between free electron spheres has to be 0·107 of the sphere diameter; the period shows that the central diameter of the neck for gold is 0·18 that of the sphere. The variation of the neck period with field direction away from [111] suggests (as is very reasonable) that the neck is really more like a hyperboloid of revolution than a cylinder, and a closer study of this variation should provide a detailed picture of the shape of the neck. Following the discovery of the neck period in gold it was looked for more carefully in copper and was eventually shown up in collaboration with Mr. M. G. Priestley who has designed a new magnetic field coil to give $1{\cdot}6 \times 10^5$ gauss rather than the $1{\cdot}2 \times 10^5$ gauss available in the standard equipment. The higher field revealed long period oscillations in a [111] copper whisker of period about 24 times that of the belly period (i.e. neck diameter 0·20 that of the sphere); the amplitude was feeble and no study of the variation of this period with orientation has yet been attempted. Probably the feebleness of these neck oscillations in copper even in the higher field is associated with the fact that the effective mass of the electrons is higher in copper than in gold (see table 3). The neck diameter in copper is rather larger than that suggested by Pippard (0·16 of sphere diameter) but agrees better with the estimate of Gavenda and Morse (1959) (0·195 of sphere diameter) based on magneto-acoustic resonance. Subsequently the neck period was found also close to the [111] direction in a silver

Table 1. Belly Periods (all in units of 10^{-9} G^{-1})

	P_{111}	P_{100}	p_{111}	p_{100}	p_{F}
Cu	1·608 (1·681)	1·557 (1·698)	± 1·00 (−0·46)	± 0·26 (−0·32)	1·637
Ag	2·00	1·96			2·09
Au	2·05	1·95			2·09

Notes.—p stands for $(1/P)(d^2P/d\theta^2)$ where θ is a small angle away from a symmetry direction; the sign of the experimental values of p has not been determined and the values are probably accurate to 20%; P_{F} is the free electron sphere value. The figures in brackets are estimates based on Pippard's model. The experimental values of P, both absolute and relative, have been more carefully determined for Cu than for Ag and Au; the absolute values for Cu should be within 2 or 3% of the true values, while those for Ag and Au may be somewhat more in error.

crystal; the period was about 51 times that of the belly period, corresponding to a neck diameter of about 0·14 that of the sphere. No study of the variation of this period with orientation has yet been made.

Further confirmation of the topology came from a gold crystal in which the field was close to a [110] direction, when weak but quite definite oscillations were observed with a period about 2·4 times the belly period, though the belly period did not itself occur. For this orientation there can be no extremal closed circuit around the belly with the model under discussion, but if we follow a path round four adjoining cells by way of the necks, there is evidently an extremal closed circuit with a shape rather like a dog's bone. Its area on the simplified assumption of exact cylinders linking exact spheres is just 0·42 or 1/2·4 that of the diametral section of the sphere, which gives very satisfactory quantitative confirmation. This 'dog's bone' period has been looked for in copper but not yet found, perhaps because of the higher effective mass or of inadequate specimen perfection. No dog's bone period has yet been found in silver either, though it is re-assuring that the belly period in both copper and silver is absent in a range of directions round [110] where no extremal closed circuits round the belly should be possible.

Table 2. Miscellaneous Periods (all in units of 10^{-9} G^{-1})

	Neck [111]	Dog's bone [110]	4-cornered Rosette [100]
Cu	38	—	3·8 (4·1)
Ag	101	—	4·8 (4·9)
Au	62	4·7 (4·7)	—

NOTES.—The neck periods were measured absolutely; the others were found by comparison with belly periods using the resonant peak method. The accuracy of the period values is probably of order 3%: the figures in brackets are estimates based on the sphere and cylinders model assuming the diametral area of the sphere to be given by the mean of P_{111} and P_{100} as given in table 1. In Au the variation of the neck period has been studied as H moves away from [111] in a [110] plane; it falls to about 55 at about 13° from [111] (towards [100]) and the oscillations then vanish. A period of about $\frac{1}{2}$ P_{111} has been observed at about 9° from [111] (towards [100]); this period occurs just beyond the angle at which main belly oscillations disappear.

The discovery of the 'neck' and the 'dog's bone' stimulated thinking about other possible types of closed circuit and two have in fact shown up. In the [100] direction in both copper and silver a period about 2·4 times the belly period was observed which can probably be associated with a closed circuit alternately above and below a diametral plane and passing around four necks through four adjacent cells; this has not yet been looked for in gold. Also, in gold, in a direction about 9° off [111] towards [100], where the belly period disappears rather abruptly, a period almost exactly half that of the belly shows up in a narrow angular range. This can be interpreted as a circuit running through two adjacent cells through the joining neck and just missing the opposite necks on either side. Similar oscillations of $\frac{1}{3}$, $\frac{1}{4}$, etc., of the belly period should in principle also show up but they have not yet been carefully looked for. A summary of all the periods observed so far which support the hypothesis of multiple connectivity is given in table 2.

Some results have also been obtained on the effective electron masses deduced from the temperature variation of the amplitude of the de Haas–van Alphen oscillations, and these are shown in table 3. The results for copper agree reasonably with the cyclotron resonance data, though there are some experimental features which are not yet fully understood ; the results for silver and gold are based on only rough experiments and have no great accuracy. Studies of the variation of amplitude with field, which in principle could give information about relaxation times, have not proved possible because the field variation is considerably modified by slight specimen imperfections (e.g. mosaic structure and bending) which cause complicated interference effects.

Table 3. Effective Masses (in terms of the free electron mass)

	[111] belly	[111] neck	[100] belly	[110] dog's bone
Cu	1·30 (1·30)		1·38 (1·32)	
Ag			0·71	
Au	0·9	0·9	—	1·1

NOTES.—The values in brackets are the cyclotron resonance data of Langenberg and Moore (1959). In Cu, where the most thorough observations have been made, a complication arose in that the variation of log A/T against T for [111] was found to fall into two linear portions of different slope (A is the amplitude); the value 1·30 corresponds to the low temperature portion; above about 1·8°K a value of 1·63 was obtained and it is possible that this is due to eddy current heating effects which falsify the temperatures. The other values were obtained from a more limited range of temperatures (but below 2°K) and the complication was not observed. The values for Au, especially for [110], are very rough and are included only to give some idea of the magnitudes.

No attempt will be made here to discuss the theoretical implications of the results or to relate them to the results of experiments of other kinds. It should however be mentioned that the idea of contact between the Fermi surface and the B.Z. in copper has been suggested not only by the anomalous skin effect results (Pippard 1957) but also by recent results on cyclotron resonance (Langenberg and Moore 1959) and magneto-acoustic resonance (Gavenda and Morse 1959) while contact for all three metals has been suggested on the basis of magneto-resistance data (Alekseevski and Gaidukov 1959, Gaidukov 1959).

ACKNOWLEDGMENTS

In conclusion it is a pleasure to acknowledge the help and advice I have received from many people ; Mr. H. L. Davies constructed most of the equipment, prepared all the silver and gold crystals and assisted in the experiments and I should like to thank him warmly for his willing and patient collaboration. The whole research was started off by the use of copper whiskers and I am very grateful to the General Electric of Schenectady, N.Y., and in particular to Mrs. E. Fontanella, for their generosity in preparing and supplying all the whiskers used in these experiments. I have also benefited greatly from many discussions with Dr. A. B. Pippard, Dr. V. Heine, Mr. M. G. Priestley and Mr. V. M. Morton and I should like to thank them for many valuable suggestions both theoretical and practical. Finally I should like to thank Mr. H. V. Beck, Dr. J. Ashmead, Dr. C. J. Adkins and Mr. F. T. Sadler for help with design and construction of particular items of the measuring equipment.

Note added in proof.—Since this paper was written the dog's bone oscillations have been found along [110] in silver; as in gold, the period was about 2·4 times the belly period.

REFERENCES

ALEKSEEVSKI, N. E., and GAIDUKOV, YU. P., 1959, *J. exp. theor. Phys.*, **37,** 672.
GAIDUKOV, YU. P., 1959, *J. exp. theor. Phys.*, **37,** 1281.
GAVENDA, J. D., and MORSE, R. W., 1959, *Bull. Amer. phys. Soc.*, **4,** 463.
LANGENBERG, D. N., and MOORE, T. W., 1959, *Phys. Rev. Letters*, **3,** 328.
PIPPARD, A. B., 1957, *Phil. Trans. roy. Soc.* A, **250,** 325.
SHOENBERG, D., 1959, *Nature, Lond.*, **183,** 171.

Magnetoresistance of Copper, Silver and Gold†

By M. G. Priestley
Royal Society Mond Laboratory, Cambridge

[Received January 18, 1960]

Abstract

It is shown that the magnetoresistance measurements of Alekseevskii and Gaidukov on single crystals of copper, silver and gold are consistent with the Fermi surfaces of these metals proposed on the basis of anomalous skin effect and de Haas–van Alphen effect measurements.

The present note discusses the extent to which the magnetoresistance results obtained by Alekseevskii and Gaidukov (1959) and Gaidukov (1959) for copper, silver and gold single crystals are consistent with the Fermi surfaces for these metals proposed as a result of anomalous skin effect and de Haas–van Alphen effect measurements (Pippard 1957, Shoenberg 1960). Each metal has a multiply-connected Fermi surface, which may be thought of roughly as a body-centred lattice of spheres which are extended so as to make contact with each other through 'necks' along the [111] directions. Shoenberg's de Haas–van Alphen experiments show that for silver, gold and copper respectively the areas of contact are 2·1, 3·2 and 4·3% of the relevant free electron sphere extremal area. The discussion will be limited mainly to gold since sufficiently detailed experimental results have been published only for this metal (Gaidukov 1959); such results as are available for silver and copper show the same qualitative features.

The figure shows a stereographic plot of Gaidukov's gold results as a function of magnetic field (H) direction. The essential feature of these results is that the transverse magnetoresistance increases approximately as H^2 over the shaded regions (marked I) and along the lines shown (which are [111] and [110] zones), but saturates over the rest of the stereogram (marked II).

We shall now show that these results can be explained in detail on the basis of the Fermi surface described above by using the theory of Lifshitz and Peschanskii (1958). According to this theory non-saturation is characteristic of the existence of open orbits, which can be of two types.

(1) Those whose axis is a line which can be drawn inside the Fermi surface and which does not intersect it in the extended zone scheme.

---

† Communicated by the Author.

These give rise to a one-dimensional set of field directions. (This type has also been considered by Ziman (1958).)

(2) Those which mark the boundary between hole and electron orbits when a plane is drawn through the extended zone scheme perpendicular to the direction of the magnetic field. These occur over a two-dimensional range of field directions.

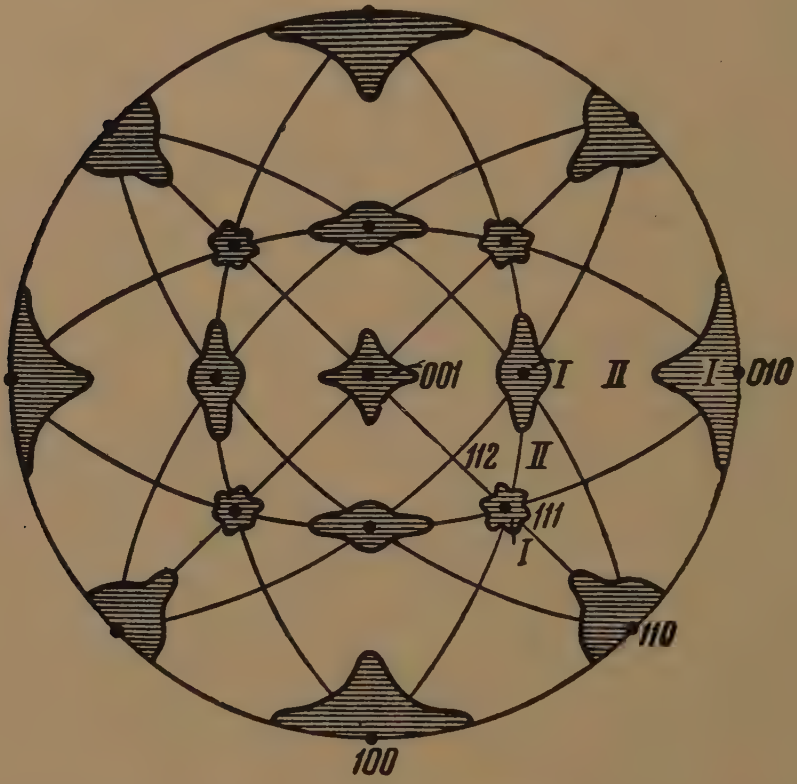

The lines of the stereogram are associated with type (1) open orbits, and the shaded regions with type (2). Since type (2) open orbits mark the boundary between hole orbits and electron orbits, and electron orbits exist for any field direction†, the regions over which the hole orbits and the open orbits exist are identical. Thus the shaded regions should be identical with the regions over which de Haas–van Alphen periods from holes are observed. The boundaries of this region also represent the singular points in the effective mass data from cyclotron resonance experiments‡. As yet such singular points have been observed only in copper (Langenberg and Moore 1959).

---

† This statement is true in the present case, but would not be true if the necks were too large.

‡ I am indebted to Dr. J. C. Phillips for this observation.

The question of the size and shape of the shaded regions thus reduces to the calculation of the regions over which the hole orbits exist. Since the points at the centre of the necks form a simple cubic lattice and a hole orbit must enter and leave each Brillouin zone via a neck, the central directions for the hole orbits are limited to those zone axes with no index greater than 1, i.e. [100], [110] and [111]. The first two of these have been observed in the de Haas–van Alphen effect (Shoenberg 1960); the [100] 'four cornered rosette' type of orbit in copper and silver, and the [110] 'dog's bone' type in gold. The [111] type of orbit is a large 'rosette' which passes through six necks. Further work may be expected to show up all three types of orbit in each metal.

The angular ranges over which these hole orbits exist can easily be calculated on the assumption that the plane of the limiting hole orbit touches the Fermi surface neck at a negligible distance from the zone boundary. Pippard's proposed surface for copper (1957) suggests that this is a reasonable approximation. The area of the neck is taken from the de Haas–van Alphen results and the contact is assumed to be circular. The results of the calculation are compared with the magnetoresistance data and other available evidence in the table and it can be seen that the agreement is quite satisfactory, bearing in mind the possible errors of the data and the somewhat crude approximation of the calculation. It is likely that much more detailed information on the shape of the neck will soon be available from the de Haas–van Alphen effect, thus providing a basis for a more exact calculation. It can easily be seen that the approximation made above leads to exaggerated estimates of the sizes of the [100] and [111] regions but has little effect on the [110] region. Any departure from the assumption of a circular contact with the (111) zone face would increase the sizes of all the regions.

One other feature of the experimental results calls for comment. Gaidukov states that measurements with H in a (100) plane showed saturation and concludes that this is because there is no open direction along [100], but a detailed examination of his results enables an alternative explanation to be put forward. Only two of his specimens, Au–1 and Au–6, provide evidence on this point since for the others the field directions do not intersect the [100] zone outside the shaded regions. Au–6 is recorded in his table 2 as showing a maximum in the magnetoresistance when the field lies in the [010] zone, and this appears to contradict his statement. Au–1 is recorded as showing saturation, but according to the theory,

$$\Delta\rho_H/\rho_0 \propto H^2 \cos^2\alpha$$

where α is the angle between the current and the axis of the open orbit. Now for Au–1, $\alpha = 84°$, i.e. $\cos^2\alpha \sim 10^{-2}$ and this would probably be sufficiently small to mask any maximum which might be expected. Thus Gaidukov's results provide no clear indication as to whether gold has an open direction along [100]. It should perhaps be pointed out that

Pippard's copper Fermi surface (1957) does have an open direction along [100]. Further magnetoresistance experiments with specimens of suitably chosen orientation should clear up this point.

Region	Measured in plane	' Radius ' of region in degrees		
		Gaidukov's gold data		Calculated
		Text	Stereogram	
[100]	(100)	13	15	12·9
	(110)	7·5	9	9·2
[110]	(110)	13	15	15·7
	(100)	7·5	8	11·2
[111]	(110)	6	6	5·3
	(211)	5	5	4·6

Notes.

There are some discrepancies between the experimental results as quoted in the text of Gaidukov's paper and those shown in the detailed stereogram (Gaidukov's fig. 5) and therefore both sets are quoted here.

To obtain the corresponding angles for silver and copper the tangents of the angles in the ' calculated ' column should be multiplied by 0·80 and 1·17 respectively.

The few results for silver and copper which are published in Alekseevskii and Gaidukov (1959) show similar qualitative behaviour but it is difficult to estimate the sizes of the angular regions from their diagrams.

The [110] de Haas–van Alphen hole period in gold has been observed up to about 10° from [110] in a plane whose axis is 29° from [100] in a (110) plane; beyond this angle the period disappears abruptly (Shoenberg, private communication). The calculated angle at which the orbit should disappear in this plane is 9·2°.

Langenberg and Moore observed an effective mass singularity in copper at 18° ± 1° from [110] in a (110) plane. The calculated value is 18·2°.

ACKNOWLEDGMENTS

I should like to thank Dr. D. Shoenberg for drawing attention to the problem and for discussion of his experimental results and also Dr. A. B. Pippard for a very helpful discussion which clarified several obscure points.

REFERENCES

ALEKSEEVSKII, N. E., and GAIDUKOV, YU. P., 1959, *Zh. eksper. i. teor. fiz.*, **37**, 672.
GAIDUKOV, YU, P., 1959, *Zh. eksper. i teor. fiz.*, **37**, 1281.
LANGENBERG, D. N., and MOORE, T. W., 1959, *Phys. Rev. Letters*, **3**, 328.
LIFSHITZ, I. M., and PESCHANSKII, V. G., 1958, *Zh. eksper. i teor. fiz.*, **35**, 1251.
PIPPARD, A. B., 1957, *Phil. Trans.* A, **250**, 325.
SHOENBERG, D., 1960, *Phil. Mag.*, **5**, 105.
ZIMAN, J. M., 1958, *Phil. Mag.*, **3**, 1117.

The *g*-factor and de Haas–van Alphen Effect of Electrons in Bismuth†

By M. H. COHEN‡
Cavendish Laboratory, Cambridge

and E. I. BLOUNT
Westinghouse Research Laboratories, Pittsburgh, Pennsylvania

[Received in revised form June 25, 1959]

ABSTRACT

A theory of the *g*-factor of conduction electrons is developed which is valid for low symmetry and arbitrary strength of spin–orbit coupling. Application to bismuth shows that $m_s \equiv 2/g \simeq m_0$ for most orientations, where m_0 is the effective mass entering the cyclotron frequency. Thus g is 260 when $\mathbf{H}$ is in the direction of smallest m_0. Further, the lifting of the spin degeneracy by the magnetic field introduces a factor $\cos r\pi m_0/m_s$ into the rth oscillatory term in the susceptibility. This explains the apparent phase shift of $r\pi$ observed in the de Haas–van Alphen oscillations of Bi.

§ 1. INTRODUCTION

THE *g*-factor of conduction electrons can differ from the free electron value of 2·0023 because of spin–orbit coupling (Yafet 1952, 1957). Furthermore, the theoretical treatment of Luttinger (1956) demonstrates clearly that the *g*-factor can greatly exceed 2 when there is a 3-fold orbital degeneracy or when the spin–orbit coupling becomes large compared to the pertinent band gaps. Roth *et al.* (1958) have calculated and measured a value of 50 for the *g*-factor of electrons in InSb, for which the pertinent band gap is 0·23 ev (Roberts and Quarrington 1955) and the spin–orbit splitting is 0·9 ev (Kane 1957). With a gap of perhaps a few hundredths of an electron volt and an atomic spin–orbit splitting of 1·86 ev (Condon and Shortley 1935, p. 179), electrons in bismuth should have an even larger *g*-factor. However, the results of Luttinger (1956) and their application to InSb by Roth *et al.* (1958) are not suited to Bi because of the low symmetry of the conduction-electron wave functions in that substance. Further, Yafet's (1957) treatment of *g*-values pertains too directly to spin-resonance in metals for our present purposes. Accordingly the necessary theory of the magnetic-moment operator and the *g*-factor are developed in § 2 of this paper. In § 3 it is shown that for conduction electrons of low symmetry, the splittings of the orbital and spin levels by a magnetic field are practically equal when the band gap is very small. In bismuth, however, the conduction-electron wave numbers lie on reflection planes or 2-fold axes in k-space so that the splittings of orbital and spin levels are equal for most orientations of magnetic field but not all (§ 4). The maximum value of the g-factor is shown to be 260 for electrons in bismuth.

---

† Communicated by the Authors.

‡ Guggenheim Fellow 1957–1958, on leave from the Institute for the Study of Metals, University of Chicago.

Such large g-factors as are found in InSb and Bi imply that the electron spin can play a significant role in the de Haas–van Alphen effect (Shoenberg 1952, 1957). Electron spin was first introduced into the theory of the de Haas–van Alphen effect Akhieser (1939) for free electrons. He found that the oscillatory term in the susceptibility corresponding to the $(r-1)$th harmonic ($r=1$ for fundamental) obtained without spin is multiplied by

$$\cos r\pi=(-1)^r \quad . \quad . \quad . \quad . \quad . \quad . \quad . \quad (1)$$

when the lifting of the spin degeneracy by the magnetic field is taken into account. Dingle (1952) and Sondheimer and Wilson (1951) have proved that when the orbital effective mass m_0 of electrons in the crystal differs from the free electron mass m, (1) must be replaced by

$$\cos r\pi m_0/m. \quad . \quad . \quad . \quad . \quad . \quad . \quad . \quad . \quad (2)$$

The work of Lifshitz and Kosevitch (1955) shows that expression (2) holds for an arbitrarily shaped Fermi surface provided that an appropriate redefinition of m_0 is made. For substances like bismuth in which m_0 is much less than m, the electron spin would have little effect according to (2). However, eqn. (2) is derived on the assumption of a g-factor of 2. The generalization of (2) valid for arbitrary g-factor is given in § 3, and it is shown there that the large g-factor of electrons in Bi is responsible for the phase shifts in the de Haas–van Alphen oscillations observed by Shoenberg (1939) and by Dhillon and Shoenberg (1955).

Other implications of the large g-factor in Bi are discussed in § 6.

§ 2. THEORY OF THE g-FACTOR

2.1. *The Magnetic-moment Operator*

We employ a simple one-electron Hamiltonian (Foldy and Wouthuysen 1950) similar to that used by Elliott (1954 a, b), Dresselhaus (1955 a, b) and others:

$$\mathscr{H}=\left(\mathbf{p}+\frac{e}{c}\mathbf{A}\right)^2\Big/2m+V+\frac{1}{8}\lambda\!\!\!^{-2}\nabla^2V+\left(\mathbf{p}+\frac{e}{c}\mathbf{A}\right).(\lambda\!\!\!^{-}/2mc)\mathbf{s}\times\nabla V. \quad (3)$$

In eqn. (3), V is the crystal potential, $\mathbf{A}=\frac{1}{2}\mathbf{H}\times\mathbf{r}$ is the vector potential for $\mathbf{H}$ a constant magnetic field, and $\lambda\!\!\!^{-}$ is the Compton wavelength over 2π. The eigenfunctions of $\mathscr{H}$ are of the Bloch form

$$\left.\begin{aligned}\mathscr{H}\psi_{\mathbf{k}n\rho}&=E_n(k)\psi_{\mathbf{k}n\rho},\\ \psi_{\mathbf{k}n\rho}&=(\Delta/(2\pi)^3)^{1/2}\exp(i\mathbf{k}.\mathbf{r})u_{\mathbf{k}n\rho}\end{aligned}\right\} \quad . \quad . \quad . \quad . \quad (4)$$

when $\mathbf{H}=0$, where $u_{\mathbf{k}n\rho}$ is a periodic two-component function normalized to unity over the volume Δ of a unit cell, and $\psi_{\mathbf{k}n\rho}$ is normalized to $\delta(\mathbf{k}-\mathbf{k}')$ over the infinite crystal. The index ρ, $\rho=1$ or 2, distinguishes the two independent eigenfunctions

$$\psi_{\mathbf{k}n1} \quad \text{and} \quad \psi_{\mathbf{k}n2} \quad (=U\psi_{\mathbf{k}n1}) \qquad (5)$$

which belong to a general wave vector $\mathbf{k}$ and energy $E_n(\mathbf{k})$ if the crystal has inversion symmetry. The operator U in (5) is

$$U=(i\sigma_y)CI, \quad U^{-1}=-U, \qquad (6)$$

where I is the inversion operator, $i\sigma_yC$ the time reversal operator, and $C\psi=\psi^*$. We work in the effective-mass approximation for conduction electrons; that is, we consider only states in the neighbourhood of the energy minimum in the conduction band (index o). By measuring $\mathbf{k}$ from the position of the minimum, confining ourselves to small $\mathbf{k}$, and setting $E_0(0)=0$, we get when $\mathbf{H}=0$

$$E_0(\mathbf{k})=\hbar^2\mathbf{k}\,.\,\boldsymbol{\alpha}\,.\,\mathbf{k}/2m. \qquad (7)$$

The components of the inverse effective-mass tensor $\boldsymbol{\alpha}$ are given by the sum rule (Dresselhaus 1955 a, b, Luttinger and Kohn 1955, Luttinger 1956)

$$\alpha_{ij}=\delta_{ij}+m\sum_{n\rho}{}' \frac{\langle o1|v_i|n\rho\rangle\langle n\rho|v_j|o1\rangle+\langle o1|v_j|n\rho\rangle\langle n\rho|v_i|o1\rangle}{(E_0-E_n)}. \qquad (8)$$

The matrix elements

$$\langle o1|\mathbf{v}|n\rho\rangle=(u_{oo1},\ \mathbf{v}u_{on\rho}) \qquad (9)$$

of the velocity operator

$$\mathbf{v}=\mathbf{p}/m+(\lambda\!\!\!^{-}/2mc)\mathbf{s}\times\nabla V. \qquad (10)$$

involve integration only over a unit cell.

The effective mass Hamiltonian becomes

$$\langle o\rho|\mathscr{H}|o\rho'\rangle=\frac{1}{2m}\left(\mathbf{p}_c+\frac{e}{c}\mathbf{A}_c\right).\boldsymbol{\alpha}.\left(\mathbf{p}_c+\frac{e}{c}\mathbf{A}_c\right)\delta_{\rho\rho'} \qquad (11)$$
$$-\langle o\rho|\boldsymbol{\mu}|o\rho'\rangle.\mathbf{H}$$

when $\mathbf{H}\neq 0$. The first term in (11) is the usual effective-mass result implying a free-electron like orbital motion from cell to cell (Luttinger and Kohn 1955). In this term, $\mathbf{p}_c=\hbar\mathbf{k}$ is the crystal-momentum operator, and $\mathbf{A}_c$ is obtained by substitution of the crystal-coordinate operator $\mathbf{x}_c=i\hbar\partial/\partial\mathbf{p}_c$ for $\mathbf{r}$ in $\mathbf{A}$ (Adams 1953 a). The second term in (11) shows that an electron carries with it an 'intrinsic' magnetic moment

$$\boldsymbol{\mu}=\boldsymbol{\mu}_l+\boldsymbol{\mu}_s \qquad (12)$$

in this free-electron like motion, partly from the spin

$$\boldsymbol{\mu}_s=-2\beta\mathbf{s} \qquad (13)$$

and partly from unquenched orbital motion

$$\langle o\rho|\boldsymbol{\mu}_l|o\rho'\rangle=-\frac{e\hbar}{2ci}\sum_{n\tau}\frac{\langle o\rho|\mathbf{v}|n\tau\rangle\times\langle n\tau|\mathbf{v}|o\rho'\rangle}{(E_0-E_n)}. \qquad (14)$$

Equation (14) is the result obtained directly from the procedures of Luttinger and Kohn (1955) as generalized by Luttinger (1956); its meaning is clearer when it is put into the form obtained directly from the procedures of Adams (1952, 1953 a, b), eqn. (18) below. The position operator $\mathbf{r}$ becomes $\mathbf{x}_c+\mathbf{X}$ in the present representation (Adams 1952, 1953 a) where

$$\begin{aligned} \langle n\rho|\mathbf{X}|n'\rho'\rangle &= (u_{\mathbf{k}n\rho}, i\partial u_{\mathbf{k}n\rho'}/\partial\mathbf{k}), \qquad (15) \\ &= \hbar\langle n\rho|\mathbf{v}|n'\rho'\rangle/i(E_n-E_{n'}), \quad n\neq n'. \qquad (16) \end{aligned}$$

We have supposed so far that

$$\langle n\rho|\mathbf{v}|n\rho'\rangle=\hbar^{-1}\partial E_n/\partial k\delta_{\rho\rho'} \qquad (17)$$

vanishes for n, $\mathbf{k}=0$. Therefore, $\langle o\rho|\boldsymbol{\mu}_l|o\rho'\rangle$ is just

$$\langle o\rho|\boldsymbol{\mu}_l|o\rho'\rangle=-\beta\langle o\rho|\mathbf{l}|o\rho'\rangle, \qquad (18)$$

where

$$\mathbf{l}=\hbar^{-1}\mathbf{X}\times m\mathbf{v} \qquad (19)$$

has the nature of an orbital angular momentum. We note that $\langle n\rho|\mathbf{X}|n'\rho'\rangle$ differs from $(u_{\mathbf{k}n\rho}, \mathbf{r}u_{\mathbf{k}n'\rho'})$ only by an integral over the surface of the unit cell (cf. Kjeldaas and Kohn 1957, Yafet, 1957) so that $\mathbf{l}$ goes over into the ordinary orbital angular momentum in the tight binding limit. Finally, we have from (12), (13) and (18)

$$\boldsymbol{\mu}=-\beta(\mathbf{l}+2\mathbf{s}). \qquad (20)$$

2.2. *The g-factor*

The 2×2 matrix with elements $\langle o\rho|\boldsymbol{\mu}|o\rho'\rangle$ can be expressed as a linear combination of the unit matrix and the three matrices

$$\mathbf{s}_i'=\tfrac{1}{2}\sigma_i, \quad i=x, y, z \qquad (21)$$

where the σ_i are the three Pauli matrices. The electron spin operator s_i does not have the form (21) in the present representation. From eqns. (5) and (6) it follows that the coefficient of the unit matrix vanishes. We have, then,

$$\langle o\cdot|\mu_i|o\cdot\rangle=-\beta\langle o\cdot|l_i+2s_i|o\cdot\rangle=-\sum_j G_{ij}s_j', \qquad (22)$$

$$\left.\begin{aligned} -\beta G_{ix} &= 2\,\mathrm{Re}\langle o1|\mu_i|o2\rangle, \\ -\beta G_{iy} &= -2\,\mathrm{Im}\langle o1|\mu_i|o2\rangle, \\ -\beta G_{iz} &= 2\langle o1|\mu_i|o1\rangle. \end{aligned}\right\} \qquad (23)$$

Strictly speaking, the coefficients G_{ij} are not the components of a second-rank tensor; however, the formal structure of eqn. (22) permits them to be so regarded. Even so, G_{ij} is not symmetric and cannot be diagonalized for a point in k-space having symmetry lower than orthorhombic.

The 'spin' Hamiltonian

$$-\langle o.|\boldsymbol{\mu}|o.\rangle.\mathbf{H}=\beta\sum_{ij}G_{ij}H_i s_j' \qquad (24)$$

has the eigenvalues

$$E_s=\pm\tfrac{1}{2}g\beta H, \qquad (25)$$

where

$$g=\left[\sum_{ijl}\lambda_i\lambda_j G_{il}G_{jl}\right]^{1/2} \qquad (26)$$

is the usual spectroscopic splitting factor. In (26) the λ_i are the direction cosines of **H** relative to the axes x, y, z. The quantity

$$Q_{ij} = \sum_l G_{il} G_{jl} \quad \ldots \ldots \quad (27)$$

is a symmetric second-rank tensor and can be diagonalized. We designate the principal components of Q_{ij} as g_1^2, g_2^2 and g_3^2 so that (26) becomes

$$g = [(\lambda_1')^2 g_1^2 + (\lambda_2')^2 g_2^2 + (\lambda_3')^2 g_3^2]^{1/2}. \quad \ldots \quad (28)$$

Here the λ_i' are the direction cosines of **H** relative to the principal axes of Q_{ij}. It must be emphasized that despite the simple form of (28), the transformation which diagonalizes the Hamiltonian (24) does not in general diagonalize G_{ij}. This differs from the customary situation in electronic paramagnetism (Bleany and Stevens 1953) because of the low symmetry with which we are concerned here. It is convenient to define a spin effective mass m_s in analogy with the more familiar orbital effective mass,

$$m_s/m = 2/g = 2[(\lambda_1')^2 g_1^2 + (\lambda_2')^2 g_2^2 + (\lambda_3')^2 g_3^2]^{-1/2}. \quad \ldots \quad (29)$$

The energy levels (25) are then just like those of a free electron except that m_s replaces the free-electron mass in the Bohr magneton. The signs in eqn. (25) derive from the signs of the G_{ij} and hence relate to the effective spin operator s' and not the true spin s. The sense of s_z' is a matter of choice and can be related to that of s_z only when the parentage of the $\psi_{on\rho}$ in terms of orbital and spin functions is particularly simple. Such is the case for conduction electrons in InSb, for which Roth *et al.* (1958) were able to assign a negative value to g itself, but not, e.g. for Bi. For convenience, therefore, we leave the signs unspecified in eqn. (25) and define g as a positive quantity in eqn. (26).

In addition to (25), the energy contains the orbital eigenvalues given by

$$(n+\tfrac{1}{2})h\omega_c + \hbar^2 k_z^2/2m_z, \quad n = 0, 1, 2, \ldots \quad \ldots \quad (30)$$

when **H** is in the z-direction, where ω_c is the cyclotron frequency,

$$\omega_c = eH/m_0 c. \quad \ldots \ldots \quad (31)$$

If α_i, $i = 1, 2, 3$, are the principal components of $\boldsymbol{\alpha}$ and λ_i the direction cosines of **H** relative to its principal axes, we have for m_0 and m_z

$$m_0 = m[\lambda_1^2\alpha_2\alpha_3 + \lambda_2^2\alpha_3\alpha_1 + \lambda_3^2\alpha_1\alpha_2]^{-1/2}, \quad \ldots \quad (32)$$

$$m_z = m(\alpha^{-1})_{zz} = m[\lambda_1^2/\alpha_1 + \lambda_2^2/\alpha_2 + \lambda_3^2/\alpha_3]. \quad \ldots \quad (33)$$

Eqns. (29) and (32) provide a convenient basis for the comparison of the splitting of the spin and orbital levels by a magnetic field; the two splittings are equal when the two effective masses are equal.

§ 3. THE ONE-LEVEL CASE

The expressions for the orbital effective mass, eqn. (32), and the spin effective mass, eqn. (29), are closely related in structure, and related sum rules hold for the quantities entering both, eqns. (8) and (14), respectively.

The condition that m_0 be small is simply that one or more band gaps entering the sum rule (8) be small. The same condition is necessary for m_s to be small (or g large) but is not sufficient. The operator μ_k vanishes in the absence of spin–orbit coupling, as is shown by a simple application of the operator U, eqns. (5) and (6). Thus we must also require the two spin states of given wave number to be completely mixed, for which the spin–orbit coupling must be comparable to or larger than the band gaps. These conditions are met in InSb, for which $m_0=0{\cdot}013m$ and $m_s=3m_0$ (Roth *et al.* 1958) and *a fortiori* in Bi, for which the result $m_s=m_0$ at most orientations of H is obtained in § 4. However, before considering any particular substance, we treat the case of electrons of small effective mass in a crystal whose symmetry operations include inversion.

If the effective-mass components are small, or $\alpha_{ij}>1$, then at least one level with velocity matrix elements of normal size almost certainly lies within a few tenths of a volt or less of E_0. We restrict ourselves to the *one-level case* in which there is only one such level, E_a, just below E_0. This level dominates the sum rules (8) and (14), and we may neglect the δ_{ij} in (8), the contributions of all other levels to both (8) and (14), and (if spin–orbit coupling is strong) μ_s in (12). Under these circumstances,

$$m_0=m_s, \qquad \text{(34)}$$

which we now proceed to demonstrate.

Take the z-axis along $\mathbf{H}$, and let x and y be arbitrary. Equation (32) then becomes

$$m_0=m[\alpha_{xx}\alpha_{yy}-(\alpha_{xy})^2]^{-1/2}, \qquad \text{(35)}$$

and eqn. (29) becomes

$$m_s=2m[G_{zz}{}^2+G_{zx}{}^2+G_{zy}{}^2]^{-1/2}. \qquad \text{(36)}$$

We define

$$\mathbf{t}=\langle o1|\mathbf{v}|a1\rangle \quad \text{and} \quad \mathbf{u}=\langle o1|\mathbf{v}|a2\rangle. \qquad \text{(37)}$$

The relations

$$\langle a1|\mathbf{v}|o2\rangle=-\mathbf{u} \quad \text{and} \quad \langle a2|\mathbf{v}|o2\rangle=\mathbf{t} \qquad \text{(38)}$$

are readily established by use of the operator U. With the aid of (37) and (38), we may write the contribution of the level E_a to α_{ij} as

$$\alpha_{ij}=m(t_it_j{}^*+t_jt_i{}^*+u_iu_j{}^*+u_ju_i{}^*)/(E_0-E_a) \qquad \text{(39)}$$

and to G_{ij} as

$$\left.\begin{aligned} G_{iz}&=2m(t_jt_k{}^*-t_kt_j{}^*+u_ju_k{}^*-u_ku_j{}^*)/i(E_0-E_a),\\ G_{ix}-iG_{iy}&=4m(u_jt_k-u_kt_j)/i(E_0-E_a). \end{aligned}\right\} \qquad \text{(40)}$$

Substitutions of (39) into (35) and of (40) into (36) and comparison of the two results leads directly to (34). Thus, we have proved that the splittings of the spin and orbital levels by a magnetic field are equal in the one-level case.

In the absence of spin–orbit coupling, $\mathbf{u}$ vanishes and (38) shows that $\mathbf{t}$ is real. From eqn. (39) we see that the level E_a can then contribute to only a single component of α. The contributions of E_a to the other components of α remain small as long as the spin–orbit splitting is small compared with the band gap E_0-E_a. The above proof of eqn. (34) is valid only if all the components of α are determined by the level E_a. The condition for the equality of m_0 and m_s in the one-level case is therefore that the spin–orbit splitting be comparable to or larger than the band gap (E_0-E_a).

Further, our considerations do not apply to electrons near points of full cubic or tetrahedral symmetry if one of the two levels is 4-fold degenerate. Specifically, eqn. (34) does not apply to InSb, where the conduction electrons are near $k=0$ and the lower level is 4-fold degenerate.

§ 4. BISMUTH

4.1. *Band Structure*

Electrons in bismuth occupy three or six ellipsoidal energy surfaces according to the de Haas–van Alphen effect (Shoenberg 1939, 1957) and cyclotron resonance (Aubrey and Chambers 1957). One set of ellipsoids is given by

$$E(\mathbf{k})=(\hbar^2/2m)(\alpha_{xx}k_x{}^2+\alpha_{yy}k_y{}^2+\alpha_{zz}k_z{}^2+2\alpha_{yz}k_yk_z), \quad . \quad . \quad (41)$$

where x and z are chosen along a dyad axis and the triad axis respectively, and $\mathbf{k}$ is measured from the position of the nearest minimum in the conduction band. Two other sets are obtained by rotation of ± 120° around the triad axis, and the remaining three are obtained from the first three by inversion. The six minima coalesce into three only if they happen to lie at the centres of zone faces. One principal axis of each ellipsoid lies along a dyad axis, but the non-vanishing of α_{yz} implies that neither remaining axis lies along the triad axis. A symmetry argument then shows that the six energy minima lie either in the three reflection planes normal to the dyad axes or on the dyad axes, the two minima in each plane or on each axis being connected by inversion. The best values available for the α_{ij} derive from a combination of de Haas–van Alphen and cyclotron resonance data

$$\alpha_{xx}=202, \quad \alpha_{yy}=1{\cdot}67, \quad \alpha_{zz}=83{\cdot}3, \quad \alpha_{yz}=8{\cdot}33\dagger, \quad . \quad . \quad (42)$$

according to Aubrey (private communication). These lead to the principal values

$$\alpha_1=202, \quad \alpha_2=0{\cdot}83, \quad \alpha_3=84{\cdot}2 \quad . \quad . \quad . \quad . \quad . \quad . \quad (43)$$

with the principal axis 3 tipped 5·80° from the triad axis. The Fermi energy is 0·0177 ev at 4°K (Dhillon and Shoenberg 1955).

4.2. *Relation between m_0 and m_s*

We infer from the two large principal values, α_1 and α_3, that at least one level lies just below E_0. Let us assume that we are actually dealing with

---

† G. Smith (private communication) has pointed out that α_{yz} should be positive in the right-handed coordinate system used here.

a one-level case, that only one band gap is very small and all other contributions to (8) are negligible. A few hundredths of an electron volt is a reasonable guess for this band gap $E_g = E_0 - E_a$ on the basis of eqns. (39) and (32), whereas an appropriate measure of the spin–orbit splitting is 1·86 ev in atomic Bi (Condon and Shortley 1935, p. 179). We can therefore take over the results of the preceding section for bismuth, eqn. (34),

$$m_0 \simeq m_s \quad \text{(Bi)}. \qquad (44)$$

However, eqn. (34) was derived on the assumption that the level E_a determines all the components of α_{ij}. This is clearly not true for Bi where α_2 is small. Thus (44) holds only for orientations of the magnetic field such that α_2 does not contribute appreciably to m_0 in eqn. (32). Substitution of (43) into (32) shows that **H** must not lie within about 5° of the 1, 3 plane for (44) to be valid.

We now explore the implications of the small value of α_2 in more detail. For states at the minimum in the conduction band the group of **k** (Bouckaert *et al.* 1936) contains only the unit operator E and the reflection operator σ or 2-fold rotation C_2. (Addition of inversion does not affect our arguments.) The character table of the double group (Elliott 1954 b) is

	R_1	R_2	R_3	R_4
E	1	1	1	1
$\bar{E}$	1	1	-1	-1
σ or C_2	1	-1	$-i$	i
σ or $\bar{C}_2$	1	-1	i	$-i$

The representations R_3 and R_4 are degenerate by time reversal (Elliott 1954 b). A Bloch function can transform either as R_3 or R_4; we make the arbitrary identification that ψ_{nk1} transforms as R_3 and ψ_{nk2} as R_4. The x, y and z components of **v** transform as R_2, R_1 and R_1, respectively. From the multiplications rules $R_1 \times (R_3, R_4) = (R_3, R_4)$ and $R_2 \times (R_3, R_4) = (R_4, R_3)$, we obtain $\langle o1|v_x|n2\rangle$, $\langle o1|v_y|n1\rangle$ and $\langle o1|v_z|n1\rangle$ as the non-vanishing matrix elements of **v** entering (8) and (14). In the one-level case, (8) becomes

$$\left.\begin{aligned}
\alpha_{xx} &= 2m|\langle o1|v_x|a2\rangle|^2/E_g,\\
\alpha_{yy} &= 2m|\langle o1|v_y|a1\rangle|^2/E_g,\\
\alpha_{zz} &= 2m|\langle o1|v_z|a1\rangle|^2/E_g,\\
\alpha_{yz} &= 2m\,\mathrm{Re}(\langle o1|v_y|a1\rangle\langle a1|v_z|o1\rangle)/E_g,\\
\alpha_{xy} &= \alpha_{xz} = 0.
\end{aligned}\right\} \qquad (45)$$

From (45), we see that in general α_1, α_2 and α_3 are all large. The small value of α_2 is thus peculiar to Bi and not a consequence of the reflection or rotation symmetry. We can infer that $\langle o1|v_y|a1\rangle$ vanishes or becomes very small when the y-axis is brought into coincidence with axis 2 by rotation around x. The phases of $\langle o1|v_y|a1\rangle$ and $\langle o1|v_z|a1\rangle$ must therefore differ by nearly 0 or π; in other words, the vector **t** is real apart from a phase factor. This special circumstance is probably related to the small size of E_g, a qualitative explanation for which has been given by Blount (1956)†.

If we now assume that the phases of $\langle o1|v_y|a1\rangle$ and $\langle o1|v_z|a1\rangle$ differ by precisely 0 or π, then α_2 vanishes in the one-level approximation. Similarly, substitution of the non-vanishing matrix elements of **v** into (14), leads to the result

$$g_1=0, \quad g_2{}^2=4\alpha_1\alpha_3, \quad g_3=0; \quad \lambda_2'=\lambda_2 \quad . \quad . \quad . \quad . \quad . \quad (46)$$

in the one-level approximation, which is equivalent to (44). We can now see clearly that in the complete expressions (28) (or (29)) and (32), instead of (46) we must actually have $\lambda_1'=\lambda_1$, λ_2' and λ_3' very nearly equal λ_2 and λ_3, $\frac{1}{2}g_1$ and $\frac{1}{2}g_3$ of order unity, and finally $\frac{1}{2}g_2$ very nearly equal to $(\alpha_1\alpha_3)^{1/2}$. Thus, when **H** is nearly perpendicular to axis 2, m_s is of order unity and hence $\simeq 10m_0$. On the other hand, eqns. (44) and (46) hold with **H** pointing along axis 2, when g takes on the enormous value of *260*.

§ 5. THE DE HAAS–VAN ALPHEN EFFECT

We turn now to consideration of the role played by the electron spin in the de Haas–van Alphen effect. The generalization of (2) required when the spin–orbit coupling is important is simply

$$\cos r\pi m_0/m_s, \quad . \quad . \quad . \quad . \quad . \quad . \quad . \quad . \quad . \quad (47)$$

as is seen immediately upon reviewing the work of Dingle (1952) or of Sondheimer and Wilson (1951). For bismuth, the factor (47) is very nearly equal to $\cos r\pi=(-1)^r$ unless **H** comes within 5° of being perpendicular to axis λ, thus recapturing eqn. (1). This is the explanation for the phase shift of π found experimentally by Shoenberg (1939) in the fundamental at a variety of orientations of magnetic field and of the equivalent factor of $(-1)^r$ found by Dhillon and Shoenberg (1955) in the fundamental and the first six harmonics at a single orientation. All orientations of **H** at which phases were determined are within the region of validity of eqn. (44).

It would be of interest to study the harmonic content and phases of the de Haas–van Alphen oscillations at an orientation such that (44) does not hold. These can be accurately determined only when a single period is present in the quantity observed (Dhillon and Shoenberg 1955). The periods associated with all six ellipsoids become equal only when **H** is along the trigonal axis. For that orientation λ_1 vanishes, $\lambda_2{}^2\alpha_3\alpha_1$ nearly equals $\lambda_3{}^2\alpha_1\alpha_2$, and $(\lambda_3')^2(g_3/2)^2$ is negligible relative to $(\lambda_2')^2(g_2/2)^2$. It then follows from (29) and (32) that

$$m_s=\sqrt{2}m_0 \quad . \quad . \quad . \quad . \quad . \quad . \quad . \quad . \quad . \quad . \quad (48)$$

when **H** is along the trigonal axis. Thus (44) is violated and $\cos r\pi m_0/m_s$ $(=\cos r\pi/\sqrt{2})$ differs from $(-1)^r$ for an orientation giving a single period.

---

† A similar situation occurs in Sb (Shoenberg 1952, Datars and Dexter, private communication).

The phases and amplitudes of successive harmonics should vary in a way quite unlike that expected without the cos $r\pi m_0/m_s$ factor. Unfortunately the torque vanishes for this orientation, and eqn. (44) holds for those orientations at which a single period is observed by the torque method (Dhillon and Shoenberg 1955). A harmonic analysis of the temperature oscillations recently reported by Kunzler and Boyle (1959) could in principle yield an experimental test of (48). An alternative method would be a direct measurement of the differential susceptibility by the magnetic field modulation scheme commonly applied in nuclear and electron spin resonance studies.

Arsenic and antimony are similar in crystal and electronic structure to Bi and have observable de Haas–van Alphen effects (Shoenberg 1957). One set of carriers in each substance fits into the six ellipsoid scheme holding for electrons in Bi. The analysis developed here for Bi can be taken over unmodified for Sb and As. However, the effective masses and hence the band gaps are larger, while the spin–orbit splittings are smaller than for Bi. Thus, relations like (44) should hold for As and Sb, but with less accuracy than for Bi. A study of the harmonic content and phases of the de Haas–van Alphen oscillations in Sb and As like that of Dhillon and Shoenberg for Bi would therefore be of interest.

Frederikse and Hosler (1957) have observed oscillations in the galvanomagnetic properties of n-type InSb. It is reasonable to suppose that the de Haas–van Alphen effect is also observable (Shoenberg, private communication). The value of m_0 is $0{\cdot}013m$ (Dresselhaus *et al.* 1955) and that of m_s is $0{\cdot}040$ from (29) and $g=50$, or

$$m_s \simeq 3m_0 \text{ (InSb)}. \qquad \qquad (49)$$

Hence the factor (47) is very nearly equal to $\cos r\pi/3$, and the amplitudes and phases of the harmonics of the de Haas–van Alphen oscillations of electrons in InSb should vary in a way inexplicable without (47).

§ 6. OTHER IMPLICATIONS OF THE LARGE g-FACTOR IN BISMUTH

We have seen in the preceding section how the observed phase shifts in the de Haas–van Alphen oscillations confirm our result $m_0=m_s$ for Bi at most orientations of $\mathbf{H}$. An immediate consequence of this is that the Pauli spin paramagnetism is three times larger than the Landau–Peierls diamagnetism when $\mathbf{H}$ is perpendicular to the trigonal axis, just as for free electrons. Thus Jones' (1934) explanation of the stready diamagnetism of bismuth leads in fact to a net paramagnetism; the correct explanation must lie in the direction suggested by Adams (1953 b).

It would be very amusing to measure a g-factor as large as 260 directly by a spin–resonance experiment. Preliminary calculations indicate that such an experiment is feasible for Bi. Because of the large spin–orbit coupling, the spin relaxation time T_1 is probably comparable to the collision time. Zone-refined Bi should give an $\omega\tau$ of order 100 at 30 000 Mc/s so that line width from collisions should be no problem. Although Dyson's

(1955) theory is not strictly applicable to Bi at 30 000 Mc/s, it suggests that intensity should also be no problem because of the large g-factor.

The spin–orbit coupling is important not only for the magnetic properties of Bi but for the entire band structure. For example, the matrix element $\langle o1|v_x|a2\rangle$, which would vanish without spin–orbit coupling, is 60% larger than $\langle o1|v_z|a1\rangle$, and the spin–orbit splitting itself is two orders of magnitude larger than E_g. It is necessary, therefore, to take explicit cognizance of the spin–orbit coupling in constructing theories of all the electronic properties of bismuth and similar substances.

Thus far we have spoken only of electrons. However, the analysis does not depend on the sign of the effective mass and can immediately be taken over, with all results, to apply to holes.

Finally, certain limitations on our present considerations must be mentioned. A number of terms have been left out of the Hamiltonian of eqn. (11) which *are* obtained by the method of Adams (1953 b). These are of order H^2 and independent of $\mathbf{x}_c$, and so do not affect the de Haas–van Alphen effect. They are of importance only for the steady susceptibility. The multiplicative factor (47) obtains only when energy depends quadratically on wave number at the Fermi surface. In the general case, the g-factor depends on $\mathbf{k}$, which causes the orbital energy levels to depend on spin-direction and thus complicates the de Haas–van Alphen effect. This $\mathbf{k}$-dependence of g also broadens the spin resonance line and may well dominate the breadth in Bi.

ACKNOWLEDGMENTS

Part of this work was carried out at the Institute for the Study of Metals of the University of Chicago where it was supported by grant G–4918 from the National Science Foundation. We are grateful to Dr. D. Shoenberg, F.R.S. for helpful and informative discussions and to J. E. Aubrey, also of the Mond Laboratory, for permission to use his effective-mass values prior to publication.

REFERENCES

ADAMS, E. N., 1952, *Phys. Rev.*, **85,** 41; 1953 a, *J. chem. Phys.*, **21,** 2013; 1953 b, *Phys. Rev.*, **89,** 633.
AKHIESER, A., 1939, *C. R. Acad. Sci. URSS*, **23,** 974.
AUBREY, J. E., and CHAMBERS, R. G., 1957, *J. Phys. Chem. Solids*, **3,** 128.
BLEANY, B., and STEVENS, K. W. H., 1953, *Rep. Progr. Phys.*, **16,** 108 (London: The Physical Society).
BLOUNT, E. I., 1956, *Bull. Amer. phys. Soc.*, **1,** 143.
BOUCKAERT, L. P., SMOLUCHOWSKI, R., and WIGNER, E., 1936, *Phys. Rev.*, **50,** 58.
CONDON, E. V., and SHORTLEY, G. H., 1935, *The Theory of Atomic Spectra* (Cambridge: University Press), p. 179.
DHILLON, J. S., and SHOENBERG, D., 1955, *Phil. Trans.* A, **248,** 1.
DINGLE, R. B., 1952, *Proc. roy. Soc.* A, **211,** 500.
DRESSELHAUS, G., 1955 a, Thesis, University of California, Berkeley (unpublished); 1955 b, *Phys. Rev.*, **100,** 580.

Dresselhaus, G., Kip, A. F., Kittel, C., and Wagoner, G., 1955, *Phys. Rev.*, **98,** 556.

Dyson, F. J., 1955, *Phys. Rev.*, **98,** 349.

Elliott, R. J., 1954 a, *Phys. Rev.*, **96,** 266; 1954 b, *Ibid.*, **96,** 280.

Frederikse, H. P. R., and Hosler, W. R., 1957, *Phys. Rev.*, **108,** 1136.

Foldy, L. L., and Wouthysen, S. A., 1950, *Phys. Rev.*, **78,** 29.

Jones, H., 1934, *Proc. roy. Soc.* A, **147,** 396.

Kane, E. O., 1957, *J. Phys. Chem. Solids*, **1,** 249.

Kjeldaas, T., and Kohn, W., 1957, *Phys. Rev.*, **105,** 806.

Kunzler, J. E., and Boyle, W. S., 1959, *Bull. Amer. phys. Soc.*, **4,** 168.

Lifshitz, I. M., and Kosevitch, A. M., 1955, *J. exp. theor. Phys. U.S.S.R.*, **29,** 730 (Soviet Physics *J.E.T.P.*, **2,** 636 (1956)).

Luttinger, J. M., and Kohn, W., 1955, *Phys. Rev.*, **97,** 869.

Luttinger, J. M., 1956, *Phys. Rev.*, **102,** 1030.

Roberts, V., and Quarrington, J. E., 1955, *J. Electron.*, **1,** 152.

Roth, L. M., Lax, B., and Zwerdling, S., 1958, *Bull. Amer. phys. Soc.*, **3,** 128.

Shoenberg, D., 1939, *Proc. roy. Soc.* A, **170,** 341; 1952, *Phil. Trans.* A, **245,** 1; 1957, *Progress in Low Temperature Physics*, ed. C. J. Gorter (New York: Interscience Publishers, Inc.), **2,** Chap. 8.

Sondheimer, E. H., and Wilson, A. H., 1951, *Proc. roy. Soc.* A, **210,** 173.

Yafet, Y., 1952, *Phys. Rev.*, **85,** 478; 1957, *Ibid.*, **106,** 679.

The Infra-red Absorption of Hot Semiconducting Diamonds†

By C. D. Clark, P. Kemmey and E. W. J. Mitchell
Physics Research Laboratory, The University, Reading
and B. W. Henvis,
Naval Research Laboratory, Washington, D.C.

[Received September 11, 1959]

Abstract

Measurements of the absorption of p-type semiconducting diamonds have been made at temperatures in the range 450 to 600°K and over the wavelength range between 6 and 45 μ. The major effect observed is an absorption, which is present only in hot semiconducting diamonds, which increases with increasing wavelength and temperature. The increase with temperature is similar to that of the increase in carrier concentration as determined from measurements of the Hall effect.

The observed wavelength dependence differs from that predicted by the theory of intervalence band absorption for mass ratios of 1·04, 1·25, 2·5 and 5. It is possible to account for the shape of the spectrum using the single band free carrier theory of Donovan and March. However, the relaxation times deduced are small (*c.* 10^{-14} sec at 563°K) and there is a discrepancy between the calculated and observed magnitude of absorption.

§ 1. Introduction

The semiconducting diamonds which are available at the present time are p-type conductors, as shown by the work of Custers (1952), Austin and Wolfe (1956), Dyer and Wedepohl (1956) and particularly Wedepohl (1957). Measurements of the Hall constant indicate that the hole concentration is *c.* 10^{13} cm^{-3} at room temperature and, consequently, at that temperature, no optical effects are observed which are directly associated with the presence of free carriers.

Wedepohl (1957) described the characteristic infra-red spectrum which semiconducting diamonds have at room temperature. The spectrum comprises sharp lines superposed on a continuum which extends into the red end of the visible spectrum. It was found by Wedepohl that the strength of these features at room temperature was proportional to the concentration of empty acceptor levels as determined from the electrical measurements, that is, to $(N_A - N_D - p)$ where N_A is the acceptor level concentration, N_D the donor level concentration and p the hole concentration. In addition to these features, semiconducting diamonds possess the 3 to 6 μ absorption band which is found in all diamonds, and which, as shown by Stephen (1958) is probably intrinsic vibrational absorption.

---

† Communicated by Professor R. W. Ditchburn.

A typical spectrum of a semiconducting diamond at room temperature is shown in fig. 1. Beyond $7\,\mu$ there is a small band at about $7{\cdot}8\,\mu$, which will be referred to below, and some evidence of a band at $21\,\mu$, but apart from these we have not detected any absorption for wavelengths out to about $50\,\mu$.

The work described in this paper was carried out to see whether any specifically free carrier effects could be observed in this otherwise transparent region. In order that there should be sufficient free carriers present it is necessary to make measurements with the diamonds at about 300°c when the carrier concentration is *c.* $10^{16}\,\mathrm{cm}^{-3}$.

Fig. 1

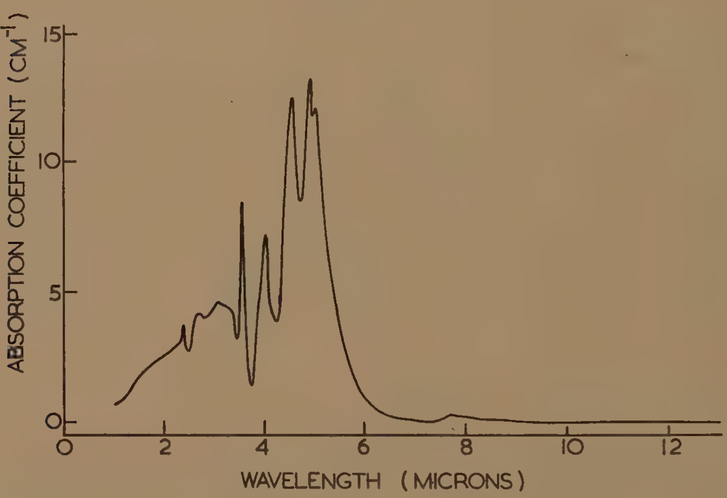

Infra-red spectrum of semiconducting diamond at room temperature.

§ 2. Experimental

The specimens used were natural type IIb diamonds of dimensions about 2 × 2 × 5 mm. Resistivity and Hall effect measurements in the temperature range 200 to 700°K were carried out as described by Wedepohl (1957).

Initially the absorption spectra of the specimens were measured for wavelengths up to $15\,\mu$ using the Grubb Parsons double beam spectrometer in the Physics Department of the N.I.R.D., Shinfield, and we are grateful to Dr. J. Goulden of that laboratory for his cooperation in this part of the work. An experimental difficulty was encountered owing to the fact that the radiation emitted by the hot specimen and its holder passed through the chopper and was recorded by the detector. A correction was made for this error by measuring separately the intensity of the emission relative to the reference beam and subtracting it from the apparent transmission curve obtained earlier. The emission was measured by putting an opaque screen on the source side of the crystal.

One specimen was measured between 10 and 24 μ on a single beam instrument using a KBr prism. This was done at the R.A.E., Farnborough, with the kind cooperation of Drs. T. S. Moss and S. D. Smith. In these measurements only the incident light was chopped and the difficulty referred to above was avoided.

The most complete sets of measurements were made at the Naval Research Laboratory, Washington, where C.D.C. and E.W.J.M. spent some time during the summer of 1958. These measurements covered the wavelength range 6 to 45 μ using a single beam Perkin Elmer spectrophotometer with NaCl, KBr, and CsI prisms. Three diamonds were measured of which two were p-type semiconductors (D22 and BP2) and one (D80) a type IIa, which served as a non-conducting control specimen.

Fig. 2

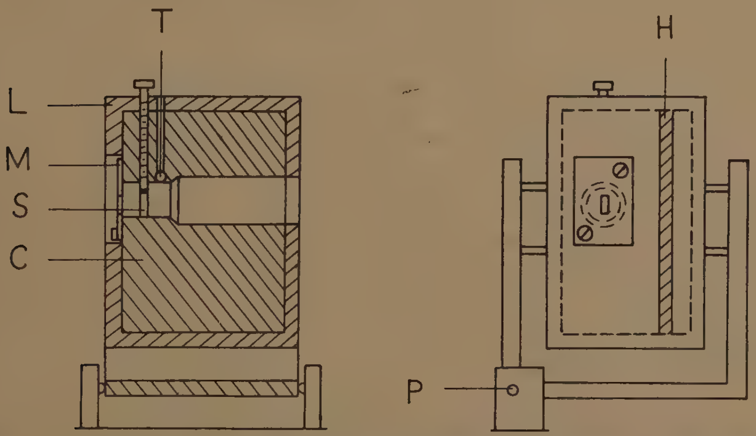

Diagram of furnace used for high temperature spectrum measurements. S: specimen; M: beam-defining mask; T: thermocouple; C: copper block; H: heating element; L: thermal insulation; P: pivot.

A diagram of the furnace used is shown in fig. 2. The crystal was clamped in a hole in a copper block. The block was lagged on the outside and was heated electrically using the element of a small soldering iron. A chromel-alumel thermocouple was used to measure the temperature as close to the diamond as possible. There was a beam defining mask attached to the furnace so that when it was in position the transmitted beam did not reach to the edges of the crystal. The furnace was mounted so that it could be pivoted out of the beam and replaced accurately to its original position. The transmission curves repeated after moving the specimen holder out and putting it back, were reproducible to within $\frac{1}{2}\%$.

The measurements were carried out in the following sequence. For a given wavelength range a record was obtained of the intensity transmitted by the specimen at room temperature. Immediately afterwards the intensity of the incident beam was recorded with the furnace completely removed from the beam. This sequence was repeated until the whole of the wavelength range had been covered.

The series of measurements of incident and transmitted intensity was then carried out with the specimen at 563°K, and later at 484°K. From the records obtained the ratios of the transmitted intensity (I_T) to the beam intensity when the specimen holder was removed (I_B), were calculated for the three temperatures.

The beam apertures in the measurements of I_T and I_B were not the same. Owing to this difference we cannot determine the exact percentage transmission (T) but only a quantity (βT) where β is the aperture ratio. In a given wavelength range β was a constant for the three temperatures of measurement. (Thermal expansion of the mask had a negligible effect.) Consequently we were able to determine for the whole wavelength range T_{563}/T_{293} and T_{484}/T_{293}. In general, referring to a ratio $T_{\text{hot}}/T_{\text{cold}}$ (T_H/T_C) we have:

$$\frac{T_H}{T_C}=\frac{(1-R)^2\exp(-\mu_H t)}{1-R^2\exp(-2\mu_H t)}\,\frac{1-R^2\exp(-2\mu_C t)}{(1-R)^2\exp(-\mu_C t)}. \quad . \quad . \quad . \quad (1)$$

Here we have assumed that the reflectivity (R) is not significantly dependent on temperature. The change in the bound electron refractive index is likely to be of the order of 0·01 which gives a change in R of 0·001 in 0·170 and this would alter the value of T_H/T_C by less than 0·2%. The extra reflectivity due to the increase in free carrier concentration at the higher temperatures can be neglected for the concentrations encountered in this work.

In eqn. (1) μ_H and μ_C are the absorption coefficients of the specimen hot and cold respectively and t is the specimen thickness. We write $\mu_H=\Delta\mu+\mu_C$ where $+\Delta\mu$ is the additional absorption at the higher temperature. Then (1) may be written:

$$\frac{T_H}{T_C}=\frac{(1-R)^2\exp(-\Delta\mu t)}{1-R^2\exp(-2\Delta\mu t)}\times\frac{1-R^2\exp(-2\mu_C t)}{1-R^2}$$
$$\times\frac{1-R^2\exp(-2\Delta\mu t)}{[1-R^2\exp(-2\Delta\mu t-2\mu_C t)]}. \quad . \quad . \quad . \quad . \quad . \quad . \quad (2)$$

Measurements on semiconducting diamonds using the double beam instrument showed that between 10 and 15 μ the value of ($\mu_C t$) was less than 0·1, while the N.R.L. measurements showed that ($\mu_C t$) did not increase as the wavelength was increased. For $(\mu_C t)=0\cdot1$ the second and third terms of eqn. (2) may be neglected provided that $(\Delta\mu\,.\,t)<2$. For $(\Delta\mu\,.\,t)=2$ the value of T_H/T_C obtained under these conditions is in error by 1%. Our results indicate that $(\Delta\mu\,.\,t)\leqslant 2$ so that we have calculated $\Delta\mu$ from:

$$\frac{T_H}{T_C}=\frac{(1-R)^2\exp(-\Delta\mu t)}{1-R^2\exp(-2\Delta\mu t)}. \quad . \quad . \quad . \quad . \quad . \quad . \quad . \quad (3)$$

In the experiments using the double beam spectrometer, in order to avoid altering the position of the crystal in the holder, T_C and T_H were not determined absolutely but $\Delta\mu$ was calculated from T_H/T_C using eqn. (3).

§ 3. Results

The observed absorption spectra are shown in fig. 3 where the results for D22 are plotted for temperatures of 563 and 484°K. The experimental points for the non-semiconducting diamond D80 are included. This curve was determined to see whether there were any effects common to IIa and IIb diamonds leading to absorption at the higher temperatures. It will be seen from fig. 3 that the amount of absorption at any wavelength in the semiconducting crystal is much greater than in D80 at the same temperature.

Fig. 3

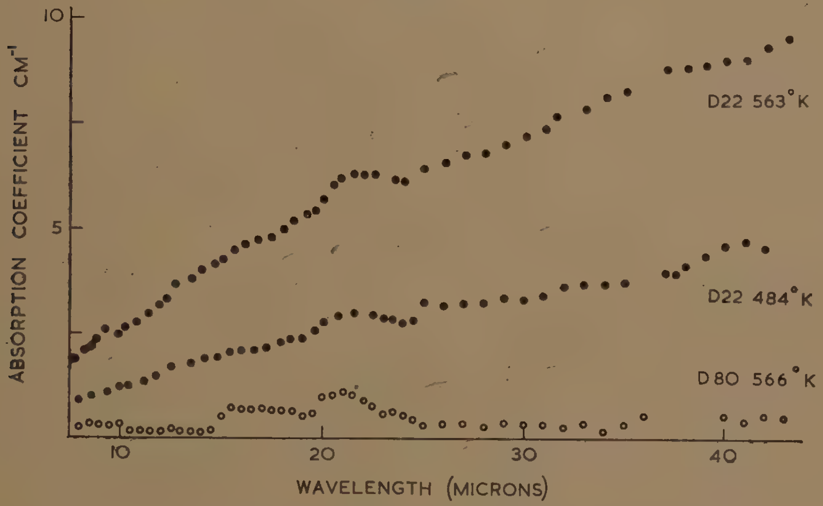

Differential absorption $\Delta\mu$ of semiconducting diamond (D22) and non-semiconducting diamond (D80).

All three spectra have a small peak near $21\,\mu$, indicating that this is not an effect specifically associated with semiconducting diamond. Sutherland *et al.* (1954) reported a band at $20{\cdot}8\,\mu$ at room temperature. Our curves show that there is some absorption in this region which changes with temperature (a band whose position and shape were independent of temperature would not appear on our $\Delta\mu$ curves).

Apart from this $21\,\mu$ band, the absorption in the semiconducting diamond increases with wavelength and is still increasing at $45\,\mu$. The rate of increase is smaller at 484 than at 563°K. Similar results over the whole range were obtained on the specimen BP2. This crystal was in the form of a plate and was unsuitable for Hall effect measurements which are required in order to determine the carrier concentration and hence the absorption cross section.

Fig. 4

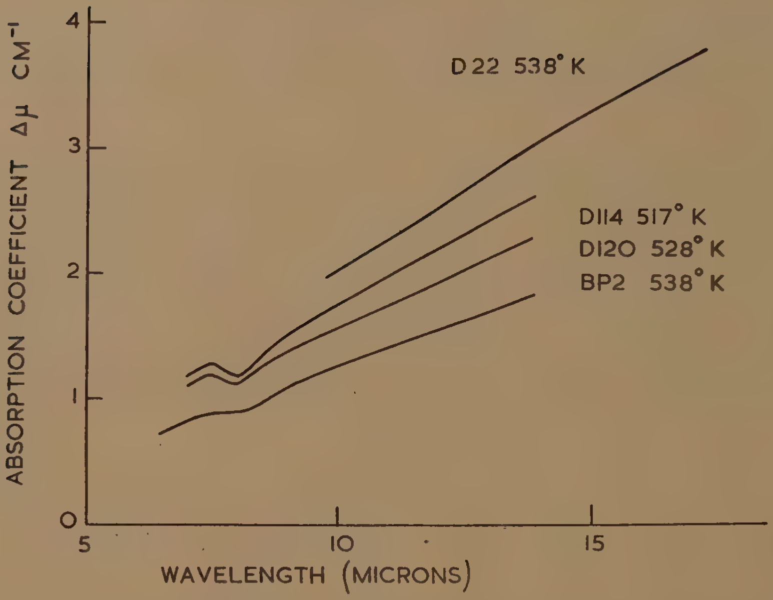

Absorption spectra of four hot semiconducting diamonds in the 5 to 20 μ range.

Fig. 5

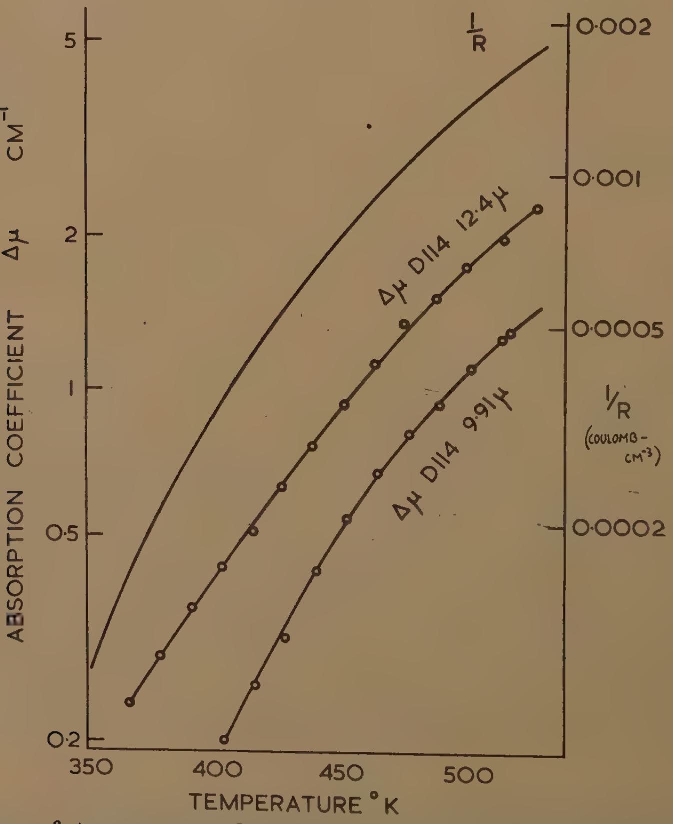

Comparison of temperature dependence of absorption at 12·4 and 9·91 μ with temperature dependence of the inverse Hall coefficient.

The spectra found for other specimens over a narrower wavelength range are shown in fig. 4. These results also indicate an absorption which increases with increasing wavelength.

Fig. 6

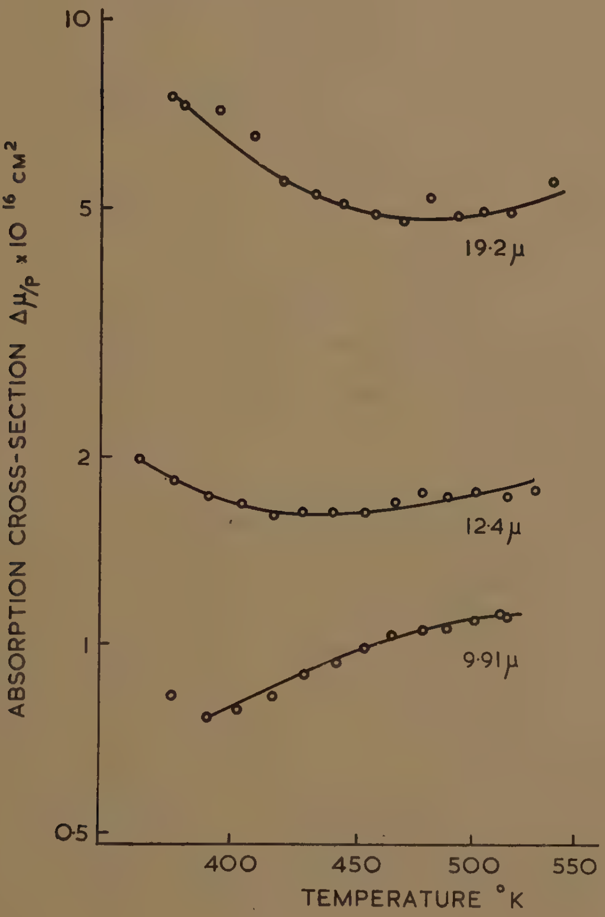

The variation with temperature of the absorption cross section at 19·2, 12·4 and 9·91 μ for specimen D114.

In two cases measurements were made at constant wavelengths as the crystals cooled. Curves of $\Delta\mu$ as a function of temperature for $\lambda = 12{\cdot}4$ and $9{\cdot}91\,\mu$ are plotted in fig. 5, which also contains the reciprocal of the Hall constant (R) as a function of temperature (right-hand ordinate). Using the Hall effect data to find the carrier concentration $[p = (3\pi/8Re)]$ we are able to calculate the absorption cross section ($\Delta\mu/p$) as a function of temperature and the results are shown in fig. 6.

§ 4. Discussion of Results

The main differences between the absorption spectra in the range 7 to 45 μ of hot and cold semiconducting diamonds are:

(i) The decrease of the absorption at about 7·8 μ with increasing temperature;

(ii) The change in the weak absorption band near 21 μ. This is also found in non-semiconducting diamonds.

(iii) The absorption which increases with increasing wavelength λ. The rate of change of absorption decreases with increasing wavelength but increases with increasing temperature.

Wedepohl (1957) attributed the differences in the electrical properties of hot and cold semiconducting diamonds to:

(*a*) Larger concentration of free holes,

(*b*) Larger concentration of ionized acceptor levels, the concentration of ionized donor levels not changing with temperature.
It is difficult to see how (*b*) could give rise to the continuously increasing absorption with wavelength, although the increase in concentration of ionized acceptor levels may provide the explanation of the feature (i) above.

In an ionized acceptor (i.e. acceptor + an electron) the binding is complete. It would, therefore, be expected that the surrounding atoms would be less disturbed from their normal lattice positions than when the centre is un-ionized and one of the bonds is broken. Hence, a possible explanation of the 7·8 μ absorption is that, in the presence of un-ionized acceptors, the lattice disturbance is sufficient for the normally forbidden 8 μ vibrational absorption to occur. As the temperature increases, the concentration of un-ionized acceptors decreases, and since we suggest that less distortion is produced by the ionized centres, we would expect the absorption to decrease.

The major effect (iii), however, seems to be associated with the presence of the free carriers. Thus for the whole wavelength range of the N.R.L. results on D22 (see fig. 6) $\Delta\mu(563°)/\Delta\mu(484°)$ is equal to $2{\cdot}05 \pm 0{\cdot}10$, compared with the ratio of the reciprocals of the Hall constants, $p(563°)/p(484°) = 2{\cdot}10 \pm 0{\cdot}2$.

There are two effects known from work on other semiconductors which could contribute: single band free carrier absorption and intervalence band transitions of the kind reported by Kahn (1955).

The absorption arising from transitions between two bands, degenerate at $k = 0$, has a maximum value, which like the width and sharpness of the absorption, depends on the effective mass ratio of the two energy bands. In order to obtain anything resembling the observed wavelength dependence it is necessary that our range should be on the high energy side of the peak. The band constants are not known for diamond so that we cannot calculate the magnitude of the absorption. However, the wavelength dependence at any given temperature is determined by the mass ratio. From eqn. (12) for the absorption coefficient for intervalence band transitions given by Kahn (1955) we have computed the wavelength dependence of the absorption for several mass ratios. Curves of a quantity y proportional to the absorption coefficient are shown in fig. 7, where

$$y=\frac{\nu^{1/2}}{(kT)^{3/2}}\left[\exp-\left(\frac{h\nu}{kT}\frac{m_2^*}{m_1^*-m_2^*}\right)-\exp-\left(\frac{h\nu}{kT}\frac{m_1^*}{m_1^*-m_2^*}\right)\right].$$

In this equation ν is the frequency, T the temperature, m_1^* and m_2^* the effective masses for the two bands.

Fig. 7

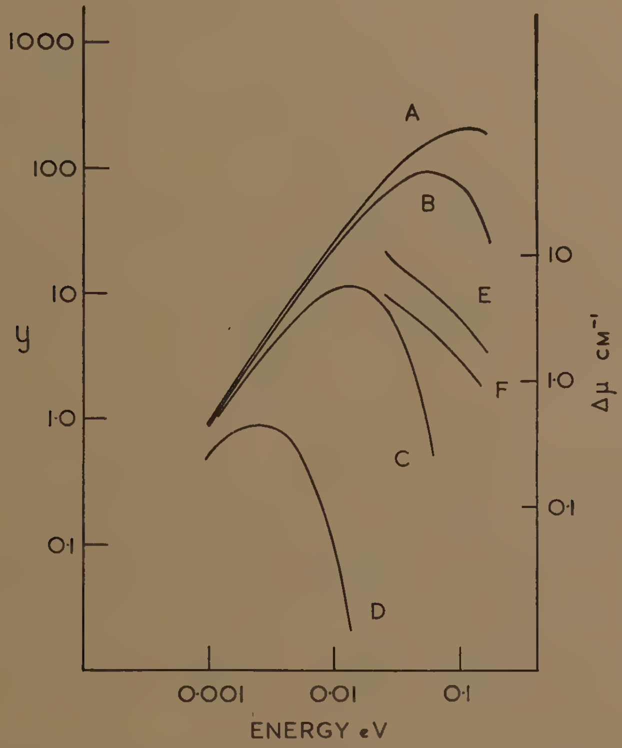

Curves A, B, C and D represent the energy dependence of interband absorption at 525°K for mass ratios 5, 2·5, 1·25 and 1·04 respectively as calculated from Kahn's equation. Curves E and F show measured absorption (right-hand ordinate) of specimen D22 at 563 and 484°K respectively.

The experimental points for D22 at 563 and 484°K are also plotted in fig. 7 and show that the absorption in the range measured increases much less rapidly with increasing wavelength than is predicted. It is, therefore, difficult to see how this type of absorption could account for our results.

4.1. *Single Band Free Carrier Absorption*

Meyer (1958) has given a quantum mechanical treatment of free electron absorption in n-type germanium, taking into account the ellipsodial energy surfaces and various possible scattering mechanisms. While the absolute value of absorption is different from earlier calculations, the wavelength dependence is not drastically altered. Thus Meyer's wavelength dependence, assuming lattice scattering, can be shown numerically to be in the range $\lambda^{1\cdot5}-\lambda^{2\cdot5}$, depending on the particular set of conditions chosen. Since we were working at temperatures between 450 and 600°K lattice scattering should be the predominant scattering mechanism in our crystals.

Under the appropriate conditions, Meyer's theory gives the same wavelength dependence as that given by the Fan *et al.* (1956) theory, in which it had been implicitly assumed that the energy surfaces were spherical. It is concluded therefore that the shape of the energy surfaces is not all important in determining the wavelength dependence of free carrier absorption.

In both theories referred to, the rate of change of absorption with wavelength is increasing with increasing wavelength, contrary to our results. These theories do not apply, however, in the region where $\omega\tau\approx1$, where ω is the circular frequency $(=2\pi c/\lambda)$ and τ the relaxation time†. The observed wavelength dependence may be obtained when $\omega\tau\approx1$ from the Drude–Zener equation:

$$\mu=\frac{4\pi Ne^2}{cm^*}\cdot\frac{\tau}{1+(\omega\tau)^2}. \qquad \ldots \ldots \quad (4)$$

The semiclassical treatment is the only one which gives the wavelength dependence of the absorption when $\omega\tau\approx1$.

Donovan and March (1956) have performed an improved semi-classical calculation in which an energy dependence of τ is included together with the Maxwell–Boltzmann spread of carrier energies in the band. They find:

$$\alpha=\frac{\mu nc}{4\pi\sigma_0}=1-u^2+u^4\exp(u^2)\int_{u^2}^{\infty}\frac{\exp(-t)}{t}\,dt. \qquad \ldots \quad (5)$$

where

$$u=\tfrac{3}{4}\pi^{1/2}(\omega\tau).$$

In fig. 8 the form of the Donovan and March function is shown, α being plotted against (u) on logarithmic scales. If the experimental curve of $\log\Delta\mu$ vs. $\log\omega$ can be made to coincide with the Donovan and March function by displacements parallel to the ordinate and abscissa, then these displacements can be used to find σ_0 and τ. The points in fig. 8 represent the experimental points for D22 originally plotted on the same log scale but now displaced to fit the theoretical curve. From the displacements we find: $\sigma_0 = 0{\cdot}065$ $(\Omega\,\mathrm{cm})^{-1}$ and $\tau = 0{\cdot}91 \times 10^{-14}$ sec. Corresponding to this value of σ_0 obtained from the wavelength dependence we have $\mu_\infty(\mathrm{opt}) = 10{\cdot}1\ \mathrm{cm}^{-1}$, since $\mu_\infty = 156\,\sigma_0$ where μ_∞ is in cm^{-1} if σ_0 is in $(\Omega\,\mathrm{cm})^{-1}$. The value of the d.c. conductivity at 563°K was 0·58 $(\Omega\,\mathrm{cm})^{-1}$ which is equivalent to $\mu_\infty(\mathrm{elec}) = 90\ \mathrm{cm}^{-1}$. These and other values are shown in the table.

---

† τ does not enter explicitly into Meyer's theory, but he refers to a condition of this kind.

Specimen	Spectrometer	Temperature (°K)	Relaxation time τ opt $\times 10^{14}$ sec	μ_∞ (opt) cm^{-1}	μ_∞ (elec) cm^{-1}
D22	N.R.L.	563	0·91	10·1	90
,,	N.R.L.	484	0·89	4·8	66
,,	N.I.R.D.	527	0·58	5·0	80
,,	N.I.R.D.	493	1·00	5·5	69
,,	R.A.E.	538	0·88	7·6	85
D114	N.I.R.D.	547	0·97	8·4	80
D120	N.I.R.D.	528	0·89	6·7	96

The most noticeable features about the parameters determined in this way are the small values of τ, and the discrepancy between the value of μ_∞ obtained from extrapolation of the optical data and the value obtained from the measured d.c. conductivity. In terms of linear frequency

Fig. 8

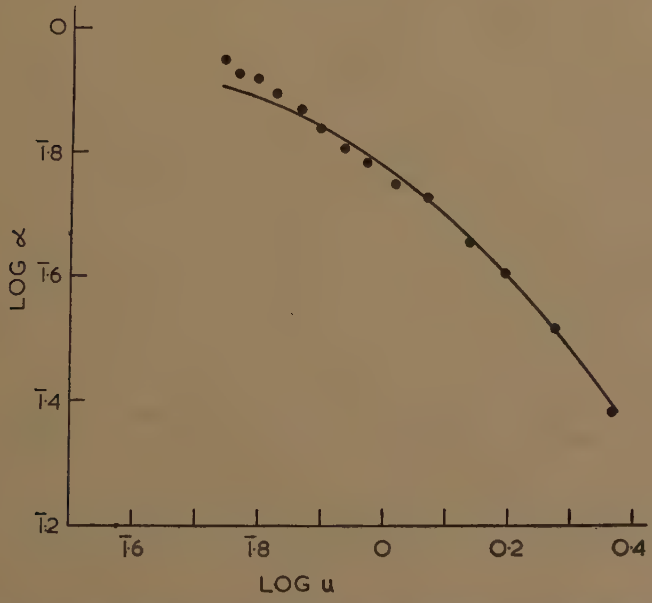

Comparison of wavelength dependence of measured absorption with the theoretical curve due to Donovan and March (1956) (solid line). The experimental points are for specimen D22 at 563°K.

$\tau = 0{\cdot}9 \times 10^{-14}$ sec is equivalent to $1{\cdot}7 \times 10^{13}$ sec^{-1} compared with the maximum vibrational frequency of $3{\cdot}5 \times 10^{13}$ sec^{-1}.

It is possible to carry out a similar analysis on the variation of absorption—expressed as $\Delta\mu/\sigma_0$(elec)—with temperature at a constant wavelength. We have from eqn. (5) that

$$\alpha = f(\omega\tau)$$

and if

$$\tau = \tau_0 T^{-x}, \quad \alpha = f(\omega \,.\, \tau_0 T^{-x}).$$

However, in this case we can only determine τ if x is known. The value of τ found will depend critically on the value of x used. In order to make a comparison with the values of τ found above we have assumed that the temperature dependence of τ is the same as the temperature dependence of the Hall mobility ($x = 2{\cdot}8$). Then from the comparison of the Donovan and March function for $\log \alpha$ and $\log (u)$ with the experimental curve of $\log(\Delta\mu/\sigma_0 \text{elec})$ and $\log(\omega \,.\, T^{-2\cdot 8})$ we can find values of (σ_0 elec/σ_0 opt) and τ_0 (and hence τ at any temperature). The values of τ at the appropriate temperature are within a factor of 3 of the values found from the wavelength dependence.

The range of ($\omega\tau$) covered in the experiments on the variation of absorption with temperature is much less than that covered in the wavelength dependence experiments. We do not attach a great deal of significance, therefore, to the values of τ deduced from the temperature dependence of absorption but note that they are of the same order of magnitude as those deduced from the wavelength dependence.

§ 5. CONCLUSIONS

The continuous infra-red absorption in hot semiconducting diamonds is considered to be associated with the presence of free carriers. Even if the valence bands have similar effective masses near $k = 0$, as indicated by the calculations of Hall (1958), it is unlikely that a major part of the absorption can be attributed to intervalence band transitions.

The wavelength dependence of the measured absorption differs from that given by the theories of free carrier absorption of Fan *et al.* (1956) and Meyer (1958). To account for the results in terms of single band free carrier absorption it is necessary that $\omega\tau \approx 1$, where the quantum mechanical treatments referred to are not valid.

Using the semiclassical theory of Donovan and March (1956) we find that the observed wavelength dependence can be obtained for $\tau \approx 1 \times 10^{-14}$ sec. However, there is a discrepancy, ranging from × 9 to × 16, between μ_∞ extrapolated from optical data and μ_∞ determined from the d.c. conductivity. Values of the same order of magnitude are obtained from the less accurate analysis of the temperature dependence data.

Thus we do not yet have an adequate interpretation of the experimental results in terms of free carrier absorption. It will probably not be possible to obtain a completely unequivocal interpretation until the valence band structure is better known. Meanwhile, an extension of measurements to the microwave region would be desirable.

ACKNOWLEDGMENTS

In addition to those people referred to in the paper we should like to thank Professors E. Burstein and R. W. Ditchburn for their interest and encouragement, Drs. G. S. Picus and M. Haas for helpful discussions, Dr. J. F. H. Custers, Director of Research, Diamond Research Laboratory, Johannesburg, for his interest in the work and also for providing the specially cut diamonds which were used, and Industrial Distributors (1946) Ltd. for financial support.

REFERENCES

AUSTIN, I. G., and WOLFE, R., 1956, *Proc. phys. Soc. Lond.* B, **69,** 329.
CUSTERS, J. F. H., 1952, *Physica*, **18,** 489.
DONOVAN, B., and MARCH, N. H., 1956, *Proc. phys. Soc. Lond.* B, **69,** 528.
DYER, H. B., and WEDEPOHL, P. T., 1956, *Proc. phys. Soc. Lond.* B, **69,** 410.
FAN, H. Y., SPITZER, W., and COLLINS, R. J., 1956, *Phys. Rev.*, **101,** 566.
HALL, G. G., 1958, *Phil. Mag.*, **3,** 429.
KAHN, A. H., 1955, *Phys. Rev.*, **97,** 1647.
MEYER, H. J. G., 1958, *Phys. Rev.*, **112,** 298.
STEPHEN, M. J., 1958, *Proc. phys. Soc. Lond.* B, **71,** 485.
SUTHERLAND, G. B. B. M., BLACKWELL, E. D., and SIMERAL, W. G., 1954, *Nature, Lond.*, **174,** 901.
WEDEPOHL, P. T., 1957, *Proc. phys. Soc. Lond.* B, **70,** 117.

The Effect of Internal Oxidation on the Damping Capacity of Copper–Silicon Alloys†

By T. B. GIBBONS and S. O'HARA
Royal College of Science and Technology, Glasgow, C.1

[Received October 20, 1959]

ABSTRACT

Damping capacity measurements have been carried out on copper–silicon alloy specimens before and after internal oxidation and the results compared with those for oxygen free, high conductivity copper specimens given the same treatment. High damping values have been noted for the fully internally oxidized copper–silicon material and it is suggested that this is caused, to some extent, by the generation of relatively free dislocations around the silica particles during the growth and subsequent cooling of these inclusions.

§ 1. INTRODUCTION

DISSOLVED impurities are known to lower the damping capacity of metals by pinning the dislocations. Hanstock (1954) has obtained large increases in the damping capacity of aluminium alloys during precipitation. Granato and Lucke (1956) have found increases in damping after internal oxidation and have suggested that the increase in damping in both these cases is due to the removal of the impurities or alloying elements from the lattice by precipitation and the consequent unlocking of pinned dislocations.

In the present work, a copper–silicon alloy, containing about 0·2% silicon, was used to determine the effect of internal oxidation on damping capacity. In all, three effects could be studied, viz. removal of silicon, entry of oxygen to the lattice, and formation of silica particles.

The amplitude dependent damping observed is best described by a static hysteresis mechanism which is frequency independent.

Granato and Lucke (1956) have described this mechanism by suggesting that the dislocation lines bell out under the applied stress and then break away from the pinning points. During the return part of the cycle, the path followed by the dislocation is different from the outgoing path and the resulting hysteresis in the dislocation stress–strain curve, gives rise to an energy loss.

A quantitative treatment of this mechanism gives the following expression for amplitude dependent damping Δ_H

$$\Delta_H = \frac{A}{\epsilon_0} \exp\left(-\frac{B}{\epsilon_0}\right)$$

---

† Communicated by the Authors.

where ϵ_0 is the measuring strain amplitude

$$A = \frac{2{\cdot}5\Omega\Lambda L_N{}^3}{\pi^2 L}\frac{K\eta\mathbf{a}}{L\epsilon_0} \text{ and } B = \frac{K\eta\mathbf{a}}{\epsilon_0}$$

where Ω is an orientation factor accounting for difference in resolved shear stress on the slip planes and applied longitudinal stress, Λ is dislocation density, L_N is dislocation network length, L is average dislocation loop length, K is Boltzmann constant, η Cottrell misfit parameter measuring the magnitude of the lattice distortion at a point defect, and $\mathbf{a}$ is a lattice parameter.

Several workers have shown that this law is not complete in itself over large ranges of strain amplitude (Niblett and Wilkes 1959).

§ 2. EXPERIMENTAL

To ensure a uniform grain size, all the specimens were vacuum annealed for 48 hours at 1040°C before internal oxidation. The internal oxidation was carried out by heating the specimens in an enclosed space with equal amounts of cuprous oxide and copper powders. This allowed the silicon to be oxidized to silica without the formation of a cuprous oxide film on the surface. Replicate samples of O.F.H.C. copper and copper–silicon were used so that the effect of oxygen in the copper could be estimated; further, a comparison of the two sets of results gave an indication of the effect of silica particles in the internally oxidized copper–silicon alloy.

Complete internal oxidation was obtained by heating the specimens at 950°C for 100 hours. The partially internally oxidized specimens were held at 900°C for 72 hours. These times were calculated from the formula suggested by Rhines and co-workers (1942), viz.

$$\log\frac{X^2 C_M}{t} = \frac{a'}{T} + b'$$

where X = depth of oxidation in centimetres in time t, C_M = original alloy concentration, T = absolute temperature, a' and b' are constants for the particular alloy.

In the partially oxidized specimens the depth of penetration was, on average, 0·13 cm, which compared favourably with the calculated depth.

The damping capacity of the specimens was measured after the initial vacuum anneal and then after internal oxidation. The apparatus used was designed to measure damping phenomena in the kilocycle range and was initially developed by Förster (1937). The bar vibrates transversely in free free motion, the damping capacity being measured from the width of the resonant peak at half the resonant amplitude. The specimens were supported a short distance from the nodes by cotton threads which vibrate and detect the vibrations of the bar. Some inaccuracy arises because the support positions and the nodes are not coincident. No correction for this has been applied, hence the individual results are not absolute but may be considered to be comparative.

§ 3. Results

The damping values for the vacuum annealed O.F.H.C. copper are given by curves 2, 3, 4, fig. 1, and curve 1, fig. 1, is typical of a vacuum annealed copper–silicon bar. The very high amplitude dependent damping of curve 2 is the result of having to push the specimen out of its graphite sheath. In general, these results are in agreement with other published work.

Fig. 1

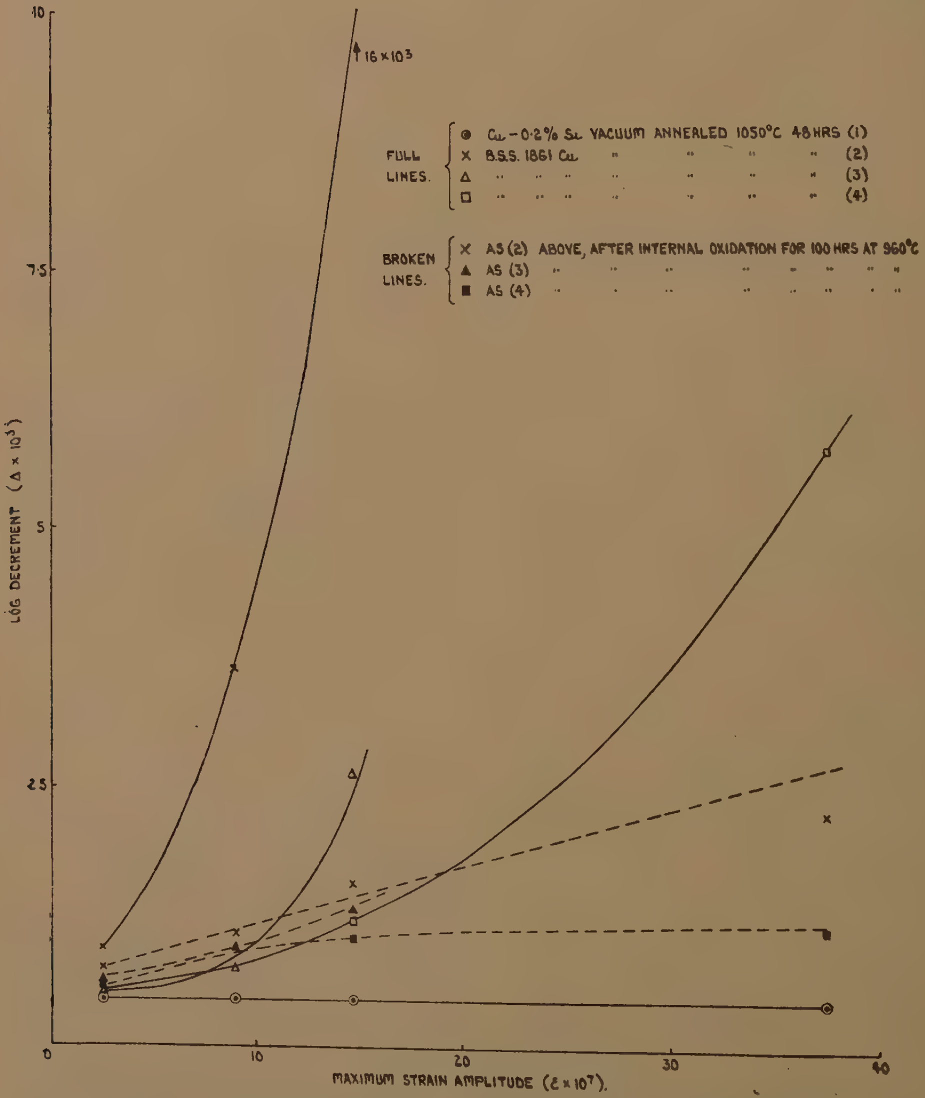

The effect of internal oxidation of these O.F.H.C. copper specimens is quite marked and is particularly noticeable in the case of curve 2. In the three cases amplitude dependent damping has been almost completely removed.

In the copper–silicon specimens, partial internal oxidation has raised the damping from amplitude independence, curve A, fig. 2, to marked amplitude dependence as shown by the broken lines, fig. 2. Complete internal oxidation has raised the curves even further—full lines, fig. 2—and the damping capacity of these specimens is very high. The effect of internal oxidation on the copper–silicon material is therefore opposite to the effect on O.F.H.C. copper.

Fig. 2

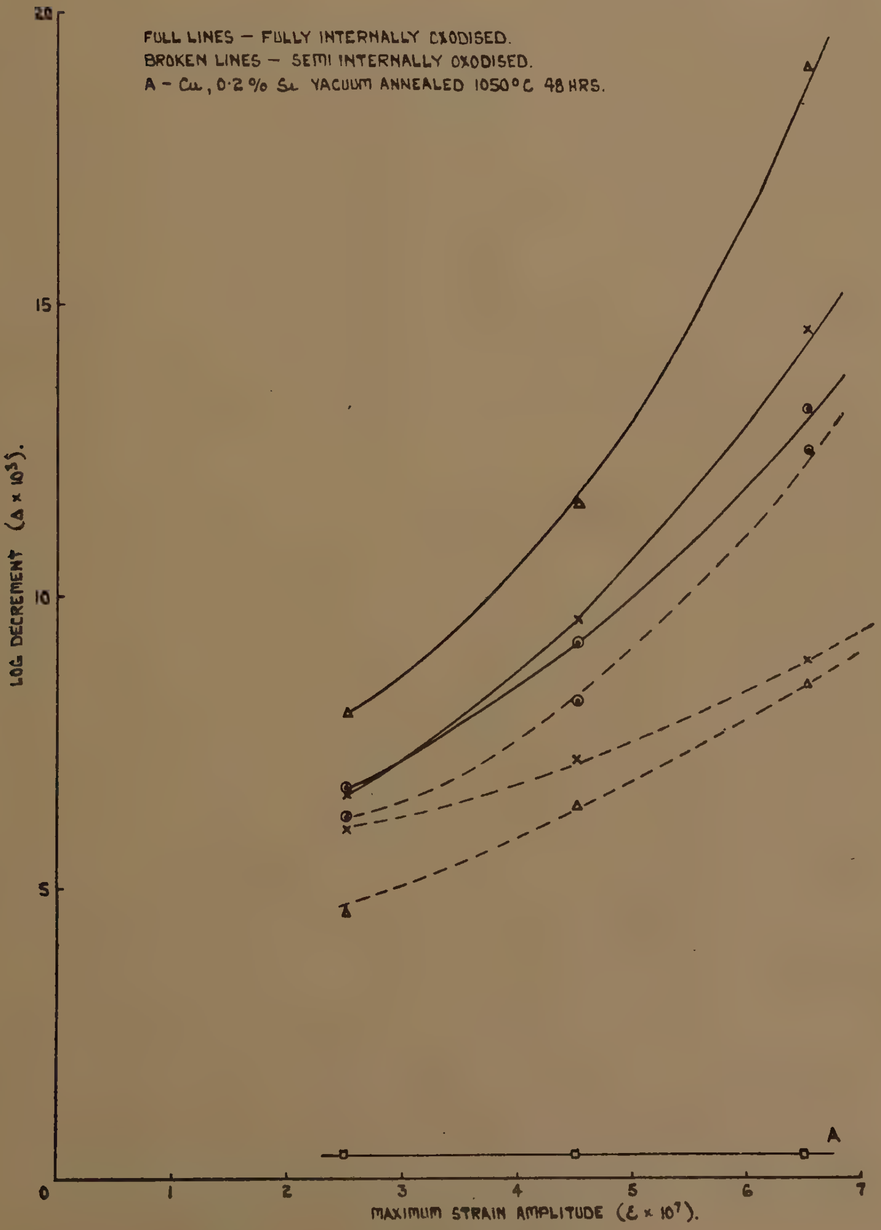

§ 4. Discussion

Perhaps the most significant difference between the fully internally oxidized copper–silicon specimens and the fully internally oxidised O.F.H.C. copper is the presence of silica particles in the former, since no oxide particles were found within the O.F.H.C. copper. The amount of oxygen present in the O.F.H.C. copper specimens, after internal oxidation, will probably be greater than in the internally oxidized copper–silicon alloy since in the latter case the oxidation front advances slowly while precipitation is taking place. It will be observed, however, that the damping values obtained for the internally oxidized copper–silicon alloy are higher than those for the vacuum annealed O.F.H.C. copper. Thus, the different amounts of oxygen present in the two sets of specimens cannot account for the high damping values of fig. 2. The high amplitude dependent damping of the copper–silicon specimens must be a direct result of the presence of silica particles. The decrease in damping capacity, on internal oxidation of annealed O.F.H.C. copper is just as expected due to the pinning effect of oxygen on the dislocation lines.

The amplitude dependent results shown in fig. 2 are characteristic of dislocation damping. It appears, therefore, that in some way, the silica particles are assisting in the creation of many loosely pinned dislocations.

Shear stresses can develop round a particle during growth at high temperature and also during cooling when the particles and matrix have different coefficients of contraction. These stresses can in turn create dislocations.

Parasnis and Mitchell (1959) have observed this effect in crystals of silver chloride. In this case, particles of what is assumed to be silver are surrounded by systems of decorated prismatic dislocation loops and more complex configurations. It is shown that the formation of these dislocations and their subsequent glide can make available the space required for the separation of further silver atoms upon the particles. Jones and Mitchell (1958) have noted systems of prismatic dislocations formed during cooling, round glass spheres in silver chloride crystals.

By direct observation of etch pits, Holden (1959) has noted large numbers of dislocations generated round precipitates formed in an iron–carbon–silicon alloy; these are believed to arise from the shear stresses developed round the particles during cooling of the alloy. Huggins (1959) has calculated the shear stresses which can arise during the formation of a precipitate and also during the anisotropic expansion or contraction of a precipitate in an isotropic matrix. He has shown that these stresses can be of large magnitudes.

In the present work, shear stresses arising during growth of the silica particles and also during cooling, may well create new dislocations around the particles. Also dislocation already in the lattice may be torn away from impurity pinning points and become free. Such a sequence of events would partly explain the high, amplitude dependent, damping results of fig. 2.

The explanation given by Granato and Lucke (1956) to account for the increase in damping after precipitation or internal oxidation is therefore oversimplified. The increased damping caused by precipitation will probably be due to a combination of three mechanisms; namely, a decrease in dissolved impurity or alloying element, the creation of dislocations round precipitates and the freeing of pinned dislocations by the shear stresses in the vicinity of the precipitates.

ACKNOWLEDGMENT

The authors would like to thank Professor Hay for his encouragement while the work was in progress.

REFERENCES

FÖRSTER, F., 1937, *Z. Metallk.*, **29,** 109.
GRANATO, A., and LUCKE, K., 1956, Reported, *Dislocations and Mechanical Properties of Crystals* (Wiley, 1957).
HANSTOCK, R. F., 1954, *J. Inst. Met.*, **83,** 11.
HOLDEN, J., 1959, *Acta Met.* (to be published).
HUGGINS, R. G., 1959, *Acta Met.*, **7,** 357.
JONES, D. A., and MITCHELL, J. W., 1958, *Phil. Mag.*, **3,** 1.
MARTIN, J. W., and SMITH, G. C., 1954, *J. Inst. Met.*, **83,** 153.
NIBLETT, D. H., and WILKES, J., 1959, *Proc. phys. Soc. Lond.*, **73,** 95.
PARASNIS, A. S., and MITCHELL, J. W., 1959, *Phil. Mag.*, **4,** 171.
RHINES, F. N., JOHNSON, W. A., and ANDERSON, W. A., 1942, *Trans. Amer. Inst. min (metall.) Engrs*, **147,** 205.

A 10 in. Diameter Liquid Hydrogen Bubble Chamber†

By Margaret H. Alston‡, D. C. Cundy, W. H. Evans,
R. W. Newport, and P. R. Williams
Nuclear Physics Research Laboratory,
University of Liverpool

[Received September 28, 1959]

Abstract

The important design features of a 10 in. hydrogen bubble chamber, its magnet and the associated control circuitry are presented.

§ 1. Introduction

A liquid hydrogen bubble chamber of 10 in. diameter and 4 in. depth has been constructed for use with the 383 Mev synchrocyclotron. The dynamic heat input is kept to a minimum by using metal bellows to provide liquid phase expansion. It has been operated in the π-meson beams of the synchrocyclotron with a repetition period of 4 sec, in a magnetic field of 8000 oersted.

§ 2. General Arrangement (fig. 1 (*a*), 1 (*b*))

The vacuum tank of 1 in. thick stainless steel (grade EN 58 B) is in the form of a cross. The vertical member contains the chamber, the liquid hydrogen reservoirs, most of the copper radiation shield and its liquid nitrogen reservoirs. The cylindrical arms of the cross, 13⅛ in. diameter and 24 in. long, house extensions bolted on to the main radiation shield which reduce the solid angle subtended at the chamber by areas at room temperature to about ⅛ steradian.

Illumination is provided by a high-speed flash tube which gives a spherical source less than ⅜ in. diameter (GE FT 230 or A.E.I. FA 5), and a plano-convex lens placed close to the chamber. This system produces a convergent beam of light which comes to a focus along the axis of the chamber and in the plane of the two camera lenses. The lenses are 10 in. apart, 45 in. from the centre of the chamber and lie symmetrically on either side of the cone of light. This arrangement ensures an essentially constant light scattering angle equal to half the stereo angle for all points photographed in the chamber. The two stereo views are taken on one frame of 35 mm film for ease of measurement and handling.

---

† Communicated by Professor H. W. B. Skinner, F.R.S.
‡ Now at the Lawrence Radiation Laboratory, University of California.

Fig. 1 (*a*)

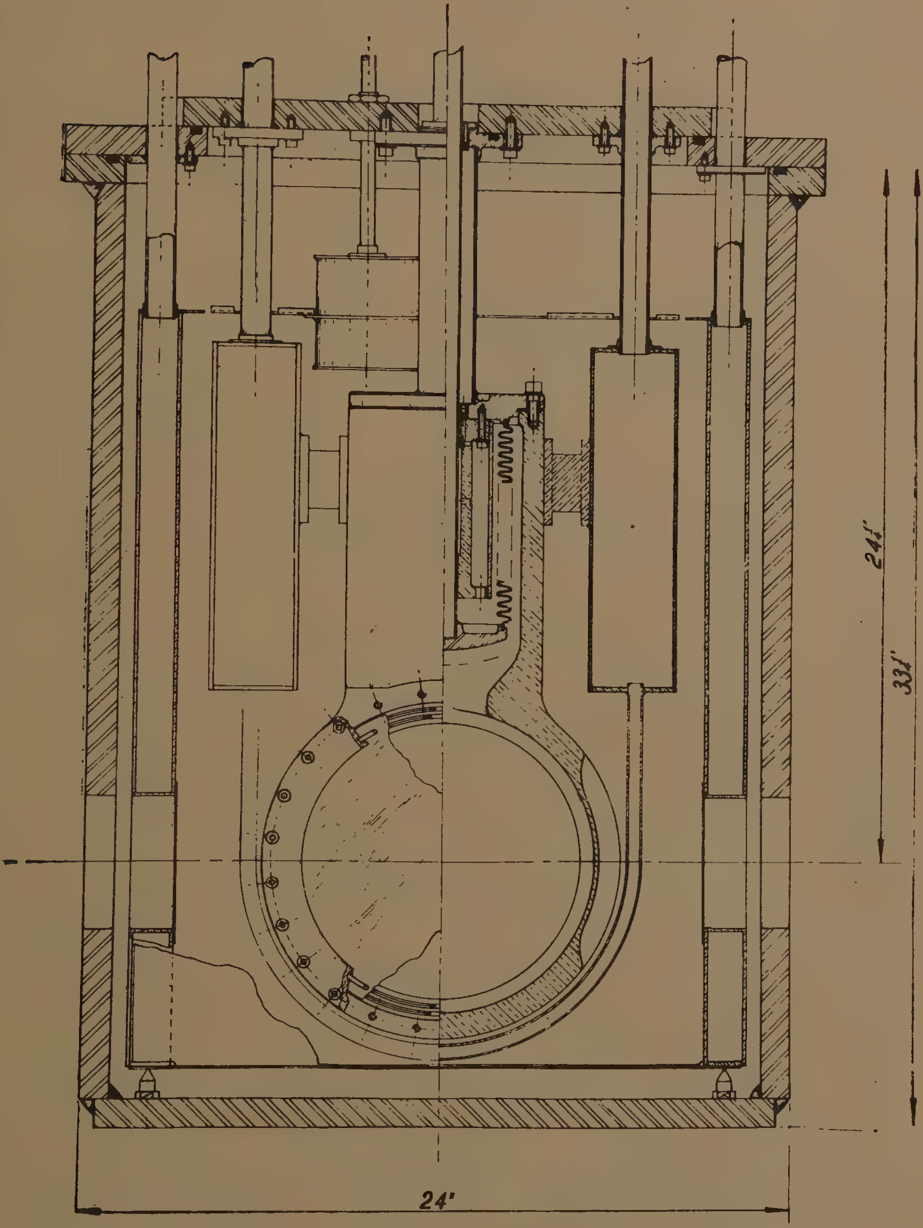

(*a*) General arrangements showing the mounting of the bubble chamber and the hydrogen reservoirs in the vacuum tank. (*b*) General arrangement showing the bubble chamber, liquid nitrogen radiation shield, the optical system and the expansion system.

Fig. 1 (*b*)

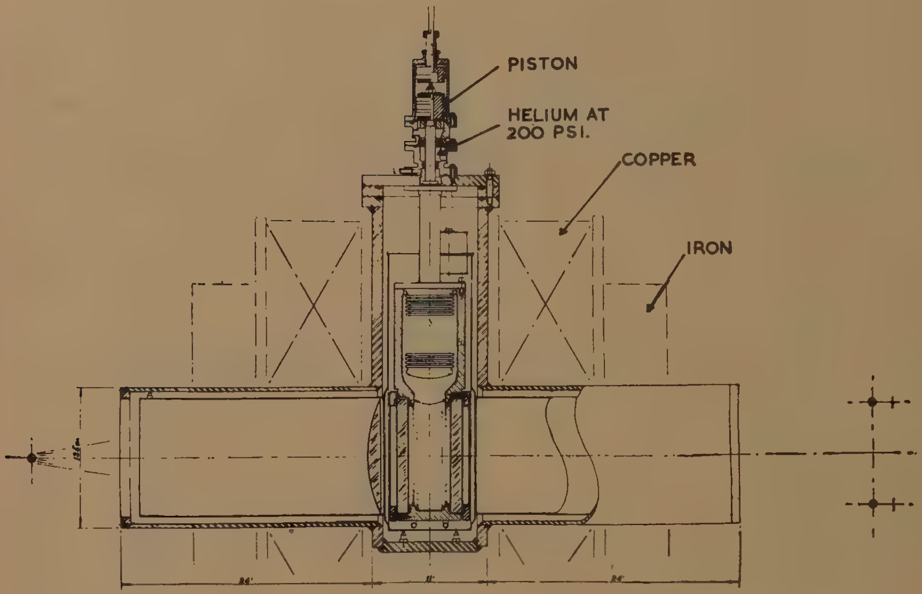

§ 3. Chamber Body (fig. 2, Pl. 19)

This was machined from a single forging of phosphorized de-oxidized copper and consists of a cylinder 10 in. in diameter 4 in. deep intersecting at right angles a second 5 in. in diameter and 10 in. deep. This second cylinder houses the bellows used for expansion. The orientation of the chamber, i.e. windows vertical with the expansion cylinder above the observed volume, was chosen so that bubbles formed during expansion rise to a position where the heat of re-compression can easily be removed (cooling takes place at the top of the expansion cylinder). Stable temperature gradients giving variable sensitivity with height are thus eliminated. This procedure also ensures that solid impurities do not collect in positions where they can obscure the field of view. It is by no means the only solution to these problems but appears to be the simplest method in practice.

The sealing of flanges and windows is achieved by using double lead ‘ 0 ’ rings with pump-outs. The whole unit and the 1 in. thick toughened-glass windows were designed to withstand 200 p.s.i.

The wall thickness is partly determined by mechanical considerations and partly by the need to keep temperature gradients in the metal to a minimum. The average thickness is 1 in. and it only departs appreciably from this in the regions of beam entry and exit where it is $\frac{1}{8}$ in. thick.

The chamber is supported by a 2 in. diameter, 0·048 in. wall stainless-steel tube welded to a flange which is in turn bolted on to the expansion cylinder.

§ 4. Expansion System

This consists of a 4-ply stainless steel bellows, each ply of 0·011 in. thickness, hard soldered to the support flange on the expansion cylinder. The bellows projects downwards into the expansion cylinder and is driven by a 1 in. diameter 0·048 in. wall stainless steel tube connected to a dished end cap on its lower end. The other end of the tube is connected to a 3-in. diameter air-driven aluminium-alloy piston at room temperature. Heat conducted along the drive tube is introduced at the bottom of the bellows and is easily removed by convective motion of the liquid hydrogen in the space between the bellows and the expansion cylinder. Helium gas is maintained in the space above the bellows to assist in the initial cooling by convection and is used to control the speed of expansion by altering the pressure. This method of control has the advantage that the expansion speed can be altered without affecting the speed of re-compression.

The drive tube is used in compression and, to reduce the tendency to buckle, cylindrical guides are provided to restrict the maximum free length to 8 in.

Failure of the bellows would result in hydrogen gas at the operating pressure entering the space above the bellows. To prevent this gas from entering the cylinder containing the air-driven piston and forming an explosive mixture with air, the drive rod passes through a small compartment containing helium gas at 200 p.s.i. and sealed by Gaco distributor seals. This pressurized helium compartment also prevents leakage of air into the bellows.

Expansion and re-compression are achieved by release of the air behind the piston and its subsequent re-introduction by means of a three-way valve. For a typical setting the cycle consists of a 8 ms expansion, a 15 ms expanded phase and an 9 ms re-compression. The system is reproducible in time to better than 0·5 ms and the particle beam traverses the bubble chamber under accurately reproducible conditions.

Under normal operating conditions the hydrogen vapour pressure is 67 p.s.i.g. and the pre-expansion pressure is 78 p.s.i.g. The expanded pressure is not accurately known but the variation of chamber pressure is displayed on one trace of a double beam oscilloscope by using a condenser gauge and the FM detector circuit described previously (Alston *et al.* 1957). The entry of the beam of particles and the position of the light flash is displayed on the second trace.

The expansion system has satisfactorily performed 10 000 cycles at room temperature and 50 000 at liquid hydrogen temperatures with a stroke of 0·7 in. corresponding to a volume expansion of $2\frac{1}{4}\%$.

§ 5. Temperature Control

The chamber is kept at the operating temperature by connecting the upper portion of the expansion cylinder to the liquid hydrogen reservoirs through two metal straps whose size is determined by the total heat input to the chamber at the operating temperature. Since the cool-down to 78°K is achieved by filling the liquid hydrogen reservoirs with liquid nitrogen and the thermal capacity of the chamber increases with temperature, the conductivity of the straps should increase correspondingly with temperature if the cool-down is to be achieved in a reasonable time. Phosphorized de-oxidized copper was chosen for the material of the straps since it has the required characteristics.

In practice the chamber is slightly over-cooled and small heaters embedded in the wall of the expansion cylinder are used in conjunction with a contact pressure-gauge connected to a vapour pressure thermometer to provide temperature control. This system regulates the vapour pressure of the hydrogen filling to 1 p.s.i.

Liquid hydrogen consumption is 1·6 litres per hour total and is constant if the chamber temperature is kept constant. The dynamic load for the chamber at 15 cycles per minute is equivalent to about 0·5 litres/hour of liquid hydrogen. This figure was calculated from the difference in the power supplied by the control heaters in the cycled and uncycled chamber. It is essential to isolate the chamber from the filling line during expansion and this is achieved by using a helium-gas operated bellows-valve placed close to the chamber.

§ 6. MAGNET

A cross section of the magnet is shown in fig. 1 (*a*). It consists of two coils, each 14½ in. ID and 44½ in. OD by 8·5 in. deep, surrounded by an iron return path but no poles. The iron end pieces are bored 14½ in. diameter to permit illumination and photography. The magnet weighs 6 tons and the gap between the coils is 14 in. Each set consists of eight double pancakes electrically in series with the cooling water in parallel. The two coils in each double pancake are joined at the centre so that the inlet and outlet water connections are on the outside. Water at 500 p.s.i. is used for cooling. Typical operating conditions are 800 amps at 240 volts giving a field of 8000 oersted with a variation of ± 2% over the illuminated volume.

§ 7. SAFETY ARRANGEMENTS

The utmost care is taken to ensure the safety of the personnel operating the chamber. The procedure adopted follows closely that employed at the UCRL. Failure of the toughened glass windows would result in the release of 6 litres of liquid hydrogen into the vacuum tank and a rapid rise in the tank pressure to about 70 p.s.i. Subsequent heat transfer from the tank to the cold hydrogen would cause a slower rise to a final pressure of around 40 atmospheres.

The tank is connected to a ‘ rupture disc ’ and a 4 in. diameter vent line. The rupture disc is constructed so that during normal operation, with the tank at high vacuum, it rests on a concave perforated plate. Should the tank pressure rise one or two pounds above atmospheric pressure the disc is forced against a sharp cutting edge and is fractured. This method of construction ensures that the performance is not strongly dependent on the unsupported strength of the disc.

The vacuum tank and all units connected to the vacuum system will withstand 150 p.s.i. High-vacuum gauges are housed in protecting brass cylinders. All hydrogen gas released is vented into the atmosphere outside the building. This applies to gas escaping from relief valves and the boil-off from the two reservoirs.

A power failure or a fault in the magnet stabilizer circuit can cause the current in the magnet to decay with a time constant of around 1·5 sec. The subsequent mechanical impulse to the chamber can be considerable (Gow, private communication). The maximum rate of current decay is reduced by using the stored rotational energy of the motor generator set. The generator is excited by means of a d.c. amplifier and a high gain amplidyne set. The output from the generator is coupled in anti-phase via a condenser to subsidiary windings in the amplidyne unit. By this means the current decay is made approximately linear and extended to 10 sec.

§ 8. COOL-DOWN PROCEDURE

The vacuum tank is first evacuated to below 10^{-5} mm mercury and the chamber is pumped through a liquid nitrogen trap to remove condensable vapours. The chamber is then filled with pure hydrogen gas which is maintained at 78 p.s.i.g. and assists in cooling the inner faces of the glass windows by convection. This gas, obtained by passing commercial hydrogen through the purifying circuit of a hydrogen liquefying plant, can be liquefied in the chamber without further cleaning.

The liquid nitrogen radiation shield is cooled at least 2 hours before the chamber. This precuation is taken to avoid condensation on the outer faces of the glass windows. No trouble due to this cause has been experienced in several days' operation.

Hydrogen condensing in the chamber is pre-cooled to 27°K through two heat exchangers at 78°K and 20°K respectively. Before cycling the chamber it is important to make sure that it is completely full of liquid hydrogen. The top of the expansion cylinder is the coldest point in the system and there is no danger that a large bubble of gaseous hydrogen be left at this point.

§ 9. OPERATING PROCEDURE WITH THE SYNCHROCYCLOTRON

In normal operation the synchrocyclotron gives one pulse of particles every 10 ms. To ensure that the particles traverse the chamber in an accurately reproducible manner the circuit shown schematically in fig. 3 is used. The pulsed-arc ion source of the synchrocyclotron is not pulsed until required. Synchronizing pulses from the accelerator appear at 10 ms intervals. These are fed into an electronic gate which is opened by the sequence unit. The next synchronizing pulse is transmitted through the gating circuit and operates a delay unit which controls the current pulse to the 3-way solenoid operated air valve. The bubble chamber is expanded after an interval governed by the setting of the delay unit and the mechanical inertia of the valves. Synchronizing pulses are also fed through the electronic gate into a 0 to 10 variable scaler, the output of which generates a pulse to trigger the synchrocyclotron pulsed-arc source. The scaler is initially set at some arbitrary figure and the dynamic pressure change in the chamber and the beam traversal time (detected by a 2-fold scintillation counter) are observed on the double beam oscilloscope. The variable delay and the scaler are then set so that the particles traverse the chamber at the correct time. A typical trace obtained is shown in fig. 4 (Pl. 20).

Fig. 3

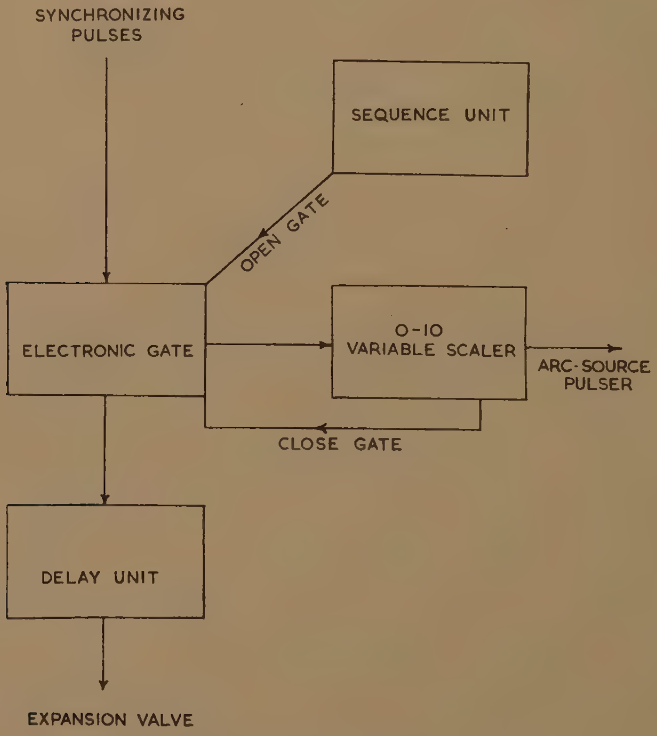

Schematic diagram of the electronic control unit.

The intensity of the circulating beam in the synchrocyclotron is recorded pulse by pulse on a commercial pen recorder, thus enabling the operator to correct for long period drifts.

Particles entering the chamber are deflected by the magnetic field around the chamber and some allowance must be made for this if the particles are to traverse the chamber symmetrically. In bubble chambers employing a vertical magnetic field the whole equipment can be rotated about a vertical axis. Bubble chambers with a horizontal field cannot in general be tilted and some other solution must be sought. A reasonably successful solution is to raise the whole equipment some inches above beam height. Any reduction necessary in the energy of the particles should be carried out as close to the chamber as possible.

An example of the pictures taken is shown in fig. 5 (Pl. 21) and a photograph of the apparatus is shown in fig. 6 (Pl. 22).

ACKNOWLEDGMENTS

We are grateful to Professor H. W. B. Skinner and Professor J. M. Cassels for their interest and encouragement ; to Professor L. W. Alvarez and his colleagues for sending us technical information on hydrogen bubble chambers ; to Mr. J. H. Craig and his staff for constructing the equipment, to Mr. A. Amery who made all the engineering drawings, to Dr. B. C. Collinge and his staff who designed and built some of the electronic equipment, to B. Halliday and Metropolitan Vickers for work on the magnet power supplies and to the synchrocyclotron and liquefier crews for their co-operation.

One of us (D.C.C.) is indebted to D.S.I.R. for a studentship ; M.H.A. and P.R.W. to the I.C.I. for Fellowships.

REFERENCE

ALSTON, MARGARET H., COLLINGE, B., EVANS, W. H., NEWPORT, R. W., and WILLIAMS, P. R., 1957, *Phil. Mag.*, **2**, 820.

Systematic Track Distortion in a 10 in. Diameter Liquid Hydrogen Bubble Chamber†

By D. C. Cundy, W. H. Evans, D. W. Hadley, P. Mason, R. W. Newport, J. R. Smith and P. R. Williams
Nuclear Physics Research Laboratory, University of Liverpool

[Received September 28, 1959]

Abstract

An investigation has been made of the dependence of systematic track distortion in a 10 in. diameter liquid hydrogen bubble chamber upon track position in the chamber, beam entry time and flash delay.

It is seen that provided photography occurs before recompression the distortions are small compared with the multiple scattering curvature, and are not significantly different from zero except at the extreme top and bottom of the chamber.

§ 1. Introduction

The bubble chamber described in the preceding paper has been placed in the pion beam of the Liverpool 156 in. synchrocyclotron, the energy of the beam traversing the chamber being 85 mev.

It is essential that distortions produced in the chamber be small, and it is useful to determine if these can be minimized by letting the beam enter the chamber at one particular instant of the sensitive time.

To detect and measure any such distortions the magnetic field was switched off, and deviations from linearity of the meson tracks were calculated in a manner very similar to that used earlier for a propane bubble chamber (Evans *et al.* 1959).

Three earlier reports of distortion measurements in hydrogen bubble chambers have been published. The first of these (Cresti) deals with the Berkeley 25 cm chamber, which had horizontal windows, and gas-phase expansion through a small diameter expansion line. Systematic general distortions were reported, these being greatest near the expansion line. Maps were plotted showing the distortion at different points in the chamber, and also the variation of curvature with flash delay.

Recently the distortion pattern in the C.E.R.N. 10 cm chamber has been investigated (Budde *et al.* 1959), the technique employed being somewhat different from that used at Liverpool, the statistics being poorer. This chamber is of similar shape to the Liverpool instrument, although of smaller size and with a different system of cooling. The results did show some systematic distortion at certain flash delays, but these were small compared with the effects of multiple scattering. At the top and bottom of the chamber radii of curvature of both signs and widely differing values were observed. It was thought that these were due to local turbulences in the liquid, which would be of diminished importance in a larger chamber.

---

† Communicated by Professor H. W. B. Skinner, F.R.S.

A full measurement of distortion in the 72 in. chamber at Berkeley, an instrument of completely different design from any of the above, has not yet been carried out. However, in a preliminary report (Alston 1959) the induced curvatures do not appear to differ significantly from zero.

§ 2. SOURCES OF DISTORTION

In addition to distortion arising from mass motions of the liquid hydrogen, spurious curvatures will be caused also by defects of the optical system and by multiple coulomb scattering.

Optical distortions arise from defects both of the camera lens and its associated optical system, and the armour plate glass windows on the chamber body and the vacuum tank, the window closest to the camera having the greatest effect.

The average curvature expected from multiple scattering can be calculated (Blackett 1954), being $3{\cdot}34\sqrt{L}$ for pions of momentum 175 MEV/c, where L is the track length in centimetres. This gives a radius of curvature of 13·3 metres for the majority of tracks measured, the extreme values being 14·9 and 11·5 metres for the longest and shortest tracks respectively.

§ 3. METHOD

Particles entered the chamber at points A, B and C on the pressure–time curve, fig. 1, at each setting the bubble growth time being varied between 1·5 and 5 msecs, although the intermediate values are not considered here.

The chamber took 8 msec to expand. Point A, occurring 4 msec later, being the earliest instant at which sensitivity was attained. Consequently such tracks consisted of widely spaced bubbles and were difficult to observe, accurate measurements being possible only on tracks with a flash delay of 5 msec. Point B occurred 14 msec after the commencement of expansion, the tracks then being of much higher quality, enabling measurements to be made at the 1·5 msec flash delay.

The time at which recompression is applied varies by about one millisecond, and photographs taken at C (21 msec after beginning of the expansion cycle) with a delay of 1·5 msec occurred sometimes before and sometimes after the application of recompression. Photographs taken with long delays occurred always after recompression.

It can be seen from fig. 1 that the pressure slowly falls during the whole of the expanded state. This is due to slight flexibility of the piston back-stop, which prevents overstressing of the drive rod.

Fig. 1

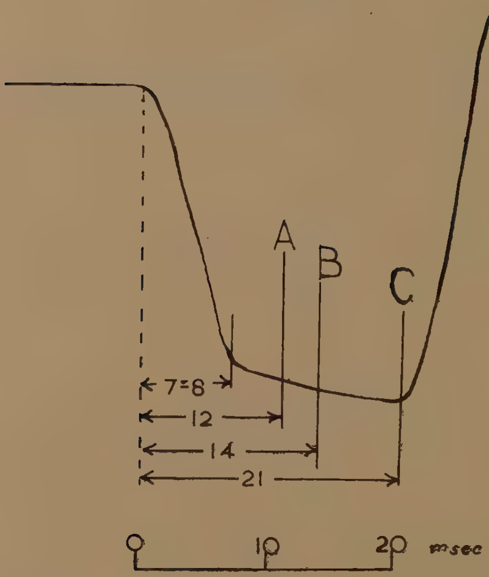

The pressure–time curve for the expansion cycle, showing time of beam entry.

Fig. 2

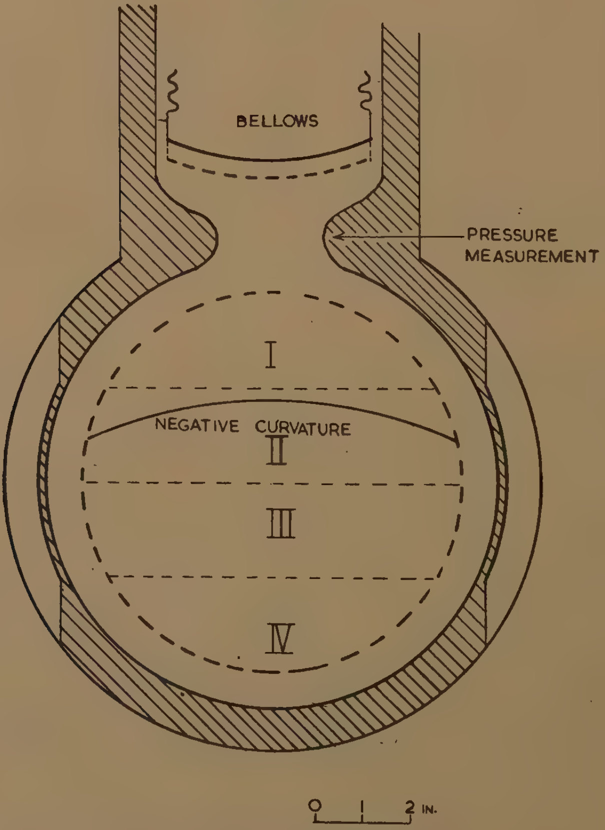
BELLOWS
PRESSURE MEASUREMENT
I
NEGATIVE CURVATURE
II
III
IV
0
1
2 IN.

Schematic section through chamber showing division into zones and position of bellows vertically above the illuminated region.

The random effects of multiple scattering may be eliminated statistically by measuring a large number of tracks traversing the same zone of the chamber, leaving only the systematic distortion caused by liquid motions.

Fig. 3

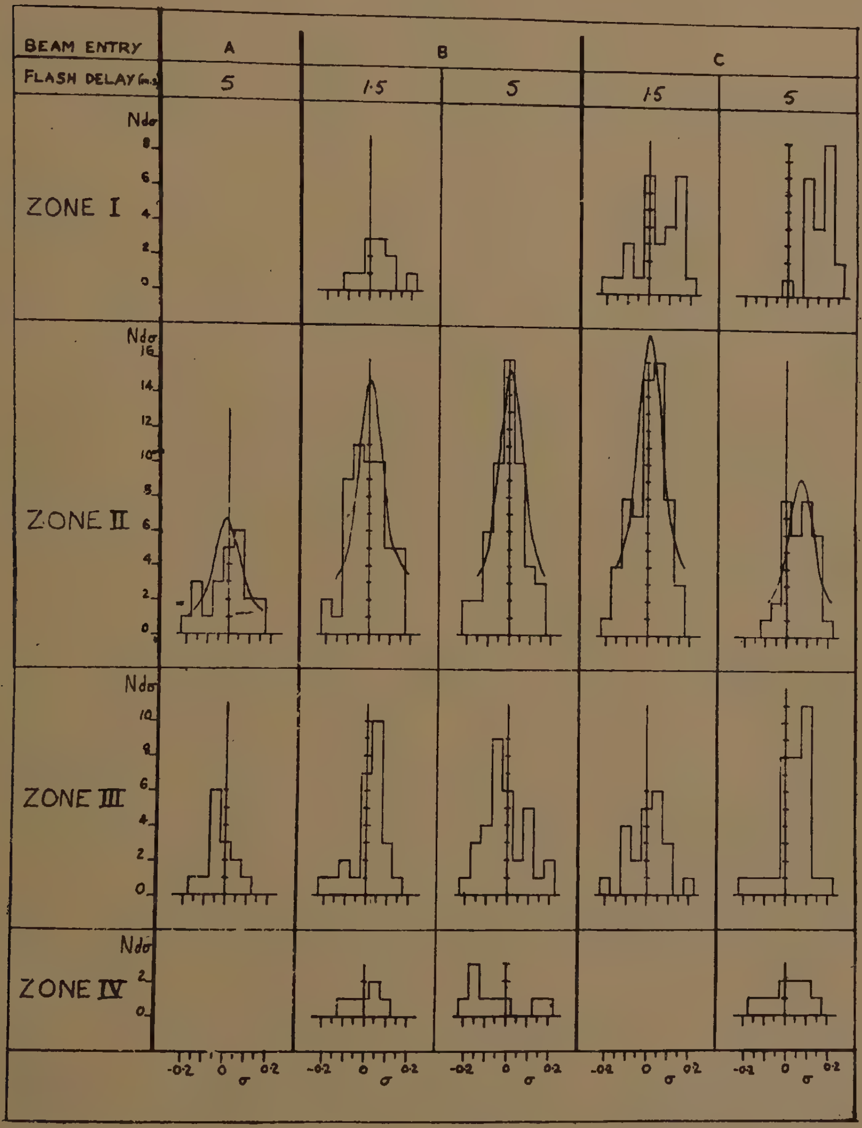

Distribution of systematic curvatures. Ordinate is number of tracks per unit range of curvature. Abscissa (σ) is curvature in reciprocal metres. The Gaussian distribution plotted in zone II has a half-width given by the multiple scattering, the mean value being that obtained from the individual readings and not from the block histogram.

The illuminated region of the chamber consisted of a circle 20 cm in diameter, which at a magnification of 1/20 gave a circular image approximately 1 cm diameter on the film. For the purpose of the analysis the chamber was divided into four horizontal zones of equal height the majority of tracks passing through the two central zones, with only a very small number within 2 cm of the top or bottom of the illuminated region.

The stereo-camera took two photographs of each expansion, with an angle of 13° between the camera axes. Initially about 60 tracks were measured on both views, the distance of each track from the chamber windows then being calculated. It was found that in all but three of these cases the tracks were at least 1 in. from the windows. Since any variations in distortion across the width of the chamber would be most significant close to the windows it was thus considered sufficiently accurate to assume the distortions to be uniform across the chamber width. Hence the remaining measurements were carried out on only one photograph of each stereo pair. Such a procedure assumed that all the tracks were parallel to the plane of the windows, but it was shown that this assumption introduced a negligible error into the final result, as did the angle of $6\frac{1}{2}°$ between the camera and bubble chamber axes (the camera used in this analysis was an earlier model than that described in the preceding paper).

Only tracks within 10° of the horizontal were measured, readings being spaced 1 mm apart on the film, except for short tracks close to the upper or lower boundaries, where readings were taken every 0·5 mm. The image width was generally 18–20 μ, readings being reproducible to within 2 μ.

Curvatures were calculated by a least squares method, negative curvature implying an upward, and positive a downward, movement of the track centre with respect to the ends. The curvatures for each zone at each expansion condition were then calculated, and are shown plotted in histogram form (fig. 3). Any curvatures (σ) having a value on the film of $|\sigma| > 5{\cdot}5\ \mathrm{m}^{-1}$ were neglected, since it was obvious from the form of the plotted distribution that these were due to single scatters which had not been detected visually.

Optical distortions were measured in the chamber position by suspending a frame carrying a grid of stretched nylon fibres. Measurement of photographs taken with this arrangement gave curvatures which were negligible compared with the errors on the main analysis.

§ 4. DISCUSSION OF RESULTS

The results of the analysis are given in the table, and illustrated graphically in fig. 3. From the histograms it can be seen that except possibly in the lowest zone (IV) where there are too few tracks, the half width of the distribution is approximately equal to the curvature arising from multiple scattering. This exception is probably caused by poor statistics, but there may possibly be an increased spread due to local vortices or turbulences in the liquid, which may not be constant from expansion to expansion.

The Variations of Track Curvature

Beam entry	A		B				C				
Flash delay	5 msec		1·5 msec		5 msec		1·5 msec		5 msec		
Zone	Curvature (m^{-1})	No. of tracks	(N)	(m^{-1})	N	(m^{-1})	N	(m^{-1})	N	(m^{-1})	N
I			—	0·018	—	−0·031	—	0·046	—	0·148	
			—	±0·020	10	±0·047	4	±0·011	28	±0·005	21
II	−0·0045		—	0·045	—	−0·0065	—	0·004	—	0·068	
	±0·020	23	—	±0·013	51	±0·011	53	±0·011	61	±0·006	32
III	−0·032		—	0·022	—	−0·008	—	0·009	—	0·042	
	±0·017	14	—	±0·014	25	±0·017	33	±0·018	20	±0·011	33
IV			—	0·011	—	−0·050	—	—	—	0·012	
			—	±0·021	6	±0·048	9	—	—	±0·032	10

At the earliest setting (A) statistically significant results could be obtained only for the two central zones of the chamber and then only with the 5 msec flash delay. Although the errors are large there is a tendency for the tracks to be slightly affected by the upward movement of the bellows at expansion, i.e. negative curvature. Photographs taken at B with 5 msec delay are not in disagreement with this possibility, although those taken at 1·5 msec delay show a slight tendency towards positive curvature. In all cases the residual curvatures are much smaller than those caused by multiple scattering, and it is not impossible that they are all zero, since the quoted errors are merely those calculated from the statistical spread of the individual points.

Tracks entering the chamber at C do, however, show an entirely different, and consistent, form of distortion. In all cases the curvature is positive, being greatest near the top of the chamber. This is consistent with the rapid downward movement of the bellows at recompression, the curvature being more pronounced at the longer delay times, when photography takes place always after the commencement of this movement. With the delay of 1·5 msec, for which recompression has sometimes not yet begun, the curvatures are still not significantly different from zero in the central zones of the chamber, and it is only close to the bellows cavity that distortion becomes appreciable. It is interesting to note that in the Saclay propane bubble chamber the particle beam enters always after the application of recompression (Bloch 1959). Distortion measurements in this chamber have not, however, yet been published.

It is seen that provided photography occurs always before the commencement of recompression the systematic distortions introduced by liquid movement are small compared with the effects of multiple scattering.

For work at high energies it would be essential to repeat the above measurements in a high energy proton beam, multiple scattering then being reduced, so that the final accuracy of the result would depend largely upon the accuracy of measurement.

ACKNOWLEDGMENTS

We wish to thank all those associated in operating the bubble chamber, the cyclotron crew for provision of beam facilities and R. Martin and S. Austin for maintaining a supply of liquid hydrogen. Miss M. Stynes assisted in the work of track measurement. D. C. C. and J. R. S. wish to thank D.S.I.R. for the receipt of research grants.

REFERENCES

ALSTON, M. H., 1959, U.C.R.L. Eng. Note 4313–03/M26.
BLACKETT, P. M. S., 1954, *Nuovo Cim. Sup.* **2,** 264.
BLOCH, M., C.E.R.N. 59–24 Pg. 15.
BUDDE, R., BURGER, A., FILTHUTH, H., GOLDSCHMIDT-CLERMONT, Y., MAYER, H. M., MORRISON, D. R. O., PEYROU, C., and TREMBLEY, J., 1959, *Nuovo Cim.*, **14,** 778.
CRESTI, M., U.C.R.L. Eng. Note 4312–07/M37.1.
EVANS, W. H., HADLEY, D. W., MORGAN, T. D. N., WILLIAMS, P. R., and KIRK, A., 1959, *J. sci. Instrum.*, **36,** 365.

The Angular Dislocation†

By Elizabeth H. Yoffe
Cavendish Laboratory, Cambridge

[Received September 22, 1959]

Abstract

The stress field of a sharply angular dislocation is calculated by Burgers' method. It is shown that more complicated configurations may be composed of angular dislocations, and the corresponding stress fields deduced by adding the fields of the components. Some examples are given, including the triangle, hexagon and tetrahedron.

§ 1. Introduction

Recent theories of work hardening depend on the elastic interaction of many dislocations. These may lie in different planes and interact with one another to form a complicated three-dimensional network of dislocation lines.

Since the equations of elasticity are linear it is possible to find the stress field due to each small part of the network, and add the results to find that of the whole. It might be thought that a straight line segment of the network would be a suitable element to consider, and this would be true if the field of such an element could be calculated. Unfortunately this is not so, since a dislocation cannot begin nor end in the interior of a perfect elastic medium, although some approximative theories have been based on the assumption that the field is similar to that of an infinite straight dislocation.

A more suitable element is the closed circuit of dislocation line, finite in extent and polygonal in shape, with a constant Burgers vector. It is found that the general network can be built up of such elements combined, where necessary, with infinite straight dislocations.

The stress field of a polygonal dislocation may be derived from the formulae of J. M. Burgers (1939) by integrating certain functions over a surface bounded by the polygon. In order to show the significance of the various terms a simple angular dislocation is considered first; that is, a dislocation composed of two semi-infinite straight arms meeting at the origin.

The stress field of the angular dislocation is derived in § 2, the triangle and hexagon are solved in detail in § 3 and § 4 and other applications are discussed in § 5.

---

† Communicated by the Author.

§ 2. THE ELASTIC FIELD OF THE ANGULAR DISLOCATION

Burgers (1939) has derived the displacements for a dislocation of arbitrary shape. His method is followed here for a dislocation line ζOZ as shown in fig. 1. The x axis is taken normal to the paper and cartesian coordinates (x, y, z) or (x, η, ζ) are used, where

$$\eta = y \cos \alpha - z \sin \alpha,$$

$$\zeta = y \sin \alpha + z \cos \alpha.$$

Also:

$$r^2 = x^2 + y^2 + z^2 = x^2 + \eta^2 + \zeta^2.$$

Fig. 1

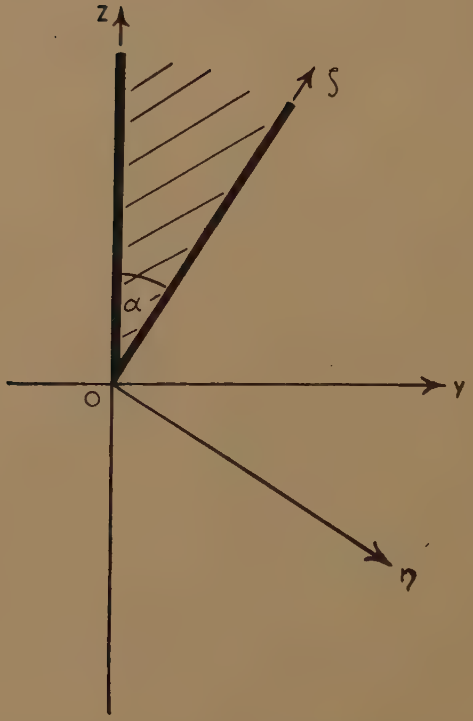

The multivalued terms in the displacements come from Burgers' function ϕ, which in this case must have a surface of discontinuity bounded by the positive z and ζ axes. In particular the surface may be the plane region shown shaded in fig. 1 and extending to infinity. At any point $P(x, y, z)$ the function ϕ has a value proportional to the solid angle subtended at P by this shaded area:

$$\phi = \frac{1}{4\pi} \int \int \frac{x}{R^3} dy' \, dz'$$

$$= \frac{1}{4\pi} \left(\tan^{-1} \frac{y}{x} - \tan^{-1} \frac{\eta}{x} + \tan^{-1} \frac{xr \sin \alpha}{x^2 \cos \alpha + y\eta} \right) \quad . \quad . \quad . \quad (1)$$

where $$R^2 = x^2 + (y-y')^2 + (z-z')^2.$$

The term $\tan^{-1} y/x$ corresponds to an infinite straight dislocation along the entire z axis, and the term $\tan^{-1} \eta/x$ to one on the ζ axis. The last term on the right-hand side corresponds to a junction of dislocations, as shown in fig. 2, since it is equal to half the solid angle subtended by the shaded areas in that figure. On adding these terms it is found that ϕ remains single valued on circling the negative z and ζ axes, but increases by unity when its circuit passes once into the paper between the positive axes.

Fig. 2

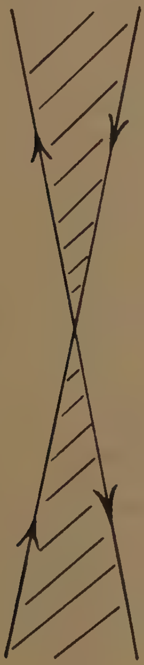

If the Burgers vector of the angular dislocation is b in the direction of x, the other terms used by Burgers are:

$$u^{**} = 0,$$

$$v^{**} = \frac{b}{4\pi}(\cos\alpha \log(r-\zeta) - \log(r-z)),$$

$$\omega^{**} = -\frac{b}{4\pi}\sin\alpha \log(r-\zeta),$$

$$\psi = \frac{b}{8\pi(1-\sigma)}(y\log(r-z) - \eta\log(r-\zeta))$$

where σ is Poisson's ratio. The complete displacements are:

$$u = b\phi + \frac{b}{8\pi(1-\sigma)}\left(\frac{xy}{r(r-z)} - \frac{x\eta}{r(r-\zeta)}\right),$$

$$v = \frac{b}{8\pi(1-\sigma)}\left(\frac{\eta\sin\alpha}{r-\zeta} - \frac{y\eta}{r(r-\zeta)} + \frac{y^2}{r(r-z)}\right.$$
$$\left. + (1-2\sigma)(\cos\alpha\log(r-\zeta) - \log(r-z))\right),$$

$$\omega = \frac{b}{8\pi(1-\sigma)}\left(\frac{\eta\cos\alpha}{r-\zeta} - \frac{y}{r} - \frac{\eta z}{r(r-\zeta)} + (1-2\sigma)\sin\alpha\log(r-\zeta)\right). \qquad (2)$$

From these expressions the components of strain and stress may be calculated in the usual way. The derivatives of the function ϕ reduce to simple forms:

$$\frac{\partial\phi}{\partial x} = \frac{1}{4\pi}\left(\frac{\eta}{r(r-\zeta)} - \frac{y}{r(r-z)}\right),$$

$$\frac{\partial\phi}{\partial y} = \frac{1}{4\pi}\left(\frac{x}{r(r-z)} - \frac{x\cos\alpha}{r(r-\zeta)}\right),$$

$$\frac{\partial\phi}{\partial z} = \frac{1}{4\pi}\frac{x\sin\alpha}{r(r-\zeta)},$$

so that the stress components are easily calculated. They consist of sums of elementary functions, and singularities on the positive z and ζ axes only. For example

$$\widehat{xx} = \frac{\mu b}{4\pi(1-\sigma)}\left(\frac{\eta}{r(r-\zeta)} - \frac{y}{r(r-z)} - \frac{x^2 y}{r^3(r-z)}\right.$$
$$\left. - \frac{x^2 y}{r^2(r-z)^2} + \frac{x^2\eta}{r^3(r-\zeta)} + \frac{x^2\eta}{r^2(r-\zeta)^2}\right),$$

$$\widehat{xz} = \frac{\mu b x}{4\pi(1-\sigma)}\left(\frac{y}{r^3} + \frac{\sin\alpha}{r(r-\zeta)} + \frac{\eta\cos\alpha}{r(r-\zeta)} + \frac{\eta z}{r^3(r-\zeta)} + \frac{\eta z}{r^2(r-\zeta)^2}\right), \qquad (3)$$

$$\widehat{zz} = \frac{\mu b}{4\pi(1-\sigma)}\left(\frac{yz}{r^3} - \frac{\eta}{r(r-\zeta)} + \frac{\eta z^2}{r^3(r-\zeta)} + \frac{\eta z^2}{r^2(r-\zeta)^2} - \frac{2\eta z\cos\alpha}{r(r-\zeta)^2} + \frac{\eta\cos^2}{(r-\zeta)^2}\right.$$
$$\left. + 2\sigma\left[\frac{y\cos\alpha}{r(r-\zeta)} - \frac{\sin\alpha\cos\alpha}{r-\zeta} - \frac{y}{r(r-z)}\right]\right).$$

If the angular dislocation has Burgers vector b in the y direction the corresponding functions are:

$$u^* = 0 = \omega^* = v^{**} = w^{**},$$

$$v^* = b\phi,$$

$$u^{**} = \frac{b}{4\pi}(\log(r-z) - \cos\alpha\log(r-\zeta)),$$

$$\psi = \frac{bx}{8\pi(1-\sigma)}(\cos\alpha\log(r-\zeta) - \log(r-z)).$$

The stress components are again readily calculated from the complete displacements:

$$\left.\begin{aligned}
u &= \frac{b}{8\pi(1-\sigma)}\left(\frac{x^2\cos\alpha}{r(r-\zeta)}-\frac{x^2}{r(r-z)}-(1-2\sigma)(\cos\alpha\log(r-\zeta)-\log(r-z))\right),\\
v &= b\phi+\frac{bx}{8\pi(1-\sigma)}\left(\frac{y\cos\alpha}{r(r-\zeta)}-\frac{\sin\alpha\cos\alpha}{r-\zeta}-\frac{y}{r(r-z)}\right),\\
w &= \frac{bx}{8\pi(1-\sigma)}\left(\frac{z\cos\alpha}{r(r-\zeta)}-\frac{\cos^2\alpha}{r-\zeta}+\frac{1}{r}\right).
\end{aligned}\right\} \quad . \; . \; . \quad (4)$$

Similarly if the Burgers vector is in the z direction the following expressions are obtained:

$$\left.\begin{aligned}
u^{**} &= \frac{b\sin\alpha}{4\pi}\log(r-\zeta) = -\frac{2(1-\sigma)\psi}{x},\\
u &= \frac{b\sin\alpha}{8\pi(1-\sigma)}\left((1-2\sigma)\log(r-\zeta)-\frac{x^2}{r(r-\zeta)}\right),\\
v &= \frac{bx\sin\alpha}{8\pi(1-\sigma)}\left(\frac{\sin\alpha}{r-\zeta}-\frac{y}{r(r-\zeta)}\right),\\
w &= b\phi+\frac{bx\sin\alpha}{8\pi(1-\sigma)}\left(\frac{\cos\alpha}{r-\zeta}-\frac{z}{r(r-\zeta)}\right).
\end{aligned}\right\} \quad . \; . \; . \quad (5)$$

The stress field of an angular dislocation of arbitrary Burgers vector is fully described by its components from eqns. (3), (4) and (5) in suitable proportion. A constant term may be added to ϕ or to any displacement without affecting the stress field.

§ 3. The Triangle

A triangular dislocation of constant Burgers vector is readily composed of three angular dislocations. These form exterior angles to the triangle, as indicated by shading in fig. 3, with the infinite segments cancelling one another.

As a particular case consider the dislocation in the form of an equilateral triangle with Burgers vector normal to its plane, in the sense that u increases by b on circling the line so as to emerge upwards from the paper inside the triangle.

Let the vertices A, B and C have coordinates $(0, 0, h)$, $(0, -\sqrt{3}h/2, -h/2)$ and $(0, \sqrt{3}h/2, -h/2)$ respectively and let

$$\begin{aligned}
\eta_1 &= -z-\frac{h}{2}, & \zeta_1 &= y,\\
\eta_2 &= \frac{\sqrt{3}y+z-h}{2}, & \zeta_2 &= -\frac{(y-\sqrt{3}z)}{2},\\
\eta_3 &= -\frac{(\sqrt{3}y-z+h)}{2}, & \zeta_3 &= -\frac{(y+\sqrt{3}z)}{2}.
\end{aligned}$$

Then the function ϕ of the angular dislocation at A is given by

$$\phi_A = \frac{1}{4\pi}\left[\tan^{-1}\frac{\eta_3}{x} - \tan^{-1}\frac{\eta_2}{x} + \tan^{-1}\left(\frac{\sqrt{3}xr_A}{2\eta_2\eta_3 - x^2}\right)\right]$$

where

$$r_A{}^2 = x^2 + y^2 + (z-h)^2.$$

Fig. 3

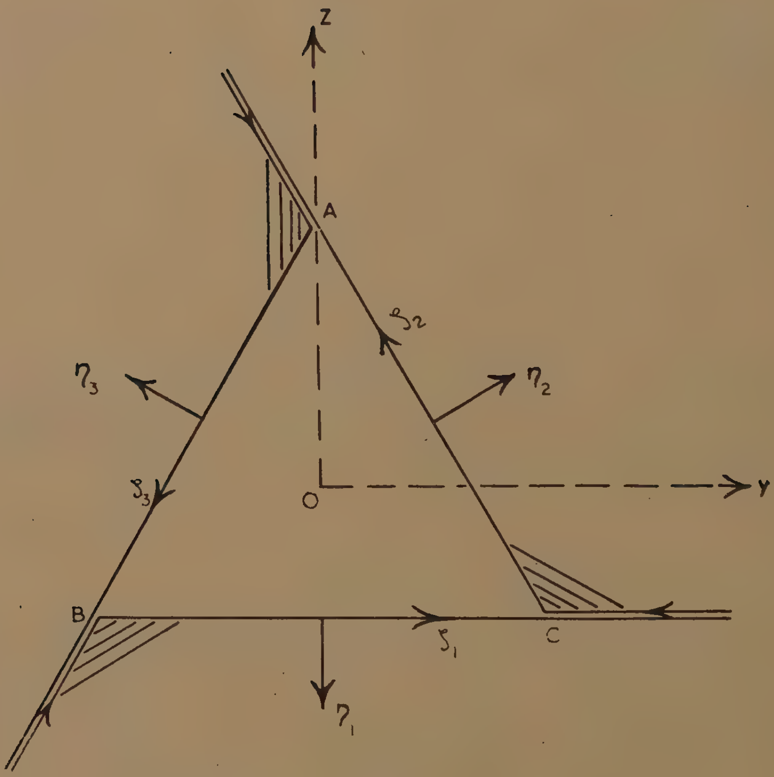

On adding similar expressions for the angular dislocations at B and C, the following function is obtained for the whole triangle:

$$\begin{aligned}\phi &= \phi_A + \phi_B + \phi_C \\ &= \frac{1}{4\pi}\left[\tan^{-1}\frac{\sqrt{3}xr_A}{2\eta_2\eta_3 - x^2} + \tan^{-1}\frac{\sqrt{3}xr_B}{2\eta_3\eta_1 - x^2} + \tan^{-1}\frac{\sqrt{3}xr_C}{2\eta_1\eta_2 - x^2}\right].\end{aligned}$$

The same result may be obtained directly by integration over the triangle, or by composing the triangle of three dislocation junctions at the vertices. It is a matter of taste whether junctions or angular dislocations are used as the primitive component of a network.

Using the results derived for angular dislocations, the normal displacement for the triangle is given by:

$$u=b\phi+\frac{bx}{8\pi(1-\sigma)}\left(\frac{\eta_3}{r_A(r_A-{}_A\zeta_3)}-\frac{\eta_2}{r_A(r_A-{}_A\zeta_2)}+\frac{\eta_1}{r_B(r_B-{}_B\zeta_1)}\right.$$
$$\left.-\frac{\eta_3}{r_B(r_B-{}_B\zeta_3)}+\frac{\eta_2}{r_C(r_C-{}_C\zeta_2)}-\frac{\eta_1}{r_C(r_C-{}_C\zeta_1)}\right)$$

where the prefix indicates the origin of the coordinate in each case,

$${}_A\zeta_2=\zeta_2-\sqrt{3}h/2,$$
$${}_B\zeta_1=\zeta_1+\sqrt{3}h/2,\quad \text{etc.}$$

The other displacements may be written down in a similar manner, but to save space will not be given here. The stress components may then be calculated as required.

From eqns. (3) it is seen that the normal stress $\widehat{xx}$ on the plane $x=0$ reduces to the simple form:

$$\widehat{xx}=\frac{\mu b}{4\pi(1-\sigma)}\left(\frac{\eta_2}{r_A(r_A-{}_A\zeta_2)}-\frac{\eta_3}{r_A(r_A-{}_A\zeta_3)}+\frac{\eta_3}{r_B(r_B-{}_B\zeta_3)}\right.$$
$$\left.-\frac{\eta_1}{r_B(r_B-{}_B\zeta_1)}+\frac{\eta_1}{r_C(r_C-{}_C\zeta_1)}-\frac{\eta_2}{r_C(r_C-{}_C\zeta_2)}\right).$$

The calculation of the elastic strain energy is therefore a simple matter in this case. If the triangle is situated in an infinite elastic body unstressed at infinity, the strain energy may be expressed as the work done against the normal stress on increasing the relative displacement from 0 to b over the surface of the triangle. That is, if the normal stress is given by

$$\widehat{xx}=bX \text{ on } x=0,$$

then

$$E=\tfrac{1}{2}b^2\iint X\,dy\,dz.$$

The integral is to be evaluated over the interior of the triangle, and may be reduced to the form

$$E=\frac{3\mu b^2}{4\pi(1-\sigma)}\int_0^{3h/2}dy\int_{y/\sqrt{3}}^{\sqrt{3}h-y/\sqrt{3}}\frac{z}{y\sqrt{(y^2+z^2)}}\,dz$$
$$=\frac{3\mu b^2}{4\pi(1-\sigma)}\,.\,\sqrt{3}h(\log 2/\sqrt{3}-1+\log h/\delta)$$
$$=\frac{C\mu b^2}{4\pi(1-\sigma)}\log\frac{0{\cdot}85R}{\delta}\quad . \; . \; . \; . \; . \; . \; . \; . \; . \; . \quad (6)$$

where C is the circumference of the triangle, R the radius of the inscribed circle and δ the core radius (of the order of b).

Corresponding results are readily obtained for Burgers vectors in other directions.

§ 4. The Hexagon

Six angular dislocations of angle $\pi/3$ and the same Burgers vector may be arranged to form a finite hexagonal dislocation in the plane $x=0$, with all the infinite segments cancelling, as shown in fig. 4.

The stress components may be calculated by adding the stresses due to the six angular dislocations, changing the origin of coordinates in each case and taking care to choose the correct Burgers vector. For instance if the Burgers vector is in the direction y at all points of the hexagon, then the stresses due to the angular dislocations at O and C are derived from eqns. (4) only, while those from A, B, D and E will include terms from both (4) and (5). The resulting expressions are long, and will not be given here, but the strain energy will be calculated for two cases of practical interest.

Fig. 4

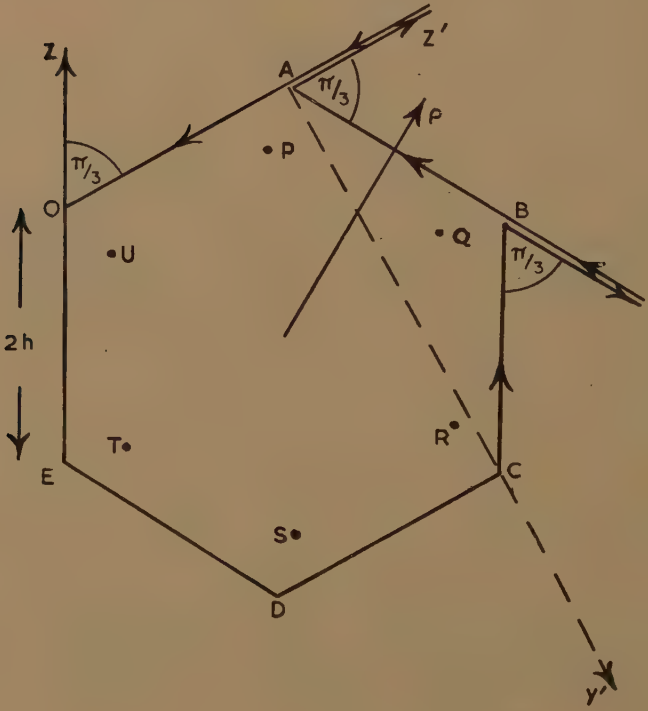

4.1. *Burgers Vector b_1 Normal to the Hexagon*

The strain energy in this case is equal to the work done against the normal stress $\widehat{xx}$ on the plane $x=0$ in forming the dislocation. From eqns. (3) this may be written

$$E=\frac{3\mu b_1^2}{4\pi(1-\sigma)}\int\int\left(\frac{\eta}{r(r-\zeta)}-\frac{y}{r(r-z)}\right)dy\,dz \qquad (7)$$

where the factor $b_1^2/2$, obtained on integrating from 0 to b_1, has been multiplied by six for the six angular dislocations. The integral is to be taken over the interior of the hexagon, and readily simplifies to the form:

$$E=\frac{-3\mu b_1^2}{4\pi(1-\sigma)}\left\{\int_0^{\sqrt{3}h}\left[\frac{2\sqrt{(y^2+z^2)}}{y}\right]_{-2h-y/\sqrt{3}}^{y/\sqrt{3}}dy\right.$$
$$\left.+\int_{\sqrt{3}h}^{2\sqrt{3}h}\left[\frac{2\sqrt{(y^2+z^2)}}{y}\right]_{-4h+y/\sqrt{3}}^{2h-y/\sqrt{3}}dy\right\}$$
$$=\frac{3\mu b_1^2}{4\pi(1-\sigma)}4h(\log\sqrt{3}h/\delta+1-\sqrt{3}+2\log 2(2+\sqrt{3})/3\sqrt{3})$$

where $2h$ is the length of a side of the hexagon, and δ is the core radius (of the order of b_1). This energy may also be written

$$E=\frac{C\mu b_1^2}{4\pi(1-\sigma)}\log\frac{0\cdot 99R}{\delta}, \qquad \dots\dots \quad (8)$$

where C is the circumference of the hexagon and R the radius of the inscribed circle.

4.2. *Burgers Vector b_2 at an Angle to the Plane of the Hexagon*

Let the vector $\mathbf{b}_2$ have components

$$\left.\begin{aligned} b_x&=\sqrt{2}b_2/\sqrt{3},\\ b_y&=b_2/2\sqrt{3},\\ b_z&=b_2/2,\end{aligned}\right\} \qquad \dots\dots \quad (9)$$

in the directions of the x, y, z axes respectively. This corresponds to the case of a face centred cubic metal with the Burgers vector ½ [110] not in the (111) plane of the hexagon, and the sides of the hexagon lying along [110] type directions in this plane. In calculating the strain energy in this case there are contributions from the stress component $\widehat{x\rho}$ as well as $\widehat{xx}$, where ρ lies along the projection of the Burgers vector in the y, z plane (see fig. 4).

An angular dislocation of Burgers vector b_x only has zero shear stresses $\widehat{xy}$, $\widehat{xz}$ in the plane $x=0$, while b_y and b_z give zero $\widehat{xx}$ on that plane. For this reason the terms in the strain energy separate and it may be written in the form

$$E=\frac{3\mu b_x^2}{4\pi(1-\sigma)}\iint\left(\frac{\eta}{r(r-\zeta)}-\frac{y}{r(r-z)}\right)dy\,dz$$
$$+\iint\left\{\int_0^{b/\sqrt{3}}\sum\widehat{x\rho}\,db_\rho\right\}dy\,dz \qquad \dots\dots \quad (10)$$

where $\sum\widehat{x\rho}$ indicates the sum of six terms from the six angular dislocations. The first term of (10) is similar to eqn. (7) with b_1 replaced by $b_x=\sqrt{2}b_2/\sqrt{3}$ and therefore its value is readily obtained from (8).

To evaluate the second term of (9) consider the shear stresses across the (yz) plane at some arbitrary point P inside the hexagon due to the angular dislocation at O. The shear stresses $\widehat{xy}$, $\widehat{xz}$ may be written in the form

$$\left.\begin{aligned}\widehat{xy}&=b_yY_2+b_zY_3,\\ \widehat{xz}&=b_yZ_2+b_zZ_3\end{aligned}\right\} \qquad \dots\dots \quad (11)$$

where Y_2 and Z_2 are derived from eqns. (4) and Y_3, Z_3 from (5). Resolving in the direction of ρ

$$\begin{aligned}\widehat{x\rho}_0 &= \widehat{xy}/2 + \widehat{xz}\sqrt{3}/2 \\ &= b_2(Y_2/4\sqrt{3} + Y_3/4 + Z_2/4 + \sqrt{3}Z_3/4). \quad . \quad . \quad . \quad (12)\end{aligned}$$

By symmetry it is found that the stresses at a corresponding point S due to the angular dislocation at C are equal to those at P due to the dislocation at O:

$$\widehat{x\rho}_C(\text{at point S}) = \widehat{x\rho}_0 \text{ (at point P)}. \quad . \quad . \quad . \quad . \quad (13)$$

For the angular dislocation at A take new axes y', z' as indicated and consider the stresses at a point Q corresponding to P and S. Then

$$\begin{aligned}\widehat{xy}' &= -b_2Y_2/2\sqrt{3} + b_2Y_3/2, \\ \widehat{xz}' &= -b_2Z_2/2\sqrt{3} + b_2Z_3/2,\end{aligned}$$

and the shear stress $\widehat{x\rho}$ at Q is given by

$$\begin{aligned}\widehat{x\rho}_A &= -\widehat{xy}'/2 + \sqrt{3}\widehat{xz}'/2 \\ &= b_2(Y_2/4\sqrt{3} - Y_3/4 - Z_2/4 + \sqrt{3}Z_3/4). \quad . \quad . \quad . \quad (14)\end{aligned}$$

The dislocation at D is found to contribute the same value of $\widehat{x\rho}$ at the corresponding point T.

Finally the angular dislocations at B and E each contribute the shear stress

$$\widehat{x\rho}_B = b_2Y_2/\sqrt{3} \quad . \quad . \quad . \quad . \quad . \quad . \quad . \quad . \quad (15)$$

at the corresponding points R and U respectively.

On changing the order of integration in the second term of (10) it becomes possible to sum the terms of $\widehat{x\rho}$ from (12), (14) and (15). It is found that Y_3 and Z_2 disappear and the integral simplifies:

$$\begin{aligned}\int_0^{b_2/\sqrt{3}} \left\{ \int\!\!\int \widehat{x\rho}\, dy\, dz \right\} db &= \int_0^{b_2/\sqrt{3}} \left\{ \int\!\!\int \sqrt{3}b(Y_2 + Z_3)\, dy\, dz \right\} db \\ &= \frac{b_2^2}{2} \int\!\!\int (Y_2 + Z_3)\, dy\, dz \\ &= \frac{(2-\sigma)\mu b_2^2}{8\pi(1-\sigma)} \int\!\!\int \left(\frac{\eta}{r(r-\zeta)} - \frac{y}{r(r-z)} \right) dy\, dz. \\ & \quad . \quad . \quad . \quad (16)\end{aligned}$$

Substituing this in eqn. (10) and comparing with (8), the strain energy of the hexagonal dislocation with $\mathbf{b}_2$ in a [110] direction is given by

$$E = (1 - \sigma/6) \frac{C\mu b_2^2}{4\pi(1-\sigma)} \log \frac{0{\cdot}99R}{\delta} \quad . \quad . \quad . \quad . \quad . \quad . \quad (17)$$

where C is the circumference of the hexagon and R the radius of the inscribed circle.

§ 5. OTHER APPLICATIONS

The angular dislocation may be used as a unit in constructing other figures of practical interest.

5.1. *Kinked Dislocation*

A simple example is the kinked dislocation shown in fig. 5, such as may arise from cross slip or prismatic slip. It may be formed by the superposition of one straight and two angular dislocations, in either of the two ways indicated in the figure.

Fig. 5

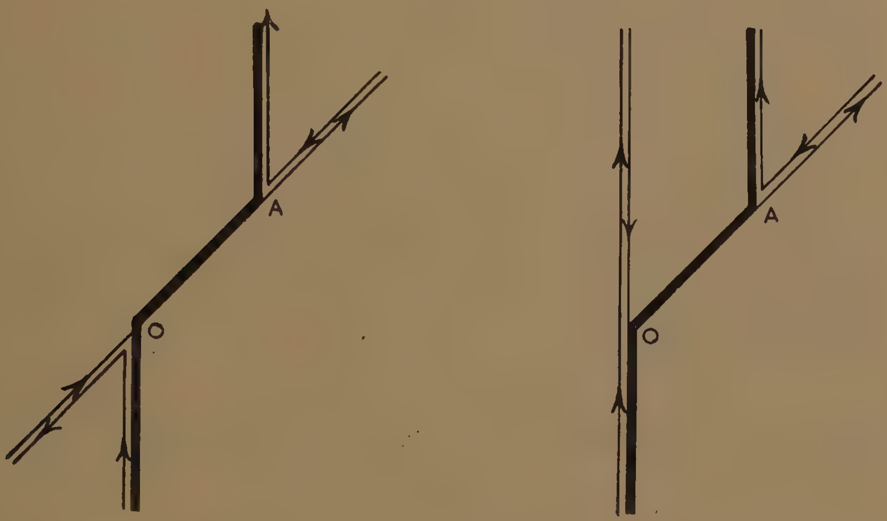

The displacements due to each angular dislocation are obtained from eqns. (2), (4) and (5) according to the Burgers vector. For example if $b_z = b$ so that the infinite segments are pure screw dislocations, and if A is the point (O, Y, Z) so that $Y/Z = \tan\alpha$, the displacements have the form

$$u = \frac{b\sin\alpha}{8\pi(1-\sigma)}\left(\frac{x^2}{r(r-\zeta)} - \frac{x^2}{r_A(r_A-\zeta_A)} + (1-2\sigma)\log\frac{r_A-\zeta_A}{r-\zeta}\right),$$

$$v = \frac{b\sin\alpha x}{8\pi(1-\sigma)}\left(\frac{y}{r(r-\zeta)} - \frac{y-Y}{r_A(r_A-\zeta_A)} - \frac{\sin\alpha}{r-\zeta} + \frac{\sin\alpha}{r_A-\zeta_A}\right),$$

$$w = b(\phi-\phi_A) + \frac{bx\sin\alpha}{8\pi(1-\sigma)}\left(\frac{z}{r(r-\zeta)} - \frac{z-Z}{r_A(r_A-\zeta_A)} - \frac{\cos\alpha}{r-\zeta} + \frac{\cos\alpha}{r_A-\zeta_A}\right)$$

where ϕ is given by eqn. (1), ϕ_A is the corresponding expression referred to the point A, and

$$r_A{}^2 = x^2 + (y-Y)^2 + (z-Z)^2,$$

$$\zeta_A = \zeta - Y\sin\alpha - Z\cos\alpha.$$

It may be of interest to examine the stress components in the case where the distance OA is small, to see by how much they differ from the stresses of a straight screw dislocation. For instance the component $\widehat{zz}$ is zero for the straight dislocation, but here it has the value

$$\widehat{zz}=\frac{\mu b x\sin\alpha}{4\pi(1-\sigma)}\left(\frac{1}{r_{\mathrm{A}}(r_{\mathrm{A}}-\zeta_{\mathrm{A}})}+\frac{\cos^2\alpha}{(r_{\mathrm{A}}-\zeta_{\mathrm{A}})^2}-\frac{1}{r(r-\zeta)}-\frac{\cos^2\alpha}{(r-\zeta)^2}\right).$$

At points on a line normal to the paper midway between O and A this reduces to

$$\widehat{zz}=-\frac{\mu b\sin\alpha}{2\pi(1-\sigma)}\left(\frac{\zeta}{rx}+\frac{\zeta r}{x^3}\right)$$

showing that there is noticeable tension and compression on opposite sides of the kink at points adjacent to it.

5.2. *Plane Polygons*

It was shown in § 3 and § 4 that a finite dislocation in the form of a triangle or hexagon may be built up of angular dislocations. The same is true of an arbitrary plane polygon, which may be obtained by varying the magnitude of the angles as shown in fig. 6. The case of the square has been worked out in detail, but will not be described here for reasons of space. The strain energy however may be compared with that of the triangle or hexagon:

$$E=\frac{C\mu b^2}{4\pi(1-\sigma)}\log\frac{0\cdot92R}{\delta} \quad . \quad . \quad . \quad . \quad . \quad . \quad . \qquad (18)$$

where C is the circumference of the square and R the radius of the inscribed circle.

5.3. *Non-planar Figures*

Angular dislocations may also be used to determine the stress field near a junction of three dislocation lines, not necessarily coplanar, and of arbitrary Burgers vectors $\mathbf{b}_1$, $\mathbf{b}_2$, $\mathbf{b}_3$. It is only necessary to rotate one angular dislocation about the z axis through a suitable angle, and then assemble the components as indicated in fig. 7. Here one of the side arms is supposed inclined to the plane of the paper. The three vertical segments cancel one another since the vector $\mathbf{b}_1-\mathbf{b}_2-\mathbf{b}_3$ must be zero.

In this manner a three dimensional network of dislocations may be built up of angular dislocations, although the labour of calculation of stress components increases steeply with the number of nodes. In certain cases however the problem simplifies to that of an assembly of plane figures each of constant Burgers vector. One example is the tetrahedron recently observed in quenched gold (Silcox and Hirsch 1959).

5.4. *The Tetrahedron*

This configuration may be composed of four equal triangular dislocations each of Burgers vector b_4 normal to its plane. The stress field is simply that obtained by adding the fields of the separate triangles as calculated in § 3.

Fig. 6

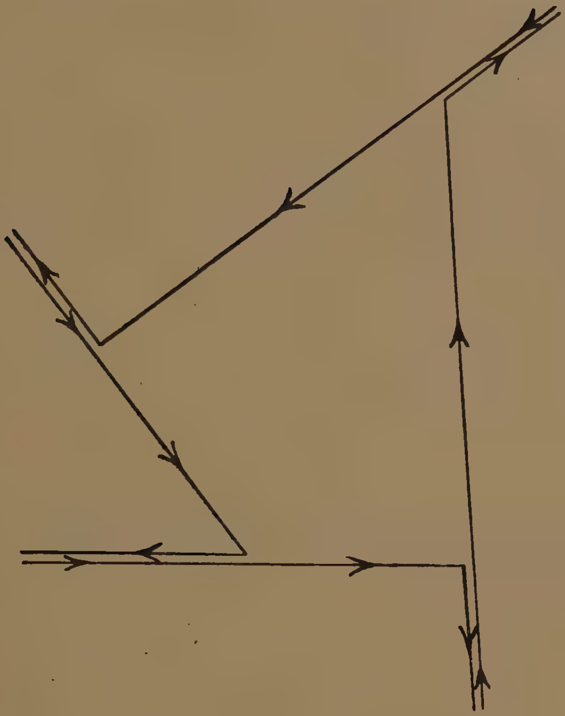

Fig. 7

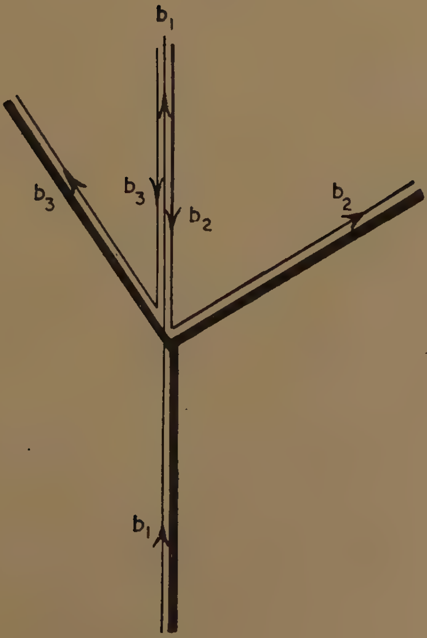
b_1
b_3
b_3
b_2
b_2
b_1

The strain energy of this tetrahedron may also be calculated. It is composed of four times the self energy of one triangle as calculated in § 3, together with twelve times the work done in forming one triangle against the normal stress due to any other triangle. That is

$$E=4\left(\tfrac{1}{2}b_4\iint \widehat{xx}\,dy\,dz\right)+12\left(\tfrac{1}{2}b_4\iint \widehat{nn}\,dS\right)$$

where S is the area of a side face of outward normal n, the base triangle being that of inward normal x. The calculation of the second integral is greatly simplified by the use of Stokes' theorem and the symmetry of the problem, whereby terms of the form

$$\iint \frac{\partial\phi}{\partial n}\,dS$$

where ϕ is harmonic, may be replaced by

$$\frac{1}{3}\iint \frac{\partial\phi}{\partial x}\,dy\,dz.$$

The second integral of the strain energy finally yields one term equal to a third of the first integral and also a term independent of the core radius δ. Using the same notation as for the triangle the strain energy of the tetrahedron is given by:

$$E=\frac{C\mu b_4}{4\pi(1-\sigma)}\left(\frac{16}{3}\log\frac{0{\cdot}85R}{\delta}-(1-2\sigma)\,3{\cdot}6\right) \quad . \quad . \quad (19)$$

where C is the circumference of a triangle, and R the radius of its inscribed circle.

According to Silcox and Hirsch (1959) such a tetrahedron can be formed in quenched Au by dissociation of a triangular Frank sessile dislocation (Burgers vector type $\frac{1}{3}[111]$). The tetrahedron consists of stair-rod edge dislocations (Burgers vector type $\frac{1}{6}$ [110]) along the [110] edges of the tetrahedron bounding the stacking faults on the (111) faces. An approximate calculation by Silcox and Hirsch indicates that this dissociation reduces the dislocation energy to one-third of that of the triangular configuration. The calculation in the present paper is based on the fact that the tetrahedron can also be considered as consisting of four triangles whose Burgers vector is one quarter that of a Frank sessile dislocation, and also normal to the plane of the triangle. The stair-rod dislocations are then formed by reactions of the type

$$\tfrac{1}{12}[111]+\tfrac{1}{12}[11\bar{1}]=\tfrac{1}{6}[110];$$

thus, to compare the energies of the triangle and tetrahedron we put $b_4=\frac{1}{4}b$, where b is the Burgers vector of the Frank sessile dislocation. Comparing eqns. (6) and (9) it is clear that the energy of the term involving the logarithm is reduced to one-third its previous value, in agreement with the result of the simple calculation, but that there is a further reduction in energy which depends on R only through C.

§ 6. CONCLUSION

In order to simplify the calculation of the stress field due to two or three dimensional networks of dislocations, Burgers' method has been used to derive formulae appropriate to an elementary component of such networks. It has been shown that any network of dislocations consisting of straight line segments may be built up of such components, so that the calculation of the stress field is tedious rather than difficult.

A network of curved segments requires further investigation, as does the extension to anisotropic media.

ACKNOWLEDGMENTS

The author wishes to thank Dr. P. B. Hirsch for very helpful discussions, advice and encouragement, Dr. J. D. Eshelby for reading the manuscript and the Atomic Energy Research Establishment, Harwell, for a grant.

REFERENCES

BURGERS, J. M., 1939, *Proc. Acad. Sci., Amst.*, **42**, 293.
SILCOX, J., and HIRSCH, P. B., 1959, *Phil. Mag.*, **4**, 72.

The Kinetics of the Growth of Precipitates from Solid Solutions†

By J. BURKE
Department of Metallurgy, University of Liverpool

[Received October 2, 1959]

ABSTRACT

Equations are derived for the rate of precipitation from an initially homogeneous solid solution on the assumptions that the process involves growth of existing nuclei and that the rate of growth is controlled by diffusion. Various forms of precipitate are considered. Impingement of the zones of the parent solution depleted in solute is allowed for by multiplying the diffusion potential by $(1-y)$ where y is the fraction of the total precipitation which has occurred. The results are appreciably different from the equations currently used to analyse kinetic data.

§ 1. INTRODUCTION

THEORETICAL treatments of the kinetics of the growth of precipitates from supersaturated solid solutions have been given by a number of authors—see the review by Hardy and Heal (1954). The results can usually be reduced to the general form

$$y=1-\exp-(t/k)^n \quad . \quad . \quad . \quad . \quad . \quad . \quad . \quad (1)$$

where y is the fraction precipitated at the time t, k is the time constant, the value of which is determined by the parameters of the system considered and n is a constant. In deriving equations of this type the procedure has been to calculate the rate of growth of one particle of the new phase as a function of time, sum over all the particles present in unit volume of the solid solution and then allow for the reduction in reaction rate consequent upon the impingement of the zones of the parent phase depleted of solute. Following Johnson and Mehl (1939), the impingement allowance usually has consisted of multiplying the overall rate of reaction by $(1-y)$. If, as is frequently the case, the growth of the new phase is determined by the rate of diffusion of the solute in the matrix, impingement will modify the diffusion potential and hence the rate of growth. Thus it would appear more satisfactory to include the impingement factor in the growth equation for each particle. Doremus (1957) employed this procedure for a limited number of precipitate shapes and his results indicate that the rate equations so derived are sufficiently different from those obtained by the former method as to completely alter the interpretation of experimental results. This has prompted a re-derivation of the rate equations for the isothermal precipitation of a solute from a supersaturated solid solution proceeding by the diffusion limited growth of existing nuclei. The same problem was discussed by Wert (1949) and by Zener (1949) using the latter method of allowing for impingement.

---

† Communicated by the Author.

Fig. 1

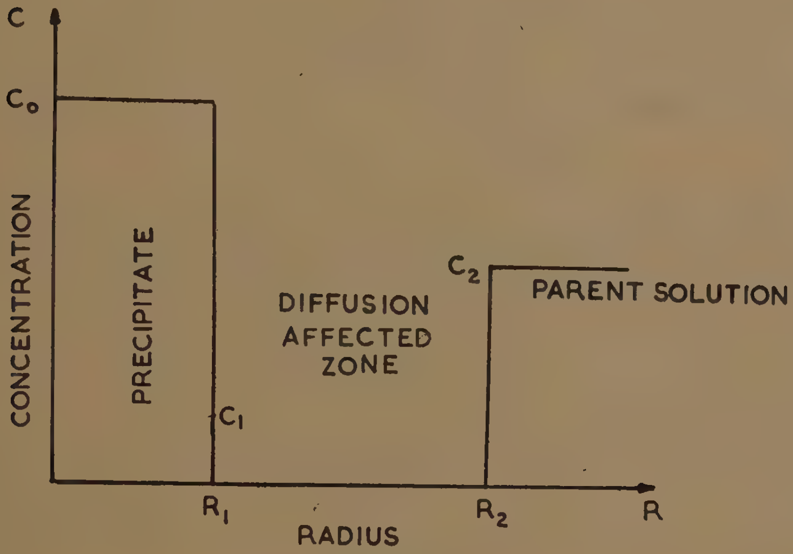

Concentration conditions around a growing particle of precipitate.

Because the rate of reaction varies with the shape of the precipitate, the following cases are considered: (*a*) spherical particles, (*b*) cylindrical particles growing in one, two or three dimensions and (*c*) discs growing in one, two or three dimensions. The following assumptions are made throughout:

(1) The reaction proceeds by the growth of a fixed number of nuclei, all of which formed at $t=0$.

(2) The supersaturated matrix is initially homogeneous.

(3) The distribution of nuclei is random.

(4) The rate of growth is determined by the rate of diffusion of solute in the matrix and the diffusion coefficient, D, is independent of concentration.

(5) The influence of the size and shape of the particles on the equilibrium matrix concentration is negligible.

§ 2. THE GROWTH OF SPHERICAL PARTICLES

Consider the conditions shown in fig. 1. An isolated particle of precipitate, radius R_1, solute concentration c_0, is in equilibrium with a solid solution, concentration c_1. Solute is being drawn from a sphere, radius R_2;

the initial concentration of the matrix is c_2. The relation between R_1 and R_2 is

$$R_1^2\,dR_1(c_0-c_1)=R_2^2\,dR_2c_2 \qquad (2)$$

and thus

$$R_2=\alpha R_1 \qquad (3)$$

where

$$\alpha=\sqrt[3]{\left(\frac{c_0-c_1}{c_2}\right)}. \qquad (4)$$

The rate of radial growth is given by

$$4\pi R_1^2\frac{dR_1}{dt}(c_0-c_1)=4\pi R_1^2D\left(\frac{\partial c}{\partial R}\right)_{R=R_1} \qquad (5)$$

where D is the diffusion coefficient for the solute in the matrix. It is assumed that after a short time a quasi-stationary state is established. The solution of Fick's equation, as given by Barrer (1941) is then

$$\frac{\partial c}{\partial R}=\frac{c_2-c_1}{(1/R_1-1/R_2)R^2}. \qquad (6)$$

Putting (6) and (3) into (5) gives

$$R_1\left(\frac{dR_1}{dt}\right)=D\frac{(c_2-c_1)}{(c_0-c_1)}\cdot\frac{\alpha}{(\alpha-1)} \qquad (7)$$

which can be written

$$R_1\left(\frac{dR_1}{dt}\right)=\beta. \qquad (8)$$

Thus for a single, isolated particle

$$R_1^2=2\beta t. \qquad (9)$$

This is of the same form as obtained by Zener (1949), but differs in the formulation of the constant β. Birchenall and Mead (1956), using a method differing slightly from the present one, obtained an expression for the radius of a graphite nodule growing in an austenite-cementite mixture which is equivalent to eqn. (7) except for the additional terms arising from the solution of the cementite.

For non-isolated particles impingement of the zones surrounding each particle results in a lowering of the rate of growth. To allow for this the right-hand side of eqns. (7) and (8) is multiplied by $(1-y)$, where y is the fraction of the total precipitation which has occurred at time t. The impingement allowance is discussed in § 9. Thus

$$R_1\left(\frac{dR_1}{dt}\right)=\beta(1-y). \qquad (10)$$

Assuming that all particles commence to grow at time $t=0$ and that there are N particles per unit volume of sample,

$$y=\tfrac{4}{3}\pi R_1^3\,.\,N\,.\left(\frac{c_0}{c_2-c_1}\right)=\gamma R_1^3 \quad \text{(say)}. \qquad (11)$$

Putting the values of R_1 and dR_1/dt from eqn. (11) into eqn. (10) gives

$$\int \frac{dy}{y^{1/3}(1-y)} = \int 3\beta\gamma^{2/3}\,dt \qquad (12)$$

which on integration yields

$$\tfrac{1}{2}\ln\left[\frac{1+y^{1/3}+y^{2/3}}{(y^{1/3}-1)^2}\right]+\sqrt{3}\left[\tan^{-1}-\left(\frac{2y^{1/3}+1}{\sqrt{3}}\right)-\frac{5\pi}{6}\right]=3\beta\gamma^{2/3}t\dagger. \qquad (13)$$

This is the rate equation for this particular model. Values of the function on the left-hand side of eqn. (13) are tabulated in table 1 to permit comparison with experimental data.

Table 1

Values of the function $f(y)=\tfrac{1}{2}\ln\left[\frac{1+y^{1/3}+y^{2/3}}{(y^{1/3}-1)^2}\right]+\sqrt{3}\left[\tan^{-1}-\left(\frac{2y^{1/3}+1}{\sqrt{3}}\right)-\frac{5\pi}{6}\right]$

y	0·1	0·2	0·3	0·4	0·5	0·6	0·7	0·8	0·9	0·95
$f(y)$	0·3371	0·5601	0·7723	0·9918	1·2297	1·5018	1·8341	2·2787	3·0040	3·7223

To illustrate the difference between this and previous methods the corresponding equation is derived using the impingement allowance employed by Johnson and Mehl (1939).

For an isolated particle

$$R_1^2=2\beta t$$

and the fraction precipitated, $y=\gamma R_1^3$

then
$$\frac{dy}{dt}=3\gamma R_1^2\,.\,\frac{dR_1}{dt}(1-y). \qquad (14)$$

In this case the impingement factor $(1-y)$ is placed in the overall rate equation. Substitution for R_1 and integration yields

$$\ln(1-y)=-(2\gamma^{2/3}\beta t)^{3/2}. \qquad (15)$$

This is identical to eqn. (1) with $n=3/2$.

The rate curves derived from eqns. (13) and (15) are compared in fig. 2. These are approximately the same at early stages of precipitation but diverge appreciably towards the end.

§ 3. CYLINDRICAL PARTICLES GROWING RADIALLY ONLY

Proceeding as before and using the steady state solution of Fick's Law for cylindrical symmetry gives the usual parabolic law for an isolated particle

$$R_c^2=2\beta_{cr}\,.\,t \qquad (16)$$

where
$$\beta_{cr}=D\left(\frac{c_1-c_2}{c_0-c_1}\right)\,.\,\frac{1}{\ln\sqrt{\left(\frac{c_2}{c_0-c_1}\right)}}. \qquad (17)$$

---

† $\sqrt{3}(5\pi/6)$ is the integration constant.

Fig. 2

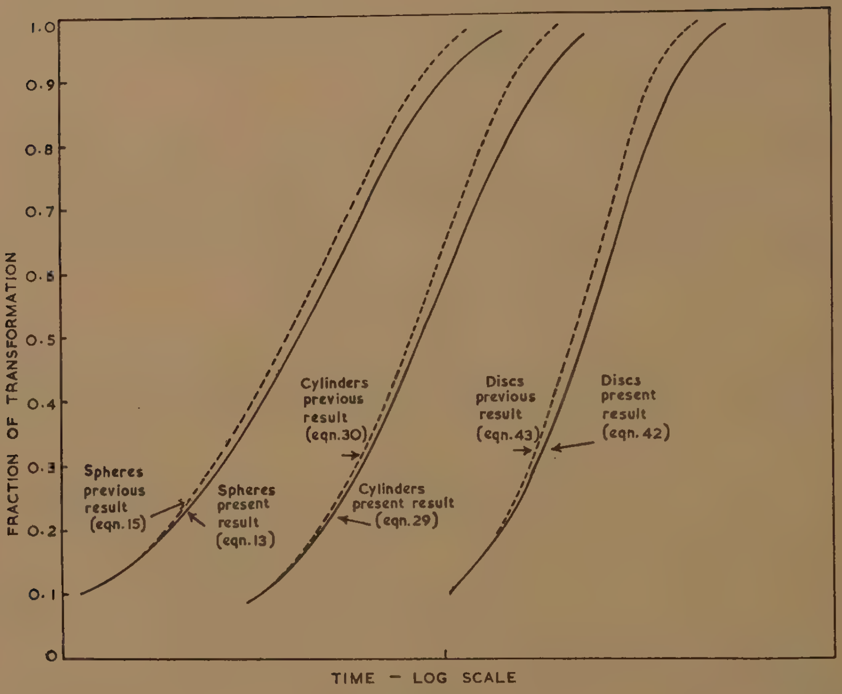

A comparison of the rate curves obtained using the Johnson–Mehl impingement factor (broken curves) and the present equations for various shapes of precipitate. The positions on the time axis are arbitrary.

Allowing for impingement

$$R_c \frac{dR_c}{dt} = \beta_{cr}(1-y); \qquad \ldots\ldots \qquad (18)$$

y is the fraction of the total precipitation which has occurred at time t and is given by

$$y = 2\pi R_c^2 L \, . \, N \left(\frac{c_0}{c_2 - c_1} \right) = \gamma_{cr} \, . \, R_c^2 \qquad \ldots\ldots \qquad (19)$$

in which $2L$ is the length of the particle, assumed constant. Putting eqn. (19) into eqn. (18) gives

$$\frac{dy}{(1-y)} = 2\gamma_{cr} \, . \, \beta_{cr} \, . \, dt$$

and integrating

$$\ln\left(\frac{1}{1-y}\right) = 2\gamma_{cr} \, . \, \beta_{cr} \, . \, t\dagger. \qquad \ldots\ldots \qquad (20)$$

The applicability of this equation in any case can be checked by plotting $\ln(1/1-y)$ as a function of time.

---

† The integration constant is zero.

§ 4. CYLINDRICAL PARTICLES GROWING AXIALLY ONLY

As pointed out by Wert the concentration conditions around the ends of a cylindrical particle growing axially remain unchanged. Thus the axial rate of growth is constant and it is possible to write

$$L=\beta_{ca}\,.\,t. \qquad (21)$$

For non-isolated particles

$$\frac{dL}{dt}=\beta_{ca}(1-y) \qquad (22)$$

which gives a rate equation

$$\ln\left(\frac{1}{1-y}\right)=\gamma_{ca}\cdot\beta_{ca}\cdot t, \qquad (23)$$

where

$$\gamma_{ca}=2\pi R_c^{\,2}\,.\,N\left(\frac{c_0}{c_2-c_1}\right) \qquad (24)$$

and R_c is the radius, assumed constant.

§ 5. CYLINDRICAL PARTICLES GROWING IN ALL DIRECTIONS

The volume of such a particle growing from negligible initial dimensions is $2\pi R_c^{\,2}L$ and the fraction precipitated y is

$$2\pi N\left(\frac{c_0}{c_2-c_1}\right).\,R_c^{\,2}L, \quad \text{say} \quad \gamma_c\,.\,R_c^{\,2}\,.\,L.$$

The rate of reaction is given by

$$\frac{dy}{dt}=\left(\frac{\partial y}{\partial R_c}\right)_L\cdot\frac{\partial R_c}{\partial t}+\left(\frac{\partial y}{\partial L}\right)_{R_c}\cdot\frac{\partial L}{\partial t}. \qquad (25)$$

Noting that eqns. (18) and (22) can be put into the integral forms

$$R_c^{\,2}=2\beta_{cr}\int_0^t(1-y)\,dt, \qquad (26)$$

$$L=\beta_{ca}\int_0^t(1-y)\,dt, \qquad (27)$$

and carrying out the operations indicated by the right-hand side of (25) gives an integral equation

$$\frac{dy}{dt}=4\beta_{cr}\cdot\beta_{ca}\gamma_c(1-y)\int_0^t(1-y)\,dt. \qquad (28)$$

The solution is

$$y=\tanh^2\sqrt{[2\beta_{cr}\cdot\beta_{ca}\cdot\gamma_c]}\,.\,t. \qquad (29)$$

Using the previous method of allowing for impingement gives for this form of precipitate

$$y=1-\exp-(2\beta_{cr}\cdot\beta_{ca}\cdot\gamma_c)\,.\,t^2. \qquad (30)$$

Graphs of eqns. (29) and (30) are plotted in fig. 2 from which it can be seen that there is again an appreciable difference in the two results, especially during the later stages of the process.

§ 6. DISCS GROWING ONLY ON ITS FACES

If X is the half-thickness of the disc

$$X\left(\frac{dX}{dt}\right)=\beta_{df}(1-y) \quad \ldots \ldots \quad (31)$$

where

$$\beta_{df}=D\left(\frac{c_2-c_1}{c_0-c_1}\right)\frac{1}{\left\{\dfrac{c_0-c_1}{c_2}-1\right\}}. \quad \ldots \quad (32)$$

Volume of disc is $2\pi R_d^2X$ where R_d is the radius, assumed constant.

$$y=2\pi R_d^2 . X . N\left(\frac{c_0}{c_2-c_1}\right)=\gamma_{df} . X. \quad \ldots \quad (33)$$

This yields a rate equation

$$y+\ln(1-y)=-\beta_{df} . \gamma_{df}^2 . t. \quad \ldots \ldots \quad (34)$$

§ 7. DISCS GROWING RADIALLY ONLY

Again following Zener and Wert it is assumed that the rate of radial growth is constant. For non-isolated particles

$$\frac{dR_d}{dt}=\beta_{dr}(1-y) \quad \ldots \ldots \quad (35)$$

and

$$y=2\pi R_d^2X . N . \left(\frac{c_0}{c_2-c_1}\right)=\gamma_{dr} . R_d^2. \quad \ldots \quad (36)$$

This gives

$$\frac{dy}{\sqrt{y} . (1-y)}=2\sqrt{(\gamma_{dr})} . \beta_{dr} . dt.$$

Integrating

$$y=\tanh^2\sqrt{(\gamma_{dr})} . \beta_{dr} . t. \quad \ldots \ldots \quad (37)$$

§ 8. DISCS GROWING IN THREE DIMENSIONS

Following the same procedure as used for cylinders growing in three dimensions leads to

$$\frac{dy}{dt}=\frac{5}{\sqrt{2}}\gamma_d . \beta_{dr}^2\sqrt{\beta_{df}}(1-y)\left[\int_0^t(1-y)\,dt\right]^{3/2} \quad \ldots \quad (38)$$

where

$$\gamma_d=2\pi N . \left(\frac{c_0}{c_2-c_1}\right).$$

This equation can be solved by writing $x=(1-y)$ and differentiating to remove the integral. The result is

$$x\frac{d^2x}{dt^2}-\left(\frac{dx}{dt}\right)^2+\tfrac{3}{2}A^{2/3} . x^{8/3} . \left(-\frac{dx}{dt}\right)^{1/3}=0 \quad \ldots \quad (39)$$

where

$$A=\frac{5}{\sqrt{2}} . \gamma_d . \beta_{dr}^2 . \sqrt{\beta_{df}}.$$

Substitution of $z^{3/5}=(-dx/dt)$ yields a linear, first-order equation, the solution of which is

$$z=5/2A^{2/3}\,.\,x^{5/3}(1-x). \qquad (40)$$

Thus

$$\frac{dy}{(1-y)y^{3/5}}=\int(5/2A^{2/3})^{3/5}\,.\,dt. \qquad (41)$$

This equation has not been integrated analytically. It can be solved numerically or by expanding $(1-y)^{-1}$ and integrating term by term which gives

$$y^{2/5}\left(1+\frac{2}{7}y+\frac{1}{6}y^2+\ldots+\frac{2}{5n-3}y^{n-1}+\ldots\right)=[\sqrt{(2\beta_{df})}\beta_{dr}{}^2\cdot\gamma_d]^{2/5}t\dagger \qquad (42)$$

which is the rate equation for this particular model. The series converges rapidly at low values of y; at $y=0{\cdot}9$ ten terms gives an accuracy better than 1%. A table of values of this series is given in table 2.

Table 2

Value of the series $f(y)=y^{2/5}\left(1+\frac{2}{7}y+\frac{1}{6}y^2+\ldots+\frac{2}{5n-3}y^{n-1}+\ldots\right)$

y	0·1	0·2	0·3	0·4	0·5	0·6	0·7	0·8	0·9	0·95
$f(y)$	0·4101	0·5588	0·6819	0·7960	0·9132	1·0348	1·1759	1·3651	1·6177	1·8128

Values accurate to within 1%.

It can be simply shown that the corresponding equation using the previous impingement factor is

$$y=1-\exp-[\sqrt{(2\beta_{df})}\cdot\beta_{dr}{}^2\cdot\gamma_d]\,.\,t^{5/2}. \qquad (43)$$

Graphs of eqns. (42) and (43) are shown in fig. 2.

§ 9. DISCUSSION

The results of widest interest are the equations giving the fraction transformed as a function of time for the spherical, disc-like and cylindrical particles growing in three dimensions. The results are grouped in fig. 2 together with the corresponding rate curves derived on the basis of the Johnson–Mehl impingement factor. It is clear from the derivation of the equations that the values of the various constants do not affect the shape of the curves, only the position on the time axis; the shape of the curve is determined by the shape of the precipitate. The present results indicate a slower rate of reaction in all cases; the divergence becomes marked for y greater than 0·5.

Although the present method of allowing for impingment is considered to be more satisfactory than previous methods in which a correction is

---

† The constant of integration is zero in this equation.

applied to the integrated rate of transformation, the use of $(1-y)$ as the impingement factor is quite arbitrary. It is difficult to conceive an analytical method which is not dependent upon equally arbitrary assumptions concerning the distribution of precipitate and the behaviour of the surfaces of the diffusion zones after impingement. Indeed, the treatment of the simplest idealized model would be formidable since non-radial diffusion is inevitable after contact of the diffusion zones. In the absence of an analytical treatment a factor is required which expresses the fact that the rate of growth decreases as the matrix is consumed; the growth rate is thus some function of $(1-y)$. The exact function will possibly vary from system to system. Here it was decided to use the simplest possible function viz. $(1-y)$. It is reasonable because it allows for immediate impingement which must occur in a random distribution of nuclei; and because it allows for the fact that impingement dominates towards the end of the reaction. Other factors have been suggested e.g. $(1-y)^2$, Mishima (1951). Doremus (1957) used both $(1-y)$ and $(1-y)^2$. The effect of the latter on the present equations is being examined.

Another consequence of the present method of allowing for impingement is important in connection with experimental measurement of rates of growth of precipitates. Such results are normally intepreted in terms of the parabolic law eqn. (9). However, eqn. (10) is more appropriate. Substituting the value of y from eqn. (11) into eqn. (10) gives

$$\int \frac{R_1 dR_1}{(1-\gamma R_1{}^3)} = \int \beta\, dt, \qquad (44)$$

integration gives

$$-\frac{1}{3\gamma A}\left[\frac{1}{2}\ln\left\{\frac{A^2-AR_1-R_1{}^2}{(A+R_1)^2}\right\}+\sqrt{3}\left\{\tan^{-1}\left(\frac{2R_1-A}{A\sqrt{3}}\right)-\frac{5\pi}{6}\right\}\right]$$
$$=\beta\gamma^{2/3}t, \quad A^3=-1/\gamma. \qquad (45)$$

A simple and more revealing way of integrating (44) is by series expansion of the denominator. The result is

$$R_1{}^2\left(1+\frac{2}{5}\gamma R_1{}^3+\frac{1}{4}\gamma^2 R_1{}^6+\ldots+\frac{2}{3n-1}\gamma^{3(n-1)}+\ldots\right)=2\beta t. \qquad (46)$$

Thus the law differs from the usual parabolic law by the second and subsequent terms of the series. The two forms of growth curve are compared in fig. 3 using values of R_1, γ and β which would permit microscopic (optical) measurement of growth rates in a typical metal system. The curves are almost identical at small R but diverge considerably as the size of the particle increases. Thus the fitting of growth data to parabolic curves with the subsequent conclusion that the rate of growth is governed by diffusion is open to considerable criticism.

In the cases of eutectoid transformations and re-crystallization the Johnson-Mehl equation will probably give a better representation of experimental data than the present equations. In these reactions only short range diffusion is involved, the re-distribution of the components

Fig. 7

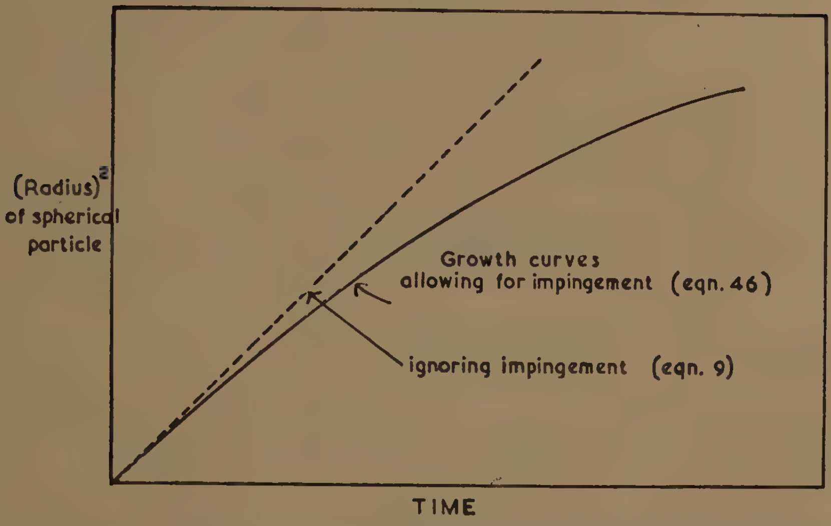

Hypothetical growth curves, (*a*) ignoring impingement (broken curve) and (*b*) considering impingement (eqn. (46)).

occurring in the parent solution adjacent to the interface. Impingement consists of direct contact between grains of the new phase and the diffusion potential is not affected.

ACKNOWLEDGMENTS

The author is grateful to Mr. A. Young of the Department of Applied Mathematics for help with the solutions of eqns. (28) and (38).

REFERENCES

BARRER, R. M., 1941, *Diffusion in and through Solids* (Cambridge : University Press).
BIRCHENALL, C. E., and MEAD, H. W., 1956, *Trans. A.I.M.M.E.*, **206** (*J. Metals*, **8**, 1004).
DOREMUS, R. H., 1957, *Acta Met.*, **5**, 293.
HARDY, H. T., and HEAL, T. J., 1954, *Progress in Metal Physics*, **5**, 143.
JOHNSON, W. A., and MEHL, R. F., 1939, *A.I.M.M.E.*, **135**, 416.
MISHIMA, T., 1951, *Proc. First World Met. Congress* 1950, *Cleveland*, (American Society of Metals), p. 668.
WERT, C., 1949, *J. appl. Phys.*, **20**, 943.
ZENER, C., 1949, *J. appl. Phys.*, **20**, 950.

CORRESPONDENCE

Density and Expansivity of Solid Krypton

By B. F. Figgins and B. L. Smith
Department of Physics, Queen Mary College (University of London),
London, E.1

[Received January 11, 1960]

The theoretical study of ideal crystal lattices is considerably strengthened when use can be made of experimental values for the thermodynamic properties of the solidified inert gases (Dobbs and Jones 1957) and in an earlier paper (Dobbs *et al*, 1956) experimental values of the density and expansivity of solid argon were reported. In the present note we give the corresponding figures for krypton.

The same two methods were used as in the earlier work. Debye–Scherrer powder photographs were taken between 20°K and 90°K and a bulk density method gave results between 70°K and the melting point ($T_m = 116$°K) where the large grain size made the x-ray method inaccurate. Using krypton supplied by the British Oxygen Company and stated to contain up to $\frac{1}{2}$% xenon and of the order 0·001% of other impurities, good agreement was not obtained where the two methods overlapped. However, when krypton supplied by the Air Reduction Sales Company and stated to be 99·98% pure was used for the bulk density method agreement was complete within the experimental accuracy ($\pm 0{\cdot}001$ Å at 20°K rising to $\pm 0{\cdot}003$ Å at 90°K for the lattice parameter from x-ray measurements and $\pm 0{\cdot}0025$ Å as deduced from bulk density measurements).

The present results are shown in the figure, together with the results of earlier workers at isolated temperatures or over narrow ranges of temperatures. It will be seen that large discrepancies occur between the various sets of results but, as already stated, there is good agreement between our results obtained by the two methods. The following table shows our values for the density and derived values of the expansivity and Gruneisen parameter $\gamma = \alpha V/\kappa_s C_p$.

T°K	20	40	60	80	90
(g cm^{-3})	3·078	3·040	2·988	2·926	2·893
$\alpha \times 10^4$ (deg^{-1} c)	4·8	7·7	9·7	11·0	11·2
γ	2·1	2·2	2·5	2·5	2·1

In order to calculate γ we have used the specific heat values of Clusius (1936) and the value of compressibility obtained by Stewart at 77°K

(1955). The latter value was corrected for temperature variation by a comparison with the results of Barker and Dobbs (1955) for argon, using a reduced temperature T/T_m.

An estimate of the density at absolute zero made by an extrapolation of our curve leads to a value of 3·09 g cm^{-3} which is to be compared with the best previous estimate (see for example Dobbs and Jones 1957) of 3·01 g cm^{-3}. The average value of the Gruneisen parameter is about 2·3 and it appears to have a maximum value of about 2·6. It is interesting to note that roughly the same variation of γ with reduced temperature was observed for argon.

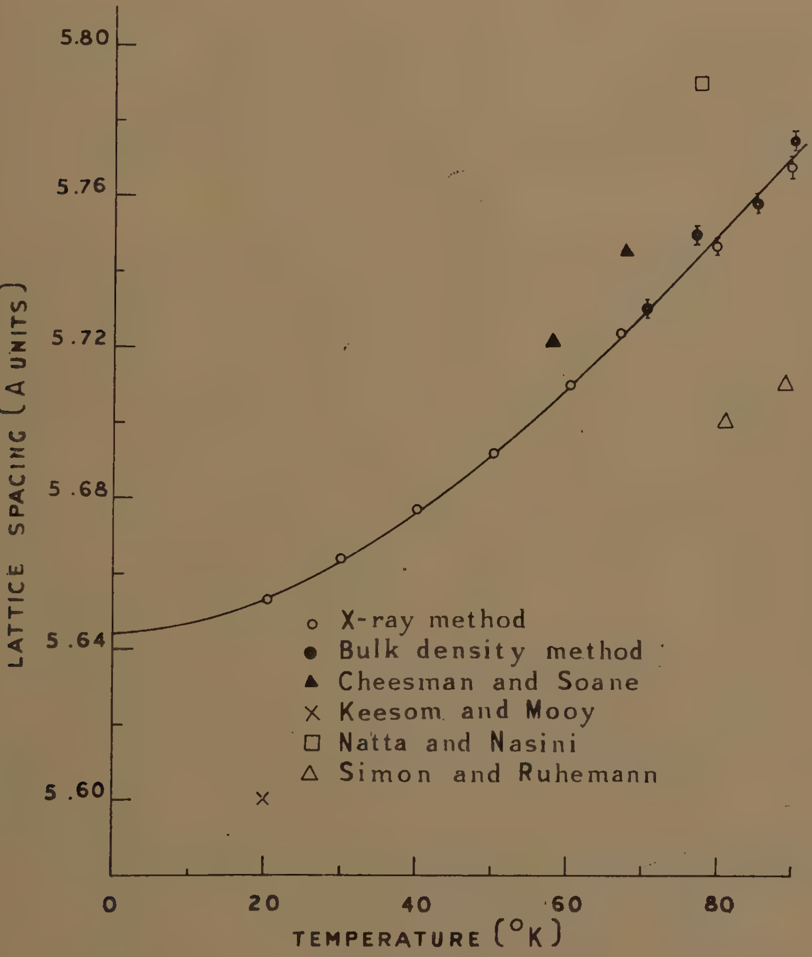

ACKNOWLEDGMENTS

We wish to acknowledge the valuable help and advice of Dr. E. R. Dobbs and of Professor G. O. Jones. We are indebted to the British Oxygen Company for a Research Fellowship (to B.F.F.) and to the D.S.I.R. for a maintenance grant (to B.L.S.)

References

Barker, J. R., and Dobbs, E. R., 1955, *Phil. Mag.*, **46**, 1069.
Cheesman, G. H., and Soane, C. M., 1957, *Proc. phys. Soc., Lond.* B, **70**, 700.
Clusius, K., 1936, *Z. phys. Chem.* B, **31**, 459.
Dobbs, E. R., Figgins, B. F., Jones, G. O., Piercey, D. C., and Riley, D. P., 1956, *Nature, Lond.*, **178**, 483.
Dobbs, E. R., and Jones, G. O., 1957, *Rep. Prog. Phys.*, **20**, 516.
Keesom, W. H., and Mooy, H. H., 1931, *Leiden Commun.* 2096.
Natta, G., and Nasini, A., 1930, *Accad. Lincei. Atti.*, **12**, 141.
Simon, F., and Ruhemann, B., 1932, *Z. phys. Chem.* B, **15**, 389.
Stewart, J. W., 1955, *Phys. Rev.*, **97**, 578.

An Anomaly in the Heat Capacity of Chromium at 38·5°c

By R. H. Beaumont†, H. Chihara† and J. A. Morrison
Division of Pure Chemistry, National Research Council,
Ottawa, Canada

[Received December 28, 1959]

Several properties of pure chromium metal show an anomalous temperature dependence in a broad temperature region below 50°c (Sully 1954); the temperature coefficients of some (e.g. Young's modulus, expansivity) undergo an abrupt reversal of sign at about 38°c. Different interpretations of the phenomena have been discussed (Pursey 1958, Neumann and Stevens 1959), but none seems to have been fully substantiated.

Although the general trend of the heat capacity curve of chromium is known between 56° and 1100°k (Anderson 1937, Armstrong and Grayson-Smith 1950), no detailed results are available for the region where an anomaly, corresponding to the anomalies in other properties, would be expected to occur. In view of the possibility that the heat capacity could yield useful additional information, we have made closely spaced measurements in the region $-5°$ to 51°c; the results are described in this note. Clear evidence has been obtained of a lambda type anomaly, the maximum occurring at $38{\cdot}5 \pm 0{\cdot}3$°c.

The specimen of ductile chromium (99·998% pure) used was part of that employed by Rayne and Kemp (1956) in heat capacity measurements below 4·2°k‡. It was in the form of a cylinder, diameter 2·5 cm and height 3·8 cm, and weighed 135·2 g. A copper holder was attached by means of a copper screw which passed through the holder and into a hole tapped in the base of the specimen. A platinum thermometer (T–4, Los and Morrison 1951) and a manganin heater were cast with Woods metal into a well in the holder at one side of the chromium cylinder. The holder and specimen were suspended by three nylon threads within the adiabatic shield of an assembly used previously for heat capacity measurements (calorimeter II: Flubacher *et al.* 1959). Thermal contact between the holder and the specimen was satisfactory throughout. During input of energy, the temperature difference between the heating element and its surroundings was not greater than 0·2°c. Also, the half life for the process of distribution of energy after heating was only 1 to 2 min.

---

† National Research Council Postdoctorate Research Fellow.

‡ This specimen was originally produced by the Aeronautics Research Laboratory, Melbourne and its mode of preparation has been described (Wain *et al.* 1954–55).

The experimental results are shown in fig. 1, and are compared with results of measurements on other specimens in fig. 2. In estimating the absolute accuracy, only the comparison with the work of Anderson (1937) is useful. In the region where the two sets of measurements overlap there is a small systematic difference of 0·5 to 1%. This may reflect a variation from specimen to specimen but the difference is within the accuracy quoted by Anderson (1930) for his method. For our present purposes the precision of the measurements is more important. Below 38·5°c, the root mean square deviation of our results from a smooth curve (fig. 1) is 0·13%.

The general shape of the heat capacity curve displayed in fig. 1, is clearly that of a lambda type anomaly. Within the precision available in the measurements, the heat capacity remains finite throughout the transition region. If, as seems reasonable, the contribution of the undisturbed state can be represented by the light dashed curve in fig. 1, estimates of the enthalpy and entropy associated with the transition can be made. These are small; the change in enthalpy amounts to 1·4 cal/g atom and the change in entropy to 0·0044 cal/g atom deg.

It is important to establish whether the magnitude of the excess heat capacity is consistent with the changes in the expansivity and compressibility of chromium which have been observed previously. The three quantities are related (Prigogine and Defay 1954) and at the lambda point the relationship takes the form

$$\Delta C_p = \frac{V_\lambda T_\lambda (\Delta\alpha)^2}{\Delta\chi}, \quad \quad (1)$$

where ΔC_p, $\Delta\alpha$ and $\Delta\chi$ refer to differences between the observed heat capacity, expansivity and compressibility and the values attributable to the undisturbed state. V_λ is the atomic volume at the transition temperature T_λ.

Two of the three quantities required for the estimation of ΔC_p from eqn. (1) are directly accessible. With adequate accuracy the density can be taken as 7·18 g/cm³ (Sully 1954). The expansivity of chromium (99·8% pure) has been measured by Fine *et al.* (1951) and a value of $\Delta\alpha$ can be obtained from their graph.

In order to compute $\Delta\chi$, a knowledge of both Poisson's ratio (μ) and Young's modulus (E) is required, since

$$\chi = \frac{3(1-2\mu)}{E}. \quad \quad (2)$$

Fig. 1

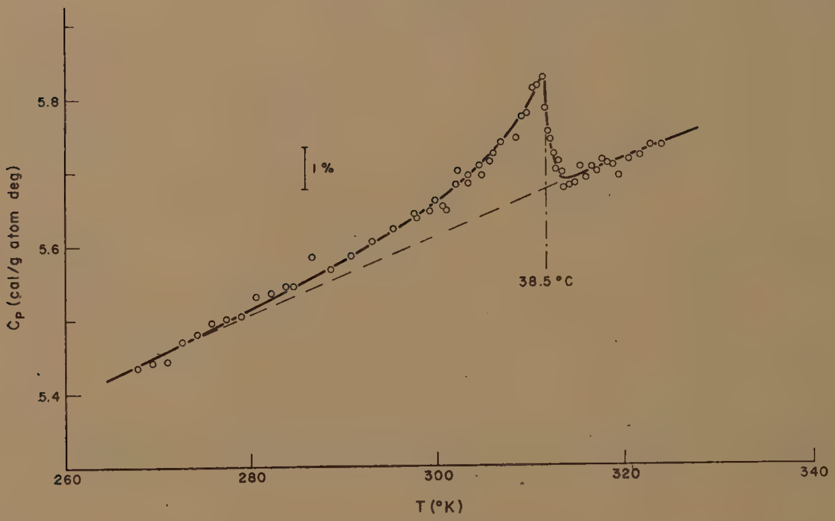

Measured heat capacities of chromium.

Fig. 2

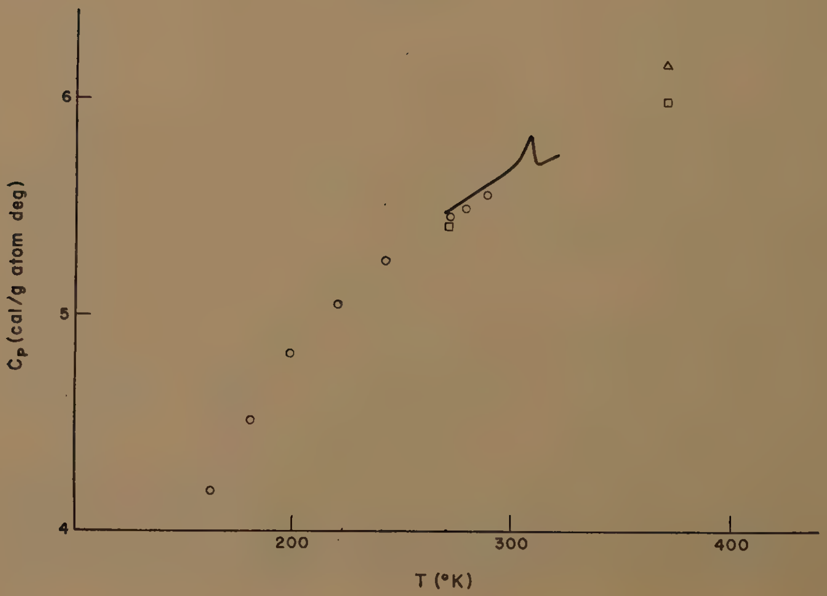

A comparison of different measurements of the heat capacity of chromium.

——Present results.

□ Armstrong and Grayson-Smith (1950).

○ Anderson (1937).

△ Umino (1926).

E has been determined by Fine *et al.* (1951) and by Pursey (1958), and the two sets of results are in substantial agreement. There is therefore no difficulty in making an estimate of the change in E at the lambda point. μ for pure chromium outside the transition region appears to be about one-third but its actual value at 38°C has not been measured. However, Pursey (1958) has established that the change in μ for the transition in chromium containing metallic impurities is about 0·2. There is evidence (Neumann and Stevens 1959) that such impurities enhance the anomaly. Therefore, it seems reasonable to suppose that μ for pure chromium at 38°C lies between 0·13 and 0·33. These values lead to lower and upper bounds on ΔC_p of 0·05 and 0·30 cal/g atom deg. respectively; direct experiment gives $\Delta C_p = 0{\cdot}15$ cal/g atom deg.

This excellent agreement between the experimental and calculated values of ΔC_p shows that the different bulk measurements on relatively pure chromium are consistent. Furthermore, since the measurements have been made on different specimens, the agreement indicates that the anomaly in chromium at 38·5°C is not to be ascribed to the presence of small amounts of impurities such as oxygen or nitrogen in the lattice. Instead, the anomaly must be the reflection of a change in the chromium lattice itself. Neutron diffraction studies by Dr. G. E. Bacon of Harwell (private communication) have recently confirmed that high purity chromium becomes weakly antiferromagnetic below about 40°C (see also, Corliss *et al.* 1959). The shape and position of the heat capacity anomaly are consistent with an antiferromagnetic transition.

ACKNOWLEDGMENT

We should like to thank Dr. G. K. White for suggesting the problem and for helpful correspondence.

REFERENCES

ANDERSON, C. T., 1930, *J. Amer. chem. Soc.*, **52**, 2712; 1937, *Ibid.*, **59**, 488.
ARMSTRONG, L. D., and GRAYSON-SMITH, H., 1950, *Canad. J. Res.*, A, **28**, 51.
CORLISS, L. M., HASTINGS, J. M., and WEISS, R. J., 1959, *Phys. Rev. Letters*, **3**, 211.
FINE, M. E., GREINER, E. S., and ELLIS, W. C., 1951, *J. Metals* (*Trans. A.I.M.E.*, **191**), 56.
FLUBACHER, P., LEADBETTER, A. J., and MORRISON, J. A., 1959, *Phil. Mag.*, **4**, 273.
LOS, J. M., and MORRISON, J. A., 1951, *Canad. J. Phys.*, **29**, 142.
NEUMANN, M. M., and STEVENS, K. W. H., 1959, *Proc. phys. Soc. Lond.*, **74**, 290.
PRIGOGINE, I., and DEFAY, R. 1954 *Chemical Thermodynamics* (Translated by D. H. Everett) (London: Longmans Green and Co.), p. 296 et seq.
PURSEY, H., 1958, *J. Inst. Met.*, **86**, 362.
RAYNE, J. A., and KEMP, W. R. G., 1956, *Phil. Mag.*, **1**, 918.
SULLY, A. H., 1954, *Chromium* (London: Butterworths Scientific Publications), chap. 3.
UMINO, S., 1926, *Sci. Rep. Tôhoku Univ.*, **15**, 597.
WAIN, H. L., HENDERSON, F., and JOHNSTONE, S. T. M., 1954–55, *J. Inst. Met.*, **83**, 133.

Direct Observation of Dislocations in Magnesium Oxide

By J. Washburn†, A. Kelly and G. K. Williamson‡
Department of Metallurgy, University of Cambridge

[Received February 9, 1960]

Dislocations have been observed in thin metal foils by electron transmission microscopy for a number of years. We have recently observed directly the motion of dislocations in thin crystals of magnesium oxide, a ceramic material of high melting point. Large crystals, supplied by the Norton Company, were prepared by cleavage followed by chemical polishing, to produce a thin specimen. From the measured separations of the traces of (110) slip planes on the two surfaces of the specimen the thickness was found to be 3000 to 5000 Å.

Direct evidence for the double cross-slip of individual screw dislocations from a given (101) slip plane into nearby parallel glide planes is shown in fig. 1 (*a*), (*b*), (*c*) (Pls. 23 and 24). The beam current was momentarily increased between exposures to move the dislocations. Multiplication of dislocations took place at the tip of a short crack near one edge of the specimen. The thermal stresses due to local heating of the crystal by the beam tended to drive screw dislocations along the (101) plane into the crystal. The paths taken by individual moving dislocations were clearly delineated at the surface by a contrast effect similar to that seen in metal foils (Hirsch *et al.* 1956). It has been suggested for metals that this effect is associated with the presence of an oxide film. This cannot be the case for magnesium oxide but films of magnesium hydroxide or deposited carbon may have been present. The paths taken by some of the dislocations show that motion was not confined to a single (101) slip plane. The band spread sideways as the dislocations moved away from the edge by frequent cross-slip, probably into (010) and then back into (101). The double cross-slip took place on a very fine scale resulting in what appeared to be noncrystallographic glide paths. All the dislocations were retarded at their intersections with the surfaces and many were also held back at one or two interior points along their length. They were bowed out between these locking points which may have been jogs consisting of short segments of edge dislocation connecting a length of dislocation in the original slip plane with another part which had undergone double cross-slip into a parallel plane. They could also have been formed by cutting of an intersecting screw dislocation by the moving dislocation.

---

† National Science Foundation fellow on leave from University of California.
‡ On secondment from C.E.G.B., Berkeley Nuclear Laboratories.

Plastic deformation associated with the propagation of cracks was also observed. Figure 2 (Pl. 24) shows a crack on a (100) plane at right angles to the plane of the foil. A row of dislocations extending from the crack surface to either the top or bottom surface of the foil can be seen on both sides of the crack.

Dislocation pile-ups consisting of a large number of dislocations lying on a single slip plane held up behind an immobile dislocation have not been observed and perhaps would not be expected in this material due to the manifest ease of cross-slip.

One particularly encouraging aspect of this work is that it has been possible to study imperfections in a refractory ceramic material using electron transmission microscopy in the same way as with metal specimens.

REFERENCE

HIRSCH, P. B., HORNE, R. W., and WHELAN, M. J., 1956, *Phil. Mag.*, **1**, 677.

REVIEWS OF BOOKS

Concepts of Classical Optics. By JOHN STRONG. (San Francisco: W. H. Freeman; London: Bailey Bros. and Swinfern, 1958.) [Pp. xxii + 692.] 80*s*.

THIS excellent textbook deals with the subject in an agreeably matter of fact way. The necessary mathematics is there, but the emphasis is on physical insight; laboratory work is kept constantly before the reader's mind by Roger Hayward's illuminating diagrams. The book could provide an ideal refresher course for technologists who found optics dull in their undergraduate days.

The first three chapters deal with light as wave motion, with superposition of wave motions and with electromagnetic waves; the next four with the interaction of light and matter. Then follow accounts, all very well written, of interference, diffraction and coherence. Chapter 12 discusses reflection-reducing overcoats on optical surfaces, interference filters, and multiple beam interferometry. Chapters 13–16 deal with the simpler properties of optical systems, and with the testing of optical surfaces. They keep closely in touch with practical problems and give an excellent introduction to optical design.

The book ends with seventeen appendices contributed by (or quoted by permission of) various authors. Although the presentation in some of the appendices is below the high standard of the main text, they bring the reader into closer touch with the growing edge of the subject and add to the vitality and interest which characterize the whole work. E. H. L.

Theory and Applications of Nuclear Induction. By A. K. SAHA and T. P. DAS. (Saha Institute of Nuclear Physics, Calcutta, India.) [Pp. 516.] 40*s*.

NUCLEAR Induction is another name for Nuclear Magnetic Resonance. It used to be said that one's preference for the name of this ever-growing field of study was determined by whether one was situated West or East of the Mississippi. At the present time when the name Nuclear Magnetic Resonance has gained almost universal usage, the authors' choice of title provides a salutary reminder of the alternative approaches to the understanding of the phenomenon.

Six or seven years ago the whole of Nuclear Magnetic Resonance could be reviewed in a book of modest dimensions. The enormous recent growth of activity, particularly in high-resolution chemical applications, makes comprehensive coverage impossible today. Nevertheless this substantial work traverses much ground: Basic theory, experimental methods, relaxation mechanisms, dipolar-broadened spectra, quadrupole-split spectra, chemical shift, electron-coupled nuclear interactions, spin echoes, Overhauser effect, pure quadrupole resonance; indeed all the main topics find their place. The book is addressed to physicists and an account of purely chemical applications is not included. The emphasis throughout is on theory, which occupies the majority of the book. The theoretical treatment is of a high standard and the book is not appropriate as a first introduction to the general reader or to the researcher newly entering the field. On the other hand to the reader already familiar with the subject the presentation of the theory will make stimulating reading. The material of the experimental sections seems rather less well organized, and contains a surprising amount of constructional detail of early apparatus. There are four pages of errata at the end.

The writing and publication of this book in India is commendable and is to be welcomed as a useful addition to the literature of the subject. E. R. A.

Electron Physics: The Physics of the Free Electron. By O. Klemperer. (London: Butterworth's Scientific Publications, 1959.) [Pp. 248 + xi.] 32*s*. 6*d*.

With the present-day preoccupation with nuclear phenomena on the one side and with electronic gadgetry on the other, the electron has become something of a Cinderella particle in University courses. Even pre-war texts which did it liberal justice, such as Barton Hoag, have been so swollen with information about the nucleus that the electron has been squeezed out of the original picture in more senses than one. The balance is somewhat restored by the present book, which is based on courses given by the author to Honours students at Imperial College, London.

The fundamental properties of the electron—charge, mass, wavelength, spin and magnetic moment—are discussed in Part II of the book, primarily from the phenomenological standpoint. All the main experiments are described, and at the same time the wave nature of the electron is discussed and the treatment is up-to-date enough to include electron spin resonance and radio frequency spectroscopy. Part I is devoted to the propagation and detection of the electron, much of it clearly condensed from the author's extensive monograph on Electron Optics. The mathematical and the experimental study of trajectories in electrical and magnetic fields are both treated in a clear and concise manner. Space charge flow has a chapter to itself, and that on methods of detection provides an introduction to the principles of different types of counter, even if too short to be very informative about practical matters. However, like the other chapters, it ends with a selected list of references through which details can be hunted up. There are also short selections of problems, mostly from the Special B.Sc. examinations of London University.

The author mentions in his preface that he has had in mind those going on to specialize in electronic engineering, and both his choice of topics and level of treatment seem eminently suited to such students. The book should also find a place in courses in applied physics, and may not be out of place in the reading of the practically minded student of pure physics. He will find here, for instance, an excellent short account of electron optics and an up-to-date discussion of the different methods of measuring e/m. However, as may be inevitable in such an effort of compression, some sections are short to the point of scrappiness. In practice, of course, lectures on electron physics will be dovetailed in with other courses; without this, the average man would not make much of the treatment of the Lamb-Retherford shift, for instance. To get full benefit from the text, a student had best follow up some of the references given and should certainly work through the problems. V. E. C.

Mécanique Quantique, Tome II. By A. Messiah. (Dunod: Paris.) [Pp. 540.] 48 New Francs.

The second volume of this comprehensive treatise takes us though symmetry and invariance, through methods of approximation and collision theory, to the Dirac electron and the elements of quantized fields. On the whole there is probably more here than one might expect every theoretical physicist to know, but it is all said with such accuracy and clarity that there is no excuse for him not knowing it if he has to. Every difficulty is explained, every approximation is justified. In a course of lectures this would be intolerable; in a text book it is invaluable. Moreover there are a number of topics here set forth explicitly which are not at all easy to find in the literature or in the other books. In the problems which are discussed it is entirely up to date, and the general approach reflects standard enlightened opinion amongst professional research workers.

The printing and the writing are impeccable ; great trouble has obviously been taken to eliminate errors and ambiguities. Perhaps I have been misled by the elegant simplicity of the French language. I challenge the author to produce an English translation of like excellence. It will surely become one of the most useful books on the subject. J. M. Z.

Fracture. By B. L. AVERBACH, D. K. FELBECK, G. T. HAHN and D. A. THOMAS (Editors). (Technology Press and John Wiley and Sons, New York.) [Pp. 646.] (No price given by publishers.)

Now that the plastic properties of solids are beginning to be understood people are taking an increased interest in the atomic mechanisms of fracture, a subject that has languished since the great papers of A. A. Griffith. A conference on it was held in April 1959 at Swampscott, U.S.A., and the proceedings are summarized in this book. Particularly valuable features, fully brought out in the book, were the wide survey of various types of fracture produced in different materials under different conditions of temperature and stressing, and the highly critical appraisals of what is really understood in this field. The main advances made at the conference were the recognition that brittle cracks in steel are often nucleated by plastic deformation, that it is usually easier to nucleate them than grow them, and that in ‘ ductile fracture ’ the material probably does not fracture at all but flows plastically into two halves. By contrast, the conference also showed that we still have some way to go in understanding creep fractures and that as regards understanding fatigue fractures, in spite of brilliant observations with the microscope, we are not sure whether we even have started yet. These and many other points are fully brought out in the 28 articles and discussions contributed by those at the conference. This book will undoubtedly become and remain the standard work on the theory of fracture until, at least, another similarly successful conference is held. A. H. C.

Advances in Electronics and Electron Physics, Vol. XI. Edited by L. MARTON. (Academic Press.) [Pp. xi+523.] $15.00.

THE volume under review is the eleventh of an annual series which has become well established. It follows more or less the form of previous issues, consisting of a number of review articles. The variety of subjects covered in this case is unusually large, ranging from Parity Nonconservation to Radio Telemetering. The articles, however, fall into one or two groups of more closely related subjects.

The first article on *Recent Advances in Photoemission* by P. Görlich gives a short up-to-date account of the interesting advances made in the past few years in the development of compound alkali metal cathodes with a short discussion of the theory of their operation. This may be grouped with the article by O. Hachenberg and W. Brauer on *Secondary Electron Emission from Solids*, which after an all too brief review of recent experimental data gives a rather protracted and sometimes obscure account of developments in the theory. It is interesting to note that data for a number of semiconductors and a good many insulators is given; too often this data is restricted to metals. Less closely related to this group is a long article by R. Clark Jones on *Quantum Efficiency of Detectors for Visible and Infrared Radiation.* This collects together much of the extensive material which the author has written on this subject. For the specialist in this field the article will provide a useful reference but for others it will make rather difficult reading. The article on *Electron Diffraction Structure Analysis and the Investigation of Semiconducting Materials* by Z. G. Pinsker (translated by L. B. Leder) gives an account mainly of Russian work in this field. There is not a great deal of information available on this particular aspect of crystal analysis and the article is a useful addition to the literature on semiconductors.

Articles of a more "electronic" type are those on *Radio Telemetering by* H. B. Riblet, dealing mainly with American practice, and on *Operational Amplifiers* by R. L. Konigsberg. The latter article is mainly theoretical; it covers a good deal of ground well-known to specialists in the field but makes very difficult reading for those not already familiar with it. It is rather typical of a great many articles in this particular field which contain much more abstract theory than practical guidance. Allied to this group of articles is that by G. E. Barlow, J. A. Overstone and F. F. Thonemann on *Automatic Data Processing in the Physical Sciences*. This is rather more discussive than informative, though some interesting examples of data processing are rather briefly described.

Finally, there is an article on *Parity Nonconservation in Weak Interactions*, by R. M. Sternheimer. This is rather more closely allied to Nuclear Physics than to Electronics and will hardly appeal to most electronics engineers. It gives quite a good account of recent work in this field but an extensive knowledge of the theoretical background of quantum mechanics is necessary in order fully to appreciate it.

As with previous issues the volume gives good value for money and both electronics engineers and physicists concerned with electronic techniques will wish to have it available for consultation. P. A. S.

Optics and Spectroscopy (*Optika i Spektroskopia*). Scientific articles translated on the initiative of the Optical Society of America. (The Optical Society of America.) [Pp. 84 per volume.]

THIS monthly journal of the U.S.S.R. Academy of Sciences commenced publication in 1956. It publishes work in all branches of optics and spectroscopy, (including x-ray, ultra-violet, visible, infra-red and microwave), thin film optics, filters, detectors, diffraction gratings and electroluminescence, and their many other applications in science and industry. The English translation starts from Volume 6, January 1959. At present it appears about six months after the Russian original but it is hoped to reduce the interval to four months. The printing of the translation is clear though rather small.

A typical number contains fourteen papers of average length equivalent to 3800 words and about an equal number of "brief reports" of average length about 1250 words. News items, book reviews and very brief letters are also included. About 40% of the space is occupied by papers on molecular spectroscopy which would be suitable for the Journal of the Faraday Society or the Journal of Chemical Physics. Another 25% of the material is in the field of Solid State Physics (absorption spectra and luminescence). Only about 30% falls within the field of J.O.S.A. or Optica Acta. About half the papers refer almost entirely to Russian journals (including earlier numbers of this journal) and in some cases this is at present a serious obstacle to understanding.

The general scientific standard is high and the translation is very welcome.

R. W. D.

Experimental Nuclear Physics, Vol. III (Editor: E. SEGRÈ). By E. SEGRÈ, G. C. HANNA, M. DEUTSCH, O. KOFOED-HANSEN and E. M. MCMILLAN. (New York: John Wiley and Sons, Inc.; London: Chapman and Hall.) [Pp. x+811.] 184*s*.

THIS is the third and final volume in the series. Segrè writes on Radioactive Decay, Hanna on Alpha-Radioactivity, Deutsch and Kofoed-Hansen two parts on Gamma-rays and Beta-rays and McMillan on Particle Accelerators. The case for this type of venture, made by Segrè in his Preface, is that "... a summary in book form is becoming even more necessary than it was a few years ago owing to the tremendous swelling of the literature". This is indeed a case for a series of summaries prepared by dedicated practitioners of their various fields, but book form imposes unwelcome rigidity and the hard covers give a false air of permanence. When we add to the enormous delays that attend such publications, at least in America, the prohibitive cost, the purpose of such publications as against the standard review series is difficult to see. Books there must still be, but the time has surely come when individual publications on the various sections of the subject, written at an epoch appropriate to each, should take the place of these compendious edited works that themselves arise from the impossibility that a single-author book entitled ‘ Nuclear Physics ’ can ever again take us to the frontiers of knowledge.

Hanna's article is beautifully and conscientiously composed. It is droll that his final ‘ Note added in proof ’ (referring to work done in 1957) should take us back more than 20 years. The chapter on Gamma-rays (for which compilation of material finished in the summer of 1955) is a rather personal account of the subject but contains much valuable information. Beta-rays similarly are cut off in the summer of 1955 for the most part but parity is mercifully caught in time and even V-A. McMillan's article is a delight. It is written from an intimacy with his material that few other than the author can command and that we shall never see again in the field of particle accelerators. D. H. W.

Principles of Optics. By Max Born and Emil Wolf. (London : Pergamon Press, 1959.) [Pp. 803.] £6.

This is a monumental work which should immediately become a standard text. It is intended to fill the same place for the English speaking world as Born's ‘ Optik ’ has held for German readers. It is, however, much more than a translation; it has been largely rewritten and is completely up to date. The aim, as in the earlier work, is to present optics deductively as a system based on Maxwell's equations. The field covered is narrower than in the earlier work, as classical molecular optics is largely omitted. The discussion is therefore limited to situations in which the atomistic structure of matter plays no decisive part. Within this limitation, the treatment is thorough and comprehensive. There are specialist contributions from seven additional authors : A. B. Bhatia, P. C. Clemmov, D. Gabor, A. R. Stokes, A. M. Taylor, P. A. Wayman and W. L. Wilcock.

Many topics are here presented in a systematic manner for the first time : for example, the treatment of partially coherent light is particularly valuable. The presentation is exceptionally clear, and the printing and illustrations reach a high standard. This book will be needed in every physics library.

B. H. B.

Applications of Thermo-Electricity. By H. J. Goldsmid. (London : Methuen.) [Pp. 118.] 10*s*. 6*d*.

This is a neat little book about the practical problem of applying the thermoelectric effect. It deals with the theoretical estimation of the efficiency of thermocouples, and the figure of merit of thermoelectric materials. Attention is then focused on the Bi_2Te_3 type of compound, whose properties are discussed in detail. Finally there is a survey of devices which have been designed or constructed using the Peltier or Seebeck effects. Obviously, with the rapid development of the art (no doubt by the author himself), this part of the text will soon be dated. Meanwhile, it will hold its own as an intelligible and useful review of an interesting application of solid state physics. There is much to be said for its publication here under its own covers at a reasonable price, instead of it being, perhaps, one of a miscellaneous collection of review articles in an expensive and clumsy volume. J. M. Z.

Journal of Nuclear Energy: Part C. Ed. J. V. Dunworth. (London: Pergamon Press.) £7 per volume.

The colossal growth of plasma physics over the last few years may appear to some as a symptom of the instability of plasma physicists, but the present scale of plasma research justifies the initiation by the Pergamon Press of this new journal, which is comfortably shared with accelerator physics; thermonuclear research is also featured. It is indeed a great benefit to workers in these fields, to have most of their literature concentrated in relatively few journals, and this one offers two other excellent services, namely abstracts of Russian papers and a list of titles of papers from ~100 journals.

While welcoming the new journal, it is fitting to recall our past debt to the dear old *Phil. Mag.* J. W. D.

Theory of Space Time and Gravitation. By V. Fock. (Pergamon Press, 1959.)

This is an outstandingly good book and its publication in English is a major event in the history of relativity. The book is entirely different from all other treatments of general relativity because the theory is treated as the theory of gravitation and the inconsistencies and the emptyness of the general principle of relativity are made clear. Since Professor Fock's Copenhagen lectures, these views have become more widely understood and, in particular, have completely convinced the reviewer. In addition to this uniquely distinguished treatment of the foundations of Einstein's theory of gravitation, the book also contains a superb description of special relativity and a detailed discussion of modern developments in the theory of gravitation due to Professor Fock and others. Although these later chapters are of primary interest to the specialist, the book can be thoroughly recommended to all physicists for its other parts. The author's views on harmonic co-ordinate systems are set out with studied moderation. The translation by Professor Kemmer is worthy of the book and an outstanding model of what a translation should be, conveying the most difficult views with a precision of language only too rarely met in translations.

H. B.

The Study of Elementary Particles by the Photographic Method. By C. F. Powell P. H. Fowler, and D. H. Perkins. (Pergamon Press, 1960.) [Pp. 650+xxxv.] £12 10*s*. 0*d*.

The last fifteen years have seen the discovery of a host of unstable particles, which are apparently fundamental to the structure of matter. In the forefront of the techniques for their detection has been the use of nuclear emulsions, pioneered by Professor Powell and his co-workers at Bristol. In this massive book, the authors have succeeded in presenting a detailed history of the discovery of the new particles, and have demonstrated the methods used for their identification by including an extensive collection of microphotographs taken largely from their own experiments. The presentation throughout is lucid, and should be intelligible to anyone with a knowledge of the rudiments of nuclear physics. It sets before the general reader many photographs of historical interest, and imparts much of the excitement of the original discoveries, while the research worker will benefit from the exhaustive discussion of the techniques of measurement and their limitations.

After a general introduction to the history of emulsions, there is an account of their manufacture and processing, including the theory of track formation. In §§ 3 to 5 attention is focused on track densities, scattering, δ-rays, and a multitude of other tricks used to deduce particle momenta and energies. The accuracy possible in emulsions is impressive, particularly when one comes to hyperfragments, " which it is possible to study in detail only with the photographic method ", as the authors say with obvious pride. The excellent reproduction of 190 microphotographs enables the reader to judge this for himself, and perhaps justifies the lavishness of the production, which has made the price of the book so regrettably high.

Sections 6 to 12 deal in turn with each of the new particles. The detailed discussion of events will appeal to all readers with detective instincts. Complementary information from counter experiments and cloud chambers is included with plentiful diagrams wherever these techniques are superior to emulsions, although the section on hyperons seems rather brief compared with that on K-mesons. The emphasis throughout is on experimental technique, and it seems a pity that a little more space could not have been given to the theoretical schemes into which the elementary particles and their interactions have been fitted. A brief description of the Gell–Mann–Nishijima scheme is given, but the discovery of the non-conservation of parity, in which π- and K-mesons played such an important part, is restricted to five pages. Rather, to the theoreticians, this book will provide an insight into the reliability of experimental data, an invaluable contribution in these days when theoreticians and experimenters are so remote from each other.

Sections 13 to 16 describe interactions of very energetic particles in cosmic rays, and provide the only compact summary of this work of which I am aware. The cosmic rays are the only source of particles with energies above 30 BeV, and emulsions will doubtless still be used for their investigation.

References are conveniently located at the end of each section, and there are good author and subject indexes. D. V. B.

BOOK NOTICES

Advances in Catalysis and Related Subjects, Vol. XI. Edited by D. D. ELEY, P. W. SELWOOD and P. B. WEISZ. (Academic Press.) [Pp. x+384.] $12.50.

Modern Physics, Fourth Edition. By H. A. WILSON. (Blackie & Son.) [Pp. xv+473.] 40*s*.

The Theory of Homogeneous Turbulence. By G. K. BATCHELOR. (Cambridge: University Press, 1959.) Students' Edition. [Pp. xi+197.] 18*s*. 6*d*.

Regression Analysis. By E. J. WILLIAMS. (John Wiley & Sons.) [Pp. ix+214.] 60*s*.

Classical Dynamics. By R. H. ATKIN. (Heinemann.) [Pp. ix+273.] 30*s*.

Annual Review of Nuclear Science, Vol. 9. Edited by E. SEGRÈ and L. I. SCHIFF. (Annual Reviews, Inc., 1959.) [Pp. vii+625.]

CORRIGENDA

The Effect of Quenching on the Formation of G.P. Zones and θ' in Al–Cu Alloys, by J. M. SILCOCK, 1959, *Phil. Mag.*, 4, 1187.

1. Table 1, column 1, the third temperature should be 300° not 200°.
2. Table 3, column 3, second figure down should be 90 not 30.

[*The Editors do not hold themselves responsible for the views expressed by their correspondents.*]

Fig. 2

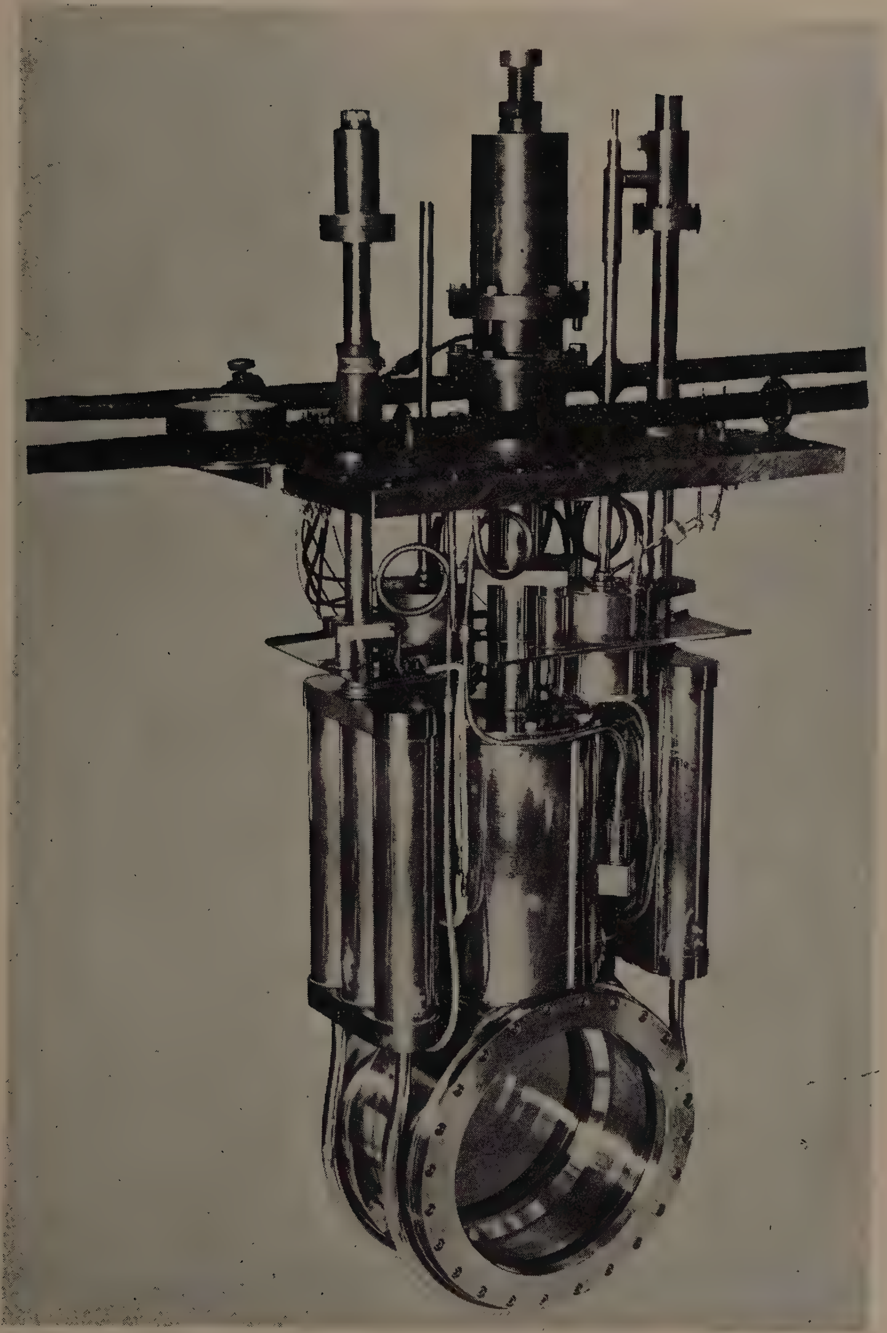

A photograph of the bubble chamber.

Fig. 4

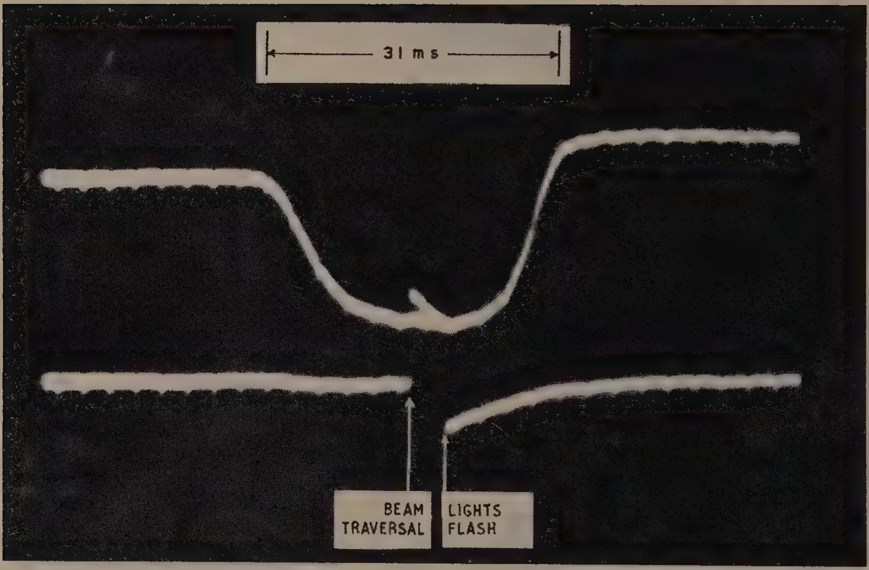

A typical oscilloscope trace showing the expansion cycle.

Fig. 5

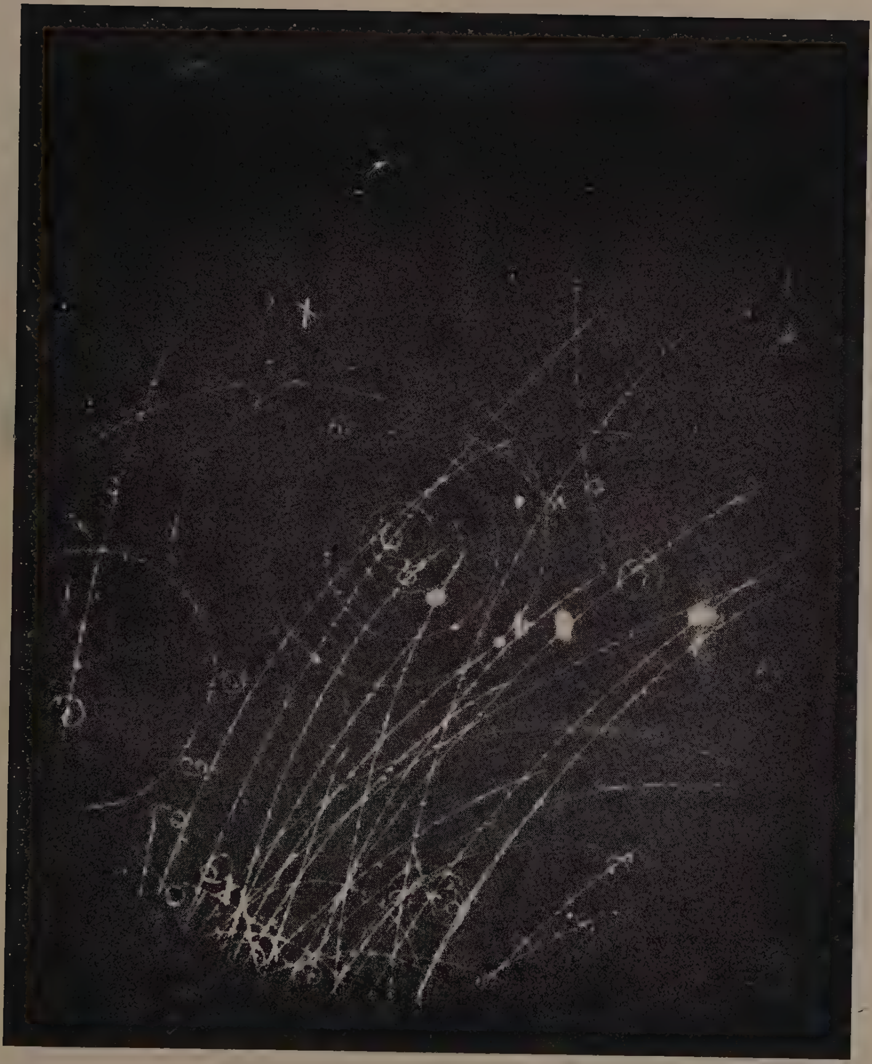

π^--mesons stopping in the chamber taken on Kodak R55 recording film at a magnification of 1/20.

Fig. 6

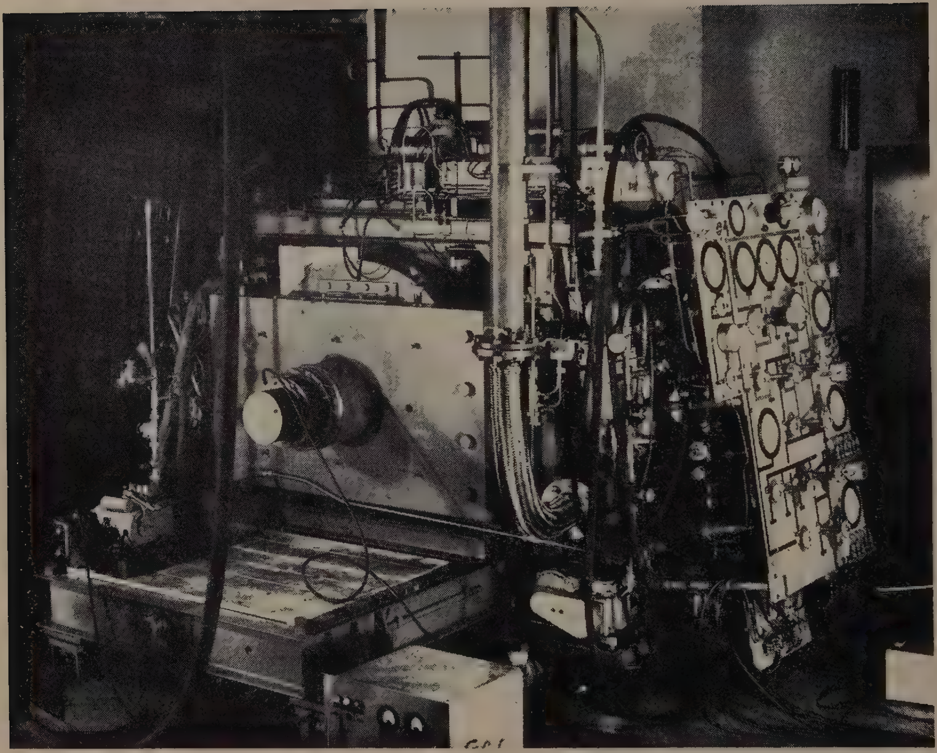

Photograph of the apparatus assembled in the π-meson beam of the 156 in. synchrocyclotron.

Fig. 1

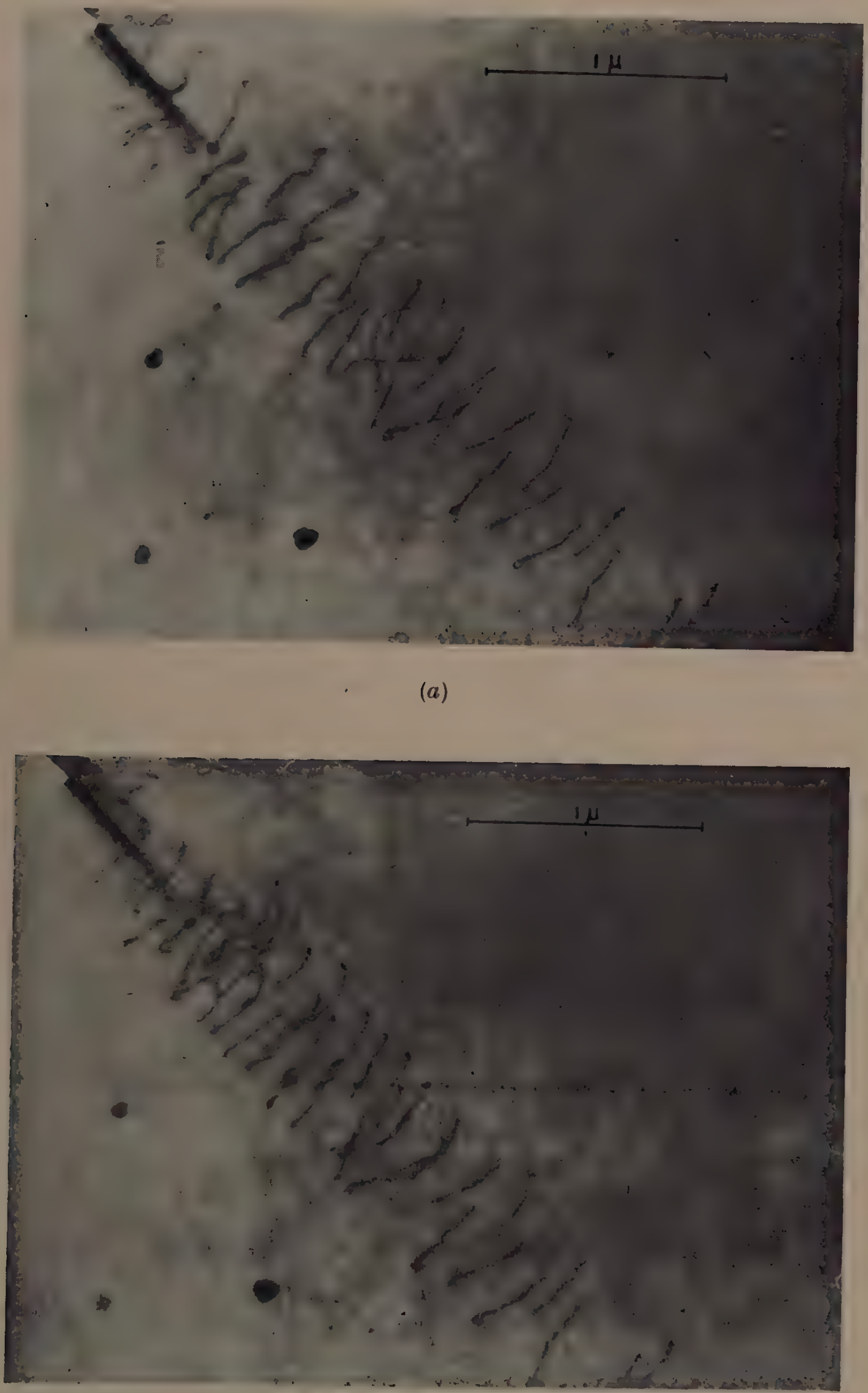

(*a*)

(*b*)

Fig. 1 (*continued*)

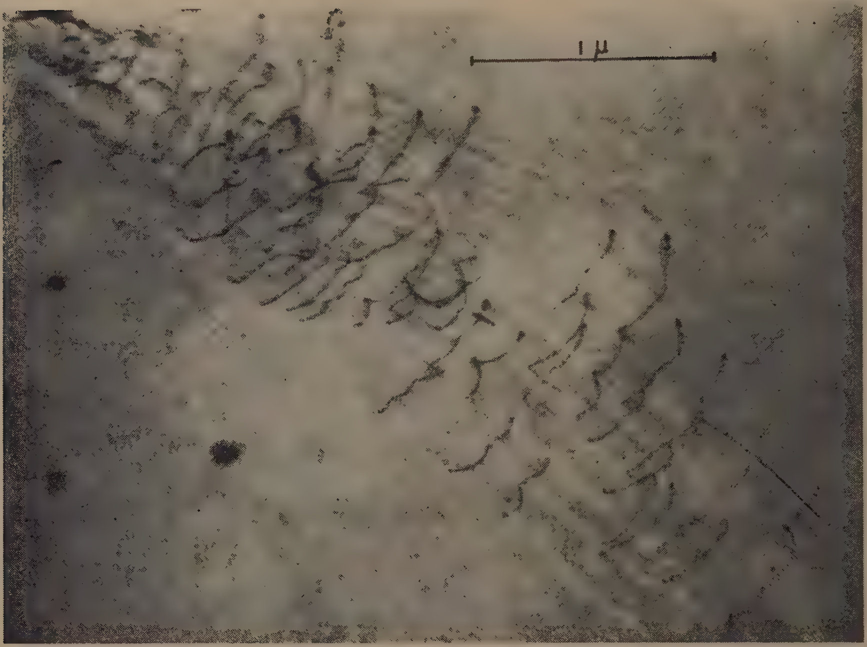

(*c*)

Three successive photographs of the same area of a magnesium oxide crystal showing dislocations moving into the specimen from a crack in the top left hand corner of the micrograph.

Fig. 2

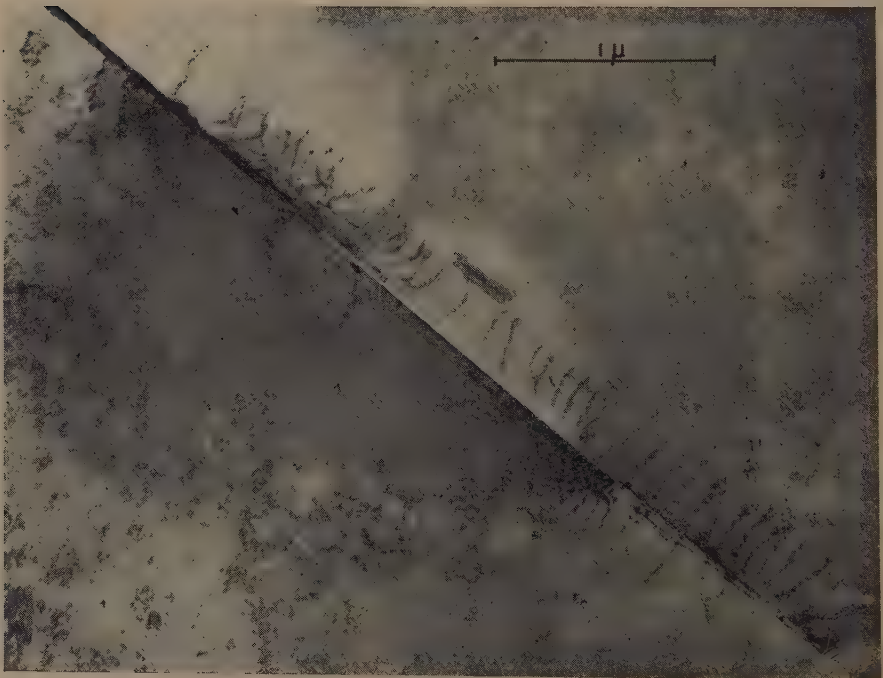

Dislocations associated with a crack in magnesium oxide.

Point Defects in Platinum†

By G. R. PIERCY
Atomic Energy of Canada Limited, Chalk River, Ontario

[Received August 24, 1959]

ABSTRACT

An investigation was made of the mobility and types of point defect introduced in platinum by deformation in liquid nitrogen, quenching into water from 1600°C, or reactor irradiation at 50°C. In all cases the activation energy for motion of the defect was determined from measurements of electrical resistivity. Measurements of density, hardness, and x-ray line broadening were also made where applicable.

These experiments indicated that the principal defects remaining in platinum after irradiation were single vacant lattice sites and after quenching were pairs of vacant lattice sites. Those present after deformation in liquid nitrogen were single vacant lattice sites and another type of defect, perhaps interstitial atoms.

§ 1. INTRODUCTION

ALTHOUGH an equilibrium number of the point defects, vacancies and interstitial atoms are present in a metal, a larger concentration is thought to be introduced by cold working, quenching, or irradiating. The concentration, distribution and type of the extra defects retained in the sample will depend on the temperature and method of production. If the defects are mobile at the temperature of production, they will move about the lattice until they reach a position of lower energy where they are trapped or annihilated. Foreign atoms are expected to act as trapping centres, while grain boundaries voids, free surfaces, and perhaps dislocations will act as annihilation centres or sinks. An interesting review on the effect of lattice defects on some physical properties of metals was recently given by Broom and Ham (1958).

Many different physical properties have been measured to detect vacancies and interstitital atoms. Electrical resistivity, which is very sensitive to their presence, is often used to measure their mobility. From this the activation energy required for one atomic jump of the defect can be calculated and the type of defect can be inferred. Also, the number of jumps required by the defect to reach the sink can be determined, from which the type of sink can be inferred. Unfortunately, all point defects increase the resistivity so that changes in other physical properties are necessary to determine exactly what type of defect is present. Changes in density and lattice parameter should discriminate between vacancies and interstitial atoms. The x-ray line width is unchanged by point defects but indicates the amount of lattice strain produced by dislocations in deformed samples.

---

† Communicated by the Author.

In the present experiments the point defects were introduced by cold work at −196°c, by quenching from above 1600°c, and by fast neutron irradiation at 50°c. The electrical resistivity, density, lattice parameter, hardness, and x-ray line width were measured before and after the defects were introduced into the sample. In addition, the mobility of the defects was determined from changes of electrical resistivity due to heat treatment.

§ 2. CHOICE OF MATERIAL

The choice of sample material for these experiments was mainly determined by the irradiation conditions. The sample should have a high melting point in order to retain a maximum amount of radiation damage at 50°c, the temperature of irradiation. In addition it should have a low gamma activity after irradiation. These two conditions, combined with the usual requirements of simple crystal structure, high purity, and good surface properties, made platinum the obvious choice.

The platinum used was Johnson Matthey and Mallory thermocouple grade (99·99%), so that direct comparison could be made with the platinum self-diffusion experiments of Kidson and Ross (1957), which were made on similar material.

§ 3. METHODS FOR INTRODUCING DEFECTS INTO PLATINUM

3.1. *Deformation*

The 0·010 in. diameter platinum wires were annealed in air at 900°c. for 30 min, and then extended 8% in liquid nitrogen. They were removed from the extension apparatus while immersed in liquid nitrogen. Since the potential leads were silver-soldered to the sample before the extension, the resistivity could be measured after any recovery anneal above −196°c.

The hardness samples were 0·1 in. thick platinum flats rolled to 8% reduction with the sample immersed in liquid nitrogen between each pass.

3.2. *Quenching*

An electric current was used to heat a 4 in. long 0·010 in. diameter platinum wire. The potential leads of 0·003 in. diameter platinum wire were spot-welded one inch from the ends of the sample. The temperature of the heated sample was determined from its resistance. The calibration curve for resistance against temperature is shown in fig. 1.

The sample was cooled rapidly (quenched) by sudden immersion into cold water. To reduce the deformation during this quench, the axis of the wire sample was perpendicular to the surface of the water. The time taken to cool the sample was measured by retaining the heating current and recording the voltage across the sample on an oscillograph. A typical quench, shown in fig. 2 (Pl. 25), gives a time of 0·02 sec to cool from 1600°C to 20°C.

Fig. 1

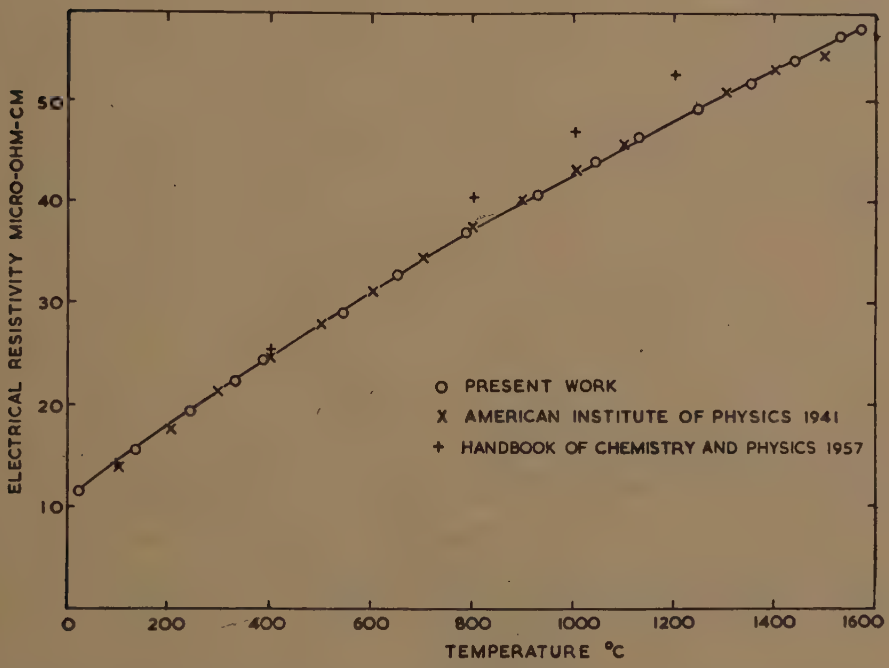

Electrical resistivity of thermocouple grade platinum. No correction was made for the change in sample dimensions with temperature.

3.3. *Fast Neutron Radiation*

The 0·010 in. diameter platinum wire was annealed in air at 900°C for 30 min and then irradiated at 50°C inside a uranium tube in the NRX reactor (Cook and Cushing 1953). Half the fast neutrons hitting the sample were from the uranium tube and had a fission energy spectrum. The other half from neighbouring fuel rods had the ususal E^{-1} spectrum. The definition of fast neutrons used in this report is neutrons with energy above 1200 ev. This is the minimum energy neutron capable of knocking a platinum atom from its lattice site.

After irradiation, the platinum wires were decontaminated and platinum potential leads spot-welded on.

§ 4. METHODS FOR DETECTING DEFECTS IN PLATINUM

4.1. *Electrical Resistivity*

Potential leads were spot-welded to the wire samples, which were 0·010 in. in diameter, and the electrical resistances measured in liquid nitrogen. The values obtained were corrected to a constant nitrogen bath temperature by measuring the resistance of an annealed sample in the same bath. The electrical circuit was made completely of copper with low thermal e.m.f. solder at all joints. A 100 mA current was used with the bath vigorously stirred to prevent temperature fluctuations due to gas bubbles forming on the sample. The potential was read to 0·1 microvolt. By reversing the sample current and potentiometer battery to eliminate stray e.m.f.'s, the resistance values were reproduceable to one part in thirty thousand.

The samples were annealed in silicone oil up to 250°C and in molten salt between 250° and 900°C.

Fig. 3

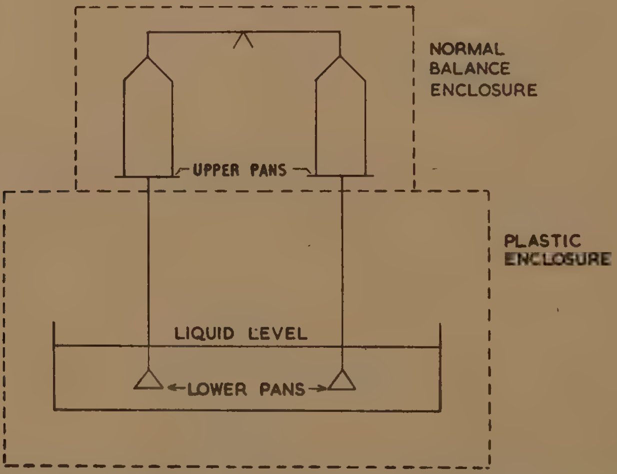

Schematic diagram showing the balance assembly for density measurements.

4.2. *X-ray Line Width*

A long 0·010 in. diameter platinum wire was extended 8% in liquid nitrogen. Sections of it were spot-welded side by side on a platinum frame to fit the diffractometer. The half widths of the (331), (420) and (422) x-ray lines were then measured after annealing the wire sample assembly at successively higher temperatures.

4.3. *Density*

The density of platinum was determined by weighing a 13 g sample in air and water with a weight sensitivity of 0·01 milligrams. The density of the sample was directly compared with an annealed reference sample of the same size using the system shown in fig. 3. The sample was put in the upper left pan and the reference sample in the upper right pan to obtain the difference between their weights in air. The sample was then placed under the liquid in the lower left pan and the standard in the lower right pan, to obtain the difference between their weights in liquid. The calculations for this method of density determination are given elsewhere (Piercy 1958). This is a very sensitive method for measuring changes in density since the measurements are not strongly dependent on the liquid density, air density, or temperature. Of course, the absolute value depends on the accuracy of the density taken for the reference sample.

Distilled water with the air removed was used for the density measurements. However, hysteresis in the contact angle between water and the 0·003 in. tantalum wire, caused the measured weight to depend on the direction of vertical motion of the balance pan. This effect was markedly reduced by using a solution of 0·08% wetting agent (Kodak Photoflo) in distilled water, which resulted in a density reproducibility of 0·005% for a 13 g platinum sample. The addition of the wetting agent did not affect the absolute value within this limit of error.

4.4. *Reaction Kinetics*

Once the excess point defects were introduced into the sample, the preliminary investigation of measuring the drop in resistivity due to annealing the sample for equal times at successively higher temperatures (an isochronal anneal) determined the minimum temperatures at which these defects were mobile. The decrease in resistance for each 5 min anneal was plotted as a function of the annealing temperature, a typical result for deformed platinum being shown in fig. 4. Once the temperature range for recovery was known, the activation energy was found by measuring the change in slope of the isothermal resistivity–time curve when the temperature was raised by 10°c. The value for the activation energy ΔH_2 was calculated from the usual equation

$$\Delta H_2 = \frac{T_1 T_2}{T_2 - T_1} K \log_e (S_2/S_1) \quad . \quad . \quad . \quad . \quad . \quad . \quad (1)$$

where K is Boltzmann's constant, S_1 is the final slope of the resistivity–time curve at absolute temperature T_1 and S_2 is the initial slope after raising the temperature from T_1 to T_2. This process was repeated until there was no further drop in resistivity. A typical set of curves for irradiated platinum is shown in fig. 5.

The slope at the end of each curve was determined in the following manner: the slope at the midpoint of a curve between two experimental points A and B was assumed equal to that of the straight line joining A and B. Therefore by measuring seven experimental points on the isothermal

Fig. 4

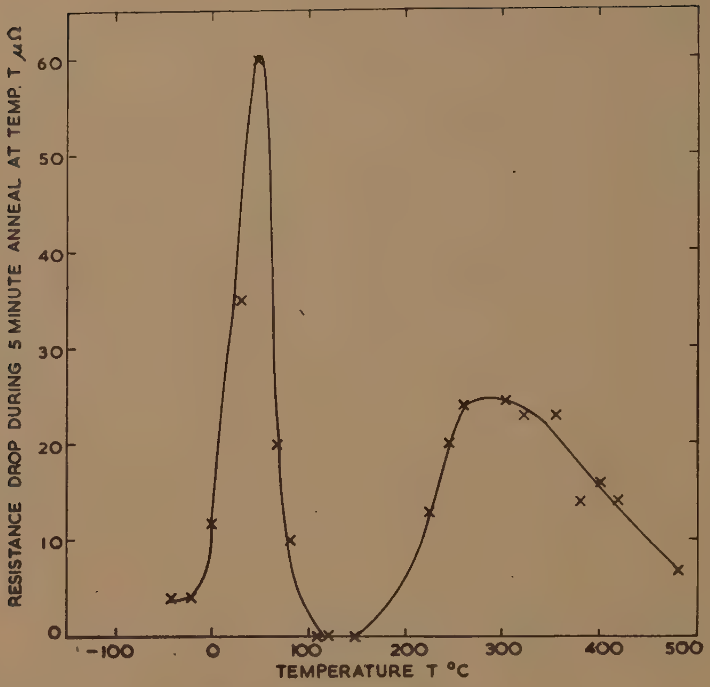

Isochronal recovery of platinum after deformation in liquid nitrogen. The drop in sample resistance for successive anneals of 5 min at temperature *T* is plotted against annealing temperature.

Fig. 5

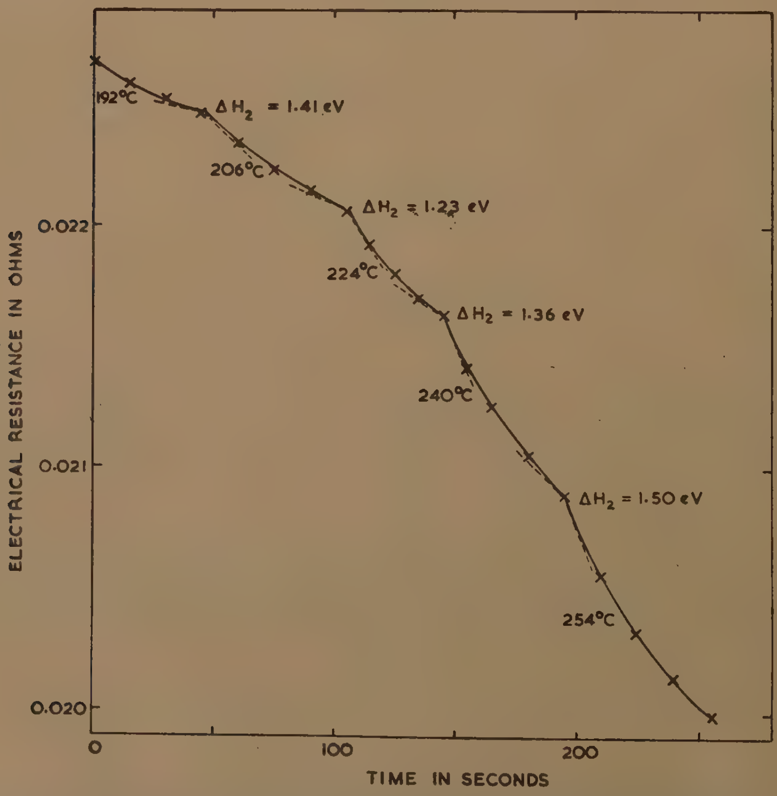

A typical set of curves to determine the activation energy required for recovery of irradiated platinum.

anneal, the values for the slope of the curve at the six intermediate points were determined. Then, by plotting the curve for these values of slope against the resistivity at these intermediate points and extrapolating the curve a short distance, the value for the slope at the end of the curve was obtained. The logarithm of the slope against the resistance at the intermediate points was usually plotted in order to have a straighter line to extrapolate. A typical example for irradiated platinum is shown in fig. 6. This is one of the few methods that determines the slope using all the experimental points equally.

Fig. 6

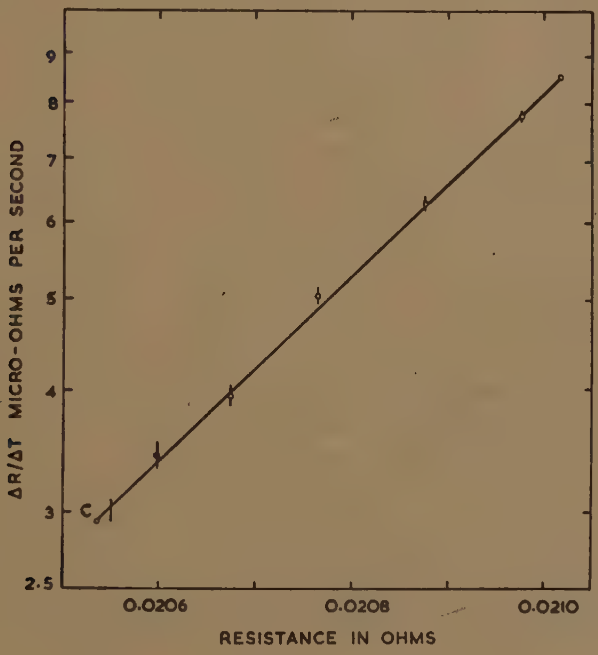

Determination of slope at the end of an isothermal annealing curve. The log of the slope found at a point midway between two experimental points is plotted against the electrical resistance at that point. The line is extrapolated to point C to obtain the slope at the end of the isothermal curve.

When the activation energy was known, the number of jumps required by the defect to reach the sink was determined from the slope of the curve obtained by plotting the logarithm of the fraction of resistivity increase remaining against the time at constant annealing temperature and applying eqn. (9) of the Appendix. The order of reaction was found from the same isothermal anneal using the method of Meechan and Brinkman (1956).

§ 5. Results and Observations

5.1. *Changes in Physical Properties*

The electrical resistivity isochronal recovery curve for platinum extended 8% in liquid nitrogen (fig. 4) has two distinct recovery stages; one below 100°c in which 0·004 micro-ohm-cm recovers, and one between 100°c and 600°c in which 0·024 micro-ohm-cm recovers. For comparison, the electrical resistivity of platinum in liquid nitrogen is 1·85 micro-ohm-cm. There was no appreciable recovery below −50°c which is contrary to the experiments of Manintveld (1954). The recovery of x-ray line width, electrical resistivity and hardness for platinum deformed 8% in liquid nitrogen are shown together in fig. 7. Because the temperature intervals are larger, this curve for the recovery of electrical resistivity does not resolve the two peaks shown in fig. 4. The x-ray line width does not change until nearly all the increase in electrical resistivity has recovered, indicating that both stages in the recovery of electrical resistivity shown in fig. 4 are mainly due to point defects, rather than to annihilation or redistribution of dislocations. However, some annihilation of dislocations

Fig. 7

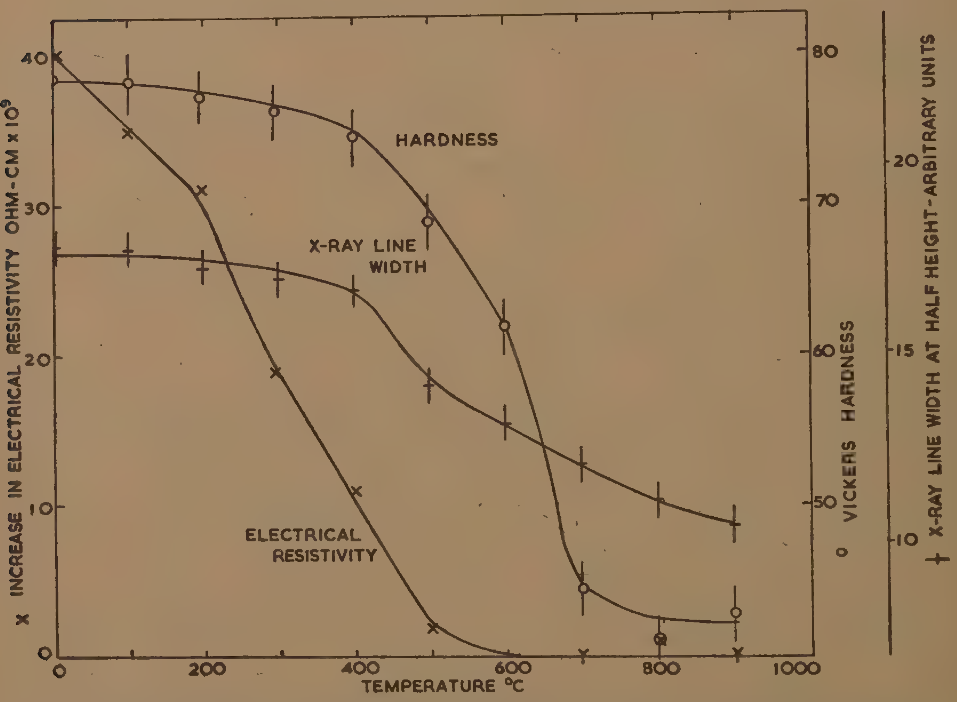

Recovery of electrical resistivity, hardness and x-ray line width of platinum samples deformed 8% in liquid nitrogen. Successive anneals for 30 min every 100°c were used.

may be occurring at the very end of the recovery of electrical resistivity. The recovery of the hardness and x-ray line width above 400°c is probably due to recrystallization.

Fig. 8

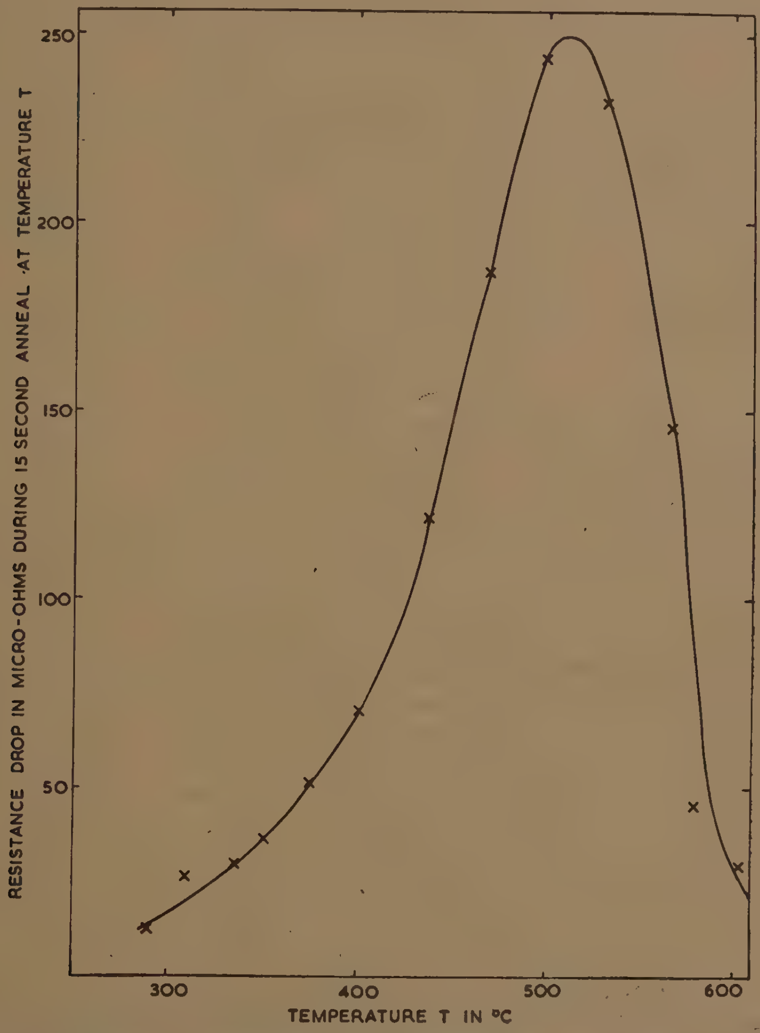

Isochronal recovery of quenched platinum showing the drop in sample resistance for successive anneals of 15 sec at temperature *T*.

The isochronal recovery of quenched platinum shown in fig. 8 has one recovery stage in the region 300 to 600°c, during which a resistivity drop of 0·12 micro-ohm-cm occurs. There was no further recovery on annealing up to 800°c. The isochronal anneal of irradiated platinum shown in fig. 9 also has only one recovery state and this occurs in the region 130–350°c. However, the large decrease of 0·48 micro-ohm-cm occurs here. There was no further recovery on annealing up to 900°c.

The recovery of the density and yield stress of irradiated platinum was examined to determine whether these recovered at the same rate as the electrical resistance. The results shown in table 1 indicate that both the density and the yield stress recover at the same rate as the electrical resistance and, therefore, are probably due to the same defect. Since the density decrease is 0·07% due to irradiation, while the lattice parameter change for the same irradiation is less than 0·005% (Tuxworth 1958 unpublished data), the defects remaining in the sample are probably single, double, or clusters of vacancies.

Fig. 9

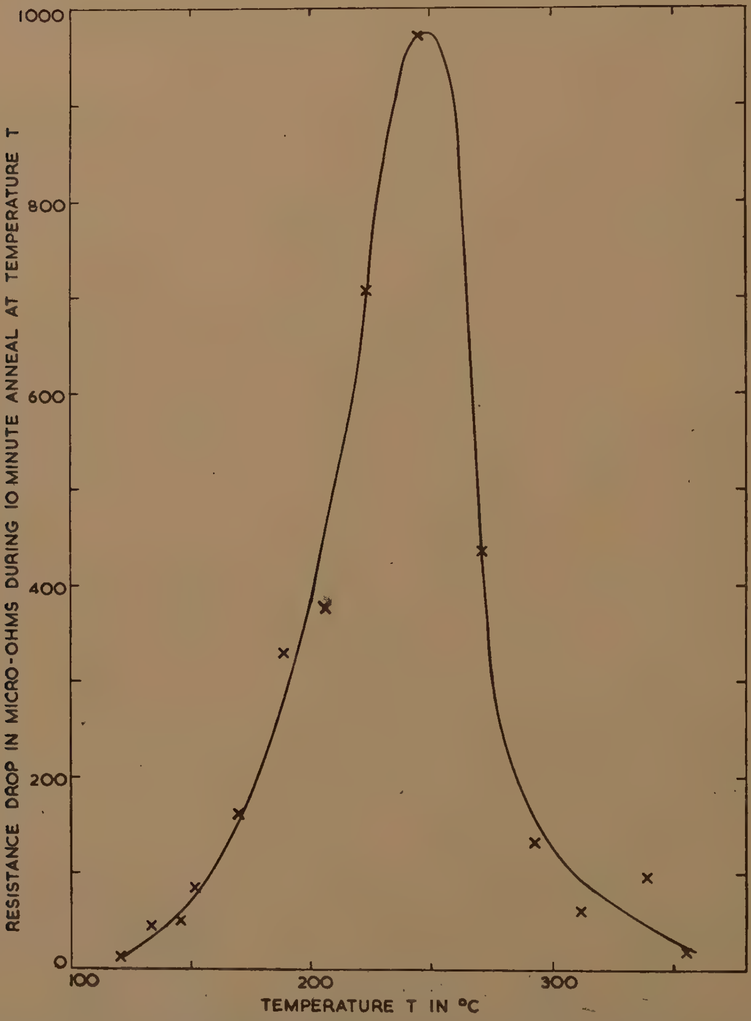

Isochronal recovery of irradiated platinum showing the drop in sample resistance for successive anneals of 10 min at temperature T.

Table 1. The Recovery of Electrical Resistivity, Density, and Mechanical Properties of Irradiated Platinum

Treatment	Electrical resistivity in liq. N_2 $\mu\Omega$ cm $\pm 0{\cdot}0001$ $\mu\Omega$ cm	% resistivity increase remaining	Density at 22·2°c g/cm^3 $\pm 0{\cdot}001$ g/cm^3	% density decrease remaining	Ultimate tensile strength p.s.i. ±1000 p.s.i.	% Ultimate strength increase remaining	Proportional limit p.s.i. ±1000 p.s.i.	% Proportional limit increase remaining
Annealed prior to irradiation	1·850	—	21·4413	—	19000	—	8000	—
Irradiated with 2×10^{20} fast n/sq. cm	2·52	100	21·4255	100	26300	100	15000	100
Irradiated plus 50 min 200°c	2·22	55	21·4335	49	23000	54	10800	40
Irradiated plus 180 hr 200°c	1·94	13	21·4396	11	20200	—	8200	—

From the results shown in table 1, the ratio of the resistivity change to fractional volume change due to irradiation is 9×10^{-4} ohm-cm. Since this is comparable with the value 3×10^{-4} ohm-cm found in gold wire that was quenched from 900°c (Bauerle and Koehler 1957), the defects in irradiated platinum are probably similar to those in quenched gold, i.e. isolated or small grouping of vacancies rather than large clusters. If one vacancy in the irradiated platinum produces an effective volume change of 0·5 atomic volumes (the number will be less than 1·0 due to relaxation about the vacancy), then the resistivity per atomic per cent vacancies when calculated from the ratio of resistivity change to fractional volume change is 4·5 micro-ohm-cm. This value, which is about three times that predicted for copper (Overhauser and Gorman 1956) is a reasonable resistivity for vacancies in platinum and will be used for later calculations of defect concentrations produced in platinum by other means. The concentration of vacancies determined for the irradiated sample by using this value is $1{\cdot}2 \times 10^{-3}$.

The defect concentration produced by fast neutrons can be calculated from the theory of Seitz and Koehler (1956), and also the theory of Brinkman (1956). Taking the total elastic scattering cross section for fast neutrons to be 5·5 barns (Langsdorf *et al.* 1957), the concentration of defects produced in platinum which is irradiated with 2×10^{20} fast neutrons per square centimetre in NRX is 0·30 when calculated from the theory of Seitz and Koehler. On the other hand, Brinkman's estimate for the concentration of defects remaining in a displacement spike is only about 0·001 (Brinkman 1954). Therefore, this should be the limiting value when all the atoms of the sample have been in at least one displacement spike, as would probably occur with the high integrated flux used here. The concentration of defects measured in this experiment, however, is expected to be much lower than the actual numbers produced, due to annihilation of the vacancies by interstitial atoms that are mobile during irradiation. Therefore, the experimental value of 0·0012 deduced from the density and resistivity change indicates that Brinkman's estimate of 0·001 for the concentration of defects remaining in a displacement spike is much too low if the displacement spike concept is applicable to platinum.

5.2. *Reaction Kinetics*

The results for the activation energy measurements on extended, quenched and irradiated platinum are given in table 2. They were all measured by the change in slope of an isothermal recovery curve when the temperature was raised.

A lattice distortion or strain will alter the distance between atoms and hence may alter the activation energy required for the atomic jump process. Since a comparison between the activation energy of recovery after cold working, quenching, and irradiating is required, and these do not produce the same lattice strain in the metal, the possible change in activation energy with lattice strain was investigated using an irradiated sample. A load equal to half the proportional limit of platinum at 400°c was hung from an irradiated sample during recovery. Although this increased the rate of recovery by a factor of two, the activation energy was still the same within experimental error.

Table 2. Activation Energy for the Recovery of Platinum after Deformation, Quenching or Irradiation

Treatment	Temperature range °c	Activation energy ev	Number of determinations
Extended 8–10% in liquid nitrogen	38 to 135	$0{\cdot}73 \pm 0{\cdot}06$†	5
Extended 8–10% in liquid nitrogen and annealed to remove lower recovery stage	230 to 360	$1{\cdot}43 \pm 0{\cdot}09$	7
Quenched from above 1600°c to 20°c in less than 0·04 sec	240 to 370	$1{\cdot}13 \pm 0{\cdot}11$	14
Irradiated at 50°c with 6×10^{19} fast neutrons per square centimetre	190 to 280	$1{\cdot}40 \pm 0{\cdot}11$	11

† The limits given are the standard deviations of all measurements taken.

The average values of activation energy from table 2 were used to calculate the order of reaction and the number of jumps required by the defect to reach the sink. These, together with the concentration of defects (based on recovery of electrical resistivity, assuming 4·5 micro-ohm-cm per atomic percent defects) are shown in table 3. The activation energy for the recovery of irradiated platinum, the only case for which two identical samples were available, was also measured by the technique of Meechan and Brinkman (1956). The result shown in fig. 10 and given in table 3 is within the limit of error of the slope change method.

§ 6. Discussion

A comparison between the present results for the reaction kinetics and other investigators are given in table 4. The values for activation energy do not agree except for quenched platinum. Since the purity of Manintveld's extended platinum was not reported, the difference in results may be due to an impurity effect. Unfortunately, his annealing experiments were not taken above 90°c. Dugdale's results on platinum irradiated or extended at room temperature (Dugdale 1952) are both the same

Table 3. Summary of Parameters for the Motion of Defects in Platinum

Treatment	Temperature range of recovery °c	Activation energy ev	Order of reaction	Number of jumps to sink† for given amount of recovery remaining	Concentration of defects‡
8–10% extension in liquid nitrogen	0 to 100	$0 \cdot 73 \pm 0 \cdot 06$	1·8 to 2·2	7×10^6 for 50% remaining 2×10^7 for 25% remaining	1×10^{-5}
	200 to 400	$1 \cdot 43 \pm 0 \cdot 09$	5·05	3×10^4 for 75% remaining 1×10^5 for 50% remaining 7×10^6 for 25% remaining	6×10^{-5}
Quenched from above 1600°c to 20°c in 0·03 sec	300 to 500	$1 \cdot 13 \pm 0 \cdot 12$	1·46	6×10^8 for 75% remaining 8×10^8 for 50% remaining 1×10^9 for 25% remaining	3×10^{-4}
Irradiated with 6×10^{19} fast n/sq. cm at 50°c	150 to 400	$1 \cdot 40 \pm 0 \cdot 11$ $1 \cdot 46 \pm 0 \cdot 05$§	2·8	1×10^3 for 75% remaining 2×10^3 for 50% remaining 7×10^3 for 25% remaining	$1 \cdot 2 \times 10^{-3}$

† Number of jumps calculated with eqn. (9) of the Appendix.

‡ The concentration is calculated from electrical resistivity measurements assuming 4·5 micro-ohm-centimetres per atom percent defects.

§ By the method of Meechan and Brinkman (Meechan 1956)—all others by the slope–change method from table 2.

Fig. 10

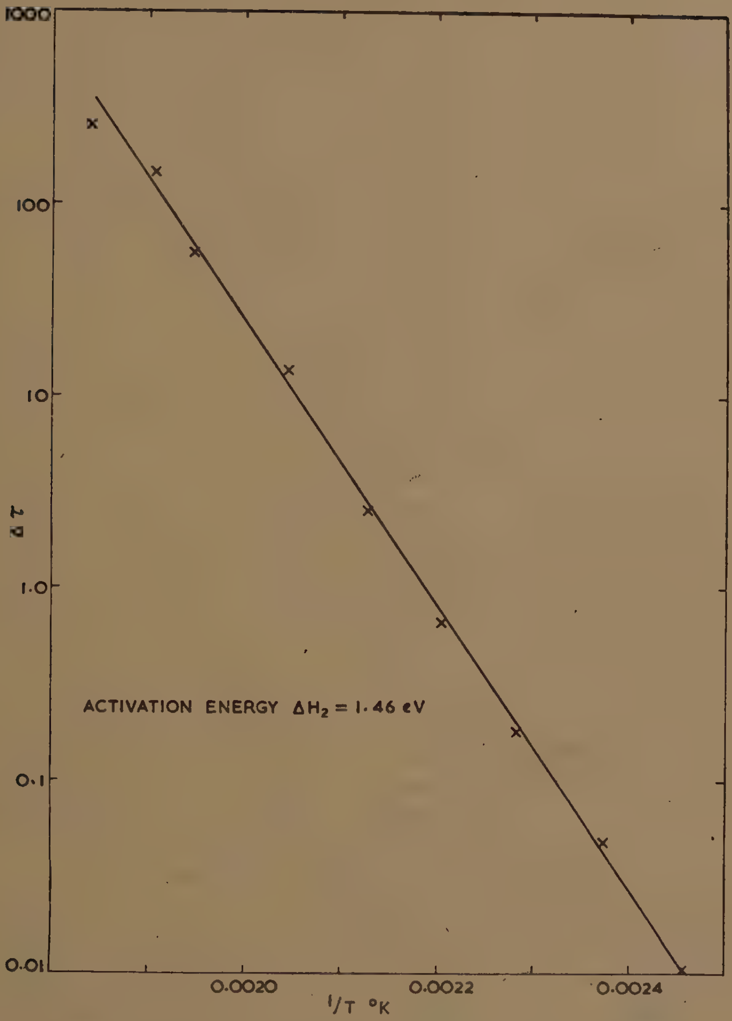

Activation energy for the recovery of irradiated platinum determined by the method of Meechan and Brinkman (Meechan 1956). The time $\Delta\tau$ required at 196°c for the same recovery occurring 10 min at temperature T of the isochronal anneal is plotted against $1/T$. The slope of the line gives an activation energy of 1·46 ev for the whole recovery process.

but are significantly below those reported here. However, he made only three activation energy measurements and all were taken after about 8% recovery. Once again, the difference may be due to sample impurity since his is unspecified. Because of these discrepancies, no single model can explain all the past results. Therefore a model will be proposed to explain the results of the present experiments in which point defects were produced by three methods and in which all measurements were made under the same conditions.

Since the density of platinum decreased after irradiation while the lattice parameter showed no significant change, the defects remaining after a room temperature irradiation are probably vacancies, divacancies or vacancy clusters. Because the changes in density and electrical resistance recover at the same rate after irradiation, they are probably caused by the same point defect. Therefore, the recovery of electrical resistivity in irradiated platinum that requires an activation energy of 1·43 ev is probably due to vacancies, divacancies, or vacancy clusters.

There are several arguments that strongly suggest the defects in irradiated platinum are isolated or small groups of vacancies rather than large clusters. The first, mentioned previously, is the agreement between the ratio of density decrease to resistivity increase in irradiated platinum with that found in quenched gold. The second, is the excellent agreement between the migration energy for defects produced by irradiation (1·43 ev) with those produced by quenching platinum from temperatures substantially below the melting point, 1·42 ev (Ascoli *et al.* 1958). A quench from these temperatures is expected to leave single vacancies while a quench from near the melting point may leave double vacancies (Koehler *et al.* 1957). The lower values of 1·1 ev required for defect migration after quenching from near the melting point as shown in table 4 are probably due to double vacancies.

Table 4. A Summary of Activation Energies Measured for the Recovery of Platinum

Method of introducing defects	Recovery temperature range examined °C	Activation energy ev	Reference
Extended at −196°C	−150 to −70	0·22	Manintveld 1954
	−10 to 70	0·99	,,
Extended at 20°C	70 to 100	1·19	Dugdale 1952
Extended at −196°C	0 to 100	0·73	Present work
	200 to 400	1·43	,, ,,
Quenching from above 1600°C	—	1·1	Lazarev and Ovcharenko 1955
	300 to 500	1·10	Bradshaw and Pearson 1956
	300 to 500	1·13	Present work
Quenching from 1100°C to 1400°C	450 to 580	1·42	Ascoli *et al.* 1958
	—	1·48	Bacchella *et al.* 1959
Reactor irradiation at 50°C	70 to 90	1·19	Dugdale 1952
	100 to 300	1·43	Present work

The third argument that suggests the defects produced by irradiation are single vacancies, is the qualitative agreement between the measured migration energy of 1·43 ± 0·1 ev and the calculated migration energy of 1·65 ± 0·15 ev from the energy of self-diffusion in platinum of 2·96 ± 0·06 ev (Kidson and Ross 1957) less the formation energy of vacancies in platinum 1·30 ± 0·1 ev (Bradshaw and Pearson 1956, Ascoli *et al.* 1958, Bacchella *et al.* 1959).

The activation energy required for recovery of the electrical resistivity after 8% extension in liquid nitrogen was 0·73 and 1·43 ev. The higher value has already been attributed to the migration of single vacancies and the lower one is perhaps due to the release of interstitial atoms from trapping sites. Both vacancies and interstitial atoms may be produced by the crossing of screw dislocations during deformation.

The order of reaction is a measure of the rate of change of the number of jumps required by a defect to reach the sink during the recovery process. Once it rises above the value two, its interpretation becomes vague and in many cases may be caused by a nonrandom initial distribution of defects. This nonrandom distribution of defects is one possible explanation for the high order of reaction and the low number of jumps required for the recovery of irradiated platinum. If the damage from a fast neutron is concentrated in one small volume the local concentration of defects may be very high. Therefore the vacancies would require only a small number of jumps before combining with another vacancy, after which they could move more rapidly. Also, if the damage from fast neutrons is concentrated in a small volume, there may be other traps for vacancies such as dislocation rings or clusters of interstitial atoms that are produced by the same neutron. Therefore the vacancies would again require only a small number of jumps before reaching these sinks.

From the number of jumps required for the defect to reach a sink in the recovery of quenched and deformed platinum, an interpretation of the type of sink can be made. In the quenched sample with a defect concentration of 3×10^{-4}, the number of jumps (8×10^{8}) is much too high for recombination of defects. The low order of reaction 1·46 also discourages this interpretation. However, if the defects are going to dislocations, an argument which agrees with the observed number of jumps, an order of reaction equal to 1·0 might be expected. The higher order of reaction observed (1·46) may be caused by the change in dislocation network due to extensive climb of dislocations which absorb defects. Thus, the last defects will migrate to a much different distribution and perhaps even different type of dislocation network than was initially present.

The eight per cent extension of platinum is expected to increase the dislocation density from 10^{8} to about 10^{10} lines per square centimetre. Therefore, the number of jumps required by the defect to reach a dislocation will be reduced from 10^{7} to 10^{5} (Lomer and Cottrell 1955) which is similar to the number of jumps required for the defects to combine. The recovery of extended platinum at 60°c appears to be by defects combining since the order of reaction is close to two. However, the high order of reaction (5·05) for the recovery of deformed platinum at 300°c, which is reflected in the large increase in number of jumps during recovery, indicates the defects are diffusing to several different types of exhaustible sinks or the sink concentration is decreasing during the recovery. The latter view is perhaps more favourable, since the experiment on the recovery of x-ray line broadening shown in fig. 7 indicated that some reduction in the dislocation density may occur during the recovery of the electrical resistivity. However, because of the unique activation energy and the large drop in line broadening on annealing at higher temperatures, the main recovery of electrical resistivity in the region of 300°c is thought to be due to vacancies rather than to dislocations.

§ 7. CONCLUSIONS

An interpretation of the point defects in platinum consistent with all our experimental results is the following:

(1) The principal lattice defects remaining in platinum after fast neutron irradiation are single vacancies with an activation energy for migration of 1·43 ev.

(2) The principal lattice defects remaining in platinum after quenching from above 1600°c are divacancies with an activation energy for migration of 1·13 ev.

(3) The two principal lattice defects remaining in platinum after an extension of 8% in liquid nitrogen are an unknown defect, perhaps interstitial atoms, with an activation energy for migration of 0·73 ev, and single vacancies with an activation energy for migration of 1·43 ev.

ACKNOWLEDGMENTS

The author is indebted to Mr. E. C. W. Perryman for suggesting this problem, and to Mrs. M. Kendall, Mrs. M. Rees, and Mr. A. Quenneville for taking most of the measurements. Thanks are also due to the x-ray group for the measurements of line broadening. The cooperation of the NRX staff in making the irradiation space available is gratefully acknowledged.

APPENDIX

NUMBER OF JUMPS REQUIRED BY DEFECT TO REACH SINK

The average number of jumps required by defects to reach a sink can be calculated from the recovery of electrical resistivity at constant temperature T. If the defect concentration is assumed proportional to the additional resistivity R above that for the fully recovered sample, the recovery rate depends on three factors

$$dR/dt = -R\Gamma p \quad . \quad . \quad . \quad . \quad . \quad . \quad . \quad . \quad (1)$$

where t is the time, Γ the defect jump frequency, and p the probability per jump that a defect reaches a sink.

The jump frequency Γ also depends on three factors

$$\Gamma = Z(\alpha\nu)\exp(-\Delta F_2/KT) \qquad (2)$$

where Z is the number of adjacent sites to which the defect may go, $\alpha\nu$ is the frequency of attempts by the defect to move to each adjacent site, and $\exp(-\Delta F_2/KT)$ is the fraction of time that a defect has sufficient free energy to jump. ν is the vibration frequency of the atom, and α is the fraction of these vibrations in each jump direction. The free energy required by the defect to jump is

$$\Delta F_2 = \Delta H_2 - T\Delta S_2 \qquad (3)$$

where ΔH_2 is the activation energy required to move the defect one jump and ΔS_2 is the entropy change produced by the defect moving from one site to the saddle point midway between sites.

The probability per jump that a defect reaches a sink is equal to the fraction of lattice sites from which the defect is directly attracted to the sink. This depends on the concentration of sink sites, their distribution, and the maximum distance of attraction between the defect and sink. Therefore

$$p = j^{-1} = \beta C_s \qquad (4)$$

where j is the average number of jumps required by the defect to reach the sink, C_s is the concentration of sink sites and β is a term depending on the sink distribution and the maximum distance of attraction between defect and sink. The term βC_s could well be called the 'effective sink concentration'.

Putting eqns. (2), (3), (4) into eqn. (1) gives:

$$S = -\frac{1}{R}\frac{dR}{dt} = -\frac{d(\ln R)}{dt} = Z\alpha\nu j^{-1}\exp(\Delta S_2/K)\exp(-\Delta H_2/KT) \qquad (5)$$

where S is the slope of the graph $\ln R$ vs. time. Solving for j gives:

$$j = Z\alpha\nu S^{-1}\exp(\Delta S_2/K)\exp(-\Delta H_2/KT). \qquad (6)$$

ΔH_2 is calculated from other experiments using eqn. (1) of the main text. Unfortunately the frequency factor $Z\alpha\nu\exp(\Delta S_2/K)$ has not been measured directly, but each factor can be estimated. Because the total vibrational energy is considered in the ΔH_2 term in eqn. (6), ν must be the frequency of the resultant vibration containing the total vibrational energy of the atom making the jump and α is the fraction of these resultant vibrations in each jump direction. The Debye frequency is usually used for ν. Bradshaw and Pearson (1956) and LeClaire (1953) take $\alpha = 1$ but the value $\alpha = Z^{-1}$ assumed by Jost (1952) seems more reasonable for vacancy diffusion since only the resultant vibration is considered. Because there are Z possible jump directions, the fraction of the resultant vibrations in any one jump direction will be about Z^{-1}. If the resultant vibration of an atom adjacent to a vacancy is always in the direction of the vacancy, then $\alpha=1$. This is unlikely, however, because each atom vibrates in phase with its nearest neighbours and the wavelength of vibration is usually greater than three to four atoms. The remaining factor, $\exp(\Delta S_2/K)$, was assumed by Bradshaw and Pearson (1956) to lie between one and ten.

Because of uncertainty in the choice of these parameters for the frequency factor, a more direct value was taken from the self diffusion measurements of Kidson and Ross (1957). Their measured value for D_0 was $0{\cdot}33\ \mathrm{cm}^2\,\mathrm{sec}^{-1}$ which gives (LeClaire 1953)

$$\alpha\nu \exp[(\Delta S_1+\Delta S_2)/K]=D_0/a^2=2{\cdot}2\times10^{14} \quad . \quad . \quad . \quad . \quad (7)$$

where $a=3{\cdot}9\times10^{-8}$ cm is the lattice parameter and ΔS_1 is the vibrational entropy due to a vacancy at a lattice site. The left side of eqn. (7) is similar to the frequency factor in eqn. (6) except for the added ΔS_1 term. However, from calculations on the relative values of ΔS_1 and ΔS_2 (Huntington *et al.* 1955)

$$\exp(\Delta S_2/K)=0{\cdot}24\exp[(\Delta S_1+\Delta S_2)/K]. \quad . \quad . \quad . \quad (8)$$

Therefore by combining eqns. (7) and (8) with (6) and taking $Z=12$ for f.c.c. lattices, j becomes

$$j=6{\cdot}3\times10^{14}\,S^{-1}\exp(-\Delta H_2/KT) \quad . \quad . \quad . \quad . \quad . \quad (9)$$

where S is the slope of $\ln R$ vs. time and ΔH_2 is the activation energy for recovery at temperature T. This equation was used to calculate the number of jumps required by the defect to reach the sink for all recovery stages investigated. The frequency factor may be incorrect if recovery other than vacancy diffusion occurs. This frequency factor is the same as that of Bradshaw and Pearson's (1956) using their assumptions ($B=\exp(\Delta S_2/K)=5$, $\alpha=1$, $\nu=10^{13}$) and including the extra Z term discussed in his later paper (Bradshaw and Pearson 1957).

An estimate of $B=\exp(\Delta S_2/K)$ can be made from eqns. (7) and (8). If $\alpha=Z^{-1}$, which seems reasonable for vacancy diffusion, and $\nu=5\times10^{12}$, the Debye frequency for platinum (Seitz 1940); then a value for B of 125 is required to match the diffusion results.

REFERENCES

American Institute of Physics, 1941, *Temperature, Its Measurement and Control in Science and Industry* (New York: Reinhold).

Ascoli, A., Asdente, M., Germagnoli, E., and Manara, A., 1958, *J. Phys. and Chem. of Solids*, **6**, 59.

Bacchella, G. L., Germagnoli, E., and Granata, S., 1959, *J. appl. Phys.*, **30**, 748.

Bauerle, J. E., and Koehler, J. S., 1957, *Phys. Rev.*, **107**, 1493.

Bradshaw, F. J., and Pearson, S., 1956, *Phil. Mag.*, **1**, 812; 1957, *Ibid.* **2**, 379.

Brinkman, J. A., 1954, *J. appl. Phys.*, **25**, 961; 1956, *Amer. J. Phys.*, **24**, 246.

Broom, T., and Ham, R. K., 1958, *Vacancies and other point defects in Metals and Alloys* (Inst. of Metals Monograph 23).

Cook, L. G., and Cushing, R. L., 1953, *Acta Met.*, **1,** 539.

Dugdale, R. A., 1952, *Phil. Mag.*, **43,** 912.

Handbook of Chemistry and Physics, 1957 39th Ed. (Cleveland : Chemical Rubber).

Huntington, H. B., Shirn, G. A., and Wajda, E. S., 1955, *Phys. Rev.*, **99,** 1085.

Jost, W., 1952, *Diffusion in Solids, Liquids and Gases* (New York : Academic Press), p. 135.

Kidson, G. V., and Ross, R., 1957, Proc. of 1957 UNESCO Radio-isotope Conference in Paris.

Koehler, J. S., Seitz, F., and Bauerle, J. E., 1957, *Phys. Rev.*, **107,** 1499.

Langsdorf, Jr., A., Lane, R. O., and Monahan, J. E., 1957, *Phys. Rev.*, **107,** 1077.

Lazarev, B. G., and Ovcharenko, O. N., 1955, *Dokl. Akad. Nauk, S.S.S.R.*, **100,** 875 or AERE Lib/Trans. 602.

LeClaire, A. D., 1953, *Acta Met.*, **1,** 438.

Lomer, W. M., and Cottrell, A. H., 1955, *Phil. Mag.*, **46,** 711.

Manintveld, J. A., 1954, *Thesis*, Technische Hoge School, Delft.

Meechan, C. J., and Brinkman, J. A., 1956, *Phys. Rev.*, **103,** 1193.

Overhauser, A. W., and Gorman, R. L., 1956, *Phys. Rev.*, **102,** 676.

Piercy, G. R., 1958, Chalk River, Report CRMet-782.

Seitz, F., 1940, *Modern Theory of Solids* (New York : McGraw-Hill), p. 111.

Seitz, F., and Koehler, J. S., 1956, *Solid State Physics*, Vol. 2 (New York : Academic Press).

Study of Adsorbed Gas Films by Electron Diffraction†

By L. H. GERMER, E. J. SCHEIBNER‡ and C. D. HARTMAN
Bell Telephone Laboratories, Inc., Murray Hill, New Jersey

[Received September 30, 1959]

ABSTRACT

Diffraction patterns of low energy electrons produced by a (111) face of a crystal of nickel have been accelerated sufficiently to show on a fluorescent screen, where they can be photographed. Various gases at low controlled pressures have been admitted to a clean surface, and the arrangements of atoms or molecules upon the surface deduced from their diffraction patterns. Molecules of CO are adsorbed at low pressures as monolayers. They form a single two-dimensional crystal having a spacing between molecules double that between surface nickel atoms ; these molecules are completely removed from the surface by heating to 175°C. Experiments with nitrogen have produced a polycrystalline monolayer having the same structure as the CO crystal. (Because of low sticking probability adequate experiments to prove that the layer is really nitrogen are difficult and have not yet been satisfactorily completed. A new type of experimental equipment seems to be required which is now being constructed.) Crystal growth in this monolayer is induced by heating to 125°C ; heating above 200°C results in transformation into one or the other of two polymorphic forms either of which is more stable than the original structure ; heating to 300°C results in melting the monolayer without removing it, the crystalline structure returning upon cooling. Oxygen can be adsorbed in a layer several atoms or molecules thick ; this shows no structure until annealed at 125°C after which the structure is that of the most complex of the polymorphic forms assigned to nitrogen ; this complex structure is polycrystalline with very small individual crystals ; its diffraction pattern is unchanged when the oxygen is reduced to a single monolayer by heating. No diffraction pattern has been obtained from hydrogen, although the presence of hydrogen is proved by rise in pressure when the crystal is subsequently heated.

§ 1. INTRODUCTION

THE arrangement of foreign atoms adsorbed as a single monolayer upon a crystal surface can be determined by the diffraction of very low energy electrons, of the order of 50 v. This has been known for a long time (Davisson and Germer 1927, Germer 1929) and a great deal of work in this field has been carried out by Farnsworth *et al.* (1929 to 1959). Up to the present time all observations of this sort have been obtained by the laborious method of discovering the features of a diffraction pattern by capturing scattered electrons in a Faraday box which is moved about over the entire field of the pattern.

---

† Communicated by the Authors.

‡ Now at Georgia Institute of Technology, Atlanta, Georgia.

Ehrenberg (1934) showed that diffraction patterns produced by low energy electrons can be accelerated through a considerable potential difference so that the entire pattern can be seen on a fluorescent screen. This represented potentially a very great improvement in the experimental procedure over the earlier method. Nevertheless, Ehrenberg did not develop the technique to a point where it had practical usefulness, and he did not discover patterns due to adsorbed atoms.

We have improved this means of observing a diffraction pattern of low-energy electrons sufficiently to make it a valuable research tool, and by means of it we have determined the arrangements of various kinds of atoms and molecules upon a crystal surface. With this new technique, experiments which were very difficult by the older method are now quite easy, and a vast number of experiments can be carried out which were impossible up to this time (American Crystallographic Association 1959).

Fig. 1

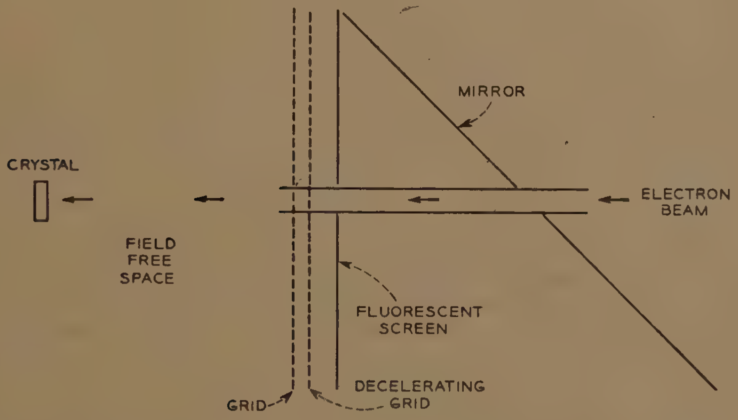

Sketch of the arrangement of the electron diffraction tube, drawn to scale.

Details of the experimental tube will be published elsewhere. For the present purpose, the sketch of fig. 1 will suffice. Electrons emerging from the gun strike the crystal at normal incidence. The diffraction pattern moves in a field free space until it reaches a fine-mesh grid. Between this grid and a second grid is a decelerating field which removes most of the slow electrons. Beyond the second grid the pattern is accelerated by 1000 or 2000 v to a fluorescent screen. The pattern can be observed directly on the screen, or by its reflection in the mirror which is inclined by 45° to the direction of the primary beam. The reflection can be photographed.

The experimental tube of fig. 1 is attached to vacuum pumps and to a Granville–Phillips type vacuum valve through which various gases can be admitted at low controlled pressures. The crystal can be outgassed by electron bombardment and the pressure of residual gas reduced to about 2×10^{-10} mm Hg. Diffraction patterns can be observed when the surface of the crystal is completely clean and the gradual development of new patterns noted as atoms or molecules of any one of a number of gases settle upon the surface The observation of these changes is made easy by the fact that the separations of adsorbed gas atoms is greater than the separations of nickel atoms in the surface layer, and, as a consequence of this, diffraction patterns from adsorbed gas atoms are observed in general in a range of voltages lower than the lowest voltages for which the nickel lattice can give any pattern. Thus in most cases there is no superposition of a diffraction pattern from adsorbed gas atoms upon a pattern arising from the nickel crystal and hence no possible confusion.

§ 2. DIFFRACTION PATTERNS FROM A CLEAN CRYSTAL

Representative diffraction patterns from a clean (111) face of a nickel crystal are reproduced in fig. 2 (Pl. 26). The first three of these, fig. 2(A), (B) and (C), represent respectively (533), (644) and (466) reflections from the lattice of the crystal, the patterns being taken at the electron beam voltages, 129, 200, and 262, for which the diffraction spots are strongest. Each pattern has threefold symmetry (except for some skewness due to an imperfect electron beam, and the fact that the spot at about 10 o'clock in fig. 2(C) is obscured by the position of the electron gun). In each case the diffraction spots appear in one or the other of the two principal azimuths of the crystal, designated A and B in the sketch of fig. 3. These are the azimuth designations used in earlier experiments (Davisson 1928 a, b, 1929, Germer 1928). The A azimuth has also been called the (111) azimuth, and the B azimuth the (100) azimuth (Davisson and Germer 1927).

In each of these three patterns, weak diffraction spots are seen in the other principal azimuth. This occurs because of the poor resolving power due to limited penetration of the electron beam into the crystal. This effect is shown in exaggerated form in fig. 2(D) in which the diffraction spots appear with equal intensities in the two azimuths; the beam voltage in this case is intermediate between 106 v, at which (244) reflections appear at maximum intensities in the A azimuth, and 129 v, at which (533) reflections appear at maximum intensities in the B azimuth.

For each diffraction pattern the tangent of the angle ϕ between the primary beam and a diffraction beam is obtained by dividing the distance of a diffraction spot from the center of the pattern (measured on such a photograph as those of fig. 2) by 44 mm, the distance from the crystal face to the fine-mesh grid, and multiplying by the photographic enlargement of the pattern. The latter is the ratio of the diameter of the grid measured on the photograph (easily seen on fig. 2(D)) to 67·5 mm, the true diameter of the grid.

The lowest voltage diffraction beams from a clean crystal appear at maximum intensity at 106 v, in the A azimuth. When the voltage of the primary beam, V, is increased steadily from this value to 400, the limit of our observations, sets of three diffraction beams appear alternatively in the two principal azimuths, each set increasing gradually in intensity to a

Fig. 3

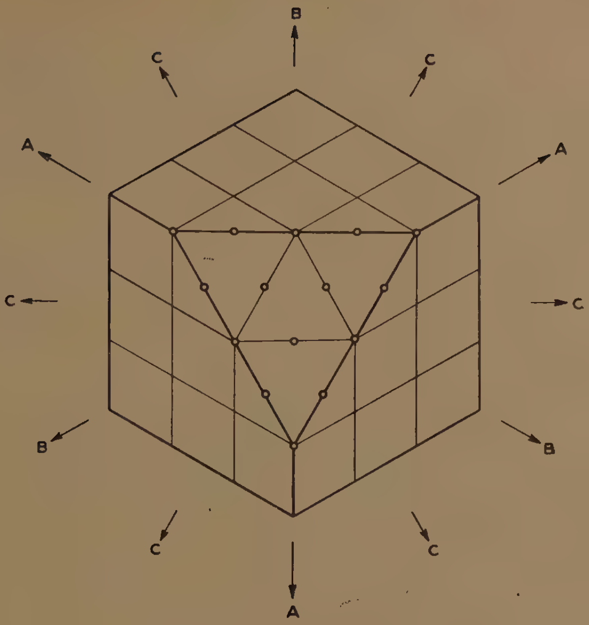

DESIGNATION OF AZIMUTHS

Sketch showing the designations of azimuths of the crystal. The orientation is the same as that of all of the diffraction patterns reproduced in this paper.

Fig. 4

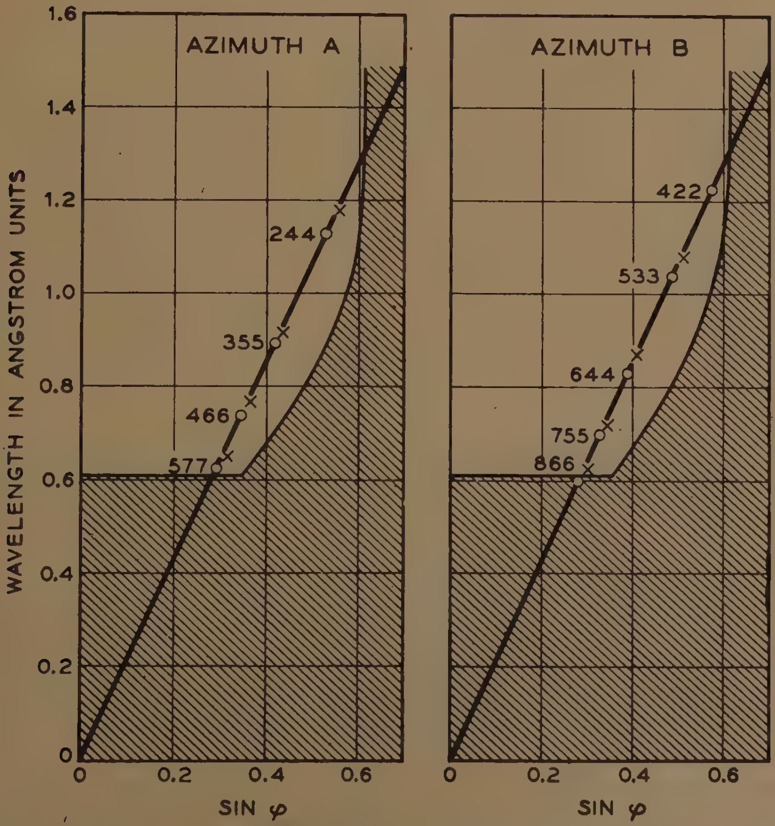

Plots of all diffraction beams observed from the nickel crystal. Observed diffraction beams plotted as crosses; calculated diffraction beams for zero inner potential plotted as open circles (see table 1). Inaccessible region marked by cross-hatching.

maximum value then decreasing in intensity and disappearing. For each such set of beams the electron wave-length at maximum intensity, calculated from $\lambda = (150/V)^{1/2}$, has been plotted in fig. 4 against the sine of the co-latitude angle, ϕ, measured as described above. The observed diffraction beams at maximum intensity are plotted as crosses and the calculated positions of all possible Laue x-ray diffraction beams in this wavelength range are plotted as open circles. The region of the plot which is inaccessible to observation is marked off by cross hatching. The lines in fig. 4 upon which the experimental points fall have a slope of 2·15 Å which is the spacing of lines of surface atoms in the A and B azimuths.

The correct correlation between observed and calculated diffraction beams is quite clear. All possible diffraction beams are found. These are written down in table 1, with the potentials at which they are observed at maximum intensity, and the theoretical potentials for zero value of the inner work function. The experimental values of inner potential probably do not differ from the average value of 16 v by more than the possible experimental errors of finding the potential for maximum intensity. Thus the experiments supply no data on variation of inner potential with angle or voltage.

Table 1. Laue Diffraction Beams from a Nickel Crystal (See fig. 4)

Azimuth A				Azimuth B			
Reflection	Voltage Obs.	Voltage Calc.	Inner Potential	Reflection	Voltage Obs.	Voltage Calc.	Inner Potential
244	106	119	13	533	129	140	11
355	178	188	10	644	200	215	15
466	262	276	14	755	294	310	16
577	355	383	28	866	403	424	21

Average inner potential 16 v.

§ 3. ADSORBED LAYERS

The nickel crystal had received considerable heating before the diffraction patterns of fig. 2 were obtained. A very brief summary of this heating seems to be a necessary prelude to an account of the diffraction patterns obtained from gas films deposited upon a clean surface.

Before the crystal was heated at all, no diffraction pattern could be observed. After heating to only 500°c, all of the Laue diffraction beams listed above were found, but there were in addition very elaborate patterns at low voltages. An example of one of these patterns is reproduced as fig. 5 (Pl. 28). (The structure giving rise to these complex patterns was later identified as having the unit cell of the 'Q-structure' which is shown in fig. 6). Low voltage diffraction patterns were entirely eliminated only after the crystal had been heated a number of times at maximum temperatures of 830°c. There were finally no traces of patterns other than the normal Laue beams from the nickel crystal, not even a 'muddy' appearance of an annular region of the fluorescent screen, appearing at low voltages, which was later associated with less than a monolayer of gas on the surface.

Fig. 6

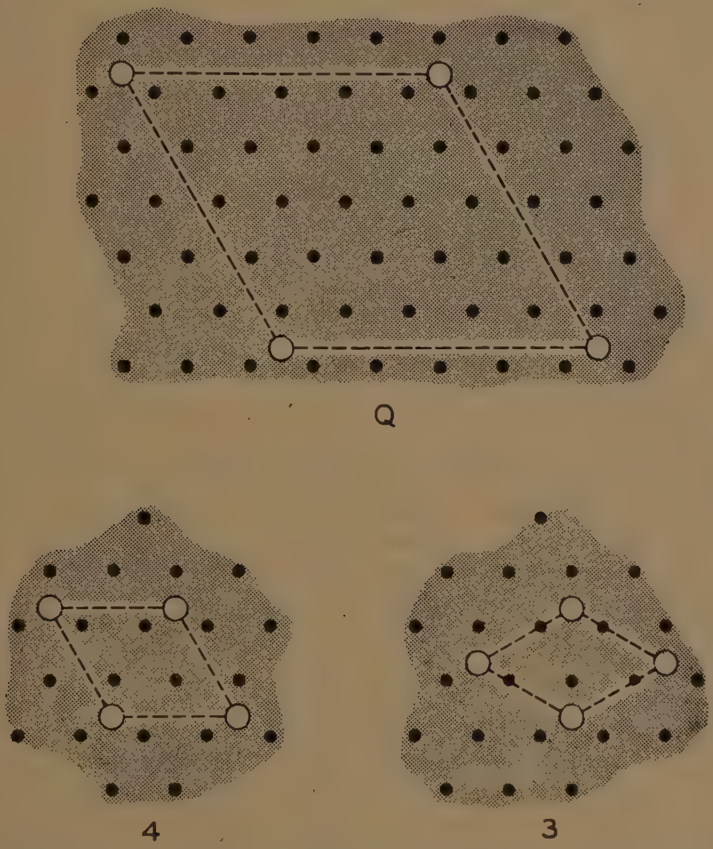

Sketches of the three different arrangements which atoms, which are presumably nitrogen, can take up upon the (111) surface of a nickel crystal. Black dots represent surface nickel atoms, open circles adsorbed atoms. The unit cells of the three different structures are drawn in; in the case of the Q structure, locations of atoms within the unit cell are not known.

3.1. *Nitrogen on Nickel*

Nitrogen was the first gas which was admitted to the experimental tube with the nickel crystal in a condition believed to be clean. Three different types of low voltage diffraction patterns have been observed after the admission of nitrogen, corresponding to three different arrangements of atoms in a monolayer on the surface. One of these structures is not yet completely understood, although its two-dimensional unit cell is known. Sketches of these structures are shown in fig. 6.

Because of the rather low sticking probability observed in these experiments it has not been established with certainty that the adsorbed gas is nitrogen rather than an impurity gas present in small amount but having sticking probability close to unity. This uncertainty is aggravated by uncontrolled fluctuations of pressure incidental to the method of cleaning the crystal at high temperatures. The bombarding tungsten ribbon adsorbs gas readily, and the release of this gas whenever the ribbon is heated raises the pressure to undesirably high values. A nickel crystal which can be heated by conduction will reduce this difficulty, and this seems to be essential for better control of gas pressure.

In all of the following experiments with nitrogen the adsorbed gas will be spoken of as nitrogen, which we now doubt. Presumptive evidence that it is atomic rather than molecular is furnished by the low sticking probability and by the fact that it is not removed until crystal temperatures above 400°c are reached.

In the sketches of fig. 6 the black dots represent the centers of nickel atoms lying in the surface layer, and the open circles the positions of adsorbed nitrogen atoms. In the structure marked 4 the separations between adjacent nitrogen atoms is double that between nickel atoms in the surface layer ; the ratio of the number of nickel atoms to the number of nitrogen atoms is 4, which number has been chosen to designate the structure. In the structure marked 3 the corresponding ratio of distances is $3^{1/2}$, and the ratio of the numbers of atoms is 3.

The structure marked Q is much more complex with a two-dimensional hexagonal unit cell having an edge of 12·4 Å, five times larger than the separation of adjacent nickel atoms. The relative intensities of different diffraction spots of a pattern representing the Q structure are not the same in different experiments. For example, the (22) and (33) reflections are sometimes strong and sometimes weak. This seems to mean that the locations of atoms within the unit cell of this structure is not always the same. Furthermore, there is, in general, no single arrangement in the different unit cells which can account for the observed intensities, which is interpreted to mean that the arrangement is not the same in all the unit cells.

In all three of these structures it has been assumed that adsorbed atoms are located between surface nickel atoms as indicated, although the diffraction patterns do not establish this fact. As the sketches of fig. 6 are reproduced here, there is no distinction between the centres of small triangles of nickel atoms having their apices up and down. If we identify azimuths in fig. 6 with those marked on fig. 3 (and with the approximate orientation of the diffraction patterns of fig. 2(A), (B) and (C), then the placing of atoms at the centres of triangles with apices upward (as is done) is equivalent to placing them above nickel atoms of the second layer below the surface rather than above atoms only one layer below. There is some experimental evidence that this is the correct placement.

Representative diffraction patterns from which the 4, 3 and Q structures have been deduced are reproduced respectively in figs. 7, 8 and 9 (Pls. 27–29). Data relating to the patterns representing the 4 and 3 structures are assembled in table 2, and data relating to the patterns from the Q structure in table 3.

The experimental conditions under which atoms take up these different arrangements on the crystal surface are imperfectly understood, and the clarification must wait upon further work. The observations which are now available are summarized below, together with the difficulties encountered in understanding the factors involved.

Table 2. Patterns Representing the 4 and 3 Structures

(1)	(2) Voltage and wave length	(3) Range of Observable spacings	(4) Calculated beams within this range	(5)	(6)	(7) Observed beams	(8)
			Miller indices	Spacing	Azimuth	Spacing	Azimuth
The 4—structure							
Fig. 7(A)	52 v 1·69 Å	From 6·8 Å to 2·9 Å	(10)	4·30 Å	A, B	4·30 Å	A, B
Fig. 7(B)	57 v 1·615 Å	From 6·5 Å to 7 Å	(10)	4·30 Å	A, B	4·45 Å	A strong B weak
Fig. 7(C)	65 v 1·52 Å	From 6·1 Å to 2·6 Å	(10)	4·30 Å	A, B	4·21 Å	B strong A weak
Fig. 7(D)	77 v 1·40 Å	From 5·7 Å to 2·4 Å	(10) (11)	4·30 Å 2·48 Å	A, B C	4·51 Å 2·46 Å	A, B C
The 3—structure							
Fig. 8	62 v 1·555 Å	From 6·3 Å to 2·6 Å	(10)	3·72 Å	C	3·76 Å	C

The 4 structure seems to be favoured by deposition at very low pressure upon a crystal at room temperature. At an appropriate electron beam voltage, the pattern representing this structure makes its appearance on the fluorescent screen rather gradually. The diffraction spots are initially very diffuse, presumably representing simultaneous nucleation of individual two-dimensional crystallites at many different points on the surface. The two-dimensional layer of atoms is then polycrystalline, however with almost certainly all of the crystals similarly oriented and representing only lateral displacements with respect to each other without rotation. There can be only four, or possibly eight, different kinds of crystallites. Since all of these two-dimensional crystallites are simply related to the structure of the underlying nickel, and therefore to each other, it is not at present clear why they do not conspire to give a sharp pattern.

Table 3. Patterns Representing the Q Structure

(1)	(2) Voltage and wave-length	(3) Range of observable spacings	(4)	(5) Calculated beams within this range	(6)	(7)	(8) Observed beams
			Miller indices	Spacing	Azimuth†	Spacing	Azimuth†
Fig. 9(A)	48 v 1·75 Å	6 Å	(20)	5·37 Å	A, B	5·32 Å	A and B
			(21)	4·06 Å	19°		
		3·5 Å	(30)	3·59 Å	A, B		
Fig. 9(B)	75 v 1·415 Å	5·8 Å	(20)	5·37 Å	A, B	Just detectable	
			(21)	4·06 Å	19°	Just detectable	
			(30)	3·59 Å	A, B	3·58 Å	A, B weak
			(22)	3·10 Å	C	3·10 Å	C strong
		2·7 Å	(31)	2·99 Å	14°	not seen	
Fig. 9(D)	120 v 1·12 Å		(10)	10·75 Å	A, B	‡	
			(11)	6·22 Å	C	‡	
			(20)	5·37 Å	A, B	5·59 Å	A, B
			(21)	4·06 Å	19°		
			(30)	3·59 Å	A, B	3·70 Å	A, B
			(22)	3·10 Å	C	3·15 Å	C
			(31)	2·99 Å	14°		
			(40)	2·69 Å	A, B	2·71 Å	A, B
			(32)	2·47 Å	23°	2·47 Å	23°
			(41)	2·35 Å	11°	2·35 Å	11°
			(50)	2·15 Å	A, B	2·15 Å	A, B
			(33)	2·07 Å	C	2·08 Å	C
			(42)	2·03 Å	19°	2·05 Å	20°
			(51)	1·93 Å	9°	1·94 Å	8°
			(60)	1·79 Å	A, B	1·82 Å	A, B
			(43)	1·77 Å	25°	1·81 Å	25°
			(52)	1·72 Å	16°	1·77 Å	16°

† Azimuths other than that A, B and C are designated by the angle which they make with the A and B azimuths.

‡ It should be pointed out that there are other diffraction patterns from the Q structure taken at 10 v and at 15 v (not reproduced here), which show the (10) and (11) reflections unmistakably and very strongly.

With the crystal at room temperature, this type of structure seems to last indefinitely. If the crystal is warmed to 100°c above room temperature the diffraction spots become considerably sharper, presumably corresponding to crystal growth. The spots can, however, never be made as sharp as one would expect them to be for the entire surface arranged in a single two-dimensional array. The patterns of fig. 7 are of intermediate sharpness.

At a temperature 225°c the patterns due to adsorbed gas atoms are very weak, and at slightly higher temperatures entirely missing, although the Laue spots from the nickel crystal are not greatly changed. This change with temperature seems to be due to melting the two-dimensional crystal of atoms so that they move about freely over the surface. A pattern reappears at once on allowing the crystal to cool. The pattern which appears after cooling is, however, never the 4 pattern. If the heating has been quite moderate, 225°c, the new arrangement is that of the Q structure. If the heating has been more severe, at temperatures which may be as high as 400°c, the pattern may be the Q or the 3. There seems to be no heat treatment which can produce the reverse change, from the Q or 3 pattern back to the 4. Thus the arrangement of atoms represented by the 4 pattern seems to be the least stable of the three arrangements.

Whether the spots of a Q type diffraction pattern are fuzzy, as in fig. 9(C), or sharp, as in fig. 9(D), is determined by the temperature to which the crystal has been raised after deposition of the gas. Maximum temperatures of the order of 225°c lead to patterns with diffuse spots (like fig. 9(C)), but sharp spots are found after heating at 300°c or 400°c.

Understanding the factors which determine the structure of adsorbed atoms is made difficult by inadequate independent control of temperature and gas pressure. The nickel crystal is heated by electron bombardment from a tungsten ribbon. Whenever this ribbon is heated the gas pressure rises (often by a factor greater than 10) because of the adsorbed nitrogen which it gives up, and whenever the ribbon is cooled there is a decrease of pressure (often by a factor of 10). A thin nickel crystal, which can be heated by conduction, is now being prepared. We expect that the factors which determine the different structures of adsorbed atoms can be found out from experiments with this crystal.

3.2. *CO on Nickel*

Carbon monoxide molecules arrange themselves on the surface of the nickel crystal in the 4-structure. Except for this one point the behaviours of carbon monoxide and nitrogen are, however, quite different. The probability that a CO molecule which strikes the surface will stick to it is very high. Yet the CO is held very weakly, and molecules of CO are completely removed by heating the crystal to only 175°c. Other differences in the behaviour of the two gases are the absence of polymorphic forms of two-dimensional CO crystals, and the greater tendency of CO molecules to arrange themslves in an almost perfect two-dimensional array, rather than imperfectly. A typical pattern from a monolayer of CO molecules is reproduced as fig. 10 (Pl. 30).

At an appropriate electron beam voltage and a suitably low CO pressure, the gradual development of a diffraction pattern can be observed quite clearly. An annular ring of nebulous character shows up first on the fluorescent screen. This ring seems at first circular, then assumes an angular appearance which soon can be identified as hexagonal. Finally, the sides of the ring clear up and only six diffraction spots are left. Initially the spots are diffuse, but they rapidly become quite sharp. In the case of nitrogen, the development of a diffraction pattern is less easily followed.

The sticking probability measurements for CO, which are very crude, were made by observing the time required for the 4 pattern to appear at maximum intensity and sharpness upon the fluorescent screen immediately after the crystal had cooled from high temperature. A simultaneous record was made of the CO pressure, which was necessarily always changing rapidly. In a number of tests, values of the integrated product of the pressure and the time were found in the range 0·4 to 6×10^{-6} mm Hg sec. The theoretical value for CO molecules striking the surface at 300°K and forming a complete monolayer with the 4 arrangement is $1{\cdot}3 \times 10^{-6}$ mm Hg sec for sticking probability unity. Although the observations were extremely crude, they do prove that the sticking probability is very high and of the order of unity. They indicate also that CO molecules are fairly free to move about over the surface at room temperature.

The diffraction patterns from monolayers of CO molecules were always quite sharp and no change of sharpness was produced by warming the crystal after deposition or by deposition upon a warm crystal. There was, however, no deposition of CO upon the crystal at temperatures in excess of 150°C, and this temperature was just high enough to clean the surface completely.

In a series of interesting experiments, CO was deposited first upon a clean crystal surface, then the surface layer was removed by heating to 175°C after which a new layer of CO molecules was deposited. It was found that after two of these cycles the surface could be only partially cleaned at this low temperature, and the situation became worse after another cycle. The obvious conclusion from these tests is that we were observing the effects of impurities in the CO (from residual gas in the tube), which could not be removed at 175°C. Behaviour was normal again after the crystal had been heated above 800°C.

In some experiments the Q structure was observed, but this was only after the crystal had been exposed over night to CO at an exceptionally high pressure (2×10^{-8} mm Hg as an average value). It seems altogether probable that this structure was due not at all to CO but to impurities.

3.3. *Oxygen on Nickel*

The behaviour of oxygen is very different from that of nitrogen or CO. Exposure of the clean crystal surface to oxygen results in gradual weakening and final disappearance of Laue beams from the nickel, without the appearance of any new diffraction beams at low voltages. When a crystal which shows no diffraction patterns of any sort, after for example having been exposed to oxygen at the comparatively high pressure of 5×10^{-8} mm Hg for 16 hours, is heated to progressively higher temperatures, the following series of changes can be observed.

After heating at 200°c, diffuse low voltage beams can be seen (fig. 11(A) Pl. 30) but the amount of oxygen on the surface is still so great that no Laue beams from the nickel are seen up to the limit of the observations at 400 v. Some sharpening of the oxygen diffraction pattern can be produced by further heating (fig. 11(B)), still without removing enough of the oxygen to permit the appearance of diffraction patterns from the nickel. More vigorous heating (probably† above 500°c) results in re-appearance of the nickel diffraction beams at apparently full intensity, *but with no change in the oxygen diffraction pattern* which is now almost certainly the pattern from a single monolayer. Finally the diffraction pattern from the oxygen is destroyed by heating at a bright cherry red.

The two dimensional spacings corresponding to the spots of fig. 11 are written down in table 4. The spots can be indexed as (22) and (40) reflections of the Q structure (see table 3). We do not understand how a thick layer of annealed oxygen can give the same type of Q pattern which is produced by a single monolayer.

Table 4. Patterns from Oxygen on Nickel

	Voltage and wave-length	Observed Beams		Miller indices (see table 3)
		Spacing	Azimuth	
Fig. 11(A)	82 v 1·35 Å	2·66 Å	A, B	(40)
Fig. 11(B)	82 v 1·35 Å	3·17 Å 2·66 Å	C A, B	(22) (40)

3.4. *Hydrogen on Nickel*

No evidence has been obtained of any diffraction pattern due to hydrogen. In one test hydrogen flowed through the experimental tube for 65 hours at an average pressure of 2×10^{-7} mm Hg. At the end of this time no low voltage diffraction features could be found; the Laue beams from the nickel lattice seemed to be even stronger than they were initially; and there was a considerable improvement in the apparent resolving power of the crystal, shown by each Laue beam being observable over a narrower range of wavelengths. It was shown, by observing a rise in pressure when the crystal was heated, that there was considerable adsorbed hydrogen.

It seems altogether possible that hydrogen atoms or molecules may be as close together on the surface as are surface nickel atoms, and with the same lateral arrangement. If this were true, their presence would result only in modification of the intensities of diffraction beams attributed to the lattice of the crystal. The improved resolving power of the crystal remains to be explained.

---

† The thermocouple attached to the crystal was out of order when this test was carried out.

§ 4. DISCUSSION

Many observations of relative intensities of diffraction beams from adsorbed gas layers require clarification. Most of this will have to await further work.

Perhaps the simplest of these observations upon relative intensities is shown in the patterns of fig. 7. One notes that diffraction patterns representing the 4 structure are strong at some voltages in the A azimuth and at other voltages in the B azimuth. " It will be noticed that the nickel atoms in the surface are of two sorts—those that are adjacent to gas atoms and those that are not. One-fourth of the nickel atoms are of this latter class, and they together form a layer of the same structure, orientation and scale factor as the gas atoms. If the two classes of nickel atoms scatter radiation in different amounts—if, for example, the gas atoms shield the adjacent nickel atoms more effectively than the non-adjacent—then, of course, the layer of nickel atoms as a whole will give rise to a differential diffraction beam capable of interference with that due to the gas layer."† This accounts for the variation of intensity with azimuth, and its change with voltage. In principle, one can work out from it the distance between the adsorbed nitrogen atoms and the surface nickel atoms. The electron wavelength is, however, too short to give any respectable precision to such a calculation. The data are consistent with a separation of 3 Å which is a reasonable value.

It has already been pointed out that in different experiments, which have led to atoms arranged on the surface in the Q structure, relative intensities of diffraction spots have been widely different. This has been interpreted to mean that there are a number of different possible arrangements of atoms within the large two-dimensional hexagonal unit cell ($a_0 = 12{\cdot}4$ Å) of the Q structure. And even one single diffraction pattern must be interpreted to arise from a structure in which there are different arrangements within the unit cell on different parts of the effective surface. It is hoped and expected that the distributions of arrangements giving rise to particular patterns can be found out.

In each diffraction pattern from a monolayer of adsorbed atoms or molecules, of whatever sort, it has been observed in general that the pattern appears most strongly at some particular electron wavelength. A single diffraction spot of the pattern can always be traced over a range of electron wavelengths, satisfying always the appropriate plane grating formula, but its intensity varies greatly. Such variation is not consistent with a pattern produced by a single atomically flat plane of atoms. The probable interpretation of this variation, which has not yet received theoretical quantitative confirmation, is that the variation is due to atomic steps on the surface within a distance appropriate to the wave-front of an electron. One single step, for example, would result in diffraction from two monolayers of atoms with a spacing of 2·03 Å (the separation of (111) planes of nickel atoms). This interpretation should be amenable to easy confirmation.

---

† The quotation is from Davisson and Germer (1927).

That this interpretation is correct is suggested by the experimentally observed fact that quite flat crystal surfaces are required for the observation of any diffraction patterns from adsorbed monolayers. In earlier experiments, before the use of the present nickel crystal, tests were carried out upon a tungsten single crystal. Excellent Laue diffraction beams were obtained from this crystal. Single monolayers of adsorbed gas atoms were deposited upon its surface by well-known techniques, but in no case could any diffraction pattern at all be obtained from one of these monolayers. Tungsten crystals, of the type used in these experiments, are known to be notoriously rough. It is now believed that this was the cause of the failure of the tungsten experiments. It seems probable that the method of investigation outlined in this paper will be applicable only to selected crystal surfaces which can be made exceptionally flat on an atomic scale.

The remarkable anomalous improvement in the resolving power of the nickel crystal, which is produced by hydrogen, is not understood. Is it possible that this improvement is the result of a change to normal spacing of an abnormal spacing between the first and second layers of nickel atoms? Accurate intensity measurements are required to settle this question.

§ 5. NEW EXPERIMENTS

A number of continuations of the present experiments immediately suggest themselves:

1. The most pressing of these is the certain identification of the gas giving rise to the patterns assigned to nitrogen. This will require a nickel crystal which can be heated by conduction in order to avoid the fluctuations in pressure taking place on heating and cooling the tungsten ribbon used in bombarding the crystal.

2. Such a crystal, which can be heated by conduction, should be valuable in other experiments also; for example, in understanding the factors which determine the transitions between the crystalline forms of the 4, Q and 3 structures, and by the flash filament technique in finding just when we have a monolayer of adsorbed atoms in those cases in which it is now uncertain, and finally in determining unambiguously whether a gas is adsorbed as atoms or molecules.

3. Repetition of some of these tests upon a (100) face of a nickel crystal. This would seem to require preparation of an unusual surface without (111) facets. Present electropolishing techniques offer promise that a satisfactory (100) surface can be obtained.

4. Tests of the reaction of one gas with another upon a crystal surface. For example, will gas atoms (presumed to be nitrogen) adsorbed upon a nickel surface in the unstable 4 structure react more readily with hydrogen than will atoms in the other two more stable arrangements? Experiments of this sort require a considerable battery of valves with appropriate auxiliary pumps and gas bulbs. These are now being installed.

5. Studies of surface states of silicon crystals. The (111) surface of silicon can be made remarkably smooth on an atomic scale, and such surfaces should be very favourable also for studies of adsorption and catalytic reaction.

REFERENCES

American Crystallographic Association—Program and Abstracts, Annual Meeting July 19–24, 1959.

DAVISSON, C. J., 1928 a, *Bell Syst. tech. J.*, **7,** 90 ; 1928 b, *J. Franklin Inst.*, **205,** 597 ; 1929, *Sci. Monthly*, **28,** 41.

DAVISSON, C. J., and GERMER, L. H., 1927, *Phys. Rev.*, **30,** 705.

EHRENBERG, W., 1934, *Phil. Mag.*, **18,** 878.

FARNSWORTH, H. E. *et al.*, 1929, *Nature, Lond.*, **123,** 941 to 1959, *J. appl. Phys.*, **30,** 675. Many papers.

GERMER, L. H., 1928, *J. chem. Educ.*, **5,** 1041 ; 1929, *Z. Phys.*, **54,** 408.

The Hardening of Lithium Fluoride by Electron Irradiation†

By A. D. WHAPHAM and M. J. MAKIN
Metallurgy Division, Atomic Energy Research Establishment, Harwell

[Received October 1, 1959]

ABSTRACT

A study has been made of the effect of 1 MEV electron irradiation on the mechanical properties of lithium fluoride single crystals tested in compression. The yield point, σ, has been shown to vary with the irradiation dose, ϕ, according to the law $\sigma=\sigma_u+A[1-\exp(-B\phi)]^{1/2}$, where σ_u, A and B are constants. This relationship has been derived theoretically by considering the passage of dislocations through radiation induced obstacles dispersed in the slip plane, together with the capture of point defects by existing obstacles. The empirical relationship $\sigma=k\phi^{1/3}$, previously used for radiation hardening in metals, is capable of representing only the medium dose results, but clearly does not fit at either low or high doses.

A new mechanism of cracking in heavily irradiated lithium fluoride, similar to that proposed by Cottrell for alpha iron, has been observed. With compression along a [001] axis, cracks are initiated at the intersections of orthogonal {110} type slip planes and extend on the (100) cleavage plane passing through the intersection and parallel to the compression axis.

§ 1. INTRODUCTION

Two types of irradiation hardening are theoretically possible in crystalline solids which normally deform by a slip process. Either (*a*) the nucleation of slip may be made more difficult by making dislocation sources harder to operate (source hardening), or (*b*) the stress for the propagation of slip may be increased (lattice hardening) by an increase in the stress required to move dislocations through the crystal. In well-annealed metals such as copper and nickel both types of hardening occur after neutron irradiation. In lithium fluoride the existence of lattice hardening after electron irradiation has been proved by observing the dislocation patterns (revealed by etching) produced by hardness indentations (Whapham 1958). In unirradiated material dislocations glide appreciable distances away from the indentation whereas after irradiation dislocations can be seen only in the immediate vicinity of the indentation, the irradiation induced lattice hardening preventing these dislocations from moving away.

Work preliminary to the present investigation has shown that it is the stress necessary to move dislocations that governs the plastic deformation of lithium fluoride. The mechanism of deformation of stressed crystals was investigated by etching to reveal the slip dislocations. It was found that in all specimens, both unirradiated and electron-irradiated, individual slip planes extended from their point of origin slowly, with progressive increase of stress. If the operation of dislocation sources determined the stress at which plastic deformation occurred then complete slip lines would be expected to form abruptly. This work also showed that dislocations in the compression specimens move at stresses well below the macroscopic yield stress at normal strain rates. In unirradiated material dislocation movement is first seen at a resolved shear stress of $0{\cdot}13\,\mathrm{kg/mm^2}$, whereas the macroscopic yield occurs at a shear stress of $0{\cdot}5\,\mathrm{kg/mm^2}$ when the applied strain rate is 10^{-4} per sec. In the electron-irradiated material, dislocation movement also starts at stresses roughly $0{\cdot}4\,\mathrm{kg/mm^2}$ less than the value at the macroscopic yield.

---

† Communicated by the Author.

Gilman and Johnston, who have measured the yield stress of lithium fluoride during bend tests (Gilman and Johnston 1956, 1958), and the stress dependence of dislocation velocity as a function of neutron irradiation (Johnston and Gilman 1958), concluded that the irradiation hardening is governed by the resistance to motion of dislocations through the crystal lattice. In addition the form of the stress–strain curve can be explained in terms of the variation of dislocation velocity with stress and the multiplication of dislocations. It is therefore apparent that the yield point at a given strain rate is a measure of the lattice hardening. No direct measurement of an increase in stress required to operate dislocation sources in lithium fluoride has yet been made.

The present experiments were undertaken to determine in detail the dependence of the lattice hardening on the irradiation dose, and to compare this with a theoretically predicted relationship.

1.1. *Dependence of Lattice Hardening on Irradiation Dose*

Lattice hardening must be caused by 'obstacles' of some kind distributed throughout the crystal lattice which oppose the motion of dislocations across the glide plane. It is not necessary to specify at this stage the nature of these obstacles except to point out that they are unlikely to be individual point defects during room temperature irradiation in view of the low temperatures at which these become mobile in most crystalline materials. It is more probable that each obstacle is a cluster or aggregate of defects of some kind.

If N is the number of dislocations per unit volume held up against N_z obstacles per unit area of glide plane then the strain rate $\dot{\epsilon}$ at a temperature T and stress σ is given by

$$\dot{\epsilon}=\frac{N\mathbf{b}\nu_0}{N_z}\exp\left(-\frac{U(\sigma)}{kT}\right), \quad . \quad . \quad . \quad . \quad . \quad . \quad . \quad (1)$$

where U is the activation energy for cutting through the obstacles, $\mathbf{b}$ is the Burgers vector and ν_0 the frequency with which a dislocation line attempts to pass the obstacle. Solving eqn. (1) for σ gives the lattice hardening stress as a function of N_z. To do this is is first necessary to determine the stress dependence of the function $U(\sigma)$. Various equations can be chosen to represent the energy profile of the obstacle which is expected to be as shown in fig. 1. Application of stress to the crystal modifies the shape of the potential energy–distance curve as in fig. 2 by introducing a variation in potential energy with distance of $\sigma l_0'\mathbf{b}$ where l_0' is the average distance between obstacles in the slip plane. Mott and

Fig. 1

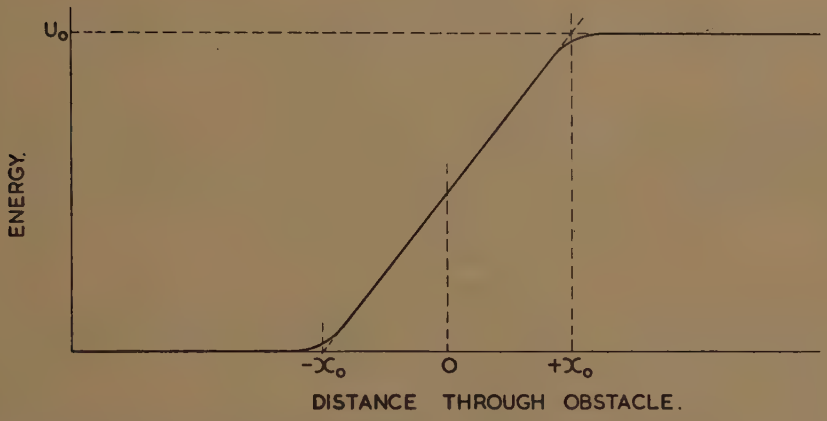
U₀
ENERGY.
-x₀
0
+x₀
DISTANCE THROUGH OBSTACLE.

Energy profile of a dislocation cutting through an obstacle at zero externally applied stress.

Fig. 2

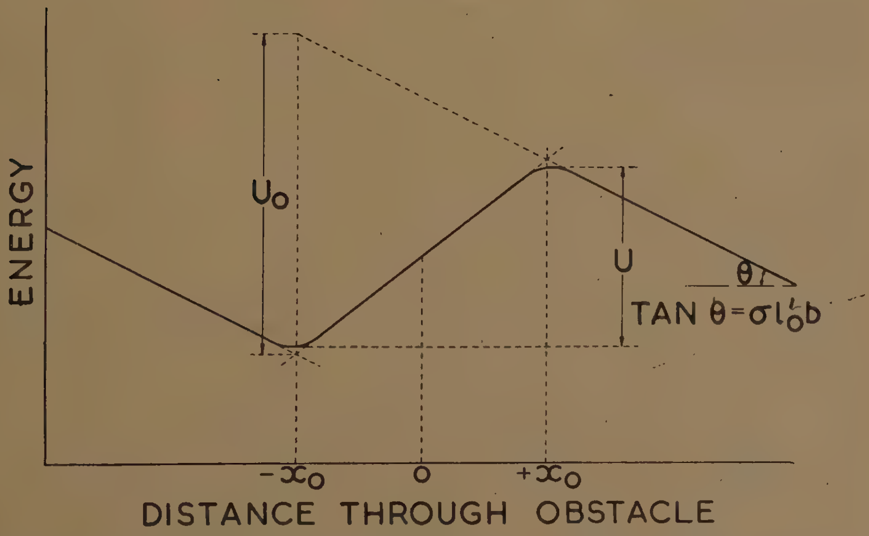
ENERGY
U₀
U
θ
TAN θ=σl₀′b
-x₀
0
+x₀
DISTANCE THROUGH OBSTACLE

Energy profile of a dislocation cutting through an obstacle when an external stress σ is applied.

Nabarro (1948) and also Seeger (1958) have shown that a good approximation to the new value of U is given by

$$U=U_0\left(1-\frac{\sigma}{\sigma_0}\right)^{3/2},$$

where U_0 is the activation energy at zero stress and σ_0 is the stress required to overcome the barrier without thermal activation.

When $U=0$,

$$\sigma_0 l_0'\mathbf{b}=\frac{U_0}{2x_0}$$

and hence

$$U=U_0\left(1-\frac{2x_0\mathbf{b}l_0'\sigma}{U_0}\right)^{3/2}. \quad \ldots\ldots\ldots \quad (2)$$

Seeger derives an almost identical expression for U except for the constant 4 instead of 2.

In the simplest case, where no allowance is made for a stress dependence of l_0'

$$l_0'=\frac{1}{N_z^{1/2}}$$

and

$$U=U_0\left(1-\frac{2x_0\mathbf{b}\sigma}{U_0 N_z^{1/2}}\right)^{3/2}.$$

Substituting for U in eqn. (1)

$$\sigma=N_z^{1/2}\frac{U_0}{2x_0\mathbf{b}}\left[1-\left\{\frac{kT}{U_0}\ln\left(\frac{N\mathbf{b}\nu_0}{N_z\dot{\epsilon}}\right)\right\}^{2/3}\right]$$

is obtained and if N_z is proportional to the irradiation dose, ϕ, initially,

$$\sigma\propto\phi^{1/2}.$$

Friedel (1956) has suggested that l_0' should decrease with increasing stress due to the greater probability of a dislocation bowing out sufficiently to meet another obstacle at high stresses. Friedel calculates that

$$(l_0')^3=\frac{G\mathbf{b}}{\sigma N_z}.$$

Inserting this into eqn. (2), we obtain

$$U=U_0\left[1-\frac{2x_0\mathbf{b}^{4/3}G^{1/3}\sigma^{2/3}}{U_0 N_z^{1/3}}\right]^{3/2}.$$

Substituting this modified expression for U into eqn. 1, the expression for σ becomes

$$\sigma=\left[\frac{N_z}{G\mathbf{b}}\right]^{1/2}\left[\frac{U_0}{2x_0\mathbf{b}}\right]^{3/2}\left[1-\left\{\frac{kT}{U_0}\ln\left(\frac{N\mathbf{b}\nu_0}{N_z\dot{\epsilon}}\right)\right\}^{2/3}\right]^{3/2}.$$

In this expression also

$$\sigma\propto N_z^{1/2}.$$

In both cases therefore dislocation theory predicts a dependence of lattice hardening on $N_z^{1/2}$.

Initially the number of obstacles N_z is expected to be proportional to the irradiation dose ϕ but, as the concentration of obstacles increases, there is an increasing probability that new defects will be captured by existing obstacles rather than nucleating new ones. Hence the number of new obstacles formed during a given increment of dose decreases as the dose increases. If there is a volume v associated with each obstacle within which capture will occur, then the rate at which new obstacles are formed $\dot{N}_z$, can be written

$$\dot{N}_z = a\dot{\phi}(1 - vN_z),$$

where a is the number of obstacles produced per electron and $\dot{\phi}$ is the dose rate. Integrating, the number of obstacles N_z is given by

$$N_z = \frac{1}{v}\left[1 - \exp(-av\phi)\right]$$

and hence the lattice hardening is given by

$$\sigma_i \propto \frac{1}{v^{1/2}}\left[1 - \exp(-av\phi)\right]^{1/2}$$

or

$$\sigma_i = A\left[1 - \exp(-B\phi)\right]^{1/2}. \quad \ldots\ldots\ldots \quad (3)$$

This formula predicts that initially the lattice hardening σ_i will be proportional to $\phi^{1/2}$ and that at large doses σ_i will saturate at a constant value A. The relationship does not depend upon the properties of any particular material and is intended to apply generally to crystalline solids which deform by slip.

The alternative relationship which has been fitted to the hardening of copper single crystals by neutron irradiation (Blewitt 1956) is that

$$\sigma_i \propto \phi^{1/3}.$$

This relationship has no sound basis in dislocation theory and is purely an empirical one which happens to fit the experimental data over the range of doses used. The importance of deciding between these two expressions is of considerable technological as well as fundamental interest since the $\phi^{1/3}$ relationship predicts a continually increasing hardening with neutron exposure instead of the saturation expected in the new theory. In metals very high neutron doses are required to decide between the two theories since at low doses by a suitable choice of constants the two relations are very similar. In lithium fluoride damaged by electron irradiation however, only comparatively short irradiation times are required to introduce enough damage to decide which relationship is more correct.

§ 2. EXPERIMENTAL

Specimens, 2·4 × 2·4 × 20 mm in size and bounded by (100) cleavage surfaces, were cleaved from two single crystal blocks 1½ in. × 1½ in. × ½ in. selected from a batch of material supplied by the Harshaw Chemical Company. The cleaved specimens contain fresh surface dislocations caused by the cleavage process and dust scratches, together with about 10^5

aged dislocations per cm². Roughly half the aged dislocations are contained in low-angle boundaries and half are randomly distributed through the crystal. The two crystal blocks used in this work were of similar purity and had been subjected to similar thermal treatment and the yield stresses, which are very sensitive to these factors, were practically identical ($0{\cdot}498 \pm 0{\cdot}010$ and $0{\cdot}493 \pm 0{\cdot}010$ kg/mm² respectively).

The specimens were irradiated, three at a time, in a beam of 1 MEV electrons produced by a Van de Graaff generator. As the penetration of the electron beam in lithium fluoride is only 1·2 mm and specimens thicker than this were required in order to perform satisfactory tests, the 2·4 mm thick specimens were irradiated firstly on one face and then turned round to irradiate the opposite face. Using this technique the radiation dose was fairly uniform throughout the crystal, as shown by optical absorption, and consistent results were obtained with them. Crystals thicker than those used show a light band in the centre, where the irradiated regions do not overlap and thinner ones show enhanced absorption in the centre.

The maximum dose used was 10^{16} electrons/cm² since, above this dose cracking, produced by radiation-expansion of the lattice, was encountered. It is unlikely that strains present in specimens which had not cracked could affect the yield point since most of the stress–strain curves showed an easy glide region of $1\frac{1}{2}\%$ even at the highest doses used. This deformation should eliminate any non-homogeneous strain present.

Care was taken to ensure that the temperature rise during irradiation was not excessive. Variation of the beam current below the maximum of 0·54 μA/cm² did not have any observable effect in subsequent testing. Theoretically it is estimated that the maximum temperature rise was about 10°C.

After irradiation, steel end pieces and two brass cross pieces, 10 mm apart, were fitted to the specimens, using a synthetic resin adhesive. Mounted in this way they were placed in a special compression jig designed to produce axial loading and tested at a strain rate of 10^{-4} sec. The strain of the 10 mm central section of the specimens was measured by a capacitative strain measuring head attached to the two brass cross pieces. With this arrangement strains from 0·01% to 10% could be measured.

Representative stress–strain curves are shown in fig. 3. The unirradiated crystal yields at $0{\cdot}496 \pm 0{\cdot}010$ kg/mm². Out of ten tests, three of the stress–strain curves show a flat easy glide of 0·3%, six showed a rate of hardening in this region which is between one-quarter and three-quarters of the following linear hardening rate, while one did not show any sign of an easy glide region. The rate of work hardening in the linear hardening region varied from test to test between the limits 0·07 and 0·18 kg/mm² % strain. The curves with the flat easy glide region are very similar to that shown by Gilman and Johnston (1956).

After 10% strain the specimens were considerably bulged. Though, in the early stages of deformation, slip on all systems could be seen (by etching to reveal dislocations), in heavily strained specimens gross slip occurred only on one or two systems since, while one pair of crystal faces were considerably bulged, the pair at right angles were macroscopically flat.

Fig. 3

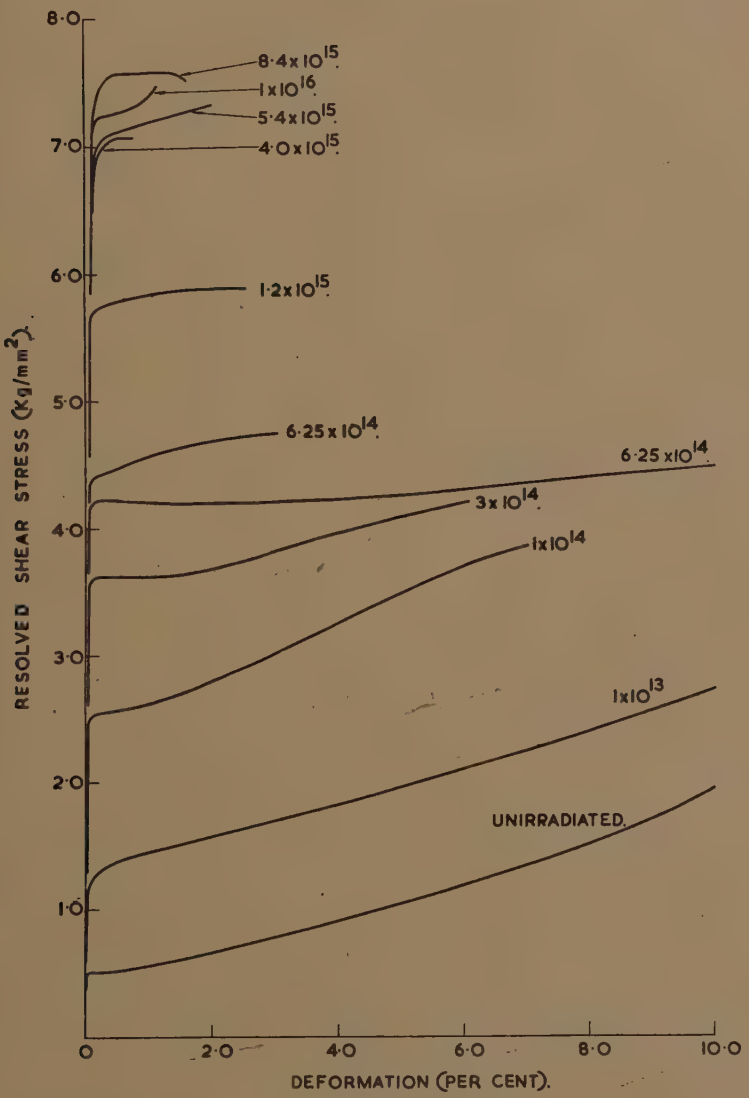

Stress–strain curves of irradiated lithium fluoride specimens tested in compression.

It is seen from the graphs that 1 MeV electron irradiation considerably increases the yield point. A dose of 10^{12} electrons/cm^2 just produces an increase clearly beyond experimental error and at 10^{16} electrons/cm^2 the yield stress is raised to 15 times the unirradiated value. The easy glide region increases to $1\frac{1}{2}\%$ strain, even at a dose of 10^{12} electrons/cm^2 and remains at approximately this value for doses up to 3×10^{14} electrons/cm^2 though, as in the unirradiated case, the occasional test will show no sign of easy glide (e.g. the test illustrated in fig. 3 for a specimen irradiation of 10^{13} electrons/cm^3). At doses above 3×10^{14} easy glide regions of several per cent were obtained (8% in the case of one specimen which had been given a dose of 10^{15} electrons/cm^2). One specimen which had been given a dose of $6{\cdot}25 \times 10^{14}$ electrons/cm^2, showed an easy glide region of about 4% and in the subsequent stage of up to 10% strain the hardening was only 0·05 kg/mm^2 % strain, whereas another specimen did not show any easy glide but a hardening rate of 0·15 kg mm^2 % strain. On examination of these two specimens after testing, the one which gave 4% easy glide showed deformation predominantly on only one set of {110} slip planes whereas the other specimen showed considerable intersecting slip. This dependence of the hardening rate on the degree of intersecting slip is well known in unirradiated materials. On deformation of irradiated crystals fewer slip lines are formed for a given strain but each line contains a higher linear density of dislocations than is found in the unirradiated crystals. After irradiation, therefore, a greater strain is expected before slip on intersecting planes produces hardening. This is in agreement with the longer easy glide region in irradiated crystals.

No cracks were observed in unirradiated crystals and crystals given an irradiation dose of up to 3×10^{12} electrons/cm^2 when they were tested up to 11% strain. Cracks were first observed at $10\frac{1}{2}\%$ strain in specimens given a dose of 10^{13} electrons/cm^2, 6% strain with a dose of 3×10^{14}, 3% strain at $1{\cdot}5 \times 10^{15}$ and a specimen irradiated to 3×10^{15} electrons/cm^2 which had been given only 0·3% strain showed many cracks. Even in these highly irradiated specimens which developed cracks in the early stages of deformation, strains of 1 or 2% could be obtained before the compression specimens shattered. The mechanism of cracking in the low dose crystals ($< 10^{15}$ electrons/cm^2) is complicated, the cracks not being confined to the {001} cleavage plane. After high doses, however, a new mechanism appears to operate. The cracks occur entirely in the {001} type planes and are initiated at the intersection of orthogonal slip planes as shown in figs. 4 and 5 (Pl. 31). Even at a magnification of 500 there is no evidence of cracking on other planes at the point of initiation. The cracks occur in the crystal in the form of slits, which sometimes extend to the crystal surfaces. This type of cracking is different from that observed by Stokes *et al.* (1958, 1959) in unirradiated MgO and is similar to that proposed by Cottrell (1958) for alpha iron. In this mechanism slip dislocations on orthogonal {110} type planes coalesce to form a new dislocation on the intersection of the planes. In fig. 6 the dislocation reaction is

$$\frac{a}{2}[10\bar{1}] + \frac{a}{2}[\bar{1}0\bar{1}] \rightarrow a[00\bar{1}].$$

The new dislocation lies in the (100) cleavage plane and is equivalent to an extra half plane inserted between (100) planes. Other slip dislocations following the original ones may also react together to form more $a[00\bar{1}]$ dislocations so increasing the number of extra half planes on one side of the intersection until a crack forms as in fig. 6.

Fig. 6

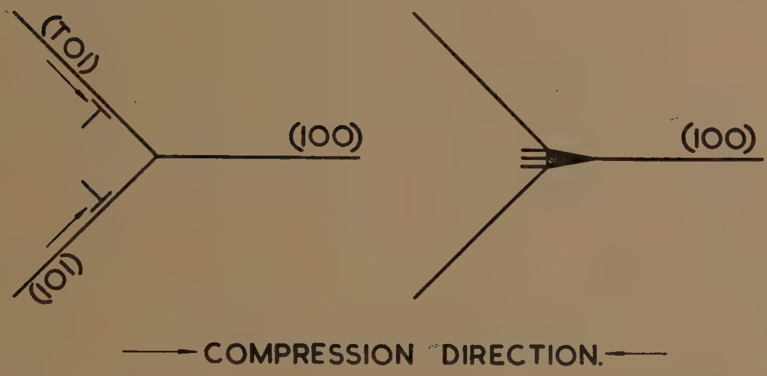

Coalescence of slip dislocations on two slip systems to form new dislocations with extra half planes on the (100) cleavage plane to form a (100) crack.

An interesting feature of crystals which have been irradiated to doses of 10^{14} electrons/cm^2 and above is that the slip traces show an enhanced optical absorption. This is seen clearly in fig. 4. The enhanced darkening of deformed crystals on irradiation has been reported, but this is the first observation of enhanced darkening by deformation of irradiated crystals. If, for example, the irradiation dose given to the crystal has produced a light brown colouration in it, slip produced by subsequent deformation is observed as dark brown planes extending through the crystal. The optical density in other regions, even near the slip planes, is not changed. It is possible that this enhanced optical absorption is due to colloidal lithium.

The rate of work-hardening in the linear hardening stage of the stress–strain curves for irradiated crystals is essentially the same as in the unirradiated case. There is a considerable scatter of individual hardening rates however, which would obscure a small effect.

The mean of the critical resolved shear stresses for the easy glide region is plotted against the irradiation dose ϕ in fig. 7, against $\phi^{1/2}$ in fig. 8 and $\phi^{1/3}$ in fig. 9. Only in fig. 8 is the initial part of the curve linear indicating that at low doses ($< 10^{14}$ electrons/cm^2) the correct relationship for the dose dependence of the critical shear stress is

$$\sigma \propto \phi^{1/2}.$$

At doses greater than 10^{14} electrons/cm^2, however, the critical shear stress increases less rapidly than the $\phi^{1/2}$ relationship and finally reaches a saturation value of 7·63 kg/mm^2. After 5×10^{15} electrons/cm^2 the critical

Fig. 7

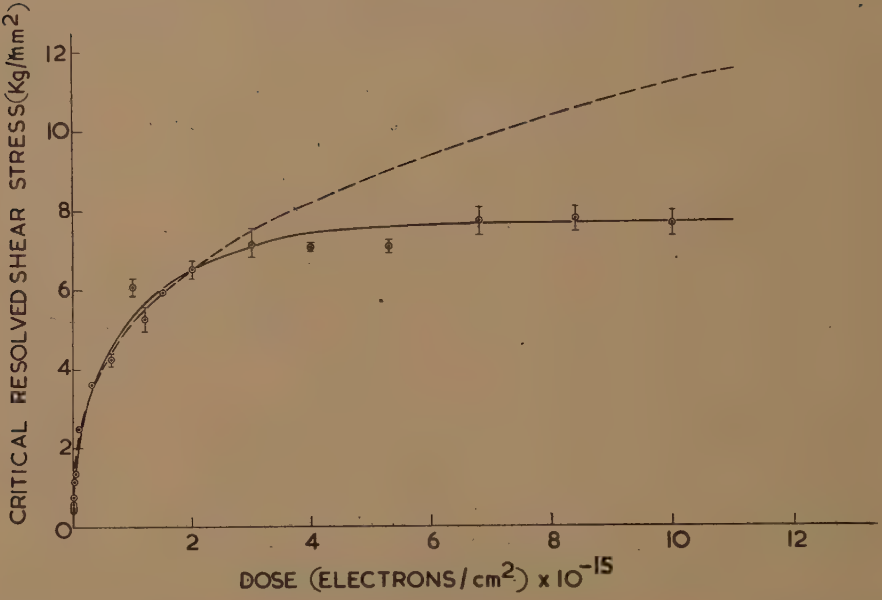

Plot of the critical resolved shear stress versus irradiation dose. The relation $\sigma = 0{\cdot}5 + 7{\cdot}13[1 - \exp(-6{\cdot}18 \times 10^{-16}\phi)]^{1/2}$ is shown as a solid line; the broken line is $\sigma = 5{\cdot}18 \times 10^{-5}\phi^{1/3}$.

Fig. 8

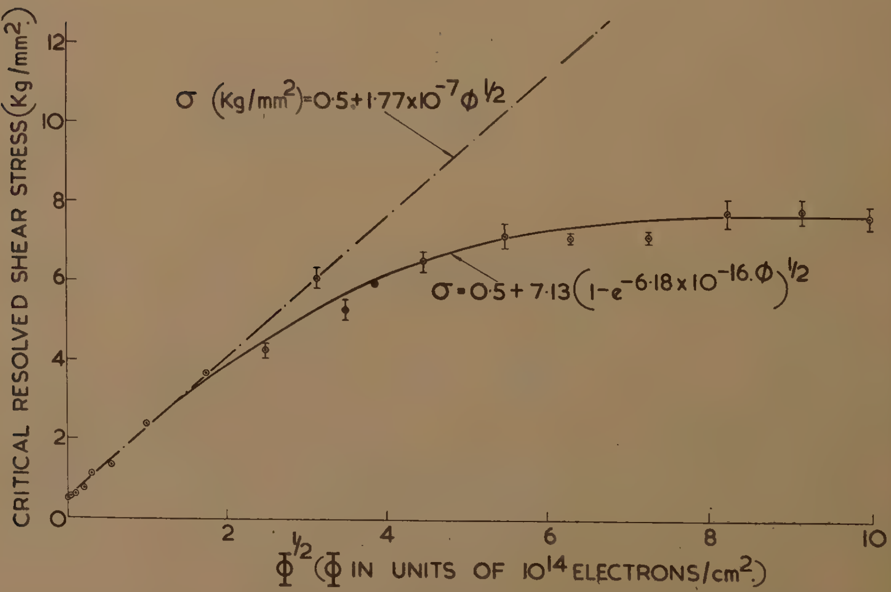

Plot of the critical resolved shear stress versus the square root of the irradiation dose.

shear stress is within experimental error of the saturated value. The results have been fitted to an equation of the type

$$\sigma = \sigma_u + \sigma_i = \sigma_u + A[1 - \exp(-B\phi)]^{1/2}$$

where σ_u = critical shear stress of unirradiated material and σ_i has been derived theoretically earlier in the paper.

This gives

$$\sigma = 0{\cdot}5 + 7{\cdot}13[1 - \exp(-6{\cdot}18 \times 10^{-16}\phi)]^{1/2}\ \mathrm{kg/mm^2}.$$

This relationship is plotted as a continuous line in each graph and represents the experimental points very accurately.

Fig. 9

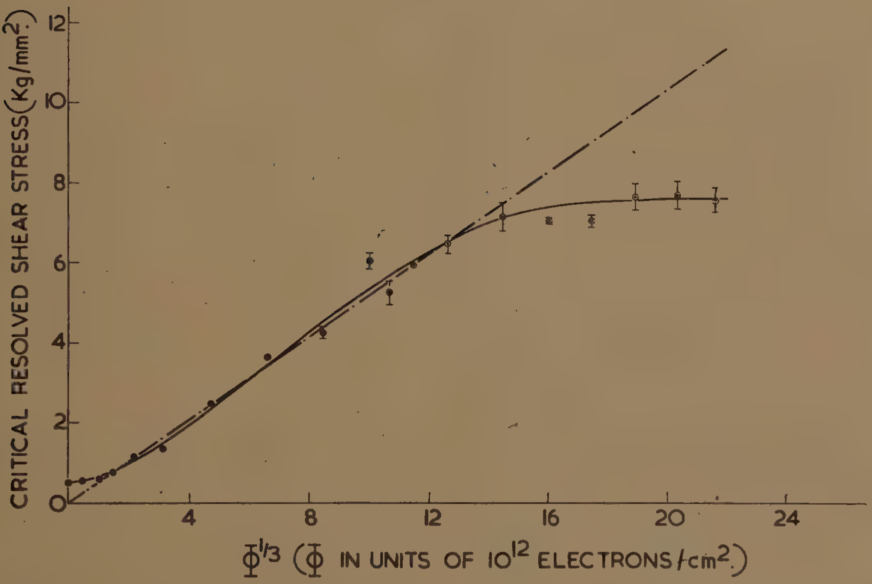

Plot of the critical resolved shear stress versus the cube root of the irradiation dose.

It is seen from fig. 9 that the previously used relation to describe the dose dependence of irradiation hardening in copper, namely

$$\sigma \propto \phi^{1/3},$$

does represent the experimental results between $\phi = 10^{12}$ electrons/cm² and 3×10^{15} electrons/cm². An incubation period is observed at low doses however, and above 4×10^{15} electrons/cm² it becomes quite clear that the cube root relationship is not the correct one.

§ 3. Discussion

The most important result of this work is the establishment of the equation

$$\sigma = \sigma_u + A[1 - \exp(-B\phi)]^{1/2}$$

as the correct relationship between irradiation hardening and electron dose in lithium fluoride crystals. This equation has been derived from dislocation theory by considering the passage of dislocations through obstacles dispersed in the slip plane coupled with a saturation in the number of obstacles due to the probability of the capture of point defects by existing obstacles. At present it is not possible to determine unequivocably the volume v over which capture will occur because in the equation only the product av can be measured. An estimate of the value of a depends upon the number of defects which form an obstacle and the number of defects produced per unit irradiation dose.

Number of defects per electron	Number of point defects in a cluster (n_c)	Number of clusters per electron (a)	Volume of sphere of influence around a cluster (v in 10^{-18} cm^3)	Radius of sphere of influence around a cluster (r)
200	1	200	3	90 Å
	2	100	6	110 Å
	5	40	15	160 Å
	10	20	30	190 Å
	20	10	60	240 Å

Table showing how the volume v and radius r of the sphere of influence around a cluster varies with the value assumed for the number of point defects in a cluster n_c.

Values of v and the corresponding radius r based upon obstacles of various numbers of defects are given in the table. In this table it has been assumed that the cross section for the production of point defects in lithium fluoride is the same as the value (3000 barns) measured for the production of F centres in KCl by electron irradiation (Varley 1954 a, b, 1956). The number of point defects estimated in this way will be a lower limit as it is possible that there may be some negative ion vacancies without an associated electron, in addition to the F centres. Here n_c is the *minimum* number of point defects which can form an obstacle which will oppose dislocation movement. It is an essential part of the theory that new defects will attach themselves to these obstacles making them grow in size as the irradiation dose increases. The volume v will be constant throughout the irradiation and will correspond to the minimum size obstacle. It is seen from the table that the most probable value of r lies between 100 and 250 Å.

It is not certain whether individual point defects could produce hardening ($n_c=1$). Gilman and Johnston (1958) notes the correlation between the onset of radiation hardening and the appearance of the 4500 Å absorption band in neutron irradiated lithium fluoride. This 4500 Å band has been ascribed to M centres (F-centre + metal-halogen vacancy pair) or some sort of electron excess centres which are larger than F centres. The etching effect in both neutron and electron-irradiated lithium fluoride observed by Gilman and Johnston (1958) is strong evidence that the obstacles grow in size with irradiation. A threshold dose is necessary for this etching effect to occur. This would be expected if obstacles could only produce an etching effect after they had grown to a critical size.

The investigations of the small angle scattering of x-rays by neutron irradiated lithium fluoride by Lambert and Guinier (1957 a) and Smallman and Willis (1957) show that small cavities having an average radius of gyration of 10–20 Å are present after exposures of greater than 5×10^{16} neutrons/cm^2. Though no small angle scattering work has been done on electron irradiated lithium fluoride the larger cavities produced by subsequent annealing were observed and are shown in fig. 10 (Pl. 32). Further evidence of the nature of the defects in irradiated lithium fluoride is provided by the observation by Lambert and Guinier (1957 b) of diffuse x-ray streaks along $\{100\}$ directions in neutron irradiated material. These authors interpret these streaks to be caused by thin platelets of lithium metal lying on $\{100\}$ planes.

The lattice hardening introduced by irradiation is on the new theory additive to the initial critical shear stress of the material. Careful analysis of the results show that the experimental formula is of the form

$$\sigma=\sigma_u+f(\phi) \quad \text{and not} \quad \sigma=f(\phi+\phi_u),$$

where ϕ_u is a 'virtual' dose required to produce the critical shear stress of the unirradiated crystal. This indicates that lattice hardening introduced by irradiation is fundamentally different from the hardening responsible for the initial critical shear stress of the material.

The new relationship derived for the dose dependence of the lattice hardening component of irradiation hardening,

$$\sigma_i=A[1-\exp(-B\phi)]^{1/2}$$

has been verified experimentally only for lithium fluoride at present. It is expected that the formula will apply generally to crystalline solids which deform by slip, however. Preliminary results on single and polycrystals of copper indicate that the equation fits the results up to the highest doses so far tested (10^{20} neutrons/cm^2). The divergence between eqn. (3) and $\sigma_i \propto \phi^{1/3}$ becomes large, however, only at high doses and the present data does not yet enable a definite decision to be made between the two relationships.

The decision between these theories is of considerable technological importance since the $\phi^{1/3}$ relationship predicts a continually increasing hardening with dose instead of saturation expected in the new theory. The two theories make considerably different predictions, therefore, when extrapolated to very high doses.

ACKNOWLEDGMENTS

The authors wish to thank Dr. J. H. O. Varley for discussions on the production of defects by irradiation, Mr. S. A. Manthorpe for experimental assistance and Dr. W. G. Burns for cooperation in irradiating the specimens.

REFERENCES

BLEWITT, T. H., 1956, *Dislocations and Mechanical Properties of Crystals*, Ed. J. C. Fisher (New York : Wiley), p. 573.
COTTRELL, A. H., 1958, *Trans. Met. Soc. A.I.M.E.*, **212,** 192.
FRIEDEL, J., 1956, *Les Dislocations* (Paris : Gauthier-Villars).
GILMAN, J. J., and JOHNSTON, W. G., 1956, *Dislocations and Mechanical Properties of Crystals*, Ed. J. C. Fisher (New York : Wiley), p. 116 ; 1958, *J. appl. Phys.*, **29,** 877.
JOHNSTON, W. G., and GILMAN, J. J., 1958, *J. appl. Phys.*, **30,** 129.
LAMBERT, M., and GUINIER, A., 1957 a, *Compt. Rend.*, **244,** 2791 ; 1957 b, *Ibid.*, **245,** 536.
MOTT, N. F., and NABARRO, F. R. N., 1948, *Report on the Bristol Conference on the Strength of Solids* (London : Physical Society), p. 1.
SEEGER, A. K., 1958, Second United Nations International Conference on the Peaceful Uses of Atomic Energy, A/CONF. 15/P/998.
SMALLMAN, R. E., and WILLIS, B. T. M., 1957, *Phil. Mag.*, **2,** 1018.
STOKES R. J., JOHNSTON, T. L., and LI, C. H., 1958, *Phil. Mag.*, **3,** 718 ; 1959, *Ibid.*, **4,** 137.
VARLEY, J. H. O., 1954 a, *Nature, Lond.*, **174,** 886 ; 1954 b, *J. nucl. Energy*, **1,** 130 ; 1956, *Progr. nucl. Energy*, **1,** 672.
WHAPHAM, A. D., 1958, *Phil. Mag.*, **3,** 103.

The Electrical Resistivity of Stacking Faults†

By A. Howie
Crystallographic Laboratory, Cavendish Laboratory, Cambridge

[Received October 2, 1959]

Abstract

The scattering of electrons and x-rays by stacking faults is due to a phase change in the diffraction by crystal planes which do not lie parallel to the fault. A simple model of the process in copper estimates a resistivity $\rho \simeq 1 \times 10^{-12}\,\beta$ ohm-cm for a total stacking fault density of β cm^{-1} on all planes. A wave matching calculation in which Tamm surface waves are used confirms the order of magnitude of the effect and is also in agreement with the prediction of the simple model that the distance over which scattering from two faults could interfere is less than the lattice spacing. These results are consistent with the available experimental data and it is concluded that the effect explains the resistivity caused by extended dislocations in cold worked metals and by tetrahedra of stacking faults in quenched metals.

§ 1. Introduction

1.1. *Resistivity of Dislocations: Experimental Data and Theoretical Predictions*

Dislocations and point defects created during plastic deformation of a metal cause an increase in the residual electrical resistivity. The part of this resistivity increase which remains after annealing at temperatures at which point defects can diffuse is ascribed to the scattering of conduction electrons by dislocations.

From the results of Clarebrough *et al.* (1955) for the changes in density, stored energy and electrical resistivity of cold-worked copper during recrystallization, Seeger and Stehle (1956) quote for the observed resistivity increase a figure $\rho = 2{\cdot}5 \times 10^{-6}$ ohm-cm per 1% density change. If we assume that each atomic length of dislocation in the crystal increases the volume by 1·5 atomic volumes (Stehle and Seeger 1956) the dislocation density to be associated with this change in resistivity is approximately 10^{13} cm^{-2}. Thus the experimental figure for the resistivity increase in copper due to a dislocation density of N cm^{-2} is $\rho = 2{\cdot}5 \times 10^{-19} N$ ohm-cm. More recent results of Clarebrough *et al.* (1957) for copper deformed in compression confirm this result and also indicate that the dislocation densities deduced by the above method from the density change are in reasonable agreement with those deduced from the stored energy release on recrystallization.

---

† Communicated by the Author.

The scattering of conduction electrons in copper by dislocation strain fields has been calculated by Hunter and Nabarro (1953) and for a dislocation density of N cm^{-2} they find a resistivity increase $\rho = 3{\cdot}8 \times 10^{-21} N$ ohm-cm which is almost two orders of magnitude smaller than the experimental figure given above. A slightly higher estmate of $\rho = 6{\cdot}0 \times 10^{-21} N$ ohm-cm was obtained by Seeger and Stehle (1956) by considering the additional scattering effects due to anharmonic displacements and the resulting redistribution of electric charge. There might also be considerable scattering of electrons by the dislocation core where the atomic positions and electron charge distribution are not well known. Harrison (1958) has calculated the scattering from a hollow core and obtains a resistivity $\rho = 5 \times 10^{-20} N$ ohm-cm.

It appears therefore that even with such an extreme model of the core it is still not possible to account for almost four-fifths of the experimental value for the resistivity. Later we shall quote an example where scattering from the dislocation core is even less able to explain the observed results.

1.2. *Resistivity of Stacking Faults: Experimental Evidence*

A possible explanation of these anomalous dislocation resistivity results was first advanced by Broom (1952). Dislocations in the face-centred cubic lattice may dissociate, in a manner proposed by Heidenreich and Shockley (1948), into two partial dislocations separated by a ribbon of stacking fault whose width is determined by the balance between the repulsion between the two partials and the surface tension of the stacking fault. Broom suggested that stacking faults may be effective in scattering electrons and that in the case of wide ribbons most of the observed resistivity might be due to the faults. A study of the increased resistivity of nickel–cobalt wires of various alloy compositions after a standard cold drawing treatment (Broom and Barrett 1953) showed a maximum resistivity for the alloy near the transformation composition where the stacking fault energy might be expected to be low and the fault ribbons wide. If we can asume that the dislocation and point defect densities in all the wires were similar this is strong evidence in favour of a large resistivity due to scattering from stacking faults. Broom and Barrett were also able to confirm the presence of wide faults from x-ray diffraction measurements. The displacement and broadening of the diffraction peaks as a result of the presence of stacking faults has been calculated for a random distribution of parallel faults by Paterson (1952) in terms of a faulting probability α. Unfortunately the interpretation of α is obscure when the faults have a limited width. Nevertheless it has proved possible (Christian and Spreadborough 1956) to establish a strong correlation in several alloys between the manifestation of a large resistivity increase after cold work and a large probability of faulting α in alloy filings. The experimental evidence in favour of a large resistivity due to stacking faults produced in plastic deformation is thus fairly convincing if not altogether conclusive.

To obtain an estimate of the stacking fault resistivity required to explain the experimental results we shall assume that scattering due to the dislocation core and strain field is correctly given by the theoretical predictions quoted above and is thus responsible for not more than one-fifth of the total effect. If we assume the average stacking fault ribbon width in copper (Seeger and Schoeck 1953) to be 25 Å it follows that with a dislocation density of N cm^{-2} there is associated a stacking fault density $\beta = 2{\cdot}5 \times 10^{-7} N$ cm^{-1} considered to be equally distributed over all four slip planes. Substituting for N in the experimental value for ρ given above we find for the resistivity due to such a fault density, β (when the resistivity is entirely due to faults)

$$\rho = 1 \times 10^{-12} \beta \text{ ohm-cm.} \qquad \qquad (1)$$

This figure is however subject to serious qualifications in view of recent suggestions (Seeger *et al.* 1959) that the stacking fault energy of copper is much higher than hitherto supposed. The equilibrium width of the stacking fault ribbon would then be much less than 25 Å. Seeger (private communication) has also made new calculations of the resistivity due to the dislocation strain field and finds that the estimate should be considerably increased. The effect of these two changes is apparently to leave the predicted value for the resistivity due to stacking faults unchanged. In view of these uncertainties it is fortunate that estimates of the stacking fault resistivity can also be obtained from observations on quenched gold.

A critical study was made by Bauerle and Koehler (1957) of the annealing of the resistivity increase observed in gold wires after rapid quenching from high temperatures. It seems probable that the part of the resistivity which anneals out at temperatures above 500°C is due to scattering from tetrahedra of stacking faults of the type observed in foils of quenched gold by Silcox and Hirsch (1959) using the transmission electron microscope technique. Silcox (private communication) finds, on the basis of Bauerle and Koehler's data and the microscope observations, that a residual resistivity of $\rho = 6 \times 10^{-9}$ ohm cm, found after quenching from 900°C and then annealing at 40°C, is to be associated with a total stacking fault density $\beta = 1{\cdot}2 \times 10^{4}$ cm^{-1} arranged in the form of tetrahedra. The resistivity of stacking faults is then

$$\rho = 0{\cdot}5 \times 10^{-12} \beta \text{ ohm-cm} \qquad \qquad (2)$$

where β is again the total fault density on all four slip planes.

It should be noted that almost all the resistivity due to the tetrahedra of stacking faults must come from the stacking faults themselves. The dislocation line length (along the edges of the tetrahedron of average length 300 Å) associated with a given area of fault is smaller by a factor of almost ten than the dislocation line length associated with the same area of fault in the deformed metal. In addition the dislocations on the edges of the tetrahedron have the small Burger's vector $\frac{1}{6}$ [110] and are arranged so that their long range stress fields cancel. The conclusion is that the dislocations associated with the tetrahedra cannot contribute more than a negligible amount to the scattering. Therefore although estimate (1) for the stacking fault resistivity is of more direct interest since it refers to copper (the metal to which the calculations given later apply) the quenching data for gold are probably the most reliable evidence in favour of a stacking fault resistivity of this order of magnitude.

1.3. *Theory of Resistivity of Stacking Faults*

A critical survey of previous attempts to investigate the scattering of conduction electrons by stacking faults has been given by Seeger (1956). He points out that in the free electron approximation (in which the potential is assumed to be constant inside the metal) electrons do not feel the presence of a stacking fault at all. For this reason a treatment by Klemens (1953), in which the fault was replaced by a scattering potential and a large reflection coefficient $R=\frac{1}{2}$ estimated for electrons incident normal to the fault, cannot be valid since free electrons are scattered by such a potential. Another estimate of $R=0{\cdot}4$ by Klemens (1956) was obtained by means of a deformation potential method but this approach holds only for slowly varying strains and is far outside the range of its applicability when used in the case of a stacking fault where the shear is infinite at the fault and zero everywhere else. An alternative approach to the problem is to use Bloch wave functions in the perfect crystal on either side of the fault and match these functions at the fault. Such methods have been used by Blatt *et al.* (1956) and Tweedale (see contributions of Ziman to the discussion at the end of the papers by Klemens (1956) and Seeger (1956)). Tweedale was able to perform a more complete calculation and estimated a very small reflection coefficient R of the order of 10^{-3} to 10^{-4}. However, as Seeger has pointed out, in neither of these investigations were surface waves at the fault considered and these waves are an essential feature of the problem.

Seeger considered the scattering from the fault in terms of a diffraction mechanism and obtained a reflection coefficient R between $\frac{1}{10}$ and $\frac{1}{2}$. Unfortunately the calculation entailed a rather implausible use of perturbation theory (see § 3.1) and certain important principles of the diffraction process are obscured.

Ziman (1958) has also emphasized the part played by diffraction in the problem and has predicted a reflection coefficient proportional to the intensity of the diffracted crystal wave. He has pointed out that in view of recent results in connection with the Fermi surface in copper (see § 2) the intensity of the diffracted beam may be large. However, he has not considered in detail the effectiveness of the various diffracted beams in contributing to the resistivity.

In this paper the scattering from stacking faults as a diffraction phenomenon is examined more closely. In § 2 the necessary preliminary description of the part played by diffraction in the propagation of conduction electrons is given in terms of a specific model of the Fermi surface in copper. It then proves possible (see § 3) to build up a simple physical picture of the effect of the fault and, by considering the equilibrium form of the crystal waves at large distances on either side of the fault, to derive an expression for the scattering and hence to deduce the resistivity. In § 4 a wave matching treatment is employed using both Bloch waves and surface waves and an estimate for the transmission coefficient of the fault is obtained. The results of these calculations are discussed.

§ 2. THE FERMI SURFACE IN COPPER ; TWO BEAM APPROXIMATION

It will be necessary in the calculations which follow to have a description of the conduction electrons in copper. The Fermi surface in copper has recently been determined by Pippard (1957) on the basis of the anomalous skin effect. Figure 2 shows a section and fig. 3 a stereographic contour map of the surface which is approximately spherical, as would be expected in a monovalent metal, but is attracted to the nearest faces (the (111) faces) of the Brillouin zone rather more strongly than had been generally supposed. This means that for conduction electrons travelling near the [111] direction diffraction from (111) planes in the crystal is important.

It is proposed in the following treatment to apply the approximation of only two strong crystal beams—a direct beam and a diffracted beam from one set of crystal planes. The wave function is then written

$$\psi(\mathbf{r})=\exp(i\mathbf{k}\,.\,\mathbf{r})+C(\mathbf{k})\exp[i(\mathbf{k}+\mathbf{g})\,.\,\mathbf{r}] \quad . \quad . \quad . \quad (3)$$

where $\mathbf{k}$ is the wave vector $|\mathbf{k}|=2\pi/\lambda$, λ being the wavelength, $\mathbf{g}/2\pi$ is a reciprocal lattice vector (in our case $\mathbf{g}=2\pi/a$ [111] and $C(\mathbf{k})$ is the ratio of the amplitudes of the diffracted and direct beams and thus a measure of the importance of diffraction (or the effect of the Brillouin zone). If the crystal potential is given by

$$V(\mathbf{r})=\sum_{\mathbf{g}} V_{\mathbf{g}} \exp(i\mathbf{g}\,.\,\mathbf{r})=\frac{\hbar^2}{2m}\sum_{\mathbf{g}} U_{\mathbf{g}} \exp(i\mathbf{g}\,.\,\mathbf{r}) \quad . \quad . \quad (4)$$

the energy E, inside the Brillouin zone, is obtained from the expression

$$\begin{aligned}\gamma&=\frac{2mE}{\hbar^2}-U_0\\ &=\tfrac{1}{2}\{\mathbf{k}^2+(\mathbf{k}+\mathbf{g})^2\}-\sqrt{\{[\tfrac{1}{2}\{(\mathbf{k}+\mathbf{g})^2-\mathbf{k}^2\}]^2+|U_{\mathbf{g}}|^2\}} \quad . \quad . \quad . \quad (5)\end{aligned}$$

and the constant $C(\mathbf{k})$ in eqn. (3) can be written in the alternative forms

$$C(\mathbf{k})=-\frac{\mathbf{k}^2-\gamma}{U_{-\mathbf{g}}}, \quad . \quad . \quad . \quad . \quad . \quad . \quad . \quad . \quad . \quad . \quad . \quad . \quad . \quad . \quad . \quad (6)$$

$$C(\mathbf{k})=-\frac{U_{\mathbf{g}}}{\tfrac{1}{2}\{(\mathbf{k}+\mathbf{g})^2-\mathbf{k}^2\}+\sqrt{\{[\tfrac{1}{2}\{(\mathbf{k}+\mathbf{g})^2-\mathbf{k}^2\}]^2+|U_{\mathbf{g}}|^2\}}} \quad . \quad . \quad (7)$$

These two expressions for $C(\mathbf{k})$ will only be equivalent when the two-beam approximation is valid and all other diffracted beams have negligibly small amplitudes. It should be emphasized that this condition does not necessarily correspond to almost free electrons. In fact the two-beam approximation is best in the vicinity of the Brillouin zone where the amplitudes of the two beams are nearly equal.

We shall assume that the surface near the zone has the form deduced by Pippard using a one dimensional Kronig–Penney model and shall use eqns. (6) and (7) to obtain values of $C(\mathbf{k})$ for wave vectors $\mathbf{k}$ on the Fermi surface where $(\hbar^2/2m)\gamma = 5{\cdot}56$ ev. At the Brillouin zone $|C(\mathbf{k})| = 1$. This follows automatically from eqn. (7) but not from eqn. (6) unless $|U_{\mathbf{g}}|$ is chosen correctly. From the value of $\mathbf{k}$ where the surface meets the zone we find $(\hbar^2/2m)|U_{\mathbf{g}}| = 3{\cdot}25$ ev so that the energy gap at the zone is 6·5 ev and compares well with Pippard's prediction of 7·5 ev on the basis of the Kronig–Penney model. We can now write eqn. (7) in a more useful form by expressing d, the distance from the end of the vector $\mathbf{k}$ to the Brillouin zone measured normal to the zone, as a fraction ϵ of the distance $\Gamma L = \frac{1}{2}|\mathbf{g}|$ (fig. 2). Then $(\mathbf{k}+\mathbf{g})^2 - \mathbf{k}^2 = 2|\mathbf{g}|d = \epsilon\mathbf{g}^2$ and using the figure deduced for $(\hbar^2/2m)|U_{\mathbf{g}}|$ and also the value for $(\hbar^2/2m)\mathbf{g}^2 = 34{\cdot}4$ ev eqn. (7) can be written

$$|C(\mathbf{k})| = \frac{1}{(5{\cdot}3\epsilon) + \sqrt{[(5{\cdot}3\epsilon)^2 + 1]}} . \quad . \quad . \quad . \quad . \quad . \quad (8)$$

The surface can then be divided into rings (fig. 2) which are parallel to the zone and correspond to increments of ϵ. A value of $|C(\mathbf{k})|$ can then be obtained for the middle of each ring using eqn. (8) and these are the first of the three values of $|C(\mathbf{k})|$ for each ring given in table 1. The second and third figures for each ring are obtained from eqn. (6), the second from points $\mathbf{k}$ on the surface between [111] and [110] and the third for points between [111] and [001]. These values of $|C(\mathbf{k})|$ are in very good agreement for the first three rings and the first two figures are in fair agreement for all the rings. The deviation of the third value of $|C(\mathbf{k})|$ for the rings furthest from the 111) Brillouin zone is due to the attraction of the Fermi surface towards the (002) Brillouin zone. In addition to this check on the usefulness of the two beam approximation we can make an estimate of the importance of the beams neglected by the theory. For electrons travelling in the [110] direction there are, by symmetry, two diffracted beams of equal amplitude. The two beam approximation holds less well for such electrons than for electrons travelling in other directions since it ignores one of these two diffracted beams entirely. The amplitude of the other diffracted beam is (using eqn. (8)) approximately $\frac{1}{4}$ of the amplitude or $\frac{1}{16}$ of the intensity of the direct beam. We may argue roughly therefore that the diffracted beams ignored in the two beam approximation all have intensities less than $\frac{1}{16}$ of the intensity of the direct beam.

§ 3. A CALCULATION OF THE RESISTIVITY OF STACKING FAULTS IN TERMS OF ELECTRON DIFFRACTION

3.1. *The Effect of Stacking Faults on the Diffracted Beams*

Seeger (1956) investigated the scattering in a crystal containing a fault as shown in fig. 1. He used a perturbation potential $V'(\mathbf{r})$.

$$V'(\mathbf{r}) = 0 \text{ in region I,}$$
$$V'(\mathbf{r}) = -V(\mathbf{r}) + V(\mathbf{r}+\mathbf{R}) \text{ in region II}$$

where $V(\mathbf{r})$ is the potential in the perfect crystal and $\mathbf{R}$ is the displacement vector associated with the fault. Since $V'(\mathbf{r})$ is either zero or has the same periodicity as the lattice the scattering will be from states of wave vector $\mathbf{k}$ to those of wave vector $\mathbf{k}' = \mathbf{k} + \mathbf{g}$ where $(1/2\pi)\mathbf{g}$ is a reciprocal lattice vector. Perturbation theory therefore demonstrates the intimate connection between the scattering from the fault and the normal process of Bragg diffraction in the crystal. However, there is no justification for its further use since the perturbation potential $V'(\mathbf{r})$ is as large as the crystal potential itself.

Fig. 1

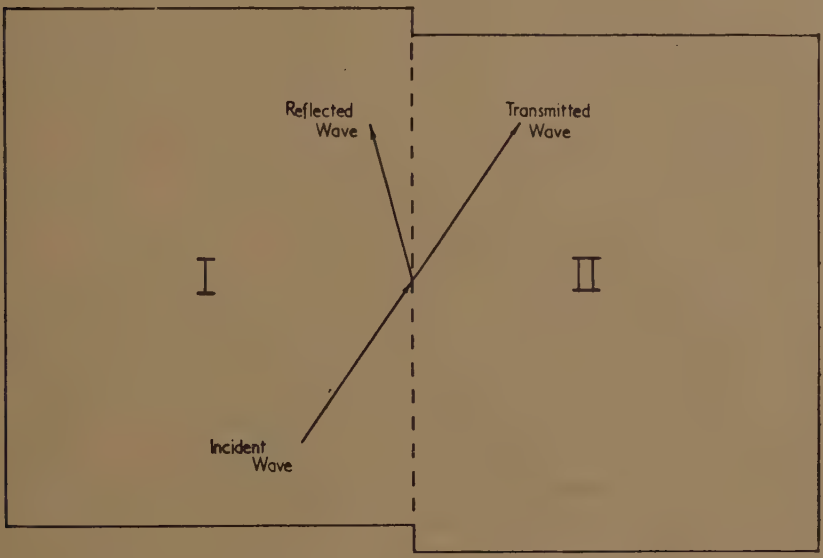

Schematic diagram of a stacking fault which lies on a (111) plane and produces a shear so that the crystal in region II is translated relative to the crystal in region I by a constant amount $\mathbf{R} = (a/6)[11\bar{2}]$. The incident, reflected and transmitted waves used in the wave matching calculation are shown, but not the Tamm waves.

We can obtain a more precise description of the effect of the fault by noting that if the crystal potential in region I (fig. 1) is $V(\mathbf{r})$ (eqn. (4)) and the crystal potential in region II is $V(\mathbf{r}+\mathbf{R})$ then

$$V(\mathbf{r}+\mathbf{R}) = \frac{\hbar^2}{2m} \sum_{\mathbf{g}} U_{\mathbf{g}} \exp\left[i\mathbf{g}\,.\,(\mathbf{r}+\mathbf{R})\right].$$

It then follows that in region I $C(\mathbf{k})$ is given by eqn. (7) and in region II

$$C(\mathbf{k}) = -\frac{U_{\mathbf{g}} \exp(i\mathbf{g}\,.\,\mathbf{R})}{\frac{1}{2}\{(\mathbf{k}+\mathbf{g})^2 - \mathbf{k}^2\} + \sqrt{\{[\frac{1}{2}\{(\mathbf{k}+\mathbf{g})^2 - \mathbf{k}^2\}]^2 + |U_{\mathbf{g}}|^2\}}}. \qquad (9)$$

Thus we see immediately that the effect of the fault is to leave the relative amplitudes of the direct and diffracted beams unchanged but to alter the relative phases of the two beams by an angle $\alpha = \mathbf{g}\,.\,\mathbf{R}$ on one side of the fault. It is worth noting that the importance of this phase effect for the scattering of high energy (100 kv) electrons in thin foils containing stacking faults has already been realized (Whelan and Hirsch 1957) and applied to explain the contrast effects in the electron microscope image due to such specimens. The phase angle α can be shown to take the values 0°, ±120° depending on the diffracting planes involved. If these planes are parallel to the fault **g** and **R** are mutually perpendicular so that $\alpha = 0$ and the fault has no effect. This point has been fully appreciated in the investigations made of the scattering effect of stacking faults on x-rays (Paterson 1952) and high energy electrons (Whelan and Hirsch 1957). However, it does not appear to be noted in any of the literature dealing with the scattering of conduction electrons by stacking faults. We see immediately that a fault on a (111) plane will have no effect on conduction electrons travelling in the [111] direction since these electrons will be diffracted by planes parallel to the fault. The electrons most strongly affected by the fault will be those travelling in the $[\bar{1}11]$, $[1\bar{1}1]$ and $[11\bar{1}]$ directions. In Seeger's calculation in which a spherical Fermi surface was used many of the diffraction effects are averaged over angles so that the simple physical picture outlined above is obscured.

Equations (7) and (9) describe the equilibrium situation between the direct and diffracted crystal waves at large distances on either side of the fault and show that is it only the phase relation between the two beams that is different on opposite sides of the fault. The detailed way in which the crystal waves change from one equilibrium situation to the other as the electron passes through the fault involves multiple Bragg scattering and interference between direct and diffracted beams from either side of the fault. Without, however, inquiring closely into these processes whose study belongs to the dynamical theory of diffraction, it is possible to come to two important conclusions.

Firstly we see that the distance required to set up the new equilibrium will depend on how strongly the direct beam is diffracted. According to the dynamical theory the direct beam (when not maintained by an applied field) will be completely diffracted after travelling a distance known as the extinction distance t_0 given by $t_0 = \lambda E/|V_{\mathbf{g}}|$ (Heidenreich 1949). The extinction distance is therefore a good measure of the distance travelled by the electron before equilibrium is restored. For conduction electrons in copper diffracting from (111) planes the extinction distance is of the order of the lattice spacing.

The second conclusion is that a knowledge of what the final result of the scattering must be is sufficient to derive an expression for it. We make the assumption that the direct beam is maintained constant by the field and thus suffers no depletion as a result of the scattering. The diffracted beams, however, are purely secondary effects due to the presence of the crystal and their amplitudes and phases relative to the direct beam on either side of the fault are determined by eqns. (7) and (9) which express the conditions for dynamical equilibrium between the direct and diffracted beams in each region. We assert, therefore, that irrespective of the detailed mechanism of the scattering, the nett effect is that enough additional electrons are scattered from the direct to the diffracted beam to set up equilibrium again. The additional intensity scattered into the diffracted beam is then

$$\begin{aligned} A(\mathbf{k},\mathbf{k}+\mathbf{g}) &= |C(\mathbf{k})|^2|\exp(i\mathbf{g}.\mathbf{R})-1|^2 \\ &= 4|C(\mathbf{k})|^2\sin^2\tfrac{1}{2}\alpha. \qquad (10) \end{aligned}$$

Fig. 2

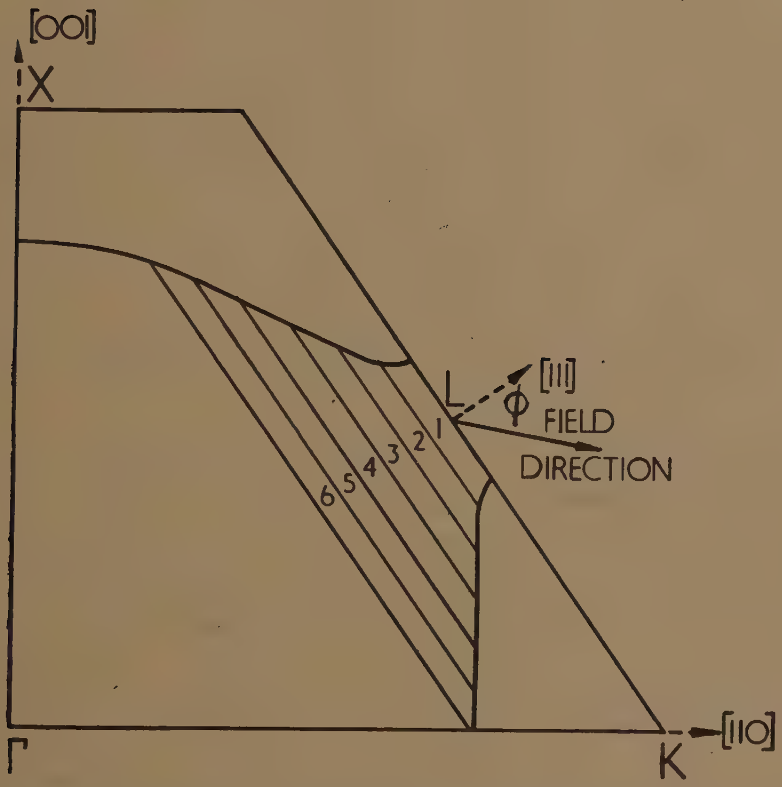

Section of the Fermi surface in copper as determined by Pippard. The surface is divided into rings near the [111] direction (see text).

It is not permissible to regard this as a scattering probability since it may well be greater than unity. Values of A ($\mathbf{k}$, $\mathbf{k}+\mathbf{g}$) greater than unity would of course be physically unreasonable in the absence of an applied field when there is only a definite number of electrons in the direct beam and any scattering diminishes that number. However, in the presence of the applied field the number of electrons in the direct beam is maintained constant by the acceleration of new electrons by the field and thus, since the effect of the fault extends for an infinite distance behind it, the scattering will continue until eqn. (10) is satisfied.

The rest of the calculation consists of evaluating $A(\mathbf{k}, \mathbf{k}+\mathbf{g})$ for various values of $\mathbf{k}$ on the Fermi surface and then of estimating the total scattering produced, for several directions of the applied field, by a given density of stacking faults equally distributed on all four sets of (111) planes. Table 1 gives the value of ϵ and hence, by eqn. (8), of $|C(\mathbf{k})|$ for each ring on the Fermi surface near the Brillouin zone (see fig. 2). The simplest assumptions are made about the current distribution over the surface.

Table 1

Ring No.	1	2	3	4	5	6
ϵ	0·025	0·075	0·125	0·175	0·225	0·275
$\|C(\mathbf{k})\|$	0·87 0·86 0·86	0·68 0·65 0·65	0·54 0·53 0·53	0·44 0·39 0·44	0·36 0·31 0·41	0·31 0·27 0·41
f	0·014	0·035	0·046	0·060	0·074	0·086
$f\|C(\mathbf{k})\|^2$	0·011	0·016	0·013	0·011	0·010	0·008

The first row of values of $|C(\mathbf{k})|$ are used in the calculation.

Table 2

Field Direction	Ring No.	γ_1	γ_2	γ_3	γ_4
[100]	1	0·30	0·30	0·30	0·30
	2–6	0·39	0·39	0·39	0·39
[110]	1	0·30	0	0	0·30
	2–6	0·71	0	0	0·71
[111]	1	0	0·20	0·20	0·20
	2–6	0·82	0·20	0·20	0·20

The number of current carriers from each ring is taken to be proportional to the area of the ring projected in the direction of the applied field. The velocity of the electrons assumed parallel to $\mathbf{k}$ must also be projected in the field direction. The product γ of these two projection factors has been evaluated for various rings and field directions and is given in table 2. γ_1, γ_2, γ_3 and γ_4 apply to electrons near the (111), $(\bar{1}11)$, $(1\bar{1}1)$ and $(11\bar{1})$ Brillouin zones respectively. The area of each ring is given in table 1 as a fraction, f, of $\frac{1}{8}S$. S is the total area of the Fermi surface and the factor

$\frac{1}{3}$ is the average value of the projection factor $\gamma = \cos^2\phi$ for a spherical surface.

The faults are assumed equally distributed on all four slip planes and each fault area must be projected in the direction of propagation of the electrons considered. This projection factor, multipled by the appropriate value of $4\sin^2\alpha/2 = 0$ or 3, gives a further factor of $\frac{3}{4}$ for each Brillouin zone. The fraction of the current scattered for unit area of stacking fault evenly distributed over all four slip planes is now given by

$$\chi = 2 \sum_{\text{rings}} f|C(\mathbf{k})|^2 \sum_i \tfrac{3}{4}\gamma_i.$$

The factor 2 takes account of the four zones on the other side of the Fermi surface. We find that χ varies by about 10% for the three field directions taken (being greatest for the [100] direction) and an average figure is $\chi \doteq 0{\cdot}15$. This fraction of the current is, to a fair approximation, scattered to the other side of the Fermi sphere, i.e. it is reversed in sign. Thus for the rate of change of current due to scattering we have

$$\left(\frac{\partial \mathbf{J}}{\partial t}\right)_{\text{scattering}} = -2\chi \mathbf{J} A$$

where A is the area of fault encountered per second. If v is the Fermi velocity then the average velocity, $\overline{|v|}$. in any direction is $\frac{1}{2}v$ for a spherical Fermi surface and, if β is the density of stacking faults, $A = \frac{1}{2}\beta v$.

So

$$\left(\frac{\partial \mathbf{J}}{\partial t}\right)_{\text{scattering}} = -\chi\beta v \mathbf{J}.$$

If the rate of displacement $\dot{\delta\mathbf{k}}$ of the Fermi surface by the applied field $\mathbf{F}$ is given by $\dot{\delta\mathbf{k}} = e\mathbf{F}/\hbar$ the current increases according to the relation

$$\left(\frac{\partial \mathbf{J}}{\partial t}\right)_{\text{field}} = \frac{e}{4\pi^3}\int_{\text{Fermi surface}} \mathbf{v}\, ds \,.\, \dot{\delta\mathbf{k}}$$

$$= \frac{e^2 vS\mathbf{F}}{12\pi^3\hbar} \text{ for a spherical Fermi surface of area } S$$

$$= \frac{e^2 vS\rho\mathbf{J}}{12\pi^3\hbar} \text{ where } \rho \text{ is the resistivity.}$$

In equilibrium

$$\left(\frac{\partial \mathbf{J}}{\partial t}\right)_{\text{scattering}} = -\left(\frac{\partial \mathbf{J}}{\partial t}\right)_{\text{field}}$$

so

$$\rho = \frac{12\pi^3\chi\hbar\beta}{e^2 S} \text{ e.s.u.}$$

Taking the area of the Fermi surface $S = 2{\cdot}2 \times 10^{17}\,\text{cm}^{-2}$ and $\chi = 0{\cdot}15$ as found previously we obtain

$$\rho = 1{\cdot}05 \times 10^{-12}\beta \text{ ohm-cm.}$$

It appears therefore that the stacking fault resistivity predicted by this simple model is in good agreement with the existing experimental results (eqns. (1), (2)). Doubtless the answer would be altered if a better approximation than the two beam approximation were used or if account were taken of the variations of electron velocity over the Fermi surface but it is not expected that these refinements would affect the general order of magnitude of the result.

§ 4. MATCHING OF BLOCH WAVE FUNCTIONS AT STACKING FAULTS

4.1. *Reflection of Electrons at a Stacking Fault*

It is possible to obtain a useful check on the results derived in the last section in terms of a more formal mathematical procedure in which the various crystal waves that can propagate in the perfect crystal on either side of the fault are matched so that the wave function and its derivative normal to the fault are continuous across the fault. In addition to a wave incident on the fault in region I (fig. 1) and a transmitted wave in region II it is necessary to have a reflected wave travelling back into region I. For this reason it is possible to refer to the reflectivity of the fault although the details of the way in which the reflected wave arises from the processes of multiple diffraction which operate at the fault are not clear. Since the waves must match at all points on the fault plane it follows that all the waves used must have the same tangential components of wave vector. Consequently if the incident, reflected and transmitted waves each have a direct beam and any number m of associated diffracted beams the requirements of continuity of the wave function and its derivative will yield $2(m+1)$ equations (two for each component beam) to be satisfied. Since it is possible to choose only the amplitudes of the direct components of the reflected and transmitted waves the problem can only be solved in the case $m=0$ which corresponds to the free electron approximation when the fault has no effect. As Seeger (1956) has pointed out it is necessary to employ in the matching technique not only the waves which propagate in an infinite crystal but also waves localized at the surface of the fault. These waves will now be discussed.

4.2. *Tamm Surface Waves*

Tamm (1932) first pointed out that it is only in an infinite crystal that all the components of **k**, the wave vector of a Bloch wave function $\exp(i\mathbf{k}\,.\,\mathbf{r})U_{\mathbf{k}}(\mathbf{r})$ need be real. In a finite crystal there are localized surface states corresponding to complex components of **k** normal to the surface. Such states have energies in the forbidden bands. Later authors (for references see Shockley 1939) have investigated some of their properties but they do not appear to have been extensively used. Attention seems moreover to have been restricted to the case when the Bragg diffracting planes are parallel to the surface in question. We shall require waves which are attenuated in the [111] direction and suffer diffraction from $(\bar{1}11)$, $(1\bar{1}1)$ or $(11\bar{1})$ planes.

The conventional two-beam approximation used in § 2.2 leads to a dispersion equation

$$\{k_1^2+k_2^2+k_3^2-\gamma\}\{(k_1+g_1)^2+(k_2+g_2)^2+k_3^2-\gamma\}+|U_g|^2=0 \quad . \quad (11)$$

where $\gamma=(2m/\hbar^2)E_F-U_0$ (E_F being the Fermi energy) and the axes (x, y, z) have been chosen so that

$$\mathbf{k}=(k_1, k_2, k_3)$$

and

$$\mathbf{g}=(g_1, g_2, 0).$$

Equation (11) is normally regarded as a quadratic equation for γ whose solution is given in eqn. (5). However, if we wish to match waves of known energy on the plane $x=0$ it can be used as a quartic equation in k_1, the component of $\mathbf{k}$ normal to this plane. In such wave matching calculations all allowed waves must have the same tangential components of $\mathbf{k}$; i.e. k_2 and k_3 can also be taken as fixed. In the cases that we consider two of the roots of eqn. (11) are real and two complex. If the roots are written k_1, k_1', $p \pm iq$ we see that k_1 and k_1' represent incident and reflected waves respectively and the two complex roots describe surface waves decaying in opposite directions. Before any matching calculation can be performed it is therefore necessary to know the reflected wave vector $\mathbf{k}'=(k_1', k_2, k_3)$

Fig. 3

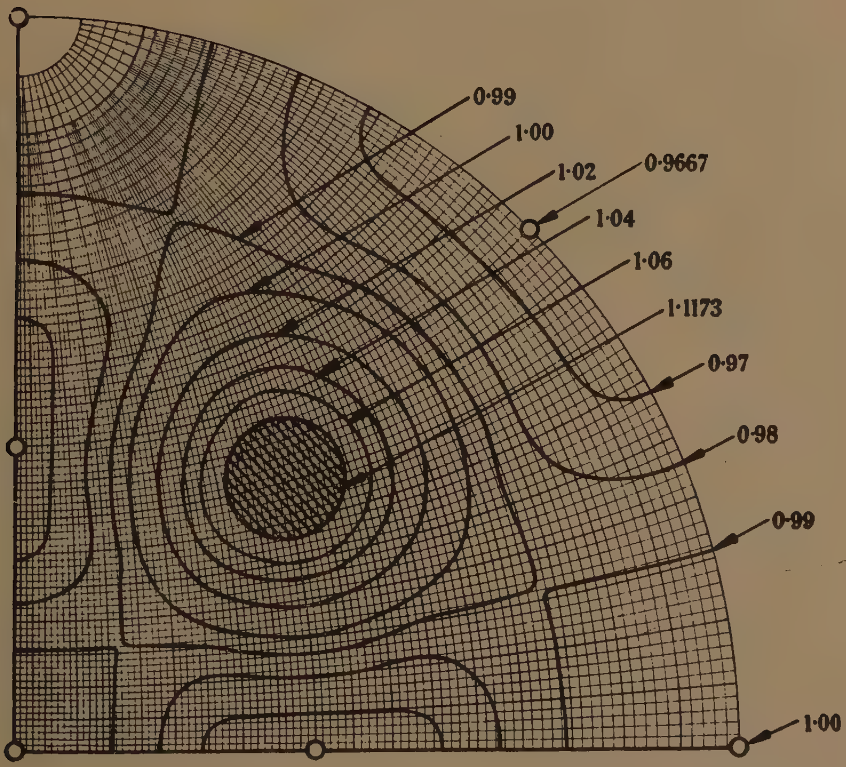

[By courtesy of the Royal Society]

Stereographic map showing contours of equal radius vector on Pippard's Fermi surface. To express the distances in the units of $|\mathbf{g}|$ used in the text the figures given should be multiplied by 0·45.

and the Tamm wave vectors $\mathbf{p}_{\pm}=(p\pm iq, k_2, k_3)$ associated with any incident wave vector (k_1, k_2, k_3) and energy E_F and also to know the amplitude of the diffracted wave connected with each one of these waves.

Fig. 4

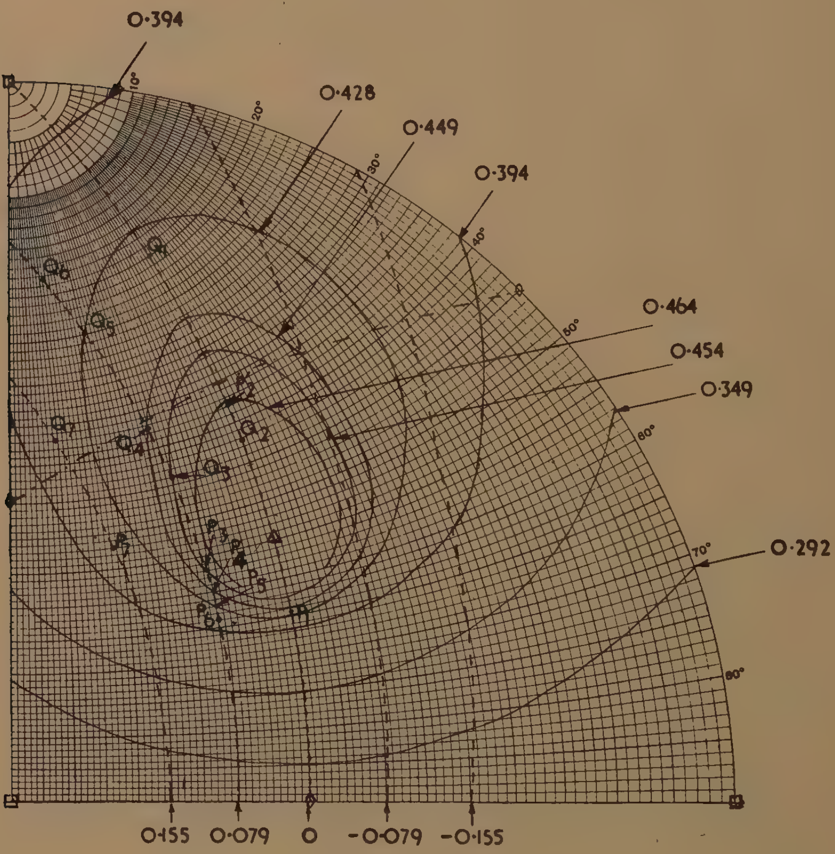

Stereographic contour map for Pippard's Fermi surface showing as solid lines the contours of constant k_2 (component of $\mathbf{k}$ parallel to $[\bar{2}11]$ and as dotted lines the contours of constant k_3 (component of $\mathbf{k}$ parallel to $[0\bar{1}1]$). The two points of intersection P and Q of any two contours correspond to a pair of incident and reflected waves. Note how these points do not always lie on opposite sides of the line $k_1=0$ (the (111) plane shown with alternate dots and dashes). In these cases refraction occurs (see text). The positions of the points P_i and Q_i used in the matching are shown. The point P_2 cannot be shown because it is on the other side of the Brillouin zone. It is represented by the point P_2' which has a wave vector directly opposite to that of the diffracted wave associated with P_2.

The method used to find the roots of the quartic eqn. (11) was again based on Pippard's model of the Fermi surface of copper. We take a stacking fault on a (111) plane and consider electrons moving near the

$[\bar{1}11]$ direction. It is convenient to take axis x, y, z along $[111]$, $[\bar{2}11]$ and $[0\bar{1}1]$ respectively. With the aid of the stereographic contour map (fig. 3) that Pippard (1957) has given, a map showing contours of equal k_2 and equal k_3 in the vicinity of the $[\bar{1}11]$ direction has been constructed (fig. 4). If the Fermi surface were spherical the contours of equal k_2 and k_3 would be small circles about $[\bar{2}11]$ and $[0\bar{1}1]$ respectively but they are distorted by the attraction of the surface to the zone boundary. A given pair of contours k_2 = constant and k_3 = constant intersect in two points corresponding to the incident and reflected waves. By measuring the angles to these points from $[111]$ and using fig. 3 the values of k_1 and k_1' are quickly obtained. Reference to the line $k_1=0$ (the (111) plane) in fig. 4 shows that one effect of the deviation of the Fermi surface from spherical form is that $k_1 \neq -k_1'$, i.e. the reflection is no longer specular. Indeed for some points k_1 and k_1' both have the same sign so that it appears that the direct beam is refracted rather than reflected. It is interesting to note, however, that the current $\mathbf{J}$, which on the average flows in the direction $\mathbf{k}+|C(\mathbf{k})|^2(\mathbf{k}+\mathbf{g})$ is in all cases reflected (though not necessarily specularly reflected) at the fault. After k_1 and k_1' have been determined by this method p and q (the real and imaginary parts of the Tamm wave vector component normal to the fault) are obtained from the relations between the roots of eqn. (11)

Table 3

Point	P_1	P_2	P_3	P_4	P_5	P_6	P_7
k_2	0·435	0·478	0·454	0·449	0·428	0·412	0·412
k_3	0	0	0·079	0·079	0·079	0·079	0·155
k_1	0·226	0·268	0·164	0·194	0·201	0·214	0·118
k_1	−0·099	0·087	0·081	0·012	−0·099	−0·145	−0·042
p	0·270	0·155	0·211	0·230	0·282	0·298	0·295
q	0·327	0·257	0·268	0·295	0·350	0·380	0·388
$C(\mathbf{k})$	0·845	1·50	0·833	0·910	0·726	0·650	0·500
$C(\mathbf{k}')$	0·403	0·795	0·607	0·490	0·403	0·382	0·371
$C(\mathbf{p}_\pm)$	$-0{\cdot}070$ $\pm 1{\cdot}90i$	$0{\cdot}264$ $\pm 0{\cdot}857i$	$0{\cdot}253$ $\pm 1{\cdot}22i$	$0{\cdot}124$ $\pm 1{\cdot}46i$	$-0{\cdot}165$ $\pm 2{\cdot}12i$	$-0{\cdot}435$ $\pm 2{\cdot}43i$	$-0{\cdot}328$ $\pm 2{\cdot}47i$

$$\left.\begin{aligned} k_1+k_1'+2p &= -2g_1, \\ 2p(k_1+k_1')+k_1k_1'+p^2+q^2 &= g_1^2+k_2^2+(k_2+g_2)^2+2(k_3^2-\gamma) \end{aligned}\right\}. \quad (12)$$

Values of k_1, k_2, k_3, k_1', p and q in units of $|\mathbf{g}|$ for several points $P_1, P_2 \ldots P_7$ on the Fermi surface near the $[\bar{1}11]$ direction are given in table 3. These points correspond to different incident wave vectors $\mathbf{k}$ and are shown in fig. 4 together with the associated points $Q_1, Q_2 \ldots Q_7$ which correspond to the reflected wave vector $\mathbf{k}'$. It should be noted that all the values of $|q|$ are in the range $\frac{1}{4}|\mathbf{g}|$ to $\frac{2}{3}|\mathbf{g}|$ so that $1/|q|$ the 'penetration depth' of the Tamm waves, is rather less than a lattice spacing. Thus $1/|q| \sim t_0$ the extinction distance (see § 3.1).

Values of $C(\mathbf{k})$, $C(\mathbf{k}')$, $C(\mathbf{p}_+)$ and $C(\mathbf{p}_-)$, the last two quantities describing the diffracted component of the Tamm waves, are also given in table 3 and have been calculated from eqns. (6) and (7) with the origin of $\mathbf{r}$ so chosen that $U_\mathbf{g}$ (eqns. (4), (6), (7)) is real and negative. It should be noted that because of the symmetry of the problem the situation is the same in the vicinity of the $(\bar{1}11)$, $(1\bar{1}1)$ and $(11\bar{1})$ zones and also that the problem is symmetrical in $\pm k_3$.

4.3. *Matching of Waves at the Fault*

The waves to be matched are two beam solutions of the Schrödinger equation in region I and II of the crystal shown in fig. 1. In region I we have:

An incident wave

$$\psi_\mathrm{I}(\mathbf{r}) = \exp(i\mathbf{k}\,.\,\mathbf{r}) + C(\mathbf{k}) \exp[i(\mathbf{k}+\mathbf{g})\,.\,\mathbf{r}].$$

A reflected wave

$$\psi_\mathrm{I}'(\mathbf{r}) = R\{\exp(i\mathbf{k}'\,.\,\mathbf{r}) + C(\mathbf{k}') \exp[i(\mathbf{k}'+\mathbf{g})\,.\,\mathbf{r}]\}$$

and a Tamm wave

$$\phi_\mathrm{I}(\mathbf{r}) = A\{\exp(i\mathbf{p}_-\,.\,\mathbf{r}) + C(\mathbf{p}_-) \exp[i(\mathbf{p}_-+\mathbf{g})\,.\,\mathbf{r}]\},$$

Because of the fact that the current which is the important physical quantity, is always reflected at the fault the wave $\psi_\mathrm{I}'(\mathbf{r})$ is always considered to propagate in region I.

In region II we have:

A transmitted wave

$$\psi_\mathrm{II}(\mathbf{r}) = T\{\exp(i\mathbf{k}\,.\,\mathbf{r}) + C(\mathbf{k}) \exp(i\alpha) \exp[i(\mathbf{k}+\mathbf{g})\,.\,\mathbf{r}]\}$$

and a Tamm wave

$$\phi_\mathrm{II}(\mathbf{r}) = B\{\exp(i\mathbf{p}_+\,.\,\mathbf{r}) + C(\mathbf{p}_+) \exp(i\alpha) \exp[i(\mathbf{p}_++\mathbf{g})\,.\,\mathbf{r}]\}$$

where the phase factor α is $-120°$. The requirement that the wave function be continuous at the fault gives the two equations:

$$\left.\begin{aligned} 1+R+A &= B+T, \\ C(\mathbf{k}) + RC(\mathbf{k}') + AC(\mathbf{p}_-) &= B\exp(i\alpha)C(\mathbf{p}_+) + T\exp(i\alpha)C(\mathbf{k}). \end{aligned}\right\}$$

The requirement that the normal derivative of the wave function be continuous at the fault yields two further equations:

$$k_1 + Rk_1' + A(p-iq) = B(p+iq) + Tk_1,$$

$$(k_1+g_1)C(\mathbf{k}) + R(k_1'+g_1)C(k') + A(p-iq+g_1)C(\mathbf{p}_-)$$
$$= B(p+iq+g_1)\exp(i\alpha)C(p_+) + T(k_1+g_1)\exp(i\alpha)C(\mathbf{k}).$$

The solutions to these equations for the real (R_1, A_1, B_1, T_1) and imaginary (R_2, A_2, B_2, T_2) parts of the wave amplitudes have been obtained on a computer and are given in full in table 4. The first set of seven values refer to the situation when the points $P_1, P_2, \ldots P_7$ in table 3 represent the incident beam. The second set of seven refers to the situation when these points represent the reflected beam and the incident beam is represented by the points $Q_1, Q, \ldots Q_7$ (see fig. 4).

Table 4

Point	R_1	R_2	T_1	T_2	A_1	A_2	B_1	B_2
P_1	−0·262	−0·383	+0·218	−0·863	−0·102	−0·335	−0·336	+0·289
P_2	−0·481	−0·417	−0·892	+0·069	−0·664	−0·239	+0·264	+1·008
P_3	−0·746	−0·406	−0·456	−0·401	−0·292	−0·051	−0·161	+0·391
P_4	−0·519	−0·455	−0·354	−0·725	−0·298	−0·252	−0·285	+0·457
P_5	−0·235	−0·377	+0·383	−0·791	−0·077	−0·264	−0·283	+0·188
P_6	−0·149	−0·324	+0·620	−0·670	−0·001	−0·218	−0·226	+0·135
P_7	−0·359	−0·456	+0·407	−0·686	−0·075	−0·136	−0·161	+0·090
Q_1	−0·251	+0·369	+0·884	−0·113	−0·022	−0·192	−0·172	−0·280
Q_2	−0·230	+0·208	+0·055	−0·900	−0·430	−0·377	−0·777	−0·118
Q_3	−0·654	+0·353	+0·583	−0·164	−0·047	−0·215	−0·168	−0·316
Q_4	−0·404	+0·336	+0·746	−0·238	−0·027	−0·218	−0·219	−0·332
Q_5	−0·271	+0·436	+0·879	−0·004	+0·023	−0·185	−0·157	−0·238
Q_6	−0·196	+0·427	+0·912	+0·031	+0·025	−0·168	−0·156	−0·186
Q_7	−0·388	+0·493	+0·762	+0·236	+0·065	−0·114	−0·081	−0·146

In view of the large number of manipulations that have been performed with quantities (the $C(\mathbf{k})$'s for instance) that cannot be accurately known less significance is attached to individual figures in table 4 than to the general order of magnitude of the results. Values of $|R|^2 = R_1^2 + R_2^2$ (the second row of values referring to the second set of results in table 4) and of $|T|^2 = T_1^2 + T_2^2$ are given in table 5. For some reason, not at present understood, the values of $|T|^2$ seem to be almost the same irrespective of whether $\mathbf{k}$ describes the incident or reflected beam and only one set is given.

The table shows that there is certainly a rough correlation between high values of $|R|^2$ and low values of $|T|^2$. However, it is difficult to interpret the values of $|R|^2$ directly since the velocity of the reflected electrons may be quite different to that of the incident electrons. It should also be born in mind that the waves used were not normalized. Neither of these difficulties apply to the interpretation of the values of $|T|^2$ which show immediately that over a large area (perhaps almost all) of the Fermi surface the 'transmission coefficient' of the fault will be of the order of 0·75 say. Moreover we may regard the fraction of the electrons not transmitted (25% say) as being scattered through a fairly large angle (40° which is the scattering angle for specular reflection in a (111) plane from the $[\bar{1}11]$ incident direction, might be taken as a typical angle). This is to be compared with the results of the diffraction calculation made in § 3 where it was shown that a fraction $\chi = 0{\cdot}15$ of the electrons were scattered through an angle of almost 180°. On the basis of these approximate considerations it appears that the resistivity predicted by the wave matching calculation would be rather less (perhaps by a factor of 4) than that obtained from the diffraction calculation.

Table 5

Point	P_1	P_2	P_3	P_4	P_5	P_6	P_7
$\|R\|^2$	0·21	0·40	0·72	0·48	0·20	0·13	0·34
$\|R\|^2$	0·20	0·10	0·56	0·28	0·26	0·22	0·40
$\|T\|^2$	0·79	0·80	0·37	0·65	0·77	0·83	0·64

It should be noted (see table 4) that the Tamm waves used in the wave matching calculation have in most cases rather small intensities. For the points P_1, P_5, P_6, P_7 $|A|^2$ and $|B|^2$ have values of the order of 0·1 and often less. For the other points P_2, P_3, P_4 higher values occur the largest being $|B|^2 = 1{\cdot}1$ for P_4. The reason why these higher values should be associated with the cases when the direct beam is refracted at the fault is not understood. It would of course be of interest to compute the total charge density bound in surface states at the fault but this involves not only the electrons considered so far but also those inside the Fermi surface with lower energies. It seems unlikely that the average Tamm wave intensity for all these electrons is greater than one tenth of the intensity of the unattenuated waves. Since the Tamm waves appear to have a penetration depth' of about one-third of a lattice distance a tentative estimate would be that for every thirty atoms at the fault one electron is bound in the surface states. As a result of this charge density at the fault the wave functions would be modified in such a way as to keep the Fermi level constant throughout the metal. The charge density would then be replaced by a scattering potential. Possibly the extra scattering produced would become important for wide ribbons of stacking fault but for ribbon widths of the order of ten atomic spacings we would expect the charge to behave rather like a line of vacancies. The charge density quoted above would be equivalent to one vacancy every three atomic distances along the dislocation and this would increase the scattering by only a few per cent.

§ 5. CONCLUSIONS

The scattering of conduction electrons by stacking faults has been shown to be due to a phase change in the diffraction from those crystal planes which do not contain the displacement vector of the fault. By using a simple physical model it has been possible to obtain an estimate of the magnitude of the effect which agrees well with experimental data and has been roughly confirmed by a wave matching calculation. The resistivity of extended dislocations in copper is therefore mainly due to the stacking fault ribbon.

The two calculations are also in agreement that the scattering from two faults should be independent provided they are further apart than one lattice spacing. This means for instance that it is justifiable to compute the effective area of a tetrahedron of stacking faults simply by adding up the areas of the faces.

It is of great importance to know whether the resistivity of stacking faults depends critically on the shape of the Fermi surface and thus varies greatly from one metal to another. We know that the resistivity will be proportional to an average value of the intensity of the diffracted beam for the electrons at the Fermi level but since the calculations described have dealt with a specific model of the Fermi surface it is not easy to draw any other general conclusions. However it is possible to calculate the stacking fault resistivity corresponding to any particular model of the Fermi surface. For instance, a rough estimate based on the Fermi surface proposed by Heine (1957) indicates that in aluminium, where the electrons are almost free, the stacking fault resistivity may be only about one-tenth of the value in copper. A low value of stacking fault resistivity might also be expected in nickel where the Fermi surface is a sphere containing 0·5 electrons per atom and does not come near any of the Brillouin zones. However, it should be borne in mind that the two-beam approximation does not provide a very good description of the conduction electrons in such a metal. In gold and silver the Fermi surface is probably rather similar to that in copper although, if the energy gap at the Brillouin zones is much less than the value of 6·5 ev assumed for copper, the surface may not make contact with the zone. Ziman (1959) has calculated that if the energy gap at the zone in copper were reduced to 5·6 ev contact would just occur. For such a Fermi surface the stacking fault resistivity would be about three-quarters of the value calculated for Pippard's model of the Fermi surface. It thus appears that the stacking fault resistivity in these metals will still be considerable even if the Fermi surface does not touch the zone but only comes very close to it.

The wave matching technique using Tamm waves could be greatly improved in power and scope if three beams could be considered instead of two. At present the method is restricted to regions of the Fermi surface where both the incident and reflected beams are diffracted by the same set of planes. It would be interesting to apply the technique to simple tilt and twist boundaries as well as to stacking faults. Such studies would give useful information about the resistivity of undissociated dislocations (composing the boundary).

In connection with the resistivity from undissociated dislocations it should be noted that there exists a diffraction effect somewhat similar to that due to stacking faults. A dislocation of Burger's vector 1/2 [110] produces a phase change in the diffracted beam which is zero for the $(\bar{1}11)$ and $(1\bar{1}1)$ reflections and 180° for the (111) and $(11\bar{1})$ reflections. This phase change is not, however, abrupt as in the case of the stacking fault (except near the centre of the dislocation) but takes place gradually so that the crystal waves can adapt themselves continuously to the changing conditions. However, if the phase change is significant over a distance comparable to the extinction distance the crystal waves will not be able to change rapidly enough and a large scattering will result. This will be true for electrons passing within about an extinction distance of the dislocation so that an undissociated dislocation should behave like a stacking fault of width one or two extinction distances. It is of interest to note that the close connection between the extinction distance and the distance from the dislocation within which this diffraction phase change produces strong scattering is also found in the case of high energy electrons passing through thin foils (Hirsch *et al.* 1960). For these electrons the extinction distances are about one hundred Angstroms and the image of the dislocation which is observed in the electron microscope as a result of the scattering is approximately of this width.

In copper this type of scattering might be responsible for about one-fifth of the resistivity due to the dislocations (assuming the stacking fault ribbon width to be ten atomic spacings and the extinction distance to be one atomic spacing). In aluminium where the ribbon width is only about one atomic spacing but the extinction distance is perhaps ten atomic spacings the effect is much more important and using these figures together with the estimate given above for the stacking fault resistivity in aluminium one can estimate a rough figure for the resistivity due to a dislocation density of N cm^{-2} in this metal of $\rho = 5 \times 10^{-20} N$ ohm-cm. The effect may also be of importance in nickel. Thus, although detailed calculations have not been carried out, the diffraction scattering from dislocations is expected to make a contribution to the resistivity several times greater than that which would be predicted on the Hunter–Nabarro treatment.

ACKNOWLEDGMENTS

My thanks are due to Professor N. F. Mott, F.R.S., and Dr. W. H. Taylor for their interest and encouragement, and to Drs. P. B. Hirsch and M. J. Whelan for many stimulating discussions about diffraction by stacking faults and dislocations. I am also grateful to Dr. J. Friedel, Dr. W. M. Lomer, Professor A. Seeger and Dr. J. M. Ziman for valuable comments and to Mr. C. Hunter for assistance with the use of the high speed computer. Finally I wish to thank the Master and Fellows of Trinity College for a Research Studentship.

REFERENCES

BLATT, F. J., HAM, F. S., and KOEHLER, J. S., 1956, *Bull. Amer. phys. Soc.*, **1**, 114.

BAUERLE, J. E., and KOEHLER, J. S., 1957, *Phys. Rev.*, **107**, 1493.

BROOM, T., 1952, *Proc. phys. Soc. Lond.* B, **65**, 871.

BROOM, T., and BARRETT, C. S., 1953, *Acta Met.*, **1**, 305.

CHRISTIAN, J. W., and SPREADBOROUGH, J., 1956, *Phil. Mag.*, **1**, 1069.

CLAREBROUGH, L. M., HARGREAVES, M. E., and WEST, G. W., 1955, *Proc. roy. Soc.* A, **232**, 255; 1957, *Acta Met.*, **5**, 738.

HARRISON, W. A., 1958, *J. Phys. Chem. Solids*, **5**, 44.

HEIDENREICH, R. D., 1949, *J. appl. Phys.*, **20**, 993.

HEIDENREICH, R. D., and SHOCKLEY, W., 1948, *Report on a Conference on Strength of Solids* (London: The Physical Society).

HEINE, V., 1957, *Proc. roy. Soc.* A, **240**, 340.

HIRSCH, P. B., HOWIE, A., and WHELAN, M. J., 1960, *Phil. Trans.* A (to be published).

HUNTER, S. C., and NABARRO, F. R. N., 1953, *Proc. roy. Soc.* A, **220**, 542.

KLEMENS, P. G., 1953, *Aust. J. Phys.*, **6**, 122; 1956, *Canad. J. Phys.*, **34**, 1212.

PATERSON, M. S., 1952, *J. appl. Phys.*, **23**, 805.

PIPPARD, A. B., 1957, *Phil. Trans.* A, **250**, 325.

SEEGER, A., 1956, *Canad. J. Phys.*, **34**, 1219.

SEEGER, A., BERNER, R., and WOLF, H., 1959, *Z. Phys.*, **155**, 247.

SEEGER, A., and SCHOECK, G., 1953, *Acta Met.*, **1**, 519.

SEEGER, A., and STEHLE, H., 1956, *Z. Phys.*, **146**, 242.

SHOCKLEY, W., 1939, *Phys. Rev.*, **56**, 317.

SILCOX, J., and HIRSCH, P. B., 1959, *Phil. Mag.*, **4**, 72.

STEHLE, H., and SEEGER, A., 1956, *Z. Phys.*, **146**, 217.

TAMM, I., 1932, *Phys. Z. Sowjet.*, **1**, 733.

WHELAN, M. J., and HIRSCH, P. B., 1957, *Phil. Mag.*, **2**, 1121, 1303.

ZIMAN, J. M., 1958, *Nuovo Cim.* Suppl. **7**, 353; 1959, *Proc. roy. Soc.* A, **252**, 63.

Infra-red Measurements of the Optical Constants of Liquid Silver†

By J. N. Hodgson
University College of North Staffordshire, Keele, Staffordshire

[Received October 22, 1959]

Abstract

The optical constants of liquid silver have been measured in the infra-red between wave numbers 4000 and 17 000 cm^{-1}. The results are compared with the Drude theory and lead to a value of about 1·1 for the effective number of free electrons per atom. The electrical conductivity of the surface layer, calculated from optical constants, differs by less than 10% from the bulk conductivity. Some results on the temperature variation of the optical constants are presented. The optical constants of liquid copper have also been measured at two wave numbers in the infra-red.

§ 1. Introduction

The programme of infra-red measurements of the optical constants of liquid metals, which was begun with mercury, Hodgson (1959), has been continued with silver. Silver has been chosen as a typical monovalent metal. It has the lowest melting point (961°c) of the monovalent noble metals but a new furnace was needed to reach this temperature. The new furnace will maintain temperatures up to 1050°c but the heating coil fused when the temperature was raised above this value. Attempts to measure liquid copper (M.P. 1083°c) were only partly successful for this reason.

The optical constants of solid silver have been previously measured over a wide spectrum range from infra-red to ultra-violet; references in Schulz (1957). The infra-red values of the dielectric constant, ϵ, at wave numbers less than 10^4 cm^{-1}, are in agreement with the Drude free electron formula assuming about 1·0 free electron per atom. At wave numbers above 10^4 cm^{-1} the values of ϵ deviate from the free electron curve due to inter-band transitions. The infra-red values of the conductivity, σ, agree with the Drude free electron formula if the relaxation time is treated as an adjustable parameter. The required relaxation time is several times smaller than the value deduced from the static conductivity. The ratio varies for different silver surfaces and is probably connected with surface imperfections.

---

† Communicated by the Author.

§ 2. APPARATUS AND FURNACE DESIGN

The apparatus and method used for measuring optical constants were the same as previously reported (Hodgson 1959). The silver was melted in a furnace inside a water-cooled brass tank, filled with hydrogen at a pressure of about 2 cm Hg. The furnace consisted of a silica tube, 3 cm diameter by 7 cm long, wound with a heating coil of nichrome wire. The tube was supported in a steel frame and thermally insulated with alumina cement. The temperature inside the silica tube was measured with a chromel–alumel thermocouple. The melting point of silver was reached with just under 1 kw power dissipation in the heating coil. A steel crucible was used at first to contain the silver in the silica tube. Two series of measurements were made with this crucible but it gradually deformed. There was also a possibility of contamination of the liquid silver by the steel. A second crucible was made from hard carbon rod. This crucible was unaffected by liquid silver and has been used for most measurements. The water cooling did not extend to the baseplate of the brass tank and it was feared that the rubber seals of the electrodes might overheat. The rubber O-rings were therefore replaced by lead O-rings which have functioned satisfactorily. The two Pyrex windows on the tank were held against silicone rubber O-rings by atmospheric pressure.

§ 3. MEASUREMENTS ON LIQUID SILVER

About 100 g of silver were needed to fill the steel or carbon crucibles. The silver used was of purity greater than 99·98%. A steel and a carbon crucible were filled with separate lots of silver. The curvature of the surface of liquid silver due to surface tension was greater than with mercury and the reflecting area was limited to the flat central part of the liquid surface. The surface was very sensitive to vibration and the supporting table had to be well insulated from the vibration of the vacuum pump. When first melted the silver had a cloudy surface but the cloudy areas soon moved to each end of the silver blob leaving a clear area in the middle. This clear area showed no scattered light even at angles close to the reflected beam. The impossibility of cleaning a liquid silver surface *in situ* was a disadvantage of this apparatus. A surface cleaning method similar to that used for mercury would be difficult to apply.

Optical constants were measured at eight points in the infra-red spectrum. The experimental errors have been estimated by taking probable errors of the measured angles and calculating the corresponding errors in ϵ and σ. In fig. 1, the errors lie within the plotted circles. The ribbon filament lamp used as radiation source in the infra-red measurements was replaced by a mercury lamp for visible and ultra-violet measurements. The angle of incidence (81·5°) was unsuitable for measurements on silver in this spectrum range. The accuracy of the results is therefore low, but much better for ϵ than σ. The experimental values of $-\epsilon$ and σ/c in fig. 2 have probable errors $\pm 0{\cdot}4$ and $\pm 0{\cdot}2 \times 10^4$, respectively.

Four sets of infra-red measurements were made over a period of several months, two on silver in the steel crucible and two on silver in the carbon crucible. These sets of measurements show differences which will be described later. The points of fig. 1 represent a typical set of results. An attempt was made to measure the temperature variation of ϵ and σ over the limited temperature range available, about 100°C.

Fig 1

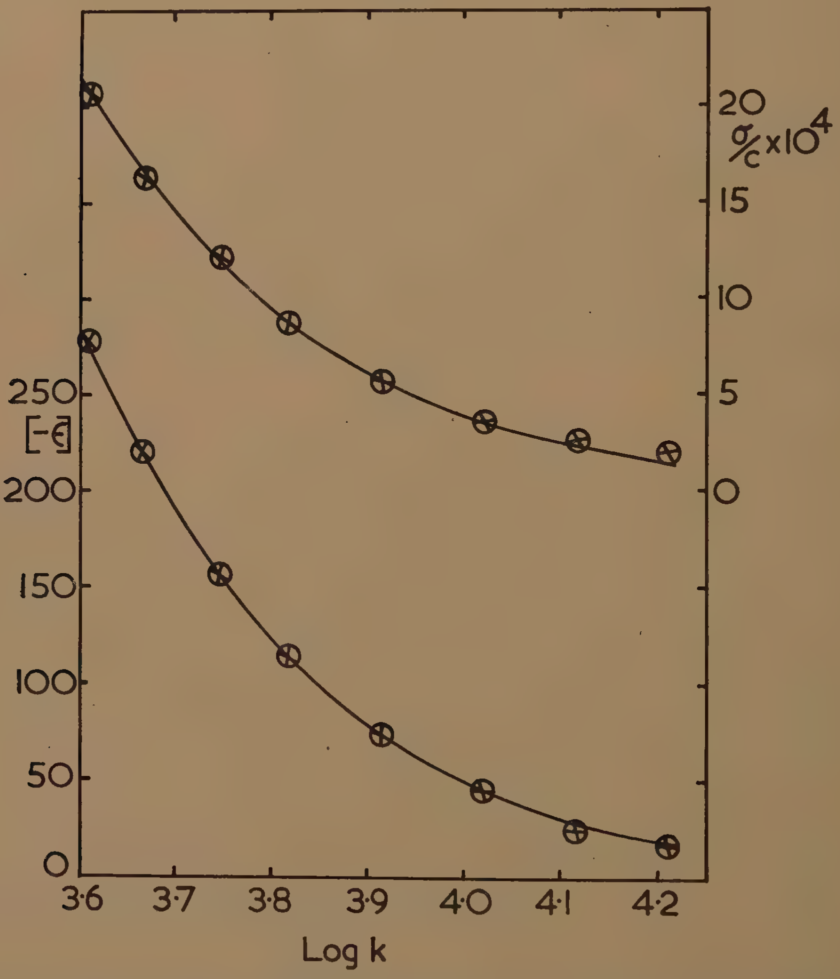

Liquid silver (infra-red). Experimental points for liquid silver (Ag–1); theoretical curves calculated from (3) and (4) with $k_0^2=5{\cdot}26\times10^9$, $k_R=1{\cdot}51\times10^3$, (i.e. $N_0=1{\cdot}13$, $\sigma_0/\mathbf{c}=174\times10^4$).

§ 4. Discussion

The number of atoms per cm³ (N_A) and the static electrical conductivity in e.s.u. (σ_0) for liquid silver, have been calculated from data in *Metals*

Reference Book (Smithells 1955). At a temperature t°C between the melting point and 1100°C:

$$N_A = 5{\cdot}20 \times 10^{22}[1 - 9 \times 10^{-5}(t - 961)], \quad . \; . \; . \; . \; . \quad (1)$$

$$\sigma_0/\mathbf{c} = 1{\cdot}82 \times 10^{6}[1 - 5{\cdot}8 \times 10^{-4}(t - 961)]. \quad . \; . \; . \; . \; . \quad (2)$$

The ratio of the conductivity of the solid to the conductivity of the liquid at the melting point is 2·1. This agrees with the theory of Mott (1934) who assumed no change in the number of conduction electrons per atom when a metal melts.

Fig. 2

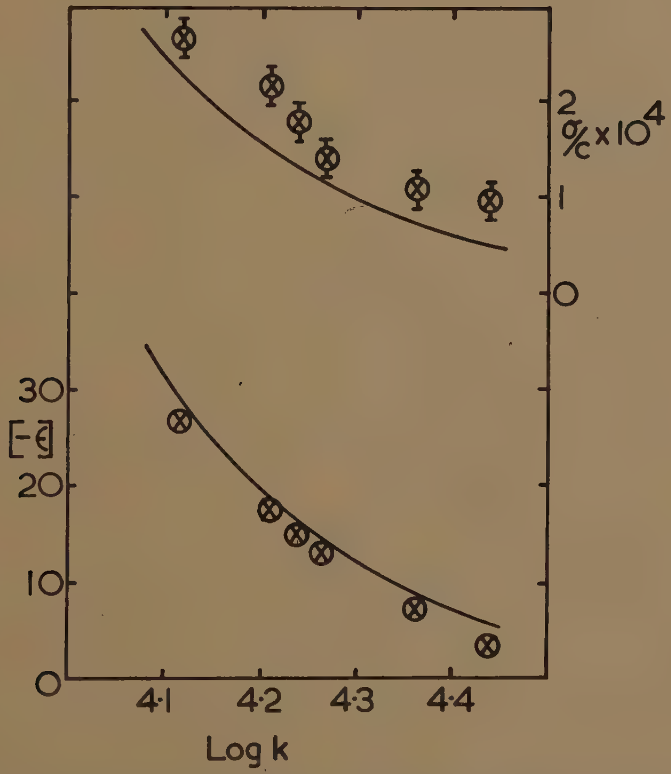

Liquid silver (visible and ultra-violet). Experimental points for liquid silver: theoretical curves continued from fig. 1.

The experimental values of ϵ, the dielectric constant, and σ, the conductivity in e.s.u., have been compared with Drude's free electron formulae:

$$1 - \epsilon = k_0^2/(k^2 + k_R^2), \quad . \; . \; . \; . \; . \; . \; . \quad (3)$$

$$\sigma/\mathbf{c} = \tfrac{1}{2}k_0^2 k_R/(k^2 + k_R^2) \quad . \; . \; . \; . \; . \; . \; . \quad (4)$$

k is the wave number in cm^{-1}; $k_0^2 = (N\mathbf{e}^2)/(\pi \boldsymbol{m}^* \mathbf{c}^2)$, where N is the number of free electrons per cm^3 of charge $-\mathbf{e}$ and effective mass $\boldsymbol{m}^*$; $k_R = 1/(2\pi \mathbf{c}\tau)$, where τ is the relaxation time. The effective number of free electrons per atom is defined by:

$$N_0 = \left(\frac{N}{m^*}\right) \Big/ \left(\frac{N_A}{m}\right). \qquad (5)$$

When $k=0$, then:

$$\sigma_0/c = \tfrac{1}{2}k_0^2/k_R. \qquad (6)$$

The formula (3) for ϵ does not include a small term due to ion core polarization. Using the value of polarizability of the Ag$^+$ ion given by Van Vleck (1932), the ion core contribution to ϵ has been estimated as 1·1.

Values of k_0^2 and k_R were calculated by means of (3) and (4) for each pair of experimental values of ϵ and σ at the same wave number, k. For $\log k$ between 3·6 and 4·0, these values of k_0^2 and k_R are constant, within experimental error, for each set of measurements. This may be seen in fig. 1 where the experimental values Ag–1 are compared with curves calculated from formulae (3) and (4). Average values of k_0^2 and k_R for each set of measurements are given in the table. Ag–1 and Ag–2 refer to liquid silver in a steel crucible; Ag–3 and Ag–4 refer to liquid silver in a carbon crucible. The temperatures used for Ag–1 and Ag–2 are uncertain because of a fault in the thermocouple circuit. N_0 and σ_0/c were calculated by means of (5) and (6). The reason for the variations in k_0^2 and k_R for different sets of measurements has not been found and requires further investigation.

Experimental Values for Liquid Silver

	k_0^2	k_R	N_0	σ_0/c	t
Ag–1	5·26	1·51	1·13	174	—
Ag–2	5·44	1·66	1·17	164	—
Ag–3	5·02	1·53	1·09	164	1020
Ag–4	5·34	1·44	1·15	185	1000
	$\times 10^9$ cm^{-2}	$\times 10^3$ cm^{-1}		$\times 10^4$	°C

The infra-red values of σ_0/c do not differ by more than 10% from the electrical values given by formula (2). This indicates that for liquid silver the surface layer has nearly the same conductivity as the bulk metal. The values of N_0 for liquid silver are larger than the accepted optical value for solid silver, $N_0=1{\cdot}03$ ($m^*/m=0{\cdot}97$), quoted by Schulz (1957). This value is probably uncertain by at least ±3%. The experimental points at wave numbers greater than 10^4 cm^{-1} deviate from the infra-red theoretical curves as shown in fig. 2.

The temperature variation of the optical constants was measured at $\log k = 3{\cdot}748$ and 4·020. The constants were measured initially at about 1000°C, then at about 1090°C, and finally again at about 1000°C. The initial and final values agreed within experimental error and the measurements were repeated with consistent results. Values of k_0^2, k_R, and

σ_0/c (infra-red) were calculated from the experimental values of ϵ and σ. The temperature coefficients have been calculated as fractions of the initial values (i.e. near the melting point).

Parameter	k_0^2	k_R	σ_0/c
Temperature coefficient per °c	-2×10^{-4}	$+6\times10^{-4}$	-8×10^{-4}
		(probable error $\pm1\times10^{-4}$)	

The coefficients of k_0^2 and σ_0/c are of the same order as the coefficients of N_A and σ_0/c (electrical) in formulae (1) and (2).

§ 5. MEASUREMENTS ON LIQUID COPPER

Pieces of sheet copper of 99·998% purity were melted in a carbon crucible. The furnace maintained a temperature sufficient to melt copper for only a few minutes before the heating coil fused. Measurements of the optical constants of liquid copper were obtained at two wave numbers.

log k	$-\epsilon$	σ/c	k_R	k_0^2
3·645	209	30·7	2·94	5·91
3·748	146	22·3	3·05	5·97
		$\times10^4$	$\times10^3$ cm^{-1}	$\times10^9$ cm^{-2}

The average values of k_0^2 and k_R lead to $N_0=0·84$ and σ_0/c (infra-red) $=99\times10^4$, compared with σ_0/c (electrical) $=141\times10^4$ at the melting point.

§ 6. CONCLUSION

The infra-red optical constants of liquid silver can be explained by the simple Drude free electron theory. The number of free electrons per atom is about 1·1 and their relaxation time about 7×10^{-15} sec. The value of the static electrical conductivity derived from the infra-red measurements agrees fairly well with the electrically measured value. These results are in contrast to those for liquid mercury, which cannot be represented by the free electron formulae.

ACKNOWLEDGMENT

I would like to thank Professor D. J. E. Ingram for valuable discussion of this paper.

REFERENCES

HODGSON, J. N., 1959, *Phil. Mag.*, **4**, 183.
MOTT, N. F., 1934, *Proc. roy. Soc.* A, **146**, 465.
SCHULZ, L. G., 1957, *Advanc. Phys.*, **6**, 102.
SMITHELLS, C. J., 1955, *Metals Reference Book* (Butterworths), p. 639.
VAN VLECK, J. H., 1932, *Electric and Magnetic Susceptibilities* (Oxford: University Press), p. 225.

The Damage and Recovery of Neutron Irradiated Tungsten†

By M. W. Thompson

Atomic Energy Research Establishment, Harwell, Berks.

[Received October 6, 1959]

Abstract

Residual electrical resistivity has been used as an index of the damage present in tungsten irradiated in a nuclear reactor at 4°K and 77°K. A comparison was made between four different types of specimen prepared from cold-drawn wire respectively annealed before irradiation at 2000, 1500, 800°C and not at all. A fifth type of specimen was prepared from wire in a different state of purity.

Four stages of recovery have been identified, the first occurring below −170°C, the second between −170 and 350°C with an activation energy rising from 0·25 to 1·7 ev, the third between 350 and 450°C with a single activation energy of 1·7 ev and the fourth above 450°C. Second-stage recovery was enhanced by the presence of cold-work, affected by impurities and in well-annealed samples after light irradiations it was suppressed.

A comparison of recovery with that in other metals leads to the conclusion that vacancies in tungsten migrate at 400°C with an activation energy of 1·7 ev. The general suggestion is advanced that vacancy migration occurs in all metals at a temperature approximately 20% of the absolute melting point T_m°K, with an activation energy roughly $5 \times 10^{-4} T_m$ ev.

Recovery in tungsten above −170°C is attributed to the release of interstitials from traps associated with impurity atoms and dislocation lines. The free interstitial is assumed to become mobile below −170°C.

The resistance *versus* dose curve for cold-worked tungsten shows acceleration and this is considered as evidence for the action of spikes on the unstable arrays of vacancies produced by deformation.

A quantitative theory of damage and recovery developed from the above model predicts the observed behaviour of the five types of tungsten specimen.

§ 1. Introduction

In this paper experiments are presented in which neutron irradiation damage has been studied by observing changes in the electrical resistivity of tungsten. It has previously been shown that after irradiation at −196°C this damage recovers by thermal annealing in two main stages at −80°C and at 350°C, the activation energies associated with these stages being 0·5 ev and 1·7 ev (Kinchin and Thompson 1958). Later work showed that the low-temperature recovery was not observed after very short irradiations and this led to the suggestion that low-temperature recovery was due to a mobile defect being released from trapping centres (Thompson 1958 a).

---

† Communicated by the Author.

The following experiments have been designed to determine both the nature of the mobile defect and of its traps:

(i) The effect of neutron dose on recovery.
(ii) A comparison of annealed and cold worked tungsten.
(iii) A comparison of material from different manufacturers.
(iv) Recovery after irradiation in liquid helium.

§ 2. EXPERIMENTAL

2.1. *Specimens*

In table 1 the various types of specimen which have been used are listed with some physical properties. Specimens made of Johnson Matthey tungsten annealed at 1500°C were used for reference in all comparative experiments. Specimens made direct from manufactured wire were found to be in a sufficiently cold-worked state for experiment (ii).

Table 1. Specimens

Type	A	B	C	D	E
Experiment	(i)	(i), (ii), (iii) & (iv)	(ii)	(ii)	(iii)
Manufacture	Johnson-Matthey Co., London				Tungsten Mfg. Co. London
Spec. analysis	0·005% Fe				spec. pure
Temp. of pre-irradiation anneal, °C	2000	1500	500	No anneal	1500
Grain size, microns	100	10	needles 1 × 25	needles 1 × 25	10
Residual resistivity micro-ohm cm	0·04	0·06	0·30	0·36	0·09

The specimens were made from 0·008 in. diameter wire which had been cleaned electrolytically in caustic soda solution using a nickel anode. A 7 cm length of wire had potential leads of the same wire spot welded at a distance of 1 cm from either end. The resulting specimen was spot welded to leads passing through a pressed glass seal which was subsequently fused into a lead glass envelope using a purified argon atmosphere to prevent oxidation. The envelope was evacuated and outgassed at 350°C after which type A, B and E specimens were given a pre-irradiation anneal by passing a current before finally sealing off. In the case of type C specimens the pre-irradiation anneal was given to the wire before mounting.

2.2. *Resistance Measurements*

All resistance measurements were carried out in liquid helium using a potentiometer to compare the voltage drop across the specimen with that across a standard resistance carrying the same current. In order to eliminate drifts a regulating device (Thompson 1958 b) held this current constant to 0·001%. The residual resistance of the specimen was measured to an accuracy of 0·003%. Because of uncertainties in the dimensions absolute resistivity could only be measured to a few per cent.

2.3. *Irradiations*

Irradiations were carried out in three vertical holes of the BEPO reactor at Harwell. These holes, TE.1, TE.3 and TE.13, penetrate the reactor core transverse to the fuel channels and have approximately the same thermal neutron flux of 10^{12} neutrons cm^{-2} sec^{-1}. Using sulphur detectors (Martin and Stanwix 1956) alongside the resistance specimens, the flux of neutrons with energies in excess of 1 MeV was measured and found to be 3×10^{10} in TE.1 and TE.13 but $1{\cdot}2 \times 10^{11}$ in TE.3. However, in spite of these variations the resistance increase for a given time and a given type of specimen, was constant to within 10% in any of the holes used. This implies that damage is chiefly due to neutrons below 1 MeV in these holes. In view of this constant resistance increase all irradiation doses have been specified as times rather than integrated neutron fluxes.

Short irradiations in liquid nitrogen were carried out in an open lead glass dewar which was lowered into the TE.13 hole whilst the reactor ran at full power. The 12-hour irradiation was carried out in a liquid nitrogen cryostat (Thompson and Jefferson-Loveday 1958) in hole TE.1. Irradiations lasting 1 week were performed with the nitrogen cryostat in hole TE.3. After all these irradiations the specimens were removed from the pile in liquid nitrogen and mounted in the laboratory cryostat without warming up.

An irradiation lasting $8\frac{1}{2}$ min was carried out in liquid helium using two concentric dewars, the outer one containing liquid nitrogen and the inner one about 200 cm^3 of liquid helium. This assembly was lowered into the TE.13 hole, a carbon resistance thermometer indicating when two-thirds of the liquid helium had boiled away. At this stage the dewars were removed from the pile and topped up with liquid. After waiting an hour for radioactivity to decay the complete assembly was removed to the laboratory where the residual resistance of the specimen was measured *in situ* through leads which had been attached before irradiation.

2.4. *Annealing After Irradiation*

After irradiation in liquid nitrogen the specimens were attached to measuring leads and placed in a cryostat-furnace assembly mounted above a liquid helium bath (Stubbs and Thompson 1958). This apparatus enabled resistance measurements to be made in liquid helium between 30 min annealing periods at successively higher temperatures in the range −196 to 200°C. For annealing at higher temperatures specimens were removed to a separate furnace. Temperature was in all cases measured and controlled to ±0·1°C.

Recovery curves were obtained by plotting $(R_T - R_0)/(R_I - R_0)$. Where R_T is the residual resistance after annealing at temperature T and R_0 and R_I are the values before and after irradiation.

§ 3. Results

3.1. *The Effect of Neutron Dose*

In fig. 1 the recovery curves for a Johnson-Matthey specimen annealed before irradiation at 1500°C and irradiated at −196°C for 1, 12 and 140 hours are compared. Before each successive irradiation current was passed through the specimen to heat it to 150°C and to restore its residual resistance to R_0. To check reproducibility two other specimens were irradiated for 1 hour and 140 hours, their results are also plotted in fig. 1. The increase of resistivity of the first specimen with irradiation is shown in fig. 4 (*b*).

Apparently the effect of decreasing dose is to reduce the proportion of recovery at low temperatures. The increase of resistance with irradiation time shows slight deceleration.

3.2. *Comparison of Annealed and Cold-worked Tungsten*

The recovery curves for Johnson-Matthey tungsten wire in the cold-worked, 500°C annealed, 1500°C annealed and 2000°C annealed states are compared in fig. 2 after 140 hour irradiations at −196°C. In fig. 3 the comparison is made after a 1-hour irradiation. The increase of resistivity with irradiation time is shown in fig. 4 for the four types of specimen.

The presence of cold-work evidently introduced its own recovery above 250°C (which is in agreement with the findings of Schultz (1959)) and enhanced recovery in irradiated specimens below 30°C. Although there is little difference between the recovery of 1500°C annealed and 2000°C annealed specimens those which were annealed at 500°C before irradiation showed rather less recovery in the range 350 to 450°C. The resistance of cold-worked specimens increased more slowly with irradiation time than that of annealed specimens and showed acceleration rather than deceleration.

3.3. *Comparison of Material from Two Manufacturers*

In view of the difficulty experienced in obtaining tungsten with controlled impurities, it was decided to compare two materials from different manufacturers. In fig. 5 the recovery of tungsten supplied by Johnson-Matthey

Fig. 1

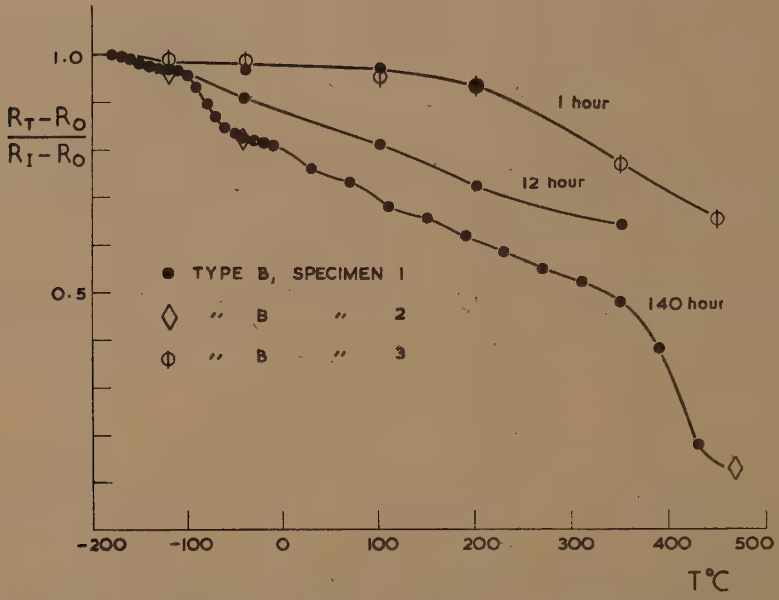

The effect of irradiation time on recovery for specimens of type B.

Fig. 2

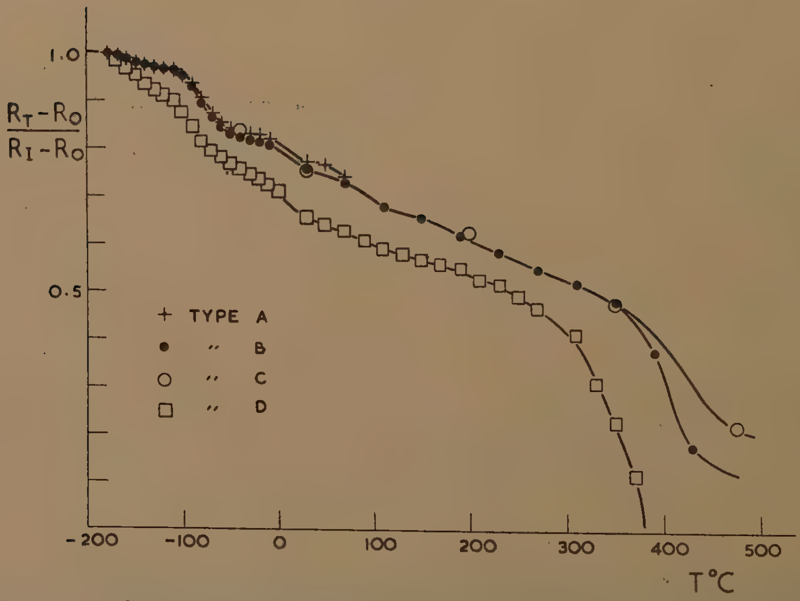

Recovery as a function of annealing treatment before irradiation; specimens of type A, B, C and D after 140 hour irradiations at −196°c.

Fig. 3

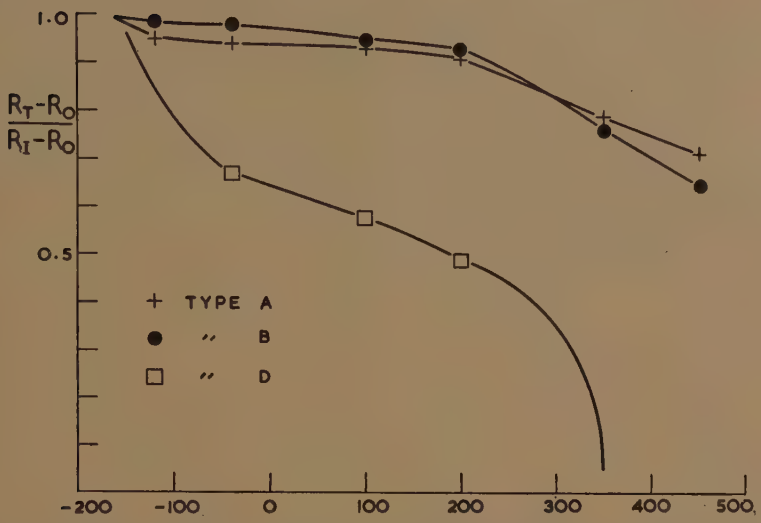

Recovery as a function of annealing treatment before irradiation; specimens o type A, B and D after 1 hour irradiations at −196°c.

Fig. 4

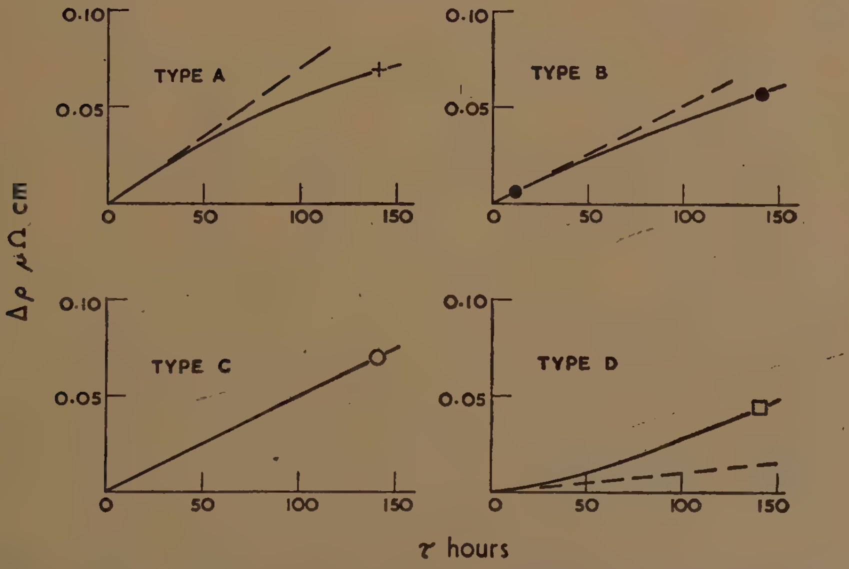

Resistance increase *versus* irradiation time at −196°c for four types of specimen A, B, C and D. Slope at the origin is estimated from increase observed after 1-hour irradiations.

is compared with that from the Tungsten Manufacturing Co. after both specimens had been irradiated together in liquid nitrogen for 1 hour. Both were annealed at 1500°c before irradiation. Whereas the Johnson-Matthey specimen increased by $5{\cdot}4\times10^{-4}$ micro-ohm-cm the other increased by only $1{\cdot}7\times10^{-4}$ micro-ohm-cm in the same time. From the residual resistivities, given in table 1, it is clear that this second specimen was in a different state of purity from the Johnson-Matthey specimen. The effect of these impurities is evidently to enhance recovery after short irradiations, particularly above 0°c.

Fig. 5

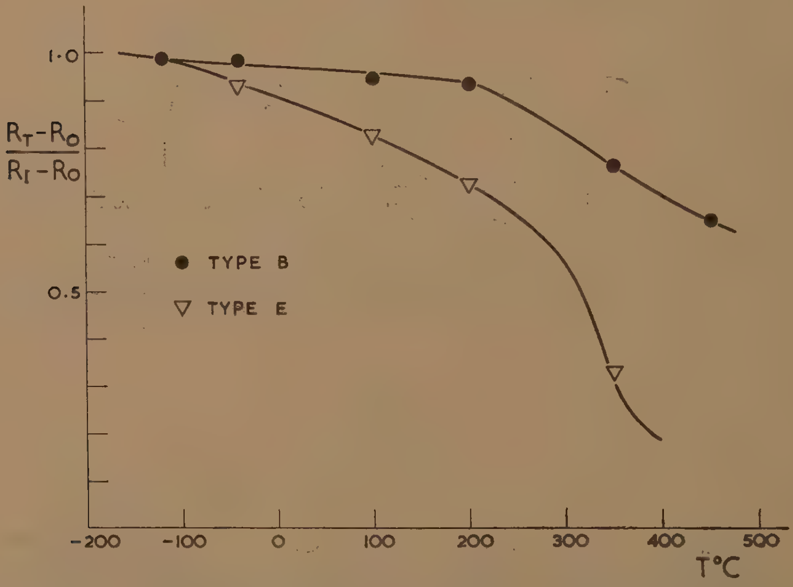

Comparison of recovery in materials of different purity but the same pre-irradiation annealing treatment; specimens of type B and E irradiated for 1 hour at −196°c.

3.4. *Recovery after Irradiation at* 4°K

After $8\frac{1}{2}$ min irradiation in liquid helium the resistivity of a Johnson-Matthey specimen annealed before irradiation at 1500°c increased by 0·0028 micro-ohm-cm. Of this increase 30% annealed after 30 min at −196°c and a further 20% after 30 min at 25°c. Since it is known that for short irradiations little recovery occurs in the range −120 to 100°c the recovery curve may be sketched as in fig. 6.

§ 4. Discussion

4.1. *The Resistivity Increase*

The observed change of resistivity with irradiation time may be interpreted using a model based on the following three postulates.

(i) Irradiation produces interstitial atoms and vacant lattice sites in equal numbers, the former defect being mobile at liquid nitrogen temperature. An attempt to justify this assumption will be made in § 4.2.

(ii) It also produces 'spike' regions of temporary local disorder containing of the order 10^5 atoms. The existence of such regions has been demonstrated in the III-V compounds by Gonser and Okkerse (1958). In tungsten the recoiling atom from a neutron collision is in the energy range (10^4 ev) where it behaves like a hard sphere with a mean free path of a few angstrom units. It therefore enters the spike region straight away and we may expect that all interstitials and vacancies are left as debris after the spikes have subsided. Thus it is unlikely that further spikes will affect the vacancies already present.

Fig. 6

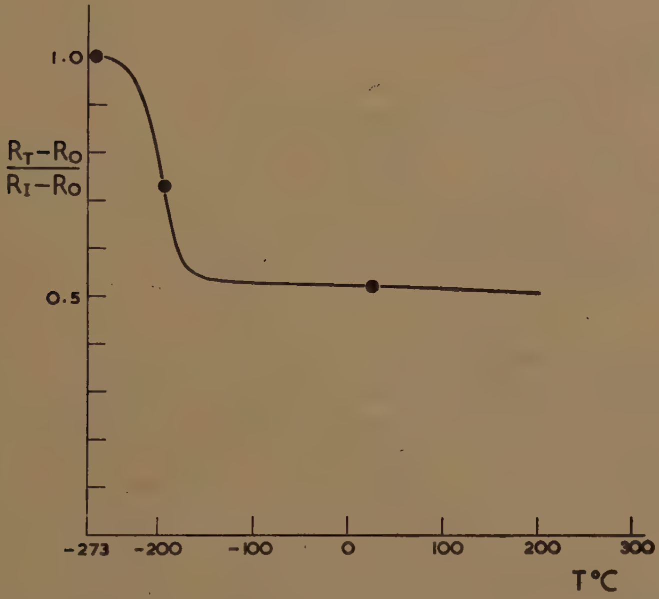

Recovery after an irradiation of 8 min at 4°K; B type specimen.

(iii) In a perfect infinite crystal at a temperature where only interstitials are mobile mutual annihilation would prevent the accumulation of defects. In a real specimen however, in addition to vacancies there will be the following sinks for interstitials: surfaces and suitable grain boundaries, dislocations and foreign atoms of favourable size. These last two may only be temporary sinks, or traps, from which the interstitial is activated by heating the specimen (Lomer and Cottrell 1955, Blewitt *et al.* 1957). It follows, therefore, that the number of vacancies present at any stage is equal to the number of interstitials which have either been trapped on temporary sinks or been lost to the permanent sinks.

Let C be the total concentration per atom of interstitials or vacancies produced by irradiation, T_r be the initial concentration of the rth type of trap, C_r the concentration per atom of interstitials on the rth trap and C_b the concentration lost to boundary sinks of which there is a constant concentration B. B must be regarded as an effective concentration which would apply if the sinks were uniformly distributed through the crystal. Consider the situation as C increases to $C+dC$. The extra dC interstitials have the choice of (T_r-C_r) unfilled traps of type r, of any other unfilled trap, of finding a boundary sink, or of annihilating the vacancies present at a concentration $(\sum C_r+C_b)$. It follows from simple proportion that the increase in the concentration trapped on the rth trap is:

$$dC_r=\frac{(T_r-C_r)dC}{B+\sum(T_r-C_r)+\sum C_r+C_b};$$

$$\frac{dC_r}{dC}=\frac{(T_r-C_r)}{B+C_b+\sum T_r}. \qquad (1)$$

Similarly

$$\frac{dC_b}{dC}=\frac{B}{B+C_b+\sum T_r}. \qquad (2)$$

Hence

$$C_b=(B+\sum T_r)\left\{\left[1+\frac{2BC}{(B+\sum T_r)^2}\right]^{1/2}-1\right\} \qquad (3)$$

Solving (1) we obtain for C_r

$$C_r=T_r\left[1-\exp\left(-\frac{C_b}{B}\right)\right]. \qquad (4)$$

Now if the resistivity change due to interstitials being trapped on the rth trap is a_rC_r and that due to a concentration V of vacancies is bV, then we may write for the resistivity increase:

$$\Delta\rho=\sum a_rC_r+\sum bC_r+bC_b$$

or

$$\Delta\rho=b\left\{\left[1-\exp\left(-\frac{C_b}{B}\right)\right]\sum T_r\left(1+\frac{a_r}{b}\right)+C_b\right\}. \qquad (5)$$

In this expression the first set of terms, arising from the trapped interstitials and their associated vacancies, saturate with the same period as C increases. The term bC_b which is due to the vacancies left behind by interstitials lost to boundaries, shows slight deceleration without saturation.

Let us apply this analysis to predict the resistivity increase of an annealed sample of tungsten. First the relation, between C and irradiation time may be established as:

$$C=n\sigma\phi \qquad (6)$$

Where n is the number of interstitial-vacancy pairs per neutron hit, σ is the total fast neutron cross section ($\sim 10^{-23}\,\mathrm{cm}^2$), ϕ is the fast neutron flux ($\sim 3\times 10^{11}$ neutron $\mathrm{cm}^{-2}\,\mathrm{sec}^{-1}$), and τ is the irradiation time. Taking n as 30 the value of C is of the order 10^{-4} for a 140-hour irradiation.

The concentration of traps, $\sum T_r$ may be estimated as follows; the residual resistivity of the tungsten suggests an impurity concentration of 10^{-4}, assuming the reasonable value of 500 microhm cm per unit concentration of impurities. This concentration is not in contradiction with the spectrographic analysis. Those traps which are due to impurities will have this order of concentration. Dislocations might also provide traps, a density of 10^{10} lines cm^{-2} producing a concentration of order 10^{-4} if ten trapping sites exist in each atomic plane, pierced by a dislocation. It would appear then that 10^{-4} is a reasonable value for $\sum T_r$.

Fig. 7

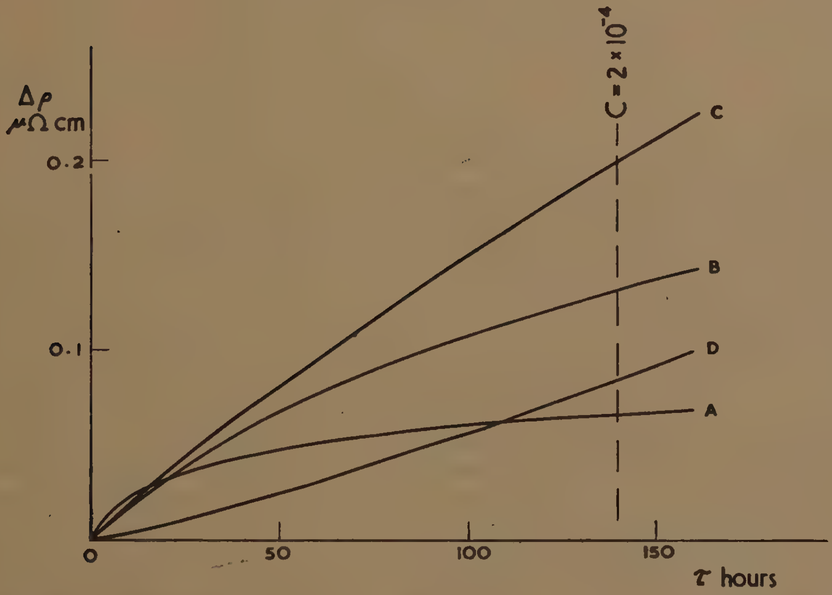

Resistance increase as a function of irradiation time calculated from theory for A, B, C and D type specimens with the sink concentrations given in table 2.

The value of B, the effective concentration of permanent sinks, will depend primarily on grain size. An order of magnitude may be obtained as the ratio of lattice sites at the grain surface to the total of sites in the grain

$$\text{i.e. } B \sim 6/dA^{1/3}$$

where d is the linear grain size and A the density of atoms. For 10 micron grains B is of the order of 10^{-4}.

In previous work (Kinchin and Thompson 1958) a value of 2×10^3 microhm cm was deduced for the resistivity increase in molybdenum per unit concentration of interstitials and vacancies. For the purposes of the present order of magnitude calculation let us take $a_r = b = 10^3$ microhm cm for tungsten which behaves similarly to molybdenum. We may then sketch $\Delta\rho$ as a function of C for specimen types A, B and C as in fig. 7 using the estimates of table 2.

Table 2. Estimated Sink Concentrations ($\times 10^4$) for Four Types of Specimen

Type	B	ΣT_r	T_1	V_0'	Temp. of annealing °c
A	0·05	0·20	0·05	0	2000
B	0·50	0·30	0·15	0	1500
C	5·00	1·00	—	0	500
D	5·00	1·00	—	2·00	None

A comparison of the curves in fig. 7 with the results of fig. 4 shows that the theory explains the qualitative effects and gives the correct order of magnitude of the resistivity change. Expressed in physical terms, an increase in grain size favours both the trapping process and annihilation of vacancies. Consequently there is a greater tendency to saturate and a greater initial rate of increase.

In the publication referred to above, the change in resistivity of tungsten irradiated at 30°c was reported to show an initial deceleration up to 5 weeks irradiation followed by steady rise. Here again there is agreement with the behaviour of the two terms in eqn. (5) the first of which might be expected to saturate after about five weeks' irradiation.

Let us now consider the resistivity increase in cold-worked tungsten. The acceleration with irradiation time suggests that there is a process occurring simultaneously with the accumulation of vacancies and trapped interstitials, which causes a decrease in resistivity. This process might be the action of spikes on unstable defect configurations produced by cold-work. For instance it has been suggested that vacancies are produced in strings during cold-work (Cottrell 1957) and the effect of a spike on such an array might well be to cause aggregation with an associated decrease in resistivity.

Suppose that such a process occurs and that one spike containing S atoms is produced per neutron hit. From our previous definition there will be n interstitials and vacancies associated with each spike. The concentration of spikes is thus C/n and the concentration of lattice sites affected by spikes is SC/n. The effect of increasing C by dC will be to increase the concentration of spike sites by SdC/n. If V' is the concentration of vacancies due to cold work then a concentration V' of these extra spike sites will be strings of vacancies and the concentration of vacancies aggregated will be:

$$\frac{SV'}{n}dC.$$

The concentration of cold-work vacancies will be further reduced by annihilation with radiation-produced interstitials. We shall neglect the effect of this annihilation on the aggregation process. By an argument analogous to that used above the following equations may be shown to govern the concentrations V, V', C_r and C_b:

$$\frac{dV}{dC}=\frac{\sum(T_r-C_r)+B+V'}{B+\sum(T_r-C_r)+V+V'}, \qquad (6)$$

$$\frac{dV'}{dC}=-\frac{SV'}{n}-\frac{V'}{B+\sum(T_r-C_r)+V+V'}, \qquad (7)$$

$$\frac{dC_r}{dC}=\frac{T_r-C_r}{B+\sum(T_r-C_r)+V+V'}, \qquad (8)$$

$$\frac{dC_b}{dC}=\frac{B}{B+\sum(T_r-C_r)+V+V'}, \qquad (9)$$

with the boundary conditions

$$C=0;\; V=C_r=C_b=0$$

and $$V'=V'_0.$$

A numerical solution of these equations has been obtained for the case of cold-worked tungsten using the values of V_0', B and $\sum T_r$ in table 2, taking S as 10^5 and n as 30. The value of V_0' was deduced from the residual resistivity difference of type C and D specimens. From this solution $\Delta\rho$ has been calculated as a function of C and values are shown in fig. 7. The predicted acceleration with C is in agreement with the observations recorded in fig. 6.

4.2. *Recovery*

Blewitt (private communication) has shown that tungsten irradiated at 20°K for 1 week in the Oak Ridge pile recovers about 50% of its resistivity increase after annealing at liquid nitrogen temperature. Since this is in substantial agreement with the tungsten irradiated at low temperatures for 8 min it appears that the effect of dose on this part of the recovery curve is small. An approximate recovery curve between 4°K and 500°C for a 140-hour irradiation may then be sketched as in fig. 8. Recovery below −170° has been designated stage I, that between −170 and 350°C as stage II, that between 350 and 450°C as stage III and above 450°C as stage IV.

Previous work (Kinchin and Thompson 1958) has shown that activation energies in stage II rise from 0·25 to 1·7 ev and that stage III proceeds at 1·7 ev.

Recovery curves of this type have been observed in other metals, the difference being that in some cases, notably gold, stage I is absent (Cooper *et al.* 1954) and that in the case of electron irradiation stage II is greatly reduced (Corbett *et al.* 1957). However, in all reported cases of irradiated, quenched or cold-worked metals stages III occurs at an absolute temperature roughly 20% that of the melting point. Table 3 lists some typical activation energies and temperatures for stage III in Ag, Al, Au, Cu, Mo, Nb, Ni, Pt. and W.

It will be noticed that the ratio of activation energy to absolute melting temperature varies little with the type of damage in a given metal or from element to element. It has long been established that such a relation exists between self diffusion activation energies (Kidson and Ross 1957) where vacancy formation and migration is the common mechanism. This suggests that the same stage III recovery mechanism operates after irradiation, cold work or quenching and that this mechanism is the same for all the above metals.

Fig. 8

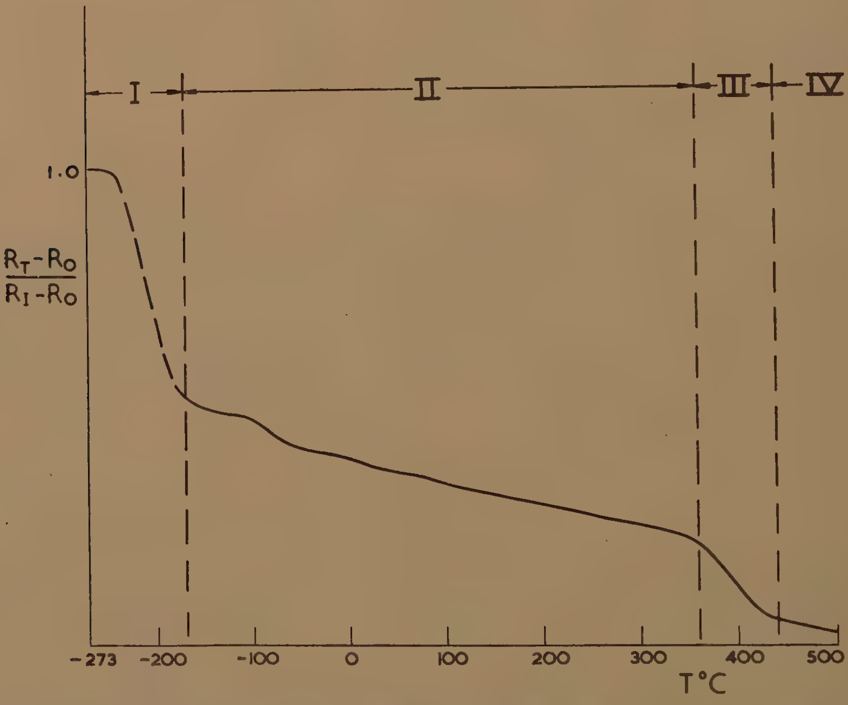

A schematic recovery curve for annealed tungsten after a 140-hour irradiation at 4°K.

Since stage III recovery after quenching is generally attributed to the migration of vacancies (Koehler *et al.* 1957) it is assumed that this is also the case in irradiated and cold-worked material. In particular, let us attribute stage III in tungsten to vacancy migration.

In order to explain the low temperature recovery it is necessary to postulate that interstitial migration occurs either in stage I or at some even lower temperature. For the purposes of this discussion let us assign stage I to interstitial migration.

Specimen types C and D have the same grain size and impurities and should have roughly the same dislocation density. Type D, however,

Table 3

Metal	T_m °K	Damage	E ev	T°K	$\frac{E}{T_m}\times 10^4$	$\frac{T}{T_m}$	Reference
Ag f.c.c.	1234	C.W.	0·65	230	5·3	0·17	Manintveld 1952
Al f.c.c.	933	Irrad.	0·55	190	5·9	0·20	McReynolds *et al.* 1955
		Quench	0·44	300	4·7	0·32	Bradshaw and Pearson 1957 b
		Quench	0·52	270	5·6	0·30	de Sorbo and Turnbull 1959
Au f.c.c.	1336	C.W.	0·69	290	5·2	0·22	Manintveld 1952
		Quench	0·82	310	6·1	0·23	Baurle and Koehler 1957
		Quench	0·68	370	5·1	0·28	Bradshaw and Pearson 1957 a
Cu f.c.c.	1356	Irrad.	0·68	250	5·0	0·19	Overhauser 1955
		C.W.	0·67	230	5·0	0·17	Eggleston 1952
Mo b.c.c.	2893	Irrad.	1·3	420	4·5	0·15	Kinchin and Thompson 1958
		C.W.	1·26	430	4·4	0·15	Martin 1957
Nb b.c.c.	2220	Irrad.	1·3	420	5·9	0·19	Makin 1959
Ni f.c.c	1728	C.W.	1·0	500	5·8	0·28	Nicholas 1955
Pt f.c.c.	2047	Irrad.	1·2	420	5·9	0·21	Dugdale 1952
		Quench	1·1	570	5·4	0·29	Bradshaw and Pearson 1956
W b.c.c.	3643	Irrad.	1·7	670	4·7	0·18	Kinchin and Thompson 1958
		C.W.	1·7	620	4·7	0·17	Schultz 1959

has an initial concentration of vacancies formed during deformation. The recovery curves of fig. 2 show that the effect of these vacancies is to enhance stage II recovery. This is evidence that stage II is in some way associated with interstitial migration resulting in vacancy annihilation.

It was pointed out in an earlier publication (Thompson 1958 a) that the absence of stage II in lightly irradiated tungsten may be explained by assuming that this stage is due to the thermal activation of interstitials from traps in the lattice. After a one hour irradiation $C \sim 10^{-6}$ whereas $\sum T_r \sim 10^{-4}$. Under these conditions interstitials being activated from the shallowest traps will become attached to deeper traps rather than annihilating the small concentration of vacancies present. Provided that the resistivity change associated with those interstitials which reach boundaries is balanced by that due to interstitials changing traps there will be no net recovery observed. In the case of type E specimens, which have a different set of impurities, the presence of stage II recovery after light irradiations might indicate that the decrease in resistivity due to migration to boundaries is not balanced by an increase due to changing traps. If the trapping mechanism of stage II recovery is accepted, then this difference in behaviour between types B and E is clear evidence that impurity atoms are capable of trapping interstitials. A similar conclusion has been reached by Blewitt *et al.* (1957) and Martin (1959, private communication) during studies of neutron-irradiated doped copper. The role of dislocations in recovery is not obvious from the experimental results, owing to simultaneous changes in grain size, but will be considered in the analysis which follows.

Using the three postulates of § 4·1 let us develop a quantitative theory of stage II recovery for comparison with the experimental observations. In order to simplify the analysis the following substitutions will be made:

$$x=\frac{C_b}{B},$$

$$t=1+\frac{\sum T_r}{B},$$

$$E \doteq 1-\exp(-x).$$

It follows from eqns. (3) and (4) that after irradiation the following concentrations of sinks for interstitials will be present:

Vacancies:	$B(x+(t-1)E)$,
Unfilled traps:	$B(t-1)(1-E)$,
Boundary sinks:	B;

$\therefore$ total concentration of sinks $=B(t+x)$.

Now suppose that the temperature of the specimen is raised sufficiently to liberate the interstitials from the first trap (T_1) and that these constitute a small proportion of the total number of trapped interstitials, i.e.

$$T_1=\alpha\sum T_r,$$

The total concentration of released interstitials is found from eqn. (4) as

$$\alpha B(t-1)E.$$

Then the concentration of these which annihilate vacancies is

$$\alpha B(t-1)E\left[\frac{x+(t-1)E}{t+x}\right]$$

the concentration going to the rth unfilled trap ($r \neq 1$) is

$$\alpha B(t-1)E\left[\frac{(1-E)(t_r-1)}{t+x}\right], \quad t_r = 1+\frac{T_r}{B}$$

and the concentration lost to boundaries is

$$\alpha B(t-1)E\left[\frac{1}{t+x}\right].$$

Now (a_1+b) is the resistivity change due to unit concentration of released interstitials annihilating vacancies. a_1 is that due to unit concentration migrating to boundaries and (a_1-a_r) is that due to unit concentration becoming trapped on the rth type of trap. The net recovery of resistivity is then

$$(\Delta\rho)_1 = -\frac{\alpha B(t-1)E}{t+x}\{(a_1+b)(x+(t-1)E) + \sum(t_r-1)(a_1-a_r)(1-E)+a_1\}.$$

The total change in resistivity due to irradiation is given by eqn. (5). We may therefore write the proportion of recovery due to interstitials being released from trap 1 as

$$\frac{(\Delta\rho)_1}{\Delta\rho} = -\frac{\alpha(t-1)E}{t-x}\,\frac{[1+a_1/b](x+(t-1)E)+\sum(t_r-1)\,(a_1-a_r/b)\,(1-E)+a_1/b}{E\sum(t_r-1)[1+a_r/b]+x}. \qquad (7)$$

From experiment it is known that for A and B type specimens recovery is zero for small doses, i.e.

$$\frac{(\Delta\rho)_1}{\Delta\rho} \to 0 \text{ as } x \to 0.$$

Putting this condition into eqn. (7) we conclude that

$$\sum(t_r-1)(a_1-a_r) = -a_1, \text{ in A and B type specimens.} \qquad (8)$$

In physical terms, the resistivity change due to released interstitials migrating to boundaries is compensated by that due to changing traps. Under these special circumstances equation (7) becomes:

$$\frac{\Delta(\rho_p)_1}{\Delta\rho} = \frac{\alpha(t-1)E}{t+x}\,\frac{[1+a_1/b](x+(t-1)E)+(a_1/b)E}{\sum(t_r-1)[1+a_r/b]E+x}. \qquad (7a)$$

In fig. 9 observed values of $(\Delta\rho)1/\Delta\rho$ for the recovery occurring between -120 and -40°C are plotted as a function of irradiation time for A, B, C and D type specimens. The expression (7 *a*) has been made to agree with the type A and B experimental points at 140 hours by choosing suitable values for T_1. It will be seen that the remaining points then fall on the theoretical curves. This indicates that the theory predicts at least the correct functional dependence of recovery on irradiation time. The selected values of T_1 are shown in table 2 and it will be noticed that there is a factor of 3 between the values for specimen types A and B. Because the coefficients a_r are unknown for types C and D and because there is no simplifying relation like (8), it is not possible to tabulate the expression (7) for these other specimens.

Let us now consider the evidence for traps being associated with dislocation lines. The theoretical curves of resistance increase were obtained by assuming a decrease in $\sum T_r$ with increasing pre-irradiation annealing temperature. The temperatures involved strongly suggest that part of the trap concentration follows the dislocation density with the implication that dislocations provide trapping sites. The further fact that T_1 varies with pre-irradiation annealing temperature in a similar way, strengthens this suggestion.

Fig. 9

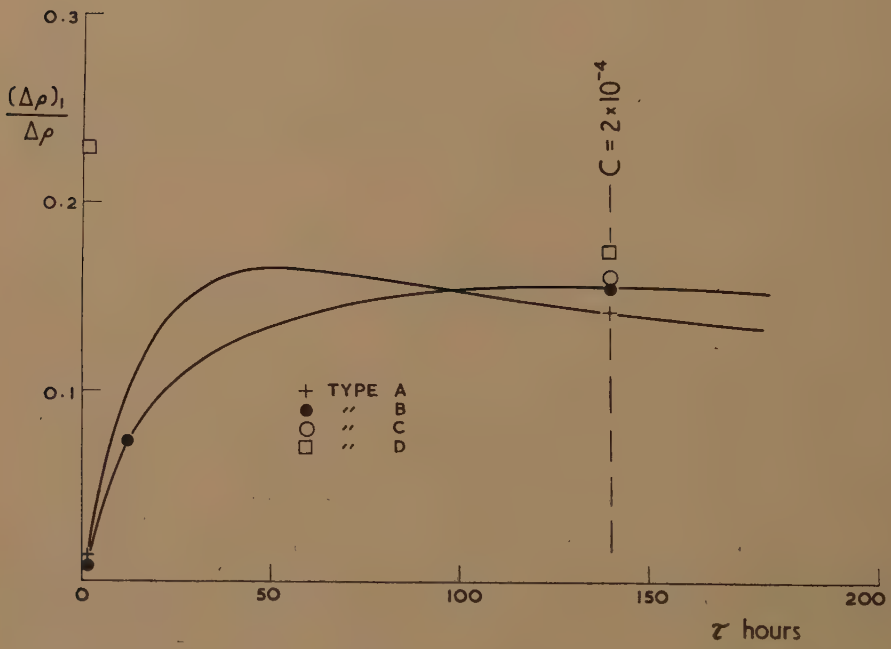

Recovery between −120 and −40°c as a function of irradiation time: the solid lines represent theoretical curves which have been fitted to the observations at $\tau=140$ using the sink concentrations given in table 2.

4.3. *Summary of Conclusions*

A quantitative theory which is consistent with the experimental facts may be derived from the following postulates:

1. Interstitials and vacancies are produced by irradiation in equal numbers.
2. Interstitials are mobile at 77°K, stage I recovery between 4°K and 77°K being tentatively assigned to interstitials first becoming mobile.

3. Vacancies become mobile between 350°c and 450°c and this mechanism is responsible for stage III recovery.
4. Three types of sink compete for interstitials:
    (*a*) Vacancies.
    (*b*) Grain boundaries.
    (*c*) Traps.

   Thermal activation of interstitials from traps is responsible for stage II recovery (−196 to 350°c). These traps are associated both with impurities and dislocations, the concentration depending on pre-irradiation annealing treatment.
5. Irradiation produces spike regions of temporary disorder containing 10^5 atoms.
6. Cold-work produces vacancies in strings and the action of spikes on these is to cause aggregation.

ACKNOWLEDGMENTS

I should like to thank Miss J. Stubbs for her invaluable assistance throughout this work and Dr. T. H. Blewitt and Mr. D. G. Martin for permission to refer to unpublished work.

List of Symbols

R_0 = resistance of specimen before irradiation.
R_I = resistance of specimen after irradiation.
R_T = resistance of specimen after annealing for 30 min at T°c.
τ = Irradiation time.
n = the number of interstitials and vacancies per neutron hit.
S = the number of atoms affected by a spike.
C = total concentration of interstitials and vacancies produced.
C_r = total concentration of interstitials on the rth trap.
C_b = total concentration of interstitials lost to boundaries.
V = total concentration of vacancies present due to irradiation.
V' = total concentration of vacancies present due to cold work (initial value V_0').
T_r = total concentration of traps of the rth type.
B = total concentration of boundary sinks.
a_r = resistivity due to unit concentration of interstitials on the rth trap.
b = resistivity due to unit concentration of vacancies.
$x = C_b/B$.
$t_r = 1 + T_r/B$.
$t = 1 + \sum T_r/B$.
$\alpha = T_1/\sum T_r$.
$E = 1 - \exp(-x)$.

REFERENCES

BAURLE, J. E., and KOEHLER, J. S., 1957, *Phys. Rev.*, **107,** 1493.

BLEWITT, T. H., COLTMAN, R. R., KLABUNDE, C. E., and NOGGLE, T. S., 1957, *J. appl. Phys.*, **28,** 639.

BRADSHAW, F. J., and PEARSON, S., 1956, *Phil. Mag.*, **1,** 812; 1957 a, *Ibid.*, **2,** 379; 1957 b, *Ibid.*, **2,** 570.

COOPER, H. C., KOEHLER, J. S., and MARX, J. W., 1954, *Phys. Rev.*, **94,** 496.

CORBETT, J. W., DENNEY, J. M., FISKE, M. D., and WALKER, R. M., 1957, *Phys. Rev.*, **108,** 954.

COTTRELL, A. H., 1957, *Symposium on Point Defects* (London: Inst. of Metals), p. 26.

DUGDALE, R. A., 1952, *Phil. Mag.*, **43,** 912.

EGGLESTON, J., 1952, *J. appl. Phys.*, **23,** 1400.

GONSER, U., and OKKERSE, B., 1958, *Phys. Rev.*, **109,** 663.

KIDSON, G., and ROSS, R., 1957, Conf. sur l'utilisation des radioisotopes dans la recherche Scientifique, UNESCO/NS/RIG/**216.**

KINCHIN, G., and THOMPSON, M. W., 1958, *J. nucl. Energy*, **6,** 275.

KOEHLER, J. S., SEITZ, F., and BAURLE, J. E., 1957, *Phys. Rev.*, **107,** 1499.

LOMER, W. M., and COTTRELL, A. H., 1955, *Phil. Mag.*, **46,** 711.

MCREYNOLDS, A. W., AUGUSTYNIAK, W., MCKEOWN, M., and ROSENBLATT, D. B., 1955, *Phys. Rev.*, **94,** 1417.

MAKIN, M. J., 1959, *Acta Met.*, **7,** 361.

MANINTVELD, J. A., 1952, *Nature, Lond.*, **169,** 623.

MARTIN, D. C., and STANWIX, P., 1956, U.K. Atomic Energy Authority report, AERE-M/M-138; 1957, *Acta Met.*, **5,** 371.

NICHOLAS, J. F., 1955, *Phil. Mag.*, **46,** 88.

OVERHAUSER, A. W., 1955, *Phys. Rev.*, **90,** 393.

SCHULTZ, H., 1959, *Z. Naturf.*, **14,** 4, 361.

DE SORBO, W., and TURNBULL, D., 1959, *Acta Met.*, **7,** 83.

STUBBS, M. J., and THOMPSON, M. W., 1958, *J. sci. Instrum.*, **35,** 68.

THOMPSON, M. W., 1958 a, *Phil. Mag.*, **3,** 28, 421; 1958 b, *J. sci. Instrum.*, **34,** 515.

THOMPSON, M. W., and JEFFERSON-LOVEDAY, D. W., 1958, *J. sci. Instrum.*, **35,** 397.

CORRESPONDENCE

A Possible Example of the Muon Radiative Decay with Internal Conversion of the γ–ray

By Valerie Mayes
H. H. Wills Physical Laboratory, University of Bristol

[Received March 30, 1960]

In making an area scan for π–μ–e, in a stack which had been exposed to the cosmic rays at an altitude of approximately 13 kilometres, an event was found (Pl. 33) in which three relativistic electrons escaped from the decay of a μ-meson at rest. A similar event has been observed by I. I. Gurevich *et al.* (1959). The nature of the μ-meson was established from its origin and from its range, 613 μ. (The average range for μ-mesons from π–μ decay in G5 emulsion is 595 μ.) The pair and positron tracks dipped steeply down into the emulsion at angles to the emulsion plane of approximately 70° and 45° respectively. It was not possible to follow the electron tracks in more than one emulsion because the stack consisted of alternate layers of 600 μ emulsion and 1·6 mm tungsten. The recorded track lengths were $\mathrm{Le}_1 = 188\,\mu$, $\mathrm{Le}_2 = 186\,\mu$, $\mathrm{Le}_3 = 242\,\mu$. The short length of the tracks and their steepness made energy determinations difficult. Apparent values for the energy of the pair and of the positron were obtained from scattering measurements, these gave

$$\mathrm{E\ pair} = 40 \pm 16\ \mathrm{Mev},$$

$$\mathrm{E\ positron} = 18 \pm 5\ \mathrm{Mev}.$$

From the opening angle of the pair an estimate of E pair of approximately 25 Mev was obtained. The angles between the tracks are

$$\psi e_1 e_2 \sim 5^\circ, \quad \psi e_1 e_3 \sim 60^\circ, \quad \psi e_2 e_3 \sim 58^\circ.$$

Since the electron tracks are not coplanar and the directions of the pair and of the positron are not collinear, the event cannot be identified with either $\mu \rightarrow 3e$ or $\mu \rightarrow e + \gamma$ with subsequent conversion of the γ-ray. The event can be identified, however, with either (1) $\mu^+ \rightarrow e^+ + (e^+ + e^-) + \nu + \bar{\nu}$ or (2) the coincidence of a converting γ-ray with the decay point of a μ-meson. The probability of radiative decay has been assessed by N. Tzoar and A. Klein (1958) as 10^{-5} per μ-meson and hence that of (1) is of the order of 10^{-7} per μ-meson. The probability of finding a background electron pair within 10 cubic microns of the μ^+ decay was determined from the density of π^+ in the emulsion and was of the order of 10^{-9} per

μ-meson, i.e. several orders of magnitudes smaller than the theoretical probability of radiative decay with internal conversion. In order to check that this did not underestimate the probability of coincidence, an area scan for electron pairs was made. This showed that the density of pairs was not greater than the density of π^+ (400 per cm^3) in the vicinity of this event.

The probability of a positron producing an electron pair, either by conversion of bremsstrahlung or by trident production (i.e. direct pair production in the field of a nucleus), in the first few microns of its path after normal μ decay, is of the same order of magnitude as the probability of radiative decay with internal conversion. In this event, however, the positron and electron pair were separated by approximately 60° and in the above two processes, at this energy, the electrons would be collimated within a few degrees. In the event observed by Gurevich *et al.* the pair and positron were indistinguishable, all three tracks lying within approximately 10° of one another.

Acknowledgments

It is my pleasure to thank Professor C. F. Powell for the facilities of this laboratory. I am indebted to Dr. D. H. Perkins and Dr. P. H. Fowler who interpreted this event and to Dr. K. Pinkau for helpful advice. Mr. W. Harbor photographed the event and I am grateful to him for his skill and patience. My thanks are due to D.S.I.R. for a maintenance grant.

References

Gurevich, I. I., *et al.*, 1959, *J. exp. theor. Phys.*, **37**, 318 (translation, *Soviet Phys.*, **37**, 225, 1960).
Tzoar, N., and Klein, A., 1958, *Nuovo Cim.*, **8**, 482.

Direct Electron Microscopy of Thin Foils of Internally Oxidized Dilute Copper Alloys

By M. F. Ashby and G. C. Smith
Department of Metallurgy, University of Cambridge

[Received February 26, 1960]

Several workers (Bollman 1956, Hirsch *et al.* 1956, Nicholson *et al.* 1957, Nicholson and Nutting 1958, Whelan *et al.* 1957) have developed techniques for examining thin metal foils by direct electron transmission. This paper describes the application of these techniques to the examination of an internally oxidised copper 0·25% aluminium alloy. The authors have obtained electron micrographs which show the internal oxide particles in the copper matrix and the interaction of dislocations with these particles.

This alloy, rolled to a strip 200 microns thick, was internally oxidized by placing it in cuprous oxide and heating for 20 min at 950°C, producing a dispersion of alumina in a pure copper matrix. Electron diffraction of electropolished specimens, using a reflection technique, showed the dispersion to be of γ high temperature alumina. This analysis was confirmed by preparing carbon extraction replicas from the specimen surface, and photographing diffraction patterns from them, using a selected area electron diffraction technique.

Satisfactory foils of this internally oxidised strip were obtained by using the Bollman (1956) technique. The bath used was a methyl alcohol: concentrated nitric acid mixture in the proportion 2 : 1, at a potential of 9 volts and a temperature of −20°C. Figure 1 (Pl. 34) is an electron micrograph of a foil of an unstrained specimen produced in this way. Many of the alumina particles, of diameter about 300 Å, are clearly defined as triangular plates or tetrahedra, and there is evidence of precipitation along preferred planes in the copper matrix. Pronounced contrast effects can be seen around the particles in the twin, where the lattice orientation is favourable for diffraction contrast. Two explanations in terms of strain fields are possible. Firstly, Nicholson and Nutting (1958) have shown that coherency strains can give rise to this type of strain pattern, so the alumina particles may be coherent with the copper matrix ; attempts to fit the alumina and copper lattices to allow coherency have so far proved unsatisfactory. Secondly, while the material is cooling after the internal oxidation process, the considerable difference in coefficient of thermal expansion of copper and alumina must produce strain fields around the particles. This second explanation seems the more probable one. The dark rings surrounding some of the particles in fig. 1 are due to carbon contamination of the foil in the microscope ; carbon builds up round particles which project from the surface of the foil.

Other foils, also internally oxidized, were strained in tension by amounts varying from 0·5 to 6·0%. From among these foils, two, strained 4%, have been selected for illustration (figs. 2 and 3, Pl. 34).

Dislocations are visible in fig. 2 bowed out between points where alumina particles prevent their movement. At first sight this pattern of dislocations seems consistent with Orowan's theory of hardening of metal by a dispersed phase (Orowan 1947). The foil is of the order of 1000 Å thick, so that any one particle will not intersect all the slip planes in the plane of the foil. However, by measuring the distance apart ($2R$) of particles between which a single dislocation is bowing out, an estimate of the yield stress (σ) of the material can be calculated, using the relationship:

$$\sigma = \frac{\alpha G \mathbf{b}}{R}$$

(where α is a constant approximately equal to $\frac{1}{2}$; G is the shear modulus of the matrix; and **b** is the Burgers vector of the dislocation.) The mean calculated yield stress was 1·4 × 10⁴ p.s.i. The measured yield stress was 1·58 × 10⁴ p.s.i.

Heavily jogged dislocations and triangular dislocation loops attached to particles can be seen in fig. 3. These loops have not collapsed onto the particles, but bow out from them. A stable configuration such as that seen in fig. 3 can be explained by supposing the loops to be prismatic, i.e. that all parts of the loop do not lie in the same slip plane. The authors have used a modification of Orowan's theory first proposed by Hirsch (1957) to explain the formation of these loops. This is illustrated schematically in fig. 4.

Fig. 4

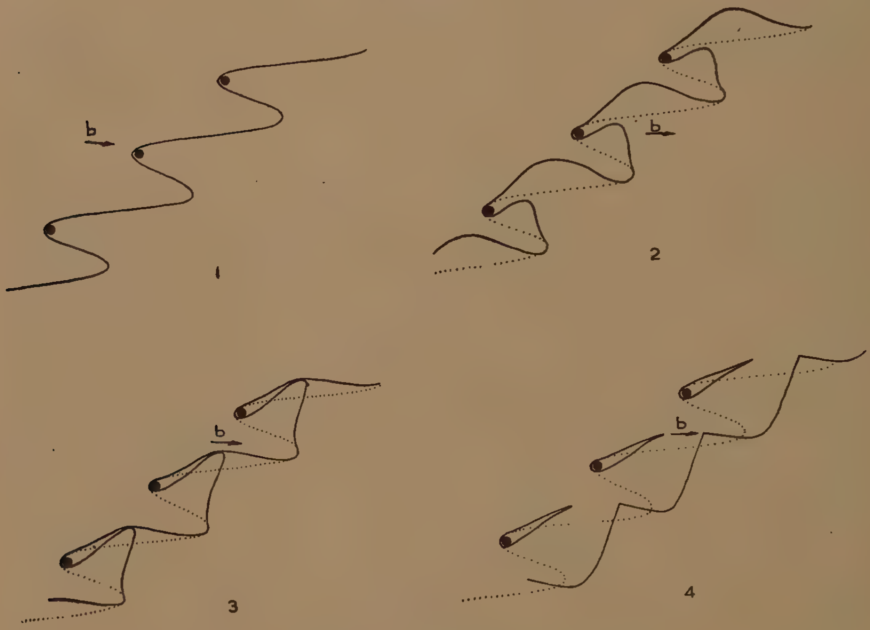

In 1 a pure edge dislocation, moving in the direction of its Burgers vector (**b**), has been held up by a set of particles intersecting the slip plane. As the applied stress rises, the screw components of the dislocation, formed when the dislocation took up the shape shown in 1, cross slip, as shown in 2. These screw components are of opposite sign on each side of a single particle; they attract each other, as in 3; and annihilate each other, as in 4. The process leaves a prismatic loop round each particle and corresponding prismatic jogs in the dislocation line. The loops can move on the surface of a cylinder whose axis is parallel to the Burgers vector, but they cannot collapse completely. This diagram shows the simplest form of this type of interaction. Any dislocation with an edge component should behave in a similar way.

A prediction from this mechanism is that the direction of elongation of the loops projected on to a slip plane will be parallel to a slip direction in the matrix metal. This prediction could be checked by electron diffraction experiments : these have not yet been tried. Inspection of fig. 3 shows that the loops appear to have a common direction of elongation.

ACKNOWLEDGMENT

The authors are indebted to Dr. P. B. Hirsch and Dr. A. Kelly for many helpful discussions and to Mr. R. S. M. Revell for his help in obtaining the electron micrographs. All electron micrographs were taken on a Metropolitan-Vickers E.M.6.

REFERENCES

BOLLMANN, W., 1956, *Phys. Rev.*, **103,** 1588.
HIRSCH, P. B., 1957, *J. Inst. Met.*, **86,** 13.
HIRSCH, P. B., HORNE, R. W., and WHELAN, M. J., 1956, *Phil. Mag.*, **1,** 677.
NICHOLSON, R. B., THOMAS, G., and NUTTING, J., 1957, *Brit. J. appl. Phys.*, **9,** 25.
NICHOLSON, R. B., and NUTTING, J., 1958, *Phil. Mag.*, **3,** 531.
OROWAN, E., 1947, Discussion, *Symposium on Internal Stresses* (London : Inst. Metals).
THOMAS, G., NUTTING, J., and HIRSCH, P. B., 1957, *J. Inst. Met.*, **86,** 7.
WHELAN, M. J., HIRSCH, P. B., HORNE, R. W., and BOLLMANN, W., 1957, *Proc. roy. Soc.*, **240,** 525.

REVIEWS OF BOOKS

Manual of Mathematical Physics. By PAUL I. RICHARDS. (London: Pergamon, 1960.) [Pp. 486.] £5 10*s*. 0*d*.

MOST dictionaries of mathematics or physics are useless: the topics are too intimately linked in logical chains; a single word, or phrase, cannot be pulled out and discussed in isolation; it carries with it strands of meaning connected with every other word in the list. This Manual is something different—it is a cryptic summary of the most important subjects in Mathematical Physics, more or less logically derived. It might be, as it were, the notes one prepares before an examination, reminding one of all the formulae and their relations, without going into all the rigorous details. The idea is a good one, and it seems to have been undertaken very conscientiously. Thus, the general pattern is sound, the style is extraordinarily easy for such a condensed work, and all is well indexed and complete with cross references. It is impossible to do more than check one's own field; it seemed sensible though I must admit that there were a few typographical errors in the formulae. The level is that of the well-educated theoretical physicist who is not a specialist in the particular field in which he is seeking guidance. As a work of reference it should be very handy, in a library or in the private collection of the experienced research worker. J. M. Z.

Fluid Mechanics. By L. D. LANDAU and E. M. LIFSHITZ. (Pergamon Press, 1960.) [Pp. xii+536.] £5 5*s*. 0*d*.

THIS book provides a concise and, on the whole, clear account of the fundamental physical phenomena associated with the mechanics of moving fluids. The structure of fluids is not considered, except in so far as it determines the macroscopic variables of state and the various transport coefficients of mass, momentum and energy. It is written from the standpoint of the theoretical physicist, and little mention is made of many aspects of fluid mechanics related to phenomena of geophysical and engineering interest. Not much space is devoted to the detailed solution of particular problems or the presentation of empirical results, except where these illuminate the topics. On the other hand, there are accounts of subjects, such as thermal diffusion, geometrical acoustics, relativistic fluid mechanics, and the dynamics of superfluids, which are not usually included in treatises on fluid mechanics.

The book starts with the motion of an ideal, but not necessarily uniform, fluid, and this is followed by accounts of the motion of a viscous fluid, turbulence, and boundary layers. These first four chapters are not altogether satisfactory, although the good features outweigh the bad. They make very interesting reading for the fluid dynamicist and contain some important new material, in particular a proof that a laminar boundary layer can separate only at a point where the wall stress is zero; but the arrangement of the material is somewhat arbitrary and occasionally the ideas are not presented clearly. There are next three brief chapters on some flows in which temperature gradients, diffusion, and surface effects, are important. These are followed by seven chapters on the motion of a compressible fluid or gas dynamics, which constitute a first class and stimulating account of the subject as it was a few years ago. The book concludes with chapters on relativistic fluid dynamics, the dynamics of superfluids, and fluctuations in fluid dynamics.

This book, although not without some flaws, is a stimulating and welcome addition to the growing list of treatises on fluid mechanics. One serious fault, however, is that it is useless as a bibliography, since only the author and date are given for most of the original papers referred to. P. G. S.

Quantum Particle Dynamics. By J. McConnell. (North Holland Publishing Company, 1960.) [Pp. 266.] 40*s*.

This second revised edition, appearing only two years after the first edition, is a readable and well presented account of quantum mechanics, quantum field theory and elementary particles. In a book of such short length certain topics have to be left out. This is especially noticeable in the last two chapters on nuclear physics and elementary particles. This may reduce the value of the book for those who wish to understand the modern theory of elementary particles. But it is still a valuable guide to the earlier stages in the development of this theory.

The first half of the book is a detailed discussion of quantum mechanics. Chapter headings show the ground covered: Special Theory of Relativity, Introduction to Quantum Theory, Schrödinger's Wave Mechanics, Heisenberg's Matrix Mechanics, Angular Momentum Systems, of Particles, The Dirac Equation. Then a careful discussion of quantisation of the electromagnetic field is given, and applied to the photoelectric and Compton effects, Bremsstrahling and Electron Pair Production. Finally in the last two chapters a brief consideration of nuclear forces and an even briefer one of elementary particles is given. The manner in which the topics are discussed makes this book very suitable for undergraduate level. The last two brief chapters should certainly whet the appetite of the interested reader for more detailed discussions of recent work in elementary particle physics. J. G. T.

Taylor Memorial Manual of Advanced Undergraduate Experiments in Physics. American Association of Physics Teachers (Editor-in-Chief: Thomas B. Brown.) (Reading, Mass.: Addison-Wesley, 1959.) [Pp. 550 with 241 line diagrams.] 72*s*.

This manual, dedicated to one of the foremost teachers of experimental physics in the United States, is designed primarily as an aid to those responsible for arranging advanced practical courses in universities and colleges. It is therefore much more a compendium of principles for the teacher than a working text-book for the individual student. The latter type of book is regrettably lacking, at least in Great Britain, and the former non-existent in the reviewer's experience until now. The nearest equivalent in the past would be the series of books on experimental physics by Searle, which had the advantages and disadvantages of their single authorship. The new Manual is a cooperative effort, in which contributions from 191 individual physicists have been co-ordinated and boiled down by a board of eight editors. The result is a mine of information, which any University physics department will do well to quarry, and not least those (not a few) brought up on and still anchored to ' Searle '. Whilst it is true that the basic philosophy of experimental physics can be distilled out of almost any experiment, it is equally true that the individual student's interest is likely to be more readily aroused by examples related to a modern context. Also a considerable number of new practical techniques have come out of modern physics and ought now to find a place in an undergraduate course. It will be helpful to many, for instance, to look through the section on non-linear oscillators, which includes a simple illustration of a relaxation oscillation, and the next section in which servomechanisms are discussed.

All the main branches of physics are covered, the chapters on electricity and magnetism and on nuclear physics being particularly extensive. The former includes microwave optics and the latter a section on health hazards. Inevitably in such an encyclopaedia the level and the detail of treatment vary considerably. Much of the Optics chapter is hardly more than a statement of physical principles, with little in the way of information about apparatus and its setting up. In the chapters on Heat, on Acoustics, and to a lesser extent in those on Electronics and Atomic Physics, there is much more practical detail. Of intent, however, ‘ old, familiar experiments ’ are given little more than a mention and a reference, so as to make space for the less familiar and the new.

The Manual has clearly been a labour of love by the friends and colleagues of Professor Ll. W. Taylor. In creating such a memorial, they must be congratulated on performing also a valuable service to Physics. It should serve as a guide and reference book to all who are involved in bringing up to date the advanced practical teaching of the subject, and in this instance ‘ advanced undergraduate ’ seems indeed to mean the same thing in both Britain and the United States.

V. E. C.

CORRIGENDA

Magnetoresistance of Copper, Silver and Gold, by M. G. PRIESTLEY, 1960, *Phil. Mag.*, **5**, 111.

On p. 114 of this paper the last two lines of the table should read as follows:

[111]	(110)	5	5	6·1
	(211)	6	6	5·3

[*The Editors do not hold themselves responsible for the views expressed by their correspondents.*]

Fig. 2

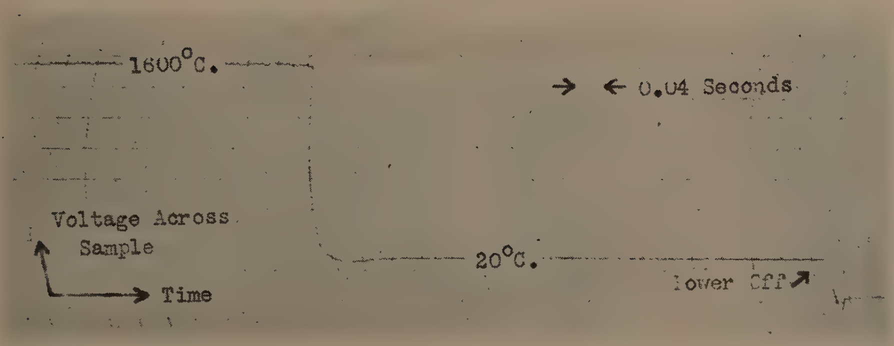

Relative temperature of platinum wire *vs* time when quenched into water. The temperature is measured by the resistance of the sample which is proportional to the voltage if the heating current is left on during the quench.

Fig. 2

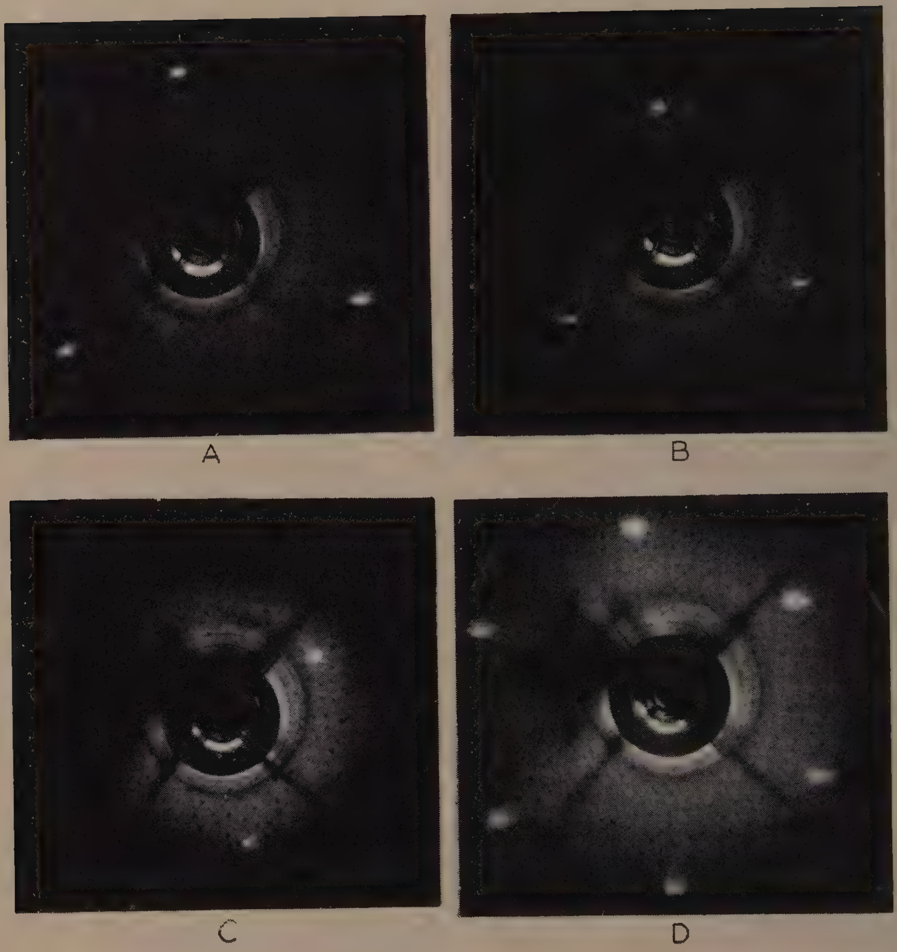

Representative diffraction patterns from the (111) face of a clean nickel crystal (see table 1). (A) (533) reflections at 129 v; (B) (644) reflections at 200 v; (C) (466) reflections at 262 v; (D) reflections in both of the principal azimuths at 120 v.

Fig. 7

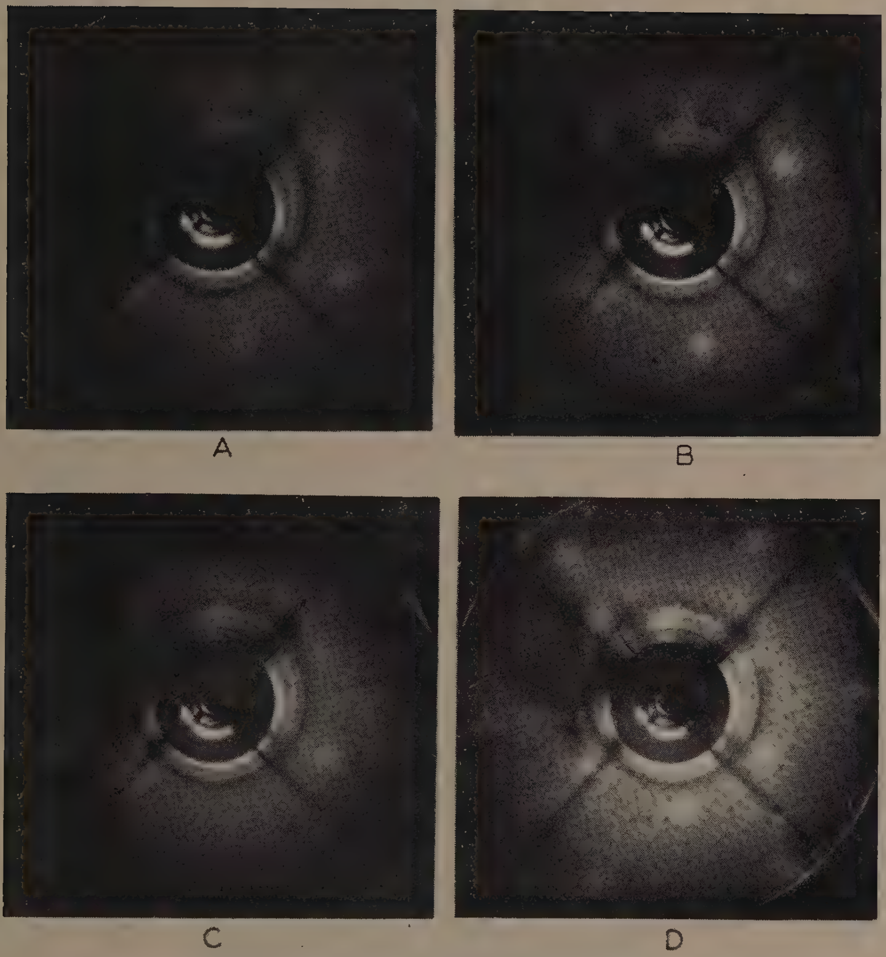

Diffraction patterns representing a monolayer of nitrogen atoms on a (111) nickel surface, arranged in the 4 structure (see table 2). (A) 52 v, diffraction beams strong in B azimuth ; (B) 57 v, diffraction beams strong in A azimuth ; (C) 65 v, diffraction beams strong in B azimuth ; (D) 77 v, diffraction beams in A and B azimuths equally strong.

Fig. 5

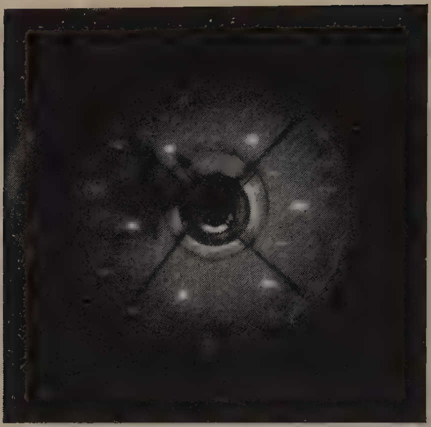

Diffraction pattern from unknown material upon crystal, before it had been thoroughly cleaned. Taken at 78 v, 1·39 Å.

Fig. 8

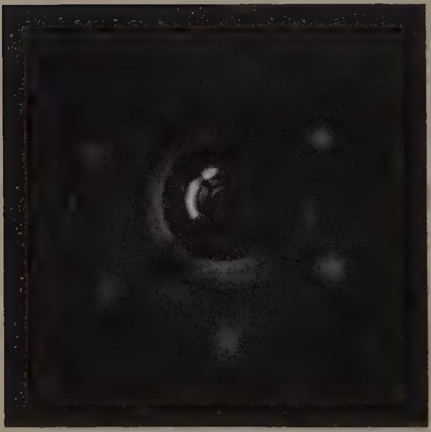

Diffraction pattern from a monolayer of nitrogen atoms on a (111) nickel face, arranged in the 3 structure. 62 v (see table 2).

Fig. 9

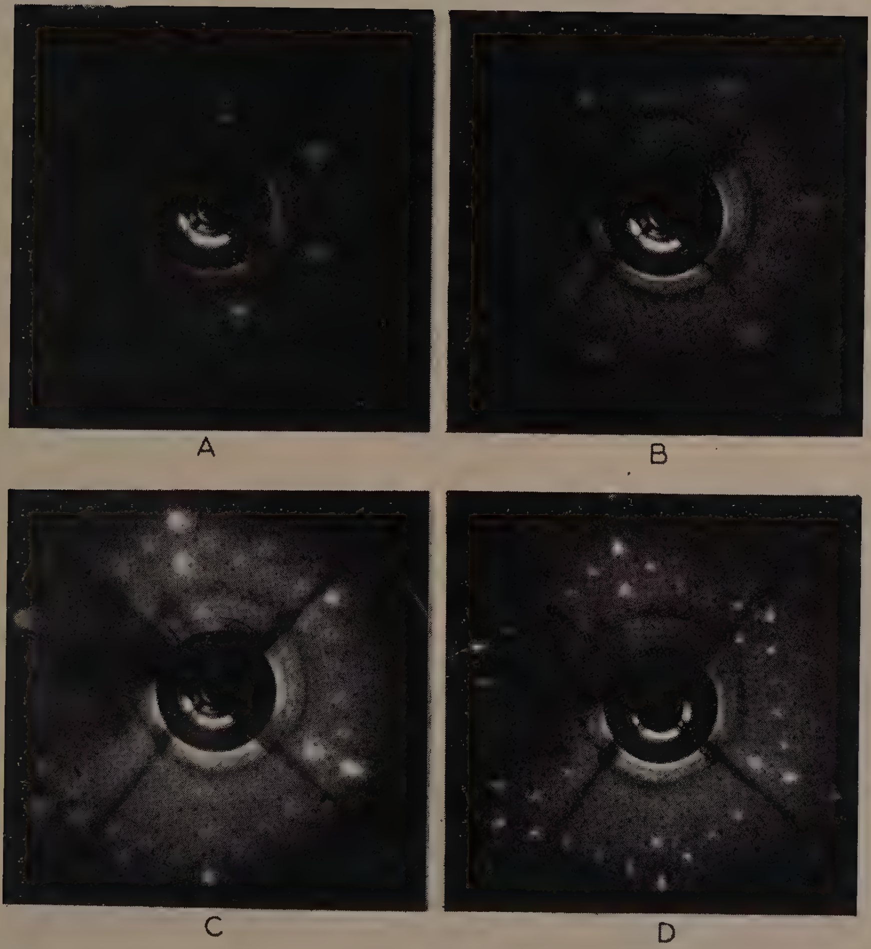

A B C D

Diffraction patterns from nitrogen atoms arranged in the Q structure (see table 3). (A) 48 v; (B) 75 v; (C) 120 v, pattern diffuse; (D) 120 v, pattern sharp after heating to 375°c.

Fig. 10

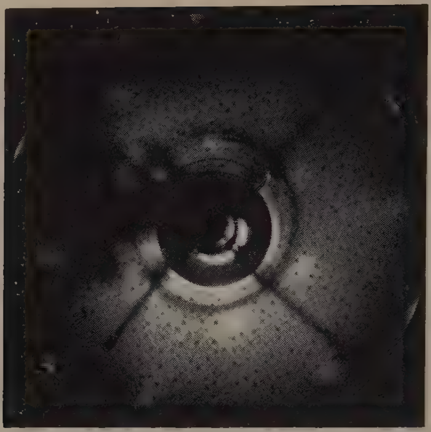

Diffraction pattern from a monolayer of CO molecules arranged in the 4 structure. The pattern is as sharp as one would expect from a single two-dimensional crystal.

Fig. 11

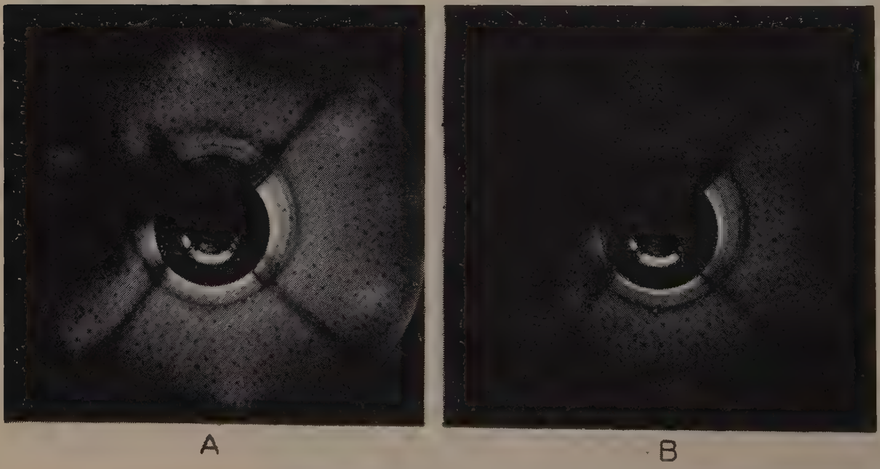

Diffraction patterns from a heavy layer of oxygen on the crystal surface, so much oxygen that no patterns at all appear from the crystal itself. 82 v, 1·35 Å. Before anneal even the oxygen gave no pattern. (A) after anneal at 200°c; (B) after further anneal. Heating the crystal sufficiently to bring back the Laue beams to full intensity resulted in no further change of the oxygen pattern. Apparently the Q structure (see table 4).

Fig. 4

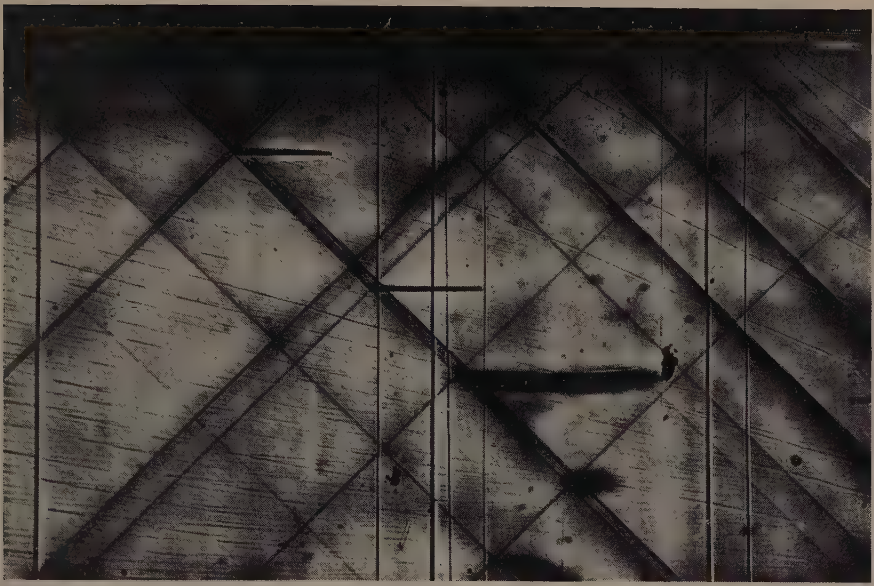

Group of three cracks seen in a lithium fluoride specimen which had been irradiated with 4×10^{15} 1 MeV electrons/cm^2 and then compressed 0·7% along [001]. The cracks which form on the usual (100) cleavage planes parallel to the compression axis, are initiated at slip-plane intersections. The slip planes are made visible by enhanced optical absorption produced by deformation of the irradiated crystal. (90 × .)

Fig. 5

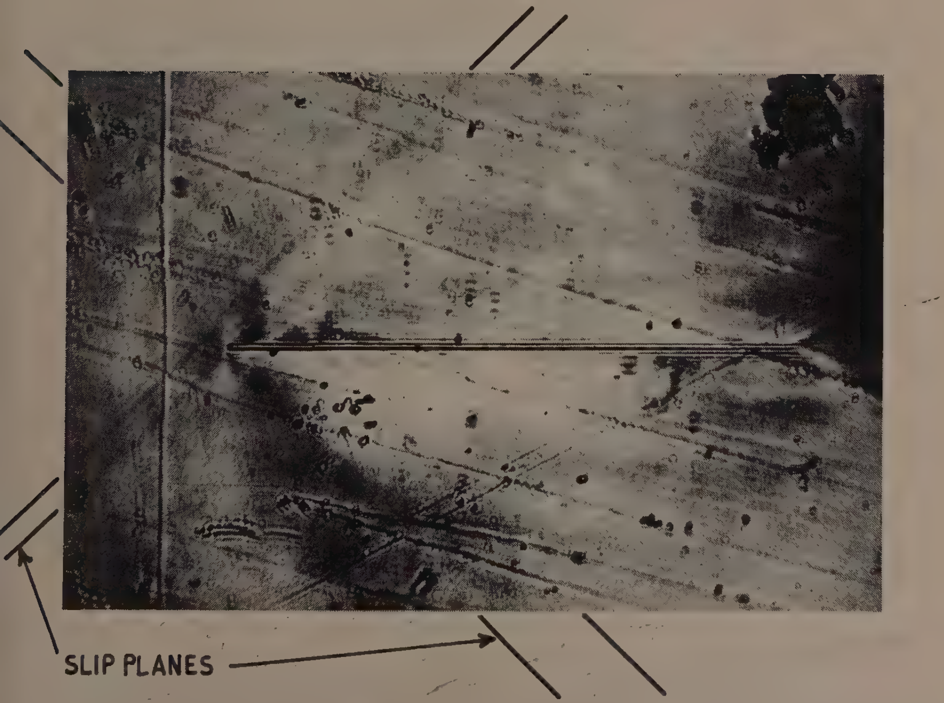

The upper crack of the group of three in fig. 4 at higher magnification. There is no sign of any component of the crack on any plane other than (100). (500 × .)

Fig. 10

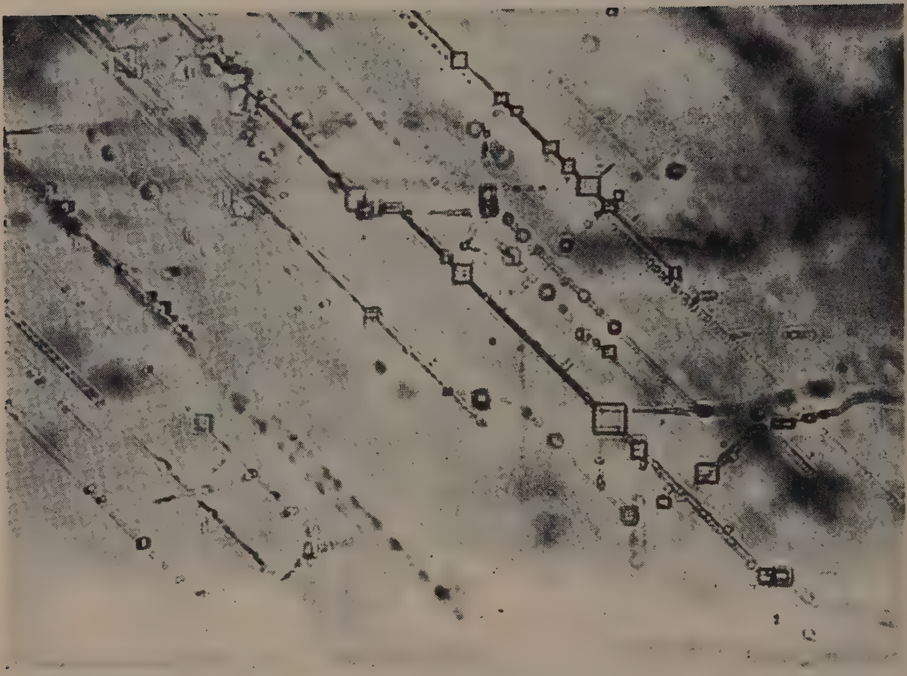

Lithium fluoride single crystal annealed for ½ hr at 700°c after an irradiation dose of 2×10^{16} 1 MeV electrons/cm^2, showing the rectangular cavities produced by vacancy condensation. The diagonal lines lie on {110} slip planes and are thought to result from non homogeneous, radiation-induced expansion of the crystal lattice.

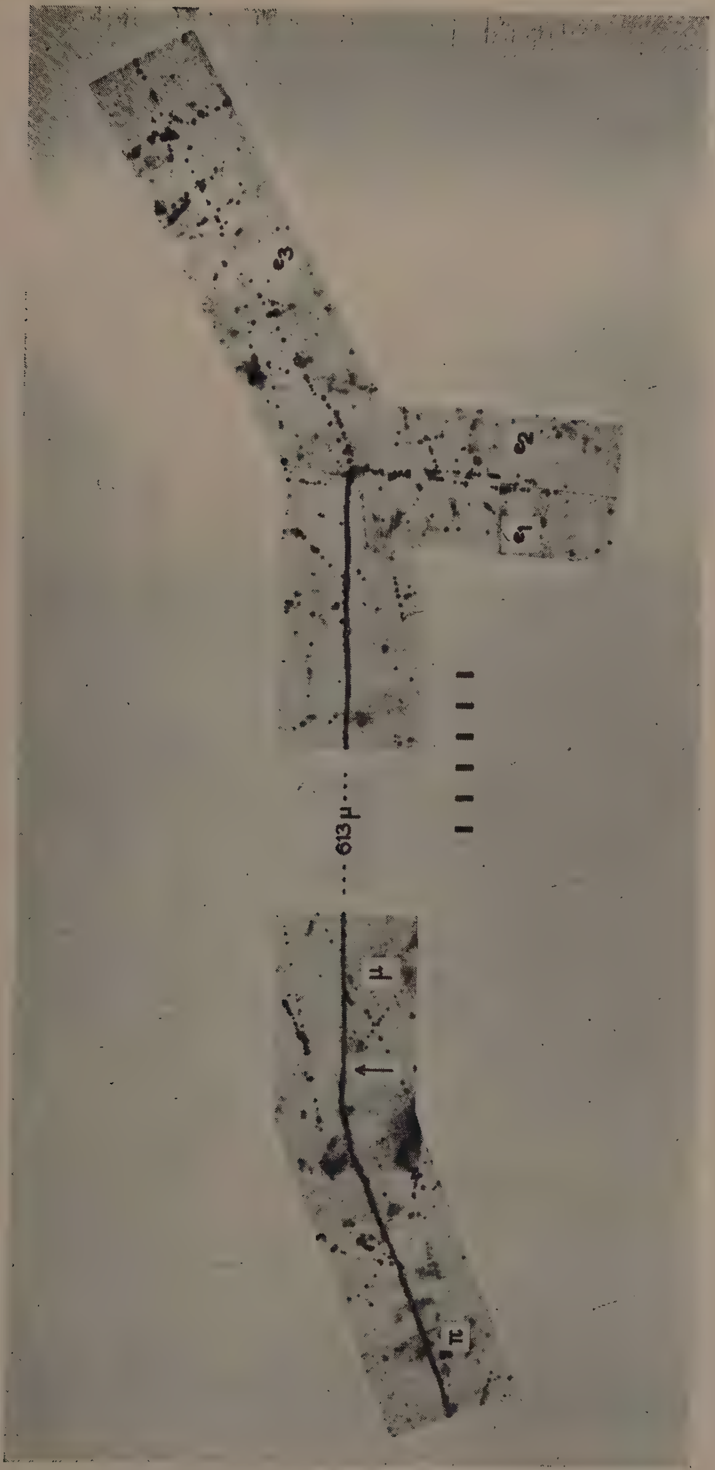

Decay of μ^+ meson which is consistent with $\mu^+ \rightarrow e^+ + (e^+ + e^-) + \nu + \bar{\nu}$.
The 613 μ refers to the total range of the μ-meson.

The scale shows 10 μ intervals.

Fig. 1

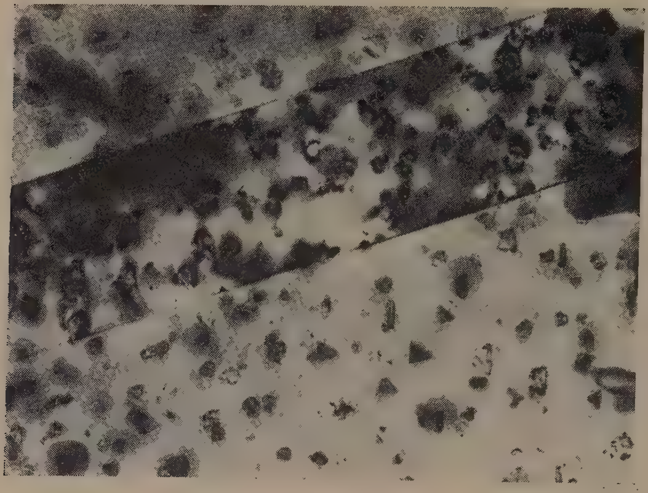

×60 000

Fig. 2

×60 000

Fig. 3

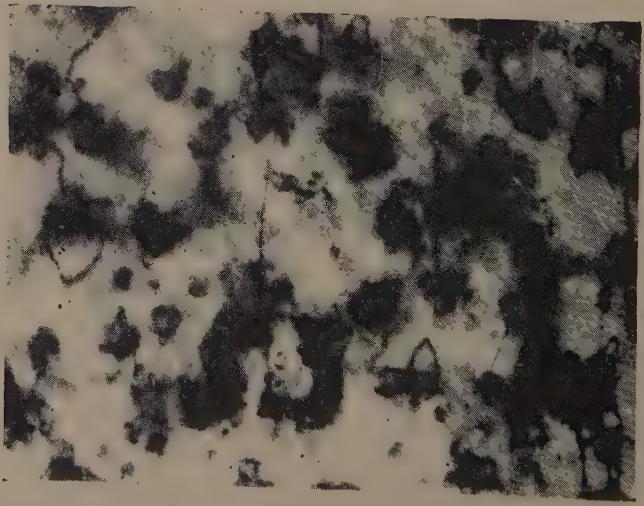

Observations on Extensive Air Showers
VIII. The Distribution in Declination and Curvature of the Shower Front†

By E. F. Bradley and N. A. Porter‡
Atomic Energy Research Establishment, Harwell

[Received November 9, 1959]

Abstract

A directional Čerenkov counter has been used at latitude 52° N to separate shower directions into two classes, incident from North and South of the East–West plane through the zenith. Evidence from some previous experiments indicates a Northern excess of approximately 30%. No excess has been observed; out of 526 showers, each containing at least 3×10^6 particles at sea level, 261 were incident from the North, and 265 from the South. The apparent direction of a shower was found to be dependent on the position of its axis relative to the detector. A directional radius of curvature was measured, making reasonable assumptions, and found to be $1625 \pm^{505}_{290}$ metres.

§ 1. Introduction

A number of experiments on large air showers have shown marked anisotropies in the distribution of shower directions in declination, though without appreciable effects in right ascension (McCusker 1959). The assignment of declination coordinates to showers may be strongly affected by small systematic errors in measurement, and these errors are not, as in the case of right ascension, eliminated by the rotation of the earth. Nevertheless, the statistical significance of the effects is high, and the distributions observed in different experiments are rather similar, showing an anomalously large number of showers from Northern directions.

An experiment has been carried out with a directional Čerenkov counter on the Culham array, latitude 52° N (Cranshaw and Galbraith 1957 a, b) to divide shower directions into two classes, incident North and South of the East–West zenith plane in laboratory coordinates. If the distribution of shower directions is isotropic, the same number of showers should be observed in the two classes. A distribution similar to that given by the M.I.T. group (Clark *et al.* 1957) for showers containing more than 2×10^6 particles, would give rise to a ratio in numbers $N/S \approx 1{\cdot}30$.

---

† Communicated by the Authors.
‡ Now at University College, Dublin.

§ 2. EXPERIMENTAL METHOD

The detector was a laminated parallelopiped of Perspex (refractive index 1·49) with dimensions $80 \times 53 \times 12{\cdot}5\,\mathrm{cm}^3$. It was supported along two lower edges in a horizontal steel tube (fig. 1) so that Čerenkov light produced by charged particles in it was retained only by multiple total internal reflection. Three 5 in. photomultipliers connected in parallel, were mounted in optical contact at each of the end faces. Signals from each of the two sets of photomultipliers were amplified separately and displayed on a recording oscilloscope.

Fig. 1

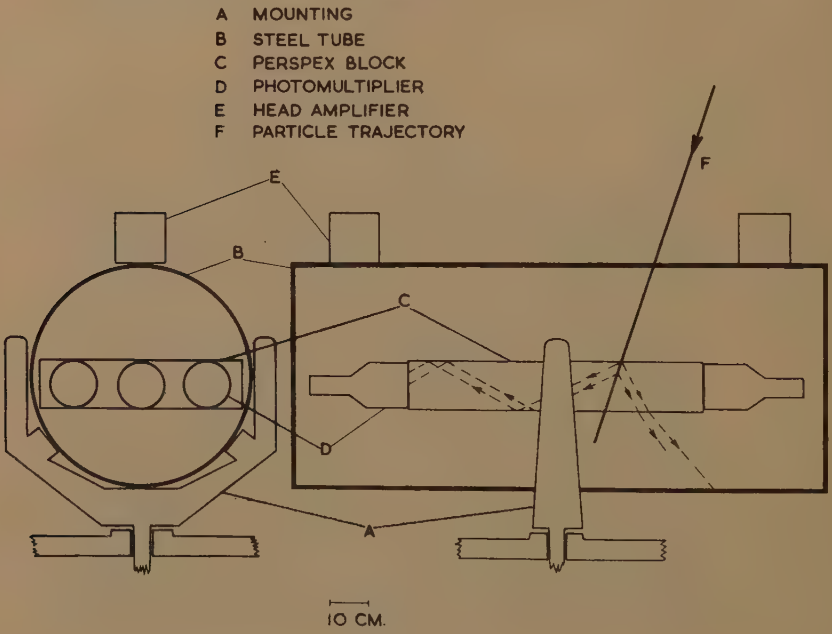

A particle incident normally on the block gave a signal approximately equal in the two sets of photomultipliers, since all the light was retained, and collected in approximately equal parts at both ends roughly independent of the position. A particle incident obliquely at the upper face of the block, however, gave a signal larger in the photomultipliers towards which it was directed, since some of the Čerenkov light was lost at the lower surface of the block. Showers could therefore be assigned to northerly or southerly directions from the ratio of signals in the two sets. The theory of the detector has been considered in the book by Jelley (1958, pp. 138–141).

In a subsidiary experiment, carried out with a Geiger telescope selecting μ-mesons, the directional response was determined. For showers, averaging over all azimuth and zenith angles, and using the zenith distribution found by the M.I.T. group, the mean signal in the preferred channel was then calculated to be roughly three times that in the other channel.

Statistical fluctuations in the number of photo-electrons produced, together with variations in mean pulse height over the surface of the block, gave rise to an uncertainty in the assignment of showers into the two classes. The probability, averaged over all zenith and azimuth angles, that a single particle was assigned to the wrong class, was 0·07. If more than one shower particle was observed this probability was considerably less. The contribution from these sources to the total statistical error is roughly 27% of the Poisson error in N/S.

In addition to the uncertainties in measurement of particle directions, the mean direction of the particles observed in any region of the shower will not correspond exactly to the axial direction. Two effects occur: (*a*) a systematic tendency for particle directions to diverge from the axial direction, increasing with distance of observation from the axis; and (*b*) the fluctuations of individual particles about the mean direction. The systematic effect was detected experimentally, and has been used to estimate the directional radius of curvature, i.e. the mean height (in the case of a vertical shower) at which particle directions projected from sea-level approach most nearly to the axis. The directional radius of curvature is comparable in magnitude with the radius of the shower front, which has been measured by several workers (Bassi *et al.* 1953, Greisen 1957) and is between 1·5 and 2·5 km. The relation between the two depends on the nature of the cascade process, on which very little reliable information is available. Particles deflected by multiple scattering alone, and reaching sea level without bremsstrahlung or appreciable loss of energy by ionization will project back to a height $2h/3$, where h is the height at which they left the axis (Scott 1949). Physically the process is more complex, since discontinuous losses of energy occur in bremsstrahlung, and in part of the trajectory the energy is carried by γ-rays. It would be expected, however, that the directional radius of curvature would lie between $2h/3$ and h, the radius of the shower front. Monte Carlo calculations are in progress on this problem.

The effects of fluctuations in individual particle directions on the overall N/S ratio is small, if the r.m.s. deviation is taken to be 10°, a value expected from electromagnetic cascade theory, and compatible with cloud chamber observations. In the present case, roughly half the events were single particle observations, and the contribution to statistical errors from fluctuations of this kind will be approximately 25% of the Poisson distribution in N/S.

If a true N/S excess exists, the mean value observed will be reduced somewhat because of these fluctuations. For a true value 1·30, the experimentally expected value is 1·24.

The detector was mounted in a caravan at the centre of the array. It was rotated through 180°, about a vertical axis, every 24 hours, so that the two sets of photomultipliers faced alternately North and South.

§ 3. Results

3.1. *North/South Ratio*

3075 showers have been observed on the array during one run. 673 of these could be assigned in direction, 16 gave signals which saturated both channels of the detector, 17 gave pulses equal in both channels, within the errors of measurement, and 2369 gave no signal in either channel. The distribution of assignable shower directions, in relation to the position of the core on the array, is shown in fig. 2. Taking only showers which fell in the circular area of 320 metres radius, the distribution of shower cores was almost uniform about the East–West line, 255 falling North, and 271 South.

Fig. 2

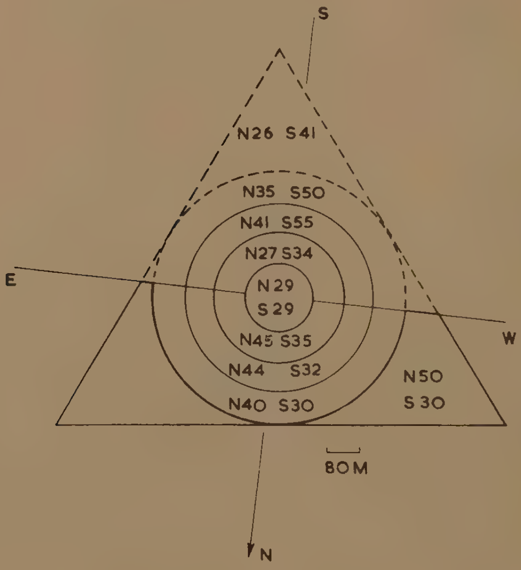

The direction of showers in this area were: 261 northerly, 265 southerly. These figures may therefore be used to determine the North/South ratio:

$$\mathrm{N/S} = 0\cdot99 \pm 0\cdot12.$$

The probability that this result be consistent with a true value $\mathrm{N/S} \geqslant 1\cdot30$, is about 0·01 on a χ^2-test. Over the whole array, 337 showers were assigned to northerly directions, and 336 to southerly directions. The statistical error includes that due to uncertainties in classification of direction, and to the difference in numbers of showers falling North and South of the East–West line.

3.2. *Radius of Curvature*

It may be seen from fig. 2 that showers falling North of the detector show a northerly directional excess, and showers falling South, a southerly excess. Assuming a zenith angle distribution $dN d\theta = K \cos^{11}\theta \, d\theta$, which is similar to that found by Clark *et al.* (1957) and integrating numerically over each half annulus for zenith, azimuth, *direction* and distance from the detector, the directional radius of curvature may be found. Values are shown as a function of distance from the shower axis, in the table:

Directional Radii of Curvature

Distance from axis, metres	Directional radius metres
80–160	1040^{+1490}_{-350}
160–240	1380^{+830}_{-345}
240–320	1840^{+1130}_{-460}
>320	1925^{+1155}_{-565}
Weighted mean value 80–320	1625^{+505}_{-290}

An increase of radius of curvature with increasing distance from the core would be expected, but the measurements are insufficiently accurate to establish it. The differences in total numbers of showers falling in corresponding North and South half-annuli arise from the granular structure of the array, and have no systematic effect on either the North/South ratio or the curvature measurements.

§ 4. Discussion

It is unlikely that a broad anisotropy could be masked in the present experiment by systematic errors. The rotation of the counter serves to eliminate errors due to differences in response of the two channels, or departure of the counter from the horizontal. Residual errors could arise from the following causes:

(*a*) Departure of the axis of rotation from the vertical. This has been tested, and is less than 0·25°, corresponding to a maximum error of 0·5% in N/S.

(*b*) Change of gain of the photomultipliers with rotation in the earth's magnetic field. Since both the caravan and counter housing are steel this effect is small, and an upper limit of 2% may be set by the change in response to vertical μ-mesons observed in the two positions.

(*c*) Asymmetries in the external surroundings of the detector. These are difficult to calculate, but believed to be small. The caravan was aligned along an East–West line, so that the distribution of absorbing material was symmetric at zenith angles up to 45°. There is no reason to believe that the main array has any preferred direction of selection.

Finally, the observation of directional asymmetries, related to the position of the shower core, lend confidence to the belief that the directional discrimination of the detector is reliable. If Coulomb scattering is assumed to be dominant in causing the lateral spread of the particles, the directional radius of curvature found corresponds to a mean radius of curvature of the shower front of $2440 \pm^{760}_{430}$ metres, consistent with the value of 2600 metres found by Bassi *et al.* (1953). This value is larger than that found by Greisen (1957) but since it is reasonable to suppose that the radius of curvature will change with distance from the core, the discrepancy is not serious.

§ 5. CONCLUSIONS

The results are inconsistent with the existence of a broad anisotropy in the declination distribution of showers which has an amplitude comparable with that pointed out by McCusker, but do not exclude the possibility of point sources which make small contributions to the total flux.

ACKNOWLEDGMENTS

The authors would like to thank Professor C. B. A. McCusker for communication of results before publication; Dr. T. E. Cranshaw, Dr. W. Galbraith, and Dr. G. W. Clark for discussion of this paper in manuscript.

REFERENCES

BASSI, P., CLARK, G. W., and ROSSI, B., 1953, *Phys. Rev.*, **92**, 441.
CLARK, G., EARL, J., KRAUSHAAR, W., LINSLEY, J., ROSSI, B., and SCHERB, F., 1957, *Nature, Lond.*, **180**, 356, 406.
CRANSHAW, T. E., and GALBRAITH, W., 1957 a, *Phil. Mag.*, **2**, 797; 1957 b, *Ibid.*, **2**, 804.
GREISEN, K., 1957, *Nuovo Cim.* Suppl., VIII, 681.
JELLEY, J. V., 1958, *Čerenkov Radiation* (London : Pergamon).
McCUSKER, C. B. A., 1959, *Phys. Rev.*, **116**, 177.
SCOTT, W. T., 1949, *Phys. Rev.*, **76**, 212.

The Relative Abundances of the Heavy Nuclei in the Primary Cosmic Radiation†

By C. J. WADDINGTON
H. H. Wills Physical Laboratory, University of Bristol

[Received December 22, 1959]

ABSTRACT

In an attempt to resolve the present controversy about the relative abundances of the heavy, $Z \geqslant 6$, nuclei in the primary cosmic radiation, the magnitude of the corrections introduced by the overlying atmosphere has been redetermined. For this reason it has been necessary to use nuclear emulsions to determine the fragmentation parameters of nuclei having $20 \leqslant Z \leqslant 28$. The results of this work show that the relative abundances calculated previously by considering the diffusion of nuclei through the atmosphere were not seriously in error, and that outside the atmosphere the ratio of H, $Z \geqslant 10$, to M, $6 \leqslant Z \leqslant 9$, nuclei is $0{\cdot}38 \pm 0{\cdot}04$. The significance of this result is considered briefly.

§ 1. INTRODUCTION

DURING recent years determinations of the chemical abundances of the nuclei in the primary cosmic radiation have been the cause of considerable controversy. In particular, the vexed question of the abundances of those nuclei with $3 \leqslant Z \leqslant 5$, the L-nuclei, has been the subject of many experiments, overshadowing, to some extent, the equally important determinations of the abundances of the heavier nuclei. For these heavier nuclei it was generally assumed, without much discussion, that the ratio $R(x)$, at a depth in the atmosphere of x g/cm^2, of those nuclei with $Z \geqslant 10$, H-nuclei, to those with $6 \leqslant Z \leqslant 9$, M-nuclei, was about 0·4 at the top of the atmosphere, R_0. However, in a recent experiment, Appa Rao *et al.* (1958) have presented evidence that the true value of R_0 may well be less than 0·3, and indeed their results can be interpreted as predicting $R_0 \leqslant 0{\cdot}2$.

These authors consider that in previous experiments the corrections that have had to be made for the effects of the residual atmosphere above the points of detection have been seriously miscalculated. In particular, they remark that since nuclei with mass numbers as high as 56 to 58 do occur in the primary radiation, the H group includes nuclei covering a wide range of masses. Thus it is not permissible to assume that the behaviour of this group can be represented by a constant mean free path for interaction, nor that the mean mass of the nuclei in the group will not change rapidly as they traverse matter. Both these assumptions had been implicit in the calculations made in earlier papers. Instead, these authors measured directly the variation of $R(x)$ with x, the depth in the atmosphere, and thus obtained a growth curve, which, when extrapolated to the top of the atmosphere, suggested that $R_0 \leqslant 0{\cdot}2$. By considering the ratio $H/(H+M)$ instead of R, these authors obtained a value for R_0 of 0·29, but the superiority of this result over that obtained by considering R is not at all clear.

---

† Communicated by the Author.

Because of the discrepancy between these results and those obtained previously, it was felt that it would be valuable to refine the earlier calculations on the effects of the overlying atmosphere, in order to see whether this divergence could be resolved. Such a refinement can be achieved by separating the H-nuclei into two groups, so that the assumptions of constant mean free path and mean charge or mass are more closely satisfied. In making these corrections it is usual to consider that a diffusion of the nuclei occurs as they pass through the atmosphere, Kaplon *et al.* (1954), and it is necessary to know the interaction mean free paths of each component, together with the number of fragments belonging to the lighter components produced in typical interactions, the fragmentation parameters. It was thus necessary to determine these quantities for the two groups of nuclei being considered, those with $10 \leqslant Z \leqslant 19$, $\mathscr{H}$-nuclei, and those with $20 \leqslant Z \leqslant 28$, $\mathscr{V}\mathscr{H}$-nuclei. Values for these quantities have been derived and are presented in this paper, together with the results obtained by using them to correct previous experimental data for the effects of the overlying atmosphere.

§ 2. EXPERIMENTAL DETAILS

Three stacks of nuclear emulsions were used. Of these, two, the G and I stacks, were exposed over Northern Italy at an altitude of about 100 000 feet, while the third, the T stack, was exposed over Texas, U.S.A., at about 125 000 feet. Details of the physical dimensions and exposure characteristics of these stacks are given in table 1. Since the geomagnetic cut-off energy for vertical incidence over Northern Italy and Texas are, in both cases, about 1·5 BeV per nucleon, Fowler and Waddington (1957) and Freier *et al.* (1959), only a few of the nuclei recorded were non-relativistic.

The top edges and sides of the emulsions were scanned for the tracks of nuclei which satisfied the following conditions:

(i) The tracks should have a projected length of at least 1 mm in a 600 micron emulsion.

(ii) The tracks should not make an angle with the vertical of more than 60°.

(iii) The tracks should be at least as heavy as those produced by silicon nuclei, $Z = 14$.

Due to the relative thinness of the T stack, which only consisted of 70 emulsions, condition (i) was modified for those tracks found on the top edges of this stack; the minimum length required being set at 2 mm per emulsion.

The charges of the nuclei were roughly measured by counting on each track 100 δ-rays which extended more than 2·7 microns from the core of the track. These measurements, while naturally insufficient to give resolution between individual charges did, in each stack, show a separation between a group of the heaviest nuclei and those of lower charge. Due to the apparent low relative abundance of those elements having $15 \leqslant Z \leqslant 19$, in the cosmic radiation, see e.g. Waddington (1960), this heavy group has been assumed to be due to $\mathscr{V}\mathscr{H}$-nuclei, and the others to $\mathscr{H}$-nuclei. Confidence in this interpretation was increased by the observation of several interactions of the type where α-particles were the only products other than the residual nucleus. In each case there was a measurable decrease in the apparent charge, of an amount consistent with the assumption that this group of heavy nuclei did not have a range of charges much greater than six.

Table 1. Physical Dimensions and Flight Characteristics of Emulsion Stacks

	Volume cm cm cm No.	Date of exposure	Duration of exposure (hours)	Altitude (feet)	Location
G	27 × 37 × 0·06 × 250	12.10.54	6·0	85 000	N. Italy
I	25 × 38 × 0·06 × 60	20. 9.55	6·67	100 000	N. Italy
T	20 × 15 × 0·06 × 70	8. 2.59	15·2	125 000	Texas

Some of these apparent $\mathscr{V}\mathscr{H}$-nuclei were actually nuclei of lower charge which had lost sufficient energy by ionization for their tracks to appear as heavy as those of relativistic $\mathscr{V}\mathscr{H}$-nuclei. A number of these could be eliminated because they were brought to rest before going 10 cm, the approximate range of a 1 Bev per nucleon $\mathscr{V}\mathscr{H}$-nucleus, others because in their interactions they produced α-particles, whose grain density showed that they were of low energy. Of the 278 nuclei which were assumed, from the original δ-ray count, to be $\mathscr{V}\mathscr{H}$-nuclei, 165 provided an indication of the velocity. About 22% of these were non-relativistic, and just over 4% appeared to be actually $\mathscr{H}$-nuclei. Thus probably less than 5 of the 113 nuclei whose velocities were unknown could have been $\mathscr{H}$-nuclei.

The 184 interactions observed as a result of tracing the tracks of the $\mathscr{V}\mathscr{H}$-nuclei through the emulsions from the point of location in the stack were analysed if they satisfied the following conditions.

(i) Provided the potential range in the stack after the point of interaction was greater than 2·0 cm the interaction was fully analysed. This condition was necessary in order to provide sufficient range for the definite identification of any α-particles emerging from the interaction.

(ii) If the potential range was between 20 and 5 mm, then only those fragments of the incident nucleus with $Z \geqslant 3$ were considered.

(iii) Interactions within 5 mm of the exit point from the stack were not analysed.

Each interaction was classified in terms of the number of black and grey tracks produced by particles emitted from the target nucleus, N_h; the number and type of fragments having $Z \geqslant 3$ emitted by the incident nucleus, n_Δ; the number of α-particles from the incident nucleus, n_α; and the number of tracks producing less than 1·4 times the minimum ionization, n_s. Due to the rather low minimum in some of these emulsions, and the complexity of some of the interactions, these values of n_s cannot be regarded as very reliable, and no estimates of the meson multiplicity are possible from these data. In every case where $n_\alpha \geqslant 1$, 500 grains were counted on at least one α-particle in order to have a measure of the velocity of the primary nucleus. The analysed interactions are listed in table 2.

The charges of the secondary nuclei were determined either by counting 100 δ-rays of more than four grains on the tracks of nuclei with $Z \leqslant 10$, or by counting 100 δ-rays which projected more than 2·7 microns from the track. Normalizing these measurements against those made previously in the I and G stacks, see Rajopadhye and Waddington (1958), and using charge indicating interactions in the T-stack, it was possible to determine Z in the range 3–10 to within plus or minus half a charge, and above 10 to assign the nuclei to a charge group.

§ 3. RESULTS

3.1. *Mean Free Path*

After suitable corrections had been made to the observed path lengths to eliminate systematic biases, 174 nuclear interactions were observed in a total path length of 1519·6 cm. The resulting mean free path is 8·72 cm, or 33·3 ± 2·5 g/cm² in nuclear emulsion having a density of 3·82 g/cm³. This value may be compared with those of 29·4 g/cm² for $\mathscr{V}\mathscr{H}$-nuclei having a mean mass number $\bar{A}=54$, and 39·2 g/cm² for $\mathscr{H}$-nuclei having $\bar{A}=27$, which are calculated from the semi-empirical relation proposed by Bradt and Peters (1950) for the cross section, σ, of

$$\sigma=\pi(1{\cdot}45\times10^{-13})^2(A_1^{1/3}+A_2^{1/3}-2\Delta R)^2. \qquad . \quad . \quad . \quad (1)$$

Thus the mean free path obtained experimentally appears to be significantly different from that predicted for $\mathscr{V}\mathscr{H}$-nuclei, corresponding to $\bar{A}=40\pm7$. This discrepancy, if real, could be due to: (*a*) failure of eqn. (1) to give the true mean free path for these heavy nuclei; (*b*) a failure to detect some of the nuclear interactions produced; (*c*) the inclusion of a number of $\mathscr{H}$-nuclei in the sample considered. Of these possibilities (*b*) appears to be the most likely since; (*a*) eqn. (1) has been experimentally confirmed over a range of incident and target nuclei which extends from α-particles passing through air to H-nuclei passing through lead, see e.g.

Table 2. Interactions marked with * are those which occurred between 20 and 5 mm of an Exit Point

N_h	n_Δ	n_α	n_s	N_h	n_Δ	n_α	n_s
0	$\mathscr{H}$ + Be	0	4	2	Li	1	21
0	$\mathscr{H}$ + Li	1	?	3	$\mathscr{VH}$		5
0	$\mathscr{H}$	3	11	3	$\mathscr{VH}$		2
0	$\mathscr{H}$	3	5	3*	$\mathscr{VH}$		2
0	$\mathscr{H}$	3	4	3	$\mathscr{VH}$		2
0	$\mathscr{H}$	2	2	3	$\mathscr{VH}$		1
0	$\mathscr{H}$	1	7	3	$\mathscr{VH}$		0
0	$\mathscr{H}$	1	4	3*	$\mathscr{VH}$		0
0	$\mathscr{H}$	1	0	3	$\mathscr{H}$	3	10
0	C+N	2	5	3	$\mathscr{H}$	3	6
0	Be+Li	0	52	3	$\mathscr{H}$	1	7
0	C	4	7	3	$\mathscr{H}$		19
0	C	1	14	3	$\mathscr{H}$		13
0		2	25	3	$\mathscr{H}$		10
0		2	24	3	Be+Be	1	16
0			?	3*	Li	7	7
1	$\mathscr{VH}$		2 p	3	Li	4	18
1*	$\mathscr{VH}$		1 p	3*		4	14
1	$\mathscr{H}$ + Li	1	17 not p	3		3	22
1	$\mathscr{H}$	4	6 p	3			15
1	$\mathscr{H}$	3	3 p	4	$\mathscr{VH}$		3
1	$\mathscr{H}$	2	0 p	4	$\mathscr{H}$	2	9
1	$\mathscr{H}$		3 not p	4*	$\mathscr{H}$	2	7
1	$\mathscr{H}$		1 p	4	$\mathscr{H}$	2	4
1	C+Li	4	16 p	4	$\mathscr{H}$	1	7
1	F	2	8 p	4	$\mathscr{H}$		9
1	O	1	16 not p	4	$\mathscr{H}$		8
1	Li	5	8 not p	4	C	5	13
1	Li	3	13 not p	4	B	4	20
1		3	17 p	4	B	1	25
1		1	29 p	4	Be	3	13
1		1	24 p	4		6	18
1			25 p	4		5	17
?	$\mathscr{H}$		4	4		2	22
2*	$\mathscr{VH}$		4	5	$\mathscr{VH}$		2
2	$\mathscr{VH}$		0	5	$\mathscr{H}$	3	3
2	$\mathscr{H}$	2	8	5	$\mathscr{H}$	2	4
2	$\mathscr{H}$	2	2	5	$\mathscr{H}$	1	16
2	$\mathscr{H}$	1	15	5	$\mathscr{H}$	1	9
2	$\mathscr{H}$	1	10	5*	C+N+Li		10
2	$\mathscr{H}$	1	4	5	B+Li	2	12
2	$\mathscr{H}$	1	3	5	C	4	12
2	Li	3	17	5	Li	4	17

Table 2 (*continued*)

N_h	n_Δ	n_α	n_s	N_h	n_Δ	n_α	n_s
6	$\mathscr{VH}$		4	13	Be + Be	1	12
6*	$\mathscr{VH}$		4	13		4	20
6	$\mathscr{VH}$		2	13*			60
6	$\mathscr{VH}$		0	14	$\mathscr{H}$	2	8
6	$\mathscr{H}$	2	7	14*	Li	4	7
6	$\mathscr{H}$		7	14		1	24
6	$\mathscr{H}$		4	15		1	45
6*	F	2	14	15			?
6	O	2	6	16	$\mathscr{H}$	2	10
6*	B + Li	2	9	16	O	2	12
6		4	33	16		3	51
6			53	16*			100
7	$\mathscr{H}$	3	7	16			28
7	$\mathscr{H}$	3	4	17	Be	3	20
7*	$\mathscr{H}$	2	7	17		2	31
7	$\mathscr{H}$	1	8	17		2	20
7	$\mathscr{H}$	1	4	18	$\mathscr{H}$	2	6
7	N	3	10	18		4	34
7	C	2	13	19	Li		38
7	Be	3	18	19		2	30
7		1	39	19		2	25
8	$\mathscr{VH}$		4	19		1	42
8	$\mathscr{H}$		2	20			39
8	$\mathscr{H}$		2	21*		7	9
8	C	2	11	21*		4	25
8		4	12	21*		2	19
8			100	21		2	?
9	$\mathscr{H}$	1	11	21			27
9*	$\mathscr{H}$		6	21			25
10	$\mathscr{H}$	1	15	21			25
10	C	3	10	22		1	21
10	B	4	9	23	B	1	16
10		3	44	23			45
10			100	23			24
11	$\mathscr{VH}$		4	24		1	32
11*	$\mathscr{VH}$		1	24			34
11	$\mathscr{H}$		7	25	B	1	42
11		4	22	25		2	23
11			120	26		3	10
12	$\mathscr{H}$	1	7	27		2	29
12	O	1	10	30	N		16
12		4	43	31			35
13*	$\mathscr{H}$	2	13	32		4	14
13	$\mathscr{H}$	2	7	37		1	23

Rajopadhye and Waddington (1958); (*c*) the selection of $\mathscr{V}\mathscr{H}$-nuclei appears stringent enough to eliminate most, if not all, of the $\mathscr{H}$-nuclei, whereas the observed mean free path suggests a contamination of over 60% with nuclei having $\bar{A}=32$. Such an effect is in contradiction to our present ideas regarding the relative abundances of $\mathscr{V}\mathscr{H}$-nuclei and nuclei with $15 \leqslant Z \leqslant 19$. On the other hand, it is quite plausible that interactions should be missed while following along the tracks of $\mathscr{V}\mathscr{H}$-nuclei.

Fig. 1

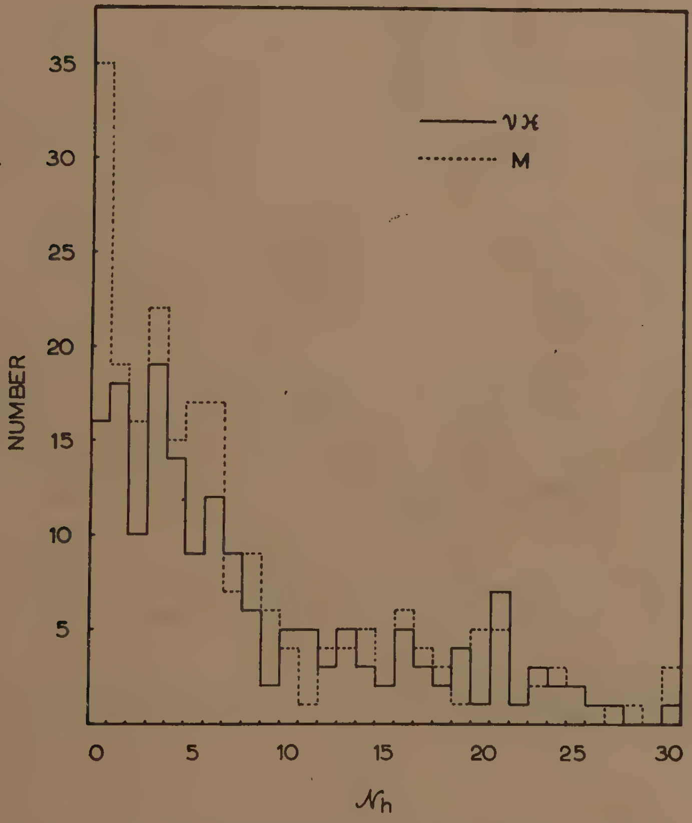

Comparison of the N_h distributions of interactions in emulsion produced by $\mathscr{V}\mathscr{H}$ and M-nuclei.

Those interactions which are most likely to be missed by an observer tracing along the track are those where the change in charge is small, there are no emitted α-particles from the incident nucleus, and there are no black or grey tracks due to evaporation fragments from the target nucleus, i.e. stars of the type $0+\mathscr{V}\mathscr{H}+n_s$. Such events will be particularly difficult to detect for $\mathscr{V}\mathscr{H}$-nuclei, since a small change of charge on such a track is much less easily recognizable than it would be on the track of a nucleus of lower charge. As a consequence an indication of whether any missing has occurred can be obtained by comparing the N_h distribution observed in this experiment with that observed previously for M-nuclei, Fowler *et al.* (1957), Rajopadhye and Waddington (1958), fig. 1. The significance of the lack of interactions with $N_h=0$ apparent from this comparison is enhanced when it is remembered that according to the accepted cross sections M-nuclei will make only 10% of their interactions with the hydrogen in emulsion, whereas the $\mathscr{V}\mathscr{H}$-nuclei will make 15%. Thus the relative number of $N_h=0$ interactions might be expected to be greater for $\mathscr{V}\mathscr{H}$-nuclei than for M-nuclei, the opposite to what is actually observed. It seems therefore that there has been a bias against finding interactions of the type with $N_h=0$.

The magnitude of these detection losses can be estimated, although not in a very statistically significant manner, in the following way:

(i) A lower limit can be obtained by considering the number of interactions with the hydrogen in emulsion that should be observed among those produced by $\mathscr{V}\mathscr{H}$-nuclei. About 27 of the 174 interactions in this sample could be expected to be with hydrogen, whereas only 26 which could possibly be such interactions were observed. Thus it is just feasible that no interactions at all were missed.

(ii) An upper limit can be obtained from a comparison with the interactions produced by M-nuclei. Of these some 10% resemble, but are not, interactions with hydrogen. The proportion of these spurious hydrogen interactions among the $\mathscr{V}\mathscr{H}$-nuclei should not be greater, and thus an upper limit to the number of missed interactions is about 20.

(iii) Another estimate of the upper limit can be obtained from the observed value of the mean free path. In order for this to have been 29·4 g/cm², the predicted value, 23 interactions must have been missed.

In the light of these considerations it has been decided to assume, arbitrarily, that the loss of interactions amounted to 15 ± 5, all of the type $0+\mathscr{V}\mathscr{H}+n_s$.

3.2. *Fragmentation Parameters*

Table 3 (*a*) shows the fragmentation parameters, P_{ij}, observed in emulsion, both for the case where no correction is made for detection losses, and for that where a correction of the amount assumed above is made. Similar figures are given for those interactions which have $N_h \leqslant 7$. Table 3 (*b*) shows the results obtained when the data of this experiment are combined with those published previously, Fowler *et al.* (1957), Cester *et al.* (1958), Puschel (1958) and Rajopadhye and Waddington (1958). A study of these other experiments suggests the presence of a detection loss similar to that observed in this experiment, and thus a correction of 21 ± 7 interactions was applied to the combined data.

Since the fragmentation parameters for $\mathscr{H}$-nuclei have not been determined in this experiment, it has been necessary to extract them from the published data, and their values are shown in table 3 (*c*). Considerations of the N_h distribution, and of the mean free path obtained for these nuclei, do not suggest any serious failures to detect interactions. This can be explained when it is remembered that such nuclei have a much lower mean charge, $\bar{Z} \sim 12$, cf. $\bar{Z} \sim 25$ for $\mathscr{V}\mathscr{H}$-nuclei, and thus interactions resulting in a small change in charge are much easier to detect, so that detection losses should be small.

Table 3. Fragmentation Parameters of $\mathscr{V}\mathscr{H}$-nuclei: Corrected Values shown in Brackets

(*a*) As observed in this experiment					
	$\mathscr{V}\mathscr{H}$	$\mathscr{H}$	M	L	α
All	0·12 ± 0·03 (0·18 ± 0·04)	0·33 ± 0·05 (0·31 ± 0·05)	0·12 ± 0·03 (0·11 ± 0·03)	0·18 ± 0·03 (0·17 ± 0·03)	1·54 ± 0·16 (1·40 ± 0·14)
$N_h \leqslant 7$	0·18 ± 0·04 (0·26 ± 0·06)	0·43 ± 0·08 (0·38 ± 0·07)	0·14 ± 0·04 (0·17 ± 0·03)	0·22 ± 0·05 (0·20 ± 0·04)	1·63 ± 0·20 (1·42 ± 0·18)
(*b*) Results from all experiments					
All	0·12 ± 0·02 (0·19 ± 0·03)	0·34 ± 0·04 (0·31 ± 0·04)	0·13 ± 0·02 (0·12 ± 0·02)	0·17 ± 0·03 (0·16 ± 0·03)	1·51 ± 0·13 (1·38 ± 0·11)
$N_h \leqslant 7$	0·15 ± 0·03 (0·26 ± 0·05)	0·41 ± 0·06 (0·36 ± 0·06)	0·13 ± 0·03 (0·11 ± 0·03)	0·18 ± 0·04 (0·16 ± 0·04)	1·55 ± 0·17 (1·34 ± 0·15)
(*c*) Fragmentation parameters of $\mathscr{H}$-nuclei, uncorrected for any loss					
	$\mathscr{H}$	M	L	α	
All	0·11 ± 0·02	0·29 ± 0·04	0·17 ± 0·03	1·18 ± 0·13	
$N_h \leqslant 7$	0·15 ± 0·04	0·41 ± 0·08	0·20 ± 0·05	1·32 ± 0·18	

§ 4. Discussion

It has been generally assumed that the fragmentation parameters obtained from those interactions in emulsions which have $N_h \leqslant 7$ are upper limits to the values applicable for air, Rajopadhye and Waddington (1958), Lorhmann and Teucher (1959), Cester *et al.* (1958). While the validity of this assumption has been contested, it will be accepted in this discussion. However, in order to verify that no gross errors are introduced, absolute limits to these maximum parameters will also be established.

The interaction mean free paths in air have been calculated from eqn. (1), and in view of the considerable evidence supporting the validity of this equation can hardly be seriously in error. Thus, using these mean free path values, and the corrected fragmentation parameters for $N_h \leqslant 7$, it is possible to calculate the extrapolation of an observed charge distribution from a point of observation within the atmosphere, to the top of the atmosphere. For example, with $R = 0{\cdot}35$ and a ratio of $\mathscr{V}\mathscr{H}/\mathscr{H}$, $S = 0{\cdot}24$ at 12 g/cm², Hillier and Rajopadhye (1958), the calculated value of R_0 was 0·41. This value may be compared with that of $R_0 = 0{\cdot}43$ found from the same data when H-nuclei are not separated into two groups, but considered as a whole.

A number of assumptions have to be made in this calculation. These will now be considered.

(i) Sensitivity of R_0 on the ratio S. When all the available data on the relative abundances of these nuclei are gathered together, Waddington (1960), S appears to have a value of $0{\cdot}23 \pm 0{\cdot}03$ at a depth in the atmosphere of about 14 g/cm². R_0 should vary with S, but is not very sensitive to small changes. For example, even if the true value of S is as low as 0·17, a fluctuation of two standard deviations, R_0 is only lowered from 0·41 to 0·40.

(ii) Fragmentation parameters in air. The assumption that the overall effect of those interactions in emulsions with $N_h \leqslant 7$ is similar to that produced in air is not easily justified. However, it is possible to obtain a lower limit for the extrapolated value of R by making extreme assumptions in the derivation of the fragmentation parameters. For R_0 to be a lower limit, $P_{\mathscr{V}\mathscr{H}.\mathscr{V}\mathscr{H}}$, $P_{\mathscr{V}\mathscr{H}.\mathscr{H}}$ and $P_{\mathscr{H}.\mathscr{H}}$ must take maximum values, while $P_{\mathscr{V}\mathscr{H}.M}$ and $P_{\mathscr{H}.M}$ take minimum values. From the emulsion data these limiting values can be obtained in the following manner. Since all the interactions with those nuclei in emulsion which resemble those in air must have $N_h \leqslant 7$ it may be assumed that all the observed fragments produced from such interactions do come only from the air-like nuclei. Since the abundance of these nuclei in emulsion is known, the relative number of $N_h \leqslant 7$ interactions due to air-like target nuclei can be calculated. Thus the extreme upper limits for these fragmentation parameters are $P_{\mathscr{V}\mathscr{H}.\mathscr{V}\mathscr{H}}; \leqslant 0{\cdot}50$, $P_{\mathscr{H}.\mathscr{H}} \leqslant 0{\cdot}70$ and $P_{\mathscr{H}.\mathscr{H}} \leqslant 0{\cdot}40$. Notice that this procedure implies that *no* $\mathscr{V}\mathscr{H}$ or $\mathscr{H}$ fragments are produced by interactions with the hydrogen in emulsion nor by peripheral collisions with heavy nuclei. From the emulsion data $P_{\mathscr{V}\mathscr{H}.M}$ and $P_{\mathscr{H}.M}$ can be allowed to tend to zero. Using these values an R of 0·35 at 12 g/cm² gives $R_0 \geqslant 0{\cdot}31$. Thus, even by making these extreme assumptions it is hardly possible to allow R_0 to be as low as Appa Rao *et al.* claim.

(iii) Mean free paths in air. The values taken depend on eqn. (1) the validity of which has been discussed in § 3.1, from which it appeared that these values can hardly be seriously in error. Furthermore, R_0 is not very sensitive to small changes in these values.

(iv) The constancy of the mean mass in the $\mathscr{V}\mathscr{H}$ and $\mathscr{H}$ groups of nuclei. While it is not possible to calculate the change in the mean mass introduced by passage through 12 g/cm² of atmosphere precisely, due to a lack of knowledge of the necessary parameters, it is possible to show that this change must be small. For example, consider an incident $\mathscr{V}\mathscr{H}$-group composed of 50% Fe and 50% Ca, with $\bar{A}=48$, and assume $P_{\mathrm{Fe\,.\,Ca}}=0{\cdot}30$. Then passage through 12 g/cm² will result in a group of 42% Fe and 58% Ca with $\bar{A}=46{\cdot}7$. Similarly, consider an incident

Fig. 2

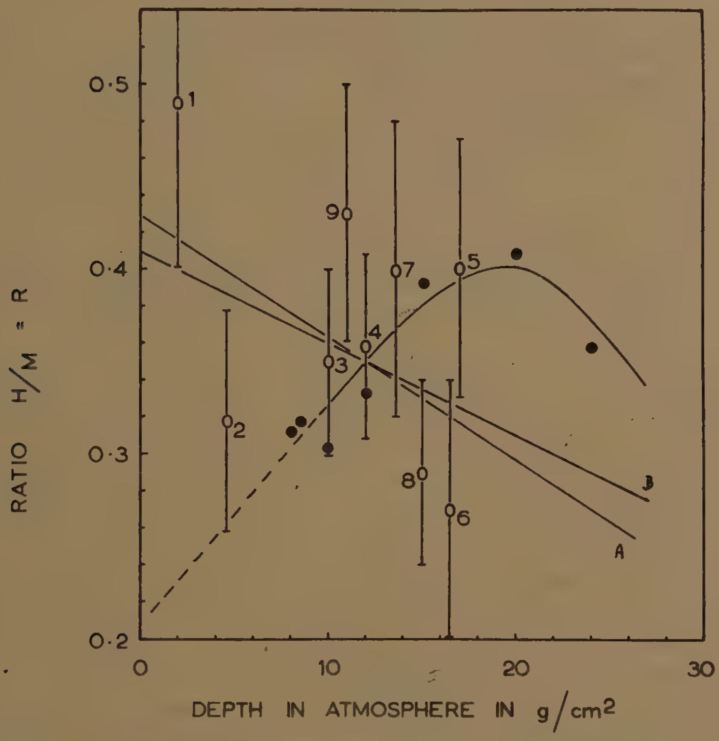

The variation of the ratio R in the atmosphere. Points shown as ● are due to Appa Rao *et al.* (1958), while the other experimental points are : 1. Yagoda (1958) ; 2. Freier *et al.* (1959) ; 3. Koshiba *et al.* (1958) ; 4. Waddington (1957) ; 5. Cester *et al.* (1958) ; 6. Waddington (1958) ; 7. Jain *et al.* (1959) ; 8. Von Friesen *et al.* (1959) ; 9. Biswas *et al.* (1959). These last two points are stated by the authors to be preliminary. Also shown are the diffusion growth curves calculated without separating the H-nuclei into two groups, A ; and by separating them into $\mathscr{V}\mathscr{H}$ and $\mathscr{H}$-nuclei, B ; both normalized to $R=0{\cdot}35$ at 12 g/cm². The growth curve constructed by Appa Rao *et al.* (1958) is also shown, with the least extreme extension to 0 g/cm² shown as a dashed line.

$\mathscr{H}$-group composed of 70% Ne, 30% S with $\bar{A}=23{\cdot}6$ and assume $P_{\mathscr{V}\mathscr{H}\,.\,\mathrm{S}}=P_{\mathscr{V}\mathscr{H}\,.\,\mathrm{Ne}}=P_{\mathrm{S\,.\,Ne}}=0{\cdot}20$. Then passage through 12 g/cm² will result in a group of 31% S, 69% Ne with $\bar{A}=23{\cdot}7$. Thus it appears that the assumption of constant mean mass in these two groups cannot be seriously incorrect for transmissions through reasonable amounts of matter.

The available experimental data on the values of R obtained in a number of experiments are shown in fig. 2, where R is plotted against the depth in the atmosphere. Also shown are the two diffusion growth curves for H-nuclei and for $\mathscr{V}\mathscr{H}$ plus $\mathscr{H}$-nuclei, arbitrarily normalized to $R=0{\cdot}35$ at 12 g/cm², and the growth curve determined by Appa Rao *et al.* Notice that in fact these diffusion curves should not be quite linear, but are drawn so for convenience, and that due to the arbitrary normalization they may be shifted parallel to themselves. The spread of the experimental values, and their concentration in the region where the values of R predicted by the various curves are closely similar, makes it difficult to draw any firm conclusions from these data, although they appear to fit the diffusion curves somewhat better than those of Appa Rao *et al.*

§ 5. CONCLUSIONS

From the above analysis it appears difficult to accept the value of R_0 predicted by Appa Rao *et al.*, and it would seem that the best value of R_0 available at this time is $R_0=0{\cdot}38\pm0{\cdot}04$, where the uncertainty is mainly due to the difficulty of normalizing the diffusion growth curves.

This figure may be compared with those calculated from the cosmic abundances determined by Cameron (1959) and Suess and Urey (1956) of 0·1 and 0·37 respectively. The difference between these figures is almost entirely due to the uncertain abundance of ^{20}Ne, but the true value probably lies within these limits. Thus it can be seen that, if account is taken of the degradation in mass produced by passage through the interstellar material between the source and the earth, the cosmic radiation is anomalously rich in heavy nuclei. It must be concluded, therefore, that either the source of this radiation is a region with an abundance of heavy elements which is greater than normal, or the acceleration mechanism preferentially accelerates heavy nuclei. This conclusion would not follow if R_0 was appreciably lower than the value obtained here.

ACKNOWLEDGMENTS

The author is grateful to Professor C. F. Powell, F.R.S., for the facilities of his laboratory, and to the Royal Society for the award of a Mackinnon Research Studentship. The existence of sufficient experimental material in this laboratory to permit this investigation was first pointed out by Dr. P. H. Fowler, while Dr. M. W. Friedlander very kindly arranged for the exposure of the T-stack in Texas. Finally the contribution of the observing staff of this laboratory must be acknowledged with deep gratitude.

REFERENCES

APPA RAO, M. V. K., BISWAS, S., DANIEL, R. R., NEELANKANTON, K. A., and PETERS, B., 1958, *Phys. Rev.*, **110**, 751.

BISWAS, S., LAVAKARA, P. J., NEELANKANTO, K. A., and SHUKLU, P. G., 1959, Report to 1959 I.U.P.A.P. Moscow Conference.

BRADT, H. L., and PETERS, B., 1950, *Phys. Rev.*, **77**, 54.

Cameron, A. G. W., 1959, *Ap. J.*, **129,** 676.
Cester, R., Debeneslitti, A., Garelli, C. M., Quassiati, B., Tallone, L., and Vigioni, M., 1958, *Nuovo Cim.*, **7,** 371.
Fowler, P. H., Hillier, R. R., and Waddington, C. J., 1957, *Phil. Mag.*, **2,** 293.
Fowler, P. H., and Waddington, C. J., 1956, *Phil. Mag.*, **1,** 637.
Freier, P. S., Ney, E. P., and Waddington, C. J., 1959, *Phys. Rev.*, **113,** 921.
Hillier, R. R., and Rajopadhye, V. Y., 1958, *Nuovo Cim.*, Suppl., **8,** 520.
Jain, P. L., Lohrmann, E., and Teucher, M. W., 1959, *Phys. Rev.*, **115,** 643.
Kaplon, M. F., Noon, J. H., and Racette, G. W., 1954, *Phys. Rev.*, **96,** 1408.
Koshiba, M., Schultz, G., and Schein, M., 1958, *Nuovo Cim.*, **9,** 1.
Lohrmann, E., and Teucher, M. W., 1959, *Phys. Rev.*, **115**, 636.
Puschel, W., 1958, *Z. Naturf.*, A, **13,** 801.
Rajopadhye, V. Y., and Waddington, C. J., 1958, *Phil. Mag.*, **3,** 25.
Suess, H. E., and Urey, H. C., 1956, *Rev. mod. Phys.*, **28,** 53.
Von Friesen, S., Waldeskog, B., Mathiesen, O., and Kristansen, K., 1959, Report to 1959 I.U.P.A.A. Moscow Conference.
Waddington, C. J., 1957, *Phil. Mag.*, **2,** 1059 ; 1958, *Nuovo Cim.*, Suppl., **8,** 518 ; 1960, *Prog. Nucl. Phys.*, **8** (to be published).
Yagoda, H., 1958, Preprint, Air Force Cambridge Research Center.

The Observation of Sharp Internal Friction Peaks in Beryllium†

By E. W. Dickson
Tube Investments Research Laboratories, Hinxton Hall, Cambridge‡

[Received October 27, 1959]

Abstract

Measurements have been made as a function of strain and temperature with specimens of commercially pure beryllium. Very sharp internal friction peaks were observed which are similar to those reported as occurring in aluminium. The previously suggested mechanism giving rise to these maxima is discussed in terms of the evidence obtained here.

§ 1. Introduction

The brittleness of beryllium is the major drawback to its extensive use in nuclear reactors and in other fields. It has low neutron absorption, low density and a high modulus of elasticity which are all very attractive properties, but in its present commercial form the metal is brittle and fabrication is difficult. It has been suggested that impurities in beryllium are responsible for its brittle behaviour but no one has yet been able to produce very pure beryllium to test this point directly.

Internal friction measurements provide a very sensitive test for the study of dislocations and their interaction with impurity atoms. This interaction determines to a large extent the mechanical properties of the metal. Granato and Lücke (1956) have developed a dislocation-pinning point model that can be compared quantitatively with internal friction data and it was hoped by this means to obtain information about the behaviour of impurities in beryllium. The main result of the experiments was the observation of very sharp internal friction peaks as the specimen temperature was changed. Similar peaks have been observed in aluminium (Birnbaum and Levy 1956, Filmer *et al.* 1958) and the mechanism which is suggested to be the cause of the internal friction peaks is discussed in relation to the evidence obtained in these experiments.

§ 2. Apparatus

The apparatus used in these experiments is described fully elsewhere (Dickson and Strauch 1959). A specimen in the form of a cylindrical rod 20 cm long and 6 mm diameter was clamped at its mid-point and set into longitudinal oscillation. The internal friction was determined from the rate of decay of the oscillations when the driving force was switched off. Mechanical oscillations of the rod were induced and detected electrostatically. An electrode was placed close to each end of the specimen and biased with a d.c. voltage relative to the specimen. Application of an oscillatory voltage to one of the electrodes at the resonant frequency of the specimen induced the mechanical vibrations. The other electrode formed part of a condenser microphone which produced a signal whose amplitude was directly proportional to the amplitude of oscillation of the beryllium rod. The detection electrode was connected through a phase shifter and amplifier to the driving electrode and when this circuit was completed it formed a regenerative loop in which the oscillations built up from noise levels. The advantages of this circuit were that specimens having a very low internal friction could be maintained at a fixed amplitude of oscillation indefinitely and a precise determination of the resonant frequency of the specimen was possible.

---

† Communicated by the Author.

‡ Now at Associated Engineering Ltd., 60 Kenilworth Road, Leamington Spa.

The internal friction could be measured in the strain range 10^{-6} to 10^{-8}. A film record was made of the decaying signal from the detecting electrode and by measuring the time taken for the oscillations to decay through a small amplitude range at selected points on the film record the variation of internal friction with strain could be determined. The internal friction coefficient, ϕ, is given by $\phi = (1/\pi f t) \log_e (A/B)$ in which f is the frequency of the oscillations and t the time for them to decay from amplitude A to amplitude B. In all these experiments the frequency of the oscillations was ~ 30 kc/s. Where the internal friction was found to be independent of strain amplitude a stop watch was used to measure the time interval in a strain range such that $A/B = 10$.

The specimen was enclosed in a stainless steel container evacuated to a pressure of 10^{-5} mm Hg. The temperature control system was of the saturable reactor type providing continuous regulation of the heat supply to the furnace and its stability allowed measurements to be made at intervals of 0·25°c.

§ 3. Specimens

The rods were supplied by the Brush Beryllium Corporation and were QMV grade. They had been manufactured by the warm extrusion of a hot pressed powder billet and the grain size was 0·02 mm. The chemical analysis provided by the manufacturers showed the major impurities to be BeO 1·16%, Al 0·15%, Fe 0·1%, Mn 0·013%, Ni 0·01%. Smaller amounts of Ag, Cd, Co and Li were also present. The density, ρ, of each rod was measured and found to be $1{\cdot}847 < \rho < 1{\cdot}852$ g/cm^3. This is greater than the theoretical density of 1·848 g/cm^3 calculated on the basis of the lattice constants because of the presence of the impurities. The texture of the rods was not determined but it is well known that rod extrusion produces a fibre texture in which most of the grains have their c axis perpendicular to the rod axis (Kaufmann *et al.* 1950).

The only specimen preparation carried out was mechanical polishing of the ends of the rods so that they were plane and perpendicular to the longitudinal rod axis.

§ 4. Experimental Results

From measurements of the resonant frequency, density and dimensions of each of the nine specimens the velocity of sound in beryllium, v, was calculated and found to be $1{\cdot}26 \times 10^6 < v < 1{\cdot}27 \times 10^6$ cm/sec and the dynamic Young's modulus E, $2{\cdot}89 \times 10^{12} < E < 2{\cdot}94 \times 10^{12}$ dynes/cm^2. These measurements were made at room temperature and show good agreement with the results of Overton (1950), $v = 1{\cdot}26 \times 10^6$ cm/sec and Gold (1950), $E = 2{\cdot}965 \times 10^{12}$ dynes/cm^2.

Fig. 1

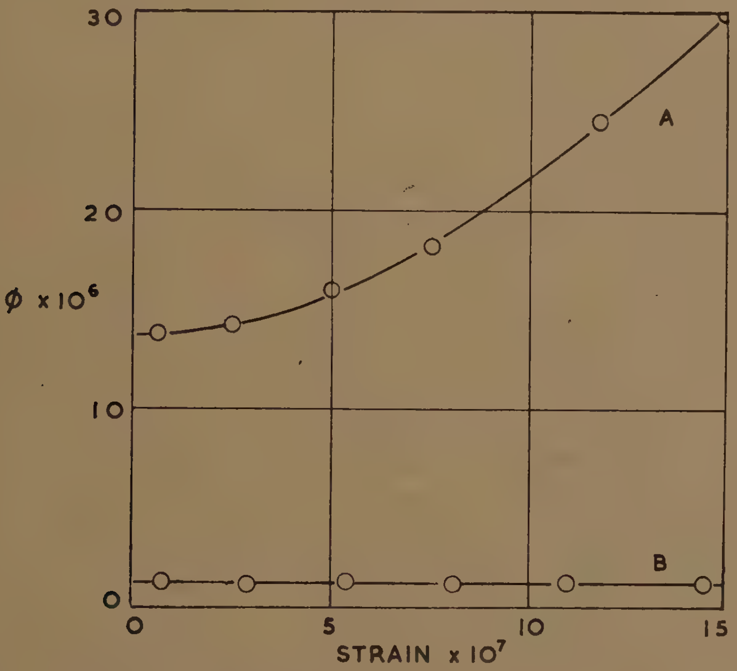

Strain dependence of internal friction. Specimen in 'as received' condition, curve A, and after three-hour anneal at 500°c, curve B.

All the specimens in the 'as received' condition showed a strain dependence of the internal friction at room temperature as illustrated in fig. 1, graph A. The internal friction became independent of strain after a three-hour anneal at 500°c, fig. 1, graph B. It is generally known that, especially with single crystals, the work done on the specimen during mounting in the apparatus can increase the measured values of the internal friction. To check this point one specimen was removed from and remounted in the apparatus three times. The results obtained on each occasion were in agreement within the experimental error of 5%. From this it was concluded that the observed effect was genuine. The elimination of the strain dependence of the internal friction could be due to the segregation of impurities to dislocations. However, attempts to prove this point and determine the kinetics by quenching and ageing experiments were not successful due to the high sensitivity of the internal friction to temperature under certain circumstances.

In a first attempt to measure the temperature dependence the specimen used was that which had previously been annealed for three hours at 500°c and the readings, taken every 10°c, showed a much larger scatter than could be attributed to experimental error. More careful measurements were then taken at intervals of 0·25°c as the beryllium rod was cooled down from 300°c at approximately 5°c per hour. The results, fig. 2, show the existence of some very sharp internal friction peaks in the temperature ranges 20–60°c and 260–290°c. Part of this graph is shown on a larger scale in fig. 3 in which all the experimental points are plotted. The experiment was repeated several times in the temperature range 20–50°c

Fig. 2

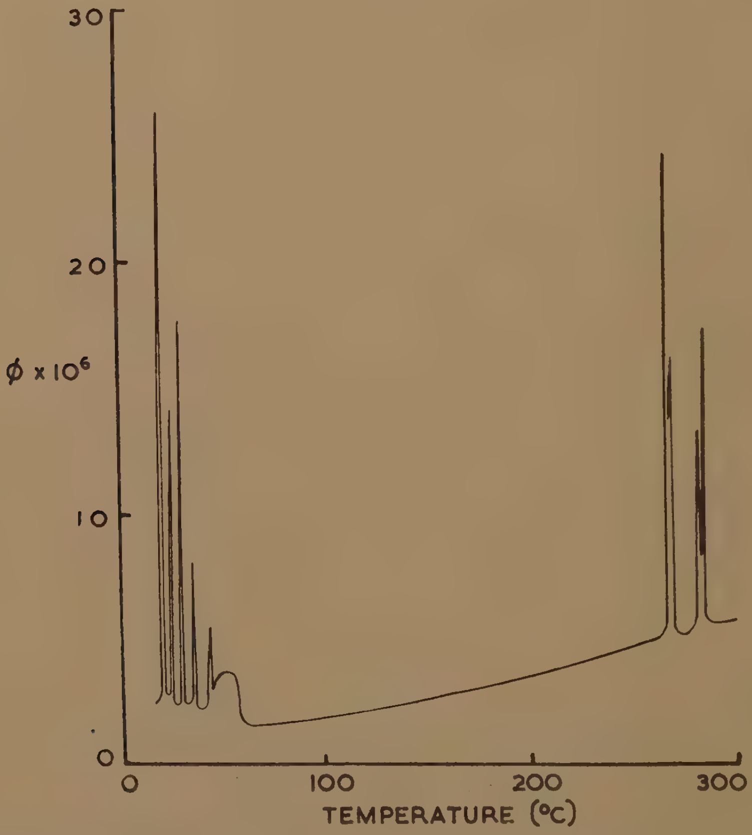

Temperature dependence of internal friction after three-hour anneal at 500°c.

and the major peaks were found to be reproducible on both heating and cooling cycles. The internal friction values as plotted were calculated from the time taken for the oscillations to decay by a factor of ten in amplitude and represent the average internal friction in the strain range 10^{-6} to 10^{-7}. Film records of the decay taken at various temperatures, including the tops of the sharp peaks, showed no strain dependence of the internal friction. The maximum strain in the specimen during these experiments did not exceed 1×10^{-6}.

Fig. 3

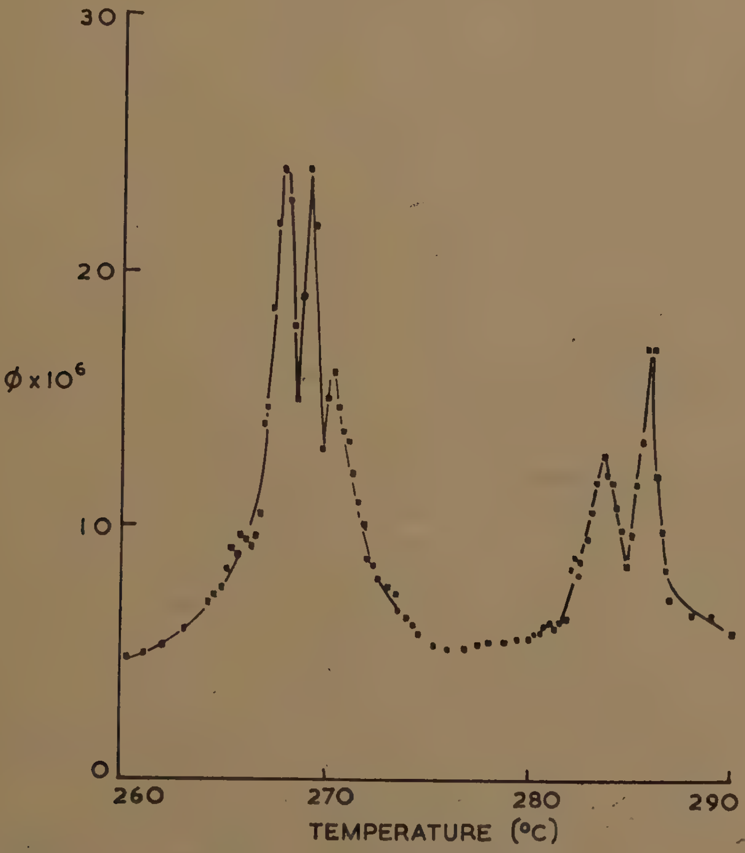

Detail of some of the sharp internal friction peaks shown in fig. 2.

A second specimen was mounted in the apparatus and annealed *in situ* for 20 hours at 235°c. Measurements of the internal friction which were taken as the specimen was slowly cooled to room temperature are shown in fig. 4. Sharp peaks similar to those shown in fig. 2 were observed near room temperature and in the temperature range 170–230°c. After a further anneal *in situ* for 50 hours at 350°c measurements were again made as the rod was slowly cooled to room temperature. The background internal friction was reduced by this heat treatment as shown in fig. 5 and the sharp peaks were now observed in a broad temperature region extending from 30–160°C. When this specimen was further heated to 300°C and furnace cooled to room temperature, the cooling rate being 200°C per hour at 300°C, only two small peaks at 30°C and 50°C were observed between room temperature and 70°C. It was again found that the internal friction in

Fig. 4

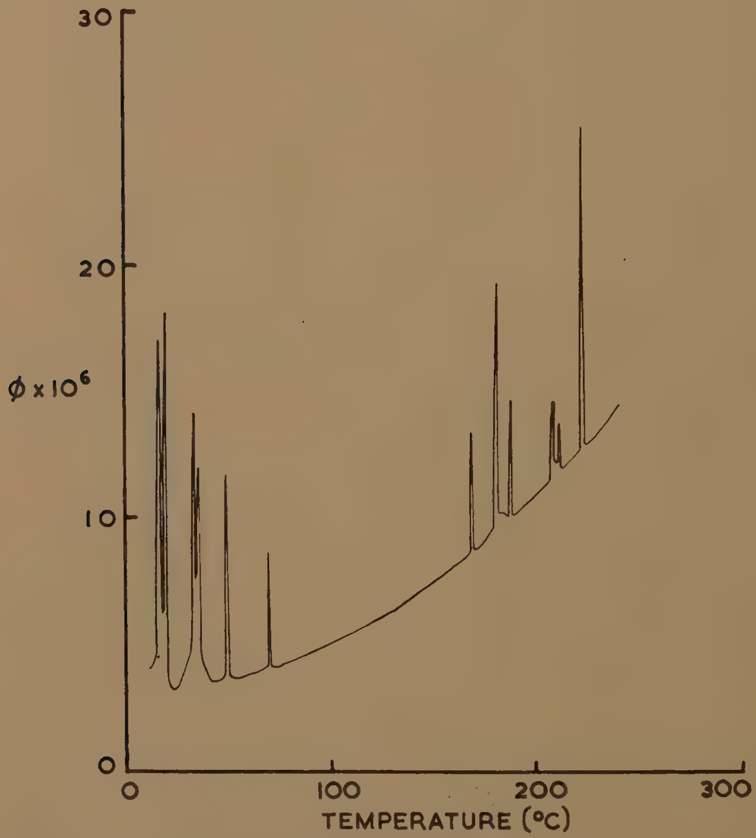

Temperature dependence of internal friction. Specimen in 'as received' condition annealed for 20 hours at 235°C before measurements made.

this temperature range was repeatable on both heating and cooling. Finally a very slow cool from 300°C produced sharp peaks once more in this low temperature region.

All these observations were made without removing the beryllium rod from the apparatus. Since it was found possible to alter the temperature region in which the sharp peaks were observed and also to repeat the measurements made during cooling and heating cycles in the range 20°C to 70°c it is thought that they were due to energy absorption by the specimen and not energy losses in the apparatus. When the apparatus was used with specimens of other metals these effects were not observed.

§ 5. Discussion

The very low values of internal friction, $\phi = 1 \times 10^{-6}$, were probably due to the highly preferred orientation of the polycrystalline specimens. In this experiment the shear stress is a maximum on planes at 45° to the longitudinal specimen axis and is very small across the basal planes of the individual grains since their c axis is perpendicular to the specimen axis. Dislocations can only be moved by a shear stress and thus the dislocation movement in the basal plane, which is the primary slip system at the temperatures involved, is very small. The effect of crystallographic

Fig. 5

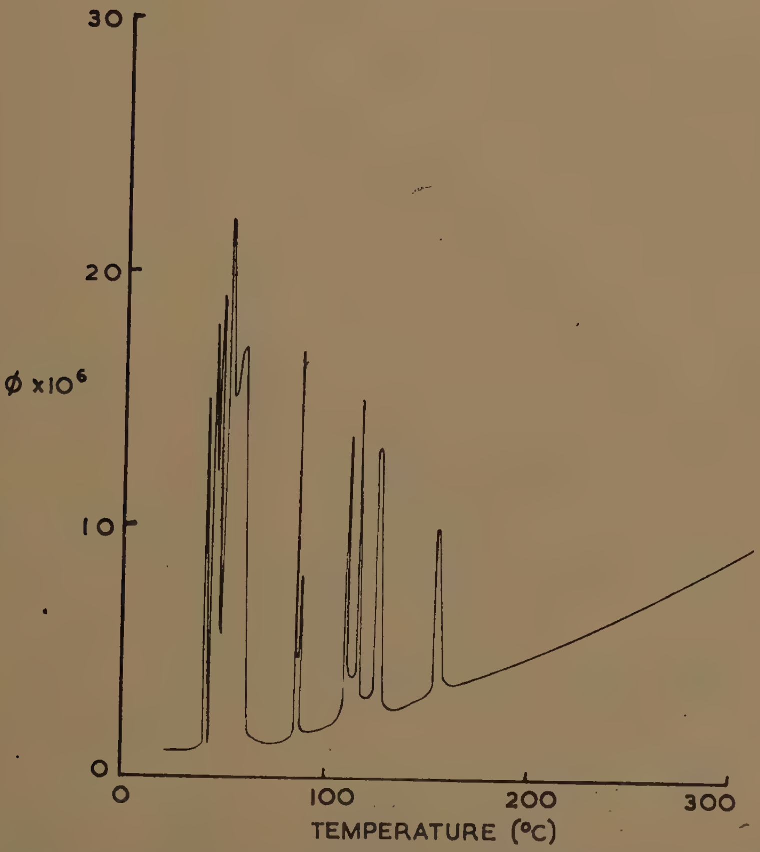

Temperature dependence of internal friction. The specimen used to obtain the results shown in fig. 4 was annealed for 50 hours at 350°c prior to these measurements.

orientation on internal friction has been demonstrated by Read (1941) using specimens of zinc.

Quenching and ageing experiments were carried out and there was some evidence that impurities were put into solution and then segregated to the dislocations, pinning them and so reducing the internal friction. These results were not satisfactory because of the irregular nature of the temperature dependence of the internal friction.

Sharp internal friction peaks very similar to those reported here have been observed with single crystal specimens of aluminium by Birnbaum and Levy (1956) and by Filmer *et al.* (1958) who used polycrystalline aluminium. Birnbaum and Levy attributed the sudden changes in internal friction to 'avalanches' of dislocations freed by the oscillating stress from loose pinning joints. Filmer *et al.* pointed out however that the freed dislocations must have moved to another stable configuration in order to produce a peak in the internal friction results and not a step.

This explanation of the phenomenon can be tentatively applied to the results on beryllium. However, the fact that the peaks were repeatable on heating and cooling cycles shows that the mechanism must be reversible. On the basis of the previously proposed model this fact implies that several pinning point configurations are possible on the dislocation lines and each configuration is stable in a particular temperature zone. As the temperature of the specimen is changed from one of these zones to another the dislocations are freed at the transition temperature and their increased mobility produces high values of internal friction. The position of the internal friction peaks on the temperature scale and their magnitude were altered by heat treatment at temperatures in excess of 150°C. This evidence is in agreement with the results on polycrystalline aluminium where it was found possible to eliminate some of the peaks and reduce the magnitude of others by annealing the specimen for 11 hours at 60°C.

If the internal friction peaks are due to the freeing of dislocations from pinning points whose energy is precisely defined then each observed internal friction peak would characterize a particular type of pinning point. The multiplicity of the peaks observed in these experiments and the variation in the temperature ranges in which they occur makes a mechanism of this type less feasible.

The evidence obtained here that the internal friction was independent of strain in the neighbourhood of the maximum values recorded implies that if the effect is due to dislocation breakaway the pinning points concerned are completely ineffective under these particular experimental conditions. The dislocation loops are not re-pinned at the zero point of the stress cycle. Considering the equation proposed by Granato and Lücke (1956) the strain independent internal friction is proportional to L^4t where L is the average length of dislocation loop which vibrates under the action of the applied oscillatory stress and t is a factor which depends on the distribution of loop lengths assumed. The magnitude of the internal friction peaks could be accounted for by an increase of a factor of two in the average loop length. An alternative explanation could be based on the factor t. As stated by Granato and Lücke (1957), $t=1$ when the pinning points are equispaced along the dislocation lines and when they are randomly distributed $t=120$. A disturbance of the distribution of pinning points could give rise to an internal friction peak. However, it is difficult to visualize a mechanism whereby the distribution of pinning points could be suitably disturbed on all the active dislocations simultaneously.

An alternative interpretation of the lack of strain dependence of the internal friction is that the sharp peaks were due to a relaxation process. Some of the peaks do have a shape consistent with a process of this type but the activation energy calculated from the shape of the peak is extremely high and far in excess of the sublimation energy of beryllium. A relaxation process should be accompanied by a change in the resonant frequency of the specimen. This was not observed in these experiments where the accuracy of frequency measurements was only $\pm 0{\cdot}4\%$.

There is clearly a need for much more experimental evidence before a satisfactory explanation for the occurrence of the sharp internal friction peaks is obtained. It is for this reason that the results obtained in this investigation have been reported in full detail.

ACKNOWLEDGMENTS

I would like to thank Dr. T. P. Hughes for his interest and encouragement in this work and the Chairman of Tube Investments Ltd. for permission to publish this paper.

REFERENCES

BIRNBAUM, H., and LEVY, M., 1956, *Acta. Met.*, **4,** 84.
DICKSON, E. W., and STRAUCH, H., 1959, *J. sci. Instrum*, **36**, 425.
FILMER, A. J., HUTTON, G. J., and HUTCHISON, T. S., 1958, *J. appl. Phys.*, **29,** 146.
GOLD, L., 1950, *Phys. Rev.*, **77,** 390.
GRANATO, A., and LÜCKE, K., 1956, *J. appl. Phys.*, **27,** 583, **27,** 789; 1957, *Dislocations and Mechanical Properties of Crystals* (New York : John Wiley & Sons), p. 437.
KAUFMANN, A. R., GORDON, P., and LILLIE, D. W., 1950, *Trans. Amer. Soc. Metals*, **42,** 785.
OVERTON, W. C., 1950, *J. chem. Phys.*, **18,** 113.
READ, T. A., 1941, *Trans. Amer. Inst. min (metall.) Engrs*, **143,** 30.

Ferromagnetism in Pd-rich Palladium–Iron Alloys†

By J. CRANGLE
Department of Physics, The University, Sheffield 10

[Received January 12, 1960]

ABSTRACT

Ferromagnetism has been detected in disordered solid solution alloys of Fe in Pd at compositions down to 1·25 atomic % of iron. Data are presented on magnetic moments and on Curie points. It is shown that part of the observed magnetic moment must be associated with the Pd atoms, and cannot be completely localized on iron atoms.

§ 1. INTRODUCTION

ACCORDING to the phase diagram of the alloy system palladium–iron published by Hansen (1958), a continuous region of solid solution having the face-centred cubic structure exists over the whole composition range at high temperatures. At lower temperatures the face-centred cubic phase is still stable between 0 and 60 atomic % of iron but there are two superlattice structures, centred round the FePd and $FePd_3$ compositions respectively.

Fallot (1938) showed that both these superlattices are ferromagnetic, with Curie points of about 750°K for FePd and about 530°K for $FePd_3$. Also, he showed that the disordered face-centred cubic structure obtained by quenching from high temperatures (and so suppressing the formation of the superlattices) is ferromagnetic down to not more than 12 atomic % of iron.

In view of the interest inherent in the question of whether long-range interactions between magnetic iron atoms in a non-magnetic palladium matrix are alone responsible for the ferromagnetic state, and whether palladium atoms themselves contribute any magnetic moment, it seemed desirable to extend and improve upon Fallot's measurements.

After the present work had been started, Gerstenberg (1958) published measurements on the paramagnetic susceptibility of PdFe alloys containing 1, 3, 5 and 7 atomic % of iron. In all cases the Curie–Weiss law was obeyed, and the extrapolated paramagnetic Curie point was positive. This implied that ferromagnetism persisted down to 1% of iron.

§ 9. PREPARATION OF THE ALLOYS

A series of five alloys containing 1–16 atomic % of iron was prepared from pure palladium lent by the Mond Nickel Company, and Johnson-Matthey spectrographic iron. The preparation was by melting in an

---

† Communicated by Professor W. Sucksmith, F.R.S.

argon arc furnace. The negative electrode of a direct current arc was a water-cooled tungsten rod and the positive electrode consisted of the specimen to be melted, which rested on a water-cooled copper base. Mostly the alloys weighed 2–3 g. All the compositions were chosen so as to lie outside the range of superlattice stability.

The alloys were analysed chemically for the iron content and spectrographically for the presence of significant impurities. The compositions are given in table 1. The probable error in atomic percentages is ± 0·05%. All the alloys contained spectrographic traces of silver and copper, and that with 1·25% of iron had also a similar trace of silicon.

Table 1

Iron content, atomic %	1·25	3·16	5·11	9·78	15·75
σ_0, c.g.s. units/g	4·9	13·1	18·8	31·9	45·3
Bohr magneton number p	0·093	0·246	0·350	0·581	0·800
Curie point θ, °K	66	122	162	236	377

§ 3. MAGNETIC TECHNIQUES

Intensity of magnetization in strong fields was measured as a function of temperature and of field in a Sucksmith ring balance (Sucksmith 1939). The magnetization at room temperature of BISRA pure iron 'AH', to which the absolute data of Weiss and Forrer (1926) were assumed to apply, was used as a standard to which other measurements could be referred. Magnetic isothermals were obtained for a range of eight applied fields between 4 and 13 kilo-oersteds, at temperatures down to a minimum of about 20°K and up to the respective Curie temperatures.

Above room temperature, a small evacuated electric furnace was attached to the balance. At lower temperatures, the specimen mount was enclosed by a metal tube, in which a high vacuum could be maintained. This tube was in turn surrounded by a shaped Dewar vessel capable of containing either liquid nitrogen or liquid hydrogen. The specimen was mounted inside the balance at the end of a thin-walled tube of silica, and its rate of heat transfer with the surroundings was small. Thus it was usually possible to make the measurements at selected temperatures below room temperature while the temperature was drifting slowly. More rapid changes of temperature were achieved by the temporary admission of helium at low pressure.

Temperatures were measured by means of a thermocouple of 'Pallador', placed in good thermal contact with the specimen.

§ 4. Results

Spontaneous magnetizations σ_T at the various temperatures T were estimated by plotting the magnetization against the effective field (corrected for demagnetizing factor) at constant temperatures, and extrapolating their linear parts to the magnetization in zero field. An example of a set of these magnetic isothermals, for the 15·8% alloy, is given in fig. 1. Their general form is not unlike that found (Weiss and Forrer 1926) in say, nickel, and in this respect the alloys seem to show normal ferromagnetic behaviour. The values of σ_T obtained are plotted as a function of temperature for each of the present alloys in fig. 2. The spontaneous magnetizations σ_0 at zero temperature were estimated by drawing the linear parts of graphs of σ_T against T^2 to where $T^2=0$. Values of σ_0 were converted to Bohr magneton numbers p, assuming the magnetic moment of the Bohr magneton to be 5586 c.g.s. units per gram molecular unit (table 1). The respective Curie points were found by plotting $\sigma_T{}^2$ against T and extrapolating the part with steepest slope to the temperature axis. They are plotted against composition in fig. 3.

Fig. 1

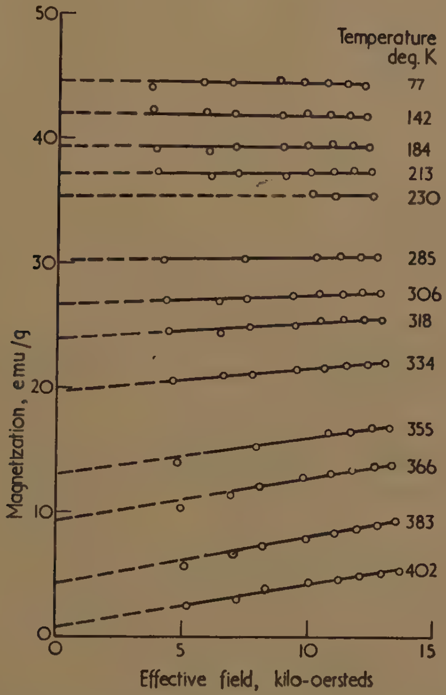

Magnetic isothermals for the 15·8 atomic % Pd–Fe alloy.

Fig. 2

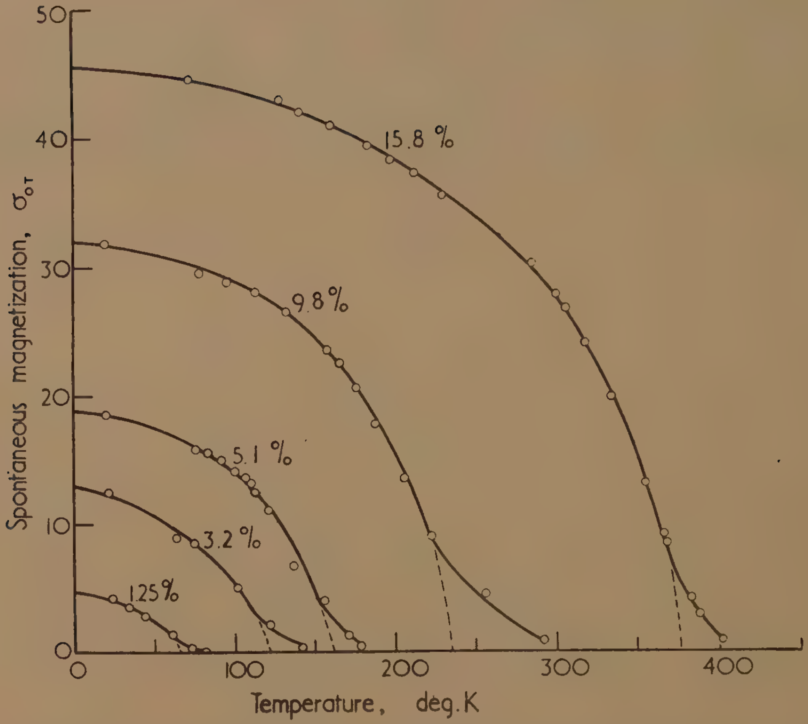

The variation of spontaneous magnetization with temperature for Pd–Fe alloys.

Fig. 3

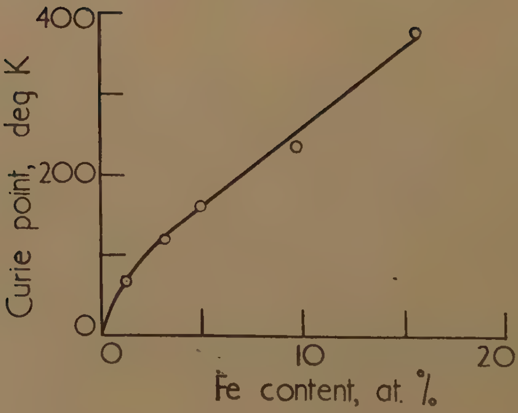

The variation of Curie point with iron content.

The magneton numbers of the present alloys and also those of Fallot's alloys are shown in fig. 4.

Fig. 4

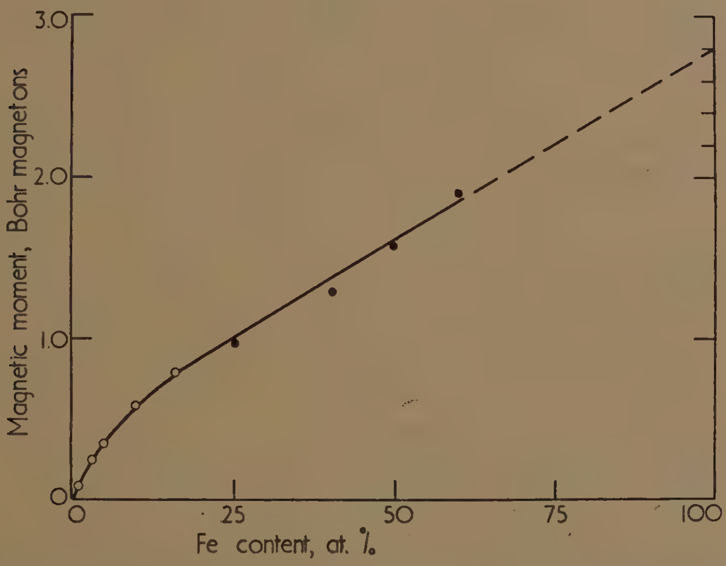

Bohr magneton numbers plotted against iron content. The open points are present measurements; the black ones are due to Fallot (1938).

§ 5. Discussion

The first remarkable feature of the measurements is that ferromagnetism persists down to such low iron contents. In fig. 3, the Curie point of the alloys appears to extrapolate to zero at zero iron concentration; and at 1·25% of iron the Curie point has already risen to over 60°K.

Sato *et al.* (1959) have theoretically demonstrated how, when ferromagnetic ordering arises from nearest-neighbour interactions between magnetic atoms dissolved in a non-magnetic matrix, the Curie point remains zero and no ferromagnetic state occurs until a finite concentration C_0 of the magnetic solute is attained. Their estimate of C_0 was of the order of $1/z$, where z is the coordination number of the crystal structure. Thus for a face-centred cubic structure ($z=12$), C_0 should be of the order of 8%, agreeing with the experimental observations in Au-rich gold–iron solid solutions (Kaufmann *et al.* 1945), where ferromagnetism does start at about 8 atomic %. Thus it appears that in the most dilute Pd–Fe alloys the ferro-magnetism cannot be a result of only nearest neighbour interactions between iron atoms. Some longer-range mechanism must be active.

The second remarkable feature of the observations concerns the magnitude of the magnetic moments. The dependence of measured magnetic moment on applied field, as typified by fig. 1, introduces little uncertainty (especially at low temperatures) into the estimates of the values of the spontaneous magnetization σ_T: the spontaneous magnetization varies regularly with temperature (fig. 2) and there is little room for doubt in the estimation of its value σ_0 at $T=0$. Yet if we suppose that the whole of the magnetic moment p shown for each alloy in table 1 is located on iron atoms, we find that the moment per iron atom would be as shown in table 2.

Table 2

Fe content, atomic %	1·25	3·16	5·11	9·78	15·75
Ratio $\dfrac{\text{Total magnetic moment}}{\text{iron content}}$	7·4	7·8	6·9	5·9	5·1

The experimentally observed magneton number p is related to the difference n between the numbers per atom of electrons with positive and negative spin by $p=\frac{1}{2}g\,.\,n$, where g is the spectroscopic splitting factor. Experimental g values are not available for these alloys. But in pure iron, g is about 2·1 (see Bagguley and Owen 1957). Thus taking this value for g, we must infer that the values given in table 2 require that there should be a difference between the numbers of electrons with positive and negative spin of up to about seven per iron atom. This is clearly impossible in either an atomic $3d$ level or a $3d$ band in which the Pauli exclusion principle dictates that vacancies can exist for only five electrons per atom with positive and five with negative spin.

We must therefore conclude that some of the magnetic moment which is present is not located on iron atoms. The present observations give no direct information beyond this on the question of the source of the magnetic moment in the alloys.

It is useful to discuss these alloys in terms of a model in which there is some characteristic localization of magnetic moment on each of the kinds of atom present. Wohlfarth (1954, 1956) has extended the simplified collective electron theory of ferromagnetism to the related alloys of palladium containing nickel or cobalt in solution. He discussed the alloys in terms of a common energy band ('d-band') to which both solute and solvent atoms contribute, and which is responsible for the magnetic properties. The variation of magnetic moment with composition is accounted for by a variation of the Fermi level as the electron concentration of the alloy is changed by altering the composition. This model seems to be oversimplified in a case where solute and solvent have atomic numbers differing by as much as do iron and palladium. Any refinement of the model seems to lead towards some characteristic localization of d-electrons, and hence of magnetic moment. There is good experimental evidence for such localization in binary alloys of pairs of elements both taken from the first transition series, from observations on ferromagnetic disorder scattering and ferromagnetic superlattice scattering of neutrons (Shull and Wilkinson 1955).

Within the framework of this localized model, the simplest interpretation of a linear variation of alloy magnetic moment with composition is that it corresponds to a proportional combination of individual magnetic moments which do not each change with alloy composition. These individual moments are simply the respective extrapolations of the line to the 0% and 100% compositions. Adopting this procedure here, the straight part of fig. 4 may be extrapolated over that part of the phase diagram in which the face-centred cubic phase is unstable, to 100% of iron. A moment of 2·8 Bohr magnetons may thus be tentatively ascribed to each atom of iron in the face-centred cubic alloy. Some support for the procedure is given by applying it similarly to the face-centred cubic ferromagnetic phase in the following alloy systems; Ni–Fe, Co–Fe and Au–Fe. In each case the same moment is obtained, within the limits of experimental error.

Fig. 5

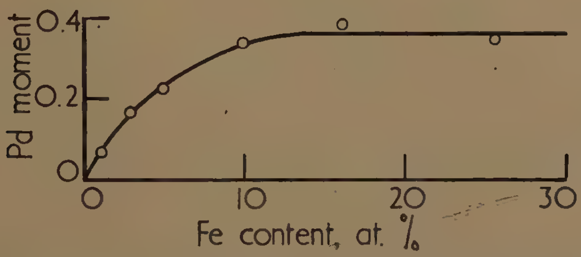

Estimated variation of moment per Pd atom, if the moment per iron atom remains about 2·8 Bohr magnetons at all compositions.

It thus seems reasonable to suggest that the iron moment in the Pd–Fe alloys may be about 2·8 Bohr magnetons, and not as great as its theoretical maximum of five. If this is the case, the moment per palladium atom for alloys with more than 10% of iron is of the order of 0·4 magnetons, and is roughly independent of composition. Of course, if the iron moment is actually lower than 2·8 units, the palladium moment must be correspondingly higher, but the main principles of this discussion remain unaffected.

In pure palladium ferromagnetism does not occur, nor has antiferromagnetism been found. Thus it seems that at $T=0$ the incompletely filled 4d band is unpolarized; there are equal numbers of electrons with either direction of spin. As iron is added to palladium in the range 0–10%, polarization of the palladium 4d band must therefore develop. A possible course of its development is shown in fig. 5, the form of which is based on an assumption of the moment on each iron atom remaining constant at 2·8 magnetons over this composition range. If the mean iron moment tends to zero at zero concentration, of course, the palladium moment will rise more steeply than is shown in fig. 5, and become constant at a lower composition.

The explanation of the observed behaviour would seem to lie in two possible directions. Either on the one hand it is due to an intrinsic tendency towards ferromagnetism in pure palladium; the decrease in lattice parameter associated with alloying here permits Pd–Pd interactions to produce a ferromagnetic state: or on the other hand Pd–Fe interactions produce a resultant moment on the palladium atoms, and are primarily responsible for the ferromagnetic state. The present experiments do not appear to distinquish between these two cases.

The former possibility is that discussed by Wohlfarth (1956) in relation to the ferromagnetic behaviour of Ni–Pd alloys. That such small concentrations of iron produce ferromagnetism suggests that if this is the dominant mechanism, palladium is on the verge of being a ferromagnetic element. In this case, it is at first sight surprising that a non-magnetic solute such as copper, which also reduces the inter-atomic distance, produces no tendency towards ferromagnetism (Svensson 1932).

If the latter possibility is considered for the case of nearest-neighbour Pd–Fe interactions only, with no Pd–Pd interactions, it appears that ferromagnetic ordering throughout a disordered face-centred cubic crystal should occur if one of the twelve Pd atoms which are nearest neighbours to a given iron atom has another iron atom as a near neighbour. That is, there should be ferromagnetism down to compositions of the order of 2% of iron. For ferro-magnetism to occur at much lower compositions, Pd–Pd interactions must also be present. This seems more likely to occur when those Pd atoms which are subjected to Pd–Fe interactions have a magnetic moment induced on them than otherwise.

Further work is in progress on more dilute Pd–Fe alloys.

ACKNOWLEDGMENTS

The author is grateful to Professor W. Sucksmith, F.R.S. for his interest and advice during the course of this work, and to the Mond Nickel Company for the loan of the pure palladium.

REFERENCES

BAGGULEY, D. M. S., and OWEN, J., 1957, *Rep. Prog. Phys.*, **20**, 304.
FALLOT, M., 1938, *Ann. Phys., Paris*, **10**, 291.
GERSTENBERG, D., 1958, *Ann. Phys., Lpz.*, **2**, 236.
HANSEN, M., 1958, *Constitution of Binary Alloys* (New York: McGraw-Hill).
KAUFMANN, A. R., PAN, S. T., and CLARK, J. R., 1945, *Rev. mod. Phys.*, **17**, 87.
SATO, H., ARROTT, A., and KIKUCHI, R., 1959, *J. Phys. Chem. Solids*, **10**, 19.
SHULL, C. G., and WILKINSON, M. K., 1955, *Phys. Rev.*, **97**, 304.
SUCKSMITH, W., 1939, *Proc. roy. Soc.* A, **170**, 551.
SVENSSON, B., 1932, *Ann. Phys., Lpz.*, **14**, 699.
WEISS, P., and FORRER, R., 1926, *Ann. Phys., Paris*, **5**, 153; 1929, *Ibid.*, **12**, 279.
WOHLFARTH, E. P., 1954, *Phil. Mag.*, **45**, 647; 1956, *J. Phys. Chem. Solids.*, **1**, 35.

Kinetics of Ordering in Fe_3Al†

By R. Feder‡ and R. W. Cahn
Department of Physical Metallurgy, University of Birmingham, England

[Received November 12, 1959]

Abstract

The resistance changes produced by thermal treatment of Fe_3Al have been measured and the annealing kinetics analysed. It was found that an increase in long-range order produced a large decrease in resistance. It was found that the rate at which ordering takes place is a function of the initial quenching temperature. All curves were fitted to the standard rate equation giving an order of reaction $n=2{\cdot}2$ for specimens quenched from 620°c and $n=1{\cdot}5$ for specimens quenched from 530°c. The activation energy obtained from resistivity kinetics was found to be much lower than the mean activation energy for diffusion.

§ 1. Introduction

In the course of a series of experiments on the effect of ordering on the electrical resistivity of the alloy Fe_3Al, some data were obtained on the isothermal change of resistivity of an initially disordered alloy. The mathematical form of these isothermal annealing curves is to be analysed in the present paper.

The experiments were limited to two compositions both close to the stoichiometric alloy Fe_3Al. This alloy has a critical temperature of about 540°c. The characteristic (DO_3) superlattice disappears at this temperature, but according to recent data (Taylor and Jones 1958) an imperfect form of order of the CsCl (B2) type persists to above 700°c. This imperfect order has little effect on the physical properties; the alloy in this condition behaves almost as if it were disordered.

The only extant studies of ordering kinetics in Fe_3Al were carried out by Rode (1957) who measured resistivity and saturation magnetization, and by McQueen and Kuczynski (1959), who measured resistivity. However, none of these attempted any analysis of the form of his isothermal curves; this is the chief purpose of the present paper.

§ 2. Experimental Procedure

Resistance specimens were formed from Fe_3Al alloys containing 24·8 at.% and 25·5 at % aluminium. Purity of the constituents was better than 99·99%. Specimens were milled from 7 cm × 1 cm × 0·1 cm strips into the form shown in fig. 1, giving an effective length of approximately 35 cm. By means of etchants the cross-sectional area of the specimens was reduced until the resistance reached a value between 0·1 and 0·2 ohms at 77°K. Current and potential leads were brazed to the specimens. Cold work was removed by vacuum annealing the specimens at 800°C for 4 hours.

---

† Communicated by the Authors.
‡ Now at Frankford Arsenal, Philadelphia, Pa.

The resistance measurements were made with a potentiometer by comparing the potential drop across the sample with the potential drop across a known resistance in series. Proper precautions against spurious thermal e.m.f.'s of thermoelectric origin were taken by the use of a reversing circuit. No attempts were made to obtain absolute values of the resistivity in view of the complex shape of the specimen. All resistance measurements were made at liquid nitrogen temperature.

Fig. 1

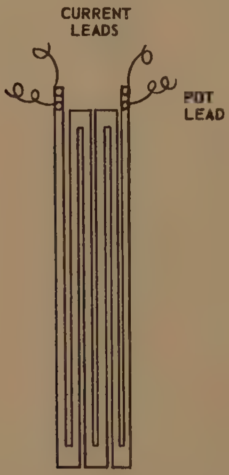

Shape of specimen used for resistivity studies.

For the kinetic studies, specimens were brine quenched from 620°C and 530°C, temperatures respectively above and below the critical temperature (538°C). The brine quench was introduced to maintain the at-temperature state as efficiently as possible. The specimens were then inserted into a preheated slotted copper block inside the furnace in order to bring them quickly to the desired temperature of isothermal ordering. The specimen was withdrawn at intervals and quenched and the resistance was measured at 77°K before continuing the isothermal anneal. The kinetics of isothermal anneals were obtained for 295°C, 322°C, 353° and 375°C.

§ 3. Experimental Results

Figure 2 shows the per cent change in resistivity (measured at 77°C) of 24·8 and 25·5% iron–aluminium as a function of the annealing temperature for infinite time. The data were so adjusted that a zero change refers to the resistance of the specimen in the condition 'as quenched from 620°C'. Each datum point represents the equilibrium value of the resistance for the temperature of its abscissa. Data points were obtained for temperatures above the critical temperature ($T_c = 538$°C), where times to attain equilibrium were of the order of a few seconds, to temperatures well below T_c involving times of the order of 10 hours.

Fig. 2

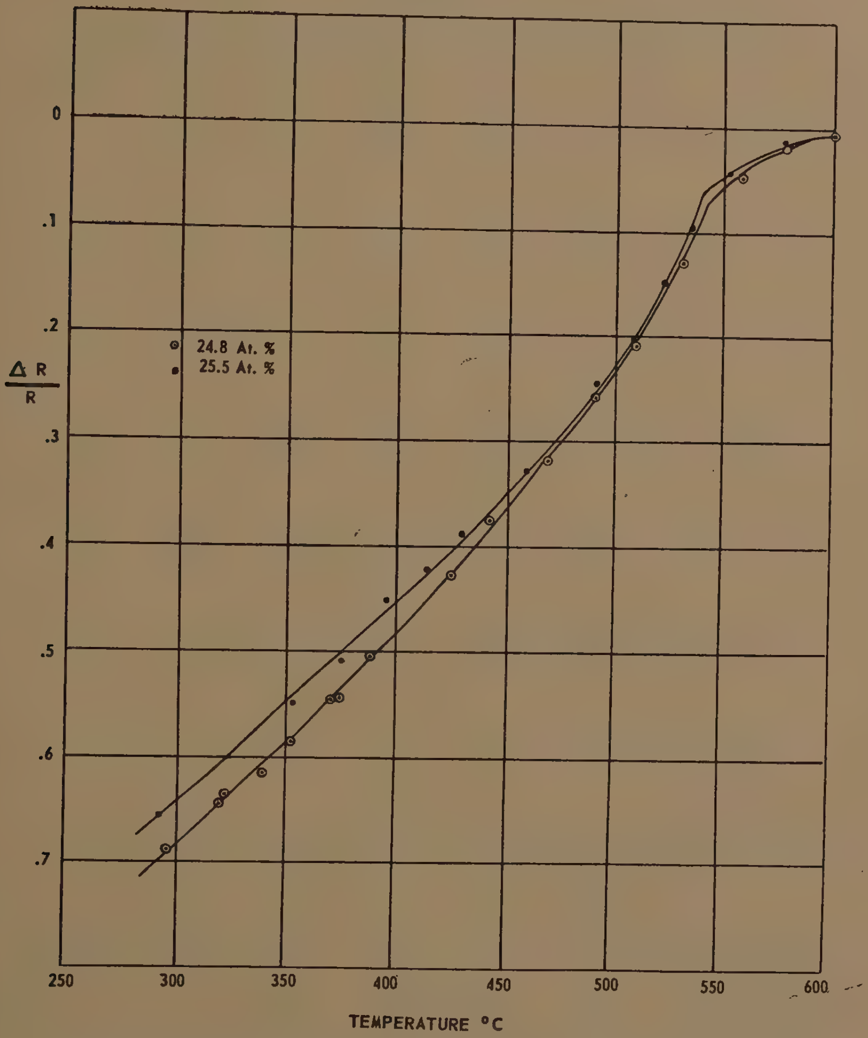

Equilibrium values of resistance. (All measurements made at 77°K.)

Isothermal data for the 24·8% aluminium alloy are shown in fig. 3 as a plot of the per cent changes in resistivity from an initial quench from 620°C. Similar data were obtained for 25·5% aluminium. Each value of the change in resistance was measured at 77°c after the specimen was held at temperature for the time indicated and then brine quenched. It should be noted that as the temperature of anneal is increased the initial slope, related to the rate of reaction, has also increased. The equilibrium resistance for higher temperatures is reached in a shorter period of time but the total resistance change is smaller, thus giving rise to a 'cross over' effect, i.e. the higher the temperature the greater is the equilibrium resistance. The final values of these curves are plotted in fig. 2 and the curves of fig. 3 indicate the method used to determine the time necessary to attain equilibrium.

Fig. 3

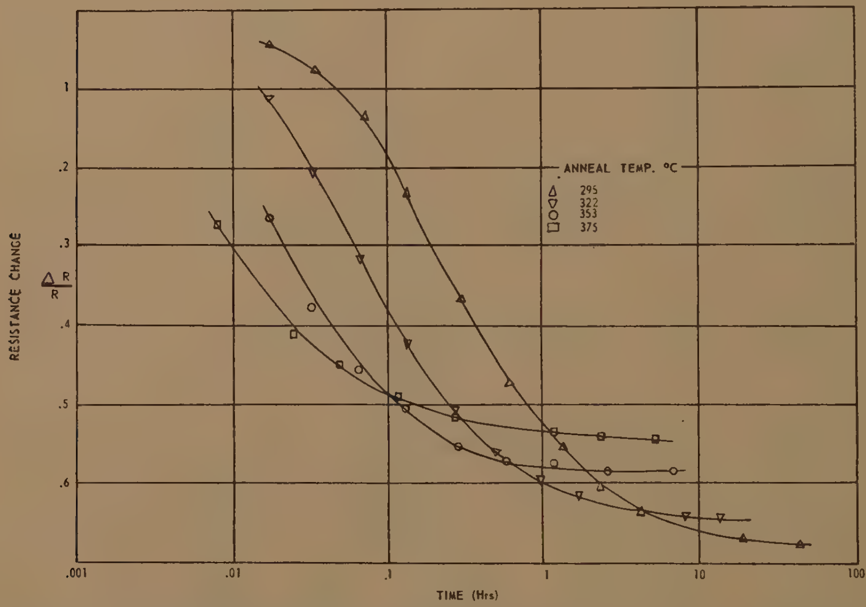

Isotherms of resistance change vs. annealing time for 24·8 at. % alloy specimens. Initially quenched from 620°c and measured at 77°K.

Similarly, isothermal annealing curves were obtained for specimens quenched from just below the critical temperature ($T_q = 530$°c) after 10 hours of soaking at temperature. Again only the results for the 24·8% aluminium alloy are shown in fig. 4. The data were adjusted so that the ordinate origin corresponds to the resistance for the 620°c quench. This may be done by utilizing $\Delta R/R$ for a change in temperature from 620°c to 530°c from fig. 2.

The isothermal annealing curves were analysed by standard techniques based on integrated rate equations for the order of reaction n. n is defined by the following standard differential equation.

$$\frac{d\rho}{dt} = -\frac{1}{\tau_n}(\rho_t - \rho_\infty)^n \quad . \quad . \quad . \quad . \quad . \quad . \quad . \quad . \quad (1)$$

where $d\rho/dt$ is the rate of change of resistivity, τ_n is the rate constant, ρ_t is the resistivity at time t and ρ_∞ is the resistivity for infinite time. A high order of reaction is characterized by a reaction rate which decreases rapidly with increasing time. According to Parkens *et al.* (1951) solid state rate processes are normally regarded as being of first order. From this point of view, the experimental curves which are characterized by higher order ($n > 1$) indicate that a distribution of activation energies is involved. Activation energies are obtained from the rate constant τ, which can be represented by an Arrhenius equation

$$\tau = \tau_0 \exp(H/KT).$$

Fig. 4

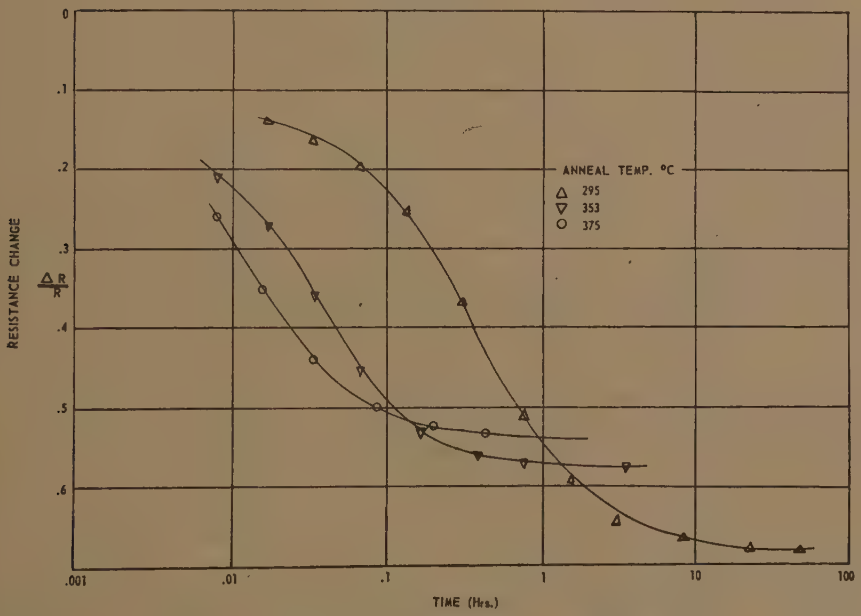

Isotherms of resistance change vs. annealing time for 24·8 at. % alloy. Specimens initially quenched from 530°C and measured at 77°K.

The triangles in fig. 5 show a typical isothermal (295°C) anneal curve of the 24·8% aluminium alloy quenched from 620°C. One of the lines represents a first order decay curve of the form $d\rho/dt = -(1/\tau)(\rho_t - \rho_\infty)$. Integration of this equation leads to the identification of a relaxation time τ_1, as the time required to achieve all but $1/e$ of the total change in the resistance at any given temperature. Each computed curve has been fitted to the experimental curve at $t = 0$, $t = \tau_1$ or τ_2 and $t = \infty$. (The relaxation time τ_2 corresponding to the second order equation is derived in the way explained in the Appendix.) It is seen that the first-order curve does not fit the data very closely. A mathematical second-order curve, represented by the open circles, makes a very good fit over the entire experimental curve.

Fig. 5

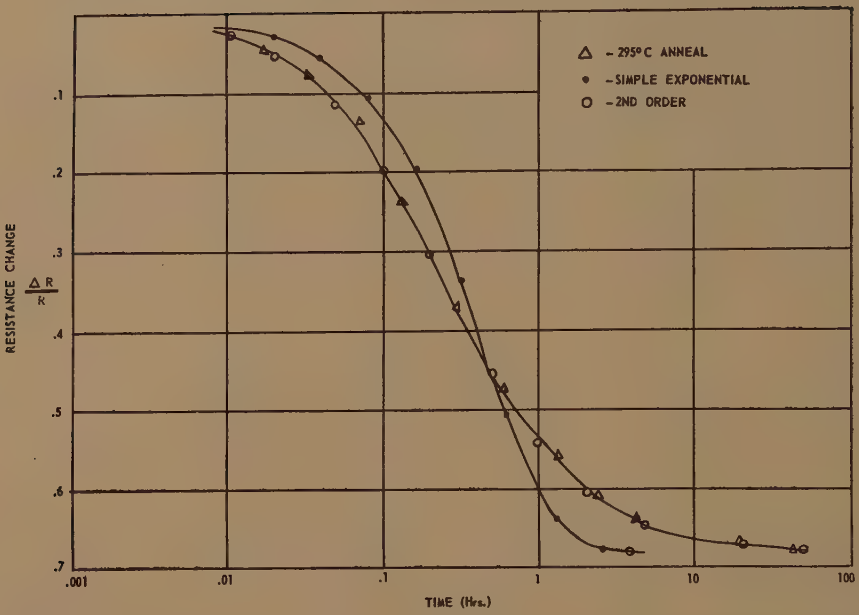

Comparison of first- and second-order curves for a 295°c isothermal anneal. 24·8% specimen, initially quenched from 620°c.

Fig. 6

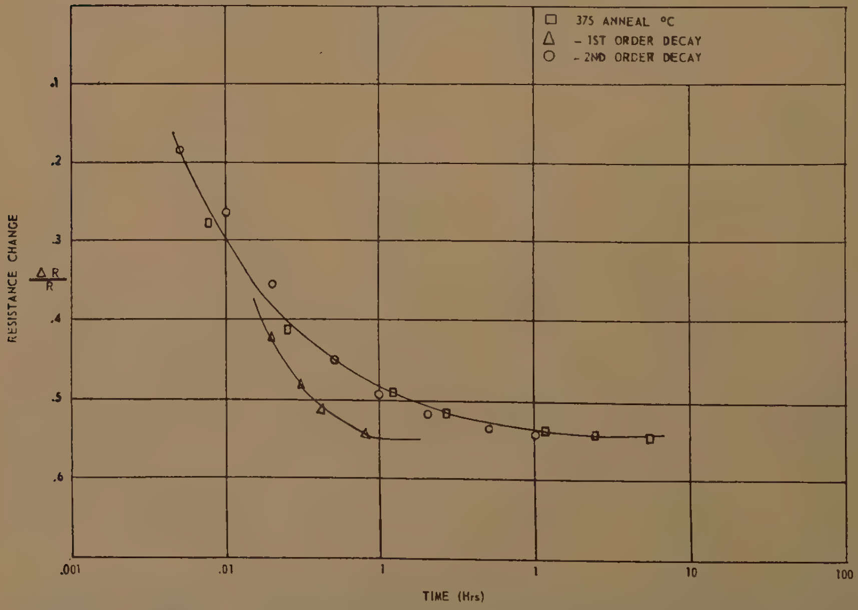

Comparison of first- and second-order curves for a 375°c isothermal anneal. 24·8% specimen, initially quenched from 620°c.

For comparison purposes, mathematical first-order and second-order curves were plotted and compared with a 375°c anneal curve as shown in fig. 6. The second-order curve indicates a good fit for times greater than τ and a poor fit for the times less than τ. On the other hand, the second-order curve as fitted to the 295°c anneal (in fig. 5) indicates a good fit throughout the entire curve. A more exact determination of the reaction order from the experimental data was obtained by means of a graphical method (Chang 1957) and also by an analytical method (Rothwarf and Steinberg 1959, private communication). The average order of reaction was 2·2 (i.e. the value of n in the formulae given in the Appendix is 2·2). Similar analyses made on specimens quenched from 530°c, below the critical temperature (fig. 4), gave 1·5 for the order of reaction. The difference in ordering rates can be seen very clearly in fig. 7, which is a plot of the 295°c isothermals (normalized at $t=0$ and $t=\infty$) indicating an increase in the rate of ordering with an increase in quenching temperature. This is to be expected for reaction orders greater than unity. Figure 8 shows a plot of the relaxation time τ as a function of the reciprocal temperature for all isothermal curves measured in these experiments. The upper plot gives the activation energy for specimens quenched from 530°c and the lower plot gives the activation energy for specimens quenched from 620°c. The two plots were obtained from the original isothermals by assuming an order of reaction of 1·5 and 2·0 respectively†. The activation energy is obtained from the slopes of the straight lines. Since each set of points lies

Fig. 7

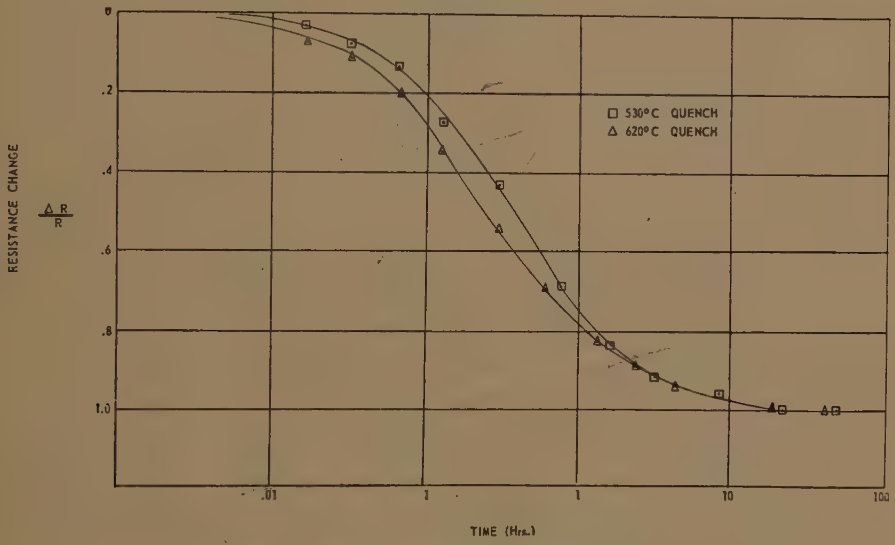

Normalized 295°c isotherms measured at 77°K.

---

† τ_0, the value of τ for $1/T=0$, is also shown in the figure.

on a straight line and the lines are reasonably parallel, one can infer that the rate of annealing is determined by a single activation process over the temperature range investigated.

§ 4. Discussion

The results summarized in the previous section indicate that, in the 24·8 at. % Fe/Al alloy, the rate at which ordering takes place is a function of the initial quenching temperature. In the table, (A) gives the values of the order of reaction as a function of annealing temperature for different quenches; (B) gives similar results for the specimens of 25·5 at. % Fe/Al treated in the same fashion. Except for one 295°C annealed specimen in (B) there is a strong correspondence of order of reaction with quenching temperature. Within experimental error there is no correlation of n with annealing temperature.

Fig. 8

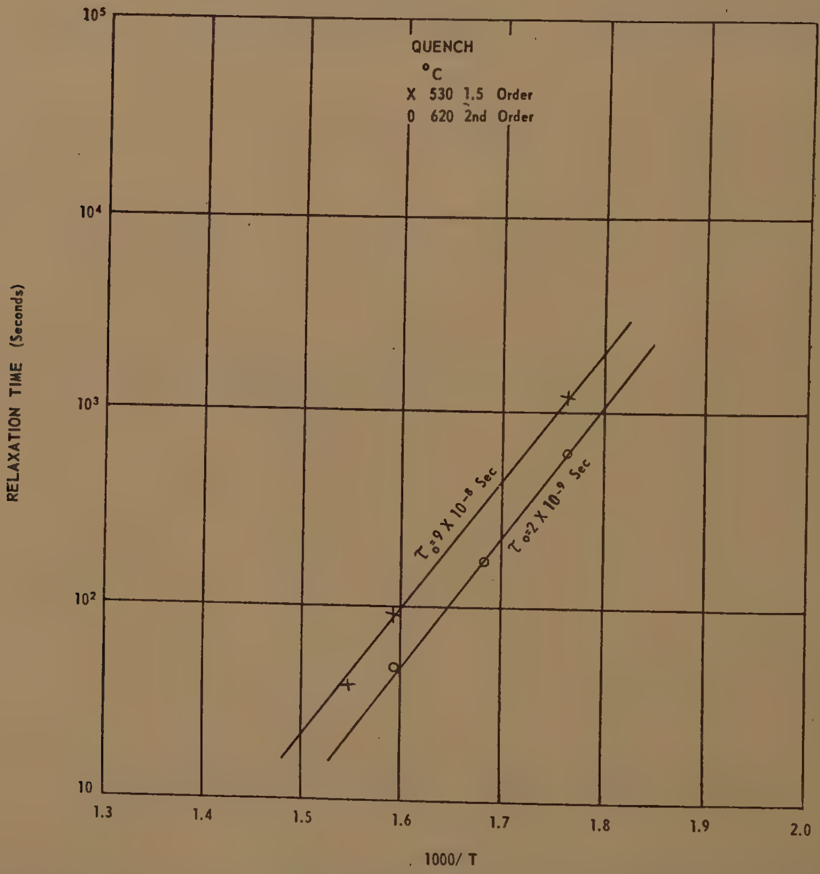

Variation of relaxation time with reciprocal absolute temperature for a 24·8 at. % FeAl alloy.

By way of example, the 295°C anneal for both quenches (24·8 at. % alloy) was normalized and plotted as a function of time (see fig. 7). The specimen quenched from the higher temperature is seen to have a faster initial ordering (indicative of a higher order of reaction) prior to the inflection point and a slowly decreasing rate of approach to equilibrium. This is similar to the experimental results reported by Brinkman *et al.* (1954) for Cu_3Au, and by Kuczynski *et al.* (1955) for CuAu. It is possible that the initial increase in rate of ordering should be attributed to an increase in the density of quenched-in vacancies. The result of this however would be that the process was no longer singly activated; i.e. no single value of n would be adequate for the entire curve. This is contrary to our findings.

Anneal °C	n, quench 620°C	n, quench 530°C
(A) (24·8%)		
295	2·25	1·6
322	2·20	
353	2·25	1·4
375	2·3	1·6
(B) (25·5%)		
295	2·3	1·95
353	2·3	1·4
375	2·5	1·4
383		1·5

The initial states should of course be influenced by the differences in atomic arrangement which exist at different quenching temperatures. For ordering temperatures well below T_c, however, nucleation is not rate-determining (see for instance Burns and Quimby 1955), and the growth rate of ordered regions will depend on the free energy difference between the initial and final states. This will be the greater, the higher the temperature from which the alloy is quenched.

The fact that a well-defined single activation energy is obtained by the present method is no doubt due to the narrowness of the range of temperatures investigated. According to Burns and Quimby's (1955) resistivity kinetic data for Cu_3Au, as interpreted by Vineyard (1956), a plot such as that in fig. 8 should give curved lines whose slopes diminish as T approaches T_c. However, the curve approximates to a straight line at low temperatures. According to Vineyard's theory, if the temperature range is one in which the equilibrium degree of order is almost constant, then the deduced activation energy for ordering should be the mean of the activation energies for self-diffusion of the two components in the alloy.

The values of the rate constant plotted in fig. 8 give a well-defined activation energy of 31 kcal/mole. Similar results were obtained for the 25·5 at. % alloy. This is to be compared with a value of 29·5 kcal/mole reported by Rode (1957). It is known that self-diffusion in pure iron has an activation energy of about 73 kcal/mole (Birchenall and Mehl 1950). The mean activation energy for diffusion of aluminium in iron is 57·3–58·6 kcal/mole (Gröbner 1955, Shyne 1958). The apparent activation energy obtained for Fe_3Al is, therefore, a good deal lower than that for any diffusion process (unless indeed the activation energies for solute and self-diffusion are sharp functions of composition or of the state of order, which cannot be entirely excluded). However, this disparity is not really surprising, since the degree of order is still changing appreciably with temperature in the range 295°C–375°C. A comparison with the corresponding data for Cu_3Au (cf. fig. 4 in Vineyard's paper) shows that in this case also the apparent activation energy deduced from resistivity kinetics is much lower than the mean activation energy for diffusion, in a temperature range in which the rate of change of degree of order with temperature is variable. What is rather surprising is the fact that the plots in fig. 8 of the present paper are such good straight lines; on the basis of Vineyard's theory these plots would be expected to be considerably curved. In spite of the fact that a well-defined activation energy is found from fig. 8, it appears probable that this has no real physical significance.

ACKNOWLEDGMENTS

We are grateful to Professor G. V. Raynor for his support, and the provision of laboratory facilities. One of us (R. F.) is indebted to the Secretary of the U.S. Army for a Fellowship.

APPENDIX

The general nth order rate equation is

$$\frac{d\rho}{dt} = -\frac{1}{\tau_n}(\rho_t - \rho_\infty)^n. \quad \ldots \quad (1)$$

Integration of this leads to the following equation:

$$(\rho_t - \rho_\infty)^{-(n-1)} = \frac{(n-1)t}{\tau_n} + (\rho_0 - \rho_\infty)^{-(n-1)} \quad \ldots \quad (2)$$

where ρ_0 = initial resistance, ρ_∞ = resistance at infinite time, ρ_t = resistance at any time t.

Equation (2) is equivalent to

$$(\rho_t - \rho_\infty) = \left[\frac{(n-1)t}{\tau_n} + (\rho_0 - \rho_\infty)^{-n-1}\right]^{-(1/n-1)}.$$

Solving for ρ_t, one obtains

$$\rho_t = \rho_\infty + (\rho_0 - \rho_\infty)\left[\frac{(n-1)(\rho_0 - \rho_\infty)^{n-1}t}{\tau_n} + 1\right]^{-(1/n-1)}. \quad \ldots \quad (3)$$

For the special case of a first order equation ($n=1$), equation (3) becomes

$$\rho_t=\rho_\infty+(\rho_0-\rho_\infty)\exp(-t/\tau_1). \qquad (4)$$

Theoretical curves were, as a matter of convenience, always fitted to experimental data at $t=0$, $t=\infty$, and a time t' at which all but $1/e$ of the total resistance change has been completed. For a first-order reaction, $t'=\tau_1$. Using this fact, one can calculate the relaxation time τ_n for any desired order of reaction, as fitted to the experimental data :

Values of ρ_t, computed from eqns. (3) and (4), are set equal. We then have

$$\exp(t/\tau_1)=\left[\frac{(n-1)(\rho_0-\rho_\infty)^{n-1}t}{\tau_n}+1\right]^{1/(n-1)} \qquad (5)$$

and solving this for τ_n,

$$\tau_n=\frac{(n-1)(\rho_0-\rho_\infty)^{n-1}t}{\exp\{(n-1)t/\tau_1\}-1}. \qquad (6)$$

Curve fitting is carried out at $t=t'$, and this value of t must therefore be substituted into eqns. (5) and (6). Since $t'=\tau_1$, we finally obtain

$$\tau_n=\frac{t'(n-1)(\rho_0-\rho_\infty)^{(n-1)}}{\exp(n-1)-1}. \qquad (7)$$

t' is known from curve-fitting, and thus τ_n can be calculated from eqn. (7). Using this value of τ_n in eqn. (3), the computed nth order curve can be compared with the data points ; this is done for various values of n until a good fit is obtained throughout. (If this proves possible for some one value of n, then the reaction is a 'singly activated' one). A fit may be obtained for a non-integral value of n. It appears reasonable to ascribe such a non-integral order of reaction to a single step process. This assumption is made since it is not possible to derive an expression of the form of eqn. (3) for the sum of several independent processes each characterized by an integral value of n. In view of this, only two physical interpretations remain for a reaction of non-integral order. Either the reaction is in fact occurring as a single-step process, or some type of coupling exists between two or more distinct processes.

REFERENCES

BIRCHENALL, C., and MEHL, R. F., 1950, *Trans. Amer. Inst. min. (metall.) Engrs*, **188**, 144.

BRINKMAN, J. A., DIXON, C. E., and MEECHAN, C. J., 1954, *Acta Met.*, **2**, 38.

BURNS, F. P., and QUIMBY, S. L., 1955, *Phys. Rev.*, **97**, 1567.

CHANG, WEN-HSUAN, 1957, *J. chem. Phys.*, **61**, 819.

GRÖBNER, P., 1955, *Hutn. List.*, **10**, 200.

KUCZYNSKI, G. C., HOCHMAN, R. F., and DOYAMA, M., 1955, *J. appl. Phys.*, **26**, 871.

PARKENS, W. E., DIENES, G. J., and BROWN, F. W., 1951, *J. appl. Phys.*, **22**, 1012.

RODE, V. E., 1957, *Bull. Acad. Sci. U.S.S.R., Phys. Ser.*, **21**, 1234.

SHYNE, J. C., 1958, *Ford Scientific Laboratory Report*, SL 2–89.

TAYLOR, A., and JONES, R. M., 1958, *J. Phys. Chem. Solids*, **6**, 16.

VINEYARD, G. H., 1956, *Phys. Rev.*, **102**, 981.

The Refractive Indices of Liquid and Solid Argon†

By G. O. Jones and B. L. Smith
Department of Physics, Queen Mary College
(University of London), London, E.1

[Received January 27, 1960]

ABSTRACT

The refractive indices of liquid and solid argon have been measured as a function of temperature between 74° and 95°K. The results, represented by the Lorentz–Lorenz function, are expressed as a function of density, and their significance discussed.

THE theory of dielectric materials, based on the Lorentz local field model, predicts that for a non-polar material the Clausius–Mossotti function $(\epsilon-1)/(\epsilon+2)\rho$, or its equivalent, the Lorentz–Lorenz function

$$(n^2-1)/(n^2+2)\rho,$$

should be independent of density (ρ). Measurements at low densities on the compressed gases argon (see for example Michels and Botzen 1949, Michels *et al.* 1951) and carbon dioxide (Michels and Kleerekoper 1939) show that although these functions are indeed nearly independent of density, they increase slowly with increasing density up to 2–300 Amagats and decrease at higher density. Measurements on liquids such as benzene (see for example Gibson and Kincaid 1938) suggest that the decrease is continued at higher density. The specific influence of temperature is very small.

In view of the crude nature of the model, and the over-simplification involved in assigning a polarizability to each atom, better agreement over such a wide range of density would hardly be expected. However, modifications to the theory, such as that of Jansen (1958), who analysed the effect of pair interactions upon the polarizability, or of ten Seldam and de Groot (1952), who considered the effect of compression on the atomic polarizability, can be made to account for slow variations of these functions.

In order to provide suitable data for the development of a more exact theory we have measured the refractive index of liquid argon (from 84–95°K) and more particularly of solid argon (from 74–84°K) in equilibrium with vapour. No accurate data appear to exist for non-polar

---

† Communicated by the Authors.

Fig. 1

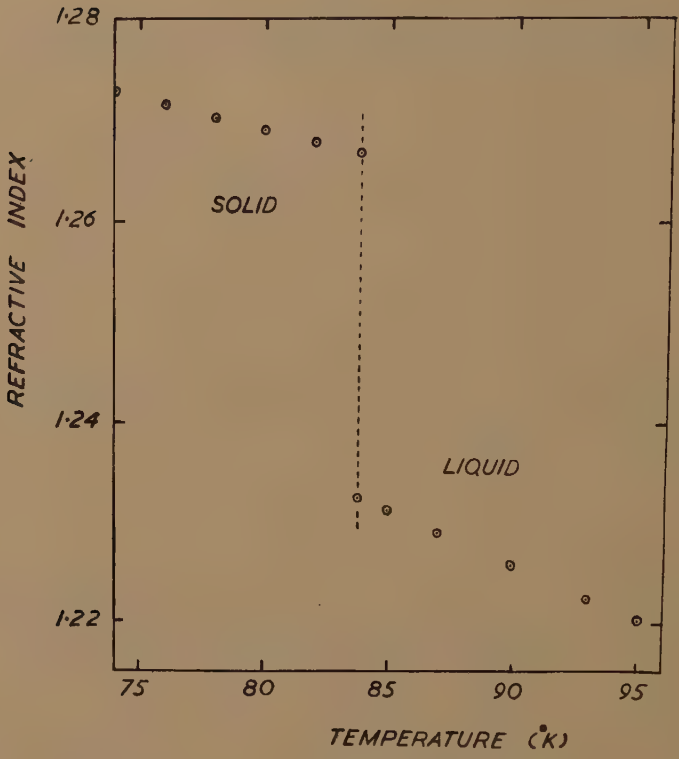
1·28
1·26
1·24
1·22
REFRACTIVE INDEX
SOLID
LIQUID
75
80
85
90
95
TEMPERATURE (°K)

Fig. 2

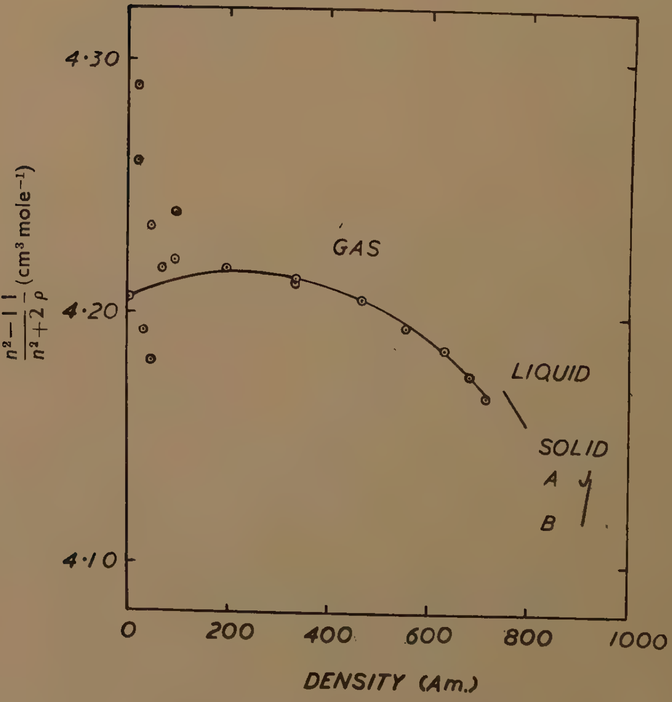
4·30
4·20
4·10
$\frac{n^2-1}{n^2+2}\frac{1}{\rho}$ (cm³ mole⁻¹)
GAS
LIQUID
SOLID
A
B
0
200
400
600
800
1000
DENSITY (Am.)

solids and argon is especially suitable because of the nature of the interatomic force, which more nearly justifies the use of an atomic polarizability and which, being spherically symmetrical, offers better hope of an accurate treatment of pair interactions. Also, solid argon has the cubic symmetry of the Lorentz model.

The spectrometric method of minimum deviation was employed. The specimen was condensed into a hollow Perspex prism contained in a simple cryostat and located at the axis of rotation of a spectrometer mounted outside the cryostat on a co-axial turntable. Measurements were made at several wavelengths and those at 5893 Å are shown in fig. 1. At the triple point (83·8°K) the refractive index of the solid is 1·2670 ± 0·0005 and of the liquid 1·2330 ± 0·0005. Since the nearest absorption band is in the ultra-violet, dispersion is small.

In fig. 2 the Lorentz–Lorenz function is plotted against density for the data of fig. 1 and for those of Michels and Botzen at 5876 Å. For our computations the density of the liquid (ρ_L) was taken from the data of Piercey (1957) and of Mathias *et al.* (1912), and the density of the solid (ρ_S) from the results of Dobbs *et al.* (1956). In the results of these authors as plotted, the experimental curve for solid argon was drawn through the point corresponding to the value (1·621 g c.c.$^{-1}$) quoted by Clusius and Weigand (1940) at the triple point. However, the recent measurements of ρ_L by Piercey indicate that the extrapolated value for ρ_L at the triple point from which Clusius and Weigand derived their estimate of ρ_S was too low. We have therefore drawn two curves to represent the behaviour of the solid. Curve A makes use of the values of density obtained from the published curve of Dobbs *et al.* and curve B of values obtained by attaching slightly more weight to their results and re-drawing their curve to a higher value (1·6275 g c.c.$^{-1}$) at the triple point. The differences between these two curves then illustrate the limiting interpretations which can reasonably be given to the results for refractive index.

It will be seen that for liquid argon the Lorentz–Lorenz function decreases by about 0·3% over the range of densities studied, roughly as would be expected from the behaviour of the gas at lower densities. For solid argon the results appear to indicate an increase with increasing density, at least at the higher densities, and point to the desirability of obtaining still more accurate values of the density near the triple point. At present no appropriate theoretical treatment exists by which the effect of pair interactions upon the polarizability at large amplitudes of vibration may be evaluated.

ACKNOWLEDGMENTS

We are grateful to Dr. E. R. Dobbs for helpful discussions and to the D.S.I.R. for a research studentship awarded to one of us.

REFERENCES

CLUSIUS, K., and WEIGAND, K., 1940, *Z. phys. Chem.* B, **46,** 1.

DOBBS, E. R., FIGGINS, B. F., JONES, G. O., PIERCEY, D. C., and RILEY, D. P., 1956, *Nature, Lond.*, **178,** 483.

JANSEN, L., 1958, *Phys. Rev.*, **112,** 434.

GIBSON, R. E., and KINCAID, J. F., 1938, *J. Amer. chem. Soc.*, **60,** 511.

MATHIAS, E., ONNES, H., and CROMMELIN, C. A., 1912, Leiden Comm. 131(a).

MICHELS, A., and BOTZEN, A., 1949, *Physica*, **15,** 769.

MICHELS, A., and KLEEREKOPER, L., 1939, *Physica*, **6,** 586.

MICHELS, A., TEN SELDAM, C. A., and OVERDIJK, S. D. J., 1951, *Physica*, **17,** 781.

PIERCEY, D. C., 1957, M.Sc. Thesis, University of London.

TEN SELDAM, C. A., and DE GROOT, S. R., 1952, *Physica*, **18,** 910.

Isotopic Spin Selection Rules
XIII: The 6·92 MeV State of ^{16}O Revisited†

By R. E. Pixley, J. V. Kane and D. H. Wilkinson‡
Brookhaven National Laboratory, Upton, N.Y., U.S.A.

[Received January 16, 1960]

Abstract

The status of the possible E1–E3 cascade between the 2+ state at 6·92 Mev, the 3− state at 6·14 Mev and the 0+ ground state of ^{16}O is reviewed in the light of recent improvements in our knowledge of radiative transitions and isotopic spin impurities. It is concluded that the present limit of 5×10^{-3} on the relative intensity, although clearly demonstrating the efficacy of the isotopic spin selection rule, is not sharp enough to be a significant test for detailed models of the nuclear structure, for which purpose an improvement by an order of magnitude would be required. It is shown by a coincidence method, using the reaction $^{19}F(p, \alpha)^{16}O$, that the relative intensity is less than 4×10^{-4}. This corresponds to $\alpha_0^2(1) < 2 \times 10^{-3}$, a low figure.

§ 1. Introduction

The first paper of this series (Wilkinson and Jones 1953) pointed out that the E1 transition between the 2+ state of ^{16}O at 6·92 Mev and the 3− state at 6·14 Mev is subject to the isotopic spin selection rule forbidding E1 transitions of $\Delta T = 0$ in nuclei of $T_z = 0$. Consequently what might have been expected as favourable competition with the E2 transition to the ground state is strongly inhibited: the experimental result of that paper was that the E1 transition is no more than 5×10^{-3} of the E2. Since that time our understanding both of the most probable speeds for uninhibited E1 transitions in the light nuclei (Wilkinson 1958) and also of the empirical and theoretical behaviour of isotopic spin impurity (MacDonald 1956, Wilkinson 1958) has greatly increased. The situation relative to ^{16}O was summarized some time ago (Wilkinson 1956). From this summary it appeared that the 1953 experimental limit on the E1 versus E2 branching ratio although clearly demonstrating the T-forbiddenness was not sharp enough to test our later and more detailed ideas about isotopic spin purity since it implied that $\alpha_0^2(1)$ (the intensity of the $T = 1$ impurity) is less than a few per cent whereas the expectation for $\alpha_0^2(1)$ at that excitation is 10^{-3} to 10^{-2}. Since 1956 the situation has been made quite definite by the measurement of the mean lifetime of the 6·92 MeV state as $(1{\cdot}2 \pm 0{\cdot}3) \times 10^{-14}$ sec (Swann and Metzger 1957). This enables us to interpret the branching ratio in terms of an actual rather than an estimated lifetime; no sensible change was introduced into the earlier analysis.

---

† Communicated by the Authors. Work performed under the auspices of the United States Atomic Energy Commission.

‡ Permanent address: Clarendon Laboratory, Oxford, England.

If we use the systematics (Wilkinson 1958) to estimate the most likely mean lifetime for an 0·78 MeV uninhibited E1 transition in ^{16}O we find about $6{\cdot}6 \times 10^{-14}$ sec. So were the E1 unaffected by the isotopic spin rule we should expect its strength relative to the E2 to be about 0·18. The old limit of 5×10^{-3} therefore corresponds, using the newer data and systematics, to $\alpha_0^2(1) < 0{\cdot}028$ (with the inevitable uncertainty introduced by guessing the speed of the uninhibited E1 transition mixed in through the isotopic spin impurities). It is therefore clear than an improvement by an order of magnitude in sensitivity to the E1 branch would be very interesting and would bring us to the point where the cascade should probably show up unless it is in fact further inhibited by something peculiar to the ^{16}O structure and having nothing to do with isotopic spin. We do not expect this for the following reason. The E2 transition is strong ($|M|^2 \simeq 0{\cdot}7$) and so must contain strong components differing from the (closed shell) ground state of ^{16}O by a single particle: $1p^{-1}(2p, 1f)$ and $1s^{-1}1d$. The 3 – state is well contained by the independent particle treatment of Elliott and Flowers (1957) which describes it as $1p^{-1}1d$. The Coulomb perturbation will mix in the $T=1$ parts of these same configurations (cf. the explicit treatment of the 1 – state at 7·12 MeV made by Elliott and Flowers) and so it is difficult to see how the E1 transition can be additionally inhibited on grounds of nuclear structure since the descriptions of the two states given above differ in all components by one-particle one-quantum jumps of the equivalent oscillator. An additional important component in the isotopic spin impurity of well-spaced states is thought to come from the Coulomb mixing of one-particle two-quantum excitations of the type $(n, j) \rightarrow (n+1, j)$ (MacDonald 1956). If we apply this recipe to generate $T=1$ impurities for the two states in question we find:

$$2+\ (T=0):\ 1p^{-1}(2p, 1f) + 1s^{-1}1d;$$
$$3-\ (T=1):\ 1s^{-1}1p^{-1}2s1d + 1p^{-2}1d2p;$$

and

$$2+\ (T=1):\ 1s^{-1}1p^{-1}2s(2p, 1f) + 1p^{-2}2p(2p, 1f) + 1s^{-2}2s1d + 1s^{-1}1p^{-1}1d2p;$$
$$3-\ (T=0):\ 1p^{-1}1d.$$

The $2+\ (T=1) \rightarrow 3-\ (T=0)$ transitions are forbidden but the $2+\ (T=0) \rightarrow 3-\ (T=1)$ are allowed unless the 2+ state is entirely $1p^{-1}1f$. This last possibility can be discounted since interaction between configurations is clearly needed to produce the large downward energy displacement implied by this state of two-quantum excitation appearing at so low an energy as 7 MeV. We therefore have no reason to anticipate a strong additional inhibition of the E1 transition and it becomes interesting to press the matter further.

§ 2. Experiment

The 6·92 MeV 2+ ^{16}O state was populated by using the resonance in ^{19}F(p, α)^{16}O at a proton energy of about 2·4 MeV. The target of BaF_2 was about 50 kev thick. At this resonance the 6·92 MeV state is fed about three times more strongly than the 1− state at 7·12 MeV while the feeding of the 6·14 MeV 3− state is relatively weak (Swann and Metzger 1957). Coincidences between the 0·78 MeV E1 transition and the 6·14 MeV E3 to the ground state were sought using a coincidence resolving time of about 0·1 μsec.

Fig. 1

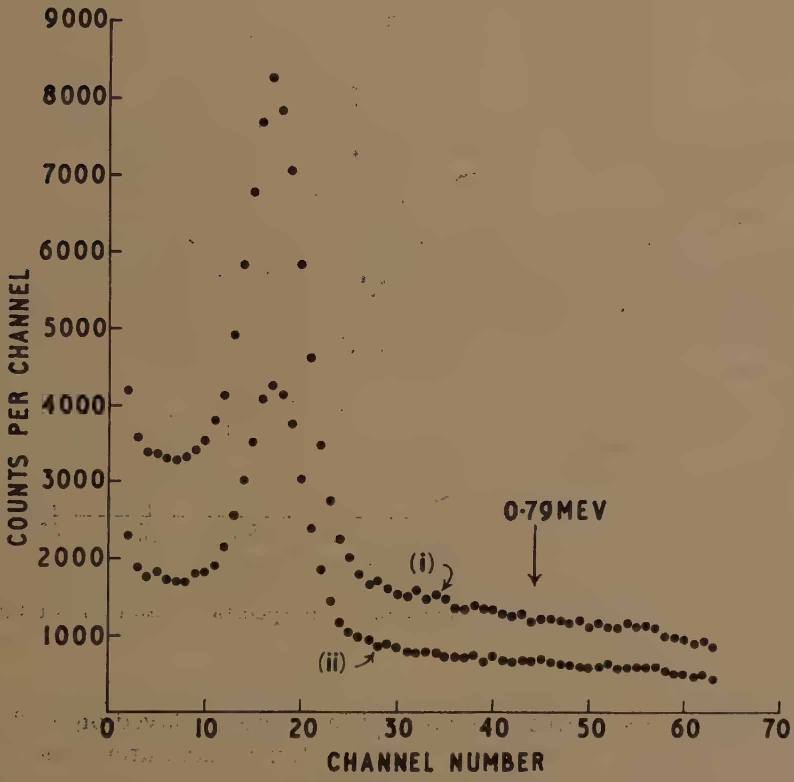

Low energy spectrum seen in coincidence with (i) the 5·4–6·5 MeV bracket in the high-energy crystal; (ii) the 6·7–7·7 MeV bracket. The peaks at channel 17 are due to annihilation radiation; the arrow indicates the expected position of the 0·78 MeV line which might show in curve (i) but not in curve (ii).

The high energy gamma-rays were detected in a 5 in. × 5 in. cylindrical NaI(Tl) crystal placed at 80° to the proton beam. The gamma-rays were collimated by a hole in the form of a truncated cone of height 2¼ in. base diameter 1¾ in. and entrance diameter ½ in. through a lead shield. The entrance was 7/16 in. from the centre of the BaF_2 target. The low energy gamma-ray was sought in a 3 in. × 3 in. cylindrical NaI(Tl) crystal placed 'out of sight' of the irradiated face of the larger crystal. The smaller crystal was $1\frac{11}{16}$ in. from the centre of the target and was placed at about 45° to the proton beam on the side away from the larger crystal. This arrangement was adopted to minimize coincidences due to scattering between the crystals and to the detection of annihilation radiation following pair conversion in the larger crystal. The smaller crystal was that used in the research on cascade de-excitation in ^{13}C (No. XIV of this series) and had a resolution of 7·6% for gamma-rays of 0·78 MEV (see fig. 3 of paper XIV).

Fig. 2

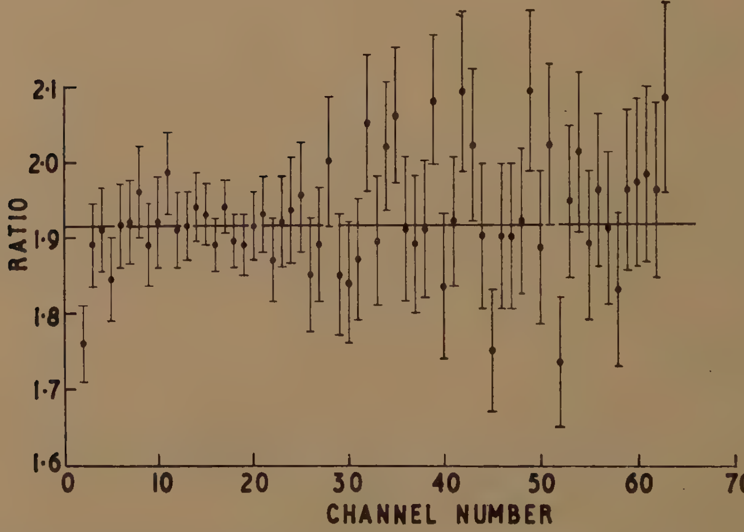

The ratio channel by channel of the counts in spectra (i) and (ii) of fig. 1

The coincidences between the two crystals were displayed on a 32 × 64 channel kicksorter made at Brookhaven National Laboratory under the direction of Mr. R. Chase. The 32 channel axis displayed the pulses in the larger crystal between energies of approximately 4 and 8 MEV; the energy range of the smaller crystal's display along the 64 channel axis was approximately 0·35 to 1·0 MEV. For purposes of display and discussion here we present severally in fig. 1 the low-energy spectra summed between channels 15–23 and between channels 24–31 of the high energy arm. The lower range corresponds to the energy spread 5·4–6·5 MEV in the larger crystal and the upper corresponds to 6·7–7·7 MEV. If the E1–E3 cascade is present the 0·78 MEV line will be seen in coincidence with the 5·4–6·5 MEV range of the larger crystal but will not be seen in coincidence with the 6·7–7·7 MEV bracket.

It is clear from fig. 1 that no strong 0·78 MeV line is present. The peak seen at channel 17 in both spectra is due to annihilation radiation. The form of the two low-energy spectra in coincidence with the two high energy brackets are effectively identical as is seen in fig. 2 where their ratio is displayed. This suggests a method of analysis that does not depend on assumptions about the form of the background underlying the possible 0·78 MeV peak. We consider the channel range 40–49 that straddles the position expected for the 0·78 MeV peak. From the total number of counts in this range of the spectrum in coincidence with the 5·4–6·5 MeV bracket we subtract the corresponding total number taken from the spectrum in coincidence with the 6·7–7·7 MeV bracket multiplied by the mean ratio for the entire spectra derived from the data presented in fig. 2. The difference so derived is 87 ± 190 counts.

An alternative though not so direct treatment of the data is to analyse that portion of pulse spectrum (i) of fig. 1 that excludes the peak region in polynomial form and then use this analysis to predict the number of counts expected for the peak region in the absence of a peak. This has been done by Dr. P. E. Hodgson of the Clarendon Laboratory, Oxford to whom our best thanks are due. Channels 28–39 and 50–63 were used to derive a best polynomial fit (4th order). This polynomial fit thus predicts 12204 ± 72 counts for the peak region of channels 40–49. The observed number is 12250. The difference of 46 ± 132 counts is to be compared with the 87 ± 190 of the direct method. We say that the difference is zero within a standard deviation of 190 counts, preferring to use the indirect solution as strong confirmation of the direct method.

Both crystals were carefully calibrated for their response to a range of monochromatic gamma-rays so that their efficiencies within the various energy ranges of interest were known. By these means we can say that the E1–E3 branch relative to the E2 transition to ground from the 6·92 MeV state is zero within a standard deviation of $2{\cdot}3 \times 10^{-4}$.

§ 3. DISCUSSION

It appears that the branching ratio is most probably less than 4×10^{-4}. This, following the considerations of § 1, corresponds to a probable upper limit on the isotopic spin impurity by intensity of about 2×10^{-3}. This figure is quite low in the expected range $10^{-3} < \alpha^2 < 10^{-2}$ though not so low as to be disturbing in view of the possible vagaries of the many matrix elements involved in the comparison with a very approximate theoretical model. It is, however, low enough to be interesting and to be a useful test of detailed attempts to describe the 2+ state. So far no thoroughgoing theoretical comparison is available for this transition as it is for the forbidden E1 transition to ground from the 1 − state at 7·12 MeV which has $\alpha_0^2(1) \simeq 7 \times 10^{-3}$ expressed under our present conventions outlined in § 1 (Wilkinson 1958) and which is well described by the independent particle model (Elliott and Flowers 1957).

REFERENCES

ELLIOTT, J. P., and FLOWERS, B. H., 1957, *Proc. roy. Soc.* A, **242,** 62.
MACDONALD, W. M., 1956, *Phys. Rev.*, **101,** 271.
SWANN, C. P., and METZGER, F. R., 1957, *Phys. Rev.*, **108,** 982.
WILKINSON, D. H., 1956, *Phil. Mag.*, **1,** 379; 1958, *Proceedings of the Rehovoth Conference on Nuclear Structure* (Amsterdam : New-Holland), p 175.
WILKINSON, D. H., and JONES, G. A., 1953, *Phil. Mag.*, **44,** 542.

Isotopic Spin Selection Rules
XIV: Transitions between Mirror States in ^{13}C and ^{13}N†

By J. V. Kane, R. E. Pixley and D. H. Wilkinson‡
Brookhaven National Laboratory, Upton, N.Y., U.S.A.

[Received January 16, 1960]

Abstract

The 3·68 Mev 3/2− state of ^{13}C is shown, by a coincidence technique to cascade via the 3·09 Mev 1/2+ state with a probability of $(6 \cdot 5 \pm 1 \cdot 0) \times 10^{-3}$. The rule that corresponding E1 transitions in mirror nuclei have the same reduced speed, i.e. are mirror transitions, is used to deduce the speed of this weak branch from data available in ^{13}N and hence to determine the radiative width of the M1 transition to ground from the 3·68 Mev state. This is (0·40–0·75) ev. The speed of this transition, which is not a mirror transition to the corresponding one in ^{13}N, is compared with the prediction of the independent particle model. Agreement is obtained within the range of the intermediate coupling parameter a/K that satisfies other data in the $A=13$ system.

§ 1. Introduction

The close comparison between the energies of excitation of corresponding states in mirror nuclei is due to the charge independence or charge symmetry of the specifically nuclear part of the nucleon–nucleon interaction. The charge-dependent Coulomb energy is considerable and produces a gross mass difference of several million electron volts between the members of the isobaric multiplet; it does not, however, affect the comparison between the level structures of the several T_z nuclei since it is, to a good first approximation, independent of the energy of excitation at least when that energy is low. Because of this one often tends to lose sight of the very real differences between mirror nuclei for those phenomena that are essentially charge-dependent in character. In particular we have no *a priori* reason to expect that the reduced speed of the electromagnetic transition between a given pair of states in a given nucleus will be unchanged for the corresponding transition between the mirror states in the mirror nucleus. The states are mirror states but the corresponding transitions are not in general mirror transitions.

---

† Communicated by the Authors. Work performed under the auspices of the United States Atomic Energy Commission.

‡ Permanent address: Clarendon Laboratory, Oxford, England.

There are several classes of exception to this general expectation that the reduced speed will depend on T_z and they have been discussed by Morpurgo (1959). The one of interest to us here is that the reduced speed is independent of T_z for E1 transitions. This rule is closely connected with the familiar isotopic spin selection rule on E1 transitions and may be easily understood by considering the Hamiltonian H of the electromagnetic interaction as split up in the usual way :

$$H = H_0 + H_1.$$

For $\Delta T = 0$, M_1 is proportional to T_z; for $\Delta T = \pm 1 M_1$ depends on T_z^2. In general, then, corresponding transitions between states with $\Delta T = \pm 1$ have the same reduced speed in the mirror nucleus, i.e. are mirror transitions, since then $M_0 = 0$, but for $\Delta T = 0$ the corresponding transitions have different reduced speeds since generally both M_0 and M_1 contribute. For E1 transitions, however, M_0 makes no contribution owing to conservation of total momentum (cf. the derivation of the E1 isotopic spin selection rule—e.g. MacDonald 1955) and so the reduced E1 speed is the same in both members of the mirror pair[†].

Accordingly we can in general make no model-independent remark about the relative speeds of the corresponding transitions in the members of a mirror pair although Morpungo (1959) has given reasons why we should not expect the speeds of corresponding M1 transitions to be greatly different in reasonable circumstances.

This situation is to be welcomed since it gives added opportunity for the testing of nuclear models which must be required to account for the differences between mirror nuclei as well as their similarities.

At present there exist almost no data on the comparison of corresponding but non-mirror transitions (e.g. M1) in nuclei for which a detailed model exists to be tested by the results. It is the purpose of this paper to provide one such comparison in a case which has received extensive theoretical treatment.

§ 2. STATES OF ^{13}C AND ^{13}N

The low-lying odd-parity states of $A = 13$ made from p^9 have been extensively treated on the independent particle model (IPM)—Inglis (1953), Kurath (1956), Lane (1953, 1955). Lane in particular has emphasized that a substantial group of experimental data is unified within the IPM by receiving satisfactory theoretical explanation for essentially the same value of the intermediate coupling parameter a/K. These data are: (i) the energy of the first odd parity excited state (3/2 –) at 3·68 MEV in ^{13}C and 3·51 MEV in ^{13}N; the magnetic moment of the ground state of ^{13}C; the beta-decay between the ground states; the reduced nucleon width of the 3/2 – state of ^{13}N; the speed of the M1 transition to ground from the 3/2 – state of ^{13}N. All these data are accounted for at a/K values between 4·8 and 5·5†.

[†] This situation can be understood qualitatively because the spin part of the matrix element is negligibly small for E1 transitions while the space part (radiation due directly to the acceleration of charge) is very much the same for a ‘radiating proton’ or ‘radiating neutron’ (the ‘effective charge’ concept) owing to the contribution from the charge on the rest of the nucleus. For, say, an M1 transition, however, the spin contribution is large and, since the magnetic moments of neutron and proton are very different we have very different contributions from the ‘radiating proton’ and the ‘radiating neutron’.

Fig. 1

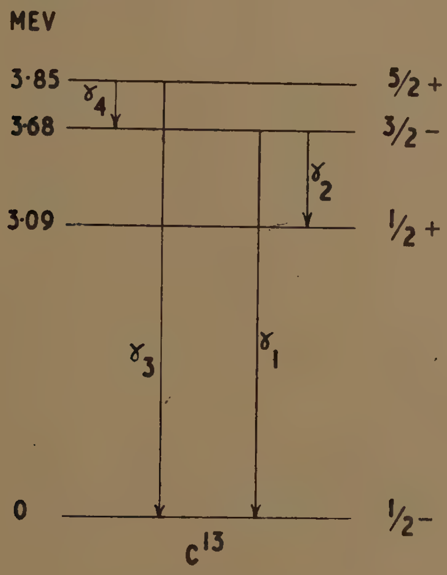

Level scheme of ^{13}C.

The purpose of this paper is to estimate the strength of the corresponding but non-mirror M1 transition from the 3/2 – state of ^{13}C at 3·68 MEV to the 1/2 – ground state and to compare it with the same IPM calculation as accounts for the transition in ^{13}N. If the calculation is satisfactory (and charge-symmetry holds) the transition in ^{13}C should be explained by the IPM theory for the same a/K value as is required in ^{13}N.

The ^{13}N transition has a width of about 0·7 ev (Seagrave 1951) and so we anticipate that the lifetime of the corresponding ^{13}C transition will be much too short for direct measurement. The state is accessible to resonance fluorescence but this technique is difficult to use in this case. In this paper we estimate the radiative width by an application of the rule, enunciated above, that E1 transition strengths are the same in mirror nuclei. Refer to fig. 1. The gamma-ray labelled γ_2 is an E1 transition whose mirror transition in ^{13}N, between the 3·51 MEV and 2·37 MEV states, has a measured width (about 0·04 ev; Woodbury *et al.* 1954). We may now transfer this reduced speed to ^{13}C and so by a measurement of the branching ratio of γ_2 versus γ_1 determine the speed of the M1 transition γ_1.

---

† See Lane (1955) for remarks on the comparative insensitivity of these results to other details of the calculation such as the L/K value and the exchange mixture. See however Skyrme (1958) for comments on some difficulties.

§ 3. EXPERIMENTAL DETAILS

We seek to prepare the 3·68 MEV state of ^{13}C in a well-defined manner and to measure the relative intensity of its cascade de-excitation. This latter probability is already known to be very low ($< 3\%$) from the work of Mackin *et al.* (1956). The state may be conveniently reached using the reaction ^{12}C(d, p)^{13}C but the relative populations of the various ^{13}C states have not been well studied and this bombardment has the added disadvantage of producing large quantities of neutrons which are always a nuisance when gamma-ray measurements of some delicacy are to be attempted. We have chosen to use the reaction ^{10}B(α, p)^{13}C. At the well-studied 4+ resonance at $E = 1{\cdot}64$ MEV (Shire *et al.* 1953, Stanley 1954) the proton cross sections for directly populating the 3·85 MEV and 3·68 MEV states are respectively 52 and 2·4 mb while the total neutron-producing cross section from ^{10}B(α, n)^{13}N is only 3·2 mb. The 3·68 MEV state is chiefly populated indirectly via the 170 kev E1 transition from the 3·85 MEV state labelled γ_4 in fig. 1 which constitutes 0·24 ± 0·05 of the transitions from the 3·85 MEV state (Mackin *e tal.* 1956).

Our experiment consisted in searching for coincidences between γ_2 and the subsequent 3·1 MEV gamma-ray and comparing their abundance with the γ_4–γ_1 coincidences. Since the 3·68 MEV level is populated chiefly via γ_4 the rather large error in the γ_4–γ_3 branching ratio is not reflected in the accuracy with which we determine γ_2 versus γ_1. γ_4 is used as a tracer for γ_1 and we do not have to compare absolute coincidence rates with absolute single counting rates as we should had we chosen conditions in which the 3·68 MEV level were populated chiefly directly. There is, however, a penalty to be paid for the use of this trick. An alternative transition from the intensely-populated 3·85 MEV state is the E2, not marked on fig. 1, to the 1/2+ state at 3·09 MEV. This is of higher energy than γ_2 and will also be found in coincidence with the 3·09 MEV transition; if, therefore, it were much more intense than γ_2 it would consitute a severe obscuration. In fact it is somewhat more intense, but not greatly so and can be subtracted with good accuracy from the gross high–low coincidence distribution. Its study will be described in another publication: it has no points of interest in common with the gamma-rays of our present report.

A light air-cooled target assembly bore a separated elemental ^{10}B target of measured thickness approximately 40 kev for alpha-particles of 1·6 MEV. The neighbouring resonances to that at 1·64 MEV are at 1·52 and 1·68 MEV. The 1·64 MEV resonance has a laboratory width of about 20 kev; the widths of its neighbours on the high and low energy sides are about 7 and 20 kev respectively. The yield from the desired resonance was thus optimized while giving it rather complete separation from neighbour states.

The high energy gamma-rays were detected in a 5 in. × 5 in. cylindrical NaI(Tl) crystal placed at approximately 80° to the alpha particle beam. A lead collimator in the form of a hollow truncated core of height $2\frac{1}{4}$ in., base diameter $1\frac{3}{4}$ in. and entrance diameter $\frac{1}{2}$ in. was placed directly in front of this crystal. The entrance to this collimator was 7/16 in. from the centre of the ^{10}B target. The low energy gamma-rays were detected at 90° to the alpha-particle beam, opposite the high energy detector, in a 3 in. × 3 in. cylindrical NaI(Tl) crystal whose front face was 7/16 in. from the centre of the ^{10}B target. A coincidence resolving time of about 0·1 μsec was used and a convenient beam current was found to be 1 μA.

Fig. 2

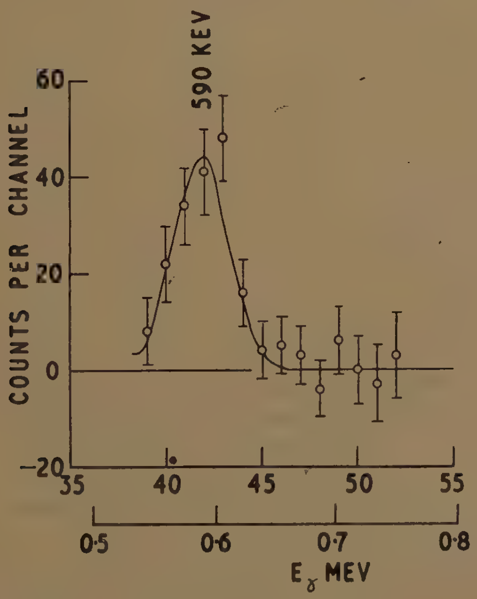

590 kev transition between the 3·68 and 3·09 Mev states of ^{13}C seen in coincidence with gamma-rays of energy greater than 1·55 Mev. The 765 kev transition between the 3·86 and 3·09 Mev states seen in coincidence at the same time has been subtracted out.

A large number of coincidence runs was taken, displaying the coincidence counts in the 3 in. × 3 in. crystal on a bias of 1·55 Mev in the larger crystal. The beam current was held constant to better than 5% during this set of runs. The bias on the large crystal as well as its response to a number of gamma-rays of both lower and higher energy than those of interest here were accurately determined since the quantitative interpretation of the results depends on a knowledge of the relative efficiency of the larger crystal, above its bias, to gamma-rays of 3·1 and 3·7 Mev.

Calibration runs for the smaller crystal were made using several standard sources placed successively at the position of the target. The first purpose of these runs was to provide an accurate energy calibration of the crystal (for this purpose the alpha-particle bombardment continued at its usual level to avoid any possible effect of rate-dependent gain—the calibration sources made only a slight change in the current in the photomultiplier). The second purpose was to determine the shape of the pulse distribution for various monochromatic gamma-rays to enable an accurate decomposition of the coincidence spectrum to be made (for this purpose there was no beam on the target and the ^{13}N was allowed to die away).

Fig. 3

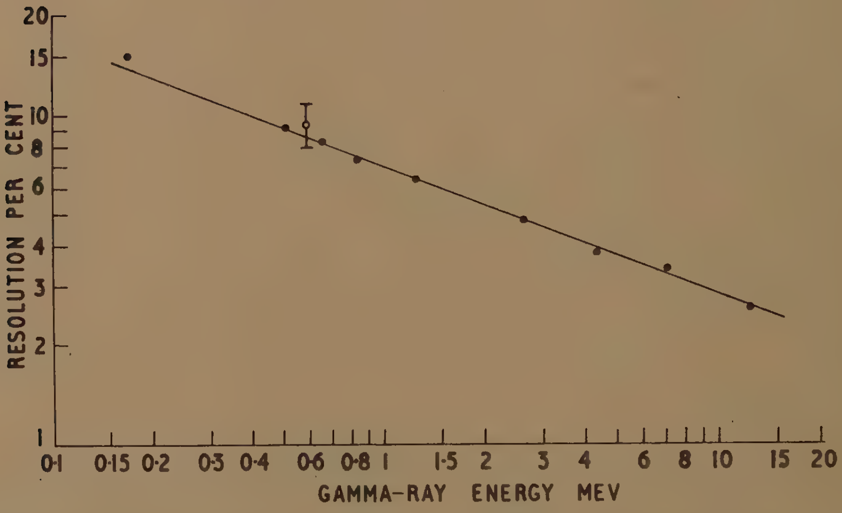

Experimentally-determined resolution (full-width at half-maximum) of the 3 in. × 3 in. NaI(Tl) crystal shown as the full-points. The observed width of the line of fig. 2 is shown as the point with the error limits.

The coincidence spectrum in the smaller crystal revealed clear peaks at 508 ± 7 kev, 590 ± 15 kev and 765 ± 8 kev. The first is due to annihilation radiation, the second compares well in energy with the 595 ± 9 kev expected for γ_2 and the third with the 765 ± 12 kev expected for the E2 transition between the 5/2+ and 1/2+ states (Ajzenberg-Selove and Lauritsen 1959). The measured shapes of the pulse distributions in the smaller crystal were used to construct that to be expected for the 765 kev transition which was then subtracted from the gross distribution to reveal that shown in fig. 2. This distribution does not go below channel 39 since then the effect of the annihilation radiation becomes severe (a slight allowance for this has to be made also in channels 39 and 40). The accurate agreement in position of this peak with that expected leaves little doubt that it is real. As a further check we may compare the observed width of the distribution of fig. 2, namely (9·2 ± 1·3)% with that to be expected from the known performance of the crystal. Figure 3 shows this comparison from which we see that the distribution of fig. 2 fits in very well.

§ 4. RESULTS

The peak of fig. 2, compared with the very much more intense 170 kev γ_4–γ_1 coincidence peak gives us the γ_2 versus γ_1 branching ratio after suitable correction for peak-to-total ratios, relative absorption efficiencies of the various radiations in the smaller crystal, the slightly different efficiency of the larger crystal above the 1·55 MEV bias for the 3·1 and 3·7 MEV lines, the direct feeding of the 3·68 MEV state by the proton transition and a few insignificant effects of absorption in the target assembly, crystal covering and so on. The angular correlations involved can be computed from data in the literature which fix the channel spin ratios (Stanley 1954): they are not strong and are effectively integrated out by the very bad geometry (± 74°) of the smaller crystal. The final value for the relative strength of the cascade de-excitation is $(6{\cdot}5 \pm 1{\cdot}0) \times 10^{-3}$, consistent with the earlier limit.

The radiative width of the mirror E1 transition was computed from the data presented by Woodbury *et al.* (1954) as 0·04 ev. Our earlier discussion in §§ 1 and 2 implied that the reduced speed corresponding to this width may be directly transferred to ^{13}C and applied to the mirror transition. This is not quite true however because the corresponding states in the two nuclei are not quite true mirror states: in ^{13}C they are both bound while in ^{13}N they are both in the continuum. In terms of the proton capture by ^{12}C to form the 3/2 – state of ^{13}N both the regular (F) and irregular (G) parts of the proton wave function resonate and contribute to the radiative width. In the corresponding case of ^{13}C the contribution from the exterior region (F) is quite different and presumably much smaller than for ^{13}N since the neutron wave function cuts off sharply from the nuclear surface owing to the binding whereas the proton wave function is not cut off. We should therefore take that portion of the radiative width in the ^{13}N case that is associated with G and transfer this to ^{13}C as a measure of the transition speed there rather than use the whole width. The separation of the F and G contributions is not simple and leads to large uncertainties but it seems likely that that part of the width in ^{13}N associated with G lies between 0·02 and 0·035 ev. We are very grateful to Professor R. F. Christy of the California Institute of Technology for drawing our attention to this very interesting effect.

When these figures are transferred to ^{13}C and corrected for the different energy of the transition they imply, together with the presently measured branching ratio, a width for the ground state M1 transition from the 3·68 MEV level of:

$$\Gamma_\gamma = (0{\cdot}40\text{–}0{\cdot}75)\,\text{ev}.$$

§ 5. DISCUSSION

We may now compare this result with the IPM theory. This latter has been very kindly furnished by Dr. Dieter Kurath of the Argonne National Laboratory, whom we thank. Figure 4 shows the calculated radiative width as a function of a/K. Also shown is the value in the jj limit ($a/K=\infty$). The upper and lower limits of the heavy box are those of our present result; the sides of the box show the limits on a/K within which the other properties of the $A=13$ system discussed above are explained by the IPM. For consistency with the IPM and charge symmetry the theoretical line of fig. 4 should pass through the box as it indeed does.

Fig. 4

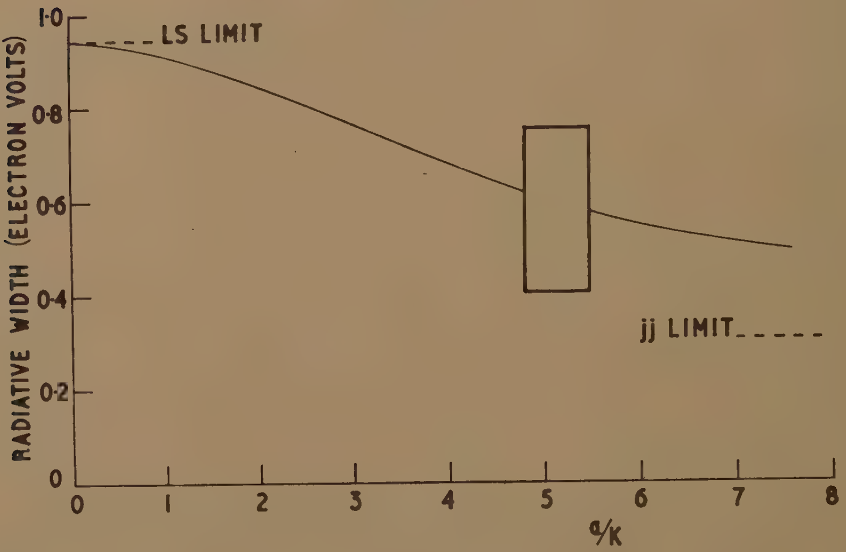

The prediction of the independent particle model for the M1 radiative width of the ground state transition from the 3·68 MeV state of ^{13}C shown as the full line (due to Dr. D. Kurath). The heavy box shows (top and bottom) the error limits of the present measurement and (side to side) the limits on a/K needed to explain other data in the $A=13$ system.

References

Ajzenberg-Selove, F., and Lauritsen, T., 1959, *Nucl. Phys.*, **11,** 1.
Inglis, D. R., 1953, *Rev. mod. Phys.*, **25,** 390.
Kurath, D., 1956, *Phys. Rev.*, **101,** 216.
Lane, A. M., 1953, *Proc. phys. Soc. Lond.* A, **66,** 977; 1955, *Ibid.*, **68,** 197.
MacDonald, W. M., 1955, *Phys. Rev.*, **98,** 60.
Mackin, R. J., Mills, W. R., and Thirion, J., 1956, *Phys. Rev.*, **102,** 802.
Morpurgo, G., 1959, *Phys. Rev.*, **114,** 1075.
Seagrave, J. D., 1951, *Phys. Rev.*, **84,** 1219.
Shire, E. S., Wormald, J. R., Lindsay-Jones, G., Lunden, A., and Stanley, A. G., 1953, *Phil. Mag.*, **44,** 1197.
Skyrme, T. H. R., 1958, *Proc. Rehovoth Conference on Nuclear Structure* (Amsterdam: North-Holland), p. 20.
Stanley, A. G., 1954, *Phil. Mag.*, **45,** 430.
Woodbury, H. H., Tollestrup, A. V., and Day, R. B., 1954, *Phys. Rev.*, **93,** 1311.

Microtwinning in Epitaxial Nickel–Iron Films†

By R. D. Burbank and R. D. Heidenreich
Bell Telephone Laboratories, Incorporated, Murray Hill, New Jersey

[Received October 1, 1959]

Abstract

Thin films of permalloy (81% Ni, 19% Fe) grown by evaporation on rock salt cleavage faces have been studied in the electron microscope. Selected area diffraction patterns indicate the presence of microtwinning on all types of {111} planes. The diffraction patterns are also subject to the effects of multiple diffraction, film deformation, and an 'effective aperture' in the optical behaviour of the electron microscope when used for selected area diffraction. Electron micrographs reveal a 'film' that consists of discrete particles, three-dimensional in character, with irregular shapes suggestive of hemispheres of various sizes which have coalesced, side by side. The irregular shapes fit together like pieces of a jig-saw puzzle to cover the film area. Twinned components can be identified with dark field illumination. The three-dimensional particles seem to be a consequence of isotropic growth of crystal nuclei that are in epitaxial orientation but distributed at random over the substrate surface. Microtwinning appears to be a relief mechanism for reduction of the strain energies which accumulate at the boundaries between growing crystal nuclei.

§ 1. Introduction

The magnetic properties of thin, evaporated films of alloys of nickel and iron are of considerable interest for switching applications. The parameters of interest such as coercive force and anisotropy are unfortunately quite difficult to control within the limits desired. The work described herein was a direct consequence of an investigation into the effect of the substrate on the magnetic properties of the deposited films. The alloy of interest here is permalloy with nearly zero magnetostriction (81% Ni, 19% Fe) and the substrate is a freshly cleaved NaCl single crystal. The magnetic measurements will be discussed elsewhere since they are not pertinent to the structural problems posed by these films. This paper is therefore concerned only with electron diffraction and microscopy results.

§ 2. Experimental

Films of Ni–Fe alloy having a composition near 80:20 (Permalloy) and in the range 400–800 Å thick for this purpose were prepared by subliming a Ni–Fe alloy under carefully controlled conditions‡. The results to be discussed in this paper were obtained from films deposited on fresh NaCl (100) cleavages maintained at about 320°c. The time required to lay down the film was of the order of one hour.

---

† Communicated by the Author.

‡ All evaporated films in this work were prepared by F. W. Reynolds and G. R. Stillwell.

Following evaporation, a plastic lacquer film was applied to the surface to act as reinforcement during removal[†]. The composite film was floated off the NaCl in water, caught on a copper mesh and then the plastic removed by immersion in a solvent. Specimens for the Siemens Elmiskop I were punched from the screen and examined in the instrument. Micrographs at 20 000 × or 40 000 × and selected area diffraction patterns using a $50\,\mu$ aperture were taken using 100 kv electrons.

Figure 1 (Pl. 35) is representative of the micrographs from a film deposited at 320°c and does not appear even to approximate a single crystal. Selected area diffraction patterns indicated a gross approximation to a single crystal with a cube face in parallel orientation to the base NaCl. The alloy is face-centred cubic with $a \cong 3{\cdot}55$ Å.

The appearance of the selected area patterns varies considerably over the area of the film due to local bending and sagging of the film between wires of the support grid. The zone axis of the diffraction pattern thus varies from point to point being usually a few degrees from [001]. When the orientation is almost coincident with the [001] axis the pattern consists of a simple square array of intense spots. Patterns have also been obtained with the orientation inclined by as much as 11° to the [001] axis. However, the most interesting and informative patterns occur at intermediate orientations of about 5° to 7°. Figure 2 (Pl. 36) is typical of such patterns. A primary array generated by 200 and 020 vectors is discernible in the central region of the pattern. However, many of the integer points such as the rows of $2k0$ and $\bar{2}k0$ are surrounded by four extra spots. Other integer points such as the rows $4k0$ and $\bar{4}k0$ are very weak and form part of a new square array whose edges are parallel to the 220 and $2\bar{2}0$ vectors. The spots along these diagonals are spaced at intervals of one-sixth of the 220 vector. This complex array arises from the f.c.c. alloy as evidenced by the spotty f.c.c. rings which intersect the orderly array of spots.

An important factor to be taken into account in all selected area patterns is the fact that regions of the specimen near the edge of the selected area aperture do not contribute uniformly to the entire diffraction pattern. Rather, a region near the edge produces only a partial diffraction pattern. The asymmetry present in patterns such as fig. 2 indicates that this must be so. The effect can be observed directly if a specimen is adjusted so that it just projects along one edge of the selected area aperture. A regular array of spots or rings will be recorded over a limited sector of the pattern while the remainder is blank. As the projection of the specimen in the aperture is increased the size of the sector increases. If the foil is moved to cover half or more of the selected area aperture, the diffraction pattern becomes more nearly normal in that a full field is seen. However, in interpreting intensities in these patterns, it must be kept in mind that each element of volume of the sample does not contribute uniformly to the entire diffraction pattern but maintains a geometric relation with a portion of the pattern. The instrument behaves as though there were an extra aperture between the lens system and the photographic plate. Such an aperture would transmit only a fraction of the diffracted beams originating near the periphery of the selected area†.

[†] The technique of removal and handling was carried out by Miss S. E. Koonce.

§ 3. INTERPRETATION OF SELECTED AREA DIFFRACTION

The instrumental response discussed in the previous section has several consequences that must be considered when dealing with films which deviate from planarity. In fig. 3 (*a*) a foil is shown which is deformed into a portion of a cylindrical surface of constant radius. The cylinder axis is normal to the plane of the figure. In the reciprocal lattice the points hkl and $\bar{h}\bar{k}\bar{l}$ have become short arcs. With the 'effective aperture' in place only the lower half of each arc can be transmitted. The horizontal dotted line represents the mean plane of the specimen and the plane of the zero level of the reciprocal lattice. If the 'plane of reflection' (a more descriptive term than 'sphere of reflection' for 100 kv electrons) is inclined at a slight angle to the plane of the zero level it is quite possible for hkl to reflect strongly while $\bar{h}\bar{k}\bar{l}$ is absent. Figure 3 (*b*) illustrates a more general cylindrical deformation. The effect on the reciprocal lattice points is obvious. In all deformations of this type the arcs of the reciprocal lattice points will be normal to the plane of reflection. Consequently, the diffraction patterns, although asymmetric will consist of spots rather than streaks. Metal foils may deform in ways that will produce bumps, hollows, or saddle points. If so, the reciprocal lattice points will become curved surfaces like spherical caps. The surfaces will again be normal to the plane of reflection. If the entire specimen contributed uniformly to the diffraction pattern it would display streaks or arcs. However, when only a limited region of the specimen contributes to a particular region of the diffraction pattern it is likely to display only spots. Because of the 'effective aperture' any given interpretation of a diffraction pattern will apply to only a restricted portion of the pattern if the film is non-planar.

---

† We are grateful to Dr. M. J. Whelan for directing our attention to a paper to be published by A. W. Agar on the accuracy of selected area microdiffraction in the electron microscope. Agar examined in a systematic manner how specimen areas *outside* the area defined by the selector aperture contribute to the observed diffraction because of spherical aberration in the objective lens. Agar did not consider the effects obtained when only part of the selected area is filled by the specimen. We believe that a systematic examination of how specimen areas *inside* the selected area contribute to the observed diffraction would show that spherical aberration also causes what we have loosely called an 'effective aperture'. It is apparent that a definitive interpretation of a diffraction pattern must take account of *all* contributions from both inside and outside the area defined by the selector aperture.

It is well known that twinning on all four {111} planes is characteristic of epitaxial growth of most of the f.c.c. metals on NaCl (see for example the excellent review article by Pashley (1956)). The effect of twinning on the reciprocal lattice is to produce a compound lattice consisting of the original lattice plus the superposition of four twinned lattices. A portion of such a compound lattice is illustrated in fig. 4. The view is along the [001] direction of the original lattice. The triple integers are Miller indices of points in the parent lattice. The single integers indicate coordinates along the [001] direction in units of one-sixth of the 002 vector.

Fig. 3

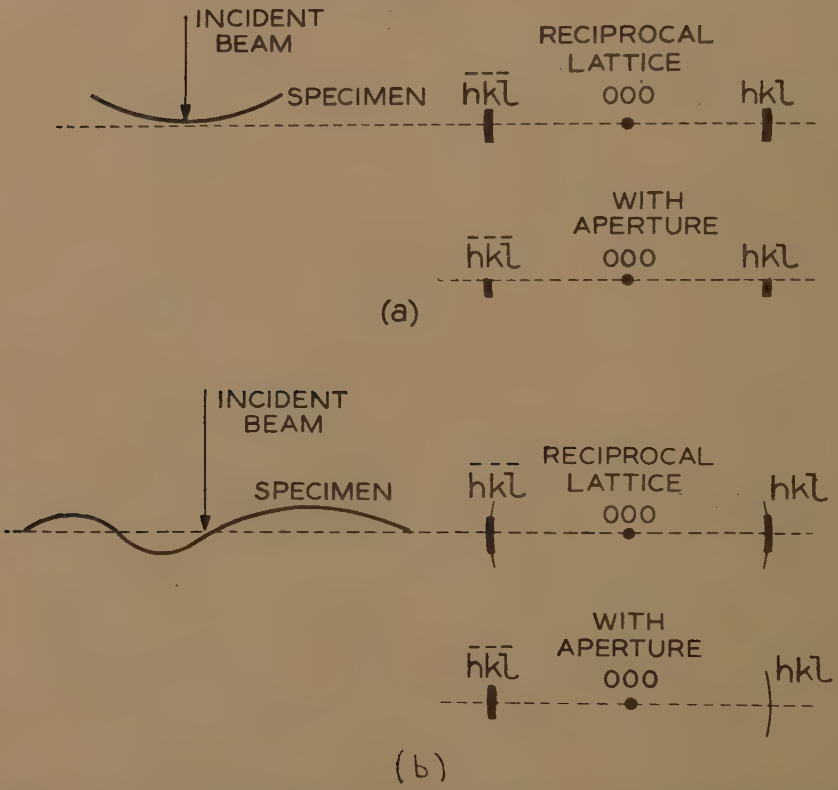
INCIDENT BEAM
SPECIMEN
RECIPROCAL LATTICE
$\bar{h}\bar{k}\bar{l}$
000
hkl
WITH APERTURE
$\bar{h}\bar{k}\bar{l}$
000
hkl
(a)
INCIDENT BEAM
SPECIMEN
RECIPROCAL LATTICE
$\bar{h}\bar{k}\bar{l}$
000
hkl
WITH APERTURE
$\bar{h}\bar{k}\bar{l}$
000
hkl
(b)

Formation of asymmetric diffraction pattern when a non-planar specimen is subjected to the 'effective aperture' of the electron microscope. (*a*) Simple cylindrical deformation. (*b*) More general cylindrical deformation.

The type of pattern shown in fig. 2 is caused by several factors including film deformation, inclined plane of reflection, double diffraction and an 'effective aperture'.

To see the effects of a deformed film and inclined plane of reflection consider fig. 5. The view is along the [010] direction of the compound

Fig. 4

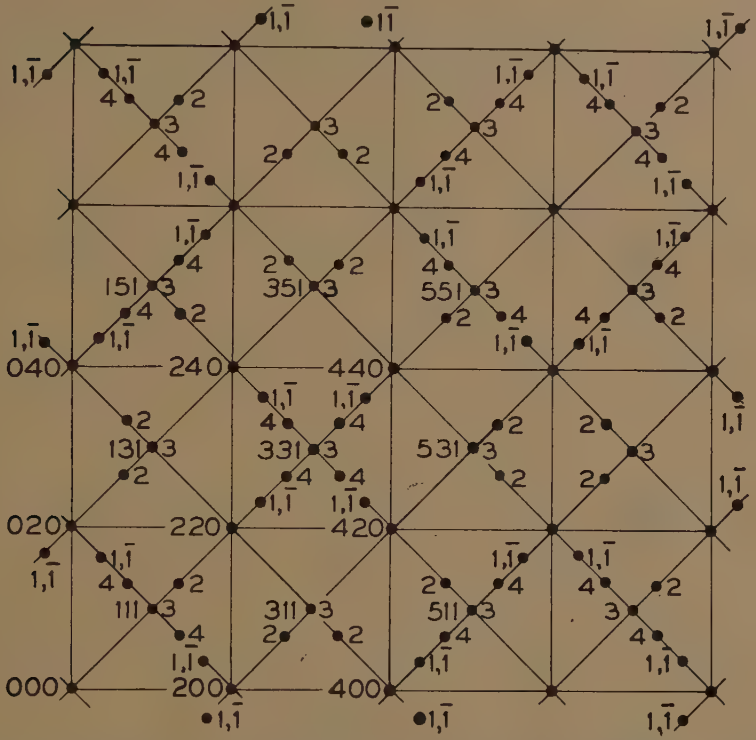
000
200
400
020
220
420
040
240
440
111
311
511
131
331
531
151
351
551
1,$\bar{1}$
1
2
3
4

Compound reciprocal lattice formed from twinning on (111), $(\bar{1}\bar{1}1)$, $(1\bar{1}1)$, and $(\bar{1}11)$ planes. View along [001] zone axis. Triple integers are Miller indices of parent spots. Single integers indicate coordinates of spots along [001] in units of one-sixth of the 002 vector.

Fig 5

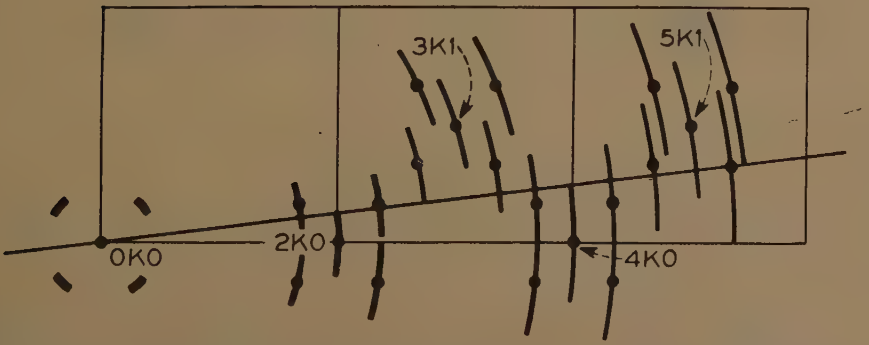
0K0
2K0
3K1
4K0
5K1

Lattice of fig. 4 viewed along [010] direction. Plane of reflection inclined at 7° to the zero level. Spots spread into arcs by cylindrical deformation of specimen of ±7°.

lattice of fig. 4. Rows of spots are seen end-on and rows of integer spots are labelled as $0k0$, $2k0$, $3k1$, etc. The film is given a cylindrical deformation of ±7° with the cylinder axis along the [010] direction. The plane of reflection is inclined at 7° to the plane of $hk0$ reflections. Each lattice point is spread into an arc whose length varies directly with the distance

Fig. 6

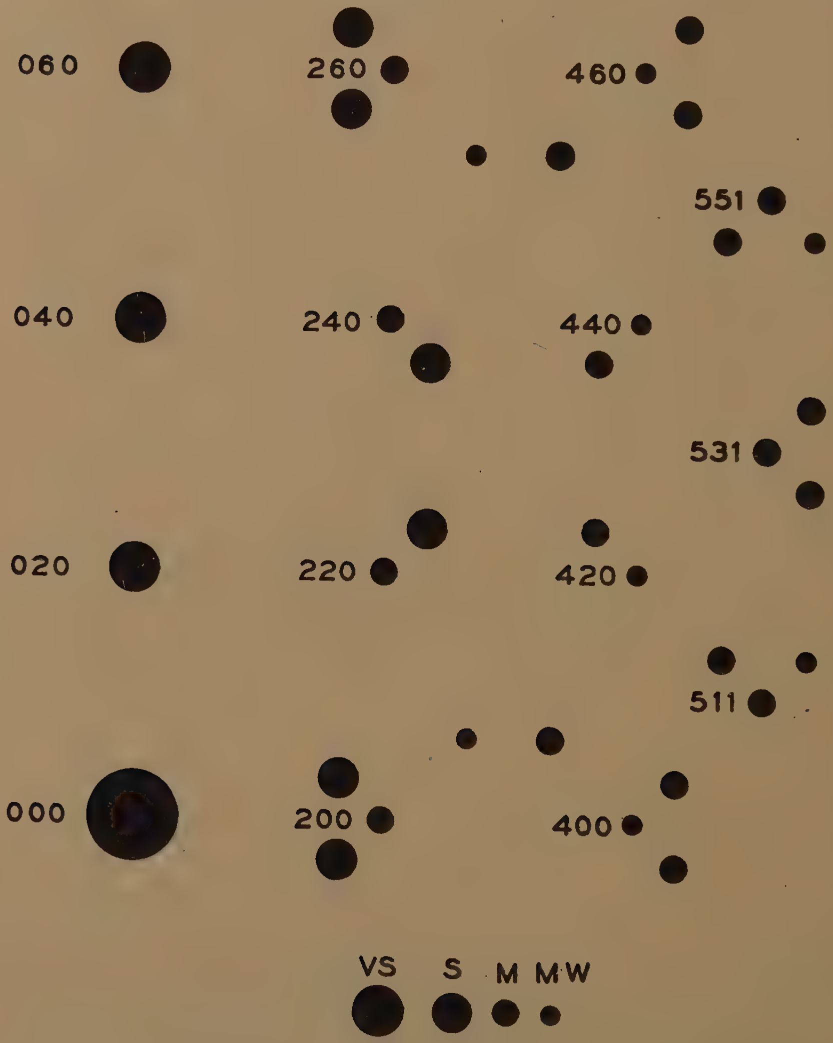

Diffraction pattern predicted when effects of fig. 5 are combined with fig. 4.

of the lattice point from the origin. The arcs fall on a series of cylinders concentric around the origin. All points of fig. 4 are assumed to have the same intensity before arcing. After arcing assume a very strong intensity on the innermost cylinder, strong on the next three cylinders, medium on the remainder. When an arc just touches the plane of reflection assume its intensity falls one grade. Thus, assign medium intensity to the $2k0$ arc, medium weak intensity to three other arcs.

Fig. 7

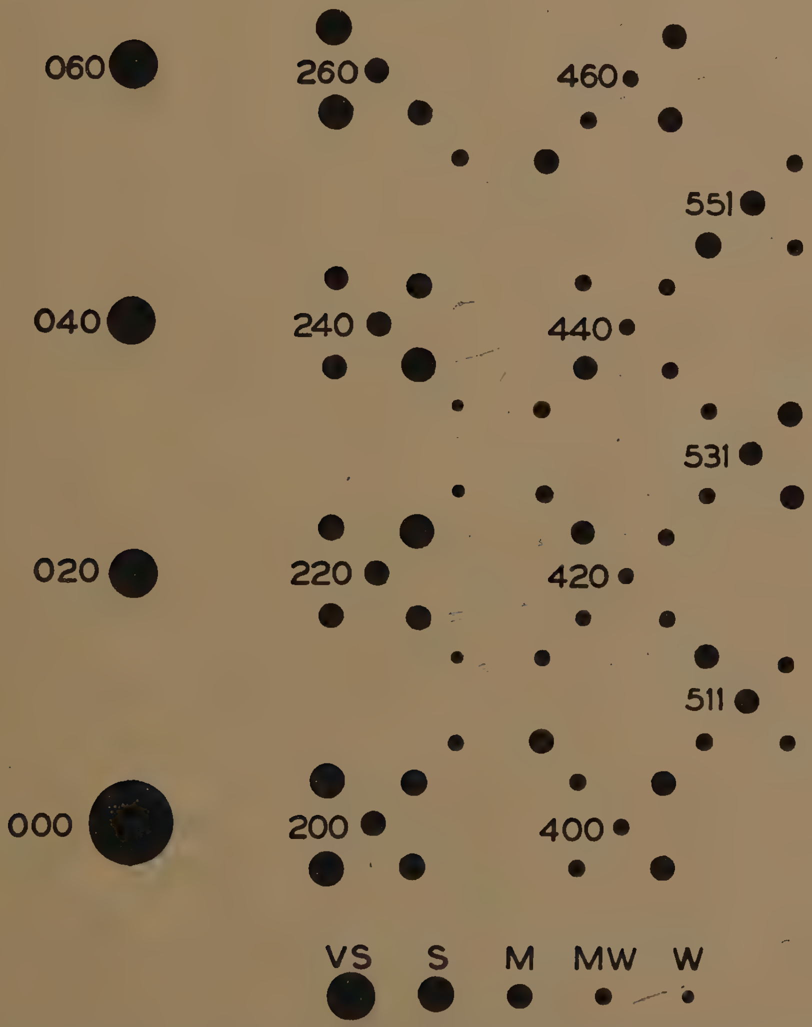

Diffraction pattern predicted from fig. 6 by double diffraction from 020 and 0$\bar{2}$0 reflections. Compare with upper right quadrant of fig. 2.

Combining the effects of fig. 5 with fig. 4 the pattern of fig. 6 is obtained. This represents the effects of microtwinning, film deformation, and inclination to the plane of reflection. Now consider the effect of double diffraction on fig. 6. Assume that when two reflections occur in succession the intensity of the double reflection is as follows:

vs + s → m
vs + m → mw
vs + mw → w
vs + w → vw
vs + vw → vvw
s + s → mw
s + m → w
s + mw → vw
s + w → vvw
m + m → vw
m + mw → vvw

Every reflection in fig. 6 is the source of a new incident electron beam. By superposition[†] of all the new patterns created the total effect of double diffraction is obtained. The major part of the effect is obtained by considering only very strong reflections. In fig. 7 the result is shown of superposing fig. 6 with the reflections obtained by double diffraction from the 020 and 0$\bar{2}$0 reflections. A considerable area of this pattern agrees very well with the upper right hand quadrant of fig. 2.

The other regions of fig. 2 do not agree with fig. 7 because the deformation of the specimen film is not of a cylindrical form parallel to [010] except in the central region of the specimen. The appearance of the 040 and 060 reflections in fig. 2 suggests that there is a cylindrical deformation parallel to [100] in the outer region of the specimen. At its simplest the deformation of the film must be of an oblong dish shape or a saddle shape.

Some of the earlier workers who observed microtwinning of f.c.c. metals on rock salt did not take account of double diffraction (see for example Menzer (1938 a, b) and Göttsche (1953)). To explain the non-integral spots which do not arise directly from twin orientations they postulated microstructures that would give the scattering power of the (111) planes a periodicity three times that of a normal lattice. However, as long ago as 1940 Thirsk and Whitmore stated that the non-integral spots which do not arise directly from twinning could be accounted for by double diffraction.

§ 4. ELECTRON MICROSCOPY OF MICROTWINNING

Figure 1 is a typical micrograph of a 'thick' film in the 400–800 Å range taken with bright field illumination. The film appears to be made up of particles that tend to be equidimensional, ranging from 300–700 Å in diameter. There are a variety of contrast effects including regular fringe systems over very limited areas. Figure 8 (Pl. 37) is a micrograph of a thick film taken with dark field illumination containing both twin spots and double diffraction spots. It would appear that a large fraction of the film belongs to twinned lattices, possibly 30 to 40%. Many of the details observed in fig. 8 are presumably Moiré patterns formed by the double diffraction spots in the illumination.

[†] The superposition consists of a translation, without rotation, from 000 to the point being considered as a new incident beam.

The absence of any simple pattern in figs. 1 and 8 suggests that the thickness of the film has caused an excess of details to overlap. Films were then chemically etched to an estimated 100–200 Å thickness. Figure 9 (*a*) (Pl. 38) shows a bright field micrograph of such an etched film. Figure 9 (*b*) shows a corresponding dark field micrograph. The illumination contained twin spots from two of the four twinned lattices and a negligible component of double diffraction. Several twinned regions in fig. 9 (*a*) are indicated by numbered arrows. Their identification as twins is confirmed by comparison with the corresponding regions in fig. 9 (*b*). A region such as that indicated by arrow 1 has dimensions of the order of 500 Å × 750 Å. Arrow 4 indicates a region of twin bands that are approximately 50 Å wide.

'Thin' films in the 100–200 Å range were then made by direct sublimation. Figure 10 (Pl. 39) is typical of the resulting microstructure. The film consists of discrete particles, three-dimensional in character, with rather irregular shapes. Many of the shapes are suggestive of an agglomeration of hemispheres of various sizes which have coalesced, side by side in one plane. The irregular shapes fit together to cover the area of the film in the same manner as the pieces of a jig-saw puzzle. In a few places a sequence of parallel twin bands is observed. The twin bands run about 25 Å in width. Figure 11 (Pl. 40) is a more limited area of thin film at higher magnification. Contrast details down to 10 Å or less are distributed in an irregular manner throughout the micrograph.

The various electron micrographs do not provide any simple picture of the microtwinning. Twinned regions can be recognized but they occur in no recognizable pattern. The width of a twinned region can apparently vary from 25 Å to 500 Å. The contrast details observed in the micrographs arise from a complex mixture of effects of crystal thicknesses, dynamic interactions, multiple diffraction, twin boundaries, etc.

The following features of the epitaxial growth appear to be consistent with the microscopic and diffraction evidence:

1. The nuclei are distributed at random over the substrate surface.
2. The nuclei undergo three-dimensional growth.
3. The principal influence of the substrate is maintaining a parallel orientation between the two cubic phases.
4. The misfit in lattice spacing of the two cubic phases is of minor importance.
5. The lattices of the nuclei have no optical phase relation with the lattice of the substrate.
6. The most important strain energies are intra-phase rather than inter-phase, i.e. intergranular rather than between film and substrate.

In a general way the process of film growth and microtwinning can be suggested from the considerations listed above. The nuclei grow isotropically. Ultimately contact will occur between a given pair of nuclei.

Only in rare instances will there be an integral lattice vector separation between the nuclei. In general then, a boundary of increasingly higher energy will be formed as the nuclei come into contact and continue to grow. The strain energy will accumulate to provide the driving force for the possible occurrence of faulting, twinning, recrystallization or other relief processes. With a random distribution in size of nuclei one of a given pair will usually be larger than the other and will probably be more firmly anchored to the substrate, and hence more stable. If the difference in stability between a pair of nuclei and the boundary energy both become sufficient then the larger grain may assimilate the less stable one. This might occur in a variety of ways. However, in view of the experimental evidence the conditions would appear to be especially favourable for the widespread occurrence of microtwinning on all {111} planes. Presumably only one orientation of {111} would be active at a particular grain boundary. Stacking fault energies must be low and the driving forces high under the conditions of the experiment. The transition from vapour state to epitaxial growth is equivalent to quenching in an extreme form. Hence it is not surprising that the driving forces are readily available in the energy built up in the grain boundaries.

Reflection electron diffraction patterns from 600–800 Å epitaxial Ni–Fe films indicate that the microtwinned material occurs as a sandwich between the sodium chloride on the one side and single crystal alloy on the top side. Apparently the layer of twinned material serves the purpose of accommodating the cubic alloy to the cubic substrate with minimum strain energy. From this point of view it would not be surprising if microtwinning were widespread at the interfaces in diffusionless transformations in bulk alloys. Thin sections of transformation products in steels have been observed to exhibit a fine line structure in martensitic plates (Kelly and Nutting 1959, Nishiyama *et al.* 1959) which may well be microtwinning.

ACKNOWLEDGMENTS

We wish to express our thanks to F. W. Reynolds and G. R. Stillwell for the preparation of the evaporated films used in this work, and to Miss S. E. Koonce for the preparation of specimens for the electron microscope.

REFERENCES

GÖTTSCHE, H., 1953, *Z. Phys.*, **134**, 517.
KELLY, P. M., and NUTTING, J., 1959, *J. Iron St. Inst.*, **192**, 246.
MENZER, G., 1938 a, *Naturwissenschaften*, **26**, 385; 1938 b, *Z. Krist.*, **99**, 378, 410.
NISHIYAMA, Z., SHIMIZU, K., and KAWANAKA, R., 1959, *Mem. Inst. sci. Res. Osaka Univ.*, **16**, 87.
PASHLEY, D. W., 1956, *Advanc. Phys.*, **5**, 173.
THIRSK, H. R., and WHITMORE, E. J., 1940, *Trans. Faraday Soc.*, **36**, 565.

Eutectic Compositions and Liquid Immiscibility in Certain Binary Alloys†

By W. HUME-ROTHERY and E. ANDERSON
Department of Metallurgy, University of Oxford

[Received November 3, 1959]

ABSTRACT

An examination is made of the compositions of eutectic points in the metallurgical equilibrium diagrams given in Hansen's text-book on *The Constitution of Binary Alloys*. A large number of eutectics occur at almost 0% of the solute element. With increasing atomic percentage of solute, the number of eutectics in a given composition range diminishes rapidly, until a recovery sets in at 8–10 atomic % solute. There are very few eutectics in the equiatomic region, and at intermediate compositions the eutectic composition distribution curves show a series of peaks at intervals of 7–8 atomic %. Stockdale's suggestion that eutectic points occur at whole number ratios of the two kinds of atom is not confirmed, but certain regions of composition are favoured, and these include the atomic ratios of approximately 1 : 6, 1 : 3, 1 : 2 and 2 : 3. The reason for this is discussed, and free energy curves are described; some of these lead to liquid immiscibility, and examples of this are discussed.

§ 1. INTRODUCTION

IN 1935 Stockdale (1935) suggested that, in binary metallurgical equilibrium diagrams, the compositions of eutectic points corresponded with simple whole number ratios of the two kinds of atom. Although supported by considerable evidence the idea was not accepted, partly because such large whole numbers were used that the experimental accuracy was often not sufficiently great to distinguish between adjacent possible ratios. In the meantime much accurate experimental work has been carried out, and in the present paper we re-examine the data, and discuss the results. These suggest certain types of free-energy/composition curves which, in their turn, have led to an interpretation of the phenomena of liquid immiscibility in certain alloy systems.

§ 2. EXPERIMENTAL DATA

Experimental data on the constitution of binary alloys have been critically reviewed by Hansen (1958) in the second edition of his book *The Constitution of Binary Alloys*, where the composition of eutectic points which have been established with reasonable accuracy are given in atomic percentages. We have accepted these values, except in a very few cases where new experimental data are known to us. In very rare cases where experimental points are given which establish the eutectic, we have accepted the composition, since the omission of a numerical value appears accidental. There are occasional systems of the transuranic elements for which Hansen gives a numerical value, but the text makes it clear that the whole diagram is approximate only, and these have been omitted completely. These details are discussed in the Appendix, and do not affect the conclusions described below.

---

† Communicated by the Authors.

Apart from these reasonably well-established (W. E.) eutectic points, Hansen's book gives many eutectics for which he gives an approximate value (e.g. ~12 atomic %), or where the composition is not indicated. For some purposes, these are of interest, and we have again accepted Hansen's value throughout, except that we have ignored some systems where the description makes it clear that the composition is quite uncertain. It is convenient to distinguish between the well-established (W. E.) eutectics, and the total number of eutectic points.

Fig. 1

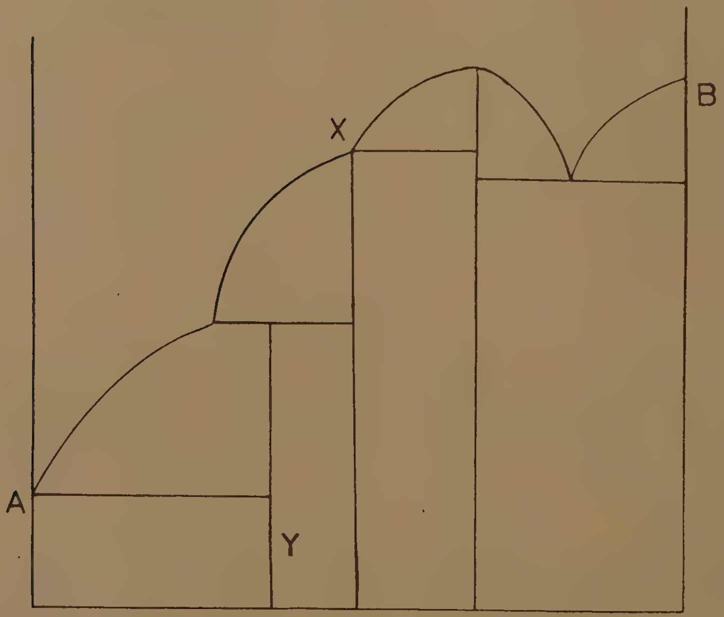

§ 3.

3.1. *The* 0% *Eutectics*

In the hypothetical diagram of fig. 1, the solidus horizontal at A is at a temperature indistinguishable from that of the melting point of the pure metal. Many such examples exist, and may be called the '0% Eutectics'. We think that these may properly be classed as eutectics, because in the cases where experimental accuracy has detected a slight difference between the temperatures of the horizontal and of the melting point of the pure metal, the number of systems in which a slight depression of the liquidus has been found (fig. 2 (*a*)) greatly exceeds that in which the liquidus rises to a peritectic horizontal just above the melting point of the pure metal (fig. 2 (*b*)). The peritectic kind of diagram (fig. 2 (*b*)) requires the solubility of B in A to be greater in the solid than in the liquid, and where the solubility is restricted this is less probable than the case of fig. 2 (*a*).

3.2. *The C.M.P. Eutectics*

In fig. 1, the equilibrium relations are such that a phase X melts at constant temperature, but without a maximum in the liquidus. The free energy relations are of the same form if points such as X are regarded as the extreme limit of eutectic or peritectic diagrams, and we refer to them as 'constant-melting-point', or C.M.P. eutectics.

Fig. 2

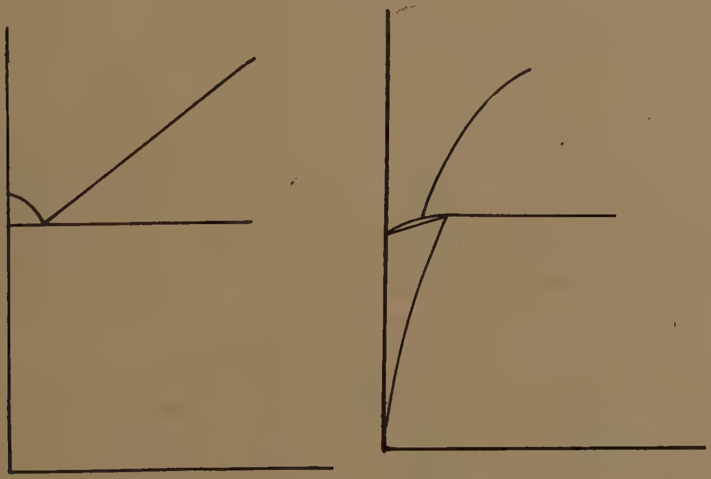

§ 4. THE STOCKDALE HYPOTHESIS

Hansen's data for the W.E. eutectics make it clear that Stockdale's hypothesis in its original form cannot be maintained. Eutectics are distributed over a very wide range of compositions, and agreement with exact whole number ratios is an exception rather than a rule, unless unduly large integers are employed. The distribution of eutectics over the whole range of compositions is, however, very uneven, and some of the fluctuations are greater than would be expected from a random distribution.

§ 5. THE EUTECTIC COMPOSITION DISTRIBUTION CURVES

To examine the problem further, we have drawn diagrams showing the number of eutectic points lying within ± 1 and ± 2 atomic % of each whole-number atomic percentage of solute. Since there is no reason why a given system should be called AB rather than BA we have expressed the compositions as lying between 0 and 50. If, for example, a particular system

AB has eutectics at 26 and 90 atomic % of B, the eutectic compositions are called 26 and 10. This procedure means that, for statistical examination, we must double the number of points at exactly 50 atomic %, and this has been done in drawing the diagrams.

Figure 3 shows the composition distribution curve for the W.E. eutectic points, and fig. 4 the corresponding curve for all the eutectic points. In fig. 3 the composition 20 atomic % corresponds to values of 23 and 37 on the ±1 and ±2 curves respectively, and this means that there are 23 eutectic points in the range 19–20–21 atomic %, and 37 in the range 18–19–20–21–22 atomic %. For each curve the full lines include the C.M.P. eutectics, and the dotted lines show how the numbers are reduced if the C.M.P. eutectics are excluded. From these diagrams the following conclusions may be drawn.

Fig. 3

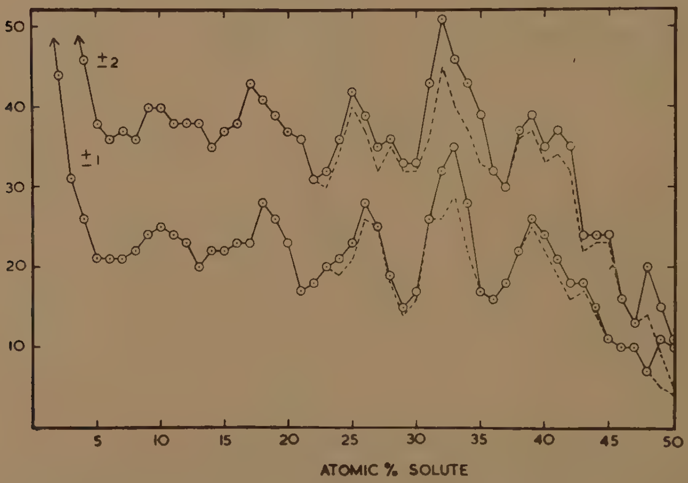

The eutectic composition distribution curves for W.E. eutectics.

(*a*) There is a very large number of 0% Eutectic Points.

(*b*) With increasing percentage of solute, the distribution curve first falls rapidly, and then rises in the range 8–10 atomic %.

(*c*) There are very few eutectics in the equiatomic region.

(*d*) In the intervening region, the distribution curve shows a remarkable series of peaks and valleys, the peaks being separated by differences of the order 7–8 atomic %. This tendency is clearly apparent if the C.M.P. eutectics are excluded, and is accentuated by their inclusion. The magnitude and approximately regular spacing of the peaks makes it improbable that they are due to random fluctuations. The relative heights of the peaks are greater for the W.E. eutectics than for the total number. This can be understood because, if the peaks are due to a genuine effect, any error in the compositions of the eutectics will tend to smear out the sharpness of the peaks, and to increase the general background. The last three peaks are in the regions of 25, 33 and 40 atomic %, and are thus near to the simple whole number ratios 3 : 1, 2 : 1 and 3 : 2.

The eutectic distribution curves of figs. 3 and 4 are admittedly statistical, and the variation of experimental accuracy makes their value difficult to assess. It has been suggested that the small number of eutectic points in the equiatomic region may be due to the existence of a large number of intermediate phases with liquidus curves rising to maxima at the composition AB, since a maximum on the liquidus curve automatically prevents the formation of a eutectic at the composition concerned. Examination of the systems which do *not* contain AB liquidus maxima shows that this suggestion is incorrect, and that the small number of eutectic points in the equiatomic region cannot be ascribed to this cause alone. Further, examination shows that the three most common compositions giving rise to maxima on liquidus curves are AB, A_2B and A_3B. The last two of these correspond with 33 and 25 atomic % solute respectively, so that the appearance of peaks on the eutectic distribution curves at these

Fig. 4

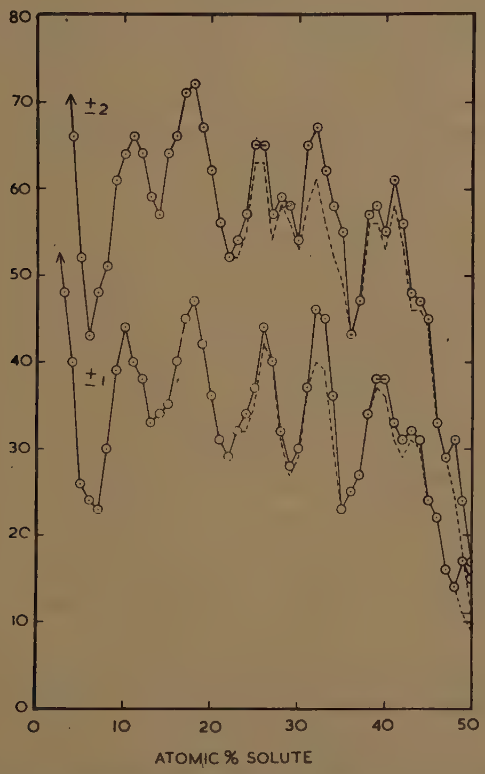

The eutectic composition distribution curves for all eutectic points.

compositions is even more remarkable than might at first appear, since the existence of the A_2B and A_3B maxima on liquidus curves must tend to diminish the number of eutectics at these compositions.

§ 6. EUTECTIC FREE-ENERGY CURVES

In the typical eutectic equilibrium, the relation between the free-energy curves and compositions is of the form shown in fig. 5, where XEY is the common tangent to the curves, and E is the composition of the liquid in equilibrium with solid X and solid Y.

If, as was imagined by Stockdale, liquid alloys can take up ordered structures of the two kinds of atom, the free-energy/composition curve—for abbreviation we shall call this the G/C curve—for the liquid phase may show a minimum at the composition which enables the two kinds of atom to pack together conveniently, and we may expect this to correspond with a whole number ratio related to the geometry of the structure. Figure 5 makes it clear that the composition of the point E only occurs at the minimum on the curve if the tangent is horizontal, and all three phases have the same free energy. This is an unlikely occurrence, and we can, therefore, understand why Stockdale's hypothesis is not, in general, confirmed.

Fig. 5

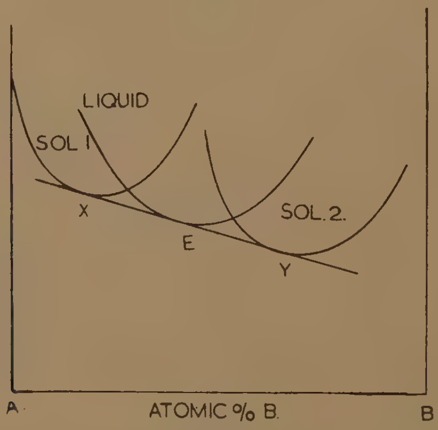

Figure 5 shows, however, that if the G/C curve for the liquid shows a rapid change in curvature at one point, tangents over a wide range of angles will strike the curve near this point, and eutectic compositions in this region will be favoured. If liquids have a structure, it may for example be possible for a liquid to accommodate a certain proportion of solute atoms easily, but for a larger proportion to result in a marked increase in free energy. The resulting G/C curve may then be of the form of fig. 6, and eutectic points in the region of X will be favoured. In such a case, if the rise in the G/C curve after X is the result of the geometry of the packing of atoms, X may correspond to a simple whole-number ratio of atoms.

Alternatively if, as in the Jones theory of α/β brasses, the bend at X is due to an electronic factor, we may expect a characteristic composition which is not a whole-number ratio.

Another possibility is for a particular ratio of the two kinds of atom to facilitate the packing of the atoms in the structure to such an extent that a marked fall occurs in the G/C curve, as shown in fig. 7. In this case, tangents over a wide range of angles can touch the curve in the region of X, whilst the inflections in the curve may result in the formation of immiscible liquids—examples of this are described on p. 397.

Fig. 6

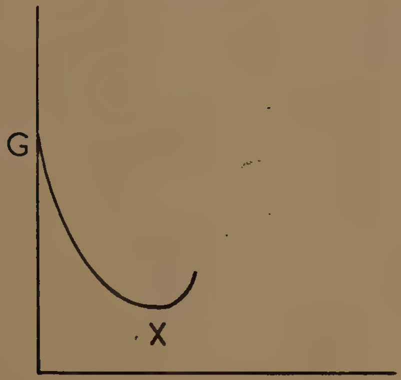

Fig. 7

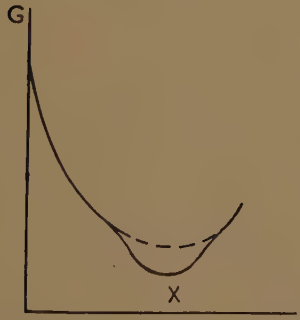

§ 7. THE 0% EUTECTIC REGION

In diagrams such as fig. 5, the free energies have to be measured with reference to arbitrary zeros for both constituents. The choice of zeros affects the slope of the line XEY in fig. 5, but not the compositions of the tangent points X, E and Y. For many purposes it is convenient to choose the zeros so that, at the temperature concerned, the values of G for the pure liquids A and B are equal. This can be done by an arbitrary choice of the zeros at each temperature, in which case the zeros change with the temperature. Alternatively we may take a fixed zero (such as the energies of isolated atoms), and denote ΔG the difference between the free energy of the alloy concerned, and of the corresponding point on the straight line joining the values for pure A and pure B. ΔG will then be zero for pure A and B, and curves connecting ΔG with C will resemble those for curves of G against C, with zeros adjusted to make the values for the pure liquids A and B equal.

Fig. 8

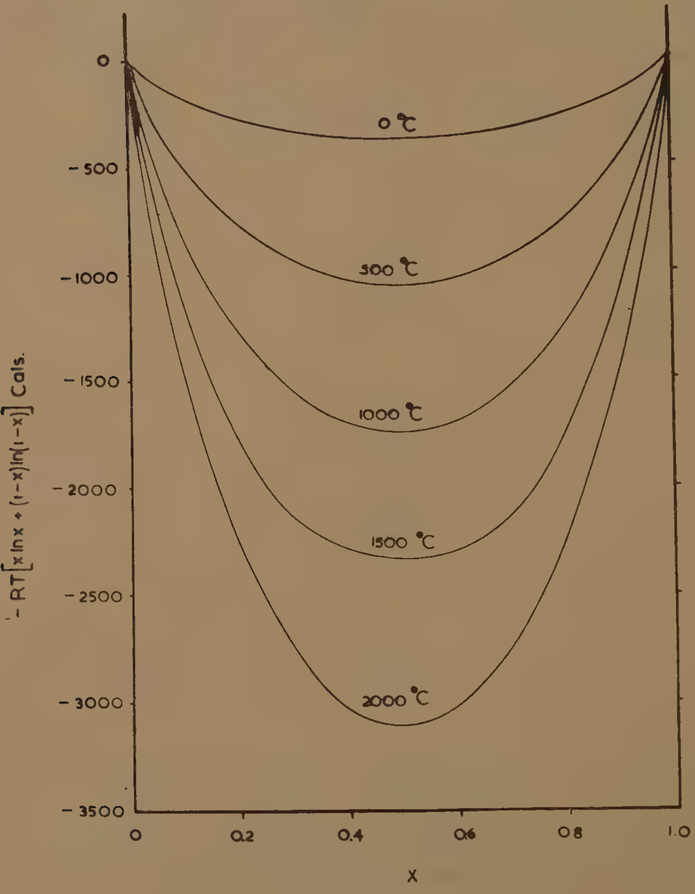

$\Delta G/C$ curves for ideal liquid solutions.

In a liquid solution the configurational entropy which results from the random mixing of A and B produces a free-energy term of the form:

$$RT\{x \ln x + (1-x)\ln(1-x)\}$$

where x is the atomic fraction of B. This gives a $\Delta G/C$ curve (i.e. a curve of ΔG plotted against the composition in atomic fractions) which is vertical at $x=0$ and $x=1$, and is symmetrical about the equiatomic composition ($x=0{\cdot}5$). Examples of these curves are shown in fig. 8. In ideal liquid solutions where there is no heat or volume change on mixing, the $\Delta G/C$

curves are of the form of fig. 8. In non ideal solutions, the $\Delta G/C$ curves will show other shapes, but as long as miscibility occurs the curves will always be vertical at $x=0$ and $x=1$.

We may consider, for simplicity, a 0% eutectic system in which the two solid phases in equilibrium with the liquid are the pure metals A and B. Since the configurational entropy term is included in the total $\Delta G/C$ curve, the tangent at 0% B will be vertical, and will not meet the ΔG curve for solid B. We may thus conclude that, if mixing of the two metals occurs, the eutectic can never be at exactly 0% solute, and we may imagine that

Fig. 9

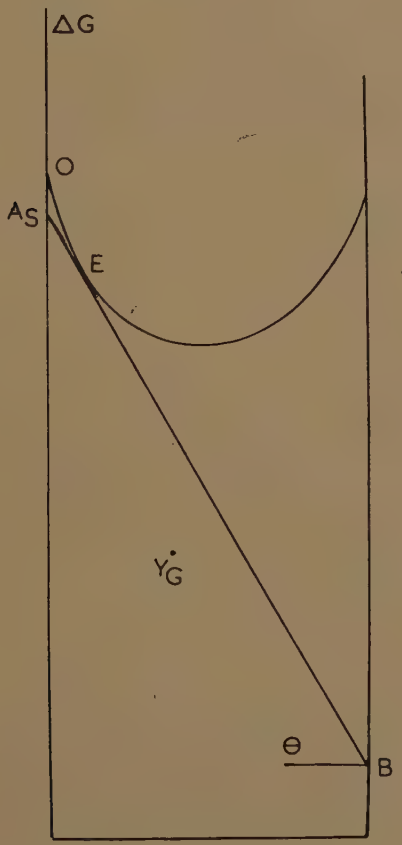

in fig. 9, the curve refers to a temperature just below the melting point of A, and that the point A_s gives the value of ΔG for pure solid A. *E* is the composition of the (very nearly) 0% eutectic, and the tangent *AEB* is very nearly vertical. For pure B, ΔG at the eutectic temperature must have a large negative value, and unless there are very abnormal effects, this means that B must be a long way below its melting point.

We expect, therefore, to find 0% eutectics mainly in systems where one metal is of very much higher melting point than the other. This is in agreement with the data, and the conclusion is irrespective of the existence of intermediate phases. Consider, for example, the system of fig. 1, where the 0% eutectic involves pure A, and the compound Y, whilst the melting point of B is much higher than that of A. Then, if fig. 9 refers to this system at the temperature of the (almost) 0% eutectic, the point B will lie considerably below 0, and if Y_G is the value of ΔG for solid Y, Y_G must lie below AB, for if it were above AB, the eutectic would consist of (B + A + Liquid) instead of (Y + A + Liquid). In such diagrams it is common practice so say that Y is an unstable compound which decomposes on melting, but the above considerations show that, at the temperature of the 0% eutectic, the nearly vertical slope of the tangent means that the value of ΔG for solid Y is large and negative.

A simple geometrical argument based on figs. 8 and 9 will show that the liquidus rising from a 0% eutectic will have the form of fig. 10 (*a*), and not that of fig. 10 (*b*).

Fig. 10

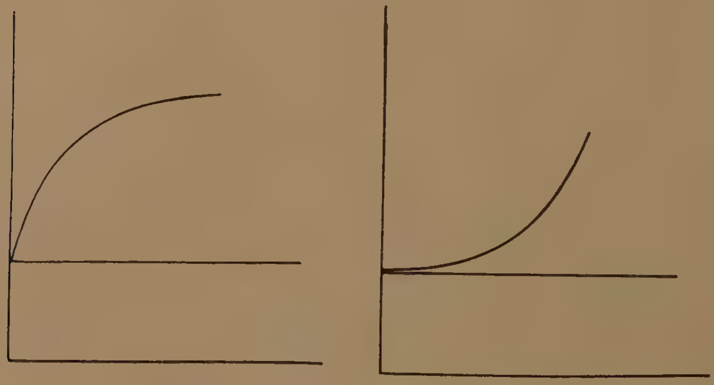

(*a*) (*b*)

§ 8. MODELS OF LIQUID STRUCTURE

Figure 5 makes it clear that, for a given $\Delta G/C$ curve for the liquid solution, a given eutectic composition may arise by chance if the curves for the two solid phases are of the appropriate shapes and levels. In attempting to explain the eutectic distribution curves, we must therefore expect to find some exceptions if we correlate points such as X in fig. 7 with particular models of the liquid state, and the existence of exceptions does not necessarily mean that the correlation is incorrect.

Frank (1952) has emphasized the importance of the work which has shown that small drops of liquid metals can undergo marked supercooling. From this he concludes that, although the coordination number in a liquid metal is high, the atomic arrangement must be different from the cubic, or hexagonal packing of spheres, since either of the latter would provide nuclei for the growth of the solid crystal. Frank, therefore suggests that the structure of liquid metals is based on the icosahedral packing of 12 atoms round a central atom as shown in fig. 11 (Pl. 41). The characteristic of this is that, if the model is held with one atom at the top, the central sphere is in contact with one sphere vertically above, and one vertically below, and with two sets of five spheres in horizontal planes. These last atoms are at the corners of two regular pentagons which are rotated through 36° about the vertical axis.

In this model the central sphere is in contact with its 12 neighbours, but the latter are not quite in contact with each other. For convenience we shall call these Frank units.

We also suggest that it may be possible for Frank units to join together in chains, in which one sphere is held in common between adjacent units. Figure 12 (Pl. 41) shows one of these chains which has been slightly bent so as to show the packing structure. In this case, the structure of the chain may be written 1–5–1–5–1 . . . where each central sphere is in contact with two sets of five, and with one sphere above and one below, but the side spheres are not in contact with each other. For convenience we shall refer to these as pentagonal chains.

§ 9. PEAKS ON EUTECTIC DISTRIBUTION CURVES

The considerations of § 7 enable us to understand the large number of eutectics at very small concentrations of solute, and the general form of the resulting liquidus curves. The distribution curves of figs. 3 and 4 show that, with increasing percentage of solute, there is at first a rapid fall in the eutectic distribution curve, until a recovery sets in at 8–10 atomic % of solute. If, therefore, we are correct in suggesting that a large number of eutectics is favoured by a marked bend in the $\Delta G/C$ curve, we may seek for some reason why a point such as X in fig. 6 occurs at the composition 8–10 atomic % of solute.

In general, when a solute B is added to a liquid metal A, mixing will be encouraged if there is a tendency for B atoms to prefer A rather than B neighbours. If a liquid consists of individual Frank units with solute atoms at their centres, we can substitute up to 1 atom in 13 (7·7 atomic %) without involving B–B closest distances of approach. We cannot, however, substitute more than 1 atom in 13 without introducing B–B contacts, unless very definite long range order exists. It is of course clear that the same conclusion would be reached if the liquid consisted of groups of 13 with a central atom surrounded by 12 others in hexagonal or cubic close-packing, but these arrangements would provide nuclei for crystallization which the Frank units avoid.

If a liquid consists of individual pentagonal chains with solute atoms down the centre of the chains, it is possible to avoid B–B contacts by a stacking sequence of the type 1–5–**1**–5–1–5–**1**–5–1–5–**1** . . ., where the bold figures **1** refer to the solute atoms. This corresponds to 1 solute atom in 12 (i.e. 8·3 atomic %).

If, therefore, a marked increase in G results from two solute atoms becoming closest neighbours, we may perhaps understand why a $\Delta G/C$ curve of the type of fig. 6 occurs with the point X at about 8 atomic % solute. It is not justifiable to claim more than a very rough approximation because, although the above argument is not affected by interchange between the outer solvent atoms of Frank units or of pentagonal chains, no allowance has been made for the sharing of atoms or for the odd atoms which may cement the units or chains together.

If the above interpretation is correct we may expect the sudden increase in G at the point X of fig. 6 to be favoured by a large electrochemical factor, because this will favour AB closest distances of approach. We should also expect the effect of two relatively large solute atoms in contact to produce a more marked increase in G than that of two relatively small atoms. For, in both Frank units and pentagonal chains, if a central atom is small, this may weaken the bonds to its 12 neighbours, but the remaining atoms will be able to collapse in upon each other. If, on the other hand, the central atom B is large, it may remain in contact with its 12 neighbours, but a great number of A–A distances must be increased.

If, therefore, we interpret the rise in the eutectic distribution curve at 8–10% solute on the above lines, we expect to find a preponderance of systems in which either the electrochemical factor is considerable, or in which the solute atom has a markedly larger atomic diameter than that of the solvent. As shown in table 1 this conclusion is confirmed for the 8% and 9% eutectics. We suggest, therefore, that the first break in the steeply falling eutectic distribution curve is the result of the introduction of close distances of approach between solute atoms.

If we accept the concept of a pentagonal chain, it is clear that, if the atoms down the centre of the chain were smaller than those in the pentagonal layers, those in the pentagonal layers could close up until they were in contact, and the pentagons rested on each other. This would give a packing sequence 1–**5**–1–**5**–1 . . . , where the small figure 1 indicates the smaller atom. We might thus expect a particularly stable structure with a sharp valley in the $\Delta G/C$ curve at a ratio of 1 small : 5 large atoms, i.e. 17 atomic % of the smaller atom. Figures 3 and 4 show that the eutectic distribution curves exhibit maxima in the region of 18 atomic %. Table 2 shows that if we represent the 17, 18 and 19% eutectics in the form $A_{83}B_{17}$, $A_{82}B_{18}$ and $A_{81}B_{19}$ respectively, there is a large majority of cases in which the B atom is the smaller. The above argument is again only a rough approximation, but it is at least suggestive that the peak in the eutectic distribution curve comes at approximately the ratio of 1 atom in 6.

In the above interpretation of the 18% eutectic peak, we have allowed smaller atoms down the centre of the chain to be closest neighbours, in order to allow a closing up of the pentagonal rings. We may now consider what the condition will be if no two B atoms are closest neighbours. If the

B atoms are down the centres of the chain, the best that can be done is a sequence such as:

$$1A\text{–}5A\text{–}1B\text{–}5A\text{–}1A\text{–}5A\text{–}1B\text{–}5A\text{–}1A\ \ldots$$

which corresponds to 8·3 atomic % B (see p. 394). If B atoms are in the pentagonal rings, then as shown in fig. 13 one pentagonal ring can hold

Table 1

Eutectic composition	Systems with B the larger atom, and size factor (%)		Systems with B the smaller atom, and size factor (%)	
$A_{92}B_8$ Total number of eutectics 11	AgTe	?	AlPd	– 4
	CuCe	43	AuCd	– 3
	CuPr	43	BiZn	–14
	CuU	18		
	ZnMg	20		
	AgTh	25		
	CuTh	41		
	CoZr	26		
$A_{91}B_9$ Total number of eutectics 13	CuLa	47	PbPd	–21
	HgTl	14	ZrSi	–26
	PbK	32	USi	–22
	SnMg	14		
	AuLa	29		
	CuCa	55		
	NiCe	46		
	CrPb	40		
	NiU	20		
	SiZr	34		

For the $A_{92}B_8$ and $A_{91}B_9$ eutectics there are 17 examples where B is the larger atom, and 6 where it is the smaller atom. In the case of the eutectic $Ag_{92}Te_8$, the Te is probably the larger atom, but the widely differing distances of approach in the crystal of Te make it impossible to estimate the size-factor.

The symbols are arranged so that the second element is the B element.

In all cases the size-factor is with reference to the A element.

two B atoms, but the pentagonal ring on either side can hold only one B atom if B–B closest neighbours are to be avoided. This permits a stacking sequence:

$$1A\text{–}\frac{3A}{2B}\text{–}1A\text{–}\frac{4A}{1B}\text{–}1A\text{–}\frac{3A}{2B}\text{–}1A\text{–}\frac{4A}{1B}\text{–}1A$$

which accommodates 3B atoms in 12, or 25 atomic % of B, but the introduction of more B atoms must result in B–B closest neighbours. We can, thus, perhaps, understand a sudden increase in free energy in this region and it is perhaps significant that, of the 36 eutectic points which occur at 24, 25, or 26 atomic %, no fewer than 23 are systems where the electrochemical factor is large, and this number would be increased if Ge and Sb

Table 2

Eutectic composition	Systems with B the larger atom, and size factor (%)	Systems with B the smaller atom, and size factor (%)
$A_{83}B_{17}$ Total number of eutectics 16	AgBa 51 AuNa 29 GaIn 33 BeCu 14 ZnU 13	AlCu −11 PrAu −21 FeC −39 LaMn −28 PbLi −11 MnAs −6 FeB −29 SbGe −16 KHg −54 MoSi −14 TiSn −3
$A_{82}B_{18}$ Total number of eutectics 15	CuAl 12 NiW 10 HgCs 75	FeP −15 MgAg −10 BaPb −20 CuAs −1 ThNb −21 PbSb −17 CeNi −31 NbSi −18 MgHg −7 VS −21 ZrSb −9 UV −10
$A_{81}B_{19}$ Total number of eutectics 16	CdNa 25 CuSb 14 MgPb 10 SiCe 55 NiSn 13	TlAs −26 BiAu −7 NiB ~ −28 CaSn −29 UCr −17 MgGa −24 NiP −12 WC −44 SbMn −8 ThV −27 PdP −21

For the $A_{83}B_{17}$, $A_{82}B_{18}$ and $A_{81}B_{19}$ eutectics there are 34 examples where B is the smaller atom, and 13 examples where B is the larger atom.

The symbols are arranged so that the second element is the B element.

In all cases the size-factor is with reference to the A element.

were regarded as electronegative in the systems CoGe, GeMn, GeFe, and CoSb. In this way, we can perhaps understand the peak at approximately 25 atomic % in the eutectic distribution curve.

The above discussion is admittedly speculative and incomplete. It is included to suggest a way in which the position of the peaks on the eutectic distribution curve may be interpreted on the assumption that they are due to the existence of bends on the G/C curves. The discussion has deliberately been confined to the icosahedral units and pentagonal chains because these avoid the introduction of nuclei for crystallization.

§ 10. TYPES OF LIQUID IMMISCIBILITY

As pointed out above (p. 389) the existence of a sharp valley in the $\Delta G/C$ curve leads to the formation of liquid immiscibility, unless solid phases intervene.

Fig. 13

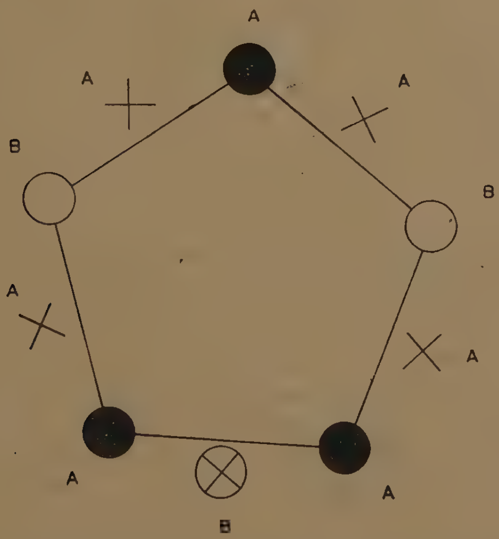

● A atoms, and ○ B atoms in one pentagonal layer. × A atoms in adjacent layer. ⊗ B atom in adjacent pentagonal layer.

We may consider first the case of fig. 14 (*a*) where convenient atomic packing gives a marked trough in the $\Delta G/C$ curve for the liquid, and where a solid phase X exists whose composition is the same as that of the minimum in the curve for the liquid. In this case decreasing temperature will eventually produce a condition in which the ΔG curve for the solid falls slightly below the minimum as shown in fig. 14 (*a*). At this temperature, alloys with compositions between X and y will consist of (Solid X + Liquid y) whilst those between y and d will consist of a single liquid phase, and those between d and c will consist of two liquid phases. A similar condition of affairs will exist on the opposite side of X, where two liquid phases will exist between a and b, a single liquid phase between b and x, whilst between x and X the alloys will consist of (Liquid x + Solid X).

Fig. 14

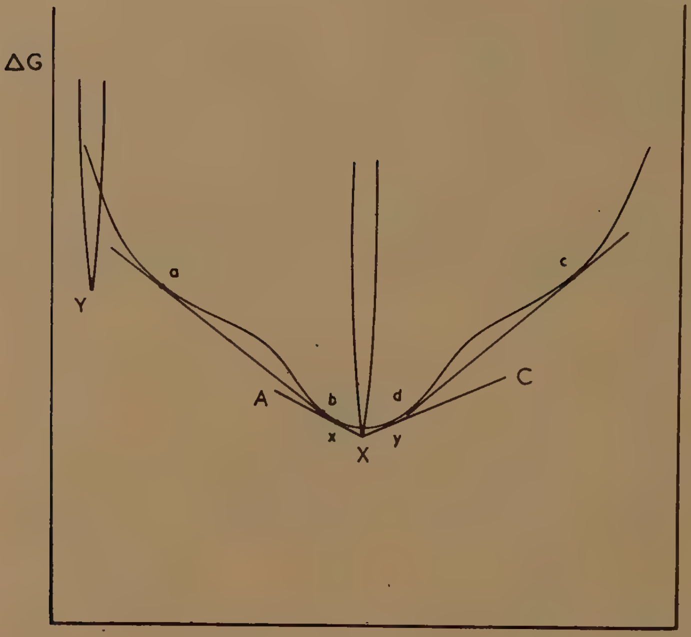

(*a*)

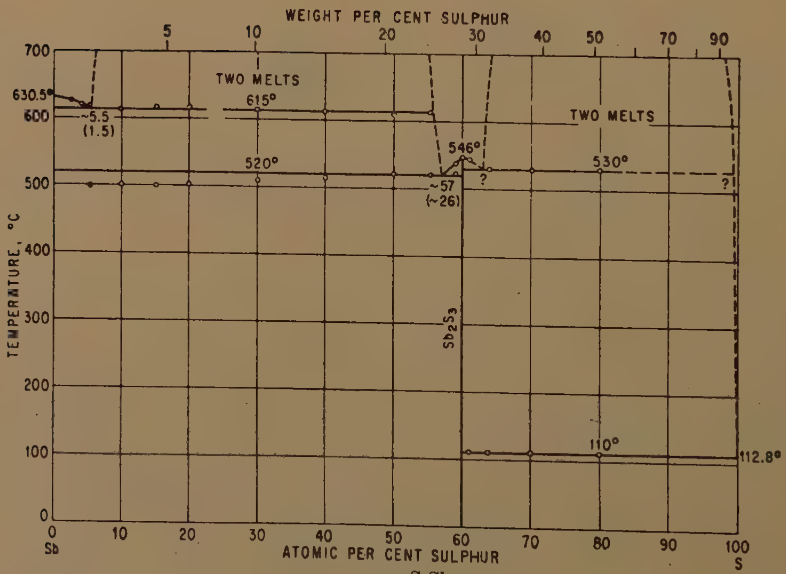

S-Sb

(*b*)

By permission from *The Constitution of Binary Alloys*, by M. Hansen.
Copyright, 1958. McGraw-Hill Book Company, Inc.

Alternatively, if the ΔG curve for a solid phase Y lies slightly below ab, the region of liquid immiscibility will be replaced by a $(Y + \text{Liquid})$ field, and on lowering the temperature there will be a eutectic of $(Y + X + \text{Liquid})$. If on raising the temperature, the ΔG curve for Y rises above ab, the phenomenon of liquid immiscibility will appear.

These characteristics are shown most strikingly by some alloys of S, Se and Te. Figure 14 (*b*) shows the system S–Sb which clearly resembles the case discussed above. In this case X in fig. 14 (*a*) is the compound Sb_2S_3 in fig. 14 (*b*), and Y is pure Sb. 520°c is the temperature of the $(X + Y + \text{Liq})$ eutectic of fig. 14 (*a*), and 615°c is the temperature at which Y in fig. 14 (*a*) lies on the projection of the straight line ba. The system AgSe is another example of this kind of diagram.

Fig. 15

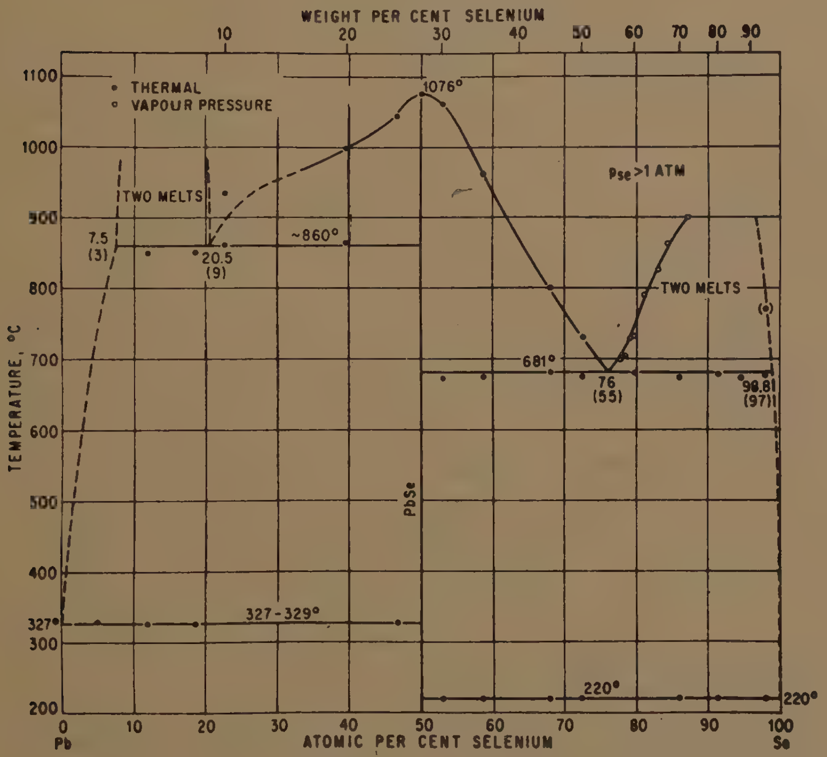

Pb-Se.

By permission from *The Constitution of Binary Alloys*, by M. Hansen. Copyright, 1958. McGraw-Hill Book Company, Inc.

If the present interpretation is correct, the formation of immiscible liquids in this kind of system is not due to a reluctance of the two kinds of atom to pack together to form a liquid. On the contrary, they form a liquid of great stability (i.e. low ΔG in fig. 14 (*a*)), and the liquid immiscibility results from the consequent inflection in the ΔG curve. In some of these cases it is possible that there are definite compound molecules in the liquid, or definite ratios of oppositely charged ions. This may be the reason why the depression of the liquidus in Ag-rich AgSe alloys is not that given by van't Hoff's equation. It seems, however, quite possible that purely geometrical packing factors may lead to a sharp valley in the ΔG curve, with the resulting formation of immiscible liquids.

If in fig. 14 (*a*) the compound *X* becomes increasingly stable, and the trough in the liquid curve is broader, the regions of liquid immiscibility will be displaced outwards from *X*. The system PbSe shown in fig. 15 appears to be an example of this kind.

Fig. 16

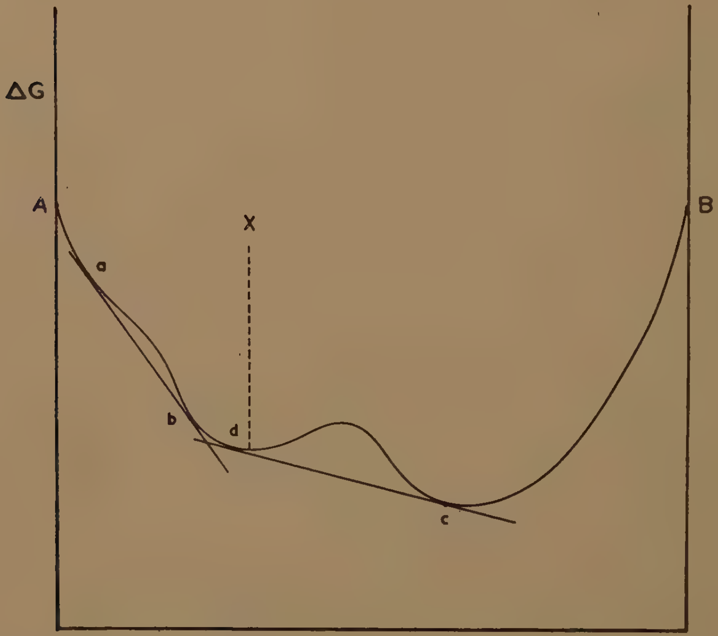

The above argument depends on the assumption that in fig. 14 (*a*) the trough in the curve is such that *a* and *c* lie above *b* and *d* respectively. There is also the possibility of a curve such as that of fig. 16 where, on drawing the tangents, *a* is above *b*, but *c* is below *d*. In this case, if the compound *X* has the same composition as the minimum in the curve, the point *d* will lie to the left of *X*. On lowering the temperature the ΔG point for *X* will eventually meet the line *dc*, and the equilibrium diagram will be of the form of fig. 17, in which the compound *X* lies under and near to the edge of one of the regions of liquid immiscibility. There appears to be no simple example of this, but in the system PSn, the general effect is found with the complication of an additional compound in the region between the two fields of liquid immiscibility (see fig. 18).

Fig. 17

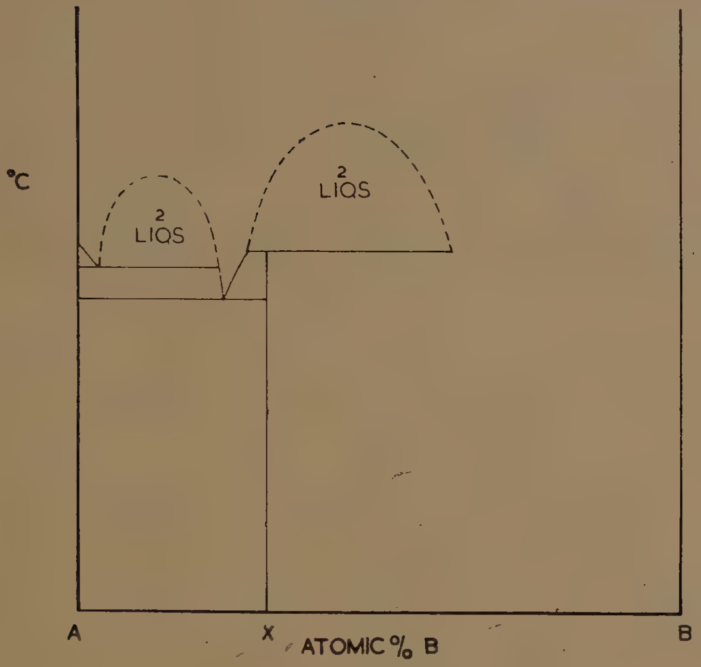
°C
2 LIQS
2 LIQS
A
X
ATOMIC % B
B

Fig. 18

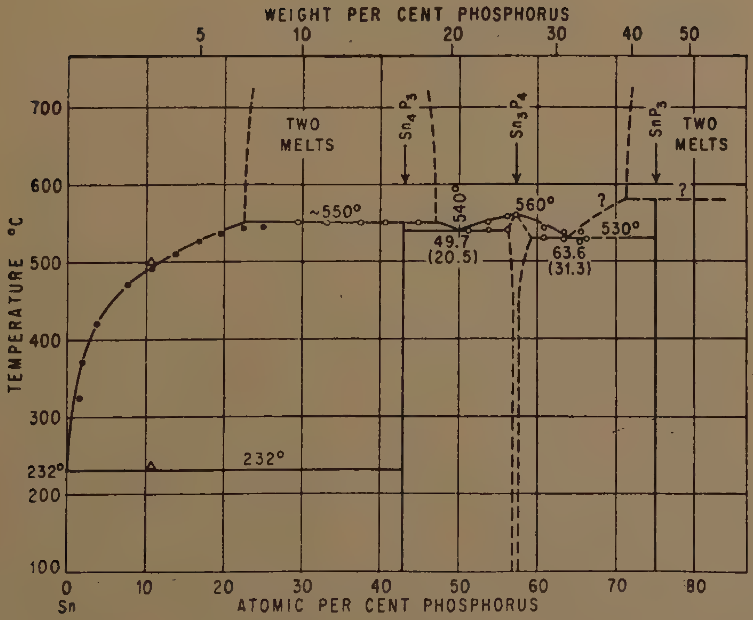

P-Sn

By permission from *The Constitution of Binary Alloys*, by M. Hansen.
Copyright, 1958. McGraw-Hill Book Company, Inc.

It is clear that, if our interpretation is correct, the formation of two separate fields of liquid immiscibility requires inflections on both sides of the minimum in the curve of fig. 14 (*a*). If the inflection occurred on one side only as in fig. 19, the above argument would lead to the existence of a region of liquid immiscibility on only one side of the compound. This is a characteristic of systems such as CuSe (see fig. 20).

If our interpretation is correct, liquid immiscibility of the above types is to be distinguished from the more ordinary type for which the $\Delta G/C$ curves are of the form of fig. 21. Here, at each side of the diagram, the free energy first falls and then rises, which is an expression of the fact that the two kinds of atom 'do not like to mix'. In contrast to this, the liquid immiscibility referred to above results from the two kinds of atom having such a strong tendency to mix at a particular composition, that the free energy falls, and produces an inflection in the $\Delta G/C$ curve.

Fig. 19

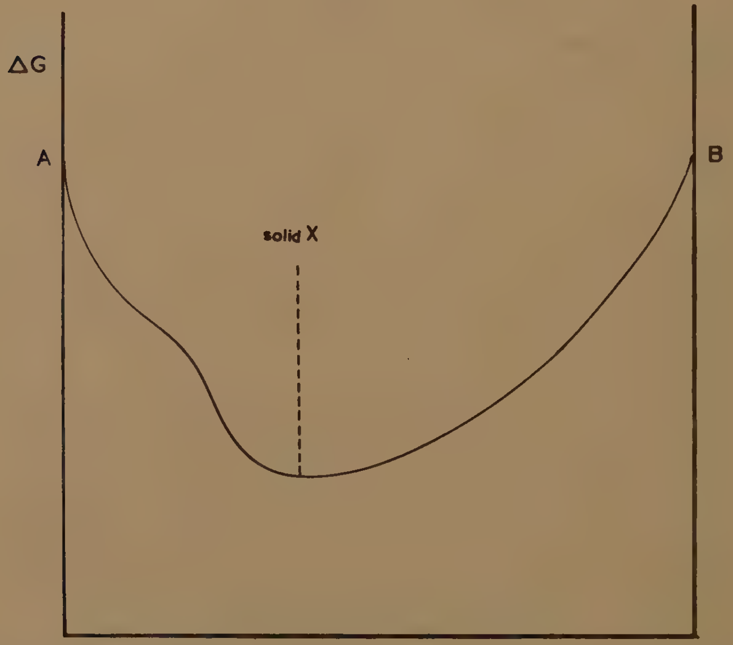

§ 11. OTHER EVIDENCE FOR ORDERED STRUCTURES IN LIQUID ALLOYS

If the $\Delta G/C$ curves for liquid alloys contain inflections of the types discussed above, these should be revealed by irregularities in the curves connecting various physical properties with the composition. In connection with the electrical resistivity of the liquid alloy, two effects may be expected. On the one hand, the development of ordered structures at particular compositions should lead to minima at the compositions concerned. On the other hand maxima in the resistivity/composition curves

Fig. 20

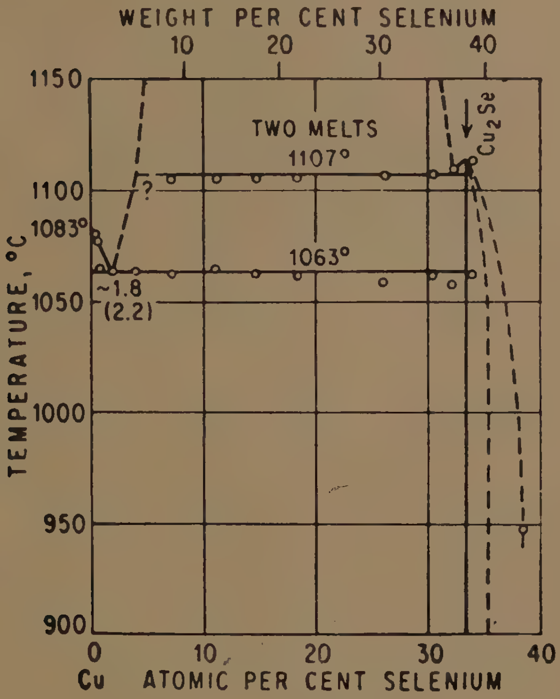

Cu-Se

By permission from *The Constitution of Binary Alloys*, by M. Hansen.
Copyright, 1958. McGraw-Hill Book Company, Inc.

Fig. 21

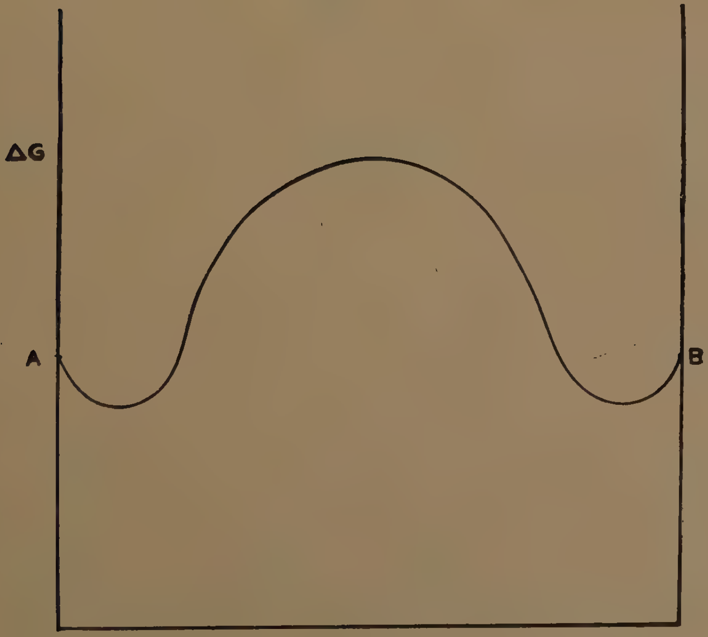

may be expected at compositions at which definite molecules or polar structures are formed with the conduction electrons bound into stable groups.

In a recent paper, Roll and Motz (1957) have examined the electrical resistivity of a number of alloy systems in the liquid state, and many of the isothermal curves show a maximum or minimum resistance at 25 or 32 atomic % of solute. These are two of the compositions corresponding to maxima on the eutectic distribution curve. Similar effects are shown in corresponding curves by other authors, and it is hoped to discuss these later.

The liquidus curves for the freezing of solid solutions should also show inflections if ordered structures exist in either the solid or the liquid solutions. If a system is chosen in which the solid solution is of negligible extent, any inflections in the liquidus curve may reasonably be taken to suggest ordered structures in the liquid. Examination of the very careful curves of Heycock and Neville (1897 a, b) suggests that some of these may be built up of segments with relatively sharp changes of direction. The conclusive establishment of this is a matter of difficulty, because highly accurate experimental data are required, and there is a natural tendency for authors to draw smooth curves through their experimental points. It is hoped to examine this question in detail later.

APPENDIX

The data from Hansen's text-book have been accepted with very few exceptions, and the following points may be noted:

(1) For alloys of Pu, several diagrams are reproduced on which eutectic compositions are indicated. These are described as being based on specimens weighing a few hundred milligrams, and we understand that further work is required before they are significant.

(2) The following eutectics (in atomic %) are not numbered in Hansen's book, but appear to be well established:

AuSn (6 Au)
BiTl (7 Bi)
CuSi (20 and 30 Si)
MgZn (30 Zn)
AuCd (30 Au)
GeNi (28 Ge)
CuIn (26 In)
AlNi (24 Al)
AuZn (34 Zn, and 37 Au)
MnPd (27 Pd, and 32 Mn)
AlMg (42 Mg)

(3) The following eutectics are included as the result of recent work in the authors' laboratory:

MnTi (10 Ti)
FeTi (16 Ti)
CuGe (22 Ge, and 37 Ge)
AlFe (32 Fe, and 26 Fe)

(4) The following eutectics have been omitted either because of inconsistent results of different investigators, or because of uncertain evidence:

SiU (47 Si). The eutectics at 9 Si and 14 U have been accepted in the total number
KSe equiatomic C.M.P. eutectic
LaMg equiatomic C.M.P. eutectic
AsSn (45 As)
MnPt (40 Mn)
CuTi (34 Ti). The eutectic at 43 Cu is accepted as well established
AuBe (20 Be)
AlLa (La-rich eutectic)
LiNa (4 Li)
AlU (6 Al)

(5) In the system AsTe the 25 As eutectic has been included because the original text suggests that the composition was established at least approximately, although figures were not given.

(6) The following equilibrium diagrams have been ignored:

BZr
BeZr
SiV
SiW

(7) It may be pointed out that the present paper refers to eutectic points only; monotectic points have not been included.

ACKNOWLEDGMENTS

The authors must acknowledge the benefit received from discussions with Professor J. D. Bernal, F.R.S., and from Dr. J. W. Christian.

REFERENCES

FRANK, F. C., 1952, *Proc. roy. Soc.* A, **215,** 43.
HANSEN, M., 1958, *The Constitution of Binary Alloys*, Second Edition (McGraw-Hill Book Co., Inc.).
HEYCOCK, C. T., and NEVILLE, F. H., 1897 a, *Phil. Trans.* A, **189,** 32; 1897 b, *J. chem. Soc.*, **71,** 407.
ROLL, A., and MOTZ, H., 1957, *Z. Metallk.*, **48,** 495.
STOCKDALE, D., 1935, *Proc. roy. Soc.* A, **152,** 81.

CORRESPONDENCE

An Observation of Crack Formation in MgO

By W. G. Johnston
General Electric Research Laboratory, Schenectady, N.Y.

[Received March 7, 1960]

Stokes *et al.* (1959) have recently described the formation of cracks at the intersection of glide bands in MgO single crystals. Those authors proposed that under certain circumstances, edge dislocations moving on a (110) plane pile up at an intersecting glide band, and coalesce to form a Stroh-crack (Stroh 1955). It is the purpose of this note to present an observation of crack formation in MgO that supports in quite some detail the proposal of Stokes *et al.*

Fig. 2

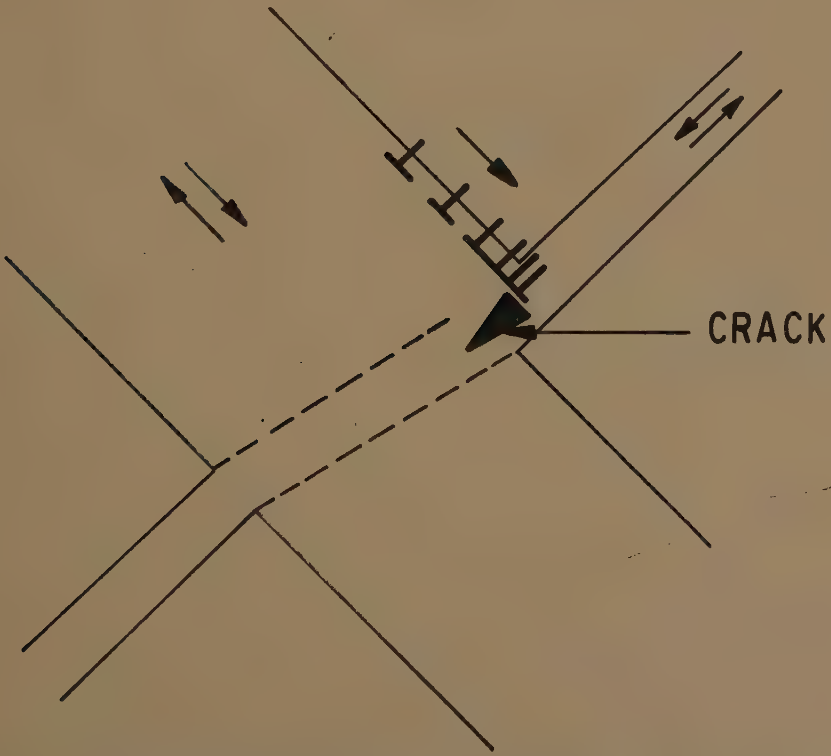

Schematic drawing of the glide band intersection of fig. 1, showing the type of dislocation that is piled up.

In fig. 1 (Pl. 42) is shown a slit-type crack such as described by Stokes *et al.* The crack formed along the intersection of two glide bands in an MgO crystal that was deformed in $2\frac{1}{2}\%$ in compression, and it extended all the way through the $\frac{1}{8}$ in. square crystal. The crystal was compressed at a strain rate of 10^{-4} $\sec^{-1}$, and the compression axis was parallel to the $\langle 100 \rangle$ crystal edge that appears in fig. 1. The crystal was then etched for 30 sec in sulphuric acid at 55°c. The dislocations in the intersecting glide bands, were predominantly edge dislocations, their Burgers vectors being parallel to the arrows alongside the bands.

The wide glide band intersects several lighter glide bands, and it is deduced from the offset of those light bands perpendicular to the wide band that they were present before the wide band formed. The light bands were possible obstacles for the wide band, and it is in fact seen that part of the wide band has been blocked by a light band, and that a crack has formed at the blocking point. The type of edge dislocation that would pile up at such a blocking point is depicted in fig. 2. That type of dislocation would lead to the formation of a Stroh crack that would spread into the wide band, as this crack appears to do.

The observation presented here supports the proposal of Stokes *et al.* for crack formation in MgO. However, it is not clear that conclusive proof for the operation of Stroh's mechanism for crack formation can be obtained from observation of dislocation distributions in a cracked crystal. It would seem that the only conclusive proof would be an observation of the actual coalescence of dislocations, such that as the dislocations disappeared, a crack would appear. Although such an observation may eventually be made by electron microscopic observation of a thin crystal, it does not seem possible by etch pit methods.

REFERENCES

STOKES, R. J., JOHNSTON, T. L., and LI, C. H., 1959, *Phil. Mag.*, **4**, 920.
STROH, A. N., 1955, *Proc. roy. Soc.* A, **232**, 548.

Upper Limit to Anisotropy of Inertial Mass from Nuclear Resonance

By R. W. P. Drever
Department of Natural Philosophy, University of Glasgow

[Received April 14, 1960]

It has been pointed out by Bondi (1952) and Cocconi and Salpeter (1958) that if inertial mass is taken to arise from gravitational interaction with distant matter one would expect the concentration of matter near the centre of our own Galaxy to cause some anisotropy of inertia at the earth. This anisotropy might be as large as one part in 10^7; and Cocconi and Salpeter suggested that it could be detected from the shifts in atomic energy levels which might result. In a single-electron atom in a magnetic field parallel to the direction of the centre of the Galaxy they find that the energy of a $p_{3/2}$ state with magnetic quantum number $m_j = \pm 1/2$ would be altered by an amount $T \, . \, \Delta M/5M$, where T is the mean kinetic energy of the electron and $\Delta M/M$ is the fractional difference between the inertial masses of a body (the electron) for accelerations parallel to the direction of the centre of the Galaxy, and perpendicular to it. A $p_{3/2}$ state for which $m_j = \pm 3/2$ would show an energy shift of equal magnitude in the opposite direction. If the magnetic field is perpendicular to the direction of the centre of the Galaxy then both these energy shifts would be reversed.

The high energy resolution obtained in studies of recoil-less resonance scattering of gamma rays suggests that this technique might provide a more sensitive method of searching for anisotropy of inertia, and in fact this idea has already been put forward by Cocconi and Salpeter (1960). In such an experiment one would look for changes in nuclear energy levels, and as the kinetic energy of the nucleon involved (in a shell-model picture) is of the order of 10 MEV the effects would be expected to be larger than in the atomic case. If it is assumed that the same calculation of energy shifts applies directly both to the atom and the nucleus, it is already possible to put a tentative upper limit to the magnitude of $\Delta M/M$ for a nucleon of about 10^{-14} from the sharpness of the lines observed in ^{57}Fe, as Cocconi and Salpeter point out. We would like to suggest here that even more sensitive checks on anisotropy of inertia can be made by nuclear magnetic resonance and nuclear quadrupole resonance techniques.

In a pure magnetic resonance experiment on a nucleus with total angular momentum quantum number $I = 3/2$, for example, the three magnetic dipole transitions between the magnetic sub-levels are normally taken to have the same resonance frequency. Anisotropy of inertia would be expected to shift the levels having magnetic quantum numbers $m_I = \pm 3/2$ in one direction, and those for which $m_I = \pm 1/2$ in the opposite direction, turning the line into a triplet. With the direction of the magnetic field fixed relative to the earth, the spacing of the outer components of the triplet would vary with time as the angle between the magnetic field and the direction of the centre of the Galaxy changes. In practice one might either work with a liquid specimen and look for small diurnal changes in the breadth of the composite resonance line, or use a single crystal in which the line is already split by a weak quadrupole interaction and look for changes in the splitting. One could hope to detect easily changes of the order of 100 cycles/sec, corresponding to values of $\Delta M/M$ of about 10^{-19}. Even from the consistency of the original results of Pound (1950) on quadrupole interactions in magnetic resonance one can probably set an upper limit to the magnitude of $\Delta M/M$ of the order of 10^{-17}.

Similar experiments can be made using pure quadrupole resonance. With a nucleus having $I = 3/2$ a single resonance corresponding to transitions between the states with $m_I = \pm 3/2$ and $m_I = \pm 1/2$ is normally expected. Anisotropy of inertia would shift the upper and lower states in opposite directions, altering the resonance frequency by an amount depending on the angle between the axis of electrical symmetry and the direction of the centre of the Galaxy. Small shifts of this kind might be detected using a single crystal of a material in which the nucleus being studied may be situated at several chemically equivalent sites in the unit cell, the axes of electrical symmetry at these sites being equally inclined to a fixed direction in the crystal. Such a crystal can be oriented so that at a certain time of day all the axes make equal angles with the direction of the centre of the Galaxy (and possibly also with the plane of the Galaxy), when the resonance frequencies at all the sites would coincide; while a few hours later the angles made by the axes with this direction might vary over a wide range, at which time one would expect separation of the resonance frequencies to broaden the composite line observed. An experiment of this kind might be almost as sensitive as one using magnetic resonance; and again one can already set an upper limit to anisotropy of inertia from present data. In this case experiments with polycrystalline specimens are the most definite, for in these anisotropy of inertia should lead to broadening of the resonance for any orientation of the apparatus. Measured line breadths (Krüger and Meyer–Berkhout 1952) of 10 kc/sec with ^{63}Cu and ^{65}Cu (each a nucleus with an unpaired $p_{3/2}$ proton) thus put an upper limit to the magnitude of $\Delta M/M$ of about 2×10^{-17}.

It might be remarked that as we have applied the calculation of Cocconi and Salpeter without considering details of nuclear structure the above limits to $\Delta M/M$ are not to be considered precise. Nevertheless it would appear that a very sensitive search for anisotropy of inertia can be made by nuclear resonance methods; and that even from data already available one can put an upper limit to anisotropy of inertia of the order of a few parts in 10^{17}, a limit lower by a factor of about 10^{10} than the anisotropy which one might expect from the theories of inertia of Sciama (1953) and Kaempffer (1958) based on Mach's principle.

ACKNOWLEDGMENTS

The author would like to thank Drs. G. A. P. Wyllie, W. K. Burton, G. M. Lewis and K. M. Guggenheimer for valuable discussions.

Note.—Since this paper was written it has been heard that a nuclear magnetic resonance experiment like the one suggested here is being performed at Yale University. Results already obtained (Hughes *et al.* 1960) set an upper limit of 10^{-20} to the magnitude of $\Delta M/M$.

REFERENCES

BONDI, H., 1952, *Cosmology* (Cambridge: University Press), p. 30.
COCCONI, G., and SALPETER, E., 1958, *Nuovo Cim.*, **10**, 646; 1960, *Phys. Rev. Letters*, **4**, 176.
HUGHES, V. W., ROBINSON, H. G., and BELTRAN-LOPEZ, V., 1960, *Phys. Rev. Letters*, **4**, 342.
KAEMPFFER, F. A., 1958, *Canad. J. Phys.*, **36**, 151.
KRÜGER, H., and MEYER-BERKHOUT, U., 1952, *Z. Phys.*, **132**, 171.
POUND, R. V., 1950, *Phys. Rev.*, **79**, 685.
SCIAMA, D. W., 1953, *Mon. Not. R. astr. Soc.*, **113**, 34.

The Embrittlement of Molybdenum by Neutron Irradiation

By A. A. JOHNSON
Physical Metallurgy Department, Imperial College, London, S.W.7

[Received November 24, 1959]

IN a recent series of experiments on EN2 steel Hull and Mogford (1958) studied the effect of neutron irradiation on the parameters σ_i and k_y in the Petch relation

$$\sigma_y = \sigma_i + k_y d^{-1/2} \quad \ldots\ldots\ldots \quad (1)$$

between yield stress, σ_y, and grain diameter, $2d$. They found that irradiation increased the lattice friction stress, σ_i, but that k_y, which is a measure of the stress required to free a dislocation from its impurity atmosphere, was unaltered. This simple phenomenological description of irradiation hardening in EN2 steel makes it possible to predict its brittle fracture properties after irradiation once the dependence of σ_i on integrated neutron flux has been measured. For example, at a given temperature brittle fracture occurs if

$$(\sigma_i d^{1/2} + k_y) k_y \geqslant \beta \mu \gamma \quad \ldots\ldots\ldots \quad (2)$$

where β is a constant which is nearly unity, μ the rigidity modulus, and γ the effective surface energy for fracture (Cottrell 1958). For the special case of σ_i varying and k_y constant this reduces to

$$\sigma_i d^{1/2} \geqslant a \text{ constant} \quad \ldots\ldots\ldots \quad (3)$$

a result which was verified experimentally by Hull and Mogford.

To establish whether or not the same simple type of irradiation embrittlement occurs in other body-centred cubic metals the writer has applied the same method as that used by Hull and Mogford to molybdenum. Twenty molybdenum tensile specimens, each having a different grain size, were prepared from an arc-cast ingot. The method of preparation and the tensile properties of unirradiated specimens from the same ingot have been described in an earlier paper (Johnson 1959). The specimens were placed in a sealed argon filled aluminium canister and irradiated in BEPO for six months. The irradiation temperature was 40°–50°C and the integrated epithermal neutron flux about 2×10^{19} n.v.t. Probably about 1 epithermal neutron in 10 had an energy greater than 1 MeV.

The irradiated specimens were tested in a modified Hounsfield tensometer at a strain rate of $0{\cdot}88 \times 10^{-4}\,\text{sec}^{-1}$. Nine were completely brittle and careful metallographic examination showed that they had failed by transcrystalline cleavage. The dependence of brittle fracture stress, σ_f, on grain size is shown in fig. 1. The results do not seem to fit the relation

$$\sigma_f = \sigma_i + k_f d^{-1/2} \quad \text{. . . . .} \quad (4)$$

which describes the behaviour of brittle unirradiated metals (e.g. Petch 1953). One result was rejected because the specimen fractured at a shoulder.

All of the remaining specimens showed pronounced yield points (fig. 2) and increased yield stresses. The changes in yield stress were greatest for large grain sizes (fig. 3) and hence cannot be due solely to a change in lattice friction stress. The strain to fracture and reduction in area at fracture were slightly decreased by irradiation for all grain sizes, but the fracture stresses were unchanged.

These results show clearly that the mechanism of irradiation embrittlement in molybdenum is more complex than that in EN2 steel.

Fig. 1

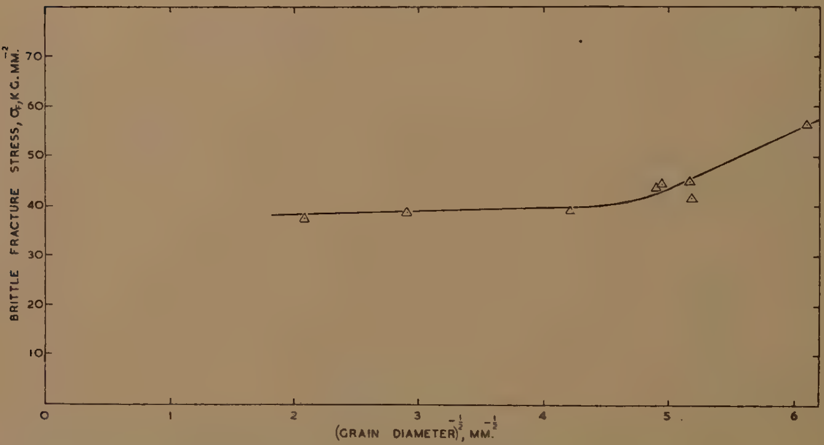

The effect of grain size on the brittle fracture stress of irradiated molybdenum.

Unfortunately, because the effects of irradiation cannot be described in terms of changes in σ_i and k_y, no straightforward interpretation of the results can be given. It seems likely that the effect of irradiation on the two materials is different because in molybdenum point defects created during irradiation can cause dislocation climb, whereas in EN2 steel climb is inhibited by a precipitate of cementite on the dislocations. If this were so all the edge dislocations in irradiated molybdenum would become jogged and the screws would tend to be wound up into spirals. This would have two effects on the mechanical properties. First, the presence of jogs on the dislocation lines in Frank–Read sources would make the sources more difficult to operate, and k_y would therefore increase. Secondly, if dislocation sub-boundaries were present they would become more opaque to slip dislocations and might then be expected to contribute to the mechanical properties in much the same way as grain boundaries.

Fig 2

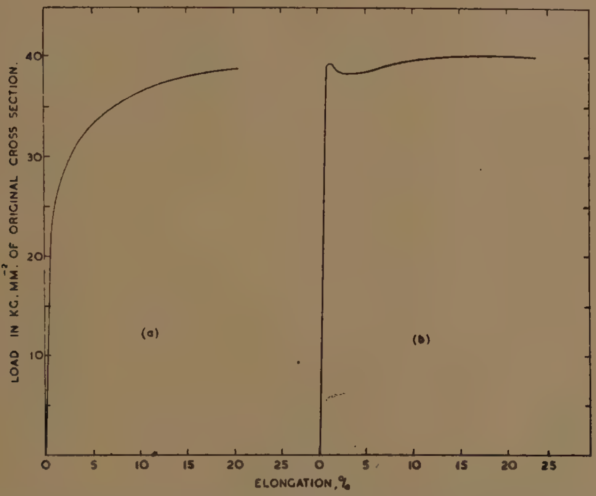

Typical load-elongation curves for coarse grained molybdenum specimens, (*a*) before irradiation and, (*b*) after irradiation.

Fig. 3

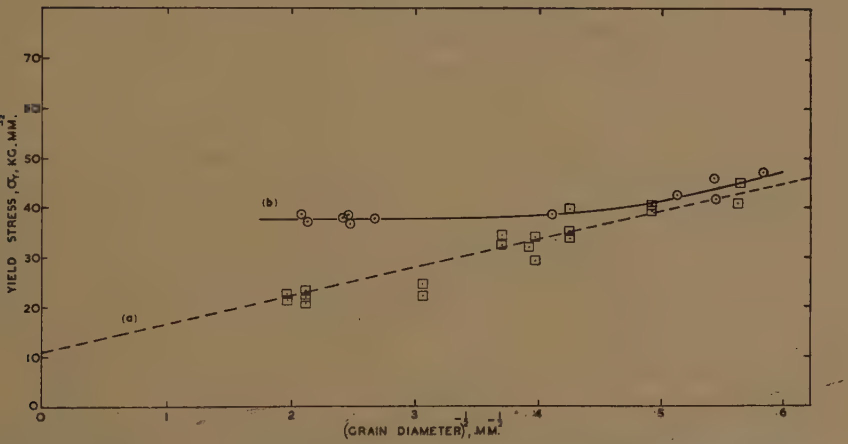

The effect of grain size on the yield stress of molybdenum, (*a*) before irradiation, and, (*b*) after irradiation.

The specimens used in the investigation were examined for sub-structure by taking back-reflection x-ray photographs. Splitting of the spots showed that in coarse-grained specimens there were four or five sub-grains in a section through each grain and that the number of sub-grains per grain decreased with decreasing grain size. The yield stresses of the irradiated specimens can therefore be explained semi-quantitatively by substituting estimated sub-grain diameters for grain diameters in eqn. (1). If this supposed strengthening of sub-boundaries were the only effect of irradiation the ductility of all the specimens would be increased whereas, in fact, some of all grain sizes become brittle. Because of the uncertainty in measuring the sub-grain diameters it is not possible to say from the results whether or not k_y has increased, but if we assume that it has, it helps us to understand the occurrence of brittle specimens because the brittle fracture criterion, eqn. (2), is very sensitive to changes in k_y. We are, however, left with the difficulty that no single value of k_y will satisfy eqn. (2) for all the sub-grain diameters simultaneously.

ACKNOWLEDGMENTS

This work was financed jointly by U.S. Navy Department, Contract No. N.62558(24)1177, and the Central Electricity Generating Board, and was carried out during the tenure of an I.C.I. Research Fellowship awarded by the University of London. The author is indebted to Professor J. G. Ball for his continued interest and encouragement, to Dr. H. M. Finniston and Mr. N. H. Hancock for the provision of irradiation facilities at A.E.R.E., Harwell, and to Mr. E. Bullen for taking the x-ray photographs.

REFERENCES

COTTRELL, A. H., 1958, *Trans. Met. Soc. A.I.M.E.*, **212,** 192.
HULL, D., and MOGFORD, I. L., 1958, *Phil. Mag.*, **3,** 1213.
JOHNSON, A. A., 1959, *Phil. Mag.*, **4,** 194.
PETCH, N. J., 1953, *J. Iron. St. Inst.*, **173,** 25.

On Microcreep in Zinc Whiskers

By P. B. Price†
Physics and Chemistry of Solids Laboratory,
Cavendish Laboratory, Cambridge

[Received April 6, 1960]

In a recent paper Cabrera and Price (1958) reported that microcreep was sometimes observed in zinc whiskers grown from the vapour when they were stressed in tension to elastic strains of the order of a few tenths of 1%, whereas large-scale plastic deformation did not occur until the elastic strain was raised to ~1%. They concluded that whiskers in which creep occurred contained dislocations which were arranged so that they were difficult to move until the applied stress was fairly high. It was impossible to verify directly the existence of dislocations in these whiskers, because they were too small (1 to 7 μ diameter) for etch-pit techniques (Coleman 1958) or X-ray transmission techniques (Webb 1958) to be applied and too thick to be examined by transmission electron microscope techniques (Hirsch *et al.* 1956).

In the present investigation of the mechanical properties of zinc whiskers and platelets, this difficulty was overcome by selecting only crystals which were thin enough to be examined by transmission electron microscopy, using a Siemens Elmiskop 1 operated at 100 kv and 10 to 40 μA beam current. It was found that any dislocations which were present could be detected in crystals up to $\sim\frac{1}{2}\,\mu$ in thickness, provided the crystals were tilted with the stereo-control to produce maximum contrast. This paper describes those results of the investigation which pertain to microcreep.

Zinc whiskers and platelets of a wide range of sizes were grown from the vapour, in an atmosphere of argon, both by the technique of Coleman and Sears (1957) and by the technique of Price (1960). Those in the latter group were known to have grown at supersaturations in the range $\sigma=0{\cdot}5$ to 2, where $\sigma=(p-p_{\text{eq}})/p_{\text{eq}}$. Most of the crystals were cooled slowly from about 400°c to room temperature after growth, but one group was grown in a silica tube, then quenched in water at room temperature.

Sixty crystals, ranging in thickness from a few hundred angstroms to about one-half micron, were examined by transmission electron microscopy before being subjected to tensile tests. Their lengths varied from $\sim 0{\cdot}5$ to 3 mm and their widths from $0{\cdot}1\,\mu$ to 2 mm. Each crystal was mounted with its largest faces perpendicular to the electron beam; electron diffraction patterns showed that these faces were always parallel to the basal plane. Of the sixty crystals studied, all but a very few were found to contain no dislocations. Examples of dislocation-free crystals are shown in figs. 1 and 2†. In no case was an axial screw dislocation ever observed. This does not, of course, eliminate the possibility that dislocations were present during growth but were removed from the crystals by climb during the cooling-down period. The only structural details which could be seen were growth steps. Occasionally surface corrosion pits developed on crystals which had been exposed to air for a long time (fig. 1).

---

† National Science Foundation Post-doctoral Fellow, 1959–60.

In some crystals, however, dislocations were observed. Figure 3 shows a network of dislocations, lying predominantly on basal planes, which are believed to have been produced as a result of high stresses set up near the end of a large platelet where it was glued to the specimen holder. Most of these dislocations originate at the line of contact with the specimen holder and extend for a considerable distance into the platelet before finally emerging on a surface. This observation makes it clear that one must be extremely careful in handling and mounting these crystals.

After the dislocation arrangements in the crystals were determined, they were deformed in tension, either inside the electron microscope or in a high-sensitivity microtensile testing machine, capable of measuring extensions of less than 100Å reproducibly (Marsh 1959). The results of tensile experiments carried out inside the electron microscope will be reported in another paper. The results of tests performed in the microtensile machine were as follows:

(1) Whiskers and platelets could be extended to high elastic strains, $\sim 2 \times 10^{-3}$ to 2×10^{-2}, before yield occurred, whether they contained dislocations or not, provided the strain rate was reasonably high ($\gtrsim 10^{-5}\,\mathrm{sec}^{-1}$).

(2) Dislocation-free crystals showed no detectable plastic behaviour below the yield point when left for several hours at high elastic strains.

(3) Microcreep was always observed below the yield point in crystals containing dislocations. The creep strain usually reached a maximum value of 10^{-4} to 10^{-3} after about one hour at a constant elastic strain of 10^{-4} to 10^{-3}. This is in order of magnitude agreement with the observations of Cabrera and Price (1958) on crystals 1 to 7 μ in thickness.

From these results it can be inferred that those whiskers tested by Cabrera and Price which showed microcreep also contained dislocations, which may have been grown in or introduced by stresses at the grips.

As fig. 3 shows, dislocations produced near the grips lie predominantly on basal planes, which are parallel to the axis of tension and therefore are not under a shear stress. Only those components which are on nonbasal planes will have a force exerted on them. It is suggested that, under a sufficiently high applied stress, these components will move, dragging the basal components with them and producing the observed microcreep. The creep stops when the dislocations have moved out of the crystal or have reached a more stable configuration. A higher stress is then required to produce yield, either through the nucleation of a twin or through the production of new dislocations on nonbasal planes.

---

† All figures are shown as plates.

Studies of the processes of slip and deformation twinning in these crystals, using the transmission electron microscope technique, are in progress; the results will be reported later.

ACKNOWLEDGMENTS

I am indebted to Professor N. F. Mott, F.R.S., and Dr. F. P. Bowden, F.R.S., for their interest and encouragement and for making available the facilities of this laboratory. I am grateful to Dr. P. B. Hirsch for many useful discussions and for reviewing the manuscript. This work was carried out during the tenure of a post-doctoral fellowship awarded by the U.S. National Science Foundation.

REFERENCES

CABRERA, N., and PRICE, P. B., 1958, *Report of the Cooperstown Conference on the Growth and Perfection of Crystals*, Ed. Doremus, Roberts and Turnbull (New York: Wiley), p. 204.
COLEMAN, R. V., 1958, *Report of the Cooperstown Conference on the Growth and Perfection of Crystals*, Ed. Doremus, Roberts and Turnbull (New York: Wiley), p. 239.
COLEMAN, R. V., and SEARS, G. W., 1957, *Acta Met.*, **5**, 131.
HIRSCH, P. B., HORNE, R. W., and WHELAN, M. J., 1956, *Phil. Mag.*, **1**, 677.
MARSH, D. M., 1959, unpublished. For an account of an earlier model see Marsh, D. M., 1959, *J. sci. Instrum.*, **36**, 165.
PRICE, P. B., 1960, *Phil. Mag.* (in the press).
WEBB, W. W., 1958, *Report of the Cooperstown Conference on the Growth and Perfection of Crystals*, Ed. Doremus, Roberts and Turnbull (New York: Wiley), p. 230.

REVIEWS OF BOOKS

A Degree Physics, Part III, Optics. By C. J. Smith. (London: Edward Arnold Ltd.) [Pp. 736.] Price £3 3*s*.

This book is a further volume in a series published under the title *A Degree Physics*, all by the same author. The first two volumes covered " General Properties of Matter ", and " Electricity and Magnetism ". The series is intended to cover rather more than is usually required by candidates taking physics at the B.Sc. General Degree level.

The book will undoubtedly be of great value to the class of students for whom it is intended. The style is readily understandable, and the diagrams are admirably clear. There is only one minor criticism which might be made; it is a pity that vector diagrams are not used more frequently in place of, or in addition to, a purely mathematical approach. The value of the vector diagram to the student is that it gives an immediate grasp of the problem, and shows clearly what happens when different quantities are varied. Examples of problems where vector diagrams might have been used with advantage occur on pages 47, 462, 469, 544, 570, 574 and 582. The usual phase amplitude diagram for circular division of a wavefront (page 569) is not given at all. The Cornu spiral, appropriate to strip division of a wavefront, is discussed, but it is first introduced as a plot of the Fresnel integrals and not as a phase amplitude diagram. This approach *via* the Fresnel integrals seems unnecessarily difficult at this fairly elementary level.

Quite a large part of the book is devoted to geometrical optics, including a detailed treatment of aberrations. Possibly the choice of subject matter was dictated by the requirements of a particular examination syllabus. If so, it seems a pity that so much geometrical optics should be demanded, for this subject, though technically important, seems to be of less educational value than physical optics. In physical optics, the student meets new methods and concepts which are of importance in many branches of physics, including modern physics. Geometrical optics, on the other hand, is a more or less self-contained subject and one, moreover, which any physicist should be able to learn quite easily if he should ever need to use it. With the constant expansion of knowledge examination syllabuses should be frequently revised, and something left out to make room for the new. Much of geometrical optics would seem to be overdue for omission.

The collections of examples at the end of each chapter form a valuable part of the book, and the answers to these are provided. B. H. B.

Physics of the Earth's Interior. By Beno Gutenberg. (Academic Press.) [Pp. 226.] Price $8.50.

This book is the first volume of the *International Geophysics Series*. It was published a few weeks before the lamented death of its author. For 50 years he has been not only one of the foremost workers in seismology, but also the author and editor of books bringing together and summarising our knowledge about the earth. The first of these was the enormous *Handbuch der Geophysik*. In this the wonder was that, even in Germany, so much could be written about a subject of which so little was known. The present book gives an admirable review of all that is now known about the inside of the earth in a mere 226 pages.

The subject is the interior of the earth; in keeping with this, topics connected with the crust of the earth, such as mountain building and isostasy are concentrated in one chapter near the start of the book. The main theme is the deduction of the properties and state of the materials within the earth from the study of seismology, gravity and other physical observations at the surface. The detail with which the various topics are treated has been influenced by Gutenberg's own interests ; the emphasis throughout is strongly on the physical side, chemical considerations and even the chemical nature of the materials concerned being barely mentioned.

The book should form a valuable introduction to the study of the earth's interior and a starting point from which the reader can appreciate the papers appearing in the journals. E. C. B.

Les Traceurs Radioactifs en Métallurgie Physique. By C. Leymonie. (Dunod.) [Pp. 240.] Price 32 NF, about £2 6*s*.

This is an excellent little book dealing with the use of radioactive tracers in metallurgy and metal physics. About one-third of the book is devoted to the measurement of diffusion coefficients and many excellent tables of values are included and an adequate discussion given of the various values obtained. This will make it an excellent reference for the latest values up to about the end of 1958. Chapters are also devoted to the study of segration in castings and in the solid state, to corrosion and oxidation of metals and to the study of the equilibrium between vapour and a condensed phase. Some new points are made in discussing the results of various workers and the author is to be congratulated on his familiarity with Russian work.

This book will appeal to the specialist and would be of use to anyone interested in applying tracer techniques. However, it is expensive for what it contains. The preparation is good but there are a number of misprints and it is annoying to find the name of one very eminent physicist continuously mis-spelt. A. K.

Introduction to Mathematical Physics. By William Band. (Princeton, N.J.: Van Nostrand Co. Inc.) [Pp. 326.] Price £2 14*s*. 6*d*.

This book of about 325 pages surveys most of the main topics of mathematical physics. Starting from vector and tensor analysis, it works through the dynamics of continuous media to the kinetic theory of gases and classical electrodynamics. The last third of the book is concerned with the theory of relativity and wave mechanics.

No student would expect to learn so many subjects by reading so few pages. However, the book is clearly written, and it is certainly of value as a reference book or dictionary of mathematical physics in which the initiated can find concise discussion and useful formulae. J. H.

Theory of Elasticity. By L. D. Landau and E. M. Lifshitz. Translated by J. B. Sykes and W. H. Reid. (Pergamon Press, 1959.) [Pp. 134.] Price £2.

This impressive book is Volume VII of the splendid series of texts on Theoretical Physics by Landau and Lifshitz. It deals concisely with a restricted number of topics which have been selected primarily on account of their interest to physicists.

In Chapter I the authors derive the fundamental equations of infinitesimal elastic theory, under both isothermal and adiabatic conditions, and include a brief discussion of the elastic properties of crystals. Chapter II gives an account of the equilibrium of rods and plates, deriving the basic equations from first principles. Chapter III deals with elastic waves in isotropic and anisotropic media, surface waves, and the vibration of rods and plates. Chapter IV contains sections on thermal conduction and viscosity in solids, and on the absorption of sound.

Throughout the book the theory is illustrated by well-chosen problems (about 80 in all), in which the method of attack is sketched and the result quoted but left for the reader to derive. This method enables the authors to pack in an enormous amount of material of great interest.

The reader is assumed to be on familiar terms with vectors, tensors, potential theory, and thermodynamics. Unsuitable for a beginner, the book will be of great value, in its power and freshness, to readers already acquainted with the subject. The translation is excellent and the layout clear and pleasing.

E. R. L.

The Classical Theory of Fields. (Course of Theoretical Physics, Vol. 2.) By L. D. Landau and E. M. Lifshitz. Translated by Morton Hamermesh. (Addison-Wesley Publishing Co. Inc. and Pergamon Press.) [Pp. 354.] Price £3 10*s*.

The second edition of the second volume of the authors' Course in Theoretical Physics was excellently translated in 1951, and is now re-issued in a binding uniform with the other volumes. In the first forty pages, the transformations and mechanical equations of special relativity are deduced from the principles of a finite invariant maximum signal velocity and of least action, while in the rest of the book, the electromagnetic and gravitational fields which carry the signals are discussed. The equations of motion of the fields and of particles in the fields are derived from the action principle and invariance considerations, and the Riemannian world geometry necessary for the gravitational case is explained very clearly. There are applications, or rather specializations, to static solutions, wave motion (including, in a chapter on optics, the geometrical limit and examples of diffraction) and radiation problems.

The treatment of the two fields in the same way is logical and illuminating, particularly since it is uncommon in text-books in this country. The book gives an impression of formality at a first reading, which is partly due to the nature of the subject and the deductive presentation; but in fact, the physically interesting applications are treated quite fully, being disguised by the label 'problems' and small print. This possibly reflects a different method of teaching in Russia. The volume's place in the Course as a whole will become clearer when the volume on macroscopic electrodynamics appears. At present one can say that it forms very valuable additional reading to a course on electromagnetic theory, and a first-rate introduction to the rather esoteric subject, as it is often considered, of general relativity. D. J. C.

Recent Research in Molecular Beams. Edited by I. Esterman. (New York: Academic Press.) First edition. [Pp. 190, 80 diagrams, 15 tables.] Price £2 12*s*.

The molecular beam technique has progressed a long way since the basic principles were laid down by Otto Stern and his collaborators in Hamberg in the early 1920's, and most of the problems listed by Stern at that time as suitable for molecular beam investigation have now been solved with considerable success by techniques which can be traced back to roots planted during the early period. This volume contains a collection of ten papers, all of them written by research workers active in the fields concerned, dedicated to Otto Stern on the occasion of his 70th birthday as a public recognition of the way they have been stimulated by his personality and his work.

In the first paper I. Estermann reviews the early molecular beam work in Hamburg and traces the development of the technique in the 1930's. Recent research with radioactive atoms is reviewed in papers by W. Nierenberg and

V. Cohen, and various aspects of accurate atomic and nuclear resonance experiments are covered in three papers by V. Hughes, P. Kusch and N. Ramsey. Applications of the beam technique to chemistry are discussed by S. Datz and E. Taylor, scattering at solid surfaces is reviewed by F. C. Hurlbut and new work on the velocity distribution in atomic potassium beams is described by P. Marcus and J. McFree. The final paper is on a Stern-Gerlach experiment with polarised neutrons.

The treatment in most of the papers is by no means comprehensive but the book should be very useful to the beam specialists as an addition to N. Ramsey's text-book on the subject. The general reader will find the reviews an excellent source of recent data and an introduction to modern beam techniques.

K. F. S.

Introduction to Quantum Field Theory. By F. Mandl. (Interscience Publishers.) [Pp. 202.] Price £1 14*s.*

The many textbooks now in existence dealing with quantum field theory are mainly addressed to the elementary particle physicist and develop the subject in considerable detail. Here is a book treating the basic ideas of second quantization, Feynman graphs, and renormalization theory, in as simple a manner as possible, accurately in terms of its level of sophistication, and with great clarity. It will serve as simple first reading for everyone and as a convenient account of field theory techniques for those to whom the subject is an occasional aid rather than a prime interest. This reviewer's only regret is that more attention has not been given to the qualitative ideas that underly the field theoretic formalism, and in particular to the nature of the vacuum. The backdrop of modern physics is not an empty void but a chaos of fluctuations and most of the characteristic field theory phenomena find their origin in this fact.

J. C. P.

Analysis of Deformation. Vol. IV. Waves and Vibrations. By K. H. Swainger. (London: Chapman & Hall, Ltd., 1959.) [Pp. xxvii+370.] Price £3 15*s.*

Dr. Swainger believes that classical theories of elasticity, plasticity and fluid flow are wrong at various points. This is the fourth volume of his attempt to correct them. Unfortunately he has cast his work into a form which might have been designed to give maximum difficulty to the reader. He invents his own notation for every quantity concerned (the summary of "Principal Notation" occupies six pages), uses dyadics, 'triadics' and 'quadadics' instead of Fensors, employs words with novel restricted meanings of his own, and writes in a contorted and obscure style.

The present volume deals with body and surface waves in isotropic fluids and elastic, visco-elastic or plastic solids. There is also a long chapter on geophysics, containing the author's theories of the constitution of the earth.

E. R. L.

[*The Editors do not hold themselves responsible for the views expressed by their correspondents.*]

Fig. 1

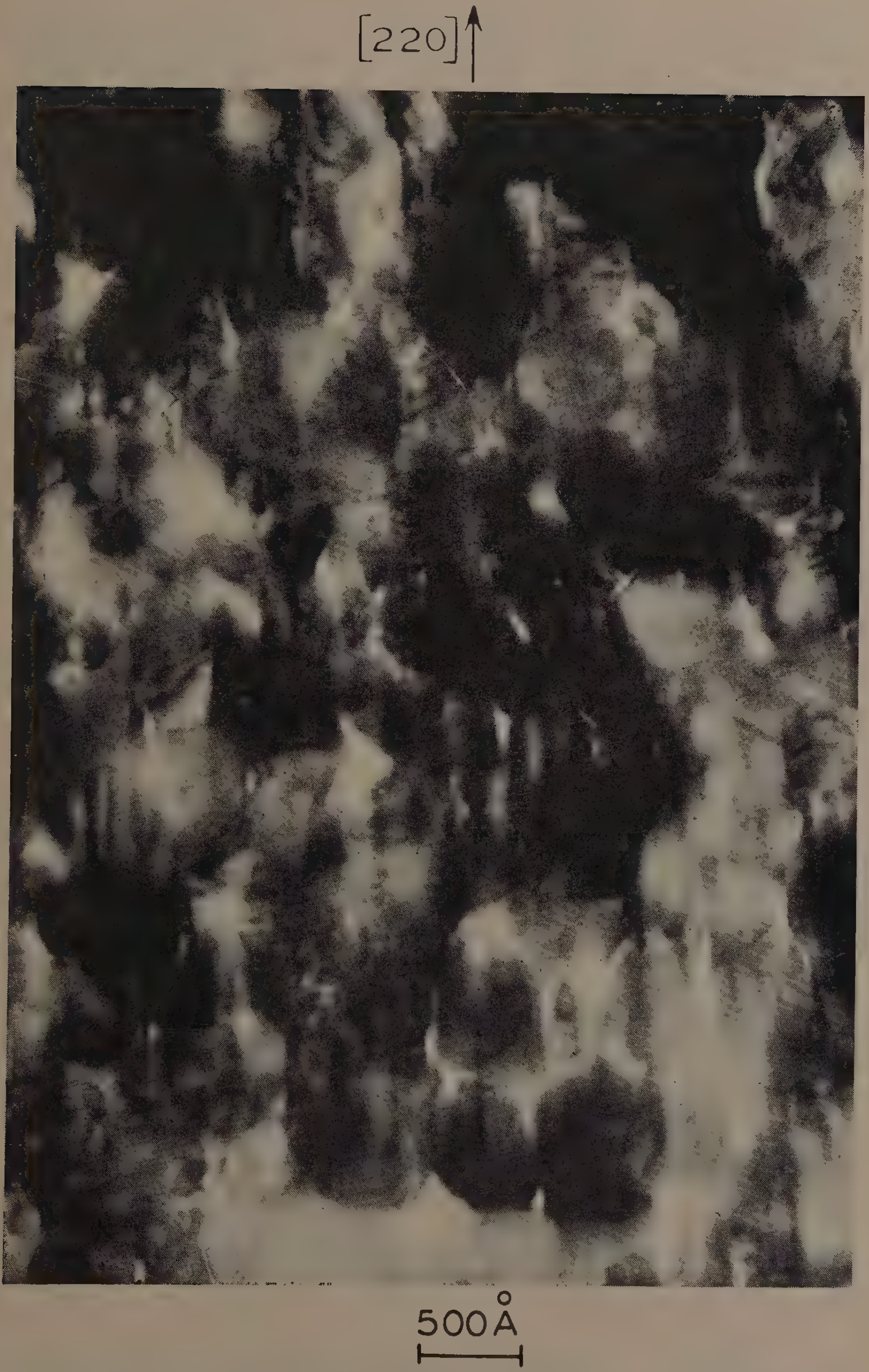

Electron micrograph of 'thick film' of 81%Ni–19%Fe. ~600 Å deposit on NaCl (100) at 320°c. Bright field illumination. Electronic magnification : 40 000×.

Fig. 2

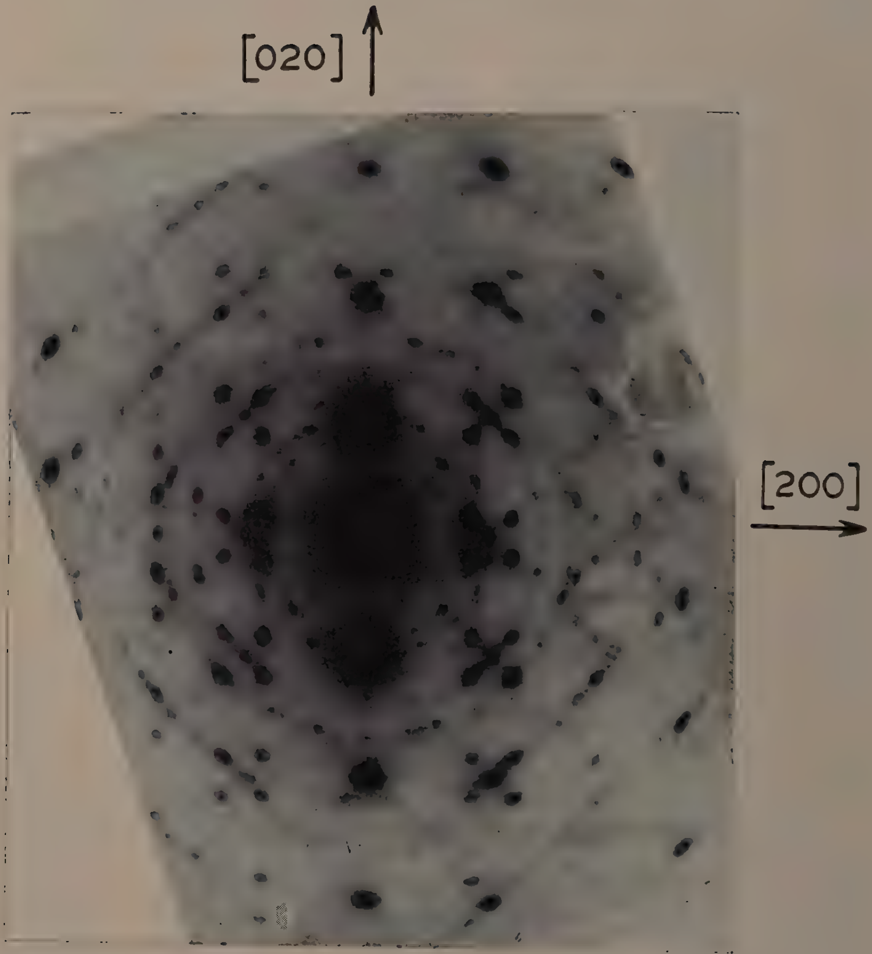

Selected area diffraction of 81%Ni–19%Fe film. About 7° inclination to [001] zone axis. Many extra spots caused by twin lattices and double diffraction. Asymmetry of pattern caused by specimen deformation and 'effective aperture' of the electron microscope.

Fig. 8

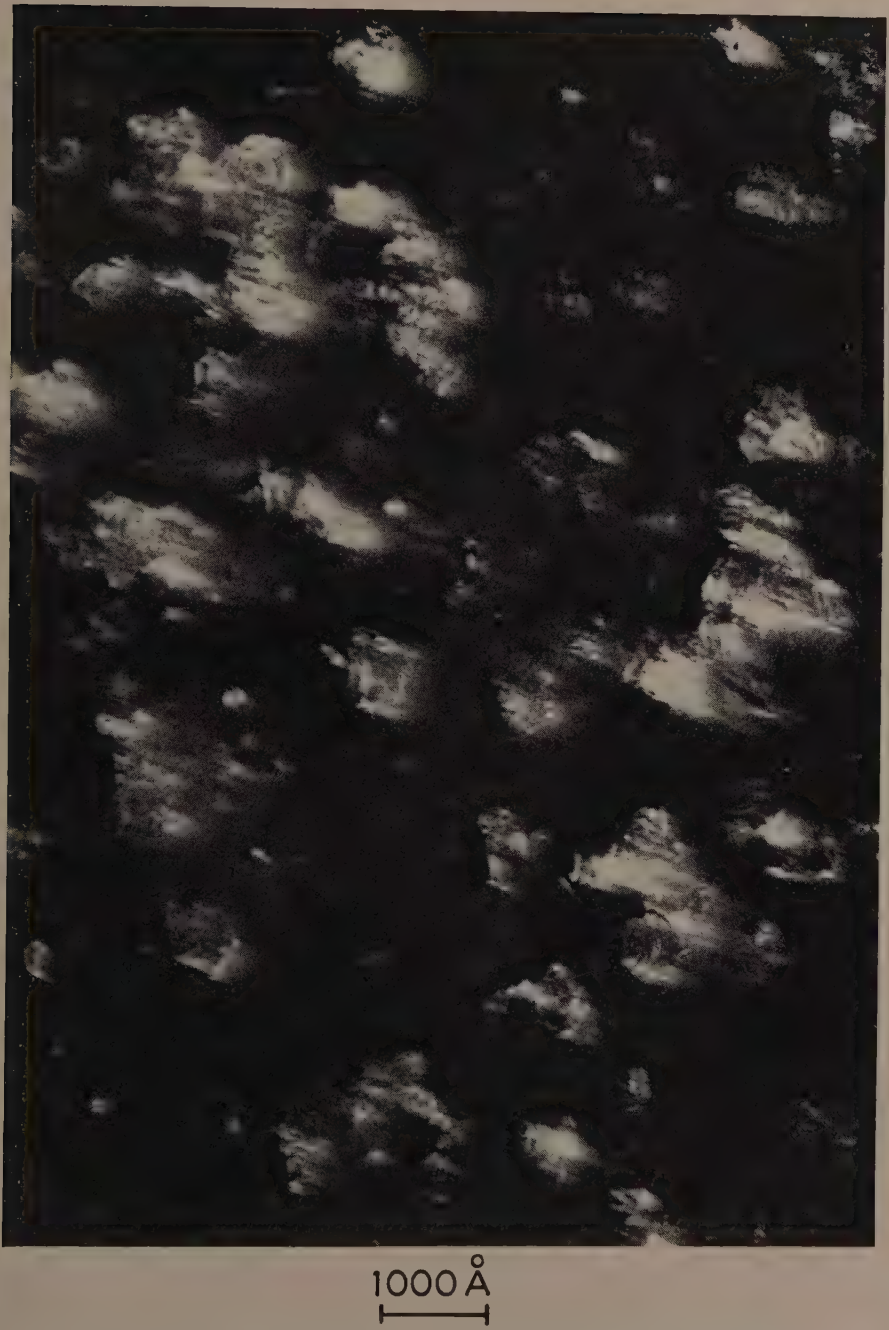

Electron micrograph of 'thick film' of 81%Ni–19%Fe. ~600 Å deposit on NaCl (100) at 320°c. Dark field illumination from both twin spots and double diffraction spots. Electronic magnification: 20 000 ×.

Fig. 9

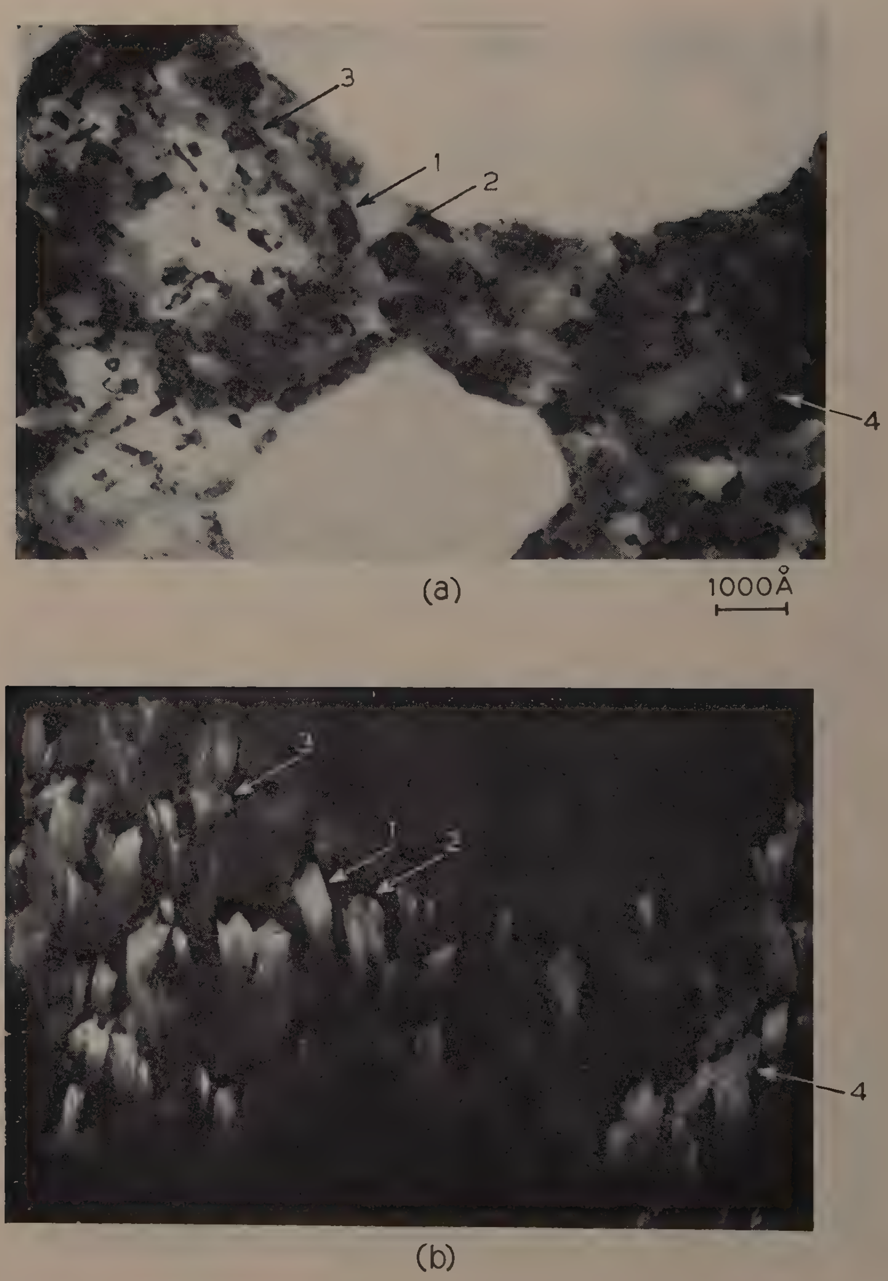

(a)

(b)

Electron micrographs of 'thick film' of 81%Ni–19%Fe after etching to 100–200 Å thickness. Electronic magnification: 20 000×. (*a*) Bright field illumination. (*b*) Dark field illumination from twin spots from two of the four twinned lattices. Several twinned regions indicated by numbered arrows.

Fig. 10

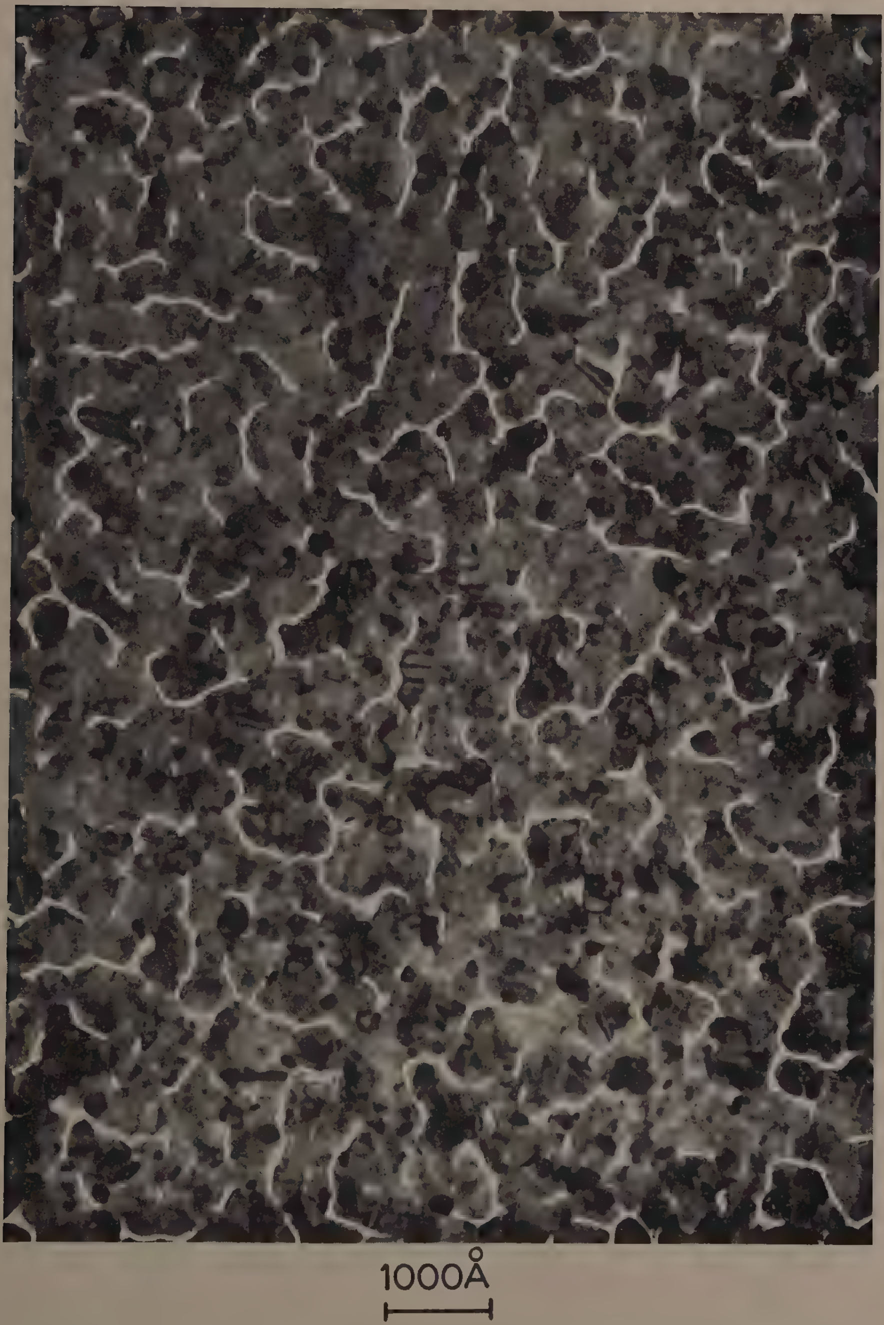

Electron micrograph of ‘thin film’ of 81%Ni–19%Fe. ~100–200 Å deposit on NaCl (100) at 320°c. Bright field illumination. Electronic magnification: 20 000×. A crystallite made up of twin bands is located near the centre of the micrograph.

Fig. 11

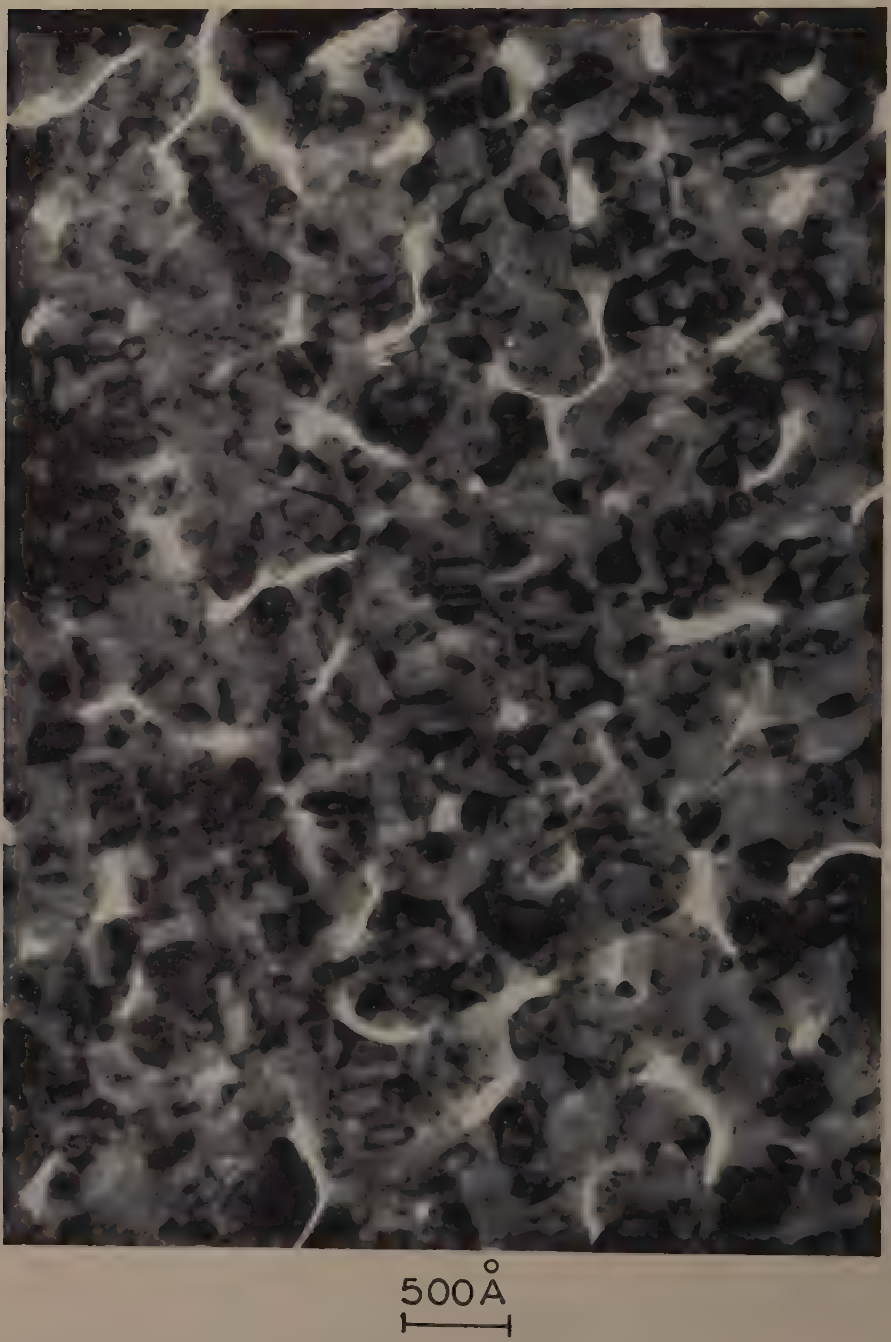

Electron micrograph of 'thin film' of 81%Ni–19%Fe. ~100–200 Å deposit on NaCl (100) at 320 c. Bright field illumination. Electronic magnification: 40 000 ×.

Fig. 11

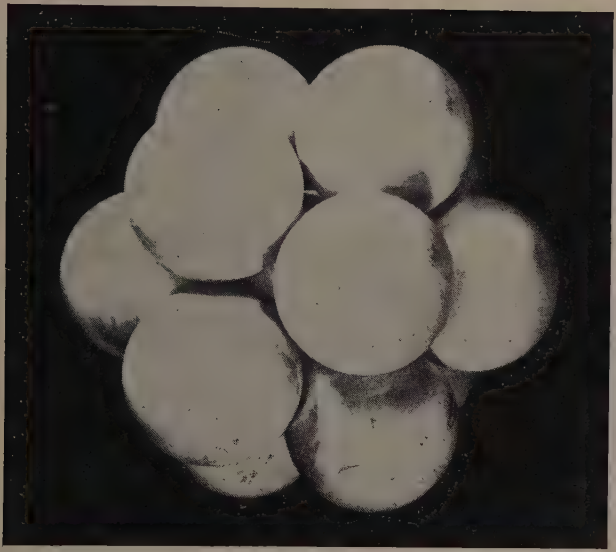

The Frank unit.

Fig. 12

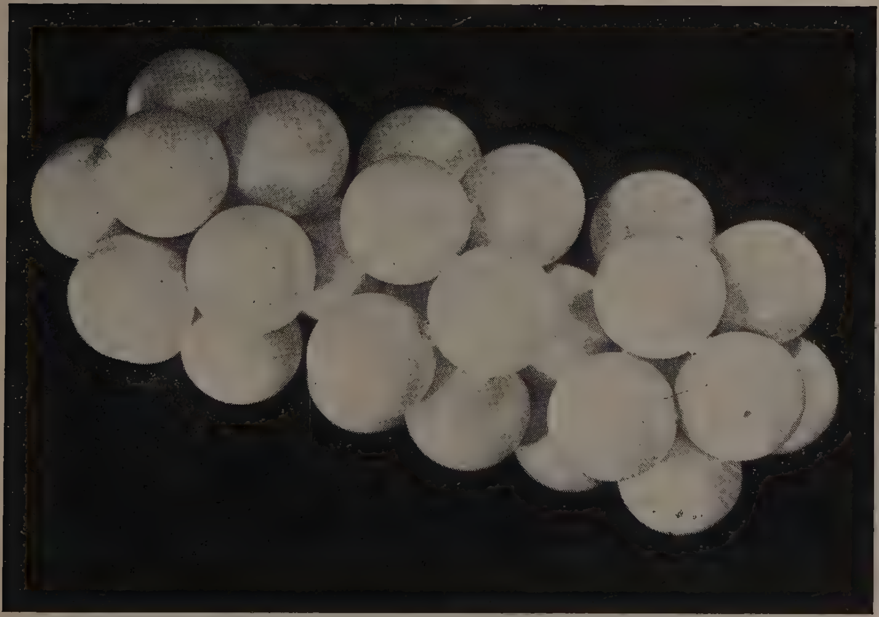

To illustrate the formation of pentagonal chains.

Fig. 1

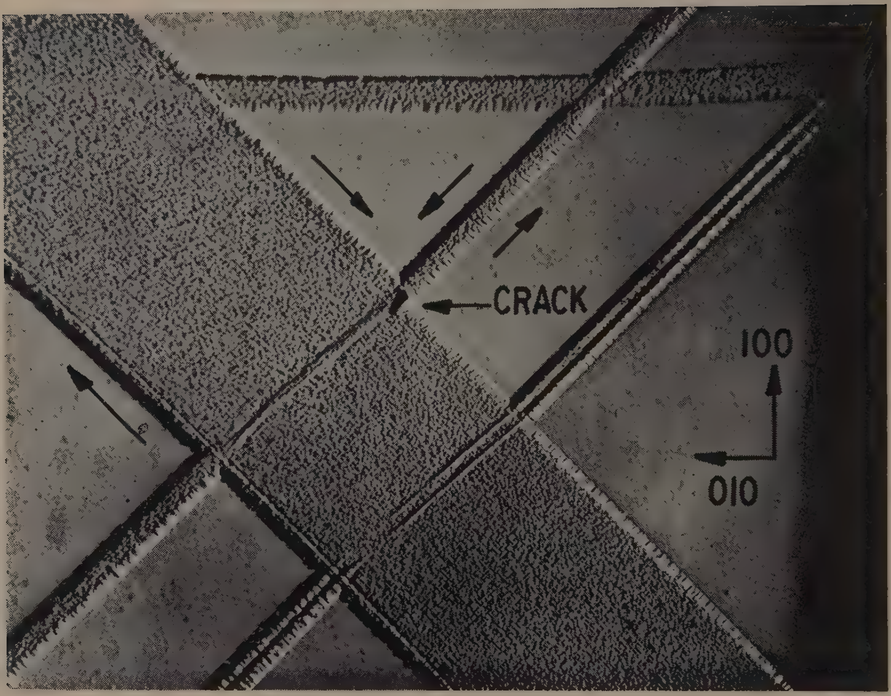

Crack at the intersection of glide bands in a MgO single crystal. The arrows alongside the bands indicate the shear within the bands. The crack has not been re-touched. Magnification: 500.

Fig. 1

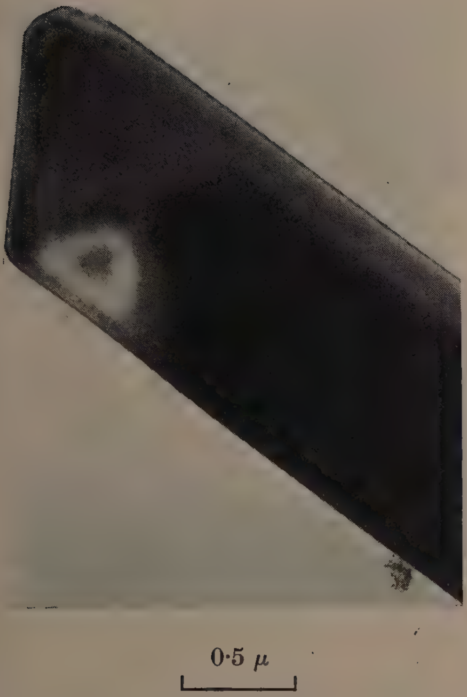

Dislocation-free zinc whisker. The basal plane is parallel to the plane of the paper.

Fig. 2

Dislocation-free zinc platelet. The growth steps are parallel to $\langle 11\bar{2}0 \rangle$ directions.

Fig. 3

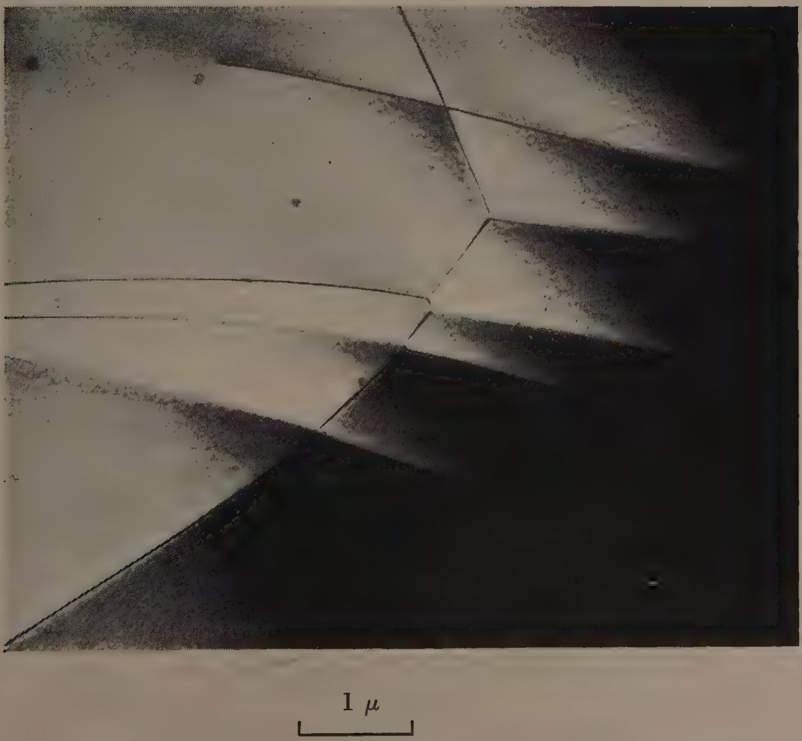

Dislocations, lying predominantly in basal planes, in a zinc platelet.

Some Effects of Vibration on the Internal Friction of Sodium Chloride†

By R. W. WHITWORTH‡
Department of Physical Metallurgy, University of Birmingham

[Received December 23, 1959]

ABSTRACT

The room temperature internal friction of single crystals of NaCl vibrating at a frequency of 90 kc/s has been measured at strain amplitudes up to $2\cdot7\times10^{-4}$. The damping of plastically deformed crystals increased with increasing strain amplitude, and can be attributed to the motion of the dislocations introduced by the deformation. Vibration of specimens at high amplitudes changed their internal friction in three distinct ways.

(*a*) When deformed specimens were annealed at 100 to 200°C the internal friction was reduced, but subsequent vibration at high amplitudes caused the damping to rise towards its value before annealing.

(*b*) While lightly deformed crystals were being driven at very high amplitudes the damping was observed to decrease; the value at lower amplitudes was afterwards found to be less than that determined before this vibration.

(*c*) At the highest amplitudes attained in these experiments new dislocations were produced in the crystals, and their presence has been shown by etching experiments; an increase in the damping was associated with the introduction of these dislocations.

These observations are discussed in terms of current theories.

§ 1. INTRODUCTION

THE internal friction of metals and ionic crystals in vibration at frequencies of 10–100 kc/s has been studied by many workers, and has been reviewed by Nowick (1953). The damping is normally found to rise with increasing strain amplitude in the specimen, and following the suggestion of Read (1940), a considerable amount of evidence has been produced to show that in many cases this internal friction is due to the motion of dislocations. Various theories, such as those of Granato and Lücke (1956), Nowick (1954) and Weertman (1955), have been proposed to explain how the dislocations give rise to damping, but the details of this subject are not yet fully understood.

One effect which is often reported in experiments on this type of damping is a change in the internal friction produced by driving the specimens at sufficiently high strain amplitudes. Most of these observations fall into one of the following categories of behaviour.

---

† Communicated by the Author.
‡ Now at Department of Metallurgy, Imperial College, London, S.W.7.

I. After vibrating the specimen at a strain amplitude in the amplitude-dependent region the internal friction at lower amplitudes is increased above its original value (e.g. Swift and Richardson (1947) in Zn, and Beshers (1959) in Cu).

II. The internal friction is reproducible in the amplitude-dependent region until the strain amplitude is raised above some high critical value; the damping then rises very steeply with amplitude, and is subsequently found to have increased at all lower amplitudes (e.g. Mason (1956) in Pb).

III. As the driving force applied to the specimen is increased the amplitude of resonance rises to a maximum value and then starts to fall, resulting in a double valued decrement *vs.* strain amplitude curve (e.g. Frankl (1953) in NaCl, and Birnbaum (1955) in Ag and Al).

IV. The internal friction rises with increasing strain amplitude, but when the amplitude is subsequently reduced the damping continues to rise (e.g. Hiki (1958) in Pb).

V. In some fatigue tests on specimens vibrating at 100–1000 c/s the internal friction is found to decrease with time during the early part of the test (e.g. Wadsworth (1957) in Cu, Al and Cd, and Broom and Ham (1959) in Cu).

The present paper reports a series of experiments on the internal friction of single crystals of sodium chloride, in which vibration of the specimens at high amplitudes has been observed to change the damping in three quite distinct ways. An increase in the damping of type I has been observed in deformed crystals which had been lightly annealed, and this effect is attributed to the motion of dislocations which were pinned during the anneal. Increases of type II have also been observed, and are shown to be due to the creation of new dislocations. The third effect is a decrease in the damping of lightly deformed crystals vibrating at sufficiently high amplitudes, and this may be similar to the changes of type V previously observed only at lower frequencies. This classification of effects is purely phenomenological, and is not intended to imply that the explanations are necessarily the same in all materials.

Before describing these changes of damping in detail it is necessary to consider the internal friction of sodium chloride observed under conditions where it is not changed by vibration. This is done in § 3, where results of measurements over a wide range of strain amplitudes are reported and discussed in terms of existing theories. The changes in this internal friction which can be produced by vibration are then described in § 4, and some possible interpretations of these effects are considered in § 5.

Previous experiments on the internal friction of sodium chloride have been reported in detail by Frankl (1953), who observed some increases in damping as a result of vibration, and also by Gordon and Nowick (1956), though they did not use high enough strain amplitudes to produce any changes in the damping. Birnbaum (1955) has presented some complicated results on one specimen with a high impurity content.

§ 2. EXPERIMENTAL DETAILS

All the internal friction measurements described here were made on specimens vibrating in their fundamental longitudinal mode at frequencies of about 90 kc/s and at temperatures between 18 and 25°c. The apparatus used was a three-component piezoelectric resonator similar to that described by Marx (1951). It consists of two $-18{\cdot}5°$ X-cut quartz bars and the sodium chloride specimen, all cut to have the same longitudinal resonant frequency, cemented end to end, and suspended *in vacuo*. This resonator is driven by applying a variable frequency a.c. potential difference, V_d, to plating on the X faces of the central quartz crystal, and the potential difference developed across plating on the centre of the X faces of the other quartz crystal is measured with a high impedance valve voltmeter. This p.d. is proportional to the amplitude of vibration of the resonator, and reaches a maximum value, V_g, when the frequency of the driving voltage equals the resonant frequency of the system. The value of V_d/V_g is then proportional to the decrement of the resonator, and from it the decrement, δ, of the specimen can be calculated, after allowing for the damping of the quartz bars, which is equivalent to a specimen decrement of 9×10^{-5}. In order to obtain absolute values of δ and the maximum strain amplitude in the specimen, ϵ, the resonator was calibrated in an a.c. bridge as indicated by Marx; however, there may be errors in this calibration which could lead to systematic errors of about 40% in all the values of δ and ϵ. Nevertheless, the relative accuracy of individual damping measurements should be about ± 2%, except at the lowest values of δ, where it is difficult to keep the frequency on resonance and the damping of the quartz bars is larger than that of the specimen. The frequency control of the oscillator was only sensitive enough to measure modulus changes in heavily deformed crystals.

As the results obtained sometimes depended on the time for which a crystal was vibrated, the following procedure was adopted unless otherwise stated. At some definite time a predetermined a.c. voltage between 0·001 and 100 v was applied to the driver crystal from a low impedance source. During the following minute the frequency was adjusted in order to find the maximum p.d. across the gauge crystal, and if this changed appreciably during the minute the change was recorded. At the end of the minute the driving voltage was turned off, and one minute later the next larger driving voltage was applied. This procedure was repeated until the highest amplitude to be used was reached.

All quantitative results quoted in this paper were obtained using specimens cleaved from one large single crystal grown in this laboratory by the Kyropoulos method. The crystal was pulled from a melt of Analar grade sodium chloride contained in a silica vessel, and it seems probable that the total impurity concentration in the specimens was less than about 0·01%. Qualitatively similar results have also been obtained on the damping of specimens taken from three other crystals including one from the Harshaw Chemical Company. The specimens had {100} faces, and measured about $0{\cdot}5 \times 0{\cdot}5 \times 2{\cdot}52$ cm in size, the length being chosen to give the correct resonant frequency to within 0·3% when the crystal was mounted on the resonator. After cleavage the specimens were annealed for about 1 hour at 650°c to remove the internal stresses produced by the cleavage damage, and then cooled to room temperature over a period of two days.

The joints between the specimens and the quartz bar were made with beeswax, melted at about 70°c in a stream of hot air; using great care joints can be made in this manner with very little associated plastic deformation of the specimens. The joints contributed only a small amount to the damping of the resonator, but, as this contribution is not known, little reliance can be placed on the measured values of the amplitude-independent decrement of the crystals at low strain amplitudes. The joints do not appear to give rise to any significant amplitude-dependent damping.

§ 3. THE INTERNAL FRICTION OF SODIUM CHLORIDE

3.1. *Experimental Results*

The internal friction of specimens annealed at 650°c and slowly cooled was found to be very low, that of a typical crystal being 10^{-5} at low amplitudes, and rising to about 10^{-4} at $\epsilon = 4 \times 10^{-5}$. However, using even great care it was impossible to avoid deforming the crystal very slightly during mounting, and it is known that deformation gives rise to amplitude-dependent damping. This difficulty can be overcome in slightly impure crystals, which are less easily deformed, and in such crystals the damping was found to be independent of amplitude in this region. It therefore seems probable that the damping of a truly undeformed 'pure' crystal would also be amplitude-independent and so small as to be insignificantly different from zero when measured with the present apparatus.

Plastic deformation of such a pure annealed crystal increases its internal friction. This is shown by fig. 1, in which the decrement δ is given as a function of the strain amplitude ϵ for three typical specimens deformed in compression along their long axes. For convenience δ is plotted on a linear scale and ϵ on a logarithmic one. The plastic strain in each specimen is given below the figure, together with the stress required to produce this deformation and the actual magnitude of δ_0, the amplitude-independent decrement at the lowest amplitudes; δ_0 may however include an uncertain contribution from the beeswax joint. The measurements were made within 2 hours of the deformation of the specimens, and, after mounting, each specimen was vibrated at the highest amplitude to be used and then allowed to rest for 20 min before its damping was measured. This driving at high amplitude was found to produce an increase in δ_0, which disappeared in about 20 min, and measurements made over a period of a few hours after this treatment were reproducible to within a few per cent. On leaving the crystal to stand at room temperatures for several hours or days the value of δ was found to decrease at all amplitudes. A number of measurements were made on crystals other than those shown in fig. 1, and for the same amount of deformation the values of δ were found to be the same as those shown within a factor of about 2. There does not seem to be any simple connection between the value of δ_0 and the rate of rise of δ at the higher amplitudes.

Fig. 1

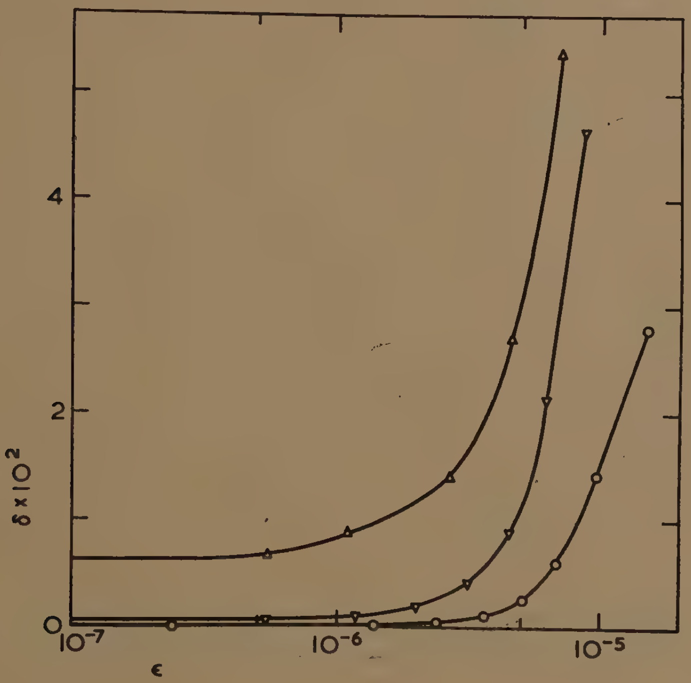

The internal friction of deformed crystals.

Symbol	Deformation %	Stress required g/mm²	δ_0
○	0·2	62	9×10^{-5}
▽	1·1	87	$5{\cdot}4 \times 10^{-4}$
△	6·7	400	$6{\cdot}2 \times 10^{-3}$

The effect of annealing a deformed crystal is to reduce its internal friction. The reduction occurs only very slowly at room temperature, but large effects can be obtained by annealing for an hour at 100 to 200°c. The magnitude of the reduction obtained by a given anneal varies between specimens cleaved from different melt grown crystals, and this suggests that the effect depends in some way on the impurities present. Similar decreases in damping are produced by irradiation with x-rays.

The motion of the dislocations which is believed to give rise to the integral friction observed in these experiments would also be expected to give rise to a decrease in the elastic modulus of the specimen, and this would produce a change in its resonant frequency. While the apparatus was not primarily designed to measure such frequency changes, it was found possible to make a few rough measurements of the way in which the resonant frequency varied with strain amplitude. These measurements show that when δ is greater than δ_0 the value of Young's modulus, E, is reduced by an amount ΔE below its value observed at the lowest amplitudes. For four specimens deformed between 4 and 7% the ratio $(\delta-\delta_0)/(\Delta E/E)$ was fairly constant, and took values between 1·0 and 2·2 for values of ϵ from 2×10^{-6} to 10^{-5}. For specimens deformed 1% and less the results are less reliable, but $(\delta-\delta_0)/(\Delta E/E)$ was found to lie between 2 and 6 in the two crystals where it was measured.

3.2. *Discussion of the Damping Mechanism*

The internal friction of sodium chloride measured in experiments of this type is due to the motion of those dislocations which are introduced into the specimen after it has been annealed. This conclusion was reached by Gordon and Nowick (1956), and is confirmed by the present results, which show that deformation increases the very small internal friction of an annealed crystal. This damping can be subsequently reduced by annealing the specimen or irradiating it with x-rays. The effect of such treatments on the ease with which the dislocations move has been studied by R. W. Davidge (private communication), using an etching technique similar to that of Johnston and Gilman (1959, § III E). His results show that dislocations present before annealing do not move under a static or 90 kc/s stress, while those introduced after annealing move even on gentle handling of the specimen. The motion of these 'fresh' dislocations under an applied stress can be prevented by those annealing or irradiation treatments which also produce a considerable decrease in the internal friction.

Before considering the mechanism by which moving dislocations give rise to internal friction it is of interest to make a rough calculation of the distances through which the dislocations move in the vibrating crystal. In the Appendix it is shown that, when there is a total length of dislocation line Λ per unit volume which is capable of moving under the applied stress, the average amplitude of motion of the dislocations, x, at a strain amplitude ϵ, must satisfy the inequality

$$x \gtrsim \frac{2}{\pi}\frac{\epsilon\delta}{\Lambda b},$$

where b is the Burgers vector of the dislocations. Internal friction measurements have been made on two lightly deformed crystals which were subsequently etched in order to estimate Λ. In one of these crystals (for which further results will later be given in fig. 3) Λ was of the order of $2\times10^4\,\text{cm}^{-2}$, and it was found that $\delta=2{\cdot}4\times10^{-3}$ at $\epsilon=1{\cdot}5\times10^{-5}$; this gives a value of $x\gtrsim 800b$. In the other crystal Λ was of the order of $4\times10^5\,\text{cm}^{-2}$, and, again at $\epsilon=1{\cdot}5\times10^{-5}$, x was estimated to be $\gtrsim 160b$.

These results indicate that the model which must be used for the amplitude-dependent damping of these specimens is one in which dislocations can move large distances through the lattice. For this motion to be obtained by the bowing of loops against their line tension, loops of length at least $10^4 b$ would have to be able to move freely over the slip plane. It is difficult to estimate dislocation densities in the more heavily deformed specimens, but it seems probable that x is smaller in a heavily deformed crystal than in a lightly deformed one tested at the same strain amplitude.

No satisfactory empirical equation has been found which relates the internal friction determined in these experiments to the strain amplitude. However, it has been observed that for $\epsilon < 10^{-5}$, $(\delta - \delta_0)$ varies roughly as ϵ^n, with n varying from specimen to specimen between about 1·7 and 2·3. Coupled with the fact that $(\delta - \delta_0)/(\Delta E/E)$ lies between 1 and 6, this result is rather similar to that given by the simple phenomenological hysteresis model of Nowick (1950).

Various authors have proposed more detailed models to describe the internal friction of solids due to the motion of dislocations. The theory which has been studied in most detail is that of Granato and Lücke (1956), who consider the motion of dislocation loops which are pinned firmly at their ends and more weakly at points along their length. When a large-enough stress is applied some of these loops break away from their pinning points and move freely through the lattice, returning to their pinned positions when the stress falls to zero. Granato and Lücke have calculated the form of the variation of δ with ϵ to be expected on this model, and comparison of the present measurements with their theory shows that their equation is far from being satisfied in the amplitude-dependent region. This suggests that their model is not applicable to sodium chloride. Such a conclusion is to be expected when it is realized that the fresh dislocations probably lie on the slip planes in long loops rather than in a network in which loops are strongly pinned at their ends (cf. Gilman and Johnston 1957).

Nowick (1954) suggested that the internal friction of annealed and lightly deformed metals is due to the hysteresis in the motion of dislocation lines which is caused by their interaction with obstacles such as impurity atoms lying on the slip plane. Weertman (1955) has discussed this model in the case where the interaction between the dislocations and impurities is due to the long range elastic stresses around them, but rough calculations suggest that this elastic interaction is too small to account for the flow stress and damping of sodium chloride. However, a hysteresis model of the type considered by Nowick may be applicable in this case if the dislocations have a strong short range interaction with impurities, point defects, clusters, etc. distributed over the slip plane. The interaction is likely to be of a predominantly short range character if the binding energy arises mainly from electrostatic forces at the dislocation core, as has been shown to be the case for vacancies by Bassani and Thomson (1956).

In this model the defects which cause the pinning are assumed to be fairly immobile, and we will consider a long dislocation line lying in its slip plane at a position where it is pinned at a number of points along its length. When a stress is applied to the crystal the dislocation bows out between the pinning points, and may break away from some of them with or without the aid of thermal activation. However, it cannot move far before it reaches a defect on the slip plane, where it will probably become pinned; this will happen because the time period of atomic vibrations is much less than the time the dislocation takes to cross the defect (unless it is moving at a velocity near that of sound). Subsequently the dislocation may break away at this or at other pinning points, and so move through the lattice in a series of jumps. When the stress is reversed the dislocation will move in the reverse direction, but in general there is no reason why it should follow a path given by the reversed sequence of forward jumps, nor why it should return exactly to its original position. This motion of the dislocation line will give rise to hysteresis in the stress–strain curve in vibration and so to internal friction. Higher applied stresses will cause larger lengths of dislocation line to move, and the damping produced by this mechanism should therefore be amplitude-dependent. Provided the impurities etc. present are not too strongly clustered this model seems not unreasonable in comparison with the distances moved by the dislocations calculated above.

§ 4. CHANGES IN INTERNAL FRICTION PRODUCED BY VIBRATION

4.1. *Changes of Type I: Increases in the Damping of Annealed Crystals*

As has already been stated, the effect of annealing a deformed crystal is to decrease its internal friction. After annealing at a sufficiently high temperature the damping is reduced almost to zero, but after a low temperature anneal the damping may still be fairly large and amplitude-dependent. Many such lightly annealed crystals have been vibrated on the resonator at amplitudes in the amplitude-dependent region, and it has been found that after such treatment the damping at lower amplitudes is greater than that observed immediately after the anneal. This is an effect similar to type I referred to in the Introduction.

Figure 2 (*a*, *b*, *c* and *d*) shows the results of measurements made to study this effect on four specimens which were annealed at different temperatures between 100 and 170°C. Each specimen was first deformed by 0·2%, mounted on the resonator, and vibrated at the highest amplitude attainable. After an interval of 20 min, δ was measured as a function of ϵ, and the results are shown in the upper curve on the appropriate figure. The crystal was then removed from the resonator, heated to its annealing temperature, held there for 1 hour, furnace cooled in 1 to 2 hours, and carefully remounted. Internal friction measurements were then made as a function of increasing ϵ, and gave the results shown by the lowest curve for each specimen. These curves show that the damping was reduced by the annealing, and also that it rose abnormally rapidly at high amplitudes; in some cases it was even observed to rise with time during measurements at a constant driving voltage. 20 min after taking these readings the damping was again measured, and the results were found to lie between those obtained before and after annealing. They are shown by the middle curves on the figure, and, provided the amplitude was not increased above its value at the end of the previous series of measurements, these curves were fairly reproducible. However, if the amplitude was raised above that used previously, the damping at all lower amplitudes was once more increased. This is shown in fig. 2 (*b*). After annealing this specimen, its damping was measured, and the results are shown by the points △. These

Fig. 2

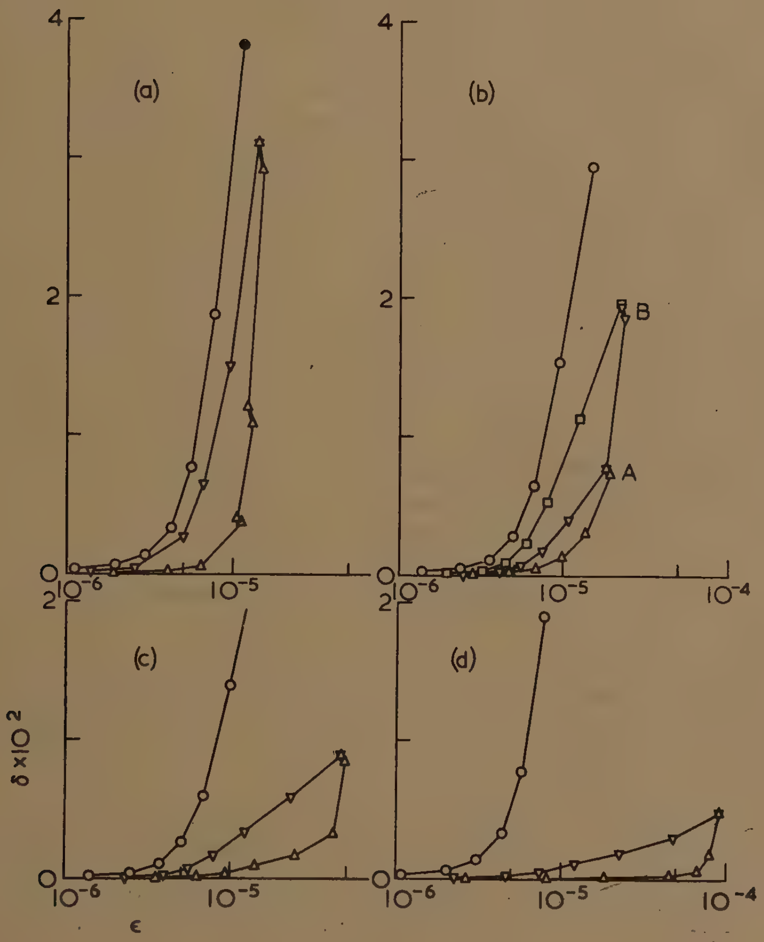

The internal friction of specimens deformed 0·2%, annealed and vibrated on the resonator. ○, before anneal; △, after 1 hour anneal at temperature stated below; ▽, repeat measurements; □, (only) second repeat.

Annealing temperatures: (*a*) 102°c, (*b*) 127°c, (*c*) 146°c, (*d*) 167°c.

Thick lines with negative slope indicate changes of δ during measurements at fixed V_d.

measurements were stopped at the point marked A, and the next series of readings gave the points ▽. In this series the crystal was driven to the point B where the amplitude is higher than at A, and this further increased the damping so that subsequent measurements yielded the points □.

Several specimens were tested in addition to those shown in fig. 2. One of these was deformed 0·2% and annealed for 1 hour at 198°c, after which the damping in the first series of measurements only exceeded 10^{-4} at values of ϵ greater than 10^{-4}. Another crystal was annealed for 20 hours at 123°c, and gave results fairly similar to those obtained after a 1 hour anneal at 146°c. Experiments were also performed on specimens deformed 1·1% and 4·3% and then annealed; these too showed an increase in the damping produced by vibration.

The damping of a deformed crystal can be reduced by x-irradiation as well as by annealing, and to study this a deformed crystal was lightly irradiated, bleached and tested on the resonator. When this specimen was vibrated at a high-enough amplitude, its damping was increased in just the same manner as that of an annealed crystal. This effect in x-irradiated crystals has previously been observed by Frankl (1953).

In the above experiments increases in damping produced by vibration have only been observed in crystals in which the damping had previously been reduced in some way; moreover the damping was never increased above that found in the specimen immediately after deformation. It will be recalled, however, that all measurements reported on such freshly deformed crystals were made after the specimen had been driven at the highest amplitude to be used. This was done because there is a small increase in the damping on first testing the specimen after mounting,and this may amount to a change in δ of up to 20%. Subsidiary experiments suggest that this increase in δ occurs as a consequence of the slight anneal given to the crystal in mounting it at about 70°c.

4.2. *Changes of Type V: Decreases in Damping at High Amplitudes*

This section describes some decreases in the damping of freshly deformed crystals, which have been observed to occur when specimens are vibrated at very high amplitudes. The strain amplitude at which measurements can be made in a deformed crystal is limited by the magnitude of its internal friction, and so it has only been possible to observe these decreases in specimens in which the density of fresh dislocations was fairly low. Figure 3 shows some results obtained on one such specimen. It was deformed longitudinally in compression under a stress of 26 g/mm², when slip occurred in some 50 slip bands, and etching showed that the density of dislocations introduced was of the order of 2×10^4 cm^{-2}. After mounting, the damping was measured as a function of increasing ϵ, giving the results shown in the upper curve. At amplitudes higher than 3×10^{-5} the value of ϵ rose at constant driving voltage, corresponding to a decrease in δ during the measurements; these decreases are shown on the figure by thick lines against which the time taken for the change is marked. Points linked by thin lines correspond to changes in the driving voltage, but there may be some decrease in δ before a reading can be made. Where it is felt that an appreciable decrease has occurred the line is shown broken. The rate of fall of δ has not been studied in detail. However, it was noticed that at constant driving voltage ϵ rose slowly to a value of about $1{\cdot}3 \times 10^{-4}$, and then at an increasing rate until it reached about $2{\cdot}7 \times 10^{-4}$; after this little further change occurred. When this point had been reached a new series of measurements was made as a function of increasing ϵ. These are plotted as the lower curve in fig. 3, and show that the damping has been reduced by a large amount as a result of driving the specimen at high amplitudes.

Fig. 3

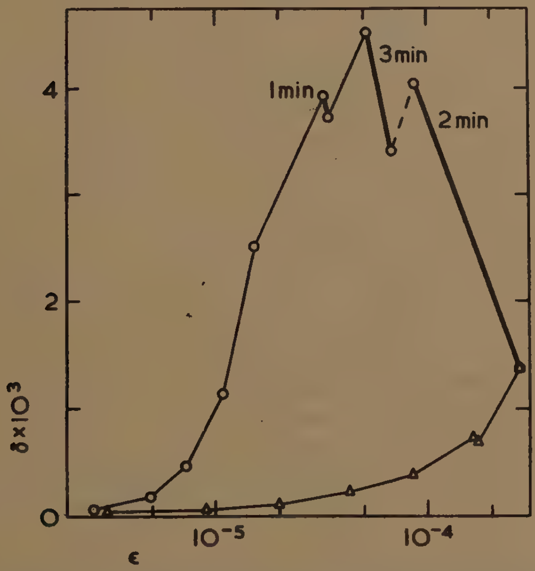

The internal friction at high amplitudes of a specimen lightly deformed in compression. ○, first series of measurements; △, subsequent measurements.

This reduction in damping has been observed in many specimens, including both lightly deformed crystals and crystals which were heavily deformed over a small region. The results of a more detailed series of measurements on a specimen of the latter type are shown in fig. 4. This specimen was locally deformed by dropping a 5 mm diameter steel ball on to the centre of one face from a height of 9·5 cm. It was then mounted on the resonator, and five series of damping measurements were made as a function of increasing ϵ, each series being taken to a higher final amplitude than the previous one. The first series stopped at the point A, and the results of the second series show that a small type I increase in damping occurred during the first measurements. The second series extended to the point B, where the hardening process was interrupted; this left the crystal in a state where its damping was given by the third curve, which joins the second at B. An increase in the driving voltage at B produced very rapid hardening to the point C, and the fourth series of readings then gave the lowest values of δ observed in this specimen. A further increase in the driving voltage at C produced very little change in ϵ, the value of δ rising to that at D. A corresponding increase was then found in all values of δ determined in the fifth and final series of measurements.

Fig. 4

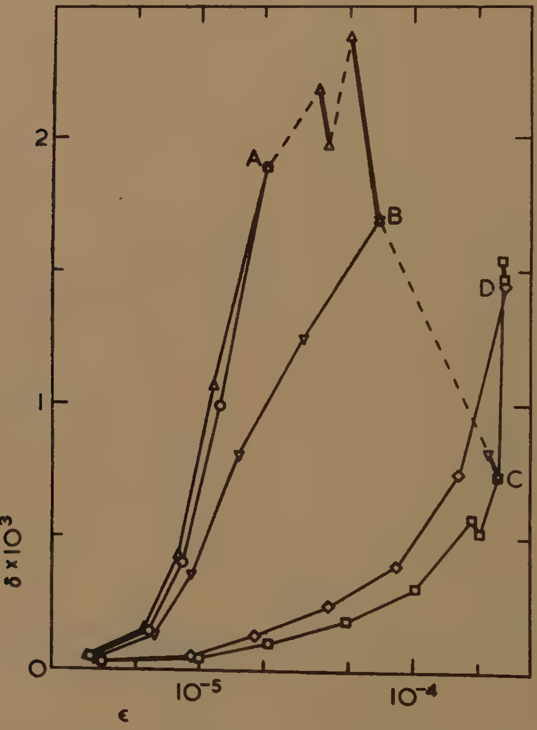

Five series of damping measurements on a locally deformed crystal. ○, 1st series to A, △, 2nd series to B, ▽, 3rd series to C, □, 4th series to D, ◇, 5th series to D,

4.3. *Changes of Type II: Increase in Damping and Creation of New Dislocations at the Highest Amplitudes*

Whenever a specimen was driven at a strain amplitude of about $2 \cdot 7 \times 10^{-4}$ its internal friction was increased at that and all lower amplitudes. A typical example of this is the rise of damping observed between points C and D in fig. 4, which has just been described. The effect has also been observed in specimens which were not given any deformation before testing, and in all cases the stress amplitude ($\sim 1100\,\mathrm{g/mm^2}$) at which the increase occurred was constant to within a few per cent. This increase in damping is similar to the type II effects mentioned in the Introduction.

Some simple etching experiments have been performed which show that these increases in damping are associated with the creation of new dislocations in the crystals. The specimens were etched using a method developed by R. W. Davidge (private communication), which is believed to reveal all the dislocations in the crystal; the interpretation of the observations is in many ways similar to that of Gilman and Johnston (1957). Fully annealed specimens were carefully mounted on the resonator and etched; they were then vibrated at a high amplitude and re-etched. After this treatment a large pyramidal etch pit indicates the position of a dislocation present in the same place before and after vibration; a large flat-bottomed pit represents the original position of a dislocation which has moved during the vibration, and a small pyramidal pit represents a dislocation not present at that position prior to vibration. Only very rarely has an apparently annealed-in dislocation been seen to move during vibration. However, dislocations introduced by handling, which occur on slip planes, move very easily even as a result of moving the resonator assembly about. After vibration at strain amplitudes up to $2{\cdot}0 \times 10^{-4}$, very few new dislocations were seen which could not be accounted for by the movement or multiplication of dislocations produced by handling before the first etch. However, when the specimens had been vibrated at an amplitude of $2{\cdot}7 \times 10^{-4}$ so that their damping was considerably increased, the appearance of the central part of the etched crystal was quite different, containing a large number of new etch pits lying on slip planes. These new pits were not apparently related to fresh dislocations present before vibration. Figure 5 (*a*) (Pl. 44) shows a typical region from such a specimen, the new dislocations being seen as small pits lying in straight lines. Figure 5 (*b*) shows an interesting but rather unusual region of the same specimen in which a large number of dislocations seem to have originated at a sub-grain boundary.

§ 5. DISCUSSION

5.1. *Increases in the Damping of Annealed Crystals*

As has already been explained, the internal friction of a deformed crystal is reduced by annealing or x-irradiation. Comparison with etching experiments suggests very strongly that this reduction is due to the pinning of dislocations, presumably by point defects or impurity atoms. As described in § 4.1 vibration of such a crystal at high amplitudes gives rise to a type I increase in its internal friction. It is very unlikely that this increase is due to the creation of new dislocations, because that effect has been observed at much higher amplitudes and gives rise to a type II increase in damping. The only alternative explanation of the type I increase in sodium chloride seems to be that the existing dislocations are unpinned by the vibration, and a simple account of this process can be given in terms of the model of damping considered at the end of § 3.2.

After annealing, the dislocations in the crystal will all be pinned at rather more points than previously, and therefore fewer dislocations will move from their initial positions at any given stress. However, after one of these dislocations has been broken away from its pinned position by the applied stress, it will move on its slip plane in the manner already described. If the interaction with its pinning points is of a short range character, there is in general no reason why it should return to the precise position where it will once more be fully pinned, and high amplitude vibration will therefore lead to a permanent increase in the damping of the specimen. On the basis of the theory of Granato and Lücke (1956), however, this effect would not be expected to occur, because in their model the dislocations return to their pinned positions after every half cycle of the stress.

5.2. *Decreases in Damping at High Amplitudes*

No satisfactory explanation has yet been found for the decreases in damping which are produced by vibration at high amplitudes, but two possibilities require brief consideration. In the Introduction attention was drawn to a similar effect (type V) observed in the fatigue of metals at lower frequencies, and Broom and Ham (1959) have attributed this effect to the production of vacancies by the motion of dislocations under the alternating stress. Subsequent experiments by Davidge *et al.* (1959) have shown that vacancies are produced by fatigue in sodium chloride crystals deformed more than 2%. In all these fatigue experiments the amplitude of motion of the dislocations is almost certainly great enough to produce many interactions between dislocations on intersecting slip planes, and it is probably these interactions which lead to the generation of vacancies. It is possible that the decrease in damping observed in the present experiments is also due to the production of vacancies or of jogs on dislocations. However, it is uncertain whether the number of dislocation interactions which can occur is sufficient to explain the observations. This can be seen from the fact that the average amplitude of motion of the dislocations at the stress where the damping begins to decrease in the specimen of fig. 3 is probably $\gtrsim 3000b$, while the separation of annealed-in dislocations other than those in sub-grain boundaries may be ten to a hundred times larger than this.

An alternative explanation of the decrease in damping can be given in terms of the model of internal friction considered above, in which the dislocations move from one pinned position to another in a series of jumps. As the amplitude is raised each dislocation will move over an increasingly large area of the slip plane, and may by chance come to lie in a configuration where the density of pinning points along its length is so high that the applied stress cannot break it away. It will then play no further part in the damping, and if a growing number of dislocations become trapped in this way, the damping of the crystal will decrease.

In both of these models the dislocations have to move a considerable distance across their slip planes at the stress where the damping starts to decrease, and this stress may therefore be related to the static stress necessary to move a dislocation. In this connection it is interesting to note that the stress amplitude at which the decrease starts is about 130 g/mm^2, while C. W. A. Newey (private communication) has shown that the static flow stress of a similar crystal is about 300 g/mm^2 at 78°K and 54 g/mm^2 at room temperature.

5.3. *The Creation of New Dislocations by Vibration*

The production of new dislocations by vibration described in § 4.3 occurs at a fairly well-defined stress amplitude of 1100 g/mm^2. This is higher than the value of the flow stress extrapolated to absolute zero, and much lower than the stress required theoretically to nucleate new dislocations in a perfect lattice ($\sim 2\mu/100 \simeq 4 \times 10^4$ g/mm^2). The etching experiments show that the new dislocations do not appear to be created by the movement of dislocations already present, and it seems probable that they are in fact nucleated at precipitates or other defects in the lattice; this has been shown to be the case in lithium fluoride by Gilman (1959). In this connection it is interesting to note the apparent nucleation at a sub-grain boundary shown in fig. 5 (*b*).

The fact that the dislocations are formed only at a stress higher than the flow stress can be understood when it is realized that the process requires the nucleation of a small loop, which then expands under the applied stress. If this stress is oscillatory the loop must expand so far during the first half cycle that it reaches a position from which it is not collapsed by the combined line tension and reverse stress in the second half cycle. In order to expand the loop sufficiently rapidly in the first half cycle a high stress is required, and the stress required to form new dislocations in vibration may be governed more by the stress needed to move the dislocation than by that required to nucleate the loop initially. Figure 5 shows that when new dislocations are created they move relatively large distances ($\sim$0·01 cm) from their point of formation, as might be expected from the above considerations.

ACKNOWLEDGMENTS

This work was carried out during the tenure of a University Research Fellowship at Birmingham University, and the author wishes to thank Professor G. V. Raynor, F.R.S. for providing research facilities in the Department of Physical Metallurgy; Dr. P. L. Pratt for suggesting the project and for his continued encouragement and advice; Mr. R. W. Davidge for making available his etching technique and giving invaluable assistance with the experiments; and many other members of the department for valuable discussions.

APPENDIX

Calculation of the Amplitude of Motion of Dislocations in a Vibrating Specimen

If the alternating stress is assumed to be uniform and represented by $\sigma=\sigma_0 \exp(i\omega t)$, the corresponding compressive strain $\epsilon_0 \exp(i\omega t)$ can be divided into two parts; an elastic part $\epsilon'=\epsilon_1' \exp(i\omega t)$, and a non-elastic part due to the motion of the dislocations $\epsilon''=(\epsilon_1''-i\epsilon_2'')\exp(i\omega t)$. It can then be shown (Nowick 1953) that

$$\delta=\pi\epsilon_2''/\epsilon_1' \quad \text{and} \quad \Delta E/E=\epsilon_1''/\epsilon_1'.$$

The strain amplitude due to the motion of the dislocations, ϵ_d, is then given by

$$\epsilon_d=(\epsilon_1''^2+\epsilon_2''^2)^{1/2}=\epsilon_1'[(\Delta E/E)^2+(\delta/\pi)^2]^{1/2}.$$

The present results on heavily deformed crystals show that $\Delta E/E \sim \delta/\pi$, so that $\epsilon_d \sim \epsilon_1'\delta/\pi$; however, even if this is not the case in lightly deformed crystals the inequality $\epsilon_d \gtrsim \epsilon_0\delta/\pi$ must be satisfied.

This dislocation strain can be considered as due to a total length of dislocation line Λ per unit volume moving a distance x on $\{110\}$ planes, and it follows that $\epsilon_d=\frac{1}{2}\Lambda bx$, where b is the Burgers vector of the dislocations. Equating these values of ϵ_d, we find that

$$x \gtrsim \frac{2}{\pi}\frac{\epsilon_0\delta}{\Lambda b}.$$

References

Bassani, F., and Thomson, R., 1956, *Phys. Rev.*, **102,** 1264.
Beshers, D. N., 1959, *J. appl. Phys.*, **30,** 252.
Birnbaum, H. K., 1955, *Acta Met.*, **3,** 297.
Broom, T., and Ham, R. K., 1959, *Proc. roy. Soc.* A, **251,** 186.
Davidge, R. W., Silverstone, C. E., and Pratt, P. L., 1959, *Phil. Mag.*, **4,** 985.
Frankl, D. R., 1953, *Phys. Rev.*, **92,** 573.
Gilman, J. J., 1959, *J. appl. Phys.*, **30,** 1584.
Gilman, J. J., and Johnston, W. G., 1957, *Dislocations and Mechanical Properties of Crystals* (New York: Wiley), p. 116.
Gordon, R. D., and Nowick, A. S., 1956, *Acta Met.*, **4,** 514.
Granato, A., and Lücke, K., 1956, *J. appl. Phys.*, **27,** 583 and 789.
Johnston, W. G., and Gilman, J. J., 1959, *J. appl. Phys.*, **30,** 129.
Hiki, Y., 1958, *J. phys. Soc., Japan*, **13,** 1138.
Marx, J., 1951, *Rev. sci. Instrum.*, **22,** 503.
Mason, W. P., 1956, *J. acoust. Soc. Amer.*, **28,** 1207.
Nowick, A. S., 1950, *Phys. Rev.*, **80,** 249; 1953, *Prog. Metal Physics*, **4,** 1; 1954, *J. appl. Phys.*, **25,** 1129.
Read, T. A., 1940, *Phys. Rev.*, **58,** 371.
Swift, I. H., and Richardson, J. E., 1947, *J. appl. Phys.*, **18,** 417.
Wadsworth, N. J., 1957, *Dislocations and Mechanical Properties of Crystals* (New York: Wiley), p. 479.
Weertman, J., 1955, *J. appl. Phys.*, **26,** 202.

Reverse Bending of Crystals of Silver Chloride†

By M. T. SPRACKLING
H. H. Wills Physics Laboratory, University of Bristol

[Received November 12, 1959]

ABSTRACT

The reverse bending of single crystal bars of silver chloride that have already been singly bent has been studied by using the photoelastic effect. There is no indication of the preferential deformation at a certain place on the bar found when annealed crystals are bent. This is also true if the crystals are first heated at temperatures between room temperature and 375°c, but if they are heated at higher temperatures and as a result all detectable long-range stresses are removed from the crystal the sharp yield point of the first bending is recovered. The result, are considered in terms of a simple dislocation model.

§ 1. INTRODUCTION

IN a previous paper (Nye *et al.* 1957) an account was given of some photoelastic observations on the deformation of single crystal bars of silver chloride. These indicate the existence of a sharp yield point in the bending test, which is manifested by plastic deformation starting at a particular place and the propagation of plasticity longitudinally down the bar rather than transversely. The latter is the conventional view.

The observations were interpreted by means of a simple dislocation model (Read 1957) in which σ_c is the stress necessary to generate dislocations and σ_0 is the stress necessary to move them through the crystal. (We interpret σ_c not literally as the stress needed to generate dislocations but as the stress necessary to create a mobile dislocation (that is, one which can move under a stress σ_0) or to "cause a dislocation to break away from a locked position"). On this model the curve of bending moment versus curvature goes through a sharp maximum at the elastic limit if σ_0/σ_c is less than 0·6. We should then expect instability in a bending test; when deformation started at a certain place it would continue there preferentially. Thus the non-uniform deformation of the silver chloride bars can be interpreted to mean that in this crystal σ_0/σ_c is less than about 0·6.

In this paper we describe the effect of applying reversed bending couples to bars that have already been plastically bent.

§ 2. EXPERIMENTS ON REVERSE BENDING

When an annealed single crystal of silver chloride is deformed plastically in bending along its complete length (Nye *et al.* 1957), so that its upper side is convex, after the deforming couples have been removed the appearance between crossed nicols is shown in fig. 1†. The distribution of longitudinal stress σ, inferred from birefringence measurements, is shown at the side of fig. 1.

---

† Communicated by the Author.

When a bar that has been bent plastically along its complete length is subject to reverse bending couples the photoelastic pattern changes as the couple increases as shown in figs. 2, 3, 4 and 5 respectively. The corresponding distributions of longitudinal stress are shown at the sides of the figures. It can be seen that the two broad outer dark bands move towards the narrow dark band which represents the neutral plane of bending. This process continues as the reversed load is increased and the three bands finally coalesce to form one narrow central band.

In this deformation there is no indication of a sharp yield point. The two broad dark bands remain parallel to the narrow central band along the complete length of the bar during reverse bending; there is no tendency for the bar to deform preferentially at any place. This is in complete contrast to the behaviour of an annealed bar.

An annealed bar can be bent so that only part of the bar deforms plastically (Nye *et al.* 1957). When such an elastic–plastic bar is subject to reverse bending couples the two dark broad bands in the plastic region move towards the narrow central band with increasing load. but they do not remain parallel to this band. They are always slightly closer to the central band in the part of the plastic region nearest the elastic–plastic junction. The ultimate coalescence is first achieved at the elastic–plastic junction. During the whole of this process the initially elastically bent region of the bar remains elastic and deforms plastically only when the three bands in the plastic region have coalesced. Hence, while the reverse bending of the plastic region is taking place, the maximum stress in the elastic region of the bar is always less than the stress σ_c needed to generate dislocations in the annealed material.

Figures 2–5 show that as the reverse couples are increased two well-defined regions of approximately constant stress σ_R appear, close to the edges of the bar at first, but spreading towards the middle of the bar as the deformation continues, until a stage is reached when the stress is uniform over almost the whole of the bar.

The 'discontinuity' in stress on crossing the neutral plane of bending found in singly-bent bars seems to become gradually smaller with increasing reverse loading, and finally disappears, to be replaced by a new discontinuity of opposite sign.

In the first bending we observed a uniform longitudinal stress σ_P over most of the plastic region which was identified with the σ_0 of Read's model. Measurements of σ_P resulting from the first bending and σ_R resulting from the reverse bending have been made and the results for σ_R/σ_P in six different specimens are 1·11, 1·03, 1·02, 1·10, 1·04, 1·18; mean = 1·08.

---

† All figures are shown as plates.

§ 3. EFFECT OF HEATING

A number of singly-bent crystals were tested in reverse bending after being heated. Temperatures ranging from about 375°C to room temperature were used (m.p. of silver chloride = 455°C).

Specimens that were not heated were left at room temperature for three weeks before retesting and those that received heat treatment were heated for eight hours followed by furnace cooling. In none of these cases was there complete annealing as judged from the photoelastic pattern. This was reduced in intensity but the main features were unchanged, indicating that there was no large-scale redistribution of stress. None of these specimens recovered the sharp yield point and associated inhomogeneous deformation of the first testing: their behaviour under reversed couples was similar to that of specimens that were untreated.

After heating for twelve hours at 400°C some specimens annealed completely (i.e. they contained no detectable long-range internal stresses) while others still showed the photoelastic pattern, but greatly reduced in intensity.

The crystals that appeared to be fully annealed, and these only, showed a yield point when tested in reverse bending and their behaviour was similar to that in the first bending: plastic yielding started at a certain place on the bar and the plastic region progressed longitudinally down the bar.

§ 4. CONCLUSIONS

The experiments on the reverse bending of bars already plastically bent show that the sharp yield point appears only in the first bending. When the bar is bent under reverse couples it behaves in the conventional manner, with no indication of preferential deformation at any place.

We may interpret this in terms of Read's (1957) dislocation model of bending. On this model, the absence of any instability in the deformation means that the ratio of the stress needed to propagate dislocations through the material to the stress needed to generate them lies between about 0·67 and 1. We may identify the uniform stress σ_R with the theoretical stress needed to propagate dislocations through the singly-bent material. Thus if σ_c' is the stress needed to generate dislocations in the singly-bent material we have $0{\cdot}67 \leqslant \sigma_R/\sigma_c' \leqslant 1$. Experimentally, σ_R is only slightly (about 8%) greater than σ_P, the stress needed to move dislocations in the annealed material. The model therefore gives two extreme possibilities: either $\sigma_c \simeq \sigma_c'$ and the slight difference between σ_R and σ_P is sufficient to raise the ratio σ_R/σ_c' above the critical value of 0·67, or alternatively, σ_c' is appreciably less than σ_c. The latter explanation seems more likely.

The experiments on heating show that in bending tests the crystals fail to recover the yield point unless they are fully annealed, that is, all long-range internal stresses are removed. Incomplete annealing by heating over a range of temperatures to within 50°C of the melting point does not produce recovery of the yield point.

If the yield point of the first bending is determined by the stress needed to break away from locking atmospheres of impurity atoms (Cottrell 1948) or vacancies, then our experiments show that these atmospheres do not form below about 400°C.

An alternative suggestion is that the yield point is determined by the stress needed to break-up stable (low-energy) arrays of dislocations, with no associated long-range stresses, within the crystal. Following deformation, the dislocations would only collect into arrays of this type after complete annealing of the crystal.

ACKNOWLEDGMENTS

I should like to thank Dr. J. F. Nye for his encouragement in the course of the work and his comments on the manuscript of this paper. The work was carried out during the tenure of a maintenance grant from the Department of Scientific and Industrial Research.

REFERENCES

COTTRELL, A. H., 1948, *Report on Strength of Solids* (London: The Physical Society).
NYE, J. F., SPENCE, R. D., and SPRACKLING, M. T., 1957, *Phil. Mag.*, **2**, 772.
READ, W. J., Jr., 1957, *Acta Met.*, **5**, 83.

The Generation of Dislocation Loops at the Surfaces of Crystals of Silver Bromide†

By J. T. Bartlett and J. W. Mitchell‡
H. H. Wills Physics Laboratory, University of Bristol

[Received January 18, 1960]

Abstract

A method for preparing chemically sensitized, dislocation-free, silver bromide single crystals is described in this paper. When these crystals are strained beyond the elastic limit and exposed to light, both the dislocation loops which are generated at the surfaces, and the surface terraces which may be associated with them, are made visible by the separation of particles of silver. The glide planes of the dislocations may then be determined from microscopic measurements and the Burgers vectors of the dislocations may be inferred if the stress distribution responsible for the deformation is at least qualitatively known. This provides a powerful method for studying dislocation interactions and the fundamental processes of plastic deformation.

§ 1. Introduction

During the course of the experimental work on dislocations in crystals of silver halides, which has been carried out at Bristol (Mitchell 1957 a, 1958 b), it has been observed from time to time that both dislocation loops generated at the surfaces of crystals, and surface terraces associated with them, can be made visible by the separation of particles of silver (see, for example, Jones 1959). It soon became clear, however, that a particularly favourable state of chemical sensitization had to be established before particles of photolytic silver would separate preferentially along the surface terraces during illumination. Until recently, we have not been able to define the conditions under which the required state of sensitization could be reproducibly achieved and an account of this work has consequently not previously been published. Our systematic investigations have now resulted in the development of a technique for sensitization which leads to reliable decoration of both dislocation loops and surface terraces when plastically deformed crystals are exposed to light.

The purpose of this paper is to describe the method which has been used for the production of dislocation-free, chemically sensitized crystals of silver bromide and some of the observations which have been made with them. The normal mode of plastic deformation involves the generation of dislocation loops at the surfaces as shown in the figures accompanying this paper. Observations on interactions between dislocations in silver bromide crystals will be presented in subsequent papers.

---

† Communicated by the Authors.

‡ Now at the Department of Physics, University of Virginia, Charlottesville, Virginia.

§ 2. Experimental Methods

Globules of high purity silver bromide were first prepared and sheets with a thickness of 400 microns and optically flat, plane-parallel surfaces were then made and cut into strips of convenient width (about 5 mm). The methods employed up to this point have already been described in detail by Clark and Mitchell (1956). It was known from previous work that the required sensitization was associated with the presence of traces of silver iodide in the crystals but it proved impossible to prepare satisfactory sheet crystals from globules of silver bromo-iodide. The sensitization was therefore carried out by annealing the strips for eight hours at 380°c in a sealed tube containing sections of crystals of silver bromide with 5 mol % silver iodide, bromine and oxygen. The pressure of bromine was about 700 mm Hg at 380°c and the pressure of oxygen, between 1 and 10 mm Hg, the precise value within this range being unimportant. The sealed tubes were allowed to cool slowly to room temperature. The crystals were then removed, strained, and the dislocations and associated surface terraces made visible by exposing them to radiation from a medium pressure mercury vapour lamp with a glass envelope. For microscopic examination, the crystals were mounted in Canada balsam on 3 in. × 1 in. glass slides and protected with a thin cover-glass. The orientations of the surfaces of the crystals were determined from back-reflection Laue x-ray diffraction photographs. The glide planes of the dislocations were established from measurements made with a calibrated micrometer eyepiece used in conjunction with the calibrated fine focusing knob of the microscope. The depth measurements had, of course, to be corrected for the refractive index of the silver halide. The points of intersection of dislocations with the surfaces of the crystals could also be made visible by etching with a 3 to 7 N solution of sodium thiosulphate for the shortest possible time and then examining them with the phase contrast microscope (Jones and Mitchell 1957).

§ 3. Experimental Observations

The etching method is a convenient one for following the process of recrystallization during annealing. The dislocations are made visible on $\{100\}$ and $\{111\}$ but not on $\{110\}$ surfaces (Jones and Mitchell 1957, Mitchell 1958 b, Jones 1959, Parasnis 1959). In the present work we found that large areas around the edges of the strips which had been cut with the razor blade recrystallized during annealing. Compared with any remaining polygonized areas in the centres of the sheets, there was always a low density of dislocations in the recrystallized areas. The majority of the residual dislocations in these areas were edge dislocations running normal to the surfaces from one side of the crystal to the other and arranged in small angle tilt sub-boundaries with the axis of tilt also normal to the surface. These sub-boundaries were not eliminated by long periods of annealing (see Mitchell 1958 b). Our observations show that small areas which are free from dislocations appear at the heavily deformed cut edges of the crystals during the early stages of the annealing process. The interface between these areas and the central area, where there is always a high density of dislocations, then advances into the crystals, and large areas are swept free from dislocations under favourable circumstances. The lattice disorder is of the Frenkel type so that dislocation loops will not be formed by the condensation of lattice defects during cooling as might occur in crystals of alkali halides. All the studies on the generation of dislocations at the surfaces of crystals and on interactions between dislocations which will be described in this and subsequent papers have been made in recrystallized areas of the annealed crystals.

Microscopic observations and quantitative measurements have now been made on many dislocation loops generated at the surfaces of silver bromide crystals under the influence of applied stresses. It has been established by direct observation that the glide planes frequently do not coincide with low index crystallographic planes but that they always contain a ⟨110⟩ direction. This is consistent with the conclusion of Nye (1948 a, b, 1949) that the silver halides deform plastically by pencil glide and with the observations of Jones and Mitchell (1958) on prismatic slip. For a given ⟨110⟩ Burgers vector, we have, however, found that slip occurs on planes with poles between the poles of the {111} and {110} planes with far higher probability than on planes with poles between {110} and {100}. No glide planes with poles near those of the {100} planes have ever been observed. This is a little surprising in view of the circular contours of the stress-generated prismatic and helical prismatic dislocations studied by Jones and Mitchell (1958, see also, Mitchell 1958 b).

Fig. 2

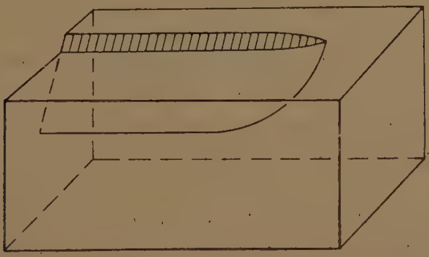

Diagram showing a dislocation loop of the type illustrated in fig. 1 (*a*), (*b*) and (*c*) (Pl. 48).

The most interesting observations have been made on crystals with surfaces parallel to (001) crystallographic planes. When these crystals are stressed along the [010] direction, dislocation loops may be nucleated at the surface on either the (0$\bar{1}$1) and (011) or the (110) and ($\bar{1}$10) planes. In the first case, the dislocation loops lie on planes making angles of 45° with the surface of the crystal. They meet the surface in the screw orientation and their two points of intersection with the surface are joined by a length of surface terrace with a height determined by the resolved component of the Burgers vector normal to the surface. The dislocation line is in the edge orientation where the loop is parallel to the surface. This case, which represents the usual mode of deformation under the conditions of our experiments, is illustrated in fig. 1 (*a*), (*b*) and (*c*) (Pl. 48), and fig. 2. In the second case, the dislocation loops lie on the (110) or ($\bar{1}$10) planes which are normal to the surface of the crystal but make angles of 45° with the direction of the applied stress. The dislocation loops which are generated at the surface on these planes meet the surface in the edge orientation and are in the screw orientation when they are parallel to the surface. This case is illustrated in fig. 3 (Pl. 48). The reason why dislocation loops of the first type are nucleated with higher frequency than those of the second may be that the attractive interaction between screw components at the surface will be less than that between edge components (see Eshelby and Stroh 1951) so that the first type should be generated in a dislocation free crystal by the application of a lower stress than the second.

The formation of these two types of dislocation loop can also be inferred, as in the earlier experiments of Gilman and Johnston (1956, 1957) on lithium fluoride crystals, by etching the strained silver bromide crystals with a 3 to 7 N solution of sodium thiosulphate which produces localized depressions where the dislocations meet the surface. In the case of silver halide crystals, this is, however, a less satisfactory technique. The etch pits coalesce at quite low dislocation densities and the resolution is lower than that which can be achieved by the separation of silver during exposure to light, quite apart from the substantial advantage that this allows the observation of surface terraces and of dislocation loops on glide planes below the surfaces of the crystals. The surface dislocation loops on glide planes in lithium fluoride crystals have recently also been observed directly by x-ray extinction contrast in the experiments of Newkirk (1959).

Two dislocation loops which were generated by straining a crystal to a very small extent are illustrated in fig. 1 (*a*), (*b*) and (*c*). Only a section of each loop is included in the photomicrograph. In fig. 1 (*a*), the microscope is focused on the surface of the specimen and it can be seen that specks of silver have been formed preferentially during exposure along the edges of the surface terraces associated with the dislocation loops. The effect of the surface terrace is clearly to increase the probability for the formation of nuclei of silver by the combination of conduction electrons and silver ions during exposure (Mitchell 1957 b, 1958 a). The surface density of particles of silver is greater along the edges of the terraces, and the size of the particles correspondingly smaller, than elsewhere on the sensitized surface. The microscope is focused 3 microns below the surface in fig. 1 (*b*) and the focal plane intercepts the dislocation loops in a position where they are essentially in the screw orientation. In fig. 1 (*c*), the microscope is focused on the dislocation lines 6 microns below the surface where they are parallel to the surface and in the edge orientation. One such dislocation loop is illustrated diagrammatically in fig. 2 which is based on the standard illustrations which appear in monographs on dislocations (see, for example, Read 1953, pp. 2, 15 and 18) but has been redrawn to correspond to the loops in fig. 1. The glide plane of the dislocation is defined by the surface terrace and the dislocation line below the surface. It may be determined by microscopic observations after the orientation of the crystal has been established from a Laue back-reflection x-ray diffraction photograph. In the case of the specimen of fig. 1, the surface was almost parallel to the (001) crystallographic planes and the glide planes of the two dislocations in the photomicrographs were very close to (011) planes which contain $\frac{1}{2}[0\bar{1}1]$ Burgers vectors. Neither the two surface terraces nor the two dislocations where they are in the edge orientation are parallel to each other from which it is evident that the glide planes do not coincide precisely with the low index (011) planes. These dislocation loops usually expand by the outward motion of the screw components which is frequently accompanied by extensive cross-slipping. Regular successions of parallel dislocation loops of this kind lying on the same glide plane are not observed.

Such successions are typical of the second mode of deformation which is illustrated in fig. 3. The glide plane is here the (110) plane and the dislocations have a Burgers vector $\frac{1}{2}[\bar{1}10]$. The leading sections of the dislocation loops are in the edge orientation and therefore cannot cross-slip as they glide outwards. Well-defined slip planes now appear but there are no surface terraces associated with the individual dislocation loops which are in the screw orientation and very feebly decorated where they are parallel to the surface.

The heavy decoration of the dislocation loops near the surface in fig. 1 (*b*), where they are in the screw orientation, is probably due to cross-slipping on a microscale which would introduce a high linear density of jogs and edge components. Such cross-slipping and jogging will be much less likely to occur in the case shown in fig. 3; here the dislocation lines will tend to minimize their length where they are in the screw orientation by remaining on the glide planes.

It is surprising that the monatomic steps which are associated with dislocation loops of the type illustrated in fig. 1 can be revealed by the preferential separation of surface particles of photolytic silver, as there must be a high density of such steps or terraces on crystal surfaces which do not coincide accurately with crystallographic planes. The situation must be that surface nuclei for the separation of silver are formed during the exposure of the sensitized crystals with higher probability along the newly formed surface terraces where, on account of the cross-slip on a microscale which has just been discussed, there may be a relatively high density of kink sites (Mitchell 1957 b, 1958 a).

ACKNOWLEDGMENTS

This work was carried out during the tenure of a Research Studentship awarded by the Department of Scientific and Industrial Research to

J. T. Bartlett. The photomicrographs were taken with equipment purchased with a special grant from the Department of Scientific and Industrial Research. This assistance is gratefully acknowledged. We are also grateful to Kodak, Ltd., for financial support and to J. H. Burrow and G. D. Freke for much valuable assistance.

References

Clark, P. V. McD., and Mitchell, J. W., 1956, *J. photogr. Sci.*, **4,** 1.

Eshelby, J. D., and Stroh, A. N., 1951, *Phil. Mag.*, **42,** 1401.

Gilman, J. J., and Johnston, W. G., 1956, *J. appl. Phys.*, **27,** 1018; 1957, *Dislocations and the Mechanical Properties of Crystals* (New York: John Wiley), p. 116.

Jones, D. A., 1959, Ph.D. Thesis, University of Bristol.

Jones, D. A., and Mitchell, J. W., 1957, *Phil. Mag.*, **2,** 1047 ; 1958, *Ibid.*, **3,** 1.

Mitchell, J. W., 1957 a, *Dislocations and the Mechanical Properties of Crystals* (New York : John Wiley), p. 69 ; 1957 b, *Rep. Progr. Phys.* (London : Physical Society), **20,** 433 ; 1958 a, *J. photogr. Sci.*, **6,** 57 ; 1958 b, *Growth and Perfection of Crystals* (New York : John Wiley), p. 386.

Newkirk, J. B., 1959, *Trans. Amer. Inst. min. (metall.) Engrs*, **215,** 483.

Nye, J. F., 1948 a, *Nature, Lond.*, **161,** 367 ; 1948 b, *Ibid.*, **162,** 299 ; 1949, *Proc. roy. Soc.* A, **198,** 190.

Parasnis, A. S., 1959, Ph.D. Thesis, University of Bristol.

Read, W. T., Jr., 1953, *Dislocations in Crystals* (New York: McGraw-Hill).

The Electrical Resistance of Iron–Aluminium Alloys and its Dependence on Crystallographic Order†

By R. W. Cahn and R. Feder‡
Department of Physical Metallurgy, University of Birmingham

[Received January 18, 1960]

Abstract

The electrical resistance of two iron–aluminium alloys, bordering on the composition Fe_3Al, was measured at room and liquid nitrogen temperatures after inducing various states of order. By means of an analysis based on values of residual resistivity and of the temperature coefficient of resistivity, the influence of order on electronic factors in the conductivity, and on the perturbations of the lattice that produce scattering, were separately estimated. The freedom of conduction electrons diminishes as the order increases, and the decrease in low temperature resistivity associated with increasing order is due to the greatly reduced scattering potential. These conclusions permitted a qualitative interpretation of the form of the anomalous resistance/temperature relation at high temperatures.

§ 1. Introduction

The present study arose from the wish to interpret the anomalous form of the resistance–temperature curves for a number of iron–aluminium alloys, first published by Bennett (1952). An example of such a curve, for nearly stoichiometric Fe_3Al, is shown in fig. 1, which is based upon measurements by the present authors. On this graph, θ_c represents the ferromagnetic Curie temperature and T_c the temperature at which crystallographic ordering sets in (Bradley and Jay 1932, Taylor and Jones 1958, McQueen and Kuczynski 1959). Bennett attributed the resistance hump just below T_c to the influence of antiphase domain boundaries, which can scatter conduction electrons and thus increase resistivity§. This, however, seemed improbable since a curve such as that in fig. 1 can be traced reversibly, whereas a structure of small antiphase domains is unstable; the domains quickly grow at high temperatures, and the resistance hump would be expected progressively to disappear if it were associated with the presence of domain boundaries.

The present experiments were designed to disentangle the various factors that determine the electrical resistance so as to achieve an understanding of the resistance at high temperatures.

---

† Communicated by the Authors.

‡ Now at Frankford Arsenal, Philadelphia, Pennsylvania.

§ Other, non-stoichiometric alloys show more pronounced humps on the resistance/temperature curves.

Fig. 1

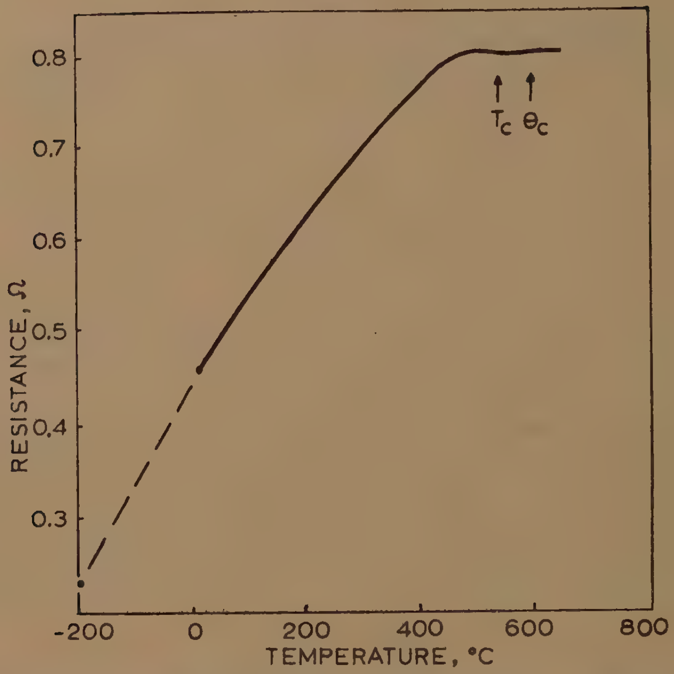

Equilibrium resistance-temperature curve of alloy containing 24·8 at. % aluminium.

§ 2. Analysis of the Electrical Resistance of an Iron-base Ordering Alloy

Since it is necessary to take into account the ferromagnetic resistivity component, an appropriate framework for analysis is provided by Coles' (1958) theory of spin–disorder terms in the resistivity. According to the quantum mechanical model for iron recently advanced by Mott and Stevens (1957), two 3*d* electrons with unpaired spins are located on each atom in body-centred cubic iron. These electrons do not themselves take part in conduction but, interacting by exchange with conduction electrons, they scatter these and contribute to the electrical resistivity. Their scattering power diminishes progressively as the spins become aligned, i.e. as the saturation magnetic moment increases with falling temperature. It is therefore possible, as a crude approximation, to express the total resistivity at a given temperature in the form

$$\rho = F \times (P_A + P_S + P_T). \qquad (1)$$

Here P_S and P_T represent the scattering perturbations due to *spin* disorder (*non*-alignment of spins) and *thermal* disorder, respectively, while P_A represents scattering due to *atomic* (i.e. crystallographic) disorder.

The factor F expresses the freedom of the conduction electrons†; it depends on the concentration, effective masses, etc. of conduction electrons, and hence on the Brillouin zone structure. When the electrons responsible for the magnetic moment are bound to individual atoms and do not enter energy bands, then neither the zone structure nor the freedom of conduction electrons will be affected by alignment of their spins, (i.e. onset of ferromagnetism) and therefore F will remain unaffected. Coles showed that this separation of resistivity into terms provided a self-consistent analysis of the resistance of iron itself, and also of iron–ruthenium solid solutions.

2.1. *Influence of Crystallographic Order*

Not only P_A, but also F will vary when the state of order changes, because any change in lattice periodicity will influence the Brillouin zone structure. To apply eqn. (1) to our alloys, therefore, it is necessary to find how P_A and F vary with order below the critical temperature T_c. We can get an approximate idea of this by obtaining data on resistivity, at room temperature and below, of alloys quenched from different temperatures and which are, consequently, in different states of order. The specimen remains in the state of order corresponding to the quenching temperature, and retains corresponding values of P_A and F, since the rate of diffusion is vanishingly small at room temperature. We have

(i)
$$\rho_0^{QT} = F^{QT} P_A^{QT}. \qquad (2)$$

Here the suffix 0 indicates the residual resistivity (at 0°K) while the superfix QT denotes the fact that the quantities refer to an alloy quenched from temperature T. The terms in P_S and P_T disappear because zero point thermal energy and residual spin disorder at absolute zero are small enough to be neglected in comparison with P_A. (The state of *spin* disorder characteristic of the quenching temperature is, of course, not frozen in by quenching.)

(ii) The temperature coefficient $\partial\rho/\partial T$, at or below room temperature, of an alloy quenched from temperature T is given by

$$\left(\frac{\partial\rho}{\partial T}\right)^{QT} = F^{QT}\frac{\partial}{\partial T}(P_S^{QT}+P_T^{QT}+P_A^{QT}). \qquad (3)$$

P_S will vary somewhat with temperature below room temperature, but the observed variation of the saturation magnetic moment with temperature is slight below 20°c (Taylor and Jones 1958), and this implies that the alignment of spins is already far advanced at this temperature. P_S will therefore be small throughout the range of temperatures in question. Moreover, this remains true for *all states of order*, since in Fe_3Al the saturation magnetic moment at room temperature varies by less than 10% between complete disorder and full order (Masumoto and Saito 1952, Rode

---

† A large value of F implies a low degree of freedom.

1957). At or below room temperature, we therefore have $\partial P_S/\partial T \approx 0$, irrespective of quenching temperature; and to an even better approximation, $\partial P_S/\partial T$ is small and constant for all quenching temperatures.

$\partial P_T/\partial T$ is also taken to be virtually independent of the state of order. The thermal perturbation P_T due to lattice vibrations is closely correlated with elastic properties, and we can estimate how much P_T varies with order by noting to what extent an elastic modulus changes with order. Yamamoto and Taniguchi (1956) showed that the change, due to ordering, of the *intrinsic* Young's modulus at room temperature (i.e. corrected for the irrelevant ferromagnetic ΔE-effect) is only 1–3% for alloys near the composition Fe_3Al. (By way of comparison, the corresponding change for Cu_3Au is about 50% (Lord 1953).) From this we can conclude that the thermal perturbation is virtually independent of order, and hence $\partial P_T/\partial T$ is independent of quenching temperature for Fe_3Al†.

P_A is determined by the quenching temperature; it does not vary with temperature below 20°C, and therefore $\partial P_A/\partial T = 0$.

From the foregoing, it follows that

$$\alpha^{QT} = \left(\frac{\partial \rho}{\partial T}\right)^{QT} \approx F^{QT} . \left(\frac{\partial P_T}{\partial T}\right)^{QT} \approx K . F^{QT} \quad . \quad . \quad . \quad . \quad (4)$$

where K is a constant.

If we take into account the small but appreciable term in $\partial P_S/\partial T$ then we have (since $\partial P_S/\partial T$ is, as argued above, nearly independent of the state of order) that

$$\alpha^{QT} = F^{QT} \left\{ \left(\frac{\partial P_T}{\partial T}\right)^{QT} + \left(\frac{\partial P_S}{\partial T}\right)^{QT} \right\} \approx K' . F^{QT}$$

where K' is another constant.

2.2. *Principle of Present Experiments*

Relations (2) and (4) permit independent estimates to be obtained of F^{QT} and $P_A{}^{QT}$ for alloys quenched from different temperatures, by measuring resistance at room temperature and in liquid nitrogen, extrapolating to 0°K to obtain an approximate value of $\rho_0{}^T$‡, and obtaining a mean value of α^{QT} from the resistance values at 293°K and 77°K. These values of F^{QT} and $P_A{}^{QT}$ can then be used to estimate a set of values of resistance at high temperatures, for comparison with observation. This has been done.

2.3. *The Alloy Fe_3Al*

Some remarks are in order concerning the applicability of eqns. (1)–(4) to the case of Fe_3Al. In the first place, there is some doubt about the quantum mechanical state of the electrons responsible for the atomic magnetic moments. The hypothesis that in iron (and iron alloys) they are in non-conducting states is largely based upon the X-ray diffraction data due to Weiss and de Marco (1958) and Weiss and Freeman (1959), and these have recently been challenged by Batterman (1959). Coles' analysis of various resistivity data does provide clear-cut support for the hypothesis; however, the present analysis stands or falls by its correctness.

---

† The Debye temperature of Fe_3Al was also found to be unaffected by ordering (Nemnonov and Finkel'shtein, 1959).

‡ It would have been better to make measurements at several temperatures, down to 20°K or below, but the necessary equipment was not available.

The formulation of eqn. (1) is open to the criticism that the P_A and P_S terms are not entirely independent, since at high temperatures the spins are disordered in both distribution and orientation. P_S at moderate temperatures is almost independent of the state of order, so that this objection is not too serious†; however, at temperatures near T_c the spin disorder does depend appreciably on the state of atomic order, and this will limit the accuracy with which the above analysis can be used to interpret the high temperature resistivity.

Nathans *et al.* (1958) have direct experimental evidence, from neutron diffraction, about the distribution of spins on different iron sites in fully ordered Fe_3Al, and find that iron atoms in crystallographically distinct sites have slightly different moments; this cannot be the case in the disordered alloy. This variation of the atomic magnetic moments with order must again limit the accuracy of the analysis.

In view of the foregoing, the conclusions reached from the present experiments should be regarded as semi-quantitative at best.

§ 3. EXPERIMENTAL METHODS

Two alloys containing 24·8 at. % and 25·5 at. % aluminium, balance iron, were vacuum melted and chill cast *in vacuo*, using constituents of 99·99% purity. The more dilute alloy also contained about 0·03% carbon owing to the use of graphite as deoxidiser; the carbon content of the other was negligible. The ingots were hot rolled to strip 1 mm thick, and resistance specimens of the form shown in fig. 2 were milled from the strip. The resistance was roughly 0·5 Ω at room temperature. This form of specimen was compact and could readily be heated to a uniform temperature and quenched.

Current and potential leads were brazed to the specimen, as illustrated. For resistance measurements at high temperatures (to obtain data such as those of fig. 1), the specimens were placed, together with a mica insulation, into a block which ensured temperature uniformity within ± 2°C. Smooth heating and cooling rates of 1–2°C/min were obtained by means of a motor-driven rheostat, and such a rate was known (Lawley *et al.* 1960) to be sufficiently slow to maintain equilibrium order down to about 350°C. Measurements were taken up to 600°C; at this temperature oxidation was negligible. All specimens were 'wiped clear' before use by means of a vacuum anneal at 800°C followed by a quench into silicone oil. X-ray studies had shown that this treatment expunges any effects caused by preceding heat-treatments.

---

† Formally, a scattering potential arising from the distributional disorder of spins is concealed in P_A; at moderate temperatures the magnetic moment per iron atom is almost independent of order, and there is therefore no point in trying to separate out the concealed term, which will be a constant fraction of P_A.

To achieve different states of order, each specimen was first heated to 670°C in air and brine quenched, and its resistance measured at 293°K and 77°K. The specimen was then reheated to 650°C, quenched and remeasured. Successive equilibrations were carried out at temperature intervals of about 20°C; the times required to equilibrate the specimen at each temperature were estimated from kinetic data (Feder and Cahn 1960) and from x-ray kinetic studies (Lawley *et al.* 1960).

Fig. 2

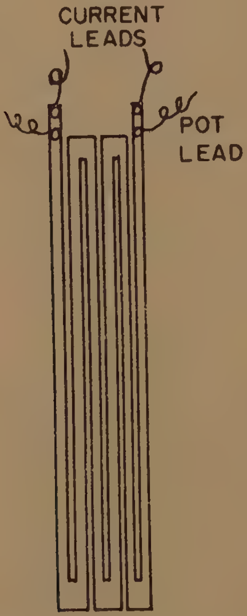

Form of resistance specimens.

The resistance was measured by the double potentiometer method, using a standard resistor in series with the specimen; a reversible circuit was used to correct for spurious e.m.f.'s of thermoelectric origins. No attempt was made to express results in terms of absolute resistivities, in view of the complex shape of the specimens.

§ 4. Experimental Results

In fig. 1 the equilibrium ρ versus T curves for the two alloys are reproduced. The influence of various thermal pretreatments in producing deviations from this curve was also studied and will be reported separately.

In fig. 3 are plotted the results of resistance measurements at 293°K and 77°K of specimens quenched from successively lower temperatures. For comparison, the graph also shows the resistance of the same alloys *at* the temperatures from which they were quenched.

The dashed curves in fig. 3 refer to repeat measurements on the same specimens, made after a preliminary 40-hour anneal at 530°c. This was intended to find whether the initial state of order, which had been found to affect ordering kinetics (Feder and Cahn 1960) also affected the *equilibrium* value of the resistance. The asymptotic final values of resistance found in Feder and Cahn's isothermal anneals by experiments are also included in fig. 3 and it will be seen that these fell on, or close to, the corresponding curves.

Fig. 3

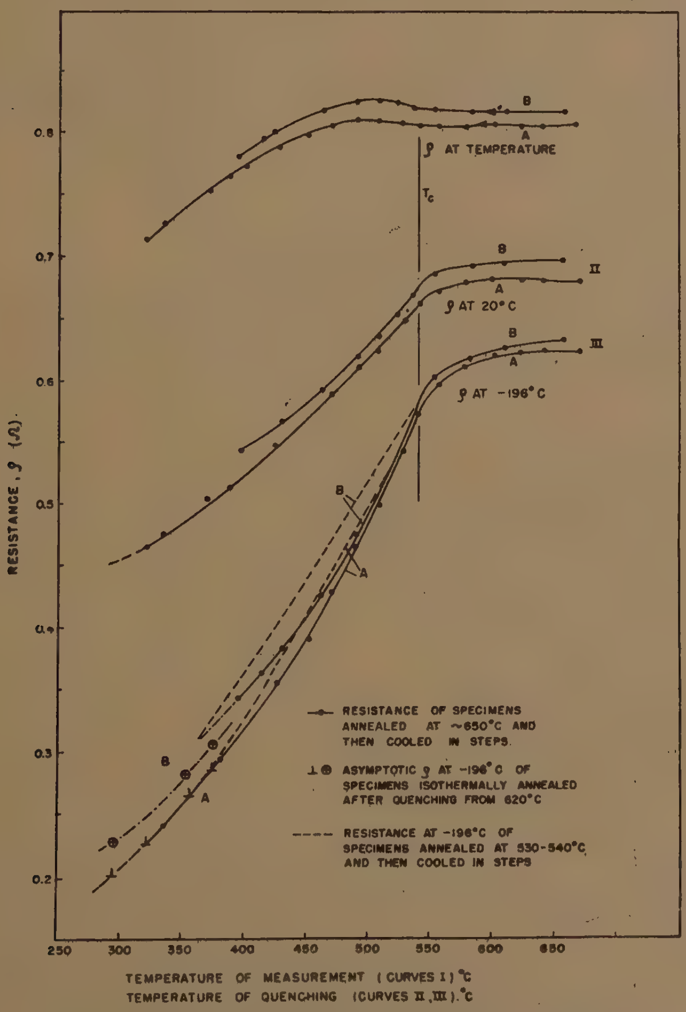

Resistance at temperature, and at 293°K and 77°K, of alloys A (24·8 at. % aluminium) and B (25·5 at. % aluminium), quenched from successively lower temperatures. Asymptotic resistance values from isothermal annealing experiments are included for comparison.

Fig. 4

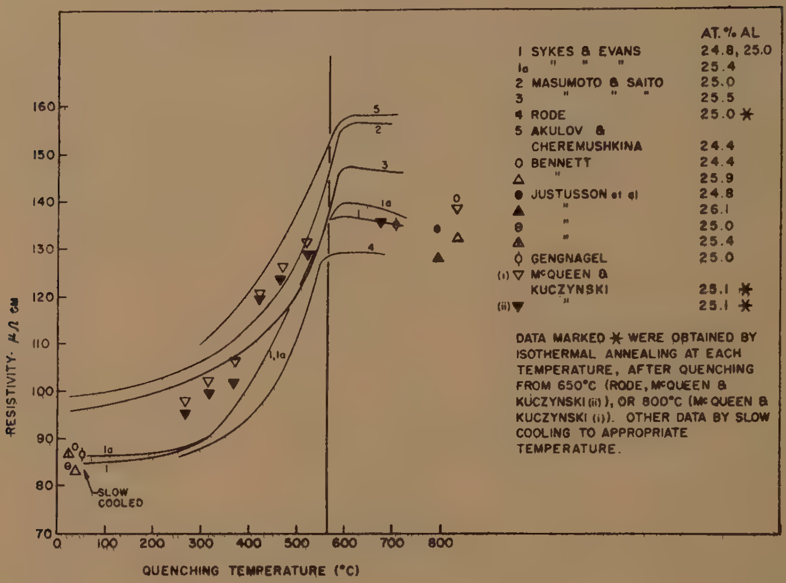

Published data on room temperature resistivity of Fe_3Al quenched from different temperatures. Exact alloy composition is listed for each set of data.

Fig. 5

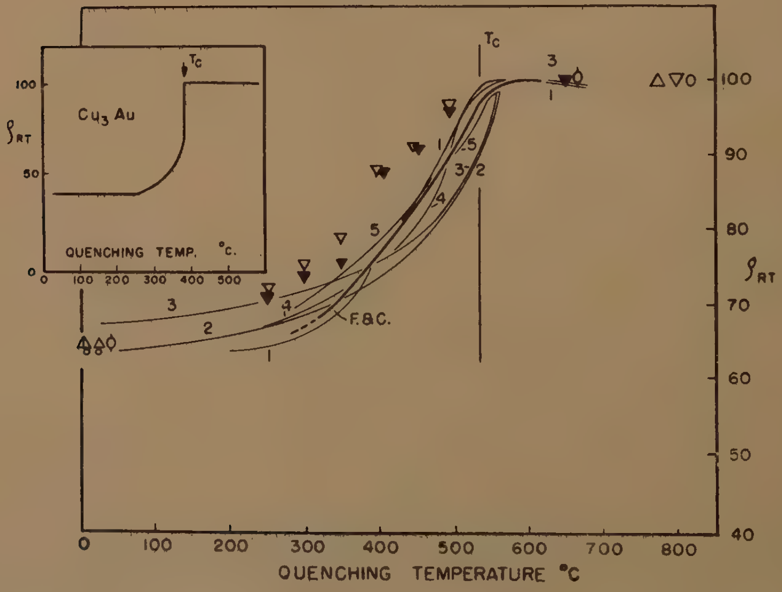

Data of fig. 4, normalized at 600°c. Inset : Data for Cu_3Au after Wright and Thomas (1958).

For comparison with these data, other published data on the room temperature resistivities are shown in fig. 4. The corresponding references will be found at the end of the paper. These data have been replotted in fig. 5, together with the present results, after normalizing the resistivity of all alloys at 600°c. Except for the recent isothermal data of McQueen and Kuczynski (1959) and those of Masumoto and Saito (1957), the various normalized plots are in fair agreement. Our own results agree best with Sykes and Evans' (1935) classical data.

A curve for Cu_3Au (Wright and Thomas 1958) has been included in fig. 5 to emphasize the difference between this alloy, in which there is a brusque discontinuity of order at T_c, and Fe_3Al, in which order appears gradually.

§ 5. Interpretation of Results

In fig. 6, the data for the 24·8 at. % alloy are replotted in a different form. Straight-line extrapolation was used to obtain estimated residual restivities

Fig. 6

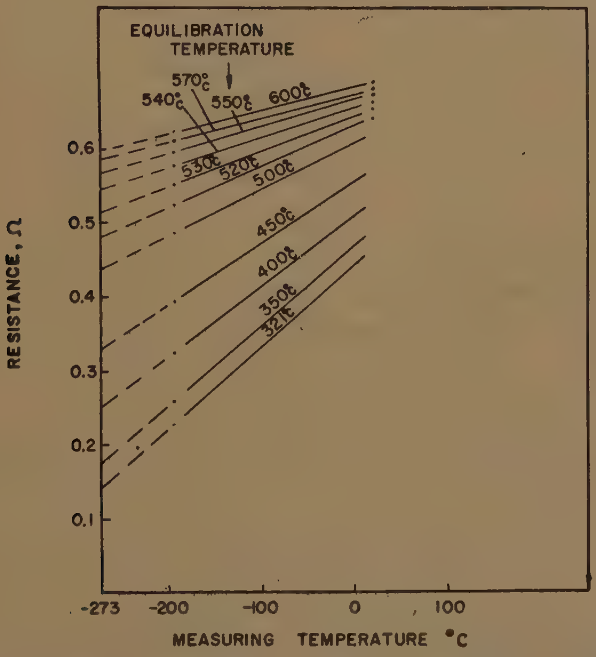

Resistance of alloy containing 24·8 at. % aluminium, quenched from different temperatures, and measured at 77°K and 293°K.

$\rho_0{}^{QT}$: for the degree of reliability of the proposed analysis, this form of extrapolation was considered adequate. From this plot values of the mean temperature coefficients of resistance were also obtained.

According to eqns. (2) and (4),

$$F_T{}^{QT} \propto \left(\frac{d\rho}{dT}\right)^{QT} \quad \text{and} \quad F_T{}^{QT} . P_A{}^{QT} \approx \rho_0{}^{QT}$$

Hence,

$$P_A^{QT} \propto \left\{ \rho_0{}^T \Big/ \left(\frac{d\rho}{dT} \right)^{QT} \right\},$$

Plots of these three quantities against quenching temperature are shown in fig. 7. Corresponding plots for the other alloy are very similar.

Fig. 7

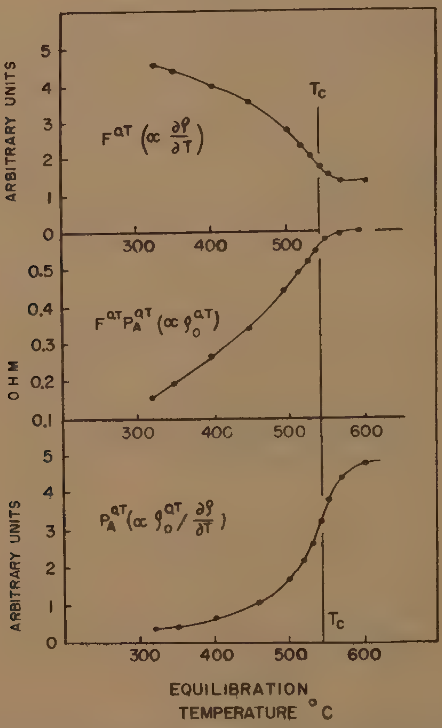

Resistivity parameters F^{QT}, $(F^{QT} \,.\, P_A{}^{QT})$ and $P_A{}^{QT}$ (alloy containing 24·8 at. % aluminium) as function of quenching temperature.

The implication of these curves is that the decrease of resistance of quenched alloys with increasing order takes place *in spite of* a decreased freedom of conduction electrons, since F increases by a factor of almost 4. This increase in F is overcompensated by the very sharp decrease of P_A as atomic order builds up.

This is exactly what Coles (1958) has proposed for the case of Cu_3Au. The postulated increase of F when Cu_3Au orders, which is supported by the observed change of the Hall coefficient, is explained by the creation of new Brillouin zones corresponding to the superlattice (Slater 1951), as a result of which the Fermi level is brought closer to a plane of energy discontinuity and the electron mobility correspondingly diminished. Coles reports that preliminary experimental results on Cu_3Au show F to increase by a factor of nearly 2 on ordering. Fe_3Al has the advantages over Cu_3Au, as an experimental material, that all degrees of order can be obtained, and that the thermal perturbations hardly depend on order; however, Cu_3Au is free of the complications arising from spin disorder, and lends itself better to an interpretation of the results in terms of Brillouin zones.

In fig. 7, the slight variation of F^{QT} and $\rho_0{}^{QT}$, and rather greater variation of $P_A{}^{QT}$, for quenching temperatures *above* T_c, is due partly to the finite rate of quenching which allows some increase of order during the quench, and partly to a very imperfect type of order which persists in the range 540–740°C (Taylor and Jones 1958, McQueen and Kuczynski 1959). This order however is so slight that it has little influence on physical properties, and is here ignored.

Note that, as the quenching temperature diminishes, P_A appears to approach asymptotically a value distinctly above zero. This implies that order never becomes perfect. This indeed is the conclusion from X-ray data (Lawley *et al.* 1960) and also from neutron diffraction (Nathans *et al.* 1958). The maximum value of the Bragg–Williams order parameter S appears to be roughly 0·8. Because of the experimental uncertainties in the experimental X-ray determination of S as a function of temperature, and the complication arising from slight order above T_c, no useful purpose would be served by seeking an exact correlation of S with P_A and F. Very roughly, P_A and F appear to be linear functions of S. ρ_0 and S^2 approximate to a linear relationship, as required by Muto's (1936) theory.

5.1. *Analysis of Resistance–Temperature Curves*

The present experiments have established that the slight humps in the ρ/T curves just below T_c are not due to the presence of small antiphase domains of order, as had been proposed by Bennett (1952). The following reasons can be adduced:

Exactly the same ρ/T curve was traced out on heating and cooling, starting with initially ordered and initially disordered alloy, respectively.

The plot of room temperature resistance as a function of quenching temperature exhibits no hump (fig. 3). Yet data on Cu_3Au (Burns and Quimby 1955, Wright and Thomas 1958) show that such a plot should possess a slight hump if small domains are present. (Such a hump is, however, restricted to quenching temperatures very close to T_c.)

X-ray studies (Lawley *et al.* 1960) show that slowly cooled Fe_3Al has a large domain size.

Some other interpretation of the form of the curves near T_c is therefore required, and this can be attempted by making use of the values of P_A and F which have been determined for various states of order. However, the complications of estimating the high-temperature resistance are such that only a semi-quantitative treatment is possible.

At a particular temperature T, the resistance is expressed by

$$\rho^T = F'^T(P_A{}^T + P_S{}^T + P_T{}^T). \quad \ldots\ldots \quad (5)$$

Here, the superfix T represents the value of the corresponding term *at* temperature T; $P_A{}^T$ is the atomic disorder scattering potential, which is purely configurational and can be taken direct from the graph of $P_A{}^{QT}$ as a function of equilibration temperature, fig. 7. The meaning of the dash in F'^T is explained below. The spin disorder scattering potential $P_S{}^T$ will be left aside for the moment. The thermal vibration scattering potential $P_T{}^T$ depends upon the mean square displacement of the vibrating atoms, and a quite general treatment (Mott and Jones 1936, p. 243) shows that at 'high' temperatures (i.e. near and above the Debye characteristic temperature), $\partial P_T/\partial T$ remains constant. For present purposes, therefore, $\partial P_T/\partial T$ is independent of temperature above 100°c.

The 'electrical freedom', F^{QT}, as plotted in fig. 7 for various equilibration temperatures, cannot be used direct in eqn. (5), because, *even for a fixed configuration of the alloy*, F must decrease with rise of temperature. This is a consequence of the quantum theory of the electrical resistance of transition metals (Mott and Jones 1936, p. 268). Much of the resistance arises from *s–d* and *p–d* scattering transitions. The transition probability, and F, depends on the number of energy states in the d band within an energy range of about kT at the Fermi surface. When the d band is nearly full, $N(E)$ is a steeply falling function of E and therefore the number of available states does not increase proportionately to T. The resistance of a pure transition metal therefore does not rise proportionately to T. In terms of the present formalism, this implies that for iron *or* for an iron alloy, the 'electronic freedom' F falls with rising temperature. We will reserve the symbol F for the configurationally determined value, determined from measurements at 20°c and 196°c of a quenched alloy as plotted in fig. 7. The true value, at any higher temperature, will be termed F' and is lower than F for the same state of order.

In fig. 8, curve 1 represents the observed ρ^T versus T data for the 24·8 at. % alloy. Curve 2 represents the predicted resistance, omitting the spin disorder term and using the configurational (temperature-invariant) values of F^{QT}. This curve has been computed from the data of fig. 6 by simply extrapolating each line to the corresponding temperature†. It was then arbitrarily assumed that over the limited temperature range 300–600°c, $(F-F')$ for a given configuration varies proportionately to absolute temperature and that $F'/F=\frac{2}{3}$ at 600°c. In spite of the arbitrariness of this correction, the corrected curve, 3, is expected to give the right general form of the configurational and thermal terms in the resistance.

The difference between this computed curve and the observed curve corresponds to the spin disorder term $F'P_S$. P_S will presumably rise increasingly rapidly with temperature as the temperature approaches the Curie point θ_c (except for a short plateau near T_c on which the spontaneous magnetization is almost constant with temperature†). This is borne out by the curve 4 of fig. 8, which represents the difference ($\approx F'P_s$) between curves 1 and 3, and by curve 5, in which P_s (derived from curve 4) is plotted against T. The general shape of curves 4 and 5, which will not depend sensitively on the exact value of the correction factors F'/F used to construct curve 3, is similar to that of the plot of spontaneous magnetization against temperature.

---

† This simple extrapolation procedure is justified since $F^T=F^{QT}$ and is *ex hypothesi* independent of temperature for a given state of order, and $\partial P_T/\partial T$, which together with F_T determines the slope of the lines of fig. 6, is also approximately independent of temperature.

Fig. 8

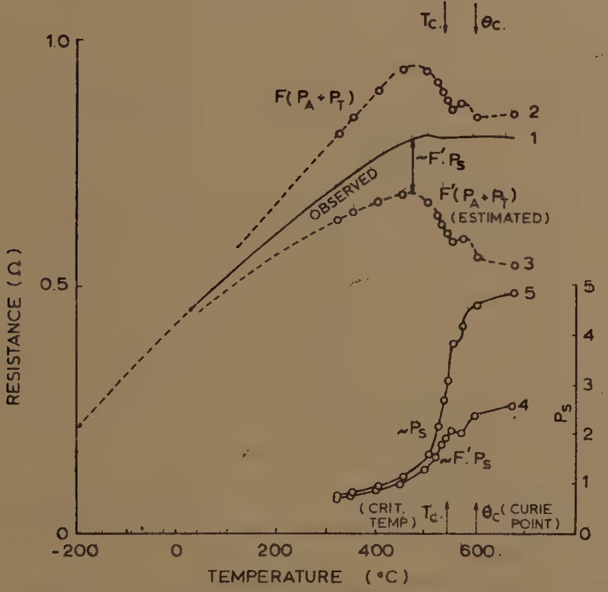

Observed and computed high-temperature resistivity values for alloy containing 24·8 at. % aluminium.

The foregoing analysis, in spite of the inevitable assumptions and approximations, is adequate for interpreting the general shape of the observed ρ^T versus T curve, and in particular the slight hump and the level part of the curve. In fact, if it were not for the counteracting influence of the spin disorder term, there would be a much more pronounced hump, as in curve 3. The hump, then, is due to the effect of atomic ordering on the various terms that determine the electrical resistance.

§ 6. DISCUSSION AND CONCLUSIONS

The present experimental data have some bearing on the proposal advanced by Haworth (1938) that, in alloys not readily amenable to study by x-ray diffraction, the thermal coefficient of resistivity α might be taken as a criterion of the existence of order. If suitable heat treatment causes a substantial increase in this coefficient, then this, it was argued, should be regarded as evidence of order, and various known alloys were adduced in evidence. On this criterion, Ni_3Fe was at that time stated to be incapable of ordering, since α *decreases* slightly on slow cooling. Yet it is known by evidence from x-ray (Wakelin and Yates 1953) and neutron diffraction (Lyaschenko *et al.* 1957) that this alloy can in fact acquire long range order. The present analysis shows that the decrease in α may be due to a reduction in $\partial P_T/\partial T$ resulting from an altered Debye temperature, or from a fall in $\partial P_S/\partial T$ due to an altered Curie temperature, and these may outweigh any change in F that occurs. Evidently, α is not a good criterion; a decrease of the residual resistivity ρ_0 is a much safer criterion for the presence of atomic order, since this depends on P_A, which is highly sensitive to the state of order. Even here, however, a large increase of F due to ordering might lead to mistaken conclusions.

---

† This plateau is deduced from magnetic data by Crangle (private communication) and Ivanovsky and Denisov (1957).

It should be possible to apply the present analysis to some other alloys which show interesting resistance anomalies. A promising candidate is the alloy U_2Mo. This is based on the body-centred cubic γ-uranium lattice, with partial long range-order of the C 11b ($MoSi_2$) type. The degree of order depends on temperature. The resistivity is almost constant over a wide range of temperature (Bostrom and Halteman 1957), and the low-temperature ρ/T curves of an alloy of somewhat different composition, quenched from various temperatures (Loasby 1959), bear a marked resemblance to the data of our fig. 2. If measurements of this type could be correlated with high temperature measurements on the stoichiometric alloy, interesting conclusions might emerge as to the electronic structure of metallic uranium.

In résumé, we list the conclusions of the present study:

(1) As the alloy Fe_3Al is progressively ordered, the freedom of conduction electrons (F) decreases considerably, but the reduction of the electron scattering (P_A) associated with atomic disorder is more than enough to compensate for this; in consequence, the residual resistivity falls sharply with increasing order.

(2) The slight maximum in resistance at about 500°c in the resistance–temperature curve of Fe_3Al has been rationalized without recourse to the discredited notion that antiphase domain boundaries are implicated. An analysis based on Coles' theory of resistivity of iron alloys, in conjunction with present experimental results on quenched alloys, shows that the maximum is due to the way in which F and P_A change with order. Moreover, the form of the entire resistance–temperature curve has been satisfactorily interpreted.

The fact that this interpretation proved feasible can be taken as presumptive evidence in favour of Mott and Stevens' model of the electronic structure of body-centred cubic iron.

ACKNOWLEDGMENTS

We are grateful to Professor G. V. Raynor, F.R.S., for his support and the provision of laboratory facilities. Thanks are due to Professor J. D. Fast of Eindhoven, who kindly arranged the casting of one of the alloys, and the British Iron and Steel Research Association who presented specially pure iron for casting the other. We are much indebted to Dr. B. R. Coles, Professor G. V. Raynor, Professor A. D. McQuillan and Dr. J. Friedel for their comments on the paper. One of us (R. F.) is indebted to the Secretary of the U.S. Army for a Fellowship.

REFERENCES

AKULOV, N. S., and CHEREMUSHKINA, A. V., 1955, *C.R. Acad. Sci. U.R.S.S.*, **102**, 45.
BATTERMAN, B. V., 1959, *J. appl. Phys.*, **30**, 508.
BENNETT, W. D., 1952, *J. Iron St. Inst.*, **171**, 372.
BOSTROM, W. A., and HALTEMAN, E. K., 1957, *Proc. 2nd Nuclear Engineering and Science Conference*, (ASME).
BRADLEY, A. K., and JAY, A. H., 1932, *Proc. roy. Soc.* A, **136**, 210.
BURNS, F. P., and QUIMBY, S. L., 1955, *Phys. Rev.*, **97**, 1597.
COLES, B. R., 1958, *Advanc. Phys.*, **7**, 40.
FEDER, R., and CAHN, R. W., 1960, *Phil. Mag.*, **5**, 343.
GENGNAGEL, W., 1958, *Naturwissenschaften*, **45**, 81.
HAWORTH, F. E., 1938, *Phys. Rev.*, **54**, 693.
IVANOVSKY, V. I., and DENISOV, P. P., 1957, *Fizika Metallov i Metallovedenie*, **4**, 550.
JUSTUSSON, W., ZACKAY, V. F., and MORGAN, E. R., 1957, *Trans. Amer. Soc. Metals*, **49**, 905.
LAWLEY, A., DAVIES, R. G., and CAHN, R. W., 1960 (submitted to *Acta Met.*).
LOASBY, R. G., 1959, *Proc. phys. Soc. Lond.*, **72**, 470.
LORD, N. W., 1953, *J. chem. Phys.*, **21**, 692.
LYASCHENKO, B. G., LITVIN, D. F., PUZEY, I. M., and ABOV, U. G., 1957, *Kristallografiya*, **2**, 64.
MASUMOTO, H., and SAITO, H., 1952, *Sci. Rep. Res. Inst. Tohoku Univ.* A, **4**, 321 ; 1957, *Ibid.* A, **9**, 338.
MCQUEEN, H. J., and KUCZYNSKI, G. C., 1959, *Trans. Met. Soc. Amer. Inst. min. (metall.) Engrs*, **215**, 619.
MOTT, N. F., and JONES, H., 1936, *The Theory of the Properties of Metals and Alloys* (Oxford : University Press).
MOTT, N. F., and STEVENS, K. W. H., 1957, *Phil. Mag.*, **2**, 1364.
MUTO, T., 1936, *Sci. Pap. Inst. phys. chem. Res. Tokyo*, **30**, 99.
NATHANS, R., PIGGOTT, M. T., and SHULL, C. G., 1958, *J. Phys. Chem. Solids*, **6**, 38.
NEMNONOV, S. A., and FINKEL'SHTEIN, L. D., 1959, *Fizika Metallov i Metallovedenie*, **7**, 944.
RODE, V. E., 1957, *Bull. Acad. Sci. U.S.S.R., Phys. Ser.*, **21**, 1234.
SLATER, J. C., 1951, *Phys. Rev.*, **84**, 179.
SYKES, C., and EVANS, H., 1935, *J. Iron St. Inst.*, **131**, 225.
TAYLOR, A., and JONES, R. M., 1958, *J. Phys. Chem. Solids*, **6**, 16.
WAKELIN, R. J., and YATES, E. L., 1953, *Proc. phys. Soc. Lond.* B, **66**, 221.
WEISS, R. J., and DE MARCO, J. J., 1958, *Rev. mod. Phys.*, **30**, 59.
WEISS, R. J., and FREEMAN, A. J., 1959, *J. Phys. Chem. Solids*, **10**, 147.
WRIGHT, P., and THOMAS, K., 1958, *Brit. J. appl. Phys.*, **9**, 330.
YAMAMOTO, M., and TANIGUCHI, S., 1956, *Sci. Rep. Res. Inst. Tohoku Univ.* A, **8**, 193.

Nuclear Magnetic Resonance in Lithium and Dilute Lithium–Magnesium Alloys†

By D. G. Hughes‡
Division of Pure Physics, National Research Council, Ottawa

[Received December 12, 1959]

Abstract

The Knight shift and line-width of the ^{7}Li resonance in dilute Li–Mg alloys has been investigated. The observed rapid fall in Knight shift with alloying concentration is interpreted using Drain's theory. Linewidth measurements show that the activation energy of self-diffusion of the ^{7}Li atoms increases from 13·1 ± 0·2 kcal/mole for pure lithium to 14·5 ± 0·3 kcal/mole for the 10 at. % magnesium alloy.

§ 1. Knight Shift Measurements

A study has been made of the ^{7}Li nuclear magnetic resonance signal in lithium and some dilute lithium–magnesium alloys (up to 10 at. % Mg). The experiments were carried out using a marginal-oscillator spectrometer and a fixed magnetic field of 6750 gauss.

Figure 1 shows the observed variation of Knight shift with alloying concentration. All these Knight shift measurements were taken at about 75°c where the nuclear dipole–dipole contributions to line-widths are negligible because of rapid thermal diffusion of the lithium atoms (Gutowsky and McGarvey 1952). The line-widths of the 2·1%, 4·4% and 10% magnesium alloys and of pure (99·9%) lithium were approximately 100 c/s (0·06 gauss), determined mainly by magnetic field inhomogeneity and modulation frequency broadening (Cagnac *et al.* 1955). The narrow lines obtained from these samples indicate that no appreciable contamination had occurred and that the alloys were quite homogeneous. However, the 0·2% and 0·8% magnesium alloys showed line-widths of 240 c/s (0·15 gauss) and 190 c/s (0·12 gauss) respectively. The lines were nevertheless fairly symmetrical and it is felt that the line centres were not appreciably perturbed by the broadening. It may also be mentioned that our value for the Knight shift of pure lithium of 0·0263 ± 0·0001% is in agreement with the value of 0·0261 ± 0·0002% reported by Gutowsky and McGarvey (1952). There is however an unexplained discrepancy between the value reported here and Knight's value of 0·0249% (Knight 1956). (In our work and in Knight's measurements the Knight shift was measured relative to an aqueous solution of LiCl.) The decrease in lattice parameter which occurs when magnesium is introduced into lithium (Levinson 1955) is expected to have an explicit effect on the Knight shift (Benedek and Kushida 1958) but this is negligible compared to the magnitudes involved here. It can be concluded from the results that the Knight shift falls almost linearly with increasing concentration of magnesium.

---

† Communicated by the Author.
‡ National Research Council Postdoctorate Fellow.

Fig. 1

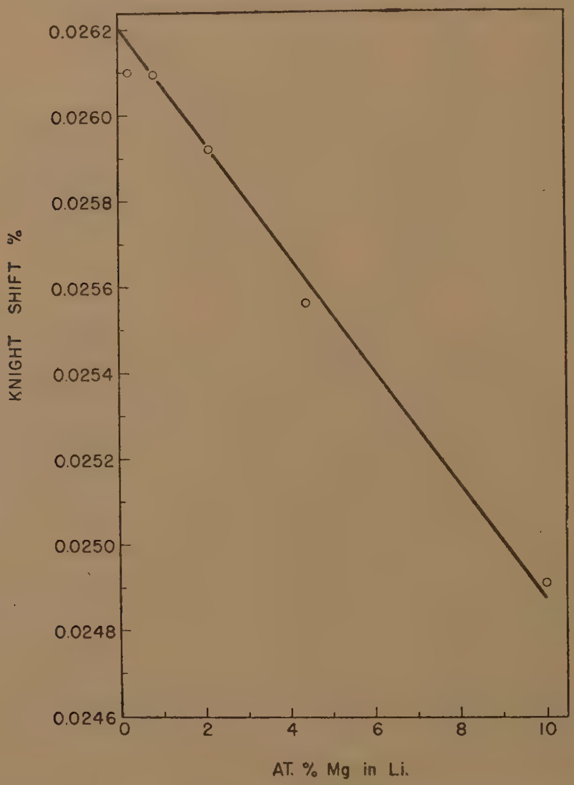

Variation of the ^{7}Li Knight shift with alloying concentration for the Li–Mg system.

It is interesting to compare the present results with those obtained by Drain (1959) for the silver–cadmium system: in both cases the introduction of a divalent metal reduces the Knight shift of a monovalent metal. Moreover, the theory given by Drain is relevant to the present system. In his theory Drain relates the density of states $N(\zeta)$ of an alloy to the density of states, $N_A(\zeta)$ and $N_B(\zeta)$, of the pure constituents by the following formula:

$$N(\zeta)=(1-c)\frac{N_A(\zeta)(\Delta H/H)_A}{(\Delta H/H)_{AA}}+c\frac{N_B(\zeta)(\Delta H/H)_B}{(\Delta H/H)_{BB}}.$$

Here c is the atomic concentration of constituent B in A, $(\Delta H/H)_{\mathrm{AA}}$ and $(\Delta H/H)_{\mathrm{BB}}$ are the Knight shifts in the pure metals, and $(\Delta H/H)_{\mathrm{A}}$ and $(\Delta H/H)_{\mathrm{B}}$ are the Knight shifts of the A and B nuclei in the alloy. In the present case:

$(\Delta H/H)_{\mathrm{AA}}=0{\cdot}0263\%$ for pure lithium,
$(\Delta H/H)_{\mathrm{BB}}=0{\cdot}28\%$ for pure magnesium (predicted value, see Knight 1956),
$N_{\mathrm{A}}(\zeta)=0{\cdot}37$ levels/atom ev (from specific heat data, Roberts 1957) for pure lithium†, and
$N_{\mathrm{B}}(\zeta)=0{\cdot}29$ levels/atom ev (from specific heat data, Estermann *et al.* 1952) for pure magnesium.

However, $(\Delta H/H)_{\mathrm{B}}$ (the Knight shift of magnesium in small quantities in lithium) has not been measured and may well be difficult to measure since ^{25}Mg, the only stable magnesium isotope with non-zero nuclear spin, is only about 10% abundant and its spin number of $\frac{5}{2}$ is expected to give rise to serious quadrupole broadening. We therefore make some estimate of this quantity. If we assume an unusually high value of 0·56% for $(\Delta H/H)_{\mathrm{B}}$, then $N(\zeta)=0{\cdot}37$ levels/atom ev for the 10 at. % Mg alloy, i.e. the density of states in this alloy is the same as in pure lithium. If however we assume that $(\Delta H/H)_{\mathrm{B}}=0{\cdot}28\%$ (the same as in pure magnesium) then $N(\zeta)=0{\cdot}34$ levels/atom ev and the density of states has fallen by nearly 10%. This means that unless the Knight shift of magnesium in lithium is greater than about 0·56% (which we feel is rather unlikely), Drain's theory suggests a fall in the density of states with increasing electron/atom ratio.

Such a fall is consistent with the predictions of the rigid band model (for references see Cohen and Heine 1958) assuming contact of the Fermi surface with the first Brillouin zone. If instead of accepting the rigid band model, we apply the ideas of Cohen and Heine (1958) then we find that the introduction of magnesium into lithium is expected to reduce the distortion of the Fermi surface. Any such 'sphericalizing' of the Fermi surface will reduce contact, *increase* the density of states and make the conduction electron wave functions more s-like in character. But we have already seen that the present results when interpreted on the basis of Drain's assumptions indicate that the density of states if anything *decreases* on alloying. This is therefore not in accord with Cohen and Heine's theory and it would seem that the rigid band model is adequate to explain the results reported here. It must however be emphasized that the conclusions drawn are highly tentative in view of the lack of direct experimental evidence on the Knight shift of ^{25}Mg in both magnesium and lithium.

---

† There is some uncertainty in this value due to the martensitic transformation which occurs in lithium at low temperatures. However, this uncertainty is not expected to exceed about 10% (Dugdale and Gugan 1960).

§ 2. Line-width Measurements

The ^{7}Li line-width has been investigated for various Li–Mg alloys (up to 10 at. % Mg) between room temperature and 200°c. No evidence of any appreciable quadrupolar broadening was found. The dipolar broadening observed above room temperature in these alloys suggested that the activation energy of self-diffusion of the lithium atoms increases with increasing concentration of magnesium. Measurements of the ^{7}Li line-width have thus been made on pure lithium and a 10 at. % Mg alloy in the temperature range where line narrowing by self-diffusion occurs. Figure 2 shows these line-width data. The rigid lattice value of the line-width of about 10·3 kc/s (6·2 gauss) for pure lithium and about 9·8 kc/s (5·9 gauss) for the 10% alloy can be explained on the basis of nuclear dipole–dipole interactions alone.

Fig. 2

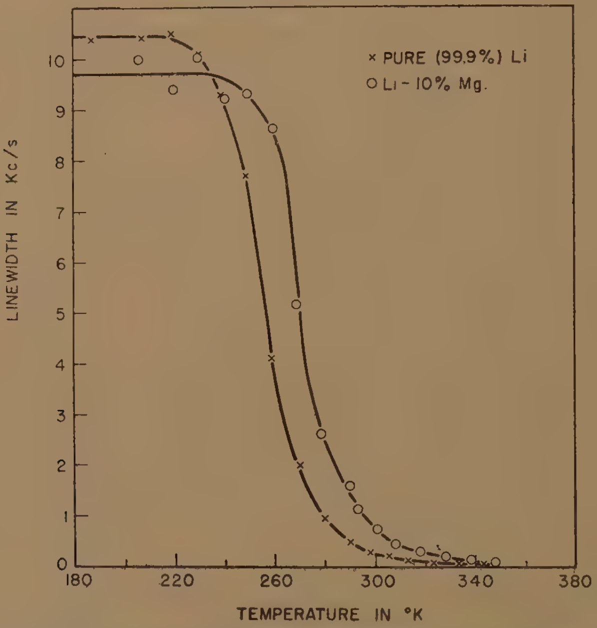

Variation of the ^{7}Li line-width with temperature for pure Li and Li–10% Mg.

From the line-width data, the activation energy of self-diffusion for ^{7}Li nuclei was calculated for both samples using the method given by Holcolm and Norberg (1955). From the region where the line-width shows an exponential dependence on temperature the following activation energies were determined: for pure lithium: 13·1 ± 0·2 kcal/mole; for the 10 at. % Mg alloy: 14·5 ± 0·3 kcal/mole. The error limits are estimated from the experimental scatter observed in the plots. The former value is in agreement with the value for pure lithium obtained by Holcolm and Norberg (1955) using pulse techniques.

The observed increase in activation energy is consistent with a picture of the alloy as more closely packed than pure lithium. Despite the larger size of the magnesium atom and ion the lattice parameter decreases with increasing magnesium concentration (Levinson 1955). Again, the van Liempt relation (van Liempt 1935), which might be expected to hold for a dilute alloy, predicts an increase in the activation energy of self-diffusion of the lithium atoms since the melting point (solidus and liquidus curves) rises with increasing concentration of magnesium.

In conclusion it may be mentioned that no line broadening arising from a dependence of Knight shift on nuclear environment has been observed for the Li–Mg system. This is in contrast to Drain's results on Ag–Cd alloys. However, such a broadening would not be expected at high temperatures due to rapid thermal diffusion and at low temperatures it is probably too small in the case of the Li–Mg alloys to be seen against the nuclear dipole–dipole broadening. The anomalous line broadening (referred to earlier) found in the 0·2% and 0·8% alloys is virtually temperature independent even in the liquid state. Its temperature independence rules out quadrupolar interactions and the type of broadening observed by Drain. It may however be related to the unexplained broadening observed in lithium samples by Holcolm and Norberg (1955). Further experiments are in progress to determine whether the effect is genuine or whether it is caused by simple contamination.

ACKNOWLEDGMENTS

I wish to thank Dr. J. S. Dugdale and Dr. D. K. C. MacDonald for their interest and stimulating discussions, and Dr. Drain for correspondence.

I am also indebted to the National Research Council for the award of a Postdoctorate Fellowship.

REFERENCES

BENEDEK, G. B., and KUSHIDA, T., 1958, *J. Phys. Chem. Solids*, **5**, 241.
CAGNAC, B., MANUS, C., BÉNÉ, G., and EXTERMANN, R., 1955, *Helv. Phys. Acta.*, **28**, 626.
COHEN, M. H., and HEINE, V., 1958, *Advanc. Phys.*, **7**, 395.
DRAIN, L. E., 1959, *Phil. Mag.*, **4**, 484.
DUGDALE, J. S., and GUGAN, D., 1960 (to be published).
ESTERMANN, I., FRIEDBERG, S. A., and GOLDMAN, J. E., 1952, *Phys. Rev.*, **87**, 582.
GUTOWSKY, H. S., and MCGARVEY, B. R., 1952, *J. chem. Phys.*, **20**, 1472.
HOLCOLM, D. F., and NORBERG, R. E., 1955, *Phys. Rev.*, **98**, 1074.
KNIGHT, W. D., 1956, *Solid State Physics*, Vol. 2 (New York: Academic Press Inc.).
LEVINSON, D. W., 1955, *Acta Met.*, **3**, 294.
ROBERTS, L. M., 1957, *Proc. phys. Soc. Lond.* B, **70**, 744.
VAN LIEMPT, J., 1935, *Z. Phys.*, **96**, 534.

On the Growth of Cadmium Crystals from the Vapour†

By P. B. PRICE‡
H. H. Wills Physical Laboratory, University of Bristol

[Received February 18, 1960]

ABSTRACT

Crystals of cadmium were grown from the vapour on a quartz fibre in an argon diffusion cell designed so that the temperature, T, could be measured and the supersaturation, σ, calculated at every point. A critical σ of $\sim 0{\cdot}4$ for nucleation was observed below which no crystals grew and above which the density of crystals increased with σ. For $\sigma \lesssim 2$, crystals grew as whiskers and thin platelets independently of σ and T; for $2 \lesssim \sigma \lesssim 10^2$ the end products were thick hexagonal plates; for $\sigma \gtrsim 10^2$ and $T \lesssim 250°\text{c}$ spike and leaf dendrites appeared and grew to large dimensions. The observed dependence of whisker growth rates on σ and whisker radius showed that growth was probably controlled by the diffusion of cadmium vapour through argon. Evidence for both tip growth and non-tip growth of whiskers is presented.

§ 1. INTRODUCTION

AT the present time a great deal of effort is being directed to studies of the unusual properties of single crystal whiskers of various materials (Doremus *et al.* 1958). However, with the exceptions of the work of Gomer (1958) on mercury whiskers and the work of Price *et al.* (1958) on electro-deposited silver whiskers, very little experimental work is being devoted to studies of the growth of whiskers under carefully controlled conditions. Because of the interesting results which studies of the mechanical properties of vapour-grown zinc and cadmium whiskers have yielded (Cabrera and Price 1958, Coleman *et al.* 1957), it was felt that a careful investigation of the kinetics of growth of these whiskers would be worthwhile.

This paper describes the results of a study of the growth rates and habits of whiskers and other small crystals of cadmium which were grown from the vapour in an atmosphere of argon under the simplest possible conditions, in which all the variables were fixed except the temperature, which was measured, and the supersaturation, which was calculated. The crystals were grown and observed in a closed cell in which convection was eliminated and the impurity content was very low. The geometry of the cell was such that the isothermals were plane, horizontal surfaces and the temperature varied linearly from top to bottom. The supersaturation was then a function of the temperatures of the top and bottom and of vertical position in the cell. The crystals grew on a quartz fibre so thin that cadmium atoms were removed from the diffusing vapour at a very low rate. As long as the density of crystals on the fibre was low, each crystal could be considered to act as an independent sink for the cadmium, which simplified the analysis of the observed growth rates.

---

† Communicated by J. W. Mitchell, F.R.S.

‡ Fulbright Fellow, 1958–59. Present address: Cavendish Laboratory, University of Cambridge.

A study of this nature is of importance because of the lack of quantitative information on the kinetics of crystal growth when diffusion of the material through a gas is the rate-controlling process. The main interest in diffusion-controlled growth in the past has been in the radical habit changes undergone by ice crystals falling through air at different temperatures. Reynolds (1952) and Mason (1953) have made rough measurements of rates of mass increase of ice crystals falling through a supercooled water cloud, but individual crystals were not followed during growth, so that there was considerable scatter in their data. Hallett and Mason (1958) have designed a diffusion cloud chamber in which the temperature and supersaturation can be controlled during the growth of ice crystals but, being interested mainly in crystal habit, they have not made growth rate measurements.

The cadmium vapour–argon system seems to be ideally suited for studies of growth rates and crystal habit. Both gases are monatomic, which simplifies the analysis, and cadmium has a high triple point pressure ($\sim 10^{-1}$ mm), does not react with glass, and is a stable solid at room temperature, so that crystals can be studied microscopically after growth.

§ 2. Experimental Details

2.1. *The Diffusion Cell*

The growth cell, shown in fig. 1, was designed to facilitate the interpretation of the results. Two Pyrex discs were sealed to the ends of a Pyrex cylinder 7 cm in diameter and 3·5 cm in length. Then a portion of the curved cell wall was ground away and replaced by an optically flat observation window about 3·5 cm by 3 cm. To the bottom of the cell was attached a small Pyrex tube containing a thin quartz fibre ending in a quartz sheath. An iron slug was sealed into the sheath so that the fibre could be raised to various positions along the axis of the cell by means of a small, d.c.-operated solenoid.

The top and bottom surfaces of the cell were maintained at fixed temperatures by pairs of aluminium discs heated internally by soldering iron elements. Temperature measurement to about 1°c was achieved with the use of two low heat capacity chromel–alumel thermocouples passing through small holes in the discs and making contact with the glass surfaces. The sides of the cell were also heated by a widely spaced wire coil wound on a cylindrical Pyrex frame which just fitted over the cell. The front portion of this frame was optically flat, so that crystals could be viewed and photographed through the frame and cell during growth.

Temperature profiles along the axis of the cell were measured for various voltages on the disc and ‘ cage ’ heaters by inserting a thermocouple into the cell through the tube which normally contained the fibre. These measurements were made in air; it was then assumed that the temperature distribution under the same conditions was the same when the cell was filled with argon and cadmium and sealed off. By proper adjustment of the relative voltages on the heaters, the temperature could be made to decrease linearly from the top to the bottom of the cell with any gradient desired and with plane, horizontal isothermals except near the cell walls. To obtain a very steep gradient it was necessary to replace the bottom disc heater by a water-cooled copper block whose temperature was varied by varying the rate of flow of the water.

Fig. 1

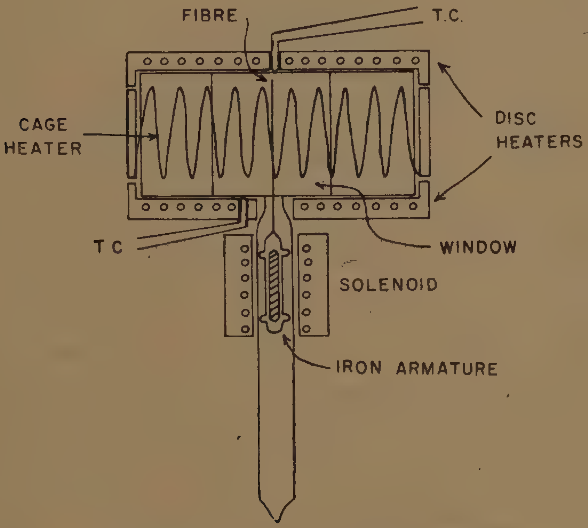

Diffusion cell for crystal growth.

A diffusion cell was prepared for crystal growth experiments by joining the small tube containing the fibre and iron slug through a constriction to a high vacuum system and to a three-stage distillation train containing high-purity cadmium (99·999%)†. The cell and connecting tubing were baked out at 500°c for 24 hours. The cadmium was then further purified by successive distillations and finally a small quantity was condensed into a layer on the top and a layer on the bottom of the cell. Then high-purity argon at a pressure of 600 mm of Hg at 20°c was introduced from a Pyrex flask by means of a break-seal arrangement and the cell sealed off.

2.2. *Experimental Procedure*

During an experiment cadmium vapour diffuses from the hot top surface through an atmosphere of argon along vertical flow lines to the bottom cooler surface. The presence of the argon, whose temperature varies linearly down the cell, causes the partial pressure and the temperature of the cadmium vapour also to vary linearly. A knowledge of the temperatures of the top and the bottom of the cell thus allows one to calculate the supersaturation of cadmium vapour as a function of position in the cell. This is done in the Appendix.

---

† Kindly supplied by the Imperial Smelting Corporation Ltd.

Let us now consider the effect of raising a fibre into the cell. If the fibre is very thin, so that it removes cadmium atoms from the diffusing vapour at a very low rate, the flow lines of the vapour will not be appreciably affected by the few crystals which can grow on the fibre except in the immediate vicinity of a crystal. This means that the interaction between neighbouring crystals and the reduction in cadmium vapour pressure near the fibre can be neglected in calculations of the supersaturation. This is a tremendous advantage over the usual whisker growth arrangement (cf. Cabrera and Price 1958), in which vapour flows through a long tube, depositing on the walls in the form of crystals as it goes and gradually decreasing in pressure until it reaches the end of the tube.

Crystals were grown in a series of temperature gradients, with the top surface of the cell usually held at the melting point of cadmium, about 320°C. The crystals grew at various temperatures and at calculated supersaturations varying from about 10^{-1} to 10^4. In this paper the supersaturation is defined as $\sigma = (p - p_{\text{eq}})/p_{\text{eq}}$, where p and p_{eq} are the actual and equilibrium partial pressures of cadmium vapour.

The procedure was to allow the temperature distribution in the cell to reach a steady state, then to torch the tube containing the fibre in order to evaporate any cadmium which might have diffused down from the cell and to heat the fibre above the temperature of the cell, and then quickly to raise it into position in the cell by means of the solenoid. In this way the experiment was started with the vapour phase in the immediate vicinity of the fibre in a temporarily undersaturated condition. Without the preheating, the vapour near the cold fibre would have initially been in a highly supersaturated condition, making nucleation of crystals easier.

Crystals were observed and photographed at magnifications of × 12·5 and × 35, both by reflected light and by transmitted light. A stereoscopic microscope was mounted as a cathetometer so that the position of a given crystal on the fibre could be determined to ± 0·05 mm. Growth rates were determined by measuring the dimensions of the crystals with a micrometer eyepiece as a function of time, the sensitivity being 1 division = 2·7 microns at × 35. Only those crystals were selected for measurements which were extending in directions nearly perpendicular to the axis of the microscope. The radii of thick whiskers were measured with the eyepiece; the radii of very thin whiskers were estimated to an accuracy of about ± 25% by observing the amounts by which they sagged under their own weight.

§ 3. OBSERVATIONS

3.1. *Crystal Habit*

3.1.1. *Low supersaturations*

It is shown in the Appendix that the supersaturation varies from zero at the top of the cell, through a maximum value, $\sigma_{\max}$, at some point $z_{\max}$

along the axis, then back to zero at the bottom. It was experimentally observed that no deposition occurred when $\sigma_{\max}$ was less than about 0·4. As $\sigma_{\max}$ was increased above this critical value, the number of crystals increased from only one or a few, located near the calculated value of $z_{\max}$ on the fibre, to a very large quantity at high supersaturation. Once nucleated, crystals continued to increase in size, even if σ was reduced to values as low as 0·12. This suggests that there is a large free energy barrier to nucleation but only a small one to the continued growth of these crystals.

At low supersaturations ($\sigma \lesssim 2$) the predominant habits were found to be whiskers and thin platelets. Figure 2† shows a typical group of crystals after 75 min of growth in a cell in which $\sigma_{\max}$ was $\sim 0{\cdot}95$. In the region included in the picture, the temperature, T, was decreasing downward from 295°C to 290°C and σ was increasing from 0·65 to 0·75.

Observations of many crystals which grew at low σ showed that there was no systematic variation of habit with either σ or T. The crystal habit seemed to be determined at a very early stage in the growth process, even before the crystal was observable in the microscope. This is suggested by fig. 3, which shows a random distribution of whiskers and platelets 5 min after the beginning of growth, when $\sigma_{\max}$ was $\sim 1{\cdot}4$.

3.1.2. *Intermediate supersaturations*

For $\sigma \gtrsim 2$ the density of crystals was rather high, and most of the whiskers and thin platelets eventually disappeared, both by growing into neighbouring crystals and by fairly rapid thickening. Under these conditions thick hexagonal plates occurred as end products. In fig. 4 ($\sigma_{\max} \simeq 3$), for example, only one whisker is left after a period of growth of a few hours. Figure 5 shows the appearance of a fibre after one day of growth at $\sigma_{\max} \simeq 8$.

3.1.3. *High supersaturations*

The higher the supersaturation the smaller was the average plate size, since the closely spaced crystals grew into each other and competed for cadmium atoms. When $\sigma_{\max}$ approached or exceeded about 10^2 and when T was less than ~ 250°C, a few large crystals with very interesting dendritic habits appeared in the deposit. Figure 6 shows a portion of a fibre at $z_{\max}$ when the bottom was water-cooled to produce a maximum supersaturation of ~ 110 at a temperature of ~ 180°C. Near the centre are four leaf-shaped crystals, only one of which is in focus, and toward the top of the picture are two polycrystalline, spike-shaped dendrites which, instead of having smooth sides as the whiskers do, are covered with overgrowth in the form of tiny hexagonal plates and irregular microscopic crystals. Figure 7 shows a cadmium 'snowflake', which also grew at high supersaturation. The morphology and growth mechanism of the leaf dendrites are discussed in detail in another paper (Price 1959).

---

† Figures 2 to 7 are shown as plates.

3.2. *Whisker Growth Rates*

Because of the absence of distinguishing marks on most of the whiskers, it was impossible to decide on the basis of observations where material was added to them during growth. It was occasionally observed, however,

Fig. 8

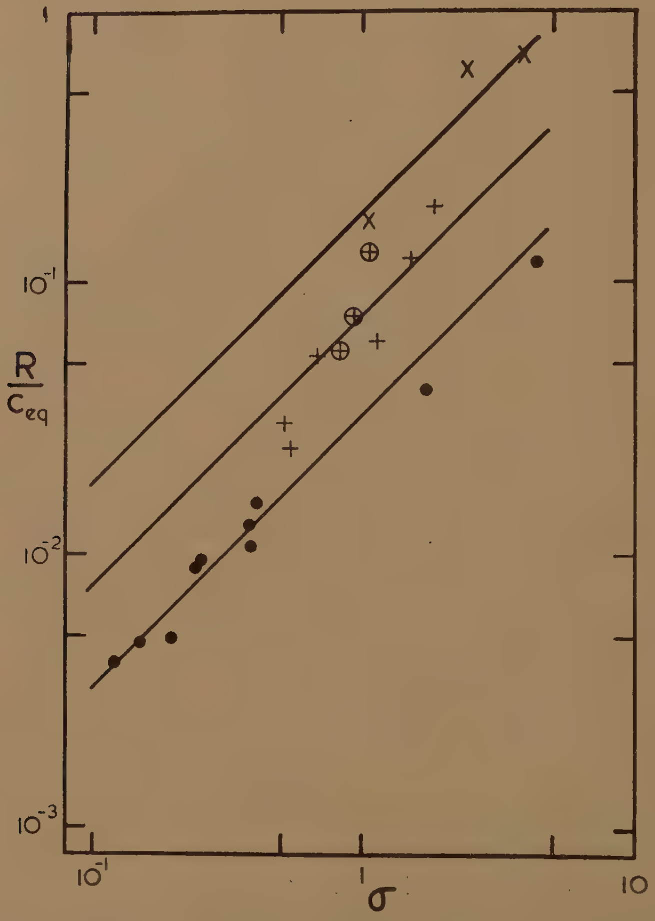

Growth rates of cadmium whiskers. Whisker radii are indicated by ● for $r_w=2\ \mu$, + for $r_w=1\ \mu$, and × for $r_w=\frac{1}{2}\ \mu$. ⊕ denotes non-tip growth for whiskers with $r_w=1\ \mu$. The units for R/c_{eq} are $\mu^4\ \text{min}^{-1}$.

that two adjacent whiskers crossed each other during growth and formed a figure X whose acute angles were gradually filled in with cadmium. The fact that these joined whiskers continued to grow in length beyond the joint and that the sections below the joint remained straight was evidence for tip growth. On the other hand, it was observed several times, particularly at rather high supersaturations ($\sigma \gtrsim 0{\cdot}8$), that a whisker would grow with a speck of cadmium at its tip. The speck remained the same size and stayed at the tip as the whisker lengthened. This seemed to indicate that material was not being added at the tip.

Some preliminary measurements were made of the axial growth rates of whiskers with no distinguishing marks and whiskers with observable specks at their tips, as a function of σ and whisker radius, r. Rates varied from a few tenths of a micron per minute to as much as 160 μ/min. The results are displayed in fig. 8, with $\log(R/c_{\mathrm{eq}})$ plotted as a function of $\log \sigma$ and with individual points labelled according to the estimated values of r. R is the observed growth rate in μ/min, $c_{\mathrm{eq}} = (p_{\mathrm{eq}}/kT)$ is the equilibrium density of cadmium vapour in atoms per μ^3, and r is in microns.

Fig. 9

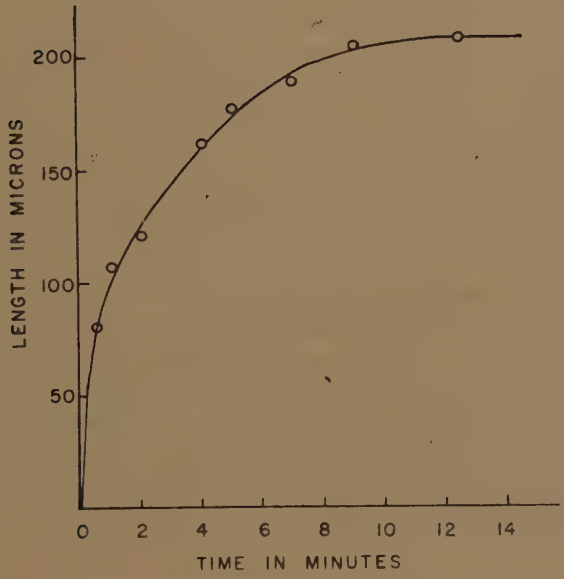

Growth rate curve of a whisker which thickens during growth at $\sigma \simeq 2{\cdot}4$.

Usually the curve of whisker length as a function of time was linear over the entire period of observation, and the whisker appeared to grow at constant radius. At high supersaturation, however ($\sigma \gtrsim 1$), a whisker was often observed to extend itself axially at a decreasing rate and radially at an increasing rate until the two rates were about the same. It then gradually grew into a bulk crystal. Figure 9 shows the change in axial growth rate for a typical whisker when σ was $\sim 2{\cdot}4$.

§ 4. INTERPRETATION OF THE RESULTS

4.1. *Crystal Habit*

The observation that whiskers and thin platelets are stable growth forms only when $\sigma \lesssim 2$ is very significant and is probably connected with the onset of surface nucleation. In fact, this is not an unreasonable value for the critical σ at which the rate of surface nucleation becomes appreciable.

This implies that at low supersaturation whiskers grow axially and thin platelets grow laterally by a dislocation mechanism. Subsequent thickening at higher supersaturation is then due to nucleation of new layers, probably where the crystal is attached to the substrate.

Since there seems to be no systematic variation of habit with either σ or T in the region of low supersaturation, and since it appears always to be determined at a submicroscopic stage of development, the dislocation configuration is probably introduced at or soon after nucleation and is responsible for the habit.

Cabrera and Price (1958) found that vapour-deposited cadmium whiskers generally grew in a $\langle 11\bar{2}0\rangle$ or a $\langle 11\bar{2}3\rangle$ direction, and that all cadmium platelets were basally oriented. It will be assumed that the crystals described above have the same orientations. Then it is proposed that a whisker develops from a nucleus containing a pure screw dislocation with a Burgers vector of $\frac{1}{3}\langle 11\bar{2}0\rangle$ or $\frac{1}{3}\langle 11\bar{2}3\rangle$ and that a platelet can develop when the nucleus has a system of one, two, or perhaps three $\langle 11\bar{2}0\rangle$ dislocations. Experiments on the plastic deformation of whiskers and platelets of zinc (Price 1960) confirm the existence of dislocations of both types.

4.2. *Whisker Growth Rates*

Although the measurements of axial growth rates of whiskers are only preliminary, it is possible from a study of fig. 8 to draw some general conclusions about the functional relationship between R, σ and r. It will be noticed that the points corresponding to whiskers of radii $\frac{1}{2}$, 1 and 2 μ fall into three groups which lie roughly along straight lines of unit slope. The equation

$$R = \frac{\alpha\sigma c_{\text{eq}}}{r^{\beta}} \quad . \; . \; . \; . \; . \; . \; . \; . \; . \quad (1)$$

can therefore be used to describe the relationship empirically, with α and β adjustable constants. For the three lines drawn in fig. 8, which were chosen to give the best fit to the data, the relation is

$$R = \frac{0{\cdot}076\sigma c_{\text{eq}}}{r^{1{\cdot}2}}\ \mu\,\text{min}^{-1}. \quad . \; . \; . \; . \; . \; . \quad (2)$$

This equation is also valid for the growth rates of whiskers with observable specks at their tips (indicated in fig. 8 by circles). Furthermore, it is in agreement with the qualitative observation that thickening whiskers grow at decreasing rates.

If diffusion of cadmium vapour through the argon is the rate-controlling process, and if it is assumed that there is a spherical diffusion field around the tip of each growing whisker, than it can be shown that the growth rate is given by

$$R=\frac{4D\Omega\sigma c_{\mathrm{eq}}}{r} \quad . \; . \; . \; . \; . \; . \; . \; . \quad (3)$$

where D is the diffusion coefficient of cadmium in argon and Ω is the atomic volume. For $D \simeq 0{\cdot}2\,\mathrm{cm}^2/\mathrm{sec}$, the equation becomes

$$R=\frac{0{\cdot}1\sigma c_{\mathrm{eq}}}{r}\,\mu\,\mathrm{min}^{-1} \quad . \; . \; . \; . \; . \; . \; . \quad (4)$$

which, although it differs from eqn. (2) in the value of the exponent of r, gives order of magnitude agreement with all the observed growth rates.

Because of the limited range of values of r for which data were obtained, and because of uncertainty in the measurements of r, it is impossible to decide exactly how R depends on r. It seems fairly certain, however, from the correspondence between (2) and (4), that R is determined by the rate of diffusion of material through the inert gas, both for the tip growing and the non-tip growing whiskers.

Let us now consider briefly how a whisker might grow by the addition of atoms at points other than the tip. One possible mechanism could operate if the whisker had a pure screw dislocation along the axis which suddenly became a pure edge dislocation and ran out to the lateral surface. If the temperature were sufficiently high, the edge dislocation would maintain the equilibrium concentration of vacancies around it. At the surface, on the other hand, there would be an understaturation in surface vacancies corresponding with the supersaturation in adsorbed surface atoms. A concentration gradient would therefore be established in which vacancies would diffuse to the surface from the edge dislocation and thus cause it to climb. Every rotation of the edge dislocation around the axis would incorporate a new plane of atoms so that the whisker would be continuously lengthened. This is one possible mechanism, similar to the one suggested by Frank (1953) to explain the growth of tin whiskers on plated surfaces. Other mechanisms for the non-tip growth of whiskers may be envisaged but it seems desirable to defer further speculation until more observations and quantitative measurements are available.

§ 5. SUMMARY

Cadmium crystals were grown from the vapour on a quartz fibre in an argon diffusion cell which was designed so that the temperature could be measured and the supersaturation calculated at every point. Crystal habits and growth rates were studied as a function of σ and T. A critical σ of $\sim 0{\cdot}4$ for nucleation was observed below which no crystals grew and above which the density of crystals increased with σ.

At low supersaturations ($\sigma \lesssim 2$) the crystal habit appeared to be determined at a very early stage in growth and was independent of σ and T,

consisting mainly of whiskers and thin platelets. For $\sigma \gtrsim 2$ the frequency of two-dimensional nucleation was so high and the density of crystals on the fibre so great that whiskers and thin platelets thickened and grew into each other, leaving as the stable growth forms mainly thick hexagonal plates. The average plate dimensions decreased as the density increased, because of increased competition for the vapour. At very high supersaturations ($\sigma \gtrsim 10^2$) crystals with dendritic habits grew to large dimensions from the deposit.

Axial growth rates of whiskers were measured as a function of σ and r and found to give fair agreement with rates derived assuming growth to be controlled by the diffusion of cadmium vapour through argon. Growth rates were accurately linear except at high supersaturations ($\sigma \gtrsim 1$), in which case the rates decreased as the whiskers thickened.

Some whiskers were observed to grow with observable specks of cadmium at their tips, which was interpreted as evidence for non-tip growth.

ACKNOWLEDGMENTS

It was a pleasure to work under the direction of Dr. J. W. Mitchell and Professor F. C. Frank, to whom I am indebted for many valuable discussions. The growth cells were constructed by J. H. Burrow, who was to a large extent responsible for the success of the experiments. The photomicrographs were taken with equipment purchased with the assistance of a grant from the Department of Scientific and Industrial Research. The work was carried out during the tenure of a Fulbright grant from the U.S. Government and was a continuation of research begun at the University of Virginia with Professor N. Cabrera, to whom I am grateful for reviewing the manuscript.

APPENDIX

DETERMINATION OF SUPERSATURATION IN THE CELL

The top and bottom surfaces of the cell may be regarded as two infinite parallel plane layers of cadmium held at fixed temperatures T_a and T_{-a} at the vertical position coordinates a and $-a$. Assuming a steady state with the vapour being transported downwards by diffusion through the gas, and assuming the diffusion constant to be independent of temperature, the diffusion equation predicts a linear variation of the vapour density of cadmium between the two layers. Using the boundary conditions that the partial vapour pressures of cadmium at a and $-a$ will be the equilibrium vapour pressures at T_a and T_{-a}, the actual values of the partial vapour pressure p at any level are determined. Since p_{eq} varies exponentially with temperature, whereas p varies linearly, it is obvious that the gas will be supersaturated with cadmium vapour at every point in the cell except at the top and bottom.

The supersaturation curve can be obtained graphically from a table of p_{eq} as a function of T (Honig 1957) for any values of T_a and T_{-a}, but it is interesting to get an analytic expression for the supersaturation as a function of temperature and position in the cell. For convenience the saturation ratio, defined by $\alpha=\sigma+1=(p/p_{\mathrm{eq}})$, will be used. Assuming that $\Delta T/T_0$ is small, where

$$\Delta T=T_a-T_{-a} \quad \text{and} \quad T_0=\frac{T_a+T_a}{2},$$

the result is

$$\alpha \simeq \cosh \beta a[1+(z/a)\tanh \beta a]\exp(-\beta z), \qquad (1)$$

where $\beta=q\Delta T/2akT_0^2$, with q=latent heat of condensation and k=Boltzmann's constant. This expression is accurate to within 6% for $\Delta T/T_0 \lesssim 0{\cdot}1$. For temperature differences greater than this it is better to solve for α graphically.

Fig. 10

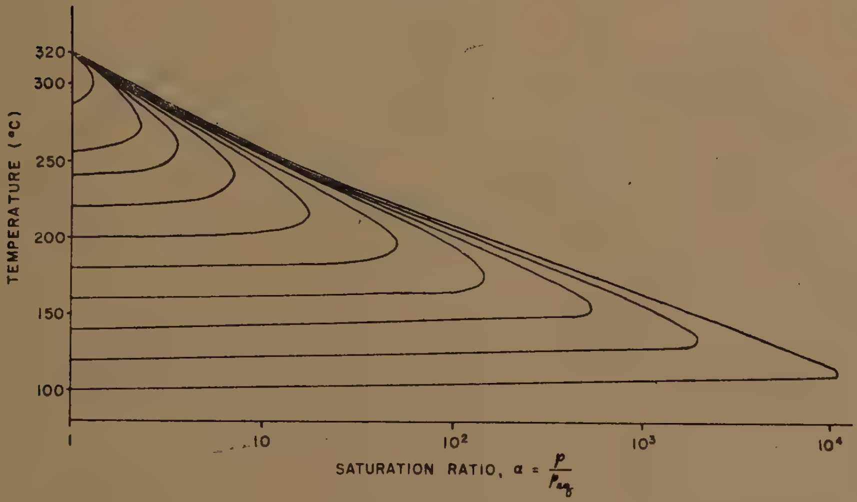

α-curves for different values of T_a and T_{-a}.

The saturation ratio varies from one at the top of the cell, through some maximum value $\alpha_{\max}$ at the position $z_{\max}$, to one at the bottom. Differentiation of (1) gives

$$\alpha_{\max}=(1/\beta a)\sinh \beta a \exp(\beta a \coth \beta a-1), \qquad (2)$$

$$z_{\max}=(1/\beta)-a \coth \beta a. \qquad (3)$$

Since $\coth \beta a$ is always greater than βa, $z_{\max}$ is always below the middle of the cell, and as βa increases (i.e. ΔT increasing), $\alpha_{\max}$ increases and $z_{\max}$ approaches $-a$.

It is seen from (1) that α is a function only of z/a and $\Delta T/T_0^2$, so that there is no point in using cells of different dimensions. The only way to vary α and T independently is to vary T_0, which means varying the fixed temperatures of the top and bottom of the cell. This is of limited usefulness, because for low values of T_a growth proceeds only very slowly due to the low vapour pressure of the source, whereas for high values of T_a part of the fibre is above the melting point of cadmium. There are thus certain practical limitations on the values of the growth parameters which can be achieved independently.

Figure 10 shows a series of α curves plotted on the same graph, with the saturation ratio as the abscissa on a logarithmic scale, with T_a for each curve fixed at the melting point of cadmium, about 320°C, and with T_{-a} varying from 300° to 100°C in 20° intervals along the ordinate axis. The curves give an idea of the behaviour of α for different values of ΔT ranging from 20° to 220°, showing qualitatively the behaviour of α_{max} and z_{max}. It is to be noted that, since the temperature varies linearly with cell height, the ordinate can also be taken as a measure of position in the cell, with the top of the cell at 320° for each curve but with the bottom of the cell at a point on the ordinate determined by the value of ΔT for a particular curve.

REFERENCES

CABRERA, N., and PRICE, P. B., 1958, *Growth and Perfection of Crystals* (New York: Wiley), p. 204.
COLEMAN, R. V., PRICE, P. B., and CABRERA, N., 1957, *J. appl. Phys.*, **28**, 1360.
DOREMUS, R. H., ROBERTS, B. W., and TURNBULL, D., 1958, editors of *Growth and Perfection of Crystals* (New York: Wiley).
FRANK, F. C., 1953, *Phil. Mag.*, **44**, 854.
GOMER, R., 1958, *J. chem. Phys.*, **28**, 457.
HALLETT, J., and MASON, B. J., 1958, *Proc. roy. Soc.* A, **247**, 440.
HONIG, R. E., 1957, *R.C.A. Rev.*, **18**, 195.
MASON, B. J., 1953, *Quart. J. R. met. Soc.*, **79**, 104.
PRICE, P. B., 1959, *Phil. Mag.*, **4**, 1229; 1960, *Phil. Mag.* (in the press).
PRICE, P. B., VERMILYEA, D. A., and WEBB, M. B., 1958, *Acta Met.*, **6**, 524.
REYNOLDS, S. E., 1952, *J. Met.*, **9**, 36.

The Dislocation Distribution, Flow Stress, and Stored Energy in Cold-worked Polycrystalline Silver†

By J. E. Bailey and P. B. Hirsch
Crystallographic Laboratory, Cavendish Laboratory, Cambridge

[Received January 5, 1960]

Abstract

Distribution and densities of dislocations, determined by electron transmission microscopy, flow stress and stored energy measurements (by microcalorimetry) on cold-worked polycrystalline silver are correlated with each other. The dislocations are arranged in dense networks forming the boundaries of an otherwise relatively dislocation-free cell structure. The flow stress is explained quantitatively in terms of the forest intersection mechanism at the boundaries. The stored energy after recovery is of the same order as the total self-energy of the dislocation arrangement, so that the long-range stresses must be largely relaxed. The considerable energy release during the recovery stage produces no observable change in dislocation distribution. This recovery stage is thought to be due to the relief of long-range stresses or to the removal of point defects.

While the values of flow stress and stored energy can be accounted for in terms of the observed non-uniform distribution of dislocations (cell structure), they are not compatible with each other on a model based on a uniform distribution of pile-ups; nor are pile-ups observed on the electron micrographs.

§ 1. INTRODUCTION

THEORIES of flow stress and work hardening depend on the particular dislocation distributions assumed in the model of a cold-worked metal (Seeger 1957, Friedel 1955, Hirsch 1958). The present paper describes a direct correlation between the experimentally determined distribution and density of dislocations, the flow stress and the stored energy in cold-worked polycrystalline silver. The distribution and density of dislocations are determined by means of the transmission electron microscope technique (Hirsch *et al.* 1956), the flow stress is measured on a conventional straining machine, and the stored energy using an isothermal calorimeter (Bailey 1959).

§ 2. FLOW STRESS AND STORED ENERGY MEASUREMENTS

The silver for all the experiments was supplied by the Sheffield Smelting Company; the purity is 99·99%, the major part of the impurity being copper together with traces of silicon, magnesium and iron.

The calorimetry experiments were carried out using specimens of about 13 mm diameter cut from tensile specimens. The grain size of the specimens was $\sim 12\,\mu$. The specimens were extended at a rate of $\sim 10^{-2}$/min; fig. 1 shows the stress–strain data of the tensile specimens. It was found

---

† Communicated by the Authors.

Fig. 1

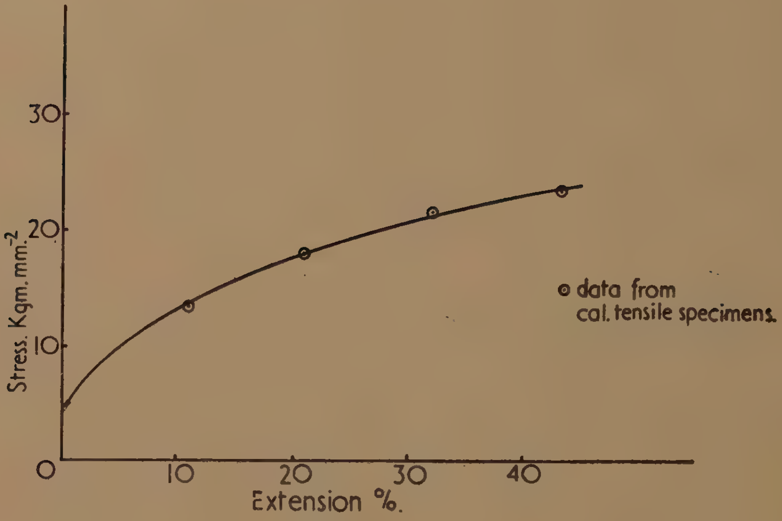

Stress–strain curves of the silver foils (full curve) and calorimetry tensile specimens (points).

Fig. 2

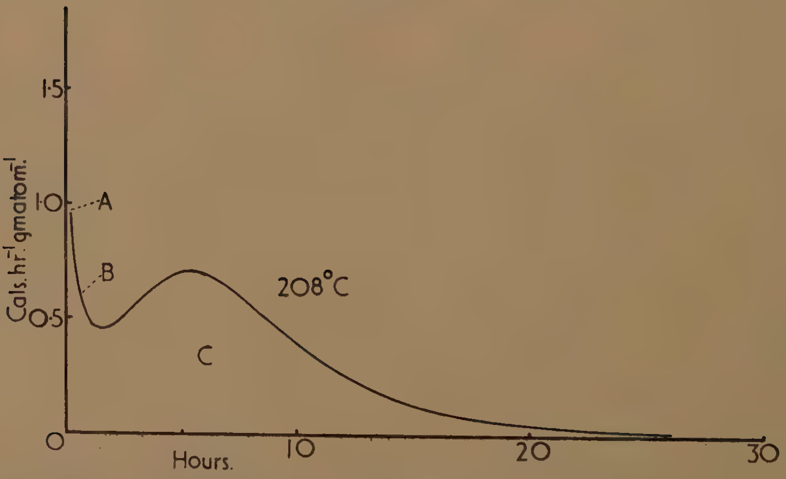

Energy release curve for silver deformed 43% in tension and annealed at 208°c, showing the recovery stage B and recrystallization stage C. Measurements cannot be made over the first fifteen minutes (region A).

impracticable to prepare electron microscope specimens from those used for calorimetry because of their large size. To overcome this difficulty a calorimeter specimen was rolled into sheet 0·005 in. thick. After suitable annealing treatments the silver foil had a grain size of $\sim 20\,\mu$. These foils were extended at a rate of $1{\cdot}5\times10^{-4}$/min; fig. 1 shows a stress–strain curve. It is clear from fig. 1 that the stress–strain curves of both types of specimen are almost identical. It is reasonable to assume therefore that the dislocation distributions are closely similar in both types of specimen for a given degree of deformation.

Table 1. Values of E_P, E_R, E_T and E^* at different temperatures for a given deformation

Deformation (% extension)	Temperature (°c)	E_T (cals/g atom)	E_P (cals/g atom)	E_R (cals/g atom)	E^* (cals/g atom)
32	253	8·10	3·34	4·76	7·60
32	245	7·75	2·91	4·84	7·25
32	229	7·54	2·78	4·76	7·14
32	209·5	7·60	2·44	5·16	7·40

Table 2. Average values of the total stored energy, E_T, and the energies evolved during recovery, E_P, and recrystallization, E_R

Deformation (% extension)	E_T (cals/g atom)	E_R (cals/g atom)	E_P (cals/g atom)
11	2·70	1·25	1·45
21	5·10	2·83	2·27
32	7·75	4·9	2·85
43	7·27	6·03	1·24

The stored energy was determined by measuring the heat evolved as a function of time in an isothermal calorimeter. A typical heat release curve is shown in fig. 2. The energy released in region A, corresponding to the first 15 min, could not be measured; this is the time interval in which the specimen reaches the equilibrium temperature of the calorimeter. Region B corresponds to a recovery stage, and region C is accompanied by recrystallization (checked by x-ray diffraction methods). The composite curves can always be analysed in terms of two overlapping components; one of these (C) has the usual recrystallization kinetics (Burke and Turnbull 1952), while region B can be fitted to a law $dQ/dt = A/(t+t_0)$, where dQ/dt is the rate of release energy, A and t_0 are constants depending on temperature and prior deformation. The total stored energy is obtained by integrating the area under the curve; the energy is in two parts, one released during recovery, E_P, and the other during recrystallization, E_R. The part released during recrystallization is usually accurate to ~5%. In order to determine the energy released during recovery, curve B is extrapolated to zero time using the above law. Table 1 gives values of E_P, E_R, the total stored energy E_T ($=E_P+E_R$) and the energy released after the first 15 min E^*, at different temperatures for a given deformation. It is clear from the agreement between the results obtained at the different temperatures that the values of E_T are accurate to about 10%. Similar results have been obtained for specimens deformed by different amounts; however, for the smallest deformation studied (11% extension) the errors are somewhat larger (Bailey 1959). The energy released during the first 15 min does not usually exceed about 20% of the total energy, except again for the specimens with the smallest deformation. The general agreement between values obtained at different temperatures suggests that the extrapolation technique used is satisfactory.

Table 2 shows the average values of E_P, E_R and E_T for each deformation.

§ 3. ELECTRON MICROSCOPE OBSERVATIONS

Electron microscope specimens were prepared by electropolishing the silver sheet of thickness 0·005 in. mentioned above, after various deformations. A polishing bath recommended for gold by Jacquet (1956) was found to be suitable. Its constituents are, per litre: 67·5 g potassium cyanide; 15 g Rochelle salt; 19·5 cm³ orthophosphoric acid; 2·5 cm³ ammonia; 15 g potassium ferrocyanide. The voltage required across the cell is about 4 v; a stainless-steel cathode is used and the specimen is agitated slightly to avoid etching. The specimen is removed rapidly after polishing, washed in distilled water and stored in absolute alcohol until required.

Typical areas of specimens deformed 10, 20 and 30% in tension are shown in fig. 3 (*a*), (*b*) and (*c*) (Pl. 52). The dislocations are arranged mainly in complex bands separating relatively dislocation-free areas. This cell structure becomes more pronounced with increasing deformation; i.e. at low deformation the dislocation density is rather more uniform, while at the higher deformation there is clearer distinction between the cell walls containing a high density of dislocations, and the relatively dislocation-free interior. After 30% deformation the diameter of the cells is ~1 μ. It is difficult to decide from the micrographs whether there is a significant decrease in cell size with increasing deformation over the range of extensions investigated, i.e. 10–30%. The cell boundaries appear to be regions of complex 3-dimensional networks; they are not single plane low angle boundaries. Figure 4 (Pl. 53) shows the nature of the cell boundaries at high magnification. The dislocation density in the cell walls increases with increasing deformation. It is not clear however whether there is any significant change in the thickness of the cell walls with increasing deformation.

The misorientations across the boundaries are less than 1°; this is evident from diffraction patterns, an example of which, from an area of $\frac{4}{3}\mu$ in diameter of a specimen extended 30%, is shown in fig. 3 (*d*). Similar single crystal patterns are obtained also from specimens deformed 10 or 20 %; areas completely within one grain were chosen for these experiments. A study of the orientation of the cell boundaries failed to reveal any tendency for them to follow any particularly simple crystallographic directions. There is no evidence on the micrographs for groups of piled-up dislocations.

The original grain boundaries are still clearly visible after deformation. No large discontinuities or steps were observed. With increasing deformation, however, there appears to be a tendency to roughening of the boundaries on a scale of about 100 Å.

Table 3. Dislocation densities in silver foil deformed in tension

Extension (%)	Dislocation density (cm/cm³)	Mean dislocation density (cm/cm³)
32	$6{\cdot}0\times10^{10}$ $8{\cdot}0\times10^{10}$ $7{\cdot}5\times10^{10}$ $5{\cdot}2\times10^{10}$ $7{\cdot}8\times10^{10}$ $7{\cdot}0\times10^{10}$ $7{\cdot}0\times10^{10}$	$6{\cdot}8\times10^{10}$
21	$5{\cdot}5\times10^{10}$ $4{\cdot}0\times10^{10}$ $6{\cdot}2\times10^{10}$ $5{\cdot}0\times10^{10}$	$5{\cdot}2\times10^{10}$
11	$2{\cdot}0\times10^{10}$ $2{\cdot}0\times10^{10}$ $2{\cdot}5\times10^{10}$ $2{\cdot}5\times10^{10}$	$2{\cdot}2\times10^{10}$

Dislocation densities were estimated by measuring the total projected length of dislocation line in a given area on a micrograph. A typical area was selected in the electron microscope, a micrograph and diffraction pattern taken, and the electron beam was then increased to allow some dislocations to move to produce slip traces. Since the orientation of the foil is known from the diffraction pattern, the particular (111) plane corresponding to a given slip trace can be determined. From the widths of the slip trace and the orientation of this (111) plane, the local thickness of the specimen can be calculated. In this way the total projected length of dislocation line in a given volume of specimen is determined. Assuming that the dislocation segments are randomly orientated, the mean length of dislocation line, R, can be derived from the mean projected length, R_P, by using the relation $R=(4/\pi)R_P$.

An important source of error arises from the difficulty of resolving individual dislocations in regions of very high dislocation density. Such areas are interpreted as bands of high dislocation density inclined almost perpendicularly to the foil surface, so that the dislocations overlap in projection. This effect was allowed for by assuming that the denstiy in these bands is similar to that in bands lying more parallel to the surface, in which the dislocation overlap is negligible, and which are thought to correspond to the regions on the micrographs in which the dislocations can be resolved. The measurements were repeated for several areas of a specimen. Table 3 shows the results; from the spread of values the error appears to be about 25%. In addition there is the possibility of systematic errors. After the specimen is thinned dislocations which are free to move may shorten their lengths by gliding into an orientation such that they traverse the foil along the shortest distance in the slip plane. The magnitude of this effect is difficult to estimate. but since most of the dislocations occur in close mesh networks this error is likely to be small. Furthermore, certain dislocations may be invisible (Hirsch *et al.* 1959); the magnitude of this effect depends on orientation and has not yet been studied rigorously; however the error is not likely to exceed 20%. We conclude that the estimates of the densities of visible dislocations are probably accurate to 25% but that they may underestimate the true dislocation densities by about 20%. In spite of these errors the increase in dislocation density with increasing deformation is clearly established.

Attempts were made to estimate the dislocation densities in the dense areas. This is very difficult to do with any precision. However, it appears that for all three deformations the dislocation densities in these areas are about five times the average values.

Electron microscope observations were also carried out on specimens which had recovered but not recrystallized. No significant difference could be detected between the dislocation distributions and densities before and after recovery.

§ 4. Discussion

4.1. *Energy of a Dislocation*

Since the stored energies and dislocation densities are known for comparable specimens, the energy associated with a dislocation can be calculated. Table 4 shows the values of energy per atom plane of dislocation before and after recovery for three different deformations. The differences between the values for different deformations are not significant; the average values are 8·3 ev before and 4·5 ev after recovery. Thus about half the total stored energy is released before recrystallization, apparently without change in the dislocation density.

It is instructive to compare these values with theoretical estimates. The dislocations are found to be arranged in complex networks which are almost certainly not stress free. The energy associated with a dislocation consists of its self-energy and the energy of interaction with other dislocations. The self-energy (per unit length) is given approximately by

$$E_1 = \frac{G\mathbf{b}^2}{4\pi K} \ln \frac{R}{r_0} + \text{core energy}$$

where G is the shear modulus, **b** the Burgers vector, $K=1$ for a screw, $1-\nu$ for an edge dislocation, ν Poisson's ratio, R the radius of the volume over which the stress field extends, and r_0 the core radius. A reasonable value for the core energy is $G\mathbf{b}^2/10$ so that we may write

$$E_1 = \frac{G\mathbf{b}^2}{4\pi K}\left(\ln \frac{R}{r_0} + 1\right).$$

The value of R is uncertain; however, a lower limit is given by the length of a dislocation segment in the networks, i.e. about 200 Å, and an upper limit by the size of the cells, i.e. about 1 μ after heavy deformation. The mean of the values for E_1 for edge and screw dislocations, of several values of R are shown in table 5 (r_0 is taken as $\mathbf{b}/2$). Values using the more detailed energy expression due to Schoeck and Seeger (1953) are also shown. These are somewhat smaller than the values calculated on the above formulation. Comparison of experimental and theoretical values of dislocation energy shows that the experimental values before recovery are somewhat larger

Table 4. Energy per atom plane of dislocation before and after recovery

Deformation (% extension)	Dislocation density, N (cm/cm^3)	Total stored energy, E_T (cals/g atom)	$L_T=E_T/N$ (ev/atom plane)	E_R (cals/g atom)	$L_R=E_R/N$ (ev/atom plane)
10	$2{\cdot}2\times10^{10}$	2·7	$9{\cdot}1\pm2{\cdot}5$	1·25	$4{\cdot}2\pm1{\cdot}0$
20	$5{\cdot}2\times10^{10}$	5·10	$7{\cdot}3\pm2{\cdot}5$	2·8	$4{\cdot}0\pm1{\cdot}0$
30	$6{\cdot}8\times10^{10}$	7·7	$8{\cdot}4\pm2{\cdot}5$	4·9	$5{\cdot}3\pm1{\cdot}0$

Table 5. The energy per atom plane of dislocations occurring singly, E_1, and in groups of 2, 3, 4 (E_2, E_3 and E_4) whose stress fields extend over a distance R

R (Å)	E_1 (simple formula) (ev/atom plane)	E_1 (Schoeck and Seeger) (ev/atom plane)	E_2 (ev/atom plane)	E_3 (ev/atom plane)	E_4 (ev/atom plane)
200	2·66	1·90	—	—	—
1000	3·38	2·61	4·1	4·62	5·16
10000	4·4	3·63	6·16	7·7	9·3

than the theoretical values of E_1. The energy released during recovery may be due partly to point defects and partly to a reduction of interaction energy accompanying small displacements of the dislocations. This interaction energy is presumably associated with the networks. It is possible for example that the networks contain groups of a few (say 2, 3 or 4) dislocations on the same slip plane, at distances of about 200 Å from each other. The interaction energy for two dislocations at a distance r apart is $(G\mathbf{b}^2/2\pi K)\ln(R/r)$; hence the total energy associated with each dislocation of the pair is

$$E_2=\frac{G\mathbf{b}^2}{4\pi K}\left(\ln\frac{R}{r_0}+1+\ln\frac{R}{r}\right).$$

A similar calculation for three and four dislocations spaced at a distance r gives

$$E_3=\frac{G\mathbf{b}^2}{4\pi K}\left(\ln\frac{R}{r_0}+1+2\ln\frac{R}{r}-\frac{2}{3}\ln 2\right)$$

and

$$E_4=\frac{G\mathbf{b}^2}{4\pi K}\left(\ln\frac{R}{r_0}+1+3\ln\frac{R}{r}-\ln 2-\frac{1}{2}\ln 3\right).$$

Values of E_2, E_3 and E_4 are shown in table 5, for $r_0=\frac{1}{2}\mathbf{b}$, $r=200$ Å, and $R=1000$ Å or 10 000 Å. It is clear from these results that the interaction energy can be accounted for in terms of interactions between groups of only three or four dislocations whose long-range stresses do not cancel and extend over the region of the cells (i.e. $\sim 1\,\mu$). After recovery there may still be some interaction energy but the extent of the long-range stress field must be reduced. The electron microscope observations show no observable difference between the dislocation arrangements before and after recovery. Therefore, if the release in energy during recovery corresponds to a reduction in the interaction energy, this must be brought about by slight movements and re-arrangements of the dislocations in the cell boundaries, for example, by climb, by cutting through other dislocations or by cross-slip.

After recovery the difference between experimental and calculated values of self-energy is hardly significant in view of the experimental errors. It may be concluded that after recovery the experimental value agrees with the theoretical value of the self-energy to within a factor of 2.

Summarizing, it appears that the stored energy values are quite compatible with the observed dislocation distributions, that any long-rauge stresses are at the most of the order of those expected from three or four dislocations piled up in the cell boundaries, and that after recovery the dislocation energy agrees to within a factor 2 with the theoretical value of the self-energy.

4.2. *Comparison of Stored Energy and Flow Stress*

There are at present two main theories which attempt to account for the flow stress of pure metals. In the first, due to Friedel (1955) and Seeger (1957), the flow stress is determined by long-range stresses due to groups of piled-up dislocations; in the second, due to Cottrell (1953), Basinski (1959) and Hirsch (1958), the flow stress is determined by short-range interactions between crossing dislocations.

According to Seeger *et al.* (1957) the temperature-independent part of the flow stress τ_g is given by a relation of the form:

$$\tau_g = \frac{G\mathbf{b}n}{2\pi K} N_G^{1/2}, \qquad \ldots \ldots \ldots \qquad (1)$$

where N_G is the density of piled-up groups of either edge or screw dislocations. The stored energy per unit volume on this model is essentially the energy of $2N_G$ large dislocations of Burgers vector $n\mathbf{b}$ (the factor 2 taking account of edge and screw dislocations), i.e.

$$E_G = \frac{G(n\mathbf{b})^2}{4\pi K} 2N_G \ln\left(\frac{R}{r_0}\right). \qquad \ldots \ldots \qquad (2)$$

Eliminating N_G between eqns. (1) and (2) gives the relationship between E_G and τ_g as:

$$E_G = \frac{2\pi K}{G} \tau_g^2 \ln\left(\frac{R}{r_0}\right).$$

The values of E_G have been calculated from the stress–strain data for the silver used in the stored energy measurements and compared with the experimental values for the stored energy E_T and E_R, before and after recovery, in table 6. For this calculation R was taken as $1\,\mu$, and the flow stress as one-half of the tensile stress.

Table 6. Values of the energy stored, E_G, as calculated from a 'pile-up' model compared with the experimental values of the energy stored prior to recovery, E_T, and prior to recrystallization, E_R

Deformation (%)	Flow stress (kg/mm²)	E_G (cals/g atom)	E_T (cals/g atom)	E_R (cals/g atom)
11	6·66	21·2	2·7	1·25
21	8·9	37·0	5·1	2·83
32	10·67	54·0	7·75	3·7
43	11·58	64·0	7·27	4·9

It is clear from the large discrepancy between E_G and E_T that the pile-up model cannot account satisfactorily for the flow stress and the stored energy.

It should be emphasized that this conclusion follows directly from the flow stress and stored energy results, and does not depend on any direct microscopic examination of the dislocation structure.

The flow stress and stored energy results might be reconciled by assuming that the pile-ups occur only in certain small regions of the metal, the other regions containing only few dislocations. There is however no evidence at all for such an arrangement. It appears therefore that the simple pile-up or long-range stress theory of flow stress must be abandoned for the case of polycrystalline silver. This conclusion is independent of the number of dislocations in the pile-up; thus any model of flow stress based on a Taylor-type distribution of dislocations throughout the volume of the metal is ruled out.

The significance of the electron microscope observations reported in § 3 will now be appreciated. The dislocations are found to occur in dense networks in bands forming the boundaries of a cell structure, the cells being relatively free of dislocations. On the forest theory the flow stress is determined by the stress required for dislocations to cut through the dense regions of the forest in the boundaries, i.e.

$$\tau_g = \frac{G\mathbf{b}}{2\pi K}\frac{1}{l_f} \quad . \quad . \quad . \quad . \quad . \quad . \quad . \quad . \quad (3)$$

where l_f is the spacing between forest dislocations in the boundary. The dislocation density in the boundaries N_f will be $\sim 1/l_f^2$, and observations indicate that $N_f \sim 5N$, where N is the average dislocation density. It is clear at once that on this model the energy will be much smaller for a given flow stress since only part of the volume of the metal is occupied by dislocations.

In fact the energy, E_F, is given by

$$E_F = \frac{NG\mathbf{b}^2}{4\pi K}\ln\frac{R}{r_0}$$

and substituting from eqn. (3) we obtain

$$E_F = \frac{1}{m}\frac{\pi K}{G}\tau_g^2 \ln\frac{R}{r_0}$$

where we have put $N_f = mN$. Putting $m \sim 5$, E_F is $\sim E_G/10$, when $R \sim 1\,\mu$, or somewhat less for smaller values of R. Thus the values of E_F are fairly close to but rather smaller than the experimental values E_T, the remaining discrepancy being possibly due to the presence of some long-range stresses, or due to a contribution to E_T from point defects. The agreement between E_F and E_R is satisfactory.

It is clear then that the essentially non-uniform distribution of dislocations observed can account both for the flow stress in terms of a forest intersection mechanism and for the stored energy.

4.3. *Relation between Flow Stress and Dislocation Density*

Figure 5 shows a plot of the square root of the average dislocation density, N, against the tensile stress, σ. It appears that $\sigma \propto N^{1/2}$; taking the flow stress τ_g as $\frac{1}{2}\sigma$, from the slope of fig. 5 we find

$$\frac{\tau_g}{N^{1/2}}=4\cdot1\times10^3\,\text{dynes/cm.}$$

The significance of this relation is not clear since according to the forest model the flow stress is determined by the local dislocation density in the cell boundaries, N_f. Although precise measurements are difficult, it appears that approximately $N_f \sim 5N$ for all deformations examined so that

Fig. 5

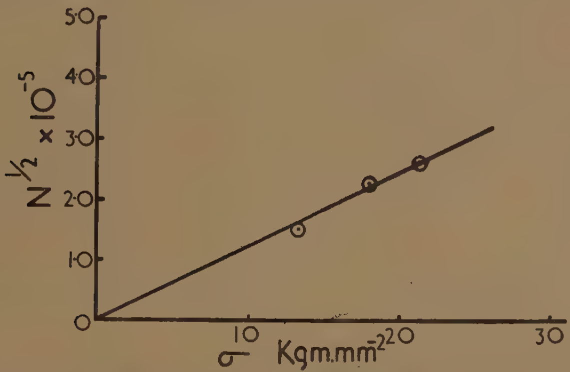

Plot of the square root of the average dislocation density, N, against the tensile stress, σ.

$$\tau_g \sim 1\cdot8\times10^3 N_f^{1/2}.$$

This expression should be compared with the approximate theoretical relation for the flow stress on the forest theory, i.e.

$$\tau_g \sim \frac{G\mathbf{b}N_f^{1/2}}{2\pi K}=1\cdot3\times10^3 N_f^{1/2}.$$

In view of the inaccuracy in determining the ratio N_f/N, and of the precise form of the theoretical expression for the dislocation intersection mechanism, the agreement between theory and experiment can be considered to be satisfactory.

§ 5. CONCLUSION

Electron transmission micrographs of deformed polycrystalline silver show that the dislocations are arranged non-uniformly in dense bands forming the boundaries of a cell structure. Only a fraction of the volume of the metal is occupied by dislocations; a reasonable measure of this fraction is N_f/N, i.e. about 20%. The experimental values of flow stress can be accounted for satisfactorily in terms of this arrangement on the assumption that it is determined by the stress required for a dislocation to penetrate the dense forest in the boundaries. Thus, although the flow stress may be high if the local dislocation density is large, the energy associated with this distribution of dislocations is relatively small since only part of the volume of the metal is occupied by dislocations. In fact, the experimentally measured values of stored energy are compatible with the observed dislocation distribution, provided that the long-range stresses associated with the networks are relatively small (particularly after recovery). The values of flow stress and stored energy are not compatible with each other if the flow stress is attributed to long-range stresses from pile-ups, and no pile-ups are observed on the electron micrographs. During recovery there is a considerable energy release but no observable decrease in dislocation density. It is not yet clear whether this release of energy is due to the relief of long-range stresses or due to the disappearance of point defects. In the latter case it might be expected that the release of stored energy during recovery would be associated with a decrease in the resistivity; it is proposed to carry out such measurements.

Electron microscope observations on the dislocation distributions in cold-worked polycrystalline Ni, Cu, Au, Al (Hirsch 1958) showed that the arrangements are rather similar to those in Ag. There is no reason to doubt that in these metals also the flow stress is determined essentially by the dislocation intersection mechanism at the boundaries. On the other hand, pile-ups are observed in stainless steel (Whelan *et al.* 1957) and α-brass (Hirsch 1958) and in these cases the long-range stresses may be important. Further experiments are needed to clarify this point.

The application of the 'forest theory' to single crystals will be discussed elsewhere.

ACKNOWLEDGMENTS

We wish to thank Professor N. F. Mott, F.R.S., and Dr. W. H. Taylor for stimulating discussions, and for constant help and encouragement. Our thanks are also due to Dr. O. Krisement for his help and advice on the problem of calorimetry, to Dr. G. C. Smith and Mr. S. Charter for facilities provided for straining calorimeter specimens, to Messrs. C. K. Jackson and G. Rickards for assistance in electron microscopy, and to other members of the metal physics group for useful discussions. One of us (J. E. Bailey) acknowledges the receipt of a maintenance grant from the Admiralty.

REFERENCES

BAILEY, J. E., 1959, Ph.D. Dissertation, University of Cambridge.
BASINSKI, Z. S., 1959, *Phil. Mag.*, **4**, 393.
BURKE, J. E., and TURNBULL, D., 1952, *Progress in Metal Physics*, **3** (London : Pergamon Press).
COTTRELL, A. H., 1953, *Dislocations and plastic flow in crystals* (Oxford : Clarendon Press).
FRIEDEL, J., 1955, *Phil. Mag.*, **46**, 1169.
HIRSCH, P. B., 1958, *Report on Symposium on Internal Stresses & Fatigue in Metals* (Detroit : General Motor Labs.).

Hirsch, P. B., Horne, R. W., and Whelan, M. J., 1956, *Phil. Mag.*, **1**, 677.

Hirsch, P. B., Howie, A., and Whelan, M. J., 1959, *Phil. Trans.* (in the press).

Jacquet, P. A., 1956, Electrolytic & Chemical Polishing: Metallurgical Reviews, **1**, 2.

Seeger, A., 1957, *Report of Lake Placid Conference on Dislocations & Mechanical Properties of Crystals* (New York: Wiley), p. 243.

Seeger, A., Diehl, J., Mader, S., and Rebstock, H., 1957, *Phil. Mag.*, **2**, 323.

Seeger, A., and Schoek, G., 1953, *Acta Met.*, **1**, 519.

Whelan, M. J., Hirsch, P. B., Horne, R. W., and Bollman, W., 1957, *Proc. roy. Soc.* A, **240**, 524.

Investigation of the Annealing of Nickel Deformed by Compression by X-ray and Stored Energy Measurements†

By D. MICHELL and E. LOVEGROVE
Division of Tribophysics,
Commonwealth Scientific and Industrial Research Organization,
University of Melbourne, Australia

[Received December 15, 1959]

ABSTRACT

X-ray diffraction patterns from bulk specimens of nickel deformed by compression have been measured with a Geiger-counter spectrometer. A composite specimen has been used to overcome the effects of preferred orientations.

The results indicate that during the annealing there is no change in the background intensity. No evidence has been found for stacking faults or changes in lattice parameter. The integrated intensities of all lines remain constant up to a temperature of annealing of about 480°c. A large decrease (30–75%) in the integrated intensity of all lines occurs on annealing to 600°c and this is attributed to extinction; an estimate of 2–4 μ is obtained for the size of the 'perfect' regions required to produce this effect.

The diffraction profiles are analysed by a number of methods. The broadening produced by the particle size effect is small. The stored energies derived from the various methods of analysis range from 0·04–2·4 cal/g. Best agreement is obtained between values of stored energy measured using a calorimetric method (0·28 cal/g) and those derived from x-ray measurements if it is assumed that the distribution of strain is Gaussian.

§ 1. INTRODUCTION

IN the study of the deformation of metals and their subsequent recovery on annealing it is desirable to compare the results of x-ray determinations with measurements of other properties such as stored energy, electrical resistivity, density, etc. Measurements of the latter properties are generally made on bulk specimens, whereas most accurate measurements of the x-ray diffraction patterns have been made on powdered specimens since there is then no complication due to preferred orientations or original grain size. However, it has been shown (Michell and Haig 1957, Clarebrough *et al.* 1955) that the energy stored in nickel deformed by grinding is considerably greater than in bulk specimens of nickel deformed to fracture by torsion. Thus it is evident that if the comparison between various properties is to be meaningful, the measurements should all be made on the one type of specimen.

In the present work the x-ray diffraction patterns from bulk specimens of nickel deformed by compression have been investigated after various stages of annealing, using a Geiger-counter spectrometer. The effects of preferred orientation have been eliminated by using a composite specimen consisting of a number of sections cut in selected orientations from the deformed material. The results have been compared with measurements of the energy stored in similar specimens deformed in the same manner.

---

† Communicated by Dr. W. Boas.

§ 2. Material and Deformation

The nickel used in the present experiments was taken from a bar of purity 99·85%, batch *M* of Clarebrough *et al.* (1960). As the grain size (1 mm) of the nickel supplied was too large to produce continuous Debye–Scherrer rings it was refined by annealing the bar for 30 min at 700°c in an atmosphere of nitrogen, deforming it by three successive compressions of 25% perpendicular to each other and then heating it at the rate of 6°c per min to 660°c in an atmosphere of nitrogen. Two such cycles of deformation and annealing produced a final grain size of 30–40 μ.

Fig. 1

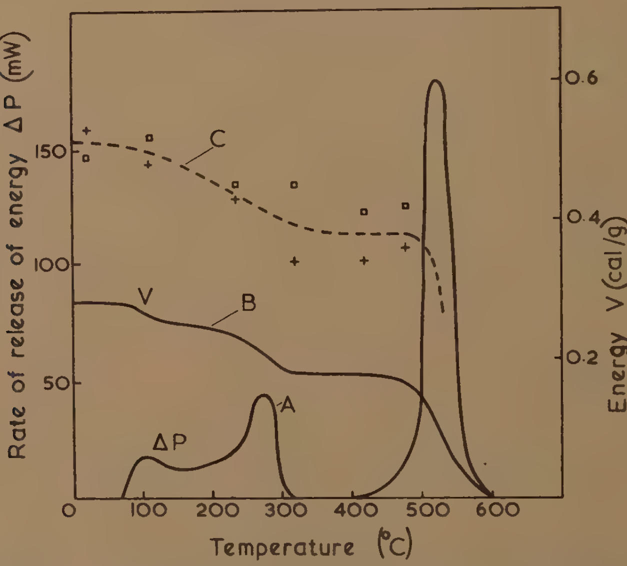

Release of energy from deformed nickel during annealing as a function of temperature.

(A) Rate of release of energy from nickel deformed by 25% cubic compression. (B) Stored energy remaining in the nickel (computed from A). (C) Calculated stored energy from Warren–Averbach analyses assuming Gaussian strain distribution. + For 111 and 222 reflections; □ for 300 and 400 reflections.

After grain refinement the nickel was in the form of rectangular blocks 1 in. × 1 in. × 2 in., the size required for the preparation of stored energy specimens. In order to preserve this shape and at the same time introduce a high degree of deformation with a minimum of preferred orientation, the final deformation also consisted of three compressions, perpendicular to each other, each of 25%.

§ 3. Stored Energy

Specimens of deformed metal were prepared for the determination of stored energy. The technique and apparatus used in making these measurements were as described by Clarebrough *et al.* (1952). The energy stored and the manner of its release are shown in fig. 1.

§ 4. X-ray Measurements

4.1. *Preparation of Specimens for X-ray Work*

Preliminary x-ray measurements made on specimens deformed in the manner described in § 2 showed that the degree of preferred orientation was such that the measurement of one element of length of a Debye–Scherrer ring could not be taken as typical of the whole ring. The following method of preparing specimens was therefore developed to minimise the effect of this preferred orientation.

If a specimen consisting of a sphere of polycrystalline metal is oscillated about its centre in such a way that all directions within the sphere are presented with equal probability to the x-ray beam, then the distribution of intensity around a Debye–Scherrer ring will be uniform and representative of the average intensity diffracted by all grains within the bulk material even if preferred orientations are present. Spherical specimens have been used in x-ray work (e.g. Mitchell and Rowland 1954), but they are undesirable in work involving the measurements of line shapes since they introduce more instrumental broadening than is obtained with flat specimens. An approximation to the use of a sphere which does not introduce additional instrumental broadening, consists of assembling in the one plane a number of flat sections, cut in selected orientations from the bulk material and presenting these with equal probability to the x-ray beam. The number of sections required is dependent on the extent and nature of the preferred orientation present in the deformed bar and the perfection to which the averaging effect is required. In the present case, ten sections were chosen corresponding to the faces of an icosahedron. However, specimens having any number of sections could be prepared by using other methods of selection.

The specimen prepared in this manner is shown in fig. 2. It consists of ten sections cut from a bar of nickel in the planes whose normals are shown in the stereographic projection, fig. 3, where the axes *a*, *b* and *c* represent the directions of the three compressions. It is desirable that no two sections are equivalent even if the resultant texture in the bar has cubic symmetry, or radial symmetry with respect to one of the directions of deformation. To avoid this, the orientation of the icosahedron relative to the axes *a*, *b* and *c* was selected so that when the normals shown in fig. 3 were referred to a unit stereographic triangle, no two were coincident (fig. 4), indicating that no two faces had the same relation to the directions of compression.

The sections were milled from the deformed bar, cut to approximately the required shape and then ground to the final dimensions. At all times the lightest of cuts were taken and copious quantities of coolant used.

Fig. 2

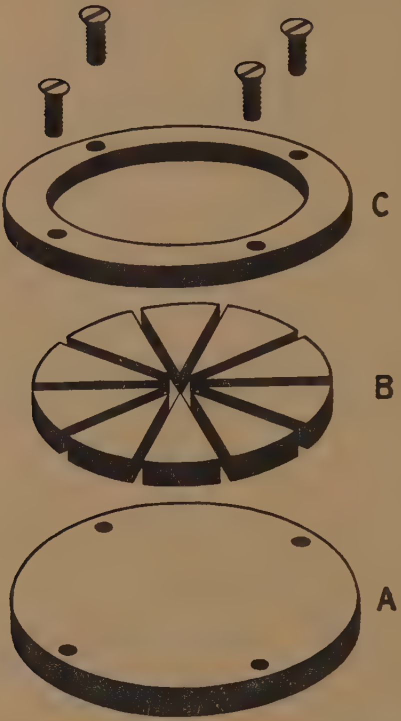

Unassembled components of composite specimen.
(A) Backing plate. (B) The ten sectors from the deformed bar. (C) Annular clamping ring and screws.

Fig. 3

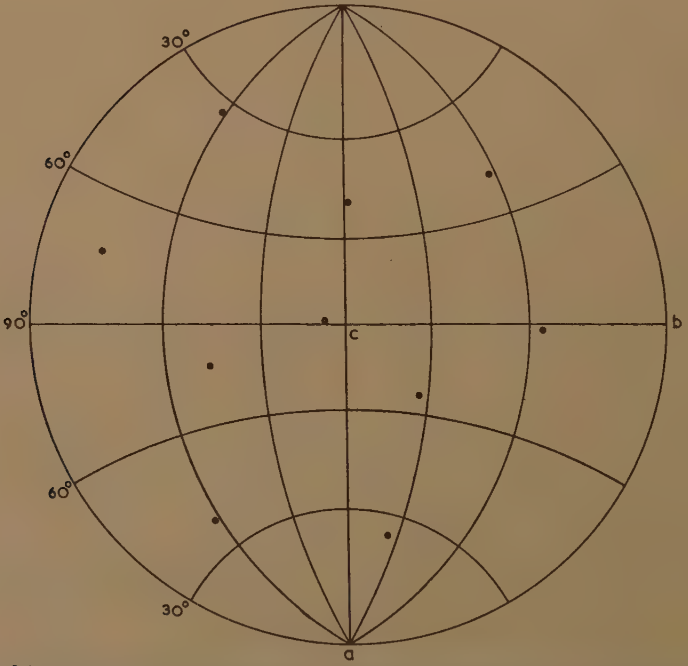

Stereographic projection showing the directions selected for the sections of the composite specimen. The *a*, *b* and *c* axes correspond to the directions of deformation.

An annular ring of wedge-shaped cross section C, together with four screws, was used to clamp the sectors B to a backing plate A (fig. 2). After assembly the complete specimen was again lightly ground, polished on metallographic papers and approximately 10 μ of the surface was removed by electropolishing. Preliminary measurements on a specimen deformed and machined in the same manner established that this treatment did not introduce any measurable change in the diffraction lines, nor did the removal of an additional 100 μ of surface by electropolishing.

Fig. 4

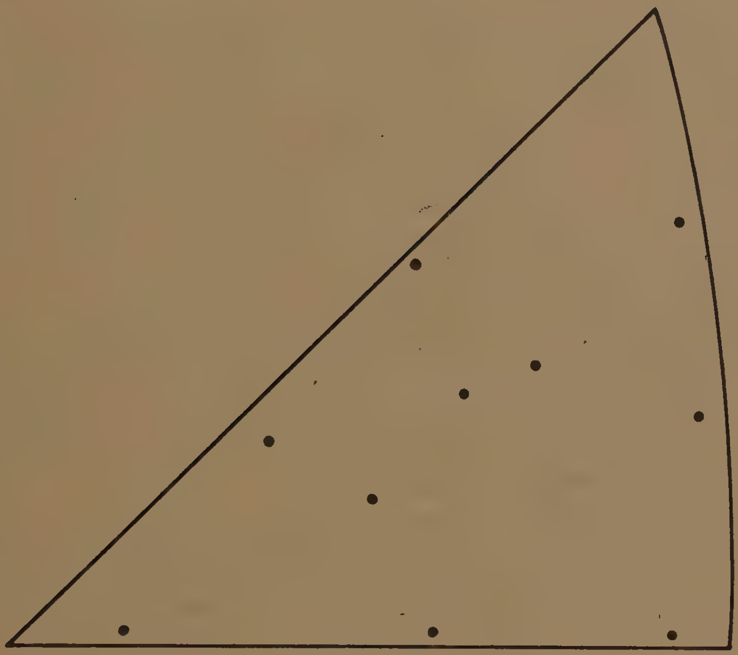

The directions selected for the sections referred to a unit stereographic triangle.

X-ray photographs made by a glancing incidence technique were used to investigate the effect of the preferred orientations in the individual sectors on the resultant Debye–Scherrer rings. Individually, the sectors produced rings whose intensities varied markedly round their peripheries but on rotating the specimen in its own plane, so that the sectors were presented in turn to the incident beam, Debye–Scherrer rings were obtained which showed no variation in intensity around their peripheries. The x-ray patterns obtained for the 111 and 200 reflections are shown in fig. 5 (Pl. 54). The central pattern is that obtained whilst rotating the composite specimen and the outer ten patterns are those obtained from the individual sectors.

4.2. *Experimental Method*

The diffraction pattern for the deformed specimen was measured first. The specimen with a thermocouple attached was then placed in a stainless steel tube and heated in an atmosphere of nitrogen at a rate of 6°c per min to 110°c. The tube was then cooled rapidly with water to room temperature and the diffraction pattern measured. The specimen was then replaced in the stainless steel tube and heated in nitrogen as quickly as possible to 110°c and then at 6°c per min to 235°c. It was then withdrawn, cooled as before and the diffraction pattern measured. This process was repeated for temperatures of 320°c, 420°c, 480°c, 540°c, 600°c and 700°c.

The x-ray diffraction patterns were measured with a Geiger-counter spectrometer using monochromatic Cu Kα radiation obtained by reflection from a crystal of lithium fluoride (Michell and Haig 1957). The 111, 222, 200 and 400 lines were measured in detail. Sufficient counting time was spent on the 311 line to enable graphical resolution of the tail of the 222 line to be made. The 331 line was measured in detail for the specimen in the deformed state, after the anneal to 420°c and in the fully annealed state. The total counting time spent on each pattern was approximately 45 hours and more than half of this was spent in measuring the background intensities and the tail regions to the lines.

Before and after each pattern was measured, the peaks of the 111 and 331 lines of a reference specimen of annealed nickel were scanned so that corrections could be applied for changes in sensitivity of the spectrometer. As the standard deviation of the reference peaks observed during the nine weeks of the experiment was only 1·2%, no corrections have been made for this effect.

All measurements have been corrected for the dead time of the counter (600 μs), for the wave shape of the x-ray output from the monochromator and for the background level of the counter in the absence of x-rays (constant at 45 counts per min).

§ 5. RESULTS OF THE X-RAY MEASUREMENTS

The diffraction pattern obtained after heating the specimen to 700°c has not been analysed in detail since it was not significantly different from that obtained after heating to 600°c.

5.1. *Background Level*

The background levels of the diffraction patterns were determined by the method employed by Hall and Williamson (1951) and Michell and Haig (1957). At angles of 35°, 64°, 110° and 127° in 2θ there appeared to be no overlapping of the tails of adjoining lines. The intensities at these angles are shown in fig. 6. Since the probable error in each of these intensities is less than one count per min, it is apparent that the intensity at each of these angles is effectively independent of the temperature of annealing and has therefore been taken as the background level at that

Fig. 6

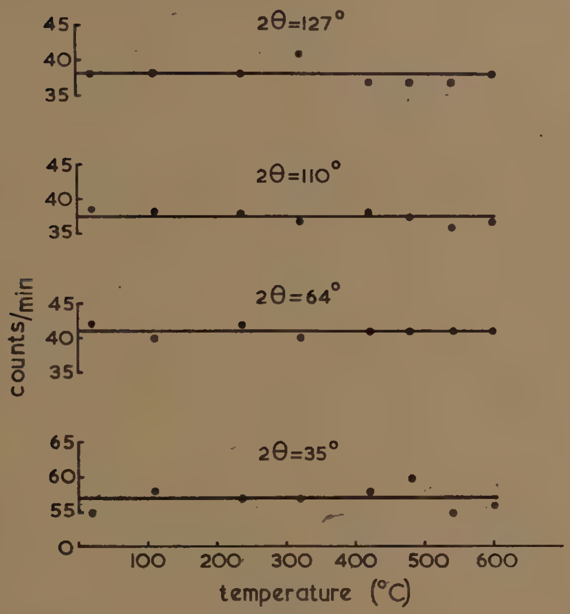

Corrected x-ray intensities at 35°, 64°, 110°, and 127° in 2θ as functions of the temperature of annealing.

Fig. 7

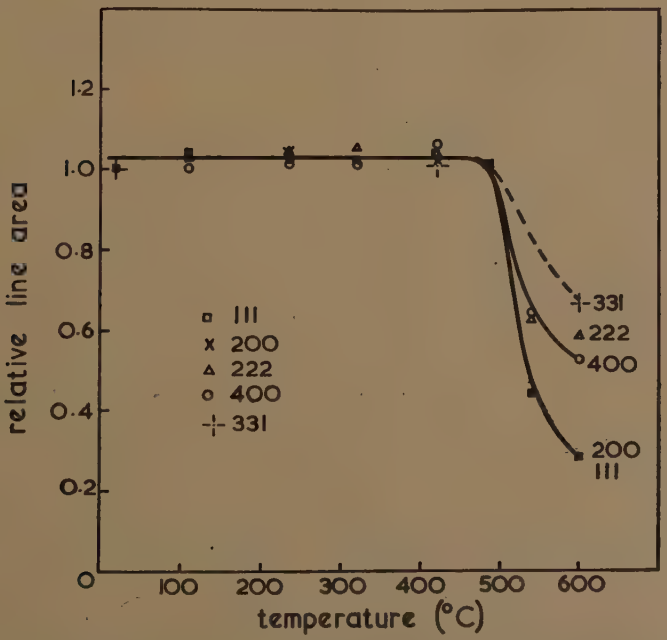

Integrated intensities of the 111, 200, 222, 400, and 331 reflections relative to the integrated intensities from the deformed specimen, as functions of the temperature of annealing.

particular angle. The background level at other angles has been taken to be that found by linear interpolation between these values.

5.2. *Integrated Intensities of the Lines*

The areas of the 111, 200, 222 and 400 lines above the background level have been computed and their variation with the temperature of annealing is shown in fig. 7. In no case does any significant change in area occur at temperatures of annealing below 480°C but in all cases a marked decrease in the areas of all lines occurs on annealing to 600°C.

5.3. *Position of the Maxima of the Diffraction Lines*

Examination of the positions of the peaks of the resolved α_1 components of the measured lines, as a function of temperature of annealing, shows no evidence for stacking faults (Paterson 1952) or change in lattice parameter, within the experimental error of $\pm 0{\cdot}01°$ in 2θ.

5.4. *Shape of the Diffraction Lines*

Inspection of the line profiles when plotted on an extended intensity scale and compressed angular scale shows that in the deformed state the lines have tails which extend for several degrees. Only small changes in the line shapes occur during annealing to 480°C and the maximum change in peak height is approximately 10%. On heating above 480°C, the line shapes change markedly particularly in the central regions. The width of all lines decreases but the peak height does not increase correspondingly since the integrated intensity decreases. In fact, the peak height of the 111 line decreases from 24 000 c.p.m. at 480°C to 8500 c.p.m. at 600°C. The decrease in intensity in the tail regions of the lines, after heating the specimen to 600°C, appears to be much less than the decrease in intensity in the central regions of the lines.

The decrease in integrated intensity cannot be due to a change in texture since X-ray photographs show that the 111 and 200 Debye–Scherrer rings are still uniform. However, the following experiment shows that it can be attributed to extinction.

The annealed specimen was lightly ground on 600 carborundum paper to reduce the perfection of the crystals at the surface and thus reduce any extinction. After this treatment the integrated intensities of the lines were found to have increased to about the values obtained for the deformed specimens and the peak height of the 111 line was approximately 27 000 c.p.m. The breadth of the 331 line was only slightly greater than that from the annealed specimen, indicating that the strains introduced by the grinding were less than 1% of those introduced by the original deformation. The surface layer was then removed in stages by electro-polishing and measurements of the peak heights of the lines and the breadth of the 331 line made at each stage. At first, the peak heights of the lines increased and the breadth of the 331 line decreased, but after the removal of 10–20 μ of surface the peak heights began to decrease until after the removal of approximately 100 μ of surface the peak of the 111 line was 9900 c.p.m. The initial increase in peak height is probably due to a decrease in line breadth following the removal of the more severely deformed surface layer. However, the removal of additional surface material exposes more perfect grains and, although the line breadth continues to decrease, the rapid decrease in integrated intensity substantially reduces the peak height. It may therefore be concluded that the decrease in intensity on annealing to 600°c is due to extinction.

§ 6. ANALYSIS OF THE DIFFRACTION PATTERNS

6.1. *Extinction*

It is difficult to calculate the integrated intensity from a crystal when its state of perfection is unknown. However, equations for the two extreme cases (i.e. the ideally perfect and the ideally imperfect mosaic) have been derived (James 1948).

Some idea of the extent of perfection in the grains of the nickel specimen may be gained by comparing the ratio of the theoretical integrated intensities of the ideally imperfect crystal (ρ_{mosaic}) and the ideally perfect crystal (ρ_{perfect}) with the ratio of the areas of the lines after deformation (A_{deformed}) and after heating to 600°c (A_{annealed}). These ratios are listed in table 1.

Table 1. Comparison of the Theoretical and Measured Relative Intensities from 'Perfect' and 'Imperfect' Nickel

Line	$\dfrac{\rho_{\text{mosaic}}}{\rho_{\text{perfect}}}$ Theoretical	$\dfrac{A_{\text{deformed}}}{A_{\text{annealed}}}$ Measured
111	8·8	3·6
200	7·9	3·6
222	5·5	1·8
400	4·6	1·9
331	4·3	1·5

The integrated intensities in the deformed state are probably given by the equation relating to the ideal mosaic and the results indicate that in the annealed state, although the perfection of the grains has increased, either the size or the degree of perfection of the perfect regions is less than that assumed in the derivation of the equation for intensity reflected by an ideally perfect crystal.

The decrease in the integrated intensity from crystals more perfect than the ideal mosaic may be due to either primary or secondary extinction. The application of a number of formulae for extinction (Williamson and Smallman 1955) to the results for the nickel failed to produce conclusive evidence for the type of extinction present. It seems reasonable to assume, however, that on annealing to 600°C, regions of high perfection were produced and that considerable primary extinction was present. That the decrease in intensity for bulk specimens was considerably greater than the corresponding change in intensity previously observed from nickel powder (Michell and Haig 1957) may be attributed to the fact that the grain size of the powder after recrystallization was 2–3 μ compared with 30–40 μ for the bulk material. This larger grain size, together with the higher purity of the nickel (99·85%) used in the present experiments, would probably lead to the production of regions of greater perfection in the annealed state than those produced in the powder of lower purity (99·6%).

If the whole decrease in integrated intensity is attributed to primary extinction, an estimate of 2–4 μ for the size of the perfect regions is obtained from the classical Darwin formula. In order to ascertain whether a substructure of this dimension was present, the specimen was examined with an optical microscope and an x-ray micro-beam technique capable of resolving misorientations of the order of 20 min of arc. No substructure was detected either in the fully annealed state, after lightly grinding the surface, or during various stages of the removal of the surface layer by electropolishing. Although the results of these experiments were negative, the possibility of a substructure cannot be excluded since misorientations of only 20–30 sec between subgrains would be sufficient to produce a mosaic as detected by x-rays.

6.2. *Integral Line Breadths*

The integral breadths have been calculated for all the measured lines. For a line from a deformed specimen the integral breadth is usually corrected for instrumental broadening by subtracting the integral breadth of the corresponding line from an annealed specimen. However, in this work extinction rendered the integral breadths of the lines in the annealed state unsuitable since it appears to reduce the intensity of the central region of the lines far more than the extremities; neither could the line shapes measured after lightly grinding the surface of the annealed specimen be used, since the grinding broadened the lines by a measurable amount. Similarly, the lines from annealed powder specimens were unsuitable since, in some cases, they were broader than the corresponding lines from the solid specimen after surface deformation by grinding. This effect is probably due to the lower density of the powder specimens which results in greater penetration of the x-rays into the surface.

The integral breadths finally used as corrections for instrumental broadening were obtained in the following way. In the absence of extinction, the general equation of a line profile of a particular reflection was assumed to vary throughout the annealing treatment only by scale factors. Therefore, the ratio of breadth at half height to integral breadth, for the reflection, should be independent of the state of annealing. This constant was evaluated from the ratio in the deformed states and applied to the breadth at half height in the annealed state. As the grinding experiments indicated that the breadth at half height was affected much less by extinction than the integral breadth, there resulted an estimate of the integral breadth which would have occurred, but for extinction, in the annealed state.

The derived value for the 111 line was 10% lower than that obtained from the measured profile, but in the case of the high angle lines which were least affected by extinction, there was good agreement between the calculated and observed integral breadths.

Fig. 8

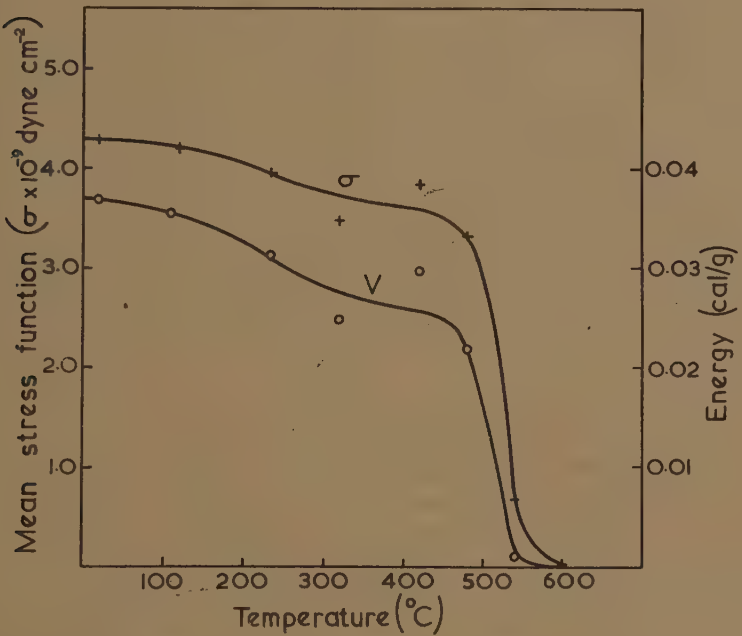

Results of the analysis of the line breadths. Mean stress function, σ, and calculated stored energy, V, as functions of the temperature of annealing.

The integral breadths β of the lines after correction for instrumental broadening were investigated by the method proposed by Hall (1949) and Mazur (1949) and used by Michell and Haig (1957) to give values of 'apparent particle size' t and mean stress function σ. The results indicated that particle size broadening was small. Although no significance could be attached to the variation of particle size with annealing temperature, a minimum estimate of particle size in the deformed state was 10^4 Å. The 'mean stress functions' are shown in fig. 8 as a function of annealing temperature. The r.m.s. stress, $\sigma_{\text{r.m.s.}}$, will depend on the actual stress distribution but, as this distribution is unknown, we assume that $\sigma_{\text{r.m.s.}}$ is equal to the 'mean stress function'. Values of stored energy V have then been computed from the equation $V = 3\sigma_{\text{r.m.s.}}{}^2/2E$, where E is an average value of Young's modulus: (see Stibitz (1936), Faulkner (1960)), and are plotted as a function of temperature in fig. 8.

6.3. *Fourier Analyses of the Line Profiles*

The Fourier coefficients A_n($n = 1$ corresponds to the repeat distance a_3 of the unit cell) for the low angle halves of the resolved α_1 components of the measured lines were determined directly with an electronic computer (CSIRAC) and were corrected for instrumental broadening by the method of Stokes (1948). In this correction a knowledge of the line shapes obtained from the annealed material in the absence of extinction is required. As these line shapes could not be measured directly they were approximated in the following way. The peak heights were calculated from the integral breadths derived in § 6.2 and the integrated intensities in the deformed state. The region over which the intensities remained substantially unaffected by extinction was determined from the grinding experiments. Between this region and the peak, the measured ordinates were adjusted by a factor which varied linearly with 2θ, decreasing from the value, calculated peak height/measured peak height, at the peak of the line to unity at the region unaffected by extinction. This method of adjustment for extinction was the most satisfactory of several which were tried as it gave the best agreement with the line shapes measured on surface ground specimens.

Fig. 9

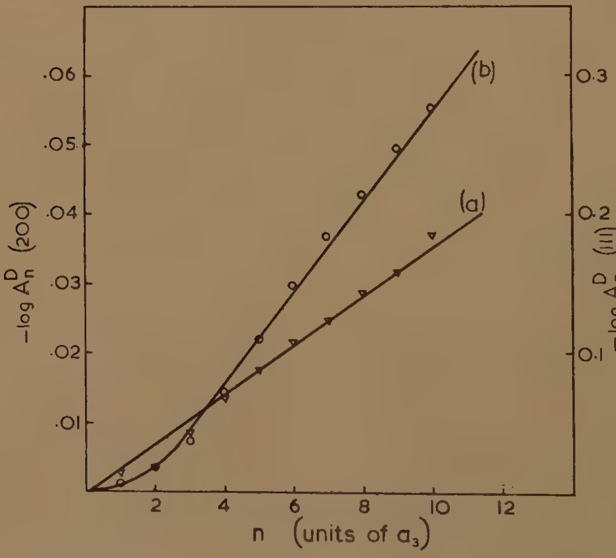

Logarithm of the Fourier coefficients of the strain broadening, $\log A_n{}^D$, after separation of the particle size effects by method 1 (a), as a function of the order n of the coefficients; (a) 111 and 222 reflections, and (b) 200 and 400 reflections.

Fig. 10

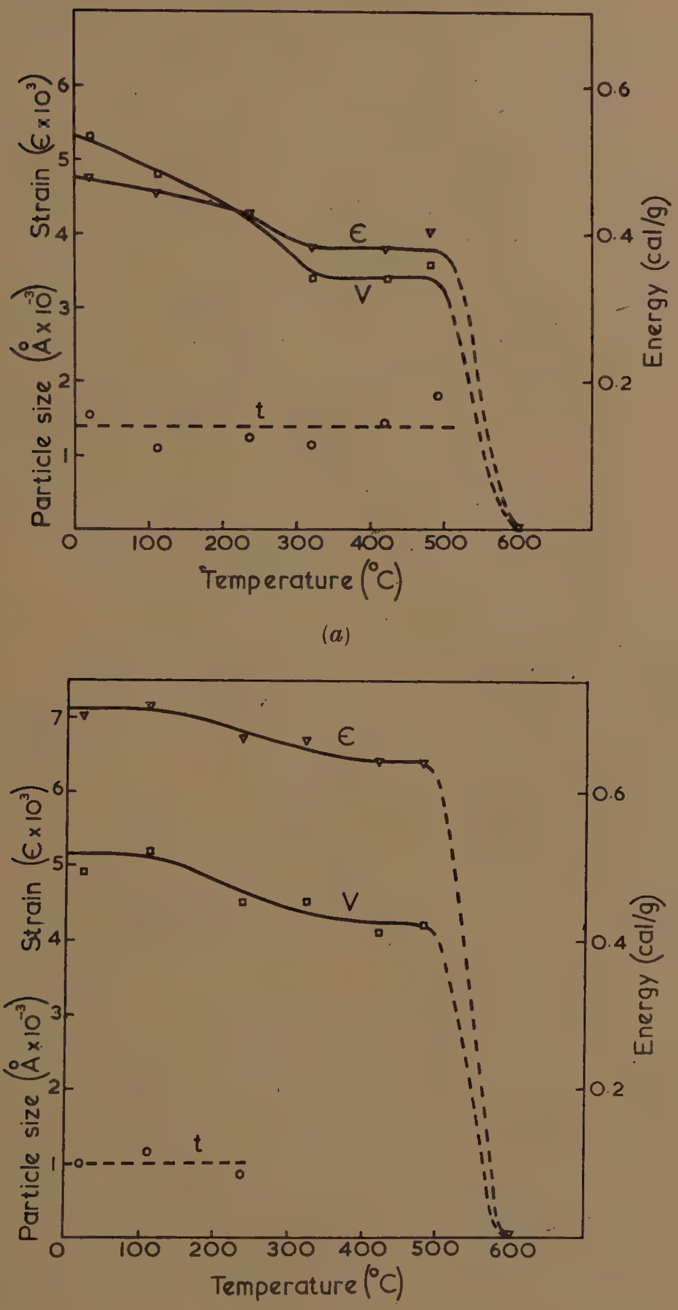

(*a*)

(*b*)

Results of the Fourier analysis (Gaussian distribution of strain). Apparent particle size, t, root mean square strain ϵ, and stored energy, V, as functions of the temperature of annealing: (*a*) for the 111 and 222 reflections, and (*b*) for the 200 and 400 reflections. No reliable estimate of t could be made for temperatures above 235°C for case (*b*).

Table 2. Summary of Results of Analyses

(*a*) 111–222 reflections

Annealing temperature (°c)	Analysis 1 *a* Gaussian strain distribution Broadening due to strain and particle size			Analysis 1 *b* Gaussian strain distribution Broadening due to strain only		Analysis 2 *a* Cauchy strain distribution Broadening due to strain and particle size			Analysis 2 *b* Cauchy strain distribution Broadening due to strain only	
	r.m.s. strain ($\times 10^3$)	Stored energy (cal/g)	Particle size (Å)	r.m.s. strain ($\times 10^3$)	Stored energy (cal/g)	r.m.s. strain ($\times 10^3$)	Stored energy (cal/g)	Particle size (Å)	r.m.s. strain ($\times 10^3$)	Stored energy (cal/g)
20	4·75	0·53	1540	5·37	0·68	9·0	1·92	No real values obtainable	8·4	1·66
110	4·52	0·48	1100	5·37	0·68	8·6	1·75		8·4	1·66
235	4·28	0·43	1280	5·06	0·61	8·1	1·55		7·9	1·48
320	3·80	0·34	1160	4·80	0·55	7·2	1·22		7·5	1·33
420	3·80	0·34	1440	4·80	0·55	7·2	1·22		7·5	1·33
480	3·92	0·36	1800	4·72	0·53	7·4	1·30		7·4	1·30

(*b*) 200–400 reflections

Annealing temperature (°c)	Analysis 1 *a* Gaussian strain distribution Broadening due to strain and particle size			Analysis 1 *b* Gaussian strain distribution Broadening due to strain only		Analysis 2 *a* Cauchy strain distribution Broadening due to strain and particle size			Analysis 2 *b* Cauchy strain distribution Broadening due to strain only	
	r.m.s. strain ($\times 10^3$)	Stored energy (cal/g)	Particle size (Å)	r.m.s. strain ($\times 10^3$)	Stored energy (cal/g)	r.m.s. strain ($\times 10^3$)	Stored energy (cal/g)	Particle size (Å)	r.m.s. strain ($\times 10^3$)	Stored energy (cal/g)
20	7·0	0·49	1000	7·3	0·53	15·2	2·30	No real values obtainable	13·0	1·69
110	7·2	0·52	1160	7·4	0·55	15·6	2·44		13·2	1·74
235	6·7	0·45	840	6·9	0·48	14·5	2·10		12·3	1·51
320	6·7	0·45	—	7·2	0·52	14·5	2·10		12·8	1·64
420	6·4	0·41	—	7·1	0·50	13·9	1·92		12·6	1·59
480	6·5	0·42	—	7·15	0·51	14·1	1·98		12·6	1·59

(*c*) 331 reflection

Annealing temperature (°c)		Analysis 1 *b* Gaussian strain distribution Broadening due to strain only			Analysis 2 *b* Cauchy strain distribution Broadening due to strain only	
		r.m.s. strain ($\times 10^3$)	Stored energy (cal/g)		r.m.s. strain ($\times 10^3$)	Stored energy (cal/g)
20		4·1	0·32		11·3	2·4
420		4·1	0·32		11·3	2·4

The derived coefficients of the lines, from the nickel when annealed to various temperatures up to 600°c, were analysed by the following methods:

1. The methods of Warren and Averbach (1949, 1950, 1952) for strain distributions which are Gaussian.

(*a*) The broadening was attributed to the simultaneous effects of small particle size and strain, and values of the strain coefficients A_n^D and the particle size coefficients A_n^P were deduced. As shown in fig. 9, $\log A_n^D$ is a linear function of n over the range $n=2$ to $n=10$, and for the coefficients derived from the 111 and 222 lines a reasonable line of fit can be drawn through the origin (curve (*a*)). This indicates that for the range of n considered here the profile for these reflections may be represented by a Cauchy function. Williamson and Smallman (1954) have pointed out that an incorrect choice of background level or inaccurate measurements in the tail regions may cause the plot of $-\log A_n^D$ against n for a Cauchy profile to be of the form shown in fig. 9, curve (*b*), and that the linear section is approximately parallel to the straight line through the origin representing the same Cauchy profile without tail or background errors. The broadening profile we derived from the coefficients A_n^D for the 200 and 400 lines was a reasonable approximation to a Cauchy profile of the same breadth which had been analysed with an assumed background level too high by $1-2\%$ (i.e. $1-2$ counts per min). As such an error in assumed background level was within the experimental accuracy, the values of $\log A_n^D$ for $n=1$ were derived from the slopes of the linear sections of the curves.

Using this method, the coefficients of the 111 and 222, and 200 and 400 reflections were analysed. The results are shown in fig. 10 and also in table 2.

(*b*) All the broadening was attributed to strain and values of strain were obtained from the coefficients to the 222, 400, and 331 reflections.

2. The methods suggested by Williamson and Smallman (1954), based on the assumption that the strain distribution was a Cauchy function.

(*a*) The broadening was attributed to the simultaneous effects of small particle size and strain. Separation of these effects by a plot of $\log A_n$ against $l_0=\sqrt{(h^2+k^2+l^2)}$ where h, k, l are the usual indices of reflection, resulted in nonsensical values of particle size ($A_n^P>1$) for the 111 and 222, and 200 and 400 reflections and therefore the derived values of strain are also doubtful.

(*b*) The 222, 400, and 331 coefficients were analysed, attributing all broadening to strain. The r.m.s. strain ϵ was calculated for a cut-off strain of 0·2.

In calculating stored energy from strain, Stibitz's equation has not been used since Faulkner (1960) using the same assumptions has shown it to be incorrect. Faulkner obtains the equation:

Energy stored in an isotropic material

$$V=\frac{15E}{2(3-4\nu+8\nu^2)}\overline{\left(\frac{\Delta D}{D}\right)^2},$$

where E is an average value of Young's modulus, ν is Poisson's ratio and $\overline{(\Delta D/D)^2}$ is the mean square value of the strain. This equation leads to energies of 2–3 times those obtained from Stibitz's equation. Since nickel is anisotropic only approximate values of energy have been obtained from the derived strains using the value of Young's modulus E_{hkl} appropriate to the direction of the strains.

The results of all the Fourier analyses are summarized in table 2.

§ 7. Discussion

7.1. *Stored Energy*

The rate of release of energy ΔP as a function of temperature (fig. 1, curve A) is very similar to that obtained for specimens deformed by unidirectional compression. According to Clarebrough *et al.* (1960) the evolution of energy between 420 and 590°c is associated with the removal of dislocations during recrystallization, whereas the peak in the ΔP curve at 250°c is associated with the removal of vacancies. However, the ΔP curves for nickel of this purity (99·85% Ni) differ from those obtained for nickel of lower purity (99·6% Ni) used in previous work (Clarebrough *et al.* 1955, Michell and Haig 1957) in that the plateau region associated with the re-arrangement and annihilation of dislocations is absent. It is considered that in the higher purity nickel used here re-arrangement and annihilation of dislocations is complete by 300°c.

7.2. *X-ray Measurements*

The measurements made on bulk specimens of nickel indicate that any change in the background level is less than the experimental error, and that there is no detectable change in the position of the lines, which might be attributed either to variations in lattice parameter or to changes in stacking fault density. In these respects the results are in agreement with those of Michell and Haig (1957) from powdered nickel.

The large decrease of 30–75% in integrated intensity which occurred in all lines when the specimen was heated to temperatures above 480°c is attributed to extinction. Precise treatment of this phenomenon is difficult since the separation of extinction into two simple types is probably unjustified. However, the observed decrease in intensity may be explained qualitatively in terms of primary extinction. If the imperfections in the grains are due to dislocations, then an average spacing of 3 μ between dislocations would produce misorientated blocks of the requisite size and result in a minimum dislocation density of 10^7 lines per cm^2 which is of the order of that expected for annealed specimens.

The decrease in intensity of the central portion of the lines without a corresponding decrease in the tails observed after heating above 480°c suggests that even in the annealed state there are some regions within the grains which are more perfect than others. Since the tails are produced by the less perfect regions, it seems reasonable to deduce that they are less affected by extinction than the central portion of the lines which is more dependent on the perfect regions.

The assumptions made in correcting the integral breadths for instrumental broadening in the line broadening analyses (§ 6.2) are not serious, but those made in approximating to the line profiles (§ 6·3) in the annealed state are of greater consequence. The approximations made should not introduce an error greater than 10% in the values of stored energy shown in table 2 but may introduce a considerable error in the value of the 'apparent particle size'. Since the broadening due to the 'particle size' effect is small anyway, too much reliance should not be placed on these values. The various methods of analysis give qualitatively similar results indicating that there is a small decrease in lattice strain on annealing below 480°c and then a sharp decrease on annealing above 480°c. This is in general agreement with the measured release of stored energy.

Quantitatively, however, the various methods give different values of lattice strain and energy. The energies derived from the line broadening analyses (§ 6.2) are an order of magnitude too small, but from the line shape analysis (§ 6.3), assuming a Cauchy strain distribution, the energies are 5–10 times greater than the measured values. The results from the Warren and Averbach treatment (fig. 1 C) are almost twice the measured values of stored energy (fig. 1 B) but suggest that in the present work a Gaussian distribution of strain is the most reasonable approximation to that present in the metal.

The disagreement between the measured and calculated energies is disappointing but it should be remembered that the value of strain derived from the Warren and Averbach type of analysis is dependent on the distance L over which the strain is calculated. If the high strain in the immediate neighbourhood of a dislocation is to be included, this distance should be small and it seems likely that energies calculated from

$$\frac{\langle \Delta L^2 \rangle^{1/2}}{L} \quad \text{for} \quad L \to 0$$

will include almost all the energy associated with isolated dislocations, low angle boundaries, etc. In practice, it is difficult to determine accurately values of

$$\frac{\langle \Delta L^2 \rangle^{1/2}}{L} \quad \text{for} \quad L \to 0$$

due to the difficulties in measuring the tails of the line profiles and it is necessary to choose some finite value of L over which the displacements are averaged. In the present work, this distance has been selected as a_3 (6 – 7 Å for the 111 and 200 reflections and 15 Å for the 331 reflection) and values of $\langle \Delta L^2 \rangle^{1/2}$, $(L = a_3)$ have been obtained by assuming that $-\log A_n{}^D$ (or ΔL^2) is proportional to L. Although this assumption is within the experimental accuracy, it seems unlikely that it is correct since it leads to

$$\frac{\langle \Delta L^2 \rangle^{1/2}}{L} \to \infty \quad \text{for} \quad L \to 0.$$

This assumption almost certainly leads to values of

$$\frac{\langle \Delta L^2 \rangle^{1/2}}{L}, \quad \text{for} \quad L = a_3,$$

which are too high.

Values of strain derived from a Cauchy strain distribution cut off at a strain of 0·2 lead to energies considerably in excess of those measured directly and it seems that for bulk specimens of nickel this distribution is too extreme. Michell and Haig (1957) postulated a strain distribution based on the Gay, Hirsch and Kelly model for a deformed metal. It was suggested that the distribution may be a weighted sum of two simple distributions, one for the comparatively low strain regions within the particles and another for the highly strained boundary regions. For powder where the volumes of the two regions are of comparable magnitude, the resulting strain distribution probably has large tails due to the highly strained boundary regions. For the bulk specimens of nickel, the 'particle size' is considerably larger than for the powder and, since the strain is lower, the contribution of the boundary regions to the composite strain distribution is probably much less than that from the particles themselves. The resultant distribution thus approximates to the simple one representing the particles alone. It appears from this work that a Gaussian function is a reasonable approximation to the strain distribution in bulk specimens of nickel.

ACKNOWLEDGMENTS

We wish to thank Dr. Boas for his continued interest and encouragement. The stored energy measurements were made by L. M. Clarebrough, M. E. Hargreaves and G. W. West, and the authors are particularly grateful for this cooperation. We should also like to thank J. F. Nicholas for many helpful discussions, G. J. Ogilvie for a number of valuable suggestions concerning specimen preparation, and D. L. Grubb who constructed the specimens with care and patience.

REFERENCES

CLAREBROUGH, L. M., HARGREAVES, M. E., LORETTO, M. H., and WEST, G. W., 1960, *Acta Met.* (in press).
CLAREBROUGH, L. M., HARGREAVES, M. E., MICHELL, D., and WEST, G. W., 1952, *Proc. roy. Soc.* A, **215,** 507.
CLAREBROUGH, L. M., HARGREAVES, M. E., and WEST, G. W., 1955, *Proc. roy. Soc.* A, **232,** 252.
FAULKNER, E. A., 1960, *Phil. Mag.*, **5,** 519.
GAY, P., HIRSCH, P. B., and KELLY, A., 1954, *Acta Cryst.*, **7,** 41.
HALL, W. H., 1949, *Proc. phys. Soc. Lond.* A, **62,** 741.
HALL, W. H., and WILLIAMSON, G. K., 1951, *Proc. phys. Soc. Lond.* B, **64,** 937, 946.
JAMES, R. W., 1948, *The Optical Principles of the Diffraction of X-rays. The Crystalline State*, Vol. II (London : G. Bell and Sons), p. 269.
MAZUR, J., 1949, *Nature, Lond.*, **164,** 358.

Michell, D., and Haig, F. D., 1957, *Phil. Mag.*, **2,** 15.
Mitchell, C. M., and Rowland, J. F., 1954, *Acta Met.*, **2,** 559.
Paterson, M. S., 1952, *J. appl. Phys.*, **23,** 805.
Stibitz, G. R., 1936, *Phys. Rev.*, **49,** 862.
Stokes, A. R., 1948, *Proc. phys. Soc. Lond.*, **61,** 382.
Warren, B. E., and Averbach, B. L., 1949, *J. appl. Phys.*, **20,** 1066 ; 1950, *Ibid.*, **21,** 595 ; 1952, *Ibid.*, **23,** 497.
Williamson, G. K., and Smallman, R. E., 1954, *Acta Cryst.*, **7,** 574 ; 1955, *Proc. phys. Soc. Lond.*, **68,** 577.

Calculation of Stored Energy from Broadening of X-ray Diffraction Lines†

By E. A. Faulkner
Division of Tribophysics, Commonwealth Scientific and Industrial
Research Organization, University of Melbourne

[Received February 16, 1960]

Abstract

A new calculation is made of the stored energy in a deformed isotropic material, in terms of the mean-square lattice strain. An isotropic stress distribution is assumed.

From the broadening of x-ray reflections in deformed metals it is possible to deduce $\overline{(\Delta d/d)^2}$, the mean-square variation in the separation d of the lattice planes contributing to the reflection. From this a calculation may be made of the energy stored in the material, if assumptions are made about the distribution of the stress components in the specimen. In this note this calculation will be carried out for an isotropic material, with assumptions leading to an isotropic stress distribution. An equation due to Stibitz (1937), which is based on the same assumptions and which has been widely quoted, will be shown to be incorrect.

The stress at any point in a crystal may be specified by the directions of the principal stress axes (x', y', z') and the magnitudes of the principal stresses $(f_{x'x'}, f_{y'y'}, f_{z'z'})$. We may define a mean-square principal stress f^2, and a stress correlation constant C, by the relations

$$\left.\begin{aligned} \overline{f^2_{x'x'}}+\overline{f^2_{y'y'}}+\overline{f^2_{z'z'}}&=3f^2,\\ \overline{f_{x'x'}f_{y'y'}}+\overline{f_{y'y'}f_{z'z'}}+\overline{f_{z'z'}f_{x'x'}}&=3Cf^2. \end{aligned}\right\} \quad . \quad . \quad . \quad (1)$$

The corresponding principal strains are given by expressions like

$$e_{z'z'}=(f_{z'z'}-\nu f_{x'x'}-\nu f_{y'y'})/E, \quad . \quad . \quad . \quad . \quad . \quad (2)$$

where E is Young's modulus and ν is Poisson's ratio.

The quantity $\Delta d/d$ is equal to the strain component $e_{z''z''}$ where the z'' axis is the direction of the normal to the planes concerned in the reflection. If (l, m, n) are the direction cosines of the z'' axis relative to the principal stress axes at any point, we have for the mean-square value of $\Delta d/d$ over all parts of the crystal

$$\overline{\left(\frac{\Delta d}{d}\right)^2}=\overline{e^2_{z''z''}}=\overline{(n^2e_{z'z'}+l^2e_{x'x'}+m^2e_{y'y'})^2}. \quad . \quad . \quad . \quad . \quad (3)$$

---

† Communicated by Dr. W. Boas.

We now assume that there is no correlation between the magnitudes of the principal stress components and the direction cosines of their axes, and, furthermore, that the axes are isotropically distributed; this implies an isotropic distribution of both stress and strain. Combining eqns. (1), (2), and (3), and using this assumption, we obtain

$$\overline{\left(\frac{\Delta d}{d}\right)^2} = \frac{f^2}{5E^2}[3-4\nu+8\nu^2+2C(1-8\nu+6\nu^2)]. \quad . \quad . \quad . \quad (4)$$

The stored energy is given by

$$V=\tfrac{1}{2}(\overline{f_{x'x'}e_{x'x'}}+\overline{f_{y'y'}e_{y'y'}}+\overline{f_{z'z'}e_{z'z'}})=\frac{3f^2}{2E}(1-2C\nu), \quad . \quad . \quad (5)$$

so the resulting expression for the stored energy in terms of the mean-square variation in the separation of the lattice planes is

$$V=\frac{15E}{2}\,\frac{1-2C\nu}{3-4\nu+8\nu^2+2C(1-8\nu+6\nu^2)}\overline{\left(\frac{\Delta d}{d}\right)^2}. \quad . \quad . \quad . \quad (6)$$

It is now necessary to make a further assumption about the strain distribution in the crystal, in order to assign a value to the constant C. There are several relatively simple assumptions which may be made, of which two will be discussed here:

(*a*) The three principal stress components are independently distributed, so that the mean value of products such as $f_{x'x'}f_{y'y'}$ is zero. This is the assumption that was made by Stibitz (1937) and corresponds to $C=0$. Equation (6) becomes

$$V=\frac{15E}{2(3-4\nu+8\nu^2)}\overline{\left(\frac{\Delta d}{d}\right)^2}=2{\cdot}93E\overline{\left(\frac{\Delta d}{d}\right)^2} \quad . \quad . \quad . \quad (6a)$$

where the expression has been evaluated for the typical case of $\nu=\frac{1}{3}$ in order to facilitate comparison with other results.

(*b*) Only shear stresses are present in the material, so that at every point the hydrostatic component $(f_{x'x'}+f_{y'y'}+f_{z'z'})$ is zero. This gives $C=-\frac{1}{2}$ and

$$V=\frac{15E}{4(1+\nu)}\overline{\left(\frac{\Delta d}{d}\right)^2}=2{\cdot}81E\overline{\left(\frac{\Delta d}{d}\right)^2}. \quad . \quad . \quad . \quad . \quad (6b)$$

A consideration of the strain field of an isolated dislocation in isotropic material shows that assumption (*b*) is probably the more realistic one; however, for $\nu=\frac{1}{3}$ the numerical coefficients are so similar that it is immaterial which of the two is adopted.

It will be seen that eqn. (6*a*) is different from the result

$$V=\frac{3E}{2(1+2\nu^2)}\overline{\left(\frac{\Delta d}{d}\right)^2}$$

which was obtained by Stibitz (1937) using the same assumptions and which, for $\nu=\frac{1}{3}$ gives

$$V=1{\cdot}23E\overline{\left(\frac{\Delta d}{d}\right)^2}.$$

In his approach to the problem, Stibitz treated the principal strains like the components of a vector, so his calculation leads to the result $\overline{e^2_{z''z''}} = \overline{e^2_{z'z'}}$ because in this case all sets of axes are equivalent. In fact, the principal axes (x', y', z') are not equivalent to any other set of axes because they are chosen so as to make $e_{x'y'} = e_{y'z'} = e_{z'x'} = 0$; the quantity $(e^2_{xx} + e^2_{yy} + e^2_{zz} + \frac{1}{2}e^2_{xy} + \frac{1}{2}e^2_{yz} + \frac{1}{2}e^2_{zx})$ is invariant under a rotation of axes, so that the value of $\overline{e^2_{z''z''}}$, where the z'' axis has no particular relation to the principal axes, must always be less than $\overline{e^2_{z'z'}}$.

There has been very little work in which a direct comparison has been made between calorimetrically measured values of stored energy and values calculated from x-ray line broadening. However, Michell and Haig (1957) made x-ray and calorimetric measurements on nickel which had been deformed by grinding, and calculated values of stored energy from the x-ray observations. On the assumption that the strain distribution function was of the Cauchy type with strain cut-off values of 0·2, and using Stibitz' equation with $\nu = 0{\cdot}3$, they obtained values of V which were lower than the calorimetrically measured values by a factor of about 2·5. The use of the corrected expression (6 *b*) would raise the calculated values by a factor of 2·3 and so give a much better agreement between the two figures.

REFERENCES

MICHELL, D., and HAIG, F. D., 1957, *Phil. Mag.*, **2**, 15.

STIBITZ, G. R., 1937, *Phys. Rev.*, **52**, 619.

CORRESPONDENCE

Statistical Methods in Rock Magnetism

By S. K. Runcorn
King's College, Newcastle upon Tyne

[Received February 18, 1960]

Research workers in palaeomagnetism have hitherto found it useful in their assessment of the precision of a set of directions of magnetization determined from a geological formation to use the statistical method introduced by Fisher (1953). Fisher takes as a standard frequency distribution function $f(\theta)$ the following:

$$f(\theta)=\frac{1}{2\sinh K}\exp(K\cos\theta) \quad . \quad . \quad . \quad . \quad . \quad . \quad . \quad (1)$$

where K is a statistic of precision and θ the angle with the true direction. Fisher shows that the maximum likelihood estimate of the true direction is the vector mean direction and of K is $N-1/N-R$ where R is the length of the vector sum of the N directions, each represented by unit vectors.

Fisher further shows how an angle of confidence, α, may be calculated such that the mean direction makes an angle less than the true direction with a probability of 95%.

Wilson (1959) objects to this usage on the ground that all distributions of directions of magnetizations may not follow this law and that, in consequence, the angle of confidence calculated above may "contain falsely implied precision". He proposes instead that workers in this subject should use the following mean cosine, which is the analogue of the variance in Gaussian statistics:

$$1-\tfrac{1}{2}\delta^2=\overline{\cos\delta}=\frac{S\cos\delta_i}{N} \quad . \quad . \quad . \quad . \quad . \quad . \quad . \quad (2)$$

where δ_i is the angular deviation of a single reading from the vector mean, and the following expression to correspond to the standard error of the mean of Gaussian statistics:

$$\epsilon=\frac{\delta}{\sqrt{N}}=\sqrt{\left\{\frac{\overline{\cos\delta}}{N}\right\}}. \quad . \quad . \quad . \quad . \quad . \quad . \quad . \quad (3)$$

In this way Wilson believes that the assumption of law (1) has been avoided. This view is wrong. It is, of course, possible to define a quantity from the sample of directions determined by eqn. (2) without assuming it is a sample drawn from an infinite population described by (1), just as it is possible to define a standard deviation in statistics of a single variation, without assuming the sample to have been drawn randomly from a population following the normal law. But while both these quantities are dependent on the scatter of the measurements, their real significance depends on the probability distribution law, for one can think of such laws which would have only one per cent or as many as ninety-nine per cent of the observations lying outside the 'standard deviation' defined in this way!

We use the statistical methods based on the Gaussian law in the case of one variate and on law (1) in the case of dispersion on a spherical surface because, in physics and geophysics, scatter is usually due to a number of unrelated causes. Where one has good reason to believe the scatter is due to a single cause, such as the varying amounts of magnetization along the present field sometimes superposed on the original direction of magnetization of a rock, common sense prevents use of the statistical methods in the straightforward form described above.

REFERENCES

FISHER, R. A., 1953, *Proc. roy. Soc.* A, **217**, 295.
WILSON, R. L., 1959, *Phil. Mag.*, **4**, 750.

The K Emission Spectrum of Metallic Lithium

By R. S. Crisp and S. E. Williams
University of Western Australia, Nedlands, Western Australia

[Received March 17, 1960]

Several authors have published lithium K spectra obtained from solid and evaporated targets. Although it has been well established that the maximum intensity does not occur at the high-energy edge as in sodium, it has also been concluded that Li does not exhibit the high-energy edge which, as a conductor, it should possess (Catterall and Trotter 1959).

We have previously published (Fisher *et al.* 1958) a K spectrum taken from a solid target of Li which indicates the existence of such an edge, though the resolution in this case was only 0·23 ev, the vacuum conditions not very good, the target energy 24 w, and the target temperature unknown. The width of the edge from 5% to about 80% of the maximum intensity is 0·47 ev, including the instrumental width.

Technical improvements made since this spectrum was obtained have enabled us to record the Li K spectrum in the third order of a 1 m glass grating under improved vacuum conditions in which there was virtually no target contamination and for which the Li, an evaporated layer on a copper target, was essentially at the cooling water temperature. The target energy was 4 w. The spectrum as directly recorded (one of several) s shown in fig. 1. The resolution of 0·9 Å is calculated according to the criteria of Fisher (1954), the slit widths being 40 μ and the 1 m grating having 576 grooves per millimetre. This is equivalent to an energy resolution of 0·07 ev using the third order of Li K.

The spectrum clearly shows a high-energy edge, characteristic of an unfilled band, which extends to 75% of the maximum intensity where a discontinuity of slope can be seen. From this point to the maximum there occurs the ‘ roll over ’ which has been attributed to the anisotropy of the Fermi surface. The first order spectrum also shows an edge extending to the same proportion of the maximum intensity. The width of the edge, including the instrumental window, is 0·30 ev. Our spectrum agrees with that of Skinner (1940) who found that at 300°K the edge width of Li K was 0·3 ev.

The spectrum obtained by Catterall and Trotter (1959) shows an edge width (to 75% of maximum intensity) of 0·55 ev, their resolution being given as 0·2 ev. The spectrum of Bedo and Tomboulian (1958), which has been plotted as a density of states curve, shows about the same width, though the instrumental window is given as 0·06 ev. A spectrum obtained by Bedo and published by Tomboulian (1957) suggests the presence of an edge.

Fig. 1

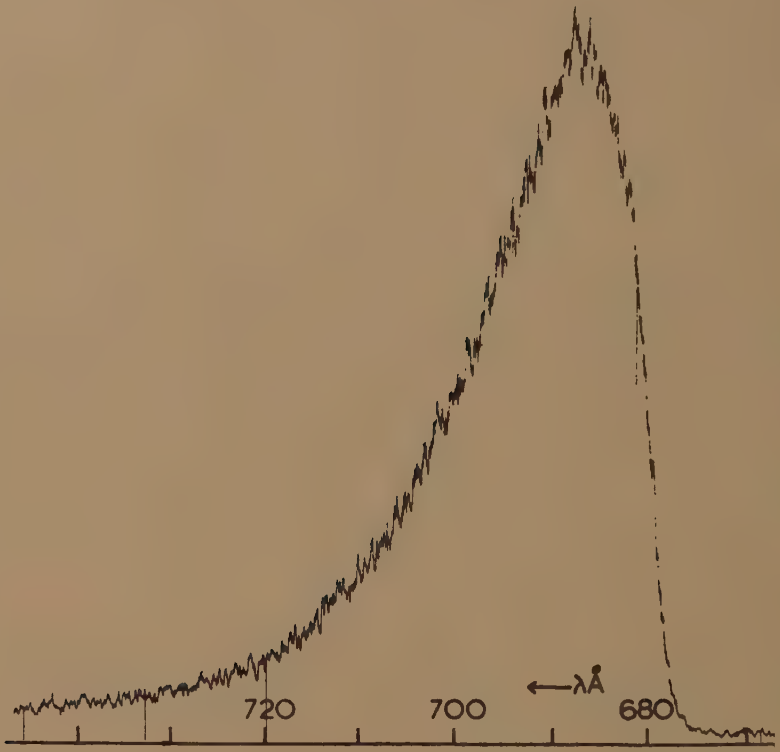

Recorder trace of Li K; 3rd order, target current 1 mA, volts 4000, target chamber pressure 10^{-6} mm, maximum count rate 640 per sec. Resolution 0·9 A. Scanning speed 8 A per min.

Fig. 2

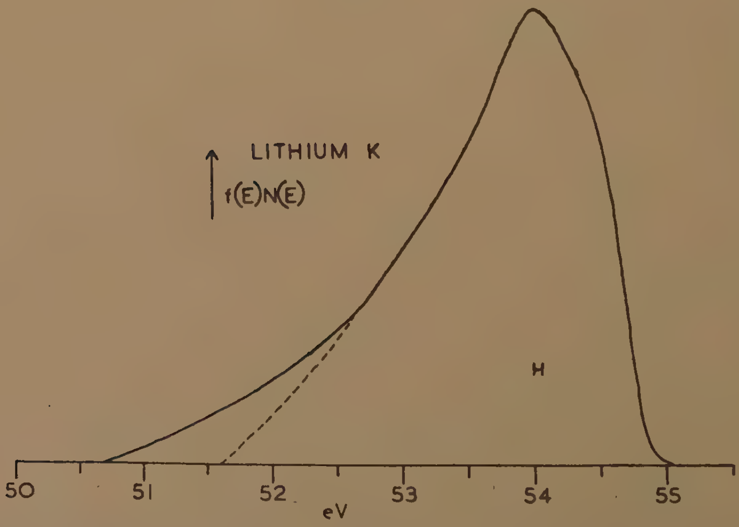

Density of states curve for Li K reduced from fig. 1, using $f(E)N(E)=\lambda^3 I(\lambda)$ (Crisp 1958). Width of the instrumental window is indicated.

The excess 'edge width' appearing in some of the published spectra would require the target temperature to be well over 700°K if temperature effects are to be invoked. The high-energy edge side of our spectrum shows a change of slope at 75% of maximum intensity and a marked lack of symmetry about the axis of half maximum intensity. These features can hardly arise from insufficient resolving power which would smooth the curve to a symmetrical form in which the presence of a true edge would be less apparent.

It would therefore appear unnecessary to seek a theoretical explanation for the non-appearance of a high energy edge in Li as some authors have done.

Figure 2 shows the density of states curve reduced from the intensity curve according to the formula $f(E)N(E)=\lambda^3 I(\lambda)$ which is accurate in the case of an instrument counting photons passing through a 'window' of fixed width (Crisp 1958).

Measurements on first-order spectra of sodium L (resolution 0·065 ev) and potassium M (resolution 0·024 ev) show edge widths of 0·21 ev and 0·19 ev respectively for evaporated layers on a copper target cooled to about 15°C. The relevant spectra will be published at a later date.

REFERENCES

BEDO, D. E., and TOMBOULIAN, D. H., 1958, *Phys. Rev.*, **109**, 35.
CATTERALL, J. A., and TROTTER, J., 1959, *Phil. Mag.*, **4**, 1164.
CRISP, R. S., 1958, *Aust. J. Phys.*, **11**, 449.
FISHER, P., 1954, *J. opt. Soc. Amer.*, **44**, 665.
FISHER, P., CRISP, R. S., and WILLIAMS, S. E., 1958, *Opt. Acta*, **5**, 31.
SKINNER, H. W. B., 1940, *Phil. Trans. roy. Soc.*, **239**, 95.
TOMBOULIAN, D. H., 1957, *Handb. Phys.*, **30**, 246.

Diamagnetic Shielding of Nuclei in Metals

By T. P. Das†
Department of Chemistry, Columbia University, New York

and E. H. Sondheimer
Department of Mathematics, Queen Mary College, London

[Received April 7, 1960]

Nuclei in metals are generally found to have a larger Larmor frequency at a given magnetic field than in ions in solution or in non-metallic solids (Knight 1949). This paramagnetic Knight shift is usually explained as arising from the alinement of conduction electron spins in a magnetic field, which also gives rise to the Pauli spin paramagnetic susceptibility χ_p. The purpose of the present note is to point out that, in addition to their contribution to the paramagnetic shift through their spins, the conduction electrons may also produce an appreciable diamagnetic shift due to their orbital motion in a magnetic field. This orbital motion is known to produce the Landau diamagnetic contribution χ_d to the susceptibility (Landau 1930).

We have calculated the diamagnetic contribution to the nuclear resonance shift, for the case of free electrons, by an adaptation of the methods used by Sondheimer and Wilson (1951) and Hebborn and Sondheimer (1959) to calculate the diamagnetic susceptibility. We use perturbation theory to calculate the partition function $Tr \exp(-\mathscr{H}/kT)$ for an electron gas in the presence of the dipole field of a nucleus of magnetic moment μ_N (considered as fixed in direction) and a uniform applied magnetic field H. Plane waves are chosen as basis functions and all magnetic field terms in the electronic Hamiltonian $\mathscr{H}$ are treated as small, so that the partition function (and hence the free energy) is obtained as a series in ascending powers of μ_N and H. Then, if F' is the term in the free energy which is proportional to $\mu_N H$, we obtain the shielding constant σ_d as $-\mu_N^{-1}\partial F'/\partial H$. A lengthy but straightforward calculation gives, for a degenerate Fermi gas.

$$\sigma_d = -\frac{4\pi n \mu_0^2}{3\zeta}, \qquad (1)$$

where n is the electron density, μ_0 is the Bohr magneton and ζ is the Fermi level. Comparing this with the expression for the paramagnetic shielding constant

$$\sigma_p = \frac{8\pi}{3}\chi_p \langle |\psi_F(0)|^2 \rangle \Delta, \qquad (2)$$

---

† Supported by the U.S. Atomic Energy Commission Contract AT(30–1)–2498 with Columbia University, New York.

where Δ is the atomic volume and $\langle|\psi_F(0)|^2\rangle$ is the average value of the wave-function density at the nucleus for electrons at the Fermi surface (Townes *et al.* 1950), we have, since $\chi_d = -n\mu_0^2/2\zeta$ for free electrons,

$$\frac{\sigma_d}{\sigma_p} = \frac{\chi_d}{\chi_p\langle|\psi_F(0)|^2\rangle\Delta}. \qquad (3)$$

This ratio has the value $-\frac{1}{3}$ for free electrons, since $\langle|\psi_F(0)|^2\rangle = 1/\Delta$ and $\chi_d = -\frac{1}{3}\chi_p$ in this case. The equality of σ_d/σ_p and χ_d/χ_p for free electrons is a consequence of the fact (pointed out to us by Dr. A. B. Pippard) that, when the electron density is constant, the part of the field at a nucleus contributed by the electrons within the Lorentz sphere is simply

$$(8\pi/3)(\chi_p + \chi_d)H,$$

so that the frequency shift is a pure susceptibility effect.

For Bloch electrons in an actual metal this conclusion is no longer valid, and the treatment given above must be generalized to include the periodic lattice potential in $\mathscr{H}$; Bloch wave functions must then be used to evaluate the matrix elements required in the calculation of the partition function. This problem will be discussed in a later paper. It is usually assumed that σ_d is always negligibly small compared with σ_p, since in real metals $\langle|\psi_F(0)|^2\rangle\Delta$ is in general large compared with unity. However, if we assume, for an order-of-magnitude estimate, that eqn. (3) still applies and that the dominant contribution to χ_d comes from the usual Landau-Peierls expression (Peierls 1933) evaluated for electrons with an effective mass m^*, we obtain

$$\frac{\sigma_d}{\sigma_p} = -\frac{1}{3}\frac{(m/m^*)^2}{\langle|\psi_F(0)|^2\rangle\Delta}. \qquad (4)$$

This suggests that σ_d may be comparable in magnitude with σ_p whenever m^* is small, as is frequently the case in multivalent metals in which high-curvature portions of the Fermi surface lie close to a zone boundary. For the case of beryllium metal, as an example, the observed Knight shift $\sigma = \sigma_d + \sigma_p$ is practically zero, while the theoretical value of σ_p is predicted to be 0·01%. Assuming that $\sigma_d = -\sigma_p$ and taking $\Delta = 7{\cdot}8 \times 10^{-24}\,\mathrm{cm}^3$ and $\langle|\psi_F(0)|^2\rangle = 1{\cdot}03 a_0^{-3}$, where a_0 is the Bohr radius (Pomerantz and Das 1960), we obtain from eqn. (4) $m^* \approx 0{\cdot}08\,m$, which agrees in order of magnitude with estimates obtained from the de Haas–van Alphen effect (Shoenberg 1957).

We have so far regarded the applied magnetic field as so small that only the non-oscillatory part of χ_d need be considered. If we assume that eqn. (3) remains valid for all values of H and substitute the complete expression for χ in the effective mass approximation (Sondheimer and Wilson 1951) we obtain

$$\sigma = \frac{64\pi^2 m^{*3/2}}{9h^3}\mu_0^{*2}(2\zeta)^{1/2}\left[3\frac{m^{*2}}{m^2}\langle|\psi_F(0)|^2\rangle\Delta - 1 - \frac{3\pi kT}{\mu_0^*H}\left(\frac{\zeta}{\mu_0^*H}\right)^{1/2}\sum_{r=1}^{\infty}\frac{(-1)^{r+1}\cos\left(\frac{r\pi m^*}{m}\right)\sin\left(\frac{1}{4}\pi - \frac{r\pi\zeta}{\mu_0^*H}\right)}{r^{1/2}\sinh(r\pi^2kT/\mu_0^*H)}\right], \qquad (5)$$

where $\mu_0^* = e\hbar/2m^*c$. Whilst this equation cannot be expected to be in any way quantitatively reliable, it suggests that there may be oscillations in σ as a function of $1/H$ when $\pi^2 kT/\mu_0^* H$ is of order unity. These oscillations, like the de Haas–van Alphen oscillations in the magnetic suceptibility, are due to the quasi-periodic character of the density of states function for a degenerate Fermi gas in a magnetic field, and should be observable under conditions similar to those required to observe the de Haas–van Alphen effect (see Shoenberg 1957). The field stability and homogeneity necessary for this purpose should be readily obtainable with the magnets currently available for nuclear magnetic resonance experiments. The amplitude of the oscillations in σ is estimated to be of the same order as σ_d, that is about 10^{-4}, for metallic beryllium at 4°K in a field of the order of 20 kG. One would also expect oscillations in the shielding of ^{25}Mg, ^{67}Zn and ^{199,201}Hg nuclei in the metals and for ^{13}C in graphite since the effective masses in all these cases are small.

ACKNOWLEDGMENTS

The authors are grateful to Professor M. Bloom and Professor R. Barrie for helpful discussions about the oscillations in shielding at high fields and low temperatures.

REFERENCES

HEBBORN, J. E., and SONDHEIMER, E. H., 1959, *Phys. Rev. Letters*, **2**, 150.
KNIGHT, W. D., 1949, *Phys. Rev.*, **76**, 1259.
LANDAU, L., 1930, *Z. Phys.*, **64**, 629.
PEIERLS, R., 1933, *Z. Phys.*, **80**, 763.
POMERANTZ, M., and DAS, T. P., 1960, *Phys. Rev.* (in the press).
SHOENBERG, D., 1957, *Progress in Low Temperature Physics*, **2**, 226.
SONDHEIMER, E. H., and WILSON, A. H., 1951, *Proc. Roy. Soc.* A, **210**, 173.
TOWNES, C. H., HERRING, C., and KNIGHT, W. D., 1950, *Phys. Rev.*, **77**, 852.

Direct Evidence for the Presence of Quarter-dislocations in Talc Monocrystals

By S. Amelinckx and P. Delavignette
S.C.K. Mol-Donk, Belgium

[Received January 26, 1960]

Quarter dislocations have been postulated first, on a geometrical basis, by Kronberg (1957) to account for the plastic behaviour of sapphire. Evidence for the existence of half-dislocations, so called Shockley partials, in stainless steel has been presented by Whelan (1958) who also discussed their interactions.

We present here direct evidence that quarter-disolocations exist in talc, and probably in the related clay minerals.

Thin cleavage foils of talc monocrystals were examined in transmission electron microscopy using the technique developed by Hirsch and Whelan (1959) for metal foils. The cleavage plane in talc is also the glide-plane; the crystals are extremely soft as a consequence of glide on this plane.

An examination of the talc structure (Wells 1950) indicates that glide takes place between the two successive oxygen sheets, which have the ring structure shown in fig. 1. These oxygen layers establish the contact between electrically neutral multilayers; their bonding is therefore very weak. Glide between these planes requires dislocations with a Burgers vector AA_1, AA_2 or AA_3 as shown in fig. 1. Dislocations with a Burgers vector AA_1 are not stable according to the 'square of the Burgers vectors' criterium; they will split into four partials with 'Burgers' vectors $A\alpha$, $\alpha\beta$, $\beta\gamma$, γA_1 as indicated in the same fig. 1. Between the four partial dislocations ribbons of stacking faults are present. They are of a different kind but have probably very nearly the same stacking fault energy. The configuration of partials is therefore mainly determined by their elastic interaction. All successive partials repel, the equilibrium separation is therefore given approximately by fig. 2.

All the characteristics of the described dislocation ribbons were actually observed as shown in fig. 3 (*a*), (*b*), (*c*) and (*d*) (Pls. 55 and 56). These figures refer to the same area, but show a different contrast, due to a different inclination of the foil. Figure 3 (*a*) reveals only two of the partial dislocations, whilst fig. 3 (*b*) shows in one area three of them and in another area all four. In fig. 3(*c*) on the other hand the contrast is such as to reveal the stacking faults between 1 and 2 and between 3 and 4. Whilst finally fig. 3 (*d*) shows the stacking fault ribbons between the three pairs of dislocations, with a slightly darker contrast between partials 2 and 3. Since the plane of the stacking fault is exactly parallel to the foil surfaces only a uniform contrast is observed in the cases here considered.

Fig. 1

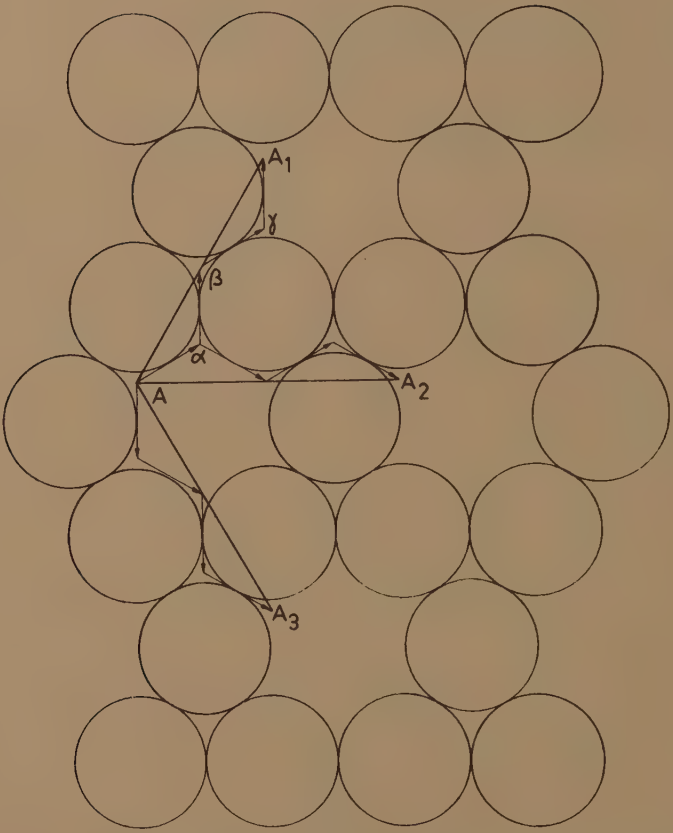

Ring structure of oxygen layers in the talc structure, glide occurs between two such layers. Possible Burgers vectors are AA_1, AA_2 and AA_3; AA_1 which is not stable splits into four partial dislocations.

Fig. 2

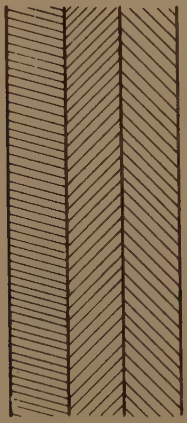

Schematic representation of the configuration of partials and stacking faults in a fourfold dislocation ribbon.

The fact that stacking fault contrast of the expected kind is observed between the individual lines is an indication that we have very probably to do with the real effect and not, e.g., with the formation of a double image as described by Hirsch and Whelan (1959). Further evidence follows from a consideration of the particular kinds of nodes which are observed.

A more detailed account of these observations will be published elsewhere.

ACKNOWLEDGMENTS

We are indebted to Mr. Goens, Director of the C.E.N. Mol, for permission to publish this paper. We also wish to thank Mr. Nicasy for his skilful preparation of specimens and Mr. Beyens for careful photographic work.

REFERENCES

HIRSCH, P. B., and WHELAN, M. J., 1959, *J. Inst. Met.*, **87**, 392, 406.
KRONBERG, M. L., 1957, *Acta Met.*, **5**, 507.
WELLS, A. F., 1950, *Structural Inorganic Chemistry* (Oxford: University Press), p. 580.
WHELAN, M. J., 1958, *Proc. roy. Soc.* A, **249**, 114.

[*The Editors do not hold themselves responsible for the views expressed by their correspondents.*]

Fig. 5

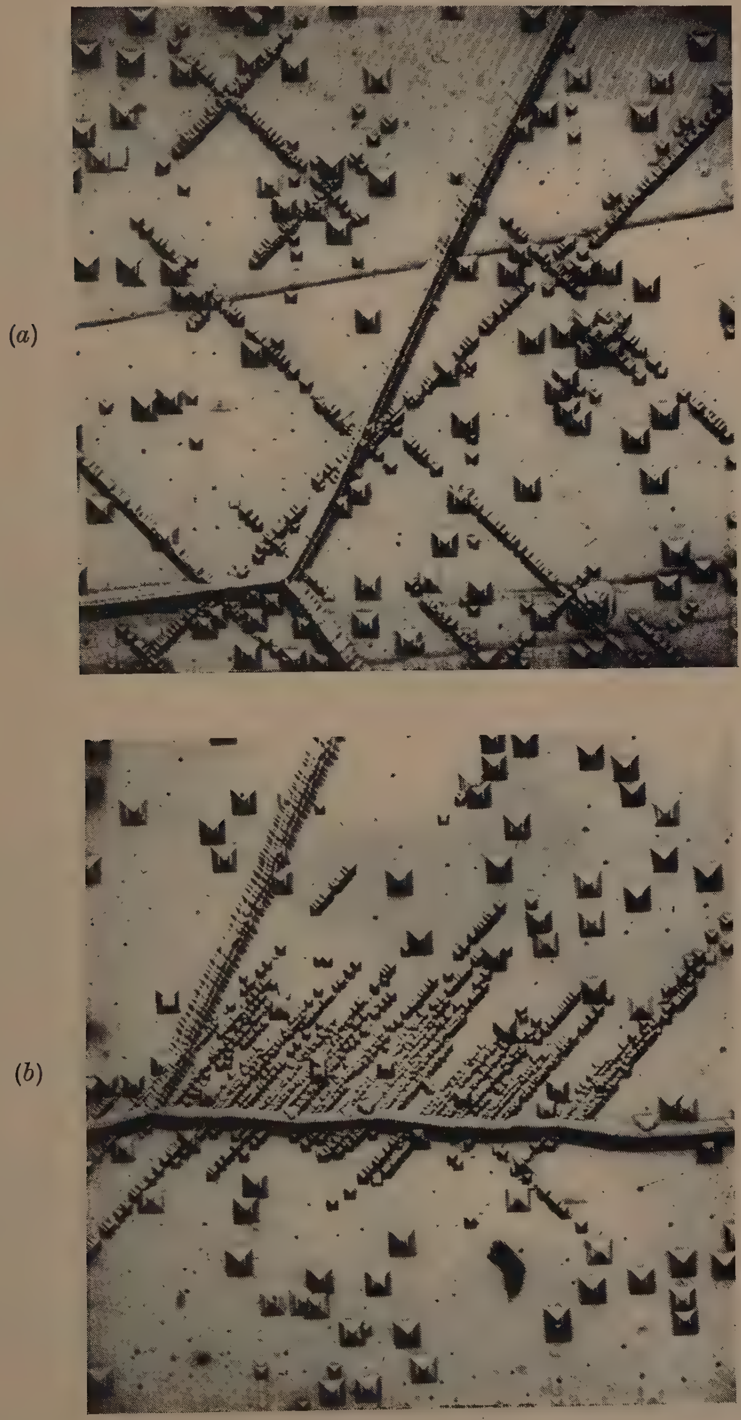

Etch pits on specimen driven at $\epsilon = 2 \cdot 7 \times 10^{-4}$, showing dislocations produced by the vibration. In (*b*) the dislocations seem to originate from a sub-grain boundary. Stress direction horizontal. Mag. ×180.

Fig. 1

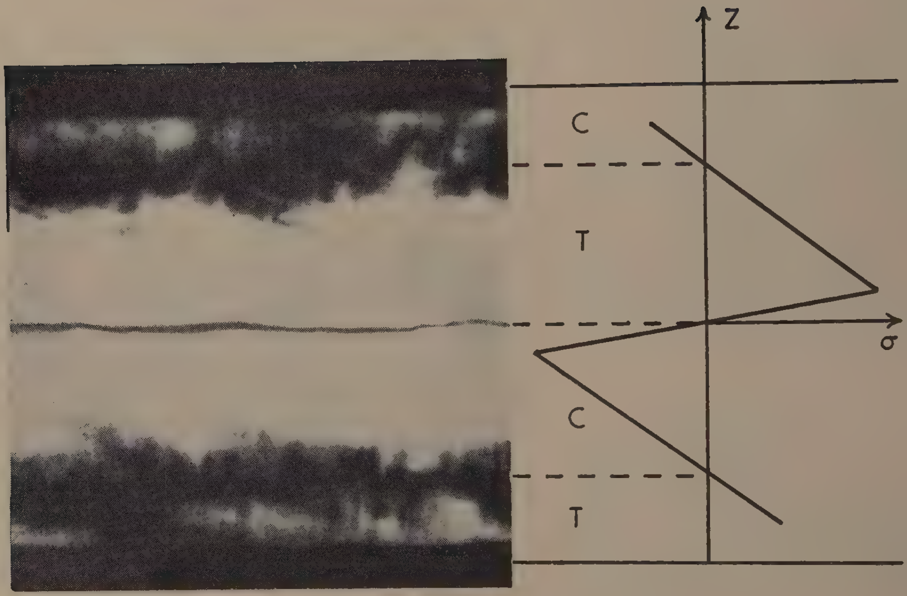

Figs. 1–5

Successive stages in the reverse bending of a singly-bent bar (external couples still applied). T = tension, C = compression. Photographs taken with crossed nicols at 45° to the extinction directions.

Fig. 2

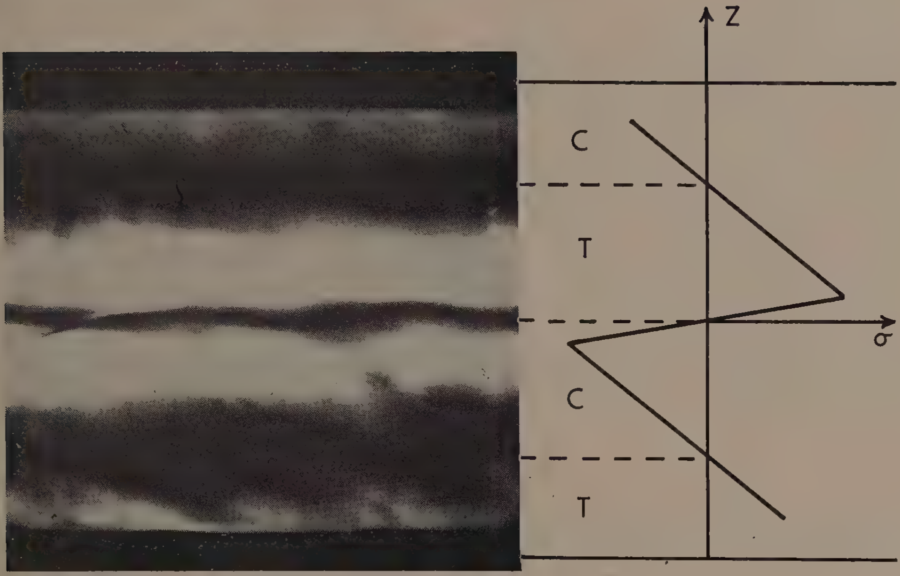

Fig. 3

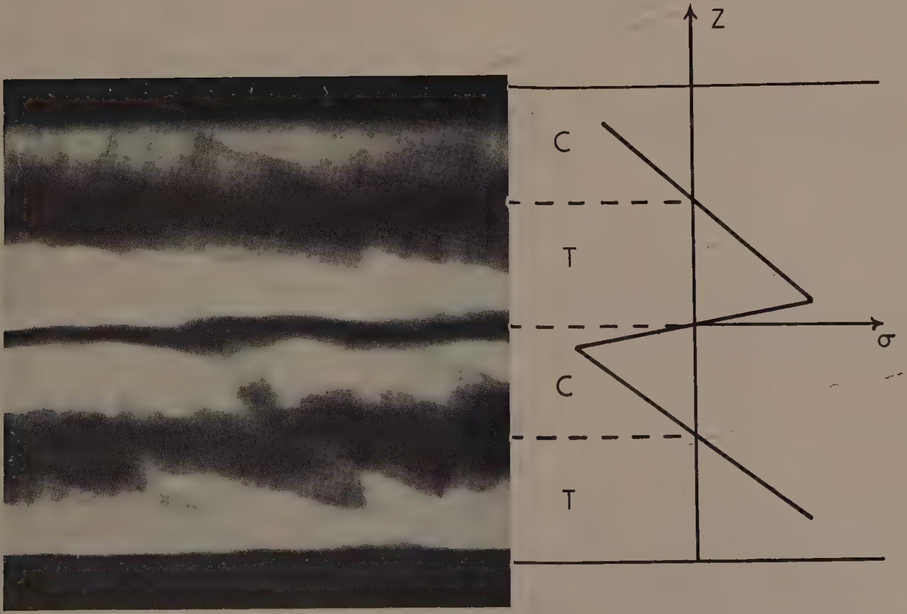

Fig. 4

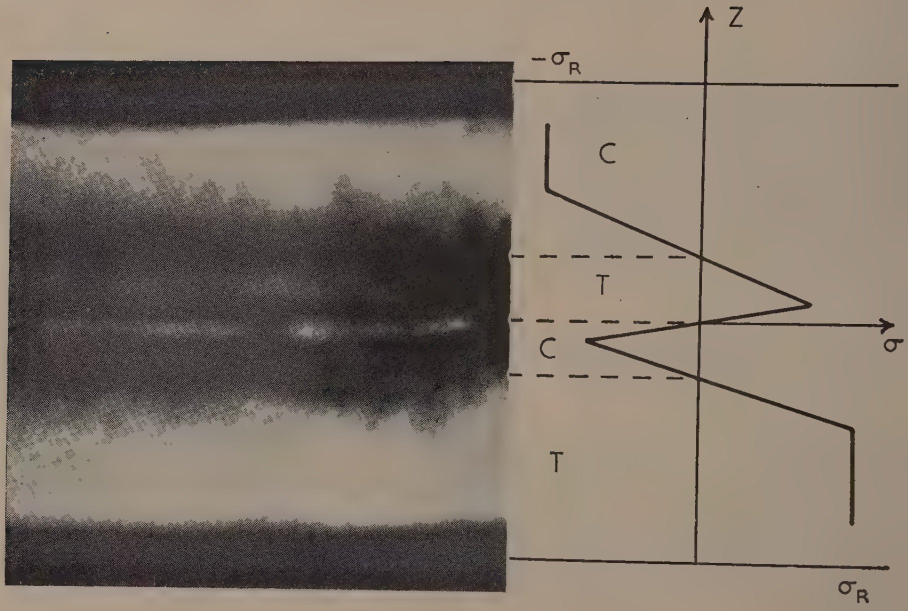
Z
$-\sigma_R$
C
T
C
σ
T
σ_R

Fig. 5

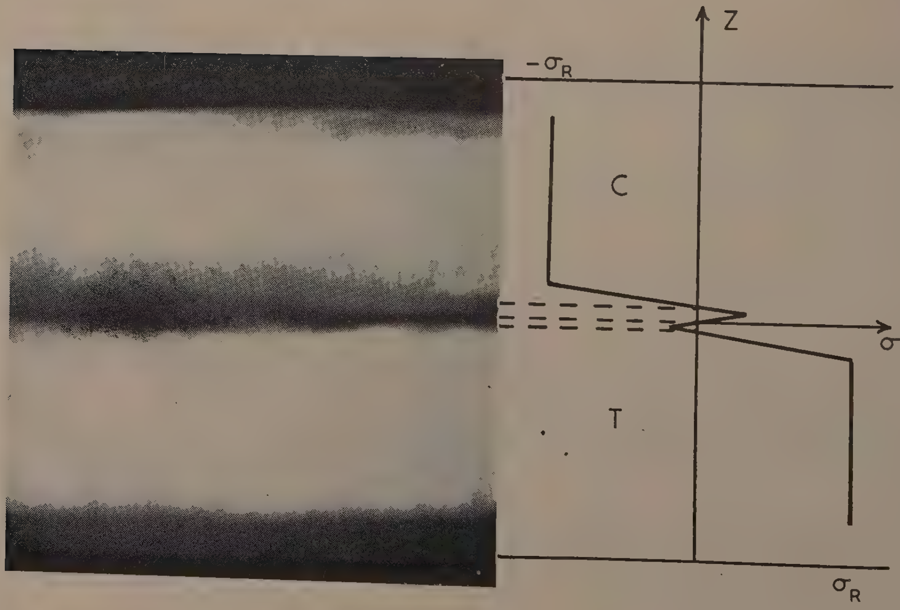
Z
$-\sigma_R$
C
σ
T
σ_R

Fig. 1

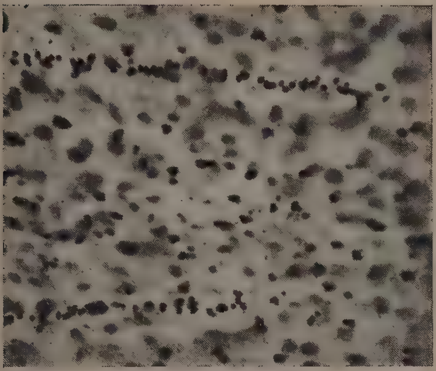

(*a*) Monatomic terraces on the surface of a crystal of silver bromide, associated with dislocation loops and decorated by the separation of particles of silver. ×1050.

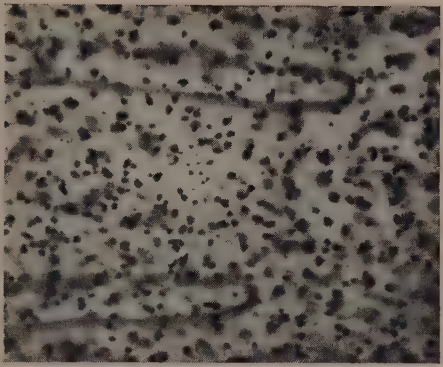

(*b*) Segments of the loops where the dislocations are in the screw orientation and define the ends of the surface terraces. 3 microns below figure 1 (*a*). ×1050.

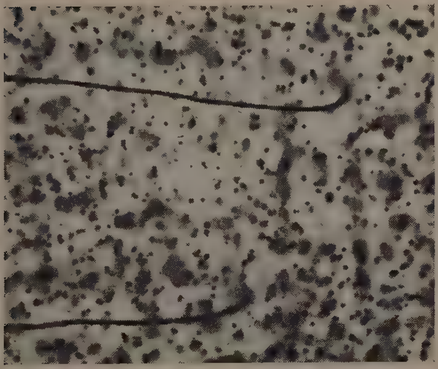

(*c*) Segments of the loops where the dislocations are in the edge orientation and are parallel to the corresponding surface terraces. 6 microns below fig. 1 (*a*). ×1050.

Fig. 3

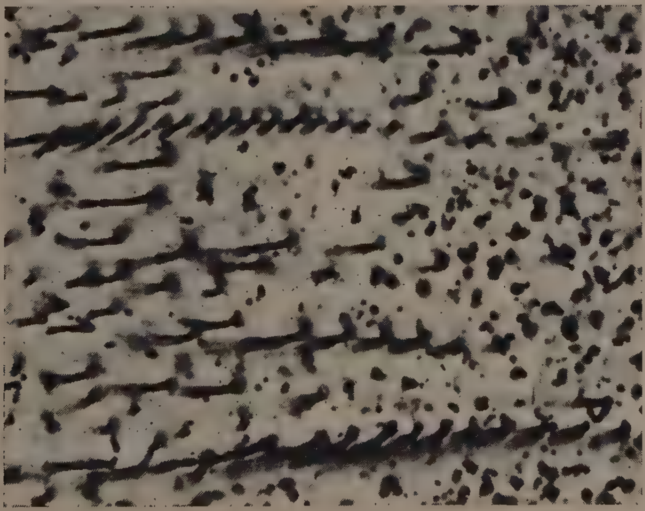

Successions of dislocation loops meeting the surface in the edge orientation and tending to lie on (110) glide planes. There are no surface terraces to be decorated and the loops are only very faintly visible where they are in the screw orientation below the surface. ×1425.

Fig. 2

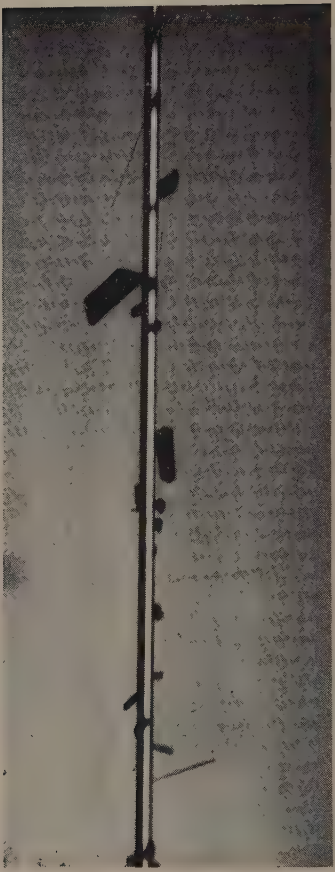

Cadmium crystals on a quartz fibre after 75 min of growth at $\sigma \simeq 0{\cdot}7$. ×28.

Fig. 3

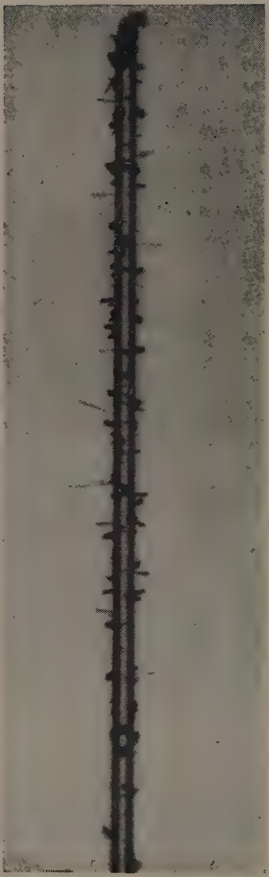

Random distribution of whiskers and platelets 5 min after beginning of growth, when $\sigma_{\max}$ was $\sim 1{\cdot}4$. ×46.

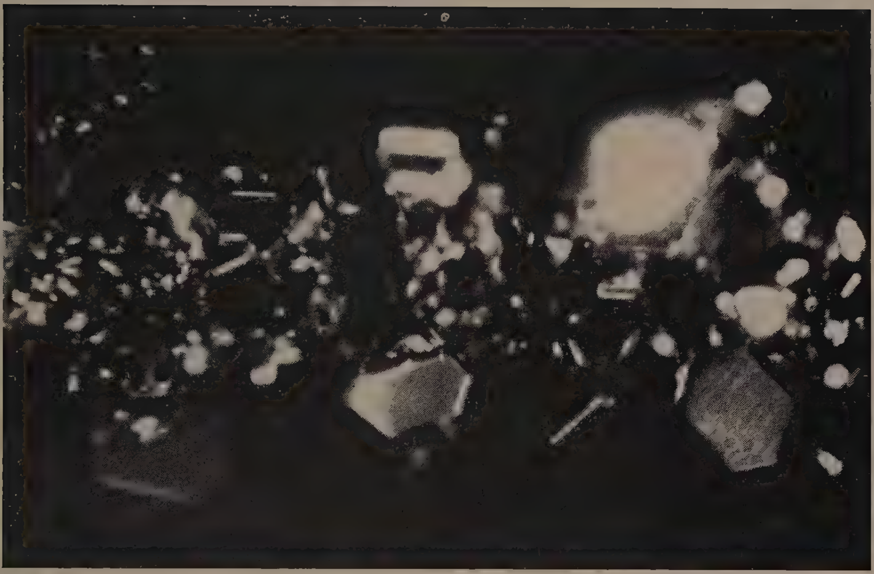

High density of hexagonal plates after one day of growth when σ_{max} was ~8. ×100.

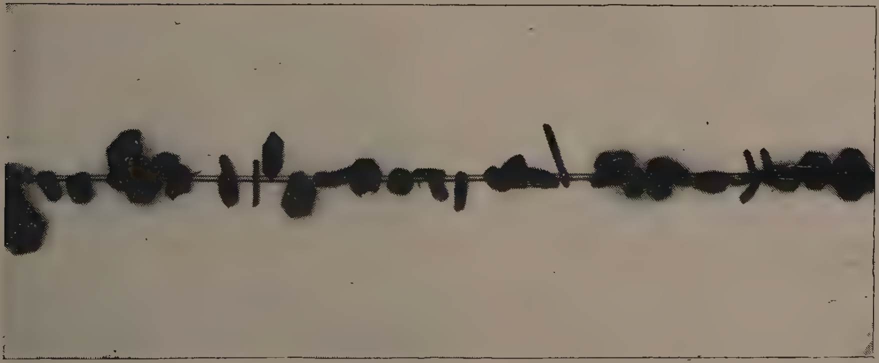

Platelet growth when σ_{max} was ~3. ×11.

Fig. 7

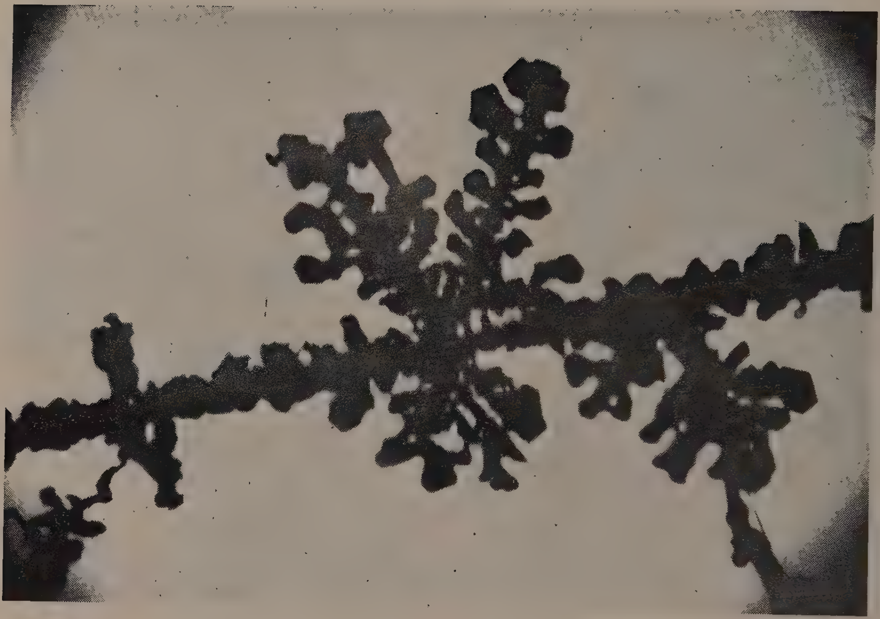

A cadmium 'snowflake'. ×45.

Fig. 6

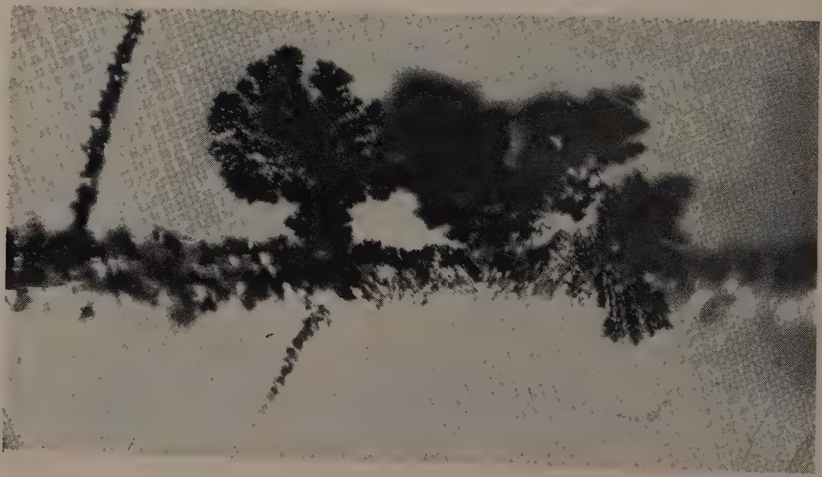

Dendritic growth at $\sigma_{\max}\sim 110$ and $T\sim 180$°c. ×28.

Fig. 3

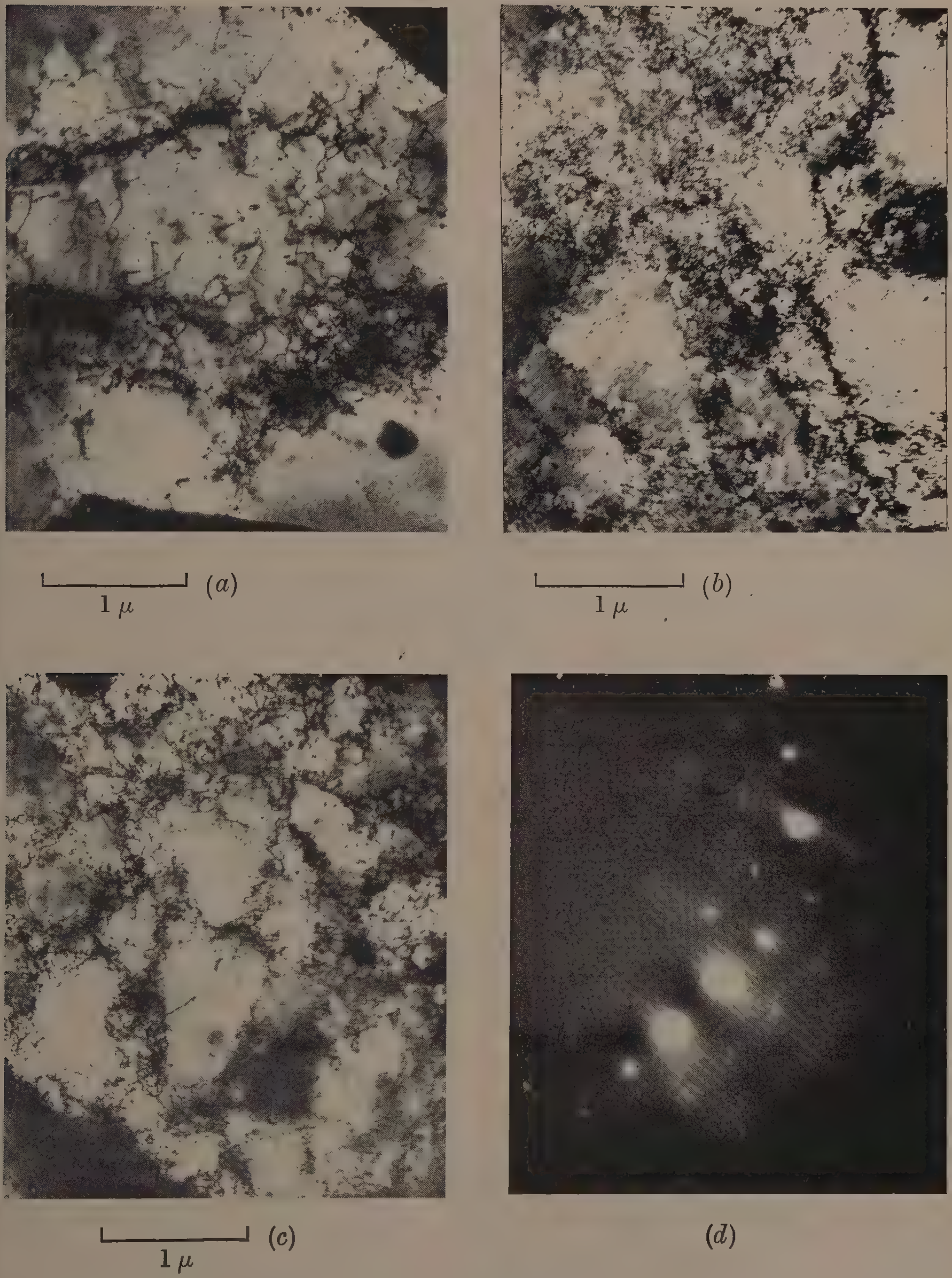

(*a*) Micrograph of polycrystalline silver deformed 10% in tension (×20 000).
(*b*) Micrograph of polycrystalline silver deformed 20% in tension (×20 000).
(*c*) Micrograph of polycrystalline silver deformed 30% in tension (×20 000).
(*d*) Electron diffraction pattern from an area $\frac{4}{3}\,\mu$ diameter, of silver deformed 30% in tension.

Fig. 4

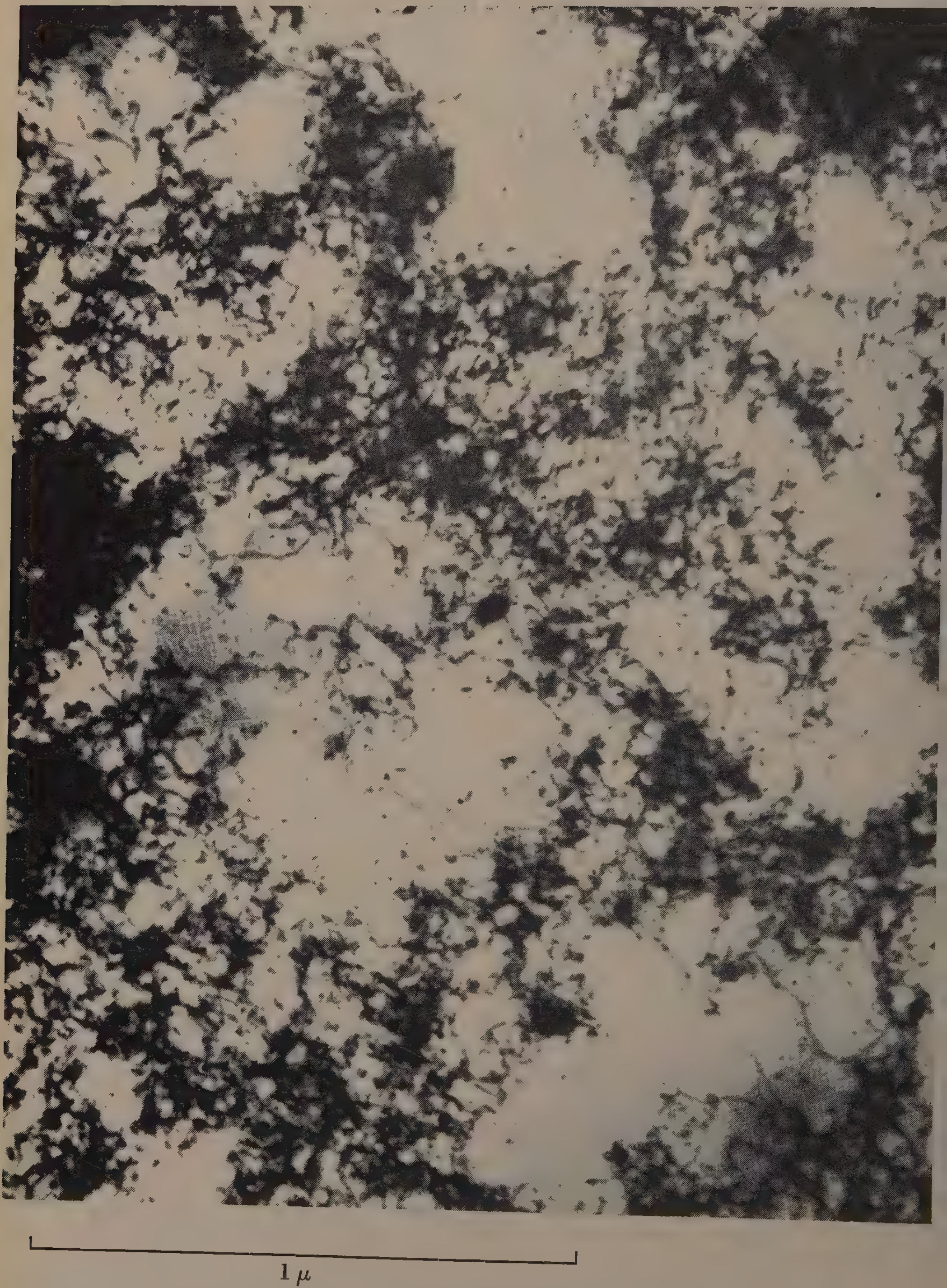

Micrograph of polycrystalline silver deformed 25% in tension, showing the complex networks in the cell boundaries (×80 000).

Fig. 5

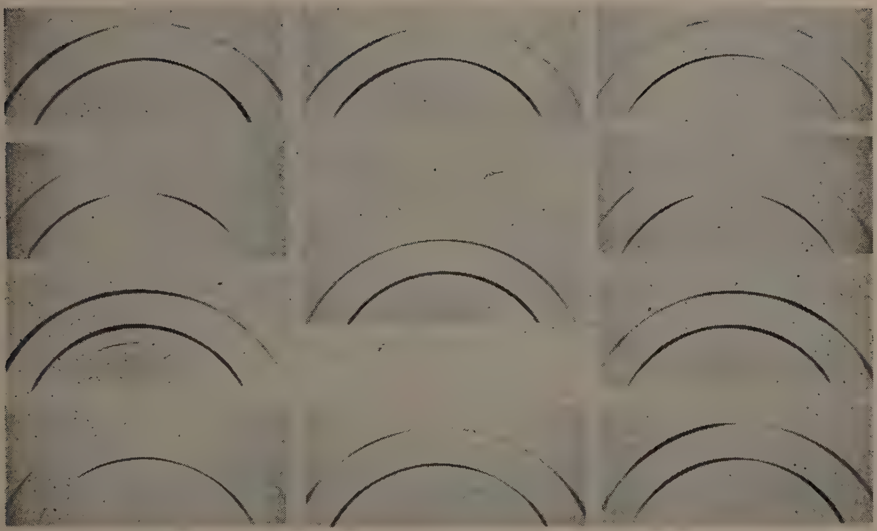

The x-ray patterns obtained for the 111 and 200 reflections from the nickel composite specimen. The central pattern is that obtained by rotating the specimen, and the outer ten patterns are those obtained from the individual sectors.

Fig. 3

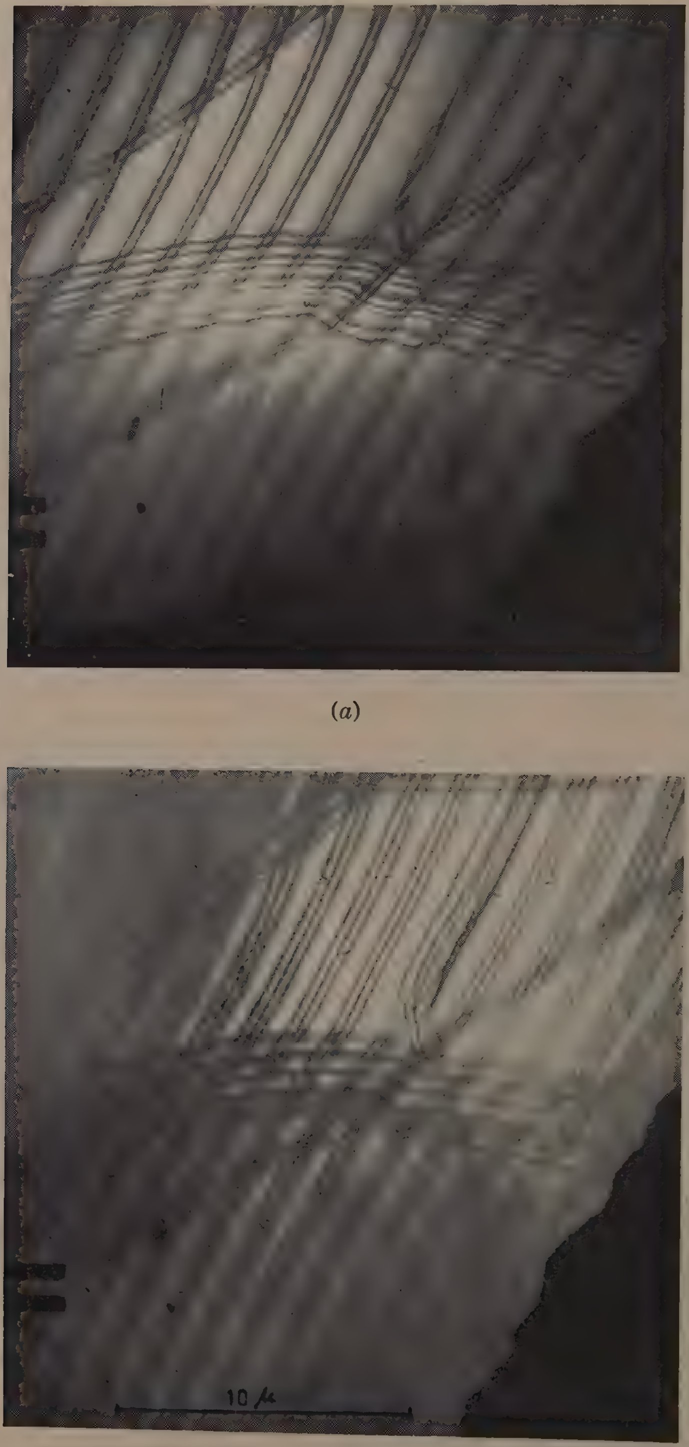

(*a*)

(*b*)

Two images of the same area, showing different features :

(*a*) Two partials are visible from the main family of dislocations.

(*b*) Three partials are visible in one area, all four are visible in a second area.

(Fig. 3 *continued*)

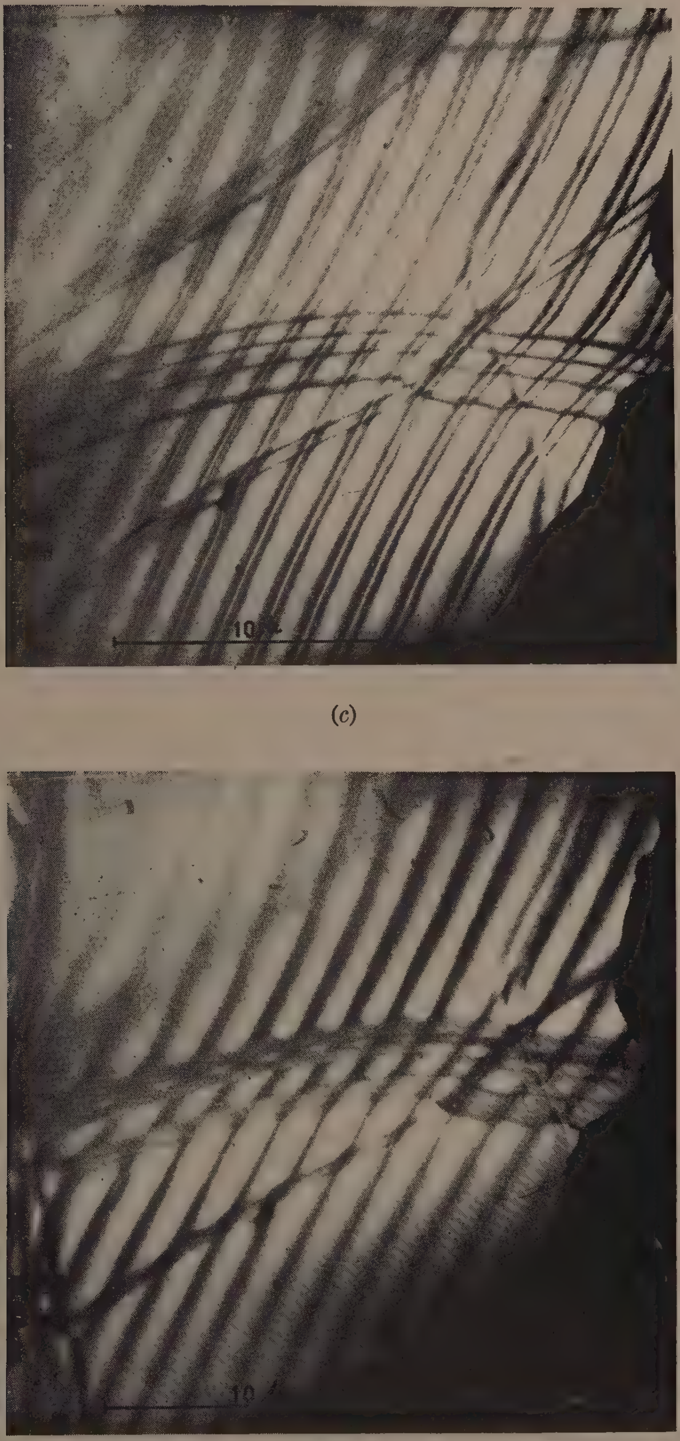

(*c*)

(*d*)

Two images of the same area, showing different features :

(*c*) The two external stacking fault ribbons have dark contrast.
(*d*) The central stacking fault ribbon has dark contrast; the two external ribbons have a somewhat lighter shade.

Nuclear Interactions of 5·7 BeV Protons in Photographic Emulsion[†]

By V. Y. Rajopadhye
H. H. Wills Physical Laboratory, University of Bristol[‡]

[Received October 1, 1959]

Abstract

Tracks produced by 5·7 BeV protons in nuclear emulsions have been followed till they interact with emulsion nuclei, and a mean free path of 35·6 ± 2·4 cm has been obtained. About 24% of the shower tracks are found to be protons, all of which emerge at angles less than 20° with the direction of the primary. The mean multiplicity of pion production is found to be 2·6 ± 0·3, the coefficient of inelasticity 0·49 ± 0·07, and the transverse momentum of pions 220 ± 30 MeV/c.

The angular distribution of the shower tracks has been analysed on the assumption that the pions are produced in a single collision system with a forward–backward symmetry in the centre of mass reference frame. The mass of the particle with which the incident proton forms such a collision, is shown to have an upper limit of 1·08 ± 0·15 proton mass units. Hence the meson production on an average may be considered as arising in a nucleon–nucleon collision even with a complex target nucleus. The angular distribution of the pions in the C-system is found to be isotropic, within the limits of experimental errors.

§ 1. Introduction

High energy protons and α-particles from cosmic radiation have provided extensive data on multiple meson production. Such observations have been made both with cloud chambers and photographic emulsions. In those cases where few or no heavily ionizing prongs are associated with the event, it has been customary to assume that the secondary particles are created in a single collision of the incident proton with an individual nucleon of the target nucleus. The energy of the incident proton is then estimated from the median angle of the shower tracks, i.e. the angle which contains half the number of shower tracks (Dilworth *et al.* 1953).

During recent years, beams of high energy protons have become available, and diffusion chambers and bubble chambers filled with liquid hydrogen have been used to investigate proton–proton interactions at various energies. These energies, though small as compared with those available in the cosmic radiation, are much above the threshold for multiple meson production. While photographic emulsion is not the ideal medium for studying such nucleon–nucleon collisions, it has nevertheless often been used for this purpose (Duke *et al.* 1955, Cester *et al.* 1956, Kalbach *et al.* 1959). Moreover, proton–nucleus collisions in the emulsion are capable of providing a wealth of useful information. It is intended to give here an analysis of such collisions, initiated by 5·7 Bev protons, in relation to various aspects of meson production, such as multiplicity, angular distribution, inelasticity, etc. Although heavy mesons, hyperons and anti-nucleons, can be produced at this energy, the cross section for their production is very much smaller than for π mesons; hence it is assumed that all the newly created particles are π mesons. The primary energy being known, the angular distribution has been used to examine the hypothesis of nucleon–nucleon collision.

[†] Communicated by the Author.
[‡] On leave of absence from the S. P. College, Poona, India.

Fig. 1

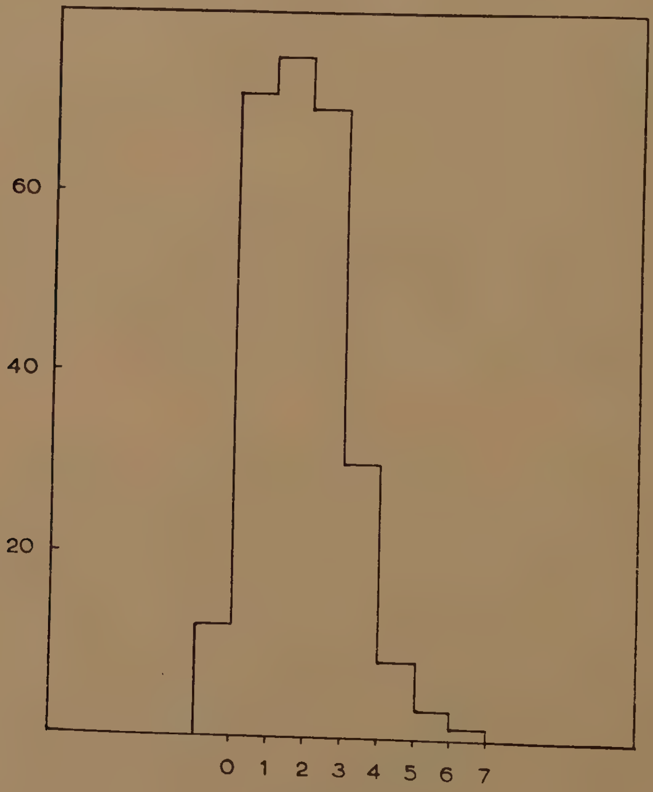

n_s distribution

§ 2. Experimental

A small stack of Ilford G5 emulsions (10 cm × 4 cm × 400 μ) was exposed to a single pulse of the 5·7 Bev proton beam from the Berkeley bevatron. The tracks were parallel to the shorter edge and had negligible dip. The beam had a high flux density of $\sim 5\times10^5$ particles per cm^2. Only two plates of the stack were used in this experiment.

Adopting a procedure of scanning along the track, 266 interactions have been obtained. An interaction has been defined as an event where the beam track seems to terminate, with or without the association of secondary track(s) of any degree of ionization. Events that look like a mere deflection of the incident track were ignored, as they would require a detailed examination, which is often inconclusive, to decide between meson production and elastic scatter. Each interaction was classified according to the number of N_h of the heavily ionizing prongs (black and grey) and the number, n_s, of the shower tracks, i.e. tracks with a blob density less than 1·4 times that of the beam proton tracks. The projected and dip angles of each shower track were measured and the space angle calculated.

Fig. 2

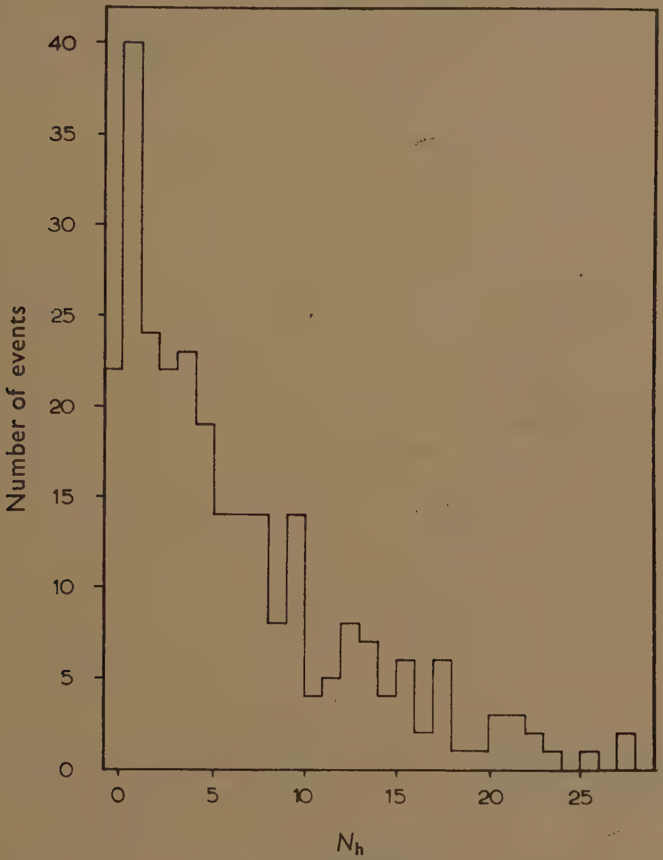

N_h distribution.

§ 3. PRELIMINARY RESULTS

3.1. n_s *and* N_h *Distributions*

The n_s distribution is shown in fig. 1. Our mean value of n_s is 2·3, as compared with 2·1, of Schein *et al.* (1956). Events in which n_s is 1, 2 or 3 are equally abundant and these together constitute 60% of the total.

The N_h distribution is shown in fig. 2. There is a high proportion (viz. 23%) of events in which $N_h \leqslant 1$: Half the number of events are included in the interval $N_h \leqslant 4$.

The observations do not show any correlation between N_h and n_s. The mean multiplicity n_s does not seem to vary with N_h, as may be seen from the table below.

Table 1. Variation of n_s with N_h

N_h	0, 1	2, 3	4–6	7–10	>11
Mean n_s	2·4	2·2	2·5	2·3	2·2

3.2. *Mean Free Path*

A total track length of 75·9 m was followed and 213 interactions obtained, thus giving a mean free path of 35·6 ± 2·4 cm. (53 additional interactions

Fig. 3

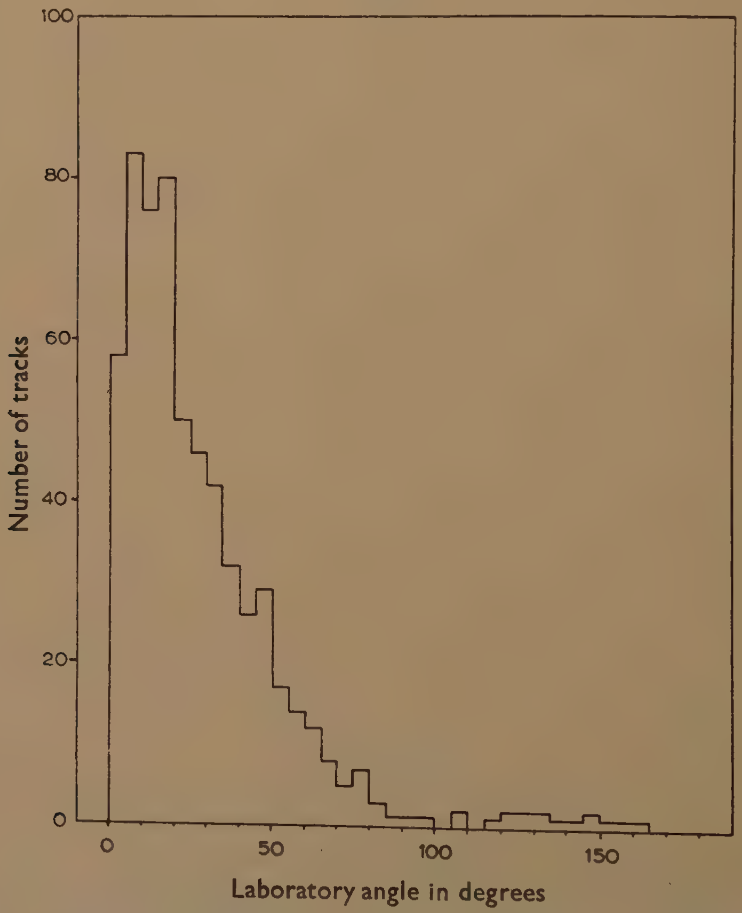

Differential angular distribution of all the shower tracks of the composite star.

were found, but the path length for these was not recorded. All the 266 interactions have been used for the further analysis.) The mean free path is in good agreement with other observations at the same energy. Cavanaugh *et al.* (1955), obtain 37·6 ± 5·3 cm from 50 events and the Bombay group (Appa Rao *et al.* 1956) find 34·7 ± 3·4 cm from 103 events.

§ 4. MEDIAN ANGLE OF THE π MESONS

Since the average number of shower tracks per star is small, all the events have been grouped together to form a 'composite star', to which it is possible to apply statistical considerations. The angular distribution of this composite star is shown in fig. 3.

Measurements on the blob density, b, and multiple Coulomb scattering, $\bar{\alpha}$, were made on all secondary tracks longer than 5 mm with a view to identifying the particles producing them. The blob density was normalized to that of nearby proton tracks at the appropriate depth. 1000 blobs were counted on the shower tracks and 3000 on the proton tracks.

Fig. 4

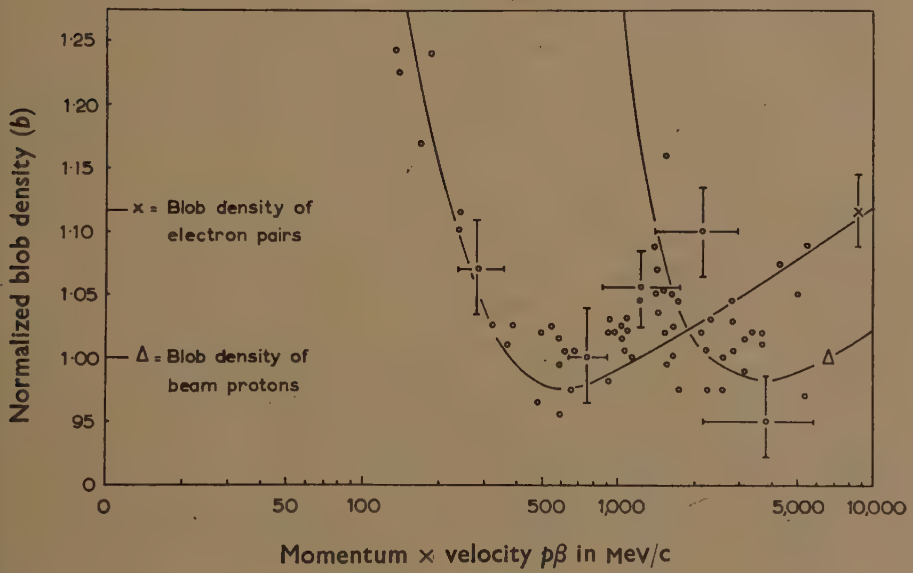

Curves showing the blob density *vs.* momentum × velocity for protons and pions The plateau value of the blob density has been obtained from tracks of electron pairs.

It is necessary to ascertain that the scattering measurements even after correction for the stage noise and reading errors, are not seriously affected by the existence of distortion, which commonly occurs on account of the differential shear of the emulsion during processing. The effect of such distortion is to impart a curvature to straight tracks. Observations were made on a number of steep grey tracks to determine the magnitude of this effect in several regions. It was then concluded that the curvature due to this cause, imposed on tracks longer than 5 mm, would introduce an error in the scattering measurement much less than that due to statistical fluctuations arising from the use of a finite number of independent cells.

The second effect to be considered is the spurious scattering (Biswas *et al.* 1955) which becomes an important source of noise in measurements using large cell sizes. Spurious scattering is believed to be caused by local dislocations in the emulsion, completely unrelated to the differential shear mentioned above. From scattering measurements on a large number of beam proton tracks it was found that the spurious scattering in these plates was fairly small, and thus the scattering measurements may be considered to give a satisfactory estimate of the energy of the particle, subject only to the statistical errors associated with the measurements.

The results of the measurements of blob density and $p\beta$ from scattering on 64 tracks which satisfied the length criterion are shown in fig. 4. The plateau value of the blob density was determined from the tracks of electron pairs materialising from the γ-rays created in π^0-decay. The plateau value of ionization and the shape of the ionization curve are believed to be sensitive to the development of the emulsion. The curves shown in the diagram are similar to those of Shapiro and Stiller (1952), where the rise in the blob density is more gradual than that obtained by Daniel *et al.* (1952). However, the uncertainty in the shape of the curves, and the statistical errors associated with the measurements of blob density and scattering, do not allow an unambiguous identification of all the tracks into those due to protons or pions. Cester *et al.* (1956) have arrived at a similar conclusion, while investigating the interactions of 3 BeV protons in emulsion. In spite of these difficulties, it is possible to obtain upper and lower limits to the median angle of the π mesons.

(*a*) In the sample of measured tracks, all those with $p\beta \leqslant 1200$ MeV/c can be classified with confidence as π mesons. If the remaining, (i.e. tracks with $p\beta > 1200$ MeV/c) are all assumed to be protons, one obtains an upper limit to the number of protons in the sample. The angular distribution of the measured tracks is given below.

Table 2. Angular Distribution of the Measured Shower Tracks

Angle	0–10°	10°–20°	20°–30°	>30°	Total
Number of tracks with $p\beta > 1200$ MeV/c	32	2	0	0	34
Total number of tracks	43	6	4	11	64

Assuming this upper limit to the fraction of protons also holds in the corresponding angular intervals of all the shower tracks (of the composite star), one obtains an upper limit to the number of protons as 157†. The median angle of the remaining, considered to be π mesons, would then be $28{\cdot}9° \pm 1{\cdot}6°$, since none of the tracks that could be ascribed to protons, are observed at angles greater than 20°. This median angle is an upper limit to the true median angle of the pions alone, since under the assumption, the number of pions at small angles is underestimated.

---

† Total number of shower particles is 606.

(*b*) If all the shower tracks of the composite star are considered to be π mesons, the median angle would be $20{\cdot}7° \pm 0{\cdot}8°$. This represents a lower limit to the true median angle of the pions since the number of pions at small angles is over estimated in this case.

An independent estimate of the median angle may be obtained in the following way:

(*c*) From statistical considerations, the incident proton will re-emerge as a proton in about half the number of collisions, and as a neutron in the other half. If in all cases, the secondary protons are relativistic, approximately 133 shower tracks emitted at small angles could be ascribed to such protons. The median angle of the remaining, all assumed to be pions, would be $27{\cdot}7° \pm 1{\cdot}6°$.

(*d*) Notwithstanding the remarks made above, about the use of $(b^*, p\beta)$ curves, it would be interesting to see what proportions of protons among the shower tracks is predicted if the tracks are identified (as protons or pions) with their aid in the best possible way. When this is done, the following angular distribution is obtained.

Table 3

Interval	0–10°	10°–20°	20°–30°	> 30°	Total
Number of protons	21	2	0	0	23
Number of pions	22	4	4	11	41
Total	43	6	4	11	64

Assuming the same proportions of protons and pions to hold for all the shower tracks in the corresponding angular intervals, the total number of protons among the shower tracks is estimated (all of these are within 20°) to be 121; the median angle of the pions would then be $26{\cdot}9° \pm 1{\cdot}6°$.

The median angle in the neighbourhood of this value does not seem to be very sensitive to the errors in the estimate of the number of protons. In fact the results under assumptions (*a*), (*c*) and (*d*) are equal within limits of experimental errors.

§ 5. KINEMATICS OF MESON PRODUCTION

Let it be assumed that the incident proton, colliding with a particle or group of particles within the target nucleus (hereafter designated as the collision partner) produces all the mesons in a single encounter. We can then define the C-system, i.e. the coordinate system in which the centre of mass of the colliding particles is at rest. This system has a velocity β_c (in units of velocity of light) with respect to the laboratory system in which the target nucleus is at rest. β_c is given by the relation,

$$\beta_c = \frac{pc}{E+E_2} \qquad \text{. . . . . (1)}$$

where p and E are the momentum and total energy of the incident proton and E_2 the rest energy of the collision partner.

A meson emitted with a velocity β^* in the C-system at an angle ϕ to the shower axis, i.e. the direction of motion of the incident proton, will appear in the laboratory system to be ejected at an angle θ. The relation between θ and ϕ is

$$\gamma_c \tan\theta = \frac{\sin\phi}{\beta_c/\beta^* + \cos\phi} \qquad \text{. . . . . (2)}$$

where

$$\gamma_c = 1/\sqrt{(1-\beta_c^2)}. \qquad \text{. . . . . . (2a)}$$

Assuming forward–backward symmetry in the C-system, half the mesons would be emitted within an angle η in the laboratory system (which corresponds to $\pi/2$ in the C-system), given by

$$\gamma_c\beta_c \tan\eta = \beta^*. \qquad \text{. . . . . (3)}$$

The total energy of the meson in the C-system, γ^*, expressed in terms of the energy (γ) and momentum ($\beta\gamma$) in the L-system provides another useful relation, viz:

$$\gamma^* = \gamma\gamma_c(1-\beta_c\beta\cos\theta) \qquad \text{. . . . . . . (4)}$$

where $\gamma\beta_x = \gamma\beta\cos\theta$ is the component along the shower axis, of the momentum of the meson in the L-system.

The measurements of the angles of emission, and multiple Coulomb scattering of the identified pions (see table 3) provide the values of γ, β and β_x. It will be recalled that the tracks available for the measurements are biased in favour of those emitted at small angles, because of the selection criterion. The geometrical loss for large angles has to be corrected for by means of an appropriate weight factor, and the true (weighted) mean values of γ, β and β_x determined.

It has been found that these values are very little affected by the errors of identification of the shower tracks. The ambiguity of identification occurs only for tracks of high energy and these are mostly emitted at small angles. The more serious errors in the mean values of β and β_x arise mostly due to the small numbers of tracks at wide angles, and the corresponding large weight factors, apart from the large statistical errors in the measurement of Coulomb scattering.

Equations (3) and (4) may now be solved for the two unknowns, β_c and β^* with the appropriate value of the median angle η. For this purpose it was found convenient to start with an assumed value of β_c (chosen appropriate to a proton–nucleon collision) and work by the method of successive approximations. The mass of the collision partner is then obtained by substituting in (1) the final convergent value of β_c.

From the lower and upper limits of the median angle (viz. 20·7° and 28·9°) the limits for the mass of the collision partner M in units of proton mass are found to be:

$$M_{\min}=0{\cdot}46 \pm 0{\cdot}05,$$
$$M_{\max}=1{\cdot}08 \pm 0{\cdot}15.$$

The median angles obtained under assumptions (*c*) and (*d*) give for M the values of $0{\cdot}98 \pm 0{\cdot}15$ and $0{\cdot}91 \pm 0{\cdot}15$ proton mass units respectively. Hence one may conclude that the meson production, on an average, occurs as if the incident proton suffers a collision with a particle of protonic mass, within the complex target nucleus.

§ 6. Isotropy of Emission

Conversion from the measured angles to the C-system angles may now be done by means of the transformation eqn. (2) of the previous section, with β_c, γ_c chosen appropriate to a proton–nucleon collision. β^* may be obtained in several ways, e.g. using eqn. (3), and the median angle under assumption (*c*) which, as we have seen earlier, gives a value of M very nearly equal to unity.

Fig. 5

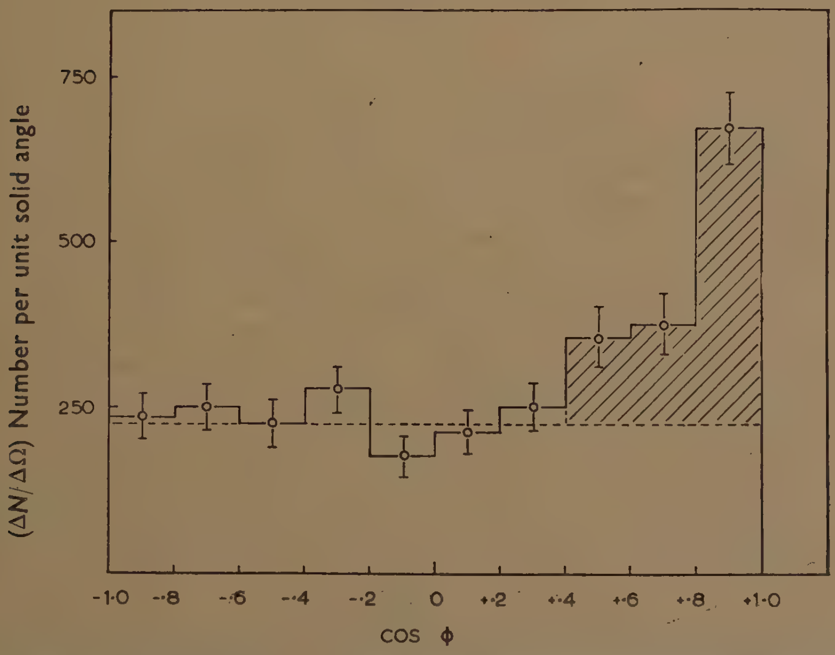

C-system angular distribution. The shaded portion represents the contribution due to protons. The number of these is estimated to be 145 ± 20.

This allows the C-system angular distribution to be determined for all the shower tracks of the composite star. This is shown in fig. 5. When the peak in the forward direction is interpreted as due to fast protons, the isotropic character of the distribution for the pions becomes immediately obvious. The number of protons in the forward peak is then estimated to 145 ± 20, all of which are confined to the interval $1 \geqslant \cos\phi \geqslant 0{\cdot}4$, which corresponds to 0–19° in the laboratory system. Both these conclusions are consistent with the observations made earlier.

The values of β^* obtained in various ways do not seem to differ from one another by more than a few per cent. To allow for a possible small uncertainty in the value of β^*, the C-system angular distribution has also been determined for two more values of β_c/β^*, viz. 1 and 0·92, and in all cases it is found to be closely similar. Thus it may be concluded that isotropy obtained is a genuine effect.

Fig. 6

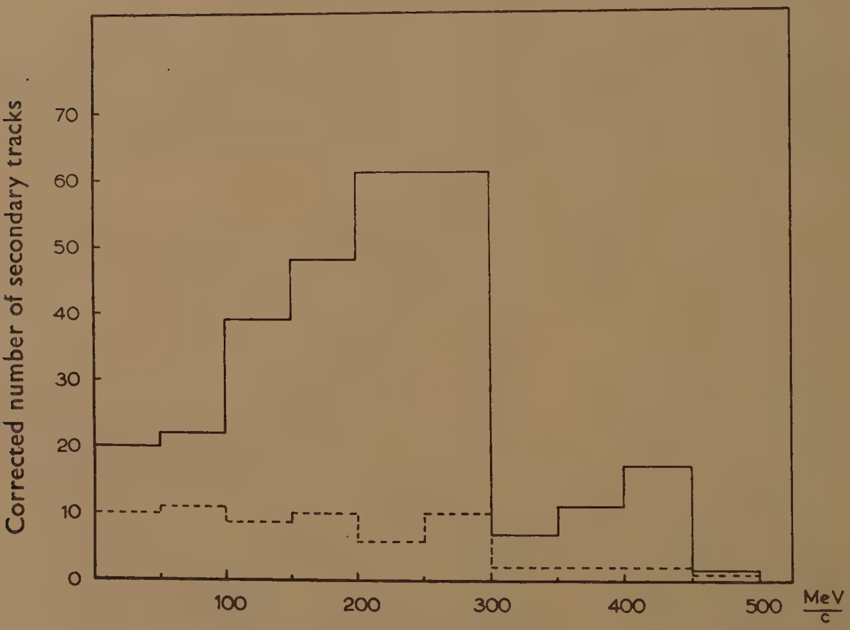

$P_\perp$ histogram for all shower tracks, corrected for the geometric loss. The dotted line represents the actual number of tracks measured.

Isotropy of emission for pions produced in 6 Bev proton interactions has been obtained by King (1958) and Kalbach *et al.* (1959). However, Daniel *et al.* (1959) have obtained a forward–backward peaking, an effect probably due to their small statistics, involving the use of only those tracks, which were identified as mesons by (b^*, $p\beta$) curves, and the large weight factors to correct the geometrical loss.

§ 7. TRANSVERSE MOMENTUM

The importance of this dynamical quantity for the understanding of high energy nuclear interactions was first realized by Nishimura (Koba 1956). Extensive measurements on the transverse momentum $P_\perp$, on the charged and neutral pions emitted from jets were made by Edwards *et al.* (1958). They find $P_\perp$ to be 500 Mev/c, over a very wide range of primary energies. Recent observations by the Japanese Emulsion Group (1959) on the $P_\perp$ of neutral pions in jets with primary energies $10^{12} \div 10^{14}$ ev show a narrow distribution with a peak at about 400 Mev/c. They also find no significant variation with either primary energy or pion energy.

In the present experiment, the transverse momentum of all the secondary particles has been determined from the measurements of the Coulomb scattering and the angle of emission. It does not seem to depend upon the identity (π or p) assigned to the particle when $p\beta_\perp > 1200$ Mev/c and thus it has the same value for all secondary tracks. The histogram of $P_\perp$, for all shower tracks, in which the observations are duly weighted to compensate for the geometrical loss is shown in fig. 6 from which the mean value of $P_\perp$ is found to be 220 ± 30 Mev/c, somewhat smaller than that observed in 'jets'. It should be noted that a large number of tracks available for measurements are emitted at small angles. Constancy of $P_\perp$ would require very high energies for the mesons emitted at small angles. This is clearly impossible in view of the finite energy of the incident proton. With the small statistics available, it is not possible to draw any conclusions regarding the variation, if any, of the transverse momentum with the angles of emission.

§ 8. ENERGY BALANCE

It is possible to see how the kinetic energy of the incident proton is accounted for in the interaction. It is convenient to consider all the interactions together and utilize the results of the scattering measurements on the sample of 64 tracks.

As a starting point, the average kinetic energy of the protons and the total energy of the pions, in the different angular intervals may be determined under assumption (*a*), § 4. The relative numbers of protons and pions shown in table 2 then allows the energy of all the shower tracks of the composite star to be calculated. A correction has to be made for the energy carried away by the neutrons, and π^0 mesons emitted. About 66% of the collisions would be with the heavy nuclei Ag and Br, in which the neutron proton ratio is 13 : 10 and thus collisions with neutrons would be more numerous in that ratio. In the case of light nuclei C, N and O, probability of a collision with a proton or a neutron is the same. From all these considerations, the energy released per star, that accounts only for all shower particles (charged and neutral) is found to be $3·5 \pm 0·8$ Mev.

Thus a lower limit is set for the energy of the shower tracks, since the assumption (*a*) causes the average energy of both pion and proton groups to be underestimated. Assumption (*d*), which gives a higher proportion of pions, may now be used as comparison, to calculate the average energy of protons and pions. From this, one obtains the total energy of the shower tracks per star to be $4·1 \pm 1·1$ Bev.

To this must be added the energy of the black and grey tracks. From a study of 9 Bev proton stars in emulsion Beliakov *et al.* (1958) have found the energy (E') of black and grey tracks in light and heavy nuclei to be respectively 470 ± 70 and 1400 ± 120 Mev. Considering the proportion of light and heavy nuclei in emulsion, the average energy per star is ~1 Bev. This is in good agreement with that deduced from cosmic ray data (Camerini *et al.* (1951), Powell *et al.* (1959)). The latter give $E' = 124N_h + 30$ Mev which corresponds to 860 Mev in the present experiment. Thus the total energy released per star agrees well with the primary energy.

Fig. 7

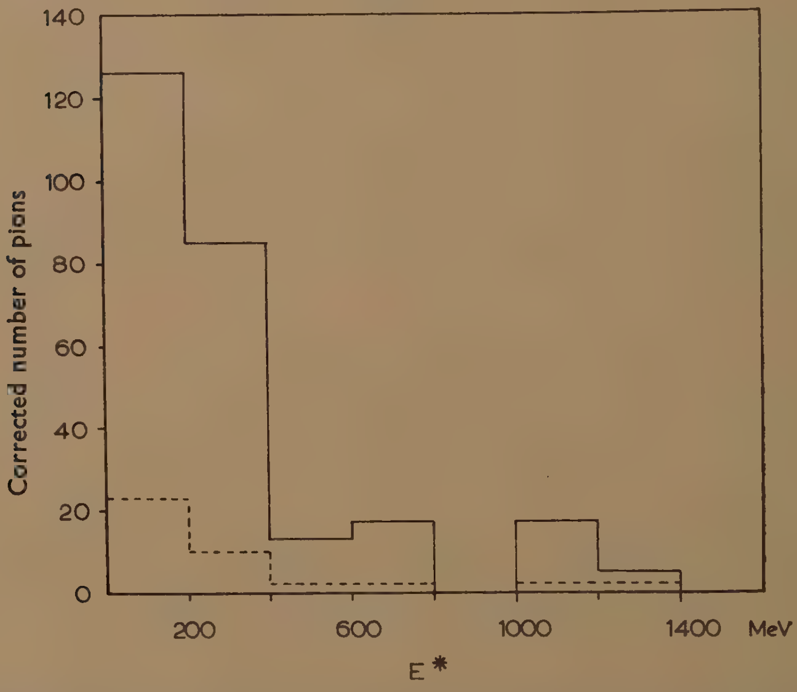

Histogram of the C-system kinetic energy for the mesons, corrected for the geometric loss. The dotted line shows the actual number of tracks.

§ 9. Pion Multiplicity and Inelasticity of Collision

The number of tracks considered to be due to protons among the 606 shower tracks varies according to the assumptions made, but it seems to lie between fairly definite limits of 121 and 157. The number of mesons then would be uncertain to that extent. Mesons emitted backwards in the C-system would appear slow in the laboratory system, and would produce grey tracks. These have not been considered in the present analysis, as their number is presumably small. Assuming the number of protons to be 145 ± 20 as obtained from fig. 5, the number of charged mesons per star is found to be 1·7. According to the principle of charge independence in meson production, the ratio of neutral to charged mesons is 1 : 2. Thus the total pion multiplicity would be 2·6 ± 0·3. This may be compared with 2·5 as predicted by Fermi's theory.

The inelasticity of collision is defined as the fraction of the available energy in the C-system, that is radiated off as mesons. The average energy of the mesons may be computed in several ways. When combined with the mean multiplicity, this would allow the inelasticity to be determined.

The average velocity of the mesons, β^*, has been found to be 0·91. This corresponds to a kinetic energy 210 Mev.

The eqns. (3) and (4) of § 5, when solved for β^* and β_c, with the median angle 26·9° under assumption (*d*) and 27·7° under assumption (*c*), give β^* as 0·935 and 0·931 respectively. These correspond to energies of 285 and 250 Mev.

On the basis of the identification of mesons made under assumption (*d*), their energies and momenta have been calculated from the measurements of multiple Coulomb scattering. Since the mesons are assumed to be produced in a nucleon–nucleon collision, their C-system energy can be calculated by means of appropriate Lorentz transformation equations. Figure 7 shows the C-system energy spectrum of the mesons, thus obtained, with due corrections for the geometrical loss. The weighted mean kinetic energy is found to be 280 ± 80 Mev.

The errors of identification of the tracks do not seem to affect the mean value obtained above. Using assumption (*a*), for discriminating pions from protons we get nearly the same spectrum, and the same mean energy. The small weight factors associated with the tracks at small angle do not alter noticeably the spectrum by their inclusion or exclusion.

All these results may not be considered inconsistent with one another, since the statistical errors are rather large. Taking the mean energy as 280 ± 80 Mev, the inelasticity would be 0·52 ± 0·15.

Since the statistical errors in the mean energy derived above are too high, we have preferred to use the results of Kalbach *et al.* (1959) who find the mean energy to be 236 ± 20 Mev, from measurements on 143 pion tracks. This gives the inelasticity as 0·49 ± 0·07.

§ 10. DISCUSSION

The median angle method for the analysis of meson showers is based on the assumption of an on-the-average forward–backward symmetry in the C-system. With events of low multiplicity as in the present experiment, the median angle of the shower tracks would be considerably smaller than that for the mesons only, because the proton often emerges from the interaction with only a small change of direction. The primary energy deduced from the median angle of the shower tracks would then be overestimated (Haber-Schaim 1956). At 6 Bev primary energy, the mean velocity of the mesons β^*, in the C-system is found to be somewhat higher than the velocity of the C-system itself. Ignoring this would have the effect of under-estimating the primary energy. The error involved, however, is of the same order as that due to the statistical error in the median angle.

The fluctuations in the median angle with N_h observed by Haber-Schaim, (1956) are probably due to the small statistical weight of his data. In the present experiment, the variation of the median angle with N_h is found to be as follows:

Table 4. Variation of the Median Angle of Shower Tracks with N_h

N_h	0	1	$\leqslant 4$	$\geqslant 5$
Median angle	$16 \cdot 3 \pm 2 \cdot 0$	$14 \cdot 0 \pm 1 \cdot 7$	$17 \cdot 5 \pm 1 \cdot 0$	$25 \cdot 0 \pm 1 \cdot 4$

A difference between the median angles for small and large N_h groups has been also found by Beliakov *et al.* (1958), in a study of 9 Bev proton stars. For collision with protons, light and heavy nuclei they find the median angles for shower tracks to be respectively 18°, 25°, and 28°.

Events with small N_h are generally considered to be good approximations to nucleon–nucleon collisions. The number of such events is not very large in this experiment. However, adopting the same procedure as before, the C-system angular distribution for pions, in these events has been determined. A plot similar to fig. 5 shows isotropy of emission for pions, allows the number of protons in the forward peak and hence the median angle of the pions to be determined. Although the median angle of the *shower tracks* is observed to depend upon the N_h group, there is no evidence that the median angle of the *pions* shows a similar behaviour. The total multiplicity of the pions for the small N_h group is found to be $2 \cdot 04 \pm 0 \cdot 36$ which, although lower than Fermi's prediction, is in agreement with Daniel *et al.* (1959), who made a more detailed examination of events with $N_h \leqslant 4$. The uncertainty in the number of protons causes large errors, and a comparison with theory loses much of the significance.

Considering all events, an upper limit to the number of fast protons per star is found to be $0 \cdot 59 \pm 0 \cdot 06$. For events of small N_h, the corresponding figure seems to be significantly higher, although the uncertainty in the number of protons estimated introduces a relatively greater error.

It is to be noted that the conclusions of the experiment are based on the analysis of shower tracks only, and from events of all N_h grouped together. Slow mesons, of which the number is presumably small, are not considered. Since an upper limit to the proton contamination of the shower tracks could be set up, it was possible to deduce that the meson production occurs as if the incident proton suffered a collision with a particle of mass no greater than 1·08 ± 0·15 proton mass units. Thus the hypothesis of a nucleon–nucleon collision seems to be justified. Moreover all the fast protons are found to be emitted at angles less than 20° and the majority of them at very small angles.

ACKNOWLEDGMENTS

It is a pleasure to thank Professor C. F. Powell, F.R.S., for the hospitality of his laboratory, and Dr. D. H. Perkins, who suggested this problem and gave valuable advice on many occasions. The author wishes to thank Dr. W. O. Lock of the University of Birmingham for the loan of the plates; the members of the Radiation Laboratory University of California who made the exposure; his colleagues in the laboratory, particularly, Dr. J. W. F. Juritz and Dr. C. J. Waddington for helpful comments; and Dr. R. R. Daniel of the Tata Institute of Fundamental Research, Bombay, for a preprint of a similar investigation, and a personal discussion. He also wishes to thank his wife for some contribution to the scanning effort. A fellowship under the Colombo plan is gratefully acknowledged.

REFERENCES

APPA RAO, DANIEL, and NEELKANTAN, 1956, *Proc. Indian Acad. Sci.* A, **43,** 181.

BELIAKOV, VAN SHUFEN, GLAGOLEV, DALKHAZHAV, KIRILLOVA, MARKOV, LEBEDEV, TOLSTOV, TSYGANOV, SHAFRANOVA, JAO TSYNG-SE, BANNIK, BAJAT JAN, GRAMENITSKIJ, DANSYZ, KOSTANASHVILI, LYUBIMOV, NONOFILOV, PODGORETSKI, SKSHIPCHAK, TUVDENDORGE, SHAHULSHVILI, BOGASHEV, BUNYATOV, VISHKI YU, MEREKOV, SIDOROV, 1958, *Cern High Energy Conference Report*, p. 309.

BISWAS, PETERS, and RAMA, 1955, *Proc. Indian Acad. Sci.* A, **41,** 156.

CAMERINI, DAVIES, FRANZINETTI, LOCK, PERKINS, and YEKUTIELI, 1951, *Phil. Mag.*, **52,** 1261.

CAVANAUGH, HASKIN, and SCHIEN, 1955, *Phys. Rev.*, **110,** 1263.

CESTER, HOANG, and KERNAN, 1956, *Phys. Rev.*, **103,** 1443.

DANIEL, DAVIES, MULVEY, and PERKINS, 1952, *Phil. Mag.*, **43,** 753.

DANIEL, KAMESHWAR RAO, MALHOTRA, and TSUZUKI, 1959, Preprint.

DILWORTH, GOLDSACK, HOANG, and SCARSI, 1953, *Nuov. Cim.*, **10,** 1259.

DUKE, LOCK, MARCH, MCEVAN, HUGHES, and MUIRHEAD, 1955, *Phil. Mag.*, **46,** 877; 1957, *Ibid.*, **2,** 204.

EDWARDS, LOSTY, PERKINS, PINKAU, and REYNOLDS, 1958, *Phil. Mag.*, **3,** 237.

HABER-SCHAIM, 1956, *Nuovo Cim.*, **4,** 669.

JAPANESE EMULSION GROUP, 1959, *Nuovo Cim. Suppl.*, **11,** 125.

KALBACH, LORD, and TSAO, 1959, *Phys. Rev.*, **113,** 325.

KING, 1958, *Phys. Rev.*, **109,** 1344.

KOBA, 1956, *Proc. VI Rochester Conf. Report*, **4,** 43.

POWELL, FOWLER, and PERKINS, 1959, *Emulsion Method Atlas* (Pergamon Press), p. 464 (to be published).

SCHEIN, HASKIN, and GLASER, 1956, *Nuovo Cim.*, **3,** 131.

SHAPIRO, and STILLER, 1952, *Phys. Rev.*, **87,** 682.

A Statistical Theory of Ionospheric Drifts†

By J. P. Dougherty
Cavendish Laboratory, Cambridge

[Received January 8, 1960]

Abstract

An attempt is made to interpret the horizontal 'drift velocities' observed in ionospheric fading-wave experiments by examining statistically the fluctuations in space and time of the density of ions and electrons. The ionization is assumed to be convected by a turbulent flow in the neutral air, but the magnetic field and the dynamo electric field are also taken into account. The drift velocity to be calculated is defined by means of the space-time correlation function.

For the D region and lower E region, the estimation of this drift velocity is found to be mathematically practicable, using certain assumptions. Results are obtained which show the relative importance of the mean aerodynamic velocity and of the electric field in determining the drift of irregularities in electron density.

For higher regions, the theoretical problem is much less tractable, for reasons discussed here; but it is pointed out that in this case it is unlikely that the irregular behaviour can be ascribed to turbulence anyway, and that the problem of the drift velocity cannot properly be investigated until a satisfactory explanation of the cause of the irregularities is available.

Some remarks are offered on the relation of this theory to the observations and to the dynamo theory.

§ 1. Introduction

Observations of the fading of radio waves reflected from the ionosphere reveal that the density of ionization has random, or 'irregular' fluctuations superposed on the gradual variation with height. If two or more spaced receivers are used, comparison of the records reveals a noticeable impression of large-scale movement of the irregularities. The procedure for evaluating the velocity from the fading records was given by Briggs *et al.* (1950). Further random movements are superposed on this general 'drift'.

In the E region, since the gas is lightly ionized and collisions are frequent, the movements of the ionization are related to those of the neutral air. It is thought that in this region the air may often be in turbulent motion; if so its movement is described in terms of a mean 'wind' on which are superposed irregular turbulent velocities. It might then be expected (and indeed has sometimes been assumed) that the mean 'wind' in the neutral air is equal to the mean 'drift' of the ionospheric irregularities. This would be the case if the density of the plasma behaved as a simple convected function, like temperature, but unfortunately the Earth's magnetic field makes the ionospheric problem much more complicated than that. The purpose of this paper is to investigate the relation between the two mean velocities. It will be shown that in general they are not the same, and that the relationship between them depends on the height.

---

† Communicated by the Author.

Clemmow *et al.* (1955) and Clemmow and Johnson (1959) gave idealized solutions of the relevant equations which showed clearly that results of this kind must be expected, and this investigation began as an attempt to generalize their work. The present approach, however, differs from theirs in several respects. In their formulation, only a uniform motion of the air was permitted; a model 'irregularity' of cylindrical or sinusoidal form was introduced at time $t=0$ (in the plasma only), and its subsequent behaviour in imposed electric and magnetic fields was found. The present paper attempts instead to discuss the problem statistically. The situation is supposed to be one of equilibrium: the turbulent flow continually creates and distorts irregularities, but these, if left to themselves, would gradually be smoothed out by diffusion. It is therefore necessary to make some assumptions about the nature of the air turbulence, and this in itself poses some difficult problems arising from the effect of the buoyancy forces. By restricting attention to the problem of the drift velocity, these assumptions are kept to a minimum, and we shall only consider the simplest which can reasonably be made. This will at least make clear the nature of the problem, and it will also become apparent that to discuss further features of the radio fading, i.e. to discuss the random movements in addition to the statistically defined 'mean drift', would require much deeper analysis. This has recently been initiated by Münch and Wheelon (1958), but so far their discussion of temporal correlations concerns only the components of turbulent velocity and not the density of a plasma convected in a magnetic field.

§ 2. Outline of the Method

To carry out this programme, we have first to decide upon the assumed form of motion of the neutral air (assuming that the reaction of the plasma on it is negligible). § 3 is taken up with a discussion of this, together with some points concerning the interpretation of the fading pattern on the ground.

The standard dynamical equations for ions and electrons together with Maxwell's equations then determine, in theory, the motion of plasma in external electric and magnetic fields. It is convenient to write all field quantities as a mean part together with a random part whose mean is zero. The mean electric field is then the field of the 'atmospheric dynamo' (Baker and Martyn 1953). This is not genuinely external of course, but it is arbitrary so far as our equations are concerned since we suppose all mean quantities to vary so slowly (with height, with horizontal distance, and with time) that they may be regarded as constant in a sample of space-time large enough to be statistically significant. The random parts are supposed statistically stationary in such a sample, and the equations governing them are developed in § 5. As in ordinary turbulence theory, it is useful to work with the Fourier transforms of the random quantities, so we derive in § 6 an 'equation of motion' for each Fourier component $N(\mathbf{k}, t)$ of the density fluctuation $n(\mathbf{x}, t)$ of the plasma. This exhibits the temporal changes in $N(\mathbf{k}, t)$ as being due to a 'convection' dependent on the mean wind and electric field, and on the direction of $\mathbf{k}$; a 'decay' due to diffusion, also directionally dependent; an 'intermodulation' with other Fourier components via their electrostatic fields; and a complicated process of 'production' by the turbulent flow, which includes amongst other things the mechanism first described by Dungey (1956).

Before entering into these dynamical considerations, however, we give in § 4 the natural definition for the 'drift' velocity of the pattern of a random scalar function in terms of its space-time correlation function. This is a straightforward generalization of that given by Briggs *et al.* (1950) for an isotropic pattern in the amplitude of the signal on the ground. Since the statistical definition of the drift is thereby the same as the one used in analysing the records, it seems reasonable to identify the two, assuming the fading to be due to small structure in the ionosphere, as discussed in § 3.

The results of § 6 are applied in §§ 7 and 8 to the drift so defined; a tentative explicit expression for it for heights up to about 120 km is found assuming an isotropic spectrum, as predicted by Howells (1960). Other literature on turbulent convection (Villars and Weisskopf 1955, Gallet 1955, 1957, Wheelon 1957, Batchelor 1959, and, with the magnetic field included, Howells 1960) concentrates on trying to estimate the spectrum function of $k(=|\mathbf{k}|)$, apparently without general agreement. So it is interesting to note that our result is independent of this. A graphical representation of the way the result depends on height, through the E region, is given, from which one can deduce the relative importance of wind and electric field in determining the drift.

For greater heights, a peculiar difficulty enters and the whole situation becomes rather obscure. The reason for this is discussed in § 9. This also provides an opportunity to make some remarks on the analogous problem for the F region.

A general discussion of the result and its relation with both the radio observations and the dynamo theory is provided in the concluding section.

§ 3. MECHANICS OF THE NON-IONIZED AIR IN THE LOWER IONOSPHERE

As we have already hinted, no adequate theory of the motion of the neutral air in the E region exists—indeed if it were not for the kind of difficulty which it is the purpose of the present paper to try to overcome, one would hope to use the radio observations to help to elucidate some features of the air motion. To make progress we have to adopt some idealized model, so some explanation is due on the question of how likely this is to be near the truth.

Present indications (mainly from data concerning the rate of deformation and diffusion of meteor trails) are that the air motion is to be pictured somewhat as follows. At the smallest scales, kinetic energy is converted into heat by the action of viscosity and we have a 'dissipation range' in the ordinary way, with buoyancy forces quite unimportant. At rather larger scales, dissipation gradually becomes less important, and buoyancy more important, but there may be an 'equilibrium range' in which neither is very effective, the main feature being the interaction among all pairs of Fourier components of the velocity field, arising from the non-linear inertial term in the Navier–Stokes equation. So far, the energy spectrum function would be roughly isotropic. But at still larger scales the effect of buoyancy becomes the dominant feature, and the spectrum becomes anisotropic. The large 'flat' eddies of about 6 km depth and up to 150 km in horizontal extent, observed by Greenhow and Neufeld (1959) come under this heading. Most of the kinetic energy resides in these eddies. An alternative description of the large-scale motions is obtained by ignoring the non-linear term so that one obtains the linearized theory of 'gravity waves' in a stratified medium (Hines 1959). This gives a useful insight into the general effect of the buoyancy forces and one can easily re-examine the non-linear term later, to establish the error involved, which, if small, can be interpreted as coupling between the various modes. (There is of course another class of motions, associated with compressibility, which at small scales are sound waves, but which at scales comparable with a scale-height are also profoundly modified by buoyancy. This is why Hines has 'two turbulent sequences'.) Finally, on a scale still larger than the large eddies or gravity waves, are the world-wide meteorological motions.

If this description is correct, the usual notion of degradation of energy from larger to smaller scales and finally into the dissipation range, may be used, but care should be exercised in estimating ϵ, the rate of dissipation per unit mass, from the characteristic size L and velocity V of the energy containing eddies. For isotropic turbulence in a uniform fluid one usually writes $\epsilon \approx V^3/L$, but recently reported observations of meteor trails indicate that ϵ is much smaller than V^3/L if the latter refers to the large gravity-dominated eddies. A qualitative explanation appears to be that gravity and the density stratification enable the flow to take on a more ordered structure whereby the excitation of smaller-scale motion through the non-linear terms is less than would be the case for a flow of comparable V and L in a uniform fluid (assuming no special boundary conditions). Thus in our case, to apply the above formula, V and L should refer to the rather smaller-scale (and less energetic) part of the spectrum where buoyancy is just beginning to be dominant, say $V \approx 1$ m/sec, L somewhat less than 1 km, as a very rough estimate. Indeed it might be better not to follow the terminology of the authors just cited, and reserve the word 'turbulence' for the approximately isotropic part of the spectrum, so excluding the gravity waves.

The reader will find more discussion of many of these points in the Proceedings of the International Symposium on Fluid Mechanics in the Ionosphere (*Journal of Geophysical Research*, December 1959) (and the author is indebted to many of the speakers at this meeting for making clearer these ideas).

This description has been given in some detail partly to emphasize the great complexity of the problem even before introducing the plasma in a magnetic field, and partly to show the significance of a fundamental assumption we shall make. This is to suppose that the radio fading, and the associated measurements of drift velocity, are to be explained in terms of the small scale, roughly isotropic, part of the spectrum. The wavelength for reflection from the E layer is about 100 m, and the size of a Fresnel zone is about 5 km. So any quite small structure in the distribution of plasma density is certainly effective in producing small-scale structure in the radio-wave diffraction pattern on the ground. On the other hand it is quite true that even with large-scale variations only, small-scale structure can appear in the diffraction pattern, as for example in an interference pattern due to specular reflection from a small number of points in a 'wavy' ionosphere. The theoretical problem of interpreting the observed distribution of signal on the ground in terms of its cause in the ionosphere is discussed by Ratcliffe (1956), who points out that the fading pattern does not contain enough information to distinguish between these possibilities. Briggs (private communication) suggests to the author that the highly irregular appearance of records obtained by him (by the rapid frequency-change method) for E region contrast rather markedly with those for the F region, when displayed as a panoramic record. The F region ones are more regular suggesting specular reflection, thus leading one to think that in the E region it is the small-scale fluctuations which are responsible for the fading. If it is subsequently shown that large structure plays an important rôle, it will be necessary to study the convection of plasma by gravity waves in a magnetic field instead of turbulent convection as in this paper. Such a study is in any case relevant to the part of the ionosphere where viscosity is so large that no equilibrium range exists at all, and work on this problem has already been published by Hines (1955, 1956). Estimates of the height at which this might begin to be the case vary; one, due to Stewart, is at about 120 km (remarks at International Symposium, loc. cit.)

Our model, then, is that the flow of neutral air consists of roughly isotropic inertial and dissipation ranges of turbulence, superposed on some uniform mean flow; the latter may incorporate, besides meteorological 'winds', flow due to any gravity waves having a scale larger than a region scanned in making an observation by radio and uniform throughout the time required to make a fading record. Although this is rather an idealization, it enables us to concentrate on the special effect of the magnetic field on the convective process.

§ 4. THE DRIFT VELOCITY OF A RANDOM SCALAR FIELD

Suppose we have an ensemble of realizations of a random scalar $n(\mathbf{x}, t)$, stationary in space and time, with mean zero. Although n will later refer to the ionization density, it will be convenient here to suppose the variance has been made unity by normalization. Our standard notation for Fourier transforms will be to use the corresponding capital letter, as in

$$n(\mathbf{x},t)=\int N(\mathbf{k},t)\exp(i\mathbf{k}\,.\,\mathbf{x})d^3k. \qquad . \quad . \quad . \quad . \quad . \quad . \quad (1)$$

The space-time correlation function is defined by the ensemble average

$$\rho(\boldsymbol{\xi},\tau)=\overline{n(\mathbf{x},t)n(\mathbf{x}+\boldsymbol{\xi},t+\tau)} \qquad . \quad . \quad . \quad . \quad . \quad . \quad (2)$$

and is independent of $\mathbf{x}$ and t (by the stationary property). By Schwartz's inequality this has a maximum (namely unity) at $\boldsymbol{\xi}=0, \tau=0$, so assuming a Taylor expansion exists, we have

$$\rho(\boldsymbol{\xi},\tau)=1-\tfrac{1}{2}[a_{ij}\xi_i\xi_j-2b_i\xi_i\tau+c\tau^2]+\ldots \qquad . \quad . \quad . \quad (3)$$

where the quadratic form in brackets must be positive definite. (Summation over i, j, being assumed as usual). The coefficients a_{ij}, b_i, c are given by the second partial derivatives of ρ.

With a suitable ergodic assumption, it is immaterial whether the average in (2) is taken over space, time, or the ensemble of realizations. Imagine, for a particular realization, an observer calculating the 'cross correlation' between the values of $n(\mathbf{x},t)$ at pairs of points separated by $\boldsymbol{\xi}$ and at two instants t and $t+\tau$, where τ is small; the averaging process being performed only over values of $\mathbf{x}$. He then selects the value of $\boldsymbol{\xi}$ which *maximizes* the correlation, and defines $\boldsymbol{\xi}/\tau=\mathbf{W}$ to be the drift velocity during the interval. An instantaneous drift is clearly provided by $\lim_{\tau\to 0}\mathbf{W}$ if the limit exists, which it does if (3) is valid; in fact one easily finds

$$\mathbf{W}=\mathbf{a}^{-1}\,.\,\mathbf{b} \qquad . \quad . \quad . \quad . \quad . \quad . \quad . \quad . \quad . \quad . \quad (4)$$

where $\mathbf{a}$ is the matrix $[a_{ij}]$ and $\mathbf{b}$ the column-vector $[b_i]$. The correlation for small τ given by (3) when $\boldsymbol{\xi}=\mathbf{W}\tau$ reduces to

$$\rho(\mathbf{W}\tau,\tau)=1-\tfrac{1}{2}[c-\mathbf{b}\,.\,\mathbf{a}^{-1}\,.\,\mathbf{b}]\tau^2+\ldots \qquad . \quad . \quad . \quad . \quad . \quad (5)$$

so the square bracket is a measure of the random changes which remain after the drift has been removed. For $\boldsymbol{\xi}=\mathbf{W}\tau+\boldsymbol{\eta}$, say, one has

$$\rho(\boldsymbol{\xi},\tau)=1-\tfrac{1}{2}[a_{ij}\eta_i\eta_j+(c-\mathbf{b}\,.\,\mathbf{a}^{-1}\,.\,\mathbf{b})\tau^2]+\ldots. \qquad . \quad . \quad . \quad (6)$$

The problem of defining a mean drift was considered by Briggs *et al.* (1950) for the case of random diffraction patterns on the ground produced when radio waves are reflected from the ionosphere. Their approach was conditioned by the fact that one has only a small number of aerials to observe that pattern so ρ can only be obtained for two or three values of $\boldsymbol{\xi}$. If the assumption as to the nature of ρ which they were thereby forced to make is true, their V_x and V_y are the same as would be given by (4) in this two dimensional case. These authors also assumed a spatial isotropy, so $a_{ij}=a\delta_{ij}$, say, and their V_c is defined as $(ac-b^2)^{1/2}/a$ in our notation, with (6) becoming

$$\rho(\boldsymbol{\xi},\tau)=1-\tfrac{1}{2}a(\boldsymbol{\eta}^2+V_c{}^2\tau^2)+\ldots. \qquad . \quad . \quad . \quad . \quad . \quad (7)$$

When $n(\mathbf{x},t)$ is given as a Fourier transform, (1), the definition (2) of ρ becomes

$$\begin{aligned}\rho(\boldsymbol{\xi},\tau) &= \int\!\!\int \exp\,[i\mathbf{k}\,.\,(\mathbf{x}+\boldsymbol{\xi})]\exp\,(i\mathbf{k}'\,.\,\mathbf{x})\,\overline{N(\mathbf{k}',t)N(\mathbf{k},t+\tau)}\,d^3k\,d^3k' \\ &= \int\!\!\int \exp\,(i\mathbf{k}\,.\,\boldsymbol{\xi})\exp\,(i\mathbf{k}''\,.\,\mathbf{x})\,\overline{N(\mathbf{k}''-\mathbf{k},t)N(\mathbf{k},t+\tau)}\,d^3k\,d^3k''.\end{aligned}$$

At this point we extend the averaging to include an integration over $\mathbf{x}$ in a large volume $8\pi^3\sigma$, remembering $\rho(\boldsymbol{\xi},\tau)$ is actually independent of $\mathbf{x}$, to obtain

$$\rho(\boldsymbol{\xi},\tau) = (8\pi^3\sigma)^{-1}\int\!\!\int\!\!\int \exp\,(i\mathbf{k}\,.\,\boldsymbol{\xi})\exp(i\mathbf{k}''.\,\mathbf{x})\,\overline{N^*(\mathbf{k}-\mathbf{k}'',t)N(\mathbf{k},t+\tau)} \times d^3k\,d^3k''\,d^3x$$

where we have made use of the reality condition $N(-\mathbf{k},t) = N^*(\mathbf{k},t)$. The usual rule for the inversion of Fourier transforms then gives

$$\rho(\boldsymbol{\xi},\tau) = \sigma^{-1}\int \exp\,(i\mathbf{k}\,.\,\boldsymbol{\xi})\,\overline{N^*(\mathbf{k},t)N\,(\mathbf{k},t+\tau)}\,d^3k. \qquad . \quad . \quad . \quad (8)$$

Comparing with (3) and (4), we have

$$\left.\begin{aligned} a_{ij} &= -\left(\frac{\partial^2\rho}{\partial\xi_i\partial\xi_j}\right)_0 = \sigma^{-1}\int k_ik_j\,\overline{|N(\mathbf{k},t)|^2}\,d^3k, \\ b_i &= \left(\frac{\partial^2\rho}{\partial\xi_i\partial\tau}\right)_0 = i\sigma^{-1}\int \overline{k_iN^*(\mathbf{k},t)\partial N(\mathbf{k},t)/\partial t}\,d^3k. \end{aligned}\right\} \quad . \quad . \quad . \quad (9)$$

These are of course actually independent of t, since $\overline{|N(\mathbf{k},t)|^2}$ is so; this also shows incidentally that $\mathbf{b}$ as given by (9) is real, as it should be.

The above work uses Fourier integrals formally, without regard for convergence. Rigorous exposition of manipulations of this type can be given, provided the Stieltjes integral notation is used, see for instance Moyal (1952). We shall recover finite expressions on evaluating $\mathbf{a}^{-1}\,.\,\mathbf{b}$.

§ 5. DYNAMICS OF THE IONS AND ELECTRONS

Detailed considerations of the effects likely to be important in the type of disturbance to be investigated, have been given by Dungey (1956) and by Clemmow and Johnson (1959) so need not be repeated here. We shall assume:

(i) Fluctuations in the magnetic field are to be neglected. A convenient choice of axes makes $\mathbf{B} = (0, 0, B)$.

(ii) The plasma consists of electrons, and ions of one kind only, singly charged, and the dynamical processes take place so rapidly that ionization and recombination processes can be neglected. Inertial and gravitational terms are also neglected.

(iii) The number densities of ions and electrons remain almost exactly equal, the difference being much smaller even than the *perturbations* in number density. (Clemmow and Johnson do not assume this at the outset, but the result of their linearized calculation is that additional modes of oscillation exhibiting non-neutrality, but decaying very rapidly, enter the theory; they are neglected here.) This is the usual procedure, (see Spitzer 1956, p. 16) which is valid provided the length-scales of the problem are all much greater than the Debye distance, which for the ionosphere is a few millimetres. The number of variables is thus reduced by one, but Poisson's equation need not be used. This is, however, contrary to Booker's (1956) treatment, which introduces both 'ionic' and 'electronic' irregularities.

We shall write script letters for the following mean quantities: $\mathcal{N}$ for the density of ions and electrons, $\mathcal{V}^+, \mathcal{V}^-$ for their velocities, and $\mathcal{U}$ for the velocity of the neutral air. The random parts are denoted by the corresponding small letters n, $\mathbf{v}^+$, $\mathbf{v}^-$, $\mathbf{u}$. But the mean electric field is written $\mathbf{E}$, and the random part $-\nabla\phi$. Capital letters N, Φ, are the Fourier transforms as in (1). We shall frequently write symbols or whole equations with alternative signs $\pm$, for brevity, to indicate ions and electrons respectively. Thus $m^\pm$, $\pm e$ are the mass and charge, while $\nu^\pm$ are the frequencies of collisions with neutral particles (ion–electron collisions being neglected). We assume partial pressures $\mathcal{N}kT$ for ions and electrons at constant temperature T. The gyro-frequencies are $\omega^\pm = eB/m^\pm$, and as in Baker and Martyn (1953) the useful angles α are defined by

$$\tan\alpha^\pm = \omega^\pm/\nu^\pm. \qquad (10)$$

The general equations of continuity and momentum are

$$\frac{\partial\mathcal{N}}{\partial t} = -\operatorname{div}(\mathcal{N}\mathcal{V}^\pm), \qquad (11)$$

$$m^\pm\nu^\pm(\mathcal{V}^\pm - \mathcal{U}) \mp e\mathcal{V}^\pm \times \mathbf{B} = \pm e\mathbf{E} - \frac{kT}{\mathcal{N}}\nabla\mathcal{N} \qquad (12)$$

which together with $\operatorname{curl}\mathbf{E} = 0$ determine the motion of the plasma. Equation (12) may be solved for $\mathcal{V}^\pm$ in the form

$$\mathcal{V}^\pm = \mathbf{M}^\pm\left(\frac{\pm e}{m^\pm\nu^\pm}\mathbf{E} + \mathcal{U} - \frac{kT}{m^\pm\nu^\pm\mathcal{N}}\nabla\mathcal{N}\right) \qquad (13)$$

where the matrices $\mathbf{M}^\pm$ are defined by

$$\mathbf{M}^\pm = \begin{bmatrix} \cos^2\alpha^\pm & \pm\sin\alpha^\pm\cos\alpha^\pm & 0 \\ \mp\sin\alpha^\pm\cos\alpha^\pm & \cos^2\alpha^\pm & 0 \\ 0 & 0 & 1 \end{bmatrix} \qquad (14)$$

Since the script letters and $\mathbf{E}$ were defined as the steady mean values, all the derivatives in (11)–(13) are actually zero; we retained them formally so that the equations in the disturbed state are then obtained by replacing $\mathcal{U}$ by $\mathcal{U} + \mathbf{u}$, etc., and $\mathbf{E}$ by $\mathbf{E} - \nabla\phi$. One then subtracts the equations satisfied by the mean quantities,

$$\mathcal{V}^\pm = \mathbf{M}^\pm\left(\frac{\pm e}{m^\pm\nu^\pm}\mathbf{E} + \mathcal{U}\right) \qquad (15)$$

to obtain

$$\mathbf{v}^\pm = \mathbf{M}^\pm\left(\mp\frac{e}{m^\pm\nu^\pm}\nabla\phi + \mathbf{u} - \frac{kT}{m^\pm\nu^\pm(\mathcal{N} + n)}\nabla n\right) \qquad (16)$$

so using (11), and going into suffix notation,

$$
\begin{aligned}
\frac{\partial n}{\partial t} &= -\frac{\partial}{\partial x_i}\left[n\mathscr{V}_i^{\pm}+(\mathscr{N}+n)v_i^{\pm}\right] \\
&= -\mathscr{V}_i^{\pm}\frac{\partial n}{\partial x_i}-M_{ij}^{\pm}\frac{\partial}{\partial x_i}\left\{\mp\frac{e(\mathscr{N}+n)}{m^{\pm}\nu^{\pm}}\frac{\partial\phi}{\partial x_j}-\frac{kT}{m^{\pm}\nu^{\pm}}\frac{\partial n}{\partial x_j}+(\mathscr{N}+n)u_j\right\} \\
&= -\mathscr{V}_i^{\pm}\frac{\partial n}{\partial x_i}+M_{ij}^{\pm}\left\{\pm\frac{e(\mathscr{N}+n)}{m^{\pm}\nu^{\pm}}\frac{\partial^2\phi}{\partial x_i\partial x_j}\pm\frac{e}{m^{\pm}\nu^{\pm}}\frac{\partial n}{\partial x_i}\frac{\partial\phi}{\partial x_j}\right. \\
&\qquad \left.+\frac{kT}{m^{\pm}\nu^{\pm}}\frac{\partial^2 n}{\partial x_i\partial x_j}-u_j\frac{\partial n}{\partial x_i}-(\mathscr{N}+n)\frac{\partial u_j}{\partial x_i}\right\}. \qquad (17)
\end{aligned}
$$

Except in the non-magnetic case, when $\mathbf{M}^{\pm}$ become unit matrices, it is impossible to eliminate explicitly the internal potential ϕ which couples the two simultaneous diffusion equations (17) and makes the problem non-linear. We are, however, only concerned to find enough about the solutions of (17) to make an estimate of the drift velocity $\mathbf{W}$ of § 4, and to do this the equation will be converted into one satisfied by the Fourier transforms.

§ 6. THE EQUATION OF MOTION OF A FOURIER COMPONENT

One simple approximation in eqns. (17) will be made at once: the fractional changes in density are known observationally to be quite small, though the density *gradients* involved are larger than the steady gradient with height which we have already neglected. Hence we can ignore n in comparison with $\mathscr{N}$ in factors where n is not differentiated, i.e. we replace the two brackets $(\mathscr{N}+n)$ by $\mathscr{N}$ in (17).

After doing this and substituting expressions of type (1) into (17), we obtain, using some straightforward changes of variable, two coupled integral equations for $N(\mathbf{k},t)$ and $\Phi(\mathbf{k},t)$:

$$
\begin{aligned}
\frac{\partial N(\mathbf{k},t)}{\partial t} &= -i\mathscr{V}^{\pm}.\mathbf{k}N(\mathbf{k},t)+M_{ij}^{\pm}\left\{\mp\frac{\mathscr{N}e}{m^{\pm}\nu^{\pm}}k_ik_j\Phi(\mathbf{k},t)-\frac{kT}{m^{\pm}\nu^{\mp}}k_ik_jN(\mathbf{k},t)\right. \\
&\qquad \mp\frac{e}{m^{\pm}\nu^{\pm}}\int k_i'(k_j-k_j')N(\mathbf{k}',t)\Phi(\mathbf{k}-\mathbf{k}',t)d^3k' \\
&\qquad \left.-i\int k_i'U_j(\mathbf{k}-\mathbf{k}',t)N(\mathbf{k}',t)\,d^3k'-i\mathscr{N}k_iU_j(\mathbf{k},t)\right\}. \qquad (18)
\end{aligned}
$$

The terms on the right-hand side of (18) have the following interpretation. The first represents a convection of the Fourier components of wave-number $\mathbf{k}$ in the ions or electrons with the mean drifts $\mathscr{V}^{+}$ or $\mathscr{V}^{-}$ respectively ; the first in the large bracket is the effect of the Fourier component with the same $\mathbf{k}$ in the electrostatic field, set up to prevent charge separation. The term involving kT gives the effect of molecular diffusion in smoothing out the Fourier component $\mathbf{k}$, while the last term of all can be identified as Dungey's mechanism (Dungey 1956) for producing irregularities in the plasma by means of a magnetic field. We note that in the absence of the field, $M_{ij}^{\pm}$ reduce to δ_{ij}, and the term becomes small because $\mathbf{k}\,.\,\mathbf{U}(\mathbf{k},t)\approx 0$ since the turbulent velocities are much smaller than the sound velocity; the term then represents the compressions in the neutral air being repeated in the plasma, an effect rejected by Villars and Weisskopf (1955) and by Gallet (1955) as being too small to explain the strength of irregularity observed. (Maeda *et al.* 1959, suggest similarly that the compressions are repeated in the plasma via the ionizing process rather than mechanically: this seems to the present writer to be far too small an effect, for similar reasons).

To complete our description of the right-hand side of (18), there are the two integral terms representing intermodulation between all pairs of Fourier components $\mathbf{k}$ and $\mathbf{k}'$. In the first case it is through the internal electric field, while the second integral is a generalization of that arising in the non-magnetic case, whereby the turbulent velocity field acting on the local gradients in $n(\mathbf{x},t)$ due to the existing irregularities, continually redistributes irregularity throughout the spectrum $N(\mathbf{k},t)$.

The gentle gradient in the mean $\mathcal{N}$ is also involved in this last mentioned process, but (as emphasized by Batchelor (1959, p. 118) but not appreciated by some of the earlier writers) the gradients due to the irregularities themselves are much more important, except at the smallest wave numbers. So (18) is still valid in the dissipation and equilibrium ranges, but omits a term describing the 'input' at small wave number, which however is immaterial to us in what follows.

It will be seen from (18) that the difficulty of eliminating ϕ between the ion- and electron-equations is at least as great as before; we have removed spatial differentiations at the price of introducing integral equations. Nevertheless (18) supplies the equation which is sufficient for the present purpose, namely that obtained by eliminating the term in which $\Phi(\mathbf{k},t)$ appears explicitly, without regard for the term in which $\Phi(\mathbf{k}-\mathbf{k}',t)$ appears under integration. If θ is the angle between $\mathbf{k}$ and $\mathbf{B}$, so that

$$\cos\theta = k_3/k \qquad \ldots\ldots\ldots \quad (19)$$

and introducing

$$S^\pm = M_{ij}{}^\pm k_i k_j/k^2 = \cos^2\alpha^\pm \sin^2\theta + \cos^2\theta \qquad \ldots\ldots \quad (20)$$

the appropriate linear combination of equations (18) is

$$\begin{aligned}\frac{\partial N(\mathbf{k},t)}{\partial t} = {} & -i\,\mathbf{W}(\theta)\,.\,\mathbf{k}N(\mathbf{k},t) - D\chi(\theta)k^2 N(\mathbf{k},t) \\ & + P_{ij}(\theta)\int k_i'(k_j-k_j')N(\mathbf{k}',t)\Phi(\mathbf{k}-\mathbf{k}',t)\,d^3k' \\ & - Q_{ij}(\theta)\left\{i\int k_i' U_j(\mathbf{k}-\mathbf{k}',t)N(\mathbf{k}',t)\,d^3k' + i\mathcal{N}k_i U_j(\mathbf{k},t)\right\}. \end{aligned} \qquad \ldots\ldots \quad (21)$$

The following abbreviations are used in (21):

$$D = \frac{2kT}{m^+\nu^+ + m^-\nu^-}. \qquad \ldots\ldots\ldots \quad (22)$$

This is the standard "ambipolar" diffusion coefficient, and

$$\mathbf{W}(\theta)=\frac{S^+\tan\alpha^+\mathscr{V}^- + S^-\tan\alpha^-\mathscr{V}^+}{S^+\tan\alpha^+ + S^-\tan\alpha^-}, \quad . \quad . \quad . \quad . \quad . \qquad (23)$$

$$\chi(\theta)=\frac{S^+S^-(\tan\alpha^+ + \tan\alpha^-)}{S^+\tan\alpha^+ + S^-\tan\alpha^-}, \quad . \quad . \quad . \quad . \quad . \qquad (24)$$

$$\mathbf{P}(\theta)=\frac{e^2B(S^+\mathbf{M}^- - S^-\mathbf{M}^+)}{m^+\nu^+m^-\nu^-(S^+\tan\alpha^+ + S^-\tan\alpha^-)}, \quad . \quad . \quad . \qquad (25)$$

$$\mathbf{Q}(\theta)=\frac{S^+\tan\alpha^+\mathbf{M}^- + S^-\tan\alpha^-\mathbf{M}^+}{S^+\tan\alpha^+ + S^-\tan\alpha^-}. \quad . \quad . \quad . \qquad (26)$$

Equation (21) can be regarded as differing from (18) in that a common velocity of convection, $\mathbf{W}(\theta)$ has been achieved to replace $\mathscr{V}^\pm$, and a common diffusive decay as if due to a diffusivity $D\chi(\theta)$. The terms with $\mathbf{P}$ and $\mathbf{Q}$ can still be regarded as describing Dungey's process, together with the intermodulation of different Fourier components, but in practice, lack of knowledge of $\Phi(\mathbf{k},t)$ would prevent any exact use of (21) alone.

$\mathbf{W}(\theta)$ is clearly identical with the 'wave velocity' found by Clemmow and Johnson (1959) for the linearized theory in the absence of turbulence. It can be regarded as a 'compromise' drift, between $\mathscr{V}^+$ and $\mathscr{V}^-$; being in fact a weighted mean of them, the weight depending on θ and on $\alpha^\pm$. It should not be confused with the $\mathbf{W}$ (written without an argument) defined in § 4, though as we shall see, they are closely related; if it were possible for all the contributions to $N(\mathbf{k},t)$ to arise only from those values of $\mathbf{k}$ corresponding to a fixed value of θ, $\mathbf{W}$ would then be just $\mathbf{W}(\theta)$ evaluated for that θ. Note also that $\chi(\theta)$ is unity for $\theta=0$, and decreases monotonically to its value at $\theta=\frac{1}{2}\pi$.

§ 7. INTEGRAL EXPRESSIONS FOR THE DRIFT VELOCITY

Although we have now set up a complete formal scheme for tackling the problem, namely eqns. (4), (9) and (18), it is already clear that even if we had enough information about the behaviour of $\mathbf{U}(\mathbf{k},t)$, an exact use of the equations would be prohibitively complex. But besides this, little is known about the temporal behaviour of the velocity field in a turbulent flow, even in the absence of buoyancy forces. Because of the non-linearity of the Navier–Stokes equation, the equation satisfied by the $\mathbf{U}(\mathbf{k},t)$ for each realization is of a similar intractable nature, and has not been much used (but see Münch and Wheelon 1958). Clearly, then, we shall have to make some approximations or statistical assumptions if we are to make any estimate of the overal drift $\mathbf{W}$. For this reason our own estimate of it must be regarded as tentative.

The integrals (9) which we have to evaluate, extend over the whole of $\mathbf{k}$-space. Although we shall continue to write them conventionally in this way, it should be noted that our assumption discussed in § 3 makes the contribution from the large scales (small values of $\mathbf{k}$) negligible. This is now seen to be even more plausible on account of the factors k^2 and $k\partial/\partial t$ in the integrands.

As pointed out by Wheelon (1957) the diffusivity D is about twice the kinematic viscosity in this context. Hence the convective equilibrium range terminates roughly where the inertial one does. and the cutoff beyond is almost certainly very rapid (Batchelor 1959). So the dissipation range may also be omitted from our integrations as a first approximation.

By retaining the range of integration as the whole of **k**-space we are really supposing that the temporal behaviour of all Fourier components is of the same form as for those in the equilibrium range, on the grounds that those parts of the range for which this is not so are unimportant anyway.

Consider now the first of the integrals (9). To evaluate this we need only the 'spectrum density' $\overline{|N(\mathbf{k}.t)|^2}$. This has been considered recently by Howells (1960), who concludes that despite the apparent anisotropy of the situation, the spectrum is roughly isotropic in the equilibrium range. Two cases arise: (i) below about 125 km height, where $\nu^+ > \omega^+$, i.e. $\tan\alpha^+ < 1$; (ii) above that level, where the opposite holds. Case (i) has been worked out in more detail, and one can say with confidence that the spectrum is close to isotropic. Even for case (ii) the departure from isotropy appears to be fairly small. (The anisotropy of the diffusion is irrelevant here because we ignore the range in which any diffusion is important. The highly elongated irregularities suggested by Booker (1956) are therefore unlikely to occur in the parts of the ionosphere wherethere is local turbulence, though they may occur where irregularities exist for some other reason).

We can, then, write $\overline{|N(\mathbf{k},t)|^2} = g(k)$, say. Using polar angles θ, ψ, relative to the 03 axis, (9) gives (where $\mathbf{l} = \mathbf{k}/k$)

$$\begin{aligned} a_{ij} &= \sigma^{-1}\int_0^\infty k^4 g(k)\,dk \int_{\theta=0}^{\pi}\int_{\psi=0}^{2\pi} l_i l_j \sin\theta\,d\theta\,d\psi, \\ &= G\delta_{ij}, \end{aligned} \qquad (27)$$

where

$$G = \frac{4\pi}{3\sigma}\int_0^\infty k^4 g(k)\,dk. \qquad (28)$$

Turning to the second of the integrals (9), we must use the work of § 6 to estimate $\partial N(\mathbf{k}, t)/\partial t$, and we shall use the form (21) in preference to the simultaneous eqns. (18). It is helpful to picture $N(\mathbf{k}, t)$, for each fixed **k**, as a locus in the complex plane. Then the first term of (21) is a tendency for the 'vector' representing N to rotate at a definite angular velocity $-\mathbf{k}\,.\,\mathbf{W}(\theta)$; the second term need not be considered. The two integral terms are of a stochastic nature and represent some kind of 'random walk' process superposed on the rotation. The last term, if it is important, is of a more systematic nature than the integrals, because at fairly small scales $U_j(\mathbf{k}, t)$ varies nearly systematically—the usual concept of convection of the small eddies by the mean or large-scale flow makes U tend to rotate with angular frequency $-\mathbf{k}\,.\,\mathcal{U}$.

Using (18) to write eqn. (9) free of time derivatives, we obtain

$$\mathbf{b}=\sigma^{-1}\int \mathbf{k}[\mathbf{k}\,.\,\mathbf{W}(\theta)]\overline{|N(\mathbf{k},t)|^2}\,d^3k, \qquad (29)$$

$$-iD\sigma^{-1}\int \chi(\theta)\mathbf{k}k^2\overline{|N(\mathbf{k},t)|^2}\,d^3k, \qquad (30)$$

$$\left.\begin{aligned}&+i\sigma^{-1}\int\int \mathbf{k}k_i'(k_j-k_j')P_{ij}(\theta)\overline{N^*(\mathbf{k},t)N(\mathbf{k}',t)\Phi(\mathbf{k}-\mathbf{k}',t)}\,d^3k\,d^3k'\\ &+\sigma^{-1}\int\int \mathbf{k}k_i'Q_{ij}(\theta)\overline{N^*(\mathbf{k},t)N(\mathbf{k}',t)U_j(\mathbf{k}-\mathbf{k}',t)}\,d^3k\,d^3k',\end{aligned}\right\} \qquad (31)$$

$$+\sigma^{-1}\mathcal{N}\int \mathbf{k}k_iQ_{ij}(\theta)\overline{N^*(\mathbf{k},t)U_j(\mathbf{k},t)}\,d^3k. \qquad (32)$$

Here θ refers to the polar angle for the wave number $\mathbf{k}$, not $\mathbf{k}'$, and it is convenient to number separately parts of the right-hand side.

For the part (29), continuing our assumption of isotropy, integration over $|\mathbf{k}|$ in polar coordinates and making use of the definition (28) of G yields a contribution to $\mathbf{W}(=\mathbf{a}^{-1}\,.\,\mathbf{b})$ which is

$$\frac{3}{4\pi}\int_{\psi=0}^{2\pi}\int_{\theta=0}^{\pi} \mathbf{l}[\mathbf{l}\,.\,\mathbf{W}(\theta)]\sin\theta\,d\theta\,d\psi. \qquad (33)$$

The part (30) is zero since the integrand is an odd function of $\mathbf{k}$.

The part (31) shows explicitly the contribution to drift velocity of the intermodulation effects. Triple correlations of N, Φ and $\mathbf{U}$ evaluated at three different wave numbers are involved here. We shall assume that these correlations are negligible; or in other words that the interactions between different wave numbers are entirely random, showing no preferred direction in space-time. This is not to say that the non-linear effects are unimportant—they are indeed important in determining the form of the spectrum, i.e. $g(k)$, but can be ignored in the drift problem.

Finally, we have to examine part (32). For case (i) of the classification mentioned above, i.e. for heights rather less than 125 km, this term does provide a systematic correlation, but it is small, because Dungey's effect (see Dungey 1956) is itself small in this region. This can be seen explicitly in our formulation by means of eqn. (26), which shows $\mathbf{Q}$ as a weighted mean of $\mathbf{M}^+$ and $\mathbf{M}^-$. Below about 90 km, where $\nu>\omega$ for the electrons also, both $\mathbf{M}^\pm$ are very nearly the unit matrix. Between 90 and 125 km, where $\mathbf{M}^+$ is still nearly unit, $\mathbf{M}^-$ is not so, however the factor $\tan\alpha^-$ increases to such an extent that except for θ very close to $\frac{1}{2}\pi$, the mean is weighted heavily in favour of $\mathbf{M}^+$. Thus it is only near and above 125 km that $\mathbf{Q}$ differs appreciably from the unit matrix, and until that happens (32) gives zero since $\mathbf{k}\,.\,\mathbf{U}(\mathbf{k},t)\approx 0$. Since $\mathbf{U}(\mathbf{k},t)$ is isotropic, no special weight is attached to the small range of θ in which this argument fails, so as a first approximation, we can justifiably neglect (32) for case (i).

For case (ii), the position with regard to (32) is much more difficult, but some remarks are offered in § 9.

§ 8. EVALUATION OF THE DRIFT VELOCITY IN THE SIMPLE CASE

For case (i), the only surviving contribution to $\mathbf{W}$, according to the foregoing arguments, is given by (33). This is no more than a mean over all directions of the velocities for the Fourier components, each resolved along the 'wave normal'. Our statistical definition of drift has thus given a new significance to Clemmow and Johnson's 'wave velocity', originally derived by a linearized theory in the absence of turbulence. Note also that the distribution among wave numbers, $g(k)$, disappears from the drift problem once an isotropic spectrum has been assumed. This is of course to be traced back to the fact that the convection for any Fourier component $\mathbf{k}$ depends solely on θ and not on the wave number k. Since there has been some controversy (summarized by Batchelor 1959) concerning $g(k)$ even for a non-magnetic case, we can regard this as being rather fortunate.

The last step is to write $\mathbf{l}=(\sin\theta\cos\psi,\ \sin\theta\sin\psi,\ \cos\theta)$ and use (20) and (23) to carry out the integrations (33); this involves only elementary integrations, and a convenient form of the result is

$$W_{1,2}=(1-R_1)\mathscr{V}_{1,2}{}^{+}+R_1\mathscr{V}_{1,2}{}^{-} \text{ and } W_3=(1-R_3)\mathscr{V}_3{}^{+}+R_3\mathscr{V}_3{}^{-}. \quad (34)$$

Thus each component of $\mathbf{W}$ is a weighted mean of the corresponding components of $\mathscr{V}^{\pm}$, the weighting factors being R_1 for those perpendicular to the field, and R_3 for that parallel to it. R_1 and R_3 depend solely upon $\alpha^{\pm}$, i.e. upon height in the ionosphere, according to the formulae

$$R_j=\frac{\sin\alpha^{+}\cos\alpha^{-}}{\sin(\alpha^{+}+\alpha^{-})}\{1+\tan\alpha^{-}\tan(\alpha^{-}-\alpha^{+})I_j[\cos\alpha^{+}\cos\alpha^{-}\cos(\alpha^{-}-\alpha^{+})]\} \quad . \quad . \quad . \quad (35)$$

(for $j=1,3$)

where
$$I_1(x)=\frac{3x}{2}\int_0^{\pi/2}\frac{\sin^5\theta\,d\theta}{\cos^2\theta+x\sin^2\theta}$$
$$=\frac{x}{2(1-x)^2}\left\{2x-5+\frac{3}{x^{1/2}(1-x)^{1/2}}\tan^{-1}\left[\frac{1-x}{x}\right]^{1/2}\right\}. \quad (36)$$

and
$$I_3(x)=2x[1-I_1(x)]. \quad . \quad . \quad . \quad . \quad . \quad . \quad . \quad (37)$$

For small x one uses

$$I_1(x)\approx\frac{3\pi}{4}x^{1/2}-4x+\frac{9\pi}{16}+x^{3/2}\ldots$$

The first factor of (35) can also be written

$$\frac{\sin\alpha^{+}\cos\alpha^{-}}{\sin(\alpha^{+}+\alpha^{-})}=[1+\tan\alpha^{-}/\tan\alpha^{+}]^{-1}=[1+m^{+}\nu^{+}/m^{-}\nu^{-}]^{-1}\approx m^{-}\nu^{-}/m^{+}\nu^{+}, \quad . \quad . \quad . \quad (38)$$

so is approximately independent of height in the ionosphere since ν^{+}/ν^{-} is nearly constant—we shall take it to be 1/30 in the numerical work which follows, and m^{+}/m^{-} to be $5{\cdot}5\times10^4$. Then R_1 and R_3 depend only on say

$\tan \alpha^- = \omega^-/\nu^-$, since α^+ is then fixed. The figure shows the values calculated from (35). This can be applied for any atmospheric model if the two numerical parameters are as just quoted, but estimated heights are also marked on the horizontal axis, taking $\omega^- = 7{\cdot}5 \times 10^6\,\text{sec}^{-1}$ and values of ν^- based on recent atmospheric models (kindly supplied by Dr. K. Weekes).

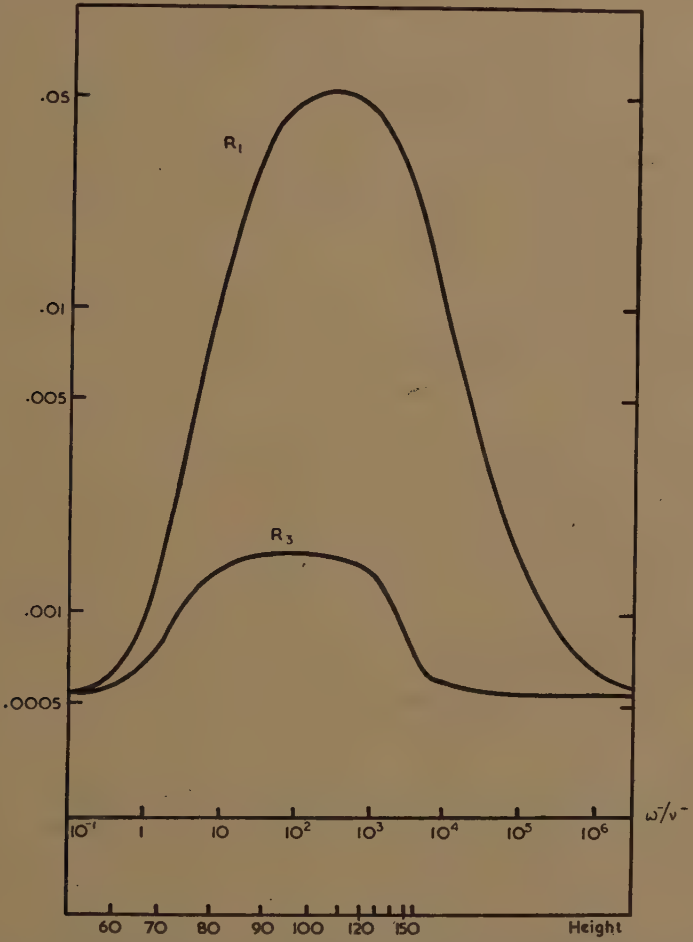

Illustrating the dependence upon height of the weighting factors R_1 and R_3 which give the relative importance of the ion-drift and electron-drift in determining the drift of the irregularities.

Consider first the lowest levels, around 70 km, where both $\alpha^\pm$ are small. The large bracket factor in (35) is then ≈ 1, (for both $j = 1, 3$) and we have $R_1 \approx R_3 \approx [1 + m^+\nu^+/m^-\nu^-]^{-1}$. But (15) has unit matrices in place of $\mathbf{M}^\pm$ in this approximation, so that, as expected, equations (33) revert to $\mathbf{W} = \mathcal{U}$, irrespective of $\mathbf{E}$.

Slightly higher in the ionosphere this simple result changes, partly because (15) becomes more complicated and partly because the coefficients R_1 and R_3 increase, especially R_1. One might have expected intuitively that however $\mathscr{V}^{\pm}$ vary in this way, the drift of irregularities would always remain approximately equal to $\mathscr{V}^{+}$ on account of the much greater mass of the ions. The coefficients R_j measure just the extent to which this must be corrected due to the motion of the electrons, an effect reaching a maximum in the middle of the region characterized by $\omega^- > \nu^-$ but $\omega^+ < \nu^+$, i.e. precisely the dynamo region. The effect is, however, fairly small unless $\mathbf{E}$ and $\mathscr{U}$ are so arranged that $\mathscr{V}^-$ is somewhat larger than $\mathscr{V}^+$. It can also be interpreted as the dynamical effect of the 'polarization' of the irregularities due to the mean current flow and the fluctuations in conductivity (cf. Clemmow and Johnson's example of a cylinder, 1955).

Above the dynamo region, the coefficients R_j decrease again to their former value, but the further complications discussed in the next section make this simple theory unreliable.

§ 9. THE UPPER E REGION AND THE F REGION

Above the dynamo region, $\mathscr{V}^{\pm}$ tend to equality, in which case the velocity given by (33) is also the same, namely

$$\mathbf{W} \approx \mathscr{V}^{+} \approx \mathscr{V}^{-} \approx (E_2/B, -E_1/B, \mathscr{U}_3) \quad . \quad . \quad . \quad (39)$$

the coefficients R_j being practically irrelevant. However, as $\mathbf{Q}$ is no longer nearly the unit matrix, the contribution from part (32) of the expression for $\mathbf{b}$ must be considered, and it has not proved possible to derive any mathematical results.

Some insight into this situation may be gained by linearizing (21), and omitting the diffusion term, for simplicity. We then have a 'small signal' theory, in which each Fourier component behaves independently and Dungey's effect may be studied in isolation. We have, for each $\mathbf{k}$,

$$\frac{\partial N}{\partial t} + i\,\mathbf{W}(\theta)\,.\,\mathbf{k}N = -i\mathscr{N}Q_{ij}k_iU_j. \quad . \quad . \quad . \quad . \quad (40)$$

Taking U_j to be proportional to $\exp(-ipt)$ where $p = \mathbf{k}\,.\,\mathscr{U}$, which as mentioned above is a good approximation for the smaller eddies, the solution for $N(t)$ consists of the particular integral proportional to $\exp(-ipt)$ and a complementary function proportional to $\exp[-i\mathbf{k}\,.\,\mathbf{W}(\theta)t]$. The former gives a finite correlation in both (29) and (32), and the latter as before in (29). But the amplitude of the complementary function is arbitrary in a linearized theory; its mean equilibrium amplitude in any situation to which the linear theory may approximate is determined by the non-linear terms. Setting all the complimentary functions zero leads of course to $\mathbf{W} = \mathscr{U}$. Presumably when both turbulent mixing and Dungey's process are important, $\mathbf{W}$ is in some sense intermediate between $\mathscr{U}$ and the value found in § 8.

As the height of the maximum electron density in the E region generally occurs at 120–130 km, no reflections can be observed from this level up to something like 180 km, and it seems most unlikely that turbulence occurs at or above this latter height. So in practice the difficulty discussed in this section is probably rarely serious.

The main point of interest in this discussion is that it has emerged that there is no unique 'velocity of irregularities' at a given level in the ionosphere. It is necessary to enquire into the details of the process producing the irregularity—in the present case we are unable to proceed without knowing in greater detail the rôles of turbulent mixing and Dungey's process. Similarly our theory for the lower E region assumes turbulent mixing as the cause, but the whole question would need to be reconsidered if, for example it were proposed that inhomogeneities in the ionizing radiation produced irregular electron density.

In the case of the F region, the difficulty becomes acute, as there is no adequate theory of the origin of the observed irregularities. Dagg (1957 a) has reviewed several explanations and criticized all of them. His own theory (1957 b), of small-scale electric fields originating in the dynamo region, is also open to criticism, however, as such electric fields would not produce compressions in the plasma (Dougherty 1959). Alfvén waves travelling along lines of force and originating in the outer ionosphere have also been suggested, (Dessler 1958) but the velocity would then be the wave velocity, which is too large to agree with the observations.

§ 10. DISCUSSION OF RESULTS

Let us now reconsider our objective, the interpretation of the drift velocities derived from fading records. To do this, we work in new axes $0x$, $0y$ and $0z$, taken along magnetic East, North, and vertically upwards, respectively. Then assuming that the fading is imposed at or near the height of reflection, the spaced-receiver experiments yield W_x and W_y appropriate to that height.

Below about 90 kms, we can with confidence say that this gives directly the wind velocity for the neutral air, $\mathscr{U}_x$ and $\mathscr{U}_y$. ($\mathscr{U}_z$ can generally be assumed to be an order of magnitude smaller.) This is true even if a magnetic field is present.

In the neighbourhood of the dynamo layer, the electric field plays an important part in determining $\mathbf{W}$, and one cannot proceed without ambiguity from W_x, W_y to $\mathscr{U}_x$, $\mathscr{U}_y$. Taking $\mathscr{U}_z=0$ and assuming E_z adjusted to make $\mathscr{V}_z^+=\mathscr{V}_z^-$ (no vertical current), we still have two further unknown quantities, E_x, E_y.

The further relations between $\mathscr{U}_x$, $\mathscr{U}_y$ and E_x, E_y must of course be provided by means of a dynamo theory of their variation over the whole globe. So the present theory can be used to find whether a proposed dynamo theory successfully predicts the drifts, and for example, their diurnal behaviour.

It is certainly possible to construct numerical examples in which the error involved in identifying the components of $\mathbf{W}$ as those of $\mathscr{U}$ would be very serious.

For much of the published data (see for example Briggs and Spencer 1954) the height to which the drift refers was not measured, except so far as to identify the region, E or F, and this makes satisfactory interpretation virtually impossible. Recently, however, Jones (1958) has reported results in which the height was estimated; simultaneous measurements at different heights near the dynamo region revealed a gradient in the velocity, which Jones expressed as a change of phase in the diurnal component of drift. A possible explanation is that although $\mathscr{U}$ and $\mathbf{E}$ are each independent of height (as assumed in the dynamo theory) the diurnal variations of $\mathscr{U}_x$, $\mathscr{U}_y$, E_x, E_y, have different phases. Since $\mathbf{W}$ depends increasingly upon $\mathbf{E}$ with increasing height, a gradual change in phase of $\mathbf{W}$ would automatically take place.

In conclusion, we may claim that a theoretical basis has been laid for relating the ionospheric drift observations to the winds and electric fields of the dynamo region.

ACKNOWLEDGMENTS

I have enjoyed many stimulating discussions with Mr. J. A. Ratcliffe, Dr. P. C. Clemmow, Dr. K. Weekes, Dr. K. G. Budden, Dr. B. H. Briggs and Dr. I. D. Howells, and my thanks are due to them all.

This work has been carried out during the tenure of a D.S.I.R. Research Studentship.

My attendance at the International Symposium on Fluid Mechanics in the Ionosphere, at Cornell University, was made possible by the United States Office of Naval Research.

REFERENCES

Baker, W. G., and Martyn, D. F., 1953, *Phil. Trans.* A, **246,** 281.
Batchelor, G. K., 1959, *J. Fluid Mech.*, **5,** 113.
Booker, H. G., 1956, *J. geophys. Res.*, **61,** 673.
Briggs, B. H., Phillips, G. J., and Shinn, D. H., 1950, *Proc. phys. Soc. Lond.* B, **63,** 106.
Briggs, B. H., and Spencer, M., 1954, *Rep. Progr. Phys.*, **17,** 245.
Clemmow, P. C., and Johnson, M. A., 1959, *J. atmos. terr. Phys.*, **16,** 21.
Clemmow, P. C., Johnson, M. A., and Weekes, K., 1955, *Rep. Ionosph. Conf.* (London: Physical Society), p. 136.
Dagg, M., 1957 a, *J. atmos. terr. Phys.*, **11,** 133; 1957 b, *Ibid.*, **11,** 139.
Dessler, A. J., 1958, *J. geophys. Res.*, **63,** 507.
Dougherty, J. P., 1959, *J. geophys. Res.*, **64,** 2215.
Dungey, J. W., 1956, *J. atmos. terr. Phys.*, **8,** 39.
Gallet, R. M., 1955, *Proc. Inst. Radio Engrs, N.Y.*, **43,** 1240; 1957, *Polar Atmos. Symp.* Pt. II (London: Pergamon Press), p. 165.
Greenhow, J. S., and Neufeld, E. L., 1959, *Proc. phys. Soc. Lond.*, **74,** 1.
Hines, C. O., 1955, *J. atmos. terr. Phys.*, **7,** 14; 1956, *Ibid.*, **9,** 56; 1959, *J. geophys. Res.*, **64,** 939.
Howells, I. D., 1960, *J. Fluid Mech.* (to be published).
Jones, I. L., 1958, *J. atmos. terr. Phys.*, **12,** 68.
Journal of Geophysical Research, 1959, International Symposium on Fluid Mechanics of Ionosphere.
Maeda, K., Kato, S., and Tsuda, T., 1959, *J. Geomagn. Geoelect.*, **10,** 91.
Moyal, J. E., 1952, *Proc. Camb. phil. Soc.*, **48,** 329.
Münch, G., and Wheelon, A. D., 1958, *Physics of Fluids*, **1,** 462.
Ratcliffe, J. A., 1956, *Rep. Progr. Phys.*, **19,** 188.
Spitzer, L., 1956, *Physics of Fully Ionized Gases* (New York: Interscience).
Villars, F., and Weisskopf, V. F., 1955, *Proc. Inst. Radio Engrs, N.Y.*, **43,** 1232.
Wheelon, A. D., 1957, *Phys. Rev.*, **105,** 1706.

Direct Observation of Defects in Evaporated Silver†

By V. A. Phillips
General Electric Research Laboratory, Schenectady, New York

[Received March 10, 1960]

Abstract

Single-crystal films of silver were made by evaporation of silver onto the cleavage surface of a heated rock-salt crystal. The crystalline defects present in the detached films were studied by transmission electron microscopy. In fresh areas of the foil, numerous simple stacking faults confined to a single plane were observed. The number varied between 5×10^9 and 1×10^{10} cm^{-2}. There was a strong tendency for the partial dislocations to lie in $\langle 110 \rangle$ directions. The morphology of the simple fault shapes resulting is considered in detail. Electron beam stressing resulted in the dissociation of whole dislocations and in the widening of faults already present. The interaction of the faults to form complex faults on several planes, and the effects of holes and dislocations were studied. Some areas showed minor defects consisting of dislocation loops and tetrahedral stacking faults. Preliminary annealing experiments indicate that the simple faults are remarkably stable at 300°c. The origin of the various defects is discussed. It is concluded that most simple faults probably form by dissociation of dislocations which may (1) grow in from the substrate, (2) nucleate at silver patch edges during growth, (3) form by impingement of patches on a $\{110\}$ plane during growth.

§ 1. Introduction

Until recently the electron microscope had not been used appreciably to study the structure of metal films condensed onto single-crystal substrates. It is, of course, well known that single-crystal films of metals may be made in this way as a result of 'epitaxy'. Pashley (1956) has reviewed the methods of achieving this. As a result of the work of Bollmann (1956 a, b), Hirsch *et al.* (1956), Whelan and Hirsch (1957 a, b) and Whelan *et al.* (1957), techniques are available for directly observing crystalline defects such as whole and partial dislocations and stacking faults.

The present work is an application of the direct observation techniques to the study of defects present in evaporated films of silver, both as-grown and after stressing in the beam of the electron microscope. This work was carried out independently of the related study of Matthews (1959) on evaporated films of gold, silver and copper, and does not overlap greatly. Pashley (1959) and Bassett and Pashley (1958–59) have investigated the structure of evaporated films, particularly of gold, but their results are complementary to the present work. A preliminary account of the present work has been given (Phillips 1959).

---

† Communicated by the Author.

§ 2. EXPERIMENTAL DETAILS

Films were prepared by evaporation of silver of 99·999% purity from a conical tungsten filament onto a freshly cleaved rock-salt crystal maintained at 300°c. The evaporation was carried out in a vacuum of about 10^{-4} mm of mercury. The films were cooled on the substrate *in vacuo* to room temperature which took about 20 min. The silver was floated off on a water surface, washed and pieces transferred to specimen grids.

Single crystal foils with an {001} plane parallel to the surface were obtained. The thickness of most foils ranged from 400–700 Å, although in the immediate vicinity of holes they were, of course, thinner.

Specimens were examined in a Siemens Elmiskop I electron microscope operated at 100 kv. Double condenser illumination was used. The samples were tilted by means of a stereo-holder to bring any defects present into contrast. A ciné film was made of the effects observable at about × 40 000 on the fluorescent screen. The improved resolution obtained by recording the image directly on plates was necessary for detailed study.

§ 3. IMAGING METHODS

Stacking faults in {001} films are readily seen by diffraction contrast and typically show extinction fringes parallel to the intersection of the {111} fault plane with the foil surfaces, that is, parallel to ⟨110⟩ directions in the plane of the film. The detailed theory of these fringe effects has been worked out by Whelan and Hirsch (1957 a, b). Figure 1 (schematic) depicts the type of electron diffraction pattern given by an {001} silver film. The 'crosses' such as that enclosed by circle B are a well-known feature of such patterns. (See for example Watanabe 1956, Ogawa *et al.* 1955.)

In the present work stacking faults were examined both in bright field and in dark field. The respective objective aperture positions for these two methods are shown by the circles A and B in fig. 1. The objective aperture size was 50 μ. Dark field images were obtained using the portion of the diffraction pattern encircled at B comprising a {200} reflection and satellite spots. The gun was tilted to bring an {002} onto the axis of the microscope. Under these conditions, individual faults contributing to this portion of the diffraction pattern are brightly imaged and individual fringes are not usually discernible. Individual dislocations may be seen in dark contrast where there is an overlapping stacking fault. Improved resolution of individual faults at moderate magnifications appears to be obtained in dark field. In bright field individual faults may be imaged in dark contrast without resolving individual fringes. This usually occurs in the vicinity of a diffuse tilt fringe as in fig. 2† and some portions of fig. 4 (*b*). The stacking fault contrast here is probably dynamical in origin. More commonly, in bright field, individual fringes are resolved at stacking faults in the way predicted by theory (Whelan 1958–59).

---

† Figures 2 to 9 are shown as plates.

§ 4. STRUCTURE OF THE FILMS

Figures 2–9 are electron micrographs of the films. Stacking faults were observed in all areas. The number of stacking faults varied from one film to another but was usually between 5×10^9 and 1×10^{10} per cm^2. This number is relatively independent of the thickness since most faults ran from surface to surface. There was a big difference in the length and complexity of the faults depending on whether or not a particular area of foil had been previously exposed to the electron beam. Exposure to the beam caused buckling, as evidenced by movement of tilt fringes across the field, and the stresses produced caused wide dissociation and frequent combination, and interaction of stacking faults both with each other and with dislocations and holes through the foil. These effects will be discussed later in more detail. Figures 2 and 4 are typical of the structure observed in areas of foil not previously irradiated. Figure 5 is typical of the appearance after exposing to the beam for some time.

Fig. 1

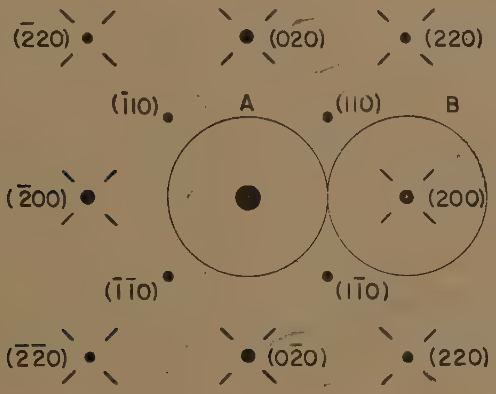

Typical electron diffraction pattern from a silver film (schematic). Circles A and B show the portions of the diffraction pattern used in the light and dark field imaging methods.

Defects which appear to be typical dislocation loops were observed in fresh areas of the films as at A in fig. 2. These loops ranged in diameter from about 100–300 Å. Smaller loops would not be recognizable but may well be present. The average number of loops in the region shown, which is about 650 Å thick, is approximately 2×10^{14} cm^{-3}. Assuming an average loop diameter of 200 Å, in order to calculate the total line length per unit volume, ρ, this loop number is equivalent to a dislocation density of $\rho/3$, that is, 4×10^8 cm^{-2}. Loops of similar sizes have been observed in quenched aluminium by Hirsch *et al.* (1958). If the loop is assumed to be a collapsed disk of vacancies, then for an average diameter of 200 Å, the corresponding initial concentration of vacancies is $1{\cdot}5 \times 10^{-5}$. Dislocation loops have been observed in quenched bulk silver by Smallman and Westmacott (1959).

A number of parallel line features will be noted in fig. 2, for example B_{1-3}. These are not due to slip contrast since this appeared to fade in less than 1/10 sec. They are instead attributed to movements of loops during the 3 sec period of the exposure. The projected direction of movement is parallel to a ⟨110⟩ direction in the plane of the film. Loops B_1 and B_2 (fig. 2) appear to have slipped out to holes through the foil. B_3 appears to have moved in a jerky fashion and is still visibile. If this interpretation is correct, it implies that the loops are prismatic loops, formed by nucleating a Shockley partial in the disk of stacking fault associated with the Frank sessile produced by collapse of a disk of vacancies on a {111} plane (Kuhlmann-Wilsdorf 1958). These would glide on a cylinder whose axis is parallel to a ⟨110⟩ direction not lying in the plane of the fault. Opposite halves of the loop would presumably glide in opposite directions as observed by Hirsch *et al.* (1958) in aluminium. Some doubt is thrown on this interpretation by the fact that the stacking-fault energy in silver is estimated (Thornton and Hirsch 1958) to be only about 35 erg cm^{-2} which is hardly sufficient to make the nucleation of a Shockley partial energetically favourable unless stress-assisted. The glissile nature of the loops would explain why they are only observed on first examination of an area, and why in similar observations on evaporated gold (Bassett and Pashley 1958–59), they apparently vanished between exposures.

Perfect dislocations were commonly seen running obliquely through the film as at D in fig. 3. Dislocations running perpendicularly to the film from surface to surface would appear as black dots in bright field as for example at C in fig. 3. Many dot-like features are also visible in fig. 6, some of which are superimposed on stacking faults. Since there is no interaction with the faults they cannot be line dislocations running right through the film but must be small defects away from the plane of the fault, possibly small loops of less than 50 Å diameter formed by vacancy condensation.

Tetrahedral stacking faults were occasionally observed confirming the finding of Matthews (1959). Smallman and Westmacott (1959) claim to have observed tetrahedra in quenched and aged bulk silver. Examples of tetrahedra are visible at E in fig. 3: the largest has a side length of about 500 Å, and the smallest about 150 Å. This agrees well with the range of sizes of tetrahedra observed by Silcox and Hirsh (1959) in quenched gold, which is to be expected since the stacking fault energy of gold and silver are about the same.

Small triangular defects such as F in fig. 3 and G in fig. 4 (*a*) were quite commonly observed. These correspond to equilateral triangles in a {111} plane, the edges of which are parallel to ⟨110⟩ directions lying in that plane. The smallest defects recognizable as of this type have side lengths of about 100 Å. The largest would have sizes limited by the thickness of the film; for example, that at A′ in fig. 4 (*a*) has a side length of about 650 Å.

The evidence is compatible with the view that the small triangular defects which do not in general intersect the film surface are Frank sessile dislocations (Frank 1949) formed by a vacancy condensation mechanism, whereas the large defects which generally intersect the film surfaces and of which A′ (fig. 4 (*a*)) is one sort are of a different type. These large defects will be discussed in §§ 5 and 6. The triangular shape of the small defects is expected, since Kuhlman-Wilsdorf (1958) has pointed out that a Frank sessile dislocation will prefer to split up into segments parallel to ⟨110⟩ directions.

§ 5. Description of Simple Stacking Faults

In areas of the films not previously exposed to the beam most of the faults were relatively short and confined to a single plane as in figs. 2 and 4 Faults confined to a single plane will be called 'simple faults'. Complex faults forming on two or more of the four possible {111} planes were usually only observed after irradiation in the beam. Matthews (1959) mainly observed complex faults and has described these rather fully. The nature of simple faults will now be described.

Most of the simple faults observed, with the exception of those ending at a hole, were straight-sided with 3–6 sides and extended from surface to surface of the film. About 5% of the partials assumed the shortest possible length parallel to a ⟨112⟩ direction so that the fault viewed in a direction perpendicular to the foil appeared 'square-ended'. A strong tendency was observed for the partial dislocations to align themselves in ⟨110⟩ directions as predicted by Kuhlmann-Wilsdorf (1958). Analysis of the directions of about 50 partials in figs. 2 and 3 showed that about 60% of them coincided with a possible [110] direction within the accuracy of measurement, and about 90% were within 15°. The direction of significant deviations was always such as to shorten the length of the partial.

The stacking faults lie on any of the four {111} planes making a 54° 44′ angle with the plane of the foil. The latter will be taken as (001), so that the (111) and $(11\bar{1})$ planes intersect the surface along $[1\bar{1}0]$ while the $(1\bar{1}1)$ and $(\bar{1}11)$ planes intersect it along [110]. It is not possible from the present micrographs to determine which of the fault boundaries is in the top surface of the foil, so that the stacking fault at T′ in fig. 2, for example, is either on the (111) or on the $(11\bar{1})$ plane if the long edge of the figure is parallel to $[1\bar{1}0]$.

Line drawings of the main possible shapes of simple fault projected onto the plane of the film are shown in figs. 10–13. The shapes have been classified according to the number of sides and the side direction. The convention adopted by Matthews (1959) is followed, viz. the intersections of the fault with the top and bottom surfaces of the film are shown by thick full and dashed lines, respectively. Fine full lines represent the extinction fringes caused by the fault. Dashed fine lines represent partial dislocations. In each of the four {111} fault planes there are three possible ⟨110⟩ directions, one of which lies in the plane of the foil. Thus in the (111) plane, the partial may be in the $[0\bar{1}1]$ or $[\bar{1}01]$ directions or may take the shortest distance through the film in the $[\bar{1}\bar{1}2]$ direction. The intercept of the (111) plane with the surfaces and also the extinction fringe direction are parallel to [1$\bar{1}$0]. The projection of either [011] or [$\bar{1}$01] perpendicular to the foil makes an angle of 45° with the [1$\bar{1}$0] direction, while the projection of [$\bar{1}\bar{1}$2] is at 90° to [1$\bar{1}$0].

Faults of type A′ may occur in two ways in each of the four planes, that is in eight ways. Similar information for all the fault types is given in brackets in figs. 10–13. Since the top and bottom fault boundaries are indistinguishable in the micrographs only a half of these possibilities would be distinguishable. Examples of 19 types of fault are identified in fig. 4 (*a*) and may be seen in fig. 4 (*b*) in light field. Examples of three more types are shown in fig. 2. Examples of G′, M′, N′, O′, P′, V′, W′, AB′, AC′ and AF′ are not shown. Of these, G′ and AB′ have been seen in other areas. The remaining types would not be expected to be common because partials parallel to [$\bar{1}\bar{1}$2] or its equivalent are relatively infrequent. Since the partials tend to deviate somewhat from ⟨110⟩ directions, many of the shapes deviate somewhat from those described.

Fig. 10

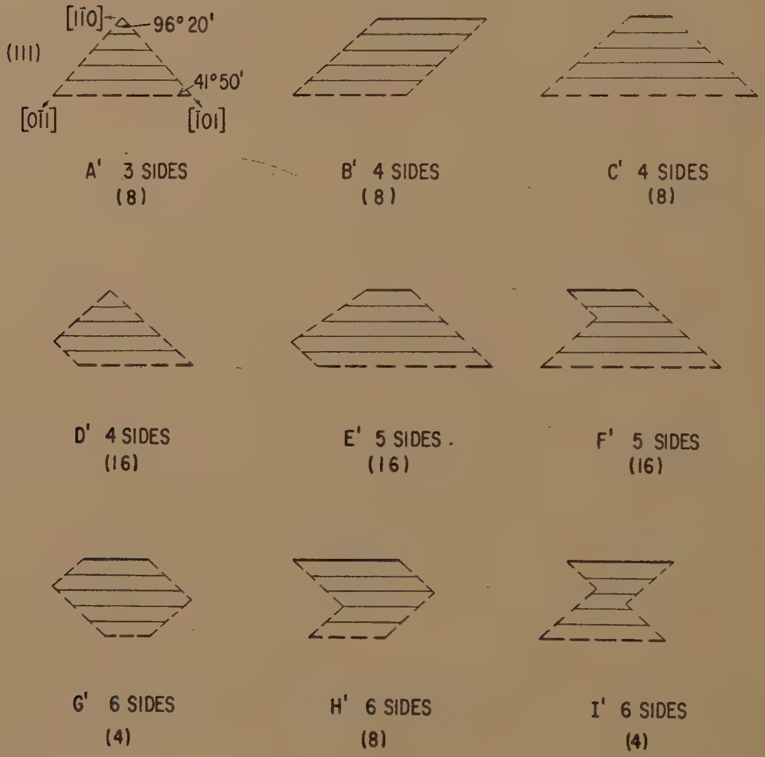
[1$\bar{1}$0]
96° 20′
(111)
41°50′
[0$\bar{1}$1]
[$\bar{1}$01]
A′ 3 SIDES (8)
B′ 4 SIDES (8)
C′ 4 SIDES (8)
D′ 4 SIDES (16)
E′ 5 SIDES (16)
F′ 5 SIDES (16)
G′ 6 SIDES (4)
H′ 6 SIDES (8)
I′ 6 SIDES (4)

Possible shapes of simple fault with partials in ⟨110⟩ directions.

Although there was a strong tendency for the partials to be straight, they were occasionally curved in a manner more typical of stainless steel (Whelan *et al.* 1957) as at fault T in fig. 6 (*c*).

Many of these simple fault types are also to be seen in a micrograph of gold grown directly on rock-salt published by Bassett and Pashley (1958–59). It is probable that they are typical of face centred cubic metals of low stacking fault energy grown epitaxially on rock-salt.

Fig. 11

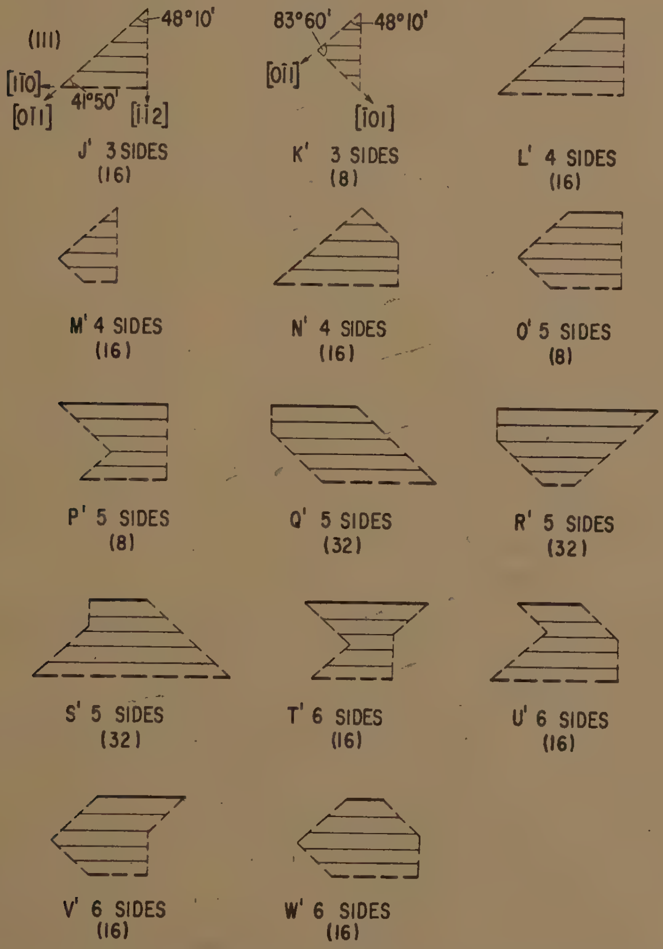
(111)
48°10'
[11̄0]
[01̄1]
41°50'
[1̄1̄2]
J' 3 SIDES
(16)
83°60'
48°10'
[01̄1]
[1̄01]
K' 3 SIDES
(8)
L' 4 SIDES
(16)
M' 4 SIDES
(16)
N' 4 SIDES
(16)
O' 5 SIDES
(8)
P' 5 SIDES
(8)
Q' 5 SIDES
(32)
R' 5 SIDES
(32)
S' 5 SIDES
(32)
T' 6 SIDES
(16)
U' 6 SIDES
(16)
V' 6 SIDES
(16)
W' 6 SIDES
(16)

Possible shapes of simple fault with one partial in ⟨110⟩ directions, other in ⟨112⟩ or ⟨110⟩ directions.

Comparison of fig. 4 (*a*) with 4 (*b*) shows that most, but not all faults are in contrast in fig. 4 (*a*). Some changes have occurred between the two exposures, for example at L and M. These will be discussed in § 6. The object I in fig. 4 is probably a twin. This is one of the very few examples observed.

H_1 in fig. 4 (*a*) is an example of a group of faults on parallel planes spaced 200–500 Å apart. H_2 appears to be a similar group of three faults more closely spaced. J_1 in fig. 4 (*a*) appears at first sight to be a similar group containing three faults, one of which is annular. However, in bright field (fig. 4 (*b*)) the contrast is such that this interpretation appears unlikely. J_2 in fig. 4 (*a*) and (*b*) is a similar example. The nature of these defects is uncertain.

Fig. 12

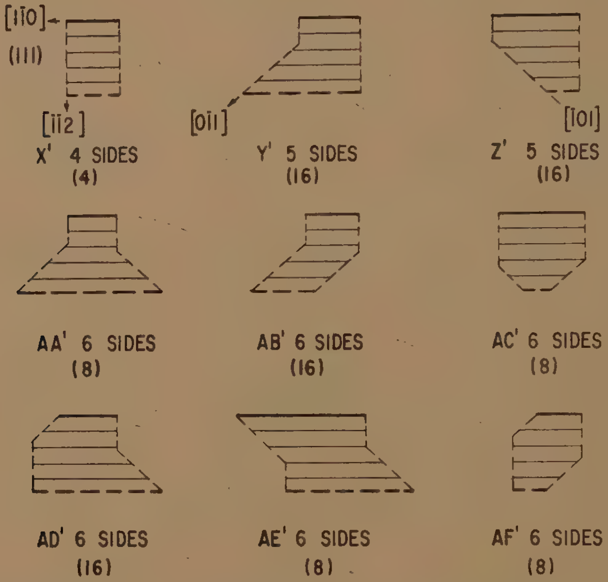

Possible shapes of simple faults with both partials in ⟨112⟩ or partly in ⟨112⟩ and partly in ⟨110⟩ directions.

The smallest defects such as K imaged in fig. 4 (*a*) are about 50 Å in diameter. Comparison with fig. 4 (*b*) shows that most of them are located at the edges of holes. These are thought to be tiny faults as discussed in § 6.

It is possible that simple planar defects are common in bulk material but have not yet been recognized. Thus the triangular defects observed in quenched and aged bulk silver by Smallman and Westmacott (1959) and Smallman *et al.* (1959–60) appear to be of type A′ although interpreted by the authors as defect tetrahedra. Similarly, some of the defects observed by Silcox and Hirsch (1959) in quenched and aged gold could be simple planar faults of types A′ and C′ rather than tetrahedra.

§ 6. Dissociation and Formation of Complex Faults

Whole dislocations lying in {111} planes tended to dissociate into two (Shockley) partials parallel to ⟨110⟩ directions and connected by stacking fault. Dislocations Q_1 and Q_2 in fig. 6 illustrate this and also show how this dissociation tends to be inhibited by the stress field associated with the dislocations R_{1-4} piled-up on a neighbouring parallel plane against a group of stacking faults. The maximum dissociation of Q_2 is about 200 Å in (*a*), 100 Å in (*b*) and 450 Å in (*c*). The dissociation of Q_1 in fig. 6 (*b*) has produced a defect of type C′ (fig. 10). Other examples of the blocking of the movement of whole dislocations by stacking faults are seen at Z in fig. 6 and at Y where the dislocation has moved out of the field between the exposures in fig. 6 (*b*) and (*c*).

Some individual dislocations such as D in fig. 3 showed no resolvable dissociation either because they did not lie in a $\{111\}$ plane or because dissociation was inhibited by the local stress field as at R_3 in fig. 6 (*b*). Dissociation to a width of less than about 100 Å would not be detectable.

Stressing in the beam caused the short simple faults typically seen in figs. 2 and 4 to widen and interact. Holes, dislocations and other faults acted as barriers to dissociation. Eventually most faults have extended as far as possible as in fig. 5 and dislocation movements become less frequent. For an average (extended) fault width of say $0{\cdot}3\,\mu$, and assuming 10^{10} faults/cm^2, an order of magnitude calculation shows that this corresponds to a plastic strain of about 5×10^{-8}. Figure 6 illustrates the structure at an intermediate stage.

Dislocation movements were very readily produced in the foil. This is attributed partly to the cleanliness of the surface, for it is probable that oxide or other contaminant layers tend to impede dislocation movement, and partly to the presence of holes which acted as stress concentrators. Holes also acted as pinning points for extended faults as at *P* in fig. 6 (*a*) where one partial has run out to the hole surface giving a fault of type AG′ in fig. 13. Other fault shapes such as AI′ in fig. 13 may be observed. Exceptionally a fault may run into two holes eliminating both partials giving a fault of type AH′ in fig. 13. Thin places in the vicinity of holes or elsewhere can similarly reduce the length of both partials and stair-rod dislocations. Movement of such partial dislocations would cause lengthening and is thus made difficult. Effects of this kind may stabilize normally unstable configurations of faults.

The widening of a fault under stress occurs when one partial is pinned and the other moved under the action of the stress. Since movement of a partial produces a shear, the stress may be locally relieved and movement stops, however, the shear produces a redistribution of the complex local stresses so that another fault is affected and expansion or contraction of this fault occurs. Thus movements tended to be rapid but to occur in stages, for example, fault S in fig. 6 (*a*) has extended a short distance in fig. 6 (*b*) and in fig. 6 (*c*) has extended to a hole where the partial will tend to be anchored due to the reduction in its length.

Combination reactions leading to complex stacking faults have been discussed by a number of authors (Cottrell 1952, Thompson 1953, Frank and Nicholas 1953, Friedel 1955, Whelan 1959). The Burgers vectors of the stable stair-rod dislocations have been listed by Frank and Nicholas

(1953). While such considerations are probably applicable to fully annealed clean films of uniform thickness, they are of doubtful value here because it is clear that the reduction in line energy of both partial and stair-rod dislocations at holes and thin places plays an important role, as also does the blocking of the movement of partials by other faults and dislocations. The formation of complex faults as a result of local stressing in the electron beam will now be considered.

A common reaction observed was the combination of two simple faults to form a one-bend fault. This has occurred at L and M between the consecutive exposures shown in fig. 4 (*a*) and (*b*). The angle between the faulted planes at L is acute (70° 32′) and at M is obtuse (109° 28′). The stair-rod dislocations (Thompson 1953) at the bends cannot here be resolved. Examples of stair-rods may be seen in fig. 6 (*a*) at the obtuse angled fault S and at the acute angled fault γ. Partial dislocations are sometimes visible, thus both partials are visible in fig. 6 (*b*) at the single bend fault W.

Another example of the formation of a single-bend acute-angled fault from two simple faults is shown in a ciné sequence (fig. 7 (*a*) to (*c*)).

Fig. 13

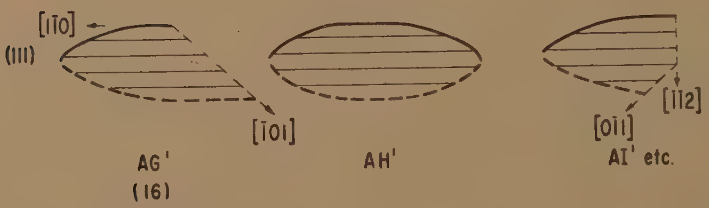

Possible shapes of simple faults running into holes—one or no partials.

The fact that the triangular fault at L in fig. 4 (*a*) combined with the other fault would suggest that it is bounded by Shockley rather than Frank partials lending some support to the distinction of two types of triangular fault in § 5.

The nucleation of dislocations at thin foil edges in stainless steel under the action of thermal stresses has been observed by Whelan *et al.* (1957). They calculate, following a private communication from Cottrell, that it is relatively easy for a dislocation to nucleate at a thin edge if it is of edge type. It was commonly observed in silver that faults tended to nucleate from the edges of holes through the films. The tiny faults K (fig. 4 (*a*)) which are located at hole edges (fig. 4 (*b*)) are thought to represent a very early stage in this process. These faults are only 50–100 Å in diameter. Figure 6 (*a*) to (*c*) shows the apparent nucleation of three successive faults from the hole edge at point W. The first and last faults to form are on parallel planes as indicated by the change in fringe contrast. A further example of simple overlapping faults is seen at X in fig. 6 (*b*); these are seen to have lengthened in fig. 6 (*c*). Another instance of fault nucleation at a hole is shown at N in fig. 9. The source of the dislocations Q_1 and Q_2 in fig. 6 is probably the hole edge to the left of Q_1.

The behaviour is frequently more complex. Comparison of fig. 8 (*a*) and (*b*) shows that the single-bend fault DEF has become a complex double-bend fault DEHGFI.

Simple faults were frequently observed to become shorter as at PQ in fig. 9 (*b*) to (*c*). Complex faults were frequently observed to contract forming simpler faults. Examples of this behaviour are seen at UT in fig. 6 (*a*) to (*c*) and at JKLM in fig. 9 (*a*) to (*c*).

Preliminary experiments have been made in which films were annealed *in vacuo* on grids for half an hour at 300°c followed by slow cooling. It appears that this treatment reduced the number of faults by a factor of 2–3. After annealing most of the faults observed are short simple faults. Whole dislocations are also present. Due to a loss in resolution occasioned by surface deterioration during annealing it was not possible to study the minor defects. Electron beam stressing caused the simple faults to widen and interact to form complex faults as before. This annealing experiment emphasizes the remarkable stability of the simple faults.

Widening and interaction processes of the kind described create complex fault patterns which impede free dislocation movement. These processes may play an important role in work hardening in bulk materials such as silver and gold if simple faults are present which may be the case as suggested in § 6. If such defects are peculiar to evaporated films then they may account for the claims that the strengths of such films may considerably exceed that of bulk material.

§ 7. ORIGIN OF INITIAL DEFECTS

The formation of the minor defects present namely dislocation loops, stacking-fault tetrahedra and small triangular defects is attributed to a vacancy collapse mechanism as discussed in § 4. The dot-like features are believed to be some kind of vacancy aggregate, perhaps unresolved loops. A vacancy concentration of about 5×10^{-5} is sufficient to account for the formation of all these defects. This seems a reasonable value for an evaporated foil.

The major defects present, namely stacking faults with their associated dislocations, could have formed by a number of alternative processes:

I. Matthews (1959) growth impingement mechanism.
II. Vacancy collapse mechanism.
III. Growth mistakes.
IV. Dissociation of whole dislocations.

These will now be considered in turn.

Matthews supposes that adjoining nuclei of silver are of different heights, grow with {111} facets, and impinge on a {111} plane with a mis-match in the stacking sequence. By suitable elaboration, the formation of both simple and complex faults can be explained. If this mechanism were important, facetting would be evident at the edges of the holes through the present films. This is not observed. A further objection to Matthews mechanism is that growth of nuclei in the case of evaporated gold (Bassett and Pashley 1958–59) and presumably in silver, seems in the early stages to occur by the growth of some nuclei at the expense of others rather than by impingement and coalescense, yet stacking faults appear to form at a very early stage in the growth before impingement becomes common.

A vacancy collapse mechanism will now be considered. In a fresh area of film, such as that shown in fig. 4, the density of major faults is about $1 \times 10^{10}\,\text{cm}^{-2}$. Assuming an average width of $0{\cdot}1\,\mu$ which is fairly typical of a fresh area and assuming that the faults formed by vacancy aggregation and collapse, this density is equivalent to an initial vacancy concentration of about 3×10^{-3}. This seems unreasonably high. Furthermore, most of the partial dislocations appear to be glissile in the plane of the associated fault. These considerations appear to rule out a vacancy collapse mechanism.

Growth mistakes could occur at an early stage during growth, possibly in laying down the first few $\{111\}$ layers, which could account for the presence of faults running from surface to surface of the films. The low stacking fault energy in silver would increase the probability of such mistakes occuring. More evidence is needed in order to properly assess the importance of this mechanism.

The most important mechanism of formation of stacking faults is thought to be the dislocation dissociation one. Dislocations might be nucleated at silver patch edges during growth since it is probable that the silver is in a state of stress. Secondly, they could form by the impingement of adjacent patches on a $\{110\}$ plane during the later stages of growth. Thirdly, it is also likely that dislocations grow from the substrate. Thus edge dislocations with a $\langle 110 \rangle$ Burgers vector emerging on a $\{100\}$ cleavage surface of the rocksalt could grow into the silver during the first stage of deposition, and as growth continued would tend to dissociate into the appropriate Shockley partials. Since there is a marked tendency for the partials to lie in $\langle 110 \rangle$ directions, it would be expected that faults formed in these ways would commonly tend to be triangular in shape (type A′). The driving force for movement of the partials into $\langle 110 \rangle$ directions presumably comes from a reduction of core energy in this orientation. Since the stacking fault energy is low, only a small stress is then required to cause further broadening of type A′ faults to form type C′. Considerable stresses arise during cooling of the film on the substrate due to differential contraction and also during stripping and drying due to surface tension effects. If both partials lay in the same $\langle 110 \rangle$ direction a fault of type B′ would be expected and could readily widen under stress. Faults such as type AG′ could result from the nucleation of a single Shockley partial at a patch edge. As demonstrated, further dissociation and interaction to form complex faults can readily occur. New faults can also be nucleated.

ACKNOWLEDGMENTS

The author is indebted to Miss E. Alessandrini who prepared the silver films and to Mr. J. A. Hugo for his assistance in the experimental work. He would like to thank his colleagues, Dr. W. G. Johnston and Dr. J. D. Livingston for criticizing the manuscript.

REFERENCES

BASSETT, G. A., and PASHLEY, D. W., 1958–59, *J. Inst. Met.*, **87,** 449.

BOLLMANN, W., 1956 a, *Phys. Rev.*, **103,** 1588 ; 1956 b, Report of First European Regional Conference on Electron Microscopy, Stockholm.

COTTRELL, A. H., 1952, *Phil. Mag.*, **43,** 645.

FRANK, F. C., 1949, *Proc. phys. Soc. Lond.* A, **62,** 202 ; 1950, *Symposium on the Plastic Deformation of Crystalline Solids, O.N.R.* (Pittsburgh : Carnegie Institute of Technology), p. 150.

FRANK, F. C., and NICHOLAS, J. F., 1953, *Phil. Mag.*, **44,** 1213.

FRIEDEL, J., 1955, *Phil. Mag.*, **46,** 1169.

HIRSCH, P. B., HORNE, R. W., and WHELAN, M. J., 1956, *Phil. Mag.*, **1,** 677.

HIRSCH, P. B., SILCOX, J., SMALLMAN, R. E., and WESTMACOTT, K. H., 1958, *Phil. Mag.*, **3,** 897.

KUHLMANN-WILSDORF, D., 1958, *Phil. Mag.*, **3,** 125.

MATTHEWS, J. W., 1959, *Phil. Mag.*, **4,** 1017.

OGAWA, S., WATANABE, D., and FUJITA, F. E., 1955, *J. Phys. Soc. Japan*, **10,** 429.

PASHLEY, D. W., 1956, *Advanc. Phys.*, **5,** 173 ; 1957, Proceedings of the Conference on Electron Microscopy held at Bangor, Wales (summarized by EMERSON, H. W., 1958, *Brit. J. appl. Phys.*, **9,** 306) ; 1959, *Phil. Mag.*, **4,** 324.

PHILLIPS, V. A., 1959, Annual Meeting of the Electron Miscrocope Society of America held at Ohio State University, Columbus, Ohio (abstracted in *J. appl. Phys.*, 1959, **30,** 2032).

SILCOX, J., and HIRSCH, P. B., 1959, *Phil. Mag.*, **4,** 72.

SMALLMAN, R. E., and WESTMACOTT, K. H., 1959, *J. appl. Phys.*, **30,** 603.

SMALLMAN, R. E., WESTMACOTT, K. H., and COILEY, J. H., 1959–60, *J. Inst. Met.*, **88,** 127.

THOMPSON, N., 1953, *Proc. phys. Soc. Lond.*, B, **66,** 481.

THORNTON, P. R., and HIRSCH, P. B., 1958, *Phil. Mag.*, **3,** 738.

WATANABE, Y., 1956, *J. Phys. Soc., Japan*, **11,** 740.

WHELAN, M. J., 1959, *Proc. roy. Soc.* A, **249,** 114.

WHELAN, M. J., and HIRSCH, P. B., 1957 a, *Phil. Mag.*, **2,** 1121 ; 1957 b, *Ibid.*, **2,** 1303.

WHELAN, M. J., HIRSCH, P. B., HORNE, R. W., and BOLLMANN, W., 1957, *Proc. roy. Soc.* A, **240,** 524.

Atmospheric Temperature Effects on the Solar Daily Variation of Cosmic Ray Intensity†

By J. J. Quenby and T. Thambyahpillai
Imperial College of Science and Technology, London

[Received January 20, 1960]

Abstract

The solar diurnal variation of the cosmic ray meson intensity caused by the periodic solar heating of the atmosphere is derived from a comparison of the ionization chamber and neutron monitor data from Huancayo. The amplitude and the time of maximum are found to be 0·11% and 05–30 hr respectively. Recent meteorological data, free from appreciable radiation errors, are found to be in rough agreement with this result. Particularly good agreement is obtained in the phases which are both later than the value given by Dorman by about 4 hr. The inclusion of this temperature correction enables the directional measurements at Mawson to be reconciled with the idea of a primary anisotropy.

§ 1. Introduction

The solar daily variation of cosmic ray intensity has been the subject of extensive investigation, chiefly because of the important information it can yield about the anisotropic distributions of the primary radiation and the modulating mechanisms responsible for their production. Continuous monitoring of the intensity, however, has been feasible only with the secondary radiation at sea-level or mountain altitudes where measurements have been made with ionization chambers, counter telescopes and neutron monitors. The intensity variations of the secondary radiation, however, are governed not only by the primary intensity variations but also by the variable conditions of the overlying atmosphere, and adequate corrections have to be applied for such atmospheric influences in order to relate the observed variations to those in the primary intensity.

The neutron-producing component of the secondary radiation is sensitive to changes of barometric pressure but is not affected to any appreciable extent by atmospheric temperature. Since effects of barometric changes can be taken adequately into account, observations of the neutron intensity provide reliable measures of the solar diurnal variations of the primary radiation entering the earth's atmosphere. In contrast, the total ionizing and μ-meson components measured by ionization chambers and counter telescopes are influenced both by pressure variations and variations of temperature throughout the atmosphere. As will be seen later, difficulties are encountered in attempting to correct for the atmospheric temperature effects.

---

† Communicated by the Authors.

In spite of these difficulties over meteorological effects, counter telescopes possess an advantage over neutron monitors in their ability to select the radiation incident from particular directions and because of this, are of particular importance in a determination of the true direction and magnitude of the anisotropy existing outside the earth's magnetic field. For instance, Brunberg and Dattner (1954) have shown how, by making some simple assumptions, the mean energy of the primary radiation giving rise to the solar daily variations and the direction of the anisotropy relative to the sun–earth line can be deduced from the directional measurements made with telescopes inclined at 30° to the vertical and pointing in the north and south directions.

Measurements of this kind made by Elliot and Dolbear (1951) and Malmfors (1949) have shown that the observed solar daily variations were of about the same magnitudes as those originating in atmospheric temperature variations. Under these circumstances, it is necessary to know the meteorological corrections with considerable accuracy in order to obtain any reliable information concerning the anisotropy.

Now, although many elegant theoretical investigations have already contributed to an understanding of atmospheric effects on the μ-meson intensity near sea-level (Olbert 1953, Maeda and Wada 1954, Trefall 1955, Dorman 1957), corrections for meteorological influences on the solar daily variations of meson intensity have not hitherto been evaluated to a high degree of accuracy. The chief difficulties encountered have been a dearth of aerological information and where radio-sonde measurements of atmospheric temperature were available, the uncertainty as to the extent to which the measurements were contaminated by insolation and lag errors.

There is general agreement that the radio-sonde measurements of the diurnal variation at high altitudes do not reflect the actual diurnal course of the air temperature (Kay 1951, Dorman 1957). However, Dorman has estimated the atmospheric contribution to the diurnal variation of meson intensity on the assumption that the radio-sonde measurements were reliable up to the 300 mb pressure level. The diurnal amplitude in the region above this isobar was estimated from cosmic ray measurements made underground at London to be $< 0{\cdot}5°\text{c}$ while the upper air soundings gave amplitudes of over 2°c. When errors of over 300% occur just above 300 mb, the limit of integration, it is conceivable that substantial radiation errors are also present in the measurements made below 300 mb and to this extent, the estimate of Dorman appears to be unreliable. An alternative estimate of the atmospheric contribution is therefore desirable.

In the following, we have attempted to deduce the 24 hr wave in meson intensity due to atmospheric temperature using only cosmic ray measurements and compare this result with the most recent meteorological data. Finally, it is shown that when this temperature correction is included, the directional measurements made at Mawson can be explained in terms of a primary anisotropy without any inconsistencies.

§ 2. COMPARISON OF NEUTRON MONITOR AND IONIZATION CHAMBER DATA FROM HUANCAYO

In this section the diurnal variation of meson intensity arising from changes of atmospheric temperature and hereafter referred to as the temperature wave, will be derived from a comparison of the ionization chamber and neutron monitor data from the equatorial station Huancayo. In this particular case where the response of the two detectors to primary intensity variations is likely to be similar, the basic cause of the difference between the two sets of results, after correction for barometric changes, is the residual atmospheric contribution left in the ion-chamber data.

We shall first examine the basis for the assumption of similarity in detector response. Rough similarities are evident in (i) Directional Sensitivity and (ii) Energy Response as defined by the differential response curves giving the number of detected secondary particles produced, as a function of the primary magnetic rigidity. These will now be described briefly under (i) and (ii)

(i) Both instruments are omni-directional in the detection of the secondary radiation and consequently the directional sensitivities to the primary radiation are determined solely by atmospheric absorption.

(ii) It is evident from the differential response curves given by Webber and Quenby (1959) that at rigidities higher than the equatorial cut-off value, the curves for an ion-chamber and a neutron monitor are similar at the atmospheric depth of Huancayo.

The following experimental result lends further support to the belief that the instrumental responses are similar. It is known that during certain periods, particularly after magnetic and cosmic-ray storms, the amplitude of the daily variation may be as great as 0·5%, whereas the temperature wave in the ion-chamber data is likely to be only 0·1% in amplitude. If the response of the two instruments to primary variations is similar, it follows that the difference between the daily variations measured by neutron monitors and meson recorders during these periods should be small.

Now, neutron monitors and wide-angled counter telescopes have concurrently been operated during 1957 and 1958 at the low-latitude stations Lae and Tokyo. The averaged results from several selected days of enhanced daily variation which followed Forbush decreases were subject to Fourier analysis and the 24 hr components are shown on harmonic dials in fig. 1. It is apparent from the diagram that the measured amplitudes are $\sim 0·6\%$ while the vectorial difference between the two detectors at any one station is $< \sim 0·1\%$. Although the data from a neutron monitor and a counter telescope have been compared here, this result should also apply to the data from a neutron monitor and ion chamber at a low-latitude station because the differences between the differential response curves of an ionization chamber and a counter telescope are negligible (Webber and Quenby 1959). It is concluded therefore, that the two types of detector at Huancayo respond in similar ways to primary intensity variations. The evidence cited above appears to be sufficient as only a qualitative similarity and not an exact correspondence in instrumental response is required for our purpose.

Let the mean solar 24 hr waves during any given month originating from primary intensity changes be represented vectorially by **N** and **I** for the measurements made by the neutron monitor and the ion chamber

Fig. 1

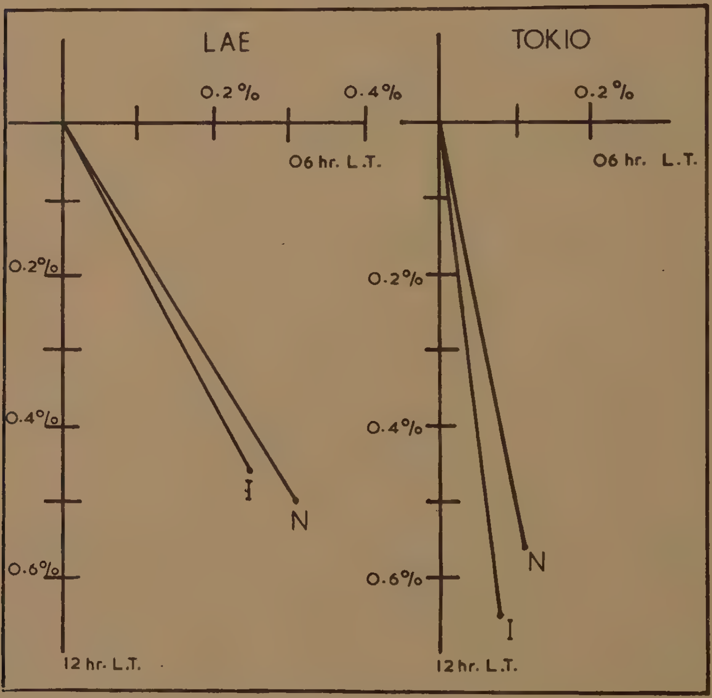

Harmonic dials, showing the 24 hr components of the daily variation measured during days of enhanced variation. Simultaneous measurements made by a neutron monitor (*N*) and a wide-angled meson telescope (*I*) at Lae and Tokyo are shown.

respectively. It will be assumed that the similarity of instrumental response leads to the following relationships:

$$|\mathbf{N}| = r|\mathbf{I}|,$$

$$\mathbf{N}.\mathbf{I} = \theta|\mathbf{N}|.|\mathbf{I}|$$

where r and θ are constants even though the rigidity dependence and the direction in space of the primary anisotropy may change in time. These conditions will be satisfied best if, as implied earlier, r and θ are both close to unity.

Since the data have already been corrected for barometric changes, the diurnal waves given by the measurements should be $\mathbf{N}$ for the neutron monitor and $\mathbf{I}+\mathbf{T}$ where $\mathbf{T}$ is the atmospheric contribution to the meson data. Moreover, for the ion-chamber, the seasonal variations of the temperature wave are likely to be small at Huancayo which is near the geographical equator. Thus for practical purposes $\mathbf{T}$ can be assumed constant.

If we now select a period of time during which the mean diurnal variation measured by the neutron monitor is zero, it can be shown that the average variation measured by the ionization chamber over this period is the temperature wave $\mathbf{T}$; i.e. if $\sum_i \mathbf{N}_i = 0$ where i denotes the monthly period, then $\sum_i \mathbf{I}_i = 0$, provided that r and θ are constant. This is easily seen when we consider a number of vectors $\mathbf{N}_i$ selected so that on addition they give a closed polygon. Even when the amplitudes of the vectors are changed uniformly by a factor r and each vector is rotated through the same angle $\cos^{-1}\theta$, the polygon will be closed. Therefore the mean 24 hr wave in the ion-chamber data is given by

$$\frac{1}{n}\sum_{i=1}^{n}(\mathbf{I}_i+\mathbf{T})=\mathbf{T}.$$

The condition $\sum_i \mathbf{N}_i = 0$ can be realized using the data from the period 1953–1955. The neutron monitor data of Conforto and Simpson (1957) have been used in our analysis together with the results of Venkatesan and Dattner (1959) after allowing for some errors in the latter analysis. The definition adopted for the diurnal vector in the former publication, though different from the conventional one, is claimed by the authors to give equivalent results.

The selected groups of months during which the mean neutron diurnal effect was nearly zero are shown in table 1 together with the actual mean values and the corresponding temperature waves from the ion-chamber data. The coefficients a_1 and b_1 are given, where the diurnal wave is represented by

$$a_1 \cos\frac{2\pi}{24}t + b_1 \sin\frac{2\pi}{24}t.$$

The atmospheric vectors are plotted on a harmonic dial in fig. 2 where the standard deviation circles are also drawn. The vectors for each group are numbered 1 to 6 and the overall mean is marked M. The individual vectors will be seen to agree within the limits of statistical accuracy but we note that they are not entirely independent of one another because some months are common to several groups. The mean temperature wave obtained in this way has an amplitude of 0·11% and a time of maximum around 05–40 hr local time.

Alternatively, r and θ can be determined from the data for two separate periods, again assuming r, θ and $\mathbf{T}$ to be constant. In order to achieve accuracy in this calculation, the measured diurnal waves during the two periods should show substantial differences. The mean diurnal waves

Table 1

Group	Selected months	Mean neutron vector (%) a_1	b_1	Atmospheric vector (%) a_1	b_1
1	October, 53 Feb., March, April, May, June, July 1954	$-0·002$	$0·01$	$0·02$	$0·11$
2	March, April, September, October, November, December 54	$-0·008$	$-0·004$	$0·00$	$0·12$
3	September, October, November, December 53; January, February, March, April, August, September 54	$-0·001$	$-0·005$	$0·01$	$0·12$
4	April, May, June, July, 53, August, September 54	$-0·01$	$+0·01$	$0·02$	$0·10$
5	March, April, May, June, August September, October, November, December, 54, January, February, March, 55.	$-0·004$	$+0·002$	$0·00$	$0·11$
6	January 54 to March 55 inclusive	$0·00$	$0·00$	$0·02$ $(+0·01,$	$0·10$ $+0·11)$

Fig. 2

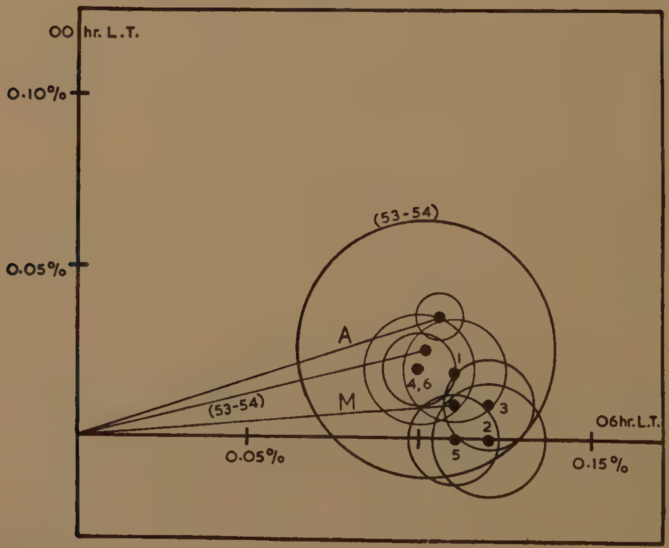

Solar time dial showing the estimated 24 hr component of the daily variation due to atmospheric temperature in the ion-chamber data from Huancayo. Vectors 1 to 6 (as in table 1) and the overall mean *M* were found by the null method. The vectors (54–54) and *A* were derived by alternative methods (vide text). The circles denote standard deviations of the estimates.

for the years 1953 and 1954 satisfy this criterion and these data yield values $r=0{\cdot}96$ and $\theta=0{\cdot}94$, consistent with our earlier assumption $r, \theta \simeq 1$. Using these values of r and θ, the temperature wave in the Huancayo ion-chamber is found to have harmonic coefficients $a_1=0{\cdot}026\%$ and $b_1=0{\cdot}102\%$.

A further estimate of the temperature effect can be obtained by assuming that the primary variations produce 24 hr waves of identical magnitude and phase in the neutron monitor and the ionization chamber, or $r=\theta=1$. Here, the vector difference between the ionization chamber and neutron monitor data gives the temperature effect and the measurements made over the years 1953 to 1955 give values $a_1=0{\cdot}035\%$ and $b_1=0{\cdot}106\%$ for this vector. The estimates given by the last two methods are also shown in fig. 2 labelled (53–54) and A respectively. Although there is substantial agreement between the estimates given by the three methods, probably the most reliable one is obtained from the null method described first.

§ 3. METEOROLOGICAL DATA

We shall now examine the evidence for a daily temperature variation in the atmosphere. The difficulties of measuring the true air temperature during daylight hours have already been indicated but in recent years temperature sensing devices with a special coating of very low absorptive power for the solar radiation spectrum have been developed (Brasefield 1948) and adopted for general use in routine upper air soundings in the U.S.A. An analysis of the upper air data obtained during the summer months of 1956 and 1957 at Washington, D.C. has been made by Harris (1959) who gives the diurnal and semi-diurnal components of the temperature variation in the atmosphere at altitude intervals of 1 km between 0·5 km and 9·5 km inclusive.

The atmospheric contribution to the solar daily variation of cosmic ray meson intensity was calculated by Dorman (1957) from the upper air data compiled by Kaminer and it is therefore interesting to compare these data from the U.S.S.R. with the more recent results of Harris. The data for the same season as Harris's results were analysed and differences between the two sets of results were found to exist in both amplitude and phase. The differences can best be seen by resolving each 24 hr wave of temperature into two components of the same periodicity, of which one has its time of maximum fixed at mid-day and the other one at 18 hr. Only the amplitudes of these components need be compared as the phases are constant. The advantage of this resolution is that the amplitude of only one of the components, viz. the one with a maximum at noon, will be sensitive to radiation errors in the measurements whilst the other will not be affected to any appreciable extent. This is because the radiation errors at times placed symmetrically with respect to noon should be roughly the same.

We have calculated the amplitudes of these components at various isobaric levels from the results of Harris and Kaminer and plotted them in fig. 3 as functions of the atmospheric pressure. It can be seen from the diagram that the two sets of results give roughly the same amplitudes at various pressure levels for the component with an 18 hr maximum. Marked discrepancies are evident, however, in the other component, with the results of Harris showing a roughly constant amplitude of ~0·1°c between 750 mb and 350 mb while the Russian data give systematically larger amplitudes which increase with altitude from 0·5°c to about 1·2°c over the same range of the atmosphere.

Fig. 3

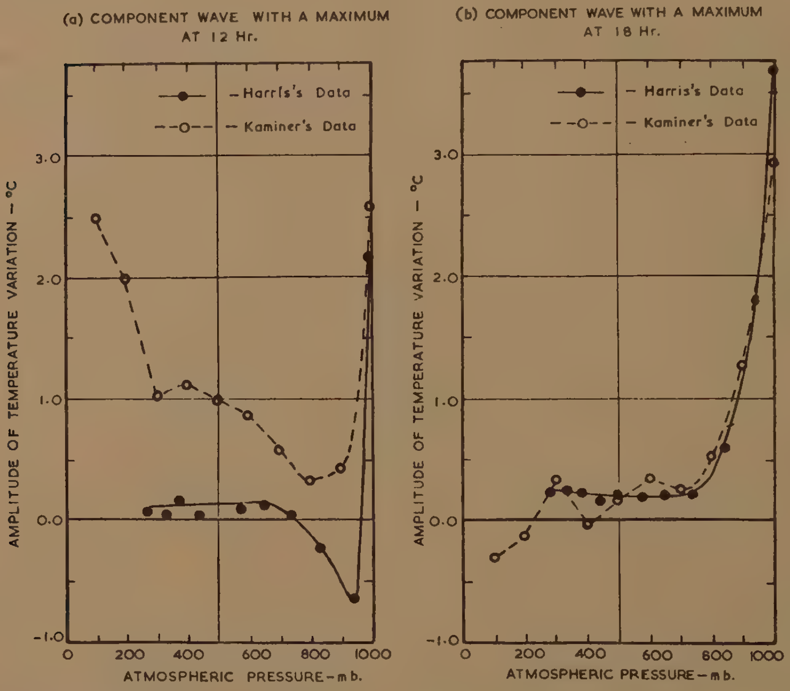

The diurnal temperature variation at various isobaric surfaces in the atmosphere according to the data of Harris (solid curve) and Kaminer (dotted curve). The amplitudes of the resolved components with a diurnal maximum at (*a*) 12 noon and (*b*) 18 hr L.T. are shown.

In determining the reasons for this divergence between the two results, factors such as the wide differences in the epochs of measurement and the geographical locations of the observing stations have to be taken into account. But there can be little doubt that at least a part of it is due to the differences in the relative amounts of radiation errors in the temperature measurements. The rough agreement between the two sets of data regarding the component which is not affected by radiation errors and the growth of the difference in the other component with increasing altitude appear to support this view.

We shall next examine the effects of the differences in aerological data on the estimates of the atmospheric contribution to the meson intensity. The temperature data of Harris together with the densities of temperature coefficients calculated by Dorman have been used to compute the percentage changes in the counting rate of a cubical meson telescope at sea-level originating in the portion of the atmosphere between sea-level and 250 mb, the limits being set by the availability of temperature data. The calculations give a first harmonic with an amplitude of 0·12% and a time of maximum at 05–30 hr, and a second harmonic with corresponding values of 0·04% and 06–30 hr respectively, The daily variation curve of meson intensity, which includes the effects of both harmonics, is shown in fig. 4 and a similar curve obtained by Dorman is also included for comparison purposes. The latter curve refers to the same season and the same range of the atmosphere, but is mainly diurnal with an amplitude of 0·22% and a maximum at 02 hr. As indicated above, the larger amplitude and the advance in phase from 05–30 hr to 02 hr must partly be due to the larger radiation errors in Kaminer's results.

Fig. 4

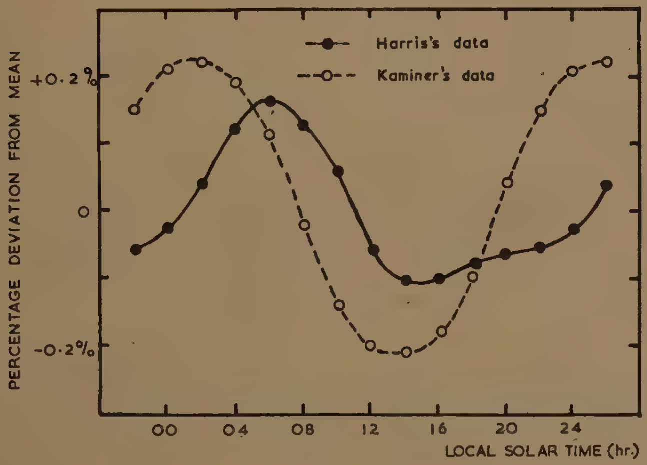

The solar daily variation due to atmospheric temperature in the counting rate of a cubical meson telescope at sea-level, calculated from the temperature data of Harris (solid curve). An earlier estimate of Dorman (dotted curve) is shown for comparison.

The contribution from that portion of the atmosphere above 250 mb cannot be estimated with any comparable accuracy but Kay (1951) has suggested that the temperature variation in the 150–80 mb region has an amplitude of < 0·5°c, reaching a maximum value in the late afternoon, and if this is accepted as correct, our diurnal amplitude of 0·12% should be increased by about 0·03 to 0·05%.

As a result of the rapid attenuation of the diurnal amplitude with height evident in Harris's data, about two-thirds of the 0·12% amplitude originates in the atmosphere below the 750 mb isobar. It is well known, however, that the daily temperature variations in the lower troposphere show a marked seasonal dependence and vary considerably with geographical location. It can be expected, therefore, that the meson intensity variations will exhibit correspondingly large fluctuations from season to season at temperate latitudes and that the annual mean of the variation will have a smaller amplitude than the summer value of about 0·16% in agreement with the suggestion of Baliga and Thambyahpillai (1959). Moreover, the magnitudes of the temperature effects may vary substantially from one cosmic ray station to another.

We conclude, however, that the temperature wave deduced in § 2 from cosmic ray data is not inconsistent with that given by aerological measurements. Of course, Huancayo is at an altitude of 3350 m above sea-level and because of the lower mean energy of the μ-mesons recorded there, the densities of temperature coefficients should be somewhat larger than at sea-level, but this cannot lead to more than a fractional change in the amplitude of the expected variation. This should, however, be offset by the integration over a smaller range of the atmosphere (0 mb to $\sim$ 650 mb) and the smaller amplitudes of the diurnal temperature variation in this range. These factors might explain the somewhat smaller amplitude of 0·11% deduced for the mountain station from cosmic ray measurements as compared with an amplitude of about 0·16% at sea-level. Moreover, the time of maximum of 05–40 hr obtained in § 2 appears to be borne out by the temperature data of Harris. The remarkable agreement between the two independent derivations with regard to the phase leaves little room for doubt that the diurnal maximum of the meson intensity variations due to atmospheric temperature occurs around 05–30 hr and not in the early hours of the morning, as has hitherto been believed (Dorman 1957).

§ 4. Directional Measurements made at Mawson

In this section we shall consider the effects of correcting solar daily variation results for atmospheric influences using the temperature vector derived above. For this purpose we have selected the measurements made during the period May 1955 to February 1956 at Mawson, Antarctica (67° 36′ S, 62° 53′ E geographic) with a vertical telescope and another inclined at 45° to the vertical and rotated at regular intervals so as to look, in turn, due geographic north, east, south and west (Parsons 1957). The data, as published, were corrected only for changes of barometric pressure. These results were believed to be inconsistent with the view that the daily variation is the result of an anisotropic distribution of the primary flux, existing outside the earth's magnetic field (Parsons) but this conclusion should be re-examined after taking into account the contribution from atmospheric temperature changes. Moreover, the dipole approximation to the earth's magnetic field used by Parsons in his discussion may not be sufficiently accurate for the purpose. Quenby and Webber (1959) have already pointed out the need for including the non-dipole part of the field in the calculation of cosmic ray cut-off rigidities and these terms are also of importance in calculating the asymptotic directions of all low energy cosmic rays.

The diurnal components of the solar daily variations measured by Parsons after the application of pressure corrections are shown in table 2 which gives the amplitudes and times of maxima for the various directions in which the telescopes were pointed. The features of interest in the results are the small amplitude of 0·014 ± 0·016% for the south direction as compared with amplitudes lying between 0·06 and 0·08% for the other directions and the appreciable spread in the times of maxima.

Table 2. The solar diurnal variations of cosmic-ray intensity at Mawson measured by telescopes pointing (*a*) in the vertical direction and (*b*) at zenith angles of 45° in various directions. The results corrected for barometer changes are shown together with the values obtained when a temperature corrections (vide text) is also included

Telescope direction	Pressure corrected		Pressure and temperature corrected	
	Ampl. (%)	Time of max. (hr (L.T.))	Ampl. (%)	Time of max. (L.T.)
North	0·081 ± 0·016	14–50 ± 00–45	0·179 ± 0·025	16–28 ± 00–32
East	0·060 ± 0·016	13–20 ± 01–00	0·147 ± 0·025	16–12 ± 00–40
South	0·014 ± 0·016	13–50 ± 04–20	0·118 ± 0·025	17–12 ± 00–45
West	0·064 ± 0·016	16–10 ± 00–55	0·172 ± 0·025	17–08 ± 00–36
Vertical	0·079 ± 0·006	13–45 ± 00–15	0·166 ± 0·020	16–04 ± 00–30

In the absence of reliable information about the temperature changes over Mawson and the differences in temperature effects for vertical and inclined telescopes, we have used the temperature vector derived for the Huancayo ion chamber (amplitude 0·11%: phase 05–40 hr) to correct all five of the 24 hr waves obtained by Mawson. This procedure can give only a rough approximation to the actual state of affairs; but the uncertainty in the amplitude of the temperature correction has no marked effect on the conclusions to be drawn from the results. The diurnal variations obtained after the temperature correction are also given in table 2 and are shown on the harmonic dial in fig. 5. As a result of the correction, the ratio of the amplitudes in the south and north directions has been increased to about two-thirds and the spread in the phases for the various directions has been reduced.

In discussing his results in terms of a primary anisotropy, Parsons has adopted the suggestion of Brunberg and Dattner (1954) that the deflection of the primary particles in the earth's magnetic field can be adequately taken into account by assuming a suitable mean value, between 20 GV and 40 GV, for the magnetic rigidity of the primary particles which are responsible for the daily variations. It is then possible to determine the asymptotic direction from which particles of this rigidity entered the earth's field before being deflected so as to be recorded by the appropriate counter telescope. This asymptotic direction is characterized by a latitude angle, measured from the geographic equatorial plane, and a longitude angle measured eastwards from the geographic meridian plane through Mawson. Using the data of Brunberg and Dattner (1953), based on the dipole approximation to the geomagnetic field, Parsons calculated these angles defining the asymptotic directions for the five telescope directions

Fig. 5

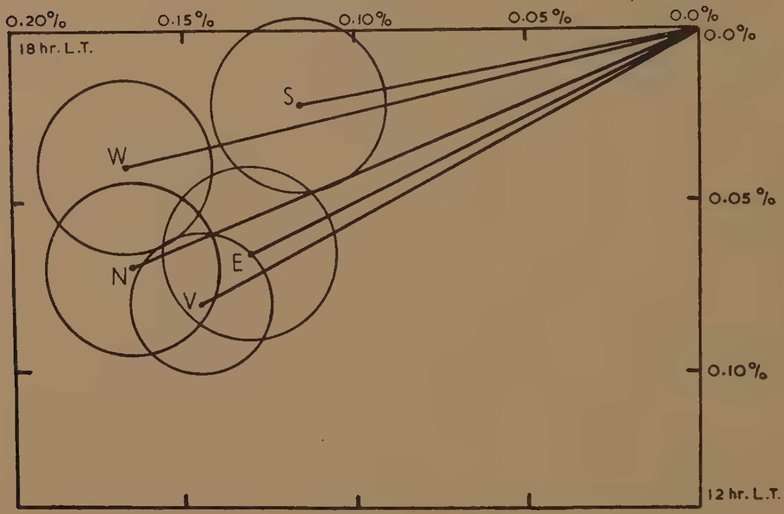

Harmonic dial representation of the cosmic ray diurnal variations at Mawson in the vertical direction (V) and at zenith angles of 45° in the north (N), east (E), south (S) and west (W) directions after correction for the effects of atmospheric pressure and temperature. Standard deviation circles are also shown.

used at Mawson and for particle rigidities of 15, 20 and 40 GV. The calculated angles of latitude and longitude are shown diagrammatically in fig. 6. Parsons has pointed out the following difficulties in reconciling his results (uncorrected for temperature effects) with an anisotropic distribution of the primaries which exists outside the earth's magnetic field. (*a*) Although the asymptotic latitude for the south pointing telescope was intermediate between those for the other telescope directions, the south telescope measured a much smaller amplitude than the other telescopes. This result cannot be explained easily because the strength of the anisotropy can be expected to show a smooth variation with latitude. It will be seen from table 2 that this difficulty is largely removed by the application of a temperature correction. (*b*) The longitude angles are

Fig. 6

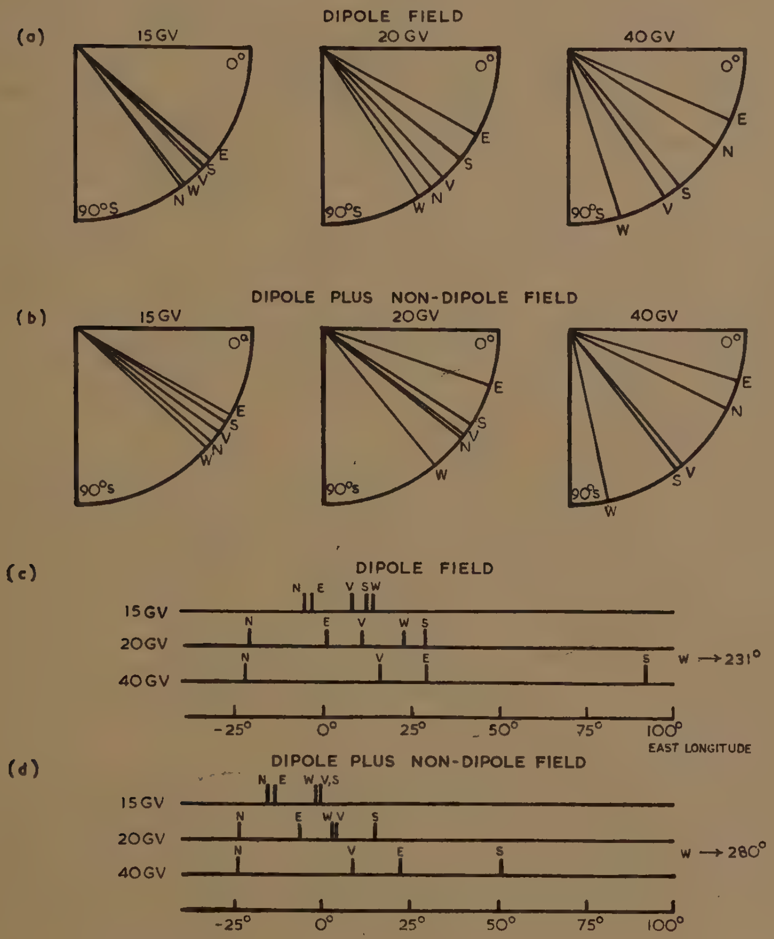

The angles of latitude and longitude defining the asymptotic directions from which primary particles enter the earth's magnetic field before being deflected so as to be recorded by the various telescopes at Mawson. Values for primary rigidities of 15, 20 and 40 GV are given.

(*a*) and (*b*), asymptotic geographic latitudes;
(*c*) and (*d*), asymptotic geographic longitudes (measured as in text);
(*a*) and (*c*), take only the dipole part of the earth's magnetic field into account;
(*b*) and (*d*), take into account the dipole and non-dipole parts of the earth's magnetic field.

different for the five telescopes and an excess of radiation entering the magnetic field from a particular direction should give rise to maxima in the measured intensity at different times. The sequence of the times of maxima should be in the order of decreasing longitude angle but the arrangement of measured times of maxima disagreed with the expected sequence.

Now, the geomagnetic latitude of Mawson on the centred dipole approximation is 73°, though the dip latitude, as defined by the angle of dip of the actual field lines, is 54°. Besides, the declinations of the horizontal components of the actual field and the field due to the centred dipole differ by 26°. Thus, the non-dipole part of the earth's magnetic field is quite large at Mawson and has to be taken into account. To do this a new dipole was fitted by requiring that the field of the fitted dipole gave a best fit to the actual field strength along the radius vector through Mawson. The angles of latitude and longitude corrected for the non-dipole field effects are also shown in fig. 6. It will be seen that there is no significant change in the distribution of latitude angles for 15 GV and 20 GV particles. Since the measured amplitudes, after temperature correction, are approximately equal within the errors, there is still no major inconsistency with the idea of a primary anisotropy.

The effect of including the non-dipole part of the earth's magnetic field is to bring the asymptotic longitudes for 15 GV and 20 GV closer to one another and this gives better agreement with the measured diurnal variations because the phases, after temperature correction, lie within a range of 20° while the standard deviations are about ± 10° on each measurement.

In order to determine the direction and the mean rigidity of the primary anisotropy, the angle θ of the direction of maximum primary intensity measured eastwards from the sun–earth line was calculated from the equation:

$$\theta = \psi_E + 15°(t_{\max} - 12)$$

where ψ_E is the appropriate longitude angle corrected for non-dipole field effects and $t_{\max}$ is the time of maximum in hours of the diurnal variation when all atmospheric influences have been eliminated. θ is plotted in fig. 7 as a function of the assumed mean rigidity of the primaries for the five telescope directions at Mawson. If the measured diurnal variations were due to a primary anisotropy, all curves should intersect at a point corresponding to the mean rigidity and the direction of the anisotropy. It will be seen from the diagram that all curves tend to converge at a primary rigidity of 10 GV and the curves separate out at higher rigidities. Thus, within the limits of statistical accuracy of the measurements, the results appear to be consistent with a primary anisotropy located roughly 70° due east of the sun–earth line, when the mean rigidity is taken to be about 10–20 GV. It is concluded, therefore, that the Mawson results can be reconciled with the idea of a primary anisotropy lying outside the earth's magnetic field, when the atmospheric influences and the deflecting action of the non-dipole part of the geomagnetic field are taken into account.

§ 5. CONCLUSIONS

Reasons have been given for believing that the corrections for atmospheric temperature effects on daily variation measurements of cosmic-ray intensity have not been evaluated accurately to date. Using purely cosmic-ray measurements, the atmospheric part of the solar diurnal variation has been found for the ionization chamber data from Huancayo.

Fig. 7

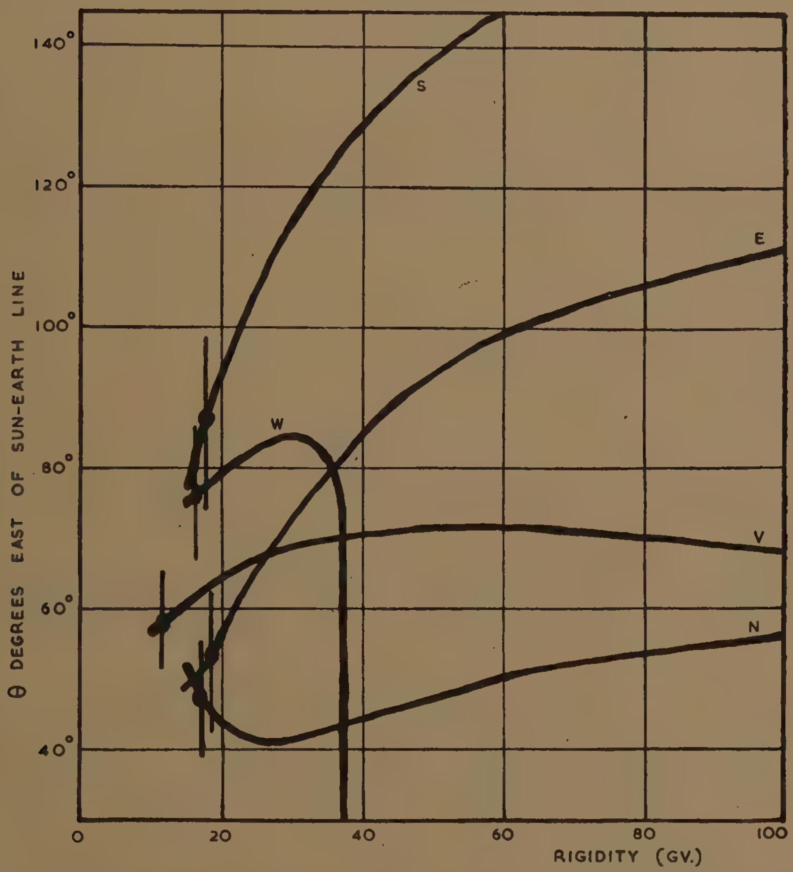

The longitude angle θ between the sun–earth line and the direction of maximum primary intensity outside the geomagnetic field, as given by each telescope at Mawson, plotted against the assumed values for the mean rigidity of the primaries producing the diurnal variation. The standard deviations of θ, which are independent of rigidity, are also shown.

This has an amplitude of 0·11% and a time of maximum around 05–40 hr L.T. Also, using some recent meteorological data, considered to be largely free from insolation errors, the atmospheric contribution has been calculated on the Dorman scheme for a cubical meson telescope operated at sea-level in temperate latitudes. The diurnal component here has an amplitude of about 0·16% and a time of maximum at 05–30 hr during the summer season. Whilst the small difference in the amplitudes given by these two independent derivations is to be expected, the remarkable agreement in phase shows that the diurnal maximum of temperature in the troposphere is reached near 18 hr and not in the early afternoon as indicated by earlier radiosonde measurements. When the latter calculation is compared with an estimate of Dorman for an ionization chamber at sea-level, it appears that the increased amplitude of 0·27% and the advance of phase to 02 hr found by Dorman are probably due to larger insolation errors in the aerological data used.

As an application of the calculated temperature effects, the directional telescope measurements made at Mawson were corrected using the Huancayo temperature vector. These corrected results are consistent with the view that the daily variation arises from a primary anisotropy outside the earth's magnetic field when the deflecting action of the geomagnetic field is taken into account. The results suggest that the primary radiation producing the daily variations possesses a mean rigidity in the range 10–20 GV and that the maximum intensity arrives from a direction 70° due east of the sun–earth line. A more comprehensive treatment of various aspects of the solar daily variation, taking into account the atmospheric effects discussed here, is now in preparation.

ACKNOWLEDGMENTS

We wish to thank Dr. H. Elliot for many valuable discussions and Professor P. Morrison for helpful comments. We are indebted to Mr. G. Wenk for the analysis summarized in fig. 1 and for calculations on the deflecting effects of the non-dipole part of the earth's magnetic field. The latter work by J. J. Quenby and G. Wenk will be published elsewhere.

REFERENCES

BALIGA, S. P., and THAMBYAHPILLAI, T., 1959, *Phil. Mag.*, **4,** 973.
BRASEFIELD, H., 1948, *J. Meteorology, Washington*, **5,** 147.
BRUNBERG, E. A., and DATTNER, A., 1953, *Tellus*, **5,** Nos. 2, 135 and 3, 269; 1954, *Ibid.*, **6,** No. 1, 73.
CONFORTO, A. M., and SIMPSON, J. A., 1957, *Nuovo Cim.*, **5,** 1052.
DORMAN, L. I., 1957, *Cosmic Ray Variations* (Moscow: State Publishing House).
ELLIOT, H., and DOLBEAR, D. W. N., 1951, *J. atmos. terr. Phys.*, **1,** 205.
HARRIS, M. F., 1959, *J. geophys. Res.*, **64,** 983.
KAY, R. H., 1951, *Quart. J. R. met. Soc.*, **77,** 427.
MEADA, K., and WADA, M., 1954, *J. sci. Res. Inst., Tokyo*, **48,** 71.
MALMFORS, K. G., 1949, *Tellus*, **1,** 2.
OLBERT, S., 1953, *Phys. Rev.*, **92,** 454.
PARSONS, N. R., 1957, *Aust. J. Phys.*, **10,** 462.
QUENBY, J. J., and WEBBER, W. R., 1959, *Phil. Mag.*, **4,** 90.
TREFALL, H., 1955, *Proc. phys. Soc. Lond.*, **68,** 625, 893.
VENKATESAN, D., and DATTNER, A., 1959, *Tellus*, **11,** 116.
WEBBER, W. R., and QUENBY, J. J., 1959, *Phil. Mag.*, **4,** 654.

Cosmic-ray Intensity Variations and the Interplanetary Magnetic Field†

By H. ELLIOT
Imperial College of Science and Technology, London

[Received January 25, 1960]

ABSTRACT

It is shown that the general characteristics of the cosmic-ray intensity variations can be explained in terms of a large-scale interplanetary magnetic field of predominantly dipole character but containing small-scale irregularities which act as scattering centres. It is suggested that the cosmic-ray data can be taken as evidence for the existence of such a field. The strength of the field, which is generated by current systems in the solar corona, is dependent on the level of solar activity but must in general be in the region of 10^{-5} to 10^{-4} gauss at the earth's orbit.

§ 1. INTRODUCTION

THE primary cosmic rays show certain characteristic variations in intensity which are rather closely correlated with solar and geomagnetic activity and it is generally believed that this relationship exists because of the modulation of the cosmic-ray flux by changing magnetic, and possibly electric, fields in interplanetary space. The central problem in the study of cosmic-ray intensity variations is that of constructing a detailed picture of these fields from the experimental data available and it is the purpose of this paper to discuss one particular model which appears to fit these data rather well. For any model to be acceptable, the configuration of fields chosen must be capable of explaining the eleven-year variation in cosmic-ray intensity over the sunspot cycle, the Forbush type decrease usually associated with great magnetic storms, the quasi-periodic 27-day variation, and the solar daily variation. Finally, it must be compatible with the propagation characteristics from sun to earth of particles accelerated to cosmic-ray energies in solar flares.

During recent years several models of the interplanetary electric and magnetic fields have been proposed but none has so far proved completely satisfactory. Broadly speaking, these proposals may be divided into two categories; those which depend on randomly orientated fields of a kind generated by the turbulent motion of highly ionized gas (Morrison 1955, Meyer *et al.* 1956, Singer 1957, Parker 1958) and those which depend on rather highly organized and uniform magnetic fields associated with solar streams (e.g. Alfvén 1954, Brunberg and Dattner 1954, Cocconi *et al.* 1957, Dorman 1957). Since these magnetic fields vary with time it follows that there must also be electric fields associated with them and in some models these electric fields play an important, even dominant, role. The possibility of an extensive interplanetary electric field capable of modulating the cosmic ray intensity has recently been discussed by Ehmert (1959).

---

† Communicated by the Author.

The modulating mechanism which will be discussed here has some features in common with these earlier models but differs from them in that it depends primarily on the existence of a general solar magnetic field which extends far out into interplanetary space beyond the earth's orbit and which is essentially non-turbulent. The screening effect of a solar dipole field on the cosmic-ray intensity at the earth was first discussed by Jánossy (1937) many years ago when it was believed that the sun possessed a dipole moment of $\sim 10^{34}$ gauss cm^3, corresponding to a polar field of about 30 gauss. We now know that the solar dipole field, as measured in the photosphere, is much smaller than this (~ 1 gauss at the pole) and that it is variable (Babcock 1959). Such a field would not in itself be capable of producing any appreciable effect on the cosmic-ray intensity at the earth. If, however, large-scale current systems exist in the solar corona the effective dipole moment of the sun may be much greater than would appear from measurements of Zeeman splitting of spectral lines originating in the photosphere. In the present model it is suggested that such currents do exist and that the field they produce is responsible for the cosmic-ray intensity variations. If we are to make a quantitative estimate of the effects of such a field on the cosmic rays, it is necessary to idealize and a close relation between the model and reality must not be expected at this stage.

§ 2. PROPOSED MODEL OF THE SOLAR MAGNETIC FIELD

In attempting to build up a picture of the interplanetary field from the cosmic-ray evidence we must begin with the simplest configuration capable of accounting for the qualitative behaviour of the cosmic rays and then elaborate it to the extent merited by the observational detail available. There are two simple models which lend themselves readily to quantitative treatment. In the first of these it is supposed that the field changes rapidly in intensity and direction as a function of space coordinates. This corresponds physically to a highly turbulent field in which the motion of the cosmic-ray particles can be treated as a diffusion problem without the necessity of any knowledge about details of their trajectories. This model has already been extensively discussed in the references given above.

At the other extreme, we can suppose that the current systems generating the field lie predominantly within the earth's orbit and possess a high degree of axial symmetry about the sun generating a nearly dipole field at points outside the earth's orbit. The motion of cosmic-ray particles in a dipole field is well understood and a quantitative treatment of this model is also possible. Close to the sun the field must be very disturbed and far from regular because of patchy photospheric fields, sunspot fields and the violent hydromagnetic motions of the solar atmosphere close to the surface. The occurrence of magnetic storms can be taken as evidence that these violent disturbances sometimes extend out as far as the earth's orbit and presumably beyond it. For the purpose of calculation we shall divide the solar field schematically into three regions as shown in fig. 1, an inner region in which the field is much disturbed and which is surrounded by another region in which the large scale axially symmetrical currents flow. These currents generate a dipole field which constitutes the third and outer region extending far beyond the earth's orbit. This dipole field will be periodically disturbed by the outward moving solar streams responsible for magnetic disturbances and auroral activity.

Fig. 1

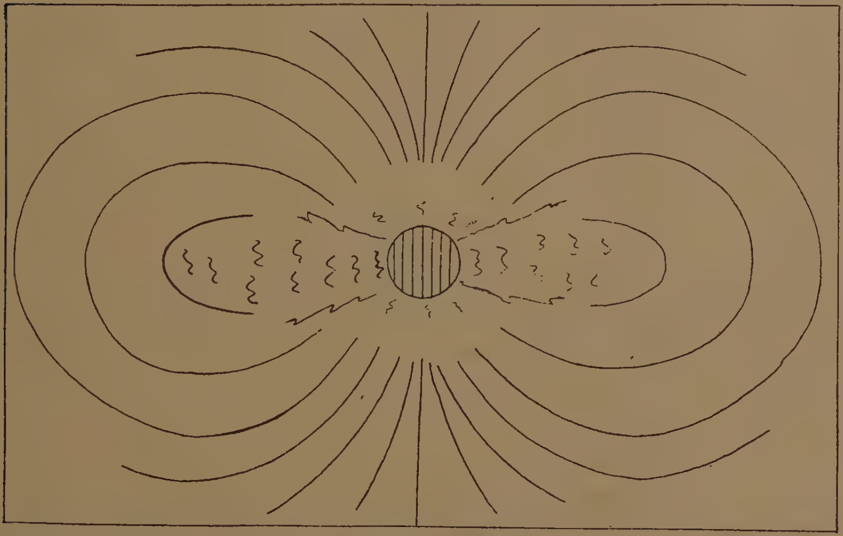

Schematic representation of the magnetic field generated by currents flowing in the solar corona.

§ 3. EFFECT OF THE SOLAR FIELD ON THE COSMIC-RAY INTENSITY

If the field outside the earth's orbit was a completely unperturbed dipole field we should have the familiar allowed and forbidden regions given by the Stormer theory. That is to say, we should have some minimum magnetic rigidity, $p_{\min}$ below which no particle could reach the earth and a maximum $p_{\max}$ above which particles could arrive from all directions. In the intervening range betewen $p_{\min}$ and $p_{\max}$ the arrival of particles would be restricted to certain directions. The values of $p_{\max}$ and $p_{\min}$ are given by

$$p_{\max}=\frac{300\,M_s}{Zr_e^2} \quad \text{and} \quad p_{\min}=(\sqrt{2}-1)^2\frac{300\,M_s}{Zr_e^2} \text{ in GV} \quad . \quad . \quad . \quad (1)$$

where r_e is the radius of the earth's orbit in centimetres (assumed circular), M_s is the dipole moment of the solar current system in gauss cm^3, Z is the particle charge in units of the electron charge e. For a singly charged particle $Z=1$ and the magnetic rigidity in GV is numerically equal to the particle momentum in GeV/c.

In reality the situation is more complicated than this because of the perturbations introduced by outward-moving solar streams. If, as seems likely, these streams can produce gradients in the field of a sufficient magnitude, particles will be scattered into forbidden regions which would otherwise be empty according to the Stormer theory. The requirement for such scattering to be effective is that the field should change by a substantial fraction in a distance corresponding to the radius of curvature of the particle trajectory in the unperturbed field. Alternatively the perturbing field, being time dependent, should change appreciably during the time the particle requires to cross the perturbing region.

Fig. 2

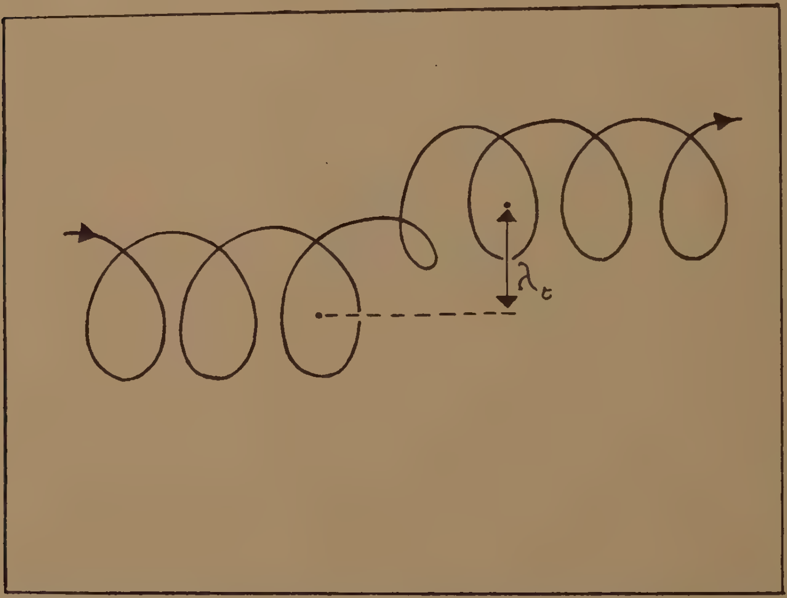

Scattering of cosmic-ray particle by irregularity in dipole field.

§ 4. SCATTERING BY MAGNETIC IRREGULARITIES

Near the equatorial plane of the solar dipole, where scattering by solar streams is most likely to occur, a cosmic-ray particle describes a nearly helical path with its axis perpendicular to the ecliptic plane. If such a particle encounters a sharp gradient in the field the radius of curvature of its trajectory at that point is changed and the particle is scattered into another orbit. As a result, the guiding centre is scattered through some distance λ_t. The projection of the trajectory in the equatorial plane is shown in fig. 2.

A detailed discussion of the scattering process is only possible if we have detailed information about the structure of the scattering region. In the absence of such information we can only make a rough schematic treatment as follows.

We suppose that the field strength in the irregularity is of the same order as that outside and that the physical dimensions of the irregularity are small compared with ρ, the radius of curvature in the unperturbed field. This means that on passing through the irregularity the particle suffers a small angular deflection

$$\theta \sim \frac{300\, B_i l}{p}$$

where B_i is the mean field strength along the particle trajectory in the perturbing field and l is its length.

Then $\lambda_t \sim \theta\rho \sim (B_i/B)\,l$ where B is the local value of the unperturbed field. If we suppose that the perturbing field B_i is linearly related to B, so that $B_i/B = \text{constant}$, it follows that λ_t is independent of particle rigidity and of position. We can then regard the motion of the cosmic-ray particle in the solar dipole field as a combination of that described by Stormer theory and diffusion with a constant transport mean free path given by λ_t above.

In the absence of absorption, the effect of the diffusion would be to fill all the forbidden regions with particles which, by Liouville's theorem, would eventually attain the same intensity as that existing in interstellar space. In fact, as we shall see, absorption by the sun reduces the intensity in the forbidden regions below that existing outside the solar system and an equilibrium intensity is reached which is dependent on the relative rates of diffusion and absorption.

§ 5. ABSORPTION OF COSMIC-RAY PARTICLES BY THE SUN

In order to estimate the extent to which particles are absorbed by the sun during their diffusion inwards we have to take into account the complete field distribution and not merely the dipole part. The simplest assumption we can make about the inner part of the field is to suppose that it is generated by a spherical current shell of radius r_c in which the currents flow along lines of latitude. If the current strength is proportional to $\cos\lambda$, where λ is the latitude, such a current system generates a dipole field outside the shell and a uniform field within it as in fig. 3.

At each scattering collision there is a finite probability that the diffusing particle can be scattered into such a direction that it will travel directly along the field lines into the sun and be absorbed. Thus, in a sense, we may regard the solar absorber as spread throughout the solar system. If the particle is to reach the sun in this way it must be scattered into a small solid angle Ω_A as shown in fig. 3, such that $\Omega_A = 2\pi\,(1-\cos\psi)$ where ψ is given by the 'trapping condition', $\sin^2\psi = B/B_0$. That is to say, a particle with a pitch angle greater than $[(\pi/2)-\psi]$ in the equatorial plane is transmitted at the surface of the sphere radius r_c and may enter the turbulent region and finally strike the sun. A particle with a pitch angle less than $[(\pi/2)-\psi]$, on the other hand, will be reflected before reaching the surface at $r = r_c$.

Thus if the particle is scattered into the solid angle

$$2\Omega_A = 4\pi\{1-\sqrt{(1-B/B_0)}\} \quad . \quad . \quad . \quad . \quad . \quad . \quad . \quad (2)$$

it will enter the turbulent region of the field. This is a necessary, but not sufficient, condition for absorption by the sun since after entering the turbulent region the particle may either strike the sun or be scattered back into the ordered dipole part of the field. If P_a is the probability that a particle entering the disturbed region will strike the sun, it follows that the absorption probability per scattering collision in the outer field is given by

$$P = \frac{2\Omega_A}{4\pi} P_a. \quad . \quad . \quad . \quad . \quad . \quad . \quad . \quad . \quad . \quad (3)$$

The probability of absorption by the sun will, of course, depend on the structure of the field close to the sun and the simplest assumption we can make is that the probability of absorption is proportional to the solid angle subtended by the sun at the point where the particle enters the turbulent region. Thus, in fig. 4, if the point of entry E is distant r' from the centre of the sun we assume that the probability of absorption is

Fig. 3

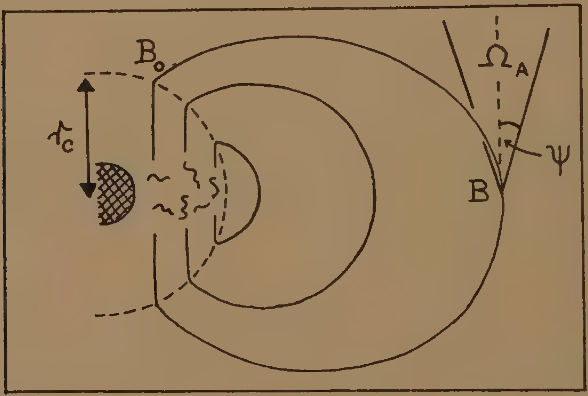

Cosmic-ray particles scattered into the solid angle Ω_A are no longer trapped by the dipole field and may be absorbed by the sun.

$$P_a(r') = \tfrac{1}{2}(1-\cos\beta)P_c \quad \text{where} \quad \cos\beta = \{1-r_s^2/r'^2\}^{1/2}$$

and P_c is the probability of a large angle scattering, i.e.

$$P_a(r') \sim \tfrac{1}{4} P_c \frac{r_s^2}{r'^2}.$$

In general the full area of the sun will not be accessible because of photospheric magnetic fields and because of this the accessible area will be to some extent dependent on particle rigidity. However, here we shall simply take the area to be a constant, A_s, so that

$$P_a(r') \sim P_c \frac{A_s}{r'^2}.$$

We must now relate this absorption probability to a particular line of force in the external dipole field. The dipole line of force which connects to E cuts the equatorial plane at C at a distance

$$r=\frac{r_C}{\cos^2\lambda}=\frac{{r_C}^3}{r'^2}$$

and therefore we can write

$$P_a(r)=P_C\frac{A_S r}{{r_C}^3}.$$

Combining this with the expression for Ω_A, we obtain for the probability of absorption per scattering collision

$$\left.\begin{aligned}&P(r)=\frac{2\Omega_A}{4\pi}P_a(r)=P_C\frac{A_S r}{{r_C}^3}\{1-\sqrt{(1-B/B_0)}\}\\ &\text{i.e.}\quad P(r)\sim P_C\frac{A_s}{2r^2}\quad\text{on putting}\quad B/B_0=\left(\frac{r_C}{r}\right)^3\end{aligned}\right\}\quad .\ .\ .\quad (4)$$

Fig. 4

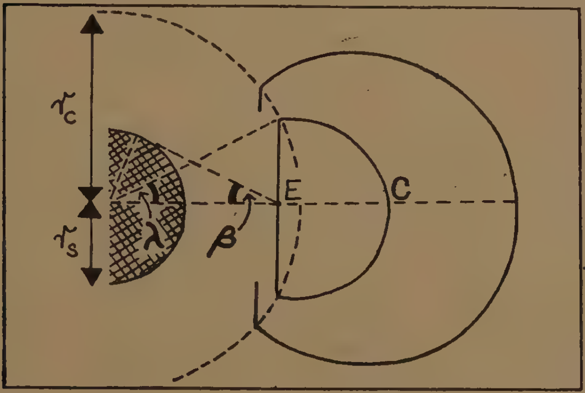

The geometry of the inner field region close to the sun.

§ 6. QUANTITATIVE DISCUSSION OF THE SCREENING BY A SOLAR DIPOLE FIELD

Our problem, then, is to calculate the cosmic ray intensity inside a diffusing medium with a transport mean free path λ_t and a probability of absorption per collision given by P in equation (4). In order to do so we must first define the outer boundary to the diffusing region. If M_S is the magnetic moment of the solar current system and λ the latitude angle measured from the equatorial plane, then according to Stormer theory, on the surface of revolution defined by

$$r=\sqrt{\left(\frac{300\,M_S}{p}\right)}\cdot\frac{\cos^2\lambda}{[1+(1-\cos^3\lambda)^{1/2}]}\quad .\ .\ .\ .\ .\quad (5)$$

particles can arrive from all directions without restriction and on this surface cosmic rays of rigidity p or greater will have the full galactic intensity.

At first sight it might seem that this surface should be taken as the outer boundary of the diffusing region. In fact it is much more realistic to take instead the surface on which particles cannot arrive directly from any direction. Inside this surface particles can only arrive by diffusion whereas, as we shall see in § 9, the flux outside this surface is very closely isotropic and of nearly full galactic intensity.

This surface, S_0, for which direct access is forbidden, is the surface of revolution generated by the curve.

$$r=\sqrt{\left(\frac{300\,M_{\mathrm{S}}}{p}\right)}\cdot\frac{\cos^2\lambda}{[1+(1+\cos^3\lambda)^{1/2}]}.$$

For λ between ± 30° we can take this to be part of the surface of a sphere of radius r_p where r_p is the value of r corresponding to $\lambda=15°$. Then

$$r_p=\sqrt{\left(\frac{45\,M_{\mathrm{S}}}{p}\right)} \quad \ldots \quad (6)$$

and the diffusing region in the dipole field is bounded by the surfaces S_0, S_1, S_2 (fig. 5).

Fig. 5

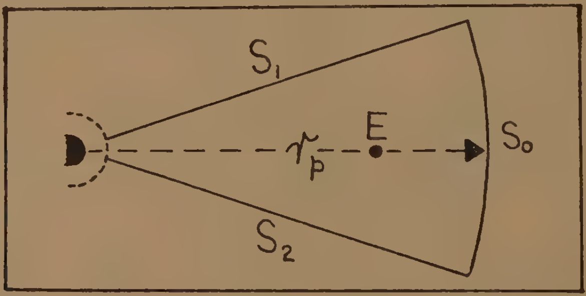

The boundaries of the region in which diffusion occurs.

Provided the absorption probability is small the net flux crossing the surfaces S_1 and S_2, fig. 5, is very nearly zero and consequently we can regard the system as spherically symmetrical so far as E is concerned.

The problem is therefore simplified to that of calculating the intensity distribution inside a diffusing spherical medium of radius $r_p=\sqrt{(45M_{\mathrm{S}}/p)}$ with a transport mean free path $\lambda_t=B_i l/B$ and a probability of absorption per collision $P=P_{\mathrm{C}}(A_{\mathrm{S}}/2r^2)$. If N is the number of scattering collisions per second and n the number of cosmic rays per unit volume, the appropriate diffusion equation is

$$N(\lambda_t^2/3)\,\nabla^2 n(r,p,t)-NP(r)\,n(r,p,t)=\frac{\partial n(r,p,t)}{\partial t}. \quad \ldots \quad (7)$$

We are interested in the stationary solution and we therefore set $\frac{\partial n}{\partial t}=0$ and put ϕ, the differential flux of particles of rigidity p, equal to nv. Then we have

$$(\lambda_t^2/3)\,\nabla^2\phi(r,p)-P(r)\,\phi(r,p)=0 \quad \ldots \quad (8)$$

or

$$\nabla^2\phi(r,p)-K\frac{\phi(r,p)}{r^2}=0 \quad \text{where} \quad K=\frac{3P_{\mathrm{C}}A_{\mathrm{S}}}{2\lambda_t^2}.$$

The solution of this equation is

$$\phi = Ar^{-\frac{1}{2}\{1-\sqrt{(1+4K)}\}} + Br^{-\frac{1}{2}\{1+\sqrt{(1+4K)}\}}$$

but since ϕ must be finite at $r=0$ it follows that $B=0$. Finally using the other boundary condition, $\phi=\phi_\infty$ at $r=r_p$, we obtain

$$\begin{aligned}\phi &= \phi_\infty\left[\frac{r_p}{r}\right]^{\frac{1}{2}\{1-\sqrt{(1+4K)}\}} \\ &= \phi_\infty\left[\frac{\sqrt{(45M_{\mathrm{s}})}}{rp^{1/2}}\right]^{\frac{1}{2}\{1-\sqrt{(1+4K)}\}} \qquad . \quad . \quad . \quad . \quad . \quad . \quad (9)\end{aligned}$$

The intensity at the earth is therefore given by

$$\phi_E = \phi_\infty\left[\frac{\sqrt{(45M_{\mathrm{s}})}}{r_{\mathrm{e}}p^{1/2}}\right]^{\frac{1}{2}\{1-\sqrt{(1+4K)}\}} \qquad . \quad . \quad . \quad . \quad . \quad . \quad (10)$$

where $r_{\mathrm{e}} = 1{\cdot}5\times10^{13}$ cm and $r_{\mathrm{e}}^2p \leqslant 45\,M_{\mathrm{s}}$.

In the calculation so far, we have taken λ_{t} to be constant but this cannot be so at low values of p when the scattering angle, θ approaches $\pi/2$. Under these circumstances, that is to say for large θ, $\lambda_{\mathrm{t}} \to \rho$. We can take this into account approximately by writing

$$\lambda'_t = \lambda_t\frac{p}{p_0+p} \quad \text{where} \quad \lambda_t = \frac{B_i l}{B} \quad \text{and} \quad p_0 = 300\,B_i l.$$

This gives λ'_{t} constant and equal to $B_i l/B$ at large values of p and $\lambda'_{\mathrm{t}} = \rho$ at $p \ll p_0$. Consequently in (10) we can replace K by

$$K' = \frac{3P_{\mathrm{c}}A_{\mathrm{s}}}{2}\frac{(p_0+p)^2}{\lambda_{\mathrm{t}}^2p^2} = K\left[\frac{p_0+p}{p}\right]^2$$

giving

$$\phi_E = \phi_\infty\left[\frac{\sqrt{(45\,M_{\mathrm{s}})}}{r_{\mathrm{e}}\,p^{1/2}}\right]^{\frac{1}{2}\{1-\sqrt{(1+4K[(p_0+p)/p]^2)}\}} \qquad . \quad . \quad . \quad (11)$$

§ 7. THE 11-YEAR VARIATION IN INTENSITY

Equation (11) gives the steady-state cosmic-ray flux at the earth in terms of the galactic flux ϕ_∞, as a function of magnetic rigidity p. It seems likely that M_{S} will vary over the solar cycle and so will the probability of capture by the sun, P, because of its dependence on Ω_A (eqn. (3)). In deducing the value of Ω_A used above we have assumed a strictly dipole field and therefore a particular relationship between B and B_0 (eqn. (2)). At the time of a major solar disturbance, however, this field must be seriously distorted by current systems associated with the outward moving solar material, indeed it has been suggested by Cocconi *et al.* (1957) that at such a time there may be a radial magnetic field connecting the earth and sun. In this extreme case, or for any increase in field strength in the region of solar emission between $\lambda = \pm 30°$, the ratio B/B_0 is increased and so is the value of Ω_A. It follows from (3) that P is also increased and consequently at sunspot maximum, when the frequency of large disturbances is greatest, the average value of K must be greater than that appropriate to a dipole field becoming say αK, where α is a numerical factor greater than 1. According to the present model it is this increase in both K and M_S with increasing solar activity which is responsible for the reduction in intensity of low-energy cosmic rays. The most convenient way of relating the predictions of the model to experimental observations is to compare the predicted variation of the ratio ϕ_E/ϕ_∞ with rigidity to that actually observed.

The differential rigidity spectrum at the earth, $\phi_E(p)$, can be measured at any particular time during the solar cycle but since we do not know $\phi_\infty(p)$, the galactic spectrum, we cannot deduce the radio $\phi_E(p)/\phi_\infty(p)$ directly from observation. There are however, two alternative plausible assumptions we can make which enable us to make a rough comparison between theory and observation. We can suppose that at sunspot minimum $K \sim 0$ in which case the galactic spectrum is simply the differential spectrum observed at the earth at that time. Alternatively, we can suppose that the galactic spectrum follows the same power law as that observed at the earth for high rigidity particles which are not affected by the solar modulation process.

Fig. 6

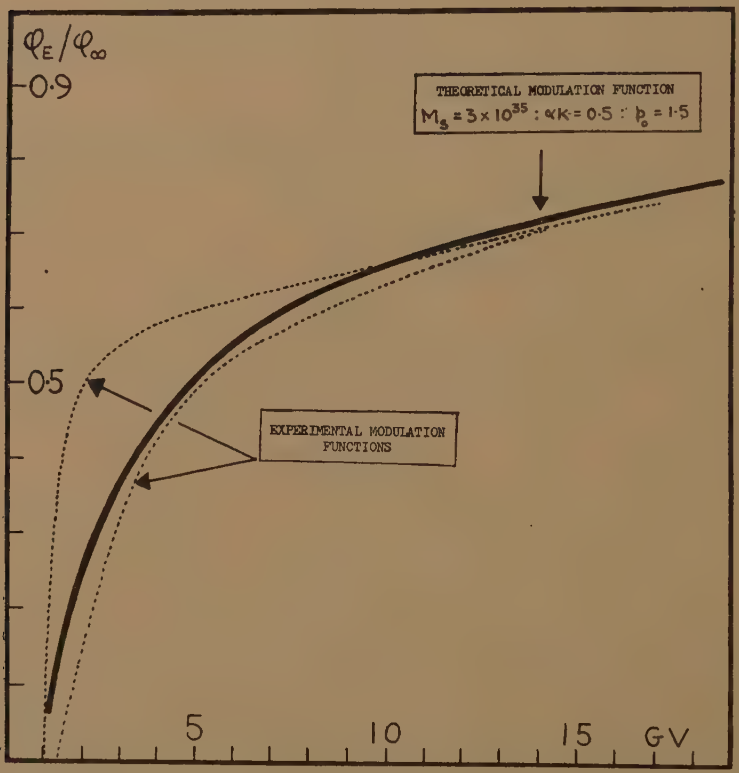

Comparison between calculated rigidity dependence of the 11-year variation and that deduced from observation.

The function $[1-\phi_E/\phi_\infty]$ deduced from experimental observations for each of these two assumptions (Elliot *et al.* 1959) is shown in fig. 6 together with that calculated for $M_s = 3\times10^{35}$, $\alpha K = 0{\cdot}5$ and $p_0 = 1{\cdot}5$ GV. It will be seen that there is reasonable agreement between theory and observation for these values of the three parameters. Using these values of αK and M and p_0 we can, with the aid of the differential response functions obtained by Webber and Quenby (1959), deduce the ratio of the change in intensity over the solar cycle for the nucleonic component and for the μ-meson intensity recorded at sea level. The calculated ratio of 3 is in rough agreement with the observed value of ~ 4 at Ottawa (Fenton *et al.* 1958).

Fig. 7

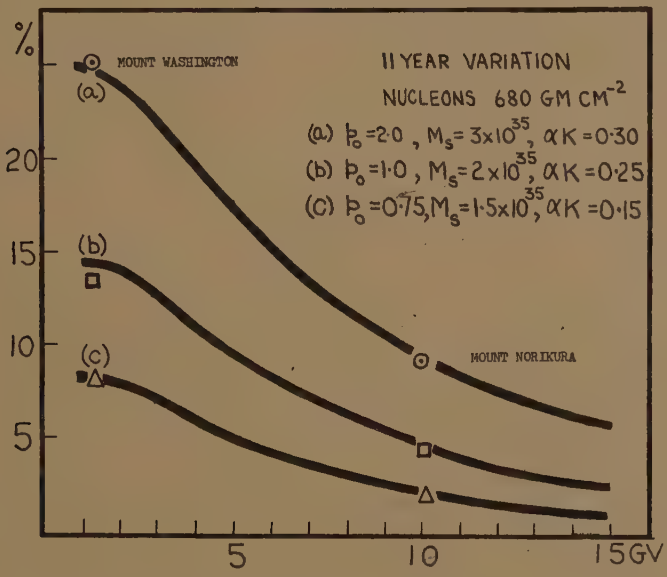

Comparison between calculated and observed rigidity dependence of the 11-year variation for nucleons at mountain altitudes.

A more detailed comparison between theory and observation is shown in fig. 7, where the calculated dependence of the long-term intensity variation on station cut-off rigidity is shown together with the observed changes at mountain stations for three different epochs of the solar cyle. It will be seen that the theoretical curves fit the data quite well provided we assume a systematic decrease in M_s, αK and p_0 with decreasing solar activity. In this calculation it has been assumed that the galactic spectrum is the same as that observed at the earth at sunspot minimum.

§ 8. Forbush-type Intensity Decreases

At the time of a great magnetic storm it frequently happens that the cosmic-ray intensity at sea level drops sharply by from 5 to 10% and then slowly recovers, over a period of several days, back to the pre-storm value.

According to the present model these Forbush decreases are closely connected with the 11-year cycle in intensity and are observed when the earth lies directly in the path of the outward-streaming material emitted by an active region on the sun. If we suppose that this solar material to some extent carries the field with it then the trapped cosmic-ray particles spiralling round the field lines must be convected outwards at the same time. It follows that on such occasions an observer at the earth will sample a subnormal cosmic-ray flux characteristic of that existing under normal conditions, at some point lying nearer to the sun. Alternatively, if we regard the outward motion of the solar gas as leading to an increased field strength in the region through which it passes illustrated in fig. 8, it follows that because grad (B) now has a tangential component, the cosmic-ray particles trapped in the field will tend to drift round the region of higher field, producing the same result, a decrease in intensity.

Fig. 8

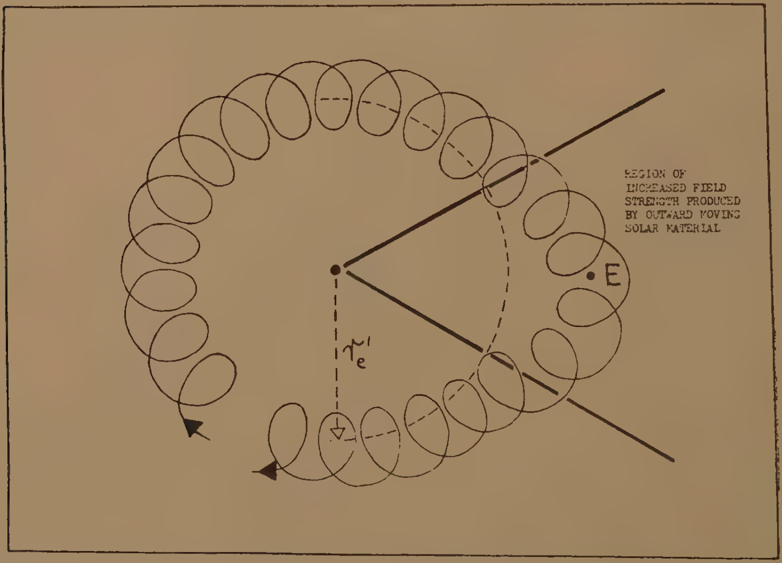

The outward convection of trapped cosmic radiation at the time of a Forbush decrease.

This will not be the only effect however. An increase in the field strength near the ecliptic plane will also lead to a greater probability of particles being absorbed by the sun. This arises from the increase in the ratio B/B_0, and therefore in Ω_A, compared with that for the unperturbed dipole field. As pointed out in the previous section, the superposition of many such events will be contributory towards the reduction in cosmic-ray intensity at sunspot maximum. Because of the time scales involved, however, this change in absorption probability is not very important in discussing the Forbush decrease and will be ignored in the following treatment.

We can obtain a rough idea of the form of the primary rigidity spectrum during a Forbush event in the following way. According to fig. 8, during the period of reduced intensity the cosmic rays received at the earth in the rigidity range $p \leqslant (45 M_S/r_e^2)$ will be those normally trapped in orbits which do not extend out beyond some distance r_e' from the sun. This distance r_e' will be related to r_e in some rather complicated way, which we shall not attempt to deduce here, by the magnitude of the perturbing field.

Fig. 9

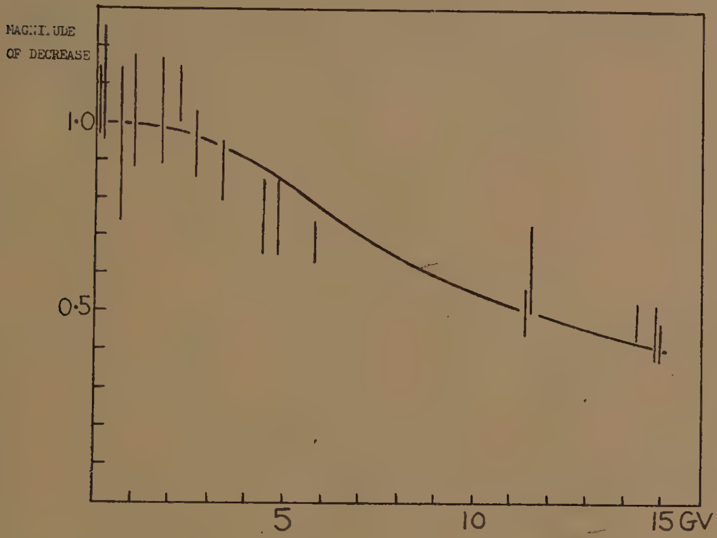

Comparison between observed and calculated change in intensity of the nucleonic component at sea level during the Forbush decrease of March 25/26, 1958. The intensity changes have been normalized to the value 1·0 at high latitudes.

It is sufficient for the present, to point out that at the time of the Forbush decrease we should observe a spectrum of the form

$$\phi_E'(p) = \phi_\infty(p)\left[\frac{\sqrt{(45\,M_S)}}{r_e'\,p^{1/2}}\right]^{\frac{1}{2}\{1-\sqrt{(1+4\alpha K[(p_0' \div p)/p]^2)}\}} \quad . \quad . \quad (12)$$

where r_e and p_0 have been replaced by r_e' and p_0', and p_0' is greater than p_0 because of the greater value of the field at r_e'. In fact $p_0' = p_0\,(r_e/r_e')^3$, and if we take $r_e/r_e' = 1{\cdot}22$, a value which gives a decrease in intensity of 5·8% in the nucleonic component at sea level at high latitudes, we find $p_0' = 3{\cdot}7$ GV. Using these values for r_e' and p_0' and taking $\alpha K = 0{\cdot}3$ and $M_S = 10^{35}$, we can calculate $\phi_E'(p)$ and the function $[1-\phi_E'(p)]$. Using this, together with the appropriate differential response functions, we can calculate the corresponding change in the μ-meson component which turns out to be 2·65%. The ratio of 2·2 between the changes in the nucleonic and meson components agrees well with the mean value of about 2·3 obtained by Fenton *et al.* (1958) for the Resolute and Ottawa stations in 1957. The change in intensity of the nucleonic component at sea level has also been calculated as a function of station magnetic cut-off rigidity using eqns. (12). The calculated dependence is shown in fig. 9 together with the observed latitude dependence for the Forbush decrease of March 25/26, 1958. Again the agreement is satisfactory.

§ 9. THE SOLAR DAILY VARIATION

In the discussion so far we have assumed the cosmic-ray flux at the earth to be isotropic at all rigidities, but in fact a large-scale solar dipole field of the kind discussed above leads to a small anisotropy which would appear as a solar daily variation in intensity. This anisotropy arises in the following way.

Fig. 10

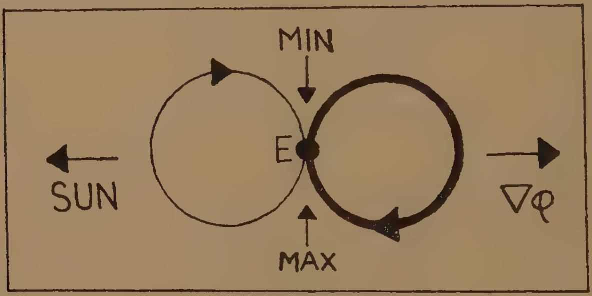

Anisotropy due to the gradient in the cosmic-ray flux.

In a uniform magnetic field in which there exists a gradient in the particle number density the flux at a point E will be anisotropic as shown in fig. 10. The fractional magnitude of the anisotropy is given by $\delta = 2\rho\,(\mathrm{grad}\,\phi)/\phi$ and an observer rotating with the earth at E and receiving radiation from directions close to the ecliptic plane would measure a sinusoidol variation in intensity with amplitude $\delta/2 = \rho\,(\mathrm{grad}\,\phi)/\phi$.

From (12) we have

$$\delta/2 = -\frac{p r_e^2}{600\,M_s}\left[1 - \sqrt{\left(1 + 4K\alpha\left\{\frac{p_0 + p}{p}\right\}^2\right)}\right].$$

Taking representative values for the three parameters $M_s = 2 \times 10^{35}$, $\alpha K = 0{\cdot}25$ and $p_0 = 1$, we can calculate $\delta/2$ as a function of p and this is shown in fig. 11 for $1 < p < 20$ GV. This calculation is valid in so far as the motion of the cosmic ray particles can be treated as a diffusion problem but it certainly breaks down for $p > 30$ GV where ρ becomes comparable with the barrier thickness. For values of $p > 48$ GV, however, we can obtain a rough estimate of the degree of anisotropy in the following way.

If the solar field was strictly dipolar in character, particles with rigidity less than

$$p_{\min} = (\sqrt{2}-1)^2 \frac{300\,M_s}{Zr_e^2}$$

could only reach the earth as a result of scattering, whereas those with rigidity greater than

$$p_{\max} = \frac{300\,M_s}{Zr_e^2}$$

could arrive freely from all directions. In the range between $p_{\min}$ and $p_{\max}$ singly charged particles could only arrive from directions lying outside a cone of semi-angle γ given by

$$\cos\gamma = 2\sqrt{\left(\frac{300\,M_s}{pr_e^2}\right)} - \frac{300\,M_s}{pr_e^2} \quad . \quad . \quad . \quad . \quad . \quad (13)$$

and with its axis in the plane of the ecliptic and perpendicular to the sun–earth line (fig. 12).

Fig. 11

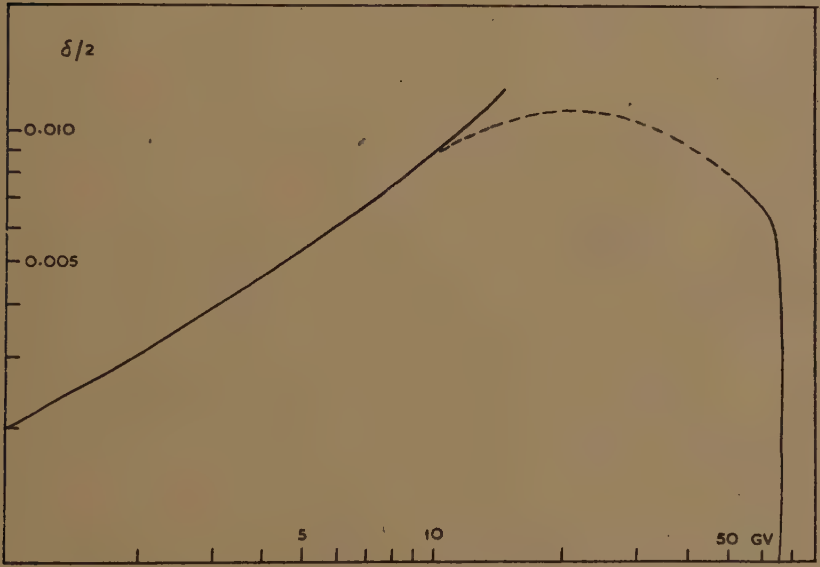

The calculated rigidity dependence of the solar daily variation.

For $M_s = 2{\cdot}0 \times 10^{35}$, $p_{\min} = 4{\cdot}6 \times 10^{10}$ and $p_{\max} = 2{\cdot}7 \times 10^{11}$ so that for this value of M_s we might expect particles in this rigidity range to be anisotropically incident on the earth. Maximum contribution to the daily intensity variation would be expected from those particles for which γ lies between about 45° and 135°, that is to say from particles with $48\,\text{GV} < p < 112\,\text{GV}$. Taking the direction of the solar dipole to be in the same sense as that of the earth and neglecting the deflection in the earth's magnetic field, maximum intensity would occur at 18 hours local time and minimum intensity at 06 hours. Primary particles in the rigidity range 48 to 112 GV produce about 20% of the μ-meson flux at sea level and if the solar field was entirely dipolar in character we should expect a large daily variation with an amplitude $\sim 10\%$. Because of scattering, however, the forbidden directions will to a large extent be filled with trapped particles and the magnitude of the anisotropy much reduced (Alfvén (1947), Kane *et al.* (1949), Treiman (1954)). The intensity in the forbidden directions will be determined by the probability of absorption by the sun and can be estimated very roughly as follows.

Fig. 12

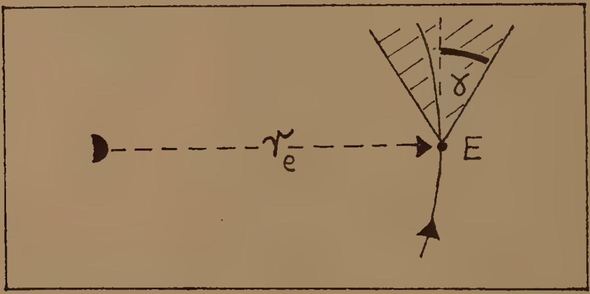

The Stormer forbidden cone at the earth due to the dipole field.

In order that a particle in the momentum range we are considering shall be transferred from an allowed into a forbidden direction it has to be scattered through an angle comparable to γ given by (13). This angular deflection will be made up for a number n, of small deviations $\theta = 300 B_i l/p$ such that

$$\cos^{-1}\left\{2\sqrt{\left(\frac{300\,M_S}{pr_e^2}\right)}-\frac{300\,M_S}{pr_e^2}\right\}=n^{1/2}\,\frac{300\,B_i l}{p}.$$

From eqn. (4) and § 7 the probability of absorption per collision, P is given by $P = P_c\,(A_S\alpha/2r_e^2)$, and taking

$$\alpha K=\frac{3P_c A_S\alpha}{2l^2}\left(\frac{B}{B_i}\right)^2=0{\cdot}25,$$

as indicated by the 11-year variation, we find

$$P=\left(\frac{B_i}{B}\right)^2\frac{l^2}{12r_e^2}.$$

The intensity in the forbidden direction at the earth, ϕ_F, is therefore given by

$$\phi_F=\phi_\infty\left(1-\frac{p^2}{12(300Br_e)^2}\left[\cos^{-1}\left\{2\sqrt{\left(\frac{300\,M_S}{pr_e^2}\right)}-\frac{300M_S}{pr_e^2}\right\}\right]^2\right). \qquad (15)$$

Putting in the value of B at the earth's orbit appropriate to $M_S = 2\times 10^{35}$ and taking $p = 5\times 10^{10}$ for instance, we obtain $(\phi_\infty - \phi_F)/\phi_\infty = 0{\cdot}016$, indicating that for this rigidity the intensity in the forbidden directions is only 1·6% less than that in the allowed directions. At $p > 67$ GV the forbidden cone has a half angle, γ, less than $\pi/2$ and in consequence can be filled to the full galactic intensity because particles can be scattered into it with a negligible probability that they will strike the sun in the process. It follows that the magnitude of the anisotropy, $\delta/2$, in primary intensity must fall from $\sim 0{\cdot}8\%$ at 50 GV to zero at $p = 67$ GV as shown in fig. 11.

In the intervening region between 20 GV and 48 GV the extent of the anisotropy is very uncertain but it seems not unreasonable to join the two branches of the curve smoothly together by the dashed line in fig. 11. Any attempt to calculate the magnitude of δ for this part of the spectrum requires a more detailed specification of the field than has been given so far and it seems likely that it is just this dependence on detail which is responsible for the great variability of the daily variation.

If, however, for the present, we accept the curve in fig. 11 as giving an approximate estimate of the degree of anisotropy for particle trajectories which lie in or near the plane of the ecliptic, we can use it to calculate the expected diurnal variation in intensity of the primary particles. In doing so we must take account of the deflection of the primary particles by the earth's magnetic field (Brunberg and Dattner 1953)). Finally, using the appropriate differential response curves (Webber and Quenby 1959), the variation of primary particle intensity can be converted into the corresponding variation for a particular component of the secondary radiation.

A calculation of this kind leads to an expected amplitude of $\sim 0{\cdot}43\%$ for the nucleonic component at Huancayo with maximum intensity occurring at 13.30 hours local time. These values are in reasonable agreement with the experimentally observed amplitude of the nucleonic variation at Huancayo of 0·3% and the time of maximum at 12.15 hours (de Moura *et al.* 1959, private communication). This calculation of the daily variation to be expected from the solar field is in the nature of a preliminary estimate but it serves to show that there is no gross inconsistency between the observed daily variation and that expected on the basis of the present model.

§ 10. THE PROPAGATION TO THE EARTH OF PARTICLES ACCELERATED IN SOLAR FLARES

It is well known that occasionally particles with energies of a few GeV can reach the earth from a solar flare and that in the early stages they do so in well defined impact zones. These impact zones soon disappear, however, leaving a slowly decaying flux of solar particles which is isotropic to a high degree. Cocconi *et al.* (1957) have shown that it is possible to account for this sequence of events if the photospheric magnetic fields can be extended by outward moving solar material into the form of long tongues which trap the solar particles and guide them to the earth.

In § 8 we have seen that distortion of the general field by outward-moving solar material can account for the Forbush decrease. In an extreme case the general field may well be dragged out into a tongue with the same capabilities of guidance and storage as those envisaged in the model proposed by Cocconi *et al.* If we accept their picture we must conclude that the present model is in no way incompatible with the propagation characteristics for solar flare particles.

§ 11. SUMMARY

It appears from the calculations given above that the general characteristics of the cosmic-ray intensity modulation process can be explained in terms of a large-scale solar field of predominantly dipole character which contains small-scale irregularities acting as scattering centres and which is occasionally very seriously distorted by outward-moving solar material. In particular this model appears to be capable of giving a semi-quantitative account of the 11-year variation, the Forbush-type decrease and the solar daily variation. The 27-day intensity variation appears to be basically the same phenomenon as the Forbush decrease (Van Heerden and Thambyahpillai 1955) and consequently does not require separate treatment.

In fitting the field model to the experimental data on the 11-year cycle three adjustable parameters have been used. The first of these M_S, determines the strength of the field, assumed to be predominantly dipole, whilst the second, αK, is a measure of the probability of absorption by the sun of particles diffusing through the dipole field. The values of M_S lie in the range 1 to 3×10^{35} gauss cm^3 and those of αK in the range 0·15 to 0·30. The third parameter, p_0 is related to the size and field strength of the scattering irregularities by the equation $p_0 = 300\, B_i l$, and if we take $B_i \sim (M_S/r_e^3)$ and $p_0 \sim 1$ GV, as indicated by the cosmic-ray data, we find $l \sim 10^{11}$ cm near the earth. No particular care has been taken in the present paper to fit the experimental data with great accuracy but it would appear that if we are to attempt a more detailed description of the interplanetary field on the basis of cosmic-ray data we shall need greater observational accuracy on the primary spectrum variations than at present exists. If however, as suggested here, there exists a dipole like field with a strength of 3 to 8×10^{-5} gauss at the earth's orbit its detection by space probe magnetometer measurements cannot be long delayed.

ACKNOWLEDGMENTS

I am indebted to my colleagues at Imperial College and particularly to Professor P. Morrison, Dr. J. J. Quenby and Dr. W. R. Webber for many helpful and stimulating discussions on this subject.

REFERENCES

ALFVEN, H., 1947, *Phys. Rev.*, **72,** 88; 1954, *Tellus*, **6,** 232.
BABCOCK, H. D., 1959, *Astrophys. J.*, **130,** 364.
BRUNBERG, E. A., and DATTNER, A., 1953, *Tellus*, **5,** 135, 269; 1954, *Ibid.*, **6,** 73.

Cocconi, G., Gold, T., Greisen, K., Hayakawa, S., and Morrison, P., 1957, I.U.P.A.P. Cosmic Ray Conference, Varenna.

Ehmert, A., 1959, I.U.P.A.P. Cosmic Ray Conference, Moscow.

Elliot, H., Hynds, R. J., Quenby, J. J., and Wenk, G., 1959, I.U.P.A.P. Cosmic Ray Conference, Moscow.

Fenton, A. G., Fenton, K. B., and Rose, D. C., 1958, *Canad. J. Phys.*, **36,** 824.

Janossy, L., 1937, *Z. Phys.*, **104,** 430.

Kane, E. O., Shanley, T. J. B., and Wheeler, J. A., 1949, *Rev. mod. Phys.*, **21,** 51.

Morrison, P., 1955, Proceedings of the I.U.P.A.P. Cosmic Ray Conference, Guanajuato.

Parker, E. N., 1958, *Phys. Rev.*, **110,** 1445.

Singer, S. F., 1957, I.U.P.A.P. Cosmic Ray Conference, Varenna, *Nuovo Cim.*, **5,** Suppl., 11.

Treiman, S. B., 1954, *Phys. Rev.*, **93,** 544.

Webber, W. R., and Quenby, J. J., 1959, *Phil. Mag.*, **4,** 654.

Electron-microscopic Observations on Radiation Damage in Graphite†

By W. BOLLMANN
Battelle Memorial Institute, Geneva, Switzerland

[Received February 4, 1960]

ABSTRACT

Transmission electron microscopy has been applied to the study of lattice defects introduced by neutron irradiation of graphite. The dark-field technique has proved to be especially useful for this purpose. The technique of preparation is described and a tentative interpretation of the observations is given.

§ 1. INTRODUCTION

A GREAT deal of research work has been done on radiation damage in graphite, and this has been reviewed up to 1956 in various papers presented to the "First Conference on Peaceful Uses of Atomic Energy" (1956). An important problem is the mechanism of energy storage. The research work presented here, which is a part of a more extended research programme, has been undertaken with the aim of studying, by means of transmission electron microscopy, lattice defects introduced by neutron irradiation.

§ 2. TECHNIQUES

For the preparation of the microscope specimens, graphite scrapings, suspended in a water–alcohol mixture, were collected with a normal 200-mesh copper grid, which was covered by a collodion foil full of holes of about 1 μ diameter. Thus, thin graphite flakes could be placed over such holes without being backed by amorphous carbon from the collodion support. Another technique was similar to that used in taking a replica : a Triafol (acetobutyrate) foil wetted, and on its surface dissolved by acetone, was pressed on to a piece of graphite. After the foil had dried on the graphite, small particles stuck to it. A small piece of the Triafol was placed on the copper–collodion grid in a Soxhlet where the Triafol was dissolved in acetone. By this method very thin specimens could be obtained. A 'dry' method was used by dusting the graphite on to a sticky copper grid (the sticky grid was prepared by dipping a normal grid into a dilute benzene solution of 'Scotch-tape' cement). In this case the graphite flakes stuck out in all directions and very thin foils which are the most interesting ones, were found to be folded. The observations were made in a Siemens Elmiskop I at 80 kv.

---

† Communicated by the Author.

The pictures are taken in dark-field illumination in the 'light' of $10\bar{1}0$ reflections selected by the aperture diaphragm, the illumination system being tilted to allow the selected beam to pass through the centre of the lenses, so that the full resolution of the microscope could be obtained. Dark-field, as compared with bright-field, has the advantage of much higher contrast because practically only those electrons which are diffracted contribute to the image, and the undeviated or diffusely scattered electrons are eliminated. Thus the influence on the image of the amorphous contamination caused by oil vapours is greatly reduced. In addition, only a small group from all the diffraction spots is selected, giving detailed information about a small component of the whole specimen. From a stack of layer-packets rotated with respect to each other, particular ones can be selected by this method. A comparison of fig. 4† and fig. 5 shows the difference in information obtained from the same area by dark-field and by bright-field illumination. In the case of the bright-field picture, none of the fine details of radiation damage can be seen. It is thought that for other applications also, dark-field transmission electron microscopy will markedly increase the amount of information obtainable, compared with the usual bright-field method. It is noteworthy, however, that even if only a part of a stack of graphite layers becomes visible by diffraction, the remainder of the material can have a harmful influence because of inelastic scattering, which introduces a chromatic error, with the effect of fading out fine details. The difference in concentration of fine details between the centre and the top of fig. 1 can be attributed to this effect. Normally, complicated moiré fringe systems are observed owing to relative rotation of superposed groups of graphite layers. The specimen has to be scanned in dark-field to choose areas with especially widely spaced moiré fringes, i.e. especially small rotation of superposed layers. The spacing of the fringe in fig. 1 corresponds to a rotation angle of 16·7′.

§ 3. Results and Discussion

The graphite studied was grade A reactor graphite irradiated by 10^{20} n/cm^2 at about 30°c. Figures 1 and 2 show the situation as it was observed in this material. Black and white dots with diameters ranging from 10 to 100 Å are visible. In another specimen of the same material small black and white loops can also be seen (fig. 3). Unirradiated graphite showed none of these dots: in this case only smooth moiré fringe systems were visible. Graphite which had been irradiated by 10^{17} n/cm^2 showed the same type of dots but at a much lower density.

To study the effects of annealing, specimens were examined of irradiated graphite (10^{20} n/cm^2), heated in vacuum for 3 hours to different temperatures, i.e. 200°, 400°, 1000°, 2200°c. The strongest annealing effect is to be expected around 200°c as the differential energy release there is a maximum (Woods *et al.* 1956). Figure 4 shows a specimen heated to 400°c. Both a certain coarsening of the loops and a decrease of the dimensions of the white and black dots are observed. In addition certain lines appear, which might be dislocations. Black and white dots were also observed in a specimen annealed at 1000°c but a specimen heated to 2200°c showed the same appearance as unirradiated material. The parallel annealing experiments of unirradiated graphite showed none of these features.

---

† All figures are shown as plates.

To obtain complete understanding of the nature of these dots, the contrast due to electron diffraction effects will have to be studied in detail. Tilting experiments have shown that the appearance of the dots can change from white to black and vice versa. The loops are reminiscent of those observed by Hirsch *et al.* (1958) in quenched aluminium, which are formed by vacancy clusters. Thus, as a tentative explanation, we suggest that the observed defects might be extrinsic and intrinsic stacking faults or groups of these corresponding to interstitial and vacancy clusters.

The difficulty in estimating the density of the dots lies in the fact that the thickness of the layer is not known. To produce the picture, fig. 1, at least three to five monatomic layers of graphite are needed, but probably there are more of them. If we suppose about 10 layers, 10^{20} n/cm^2, and a mean free path of the neutrons of about 3 cm, we observe about 5 to 10 times fewer dots than expected neutron impacts. Thus, the dots could originate from individual neutron impacts, if only the high-energy neutrons produce a visible effect. This does not mean that the dot should be at the place where the impact actually occurred, because it could mark the end of the path of an atom which has been hit, unless further rearrangement and annealing happened in the time between irradiation and observation.

Some of the properties of irradiated graphite, e.g. x-ray line broadening and differential energy release at 200°c, show a significant change for a dose of about 4 to 6×10^{20} n/cm^2 (Woods *et al.* 1956). At higher doses the x-ray lines broaden very strongly and the energy release on annealing is more and more displaced to higher temperatures at the expense of the release at 200°c. Looking at fig. 1 and considering a 6-times higher dose it becomes obvious that a significant part of the graphite lattice must be disturbed, or even destroyed, which would be compatible with the x-ray line broadening. So, the change from the low dose annealing, happening essentially at around 200°c to the high dose annealing which is displaced to higher temperature might correspond to the change from repairing an existing crystal lattice to nucleating a new one.

ACKNOWLEDGMENTS

The author wishes to thank Drs. P. B. Hirsch, J. Spreadborough, and G. Baroody for very helpful discussions, Miss R. Kollrack for the preparation of the specimens and for partly developing the preparative technique, and AGIP Nucleare, Milan, for financing the research and for permission to publish this paper.

REFERENCES

HIRSCH, P. B., SILCOX, J., SMALLMAN, R. E., and WESTMACOTT, K. H., 1958, *Phil. Mag.*, **3**, 897.
Peaceful Uses of Atomic Energy, Vol. 7, 1956 (New York : United Nations).
WOODS, W. K., BUPP, L. P., and FLETCHER, J. F., 1956, *Peaceful Uses of Atomic Energy*, Vol. 7 (New York : United Nations), p. 455.

Cross-tie Walls in Thin Permalloy Films†

By M. PRUTTON
International Computers and Tabulators Ltd., Research and Design Division,
Gunnels Wood Road, Stevenage, Herts

[Received February 15, 1960]

ABSTRACT

A solution of the non-linear differential equations of a domain boundary is reported for the case of a thin film in which the demagnetizing energy associated with the magnetization at right angles to the plane of the film is included. The solution leads to a proposal for the internal structure of the cross-tie wall which has been observed in thin films of permalloy. The effects of the magnetic poles in this model of a cross-tie wall are discussed and compared with observations. The energy density of the wall is suggested to be about 10 ergs/cm² and the correlation between cross-tie spacing and length is derived.

§ 1. INTRODUCTION

IN order to understand coercivity effects in thin films when the reversal process is one of domain wall motion it is important to have detailed knowledge of the energies of the domain boundaries. Néel (1955) has described how the energy associated with a Bloch wall rises as the thickness of a film decreases because of the increasing magnetostatic contribution to the wall energy arising from the poles on the surface of the film. When this magnetostatic energy becomes sufficiently great it is energetically favourable for the magnetization M in the boundary region to rotate in the plane of the film. Such a wall is known as a Néel wall and in permalloy films of zero magnetocrystalline anisotropy and induced uniaxial anisotropy of 1500 ergs/cm³ it occurs below a thickness of about 300 Å and decreases in energy with decreasing film thickness. Further, the Néel wall is much thicker than a Bloch wall for the same film thickness because of the low value of the induced anisotropy which provides the force tending to restrict the wall thickness.

Huber *et al.* (1958) have observed a 'cross-tie' structure domain wall in thin films of permalloy and have proposed a model for the magnetization distribution within the wall. Figure 1 is reproduced from their paper and it shows how their model includes both Néel and Bloch like segments.

---

† Communicated by the Author.

The object of this paper is to describe some calculations made to try to derive a cross-tie wall from a perfectly general set of equations for a domain wall.

Fig. 1

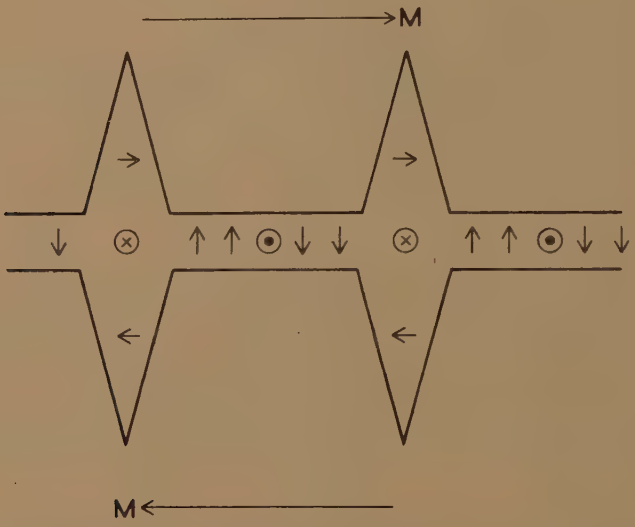

Huber, Smith and Goodenough's model for the cross-tie wall.

§ 2. SOLUTION OF THE WALL EQUATIONS

By describing the behaviours of the amplitude-constant magnetization vector **M** with two angles (θ, ϕ) defined in fig. 2 and in the presence of a

Fig. 2

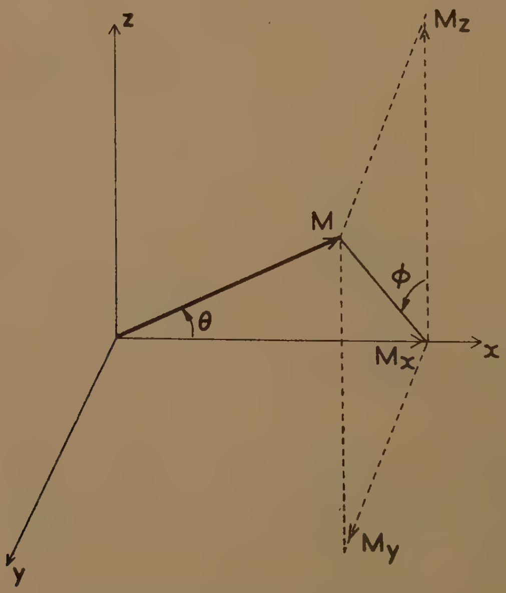

The definition of coordinate angles.

general anisotropy, $K(\theta, \phi)$ which can be chosen to include magnetostatic, magnetoelastic and magnetocrystalline terms Harrington (1958) has shown that the conditions to be satisfied by a static boundary in the absence of an applied field and in a material with exchange constant A are

$$2A\nabla^2\theta = 2A\sin\theta\cos\theta(\nabla\phi)^2 + \partial K/\partial\theta, \quad \quad (1)$$

$$2A\sin^2\theta\,\nabla^2\phi = -4A\sin\theta\cos\theta\,(\nabla\theta\,.\,\nabla\phi) + \partial K/\partial\phi. \quad \quad (2)$$

Harrington derived these equations in a semi-classical manner by formulating a Langrangian of the system and then using a variational treatment to obtain a set of Euler–Lagrange equations. It was from these Euler–Lagrange equations that eqns. (1) and (2) were deduced.

In a thin permalloy film the total anisotropy K can be represented by two terms:

(i) A term $K\sin^2\theta$ expressing the fact that such films show an induced uniaxial anisotropy and

(ii) A term proportional to the square of the component of magnetization at right angles to the plane of the film which occurs because of the magnetostatic energy associated with magnetic poles at the surface of the film. Thus the total anisotropy term can be written as

$$K(\theta, \phi) = K\sin^2\theta(1 + b\cos^2\phi) \quad \quad (3)$$

where b is a constant determined by the magnetostatic energy density of a thin film magnetized uniformly perpendicular to its plane.

The solution of eqns. (1) and (2) for a given set of boundary conditions is not straightforward and in order to proceed from the $K(\theta, \phi)$ in (3) above let us choose to find a solution in which θ varies normal to the wall and ϕ varies along the wall so that the derivatives of the two angles are orthogonal and $\nabla\theta\,.\,\nabla\phi = 0$.

Thus the two equations become:

$$A\,\partial^2\theta/\partial y^2 = A\sin\theta\cos\theta(\partial\phi/\partial x)^2 + K\sin\theta\cos\theta(1 + b\cos^2\phi), \quad \quad (4)$$

$$A\,\partial^2\phi/\partial x^2 = -bK\cos\phi\sin\phi. \quad \quad (5)$$

Equation (5) may be directly solved giving

$$x - x_0 = \sqrt{\left(\frac{A}{bK}\right)}\log\tan(\phi/2 + \pi/4) \quad \quad (6)$$

inserting $(\partial\phi/\partial x)^2$ in (4) and solving yields the result:

$$y - y_0 = \sqrt{\left(\frac{A}{K(1 + 2b\cos^2\phi)}\right)}\log\tan(\theta/2). \quad \quad (7)$$

Equations (6) and (7) together show that the wall thickness (y direction) varies with the value of ϕ and hence with the value of x. A plot of y at $\theta = 175°$ against x is shown in fig. 3 using the following values

$A = 10^{-6}$ ergs/cm
$K = 1500$ ergs/cm^3 (i.e. $H_k \sim 4$ oersteds),
$b = (4\pi M^2/K) = 8{\cdot}5 \times 10^3$.

This value of b has been used because the energy associated with the demagnetizing field normal to the plane of the film is $4\pi M^2$.

Fig. 3

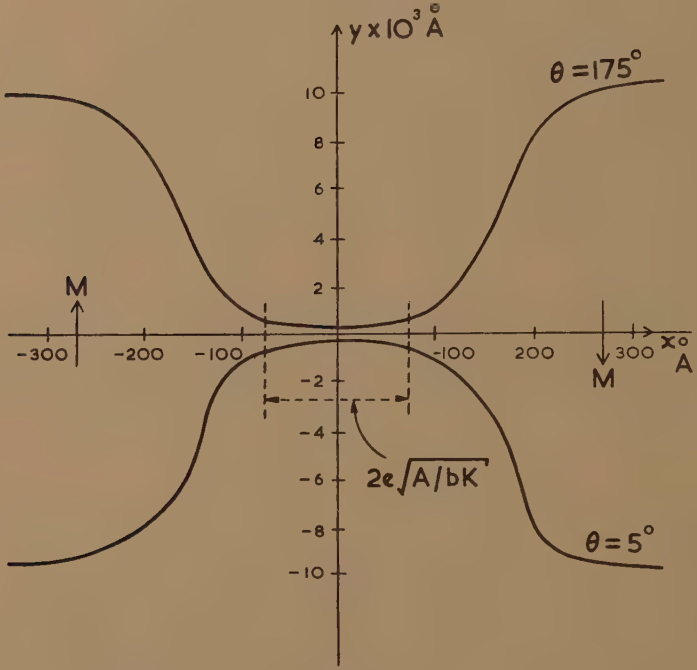

The variation of wall thickness for $\theta = 5^\circ$ and $\theta = 175^\circ$.

It is clear that the solution represented by eqns. (6) and (7) is not cyclic in x so that it cannot be the solution for a cross-tie wall. However, the following points are to be noticed.

(i) This solution contains a Bloch segment and two Néel segments and so is a compromise between pure Bloch and Néel walls in the same way as the original interpretation by Huber, Smith and Goodenough of the cross-tie wall.

(ii) Using the constants above, the distance between the centre of the Bloch segment and the Néel segment is about 300 Å which is a distance very short compared with the diameter of a typical film. The magnetostatic energy associated with the free poles in the Néel segments has not been taken into account in the calculation above and it is likely that the Néel segments will be reduced in length in order to minimize this energy. Further, there will be a magnetostatic interaction between the poles in adjacent Néel segments. This will be discussed later.

(iii) The wall thickness in the Néel region is of the order of 15 000 Å which compares reasonably with the cross-tie width as shown in the paper by Huber *et al.* and in a paper by Moon (1959).

(iv) With increasing film thickness the value of b falls and both the length and the width of the Bloch segment increase so tending to a simple Bloch wall. The wall thickness in the Néel segment decreases with increasing uniaxial anisotropy K as is expected.

It is suggested that the solution above could in fact represent one cycle of a cross-tie wall and the reason that a cyclic solution has not been found is associated with the fact that the original formulation of the domain wall equations did not take into account the energetic consequences of a non-constant value of div $\mathbf{M}$ in the wall. These magnetostatic interactions will be dependent upon the film thickness and will be important in determining the width and spacing of the Néel segments. In fig. 4 is drawn a model for the proposed structure of a cross-tie wall based upon the solution derived above. The principal difference between this model and that of Huber *et al.* is that the wide sections of the wall are Néel segments and do not contain a magnetization vector at right angles to the plane of the film at the centre of the wall. This model is still consistent with the shift observed in a powder pattern when a field is applied in a plane normal to the surface of the film.

Fig. 4

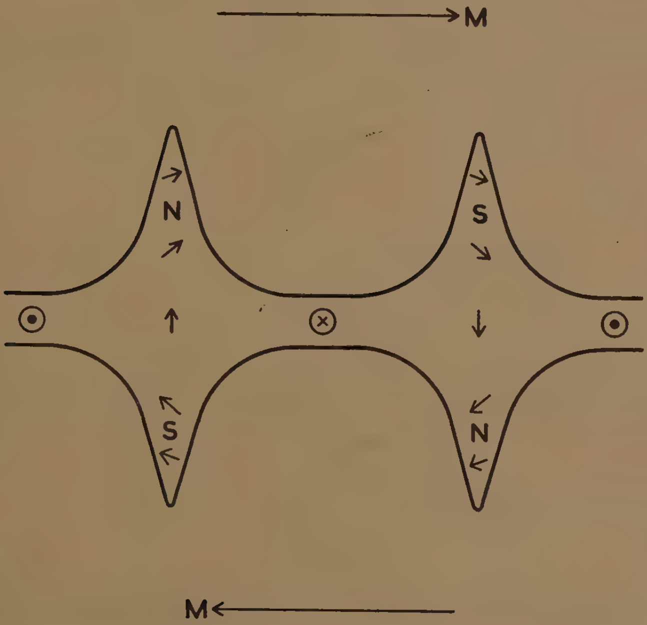

Proposed model for the magnetization distribution within a cross-tie wall.

The magnetic colloid will reveal a cross-tie type of wall structure for this magnetization distribution because it will lie in the places where the magnetic field at the surface of the film is high. Thus it will collect along the length of the wall because here the magnetization intersects the film surface and there are magnetic poles, and along the cross-ties because here there is a stray field linking the poles in the two halves of Néel segment on each side of the wall.

§ 3. THE EFFECTS OF MAGNETOSTATIC INTERACTIONS

Before attempting to evaluate the effects of magnetostatic interactions in the cross-tie wall it is convenient to consider the thickness and energy of the simple Néel type of boundary. If the energy density and width of a wall in the bulk material are written as σ_0 and a_0 respectively then the energy density in a Néel wall of width a in a film of thickness D can be written (Néel 1955) as:

$$E=\frac{\sigma_0}{2}\left(\frac{a}{a_0}+\frac{a_0}{a}\right)+\frac{2\pi aDM^2}{a+D}.$$

The equilibrium wall energy and width for a film of given thickness can be found from this equation by putting $\partial E/\partial a=0$. The variation of E and a with film thickness is shown in fig. 5. The variation in the width of the wall with changing film thickness is attributed to the fact that as the film thickness increases the area of free poles in the wall increases and as these are of opposite sign in each half of the wall they attract each other increasingly and the wall becomes thinner.

Fig. 5

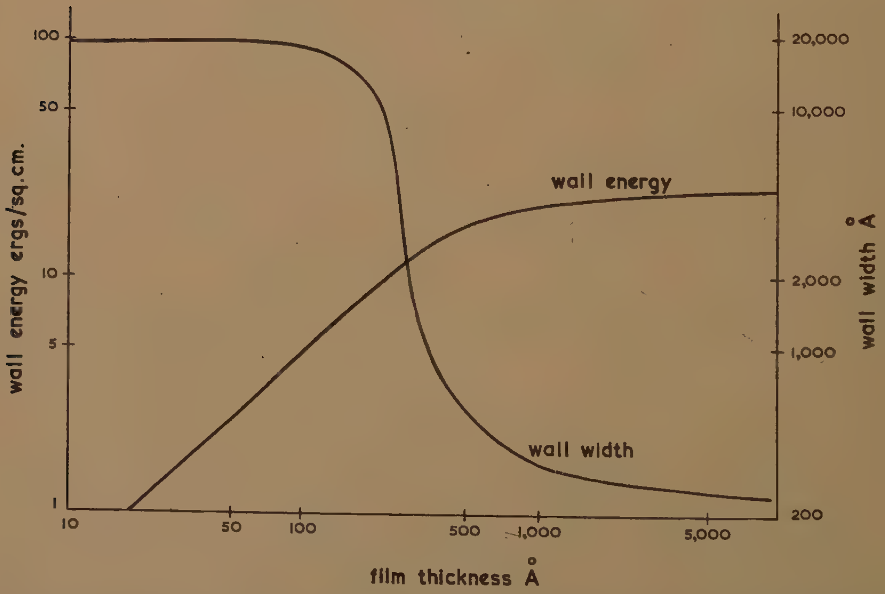

The thickness and energy density of Néel wall in permalloy film using $\sigma_0=0{\cdot}28$ ergs/cm^2, $a_0=2\times10^{-4}$ cm, $A=10^{-6}$ ergs/cm and $K=10^3$ ergs/cm^3.

Next it is instructive to consider the wall shown in fig. 4 when the free poles in the Néel segments are regarded as being at a point distance p from the axis of the wall and the cross ties are separated by a distance q. It is easily shown by considering nearest neighbours and magnetostatic effects alone that the wall is stable when

$$256p^6 = (q^2+4p^2)^3$$

i.e. $$q \sim 1{\cdot}5p.$$

The dimension p is determined primarily by the free poles in the Néel segments alone, consequently as the film thickness decreases the dimensions p and q both increase. This is consistent with the observations of Rubinstein and Spain (1959) who report that the spacing between cross ties increases as the films thickness decreases and that the larger the spacing between cross ties the longer is the cross tie.

§ 4. The Wall Energy

The sum of the exchange energy and the anisotropy energy at a point (θ, ϕ) in the wall is

$$f = 2K \sin^2\theta(1+2b\cos^2\phi).$$

Neglecting the magnetostatic contributions the wall energy per unit length can then be written

$$\sigma_l = \int_{-\infty}^{\infty} f\,dy = \int_0^{\pi} f(dy/d\theta)\,d\theta.$$

Thus

$$\sigma_l = 4\sqrt{[AK(1+2b\cos^2\phi)]}.$$

An approximate term for the average wall energy density σ_w can then be derived by assuming that the solution above is one for a cyclic wall and averaging the energy σ_l over one cycle.

Thus

$$\sigma_w = \frac{\int_{-\pi/2}^{\pi/2} \sigma_l\,(dx/d\phi)\,d\phi}{C\sqrt{(A/bK)}} \quad . \; . \; . \; . \; . \; . \; . \; . \quad (8)$$

where C is a constant which allows for the fact that the cycle length is in fact longer than $\sqrt{(A/bK)}$. It can be seen from fig. 3 (where the value of $\sqrt{(e^2A/bK)}$ is marked) that a reasonable value for C is about 2·5. Equation (8) can then be expressed as

$$\sigma_w = \frac{8M}{C}\sqrt{(2\pi A)}\int_0^1 \sqrt{\left(\frac{a^2+y^2}{1-y^2}\right)}\,dy$$

where $a = 1/2b$. The integral is a complete elliptic integral of the second kind which is equal to unity because $b \gg 1$, therefore

$$\sigma_w \sim 3M\sqrt{(2\pi A)}. \quad . \; . \; . \; . \; . \; . \; . \; . \quad (9)$$

For the values of M and A used above this means that $\sigma_w \sim 10\,\mathrm{ergs/cm^2}$ and is independent of film thickness and uniaxial anisotropy K when the magnetostatic contributions are neglected. This latter result is reasonable because in this case the energy balance is between the exchange A and the demagnetizing field $4\pi M$.

Using Néel's data for Bloch and Néel walls fig. 6 has been plotted showing the variation of wall energy with film thickness for the three types of wall.

Fig. 6

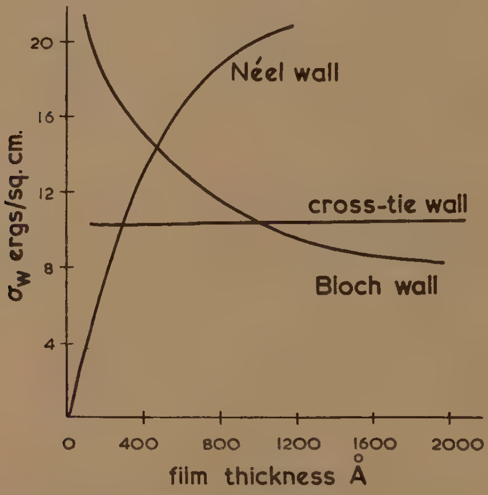

Plots of wall energy density *versus* film thickness for Bloch, Néel and cross-tie walls.

It is clear that a cross-tie wall of energy density 10 ergs/cm^2 can only be expected in thin permalloy films in the thickness range 200–1000 Å. This is in substantial agreement with the work of Methfessel *et al* (1959) who report that they can observe cross-tie walls in thin permalloy films only in the thickness range 400–900 Å.

§ 5. CONCLUSIONS

Although it has not been possible to derive a cross-tie wall directly from the general wall equations a solution describing a wall half-way between a Bloch and a Néel boundary has been found. This solution appears to be similar to one-cycle of a cross-tie wall and makes possible the presentation of a more plausible model for such a wall than that suggested by Huber, Smith and Goodenough. The energy balance in this wall is between the exchange energy and the demagnetizing energy contained in the component of the magnetization at right angles to the plane of the film. The spacing and lengths of the cross-ties are determined by the magnetostatic interactions between the cross-ties arising because they are Néel type regions and so contain magnetic poles. An approximate calculation of the energy of this wall reveals that permalloy films should only exhibit cross-tie walls when between 200 and 1000 Å thick. This is in fair agreement with observation.

ACKNOWLEDGMENTS

The author would like to thank H. Rubinstein of Laboratory for Electronics Inc., Boston, Massachusetts for a stimulating correspondence on this problem. He would also like to thank the Directors of International Computers and Tabulators Ltd., for permission to publish this paper.

RERERENCES

HARRINGTON, J. V., 1958, *M.I.T. tech. Rep.*, Lincoln Laboratory No. 166, January.

HUBER, E. E., SMITH, D. O., and GOODENOUGH, J. B., 1958, *J. appl. Phys.*, **29,** 294.

METHFESSEL, S., MIDDLEHOEK, S., and THOMAS, H., 1959, Paper 122, Detroit Conference on Magnetism and Magnetic Materials; 1960, *J. appl. Phys.*, **31,** 302 *S*.

MOON, R. M., 1959, *J. appl. Phys.*, **30,** 825.

NÉEL, L., 1955, *C. R. Acad. Sci., Paris*, **241,** 533.

RUBINSTEIN, H., and SPAIN, R. J., 1959, Paper 123, Detroit Conference on Magnetism and Magnetic Materials; 1960, *J. appl. Phys.*, **31,** 306 *S*.

The Generation of Vacancies in Metals†

By R. S. Barnes

Atomic Energy Research Establishment, Harwell, Berkshire

[Received January 7, 1960]

Abstract

The regions where injected helium atoms first appear as gas bubbles are those where thermal vacancies originate. Microscopic examination of metals, injected with helium by using them as targets for energetic alpha-particles, reveals grain boundaries as the principal suppliers of vacancies. Detailed examination distinguishes those boundaries which generate vacancies from those which merely conduct them. The behaviour and nature of these boundaries and other vacancy sources are discussed.

§ 1. Introduction

Since the concept of the vacant lattice site (or vacancy) was introduced by Frenkel, it has become increasingly clear that this point defect plays an important role in many physical processes of crystalline solids; particularly at high temperatures where the equilibrium vacancy concentration rises steeply, but even at low temperature when non-equilibrium vacancy concentrations have been introduced by quenching, deformation, or by atomic particle bombardment. A recently developed technique (Barnes *et al.* 1958) enables the sources of vacancies to be observed. These observations and some of the deductions from them will be given in this paper.

Mono-energetic alpha-particles from a cyclotron have been used to bombard a metal surface and inject a layer of helium atoms beneath the surface at a depth equal to the range of the alpha-particles in the metal (see fig. 1). The helium atoms in this layer, which is normally quite thin ($\sim 10^{-3}$ cm), are unable to migrate once their initial momentum is spent unless the temperature of the metal is sufficiently high. If the temperature is below this value the helium atoms remain dispersed in 'solution' in the metal; the concentration steadily increasing far beyond the solubility limit as the alpha-particles continue to be fired in. High concentrations of helium can be retained in solution in this way. On heating such a bombarded metal the helium atoms become mobile at some temperature and precipitate from solution with the ultimate formation of gas bubbles. Gas bubbles have been osberved on heating copper (Barnes *et al.* 1958), aluminium (Barnes 1959), beryllium (Barnes and Redding 1959) and uranium which has been injected with helium. Some study has also been made of gas inserted by other means into the metals (Ells and Perryman 1959, Mykura 1959, Rich *et al.* 1959). Figure 2† is a photomicrograph of a sectioned copper single-crystal injected with helium by bombardment with 38 MeV alpha-particles and then heated to 700°C for 1 hour. The bombarded surface is seen at the top of the figure,

---

† Communicated by the Author.

Fig. 1

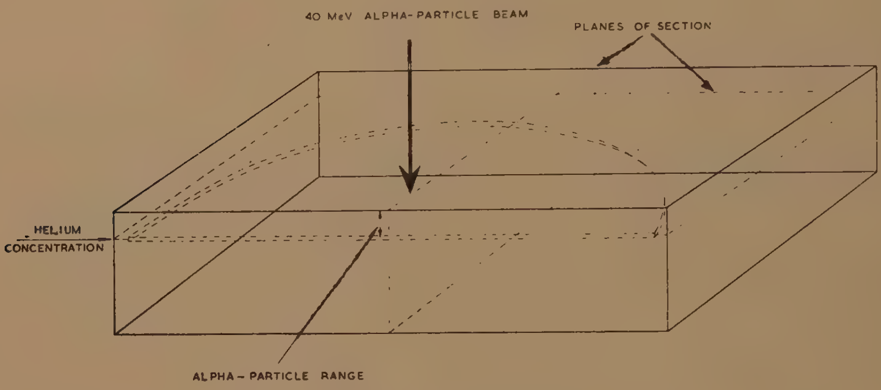

The injection of helium atoms by bombardment with alpha-particles.

and the layer containing the helium bubbles can be clearly seen at the bottom‡. It is observed that in the first instant only those helium atoms accessible to vacancies precipitate; only the periphery of the layer containing bubbles. This is the region immediately accessible to vacancies from outside the layer. After shorter times (or lower temperatures) the bubbles are even more marginal, and as the heating progresses the vacancies penetrate the layer further until the whole of the layer is filled with bubbles. These observations show that there are no vacancy sources *within* the helium layer in single crystals of copper. By heating for a time insufficient to allow the complete precipitation of the helium it is possible to outline with bubbles, the sources of the vacancies necessary for the process, and so observe these sources.

§ 2. Vacancy Sources

2.1. *Free Surface*

That the free surface of the metal is a source of vacancies is demonstrated by fig. 3. This shows that although the heat treatment has been insufficient to fill the helium layer with bubbles, near the free surface (lying on the left of the figure), the layer is filled. (The free surface has been covered with an electro-deposit of copper after the heat treatment to preserve flatness of the micrographed surface during polishing.) Vacancies have apparently formed at the free surface during heating, and have migrated inwards a distance demarked by the limit of the bubbles. The shape of this demarcation line must be an index of the concentration of the helium in the layer. If a given number of vacancies per helium atom is necessary before bubbles can form, then the penetration of the vacancies is inversely proportional to the helium concentration. If this is so the shape suggests that the helium is assymmetrically distributed about the mean range of the alpha-particles, and this is borne out by the distribution of the bubbles once they have formed.

---

† Figures 2–11 are shown as plates.

‡ In this sample the individual bubbles cannot be resolved, yet the layer can be seen, mainly due to its lower reflectivity than the rest of the electro-polished surface.

Evidence that the free surface is a source of vacancies is provided also at each heat treatment, for it is only after a sufficiently thick layer has been removed from the surface that an unbubbled region is seen. For instance, fig. 4 shows the same area (*a*) after a thin surface layer has been removed and (*b*) after much more has been removed, when the vacancies from the original surface are not contributing to the helium bubbles.

2.2. *Grain Boundaries*

Vacancies are also generated at grain boundaries within the helium layer, Figure 4 shows this in the same piece of copper as that seen in fig. 3, but after heating at 825°c for 1 hour, and the penetration of vacancies into the layer is very similar, suggesting that the grain boundary supplies vacancies at the same rate as the free surface. Both figs. 3 and 4 were of copper which had been well annealed (heated to 1050°c for 48 hours *in vacuo*) before the helium was injected. Other samples of copper with a lower temperature of anneal had much smaller grain size. This material showed similar behaviour at the grain boundaries (see fig. 5), but due to the more numerous sources the vacanices were more plentiful. Photographs of samples sectioned in a plane through the centre of the band and parallel to the bombarded surface (parallel sections) are shown in figs. 5 and 6. These show clearly that most of the grain boundaries are supplying vacancies to the helium in the surrounding metal.

2.3. *Twin Boundaries*

There are many coherent annealing twin boundaries shown in figs. 4, 5 and 6. These are never surrounded by bubbles and thus are never vacancy sources. As such a coherent twin boundary is not surrounded by bubbles, even where it intersects a grain boundary which is, suggests that it is also unable to *conduct* vacancies. However, a *non-coherent* twin boundary, although normally free of bubbles, frequently is surrounded by them if it connects with a grain boundary, suggesting that such a boundary is conducting vacancies from the true vacancy source. Not all non-coherent boundaries do this, e.g. fig. 6 shows two non-coherent boundaries (NC) of similar nature, both intersecting bubbled regions but only one of these is bubbled itself.

There are certain twin boundaries which invariably contribute vacancies to their surroundings. These are boundaries separating two individual annealing twins. In every such case the boundary contributes vacancies equally as well as a normal grain boundary. Two examples of boundaries (one being very short) between the two twins T_1 and T_2 of the parent grain P are shown in figure 6.

2.4. *Point Sources*

In addition to the vacancy sources already described there are point sources which give rise to small circular regions of bubbles (see, for example, fig. 5). These point sources can in a few cases be identified as being due to voids within the metal. Figure 7 shows two photomicrographs of a void in aluminium. The first (*a*) is of a section almost through the centre of the void and (*b*) is of a subsequent section cutting the void below its centre. Such a void would be able to contribute vacancies to its surroundings until it was completely filled in by the aluminium atoms deposited there. The bubble free zone immediately surrounding the void is presumably due to these deposited atoms.

Inclusions which at the heating temperature are surrounded by a gap due to differential expansion should behave as a void, but due to the smallness of the free volume available the number of vacancies generated there should be limited. Figure 8 illustrates this behaviour at an inclusion (I) in copper. The inclusion is surrounded by a very narrow circle of extremely small bubbles (~ 300 Å in diameter) which can only just be discerned in the figure but have been revealed by electron micrographs of replicas from this region. In comparison the void†, which lies very close to the inclusion in fig. 8, has supplied sufficient vacancies for bubbles to have formed a large distance from it.

Other point sources, which do not contain a helium free zone (see the electron micrograph of a replica in fig. 9) are less well understood. As can be seen, there are very few in material which has been well annealed (figs. 2, 3 and 4) but they are very numerous in material heated sufficient only for recrystallisation before injecting the helium (fig. 5). A piece of copper (that shown in fig. 6) which had been well annealed was cold-wrought and then recrystallized before injecting it with helium. The material was then found to contain point sources, but these were fewer in number and more irregularly sited than those seen in the rolled material treated identically, but not annealed at a high temperature (cf. fig. 6 with 5). It is unlikely that these point sources are due to voids, as it is difficult to believe that voids could be reintroduced merely by working the material.

2.5. *Dislocation Lines*

On no occasion in any of the material studied have dislocation lines themselves been identified as supplying vacancies to the helium atoms. The well-annealed material contains $\sim 10^6$ dislocation lines cm^{-2} and the recrystallized material many more, but in neither case are bubbled regions observed on a scale as fine as this. Samples have been purposely bent or cold-worked in other ways, but although slip occurred in the region containing the helium atoms, the subsequent precipitation of the helium followed the normal pattern for the undeformed material, despite the inevitable introduction of dislocations into the helium layer.

---

† The void has permitted a greater penetration of those alpha-particles which have passed through it, as is shown by bubbles lying beneath the void which have prevented locally the advance of the grain boundary running along the base of the gas layer.

§ 3. Deposition of Atoms

One consequence of the generation of vacancies is that there must be a deposition of atoms at the source. This deposition arises from the manner in which vacancies migrate and should be observable. A vacancy migrates by exchanging places with a neighbouring atom, so that although each atom only moves one jump, there is in effect always a counter flow of atoms in equal number to the flow of vacancies. Thus the generation of a vacancy at a source and its subsequent migration to a helium bubble is equivalent to the migration of an atom from the bubble to the source, where it is deposited. Thus for each vacancy generated at a source an atom of the matrix is deposited there.

The helium bubbles, which are inert markers in the crystal, will move away relative to the source as these atoms are deposited. Thus at at each source there should be a region free of bubbles containing as many atoms of the matrix as there are vacancies generated. This phenomena can be observed for instance in fig. 7 (*a*) and (*b*) which shows a zone free of bubbles, at the surface of the void†. The width of the zone free of bubbles is relatively much wider in the lower section (fig. 7 *b*) as would be expected. Eventually the void can be completely filled and will then cease to be a source of vacancies as occurs at the inclusion shown in fig. 8. The majority of point sources do not contain such a region free of bubbles suggesting that they operate in a different way.

Figure 10 (*a*) is a shadowed two-stage carbon replica of the electropolished surface of a region in the helium filled layer in copper after heating for two hours at 800°c. The individual bubbles are easily resolved and each casts a shadow. The diameter of the bubbles can be estimated from the width of these shadows, but these may over-estimate due to enlargement by the etchant. Figure 10 (*b*) shows a thin film of copper (~ 3000 Å thick) viewed in transmission in the electron microscope. The bubble size is here truely represented as the majority of them are completely embedded in the copper (diameter 3×10^{-5} cm). Both these photographs show grain boundaries running across them and at each there is a region free from bubbles, similar to that observed at the void in fig. 7.

If the explanation for this free zone is correct then the volume of the bubbles formed per unit area of grain boundary should be equal to the volume of the material deposited upon that area of the boundary. Rough estimates from fig. 10, where the average bubble radius is taken to be $1{\cdot}5 \times 10^{-5}$ cm and the number of bubbles $\sim 10^{13}$ cm^{-3} show that the volume of the deposit is about 10^{-4} cm^3 and the equivalent bubble volume $1{\cdot}3 \times 10^{-4}$ cm^3; agreement well within the accuracy. The number of vacancies generated at each atom site of the grain boundary is thus 3×10^3 during the two hours heating at 800°C and the deposited atoms produce a local volume increase around the boundary which in the above example is about 11%.

---

† No such clear zone can be seen at the free surface shown in fig. 3. This may have been etched away during the preparation for the electro-deposition, or smeared out by surface diffusion.

Not all grain boundaries show this effect, suggesting that only some of the grain boundaries (those with helium-free zones) are really acting as sources the rest are merely conducting vacancies into the crystal from elsewhere. Some local diffusion of the helium to those boundaries surrounded by bubbles occurs as some small bubbles can always be seen on the boundaries themselves. The helium free region cannot be caused by diffusion of the helium however, as this would occur at all boundaries equally.

In general the grain boundaries which are the most copious vacancy sources are those which lie in, or nearly in, the plane of the helium layer. This behaviour can be understood when it is realised that if a grain boundary is to be a true source of vacancies it must have atoms deposited upon it, and the region must *expand* laterally. A grain boundary lying perpendicular to the helium layer will be heavily restrained by the metal above and below the layer and such expansion will be difficult. Grain boundaries lying in the plane of the layer will have no such restraint.

Boundaries which do not have this helium free region frequently contribute fewer vacancies into the surrounding crystal as the distance from the real source of vacancies increases (e.g. some boundaries shown in fig. 5). This adds to the evidence that they are only conducting vacancies from this source.

§ 4. Discussion

The observations show that the first bubbles to form surround both the true vacancy sources and also those features which are merely conducting vacancies from these sources. A source can be distinguished from a vacancy conductor by the region of precipitated metal atoms, devoid of helium bubbles, adjacent to it. The vacancy sources and conductors will be discussed separately.

4.1. *Vacancy Sources*

The free surface is the most straightforward source of vacancies. On a clean surface there will be no restraint to reduce the normal atomic fluctuations which occur. A surface film, e.g. an oxide layer, may retard such a vacancy source, but if it is not a coherent one the effect should be slight.

The situation at a grain boundary is similar to that at a free surface with the added complication caused by the superimposed crystal of a different orientation. The inherent structure of a boundary is expected to determine its ability as a vacancy source. If there is a space in the boundary of approximately an atomic size then there would be little hinderence to the generation of a vacancy. Boundaries having little free space, i.e. nearly coherent boundaries, would not be good sources. However, not only must there be spaces in the boundary large enough for extra atoms to be forced in but spaces must then form elsewhere in the boundary for the process to continue.

A hydrostatic pressure (P) upon a sample generating vacancies would necessitate an extra amount of work Pa^3 (where a^3 is the volume of an atom) to be performed in generating a vacancy. A pressure of more than 10^4 atmospheres must be applied before this extra work ($\sim 7 \times 10^{-2}$ ev) is comparable with that needed to create a vacancy at a free surface (~ 1 ev). If such a pressure was applied then the number of vacancies emanating from each and every source would be limited. Such high pressures cannot be maintained within these samples, so that local pressure, e.g. those caused by unequal vacancy production at different boundaries, cannot influence the emanation of vacancies from a boundary.

However, internal pressures, although unable to prevent the formation of bubbles, can change the behaviour of a boundary from that of a source to that of a conductor by forcing the atoms which are normally deposited on the boundary to flow along it to some other boundary (not subjected to this pressure) where they are deposited. A laternal pressure of about 40 atmospheres (600 p.s.i.) is estimated to be sufficient to cause this flow of atoms out of a boundary in a typical experiment. Such pressures can be attained and maintained, and explain why boundaries lying in the plane of the helium layer contain the zone free of bubbles near to them and those lying perpendicularly do not. Such pressures around a cylindrical or spherical source would also be expected to force the atoms to escape by any possible path. If no such path existed then the deposited atoms would build up a pressure sufficient to cause the surrounding material to yield.

Thus external pressure, or pressures imposed by the material itself, can induce a vacancy source to act as a conductor. But this cannot explain why a coherent twin boundary is never a source of vacancies. This must be due to the nature of the boundary itself.

4.2. *Vacancy Conductors*

Certain crystal defects are unable to generate vacancies but can conduct them†. Such conductors are distinguished from true sources by the absence of an intervening region of deposited metal atoms between them and the helium bubbles. There is no change in volume in such a region as the vacancies are conducted in from their true source where the actual volume increase occurs. The conduction process is thus unaffected by restraining pressures except in so far as the source itself is affected.

---

† Strictly, the concept of a vacancy in a boundary is meaningless because of the absence of a simple crystallographic arrangement there. But the end effect of the diffusion of atoms (not necessarily a particular atom) along the boundary is equivalent to the diffusion of a vacancy along the boundary.

A grain boundary which appears to be a good source is sometimes converted into a poor conductor where one of the adjacent grains is twinned (fig. 11) and occasionally a change in boundary direction prevents a boundary from even conducting vacancies. These effects cannot be caused by local pressure changes and clearly show the importance of the nature of a boundary upon its behaviour.

As a conductor can only conduct a limited number of vacancies from the true source, and as the vacancies are 'pumped' away into the helium bubbles in the surrounding crystal, the supply becomes exhausted at a distance from the real source which is dependent upon the relative diffusion rates of vacancies along the conductor and through the surrounding crystal. In small grain material the penetration of vacancies from the source boundaries into the surrounding crystal is the same for all, but in large grain material the distance is very variable. This is because in the latter case the conduction paths are much longer so that exhaustion of the supply occurs more frequently.

Occasionally a conducting boundary is seen in a parallel section, where the bubbled region tapers to a point, the vacancy supply being exhausted there (see fig. 5). In some of these cases the penetration of vacancies from the adjacent vacancy source is more than the width of the unbubbled region of the helium layer, i.e. more than the penetration in a direction perpendicular to the photograph. Thus in these particular boundaries the conduction of vacancies is anisotropic. Vacancies conducted along the boundary from outside the layer are unable to travel as far as those conducted in the plane of layer. In other cases the exhaustion occurs in less than the width of the unbubbled region and here the boundary is probably a poor conductor in all directions.

The circular regions of bubbles observed in figs. 5 and 6 suggest that vacancies are emanating from a point. They cannot arise from voids which were originally present but are now completely filled as there is no central region devoid of helium bubbles (see fig. 9). The complete absence of such central regions also demonstrated that these spheres of bubbles are not caused by point *sources* of vacancies. Vacancies must be supplied to the region and then radiated from the central point. As these regions do not in general lie on any observable boundary the vacancies must be conducted in via some unseen defect, presumably dislocation lines. Certainly the number of circular regions is very much smaller and their size more non-uniform in well annealed material (in fact none can be seen in figs. 2, 3 and 4 where the number of dislocation lines is $\sim 10^6\,\mathrm{cm}^{-2}$). In this material the number of circular regions is only $\sim 10^4\,\mathrm{cm}^{-2}$ ($r \sim 2 \times 10^{-4}$ cm), i.e. the number of spherical regions is $\sim 2 \times 10^7\,\mathrm{cm}^{-3}$, whereas the number of dislocation nodes must be $\sim 10^9\,\mathrm{cm}^{-3}$, almost two orders of magnitude greater. Thus if the dislocation nodes are the originating points, only a few of them are operating. The regions might originate upon some special dislocation configuration which can climb and thus supply vacancies itself.

4.3. *Dislocation Lines*

It is surprising that the majority of the dislocation lines which are known to exist in the metal are unable to climb and thus supply vacancies to the helium atoms and permit precipitation as bubbles. Dislocations of both edge and screw character are known to be sinks for supersaturated point defects and it seems reasonable that they should behave reversibly when the vacancy concentration is depleted. The explanation may be that the dislocations are effectively locked by the helium atoms lying upon them and are thus unable to *climb*. Certainly the material in the layer containing helium is much harder (the microhardness is approximately doubled) presumably because the helium atoms impede *slip* of dislocation lines.

§ 5. STRUCTURE OF BOUNDARIES

A coherent twin boundary, which is never either a source or a conductor of vacancies, is a particularly simple boundary, lying on a (111) plane. The diagram (fig. 12) shows the atom positions of a (111) plane as dots. The plane of atoms above this is represented as crosses. The right hand side can be seen to have suffered a twinning shear, i.e. the passage of a partial dislocation with Burgers vector **b** on each plane. If the successive (111) planes in a perfect crystal are labelled ABCABC then the fault at the twin plane can be represented by the sequence ABACBA. This is a perfecty fitting boundary of very low energy and it sould be surprising if it was able

Fig. 12

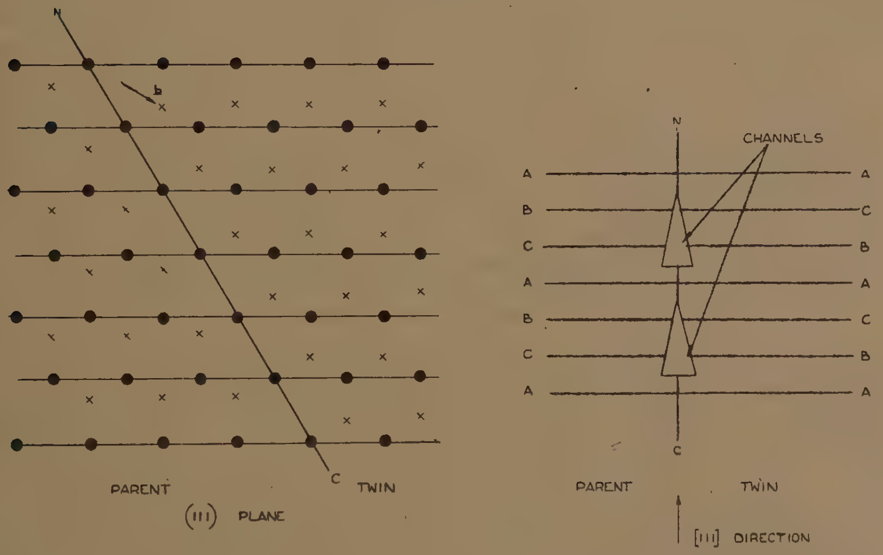

Diagram of the atomic arrangement at a non-coherent boundary NC in a face-centred-cubic crystal.

to generate or conduct vacancies, for the formation energy would be almost as high as than in perfect crystal (i.e. ~5 ev).

A non-coherent twin boundary is that which separates the twinned from the untwinned material and yet does not contain the twinning vector **b**. Such a boundary (NC) is represented in the diagram (fig. 12) and must contain an appreciably lower density of atoms than the perfect crystal. Thus a boundary of this nature might be expected to conduct vacancies particularly if it lay normal to **b**. As every third (111) plane (the B plane) is common to both the parent and twin, the non-coherent twin boundary will consist of well-defined channels, lying parallel to the (111) twin plane. It should be relatively easy for atoms (and thus effectively vacancies) to flow along these channels, but most difficult for them to flow in any other direction. The boundaries would be expected to conduct vacancies very anisotropically, as appears to be the case. Due to the tie-rod action of every third layer, it would be difficult for extra atoms to be accommodated in this boundary, and it would thus not be a source of vacancies, in the sense we have defined.

The number of possible configurations of a grain boundary is enormous. Some simple boundaries may be considered. A simple tilt boundary between two grains with a small angle of misorientation may be treated as a collection of edge dislocations and a simple twist boundary as a collection of screw dislocations. Such boundaries have low energy and appear to be unable to create vacancies, but may conduct them in the same way as it is thought that dislocation lines may. The conduction of such boundaries should be highly directional. High-energy boundaries have considerable atomic misfit along them and such boundaries should generally be good sources of vacancies. It is a general observation that low energy boundaries are rarely sources of vacancies but high energy ones frequently are.

§ 6. THE EFFECT OF DISPLACEMENT VACANCIES

A large number of vacancies is produced during the bombardment of the target with alpha-particles, and it should be explained why these are not able to permit helium bubbles to form before vacancies from grain boundaries, etc., arrive. One can conclude only that the number of vacancies involved is too small. The following simple model illustrates the situation.

Consider a unit volume of crystal with a simple cubic structure containing no vacancy or interstitial atom sinks which is bombarded with alpha-particles and has attained an equilibrium situation with N vacancies and an equal number of interstitial atoms. Consider also that the temperature is such that the interstitial atoms have a high mobility (ν atomic jumps/sec) and that the vacancies are unable to change their position by thermal activation—this is likely to be the situation in copper at room temperature. For this equilibrium state to be maintained the number of interstitial atoms combining with vacancies in time δt must be balanced by the number ($n\delta t$) being produced in that time. In time δt each interstitial atom explores $\nu\delta t$ interstitial sites and as each of these enables access to at least four new vacancy positions the number of vacancies annihilated is $4(N/N')\nu\delta t$ where N' is the number of atomic positions in the unit volume. As there are N interstitial atoms, which we shall assume behave independently,

$$4(N/N')\nu\delta t N = n\delta t$$

i.e.

$$N = \tfrac{1}{2}\sqrt{(nN'/\nu)}.$$

Substituting the values for copper at 600°K bombarded in two hours with alpha-particles sufficient to produce an atomic concentration of 10^{-3} helium atoms in the layer beneath the surface, gives a value for the equilibrium atomic concentration of vacancies to be $\sim 10^{-9}$, i.e. only one vacancy per 10^6 helium atoms. Thus it is reasonable to assume that the annihilation of the vacancies by the interstitial atoms produced at the same time, removes the vast majority of the vacancies. The remainder are so few that they are unable to assist in the formation of the helium bubbles of the size observed. Only if the number of sinks for the interstitial atoms are so numerous that more than one hundredth of the interstitial atoms are annihilated at positions other than at vacancies would these vacancies be expected to affect the observations appreciably.

§ 7. CONCLUSIONS

1. The vacancies introduced during the alpha-particle bombardment are mainly annihilated by the interstitial atoms also produced, so that those remaining are too few to permit the formation of the helium bubbles observed.
2. The necessary vacancies for bubbles to form are drawn from vacancy sources in the material by thermal activation.
3. The nature of a defect boundary in the crystal determines whether it is inherently a source, or merely a conductor of vacancies, or neither.
4. A boundary can be restrained from acting as a source, but not as a conductor, by the application of a lateral pressure.
5. Extremely high pressures are needed to prevent the supply of vacancies.
6. A boundary which conducts vacancies can do so at different rates in different directions.
7. Line defects in the crystal are unable to act as vacancy sources in the conditions of these experiments, but may conduct vacancies.

ACKNOWLEDGMENTS

I am indebted to Mr. D. J. Mazey for his patience and care in obtaining the micrographs, to Dr. J. Coiley and Mrs. B. Jenkins for their help with

the electron microscope, to Mr. G. B. Redding who prepared the targets which were bombarded at Birmingham University under the supervision of Mr. W. Hardy, and to Professor A. H. Cottrell, F.R.S. of Cambridge University for many valuable discussions during the course of this work with which he has been closely associated.

REFERENCES

BARNES, R. S., 1959, *Colloque sur la Diffusion a l'État Solide* (Amsterdam: North Holland Publishing Co.), p. 57.

BARNES, R. S., and REDDING, G. B., 1959, *J. nucl. Energy*, **A**, **10,** 32.

BARNES, R. S., REDDING, G. B., and COTTRELL, A. H., 1958, *Phil. Mag.*, **3,** 97.

ELLS, C. E., and PERRYMAN, E., 1959, *J. nucl. Materials*, **1,** 73.

MYKURA, H., 1959, *Phil. Mag.*, **4,** 907.

RICH, J. B., REDDING, G. B., and BARNES, R. S., 1959, *J. nucl. Materials*, **1,** 96.

REVIEWS OF BOOKS

Solid State Physics in Electronics and Communications. Vol. 1, Part 1, Semiconductors. Edited by M. Désirant and J. L. Michiels. (London and New York: Academic Press, 1960.) [Pp. 638.] £6 8*s*. 6*d*.

This is not a book: it is the Report of a Conference held in Brussels in June 1958. It has all the disadvantages of such a document: (*a*) eighteen months is far too long a delay; if the papers were worth publishing, they were worth publishing quickly, and three more volumes are yet to appear; (*b*) many of the papers are mere interim accounts of work in progress; they may have been worth presenting verbally at the conference, but are not worth printing; (*c*) there is no reason to suppose that any of these papers were refereed; they do not, therefore, carry the weight of work published in reputable scientific journals; (*d*) it is more lavishly and expensively printed than such ephemeral work deserves; no private person would afford to buy it for the occasional reference; (*e*) although libraries may be persuaded into purchasing it, the problem of finding papers in it by reference will be much more complicated than in the ordinary scientific journals; even the title is too long for a neat footnote, and who can guess how it will be indexed in the book stacks.

For these reasons I cannot commend the publication of such works, however admirable may be some of the actual research that is here reported (and some of it is quite interesting). Perhaps the publishers or the organizers of the conference can explain the rationale of their procedure, and tell us its advantages compared with the publication of ordinary scientific papers through the usual channels in the recognized journals. J. M. Z.

A New Method in the Theory of Superconductivity. By N. N. Bogoliubov, V. V. Tolmachev and D. V. Shirkov. (New York: Consultants Bureau, Inc.; London: Chapman & Hall, Ltd.) [Pp. 121.] Price $5.75, about £2 10*s*.

The theory of superconductivity has undergone a rapid development in the last three years. Indeed it would be fair to say that physicists now have a qualitative understanding of many of the main features of the superconducting state. The initial impetus for this development came from the now celebrated paper of Bardeen, Cooper and Schrieffer. Immediately after this Bogoliubov, Tolmachev and Shirkov developed an alternative approach to the theory. The volume under review is essentially a translation of this and several other Russian papers on the subject. As such it will be of the first importance to those theoretical physicists whose Russian is inadequate to deal with the original papers. It is stated on the jacket that the book contains a complete solution to the theoretical problems of superconductivity. This, at least in the opinion of the reviewer, is not so and it is unlikely that the authors themselves would support such a claim. The book does, however, contain a clear account of the Russian contributions to the subject. The main criticism that might be made of it is that the presentation is rather abstract and that very little physical discussion of the theoretical results is given. Nevertheless the serious student of the subject will find it particularly valuable for the clear account of the quasi particle transformation and the principle of compensation of dangerous graphs, for the discussion of the role of the coulomb interaction and for the detailed investigation of the collective modes of motion in the superconducting state. There are unfortunately several obscurities in the translation, rather too many considering the price of the book. G. V. C.

The Conceptual Foundations of the Statistical Approach in Mechanics. By P. and T. EHRENFEST. Translated by M. J. Moravcsik. (Ithaca, N.Y.: Cornell University Press.) [Pp. xii+114.] Price £1 4*s*.

THIS is a most welcome translation of one of the few classics in the field of statistical mechanics. It has been relatively difficult to get hold of the original (at any rate until the appearance last year of the Collected Works of P. Ehrenfest) and, as is pointed out by Kac and Uhlenbeck in a short preface, the original is couched in rather difficult German. Anybody who is interested in the development of statistical mechanics, and especially in its foundations, will want to possess this booklet, and luckily its price does not have to be a hindrance, as it so often is these days. It is rather unfortunate that the translation is far from smooth and reads even less easily than the original. A number of German terms were deemed to be untranslatable, but I fail to see why recurrence paradox, reversibility paradox, and equivalent would be incorrect renderings of *Wiederkehreinwand*, *Umkehreinwand* and *gleichberechtigt*, to name a few instances. A personal element is introduced by a special preface for this translation (also printed in the Collected Works) by Mrs. Ehrenfest consisting of a few remarks which were omitted in the original on her instigation, but which she feels should now be included. D. TER HAAR.

BOOK NOTICES

Confluent Hypergeometric Functions. By L. J. SLATER. (Cambridge: University Press, 1960.) [Pp. 247.] Price £3 5*s*.

A Simple Approach to Electronic Computers. By E. H. W. HERSEE. (London: Blackie & Son.) [Pp. 104.] Price 12*s*. 6*d*.

Lectures on Fourier Integrals. By S. BOCHNER. Translated by M. Tenenbaum and H. Pollard. Annals of Mathematics Studies, No. 42. (Princeton: University Press; London: Oxford University Press.) Price £2.

[*The Editors do not hold themselves responsible for the views expressed by their correspondents.*]

Fig. 2

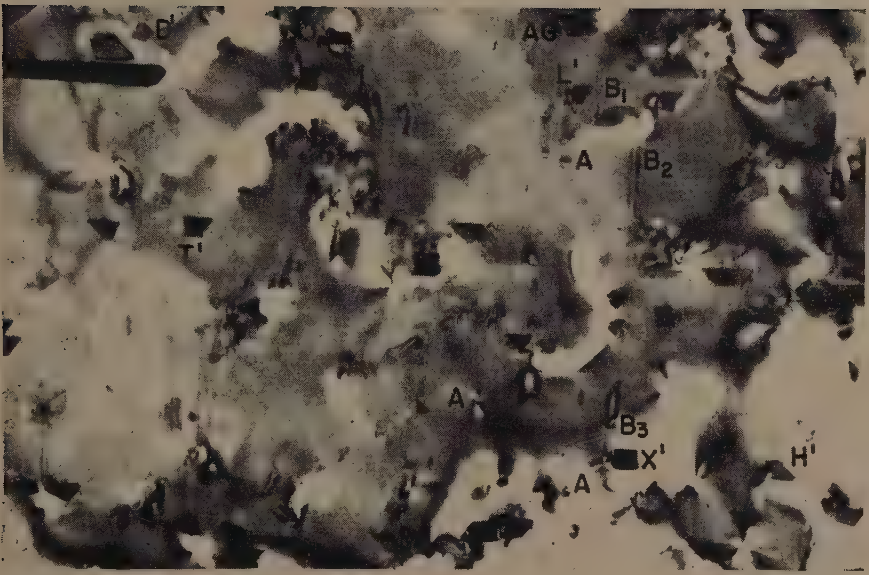

Structure of fresh area of monocrystalline film of silver made by evaporation onto heated rock salt. Note simple stacking faults AG′, D′, X′, etc., dislocation loops A, and parallel line features B_{1-3}. Holes appear in white contrast. Foil thickness about 650 Å. × 60 000.

Fig. 3

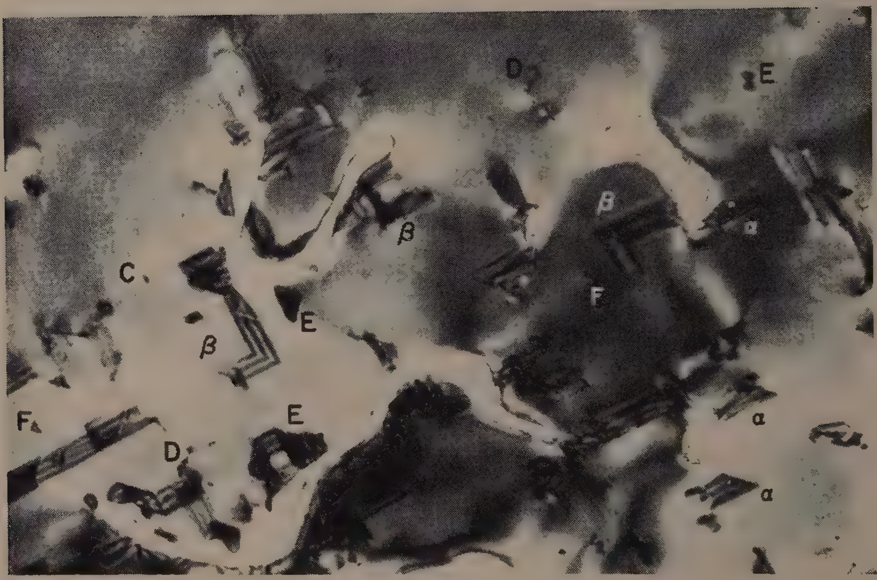

Region showing line or point defects C, whole dislocations D, stacking faults α, β, stacking-fault tetrahedra E, and triangular loops F which are probably Frank sessile dislocations. The simple stacking faults α and complex faults β show typical extinction bands. Foil thickness 500–650 Å. × 100 000.

Fig. 4 (*a*)

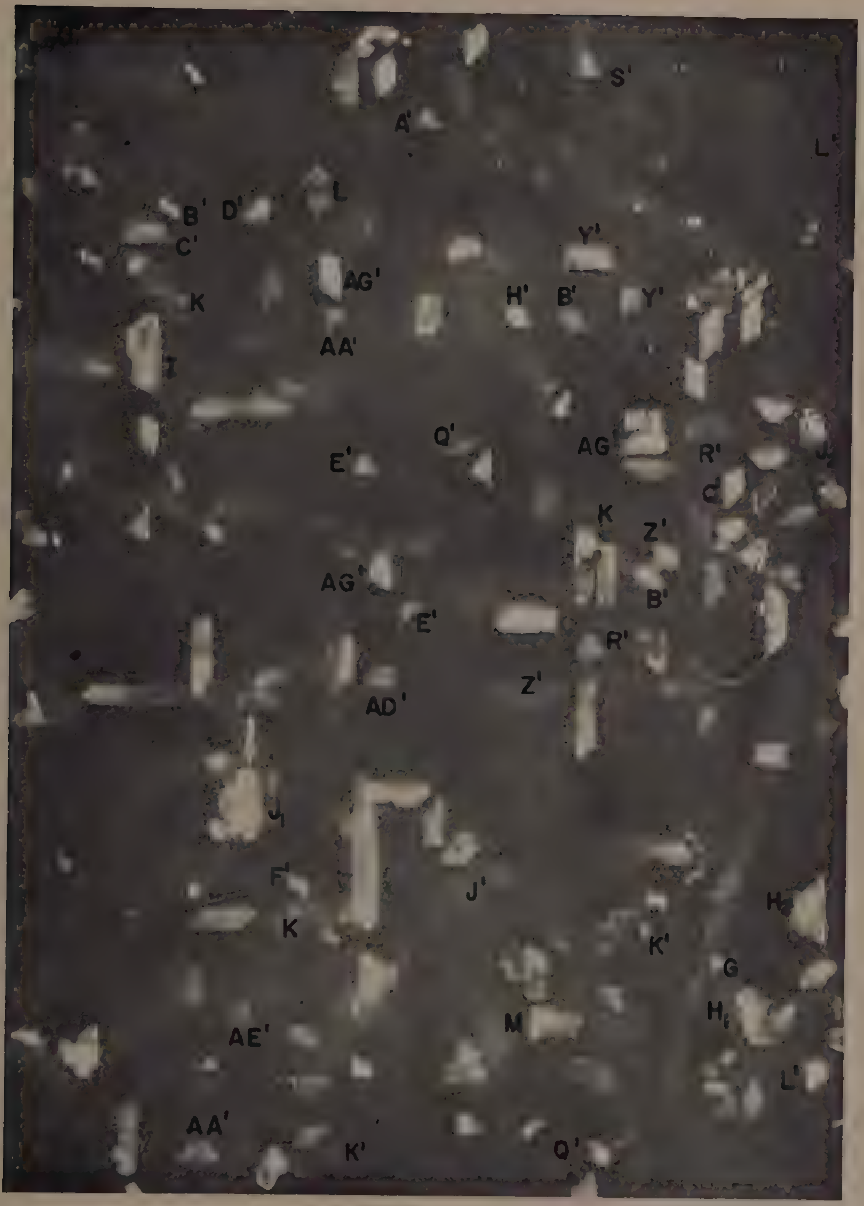
S'
A'
L'
L
B'
D'
C'
Y'
AG'
K
H'
B'
Y'
AA'
I
Q'
E'
AG
R'
J_2
C
K
Z'
AG'
B'
E'
R'
Z'
AD'
J_1
F'
J'
H_2
K
K'
G
H_1
M
AE'
L'
AA'
K'
Q'

(*a*) Dark field electron micrograph of fresh area of film showing stacking faults in white contrast. Feature I is probably a twin. The interpretation of features J_1 and J_2 is in doubt (see text). The remaining features are stacking faults and may be classified according to shape as described in the text. Note groups of parallel faults H_1 and H_2. ×60 000.

Fig. 6

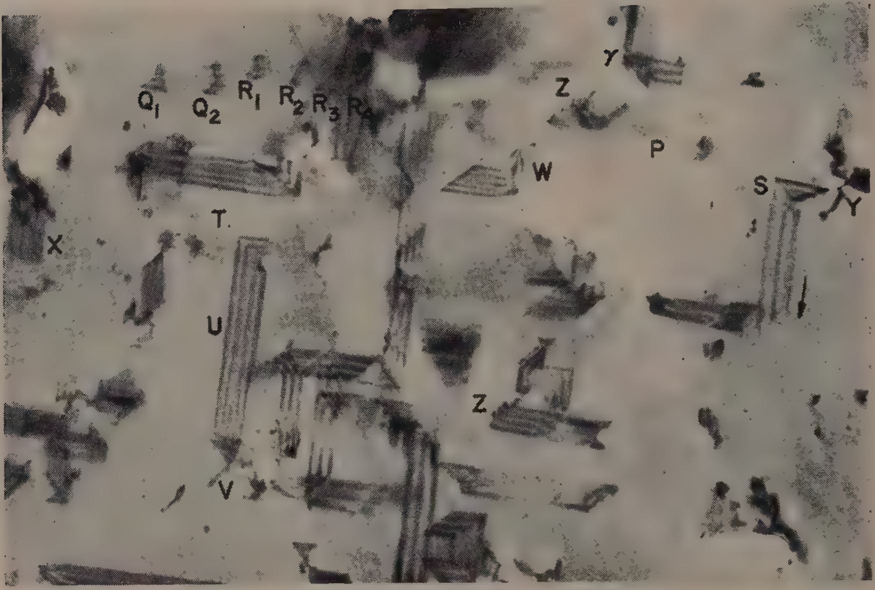

(*a*)

Sequence of micrographs showing effect of thermal stressing on structure. Note pile-up of dislocations Q_1, Q_2, R_1–R_4 against a group of stacking faults; dissociation is least at the head of the pile-up. Q_1 and Q_2 are on a different but probably parallel $\{111\}$ plane to that of R_1–R_4. The hole edge W appears to be a source of dislocations, since a second fault on a different plane has appeared between exposures (*a*) and (*b*) forming a single-bend fault, while in (*c*) a third fault on a $\{111\}$ plane parallel to that occupied by the fault in (*a*) has appeared. The single-bend fault S has widened progressively between (*a*) and (*b*) and between (*b*) and (*c*), being blocked by a hole in (*c*). Complex fault UT has changed to a simple fault T in (*c*) permitting dislocation V in (*b*) to move to a new position in (*c*). There appear to be two parallel faults at X which have extended between (*b*) and (*c*). Dislocations at Y and Z in (*a*) are held up at faults. Z has moved away in (*c*). Note the pinning of partials P and W at holes, in (*a*). Note the tendency of partials associated with faults Q_1, Q_2 and W in (*c*) to be parallel to $\langle 110 \rangle$ directions in the fault plane. Stair-rod dislocations as at the bend in fault S in (*a*) are parallel to $\langle 110 \rangle$ directions in the fault plane. × 140 000.

Fig. 6 (*continued*)

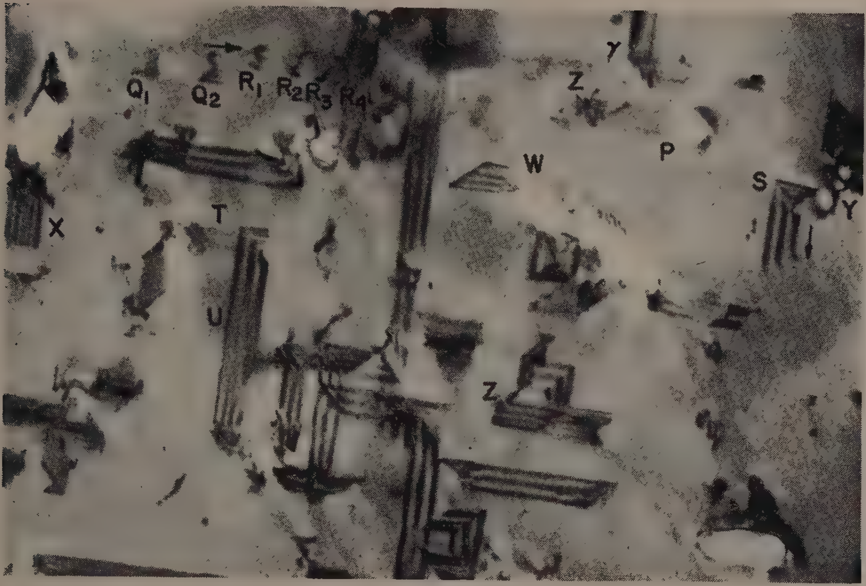
Q_1
Q_2
R_1
R_2
R_3
R_4
Y
Z
W
P
S
Y
X
T
U
Z

(*b*)

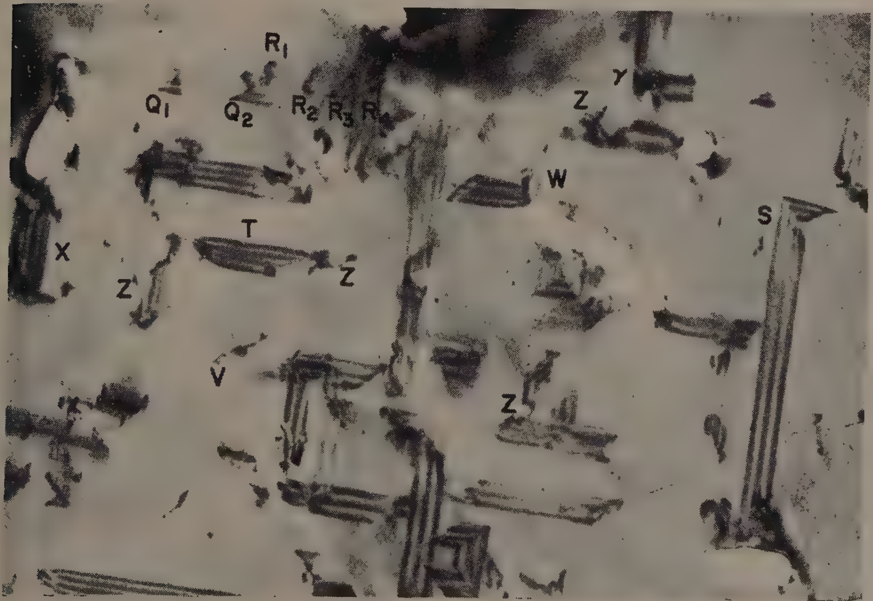
R_1
Q_1
Q_2
R_2
R_3
R_4
Y
Z
W
S
X
T
Z
Z
V
Z

(*c*)

Fig. 7

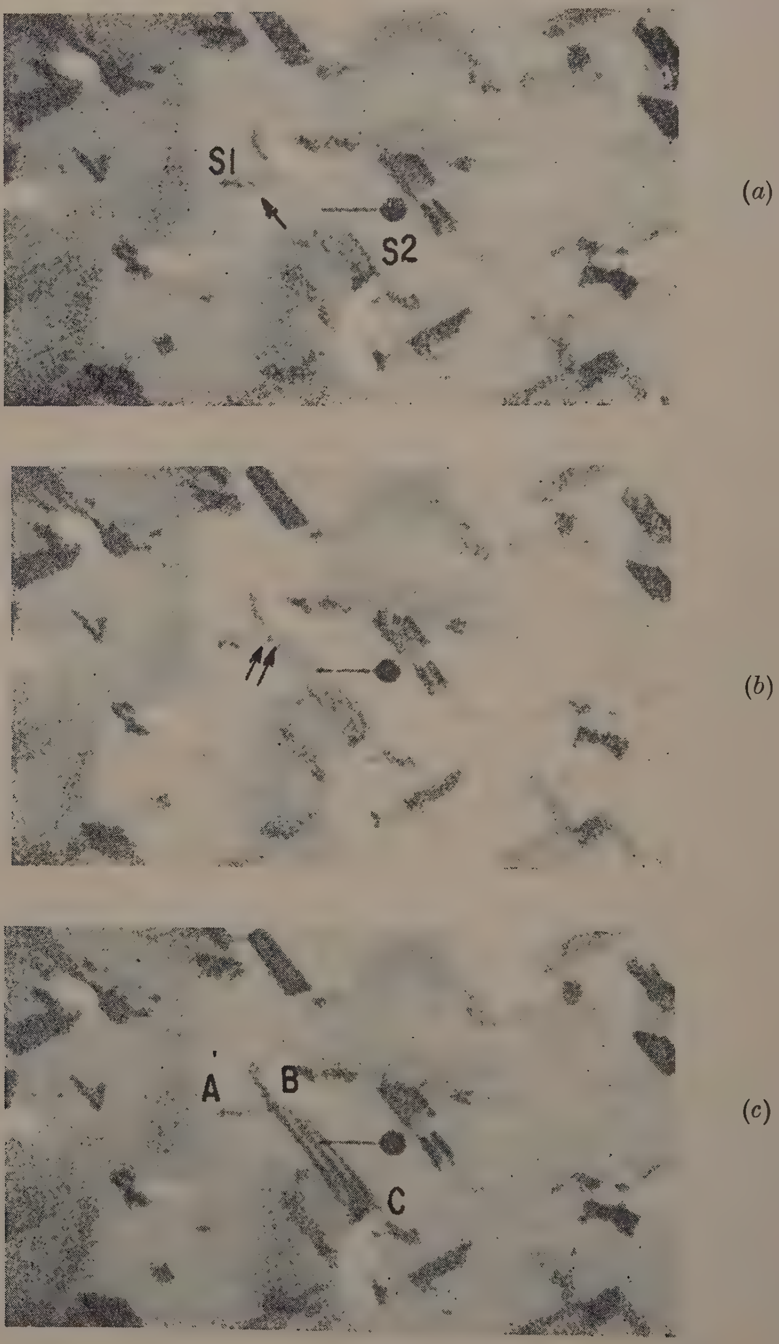

Sequence of ciné photographs showing combination of two simple faults to form a single-bend complex fault. In (*a*) the two faults S1 and S2 are visible. In (*b*) fault S2 has extended but the two partials (retouched for reproduction) indicated by arrows are separately visible. In (*c*) the two partials have combined giving a stair-rod dislocation at B (not visible) and forming a single-bend fault ABC (angle between faulted planes acute). Magnification about ×80 000 parallel to screen marker and about ×67 000 perpendicular to this.

Fig. 8

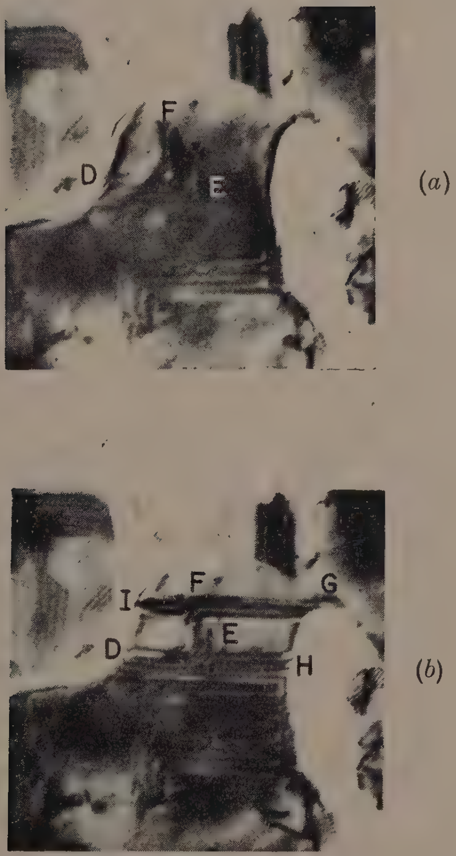

Sequence of micrographs showing conversion of single-bend fault DEF in (a) to a complex double-bend fault DEHGFI in (b). × 140 000.

Fig. 9

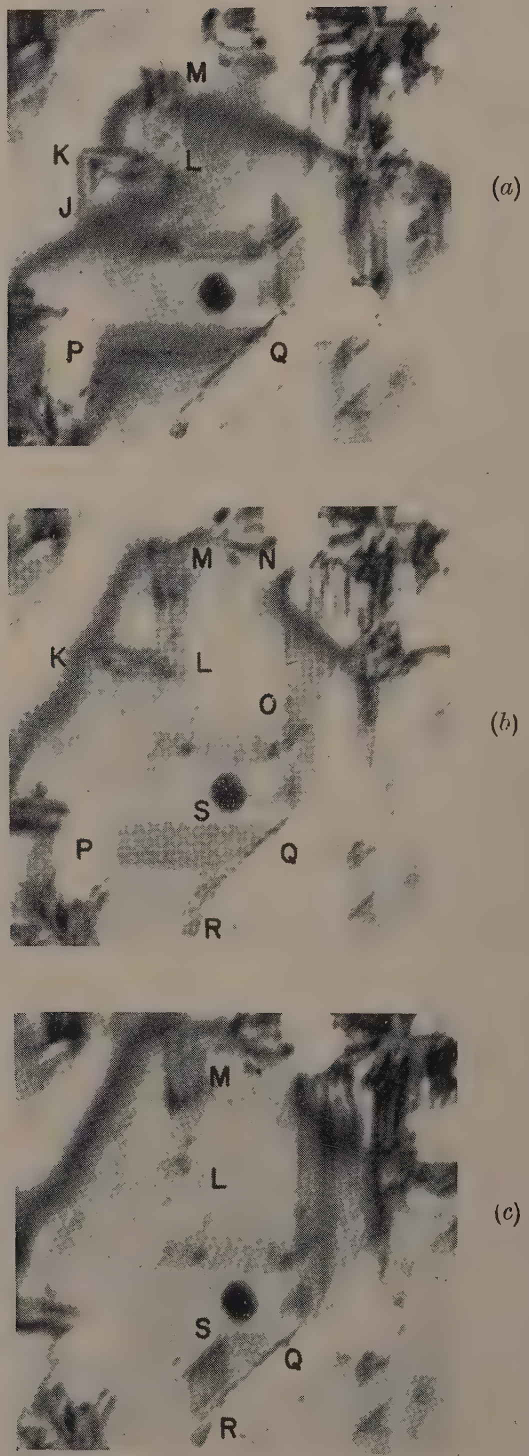

Sequence of micrographs showing changes in fault configuration. Between exposures (*a*) and (*b*): the double-bend-fault JKLM has become a single-bend fault KLM, a simple fault NO has formed between a hole at N and another complex fault at O, and a simple fault RS has formed between a hole at R and a fault PQ. Between exposures (*b*) and (*c*): the single-bend fault KLM has become a simple fault ML, fault PSQ has contracted to SQ and its partial appears to be held up at the partials of fault SR. ×140 000.

Fig. 1

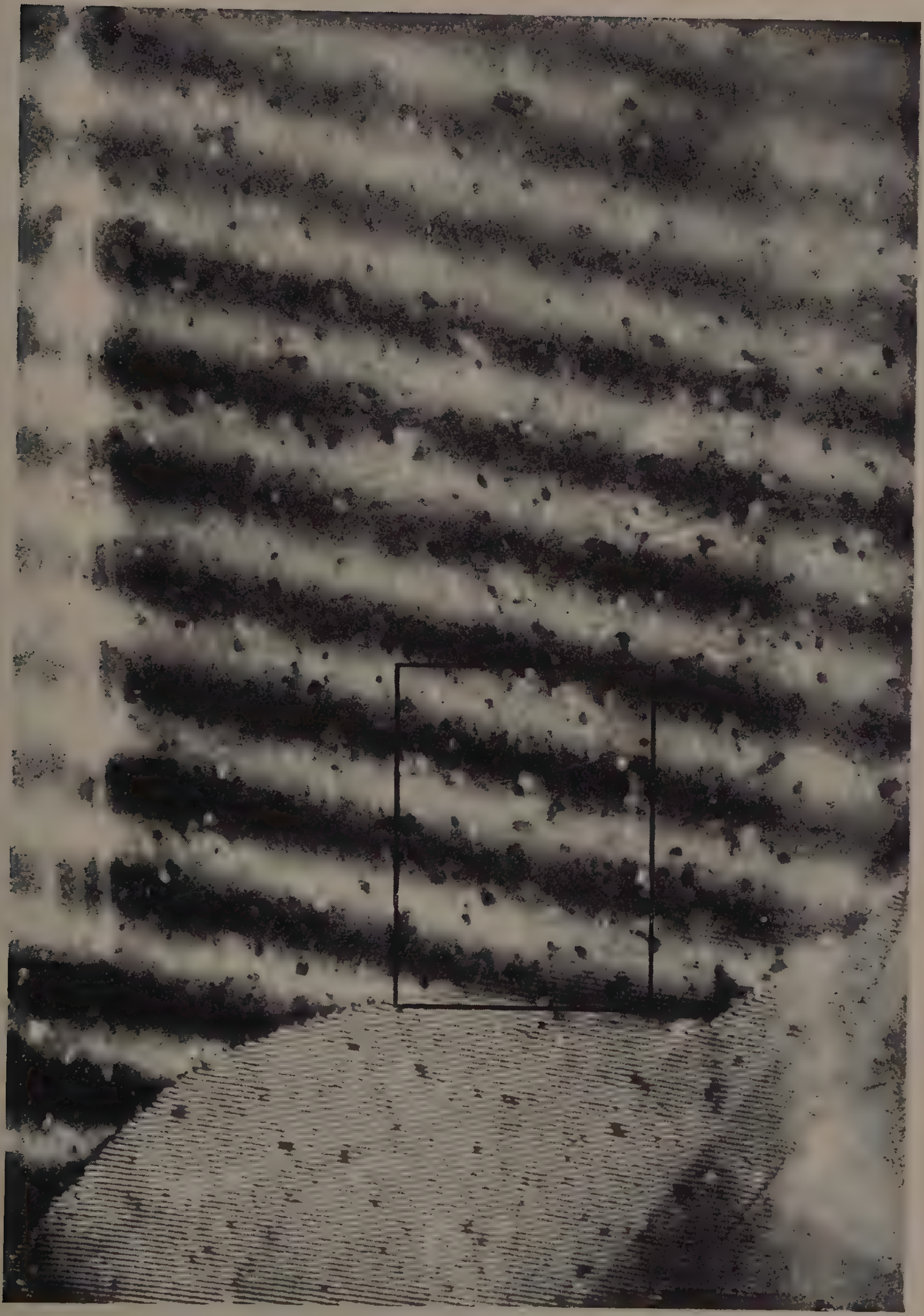

Graphite irradiated by 10^{20} n/cm^2 at 30°c, 320 000 ×.

Fig. 2

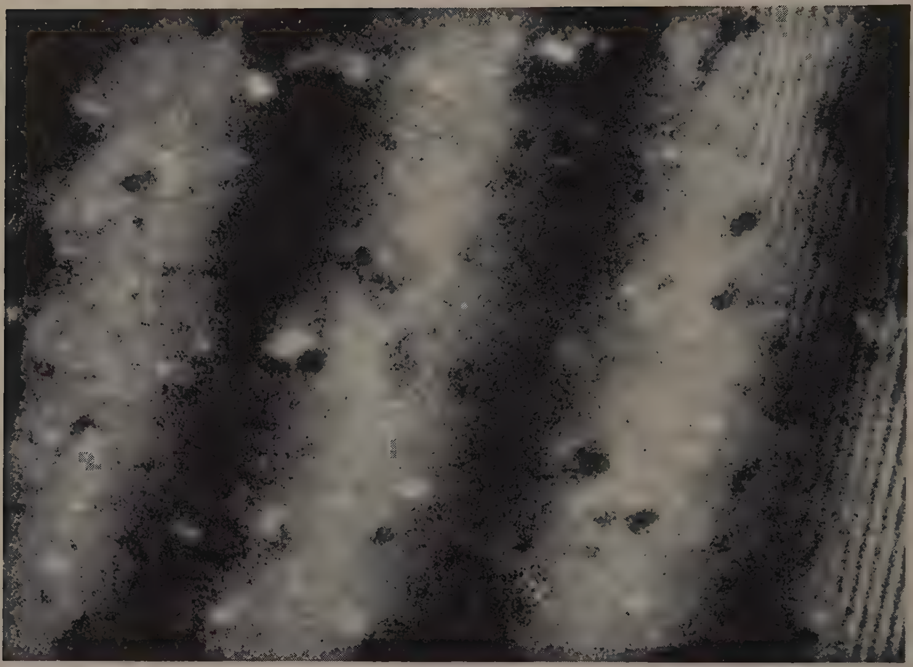

Detail of fig. 1, 800 000 ×.

Fig. 3

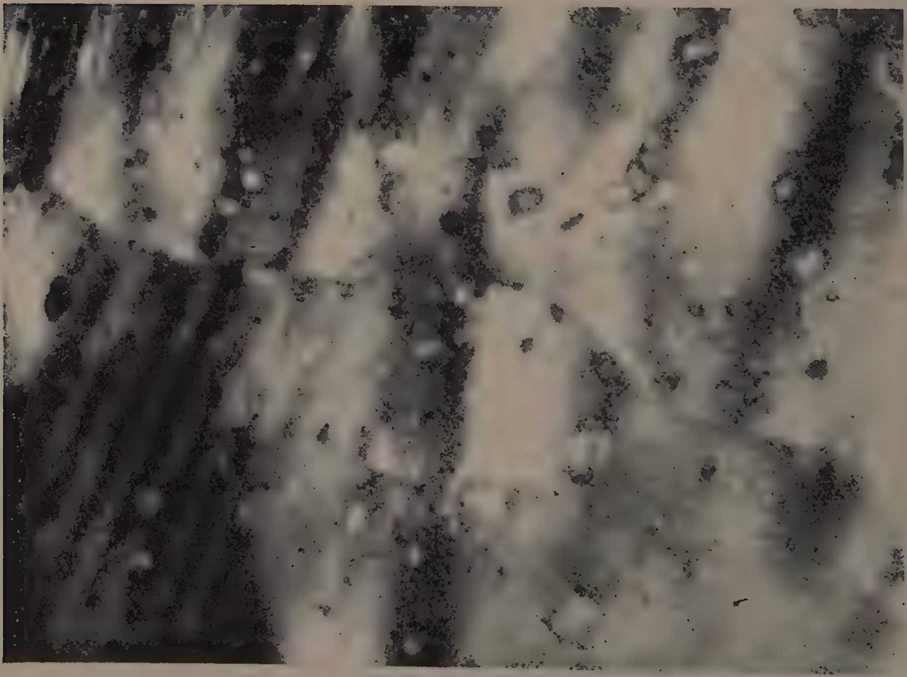

Same type of graphite as fig. 1 showing loops, 320 000 ×.

Fig. 4

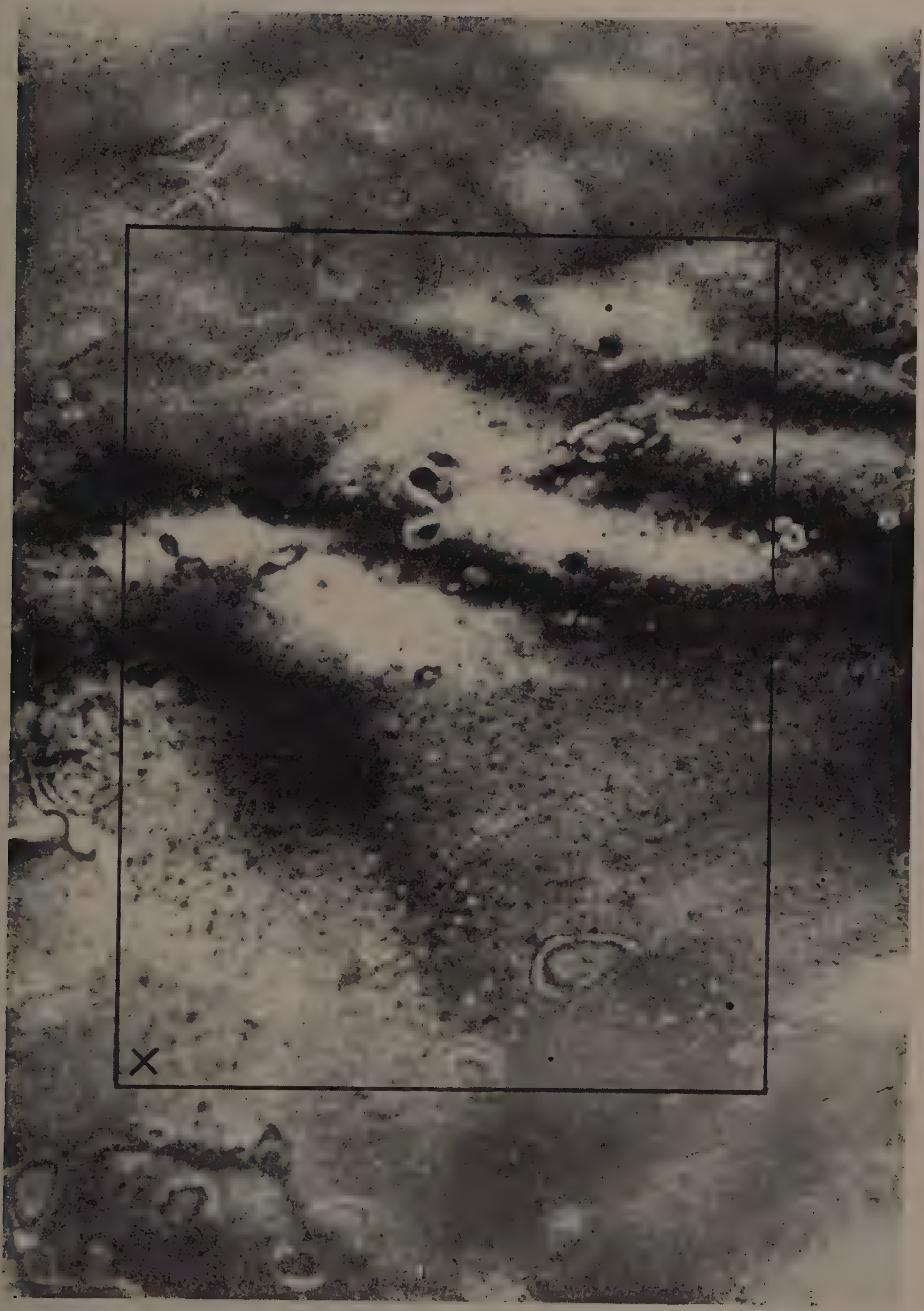

Same graphite as fig. 1 annealed at 400°c, 320 000 ×.

Fig. 5

Selected area of the specimen fig. 4 in bright-field illumination, 320 000 ×.

Fig. 2

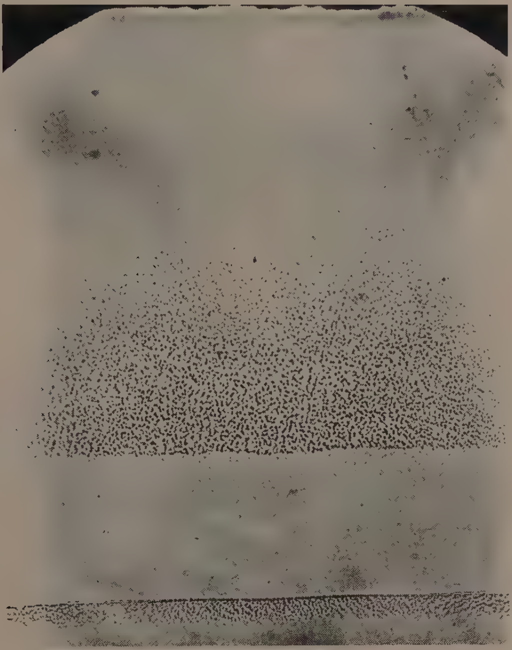

The incomplete precipitation of injected helium atoms in a single crystal of Johnson Matthey spectroscopically standardized copper during heating at 700°c for 1 hour. ×570.

Fig. 3

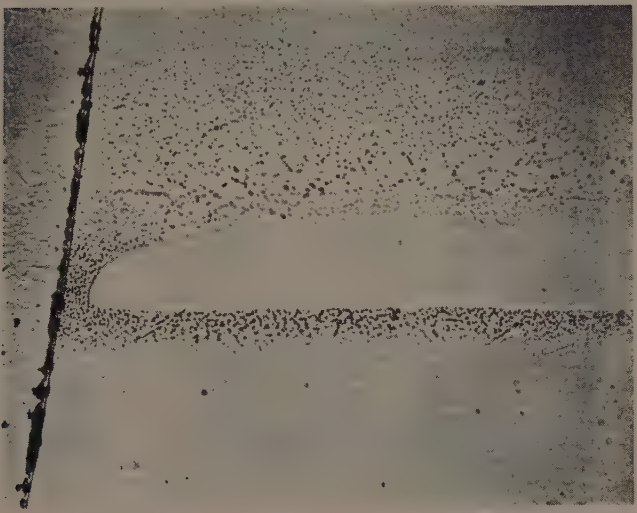

Bubbles at a free surface in copper after heating to 800°c for 1 hour. ×750.

Fig. 4

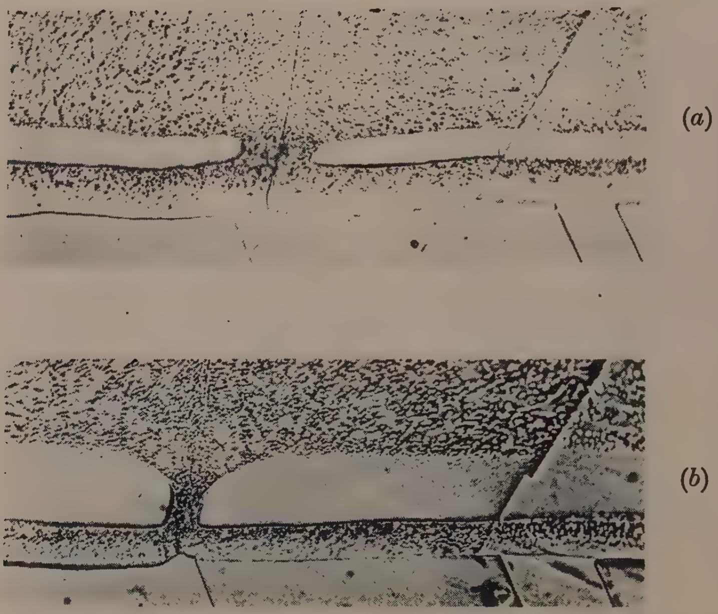

The surface exposed during heat treatment of 1 hour at 825°C (*a*) after a thin layer has been removed by mechanical and electro-polishing and (*b*) after the similar removal of a further layer. ×750.

Fig. 5

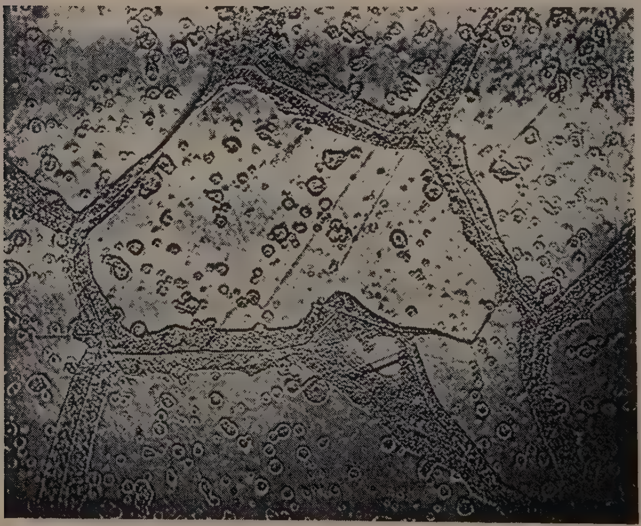

A parallel section of a similar piece of fine grain copper after an anneal of 1 hour at 750°C. ×570.

Fig. 6.

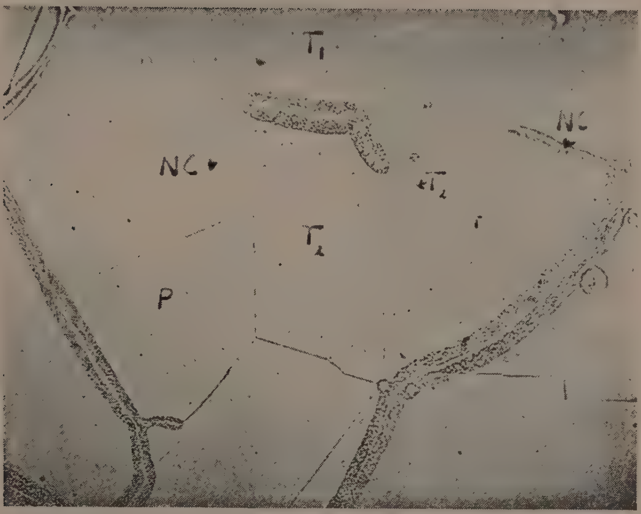

A parallel section showing bubble formation at twin boundaries. ×570.

Fig. 7

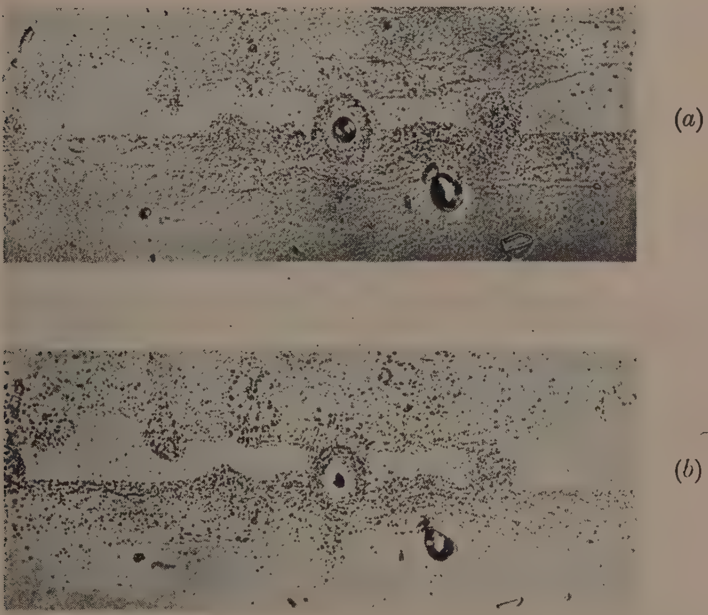

Microphotographs of a void in Johnson Matthey spectroscopically standardized aluminium (*a*) a section almost through the centre and (*b*) one below the centre. ×570.

Fig. 8

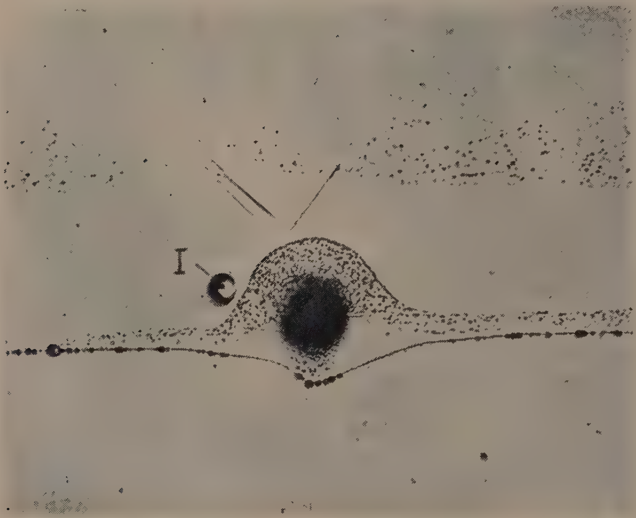

Photomicrograph of an inclusion (I) and a void in copper showing their relative ability to supply vacancies. × 1000.

Fig. 9

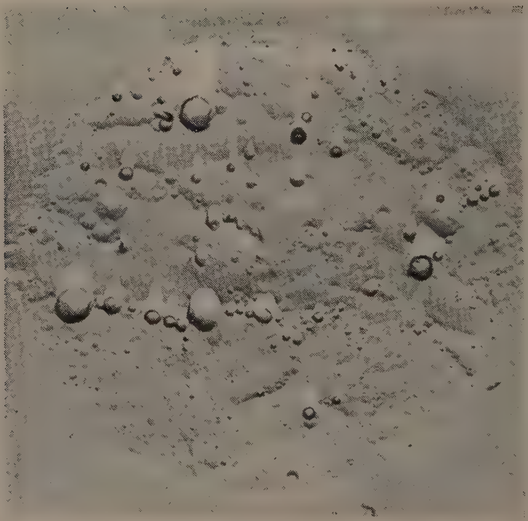

Electron micrographs of a circular region of bubbles in aluminium. × 9000.

Fig. 10

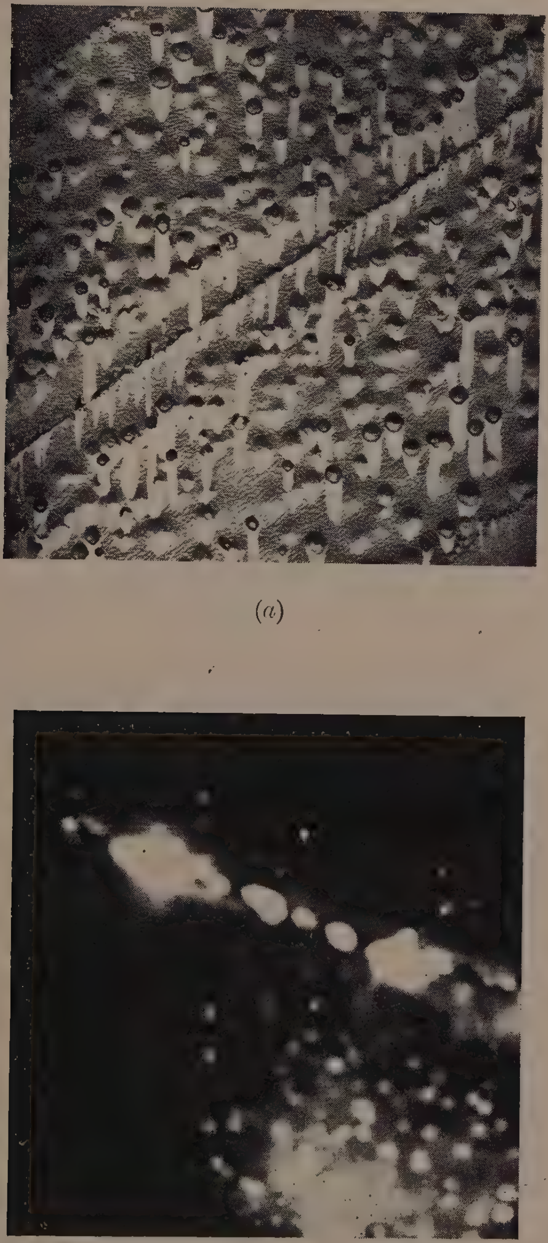

(a)

(b)

Electron micrograph of a grain boundary showing a zone with no bubbles adjacent to the boundary (*a*) shadowed carbon two-stage replica ×7000 and (*b*) transmission through a thin film of the metal extracted from the helium layer. ×12000.

Fig. 11

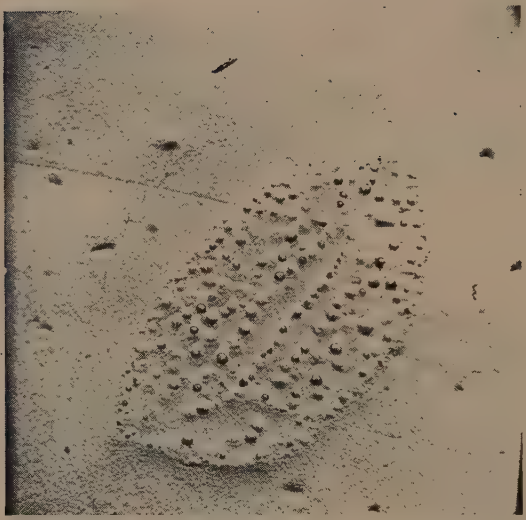

A grain boundary which is either a good vacancy source (central region) or a poor conductor, depending upon whether the adjoining grains are twinned or not. ×3000.

Creep in Face-centred Metals and Solid Solutions with special reference to α-brasses†

By P. FELTHAM and G. J. COPLEY
The University, Leeds

[Received June 24, 1959; and in revised form August 29, 1959]

ABSTRACT

The creep of α-brasses containing 10–35% Zn was studied in the range 350–650°C. The equilibrium creep rate satisfied the relation $\dot{\epsilon}=A_0(T)\exp(-H/kT)\sinh(q\sigma/kT)$, but two sets of the parameters A_0, H and of the activation volume q associated with the tensile stress σ were required, one above and one below a critical stress $\sigma_c'(T)$ above which Cottrell–Lomer locking appeared to become a less effective impediment to slip than at lower stresses. A peak in the activation energy H' (below σ_c') close to the composition represented by Cu_3Zn is interpreted in terms of local order near dislocation cores. This affects the migration of jogs and hence recovery by climb. Below σ_c', H is equal to 1·6 times the activation energy for grain boundary self-diffusion. Two models are proposed in which the climb of dislocations over intragranular obstacles or within grain boundaries are rate determining, depending on whether $\sigma<\sigma_c'$ or $\sigma>\sigma_c'$. The temperature dependence of A_0', A_0, q' and q is explained on the basis of the assumption that the dimensions of the intragranular substructure developing during creep attain lower limiting values which, at any given temperature, depend only on σ_c'.

§ 1. INTRODUCTION

IN their recent paper on the creep of face-centred cubic metals Feltham and Meakin (1959) showed that the steady, equilibrium, creep rate of oxygen-free high-conductivity copper (99·99%) of constant grain size could be represented by the relation

$$\dot{\epsilon}=A_0(T)\exp(-H/kT)\sinh(q\sigma/kT), \quad \dots \quad (1)$$

but that at any given temperature within the range 400–700°C used by them two sets of the parameters A_0, H, as well as of the activation volume q associated with the applied tensile stress σ had to be used, one below and one above a critical value of the applied stress $\sigma_c'(T)$ above which Cottrell–Lomer locking appeared to become a less effective impediment to slip than at lower stresses. While they could account quite well for the observed orders of magnitude of these parameters in terms of a model involving recovery facilitated by the climb of edge dislocations, they felt unable to advance an explanation of the pronounced temperature dependence of A_0 with the limited experimental data, relating in particular to the effect of intragranular substructures on the creep rate, then at their disposal.

---

† Communicated by the Authors.

The main object of the present work was to extend their research to alpha-brasses, utilizing the zinc content as a new variable which, through its effect on the creep rate, was expected to make a further development of the theory possible.

§ 2. MATERIALS AND METHOD

The equipment and the experimental methods were as described for copper (Feltham and Meakin 1959). Creep took place under constant stress in a vacuum better than 1 μ Hg. Rod-shaped specimens with a 10 cm gauge length and of 0·17 cm diameter were used. These were annealed *in situ* prior to creep, as in the case of copper, until a mean grain diameter $D=3\times10^{-3}$ cm was obtained. During annealing and creep each specimen was enveloped in thin foil rolled from the same type of brass from which the specimen had been drawn, and this was found to reduce zinc losses to a level at which no significant change was detectable after creep either gravimetrically or by microscopy.

The brasses used came from the same stock as those employed by Feltham and Copley (1958) in their study of grain-growth, and contained nominally 10, 20 30 and 35% of zinc by weight†.

Table 1

Brass	Cu%	Zn%	Fe%	Ni%	Sn%	Pb%	Bi%
90/10	89·68	10·29	0·030	0·000	—	0·000	0·0006
80/20	80·88	19·11	0·006	0·000	—	0·000	0·0006
70/30	71·13	28·85	0·004	0·000	0·003	0·009	0·0004
65/35	65·04	34·93	0·008	0·000	0·002	0·021	0·0003

Table 2

Brass	Annealing time (min)	Annealing temperature (°c)
90/10	20	650
80/20	20	600
70/30	20	550
65/35	15	550

Analyses of the brasses, and the annealing times and temperatures which were used to obtain the standard grain size are shown in tables 1 and 2. X-ray back-reflection photographs and electrolytic etching techniques (Jacquet 1954) showed the annealed brasses to be polygonized.

---

† As the atomic weight copper differs from that of zinc by less than 3% weight percentages are virtually equal to the corresponding atomic percentages.

The sub-grains appeared to be of the type observed by Young (1958) in copper, and by Hibbard and Dunn (1957) in silicon iron. The mutual inclination between sub-grains was of the order of $\frac{1}{2}$° (fig. 1, Pl. 77).

§ 3. Experimental Results

The creep of the brasses was similar in essence to that found in copper†, as may be seen from the recurrence of the following features, previously observed and discussed by Feltham and Meakin (1959):

(*a*) The instantaneous strain ϵ_0, measured within the first 1–2 sec after the application of the load to the specimen, obeyed the 'parabolic' work-hardening law

$$\sigma^2 = \chi_p(\epsilon_0 - \epsilon_c), \quad . \quad . \quad . \quad . \quad . \quad . \quad . \quad . \quad (2)$$

where $\chi_p(T)$ is the coefficient of work-hardening, and ϵ_c a small strain‡ (fig. 2).

Fig. 2

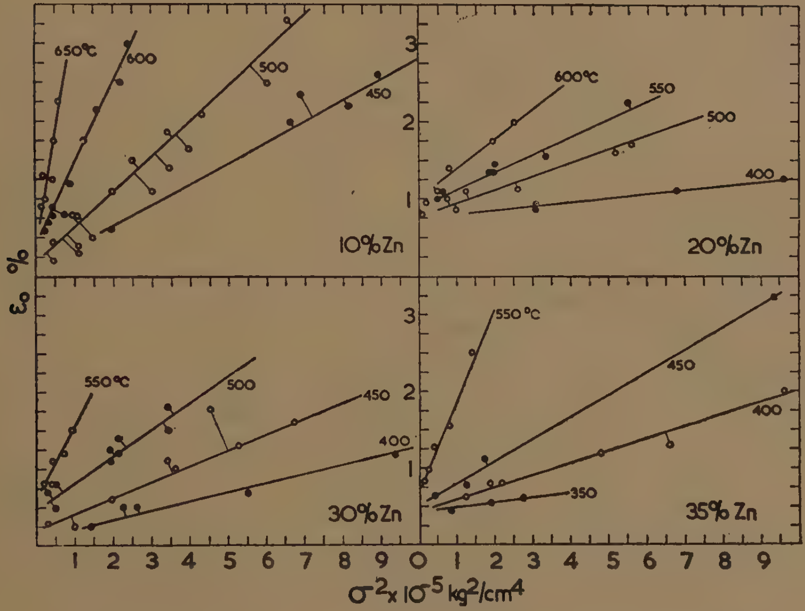

The initial strain as function of the applied stress (eqn. (2)).

(*b*) The transient stage, which follows the initial extension, consisted of two parts, the first obeying the Andrade equation

$$\epsilon_{\mathrm{tr}} = \beta(\sigma, T)t^{1/3}, \quad . \quad . \quad . \quad . \quad . \quad . \quad . \quad . \quad (3)$$

---

† All data on copper referred to in the text or diagrams are taken from the paper by Feltham and Meakin (1959). A full documentation of the experimental work discussed in the present paper has been given by Copley (1959).

‡ That the lines do not pass through the origin is probably due to the fact that the hardening is linear at low strains.

the second, subsequent, part showing a 'flattening out' with a creep rate much smaller than predicted by eqn. (3). No definite evidence of the existence of the $t^{1/3}$ stage was however obtained with the brasses containing 20, 30 and 35% of zinc, in which the whole transient stage was rather 'flat', as may be seen from the characteristic creep curves shown in fig. 3. Similarities between the transient creep of copper and the 90/10 brass are apparent from the validity of the relation

$$(\epsilon_{tr})_{max}-\epsilon_0=\lambda(T), \quad \sigma>\sigma_c' \quad . \quad . \quad . \quad . \quad . \quad . \quad . \quad (4)$$

indicated by the horizontal parts of the curves in fig. 4. Here $\lambda(T)$ is constant at any given temperature; $(\epsilon_{tr})_{max}$ is the strain at the onset of the steady stage of creep, and ϵ_0 the initial instantaneous strain referred to in equation (2). While the stress dependence of the strain $(\epsilon_{tr})_{max}$ is similar in all the brasses (fig. 5), the relation given by eqn. (4) does not seem to be applicable to all of them.

Fig. 3

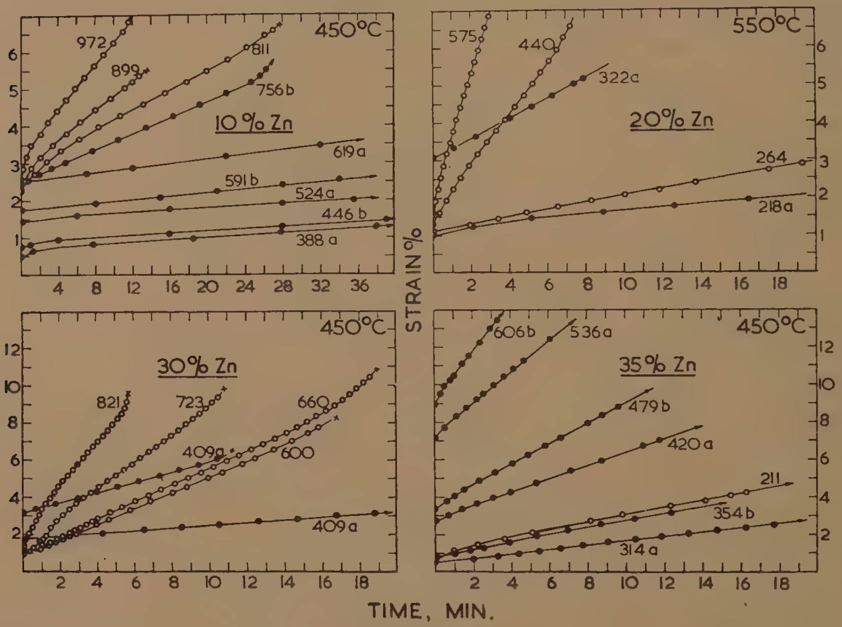

Characteristic creep curves. Figures indicate the applied tensile stress in kg/cm². Curves with the same suffix were obtained with the same specimen by changing the load during creep. The initial part of curves *a* for 35% Zn is not shown. An incubation period was sometimes observed, e.g. an almost horizontal part of curve 600 for 30% Zn. For curve 211 (35% Zn) multiply time-scale by 10.

(*c*) The equilibrium, steady, tensile strain rate could be expressed by the relation.

$$\dot{\epsilon}=\tfrac{1}{2}A_0(T)\exp\left[-(H-q\sigma)/kT\right], \quad . \quad . \quad . \quad . \quad . \quad . \quad . \quad (5)$$

Fig. 4

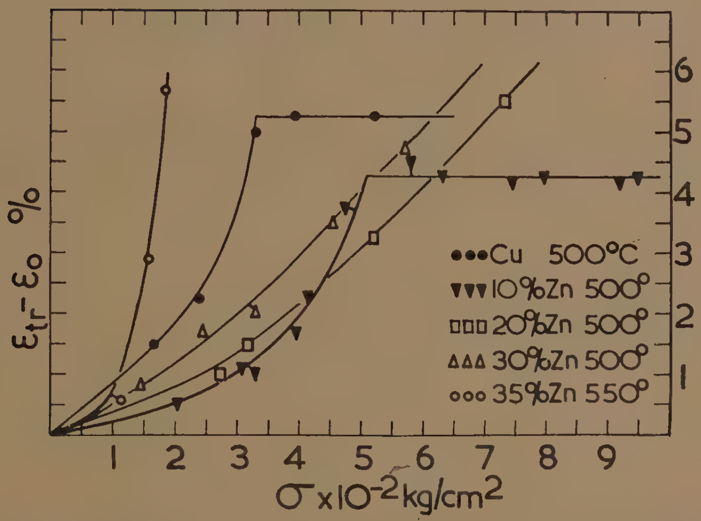

The difference between the maximum of the transient strain and the initial strain as function of the applied stress (eqn. (4)).

Fig. 5

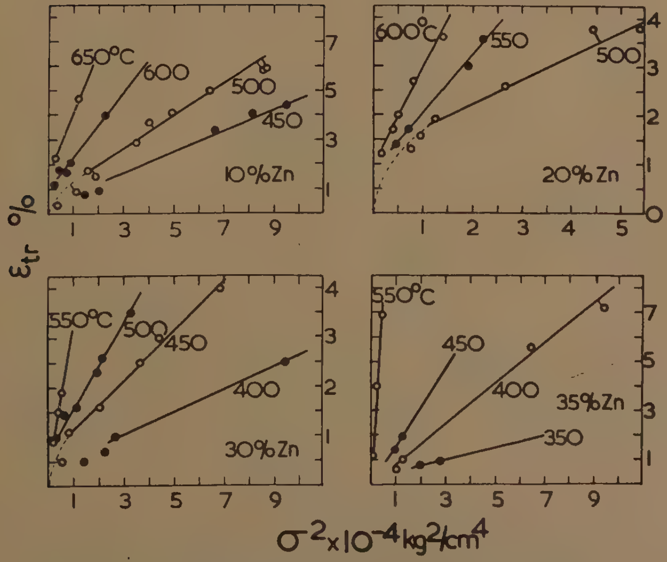

The stress dependence of the total transient strain and again two sets of the parameters were required, i.e. A_0', H' and q' below a critical tensile stress σ_c', corresponding to the breaks in the isotherms in fig. 6, and A_0, H and q above σ_c'. The values of H' and H, q' and q, and the virtual temperature independence of the products

$$A_0'(T)\exp(-H'/kT) \text{ and } A_0(T)\exp(-H/kT) \quad . \quad . \quad . \quad (6)$$

are shown in figs. 7–10; the heats of activation H' and H were determined by the temperature-cycling method (Feltham and Meakin 1959). (In the log $\dot{\epsilon}$ versus log σ representation the isotherms are cusp shaped, with the nodes at σ_c'.)

Fig. 6

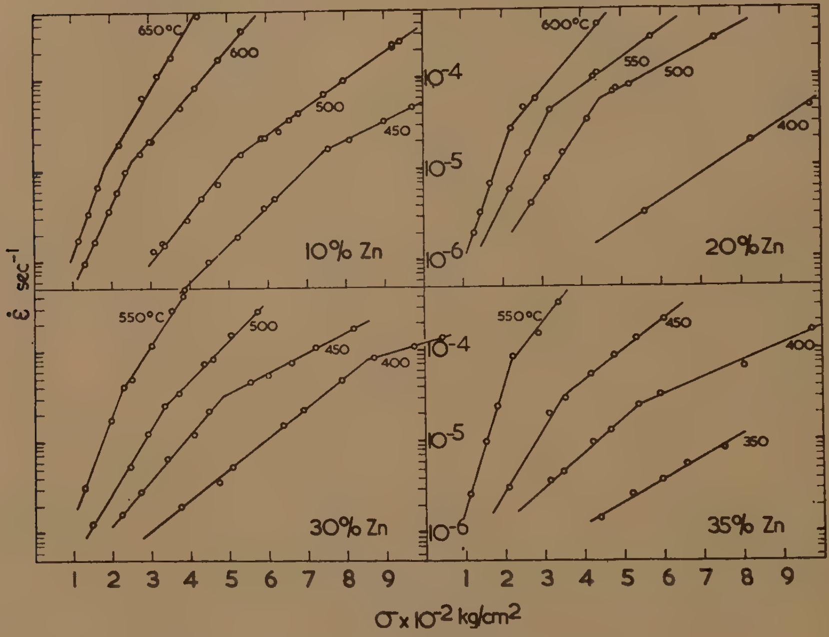

Stress versus steady strain rate isotherms.

(*d*) The temperature dependence of the critical stress σ_c' was again given by

$$\log(\sigma_c'/G) \simeq c_1 - c_2 T, \quad . \quad . \quad . \quad . \quad . \quad . \quad . \quad . \quad (7)$$

(fig. 11), where G is the shear modulus, and c_1 and c_2 constants. An equally satisfactory representation over the entire range of temperatures used was found to be

$$\sigma_c' = (\sigma_c')_0 \exp(Q/kT), \quad . \quad . \quad . \quad . \quad . \quad . \quad . \quad . \quad (8)$$

the 'activation energy' Q depending somewhat on the zinc content. Equation (8) will be used at a later stage, being more convenient than eqn. (7) (see eqn. (11) and fig. 14).

Fig. 7

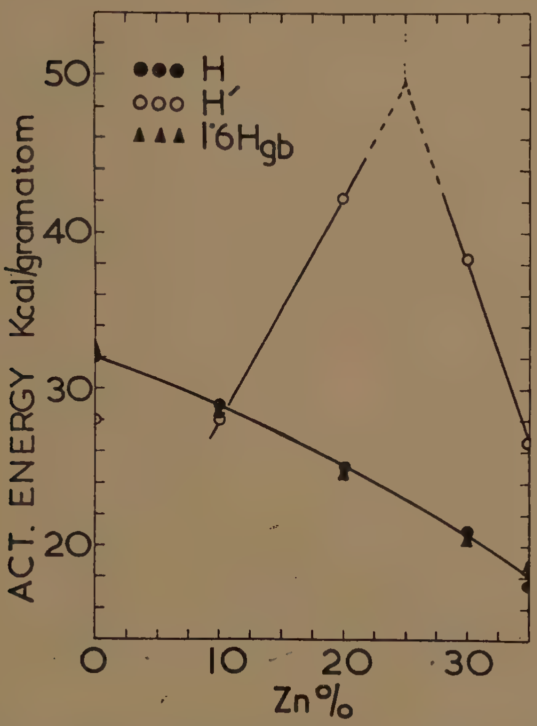

The activation energies H' and H below and above σ_c' respectively.

Fig. 8

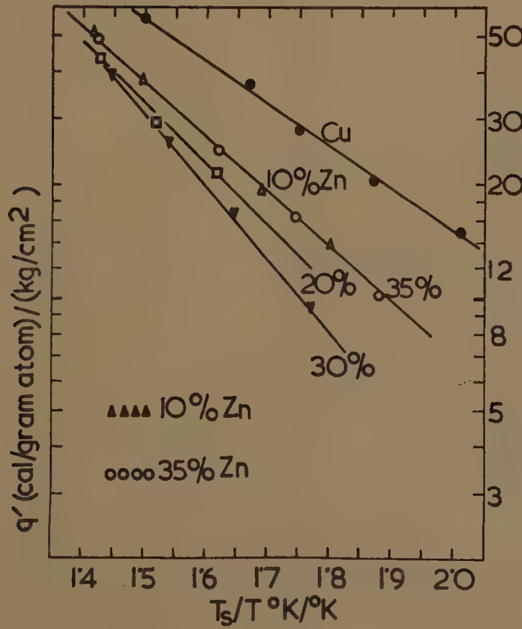

The activation volume q' obtained from fig. 6. The solidus temperatures are, with ascending zinc contents, 1356, 1305, 1253, 1191 and 1175°K.

Fig. 9

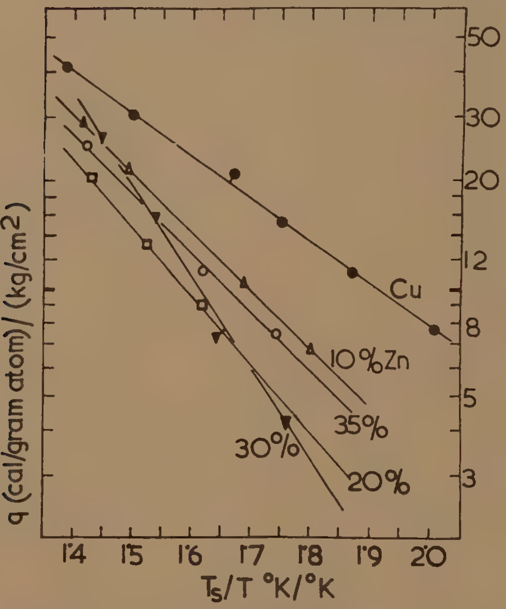

The activation volume q at stress exceeding σ_c'.

Fig. 10

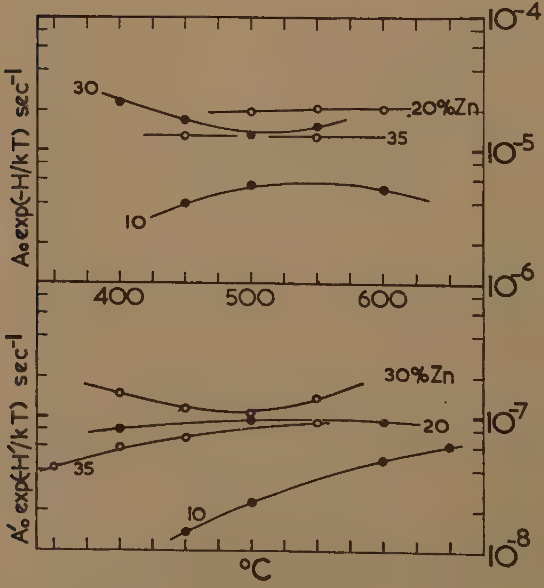

The products $A_0' \exp(-H'/kT)$ and $A_0 \exp(-H/kT)$.

(*e*) The time to fracture, t_f, can be expressed in terms of the equilibrium creep rate:

$$t_f=(K/\dot{\epsilon})^m, \tag{9}$$

where K and m are constants, and $m \simeq 1{\cdot}0$ (fig. 12).

(*f*) The formation of slip-bands was observed to take place in creep at stresses above σ_c' (fig. 13, Pl. 78); below σ_c' slip was not resolvable by optical microscopy. Intragranular cavitation, sometimes in the form of discrete adjacent voids of the string-of-beads type previously reported by Greenwood *et al.* (1954), was also observed.

Fig. 11

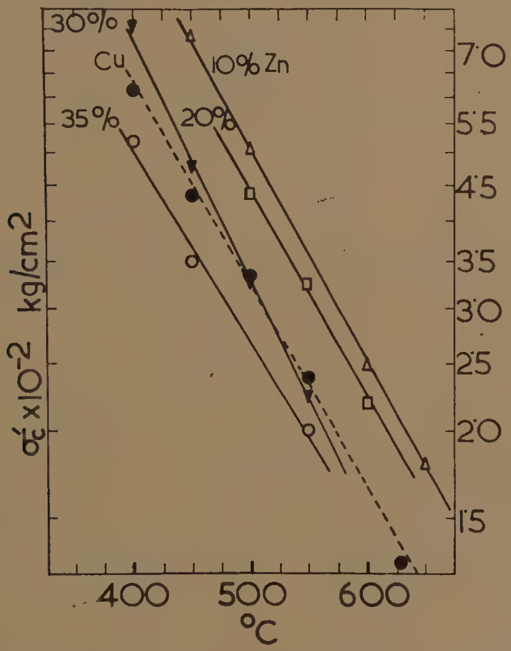

Temperature dependence of the critical tensile stress σ_c'.

(*g*) The existence of a linear relation between χ_p (eqn. (2)) and σ_c' was again confirmed, as may be inferred from the constancy of the products $\sigma_c'q'$ and $\chi_p q$ (figs. 14 and 15), and the experimentally established relation (figs. 8 and 9):

$$q' \simeq 2q. \tag{10}$$

The temperature dependence of q', and hence of q, was of the form

$$q'=q_0' \exp(-Q/kT) \tag{11}$$

as is apparent from figs. 8 and 9. Values of Q are given in table 3.

(*h*) The equilibrium strain rate was independent of the grain size below σ_c', above this stress it was a linear function of the square of the mean grain diameter (fig. 16).

(*i*) The value of H' obtained at 450°C by the thermal cycling method with a single crystal, which had been grown in an evacuated silica tube from a rod of the 65/35 brass by Bridgman's method, was found to be 45 kcal/gram atom, i.e. close or equal to the activation energy of chemical self-diffusion, and appreciably higher than H' as observed in polycrystals of the same brass.

Table 3

Brass	Cu	90/10	80/20	70/30	65/35
H' kcal/g atom	28	28	42	38·5	26·5
Q kcal/g atom	7·1	9·8	10·9	13·8	12·5
H'/Q	3·9	2·9	3·8	2·8	2·1

Fig. 12

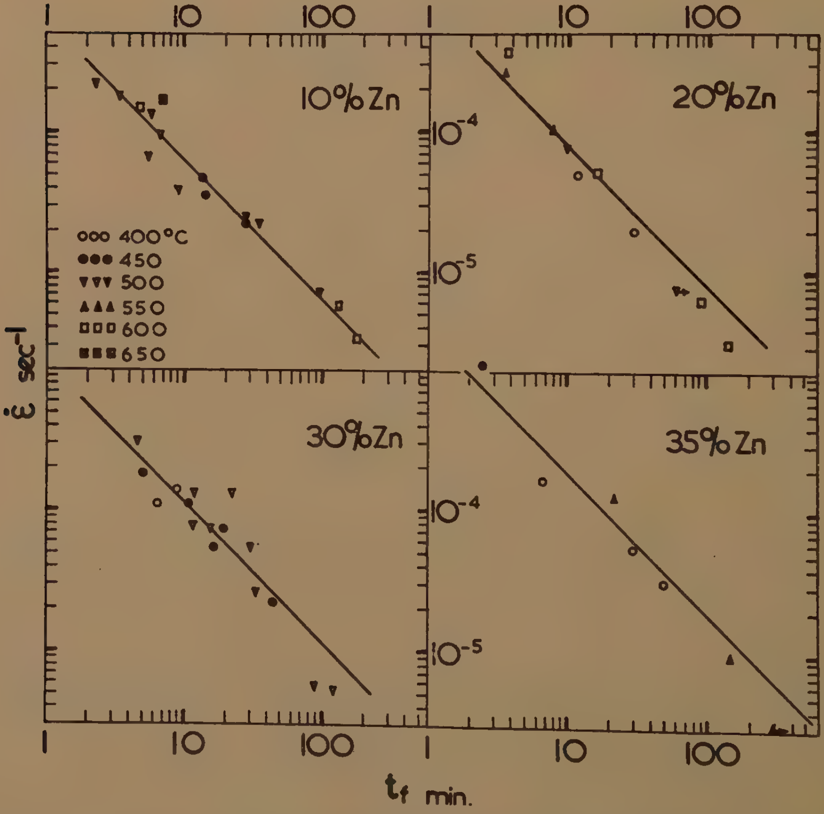

The time to fracture as function of the equilibrium creep rate. The lines correspond to $m=1$ in eqn. (9).

Of the observations which cannot be correlated with similar ones made on copper two are of particular interest. First, with the exception of the 90/10 brass, the difference between H' and H was much greater than in copper (fig. 7). While H' (below σ_c') was found to be independent of temperature it changed significantly with the zinc content, particularly at concentrations approaching the composition Cu_3Zn. Second, H (at stresses exceeding σ_c') did not show a similar maximum, but decreased uniformly with increasing zinc contents. As may be seen from fig. 7,

$$H \simeq 1 \cdot 6\, H_{gb}, \quad . \quad . \quad . \quad . \quad . \quad . \quad . \quad . \quad . \quad . \quad (12)$$

where H_{gb} is the heat of activation of grain boundary self-diffusion as determined by Feltham and Copley (1958) from grain-growth data.

Fig. 14

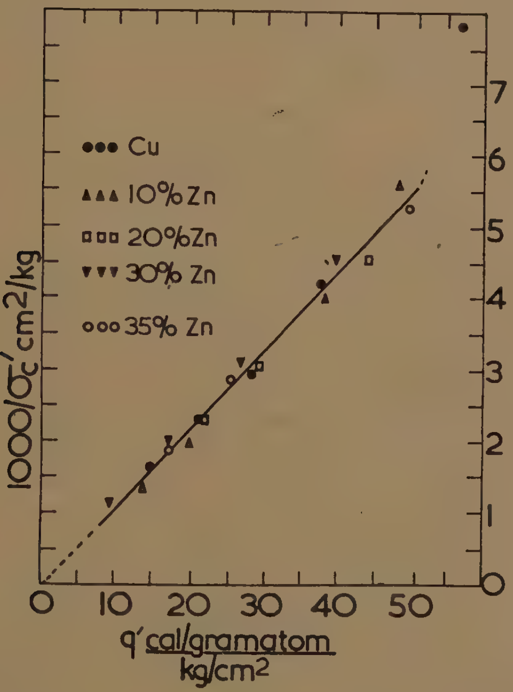

The relation between the critical stress σ_c' and q'.

A correlation of $(\epsilon_{tr})_{max}$ with σ^2, not previously attempted for copper, shows a parabolic law of the same form as eqn. (2) to be again applicable (fig. 5). The coefficients of work-hardening are generally lower (dotted lines in fig. 17) than the corresponding ones (full lines) derived from the initial extension (fig. 2).

The qualitative similarities between the characteristics of the creep of alpha-brasses and copper, indicated by the above points, suggest that the mechanisms of creep are essentially the same in polycrystals of the

Fig. 15

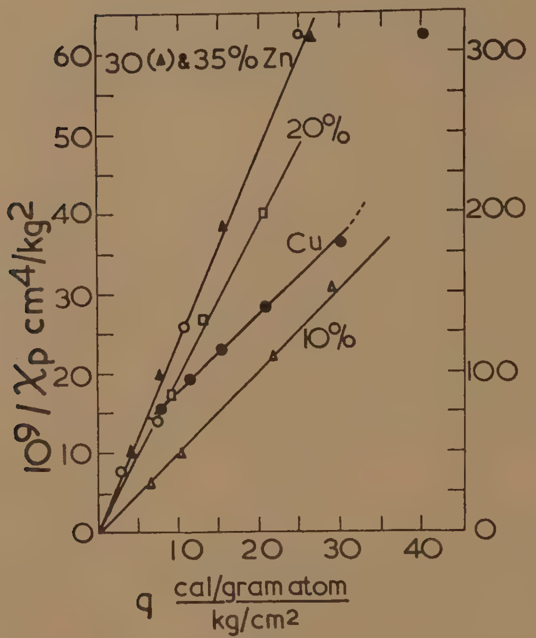

The coefficient of parabolic work-hardening (eqn. (2)) as function of the activation volume *q*. The right hand scale is for copper and the 90/10 brass only.

Fig. 16

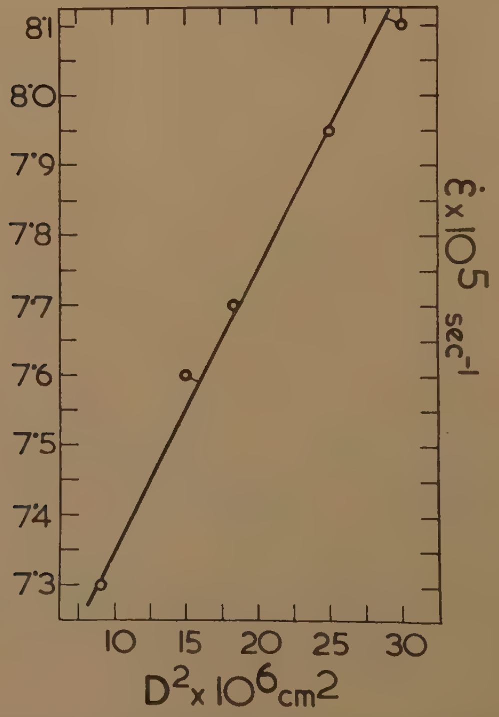

The effect of grain size on the creep rate at 500°c in 70/30 brass. The various grain sizes were obtained by annealing at 600°c for periods up to 45 min.

brasses and copper; a similar inference appears to be justified for single crystals also (point (*i*)). We shall therefore attempt to correlate the observations in terms of a model similar to that employed by Feltham and Meakin (1959) in describing the creep of copper, first however developing the model in the light of the results obtained in the present work, particularly those arising from the use of the alloy composition as a variable.

Fig. 17

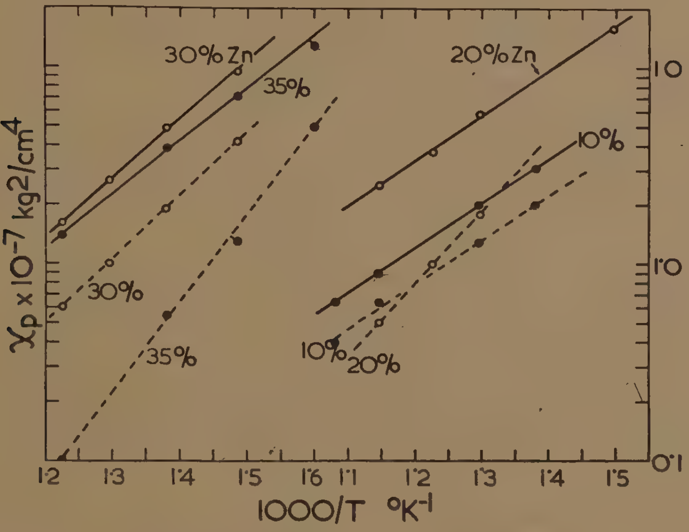

The coefficients of parabolic work-hardening obtained from fig. 2 (full line) and fig. 5 (broken line) for the initial extension and the total transient strain respectively.

§ 4. Discussion

4.1. *Dislocation Climb and Ordering*

Basing ourselves on the reasoning of Feltham and Meakin (1959) we therefore assume that the rate determining mechanism, i.e. the slowest recovery mechanism, is the climb of edge dislocations over obstacles, both above as well as below σ_c', and that the dislocations are lost mainly at sinks within the grains below σ_c', while the grain size dependence of $\dot{\epsilon}$, as well as micrography suggest that above σ_c' intergranular recovery is rate determining, the grain boundary being less permeable to the propagation of slip than the intragranular obstacles.

Of the features due to alloying the composition dependence of H' is indicative of a tendency to superlattice formation which, in view of the high temperatures, cannot be general throughout the lattice (Masumoto *et al.* 1952), but is probably located in the immediate vicinity of the dislocation cores. If the rate determining mode of recovery occurs at grain boundaries then superlattice formation would be expected to be of little consequence in view of the non-crystallographic structure of the grain interfaces, and effects due to ordering should not affect the activation energy of creep significantly. The observation that H (above σ_c') is in fact a monotone function of the zinc content thus further supports the view that the rate controlling recovery process at stresses exceeding σ_c' occurs at grain boundaries.

We shall assume that in polycrystalline brasses, as in copper, climb takes place through the migration of jogs in edge dislocations in which the jogs are due to intersection of the climbing dislocation with 'forest' dislocations, and that the applied stress assists the migration of the jog by reducing the activation energy from H' (or H) to $H' - q'\sigma$ (or $H - q\sigma$) by a mechanism of the type described by Feltham and Meakin (1959). In their work H' was identified with the activation energy for the non-conservative migration of a jog in the presence of a vacancy adjacent to it; $H(\sigma > \sigma_c')$, given by them as 32 kcal/gram atom, is close to the activation energy for grain boundary slip (33 kcal/gram atom) as found in copper by Rotherham and Pearson (1956).

The assumption that climb occurs by the migration of jogs in the presence of vacancies does not imply that the process is equally simple in copper and in the brasses; the appreciable variation of H' with zinc concentration suggests a greater complexity in the brasses than in copper, involving, in particular, disordering of the superlattice in a small volume surrounding the jog. We shall therefore write for the free energy of activation of the process:

$$E' = H_j' + zH_0'\left(1 - \frac{T}{T_s}\right) = H' - zH_0'\frac{T}{T_s} \quad . \quad . \quad . \quad . \quad (13)$$

where H_j' is about 27 kcal/gram atom, i.e. corresponding to the line which may be drawn through the values of H' for copper, and the 90/10 and 65/35 brasses for which ordering makes no or only a negligible contribution (fig. 7), T_s the solidus temperature, and z an ordering parameter with values between 0 (Cu) and 1 (for approximately 25% Zn). The second term in the bracket in eqn. (13) represents the entropy of the disordering process.

4.2. *Creep Below σ_c'*

Now if, in general, a jog has to migrate a distance l_j', i.e. l_j'/b times before the dislocation containing it (among others) has climbed by one lattice spacing b, and if this dislocation has to climb $\frac{1}{2}l_s'/b$ times before escaping over an obstacle having a stress field of wavelength l_s', then the time of escape will be given by

$$t' \simeq (1/\nu)(\tfrac{1}{2}l_j'l_s'/b^2)\exp\left[(E' - q'\sigma)/kT\right], \quad . \quad . \quad . \quad . \quad (14)$$

where ν is of order of $10^{12}\,\mathrm{sec}^{-1}$, and (Feltham and Meakin 1959):

$$q' = l_j'b^2/4 = fl_s'b^2/4 \quad . \quad . \quad . \quad . \quad . \quad . \quad . \quad . \quad (15)$$

where f is a real fraction which, in correlating the experimental results we shall later take to be equal to 1/70.

We have written σ instead of $\sigma-\sigma_y$ in eqn. (14), because the tensile yield stress σ_y (which may be defined as the stress to give a tensile creep rate of, say $10^{-8}\,\text{sec}^{-1}$) is negligible in comparison with the values of σ which have here been used, as may be seen from a rough extrapolation of the isotherms (fig. 6) to such low strain rates.

If the mean spacing of the intragranular slip zones is l_h', then the creep rate in shear is $(b/l_h')/t'$, assuming that the dislocations climb over barriers singly. On taking the tensile strain rate to be half the shear rate one obtains on substituting for t from eqn. (14):

$$\dot{\epsilon}=\tfrac{1}{2}A_0'\exp\left[-(H'-q'\sigma)/kT\right] \quad . \quad . \quad . \quad . \quad . \quad (16)$$

with

$$A_0'=2(\nu b^3/v')\exp\left(zH_0'/kT_s\right), \quad . \quad . \quad . \quad . \quad . \quad . \quad (17)$$

where we have written

$$v'=l_h'l_j'l_s'. \quad . \quad . \quad . \quad . \quad . \quad . \quad . \quad . \quad . \quad (18)$$

We shall revert to the discussion of eqn. (17) after having considered the equilibrium creep rate above σ_c'.

4.3. *The Equilibrium Creep Rate above* σ_c'

In view of the grain size effects discussed above we shall assume, following Feltham and Meakin (1959), that at stresses above σ_c' the active slip zones generally extend across the entire grain, the grain boundary now being the strongest obstacle to the propagation of slip. Transgranular slip bands as are observed above σ_c' in copper and in the brasses (fig. 13) will then be regarded as having resulted from the propagation of slip initiated by the failure of intragranular obstacles† to contain dislocations within the small glide zones active below σ_c'.

Now, if we imagine slip to spread from one such small zone across the grain it will induce the spreading of slip from similar zones situated within a volume of the grain equal to about $\bar{D}^2l_h$ where, as before, l_h is the mean distance between small slip zones, and is thus of the same order of magnitude as l_h'. We shall take the area $\bar{D}^2$ equal to aD^2-L^2, with $a\simeq\frac{1}{2}$, D the mean grain diameter, and L the length of the initial slip zone. We would therefore observe the formation of a slip band comprising on the average $N(\bar{D}^2l_h)$ active slip planes, N being the density of active slip zones per unit volume prior to the onset of band formation, i.e. below σ_c'. If, now, the average slip distance at stresses below σ_c' is L then we may write.

$$N=C/L^2l_h \quad . \quad . \quad . \quad . \quad . \quad . \quad . \quad . \quad . \quad (19)$$

---

† The role of sessile dislocations of the Cottrell–Lomer type in providing or stabilizing obstacles in face-centred metals has been discussed by Feltham and Meakin (1959). In body-centred metal sessile dislocations may form through the reaction $\frac{1}{2}a[\bar{1}\bar{1}1]+\frac{1}{2}a[11\bar{1}]=a[001]$, proposed by Cottrell (1958).

where C is a numerical constant of order unity The shear strain induced in the grain by the loss of one dislocation per active slip plane, assuming adjacent bands to be $2l_h$ apart, is then given by $N(\bar{D}^2 l_h)(b/l_h)$; the corresponding tensile strain may therefore be written, on substituting for N from eqn (19):

$$\epsilon = Cb\bar{D}^2/l_h L^2. \quad . \quad . \quad . \quad . \quad . \quad . \quad . \quad . \quad (20)$$

The formation of bands on one slip system only has been considered in deriving eqn. (20), it being assumed that the effect of the more complex geometry of deformation of actual grains would also find expression through C.

We shall assume the climb in the grain boundary to be akin to that within the grain, so that the life-time, t, of a dislocation will again be given by an equation of the same form as (14), omitting dashes from the parameters, and where now also

$$E = H + (34C_{\mathrm{Zn}})T. \quad . \quad . \quad . \quad . \quad . \quad . \quad . \quad (21)$$

The reason for using eqn. (21) is as follows:

As is apparent from fig. 7, the measured value of H is equal to 1·6 times the heat of activation of grain boundary self-diffusion in the brasses. The free energy of grain boundary self-diffusion in the brasses contains however a composition dependent entropy term (Feltham and Copley 1958):

$$E_{\mathrm{gb}} = H_{\mathrm{gb}} + (21{\cdot}2C_{\mathrm{Zn}})T \text{ kcal/gram atom}, \quad . \quad . \quad . \quad . \quad (22)$$

which leads to the corresponding entropy term in eqn. (21) on multiplying by 1·6, the observed ratio H/H_{gb}. The strain rate ϵ/t is therefore (using eqns. (14), (20) and (21)):

$$\dot{\epsilon} = \tfrac{1}{2}A_0 \exp[-(H - q\sigma)/kT], \quad . \quad . \quad . \quad . \quad . \quad (23)$$

where now

$$A_0 = 2(Cb^3\nu\bar{D}^2/L^2 v)\exp(-17C_{\mathrm{Zn}}), \quad . \quad . \quad . \quad . \quad . \quad (24)$$

with C_{Zn} expressed as a proper fraction, and

$$v = l_h l_j l_s. \quad . \quad . \quad . \quad . \quad . \quad . \quad . \quad . \quad . \quad (25)$$

From eqns. (17) and (24) one obtains

$$A_0/A_0' = C(\bar{D}/L)^2(v'/v)\exp[-17C_{\mathrm{Zn}} - (zH_0'/kT_s)]. \quad . \quad . \quad (26)$$

It is clear from eqns. (17) and (24) that the pronounced temperature dependence of A_0' and, by implication, that of A_0 (eqn. (26)), must be ascribed to v' and v respectively. This we shall now consider.

4.4. *The Temperature Dependence of A_0', A_0, q' and q*

In discussing the temperature dependence of these parameters we shall make the basic assumption that in the transient stage of creep the intragranular substructure developing by glide and polygonization finally attains a lower limiting size beyond which no further fragmentation takes place. A sub-structure with a characteristic dimension l_s' then persists throughout the steady stage of creep, l_s' being a measure of the wavelength of the intragranular stress fields. We shall also assume that the mean spacing between adjacent jogs on dislocations l_j' is given by

$$l_j'=fl_s' \text{ and } l_j=fl_s, \qquad (27)$$

as in eqn. (15), and that we may write

$$l_s'=\alpha Gb/\tau_c', \qquad (28)$$

where the shear stress

$$\tau_c' \propto \sigma_c', \qquad (29)$$

and α a dimensionless constant of order 0·1, the exact value of which is determined by the specific arrangement of the dislocations characteristic of the steady stage. As, according to Feltham and Meakin (1959), σ_c' appears to be determined by the magnitude of the stacking-fault energy†, so is then the characteristic length l_s'.

If now we take the spacing between slip zones ($\sigma < \sigma_c'$) to be of the same magnitude as the wavelength of the intragranular stress field, i.e.

$$l_h'=l_s', \quad (\text{and } l_h=l_s), \qquad (30)$$

then eqn. (17) yields, on using eqns. (18), (27) and (28),

$$A_0'=(2f^2\nu b^3/l_s'^3)\exp(zH_0'/kT_s), \qquad (31)$$

or

$$A_0'=(2\nu f^2/\alpha^3G^3)\tau'^3_c \exp(zH_0'/kT_s). \qquad (32)$$

On taking $\nu=10^{12}\,\text{sec}^{-1}$, $G=4\times10^5\,\text{kg/cm}^2$, $\alpha^3/f^2=2{\cdot}2$, one obtains for copper ($z=0$):

$$A_0'=(\tau_c'/70)^3\,\text{sec}^{-1},$$

and on taking

$$\sigma_c'=3\tau_c', \qquad (33)$$

$$A_0'=(\sigma_c'/210)^3\,\text{sec}^{-1}, \qquad (34)$$

σ_c' and τ_c' being expressed throughout in kg/cm². The values of A_0' obtained from eqn. (34) compare well with those obtained by Feltham and Meakin (1959) experimentally (table 4).

On substituting for l_s' from eqn. (15) into eqn. (31) one obtains for copper:

$$A_0'=\nu f^2b^2/32q'^3 \qquad (35)$$

which, with $f=1/70$, yields

$$A_0'\simeq 10^5/q'^3\,\text{sec}^{-1}, \qquad (36)$$

q' being given in (cal/gram atom)/(kg/cm²). Values of A_0' obtained by means of eqn. (36) are also shown in table 4. With the above value of f, α in eqn. (32) assumes the value 0·077.

---

† Feltham and Meakin found that the stress $\sigma_c(T)$ at which linear hardening terminates in copper in the range 77–293°K did not extrapolate well to the values of $\sigma_c'(T)$ obtained in creep between 400 and 700°C. This was confirmed with brasses, using σ_c values obtained by Feltham and Copley (1960); extrapolation was not possible.

As to A_0, we observe that on taking the slip distance to be $L=5\mu$ in eqn. (26), the ratio $(\bar{D}/L)^2$ is equal to about 18, so that for copper, for which $q'/q=2$ and hence $v'/v=8$,

$$A_0/A_0'=130C,$$

which, remembering that C was assumed to be of order 1, is in fair agreement with the values of this ratio in table 4.

Table 4

Brass		Temperature (°C)					
		400	450	500	550	600	650
Cu	A_0' eqn. (34)	25	8·9	2·9	1·3	0·8‡	—
	A_0' eqn. (36)	36	13·5	4·5	2·0	0·6‡	—
	A_0' (expt.)†	26 (*a*)	8·9	3·3	1·2	0·6‡	—
	A_0	$1{\cdot}6\times10^4$	2900	660	140	33‡	—
	A_0/A_0'	390	325	200	116	55	—
90/10	A_0'	—	16	3·8	—	0·3	0·056
	A_0	—	2000	730	—	82	—
	A_0/A_0'	—	125	191	—	366	—
80/20	A_0'	$3{\cdot}0\times10^6$	—	$6{\cdot}6\times10^4$	—	2600	—
	A_0	—	—	180	84	24	—
	A_0/A_0'	—	—	$2{\cdot}7\times10^2$	—	$9{\cdot}3\times10^{-3}$	—
70/30	A_0'	$2{\cdot}7\times10^5$	$3{\cdot}3\times10^4$	$4{\cdot}5\times10^3$	$1{\cdot}4\times10^3$	—	—
	A_0	140	34	12	5·6	—	—
	A_0/A_0'	52×10^{-3}	0·012	0·0027	0·004	—	—
65/35	A_0'	78 (*b*)	21	7·0	0·99	—	—
	A_0	—	97	—	0·72	—	—
	A_0/A_0'	—	0·46	—	0·73	—	—

† All remaining A_0' and A_0 are experimental values expressed in sec^{-1}.
‡ 630°C. (*a*) Previously erroneously given as 41. (*b*) 350°C.

4.5. *The Effect of Alloying on A_0' and A_0*

Assuming that the effect of alloying is expressed only through the exponential terms in eqns. (24) and (26), we find that in a 65/35 brass, in which z may be assumed to be 0, (eqn. (13)) A_0 should be approximately 365 times smaller than A_0 in copper, i.e. by $\exp(-17\times0{\cdot}35)$, on using eqn. (24). This overestimates the ratio obtained at 550°C (194) by a factor of about 2, with a bigger error at lower temperatures, presumably because of the simplifying assumption made in deriving the theoretical ratio.

In order to investigate the effect of the local ordering we shall compare the ratio A_0/A_0' for copper with that of the 70/30 brass, taking zH_0 in eqn. (26) to be equal to 11·5 kcal/gram atom (i.e. $38{\cdot}5-28$; table 3, eqn. (13)). With $T_s=1191$°K for 70/30 brass the ratio should be $1{\cdot}4\times10^4$ times greater in copper than in the brass. This compares very well with the average value of the experimentally determined ratio obtained from values given in table 4, namely $1{\cdot}8\times10^4$.

The treatment also accounts for the virtual temperature independence of the products $A_0'(T)\exp(-H'/kT)$ and $A_0(T)\exp(-H/kT)$, also observed in copper and other metals (Fastov 1950), for the temperature dependence of A_0' and A_0 is of the form $\exp(3Q/kT)$, (eqns. (10), (11), (26) and (35)), and this largely cancels the effect of the Boltzmann term containing the activation energies H' and H respectively. Further, the observation (Feltham 1957) that at temperatures corresponding to the same fraction of the melting point large values of q' are associated with metals having large stacking-fault energies can be explained if a significant part of the stress defining l_s' (eqn. 28) is due to chemical interaction of the stacking-fault region of extended dislocations with solute atoms or vacancies. For then the proportionality between σ_c' and $1/q'$ (eqns. (15), (28) and (29)), arising if α is assumed constant, shows that an increase of τ_c' with zinc content would result in a decrease in q'. The assumed constancy of α in eqn. (28) also implies invariance of the product $q'\sigma_c'$. This is born out by the data in fig. 14; it is however only approximate, as may be seen from the relation between the two parameters obtainable on equating strain rates in eqns. (5) and (16).

Allowing for the various simplifying assumptions made in developing the models of the creep mechanisms the agreement obtained with experiment may be considered satisfactory. The treatment also clearly shows, however, that further detailed studies of the modes of deformation and of the effect of intragranular substructures in creep are necessary before truly quantitative laws of the high-temperature deformation of metals can be advanced.

REFERENCES

COPLEY, G. J., 1959, Ph.D. Thesis, The University, Leeds.
COTTRELL, A. H., 1958, *Trans. met. Soc. Amer. Inst. mech. Engrs*, **212**, 192.
FASTOV, N. S., 1950, *Zhur. Tekh. Eksp. Fiz.*, **20**, 543.
FELTHAM, P., 1957, *Phil. Mag.*, **2**, 584.
FELTHAM, P., and COPLEY, G. J., 1958, *Acta Met.*, **6**, 539; 1960, *Ibid.* (to be published).
FELTHAM, P., and MEAKIN, J. D., 1959, *Acta Met.*, **7**, 614.
GREENWOOD, J. N., MILLER, D. R., and SUITER, J. W., 1954, *Acta Met.*, **2**, 250.
HIBBARD, W. R., and DUNN, C. G., 1957, *Creep and Recovery* (Cleveland: Amer. Soc. Metals.)
JACQUET, P., 1954, *Acta. Met.*, **2**, 752.
MASUMOTO, H., SAITO, H., and SUGIHARA, M., 1952, *Sci. Rep. res. Inst. Tohôku Univ.* A, **4**, 480.
ROTHERHAM, L. R., and PEARSON, G. S., 1956, *Trans. Amer. Inst. met. Engrs*, **206**, 881.
YOUNG, F. W., 1958, *J. appl. Phys.*, **29**, 760.

On Dislocations Formed by the Collapse of Vacancy Discs†

By C. Elbaum
Physics Department, Metals Research Laboratory, Brown University,
Providence, Rhode Island

[Received February 15, 1960]

Abstract

The formation of dislocations by the collapsing vacancy disc mechanism is examined for aluminium, copper, silicon and germanium. It is shown that this mechanism can be important in the case of metals. In the case of silicon and germanium dislocation loops produced by the above mechanism, during usual crystal growth from the melt, will not reach sizes detectable by means of the optical microscope.

§ 1. Introduction

The problem of the origin of dislocations in crystals in general, and in crystals grown from the melt, in particular, has been the object of considerable speculation in recent years. Among other possible mechanisms, it has been suggested that dislocations in crystals grown from the melt are likely to originate from the collapse of vacancy discs formed by the precipitation of these imperfections. This precipitation takes place under conditions of supersaturation during cooling of the crystal. (For a summary see Kuhlmann-Wilsdorf 1958.) In the following, some remarks are made concerning the likelihood of this mechanism operating in the case of metals and of silicon and germanium.

A dislocation loop may be expected to nucleate by the above mechanism when the free energy associated with this dislocation loop is equal to or smaller than the free energy associated with a vacancy disc. Collapse of the disc will occur when it reaches a size for which the above condition is satisfied. Subsequent growth of the dislocation loop thus formed can take place by climb, through the addition of vacancies from the surrounding volume. This process increases the size of the loop and thus the free energy associated with it. Growth will therefore occur only if there is a supersaturation of vacancies with respect to the dislocation loop. In order to make numerical estimates of the necessary supersaturation, the free energy associated with a dislocation loop must be examined. It should also be emphasized that the collapsing vacancy disc mechanism and subsequent growth of the dislocation loop are confined to temperatures at which the vacancy mobility is sufficient for appreciable growth of the loop to occur. Consideration must, therefore, be given to the temperature dependence of the free energy associated with a dislocation.

---

† Communicated by the Authors. This research was supported by the Office of Naval Research under Contract Nonr 562 (27).

§ 2. TEMPERATURE DEPENDENCE OF THE DISLOCATION ENERGY

By far the major part of the free energy associated with a dislocation comes from the elastic energy of the strain field around a dislocation and, for practical purposes, the free energy and the elastic energy may be considered numerically equal (Cottrell 1953). This energy, per atomic plane, is approximately proportional to $\mu\mathbf{b}^3$, where μ is the appropriate shear modulus and $\mathbf{b}$ is the Burgers vector. The temperature variation of the above product will be:

$$\frac{1}{\mu\mathbf{b}^3}\frac{d(\mu\mathbf{b}^3)}{dT}=\frac{1}{\mu}\frac{d\mu}{dT}+\frac{3}{\mathbf{b}}\frac{d\mathbf{b}}{dT}=\beta+3\alpha \quad . \; . \; . \quad (1)$$

where β is the temperature coefficient of the shear modulus (in all cases considered, the shear modulus increases with increasing temperature) and α is the linear coefficient of thermal expansion. If we call $W_{T_0}=(\mu\mathbf{b}^3)_{T_0}$ this energy at some arbitrary temperature, say room temperature, then W_T at some other temperature will be:

$$W_T+W_{T_0}[1+(\beta+3\alpha)(T-T_0)]. \quad . \; . \; . \; . \quad (2)$$

Table 1 gives the values of W_{T_0} (at room temperature) and the ratios W_T/W_{T_0} at $T=0{\cdot}9T_M$ (where T_M denotes the melting temperature), for aluminium, copper, silicon and germanium. In these calculations average values of α, in the temperature range considered, were taken from the Handbook of the American Institute of Physics (1957) and values of β from the references quoted by Huntington (1958). It was assumed that β was constant in the temperature range considered, since these temperatures are well above $\theta_D/3$, where θ_D is the Debye temperature; a linear variation of the elastic constants with temperature may, therefore, be expected.

Table 1

Element	$T=0{\cdot}9T_M$ (°K)	$\alpha\times10^6$ (per °C)	$\beta\times10^6$ (per °C)	$(\mu\mathbf{b}^3)_{300°\mathrm{K}}$ (ev)	$\frac{(\mu\mathbf{b}^3)_T}{(\mu\mathbf{b}^3)_{300°\mathrm{K}}}$
Al	840	28·7	510	3·94	0·75
Cu	1220	20·3	380	5·02	0·706
Si	1517	3·3	44	28·1	0·955
Ge	1091	7·0	90	27·2	0·95

Two points are immediately apparent: (*a*) the well-known fact that the elastic energy of a dislocation is considerably lower in aluminium and in copper than in silicon and germanium; (*b*) the ratio W_T/W_{T_0} is much smaller for aluminium and copper than for silicon and germanium. This leads to the qualitative conclusion, that in the case of a metal the generation of dislocations, by any mechanism, becomes considerably easier as the temperature increases. This does not apply to the same extent in the case of silicon and germanium.

§ 3. DISLOCATIONS FORMED BY THE COLLAPSE OF VACANCY DISCS

Special consideration will now be given to dislocations forming by the collapsing vacancy disc mechanism in the case of crystal growth from the melt. Schoeck and Tiller (1960) recently calculated the supersaturation of vacancies necessary for the growth of a dislocation loop formed by the above mechanism. Their expression is of the form:

$$\ln\frac{C}{C_0}=P\frac{\mu \mathbf{b}^4}{T}. \qquad \ldots\ldots\ldots (3)$$

Here C denotes the actual concentration of vacancies in the lattice at the temperature T and C_0 is the concentration of vacancies at T corresponding to equilibrium with respect to an external surface. P is a proportionality factor, which for a given material is a function only of the dislocation loop radius:

$$P=\frac{1}{4\pi(1-\nu)rk}\left[\ln\left(\frac{r}{\mathbf{b}}+1\cdot6\right)+\frac{1}{1+1\cdot6\mathbf{b}/r}\right]$$

where ν is Poisson's ratio (assumed to be $\frac{1}{3}$ for numerical estimates), k is Boltzmann's constant, r is the loop radius and $\mathbf{b}$ is the Burgers vector. Writing

$$\frac{C}{C_0}=\exp\left[-\frac{U_f}{R}\left(\frac{1}{T_M}-\frac{1}{T}\right)\right]$$

these authors derive from eqn. (3) the expression

$$\frac{\Delta T}{T_M}=\frac{3\mu\mathbf{b}^3}{8\pi U_f}\frac{\mathbf{b}}{r}\left[\ln\left(\frac{r}{\mathbf{b}}+1\cdot6\right)+\frac{1}{1+1\cdot6\mathbf{b}/r}\right] \qquad \ldots (4)$$

where $\Delta T=T_M-T_C$ defines the temperature drop from the melting temperature, at which a sufficient supersaturation is reached for a dislocation loop of a given radius r to form; U_f is the energy of formation of a single vacancy.

If the radius r is expressed in Burgers vectors and the temperature variation of $\mu\mathbf{b}^3$ (eqn. (2)) is taken into account, expression (4) can be rewritten in the form:

$$T_c=\frac{1-A(\mu\mathbf{b}^3)_{T_0}[1+300(\beta+3\alpha)]}{\dfrac{1}{T_M}+A\dfrac{(\mu\mathbf{b}^3)_{T_0}}{U_f}(\beta+3\alpha)} \qquad \ldots\ldots (5)$$

where A is a numerical factor which depends on the value chosen for r and $(\mu\mathbf{b}^3)_{T_0}$ is taken at 300°K. T_c is the temperature at which a sufficient vacancy supersaturation is reached to form a dislocation loop of a given radius r_c.

Calculations by Schoeck and Tiller show that a vacancy disc of a radius 5**b** or more may be considered to have collapsed and formed a dislocation loop. Assuming this to be valid, the temperatures T_c were calculated for the four elements under consideration, for $r_c=5\mathbf{b}$ and $r_c=10\mathbf{b}$, and are given in table 2. In all the calculations experimental values of U_f and U_m (U_m is the activation energy for migration of vacancies) are used, except in the case of silicon, for which no such values are available. It is assumed instead, by comparison with germanium, that the activation energy U_{SD} for self-diffusion in silicon is at least equal to the highest values of activation energy for diffusion of substitutional impurities, such as boron, gallium, indium and thallium (Fuller and Ditzenberger 1956). This activation energy is approximately 90 000 cal/mol. Again by analogy with germanium (Letaw *et al.* 1956) it is assumed that for silicon a vacancy self-diffusion mechanism is valid and that $U_f \simeq \frac{2}{3} U_{\mathrm{SD}} = 60\,000$ cal/mol and $U_m \simeq \frac{1}{3} U_{\mathrm{SD}} = 30\,000$ cal/mol. It should also be pointed out that the chosen value of U_f for silicon satisfies the empirical relation

Table 2

Element	U_f (ev)	U_m (ev)	T_c (°K)	$\frac{\Delta T}{T_M}$	$\frac{dr}{dt}$ (cm sec)	$r_{\max}$ (cm)
Al $r_c=5\mathbf{b}$	0·76	0·43	778	0·166	4·6	$2{\cdot}76\times10^{4}$
Al $r_c=10\mathbf{b}$			835	0·105	64·5	$3{\cdot}7\times10^{4}$
Cu $r_c=5\mathbf{b}$	0·9	1·1	1103	0·186	0·108	10^{3}
Cu $r_c=10\mathbf{b}$			1200	0·115	0·575	$3{\cdot}2\times10^{3}$
Si $r_c=5\mathbf{b}$	2·6	1·3	645	0·616	$3{\cdot}76\times10^{-11}$	$2{\cdot}1\times10^{-7}$
Si $r_c=10\mathbf{b}$			995	0·412	$1{\cdot}16\times10^{-7}$	$1{\cdot}45\times10^{-4}$
Ge $r_c=5\mathbf{b}$†	2	0·97	282	0·76	10^{-17}	—
Ge $r_c=10\mathbf{b}$			600	0·5	$1{\cdot}57\times10^{-9}$	$2{\cdot}75\times10^{-6}$

† Here T_c is below room temperature, hence no value for $r_{\max}$ is given.

$$(U_f/T_M)_{\text{silicon}} \simeq (U_f/T_M)_{\text{germanium}}.$$

The values of $\Delta T/T_M$ for the four elements are also given in table 2. It is seen that this ratio is much higher for silicon and germanium than for aluminium and copper. The question thus arises whether dislocation loops forming at these values of $\Delta T/T_M$ can grow to measurable sizes in the time available during crystal growth, for a temperature drop from T_C to room temperature.

An estimate will now be made of the maximum size that a dislocation loop thus formed can reach in each of the four elements. The maximum rate of growth of a circular dislocation loop, at a given temperature T, is derived as follows. When the ring grows from radius r to $r+dr$ it absorbs a volume of vacancies given by $a2\pi r\,dr$, where a is the lattice parameter. The maximum rate of growth will be achieved when this volume of vacancies will be supplied by the diffusion to the dislocation ring of all the available excess vacancies from an appropriately expressed volume element dV. Here dV is an increment in the volume of a torus of average principal radius r and of cross-sectional radius s, where $s=D_v^{1/2}t^{1/2}$ (D_v is the vacancy diffusion coefficient and t is time), i.e.

$$dV=(2\pi r)2\pi\,s ds.$$

The volume of vacancies in dV is obtained by multiplying dV by the concentration of excess vacancies $(C-C_0)$. It is assumed here that the actual vacancy concentration is given by the concentration corresponding to equilibrium with respect to an external surface at the melting temperature, thus

$$C\cong\exp(-U_f/RT_M) \quad \text{and} \quad C_0\cong\exp(-U_f/RT).$$

By equating the two volumes of vacancies we obtain:

$$a2\pi\,r dr=(C-C_0)(2\pi r)2\pi\,s ds.$$

Finally, the rate of growth is given by:

$$\frac{dr}{dt}=\frac{dr}{ds}\frac{ds}{dt}=\frac{\pi}{a}D_v(C-C_0). \qquad (7)$$

In the following it is assumed that the dislocation loop under consideration is the only available sink for vacancies in the crystal. Thus the maximum loop radius attainable in a time t_1, during which the temperature of the crystal drops from T_c to room temperature, will be given by

$$r_{\max}=r_c+\frac{\pi}{a}(C-C_0)\int_0^{t_1}D_v\,dt \qquad (8)$$

where $T=T_c$ at $t=0$.

We will now evaluate $r_{\max}$ in the case of crystal growth from the melt. Under typical laboratory conditions crystals are grown from the melt at rates v of approximately 10^{-3} cm/sec and with a temperature gradient G (along the growth direction of the crystal) of about 20°c/cm. Thus the rate of temperature decrease along the crystal will be given by $w=dT/dt=vG=2\times10^{-2}$ degrees/sec. The integral on the right-hand side of expression (8) can now be evaluated as follows:

$$D_v(T)=D_0\exp(-U_m/RT) \quad \text{and} \quad T=T_c-wt;$$

hence

$$\int_0^{t_1}D_v\,dt=D_0\int_0^{t_1}\exp\left[-\frac{U_m}{RT_c\left(1-\frac{wt}{T_c}\right)}\right]dt;$$

by expanding $(1-wt/T_c)^{-1}$ and retaining the first two terms, we obtain:

$$\int_0^{t_1}D_v\,dt=D_v(T_c)\frac{RT_c^2}{U_m w}\left[1-\exp\left(-\frac{wU_m t_1}{RT_c^2}\right)\right].$$

Hence:

$$r_{\max}=r_c+\frac{\pi}{a}(C-C_0)D_v(T_c)\frac{RT_c^{\,2}}{wU_m}\left[1-\exp\left(-\frac{wU_m t_1}{RT_c^{\,2}}\right)\right]. \qquad (9)$$

Assuming $D_0=1$, values of $r_{\max}$ (eqn. (9)), starting from $r_c=5\mathbf{b}$ and $r_c=10\mathbf{b}$, and of dr/dt (eqn. (7)), at T_c for $r_c=5\mathbf{b}$ and $r_c=10\mathbf{b}$, are given in table 2.

§ 4. DISCUSSION AND CONCLUSIONS

It appears from the values of $r_{\max}$ that in the case of aluminium and copper, the actual size of loops originating from collapsed discs will not be determined by $r_{\max}$. This size will probably depend on the presence of other vacancy sinks in the crystal, in particular on the presence of other dislocations. It should also be pointed out that for aluminium and copper, the rate dr/dt at T_c is well in excess of the usual crystal growth rate. Dislocation loops can, therefore, grow into regions where the temperature is above T_c. The rate dr/dt can thus increase until the loop reaches a region at temperature $T_{\max}$ (near T_M) at which $dr/dt(T)$ goes through a maximum, after which it drops rapidly, reaching zero at $T=T_M$. This again suggests that in aluminium and copper $r_{\max}$ is neither the limiting nor necessarily the determining factor in the ultimate size of the loops.

For silicon and germanium the values of $r_{\max}$ indicate that dislocations produced by the collapsing vacancy disc mechanism will not attain sizes visible in an optical microscope. Moreover, for these elements dr/dt is several orders of magnitude smaller than the crystal growth rate. The dislocation loops are, therefore, always in a region whose temperature decreases at the rate given by the product vG. Thus $r_{\max}$, determined from eqn. (9) appears to give an upper limit of loop size.

It is suggested that the above conclusions explain why crystals essentially free of dislocations detectable by means of the optical microscope (Dash 1959) can be produced by growth from the melt in the case of silicon and germanium. Such crystals are grown under very carefully controlled conditions, from materials of very high purity. All major known dislocation-producing mechanisms, except collapsing vacancy discs, are thus essentially eliminated, whereas the latter is not capable of producing dislocations of detectable size. It appears that for metals, even when purity and solidification conditions are similar to those of silicon and germanium, the prevention of dislocation growth from collapsed vacancy discs will be more difficult.

REFERENCES

AMERICAN INSTITUTE OF PHYSICS, 1957, *Handbook* (McGraw-Hill Co.), pp. 4–51.
COTTRELL, A. H., 1953, *Dislocations and Plastic Flow in Crystals* (Clarendon Press), p. 39.
DASH, W. C., 1959, *J. appl. Phys.*, **30**, 459.
FULLER, C. S., and DITZENBERGER, J. A., 1956, *J. appl. Phys.*, **27**, 544.
HUNTINGTON, H. B., 1958, *Solid State Physics*, **7**, 322, Editors F. Seitz and D. Turnbull.
KUHLMANN-WILSDORF, D., 1958, *Phil. Mag.*, **3**, 125.
LETAW, H. J., PAROTNOY, W. M., and SLIFKIN, L., 1956, *Phys. Rev.*, **102**, 636.
SCHOECK, G., and TILLER, W. A., 1960, *Phil. Mag.*, **5**, 43.

Palaeomagnetism of the British Carboniferous System†

By C. W. F. Everitt
Imperial College, London

and J. C. Belshé
Department of Geodesy and Geophysics, Cambridge

[Received May 23, 1960]

Abstract

Superficially conflicting evidence has been found concerning the direction and sense of the earth's magnetic field in carboniferous times. Various explanations of the results are considered here. We conclude that the discrepancies in direction occur because some sites underwent secondary remagnetization during the Triassic period. If this hypothesis is correct, the mean direction for the Carboniferous period was 200° east of true north and 27° down; placing Britain 15° south of the equator. As regards the sense of the field we conclude that it probably underwent a rapid series of inversions in the early part of the Carboniferous period and then remained reversed for a considerable time.

§ 1. Introduction

We have been independently engaged on palaeomagnetic studies of rocks from the British Carboniferous system. The investigations revealed systematic discrepancies of about 70° between the axes of magnetization in different formations, and provided strongly conflicting evidence concerning reversal of the earth's magnetic field. In the present account we propose to summarize the results and examine the discrepancies.

A map of the areas examined is given in fig. 1. They may conveniently be divided as follows: first, sedimentary formations in Derbyshire, Lancashire, Staffordshire, and South Wales; second, baked and igneous formations in the English Midlands including Derbyshire; third, baked and igneous formations in Scotland.

The sedimentary formations cover almost the complete Carboniferous period. In Derbyshire, the geological succession comprised about 14 000 ft of sediments extending from the Carboniferous limestone to the Coal Measures; the estimated time-span being about 220–280 million years. In the Lancashire Coalfield there are 20 000 ft of sediments, and in the South Wales Coalfield 15 000 ft of sediments, covering approximately the same period. Samples were taken from 46 sites in these areas, and from one site in the late Carboniferous Keele beds of Staffordshire. Further details are given in the table.

---

† Communicated by the Authors.

Fig. 1

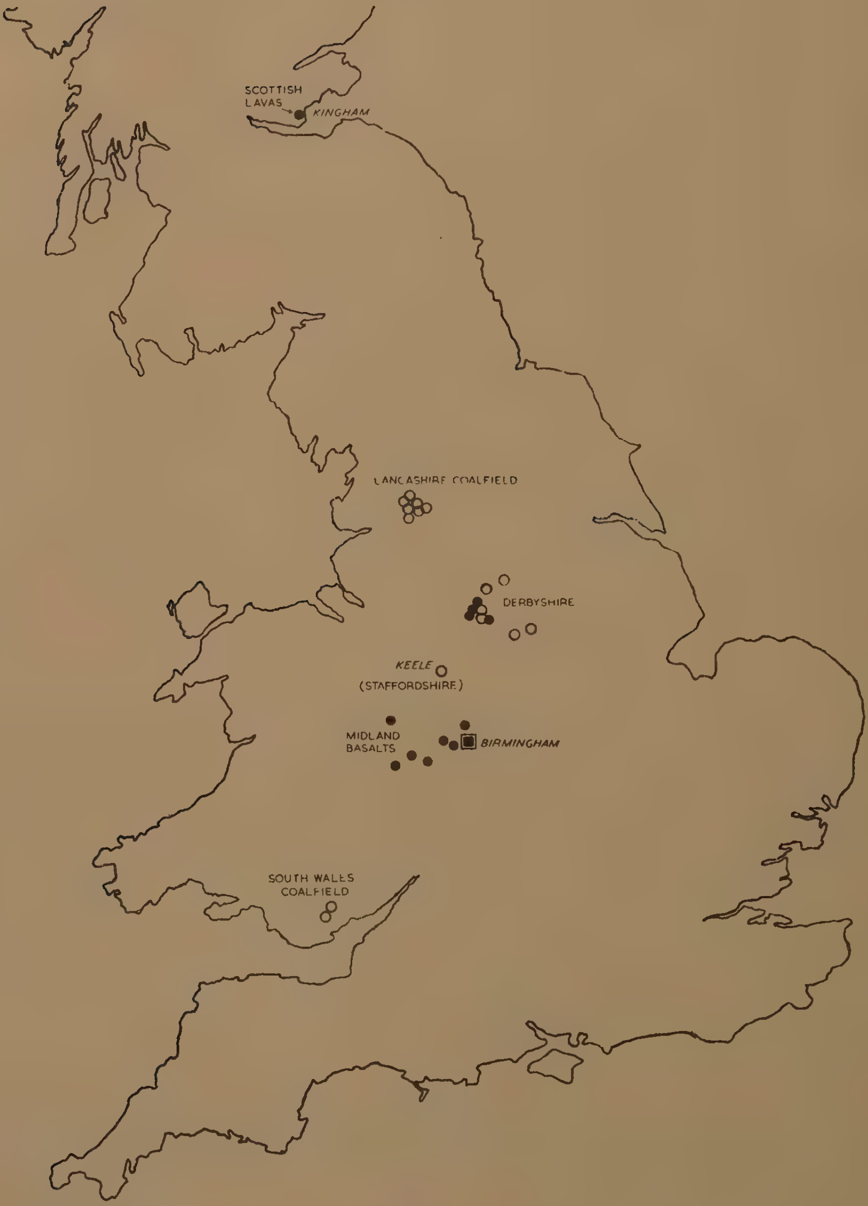
SCOTTISH LAVAS
KINGHAM
LANCASHIRE COALFIELD
DERBYSHIRE
KEELE
(STAFFORDSHIRE)
MIDLAND BASALTS
BIRMINGHAM
SOUTH WALES COALFIELD

Distribution of sites.

● Baked and igneous formations.

○ Sedimentary formations.

Region	Description	Material examined		Material accepted		Declination	Inclination	Period	Approximate age
		Sites	Samples	Sites	Samples	Degrees east of true north			Millions of years
Derbyshire	Sedimentary	22	84	3	13	37°	39° down	Carboniferous Limestone to Millstone Grit	230–280
				3	11	197°	37° down		
Lancashire	Sedimentary	12	49	4	14	24°	22° down		
				3	10	184°	23° down		
Staffordshire	Sedimentary	1	7	1	7	199°	34° down	Late Carboniferous	270
South Wales	Sedimentary	12	79	2	18	205°	49° down		
English Midlands	Baked	6	11	6	11	202°	17° down	Late Carboniferous	280
	Sills		12		12	196°	13° down		
	Baked	1	2	1	2	349°	1° down	Carboniferous Limestone	240
	Lava		5		3	357°	14° down		
Derbyshire	Baked (1)	1	6	1	6	221°	34° down	Middle Carboniferous?	260?
	Sill (1)		7		7	218°	36° down		
	Lava (2)	1	3	1	3	48°	45° up	Carboniferous Limestone	240
	Lavas (2)	2	3	2	3	200°	29° down		
(2) (3) Scotland (Kinghorn)	Beds 9–15	4	7	2	5	12°	18° up	Calciferous Sandstone	230
	Beds 16–20	4	11	3	8	170°	24° down		
	Bed 21	1	3	1	2	55°	19° down		
	Beds 25–48	13	25	10	20	13°	35° up		
	Beds 50–55	5	8	4	6	205°	41° down		
	Bed 65	1	2	1	2	15°	14° down		
	Bed 69 (4)	1	2	1	2	15°	35° up	Late Calciferous Sandstone?	240?

(1) The origin of this formation at Tideswelldale is not certain. It may be lava.

(2) The directions for two of the Derbyshire lavas and in beds 12, 15, 19, 20, 31, 32, 38, 48 from Kinghorn are values after thermal or alternating field cleaning (see text).

(3) All the results are from igneous rocks except beds 25, 45, 54 which were baked sandstones.

(4) This formation is a sill of uncertain age.

The English baked and igneous rocks were from two areas. In the first, near Birmingham, there were six late Carboniferous sills and one lava of Carboniferous Limestone age. In the second area, in Derbyshire, there were three lavas also of Carboniferous Limestone age, and one Middle or Late Carboniferous Sill.

The Scottish baked and igneous rocks were a series of lavas and interbedded sediments from Kinghorn, Fife, covering a few million years in the Calciferous Sandstone period. In the table the beds are numbered consecutively from the bottom upwards, irrespective of their nature, in accordance with the notation of Geikie (1900).

Fig. 2

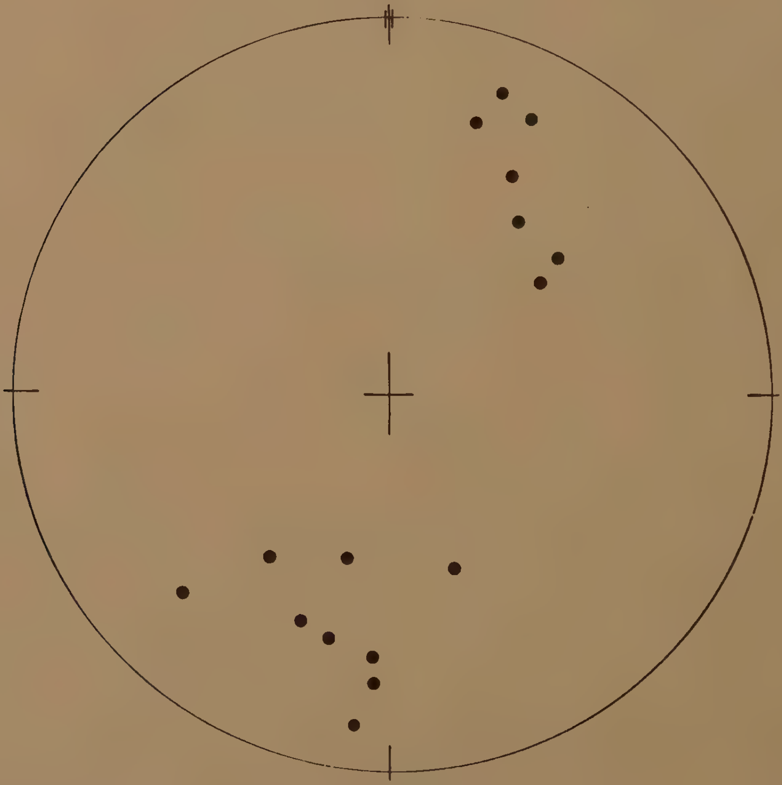

Results from sedimentary formations (lower hemisphere of Schmidt projection).

Some details of the sampling are included in the table. Several oriented blocks were collected at each site. As a rule, three to six discs $1\frac{3}{8}$ in. diameter $\frac{1}{4}$ in.–$\frac{1}{2}$ in. thick were cut from each block and measured on a Blackett magnetometer. The mean directions and, where necessary, the standard deviations were calculated by the methods given by Wilson (1959). Certain other measurements were also carried out as described in the following sections.

§ 2. Results

2.1. *Directions of Magnetization*

The main results are set out in the table and plotted on figs. 2–4. The directions are all given relative to the original bedding and flow-planes. They have been plotted on the lower hemisphere of a Schmidt projection, the sense of the magnetization being reversed for the upward dips.

Fig. 3

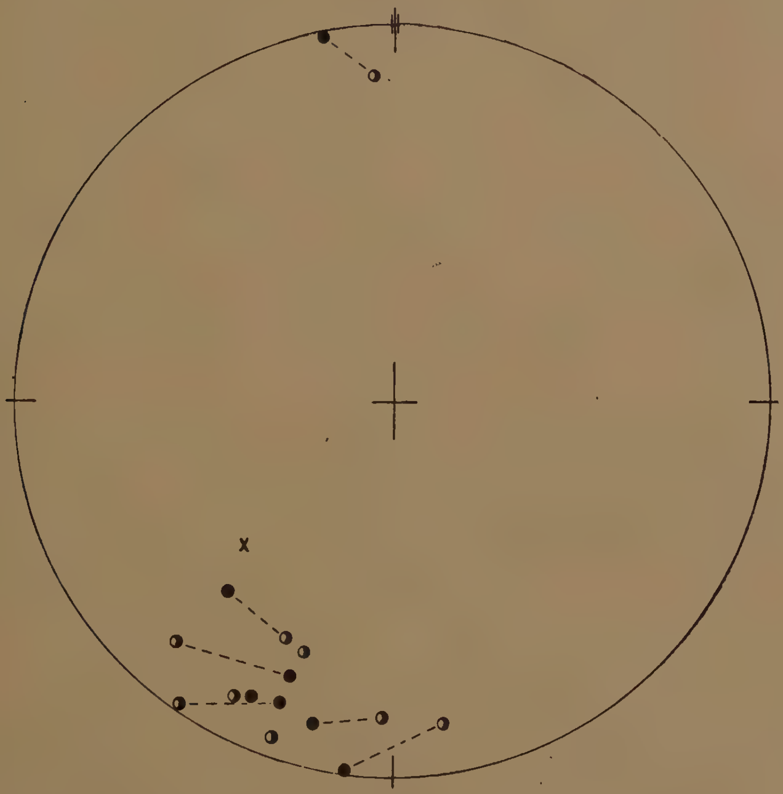

Results from English baked and igneous formations (lower hemisphere of Schmidt projection).

● Baked rocks.
◐ Igneous rocks (north magnetic pole).
× Igneous rocks (south magnetic pole).
– – – Joins results from same site.

In the sedimentary rocks the magnetization was often extremely weak and sometimes widely scattered; but at some sites there was good agreement between the mean directions of different blocks. As a first step in analysis, only the sites for which the standard deviations between individual blocks was less than 20° were accepted. Out of 47 sites, 16 fall within this category. Their directions, which are plotted in fig. 2, fall in two well-defined groups ; one with a mean azimuth 34° east of true north and a mean dip of 31° down, and the other 195° east and 35° down. The smaller angle between these two mean axes is about 70°. On the sites with scattered directions, the results still showed some tendency to group about the same two axes. Sometimes the two directions even occurred at the same site ; the most striking example being the Union Strip Mine, Derbyshire, where three blocks agreed closely at 25° east, 33° down and three others agreed at 213° east and 31° down.

Fig. 4

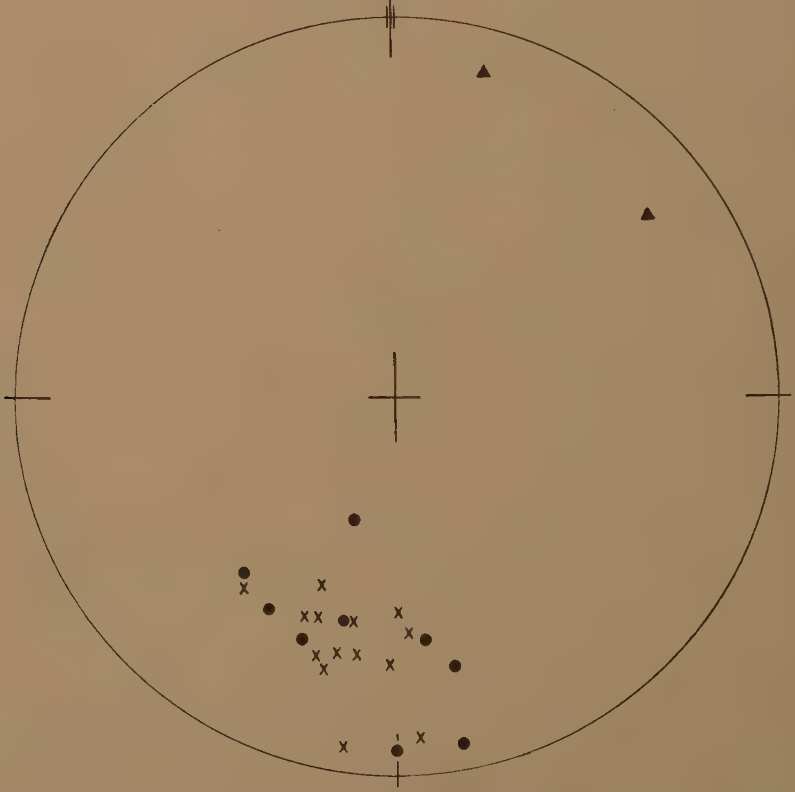

Results from Scottish baked and igneous formations (lower hemisphere of Schmidt projection).

● North pole.
× South pole.
△ Discordant directions (north pole).

Figure 3 shows the directions in the English baked and igneous rocks. In the sills and associated baked sediments the mean direction was 202° east and 19° down ; while of the lavas from Derbyshire, one was magnetized 46° east, 45° up, and two showed initial north-east downwards directions, which changed on heating to within 100°c of the Curie temperature and gave a final mean direction of 200° east and 20° down. The remaining lava, near Birmingham, gave a mean 357° east and 7° down ; but since the scatter of directions was large (standard deviation 14°), this probably only represented a reversal of the south-west downward axis.

The directions for the baked and igneous formations in Scotland contrast with the preceding data. They are given in fig. 4. The mean axis was 193° east 33° down. Along this axis, magnetizations existed in either sense ; there being successive groups of normal and reversed lavas. In two lavas (numbers 25 and 65) lying between normal and reversed groups there were discordant directions which are differently designated in fig. 4. Apart from these, which may represent an intermediate direction during the course of an earth's field reversal, there was no sign of the north-east/downwards magnetization.

The results as a whole, then, show two distinct directions ; 40 sites being magnetized along south-east/downwards axes, and 7 along a north-east/downwards axis. The angle between these two axes is about 70°. It should be remarked that some measurements by Clegg *et al.* (1954) on sediments at Frampton Cotterill Gloucestershire, also gave a north-east/downwards direction (44° east, 35° down).

2.2. *Stability*

In assessing the significance of the magnetizations we must consider not only their stability (that is whether they represent a unique direction of the earth's magnetic field) but also their age : for a stable magnetization may easily have been acquired long after the rocks were formed.

The stability of the south-west/downwards direction is demonstrated by four lines of evidence, as follows :

(1) There was close agreement in direction between igneous and sedimentary rocks of widely different type.

(2) Exact 180° reversals occurred ; showing that there had not been any secondary magnetization sufficient to disalign the two directions.

(3) The directions for the Scottish beds (which are tilted 30° eastwards) agreed with the English ones more closely relative to the bedding planes than the present horizontal. This indicates that the magnetization was acquired before tilting.

(4) There was good agreement between the directions in associated baked and igneous rocks. This line of evidence seems especially convincing since the intrinsic scatter of the baked rocks was only 2–3°.

The measurements on baked rocks also provided a test of the date of magnetization. At several sites there was a large and systematic decrease of intensity and increase of scatter with distance from the contact (Everitt and Clegg 1960), which strongly suggests that the baked material became magnetized when the igneous bodies cooled, and therefore that the magnetizations were of Carboniferous age.

Several of the Scottish lavas had widely scattered natural magnetizations. Laboratory heating experiments were carried out on six of these by Mr. R. L. Wilson. In each case, he found that the directions came into line with the mean values for adjacent beds, on heating to within 100°C of the Curie temperature. For two lavas a similar effect was achieved by alternating field demagnetization. The sites treated in this way are distinguished in a note to the table.

The stability of the north-east/downwards magnetization is not so well attested. However, there is some field evidence from measurements on two limbs of the Pendle monocline, which agreed more closely relative to the bedding-planes than to the present horizontal ; although since the direction of magnetization was only a few degrees from the strike axis, this test is not absolutely decisive. In addition, there was some laboratory evidence for stability, since the directions of magnetization showed no appreciable change on heating in zero field to 200°C.

2.3. *Age of the Magnetizations*

The evidence from baked rocks, outlined in the preceding section, strongly suggests that the south-west/downwards magnetizations were acquired at the time of formation of the igneous rocks, which—for the Kinghorn lavas at least—can confidently be assigned to the Carboniferous period.

The north-west/downwards magnetization on the other hand occurs only in the sedimentary rocks and may be assigned to any period before the folding of the Pendle monocline. The mean direction was 39° east and 35° down, which is remarkably near the figure of 34° east, 28° down given by Clegg *et al.* (1954) for the Triassic period. It is therefore conceivable that the magnetization was acquired by a secondary process during Triassic times.

There is some geological evidence to support this view. Many of the Carboniferous formations underlying the Permo-Triassic strata on either side of the Pennines are markedly reddened to depths of 1000 ft or so. According to Trotter (1953), the reddening was due to weathering of the iron minerals to hematite while the overlying strata were being formed. The beds examined here did not belong to the most severely weathered series but, as we have seen, the magnetic material in them was hematite. Although it has not been possible to relate in detail their position to the Permo-Triassic erosion surface, there does seem to be a definite connection. This may be illustrated conveniently by results from three sites in the Coal Measures of Derbyshire–Yorkshire border. At Sheffield Brick Pit, which is some way from the erosion surface, the mean direction was 207° east, 36° down ; at Hardwick Hall, which is very near the erosion surface, the direction was 50° west and 33° down ; while at Union Strip Mine, which was slightly further away than Hardwick Hall, three blocks agreed at 25° east, 33° down, and three others agreed at 213° east, 31° down. Much the simplest explanation of these results is in terms of local re-magnetization during Triassic times.

A second line of evidence is provided by the Keele beds of Staffordshire, in which the hematite is thought to be primary and should therefore retain the original Carboniferous magnetization. Their direction was indeed 199° east and 34° down.

The most obvious objection to the interpretation in terms of remagnetization is that the beds of the Pendle monocline appear to have acquired their north-east magnetization before being folded in the Hercynian orogeny, which occurred during early Permo-Triassic times. As mentioned above, the evidence is not absolutely decisive. But even if the beds were magnetized before folding, that only proves that the north-east downwards direction appeared fairly early in Permo-Triassic times : it may still have been a considerable time after the Carboniferous period ended.

2.4. *Reversals*

We have seen that at Kinghorn the normal and reversed magnetizations occur in separate groups of five or more lavas. This suggests that the earth's field underwent inversions : a view which is supported by the conjunction of concordantly magnetized baked sediments with both normal and reversed groups : and also by the absence of any positive evidence from the heating experiments for physico-chemical reversals. If so, inversions of the field occurred at the rate of about one per million years—that is, at about the same rate as found by Hospers (1953) for the Tertiary period.

If this interpretation is correct, it is puzzling that all the lavas and baked sediments showing these periodic inversions were formed during a relatively small part of the early Carboniferous, while all the later sediments and intrusions (which extend over the major part of the period) are reversed.

In assessing these results, we distinguished two questions. The first is whether the earth's field reversed at all, the second whether it underwent a rapid sequence of inversions from normal to reversed and back. There seem to be four possibilities :

(i) All the sedimentary and some igneous rocks were self-reversed.

(ii) All rocks were magnetized in a reversed field, and some early lavas and associated baked sediments underwent physico-chemical reversal to the normal direction.

(iii) Inversions of the earth's field occurred frequently throughout the period, but the sediments and intrusions by chance only became magnetized during periods of reversed field.

(iv) Inversions occurred frequently during early Carboniferous times, but afterwards the field remained continuously reversed for a considerable period.

The first explanation would require a great exercise of special pleading. Of the remaining explanations the second is the least satisfying because once the possibility of a reversed field is admitted, the main ground for believing that self-obliterating physico-chemical reversals have occurred commonly in rocks disappears. The third hypothesis is excluded, because it seems inconceivable that all the sediments became magnetized in less than a million years. Hence it is best to accept tentatively the fourth hypothesis that the earth's field underwent several inversions during the early part of the period and afterwards remained reversed.

§ 3. Conclusion

Our conclusions may be summarized as follows :

1. The results in the south-west/downwards group give a mean axis of magnetization for the Carboniferous period (age about 250 million years) of 200° east and 27° down. The standard deviation was 20°. These figures are consistent with the directions of 200° east and 35° down given by Nairn (private communication) for the continent of Europe, and 189° east and 9° up given by Creer (1957) for the early Permian in Britain (age about 200 million years).

Some of our results have already been quoted by Irving (1959) and by Blackett, Clegg and Stubbs (1960). The present results are based on more complete and accurate data, and must be regarded as superseding their figures. Broadly they confirm the picture presented by these workers but place Britain about 20° further south, and thus, for example, considerably reduce the relative displacement between England and Australia from that originally claimed by Irving.

Our final mean values for the four quantities ΔI, ϕ, ψ and λ_m defined by Blackett *et al.* (1960) are ΔI, 92° ; ϕ, 87° ; ψ, 23° ; and λ_m, 22° S.

2. Some of the sediments were probably remagnetized during Triassic times. This suggests that the effects of Permo-Triassic weathering extended to a considerably greater depth than has usually been supposed. Palaeomagnetic measurements obviously provide a powerful method of investigating such phenomena.

3. The earth's field seems to have undergone a rapid series of inversions in early Carboniferous times and afterwards to have remained reversed for a considerable period.

Acknowledgments

We wish to thank Professor P. M. S. Blackett, Dr. J. A. Clegg, and Professor S. K. Runcorn for their interest in this work.

In collecting we were helped by Dr. P. H. S. Stubbs, Mr. G. Turnbull, and Mr. M. Andrew ; and we are also especially indebted to Mr. G. W. Masse for his help in collecting and in many other ways.

C. W. F. E. is indebted to the D.S.I.R. for a Research Studentship, and J. C. B. to the U.S. Educational Commission for a Fulbright Fellowship. The work was supported by grants from D.S.I.R.

REFERENCES

BLACKETT, P. M. S., CLEGG, J. A., and STUBBS, P. H. S., 1960, *Proc. roy. Soc.* A (in the press).
CLEGG, J. A., ALMOND, M., and STUBBS, P. H. S., 1954, *Phil. Mag.*, **45,** 583.
CREER, K. M., 1957, *Phil. Trans.*, **250,** 111.
EVERITT, C. W. F., and CLEGG, J. A., 1960, (to be published).
GEIKIE, SIR A., 1900, Geological Survey Memoir for Central Western Fife
HOSPERS, J., 1953, *Kon. Ned. Acad. Wet.*, **56,** 477.
IRVING, E., 1959, *Geophys. J., R.A.S.*, **2,** 51.
TROTTER, F. M., 1953, *Proc. York. geol. Soc.*, **29,** 1.
WILSON, R. L., 1959, *Phil. Mag.*, **4,** 750.

Recovery of Quenched-in Resistivity at High Temperatures in Gold†

By M. Meshii and J. W. Kauffman
Materials Science Department, Northwestern University
Evanston, Illinois, U.S.A.

[Received September 15, 1959]

Abstract

For quenches made from 1000°c, 90% of the quenched-in resistivity anneals out in the vicinity of room temperature leaving 10% which subsequently recovers only at much higher temperatures. This remaining resistivity is associated with configurations which are formed from the quenched-in vacancies. The recovery of this remaining resistivity was studied. Two recovery regions were defined: The first region was found within a wide temperature range, 200°c to 600°c; the second region was observed within a very narrow temperature range about 630°c. Complete recovery occurred during this stage. The recovery in the temperature range 200°c to 600°c had no observable effect on the yield stress. However, the second step of the resistivity recovery observed in a narrow temperature range above 600°c corresponds to the resoftening of quench-hardening.

§ 1. Introduction

Previous studies of the annealing out of quenched-in resistivity have been confined to annealing temperatures in the neighbourhood of room temperature. However, there is a portion of the quenched-in resistivity which does not recover at these temperatures. A much higher temperature is necessary for its recovery. It is now well accepted that the room temperature recovery of quenched-in resistivity is associated with the migration of essentially random vacancies and vacancy complexes either to sinks, where they disappear, or else they migrate, finally forming stable configurations which are less effective in scattering electrons and hence contribute a smaller amount of electrical resistivity. Some of these configurations of lower electrical resistivity and lower lattice energy are responsible for quench-hardening. The purpose of the present work is to investigate the nature of this remaining resistivity and to study the correlation of this to the quench-hardening mechanism.

§ 2. Experimental Procedure

The quenching methods have been described in a previous publication (Meshii and Kauffman 1959 a). All quenches were made from 1000°c ± 10°c with a rate of 30 000°c/sec. The samples used were gold wire 0·016 in. in

---

† Communicated by the Authors. This investigation was performed with the support of the Office of Naval Research of the United States Government.

diameter. The purity was 99·999%. Subsequent to the quench the specimens were annealed in a furnace kept within ± 1°c. The resistivity measurements were then made at 4·2°K, using standard potentiometric methods.

Fig. 1

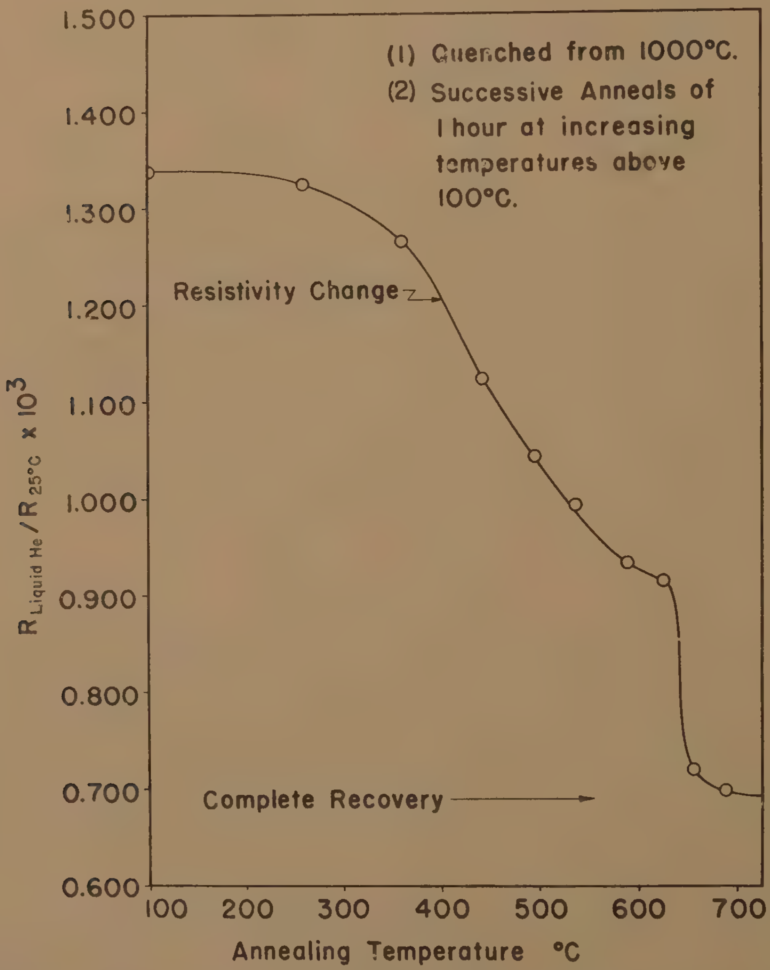

Resistivity recovery during successive isochronal annealings after complete ageing.

§ 3. Experimental Results

The recovery of the electrical resistivity upon one hour annealings at fixed temperatures is shown in fig. 1. The rate of recovery as a function of annealing temperature is shown in fig. 2. These curves do not correspond to the recovery of the yield stress of quenched gold (Meshii and Kauffman 1959 b, 1960), except for the last recovery stage above 600°c. One hour annealings below 500°c produce a considerable recovery of resistivity, while they do not affect mechanical properties. It is also seen from figs. 1 and 2 that there are at least two stages in the resistivity recovery below 600°c. About two-thirds of the quenched-in resistivity remaining after the room temperature recovery anneals out below 600°c.

Fig. 2

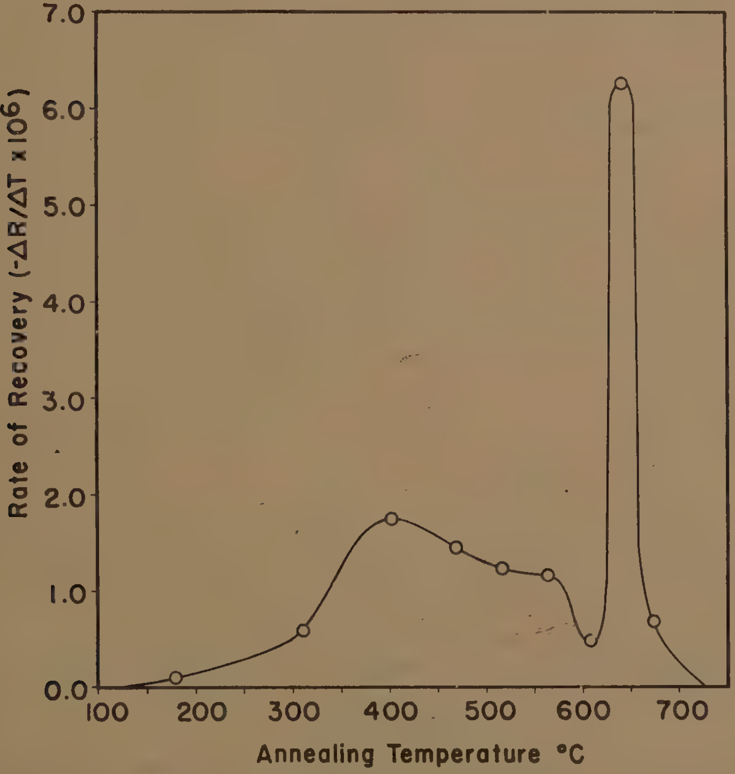

Average rate of recovery between two adjacent points in fig. 1 is plotted against average temperature.

The activation energy for the recovery of this resistivity was difficult to determine accurately, first, because the change in resistivity is small and therefore difficult to measure, and secondly, it appears that more than one process is operating and therefore a unique activation energy would not be expected. An example of the data is shown in fig. 3. From these data, using the slope intersection method, a value of 1·2 ± 0·1 ev was obtained for temperatures between 415°c and 440°c. A value of 1·5 ± 0·3 ev was found between 440°c and 484°c. These results indicate that the processes occurring below 600°c have a much lower activation energy than that associated with resoftening, where 4·7 ev was found (Meshii and Kauffman 1959 b, 1960). The recovery stage above 600°c is seen to be highly dependent on temperature. Complete recovery had occurred after a narrow temperature range. This behaviour is similar to that found for the recovery of the yield stress, both in regard to the temperature range and the apparent dependence on temperature.

Fig. 3

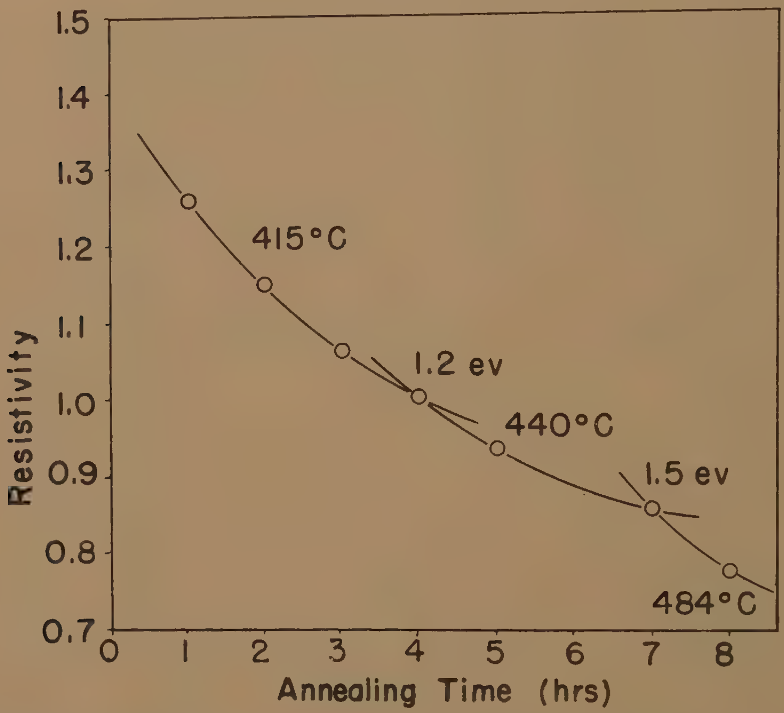

Activation energy determinations in the first stage of resistivity recovery.

§ 4. Discussion

Quench-hardening has not been found immediately after quenching, the hardening only occurs upon ageing at room temperature. Resoftening of the quench-hardening is found to occur only above 600°c. Therefore, as concluded (Meshii and Kauffman 1959 b, 1960) configurations which give rise to hardening are formed as a result of vacancy and vacancy complex migration near room temperature. The recovery of the quenched-in resistivity beteen 200°c and 600°c then has little effect on the yield stress. However, the recovery occurring about 650°c apparently corresponds to the recovery of quench-hardening.

Acknowledgment

The authors wish to thank Mr. R. Kloske for assistance in making some of the measurements.

References

Meshii, M., and Kauffman, J. W., 1959 a, *Acta Met.*, **7**, 180; 1959 b, *Bull. Amer. phys. Soc.*, **4**, 172; 1960 *Phil. Mag.*, **5** (to be published).

Localized Modes in Crystals and Sharp Details of the Optical Absorption Spectra†

By Robert Englman
Department of Physics, Israel Institute of Technology, Haifa, Israel

[Received April 12, 1960]

Abstract

A theory is put forward in qualitative terms to account for the sharp nibs frequently observed at the long wavelength end of the spectral lines of ionic crystals, in which optical absorption by a cation has taken place. The broad band is primarily due to excitation of the vibrational modes of the crystal by the Franck–Condon strain; nibs are supposed to be caused by localized modes introduced in the crystal either by the differing mass or by a change in the force constants of the absorbing ion. Experimental evidence in rocksalt-type crystal indicates the presence of T_{2g}-modes of localized vibrations.

§ 1

The shape of the absorption spectra of paramagnetic ions in crystals is not particularly well understood today. The lack of thoroughgoing research in this field results in a situation that, while the assignment of bands can be made with confidence on the basis of crystal field theory, the fine details of the absorption line (sometimes also called *structure*) are explained in an *ad hoc* manner and without relation to the broader problems involved. The questions are sharpened by recent works with paramagnetic ions in ionic crystals, appearing either substitutionally as impurities or as the host ion, and mainly for two reasons:

First, because in at least the simplest cases investigated, crystals with the NaCl structure, we should have quite a good working knowledge of the dynamical behaviour of the crystal; in contrast to ligand coordinated complexes (which historically take precedence), whose interaction with their immediate neighbours is as yet a matter of speculation. Secondly, while the numerous discrete vibrational modes of the latter can accommodate the interpretation of practically any 'structure' of the line, in a crystal, where there exist continua of vibrational modes, the very existence of discrete peaks is puzzling.

In figs. 1 and 2 we show two optical absorption lines which are typical of their kind and which exhibit sharp nibs superimposed on the broad bands. The lines are due to chromium ion in magnesium oxide (at 77°K) and chromium ion in Al_2O_3 (77°K). Both host crystals are predominantly cubic (Stahl-Brada and Low 1959)

---

† Communicated by the Author.

In the writer's view two aspects of the bands, the band-breadth and the nibs, should be distinguished. In fact, it is argued that the broadening is due to what Brillouin (1953) calls passing bands and the nibs to stopping

Fig. 1

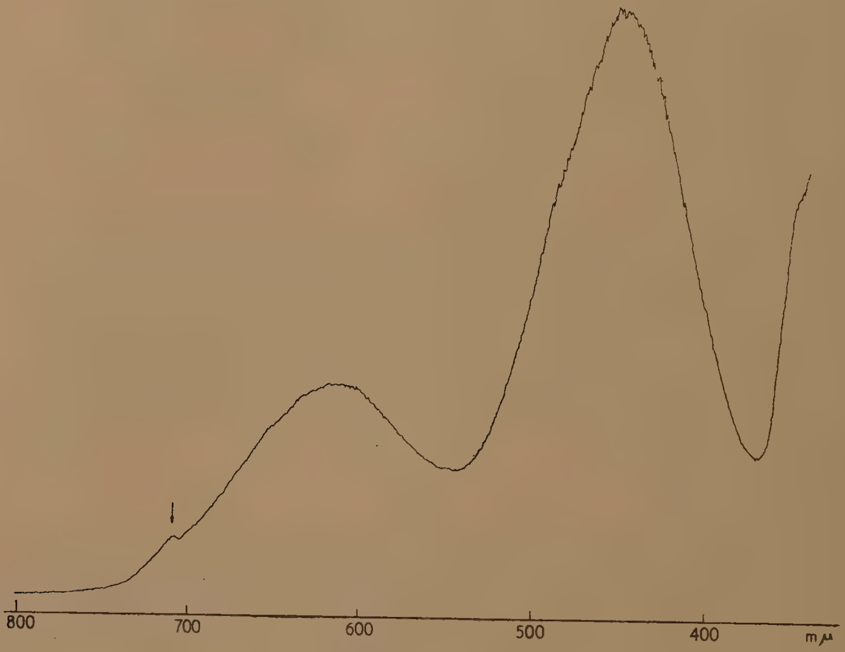

Fig. 2

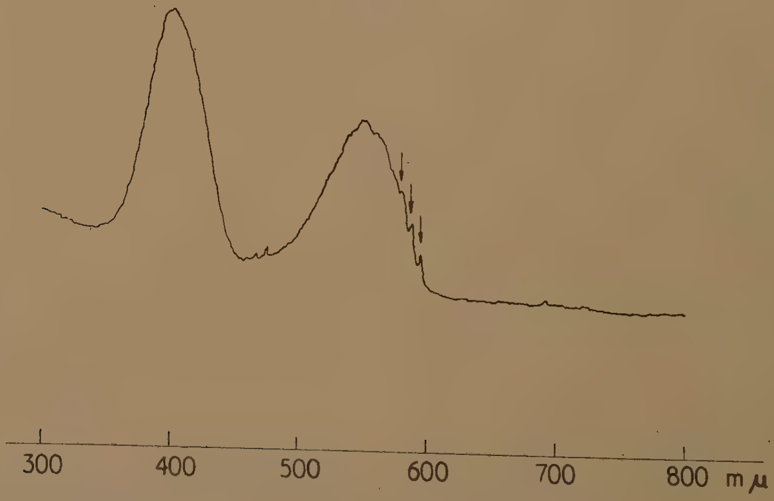

bands. The theory of the line shape should of course be put quantitatively. Nonetheless, even before this (formidable) task is achieved, good purpose is served by formulating the ideas qualitatively. Some of the conclusions are by no means trivial.

§ 2

It is well known that the optical absorption by the ion will in general leave the crystal strained, since different equilibrium dispositions will correspond to the excited and to the ground states. In a crystal this change in the equilibrium configuration will in general affect all the modes in what is presumably a continuous manner. (We expect that the relative change in the configuration on going from one mode to another of adjacent energy will tend to zero as the number of crystal points goes to infinity.) Consequently, various harmonics of each mode will be simultaneously excited with varying probabilities; the variation of the totality of probabilities will produce the rise and fall of the intensity curve. We wish now to emphasize that because of the smooth variation (throughout the continuum of modes) of the equilibrium configurations and of the excitation probabilities a smooth absorption line must result.

We have so far considered the continua, both acoustic and optic, of vibrational modes, called also passing modes, since an excitation in this mode will pass through the whole lattice. It is, however, easy to convince ourselves that other modes may also exist. For this purpose, consider the chromium ion in the MgO lattice. The chromium ($Z=24$) is just about twice as heavy as its host, Mg($Z=12$), and will not, even with the same force constant, fit in with any existing vibrational mode. It has in fact been shown (Maradudin *et al* 1958) that, while the frequencies of the continua are slightly shifted, there will now appear new frequencies spaced apart from the continua of frequencies. The modes corresponding to these frequencies will be localized round the impurity; necessarily so, since the regular lattice cannot 'pass' vibrations of such modes. The number of such *stopping* modes per impurity atom is at most six (Ledermann 1944). It is clear that the excitation of these localized modes by the local strain will be relatively highly likely.

It is also known that on introducing an atom heavier than the host the stopping mode will recede from the bottom of the optic branch, while for a lighter atom the stopping mode will emerge from the top of the acoustic (or optic) branch. We shall now consider the possible energies of these modes.

§ 3

Magnesium oxide forms a rocksalt-like structure. The six branches of such a crystal are shown in fig. 3. (Two–two transverse branches coalesce by symmetry.)

The curves are the results of Kellerman's classic calculations (Kellerman 1940) on NaCl. For our purposes there is no difference between these curves and the refined and more recent results of Cochran (1959). We shall use these curves for MgO by adjusting the vertical scale so as to fit the observed circular dispersion frequency $\omega_0 = 10{\cdot}9 \times 10^{13}\,\text{sec}^{-1}$ for MgO (Born and Huang 1956). For NaCl, $\omega_0 = 3{\cdot}09 \times 10^{13}\,\text{sec}^{-1}$.

Then the positions of stopping bands are as follows:

Longitudinal mode: 580–770 cm^{-1}; Transverse mode: 382–540 cm^{-1}.

A careful reference to fig. 1 gives a value of 500 cm^{-1} for the position of the nib from the beginning of the band. This puts the energy of this mode clearly into the upper half of the transverse stopping band. What is the nature of such a mode?

Fig. 3

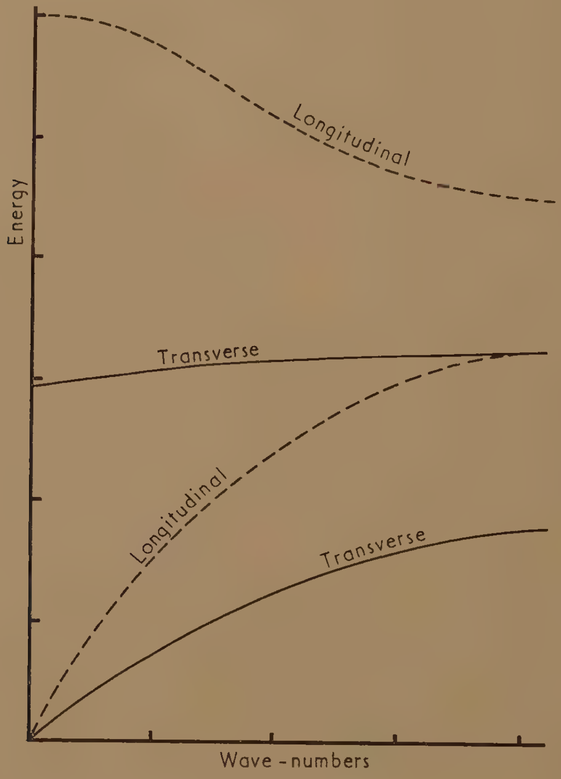

Fig. 4

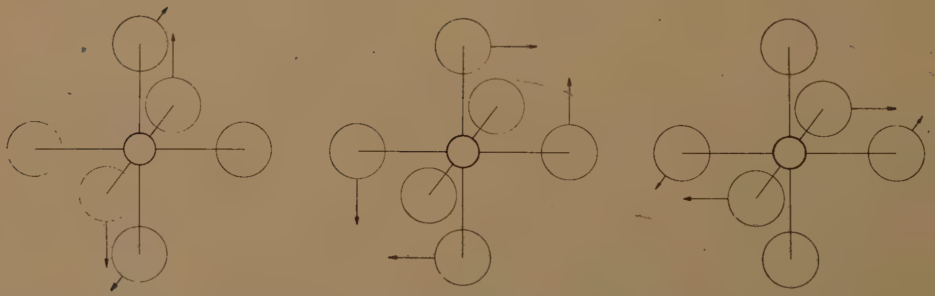

It is known (Brillouin 1953) that in a diatomic chain at the bottom of the optic band the heavy atom is stationary and the light atoms vibrate 180° out of phase. It is very plausible that the character of vibration persists also for a localized mode emerging from the bottom of the optic band. In terms of the classification (Öpik and Pryce 1957) of *localized* octahedral modes this is a T_{2g} (Q_4, Q_5, Q_6) mode. (We recall that transverse vibrations are considered.)

Now, such modes are related to trigonal distortion of the complex. It follows that these modes may be expected to be prominent whenever either the ground state or the excited state is associated with sizeable trigonal distortion. Professor Low has informed me that there is indeed a strong correlation between the appearance of the nib and a trigonal distortion of the lattice in the ground state.

§4

We shall end with a few brief remarks.

The absence of further nibs in fig. 1, cannot be construed as though no further stopping modes are excited, but rather that the rapid rise of the main band obscures any satellite peak. Accordingly the nibs will be most apparent whenever their energy, or that of their overtones, reaches the beginning, top or end of the band.

The three nibs of fig. 2 are probably not successive overtones, since their separation $\sim 130\,\mathrm{cm}^{-1}$ is too small to be fitted into the stopping band. (We assume for Al_2O_3 a roughly similar vibrational structure to that for MgO.) The first nib appears at 480–$500\,\mathrm{cm}^{-1}$.

When the absorption is on the host cation, no localized modes exist due to differences in mass. But there will be localized modes due to changes in the force constants of the absorbing ion (Englman 1960). These changes may be at the same time a decrease in one direction and increase in another, giving rise to localized modes arising both from the optical and from the acoustic branches. Thus, nibs of lower frequencies may also make their appearance.

ACKNOWLEDGMENT

My thanks are due to Professor W. Low for showing me the spectra in figs. 1 and 2.

REFERENCES

BORN, M., and HUANG, K., 1956, *Dynamical Theory of Crystal Lattices* (Oxford: The Clarendon Press).
BRILLOUIN, L., 1953, *Wave Propagation in Periodic Structures* (New York: Dover Publications, Inc.).
COCHRAN, W., 1959, *Phil. Mag.*, **4**, 1082.
ENGLMAN, R., 1960, *Mol. Phys.*, **3**, 23.
KELLERMAN, E. W., 1940, *Phil. Trans. roy. Soc.*, **238**, 513.
LEDERMANN, W., 1944, *Proc. roy. Soc.* A, **182**, 362.
MARADUDIN, A. A., MAZUR, P., MONTROLL, E. W., and WEISS, G. H., 1958, *Rev. mod. Phys.*, **30**, 175.
ÖPIK, V., and PRYCE, M. H. L., 1957, *Proc. roy. Soc.* A, **238**, 425.
STAHL-BRADA, R., and LOW, W., 1959, *Phys. Rev.*, **113**, 775.

Micro-cracks and their Relation to Flow and Fracture in Single Crystals of Magnesium Oxide†

By F. J. P. CLARKE and R. A. J. SAMBELL
Atomic Energy Research Establishment, Harwell, Berks

[Received December 4, 1959]

ABSTRACT

Evidence on mechanisms of fracture in magnesium oxide single crystals subjected to tensile loading is given. As-cleaved crystals contain micro-cracks typically 10^{-4} in. long and slip originating from near these cracks occurs during deformation. At a later stage the cracks grow gradually until they increase to a critical size when catastrophic propagation occurs. If the cracks are removed by polishing ductility is enhanced five to ten times Some crystals were reactor irradiated to doses in the range 10^{14}–10^{19} n.v t. (epithermal) and the effects of this treatment on flow and fracture are described and discussed.

§ 1. INTRODUCTION

CLEAVED single crystals of magnesium oxide are generally more ductile if chemically polished prior to stressing. The mechanisms of fracture in the polished state have been investigated by Stokes *et al.* (1959 a, b, c) and in the unpolished state by Gorum *et al.* (1958) and Washburn *et al.* (1959). The factors leading to fracture in the unpolished state are not clearly defined at present and it is the purpose of this paper to aid an understanding of the processes involved.

Reactor irradiation has been used as a means of varying the amount of slip preceding fracture, and the fracture characteristics have been examined at six different doses in the range 10^{14} to 10^{19} n.v.t. (epithermal).

§ 2. EXPERIMENTAL METHOD

Crystals of magnesium oxide were obtained from the Norton Company, Niagara Falls, and the purity of two crystals from which the specimens were cleaved is given in table 1.

All tests reported here are tensile tests made on a Hounsfield tensometer. The load was estimated by measuring the movement of the load beam with a micrometer dial gauge; the figure thus obtained gave the tensile force measurement to about 0·1 lb wt. Another dial gauge was used to measure the combined extension of the beam, specimen and specimen grips. By calibrating the apparatus initially specimen extensions alone down to 10^{-4} in. could be deduced. The rate of loading was kept constant at about 1 lb wt min^{-1}.

---

† Communicated by the Authors.

The grip part of the apparatus is shown schematically in fig. 1. Axial holes of diameter to suit each specimen, were drilled into the ends of two stainless steel rods 0·25 in. diameter and 2–3 in. long. The rod radius was reduced near these ends to allow a 4 mm microscope objective to approach the specimen. The crystal test bar typically 0·02 in. square by 1 in. long was araldited into these holes and the whole placed into a stainless steel guide collar. This collar had slots milled near the specimen to allow transmitted light microscopic examination to be made during the testing. The other ends of these rods were mounted into small brass collars soldered into Meccano universal couplings. These couplings were fixed to the load grips of the tensometer. By careful machining of the rods and collar non-axial stresses could be reduced sufficiently to prevent any preferential slip at the test piece ends for most tests and the position of fracture occurred randomly. However, in some tests on very brittle specimens there was evidence (given in the text) that non-axial loading was sufficient to give rise to special effects.

Table 1. Analysis of impurity content of crystals used

Impurity	Be	Al	Fe	Ca	Si	Ni	Mn	Ba	Crystal
Concentration (p.p.m.)	70	100	100	500	100	10	10	—	A
	—	300	600	1500	700	200	—	100	B

Fig. 1

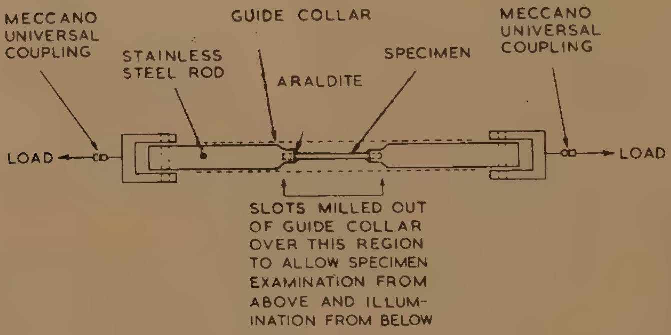
MECCANO UNIVERSAL COUPLING
GUIDE COLLAR
MECCANO UNIVERSAL COUPLING
STAINLESS STEEL ROD
SPECIMEN
ARALDITE
LOAD
LOAD
SLOTS MILLED OUT OF GUIDE COLLAR OVER THIS REGION TO ALLOW SPECIMEN EXAMINATION FROM ABOVE AND ILLUMINATION FROM BELOW

Schematic representation of load grips and associated apparatus (not to scale).

Etching and polishing were carried out in two solutions:

Solution A. Equal parts of saturated ammonium chloride and concentrated sulphuric acid.

Solution B. 88% orthophosphoric acid.

Solution A was used to etch dislocation positions, and solution B as a polishing solution. A detailed study of the action of these solutions has already been described (Ghosh and Clarke 1959).

§ 3. Experimental Results

3.1. *Unirradiated Crystal*

Figure 2 (*a*)† illustrates typical irregularities seen at the edges of a crystal after cleaving. At these high magnifications (× 2000) it is difficult to know exactly what the irregularities represent. Small lines may be revealed by etching solution A, also at the edge, as shown in fig. 2 (*b*) (typical one arrowed); these are not necessarily associated with the pre-etching irregularities. The lines are typically $\sim 10^{-4}$ in. in length and may occur as close together as 10^{-4} in. It will be argued later that these lines are etched micro-cracks and we shall call them cracks in the following description. It has not so far been found possible to control the occurrence of these cracks, but edges have been cleaved along which none has been observed. It is likely that such cracks are present in the as-cleaved and unstrained condition because dislocations, which might produce a crack nucleus, are not invariably found near them; however etching usually reveals a few dislocation loops apparently arising from near the crack tip as shown in fig. 2 (*b*). Such loops may be on one or all possible (110) slip planes, though more often slip is restricted to one such plane at this stage. If a crystal which has been etched is subsequently subjected to tensile stress (to about $0{\cdot}6 \times$ fracture stress, σ_f), any dislocation loops formed prior to etching may expand but an appreciable increase in the number of loops is not observed. If a crystal be stressed to this value *prior* to etching, however, there is an appreciable increase in the number of dislocations arising at or near a crack tip (fig. 2 (*c*)). As before these are revealed by etching, and the etching operation tends to inhibit the production by stress increase of further loops. It is not possible therefore to follow with etching techniques the changes produced in a particular slip band and associated with a particular crack, as a function of change in stress level, because the etching interferes with the mechanisms at work. It *is* possible to carry out a number of experiments on different specimens and to look for a pattern in development and this has been done.

As the crystal is further strained the amount of slip increases and new dislocation loops are activated at the edges of planes already populated, thus forming slip bands. The cracks may grow at these higher stresses but some increase in the amount of slip associated with the crack always precedes the growth of the crack in unirradiated crystals. By the time this stage is reached slip is, more often than not, occurring on orthogonal systems converging on the crack, but sometimes is still restricted to one system as shown in fig. 3 (*a*). At this stage the crack grows along (100) cleavage planes and the largest crack length obtainable prior to fracture varies with the impurity content; for a crystal of analysis B it was typically 5×10^{-3} in. At this size the crack can clearly be seen as such by examination with light reflected off its face.

---

† Figures 2 to 6 and fig. 8 are shown as plates.

While only the slip arising from a single crack has so far been mentioned, in practice several cracks grouped together are often responsible for the pattern observed especially where it occurs on orthogonal systems as fig. 3 (*b*). The cracks themselves cannot clearly be seen in this photograph but it has been confirmed that each slip system has originated at a crack tip of the type already discussed. The cracks described above lie in (100) planes. Crack configurations have been observed in which the crack lies in both (100) and (110) planes as shown in fig. 6. A suggested diagrammatic representation of the crack geometry is also given and this will be discussed in § 4.2.

A typical fracture surface is shown in fig. 4 (*a*) and is similar to those already reported (Stokes *et al.* 1959 c, Clarke 1959); the crack has spread out from the quadrant-shaped plane ABC, which has a radius between 5×10^{-3} and 8×10^{-3} in. long. This photograph was taken from a specimen from crystal B, and in a purer crystal (analysis A) the crack may spread out from a line or from a line + corner as shown in figs. 4 (*b*) and (*c*) respectively. An important feature of this quadrant-shaped area is the distribution of slip bands revealed by etching. Figure 5 photographed at the corner of the quadrant shaped area shows that these are along the crack front of increasingly large quadrant shaped areas, similar to those which can be formed by gradual cleaving (Gilman 1958).

Table 2. Comparison of fracture data for unirradiated crystals (analysis A) and those given reactor irradiation to the dose range 10^{14}–10^{16} n.v.t. (epithermal)

Specimen number	Irradiation dose (n.v.t.)	Treatment	Fracture stress (10^4 lb wt in.$^{-2}$)	Strain (10^{-4})	Comments on type of fracture
36	None	None	0·67	6·7	Line + corner
35	None	Polished	1·0	42·2	Line
37	None	Etched	0·60	24·3	Line
38	10^{14}	None	1·0	1·3	Corner
39	10^{14}	Polished	1·6	7·1	Line
40	10^{15}	None	1·3	2·8	Corner
41	10^{15}	Polished	1·7	1·8	Line + corner
42	10^{16}	None	1·5	0·35	Corner
43	10^{16}	Polished	1·9	2·5	Line

If after cleaving, the crystal edges be polished away using orthophosphoric acid as for the experiments recently reported by Stokes *et al.* (1959 a, b, c), to a depth sufficient to remove the initially present crack nuclei, the crystal exhibits considerably more ductility prior to fracture, and the fracture stress is raised (table 2). It has been shown (Stokes *et al.* 1958, Clarke 1959) that cracks may then form as a result of dislocation interaction by both the mechanism due to Cottrell (1958) and Stroh (1954).

Table 3. Comparison of fracture data for crystals (analysis A) given reactor irradiation to the dose range 10^{17}–10^{19} n.v.t. (epithermal) and unirradiated crystals (analysis B)

Specimen number	Irradiation dose (n.v.t.)	Treatment	Fracture stress (10^4 lb wt in.$^{-2}$)	Strain (10^{-4})	Comments on type of fracture
50	10^{17}	None	2·3	5·3	Line + corner
51	10^{17}	Polished	2·2	4·5	Line
52	10^{17}	None	1·9	0·47	Point away from edge
53	10^{17}	Polished	2·3	2·8	Point away from edge
48	3×10^{18}	None	4·1	Some but none measurable	Point away from edge
49	3×10^{18}	Polished	5·0	ditto	Point away from edge
58	3×10^{18}	None	4·2	ditto	Corner
45	10^{19}	None	4·2	None	Corner
47	10^{19}	Polished	7·1	Some but none measurable	Corner + line
54	10^{19}	None	4·0	None	Point away from edge
55	10^{19}	Polished	4·7	1·2	Point away from edge
56	None: impure crystal	None	1·7	0·4	Corner
57	None: impure crystal	Polished	2·0	41	Point away from edge

3.2. *Irradiated Crystal*

Irradiation increases the fracture stress; it also decreases the amount of ductility obtained before fracture (tables 2 and 3). Other characteristics of the fracture vary with the dose range and so the effects will be considered in this way. All the specimens for these results were taken from crystal A.

3.2.1. 10^{14}–10^{16} *n.v.t.*.

Unpolished specimens usually fracture from a corner and the characteristic cleavage quadrant may be seen at that corner; the radius of this quadrant is decreased as the irradiation dose, and hence the fracture stress, is increased. The change of quadrant radius, c, with fracture stress, σ_f, is such that a plot of σ_f against $c^{-1/2}$ is linear (fig. 7). Orthogonal slip systems acting on $\{110\}$ planes often intersect at the edge from which the catastrophic crack propagation has originated, in a manner similar to that observed by Washburn *et al.* (1959) and observed in unirradiated specimens. However, more rarely the crack origin corresponds to the position where only one active slip band meets the crystal edge, as in fig. 3 (*a*).

Fig. 7

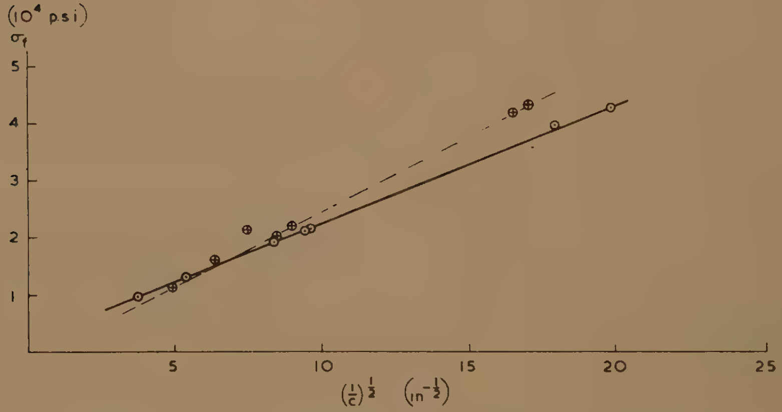

Plot of σ_f against $c^{-1/2}$ to demonstrate agreement with Griffith relation c = radius of quadrant region (ABC of fig. 4 (*a*) for example). ○, A series of measurements taken from photographs; ⊕, a series using a microscope graticule.

The amount of ductility is decreased as the irradiation dose is increased (table 2) and this is reflected in the distribution of slip bands in two ways; the bands are less numerous and they are much narrower. Irradiation seems to inhibit nucleation of new dislocation loops at the edge of existing bands.

Polished specimens usually fracture from a line as shown in fig. 4 (*b*), where the fracture has spread out catastrophically from AB. Sometimes however, (fig. 4 (*c*)) the fracture spreads out from both a line (CD) and a corner (E). The line is that of intersection of orthogonal slip systems which is generally away from the crystal edge and such specimens show the fracture characteristics reported by Stokes *et al.* (1959a, b, c). For specimens which clearly fracture from a line across the crystal face, both the ductility and fracture stress have been increased by polishing. A specimen which fractures as fig. 4(*c*) may show a slightly decreased ductility as compared with one fracturing as fig. 4(*b*). This difference in ductility is small however compared with the differences observed between pure corner and pure line-originating cracks (table 2). Polishing generally raises the fracture stress by an appreciable amount.

Typical experimental figures illustrating these various features are shown in table 2. Important features include:

(i) With the exception of specimen 41 the polished specimens are five to seven times more ductile than untreated ones, the slip being more evenly distributed along the whole length of the crystal.

(ii) There is an increase in the fracture stress with irradiation.

(iii) Polished specimens fracture at a higher stress than unpolished ones.

(iv) Etching (specimen 37) gives enhanced ductility, but less than polishing. The specimen corners were not detectably rounded by the etching treatment.

(v) For irradiations in this range the occurrence of a combined corner + line originating fracture (as specimen 41) is the exception rather than the rule.

3.2.2. 10^{17}–10^{19} *n.v.t.*

In this range the occurrence of an unambiguous corner or line originating fracture is now the exception, and in addition a new fracture configuration is observed occurring from a surface point near the centre of the face in question. A typical case is illustrated in fig. 4(*d*).

The strains observed at 10^{18} n.v.t. were usually below 10^{-4} but at 10^{17} n.v.t. they were just measurable. Unpolished specimens invariably show that the crack origin has been at a line + point (fig. 4(*c*)) or at a point (fig. 4(*a*)). This point may be at the crystal edge or away from it, but always at a surface. Polished specimens, on the other hand, have the crack origin coming from either a point or a line or both. If from a point then the point is at the crystal surface and if from a line then the line is within the crystal.

At 10^{19} n.v.t. much the same pattern of crack characteristics is observed, but for unpolished specimens there is usually no plastic deformation; none is measurable, and in addition no slip lines are revealed by etching for cases of corner-originating fracture. A polished specimen by comparison fractures at a very much higher stress and shows signs of slip.

Some typical experimental results are given in table 3. Rather more examples are given for each dose than before to demonstrate the variation due to the extra fracture characteristics. The pattern of behaviour is not nearly so clear here, but attention is drawn to these aspects:

(i) Polishing generally increases ductility if the comparison is made between corner and line-originating fracture, or between specimens both of which show point-away-from-edge originating fracture.

(ii) The general increase in fracture stress with increase in irradiation dose is maintained.

Micro-cracks have been observed along a face (fig. 8) away from an edge and it is probable that they are responsible for some of the slip and the fracture in, for example, the cases of specimens 52, 53, 54 and 55 of table 3. It has been noticed however that such cracks tend to occur nearer the araldited ends and so may be associated with stress concentrations due to non-axial loading. This defect would show up more in irradiated (and hence more brittle) specimens.

3.3. *Less Pure Crystal*

It has been shown (Anderson and Clarke 1959 a, b) that impurities increase the fracture stress but do not change the ductility. This is in contrast to the effect of irradiation which raises the fracture stress and decreases the ductility. We include some comparative results on these effects in table 3.

§ 4. DISCUSSION

4.1. *Unirradiated Crystal*

We have suggested previously (Clarke 1959) that micro-cracks may be responsible for the orthogonal slip so often associated with fracture and this is the basis of the present interpretation. Whether these micro-cracks are present before cleaving and are opened up by cleaving, or are formed during the cleaving is not certain. They cannot be detected prior to etching; the crystal edges are so imperfect when viewed at a magnification of around × 2000 however, that it would be difficult to distinguish small cracks from cleavage steps, etc. (see fig. 2 (*a*)). Etching might be expected to reveal cracks more clearly however and it is believed that the black lines at right angles to the crystal edge in fig. 2 (*b*) are cracks revealed in this way. This interpretation is consistent with:

(i) The dislocation loops originating near the line end (fig. 2 (*b*)). If the line were a crack as suggested, the tip would act as a stress concentrator and hence as a preferential source of slip. Small dislocation loops can be created by a slowly propagating cleavage crack (Gilman 1957) but the dislocations typified in fig. 2 (*b*) are not correctly oriented with respect to the crack to be related to these.

(ii) Stressing prior to etching increases the number of loops present near such black lines (fig. 2 (*c*)).

(iii) The lines continue unbroken across both faces forming the edge (see both the long and the shorter lines of fig. 3 (*a*)).

(iv) Some of the lines observed are longer after stressing at near the fracture stress (fig. 3 (*a*)). These longer lines are unambiguously cracks, since they may be seen in the unetched condition by light reflected off the crack faces.

(v) After etching, the production of more dislocations near the line end is inhibited. This could be because the etchant tends to round off the crack tip and so reduce the stress concentration there.

These cracks are initially too small to propagate as Griffith cracks, for taking

Surface energy per face, $S = 1{\cdot}5 \times 10^{-2}$ lb wt in.$^{-1}$ (2700 ergs cm^{-2}: Gilman 1959).

Young's modulus, $E = 4{\cdot}4 \times 10^{7}$ lb wt in.$^{-2}$ (3×10^{12} dyn cm^{-2}: Gilman 1959).

Fracture stress, $\sigma_f = 10^4$ lb wt in.$^{-2}$, a typical value for an unirradiated crystal of analysis B. Then if we take the form of Griffith equation to be $\sigma_f = (2ES/\pi c)^{1/2}$

(e.g. Petch 1954) the critical crack length, c, turns out to be about 4×10^{-3} in. compared with a typical initial size of 10^{-4} in.

However, it is noted that the maximum crack size seen on unirradiated crystals after stressing (5×10^{-3} in.) is close to that calculated from the Griffith equation. This suggests that the crack may propagate catastrophically as a Griffith crack when it grows to a critical size, and more evidence will be given later to support this.

The dislocation pattern of fig. 5 is similar to that reported by Gilman (1958) and would seem to indicate that at the beginning of its growth the quadrant shaped area grows in radial bursts of about 10^{-4} in. As the crack opens up, the driving force must decrease and so the crack slows down; a crack velocity is thus reached at which dislocation loops can be nucleated (Gilman 1957–1958) and the remaining crack energy is absorbed in this way. As the external stress is further increased the crack energy is again raised and the process is repeated. In fig. 3 (*a*) there is a forked dislocation pattern ahead of the crack tip. This is interpreted as representing the lines of intersection of these loops with the crystal surface; a similar pattern has been fully discussed by Washburn *et al.* (1959). At this crack size the crack front below the surface must, on this interpretation, be bowing out ahead of the surface crack. The closeness in the size of the largest cracks seen prior to fracture and the radius of a quadrant shaped area (§ 3.1) suggests that the quadrant represents the crack area prior to catastrophic propagation. The change in the size of this area as the fracture stress is raised by irradiation is consistent with this interpretation and this will be discussed more fully in § 4.2.

So far we have discussed the presence of (100) micro-cracks. It is fairly easy to cleave magnesium oxide along {110} though it is difficult to obtain large areas in this way. However, it would seem reasonable for whatever mechanism gives rise to (100) cracks to give rise also to (110) cracks and we interpret the photograph of fig. 6 in this way. Referring to the diagram of fig. 6, it is suggested that the original crack occurs over the adjacent {100} faces containing AB and BC, and occupies the quadrant-shaped area ABC in (110). At C the crack end changes from (110) to (100) and we assume for the sake of illustration that the length AC also changes as it reaches the line CD perpendicular to the face containing BCE. Then as the crack front AC sweeps out to some point such as D, the end A must also change direction across the face containing AB towards the general direction of D, if the crack plane is to be continuous and eventually complete. The line ABCE of the diagram represents the corresponding line in the photograph and it is suggested that the final part of the line in the photograph, corresponding to the continuation of the crack line BA, may be explained in this way.

4.2. *Irradiated Crystal*

It has been observed that the initial cracks present in a crystal do not normally propagate until some slip has occurred. There are two consequences of this. The first is that reactor irradiation should increase the fracture stress because the electronic re-distribution or the displaced atoms it produces might be expected to pin dislocations. This would increase the stress required to move dislocations and hence the fracture stress. The second is that it should, in principle, be possible to reach a stress below that required to move dislocations but sufficient to propagate the micro-crack as a Griffith crack without any growth having to take place. Both of these conditions are realized in practice. It is quite clear from table 3 that the fracture stress is raised by irradiation and at a dose of 10^{19} n.v.t. the crack propagates catastrophically without any detectable slip (cf. specimens 45 and 47). A corollary of this interpretation is that the length of the micro-crack prior to catastrophic crack propagation should be related to the fracture stress by the usual Griffith-type equation. More particularly a plot of fracture stress σ_f, against $c^{-1/2}$, where c is the crack length, should be linear; fig. 7, which includes data from irradiated and unirradiated specimens, shows that it is.

If dislocations are not able to move at the fracture stress for an unpolished crystal irradiated at 10^{19} n.v.t., then a polished crystal given this dose should fracture at a higher stress, above that necessary to operate dislocation sources, because dislocation interactions are now necessary to *form* crack nuclei. This would explain the unusually large differences in fracture stress between the polished and unpolished crystal results of specimens 45 and 47. However, the crack size is critical here because the fracture stress would vary with it in the case of unpolished crystals.

§ 5. CONCLUSIONS

Microcracks typically 10^{-4} in. long present after cleaving may be responsible for the fracture characteristics of as-cleaved magnesium oxide single crystals. At this size the cracks are too small to propagate as

Griffith cracks; nevertheless they do propagate and the following stages are involved:

(i) At about $0{\cdot}6\sigma_f$ slip arising from the microcrack tip begins to spread across the crystal.

(ii) The crack grows gradually as the applied stress is further raised.

(iii) When the crack reaches a critical size it propagates catastrophically, probably as a Griffith crack.

If the edges of the crystal be removed by chemically polishing to a depth sufficient to remove the micro-crack, crack nucleation then has to take place by dislocation interaction and there is an increase in the amount of slip preceding fracture; hence polished crystals exhibit greater ductility than unpolished ones.

Reactor irradiation affects the crystal in several ways:

(*a*) The fracture stress is raised.

(*b*) The amount of slip preceding fracture is decreased.

(*c*) Any slip bands produced are narrower.

(*d*) The area over which micro-cracks have to grow to cause fracture is reduced to conform to a Griffith-type relation between fracture stress and crack length.

At irradiation doses of 10^{19} n.v.t. micro-cracks can grow catastrophically in unpolished specimens at stresses below those required to operate dislocation sources.

ACKNOWLEDGMENTS

We would like to thank various of our colleagues for discussions on the subject matter of this paper. We are also grateful to Dr. P. Murray and Mr. J. Williams for their encouraging interest during the period of research.

REFERENCES

ANDERSON, P. J., and CLARKE, F. J. P., 1959 a, U.K.A.E.A. Report AERE M.491; 1959 b, E.A.E.S. Symposium on Reactor Materials, Stockholm, U.K. 6.

CLARKE, F. J. P., 1959, *Special Ceramics*: Proceedings of a Symposium held at the British Ceramic Research Association, July (London: Heywood & Co.).

COTTRELL, A. H., 1958, *Trans. Amer. Inst. min. (metall.) Engrs*, **212**, 192.

GHOSH, T. K., and CLARKE, F. J. P., 1959, U.K.A.E.A. Report AERE R.3182.

GILMAN, J. J., 1957, *Trans. Amer. Inst. min. (metall.) Engrs*, **209**, 450; 1958, *Ibid.*, **212**, 310; 1959, Fracture Conference, Swampscott, U.S.A.

GORUM, A. E., PARKER, E. R., and PASK, J. A., 1958, *J. Amer. ceram. Soc.*, **41**, 5.

PETCH, N. J., 1954, *Progr. Met. Phys.*, **5**, 1

STOKES, R. J., JOHNSTON, J. L., and LI, C. H., 1958, *Phil. Mag.*, **3**, 718; 1959 a, *Ibid.*, **4**, 137; 1959 b, *Trans. Amer. Inst. min. (metall.) Engrs*, **215**, 437; 1959 c, *Phil. Mag.*, **4**, 920.

STROH, A. N., 1954, *Proc. roy. Soc.* A, **223**, 404; 1955, *Ibid.*, **232**, 548.

WASHBURN, J., GORUM, A. E., and PARKER, E. R., 1959. *Trans. Amer. Inst. min. (metall.) Engrs*, **215**, 230.

Etching of Strained Aluminium†

By G. A. Bassett and C. Edeleanu
Tube Investments Research Laboratories, Cambridge

[Received February 15, 1960]

Abstract

The initiation of etch attack of strained aluminium has been studied by optical and electron microscopy. It is concluded that an important factor is rupture of the protective natural oxide film and its subsequent failure to repair completely in a short time. Slip, in a direction closely parallel to the specimen surface, or a deformation in compression appears to damage the oxide film more severely than deformation in tension. No correlation between etch pits and the end of dislocation lines has been found.

§ 1. Introduction

Amelinckx (1953) showed that it was possible to etch slip lines in aluminium using a $HNO_3/HCl/HF$ mixture and suggested that dislocations were being etched. Forsyth (1954) however showed that if the specimen was electropolished after straining it no longer was possible to etch the slip lines and he therefore suggested that the attack observed by Amelinckx was due to the initiation of the corrosion reaction at the steps left by the slip process. Lacombe (1947) and Lacombe and Beaugard (1948) and many others have shown that it was possible to obtain pits so distributed on the surface of aluminium that it was reasonable to assume them to indicate the position of dislocations. It seems however that such etching is only possible if the metal has impurities present and it has been suitably heat treated to allow the condensation of such impurities on the dislocations (Wyon and Crussard 1951, Forty and Frank 1955). More recently Braun *et al.* (1958) reviewed some of the earlier work and demonstrated that they could only obtain pits at grain boundaries after a period of room temperature ageing during which they suggested impurities diffused through the boundaries and into the oxide film.

Somewhat similar results have been obtained on various other metal systems and there is a fair amount of evidence that, at least in metals, dislocations are not easy to etch unless some impurity is associated with them. On the other hand many alloys tend to suffer a type of failure known as stress corrosion. The detailed mechanism of this is far from understood. One school has held that failure was due to highly enhanced corrosion due to the high stresses or strain at the tip of a crack and this view is particularly favoured by Hoar and Hines (1956) and Hoar and West (1958) whose interpretation of their electrochemical measurements is consistent with such a theory. There are however various difficulties in accepting this theory, one of which is that if strain or stress had a really marked effect on corrosion reactions the art of etching clean dislocations would presumably be well established by now. In view of this and of the fact that there are other corrosion phenomena such as the 'tunnelling' which occurs in aluminium (see for example Pearson *et al.* 1952), it was considered worth re-examining the etching of aluminium to see whether the reasons for pit localization could be established.

---

† Communicated by the Authors.

§ 2. Experimental

Two grades of aluminium have been used in the work; $\frac{1}{4}$ in. square bar in 99·99% Al and British Aluminium super purity sheet containing the following impurities:

Fe %	Si %	Cu %	Zn %
0·0010	0·0030	0·0015	0·0003

A few other batches of material including some zone-refined aluminium were used but no differences in behaviour were observed.

The specimens were annealed for at least $\frac{1}{2}$ hour at 600°c and air cooled. Electropolishing, whether for micro-examination or for thinning, was carried out in the usual 1–5 perchloric–alcohol bath at about 20 v.

Etching was carried out in freshly made up 47% HNO_3, 3% HF, 50% HCl solution (often used for this type of experiment) or in 3% NaCl at 1·5 v anodic to platinum. Unless otherwise stated it was carried out soon after stressing to avoid ageing effects of the Braun type.

Anodizing, for replica work, was carried out in a solution of 12 g disodium hydrogen phosphate 0·4 ml H_2SO_4 made up to 100 ml and at 30 v. For the optical work the anodizing was carried out in a 10% H_2SO_4 solution at various voltages up to 15 v.

2.1. *Etching in HNO_3–HCl–HF*

The initial experiments confirmed the finding of Amelinckx and Forsyth, and fig. 1† is a low magnification light micrograph showing the attack at slip lines on a specimen previously strained. Figure 2 shows a higher magnification micrograph of a less severely etched grain and in this it can be seen that the pits tend to bunch in a way which could be taken to be due to pile-ups of dislocations.

The initial experiments were carried out on bent specimens and it was very noticeable that by no means all slip lines etched up, that by far the greater number of those that did were on the compression side of the specimen and that virtually none was on the tension side. This observation was subsequently confirmed by etching specimens strained in tension and in compression. In addition specimens were strained in torsion and with these there was, if anything, a greater tendency for pitting at slip lines than in the compression specimens.

---

† All figures are shown as plates.

Examination of the pits with the electron microscope using the oxide replica technique confirmed the light microscope observations. In addition it has been frequently found that the pitting was greatest at those slip lines which showed no, or only very small, steps at the surface (i.e. slip direction was approximately in the plane of the surface). This is shown in fig. 3 in which case it is easy to appreciate that the surface was very nearly parallel to a (110) face (the etching reagent develops (100) facets) and on such a surface slip can occur making virtually no step as indeed the micrograph shows. Figure 4 shows a different example in which etching has again occurred on a slip system making a small surface step but the important thing to note is that larger slip steps are plainly visible in a different system which have not been etched at all.

Pits were sometimes observed at visible slip steps especially in the compression specimens and fig. 5 shows an example chosen since it shows stages in the development of pits at such slip traces. In this case it seems that the upper side of the slip line is high relative to the other side and that the slip has occurred in such a way that the new surface makes an acute angle with the original surface and there is an 'overhang'. At stage one, only the high side has been attacked, at two attack is starting on the lower side and this is better seen at stage three. It is interesting to note that at stage four a fifth face has started developing on the high side of the step. This development of a fifth (and sometimes of even a sixth face) is fairly frequent.

In an attempt to correlate slip direction with tendency to pit a specimen was etched in the usual way, then strained and re-etched in the hope that a few 'old' etch pits would identify the slip direction but generally the second etch destroyed the evidence and only a few cases have been found. The available evidence indicates that where steps are present pitting is more prone to occur when the step makes acute angles with the surface than when it makes an obtuse angle and this presumably explains the observed difference between compression and tension.

The observation of Braun *et al.* that a few weeks' ageing at room temperature caused the grain boundaries to etch up was confirmed. It was found in addition that a specimen strained and then allowed to age, etched only at the grain boundaries, the slip lines being ignored whether or not the specimen was polished after straining. The materials now being used are not pure enough to recrystallize at room temperature and there must be many dislocations left on slip planes so that it seems that room temperature ageing does not make dislocations prone to etching. Similar ageing experiments were then repeated but the specimens were stored in well-pumped down ampoules and in this case the strained specimen showed both grain boundary and slip line etching if no polishing was done after straining, fig. 6, but not otherwise. Again it will be noticed that not all slip bands etch up equally, presumably slip direction being important in this case also.

2.2. *Etching of Anodized Specimens*

The results on strained specimens seemed to be most easily explained by assuming that the localization of the pits was due to the rupturing of the natural oxide film on the aluminium by the slip process and that the repairing process of the cracks in the film left a local weakness. The film on aluminium is known to be highly inert even in acid and once it is 'punctured' because of some defect the attack on the metal is likely to be very rapid locally, and cause pitting before the reaction starts elsewhere. The pits therefore denote locations where the film happens to have been weak and has been punctured by the etching solution rather than where the metal is particularly reactive. Whilst it is easy to see how the incorporation of impurities in the film can cause the necessary type of weakness it is not so easy to see why a film broken mechanically should not repair effectively.

The natural film on aluminium is very thin and, at present, there seems to be no suitable technique for studying directly the manner in which it breaks. For this reason the film was thickened by anodizing in sulphuric acid and it was examined after the metal had been strained. It was found that thick films obtained by anodizing at 15 v cracked at right angles to the tensional direction and that the cracks ran with little deviation from grain to grain, fig. 7. In compression specimens the cracking occurred as a result of secondary tensional stresses and ran parallel to the compression direction showing that at least the thick films can accommodate some strain. The overall appearance was very similar to that of the cracks in the brittle lacquers sometimes used in stress analysis. With thinner films however the cracking was influenced by the slip process and with a 7 v film the cracking, as can be seen in fig. 8, occurred at slip lines. It seems reasonable to assume that the even thinner natural film breaks at slip lines by a mechanism similar to that proposed by Brame and Evans (1958) and Evans and Schwarzenberger (1959).

Etching experiments carried out on the strained anodized specimens, as might have been expected, confirmed that pits formed at cracks in the film whether or not these were at slip lines, and with the thicker films it was often possible to see the film left in position above the pits particularly if the etching were done in the sodium chloride solution as in the case shown in fig. 7. Naturally the anodized films cannot be repaired without further anodizing and these experiments only show that films can break but not show directly why the damage is not healed properly in all cases unless one makes the somewhat bold assumption that in tension the break is a clean one and is easily repaired, but when shear or compression is present the break may be less clean; portions of the film may be left under strain and that it is this debris that forms the local weakness in the film.

2.3. *Etching in NaCl*

The above experiments are somewhat far removed from stress corrosion since the reagent used would not produce this type of failure even in a susceptible alloy. To get a step nearer, etching experiments were also carried out in NaCl. In this case the etching was normally random and it was found that pitting could not be produced at the slip lines of strained specimens except as stated above when these were lightly anodized. Even in these by no means all the cracks in the film etched up. This was not entirely surprising taking account of the chemistry of the process. The NaCl solution is not a particularly reactive reagent until such time as the reaction starts when, because of a hydrolysis reaction, it becomes locally highly acid and the reaction is therefore autocatalytic (Edeleanu and Evans 1951). Because of this the first few pits which form take all the available current and no fresh pits can start.

It was considered that a way to counter the autocatalytic mechanism would be to strain a specimen by bending whilst under the solution, the etching current only being applied for the period of straining. Under such conditions metal would be immediately exposed to etching conditions where the oxide film was ruptured and there would be a minimum opportunity for the film to repair. The extensive pitting at slip lines on an electropolished specimen produced by such an experiment is shown in fig. 9. It will be noted that cross slip occurred frequently in the neighbourhood of pits presumably because of local stress raising effects.

2.4. *Transmission Electron Microscopy*

The most satisfactory manner in which to study the relation between pits and dislocations is to use transmission electron microscopy and the results so far obtained using this technique are consistent with the view expressed above that pits are formed mainly because of weaknesses in the oxide films. No evidence has so far been found to indicate that dislocations in the metal play a direct part in initiating the etching process. Figure 10 for instance shows a strained specimen prepared by thinning from both sides and etching the thin film so produced. Networks of dislocations are observed but not in any marked association with etch pits. Examples have been found where interactions between pits and dislocations have occurred and fig. 11 shows two pits in which dislocations, almost in the plane of the foil, 'outcrop'. The dislocation pattern, appears distorted in the neighbourhood of pits. It should be noted however that the 'outcrop' of dislocations in pits as in fig. 11 is a reasonably unusual occurrence and seems to be no more frequent than might be expected taking into consideration the density of dislocations. Figure 12 is more typical of unstrained material in which only two dislocations are visible. One of them does not seem to have initiated a pit whilst the other is near a pit but unlikely to have initiated it.

Dislocations in aluminium may be moved under the influence of the beam so that it is never absolutely certain that the pattern is exactly as it was whilst the etching was carried out, but the pictures were taken quickly and are thought to represent reasonably accurately the state of the original specimen. What may be significant is that the outcropping dislocation finds no difficulty in moving eventually and those in fig. 11 were seen to do so indicating that they were not anchored by 'hollowing out' on a scale smaller than could be distinguished in the micrograph.

§ 3. Discussion

For most metals the anodic reaction, that is the removal of atoms from the metals and their solvation as ions into the solution, requires a very small energy of activation (i.e. it is not highly polarized) unless oxides are present. This is presumably due to the fact that on normal surfaces there must always be frequent steps and the reaction can occur in stages as suggested by Conway and Bockris (1958). The most important surface steps are presumably those due to the emergence of dislocations since these are indestructible and under suitable conditions it should be possible to locate clean dislocations by etching but this does not appear to be at all easy, at least in the case of metals. One probable reason is that one requirement for etching dislocations is that the reaction be carried out under near equilibrium conditions which, with reactive metals such as aluminium in aqueous electrolytes is impossible. For this reason it is not considered entirely surprising that in the present case the pits have not been proved to locate dislocations but have occurred at places where the oxide film, the more important factor in controlling the anodic reaction, has been damaged.

As already stated it is not clear why air formed films do not readily repair after being damaged. They seem to do so eventually (a few weeks) if the specimen is not stored in vacuum, but a few minutes, certainly an hour or two in air, ought to be sufficient, which does not seem to be the case. The only explanation seems to be that it is the strain in the oxide debris. That such strain exists has not been possible to demonstrate in the present case but fig. 13 shows a thin tarnish film on brass broken as a result of slip. In this case the optical properties are such that an interference pattern can be seen from the light reflected from the metal and the oxide surface and it seems that the film has to some extent lifted and must have distorted and strained considerably. Damage of this type would not presumably be completely repairable by exposure to the conditions which first caused the film.

The etching of dislocations in impure metals is presumably due to a local increase in the reactivity of the oxide resulting from the incorporation of impurities in the film but it is not easy to see how this occurs in the room temperature ageing experiments leading to grain boundary etching. In this case the film grows for all intents and purposes to its maximum thickness during the first few hours and it is not easy to visualize how it subsequently becomes contaminated.

From a corrosion point of view, apart from the pit initiation, it is at least as important to consider what is likely to occur once a pit has started no matter what the reason may have been. Under normal circumstances the metal surface will not be a cube face, so that whether or not there are dislocations there will be steps present and a pit will be able to form and grow by layers of atoms 'peeling off' from the outside edges of the pit. It is relevant to consider what will happen when the pit eventually meets a dislocation (e.g. as in fig. 11).

In such cases the face on which the dislocation emerges may contain a greater length of step per unit area than other faces and might then be expected to corrode faster than the other faces. Moreover such a face would no longer require to extend to the outer surfaces since steps would now be present and the pit may elongate in the direction of the dislocation. This presumably explains the observed formation of a fifth and sixth face in certain cases. Generally the dislocation would not however be in a [100] direction so that as the pit grows the face following a dislocation would change to an alternative cube face and the growth direction of the pit would also alter through right angles. Such pits sometimes called tunnels are in fact found in aluminium as a result of corrosion in tap waters (Pearson *et al.* 1952), or by anodic attack in chlorides (Burger *et al.* 1955). The formation of tunnels of the type found in practice probably requires something more than dislocations to be present since it is difficult to explain otherwise why they remain so narrow. Up to now they have been found in solutions in which it is reasonable to expect that the autocatalytic process mentioned above is likely to be operative. In such solutions, since the overall amount of corrosion which occurs is controlled by some outside factor such as the amount of oxygen available or the current supplied, the reaction will always tend to be concentrated at only a few points and especially at any point where there is a slight advantage. At other points the reaction would halt so that once a pit has 'found' a dislocation the reaction on the faces not containing dislocations may cease entirely. Since from both the stress corrosion and tunnelling corrosion point of view the manner in which pits extend rather than how they initiate seems more important, it may still be that even though it is difficult to 'etch' clean dislocations these may play an important part in the corrosion process.

ACKNOWLEDGMENTS

We thank several laboratory colleagues for helpful discussions, Mr. T. Law for his able experimental assistance, and the Chairman of Tube Investments Ltd. for permission to publish this paper.

REFERENCES

AMELINCKX, S., 1953, *Phil. Mag.*, **44,** 1048.
BRAME, D. R., and EVANS, T., 1958, *Phil. Mag.*, **3,** 971.
BRAUN, I., FRANK, F. C., and MEYRICK, G., 1958, *Phil. Mag.*, **35,** 1312.
BURGER, F. J., FULL, F. V. G., and HARRIS, P. H., 1955, *Bull. Inst. Metals*, September, p. 6.
CONWAY, B. E., and BOCKRIS, J. O'M., 1958, *Proc. roy. Soc.* A, **248,** 394.
EDELEANU, C., and EVANS, U. R., 1951, *Trans. Faraday Soc.*, **47,** 1121.
EVANS, T., and SCHWARZENBERGER, D., 1959, *Phil. Mag.*, **4,** 889.
FORSYTH, P. J. E., 1954, *Phil. Mag.*, **45,** 344.
FORTY, A. J., and FRANK, F. C., 1955, *J. phys. Soc., Japan*, **10,** 656.
HOAR, T. P., and HINES, J. G., 1956, *J. Iron St. Inst.*, **182,** 124.
HOAR, T. P., and WEST, J. M., 1958, *Nature, Lond.*, **181,** 835.
LACOMBE, P., 1947, *Strength of Solids*, Report on Bristol Conference (London : The Physical Society).
LACOMBE, P., and BEAUGARD, L., 1948, *J. Inst. Metals*, **78,** 7.
PEARSON, E. C., HUFF, H. J., and HAY, R. H., 1952, *Canad. J. Tech.*, **30,** 311.
WYON, G., and CRUSSARD, C., 1951, *Rev. Metall.*, **48,** 121.

The Anhysteretic Remanence of Magnetic Recording Tapes†

By E. P. WOHLFARTH
Department of Mathematics, Imperial College, London

[Received March 24, 1960]

ABSTRACT

The anhysteretic properties of magnetic tapes are discussed by introducing the idea of internal demagnetization spectra.

§ 1. INTRODUCTION

RECENT discussions (Schwantke 1958, Woodward and Della Torre 1960, Daniel and Levine 1960) of the physics of the process of magnetic tape recording with high-frequency bias have emphasized again (Greiner 1953, Westmijze 1953, Wohlfarth 1960) the close correspondence between this process and that of the acquisition of the anhysteretic remanent magnetization (Wohlfarth 1957). The initial slope s of a curve relating this magnetization $I_{ar}(H)$ with direct field H (reduced to zero after the previous application and slow reduction of an alternating field of high initial amplitude) gives to some extent (Daniel and Levine 1960) a measure of the sensitivity of the tape under recording conditions. However, the $I_{ar}(H)$ curves of actual tape materials are only linear in H up to certain field strengths H_0, where

$$sH_0/I_{ar}(\infty)=I_{ar}(H_0)/I_{ar}(\infty)=j_b<1, \quad . \quad . \quad . \quad . \quad . \quad (1)$$

say, and where $I_{ar}(\infty)$ is the static saturation remanence. If j_b is considerably less than 1, then, for distortion-free recording, only a small fraction of the maximum possible signal is, in fact, useful.

The values of the initial slope s and of the ratio j_b may be discussed as follows: Although s is ideally infinite, it assumes finite values due to the action of internal demagnetization effects (Néel 1943, Wohlfarth 1957; see also Daniel and Levine 1960). These effects arise as a result of the interactions between the magnetic particles on the tape, the presence of non-magnetic cavities inside the particles (Osmond 1953, Wohlfarth 1959), and for other reasons. The magnetostatic problems raised by these effects are very complex (see, for example, Wohlfarth 1955, Brown and Morrish 1957), and it has been customary to analyse them formally in terms of an internal demagnetization coefficient N_i, such that $s=1/N_i$ (here external demagnetization effects are either assumed to be negligibly small, as with longitudinal magnetization in thin tape specimens, or to have been allowed for). However, if N_i were constant throughout the material, then the ratio j_b in relation (1) would equal 1 (Wohlfarth 1957). In order to interpret observed values $j_b<1$ it is thus necessary to introduce the idea of *internal demagnetization spectra*, such that $n(N_i)dN_i$ gives the relative volume of the

---

† Communicated by the Author.

magnetic material with internal demagnetization coefficients in the range dN_i. The form of this distribution function is determined by such properties of the tape as the dispersion and orientation of the magnetic particles, which in their turn determine other effects such as noise (Howling 1956). It is shown here that $n(N_i)$ may be estimated for a magnetic tape (or, indeed, for any other heterogeneous magnetic material) from accurate measurements of the anhysteretic remanence curve over a wide range of the direct field strength.

§ 2. CALCULATION OF THE INTERNAL DEMAGNETIZATION SPECTRUM

Let where

$$\left.\begin{aligned} j_{ar}(h)&=I_{ar}(H)/I_{ar}(\infty), \\ h&=H/I_{ar}(\infty), \end{aligned}\right\} \qquad (2)$$

and where $I_{ar}(H)$ is the anhysteretic remanent moment per unit volume of the magnetic material of the tape. Then, in terms of the distribution function $n(N_i)$,

$$j_{ar}(h)=\int_0^h n(N_i)dN_i+h\int_h^\infty n(N_i)d(\ln N_i), \qquad (3)$$

so that

$$n(h)=-hd^2j_{ar}(h)/dh^2, \qquad (4)$$

satisfying the normalization condition

$$\int_0^\infty n(N_i)dN_i=1. \qquad (5)$$

Fig. 1

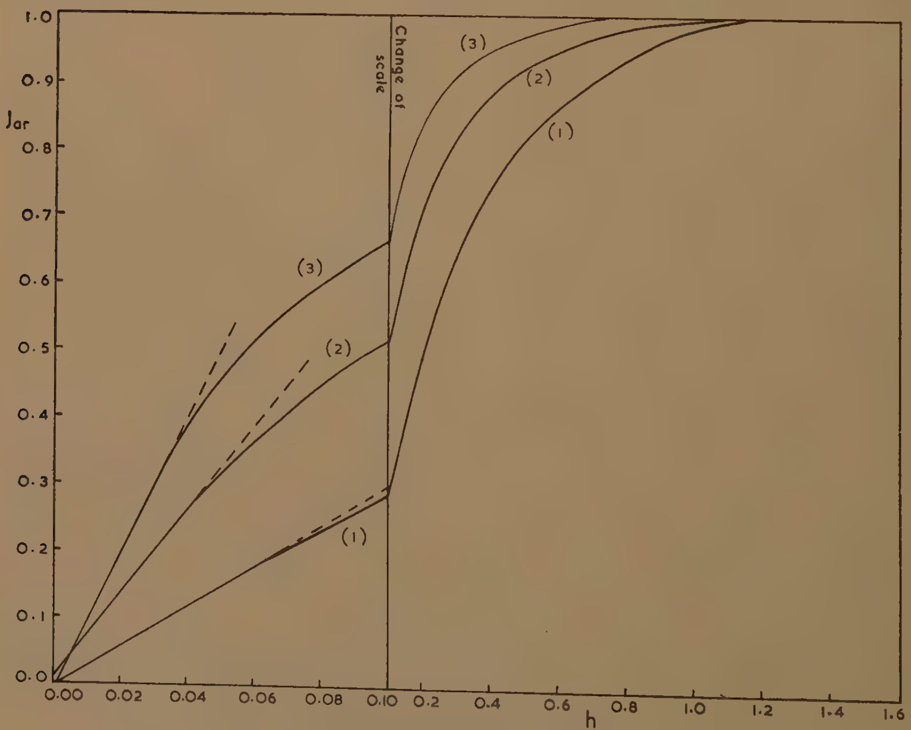

Reduced anhysteretic remanence curves.

Figure 1 shows $j_{ar}(h)$ curves for three distinct types of tape, and the table summarizes their relevant properties. Here s is the initial slope of the anhysteretic remanence curve $(dj_{ar}/dh)_{h\to 0}$ and $1/s$ gives the value of N_i which would have been calculated as the *unique* internal demagnetization coefficient in the absence of this analysis. Also N_0 gives the reduced field $H_0/I_{ar}(\infty)$ up to which the $j_{ar}(h)$ curve is linear, and N_1 the reduced field $H_1/I_{ar}(\infty)$ beyond which $j_{ar}(h)$ is equal to 1. Hence, from relation (4),

$$n(N_i)=0 \text{ for } \left.\begin{array}{l} N_i<N_0, \\ N_i>N_1. \end{array}\right\} \qquad (6)$$

Also, in the table, $j_b=j_{ar}(N_0)=N_0 s$ gives the relative extent of the linear portion of the curve along the j_{ar} axis, defined by relation (1), and $d=(N_1-N_0)$ is the width of the internal demagnetization spectrum. The quantities sd and $(\beta+1)/(\alpha+1)$ are used in the following analysis. Finally, N_m gives the most probable value of N_i, defined as that where $n(N_i)$ is a maximum. It appears that N_m is quite different from $1/s$, so that this last quantity has no direct significance, although $N_m s=0{\cdot}58\pm 0{\cdot}05$ for all three tapes.

Properties of Magnetic Tapes

Tape	s	$1/s$	N_0 $=H_0/I_{ar}(\infty)$	N_1 $=H_1/I_{ar}(\infty)$	j_b $=N_0 s$	d $=(N_1-N_0)$	sd	$\frac{\beta+1}{\alpha+1}$ (calc.)	N_m
1	3·1	0·32	0·055	1·12	0·17	1·06	3·3	3·0	0·19
2	6·2	0·16	0·043	1·10	0·27	1·06	6·6	8·0	0·10
3	10·6	0·09	0·028	0·80	0·29	0·77	8·2	10·6	0·05

The various quantities in the table could all be obtained from the measurements with reasonable accuracy.

Figure 2 shows the $n(N_i)$ curves for the three tape specimens obtained from fig. 1 and relation (4). The calculations were carried out by a combination of graphical interpolation and numerical differentiation, and, although the results are necessarily not too accurate, the normalization condition (5) was easily satisfied to within about 5%. If this analysis is applied more widely it should be possible to develop more accurate methods of calculation or even of automation.

§ 3. ANALYSIS OF THE RESULTS

As there is no simple theoretical formula for the curves of fig. 2, and since direct numerical calculations based on these curves are not sufficiently accurate, the results described in § 2 were analysed on the basis of an approximate though general expression for the distribution function, of the form

$$n(N_i)=AN_i(N_i-N_0)^{\alpha}(N_1-N_i)^{\beta}\gtrless 0, \qquad (7)$$

where A is the normalizing constant. Relation (7) satisfies (6), and, with

$0<\alpha\ll 1$, $\beta\gg 1$, describes the curves of fig. 2 qualitatively quite well. It then follows from (3) and (7) that

$$s=(\alpha+\beta+2)[N_0(\beta+1)+N_1(\alpha+1)]^{-1}, \qquad (8)$$

so that

$$j_b=1-sd[1+(\beta+1)/(\alpha+1)]^{-1}\geqslant 0. \qquad (9)$$

Fig. 2

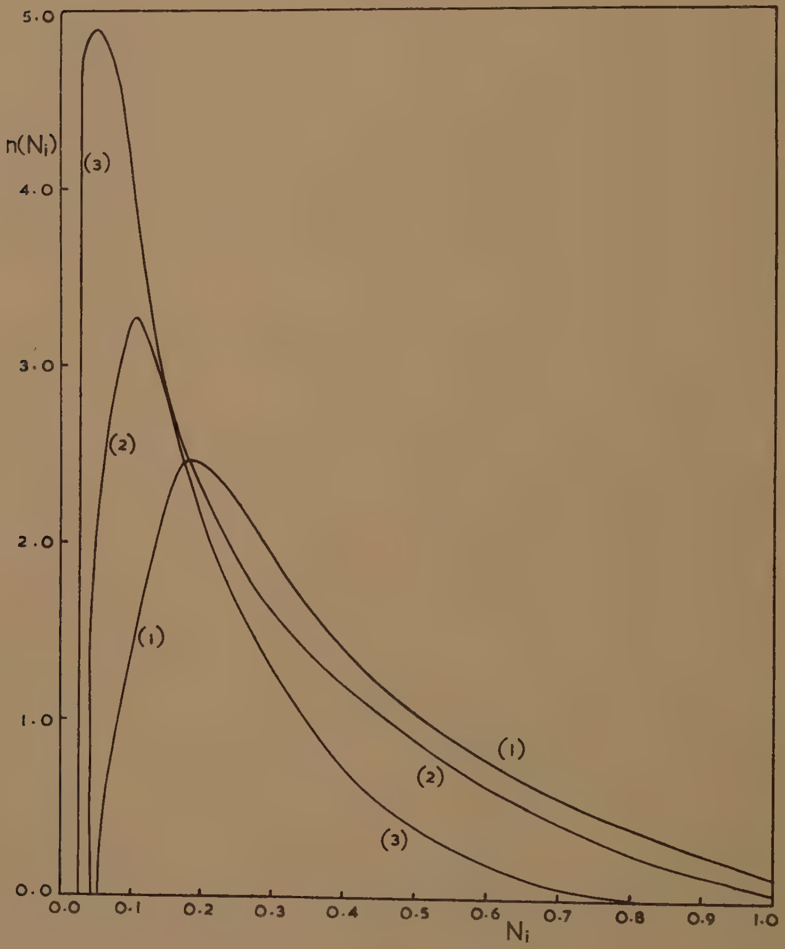

Internal demagnetization spectra. N_i, internal demagnetization coefficient; $n(N_i)$, distribution function, referred to the volume of the magnetic material.

Other approximations to $n(N_i)$ were also investigated; in all cases j_b depends only on the product sd and a form factor. Relation (9) shows that for large values of j_b, which are desirable, it is necessary to have a tape material with the following properties.

(1) Low anhysteretic slope s; this is unfortunate as it implies that high j_b, i.e. high signal, and high sensitivity are difficult to obtain simultaneously.

(2) A low value of the width, d, of the internal demagnetization spectrum; this result is to be expected on general grounds and could be brought about by good dispersion, orientation, etc. of the tape particles.

(3) A high value of the form factor $(\beta+1)/(\alpha+1)$, i.e. a rapid rise followed by a rapid decay of the distribution function $n(N_i)$; this state of affairs could again be brought about by good dispersion. Using relation (9) and the observed values of s, $d=(N_1-N_0)$ and $j_b=N_0 s$, all of which characterize the *extreme regions* of the anhysteretic remanence curve, it is now possible to calculate the values of the form factor, and the results are also shown in the table. They may then be compared with the actual form of the distribution function, obtained from the anhysteretic remanence curve over the *whole range* of the direct field strength from relation (4).

Although *specimen* 1 has a low anhysteretic slope s, it has nevertheless also a very low value of j_b. The calculated value of the form factor $(\beta+1)/(\alpha+1)$ is thus also low, as given in the table, and fig. 2 shows that the form of the $n(N_i)$ curve over the whole range agrees qualitatively with this result.

Specimen 2 has the same value of the width d as specimen 1 but a much higher slope s. In order to interpret the observed value of j_b it is thus found that the calculated form factor is much higher than for specimen 1, agreeing with the much peakier appearance of the $n(N_i)$ curve of fig. 2.

Finally, *specimen* 3 has the largest s and j_b and the smallest d, and thus, in agreement with fig. 2, the largest corresponding value of $(\beta+1)/(\alpha+1)$.

§ 4. DISCUSSION

The results for the three tape specimens can be correlated qualitatively by means of an analysis based on the idea of internal demagnetization spectra. Some correlation is also possible with the actual dispersion and orientation of the tape particles.

This method should also be useful for other magnetic materials such as sintered cubic (Brož and Šternberk 1959) and hexagonal ferrites (Stuijts and Wijn 1958), permanent magnet alloys (Gould and McCaig 1954), other heterogeneous alloys (Kranz 1956) and anisotropic thin magnetic films, for which a structural orientation of imperfections has been tentatively suggested (Wohlfarth 1959, unpublished) to account, in part, for the magnetic annealing mechanism.

ACKNOWLEDGMENTS

I am indebted to Dr. R. R. Pearce and Dr. P. M. Griffiths of the Research Laboratories of Electric and Musical Industries Ltd. for supplying the experimental data on which this analysis is based, and to them and Dr. A. N. Gordon for helpful discussions.

References

Brown, W. F., and Morrish, A. H., 1957, *Phys. Rev.*, **105,** 1198.
Brož, J., and Šternberk, J., 1959, *Czech. J. Phys.*, **9,** 666.
Daniel, E. D., and Levine, I., 1960, *J. acoust. Soc. Amer.*, **32,** 1, 258.
Gould, J. E., and McCaig, M., 1954, *Proc. phys. Soc. Lond.* B, **67,** 584.
Greiner, J., 1953, *Der Aufzeichnungsvorgang beim Magnettonverfahren mit Wechselstromvormagnetisierung* (Berlin: VEB).
Howling, D. H., 1956, *J. acoust. Soc. Amer.*, **28,** 977.
Kranz, J., 1956, *Beiträge zur Theorie des Ferromagnetismus und der Magnetisierungskurve* (Berlin: Springer), p. 180.
Néel, L., 1943, *Cahiers Phys.*, **17,** 47.
Osmond, W. P., 1953, *Proc. phys. Soc. Lond.* B, **66,** 265.
Schwantke, G., 1958, *Frequenz,* **12,** 355, 383.
Stuijts, A. L., and Wijn, H. P. J., 1958, *Philips tech. Rev.*, **19,** 209.
Westmijze, W. K., 1953, *Philips res. Rep.*, **8,** 245.
Wohlfarth, E. P., 1955, *Proc. roy. Soc.* A, **232,** 208; 1957, *Phil. Mag.*, **2,** 719; 1959, *J. appl. Phys.*, **30,** 1465; 1960, *Symposium on Solid State Physics,* **3,** 223 (Brussels, 1958).
Woodward, J. G., and Della Torre, E., 1960, *J. appl. Phys.*, **31,** 56.

An Electron Spin Resonance Investigation of Photographic Processes in Crystals of AgCl containing Traces of CuCl†

By I. S. CICCARELLO, M. B. PALMA-VITTORELLI, and M. U. PALMA
Istituto di Fisica dell'Università di Palermo

[Received March 7, 1960]

ABSTRACT

An electron spin resonance spectrum, due to the formation of cupric ions during illumination, has been observed in crystals of silver chloride containing 0·1 mol % of cuprous chloride, which have been quenched to −183°C immediately following irradiation. The spectrum fades rapidly if the crystals are kept at any temperature above −140°C after the end of illumination. An interpretation of this behaviour is given which is based upon the Mitchell theory of the photochemical process in crystals of silver halides.

§ 1. INTRODUCTION

EXPERIMENTAL work on crystals of silver halides containing traces of cuprous halides (Clark and Mitchell 1956, Moser *et al.*, 1957) has given results of considerable interest in connection with the mechanism of the formation of photolytic silver and has revealed new dislocation phenomena of great interest for the physics of solids (Parasnis and Mitchell 1959).

The observations which have been made, particularly: (*a*) the enhancement of the photochemical sensitivity, (*b*) the appearance of a transient coloration upon illumination, and (*c*) the regression of the silver nuclei upon storage or appropriate heat treatment (Parasnis and Mitchell 1959), indicate that an experimental study of the behaviour of the positive holes which are liberated during illumination and involved in regression would be of great interest.

Such an experimental study may be carried out with Electron Spin Resonance (E.S.R.) techniques and a preliminary account of experiments on the behaviour of crystals of silver chloride containing traces of CuCl will be presented in this paper.

§ 2. EXPERIMENTAL METHODS AND RESULTS

Silver chloride single crystals of high purity containing about 0·1 mol % of cuprous chloride have been used for the present investigation. They have been generously supplied by Professor J. W. Mitchell‡ and Dr. E. A.

---

† Partially supported by the Comitato Regionale Ricerche Nucleari, Palermo. Communicated by J. W. Mitchell.

‡ Now at the Department of Physics, University of Virginia, Charlottesville, Virginia.

Braun of the University of Bristol. The methods used for the preparation of the specimens have been described by Clark and Mitchell (1956) and by Parasnis and Mitchell (1959). Specimens in the form of rectangular parallelepipeds were cut from single crystals. Their surfaces were carefully polished on soft cloth soaked in a 5% solution of potassium cyanide and then, after thorough washing, they were annealed at a temperature of 420°c in an atmosphere of nitrogen.

The E.S.R. measurements were made in the 3 cm band, using the spectrometer which has been previously described; in this spectrometer a high sensitivity is achieved by the accurate stabilization of both the magnetic field and the microwave frequency (Palma-Vittorelli and Palma 1958). The use of the rotatable magnet, and of a rotatable sample holder inside the microwave cavity permit the steady magnetic field to be oriented along any direction in the crystal, for any initial orientation of the crystal in the holder. All the measurements in any plane of the crystal may thus be performed without removing the crystal from the microwave cavity, which is maintained at a constant and controlled temperature.

The crystals were irradiated for 10 to 20 sec at a distance of about 10 cm from a 500 w Hanau mercury vapour lamp with quartz envelope (S 500/PL 324).

The most important experimental results are:

(*a*) No E.S.R. has been observed either at room temperature or at liquid oxygen temperature, with non-irradiated crystals of silver chloride containing 0·1 mol % of cuprous chloride.

(*b*) An E.S.R. signal has been observed in the same crystals when they have been irradiated at room temperature and then cooled rapidly to liquid air temperature. For these experiments, the microwave cavity was surrounded by a Dewar vessel filled with liquid oxygen, and the crystal (already fixed on its holder) was dropped into the cavity at the end of the period of irradiation, within an extremely short interval of time.

The E.S.R. spectra obtained under these conditions are similar to those obtained by Tucker (1958) with crystals of AgCl containing traces of CuCl which had been exposed to an atmosphere of chlorine. The figure shows the spectrum obtained at liquid oxygen temperature in the direction which gives the best resolution; it is assumed, by comparison with the results of Tucker (1958), that this is a ⟨100⟩ direction. The main lines (indicated by arrows) are attributed to cupric ions formed by the trapping of positive holes by cuprous ions occupying cation lattice sites and subjected to a crystalline electric field having a symmetry axis along a ⟨100⟩ direction. For such a symmetry, the E.S.R. spectrum is described (Bleaney, Bowers and Ingram 1955, Bleaney, Bowers and Pryce 1955, Tucker 1958) by the following spin Hamiltonian:

$$\mathscr{H} = g_{\parallel}\beta H_z S_z + g_{\perp}\beta(H_x S_x + H_y S_y) + A S_z I_z + B(S_x I_x + S_y I_y) \\ + P\left[I_z^2 - \tfrac{1}{3}I(I+1)\right]$$

which in our case fits the experimental results with the following values: $S=\frac{1}{2}$, $I=\frac{3}{2}$ and

$$g_{\parallel}=2{\cdot}28\pm0{\cdot}01, \qquad A=115\pm10\,\text{gauss},$$
$$g_{\perp}=2{\cdot}066\pm0{\cdot}003, \qquad B=40\pm5\,\text{gauss},$$
$$P=8{\cdot}5\pm3\,\text{gauss}.$$

The two central lines of the four $\Delta M_I=\pm2$ lines, which are allowed on account of the nuclear quadrupole interaction, are almost coincident, and are not resolved. The other barely-resolved lines, which are not indicated by arrows, are attributable to cupric ions in different configurations (see, for instance, Tucker 1958).

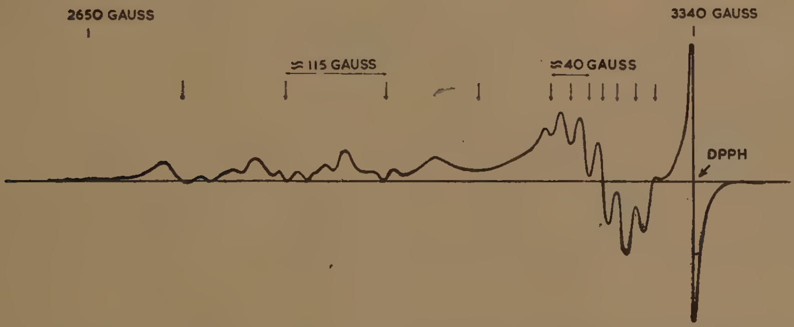

E.S.R. spectrum (derivative) of a silver chloride crystal containing about 0·1 mol % of CuCl, after illumination at room temperature and rapid cooling to liquid air temperature. The crystal is assumed to have had a ⟨100⟩ direction parallel to the steady magnetic field.

(*c*) No significant change in the spectrum is observed when the temperature of the cavity containing the specimen is raised to about −160°c for several hours. The same is true when the temperature is raised to −145°c for 30 min. If the temperature is, however, raised to −120°c for 30 min, the E.S.R. signal fades and is barely detectable. The fading is not reversible, and the spectrum shown in the figure cannot be obtained if the temperature is lowered again to −183°c.

If the specimen is not cooled rapidly immediately after irradiation, erratic and non-reproducible results (including the absence of an E.S.R. signal) are obtained.

§ 3. Discussion of the Results

The features of the hyperfine structure of the E.S.R. spectrum which is reproduced in the figure and the measured values of the parameters of the spin Hamiltonian leave little doubt that the spectrum is due to the formation of cupric ions during the exposure of the crystals at room temperature.

The striking observation is that the E.S.R. signal fades extremely rapidly at room temperature and this probably accounts for the negative results reported by Tucker (1958) in his study of similar crystals.

The absorption of light with a wavelength near the edge of the absorption band of the crystals results in the liberation of conduction electrons and positive holes. According to the Mitchell theory of photochemical processes in crystals of silver halides, the positive holes are trapped before the electrons, and the trapping of the positive hole is followed by the passage of a silver ion from a neighbouring site into an interstitial position and its diffusion away. The conduction electrons then combine with silver ions at sites on external and internal surfaces and along dislocation lines to form the groups of silver atoms of the surface and internal latent images and, ultimately, particles of photolytic silver (Mitchell 1957 a, b, 1958).

We believe that our experimental observations provide supporting evidence for the operation, in these crystals, of the two stages in the Mitchell theory which are concerned with the positive holes. In crystals of silver chloride containing cuprous chloride, the positive holes would be trapped by the substitutional cuprous ions, Cu^+, to form the cupric ions, Cu^{++}, which are responsible for the E.S.R. signal. This corresponds with the first stage in the Mitchell mechanism. The signal fades rapidly at temperatures down to about $-130°$C but does not fade at temperatures below $-145°$C. In accordance with the second stage of the Mitchell mechanism, we believe that this fading might be related to the passage of a silver ion from one of the twelve possible sites around the cupric ion into an interstitial position and to its diffusion away, which occurs with a lowering of the free energy. In the resulting association complex, consisting of the cupric ion and the adjacent vacant silver ion lattice site, the positive hole might be shared between the cuprous ion and the six chloride ions surrounding the vacant silver ion lattice site. It is of interest to remark that the temperature below which the signal does not fade corresponds with that at which silver ions on lattice sites adjacent to cupric ions might be expected to be unable to jump into interstitial positions to diffuse away.

ACKNOWLEDGMENTS

We are deeply indebted to Professor J. W. Mitchell for his cooperation, for valuable discussions and suggestions, and for his communication of experimental and theoretical results. Dr. E. Braun and Professor J. W. Mitchell kindly supplied the crystals used for the present work.

We also wish to thank Professor F. G. Fumi[†] and Dr. M. P. Tosi of his group for many valuable discussions.

Finally, we wish to express our deep appreciation of all the friendly assistance which we have received from the Director of the Institute, Professor M. Santangelo.

[†] Now at Cornell University, Ithaca, New York.

REFERENCES

BLEANEY, B., BOWERS, K. D., and INGRAM, D. J. E., 1955, *Proc. roy. Soc.* A, **228,** 147.

BLEANEY, B., BOWERS, K. D., and PRYCE, M. H. L., 1955, *Proc. roy. Soc.* A, **228,** 166.

CLARK, P. V. McD., and MITCHELL, J. W., 1956, *J. photogr. Sci.*, **4,** 1.

MITCHELL, J. W., 1957 a, *Die Photographische Empfindlichkeit* (Darmstadt: Helwich); 1957 b, *Rep. Progr. Phys.*, **20,** 433 (London: Physical Society); 1958, *J. photogr. Sci.*, **6,** 57.

MOSER, F., NAIL, N. R., and URBACH, F., 1957, *J. Phys. Chem. Solids*, **3,** 153.

PALMA-VITTORELLI, M. B., and PALMA, M. U., 1958, *Nuovo Cim.*, Suppl. **7,** 139.

PARASNIS, A. S., and MITCHELL, J. W., 1959, *Phil. Mag.*, **4,** 171.

TUCKER, R. F., JR., 1958, *Phys. Rev.*, **112,** 725.

Dislocation Nets in Bismuth and Antimony Tellurides†

By P. DELAVIGNETTE and S. AMELINCKX
Centre d'Etude de l'Energie Nucléaire, Mol-Donk, Belgium

[Received February 24, 1960]

ABSTRACT

The electron microscopic examination of thin foils of bismuth and antimony telluride, prepared by repeated cleavage, reveals the presence of extended dislocation patterns. Since the *c*-plane is simultaneously glide and cleavage plane, the dislocation arrangements are preferentially situated in the plane of observation. This is a considerable advantage if one wishes to study the configurations due to glide, since one might hope that the typical thin foil behaviour would not apply to the glide planes parallel to the foil. Sets of concentric dislocation lines are often observed, but they invariably originate in some invisible source, outside the crystal.

In the *c*-plane very extended nets are often observed. The multiplication of dislocations and the resulting formation of networks, as well as the elimination of dislocations are observed whilst in progress. The latter phenomenon is due to a combination of glide and climb. Some contrast effects are also mentioned.

§ 1. INTRODUCTION

THE electron microscopic examination in transmission of thin metal foils as developed by Hirsch *et al.* (1956, 1958), Whelan and Hirsch (1957 a, b), Bollmann (1956), and others has opened up a new field in making possible the direct observation of 'clean' dislocations.

Most of the work on thin foils so far has been confined to metals, although some work has been done on semiconductors (Geach *et al.* 1957). Networks of dislocations, as observed in these foils, have been described and analysed for the case of aluminium and stainless steel by Whelan and Hirsch (1957 a), It is however surprising that in general well-developed networks, containing large numbers of meshes, as e.g. observed by decoration techniques in the alkali halides (Amelinckx 1956, 1958) have not been found in the electron microscopic studies, as yet. The object of this paper is to describe observations of some very well-developed networks, which are fairly regularly found in the basal plane of bismuth and antimony telluride single crystal flakes. In these materials it was possible to observe the actual formation of networks whilst in progress.

We will describe in this paper features common to both substances; phenomena typical of Sb_2Te_3 not found in Bi_2Te_3 will be described in a later paper.

---

† Communicated by the Authors.

§ 2. EXPERIMENTAL

The tellurides used for these observations were prepared for semiconductor application. They consisted of small single crystal blocks and were made by melting together the elements in the stoichiometric proportions, in a quartz tube. Specimens, sufficiently thin to transmit electrons were prepared by repeated cleavage. In electron diffraction these cleavage flakes showed excellent hexagonal cross-grating patterns, typical of the basal plane. This allowed complete orientation of the foil. The specimens are very stable except for melting and they can be examined up to several days after their preparation.

A satisfactory method for preparing these cleavage flakes consisted in sticking a crystal flake with one face to ‘palavit’, a rapidly setting plastic, used in dental surgery, and pulling off flakes at the other side by means of scotch tape. Sufficiently thin flakes adhering to the palavit are then selected and thoroughly washed, mounted on grids and examined with a standard Philips microscope operated at 100 kv. By tilting the specimens with respect to the electron beam a suitable contrast can be obtained.

Burgers vectors of dislocations were determined by the use of selected diffracted beams to produce a dark field image. The procedure is as follows. A diffraction pattern is produced at zero magnification; by means of the 25 μ object diaphragm a particularly intense spot can be selected. The image due to this spot is then magnified without tilting the specimen so as to allow observation of the dislocation pattern. If the selected spot corresponds to a reflection against a set of crystal planes passing through the Burgers vector, the dislocation is not visible. It is clear that this procedure allows a determination of the direction of the Burgers vector. An example of such an image is visible in fig. 1† whilst fig. 2 shows a similar field in normal conditions. It is clear that one set of lines is lacking in fig. 1. This information combined with a knowledge of the structure is sufficient to asign plausible Burgers vectors to the different segments of the net.

Although the specimens were not intentionally deformed the way of preparing them certainly introduces large numbers of dislocations.

§ 3. THE CRYSTAL STRUCTURE OF BISMUTH AND ANTIMONY TELLURIDE; BURGERS VECTORS

Bismuth telluride has a close-packed layer structure (Lange 1939), Francombe 1958); it can schematically be described by the layer sequence

$$\ldots . [\text{Te–Bi–Te–Bi–Te}]\text{Te–Bi–Te–Bi–Te}|\text{Te–Bi–Te–Bi–Te–}|\ldots .$$
$$\longleftarrow 10\,\text{Å} \longrightarrow$$

One-third of the hexagonal unit cell has been indicated by brackets; its total height is about 30 Å. Each of these layers is close-packed and the stacking of the layers is further cubic close-packed: i.e. (see fig. 3)

$$\begin{array}{l}\text{Te Bi Te Bi Te Te Bi Te Bi Te Te Bi Te Bi Te}\\ A_1 B_1 C_1 A_2 B_2 | C_2 A_3 B_3 C_3 A_4 | B_4 C_4 A_5 B_5 C_5 | \ldots .\end{array}$$

---

† Figures 1, 2, 7–10, 13, 14, 16, 21, 22, 24, 25 are shown as plates.

The structure of Sb_2Te_3 is not described in the literature, but it is probably the same, antimony being substituted for bismuth (fig. 3).

The pronounced layer structure explains why there is an extremely perfect cleavage along the basal plane. Cleavage probably takes place between two tellurium layers, since the bonds are weakest there. The main glide plane is also the basal plane and specimens deform quite easily by glide along this plane. This could be observed directly in the microscope.

Fig. 3

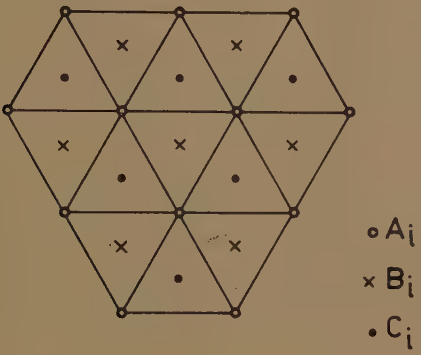

Schematic view of different sites in cubic close-packed structures to which is referred in the description on the structure of bismuth and antimony telluride.

Fig. 4

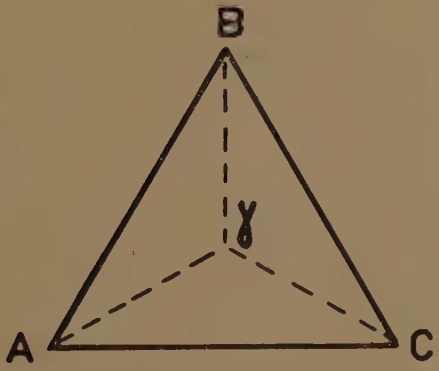

Notation used for Burgers vectors in the basal plane.

The location of the glide plane is probably the same as the one of the cleavage plane, i.e. between the two Te-layers. The fact that both cleavage plane and glide plane are parallel to the *c*-plane, makes Bi_2Te_3 and Sb_2Te_3 excellent materials for the preparation of foils that will have extensive dislocations arrangement in the plane of the foil.

The c-plane being the main glide plane, the distribution of Burgers vectors is similar to the one found in the hexagonal metals, i.e. there are six possible basal plane Burgers vectors which connect nearest neighbours in this plane. They can all be given a name by referring to fig. 4, e.g. AB, BC.... In principle the possibility of dissociated dislocations exists, e.g. AB may dissociate into Shockley partials according to the reaction:

$$AB \rightarrow A\gamma + \gamma B.$$

With the microscope at our disposal it was difficult to decide unambiguously whether the dislocations were single or dissociated. There are indications that sometimes dissociation occurs.

The direction of these Burgers vectors agree with those found by using the selected beam method. This cannot be considered as a proof that glide is between the two tellurium layers.

§ 4. Possible Dislocation Arrangements

Practically only dislocations with Burgers vector in the basal plane are easily formed; they are presumably also the only ones that are observed over an appreciable length, since the plane of observation is in all cases the c-plane. The number of essentially different dislocation patterns is therefore rather restricted.

If glide on only one slip system has taken place the only possible arrangement is a set of parallel lines or concentric loops. If glide has taken place on several parallel glide planes of the same set, tilt boundaries in planes perpendicular to the Burgers vector might eventually form. The probability to observe them is however small in view of the small thickness of the foil.

If slip on two systems has taken place along the same or neighbouring glide planes, stable hexagonal nets form after some anneal.

Using the notation introduced in §3, which is an adaptation of Thompson's notation (Thompson 1953), the lettering pattern becomes as shown in fig. 5. One could now distinguish a number of singularities which give rise to deviations from the normal hexagonal grid. They have been analysed by Amelinckx (1956) and Frank (1955) for the case of the face-centred cubic lattice, more specifically for the sodium chloride structure. Since in the present case we are restricted to co-planar Burgers vectors, very few observable singularities result. Some possibilities are nevertheless shown in fig. 6.

Since we have no dislocations with mutually perpendicular Burgers vectors, square grids are not to be expected.

§ 5. Results of Observations

5.1. *Sets of Parallel Lines* (*Straight or Curved*)

Sets of parallel curved lines apparently originating from some invisible centre are frequently observed. These centres are very probably the dislocation sources which operated during deformation. Sources situated in the bulk material have however not been found. Invariably the origin is somewhere out of the foil or at its surface. Examples of sets of lines are visible in fig. 7.

When a dislocation with a different Burgers vector is present in the same or nearby glide plane, zig-zag lines result, as shown in fig. 8, A, B, C and D.

Fig. 5

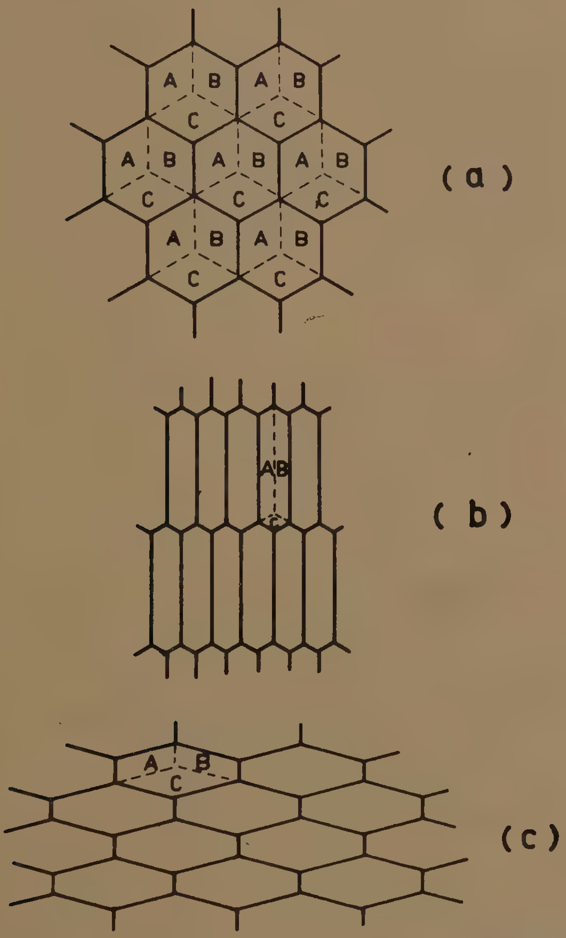

Differently shaped networks as observed in both tellurides.

In a few cases the dislocation lines seem to be interrupted; see e.g. fig. 9, arrows A. This is due to the fact that locally segments of dislocation lines left the crystal. It is clear that this is the combined effect of glide and climb. The argument is that if it were due to pure glide it would require cross slip of a dislocation in the screw orientation. In that case all missing segments would have to have well-defined screw orientations, i.e. parallel to Burgers vectors, which obviously is only approximately the case.

We have actually observed the process taking place. Figure 10 gives an example which could be photographed. It is obvious that the segment A has shortened in the interval of time, i.e. 20 sec between the two exposures.

Fig. 6

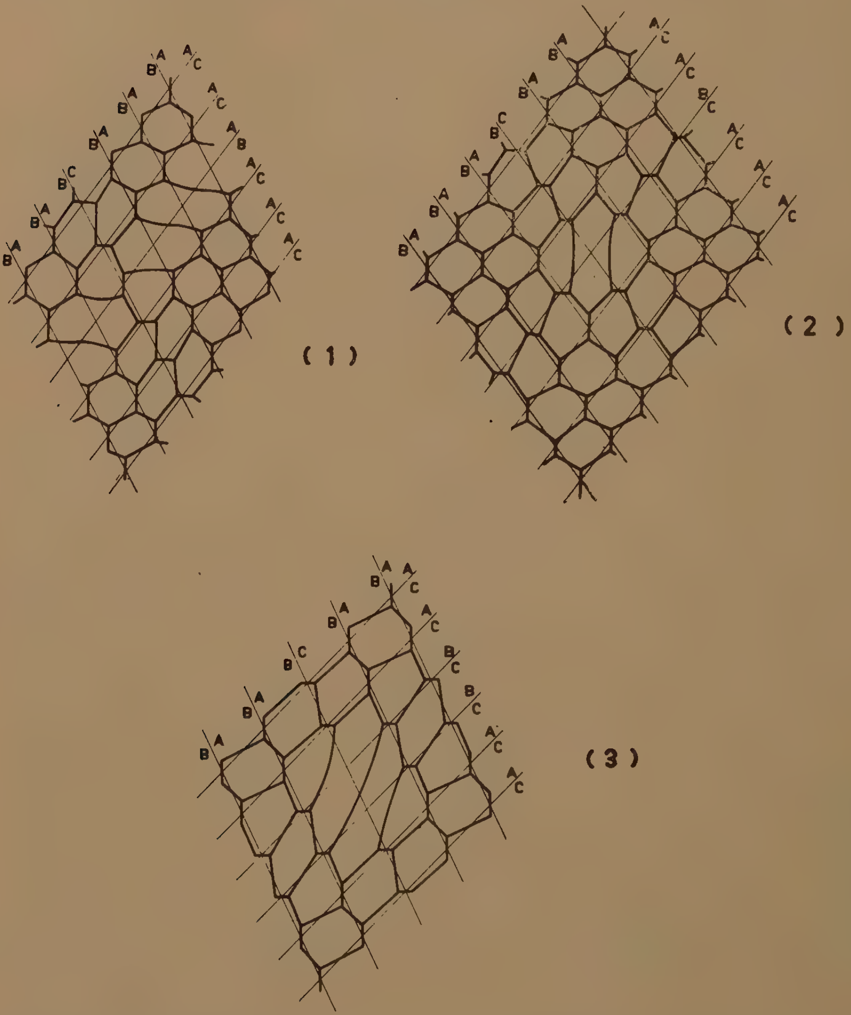

Possible singularities in networks consisting only of dislocations with a basal plane Burgers vector.

The geometry of the process can be pictured as in fig. 11. As driving forces one can consider the line tension of the dislocations and the image force on it; the first tends to shorten the line; the second tends to pull it out of the crystal. They both induce it to climb out of the crystal. The necessary activation for climb is provided by the heating of the sample with the electron beam. This is supported by the observation that most of the movement takes place at the beginning of the irradiation with the beam, i.e. during the temperature rise. Extensive glide motions in the c-plane were observed also.

5.2. *Hexagonal Nets*

Very extended nets, of which examples are shown in fig. 2, have been observed with a surprisingly good contrast. The shape of the meshes ranges from perfectly hexagonal to very elongated. These different shapes are shown schematically in fig. 5. Very elongated hexagons are present between lines B and C in fig. 8; hexagons of the type (c) are visible in the left top region of fig. 9. The nets result from the intersection of two systems of glide loops in the same or neighbouring glide planes. It is known (Amelinckx 1956) that crossed sets of screw dislocations in parallel glide planes exert a pronounced attraction, one on the other, which, after interaction and rearrangement, results in the formation of the hexagonal grids.

Fig. 11

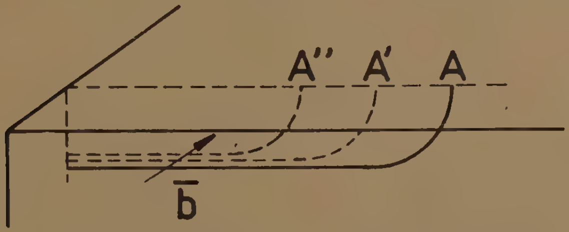

Movement of dislocations by climb.

The initial stage in the formation of such a grid is visible in fig. 9. The net with fine meshes is not yet formed, i.e. new segments have not yet been formed at the intersecting points. This can be deduced from the absence of certain sections of lines. We will present further successive stages in the formation of an hexagonal grid.

In a number of nets 'holes' are frequently observed. Such 'holes' could eventually result from intersecting singular lines in the net (Amelinckx 1958, Frank 1955). A careful analysis of all possibilities shows however that, if only co-planar Burgers vectors are available, which is the case here, such holes are not to be expected. The holes, in the present case, result from the fact that the foils are so thin that certain segments of dislocation line of the network are so near to the surface that they are pulled out of the crystal by the image force, in the way discussed previously. The remaining segments are then practically normal to the foil and their visibility is small. This process is schematized in fig. 12 for a single segment leaving the foil; observed examples are visible in fig. 13, as indicated by the arrows A. If a whole node leaves the foil, more complex holes may form as shown schematically in fig. 12 (b) and observed in fig. 13, arrows B and C. In a few cases a complete net gradually left the foil. The high contrast is probably due to the proximity of the net to the foil surface, which in turn makes possible the described phenomena.

5.3. *Square Grids*

The photograph of fig. 14 shows what is apparently a square grid of dislocations. We know however that the plane of observation is the c-plane and hence that Burgers vectors of dislocations in that plane enclose

Fig. 12

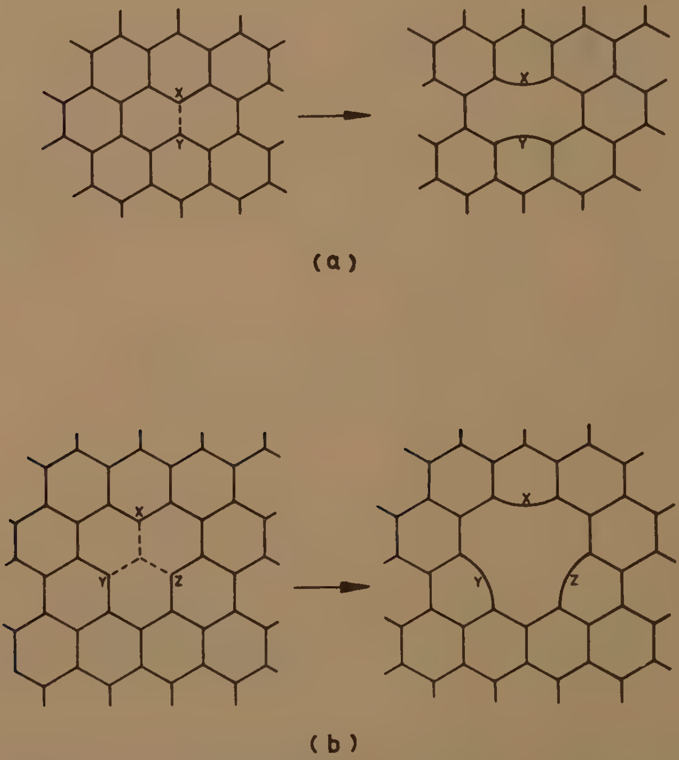

Holes in hexagonal nets resulting from the elimination of certain segments out of the foil. (*a*) segments XY left the foil ; (*b*) node XYZ left the foil.

angles of 60° or 120°. Therefore the square grid cannot be a stable arrangement. The observed pattern is therefore most probably composed of two roughly mutually perpendicular sets of dislocations in parallel glide planes. Such arrangements would, if climb should occur, give rise to hexagonal grids; they were therefore most probably introduced during deformation.

5.4. *Interactions between Dislocations in Parallel Glide Planes*

As pointed out by Read (1953) and shown experimentally by one of the present authors (Amelinckx 1956), dislocations in parallel glide planes exert at their crossing point large local forces which in general have a component of attraction (or repulsion) and a torque. The torque tends to twist the dislocations into typical configurations of which examples are shown in fig. 15. Depending on the character of the dislocation lines the configuration may be symmetrical or asymmetrical. Observed examples can be found in fig. 16, at the points marked A. The same set of crossing lines may produce in different regions, different configurations; i.e. in one region it may be symmetrical, in the other asymmetrical. The reason for this is obviously that the direction of the lines, and hence their character, changes. Examples of asymmetrical twisting are visible in fig. 14 in the marked square.

Fig. 15

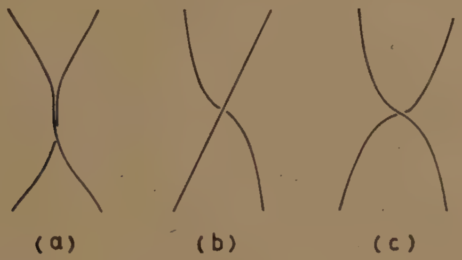

Twisting of dislocations at crossing points. Depending on the character of the dislocations the configuration is either symmetrical (*a*) and (*c*) or asymmetrical (*b*). Observed examples can be found in figs. 14 and 16.

Fig. 17

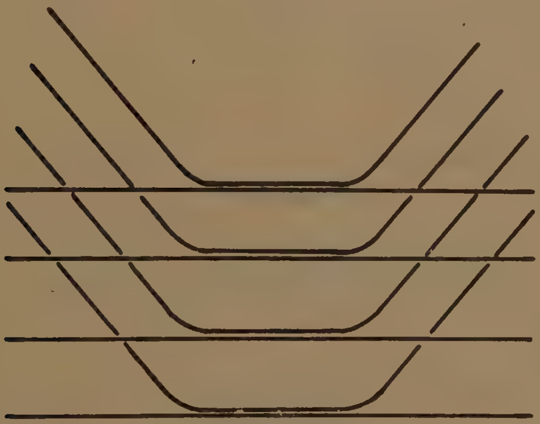

Lining up of dislocations as observed in the marked regions of fig. 16.

In a few cases dislocations of apparently the same system of parallel lines, i.e. with the same Burgers vector, also show interactions, proving that they are not in the same but in parallel glide planes. Examples of this are visible in fig. 16 in the region indicated by the arrows A. Another striking feature is that equidistancy is conserved although the dislocations are not all in the same glide plane. This can of course be understood since dislocations of the same sign and Burgers vector, but in parallel glide planes, repel one another unless they can line up in a plane perpendicular to the Burgers vector. Examples of lining up can be observed in fig. 16 in the region surrounded by a square, as is schematized in fig. 17.

Fig. 18

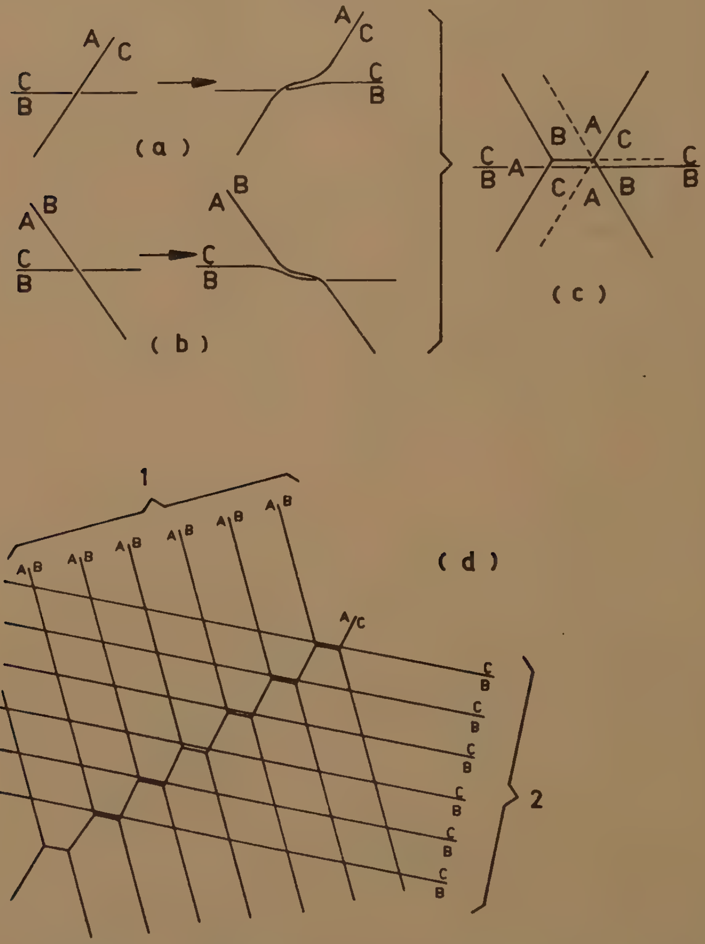

Interaction of segments of zig-zag lines A, B, C and D of fig. 8 with the dislocations of set (2). Figures (*a*), (*b*) and (*c*) show why the presence of the set (2) with Burgers vectors CB, catalyzes the formation of segments with Burgers vector BC at the crossing points of set (1) and the singular line (with Burgers vector AC).

We will now discuss in particular fig. 8 and the corresponding fig. 18. The field is covered by a lozenge-shaped network. As pointed out previously, this is most probably formed by two crossed sets of dislocations in parallel glide planes. One family of lines (1) is intersected by singular lines, marked B, C and D on fig. 8. These singular lines formed zig-zag lines as a result of interaction. The remarkable feature is that one family of segments of the zig-zag line is invariably above a line of the set (2). By allocating suitable Burgers vectors, as shown, this behaviour can be completely understood. The distribution of Burgers vectors is such that the presence of the set (2) with Burgers vector CB catalyzes the formation of a segment of dislocations BC at the crossing point. This can be explained by referring to fig. 18.

Suppose for simplicity that a dislocation with Burgers vector AC is crossed by a dislocation with a Burgers vector CD (see fig. 18 (*a*)). At the crossing point dislocations will exert a torque one on the other in such a way that they tend to adopt the configuration shown in fig. 18 (*a*). If dislocations with a Burgers vector CB and AB cross, the torque at the crossing point is such that the configuration shown in fig. 18 (*b*) tends to develop. The result of the crossing of the three dislocations is now that *no* net torque is exerted on CB, but that the dislocations with Burgers vectors AB and AC develop parallel segments which will combine into a single segment with Burgers vector BC (fig. 18 (*c*)). Parallel to this segment are dislocations with Burgers vector CB, in a parallel glide plane. The equilibrium configuration of these two dislocations is one parallel to the other in such a way that the plane through both of them forms an angle of 45° with the slip plane (the *c*-plane). Since the dislocations are in nearby glide planes this effectively means that they will be observed one on top of the other (fig. 18 (*d*)).

§ 6. DISLOCATION MOVEMENTS

As a result of the small thermal conductivity of the tellurides the specimens become rather hot, and in many cases, when thermal contact with the supporting grid is not good, they can be melted by means of the electron beam. At temperatures not too far from the melting point, extensive rearrangements of dislocations take place, especially in the neighbourhood of the contact with the grid, where thermal gradients are largest. The rearrangement goes in two ways: usually dislocations are eliminated, but in a number of cases dislocations are introduced and we were able to observe the actual formation of networks whilst in progress. We will now discuss the different types of rearrangements separately.

6.1. *Rearrangements by Glide in the Basal Plane*

The main glide plane is the *c*-plane; glide on it has usually jerky character. No evidence for Frank–Read sources was however found, although circumstances were almost ideal. In a number of cases segments lying in the foil over an appreciable length, and leaving the foil at their end points were observed. Such segments have the geometry of a Frank–Read source; they have however been observed to move as a whole, without multiplication.

6.2. *Elimination of Dislocations by Glide on other Glide Planes*

The glide planes different from the *c*-plane have traces along the close-packed directions of the basal plane; they are therefore very likely the traces of the octahedral planes of the pseudo cubic stacking. The second rearrangement process consists in a combination of glide on this system, using the same basal Burgers vectors, and climb, resulting in the elimination of the dislocation out of the foil. It proceeds in the way schematized in fig. 19. Once a small segment of dislocation has left the foil, the line tension of the dislocation tends to pull it completely out.

Fig. 19

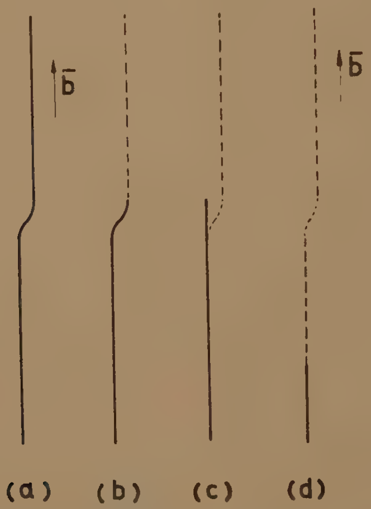

Illustrating the mechanism of elimination of dislocations out of a foil. The pure screw segments glide on non-basal slip planes; the edge sections slip on the basal plane or climb. Observed sequences can be found in figs. 10 and 21.

Two different cases arise. If the dislocations had, originally, both end points in the same face, it disappears completely, without leaving a trace, as opposed to the observations by Hirsch *et al.* (1956), in the case of aluminium. This is of course natural, if Hirsch's explanation based on the presence of an oxide film is right, since no surface step is raised in our case. If the dislocation had originally its two end points at opposite faces of the foil, it is reduced to a small segment of dislocation perpendicular to the foil.

The dislocations that are capable of this type of behaviour are those having large screw sections which can cross glide easily. Whilst gliding out of the foil some segments get stuck for a short while, as shown in fig. 19 (*b*), then glide further out. The stopping points are found to be small segments which are not pure screws and have therefore to climb a small distance or to cross glide on the *c*-plane, as represented in fig. 19 (*c*).

A process of elimination which was actually observed, but could not be photographed as yet, is summarized in fig. 20. Dislocation (3) of a set of parallel screws (1), (2), (3) was suddenly reduced by glide, to a dot dislocation, connecting upper and lower face. It then climbed slowly towards the next screw (2) of the set. On reaching it, the latter dislocation broke up into two parts (2′) and (2″) which suddenly disappeared by glide. This process is of course due to mutual annihilation at the intersection point, followed by the formation of two dislocation segments (2′) and (2″) connected to the surface of the foil. This is represented schematically in fig. 20 (*d*), (*e*).

Fig. 20

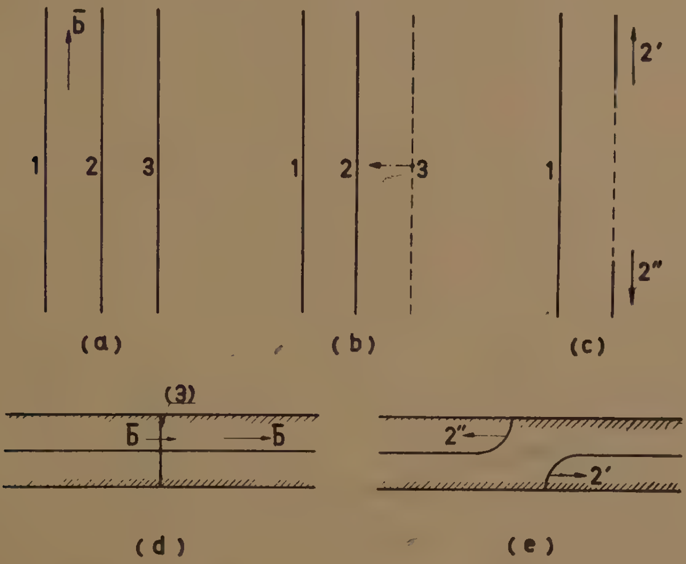

Illustrating a process of elimination of dislocations out of a foil. (*a*) dislocation (3) reduces to a segment perpendicular to the foil; (*b*) dislocation (3) climbs towards dislocation (2); (*c*) on intersecting dislocations (2), the two segments 2′ and 2″ are formed, they glide out of the foil; (*d*) and (*e*) illustrate in cross section the process happening in (*c*).

Sequences of pictures illustrating the elimination of dislocations by means of the described processes are reproduced as fig. 10 (*a*), (*b*), (*c*), (*d*). The sections of dislocations marked B and C disappeared between the exposures (*a*) and (*b*). The node X was at the same time displaced along the dislocation marked (3).

Between exposures (*b*) and (*c*) the dislocations D and E disappeared and the dislocation A shortened considerably.

In the interval of time between the exposures (*c*) and (*d*) dislocation A shortened further and a number of other dislocations disappeared. Many more changes apart from those described can be found. It is evident that the disappearing segments have a certain preferred orientation but are not parallel to the same direction over the whole length, as is consistent with the process described.

A second series of pictures (fig. 21 (*a*), (*b*), (*c*), (*d*) and (*e*)) illustrates the elimination of dislocations out of a regular sequence of parallel dislocations. The larger part of the motions is here conservative, i.e. glide along a glide plane that intersects the basal plane along a line parallel to the general direction of the dislocations. The process is therefore very rapid; the dislocations retract suddenly.

6.3. *Movement of Dislocations Resulting in the Formation of Networks*

Some of the networks, observed in these single crystal foils, actually formed during the observation. A sequence of photographs of the same area illustrating this process is shown in fig. 22 (*a*), (*b*), (*c*) and (*d*). The time interval between successive pictures was only of the order of half a minute or one minute maximum. At the end of the observation period the area was completely filled with a dense network. The most striking feature is the absence of extensive glide in the *c*-plane, most glide being on planes intersecting the basal plane along directions enclosing roughly angles of 60°. No activity of sources was observed, every dislocation developing separately. In cases where the origin could be identified it turned out to be a dislocation segment connecting upper and lower face of the foil (see 1 and 2 of fig. 22). In most cases the origin was not obvious.

It can be seen clearly that the segments of dislocation 1 and 2 are lengthening at both ends between exposures (*a*) and (*b*). The three possible shapes of the features 1 and 2 are:

(1) a segment connecting top and bottom face,

(2) a half loop ending with both ends in top or bottom face,

(3) a loop inside the crystal and lying in a plane perpendicular to the observation plane.

The first possibility is the more likely one. A half loop, for example, would be rather unstable. Buckling of the foil under the thermal gradients now creates an inhomogeneous shear stress, i.e. a shear stress changing sign at the neutral plane. This type of stress distribution tends to move both ends of the dislocation in opposite senses. This movement results necessarily in intersection 1 with the transverse set of lines 3, 4, 5 and 6, already present in the foil, and hence in the formation of three-fold nodes as shown in fig. 23. The general directions of the dislocations are such that they have mainly screw character. This is in fact implied in the description of the movement; this then fixes their Burgers vector. The non-rectilinear character of the dislocations 1 and 2 is due to some cross slip on the basal plane.

§ 7. CONTRAST EFFECTS

As pointed out by Whelan (1959) dislocations are pictured under certain conditions of observation as double lines. This occurs when two different Bragg reflections collaborate to the contrast. A striking example of this is visible in fig. 7 where even a threefold contrast is visible in one area marked A. This photograph shows that the double contrast is depending on the Burgers vector, on the orientation of the line and of course on the orientation of the foil.

In a number of cases (see figs. 13 and 14) dislocations show banded contrast, as if they consisted of a ribbon of stacking faults. This is however not the case since no contracted or extended nodes are seen in fig. 13.

A remarkable contrast effect was found, which as far as we know, is not yet described. An example is shown in fig. 24. The dislocation lines AB and CD separate a dark and a light region. That the dividing line is indeed a dislocation is shown by the fact that such lines often glide in the basal plane; the contrast accompanies them during this process. Sometimes the dislocation line itself does not produce any contrast.

Fig. 23

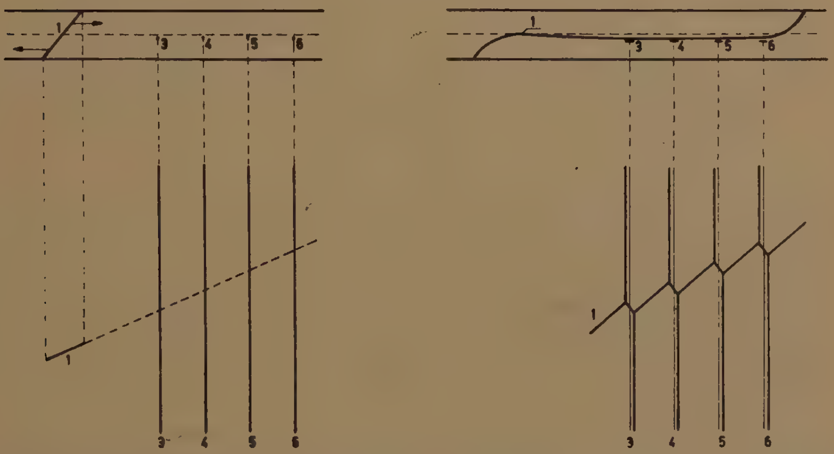

Illustrating the formation of networks. Dislocation 1 glides and intersects dislocations (3), (4), (5), (6). The observed sequence is shown in fig. 22.

In other cases only parts of the dividing line are formed by a visible dislocaion line. This particular form of contrast is only seen near to a broad extinction contour. Overlapping regions produce different shades of contrast, as shown also in fig. 24.

The presence of a dislocation line producing this type of contrast may change the contrast of other dislocations intersecting it. In fig. 25, for example, the line AB is a dislocation line. In the region above AB dislocation lines are pictured as white lines, they exhibit so-called dark field contrast. In the region below AB they have normal contrast. The left part of the same photograph also exhibits the same type of contrast as shown in fig. 24. Different parts of the meshes of the network have a different shade, the shade changing discontinuously at dislocation lines.

Dislocation lines often change contrast discontinuously, a broad line may become suddenly fine, without changing direction (see, e.g., fig. 10 (*a*), arrows Y). The simplest explanation is to assume that this is due to a change in Burgers vector as a consequence of branching in a plane perpendicular to the *c*-plane. This is shown schematically in fig. 26.

Fig. 26

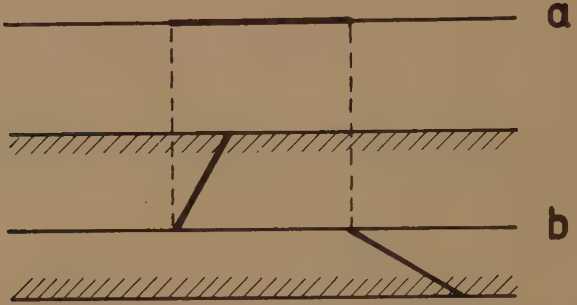

Illustrating the discontinuous change in contrast of certain dislocations: (*a*) top view as seen in microscope; (*b*) cross section of foil. Observed examples can be found in fig. 10.

ACKNOWLEDGMENTS

We would like to express our thanks to Mr. Goens, director of the C.E.N. (Centre d'Etude de l'Energie Nucléaire), Mol, Belgium, for his permission to publish this paper.

We also thank Mr. Beyens for his careful photographic work, Mr. Nicasy for skilful preparation of specimens and Mr. Biermans for preparing the drawings.

REFERENCES

AMELINCKX, S., 1956, *Phil. Mag.*, **1,** 269; 1957, *Dislocations and Mechanical Properties of Crystals* (New York: Wiley and Sons), p. 3; 1958, *Acta Met.*, **6,** 34.
BOLLMANN, W., 1956, *Phys. Rev.*, **103,** 1588.
FRANCOMBE, M. H., 1958, *Brit. J. appl. Phys.*, **9,** 415.
FRANK, F. C., 1955, *Rep. Bristol Conf. on Defects in Crystalline Solids* (London: The Physical Society), p. 159
GEACH, G. A., IRVING, B. A., and PHILIPS, R., 1957, *Research*, **10,** 411.
HIRSCH, P. B., HORNE, R. W., and WHELAN, M. J., 1956, *Phil. Mag.*, **1,** 677.
HIRSCH, P. B., SILCOX, J., SMALLMAN, R. E., and WESTMACOTT, K. H., 1958, *Phil. Mag.*, **3,** 897.
LANGE, P. W., 1939, *Naturwissenschaften*, **27,** 133.
READ, W. T., 1953, *Dislocations in Crystals* (New York: McGraw-Hill).
THOMPSON, N., 1953, *Proc. phys. Soc. Lond.* B, **66,** 481.
WHELAN, M. J., and HIRSCH, P. B., 1957 a, *Phil. Mag.*, **2,** 1121; 1957 b, *Ibid.*, **2,** 1303.
WHELAN, M. J., 1959, *J. Inst. Met.*, **12,** 392.

Effect of Temperature on Yield and Flow Stress of B.C.C. Metals†

By Hans Conrad
Metallurgy Department, Westinghouse Research Laboratories,
Pittsburgh 35, Pennsylvania‡

[Received November 16, 1959]

Abstract

A comparison of data on yielding and flow of b.c.c. metals indicates that the proportional limit, the lower yield stress, the friction stress of Heslop and Petch, and the flow stress after some strain beyond the Lüders strain all exhibit the same strong temperature dependence. This suggests that they all represent the same deformation mechanism. Furthermore, in iron the temperature dependence of these parameters depends on the total interstitial content and on the presence of grain boundaries. Only when both are present does one observe the very strong temperature dependence normally associated with commercial irons and steels.

The strong temperature dependence of the lower yield stress, σ_{LY}, in b.c.c. metals has been attributed to the tearing of dislocations from their atmosphere of interstitial atoms (Cottrell and Bilby 1949, Fisher 1955). Subsequent deformation is then assumed to occur by the motion of free dislocations. If this is so, it is rather interesting that the proportional limit, σ_{P}, and the flow stress after some strain beyond the Lüders strain, σ_{ϵ}, show the same strong temperature dependence as the initial lower yield stress ; for example, see fig. 1 for molybdenum. Also Heslop and Petch (1956) have recently shown that the lattice friction stress§, σ_{00}, in iron shows a strong temperature dependence. Further, Conrad and Schoeck (1960) have found that the temperature dependence of the reversible flow stress ||, σ_{fl} for strained electrolytic iron is independent of strain and is practically identical to that for the initial lower yield stress and for the lower yield stress after strain-ageing. This all suggests rather strongly that the proportional limit, the lower yield stress and subsequent plastic flow in b.c.c. metals are controlled by the same mechanism.

---

† Communicated by the Author.

‡ Present address : Research Laboratories, Atomics International, Canoga Park, California.

§ σ_{00} was obtained as follows : Plots of σ_{LY} versus (grain size)$^{-1/2}$ were extrapolated to infinite grain size to yield σ_0. Plots of σ_0 versus (C+N) content in solution were extrapolated to zero concentration to give σ_{00}.

|| σ_{fl} was obtained by making a rapid change in temperature and noting the change in flow stress.

Fig. 1

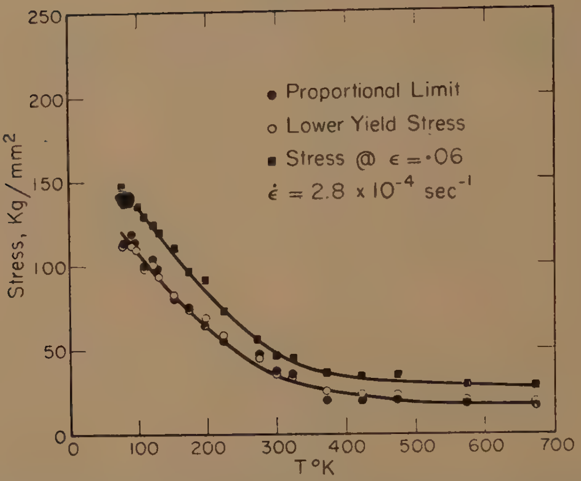

Effect of temperature on the proportional limit, yield stress and stress after strain of 0·06 for molybdenum in compression (data from Alers *et al.* 1958).

Fig. 2

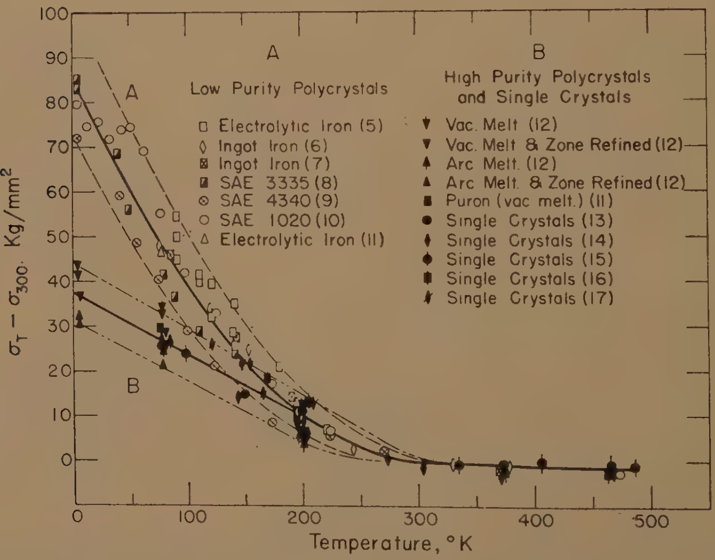

(5) Conrad and Schoeck (1960); (6) Geil and Carwile (1950); (7) McAdam and Mebs (1943); (8) Olleman (1955); (9) Wessel (1957); (10) Wessel (1956); (11) Wiener (unpublished research); (12) Smith and Rutherford (1957); (13) Allen *et al.* (1956); (14) Cox *et al.* (1957); (15) Paxton and Churchman (1953); (16) Vogel and Brick (1953); (17) Steijn and Brick (1954).

Effect of temperature on the lower yield stress of iron and several steels in tension.

When comparing the data in the literature for iron one finds that the temperature dependence of the yield stress is dependent on the purity and the form; i.e. whether it is single or polycrystalline. In the present note data for iron has been assembled to illustrate these effects and to point out certain features which have not been previously defined explicitly.

Figure 2 shows the effect of temperature on the lower yield stress of iron single and polycrystalline specimens of various impurity contents. The temperature independent component of the stress has been removed by plotting the difference between the yield stress at temperature T and the yield stress at 300°K versus the temperature. Pertinent data for the various materials are listed in the table. It is seen from fig. 2 that the data points lie in two scatter bands, one with the strong temperature dependence generally associated with b.c.c. metals (Band A), and the other with a somewhat weaker temperature dependence, especially at the low temperatures (Band B). The temperature dependence of Band B is, however, still greater than that generally observed for f.c.c. and c.p.h. metals. In Band A lie the data points for all polycrystalline materials of low purity, i.e. $(C+N) > 0{\cdot}01$ wt %. In Band B lie the data points for high purity polycrystals, $(C+N) < 0{\cdot}01$ wt %, and for single crystals of both low and high purity.

Fig. 3

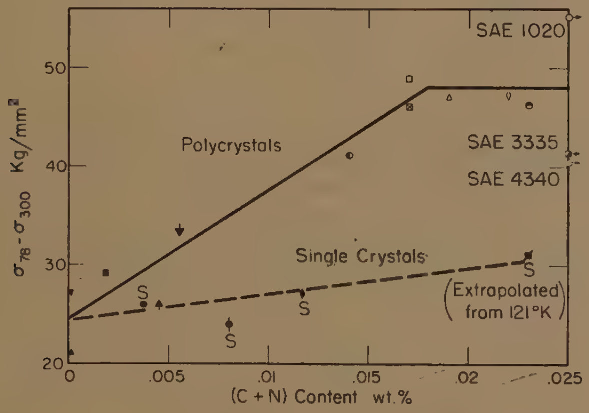

Effect of C+N content on the difference in yield stress at 78°K and 300°K for single (S) and polycrystalline specimens of iron (refer to table and fig. 2 for symbols).

The effect of interstitial content and grain boundaries on the temperature dependence of the yield stress is further shown in fig. 3, where the difference between the yield stress at 78°K and at 300°K is plotted versus the carbon plus nitrogen content. It is here seen that the temperature dependence of the yield stress for polycrystalline iron depends sensitively on the interstitial content up to $\sim 0{\cdot}015$ wt %, while that for the single crystals shows only a very slight dependence. Above $0{\cdot}015\%$ there does not appear to be any further effect of interstitial content for the polycrystals. Thus the strong

Information Pertaining to Figs. 2 and 3

Symbol	Material	Reference	C (wt %)	N (wt %)	C(%)+N(%)	A.S.T.M. G.S.	Strain rate (sec^{-1})
		(*a*) Low purity polycrystals					
◇	Ingot iron	Geil and Carwile (1950)	0·02	0·002	0·022	2–3	Very low
☒	Igot iron	McAdam and Mebs (1943)	0·015	—	∼0·015	—	Very low
□	Electrolytic iron	Conrad and Schoeck (1960)	0·014	0·003	0·017	3–8	$1{\cdot}7\times10^{-3}$
△	Electrolytic iron	Wiener (unpublished research)	0·012	0·007	0·019	5	$2{\cdot}7\times10^{-4}$
◓	Electrolytic iron deoxidized with C	Steijn and Brick (1954)	0·023	—	∼0·023	5	$1{\cdot}7\times10^{-4}$
◐	Carbonized pure iron	Hall (1953)	0·014	0·0002	0·014	2	—
◪	SAE 3335	Olleman (1955)	0·34	—	∼0·34	9	$2{\cdot}8\times10^{-4}$
⊗	SAE 4340	Wessel (1957)	0·30	—	∼0·30	1	$2{\cdot}8\times10^{-4}$
○	SAE 1020	Wessel (1956)	0·24	—	∼0·24	5	$2{\cdot}1\times10^{-3}$

Information Pertaining to Figs. 2 and 3 (*continued*)

Symbol	Material	Reference	C (%)	N (%)	C(%)+N (%)	A.S.T.M. G.S.	Strain rate (sec^{-1})
		(*b*) High purity polycrystals					
▼	Vac melt iron	Smith and Rutherford (1957)	0·005	0·0005	0·0055	8	1×10^{-5}
▼	Vac melt and zone ref.	Smith and Rutherford (1957)	0·00009	No trace	0·0001	5–6	1×10^{-5}
▲	Arc melt iron	Smith and Rutherford (1957)	0·004	0·00009	0·004	3–5	1×10^{-5}
▲	Arc melt and zone ref.	Smith and Rutherford (1957)	0·00009	No trace	0·0001	3–5	1×10^{-5}
■	Puron	Wiener (unpublished research)	0·0008	0·001	0·0018	7·5	$2{\cdot}7 \times 10^{-4}$
		(*c*) Single crystals					
●	Vac melted iron	Allen *et al.* (1956)	0·0027	0·001	0·0037	—	—
◆	Decarb SAE 1008	Cox *et al.* (1957)	0·010	0·0018	0·0118	—	$8{\cdot}3 \times 10^{-5}$
●	Decarb Armco iron	Paxton and Churchman (1953)	0·003	0·005	0·008	—	$3{\cdot}3 \times 10^{-5}$
■	Ingot iron	Vogel and Brick (1953)	—	—	~0·01	—	$1{\cdot}7 \times 10^{-4}$
■	Electrolytic Iron deoxidized with C	Steijn and Brick (1954)	0·023	—	~0·023	—	$1{\cdot}7 \times 10^{-4}$

temperature dependence of the lower yield stress (Band A) is associated with the combined effect of interstitial impurities and grain boundaries. If either is missing a lower temperature dependence results (Band B). It is noteworthy that the temperature dependence of the yield stress for C+N=0% (Band B) is approximately linear.

Figure 4 compares the effect of temperature on the lower yield stress, σ_{LY}, taken from fig. 2 with the effect of temperature on the lattice friction stress, σ_{00}, derived by Heslop and Petch (1956) from material with a total C+N content† of 0·16%, and the reversible flow stress after a strain of 5%, σ_{f1}, determined by Conrad and Schoeck (1960) for electrolytic iron with C+N content of 0·017%. It is seen that the data points for σ_{00} and σ_{f1} fall (with one exception) into Band A, as might be expected in view of the interstitial contents of the materials for which these quantities were determined. Since the values for σ_{00} were obtained by extrapolating σ_0 to (C+N) in solution = 0%, it appears that the total impurity content governs the temperature dependence of σ_{00} rather than the amount in solution. The value for σ_{00} at the lowest temperature, 77°K, falls outside Band A. This may be due to the occurrence of twinning which has been observed at this temperature (Deronja and Gensamer 1959, Hahn *et al.* 1959, Owen *et al.* 1958). It is anticipated that σ_{00} and σ_{f1} determined on high purity polycrystals or on single crystals of the purity listed in the table will fall into Band B.

Fig. 4

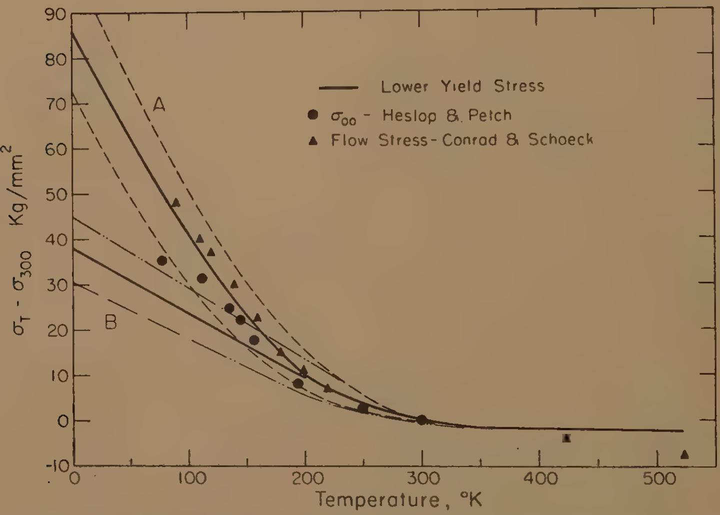

Effect of temperature on the lower yield stress σ_{LY}, the frictional stress σ_{00} and the flow strews σ_{f1} of iron in tension.

---

† However, the amount in solution was only approximately 0·005 to 0·025%.

In conclusion, the available data on the effect of temperature on the deformation of b.c.c. metals indicate the following:

1. The proportional limit σ_p, the lattice friction stress σ_{00}, and the reversible flow stress σ_{f1} show a temperature dependence similar to that for the lower yield stress σ_{LY}.
2. The temperature dependence of the flow parameters σ_{LY}, σ_{f1}, σ_{00}, in polycrystalline iron is determined by the total interstitial content rather than that in solution.
3. In iron the presence of both grain boundaries and interstitial impurities are required to give the very strong temperature dependence of the stress normally attributed to b.c.c. metals.

REFERENCES

ALERS, G., ARMSTRONG, R. W., and BECHTOLD, J. H., 1958, *Trans. Amer. Inst. min. (metall.) Engrs*, **212,** 523.

ALLEN, N. P., HOPKINS, B. E., and MCLENNAN, J. E., 1956, *Proc. roy. Soc.*, **234,** 221.

CONRAD, H., and SCHOECK, G., 1960, *Acta Met.* (to be published).

COTTRELL, A. H., and BILBY, B. A., 1949, *Proc. phys. Soc. Lond.* A, **62,** 49.

COX, J. J., HORNE, G. T., and MEHL, R. E., 1957, *Trans. Amer. Soc. Metals*, **49,** 118.

DERONJA, F. S., and GENSAMER, M., 1959, *Trans. Amer. Soc. Metals*, **51,** 667.

FISHER, J. C., 1955, *Trans. Amer, Soc. Metals*, **47,** 451.

GEIL, G. W., and CARWILE, N. L., 1950, *J. Res. nat. Bur. Stand.*, **54,** 129.

HAHN, G. T., AVERBACH, B. L., OWEN, W. S., and COHEN, M., 1959, Swampsott Conference on Fracture, N.A.S.

HALL, L. D., 1953, *A.S.T.M. Stand.*, No. 158, p. 374.

HESLOP, J., and PETCH, N. J., 1956, *Phil. Mag.*, **1,** 866.

MCADAM, D. J., and MEBS, R. W., 1943, *Proc. Amer. Soc. Test. Mater.*, **32,** 661.

OLLEMAN, R., 1955, Ph.D. Thesis, University of Pittsburgh.

OWEN, W. S., COHEN, M., and AVERBACH, B. L., 1958, *Trans. Amer. Soc. Metals*, **50,** 517.

PAXTON, H. W., and CHURCHMAN, A. T., 1953, *Acta Met.*, **1,** 473.

SMITH, R. L., and RUTHERFORD, J. L., 1957, *Trans. Amer. Inst. min. (metall.) Engrs*, **209,** 857.

STEIJN, R. P., and BRICK, R. M., 1954, *Trans. Amer. Soc. Metals*, **46,** 1406.

VOGEL, F. L., and BRICK, R. M., 1953, *Trans. Amer. Inst. min. (metall.) Engrs*, **197,** 700.

WESSEL, E. T., 1956, *Proc. Amer. Soc. Test. Mater.*, **56,** 540; 1957, *Trans. Amer. Soc. Metals*, **49,** 149.

WIENER, G. W. (unpublished research, Westinghouse Research Laboratories).

CORRESPONDENCE

On the Residual Resistance of Binary Alloys

By E. VERBOVEN[†]
Instituut voor theoretische fysica der Rijksuniversiteit, Utrecht, Netherland[‡]

[Received May 23, 1960]

IT is well known that the electrical resistance of binary alloys may be divided into two parts: the thermal resistance and the residual resistance. This letter will be devoted to the residual resistance of disordered binary alloys. A first theoretical description of this property has been given by Nordheim (1931). His derivation is based on the quantum mechanical Boltzmann equation. He found the residual resistance ρ_0 to be proportional to the product of the concentrations m_A, m_B of the two metals ($m_A + m_B = 1$), so that

$$\rho_0 \sim m_A m_B (\Delta Z)^2 \qquad \qquad (1)$$

where ΔZ is the difference in the effective charges of the two ions. Formula (1) is verified in practice to a high degree of accuracy for alloys of good conductors. A serious discrepancy is present for alloys of a good conductor and a transition metal. This effect was explained by Mott (1935) as an interband scattering of the s-electrons to the d-band. For a typical alloy such as Ag–Pd this scattering must be very important in order to explain the observed deviation from the parabolic law (1) in the region of high Pd-concentrations. However this mechanism cannot explain the deviation for lower Pd-concentrations.

Here we want to give another explanation for the deviation just discussed. The starting point is a simplified version of the Kubo-formula:

$$\sigma_{\mu\nu} = -\mathrm{Tr}_e \left\{ \frac{\partial f}{\partial H} \lim_{T\to\infty} \int_0^T dt\, \tfrac{1}{2}[j_\mu(t) j_\nu(0) + j_\mu(0) j_\nu(t)] \right\} \qquad (2)$$

which gives a closed expression for the conductivity tensor in terms of an equilibrium correlation between currents. This formula has been evaluated by perturbation theory to second order by Verboven (1960). The lowest order term reproduces the usual formula for the conductivity. In our case it gives the Nordheim result. The first higher order term in the conductivity introduces new effects. Its importance is governed by the dimensionless parameter $(\hbar/\tau(\eta)\eta)^{1/2}$, where $\tau(\eta)$ is the relaxation time taken at the Fermi surface and η the Fermi energy. Going over to the resistivity the additional term found there is

$$\rho_1 \sim m_A m_B (m_B - m_A)(\Delta Z)^3 \qquad (3)$$

[†] Aspirant of N.F.W.O., Belgium.

[‡] On leave of absence from the University of Louvain.

Fig. 1

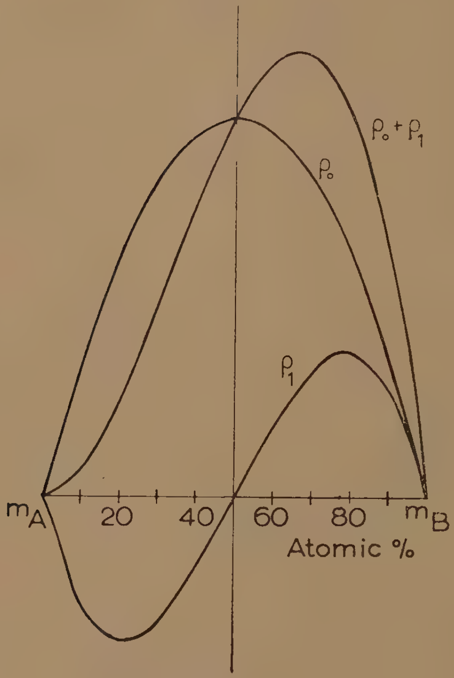

Theoretical curves.

Fig. 2

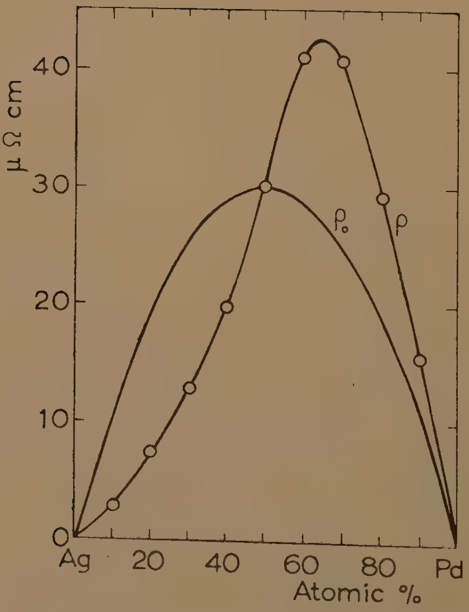

Residual resistance of Ag–Pd and ρ_0.

which contains the whole effect of ternary collisions. The sign depends on ΔZ. In the case of Ag–Pd this is negative. In fig. 1 we represent $m_A . m_B$, $m_A . m_B(m_A - m_B)$ and their sum in arbitrary units. In fig. 2 we plot the residual resistance ρ of Ag–Pd. The parabola ρ_0 is constructed in such a way that it joins this curve in $m_A = \frac{1}{2}$. In fig. 3 we draw $(\rho - \rho_0)/\rho_0$ for Ag–Pd. It is seen that we have a deviation from the straight line predicted from (1) and (2) in the region of high Pd-concentrations. We interpret it as the additional part of the residual resistance due to the interband scattering. For alloys of good conductors the dimensionless parameter mentioned above is too small to give an important contribution.

Fig. 3

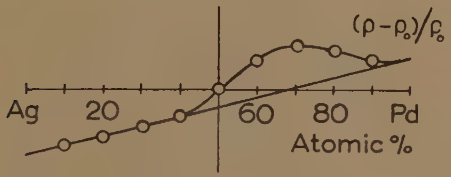

$(\rho - \rho_0)/\rho_0$ for Ag–Pd.

REFERENCES

MOTT, N. F., 1935, *Proc. phys. Soc. Lond.*, **47**, 571.
NORDHEIM, L., 1931, *Ann. Phys., Lpz.*, **9**, 607.
VERBOVEN, E., 1960, *Physica* (to be published).

A Note on the Selection Rules for Optical Transitions in Alloys

By J. M. Ziman
Cavendish Laboratory, University of Cambridge

[Received June 22, 1960]

It is well known (e.g. Mott and Jones 1936, p. 99) that direct optical transitions in solids are 'vertical', i.e. between states of nearly the same reduced **k**-vector. Indirect transitions in which a phonon is emitted or absorbed with the photon, have also been studied (Bardeen *et al.* 1955). These depend on the temperature, but allow the initial and final states to differ by any **k**-vector. The purpose of this note is to point out that one can also have indirect transitions involving the virtual scattering of the electron by *impurities*, and that in an alloy the transition probability for such processes may be comparable with the rate for direct transitions, so that an absorption edge may represent the minimum band gap, rather than the minimum energy difference between states lying directly 'above' each other in a reduced zone.

We use time-dependent perturbation theory, which tells us that in first order the transition probability is proportional to the square of the matrix element

$$\langle \mathbf{k}|P|\mathbf{k}'\rangle = \left(\frac{eE_0\hbar}{2\pi m\nu i}\right)\int \psi_{\mathbf{k}}{}^{*}\nabla\psi_{\mathbf{k}'}\,d\mathbf{r} \quad . \quad . \quad . \quad . \quad (1)$$

between the states $|\mathbf{k}\rangle$ and $|\mathbf{k}'\rangle$. In second order (Schiff 1955, p. 202) this matrix element is replaced by the sum of two terms like

$$\frac{\langle \mathbf{k}|P|\mathbf{k}''\rangle\langle \mathbf{k}''|Q|\mathbf{k}'\rangle}{\Delta\mathscr{E}} \quad . \quad . \quad . \quad . \quad . \quad . \quad (2)$$

where $\langle \mathbf{k}''|Q|\mathbf{k}'\rangle$ is the matrix element for the scattering of electrons by impurities, phonons, etc. Of course the intermediate state $|\mathbf{k}''\rangle$ must lie directly 'above' $|\mathbf{k}\rangle$ but the change of wave vector from $\mathbf{k}''$ to $\mathbf{k}'$ is not prescribed. Thus we may think of $|\mathbf{k}\rangle$ being the highest occupied state in one band, and $|\mathbf{k}'\rangle$ as the lowest empty state in the next band. We need not worry that the scattering from $|\mathbf{k}''\rangle$ to $|\mathbf{k}'\rangle$ is virtual with an energy change $\Delta\mathscr{E} = \mathscr{E}_{\mathbf{k}''} - \mathscr{E}_{\mathbf{k}'}$; the photon energy will be just the difference between the energies of initial and final states, i.e. the true band gap.

A typical model of an impurity is a screened coulomb potential, of charge Ze and screening constant q. In Born approximation this has the matrix element (e.g. Ziman 1960, p. 224)

$$\langle \mathbf{k}''|Q|\mathbf{k}'\rangle = 4\pi Ze^2/\{q^2 + |\mathbf{k}'' - \mathbf{k}'|^2\}. \quad . \quad . \quad . \quad . \quad . \quad (3)$$

If we use the Thomas–Fermi approximation, we can write (Ziman 1960, p.161)

$$q^2 = 4\pi \mathbf{e}^2 \mathcal{N}(\mathcal{E}) \qquad (4)$$

in terms of the density of states at the Fermi level. This value of q^2 is large enough to make it the dominant term in (3) if the scattering is not through too large a distance in the zone. Putting (4) and (3) into (2), and supposing a relative concentration x of impurity atoms amongst the N atoms of the crystal, we have

$$\frac{\langle \mathbf{k}''|Q|\mathbf{k}'\rangle}{\Delta\mathcal{E}} \sim \left(\frac{xZ}{\mathcal{N}(\mathcal{E})}\cdot\frac{N}{\Delta\mathcal{E}}\right). \qquad (5)$$

For a monovalent free-electron system this simplifies because $\mathcal{N}(\mathcal{E}) = 3N/2\mathcal{E}_F$ where $\mathcal{E}_F$ is the Fermi energy. Other things being equal, the ratio of indirect transitions to direct transitions should be the square of (5), i.e.

$$\left(\frac{2}{3}\frac{\mathcal{E}_F}{\Delta\mathcal{E}}xZ\right)^2. \qquad (6)$$

In alloys of the noble metals, where xZ can be 0·3 or more before we reach the α-phase boundary, and where $\mathcal{E}_F$ is, say, 6 ev we can allow $\Delta\mathcal{E}$ to be as much as 1 ev and still have this ratio near unity. Of course there are a number of complicated correction factors, but these would not alter the general conclusion that we may really be watching indirect transitions across the band gap when we see absorption edges in alloys. This is important in the interpretation of experiments like those of Biondi and Rayne (1959) where the rigid-band model is being tested.

REFERENCES

BARDEEN, J., BLATT, F. J., and HALL, L. M., 1955, *Photoconductivity Conference* (New York), p. 146.

BIONDI, M. A., and RAYNE, J. A., 1959, *Phys. Rev.*, **115,** 1522.

MOTT, N. F., and JONES, H., 1936, *The Theory of the Properties of Metals and Alloys* (Oxford).

SCHIFF, L. I., 1955, *Quantum Mechanics* (New York).

ZIMAN, J. M., 1960, *Electrons and Phonons* (Oxford).

The Shear Component of Ductile Fracture

By K. E. Puttick
Davy Faraday Research Laboratory, The Royal Institution,
21 Albemarle Street, London, W.1

[Received June 13, 1960]

There are two well-defined stages in the fracture of a cylindrical test piece of a ductile metal. The first stage begins on the axis in the centre of the necked region, and the general directions of propagation of the crack lie in a plane normal to the tensile axis; this is usually called the 'tensile' part of the break, although it does not obey a simple tensile stress criterion. In the second and final stage the directions of propagation lie on the surface of a cone. It is generally supposed that this cone fracture represents slipping-off by intense local shear on a surface of maximum shear stress, but the details of the process are not at all well understood; in particular, what determines the localization of flow, and the geometry of the actual process of separation?

To answer these questions fully we need to know how the tensile stage of the fracture is propagated, and although it has been shown that the essential process is the coalescence of inclusion holes with the growing central fissure, the distribution of stress and strain in the neck at this stage is obscure. However, experience with controlled cracks made to grow slowly indicates that the material in the neck only undergoes a very small increment of total strain during this period, so that the spring of the testing machine cannot relax much, and the applied load is probably sensibly constant during this period in a normal test. The stress on the uncracked material ahead of the fracture is thus rising during its lateral spread. Also, metallographic examination of the crack shows that it is wide in the centre and narrow at the tip, so that it is an internal notch whose effect must become progressively more severe as it approaches the surface. No theoretical solution of this problem for a cylindrical specimen is possible at present; the most one can do, as Zener (1948) has suggested, is to use known solutions in analogous plane strain problems as a guide in interpreting observations.

Consider, then, the case of a sheet specimen in plane strain containing a prismatic crack whose tip is approximately wedge-shaped. The incipient zone of deformation is the region of maximum stress ahead of the crack bounded by two planes passing through its edge and intersecting the free surface at 45° (fig. 1). When the specimen is stressed in tension, plastic deformation is initially confined to shearing along these planes of maximum shear stress. If the crack propagates toward the surface, finite plastic deformation can occur without large discontinuities in displacement, as is shown in fig. 2. At any instant deformation is taking place only along planes OA, OB, O′A′, O′B′; the material which has already undergone deformation is contained within the shaded regions, having suffered a shear the magnitude of which is a function of the angle at the tip of the crack. The two ends of the specimen move outwards exerting little constraint on the wedges of material OAB, O′A′B′, which move inwards as rigid bodies. The pattern of flow is, in fact, essentially that described by Hill (1953) for the final stage of separation during the cutting of thin sheets by wedge-shaped tools.

Fig. 1

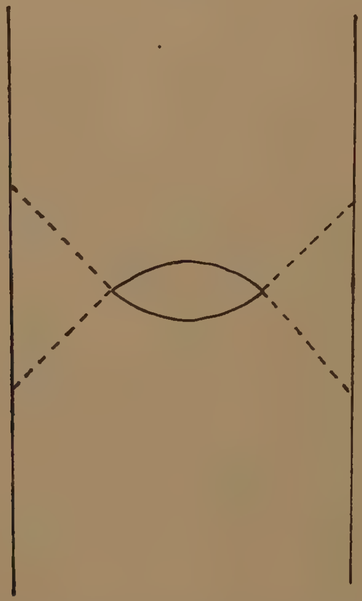

In the case of a cylindrical specimen containing a lens-shaped crack the deformation must be more complex than this, because the surfaces of maximum shear stress are cones, not planes, and the region bounded by them is a ring. In order to allow local shear deformation some plastic flow must take place within this ring to allow it to contract. However, deformation in the region is constrained by the material outside it, so that yielding develops radial and circumferential stresses in addition to the axial tension. Nevertheless, these diminish in intensity as the crack approaches the surface, and it seems reasonable to suppose that the crack initiates narrow zones of shear when it attains some critical size.

We now have to consider the actual process of separation. The usual hypothesis is that put forward by Zener (1948) that, at the high strain rate prevailing, adiabatic heating reduces the slope of the stress–strain curve of the material in the neighbourhood of the crack to a negative value. The resulting instability localizes the shear strain to such an extent that the two halves of the specimen slip off along a shear surface. The main difficulty in accepting this explanation is that bodies in contact along conical surfaces cannot slide rigidly on each other; complete slipping off would require considerable plastic distortions outside the shear zone which are not, in fact, observed.

Fig. 2

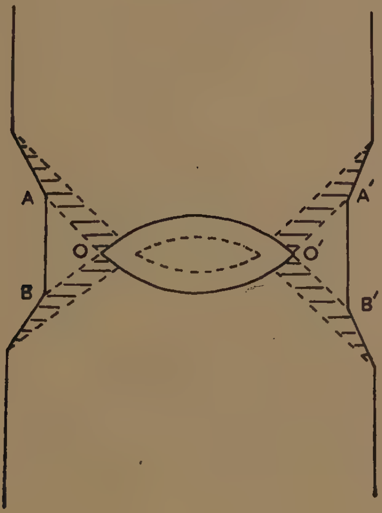

Direct observation of the actual process is hampered by the fact that the fracture is normally very fast in this stage and difficult to control. However, one occasionally finds a fractured specimen in which can be observed the zone of shear complementary to that along which the separation has occurred (that this complementary zone is not usually found is no doubt because a real crack is rarely ideally symmetrical). Figure 3 (*a*) (Pl. 101) shows such a specimen of copper sectioned and polished to reveal the inclusion holes, fig. 3 (*b*) (Pl. 101) the same section etched to show the grain flow. The local shear is clearly visible and is about 20°; along the shear zone the inclusion holes, which have been considerably elongated along the tensile axis by the previous deformation, have been reoriented. Such a reorientation, effectively producing a number of cracks inclined to the direction of the maximum principal tensile stress, must result in a considerable local magnification both of tensile and shear stresses, so that the zone represents a preferential path for the main fracture. It seems likely, in fact, that the final process of separation along the cone is essentially a tensile failure requiring little deformation elsewhere to accommodate it.

I suggest, therefore, that it is unnecessary to invoke adiabatic heating to explain the shear component of ductile fracture; as soon as the crack grows to a sufficient size and sharpness to initiate far reaching zones of localized shear it will tend to follow them. In the absence of a detailed analysis of the strain around the growing crack it is impossible to make any quantitative estimate of 'sufficient size', but qualitatively, the simplest hypothesis is that localized shear is initiated when the shear stress ahead of the crack attains a critical value. If so, one might expect that by using a very hard machine so that the crack grows slowly under decreasing load, maintaining a constant stress on the uncracked material around it, the shear cone could be eliminated. I have, in fact, found that it is possible to do this; a specimen of ductile Armco iron tested in such a way broke with a tensile fracture right across the minimum section of the neck, while the same material in a normal test developed ordinary cup-and-cone fracture.

ACKNOWLEDGMENT

I wish to thank Mr. A. P. Green and Professor R. King for valuable discussions on this subject.

REFERENCES

HILL, R., 1953, *J. Mech. phys. Solids*, **1**, 265.
ZENER, C., 1948, *Fracturing of Metals* (American Society of Metals), p. 3.

REVIEWS OF BOOKS

The Electric Arc. By J. M. Somerville. (London: Methuen & Co. Ltd., 1960.) [Pp. ix+150.] 12*s*. 6*d*.

The electric arc is one of the most common forms of electrical discharge. It can be regarded as the final phase of the transition from a state of insulation of a gas to that of conduction, the initial state being the electrical breakdown process which is followed by the, possibly transitory, glow discharge. Whether in a useful application, as in a mercury arc rectifier, or, in its undesirable aspects, when it occurs in electrical contacts, the arc is of interest to physicists and electrical engineers alike. Investigation of the mechanism of operation of an arc discharge must range over a variety of interesting branches of physics involving the evaporation of metals, thermionic and cold electron emission from metals, ionization of atoms, and the diffusion and recombination of ions in gases and vapours. A modern book on the subject is therefore to be welcomed. This monograph *The Electric Arc* by Professor Somerville is for the non-specialist, and aims to give a concise account of arc phenomena and to make clear the basic physical processes. It can be said at once that it succeeds in this aim and can be recommended to students.

The subject matter is confined to basic physical processes; discussion of numerous practical applications of interest to the electrical engineer is omitted. The treatment is in two parts: Part I, of 87 pages, on the stable arc is equally divided between a treatment of the long luminous column and electrode effects; while Part II, of 34 pages, on the approach to the stable arc, mainly deals with the formation of the spark channel, its early development and expansion, electrode phenomena in sparks, and ends with a brief qualitative summary of the glow to arc transition, the very short arc, the vacuum arc and the drawn arc. However, copious references are given to enable the interested reader to pursue further these aspects of the subject. Thus, the main treatment of the arc is to be found in Part I and the reader will find this a very helpful introduction to an account of the phenomena and basic physics of the steady state arc column. F. LL. J.

Fast Neutron Physics. Part I, Techniques. Edited by J. B. Marion and J. L. Fowler. (New York: Interscience Publishers, 1960.) [Pp. 983.] £10 18*s*.

Fast neutron measurements are among the most difficult facing the nuclear physicist. However, because of their obvious connection with nuclear weapons much effort has been expended upon them both during and since the last war. The development of reactors in which fast neutrons play an important part has also intensified the practical interest in such measurements. Their importance as a tool for studying basic nuclear structure is also very great since fast neutrons interact only through the nuclear forces uncomplicated by the electrostatic forces.

This book records in practical and useful form the accumulated technical experience of over 30 experts in the fast neutron field. It is interesting that in general the old techniques have been refined and that there has been no dramatic ‘ break through ’ in method. A second volume will review experiments and theory. In this volume neutron sources of all types, recoil detection methods and detection by neutron-induced methods are the subject of many individual contributions. In addition many special problems receive individual treatment

such as shielding, target preparation, radiation hazards and computing techniques associated with fast neutron measurements. In spite of the large number of individual contributors the overall style and method of presentation is remarkably uniform. Although the theoretical background to the various techniques receives adequate treatment, most of the material is severely practical making it a handbook in the literal sense of the term. It is thus most regrettable that the price will prevent it reaching many research workers' shelves.
E. B. P.

Irreducible Tensorial Sets. Vol. 4, Pure and Applied Physics. By U. Fano and G. Racah. (New York: Academic Press Inc., 1959.) [Pp. vii + 171.] $ 6.80.

The kind of group theory which is applied to physics is seldom more than organized common sense. Of recent years, however, advances have been made in several branches of physical theory which have been greatly helped by mathematical techniques, of which it can be said that the organization of common sense is of such a high order than it can well be dignified by the name of group theory. These techniques, originally developed for the study of atomic spectroscopy, have found applications in nuclear theory and solid state physics as well, and are likely to be increasingly useful in the future as theoretical physicists become familiar with them.

Whenever the behaviour of a physical system is invariant under the operation of transformations which form a group (e.g. rotations about the nucleus in the case of the electrons in an atom), the various physical characteristics of the system can be classified in terms of the *representations* of the group. That is to say, they fall into sets of quantities (irreducible tensorial sets) which transform according to standard patterns. Physical calculations involving algebraic manipulations of these quantities are made much easier if they can be related to standard prototypes. When they involve the products of three or more quantities, the saving in labour and the gain in physical insight can be considerable. This is the basic task of the book. The methods as developed are specifically applied to the group of rotations in three dimensions, but they are in fact quite general. The chapters are short and each is easily digested, so that a difficult and abstract subject is made easy to assimilate. These methods have been steadily gaining in importance, and this systematic exposition of them is welcome.
M. H. L. P.

[*The Editors do not hold themselves responsible for the views expressed by their correspondents.*]

Fig. 1

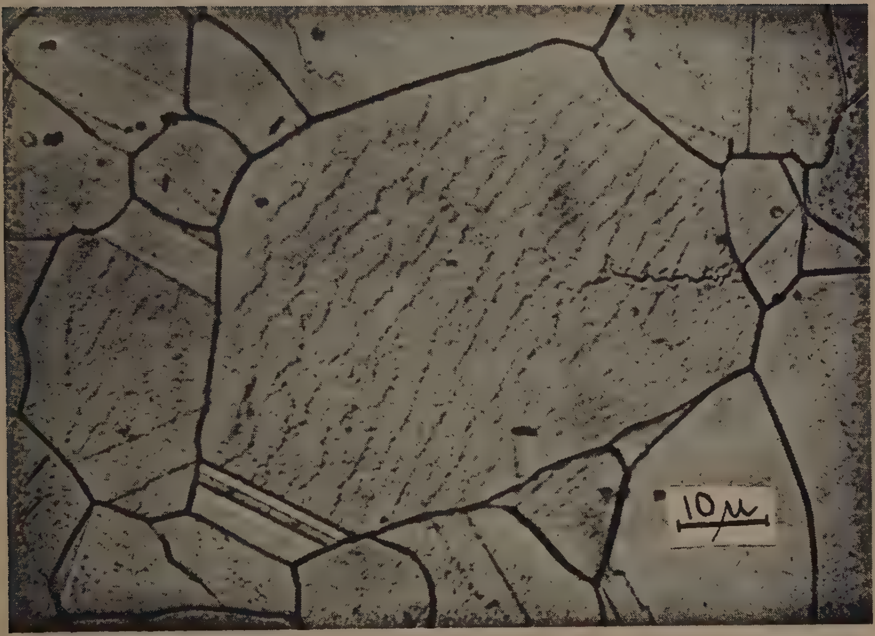

Substructure in 70/30 brass annealed for 20 min at 550°c.

Fig. 13

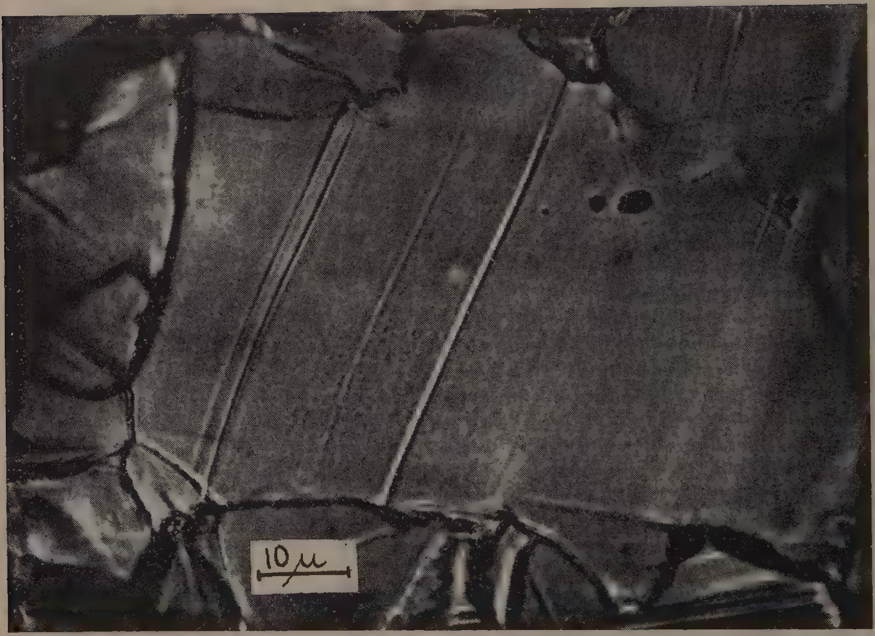

Transgranular slip bands developed during creep at 500°c at a stress of 500 kg/cm^2 in 70/30 brass. The specimen was examined after the initial extension had taken place, re-electropolished, and returned to the furnace. Bands were not observed after the initial extension. The immediate extension on re-loading was very small.

Fig. 2

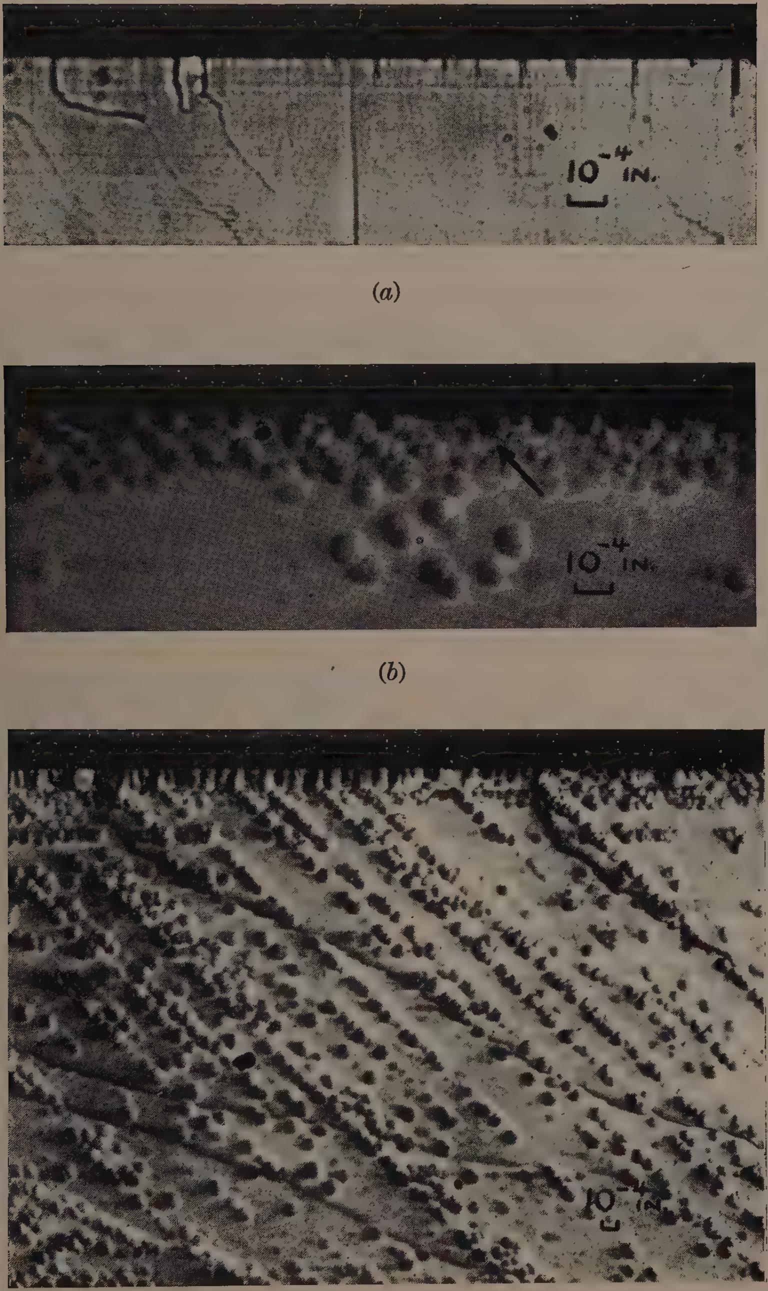

(*a*)

(*b*)

(*c*)

(*a*) Crystal edge prior to etching; (*b*) crystal edge after etching showing typical micro-cracks; (*c*) development of slip after stressing.

Fig. 3

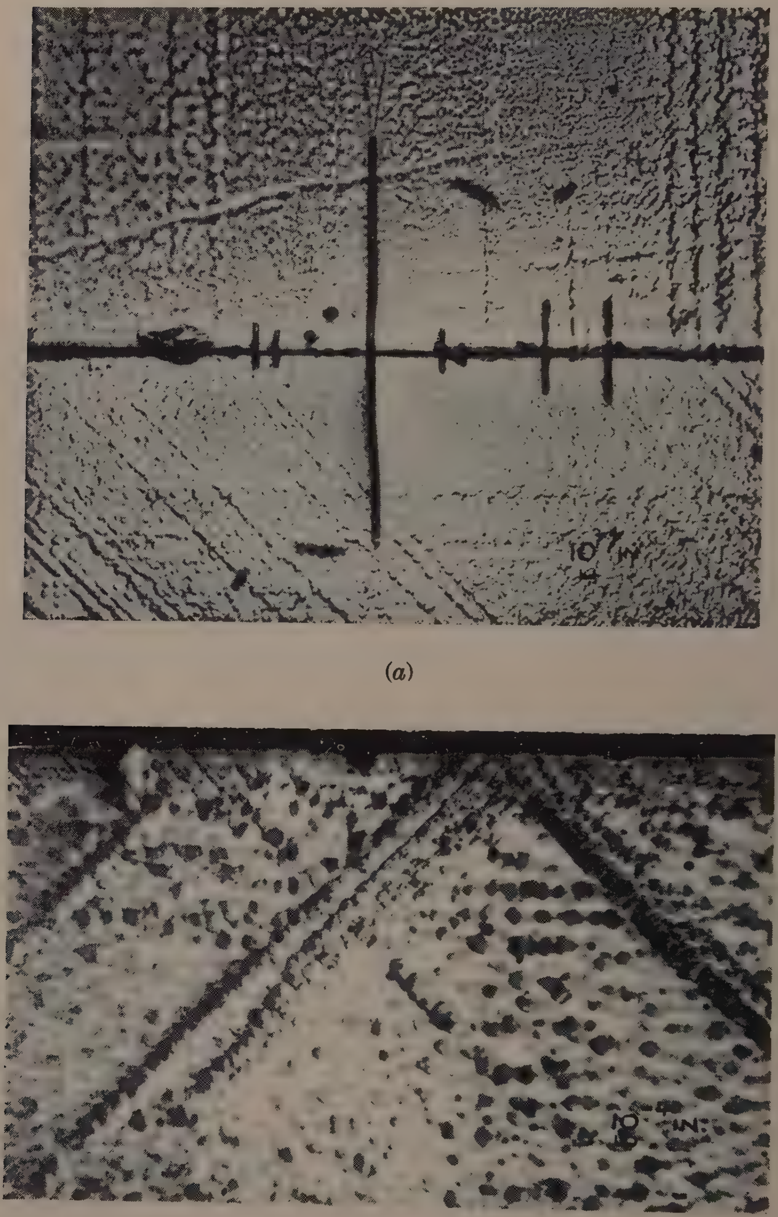

(*a*) Two adjacent faces are laid out flat to show the development of a micro-crack. All cracks are continuous—any appearance that this is not true is due to slightly different magnifications of the two photographs; (*b*) early stage in the development of orthogonal slip originating at a number of edge micro-cracks.

Fig. 4

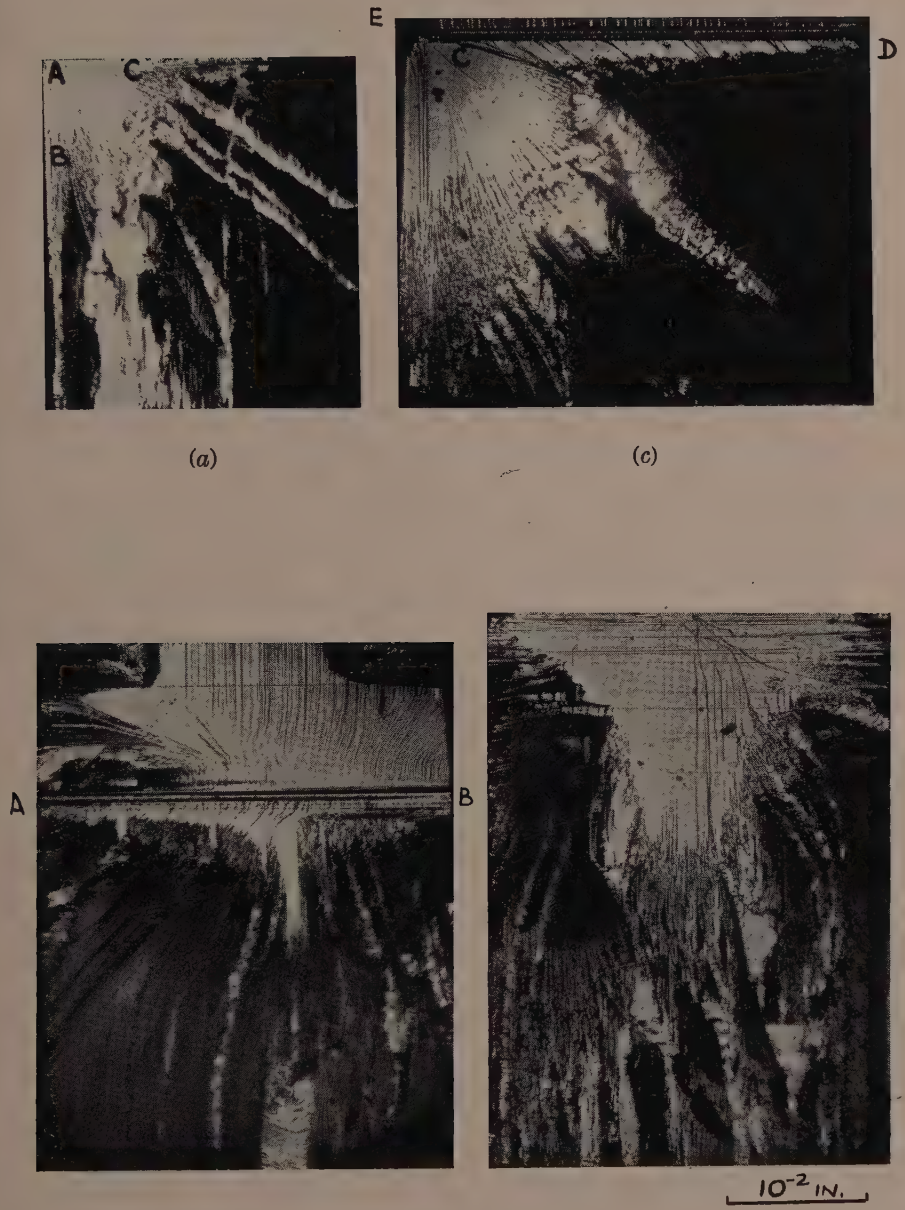

(a) (c)

(b) (d)

Various characteristic fracture faces.

(a) Corner originating fracture; (b) line originating fracture; (c) corner+line originating fracture; (d) fracture originating at a point on a face away from the edge.

Fig. 5

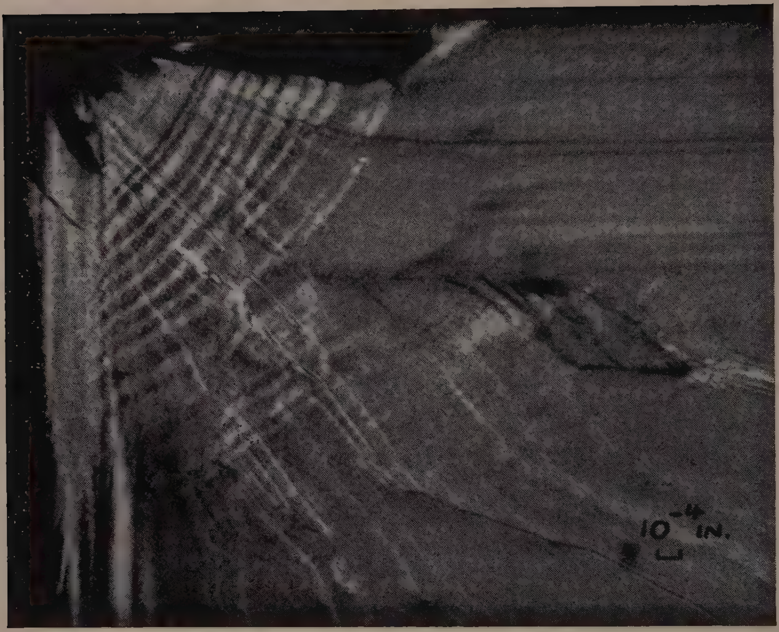

Slip configuration revealed by etching at the extreme corner (e.g. A in fig 4 (*a*)) of a crystal with fracture characteristics similar to fig. 4 (*a*).

Fig. 6

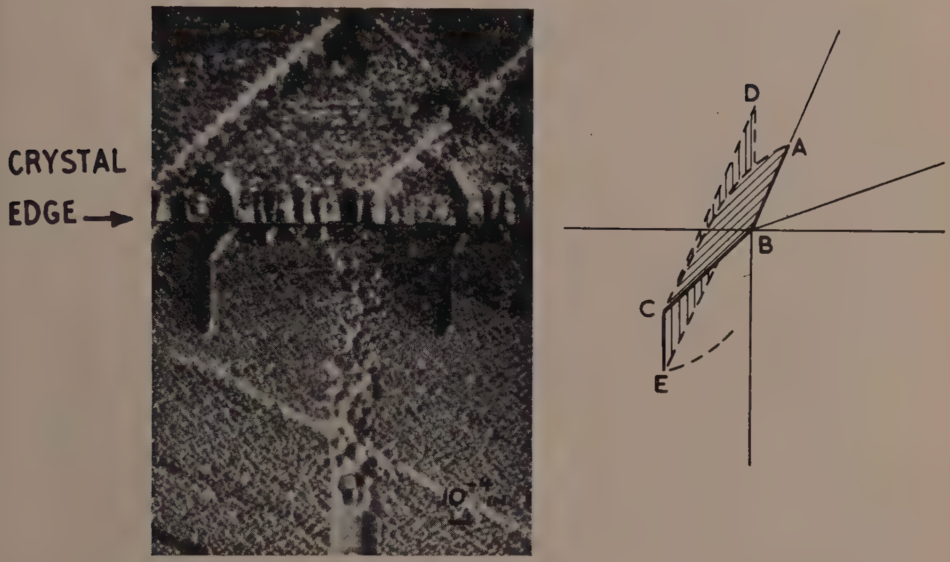
CRYSTAL EDGE
10⁻⁴
D
A
B
C
E

The photograph comprises those of two adjacent faces laid out flat to show the crack configuration. At the side is a schematic representation of the crack.

Fig. 8

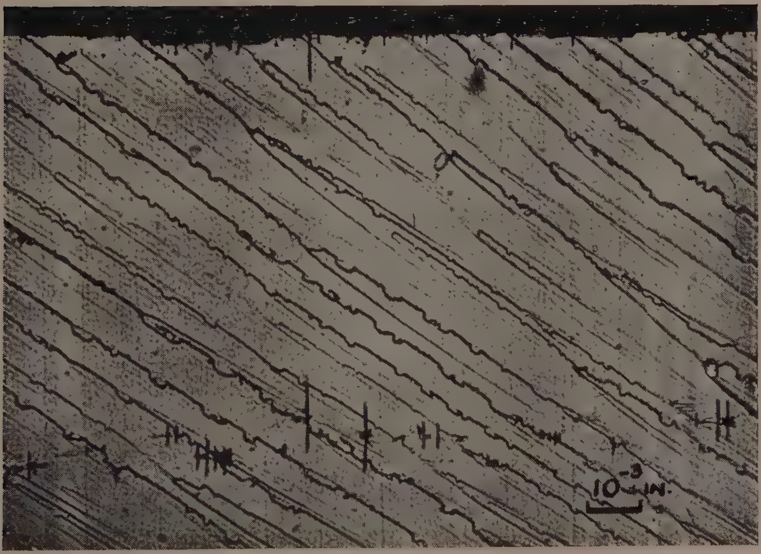

(100) cracks occurring away from crystal edge.

Fig. 1

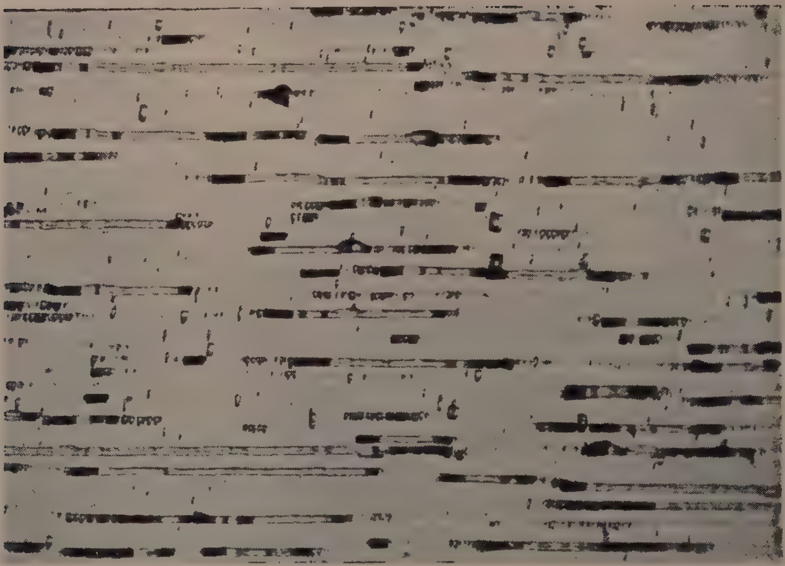

Etching pits on aluminium strained after electropolishing. × 600.

Fig. 2

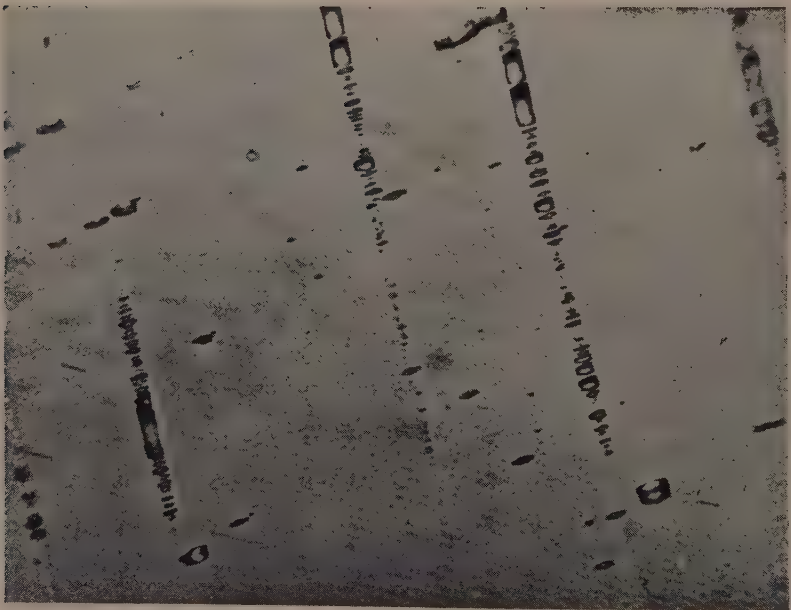

Bunching effect observable on specimen shown in fig. 1. × 1000.

Fig. 3

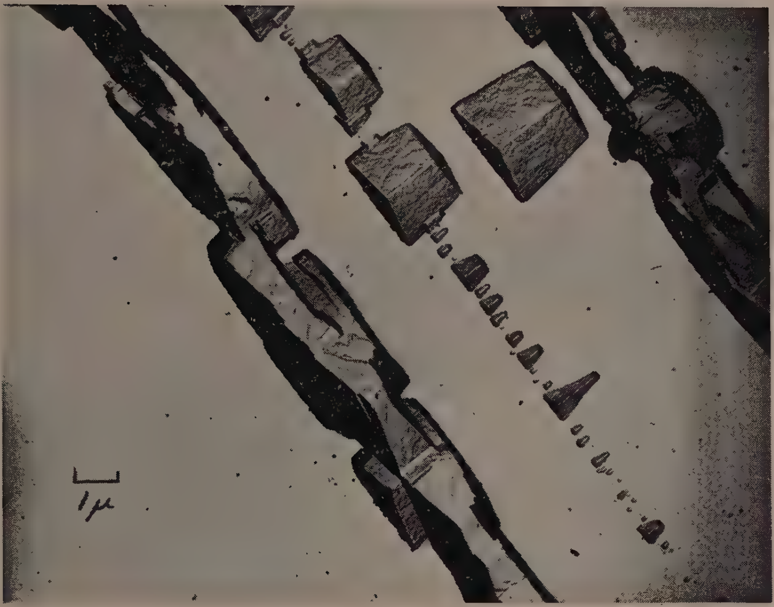

Pits formed along slip trace making no visible surface step.
Anodic film replica. ×6000.

Fig. 4

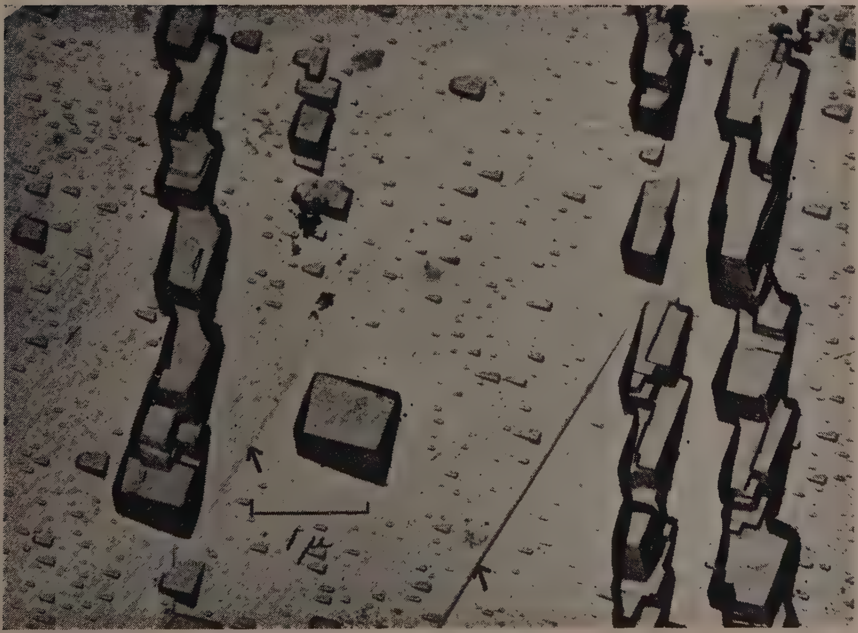

Absence of pits on slip trace making large surface step. ×16 000.

Fig. 5

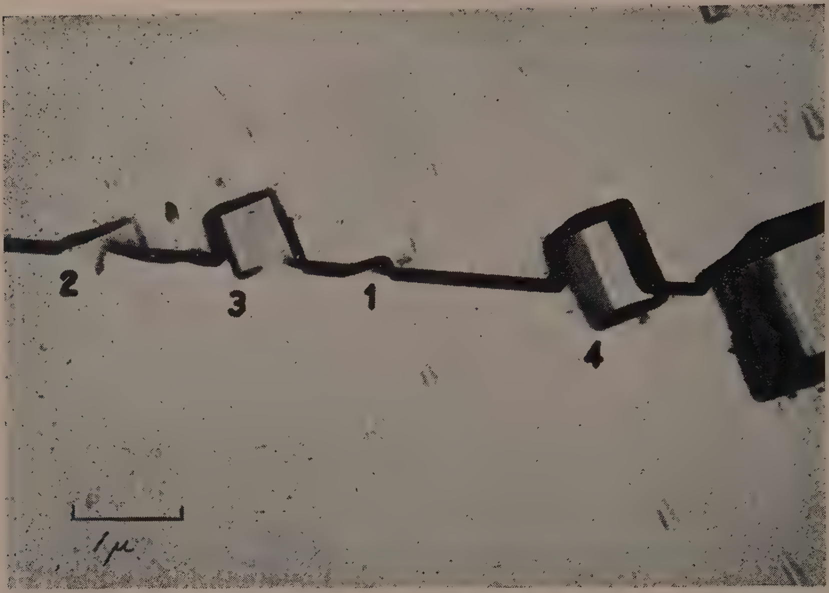

Stages in pit formation at compression slip step making acute angle with surface. × 16 000.

Fig. 6

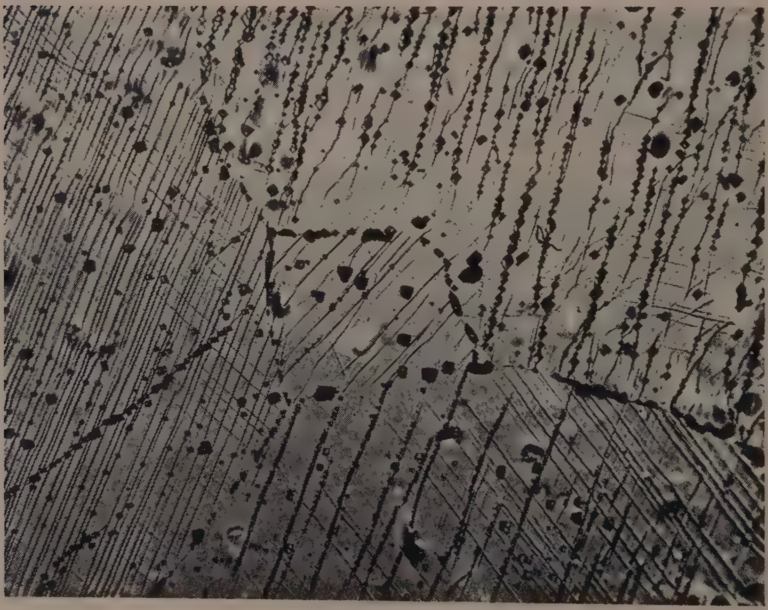

Pitting on both grain boundaries and at slip on specimen aged in vacuum for 32 days. Note that not all slip traces are etched. × 350.

Fig. 7

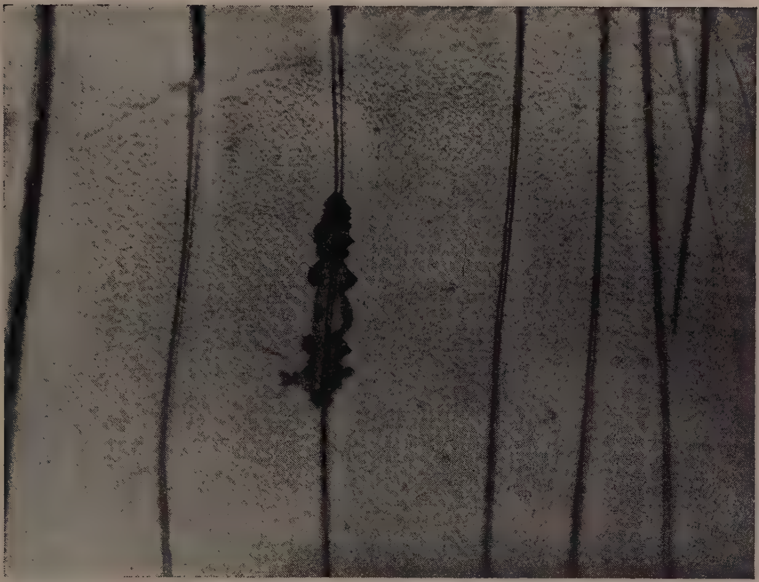

Cracks formed in heavy anodic film showing that there is no relation between cracks and structure and the manner in which etching pits are formed under the film. ×650.

Fig. 8

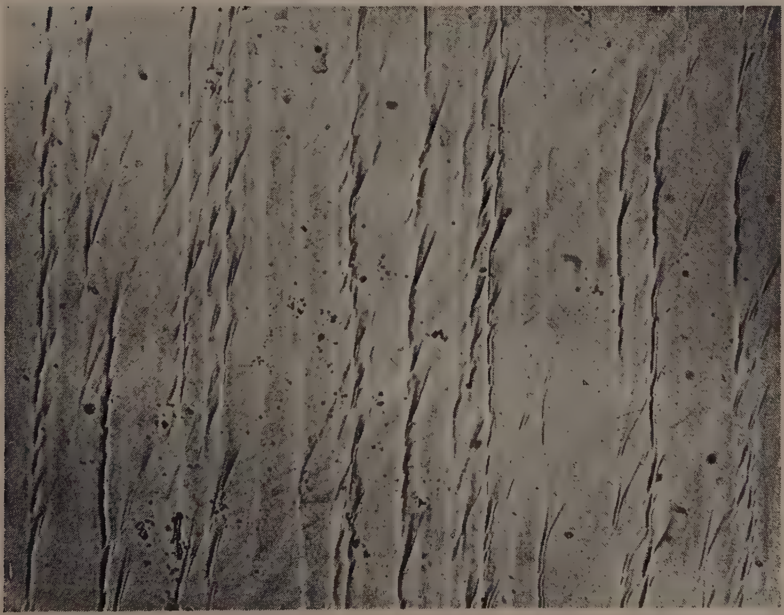

Cracking in thin anodic film showing relation with slip. ×650.

Fig. 9

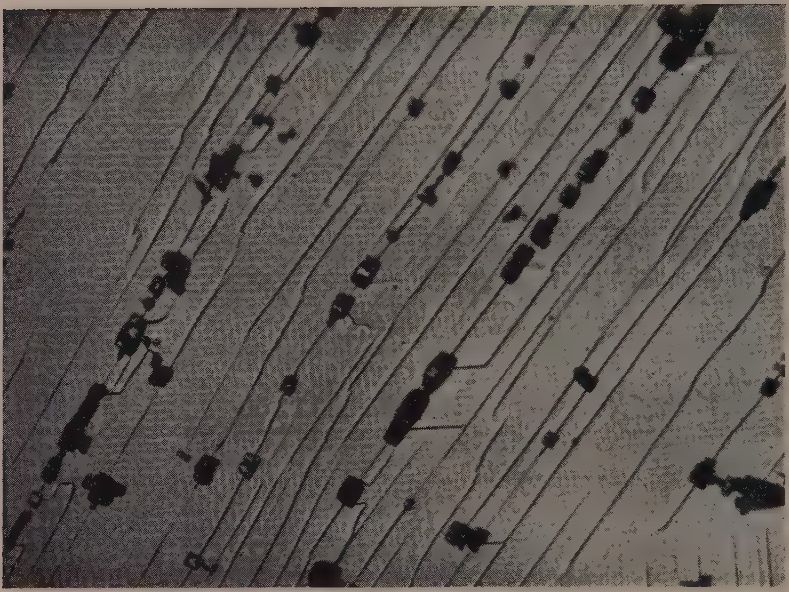

Pits formed by anodic attack in sodium chloride during bending the specimen. ×300.

Fig. 10

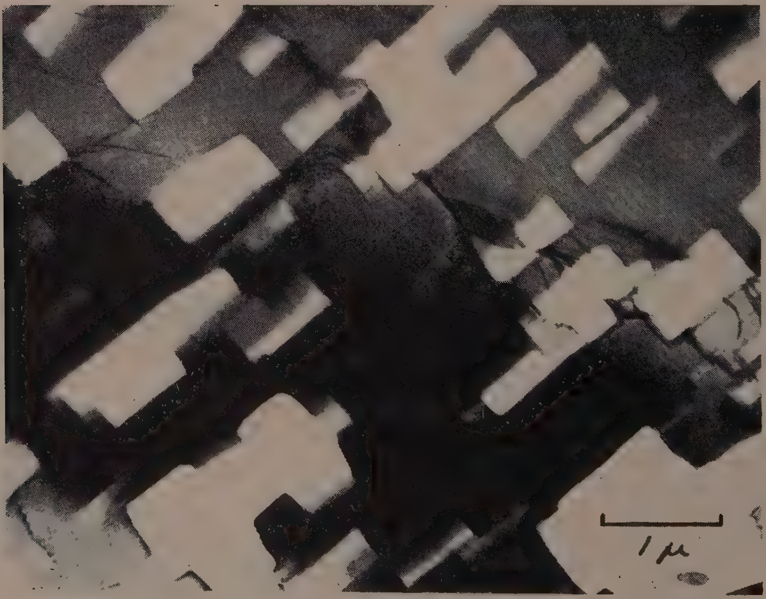

Transmission electron micrograph showing pits in thin foil containing many dislocations. ×16 000.

Fig. 11

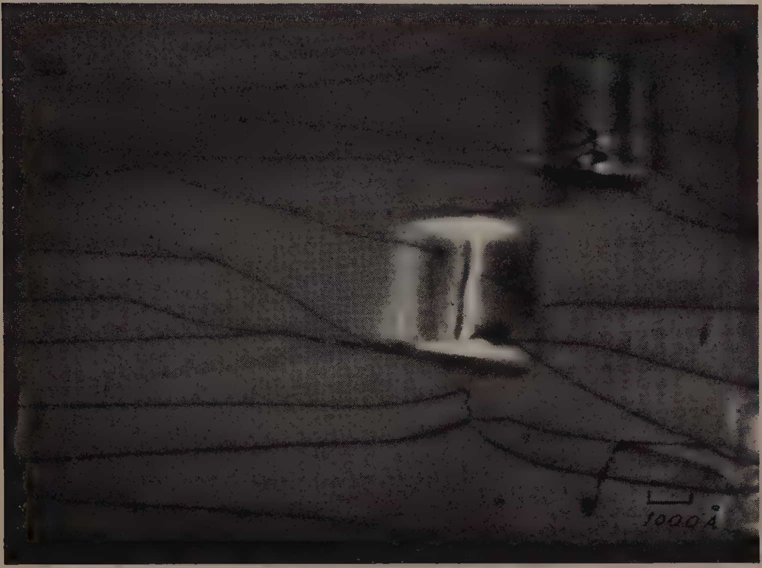

Small pits in thin foil containing long dislocations roughly in the plane of the foil. × 60 000.

Fig. 12

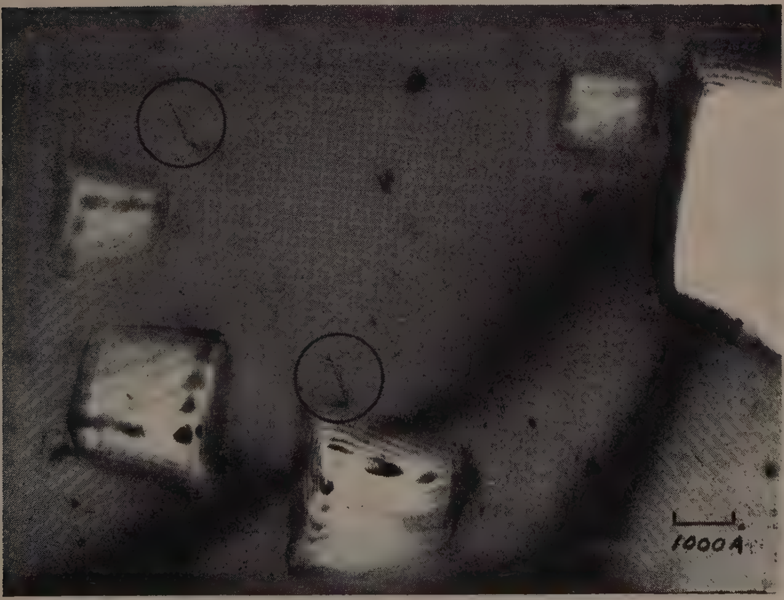

Pits in annealed aluminium showing two dislocations which have not been attacked. × 80 000.

Fig. 13

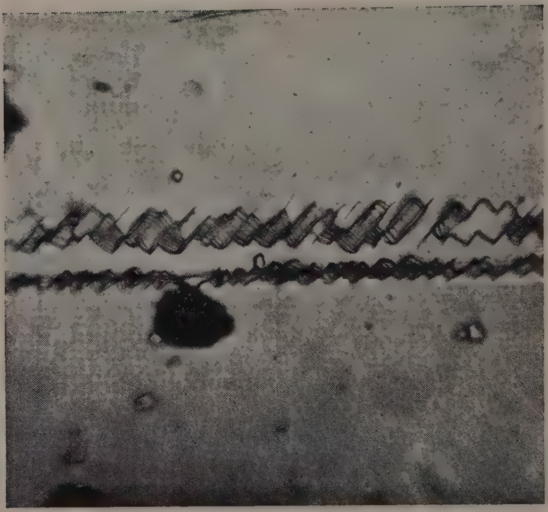

Mode of cracking of light tarnish film on brass. The interference effects are due to lifting of the film. ×2000.

Fig. 1

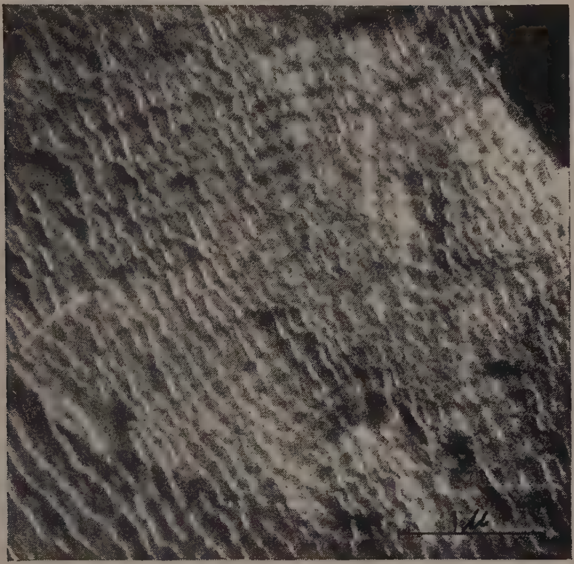

Dark field image of hexagonal network to show the disappearance of one set of lines.

Fig. 2

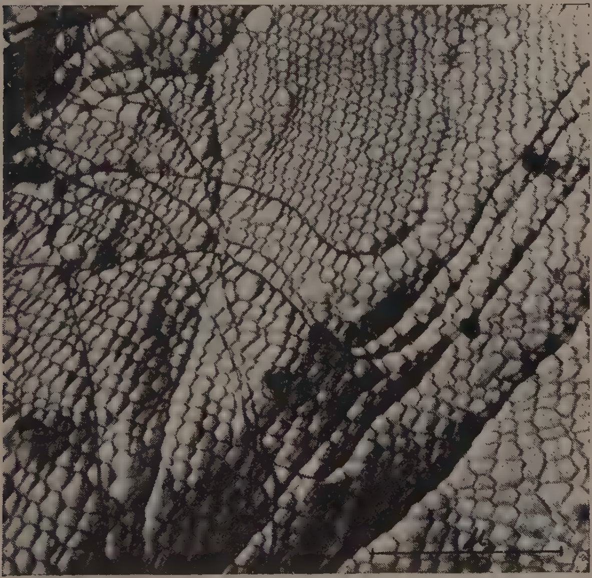

Hexagonal net in the basal plane of bismuth telluride. The net extended over an area equivalent to several times the field shown.

Fig. 7

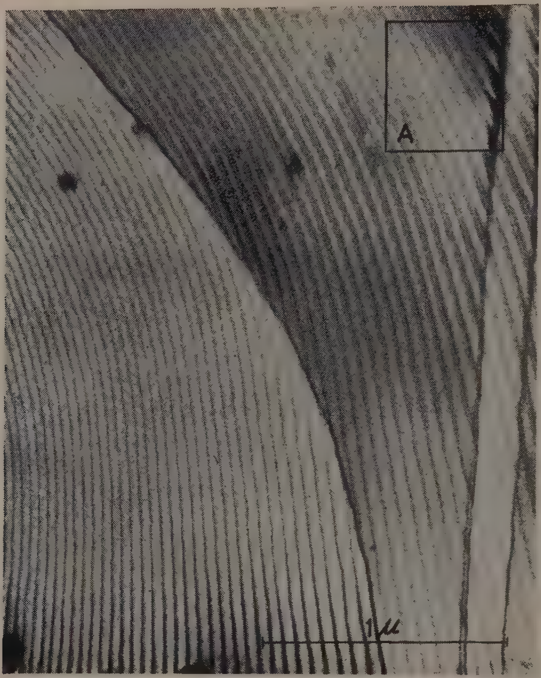

Set of parallel dislocation lines originating from some invisible source far to the left. Note that a number of dislocations have a double contrast in region A, a third line is faintly visible. It is believed that this is also an electron optical effect.

Fig. 8

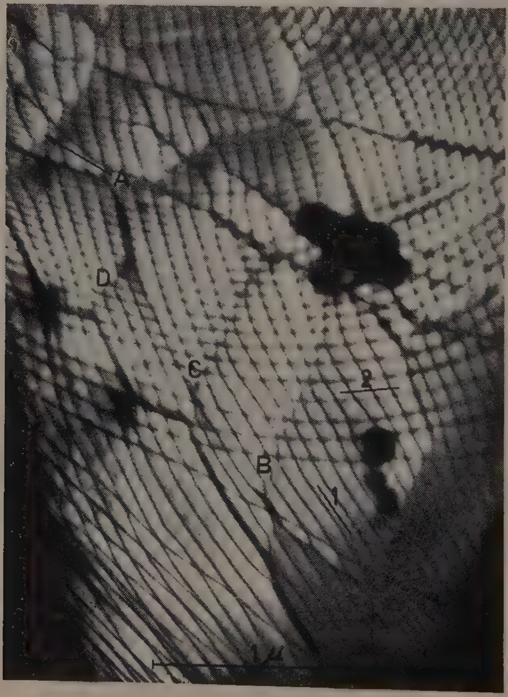

Networks with lozenge-shaped meshes resulting from the crossing of sets (1) and (2). Singular lines A, B, C and D interacted with (2) but not with set (1), and formed a zig-zag line. One family of segments of the zig-zag line lined up with lines of set (2). For detailed explanation see also fig. 18.

Fig. 9

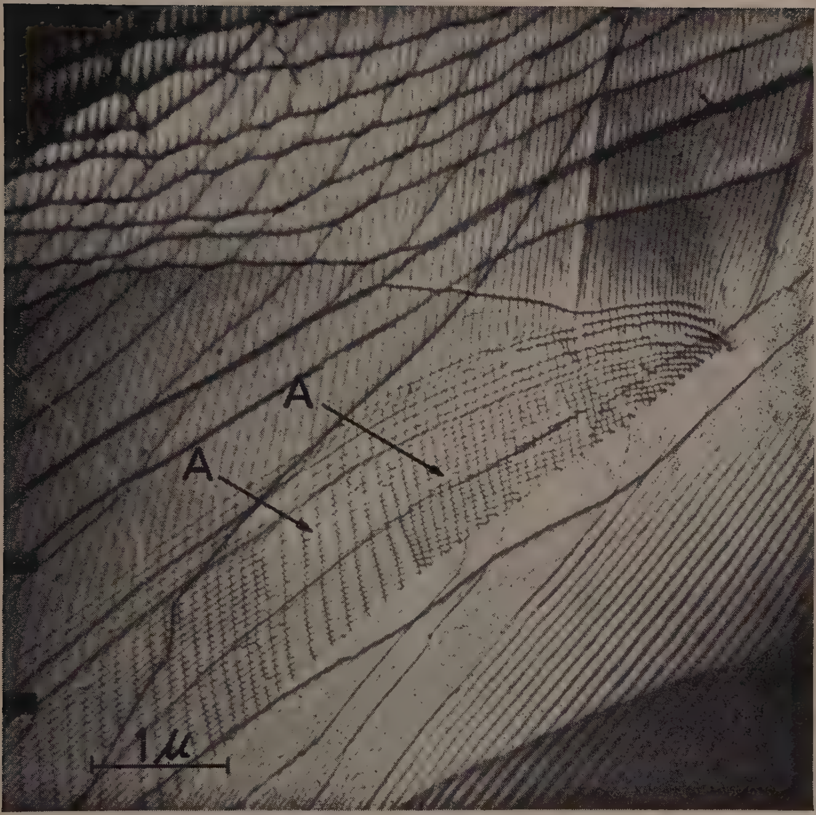

In the central region crossing sets of lines giving rise apparently to a network. Meshes have however not formed, as can be deduced from the absence of certain segments marked A. Segments are also lacking in the parallel set of lines ; the lacking segment left the foil.

Fig. 10

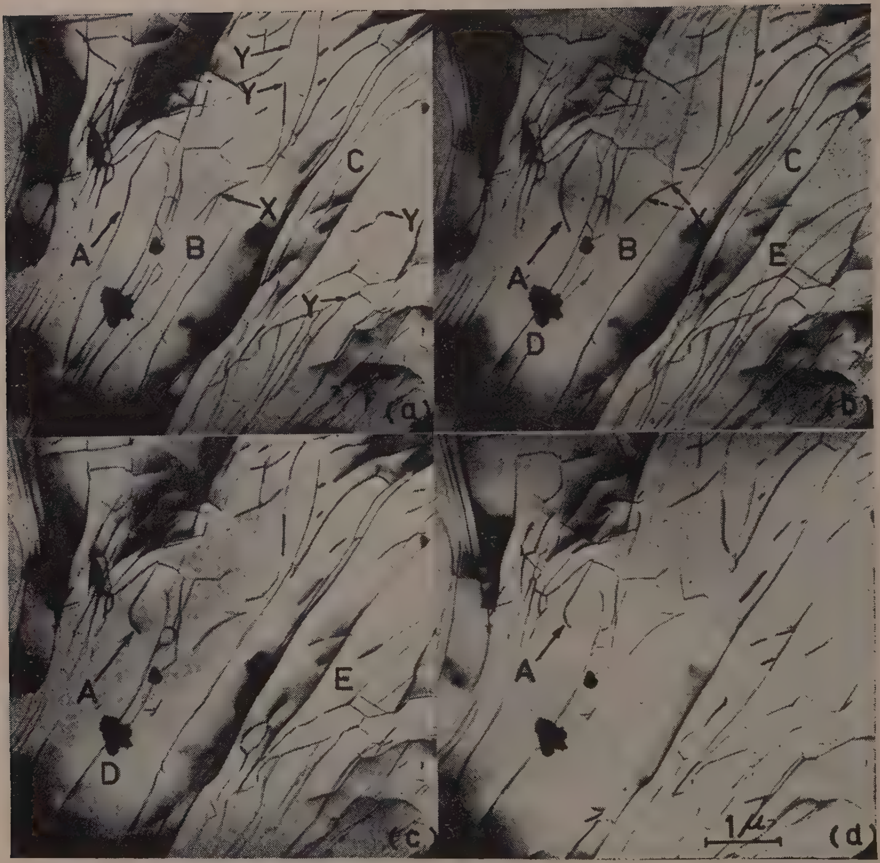

Successive stages in the elimination of dislocations out of the foil. Between exposures (*a*) and (*b*) the lines marked A, B and C disappeared; in further stages A shortens gradually. Between (*b*) and (*c*) the lines marked D and E left the foil. Note also the changing contrast along certain lines; compare with fig. 26.

Fig. 13

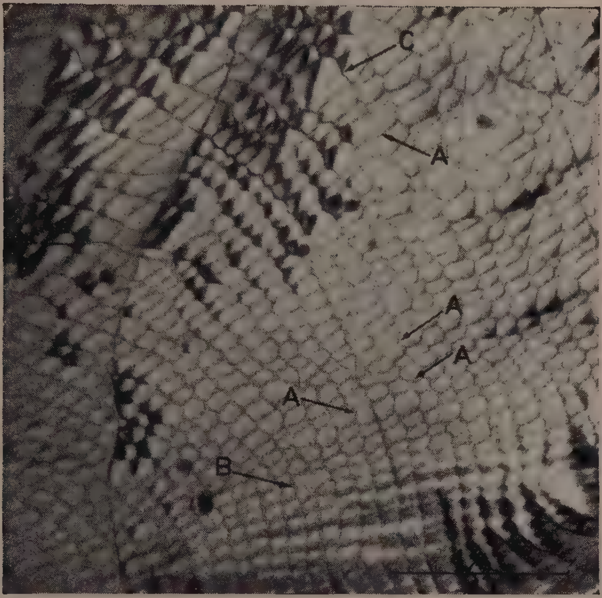

Hexagonal network in the basal plane of bismuth telluride. The dislocations all exhibit a banded contrast. A number of segments left the foil, as shown schematically in fig. 12, and gave rise to ‘ holes ’ in the net. At the spots marked A a single segment left the foil, whilst at the spot B a node left the foil. A more complicated hole is visible in C.

Fig. 14

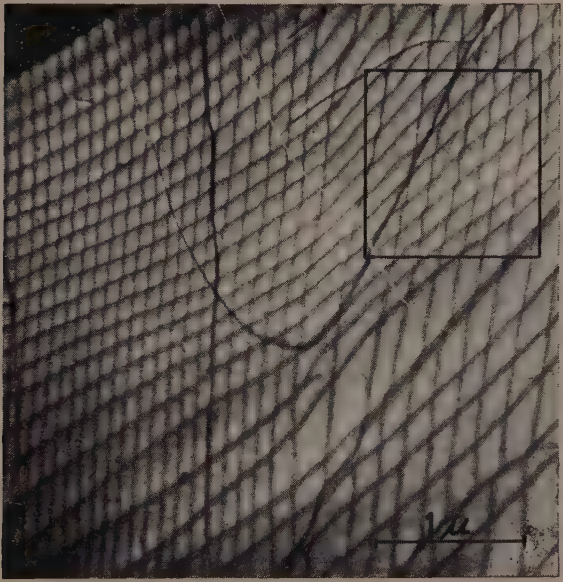

Two crossing sets of lines. Note in the square the asymmetrical twisting of dislocations at the crossing points. In the right bottom corner dislocations are pictured as wide bands resembling stacking-fault ribbons. It was however not possible to decide unambiguously whether splitting into partials really occurs or not.

Fig. 16

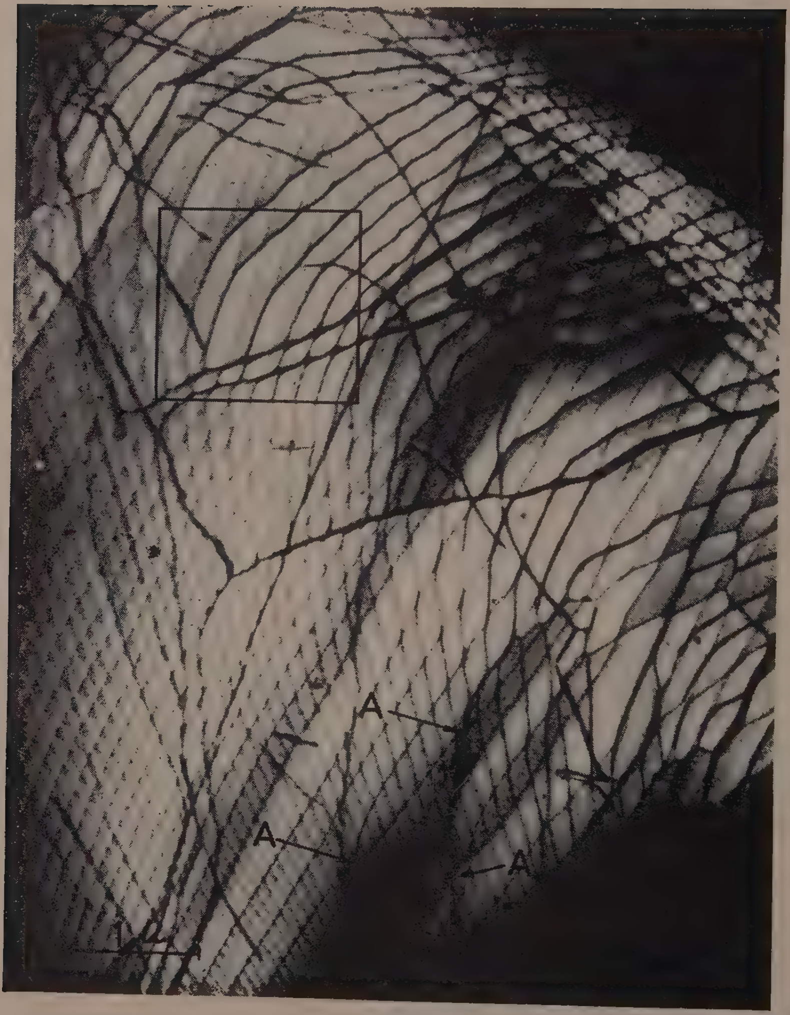

Crossing sets of dislocations showing elastic interactions. At the point marked A twisting at the crossing points is clearly visible. Note also lining up 'one on top of the other' in the region marked by a square.

Fig. 21

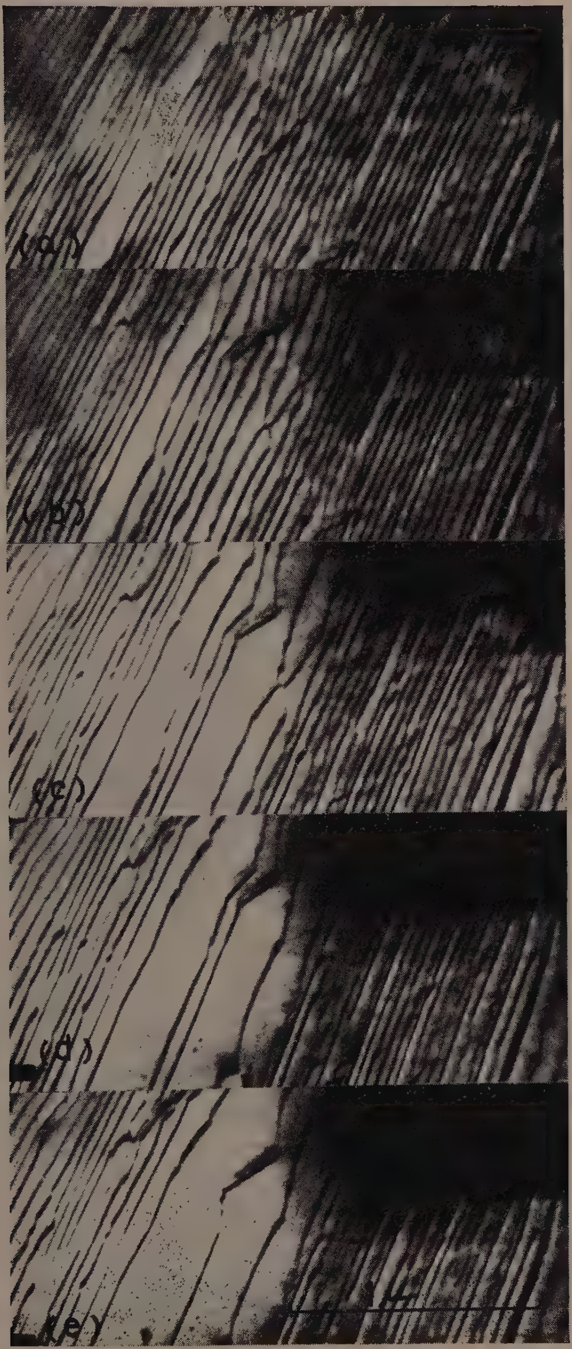

Elimination of dislocation lines by a combination of climb and glide, out of an antimony telluride foil. (*a*) 0 sec ; (*b*) 45 sec ; (*c*) 1 min, 30 sec ; (*d*) 2 min, 30 sec ; (*e*) 4 min.

P. DELAVIGNETTE and S. AMELINCKX Phil. Mag. Ser. 8, Vol. 5, Pl. 98.

Fig. 22

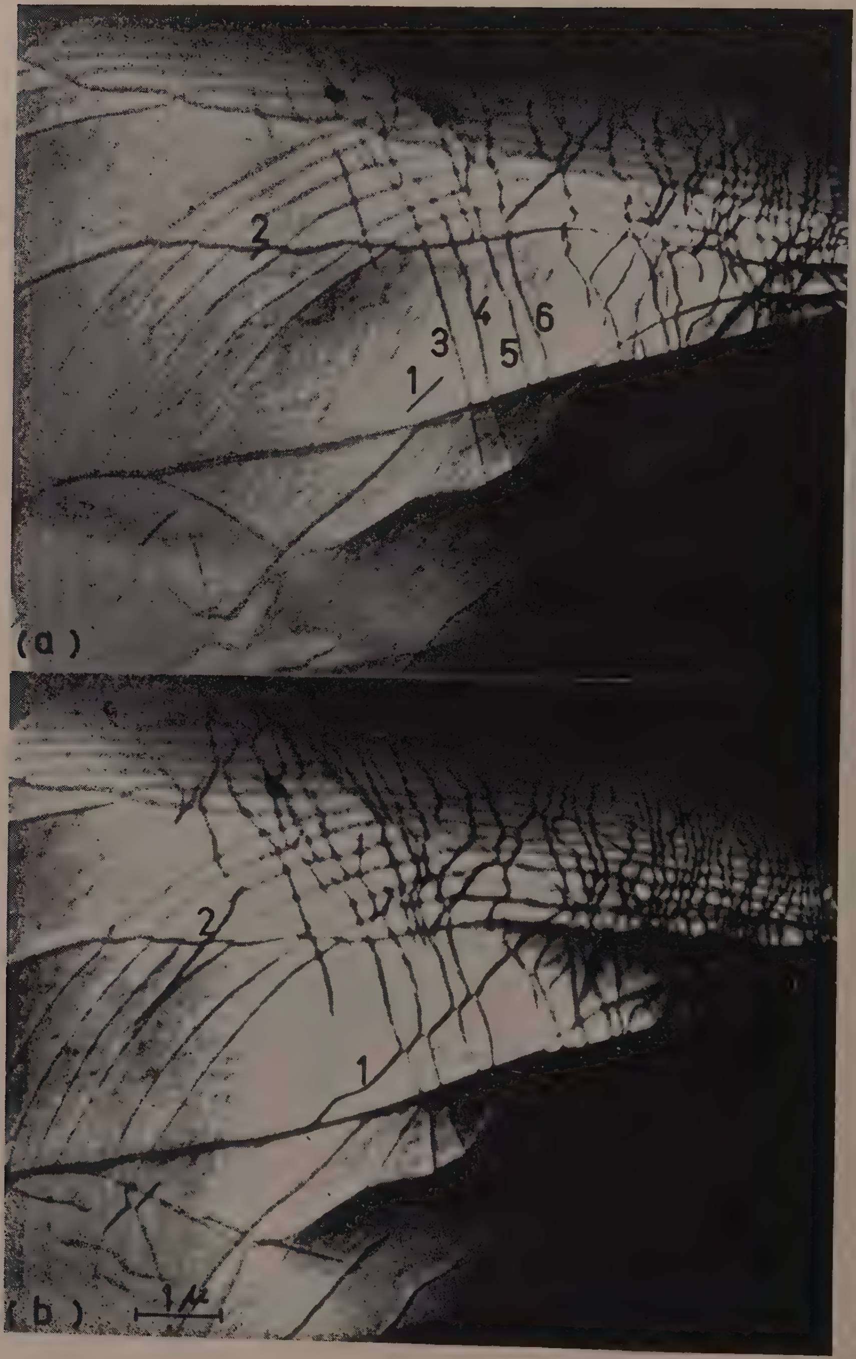
2
3
4
5
6
1
(a)
2
1
(b)
1 μ

Fig. 22 (*continued*)

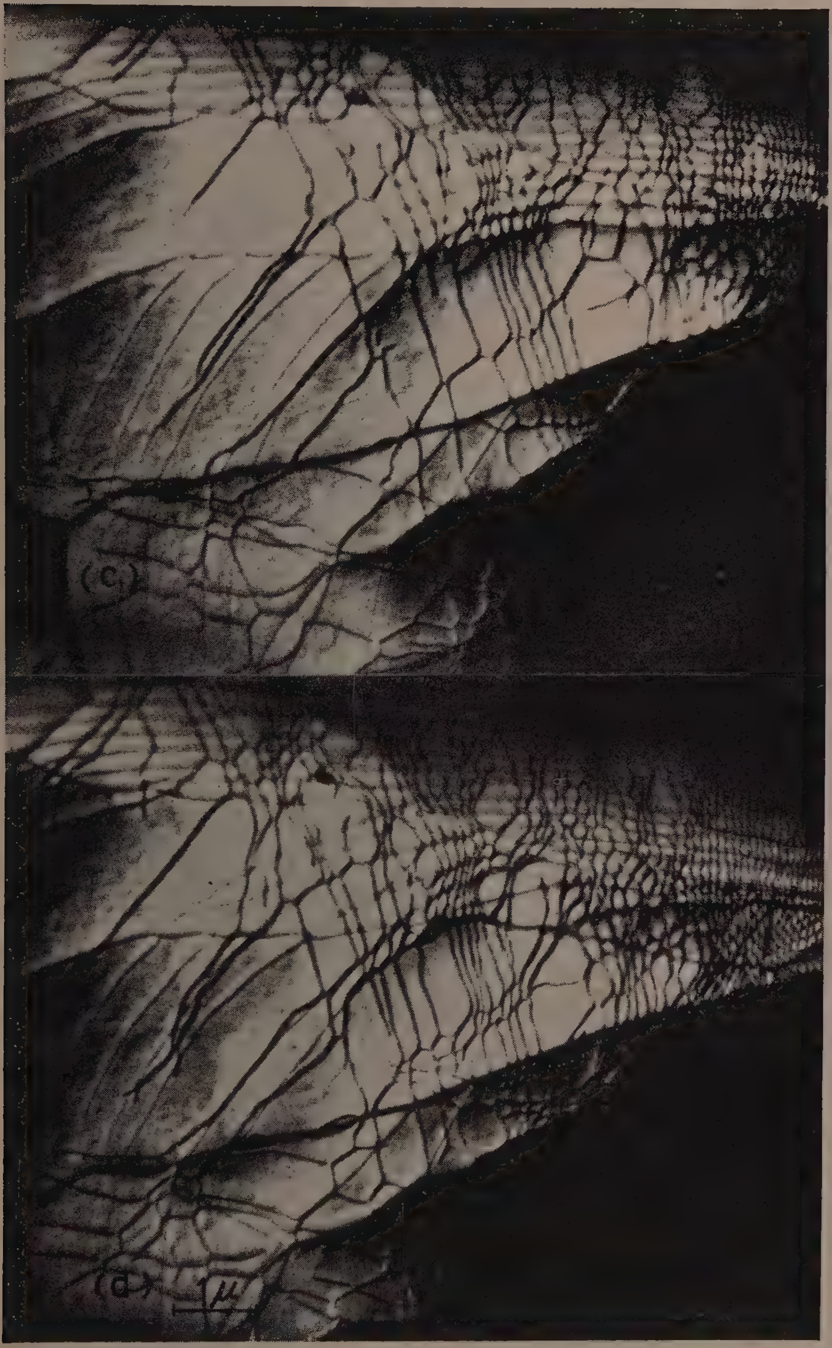

Formation of hexagonal networks in the basal plane of bismuth telluride. Note the lengthening of the segments (1) and (2) between stage (*a*) and (*b*). This results in the intersection of (1) with the set (3), (4), (5) and (6). The same process is repeated and the result is a network as shown in (*d*). In the final stage the whole area was covered with a network as dense as the area shown in the right top part of (*d*). The process is also illustrated schematically in fig. 23.

Fig. 24

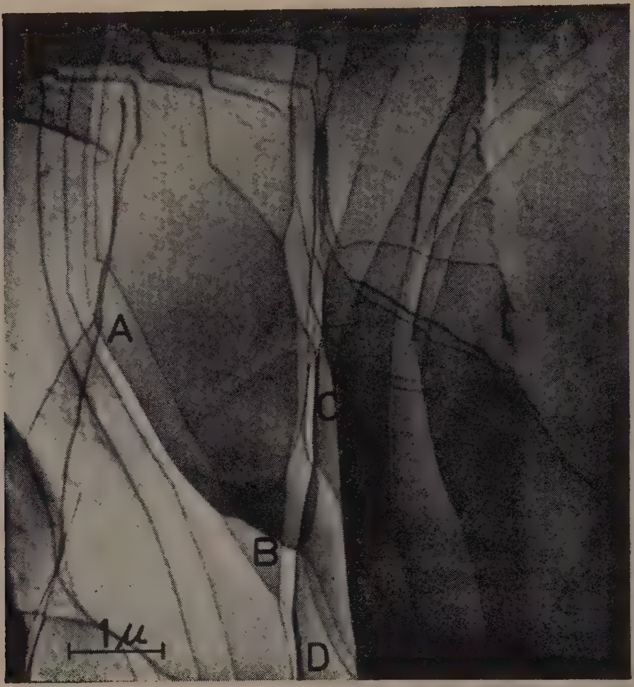

Discontinuous change in contrast at dislocation lines AB and CD. Overlapping regions show a different shade.

Fig. 25

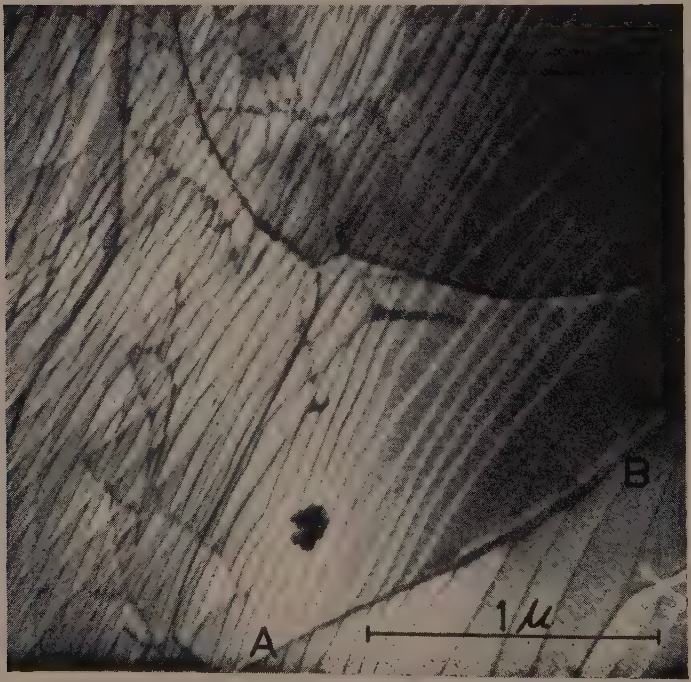

Illustrating contrast effects. Dislocations exhibiting a normal contrast acquire a dark field contrast on intersecting AB. In the left part of the photograph contrast effects similar to those illustrated in fig. 24 are visible.

Fig. 3

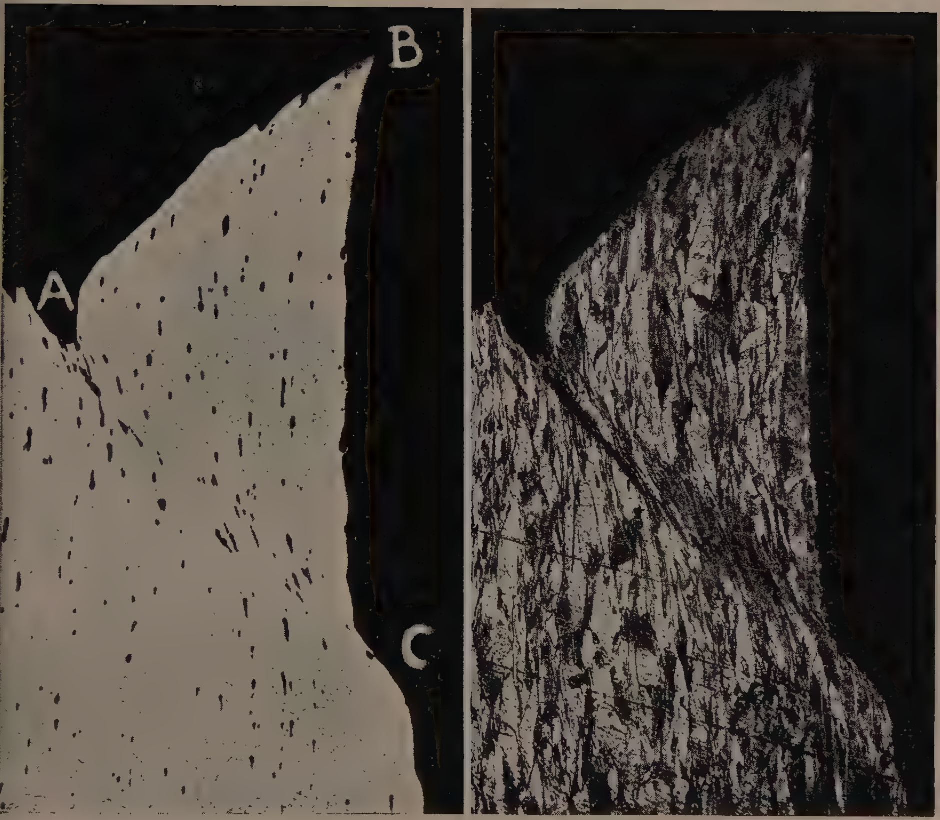

(*a*) (*b*)

Section of broken copper tensile test piece, showing 'cone' fracture surface AB and complementary narrow zone of shear AC. Notice the surface step formed by the shear at C. ×70. (*a*) Polished, showing re-orientation of inclusion holes. (*b*) Etched, showing grain flow.

The Thermoelectric Power of Pure Copper†

By A. V. Gold‡, D. K. C. MacDonald, W. B. Pearson
and I. M. Templeton
Division of Pure Physics, National Research Council, Ottawa, Canada

[Received February 24, 1960]

Abstract

Measurements of the absolute thermoelectric power S of very pure copper samples (with residual resistivity ratios as low as $3{\cdot}1\times10^{-4}$) have been carried out between ~0·1°K and ~350°K. Several specimens were found to exhibit marked negative anomalies in S between 8°K and 9°K, whereas a very pure sample of 'natural' copper gave small but positive values of S at low temperatures. By emphasizing that S depends on the *relative* importance of the various scattering mechanisms we have been able to show that the anomalies occur whenever scattering by traces of *iron* becomes dominant, other impurities being of only minor importance. Moreover we are able to account for the occurrences of similar anomalies, as well as the resistance minima, in dilute alloys of oxygen-containing copper with various solutes (e.g. Ga, Ge, Sn . . .) *not* in terms of these particular solutes *directly*, but only in so far as they separate traces of iron from its oxide, thereby bringing it into solid solution. At about 70°K there is a positive peak in S which we ascribe to an Umklapp phonon-drag component.

§ 1. Introduction

The absolute thermoelectric power, S, of a well-annealed copper specimen was shown by MacDonald and Pearson (1953) to be very small and negative below about 14°K, a typical value for S being about $-0{\cdot}04\,\mu$v/deg. at 5°K. However, extrapolation of thermoelectric data obtained recently (MacDonald *et al.* 1960) below 1°K on a sample of similar purity, but obtained from a different source, indicated a probable value of about $-3{\cdot}0\,\mu$v/deg. at 5°K, *i.e. differing by about two orders of magnitude from the previous result.* These contradictory results on specimens of almost identical residual resistivity are rendered even more astonishing when one bears in mind the prediction of conventional theory (Wilson 1953) that at low temperatures the thermoelectric power should be small ($S\doteqdot-0{\cdot}05\,\mu$v/deg. at 5°K for the free electron model) and *independent* of the amount and nature of impurities present, provided that the impurity concentration is not sufficient to alter appreciably the band structure of the otherwise pure metal. We have therefore been prompted to remeasure S for a variety of the purest samples of copper which we have been able to obtain to date, including a very pure sample of 'natural' copper. Our attention was at first confined to the temperature region between 2°K and 20°K, but in view of the diversity of the results obtained, we have also carried out measurements on the same samples between 80°K and 400°K; at such relatively high temperatures one would certainly expect a similar behaviour for all pure samples since the thermal scattering of the electrons far outweighs the scattering due to impurities.

---

† Communicated by the Authors.
‡ National Research Council Postdoctorate Fellow.

§ 2. EXPERIMENTAL

The experimental method for the measurement of S between 2°K and 20°K consists of the improved technique used by Christian *et al.* (1958) for the determination of the absolute thermoelectric power of lead, the superconducting Nb_3Sn specimen used in these experiments being replaced by the present copper samples. Thus S at any temperature is obtained as the difference between the observed thermoelectric power and the absolute value for lead. In order to make quite sure of our results, especially in cases where $S_{\text{obs}} \doteqdot S_{\text{Pb}}$ so that S is given by the difference between two large and nearly equal quantities, we have recalibrated the lead wiring of the apparatus against a fresh Nb_3Sn superconductor. In addition we have measured S for one sample directly against Nb_3Sn, but this procedure is in general impracticable, requiring samples in the form of long, thin wires. The measurements between 80°K and 400°K were also made relative to lead, the specimen being housed in an evacuated container which could be immersed in various constant-temperature baths. One end of the specimen was anchored to the container, and the temperature gradient, established by a heater at the other end, was measured by copper–constantan thermocouples. A sensitive galvanometer amplifier (MacDonald 1947) was used to measure the potentials from both the specimen and the thermocouples. In addition we have used the method of MacDonald and Pearson (1953) to follow S for two samples from 4·2°K to room temperature and have extended measurements on two further samples to temperatures below 1°K using the technique of MacDonald *et al.* (1960).

Most of the specimens were some 6 or 7 cm long, and 0·1 mm to 0·5 mm in diameter, with the lead potential wires and small copper thermal probes attached about 1 cm from either end with pure lead as solder. The 'natural' copper sample was of unfavourable dimensions being in the form of an irregular L-shaped 'wire', of length 8 mm and mean thickness about 0·3 mm, though there were several thinner spots. Details of the specimens concerning source, preparation, and residual resistance ratio are given in the table.

§ 3. RESULTS

Figure 1 illustrates the remarkable diversity of thermoelectric power which we have found in the various 'pure' copper samples below 20°K. Sample Cu 1 was prepared from the same commercial copper containing

Sample Cu	Source	Code in figs. 1, 2 and 3	$10^3 \times \rho$ ($\rho = R_{4\cdot 2}/(R_{293}-R_{4\cdot 2})$)	S_{anom} (μv/deg.°c)	T_{anom} (°K)
1	'J.T.H.' commercial Cu containing oxygen. 0·002% Fe (present as oxide), traces Ca, Al and Mg	□	2·23	− 0·05	~5·5
2	A.S. and R. batch 'A' (long drawn wire; measured directly against Nb_3Sn)	+	2·75	− 3·2	9·5
3	A.S. and R. batch 'B' (drawn wire)	×	1·21	− 4·6	8·0
4	Do. (etched rod bent in mounting)	○	0·97	− 5·8	8·5
5	Do. (etched rod)	●	0·86	− 6·0	8·5
6	Do. (long drawn wire)	—·—·	1·05	− 5·2	~8·7
7	A.S. and R. batch 'C'† (drawn wire)	△	0·65	− 1·8	~7·8
8	Do. (etched rod)	▽	0·48	− 2·9	~8·1
9	Natural copper from Keweenaw Peninsula, Lake Superior‡	◇	0·31	Positive *S* below 13°K	
10	'J.T.H.' Cu+0·054 wt % Fe (drawn wire)	⬙	320§	~ −16·0	
11	A.S. and R. Cu (batch B)+0·01% Sn (long drawn wire)	—··—··	25·2	− 1·58	14
Kropschot and Blatt (1959)	A.S. and R. (drawn wire)		1·85	− 1·9	~10
Powell *et al.* (1959)	A.S. and R. (drawn wire)		0·67		

Notes: Specimens 1–11 have been vacuum annealed at 530°c for 24 hours. Chemical analyses on A.S. and R. batches B and C give ~0·0001% Fe; spectrographic analyses by American Smelting and Refining Co. give similar amounts of As, Ni, Pb, S, Sb, Se, Sn and Te.

† Kindly supplied by Dr. J. Babiskin.

‡ Kindly supplied by Professor A. F. Kip and Dr. D. Langenberg.

§ At resistance minimum (26°K; Pearson 1955).

oxygen as used by MacDonald and Pearson (1953) and our findings of small and negative values of S confirm the results obtained earlier by a less accurate experimental technique. The results for this sample are also shown on a more expanded scale in fig. 2 (*a*). Samples Cu 2 to Cu 8, on the other hand, all exhibit a marked negative anomaly in S which reaches a maximum size between 8°K and 9°K. These samples were prepared from

Fig. 1

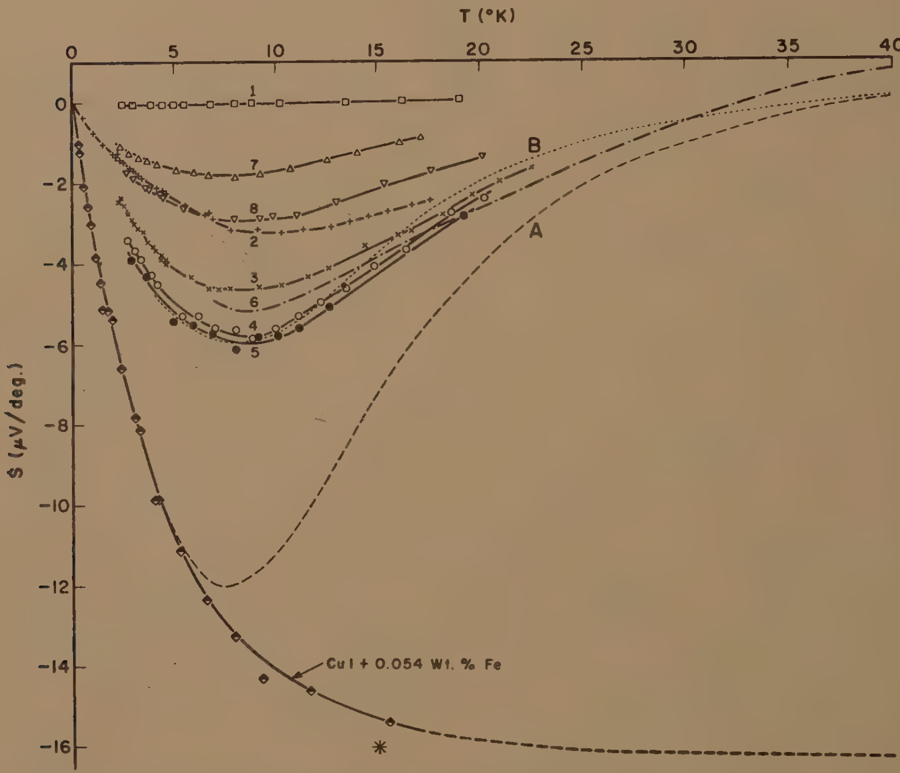

The low-temperature anomaly in S. Details of the specimens are given in the table. With this highly compressed scale of ordinates a linear extrapolation of the high-temperature results (fig. 3) and the free-electron variation of S (Wilson 1953) would both be indistinguishable from a horizontal line through the origin. A, B: calculated from eqn. (3) for a specimen with $\rho = 0{\cdot}67 \times 10^{-3}$ and assuming, respectively, 100% and 50% of the impurity scattering to be due to iron. *, characteristic value of $S_{15°\mathrm{K}}$ for Fe in Cu from fig. 4.

various batches of copper refined by American Smelting and Refining Co., and all have residual resistivities comparable with or lower than that of Cu 1. The extreme cases of Cu 1 and Cu 5 have values of S which differ by a factor of 120 at the anomaly! In samples taken from the *same* batch, the observed minimum value of S appears to increase as the purity of the metal, gauged by the residual resistivity, increases (see table).

When, however, samples taken from *different* batches are compared there is generally speaking no correlation between overall purity and thermoelectric power.

Fig. 2

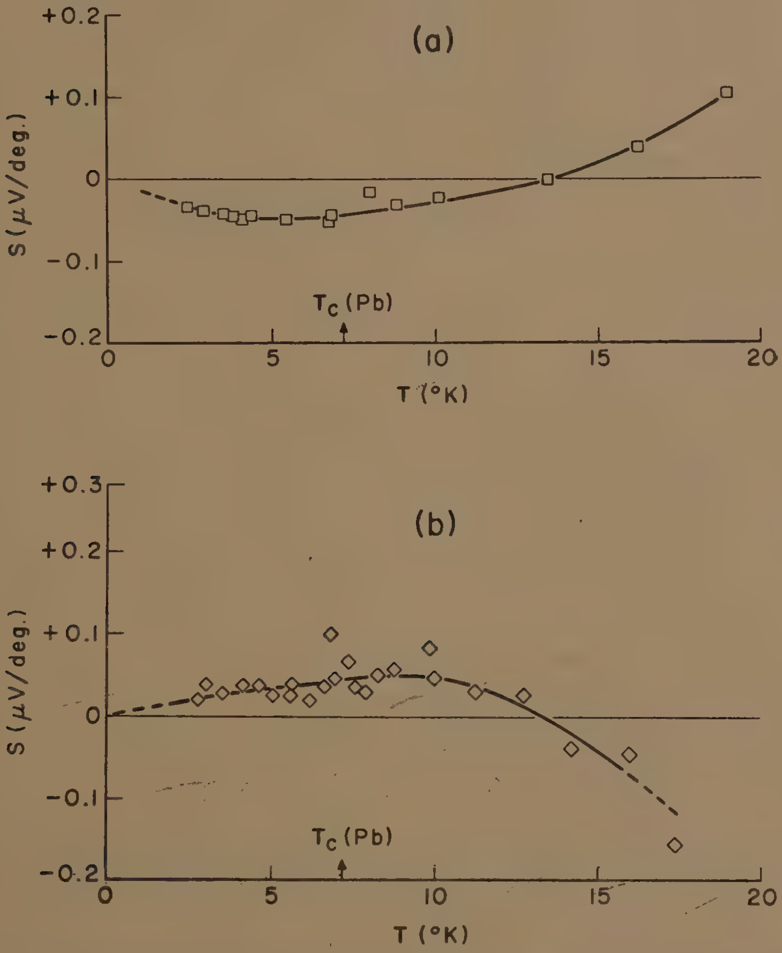

Low-temperature variation of S for (*a*) Cu 1 and (*b*) Cu 9 (natural copper), with the scale of the ordinates considerably expanded.

In addition to these remarkable results, we have now found a small but *positive* thermoelectric power at low temperatures for the 'natural' sample Cu 9, which, according to residual resistivity, is the purest of all our samples. The data for this specimen are presented on an enlarged scale in fig. 2 (*b*). Measurement of S for this very pure and inconveniently shaped sample was not easy because of the difficulty in setting up an adequate temperature gradient. We are in no doubt whatsoever that S is indeed positive below 7·2°K, where direct measurements are made relative to superconducting lead with zero thermoelectric power. However, we cannot be too sure of the reliability of the results above 7·2°K since S is then obtained as the difference between two large and nearly equal observed quantities. Because of the unfavourable dimensions of the specimen, with the lead solder joints for the potential and thermal probes occupying some 20% of its length, the experimentally observed thermoelectric power might contain a systematic error as great as 10%; such an error would result in a displacement of the value of S at, say, 18°K upwards or downwards by about 0·08 μv/deg. However, since the values of S turn out to be more or less the same when measurements are made either just below or just above 7·2°K, we are inclined to think that any error is not as large as this and that S does indeed change sign near 13°K.

Fig. 3

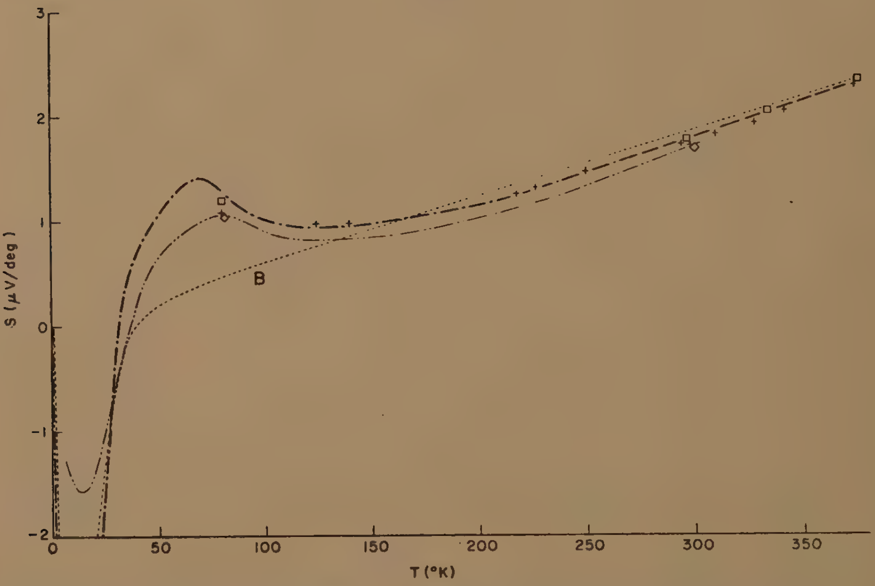

Variation of S with T up to 400°K. Details of the specimens are given in the table. —·—, Cu 6; —··—··, Cu+0·01% Sn; B, calculated from eqn. (3) for a specimen with $\rho=0{\cdot}67\times10^{-3}$, assuming that 50% of the impurity scattering is due to iron and that $S=+5{\cdot}4\times10^{-3}T$ μv/deg. at high temperatures.

In contrast to the striking differences found at temperatures below 20°K, the thermoelectric powers above 100°K (fig. 3) do not differ significantly from sample to sample and are positive. Thus the data from Cu 1 (no low-temperature anomaly) and Cu 6 (large anomaly) are virtually indistinguishable at the higher temperatures. Also shown in fig. 3 is the curve obtained for an alloy with 0·01% Sn (see table). The results given recently by Kropschot and Blatt (1959) for a pure specimen with residual resistivity similar to that of some of our samples (see table) fall close to our Cu–Sn curve, while the earlier work of Borelius *et al.* (1930) (see also Nyström (1947)) for a nominally pure specimen of unknown residual resistivity gives slightly greater values of S than the present results.

§ 4. DISCUSSION

4.1. *The Anomalous Scattering and the Resistance Minimum*

The low-temperature anomalies found in samples Cu 2 to Cu 8 bear considerable resemblance to the results obtained when material similar to that of Cu 1 is alloyed with very small amounts of iron (see fig. 1, also Borelius *et al.* 1932, Pearson 1955), and we shall now propose, and justify as we proceed, that the anomalies in S arise specifically from some anomalous scattering of the conduction electrons by traces of *iron* rather than from scattering by other impurities, phonon-drag effects, or because of basic peculiarities in the electronic structure alone. Starting from this single hypothesis we are able to account for and coordinate a considerable range of hitherto unexplained experimental facts relating not only to the thermoelectric power in 'pure' copper but also to the thermoelectric power and the resistance minimum in several dilute copper alloys.

The presence of traces of around 0·0001% iron in the samples showing the anomaly in S has been established by chemical analysis (see table); from this fact, together with the residual resistivities of the samples and the known scattering cross section for iron in copper (cf. Pearson 1955), we conclude that scattering by iron is the dominant impurity scattering. Reasons will shortly be given why we believe the other impurities (e.g. As, Ni, ...; see table) to be of only secondary importance as far as the anomaly in S is concerned. The commercial copper Cu 1 is known to contain about 0·002% iron, *present as oxide* (MacDonald and Pearson 1955 a); if, however, this copper is melted under reducing conditions, a sizeable anomaly of about $-9\,\mu$v/deg. results, consistent with the supposition that the iron has now entered into solid solution.

On the other hand, it is tempting to regard the small yet positive S in our purest sample Cu 9 as being close to the true 'diffusion' thermoelectric power of pure copper, unaffected by any anomalous impurity scattering. In this connection it is worth noting that the values of slopes, dS/dT, at high and low temperatures are both approximately $+5\times10^{-3}T\,\mu$v/deg^2. This is, broadly speaking, in agreement with conventional theory (Wilson 1953) which predicts the slopes at high and low temperatures to be of the same (albeit negative) sign, with the former three times the latter.

As a starting point for further discussion of the low-temperature results we shall now make use of an expression, originally proposed by Kohler (1949)†, for thermoelectric power of a single-band conductor where two or more scattering mechanisms are present. If we assume these scattering mechanisms to operate independently of one another, each giving rise to a characteristic thermoelectric power $S_i(T)$ and a thermal resistivity $W_i(T)$, then, subject to certain restrictions, the resultant thermoelectric power should be given by:

---

† Kohler derived this result from his theory of electron transport based on a variational principle. The result can be derived in a direct manner with similar restrictions from a rather general model (Appendix I).

$$S=\sum_i W_i S_i \Big/ \sum_i W_i. \qquad \qquad (1)$$

Thus, unlike the thermal and electrical resistivities, the resultant thermoelectric power does *not* depend on the *total* amount of scattering but on the *relative* amounts of scattering, as gauged by the thermal resistivities W_i, of the individual mechanisms.

An application of (1), of which we shall make considerable use in what follows, concerns the low-temperature thermoelectric power in a metal in which two types of impurity are present. Since we are concerned with the residual resistance region, we may write $W_i=\rho_i/L_0T$ (L_0 is the Lorenz constant $=\pi^2k^2/3e^2$) and we obtain a relation which was in essence given by Nordheim and Gorter (1935; eqn. (9)):

$$S=\sum_i \rho_i S_i \Big/ \sum_i \rho_i=\frac{\rho_a}{\rho}S_a+\frac{\rho_b}{\rho}S_b=S_a+\frac{\rho_b}{\rho}(S_b-S_a), \qquad (2a)$$

where S_a, S_b and ρ_a, ρ_b are the thermoelectric powers and electrical resistivities (or corresponding residual resistance ratios) which would be obtained if each of the impurities a, b were to be present by itself. Thus if we now start with a 'pure' metal with parameters S_a, ρ_a and measure the changes in S and ρ as the impurity b is added, then a plot of S against the total inverse residual resistance ratio $1/\rho$ should yield a straight line with intercept S_b as $1/\rho\to 0$, this value being independent of the parameters S_a, ρ_a of the starting material. We must emphasize that these conclusions assume that the only role of the added solute impurities is to scatter the electrons. In other words, we are specifically excluding any modification of the Fermi surface due to alloying. These predictions appear strikingly confirmed in fig. 4, which shows the effects of adding small amounts of nickel to the copper of samples Cu 1 and Cu 2. Although the two 'pure' starting metals have considerably different values of S_a, both plots extrapolate to approximately the same value of $S_b \doteqdot -1{\cdot}2\,\mu$v/deg., which is then the characteristic value of S for nickel in copper at 15°K. Thus, by constructing such S *versus* $1/\rho$ plots at a fixed temperature for any particular solute, we can determine the concentration-independent characteristic value of S for the solute at that temperature. In other words, when the scattering by the solute *dominates* the impurity scattering the observed thermoelectric power will be the characteristic thermoelectric power for that solute in the solvent considered.

We have determined the characteristic thermoelectric powers for the solutes Ag, Au, Cr, Ga, Ge, In, Si and Sn in copper (see fig. 5), as well as that due to physical imperfections introduced by cold-working pure copper

(Pearson 1960), and find that the characteristic values are all small, lying in the range between +1 and −1 μv/deg. at 15°K. However, there is one glaring exception to this scheme, namely *iron*, for which one finds the anomalously high value of −16·2 μv/deg. at 15°K (fig. 4)†.

Fig. 4

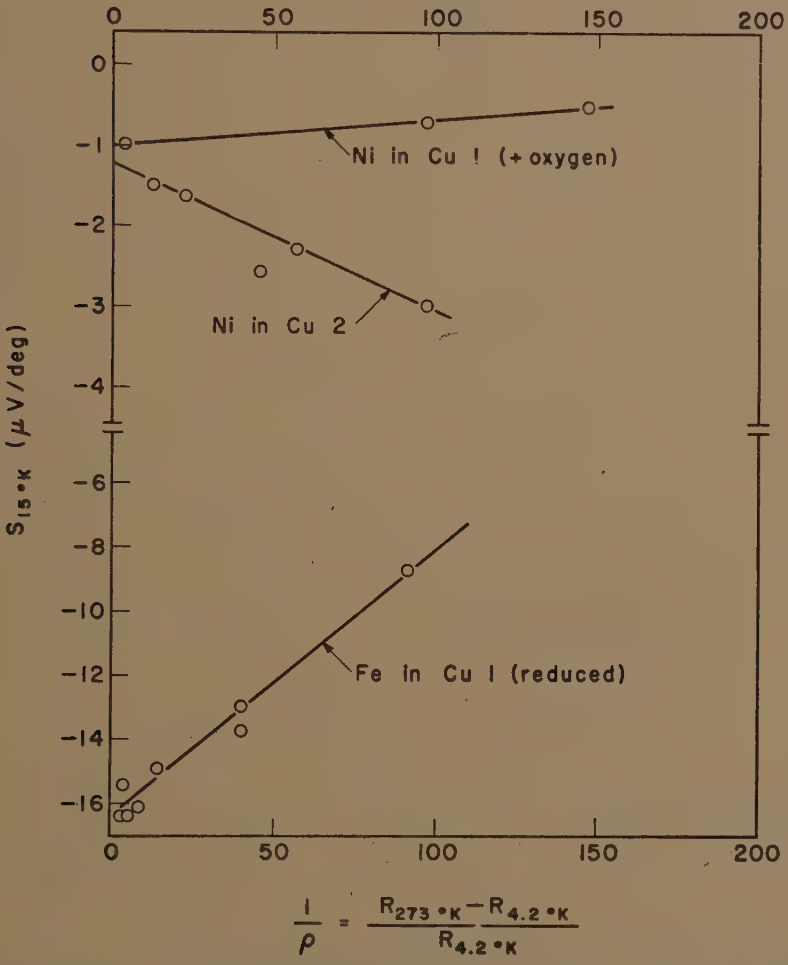

Variation of $S_{15°K}$ with inverse residual resistance ratio for dilute Cu–Ni and Cu–Fe alloys.

These results thus lay the foundation for our hypothesis that the low-temperature anomaly is primarily due to the dominant scattering of

---

† There is some evidence that the solutes Co, Mn and perhaps Bi and Pb, may have somewhat greater (negative) characteristic values of S at 15°K than −1 μv/deg.; we intend to re-investigate these alloys using our present much purer copper.

Fig. 5

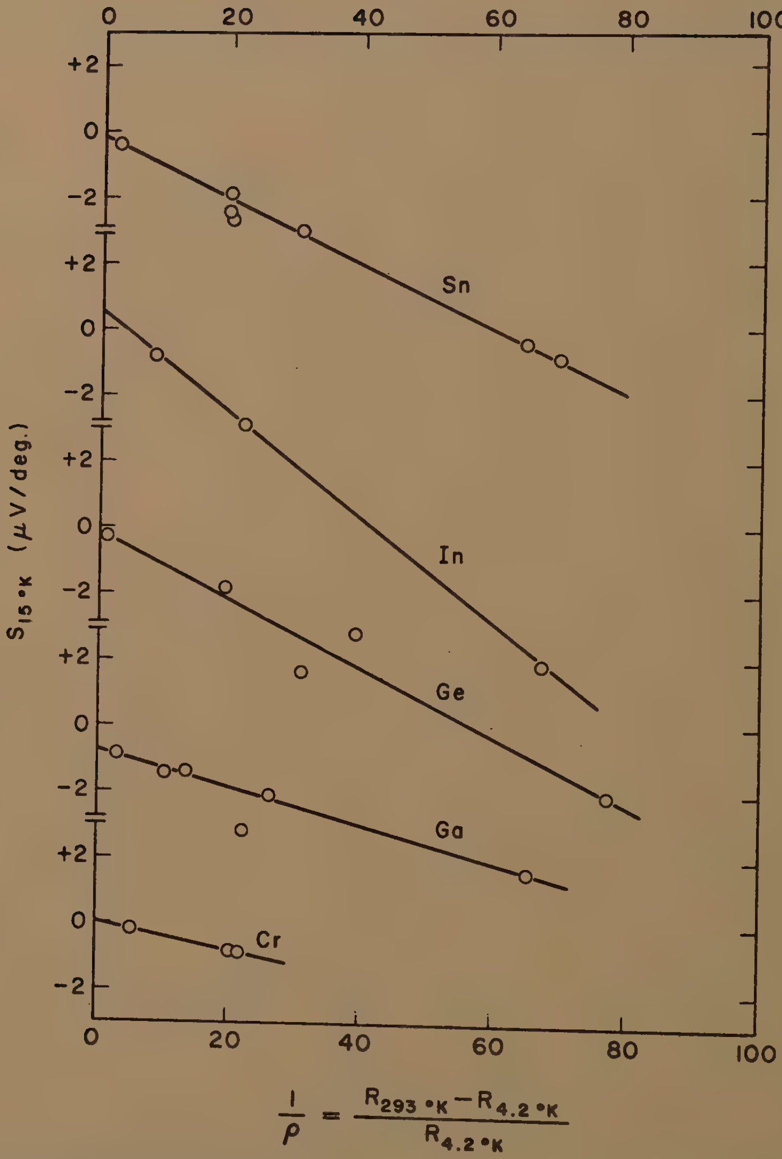

Variation of $S_{15°\text{K}}$ with inverse residual resistance ratio for dilute alloys of Cr in A.S. & R. Cu and Sn, In, Ge and Ga in Cu 1 (containing oxygen). The data for the latter four alloy series correspond to the region B C in fig. 10 (Appendix II); they were obtained by a less accurate experimental technique than that used for the Cu–Cr, Cu–Ni and Cu–Fe alloys which might give rise to errors corresponding to displacing the lines upwards or downwards by $\pm 0{\cdot}5\,\mu$v/deg. The same remarks hold for the data on alloys with the solutes Ag, Au and Si (not shown in figs. 4 and 5), all of which yield characteristic values of close to zero at 15°K.

small traces of iron and we shall now give a more quantitative discussion of the temperature dependence of S in the neighbourhood of the anomaly. Applying eqn. (1) to the case of impurity and thermal scattering, we have:

$$S = \frac{W_{\mathrm{imp}}}{W_{\mathrm{imp}} + W_{\mathrm{th}}} S_{\mathrm{imp(Fe)}} + \frac{W_{\mathrm{th}}}{W_{\mathrm{imp}} + W_{\mathrm{th}}} S_{\mathrm{th}}. \quad . \quad . \quad . \quad (3)$$

Since the characteristic value of S for iron in copper of $-16{\cdot}2\,\mu$v/deg. at 15°K lies close to the curve for the 0·054% Fe alloy in fig. 1, we shall take the curve for this particular alloy to approximate to the true curve of $S_{\mathrm{imp(Fe)}}$, when all other scattering mechanisms are dominated by the scattering from iron. This curve 'saturates' at a value of about $-16\,\mu$v/deg., at least up to the limit of the impurity scattering region which occurs at about 100°K for this iron concentration (cf. fig. 2 of Borelius *et al.* (1932)). For the purely thermal scattering component we shall take $S_{\mathrm{th}} = +5{\cdot}4 \times 10^{-3} T\,\mu$v/deg. from the Thomson heat measurements of Nyström (1947) above 350°K, where impurity scattering is negligible and phonon-drag effects are assumed to be small (§ 4.2)†. The temperature dependence of the thermal resistivity components W_{imp} and W_{th} for a copper sample of similar purity to ours has been given recently by Powell *et al.* (1959) (see table) and the resulting S–T variation calculated from eqn. (3) is shown as the curve A in fig. 1.

It is pleasing that this simple analysis accounts not only for the shape of the observed curves but also for the temperature at which the anomaly occurs. The discrepancy in the actual size of the anomaly can be attributed to the effect of scattering by all the remaining traces of chemical and physical impurities present in the copper, e.g. Ag, Au, Cr, ..., etc., which alone give very small values of S and yet give rise to approximately half of the impurity scattering in the thermal resistivity. In fact the curves for Cu 4, Cu 5 and Cu 6 can be well accounted for by supposing 50% of W_{imp} to be due to iron and the remaining 50% to be due to other impurities with small (effectively zero) S_{imp} (fig. 1, curve B). Likewise the fact that S for cold-worked copper is *positive* relative to annealed copper in this temperature region (cf. Pearson 1960, van Oijen 1957) is merely a reflection of the fact that the *relative* amount of scattering due to iron is reduced by the introduction of defects. Figure 3 also shows a considerable reduction of the anomaly when material of samples Cu 3 to Cu 6 is alloyed with 0·01% Sn, this being sufficient to 'swamp' most of the effect of the iron present ($\sim$0·0001%).

We have already pointed out that, with the notable exception of iron, all of the solutes in copper studied so far have *low* characteristic thermoelectric powers ranging between $+1$ and $-1\,\mu$v/deg. at 15°K. This at first sight does not seem to be in keeping with the fact that sizeable anomalies of as much as $-10\,\mu$v/deg. can be 'produced' when copper is alloyed with *some of these very elements* (MacDonald and Pearson 1955 a, b). The copper used for these experiments was the same as that of our sample Cu 1, viz. *containing oxygen*, and we now propose that these results arise from some metallurgical phenomenon whereby the particular solutes concerned separate the iron (~0·002%) from its oxide and that it is the iron which is primarily responsible for the anomalies. For example, tin is typical of such solutes and the dependence of the size of the anomaly on tin concentration is shown in fig. 6 (curve A). At tin concentrations above about 0·005 at. % all the iron has been brought into solid solution and the addition of further tin as solute merely cuts down the relative importance of the anomalous scattering by iron; this is the sole effect of the tin in alloys which have been prepared under *reducing* conditions (curve B). A further discussion of the Cu–Sn alloys is given in Appendix II.

---

† S varies linearly with T above 350°K in accordance with eqn. (4) to within the accuracy of Nystrom's Thomson heat results and of the absolute value of S at 350°K (fig. 3).

Fig. 6

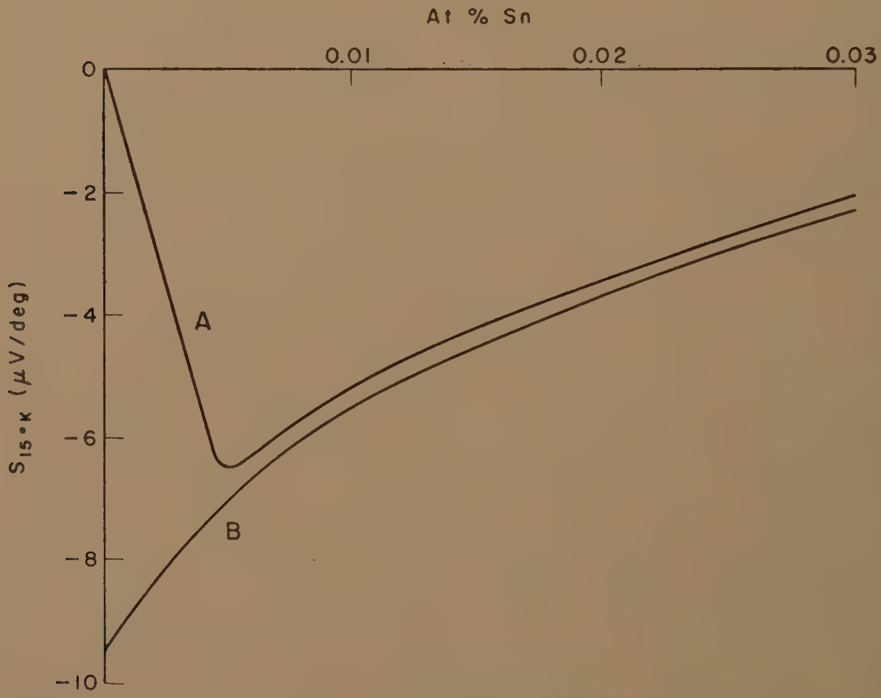

Dependence of size of the low-temperature anomaly on tin concentration in dilute alloys prepared from the oxygen-containing Cu 1 (curve A) and from the same copper, but under reducing conditions (curve B). (MacDonald and Pearson 1955a; somewhat schematic).

Similar conclusions about iron being the ‘prime mover’ in the dilute alloys studied by MacDonald and Pearson (1955 a, b) are arrived at from considerations of the resistance minimum which is closely related to the thermoelectric power anomaly. While the size of the thermoelectric power anomaly depends on the relative concentration of iron, the absolute size of the associated resistance minimum depends on the *total* amount of iron present (Pearson 1955). Thus we see from fig. 7 that the size of the resistance minimum in the Cu–Sn alloys remains constant once sufficient tin has been added to the oxygen-containing copper to bring all the iron into solid solution. Moreover, the size of the minimum obtained by reducing the initial copper is the same as the saturation value for the unreduced Cu–Sn alloys, this point lying on the straight line obtained by subsequently alloying with iron. The picture outlined so far is quite consistent with all the experimental data for various solutes in copper, but offers no explanation of the result of Pearson *et al.* (1959) that a resistance minimum can be created in oxygen-free Cu–Sn single crystals prepared from A. S. and R. copper simply by rendering them polycrystalline and annealing; the fact that the residual resistivity did not increase in this process would suggest that the specimens were not significantly contaminated by extraneous impurities†. In the present work we have found no significant evidence

Fig. 7

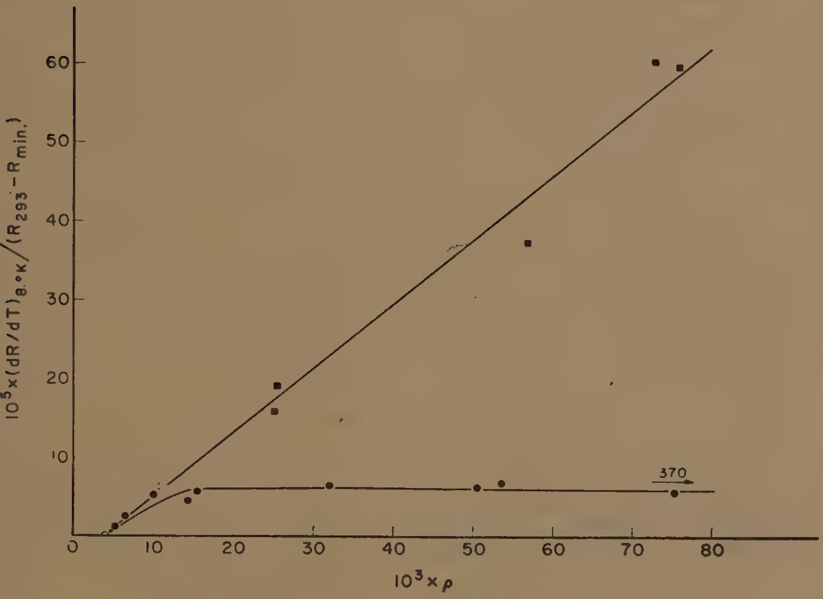

Dependence of absolute size of resistance minimum (gauged by $(dR/dT)_{8^\circ\mathrm{K}}/(R_{293}-R_{\min})$) on residual resistance ratio in dilute alloys prepared from the oxygen-containing Cu 1 ○, Cu 1; ●, Cu 1 + Sn; □, Cu 1 (reduced); ■, Cu 1 + Fe (reduced) (Pearson 1955). If instead we plot the size of the minimum, *relative* to the resistivity ρ at the minimum, against ρ, we obtain a cusp-shaped curve similar to curve A in fig. 6.

---

† Mr. E. Wallingford (private communication) has shown that no resistance minimum results if the oxygen-free A.S. and R. copper (with low iron content; see table) is alloyed with tin.

of a resistance minimum in our 'pure' copper samples, in spite of many having large thermoelectric power anomalies. This is, of course, to be expected in view of the minute quantities of iron concerned ($\sim 0{\cdot}0001\%$), the size of the minimum depending not on the relative but on the total iron concentration.

While we have so far been able to coordinate a variety of experimental facts relating to the low-temperature thermoelectric power anomalies and the resistance minima in 'pure' copper and in dilute copper alloys, we are still unable to account satisfactorily for the temperature dependence of the anomalous characteristic thermoelectric power of iron in copper (fig. 1). Let us emphasize that the 'flattening-off' of the curve at about $-16\,\mu$v/deg. is *not* due to scattering of electrons by thermal vibrations. Presumably we are concerned here with some highly energy-dependent inelastic scattering of the electrons by magnetic iron impurity ions (cf. Schmitt 1956; see also Korringa and Gerritsen 1953). Unfortunately, the recent theoretical work by Brailsford and Overhauser (1959) does not seem to be directly applicable to our case as far as calculating the thermoelectric power is concerned. These authors predict a quadratic dependence of the size of the resistance minimum on solute concentration whereas the size of the minimum in dilute Cu–Fe alloys is found to increase *linearly* with concentration (fig. 7; Pearson 1955).

4.2. *The Results at High Temperatures and Evidence for Phonon-drag*

According to the conventional theory (cf. Mott and Jones 1936, Wilson 1953) the diffusion thermoelectric power is given by the expression:

$$S=\frac{\pi^2k^2T}{3e}\left(\frac{\partial\log\sigma(E)}{\partial E}\right)_\zeta=\frac{\pi^2k^2T}{3e\zeta}\left(\frac{\partial\log\sigma(E)}{\partial\log E}\right)_\zeta, \quad . \quad . \quad . \quad (4)$$

where the derivative of the conductivity $\sigma(E)$ is taken at the Fermi level ζ and e is the electronic charge in magnitude and sign. Thus from the fact that S is positive at high temperatures (fig. 3) we infer that $(\partial\sigma(E)/\partial E)_\zeta$ is negative, of opposite sign to that predicted for free electrons (Wilson 1953). We believe that this sign reversal must in some way be connected with the fact that the Fermi surface in copper is distorted to the extent of contacting the Brillouin-zone boundary (Pippard 1957, Shoenberg 1960); S is also positive for both silver and gold, whose Fermi surfaces are now known to contact the zone faces (Shoenberg 1960). It might be worth noting that the high-temperature thermoelectric power in copper calculated from eqn. (4) for thermal scattering of free electrons, viz. $S=-8{\cdot}7\times10^{-3}T$ μv/deg. (taking $\zeta=7{\cdot}0$ ev and $(\partial\log\sigma/\partial\log E)_\zeta=2{\cdot}5$ (Jones (1956); Wilson (1953) gives $(\partial\log\sigma/\partial\log E)\zeta=3$)) is quite close to the observed result of $S\doteqdot+5{\cdot}4\times10^{-3}T$ μv/deg. (fig. 3), apart from the change in sign.

It will be seen from fig. 3 that the experimental results around 70°K lie considerably above the dashed curve B, which was calculated from eqn. (3) on the assumptions that 50% of the low-temperature impurity scattering was due to iron and that $S=+5{\cdot}4\times10^{-3}T$ μv/deg. at high temperatures. We interpret this difference as arising from a net positive Umklapp-type phonon-drag component in S. The detailed theory of phonon-drag in even the monovalent metals is complicated (Ziman 1959, Bailyn 1960), the resulting thermoelectric power depending on the relative frequencies of normal (N) and Umklapp (U) scattering processes (fig. 8), so that in what follows we shall make only a rough comparison of the phonon-drag contribution S_g with simple theory.

Fig. 8

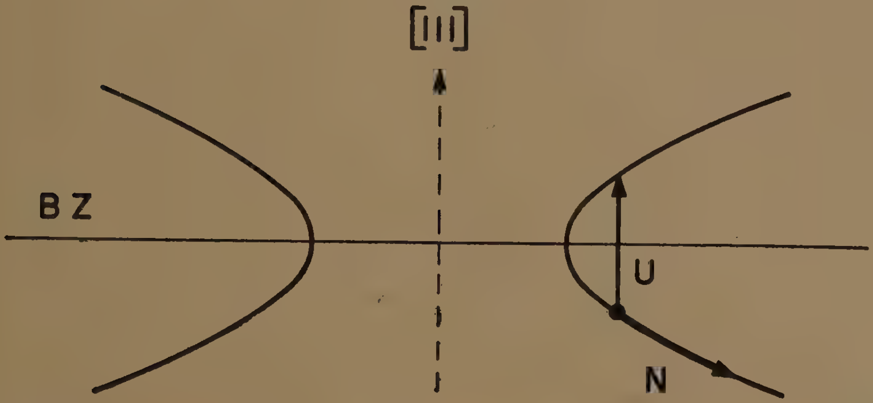

Illustrating scattering by N- and U-processes near the contact of the Fermi surface with the Brillouin zone.

A convenient expression for the phonon-drag thermoelectric power at temperatures low enough for the phonons to be scattered by electrons only, and assuming only N-scattering processes, was given by MacDonald (1954) and later in more exact form by Hanna and Sondheimer (1957) and is:

$$S_g=\frac{1}{3}\frac{1}{Ne}C_g, \qquad (5)$$

where C_g is the lattice specific heat and N is the number of electrons per unit volume. This gives for copper:

$$S_g=-1{\cdot}65\times10^{-4}T^3\,\mu\text{v/deg.}, \qquad (6)$$

assuming one electron per atom and $\theta_D=344$°K (cf. Corak *et al.* 1955). Now if the Fermi surface in copper were singly connected, the positive low-temperature contribution to S_g from U-processes would depend in an approximately exponential manner on T; since, however, the Fermi surface contacts the Brillouin zone, and so runs smoothly from one cell of the reciprocal lattice into the next, we might expect the contributions from both N- and U-processes (fig. 8) to vary more or less as T^3. Then by roughly fitting the difference between the observed curve for Cu 6 and curve B (fig. 3) to a T^3 law below the maximum we find:

$$S_{g(\mathrm{obs})} \doteqdot +1{\cdot}2 \times 10^{-5} T^3 \,\mu\mathrm{v/deg.} \qquad . \; . \; . \; . \; . \quad (7)$$

This is less than 10% of the magnitude given in eqn. (6) for N-processes alone, so that we conclude that the contributions to S_g from U-processes and N-processes very nearly cancel and that we have a small excess of the U-contribution. Although strictly it appears that Ziman's (1959) calculation is not applicable to the case where the Fermi surface touches the Brillouin zone, the observed maximum is, broadly speaking, in keeping with his general prediction of a U-type maximum in S_g at $T \sim \theta_D/10$ for monovalent metals with a distorted but singly-connected Fermi surface. At the lowest temperatures, however (i.e. where only phonons of low wave-number are excited) we would expect ultimately from fig. 8 the contribution from N-processes to be the larger, and it is suggested that this may be the reason why the results from our purest sample apparently become negative at about 13°K (fig. 2(*b*)); any such trend in the A.S. and R. samples would be masked by the large anomaly.

At temperatures above the peak at 70°K, the phonon-drag term should fall off as T^{-1} on account of phonon–phonon scattering (Hanna and Sondheimer 1957), but it is difficult to verify this precisely since this obviously depends on the exact choice of our curve B at the higher temperatures. The reduction in the phonon-drag term due to phonon–impurity scattering is illustrated by the curve for the Cu + 0·01% Sn sample (fig. 3), and Pearson (1960) has discussed the reduction due to scattering of phonons by lattice defects.

Notes added in proof:

(i) Blatt and Kropschot (1960) have recently discussed the reduction in the phonon-drag 'hump' when copper is alloyed with various solutes.

(ii) The simple derivation of Kohler's formula (Appendix I) has also been pointed out by de Vroomen (1959) and de Vroomen *et al.* (1960); Kohler's formula has also been derived, but in a more complicated way, by van Oijen (1957).

(iii) de Vroomen (1959) has independently suggested that the thermoelectric power anomalies and the resistance minima in various dilute alloys may be due to transition metal impurities.

(iv) The high-temperature part of curve B (fig. 3) has been inadvertently drawn with slope $6{\cdot}0 \times 10^{-3} \,\mu\mathrm{v/deg}^2$ rather than $5{\cdot}4 \times 10^{-3} \,\mu\mathrm{v/deg}^2$; this is of no real consequence as far as the anomaly is concerned.

ACKNOWLEDGMENTS

We are indebted to Professor A. F. Kip and Dr. D. Langenberg for kindly giving us the sample of natural copper, to Dr. J. Babiskin for kindly giving us a batch of very pure A.S. and R. copper, and to Dr. J. S. Dugdale for helpful discussions. We are also grateful to Mr. D. J. Huntley for carrying out some of the measurements, to Mr. J. W. Fisher for preparation of most of the specimens, and to Miss J. Spong for her help with the calculations.

APPENDIX I

Consider two conductors placed in series with one another as in fig. 9 (*a*) and having absolute thermoelectric powers S_1, S_2 and thermal resistances W_1, W_2, respectively. If then a (small) temperature difference, ΔT, be applied across the system as shown, this temperature difference will be divided in proportion to the thermal resistances W_1, W_2. Consequently,

Fig. 9

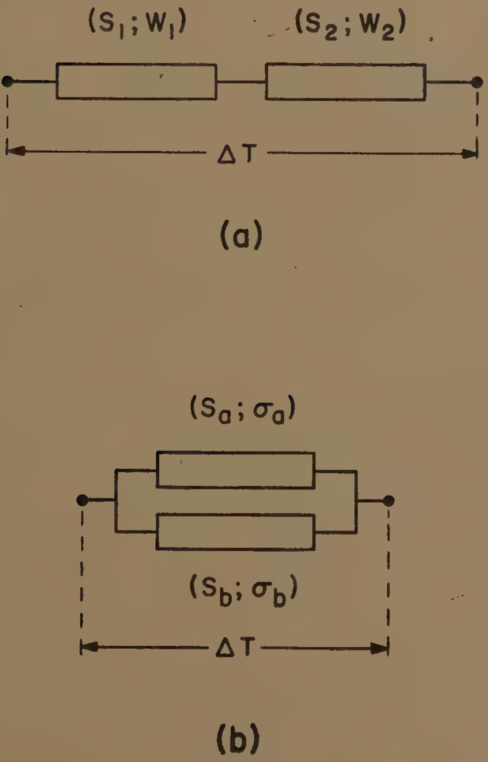

Illustrating the series and parallel circuit theorems.

a net open circuit potential difference, ΔV, will be generated across the series combination given by

$$\Delta V = S_1 \frac{W_1}{W_1+W_2} \Delta T + S_2 \frac{W_2}{W_1+W_2} \Delta T, \quad . \quad . \quad . \quad (8)$$

i.e. the absolute thermoelectric power of the conductors in series is given by

$$S = \frac{W_1 S_1}{W_1+W_2} + \frac{W_2 S_2}{W_1+W_2} \quad . \quad . \quad . \quad . \quad . \quad . \quad (9a)$$

or more generally

$$S = \sum_i W_i S_i \Big/ \sum_i W_i. \quad . \quad . \quad . \quad . \quad . \quad . \quad (9b)$$

We now suggest that this result may be applied directly to a *single* conductor with various scattering mechanisms under the following conditions:

(i) We assume that the electrical conduction in the conductor may be treated in terms of a *single* homogeneous group of charge carriers (let us say electrons). We believe that this implies in particular that matrix elements for electron scattering should *not* depend explicitly on the electron wave vector, $\mathbf{k}$.

(ii) The electron scattering mechanisms are to be assumed as being entirely independent of one another, and such that any particular scattering mechanism (say the ith), if operating entirely alone, would give rise to a characteristic thermoelectric power, $S_i(T)$, at the temperature T appropriate to the conductor and a thermal resistivity due to electron scattering, $W_i(T)$. Effectively, what we assume is that each and every electron 'collision', whatever its cause, may be considered as independent of preceding or succeeding 'collisions'.

(iii) Where we are concerned with a variation in the intensity of any electron scattering mechanism (e.g. owing to variation in concentration of a solute or in the intensity of thermal scattering) we assume that the essential characteristics of the conduction electrons remain unchanged. Effectively this means that the electron density of states function is assumed to be unaffected.

(iv) The transport of *heat* (i.e. thermal conduction) in the conductor is supposed to be determined entirely (i.e. in practice dominantly so) by the conduction electrons.

It would appear that these restrictions are effectively those which are involved when Kohler's theorem is derived from a specific analysis of electron transport, although perhaps slightly less restrictive in some aspects. In particular, it would appear that these conditions usually restrict one to applying eqn. ($9a$, b) usefully to the analysis of diffusion thermoelectric power (but see immediately below).

Recently the problem of calculating thermoelectric power *due to phonon-drag* has been in prominence. A matter of some interest has been the relative contributions from 'normal' electron–phonon process and from the Umklapp processes in a conductor otherwise free from electron scattering mechanisms. It is improbable that eqn. (9*a*, *b*) can be applied *strictly* to this situation because the electron–phonon scattering matrix elements, particularly for Umklapp processes, will presumably depend quite significantly on the electron wave vector, **k**. However, at least as a useful approximation, it appears that one might write for the thermoelectric power, S_g, due to phonon-drag:

$$S_g(T) = \frac{S_{gN}(T)W_N(T)}{W_N(T)+W_U(T)} + \frac{S_{gU}(T)W_U(T)}{W_N(T)+W_U(T)}.$$

This may be compared with the expression put forward by Ziman (1959) and Bailyn (1960).

One is tempted to try and generalize eqn. (9*a*, *b*) if lattice thermal conduction is no longer negligible in comparison with electronic thermal conduction. We suggest that if this is the case, an approximate extension of eqn. (9*a*, *b*) might run as follows: in eqn. (8) S_1 and S_2 remain as before, but W_1 and W_2 would be replaced by W_1^* and W_2^*, where

$$W_1^* = (K_1 + (1+\alpha)K_g)^{-1}; \quad W_2^* = (K_2 + (1+\alpha^{-1})K_g)^{-1}$$

and

$$K_1 = W_1^{-1}, \quad K_2 = W_2^{-1}.$$

K_g is the lattice thermal conductivity, and $\alpha = N_2/N_1$, where N_1 and N_2 are the numbers of electron scattering centres corresponding to the electronic thermal resistivities W_1 and W_2 respectively. Thus if w_1 and w_2 are the apparent electron scattering cross-sections for thermal resistance corresponding to these two mechanisms, then $\alpha = W_2 w_1 / W_1 w_2$.

This modified form of eqn. (8) means that S would no longer vary exactly as predicted in the text (p. 772) when two impurities are present at low temperatures; we should now look for deviations due to this cause from the expected linear dependence of S with $1/\rho$.

Although we make no use in this paper of a two-band model of a conductor it seems appropriate to point out here that an expression for the thermoelectric power in a two-band conductor may be derived in a rather similar manner. If we consider two conductors (*a*) and (*b*) in parallel (see fig. 9*b*) having absolute thermoelectric powers, S_a and S_b, and electric conductances, σ_a and σ_b, then it is easy to show that the absolute thermoelectric power, S, of the System is given by

$$S = \frac{\sigma_a S_a}{\sigma_a + \sigma_b} + \frac{\sigma_b S_b}{\sigma_a + \sigma_b}; \quad . \quad . \quad . \quad . \quad . \quad . \quad (10a)$$

or if a number of conductors are in parallel:

$$S = \sum_j \sigma_j S_j / \sum_j \sigma_j. \quad . \quad . \quad . \quad . \quad . \quad . \quad . \quad . \quad (10b)$$

This result may then be applied quite generally to the case of a single conductor which has two independent groups of charge carriers, *a* and *b*, with conductivities σ_a and σ_b respectively, and such that each group *if acting alone* would contribute a thermoelectric power S_a and S_b respectively. As long as the condition of independent conduction by the two groups of carriers is strictly maintained, the result of eqn. (10 *a*; *b*) should be quite general and independent of any specific mechanism of thermoelectric power production. Equation (10 *a*) has been derived previously by various authors (Sondheimer 1948, Chambers 1952†, Wilson 1953) with varying degrees of generality.

Finally let us point out that the expression given by Mott and Jones (1936) for the diffusion component of thermoelectricity will also yield corresponding expressions within the range of its validity. Mott and Jones give:

$$S=\frac{\pi^2k^2T}{3e}\left(\frac{d\log\sigma(E)}{dE}\right)_{E=\zeta} \quad . \quad . \quad . \quad . \quad . \quad . \quad (11\,a)$$

for the absolute thermoelectric power, which may also be written

$$S=-\frac{\pi^2k^2T}{3e}\left(\frac{d\log\rho(E)}{dE}\right)_{E=\zeta} . \quad . \quad . \quad . \quad . \quad . \quad . \quad (11\,b)$$

Equation (11 *a*) was derived from a Boltzmann equation analysis, the solution of which depended on the assumption of a relaxation time, and, as mentioned above, is applicable only to the diffusion component of thermoelectricity. Mott and Jones themselves say: "It is valid both for pure metals and for alloys at temperatures above the characteristic temperature θ, and at lower temperatures provided the 'Restwiderstand' ["residual resistance"] is large compared with the resistance due to the thermal motion of atoms. It is not, however, valid for *pure* metals if $T<\theta$." If eqn. (11 *a*) is now applied to a metal or other conductor, in which we assume that there are two independent bands of carriers, then we may write as before (cf. eqn. (10 *a*)):

$$S=\frac{\sigma_aS_a}{\sigma_a+\sigma_b}+\frac{\sigma_bS_b}{\sigma_a+\sigma_b} . \quad . \quad . \quad . \quad . \quad . \quad . \quad . \quad (12)$$

If, instead, we start from eqn. (11 *b*) and regard the conductor as made up of a single band of carriers which encounter two separate scattering mechanisms (both of which must satisfy the requirements of the original formula) and if we write the electrical resistivities corresponding to each of these mechanisms as ρ_1 and ρ_2, and the corresponding absolute thermoelectric powers that would be observed if either were acting independently alone as S_1 and S_2 respectively, then we may write:

$$S=\frac{\rho_1S_1}{\rho_1+\rho_2}+\frac{\rho_2S_2}{\rho_1+\rho_2} , \quad . \quad . \quad . \quad . \quad . \quad . \quad . \quad (13)$$

---

† Chambers' derivation appears to be based on the most general assumptions for a two-band model of a conductor and he points out that concern with a two-band model dates back as early as Riecke (1898). A similar equation to (10 *a*) was derived by Fowler (1936) for the case of a semiconductor with conductivity arising from two bands.

which is essentially the result of Nordheim and Gorter (1935). Equation (9*a*) (Kohler's formula) of course reduces to this when we can write $W=\rho/L_0T$ (where L_0 is a *constant*) and this is valid either in the residual resistance region where impurity scattering is entirely dominant, or at 'high' temperatures ($T \gtrsim \theta$) where the thermal scattering becomes essentially classical in character, which are just the regions of validity of the Mott and Jones formula.

APPENDIX II

We give here a further discussion of the effect of adding tin to our oxygen-containing copper in terms of the S *versus* $1/\rho$ plot of fig. 10. Curve A B C gives the variation of the size of the anomaly as the tin concentration is increased; the point C for $1/\rho \to 0$ then gives the characteristic value of $S_{15^\circ\mathrm{K}}$ (~ 0) for tin in copper. If, on the other hand, the alloys are prepared under reducing conditions, the addition of tin reduces the size of the anomaly which is already present in the starting material (D B C). Furthermore when iron is deliberately added to the reduced copper, the points lie on the continuation of the line A D (giving the characteristic value of $S_{15^\circ\mathrm{K}}$ for iron in copper at E), which is consistent with the hypothesis that hydrogen-reduction brings the iron in the initial oxygen-containing copper into solid solution. Since iron is the only impurity in the copper with a greater negative characteristic thermoelectric power than $-1\,\mu$v/deg. at 15°K, it is proposed that the tin does not in itself 'produce' the anomaly in the oxygen-containing copper A, but that it brings the iron into solid solution until the point B is reached where the amount of iron in solid solution is constant (corresponding to D). Thereafter (B C) the addition of more tin reduces the relative amount of anomalous scattering by iron so that the

Fig. 10

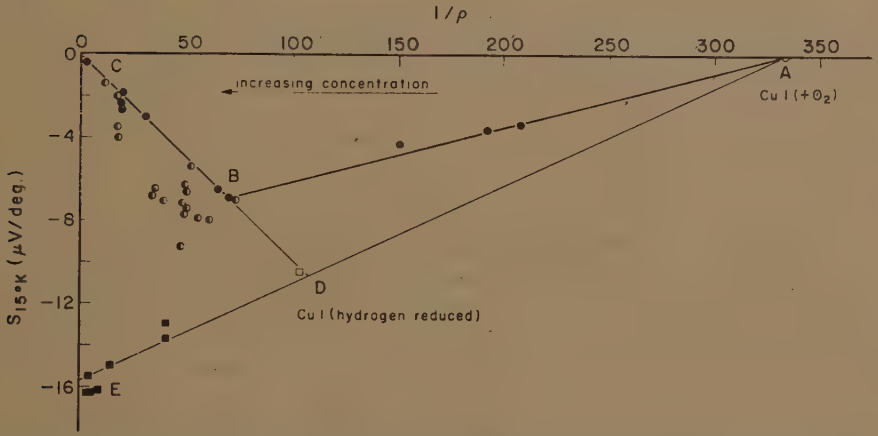

Variation of $S_{15^\circ\mathrm{K}}$ with inverse residual resistance ratio for dilute alloys prepared from the oxygen-containing Cu 1. ○, Cu 1; ●, Cu 1+Sn; □, Cu 1 (reduced); ■, Cu 1+Fe (reduced): ◐, Cu 1+Sn (reduced).

size of the anomaly decreases; likewise it is the reduction by the tin of the effectiveness of the iron scattering which results in the oxygen-containing alloys following the path A B C rather than A D C. It is interesting to note that many of the points for the *reduced* tin alloys lie *below* the line D B C, which suggests that alloying with an excess of tin is not alone sufficient to bring *all* the iron into solid solution.

REFERENCES

BAILYN, M., 1960, *Phil. Mag.* (in the press).
BLATT, F. J., and KROPSCHOT, R. H., 1960, *Phys. Rev.*, **118,** 480.
BORELIUS, G., KEESOM, W. H., JOHANNSON, C. H., and LINDE, J. O., 1930, *Proc. Acad. Sci. Amst.*, **33,** 17 (Leid. Comm. 206a); 1932, *Ibid.*, **35,** 25 (Leid. Comm. 217e).
BRAILSFORD, A. D., and OVERHAUSER, A. W., 1959, *Phys. Rev. Letter*, **6,** 331.
CHAMBERS, R. G., 1952, *Proc. phys. Soc.* A, **65,** 903.
CHRISTIAN, J. W., JAN, J.-P., PEARSON, W. B., and TEMPLETON, I. M., 1958, *Proc. roy. Soc.* A, **245,** 213.
CORAK, W. S., GARFUNKEL, M. P., SATTERTHWAITE, C. B., and WEXLER, A., 1955, *Phys. Rev.*, **98,** 1699.
DE VROOMEN, A. R., 1959, *Thesis*, University of Leiden.
DE VROOMEN, A. R., VAN BAARLE, C., and CUELENAERE, A. J., 1960, *Physica*, **26,** 19.
FOWLER, 1936, *Statistical Mechanics* (Cambridge: University Press).
HANNA, I. I., and SONDHEIMER, E. H., 1957, *Proc. roy. Soc.* A, **239,** 247.
JONES, H., 1956, *Handbuch der Pyhsik* (ed. S. Flügge), **19,** 227.
KOHLER, M., 1949, *Z. Phys.*, **126,** 481.
KORRINGA, J., and GERRITESN, A. N., 1953, *Physica*, **19,** 457.
KROPSCHOT, R. H., and BLATT, F. T., 1959, *Phys. Rev.*, **116,** 617.
MACDONALD, D. K. C., 1947, *J. sci. Instrum.*, **24,** 232; 1954, *Physica* **20,** 996.
MACDONALD, D. K. C., and PEARSON, W. B., 1953, *Proc. roy. Soc.* A, **219,** 373; 1955 a, *Acta Met.*, **3,** 392; 1955 b, *Ibid.*, **3,** 403.
MACDONALD, D. K. C., PEARSON, W. B., and TEMPLETON, I. M., 1960, *Proc. roy. Soc.* (in the press).
MOTT, N. F., and JONES, H., 1936, *Theory of Metals and Alloys* (Oxford: Clarendon Press).
NORDHEIM, L., and GORTER, C. J., 1935, *Physica*, **2,** 383.
NYSTRÖM, J., 1947, *Ark. Mat. Astr. Fys.* A, **34,** No. 27.
PEARSON, W. B., 1955, *Phil. Mag.*, **46,** 911; 1960, *Phys. Rev.* (in the press).
PEARSON, W. B., RIMEK, D. M., and TEMPLETON, I. M., 1959, *Phil. Mag.*, **4,** 612.
PIPPARD, A. B., 1957, *Phil. Trans.* A, **250,** 325.
POWELL, R. L., RODER, H. M., and HALL, W. J., 1959, *Phys. Rev.*, **115,** 314.
RIECKE, E., 1898, *Wied. Ann.*, **66,** 545, 1199.
SHOENBERG, D., 1960, *Phil. Mag.*, **5,** 105.
SONDHEIMER, E. H., 1948, *Proc. roy. Soc.* A, **193,** 484.
SCHMITT, R. W., 1956, *Phys. Rev.*, **103,** 83.
VAN OIJEN, D. J., 1957, *Thesis*, University of Delft.
WILSON, A. H., 1953, *The Theory of Metals* (Cambridge: University Press).
ZIMAN, J. M., 1959, *Phil. Mag.*, **4,** 371.

Observations of the Decomposition of Crystals of Lead Iodide in the Electron Microscope†

By A. J. Forty
H. H. Wills Physics Laboratory, University of Bristol

[Received January 24, 1960]

Abstract

Thin crystals of lead iodide grown from solution have been examined in transmission in the electron microscope. The crystals are sufficiently stable in the electron beam to allow dislocations to be observed, but it is found that after prolonged periods of observation at high beam intensities decomposition commences, and proceeds through a number of stages to completion. The initial and intermediate stages are accompanied by the climb of pre-existing dislocations, the formation of new dislocations and the creation of other features which might be interpreted as cavities in the crystal. These can be understood to some extent as a result of the formation of vacancies in the crystal under irradiation with the electron beam. In the final stage the crystals appear to decompose completely leaving an aggregate of dense crystallites which are probably metallic lead. This is presumably accompanied by the release of iodine gas. The mechanism for this final stage of decomposition is not yet understood.

§ 1. Introduction

The application of transmission electron microscopy to the study of thin crystalline films during the past few years has led to a remarkable advance in our knowledge of the formation and behaviour of dislocations and other imperfections in crystals. The observations have, however, been made almost entirely on metal crystals. This is not altogether surprising since dislocation theory finds its most direct application in attempts to explain the mechanical behaviour of metals. Moreover, metal films are relatively stable in the beam of the electron microscope whereas other inorganic crystals, such as sodium chloride, for example, are known to decompose very rapidly, presumably because of their low thermal and electrical conductivities. Recent attempts to correlate the step structure on growth surfaces of crystals with internal imperfections by direct observation have, however, indicated that there are some inorganic crystals, notably lead iodide and cadmium iodide, which are moderately stable in the electron beam for periods sufficient to allow observations on dislocations to be made, and that these can provide a useful contribution to this field of study.

The correlation expected from this study has not been found, but, as will become evident later, this is not altogether surprising since the interaction of the electron beam with the thin crystals used here leads to a slow but controllable decomposition of the crystals in such a manner as to modify existing dislocations and generate new ones. The observations which have been made on this process of decomposition are thought to be sufficiently interesting to be reported in this paper.

---

† Communicated by the Author.

It is impossible at this stage to determine whether the decomposition is induced directly by irradiation of the crystals in the electron beam or whether it occurs indirectly as a result of the heating of the crystals. In either case it can be considered to some extent to represent a form of radiation damage, and, moreover, a form of damage which can be observed directly in progress. It is not impossible that similar effects might be found in metal crystals but to a greatly lesser degree so that these have hitherto escaped observations.

§ 2. Experimental

The observations to be described have all been made on crystals of lead iodide. Cadmium iodide and other members of this family of compounds show similar effects and have also been examined in some detail. These will not be discussed here.

Large plate-like crystals of lead iodide can be grown from a solution in alcohol by saturating the solution at about 100°c in a water bath and allowing this to cool slowly to room temperature. The crystals can then be transferred to an electron microscope specimen grid by depositing a drop of the stirred solution and allowing it to evaporate, leaving several large crystals resting across the bars of the grid. An alternative but less reliable method is to place the grid in a drop of the solution between a glass slide and a cover slip, heat gently to about 100°c and then allow to cool to room temperature. In this way a few crystals grow in contact with the grid which can then be dried by extracting the excess solution with a filter paper.

The crystals have a marked platelet habit and lie flat on the specimen grid without a supporting film. Prepared in this way, a good many of them are sufficiently thin for direct transmission microscopy. It is thus possible to examine as-grown crystals without further preparation.

The crystals have been examined in a Philips 100 kv electron microscope. This allows direct transmission microscopy with facilities for tilting the specimen through large angles and for deflecting the beam through small angles. Moreover, facilities for electron diffraction are available so that crystallographic orientations and some contrast effects in the microscope image can be fairly readily determined as the observations are made.

§ 3. The Crystal Structure of Lead Iodide

In the following sections reference to directions and other special features of the lead iodide structure will frequently be made. These are summarized in fig. 1[†] which shows one unit of the structure. It will be seen that this consists of a sandwich of a hexagonal array of lead ions between two close-packed layers of iodine ions. The crystal is built of a stack of such sandwiches so that a layer sequence in the familiar *a*, *b*, *c* notation can be described as

---

[†] Figures 2–15 are shown as plates.

$$(a\gamma b)\,(a\gamma b)\,(a\gamma b)\ldots$$

where Roman letters represent iodine ions and Greek letters represent lead ions. In view of the relative sizes of the lead and iodine ions it is possible to regard this structure simply as a hexagonal close-packing of iodine ions with interstitial lead ions placed in the octahedral holes between alternate pairs of layers. The basal plane defined by the direct contact of two iodine layers without interstitial lead provides a cleavage plane and a plane of easy glide.

Fig. 1

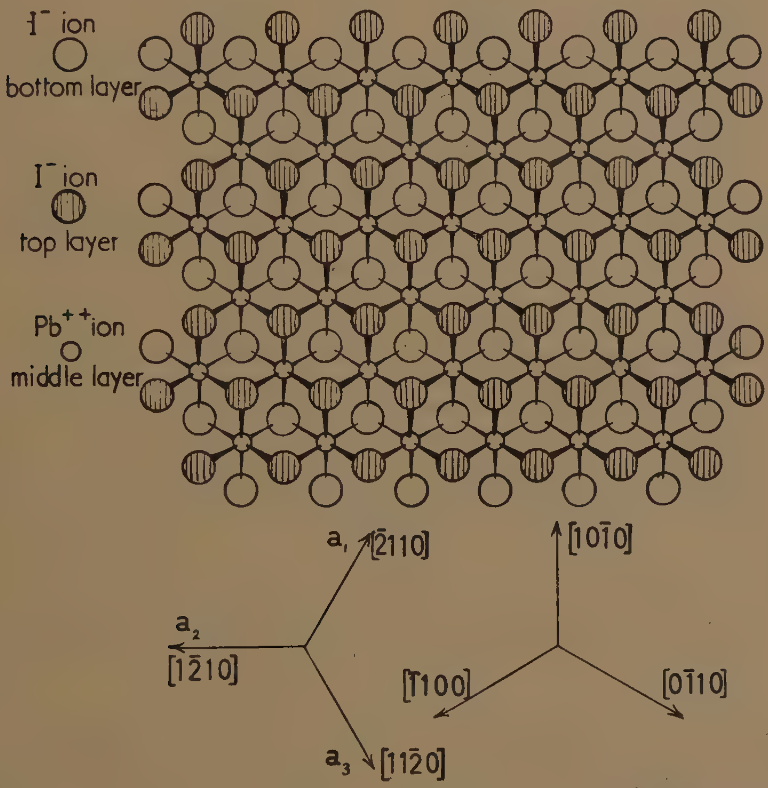

A single sandwich of lead iodide. Note the strong ionic bonding within the sandwich.

§ 4. OBSERVATIONS

Dislocations can be seen in the crystals as soon as observation commences. These are generally individual lines or wide-meshed networks of dislocations lying in the plane of the platelet. This is the basal plane (0001) and is the plane in which glide or other deformation is likely to occur most readily. It is also the plane on which the steady thickening of the platelet has taken place (Forty 1952) during growth. It is therefore possible that these pre-existing dislocations have been introduced during growth or by deformation through transferring the crystals from the solution to the specimen grid.

This simple pattern gradually becomes more complex during a prolonged period of observation as the crystal begins to decompose. The rate at which decomposition develops and proceeds depends on the intensity of the electron beam; that is, on the filament current, condenser current and the operating voltage applied. Most of the observations to be described have been made at 80 kv although some have been made at the full 100 kv. In the latter case decomposition is often catastrophic.

It is convenient to describe the observations separately in the early, intermediate and final stages of decomposition, although it must be emphasized that the process is one which evolves and progresses steadily, varying at each stage only in the degree of decomposition reached.

Decomposition invariably starts at the centre of the illuminated portion of the crystal, presumably where the beam is most intense. A zone of decomposed crystal eventually grows and spreads outwards over the whole platelet. Thus, after a prolonged exposure to the beam it is possible to observe at any one time the early stage of decomposition at places well removed from the centre with the intermediate and final stages nearer the centre.

§ 5. Dislocations in the Crystals before Decomposition

The crystals are by no means perfect even before decomposition. Figure 2, for example, shows part of a thin platelet containing an extensive array of dislocations. This array appears to be lying parallel to the basal plane although, owing to the large depth of focus of the microscope, one cannot be certain that it is confined to a single plane. It will be noticed that the dislocations are crossed by a number of extinction contours so that the contrast varies from point to point in the array. This distribution of contours is typical for these crystals and indicates a marked degree of buckling. Some of the buckling is probably a natural result of growth but some must also have been introduced by mounting the crystals across the specimen grid without a supporting film.

Arrays are usually confined to a few regions of the crystal and can often be described as large families of loops of dislocation. These may have been introduced during growth or by deformation during mounting. The latter possibility is favoured since a network introduced during growth is more likely to extend throughout the crystal and would probably show crystallographic features. Moreover, the arrays are usually localized near holes and other gross imperfections in the crystal where shear stresses can be expected to be concentrated during handling. The array shown in fig. 2, for example, can be described as a fairly complex system of several independent families of loops lying in parallel basal planes which have been generated from the large hole and tear in the crystal under the high stresses imposed during mounting. Members of these families have subsequently interacted to produce the hexagonal and more complex networks. Such a possibility has been indicated by observations on a number of simple systems where this behaviour can be followed with some certainty. Figure 3 shows one of these systems consisting of at least five families of loops all originating from a single hole in the crystal. The system is in the early stage of formation but already some interaction has occurred between families B and C. The formation of these loops in the basal plane by a glide process must mean, of course, that the Burgers vectors of the dislocations also lie in this plane. This has not been confirmed by direct diffraction studies but there is some evidence for it from observations of the climb of the dislocations which indicates that the slip direction is probably the $[10\bar{1}0]$ direction.

The arrays in the freshly prepared crystals become modified after a short period of observation in a manner which suggests that dislocation climb is occurring. This is the first indication that the electron beam is damaging the crystal and forms part of what has already been described as the early stage of decomposition. The resulting pattern of dislocations is often extremely complex but there are instances where the climb of individual dislocations can be resolved. Dislocation climb is associated with the condensation of point defects, vacancies or interstitials; the examples described in the following section serve to illustrate that, since this kind of interaction is indeed occurring, point defects are being produced in the early stage of decomposition. They also illustrate a number of interesting features of the climb process.

§ 6. THE EARLY STAGES OF DECOMPOSITION

The condensation of point defects in a crystal can lead to the climb of existing dislocations or to the formation of new prismatic loops of dislocation. Both climb and loop formation have been observed in the lead iodide crystals after short periods of exposure to the electron beam. The two processes often occur in the same region of the crystal, although climb is sometimes observed in the absence of detectable loop formation. This seems to indicate that, as might be expected, the supersaturation of defects required for nucleation of isolated aggregates is larger than that required for climb.

The climb of a dislocation in the edge orientation results only in a simple translation of the line in the climb plane. The fact that such simple translations are often observed during climb with some component in the plane of observation (i.e. in the basal plane) indicates that the climb plane is not a prismatic plane of the hexagonal structure but is inclined at some intermediate angle. This feature will be discussed more fully later when it will become apparent that such a plane might well be of the type $(10\bar{1}1)$.

The climb of a dislocation in the screw orientation, or of any dislocation having a screw component, can proceed only by the line adopting a helical configuration so as to extend it in the edge orientation. Helical dislocations have been studied extensively by Amelinckx *et al.* (1957) in crystals of fluorite internally decorated with metallic silver and have also been observed with the electron microscope in thin films of aluminium–copper alloy by Thomas and Whelan (1959). In both cases the formation of helices can be associated with conditions in which a supersaturation of vacancies is known to exist. Helical dislocations are frequently observed in the lead iodide crystals after decomposition commences and figs. 4 and 5 show examples of these. That shown in the centre of fig. 4 is clearly a rounded helix of irregular radius and pitch and is very similar to those observed by Thomas and Whelan. The dislocations shown in fig. 5 and also at the bottom of fig. 4 are more typical of those generally observed. They appear to have a characteristic zig-zag configuration which might be interpreted as the projected image of a segmented helix. This can be taken to indicate that there are preferred crystallographic planes for dislocation climb in these crystals. It is interesting to notice in fig. 5 that the zig-zags appear to form parts of a single loop of dislocation terminating on a large hole. This loop is probably one formed at the hole in the crystal by deformation prior to observation and which has subsequently climbed out of the basal plane. The zig-zags follow the parts of the dislocations in the screw orientation whilst the outermost curved portion probably represents the edge component. This appears to have climbed completely out of the crystal at one end. Such a description is consistent with the suggestion that the pre-existing dislocations lie in the basal plane and have their Burgers vector in this plane and also with the idea that the climb plane is some inclined pyramidal plane.

Figure 6 shows another mechanism by which point defects can interact with dislocations. Aggregation can occur preferentially at a point in the dislocation line, leading to a bulge if the dislocation is in the edge orientation or to a single helical loop in the line if it has a screw component. Both forms occur in fig. 6 but the large loop in the vertical line is probably the most striking feature here. There appears to be one and a half turns of helical loop. Figure 6 is especially interesting since it illustrates at the same time several long segmented helices and also the appearance of a large number of small isolated loops of dislocation. The occurrence of such loops will be discussed shortly.

Figure 7 shows a more complex example of the climb of isolated segments of the original dislocation lines. In this case chains of elongated loops protrude from the connecting dislocations, as if formed by the successive nucleation of new loops in a single plane. Alternatively, the protrusions might be accounted for by the growth of a single elongated loop on an inclined plane and the subsequent displacement of parts of it by glide in the basal plane to produce the twisted appearance. The orientation of the crystal by electron diffraction shows that the elongation of the protrusions follows the three $\langle 11\bar{2}0\rangle$ directions. Clearly these are the preferred directions for the growth of prismatic loops in lead iodide.

The occurrence of small isolated loops in the early stages of decomposition has already been pointed out in the description of fig. 6. The loops in this photograph are extremely small but nevertheless it is possible to see that the line has uniform contrast. It might be inferred from this that the loops lie in the plane of observation. There are instances, however, as in fig. 8, where loops show a variable contrast. It has been pointed out by Whelan (1959) in connection with similar observations in quenched metal films that these can be interpreted as loops inclined to the plane of observation, with the more steeply inclined parts showing poor contrast. This interpretation, together with the crystallographic orientation established from the electron diffraction pattern from this region of the crystal, indicates that the loops in fig. 8 are inclined to the basal plane about a direction close to $[11\bar{2}0]$.

§ 7. THE INTERMEDIATE STAGE OF DECOMPOSITION

After a prolonged period of observation other features appear in the crystals close to the centre of the illuminated patch. The most striking of these is the appearance of sharply defined bright patches less than one micron in diameter which form in this region and spread outwards through the crystal. They appear gradually and in comparatively small numbers at low beam intensities but catastrophically if the intensity of illumination is increased. At the same time, the dislocation climb already described becomes more pronounced. Clearly the generation of point defects is increasing. There appears to be no definite correlation between the points at which the bright patches are formed and the occurrence of other imperfections or singularities, although the edges of the crystals are favoured to some extent. The patches usually appear where the irradiation is most intense.

At high rates of formation the patches are rounded in outline but at low rates or after reduction of the beam intensity they develop a hexagonal shape with edges following the $\langle 10\bar{1}0 \rangle$ directions in the basal plane. The latter shape is illustrated in fig. 9. The bright contrast is consistently observed under most diffracting conditions, although the degree of brightness varies considerably. Such a variation is clearly illustrated in fig. 10 where patches can be seen on and either side of a strong extinction contour. Moreover, the superposition of two patches invariably leads to enhancement of the brightness (see fig. 9 for example). These observations suggest that although some of the contrast might arise from irregular diffraction of the electron beam in the neighbourhood of the patches a large part of it can be accounted for by a diminished absorption if they represent voids or cavities in the crystal. This explanation is not entirely satisfactory, however, since such a marked degree of brightness requires that the cavities should occupy a large fraction of the thickness of the crystal and, further, some evidence will be presented shortly which shows that the bright contrast can be removed and even reversed in some circumstances by a slight tilting of the crystal, favouring an interpretation in terms of a diffraction phenomenon.

At high beam intensities the bright patches drift through the crystal at speeds of several microns per second, and the direction of movement is generally outwards from the centre of the illuminated area. Their movement is frequently checked by obstacles in the crystals, such as dislocations lying in arrays ahead of the advancing patches or shallow etch pits extending into the crystal. This, together with the observation that complex clusters can always be resolved into a number of individual patches overlying each other, suggests that the bright patches represent internal imperfections disposed at various levels through the depth of the crystal.

The movement of the patches can be controlled fairly readily by adjusting the operating conditions of the microscope correctly. This allows sequences of photographs like that shown in fig. 10 (*a*), (*b*), (*c*), (*d*) to be recorded to illustrate the movement and occasional merger of patches. This particular sequence illustrates also the very interesting observation that trails of dislocation lines are often associated with the movement of patches. The trailing dislocations are sometimes single loops but are often multiple like those in fig. 10. The outward movement of patches and the extension and interaction of the trailing dislocations results in an extensive structural breakdown of the crystals. The development of this breakdown in its early stage is illustrated by fig. 10 and, in particular, by (*d*). Figure 11 shows the completed state of deformation left after a wave of bright patches has crossed a crystal in this way. This pattern has been produced entirely by the complex interaction of loops from each patch with some simultaneous modification by dislocation climb.

§ 8. THE FINAL STAGE OF DECOMPOSITION

The formation and migration of bright patches leaves the crystal in a densely dislocated condition. At this stage, electron diffraction reveals that the structure is still essentially a single crystal. If exposure to a high intensity electron beam is continued, however, the crystal rapidly breaks down into its final decomposed state. The beginning of this final stage is illustrated by fig. 12. This shows a rapidly decomposing zone at the bottom of the photograph. A wave of bright patches is leaving this zone and some of the patches are trailing loops of dislocation. In the decomposed zone itself there remains an aggregate of dense crystallites. Some of these are roughly triangular or hexagonal in outline. This characteristic form is more clearly illustrated by fig. 13 which shows a similar area where decomposition is nearing completion. In this case the crystallites appear to be similarly oriented. It is thought that the crystallites are metallic lead and this has been partially confirmed by electron diffraction from the region shown in figure 13. The crystallites are occasionally embedded in a thin film of crystalline matrix but more frequently appear to be suspended only in the carbon film which becomes deposited on the specimen during observation. Presumably lead iodide completely decomposes in the final stage to form metallic lead and iodine gas.

§ 9, DISCUSSION

It is clear that the decomposition of the crystals, at least in the early stages and probably in all stages, is proceeding by the generation of point defects, produced either directly or indirectly by the electron beam. It is unlikely that the disordering of the structure which we observe in the initial stages is a direct result of irradiation. At most, it might be expected that the electron beam will produce ionization of thermally produced defects, leading to the formation of complexes such as F-centres or V-centres. It is more likely that the defects responsible for climb are produced indirectly due to the heating of the crystals by the high energy beam, although we cannot be certain of this until the observations are repeated under more closely defined conditions in which the temperature of the crystals is recorded and varied by external control.

According to Lidiard (1957) in a discussion of Tubandt's work (1932), lead iodide is likely to develop Shottky disorder on heating to temperatures around 200–300°C. That is, it might be expected that mobile single ion vacancies of either kind will be produced during the exposure of the crystals to an electron beam of sufficient intensity to raise the temperature to this degree. We might also expect molecular vacancies (i.e. associated groups of lead and iodine ion vacancies) to be produced. Although there is no direct evidence to support this, some indication can be obtained from the observation that lead iodide evaporates in molecular form under gentle heating (Lister and Sutton 1941). The structure of lead iodide, in which there is strong ionic bonding in the sandwiches of PbI_2 but only weak binding between them, is likely to ensure that the association of lead and iodine ion vacancies thus created is preserved to some extent.

The observations of the formation of loops and the climb of dislocations to form helices and zig-zags in the early stages of decomposition can be accounted for by suggesting that vacancies are created in the centre of the illuminated patch of crystal and that these migrate and aggregate in the outer regions. The orientations of loops and zig-zags indicate that the climb plane or plane preferred for aggregation intersects the basal plane along $\langle 11\bar{2}0 \rangle$ directions and is therefore one of the family $\{10\bar{1}n\}$. The tilting of the loops clearly indicated in some of the photographs suggests that the climb planes might well be the pyramidal planes $\{10\bar{1}1\}$. It is interesting to notice that these are single planes in the crystal structure which are followed closely by slightly corrugated surfaces having a simple molecular composition, and are therefore planes in which molecular vacancies might prefer to aggregate. It might even be considered that these are the planes in which molecular vacancies are most readily created since they provide the correct geometrical conditions by which the non-linear molecules of lead iodide may leave the structure without distortion. We may conclude that decomposition in the early stages probably proceeds with the formation of mobile molecular vacancies by the evaporation of lead iodide molecules and that these aggregate to produce the climb of existing dislocations and the creation of new loops.

It is more difficult to understand the mechanism of decomposition in the intermediate stage. The remarkable degree of brightness and sharpness in the patches produced at this stage can be accounted for in terms of absorption contrast only if they represent thick prism-shaped cavities. Such cavities might be formed by the condensation of vacancies. It is interesting to notice here that the particular orientation found for the hexagonal patches is the only one for which a corresponding hexagonal prism-shaped cavity can be created in the crystal with no net configurational charge. In other words, the cavities can be formed by the condensation of molecular vacancies or equivalent numbers of single lead and iodine ion vacancies in layers parallel to the basal plane. The cavity model is consistent with a number of the observed properties of the bright patches. For example, the marked interaction between the patches and arrays of pre-existing dislocations might be explained by the elastic interaction between cavities and dislocations. This interaction might well be repulsive for a dislocation on one side of a cavity and attractive on the other, depending on the Burgers vector of the dislocation and the nature of the walls of the cavity. In the present experiments we frequently observe instances where moving bright patches initially repel dislocations but retain them by close attraction after cutting through. Many of the observations of dislocation loops being trailed behind bright patches (fig. 10 for example) may be accounted for in this way. The structural breakdown associated with the movement of patches in the intermediate stage of decomposition might therefore arise from an extension of existing dislocations rather than the creation of new ones.

The movement of the bright patches is an ordered process, all drifting in the same direction and generally outwards from the centre of decomposition. Such a movement can be accounted for by an electrolytic process if the patches represent cavities containing some iodine gas. This might indeed be the case since the internal decomposition of lead iodide to form metallic lead and iodine gas is likely to commence at the beam intensities required to induce movement of the patches (see fig. 12, for example). The crystal, being non-uniformly charged by the electron beam, is likely to carry a radial potential gradient and this can transport ions across the cavities to deposit lead iodide on the inner surfaces and remove it from the outer surfaces. Some simple calculations of the magnitude of current required to account for the simultaneous movement of a typical system of bright patches by this process have been made, and this represents only a small fraction of the total current incident on the crystal. An electrolytic process is not therefore unreasonable. A similar argument using distillation of lead iodide down the temperature gradient over the crystal can be applied but this leads to an inward movement of cavities towards the centre of illumination. It is possible that the movement observed is due to a combination of thermal and electrolytic processes.

The cavity model, although successful in accounting for many of the observed properties of the bright patches, is not completely satisfactory. One of the difficulties encountered is illustrated by fig. 14 (*a*) and (*b*). These show the change in appearance of a field containing a number of bright patches as the electron beam is deflected through a small angle. In the initial setting the patches have the usual bright contrast whereas in the second setting the brightness of some has disappeared. At the same time a complex array of dislocation loops associated with the patches has appeared. It will be noticed also that some of the patches now appear as small isolated loops (as at A, B, C for example) inclined to the plane of observation. This kind of behaviour is further illustrated by fig. 15 (*a*), (*b*) which show a complete reversal of contrast for a number of patches following a slight deflection of the electron beam. These observations are exceptional but indicate that at least some of the appearance of the patches arises from a form of diffraction contrast. No completely satisfactory explanation of this behaviour is available.

The final stage of decomposition of lead iodide is not fully understood at present. Clearly, the process involves the formation and aggregation of metallic lead and the corresponding release of iodine gas, but it is not yet clear how this is assisted, if at all, by vacancies or other defects produced in the earlier stages. This is a feature of the observations which requires further investigation under carefully controlled thermal and electrical conditions.

ACKNOWLEDGMENTS

The author wishes to thank Professor F. C. Frank for many useful and interesting discussions during the course of this work. He is also grateful to Miss E. Harris for her able assistance and instruction in the use of the Philips 100 kv electron microscope.

REFERENCES

AMELINCKX, S., BONTINCK, W., DEKEYSER, W., and SEITZ, F., 1957, *Phil. Mag.*, **2,** 355.
FORTY, A. J., 1952, *Phil. Mag.*, **43,** 72.
LIDIARD, A. B., 1957, S. Flügge's *Handbuch der Physik*, Vol. 20, p. 246.
LISTER, M. W., and SUTTON, L. E., 1941, *Trans. Faraday Soc.*, **37,** 406.
THOMAS, G., and WHELAN, M. J., 1959, *Phil. Mag.*, **4,** 511.
TUBANDT, C., 1932, *Handbuch der Experimentalphysik*, Vol. 12 (1), p. 383.
WHELAN, M. J., 1959, *J. Inst. Met.*, **87,** 392.

Dislocations with Burgers Vectors of $a\langle 100\rangle$ in Crystals of Silver Bromide†

By J. T. Bartlett and J. W. Mitchell
H. H. Wills Physics Laboratory, University of Bristol‡

[Received March 7, 1960]

Abstract

Experimental observations of the combination, in crystals of silver bromide, of two dislocations with Burgers vectors of $\frac{1}{2}a\langle 110\rangle$ at right angles to form a single dislocation with a Burgers vector of $a\langle 100\rangle$ are described in this paper. It is believed that this is the first occasion upon which the interaction has been definitely established for dislocations on glide planes.

§ 1. Introduction

The conditions under which dislocations combine or dissociate were first discussed by Frank (1949) who pointed out that cases occurred in the cubic system in which a pair of dislocations could have the same energy as a single combined dislocation.

The object of the present paper is to describe interactions of this kind in crystals of silver bromide between two dislocations with Burgers vectors of $\frac{1}{2}a\langle 110\rangle$ at right angles which combine to form a single dislocation with a Burgers vector of $a\langle 100\rangle$. Many examples of this interaction have now been observed in different crystals. Fourteen of them have been partially analysed and eight of these have been fully analysed. The experimental observations on one of these interactions are reported in detail in this paper. The intersecting dislocations were always nucleated at the surfaces of the crystals. The dislocation loops expanded on their different glide planes under the influence of the applied stress and the interactions occurred where they intersected.

Amelinckx (1958 a) has presented some evidence that dislocations with an $a\langle 100\rangle$ Burgers vector can appear in crystals of potassium chloride as a result of the above interaction. The dislocations which he observed formed segments of nets on sub-boundaries where there was a relatively high density of dislocations. They were decorated by a method (Amelinckx 1958 b) requiring the crystals to be heated to a temperature at which climb could occur through the interaction of the dislocations with mobile Schottky defects. Amelinckx suggested that the presence of a third dislocation, interaction with which would tend to bring the combining dislocations into a parallel orientation, might be a necessary condition for the reaction.

---

† Communicated by the Authors.

‡ Now at the Department of Physics, University of Virginia, Charlottesville, Va.

In the present work, the interacting dislocations were generated at the surfaces of initially dislocation-free crystals. Both the dislocation lines and the associated surface terraces were decorated with particles of colloidal silver by exposing the crystals to light at room temperature after they had been strained. This allows the glide planes to be determined and the nature of the interactions to be fully established. In these experiments, the dislocations are observed in the configuration which they have at a particular stage of their glide motion.

§ 2. Experimental Observations

Full details of the experimental method are given in our previous paper (Bartlett and Mitchell 1960). Here we will describe one of the eight examples of the interaction which has now been fully established by detailed experimental measurements. The orientations of the silver bromide crystals were determined from back-reflection Laue x-ray diffraction photographs. The orientation of the crystal in which the particular interaction which will be illustrated was observed is represented in the stereographic projection of fig. 1. It will be seen that the surface of the crystal was very nearly parallel to the (001) crystallographic planes. The relative positions of the decorated surface terraces and of the dislocation lines below the surface are shown diagrammatically in fig. 2. The decorated surface terraces are illustrated in the photomicrograph of

Fig. 1

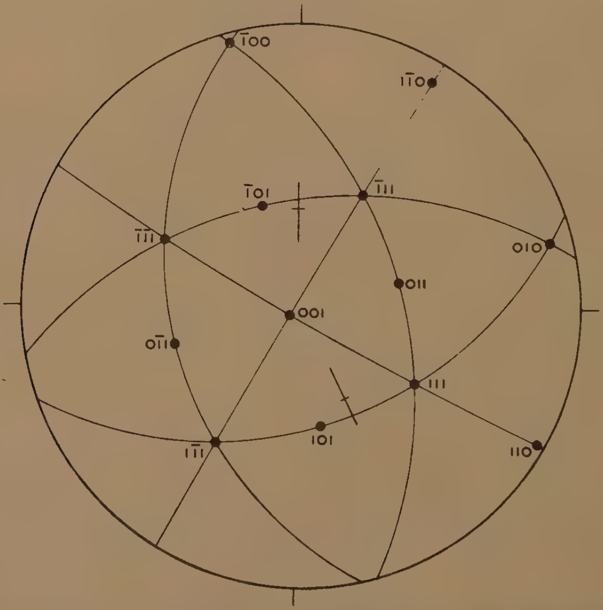

Stereographic projection showing the orientation of the crystal and the poles of the glide planes of the interacting dislocations.

fig. 3 (Pl. 109) and the corresponding dislocation lines at a distance of 4 microns below the surface are shown in fig. 4 (Pl. 109). The crystal was displaced on the microscope stage between the two photographs as will be evident from fig. 2.

Fig. 2

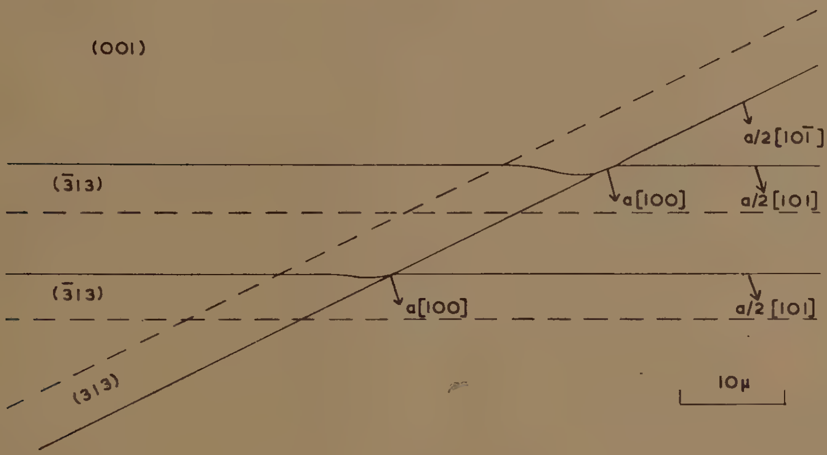

Diagram showing the relative positions of the surface terraces (dotted lines) and of the dislocation lines. The indices of the glide planes are given together with the Burgers vectors of the dislocations.

Our observations indicated that the oblique dislocation in the illustrations was the intersected dislocation and that the two parallel dislocations were the intersecting dislocations. The extremely small depth of focus of a high-power, large-aperture microscope objective is used to advantage in this work as it allows us to focus accurately upon the surface terraces and the dislocation lines. We have determined the glide planes of the intersected and intersecting dislocations from measurements with a calibrated micrometer eyepiece and the calibrated fine focusing adjustment of the microscope. Angular relationships with respect to the orientation of the crystal were measured with a microscope eyepiece with a graduated circular vernier scale. The results of these observations are presented in figs. 1 and 2. The crosses on the arcs in fig. 1 show the mean experimental values for the location of the poles of the glide planes and the lengths of the arcs indicate the spread of the individual observations. Even when the microscope is in very good adjustment, there is inevitably a considerable error in the depth measurement which has also to be corrected to allow for the relatively high refractive index of silver bromide.

As all our observations establish that the glide planes of dislocations in silver bromide crystals contain an $a\langle 110\rangle$ lattice vector, we deduce that the glide planes of the intersected and intersecting dislocations in the neighbourhood of this interaction are the (313) and ($\bar{3}$13) planes, respectively. The only possible Burgers vectors for these dislocation lines are therefore

$\frac{1}{2}a[10\bar{1}]$ and $\frac{1}{2}a[101]$ and the interaction must be represented by one of the following equations depending on the sense of the Burgers vectors:

$$\tfrac{1}{2}a[101]+\tfrac{1}{2}a[10\bar{1}]=a[100], \qquad (1)$$

$$\tfrac{1}{2}a[101]+\tfrac{1}{2}a[\bar{1}01]=a[001]. \qquad (2)$$

Our experimental observations do not allow us to distinguish between these two alternatives. For purposes of discussion, we have therefore represented the reaction as though it occurred in accordance with eqn. (1) and this is consistent with the fact that the plastic deformation resulted from the establishment of a tensile stress in the crystal. The interaction leads to the formation of a segment of dislocation line with a Burgers vector of $a[100]$ and, within the limits of experimental error, this combined dislocation is parallel to the [010] direction in the crystal. This means that its glide plane is the (001) plane. Both the combining dislocations and the resultant dislocation are almost in the pure edge orientation.

§ 3. Discussion

The resultant edge dislocation with a Burgers vector of $a[100]$ in the (001) plane could dissociate into two dislocations of mixed character as follows:

$$a[100]=\tfrac{1}{2}a[110]+\tfrac{1}{2}a[1\bar{1}0]. \qquad (3)$$

We have no experimental evidence for this dissociation but it might be possible if the energy of a dislocation were less in the screw than in the edge orientation (see, Huntington *et al.* 1955). Complete dissociation on the (001) plane is unlikely to occur as the interacting dislocations would be pinned at the nodes and the force between the two dissociated dislocations should be small. It is also evident that the resulting system could glide only with difficulty, even if dissociation did occur, as the dislocations meeting in the nodes could not move simultaneously on their three intersecting glide planes. We have, moreover, never observed dislocations with {100} glide planes in silver bromide crystals (see, Bartlett and Mitchell 1960).

Acknowledgments

This work was carried out during the tenure of a Research Studentship awarded by the Department of Scientific and Industrial Research to J. T. Bartlett. The photomicrographs were taken with equipment purchased with a special grant from the Department of Scientific and Industrial Research. This assistance is gratefully acknowledged. We are also grateful to Kodak Ltd., for financial support and to J. H. Burrow and G. D. Freke for valuable assistance.

References

Amelinckx, S., 1958 a, *Nuovo Cim.*, **7**, 569; 1958 b, *Acta Met.*, **6**, 34.
Bartlett, J. T., and Mitchell, J. W., 1960, *Phil. Mag.* **5**, 445.
Frank, F. C., 1949, *Physica*, **15**, 132.
Huntington, H. B., Dickey, J. E., and Thomson, R., 1955, *Phys. Rev.*, **100**, 1117.

The Atomic Diffusion of Platinum in Gold†

By A. J. Mortlock, A. H. Rowe and A. D. Le Claire
Metallurgy Division, Atomic Energy Research Establishment,
Harwell

[Received March 15, 1960]

Abstract

Measurements are reported of the diffusion of platinum at tracer concentrations in gold over the temperature range 800°c to close to the melting point of gold. Above about 900°c the results obtained can be fitted to the following equation: $D=(7{\cdot}6^{+4\cdot7}_{-2\cdot9})\exp[-(60\,900\pm1200)/RT]$ cm^2/sec. The magnitude of the observed activation energy relative to that corresponding to self-diffusion in gold is in qualitative agreement with current theories.

Below about 900°c the observed diffusion coefficients appear to be enhanced relative to those expected by extrapolation from higher temperatures; possible explanations of this effect are discussed.

§ 1. Introduction

In recent years careful experiments using radio-tracers have shown that activation energies for the diffusion of impurities at near-zero concentration in a given solvent may be greater or smaller than that associated with the self-diffusion of the solvent. This is in contrast to earlier experimental results which suggested that, in general, impurities diffuse with activation energies less than that for the solvent: see, for example, the collections of data given by Seitz (1943) and Le Claire (1949).

A considerable advance in the understanding of the results of these more recent experiments came when Lazarus (1954) introduced a simple electrostatic model in order to explain the observed differences in activation energies. This model was based on the earlier Mott (1936) picture of an impurity of valence $Z+1$ dissolved in a monovalent solvent and screened by the conduction electrons, the resultant potential distribution around the impurity being found by solving a linearized form of the Thomas–Fermi equation. The change in the energy of vacancy formation was considered by Lazarus to be simply the change in the lattice binding energy of a nearest neighbour in the screened potential of the impurity atom. The change in the energy of motion was supposed to be due to a corresponding change in the elastic constants controlling a particular distortion of the lattice capable of moving the impurity atom towards the adjacent vacancy.

This model yielded the following equation for ΔH, the amount per atom by which the activation energy for impurity diffusion exceeds that for solvent self-diffusion:

$$\Delta H=-[1-(q^2a^2-5qa-5)/4](Ze^2/a)\exp(-qa) \quad . \quad . \quad . \quad (1)$$

---

† Communicated by the Authors.

where q, a and e are respectively the screening parameter, interatomic spacing and electronic charge. Substitution in this shows that the activation energy for the diffusion of electropositive ($+$ve Z) impurities should be less than that for solvent self-diffusion and, for electronegative impurities ($-$ve Z), greater.

Good agreement between theory and experiment was found for the electropositive impurities, cadmium, indium, tin and antimony diffusing in silver, see Lazarus (1960), but was poor in the case of analogous impurities in copper. Similar, although scarcer data for electronegative impurities also appeared to be in poor agreement with the simple theory. For example, Mackliet (1958) found that, while nickel, cobalt and iron diffuse in copper with activation energies greater than that for copper self-diffusion, as expected, the sign of the change in activation energy in going from one element to the other was opposite to what one would expect on the basis of eqn. (1).

Alfred and March (1956) later showed how a more accurate working out of the model could be obtained if exact numerical solutions of the applied Thomas–Fermi equation were employed. Their analysis indicated that the right hand side of (1) should in fact be multiplied by a factor α which was a decreasing function of Z, being >1 for $-$ve Z's and <1 for $+$ve Z's. Application of this result produced little improvement in the agreement between theory and experiment for electropositive impurities but indicated the possibility of relatively large values of ΔH for electronegative impurities. Results recently obtained by Pierce and Lazarus (1959) on the diffusion of ruthenium in silver seem to verify this particular prediction.

Manning (1958) has pointed out that this earlier theoretical work neglects a possible temperature dependence of the correlation factor, f, which takes account of inequalities in the probability of diffusion jumping in different directions in any formula for the diffusion coefficient based on a purely random walk analysis. If f is in fact temperature dependent then the observed activation energy per atom, Q, is related to the calculated sum, H, of the energy of movement and energy of formation, by the equation

$$Q=H-k[d\ln f/d(1/T)] \quad . \quad . \quad . \quad . \quad . \quad (2)$$

where k is Boltzmann's constant and T is the temperature in degrees Kelvin.

For impurity diffusion f depends not only on the frequency of impurity–vacancy jumps but also on that of vacancy exchanges with neighbouring solvent atoms. These jump rates generally will involve several different activation energies so that f will be temperature dependent and the second term on the right in eqn. (2) may represent a small but nevertheless significant contribution to Q. For the particular case of self-diffusion f is only a geometrical constant so that the second term is zero. Thus, it is possible to write

$$\Delta Q=\Delta H-k[d\ln f/d(1/T)] \quad . \quad . \quad . \quad . \quad . \quad (2a)$$

where ΔQ is the observed difference in activation energy between impurity and solvent self-diffusion and the second term on the right continues to refer to impurity diffusion only; the relative importance of this term is greatly increased when applied in this way since its magnitude is usually of the same order as that of ΔH.

An alternative theoretical derivation of ΔQ, as opposed to ΔH only, has recently been proposed by Le Claire (1960); it also is based on the electrostatic model of the dissolved impurity. The change in the energy of vacancy formation is calculated as before but the change in the energy of motion is considered to be simply the difference in energy between the electrostatic configuration corresponding to the impurity atom at the saddle point and that with it at the equilibrium position. For this purpose the saddle point configuration is taken to correspond to a charge Ze situated between two half vacancies of charge $-\frac{1}{2}e$ each. The centroids of the supposedly hemispherical charge shapes of the half-vacancies are taken to be the effective charge centres. For electronegative impurities where the controlling jump frequency is that due to impurity atom–vacancy exchange, the correlation factor correction is negligible so that in this case

$$\Delta Q = \Delta H = (16\alpha Z e^2/11a) \exp(-11qa/16). \quad . \quad . \quad . \quad . \quad (3)$$

It is clear that particular interest attaches to new experimental data on the diffusion characteristics of electronegative impurities in the monovalent metals, as the various theories of ΔQ diverge to a greater extent in this region than for electropositive impurities. Furthermore, the lack of a correlation factor correction in this region makes for a less complicated comparison of the theoretical model with experiment. For these reasons a series of measurements has been made of the diffusion of the electronegative impurity platinum dissolved in the monovalent noble metal, gold.

§ 2. MATERIALS

The gold used was supplied by Johnson Matthey in the form of flat circular discs of about 2 cm diameter and 4 mm thick with a nominal purity of 99·98%. A full spectrographic analysis revealed that the major impurity was silver with a concentration of about 44 p.p.m. Other impurities were present in negligible concentrations, suggesting that the overall purity could be appreciably better than the nominal figure.

The platinum was also supplied by Johnson Matthey; in this case the purity was given as 99·999%.

§ 3. METHOD

The technique employed in these experiments was the fairly standard one in which a thin layer of radioactive solute is laid down on one face of a solvent metal specimen and diffused in by heat treatment. The resultant concentration versus penetration distance profile is then determined by first serially sectioning with a precision lathe and then subjecting each individual section to radioactive assay. Provided the surface concentration of solute falls to a very small level in a time which is short compared to the total diffusion time, then the calculated diffusion coefficient can be taken as applying to effectively zero concentration of solute.

§ 4. Experimental Details

The diffusion specimens were prepared in the following manner.

Where single crystals were required the as-received gold discs were remelted in a graphite crucible-mould of high purity suspended in an argon atmosphere in a vertical tube furnace. The crucible was then lowered through a sharply decreasing temperature zone, the single crystal being nucleated at a vee-shaped depression near the bottom of the crucible-mould. The near-circular discs so produced were finely ground on one face and etched with a 40% solution of boiling aqua regia. This process was repeated several times until a flat and nominally cold-work-free surface was produced. The specimen was then annealed for about three days at about 1000°c, usually in vacuum, and the single-crystallinity and freedom from large scale cold work tested by taking Laue back reflection x-ray photographs of the surfaces.

Those discs which were finally given a diffusion annealing as polycrystals were finely ground on one face but were usually not subjected subsequently to any etching or pre-diffusion annealing. The grain size of this material was about 1 mm^2.

Pile-activated platinum contains the radioactive isotopes ^{191}Pt, ^{193}Pt, ^{195}Pt, ^{197}Pt and ^{199}Pt, of which ^{199}Pt (half-life 30 min) decays to the stable isotope ^{199}Hg via the radioactive daughter ^{199}Au (half-life 3·2 days). This means that it is necessary either to remove this impurity before deposition onto the gold discs or else to discriminate against it during the radioactive assay of the sections. As an extra precaution in the present case both procedures were followed.

Before deposition onto the prepared surfaces of the gold specimens the active gold impurity was removed from the pile-activated platinum by preferential distillation, at least two days having been allowed to elapse so that practically all the gold impurity destined to be produced by decay was present. The relative absence of active gold was checked with a scintillation counter-pulse height analyser arrangement by comparing the 165 kev gamma peak due to ^{199}Au decay with the 65 kev gamma peak due to the combined decay of the remaining platinum isotopes; this technique was originally described by Kidson and Elsdon (1958). The correctness of the association of the observed 65 kev gamma peak with platinum decay was checked by half-life measurement. The observed effective half-life of this peak was found to be 3·5 days, in fair agreement with the figure of 3·7 days obtained by Kidson and Elsdon from measurements extending over 10 days. The present measurements extended over a period of 9 days following a ‘cooling’ period of about 6 days and after removal of the gold impurity.

Deposition of the purified platinum onto the gold specimens was carried out in the special vacuum evaporator described by Rowe (1959). A bead of platinum was supported in a glazed thoria crucible contained in a silica vacuum vessel. A suitable flux concentrator was mounted around this vessel and the bead heated by radio-frequency induction. Layers of not more than about 1000 Å were deposited in this way and calculation showed that in the worst case the maximum concentration of platinum in the diffusion zone fell to about 1% in a time which was negligible compared to the total annealing time.

The platinum deposited gold discs were sealed in vacuum in small silica tubes and annealed for periods ranging from a day to three weeks. Temperature uniformity in the temperature-controlled annealing furnaces was assisted by the use of hollow metal (stainless steel or nickel) blocks into which the silica tubes were placed. The temperature measurement was made with specially calibrated Pt–(Pt + 13% Rh) thermocouples which were checked regularly for drift by melting a small piece of gold wire welded across their hot junctions. Suitable corrections were also applied for the diffusion which took place during heating up, no correction being necessary for cooling down as the specimen was usually quenched in water. Overall, the stated temperatures cannot be in error by more than about ± 2°c.

Sectioning was carried out in the manner described earlier by Makin *et al.* (1957). In this case, however, the individual cuts were dissolved in aqua regia and counted as a liquid in a well-type scintillation counter, attention being restricted to the 65 kev gamma radiation due to the active platinum isotopes. By taking the ratio of the measured activity of each section to the mean measured activity of the first section, used as a standard and counted immediately before and after each other section, the relative activities of all sections were obtained in a manner independent of radioactive decay or change in counter characteristics. Subsequent measurements of the ratios corresponding to individual sections were occasionally carried out as an additional running check of their constancy in time and therefore of the purity of the diffusing metal. If there had been a contaminating radioactive impurity present with half-life and diffusion characteristics different from those of platinum, the magnitude of the ratio corresponding to a particular section would not have been independent of time.

§ 5. RESULTS

The logarithm of the relative activity of each section was plotted against the square of the penetration distance and a straight line fitted by least squares analysis. Where necessary any points corresponding to small or large penetrations which appeared to be inconsistent with the general slope of this line were neglected. The diffusion coefficient, D, was calculated from the slope of this line via the following equation

$$\ln(C/C_0) = -x^2/4Dt \quad . \quad . \quad . \quad . \quad . \quad . \quad . \quad . \quad (4)$$

in which (C/C_0) is the concentration of platinum at a penetration distance x relative to that at the surface after a diffusion annealing for effective time t.

In fig. 1 two plots are given corresponding to data obtained from the simultaneous diffusion annealing of a single crystal and a polycrystal at 1039°C. The fact that the operative diffusion coefficients are in close agreement in this case indicates that the presence of a highly worked surface layer is unimportant at relatively high temperatures. That this is so is evident when it is remembered that the single crystal had been finely ground, etched and pre-annealed prior to the final diffusion annealing whereas the polycrystal had only been finely ground.

Diffusion Coefficients of Platinum in Gold at Various Temperatures

Temperature (°C)	Diffusion coefficient (cm²/sec)	
1055·5	$7{\cdot}33 \times 10^{-10}$	
1039·0	5·67	(SC)
1039·0	5·52	
1030·2	4·42	
1007·7	3·16	
977·0	1·62	
950·9	$9{\cdot}80 \times 10^{-11}$	
925·9	6·35	
845·0	1·23	(SC)
845·0	1·23	(SC)
801·0	$5{\cdot}54 \times 10^{-12}$	(SC)
799·0	5·00	(SC)

Diffusion coefficients obtained with single crystal specimens are labelled (SC).

At low temperatures where short-circuiting diffusion is of greater importance a more exact test was felt to be necessary in order to demonstrate that the diffusion coefficients obtained were independent of the preliminary treatment of the specimen surface. Especially was this the case because x-ray evidence suggested that a small proportion of the lattice defects introduced by grinding sometimes remained after etching and pre-annealing. Also, a polycrystal annealed at 802°C had shown definite signs that material transfer via grain boundaries represented an appreciable proportion of the total transfer at these temperatures. For these reasons a comparison was made at 800°C between a single crystal specimen in the as-grown condition and one which had been worked, etched and pre-annealed: as before no significant difference in behaviour was detected. The log (C/C_0) versus x^2 plot corresponding to the as-grown single crystal is given in fig. 2 together with that obtained using the polycrystal referred to above.

Fig. 1

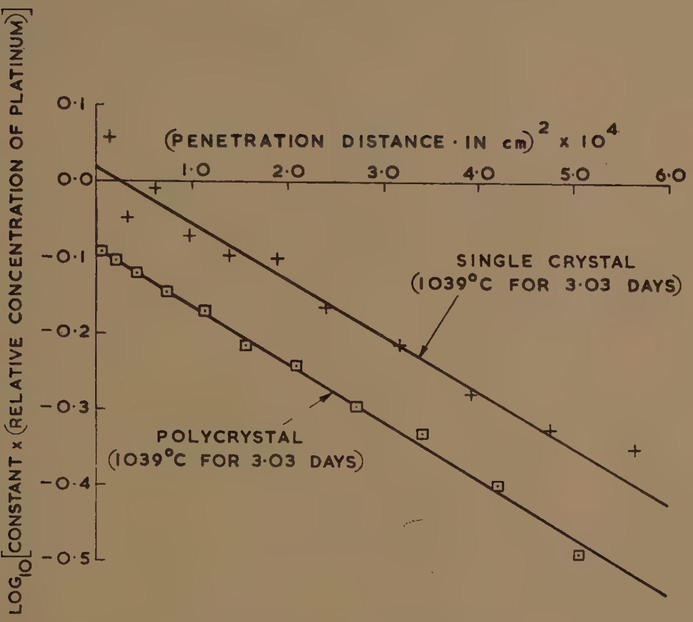

Concentration distributions for a single crystal and a polycrystal gold specimen after annealing at 1039°c.

Fig. 2

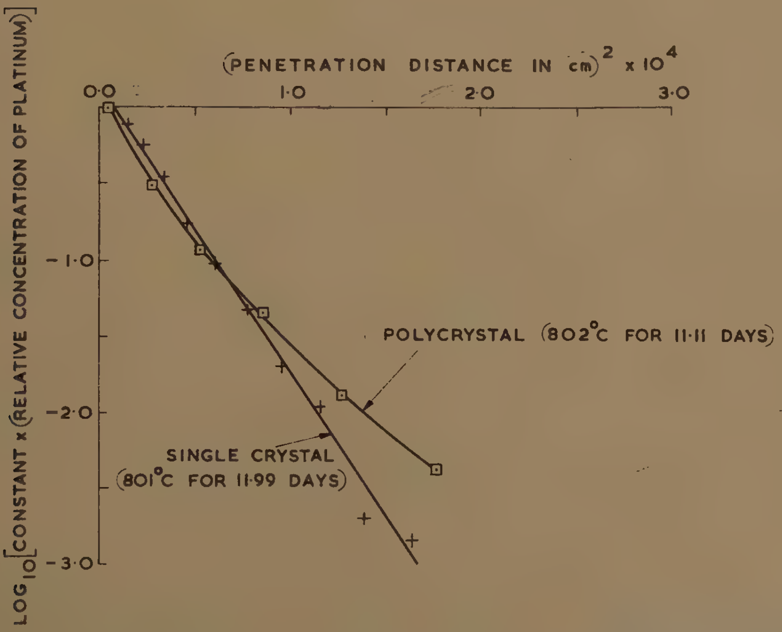

Concentration distributions for a single crystal and a polycrystal gold specimen after annealing at 801°c and 802°c respectively.

In the table the diffusion coefficients obtained and the temperatures to which they apply are listed. Figure 3 is a plot of log D versus $(1/T)$. The equation to the straight line fitted by least squares analysis to the region

Fig. 3

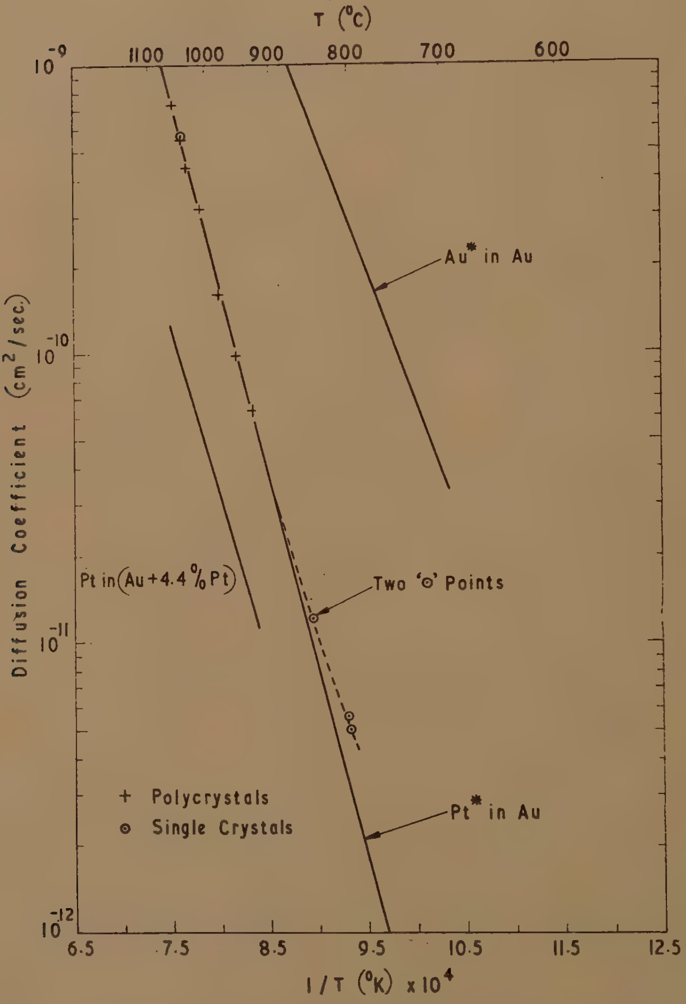

Arrhenius plot of experimental data for the diffusion of platinum in gold and, for comparison, self-diffusion in gold.

corresponding to temperatures in excess of about 900°c is:

$$D \doteqdot (7{\cdot}6^{+4\cdot7}_{-2\cdot9}) \exp\left[-(60\,900 \pm 1200)/RT\right] \text{cm}^2/\text{sec} \quad . \quad . \quad (5)$$

where R is the gas constant in calories per gramme molecule per degree Kelvin, and the errors are standard errors based on the scatter of the individual diffusion coefficients.

§ 6. Discussion

The only other data available on the diffusion of platinum in gold with which a comparison is worthwhile are those due to Bolk (1959). This author determined the partial diffusion coefficient of platinum in gold-platinum alloy at an average concentration of 4·4% platinum (atom fraction). The results obtained correspond to the equation

$$D=0{\cdot}09\exp\left[-(54\,000\pm7000)/RT\right]\,\mathrm{cm}^2/\mathrm{sec},$$

which has also been plotted in fig. 3. It is clear that the activation energy observed is not inconsistent with that found in the present investigation. No significance can be attached to the large disagreement in the pre-exponential factors because of the very low accuracies involved.

The anomalously enhanced diffusion evident at low temperatures needs some comment. It is similar to that observed by Mackliet (1958) when studying the diffusion of iron and cobalt in copper. The effect is clearly not due to the presence of short-circuiting diffusion along grain boundaries because of the use of single crystals. Also, the presence of an unwanted impurity would only be expected to enhance the overall diffusion in the manner observed if it were very fast-moving in gold compared to gold itself. This follows from the possibility that the diffusion of platinum in impure gold can be expressed as a linear function of that in pure gold and the diffusion coefficient of the impurity itself in gold: see, for example, Hart *et al.* (1957). As it is reasonable to suppose that the activation energy for the diffusion of the hypothetical impurity in impure gold is less than that for platinum in pure gold, the effective 'activation energy' for the diffusion of platinum in impure gold could then be an increasing function of temperature, as observed.

In order to settle this point a rough measurement was made of the diffusion of silver (the major impurity present) at tracer concentration in gold: a figure of $2{\cdot}7\times10^{-9}\,\mathrm{cm}^2/\mathrm{sec}$ at 900°C was obtained. This is not much different from that for self-diffusion in gold at the same temperature ($1{\cdot}5\times10^{-9}\,\mathrm{cm}^2/\mathrm{sec}$) so that the operation of this mechanism in producing the observed enhancement is unlikely.

Hart (1957) has suggested that short-circuiting diffusion along dislocations can enhance bulk self-diffusion at sufficiently low temperatures. Later, Mortlock (1960) pointed out that segregation towards these defects could amplify this effect in the case of solute diffusion. The total enhancement in D, ΔD, is then given by

$$\frac{\Delta D}{D_1}=nf_0\left(\frac{D_d}{D_1}\right)\left(\frac{C_d}{C_1}\right) \quad . \quad . \quad . \quad . \quad . \quad . \quad . \quad (6)$$

where n is the number of sites that go to make up a typical cross-sectional area of the dislocation pipe, f_0 is the fraction of all atoms situated in the cores of the pipes, D_d/D_1 is the ratio of the diffusion coefficient in the pipe to that in the lattice, and C_d/C_1 is the ratio of the fractional concentration in the pipe to that in the lattice.

A rough value of $3{\cdot}1 \times 10^4$ for D_d/D_l was found by applying the equation given by Fisher (1951) for bulk diffusion transfer via grain boundaries and lattice to the linear portion of a log C versus x plot of the data obtained with the polycrystal annealed at 802°c.

Taking n to be 10 and f_0 to be between 6×10^{-10} and 6×10^{-8} (corresponding to dislocation densities lying between 10^6 and 10^8 lines/cm^2), C_d/C_l then turns out to be in the range 4×10^3 to 4×10, to account for the observed enhancement of D. This corresponds to solute atom-dislocation binding energies of the order of a few tenths of an electron volt, which are not unreasonable. Furthermore, the average concentration levels operative in the diffusion specimens annealed at 800°c are a few tenths of a per cent, so that values of C_d/C_l not exceeding a figure in the range $\sim 10^2$ to 10^3 are allowable before the change in the overall effect produced by the dislocations becoming saturated must be considered.

The equation given above for $\Delta D/D_l$ does not take account of the fact that solute atom jumps in a dislocation pipe at right angles to the axis of the pipe do not contribute fully to the observed overall diffusion coefficient due to partial reflection from the pipe wall. At the worst only diffusion parallel to the axis of the pipe will be observed and, as the effective number of pipes which are parallel to any given direction is a third of the total, a factor k' which is less than unity but greater than a third should be introduced on the right hand side of eqn. (6). Therefore, if indeed dislocation diffusion is the whole cause of the observed diffusion coefficient enhancement, it would be more correct to regard the values of C_d/C_l calculated from eqn. (6) as lower limits.

An attempt was made to test the explanation of the observed diffusion coefficient enhancement based on the presence of dislocations by measuring the diffusion of platinum in a single crystal which had been so deformed that the dislocation density was appreciably larger than that in an as-grown crystal. The deformation was introduced by bending a special single crystal shaped in the form of a rectangular prism about an axis perpendicular to its two principal faces. One of these faces was then deposited with radioactive platinum in the usual way and the diffusion into the crystal following an annealing of about ten days duration at 800°c measured in a direction parallel to the bend axis. Unfortunately recrystallization occurred during this annealing and the penetration profile obtained was characteristic of a polycrystal at this temperature.

Before the agreement between theory and experiment can be discussed in relation to the activation energy problem, the question of the value of Z to be assigned to platinum dissolved in gold must be settled. Magnetic susceptibility data given by Vogt (1932) indicate that the rate of increase of the susceptibility of Au + Pt alloys as the platinum content is increased is considerably less than that to be expected on a simple compositional basis (which would be the case if the platinum atoms were unaffected by their surroundings), at least up to about 90% (atom) platinum. This suggests that the electronic structure of the dissolved platinum atom tends to be similar to that of gold; thus, the operative value of Z is best taken as -1.

Using this value, the initial theoretical analysis of the activation energy problem by Lazarus which was described earlier predicts that ΔQ is equal to 2·0 kcal/mol. If the correction due to Alfred and March is applied this becomes 3·0 kcal/mol. The recent treatment by Le Claire of the same problem gives 8·5 kcal/mol. If the activation energy for self-diffusion in gold is taken as 41·7 kcal/mol, Makin *et al.* (1957), then the experimental value for ΔQ comes out to be 19·2 kcal/mol. It is clear, therefore, that Le Claire's model yields the closest agreement between theory and experiment. At least part of the large discrepancy remaining can be put down to the possibility that the potential distribution around an impurity atom of negative excess valence is not in fact accurately defined by the equation $V=(\alpha Ze/a)\exp(-qa)$ given by Alfred and March (1956), March (1959, private communication).

A calculation of the total entropy of activation using the observed value for the pre-exponential factor yields a figure of 7·2 k units, k being Boltzmann's constant. The sign of this result is in agreement with theoretical calculations due to Huntingdon *et al.* (1955) which predict a magnitude of about 0·9 k units. If due account were taken of the fact that a platinum atom is smaller than a gold atom, thereby producing less crowding at the saddle point during the elementary diffusion movement, the theoretical estimate would be higher.

§ 7. PRINCIPAL CONCLUSIONS

The activation energy associated with the diffusion of platinum at tracer concentrations in gold has been measured and found to be much larger than for self-diffusion in gold. This is qualitatively consistent with current theories, but numerical agreement is poor.

The diffusion observed at temperatures below about 900°C was found to be greater than expected on the basis of extrapolation from higher temperatures. Calculations indicate that this effect could be due to short-circuiting diffusion of segregated platinum along dislocations.

ACKNOWLEDGMENTS

The assistance of Miss A. Nunley and Mr. C. Layton in carrying out some of the observations and numerical calculations is gratefully acknowledged. In addition, the authors wish to thank Dr. J. Makin and his colleagues for operating the single crystal growing furnace.

REFERENCES

ALFRED, L. C. R., and MARCH, N. H., 1956, *Phys. Rev.*, **103,** 877.
BOLK, A., 1959, *Het Kirkendall-Effect in Het Systeem Goud-Platina* (Delft: Grafisch Bedrijf Avanti): Delft Technical Institute Doctor Thesis.
FISHER, J. C., 1951, *J. appl. Phys.*, **22,** 74.
HART, E. W., 1957, *Acta Met.*, **5,** 597.
HART, E. W., HOFFMAN, R. E., and TURNBULL, D., 1957, *Acta Met.*, **5,** 74.

HUNTINGTON, H. B., SHIRN, G. A., and WAJA, E. S., 1955, *Phys. Rev.*, **99,** 1085.
KIDSON, G. V., and ELSDON, W. L., 1958, *J. appl. Radiat. Isotopes*, **3,** 252.
LAZARUS, D., 1954, *Phys. Rev.*, **93,** 973; 1960, *Advances in Solid State Physics*, Vol. 10 (New York: Academic Press Inc.).
LE CLAIRE, A. D., 1949, *Progress in Metal Physics*, Vol. 1, 370–372 (London: Butterworths Scientific Publications Ltd.); 1960, *Phil. Mag.* (to be published).
MACKLIET, C. A., 1958, *Phys. Rev.*, **109,** 1964.
MAKIN, S. M., ROWE, A. H., and LE CLAIRE, A. D., 1957, *Proc. phys. Soc. Lond.* B, **70,** 545.
MANNING, J. R., 1958, *Phys. Rev. Letters*, **1,** 365.
MORTLOCK, A. J., 1960, *Acta Met.*, **8,** 132.
MOTT, N. F., 1936, *Proc. Camb. phil. Soc.*, **32,** 281.
PIERCE, C. B., and LAZARUS, D., 1959, *Phys. Rev.*, **114,** 686.
ROWE, A. H., 1959, *A.E.R.E. Report* No. 3113.
SEITZ, F., 1943, *The Physics of Metals*, 181 (New York: McGraw-Hill Book Company, Inc.).
VOGT, E., 1932, *Ann. Phys., Lpz.*, **14,** 23.

Charged Dislocations in Lithium Fluoride†

By R. L. Sproull
European Research Associates, Brussels, Belgium‡

[Received March 14, 1960]

Abstract

The application of strong electrostatic fields to bent LiF crystals produced small motions (0·1 to 6 Å) of the bends which were analysed in terms of the motion of charged dislocations. The charge on the dislocation core was positive and of the order of 10^{-4} to 10^{-3} e.s.u./cm, and it presumably arose from the inequality of the free energies of formation of positive ion and negative ion vacancies. Estimates of the electrostatic contribution to the critical shear strength based on these values of charge substantiate the suggestion by Eshelby, Newey, Platt, and Lidiard that much of this strength may be electrostatic in origin.

§ 1. Introduction

The purpose of this experiment was to learn if dislocations in an ionic crystal could be electrostatically charged and, if so, to study the behaviour of such dislocations in an applied field. Eshelby *et al.* (1958) have recently pointed out that dislocations in ionic crystals should generally be charged and have suggested that a substantial part of the critical shear stress of such crystals is attributable to the electrostatic attraction between a dislocation and its surrounding charge cloud. They have also proposed several interesting consequences of the charge on dislocations for the mechanical behaviour of ionic crystals, including the proposal that a sufficiently strong electric field might produce plastic deformation.

The present experiment had a different objective, namely to produce *elastic* deformation by an applied electric field. It was expected that the phenomena would be somewhat simpler than plastic deformation and that the effect, if any, could be studied as a function of the field in order to distinguish it from spurious effects.

The basic plan of the experiment was to apply a strong electric field to the dislocations forming a bend in a crystal and thereby to cause the whole dislocation pattern constituting the bend to move a short distance. A crude sketch showing how the measurement was accomplished is presented in fig. 1. One end of the bent crystal was rigidly mounted, and the motion of the other end (the displacement x) was transmitted to an electromechanical transducer. Such an experiment requires the measurement of very small values of the displacement x, from a few hundredths

---

† Communicated by the Author.
‡ Present address: Cornell University, Ithaca, New York.

Fig. 1

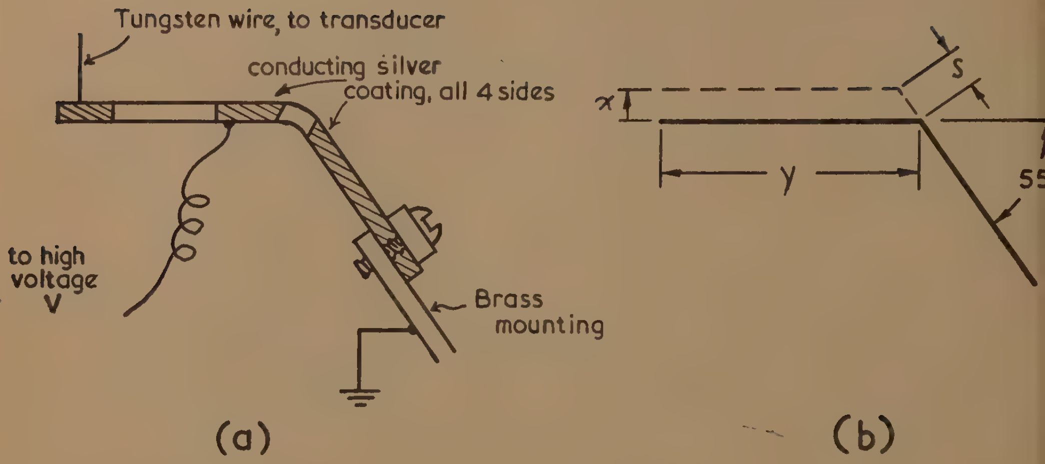
Tungsten wire, to transducer
conducting silver coating, all 4 sides
to high voltage V
Brass mounting
(a)
x
s
y
55
(b)

(*a*) Bent crystal. Motion of the left end is communicated through the tungsten wire to the transducer. (*b*) The relation between a displacement s of the bend and a displacement x of the transducer.

Fig. 2

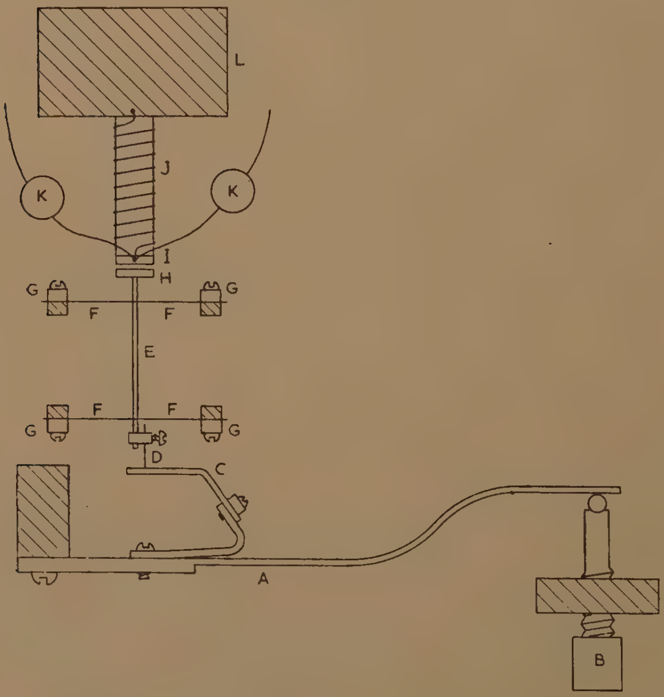
L
J
K
K
I
H
G
G
F
F
E
F
F
G
G
D
C
A
B

Schematic plan view of apparatus. The shaded parts are fastened rigidly to the base plate.

of an angstrom to several angstroms, but it proved practical to accomplish this measurement with a rather simple apparatus.

§ 2. APPARATUS AND TECHNIQUE

A schematic diagram of the apparatus appears in fig. 2. A brass bar A was rigidly mounted at the left end. The gradation in thickness and the length (18 cm) of the bar were such that 1/11 revolution of the micrometer head B moved the tip of the crystal in contact with D a distance of 1 μ. (This micrometer motion was used both for adjustment and for calibration.) The bent crystal C was clamped to the brass bar, and motion of the free end of C was transmitted through the 0·2 mm diameter tungsten wire D and the brass rod E to the 1 cm diameter plate H of a parallal plate condenser. The part E and H was supported by four 1·5 mm × 0·02 mm Cu–Be legs F; these legs confined the motion of E to one dimension and provided a light spring action to hold D against C. The other plate I of the condenser was cemented to the end of a 1 cm outside diameter quartz tube on which were wound 57 close-spaced turns of 0·03 mm diameter wire. One end of this coil J was earthed and the other was connected to I; the resonant circuit thus formed and the two 2 $\mu\mu$F coupling condensers K constituted the feed-back (frequency controlling) network of a two-transistor oscillator developed by Dr. J. Van Cakenberghe and Mr. L. Tremouroux (the circuit diagram will be provided on request). The transistors were embedded in a large brass block L to retard temperature drifts. Dust prevented use of condenser plate separations closer than 3 or 4 μ; at this separation, the oscillator frequency was about 5 Mc/s, and a typical calibration was a change of about 0·3 Mc/s per micron of motion of the crystal end (30 c/s per Å). This high value was attained partly because of the flatness of the condenser plates which (as with the rest of the apparatus) were skilfully prepared by Mr. M. Fievet, and partly because the plates could easily be made nearly parallel. Parallelism was accomplished by loosening the clamps G, holding the two plates H and I together by a loop of thread, and then tightening the clamps.

The assembly of fig. 2 (except the tip of the micrometer head) was enclosed in a massive brass box which in turn was enclosed in foamed plastic and shielded from draughts. The batteries powering the oscillator were also protected from rapid temperature changes. Thus although only crude temperature compensation was built into the apparatus, under favourable conditions a drift in one minute of < 10 c/s ($\frac{1}{3}$ Å) was often observed, and data could be taken at much higher drift rates. Frequency fluctuations superimposed on the drift, presumably microphonic in origin, were $\sim \pm 3$ c/s in each measuring period of 2 sec; averaging repeated measurements reduced uncertainty from this source. The frequency was measured with a Hewlett–Packard 524B frequency meter which usually was set to count the number of cycles in a 1 sec interval and to plot the last two or the last three digits of this number on a strip-chart recorder. Thus full scale on the recorder was 100 cycles (~3 Å) or 1000 cycles (~30 Å).

Single crystals about 1·7 × 6 × 35 mm were cleaved from LiF purchased from the Harshaw Chemical Company. Each crystal was bent by forcing it into a notch in an aluminium block pre-heated to 200°c. The crystal was cooled quickly to room temperature and contained a 55° bend about 4 mm in length; this angle was a compromise between too non-uniform an electric field (too large angles) and too small a ratio of x to the amount of motion of the bend (too small angles). Conducting silver electrodes were painted onto the crystal as sketched in fig. 1 (*a*), and the surface of the crystal in the region of the electric field was coated with a thin polystyrene solution. A 0·25 mm copper wire of which one end was embedded in the silver paint connected the high-voltage output of a radio-frequency power supply to the central electrode of the crystal (corona currents with a threshold at ~3000 v were observed when the size of this wire was decreased to 0·1 mm).

After the crystal was mounted in the measuring apparatus and the temperature allowed to stabilize for 16 hours or more, measurements were begun. The cycle of measurement was as follows: with no voltage, the frequency meter counted cycles for 1 sec; this number was transmitted to the recorder (but it took nearly 2 sec for the recorder pen to attain its final position). After 1 sec of counting, the counter was idle for 1 sec; a second count was then made. Immediately after this count was completed, the high voltage was switched on, applying a negative potential to the high-voltage lead. Two readings were made with a negative potential. Then two zero readings and two readings with a positive voltage the same in magnitude as the negative voltage completed the cycle. (Switching of the applied voltage occurred in less than $\frac{1}{3}$ sec and therefore was complete before a new count was made.) Occasionally zero readings were omitted in order to switch with maximum speed from minus-to-plus-to-minus, etc., to combat drift when the effect of reversing the voltage was very slight.

Usually 10 or 20 such cycles of eight frequency readings each were taken with 500 v, then a similar group with 1000 v, and so so. After the entire series of measurements, calibration was made in order to convert frequency changes to angstroms of motion.

§ 3. Experimental Results

Two sections of the recorder chart for a series of readings on one crystal are reproduced in fig. 3. At low voltages a *positive* potential applied to the high-voltage electrode *increased* the frequency, and a negative potential decreased the frequency. At higher voltages, decreases in frequency were produced by potentials of either sign, but the decrease was smaller in magnitude when the potential was positive. An increase in frequency corresponded to an increase in condenser plate spacing, which in turn would have been produced by motion of the bend in the crystal toward the end where it was rigidly mounted.

Fig. 3

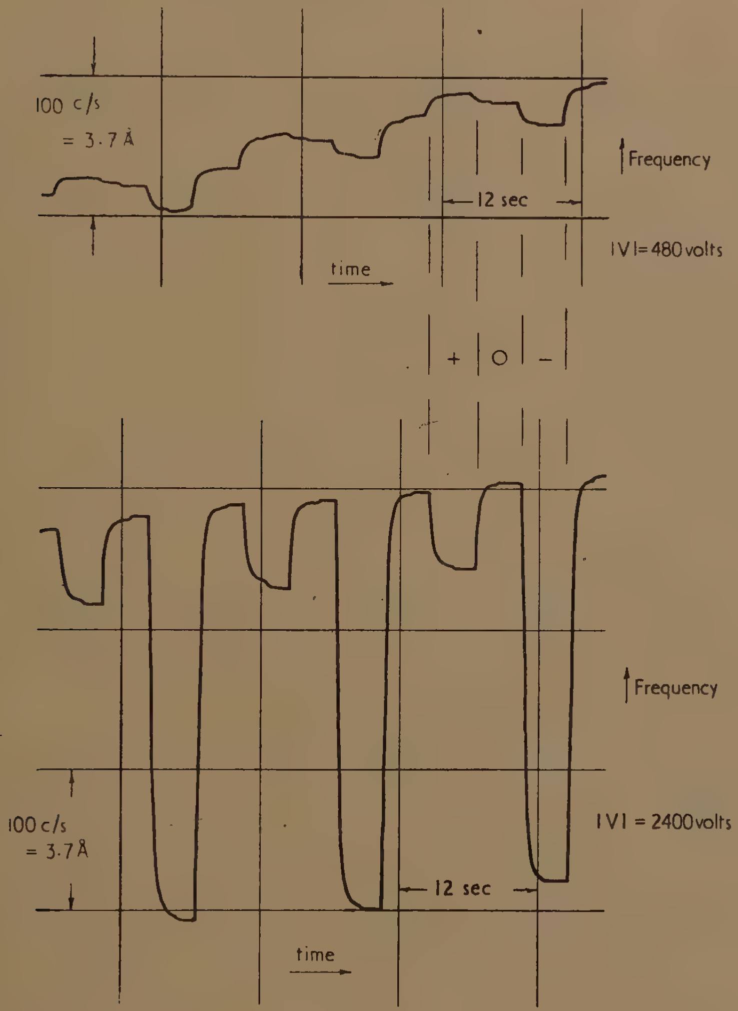

Strip-chart recordings for two magnitudes of $|V|$. The symbols O, +, and − refer to the values of V during each 4-second period.

It is clear from data like that in fig. 3 that at least two processes with different voltage dependencies occurred. Progress in separating these processes can evidently be made by determining the component of the displacement x which is an even function of voltage and the component which is an odd function. Let

$$x = aV + bV^2 + cV^3 + dV^4 + \dots .$$

Then if x_1 is the displacement at voltage V and x_2 the corresponding displacement at voltage $-V$,

$$(x_1+x_2)/2=bV^2+dV^4+\dots, \qquad (1)$$

$$(x_1-x_2)/2=aV+cV^3+\dots. \qquad (2)$$

Experimental values of the former (even) function are plotted as a function of V^2 in fig. 4. It appears that b is positive and that d and higher even coefficients are nearly zero. The value of b varied from one crystal to another or even with different electrodes on the same crystal. Analysis in the Appendix shows that this even function quite probably arose from electrostriction and is not of primary interest in this investigation.

Data for the odd function of V on the same crystal used for fig. 4 are plotted in fig. 5, in which the ordinate is $-(x_1-x_2)/2$, hereafter called $-\bar{x}$. Evidently both a and c are negative. In all the data taken, $\bar{x}$ was always a distinctly non-linear function of V, and the non-linearity was always in the same sense and about the same in magnitude. Curves nearly identical to those of fig. 5 were found for three other Harshaw LiF crystals, with the same values $\pm 30\%$ of a and c. Similar phenomena, but with smaller and more variable values of a and c, were observed on Leitz and Harshaw NaCl crystals.

Several possible disturbing effects are considered in the Appendix, and it is there shown that the displacements plotted in fig. 5 are probably not the result of heating, electrostriction, converse piezoelectric effect, or the motion of vacancies. Although there may be other spurious effects not properly considered, there are two arguments in favour of the dislocation motion interpretation of the data:

(1) $\bar{x}$ as a function of V is non-linear; furthermore, c/a has the sign and about the magnitude expected, as will be shown in § 4.

(2) A bent crystal was polygonized by heating to 600°c and slowly cooling in air. Etching carried out by Mr. M. Reynders and Dr. E. Votava, according to the Gilman and Johnston (1956) prescription, showed that most of the isolated dislocations climbed into small angle boundaries as a result of this treatment. Polygonization reduced the odd-function-of-V effect by a factor of 8 and did not change the even function. Since this treatment changed the internal arrangement of dislocations but not the external shape of the crystal, it provided some evidence to support the connection between the observed phenomena and the properties of dislocations.

The transducer motion $\bar{x}$ could have arisen either because of a change in the bend angle or a change in the bend position. The former type of motion is sensitive to the distance y defined in fig. 1 (b), whereas the latter (illustrated in that figure) is not. Only limited advantage was taken of this different behaviour because an electrostatic shield around the high-voltage electrode prevented the use of small values of y, but experiments on the same bent crystal mounted with different values of y

Fig. 4

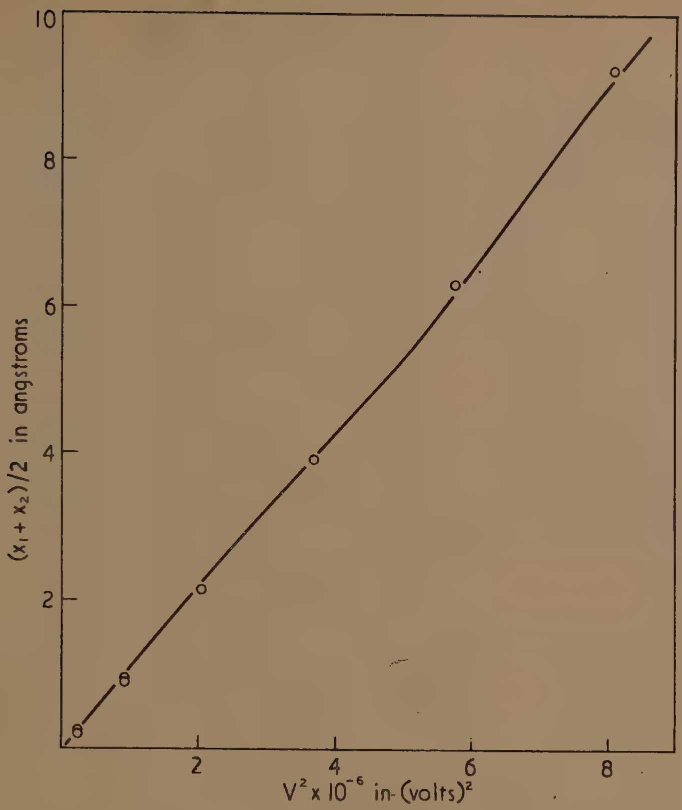

The part of x that is an even function of V plotted *vs* V^2.

Fig. 5

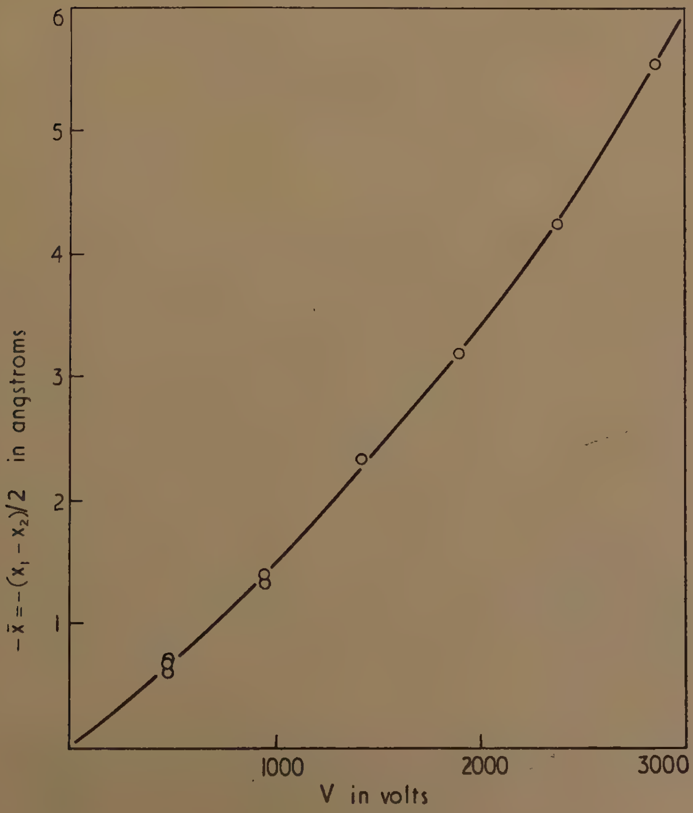

The part of x that is an odd function of V plotted *vs* V.

indicated that the motion $\bar{x}$ was of the type illustrated in fig. 1 (*b*), that is, a change in the position of the bend. A more convincing experiment consisted of bending a crystal into a half-circle of radius ~ 1 cm, mounting the crystal at one end of the diameter, and permitting the other (free) end to actuate the transducer through a tiny quartz rod. In this configuration, azimuthal electric fields failed to produce measurable displacements of the free end, whereas any change in the angle of bending would have caused larger displacements than those observed in the usual (fig. 1) configuration.

§ 4. Discussion

The data from fig. 5 at $\bar{x} = -1$ Å and $\bar{x} = -4$ Å will be considered here, but other experiments on the same crystal and on other LiF crystals gave substantially the same results. If these displacements $\bar{x}$ were produced by a motion s of the 55° bend,

$$\bar{x} = s \sin 55^\circ.$$

The edge dislocations constituting the bend move on the (110) and (110) glide planes at an angle of 45° to the (100) planes forming the surfaces of the crystal (fig. 6). The distribution of dislocations within the bend is complicated when the angle of bending is so large, but a dislocation on a (110) plane and one on a (110) plane can be approximately replaced (insofar as their effect on the external shape of the crystal is concerned) by a single dislocation of larger [010] Burgers vector, as sketched in fig. 6 by dotted lines. The motion to the left of these does not change the radius of curvature of the bend, but some dislocations at the left side move into a previously straight section of crystal, and some at the right leave a curved section and make it straight. Thus the bend as a whole moves a distance $s = r/\sqrt{2}$ along the length of the crystal when the individual dislocations move a distance r along their glide planes. Thus

Fig. 6

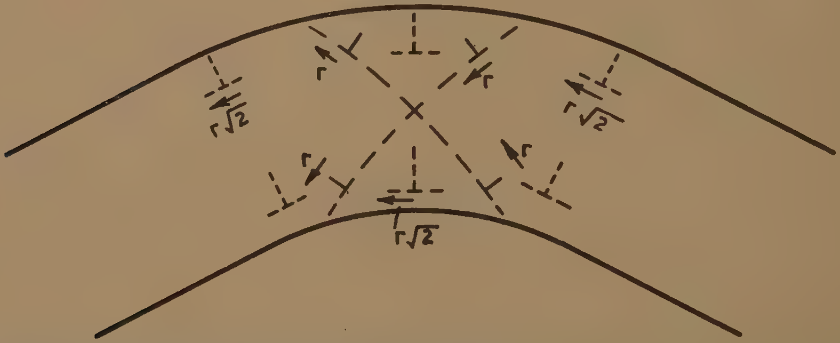

Schematic diagram showing the relation between the motion r of dislocations along glide planes and the motion s of the bend.

$$r = \sqrt{2}\bar{x}/\sin 55^\circ. \quad . \quad . \quad . \quad . \quad . \quad . \quad (3)$$

Attention will next be directed toward the theory of the motion r as a function of the applied electric field. Lehovec (1953) showed that a space-charge layer should occur at the surface of an ionic crystal because vacancies cannot be formed inside the perfect crystal and because the free energies of formation of positive and negative ion vacancies are in general different. Pratt (1957) and Eshelby *et al.* (1958) made the important advance of suggesting that a similar space-charge region should occur around a dislocation, since dislocations can serve as sources and sinks for vacancies. Equal concentrations n_+ of positive ion vacancies and n_- of negative ion vacancies must occur in the regions of the crystal remote from dislocations in order to preserve electrical neutrality. But if the free energy of formation of a positive ion vacancy, g_+, does not equal the free energy of formation of a negative ion vacancy, g_-, an electrostatic potential difference must occur between the core of the dislocation and the remote regions. If $g_+ < g_-$, as is likely in the alkali halides, the core of the dislocation becomes positively charged, and there is a negative space charge surrounding the core. Thus the further emission of positive ion vacancies (negatively charged) is opposed by the electrostatic field. The dislocation then contains an excess of jogs (Seitz 1950, 1951) of positive sign.

Fig. 7

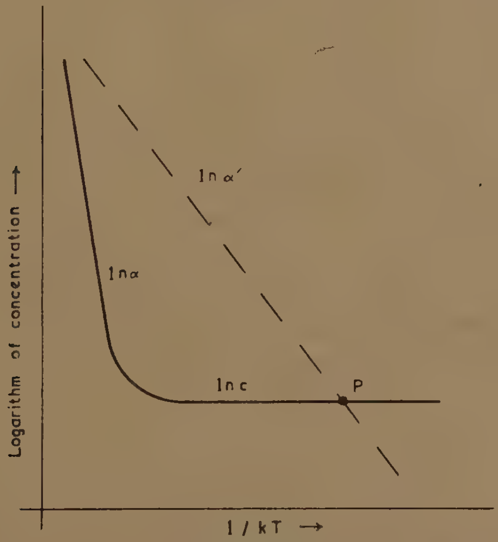

Schematic diagram of the logarithm of the concentration of positive ion vacancies as a function of reciprocal temperature.

The presence of divalent ions in an alkali halide modifies this analysis, since the concentration α of positive ion vacancies then approaches at low temperatures the concentration c of divalent ions. The situation is shown schematically in fig. 7, in which the dashed line is $\alpha'=\exp(-g_+/kT)$ and the solid line is $\alpha=\exp[-(g_++g_-)/2kT]$ at high temperatures and $\alpha=c$ at low temperatures. α' is the concentration of positive ion vacancies that would obtain in the absence of the requirement of electrical neutrality, and α is the actual concentration. Dislocations are positively charged when the temperature is above that at the 'isoelectric point' P and negatively charged below. Eshelby *et al.* (1958) have also considered the effects of vacancy–impurity association and impurity precipitation, which add complications to fig. 7.

Eshelby *et al.* (1958) found an approximate expression for the force per unit length F pulling a dislocation toward the centre of its charge cloud when the dislocation was displaced a distance r:

$$F=\frac{-2\sigma^2\kappa}{\epsilon}\left[(\kappa r)^{-1}-K_1(\kappa r)\right]. \quad . \quad . \quad . \quad (4)$$

Here σ is the dislocation charge per unit length (e.s.u./cm), ϵ is the dielectric constant, K_1 is the Bessel function of imaginary argument (Watson 1952), and κ is defined by

$$\kappa^2=8\pi e^2N\alpha/\epsilon kT,$$

with N the number of cation cites per cm³. Thus κ^{-1} is the characteristic radius of the cylindrical charge cloud surrounding a dislocation. Equation (4) was based on several approximations which limit its quantitative application, especially if the temperature is more than ~20°c from an 'isoelectric' point (the point P in fig. 7).

Eshelby *et al.* (1958) were concerned only with the maximum value (0·40) of the bracket in eqn. (4) in estimating the critical shear stress to pull the dislocation from its cloud, but the interest in the present experiment centres on small values of κr. It is therefore worthwhile to expand $K_1(\kappa r)$ about $\kappa r=0$ using

$$K_1(\kappa r)=\frac{1}{\kappa r}+\frac{\kappa r}{2}\left(\ln\frac{\kappa r}{2}+0{\cdot}0772\right)+\frac{(\kappa r)^3}{16}\left(\ln\frac{\kappa r}{2}-0{\cdot}6728\right)+\ldots \quad (5)$$

from Watson (1952). Neglecting the term in $(\kappa r)^3$ in (5) makes an error of only 1% at $\kappa r=0{\cdot}08$, and therefore only the first two terms need be retained when considering small displacements of dislocations.

The force F' on the dislocation by the electric field E is $F'=E\sigma$. In the steady state with field applied, the sum of this force and the force from eqn. (4) is zero, and

$$E\sigma=\frac{-\sigma^2\kappa^2}{\epsilon}r\left(\ln\frac{\kappa r}{2}+0{\cdot}0772\right). \quad . \quad . \quad . \quad . \quad (6)$$

The peculiar behaviour of this equation as a function of σ is caused by the assumption that no restoring force other than the electrostatic one is applied, and if σ is too small, this is clearly a poor assumption. On this assumption, however, (6) becomes

$$r\left(\ln\frac{\kappa r}{2}+0{\cdot}0772\right)=-\frac{\epsilon}{\sigma\kappa^2}E, \quad . \quad . \quad . \quad . \quad . \quad (7)$$

in which $\ln(\kappa r/2)$ is always < 0. It should be noted that $r(E)$ is distinctly non-linear even at extremely small values of κr; the logarithmic derivative is 0·81 at $\kappa r = 0{\cdot}01$ and is 0·92 at $\kappa r = 0{\cdot}00001$.

The assumption has been made in the above that the charge cloud is fixed. The data of Haven (1950) would indicate appreciable mobility for the positive ion vacancies in LiF at 22°C, however. Any motion of the charge cloud evidently reduces the magnitude of the dislocation motion but should not make a qualitative difference unless the charge cloud motion changes the shape of the crystal.

There is no requirement that the average displacement of the dislocation lines be an integral number of Burgers vectors, or even that the displacement of a single line be limited in this way, since only parts of the line may move. Although dislocations in LiF are in general loops with large screw components (Gilman and Johnston 1957), only the edge components determine the amount and position of the bend. Therefore this analysis is concerned only with these components which are the 'necessary' dislocations to produce the bend.

From the above picture of the effect of an electric field on the charged dislocations, it would be expected that the motion r (or x) would be a completely odd function of V. Thus the non-linearity of the data, analysed according to the procedure of §3, can be compared with the theory without considering possible errors by loss of terms in even powers of V.

One must resist the temptation to determine the magnitude of α by comparing the non-linearity in $r(E)$ from (7) with the non-linearity of $\bar{x}(E)$ from fig. 5, since clearly too many and too crude approximations have been made in reaching (7). Instead, α will be estimated from ionic conductivity measurements made on these crystals and from the mobility data of Haven (1950) extrapolated to 22°C. This procedure yields a very low value of α, $\alpha_1 = 2{\cdot}2 \times 10^{-7}$, which is so low compared to the probable divalent ion impurity concentration that considerable association of vacancies or precipitation of impurities must be occurring. It is quite possible that the space-charge layer could be constructed in part from less mobile species than positive ion vacancies (e.g. divalent ions, charged vacancy aggregates). It may therefore be worth while also to carry through the analysis of the data with $\alpha_2 = 10^{-5}$ which may be more typical of the concentration of charges available for forming the space-charge cloud.

The corresponding values of κ at 22°C are $\kappa_1 = 4{\cdot}2 \times 10^{-5}\ \text{cm}^{-1}$ and $\kappa_2 = 2{\cdot}8 \times 10^{-6}\ \text{cm}^{-1}$. From fig. 5, eqn. (3), and the geometry of the crystal, we obtain the pair of data points:

$$\bar{x} = 1\ \text{Å}, \quad r = 1{\cdot}73\ \text{Å}, \quad V = 710\ \text{v}, \quad E = 5{\cdot}25\ \text{e.s.u./cm};$$

$$\bar{x} = 4\ \text{Å}, \quad r = 6{\cdot}9\ \text{Å}, \quad V = 2260\ \text{v}, \quad E = 16{\cdot}7\ \text{e.s.u./cm}.$$

From the assumption $\alpha = \alpha_1$, we obtain $\sigma_1 = 2{\cdot}0 \times 10^{-3}\ \text{e.s.u./cm}$ from the 1 Å data and $\sigma_1 = 2{\cdot}1 \times 10^{-3}\ \text{e.s.u./cm}$ from the 4 Å data. The excellent agreement between these two values demonstrates the agreement between the theoretical and observed non-linearity of $r(E)$. From the assumption $\alpha=\alpha_2$, we obtain $\sigma_2=6{\cdot}6\times10^{-5}$ e.s.u./cm from the 1 Å data and $\sigma_2=8{\cdot}7\times10^{-5}$ e.s.u./cm from the 4 Å data. The non-linearity no longer is in such good agreement. Although the precise amount of non-linearity in (7) is, of course, dependent on the accuracy of the assumptions and approximations, a non-linearity of this same sense (more rapid than linear dependence of r on E) would be expected from the nature of the physical situation. The assumption that the temperature is near an isoelectric point ($\sinh p\simeq p$ in the notation of Eshelby *et al.* 1958) is well satisfied for $\alpha=\alpha_2$ but not for $\alpha=\alpha_1$.

The values of σ thus obtained are not unreasonable in that jogs in the dislocation lines could provide enough excess charge of one sign, but the σ_1 values ($\sim4\times10^6$ electrons/cm) approach the upper limit of credibility.

Eshelby *et al.* (1958) estimated the critical shear stress Y of electrostatic origin as

$$Y=0{\cdot}80\sigma^2\kappa/\epsilon\mathbf{b},$$

where **b** is the Burgers vector (2·98 Å in LiF). Values of Y corresponding to σ_1, κ_1, and σ_2, κ_2 are $Y_1=5000$ g/cm^2 and $Y_2=50$ g/cm^2. The former of these is unreasonably large, since Gilman and Johnston (1957) have found yield stresses of the order of 1000 g/cm^2 at 300°K. It is noteworthy, however, that the experimental data here for σ and reasonable values of κ predict Y values comparable to the observed yield stress. To some extent this confirms the suggestion of Eshelby *et al.* (1958) that the electrostatic stress is a substantial part of the critical shear stress in ionic crystals.

The *sign* of the charge σ is obviously of interest. It is apparent from the sense of the observed motion (first paragraph of § 3) and the analysis associated with fig. 6 that the dislocations were positively charged. Thus the isoelectric point P of fig. 7 must have been below room temperature. If no vacancy–impurity association or impurity precipitation occurred, it is possible to estimate crudely the value of g_+ for LiF. This task was carried out by using the sign and magnitude of σ, the theory of Eshelby *et al.* (1958), and the value $g_++g_-=2{\cdot}68$ ev for LiF from Haven (1950). The slope of $\ln\alpha'$ *vs.* $1/kT$ in fig. 7 was adjusted until the vertical separation of the two lines at 22°C was the value computed from the measured σ. The σ_1 results placed P about 100°C below room temperature and led to a very low value of g_+. The σ_2 results, which are probably nearer the actual situation, placed P at about 0°C and led to $g_+=0{\cdot}3$ ev. Although there appear to be no other experimental or theoretical determinations of g_+, this value is unreasonably low, and therefore a more complicated interpretation of the data involving precipitation or association may be necessary.

It remains to suggest an explanation for the substantial reduction in $r(E)$ after polygonizing the crystal. The dislocation walls after this treatment were about 0·0022 cm apart on the average, and since the curvature in the bend was about 3 radians/cm, the tilt angle in each wall was on the average approximately 0·007 radian, and the dislocations making up the wall were ~ 400 Å apart. At this separation the individual charge clouds begin to coalesce (especially under the assumption $\alpha = \alpha_1$), and the restoring force at a displacement r is greater than if the dislocations were isolated. This explanation is rather tenuous, especially if $\alpha = \alpha_2$, however, and it may be that immobilization of dislocations by Cottrell atmospheres is the real cause of the reduction in $r(E)$ in the polygonized crystals.

§ 5. CONCLUSION

Evidence has been presented here to indicate that dislocations in LiF at room temperature are charged and can be moved measurable distances by an electric field. The observed magnitude of the charge in part confirms the suggestion by Eshelby *et al.* (1958) that a substantial part of the strength of ionic crystals is electrostatic in origin. It should be possible to use experiments such as the present one to learn interesting features of vacancy formation energies, association, and precipitation in ionic crystals, and such experiments might have an important bearing on the questions of plasticity, hardening, creep, and the temperature dependence of the yield stress in non-metallic crystals. Amelinckx *et al.* (1959) have also observed the effects of charged dislocations in an ingenious experiment quite different from the present investigation.

An obviously important handicap of the present experiment was the inability to vary the temperature over an appreciable range, whereas a variation of 50° or 100° could provide a crucial test of the dislocation interpretation of the effect studied and of some of the assumptions in the analysis. Another interesting experiment would be to bend a crystal, polygonize it, and then straighten it at a temperature < 200°C; in this way it might be possible to measure the effect of isolated dislocations but with a completely rectangular crystal geometry, which should permit the application of a symmetrical electric field and minimize complicating effects. Among the additional experiments that would be worth while are studies of other ionic crystals, of alkali halides with known concentrations of divalent ion impurities, and of crystals with various heat treatments.

ACKNOWLEDGMENTS

In addition to the help acknowledged in the text, it should be noted here that the assistance of Dr. J. Van Cakenberghe, Mr. P. L. Moentack, and Mr. L. M. Tremouroux was indispensable in this investigation. The encouragement and suggestions of Dr. R. H. Gillette were invaluable. The author is also grateful to Dr. W. W. Webb for a critical study of this work and to the Union Carbide Corporation for its support.

APPENDIX

Whenever an apparatus sensitive to shape or length changes of the order of 1 Å is employed, it is obvious that many possibilities exist for spurious and subsidiary effects to complicate the data and perhaps to hide or to simulate the effect sought. It is never possible to be sure that all such disturbing effects have been avoided or accounted for, but it may be worth while to comment on some of the possible disturbances.

Heating

A temperature rise in the crystal could have caused a decrease in oscillator frequency simply by thermal expansion or by an expansion of the crystal at the inside of the bend that was greater than at the outside. Calculations based on observed currents showed that this displacement x was $< 0{\cdot}05$ Å at $V = 1500$ v. Furthermore, the displacement produced by such expansion should have had a time constant > 1 sec, instead of much < 1 sec as observed, and should have been an even function of V.

Heating by corona currents in the air around the crystal was more troublesome. In early experiments with a 0·1 mm wire connecting the high voltage to the crystal, phenomena simulating plastic deformation (continuous increase of x with time for several minutes) occurred, but these were traced to corona heating which was not the same for positive and negative V's. Corona was identified as the cause by measuring the current drawn from the high voltage supply with and without a crystal in place, and by showing that the 'plastic' effect was proportional to the power dissipated in corona (which had a distinctive voltage dependence). This effect was absent for $V < 3000$ v, even with the 0·1 mm wire, and absent at all voltages used with the 0·25 mm wire.

Electrostriction

Electrostriction is by definition (Cady 1946, Forsbergh 1956) that part of the strain in a substance produced by an electric field which is an even function of the field. No data appear to be available for LiF, but a typical magnitude in other solids is about $10^{-14}E^2$, where E is the electric field in v/cm (Cady 1946).

The longitudinal electrostriction coefficient in LiF was estimated by measuring $x(V)$ for a straight crystal mounted with its long dimension (direction of E) in the direction of the axis E (fig. 2). The strain was closely proportional to E^2, where E is the electric field in v/cm, and was about $5 \times 10^{-16}E^2$. (The transverse coefficient was estimated by a similar experiment with the straight crystal at right angles to the direction of motion of the transducer, and a value $3 \times 10^{-15}E^2$ was computed for the strain.) With the same measuring cycle described in § 2, the displacement x was always the same for positive and negative voltages.

The combination of electrostriction and polarization could have produced a displacement which was not exactly an even function of field, since the internal field would not have had the same magnitude when the external potential difference was reversed in sign. When a strong (10 000 v/cm) polarizing field had been applied for several minutes to the straight crystal described in the preceding paragraph and the usual procedure was then followed for taking data, a small effect of reversing the field was observed, the length of the crystal being greater when the applied field was opposed to the polarizing field. This effect disappeared in about 15 sec after the polarizing field was removed. A similar experiment was performed on a bent crystal. a potential difference of 2000 volts was applied for $1\frac{1}{2}$ min. and then data were taken at 500 v in the usual way. A small spurious effect of reversing V was observed in the first few cycles, but it disappeared in 30 sec. This experiment should have greatly exaggerated the effect of the combination of electrostriction and polarization. The dielectric relaxation time of LiF at room temperature can be estimated from its dielectric constant (9·27) and measurements of the ionic conductivity at room temperature (about $1{\cdot}5\times10^{-10}$ mho/cm for the LiF samples used). This time is about one minute, and therefore polarization fields cannot be sustained for long times. The cycle of taking data was ordinarily strictly timed to prevent the application of voltage of one sign for a longer time than that of the other. Occasionally a voltage of one sign would be sustained for 5 or 10 sec to accentuate any polarization–electrostriction effect, but such an effect never appeared in the experiments described in §§ 2 and 3.

There is another argument against the possibility that the combination of polarization and electrostriction may have created the observed odd-function-of-V effect in bent crystals: if the internal polarization field is E_0, the external applied field is E, and k is a constant, electrostriction would have produced a displacement

$$x=k(E+E_0)^2=kE^2+2kEE_0+kE_0{}^2.$$

Thus the contribution to x which is an odd function of E (or V) should have been strictly linear in V, and this definitely did not agree with the data.

Electrostriction is quite probably the cause of the V^2 term evident in fig. 4, since E was undoubtedly larger at the inside of the bend than at the outside, and thus electrostriction produced a decrease in oscillator frequency (increase in x). The approximate magnitude of **b** in (2) could be estimated from the electrode geometry and agreed well with the observed magnitude. Furthermore the sign of d could be changed and its magnitude increased a factor of 4 upon exaggerating the non-uniformity in field by the electrode configuration of fig. 8. In principle, then, this even function of V could be reduced to zero by careful design of the electrodes, but this process would be tedious and unnecessary.

Converse Piezoelectric Effect

Although a piezoelectric effect cannot occur in a crystal with the NaCl structure, which has a centre of symmetry, the excess of dislocations of one geometrical sign removes this symmetry. If this interpretation of the effect shown in fig. 5 be assumed, a piezoelectric coefficient of $\sim 4 \times 10^{-11}$ cm/v is computed. This is of the same order of magnitude or an order of magnitude smaller than the piezoelectric constants in crystals for which the effect is permitted by symmetry. It seems quite unreasonable to expect that the small deviation from inversion symmetry produced by bending could produce such a large coefficient.

Surface Effects

It is very difficult to analyse the possibilities of spurious deflections caused by surface charges, but the choice of LiF should have reduced the effects of water adsorption, and the polystyrene coating should also have helped. It should be noted that one crystal was measured before coating with polystyrene and again after coating; no observable changes in $x(V)$ occurred.

Fig. 8

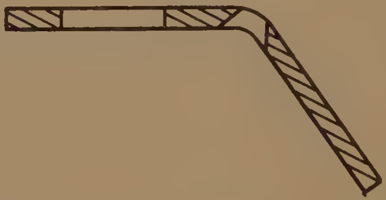

Crystal with electrodes shaped to exaggerate the electrostriction effect.

Electrostatic Effects

Electrostatic forces should have been strictly proportional to V^2. Also, in most of the experiments an electrostatic shield connected to the high voltage (and mechanically supported from the base of the apparatus, *not* from the crystal) surrounded the high-voltage electrode on the crystal. This shield did not even alter the V^2 term appreciably and had no effect at all on the odd function.

Motion of Vacancies

Since there is appreciable ionic conductivity in these crystals at room temperature, the possibility arises of a change in shape or length by ion motion. The dominant mobile species in LiF is the positive ion vacancy (Haven 1950). Whether it expands or contracts the lattice is not known with certainty, but the expansion or contraction cannot be much more than one Li^+ atom volume per vacancy. If this magnitude be assumed, the effect of ionic motion on the shape of the crystal was negligible in the present experiment. Furthermore, such a process should have produced an x which changed continuously for many minutes after the voltage was applied, whereas the observed displacements reached their terminal values in a fraction of a second.

References

Amelinckx, S., Vennik, J., and Remaut, G., 1959, *J. Phys. Chem. Solids*, **11,** 170.

Cady, W. G., 1946, *Piezoelectricity* (New York : McGraw-Hill).

Eshelby, J. D., Newey, C. W. A., Pratt, P. L., and Lidiard, A. B., 1958, *Phil. Mag.*, **3,** 75.

Forsbergh, P. W. Jr., 1956, *Encyclopedia of Physics*, Vol. **17** (Berlin : Springer), p. 264.

Gilman, J. J., and Johnston, W. G., 1956, *J. appl. Phys.*, **27,** 1018; 1957, *Dislocations and Mechanical Properties of Crystals* (New York : Wiley), p. 129.

Haven, Y., 1950, *Rec. trav. Chim. Pays-Bas*, **69,** 1471.

Lehovec, K., 1953, *J. chem. Phys.*, **21,** 1123.

Pratt, P. L., 1957, *Monogr. Ser. Inst. Metals*, **23,** 99.

Seitz, F., 1950, *Phys. Rev.*, **80,** 239; 1951, *Rev. mod. Phys.*, **23,** 341.

Watson, G. N., 1952, *Theory of Bessel Functions* (Cambridge: University Press), pp. 78, 80 and Table II.

Electron Microscope Observations on the Annealing Processes Occurring in Cold-worked Silver†

By J. E. Bailey
Crystallographic Laboratory, Cavendish Laboratory, Cambridge

[Received April 1, 1960]

Abstract

Electron microscope observations on the dislocation structure of cold-worked polycrystalline silver and on the processes occurring during annealing are described.

In silver deformed 25% in tension the dislocations are arranged in a cell structure and the stored energy is released in two stages, a recovery stage followed by recrystallization. During the recovery stage there is no observable change in the dislocation distribution but there is a possibility of small-scale dislocation rearrangements within the cell boundaries. Recrystallization occurs by the migration of the grain boundaries originally present in the metal and this process is discussed in some detail.

Observations made on heavily rolled silver annealed either inside the electron microscope on a heating stage or outside the microscope are also described.

§ 1. Introduction

Microcalorimetric experiments reported in a previous paper (Bailey and Hirsch 1960) have shown that the energy stored in cold-worked polycrystalline silver is released in two distinct annealing stages which differ in the form of their annealing kinetics. One of these stages is accompanied by recrystallization, as shown by x-ray diffraction patterns. The other process, called recovery, begins prior to recrystallization when the specimen is annealed isothermally for a short period of time. The present paper reports some results obtained using the transmission electron microscopy technique to elucidate the mechanisms occurring during recovery and recrystallization. One particular aim of the experiments was to determine the nature of the recrystallization nuclei.

Observations were made both on specimens which had just been annealed in bulk outside the microscope and then thinned by electropolishing and on specimens which had been thinned first and then annealed on a heating stage inside the electron microscope.

---

† Communicated by P. B. Hirsch.

§ 2. PREPARATION OF THE SILVER FOILS

Polycrystalline silver specimens (99·99% purity) were deformed 25% in tension in the manner described previously (Bailey and Hirsch 1960) and by cold rolling by varying amounts up to 95% reduction. The cross sections of the specimens prior to deformation were so chosen to give final foil thicknesses of ~0·005 in. The silver foils were then thinned by electropolishing (for solution used see Bailey and Hirsch 1960) and examined in the electron microscope.

Pieces of the foils, deformed 25% in tension or cold rolled to 95% reduction, were annealed in the bulk for various times at temperatures at which complete recrystallization occurred in 15–20 hours, and after thinning were examined in the electron microscope. Some of the heavily rolled specimens were thinned before annealing and examined on a heating stage (Whelan 1957) in the electron microscope.

§ 3. OBSERVATIONS ON FOILS ANNEALED IN BULK

3.1. *Dislocation Arrangement after Cold Work*

In specimens deformed 25% in tension the dislocations are arranged in a cell structure shown in fig. 1 (*a*)†, which was discussed in a previous paper (Bailey and Hirsch 1960). The misorientations across cell walls are small, ~1°, the diffraction patterns from an area covering one cell wall being typical of those from single crystals (fig. 1 (*c*)). The cell boundaries appear to consist of dense 3-dimensional networks; they are not simple dislocation walls.

Foils rolled to 20% reduction had dislocation distributions similar to those found in the extended specimens. With increasing reduction, however, the dislocation density and the misorientations across the cell boundaries increase. Figure 2 shows a series of micrographs of specimens after reductions of 20, 40, 60 and 95% and fig. 3 corresponding diffraction patterns from areas of ~$\frac{4}{3}\,\mu$ diameter. The table lists the average spread in orientation per diffraction spot or cluster of spots for these specimens. It is clear from the diffraction patterns and from the table that not only does the average range of orientations increase with greater deformation, but some of the cells develop into distinct sub-grains, the misorientation increasing considerably. Diffraction patterns were taken from areas including a single cell boundary; for the specimens rolled to 95% reduction, it appears that quite large misorientations, even up to ~10° occur. Some of the boundaries are quite well defined, e.g. fig. 4.

It is interesting to compare the misorientations in the table with those found in previous x-ray work (Gay and Kelly 1953). In the latter experiments the angular spread along a Debye–Sherrer arc from an area of specimen ~20 μ in diameter was measured. These results are also shown in the table. Although the area of examination is many times greater in the x-ray than in the electron case, the misorientations are only greater by a factor of 3 or so. This shows that the orientation does not change in the same sense across a grain but fluctuates about a mean orientation.

---

† With the exception of fig. 12, all figures are shown as plates.

It is difficult to give a precise estimate of the dislocation density in the foil rolled to 95% reduction, an order of magnitude estimate being $\sim 5 \times 10^{11}$ cm/cm^3 compared with 7×10^{10} cm/cm^3 for a specimen extended about 25% in tension.

Whereas the grain boundaries in the foils extended 25% in tension generally appear quite straight and do not show any large scale (> 1000 Å) discontinuities, it is very difficult to recognise the original grain boundaries in the rolled specimens.

Misorientations in Rolled Foils

Silver (present investigation)		Copper (Gay and Kelly 1953)	
Reduction (%)	Total angular misorientation from $1\frac{1}{2}\,\mu$ diameter region (°)	Reduction (%)	Total angular misorientation within one grain (20 μ) (°)
		10·8	$3\frac{1}{2}$
20	< 2	19·6	6
		28·9	8
40	~ 4		
		49·0	15
60	~ 7		
95	~ 12		

3.2. *Observations on Partially Annealed Specimens*

3.2.1. *Silver foil deformed 25% in tension*

The process of recrystallization was found to be very inhomogeneous on the scale of the electron microscope observations. In the same specimen large areas were recrystallized, while in others no obvious change had taken place as a result of the annealing treatment. In order to study the recrystallization mechanism at an early stage, observations were made on specimens annealed for 1 hour at 200°C; at this temperature complete recrystallization occurs in 15–20 hours. Figure 1 (*b*) shows a typical region of such a specimen which had not recrystallized. Although a small amount of stored energy (~ 5%) is released during this time (Bailey 1959), there is no observable change in dislocation distribution, as can be seen from a comparison of fig. 1 (*a*) and (*b*). Observations after much longer periods of recovery, corresponding to a larger release of stored energy (> 20%), also failed to reveal any observable change in dislocation distribution. However, small rearrangements of dislocations within the complex networks cannot be ruled out.

In other areas of similar specimens the original grain boundaries show bulges which are the result of grain boundary migration during annealing. Examples are shown in figs. 6 and 7. It should be emphasized that after deformation and before annealing, the grain boundaries are generally quite straight (fig. 5). Figure 6 (*a*) and (*b*) show an early stage of the migration process. In fig. 6 (*a*) the original position of the grain boundary is clearly along the line joining the two straight lines on either side of the bulge. The region through which the boundary has moved has a comparatively small dislocation density. This shows that most of the dislocations forming the cell structure are not connected to the boundary and presumably do not originate there. Some dislocations however, do end on the boundary and these increase in length as the boundary moves forward; examples are seen in fig. 6 (*a*). Figure 6 (*c*) shows a later stage in the migration process, the recrystallizing grain A has the same orientation as the cold-worked grain B and the original position of the grain boundary was presumably along the line joining points C and D. Figure 7 shows a case where neighbouring sections of a boundary appear to have moved into adjacent grains.

These observations suggest that recrystallization in these specimens takes place by migration of the original grain boundaries. This process will be considered in more detail in § 5. All the observations to date are consistent with this process of recrystallization. Occasionally completely enclosed recrystallizing grains are observed, as for example in fig. 8. Such grains are thought to originate from movement of original grain boundaries previously above or below the section of the specimen examined.

3.2.2. *Silver foil cold rolled to* 95% *reduction*

Whereas in the specimens deformed 25% in tension no polygonization was observed, in the heavily rolled foils sub-grains are formed as a result of short anneals. Figure 9 (*a*) shows an example of the sub-grains present after a 20 min anneal at 110°c, to be compared with the cold worked structure shown in fig. 2. These specimens recrystallize in 15–20 hours at 110°c.

Figure 9 (*b*) shows an example of the early stage of recrystallization. As in the case of the specimens deformed 25% in tension, recrystallization appears to take place by the migration of a high angle boundary. However, as the original grain boundaries cannot be distinguishd in the cold-worked metal, it is not possible to decide whether the moving boundary formed part of an original grain boundary or of a sub-grain boundary produced during deformation, or as a result of polygonization during annealing. It should be noted that in this material large misorientations across sub-grain boundaries are present after the deformation so that to some extent the difference between the original and newly formed boundaries disappears.

§ 4. OBSERVATIONS ON HEAVILY ROLLED SPECIMENS USING A HIGH TEMPERATURE STAGE

For these experiments silver cold-rolled to 95% reduction was thinned by electropolishing and placed on the mount of the high temperature stage. The foil is heated by passing a d.c. current through the specimen mount. A calibrated ammeter enables the foil to be heated to any required temperature by the operation of a variable rheostat. The high temperature stage was designed by Whelan (1957).

To avoid certain difficulties in operating the stage, e.g. specimen drift, the following procedure was usually adopted: The area selected for observation was heated to the appropriate temperature, allowed to cool down and observed again and this operation was repeated as required; during the heating and cooling operation the electron beam was switched off.

The results obtained on heating these thin foils in the electron microscope showed that they behave in many respects differently to the bulk material.

Figure 10 shows a set of micrographs taken using the technique described above. The micrographs are all taken from the same area and associated diffraction patterns were taken from the central area ($\frac{4}{3}\,\mu$ diameter). Figure 10 (*a*) shows the area at room temperature. Owing to the high dislocation density, dislocations cannot be resolved individually and the area is generally opaque. Heating for four minutes at 200°C and then cooling gave the result shown in fig. 10 (*b*). The micrograph shows clearly that some changes have occurred; sharp boundaries have appeared producing sub-grains at A, B and C. If the sequence of micrographs is followed through it is seen that more sub-grains form and that some grow slightly.

The diffraction patterns taken with the sequence of micrographs show that the greater part of the orientations present originally remains the same throughout the sequence. This observation supports the suggestion that the sub-grains form by a polygonization process. Numerous series of observations similar to these were made.

It is not possible however, to account for all the spots occurring on the diffraction patterns. Several possibilities arise: It is not certain that the diffraction aperture is placed on exactly the same area for each diffraction pattern and therefore new orientations were possibly introduced. Furthermore, during sub-grain growth, neighbouring sub-grains with a new orientation may grow into the region. Finally, the variation in the amount of buckling of the foil during the heating will cause some spots to be excluded and others to be introduced.

The results obtained on annealing these very thin foils in the electron microscope differ considerably from the results obtained on annealing the bulk material. As compared with the bulk material, in which recrystallization produces a grain size of $\sim 20\,\mu$ at 110°C, in these thin foils, a small amount of sub-grain growth occurs rapidly at higher temperatures, and results in a small sub-grain or grain size of $\sim 1\,\mu$.

Further observations on these thin foils suggest that the grain size is a function of the foil thickness. Figure 11 (*a*), (*b*) and (*c*) was taken after heating a specimen to a high temperature in the electron microscope. Figure 11 (*a*) was taken close to an edge of the foil, fig. 11 (*b*) was taken further in from the edge (from such areas most of the previously described observations have been made), fig. 11 (*c*) as far inside the specimen as possible. It is seen that the grain size ($\sim \frac{1}{2}\mu$) near the edge of the foil (fig. 11 (*a*)) increases to several microns far inside the foil (fig. 11 (*c*)). This observation that the grain size increases continuously with increasing thickness of the foil suggests that no new recrystallization mechanism is occurring in the thinner parts of the foil but that the mobility of grain boundaries decreases with decreasing foil thickness. This effect can be qualitatively accounted for if the surface of the foil resists the motion of the boundary. It is clear that the thicker the foil, the smaller will be the effect of this resistance on the migration of a grain boundary, since on the whole there will be less of its boundary in contact with the surface of the foil.

Observations were made on the foils during the heating in an attempt to gain information about the mechanism of sub-grain formation and growth. It was observed that the process occurred very rapidly and jerkily and in this respect was difficult to observe since there was no indication that a particular region was about to polygonize. Attempts to record this process with a ciné camera were unsuccessful. The rapidity and jerky manner with which the process occurred, suggested that the mechanism had some of the features of a slip process.

§ 5. DISCUSSION

According to the conventional nucleation theory (Burke and Turnbull 1952), the nucleation of new grains during recrystallization occurs by a sequence of thermal fluctuations from atomic dimensions. Now for a nucleus to grow the increase in surface free energy must be more than compensated for by the loss in the volume free energy[†]. Consider a spherical nucleus of radius R; if the nucleus is to grow then:

$$\{4\pi(R+\delta R)^2 - 4\pi R^2\}\sigma < 4\pi R^2 \delta R E$$

where E is the stored energy per unit volume and σ the surface energy; this reduces to

$$R > 2\sigma/E.$$

For silver deformed 25% in tension $E \sim 4$ cals/g atm and $\sigma \sim 500$ ergs/cm^2 and hence $R > \frac{1}{2}\mu$. To produce a nucleus of $\sim \frac{1}{2}\mu$ radius with the aid of thermal fluctuation seems a rather unlikely process. It is sometimes suggested that in local regions of the metal, the value of the stored energy is several orders of magnitude greater than the average value and hence that nuclei of atomic dimensions can grow since $2\sigma/E$ is then very much less than $\frac{1}{2}\mu$. The difficulty with this model is that the stored energy must drop rapidly in the surrounding regions in order to give the low average stored energy value observed, whereas if such a nucleus is to grow the stored energy density must fall off in such a manner that the radius of the growing nucleus is always greater than $2\sigma/E$. In a previous paper (Bailey and Hirsch 1960) it has been shown that the total stored energy can be accounted for in terms of the observed dislocation arrangement in the metal, i.e. dense dislocation arrangements in cell walls. In this model the local stored energy density is a maximum at the core of a dislocation. It is expected therefore, to be easiest to form a nucleus of atomic dimensions at the core; however, it can be easily shown that growth can occur only to atomic dimensions because the surrounding elastic strain energy density from a dislocation falls off too rapidly for the nucleus to grow. It may be thought that a nucleus of ~ 100 Å could grow in the cell walls. For polycrystalline silver deformed in tension the dislocation density N_f in the cell walls is about five times the average dislocation density N (Bailey and Hirsch 1960) and hence in the cell walls the stored energy E_f is $\sim 5E$; therefore $2\sigma/E_f$ is $\sim 1/10\,\mu$. To form a nucleus of this size by thermal fluctuations is quite unreasonable, but even worse, it could not grow out of the cell walls unless its radius $R \sim 1/2\,\mu$, i.e. the possibility of growth is still governed by the average value of the stored energy.

[†] The assumption is made throughout this discussion that the free energy is equal to the difference between the stored energy involved and surface energy absorbed.

It can be concluded therefore that for the distribution and density of dislocations observed in the cold-worked metal, recrystallization by a process of random nucleation is ruled out. For the nucleation process, R must be ~ 10 Å and hence this process would be possible only if $E \sim 10^3$ cals/g atm corresponding to a dislocation density of $\sim 10^{14}$ cm/cm^3; this value is very unlikely and so far there is no evidence for such high dislocation densities in local regions of a deformed metal. Furthermore, recrystallization occurs in materials with lower dislocation densities than those considered here. For this reason the theory due to Cahn (1950), which suggests that recrystallization nuclei are produced by the polygonization of dislocations to form sub-grains which then grow preferentially, seems particularly plausible.

In actual fact the observation is that in silver foils deformed in tension recrystallization occurs by the migration of the grain boundaries. Beck and Sperry (1950) observed this mechanism, which they called strain induced boundary migration, when annealing aluminium cold-rolled to moderate deformations. Their observations were on a much larger scale than those presented here. The grain size of the aluminium was $\sim 10^4\,\mu$ as compared with $\sim 10\,\mu$ for the silver used in this investigation and they observed regions of the grain boundaries of $\sim 10^3\,\mu$ in length to bulge out and grow into the neighbouring grains, as compared with regions $\sim 1\,\mu$ in length in the present case. These combined observations strongly suggest that for moderate deformation most polycrystalline metals recrystallize by this grain boundary migration mechanism. The problem now is to decide on the criterion for migration of the boundary. A simplified model is envisaged here (fig. 12) in which a circular area of grain boundary of diameter $2L$ bulges out into the shape of a spherical cap and migrates; such a model is in accordance with the observations. The boundary will migrate provided that there is a difference in free energy ΔF across the boundary; that is, provided that the energy released by the migration more than compensates for the increase in surface energy. Now the change in free energy will be given by:

$$\Delta F\,.\,\delta V = E\,\delta V - \sigma\delta A \qquad (1)$$

where δA is the increase in boundary area when the volume δV is swept through by the grain boundary and E is the stored energy difference across the boundary and σ the grain boundary energy. For migration ΔF must be positive, that is:

$$E > \sigma\delta A/\delta V. \qquad (2)$$

Fig. 12

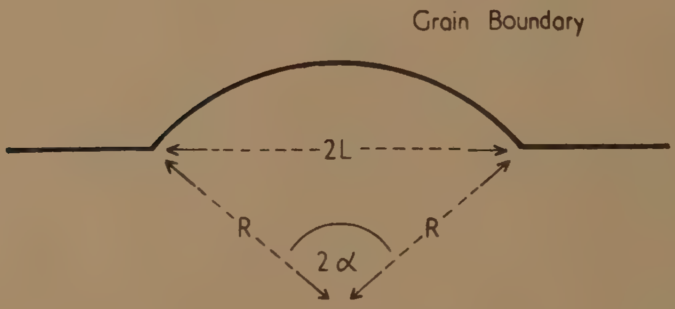

Model for the grain boundary migration process.

For the above model (fig. 12)

$$\delta A/\delta V = 2\sin\alpha/L \qquad (3)$$

which has a maximum of $2/L$ when $R = L$ and hence:

$$E \geqslant 2\sigma/L.$$

Thus provided an area of radius $> L$ moves forward there is a positive driving force. But the rate of advance or of formation of the bulge depends on the nature of the migration process on an atomic scale. For silver deformed $\sim 25\%$ in tension $E \sim 4$ cals/g atm and thus $L > \frac{1}{2}\,\mu$, which agrees favourably with the observations.

The treatments of grain boundary migration occurring in the literature (Burke and Turnbull 1952, Cole *et al.* 1954) are based on models in which an atom is transferred across the boundary and the linear rate of growth G is given by:

$$G = C\,.\,\Delta F\,.\exp(-U)/KT \qquad (4)$$

where U is the activation energy for the transfer of atoms from the cold-worked side of the boundary to the other side, T is the temperature,

K Boltzmann's constant and C a constant, at a given temperature. From eqn. (4) it is seen that G is proportional to ΔF and substituting for ΔF from eqn. (1):

$$G = B \,.\, \Delta F = B(E - \sigma \delta A / \delta V), \quad \ldots \ldots \quad (5)$$

B being a constant at a given temperature. It is clear from eqns. (5) and (3) that the migrating boundary region will initially decelerate until $R = L$ (i.e. when $\delta A / \delta V$ reaches a maximum) and will then accelerate again; further, unless $L > 2\sigma / E$ the regions of boundary decelerate and come to a halt, otherwise ΔF would become negative. The time taken by the migrating boundary to reach the position where $R = L$ may be looked upon as a nucleation period.

The process of grain boundary migration can then be considered to proceed as follows: migration may start at an area of boundary across which there is a fairly large difference in dislocation density. As soon as the boundary has moved a dislocation free region is generated on one side so that the driving force is then governed by the average value of the stored energy. Although the stored energy associated with the dislocations is responsible for the driving force for the migration process and produces a positive value of ΔF in eqn. (4), the main rate determining factor is the activation energy U which is only affected to a very small degree by the dislocations. The above model does not enquire into the mechanism by which the boundary migrates on an atomic scale. It does not imply a particular value for the activation energy or whether the activation process is affected by dislocations ending in the boundary. Although the process may be expected to be influenced where dislocations end in the boundary, most of the boundary must migrate by the normal process and therefore, the average activation energy U is not expected to be greatly affected by dislocations. The value of U might be expected to be about that for grain boundary self diffusion. The observations discussed here do not provide information on the nature of the migration process since boundary migration was not observable in the electron microscope. It is proposed to discuss this process in more detail in a later paper.

The observations on the recrystallization of heavily rolled foils (95% reduction) are less conclusive. Although recrystallization is seen to occur by the migration of high angle boundaries, it is possible that the sub-grains which are observed to form by polygonization are also able to migrate. Due to the high misorientations observed in these foils a sub-grain boundary need only migrate a small distance before becoming essentially a high-angle boundary. For this reason and the fact that the original grain boundaries were indistinguishable, it was not possible to determine whether recrystallization occurred by the migration of the old grain boundaries or by sub-grain boundaries or by both. In a sense the distinction between these two mechanisms is trivial since the straight forward interpretation of the observations presented here is that in all cases recrystallization occurs by the migration of the high angle boundaries present in the material regardless of their origin. For this reason it would seem of great interest to investigate the conditions under which deformed single crystals recrystallize.

ACKNOWLEDGMENTS

The author is indebted to Professor N. F. Mott, F.R.S., and to Dr. W. H. Taylor for their interest and encouragement. He particularly wishes to thank Dr. P. B. Hirsch for his useful criticism and for a very full discussion of the content of this paper. Thanks are also due to Messrs. C. K. Jackson and G. Rickards for assistance in electron microscopy. The author wishes to acknowledge the receipt of a maintenance grant from the Admiralty.

REFERENCES

BAILEY, J. E., 1959, Ph.D. Dissertation, University of Cambridge.
BAILEY, J. E., and HIRSCH, P. B., 1960, *Phil. Mag.*, **5,** 485.
BECK, P. A., and SPERRY, P. R., 1950, *J. appl. Phys.*, **21,** 150.
BURKE, J. E., and TURNBULL, D., 1952, *Prog. met. Phys.*, **3,** 220 (London: Pergamon Press).
CAHN, R. W., 1950, *Proc. phys. Soc. Lond.*, A, **63,** 323.
COLE, D. G., FELTHAM, P., and GILLIAM, E., 1954, *Proc. phys. Soc. Lond.*, B, **67,** 131.
GAY, P., and KELLY, A., 1953, *Acta Cryst.*, **6,** 165.
WHELAN, M. J., 1957, Ph.D. Dissertation, University of Cambridge.

Strain-broadening of Nuclear Magnetic Resonance Lines in Copper†

By E. A. FAULKNER
Division of Tribophysics, Commonwealth Scientific and Industrial Research Organization, University of Melbourne, Australia

[Received January 25, 1960]

ABSTRACT

The mean-square width of the nuclear magnetic resonance absorption line in copper sheet has been measured with an accuracy of ±4%, using specimens from a sample of copper (99·98% Cu) on which stored energy measurements had already been made (Clarebrough *et al.* 1957). Plastic deformation has been found to increase the mean-square line width by up to 40% and there is evidence that the broadening is proportional to the stored energy. There is also a small reduction in the integrated intensity of the line in deformed specimens, possibly caused by the high strains in regions near the cores of dislocations.

The results can be interpreted satisfactorily on a model where both the line width and the stored energy are calculated from the state of strain of the material.

§ 1. INTRODUCTION

SOME preliminary measurements of the nuclear magnetic resonance in rolled copper sheet have already been reported (Faulkner 1959 a). The accuracy of these experiments was severely limited by the effects of eddy-currents and preferred orientation, but they were sufficient to show that the sensitivity of the resonance line to deformation had previously been overestimated by a factor of 10 or more (Bloembergen 1955); this was confirmed by measurements on copper sheet subjected to elastic strain (Faulkner 1959 b).

The experimental technique has now been improved so that measurements of the mean-square line width in copper sheet are possible with a standard deviation of ±4%. Plastic deformation has been found to cause a definite broadening of the line, and this paper describes measurements of the line width and intensity as a function of the degree of plastic deformation by rolling. The material used was O.F.H.C. copper (99·98% Cu) on which stored energy measurements had already been made (Clarebrough *et al.* 1957) for similar amounts of deformation by compression.

All measurements were made at room temperature, on the ^{63}Cu resonance.

---

† Communicated by W. Boas.

§ 2. APPARATUS

The spectrometer is of the marginal-oscillator type, operating at 5·5 Mc/s. It is based on a Colpitts oscillator coupled to a crystal detector which is connected through a high resistance to the grid of the oscillator valve, so that this valve also acts as the first audio-frequency amplifier. This arrangement has been found more sensitive than a simple regenerative detector (Gutowsky *et al.* 1953), and gives much better control of oscillation amplitude with change of frequency. The frequency is swept at a rate of 26 kc/s per hour by a synchronous motor which drives the tuning capacitor through a reduction gear. The detector is relatively insensitive to direct pick-up from the modulation coils, so no compensating coil is necessary.

A permanent magnet is used, with a gap of 11·4 cm diameter and 3·8 cm length, in which the field is 4·9 kilogauss. The field is sinusoidally modulated at a frequency of 350 c/s with peak-to-peak amplitude of 5·0 gauss, which is nearly equal to the line width.

The audio-frequency signal is fed to a pentode preamplifier mounted in the oscillator housing, and then to a transistor amplifier with a gain of 50 dB; this is run from a transistor-stabilized direct current supply which also provides the current for the heaters of the oscillator and preamplifier valves. The output of the amplifier, which is about 1 volt peak-to-peak, is fed to a transistor phase-sensitive detector (Faulkner 1959 c) with a time-constant of 5 sec, connected to a 0–10 millivolt Varian recorder.

§ 3. EVALUATION

Three parameters are extracted from the recorded curves: these are the mean-square line width $\overline{\Delta f^2}$, the integrated intensity I, and the ‘derivative maximum’ G_{max}. In the recorded curve the abscissa is proportional to the oscillator frequency f and the ordinate to the output voltage $G'(f)$ of the phase-sensitive detector. The curve has the same general appearance as the usual ‘derivative’ curve but is not quite antisymmetric, the maximum value on the high-frequency side being about 15% greater than the corresponding value on the low-frequency side. This distortion is due to eddy currents in the specimen (Chapman *et al.* 1957). A function $G(f)$ can be defined by

$$G(f)=G(f_0'+\Delta f)=\tfrac{1}{2}[G'(f_0'+\Delta f)-G'(f_0'-\Delta f)] \quad . \quad . \quad . \quad (1)$$

where f_0' is the frequency for which $G'=0$. This process is equivalent to taking a mean of the magnitudes of G' at equal intervals from f_0', and, because the distortion is small, G should be a good measure of the output voltage in the absence of distortion.

Using the analysis of Andrew (1953), one can now calculate the mean-square line width $\overline{\Delta f^2}$ from the formula

$$\overline{\Delta f^2}=\frac{\int_0^\infty (f-f_0')^3 G(f)\,df}{3\int_0^\infty (f-f_0')G(f)\,df}-\frac{\gamma^2 h_m{}^2}{4} \quad . \quad . \quad . \quad . \quad . \quad (2)$$

where γ is the gyromagnetic ratio and h_m is the modulation amplitude; also the integrated intensity I from the formula

$$I = \int_0^\infty (f-f_0')G(f)\,df \quad . \quad . \quad . \quad . \quad . \quad . \quad . \quad . \quad (3)$$

which gives I in units which depend on the experimental parameters.

In order to carry out the integrations, the experimental curve was traced from the recorder chart on to graph paper and values of G' were read at intervals of 0·25 cm, corresponding to frequency intervals of 0·44 kc/s. This gave about 55 non-zero numerical values for each line.

The parameter which is referred to as $G_{\max}$ was obtained for each line by averaging the two highest numerical values of G. The ratio $I/G_{\max}$ for a line has the same units as the mean-square width, and has been found to be a very useful empirical measure of line width, although its value cannot be simply corrected for modulation broadening.

§ 4. SPECIMENS

A strip of copper of size 5·1 × 2·3 × 0·18 cm was machined from the bar which provided the specimens for the stored energy experiments referred to previously (Clarebrough *et al.* 1957). This was annealed for one hour at 600°C, after which strips were rolled from it of thickness 0·010, 0·005, 0·0033 and 0·0025 cm, the rolling being done in alternate directions with about 10% reduction at each pass. The thinnest of these strips had been reduced by 98·6% in thickness. The three thicker strips were recrystallized by being annealed for 10 min at 300°C and were then rolled down to a thickness of 0·0025 cm, corresponding to reductions in thickness of 75, 50 and 25%.

Each specimen consists of two pieces cut from the rolled strips, each piece measuring 6·0 × 0·6 × 0·0025 cm. These are wrapped in rice paper and wound into a tight spiral of outer radius 0·25 cm which is fitted into a glass tube; this tube can be slid into the specimen coil of the spectrometer.

In this spiral type of specimen, the effects of preferred orientation are minimized and thinner sheet can be used than in the parallel-sheet type of specimen used previously without any sacrifice of rigidity, so that eddy-current distortion of the line is greatly reduced. The specimen has good thermal contact with the wall of the glass tube, and can be heat-treated without being removed from the tube. The extra deformation involved in winding the strip has been found to be negligible compared with the deformation by rolling.

§ 5. EXPERIMENTAL PROCEDURE

Specimens were prepared from each of the rolled strips and the following experiments were done:

(1) The nuclear magnetic resonance absorption line was observed over a frequency range of 50 kc/s, which is about eight times the line width. This wide range was necessary in order to obtain an accurate zero level, because the tails of the line extended over a range of up to 25 kc/s. Lines were

recorded from two specimens of each deformation, and then a second set of strips was rolled and lines were recorded from one more specimen of each deformation. The mean-square width and integrated intensity of each line were obtained by the methods already described.

(2) Deformed specimens were heated at a rate of 6°C per minute in an oil bath, from which they were removed at suitable intervals to allow the absorption line to be recorded, and then returned to the bath for the heating to be continued. So that the experiment could be done in a reasonably short time, the frequency range was limited in these experiments to about 10 kc/s, which was sufficient to enable G_{max} to be measured but not the other line parameters. The value of G_{max} for a line can be measured with an estimated accuracy of about $\pm 1{\cdot}5\%$ in 25 min, so it will be seen that this is a convenient quantity to follow through the process of recrystallization.

§ 6. RESULTS

The observed mean-square line widths and values of I/G_{max} for the various deformations are listed in the table, with the standard deviations of eight observations on three separate specimens; the results listed under zero deformation refer to nine observations on four specimens which had been recrystallized (see below) after deformations ranging from 25 to 99%. The table also shows values of stored energy obtained by interpolation from the results given by Clarebrough *et al.* (1957) for deformation by compression, which may be assumed to be approximately equal to the stored energy in specimens which have been subjected to the same amount of deformation by rolling. In fig. 1 the observed mean-square line widths are plotted against these values of stored energy.

Deformation (%)	0	25	50	75	99
Mean-square width $(\text{kc/s})^2$	$7{\cdot}4 \pm 0{\cdot}2$	$8{\cdot}9 \pm 0{\cdot}3$	$9{\cdot}3 \pm 0{\cdot}4$	$10{\cdot}0 \pm 0{\cdot}4$	$10{\cdot}2 \pm 0{\cdot}3$
I/G_{max} $(\text{kc/s})^2$	$1{\cdot}06 \pm 0{\cdot}02$	$1{\cdot}17 \pm 0{\cdot}03$	$1{\cdot}22 \pm 0{\cdot}02$	$1{\cdot}28 \pm 0{\cdot}04$	$1{\cdot}30 \pm 0{\cdot}03$
Relative value of I/G_{max}	1·00	1·10	1·15	1·20	1·22
Stored energy (cal/g)	0·000	0·088	0·121	0·154	—
Relative value of G_{max} after recrystallization	1·00	1·12	1·21	1·27	1·33

The results of the annealing experiments are shown in fig. 2. It can be seen that a sudden increase in G_{max} occurs for each specimen in a range of temperature which is lower the higher the degree of deformation. It is found that this range of temperature corresponds to that in which the evolution of stored energy and changes in properties accompanying recrystallization have been observed (Clarebrough, Hargreaves and West, private communication). The increase in G_{max} on annealing is therefore attributed to recrystallization.

Relative values of G_{max} before and after recrystallization are obtained from the initial and final levels in these curves and are listed in the table.

Fig. 1

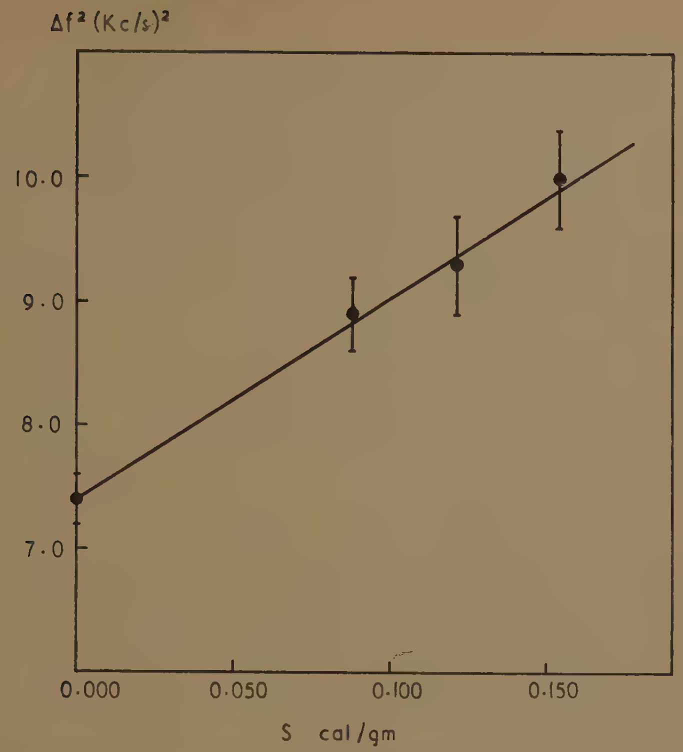

Mean-square line width in deformed and annealed copper sheet, plotted against stored energy figures. The equation of the drawn line is $\overline{\Delta f^2} = 17S + 7{\cdot}4$.

Fig. 2

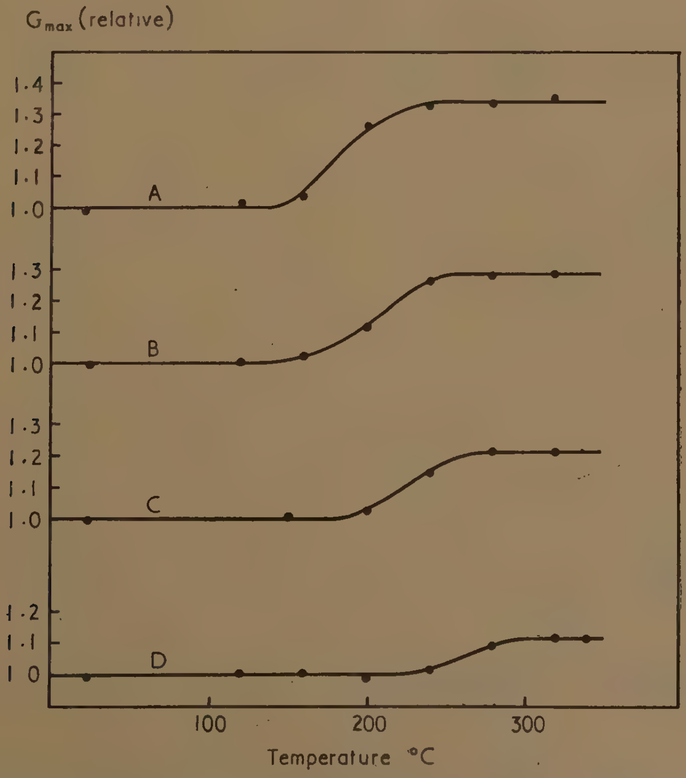

Nuclear magnetic resonance in rolled copper sheet heated at 6°c per minute. Deformation: A, 99%, B, 75%, C, 50%, D, 25%.

§ 7. DISCUSSION

Strain-broadening of nuclear magnetic resonance lines is due to electric quadrupolar interactions, as distinct from the magnetic dipolar interactions which are the cause of the line width in a strain-free cubic crystal. Since there is no correlation between these two mechanisms, the resultant mean-square line width is simply the sum of the dipolar and quadrupolar contributions:

$$\overline{\Delta f^2}=\overline{\Delta f_{\mathrm{D}}{}^2}+\overline{\Delta f_{\mathrm{Q}}{}^2}. \quad . \quad . \quad . \quad . \quad . \quad . \quad . \quad . \quad (4)$$

The quadrupolar perturbation of the nuclear magnetic energy levels at a given site depends on the electric field gradient grad grad ϕ, which is zero in the case of perfect cubic symmetry and which is linearly related, in the case of small strain, to the value of the strain tensor at the site (Cohen and Reif 1957). In first-order perturbation the frequency shift Δf of the nuclear magnetic resonance is proportional to $\phi_{z'z'}$ where z' is the direction of the applied magnetic field, the other components of grad grad ϕ being inoperative. Since the stored energy of a randomly strained isotropic material is proportional to the mean-square value of the strain, and since the strain distribution in polycrystalline rolled sheet approximates to a random one, it may reasonably be assumed that the mean-square value of $\phi_{z'z'}$ is proportional to the stored energy. These considerations lead to the following theoretical relation between the stored energy S and the quadrupolar contribution $\overline{\Delta f_{\mathrm{Q}}{}^2}$ to the mean-square line width:

$$\overline{\Delta f_{\mathrm{Q}}{}^2}=kS. \quad . \quad . \quad . \quad . \quad . \quad . \quad . \quad . \quad . \quad . \quad (5)$$

It will be seen from fig. 1 that a straight line can easily be drawn through a plot of the observed values of $\overline{\Delta f^2}$ against S. Comparison of the equation of this line with eqns. (4) and (5) leads to the result

$$k=17\ (\mathrm{kc/s})^2\ \text{per (calorie per gram)}. \quad . \quad . \quad . \quad . \quad . \quad (6)$$

The other information that can be derived from these results concerns the integrated intensity of the lines. Experiments on alloys (Bloembergen and Rowland 1953) indicate that the quadrupolar interactions rise very sharply in the neighbourhood of a solute atom so that quadrupolar interactions at the adjacent sites are sufficient to eliminate their contribution to the observed nuclear magnetic resonance line, while the resonance at other sites is only slightly affected. A similar effect may be expected near the core of a dislocation, so that the presence of dislocations will result in a reduction in the integrated intensity I of the line (which is proportional to the number of nuclei taking part in the resonance) compared with the corresponding value for a perfect crystal. Small changes in the absolute value of I are not easy to measure experimentally because of slight variations in the overall sensitivity of the apparatus from day to day but measurements of the value of $I/G_{\max}$ are not affected by such variations. A useful indication of any change in I can therefore be obtained by comparing the ratio $G_{\max}$ (recrystallized)/$G_{\max}$ (deformed) from the annealing experiments with the relative values of $I/G_{\max}$ in the deformed and annealed states.

If I remained constant during annealing, these two ratios would be equal, but it can be seen from the table that the relative change in $G_{\max}$ is always slightly more than the corresponding ratio of $I/G_{\max}$ values so it seems that I does increase by a few per cent during recrystallization.

It will be seen from the table that the line width for the 99% deformed specimen is very little more than that for the 75% deformed specimen. although the increase in $G_{\max}$ on annealing is significantly greater. In the absence of stored energy data for this degree of deformation, no attempt will be made to interpret this fact; however, it is consistent with the fact that in copper filings, which may show a much larger increase in $G_{\max}$ on annealing, there is no very marked broadening of the line at any stage in the annealing process.

The results of the earlier annealing experiments on parallel-sheet specimens (Faulkner 1959 a) agree within experimental limits with the more accurate results quoted here except for the case of 25% deformation. [In the report of these experiments the quantity $G_{\max}$ was referred to as the *intensity* of the line, following previous practice (Bloembergen and Rowland 1953).] Because of eddy-current effects, the strain-broadening of the line was not observed in these experiments and it was assumed that changes in $G_{\max}$ on annealing were largely due to variations in the integrated intensity; however, it now appears that the main cause of such changes is variation in the line width and shape.

§ 8. CALCULATION OF STRAIN-GRADIENT TENSOR

The quadrupolar perturbation of the nuclear magnetic energy levels at a given site depends on the electric field gradient grad grad ϕ, which is connected with the strain at the site by a fourth-order tensor which may be written, by the use of the Voigt notation, in terms of components F_{ij}; in the case of cubic symmetry there are only two independent components, $F_{11}=-2F_{12}$ and F_{44}. The values of these components may be calculated from the observed constant of proportionality between stored energy and line broadening in polycrystalline material if assumptions are made about (a) the relation between F_{11} and F_{44} and (b) the strain distribution in the specimen.

(a) It is reasonable to suppose that the field gradient is due to the displacement of charges in a uniformly deformed lattice, and this assumption leads to the relation (Cohen and Reif 1957) $F_{44}=F_{12}$ which has been confirmed experimentally for single crystals of InSb (Shulman *et al.* 1957) and which has been used in all the calculations in this work.

(b) There are various possible assumptions that can be made about the strain distribution in the deformed material. The simplest one is that there is only elastic shear strain, randomly distributed in direction and magnitude, and that all the stored energy resides in the regions of the crystal which contribute to the nuclear magnetic resonance, the effect of dislocation cores being ignored. This assumption will be used in the calculation which follows.

Let the strain at any lattice site in a cubic crystal have the single component $E=E_{x''y''}$, the direction cosines of the x'' and y'' axes referred to the crystal axes being (l_1, l_2, l_3) and (m_1, m_2, m_3) respectively. The strain components in the crystal axes are then

$$\left.\begin{array}{lll} E_{xx}=l_1m_1E, & E_{yy}=l_2m_2E, & E_{zz}=l_3m_3E, \\ E_{yz}=(l_2m_3+l_3m_2)E, & E_{zx}=(l_3m_1+l_1m_3)E, & E_{xy}=(l_1m_2+l_2m_1)E, \end{array}\right\} \quad (7)$$

and the components of grad grad ϕ are obtained by multiplying by the tensor F, in which $F_{11}=-2F_{12}=-2F_{44}$. This gives

$$\left.\begin{array}{l} \phi_{xx}=F_{11}(E_{xx}-\frac{1}{2}(E_{yy}+E_{zz}))=\frac{3}{2}F_{11}l_1m_1E, \\ \phi_{yz}=-\frac{1}{2}F_{11}E_{yz}=-\frac{1}{2}F_{11}(l_2m_3+l_3m_2)E, \end{array}\right\} \quad . \quad . \quad . \quad . \quad (8)$$

with corresponding expressions for the other components of grad grad ϕ.

In first-order quadrupolar perturbation of nuclear magnetic energy levels the only operative component of grad grad ϕ is $\phi_{z'z'}$ where the z' axis is the direction of the applied magnetic field, with direction cosines $(\lambda_1, \lambda_2, \lambda_3)$ referred to the crystal axes. This component is given by

$$\phi_{z'z'}=\lambda_1^2\phi_{xx}+\lambda_2^2\phi_{yy}+\lambda_3^2\phi_{zz}+2(\lambda_2\lambda_3\phi_{yz}+\lambda_3\lambda_1\phi_{zx}+\lambda_1\lambda_2\phi_{xy}) \quad . \quad . \quad (9)$$

and its mean-square value may be obtained by averaging this expression over all the sites in a randomly oriented array of crystals

$$\overline{\phi_{z'z'}^2}=\frac{1}{5}(3\overline{\phi_{xx}^2}+4\overline{\phi_{yz}^2}+2\overline{\phi_{xx}\phi_{yy}}). \quad . \quad . \quad . \quad . \quad (10)$$

The averages in this equation are obtained from eqns. (8) by assuming a random distribution of the l's and m's, the result being

$$\overline{\phi_{z'z'}^2}=\frac{1}{10}F_{11}^2\overline{E^2}. \quad . \quad . \quad . \quad . \quad . \quad . \quad . \quad . \quad (11)$$

The corresponding broadening of the nuclear magnetic resonance line can be calculated from the well-known formulae for first-order quadrupole interaction (Pound 1950): the result for copper, in c.g.s. electrostatic units, is

$$\overline{\Delta f_Q^2}=1\cdot8\times10^{-17}\overline{\phi_{z'z'}^2}=1\cdot8\times10^{-18}F_{11}^2\overline{E^2}, \quad . \quad . \quad (12)$$

allowance having been made for the fact that the central component of the line, comprising 40% of its intensity, is not broadened in first-order approximation.

The strain energy density is simply $\frac{1}{2}\mu E^2$ where μ is the shear modulus so the stored energy per unit mass is given by

$$S=\mu\overline{E^2}/2\rho \quad . \quad . \quad . \quad . \quad . \quad . \quad . \quad . \quad . \quad (13)$$

where ρ is the density. The value of F_{11} can now be found by combining eqns. (12) and (13) and putting in the observed value of $\overline{\Delta f_Q^2}/S$ from eqn. (6) which is equal to 0·41 (c/s)^2 per (erg/g), and the known values of μ and ρ for copper. The final result is

$$F_{11}=7\times10^{13}\text{ c.g.s. electrostatic units.} \quad . \quad . \quad . \quad (14)$$

This result is probably somewhat lower than the true value, because no account is taken of any reduction in integrated intensity which may be caused by the deformation; this is equivalent to ignoring the strain energy of the regions in the crystal where the strain is very high.

It is interesting to compare the result (14) with estimates of the components of F made on the assumption that the field gradient is due to the displacement of unit electronic charges e located at the lattice points of a uniformly deformed lattice. A sum over the twelve nearest neighbours in a face-centred cubic lattice gives $F_{11} = 6ea^{-3}$, where a is the nearest neighbour distance, and this is equal to $1{\cdot}75 \times 10^{14}$ c.g.s. electrostatic units for copper. The ratio of the actual value of F_{11} to this estimate has been referred to as the anti-shielding factor because its value was thought to be greater than unity; however, this calculation suggests that it is about 0·4. This is much lower than corresponding values for ionic compounds (Watkins 1952) and semi-conductors (Shulman *et al.* 1957), presumably because of the effect of conduction electrons.

ACKNOWLEDGMENT

The author wishes to acknowledge the contribution made to this work by Dr. M. E. Hargreaves, whose advice and cooperation have been invaluable. Thanks are also due to Dr. A. K. Head, Dr. J. K. Mackenzie, and Mr. G. W. West for many valuable discussions.

REFERENCES

ANDREW, E. R., 1953, *Phys. Rev.*, **91,** 425.
BLOEMBERGEN, N., 1955, *Report on the Bristol Conference*, **1** (London: The Physical Society).
BLOEMBERGEN, N., and ROWLAND, T. J., 1953, *Acta Met.*, **1,** 731.
CHAPMAN, A. C., RHODES, P., and SEYMOUR, E. F. W., 1957, *Proc. phys. Soc. Lond.*, B, **70,** 345.
CLAREBROUGH, L. M., HARGREAVES, M. E., and WEST, G. W., 1957, *Acta Met.*, **5,** 738.
COHEN, M. H., and REIF, F., 1957, *Solid State Physics*, **5,** 321 (New York: Academic Press).
FAULKNER, E. A., 1959 a, *Nature, Lond.*, **183,** 1043; 1959 b, *Ibid.*, **184,** 442; 1959 c, *J. sci. Instrum.*, **36,** 321.
GUTOWSKY, H. S., MEYER, L. H., and MCCLURE, R. E., 1953, *Rev. sci. Instrum.*, **24,** 644.
POUND, R. V., 1950, *Phys. Rev.*, **79,** 685.
SHULMAN, R. G., WYLUDA, B. J., and ANDERSON, P. W., 1957, *Phys. Rev.*, **107,** 953.
WATKINS, G. D., 1952, *Ph.D. Thesis*, Harvard University.

Observation of Interstitial Atoms in F.C.C. Metals†

By A. Seeger, P. Schiller, and H. Kronmüller
Max-Planck-Institut für Metallforschung, Stuttgart, and Institut für theoretische und angewandte Physik der Technischen Hochschule Stuttgart, Germany

[Received May 8, 1960]

For a number of years, among the outstanding problems in the study of lattice defects in f.c.c. metals there have been the properties of atoms on interstitial lattice sites as produced by cold-work or radiation damage. Considering copper as an example, the key problem was whether the energy of migration of interstitial atoms was about 0·1 ev or about 0·6 ev. In the first case, the interstitial atoms would anneal out below 60°K, whereas in the second case the so-called annealing stage III (at about 250°K) would have to be ascribed to the annealing out of the interstitial atoms. So far no specific experiment has been published that would demonstrate directly the presence or the behaviour of isolated interstitial atoms in f.c.c. metals. The two views mentioned above are based on the analysis of a large body of experimental material, the interpretation of which includes the assignment of migration and formation energies to lattice defects other than interstitials. Recent reviews emphasizing the one or the other of the two principal viewpoints are those by Seitz (1959; small migration energy of interstitials) and by Seeger (1958, 1960; large migration energy of interstitials).

A recent theoretical study of interstitials in copper (Seeger *et al.* 1960) using the model of Seeger and Mann (1960) has given the following results:

(i) The interstitialcy configuration (fig. 1 *b*; Huntington and Seitz (1942)) has a lower energy than the position in the cube centre (fig. 1 *a*), in agreement with the results of Gibson *et al.* (1960).

(ii) The energy difference between the interstitialcy configuration (fig. 1 *b*) and the configuration with cubic symmetry (fig. 1 *a*) is of the order 0·6 ev–0·7 ev. This suggests that the energy of migration of an interstitial atom is of about the same magnitude.

An experimental check of these theoretical results appears possible as follows: According to the calculations, the stable configuration of an interstitial has a tetragonal symmetry with a preferred ⟨100⟩ axis. In an unstressed cubic crystal an equal number of interstitials will have their preferred directions parallel to each of the three cube axes, whereas under the action of an applied stress or (in a ferromagnetic crystal) in the presence of a magnetic field an asymmetric distribution will have a lower free energy. The transition of a random distribution to such a partially ordered one should give rise to a relaxation phenomenon similar to the so-called Snoek–effect of carbon atoms in α-iron. Estimates show the mechanical 'relaxation strength' per atom should be about the same in both cases.

---

† Communicated by the Authors.

There are, however, two important differences between the interstitial atoms in f.c.c. metals and the carbon (or other) impurities in b.c.c. metals:

(i) The f.c.c. interstitials cannot be present in thermal equilibrium. They anneal out at temperatures at which they are sufficiently mobile. This means that there are practical upper limits to the measuring frequencies and measuring times that can be used.

Fig. 1

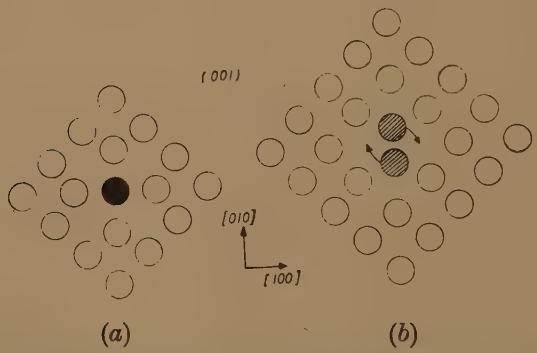

Section through a (001)-plane in a f.c.c. crystal containing an interstitial atom. (*a*) Interstitial (full circle) in cube centre, cubic symmetry of the environment. (*b*) Interstitial in interstitialcy (dumb-bell) configuration (hatched circles). Tetragonal symmetry with tetragonal axis along [010].

(ii) The activation energy of the relaxation process will in general be different from (lower than) the energy of migration of the interstitials as determined from diffusion experiments. The larger this difference the less stringent are the conditions mentioned under (i). Consider fig. 1: For interstitial migration by the interstitialcy mechanism the configuration of fig. 1 *b* must change (approximately) into that of fig. 1 *a* and may then relax into the interstitialcy configuration again, possibly with a different preferred ⟨100⟩–axis than before. However, the dumb-bell configuration of the two hatched 'half-interstitials' may 'rotate' into another ⟨100⟩–axis. The projection of such a movement on the (001)–plane is indicated by arrows in fig. 1 *b*. This movement leads over a saddle-point configuration lower in energy than that of fig. 1 *a*. Since this 'rotation' does not shift the 'centre of gravity' of the interstitialcy, it cannot contribute to the interstitial diffusion.

Keeping in mind the above mentioned complications over and above the Snoek–effect as caused by impurities, we have searched for the relaxation process due to the dumb-bell rotation. The noble metals were inconvenient for this, since the interstitial atoms anneal out in a very short time at ambient temperature. According to Sosin and Brinkman (1959), interstitials in nickel have an energy of migration of 1·03 ev. They should therefore be quite persistent at room temperature. Allowing for the different scales of temperatures or activation energies, the spectra of migration energies of point defects appear to be very similar for copper and nickel. We have therefore chosen nickel for an experimental investigation. This has the additional advantage that we are able to demonstrate the ferromagnetic analogue to the Snoek–effect (in the case of C in α–Fe called Richter-after-effect).

We have employed two different experimental techniques: (1) Internal friction as measured in the torsion pendulum (apparatus described by Bangert 1952); (2) The disaccommodation of the initial ferromagnetic susceptibility as measured in a mutual inductance bridge (Wilde 1952, Gerstner 1960).

All our measurements were performed on polycrystalline nickel wires drawn at room temperature and stored at liquid oxygen temperature. As a function of temperature the logarithmic decrement showed peaks of the order of magnitude 10^{-3} superimposed on a rather large background increasing uniformly with temperatures. The shift in the peak temperature was observed for a frequency variation by a factor of 5. The corresponding relaxation times τ are plotted as a function of the reciprocal absolute temperature in fig. 2 (full circles). The half-width of the peaks corresponds to an activation energy of 0·8 ev.

The disaccommodation of the initial susceptibility μ was measured between 0°c and 21·4°c. To a good approximation the time variation of μ was exponential. The corresponding relaxation times τ are shown as open circles in fig. 2.

The magnetic and mechanical measurements can be described by the equation

$$\tau=\tau_0 \exp\left(\frac{Q}{kT}\right) \quad . \; . \; . \; . \; . \; . \; . \; . \; . \quad (1)$$

with $Q=(0{\cdot}79\pm0{\cdot}03)$ ev. For $Q=0{\cdot}79$ ev we find $\tau_0=4\times10^{-12}$ sec. The relaxation times that can be deduced from the disaccommodation measurements of Morkowski (1959) between 10·3°c and 59·6°c agree with the relation shown in fig. 2.

We have also performed annealing experiments. The relaxation effect annealed out with an activation energy of migration of about 1 ev. Allowing for differences in the amount of cold-work, the annealing characteristics were the same as those observed in resistivity annealing studies of stage III and attributed to interstitial migration (Sosin and Brinkman 1959). We consider this as strong evidence for the assignment of both the annealing stage III and the relaxation effect reported in this note to the movement of individual interstitial atoms. Any other explanation (for instance one involving diinterstitials) appears to be far less satisfactory.

The present results are in complete agreement with the view that the migration energies of interstitials are rather high, and with the results of the calculations mentioned above. For copper, where according to Meechan and Brinkman (1956) the activation energy of interstitial migration is 0·6 ev, we expect an activation energy Q for the relaxation mechanism of about 0·45 ev. A relaxation peak in cold-worked copper with such an activation energy was observed by Hasiguti and Okuda (1959). We are not sure, however, whether this peak has the same origin as that studied in the present paper, since the annealing behaviour of the two peaks seems to be different. We are planning to undertake experiments on the noble metals in order to investigate these questions further.

Fig. 2

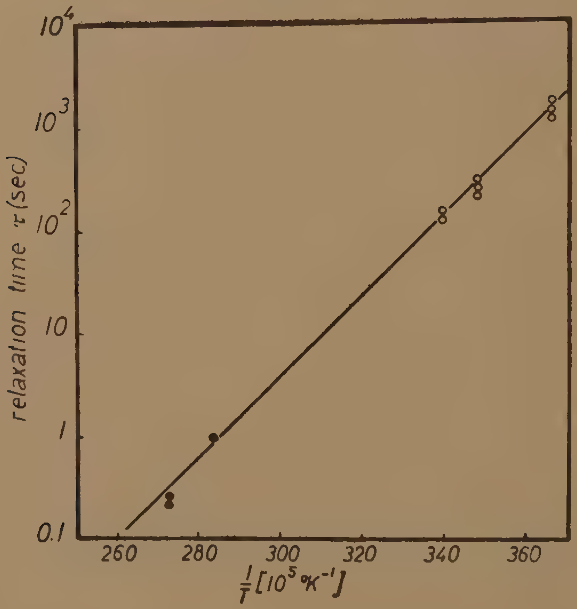

Relaxation time τ (in logarithmic scale) as a function of the reciprocal of the absolute temperature T.

The relaxation effect reported in the present paper appears not only to decide the question of the migration energy of interstitials in f.c.c. metals discussed above, but promises to provide a quantitative tool for the study of atoms on interstitial sites. Experiments on radiation damaged metals would be particularly interesting in this respect.

Note added in proof.—Experiments on pile-irradiated nickel have now been performed, and the results agree in all respects with those reported here (Kronmüller *et al.* 1960).

REFERENCES

BANGERT, L., 1952, Thesis T. H., Stuttgart.
GERSTNER, D., 1960, (to be published).
GIBSON, J. B., GOLAND, A. N., MILGRAM, M., and VINEYARD, G. H., 1960, *Bull. Amer. phys. Soc.*, **5,** 26.
HASIGUTI, R. R., and OKUDA, S., 1959, *Proc. imp. Acad. Japan.*, **35,** 284.
HUNTINGTON, H. B., and SEITZ, F., 1942, *Phys. Rev.*, **61,** 315.
KRONMÜLLER, H., SEEGER. A., and SCHILLER, P., 1960, *Z. Naturforschg.* (in the press).
MEECHAN, J. C., and BRINKMAN, J. A., 1956, *Phys. Rev.*, **103,** 1193.
MORKOWSKI, J., 1959, *Acta phys. polon.*, **18,** 75.
SEEGER, A., 1958, *Proceedings of the Second United Nations International Conference on the Peaceful Uses of Atomic Energy*, Vol. 6, 250 (Geneva); 1960, *Prog. nucl. Energ.*, Vol. 3 (in the press).
SEEGER, A., and MANN, E., 1960, *J. Phys. Chem. Solids*, **12,** 326.
SEEGER, A., MANN, E., and v. JAN, R., 1960, (to be published).
SEITZ, F., 1959, *Trans. met. Soc., A.I.M.E.*, **215,** 354.
SOSIN, A., and BRINKMAN, J. A., 1959, *Acta Met.*, **7,** 478.
WILDE, H., 1952, *Arch. elektr. Übertr.*, **6,** 354.

Lattice Vibrations of Sodium Chloride: Experimental and Theoretical Heat Capacity Data†

By J. R. Hardy
Department of Physics, University of Reading, Berkshire

and A. M. Karo
Lawrence Radiation Laboratory, University of California, Livermore, California

[Received May 3, 1960]

Abstract

Vibrational frequency spectra of sodium chloride derived from two theoretical models which allow for ionic deformability, instead of treating the ions as rigid point charges, have been used to calculate ‘ effective ’ Debye temperatures and distribution function moments.

The results are compared with those deduced from specific heat measurements. For the second, more refined, model the agreement with experiment is considerably better than that achieved when the ions are treated as rigid point charges as in the simple Born theory.

§ 1. Introduction

There has recently been a revival of interest in the theory of the lattice dynamics of the alkali halide crystals. This has been stimulated by high-precision, specific heat measurements on these materials by Morrison *et al.* (1955), Morrison and Patterson (1956), Berg and Morrison (1957), Briscoe and Squire (1957), Briscoe and Norwood (1958). At the same time preliminary results on inelastic neutron scattering in sodium iodide (Woods *et al.* 1959) have shown that the simple Born–Mayer model does not adequately describe the dynamical behaviour of this crystal. This model assumes that the crystal is composed of point charges held apart by nearest-neighbour repulsion, and it has long been known that it does not adequately describe the dielectric properties of these crystals even when the ions themselves are regarded as polarizable. Cochran (1959 a) has interpreted the frequency *versus* wave number dispersion curves for lattice vibrations obtained from neutron scattering data in terms of a model advanced by Hanlon and Lawson (1959) to explain the dielectric properties and claims good agreement with experiment for sodium iodide. A similar model for germanium reproduces the experimental dispersion curves very closely (Cochran 1959 b).

Recently one of us (Karo 1959, denoted by A hereafter, 1960) has carried out a systematic investigation of the frequency spectra of most of the alkali halides on the basis of the simple Born–Mayer model. This represents an extension of Kellermann's (1940, 1941) classic work on sodium chloride and uses improved compressibility data (Born and Huang 1954). The

---

† Communicated by the Authors.

results of this investigation are directly comparable with those of Barron *et al.* (1957) deduced from the experimental data of the last two authors. The agreement between theory and experiment is, in many respects, very good. However, in view of the large difference between the frequency spectrum of lattice normal modes calculated in this way and that calculated by one of us (Hardy 1959, denoted by B hereafter, fig. (2)†) using a more refined model of the crystal, it is obviously necessary to show that these new results can also be reconciled with the thermal data. This is the object of the present paper.

§ 2. Outline of the Theory

A typical normal mode of a perfect crystal lattice is a plane wave of frequency ω_i, and one mole of sodium chloride has a total of six L distinct modes, where L is Avogadro's number. The standard technique, originated

Fig. 1 (*a*)

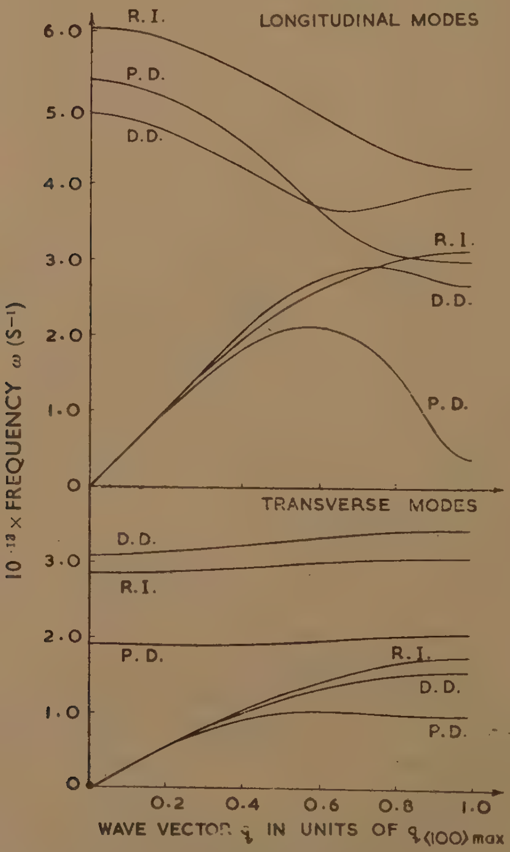

Phonon dispersion curves.
ω versus q along a ⟨100⟩ direction.

---

† The peaks A and D of the frequency spectrum in fig. 2 of reference B are wrongly assigned in the text. The former is due to transverse *acoustic* modes and the latter to longitudinal *optical* modes.

by Blackmann (1935, 1937) for determining the frequency distribution function $N(\omega)$ (number of normal modes/unit frequency at ω) is to take a sample of wave vectors chosen to satisfy the Born–von Kármán periodic boundary conditions. One then determines the corresponding ω_i's by solving the equation of motion for the model lattice in question. This was the method used in both references A and B, resulting in the determination of about 6000 frequencies in each case.

Fig. 1 (*b*)

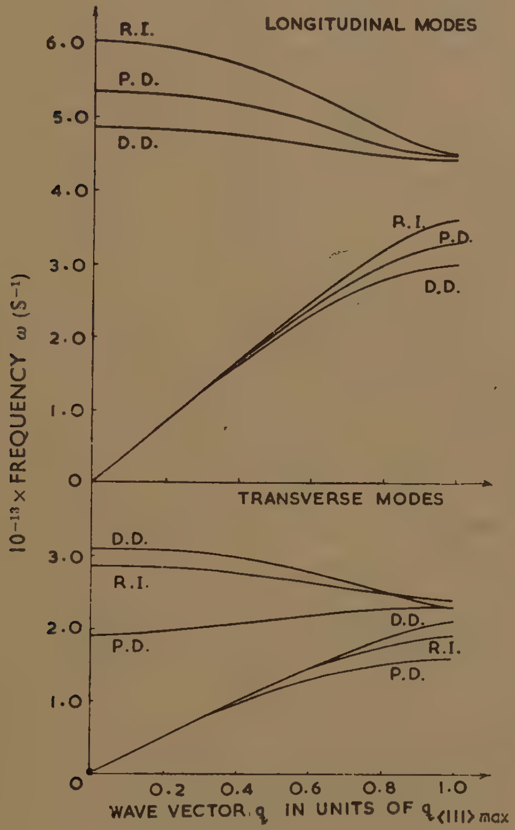

Phonon dispersion curves.
ω versus q along a $\langle 111 \rangle$ direction.

The work in B represents an attempt to construct a theoretical model which allows for the fact that the ions certainly do not behave as point charges when displaced from their equilibrium positions. There are two stages to this work. First, one assumes that each ion acquires a dipole moment proportional to the electrostatic field acting on it, and the resulting $N(\omega)$ versus ω curve is shown as fig. 1 in B. The resulting thermal data have now been calculated and will be discussed in detail in the next section, but the agreement between theory and experiment is completely destroyed.

The good agreement between Born–Mayer theory and experiment now appears rather puzzling, and the second stage of the work is to introduce a further modification of the model, which one hopes will remove this anomaly. This modification is, however, introduced quite independently, and is necessary in order to fit the observed macroscopic dielectric constants (static and optical frequencies) and the reststrahlen frequency. The new concept is that of a 'deformation' dipole (D.D.) associated with each chlorine–sodium bond. This idea was originally due to Szigeti (1950) who pointed out that overlap causes a distortion of the ionic charge distributions which can be described, to the lowest approximation, by these dipoles. Their exact location is not important when conditions are homogeneous, but, for the purpose of the calculations in B, they were assumed to lie at the centre of the chlorine ion, and to vary in magnitude with interionic separation in the same way as the overlap repulsive potential.

The advantage of this mechanism, as far as sodium chloride is concerned, is that it is possible to fit the observed reststrahlen frequency and compressibility simultaneously. This is not possible if one uses Hanlon and Lawson's (1959) model as Cochran (1959 a) does.

In fig. 1 (*a*) and (*b*) the dispersion curves for the ⟨100⟩ and ⟨111⟩ directions are shown. Those marked R.I. (rigid ions) are derived from Kellermann's (1940) data, those marked P.D. (polarization dipoles) result when ionic polarization alone is included, and those marked D.D. (deformation dipoles) follow when both polarization and deformation are taken into account. The D.D. curves for the ⟨100⟩ direction are very similar to those published by Cochran (1959 a) and, in view of the differences between the two approaches, this agreement is very encouraging.

§ 3. COMPARISON BETWEEN THE RESULTS OF THEORY AND EXPERIMENT

Barron *et al.* (1957) have analysed the sodium chloride experimental data in such a way as to extract effective Debye temperatures and certain positive and negative moments of the frequency distribution. The former quantity $\Theta_D(T)$ is defined as $\hbar\omega_m(T)/k$ where $\omega_m(T)$ is the cut-off frequency imposed on the Debye spectrum in order to fit the observed specific heat at a temperature T. The nth moment is defined as

$$\mu_n = \int_0^\infty \omega^n N(\omega)\, d\omega \Big/ \int_0^\infty N(\omega)\, d\omega$$

(this is in fact $(2\pi)^n$ times the values given by Barron *et al.*).

In fig. 2 the values of Θ_D derived from the two models (P.D. and D.D.) are compared with values of Θ_D from A. On the same figure are plotted the experimental results of Morrison and his co-workers (1955, 1956).

In the table the calculated moments of both distributions are compared with the experimental results. Also shown are the results given in (A) derived for rigid ions using both room temperature and absolute zero compressibilities. Finally in fig. 3 a plot of the function

$$\omega_D(n) = [\tfrac{1}{3}(n+3)\,\mu_n]^{1/n},$$

Fig. 2

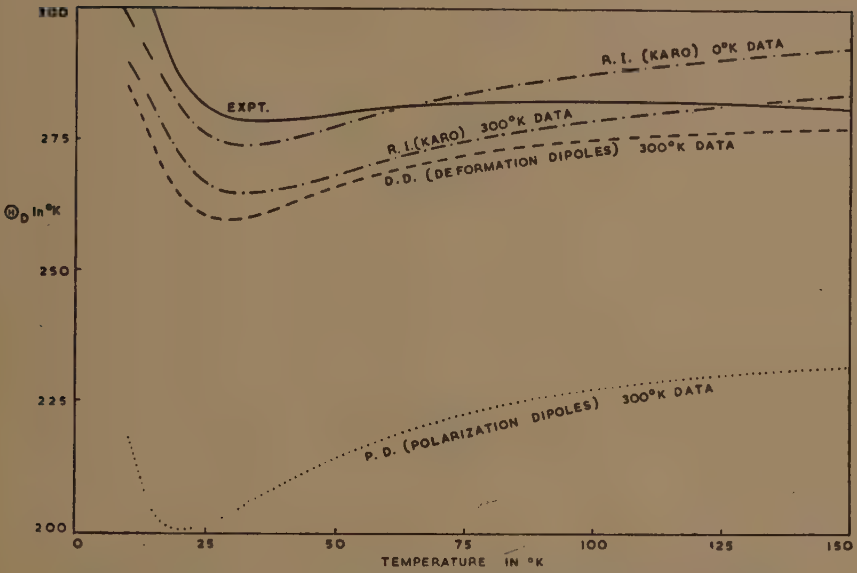

Effective Debye temperatures Θ_D versus absolute temperature.

Fig. 3

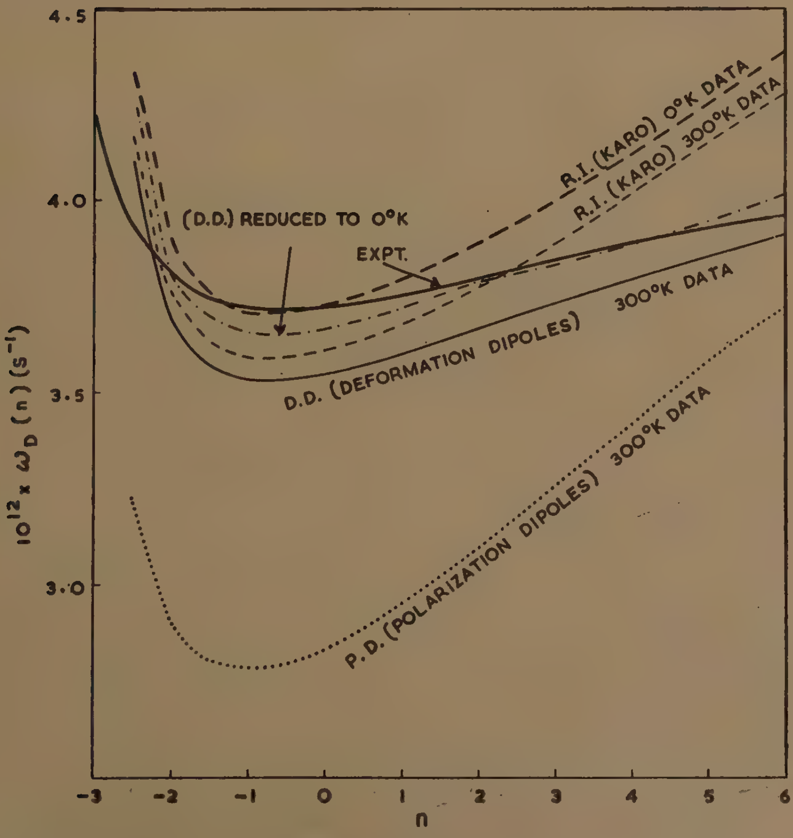

Moment function $\omega_D(n)=[\frac{1}{3}(n+3)\mu_n]^{1/n}$ as a function of n for the various data.

defined by Barron *et al.* (1957) as a means of correlating the various moments, is given for the various sets of results ($\omega_D(n)$ is in fact 2π times the function $\nu_D(n)$ used by these authors).

Moments of the Various Distribution Functions

Moment μ_n	Experimental	P.D.	D.D.	Karo 0°K data	1959 R.T. data
$10\mu_1{}^{-13}$ (s^{-1})	2·81	2·21	2·70	2·85	2·76
$10\mu_2{}^{-26}$ (s^{-2})	8·65	5·75	8·07	9·09	8·56
$10\mu_4{}^{-52}$ (s^{-4})	98·2	58·6	89·3	125	113
$10\mu_6{}^{-78}$ (s^{-6})	1,290	885	1,200	2.360	2,060
$10\mu_{-1}{}^{13}$ (s)	0·403	0·539	0·425	0·404	0·418
$10\mu_{-1\cdot5}{}^{19\cdot5}$ ($s^{3/2}$)	0·276	0·427	0·297	0·276	0·289
$10\mu_{-2}{}^{26}$ (s^2)	0·208	0·358	0·221	0·199	0·213
$10\mu_{-2\cdot5}{}^{32\cdot5}$ ($s^{5/2}$)	0·197	0·320	0·176	0·155	0·168

§ 4. DISCUSSION

When one examines the curves shown in figs. 2 and 3, one must remember that the results from B (P.D. and D.D.) are derived from spectra calculated from room temperature data. For the moments, no direct comparison can be made with experimental values, since they have been derived from an 'effective' harmonic spectrum of the crystal at absolute zero. However, it is possible to correct for this, to a first approximation, by assuming that room temperature and absolute zero results differ by the same amounts as those deduced in (A). This has been done for the moment function $\omega_D(n)$ shown in fig. 3 and the resulting curve (D.D. reduced to 0°K) is remarkably close to that determined experimentally. This is particularly striking in view of the large discrepancy between the curve P.D. and the experimental results. Furthermore the overall agreement between theory and experiment is noticeably better, particularly for large n, than that of the simple Born–Mayer theory.

The Θ_D versus T curves have not been corrected in any way; the theoretical curves are compared with the experimental curve taken directly from the results of Morrison and his co-workers (1955, 1956). However, comparison with the results of A shows that the values of Θ_D from B would be about 10°K higher if absolute zero data had been used. The use of such data is advisable below 100–150°K and for the D.D. case, much of the discrepancy between theory and experiment is removed between the minimum and 150°K. (The empirical Θ_D is too low, above about 30°K, and must be corrected to remove anharmonic effects.)

There are, however, still certain discrepancies in the D.D. curve:

(1) In the region of the minimum and below, the calculated Θ_D versus T curve is about 5–10°K too low even when corrected.

(2) The theoretical moment curve is a little too low in the intermediate range.

(3) The calculated moments increase too rapidly as $n \to -3$.

It would be unwise to draw any conclusions from (1) and (3) alone, as both effects depend critically on the low frequency end of the distribution and are strongly influenced by the coarseness of our 'net' of chosen wave vectors. Thus (2) is the only definite anomaly. This discrepancy might be removed if the first two peaks in the D.D. $N(\omega)$ versus ω curve were more distinct since this would probably raise the lower-order moments ($|n| \leqslant 1{\cdot}5$) without much affecting the others. This might happen if the calculations were carried out exactly using absolute zero data. Unfortunately the relevant information, in particular the reststrahlen frequency, does not seem to be available.

It is worth noting that these first two peaks coincide with the two proposed by Barron and Morrison (1960), and that the high central peak, found by Kellermann (1940) and in (A) is in fact split by the present theory, as they suggest might be the case, into the second and third peaks of the D.D. spectrum.

§ 5. CONCLUSION

In view of the good agreement between theory and experiment, in particular with respect to the moment curves, the results in this paper tend to confirm that the model of sodium chloride, used during calculations on the frequency spectrum of this crystal in reference B, provides a better description of its dynamical properties than any used previously in such calculations. There remains some discrepancy in the specific heat, but improvement could result when accurate low-temperature dielectric constants and reststrahlen frequency are available to use as input data, and when the calculation is carried out for more points in the reciprocal lattice.

ACKNOWLEDGMENTS

We should like to thank Dr. T. H. K. Barron and Dr. J. A. Morrison, for communicating their results to us prior to publication and for access to unpublished data.

One of us (A.M.K.) would like to acknowledge the support of the U.S. Atomic Energy Commission and the other author (J.R.H.) would like to thank A.E.I. for a Research Fellowship during the tenure of which this work was carried out.

References

Barron, T. H. K., Berg, W. T., and Morrison, J. A., 1957, *Proc. roy. Soc.* A, **242,** 478.

Barron, T. H. K., and Morrison, J. A., 1960, *Proc. roy. Soc.* (in the press).

Berg, W. T., and Morrison, J. A., 1957, *Proc. roy. Soc.* A, **242,** 476.

Blackmann, M., 1935, *Proc. roy. Soc.* A, **148,** 384; 1937, *Ibid.* A, **159,** 416.

Born, M., and Huang, K., 1954, *Dynamical Theory of Crystal Lattices* (Oxford: Clarendon Press).

Briscoe, C. V., and Norwood, M. H., 1958, *Phys. Rev.*, **112,** 45.

Briscoe, C. V., and Squire, C. F., 1957, *Phys. Rev.*, **106,** 1175.

Cochran, W., 1959 a, *Phil. Mag.*, **4,** 1082; 1959 b, *Proc. roy. Soc.* A, **253,** 260.

Hanlon, J. E., and Lawson, A. W., 1959, *Phys. Rev.*, **113,** 472.

Hardy, J. R., 1959, *Phil. Mag.*, **4,** 1278.

Karo, A. M., 1959, *J. chem. Phys.*, **31,** 1489 ; 1960, *Ibid.* (in the press).

Kellermann, E. W., 1940, *Phil. Trans. roy. Soc.*, **238,** 513 ; 1941, *Proc. roy. Soc.* A, **178,** 17.

Morrison, J. A., Patterson, D., and Dugdale, J. S., 1955, *Canad. J. Chem.*, **33,** 375.

Morrison, J. A., and Patterson, D., 1956, *Trans. Faraday Soc.*, **52,** 764.

Szigeti, B., 1950, *Proc. roy. Soc.* A, **204,** 51.

Woods, A. D. B., Cochran, W., and Brockhouse, B. N., 1959, *Bull. Amer. phys. Soc.*, **4,** 246.

CORRESPONDENCE

Measurements of Thermoelectricity below 1°K—IV

By D. K. C. MacDonald, W. B. Pearson and I. M. Templeton
Division of Pure Physics, National Research Council, Ottawa, Canada

[Received July 18, 1960]

It is well known that metals such as copper may show anomalous resistive and thermoelectric behaviour at low temperatures. It now seems clear (cf. Gold *et al.* 1960) that the large negative thermoelectric power which develops at temperatures of the order of 10°K to 20°K in certain specimens of the 'pure' metal or specially prepared dilute alloys must be attributed primarily to the presence of very small quantities of iron in solid solution. It also appears that other magnetic ions in solid solution will give rise to similar behaviour (cf. e.g. Jacobs and Schmitt 1959). It has been suggested (Schmitt 1956, cf. also Brailsford and Overhauser 1959) that, for example, the appearance of a maximum (and consequently also a minimum) in the electrical resistance at low temperatures can be explained in terms of scattering by magnetic impurity ions, if the spin degeneracy of the ground state is split and the electron scattering cross sections of the lower levels are higher than those of the upper levels. No detailed analysis appears to have been made of the thermoelectric behaviour to be expected on such a model, but it is suggested (cf. Schmitt loc. cit.) that this might be predicted if due account is taken of the inelastic electron scattering involved. One might remark that the experimental situation is to some extent complicated by the fact that electron scattering by excited lattice vibrations (phonons) becomes important above, say, 15°K in Cu in comparison with electron scattering by impurity sites.

In a previous letter to this Journal (MacDonald *et al.* 1959) we presented some data on the thermoelectric power of a number of metals at very low temperatures, and remarked in particular on the puzzling change of sign which we observed (in Ni, Pd and Fe) when the residual resistivity was altered by a relatively modest amount. Following that work we decided to have a number of alloys of the transition metals, Pd and Pt, specifically prepared with Cu, Sn and Fe as solutes in relatively small concentrations. We are grateful to Dr. J. C. Chaston of Messrs. Johnson, Matthey and Co., Wembley, for his interest in preparing a series of eighteen such alloys for us. We have now surveyed the thermoelectric power of a number of these alloys. Some of the results are shown in figs. 1 and 2 where for the present we have restricted ourselves to the most concentrated alloys (nominal 0·5 at. % solute in each case) for comparison of behaviour.

The following points seem to us noteworthy :

(i) The behaviour of the thermoelectric power is monotonic from the absolute zero (up to at least 3°K) when copper and tin are present as the dominant impurity in Pd or Pt. We note however that, when dissolved in Pd, Cu gives rise to a negative, and Sn to a positive absolute thermoelectric power.

(ii) The presence of Fe as a solute in Pd or Pt gives rise to a thermoelectric power which goes through a positive maximum (which in Pt as parent occurs at a temperature as low as about 0·5°K) and then changes sign, becoming negative (and in the case of Pt almost linear in temperature dependence above about 1°K).

Fig. 1

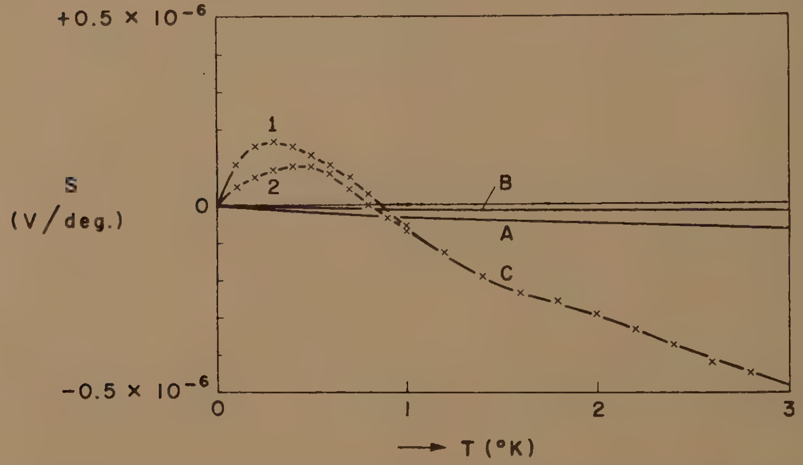

Measurements of absolute thermoelectric power of alloys of Cu, Sn and Fe in Pt. Solute concentration: 0·5 nominal at. % in each case.

A: Cu in Pt. B: Sn in Pt. C: Fe in Pt; 1: points derived from measurements of thermo-e.m.f. to ~2°K; 2: points derived from measurements of thermo-e.m.f. to ~3°K.

(iii) Comparing the monotonic temperature dependences (and in the case of the Pt alloys the relative magnitude) of the alloys containing Cu and Sn with that of the alloys containing Fe, it seems most improbable that 'phonon-drag' effects could be responsible for the anomalous behaviour of the alloys containing Fe. Apart from this direct comparison, one might expect that the amount of impurity present (0·5 nominal at. % in each case) would play some role in scattering the phonons, and we recall moreover that the characteristic temperatures (θ) of Pt and Pd are about 230°K and 270°K respectively.

(iv) We are thus led to believe that the anomalous behaviour we have observed at these very low temperatures in the alloys containing Fe cannot be attributed to 'phonon-drag', nor more generally to electron-scattering by thermal vibrations of the lattice but rather that we must seek an explanation in terms specifically of electron-scattering by Fe ions. It is thus of considerable interest to find that scattering by Fe ions can give rise to a maximum in S and also a change of *sign* at these very low temperatures, particularly as the conventional theory of 'diffusion' thermoelectricity predicts uncompromisingly that $S \propto T$ (e.g. Wilson 1953, Mott and Jones 1936).

Fig. 2

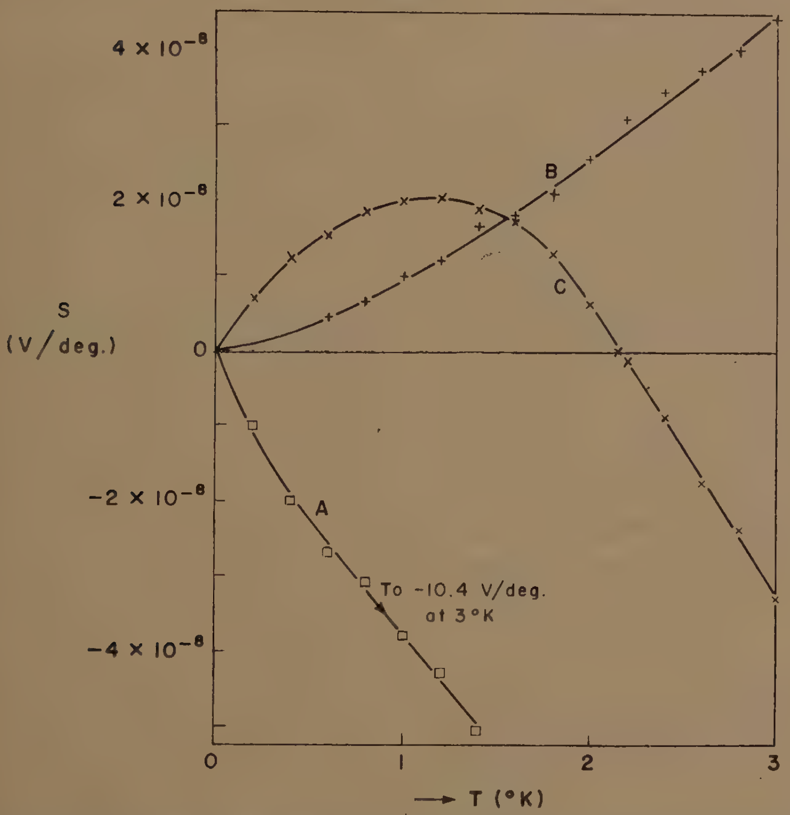

Measurements of absolute thermoelectric power of alloys of Cu, Sn and Fe in Pd. Solute concentration: 0·5 nominal at. % in each case.

A: Cu in Pd. B: Sn in Pd. C: Fe in Pd.

Since similar concentrations of Fe behave differently in different parent metals, experiments of this kind should be fruitful in studying the influence of the matrix on the interaction involved (presumably magnetic) between the scattering ions, if the general type of mechanism suggested by Schmitt and others (foregoing references) is accepted as responsible.

We are studying a number of other metals at these very low temperatures, with magnetic ions as solutes, and we hope to publish a fuller account of this work later.

ACKNOWLEDGMENT

We should like to thank Mr. J. E. Dunick for technical assistance in some of these experiments.

REFERENCES

BRAILSFORD, A. D., and OVERHAUSER, A. W., 1959, *Phys. Rev. Letters*, **3**, 331.
GOLD, A. V., MACDONALD, D. K. C., PEARSON, W. B., and TEMPLETON, I. M., 1960, *Phil. Mag.*, **5**, 765.
JACOBS, I. S., and SCHMITT, R. W., 1959, *Phys. Rev.*, **113**, 459.
MACDONALD, D. K. C., PEARSON, W. B., and TEMPLETON, I. M., 1959, *Phil. Mag.*, **4**, 380.
MOTT, N. F., and JONES, H., 1936, *Theory of Properties of Metals and Alloys* (Oxford: Clarendon Press).
SCHMITT, R. W., 1956, *Phys. Rev.*, **103**, 83.
WILSON, A. H., 1953, *Theory of Metals*, 2nd edition (Cambridge: University Press).

REVIEWS OF BOOKS

Similarity and Dimensional Methods in Mechanics. By L. I. SEDOV. Translated by M. HOLT and M. FRIEDMAN. (London: Cleaver Hume for Infosearch.) [Pp. 363.] No price given by publishers.

THIS is a translation of the 4th Russian edition (1956) of this well-known work. The chapter headings are: (1) General dimensional theory; (2) Similarity, modelling and examples of the application of dimensional analysis; (3) Application to the theory of motion of a viscous fluid and to the theory of turbulence; (4) One-dimensional unsteady motion of a gas; (5) Application to astrophysical results.

With a few exceptions the problems treated in this book are taken from fluid mechanics and illustrate the various roles played by dimensional analysis in modern applications. In its simplest form the dimensional argument follows from the known equations of motion and shows, e.g. that the drag coefficient of a sphere in steady motion (which cannot easily be calculated) is a function only of Reynolds' number; this has been verified by measurements. When several dimensionless variables enter, simplification may sometimes be achieved in limiting cases by use of intuitive physical arguments. Numerous diagrams show how far these are supported by experiments. In Chapter 3 some of the arguments are less obvious, and less use is made of the equations of motion. Boundary layers, isotropic turbulence and pipe-flow turbulence are discussed, with a short excursion into mixing-length theory. Chapter 4 is the longest in the book (150 pages). Dimensional analysis is applied to those special solutions of the equations of motion in which the scale but not the form of the solution changes with time, the *self-similar* solutions. The equations of motion then reduce to a system of ordinary differential equations. This part is mainly theoretical and few comparisons with experiment are given.

This book can be warmly recommended both as a study of dimensional analysis and as a study of certain parts of fluid mechanics. F. U.

Mathematics in Physics and Engineering. By J. IRVING and N. MULLINEUX. (New York: Academic Press Inc., 1960.) [Pp. 883.] $11.50.

THE subject-matter of this book has formed the basis of lecture courses at British universities to undergraduate and postgraduate students of mathematics, physics and engineering. Chapter headings are: 1. Introduction to Partial Differential Equations; 2. Ordinary Differential Equations: Frobenius' and Other Methods of Solution; 3. Bessel and Legendre Functions; 4. The Laplace and Other Transforms; 5. Matrices; 6. Analytical Methods in Classical and Wave Mechanics; 7. Calculus of Variations; 8. Complex Variable Theory and Conformal Transformations; 9. The Calculus of Residues; 10. Transform Theory; 11. Numerical Methods; 12. Integral Equations.

There is an appendix on certain mathematical topics which could not find a place in the text. Many examples are worked in the text, and at the end of each chapter there are problems the solutions of which are given at the end of the book. The authors intend that a good knowledge of elementary differential and integral calculus should be sufficient for an understanding of this work.

The reviewer believes that this book will appeal most to those who, trained as applied physicists or engineers, wish to take a serious interest in the mathematical side of their subject. It is clear that the authors are not only competent mathematicians but also convinced of the importance and utility of mathematics in applied science and it is to be wished that they may open the eyes of some of those engineering students who were obliged by degree requirements to learn mathematical methods without their applications, and who have naturally acquired a harmful distaste for all theory. The book appears well suited for this purpose. Technologists will probably like the authors' style. A different selection of topics might have been made by different authors. The reviewer has only one serious criticism. It seems to him that more references should have been given, to papers as well as to books.

F. U.

[*The Editors do not hold themselves responsible for the views expressed by their correspondents.*]

Fig. 2

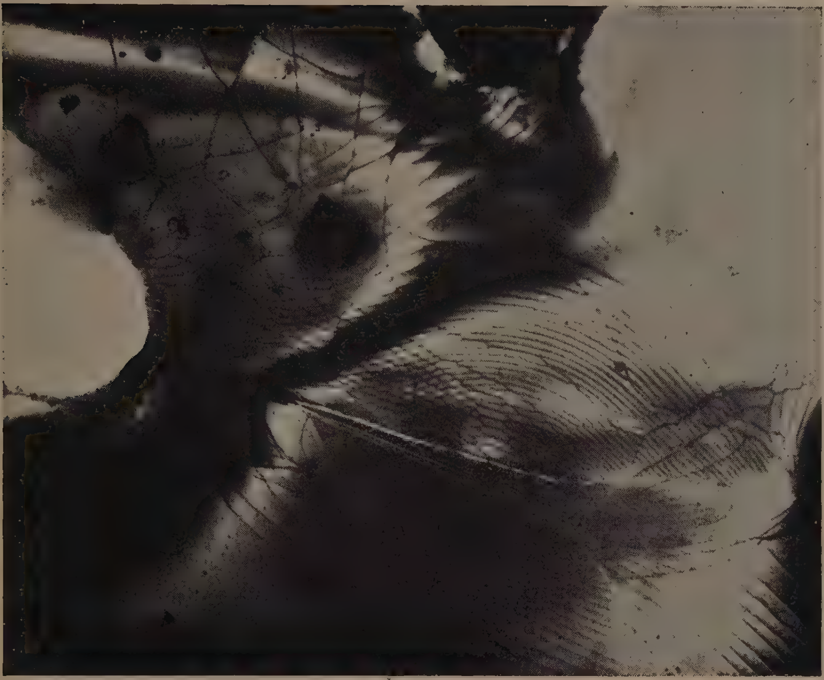

An array of dislocations associated with deformation of the crystal during mounting on specimen grid. × 10 000.

Fig. 3

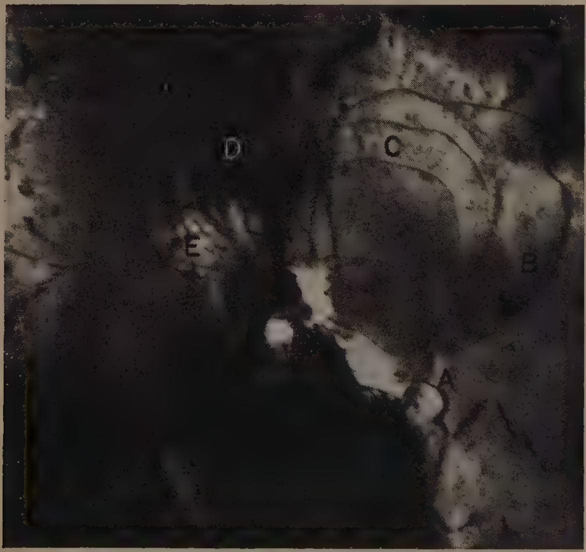

An array of pre-existing dislocations which is clearly composed of a number of families of loops A, B, C, D, E. × 18 000.

Fig. 4

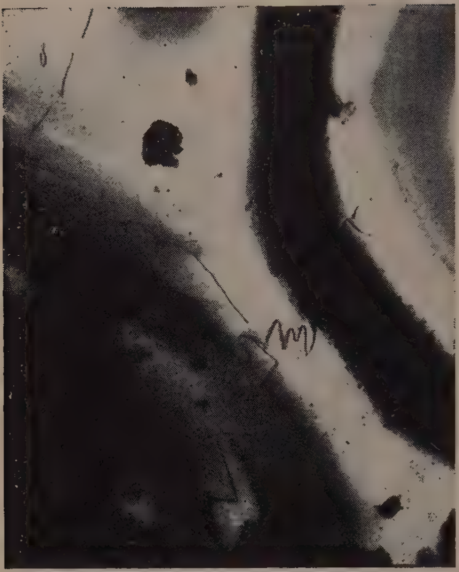

Helices produced by the climb of pre-existing dislocations. ×18 000.

Fig. 5

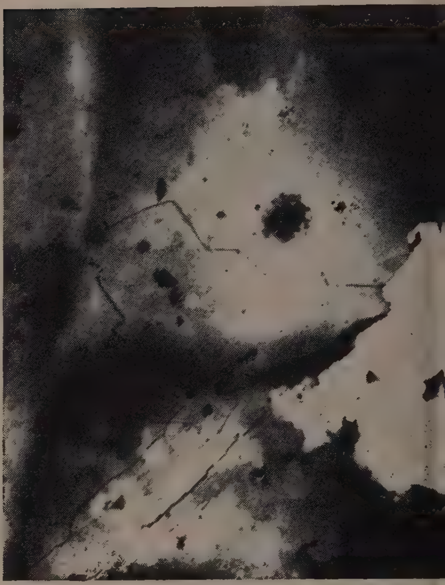

The climb of a loop of dislocation. ×18 000.

Fig. 6

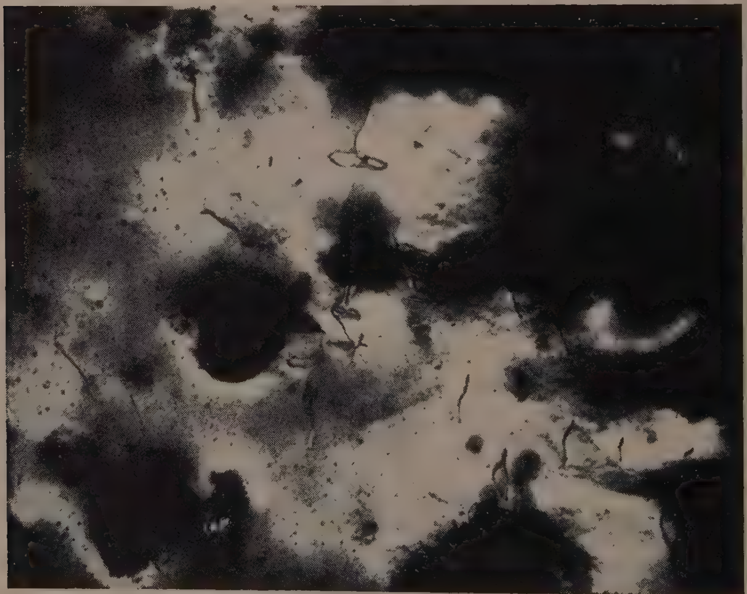

Illustrating the formation of a loop in a dislocation line by localized condensation of vacancies. Note also the large numbers of small isolated loops and the several zig-zag dislocations. ×24 000.

Fig. 7

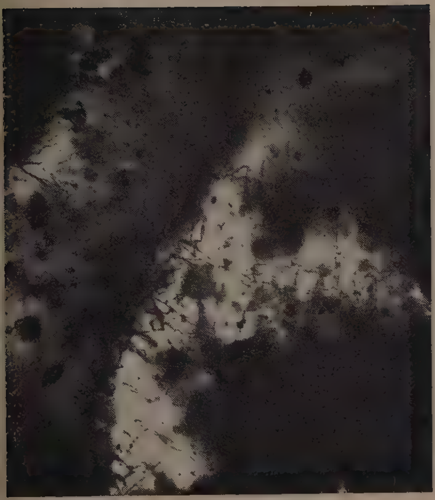

Illustrating chains of loops formed during climb from an array of pre-existing dislocations. ×15 000.

Fig. 8

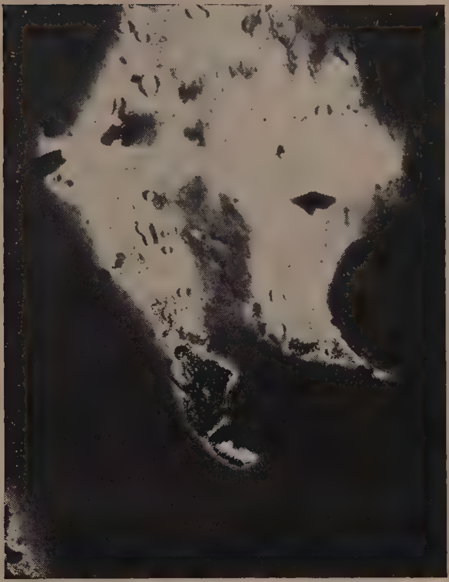

Isolated loops of dislocation, apparently lying in an inclined plane. ×24 000.

Fig. 9

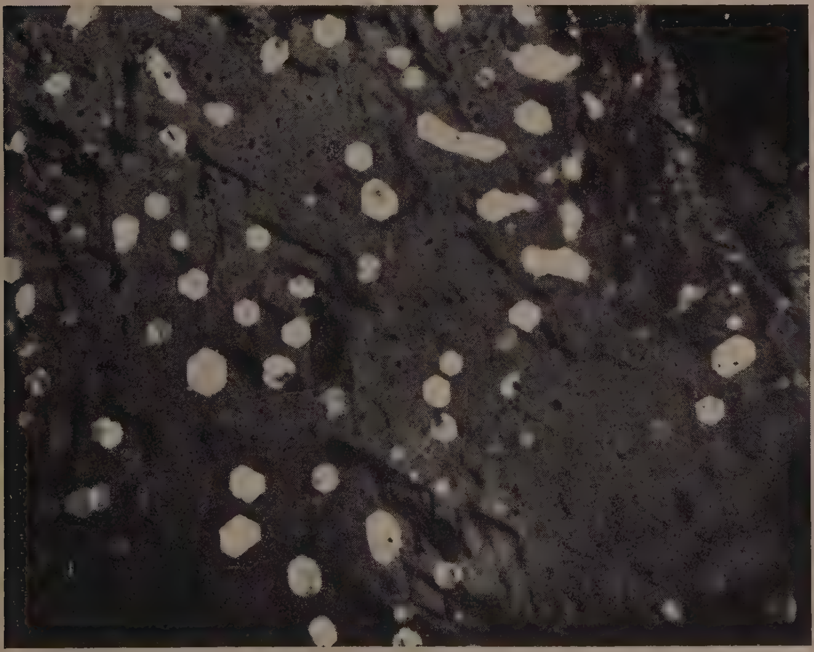

Bright patches formed during the intermediate stage of decomposition. The outlines follow $\langle 10\bar{1}0\rangle$ directions. ×20 000.

Fig. 10

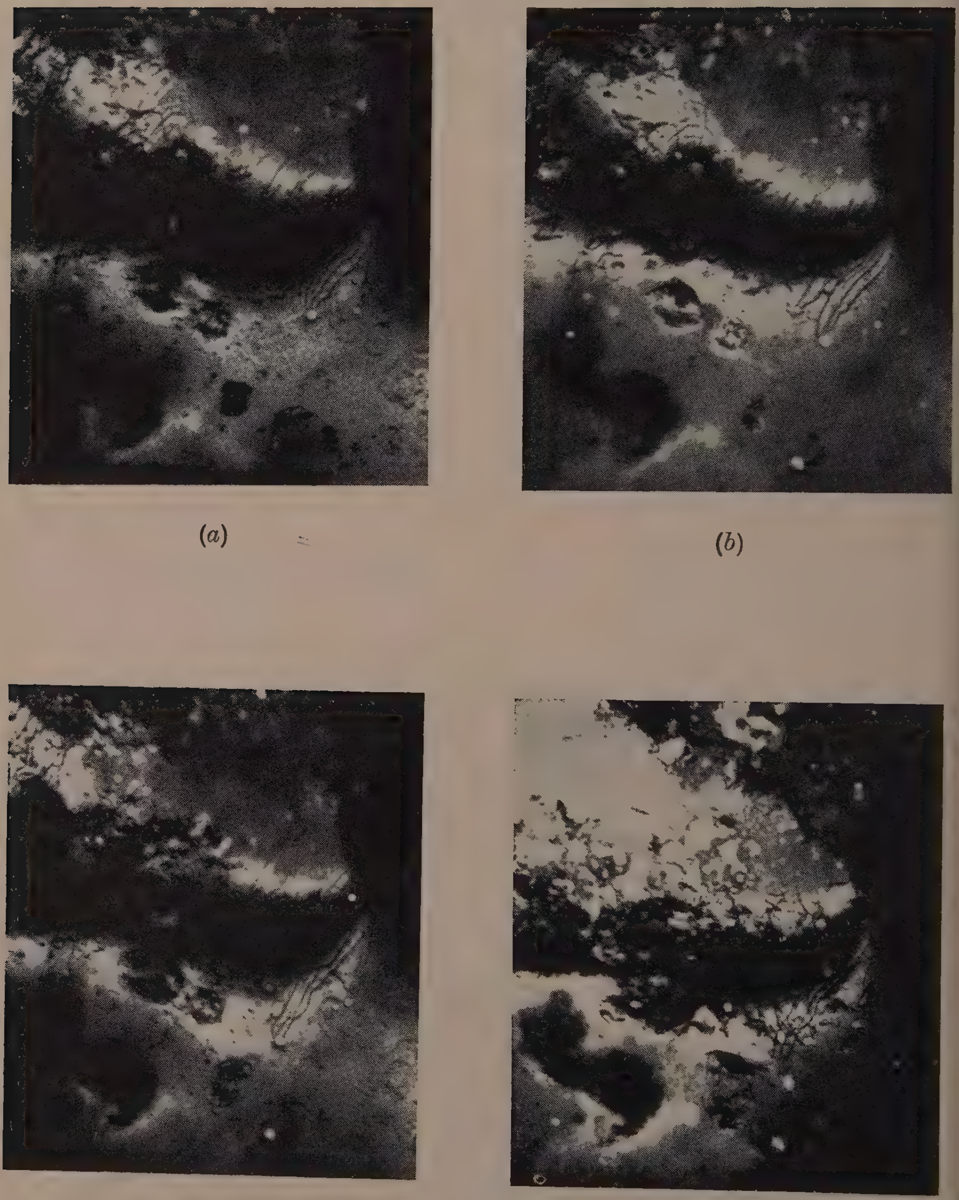

(a) (b)

(c) (d)

Sequence illustrating the movement of a number of bright patches and the extension of dislocations associated with them. × 15 000.

Fig. 11

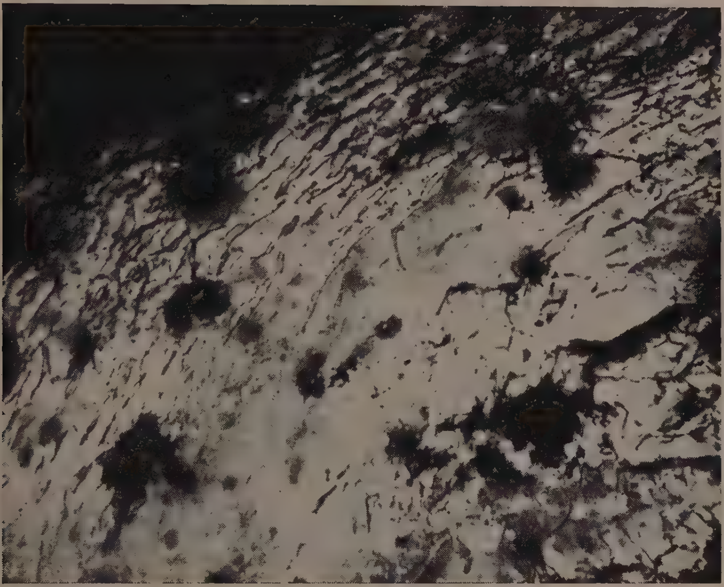

A highly dislocated region produced by the passage of a wave of bright patches. ×15 000.

Fig. 12

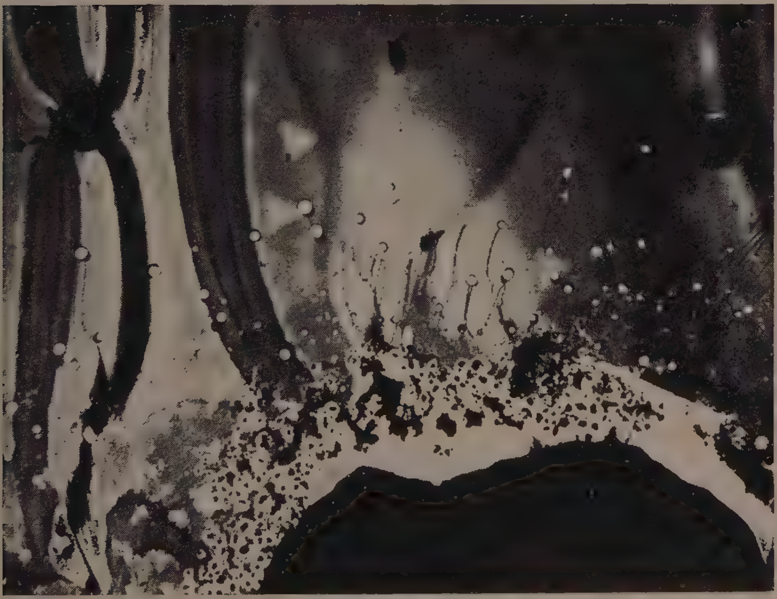

The commencement of the final stage of decomposition. A wave of bright patches is leaving a completely decomposed zone. ×15 000.

Fig. 13

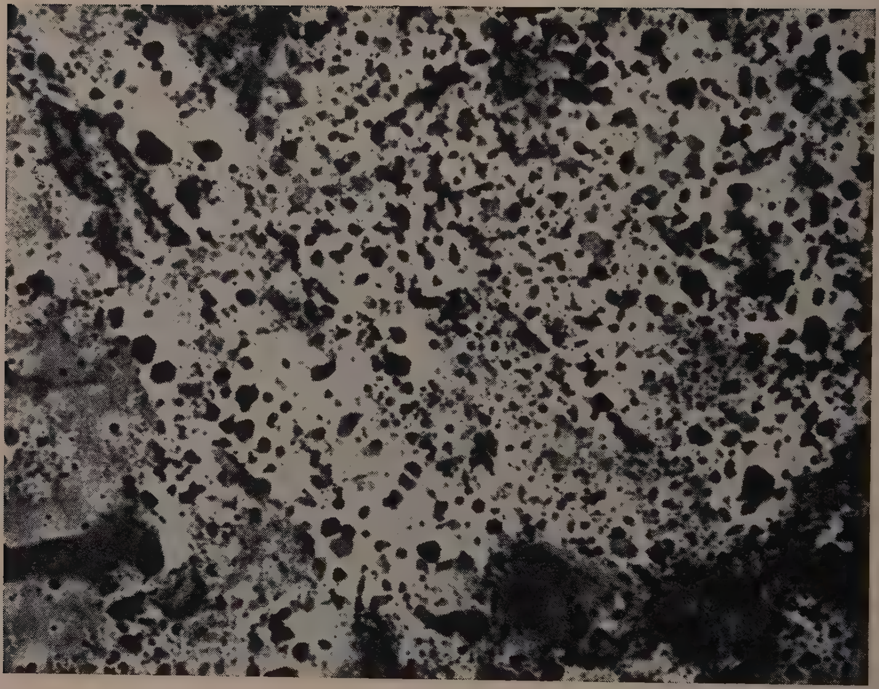

An aggregate of dense crystallites remaining after complete decomposition. × 24 000.

Fig. 14

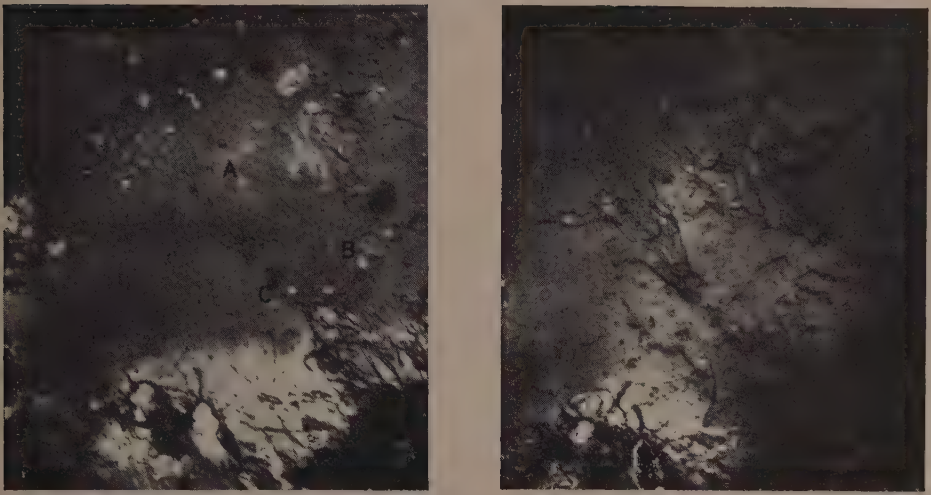

(a) (b)

Illustrating the change in appearance of bright patches after a slight deflection of the electron beam. ×15 000.

Fig. 15

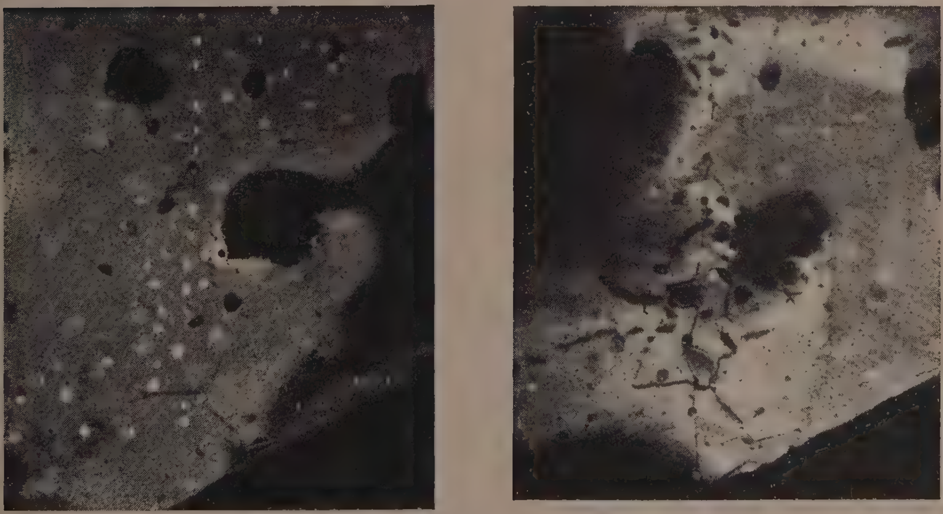

(a) (b)

Illustrating the reversal of contrast of patches after deflection of the electron beam. ×20 000.

Fig. 3

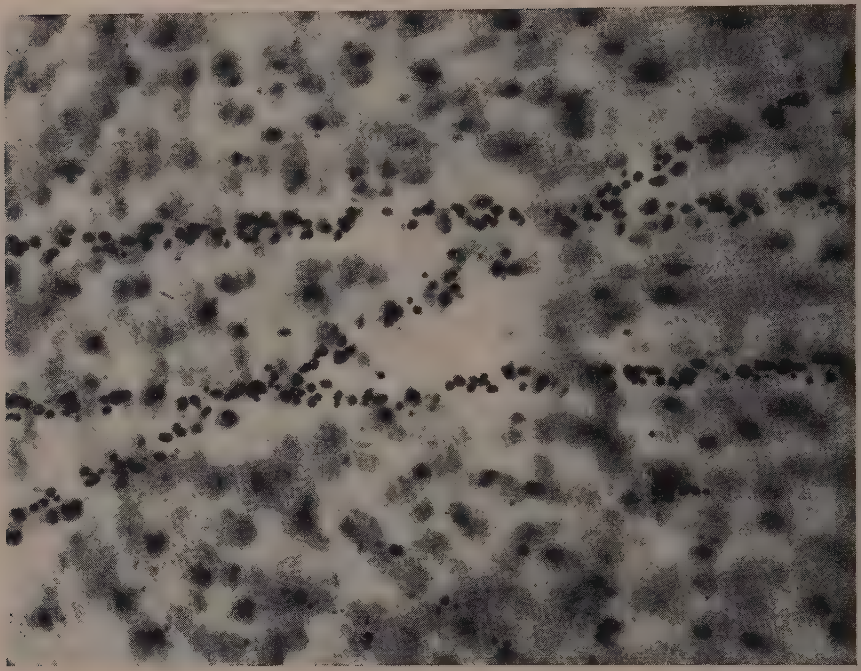

Surface terraces associated with dislocation loops made visible by the separation of particles of silver. ×1600.

Fig. 4

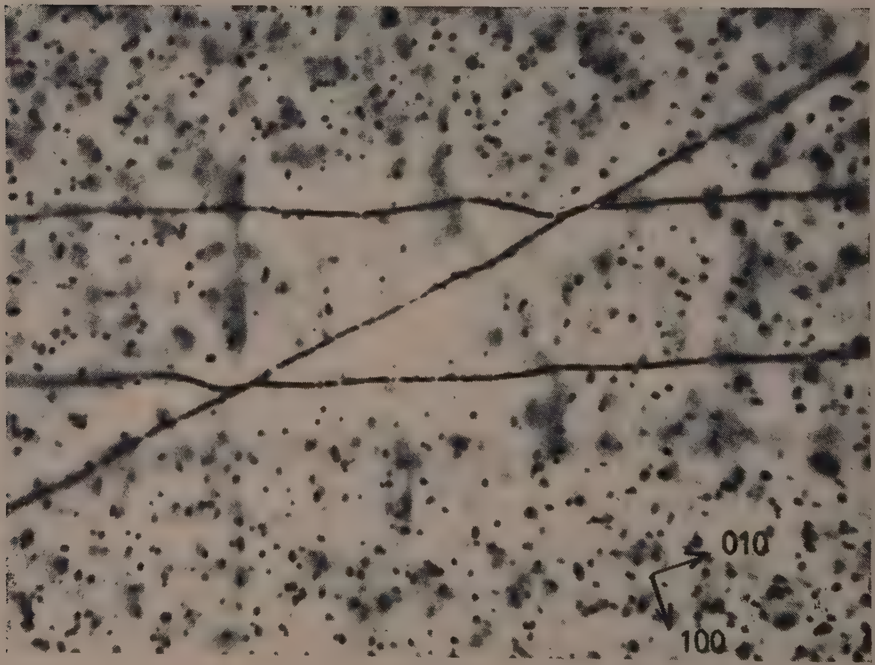

Dislocations approximately in the edge orientation corresponding with the surface terraces of fig. 3 and made visible by the separation of silver. ×1600.

Fig. 1

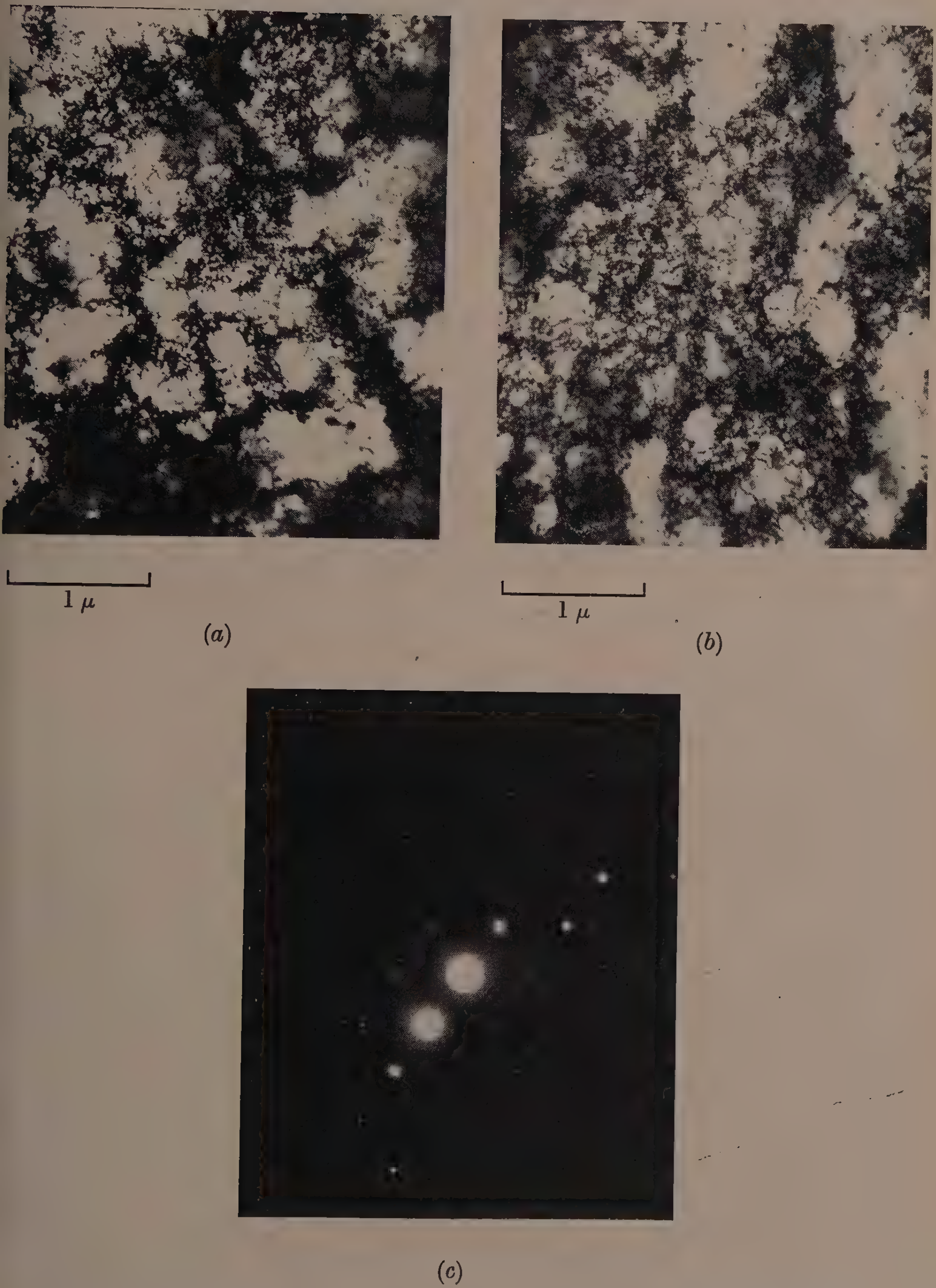

(*a*) Electron micrograph of a typical area within one grain of polycrystalline silver deformed 25% in tension. (*b*) Unrecrystallized area within one grain of polycrystalline silver deformed 25% in tension and annealed for 1 hour at 200°c. (*c*) Electron diffraction pattern from an area $\frac{4}{3}\,\mu$ in diameter within one grain of polycrystalline silver deformed 25% in tension. Mag. ×20 000.

Fig. 2

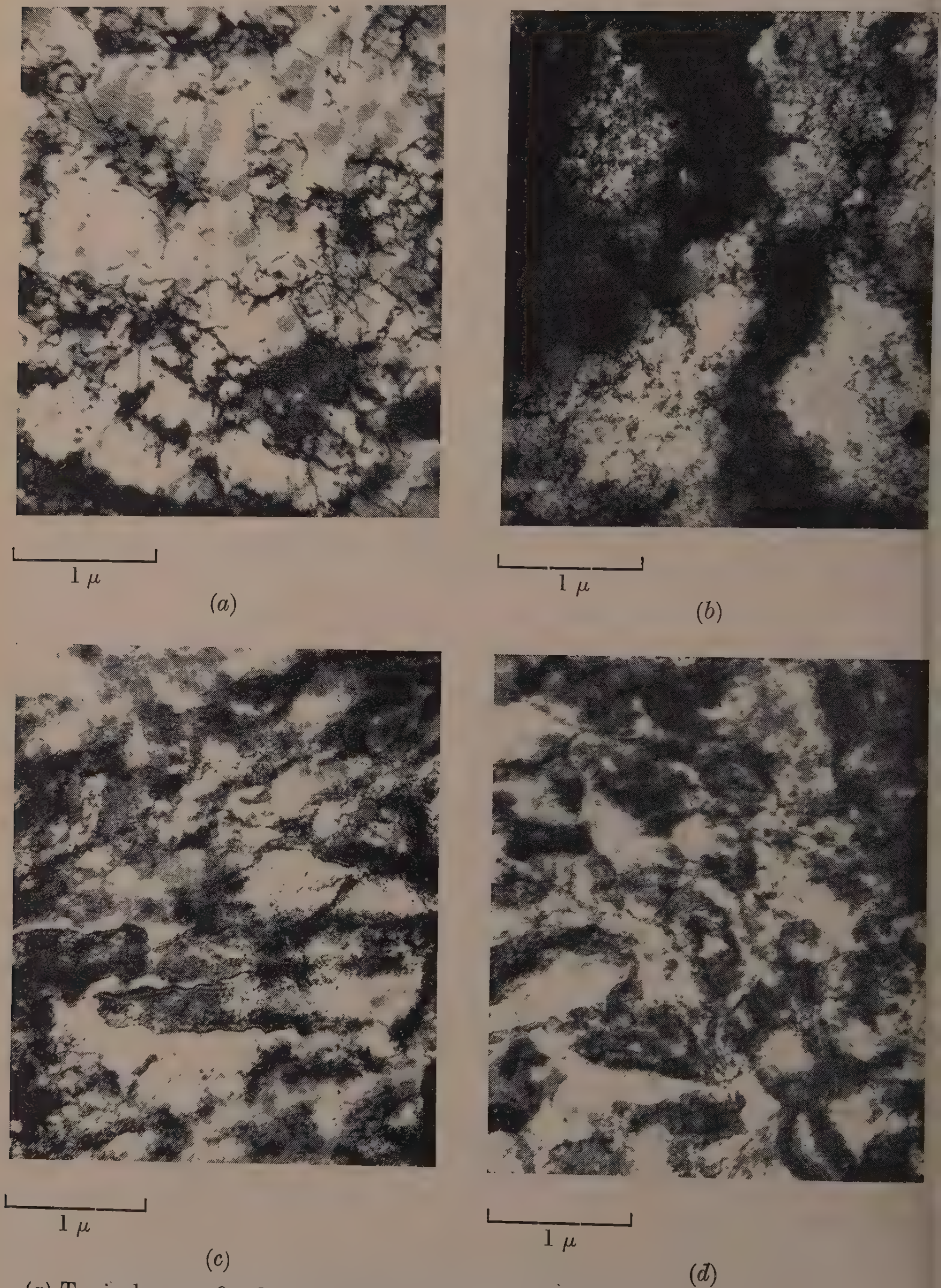

(*a*) Typical area of polycrystalline silver reduced 20% by cold rolling. (*b*) Typical area of polycrystalline silver reduced 40% by cold rolling. (*c*) Typical area of polycrystalline silver reduced 60% by cold rolling. (*d*) Typical area of polycrystalline silver reduced 95% by cold rolling. Mag. × 20 000.

Fig. 3

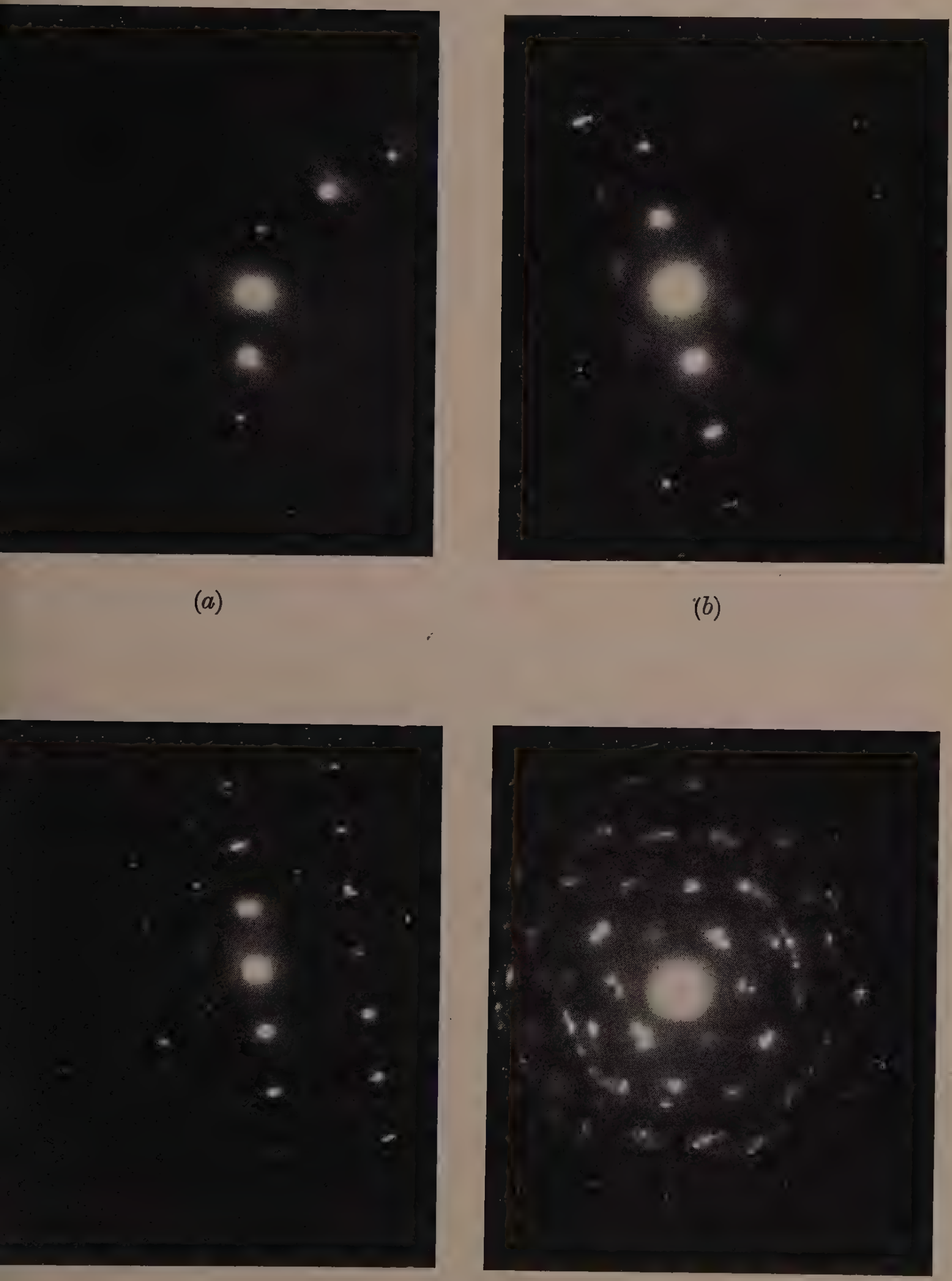

(a) (b)

(c) (d)

Set of electron diffraction patterns of the central region ($\frac{4}{3}\,\mu$ diameter) of the areas shown in fig. 2 (*a*), (*b*), (*c*) and (*d*) respectively.

Fig. 4

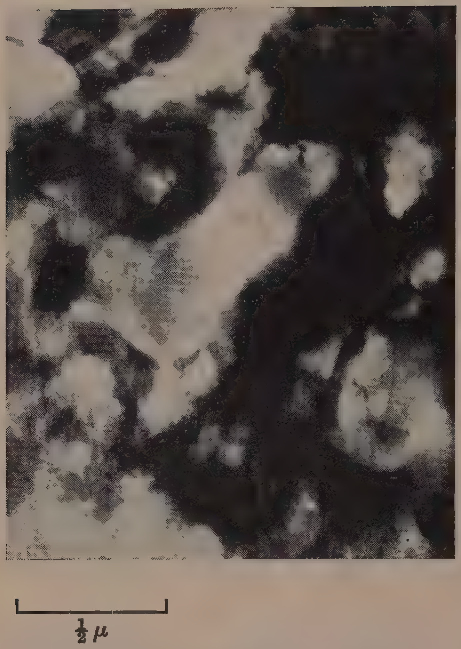

Sub-boundaries in heavily rolled (95% reduction) polycrystalline silver. Mag. × 40 000.

Fig. 5

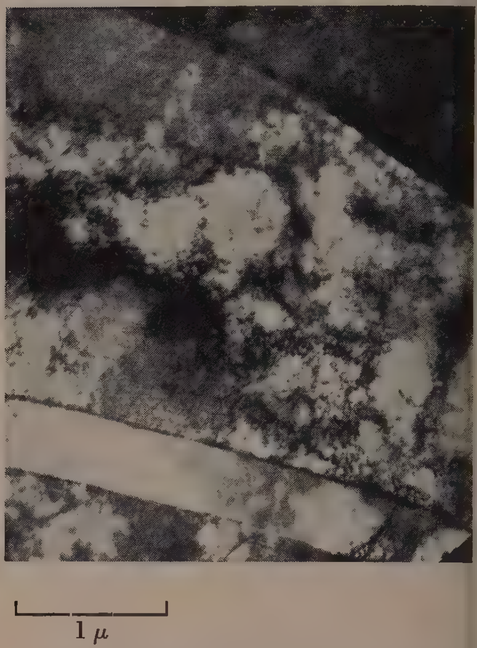

Grain boundaries in polycrystalline silver deformed 25% in tension. Mag. × 20 000.

Fig. 6

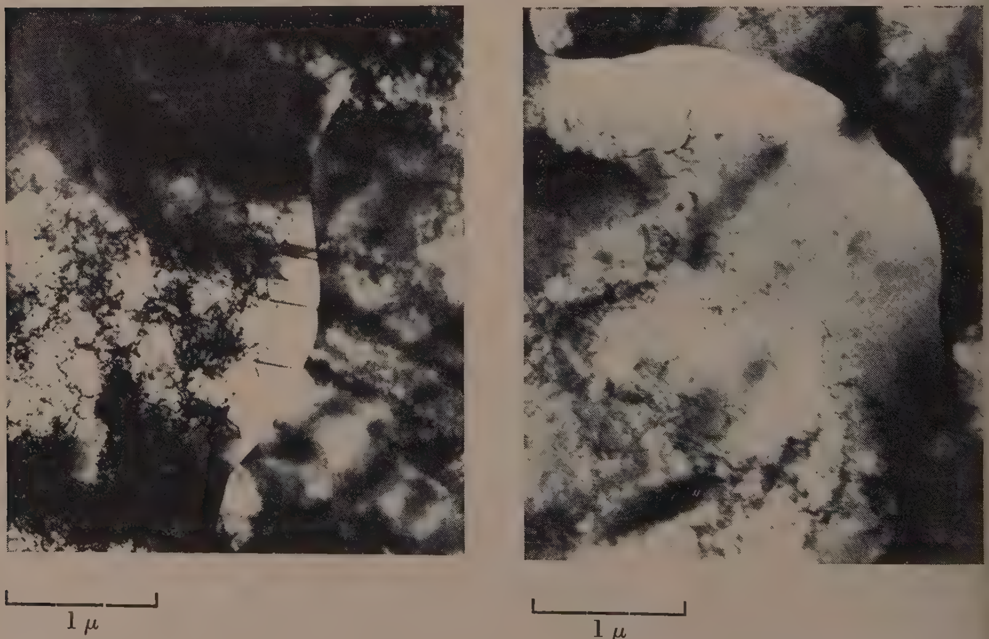

(*a*)

(*b*)

Examples of the early stage of grain boundary migration in polycrystalline silver deformed 25% in tension and annealed 1 hour at 210°c. Mag. × 20 000.

Fig. 6 (*continued*)

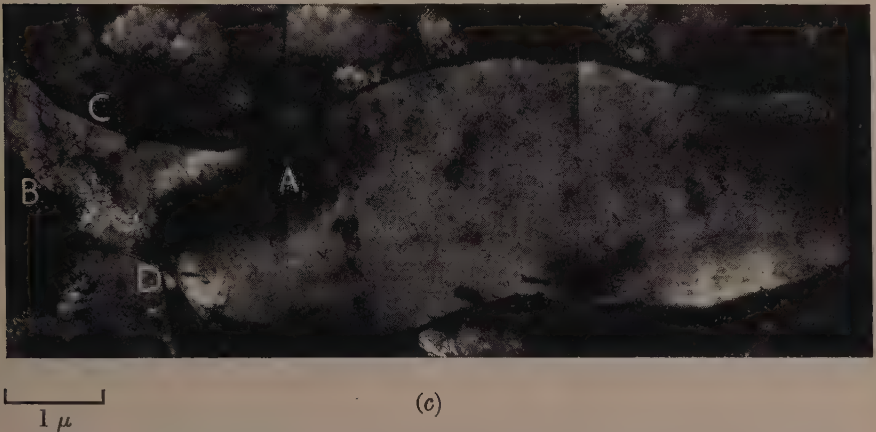

(*c*)

Advanced stage of grain boundary migration in polycrystalline silver deformed 25% in tension and annealed 1 hour at 200°c. Mag. × 13 000.

Fig. 7

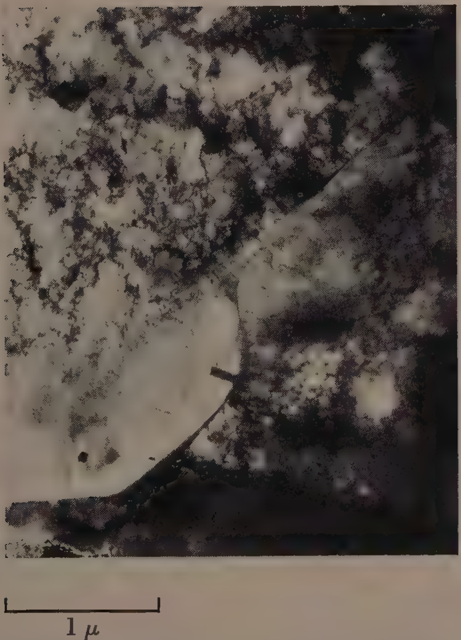

Neighbouring regions of a grain boundary attempting to migrate in opposite directions. Mag. × 20 000.

Fig. 8

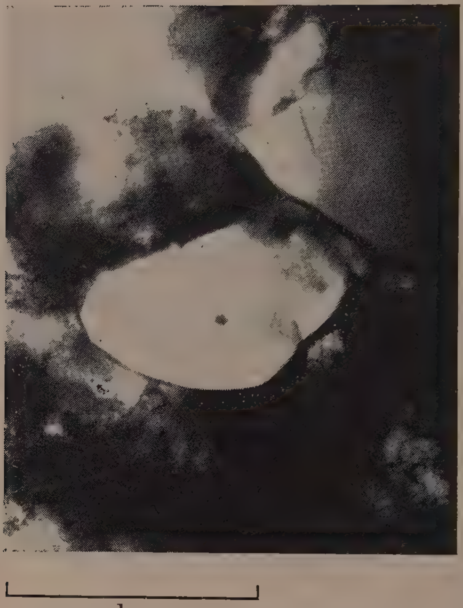

Micrograph showing completely enclosed recrystallizing grain. Mag. ×33 000.

Fig. 9

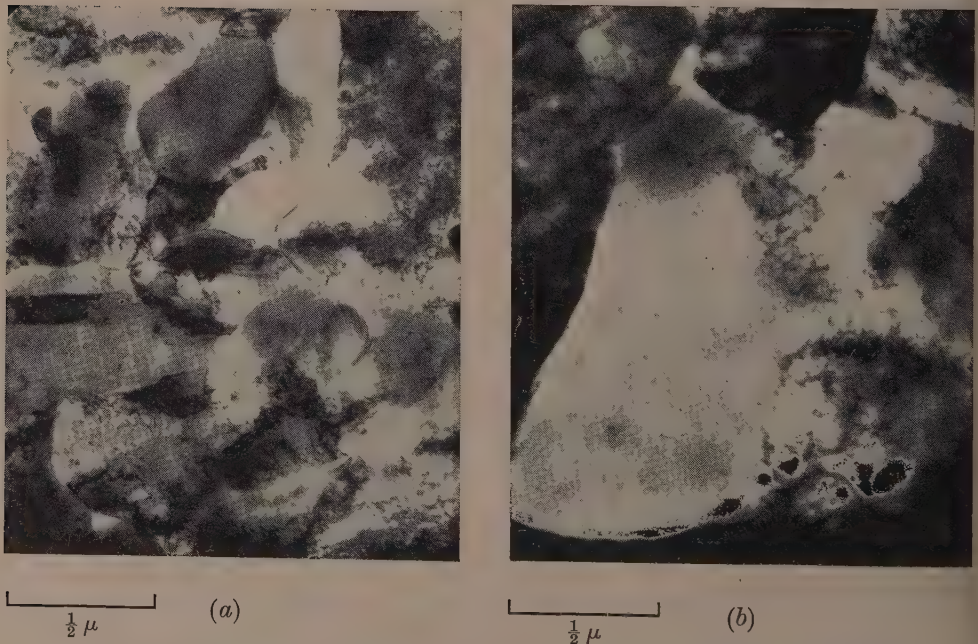

(*a*) Area of heavily rolled (95% reduction) silver foil, annealed 20 min at 110°c showing sub-grain formation. (*b*) Early stage in the growth of a recrystallizing grain in heavily rolled silver (95% reduction) after annealing for 20 min at 110°c. Mag. ×40 000.

Fig. 10

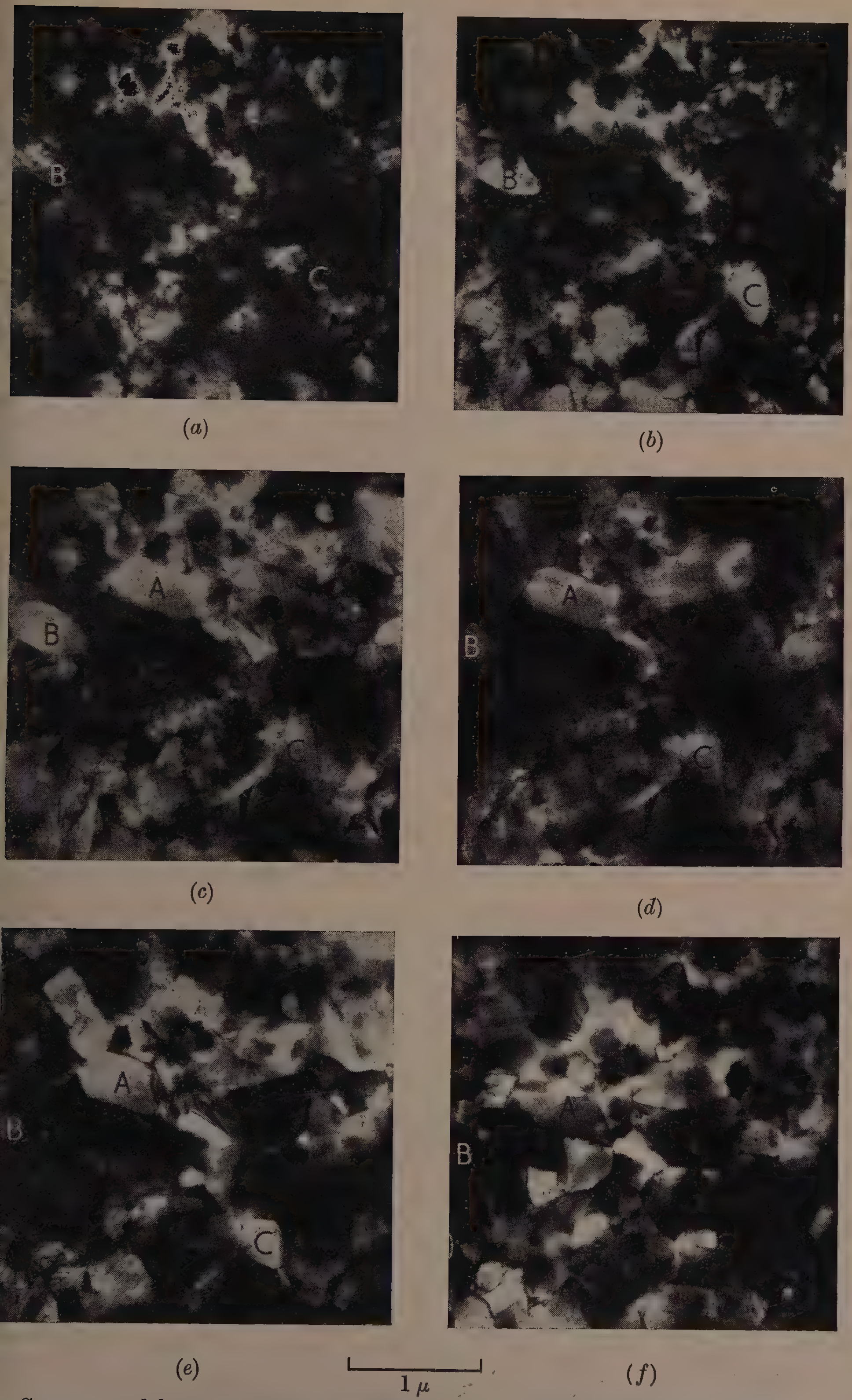

Sequence of heating stage observations on heavily rolled (95% reduction) polycrystalline silver foil, showing: (*a*) Area at room temperature. (*b*) Same area after heating for 4 min at 200°c. (*c*) Same area after heating for $1\frac{1}{2}$ min at 400°c. (*d*) Same area after heating for $\frac{3}{4}$ min at 500°c. (*e*) Same area after heating for $\frac{1}{4}$ min at 600°c. (*f*) Same area after heating for $\frac{1}{4}$ min at 700°c. Mag. ×20 000.

Fig. 11

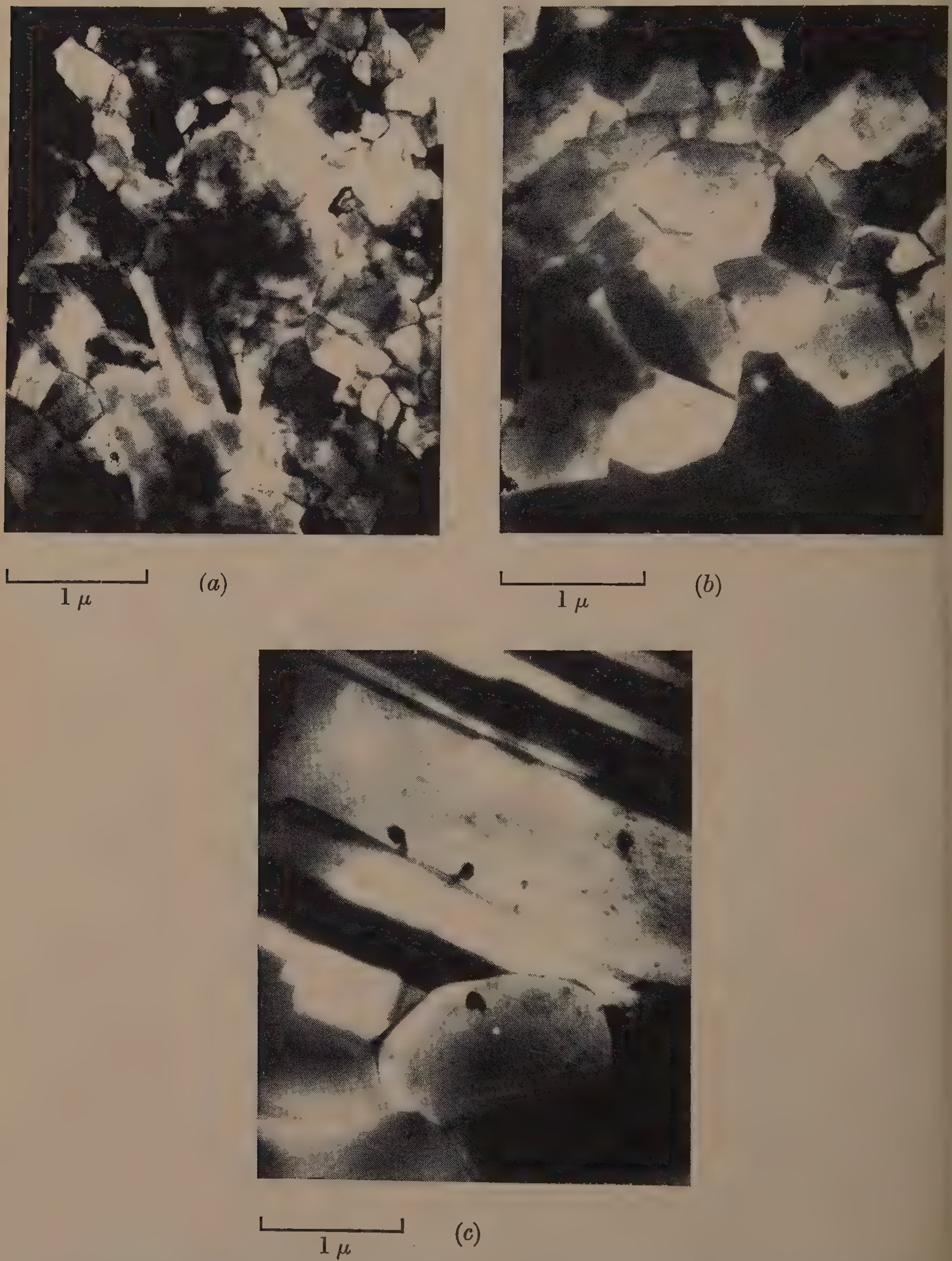

Micrographs of heavily rolled (95% reduction) polycrystalline silver foil after heating to a high temperature in the electron microscope, showing the increase of the grain size with increasing thickness of the foil. Mag. ×20 000.

Pyramidal Glide and the Formation and Climb of Dislocation Loops in Nearly Perfect Zinc Crystals†

By P. B. Price‡
Physics and Chemistry of Solids, Cavendish Laboratory, Cambridge§

[Received June 3, 1960]

Abstract

Zinc whiskers and platelets with a (0001) orientation and thin enough ($\lesssim \frac{1}{2}\mu$) to be transparent to 100 kv electrons were deformed in tension inside the electron microscope and the motion of individual dislocations followed by the transmission technique. These observations were then related to the macroscopic properties as determined by stress–strain curves. The crystals, which were found to be initially free of dislocations, deformed mainly by twinning (which is not considered here) or by pyramidal glide on the $(11\bar{2}2)$ $[\bar{1}\bar{1}23]$ system. Dislocations with three types of Burgers vectors were produced: long $\langle\bar{1}\bar{1}20\rangle$ dislocations which were easily immobilized and contributed very little to the deformation; short $\langle\bar{1}\bar{1}23\rangle$ screw dislocations which caused pyramidal glide and sometimes left behind long, narrow $\langle\bar{1}\bar{1}23\rangle$ loops which then split up into circular loops with the same Burgers vector; and circular $\langle 0001\rangle$ loops which were formed from $\langle\bar{1}\bar{1}23\rangle$ loops by the reaction $\frac{1}{3}\langle\bar{1}\bar{1}23\rangle \rightarrow \frac{1}{3}\langle\bar{1}\bar{1}20\rangle + \langle 0001\rangle$. Both types of loops were sessile but disappeared by climb at room temperature at a rate which agreed with the predicted rate. The loops impeded the motion of dislocations and were responsible for the propagation of glide as a Lüders band.

§ 1. Introduction

During an investigation at the University of Virginia of the mechanical properties of zinc whiskers (Cabrera and Price 1958), preliminary experiments showed that the mechanical properties of single crystal 'ribbons' and platelets of zinc were also extremely interesting. These studies have been continued at the University of Cambridge, using the elegant technique of transmission electron microscopy developed by Hirsch *et al.* (1956) and others, and the results appear to be important, not only for their elucidation of some of the properties of whisker-like crystals but also because of their application to the properties of metals in bulk form.

Zinc whiskers and platelets less than about $\frac{1}{2}\mu$ thick proved to be ideal specimens for this type of study because they were already transparent to 100 kv electrons without thinning and because their surfaces were extremely smooth. The crystals were deformed inside the electron microscope and the motion of individual dislocations followed during and after straining. These observations were then compared with the macroscopic behaviour as determined by tensile stress-strain curves.

---

† Communicated by Dr. P. B. Hirsch.

‡ National Science Foundation Post-Doctoral Fellow, 1959–60.

§ Permanent address: General Electric Research Laboratory, Schenectady, New York.

§ 2. EXPERIMENTAL PROCEDURE

The thin crystals were grown from zinc vapour of high purity by the technique of Coleman and Sears (1957). The investigation was limited to whiskers whose direction of growth was in the basal plane and to platelets whose largest faces were parallel to the basal plane. Thus, in the tensile tests the axis of tension was always parallel to the basal plane. All the crystals were rectangular in cross section and ranged in length from 2 to 6 mm, in width from 10 μ to 1 mm, and in thickness from 0·05 to 0·5 μ. Crystals less than about 20 μ wide were generally referred to as whiskers and wider ones as platelets.

Macroscopic properties were studied with a high sensitivity tensile testing machine, developed by Marsh (1959), which was capable of measuring extensions of less than 100 Å reproducibly. A specimen was mounted with diphenyl-carbazide and observed during deformation at low magnification (× 100). After the completion of a test it was removed and examined at high magnification in a metallurgical microscope.

The microscopic behaviour was observed in a Siemens Elmiskop 1 electron microscope during plastic deformation in a tensile straining device designed by Fisher (1959) to replace the normal stereo specimen holder. A crystal was mounted with drops of collodion to the two jaws of a tiny chuck which could be forced apart by a wedge device. The wedge was coupled directly to the normal stereo-drive, so that the crystal could be strained in tension by simply rotating the stereo-drive knob located on the outside of the microscope. The specimen gauge length was 0·8 mm and the maximum obtainable plastic strain about 6%, corresponding to four complete turns of the stereo-drive knob.

§ 3. RESULTS

3.1. *Tensile Tests and Observations in the Optical Microscope*

Since the axis of tension was always parallel to the (0001) plane, basal glide was impossible, and plastic deformation began either by the nucleation and growth of a twin or by the initiation and propagation of non-basal glide in the form of a Lüders band. In some cases both twinning and non-basal glide occurred. Only the latter is discussed here; twinning is considered in another paper (Price 1960 a).

Figure 1 is a typical stress–strain curve for a crystal which deformed by nonbasal glide. The elastic region, OY, was linear and extended to a maximum strain which ranged from about 2×10^{-3} for large platelets to 10^{-2} for whiskers. At some point on the crystal, usually at a large growth step or near one of the grips, plastic deformation started and the stress dropped to a value A, about $\frac{2}{3}$ of the yield stress. In the region of easy glide, AB, a Lüders band, clearly observable in the optical microscope at low magnification, was propagated from this point along the crystal, with most of the deformation taking place in a very localized region at the head of the band. If the stress was reduced below the flow stress, creep occurred. If the stress was completely removed and the crystal allowed to rest for about an hour in the easy glide region, further deformation took place at various points all along the band at about the same flow stress as before. Finally fracture occurred at B at a plastic strain of about 5% to 10%. Sometimes a crystal did not fracture until after the Lüders band had run along its entire length and some further glide had taken place. This only happened with narrow whiskers and was accompanied by an appreciable increase in the flow stress (not shown in fig. 1).

Figure 2† is an optical micrograph of a deformed platelet, after fracture at B, showing the appearance of the glide lines which made up the Lüders band, AC. To the right of C no evidence of plastic deformation could be detected in the optical microscope.

Fig. 1

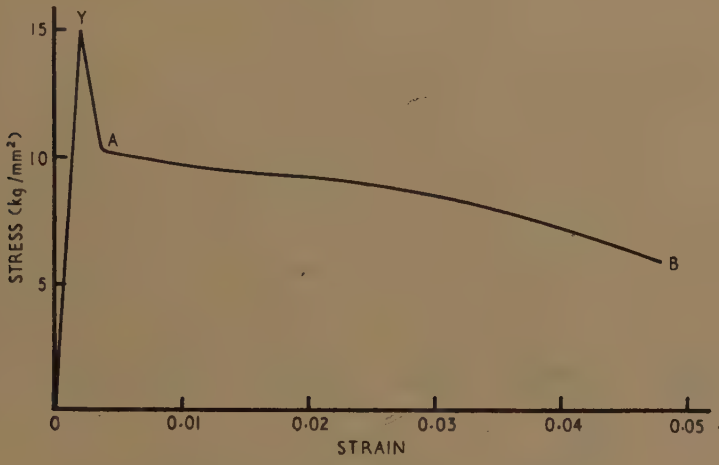

Typical stress–strain curve for a platelet.

The line D is simply a growth step running the length of the crystal. Note that the glide lines and the fractured edges are perpendicular to the edges of the crystal, which run in close-packed directions.

Two features of fig. 2 tell us that the Burgers vector of the deformation must be out of the basal plane:

(1) The crystal does not decrease in width in the deformed region AC.

(2) The glide lines are perpendicular to the axis of tension.

3.2. *Deformation Inside the Electron Microscope*

A tremendous amount of information was gained by observing the various stages of the deformation at high magnification with the transmission electron microscopic technique. Every crystal, provided it was mounted properly, was found to be initially free of dislocations (Price 1960 b). After a very small amount of plastic strain, glide traces and dislocations were usually found in a narrow zone a few microns wide and extending all the way across the crystal. As was observed in the optical microscope, this zone was always located where the applied stress was concentrated, either at a large surface step or near one of the glue joints.

---

† Figures 2, 3, 4, 6, 7, 9, 10 and 11 are shown as plates.

Figure 3 is an electron micrograph of part of a narrow deformed zone, with its boundaries indicated by arrows. Within this region were found glide traces, long dislocations lying predominantly in basal planes, short dislocations running from the top face to the bottom face, and a large number of dislocation loops ranging in diameter from a few tens of angstroms to a few thousand angstroms.

During further straining the region containing glide traces and dislocations grew, and by observations of their movement in a large number of crystals, it was possible to determine the nature of the dislocations and their role in the deformation. The results are summarized below.

3.2.1. *Prismatic glide*

The long dislocations were found to have a $\frac{1}{3}\langle\bar{1}\bar{1}20\rangle$ type Burgers vector. They glided prismatically on basal planes and on non-basal planes whose zone axis contained the Burgers vector, their non-basal components leaving traces on the surface which were in accurately straight lines parallel to this direction. Examples are shown in fig. 4 at *a*, *b*, *c*, *d* and *e*. The close-packed directions and the axis of tension are indicated in the figure by the vectors $\mathbf{a}_1$, $\mathbf{a}_2$, $\mathbf{a}_3$ and $\mathbf{T}$. The components of the $\langle\bar{1}\bar{1}20\rangle$ dislocations lying in basal planes were not subjected to a stress but were simply dragged along by the non-basal components. These dislocations were therefore easily immobilized by obstacles such as loops, other dislocations and surface imperfections, and their movement accounted for only a very small portion of the plastic strain.

3.2.2. *Pyramidal glide*

Most of the deformation resulted from the formation and movement of large numbers of the short dislocations, which produced glide lines whose integrated effect was visible in the optical microscope at low magnification. Isolated traces due to the movement of these dislocations are visible in fig. 4 at A, B, C, D, E, F and G. From the directions and widths of the traces, it was possible to identify the glide planes of the short dislocations, provided the thickness of the crystal was known. This was determined, in crystals which twinned at some stage of the deformation, by measuring the projected width of a coherent twin boundary, which was known to lie on a $\{10\bar{1}2\}$ plane.

It was found that the short dislocations always glided on pyramidal planes with a common $\langle\bar{1}\bar{1}23\rangle$ zone axis. Because of the ease with which the dislocations were able to cross-glide from one pyramidal plane to another (see trace E in fig. 4), it was concluded that their Burgers vectors were of the $\frac{1}{3}\langle\bar{1}\bar{1}23\rangle$ type and that they were of screw character. We saw in §3.1 that the direction of glide had to be out of the basal plane, and the vector $\frac{1}{3}\langle\bar{1}\bar{1}23\rangle = \mathbf{c}+\mathbf{a}$ is the smallest non-basal lattice vector along which there was a finite resolved shear stress.

The most common pyramidal glide plane was $\{11\bar{2}2\}$, which was responsible for the high density of glide lines visible in the optical microscope. One of these planes is indicated in figure 5, along with the $[\bar{1}\bar{1}23]$ glide direction. It is clear from figs. 4 and 6 that pyramidal glide was not restricted to a $(11\bar{2}2)$ plane but could occur on other pyramidal planes, such as $(10\bar{1}1)$, containing the $[\bar{1}\bar{1}23]$ direction, provided the resolved shear stress on them was sufficiently high.

Fig. 5

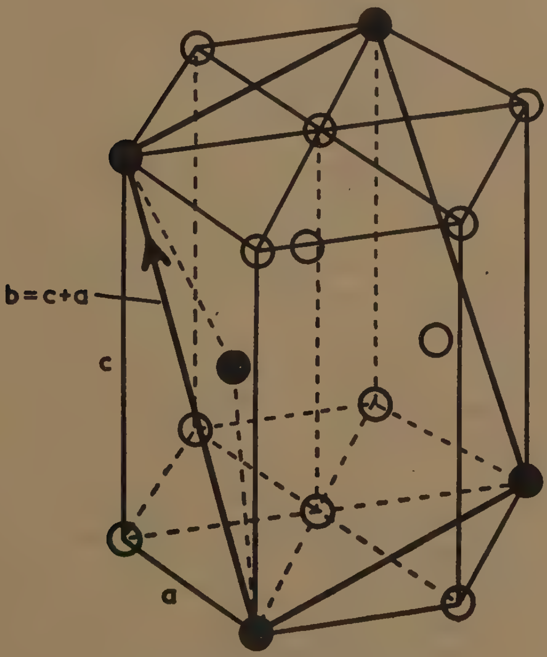

$(11\bar{2}2)$ $[\bar{1}\bar{1}23]$ glide system.

3.2.3. *Dislocation loops*

Dislocation loops, circular in shape and oriented on basal planes (see figs. 3, 4, 6, 7, 9, 10, 11) were formed during pyramidal glide, as a direct result of the motion of $\langle\bar{1}\bar{1}23\rangle$ type dislocations. This is clearly demonstrated in figs. 4 and 6, which show loops arranged in rows along the paths which individual $\langle\bar{1}\bar{1}23\rangle$ dislocations have taken.

Loops were only associated with pyramidal traces. Along some traces there were many large, closely spaced loops (fig. 6); along some were a small number of widely spaced, very tiny loops (traces B, D, G, fig. 4); and along others no loops were formed. When the deformation became so intense that many traces overlapped (fig. 7), it was no longer possible to associate loops with individual traces.

Since none of these loops was observed to glide on the basal plane, it was concluded that their Burgers vectors were out of the basal plane. The results of a detailed study of the loops are presented in § 3.3.

3.2.4. *Propagation of the Lüders band*

It was stated earlier that deformation began with the formation and movement of dislocations in a very narrow region extending across the crystal. During further straining the density of dislocations in this region increased and a large number of loops was produced, which acted as obstacles to the motion of $\langle\bar{1}\bar{1}20\rangle$ dislocations. This is demonstrated in figs. 6 and 7. The blocked $\langle\bar{1}\bar{1}20\rangle$ dislocations, in turn, made the glide of $\langle\bar{1}\bar{1}23\rangle$ dislocations difficult (fig. 3). When the density of loops was very high, all the dislocations became entangled and further glide took place at the edges of the deformed region, where few loops were present, causing it to grow in width. This process was responsible for the propagation of a deformation front which was observed optically as a Lüders band.

If, at some stage of the deformation, the crystal was allowed to rest at room temperature, the loops diminished in size and gradually disappeared, allowing the entangled dislocations to anneal out of the crystal. Within about one hour all of the loops and most of the dislocations were gone. Further straining then produced more glide and more loops in the deformed region. This explains the optical observations that new glide lines could be produced *inside* the Lüders band after a room temperature anneal.

3.2.5. *Fracture*

Usually a crystal fractured before the Lüders band extended over its entire length. Fracture was preceded either by the formation of a twin (Price 1960 a) or by a decrease in thickness of a narrow region a few microns wide and extending across the crystal. This decrease in thickness, which was obvious from the increasing transparency of the narrow region, was due to the movement of large numbers of $\langle\bar{1}\bar{1}23\rangle$ dislocations on a few pyramidal planes. Once the thinning became appreciable, all of the glide took place in this region, where the stress was highest, until the crystal simply glided in two. The observation of increasing transparency with increasing glide is, of course, further proof that the Burgers vector was out of the basal plane.

3.3. *Detailed Study of the Loops*

3.3.1. *Origin and Burgers vector*

There are two possible ways in which the loops could have originated during pyramidal glide; (1) by a dislocation mechanism involving the $\langle\bar{1}\bar{1}23\rangle$ dislocations or (2) by condensation of discs of point defects produced during glide. In many cases loops were actually observed in the process of forming by the first mechanism. This process occurred too rapidly to be photographed, but the successive stages are drawn schematically in fig. 8. During the passage of a $\langle\bar{1}\bar{1}23\rangle$ screw dislocation a long narrow loop was left behind, (*a*), which was unstable and went through configurations such as (*b*) and (*c*), finally becoming a series of circular loops, (*d*), within a period of 1 to 5 sec. The total area enclosed by the circular loops appeared to be about the same as that enclosed by the original loop. Sometimes several long narrow loops, running in the same direction, were formed at the same time on nearby planes. The long loops then split up into circular loops whose positions were determined by their mutual stress fields. As fig. 9 shows, the circular loops tended to occur in clusters, each loop of a cluster being situated in the same plane as the parent loop from which it was formed.

Fig. 8

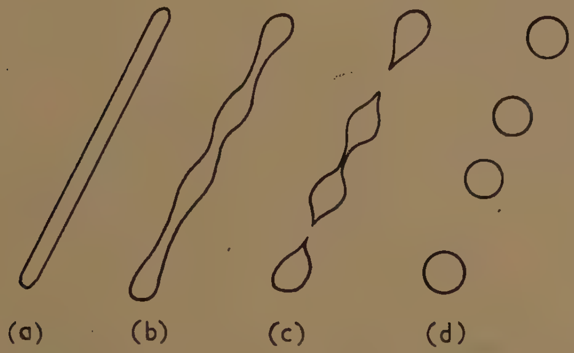

Formation of circular loops from long $\langle\bar{1}\bar{1}23\rangle$ loops.

The Burgers vector of a loop formed by the dislocation mechanism should be different from that of a loop formed by point defect condensation. In the first case one would expect the Burgers vector to be either $\frac{1}{3}\langle\bar{1}\bar{1}23\rangle$ or another lattice vector related to it by a simple dislocation reaction. In the second case the Burgers vector would be either $\frac{1}{2}\langle 0001\rangle$ or $\frac{1}{6}\langle\bar{2}023\rangle$, neither of which is a lattice vector, and the loop would enclose a stacking fault.

In order to help determine the Burgers vectors, selected area diffraction patterns were obtained for a large number of loops and compared with the corresponding micrographs. It will be noticed in figs. 3, 4, 6, 7, 9, 10 and 11 that some of the loops are fairly uniform in contrast around their periphery (figs. 6 and 9), whereas others vary in contrast, actually becoming invisible along a certain azimuth (figs. 3, 10 (*a*) and 11). It was found that the diffraction pattern of every region containing loops with varying contrast was characterized by a strong reflection from planes parallel to the azimuth along which the contrast was zero or a minimum. This is illustrated in fig. 10 (*a*), which shows loops whose contrast vanishes along a direction parallel to $(11\bar{2}0)$ planes. The diffraction pattern, fig. 10 (*b*), is in the same orientation as the micrograph. Similar results were obtained when the strong reflection was from (1010) planes. It was concluded that the Burgers vectors of the loops with invisible portions were always $\langle 0001\rangle$ and that the contrast was due to the edge component of the dislocation, that is, it resulted from displacements of atoms in the plane of, but normal to, the loops. When the displacements were parallel to reflecting planes, no contrast was produced (Howie and Whelan 1960). The possibility of a $\frac{1}{2}\langle 0001\rangle$ Burgers vector was ruled out because no stacking fault contrast was ever observed inside these loops.

Fig. 12

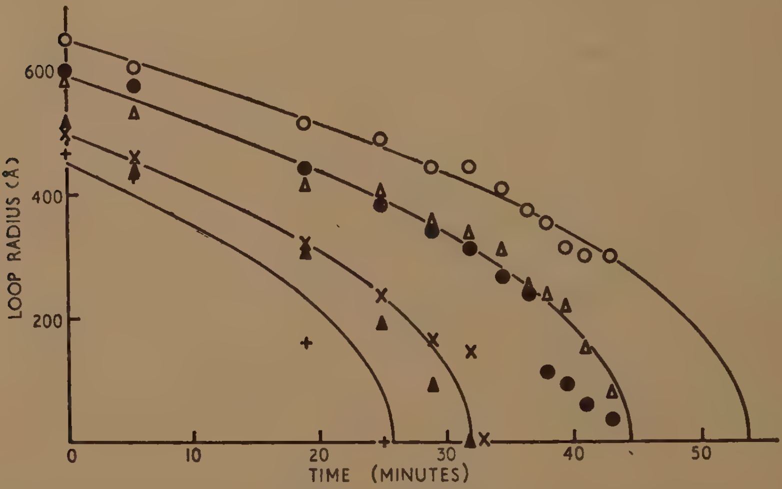

Decrease of radius with annealing time for the six largest loops in fig. 11. The parabolas drawn through the points can be made to coincide by translations along the time axis.

Evidence that the $\frac{1}{3}\langle\bar{1}\bar{1}23\rangle$ Burgers vector also occurred is seen in fig. 10 (*c*), which shows a number of loops which were formed by the dislocation mechanism. Those at A are of the $\langle 0001\rangle$ type, with vanishing contrast along a direction parallel to the $(11\bar{2}0)$ reflecting planes (see the diffraction pattern, fig. 10 (*d*)). Each of the other loops shows contrast which, although it varies around the periphery, never completely disappears, and this can only occur if the Burgers vector has a component normal to the reflecting planes. To a first approximation, this contrast is due to a superposition of the contrast from a $\langle 0001\rangle$ loop and of that from a loop with a Burgers vector in the basal plane.

The most likely explanation for the two different types of contrast is that all of the loops originally had the Burgers vector of their generating $\langle\bar{1}\bar{1}23\rangle$ dislocations, but that the three loops at A underwent a reaction of the type $\frac{1}{3}\langle\bar{1}\bar{1}23\rangle\rightarrow\frac{1}{3}\langle\bar{1}\bar{1}20\rangle+\langle 0001\rangle$. The $\langle\bar{1}\bar{1}20\rangle$ loops then disappeared by glide in the basal plane, leaving loops with a ⟨0001⟩ Burgers vector and with a lower energy.

No evidence was found in the diffraction studies that any of the loops were formed by the condensation of vacancies or interstitials.

3.3.2. *Annealing of loops at room temperature*

The kinetics of annealing of the loops at room temperature were studied by taking a series of high magnification electron micrographs of a small region containing loops over a period of about one hour and measuring the radii of the loops as a function of time. In order to minimize the temperature rise in the crystal due to bombardment by electrons, the high voltage was turned off between exposures, so that the crystal was heated for only a few seconds every five minutes or so.

Fig. 13

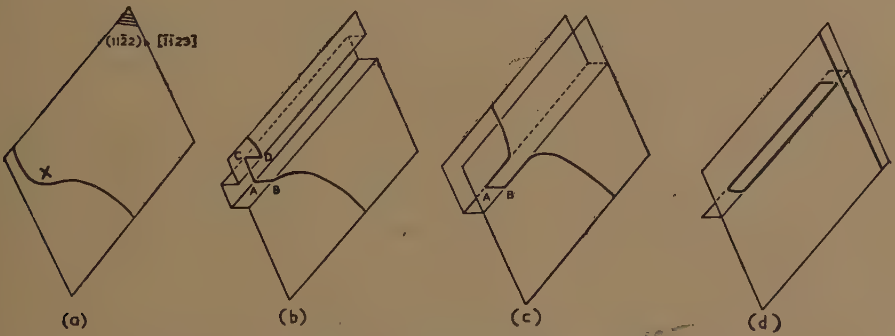

Formation of elongated loops from the multiple jog, AB.

Figure 11 shows qualitatively the behaviour of a large number of loops and fig. 12 is a plot of the radii, r, of the six largest loops in fig. 11 as a function of time, t. It is seen that the loops remained circular during annealing and that the rate of shrinking increased as the loops became smaller. From a plot of log r vs. log t it was ascertained that all of the data could be fitted fairly well by the parabolic equation

$$r^2 = A(t-\tau),$$

where $A \simeq -1{\cdot}3 \times 10^{-14}\,\mathrm{cm}^2/\mathrm{sec}$ is a constant and τ, the intercept of the parabola on the time axis, is the time at which a loop disappeared ($r=0$). The curves in fig. 12, which are parabolas obtained from this equation, are all identical except for a translation along the time axis.

§ 4. INTERPRETATION AND DISCUSSION

4.1. *Formation of Loops*

It seems fairly certain that the elongated loops which split up into circular loops were formed from multiple jogs in ⟨$\bar{1}\bar{1}$23⟩ screw dislocations. Figure 13 shows a plausible way in which this could happen (proposed by Hirsch, private communication). A fast-moving screw dislocation which is held back at some point by an obstacle at X is able to overcome the obstacle by double cross-glide along part of its length. This results in the formation of two multiple jogs, AB and CD. If this occurs near the surface of the crystal, one of the jogs, CD, may be able to glide along the dislocation to the surface, but AB will be prevented from gliding by the obstacle on one side and by a force due to the curvature of the moving dislocation on the other. AB will remain connected to the moving dislocation by two parallel lines. Eventually a long, narrow loop will be pinched off, perhaps when the dislocation cross glides again to avoid another obstacle.

This explanation is supported by evidence in fig. 4, trace E. It appears as though the dislocation encountered an obstacle at O, cross glided and acquired a multiple jog, produced a long loop which split up into a string of circular loops, then cross-glided back onto its original glide plane and lost its jog. At O, where cross glide started, the trace abruptly widened whereas it should have narrowed by an amount determined by the Burgers vector and the angle between the two cross-glide planes. The fact that the widening occurred only at one side of the trace is to be expected on the basis of the above model, in which one of the jogs glides to the surface. From the measured increase in trace width, the jog length was estimated at 200 Å. Assuming that the total area enclosed by the row of loops was the same as the area of the long loop from which they were formed, another estimate of the jog length was obtained by dividing the average area of a loop by the average spacing of loops. This gave about the same value.

Let us now consider the splitting of a long loop into circular loops. It is easy to see that the process involves a lowering of the energy, provided the circular loops exceed a certain diameter. The total energy of n circular loops with a [0001] Burgers vector is $[n\mu \mathbf{b}^2 d/4(1-\nu)]\log(d/\mathbf{b}_0)$, where μ is the shear modulus, ν is Poisson's ratio, d is the loop diameter, and $\mathbf{b}_0 \sim \mathbf{b}$. The energy of a long loop can be approximated by the interaction energy of two parallel edge dislocations of length L, separated by a distance r, and this is given by $[\mu \mathbf{b}^2 L/2\pi(1-\nu)][\log(r/\mathbf{b}_0)+\frac{1}{2}]$. On the assumption that $n\pi d^2/4 = rL$, the necessary condition for splitting is found to be

$$\frac{d}{\log(d/\mathbf{b}_0)} \geqslant \frac{2r}{\log(r/\mathbf{b}_0)+\frac{1}{2}}.$$

From measurements of loop sizes and spacings in the micrographs, estimates of the widths of elongated loops were made and found to satisfy the above inequality in all cases.

Although the energy of a long loop is lowered by splitting, this can only take place at a temperature at which jogs can easily be formed. Once the loop becomes jogged, the process may be assisted by pipe diffusion along its periphery, because of the large Burgers vector of the dislocation ($\mathbf{b} = 5{\cdot}1$ Å). Experiments are now in progress to see if zinc platelets deformed at low temperature inside the electron microscope contain elongated loops instead of circular ones.

Evidence is beginning to accumulate that dislocation loops are formed during the deformation of many ductile materials. Segall (1960) has observed loops in fatigued specimens of Al, Cu, Ni and Au which were electrolytically thinned after deformation and examined by transmission electron microscopy. He found a very high density of long, narrow loops in Cu, Ni and Au and a high density of circular loops in Al. Elongated loops have also been seen in specimens of Cu – 2·5% Al which were deformed in tension and thinned for examination by the transmission technique (Howie 1960).

Dash (1958) has etched silicon crystals deformed at high temperature and found trails of defects extending behind screw dislocations along the direction of their motion and joining them at cusps. He suggested that the trails exerted a dragging force on the dislocations and that they were formed by the nonconservative motion of jogs.

Johnston and Gilman (1960) have concluded, from etch-pit studies of deformed crystals of LiF and MgO, that moving screw dislocations with multiple jogs ranging in size from $3\mathbf{b}$ to $300\mathbf{b}$ produce defect trails from which long dislocation loops are formed. This has recently been confirmed for MgO crystals by Washburn *et al.* (private communication), who have observed, by transmission electron microscopy, elongated loops which were probably formed during the motion of jogged screw dislocations. When heated to high temperature they split up into circular loops, in the same way as the loops in zinc did at room temperature.

Circular loops have been observed in large zinc samples, thinned for transmission microscopy, by Fourdeux and Berghezan (1960) and by Brown (private communication), but most of them contained stacking faults and were believed to have been produced by vacancy condensation. The nature of the contrast at the loops observed by Brown has recently been analyzed by Howie and Whelan (1960), using the dynamical theory of electron diffraction and including a term to take account of incoherent scattering.

4.2. *Climb of Loops at Room Temperature*

Because of its prismatic nature, a loop produced by pyramidal glide can only shrink by climb. As we shall see, the observed rates of shrinking are quantitative evidence that climb does occur easily at room temperature in zinc by the diffusion of vacancies either to or from a loop, depending on whether it is of vacancy or interstitial type.

The rate of shrinking of a loop as a function of temperature and radius has been worked out by Silcox and Whelan (1959), using Friedel's theory of climb (1956). The surfaces of a thin specimen (~ 1000 Å) are very effective sources and sinks of vacancies. On the assumptions that the concentration of vacancies during annealing maintains its equilibrium value (zero chemical stress) and that the concentration of jogs in the loop is $\frac{1}{2}$, they obtain the equation

$$\frac{dr}{dt} = -\tfrac{1}{2} Z \nu_a \mathbf{b} \exp\left(-\frac{E_d}{kT}\right)\left[\exp\left(\frac{F_c \mathbf{b}^2}{kT}\right) - 1\right], \quad . \quad . \quad . \quad (1)$$

where r is the loop radius at time t; Z is an atomic coordination factor ~ 11; ν_a is an atomic vibration frequency $\sim 10^{13}$; $\mathbf{b}$ is the Burgers vector of the loop; E_d is the activation energy for self-diffusion; kT is the Boltzmann temperature factor; and $F_c = \mu \mathbf{b}^2 \log(r/\mathbf{b})/4\pi(1-\nu)r$ is the force due to the line tension and curvature of the loop.

In the range of loop radius and temperature of interest, the expression $\exp(F_c\mathbf{b}^2/kT)-1$ can be approximated quite well by $\alpha\mathbf{b}/r$, where α is determined graphically. Equation (1) is then integrated to give

$$r = r_0[1-(t/\tau)]^{1/2}, \quad \ldots \ldots \quad (2)$$

where r_0 is the initial radius, at $t=0$, and τ is the time at which $r=0$, given by

$$\tau = \frac{r_0^2}{Z\nu_a\mathbf{b}^2\alpha}\exp\left(\frac{E_d}{kT}\right). \quad \ldots \ldots \quad (3)$$

The result should apply equally well to vacancy and interstitial type loops.

Equation (2) is equivalent to the empirical equation of § 3.3.2,

$$r^2 = A(t-\tau) \quad \ldots \ldots \quad (4)$$

with

$$A = -\frac{r_0^2}{\tau} = -Z\nu_a\mathbf{b}^2\alpha\exp\left(-\frac{E_d}{kT}\right). \quad \ldots \ldots \quad (5)$$

For ⟨0001⟩ loops in zinc at ~300°K (see fig. 11), α was found to be 240, and putting $\mathbf{b}=4{\cdot}94$ Å and using the experimentally determined constant $A=-1{\cdot}3\times10^{-14}$ cm^2/sec, eqn. (5) was solved for E_d, giving $E_d=0{\cdot}93$ ev, to be compared with the value 0·95 ev, for self-diffusion parallel to the c-axis, obtained by Shirn *et al.* (1953).

The excellent agreement justifies the assumptions that the average temperature rise in the specimen due to the electron beam was negligible and that the diffusion of vacancies between the loops and the surfaces was so fast that the equilibrium concentration was maintained.

4.3. *Macroscopic Properties*

The electron microscopic observations reported here have made it possible to understand some of the macroscopic properties of zinc whiskers and platelets in the (0001) orientation. It is now clear that a wide platelet has a lower yield point that a whisker, not because of a different dislocation configuration, since neither of them initially contains any dislocations, but because of the greater effectiveness of growth steps and of the glue joints in concentrating the stresses.

The occurrence of pyramidal glide on the $(11\bar{2}2)$ $[\bar{1}\bar{1}23]$ system, which was first reported by Bell and Cahn (1957), has been definitely established, by measurements on individual glide traces, as the major mode of glide in these whiskers and platelets and the one responsible for the optically visible glide lines. The $(11\bar{2}2)$ glide plane may be favoured over other pyramidal planes because the $[\bar{1}\bar{1}23]$ dislocations can lower their energy by splitting into partials on this plane in a reaction of the type

$$\tfrac{1}{3}[\bar{1}\bar{1}23] \rightarrow \tfrac{1}{6}[\bar{2}023]+\tfrac{1}{6}[0\bar{2}23] \text{ (Frank and Nicholas 1953).}$$

It has been seen that the propagation of a deformation front or Lüders band is a result of the formation of loops, which impede dislocations and force new glide to occur at the edges of the deformed region. It should be pointed out that this localized hardening is not accompanied by an increase in the average flow stress. In these crystals, which are initially free of dislocations, the flow stress is the stress necessary for glide at the edge of the deformed region, and this should only increase after the Lüders band has completely covered the crystal, as was observed. Similarly, a room temperature anneal, which eliminates the loops, should not affect the flow stress unless the whole crystal has been deformed.

§ 5. Summary

The most important results which emerged from the investigation were the following:

(1) Zinc whiskers and platelets with a (0001) orientation were initially free of dislocations and had a sharp yield point whose value was determined by stress concentrations at large surface steps or at the grips.

(2) Pyramidal glide in $\langle\bar{1}\bar{1}23\rangle$ directions and mainly on $\{11\bar{2}2\}$ planes was the major mode of deformation in crystals which did not twin.

(3) Dislocations with three Burgers vectors were identified: (*a*) $\langle\bar{1}\bar{1}20\rangle$ dislocations which glided prismatically and were easily immobilized; (*b*) $\langle\bar{1}\bar{1}23\rangle$ dislocations, predominantly screw, which caused pyramidal glide and sometimes left behind long, narrow $\langle\bar{1}\bar{1}23\rangle$ loops which then split up into circular loops with the same Burgers vector; and (*c*) $\langle 0001\rangle$ loops which were formed from $\langle\bar{1}\bar{1}23\rangle$ loops by the reaction

$$\tfrac{1}{3}\langle\bar{1}\bar{1}23\rangle \rightarrow \tfrac{1}{3}\langle\bar{1}\bar{1}20\rangle + \langle 0001\rangle.$$

(4) Both types of loops impeded the motion of dislocations and were responsible for the propagation of the active glide region as a Lüders band.

(5) The loops diminished in size and disappeared by climb at room temperature by the diffusion of vacancies between the loops and the surfaces. From the annealing curves an activation energy for self-diffusion of 0·93 ev was obtained, in good agreement with the results of other workers.

Acknowledgments

I am indebted to Professor N. F. Mott, F.R.S., and Dr. F. P. Bowden, F.R.S., for their continued interest and encouragement and for making available the facilities of this laboratory. I am grateful to Dr. P. B. Hirsch for many valuable discussions and for reviewing the manuscript, to R. M. Fisher, who very kindly allowed me to use his straining stage, and to my colleagues in the Cavendish Laboratory for discussions.

This work was carried out during the tenure of a post-doctoral fellowship awarded by the U.S. National Science Foundation.

References

Bell, R. L., and Cahn, R. W., 1957, *Proc. roy. Soc.* A, **239,** 494.

Cabrera, N., and Price, P. B., 1958, *Report of the Cooperstown Conference on the Growth and Perfection of Crystals*, Ed. Doremus, Roberts and Turnbull (New York : Wiley), p. 204.

Coleman, R. V., and Sears, G. W., 1957, *Acta Met.*, **5,** 131.

Dash, W. C., 1958, *J. appl. Phys.*, **29,** 705.

Fisher, R. M., 1959, *Rev. sci. Instrum.*, **30,** 925.

Fourdeux, A., and Berghezan, A., 1960, *Compte rend.*, **250,** 3019.

Frank, F. C., and Nicholas, J. F., 1953, *Phil. Mag.*, **44,** 1213.

Friedel, J., 1956, *Les Dislocations* (Paris: Gauthier-Villars), p. 72.

Hirsch, P. B., Horne, R. W., and Whelan, M. J., 1956, *Phil. Mag.*, **1,** 677.

Howie, A., 1960, *Proceedings of European Regional Conference on Electron Microscopy, Delft* (to be published).

Howie, A., and Whelan, M. J.. 1960, *Proceedings of European Regional Conference on Electron Microscopy, Delft* (to be published).

Johnston, W. G., and Gilman, J. J., 1960, *J. appl. Phys.*, **31,** 632.

Marsh, D. M., 1959, unpublished. For an account of an earlier model see Marsh, D. M., 1959, *J. sci. Instrum.*, **36,** 165.

Price, P. B., 1960 a, *Proc. roy. Soc.* A (in the press); 1960 b, *Phil. Mag.*, **5,** 417.

Segall, R. L., 1960, *Ph.D. thesis*, University of Cambridge.

Shirn, G. A., Wajda, E. S., and Huntington, H. B., 1953, *Acta Met.*, **1,** 513.

Silcox, J., and Whelan, M. J., 1959, *Structure and Properties of Thin Films*, Ed. Neugebauer, Newkirk and Vermilyea (New York : Wiley), p. 164.

The Thermal Conductivity of Impure InAs at High Temperatures†

By F. W. Sheard‡
Cavendish Laboratory, Cambridge

[Received April 5, 1960]

Abstract

The addition of impurities affects both the lattice and electronic thermal conductivities of a semiconductor. At high temperatures the lattice resistance is increased by an amount independent of temperature: for the small concentrations normally present in semiconductors the impurity resistance can be derived very simply from the variational principle. The electronic contribution is normally obtained from the electrical conductivity via a Lorentz number. For a degenerate electron gas assuming polar scattering dominates an approximate calculation shows that at high temperatures the Lorentz number can be considerably reduced below the 'standard' value $\mathscr{L}_0=(\pi^2/3)(k/e)^2$. These theoretical calculations do not completely agree with the observed conductivity of impure InAs between 300 and 700°K (Stuckes 1960). The disagreement is attributed to the electronic contribution. To give agreement the Lorentz number would have to be reduced further but the precise amount is uncertain owing to experimental errors.

§ 1. Introduction

The addition of electrically active impurities to a semiconductor changes both the lattice and electronic thermal conductivities. The lattice conductivity is decreased owing to the additional phonon scattering while the extra conduction electrons increase the electronic contribution. These effects are qualitatively understood but it is nevertheless desirable to study them quantitatively for particular materials.

An absolute calculation of the electronic thermal conductivity would require knowledge of the conduction band structure which is so far only known for Ge, Si and InSb. Instead, using a simple model, one calculates the Lorentz number $\mathscr{L}=\kappa_e/\sigma T$, which at high temperatures will not be painfully sensitive to the details of band structure. Then from the measured electrical conductivity σ the electronic thermal conductivity κ_e is obtained.

However there is often doubt concerning the electron scattering mechanism. At high temperatures and in elemental semiconductors scattering by acoustic modes is likely to dominate. But in compound semiconductors the interaction of the electrons with the electric polarization of the optical modes of the lattice may be stronger and polar scattering may dominate.

---

† Communicated by the Author.

‡ Now at Physics Department, University of Nottingham.

Since the energy of an optical phonon can span a large part of the electron distribution such scattering is not describable by a simple relaxation time. A crude calculation of the Lorentz number for the case of a degenerate electron gas is given below. It is found that even at temperatures close to the optical mode temperature Θ_0, $\mathscr{L}$ can be considerably below the standard value $\mathscr{L}_0=(\pi^2/3)(k/e)^2$ valid for elastic scattering. Thus estimates of the heat transport in degenerate compound semiconductors may be considerably in error if they rely on the standard Lorentz number.

The scattering of phonons by impurities is well understood but there are difficulties in the calculation of the thermal resistance from the phonon free path. The magnitude of the impurity resistance at high temperatures is discussed in § 3.

Finally the recent data on heavily doped InAs (Stuckes 1960) are analysed.

§ 2. THE LORENTZ NUMBER FOR POLAR SCATTERING

The interaction of an electron of wave vector **k** with the electric polarization caused by an optical phonon **q** leads to a transition probability

$$\mathscr{Q}_{\mathbf{k},\mathbf{q}}^{\mathbf{k}'} \propto \frac{1}{q^2}\delta_{\mathbf{k}+\mathbf{q},\mathbf{k}'}\delta(\mathscr{E}_{\mathbf{k}}+\hbar\omega_l-\mathscr{E}_{\mathbf{k}'}) ; \quad . \quad . \quad . \quad . \quad . \quad . \quad (1)$$

k′ being the wave vector of the scattered electron and ω_l the frequency of the longitudinal optical modes (Ehrenreich 1957). The factor of proportionality need not concern us since the Lorentz number, being the ratio of the thermal and electrical conductivities, is independent of the magnitude of the transition rate.

To take account of the change in energy of an electron during a collision the variational method of calculation must be used. It was in this way that Howarth and Sondheimer (1953) obtained the electrical resistance and thermopower. We shall use the formulation in terms of entropy production (Ziman 1960, p. 280) and indicate only the calculation of the thermal resistivity W.

The relevant equation is

$$W=\frac{T^2\dot{\mathscr{S}}_{\text{scatt}}}{\mathbf{U}^2}, \quad . \quad . \quad . \quad . \quad . \quad . \quad . \quad . \quad (2)$$

where

$$\dot{\mathscr{S}}_{\text{scatt}}=\frac{1}{kT^2}\int\int\int(\Phi_{\mathbf{k}}+\Phi_{\mathbf{q}}-\Phi_{\mathbf{k}'})^2 f_{\mathbf{k}}{}^0 n_{\mathbf{q}}{}^0(1-f_{\mathbf{k}'}{}^0)\,\mathscr{Q}_{\mathbf{k},\mathbf{q}}^{\mathbf{k}'}\,d\mathbf{k}\,d\mathbf{q}\,d\mathbf{k}' \qquad (3)$$

is the rate of entropy production due to scattering processes, and

$$\mathbf{U}=\int\mathbf{v}_{\mathbf{k}}(\mathscr{E}_{\mathbf{k}}-\zeta)\Phi_{\mathbf{k}}\left(-\frac{\partial f_{\mathbf{k}}{}^0}{\partial\mathscr{E}_{\mathbf{k}}}\right)d\mathbf{k} \quad . \quad . \quad . \quad . \quad . \quad . \quad (4)$$

is the heat current for the state of the system where the deviation from the equilibrium distribution function is

$$f_{\mathbf{k}}-f_{\mathbf{k}}{}^0=-\Phi_{\mathbf{k}}\left(\frac{\partial f_{\mathbf{k}}{}^0}{\partial\mathscr{E}_{\mathbf{k}}}\right).$$

$\Phi_{\mathbf{q}}$ is likewise the deviation of the phonon system from equilibrium.

The variational principle assures us that W takes its minimum value when $\Phi_{\mathbf{k}}$, $\Phi_{\mathbf{q}}$ are solutions of the corresponding transport equations subject to the subsidiary condition that the electric current in the system is zero. Thus guessing suitable solutions yields a good approximation to the thermal resistance.

Making the usual assumption that $\Phi_{\mathbf{q}}=0$ we take for the electron distribution in the presence of a thermal gradient along a direction $\mathbf{u}$,

$$\Phi_{\mathbf{k}} \propto (\mathscr{E}_{\mathbf{k}}-\zeta)\mathbf{k}\,.\,\mathbf{u}, \qquad . \; . \; . \; . \; . \; . \; . \; . \quad (5)$$

which to a good approximation satisfies the condition of zero electric current.

The evaluation of (3) using (1) and (5) requires an integration over $\mathbf{q}$. This is performed as in the calculation by Ziman (1960, p. 434) of the mobility in the non-degenerate limit. The final integration over $\mathbf{k}$-space is converted into one over the energy $\mathscr{E}$ of the state $\mathbf{k}$ assuming simple parabolic band structure: neglecting the proportionality factors in (1) and (5) we obtain

$$\dot{\mathcal{S}}_{\text{scatt}}=\frac{n^0}{4\pi^2kT^2}\cdot\frac{2m^{*3}}{3\pi^2\hbar^6}\int\left\{2\mathscr{E}\sqrt{\left(1+\frac{\hbar\omega_l}{\mathscr{E}}\right)}(\mathscr{E}-\zeta)(\mathscr{E}-\zeta+\hbar\omega_l)\right.$$
$$\left.+(\hbar\omega_l)^2(2\mathscr{E}-\zeta+\hbar\omega_l)\ln\left(\frac{\sqrt{[1+(\hbar\omega_l/\epsilon)]}+1}{\sqrt{[1+(\hbar\omega_l/\epsilon)]}-1}\right)\right\}f_{\mathbf{k}}{}^0(1-f_{\mathbf{k}'}{}^0)\,d\mathscr{E}, \qquad . \; . \; . \quad (6)$$

where n^0 is the Bose–Einstein distribution for the phonons.

The energy $\mathscr{E}$ of an electron is measured from the bottom of the conduction band so that the limits of integration are $\mathscr{E}=0$ and ∞. Using the variable $x=(\mathscr{E}-\zeta)/kT$ the lower limit becomes $-\zeta/kT$ but may be replaced by $-\infty$ with negligible error if the gas is sufficiently degenerate. The integrals are evaluated by expanding the integrand, apart from the factor $f_{\mathbf{k}}{}^0(1-f_{\mathbf{k}'}{}^0)$, in powers of $\hbar\omega_l/\zeta$ and retaining only the lowest powers to give a non-zero result (Howarth and Sondheimer 1953). Defining $\xi=\zeta/kT$, $\alpha=\hbar\omega_l/kT$, (6) can be expressed in terms of the two integrals evaluated below:

$$\mathscr{I}_1=\int x(x+\alpha)(x+\xi)\sqrt{\left(1+\frac{x}{x+\xi}\right)}\frac{1}{(1+e^{-x})(e^{x}+e^{-\alpha})}\,dx$$
$$=\frac{\xi\alpha}{(1-e^{-\alpha})}\left(\frac{\pi^2}{3}-\frac{\alpha^2}{6}\right),$$

$$\mathscr{I}_2=\int\alpha^2(2x+\xi+\alpha)\ln\left(\frac{\sqrt{[1+(\alpha/x+\xi)]}+1}{\sqrt{[1+(\alpha/x+\xi)]}-1}\right)\frac{1}{(1+e^{-x})(e^{x}+e^{-\alpha})}\,dx$$
$$=\frac{\alpha^3\xi}{(1-e^{-\alpha})}\ln\left(\frac{4\xi}{\alpha}\right).$$

Finally

$$\dot{\mathcal{S}}_{\text{scatt}}=\frac{n^0}{4\pi^2kT^2}\cdot\frac{4m^{*3}}{3\pi^2\hbar^6}(kT)^4\frac{\xi\alpha}{(1-e^{-\alpha})}\left\{\frac{\pi^2}{3}-\frac{\alpha^2}{6}+\frac{\alpha^2}{2}\ln\left(\frac{4\xi}{\alpha}\right)\right\}. \qquad (7)$$

After a little manipulation the thermal current is found to be

$$|\mathbf{U}|=\frac{(kT)^2(2m^*\zeta)^{3/2}}{9\hbar^4}, \quad . \quad . \quad . \quad . \quad . \quad . \quad . \quad . \qquad (8)$$

provided ζ is measured from the bottom of the conduction band.

In our notation the electrical resistance, calculated for the lowest order trial function $\Phi_{\mathbf{k}}=\mathbf{k}\,.\,\mathbf{u}$, comes out to be

$$\rho=\frac{n^0}{4\pi^2kT}\cdot\frac{4m^{*3}}{3\pi^2\hbar^6}(kT)^2\frac{\xi\alpha}{(1-e^{-\alpha})}\bigg/\frac{e^2(2m^*\zeta)^3}{9\pi^4\hbar^8}. \quad . \quad . \quad . \qquad (9)$$

At high temperatures the behaviour of the electrical and thermal resistivities is given quite reliably by these formulae: σ is inversely proportional to T while κ_e approaches a constant value. But they are only qualitatively true at low temperatures where better trial functions are needed to give any accuracy.

The magnitude of the Lorentz number follows from (7), (8) and (9):

$$\mathscr{L}\doteq\frac{\rho}{WT}=\frac{\mathscr{L}_0}{1+\frac{3}{2\pi^2}\left(\frac{\Theta_0}{T}\right)^2\left\{\ln\left(\frac{4\zeta}{\hbar\,\omega_l}\right)-\frac{1}{3}\right\}}. \quad . \quad . \quad . \qquad (10)$$

It is the deviation from the high temperature limit, $\mathscr{L}\to\mathscr{L}_0$, that concerns us. This arises because of the 'vertical transitions' in which an electron is scattered vertically through the Fermi surface by a phonon of small wave number. Such processes contribute strongly to the thermal resistance because of the considerable energy change $\hbar\omega_l$ involved, but add very little to the electrical resistance owing to the small angle of scatter. Hence the Lorentz number is reduced below the value $\mathscr{L}_0$ valid for elastic collisions. But at sufficiently high temperatures the width of the Fermi surface, kT, is much greater than $\hbar\omega_l$ and the collisions are effectively elastic.

§ 3. LATTICE CONDUCTION AT HIGH TEMPERATURES

We shall now study how the lattice conductivity is limited by the various phonon scattering mechanisms paying particular attention to the effects of impurities.

Phonon–phonon U-processes provide most of the thermal resistance and a crude estimate of this has been given by Leibfried and Schlömann (1954):

$$W_{\mathrm{U}}=\frac{10\pi^3}{3(4)^{1/3}}\left(\frac{\hbar}{k}\right)^3\frac{\gamma^2}{M\Theta^2\delta}\left(\frac{T}{\Theta}\right), \quad . \quad . \quad . \quad . \quad . \quad . \qquad (11)$$

where M is the average mass, δ^3 the average volume per atom and γ is the Grüneisen ratio. They did not consider the different types of U-process in detail and this, with many other approximations, makes (11) only reliable to a factor of 2 or 3.

Adding substitutional impurities produces additional phonon scattering the cross section depending almost entirely on the mass difference ΔM between the impurity and the atom normally occupying the lattice site.

Other effects due to the accompanying strain field are small. The mean free path $\Lambda_{\mathbf{q}}$ for phonons of wave number q is given by (Berman *et al.* 1956),

$$\frac{1}{\Lambda_{\mathbf{q}}} = \frac{q^4}{4\pi} n_{\mathrm{S}} \left(\frac{\Delta M}{\mathscr{D}}\right)^2, \quad \ldots \ldots \quad (12)$$

where there are n_{S} scattering centres per unit volume in a medium of average density $\mathscr{D}$.

To obtain the thermal resistance we must average this quantity over the whole lattice spectrum taking account of the mutual interactions of the phonons by N-processes and U-processes. When N-processes outweigh the effects of impurity scattering and completely dominate the phonon distribution a simple formula can be obtained (Ziman 1960, p. 308). It derives from the variational principle and as such gives an upper limit to the thermal resistance. Within this approximation the resistances due to U-processes and impurity scattering are additive the latter being expressed as a harmonic average over the mean free path:

$$W_{\mathrm{i}} = \frac{3}{C^2} \int \frac{C_{\mathbf{q}}}{\Lambda_{\mathbf{q}} v_{\mathbf{q}}} \mathbf{dq}, \quad \ldots \ldots \quad (13)$$

where $C_{\mathbf{q}}$ is the contribution of modes of wave vector $\mathbf{q}$ to the total heat capacity C and $v_{\mathbf{q}}$ is the phonon group velocity.

At low temperatures this formula cannot be used: for, the number of N-processes occurring is limited by selection rules and in most solids the scattering by naturally occurring isotopes is sufficient to influence the phonon distribution. Even for small isotopic content the observed resistance can be many times smaller than the variational limit (13) However a more general calculation, in which both N-processes and impurity scattering were allowed to fix the form of the phonon distribution, has given good agreement with experiment over wide ranges of impurity concentration (Berman *et al.* 1959). The theory of this is now well understood.

At high temperatures N-processes are much more common especially at the higher phonon frequencies. Equation (13) will therefore hold under less stringent conditions than required for low temperatures. A simple Debye model for the solid gives

$$W_{\mathrm{i}} = \frac{\delta^3}{kv\Lambda_{\mathrm{D}}} \mathscr{J}_8\left(\frac{\Theta}{T}\right) \Big/ \frac{\Theta}{T} \left\{\mathscr{J}_4\left(\frac{\Theta}{T}\right)\right\}^2 : \quad \ldots \ldots \quad (14)$$

Λ_{D} is the mean free path for a phonon of the Debye frequency $k\Theta/\hbar$, and v is an average sound velocity. $\mathscr{J}_n(x)$ is the standard transport integral,

$$\int_0^x \{z^n e^z/(e^z - 1)^2\}\, dz,$$

which has been extensively tabulated (National Bureau of Standards 1959). This formula predicts that for $T \gtrsim 0{\cdot}6\Theta$, W_{i} is nearly constant; since we are only interested in temperatures greater than Θ we can write

$$W_{\mathrm{i}} = \frac{3\delta^3}{7kv\Lambda_{\mathrm{D}}}, \quad T \gtrsim \Theta. \quad \ldots \ldots \quad (15)$$

Finally expressing the sound velocity in terms of the Debye temperature and introducing the average mass per atom M we have from (12)

$$W_{\mathrm{i}}=\frac{9\pi}{14}(6\pi^2)^{1/3}\frac{\hbar}{k^2}\frac{\delta^4}{\Theta}n_{\mathrm{s}}\left(\frac{\Delta M}{M}\right)^2. \qquad (16)$$

Unfortunately the available experimental evidence refers to such large concentrations of imperfections that we are unable to verify (16) in detail. The measurements of Geballe and Hull (1958) on normal and isotopically pure Ge have shown clearly that the additional resistance is independent of temperature for $T>\Theta$, but the observed magnitude is five times smaller than predicted by (16). For a Ge alloy containing 10% Si (Steele and Rosi 1958) the isotope resistance is some twenty-five times smaller. But for these specimens this is not really surprising since when they are taken to low temperatures ($\Theta/10$) the variational limit (13) is too large by factors of about 30 and 130 respectively (see Berman *et al.* 1959).

Use of the simple formula (13) is therefore limited to small impurity concentrations but for a particular concentration it is a better approximation at high than at low temperatures. For semiconductors where concentrations are indeed small it is likely to be quite accurate. To derive a formula for the high-temperature impurity resistance at arbitrary concentrations would be difficult; for the U-processes, which can be neglected at low temperatures, would have to be taken explicitly into account.

A formula similar to (16) but with a smaller numerical coefficient has been given by Ambegaokar (1959). He assumes that at high temperatures the phonon spectrum is dominated by U-processes, described by an appropriate relaxation time, upon which isotope scattering is a small perturbation. This is incorrect, for accompanying the U-processes there must be more than an equal number of N-processes which cannot be taken into account by simply adding reciprocal relaxation times. By treating the N-processes properly (Klemens 1958, p. 32, Callaway 1959) one arrives by a slightly different method at (16) again.

In an n-type semiconductor the conduction electrons can also scatter phonons and contribute to the lattice resistivity. However, a rough estimate shows the effect to be negligible for the impure InAs sample considered in the next section.

§ 4. THE THERMAL CONDUCTIVITY OF IMPURE InAs

To calculate the thermal transport in heavily doped InAs we need, apart from the measured electrical conductivity, estimates of the Fermi level, the optical mode temperature and the Debye temperature.

A knowledge of the melting point T_{M}, density $\mathscr{D}$ and average atomic weight A can be used to estimate the Debye temperature from the Lindemann melting formula

$$\Theta=BT_{\mathrm{M}}^{-1/2}A^{-5/6}\mathscr{D}^{1/3}. \qquad (17)$$

The value 200 taken for B was the mean of values calculated from the known properties of Si and Ge. This gave $\Theta = 280$°K.

The optical mode energy has not been determined very accurately (Picus *et al.* 1959, Ehrenreich 1957) and we shall simply take the round figure of 350°K for Θ_0.

Since intrinsic InAs is weakly degenerate at room temperature, a sample containing 10^{19} donor impurities per cm^3 will be highly degenerate. With an effective mass of $0{\cdot}064 m_e$ (Welker and Weiss 1956) and a parabolic conduction band the Fermi energy would be 0·26 ev. However, comparison with InSb (Ehrenreich 1957, 1959) suggests the conduction band is appreciably non-parabolic, having a greater density of states, which would lower the calculated Fermi level.

Fig. 1

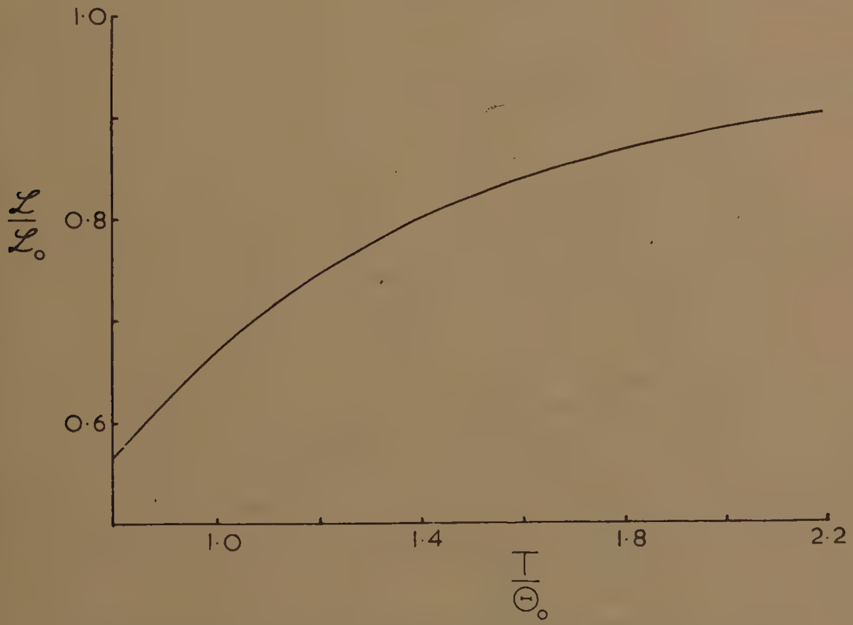

Lorentz number for polar scattering in a degenerate electron gas: $\zeta/\hbar\omega_l = 9$.

These plausible values can now be used to calculate the effects of the impurities on the electronic and lattice thermal conductivities of InAs.

The electronic contribution follows immediately from (10) with $(\zeta/\hbar\omega_l) \sim 9$, for which the behaviour of the Lorentz number is shown in fig. 1. The reduction below the asymptotic value $\mathscr{L}_0$ is surprisingly large: at $T = \Theta_0$, $\mathscr{L}/\mathscr{L}_0 \sim 0{\cdot}67$.

The extra lattice resistance is given by (16) evaluated for a concentration of 10^{19} substitutional sulphur atoms per cm^3: the result is $W_i = 0{\cdot}43$ cal^{-1} cm sec °K. In order to justify our use of the variational limit we look at the ratio of the calculated W_i to the observed Umklapp resistance at

$T=\Theta$, $W_{\text{i}}/W_{\text{U}}(\Theta)$, which clearly reflects the relative strengths of impurity scattering and phonon–phonon scattering. In the experiments previously mentioned on Ge and a Ge–Si alloy it is about 0·5 and 25 respectively. But for the InAs sample $W_{\text{i}}/W_{\text{U}}(\Theta)$ is much smaller ($\sim\frac{1}{30}$) thus justifying the assumption that the phonon system is dominated by N-processes and only slightly perturbed by the impurity scattering.

We could now compute theoretically the total thermal conductivity of the impure InAs and compare with experiment. This would involve using the very crude estimate (11) of W_{U} and the results would therefore not be of great significance. The Leibfried–Schlömann estimate has in any case been thoroughly discussed elsewhere (Klemens 1958, p. 46). Since our interest lies with the relatively small effects of the impurities we shall take W_{U} from experiment and avoid the numerical uncertainties in (11).

Table 1. Electronic and lattice contributions to the thermal conductivity of pure InAs ($n=3\times10^{16}$)

T°K	$\kappa_{\text{expt}}^{(\text{p})}$	$\kappa_{\text{e}}^{(\text{p})}$	$\kappa_{\text{L}}^{(\text{p})}$	W_{U}
300	0·0640	0·0004	0·0636	15·72
400	0·0448	0·0006	0·0442	22·60
500	0·0335	0·0010	0·0325	30·80
600	0·0280	0·0025	0·0255	39·20
700	0·0250	0·0045	0·0205	48·80

Unit of conductivity: cal cm^{-1} sec^{-1} °K^{-1}.

Table 1, taken from Stuckes (1960), summarizes the data for a fairly pure InAs sample (3×10^{16} donors cm^3) from which W_{U} was obtained in the temperature range 300 to 700°K. The electronic thermal conductivity $\kappa_{\text{e}}^{(\text{p})}$ was calculated using the relaxation time approximation and Boltzmann statistics: since it is small the error in the lattice conductivity $\kappa_{\text{L}}^{(\text{p})}$ is unlikely to be large.

Our estimate of the total conductivity of the impure specimen is thus obtained by the following algebraic manipulations: the superscripts (p) and (i) refer to the words pure and impure.

$$\left.\begin{aligned} \frac{1}{W_{\text{U}}} &= \kappa_{\text{L}}^{(\text{p})} = \kappa_{\text{expt}}^{(\text{p})} - \kappa_{\text{e}}^{(\text{p})}, \\ \frac{1}{\kappa_{\text{L}}^{(\text{i})}} &= W_{\text{L}}^{(\text{i})} = W_{\text{U}} + W_{\text{i}}, \\ \kappa_{\text{total}}^{(\text{i})} &= \kappa_{\text{L}}^{(\text{i})} + \kappa_{\text{e}}^{(\text{i})}. \end{aligned}\right\} \quad . \quad . \quad . \quad . \quad (18)$$

The result is given in table 2.

The last two columns show that there is a discrepancy which increases with temperature becoming quite large at the highest temperature. There are obviously four possible sources of this disagreement, i.e. W_{L}, W_{i}, $\kappa_{\mathrm{e}}^{(\mathrm{i})}$, $\kappa_{\mathrm{expt}}^{(\mathrm{i})}$; but what is the relative significance of each in producing the final discrepancy?

Firstly, experimental errors are by no means negligible. The measured conductivities are only accurate to 3% at the lower temperatures and 5% at the higher temperatures in the table (Stuckes 1960). At 300°K this could account for more than half the difference $\kappa_{\mathrm{total}}^{(\mathrm{i})}-\kappa_{\mathrm{expt}}^{(\mathrm{i})}$. At 700°K W_{L} also includes errors in $\kappa_{\mathrm{e}}^{(\mathrm{i})}$ and about a third of the discrepancy could be explained in this way. We are left with possible errors in the theoretical estimates of W_{i}, $\kappa_{\mathrm{e}}^{(\mathrm{i})}$ with which to explain the remainder.

Table 2. Theoretical estimate of total thermal conductivity of impure InAs ($n=10^{19}$).

T°K	$W_{\mathrm{L}}^{(\mathrm{i})}$	$\kappa_{\mathrm{L}}^{(\mathrm{i})}$	$\kappa_{\mathrm{e}}^{(\mathrm{i})}$	$\kappa_{\mathrm{total}}^{(\mathrm{i})}$	$\kappa_{\mathrm{expt}}^{(\mathrm{i})}$
300	16·15	0·0619	0·0072	0·0691	0·0630
400	23·03	0·0434	0·0111	0·0545	0·0470
500	31·23	0·0320	0·0142	0·0462	0·0377
600	39·63	0·0252	0·0165	0·0417	0·0320
700	49·23	0·0203	0·0182	0·0385	0·0285

Unit of conductivity: cal cm^{-1} sec^{-1} °K^{-1}.

The value deduced for the impurity resistance is reliable as far as the Debye model applies to InAs. It is a variational estimate and as such can only be reduced by more accurate calculation using the same model. A more realistic model, or the presence of other imperfections in the impure sample, could possibly lead to a larger W_{i}. However, if the source of the remaining discrepancy is in the impurity resistance, this would need to be strongly temperature dependent. At the highest temperature it would have to be some fifty times the value previously calculated. This is in flat contradiction to theory of §3 and the experiments of Geballe and Hull. An explanation invoking a temperature dependent impurity resistance is therefore to be rejected. One can more plausibly tamper with the magnitude of W_{i}; at 300°K, where the electronic contribution $\kappa_{\mathrm{e}}^{(\mathrm{i})}$ is of least importance, only multiplication by two is needed to bring about the required agreement.

At the higher temperatures, where $\kappa_{\mathrm{e}}^{(\mathrm{i})}$ is important, the discrepancy between theory and experiment persists. It would not however be surprising if our calculation of $\kappa_{\mathrm{e}}^{(\mathrm{i})}$ were wrong. Even the assumption of polar scattering is suspect for the dominant scattering mechanism in InAs has not been definitely established. Since the phonon scattering cross-section is known accurately no such doubts exist about W_{i}; only its magnitude is a little uncertain.

Suppose for example that we accept the latter calculation; the electronic heat transport can then be estimated from experiment according to

$$\kappa_{\mathrm{e}}^{(\mathrm{i})}\,(\mathrm{estd}) = \kappa_{\mathrm{expt}}^{(\mathrm{i})} - \frac{1}{W_{\mathrm{L}} + W_{\mathrm{i}}}, \qquad (19)$$

and compared directly with theory. This final comparison is made in table 3 and illustrated in fig. 2. The curve marked 'elastic scattering' is the result of using the standard Lorentz number $\mathscr{L}_0$. There is considerable uncertainty in the experimental curve. The dotted lines E indicate the limits to which it could be raised by a favourable combination of experimental errors. It thus appears that the reduction in the Lorentz number afforded by polar scattering is not sufficient to account for the experimental results.

Table 3. Comparison of estimated κ_{e} for impure InAs with theory

T°K	$\kappa_{\mathrm{L}}^{(\mathrm{i})}$	$\kappa_{\mathrm{expt}}^{(\mathrm{i})}$	$\kappa_{\mathrm{e}}^{(\mathrm{i})}$ (estimated)	$\kappa_{\mathrm{e}}^{(\mathrm{i})}$ (polar)	$\kappa_{\mathrm{e}}^{(\mathrm{i})}$ (elastic)
300	0·0619	0·0630	0·0011	0·0072	0·0121
400	0·0434	0·0470	0·0036	0·0111	0·0153
500	0·0320	0·0377	0·0057	0·0142	0·0176
600	0·0252	0·0320	0·0068	0·0165	0·0193
700	0·0203	0·0285	0·0082	0·0182	0·0205

Unit of conductivity: cal $\mathrm{cm}^{-1}\,\mathrm{sec}^{-1}\,{}^\circ\mathrm{K}^{-1}$.

Unfortunately the simplifications made in deriving this formula will not provide an excuse for reducing the Lorentz number still further. Briefly they are:

(1) Electron screening: This reduces the transition probability (1) especially at the lower phonon frequencies (Ehrenreich 1959). Vertical transitions, which only contribute strongly to the thermal resistance, are not so frequent and the Lorentz number is consequently increased.

(2) Trial functions: Only the simplest possible were used in the calculation. The electrical resistance is given accurately (Howarth and Sondheimer 1953) but the thermal conductivity is more sensitive to the balance of the electron system and needs a larger correction. But κ_{e} is thereby increased and so also is $\mathscr{L}$.

(3) Partial degeneracy: The electron gas may not be completely degenerate as assumed. At temperatures sufficiently high for the relaxation time approximation to be valid a partially degenerate gas has a Lorentz number slightly smaller than $\mathscr{L}_0 = 3{\cdot}29(k/e)^2$, and tending

towards the value $3(k/e)^2$ for a non-degenerate gas. This same trend will be observed at rather lower temperatures but the decrease in $\mathscr{L}$ is likely to be quite small.

(4) Band structure: We do not expect the actual band structure of InAs to greatly influence the formula for $\mathscr{L}$. The position of the Fermi level also depends on the model used but it appears logarithmically so that only serious misplacement would affect the magnitude of $\mathscr{L}$.

Fig. 2

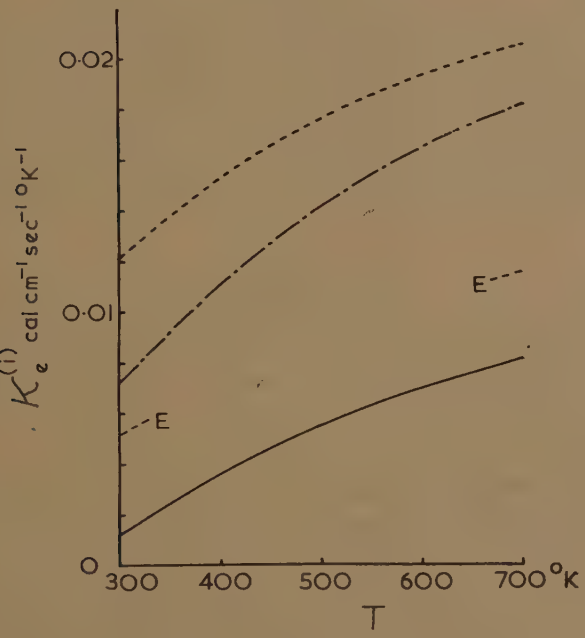

Electronic thermal conductivity of impure InAs.

———— estimated from experiment.
— — — — — polar scattering.
- - - - - - - - elastic scattering.

Experiments of greater accuracy are desirable in order to clarify the position by defining the precise reduction in the Lorentz number. Nevertheless it is clear that the electron scattering mechanism in InAs is inelastic at high temperatures.

ACKNOWLEDGMENTS

I wish to express my thanks to Dr. J. M. Ziman for his helpful advice and to Miss A. D. Stuckes for a copy of her paper before publication. I am also indebted to Industrial Distributors (1946) Ltd., for a research grant.

REFERENCES

AMBEGAOKAR, V., 1959, *Phys. Rev.*, **114,** 488.
BERMAN, R., FOSTER, E. L., and ZIMAN, J. M., 1956, *Proc. roy. Soc.* A, **237,** 344.
BERMAN, R., NETTLEY, P. T., SHEARD, F. W., SPENCER, A. N., STEVENSON. R. W. H., and ZIMAN, J. M., 1959, *Proc. roy. Soc.* A, **253,** 403.
CALLAWAY, J., 1959, *Phys. Rev.*, **113,** 1046.
EHRENREICH, H., 1957, *J. Phys. Chem. Solids*, **2,** 131; 1959, *Ibid.*, **9,** 129.
GEBALLE, T. H., and HULL, G. W., 1958, *Phys. Rev.*, **110,** 773.
HOWARTH, D. J., and SONDHEIMER, E. H., 1953, *Proc. roy. Soc.* A, **219,** 53.
KLEMENS, P. G., 1958, *Solid State Physics*, Vol. 7 (New York: Academic Press).
LEIBFREID, G., and SCHLÖMANN, E., 1954, *Nachr. Akad. Wiss. Göttingen*, IIa, No. 4, 71.
NATIONAL BUREAU OF STANDARDS, 1959, Circular No. 595.
PICUS, G., BURNSTEIN, E., HENWISS, B. W., and HASS, M., 1959, *J. Phys. Chem. Solids*, **8,** 282.
STEELE, M. C., and ROSI, F. D., 1958, *J. appl. Phys.*, **29,** 1517.
STUCKES, A. D., 1960, *Phil. Mag.*, **5,** 84.
WELKER, H., and WEISS, H., 1956, *Solid State Physics*, Vol. 3 (New York: Academic Press), p. 22.
ZIMAN, J. M., 1960, *Electrons and Phonons* (Oxford: Clarendon Press).

Nuclear Magnetic Resonance in β Brass†

By G. W. West
Division of Tribophysics,
Commonwealth Scientific and Industrial Research Organization,
University of Melbourne, Australia

[Received April 22, 1960]

Abstract

The nuclear magnetic resonance lines from β brass at room temperature have been studied as a function of composition and deformation. A simple model is proposed to explain the variation of intensity with composition. The Knight shift is 0·14%, independent of composition. Filing at room temperature eliminates the line from most specimens but it can be restored by annealing. Changes in line shape occur before, during, and after recrystallization.

§ 1. Introduction

The effects of deformation and composition on the ^{63}Cu resonance in copper and copper–zinc alloys have been studied by Bloembergen and Rowland (1953). They showed that in pure copper the components of the line due to the satellite transitions ($m=\frac{3}{2}\rightarrow\frac{1}{2}, -\frac{1}{2}\rightarrow-\frac{3}{2}$) can be almost eliminated by cold work but that there is no effect on the central component corresponding to the transition $m=\frac{1}{2}\rightarrow-\frac{1}{2}$. Furthermore, in cold-worked copper–zinc alloys they showed that the central component was unobservable when the zinc content exceeded 25%. They explained these effects in terms of quadrupole broadening but pointed out that if the composition was such that an ordered structure with cubic symmetry occurred, quadrupole broadening should be absent and a line would be expected. Following this idea, they looked for resonance from a β brass containing nearly 50% zinc. However, they could detect no resonance and suggested that ordering was not complete.

Since then resonance lines from β brass have been reported (West 1958). The present paper gives details of the variation of this resonance line with composition and with deformation and subsequent heat treatment.

§ 2. Experimental Details

The detecting apparatus was a conventional Pound–Knight–Watkins spectrometer operating at about 5·96 Mc/s and a Varian 12 in. electromagnet set at about 5250 gauss. The modulation amplitude was 3 gauss peak-to-peak and all resonance lines were obtained at room temperature.

The alloys were originally prepared from OFHC copper and pure zinc for another investigation (Clarebrough 1957). Their compositions are given in table 1.

---

† Communicated by W. Boas.

The copper–zinc equilibrium diagram (Raynor 1944) was used to determine the phase composition of each alloy. The composition of alloy C corresponds to the β phase boundary so that alloys C, D and E all contain β phase of the same composition. For alloy D approximately $\frac{8}{9}$ of the specimen volume should be β phase while for alloy E about $\frac{7}{9}$ should be. Metallographic examination showed that alloy A, after it had been annealed at 450°C for two hours and then slowly cooled in the furnace, contained a small amount of γ phase, estimated very approximately as 5%. These estimates of the amounts of the different phases present are necessary since in comparing the signals from different alloys it has been assumed that no signal was obtained from the copper atoms in α or γ phases.

Table 1. Zinc Content of Alloys

Alloy	Phases present	Atomic % zinc in alloy	Atomic % zinc in β phase
A	$\beta+\gamma$	50·05	49·5
B	β	47·64	47·64
C	β	46·15	46·15
D	$\alpha+\beta$	45·06	46·15
E	$\alpha+\beta$	43·14	46·15

The material for the resonance experiments was prepared by filing the alloys at room temperature and accepting only those particles which passed through a 160 mesh sieve. These particles were then placed for 5 min in a solution of stearic acid in benzene, washed and allowed to dry. By this treatment the particles were coated with an insulating layer which was stable at the annealing temperatures used. The specimens of brass consisted of 200 mg of powder held in glass tubes. A reference specimen of OFHC copper (99·96% Cu) was prepared in a similar manner but only particles which passed through a 300 mesh sieve were used. The reference specimen was annealed at 450°C for two hours. It contained 98·5 mg of copper, i.e. the same number of copper nuclei as would be present in 200 mg of an ideal copper-zinc alloy containing 50 atomic per cent zinc.

For all heat treatments up to 350°C the glass tubes containing the filings were immersed in silicone oil at the appropriate temperature for 5 min. For heat treatments above 350°C, in order to minimize loss of zinc, the filings were sealed in glass tubes under a pressure of argon of just less than one atmosphere and then placed in a furnace for the specified time.

§ 3. Experimental Results

3.1. *Effect of Composition*

Specimens of all compositions were annealed for two hours at 450°C and slowly cooled in the furnace. Table 2 shows relative integrated intensities, relative peak-to-peak heights of the derivative curves, and the line widths as measured between peaks on the derivative curve. The values for the brass specimens have been normalized to correspond to specimens containing the same total number of nuclei in the β phase as would be present in 200 mg of an ideal copper–zinc alloy containing 50 atomic per cent zinc.

Table 2. Results for Annealed Copper and β Brass

Alloy	Copper	A	B	C	D	E
Relative integrated intensities	2·5	0·68	0·48	0·35	0·35	0·35
Relative peak-to peak heights	1	0·57	0·35	0·25	0·21	0·17
Line width (gauss)	6	3·3	3·5	4	4	4

The lines for specimens from alloys A, B, and C, annealed at 450°c for two hours, and for the reference copper specimen under the same resonance conditions are shown in fig. 1. The lines for D and E have peak heights as indicated in table 2 but are relatively larger in the tails than the line for C, so that the integrated intensities for C, D and E are approximately equal.

The lines from these annealed specimens are symmetrical and there is a slight broadening and a decrease in peak height as the copper content increases. In order to compare the shapes of the lines, the derivative curves for a specimen from alloy A and for the copper reference specimen have been replotted in fig. 2. The scales of both axes have been adjusted so that both lines have the same peak height and coincide at half peak height. It is clear that the curve from the brass specimen has a much larger tail than that from the copper specimen.

The lines from the brass specimens occur at a frequency 5·2 kc/s below that from the copper reference specimen and any variation of frequency with change in composition is less than 0·1 kc/s. Thus the Knight shift for ^{63}Cu is only 0·14% in β brass compared with 0·23% in pure copper. If these values are substituted in the Korringa (1950) relation the calculated spin-lattice relaxation time for copper is 0·37 that for brass.

The saturation curves for a specimen from alloy A and for the copper reference are shown in fig. 3. The ratio of relaxation times from these results is given by (Andrew 1955)

$$\frac{T_1\,(\text{copper})}{T_1\,(\text{brass})} = 0{\cdot}43\,\frac{T_2\,(\text{brass})}{T_2\,(\text{copper})},$$

where T_1 = spin–lattice relaxation time, and
T_2 = spin–spin interaction time.

For this to agree with the results calculated from the Korringa relation the spin–spin interaction times for copper and brass would need to be approximately equal.

Fig. 1

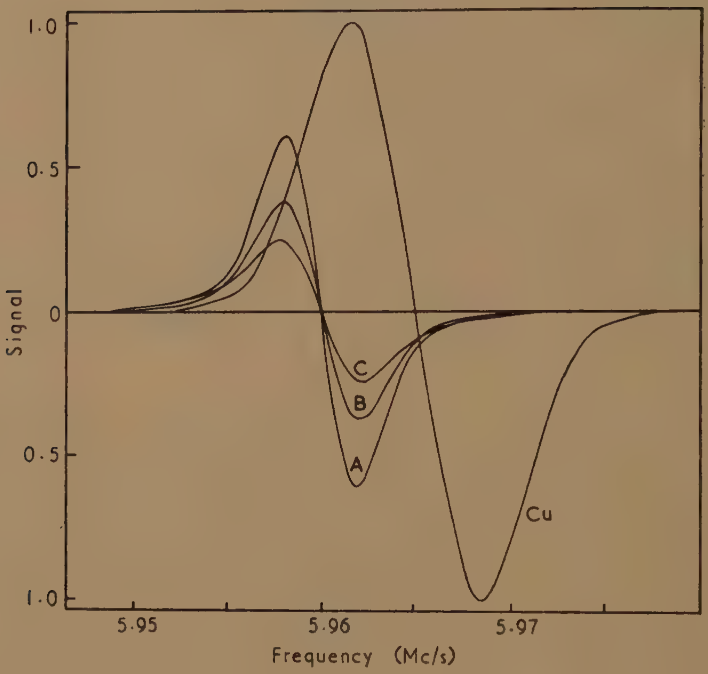

The derivatives of the ^{63}Cu resonance in β brass (alloys A, B, and C) and in pure copper.

Fig. 2

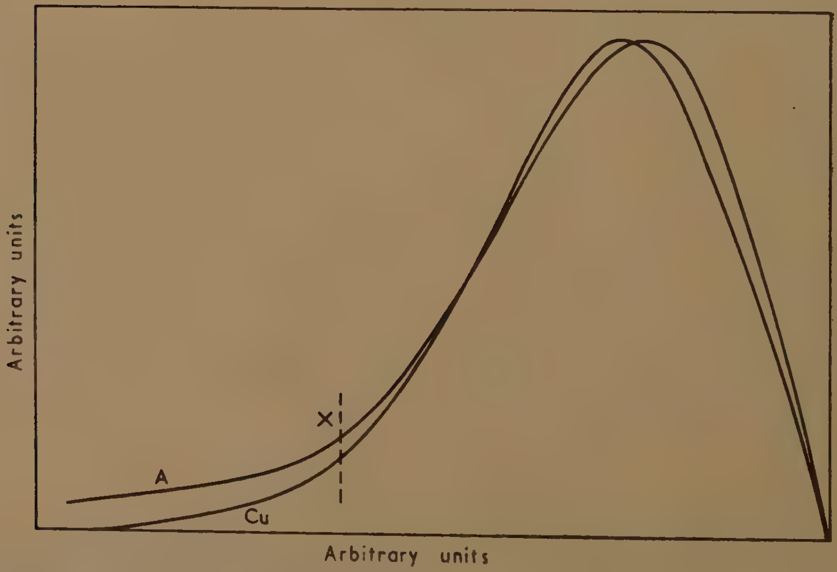

The line shapes of the ^{63}Cu resonance in β brass (50·05% zinc) and copper.

Fig. 3

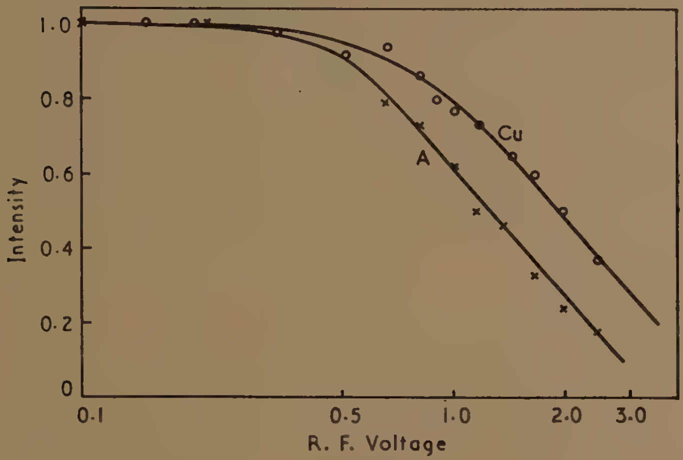

The saturation curves for the ^{63}Cu resonance in β brass and copper as a function of the radio frequency voltage across the specimen coil

○ ○ ○ Copper; × × × β brass (50·05% zinc).

Fig. 4

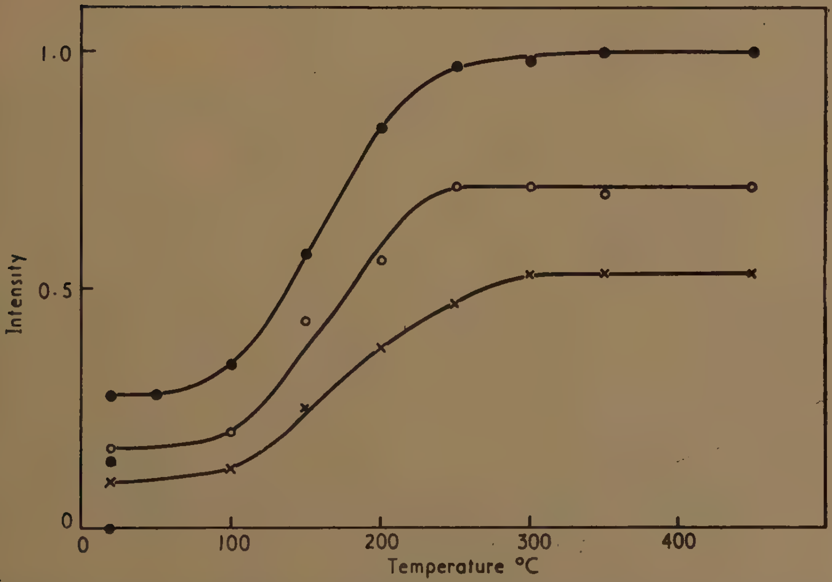

The variation of the peak-to-peak height of the derivative curve with annealing temperature for the ^{63}Cu resonance in β brass

. . . 47·64% zinc; ○ ○ ○ 46·15% zinc; × × × 45·06% zinc.

3.2. *Effect of Deformation and Annealing*

In one set of annealing experiments one specimen from each of alloys B, C, and D was filed and prepared as described in § 2. Two hours after filing, only alloy B gave an observable signal. However, after eight weeks at room temperature, the signal from alloy B had doubled in intensity and the other specimens gave observable signals. All specimens were then given 5 min annealing treatments at successively higher temperatures up to 350°c. The peak-to-peak height of the derivative curve as a function of annealing temperature is shown in fig. 4.

Fig. 5

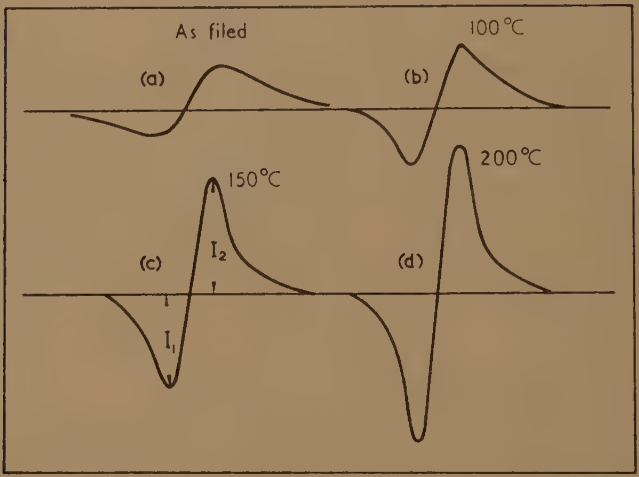

The variation of line shape with annealing temperature for the ^{63}Cu resonance in β brass (47·64%) zinc.

(*a*) as filed; (*b*) annealed at 100°c;
(*c*) annealed at 150°c; (*d*) annealed at 200°c.

In another set of annealing experiments, separate filed specimens of equal weight were annealed at various temperatures up to 450°c. The results from these agree with those from the first set and are also included in fig. 4. The lines for specimens from alloy B as filed and after annealing at 100°c, 150°c and 200°c are shown in fig. 5. Similar sets of curves are obtained from alloys C and D.

Table 3 shows the relative peak-to-peak heights of the derivative curves, the ratio of the peak values on the derivative curve (I_1/I_2 in fig. 5), and the line widths as measured between peaks for specimens from alloys B, C, and D as filed and after annealing at the temperatures shown. The points to be noted are (1) the steady increase in peak-to-peak height, even above 200°c, (2) the asymmetry of the lines which disappears after annealing at 200°c or above, (3) the steady decrease in line width on annealing up to 200°c.

X-ray back-reflection photographs of alloys B, C, and D were taken after filing and after annealing at 150°c, 200°c and 450°c. These showed that recrystallization became effectively complete between 100°c and 200°c.

Table 3. Results of Annealing Alloys B, C and D

Alloy		Filed	100°c	150°c	200°c	300°c	450°c
B	Peak-to-peak height	0·28	0·34	0·56	0·84	0·99	1·0
	Asymmetry I_1/I_2	0·7	0·8	0·8	1·0	1·0	1·0
	Line width (gauss)	6·0	4·5	3·7	3·5	3·5	3·5
C	Peak-to-peak height	0·17	0·20	0·44	0·56	0·72	0·72
	Asymmetry I_1/I_2	0·7	0·8	0·8	1·0	1·0	1·0
	Line width (gauss)	6·4	4·8	4·2	4·0	4·0	4·0
D	Peak-to-peak height	0·10	0·16	0·28	0·42	0·60	0·60
	Asymmetry I_1/I_2	0·7	0·8	0·8	1·0	1·0	1·0
	Line width (gauss)	8·0	5·6	4·8	4·0	4·0	4·0

§ 4. Discussion

4.1. *Effect of Composition*

In comparing the intensities of the resonance lines from different specimens, the following assumptions will be made:

(i) The integrated intensity is proportional to the number of copper nuclei contributing,

(ii) the satellite components have been eliminated from all lines from brass specimens, and

(iii) a nucleus will contribute to the resonance only if each of the first three shells of atoms surrounding it contains atoms of one type.

These assumptions are comparable to those used by Bloembergen and Rowland to explain their results in α brass, and as is shown below they provide a consistent explanation of the present results.

Suppose we have a fully ordered β brass containing $(N/2)\,(1+x)$ copper atoms and $(N/2)\,(1-x)$ zinc atoms. Then the $(N/2)a$-sites are occupied by copper atoms, and the $(N/2)b$-sites are occupied by $(N/2)\,(1-x)$ zinc atoms and $(N/2)x$ copper atoms. The eight nearest neighbours of each copper atom on a b-site will be copper and the probability that the eighteen next nearest neighbours (six in the second shell and twelve in the third) will be all of the one type is $(1-x)^{18}+x^{18}$. Therefore, the contribution to the resonance from copper atoms on b-sites is $(N/2)x[(1-x)^{18}+x^{18}]$. Similarly the contribution from copper atoms on a-sites is $(N/2)[x^8+(1-x)^8]$. For β brass, the possible range of x is such that the only significant contribution comes from the term $(N/2)(1-x)^8$. This corresponds to copper atoms on a-sites with eight zinc atoms in the first surrounding shell and copper atoms filling the second and third shells. Therefore, the number of copper nuclei contributing to the resonance is $(N/2)(1-x)^8$ and it follows that the integrated intensities from alloys A, B, and C should be in the ratio 1 : 0·75 : 0·57. The experimental values shown in table 2 give this ratio as 1 : 0·7 : 0·5, i.e. within experimental error of the predicted ratio.

Since the copper reference specimen contains $N/2$ nuclei the ratio of the integrated intensity for brass to that for the central component of copper will be $(1-x)^8$. The integrated intensity of the central component for copper is 0·4 that of the total, i.e. 1·0 on the scale used in table 2. The integrated intensities should on this argument be 0·92, 0·69 and 0·53, for alloys A, B, and C respectively. The fact that the measured values are lower may be due to two causes. Firstly, the long tails on the β brass lines may have caused the intensities to be underestimated. Secondly, the alloys may not be fully ordered. If it is assumed that the discrepancy is entirely due to disorder, it can be shown that long-range order parameters of 0·98, 0·97 and 0·96 for alloys A, B, and C respectively give calculated intensities corresponding to those shown in table 2.

Referring now to the shape of the lines, the large tail on the line from β brass (see fig. 2) indicates that some of the nuclei have suffered appreciable second-order quadrupolar interaction so that their resonance signal is displaced well away from the centre of the line. However, since the central portion of the line is symmetrical this part must consist of undistorted central components from other nuclei. If the curve is divided at x into a central portion plus a tail, the number of nuclei in the central portion is about 70% of the number contributing to the resonance.

The frequency of the resonance in β brass appears to be independent of composition and the discussion above has suggested that each copper nucleus contributing to the resonance is surrounded by a shell of zinc atoms. Similarly, in α phase copper–zinc alloys, Bloembergen and Rowland found that the frequency of the resonance was independent of composition. They further suggested that a copper nucleus contributes to the resonance only if it is completely surrounded by at least two shells of copper atoms. The Knight shift observed in copper will then be characteristic of a copper atom surrounded by copper atoms, and that in β brass of a copper atom surrounded by zinc atoms in the first shell. Drain (1959) has shown that in the silver-cadmium system, where quadrupolar interactions are absent, the Knight shift decreases continuously as the cadmium content increases from zero to 50%. He suggests that if it were possible to eliminate quadrupolar interaction in the copper–zinc system the behaviour would be similar. The present results agree with this prediction.

4.2. *Effect of Deformation and Annealing*

The deformation produced by filing is sufficient to render the line unobservable for specimens with low zinc content (alloys C and D). This behaviour is in sharp contrast to that of copper and α brass where filing has no apparent effect on the central component. Since the strains must be of the same order of magnitude in the two sets of alloys, this implies that the tensor giving the electric field gradient in terms of the strain is much larger for β brass.

The recovery of intensity with time at room temperature indicates that an appreciable amount of atomic movement is taking place. However, all lines from deformed specimens are asymmetric and comparatively broad. Therefore, in these lines the central components are showing the effects of second-order strain broadening. Further, these effects persist on annealing at temperatures below 200°c, i.e. any atomic re-arrangements occurring during recovery are not sufficient to eliminate second-order broadening. However, on annealing at 200°c, i.e. on recrystallization, the return to a symmetrical line and a further reduction in width indicate that second-order broadening has been reduced. The continuing increase in peak-to-peak height and constant line width on annealing at temperatures above 200°c is probably due to an increase in the degree of order in the specimens.

It is possible that some of the change during recovery may be due to the phase transformation discovered by Massalski and Barrett (1957). They have shown that filing β brass at room temperature causes a change to the hexagonal close-packed phase. Such a change would destroy the cubic symmetry around the nucleus with consequent elimination of the resonance line. The line would reappear as the hexagonal close-packed phase reverted to the body-centred cubic phase. However, it is unlikely that all the change in intensity can be attributed to this cause since only small traces of the hexagonal close-packed phase were reported.

ACKNOWLEDGMENTS

I would like to thank Mr. H. S. Voake for his valuable assistance throughout the whole of this investigation. I would also like to thank Mr. J. F. Nicholas and Mr. E. A. Faulkner for much helpful discussion and criticism.

REFERENCES

ANDREW, E. R., 1955, *Nuclear Magnetic Resonance* (Cambridge: University Press), p. 111.
BLOEMBERGEN, N., and ROWLAND, T. J., 1953, *Acta Met.*, **1**, 731.
CLAREBROUGH, L. M., 1957, *Acta Met.*, **5**, 413.
DRAIN, L. E., 1959, *Phil. Mag.*, **4**, 484.
KORRINGA, J., 1950, *Physica*, **16**, 601.
MASSALSKI, T. B., and BARRETT, C. S., 1957, *Trans. Amer. Inst. min. (metall.) Engrs*, **209**, 455.
RAYNOR, G. V., 1944, *Annotated Equilibrium Diagram*, No. 3 (London: Inst. Metals).
WEST G. W., 1958, *Nature, Lond.*, **182**, 1436.

Some Magnetic Properties of the Ising Model[†]

By D. M. Burley
Mathematics Department, The University, Glasgow, W.2[‡]

[Received May 4, 1960]

Abstract

Two properties of the Ising model are considered. Firstly, by extrapolating appropriate series expansions, the spontaneous magnetization of a ferromagnet for three-dimensional lattices is obtained. From the results accurate values for the critical temperature are found. Secondly, the high temperature susceptibility of an antiferromagnet is derived from the approximation of Kikuchi. The resulting susceptibility curves show that for loose-packed lattices a maximum value occurs at a temperature slightly above the critical point, while for the close-packed lattices no such effect is obtained.

§ 1. Introduction

Two of the fundamental properties in magnetism are the appearance of the spontaneous magnetization of a ferromagnet in zero field, and the zero field susceptibility for both a ferromagnet and antiferromagnet. The first of these properties has been studied in detail on the Ising model for two-dimensional lattices, and explicit formulae have been obtained by Yang (1952) and Potts (1952). For the three-dimensional lattices the spontaneous magnetization has been evaluated for various approximate methods and Münster and Sagel (1956) have summarized many of the results, together with the results obtained by the series expansion method of Fuchs, for the equivalent problem of the phase boundary of regular solutions. For the simple cubic lattice, Wakefield (1951) evaluated the spontaneous magnetization by extrapolating the series expansion which he obtained by calculating a large number of terms in the partition function for the assembly and then calculating the spontaneous magnetization from the free energy (F) by the equation

$$I_0/I_\infty = \partial F/\partial H|_{H=0} \quad . \quad . \quad . \quad . \quad . \quad . \quad (1)$$

where I_0 is the spontaneous magnetization in zero field at a temperature T, I_∞ is its value at absolute zero and H is the applied magnetic field. He then tried to extrapolate the resulting series. The convergence of this series is very slow in the critical region, and his method of extrapolation is doubtful there, particularly since he found that the magnetization dropped discontinuously to zero from a value of about 0·4. A better method of extrapolation will be applied and some more reliable results obtained.

[†] Communicated by the Author.

[‡] Present address: Applied Mathematics Department, The University, Sheffield, 10.

The second quantity, the zero field susceptibility, has been studied in some detail for a ferromagnet by Domb and Sykes (1957). A more interesting problem, however, is to evaluate susceptibility for an anti-ferromagnet, since on the Ising model, with only nearest-neighbour interactions, a close-packed lattice has no completely ordered state and hence no cooperative transition; also it will be shown that for loose-packed lattices the maximum value occurs not at the Néel temperature but at a temperature slightly above it. The approximate method of Kikuchi (1951) is used in the calculation of this paper. Sykes and Fisher (1958) have reported results of this nature and some detailed calculation has been given by Fisher (1959).

§ 2. SPONTANEOUS MAGNETIZATION

The method of extrapolation used in this section follows closely the method used by Domb and Sykes (1956). They showed that the partition function per spin, $\Lambda(\mu, z)$, could be written in a series expansion, at low temperatures, as

$$\Lambda(\mu, z) = 1 + \mu f_1(z) + \mu^2 f_2(z) + \ldots \qquad (2)$$

where $\mu = \exp(-2mH/kT)$ and $z = \exp(-\epsilon/kT)$, m is the magnetic moment per spin and ϵ the interaction energy between nearest neighbours. The $f_r(z)$ in the expansion are just finite polynomials, which are listed for the various lattices by Domb and Sykes (1956).

Using (1) the spontaneous magnetization can be written in terms of these $f_r(z)$ as

$$I_0/I_\infty = \lim_{r\to\infty} (1 - 2C_r), \qquad (3)$$

where

$$C_r = \sum_{i=1}^{r} i f_i(z) \Big/ \sum_{i=0}^{r} f_i(z). \qquad (4)$$

For any given z and given lattice it is found that the numbers C_r vary in a smooth and convergent manner and that the extrapolation $r \to \infty$ can be made with confidence. For small z, a very good estimate can be obtained by plotting C_r against $1/r$ and extrapolating the resulting graph; this method was found to be adequate for $T/T_c < 0{\cdot}8$ (where T_c denotes the critical temperature). For larger values of z, a more accurate method must be applied and it is essential that the polynomials $f_i(z)$ be calculated accurately to at least six figures for the various values of z in the critical region, since some differencing is employed. Fortunately a large amount of data on the $f_i(z)$ had been calculated on the digital computor and was kindly made available by Professor C. Domb. Where no data were available, the values were calculated, and from the $f_i(z)$ it is easy to compute the C_r of eqn. (4).

The method of extrapolation was chosen to cover as large a variation as possible and it was assumed that $\Delta C_r = C_r - C_{r-1}$ could be written in the form $\Delta C_r = A/r^h$. For a given lattice and a fixed value of z, a series of values of h were obtained which were seen to approach a limit h^*, and using this value of h^*, a series of values of A were obtained which approached a value of A^*. If $f_0(z)$ to $f_p(z)$ were known for the given lattice the value of C_∞ was calculated from the equation:

$$C_\infty = C_p + A^* \sum_{r=p+1}^{\infty} 1/r^{h^*}. \qquad (5)$$

Fig. 1

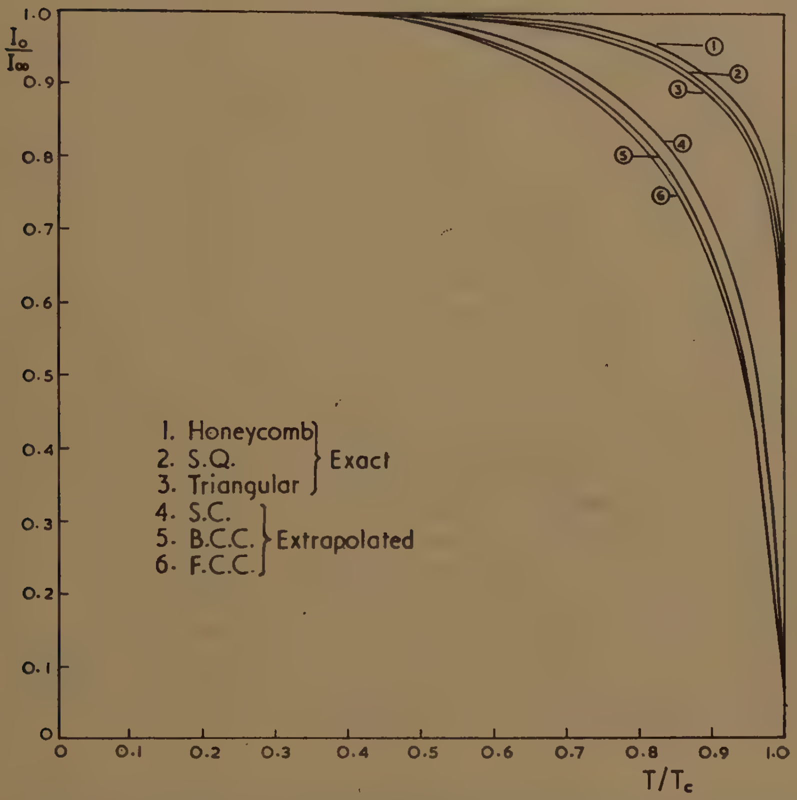

Graph of the spontaneous magnetization against reduced temperature.

In the critical region it was found that h^* was close to unity and since (5) is very sensitive to changes in h^* in this region, care had to be taken. An example of the method of calculation is given in Appendix I for the body-centred cubic lattice for the value $z^2 = 0{\cdot}529$. This value is very close to the critical point $(T/T_c = 0{\cdot}99)$ and the possible error of extrapolation is at its maximum. The value of h^* chosen for this calculation was 1·26 and the limits between which h^* could vary are 1·24 and 1·30. The computed values of C_∞ for these extreme values are 0·248 and 0·200, and the value for $h^* = 1{\cdot}26$ is $C_\infty = 0{\cdot}227$. Thus the estimated error in the critical region for the spontaneous magnetization is ± 0·04. For smaller values of z the estimated error decreases rapidly. The method was followed for the simple cubic (S.C.), body-centred cubic (B.C.C.) and face-centred cubic (F.C.C.) lattices and the results are shown in fig. 1 in comparison with the exact curves for the two-dimensional lattices; and the computed values for the three-dimensional lattices are given in Appendix II.

Since the Ising model treats spin as a classical property, quantitative agreement with experiment is not to be expected, but despite the considerable idealization of the model good qualitative agreement is obtained, the spontaneous magnetization curves going to zero at the critical temperature. The importance of the quantum nature of spin is shown well by the better quantitative agreement obtained at low temperatures from the spin wave treatment of the Heisenberg model (Dyson 1956). This work on the Ising model is important, nevertheless, on two counts. Firstly, the data obtained give a valuable yardstick by which more physically realistic models and approximate methods, used for the models, can be measured. Secondly, fig. 1 shows clearly that the dimensionality of the lattice is the most important feature to be considered and that the coordination number of the lattice only affects the fine structure of the curves.

For the two-dimensional lattices and approximate methods, for the Ising model, it is known that near the Curie point the spontaneous magnetization behaves like $I_0/I_\infty \sim A(T_c - T)^n$ and this is assumed to be the case for three-dimensional lattices also. The exact results for the two-dimensional lattices give $n = \frac{1}{8}$ and it would be extremely useful if n could be estimated for the three-dimensional lattices. In order to estimate its value, however, extremely accurate data must be obtained in the region $0{\cdot}98 < T/T_c < 1$. Such accurate results are not available from this work, but from the extrapolated curves of fig. 1 it appears certain that $n > \frac{1}{8}$. A comparison of these curves with those obtained from the Bethe and Kikuchi approximations indicates that n is between $\frac{1}{4}$ and $\frac{1}{2}$.

§ 3. CRITICAL POINTS

The critical temperature associated with a given lattice is obtained by finding the value of z for which the spontaneous magnetization becomes zero. When the values of z_c obtained by Domb and Sykes (1956) were used it was found that, instead of vanishing, the spontaneous magnetization for the body- and face-centred cubic lattices remained at a value of about 0·15. Since the possible error was estimated to be ± 0·04 it was assumed that these critical values were inaccurate. Because the spontaneous magnetization curve is so steep near the Curie point, it is very sensitive to changes in T_c and hence a recalculation of the critical values from the data obtained in the previous section, produces accurate values.

The critical temperatures obtained by Domb and Sykes (1956) were obtained by extrapolation of the maximum of the low temperature specific heat. In a later paper, Domb and Sykes (1957) studied the high-temperature susceptibility and obtained approximations to the Curie temperature by estimating the radius of convergence of the series expansion in inverse powers of temperature. The results obtained in this paper are in close agreement with the present estimates, and a comparison is made in the table, where the various values of $t_c = kT_c/q\epsilon$ are presented.

Estimated Critical Values of $t_c = kT_c/q\epsilon$

Lattice	Domb and Sykes (1956)	Domb and Sykes (1957)	Present estimate
S.C.	0·748	0·752	0·749
B.C.C.	0·784	0·794	0·793
F.C.C.	0·805	0·816	0·815

The accuracy of the present estimates for the critical temperature were obtained by plotting the values for the spontaneous magnetization against z and considering the possible errors made in the extrapolation. It was found that the critical temperatures obtained were accurate to $\pm 0{\cdot}003$ and it may be observed that, for the simple cubic lattice, both the values of Domb and Sykes are within these limits.

§ 4. HIGH-TEMPERATURE SUSCEPTIBILITY

The particular interest in this quantity is that at temperatures well above the Curie point a magnet becomes paramagnetic and the zero field susceptibility (χ_0) obeys the Curie–Weiss law.

$$\chi_0 = \frac{C}{T \pm T_p}, \qquad \qquad (6)$$

where T_p is the paramagnetic Curie temperature, the positive sign referring to an antiferromagnet and the negative sign to a ferromagnet. From the constant, C, information can be obtained about the Bohr magneton number and hence about the spin of the systems in the assembly. This constant is, therefore, of considerable interest experimentally and a theoretical reproduction of the behaviour, and a consideration of deviations from this behaviour are desirable.

On the Ising model, the ferromagnetic susceptibility has been studied in detail both from the Bethe approximation originally by Firgau (1942), and more recently by Domb and Sykes (1957) from a series expansion method. For the antiferromagnetic little has been attempted however.

Brooks and Domb (1951) calculated the susceptibility from series expansions for the simple quadratic lattice, but because of the difficulty of convergence near to the Néel point, they missed the essential feature of a maximum slightly above this point. The Bethe approximation also does not produce a maximum. In this case, the reason is linked to the fact that the approximation does not consider any closed configurations on the lattice and hence does not even differentiate between loose- and close-packed lattices. This difference is most important in the antiferromagnetic case and it is the closed configurations on a lattice which determine the behaviour of the assembly in the neighbourhood of the critical point.

The simplest method by which closed configurations can be taken into account, is by using the approximation of Kikuchi (1951). The notation and derivation of this approximation are rather long and in order to avoid reproducing Kikuchi's work, his notation will be followed exactly and his results assumed to be known. The method has to be extended a little to include the parameter $\mu=\exp(-2mH/kT)$, but the extension is trivial and modifies his equations only slightly. One of the variables (ξ_1) occurring in the approximation turns out to be exactly the magnetization of the assembly and consequently the susceptibility in zero field can be derived from the equation

$$\chi_0=(I_\infty m/kT)(\partial\xi_1/\partial\mu)|_{\mu=1}. \qquad \dots\dots \quad (7)$$

On the Bethe approximation, which may be treated in Kikuchi's notation, the long-range order, ξ_1, and the short-range order, y_2, are the only independent variables to appear in the basic equations obtained for the approximation. The derivatives with respect to μ of these two quantities can then easily be calculated. At temperatures above the Curie point, and when the magnetic field is zero (i.e. $\mu=1$) the basic equations can be solved explicitly as

$$\xi_1=0, \qquad y_2=z/2(1+z).$$

Putting these values into the calculated value of $(\partial\xi_1/\partial\mu)|_{\mu=1}$ and using (7) gives the Firgau formula

$$\chi_0=(I_\infty m/kT)\{qz-(q-2)\}^{-1}. \qquad \dots\dots \quad (8)$$

This, however, is not the susceptibility of an antiferromagnet but of a ferromagnet. In order to make the necessary conversion the simplest method is to use the variable $v=(1-z)/(1+z)=\tanh(\epsilon/2kT)$ and changing the sign ϵ just changes the sign of v. Applying this transformation to (8) gives

$$\frac{\chi_0\epsilon}{I_\infty m}=\frac{\tanh^{-1}v(1-v)}{1+(q-1)v}.$$

Since the long-range order, ξ_1, has been put explicitly equal to zero this formula is only valid above the Néel temperature, which occurs at the specific heat singularity, that is for $0\leqslant v\leqslant 1/(q-1)$.

On the Kikuchi approximation the method follows very closely the method for the Bethe approximation, but this time two long-range order parameters, ξ_1 and ξ_2, appear, although it is still the quantity $\xi_1' = (\partial\xi_1/\partial\mu)|_{\mu=1}$ which is required in order to substitute into eqn. (7). From the basic equations obtained by the approximation, in the region above the Néel point and in zero field (i.e. $\mu=1$ and $\xi_1=\xi_2=0$), explicit solutions can be obtained for the other variables occurring in the equations. It is again simple to substitute into the calculated quantity ξ_1'. Making the transformation to the antiferromagnetic problem, that is using the variable v and then changing its sign, gives for the various lattices

S.Q.

$$\frac{\chi_0\epsilon}{I_\infty m} = \frac{\tanh^{-1} v(1-2v)(1+v)}{(1+2v)(1+v-4v^2)} \quad \text{for} \quad 0 \leqslant v \leqslant \tfrac{1}{8}(\sqrt{17}-1); \qquad (9)$$

Tri.

$$\frac{\chi_0\epsilon}{I_\infty m} = \frac{\tanh^{-1} v(1+v)}{(1+3v)(1+4v)} \quad \text{for} \quad 0 \leqslant v \leqslant \tfrac{1}{4}; \qquad (10)$$

S.C.

$$\left.\begin{aligned} \frac{\chi_0\epsilon}{I_\infty m} &= \tanh^{-1} v \, \frac{(3+p)(1+p)}{(3-p)(5-p)}, \\ v &= \frac{p^4-18p^3+18p-1}{p^4+36p^3+54p^2+36p+1}, \end{aligned}\right\} \qquad (11)$$

$$\text{for} \quad 0 \leqslant v \leqslant 0{\cdot}2136 \quad \text{or} \quad \tfrac{1}{3} \leqslant p \leqslant 1;$$

F.C.C.

$$\left.\begin{aligned} \frac{\chi_0\epsilon}{I_\infty m} &= \frac{\tanh^{-1} v(t-t^2+t^3)(1+t-t^2+t^3)}{(2-t+t^2-t^3)(3-t+t^2-t^3)}, \\ v &= \frac{t^3-3t^2+t+1}{t^3+t^2+t+1}, \end{aligned}\right\} \qquad (12)$$

$$\text{for} \quad 0 \leqslant v \leqslant 0{\cdot}09975 \quad \text{or} \quad 0{\cdot}8412 \leqslant t \leqslant 1.$$

The regions of validity of the various parameters are determined as in the Bethe approximation, since the long-range order parameters are put explicitly equal to zero. The upper limits for v are found in the case of loose-packed lattices, from the specific heat singularity, and in the case of close-packed lattices, from the specific heat singularity for the corresponding ferromagnetic problem.

In order to compare these formulae with the exact series expansions it is necessary to expand the closed forms in a power series. For the two-dimensional lattices, this is very easy and it is found that for the simple quadratic lattice the expansion agrees up to v^7 with the expansions of Domb and Sykes (1957) and then the terms are too large by an amount $(16v^8-96v^9+488v^{10}-\ldots)$. This error can be attributed to the inaccurate counting of an octagon and similar larger clusters on the lattice. The expansion for the triangular lattice agrees up to the term v^5 and then is too large by an amount $(12v^6-204v^7+1944v^8-14\,388v^9+\ldots)$, again the error can be attributed to the inaccurate counting of hexagons and some larger clusters. The expansion for the three-dimensional lattices is more difficult, but as expected agreement is obtained up to v^5 for the simple cubic and up to v^3 for the face-centred cubic.

Fig. 2

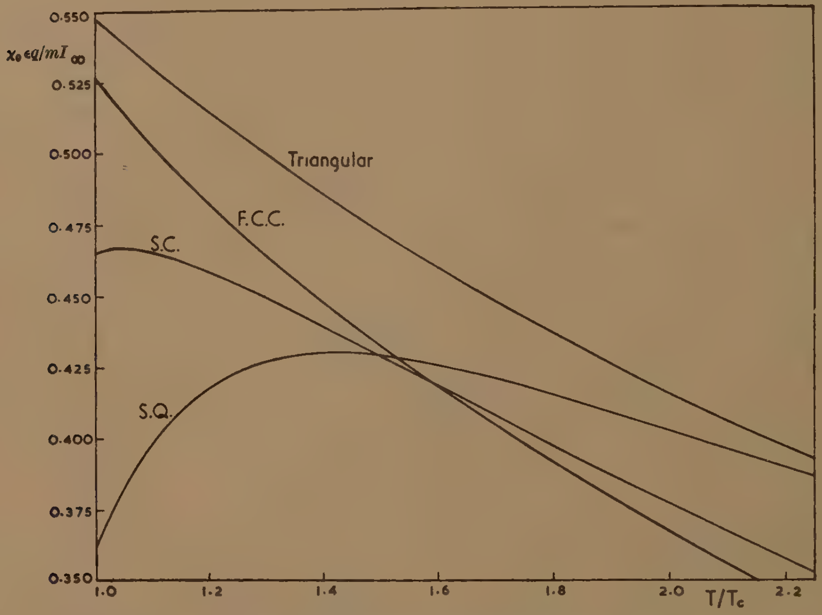

Graph of zero field susceptibility against reduced temperature for an antiferromagnet.

In fig. 2 the curves of $\chi_0\epsilon q/mI_\infty$ are plotted against T/T_c and interesting results are observed. It is noticed that, while the curves for the close-packed lattices increase monotonically up to the Néel point, for the loose-packed lattices the curves show a maximum above the critical temperature and are decreasing when they reach this point. These maxima occur at $T/T_c=1{\cdot}43$ for the simple quadratic and at $T/T_c=1{\cdot}04$ for the simple cubic lattice. How the curves continue as the temperature is decreased through the Néel point is a very interesting question, but the solution of the basic equations in this region is complicated, and this was not attempted. For the close-packed lattices an additional difficulty arises from the fact that no ordered state exists even at absolute zero. Although it was found possible to write down the basic equations for the triangular lattice they are so complicated that no solution was attempted except for $T=0$. At this point is was found that the entropy for this lattice is given by

$$S/R=\ln\tfrac{4}{3}=0{\cdot}2877 \quad . \quad . \quad . \quad . \quad . \quad . \quad . \quad (13)$$

compared with the exact value obtained by Wannier (1951) of

$$S/R = 0{\cdot}3383.$$

The agreement between the two results is not particularly good but the value (13) is almost identical to a result obtained by Wannier by considering the origin of the major part of the degeneracy. The agreement between (13) and this result is to be expected however since Wannier used just the configurations on the lattice treated correctly by the Kikuchi approximation, both methods neglecting intermediate-order parameters.

Despite the difficulty of solution in the low-temperature region, some idea of the behaviour can be obtained by writing the susceptibility in the form of Sykes and Fisher (1958). They showed that the susceptibility behaves essentially like the configurational energy, and this is only modified by a function which is small in the critical region. This was found to be the case for the Kikuchi approximation, the susceptibility being modified at the critical point by only 2% for the S.Q. lattice and ½% for the triangular lattice. The shape of the curves can thus be deduced from the configurational energy or the specific heat. For the Bethe approximation the complete curves have been calculated numerically and a sharp cusp is observed at the Néel point. For the Kikuchi approximation, the loose-packed lattices will still show a discontinuity in the gradient but this will not be so pronounced, while the exact result will show a vertical point of inflexion, with no discontinuity in slope at the Néel point. For the close-packed lattice, since there is no specific heat discontinuity, and no completely ordered state, it may be assumed that the curves pass through the corresponding ferromagnetic Curie point with no change of slope or point of inflexion in the case of the exact solution.

The striking result of this investigation is the appearance of the maximum in the susceptibility for the loose-packed lattices. Cooke *et al.* (1959) have observed experimentally such maxima for various antiferromagnetic salts at $T/T_c \simeq 1{\cdot}01$. This result is in quite good agreement with the value obtained for the simple cubic lattice, and it thus appears that the maximum is of an essentially cooperative nature. A difficulty of comparison arises, however, since the salts considered all have a face-centred cubic structure, which on the Ising model shows no antiferromagnetic transition. The stabilizing effects of second nearest neighbours with a ferromagnetic interaction and also a consideration of anisotropic effects may well provide for the antiferromagnetic transition and the associated maximum. It is hoped to study these effects in more detail.

ACKNOWLEDGMENTS

I should like to thank Professor C. Domb for his continued interest and encouragement in this work and Drs. M. F. Sykes and M. E. Fisher for many discussions on the subject. I should also like to thank the Department of Scientific and Industrial Research for a maintenance grant for the period during which most of this work was completed.

APPENDIX I

Method of Extrapolation for the Body-centred Cubic Lattice and $z^2 = 0{\cdot}529$

i	ΔCi	h	A	A^*/i^{h^*}
1	0·073631	0·982	0·07363	0·0980
2	0·037271	1·157	0·08926	0·0409
3	0·023321	1·181	0·09309	0·0246
4	0·016603	1·232	0·09523	0·0171
5	0·012611	1·220	0·09582	0·0129
6	0·010098		0·09654	0·0103

The value of h^* chosen is 1·26 which gives $A^* = 0{\cdot}0980$.

$$C_\infty = 0{\cdot}1735 + 0{\cdot}0980 \sum_{i=7}^{\infty} 1/i^{1{\cdot}26} = 0{\cdot}405.$$

APPENDIX II

Results for the Extrapolation of the Spontaneous Magnetization

S.C.		B.C.C.		F.C.C.	
T/T_c	I_0/I_∞	T/T_c	I_0/I_∞	T/T_c	I_0/I_∞
0·998	0·06	0·999	0·04	0·998	0·02
0·993	0·18	0·990	0·19	0·994	0·08
0·987	0·23	0·964	0·39	0·987	0·15
0·982	0·29	0·936	0·55	0·973	0·30
0·972	0·43	0·909	0·64	0·959	0·40
0·920	0·64	0·859	0·76	0·949	0·46
0·858	0·80	0·789	0·84	0·916	0·61
0·740	0·91	0·688	0·92	0·800	0·82
0·642	0·95	0·600	0·96	0·684	0·92
0·558	0·98	0·523	0·98	0·512	0·98

REFERENCES

Brooks, J. E., and Domb, C., 1951, *Proc. roy. Soc.* A, **207,** 343.

Cooke, A. R., Lazenby, R., McKim, F. R., Owen, J., and Wolf, W. P., 1951, *Proc. roy. Soc.* A, **250,** 97.

Domb, C., and Sykes, M. F., 1956, *Proc. roy. Soc.* A, **235,** 247 ; 1957, *Ibid.* A, **240,** 214.

Dyson, F. J., 1956, *Phys. Rev.*, **102,** 1217.

Firgau, E., 1942, *Ann. Phys., Lpz.*, **40,** 295.

Fisher, M. E., 1959, *Physica*, **25,** 521.

Kikuchi, R., 1951, *Phys. Rev.*, **81,** 988.

Münster, A., and Sagel, K., 1956, *Z. Phys. Chem., Neue Folge.*, 7, **267,** 296.

Potts, R. B., 1952, *Phys. Rev.*, **88,** 352.

Sykes, M. F., and Fisher, M. E., 1958, *Phys. Rev. Letters*, **1,** 321.

Wakefield, A. J., 1951, *Proc. Camb. phil. Soc.*, **47,** 419.

Wannier, G. H., 1950, *Phys. Rev.*, **79,** 357.

Yang, C. E., 1952, *Phys. Rev.*, **85,** 808.

The Spacing of Prismatic Dislocation Loops†

By R. Bullough and R. C. Newman

Research Laboratory, Associated Electrical Industries, Aldermaston Court, Aldermaston, Berkshire

[Received May 11, 1960]

Abstract

The stresses round a circular prismatic dislocation loop are determined and used to calculate the spacings between such loops in a row generated from a source of internal stress. The results are consistent with the available experimental observations.

§ 1. Introduction

Recent experiments by Dash (1958), Jones and Mitchell (1957) and Parasnis and Mitchell (1959) have established that stresses set up round internal defects in crystals can be relieved by the generation and motion of several co-axial prismatic dislocation loops (Seitz 1951). The diameters of the loops in such a row are approximately equal and comparable with the diameter of either an artificially introduced inclusion (Jones and Mitchell 1957) or a particle of precipitated second phase (Parasnis and Mitchell 1959); the stresses are a consequence of a differential expansion during heating in the former case and a change in volume on precipitation in the latter case.

The purpose of this paper is to investigate theoretically the relation between the separation and diameter of adjacent loops in a particular row of such loops. In § 2 the stresses and displacements associated with a single prismatic loop in an elastic medium are derived. These are obtained by 'cutting' along the cylindrical glide surface and applying suitable boundary conditions to the two curved surfaces. Finally in § 3 the equilibrium configuration of a row of loops is computed, subject to the assumption that a critical shear stress is required to move a loop and the results are compared with the available experimental observations.

§ 2. The Stresses and Displacements around the Loop

We shall consider a circular prismatic loop of strength b and radius a with its centre at the origin of a cylindrical coordinate system, $z=0$ being the plane of the loop. This dislocation is created by making a cylindrical cut over the surface $r=a$ in an infinite medium and applying a shear stress to the two sides of the cut so that the relative displacement across $r=a$ is given by

---

† Communicated by the Authors.

$$w^{\mathrm{o}}(a,z)-w^{\mathrm{i}}(a,z)=\left.\begin{array}{ll} -b/2 & z>0 \\ +b/2 & z<0 \end{array}\right\} \quad . \quad . \quad . \quad . \quad (1)$$

where w is the displacement in the z direction and the superscripts o and i refer to regions outside $(r \geqslant a)$ and inside $(r \leqslant a)$ the cut respectively. The cut is now rewelded and to ensure no additional forces are required for this procedure we must have continuity of traction across $r=a$; thus

$$\left.\begin{array}{l} p_{rr}{}^{\mathrm{i}}(a,z)=p_{rr}{}^{\mathrm{o}}(a,z), \\ p_{rz}{}^{\mathrm{i}}(a,z)=p_{rz}{}^{\mathrm{o}}(a,z). \end{array}\right\} \quad . \quad . \quad . \quad . \quad . \quad (2)$$

Finally, the radial displacement u must be continuous across $r=a$:

$$u^{\mathrm{i}}(a,z)=u^{\mathrm{o}}(a,z). \quad . \quad . \quad . \quad . \quad . \quad . \quad . \quad . \quad . \quad (3)$$

The required stresses were obtained using the method of Fourier transforms (see for example Tranter and Craggs 1945). The two relevant solutions of the transformed biharmonic equation are:

and
$$\left.\begin{array}{l} X^{\mathrm{i}}(r,\eta)=A(\eta)I_0(\eta r)+B(\eta)\eta r I_1(\eta r) \\ X^{\mathrm{o}}(r,\eta)=C(\eta)K_0(\eta r)+D(\eta)\eta r K_1(\eta r) \end{array}\right\} \quad . \quad . \quad . \quad . \quad (4)$$

where
$$\left[\frac{d^2}{dr^2}+\frac{1}{r}\frac{d}{dr}-\eta^2\right]^2 X(r,\eta)=0. \quad . \quad . \quad . \quad . \quad . \quad (5)$$

The arbitrary functions A, B, C and D were obtained by satisfying the boundary conditions (1), (2) and (3) after transformation; the expressions relating the stresses and displacements to the stress function $\chi(r,z)$, where

$$X(r,\eta)=\int_{-\infty}^{\infty}\chi(r,z)\exp(\mathrm{i}\eta z)\,dz,$$

are given in full by Sneddon (1951).

The required solution in the region $r \geqslant a$ is:

$$\left.\begin{array}{l} p_{rr}=\dfrac{2\alpha}{r}\mu\displaystyle\int_0^{\infty}\{(1-2\nu)r\eta v_{01}(\eta)+2(1-\nu)v_{11}(\eta)-a\eta v_{10}(\eta)\}\cos\eta z\,d\eta, \\ p_{rz}=2\alpha\mu\displaystyle\int_0^{\infty}\{av_{10}(\eta)-rv_{01}(\eta)\}\eta^2\sin\eta z\,d\eta, \\ p_{zz}=2\alpha\mu\displaystyle\int_0^{\infty}\{\eta r v_{11}(\eta)-2v_{01}(\eta)-\eta a v_{00}(\eta)\}\eta\cos\eta z\,d\eta, \\ w=\alpha\displaystyle\int_0^{\infty}\{\eta r v_{11}(\eta)-2(1-\nu)v_{01}(\eta)-\eta a v_{00}(\eta)\}\sin\eta z\,d\eta, \\ u=\alpha\displaystyle\int_0^{\infty}\{2(1-\nu)v_{11}(\eta)+\eta r v_{01}(\eta)-\eta a v_{10}(\eta)\}\cos\eta z\,d\eta, \end{array}\right\} \quad (6)$$

where

$$v_{ij}=K_i(r\eta)I_j(a\eta), \quad \alpha=ba/2\pi(1-\nu)$$

and μ and ν are the shear modulus and Poisson's ratio respectively. The solution for the region $r \leqslant a$ may be obtained simply by replacing v_{ij} by u_{ij} where

$$u_{ij}=(-1)^{i+j}I_i(r\eta)K_j(a\eta).$$

We have also obtained the elastic solution by making a cut through the plane of the loop and applying suitable tractions to the two planar sides of such a cut. The solution obtained using this latter model appears in a different form from that given above; for example, the shear stress on the cylindrical surface $r=a$ is

$$p_{rz}(a,z)=\pi\alpha\mu z\int_0^\infty \eta^2 J_1{}^2(a\eta)\exp(-\eta|z|)\,d\eta. \quad . \quad . \quad . \quad (7)$$

The equivalence of (7) and $p_{rz}(a,z)$ given by (6) may be demonstrated by showing that each is equal to the same line integral:

$$\frac{\alpha z}{2i}\int_{c-i\infty}^{c+i\infty}\frac{2^s\Gamma(2+\frac{1}{2}s)\Gamma(-1-s)\Gamma(1-s)a^{-s-2}|z|^s}{[\Gamma(-\frac{1}{2}s)]^2\Gamma(1-\frac{1}{2}s)}\,ds$$

by simple use of the product formula for the Mellin transform (Titchmarsh 1948); similarly the more general stresses and displacements can be related to line integrals of this type.

In order to determine the equilibrium spacing of loops in a row we shall require the variation of $p_{rz}(a,z)$ with $\rho=z/2a$. The integrals involved in (6) or (7) can be evaluated in terms of tabulated elliptic integrals (Watson 1952) and the variation is shown in fig. 1.

§ 3. THE EQUILIBRIUM CONFIGURATION OF A ROW OF LOOPS

It is assumed that when a new loop is created at the surface of the inclusion it will glide on the cylindrical surface and simultaneously cause the other loops in the row to move further away from the inclusion. The final configuration will be achieved when the shear stress on each one of the loops due to its neighbours is equal to the critical shear stress $p_{rz}{}^{\text{crit}}$ to move the loop. The shear stress distribution around a single loop, as shown in fig. 1, decreases rapidly with distance z from the loop:

$$p_{rz}(a,z)\rightarrow\frac{ba^3\mu}{(1-\nu)z^4} \quad \text{(large } z\text{)}.$$

In view of this, and since experimental observations indicate that the separation between loops is comparable with their diameters, the resultant shear stress on any loop of the row is quite well determined by the relative positions of its first and second neighbours only. In setting up the relevant difference equations for each loop it was convenient to introduce

Fig. 1

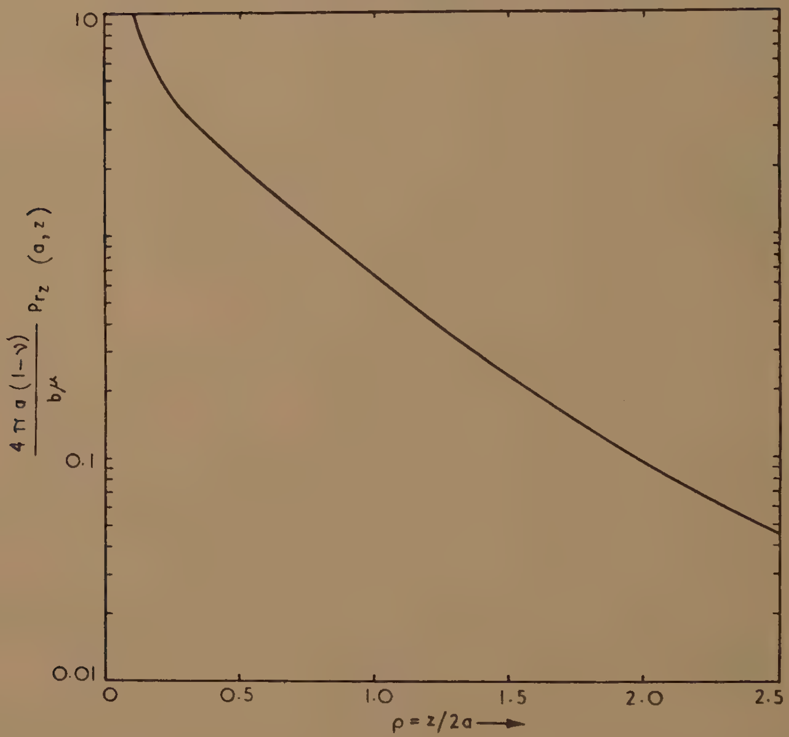

The shear stress distribution on the cylindrical glide surface $r=a$ due to a single loop of radius a and strength b situated at $z=0$.

Fig. 2

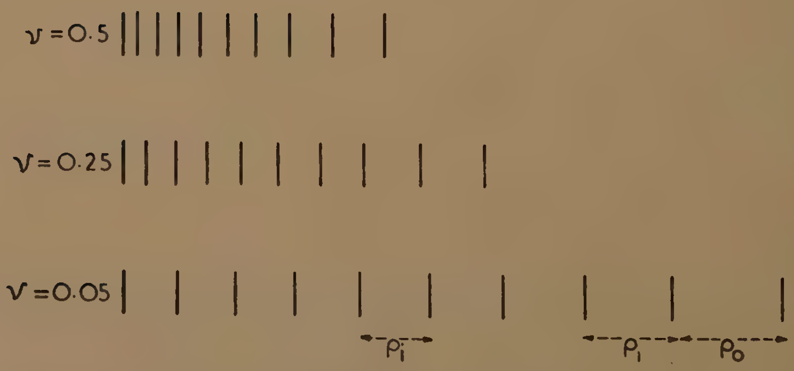
$\nu = 0.5$
$\nu = 0.25$
$\nu = 0.05$
ρ_i
ρ_i
ρ_o

Equilibrium configurations for row of ten loops drawn to scale ($\rho = z/2a$).

the dimensionless parameter v given by

$$v = \frac{4a\pi(1-\nu)}{b\mu} p_{rz}^{\text{crit}} . \qquad (8)$$

These equations were linearized and solved by a method of repeated approximation on a digital computer. Computations were made for both a row of five and ten loops with three values of v: 0·5, 0·25 and 0·05. Tabulated results for the row of ten loops are given in table 1 and shown diagrammatically in fig. 2.

Table 1. Computed spacings for the row of ten loops in units of the loop diameter

v \ ρ_i	0	1	2	3	4	5	6	7	8
0·5	1·23	0·951	0·791	0·684	0·606	0·546	0·491	0·478	0·317
0·25	1·55	1·25	1·07	0·952	0·862	0·792	0·731	0·703	0·549
0·05	2·47	2·05	1·83	1·68	1·57	1·48	1·41	1·35	1·25

Table 2. Values of p_{rz}^{crit}/μ as a function of the parameter v and the ratio $2a/b$

v \ $2a/b$	10^5	10^4	10^3
0·5	10^{-6}	10^{-5}	10^{-4}
0·25	5×10^{-7}	5×10^{-6}	5×10^{-5}
0·05	10^{-7}	10^{-6}	10^{-5}

The configuration for the row of five loops was not significantly different from the outermost five loops in the row of ten for all the v values. Hence the ten loop configurations may also be used to determine the configurations for any number of loops less than ten. It may be seen from fig. 2 or table 1 that as the critical shear stress is reduced (decreasing values of v) the variation of spacing between any two adjacent loops in the row also decreases. For a row of more than about five loops and with $v = 0·5$ it is seen from fig. 2 that the loops become closely spaced and hence in this case our neglect of third neighbour interaction is not justified near the source of the loops.

It has been assumed above that the critical shear stress to move a loop is independent of the loop diameter. This we believe is a reasonable assumption when the diameter of the loop exceeds about 10$\mathbf{b}$ (where $\mathbf{b}$ is the Burgers vector of the loop). Although it has not been possible to solve the integral equation appropriate to a Peierls loop, and hence obtain a direct indication of the dependence of the dislocation width on the loop diameter, the corresponding problem for a pair of parallel straight dislocations lying back to back has been solved and indicates that the width variation is not significant until the spacing between the lines is less than 5**b**.

In order to compare the present results with experimental observation the following procedure is adopted. From the number of loops in the row and the mean ratio of spacing to loop diameter it is possible, with the aid of fig. 2, to determine the value of the parameter v. This value of v and the measured loop diameter $2a$ enable an estimate of the critical shear stress to be made from (8). The dependence of the critical shear stress on v and the ratio $2a/b$ as given by (8) is shown in table 2 for a wide range of loop diameters.

Table 3. Application to the experimental observations of Dash (1958) and Parasnis and Mitchell (1959)

Material	Number of loops in row	Approximate loop diameter (microns)	ρ_i(mean)	Estimated value of v	Value of critical shear stress
AgCl	> 10	1·3	0·9	$\lesssim 0{\cdot}25$	$\lesssim 10^{-5}\,\mu$
Si	4	30	0·7	$\gtrsim 0{\cdot}5$	$\gtrsim 10^{-6}\,\mu$

We have applied this method to the results of Parasnis and Mitchell (1959, fig. 6) on silver chloride and Dash (1958, fig. 1) on silicon. Their results are summarized in table 3 and it is seen that these lead to not unreasonable values of the critical shear stress. A more stringent test of this theory must await further experimental observations.

ACKNOWLEDGMENTS

The authors wish to thank Mr. P. Redman for his assistance with the numerical work and Mr. D. P. R. Petrie and Mr. R. L. Rouse for their encouragement. Thanks are also due to Dr. T. E. Allibone, F.R.S., Director of the Laboratory, for permission to publish this paper.

REFERENCES

DASH, W. C., 1958, *Phys. Rev. Letters*, **1**, 11.
JONES, D. A., and MITCHELL, J. W., 1957, *Phil. Mag.*, **3**, 1.
PARASNIS, A. S., and MITCHELL, J. W., 1959, *Phil. Mag.*, **4**, 171.
SEITZ, F., 1951, *Rev. mod. Phys.*, **23**, 328.
SNEDDON, I. N., 1951, *Fourier Transforms* (New York: McGraw-Hill).
TITCHMARSH, E. C., 1948, *Introduction to the theory of Fourier Integrals* (Oxford : Clarendon Press).
TRANTER, C. J., and CRAGGS, J. W., 1945, *Phil. Mag.*, **36**, 241.
WATSON, G. N., 1952, *The theory of Bessel functions* (Cambridge : University Press).

Some Elastic and Thermal Properties of Zirconium and Tungsten†

By A. Myers

Physics Department, the University, Leeds‡

[Received March 28, 1960; and in revised form August 9, 1960]

Abstract

The longitudinal and shear wave velocities of 10 Mc/s ultrasonic waves have been measured in polycrystalline specimens of zirconium and tungsten at temperatures between 14° and 300°K and the elastic constants calculated from these measurements. The difference between the specific heats at constant pressure and at constant volume in these metals at various temperatures has been calculated by means of the thermodynamic relation involving the bulk modulus of the metal; this difference is used in the examination of a suggested method of obtaining the γ values, and hence the electronic specific heats of metals.

It is found that the γ values for zirconium and tungsten estimated by this method are greater by factors of about 1·3 and 2·8 respectively than the values obtained from low-temperature calorimetric determinations. For a number of reasons, which are discussed, close agreement is not to be expected but no satisfactory explanation for the very wide discrepancy has been found.

§ 1. Introduction

The γ value of a metal is the value of the proportionality constant relating the electronic contribution to the specific heat (C_e) to the absolute temperature (T) in the relation $C_e = \gamma T$, which is generally assumed to be valid for temperatures such that $kT \ll \epsilon_0$, where k is Boltzmann's constant and ϵ_0 is the Fermi energy.

The usual method of obtaining γ has been by means of low-temperature calorimetry (γ obtained in this way will be denoted by γ_0). Such methods of obtaining γ, although applicable to most metals, are tedious in practice and almost invariably involve measurements at liquid helium temperatures. Recently, γ values have been estimated by Clusius and Bühler (1955), Clusius and Franzosini (1956), Clusius and Losa (1955 a, b), Clusius *et al.* (1957), and Clusius and Schachinger (1947, 1952 a, b) using a method which does not involve measurements in the liquid helium temperature range. They assume that the lattice specific heat (C_L) can be represented, over an appreciable temperature range, by a single Debye term. They select a series of trial γ values and calculate the electronic specific heat which would correspond to these values; the electronic specific heat is subtracted from the total specific heat at constant volume (C_v), i.e. from the sum of the lattice and electronic contributions. The γ value, which leaves the remainder most nearly following a single term Debye curve over a sufficiently large temperature interval, is then chosen as the one to be associated with the electronic specific heat of the metal. The actual technique is to plot graphs of θ_D (the Debye characteristic temperature) against the absolute temperature for various γ values, and to select that value of γ for which the variation of θ_D with temperature is least.

---

† Communicated by the Author.

‡ For academic year 1959–60, at Physics Department, Brown University, Providence, R.I., U.S.A.

The method depends upon a knowledge of the variation of C_v with temperature. Measurements of the specific heats of metals, however, are obtained under constant pressure conditions (C_p) and these must be converted into values corresponding to constant volume conditions. This conversion can be made by means of the relation:

$$(C_p - C_v)_T = 9\alpha^2 KVT,$$

where α is the coefficient of linear expansion, K is the bulk modulus and V is the atomic volume. In order to allow the conversion of specific heat data to be made over the whole temperature range of interest, the variation of α and K with temperature is needed. Extensive data exist for the temperature dependence of the expansion coefficient of most metals but the temperature dependence of the bulk modulus is known only in a few cases. Approximate relations between C_p and C_v exist which do not involve the temperature variation of K and for most metals these relations are sufficiently accurate for the present purpose. It has been found as a result of the present investigations that this situation holds for zirconium and tungsten. It was considered necessary to show this because γ values which do not agree with γ_0 are obtained for both metals following the method used by Clusius *et al.*, and also the uncertainty introduced by using the approximate relations is not known. In addition, it has been stated (Dayal 1944) that tungsten does not obey Grüneisen's law (namely that $KV\alpha/C_v$ is a constant, independent of temperature) at temperatures below 300°K; this is involved in deriving the approximate relation. Expansion coefficient data are available for tungsten and zirconium in the appropriate temperature range but there is no corresponding information for the bulk moduli; the variations of the bulk moduli with temperature have therefore been measured. The bulk moduli are determined by measuring the ultrasonic longitudinal and shear wave velocities, the accuracy depending on the ultrasonic attenuation coefficients of the metals. The lower these, the more accurate are the velocity measurements. Tungsten and zirconium possess low attenuation coefficients and were partly chosen for this reason. These metals are also among the most readily available of the relatively few which have the following additional advantages:

(*a*) they have fairly large γ values (so that C_e will be significant in comparison to C_L);

(*b*) data is available giving the temperature dependence of α and C_p;

(*c*) the anharmonic motion of the lattice vibrations is probably small (see § 4).

§ 2. EXPERIMENTAL DETAILS

2.1. *Elastic Moduli*

The elastic moduli of metals can be obtained conveniently, having regard to the temperature range involved, by measurement of the velocities of ultrasonic longitudinal and shear waves. For an isotropic medium, and these polycrystalline materials are assumed to be effectively isotropic, the following relations hold and enable K to be determined:

$$V_L = \left\{ \frac{1}{p} [K + \tfrac{4}{3}G] \right\}^{1/2}, \quad V_S = \left\{ \frac{G}{p} \right\}^{1/2},$$

where V_L and V_S are the velocities of propagation of elastic longitudinal and shear waves respectively, G is the rigidity modulus and p is the density.

The wave velocities have been measured using a method described in a previous paper (Myers *et al.* 1959) under the name of the coincidence technique. In this a continuous sequence of pulses of oscillation (of 3–5 μsec duration) are applied across a quartz transducer cemented to one end of the specimen. Signals are received at the other end of the specimen by means of a similar quartz crystal. Because of the reflection of pulses at the ends of the specimen, several pulses are received for each pulse initially propagated. The coincidence is made between the front of any of the reflected pulses, or the directly transmitted pulse, and the front of the subsequent pulse of oscillation from the oscillator. The time taken for the wave to travel through the specimen is obtained by measurement of the pulse repetition frequency of the oscillator.

10 Mc/s longitudinal and shear waves are propagated by using X-cut and Y-cut quartz crystals respectively.

The wave is delayed on every traversal of the specimen by a small time; this is an end effect caused by the wave traversing the metal to crystal bond and also by interference effects due to reflections at the various boundaries at the ends of the specimen. The usual method of eliminating these time delays is to measure the velocity in two or more different lengths of the specimen and consider the time taken to travel a path equal to the difference in length of the specimens (Neighbours *et al.* 1952). This procedure has been followed here. In addition, the magnitudes of the end effects have been made as small as possible by using very thin bonds. Apparent delays of 0·01 to 0·03 μsec for longitudinal waves and of 0·02 to 0·06 μsec for shear waves were measured and corrected for; even if the correction were not made, the error introduced from this source would have been less than 0·3% in the transit time.

2.2. *The Specimens*

Both the zirconium and the tungsten were supplied in the form of sintered cylindrical bars of about 20 mm diameter by Murex, Ltd. Measurements were taken in both cases on two specimens about 6 and 12 cm long. The suppliers quote the purity of the zirconium as from 98 to 99%, about 1% to 2% of the impurity being hafnium and less than

0·3% being other elements. This was as pure zirconium as could readily be obtained commercially. The tungsten, on the other hand, was stated to contain only from 0·02 to 0·05% of iron and traces only of other elements, giving it a purity of about 99·95%.

The density of the zirconium specimens was 6·55 ± 0·01 g/cm^3; this is to be compared with an x-ray density for zirconium of 6·502 ± 0·002 g/cm^3. The 1 to 2% hafnium impurity was thought to be responsible for the actual density being higher than the x-ray value and measurements by de Boer and Fast (1940) on zirconium containing 0·5% hafnium confirm this to some extent by giving an x-ray density of 6·54 g/cm^3. It is probable, however, that the actual density was determined not only by the impurity but also by the porosity of the sintered metal. The purity of the tungsten was much higher than that of the zirconium and the density of 18·65 ± 0·04 g/cm^3 was noticeably low in comparison with the x-ray density of 19·270 ± 0·002 g/cm^3; this was due to porosity. It is not obvious which density should be taken in order to estimate the elastic constants of pure, non-porous specimens of polycrystalline zirconium and tungsten. Fewer objections seem to be against taking the x-ray densities and, following Overton and Gaffney (1955), these have been used. In subsequent discussions, however, the implications of this decision are considered.

2.3. *The Bonds and the Cryostat Arrangements*

Dow Corning 200 silicone fluid, of viscosity $2{\cdot}5 \times 10^6$ centistokes, was used to produce the bonds for use with longitudinal waves, and Edwards apiezon grease grade N was used for the shear waves; in both cases the bonds were effective from 300° to 14°K.

The temperature of the specimens was controlled by suspending them inside a silvered glass dewar in which the pressure between the walls can be varied. This dewar was immersed in a bath of liquid nitrogen. At the start of the experiments, the pressure in the dewar interspace was about 0·1 cm of mercury, so that the heat conduction across the walls was appreciable and the specimen cooled down. When the required temperature was reached, the interspace pressure was reduced to about 10^{-6} cm of mercury, producing an effective thermal isolation while measurements were taken.

Temperatures lower than the boiling point of liquid nitrogen were obtained by immersing the specimen in either liquid nitrogen or liquid hydrogen and reducing the pressure above the liquid.

The temperature of the specimen was measured by means of two calibrated chromel–alumel thermocouples strapped one at each end of the specimen.

§ 3. RESULTS

The wave velocities obtained for zirconium are shown in figs. 1 and 2. In these figures the full line gives the variation of the velocity with temperature after the end effects have been allowed for; these values are given at 25°K intervals in table 1. Also given in table 1 are the adiabatic elastic constants E, K and G (where E is Young's modulus) and the factor $(C_p - C_v)_T$. The values of $(C_p - C_v)_T$ have been obtained using the expansion coefficient data of Erfling (1939) and Nix and MacNair (1942) for zirconium and tungsten respectively. The values of $(C_p - C_v)_{NL}$ are those given by the Nernst–Lindemann equation: $(C_p - C_v)_{NL} = AC_p^2T$, where A is a constant which is evaluated at 300°K; this is an approximate relation

Fig. 1

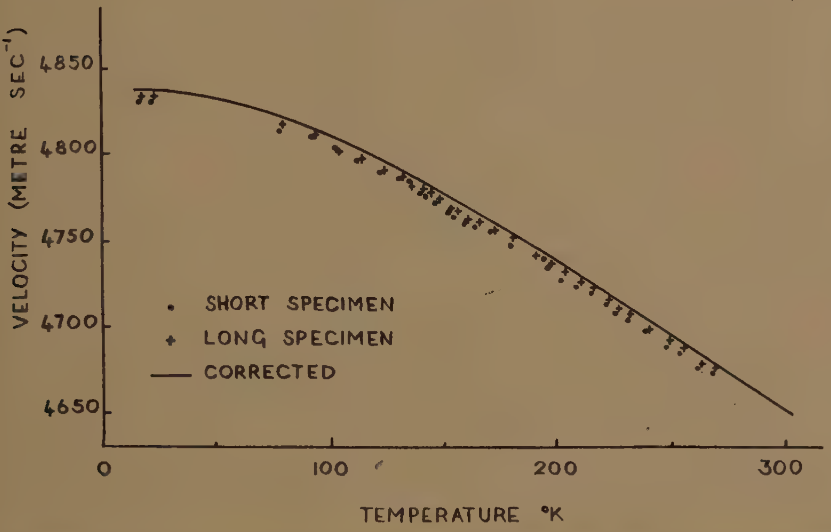

The variation of the longitudinal wave velocity in zirconium with temperature.

Fig. 2

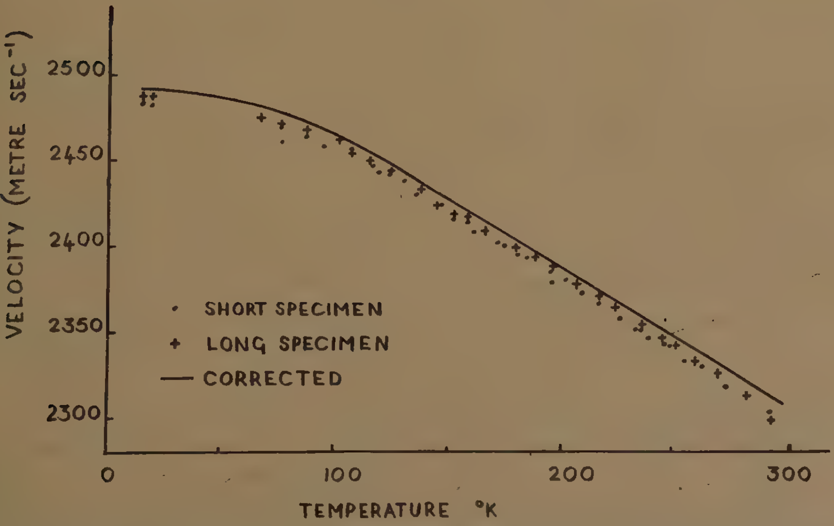

The variation of the shear wave velocity in zirconium with temperature.

much used in the conversion of specific heat data from constant pressure to constant volume conditions.

Table 1. The smoothed ultrasonic wave velocities, the elastic constants and the factor $(C_p - C_v)$, calculated by means of the thermodynamic and also by the Nernst–Lindemann relation, for zirconium and tungsten. Velocities are given in metres per second, elastic constants in units of 10^{-11} dynes per square centimetre and $(C_p - C_v)$ in calories per gram mole per °K

T	V_L	V_S	E	G	K	$(C_p-C_v)_T$	$(C_p-C_v)_{NL}$
(i) Zirconium							
	±4	±3	$\pm 0{\cdot}1_5$	±0·01	±0·06	± ~1%	± ~2%
0	4838	2484	$10{\cdot}6_2$	4·02	9·88	0·0000	0·0000
25	4836	2484	$10{\cdot}6_3$	4·02	9·86	0·0000	0·0000
50	4830	2480	$10{\cdot}5_9$	4·01	9·84	$0{\cdot}0001_8$	$0{\cdot}0006_7$
75	4822	2472	$10{\cdot}5_1$	3·98	9·81	0·0014	0·0027
100	4808	2461	$10{\cdot}4_4$	3·95	9·77	0·0044	0·0055
125	4794	2442	$10{\cdot}3_0$	3·89	9·74	0·0081	0·0086
150	4776	2423	$10{\cdot}1_4$	3·82	9·73	0·0113	0·0116
175	4758	2403	$9{\cdot}9_9$	3·76	9·69	0·0144	0·0148
200	4737	2388	$9{\cdot}8_6$	3·71	9·63	0·0178	0·0179
225	4716	2365	$9{\cdot}6_9$	3·64	9·61	0·0213	0·0211
250	4695	2345	$9{\cdot}5_5$	3·58	9·55	0·0246	0·0242
275	4672	2323	$9{\cdot}3_7$	3·51	9·50	0·0282	0·0276
300	4650	2298	$9{\cdot}1_8$	3·43	9·49	0·0300	0·0300
(ii) Tungsten							
	±5	±4	±0·7	±0·04	±0·2	± ~1·5%	± ~2·5%
0	5116	2836	$39{\cdot}7_5$	15·55	29·86	0·0000	0·0000
25	5115	2835	39·7	15·54	29·86	0·0000	0·0000
50	5114	2833	39·7	15·52	29·86	$0{\cdot}0003_9$	$0{\cdot}0004_1$
75	5112	2831	39·6	15·50	29·85	0·0019	0·0024
100	5110	2828	39·5	15·46	29·85	0·0047	0·0058
125	5107	2824	39·4	15·41	29·84	0·0083	0·0100
150	5103	2820	39·3	15·36	29·82	0·0120	0·0144
175	5099	2816	39·2	15·31	29·80	0·0162	0·0190
200	5094	2812	39·1	15·26	29·73	0·0204	0·0233
225	5089	2807	38·9	15·20	29·69	0·0246	0·0272
250	5085	2801	38·8	15·13	29·66	0·0295	0·0321
275	5079	2796	38·7	15·07	29·64	0·0354	0·0362
300	5075	2791	38·5	15·01	29·63	0·0410	0·0410

§ 4. DISCUSSION

The comparison of values of $(C_p - C_v)$ given by the Nernst–Lindemann equation with those given by the thermodynamic relation shows that the two sets of values agree well for both zirconium and tungsten at all except the lower temperatures; here it has been found that the disagreement arises not because of the variation of K with temperature, which is neglected in the Nernst–Lindemann equation but because of the assumption that C_p is proportional to α (using Grüneisen's law); thus the disagreement is due to the well-known failure of this law at low temperatures. Whereas with zirconium the assumption that C_p is proportional to α leads to an error of about 30% in the value of (C_p-C_v) at 100°K, the error introduced is only 5% if the bulk modulus is assumed not to vary with temperature. In fact a very close estimate of (C_p-C_v) can be obtained by using the relation $(C_p-C_v)=B\alpha^2T$, where B is a temperature independent constant to be evaluated at room temperature, rather than the Nernst–Lindemann relation. This situation does not necessarily hold in all metals especially those in which the bulk modulus is very temperature dependent. The magnitude of the conversion factor (C_p-C_v) is small in the two metals studied even at normal temperatures; at 100°K although the Nernst–Lindemann relation gives a value for (C_p-C_v) differing appreciably in zirconium from that given by the thermodynamic relation, the whole term represents only a small fraction, about 0·1% of C_v.

Fig. 3

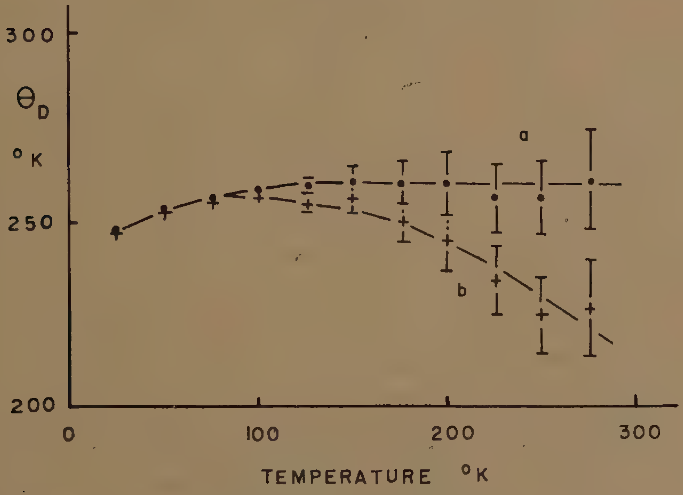

The variation of θ_D with temperature for zirconium. A γ value of $9{\cdot}1\times10^{-4}$ cal mole^{-1} deg^{-2} is assumed in curve (*a*) and a γ value of $7{\cdot}0\times10^{-4}$ cal mole^{-1} deg^{-2} is assumed in curve (*b*).

The values of $(C_p-C_v)_T$ for zirconium shown in table 1 have been used to convert the specific heat data of Skinner and Johnston (1951) to constant volume conditions; this has then been used to estimate the γ value of the metal employing the method used by Clusius. The plot of θ_D against temperature is shown in fig. 3 and a γ value of $9{\cdot}5\times10^{-4}$ cal mole^{-1} deg^{-2} is indicated. This is to be compared with the values of $6{\cdot}9\times10^{-4}$ cal mole^{-1} deg^{-2} (Estermann *et al.* 1952) and $7{\cdot}25\times10^{-4}$ cal mole^{-1} deg^{-2}

(Wolcott 1955). The zirconium used by Skinner and Johnston was of high purity and their measurements accurate.

When the method is applied to tungsten, using the specific heat data compiled by Kelley (1948), the γ value obtained is 9×10^{-4} cal mole^{-1} deg^{-2} in comparison with values of $3{\cdot}53\times10^{-4}$ cal mole^{-1} deg^{-2} (Rayne 1954) and $2{\cdot}9\times10^{-4}$ cal mole^{-1} deg^{-2} (Wolcott 1955). The plots of θ_D against temperature are shown in fig. 4 in which it can be seen that the discrepancy between the above values cannot be explained in terms of the estimated experimental uncertainty.

The specific heat data for tungsten are less accurate than those for zirconium and, in order to check the above result, the specific heat of tungsten was measured between 77° and 300°K and agreement obtained to within about 1%. It was found that the value of γ indicated was again about 9×10^{-4} cal mole^{-1} deg^{-2}.

Fig. 4

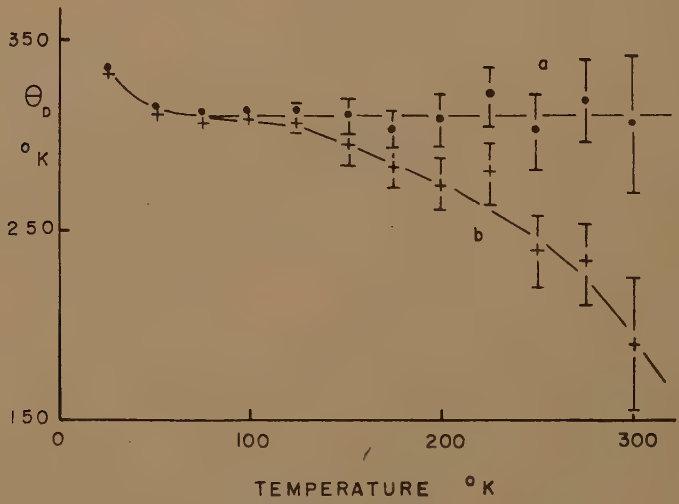

The variation of θ_D with temperature for tungsten. A γ value of $9{\cdot}0\times10^{-4}$ cal mole^{-1} deg^{-2} is assumed in curve (*a*) and a γ value of $3{\cdot}0\times10^{-4}$ cal mole^{-1} deg^{-2} is assumed in curve (*b*).

The principles involved in the calculation of γ values by the method used by Clusius have been known for some time (cf. Stoner 1938). A γ value for tungsten has been previously estimated (Wilson 1954) by considering data at 1000°K; this value is $5{\cdot}2\times10^{-4}$ cal mole^{-1} deg^{-2} and is in fairly good agreement with γ_0. In view of this the calculations were extended to 2000°K, using the specific heat data compiled by Kelley and the Nernst–Lindemann relation for (C_p-C_v) above 300°K.

It is well established that at temperatures above about $\theta_D/3$, Grüneisen's law agrees very well with experiment, so $(C_p-C_v)_{NL}$ should give reliable values in the region above 300°K; in addition, (C_p-C_v) is about three times smaller than C_e and any small deviations from Grüneisen's law will be unimportant.

At high temperatures the lattice specific heat becomes less and less dependent on the precise θ_D value chosen and ultimately approaches 3R, thus a plot of θ_D against temperature is not suitable. Instead $(C_v - C_L)/T$ has been calculated and is shown in table 2, a θ_D value of 310°K being used as this is the value generally accepted and is also the value indicated by the curves of fig. 4. $(C_v - C_L)/T$ gives the γ value of the metal provided that the lattice specific heat follows Debye's theory. It can be seen that except between about 100° and 400°K fairly good agreement with γ_0 is obtained. Thus, between 100° and 400° there is an additional contribution to the specific heat; at higher temperatures the contribution appears to decrease.

Table 2. Estimated γ values for tungsten assuming $\theta_D = 310$°K. $(C_v - C_L)$ is given in units of calories per gram mole per °K

T°K	100	200	300	400	500	600
$(C_v - C_L)/T \times 10^4 \pm \sim 10\%$	5·0	9·3	9·3	5·0	4·2	4·0
T°K	700	800	1000	1200	1500	2000
$(C_v - C_L)/T \times 10^4 \pm \sim 10\%$	3·8	4·0	4·1	4·5	4·5	4·6

One possible reason why the γ values obtained for zirconium and tungsten do not agree with their respective γ_0 values is that, in the calculation of the elastic constants from the wave velocities, incorrect densities may have been taken. If a different density were taken, $(C_v - C_L)$ would be changed by an amount proportional to the temperature and hence γ would be changed; a decrease in density would lead to an increase in the estimated value of γ and to an even worse agreement with γ_0. It is inconceivable that a higher density than the X-ray value should be used but even if it were, although a lower estimate for γ would result, the variation of $(C_v - C_L)/T$ shown in table 2 for tungsten would not be explained. Also, if the actual instead of the X-ray density were taken, since $(C_v - C_L)$ is at least three times greater than $(C_p - C_v)$, the resulting γ value would be greater by only about 3%, i.e. by less than the uncertainty in γ. Thus, the porosity of the specimens does not appreciably affect the γ value obtained, nor could it account for the temperature dependence of $(C_v - C_L)/T$ observed in table 2.

The increase of the specific heat beyond that expected, in the temperature region above about 100°K, may be due either to the Debye theory not being obeyed by tungsten or to an increase in the γ value of the metal as the temperature is increased. Increases in γ can occur when open electronic bands overlap (Elcock *et al.* 1953). It is not, however, expected that this will happen at temperatures so low in comparison to ϵ_0/k (the degeneracy temperature). Interactions between the electron gas and the lattice vibrations can also lead to an increase in γ (Buckingham and Schafroth 1954, Jones 1957). Buckingham and Schafroth find that because of modification of the density of energy levels at the Fermi surface γ is increased at lower temperatures but the increase when $T \gg \theta_D$ is zero. At intermediate temperatures the contribution to the γ value has not been evaluated. The interaction considered by Jones is one which gives a significant contribution to the electronic specific heat when the electronic energy as a function of momentum is very different from that in the free electron case. This is the situation when the Fermi surface approaches closely the Brillouin zone boundary. This interaction also leads to an increase in γ_0. It is unlikely, however, that these effects are responsible for the unusual behaviour of the apparent γ value in tungsten since the low temperature γ value obtained experimentally agrees very well with that calculated theoretically (Manning and Chodorow 1939); no account was taken, in the calculation, of the electron-lattice interactions and thus these interactions do not appear to play a significant part in determining the low temperature γ value for tungsten. Yet in both cases it is at low temperatures that the effects of such interactions are expected to be noticeable. Thus, it is presumed that the disagreement is due to a contribution to the lattice specific heat which is not given by the Debye theory. The deviations from Debye's theory may be caused either because the actual vibration spectrum of the normal modes for tungsten may not yield a specific heat which follows Debye's theory at these temperatures or because substantial contributions from anharmonicity of the lattice motion may be present. Any vibration spectrum able to yield a variation in the specific heat capable of explaining the situation would have a very different shape from that calculated theoretically for tungsten (Fine 1939). This spectrum, though based on the assumption of central forces acting between the atoms, predicts the same θ_D value as that obtained experimentally and predicts generally the same variation of θ_D at low temperatures as that experimentally observed. It also gives specific heat values which above about 50°K obey Debye's theory. It might, therefore, seem more likely that the cause of the disagreement is anharmonic motion of the lattice, which gives rise either to a positive or a negative contribution to the specific heat. Unfortunately theories of anharmonic motion are still in a rudimentary stage and it is not known if such a contribution to the specific heat could occur in tungsten. The melting point of tungsten, however, is high and the lattice vibrations at 300°K will be small in comparison to the interatomic spacing; thus, the anharmonicity is expected to be also small. This is borne out by the small values of other properties of the metal which are dependent on the anharmonicity of the lattice vibrations, e.g. the expansion coefficient and the variation of the bulk modulus with temperature. Clusius has found, however, that this method of obtaining γ works in metals for which the anharmonicity is presumably greater than in tungsten as e.g. in rhodium.

The decrease of $(C_v - C_L)/T$ in tungsten above 400°K to a value close to γ_0 is remarkable since, at these temperatures, there is the possibility of vacancy formation giving an additional contribution to the specific heat and existing contributions may be more important, e.g. anharmonicity and band overlap. Vacancy formation becomes important in the region of the melting point and gives a positive contribution to the specific heat. This would lead to increasing values of $(C_v - C_L)/T$ with increasing temperatures; table 2 does not disclose any significant contribution of this type. Reasons have been presented suggesting that the anharmonic motion in tungsten is small; in table 2 any contribution from this source, even at 2000°K, appears to be negligible. The work of Elcock, Rhodes and Teviotdale raises the question of whether or not, because of the band overlap, the γ value should be constant up to 2000°K. The density of states curve calculated by Manning and Chodorow suggests that γ should decrease below γ_0 at high temperatures but, because of the idealised bands considered by Elcock *et al.*, no numerical check can be made to determine if 2000°K is sufficiently high for such a decrease to be important. $(C_v - C_L)/T$ in table 2 does not indicate any such decrease. Though it would appear that the value of $(C_v - C_L)$ in tungsten at high temperatures corresponds to C_e, there is the unlikely possibility that this agreement is fortuitous and that cancellation of two or more of the above effects is responsible for the constancy of $(C_v - C_L)/T$.

§ 5. CONCLUSIONS

The elastic constants of zirconium and tungsten have been measured between 14° and 300°K.

It has been noted that the Nernst–Lindemann relation enables specific heat values to be converted from constant pressure to constant volume conditions with sufficient precision for most purposes in zirconium and tungsten in the temperature range extending up to 300°K.

It has been found that the method used by Clusius for obtaining the γ values of metals does not give γ values agreeing with those obtained from measurement in the liquid helium temperature range in the case of zirconium and tungsten. In zirconium this difference although small is significant. In tungsten it is much greater than in zirconium but is reduced when Clusius' method is extended to temperatures greater than θ_D. On theoretical grounds it is thought that the additional contributions to the specific heats are not of electronic origin.

ACKNOWLEDGMENTS

I am grateful for the advice and interest of Dr. L. Mackinnon and Dr. F. E. Hoare and also for the encouragement and helpful comments of Professor E. C. Stoner, F.R.S. In addition I am indebted to the Department of Scientific and Industrial Research for a maintenance grant.

REFERENCES

de Boer, J. H., and Fast, J. D., 1940, *Rec. Trav. chim. Pays-Bas*, **59**, 161.
Buckingham, M. J., and Schafroth, M. R., 1954, *Proc. phys. Soc. Lond.* A, **67**, 828.
Clusius, K., and Bühler, H. H., 1955, *Z. Naturf.* A, **10**, 930.
Clusius, K., and Franzosini, P., 1956, *Z. Naturf.* A, **11**, 957.
Clusius, K., and Losa, C. G., 1955 a, *Z. Naturf.* A, **10**, 545 ; 1955 b, *Ibid.*, **10**, 939.
Clusius, K., Losa, C. G., and Franzosini, P., 1957, *Z. Naturf.* A, **12**, 34.
Clusius, K., and Schachinger, L., 1947, *Z. Naturf.* A, **2**, 90; 1952 a, *Ibid.*, **7**, 185 ; 1952 b, *Z. angew. Phys.*, **4**, 442.
Dayal, B., 1944, *Proc. Indian Acad. Sci.* A, **20**, 192.
Elcock, E. W., Rhodes, P., and Teviotdale, A., 1953, *Proc. roy. Soc.* A, **221**, 53.
Erfling, H. D., 1939, *Ann. Phys., Lpz.*, **34**, 136.
Estermann, I., Friedberg, S. A., and Goldman, J. B., 1952, *Phys. Rev.*, **87**, 582.
Fine, P. C., 1939, *Phys. Rev.*, **56**, 355.
Jones, H., 1957, *Proc. roy. Soc.* A, **240**, 321.
Kelley, K. K., 1948, *U.S. Bur. Mines Bull.*, Nos. 476, 477.
Manning, M. F., and Chodorow, M. I., 1939, *Phys. Rev.*, **56**, 787.
Myers, A., Mackinnon, L., and Hoare, F. E., 1959, *J. acoust. Soc. Amer.*, **31**, 161.
Neighbours, J. R., Bratten, F. W., and Smith, C. S., 1952, *J. appl. Phys.*, **23**, 889.
Nix, F. C., and MacNair, D., 1942, *Phys. Rev.*, **61**, 74.
Overton, W. C., and Gaffney, J., 1955, *Phys. Rev.*, **98**, 969.
Rayne, J., 1954, *Phys. Rev.*, **95**, 1428.
Skinner, G. B., and Johnston, J. L., 1951, *J. Amer. chem. Soc.*, **73**, 4549.
Stoner, E. C., 1938, *Phil. Mag.*, **25**, 899.
Wilson, A. H., 1954, *The theory of metals* (Cambridge: University Press), p. 150.
Wolcott, N. N., 1955, Conf. de Phys. des basses temps., Paris, Sept. 2–8.

The Mechanism of Quench-hardening and its Recovery in Gold†

By M. Meshii and J. W. Kauffman
Materials Science Department, Northwestern University,
Evanston, Illinois, U.S.A.

[Received September 15, 1959]

Abstract

Resoftening characteristics of quench-hardened gold were experimentally determined. Resoftening occurred above 600°c at a highly temperature-dependent rate with an activation energy of 4·7 ev. Various quench-hardening mechanisms are considered. The processes corresponding to the observed characteristics are for quench-hardening: formation of tetrahedral stacking faults; and for resoftening: the nucleation of a Shockley partial dislocation ring on any face of the tetrahedron.

§ 1. Introduction

Pure metals can be hardened by rapid quenching from high temperatures and subsequent ageing in the neighbourhood of room temperature (Maddin and Cottrell 1955, Meshii and Kauffman 1957, 1959, Kimura *et al.* 1958, 1959). All, or nearly all, of the quench-hardening is acquired during the ageing process. During the ageing, quenched-in vacancies and vacancy complexes migrate and coagulate, eventually forming lower energy configurations. Thus, the end products resulting from the vacancy migration and coagulation are considered to be the cause of this type of hardening. Various mechanisms for quench-hardening have been put forward, such as the formation of cavities along dislocation lines (Coulomb and Friedel 1956), jog formation (Maddin and Cottrell 1955), and sessile dislocation rings collapsed from vacancy platelets (Li *et al.* 1953). However, none of these proposals has been based on systematic experimental observations.

In the present work, the nature of resoftening from quench-hardening is studied. This allows a further examination of various possible hardening mechanisms. It is found that none of the above mentioned mechanisms can correspond to the observed resoftening characteristics.

Recently, Silcox and Hirsch (1959), using an electron microscope, observed, in thin foils of gold, contrast effects caused by quenching; they explained these as tetrahedral stacking faults. Hardening due to tetrahedral stacking faults was found to be consistent with the present results. The mechanism of resoftening proposed by the present authors is the formation of a new Shockley dislocation ring on any face of the tetrahedral stacking fault, which subsequently grows, finally collapsing the tetrahedron.

---

† Communicated by the Authors. This investigation was performed with the support of the Office of Naval Research of the United States Government.

§ 2. EXPERIMENTAL PROCEDURE

The quenching methods used have been described in a previous publication (Meshii and Kauffman 1959). The samples were gold wire, 0·016 in. in diameter, of purity, as reported by the supplier, 99·999%. The purity was checked by measuring the ratio of resistivity at room temperature to that at 4·2°K. For all specimens used these ratios were between 1500 and 2500. The temperature from which the quench was begun was 1000° ± 10°C. The cooling rate used was 30 000°C/sec. After quenching, all specimens were aged one hour at 100°C so as to produce the maximum saturated hardening. Further ageing at this temperature did not produce detectable over-ageing. Following this ageing treatment, the specimens were annealed in an argon atmosphere at high temperatures controlled to within ± 1°C, except for a very short time interval when the specimen was placed into the furnace. However, this short interval was found to have a negligible effect on the annealing results.

§ 3. EXPERIMENTAL RESULTS

Ageing at 100°C for 1 hr is sufficient to saturate at maximum hardening; no further change in mechanical properties was observed by further ageing at this temperature. After the specimens gained maximum quench-hardening, they were annealed isothermally at four different temperatures—612°C, 627°C, 642°C and 657°C—for various periods of time. These data are shown in figs. 1 and 2. A large temperature dependence of the re-softening rate is evident. The times required to reach the given yield loads of 4·0 lb and 3·0 lb are shown in the table.

Annealing temperature (°C)	Time taken to reach the yield load of 4·0 lb (hrs)	Time taken to reach the yield load of 3·0 lb (hrs)
657	0·5	1·1
642	1·2	3·0
627	3·8	8·5
612	9·8	24·0

In fig. 3, logarithms of the times in the table are plotted against the reciprocal of absolute temperatures of annealing. Two straight lines are found whose slopes yield 4·7 and 4·8 ev as the activation energy of re-softening. The activation energy found here is much larger than the activation energy for self-diffusion of gold. Further, we find that the temperature for resoftening of quench-hardening is much higher than the temperature for resoftening of gold deformed to give the same degree of hardening.

Fig. 1

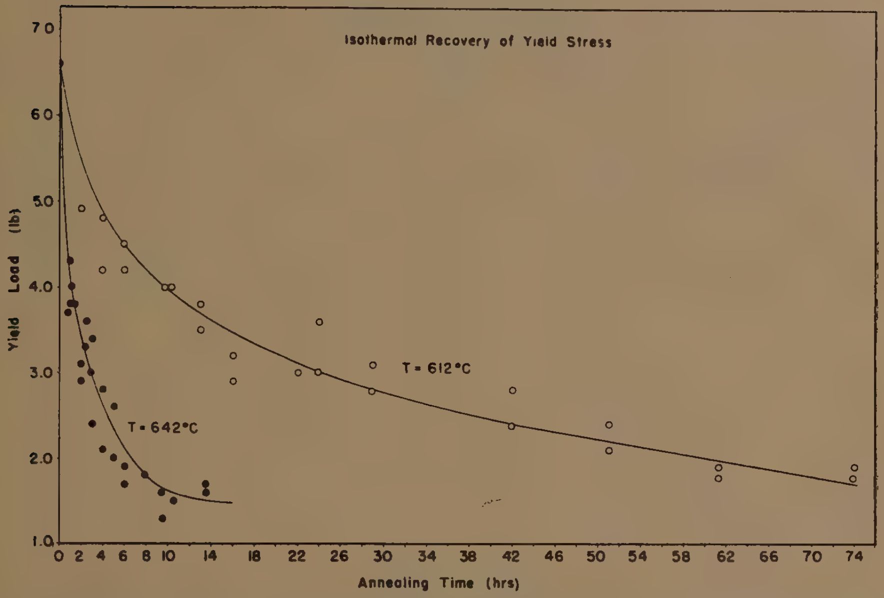

Isothermal recovery of yield stress at 612°c and 642°c. All specimens are quenched from 1000°c with an average cooling rate of 30 000°c/sec and aged at 100°c for 1 hr before annealing.

Fig. 2

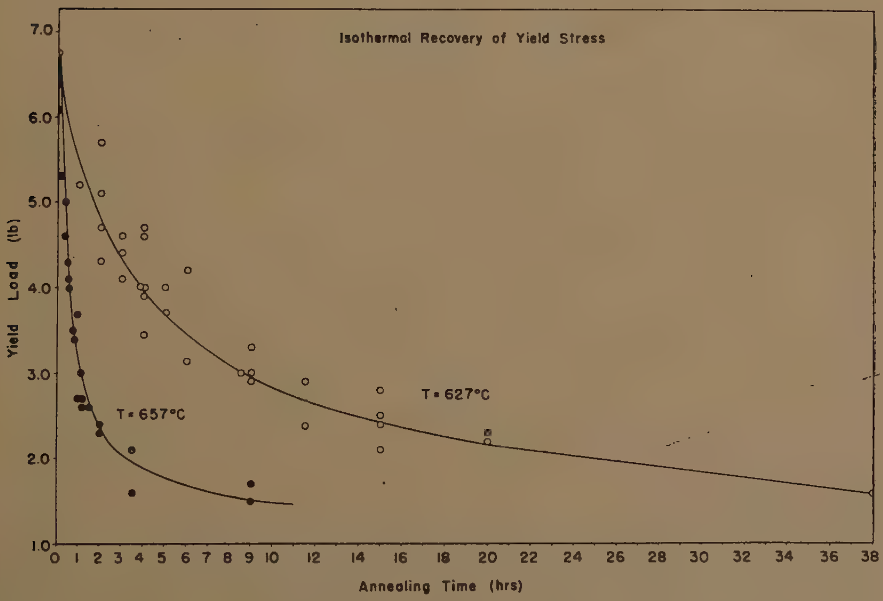

Isothermal recovery of yield stress at 627°c and 657°c. All specimens are quenched from 1000°c with an average cooling rate of 30 000°c/sec and aged at 100°c for 1 hr before annealing.

§ 4. DISCUSSION

4.1. *Primary Characteristics*

The mechanism of quench-hardening and the mechanism of the recovery of quench-hardening must correspond to the following experimental observations:

(1) Quench-hardening is persistent at high temperature, resoftening only above 600°C, while strain hardening shows appreciable resoftening at 400°C.

(2) The resoftening kinetics exhibit an activation energy of 4·7 ev, which is much higher than that of self-diffusion in gold.

Fig. 3

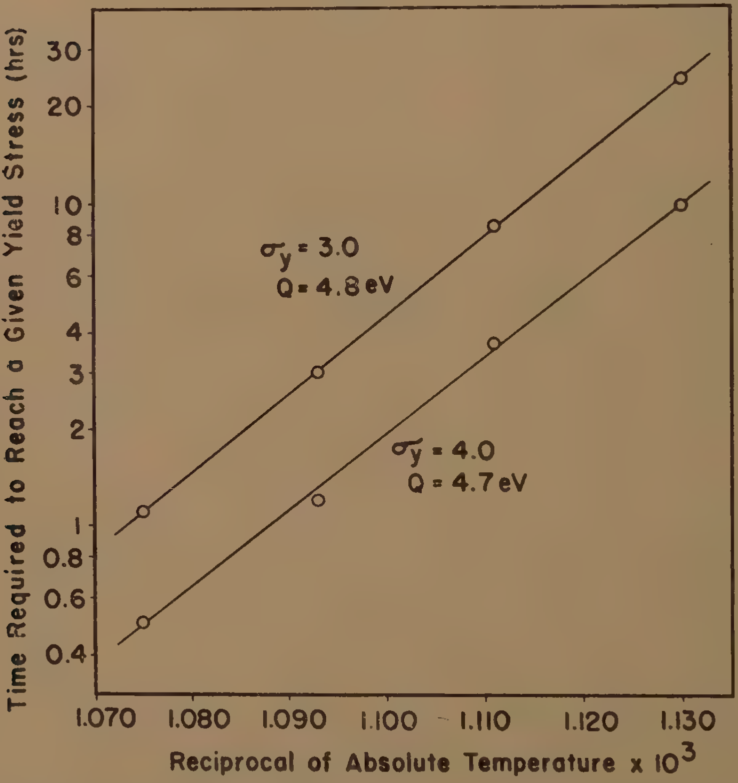

Logarithmic plot of time required to reach the degrees of recovery $\sigma_y=3{\cdot}0$ and $\sigma_y=4{\cdot}0$ against reciprocal of absolute temperature of annealing.

From the large activation energy for resoftening of quench-hardening and the high temperature necessary for resoftening, we conclude that the mechanism for resoftening of quench-hardening must not be diffusion controlled. The resoftening of strain hardening has generally been interpreted in terms of self-diffusion, and this has been confirmed by experimental and theoretical results, although there are still some uncertainties as to the detailed mechanism involved.

4.2. *The Mechanism Corresponding to the Observed Recovery Characteristics*

Several mechanisms have been proposed for quench-hardening. These involve various configurations resulting from vacancy condensation and are capable of producing various degrees of hardening. We may now quantitatively examine these mechanisms using the present experimental results. The possible hardening due to jogs and cavities formed along existing dislocations must be rejected as the main hardening mechanism for the quenched gold, because these would anneal out at lower temperatures with the activation energy of self-diffusion. The same consideration is valid for unextended or partially extended Frank sessile dislocations.

A possible configuration resulting from the migration and coagulation of quenched-in vacancies was recently observed (Silcox and Hirsch 1959) with an electron microscope. In gold foils they found configurations resulting from quenching, which have a tetrahedral appearance. They interpreted these configurations as being formed from triangular sheets of vacancies. The edges of the tetrahedra consist of stair-rod dislocations and the faces are intrinsic stacking fault planes. Since the stair-rod dislocation, by definition, is the intersection of two stacking fault planes, it follows that these dislocations must exist as straight line segments and the Burgers vector must not lie on the stacking fault plane to which it belongs. Therefore we reach the important conclusion that these stair-rod dislocations can neither glide nor climb by simple diffusion, and a mechanism for resoftening other than diffusion must be considered. In the following section, a mechanism for the disappearance of these tetrahedral configurations is proposed.

4.3. *The Disappearance of Tetrahedral Stacking Faults by Dislocation Nucleation*

A dislocation ring which nucleates on any face of a tetrahedron and subsequently grows and interacts with the stair-rod dislocations can annihilate the tetrahedral configuration. We consider the nucleation of a dislocation such as to eliminate the stacking fault as it grows. This removal of the stacking fault plane provides a driving force tending to increase the area of the dislocation ring. This type of dislocation would have a fault vector of the $\frac{1}{6}\langle 112\rangle$ type. After the new dislocation, which is a Shockley partial dislocation ring, is nucleated, its further growth proceeds, decreasing the energy. As this dislocation ring grows, it will eventually reach the edge of the stacking fault and then interact with the three stair-rod dislocations. Similar dislocation reactions have been proposed by Silcox and Hirsch (1959) to describe the tetrahedral formation. Three stair-rod dislocations are transformed into two Shockley partial dislocations and one Frank sessile dislocation. The resultant two Shockley partial dislocations can move so as to eliminate the two remaining stacking faults. The final configuration resulting from these reactions is a stacking fault plane surrounded by a Frank sessile dislocation. Thus, for resoftening to occur, we still must eliminate this final configuration. This can occur now by the evaporation of vacancies out of the Frank sessile dislocation ring. Using the activation energy for self-diffusion, one can calculate the time required for this evaporation to take place. The result is only a few seconds in the temperature range where resoftening occurs. Hence the time limiting process will be the nucleation of the original dislocation on the stacking fault plane. It is now necessary to consider in more detail the nucleation of this dislocation to see if it corresponds to the observed experimental data.

The analysis for the case of the nucleation of a dislocation ring under an external force has been made by Cottrell (1953). Using his method we have extended the calculations to the present case, which gives both the critical size for the nucleation of a Shockley partial dislocation ring on the stacking fault plane and also the activation energy required for the nucleation. Using 40 erg/cm^2 as the stacking fault energy, $4{\cdot}8 \times 10^{-7}$ cm is found for the critical radius and 6·6 ev is found for the activation energy. This calculated activation energy is in reasonable agreement with the experimentally observed value of 4·7 ev. Further, the probability of nucleation must be proportional to the area of the stacking fault and therefore to the number of tetrahedral stacking faults. Then, a first order reaction should be observed for the disappearance of the tetrahedral stacking faults and hence for their resoftening process. Here again we find agreement with the experimental data to within experimental error.

4.4. *The Case of Extended Frank Sessile Dislocations*

In the § 4.2, the Frank sessile dislocations were considered to be unextended; however, it is possible that these dislocations exist as extended dislocations and we now consider the more complex mechanisms for their removal. In the case of totally extended Frank sessile dislocations, the extended partials must combine before vacancy evaporation can take place. Then the activation energy for the disappearance of the configuration is the sum of the energies, namely, self-diffusion plus the energy difference between extended and unextended dislocations. The shape of extended Frank sessile dislocations is generally triangular. The evaporation of vacancies is most likely to take place from an apex of the triangle, because the length of the dislocation is thus shortened instead of lengthened, and because the energy for dislocation recombination is the lowest at an apex of a triangular ring. The activation energy for recombination of extended dislocations is estimated to be much smaller than that of self-diffusion for this case†.

The nucleation of a Shockley partial dislocation on the stacking fault region is an alternative mechanism for the elimination of extended Frank sessile dislocations. The stacking fault region inside a Frank sessile dislocation has the same probability of nucleation as a stacking fault on a tetrahedron. If this process should occur, the Frank sessile dislocation will be converted to a glissile dislocation of the $\frac{1}{2}\langle 110\rangle$ type. However, the vacancy mechanism is more likely, due to its lower activation energy.

---

† Appendix.

4.5. *Consideration of the Size of the Tetrahedra*

Let us next consider the effect of the size of the tetrahedra. When tetrahedra are smaller than a critical size, they become more stable than triangular rings of Frank sessile dislocations. Then a mechanism other than the nucleation of a Shockley dislocation ring must be considered for the elimination of these tetrahedra. Extended jogs have been considered previously (Silcox and Hirsch 1959). The energy to form a jog on a tetrahedron will be considerably larger than the activation energy for the present recovery mechanism. On the other hand, as shown in the present experimental results, a sudden recovery of quench-hardening occurs over a narrow temperature range with a distinct activation energy of 4·7 ev and no hardening effect remains after this recovery. These facts in conjunction with the above consideration lead us to conclude that the tetrahedra smaller than a critical size are unimportant for the mechanism of quench-hardening and its recovery in gold.

ACKNOWLEDGMENTS

The authors wish to acknowledge the discussions and the suggestions of Professor J. Takamura of Kyoto University, and Professor R. Thomson of the University of Illinois.

They would also like to thank Professor A. Kelly of Cambridge University for reading this paper.

APPENDIX

THE ENERGY OF RECOMBINATION OF AN EXTENDED FRANK DISLOCATION

The repulsive force between the partial dislocations is

$$F=\frac{\mu(\mathbf{b}_1\,.\,\mathbf{b}_2)}{2\pi(1-\nu)d}$$

where $(\mathbf{b}_1\,.\,\mathbf{b}_2)$ is $a^2/18$ in the case of Frank sessile dislocation. This force must balance the surface tension due to the stacking fault at $d=d_0$

$$\frac{\mu a^2}{36\pi(1-\nu)d_0}=\gamma,$$

$$d_0\gamma=\frac{\mu a^2}{36\pi(1-\nu)}.$$

The energy required to recombine an extended Frank dislocation consists of two terms, E_d and E_γ.

The segments of ΔL of Shockley and stair-rod dislocations recombine to ΔL of Frank dislocation. Then energy change is

$$E_d=\frac{\mu a^2}{36\pi}\log\left(\frac{r}{r_0}\right)\Delta L.$$

By the recombination of the segment ΔL, the area $\Delta L \,.\, d_0$ of the stacking fault is eliminated. The energy due to this is

$$E_\gamma = -\gamma d_0 \,.\, \Delta L.$$

Thus the total energy change is

$$E = E_d + E_\gamma = \left[\frac{\mu a^2}{36\pi}\log\left(\frac{r}{r_0}\right) - \gamma d_0\right]\Delta L = \left[\frac{\mu a^2}{36\pi}\log\left(\frac{r}{r_0}\right) - \frac{\mu a^2}{36\pi(1-\nu)}\right]\Delta L.$$

The total energy change per an atomic distance is only 0·2 ev, where we have used $\mu = 2{\cdot}8 \times 10^{11}$ erg/cm^3, $a = 4{\cdot}08 \times 10^{-8}$ cm, $r = 430 \times 10^{-8}$ cm, and $r_0 = 5{\cdot}77 \times 10^{-8}$ cm. The evaporation of vacancies from a triangular ring of Frank sessile dislocation is most likely to take place from its apex. The recombination over two atomic distances is sufficient for a vacancy to evaporate. Hence it is evident that this energy will be considerably smaller than the activation energy of self-diffusion, even though some approximations have been used in the above calculation.

REFERENCES

COTTRELL, A. H., 1953, *Dislocations and Plastic Flow in Crystals* (Oxford: Clarendon Press), p. 53.

COULOMB, P., and FRIEDEL, J., 1956, *Dislocations and Mechanical Properties of Crystals* (Lake Placid Conference) (New York: John Wiley and Sons, Inc.), p. 555.

KIMURA, H., MADDIN, R., and KUHLMANN-WILSDORF, D., 1958, *Bull. Amer. phys. Soc.*, **3,** 125; 1959, *Acta Met.*, **7,** 154.

LI, C. H., WASHBURN, J., and PARKER, E. R., 1953, *J. Metals*, **5,** 1223.

MADDIN, R., and COTTRELL, A. H., 1955, *Phil. Mag.*, **46,** 735.

MESHII, M., and KAUFFMAN, J. W., 1957, *Bull. Amer. phys. Soc.*, **2,** 145; 1959, *Acta Met.*, **7,** 180.

SEEGER, A., 1955, *Defects in Crystalline Solids* (London: Physical Society), p. 391.

SILCOX, J., and HIRSCH, P. B., 1959, *Phil. Mag.*, **4,** 72.

Unloading Effects in Aluminium and Aluminium–Zinc Single Crystals†

By A. T. Thomas
Aluminium Laboratories Limited, Banbury, Oxon, England

[Received March 28, 1960]

Abstract

Interrupted tensile tests have been carried out on single crystals of super-purity aluminium and solid solutions of aluminium–zinc. Partial load removal during an interruption of the test is shown to have several effects on subsequent plastic flow. Unloading yield points are formed during tests on both alloy and aluminium specimens, while strain ageing yield points formed during tests on alloy specimens are shown to be either enhanced or diminished, depending on the sequence of prior ageing and unloading. Finally the relationship between unloading and room temperature recovery is examined and the results suggest that the trapping of glissile dislocations, as a result of unloading, leads to a partial suppression of recovery.

§ 1. Introduction

Experimental work at different times has demonstrated that non-elastic and irreversible effects can occur when alloys and pure metals are unloaded during interruptions of tensile tests. Holden and Kunz (1952) showed how strain ageing yield points in iron are decreased in magnitude if the ageing takes place under reduced load. Their interpretation followed a suggestion by Fisher that the anchoring of a dislocation by solute atoms is more efficient if the former is in a stressed or bowed condition than if relaxed. An alternative suggestion by Paxton (1953) emphasized the sensitivity of the upper yield point to various experimental factors leading to stress concentrations. Thus the unloading is likely to disturb axiality of the specimen leading to a reduced yield point.

Another effect of unloading has been reported by Haasen and Kelly (1957) and Makin (1958) who observed the existence of yield points during tensile tests on single crystals of, respectively, high-purity aluminium and nickel, and copper, as a result of unloading during interruptions of the tests. The characteristics and mode of occurrence of these yield points suggest that strain ageing is an unlikely explanation for their formation. The yield points occur only if some of the load is removed during an interruption of test and their magnitude increases with extent of unloading. The effect is absent at low strains, occurring only after the termination of the region of easy glide, and its magnitude increases with strain. The yield point magnitude is independent of the waiting period and the yield points occur equally well at liquid air temperatures. These observations have suggested a process in which the glissile dislocations run backwards and trap one another during unloading.

---

† Communicated by the Author.

An examination of yield points in α-brass and other face-centred cubic metals by Bolling (1959) has indicated the formation of unloading yield points to be a general feature of face-centred cubic metals at temperatures where recovery is not appreciable. This work also confirmed that the magnitude of the strain ageing yield point is a function of the stress on the specimen during ageing, and ageing under reduced stress decreases the yield point. Finally, Bolling has shown that combining ageing with unloading produces interesting yield effects which he attributes to a combination of both processes.

The present study was undertaken to examine the general effects of unloading during interruptions of tensile tests on single crystals of high-purity aluminium and dilute aluminium–zinc alloys. The conditions were, therefore, examined under which yield points in alloy crystals could be enhanced or suppressed as a result of prior unloading.

§ 2. EXPERIMENTAL PROCEDURE

The materials used were super-purity aluminium (99·996%) and high-purity alloys of aluminium–0·42 at. % zinc and aluminium–0·2 at. % zinc. The alloys were made by melting together super-purity aluminium and 'Crown Special' zinc (99·986%) kindly supplied by the National Smelting Company, Avonmouth. The melting furnace was an alumina-lined crucible heated in an electrical resistance furnace, and the melt was chill cast in an iron mould producing an ingot 0·75 in. diameter × 4 in. in size. After discarding the head and tail the remainder of the cast ingot was heated for 4–5 hours at 450°C, and then extruded to $\frac{1}{8}$ in. diameter wire using a miniature extrusion press operated by an Amsler tensile testing machine. Wire drawing from $\frac{1}{8}$ in. diameter to 0·064 in. diameter was carried out using a simple draw bench. Single crystals were prepared from the drawn wire by the strain anneal method and wire crystals of approximately 5 cm in length were sectioned by a strain-free electro-erosion technique. To facilitate loading in the tensile machine, small polycrystalline loops of aluminium or the appropriate alloy were attached to the ends of the crystal by local welding, leaving a 4 cm working length. The orientation of each crystal was measured by the Laue back-reflection method and is shown in fig. 1.

Tensile tests were performed at a strain rate of 2×10^{-5} per sec in an Instron tensile testing instrument which is a recording hard beam machine. The load was measured by a load cell and the elongation by the cross-head motion. Tests were carried out either at room temperature or at 90°K with the specimen immersed in a Dewar flask containing liquid air.

In order to estimate the proportion of the applied load removed during an unloading test, a calibration test was carried out on a dummy specimen at a strain rate of 2×10^{-5} per sec to determine the rate of unloading. This was measured and found to be approximately 3 kg/min for a cross-head speed of 0·005 cm/min.

Fig. 1

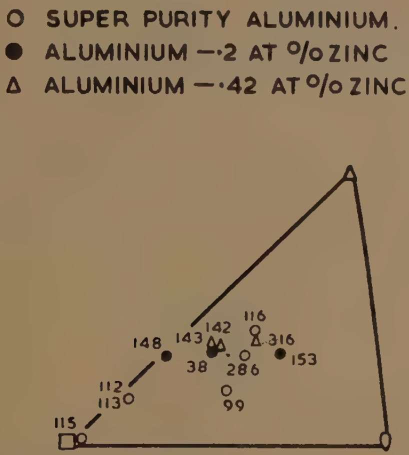
○ SUPER PURITY ALUMINIUM.
● ALUMINIUM —·2 AT % ZINC
Δ ALUMINIUM —·42 AT % ZINC
116
142
143
148
316
153
38
286
112
113
99
115

Initial orientations of the tension axes of the crystals examined.

§ 3. General Effects of Unloading

To appreciate the influence of unloading on such processes as recovery and strain ageing, it is first necessary to observe the deformation behaviour of specimens under conditions of no deliberate unloading during the interruption periods.

3.1. *Interruptions Without Unloading*

These tests were carried out to show the general nature of the strain ageing yield points in dilute aluminium–zinc alloys, and also to demonstrate some effects of room temperature recovery. A wire single crystal of aluminium–0·2 at. % zinc was strained plastically at room temperature. At frequent intervals the test was stopped and restarted after a time interval of 5 min. No load was deliberately removed during the interruption, but some creep relaxation usually occurred. This relaxation never exceeded 10% and was usually much less. Whenever a yield point was found (in this and subsequent tests) the magnitude of the yield point (Δl) and the change in flow stress (Δh) were measured. These quantities are illustrated in fig. 2.

A typical example of the relationship between the parameters Δh, Δl and load (l) on specimen for such an interrupted test is shown in fig. 3 for specimen T153 (aluminium–0·2 at. % zinc). Yield points, which at small extensions and small loads were well developed, decreased with increase of load. At a load of 4·2 kg, which corresponded to an elongation of 20%, the yield point no longer occurred. At the same time, small and positive increases in flow stress (Δh) which occurred at small loads, gradually changed to large negative values at high loads indicating a softening of the crystal during the period of interruption at this stage of the test.

Fig. 2

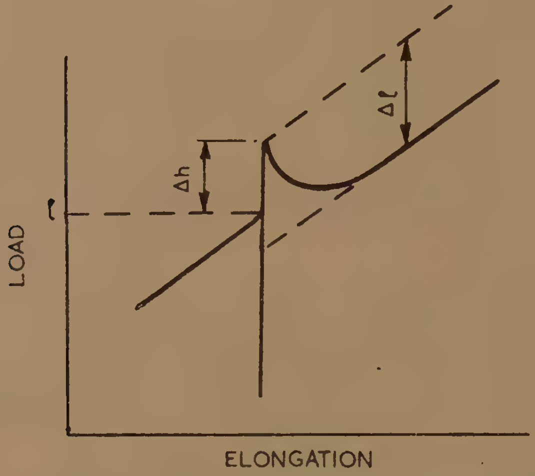

Illustrating the method adopted for measuring the magnitude of a yield point (Δl), and the change in flow stress (Δh) at a value of load (l) where the tensile test is interrupted.

Fig. 3

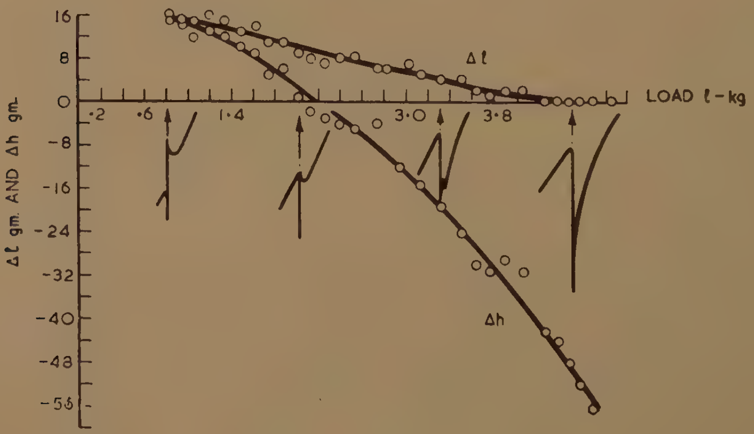

The variation of yield point (Δl) and flow stress (Δh) with load (l) expressed graphically and diagrammatically for alloy crystal T153 tested at 295°K.

Similar tests on a super-purity aluminium crystal specimen produced no yield points and no initial increases in flow stress, but progressive softening of the crystal again occurred.

Tests at 90°K produced no yield points and no softening in either specimen.

3.2. *Unloading During Interruptions*

The relation between Δl and load for an alloy crystal when a constant proportion (75%) of the load is removed and replaced during each constant time interval (5 min) is shown in fig. 4, again using specimen T153 (aluminium–0·2 at. % zinc) tested at room temperature as a typical example. After interruptions, small strain ageing yield points were obtained at the beginning of the test. These decreased with increase of load and became zero at a load of 1·2 kg. At 1·4 kg a yield point reappeared. Initially this was very small and rounded in appearance, being no more than a small undulation in the load/extension curve. As the test proceeded, the yield points became larger and sharper, but never as abrupt as the initial strain ageing yield points.The difference in appearance of the two types of yield point are well shown in fig. 6, where test (*a*) produces a strain ageing yield point and test (*g*) gives rise to an unloading yield point.

Fig. 4

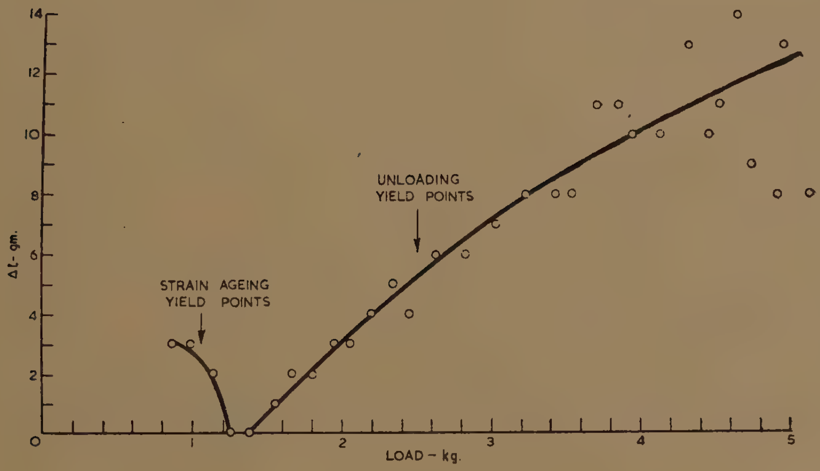

The variation of strain ageing yield point and unloading yield point (Δl) with load (l) for alloy crystal T153 tested at 295°K with 75% of applied load removed and reapplied during each 5 min interruption.

Tests on super-purity crystals indicate a similar yield point development with increase in load. A notable difference is the absence of any strain ageing yield point which is present in an alloy crystal. At liquid air temperature (90°K) yield points which develop as a result of unloading are very much larger than at room temperature for both alloy and aluminium crystals, whilst strain ageing yield points are absent at this temperature.

Unloading yield points were never observed during the easy glide or Stage I regions of the load-extension curves which is in agreement with the observations on copper single crystals by Makin (1958). It was further

Fig. 5

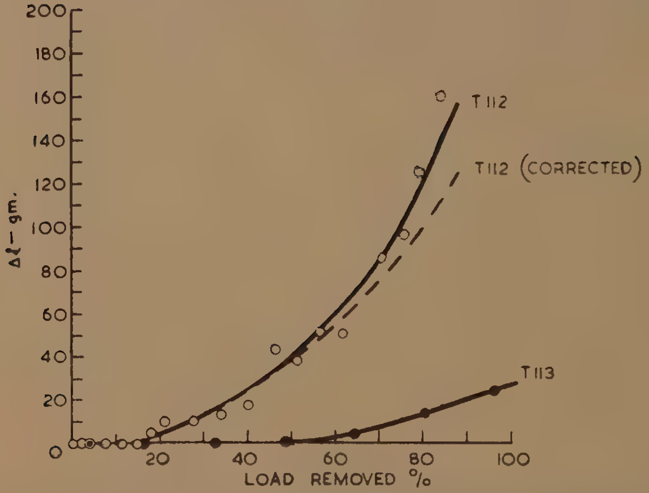

The variation of unloading yield point (Δl) with percentage load removed for the aluminium crystals T112 tested at 90°K and T113 at 295°K for time intervals of 5 min.

Fig. 6

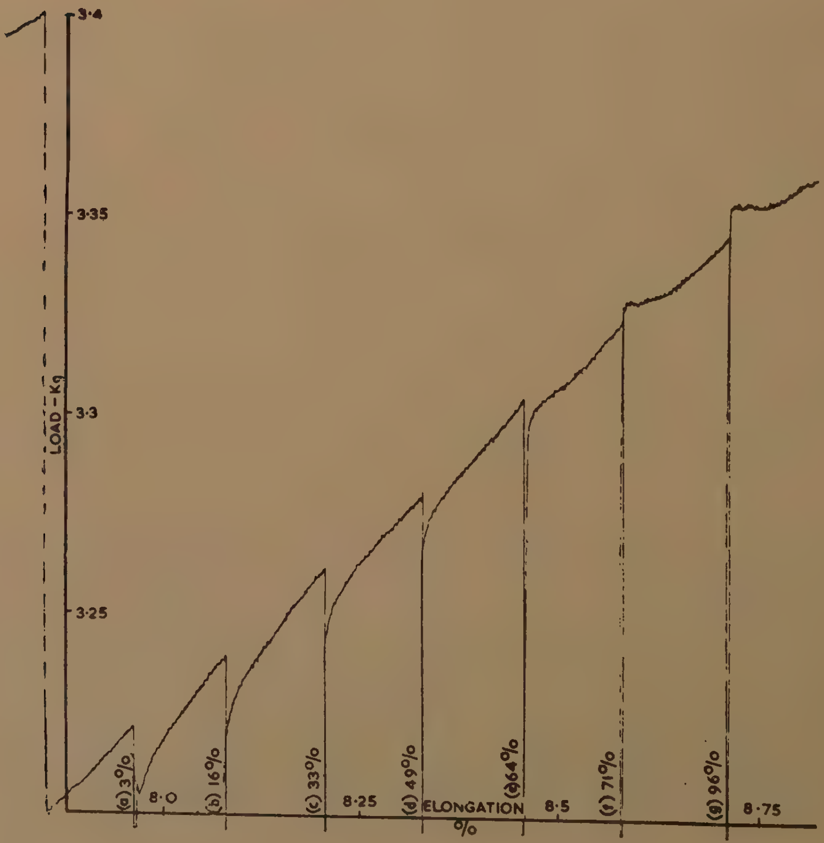

Region of a load-elongation curve for alloy crystal T142 showing a series of interruptions at constant time intervals of 3 min during which increasing percentages of load were removed and reapplied.

noted that there was a tendency for unloading yield points to appear earlier for those crystals orientated to give high rates of work hardening than for those which exhibited two-stage hardening. This indicates that the amount of cold work is an important factor for the appearance of this effect.

The results of these tests have shown that the size of the unloading yield point is dependent on the amount of load on the specimen. Other tests show that it is also dependent on the proportion of load removed in the manner illustrated in fig. 5, which shows this relationship for the aluminium crystals T112 tested at 90°K and T113 tested at 295°K. The curve for specimen T112 has been corrected to take into account the increase in the unloading yield point as a result of the increase in applied load during the test. The increase in applied load during the test at 295°K on specimen T113 was sufficiently small for this correction to be unnecessary.

In the case of the alloy crystal T153, it is possible by a study of figs. 3 and 4 to choose a load region where the strain ageing yield points are still present with the load maintained (e.g. for loads less than 4·2 kg in fig. 3), and where unloading yield points would also occur by partly removing the load during the interruption (e.g. for loads greater than 1·4 kg for 75% load removal in fig. 4). Thus in the load region between 1·4 and 4·2 kg, a sequence of interruptions with increasing load removals should produce both kinds of yield points in the subsequent plastic flow.

Figure 6 is a reproduction of an actual trace made by the recorder of the tensile machine during such a test on the alloy crystal T142 at 295°K in the load range 3·2–3·4 kg. As the proportion of load removed during the constant time interval of 3 min increased from (*a*) 3% to (*g*) 96%, the following sequence was observed:

(*a*) 3% A small sharp yield point was accompanied by a fall in flow stress.

(*b*) 16% The yield point vanished but the fall in flow stress remained.

(*c*) 33%
(*d*) 49% The fall in flow stress was becoming noticeably smaller.

(*e*) 64% The flow stress on retesting was much the same as before the interruption.

(*f*) 71% A rounded load drop was accompanied by an increase in flow stress.

(*g*) 96% Complete load removal during the interruption produced a further increase in flow stress accompanied by a large but rounded yield point.

Thus, gradually increasing load removals during constant time intervals produced, on one hand, a small sharp yield point and a softening of the crystal when the load was maintained, and on the other hand, a large rounded yield point and a hardening when most of the load was removed.

The time intervals of each interruption in this test was kept constant at 3 min. If the process responsible for the initial softening of the crystal was not taking place during unloading and reloading, it might be argued that waiting times should not include the time taken to unload and reload. If this were the case, the increasing proportion of the 3 min interval taken up by unloading and reloading would explain the gradual decrease of softening. To examine this contention, two tests (*p*) and (*q*) were carried out to compare the effect of maintaining the load for a 3 min interruption, (test *p*) and removing 92% of the load, waiting 3 min and reloading, (test *q*). The waiting period of 3 min did not, in the case of test (*q*), include the time of unloading and reloading. These tests are shown in fig. 7 for the alloy crystal specimen T142 tested at 295°K. The results of tests (*p*) and (*q*) are similar to those of tests (*a*) and (*g*) in fig. 6, and they indicate that the time taken to unload and reload is not related to the behaviour described.

Fig. 7

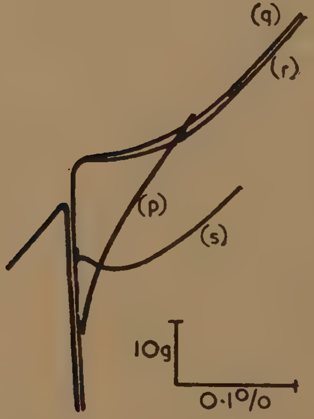

Composite diagram of the load-elongation relationships for alloy crystal T142 in the ranges 3·4 to 3·5 kg load and 9·25 to 10·0% elongation after the following tests at 295°K.

(*p*) Interruption of 3 min with 3% of load removed.
(*q*) Remove 92% of the load, wait 3 min and reload.
(*r*) Remove 92% of the load and reload where the total interruption time is 3 min.
(*s*) Remove 92% of the load, wait 60 min and reload.

This conclusion was confirmed by test (*r*), fig. 7, in which the 3-min time interval included the time taken to unload and reload, and the subsequent hardening and load drop produced was the same as for test (*q*). For long time intervals softening does occur even with the load removed. Test (*s*), fig. 7, shows that softening has occurred after a 60 min interval with 92% of the load removed. However, the rate of softening under these conditions is very much slower than with the load maintained.

§ 4. Summary of Results

An interrupted tensile test with the load maintained during the interruption produced the following effects on retesting.

(*a*) Sharp yield points were obtained with alloy crystals tested at room temperature. The magnitude of the yield point decreased with increase in applied load and eventually disappeared. No yield points were obtained with super-purity aluminium crystals or with aluminium alloy crystals tested at 90°K.

(*b*) A progressive softening of a specimen tested at room temperature, indicated by a fall in flow stress, occurred for both alloy and super-purity aluminium crystals. The effect increased with increase in applied load, and with time of interruption; it has to be noted, however, that at 90°K the effect did not occur. No softening was observed during tests at 90°K.

An interrupted tensile test with the load partly removed during the interruption produced the following effects on retesting.

(*a*) The sharp initial yield points were suppressed. The degree of suppression increased with increase of proportion of load removed and as the series of tests progressed to high loads.

(*b*) Softening at large extensions was diminished by load removal; this effect increased with increase of the proportion of load removed.

(*c*) At a certain value of applied load, large load removals completely prevented room temperature softening and, in fact, caused a hardening. Associated with the hardening was a large, but rounded, yield point, and this occurred with both alloy and aluminium specimens. This yield point increased and sharpened with the proportion of load removed and with the extent of prior cold work of the crystal.

(*d*) For crystals of different orientation, the onset of the unloading yield point occurred at lower extensions for crystals that work harden appreciably than it did for crystals which show easy glide. The unloading yield point did not occur until after the easy glide region.

(*e*) Unloading yield points were much larger and developed more easily during tests at 90°K than at 295°K.

(*f*) The magnitude of the unloading yield point was independent of time of interruption, but the hardening associated with it decreased with increase of waiting time at room temperature.

§ 5. Discussion

From the nature of the results, it is clear that a distinction must be made between two types of yield points. The initial sharp yield point, which occurred at low loads with the load maintained during the waiting period, has certain characteristics which indicate that it is a true strain-ageing yield point dependent on the presence of solute atoms for its occurrence.

It occurred only in the aluminium alloy crystals and not in the super-purity aluminium crystals; furthermore it occurred during tests at room temperature and not during tests at 90°K; it decreased with removal of load during the interruptions. Figure 6 shows the transition from the strain-ageing yield point to the unloading yield point as the load maintained on the specimen during a constant waiting time is gradually decreased.

The currently held theory of the strain-ageing yield point is due to Cottrell (1953). At temperatures at which solute atoms (zinc atoms in the case of the alloys used in this investigation) are able to diffuse through the crystal lattice, they will be attracted to positions of low energy adjacent to dislocations, where they form atmospheres which act as barriers to subsequent dislocation movement. Thus, the stress required to initiate slip is greater than that required to maintain slip, and a load relaxation will occur at the onset of plastic flow.

The softening of a crystal which occurs as a result of an interruption at room temperature after appreciable cold work is undoubtedly a recovery effect. It is well known that cold-worked aluminium and dilute aluminium alloys will recover at room temperature.

As a result of unloading, the formation of the unloading yield point, and the suppression of the recovery softening process, appear to be complementary effects, as revealed in fig. 6.

Haasen and Kelly (1957) explain the formation of the unloading yield point by suggesting that sessile dislocations are formed through the interaction of dislocations running back on intersecting slip planes as a result of unloading. The consequent anchoring of glissile dislocations would give rise to a yield point on retesting. The initial appearance of the unloading yield point only after the termination of the Stage I region of the stress–strain curve gives support to this mechanism. It is suggested that this explanation can be extended to account for the suppression of recovery softening which occurs at room temperature. With the load maintained the applied stress acting on the dislocations is balanced by the action of the back stress due to neighbouring dislocations. Thermal energy is sufficient to cause a re-distribution of dislocations forming a fairly well defined dislocation network. This would lead to a reduction in flow stress. The recovery process at room temperature cannot take place to the same extent if unloading has occurred, due to the anchoring of dislocations in the way described.

§ 6. UNLOADING, STRAIN AGEING AND RECOVERY

The tests described in the previous sections have distinguished between two types of yield point and have shown a relationship between the development of an unloading yield point and the flow stress associated with it. The tests to be described in the present sections were carried out to examine more closely the connection between unloading, recovery and strain ageing by combining unloading and reloading with a waiting period at load. Tests were carried out on both alloy and aluminium specimens at both room and liquid air temperatures. This procedure enabled the distinction to be made between yield points due to strain ageing and those due to unloading.

The testing procedure was as follows:

A specimen was strained at 295°K to 16–17% extension; the test temperature was then changed to 90°K. The stress-elongation curves for these two temperatures are shown in fig. 8. The test was frequently interrupted to carry out the following four separate tests, generally in the sequence given.

Test 1. The test was stopped and restarted after a time interval of 5 min. No load was deliberately removed during the interruption.

Test 2. The test was stopped for the purpose of removing a large percentage of the applied load which was re-applied immediately to continue the test.

Test 3. The test was stopped for an interval of 5 min. The specimen was then unloaded and reloaded immediately to continue the test.

Test 4. The test was stopped, the specimen unloaded and immediately reloaded nearly to the onset of plastic flow when an interval of 5 min was allowed to occur before the test was continued.

The diagrammatic illustration of each test is included in fig. 9. The extent of unloading in Tests 2, 3 and 4 was usually 80–90% of the applied load.

A number of crystals were tested according to the above programme and the results obtained from the super-purity aluminium specimen T286 and the aluminium–0·42 at. % zinc specimen T316 are typical. Figure 8 shows the initial orientation of these crystals together with their overall stress-elongation curves for extensions, partly at 295°K and partly at 90°K. The results of the four tests at each of the positions A, B and C, fig. 8, are illustrated in fig. 9, which is a reproduction of the load-extension curves obtained directly from the recorded chart. The details of these tests are shown in the table, which gives the load and elongation values at the commencement of each test; the load and elongation ranges over which these tests extended; and the percentage load removed where applicable. The results and interpretation of these tests are presented below in detail with reference to fig. 9.

6.1. *Super-purity Aluminium Specimen T*286

Position A

At small extensions, little or no room temperature recovery is occurring, and this would account for the absence of softening in Test 1. Tests 2, 3 and 4 indicate that unloading is having very little effect at this stage.

Fig. 8

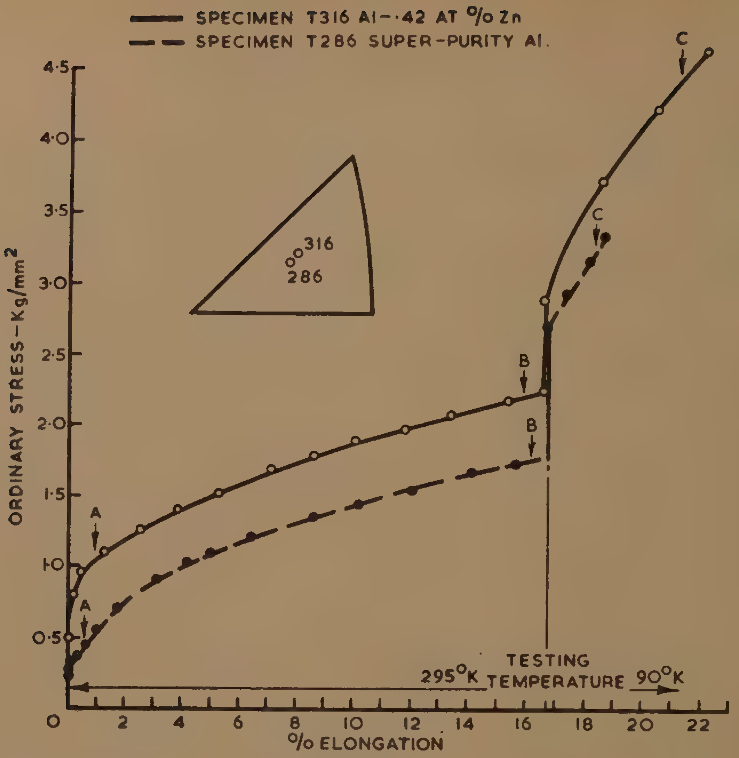

Stress-elongation curves for crystals tested at 295° K and 90°K.

Fig. 9

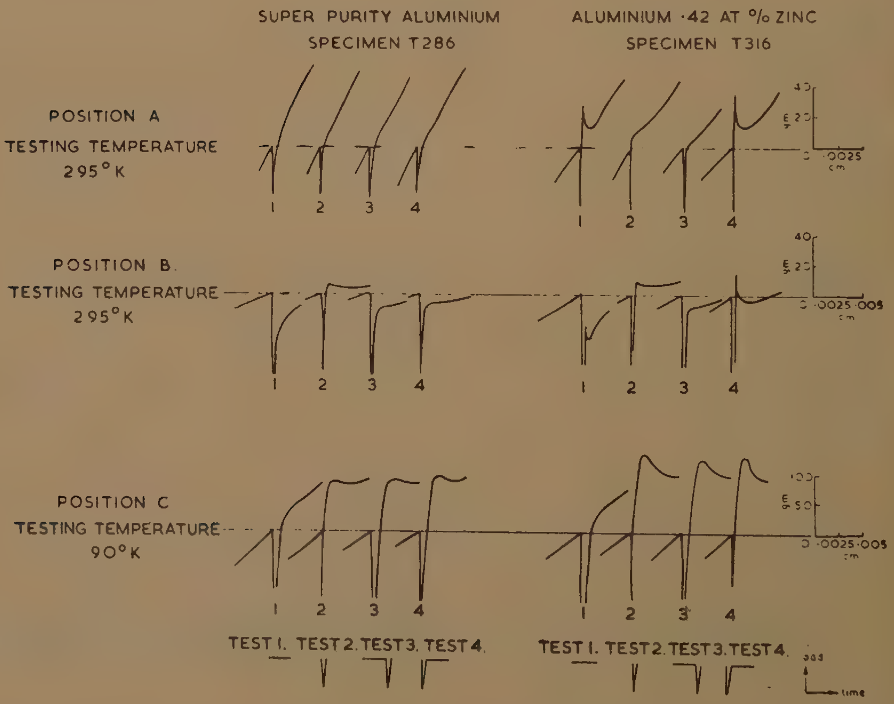

Load-extension relationships on retesting after a variety of tests performed during interruptions of tensile tests on super-purity aluminium and aluminium–zinc single crystals.

Position B

After some 16% elongation, the behaviour is now very different. Waiting 5 min without unloading (Test 1) produces a large fall in flow stress on retesting, which is indicative of the large amount of stress-assisted recovery occurring at room temperature at this extension. Unloading and reloading immediately (Test 2) produces a typical unloading yield point together with an absence of recovery softening indicated by an increase in flow stress. Tests 3 and 4, which combine a 5 min wait either before or after unloading and reloading, produce less well-developed unloading yield points with flow stresses intermediate between those obtained in Tests 1 and 2. The negligible effect of unloading during the tests at position A might be attributed to an insufficient number of intersecting slip planes present after this small extension, and the corresponding small number of blocked dislocation groups present. The trapping of dislocations as a result of unloading would tend to inhibit their movement and rearrangement associated with recovery, leading to the observed suppression of recovery softening. The intermediate flow stress values after Tests 3 and 4 suggest that some recovery is occurring after unloading and reloading (Test 4), while waiting 5 min before unloading and reloading allows slightly more recovery to occur as indicated by the slightly lower flow stress after Test 3 than after Test 4.

Position C

The same sequence of tests carried out at 90°K shows no recovery softening during Test 1, while all other tests involving unloading produce, on retesting, large unloading yield points. The similarity of results for Tests 2, 3 and 4 shows that the incorporation of a 5 min waiting period, whether before or after unloading and reloading, does not substantially affect the shape or size of the unloading yield point.

6.2. *Aluminium–0·42 at. % Zinc Specimen T*316

Position A

The main difference between the tests on the alloy specimen after a small extension compared with the corresponding tests on the super-purity specimen is the occurrence of large yield points after both Tests 1 and 4. It is noticeable that no yield points occurred after Tests 2 and 3, indicating that unloading and reloading prevents strain ageing from occurring, or as in the case of Test 3, unloading and reloading after an ageing period suppresses the occurrence of the yield point. This is in accord with earlier observations that unloading reduces the size of strain ageing yield points, the effect being greater for increased load removals and increase in specimen extension.

The occurrence of the large yield point after Test 4 shows that a 5 min ageing after unloading and reloading results in a larger yield point than is obtained by ageing for 5 min without unloading as in Test 1. Even for these small extensions, some recovery is already occurring as shown by the small difference in flow stress between Test 1 and Test 4 and also between Test 2 and Test 3.

Unloading prevents the strain ageing yield point from occurring, even when an ageing period has occurred prior to unloading. This suggests that (as a result of the removal of the applied load) the running back of dislocations along slip planes (under the action of the back stress of neighbouring dislocations) is sufficient to dissociate the dislocations from their solute atom atmospheres formed during the prior ageing period.

Position B

Test 1 illustrates two aspects of recovery which are occurring after an elongation of 16% at 295°K. These are the fall in flow stress and the reduction in size of the strain ageing yield point in comparison with the yield points obtained after tests at position A where little or no recovery was occurring. The association of these two aspects of recovery and their increase with increase in crystal extension has been observed earlier (fig. 3). It is suggested that the dislocation network formed during recovery becomes saturated with solute atoms. This would have the effect of decreasing the available solute concentration for anchoring the potential glissile dislocations, giving rise to the observed decrease in yield point size.

Unloading and reloading without waiting (Test 2) produces a yield point very similar to that produced after Test 2 at position B for the pure aluminium specimen. The size and shape of this unloading yield point can be directly compared with the larger and more abrupt strain ageing yield point.

Unloading and reloading after an ageing period (Test 3) again prevents the strain ageing yield point from occurring and a reduced unloading yield point occurs accompanied by a flow stress intermediate between those obtained after Tests 1 and 2.

Test 4 shows that a large yield point can be obtained if ageing is preceded by unloading and reloading. This might be explained, at least partly, by the suggested suppression of recovery by unloading, allowing more solute atoms to be locally available for anchoring the glissile dislocations. That this is not the complete explanation can be appreciated by reference to fig. 10, which shows how yield points arising from the four tests develop with stress for the alloy crystal during the room temperature deformation. Curves 1 and 4 represent the relationship between stress and the magnitude of the yield points formed as a result of Tests 1 and 4. Both curves rise to a maximum very soon after the initial yield point and subsequently decrease with stress. Curve 4 is substantially higher than curve 1 at all stresses. This means that yield points arising from Test 4 are considerably larger than those after Test 1, even at low stresses where recovery effects are not yet appreciable. The principal cause of the large yield point after Test 4 is, therefore, more likely to be some combination of both unloading and ageing, such as the ageing of sessile dislocations formed by prior unloading as proposed by Bolling (1959) in the case of α-brass. In contrast to curves 1 and 4, curves 2 and 3 are typical of the development of essentially unloading yield points and which correspond to the development of the unloading yield point shown in fig. 4. Curve 3 is lower than curve 2 due to the recovery softening occurring during the 5 min wait before unloading and reloading. It can also be seen in fig. 10 that curve 4 does not fall off at high stresses quite so fast as curve 1, although the difference is small. It might be expected that the difference would be greater if recovery was being appreciably reduced by prior unloading and reloading. In contrast, fig. 11 shows how changes in flow stress (Δh) vary with stress for the same tests.

Fig. 10

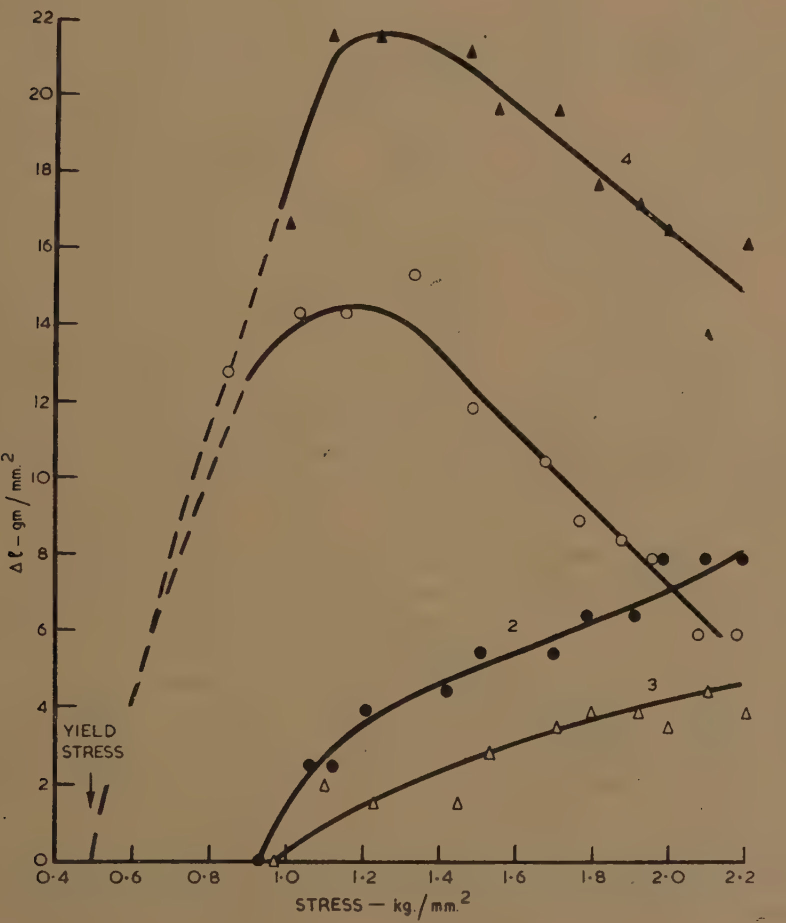

The variation of yield point size (Δl) with stress after Tests 1, 2, 3 and 4 performed during interruptions of tensile tests at 295°K on alloy crystal T316.

Curve 1 falls away considerably faster than curve 4. A further indication of the importance of unloading on recovery is shown in fig. 12, which expresses the change in flow stress as a function of time of interruption of a series of tests performed on specimen T143 after 15% elongation at room temperature. It is seen that if unloading and reloading precedes the waiting period, the subsequent recovery softening is considerably reduced. Hence, it is likely that part of the explanation for the large yield point obtained after Test 4 at large (specimen) extensions at room temperature is the partial suppression of recovery and the consequently diminished inhibiting effect of recovery on strain ageing.

Fig. 11

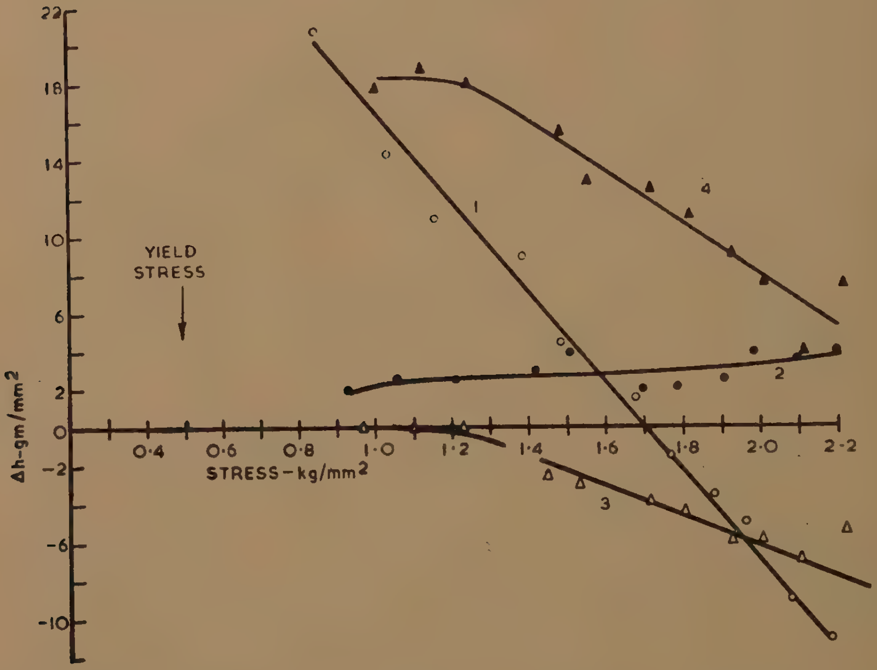

The variation of changes in flow stress (Δh) with stress after Tests 1, 2, 3 and 4 performed during interruptions of tensile tests at 295°K on alloy crystal T31·6.

Position C

Tests at 90°K are similar to the corresponding tests on the super-purity aluminium specimen. This is not unexpected as strain ageing does not occur at this temperature due to the absence of solute atom diffusion. Test 1 shows also that no recovery softening is taking place while Tests 2, 3 and 4, all of which involve unloading, exhibit large unloading yield points. The increase in size of these unloading yield points compared with tests at position C, for the super-purity aluminium crystal is due entirely to the larger applied loads and extensions operative during the alloy tests, as shown in the table.

Fig. 12

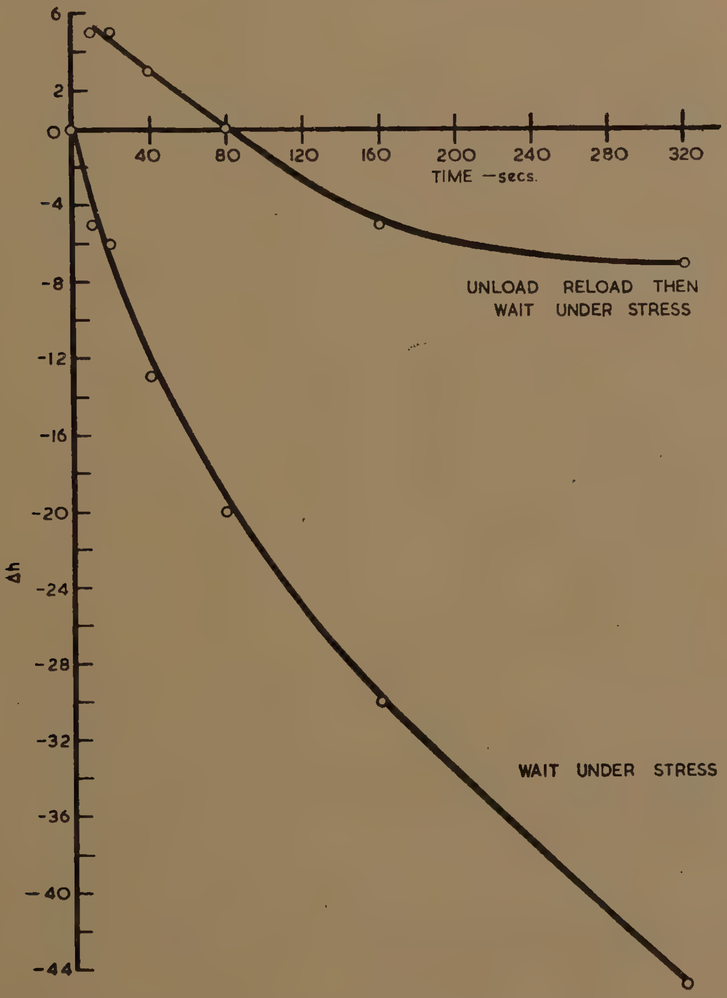

The variation of changes in flow stress (Δh) as a function of waiting time for alloy crystal T143 after 15% elongation at 295°K.

§ 7. Summary of Results

Test 1. *Test stopped and restarted after a time interval of* 5 *min during which time no load was deliberately removed*

295°K. The alloy crystal exhibited a strain ageing yield point while the aluminium crystal did not. At large extensions, a fall in flow stress

Table 1. Details of loads and elongations at which interruptions of tensile Tests occurred and the Percentage Load Removed where Applicable

Test (see fig. 9)		Super-purity aluminium (specimen T286)					0·42 at. % zinc alloy (specimen T316)						
		Load (kg)	Elong. (%)	Unload (%)	Load range (kg)	Elong. range (%)	Test (see fig. 9)		Load (kg)	Elong. (%)	Unload (%)	Load range (kg)	Elong. range (%)
A	1	0·688	0·302	—	0·186	0·361	A	1	2·068	0·81	—	0·220	0·68
	2	0·754	0·422	84·5				2	2·148	1·01	89·0		
	3	0·818	0·542	78·0				3	2·234	1·28	85·5		
	4	0·874	0·663	73·0				4	2·288	1·49	83·5		
B	1	3·364	15·65	—	0·040	0·75	B	1	4·440	15·6	—	0·068	0·8
	2	3·380	15·90	89·6				2	4·464	15·9	89·2		
	3	3·394	16·15	89·3				3	4·488	16·2	88·8		
	4	3·404	16·40	89·0				4	4·508	16·4	88·4		
C	1	5·72	17·4	—	0·58	1·1	C	1	7·80	19·0	—	1·30	2·6
	2	5·93	17·8	88·6				2	9·10	21·6	89·2		
	3	6·13	18·1	85·5				3	8·60	20·6	88·9		
	4	6·30	18·5	88·5				4	8·90	21·2	89·5		

occurred in both crystals and was accompanied, in the case of the alloy crystal, by a strain ageing yield point of diminished size. Both effects are attributed to recovery.

90°K. No yield points were observed in either specimen and no fall in flow stress occurred. This is explained by the absence of strain ageing and recovery at this temperature.

Test 2. Test stopped for the purpose of removing a large percentage of the applied load which was re-applied immediately to continue the test

295°K. No large effect was observed in either crystal at small extensions indicating that the strain ageing yield point was prevented from occurring in the alloy crystal. At large extensions, unloading yield points in both crystals occurred accompanied by an absence of recovery softening which is attributed to a suppression of recovery by unloading.

90°K. Large unloading yield points occurred in both crystals.

Test 3. Test stopped for an interval of 5 min, specimen then unloaded and reloaded immediately to continue the test

295°K. At small extensions, no yield points were observed in either specimen indicating that the effects of strain ageing in the case of the alloy crystal were eliminated as a result of subsequent unloading. At large extensions unloading yield points and increases in flow stress occurred, but to a smaller extent than in Test 2.

90°K. Large unloading yield points occurred in both crystals.

Test 4. Test stopped, specimen unloaded and immediately reloaded nearly to the onset of plastic flow, left for 5 min before the test was continued

295°K. At small extensions no yield points and no change in flow stress were observed for the aluminium crystal while at large extensions an unloading yield point and an increase in flow stress occurred. Both these effects were slightly larger than those obtained in Test 3, but not as large as in Test 2. Well developed yield points occurred for both extremes of extension for the alloy crystal accompanied by an increase in flow stress. It is suggested that the ageing of sessile dislocations is mainly responsible for this effect, whilst a contributory factor is the inhibiting effect of unloading on recovery which would otherwise reduce the strain ageing yield point at the large extension (as in Test 1).

90°K. Large unloading yield points occurred in both crystals.

§ 8. DISCUSSION

The factors governing the appearance of unloading effects implies that their explanation is closely associated with the mechanism of work hardening. According to the latest ideas on work hardening (Basinski 1959)

Lomer–Cottrell sessiles are not now considered to play such an important role than hitherto supposed. At the same time they must contribute to the general picture of work hardening and their existence can satisfactorily explain the experimental features of unloading. The increased yield point obtained if ageing is preceded by unloading and reloading has been explained in part by the ageing of sessile dislocations. This implies that the dislocations held back by sessiles are released by the break down of the latter in a way discussed by Stroh (1956), rather than by cross slipping around the obstacles. Otherwise ageing the sessiles would not be expected to enhance the yield point.

§ 9. CONCLUSIONS

Unloading yield points occur in both aluminium and dilute aluminium–zinc single crystals. Strain ageing yield points are suppressed or enhanced depending whether ageing occurs before or after unloading and reloading. The results suggest that the ageing of sessile dislocations formed by unloading is largely responsible for the enhanced yield point. In addition, room temperature recovery, which produces a fall in flow stress, and a reduced strain ageing yield point can be partially suppressed by unloading, and this effect contibutes to the enhanced yield point if ageing is preceded by unloading and reloading.

ACKNOWLEDGMENTS

The author wishes to acknowledge the assistance of Mr. E. H. Köster in the experimental work, and to Dr. A. R. Harding and Mr. G. E. G. Tucker for helpful discussions of the results and their interpretation. Thanks are due to Aluminium Laboratories Limited, Banbury for permission to publish this paper.

REFERENCES

BASINSKI, Z. S., 1959, *Phil. Mag.*, **4,** 393.
BOLLING, G. F., 1959, *Phil. Mag.*, **4,** 537.
COTTRELL, A. H., 1953, *Dislocations and Plastic Flow in Crystals* (Oxford: University Press).
HAASEN, P., and KELLY, A., 1957, *Acta Met.*, **5,** 192.
HOLDEN, A. N., and KUNZ, F. W., 1952, *J. appl. Phys.*, **23,** 799.
MAKIN, M. J., 1958, *Phil. Mag.*, **3,** 287.
PAXTON, H. W., 1953, *J. appl. Phys.*, **24,** 104.
STROH, A. N., 1956, *Phil. Mag.*, **1,** 489.

Anomalous Electron Absorption Effects in Metal Foils[†]

By H. HASHIMOTO[‡]
Metallurgy Department, Cambridge University

and A. HOWIE and M. J. WHELAN
Cavendish Laboratory, Cambridge

[Received March 22, 1960]

ABSTRACT

The dynamical theory of electron diffraction including a term to take account of absorption has been applied to explain some contrast anomalies observed at extinction contours and stacking faults on transmission electron micrographs of metal foils. The theory is at present phenomenological because the detailed mechanism of the absorption process is not understood. This paper reports some preliminary results of the theory and compares them with observations.

OBSERVATIONS by transmission electron microscopy on thin foils of several metals have revealed certain interesting contrast effects at extinction contours and stacking faults. These effects can be explained in terms of an anomalous absorption effect similar to the well-known Borrmann effect (1941, 1950) observed with x-rays.

Figure 1 (*a*) and (*b*) and fig. 2[§] show typical examples of the appearance of bend extinction contours (Heidenreich 1949) observed on transmission electron micrographs of thin and thicker areas of metal foils. Figure 1 (*a*) is a bend contour in a thin region of aluminium foil. Selected area electron diffraction patterns have shown that such a contour is produced by two lowest order Bragg reflections hkl and $\bar{h}\bar{k}\bar{l}$. For example the area of the foil labelled A in fig. 1 (*a*) gives rise to a strong 111 reflection together with a weak $\bar{1}\bar{1}\bar{1}$ reflection, while the area labelled B gives rise to a strong $\bar{1}\bar{1}\bar{1}$ reflection and a weak 111 reflection. Subsidiary maxima are visible on either side of the principal dark contours A and B. In the region lying between the two principal contours the intensity transmitted in the bright field image (fig. 1 (*a*)) is observed to be lower than that on the other sides of the principal contours. This asymmetry in the intensity transmitted on either side of a Bragg reflection increases with increasing foil thickness while the visibility of subsidiary maxima decreases. In thicker regions a bend extinction contour appears as a dark band. An example of this is shown in fig. 2, which is a bright field micrograph taken from a copper foil.

[†] Communicated by the Authors.
[‡] On leave of absence from Kyoto Technical University, Japan.
[§] Figures 1 and 2 and figs. 7 and 8 are shown as plates.

In this case no subsidiary maxima are visible. The interior of the band is very dark, while the light borders of the band show very good electron transmission. Note that the dislocations are very clearly visible in these regions. The bands can be swept across the field of view by tilting the specimen. Selected area diffraction patterns have confirmed that the transparent borders are associated with particularly strong incident and lowest order reflected waves in agreement with the observations of Kohra and Watanabe (1959) on molybdenite crystals. The intensity asymmetry in thin regions and the disappearance of subsidiary contours in thick regions are not predicted by the usual dynamical theory of diffraction (without absorption).

The presence of considerable background scattering and Kikuchi lines on selected area diffraction patterns suggest that incoherent scattering of electrons may be responsible for the contrast anomalies discussed above. A phenomenological description of the effect of incoherent scattering (hereafter referred to as absorption) can be obtained by application of the dynamical equations of electron diffraction to a crystal with complex lattice potential. The imaginary part of the lattice potential gives rise to absorption. Yoshioka (1957) has given a general quantum mechanical justification of this procedure. In considering the explanation of the observations it is important to note that both types of bend contour mentioned above are produced by two lowest order Bragg reflections, i.e. the so-called 'systematic' reflections on opposite sides of the origin of reciprocal space. The dynamical theory of electron diffraction for two strong reflections (i.e. a three-beam theory) should therefore be applied. However, numerical calculations for this case have shown that the main qualitative features of the results are unchanged by applying the usual two-beam theory to one-half of the bend contour. The theory is then identical with that of the corresponding x-ray Borrmann effect which has been treated by Zachariasen (1945), by Von Laue (1949) and by Hirsch (1952). Figure 3 (*a*) and (*b*) shows typical intensity profiles of one-half of a bend extinction contour for bright and dark field images respectively, calculated by the one strong reflection approximation (i.e. a two-beam theory). It will be noted that the intensity of the bright field image is asymmetrical about the centre of the reflection, while the peak of maximum intensity is displaced from the centre. However, in the dark field image there is no asymmetry and the peak maximum occurs at the centre of the reflection. This has been observed experimentally. Figure 1 (*b*) is the dark field image in the strong reflection from the area A in fig. 1 (*a*). To a rough approximation the image appears symmetrical. The exact symmetry of course will depend on the nature of the buckling of the foil. The vertical scale of the intensity in fig. 3 depends on the mean absorption coefficient of the material, while the shape of the curves depends on the crystal thickness t, and on two parameters t_0 and τ_0. t_0 is the extinction distance calculated from $t_0=\lambda E/V_g$, where λ is the electron wavelength, E is the electron energy in volts, V_g is the Fourier coefficient of order **g** of the real part of the complex lattice potential and **g** is the reciprocal lattice vector corresponding to the Bragg reflection. Extinction distances for low-order reflections of face-centred cubic metals are of the order of a few hundred angstroms (Whelan 1959, Hirsch *et al.* 1960). τ_0 is an absorption parameter derived from the same formula by substituting for V_g the Fourier coefficient of order **g** of the imaginary part of the complex lattice potential. The spacing between the subsidiary

Fig. 3

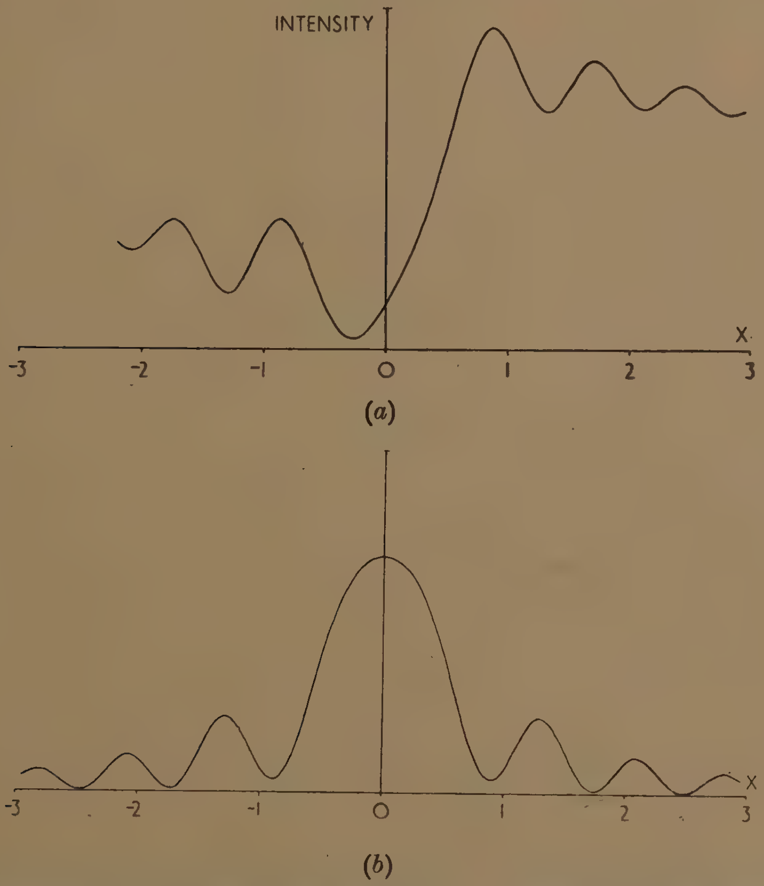

(*a*) Theoretical profile of the bright field image of one-half of a bend extinction contour in a thin region such as fig. 1 (*a*). The ordinate is the intensity transmitted on a linear scale which depends on the mean absorption coefficient. The abscissa x (see Whelan and Hirsch 1957 a) represents deviation from the Bragg angle. $x=0$ corresponds to the exact Bragg angle. Note the asymmetry of the bright field image. (*b*) Profile of the dark field image corresponding to (*a*). ($t/t_0=1{\cdot}5$, $t/\tau_0=0{\cdot}15$.)

maxima in fig. 3 (*a*) is determined by t/t_0, while the shape of the curve, i.e. the degree of asymmetry and the amplitude of the subsidiary oscillations, depends on t/τ_0. The quantity $\pi t/\tau_0$ is identical with the parameter Ak used by Zachariasen (1945) and by Hirsch (1952). Figure 3 (*a*) and (*b*) corresponds to $t/t_0=1{\cdot}5$ and $t/\tau_0=0{\cdot}15$. As t/τ_0 increases the asymmetry of the bright field image increases while the amplitude of the subsidiary oscillations decreases. Figure 4 (*a*) and (*b*) shows intensity profiles for $t/t_0=10$ and $t/\tau_0=1{\cdot}0$. Figure 4 (*a*) accounts qualitatively for the nature of one-half of the bend extinction contour observed in thick regions

Fig. 4

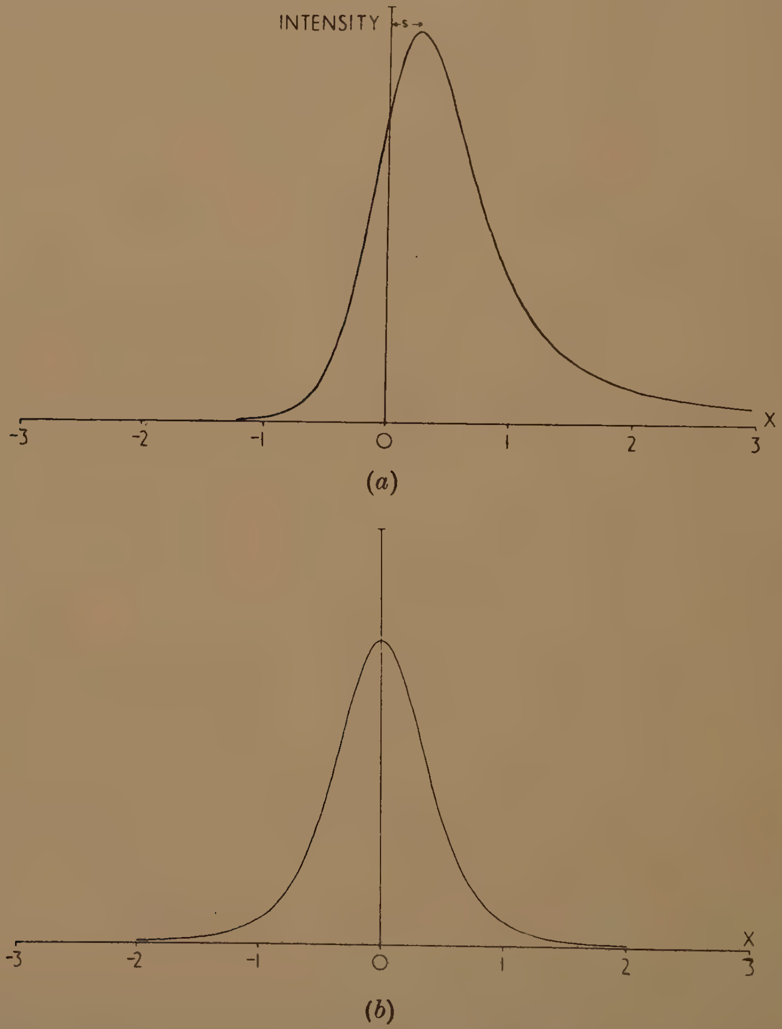

(*a*) Theoretical profile of the bright field image of one-half of a bend extinction contour in a thick region such as fig. 2. Note the absence of subsidiary maxima and the displacement *s* of the peak from the exact Bragg angle. (*b*) Profile of the dark field image corresponding to (*a*). ($t/t_0=10$, $t/\tau_0=1$.)

(fig. 2). Note that for thick crystals (fig. 4 (*a*) and (*b*)) the intensity profile of the dark field image is similar in nature to that of the bright field image except for a displacement *s* of the peak of the bright field image from the exact Bragg condition. This is the phenomenon of 'reversal' of the extinction line and has been discussed by Hirsch (1952) for the x-ray case. This effect in thick regions has also been verified experimentally.

The theory has been extended to calculate the profile of fringes observed at stacking faults in face-centred cubic metals. The formal theory can easily be obtained from that given by Whelan and Hirsch (1957 a, b) by allowing the parameters β_1 and β_2 used by those authors to become complex and by including a mean absorption coefficient. The theory leads to the following results.

(*a*) At the reflecting position for small t/τ_0, the fringe profiles exhibit alternating intensities of fringe maxima or minima depending on crystal thickness. The spacing between the intensity maxima corresponds approximately to $\frac{1}{2}t_0$ as in the theory without absorption. The difference between adjacent intensity minima is larger near the edges of the fault (fig. 5 (*a*)), while the peak intensity transmitted in the middle of the fault is smaller than that at the edges. In fact in fig. 5 (*a*) the choice of absorption parameters ($t/t_0=5, t/\tau_0=0\cdot35$) is such that the subsidiary minima are suppressed at the light fringes A near the edges of the fault although they are visible at B. The intensity profile of the bright field image is symmetrical about the centre of the fault.

(*b*) Figure 5 (*a*) shows that the theory accounts for the absence of subsidiary fringes near the edges of the fault, an effect which was tentatively attributed by Whelan and Hirsch (1957 b) to strains due to a surface oxide film. Figure 7 shows an example of a stacking fault in stainless steel where the subsidiary fringes near the edges of the fault are not visible. It is thought that this micrograph corresponds fairly closely to the condition of fig. 5 (*a*).

(*c*) The profile of the dark field image is asymmetrical about the centre of the fault (fig. 5 (*b*)). This has been verified experimentally.

(*d*) At the reflecting position for large t the subsidiary maxima or minima tend to disappear except near the centre of the fault. In this case the spacing between the main fringes near the edges of the fault corresponds to t_0. The mean intensity transmitted in the dark and bright field images and the visibility of the fringes is lower near the centre of the fault as shown in fig. 6 (*a*) and (*b*), for which $t/t_0=8, t/\tau_0=0\cdot56$. Figure 8 shows an example of the decrease in visibility of the fringes near the centre of a fault in stainless steel. It is thought that this micrograph corresponds closely to the theoretical curve of fig. 6 (*a*).

The results show that absorption effects must be considered to explain the fine detail of transmission electron micrographs of thick metal foils. At present however there is no theoretical treatment of incoherent scattering in metals which leads to a reliable estimate of the absorption parameter τ_0. The observations on aluminium and stainless steel foils can be explained on the assumption that τ_0 is about 10 to 15 times t_0. The detailed mechanism of the absorption process is also unknown.

Fig. 5

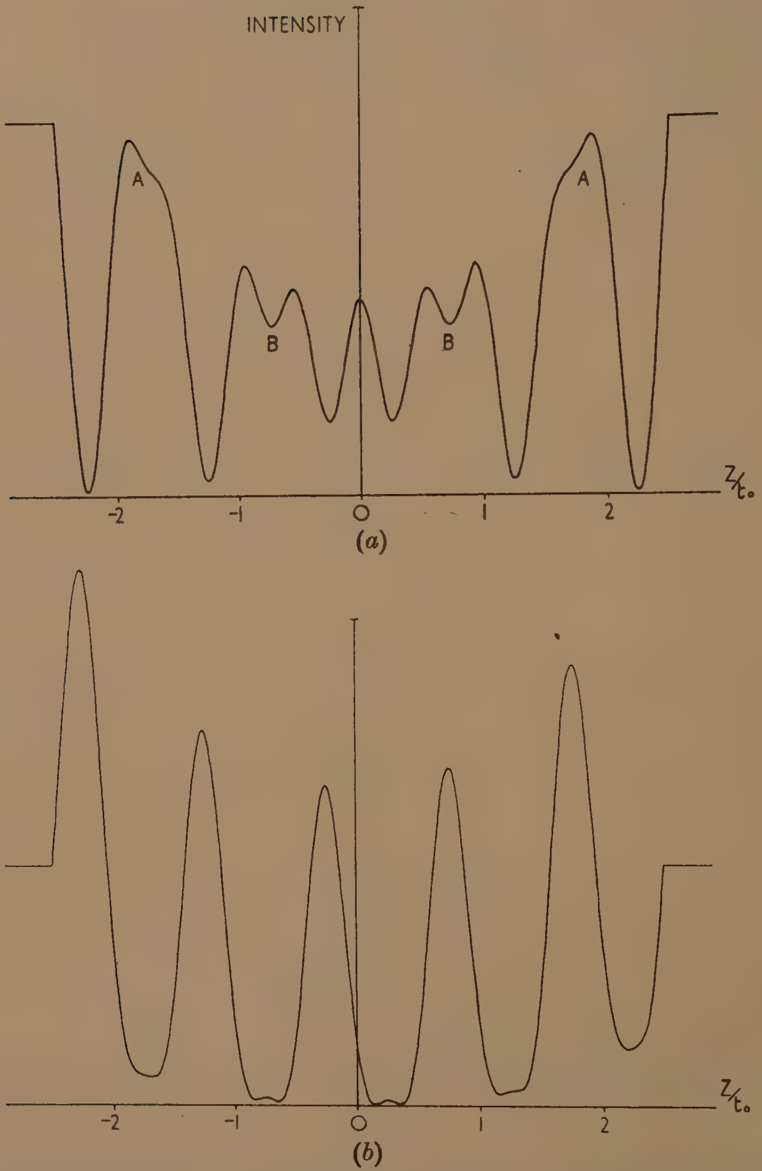

(*a*)

(*b*)

(*a*) Theoretical profile of the bright field image of the interference fringes at a stacking fault in a face-centred cubic metal. The ordinate is the intensity transmitted on a linear scale which depends on the mean absorption coefficient. The abscissa z/t_0 is proportional to distance on the image measured from the centre of the fault ($z=0$) (see Whelan and Hirsch 1957 a). The curve is calculated from the exact Bragg angle ($x=0$). Note the weak dark fringes at B and the absence of similar fringes at A. Note also that the image is symmetrical about $z=0$. Compare with fig. 7. (*b*) Dark field image corresponding to (*a*). Note the asymmetry of the image about $z=0$. ($t/t_0=5$, $t/\tau_0=0{\cdot}35$.)

It is in principle possible to estimate τ_0 from bright field and dark field micrographs. For example in thick regions the displacement s (fig. 4 (*b*)) between the peaks of dark field and bright field images is a function of t/τ_0, and provided t is known, τ_0 can be estimated if s is measured. Measurements of the intensity transmitted at extinction contours relative to that of the incident beam could also be used to determine the mean absorption coefficient. Then if τ_0 were known for several reflections, the atomic form factor for incoherent scattering could be derived.

Fig. 6

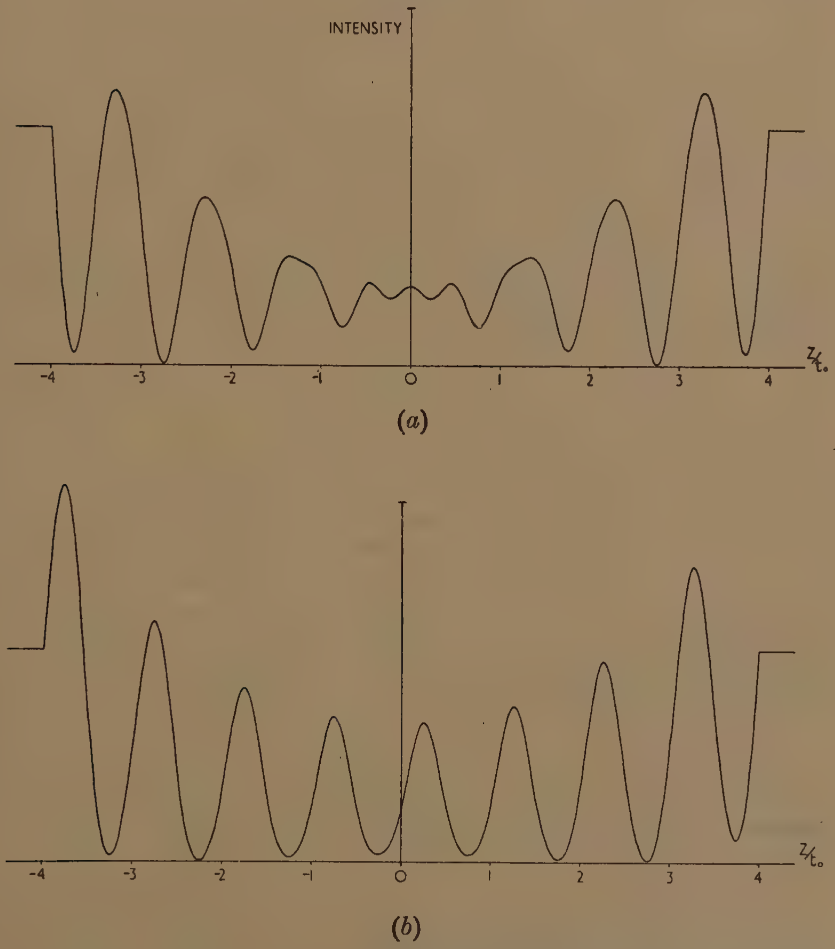

(*a*) Theoretical profile at the exact Bragg angle of the bright field image of the fringes at a stacking fault in a thicker region. Note the absence of subsidiary dark fringes except near the centre of the fault. Note also the decrease in visibility of the fringes near the centre of the fault. Compare with fig. 8. (*b*) Dark field image corresponding to (*a*). ($t/t_0=8$, $t/\tau_0=0{\cdot}56$.)

An interesting application of the results for a stacking fault arises from the symmetry and asymmetry about the centre of the fault of bright field and dark field images respectively. For certain symmetrical orientations of a f.c.c. plate crystal (e.g. (100) parallel to the surface) it is not possible from the bright field image of a stacking fault alone to decide which edge of the fault corresponds to the top or bottom surface of the crystal. However, comparison of fig. 5 (*a*) and (*b*) (or fig. 6 (*a*) and (*b*)) shows that at one edge of the fault bright field and dark field images tend to be similar in nature, whereas at the other edge they tend to be complementary. These two cases correspond to the intersection of the fault with the surfaces closest to and furthest away from the electron beam source respectively. Therefore bright field and dark field images of a fault should be sufficient to differentiate between the two edges. Similar considerations would be expected to hold for dotted (fringed) dislocation images.

The theory also accounts qualitatively for certain other contrast effects observed at dislocations, such as the dotted appearance near the surfaces of dislocations running obliquely through foils (Hirsch *et al.* 1960) and the general dark nature (free from dotted effects) of the images of dislocations in the interior of thick crystals. These effects would be analogous to the decreasing transmitted intensity and visibility of fringes at a stacking fault towards the centre of the fault. Full details of the theory outlined in this paper will be published later.

ACKNOWLEDGMENTS

Our thanks are due to Professor N. F. Mott, F.R.S. and to Professor A. H. Cottrell, F.R.S. for their encouragement. We are grateful to Drs. P. B. Hirsch, J. Nutting, to Mr. R. M. Fisher, and to a number of our colleagues for stimulating discussions. Thanks are also due to the Director and staff of the Mathematical Laboratory, Cambridge, for permision to use EDSAC 2.

Acknowledgments for financial support are due to the Japanese Ministry of Education (H.H.), to the Master and Fellows of Trinity College, Cambridge (A.H.) and to the Royal Society Mr. and Mrs. John Jaffé Donation (M.J.W.).

REFERENCES

BORRMANN, G., 1941, *Phys. Z.*, **42,** 157; 1950, *Z. Phys.*, **127,** 297.
HEIDENREICH, R. D., 1949, *J. appl. Phys.*, **20,** 993.
HIRSCH, P. B., 1952, *Acta cryst.*, **5,** 176.
HIRSCH, P. B., HOWIE, A., and WHELAN, M. J., 1960, *Phil. Trans. roy. Soc.* **252,** 499.
KOHRA, K., and WATANABE, H., 1959, *J. phys. Soc. Japan*, **14,** 1119.
LAUE, M. VON, 1949, *Acta cryst.*, **2,** 106.
WHELAN, M. J., 1959, *J. Inst. Metals*, **87,** 392.
WHELAN, M. J., and HIRSCH, P. B., 1957 a, *Phil. Mag.*, **2,** 1121; 1957 b, *Ibid.*, **2,** 1303.
YOSHIOKA, H., 1957, *J. phys. Soc. Japan*, **12,** 628.
ZACHARIASEN, W. H., 1945, *Theory of X-ray Diffraction in Crystals* (New York: Wiley & Sons), p. 135.

REVIEWS OF BOOKS

Heat and Thermodynamics. Fifth edition. By J. K. Roberts, revised by A. R. Miller. (Blackie, 1960.) [Pp. 619.] Price £2 5*s*.

The fifth edition of this well-known text-book consists essentially of the edition of 1950 together with some 25 pages of new material. The changes appear to be, for the most part, those necessitated by advances in technique or by changes in convention. For example, the section on magnetic cooling reports the successful outcome of the attempts at nuclear demagnetization, and the chapter on temperature mentions the new definition of the Thermodynamic Scale in terms of a single fixed point. J. A.

Hypersonic Flow. Edited by A. R. Collar and J. Tinkler. (Butterworths Scientific Publications, 1960.) [Pp. xv+432.] Price £3 10*s*.

This book is a record of the eleventh Colston Symposium, held at the University of Bristol in April 1959, which was devoted to Hypersonic Flow. Fifteen papers were presented, which are all reproduced here in full together with a report of the discussion after each paper. The scope of the papers range from surveys of the experimental work being carried out at various laboratories throughout the world to applied research on the design of hypersonic vehicles and the theoretical solution of particular flow problems. The book will be of great intesest to active workers in the field of hypersonic flow, but cannot be recommended to the reader who knows little about the subject and wishes to learn more.

The publishers are to be congratulated on the very attractive appearance of the book. P. G. S.

Non-Relativistic Quantum Mechanics. By R. M. Sillitto. (Edinburgh University Press, 1960.) [Pp. 230.] Price £1 15*s*.

Although there are numerous treatises on Quantum Theory, there is room for a modern teaching text for undergraduates. Here is a nice straightforward account of the standard theory, without frills but quite clear and explicit. Whilst the argument is mathematical rather than ‘ physical ’ nothing is laboured and there are no obvious omissions. It is going to be extremely useful, especially for good students who are not specializing in mathematical physics but who need to learn the key ideas from a modern standpoint. I only wonder whether the author will succeed in his attempt to put across pure matrix mechanics at an early stage before the reader has had much experience with the general properties of wave functions. The conceptual jump from energy levels and wave packets to states and operators is the most important and difficult thing to learn in the course and is, perhaps, best approached more gently. But the direct attack is certainly worth trying. J. M. Z.

Progress in Elementary Particle and Cosmic Ray Physics. Vol. V. Edited by J. G. Wilson and S. A. Wonthuysen. (Amsterdam : North-Holland Publishing Company, 1960.) [Pp. 461.] Price £4 5*s*.

The earlier volumes in this series were entitled *Progress in Cosmic Ray Physics.* With the great accelerators encroaching more and more on the high energy region, the editors felt that the title and the contents of the series should include elementary particle physics. Clearly this is a wise change.

The present volume consists of review articles on weak decays, nucleon–nucleon scattering, anti-nucleons, cosmic ray jets, the absorption of negative muons. Of these perhaps the most stimulating is the article on jets by D. H. Perkins, in which the puzzle of the high degree of elasticity in very high-energy collisions is emphasized. J. H.

Theory of Elementary Particles. By P. ROMAN. (Amsterdam : North-Holland Publishing Company, 1960.) [Pp. xii + 575.] Price £5.

THE main part of this volume consists of a very careful and very detailed discussion of those groups which are used for classifying the elementary particles and for examining the selection rules that govern their interactions. The representations of the four-dimensional orthogonal group and its sub-groups are considered in detail, and applied to spin and rotation, the Lorentz invariance of generalized field equations, and the various theories of isobaric space. The discrete operations, space inversion, time reversal and charge conjugation are also examined and there is a clear discussion of parity violation.

The mathematical apparatus which is set up is perhaps somewhat more elaborate than is necessary for the job it does, and in places the notation is too generalized and too cumbersome. Nevertheless this must be a valuable book for anyone who wishes to know what are the mathematical foundations of the symmetry principles of elementary particle physics. J. H.

Electrons and Phonons. By J. M. ZIMAN. (Oxford : The Clarendon Press, 1960.) [Pp. 554.] Price £4 4*s*.

THIS book is excellent. The author sets out to describe the bulk of the electron and phonon theory of solids with emphasis on transport phenomena. While presupposing only an elementary knowledge of wave mechanics, he succeeds beyond all expectations and, indeed, it is impossible to think of a single criticism which can be made of content or of presentation. The author's style is so lively that the reader's attention is always captured even throughout the more sophisticated sections of the book and important principles are clearly distinguished from subsidiary points in a way usually possible only in lectures.

The subject matter is logically organized and the index so good that it is easy to find the discussion of any particular problem. As a result the book will be just as valuable to the established research worker as it is to the graduate student. It is quite obviously one of those few books which we always want close to hand and despite its high cost must be regarded as indispensable to any worker or student in this field W. M.

Introduction to Statistical Thermodynamics. By T. L. HILL. (Reading, Mass. : Addison-Wesley Publishing Company, 1960.) [Pp. xiv + 508.] Price £3 14*s*.

THIS volume is intended—as its title implies—as an introductory text-book on equilibrium statistical mechanics, and as such is aimed at the same public as Rushbrooke's text-book. It is mainly meant to be used for courses for chemists—in Great Britian it would serve admirably for a final Honours Year course. The coverage of topics is very broad and gives a good idea of modern—that is, post-war—developments in statistical thermodynamics. After a short introduction on the principles of statistical mechanics (although this is called ' quantum ' statistical mechanics, quantum mechanics only is invoked in assuming quantization of energy ; the typical quantum mechanical aspects of the Fermi–Dirac and Bose–Einstein's statistics are only very briefly discussed in the very last chapter) the main part of the book is concerned with applications. These range from perfect monatomic, diatomic, and polyatomic gases to the theory of polymer and polyelectrolytic solutions and gels. A large number of exercises of a broad range of difficulty make this book even more useful, and this reviewer expects that it will be widely used by physical chemists.

D. ter Haar.

Optics of Thin Films. By Antonin Vašiček. (North-Holland Publishing Company, 1960.) [Pp. xii+403.] Price £4.

The applied optics of thin films has become an important subject in the past twenty years but there is still no good general text on it. Professor Vašiček's book is an interesting essay which recalls its author's striking personality but it is too uneven and sketchy to be useful as a text-book. It deals with Fresnel's formulae, reflection and transmission by one, two and many films, metallic films and polarization effects. The treatment is almost entirely theoretical ; there is nothing about methods of producing thin films, a very little about measuring their properties and some mention of applications.

The author points out in the preface that the book reflects his own interests and this is certainly clear from the lists of references alone. This bias results in unnecessary detail on some topics, e.g. it is hardly necessary nowadays to devote about 100 pages to deriving and discussing special formulae for one and two films when these follow immediately from the general formulae for *n* films. On the other hand, many important properties of periodic multilayers are omitted ; if the author had applied the Brillouin zone theory here he would not have made the following misleading statement (p. 238) : " Although the greatest reflectivity increases further with increasing number of films, the spectral region of this high reflectivity narrows somewhat ". It does not. Results are frequently obtained for multilayers and also for single absorbing films by considering multiple reflections and there is much discussion about the validity of this and other methods. It seems to the reviewer that provided the elementary but tedious mathematics is correctly carried out, all such phenomenological approaches must lead to the same results since they are all based ultimately on Maxwell's equations.

To sum up, those familiar with the subject of thin film optics will enjoy reading this book but it cannot rank either as a reference work, since it covers too little ground, or as a research monograph, since it is too laboured on elementary points.

W. T. W.

Foundations of Electromagnetic Theory. By John R. Reitz and Frederick J. Milford. (Addison-Wesley, 1960.) [Pp. 387.] Price £2 9*s*.

Principles of Electricity and Magnetism. By E. M. Pugh and E. W. Pugh. (Addison-Wesley, 1960.) Price £2 9*s*.

Foundations of Electromagnetic Theory is a text written for a course on electricity and magnetism for physicists, advertised as " at advanced undergraduate level ", though it does not quite cover all that might be expected in Cambridge of a final year student. It starts with electrostatics at a level including the use of Poisson's equation and the uniqueness theorem, and covers the usual range through Maxwell's equations up to the radiation from a dipole aerial and from an accelerating point charge. Two chapters on the microscopic theory of dielectrics and magnetism are included, as well as an interesting chapter on the behaviour of plasmas. However, there are also a few gaps, with no mention for example of noise, valves, the impulse response of a two-terminal system, or the formulation of magnetostatic energy in the presence of permanent magnets. The Drude formula for the conductivity of a metal contains the usual incorrect factor of $\frac{1}{2}$.

On the whole the style is extremely clear, and the book can be warmly recommended as a good text for third year students. There are also many examples, the typography is pleasing, and the diagrams are up to the usual superlative Addison-Wesley standard. It seems hardly necessary to remark these days that rationalized M.K.S. units are used.

The second book *Principles of Electricity and Magnetism* covers almost exactly the same ground but at a somewhat lower standard, particularly in the use of mathematics. The style is rather ponderous. V. H. O.

Selected Lectures in Modern Physics. Edited by H. Messel. (Macmillan, 1960.) Price 30*s*.

In January 1958 the Nuclear Research Foundation arranged a series of lectures on selected topics in physics, in the University of Sydney. The objective was a refresher course for science teachers which would stimulate interest and, eventually, encourage students to read Science or Engineering at Universities. This book is a reprint of the lectures, and it is interesting to note that a copy was issued, free, to every science teacher in the State of New South Wales.

There are 22 lectures in the book, given by 18 people and, as might be expected, the emphasis is strongly placed upon nuclear physics. The first nine lectures deal with various aspects of this subject—if we include cosmic radiation under the same general heading. There are three lectures related to astrophysics, two on relativity, and the remainder on a variety of topics. In an effort of this kind, the choice of subject matter is to some extent dictated by the interests of the lecturers available, and to some extent also by the possibility of adding a little glamour to an elementary exposition. The former factor doubtless accounts for the inclusion of a most interesting chapter on " Physics in Rainmaking " and the latter for the fact that there is no mention of solid state physics apart from one lecture on " Transistor Electronics ". In the same way, it is understandable that many of the passing references to particular pieces of research are to Australian work.

The style and standard of the individual lectures varies considerably. There is the frankly chatty and conversational style of " How to talk to an Electronic Brain " and the rather thorough and formal exposition of " Precise Measurement ". This last, although a fascinating subject is a little unexpected, in a book on " Modern Physics ", as indeed is the lecture on " The Concept of Temperature ". Some of the lectures are well written and easy to read, others are more difficult, either because of the inherent difficulty of the subject—e.g. " Strange Particles" —or because of defects of presentation. The second lecture on Nuclear Energy, dealing with reactor technology is little more than a set of lecture notes and contains the correct, but unhelpful, paragraph : " Example of gases H_2, He, CO_2, N_2, Air, A."

It would perhaps be unfair to criticize the book for a lack of balance either in subject matter or in treatment. It could form a useful addition to sixth form and University libraries, where harassed students writing essays would welcome it, and find the short reading lists appended to many of the lectures very helpful. N. T. O.

Solid State Physics. Vol. 10. Edited by F. Seitz and D. Turnball. (New York : Academic Press, 1960.) [Pp. 516.] Price $14.50.

The mixture as before—Positron Annihilation (Wallace) ; Diffusion in Metals (Lazarus) ; Wave Functions for Electron-Excess Color Centres in Alkali Halide Crystals (Gourary and Adrian) ; Continuum Theory of Stationary Dislocations (de Wit) ; Theoretical Aspects of Superconductivity (the late

Professor M. R. Schatroth). I still think that it is a mistake to ask every well known scholar in the field to write a review of his subject, instead of commissioning longer, broader, more integrated articles and books from carefully selected people. But the series continues to be useful for reference.
J. M. Z.

Introduction to Solids. By L. V. Azaroff. (McGraw-Hill, 1960.) [Pp. 460.] Price £3 14*s*.

An amusing consequence of progress in science is that it keeps making nonsense of the inter-disciplinary frontiers so firmly defended by the academic pundits. This book correctly claims to be " suitable for students of chemistry, ceramics, metallurgy, mineralogy, physics and all engineering fields dealing with solid state ". All that it does is to collect together all the physical properties of solids, and indicate their explanation. It is not a very advanced book ; there is really no mathematics, and some of the more complicated topics are blocked in rather sketchily. But the author's instinct to explain things in terms of 3-dimensional geometry is essentially sound. Solids, like works of architects, are *structures*, and this is more directly relevant, for most scientific purposes, than that they are also minimum free energy states of ensembles of solutions of the quantum-mechanical many-body problem. Here is a lively, well-written, elementary text book for ordinary undergraduates. It is what we have been needing for a long time.
J. M. Z.

Advances in Cryogenic Engineering. Vol. 5. Edited by K. D. Timmerhaus. (New York : Plenum Press Inc., 1960.) [Pp. 582.] Price $13.50.

This volume contains the papers delivered at the Conference on Cryogenic Engineering held at the University of California on September 2–4, 1959.

The primary emphasis at this conference was on the use of cryogenic liquids as fuels for missiles and the majority of the papers dealt with problems arising from this application. There can be no doubt that the book is essential reading for all engineers working in this field. Many of the papers will also be of interest to a wider public, especially the series of articles on thermal insulation and the experimental studies of the burning and explosion of hydrogen.
J. A.

Physics of the Atom. By M. Russell Wehr and James A. Richards. (Reading, Mass.: Addison-Wesley; and London, 1960.) [Pp. xi+420.] Price £2 9*s*.

Modern physics, interpreted as the contribution of the twentieth century to the subject, is gradually working its way further and further back in university and now even in school courses. Some day, perhaps, we shall have a satisfactory treatment which combines the classical approach with the modern, the older knowledge being entirely re-seen in the light of the new. Until that happens, we have an increasing number of tests from which to choose in shaping an introductory course in atomic and nuclear physics to follow the traditional grounding in heat, light, sound, electricity and magnetism. For reasons which it would be interesting to analyse, they mostly come from authors in the United States and very few from the United Kingdom. The latest addition to the ranks is also American, and it is perhaps best to compare it with its stable-mates.

Wehr and Richards have set out to write a sequel to the well-established *University Physics* of Sears-Zemansky. Twelve chapters take the student from the atomic view of matter, electricity and radiation, through relativity, x-rays and the wave-particle concept to the solid state, with nuclear physics occupying the last four chapters. The treatment is largely chronological and in this respect, as in the informal, almost colloquial style, the book is akin to Oldenberg's *Introduction to Atomic Physics*. It is distinctly more advanced, however, in that it has " not hesitated to use calculus where it is appropriate ". The amount of mathematical development is very limited, nevertheless, except in the chapter on relativity. It is thus much less suited to a university introductory course as usually understood in this country than is French's *Principles of Modern Physics*, for example. It should be much more useful to sixth forms, as a chatty and more or less painless survey for the would-be physicist of the territory he must later explore in greater detail. It should also fit well into a broad course in physical science for chemists, engineers or others who want only a nodding acquaintance with the ideas of modern physics, without a detailed mastery of its techniques. If they work through a good selection of problems at the end of each chapter, they could pick up quite a lot of these also, if they would. The text is very well set-out, the diagrams are excellent, and plenty of references are given for further reading. One can well imagine a youngster's imagination being fired on coming upon such a readable and intelligently presented account of what physics now means, after all the drudgery of the old school mill. But at the same time someone ought to warn him that it is not always so easy as it is made to sound in these pages.

V. E. G.

BOOK NOTICES

Formation and Trapping of Free Radicals. Edited by A. M. Bass and H. P. Broida. (New York and London: Academic Press, 1960.) [Pp. 522.] $16.00.

The Other Side of the Moon. Issued by the U.S.S.R. Academy of Sciences. Translated from the Russian by J. B. Sykes. (Pergamon Press, 1960.) [Pp. 36.] 10*s*. 6*d*.

Sector-focused Cyclotrons. Proceedings of an Informal Conference, Sea Island, Georgia, February 2–4, 1959. Nuclear Science Series Report, No. 26. (Washington, D.C.: National Academy of Sciences, 1959.) [Pp. 291.] $2.50.

Cosmology. By H. Bondi. Second Edition. (Cambridge: University Press, 1960.) [Pp. 182.] Price 30*s*.
This is a second edition of a well-known work.

Über neue Rechnungsgrundlagen der Atom- und Strahlungsphysik. By Karl Nowak. (Wien: Verlag Neue Physik, 1959.) [Pp. 78.] Price D.M. 7.50, 2*s*. 6*d*.

Dynamics of Climate. The Proceedings of a Conference on the Application of Numerical Integration Techniques to the Problem of the General Circulation, held October 26–28, 1955. Edited by R. L. Pfeffer. (Pergamon Press, 1960.) [Pp. 137.] Price £1 15*s*.

[*The Editors do not hold themselves responsible for the views expressed by their correspondents.*]

Fig. 2

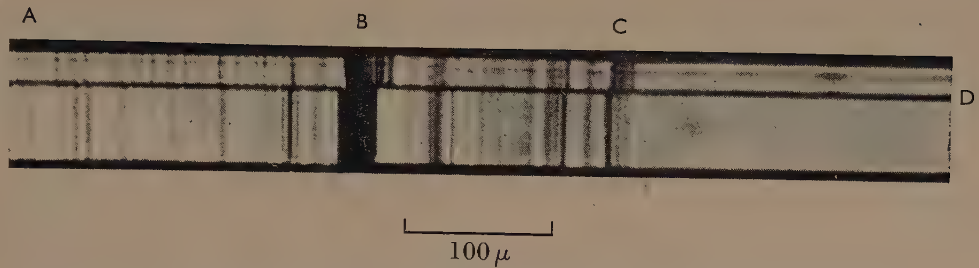

Optical micrograph of a platelet which fractured at B after deformation by pyramidal glide. Note the Lüders band, AC.

Fig. 3

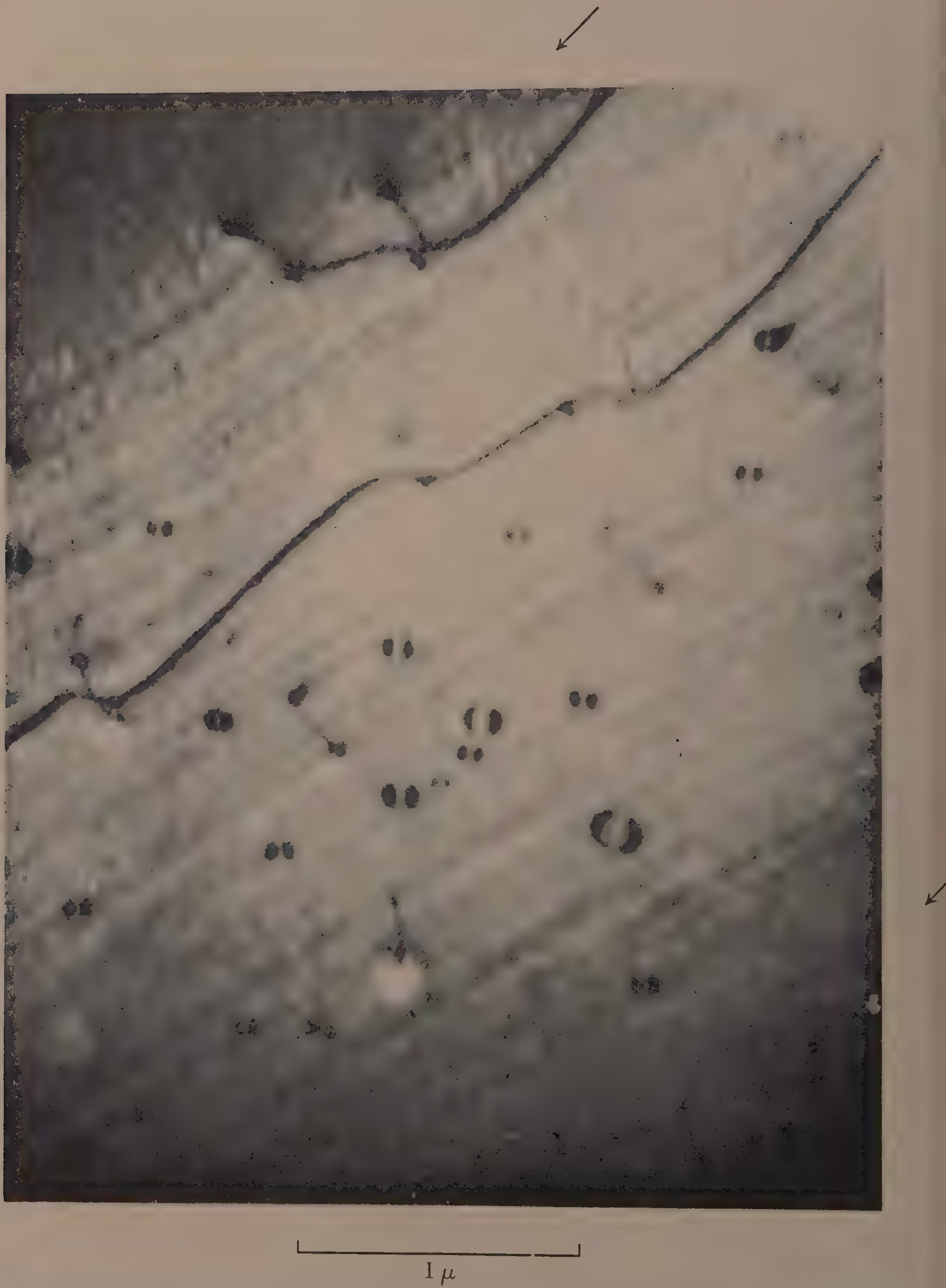

Electron micrograph showing pyramidal glide traces, $\langle\bar{1}\bar{1}20\rangle$ dislocations, $\langle\bar{1}\bar{1}23\rangle$ dislocations, and prismatic dislocation loops.

Fig. 4

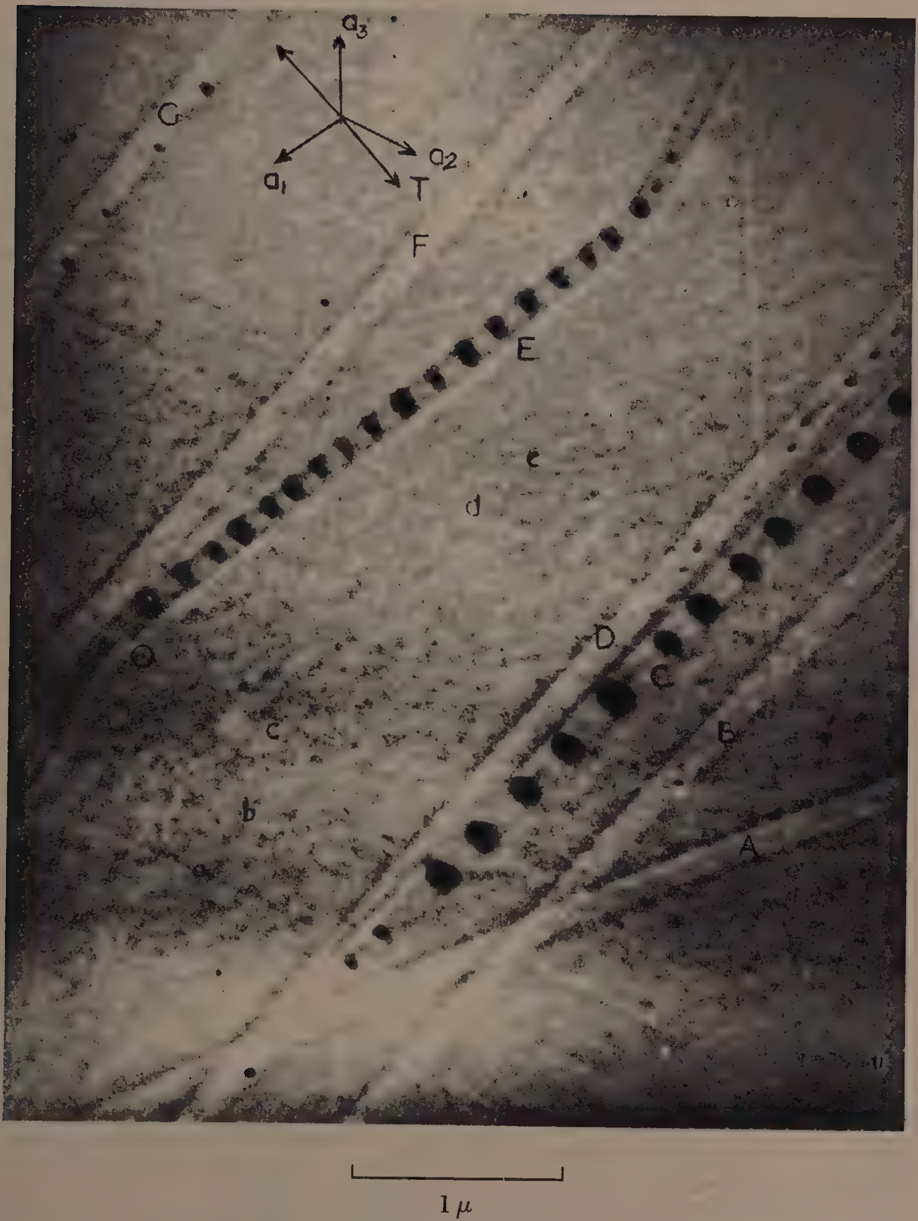

Electron micrograph showing $\langle \bar{1}120 \rangle$ traces at *a*, *b*, *c*, *d*, *e*, pyramidal traces at A, B, C, D, E, F, G, and loops along traces B, C, D, E and G. The dislocation which produced trace E has cross glided at O, acquiring a multiple jog and forming a row of loops.

Fig. 6

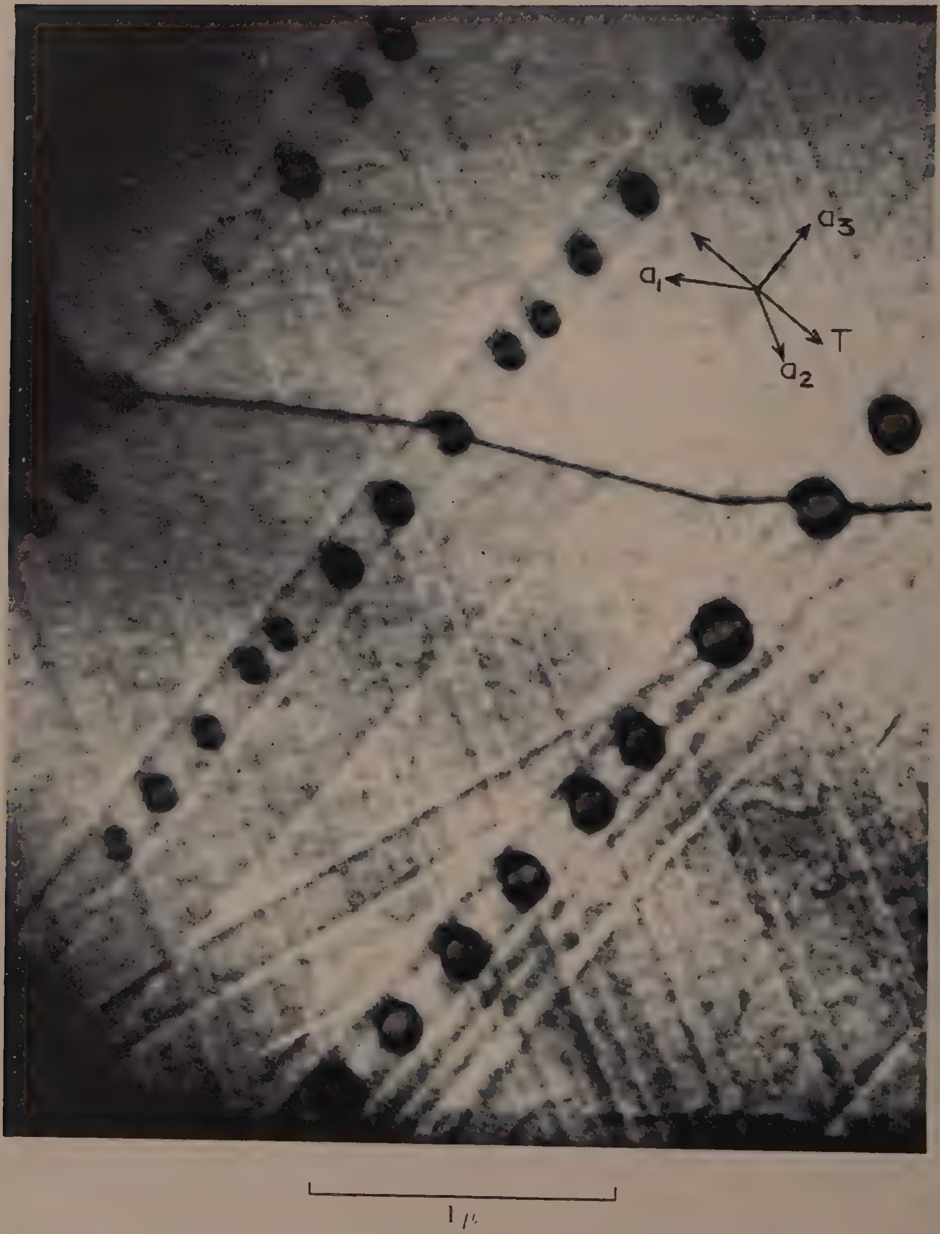

Loops along pyramidal traces. A $\langle\bar{1}\bar{1}20\rangle$ dislocation is pinned at three loops.

Fig. 7

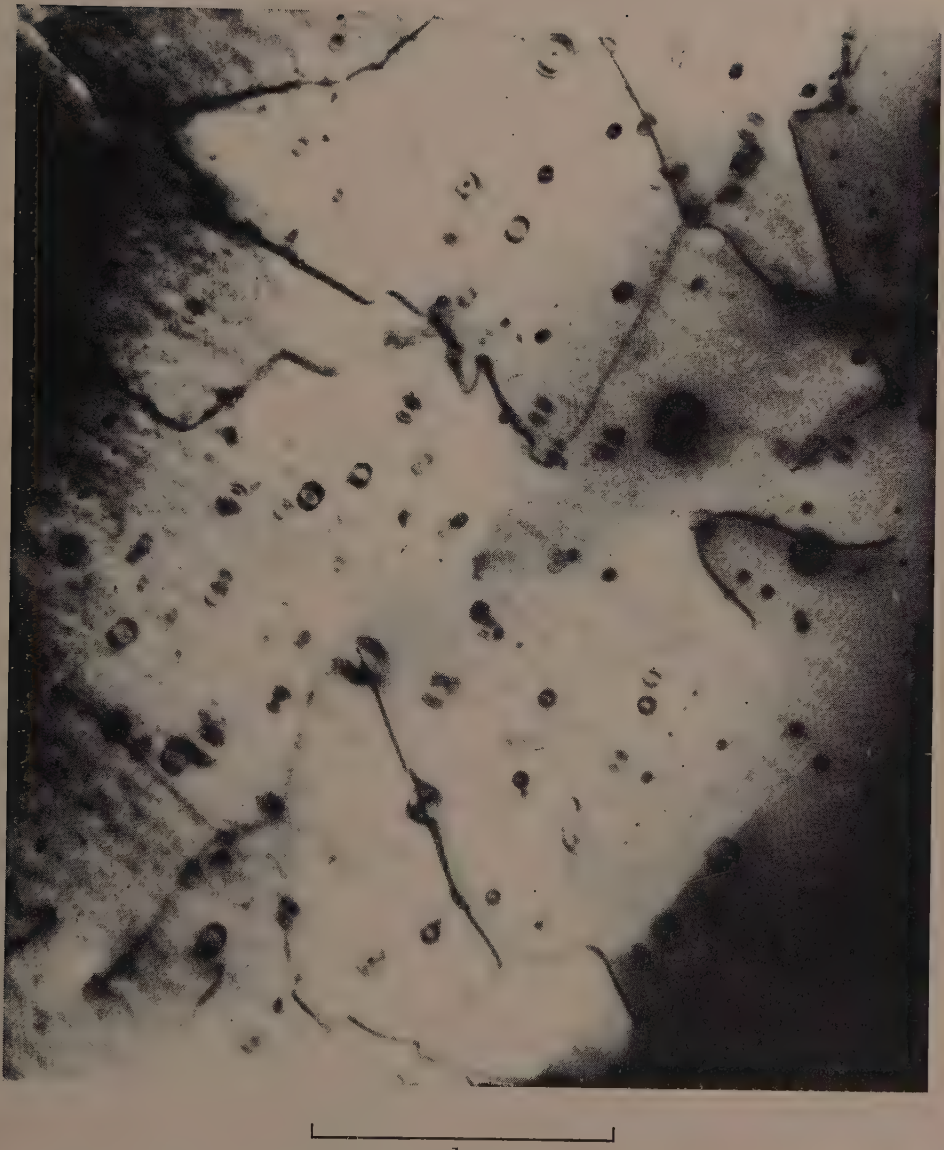

Heavily deformed region showing $\langle\bar{1}\bar{1}20\rangle$ dislocations pinned at loops.

Fig. 9

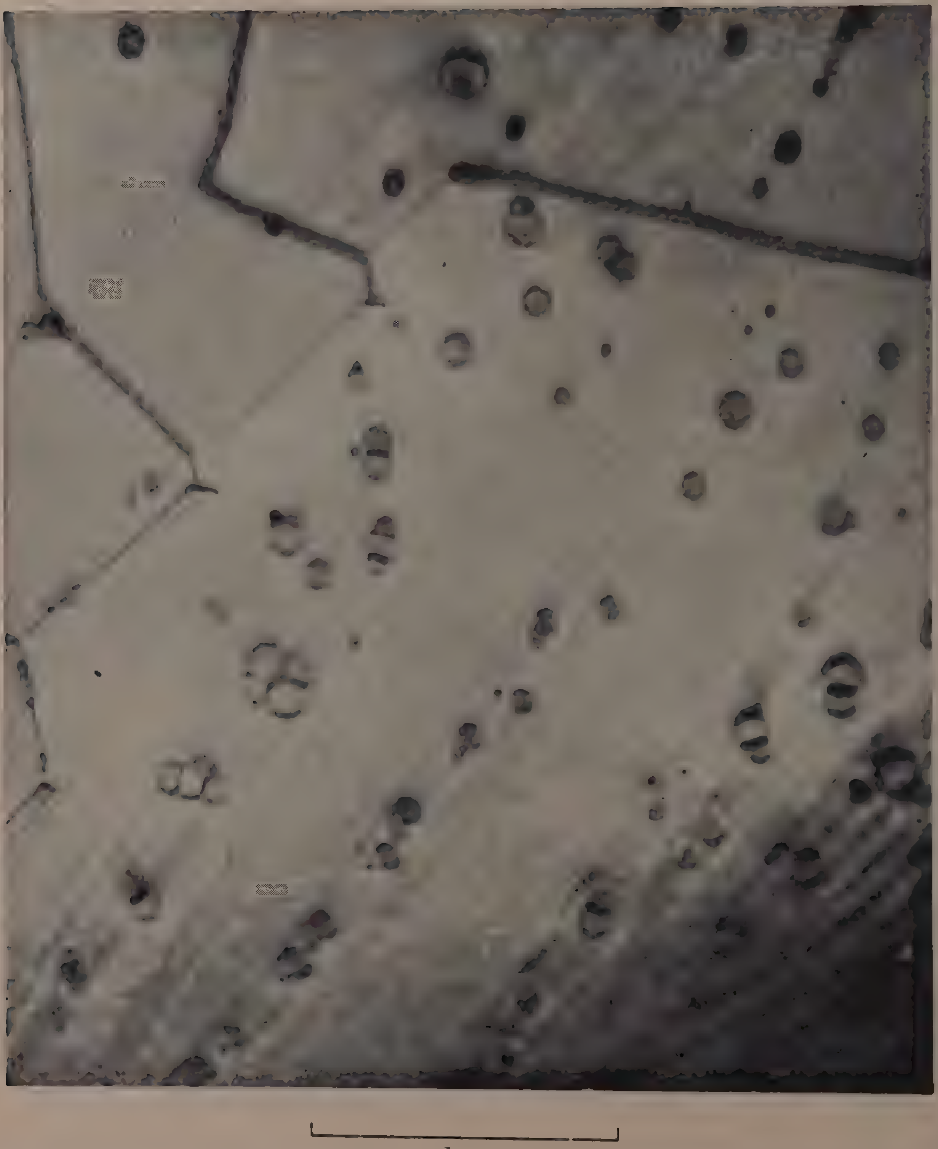

Clusters of loops along overlapping glide traces.

Fig. 10

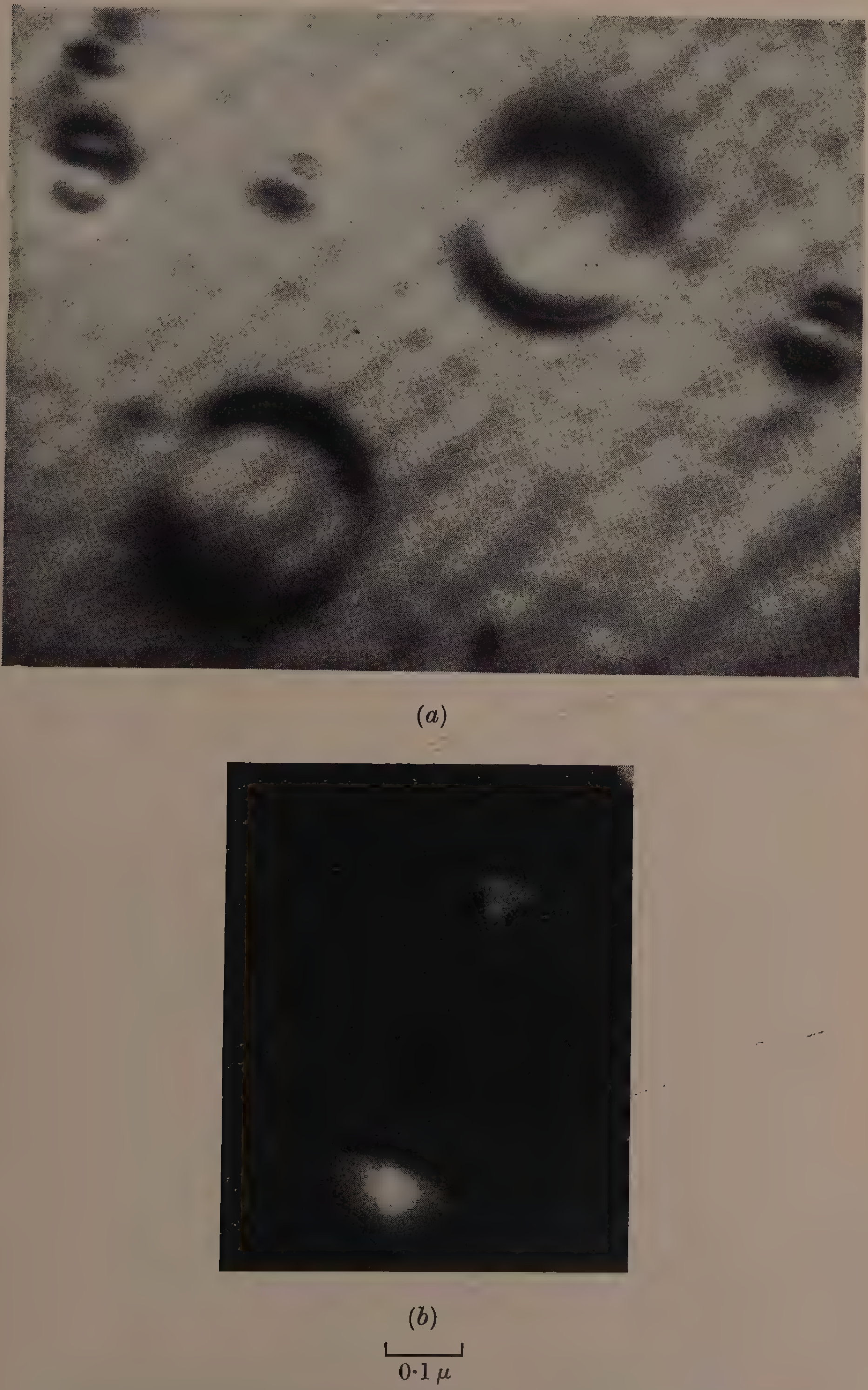

(a) ⟨0001⟩ loops with vanishing contrast along a direction parallel to strongly reflecting (11$\bar{2}$0) planes.

(b) Diffraction pattern for (a), showing the 11$\bar{2}$0 spot.

Fig. 10 (*continued*)

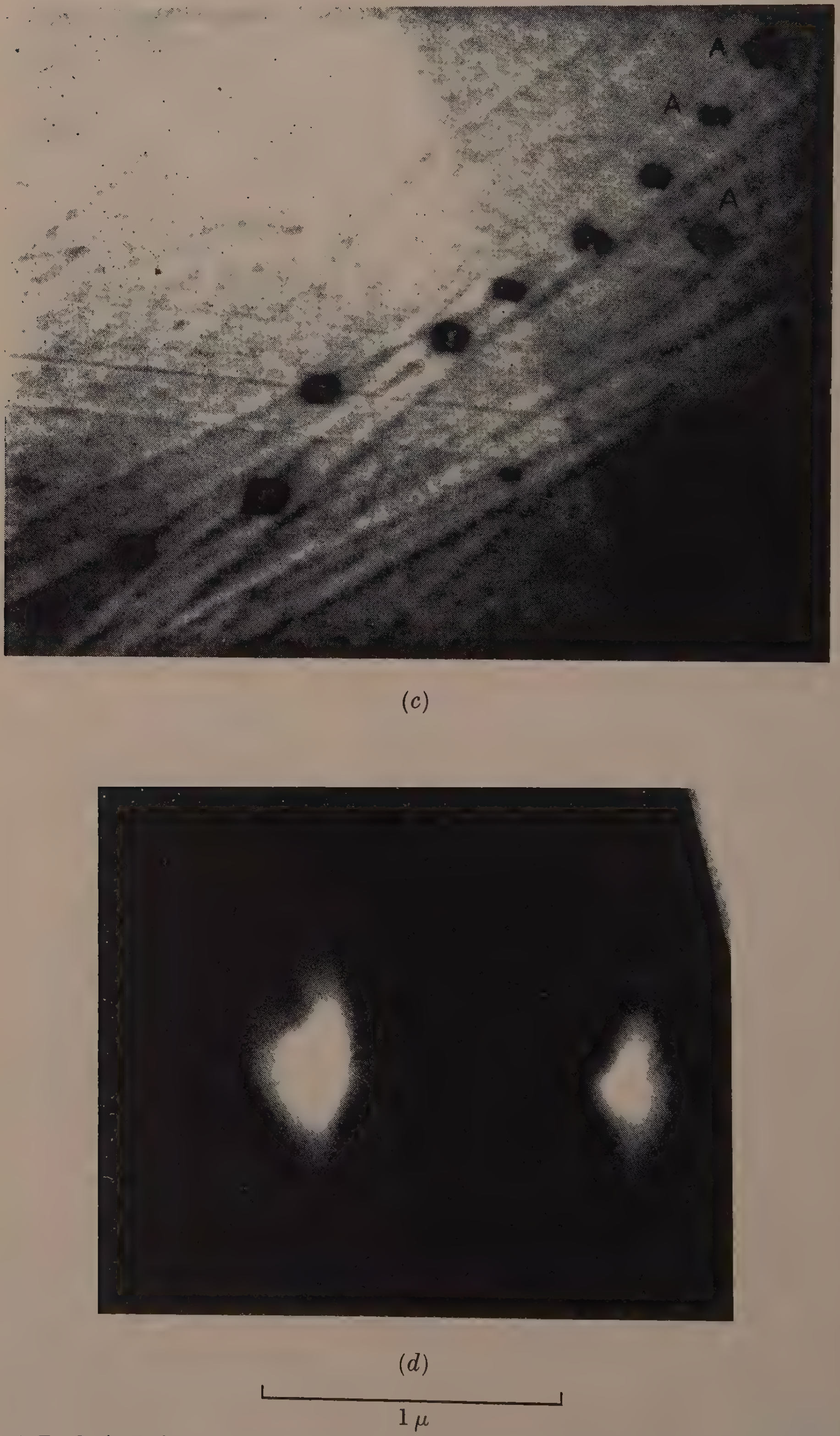

(*c*) Both ⟨0001⟩ loops (at A) and ⟨$\bar{1}\bar{1}23$⟩ loops formed by the same dislocation mechanism.

(*d*) Diffraction pattern of (*c*).

Fig. 11

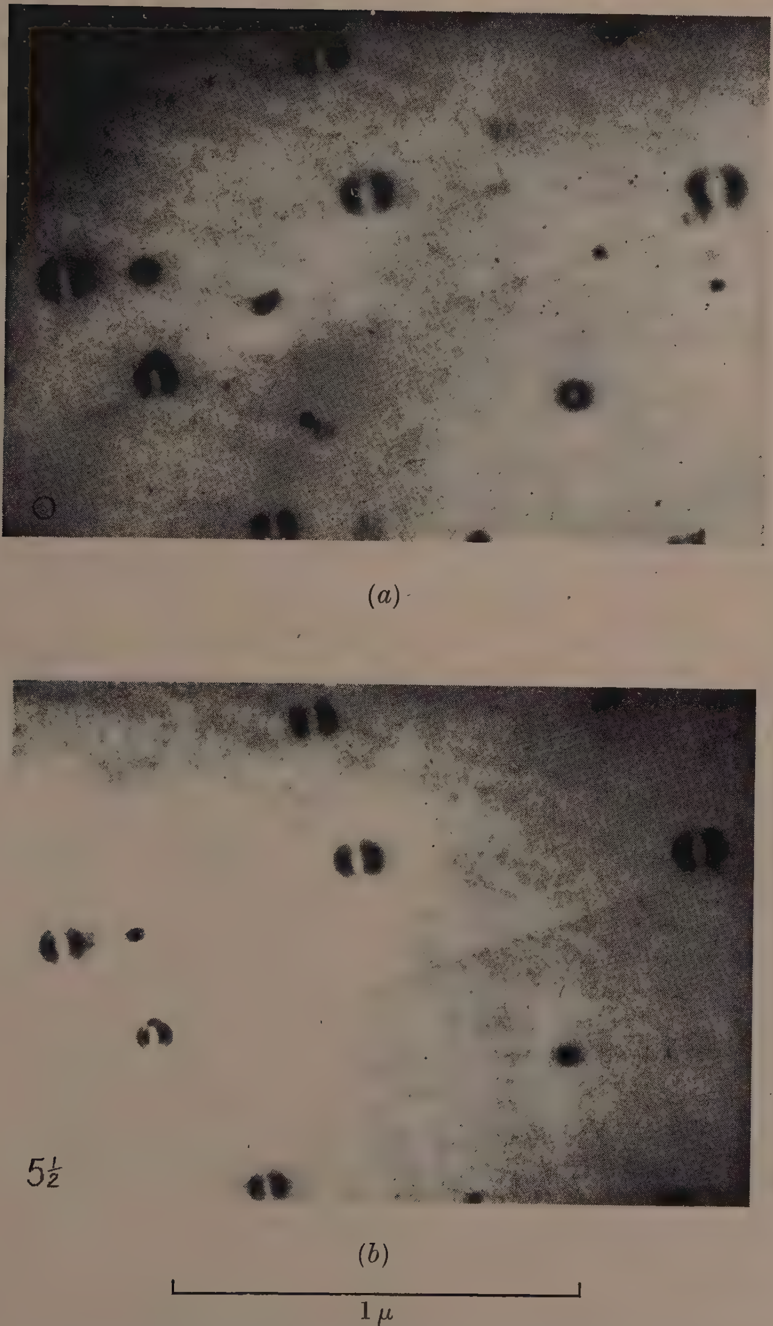

Sequence showing the annealing of loops at room temperature. The numbers refer to the time in minutes at which exposures were made.

Fig. 11 (*continued*)

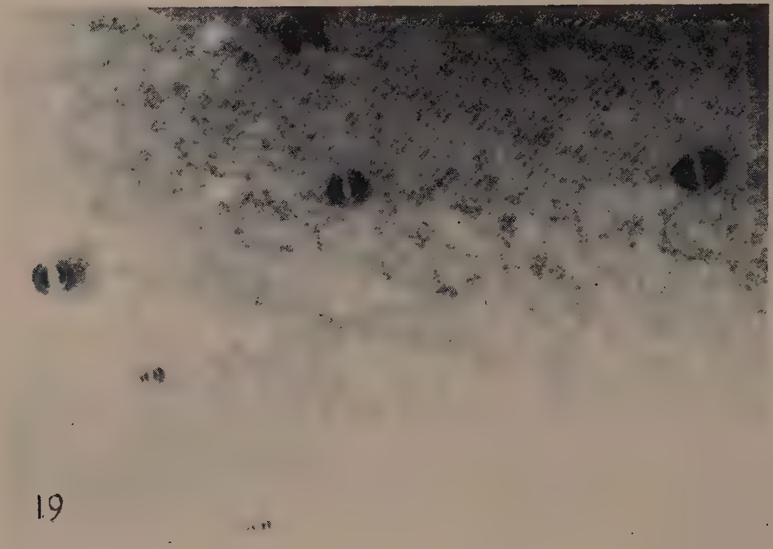

(*c*)

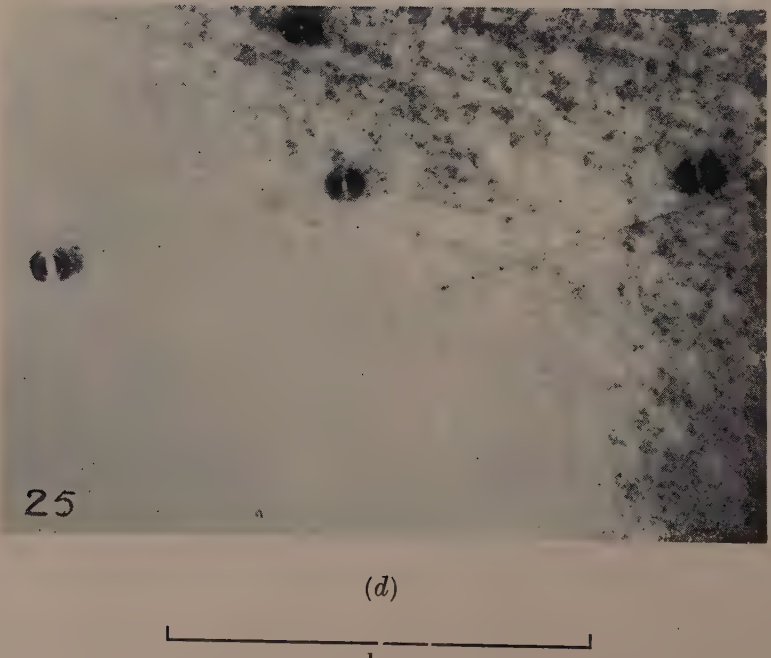

(*d*)

Fig. 11 (*continued*)

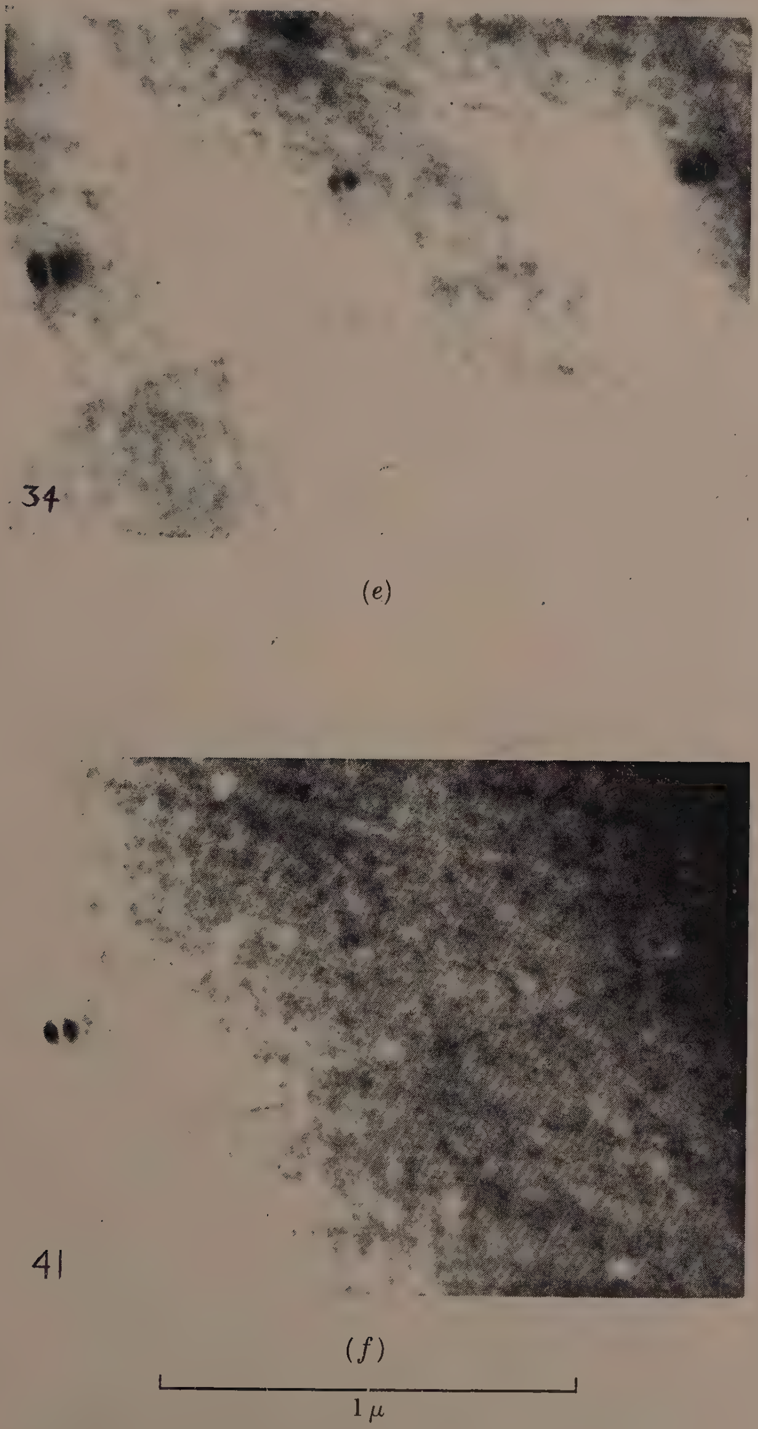

(*e*)

(*f*)

Fig. 1

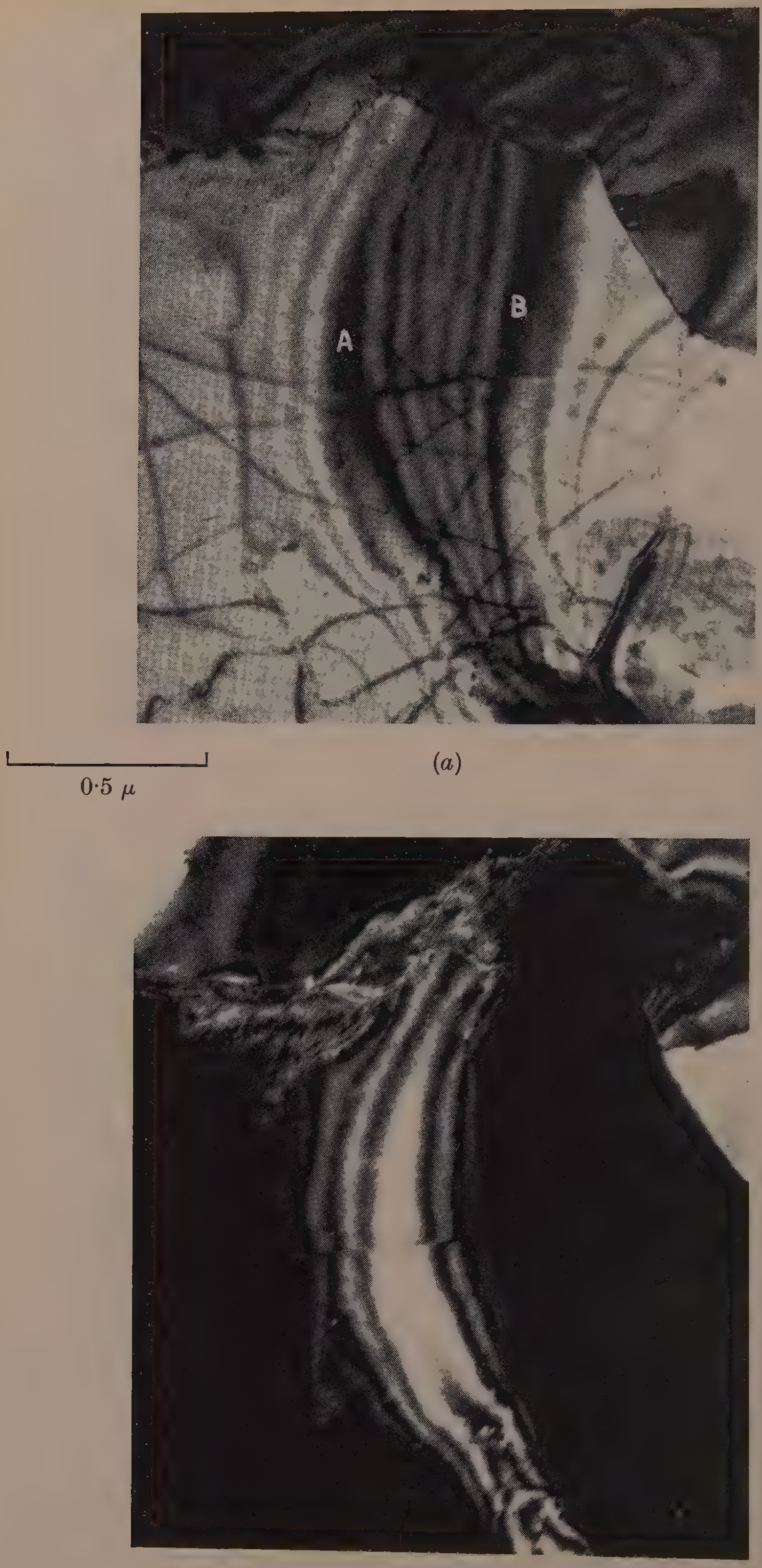

(*a*)

(*b*)

(*a*) Bright field micrograph of a bend extinction contour in aluminium foil. The contour is produced by the 111 reflection (A) and the $\overline{1}\overline{1}\overline{1}$ reflection (B). Note the difference between the intensities transmitted inside and outside the contour. Mag. × 53 000. (*b*) Dark field image of the same region in the 111 reflection.

Fig. 2

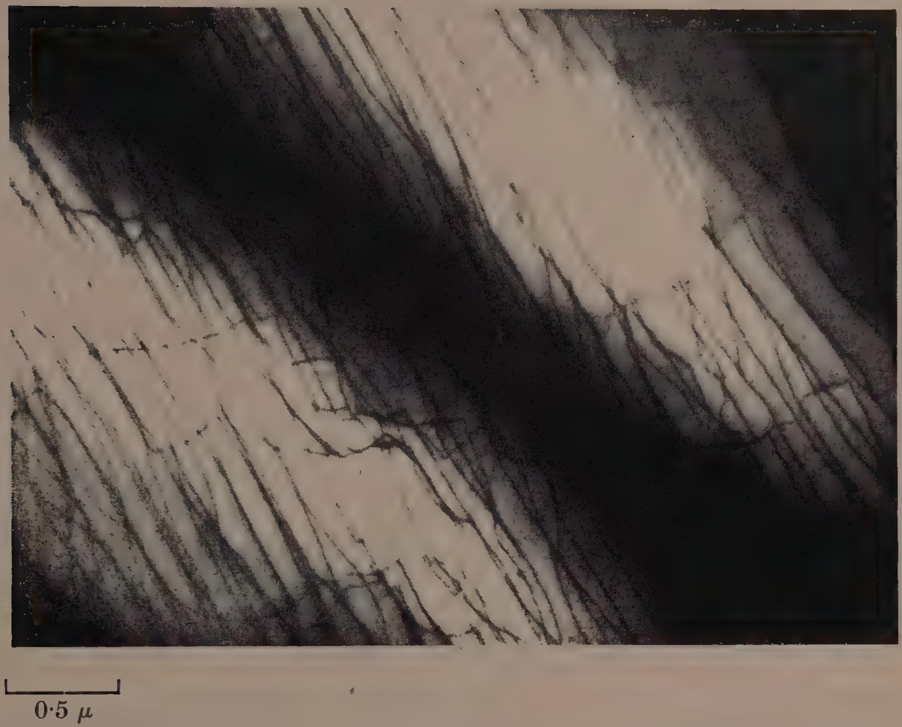

Bright field micrograph of a bend extinction contour in a thick region of copper foil (exact thickness not known). The transparent regions correspond to strong 111 and $\bar{1}\bar{1}\bar{1}$ reflections respectively. Note the absence of subsidiary maxima and minima as in fig. 1 (*a*). Mag. ×30 000.

Fig. 7

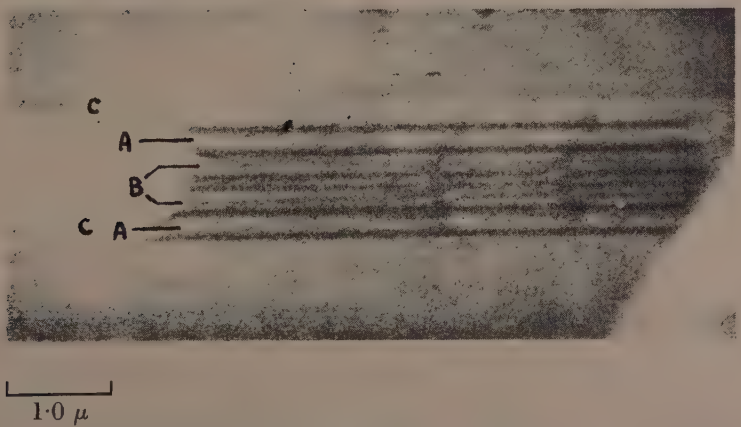

Bright field micrograph of a stacking fault in stainless steel. Note the subsidiary dark fringes B and the absence of similar fringes at A. Compare with fig. 5 (*a*). C – C is a slip trace produced by a moving dislocation and should not be confused with the fault contrast. Mag. ×130 000.

Fig. 8

Bright field micrograph of a stacking fault in stainless steel showing fringes similar to the type predicted in fig. 6 (*a*). Note the decrease in visibility of the fringes near the centre of the fault. Mag. × 130 000.

The Effects of Surface Condition on the Mechanical Properties of Lithium Fluoride Crystals†

By A. R. C. WESTWOOD
RIAS, 7212 Bellona Avenue, Baltimore 12, Maryland, U.S.A.

[Received May 23, 1960]

ABSTRACT

A comparative study has been made of the mechanical behaviour of as-cleaved, chemically polished and coated lithium fluoride crystals. Surface coatings were produced by vacuum deposition and by chemical reaction. Thin ($\not> 10\,\mu$) reacted-coatings increased the yield stress some 50% and were responsible for catastrophic stress drops observed at the critical resolved shear stress. Coatings also decreased the initial rate of work-hardening and the stress and strain to fracture. Failure occurred by the formation of Stroh-type cracks.

An explanation for these and other results is offered based on considerations of the distribution and number of operable dislocation sources, and the piling up of dislocations at intersecting slip bands and beneath surface films. Metallographic evidence is presented for the latter phenomena. Experimental observations are more consistent with a barrier-mechanism of work-hardening than with a defect-mechanism.

§ 1. INTRODUCTION

Two concepts have proved useful in understanding some of the effects of surface films on the mechanical properties of metallic crystals. The first, due to Fisher (1952), is that a dislocation line emerging unpinned at the surface, but being pinned at some interior point, can serve as a source. Such sources are formed during crystal growth and should be activated at about half the stress required to activate interior sources of similar length. It follows that Fisher-type 'surface-sources' would be responsible for the initial stages of plastic deformation. However, a surface film might be expected to restrict or prevent the operation of these surface-sources, thus causing the increased yield stresses observed with coated metal crystals (Roscoe 1936, Adams and Cottrell 1958, and many other workers). Secondly, a surface film might prevent the egress of dislocations from a crystal so that they become piled-up beneath the film (Menter and Hall 1950, Phillips and Thompson 1950). Barrett's (1953) abnormal after-effect phenomenon can be explained in this way.

The objective of the present investigation was to obtain a better understanding of the effects of surface films on the mechanical properties of ionic crystals and to examine the validity of the above concepts for such crystals. For these studies, lithium fluoride was chosen in preference to other ionic crystals in order to take advantage of the dislocation-revealing techniques developed by Gilman and Johnston (1957).

---

† Communicated by the Author.

Gilman *et al.* (1958) have demonstrated that a slowly moving cleavage crack (velocity $< 6 \times 10^{-3}$ cm/sec) can introduce many dislocation half-loops into the surface of lithium fluoride. These half-loops then serve as readily activatable sources during subsequent stressing. However, such artificially introduced surface sources, which must be distinguished from Fisher-type surface sources, can be completely removed by a short chemical polish.

To clarify the role played by these and other sources and by surface films in the yielding and work-hardening processes, comparative tests were performed on as-cleaved and chemically polished crystals in the coated and uncoated condition. In addition, some experiments aimed at providing direct evidence for the piling up of dislocations beneath a surface film were undertaken.

§ 2. Experimental Techniques

Lithium fluoride crystals were obtained from the Harshaw Chemical Company and compression specimens, approximately 12 mm–18 mm × 5 mm–6 mm square, were cleaved from these crystals. After the appropriate surface preparation, specimens were compressed in an Instron testing machine at strain rates of order 10^{-4} per sec.

For any particular test series, all specimens were cleaved from the same area of given crystal, were subjected to identical heat treatments and were subsequently handled with great care to prevent accidental surface damage. In this way, reasonable reproducibility of results was obtained ($\sim \pm 8\%$). Values of the yield stress, the critical resolved shear stress and the stress and strain to fracture were determined from the Instron recorder chart. The yield stress was taken as the stress at which stress–strain curves first deviated from linearity, and the critical resolved shear stress as the stress at which a large increase in strain occurred at almost constant stress. These two stresses are readily distinguished in the compressive stress–strain curves of lithium fluoride crystals.

Experiments were performed using specimens with a vacuum-deposited coating ($\ngtr 5\,\mu$) of chromium or with a reacted-coating produced in the following way. Freshly cleaved or chemically polished crystals were gently placed in intimate contact with pure magnesium oxide powder. They were then slowly heated to 600°–700°c and held there for 1–3 hours. At these temperatures a chemical reaction producing MgF_2 and Li_2O occurs (Ludellans and Welsh 1952) and a coherent and slightly interdiffused surface coating results†. The specimens were then furnace-cooled slowly to 300°c and finally air quenched to room temperature to avoid possible strain-ageing phenomena. Other specimens, not in contact with magnesium oxide, were given identical heat treatments for comparative tests.

---

† The reacted-coating is believed to be an alloy layer, 5–50 μ thick, of magnesium in lithium fluoride. Magnesium fluoride is soluble in lithium fluoride (~ 6 mol. % max.) at temperatures above 400°c (Haven 1950) and can be precipitated out at lower temperatures. Elastic distortion in the lattice due to differences in ionic radii is negligible since Mg^{++} and Li^{+} are similar in size—0·78 Å radius. However, to preserve electrical neutrality, each magnesium ion is expected to be associated with a cation vacancy bound to it by the coulomb forces between them.

For metallographic studies, the crystal preparation, polishing and etching techniques described by Gilman and Johnston (1957) and Johnston and Gilman (1959) were used.

§ 3. EXPERIMENTAL OBSERVATIONS

A thin film of chromium on as-grown, as-cleaved lithium fluoride crystals increased the yield stress some 12%, but no increase in critical resolved shear stress was observed and the subsequent work-hardening behaviour was not significantly affected. Examination of the chromium film after deformation revealed cracks which appeared to be associated with underlying bands of both edge and screw dislocations.

Reacted-coatings on as-cleaved specimens affected all stages of the deformation process. Table 1 displays the results of tests on specimens in the coated and uncoated conditions. The numerical values quoted are averages from tests on several specimens (3–6) in each condition and the figures in brackets are the percentage increase or decrease in value caused by the presence of the coating.

Table 1. The effect of reacted-coatings on the mechanical properties of as-cleaved lithium fluoride crystals. Change in property indicated in brackets

	Average yield stress in g/mm²	Average critical resolved shear stress in g/mm²	Average stress at fracture in g/mm²	Average glide strain at fracture in %
As-cleaved specimens from crystal block A	83	120	860	13·8
As above with thin ($\ngtr 10\,\mu$) reacted-coating	128 (+54%)	149 (+25%), stress-drops	450 (−45%)	10·5 (−24%)
As-cleaved specimen from crystal block B	138	156	950	15·9
As above with thick ($25\,\mu$–$50\,\mu$) reacted-coating	222 (+61%)	265 (+70%)	505 (−47%)	8·0 (−50%)

Thin coatings ($\ngtr 10\,\mu$) increased the yield stress by 50% and caused 'catastrophic' stress drops at the critical resolved shear stress. Thicker coatings ($\sim 25\,\mu$ and $\ngtr 50\,\mu$) increased both the yield and critical resolved shear stresses by 60–70% but stress drops were not observed. However, the stress and strain to fracture were reduced to 50% of that of uncoated specimens. Figures 1 and 2† illustrate typical stress–strain curves and demonstrate that coated specimens exhibited initially a lower rate of work-hardening than similar uncoated crystals.

---

† With the exception of figs. 1, 2 and 8, the figures are shown as plates.

In contrast, a reacted-coating on a specimen chemically polished before the reaction treatment had very little effect on its yield stress (an increase 3%) and caused only a small increase in the critical resolved shear stress (13%). Table 2 summarizes the results of these tests and, for comparison, the results of others performed with chemically polished, annealed out of contact with magnesium oxide, and finally repolished specimens.

Fig. 1

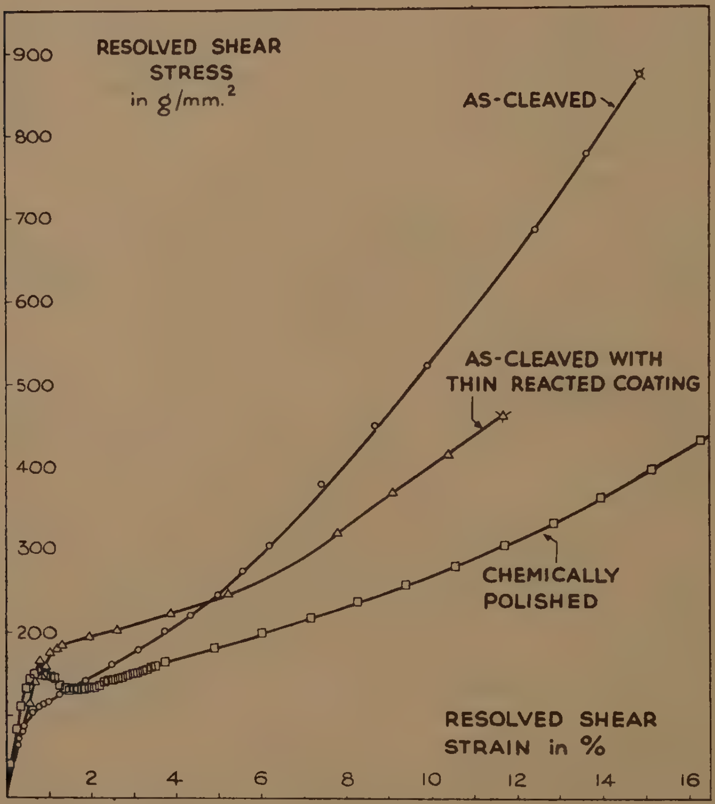

The effect of surface condition and thin reacted-coatings on the stress–strain curve of lithium fluoride crystals.

In all tests, failure was caused by nucleation of cracks (Stroh 1955) on (110) planes at slip band intersections—fig. 3. These cracks subsequently grew into slits and switched onto (100) cleavage planes in the manner described by Stokes *et al.* (1959) for magnesium oxide.

As an aid to understanding the above observations, metallographic studies were made on certain coated and deformed specimens. Evidence of dislocations piled up beneath the surface film and at other obstacles was found. Figure 4 shows edge dislocations piled up at a sub-boundary. It appears that such boundaries are not strong obstacles and usually cannot support more than 20–30 dislocations. The distribution of the dislocations in fig. 4 does not conform to the relationships derived by Eshelby *et al.* (1951), probably because the dislocations relaxed back towards their source—not in the micrograph—between the straining and etching processes. Alternatively, Hirsch *et al.* (1959) have shown that, in stainless steel, piled-up groups of dislocations can interact with others on an intersecting system to produce a network which can prevent the pile-up conforming to predicted relationships. In view of Johnston and Gilman's (1960) work on the form of dislocation loops in lithium fluoride, this alternative explanation is considered less likely.

Fig. 2

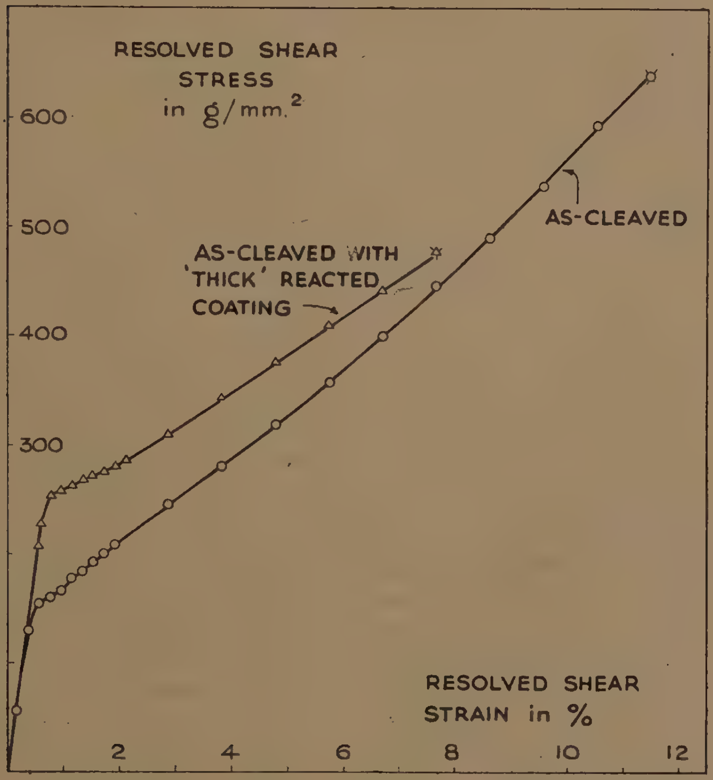

The effect of a thicker reacted-coating on the stress–strain curve of an as-cleaved lithium fluoride crystal.

Piled-up groups of screw dislocations are not common, but fig. 5 illustrates one example.

As in magnesium oxide, broad bands of edge dislocations act as barriers to edge dislocations on an intersecting slip system and are eventually responsible for the cracks which cause failure. Figure 6 shows a pile-up of edge dislocations that appear to have emanated from the half-loop source originally at A.

An example of a piled-up group of edge-dislocations beneath a reacted coating is given as fig. 7.

Table 2. The effect of 'reacted-coatings' on the yield behaviour of chemically polished lithium fluoride specimens from crystals block A

	Average yield stress. in g/mm^2	Average critical resolved shear stress in g/mm^2
Chemically polished specimens	121	127
Chemically polished and reacted specimens	125 (+3%)	143 (+13%)

§ 4. Discussion

4.1. *The Effect of Surface Films on Yielding Behaviour*

Grown-in dislocations in lithium fluoride do not contribute significantly to the deformation process (Gilman and Johnston 1957) so that a comparison of the yield behaviour of as-cleaved and chemically polished crystals in the uncoated and coated conditions can be particularly revealing—table 3. Coating an as-cleaved crystal produces the same effect on the yield stress as a chemical polishing treatment, namely it causes an increase of some 50%. This can be explained as follows. Other investigations have demonstrated that small alloying additions of divalent cations to univalent cation type ionic crystals can exert a profound influence on the yield stress of such crystals, sometimes causing a tenfold increase in this property (Edner 1931, Schoenfield 1932, Nadeau and Washburn 1960). Hardening probably results from the increased difficulty of moving a dislocation through a lattice containing either foreign ion-vacancy pairs—due to mutual interactions—or precipitate particles.

In this investigation, reacted-coatings consisted of a coherent alloy layer of magnesium in lithium fluoride. No metallographic evidence for precipitated magnesium fluoride was obtained although its presence as submicroscopic particles is possible. Coatings affected the yield stress of the test specimens by preventing the operation of artificially introduced surface-sources. This could be achieved in two ways: by solute ion locking or by preventing half-loop expansion and multiplication by virtue of the increased lattice resistance to dislocation motion caused by the presence of magnesium ion-vacancy pairs or fine precipitate particles in the surface coating.

As-cleaved and coated specimens were thus forced to utilize other sources of dislocations also available to polished crystals, that is, interior sources. Gilman (1959) has suggested that such sources are dislocations introduced during cooling from heat-treatment temperature, by precipitate particles or other stress raisers and, in polycrystals, from grain boundaries. The small effect of a coating on the yield stress of chemically polished crystals suggests that Fisher-type surface-sources—though possibly important in metal crystals—are not important in lithium fluoride crystals. This seems in accord with Gilman's (1959) studies which suggest that conventional Frank–Read sources are not responsible for dislocation multiplication in lithium fluoride.

Table 3. A comparison of the yield behaviour of as-cleaved and chemically polished crystals

	Uncoated		With 'thin' reacted-coating	
	Average yield stress in g/mm^2	Average C.R.S.S. in g/mm^2	Average yield stress in g/mm^2	Average C.R.S.S. in g/mm^2
As-cleaved crystals	83	120	128	149
Chemically polished crystals	121	125	127	143

An as-cleaved and uncoated crystal then, deforms by the operation of many sources, mainly located at the surface and these begin to operate at relatively low stresses (in these crystals, approximately 80–100 g mm^2). Multiplication proceeds probably by a cross-glide mechanism (Koehler 1952, Orowan 1954, Johnston and Gilman 1960) and at an increasing rate as the stress is raised. A chemically polished crystal, however, has fewer and relatively harder sources. Thus its yield stress is higher than a similar as-cleaved crystal, but since the multiplication rate is a very sensitive function of stress level (Johnston and Gilman 1959), when multiplication does begin it proceeds very rapidly. In some cases, the multiplication process in a chemically polished crystal reaches such a high rate that the specimen begins to deform at a greater rate than that caused by the motion of the testing machine crosshead and this is manifested by a meandering or 'casual' stress drop, fig. 8 (*a*).

The critical resolved shear stress is a more complex factor affected by such variables as strain rate, the number of dislocations present, their rate of multiplication and, in these studies, the ability of dislocations to pass out of the surface of the crystal.

Thin coatings of chromium had no significant effect on the critical resolved shear stress since they were themselves brittle and fractured during the compression test. Thus they did not constitute a real obstacle to the egress of dislocations. Relatively thin reacted-coatings however did provide an obstacle because of the increased resistance to dislocation motion in the alloyed layer and caused edge dislocations to pile up beneath the coatings —fig. 7. However, these piled-up groups were able to break through thin reacted coatings (5–10 μ) and cause a catastrophic drop in stress at the critical resolved shear stress, fig. 8 (*b*). Such catastrophic stress drops may be another manifestation of the high rate of multiplication of internal sources once they are operated—compare the casual stress drop of polished crystals, fig. 8 (*a*). The production of a burst of dislocations which pile up and then break through a surface film appears to be a more likely cause of catastrophic stress drop than a process involving the steady piling up of dislocations until a break-through stress is reached. Stress drops were not observed with specimens having a thicker reacted coating, presumably because catastrophic break-through was not possible.

Fig. 8

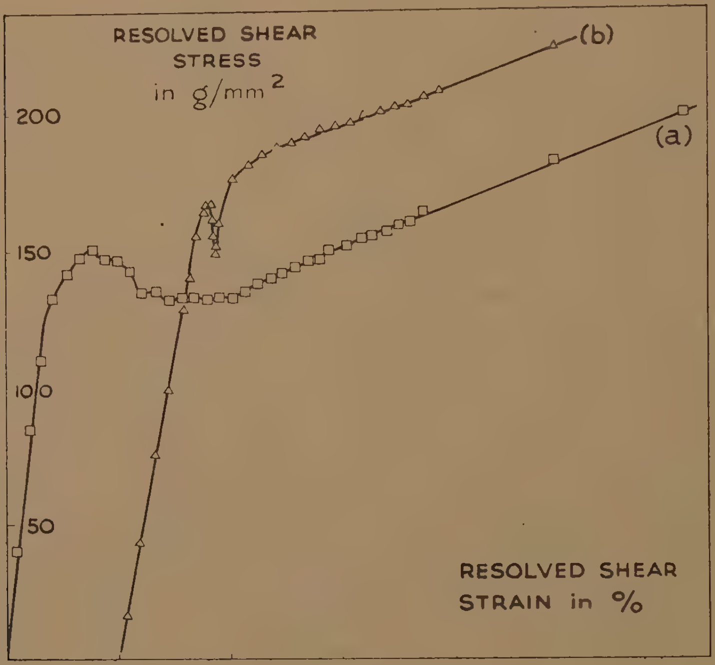

Illustrating the ‘ casual ’ and ‘ catastrophic ’ stress-drops observed with lithium fluoride crystals.

4.2. *The Effect of Surface Coatings on Work-hardening and Fracture Behaviour*

During compression tests, four glide systems, ($\langle\bar{1}01\rangle/\{101\}$), were equally oriented to the applied stress, and glide on a single system was restricted to very low strains. However, the rate of work-hardening was linear over the first three to four per cent glide strain. Gilman and Johnston (1960) have also noted this and have suggested that work-hardening at low strains in lithium fluoride results from the production of lattice defects which are left in the wakes of moving dislocations. These defects then interfere with the movement of subsequent dislocations on the same or neighbouring slip planes. However, after 3 or 4% strain, the stress–strain curves, particularly of uncoated, as-cleaved crystals, deviate markedly from linearity—fig. 1. The present work suggests that a dislocation-barrier mechanism must be responsible for at least part of the work-hardening at higher strains. The metallographic evidence of figure 6; a comparison of the work-hardening rates of as-cleaved and chemically polished crystals; observations on the effects of coatings on the stress–strain curve and the mode of fracture all appear consistent with this view. Based on this supposition, the experimental results can be explained as follows.

When an as-cleaved crystal is deformed, many sources operate and dislocations on intersecting systems soon meet and interact. Their mutual interference then results in a relatively high rate of work-hardening. Fewer sources operate in a polished crystal so that, at a similar strain, there should be more slip per source. This is evidenced by the presence of fewer, but broader, slip bands in such crystals. However, since the number of intersections is reduced, dislocation–dislocation interference effects should decrease so that a lower rate of work hardening should be, and is, observed with polished crystals; see fig. 1 and also Suzuki's (1957) studies with potassium chloride crystals.

A defect-hardening mechanism would predict the converse. More slip per source should result in greater defect-dislocation interference effects and a higher rate of work hardening for polished crystals than as-cleaved crystals. Thus the defect-mechanism does not satisfactorily explain work-hardening behaviour at higher strains.

By reducing the number of operable sources, a surface coating also reduces the initial rate of work-hardening. Specimens having a relatively thick coating (25–50 μ), probably deform by a leak out of dislocations through the film at a rate which is considerably less than the rate at which they pile-up beneath the film. In effect, the dislocations pile-up against a stable barrier so that the observed difference in fracture stress and strain between coated and uncoated specimens, table 1, may be accounted for as follows. A considerable strain is necessary to produce a sufficient number of dislocations concentrated into the thick bands which can act as a stable, rather than a temporary, barrier to edge dislocations on an intersecting system. However, for relatively thickly coated specimens, the coating itself can act as a suitable barrier. A crack nucleus then results either from the uncomplicated piling up of dislocations against this barrier or by the piling up of dislocations on a secondary system against a stabilized band of dislocations on a primary system—the stabilized band being caused by the piling up of dislocations beneath the surface coating. Observations on coated specimens showed that cracks always initiate at the surface and, apparently, just below the coating.

§ 5. Conclusions

The main conclusions from this investigation are:

(i) Metallographic evidence shows that surface coatings can act as barriers to the egress of edge-dislocations.

(ii) Tests on as-cleaved, chemically polished, coated and uncoated specimens, show that a coating can effectively restrict the operation of artificially introduced surface sources, thereby raising the yield stress. A coating also decreases the initial rate of work hardening of as-cleaved lithium fluoride crystals by reducing the number of active sources so that mutual interference effects are lessened.

(iii) A catastrophic break through of a surface film by piled-up groups of dislocations can cause a sharp stress-drop. This can be readily distinguished from the more casual stress drop observed with uncoated chemically polished specimens but it is likely that both are caused by a high rate of dislocation multiplication.

(iv) A barrier-mechanism better explains work-hardening phenomena at strains above some three to four per cent.

(v) A surface coating can act as a stable barrier to dislocations causing pile-up, coalescence and the formation of crack nuclei beneath the film. This can reduce the stress and strain to fracture of coated crystals to half of that of uncoated crystals.

ACKNOWLEDGMENTS

It is a pleasure to acknowledge the encouragement of Mr. W. W. Bender, the helpful discussions with Dr. H. M. Otte and the capable assistance of H. Opperhauser, Jr., D. Goldheim and C. Feltes in this work. We are also grateful for the financial support received from Watertown Arsenal Laboratories and in particular the continued interest of Mr. Murray Jacobson.

REFERENCES

ADAMS, M. A., and COTTRELL, A. H., 1958, *Acta. Met.*, **6,** 327.
BARRETT, C. S., 1953, *Acta Met.*, **1,** 2.
EDNER, A., 1931, *Z. Physik.*, **73,** 623.
ESHELBY, J. D., FRANK, F. C., and NABARRO, F. R. N., 1951, *Phil. Mag.*, **42,** 351.
FISHER, J. C., 1952, *Trans. Amer. Inst. min. (metall.) Engrs*, **194,** 531.
GILMAN, J. J., 1959, *J. appl. Phys.*, **30,** 1584.
GILMAN, J. J., KNUDSEN, C., and WALSH, W. P., 1958, *J. appl. Phys.*, **29,** 601.
GILMAN, J. J., and JOHNSTON, W. G., 1957, *Dislocations and the Mechanical Properties of Crystals* (New York : Wiley), p. 116 ; 1960, *J. appl. Phys.*, **31,** 687.
HAVEN, Y., 1950, *Rec. trav. Chim. Pays.-Bas.*, **69,** 1471.
HIRSCH, P. B., PARTRIDGE, P. G., and SEGALL, R. L., 1959, *Phil. Mag.*, **4,** 721.
JOHNSTON, W. G., and GILMAN, J. J., 1959, *J. appl. Phys.*, **30,** 129 ; 1960, *Ibid.*, **31,** 632.
KOEHLER, J. S., 1952, *Phys. Rev.*, **86,** 52.
LUDELLANS, W. L. W., and WELSH, A. J. E., 1952, *Acta Cryst.*, **5,** 841.
MENTER, J. M., and HALL, E. O., 1950, *Nature, Lond.*, **165,** 611.
NADEAU, J., and WASHBURN, J., 1960, 1st Tech. Report to U.S.A.E.C. Contract No. AT(11–1)–34. Project No. 28.
OROWAN, E., 1954, *Dislocations in Metals* (New York : Amer. inst. min. (metall.) Engrs), p. 104.
PHILLIPS, D. J., and THOMPSON, N., 1950, *Proc. phys. Soc. Lond.* B, **63,** 839.
ROSCOE, R., 1936, *Phil. Mag.*, **21,** 399.
SCHOENFIELD, H., 1932, *Z. Phys.*, **75,** 442.
STOKES, R. J., JOHNSTON, T. L., and LI, C. H., 1959, *Phil. Mag.*, **4,** 920.
STROH, A. N., 1955, *Proc. roy. Soc.* A, **232,** 548.
SUZUKI, T., 1957, *Dislocations and the Mechanical Properties of Crystals* (New York : Wiley), p. 215.

Electron Microscope Observations of Deformed Magnesium Oxide†

By J. Washburn‡, G. W. Groves, A. Kelly and
G. K. Williamson§
Department of Metallurgy, University of Cambridge

[Received May 9, 1960]

Abstract

Observations have been made by electron transmission microscopy of thin flakes of deformed magnesium oxide. The ease of cross slip of screw dislocations in this material has been directly verified. Cross slip leads to the formation of many markedly elongated prismatic loops of dislocation. These are observed profusely within slip bands, produced at room temperature. They are unstable at higher temperatures and break up into numbers of smaller prismatic loops. From these observations a mechanism for the widening of slip bands, observed under the optical microscope, is proposed. Certain dislocation interactions have been observed and analysed and preliminary observations made of slip band intersections.

§ 1. Introduction

The dislocation arrangement in deformed metal crystals has been extensively studied by electron transmission microscopy—see, for example, the review by Hirsch (1959). There have been no similar observations on non-metallic crystals. Etch pit techniques have been used to study dislocation motion and arrangement in deformed crystals of lithium fluoride and magnesium oxide (Gilman and Johnston 1956, Washburn *et al.* 1959, Stokes *et al.* 1959). However, very little information concerning the arrangement of dislocations within slip bands and at slip band intersections can be obtained because the density of etch pits becomes too great for optical resolution. A previous note (Washburn *et al.* 1960) reported that dislocations in magnesium oxide can be studied conveniently by electron transmission microscopy with an increase in resolving power of about two orders of magnitude.

The purpose of the present paper is to present some observations on the behaviour of dislocations in deformed magnesium oxide and to describe the dislocation networks within slip bands and at slip band intersections.

---

† Communicated by the Authors.

‡ National Science Foundation fellow on leave from the University of California.

§ On secondment from C.E.G.B. Berkeley Nuclear Laboratories.

§ 2. Experimental Procedure

Thin sheets of MgO, approximately $0{\cdot}025 \times 1 \times 2$ cm were cleaved on {100} faces from large crystals obtained from the Norton Company.

Specimens were chemically polished in 85% orthophosphoric acid at 100°c, to remove cleavage damage to the surfaces. After deforming plastically, specimens were etched for a few seconds in boiling concentrated nitric acid. The region selected for examination under the electron microscope was thinned by rotating the specimen slowly above a small jet of hot orthophosphoric acid. The specimen was removed from above the jet and washed in distilled water at the instant when a hole first appeared at some point. Clean surfaces were obtained by washing thoroughly in distilled water, and rinsing in methanol and then in ethyl ether. Areas sufficiently thin for electron transmission were revealed by the appearance of bright interference fringes in vertical optical illumination.

Observations were made with an electron microscope operating at either 80 or 100 kv. No trouble was encountered due to charging of specimens in the beam even though MgO is a poor conductor. It has been shown that the temperature rise of a metal specimen under the beam is $\leqslant 100$°c under normal operating conditions (Silcox and Whelan 1960). The temperature rise in MgO is likely to be considerably higher due to the lower thermal conductivity. Since application of the full beam current, by removing the condenser aperture, failed to evaporate a hole in the specimen if the area irradiated was close to one of the grid bars of the support it is felt that the temperature rise of the specimen under normal operating conditions was less than 800°c.

§ 3. Observations and Discussion

Most metal crystals studied in electron transmission have random crystallographic orientation with respect to the plane of the foil. In this work a $\langle 100 \rangle$ direction was always approximately parallel to the axis of the microscope, making interpretation of observations somewhat simpler. The shortest Burgers vector for a perfect dislocation in the MgO structure is $(a/2)\ \langle 110 \rangle$. Etch pit studies have shown that this is the operative slip direction in MgO and that glide of dislocations takes place most easily on {110} planes. Interpretation of results is simpler than in metals for another reason: there is only one $\langle 110 \rangle$ slip direction in each {110} slip plane. Therefore a given slip plane is expected to contain only one kind of mobile dislocation. There are six {110} slip planes. If the surface of the foil is taken as (001), the projections of the {110} planes onto (001) appear as shown in fig. 1†. The four lying at 45° to the surface have a projected width equal to the thickness of the foil and intersect the surface along $\langle 100 \rangle$ directions. The remaining two are at 90° to the surface and project as lines lying along $\langle 110 \rangle$ directions. The two different slip plane orientations relative to the foil normal will hereafter be referred to as 45° and 90° slip planes. The projection of a dislocation line lying in one of the 45° slip planes can have any direction and shape. Any dislocation in one of the 90° planes must appear either as a point or a straight line that lies exactly along ⟨110⟩. A dislocation in one of the 45° slip planes is in pure screw orientation when its projection lies along the ⟨100⟩ direction at right angles to the trace of its slip plane and in edge orientation when it lies along the trace of its slip plane. The ⟨110⟩ slip direction in the 90° planes is parallel to the surface. Therefore a dislocation in these planes is in screw orientation when it lies parallel to the foil surface and in pure edge orientation when it is at right angles to the surface of the foil.

---

† All figures are shown as plates with the exception of figs. 1, 7, 8.

Fig. 1

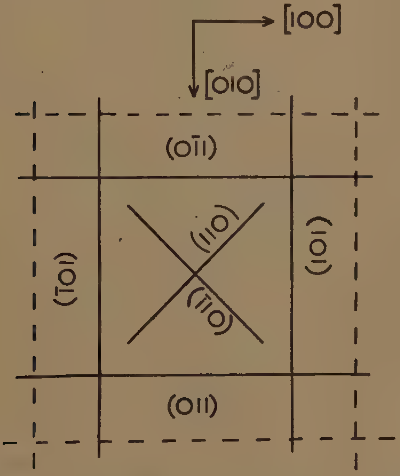

Projection of the {110} slip planes on to the (001) surface of an MgO flake.

3.1. *Motion of Screw Dislocations*

Figure 2 shows curved dislocations lying on one set of 45° planes. The diagonal line across the upper right-hand corner of the picture is a cleavage crack lying along ⟨100⟩. The dislocations had been moved by thermal stresses, generated by increasing the electron beam current, prior to taking the photograph. They appeared to be all of the same sign because they all moved towards the crack. The majority of these dislocations are approximately in screw orientation. Nearly straight screw dislocations were often found in the foils, but when they moved they frequently developed deep cusps, at points within the foil. These can be observed on some of the dislocations in fig. 2. The trails left on the surface by the ends of moving dislocations were not always parallel to the traces of the {110} slip planes.

Screw dislocations thus appear to be able to transfer easily from one {110} slip plane to a nearby parallel one. At the places where this transfer occurs jogs consisting of short segments of edge dislocation will be formed, which can only move by glide along the direction of the Burgers vector of the original screw. They will thus act as locking points and the screw will be bowed out between them. Figure 3 shows dislocations lying on 45° planes which were straight before local heating with the beam. They have all developed relatively immobile points and cusps along their length during motion.

3.2. *Dislocation Structure of Slip Bands*

The observations just described on moving dislocations were made in specimens containing a few isolated dislocations. To study the damage within slip bands crystals were bent at room temperature to produce slip on either 90° or 45° slip planes. 45° slip bands were obtained by bending about a ⟨100⟩ lying in the plane of the sheet, to an average surface strain of $\sim 5\%$. To produce slip bands on 90° planes crystals were bent about an axis at right angles to the plane of the sheet.

45° slip bands appear as shown in fig. 4. Many dislocations can be observed terminating at top and bottom surfaces of the foil—this can often be recognized by a dark blob, at the end of the dislocation line. However, there are much larger numbers of dislocation lines which appear to be entirely within the foil and appear sometimes as a single line and sometimes as a double one. Since these dislocations do not appear to terminate at a surface or a node they must consist of a closed loop of dislocation. The majority of them run roughly parallel to a ⟨100⟩ direction but deviations from this direction of up to about 30° are quite common.

All dislocations in a given slip band had the same Burgers vector. This is expected from the geometry of the MgO structure and was verified in a number of cases by tilting the specimen into a position of zero diffraction contrast. All the dislocations in a band disappeared simultaneously at a setting when there was only one strongly diffracting plane parallel to the expected Burgers vector—an example is shown in fig. 5. The dislocation lines observed which do not terminate on the surface must therefore consist of a closed loop of dislocation which is predominantly of edge character. Since the majority of these are not resolved into separate dislocation lines the separation of the two sides of the loop must be less than a few hundred angstrom units. They will be designated, plus–minus pairs.

Figure 6 shows the dislocation population within a 90° slip band. The dislocations appear as lines approximately parallel to ⟨110⟩. Sometimes these lines appear double. Although these could be dislocations of predominantly screw character lying in a 90° plane it is thought more likely, in view of the large numbers of plus–minus pairs observed in the 45° orientation of the slip plane that these are in fact also plus–minus pairs which deviate widely from a ⟨100⟩ direction. The fact that they sometimes appear as double lines, confirms this interpretation. These lines lie only approximately parallel to ⟨110⟩ which means that many dislocations do not lie exactly in the {110} slip planes, which again indicates cross slip.

The observations of plus–minus pairs and the fact that dislocations in slip bands do not lie exactly in a {110} plane are entirely consistent with the observations on moving screw dislocations and in fact the observations on the moving screws suggest the mode of genesis of the plus–minus pairs. This is illustrated in fig. 7. Lengths of screw dislocation are observed to cross slip out of one slip plane and then back to another parallel one. If different parts of the same screw dislocation cross slip by different amounts then edge dislocation segments are formed and as the two parts of the screw continue to move a plus–minus pair of dislocations will be left behind the moving one. The plus–minus pair can be terminated if the two lengths of the screw (due to changes in the local stress field) come back to the same (110) plane again. The particular plus–minus pair will then become a closed prismatic loop and cannot be eliminated by glide alone; the locking point on the screw is then eliminated.

Fig. 7

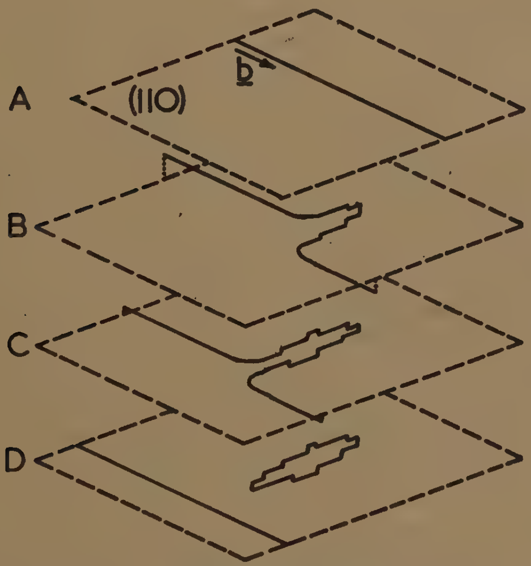

Schematic illustration of the formation of plus–minus pairs. **b** is the Burgers vector of the dislocation.

The dominant feature of slip bands observed under the electron microscope is the large number of plus–minus pairs. In view of this it is clear that when etch pits are used to study dislocation distribution in slip bands many of the pits must mark the positions of close plus–minus pairs rather than those of single dislocations.

Dislocation multiplication may take place by a modification of the process suggested for the production of plus–minus pairs. During the formation of a pair the two lengths of screw dislocation may move apart by cross slip until they are sufficiently far apart for the force between them to be very small. Each could then move independently of the other forming two sources of dislocation on widely separated, but parallel slip planes. A schematic illustration of this process is given in fig. 8. It is proposed that such a process accounts for the formation of wide slip bands in MgO, observed under the optical microscope (Washburn *et al.* 1959), and for the increase in dislocation density when a single loop of dislocation is expanded in LiF crystals (Gilman and Johnston 1956).

Fig. 8

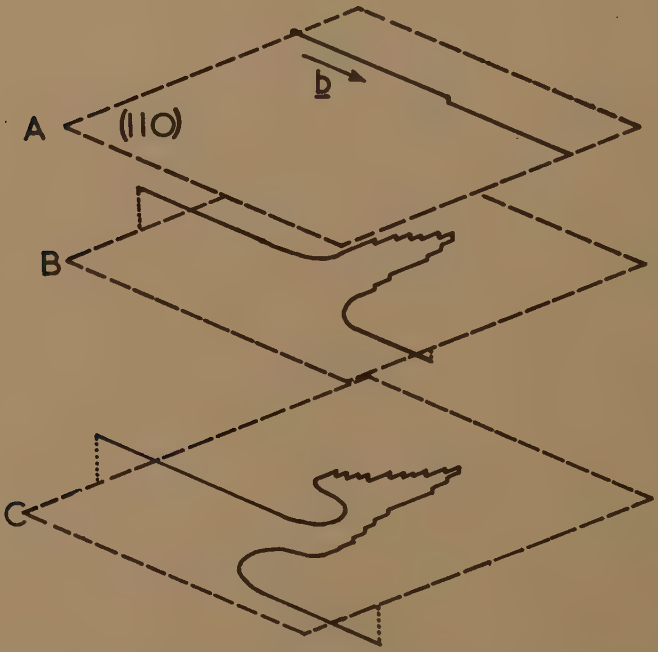

Schematic representation of a possible mechanism of dislocation multiplication.

3.3. *Stability of Plus–Minus Pairs*

The break-up of long plus–minus pairs into short lengths was observed in crystals deformed at a high temperature in an air–gas flame or could be observed directly when areas containing long pairs were heated in the microscope. An example of a pair breaking up during heating in the microscope by increasing the beam current is shown in fig. 9 (*a*) and (*b*). Since break-up is observed to have occurred in specimens which have not been heated to greater than ~1600°c the process must occur in the absence of thermally generated point defects. If a pair of straight parallel edge dislocations of separation d breaks up into a number of circular prismatic loops each of radius R such that the area of prismatic loop projected normal to the Burgers vector is conserved, the ratio of the energy of the loops to the original plus–minus pair is given to a sufficient approximation by

$$\frac{d}{R}\,\frac{\ln R/r_0}{\ln d/r_0}$$

where r_0 is the radius of the core of a dislocation. The elastic energy of the system is then reduced if a plus–minus pair breaks up into a set of loops of average radius more than a few times greater than the original separation of the two dislocations in the plus–minus pair. This condition for stability reduces to the statement that the separation of the resultant loops should always be larger than 1·57 times their diameter. When the loops could be resolved this was found to be the case†.

3.4. *Dislocation Interactions*

In MgO each slip plane contains only one type of mobile dislocation, hence dislocation interactions are not expected to be observed as frequently as in face-centred cubic metals. They should occur predominantly at intersections of {110} planes. There are three possible reactions between the dislocations with Burgers vector $(a/2)\langle 110\rangle$ in this structure. Only one of these should lead to a reduction in elastic strain energy and it has been observed in a number of samples. A clear example of interactions of this type is shown in fig. 10. If the surface of the foil is taken as (001) dislocations A and B are on 45° slip planes at right angles to one another with Burgers vectors $(a/2)\,[011]$ and $(a/2)\,[0\bar{1}1]$ respectively. Both sets of dislocations have been intersected by dislocations C with Burgers vector $(a/2)\,[10\bar{1}]$.

The reaction between A and C gives

$$(a/2)\,[011]+(a/2)\,[10\bar{1}]\rightarrow(a/2)\,[110],$$

and between B and C,

$$(a/2)\,[0\bar{1}1]+(a/2)\,[10\bar{1}]\rightarrow(a/2)\,[1\bar{1}0].$$

The first reaction gives a short length of dislocation lying along $[\bar{1}11]$ and the second one lying along $[\bar{1}\bar{1}1]$. These directions lie at 90° to one another in projection as is observed. In both cases the interaction produces a short length of dislocation which is pure edge and can only move in a {112} plane. The three dislocations meeting at any of the nodes do not have a common slip plane. This may be the reason why the angles between the dislocation lines at the nodes are not equal to 120°. Alternatively this could be because a dislocation with Burgers vector ⟨110⟩ lying in {112} has a higher energy than one lying in {110}.

---

† The break-up of long prismatic dislocations into a number of circular loops has recently been observed independently in zinc by P. B. Price (private communication).

No other interactions have so far been unambiguously identified.

3.5. *Slip Band Intersections*

The intersections between slip bands are of particular interest from the point of view of crack nucleation. Cracks have been observed under the optical microscope to form at or near two types of slip band intersections. These are: (1) slip bands intersecting along ⟨100⟩, the two slip directions being at 90° to one another (Stokes *et al.* 1958, Washburn *et al.* 1959) and (2) slip bands intersecting along ⟨111⟩; the two slip directions being at 120° to one another (Keh *et al.* 1959).

The second type of intersection was easily studied under the electron microscope. It was produced between two 45° planes by bending a crystal about the [100] axis in the plane of the sheet and then straightening it and again bending about the [010]. An example of such an intersection is shown in fig. 11. It is characterized by a dense tangle of dislocations, many of which appear to be plus–minus pairs. It is not possible to follow the course of many dislocations at the intersection and no interactions can be definitely identified. There is no evidence that dislocations are piling up against the intersection. The increase in dislocation density appears confined to the intersection itself and the dislocation arrangement in the slip bands is the same at small and large distances from the intersection.

Intersections at right angles could be recognized at the intersection of two 90° slip bands—as illustrated in fig. 12. Nothing was observed at these intersections that looked like a pile-up of edge dislocations and no cracks were seen. However, examination of orthogonal intersections of slip bands in this orientation yields only limited information because the slip bands are viewed parallel to the slip plane and normal to the slip vector of the dislocations. It has not so far been possible to recognize unambiguously an orthogonal intersection of two 45° slip bands.

The electron microscope study of slip band intersections in these crystals has revealed that the intersection is characterized by an increase in density of plus–minus pairs but so far no cracks have been observed to form at them.

Acknowledgments

The authors are grateful to Professor A. H. Cottrell, F.R.S., for his encouragement throughout this research and to the National Science Foundation for the award of a fellowship to J.W. which made this cooperation possible. G.W.G. is grateful to the United Kingdom Atomic Energy Authority for the award of a bursary, and G.K.W. to the Central Electricity Generating Board for financial support.

REFERENCES

GILMAN J. J., and JOHNSTON, W. G., 1956, *Dislocations and Mechanical Properties of Crystals* (New York: J. Wiley and Sons Inc.), p. 116.

HIRSCH, P. B., 1959, *Metallurg. Rev.*, **4,** 101.

KEH, A. S., LI, J. C. M., and CHOU, Y. T., 1959, *Acta Met.*, **7,** 694.

SILCOX, J., and WHELAN, M. J., 1960, *Phil. Mag.*; **5,** 1.

STOKES, R. J., JOHNSON, T. L., and LI, C. H., 1958, *Phil. Mag.*, **3,** 718; 1959, *Trans. Amer. Inst. min. (metall.) Engrs*, **215,** 437.

WASHBURN, J., GORUM, A. E., and PARKER, E. R., 1959, *Trans. Amer. Inst. min. (metall.) Engrs*, **215,** 230.

WASHBURN, J., KELLY, A., and WILLIAMSON, G. K., 1960, *Phil. Mag.*, **5,** 192.

Cyclotron Resonance in Lead†

By J. E. Aubrey
The Royal Society Mond Laboratory, University of Cambridge‡

[Received May 11, 1960]

Abstract

Cyclotron resonance effects of the Azbel'–Kaner type have been observed in lead specimens at 9 kMc/sec and 1·2°K, and effective mass values of the charge carriers have been deduced from the magnetic field dependence of the surface resistance of the specimens. The anisotropy of the surface conductivity of the single crystal specimens in the low field limit was found to be consistent with the existing model of the Fermi surface in lead, and from the value of the surface conductivity of a polycrystalline specimen, a value of the total Fermi surface area was found which supports the view that the fourth Brillouin zone in lead is empty.

§ 1. Introduction

The theoretical prediction of Azbel' and Kaner (1956) that cyclotron resonance might be observable in metals when the magnetic field H is applied parallel to the sample surface, was verified by Aubrey and Chambers (1957) working on bismuth, and on completion of some additional experiments on bismuth (Aubrey 1960), it was decided to make a preliminary study of lead§.

Azbel' and Kaner showed that for the simple case of a quadratic electron energy band, the surface impedance Z of the metal in the anomalous skin effect limit varies with magnetic field according to the relation

$$Z \simeq Z(0)[1-\exp(-2\pi i x)\exp(-2\pi x/\omega\tau)]^{1/3} \quad . \quad . \quad . \quad (1)$$

where $Z(0)$ is the impedance in zero field and $x=\omega/\omega_c=m^*c\omega/eH$. For $\omega\tau \gg 1$, both real and imaginary parts of Z are oscillatory functions of x with period $\Delta x=1$, and from a measurement of the period of the oscillations in H^{-1}, the effective mass m^* of the electrons can be found. In the work to be described, the field dependence of the real part, R, of Z has been investigated in the range of magnetic field 1200 gauss|| to 9000 gauss by

---

† Communicated by the Author.

‡ Present address: Department of Physics, University of Pennsylvania, Philadelphia 4, Pennsylvania, U.S.A.

§ Bezuglyi and Galkin (1958) have also done some preliminary work on lead using a very similar experimental method to that used in the present work but have published results on only one sample whose orientation was not specified.

|| The field 1200 gauss was approximately the lowest field at which the transition from the superconducting to the normal state was complete.

observing the change in the Q of a resonator of which the specimen forms the most dissipative part: the specimens were wires, 1 mm in diameter and 1·4 cm long, constituting the central conductor of a coaxial resonator, whose design has been described by Pippard (1950).

Zone-refined lead with resistance ratio $\rho(290^\circ\mathrm{K})/\rho(1{\cdot}9^\circ\mathrm{K}) = 2{\cdot}5 \times 10^4$ supplied by the Westinghouse Research Laboratories was used, and to form wire for the specimens, the lead billets were first extruded at room temperature through a 1 mm steel die. The extruded metal was etched with concentrated hydrochloric acid to remove contamination picked up from the die, and single crystals were grown on a flat plate furnace. These were subsequently electropolished using the perchloric and acetic acid mixture specified by Tegart (1956) yielding a highly specular surface whose brightness did not diminish between polishing and insertion of the specimen into the cryostat. Some care was needed in mounting the specimens to ensure that the magnetic field, provided by an air-cored solenoid, was as nearly parallel to the specimen axis as possible.

§ 2. RESULTS

Specimens whose axes had the crystallographic orientations (100), (110), (111), (210), (211), (221), were studied and curves of $R(H)/R(1200)$ versus H^{-1} for each of these orientations are given in figs. 1 to 6. Each of the curves shows maxima and minima whose positions were found to be reproducible in repetitions of the measurements under identical conditions, and the values of H^{-1} at which these occur are given in the table. It is clear that in general there is no precise periodicity in H^{-1} of the kind predicted by eqn. (1), except in fig. 4 and possibly fig. 5. Thus it is clear that the observed behaviour cannot generally be accounted for by the presence in the metal of a single group of charge carriers of unique effective mass.

Orientation	Resistance maxima $10^4 \times H^{-1}$ (gauss)$^{-1}$	Resistance minima $10^4 \times H^{-1}$ (gauss)$^{-1}$	m^*/m_0
100	2·1, 3·5, 6·6	2·6, 4·8	$1{\cdot}3,\ 0{\cdot}6_6$
110	1·8, 3·7	2·1, 4·2	$1{\cdot}6,\ 0{\cdot}7_6$
111	2·1, 3·6	2·4, 4·3	$1{\cdot}4,\ 0{\cdot}7_4$
210	1·7, 3·5 5·6, 7·7	2·0, 4·4 6·5, 8·4	$1{\cdot}7,\ 0{\cdot}7_2$ or $1{\cdot}4_4 \pm 0{\cdot}0_7$
211	1·8, 3·5 5·9, 8·4	2·3, 4·8 6·6	$1{\cdot}4,\ 0{\cdot}6_6$ or $1{\cdot}3_7 \pm 0{\cdot}1_9$
221	1·4, 2·0, 3·1 4·4, 6·5, 8·5	1·7, 2·6, 3·8 5·3, 7·3	2·0, 1·3

Fig. 1

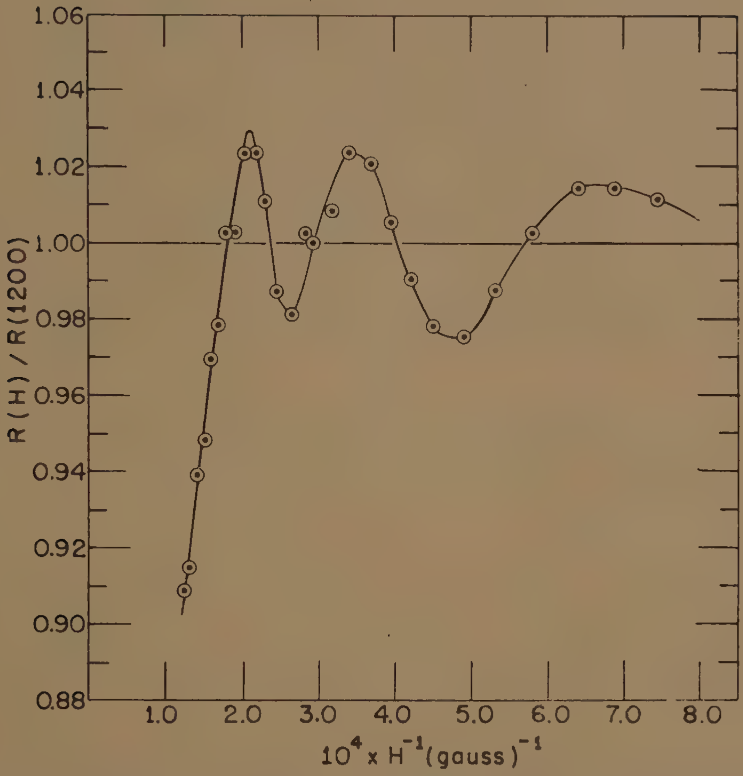

Surface resistance as a function of reciprocal field for a (100) specimen.

Fig. 2

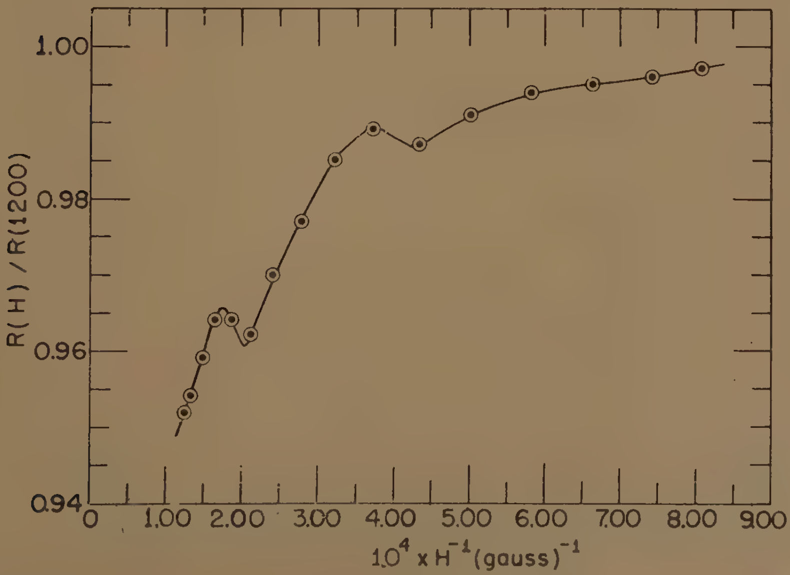

Surface resistance as a function of reciprocal field for a (110) specimen.

For a multiple band model, the form of the theoretical curve of surface resistance against reciprocal field may be most simply obtained from the approach used by Heine (1957) though the results follow also from the original form of the theory as given by Azbel' and Kaner (1957). For the present purpose it is sufficient to consider the simple case of a band structure in which the Fermi surface consists of a number of spheres, and we obtain from Heine's eqns. (6) and (12):

$$Z=2\exp(i\pi/3)\,(2\pi^2\omega^2/s)^{1/3}, \quad s=\sum_{\nu} a_{\nu} \qquad \ldots\ldots \quad (2)$$

where a_{ν} involves only the band indexed ν, and the summation is over the total number of bands.

Fig. 3

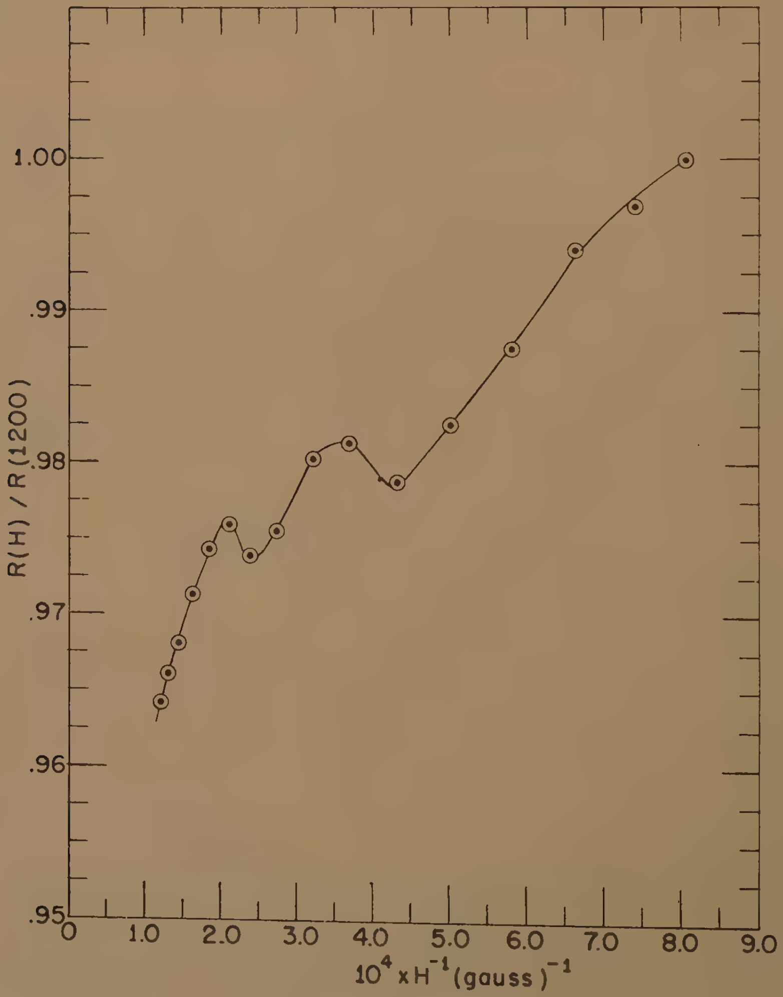

Surface resistance as a function of reciprocal field for a (111) specimen

Figure 7 shows the variation of $R(H)/R(0)$ with H^{-1} as calculated from (2) for the special case of a two band model with effective masses in the ratio 2:1, taking $\omega\tau=2\pi$ in each band, and assuming that both bands contribute equally to the effective conductivity in zero field. The number of bands is restricted here to two partly for the sake of simplicity, and partly because the two-band curve reproduces the behaviour observed in figs. 1 to 3 fairly adequately. Included in fig. 7 are curves of $R(H)/R(0)$ for the two constituent bands of the model considered separately (eqn. (1)). The fundamental resonance (i.e. the first resistance minimum), which occurs at approximately

$$x=1{\cdot}1=\frac{m^*c\omega}{eH_1} \quad . \; . \; . \; . \; . \; . \; . \; . \; . \quad (3)$$

Fig. 4

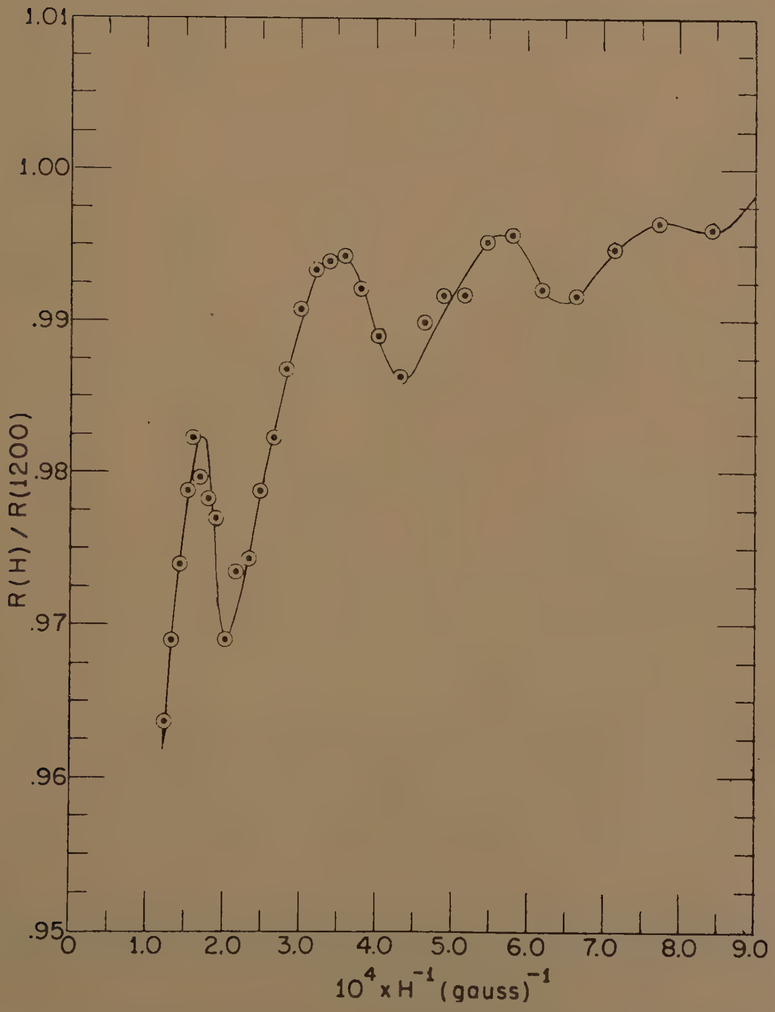

Surface resistance as a function of reciprocal field for a (210) specimen.

for each individual band alone, occurs at virtually the same position in the composite pattern†. This result is rather insensitive to the precise ratio of the effective masses used in the model and also to changes in the assumed values of $\omega\tau$ in the two bands and in their relative contributions to the effective conductivity. We shall therefore use (3) in interpreting the experimental results, i.e. we apply (3) to the positions H_1, of the first

Fig. 5

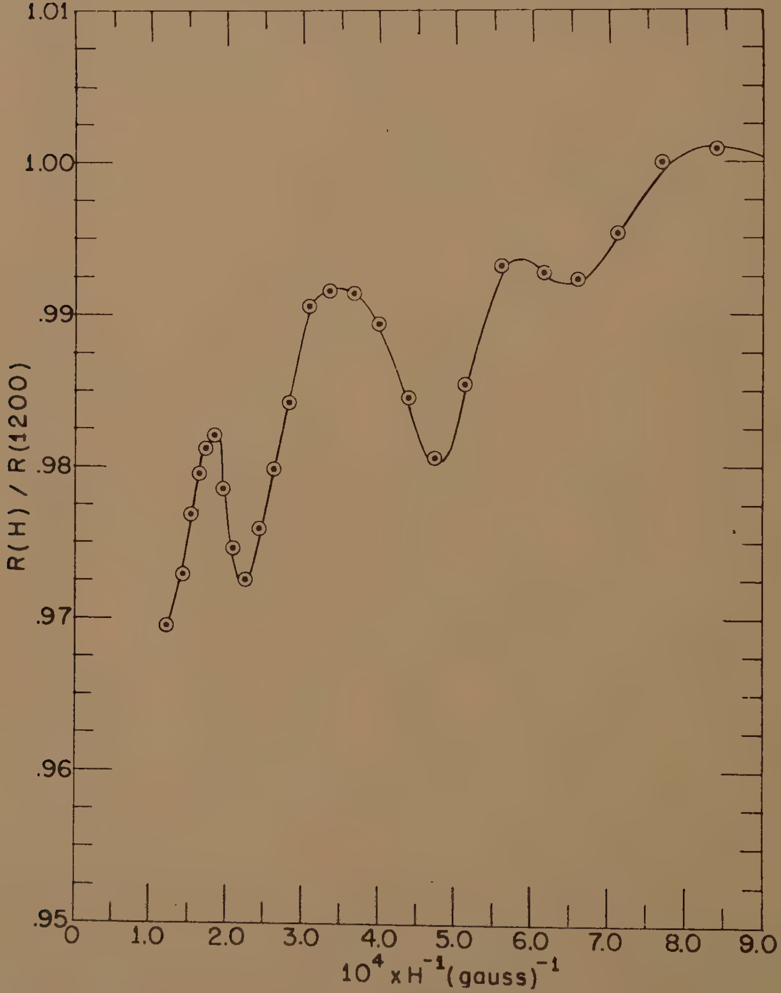

Surface resistance as a function of reciprocal field for a (211) specimen.

---

† The minima in R are related directly to maxima in the a_ν (eqn. (2)) which are themselves periodic in H^{-1} for each band. The fundamental maxima in the a_ν are sufficiently strong, with a realistic choice of $\omega\tau$, for the corresponding minima in the two-band resistance curve to appear at virtually unchanged positions with reference to the single band curves.

two resistance minima as given in the table and thus obtain the values of m^* shown in the fourth column of the table. The error in these mass values arising from the uncertainty of about $0{\cdot}2 \times 10^{-4}$ (gauss)$^{-1}$ in the positions of the resistance minima amounts to 10% for the set of larger mass values and 5% for the smaller values. A more important source of error however lies in the possibility that the phase of the oscillations in the surface resistance is not as predicted by the Azbel'–Kaner theory. Phase shifts have in fact been found in the work on bismuth (Aubrey and Chambers 1957) and also in work on zinc (Galt *et al.* 1959) and on copper (Langenberg and Moore 1959), and when present they may lead to errors, possibly of as much as 20 or 30% in the mass values calculated using eqn. (3).

Fig. 6

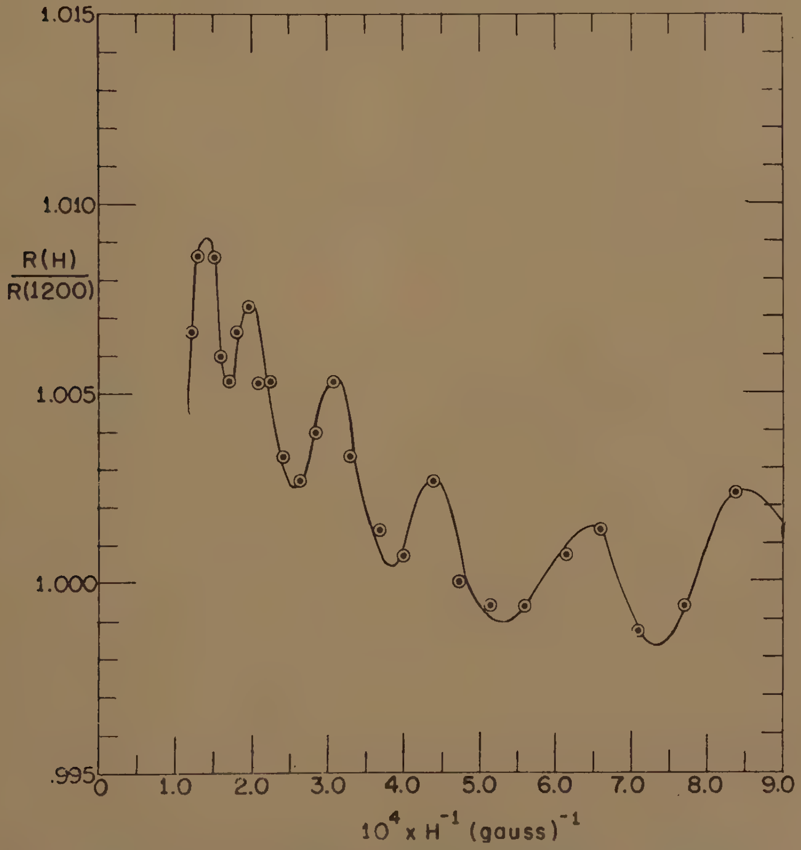

Surface resistance as a function of reciprocal field for a (221) specimen.

An alternative interpretation seems plausible for figs. 4 and 5, namely, that each of the curves reflects primarily the presence of a group of carriers with a single effective mass. The mean periods, $\Delta(H^{-1})$, are found to be

$$2{\cdot}1 \pm 0{\cdot}1 \times 10^{-4} \quad \text{and} \quad 2{\cdot}2 \pm 0{\cdot}3 \times 10^{-4}\,(\text{gauss})^{-1},$$

and the corresponding effective mass values calculated from the relation

$$m^* = \frac{e}{\omega c \Delta(H^{-1})} \quad . \quad . \quad . \quad . \quad . \quad . \quad . \quad . \quad (4)$$

are recorded as alternative values in the fourth column of the table. The fact that the value for the (210) orientation differs appreciably from the value calculated from the position of the first resistance minimum means that the curve, treated as a single Azbel'–Kaner oscillatory pattern, has a phase shift of the kind mentioned above, and confirms the possibility that there may be considerable errors in the effective mass values calculated from the positions of resistance minima using eqn. (3).

Fig. 7

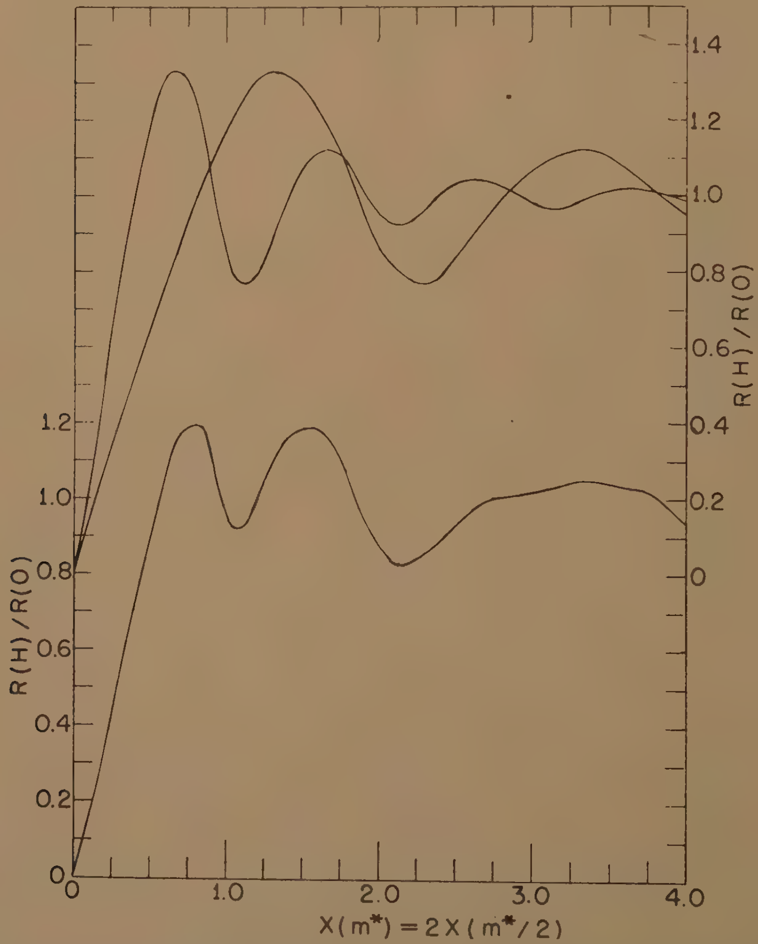

Upper curves (right-hand ordinate scale): theoretical surface resistance curves for the single band model (eqn. (1)). The abscissa

$$x(m^*) = m^* c\omega / eH = 2\, x(m^*/2).$$

Lower curve (left-hand ordinate scale): theoretical surface resistance curve for the two band model described in the text.

§ 3. Interpretation of the Results

Gold (1958) has suggested a model of the Fermi surface of lead from an analysis of the de Haas–van Alphen effect, using the free electron model as a guide. According to this model, electrons occupy the first four Brillouin zones in k-space, the first being completely filled, the second having a vacant central region, the third being occupied along the zone edges and the fourth being occupied at the zone corners. Recent considerations (Cohen and Gold 1960) have led to the suggestion that the fourth zone is in fact empty, so that portions of the Fermi surface exist in the second and third zones only. Gold finds an approximately isotropic effective mass of the order $1{\cdot}0 \pm 0{\cdot}1 m_0$ for the holes of the second zone, and a value $0{\cdot}56 \pm 0{\cdot}06 m_0$ for the electrons moving in orbits about the 'limbs' of the multiply connected surface in the third zone; it seems plausible therefore to associate the larger set of mass values, which fall in the range $1{\cdot}3$ to $2{\cdot}0 m_0$ with the second zone holes, and the set of values in the range $0{\cdot}6_5$ to $0{\cdot}7_6 m_0$ with the third zone electrons. Exact agreement between Gold's values and those found here is not to be expected since the de Haas–van Alphen values refer to electrons moving in orbits of extremal area on the Fermi surface, whereas the cyclotron resonance mass values refer to electrons moving in orbits on regions of the Fermi surface where the effective mass itself passes through extremal values (Azbel' and Kaner 1957).

§ 4. R.F. Conductivities

Useful information about the band structure can be obtained from measurements of the absolute value of the surface conductivity, Σ, at the anomalous skin effect limit in zero magnetic field†. Thus if plane single crystal specimens of a sufficient number of orientations are measured, the complete shape of the Fermi surface can in principle be found. This method is feasible in practice only if the Fermi suface has a relatively simple shape, e.g. if it consists of a single sheet, only, as in copper (Pippard 1957), or if the individual sheets have a simple analytic form, as in bismuth (Smith 1959). In the present work the measured value of Σ is an average over the azimuth of the cylindrical-shaped specimens, and all that can be attempted is a qualitative test of the compatibility of the observed anisotropy of Σ (fig. 8) with the existing model of the Fermi surface.

For a plane single crystal specimen (or at any azimuth of a cylindrical-shaped single crystal specimen), the principal components of the surface conductivity tensor are determined by integrals over the Fermi surface of the form, $\int |\rho(k_x)|\, dk_x$ and $\int |\rho(k_y)|\, dk_y$ (Pippard 1954). Here k_x and k_y are chosen as coordinates in k-space such that the corresponding axes in real space, x and y, are parallel to the principal directions of the surface impedance tensor. The quantity $|\rho(k_x)|$ is the absolute magnitude of the radius of curvature of the section of the Fermi surface in the plane k_x at the point where the normal to the section is parallel to k_y, and similarly for $|\rho(k_y)|$. Thus if $|\rho(k_x)|$ for example is large, the section dk_x about k_x makes a large contribution to the surface current, a large total surface current indicating a high value of Σ. It would seem reasonable to expect an almost isotropic contribution to the surface current from the holes of the second zone on account of the isotropy of the de Haas–van Alphen period and the distance of the Fermi surface from the Brillouin zone boundary (the surface contains approximately 0·4 holes per atom). Most of the observed anisotropy must therefore be due to the third zone electrons which occupy the multiply connected surface illustrated schematically in fig. 7 of Gold (1958). The limbs of this surface were shown as cylinders, but a more satisfactory fit of the period data (the γ oscillations in Gold's paper) can be obtained by taking a prolate spheroid with axial ratio 2·3 : 1 as the model of one of the limbs. If a Fermi surface consisting of a single prolate spheroid is considered, the surface current will be largest when the direction of current flow makes an angle of 90° with the spheroid axis, for in this case the radii of curvature of sections of the spheroid are large. This implies that the spheroid axis is normal to the metal surface, a condition which can hold only if the specimen surface is plane. For a cylindrical specimen with the spheroid axis normal to the specimen axis, the surface conductivity will vary over the azimuth, and there will be two diametrically opposite regions where Σ is large. Since six of the twelve spheroids which make up the repeat unit of the multiply connected surface have their axes normal to the direction of current flow for a (111) specimen we should expect a maximum in Σ for this orientation. Four spheroids

---

† At temperatures below 7°K this could not be observed directly because the lead specimens became superconducting in fields below about 1200 gauss. Extrapolation from higher fields, however, involved little error: see figs. 1 to 6.

Fig. 8

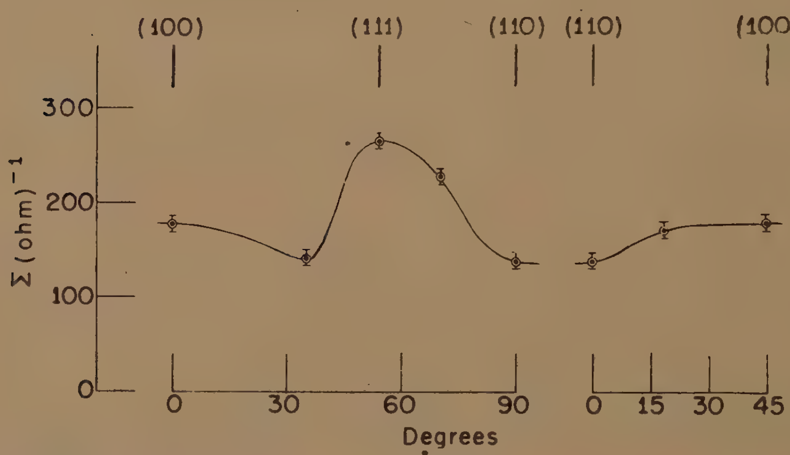

Anisotropy of the surface conductivity of the single crystal specimens.

satisfy this condition for a (100) specimen so we should again expect the surface conductivity to be large at this orientation, though not as large as at (111). These brief considerations explain the qualitative features of fig. 8, and it is likely that a model of the Fermi surface made up of twelve interconnected spheroids, and a single sphere representing holes of the second zone, would yield the observed anisotropy of Σ.

Finally, the total area of the Fermi surface, S, and the related parameter σ/l where σ is the d.c. conductivity, and l is an average value of the mean free path, can be calculated from the surface conductivity of a polycrystalline specimen. The appropriate relations are

$$S=\frac{2\pi^3 3^{3/2}\hbar c^2\omega^2\Sigma^3}{e^2} \quad . \; . \; . \; . \; . \; . \; . \; . \quad (5)$$

(Chambers 1952), and

$$\sigma/l=\sqrt{3\pi\omega^2\Sigma^3} \quad . \; . \; . \; . \; . \; . \; . \; . \; . \quad (6)$$

(Reuter and Sondheimer 1948). Σ for a polycrystalline specimen was found to be $181 \pm 6\,(\text{ohm})^{-1}$ and this leads to the values

$$S=17{\cdot}1 \pm 1{\cdot}7 \times 10^{16}\,\text{cm}^{-2},$$

$$\sigma/l=11{\cdot}1 \pm 1{\cdot}1 \times 10^{10}\,(\text{ohm cm}^2)^{-1}.$$

These are in reasonably good agreement with the value of σ/l obtained from measurements at 1·2 and 3·6 kMc/sec by Chambers (1952), namely $9{\cdot}4 \pm 0{\cdot}7 \times 10^{10}\,(\text{ohm cm}^2)^{-1}$; the somewhat higher values found here can be accounted for by the better surface finish obtained in this work. Gold's model of the Fermi surface leads to a value for S of $25{\cdot}5 \times 10^{16}\,\text{cm}^{-2}$ if the corners of the fourth zone are occupied, or $18{\cdot}6 \times 10^{16}\,\text{cm}^{-2}$ if they are unoccupied. The experimental value given above thus supports the belief that the fourth zone is empty.

ACKNOWLEDGMENTS

I wish to thank Dr. D. Shoenberg, F.R.S., and Dr. R. G. Chambers for their interest in this work and for their assistance in the preparation of the manuscript, and Dr. A. V. Gold for several stimulating discussions. I wish also to express my gratitude to the Department of Scientific and Industrial Research for the award of a maintenance grant, and to the U.S. Atomic Energy Commission for support on contract number AT(30–1)2395 during the period of writing.

REFERENCES

AUBREY, J. E., 1960, *J. Phys. Chem Solids* (to be published).
AUBREY, J. E., and CHAMBERS, R. G., 1957, *J. Phys. Chem. Solids*, **3,** 128.
AZBEL', M. YA., and KANER, E. A., 1956, *J. exp. theor. Phys., Moscow,* **3,** 772; 1957, *Ibid.*, **5,** 730.
BEZUGLYI, P., and GALKIN, A., 1958, *J. exp. theor. Phys., Moscow,* **7,** 163.
CHAMBERS, R. G., 1952, *Proc. roy. Soc.* A, **215,** 481.
COHEN, M. H., and GOLD, A. V., 1960, *Phil. Mag.* (to be published).

GALT, J. K., MERRITT, F. R., YAGER, W. A., and DAIL, H. W., JR., 1959, *Phys. Rev. Letters*, **2,** 292.
GOLD, A. V., 1958, *Phil. Trans.* A, **251,** 85.
HEINE, V., 1957, *Phys. Rev.*, **107,** 431.
LANGENBERG, D. N., and MOORE, T. W., 1959, *Phys. Rev. Letters*, **3,** 328.
PIPPARD, A. B., 1950, *Proc. roy. Soc.* A, **203,** 98; 1954, *Ibid.*, **224,** 273; 1957, *Phil. Trans.* A, **250,** 325.
REUTER, G. E. H., and SONDHEIMER, E. H., 1948, *Proc. roy. Soc.* A, **195,** 336.
SMITH, G. E., 1959, *Phys. Rev.*, **115,** 1561.
TEGART, W. J. McG., 1956, *The Electrolytic and Chemical Polishing of Metals* (Pergamon Press).

The Anisotropy of Optical Absorption Induced in Sapphire by Neutron and Electron Irradiation†

By E. W. J. MITCHELL, J. D. RIGDEN‡ and P. D. TOWNSEND
Physics Department, The University, Reading

[Received April 27, 1960]

ABSTRACT

Measurements have been made of the anisotropy of the optical absorption induced by neutron and electron irradiation. Some of the measurements were made with a six-plate fluorite polarizer, whose efficiency was found to be 65% at 2500 Å, and which could be used at shorter wavelengths than a Glan–Thomson prism.

In the spectrum induced by neutron irradiation, bands are resolved at −185°c at 1·9, 2·2, 2·8, 3·5, 4·1, 4·8 and 6·1 ev, the latter being measured both with a quartz spectrophotometer and a fluorite vacuum spectrograph. The 6·1 ev band was found to be isotropic but the 2·8, 3·5, 4·1 and 4·8 ev bands were anisotropic, having parallel to perpendicular ratios greater than 1. The anisotropy measurements reveal the presence of a band of opposite anisotropy at 5·3 ev. In order to account for the complete shape of the spectrum of the anisotropic ratio it is necessary to assume the presence of other bands having the same anisotropy as the 5·3 ev band. The 5·3 ev band did not appear in the electron irradiated specimens, although both the 4·8 ($\mu_{\parallel} < \mu_{\perp}$) and 6·1 ev (isotropic) bands were found. Possible models for these two centres are discussed.

The rate of decrease of absorption with heat treatment has been measured for temperatures up to 500°c and is compared with the rate of recovery of the neutron induced expansion studied by Martin (1959).

§ 1. INTRODUCTION

BOTH Levy (private communication, 1957) and Rigden (1958) have found that the radiation-induced absorption spectrum has more structure than originally reported by Levy and Dienes (1954). The spectrum comprises several overlapping bands which Levy has analysed into Gaussian bands having peaks at either: 6·02, 5·34, 4·84, 4·21, 3·54, 2·95 and 2·42 ev; or, 6·06, 5·82, 5·54, 4·84, 4·07, 3·44, 2·85 and 2·41 ev. It is clearly desirable to resolve these bands experimentally.

Sapphire has a rhombohedral unit cell and it is therefore likely that absorption bands associated with defects in the structure will be anisotropic. Different centres will, in general, be expected to show differing amounts of anisotropy. Thus, the study of the anisotropy of absorption, particularly at low temperatures, can be expected to give experimental information about some of the details of overlapping bands. We have therefore measured the anisotropy of absorption in polarized light from 6000–2000 Å.

---

† Communicated by the Authors.
‡ Now at National Research Council, Ottawa.

It has already been shown by Gibbs *et al.* (1957) that a band can be produced at 4·8 ev by oxidation. In fact, this band is often found in unirradiated crystals, having presumably been formed in the oxidizing conditions prevailing at growth. However, before the 4·8 ev radiation induced band is ascribed, without doubt, to the same centre it is desirable that some property in addition to peak energy should be shown to be the same. We have used optical anisotropy as an additional property and the results are presented in the paper.

§ 2. Experimental

2.1. *Materials*

The crystals used were artificial sapphires grown by the Salford Electrical Instruments Ltd. Our specimens were in the form of discs 15 mm diameter and 1 or $\frac{1}{2}$ mm thick. The optic axis (c-axis)—that is, the body diagonal of the rhombohedral cell—is in the plane of the disc. Both this axis, and the perpendicular direction lying in the plane, were determined by back reflection Laue photographs. Spectrographic analysis indicated that Na (2 ppM), Ca, Cu, Mg and Si (1 ppM) were the principal impurities.

2.2. *Method of Measurement*

The optical transmission spectra were measured in two Hilger UVISPEK spectrophotometers, the useful ranges of which were about 10 000–2100 Å and 10 000–1950 Å respectively. Measurements in the vacuum ultraviolet were made using the apparatus described by Mitchell and Paige (1956). In the sapphire measurements, however, the plate calibration was determined using a set of sectored discs which were rotated in vacuum rather than by oscillating grids. The construction and operation of this device were described by Rigden (1958) and will be published separately.

Reflection losses were calculated using the refractive indices determined by Kebler (1954) and absorption coefficients were calculated from:

$$T = (1-R)^2 \exp(-\mu x) \qquad \ldots \ldots \quad (1)$$

where T is the percentage transmission, R the reflection from a sapphire/air interface, μ (cm^{-1}) the absorption coefficient and x (cm) the specimen thickness. None of the crystals before irradiation had a transmission spectrum which could be accounted for by assuming that reflection was the only loss. The additional losses are believed to arise partly from surface scattering and in part from absorbing centres present in the crystals from growth. The former effect was eliminated as far as possible, by setting the crystal always in the same position in the mounting vice; this was particularly important in the bleaching experiments. In the unirradiated crystals the amount of absorption present was less than 3 cm^{-1} for photon energies up to 5 ev, but could be as high as 5 cm^{-1} at higher photon energies.

Much more absorption, up to 20 cm^{-1} at 6 ev, was present in one batch of crystals, which was not used in the irradiation experiments.

2.3. *Measurements using Polarized Light*

The quantity we wish to determine is the anisotropic ratio

$$(\mathscr{A}=\mu_{\mathbf{E}\parallel c}/\mu_{\mathbf{E}\perp c})$$

Fig. 1

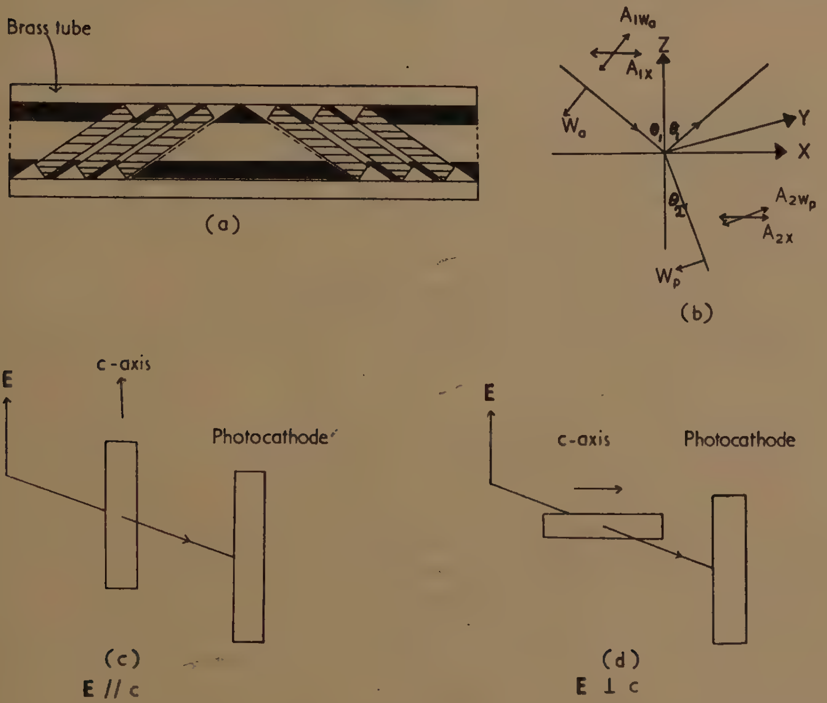

(*a*) The fluorite polarizer—CaF_2 plates separated by brass spacers in a brass tube.
(*b*) Definitions of quantities used in calculating the efficiency of the polarizer: light in medium 1 incident at θ_1 and having amplitudes A_{1y}, A_{1x} and A_{1wa}; angle of refraction θ_2 and in medium 2 the amplitudes are A_{2y}, A_{2x} and A_{2wp}; the axes w_a and w_p are perpendicular to the directions of propagation in the respective media and lie in the plane of the beams.
(*c*) and (*d*) Relative positions of **E**, *c*-axis of crystal and photocathode surface, as used for determining $\mu_{\mathbf{E}\parallel c}$ and $\mu_{\mathbf{E}\perp c}$.

as discussed by Mitchell and Paige (1955), and Mitchell and Rigden (1957). Light from the monochromator is partially polarized and the response of the photocells is sensitive to the direction of **E**. Measurements of these effects were reported by Mitchell and Paige (1955).

In determining $\mathscr{A}$ it is necessary to eliminate the anisotropy of the sensitivity of the photocell. Thus we determine $\mu_\parallel$ and $\mu_\perp$ separately.

Having determined say $\mu_{\parallel}$ one could determine $\mu_{\perp}$ by rotating the polarizer through 90° and measuring $T_{\perp}$ in the usual way—by moving the specimen in and out of the beam. The disadvantage of this procedure is that if the initial (||) direction is chosen to utilize the maximum intensity from the monochromator, the second (⊥) measurement is made with a smaller amount of energy, and therefore with less accuracy. Consequently we have determined ($\mu_{\perp}$) by rotating the crystal through 90°, and remeasuring the transmission curve in this position (fig. 1 (*c*) and (*d*)). Unless otherwise stated, the anisotropy before irradiation was found to be negligible.

2.4. *Polarizers*

Polaroid sheet was used as the polarizer in the visible region. For the ultra-violet a fluorite plate polarizer was made, some measurements being also carried out using a Glan-Thomson polarizer.

The plate polarizer contained six plates mounted in a brass tube with brass spacers as shown in fig. 1 (*a*). The plates were set at an angle (θ_1) of $(55{\cdot}5 \pm 0{\cdot}5)°$, which is the optimum polarizing angle for a refractive index of $1{\cdot}455 \pm 0{\cdot}014$ which for fluorite occurs at 2900 Å.

After crossing one interface the amplitudes of **E** in two directions y and w defined in fig. 1 (*b*), are given, for example in Ditchburn (1952), by:

$$A_{2w_p} = \frac{A_{1w_a} 2 \sin\theta_2 \cos\theta_1}{\sin(\theta_1+\theta_2)\cos(\theta_1-\theta_2)}$$

and

$$A_{2y} = \frac{A_{1y} 2 \sin\theta_2 \cos\theta_1}{\sin(\theta_1+\theta_2)} .$$

On emerging from the sixth plate the light is polarized by an amount represented by the polarization efficiency p, where

$$p = \frac{(A_{13w_a})^2 - (A_{13y})^2}{(A_{13w_a})^2 + (A_{13y})^2}$$

which can be written as:

$$p = \frac{1 - \cos^{24}(\theta_1-\theta_2)}{1 + \cos^{24}(\theta_1+\theta_2)} . \qquad \qquad (2)$$

The spectrum of the calculated efficiency is shown in fig. 2.

The spectral efficiency of the plate polarizer has been investigated using light polarized by the Glan–Thomson prism. The transmission of the plate polarizer ($T = I_T/I_0$) for both the parallel ($T_{\parallel}$) and perpendicular ($T_{\perp}$) orientations was measured in the UVISPEK. If the efficiency of the Glan–Thomson prism were 100% the quantity $p_e = (T_{\parallel} - T_{\perp})/(T_{\parallel} + T_{\perp})$ would represent the efficiency of the plate polarizer. The spectrum of p_e is shown in fig. 2, from which it will be seen that the measured efficiency is close to the calculated value, being 1 to 6% less throughout the range covered. This difference arises from the inaccuracy of setting the plates, the fact that the Glan–Thomson will not be 100% efficient and possibly some surface irregularities on the fluorite plates.

The use of a polarizer which is not 100% efficient means that the measured value of the anisotropic ratio will be less than the true value. For a true anisotropic ratio of 1·5 a 60% efficient polarizer will give a value of $\mathscr{A} = 1{\cdot}3$; and for a true value of 3·0 the measured value would be 2·0. In our measurements on sapphire a much larger uncertainty in the true value of $\mathscr{A}$ for a particular band arises because of the uncertainty about the relative amounts of the 'wings' of overlapping bands.

Fig. 2

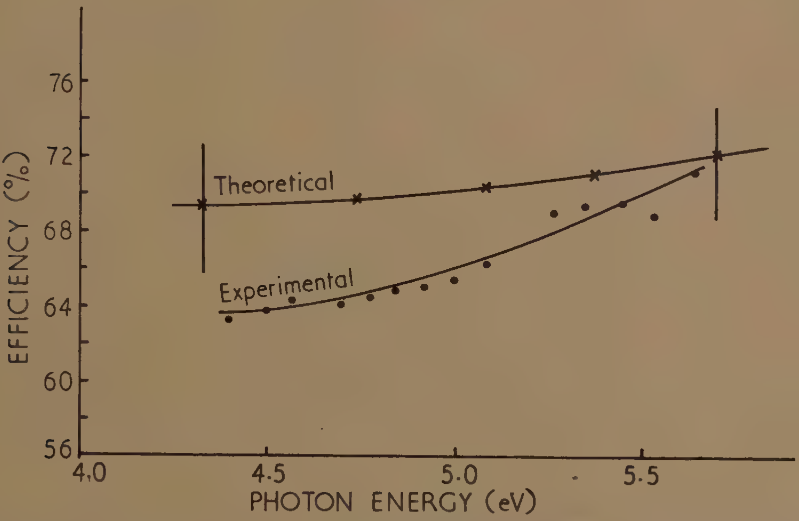

Comparison of the measured and calculated efficiencies of the fluorite plate polarizer.

2.5. *Irradiations*

Neutron irradiations were carried out at about 30°c in the Harwell pile BEPO. The specimens were irradiated with electrons from a 2 Mev Van de Graaff accelerator. For the electron irradiations the crystals were mounted in Wood's metal in a water cooled brass block.

§ 3. Results

3.1. *The Absorption Spectrum*

The spectrum measured at room temperature after reactor irradiation is shown in fig. 3. The measurements on this specimen for photon energies greater than 5·8 ev were obtained using the vacuum ultra-violet spectrograph and show the strong absorption band at 6·1 ev previously reported by Levy and Dienes (1954). For lower dose irradiations it is possible to see this peak in the spectrophotometer results. Other bands are found at 4·8, 4·1, 3·5 and 2·8 ev, the last three not being reported by Levy and Dienes (1954) but having been seen independently by Levy (1957). We shall refer later to the relative peak heights of the 6·1 and 4·8 ev bands; for the spectrum of fig. 3 the ratio of peak heights is 4·1 : 1.

Fig. 3

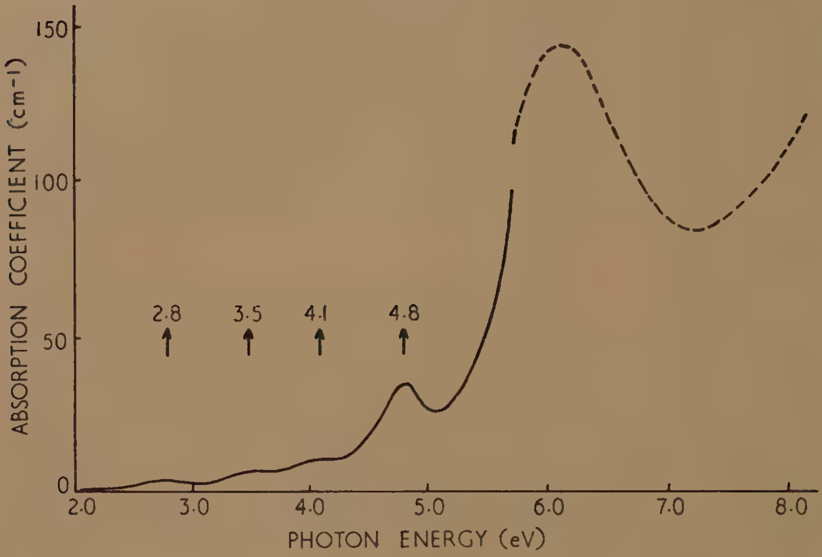

The absorption spectrum of neutron irradiated sapphire, including the vacuum ultra-violet region.

Fig. 4

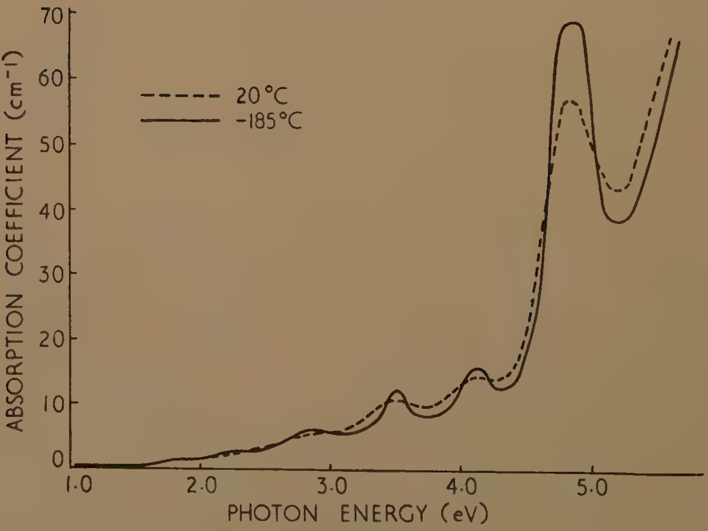

The absorption spectrum of neutron irradiated sapphire at 20°c and −185°c.

Low-temperature measurements have been made for photon energies up to 5·8 ev and as will be seen from fig. 4 the bands sharpen although the integrated absorption is within 3% of the absorption at room temperature. Additional bands are resolved at 1·9 and 2·2 ev. There was a trace of an

Fig. 5

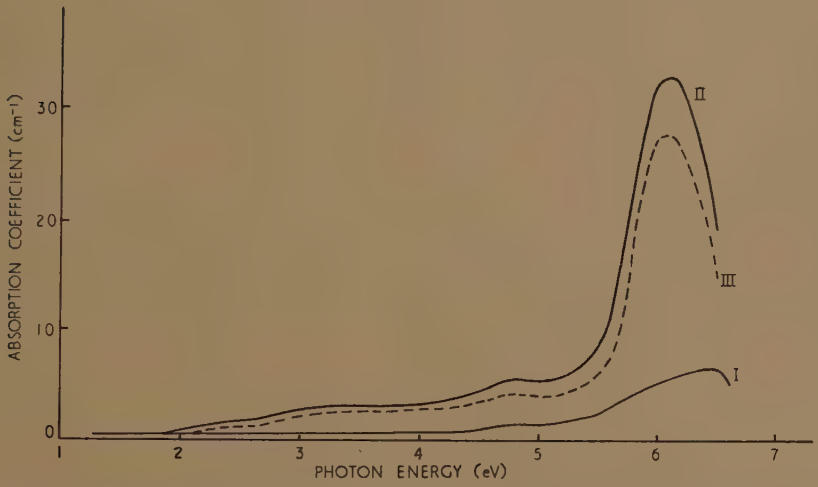

The absorption spectrum before (I) and after (II) irradiation with 2 Mev electrons (10 500 μA min cm^{-2}); the induced spectrum is curve III.

Fig. 6

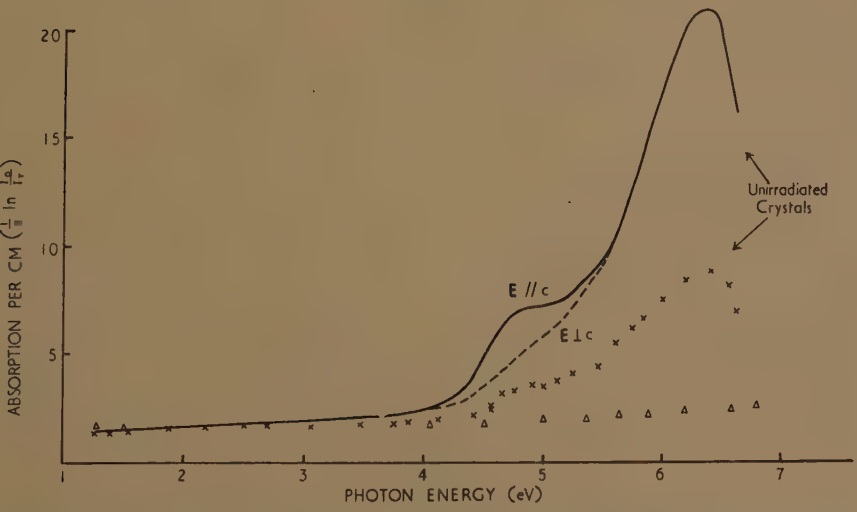

The absorption per unit length of two unirradiated crystals showing the 4·8 ev band. The points shown by △ △ △ are the calculated values of the reflection loss for a non-absorbing crystal.

absorption band at 1·9 ev in the x-ray induced absorption reported by Hunt and Schuler (1953), who found in addition weak (*ca.* 1 cm^{-1}) bands at 3·1 and 5·4 ev. Levy and Dienes (1954) also reported the presence of the 3·1 and 5·4 ev bands in γ-irradiated sapphire.

A typical spectrum induced by 2 Mev electron irradiation is shown in fig. 5. The strongest peaks of the spectrum after neutron irradiation are present (6·1 and 4·8 ev) and there is some indication of a band at 3·1 ev. It appears that the tail of the 6·1 band extends to the region of the 4·8 ev absorption. The ratio of the heights of the 6·1 and 4·8 ev peaks is 6·7. Because of the lower absorption this value has been determined from the induced spectrum and, as with the value quoted above for the neutron irradiation, no allowance has been made for overlap.

Gibbs *et al.* (1957) have reported in a brief communication that the 4·8 ev band could be produced in sapphire by heating in oxygen above 1300°C. They also found that the band could be removed by subsequent heating in hydrogen. We have found a weak band at 4·8 ev in crystals heated in air at 1400°C and the band was present before irradiation in one batch of crystals supplied by the manufacturer. The absorption spectrum of one of these crystals is shown in fig. 6.

3.2. *The Anisotropy of Absorption*

The anisotropy of the absorption induced by neutron irradiation is shown in fig. 7 and the spectrum of the anisotropic ratio ($\mathscr{A}$) in fig. 8, $\mathscr{A}$ for the 4·8 ev band being shown in more detail in fig. 9. The contribution from the 6·1 ev band appears to be isotropic and this has been confirmed at lower wavelengths using the fluorite plate polarizer. There are peaks showing positive anisotropy ($\mathscr{A}-1>0$) at 4·8, 4·1, 3·5 and 2·8 ev. These peaks were all resolved in the straight-forward absorption spectrum. It will also be seen from fig. 8 that the anisotropy is negative for photon energies near 5·3, 4·4, 3·8 and 3·3 ev, none of which energies corresponds to resolved absorption peaks.

We consider first the negative anisotropy in the region of 5·3 ev. There is no doubt that the absorption at 5·3 ev is contributed to by the low-energy tail of the 6·1 ev band and the high-energy tail of the 4·8 ev band. However, the first of these is isotropic and the second has positive anisotropy so that to obtain a negative anisotropy we have to assume that there is a strong contribution at 5·3 from a band having negative anisotropy. The assumed band obviously cannot be sharp otherwise it would be resolved in the absorption spectrum. As was pointed out above Levy (1957) had to postulate a band either at 5·34 or 5·54 ev in order to account for the observed spectrum in terms of overlapping Guassian bands. Our anisotropic measurements are consistent with a band at 5·34 ev having a negative anisotropy such that $\mathscr{A}<0·55$. It is likely that this is the same band which is resolved in γ-irradiated specimens when both 4·8 and 6·1 ev bands are absent.

Fig. 7

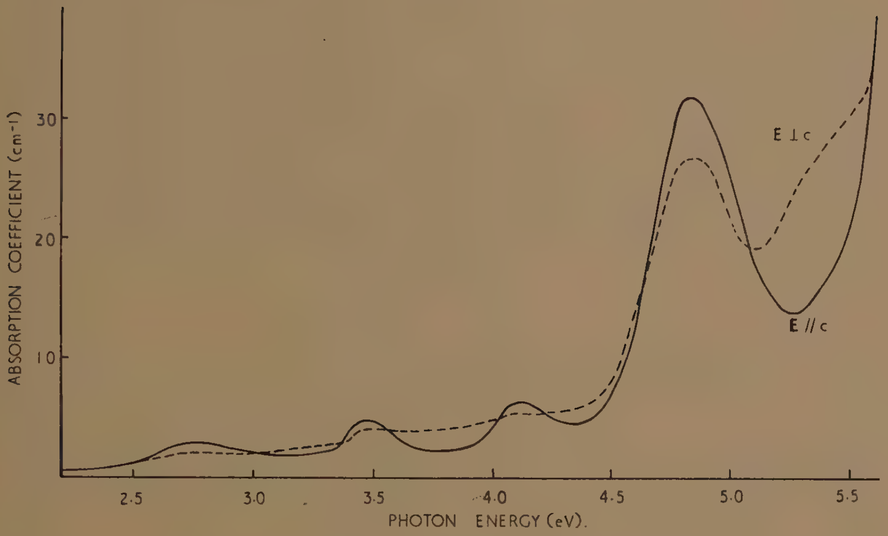

Absorption spectrum induced by neutron irradiation: – – – – – – – – – $\mathbf{E}_{\perp c}$; ———————— $\mathbf{E}_{\parallel c}$. Measurements at −185°c.

Fig. 8

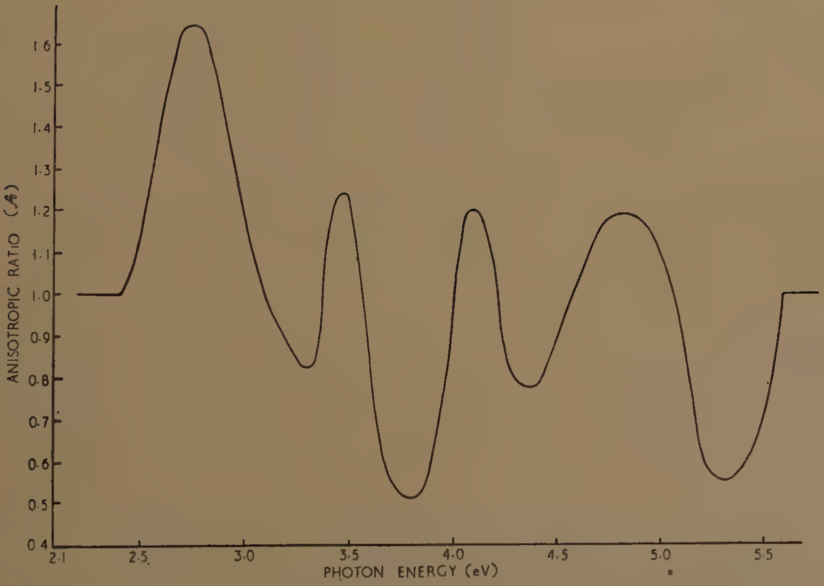

Spectrum of the anisotropic ratio of a neutron irradiated crystal.

In order to account for the remaining part of the $\mathscr{A}$-spectrum it is not necessary to assume bands of negative anisotropy at all the minima (4·4, 3·8 and 3·3 ev). One simpler possibility is that there is a wide band having negative anisotropy at 3·8 ev. The small negative anisotropy at 4·4 ev could then be accounted for by overlap from the 3·8 and 5·34 ev bands (both negative) beyond the relatively narrower, and resolved, bands at 4·1 and 4·8 ev (both positive). Similarly, the small negative anisotropy at 3·3 ev could be accounted for by the stronger contribution of the negative 3·8 ev band beyond the narrower, and resolved, band at 3·5 ev (positive anisotropy). One alternative possiblity is that there is a wide unresolved 3·1 ev band present, the band which is found in γ-irradiated crystals. Such a band having negative anisotropy would account for the rapid decrease of $\mathscr{A}$ on the high-energy side of the 2·8 ev band (positive anisotropy), and would be sufficiently wide to account for the negative anisotropy at 3·8 ev, between the much narrower bands at 3·5 and 4·1 ev (positive anisotropy). For this alternative, however, one has to assume either an additional negative band at about 4·4 ev, or that the absorption at 4·4 ev is dominated by contributions from the 3·1 and 5·4 ev bands.

Fig. 9

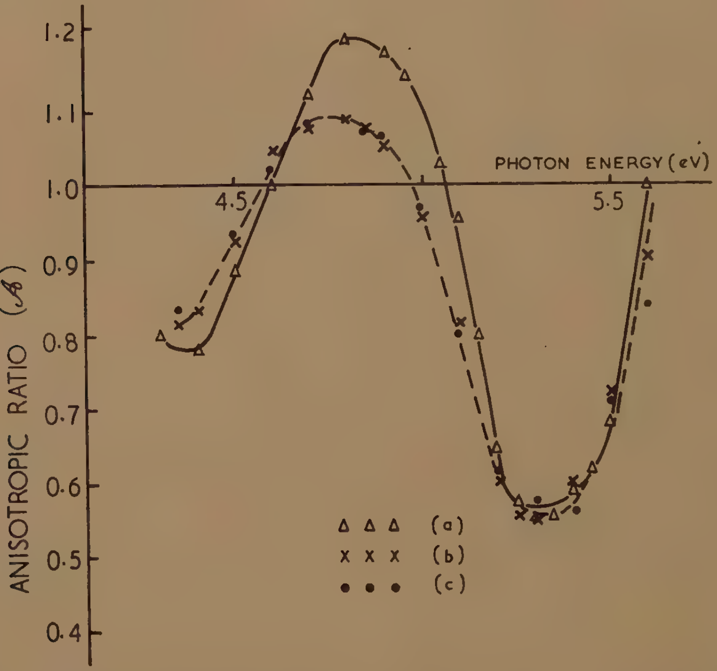

Spectrum of the anisotropic ratio in the region of 4·8 ev: (*a*) specimen R1 measured at −185°c using the Glan–Thomson; (*b*) R1 measured at 20°c using the fluorite plate polarizer; and (*c*) specimen R2A measured at 20°c with the plate polarizer.

These results of measurements of the anisotropy of absorption may be summarized as follows:

Bands of positive anisotropy:

2·8 ev $\mathscr{A} > 1{\cdot}65$,
3·47 ev $\mathscr{A} > 1{\cdot}24$,.
4·10 ev $\mathscr{A} > 1{\cdot}20$,
4·80 ev $\mathscr{A} > 1{\cdot}20$.

Bands of negative anisotropy:

5·34 ev $\mathscr{A} < 0{\cdot}55$.

At least one other $\mathscr{A} < 0{\cdot}50$,
either at 3·8 ev or 3·1 ev.

The positive bands are resolved as peaks in the absorption spectrum, the negative bands are not; in addition the isotropic 6·1 ev band is resolved in the absorption spectrum.

The anisotropy of the absorption spectrum induced by electron irradiation is shown in figs. 10 and 11. Because of the small absorption below 3 ev it was not possible to obtain experimentally reproducible results in that region. However, the fall of $\mathscr{A}$ below 3·4 ev is significant as are the values at higher photon energies. The most noticeable feature of fig. 11 is the absence of an effect which could be readily associated with a negative 5·34 ev band. The anisotropy spectrum could be accounted for by:

Bands of positive anisotropy:

3·4 ev $\mathscr{A} > 1{\cdot}6$,
4·8 ev (resolved in absorption spectrum) $\mathscr{A} > 1{\cdot}5$.

Bands of negative anisotropy:

Either 3·1 or 3·8 ev, or both, $\mathscr{A} < 1{\cdot}0$.

Neither of the negative bands is resolved in the absorption spectrum but the isotropic 6·1 ev band is resolved. We suggest that the overlap from the 3·8 ev band extends towards 5 ev and that the anisotropy of 1·5 at 5·3 ev is entirely due to overlap from the 4·8 ev band, there being also a contribution to the absorption from the isotropic 6·1 ev band. The 5·3 band if present in electron irradiated crystals, is very weak. Negative anisotropy at 5·3 ev was however obtained in such a crystal after subsequent neutron irradiation.

Finally the anisotropy has been measured of the absorption in one of the unirradiated crystals containing a band at 4·8 ev. The parallel and perperdicular curves are shown in fig. 6 from which it will be seen that the 4·8 ev band has positive anisotropy, as is found for the band induced at 4·8 ev by particle irradiation.

3.3. *The Effect of Heat Treatment on the Induced Absorption*

A neutron irradiated specimen was heated in an open furnace for 30 min at successively higher temperatures up to 500°c and the absorption spectrum measured after each heat treatment. The isochronal recovery curves for the absorption peaks 4·1, 4·8 and 6·1 ev are shown in fig. 12, the results being normalized to be 100 before heat treatment. Martin's[†] (1959) results for the recovery of the length of reactor irradiated sapphire are also shown, having also been normalized to be 100 before heat treatment.

Fig. 10

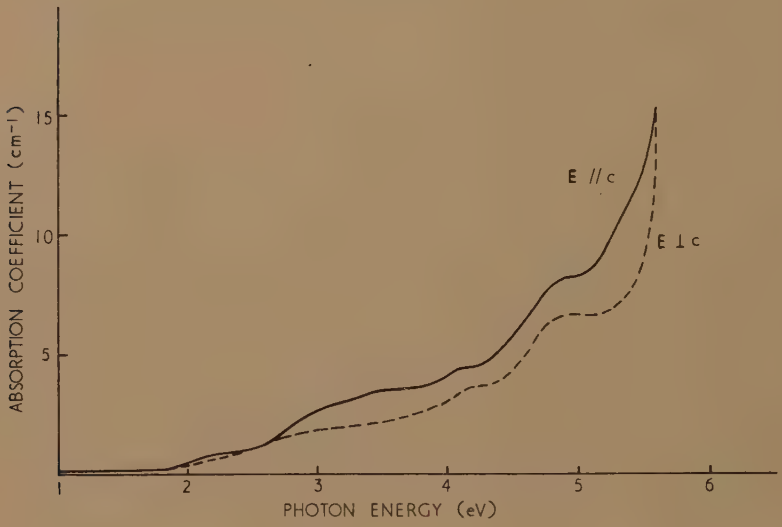

The absorption spectrum after electron irradiation: ———— $\mathbf{E}_{\parallel c}$; and - - - - - $\mathbf{E}_{\perp c}$.

Fig. 11

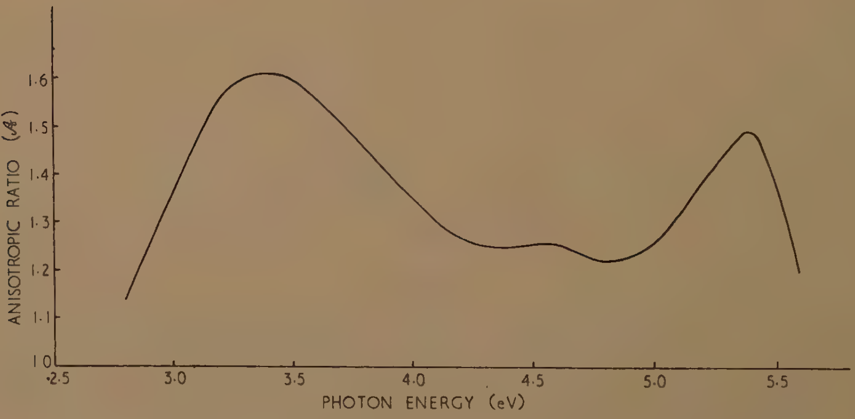

Spectrum of the anisotropic ratio of an electron irradiated crystal.

[†] The specimens used by Martin were supplied by the Salford Electrical Instruments, Ltd. and were reported to contain 3000 ppM of Si, 500 of Cr, 100 of Ni and 50 of Mn.

It will be seen that the rate of decrease of the 4·1 ev band is similar to the rate of recovery of the induced expansion parallel to the c-axis. On the other hand the 4·8 ev and 6·1 ev bands decrease at a rate similar to the rate of recovery of the *mean* induced expansion, although above 400°c the 6·1 ev band decreases more rapidly.

Fig. 12

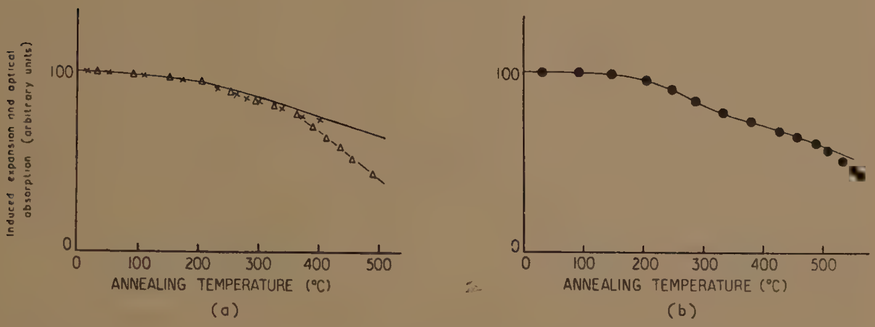

The decrease of induced expansion (Martin) and optical absorption with heat treatment: (*a*) recovery of mean expansion shown as full line; (*b*) recovery of expansion ∥ c-axis shown as full line; optical absorption data shown by × × × (4·8 ev) and △ △ △ △ (6·1 ev) on (*a*); and ● ● ● (4·1 ev) on (*b*).

§ 4. Discussion of Results

The major additional feature which is resolved by measuring the anisotropy of the induced absorption is that at 5·3 ev, a band at this energy having previously been indicated by Levy's (1957) Gaussian analysis of the partially resolved spectrum. Because of the overlapping, however, it is not possible to determine exact values of $\mathscr{A}$ for individual centres, but only to fix lower, or higher limits.

The values of $\mathscr{A}$ to be expected for transitions involving wave functions localized in particular directions may be calculated from the relation given by Mitchell and Rigden (1957). For a uniaxial crystal having 3-fold symmetry about the axis:

$$\mathscr{A} = \frac{\sum\limits_x 3n_x \cos^2\theta_x}{\sum\limits_x n_x \cdot \frac{3}{2}\sin^2\theta_x}$$

where the set x of $3n_x$ dipole oscillators makes an angle θ_x with the c-axis. In the case where there is only one set of $3n$ at θ the anisotropic ratio $\mathscr{A} = 2\cot^2\theta$. Some values are given in the table for simple directions in the α–Al_2O_3 structure.

From the table it will be seen that using these directions the only way of obtaining small values of $\mathscr{A} < 1$ (negative anisotropy) would be from wave-functions directed along the closest 0–0 directions. In order to give non-zero values these directions would have to lie slightly out of the (001) plane. Such a distortion could arise because of an adjacent Al vacancy. There are other possibilities for localized orbitals lying close to the (001) plane, e.g. the association of an Al vacancy and an interstitial impurity, or an oxygen vacancy with an impurity atom in a normal oxygen position. It is clear that the experimentally established negative anisotropy of the 5·3 ev band cannot be associated with Al–0 or Al–Al directions.

The anisotropy of the 2·8 ev band ($\mathscr{A} > 1{\cdot}65$) could be accounted for if the orbitals involved were directed either along Al–0 directions, or along some of the combinations of Al–Al directions, but not along 0–0. This band appears only after neutron irradiation and is presumably associated with a displacement, either in some stage of aggregation or single.

Anisotropic Ratios for Transitions Involving Particular Directions in Sapphire

Direction in crystal	Angle with *c*-axis	$\mathscr{A}$	Possible centre
Al–0	N.N. 3 at 46° 36′. Effect from N.N. and 3 N.N.N. at 59° 6′, assuming the 6 to be equivalent	1·79 1·16	Al vacancy; directed bonds from oxygens remaining in original directions (cf. Coulson and Kearsley 1957, diamond).
0–0	N.N. 3 at 90°. Effect from N.N. and 3 N.N.N. at 33° 48′	0 1·25	Al vacancy and a trapped hole; hole localized in N.N. 0—0 or shared along 6 edges of 0 octahedron
Al–Al	N.N. 1 at 0°. Effect from N.N. and 3 N.N.N. at 78° 25′.	∞ 2·33	0 vacancy and trapped electron shared between neighbouring Al–Al

The strongest band induced is that at 6·1 ev, which is isotropic. This centre could be an interstitial atom. If it were a substitutional centre the table shows that the transition could not be associated with the closest Al–0, Al–Al or 0–0 directions.

The positive anisotropy found for the 4·80 ev band, whether produced by irradiation or from growth is further evidence that it is the same centre involved in both cases. Gibbs *et al.* (1957) induced a band at 4·8 ev by heating in oxygen and we suggest that this is either due to interstitial oxygen, or the oxygen atoms surrounding an Al vacancy. However, the 4·8 ev band reported in this paper is not isotropic, so that we prefer the latter alternative. Finally, the 6·1 and 4·8 ev bands have always appeared together and with approximately the same relative strengths (5 ± 1). It is possible, therefore, that these two bands are associated with complementary centres. This would also be consistent with an interstitial model for the 6·1 ev band, and leads to the specific suggestion that it results from an electron trapped at an interstitial Al ion. Arnold (1960) has also suggested, in a brief communication and for different reasons, that the 6·1 ev band is associated with Al displacements.

§ 5. CONCLUSIONS

The absorption spectrum induced by irradiation as measured with unpolarized light contains unresolved bands which can be detected using polarized light. The strongest damage band (6·1 ev) is isotropic having on its low-energy side a normally unresolved band (5·3 ev) which is only induced by neutron irradiation. Because the anisotropy of the 4·8 ev band has been found to be positive in both irradiated and unirradiated specimens it is concluded that this band is associated with the centre induced by oxidation as reported by Gibbs. On the basis of the present evidence we ascribe the 4·8 ev band to a transition on an oxygen ion surrounding an Al vacancy, and the 6·1 ev band to an electron trapped at an interstitial Al ion.

Independently of these models the decrease of optical absorption with heat treatment up to 400°C involves similar processes to the recovery of linear dimensions as reported by Martin (1959).

ACKNOWLEDGMENTS

We wish to thank Professor R. W. Ditchburn for his interest and both Mr. J. W. Ryde, F.R.S., and Mr. L. A. Thomas of the G.E.C. Research Laboratories, Wembley, for arranging the supply of some of the crystals. Two of the authors (J. D. R. and P. D. T.) wish to acknowledge the receipt of D.S.I.R. maintenance grants.

REFERENCES

ARNOLD, G. W., 1960, *Bull. Amer. phys. Soc.*, **5**, 167, IAl.
COULSON, C. A., and KEARSLEY, M. J., 1957, *Proc. roy. Soc.* A, **241**, 433.
DITCHBURN, R. W., 1952, *Light* (London: Blackie),
GIBBS, P., CUTLER, I. B., and BATES, J. L., 1957, *Bull. Amer. phys. Soc.*, **2**, 300, B12.
KEBLER, R. W., 1954, *Proc. Inst. Soc. Amer.*, **9**, part 2. Paper No. 54–3–5.
LEVY, P. W., and DIENES, G. J., 1954, *Report of Bristol Conference on "Defects in Crystalline Solids"* (London: Physical Society).
MARTIN, D. G., 1959, *Phys. Chem. Solids*, **10**, 64.
MITCHELL, E. W. J., and PAIGE, E. G. S., 1955, *Phil. Mag.*, **46**, 1353; 1956, *Ibid.*, **1**, 1085.
MITCHELL, E. W. J., and RIGDEN, J. D., 1957, *Phil. Mag.*, **2**, 941.
RIGDEN, J. D., 1958, Ph.D. Thesis, University of Reading.
SCHULER, R. H., and HUNT, R. A., 1953, *Phys. Rev.*, **89**, 664.

Some Observations on the Stress-corrosion Cracking of α-brass and Similar Alloys†

By C. Edeleanu
Tube Investments Research Laboratories, Hinxton Hall, nr. Cambridge

and A. J. Forty
H. H. Wills Physics Laboratory, University of Bristol

[Received May 14, 1960]

Abstract

An attempt has been made to establish a mechanism for stress corrosion by direct observation on the propagation of cracks in α-brass tested under ammonia. The observations indicate that failure might be described by a two-stage process, of local embrittlement followed by a cleavage-like fracture. Such a model demands that the embrittled zone should have its mechanical properties modified in such a way as to allow a crack to form and reach some critical velocity, whilst the normal unattacked metal should be able to support this free-running crack for extensive failure to occur. These requirements are examined in the light of current ideas on the metal physics of fracture.

§ 1. Introduction

The failure of certain alloys under the simultaneous action of static stress and exposure to a corrosive environment is a well-known phenomenon (see, for example, the two recent symposia on the subject (Robertson 1956, Rhodin 1960)). There is as yet, however, no completely satisfactory explanation. The phenomenon presents an interesting relationship between mechanical failure and chemical attack, neither of which is sufficient alone to produce serious damage. Some explanations (for example, that put forward recently by Hoar and West 1958) emphasize the importance of the chemical attack, considering that the plastic yielding of the crystal under the applied stress enhances the rate of dissolution of metal at the tip of the crack. Others regard the failure as a purely mechanical breakdown in a material which has become embrittled by exposure to the corrosive reagent.

The present studies of crack propagation in stress corrosion were carried out in an attempt to distinguish between these processes by direct observation. We suggest below that the mechanical factor appears to be at least as important as the chemical one, although complete embrittlement is not essential ; local embrittlement of a zone at the free surface of a crystal or around the tip of a static crack is all that is necessary to initiate fracture, and this can propagate through the non-embrittled metal provided a high crack velocity is maintained.

---

† Communicated by the Authors.

Our observations on the progress of cracks in α-brass lead us to propose a model of transcrystalline stress-corrosion cracking based on the process of embrittlement followed by brittle crack propagation. It is noteworthy that those systems which exhibit transgranular failure have a number of common features, all of which are required by this model. For example, alloys like copper/zinc and copper/gold probably contain varying degrees of short-range lattice order. This is significant since short-range order should have a marked effect on the mechanical properties of the alloy as far as crack propagation is concerned. Again, the corrosive environments which lead to cracking produce only a selective attack of the alloy (for example, ferric chloride oxidizes the copper in copper/gold, ammonia selectively removes zinc from brass). This is important since it can lead to a form of embrittlement which, according to our ideas, forms a possible mechanism for the initiation and further propagation of a brittle crack.

The observations on which this paper is based deal mainly with the *propagation* of cracks in stress corrosion. This arises from two considerations. Firstly, with present techniques it is not possible to observe the initiation of a crack directly ; the crack must have propagated some distance before it becomes visible. Secondly, we consider that the propagation of the crack is equally important in determining the failure of a specimen and this, of course, can be observed directly. Our experiments and the ideas developed from them do in fact justify this approach. It will be shown in a later section how these ideas tend to indicate the kind of relationship to be expected between susceptibility to stress-corrosion and alloy structure, composition, the degree of preliminary cold work and the nature of the corrosive environment.

§ 2. EXPERIMENTAL TECHNIQUE

The system adopted for the present study is α-brass in ammonia. This is a useful system experimentally since α-brass is easily controllable in crystal form, composition and surface finish. We have used as our stock material a high purity brass supplied by I.C.I. (Metals Division), having an initial composition :

Cu	As	Sn	Ni	Fe	Mn	Bi
69·71	0·003	trace	0·01	0·01	0·05	trace

Some zinc is lost from this material during the preparation of single crystals but analyses have shown that this does not appreciably alter the composition, particularly in the central regions of the crystals where our observations of crack propagation are made.

Good single crystals can be grown fairly easily by using a closed graphite mould lowered slowly through a temperature gradient. A light mechanical polish of these crystals followed by electropolishing in a phosphoric acid bath produces surfaces which are completely satisfactory for microscope observations.

Normally, when brass is exposed to ammonia vapour the surfaces tarnish very rapidly. This is due to the presence of oxygen and the tarnishing can be minimized by fully immersing the brass in a solution of ammonia. Consequently, in order to preserve the high optical quality of the surfaces, our observations have been made using an apparatus which allows continuous viewing at high magnification whilst the specimen is deformed in bending fully immersed in ammonia. A diagram of this apparatus is shown in fig. 1†. The load applied to bend the specimen is controlled directly by the compression of the spring under the movement of the screw.

Fig. 1

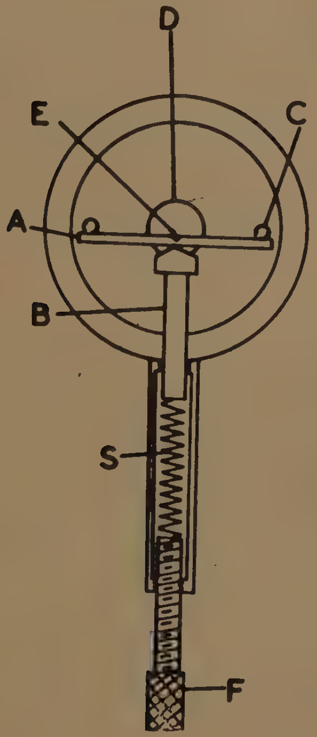

Diagram of straining apparatus. A. Brass specimen. B. Steel piston. C. Steel peg. D. Glass window (cover slip). E. Notch in specimen. F. Steel screw. S. Steel spring.

The experimental procedure is as follows. The specimen is strained in bending with a residual stress applied through the compressed spring. Ammonia is added to the cell and the surface of the specimen is continuously viewed through the glass window with a high-power water-immersion microscope objective. Areas of the polished surface can be photographed before and after the crack appears and, in this way, it is possible to correlate the mode of propagation with the grain, orientation and pre-deformation of the specimen. This kind of observation is greatly assisted by notching the specimen before straining to localize the heavily cold-worked area and therefore the area of cracking. It must be emphasized that the notching is not an essential requirement for cracking to occur but is simply used for experimental convenience ; unnotched specimens usually fail by the formation of a large number of cracks, notched specimens by one main crack running from the notch.

---

† With the exception of figs. 1 and 7, all figures are shown as plates.

The observations we have made in this way on the propagation of the cracks are obviously limited to surface traces. They have therefore been supported in a few cases by sectioning the specimens after cracking. This has confirmed that the main features of the surface traces, the discontinuities in these traces for example, are characteristic of cracking inside the crystal. That is, our observations, although confined to the surface, appear to provide a reliable indication of the mode of propagation of the complete crack.

§ 3. EXPERIMENTAL OBSERVATIONS

Failures by stress corrosion are usually classified as intergranular or transgranular cracking. With some materials, as for example with the particular α-brass used in the present experiments, there appears to be no fundamental difference between failures by these two paths. It is convenient however to describe the observations separately for single crystals (transgranular failure) and polycrystalline specimens (both intercrystalline and transgranular cracking).

Using the technique just described with single crystals it was noticed that the heavily cold-worked region appearing around the notch after the initial straining could not be prevented from tarnishing. This may be due to the increased chemical activity along slip lines in this area but entrapped air in the notch may also be partly responsible. The surface well removed from the notch is less heavily worked and less tarnished so that high-resolution microscopy is readily achieved here. The small amount of tarnishing which does occur appears to be selective and can in some cases be put to effective use for increasing the visibility of slip lines. For example, in fig. 2, which shows a surface crack initially formed by stress corrosion and then strained open by further stressing, the short slip steps around the tips of the crack are visible only as a result of the tarnishing. This micrograph provides at the same time a good illustration of the high degree of ductility remaining in the brass around the cracked region ; the fracture cannot propagate under stress alone. Moreover, localization of the slip at the tip of the crack indicates a pronounced stress-concentration effect which is characteristic of a mechanical failure, and it is consequently difficult to believe that the crack has advanced in this state purely by chemical dissolution of the brass.

The appearance of the main crack at the notch invariably follows some period of incubation which under the present experimental conditions was about 1–2 hours. It is not possible to observe its formation or even its propagation in detail in this region. However, when the crack finally emerges into the less severely deformed part of the crystal a number of interesting features of the mode of propagation become apparent. These are best illustrated by sequences of micrographs like that of figs. 3–6.

Figures 3–6 show successive stages in the propagation of a free-running crack (i.e. no increased stressing during the test). The crystal in this case has an orientation such that the crack is running closely parallel to the trace of one slip system but cuts across the principal operative slip systems. The crack appears to run in short steps, each step starting and finishing on transverse slip lines. Some of these slip lines are apparently newly produced by the crack, others (and possibly all of them) are pre-existing slip bands which are increased in size by the crack. It appears then that rapid failure occurs in each step but this is terminated at pre-existing slip bands. The stresses around the tip of the crack are relieved now by further slip in the bands and this is accompanied by a corresponding amount of sidewise opening of the crack. This opening of the crack when it reaches a slip band is shown for example in figs. 3–6 and also diagrammatically in fig. 7 (A–C).

Although the crack opens mainly in the way described there appears to be also a slight ‘ yawning ’ as well as a parallel displacement of its surfaces ; this is taken to indicate that the slip at its tip is being restricted or is non-uniform leading to a local rotation of the crystal structure.

The crack halts temporarily at each new slip band and there is a further period of incubation here, although this is not as long as that required for the appearance of the initial crack at the notch and may be as short as one minute. When the next stage in the fracture does occur it appears suddenly as a very fine crack, barely visible under the microscope. This we describe as a ‘ ghost ’ crack. The ‘ ghost ’, which terminates on a slip band, widens slowly into a visible crack by further slip. This succession of events strongly suggests that fracture is occurring, not by the propagation of a single crack, but by a discontinuous process involving the spreading, stopping and re-initiation of separate cracks. This discontinuous fracture process leads to an extremely irregularly shaped surface trace. In the particular case of figs. 3–6 we see that the trace is composed of short straight segments lying between neighbouring slip bands. Side-stepping of the trace occurs frequently ; this presumably means that the new ghost crack is re-initiated from some site further down the slip band or, alternatively, starts from the old crack but tends to spread initially along the slip direction. In either case, failure must eventually occur within the slip band otherwise the full applied load could not be transmitted to the tip of the ghost to maintain propagation.

When the main crack direction is not as closely perpendicular to slip bands as in figs. 3–6, the crack pattern is less simple. In fig. 8, for example, the segments of the trace of the crack are curved but clearly some side-stepping occurs across most of the slip bands. The side-stepping is a characteristic feature of all the specimens tested and we infer that there must be some marked relationship between the propagation of the crack and the crystal structure, and in particular the occurrence of slip bands in the crystal.

Fig. 7

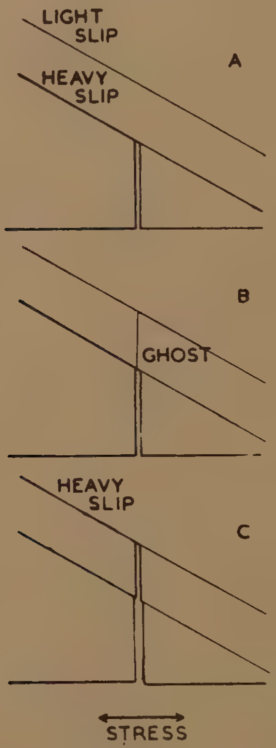

Diagrammatic representation showing stages during crack propagation.

The side-stepping is not confined to the surface traces. This has been demonstrated by taking transverse sections across the cracks. Figure 9, for example, is a micrograph showing in section one of the tested single crystals. We see that the discontinuous nature of the crack extends through the whole crystal ; the crack appears to be a rough fracture composed of a large number of cleavage-like elements. The orientation of the crack relative to the crystal structure in this particular case shows that the cleavage tends to follow the (111) plane.

Although it is not possible to discover the origin of the crack running from the notch, the origin of other minor surface cracking can sometimes be detected. This generally occurs where duplex slip has taken place. That is, where slip is held up by other slip bands, a sufficient stress can be concentrated here to start a crack under the ammonia. A large number of sites of this kind can be seen in fig. 10. Figure 11 shows how, alternatively, cracks can be formed inside heavy slip bands. Some caution must be applied however in attributing all forms of cracking along slip bands to a failure of the bulk material ; some cases have been found in which rupturing the film of tarnish on the surface as the slip steps emerge could be mistaken for cracking of the metal itself.

A number of experiments have been carried out on polycrystalline brass generally prepared by annealing the cold-rolled stock in air at 800°c. We have found that the cracking occurs predominantly near grain boundaries but that a great deal of transcrystalline cracking is also present. The careful study of intercrystalline cracking using the present technique is complicated by the fact that a slight amount of boundary etching is often present, making the detection of the ghost difficult. Observation is further complicated by the branching generally found and the difficulty of predicting which of a number of possible boundaries is likely to fail. However, such evidence as has been obtained indicates that the cracking occurs in exactly the same way as in the single crystal except that it follows a boundary instead of a cleavage plane. As in the single crystal case quite apart from the main cracking from the notch, surface cracking also is found, but in this case it is often associated with boundaries and is considerably more frequently observed.

In many cases this surface cracking develops from a series of micro-cracks formed in the neighbourhood of boundaries. That is, the cracks following the grain boundaries do not appear to be produced by a simple parting of the grains. The micro-cracks are formed at the boundaries but extend into the adjacent grains under the applied stress. This kind of failure is illustrated by figs. 12, 13 and 14. The appearance of the micro-cracks in fig. 12 strongly suggests that they might be formed by the mechanism proposed by Stroh (1957); that is, the grain boundaries sufficiently oppose slip within the grains for stresses to be concentrated here to initiate fracture. Both the correlation between the occurrence of slip lines and cracks and the shapes of the cracks agree with Stroh's ideas on the initiation of fracture in a ductile material. It should be noted however that these cracks appear only after immersion in ammonia. This implies that, since the concentration of stress at the head of slip band is not normally great enough to cause fracture under the kind of stresses applied during the test, the corrosive environment is playing an important part in modifying the mechanical properties of the crystal in the neighbourhood of grain boundaries to allow this early failure.

The micro-cracks spread under the applied stress and eventually link up to complete the intercrystalline breakdown. The inclination of the boundary to the principal stress direction seems important in determining the ease with which the eventual link up proceeds, as can be seen in figs. 13 and 14. These show two examples where boundaries lying in different orientations have reached different stages in this process. Once the micro-cracks have linked up completely to form a large intercrystalline failure it is very easy to overlook this detail in reconstructing the mechanism by which the cracking started. It may well be that this explains why this effect has not been previously reported.

§ 4. Discussion

The most important impression gained from the microscope observations is that failure of the specimen occurs by a typical fracture process ; that is the cracking is largely mechanical in character. Yet this kind of failure occurs only in the presence of ammonia. Without the ammonia or with a sudden increase of stress the crystal deforms plastically around the tip of the crack. This has been illustrated by fig. 2 and also by a cine record of the cracking process. The phenomenon of stress-corrosion cracking then might well be the development of a brittle-like fracture triggered in some way be a chemical reaction between the brass and the ammonia.

The complete failure of the specimen takes a finite time, greater than that required for a purely brittle fracture. It is apparent however that the individual steps in the cracking process occur very rapidly and might well be brittle fracture whilst the process of re-initiation of the cracks at slip bands is a slow process leading to a low overall failure rate. In other words the rate-controlling process is the re-initiation of the crack. As we shall see later this re-initiation might well be the most important aspect of the whole phenomenon of stress-corrosion cracking. Our interpretation of the phenomenon then is that a crack runs freely through the brass in a brittle fashion until it meets a slip band. Slip in this band stops the crack. Further cracking requires re-initiation of the fracture and this, being associated with a chemical process, takes time and therefore controls the rate of the whole process.

Such a model requires in the first instance that undeformed α-brass can support a free-running crack. A truly brittle fracture is possible only if the plastic yielding of the metal under the stress field imposed by the crack can be restricted. Previous work on this aspect of brittle fracture in ductile crystals (Gilman 1957, 1958, Forty 1957) has indicated that this is possible only if the crack travels faster than some critical speed which is associated with the rate at which dislocations can be generated and moved outwards from the tip of the crack. We have no measure of the speed at which the brittle bursts of fracture propagate in stress corrosion but it is possible to put some upper limit on it since it is unlikely that any brittle fracture will spread at a speed greater than one-third of the speed of sound in the crystal. It follows that if yielding is to be prevented dislocations in α-brass must move slower than this. This is in fact quite possible since it is well known that α-brass reacts sluggishly to applied stress, this being attributed to the short range ordering of the structure characteristic of all alloys of this kind (Cottrell 1953, Broom and Biggs 1954). Copper/gold, austenitic stainless steel and other materials susceptible to stress-corrosion cracking all have a characteristically low yield rate which can be attributed to the interaction of dislocations with phase domains, or impurity atmospheres.

The interpretation of our observations on the propagation of cracks in terms of short bursts of brittle fracture must clearly arouse some interest. It implies that brittle fracture is possible in a face-centred cubic metal and, moreover, that it is a cleavage-like fracture which appears to follow the $\{111\}$ planes. The foregoing discussion has shown that this can be justified only if the crack is propagated at high speed. We suggest that the important role of the chemical environment in stress corrosion of these alloys is to modify the mechanical properties of a surface layer or a zone around the tip of an exhausted crack in such a way not only to allow a new crack to form but also to reach the critical speed required for further propagation in the normal metal.

Our model also demands that deformed α-brass should be softer than the undeformed material. As we have seen, the crack is free-running until it meets a slip band, where it stops by a process of further plastic flow. This too can be explained on the basis of the existence of short-range order in our specimens ; for there is good reason to believe that the localized destruction of this order in the slip bands does in fact lead to a form of softening (as demonstrated, for example. by the yield point phenomenon in copper/gold). Softening can occur only initially and the slip bands must eventually work-harden in the normal way. This suggests that a small degree of cold work might be effective in stopping the cracks and hence possibly decreasing the susceptibility to stress corrosion, whereas heavy cold work might support cracking.

Our model proposes that, when a crack terminates at a slip band, fracture continues only by re-initiation and propagation into the next undeformed zone of the crystal. We have examined a number of mechanisms for the process of re-initiation, which may differ from alloy to alloy. One such mechanism is based on the idea that, although the shear stresses at the tip of the incident crack are relieved by slipping in a pre-existing slip band, this might not completely remove stress concentrations since the slip can be held up further down the band. If the obstacle here is strong enough a new fracture can occur. It is difficult however to understand how such a mechanism is influenced by the chemical environment, unless this aids the slip process at the tip of the crack and therefore indirectly assists the concentration of stresses inside the crystal.

An alternative mechanism, and one which is apparently more satisfactory since it utilizes the chemical environment more directly, is that of embrittlement. If the corrosive reagent produces embrittlement of the metal around the tip of the crack, then clearly a purely brittle fracture can be initiated here. Embrittlement can occur also over the surface of the specimen in early stages of the test and thus account for the initiation of cracks in the first place as well as for their subsequent re-initiation as the failure spreads. Complete embrittlement of the specimen is not essential and indeed is not reached in practice according to the observation that marked plastic deformation can be produced by an increase in stress or by removal of the ammonia during test. It is necessary only for an embrittled zone to be formed at the free surface or around the tip of an existing crack. The zone must be large enough however to support a crack which is stable at the stress level being applied and must, moreover, allow the crack to reach a critical velocity so that the brittle fracture can be maintained when it emerges from the embrittled zone and penetrates the normal metal. The critical size, according to current ideas of the cracking of brittle solids, is likely to be inversely dependent on the square of the stress applied to open the crack. On this account a very marked effect of applied stress on time to failure can be expected, which agrees with experiment (Robertson 1956).

The growth of the embrittled zone to critical size will of course account for the incubation periods found for the initiation of the original crack at the surface and for the re-initiation after its arrest at slip bands. Some evidence for the existence and growth of the zone may be derived from figs. 15 and 16. These show the results of increasing the bending stress during a test, immediately after the halting of a crack in one case (fig. 15) and after a waiting period in the other (fig. 16). We see that the increased stress is accommodated by plastic yielding around the tip of the newly halted crack in the first case but by a further burst of cracking in the other.

The localization of surface cracking around grain boundaries in polycrystalline specimens can also be accounted for by our model. It is likely that chemical reaction between the brass and ammonia would proceed more readily in the neighbourhood of a boundary and in this way a zone of embrittled material can develop here. This can restrict the slip within the grains and also resist the tendency for plastic deformation to be transferred from one grain to another so that micro-cracks may be more readily formed. There are materials, however, which fail in a truly intercrystalline fashion. In such cases a precipitation reaction is normally involved and this will affect the local mechanical properties and may also localize the corrosion in the region of grain boundaries. A good example of this class is the Al–7% Mg type of alloy.

The way in which embrittlement is produced by the chemical environment is not yet clear. It is known of course that brass can be embrittled by the process of dezincification during a vacuum anneal at high temperature, and an intergranular failure very similar to that of stress corrosion can be produced in a stressed specimen by this treatment. It is possible that a similar form of dezincification occurs when brass is immersed in ammonia. However, the electrochemistry of the brass/ammonia system is incomplete and only simple tentative results can be quoted here.

A few potential measurements have shown that zinc, as expected, is considerably more anodic than copper in ammonia and in ammonia containing copper and zinc in the 70/30 ratio. It is suggested therefore that there will be a tendency for the selective removal of zinc from the alloy especially in the strictly limited volume of solution present in a crack. This leaching process may not be merely superficial and zinc could be removed from internal lattice sites by a dislocation piping mechanism. This would leave a partly porous metal since large-scale rearrangement by diffusion is unlikely at the temperature of the test. Such material would be well suited for the initiation of a brittle fracture. This idea has been developed further in a recent publication by Forty (1960).

Evidence for embrittlement in the copper gold alloys has already been provided by the work of Robertson and Bakish (1956). This shows that the selective removal of copper by ferric chloride solution (which ultimately leads to stress corrosion cracking) leaves behind a gold sponge. These authors make the further interesting observation that immersion of a slab of material in ferric chloride for several weeks results in complete penetration by tunnelling, possibly along dislocation lines.

An alternative explanation for the formation of the embrittled zone is that both components of the alloy (Cu and Zn in our case) are removed by the ammonia but that one of them (Cu possibly) is re-plated to form an electro-deposited sponge. One difficulty here however is that the sponge in this case might not be sufficiently coherent with the unattacked brass to allow transfer of the fracture into the normal ductile material. In other words a piped embrittled zone has more attractive mechanical properties for our requirements than a sponge.

The picture we have of the phenomenon of stress corrosion cracking can now be summarized. Exposure to a corrosive environment produces a surface embrittlement. Eventually, when the embrittled zone has reached a sufficient depth this layer is cracked by the applied stress and, whenever the crack reaches a high enough speed, cracking can continue in the brass until a soft region such as a slip band is reached. Here the crack is stopped by slip occurring at its tip. Further chemical embrittlement now occurs at the tip of crack until the embrittled zone is large enough to allow a new crack to form and reach the critical velocity for fracture. The overall rate of propagation of the crack and therefore the susceptibility of the material to stress-corrosion cracking is effectively controlled by the time between halting and the initiation of the new crack, and this in turn depends on the rate of chemical embrittlement around the tip and the magnitude of the applied stress. Thus we expect in general a relationship between susceptibility to failure and applied stress. The mechanism of embrittlement is not known but it seems reasonable that the embrittled material will have mechanical properties strongly dependent on composition and state of deformation of the alloy. There should, therefore, be a relationship between susceptibility and composition. There seems to be some evidence for this in practice (Graf 1956). Further, the rate of cracking and therefore susceptibility should depend on the frequency with which soft slip bands are encountered. That is, susceptibility should depend on the degree of cold work in the specimen before testing.

One of the most important questions raised by this work is whether an undeformed crystal can support a free-running crack. This is only likely if the rate at which plastic flow can occur is small compared with the crack velocity. As we have already indicated, although this is impossible for pure metals, it might well be possible for certain types of alloy, and in particular for those alloys known to be susceptible to stress corrosion.

ACKNOWLEDGMENTS

We wish to thank the Director of the Hinxton Hall Laboratory, Dr. T. P. Hughes, and the Chairman of Tube Investments Limited for permission to publish this work.

It is a pleasure also to thank Mr. T. Law for his skilful assistance during the course of the experiments.

REFERENCES

BROOM, T., and BIGGS, W. R., 1954, *Phil. Mag.*, **45,** 246.
COTTRELL, A. H., 1953, *Relation of Properties to Microstructure* (Cleveland: American Society for Metals), p. 131.
FORTY, A. J., 1957, *Proc. roy. Soc.* A, **242,** 392; 1960, *Physical Metallurgy of Stress Corrosion Fracture*, ed. T. N. Rhodin (New York: Interscience Publishers), p. 99.
GILMAN, J. J., 1957, *Trans. Amer. Inst. min. (metall.) Engrs*, **209,** 449; 1958, *J. appl. Phys.*, **29,** 601.
GRAF, L., 1956, *Stress Corrosion Cracking and Embrittlement*, ed. W. D. Robertson (New York: J. Wiley & Sons).
HOAR, T. P., and WEST, J. M., 1958, *Nature, Lond.*, **181,** 835.
RHODIN, T. N., 1960, *Physical Metallurgy of Stress Corrosion Fracture*, ed. T. N. Rhodin (New York: Interscience Publishers).
ROBERTSON, W. D., 1956, *Stress Corrosion Cracking and Embrittlement*, ed. W. D. Robertson (New York: J. Wiley & Sons).
ROBERTSON, W. D., and BAKISH, R., 1956, *Acta Met.*, **3,** 292.
STROH, A. N., 1957, *Advanc. Phys.*, **6,** 418.

Thermal Aspects of the Growth of Thin Films by Vacuum Sublimation†

By G. Gafner
National Physical Research Laboratory,
P.O. Box 395, Pretoria, South Africa

[Received May 9, 1960]

§ 1. Introduction

It has been stated (Pashley 1956) that a knowledge of the growth mode of a layer is essential before any comprehensive theory of epitaxy can be formulated. Considerable experimental information regarding the initial stages of the overgrowth process has recently been published but interpretation of these results is hampered by the absence of quantitative information regarding the thermal situation prevailing during growth. It is to be expected that the growth temperature would markedly influence such important properties as crystallite size and perfection and the tensile stresses which might result if any differential thermal contraction of the substrate and overgrowth took place.

The following contradictory opinions are found in the literature regarding the temperature of an overgrowing layer: Hoffmann *et al.* (1954) have stated that the first and second nearest neighbours of an incident atom will undergo an instantaneous temperature rise of about 700°c when the incident atom shares its sublimation energy with them. As the relaxation time of such a thermal pulse is about 10^{-12} sec they conclude that it is incapable of producing any bulk recrystallization. This argument is undoubtedly valid for the incidence of an isolated atom but the conclusion is controversial when the film is heated by the continuous deposition of material. In contradistinction to this, Wilman (1955) has concluded, on the basis of experimental results, that the surface temperatures of overgrowths formed on metallic and other substrates at rates of 15 to 300 Å/sec may be hundreds of °c higher than the substrate temperatures. The need for a quantitative estimate of this temperature is thus apparent.

§ 2. Factors which Complicate the Mathematics

An exact mathematical representation of the thermal situation during the growth of a continuous film by vacuum sublimation is analytically intractable due to the presence of the following complications:

---

† Communicated by the Author.

1. A free boundary with continuous heat generation on it.
2. Radiative heat losses from both the free surface and the substrate underface which depend on the fourth powers of the respective, varying temperatures.
3. The composite nature of the system as two different sets of thermal constants are involved; one for the substrate and another for the overgrowth.

It follows that any analytical treatment of the problem must involve many approximations. It will be shown that it is nevertheless possible to approximate to the various situations in such a way that reliable conclusions can be drawn.

§ 3. RANGE OF THE SUBSTRATE AND DEPOSITION PARAMETERS

The range of final film thicknesses and deposition rates of interest have upper limits of 10 000 Å and 1000 Å/sec respectively. The substrate thicknesses vary from about 1 cm, in lens coating work to $<0{\cdot}01$ cm when deposition is onto thin mica cleavages. When the substrate is thick it is to be expected that the film temperature will be predominantly dependent on the conduction losses across the interface. When the substrate is thin, however, the heat generated will be rapidly distributed through the composite system and its resultant temperature will depend on the balance between radiative losses and the heat generation rate. As the total amount of heat liberated (about 2 cal), when 1 cm^2 of the thickest film of interest (10 000 Å) is formed, can uniformly heat a substantial substrate only a few °C, it is reasonable to assume a semi-infinite substrate in this instance.

§ 4. TEMPERATURE OF A CONTINUOUS LAYER GROWING ON A THICK SUBSTRATE

An upper limit to the temperature in a film growing on a semi-infinite substrate will follow from a calculation of the surface temperature of the substrate when the heat associated with the deposition rate is generated directly on it. To ensure that this calculation gives a true upper limit, the lower of the substrate and overgrowth thermal diffusivities will be accredited to the substrate and no heat losses from the system will be allowed.

The heat-flow theory of this system is given by Carslaw and Jaeger (1948, p. 56) and the relevant special case of their solution is:

$$v=\frac{2Q}{K}\left(\frac{\alpha t}{\pi}\right)^{1/2}. \qquad (1)$$

This equation relates the temperature increase v at a time t relative to that at time $t=0$, on the surface of a semi-infinite solid on which heat is generated at a constant rate Q cal/cm^2 sec subsequent to time $t=0$. K and α represent the thermal conductivity and diffusivity of the solid respectively. For solids, using the c.g.s. °C system with the unit of heat the calorie, as will be done in all the ensuing work unless otherwise stated, $\rho c \approx 0{\cdot}6$ and thus $K \approx 0{\cdot}6\alpha$. This being so (1) becomes:

$$v = \frac{2Qt^{1/2}}{0{\cdot}6(\alpha\pi)^{1/2}}. \qquad (2)$$

The highest heats of vaporization lead to a heat generation rate of about 0·2 cal/cm^2 sec when growth takes place at a rate of 1000 Å/sec. The lowest thermal diffusivity values for solids are around 0·005 cm^2/sec, so that the highest temperature rise to be expected for any film growing at a rate of 1000 Å/sec or less, on a thick substrate, to a thickness of 10 000 Å is, from (2):

$$v_{\max} = \frac{2 \times 0{\cdot}2 \times 10^{1/2}}{0{\cdot}6 \times 0{\cdot}0157^{1/2}} = 17\,^\circ\mathrm{C}. \qquad (3)$$

The general conclusion is thus that there will be no marked temperature rise at the surface of a continuous, growing, film due to the build-up of heat at the plane of generation. This conclusion is valid for all materials commonly used in vacuum sublimation work.

§ 5. TEMPERATURE OF A CONTINUOUS LAYER GROWING ON A THIN SUBSTRATE

An implication of the previous conclusion is that large surface temperatures can arise only when the thermal capacity of the substrate is small. This in turn implies that there will be a small temperature difference across the substrate. When this situation prevails, an estimate of the temperature can made as follows:

Consider unit surface area of a substrate of the infinite slab type, which has thermal capacity A and is sufficiently thin to allow the temperature drop across it to be ignored when heat is continuously generated on one of its faces at a rate Q. This heat generation is associated with the advent of new material at such a rate that the thermal capacity of the system increases at a constant rate B. The thermal capacity of the system at time t is then given by $(A+Bt)$.

Heat losses are considered to be solely radiative and can thus be represented by a term of the form $C(v^4-v_0^4)$, where v is the varying temperature of the system and v_0 is the environmental and initial substrate temperature in °K. The net heat gain rate when the temperature is v is equal to $Q-C(v^4-v_0^4)$. The rate of change of temperature with time at any instant is thus:

$$\frac{dv}{dt} = \frac{Q-C(v^4-v_0^4)}{A+Bt}. \qquad (4)$$

The solution to this differential equation is readily found, after separation of the variables, and is:

$$\arctan(zv)-\arctan(zv_0)-\frac{1}{2}\left\{\log_e\left(\frac{zv-1}{zv+1}\right)\left(\frac{zv_0+1}{zv_0-1}\right)\right\}=2z\left(\frac{Q+Cv_0^4}{B}\right)\log_e\left(1+\frac{Bt}{A}\right) \qquad (5)$$

where

C = Stefan–Boltzmann constant × number of faces × emissivity
= $1{\cdot}37\times10^{-12}\times2\times$ emissivity;
A = Initial thermal capacity of the system/cm² of surface area
= $l_s\rho_s c_s$ (in which subscript s refers to the original substrate);
B = Thermal capacity of the material deposited/cm² sec
= $l_0/\sec\,\rho_0 c_0$ (in which subscript 0 refers to the overgrowth);
Q = Heat released/sec cm² when the overgrowth thickness increases by l_0/sec;
v = Temperature of the system (°K);
v_0 = Environmental and initial temperature (°K);
$z=(Q/C+v_0^4)^{-1/4}$.

As eqn. (5) does not contain the temperature explicitly it is necessary to calculate the times at which given temperatures will be attained in order to obtain the temperature–time dependency. This has been done for a range of deposition rates, a substrate thickness of 1 mm and various substrate emissivities, on the assumption that a deposition rate of 1000 Å/sec corresponds to a heat generation rate of 0·2 cal/cm² sec and that the environmental temperature is 300°K. The results of these calculations are given in table 1.

Table 1. Times taken for the surface temperature of a thin slab to attain the stipulated values at various deposition rates and substrate emissivities

Heat generation rate in cal/sec cm²	Emissivity	Deposition in Å/sec	Time in seconds of attainment of			
			400°	500°	600°	700°K
0·2	0·02	1000	30	61	92	123
0·02	0·02	100	307	638	1031	1459
0·002	0·02	10	Max. temp. attained 303°K			
0·2	0·2	1000	31	65	104	285
0·02	0·2	100	590	Max. possible temp. 460°K		
0·002	0·2	10	Trivial temp. rises			

The times at which the temperatures listed in table 1 will be attained for different substrate thicknesses can be deduced from the table by multiplying the times in the table by the thickness of the substrate in mm. It follows that a temperature rise of 100°C or more, for example, will be attained during the deposition of a film of thickness 10 000 Å only if the substrate has a thickness of 0·03 cm or less, when the deposition rate is 1000 Å/sec and the substrate emissivity is 0·02. A maximum substrate thickness of 0·003 cm will allow the same temperature increment to be attained when the deposition rate is 100 Å/sec and the emissivity is as above. Increasing the emissivity of the system to 0·2 reduces the last mentioned maximum substrate thickness to 0·002 cm. It can thus be concluded that temperature increases of hundreds of °C will not arise unless deposition is onto very thin substrates.

§ 6. VALIDITY OF THE THICK AND THIN SUBSTRATE APPROXIMATIONS

The temperature of a continuous overgrowing layer has been calculated in approximation using two extreme models. The range of validity of these models can be estimated from a knowledge of the temperatures of, and the temperature difference between, the two substrate surfaces when heat is generated directly onto one of these surfaces and no radiative heat losses occur from either. Macey (1940) has shown that the temperature v in an infinite slab, measured with respect to the initial temperature, when heat is generated at a constant rate Q/unit area sec at $x=l$ and there is no heat loss from $x=0$, is given by

$$v=\frac{2Q(\alpha t)^{1/2}}{K}\sum_{n=0}^{\infty} i\operatorname{erf}c\frac{(2n+1)l-x}{2(\alpha t)^{1/2}}+i\operatorname{erf}c\frac{(2n+1)l+x}{2(\alpha t)^{1/2}}.$$

The temperatures at $x=0$ and $x=l$, designated v_0 and v_l respectively, have been calculated for various substrate thicknesses, and for times up to 10 sec when the heat generation rate is equal to the extreme value of 0·2 cal/cm^2 sec, taking the thermal diffusivity as 0·005 and the thermal conductivity as 0·003 both of which are extremely low values for solids. The results of these calculations are given in table 2.

These results show that the temperature differences across all substrates thinner than 1 mm are trivial. The theory which in effect gives the substrate infinite thermal conductivity and predicts the overgrowth temperature on the basis of the balance between heat generation and radiative heat loss is thus an excellent approximation to the exact situation prevailing when deposition is onto substrates of thickness 1 mm or less. In contrast to this, the fact that the far surface of a substrate, of thickness 1 cm, remains at effectively the initial temperature during the generation of the amount of heat equivalent to the deposition of 10 000 Å of metal at a rate of 1000 Å/sec shows that the semi-infinite substrate approximation is valid for the conditions pertaining to the technological process of lens blooming and mirror coating, etc.

Table 2. Surface temperatures attained by substrates of various thicknesses at various times when heat is generated onto the surface $x=l$ at a rate of 0·2 cal/cm^2 sec. Thermal diffusivity and conductivity taken as 0·005 and 0·003 respectively

Time t (sec)	l in cm =	1·0	0·1	0·01
1	v_0 °C v_l	0·0 5·3	2·2 5·5	33·3 33·6
3	v_0 v_l	0·0 5·3	8·9 12·2	100·0 100·3
6	v_0 v_l	0·0 13·0	18·9 22·2	200·1 200·4
10	v_0 v_l	0·0 16·8	32·3 35·6	333·6 333·9

§ 7. TEMPERATURE OF A THREE-DIMENSIONAL AGGREGATE DURING GROWTH

The preceding theory is relevant to growth by a continuous film mechanism. In the first stages of overgrowth, however, the experimental indications are that three-dimensional aggregates, rather than two-dimensional monolayers, are formed in many instances. The thermal situation when growth occurs in this way is markedly different from that considered previously and merits separate treatment as the three-dimensional aggregate must approximate to a point source of heat in the initial stages and thus requires a large temperature gradient to allow heat loss from it at a finite rate.

The most obvious model on which to base calculations of the temperature of such an overgrowing aggregate consists of a continuous, growing, disk source of heat which represents the base of the overgrowing aggregate, on a semi-infinite substrate. The temperature at the centre of the disk source would then approximate to the temperature of the aggregate. As the calculation based on this model cannot be handled in terms of tabulated functions, it was found necessary to use the following model instead: The heat generated as the aggregate grows is considered to be released at a point $r=0$ on the surface of semi-infinite substrate. Instead of the aggregate growing on the substrate, however, we consider the closely related hypothetical case in which the aggregate grows into the substrate, equating the volume of the ingrowing aggregate at any instant to the amount of material that has arrived at the 'catchment area' of the aggregate by that time.

The temperature v at a point r in an infinite solid in which heat is continuously liberated at the origin ($r=0$), at a rate Q subsequent to time $t=0$ is given by Carslaw and Jaeger (1948, p. 221) as

$$v=\frac{Q}{4\pi Kr}\operatorname{erf}c\frac{r}{(4\alpha t)^{1/2}}. \qquad \ldots\ldots \quad (6)$$

The equivalent temperature in the hemispherical geometry that our model is based on, i.e. on a semi-infinite, rather than an infinite, substrate will be just twice as large assuming no heat loss from the exposed surface.

When the aggregate grows as a hemisphere with material arriving at a constant rate A cm³/sec, its volume V will be given by

$$V=\tfrac{2}{3}\pi r^3=At. \qquad \ldots\ldots\ldots \quad (7)$$

The average temperature of the aggregate can be calculated from (6) and is given by

$$v=(2\pi r^3/3)^{-1}\int_0^r (Q/2\pi Kr)2\pi r^2 \operatorname{erf}c\left\{\frac{r}{(4\alpha t)^{1/2}}\right\}dr$$

$$=\frac{6Q\alpha t}{\pi r^3 K}\left\{\tfrac{1}{2}\operatorname{erf}\left\{\frac{r}{(4\alpha t)^{1/2}}\right\}+i^2\operatorname{erf}c\left\{\frac{r}{(4\alpha t)^{1/2}}\right\}-0{\cdot}25\right\}.$$

Substituting for r from (7) this becomes

$$v=\frac{4\alpha Q}{KA}\left\{\tfrac{1}{2}\operatorname{erf}\frac{(3At/2\pi)^{1/3}}{(4\alpha t)^{1/2}}+i^2\operatorname{erf}c\frac{(3At/2\pi)^{1/3}}{(4\alpha t)^{1/2}}-0{\cdot}25\right\}.$$

The highest values of Q are such that $Q\simeq 10^4 A$ cal/sec and, as before, $0{\cdot}6\alpha\simeq K$, thus giving

$$v=6{\cdot}7\times 10^4\left\{\tfrac{1}{2}\operatorname{erf}\frac{(3At/2\pi)^{1/3}}{(4\alpha t)^{1/2}}+i^2\operatorname{erf}c\frac{(3At/2\pi)^{1/3}}{(4\alpha t)^{1/2}}-0{\cdot}25\right\}. \qquad (8)$$

Equation (8) has been evaluated for various values of the time (t), with $\alpha=0{\cdot}005$ and giving A the realistic value of 10^{-13} cm³/sec which corresponds to nuclei 1 μ apart when the mean deposition rate is 1000 Å/sec or 10 μ apart when the deposition rate is 10 Å/sec. The results of the calculation show that the mean temperature of the aggregate falls to 86°c above that of the substrate after 10^{-6} sec and to 9°c above the substrate temperature after 1 sec.

In actual growth the supply of material to a nucleus would equal the volume rate of deposition of material onto the area eventually supplying the growing aggregate only after the initial transient needed to establish the flow pattern to the nucleus had passed. The temperatures calculated from (8) for very small values of the time are thus too high as instantaneous aggregation of all the material arriving in the 'catchment area' is assumed in the calculation. Neglect of the thermal capacity of the aggregate and the fact that part of the heat of vaporization is lost to the substrate as heat of adsorption before aggregation also causes over-estimation of the temperature but these factors are compensated, at least partially, by the fact that in the model adopted, heat loss to the substrate takes place through twice the area that it would be through when the aggregate grows on the substrate with a contact angle of 90°.

It can be concluded thus that growth by a three-dimensional aggregation process in which the contact angle is less than 90° can lead to high aggregation temperatures only in the earliest stages of growth when both deposition and surface migration rates are very high. It is not to be expected that the contact angle would be much larger than 90° for the materials commonly encountered in the 'overgrowth by vacuum sublimation' literature, as this would imply a large measure of re-evaporation during the migration to the nucleus process which is in turn incompatible with common experience.

§ 8. Summarized Conclusions

The temperature of an overgrowing film will be essentially that of the substrate when growth is by a continuous film mechanism. High film temperatures thus necessitate low substrate thermal capacities in order that the heat of sublimation released on formation of the film may elevate the temperature of the system appreciably. The possibility of high transient temperatures being attained in the initial stages of growth by a three-dimensional aggregation process exists when deposition is at a very high rate onto a substrate of low thermal diffusivity, and migration of the incident material is rapid. It has been shown in the extreme case, for which calculations were made, that the aggregate temperature drops to less than 100°c above substrate temperature after only 10^{-6} sec and after 1 sec is only 9°c above the substrate temperature.

Acknowledgment

The author would like to express his gratitude to Professor J. H. van der Merwe of the University of Pretoria for his interest in this work.

References

Carslaw, H. S., and Jaeger, J. C., 1948, *Conduction of Heat in Solids.*
Hoffman, R. H., Daniels, R. D., and Crittenden, E. C., 1954, *Proc. phys. Soc. Lond.* B, **67**, 497.
Macey, H. H., 1940, *Proc. phys. Soc. Lond.*, **52**, 625.
Pashley, D. W., 1956, *Advanc. Phys.*, **5**, 173.
Wilman, H., 1955, *Proc. phys. Soc. Lond.* B, **68**, 474.

The Annealing of Electron Irradiation Damage in Graphite†

By W. N. REYNOLDS and P. R. GOGGIN
Atomic Energy Research Establishment, Harwell, Berks

[Received May 26, 1960]

ABSTRACT

Samples of pure artificial graphite have been irradiated with electrons at 79°K, and a study made of the annealing characteristics of the changes in electrical conductivity, Hall effect and magneto-resistance. All three quantities show an anomalous annealing range below 120°K, and a simplified band theory calculation indicates that the concentration of both electrons and positive holes increase during irradiation and also in the anomalous annealing range.

§ 1. INTRODUCTION

WORK described by Austerman and Hove (1955) and in more detail by Austerman (1958) indicated the importance of resistivity annealing studies in irradiated graphite from about 80°K upwards. These authors exposed samples of graphite to 1·25 MeV electron beams at liquid helium temperatures and then observed the effects on resistivity at 4°K of successive 1 min anneals to temperatures up to about 280°K—the so-called pulse annealing technique. The dose they used, about 20–40 microampere-hours, was such as to cause an initial resistivity increase of about 5%. In the annealing range up to about 80°K, they found only very small resistivity changes, but from 80°K to 110°K a further sharp increase in resistivity was observed amounting to about 30–40% of the initial increase on irradiation. At higher temperatures the behaviour was more normal, the resistivity tending monotonically at a decreasing rate to the unirradiated value. Austerman suggested that the anomalous resistivity increase could be due either to a release of trapped charge carriers or to an increase in density of carrier scattering centres and that experiments could be carried out to separate these factors. He also pointed out that irradiations in liquid nitrogen at 77°K would be suitable, provided that that temperature was held to within a few degrees.

It may be doubted whether the two factors mentioned by Austerman can be separated so easily. Thus, in the work described by Eatherly (1953)‡ on the annealing of pile-irradiated graphite, an anomolous resistivity increase observed on pulse-annealing up to 1300°C was accompanied by anomalies in the magneto-resistance and Hall-effect curves. However, the interpretation of such results in terms of band theory parameters such as carrier density and mobility is now on a firmer basis, owing to recent theoretical work. The foundation of this work was laid by Slonczewski and Weiss (1958) and by McClure (1957) who generalized previous band calculations by the use of group theory. The experimental results of Galt *et al.* (1956) as analysed by Nozières (1958) on cyclotron resonance and those of Soule (1958 a) as analysed by McClure (1958) and Soule (1958 b) on the oscillatory galvanomagnetic effects in graphite have permitted elaboration of the band structure model second only to that of the commoner semiconductors.

---

† Communicated by the Authors.

‡ The authors are indebted to the Director of the USAEC Division of Classification for permission to mention some of Dr. Eatherly's results, which are only available in a classified report.

§ 2. Experimental Method

Pulse annealing studies have been made on samples of artificial graphite irradiated by means of a 4 mev electron linear accelerator at liquid nitrogen temperature. The properties studied were resistivity, Hall effect and magneto-resistivity at a field of 5600 gauss. The specimens were made of Acheson grade A pure pile graphite, cut parallel to the direction of extrusion, in rods 3 mm square and 25 mm long. A central 36 s.w.g. hole was drilled perpendicular to the length to take a thermocouple, made of 40 s.w.g. chromel–alumel wire, as shown in fig. 1. The voltage contacts were inserted into holes at 6 mm on either side of the centre, defining the useful length as 12 mm. The Hall contacts were fine beryllium–copper wire springs, and these were supported, together with the copper end-clamps for current supply on a block of Sindanyo. The whole device was mounted on 18 in.

Fig. 1

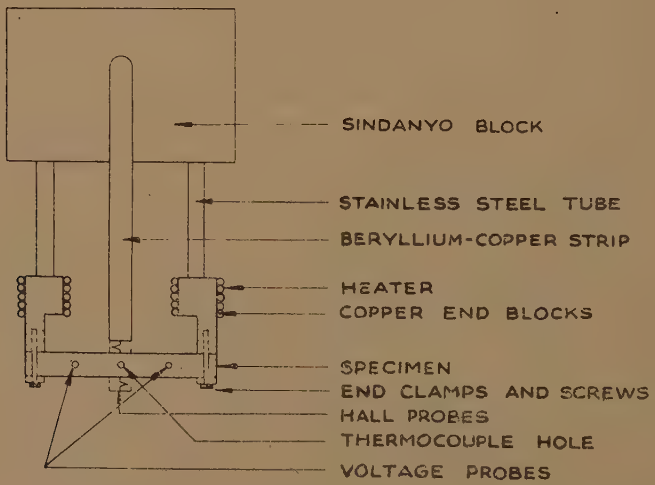

Apparatus for the electron irradiation and thermal annealing of graphite rods.

long stainless steel tubes for successive insertion into the accelerator head and the annealing vacuum chamber, and was completely wired before irradiation, the pre-irradiation values being determined under similar conditions to those for the post-irradiation and annealed values.

The irradiation chamber was a brass box screwed to the accelerator. The beam was admitted through a thin copper window and a slit the same size as the specimen in the brass wall was used as a stop. An exit window was also provided. The beam current into the specimen was in the range 10–30 μ amp, and exposures of 1–2 hours produced resistivity increases of 5–10%. The irradiation chamber was completely filled with liquid nitrogen supplied by a nitrogen pressurized siphon from a Dewar vessel, at a sufficient rate to keep it flowing out of a hole at the top in liquid form. It was found advisable to include a piece of copper gauze to reduce the risk of troublesome minor explosions, the exact cause of which was not determined. Continuous readings of both temperature and resistance were made during the runs to ensure that the temperature rise in the specimens was less than 2°C. The resistance rose linearly with the exposure time, but the change on switching the beam on or off was very small. At the end of the irradiation period, the specimen end of the apparatus was immersed in liquid nitrogen, and then transferred to the annealing chamber.

The annealing chamber was a glass vacuum system which could be pumped to better than 10^{-5} mm Hg, and was immersed in a special Dewar flask containing liquid nitrogen between the poles of an electromagnet. Heat for the annealing programme was supplied by small electrical heaters wound on the copper end clamps. The current supply for the electromagnet was carefully stabilized. The thermocouple and electrical leads were brought out through special bushes. The directions of specimen and magnet current were separately reversed for each reading. The annealing chamber was filled with pure dry nitrogen or helium gas during readings, as this was found to give more stability to the base temperature used for the pulse annealing, viz. 80°K. No difference was observed in specimen properties between readings in nitrogen and those in helium.

§ 3. RESULTS

Figures 2 (*a*), (*b*) and (*c*) show the behaviour of the resistivity change, magneto-resistivity and Hall coefficient as a function of annealing temperature at about 10°C intervals. The resistivity curve, fig. 2 (*a*) shows the same general trends as those of Austerman's curves, as well as some additional features. The resistivity rise begins at 80°K and is almost completed at 120°K. However, a further slight increase is now seen up to 160°K, at which temperature a rather sharp fall off is indicated. The fall in resistivity from 160°K to 270°K is not so simple as suggested by Austerman, and the original irradiated value is crossed slightly below, rather than above 200°K. All our curves then show a well-marked minimum at 270°K–280°K, although it is not certain that the excess resistivity falls so low in every case because, at any rate in the earlier results, we took no special care to

Fig. 2

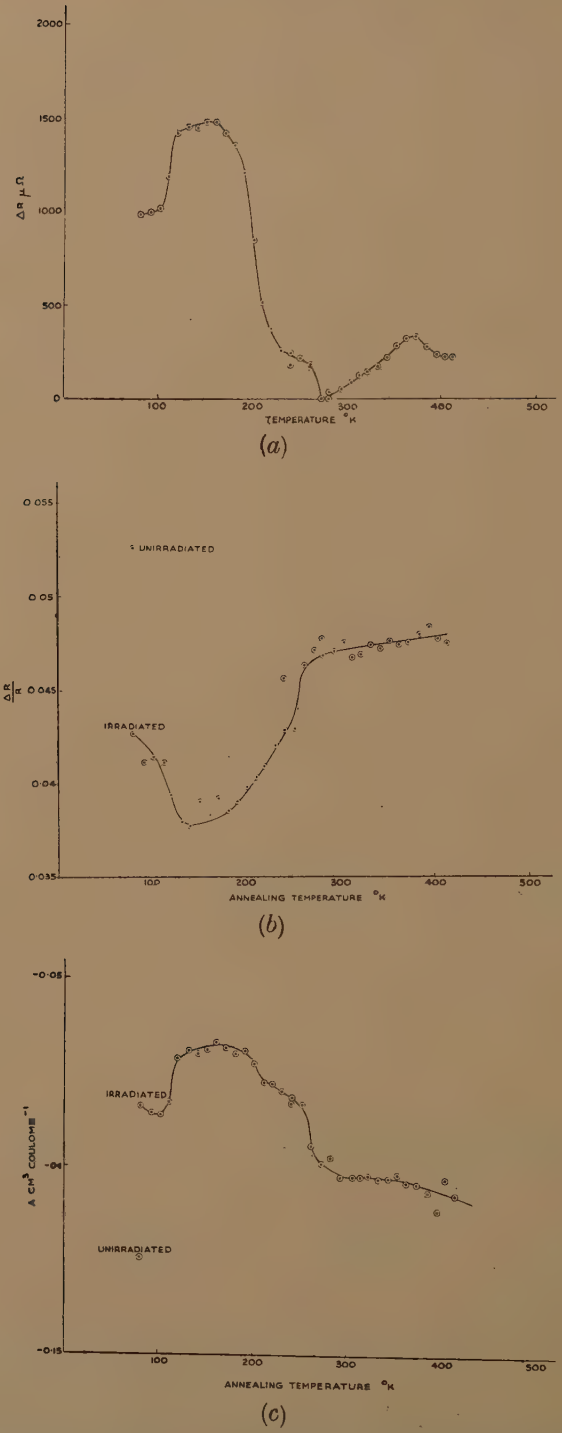

(*a*) Excess resistance ΔR due to irradiation and annealing as a function of annealing temperature. (*b*) Relative increase in specimen resistance $\Delta R/R$ in a magnetic field of 5600 gauss on irradiation and annealing as a function of annealing temperature. (*c*) Hall coefficient A in cm^3/Coulomb on irradiation and annealing as a function of annealing temperature.

study this unexpected feature. All specimens show a second maximum around 400°K, although not generally as sharp as that given here.

The magneto-resistance and Hall-effect curves in figs. 2 (*b*) and (*c*) are somewhat unexpected in that they both indicate an apparent increase of the irradiation damage effects for anneals in the 80°K to 120°K range. More straightforward annealing again commences at about 160°K, but there is no extreme value at 270°K showing that the resistance minimum is due to a fortuitous balance of the carrier densities and mobilities; its magnitude may depend critically on the local structure. In any case, the resistivity when measured alone now appears a rather unreliable guide to radiation damage annealing.

Figure 3 shows the experimental results normalized to the initial changes on irradiation. All three show the initial rise of 40–50%, but the resistivity falls away more rapidly on the high temperature side. The particular specimen illustrated was irradiated at a beam current of 14 μ amp for about 105 min. It is noteworthy that specimens given about twice this dose gave normalized resistivity and magneto-resistivity curves closely agreeing with those of fig. 3, but that the normalized Hall effect showed an initial rise of only about 20%.

§ 4. Discussion

We note first that the theory of Kinchin and Pease (1955) gives the mean number of atoms displaced per primary knock-on for 4 Mev electrons in graphite as 2·8, whereas that for 1·25 Mev electrons as used by Austerman is only slightly greater than unity. Thus, in our specimens, the damage may be more complex. However, many primary displacements must still be in the form of simple interstitial-vacancy pairs, and in view of the correspondence in the resistivity behaviour, we shall not consider these complications at present. The Kinchin and Pease theory also indicates a total density of $1{\cdot}2 \times 10^{16}$ displaced atoms/cm^3 for this specimen.

Many people have observed changes of graphite properties similar to those shown here on initial irradiation. In general, they are explained (see e.g. Hennig and Hove 1955) by supposing that the defects trap electrons, thus lowering the Fermi level and making the conduction tend from *n* to *p*-type, and also, since the charged defects act as scattering centres, decreasing carrier mobilities.

The similar sharp increase in the 80°–120°K temperature range in the normalized values of the quantities measured, as shown in fig. 3 indicates that some re-arrangement of the original damage is taking place, quite distinct from direct re-integration. This could be a dispersion of interstitial-vacancy pairs, if it is supposed that, over a certain range, there is a repulsive force between the two components, as has been suggested for example, by Wertheim (1959) in the case of silicon. In order to account for the decreasing magneto-resistance, it would then be necessary to postulate that this dispersion permitted further electron trapping, because we know (see e.g. Mott and Jones 1936) that the scattering power of a defect is proportional to the square of its change. Thus dispersion without additional trapping would be expected to give less scattering and higher mobility and magneto-resistance, but further electron trapping would account for the observed changes in both magneto-resistance and Hall effect.

Fig. 3

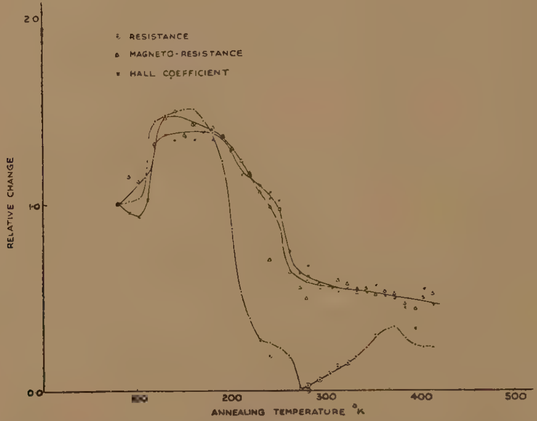

Changes in resistance, magneto-resistance and Hall coefficient normalized to to initial changes on irradiation as a function of annealing temperature.

This hypothesis may be examined in greater detail. Using unpublished expressions derived by Johnston (given in the appendix) we have calculated values of the mobilities μ_+ and μ_- and effective densities n_+ and n_- of holes and electrons respectively, corresponding to the data in fig. 2. These expressions are based on an overlapping two-band cylindrical model of graphite, using the theory of Jones and Zener (1934). A more complex model based on single crystal studies would not be appropriate in view of the uncertainties over corrections for orientation, density and crystallite boundary effects in our materials. The Jones–Zener theory solves the Boltzmann equation in terms of an expansion in powers of μB, where B is the applied magnetic field, which applies to our results since $\mu B \sim 0{\cdot}1$. In the case of Soule's (1958 a) work on single crystals, where $\mu B > 1$, the form of solution given by McClure (1956) is required.

If the relaxation times for the two types of current carrier are assumed equal, the calculations of Johnston (1955) suggest that

$$\frac{\mu_+}{\mu_-} = b \sim 0{\cdot}8$$

so that for this value of the mobility ratio we may calculate the values of μ_+, μ_-, n_+ and n_- from the three corresponding experimental values of A, the Hall coefficient, ρ the resistivity and $\Delta\rho/\rho$ the magneto-resistance observed on application of the standard field B. Figures 4 and 5 give the values obtained for μ_- as a function of annealing temperature (μ_+ is merely 0·8 of this value at any point) and n_+ and n_- respectively. The mobilities and carrier densities were all lower than those obtained from the single-crystal work at the same temperature. Crystallite boundary scattering is thought to be important in artificial graphite, and to account for the opposite sign of the temperature coefficient of resistance by limiting the carrier mean free path. This would also account for the low mobilities observed, but the low carrier densities are less easily explained.

Fig. 4

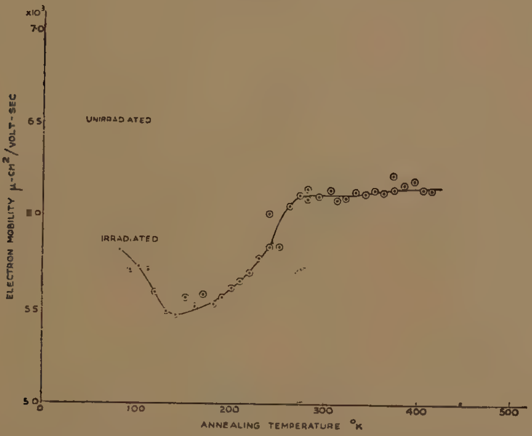

Electron mobility as a function of annealing temperature.

The most striking feature of fig. 5, however, is the increase of concentration found for both types of carrier both on irradiation and in the lower part of the annealing range. Such behaviour is not compatible with the simple two-band model and constant mobility ratio which we have used, and may be connected with the type of band distortion described by Parmenter (1955) which could cause an increase in the band overlap in graphite.

It is observed in the appendix that for the model we have used, the difference between hole and electron concentrations at any point on the annealing curve must be equal to the density of trapped electrons. Carrier scattering is presumably increased by trapped electrons, and it is therefore of interest to study the relationship between n_+ and n_- and the carrier mobilities. Figure 6 shows the value of $n_+ - n_-$ as a function of $1/\mu_-$ for an assumed value of $b = 0{\cdot}8$. It is interesting that the change in trapped electron density on irradiation is about $1{\cdot}5 \times 10^{16}/\text{cm}^3$—quite close to the calculated defect density, and the two could in fact be made equal by putting $b \sim 0{\cdot}85$. The increase in trapped carrier density in the first annealing phase would then require that some defects acquire more than one charge. The loop in the curve for later phases of annealing shows that processes other than direct re-integration are involved.

Other workers have noticed the rapid change in magneto-resistance compared with resistance for pile irradiation, which leads to the above conclusions, notably Kinchin (1954) but the only detailed work seems to be that of Eatherly (1953). He studied the resistivity, magneto-resistivity and Hall effect on AWG graphite specimens cut parallel to the axis of extrusion and irradiated up to a dose of 460 MWD. An analysis of his

Fig. 5

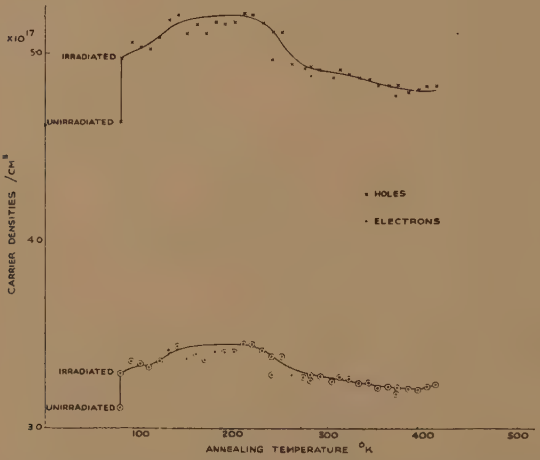

Carrier densities as a function of annealing temperature.

Fig. 6

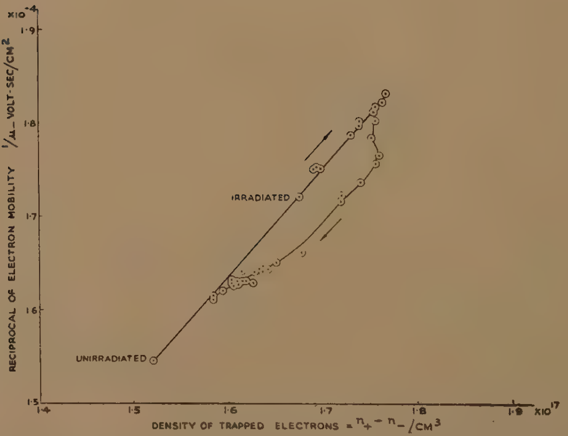

Variation of density of trapped electrons $n_t=n_+-n_-$ with electron mobility reciprocal $1/\mu_-$.

results similar to that which we have used shows that the density of holes increases monotonically and the carrier mobilities decrease monotonically with dose, but that the electron density rises to a maximum at about 3 MWD and then falls off.

§ 5. CONCLUSIONS

The extension of Austerman's work by simultaneous measurements of magneto-resistance and Hall effect has given results of considerable interest. The analysis of these results shows that the simple band-theory model cannot provide a full explanation.

Other annealing experiments, such as the study of the region around 0°C now appear to be of interest, and it would also be profitable to compare higher dose electron damage with lower dose neutron damage. However, detailed atomic mechanisms are not yet identifiable.

ACKNOWLEDGMENTS

The authors would like to express their thanks to their colleagues in the Theoretical Physics Division for discussion of the results of this work and for the performance of computations. They are particularly indebted to Dr. D. F. Johnston who derived a new approximation for the magneto-resistance relationship which he describes in the appendix.

APPENDIX

By D. F. JOHNSTON

Galvanomagnetic Formulae for an Overlapping Cylindrical Two-band Model of Graphite

Hall coefficient

$$A=\frac{E_y}{B_z I_x}=\frac{1}{e}\frac{(\mu_+{}^2 n_+ - \mu_-{}^2 n_-)}{(\mu_+ n_+ + \mu_- n_-)^2}\cdot\frac{1}{\cos^2\theta}.$$

Resistivity

$$\rho=\frac{E_x}{I_x}=\frac{1}{e(\mu_+ n_+ + \mu_- n_-)}.$$

Magneto-resistance

$$\frac{\Delta\rho}{\rho}=\frac{B^2\cos^2\theta}{\mu_+ n_+ + \mu_- n_-}\left[\mu_+{}^3 n_+ + \mu_-{}^3 n_- - \frac{(\mu_+{}^2 n_+ - \mu_-{}^2 n_-)^2}{\mu_+ n_+ + \mu_- n_-}\right]$$

where n_+ and μ_+ denote the concentration (n/cm^3) and mobility (cm^2/sec volt) respectively of the 'holes' in the lower band. Similarly n_- and μ_- denote these features for electrons in the upper band.

The magnetic field B_z is in gauss divided by 10^{-8}.

The electronic charge e is in coulombs, i.e. $e=1{\cdot}6\times10^{-19}$.

These formulae are valid only if μ_+, μ_- and B are such that $(\mu_+ B_z)^2$ and $(\mu_- B_z)^2$ are negligible relative to unity.

These formulae are derived for the case where the axis of the cylindrical energy surfaces is contained in the y–z plane at an angle θ to the z-axis. The magnetic field is such that $B_x=0=B_z$.

The energy surfaces of the model are of the form

$$\epsilon_+=\epsilon_0-\lambda_+(k_1{}^2+k_2{}^2),$$
$$\epsilon_-=\lambda_-(k_1{}^2+k_2{}^2),$$

where ϵ_0 is the 'overlap' of the two bands. We define the mobilities of 'holes' and electrons in the form

$$\mu_+ = \frac{2e\tau_+\lambda_+}{h^2}, \quad \mu_- = \frac{2e\tau_-\lambda_-}{h^2}$$

where τ_+ and τ_- are relaxation times for 'holes' and electrons respectively. The formulae have been simplified by neglecting the variation of τ_+ and τ_- near the Fermi surface.

The concentrations of 'holes' and electrons, n_+ and n_-, are defined by

$$n_+ = \frac{4\pi kT}{c\lambda_+} \ln\{1+\exp(\epsilon_0-\eta)/kT\},$$

$$n_- = \frac{4\pi kT}{c\lambda_-} \ln\{1+\exp\eta/kT\},$$

where c denotes the c-spacing in in graphite and η denotes the chemical potential. With this definition:

$$n_+ - n_- = \text{concentration of trapped electrons.}$$

Orientation and Density Corrections

We have assumed that in our polycrystalline sample of graphite, the crystallites are orientated so that their c-axes are contained in the y–z plane. Accordingly we replace $\cos^2\theta$ by $\frac{1}{2}$ in the formulae given in (1).

If α is the ratio of the observed density to the theoretical density of graphite, the true current density I_x is related to the apparent current density I_x' by the relation $I_x = I_x'/\alpha$. We have taken $\alpha = 0{\cdot}8$

REFERENCES

AUSTERMAN, S. B., 1958, Atomics International Report No. NAA–SR–2457.

AUSTERMAN, S. B., and HOVE, J. E., 1955, *Phys. Rev.*, **100,** 1214.

EATHERLY, W. P., 1953, Classified USAEC Report.

GALT, J. K., YAGER, W. A., and DAIL, H. W., 1956, *Phys. Rev.*, **103,** 1586.

HENNIG, G. R., and HOVE, J. E., 1955, First Geneva Conference Paper 7P 666.

JOHNSTON, D. F., 1955, *Proc. roy. Soc.* A, **227,** 349.

JONES, H., and ZENER, C., 1934, *Proc. roy. Soc.* A, **145,** 269.

KINCHIN, G. H., 1954, *J. nucl. Energy*, **1,** 124.

KINCHIN, G. H., and PEASE, R. S., 1955, *Rep. Progr. Phys.*, **18,** 1.

McCLURE, J. W., 1956, *Phys. Rev.*, **101,** 1642 ; 1957, *Ibid.*, **108,** 612 ; 1958, *Ibid.*, **112,** 715.

MOTT, N. F., and JONES, H., 1936, *The Theory of the Properties of Metals and Alloys* (Oxford : University Press), p. 292.

NOZIÈRES, P., 1958, *Phys. Rev.*, **109,** 1510.

PARMENTER, R. H., 1955, *Phys. Rev.*, **97,** 587.

SLONCZEWSKI, J. C., and WEISS, P. R., 1958, *Phys. Rev.*, **109,** 272.

SOULE, D. E., 1958 a, *Phys. Rev.*, **112,** 698 ; 1958 b, *Ibid.*, **112,** 708.

WERTHEIM, G. K., 1959, *Phys. Rev.*, **115,** 568.

The Phonon Drag Component of the Thermoelectric Power of the Alkali Metals at Low Temperatures†

By M. BAILYN
Northwestern University, Evanston, Illinois, U.S.A.

[Received September 6, 1959 ; and in revised form March 4, 1960]

ABSTRACT

The theory of phonon drag in the thermoelectric power is developed from an equation derived in a previous paper. It is shown that important in the understanding of the phenomena are the relative probabilities $\alpha\,(j\mathbf{q};\,\mathbf{q}+\mathbf{K})$ that a phonon of wave vector **q** and polarization j will interact with electrons via a process of umklapp type **K**, where **K** is a reciprocal lattice vector or zero. $\alpha\,(j\mathbf{q},\,\mathbf{q}+\mathbf{K})$ is the probability relative to all the processes into which the jq phonons can enter, including phonon–phonon collisions and phonon-impurity interactions. It is shown by means of a 'baby spectrum' that the use of α results in the domination of the phonon drag effect by the transverse-like phonon modes, and in the watering down of any 'bulge' effect of the Fermi surface. Rough calculations are made that show that one can get qualitative agreement with experiment over at least part of the temperature range from 2 to 20°K. It is shown that with neglect of phonon–phonon and phonon-impurity interactions the phonon drag part S_g of the thermoelectric power is the sum of two terms, a normal (negative) term S_g^-, which is exactly what would be calculated if all processes were non-umklapp processes, plus a term S_g^+ which is anomalous (positive) in sign and is the effect on the electrons of the Bragg reflections abstracted from the umklapp processes. A simple derivation of the basic equation is given.

§ 1. INTRODUCTION

IN 1958, MacDonald *et al.* measured the thermoelectric power of the alkali metals down to 2°K. They found that the magnitudes of this quantity were in all cases many times that predicted by the normal theory, in caesium as much as about 30 times larger, in sodium about 10 times larger. They also found that the sign becomes anomalous, namely positive, in caesium and rubidium, and that an oscillation takes place in potassium between 2 and 10°K. These authors showed that the phonon-drag effect might possibly explain the measured magnitudes since it had been shown by MacDonald (1954) (without the factor $\frac{1}{3}$) and Hanna and Sondheimer (1957) that on neglect of phonon–phonon interactions the phonon-drag contribution to the thermoelectric power is given by

$$S_g = -\frac{1}{3}\frac{C}{N|e|} = -\frac{77\cdot 8\kappa}{|e|}\left(\frac{T}{\Theta}\right)^3 \;\ldots\; T \ll \Theta, \quad . \;\; . \;\; . \quad (1.1)$$

where C is the specific heat of the lattice, and where N is the number of atoms per unit volume. Θ is a Debye temperature. Such a term does give large magnitudes in the temperature range considered. But it was thought that this would always be a negative contribution and hence there was no explanation of the change in sign to positive in Rb and Cs, nor of the oscillation in K.

---

† Communicated by the Author. This work was partially supported by a National Science Foundation Grant (U.S.A.).

In 1958, the author developed a theory to take into account the effect of the non-equilibrium component of the phonon distribution by means of a Variation Principle. The transport coefficients were derived, and in particular the phonon-drag term S_g in the thermoelectric power was formulated. It was found that the umklapp (UK) processes in the scattering of electrons (in monovalent metals) almost always yielded an anomalous or positive contribution to S_g, whereas the normal, non-UK processes always yielded a normal (negative) sign in S_g. It was therefore suggested that the UK contribution to the phonon-drag effect would be able to account for the anomalous sign as well as the anomalous magnitude of the measured thermoelectric power. It was cautioned however that the actual effect was the result of a 'delicate balance' between very large positive and negative contributions, and that an extremely complicated computation would be required to see if the theory in fact matched the experiment. In addition, not the ordinary electron–phonon matrix element appears, but rather one normalized in a different fashion, and consequently quite a bit more difficult to know how to handle.

There have been other approaches to the same problem. Notably, Hanna and Sondheimer (1957) considered the solution of the Boltzmann equation taking into account the non-equilibrium component of the phonons. Their expressions would correspond to a first approximation to the solution obtained by the author were it not for the fact that they did not take into account umklapp processes. For other references see Bailyn (1958).

Ziman (1959) had however developed a theory which is also a Variational Principle and which does take into account umklapp processes. By ignoring phonon–phonon processes, he was able to compute the phonon-drag term in the thermoelectric power, and found that by postulating a large effect arising from the distortion of the Fermi surface, he was able to get tolerable agreement between theory and experiment.

We have rather serious objections to both the theory and the computations of Ziman, and the purpose of this paper is to develop the theory according to the lines we originally suggested. In § 8 we compare the two approaches.

In § 2 we derive the basic expression of Bailyn (1958) in a very simple manner. This derivation evolved out of conversations with Dr. D. K. C. MacDonald. The confidence that a simple derivation was possible was entirely his. In § 3 we separate S_g into the intrinsically positive portion (S_g^+) and the intrinsically negative portion (S_g^-). In § 4 we derive an approximate expression for S_g^+ from which calculations are subsequently made. In §§ 5 and 6 we construct and discuss the phonon spectrum from which we draw a qualitative picture of the nature of the contributions to S_g^+.

§ 2. SIMPLE DERIVATION OF THE BASIC EQUATION

(With D. K. C. MacDonald)†

We regard the phonons as proceeding down a metal bar from one at temperature T_1 to the other at T_2. The length of the bar is δx. We consider a quantity $\delta N(j\mathbf{q})$ which is the net number of phonons of wave vector $\mathbf{q}$ and polarization j in the bar at any instant that must be annihilated sooner or later before reaching the cold end of the bar in order to maintain the boundary conditions of temperature. (Going in the $-x$ direction, the same number of $-q, j$ phonons must be created. q is supposed to have a positive x-component, so that $-q$ has a negative x-component.) To first order in the non-equilibrium component of the distribution, this is given by

$$\delta N(j\mathbf{q}) = \frac{\partial N_0(j\mathbf{q})}{\partial x}\,\delta x, \qquad \qquad (2.1)$$

where $N(j\mathbf{q})$ is the equilibrium number of phonons at T_1 or T_2. (It does not matter for our purpose where in the interval T_1, T_2 we evaluate $\partial N_0/\partial x$.)

Let us now define $\alpha(j\mathbf{q}\,;\ \mathbf{q}+\mathbf{K})$ to be the relative probability that any one of these excess phonons will be destroyed (i.e. will interact) by means of an UK process of type $\mathbf{K}$. A given $\mathbf{q}j$ phonon may get destroyed by (1) normal interactions, with electrons denoted by $\mathbf{K}=\mathbf{K}_0=0$, (2) umklapp interactions with electrons, denoted by $\mathbf{K}_n$ for the nth reciprocal lattice vector (a given phonon may possibly interact by means of more than one type of UK process), and (3), all the other processes not involving electrons, such as phonon–phonon interactions, boundary scattering impurity, etc. The processes in the last category are described by a probability B_0 which is the sum of the probabilities for the separate processes. The quantity α will be taken from Bailyn (1958, eqn. (69)). (See also eqns. (11) and (13) and the dagger footnote page 1593 of that reference.)

$$\alpha(j\mathbf{q}\,;\ \mathbf{q}+\mathbf{K}) = \frac{B(j\mathbf{q}\,;\ \mathbf{q}+\mathbf{K})}{B_0 + \sum\limits_{\mathbf{K}'}^{[j\mathbf{q}]} B(j\mathbf{q}\,;\mathbf{q}+\mathbf{K}')} \qquad \qquad (2.2)$$

The B's represent 'absolute probabilities'. They are given by Bailyn (1958, eqn. (65)) and are met again in (5.5) below. The $\mathbf{K}'$ sum in (2.2) means a sum over all the umklapp processes which a given phonon $\mathbf{q}j$ can enter into. There is a temperature dependence in α arising from the fact that B_0 is temperature dependent, getting in fact much larger as T gets larger. At all but the lowest temperatures, B_0 is so large that the α's become small enough to make phonon drag effects negligible.

---

† The opinions presented in the remainder of this paper are not necessarily shared by Dr. MacDonald.

To calculate the thermoelectric power, we seek the effective x-component of the force, F_x, on the electrons resulting from phonons relaxing by mechanisms (1) and (2) above. Each collision of type K_n will transfer a crystal momentum

$$P_{\mathbf{q},\mathbf{K}}=\hbar(\mathbf{q}+\mathbf{K}) \quad . \quad . \quad . \quad . \quad . \quad . \quad . \quad . \qquad (2.3)$$

into the electron system. Th probable x-component of the momentum introduced into the electron system by the *excess* $\mathbf{q}j$ phonons relaxing by $\mathbf{K}_n$-type collisions is then

$$\delta N(jq)\alpha(j\mathbf{q}\,;\ \mathbf{q}+\mathbf{K}_n)[\mathbf{P}_{\mathbf{q},\mathbf{K}}]_x. \quad . \quad . \quad . \quad . \quad . \quad . \qquad (2.4)$$

We have to use the relative probabilities α, because the number $\delta N(j\mathbf{q})$ of phonons *must* be destroyed somehow or other in order to maintain the temperature boundary conditions. Therefore the sum of probabilities for all the interactions that these excess $\mathbf{q}j$ phonons can enter into must be 1. This 'renormalization' is characteristic of all phonon–drag calculations.

A sum over n (including the normal term $n=0$) would then give the total momentum introduced by the $\mathbf{q}j$ phonons. The time it would take would be the time $\delta t(j\mathbf{q})$ taken by a $\mathbf{q}j$ phonon which managed to travel from one end of the bar to the other before being destroyed. Thus the force on the electrons from the $\mathbf{q}j$ phonons is equal to the rate of change of momentum caused by phonon destruction and is

$$F_x(j\mathbf{q})=\sum_{\mathbf{K}}^{[j\mathbf{q}]}\frac{\partial N_0}{\partial x}\frac{\delta x}{\delta t(j\mathbf{q})}[P_{\mathbf{q},\mathbf{K}}]_x\alpha(j\mathbf{q}\,;\ \mathbf{q}+\mathbf{K}). \quad . \quad . \qquad (2.5)$$

But $\delta x/\delta t(j\mathbf{q})$ is just the x-component of the drift (group) velocity $\nabla_q\omega(j\mathbf{q})$ of the $j\mathbf{q}$ phonons where $\omega(j\mathbf{q})$ is the frequency of these phonons. Further the force F_x may be set equal to $-|e|\mathscr{E}_xN$, where N is the number of electrons in the bar, and $\mathscr{E}_x$ is the average electric field that would produce this force. In the usual sense, an electric field is the same on every electron, but the force on different electrons would be different according to (2.4). We thus have here an average force (which would be the measured force). Finally we write

$$\frac{\partial N_0}{\partial x}=\frac{z}{(e^z-1)(1-e^{-z})}\frac{1}{T}\frac{dT}{dx}, \quad . \quad . \quad . \quad . \quad . \quad . \qquad (2.6)$$

where

$$z=\frac{\hbar qv(j\mathbf{q})}{\kappa T}. \quad . \quad . \quad . \quad . \quad . \quad . \quad . \quad . \quad . \qquad (2.7)$$

We have used the fact that the frequency $\omega(j\mathbf{q})$ of a phonon is $qv(j\mathbf{q})$ where $v(j\mathbf{q})$ is the phase velocity. The phonon-drag component of the thermoelectric power is just (2.5) divided by the temperature gradient:

$$S_g=\mathscr{E}_x/(dT/dx)=-(3Ne)^{-1}\sum_{j\mathbf{q}}\sum_{\mathbf{K}}^{[j\mathbf{q}]}\alpha(j\mathbf{q}\,;\ \mathbf{q}+\mathbf{K})\hbar(\mathbf{q}+\mathbf{K})\,.\,\nabla_q\omega\partial N_0/\partial T.$$

$$. \quad . \quad . \qquad (2.8)$$

We have contemplated a cubic crystal so that P_xv_x was replaced by $(1/3)\mathbf{P}\,.\,\mathbf{v}$.

This expression for free electrons follows from the γ_0/α_0 term of eqn. (86) of our 1958 article, when eqns. (79) and (77) are used. (For the extension to non-spherical energy surfaces and several bands, see Bailyn (1960), Appendix H.)

We see from (2.8) that for an UK process, $\mathbf{q}+\mathbf{K}$ is directed away from $\nabla_q\omega$ (which is generally in a direction close to that of $\mathbf{q}$), and the contribution is positive, i.e. anomalous. Normal processes ($\mathbf{K}=0$) give a normal sign.

§ 3. SIMPLIFICATION ARISING FROM NEGLECT OF PHONON–PHONON COLLISIONS

We first make a preliminary approximation, which is to neglect phonon–phonon and other relaxation processes not involving electrons. This implies

$$\sum_{\mathbf{K}}^{[j\mathbf{q}]} \alpha(j\mathbf{q};\ \mathbf{q}+\mathbf{K})=1. \quad . \quad . \quad . \quad . \quad . \quad . \quad . \quad (3.1)$$

We then go back to (2.8) and separate the right-hand side into a $j\mathbf{q}\mathbf{K}$ summation containing the $\mathbf{q}$ of the momentum factor $\mathbf{q}+\mathbf{K}$ plus a $j\mathbf{q}\mathbf{K}$ summation containing the $\mathbf{K}$ of the momentum factor. The term in $\mathbf{q}$ will then contain a sum over $\mathbf{K}$ which is exactly the left-hand side of (3.1) and hence may be let equal to 1. We thus get the separation.

$$S_g=S_g^{+}+S_g^{-}, \quad . \quad . \quad . \quad . \quad . \quad . \quad . \quad . \quad . \quad . \quad (3.2)$$

$$S_g^{-}=-\frac{1}{3N|e|}\sum_{\mathbf{q}}\sum_{j}\hbar\mathbf{q}\,.\,\nabla_q\omega\frac{\partial N_0}{\partial T}=-C/(3Ne), \qquad (3.3\,a)$$

$$S_g^{+}=-\frac{1}{3N|e|}\sum_{\mathbf{q}}\sum_{j}\sum_{\mathbf{K}\neq0}^{[j\mathbf{q}]}\alpha(j\mathbf{q};\ \mathbf{q}+\mathbf{K})\hbar\mathbf{K}\,.\,\nabla_q\omega\frac{\partial N_0}{\partial T}. \qquad (3.3\,b)$$

A number of points needs to be made apropos of these equations. First, in (3.3 *a*) C stands for the specific heat

$$C=\frac{\Delta}{8\pi^3}\sum_{j}\int d^3q\hbar\omega\frac{\partial N_0}{\partial T}, \quad . \quad . \quad . \quad . \quad . \quad . \quad . \quad (3.4)$$

(where Δ is the crystal volume); thus the relation in (3.3 *a*) is possible only if we identify

$$\mathbf{q}\,.\,\nabla_q\omega=qv \quad . \quad . \quad . \quad . \quad . \quad . \quad . \quad . \quad . \quad (3.5)$$

This is not in general true, but it is shown in the Appendix to be the case for the particular spectrum for which we make calculations. This specific heat relation (3.3 *a*), previously obtained by Hanna and Sondheimer (1957), and MacDonald (1954), is thus shown to arise in the more general considerations of this paper, provided phonon–phonon and phonon-impurity interactions are neglected, and provided the spectrum satisfies (3.5).

Second, the sum over $\mathbf{K}$ in (3.3 *b*) is set equal to 12 times the contribution from each $\mathbf{K}$. This is the case because the contribution of each $\mathbf{K}$ is the same, and there are 12 nearest neighbour $\mathbf{K}$'s. The region of $\mathbf{q}$ integration for a given $\mathbf{K}$ is the shaded volume of fig. 1. It is the overlap volume between the q-sphere of radius $q_{\max}$ centred at $q=0$, and the sphere of radius $2k_0$ (k_0 being the wave vector of the electron at the top of the Fermi sphere) centred at the origin of the reciprocal lattice vector $\mathbf{K}$. The tip of $\mathbf{K}$ is at $q=0$, (i.e. 000) and the tail is at, say, the 011 reciprocal lattice point. In UK interactions an electron wave vector changes from $\mathbf{k}$ to $\mathbf{k}'$ with $|\mathbf{k}-\mathbf{k}'|\leqslant 2k_0$ and $\mathbf{k}-\mathbf{k}'=\mathbf{q}+\mathbf{K}$. Hence the permitted q-volume for the $\mathbf{K}=011$ type of umklapp process is the overlap volume as described above.

Fig. 1

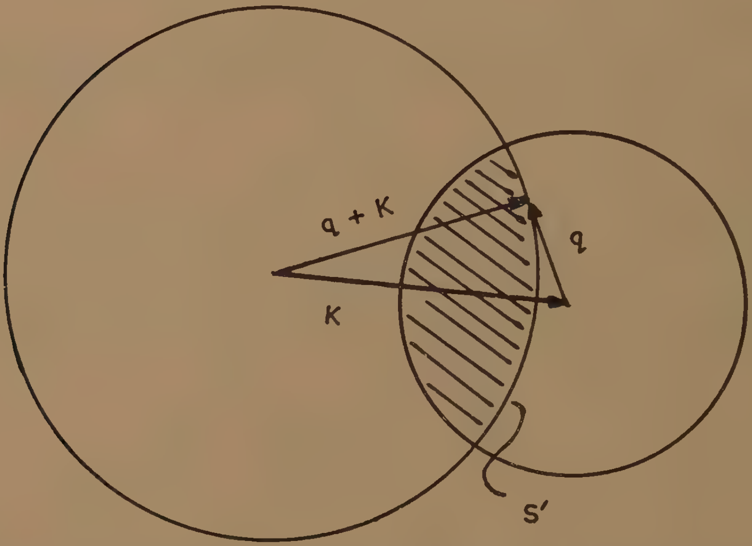

The geometry of umklapp processes. The surface S′ is the surface for which table 1 is computed. It is that part of the surface of the shaded volume that is part of the surface of the sphere of radius $|q+K|$ when $|q+K|=2k_0$.

We make the separation into $S_g{}^-$ and $S_g{}^+$ for several reasons. It has the advantage of providing the anomalous sign contribution as an extra term to be added to the 'normal' specific heat term. It has the advantage that, unless details of the electron number N are investigated, many of the complications arising from electron quantities (such as shape of Fermi surface) appear only in $S_g{}^+$†, whereas $S_g{}^-$ in principle can be computed by one of several standard methods, or can be taken from experiment. And finally it has the advantage that the two terms have a definite physical significance. $S_g{}^-$ is the contribution which would occur if for some reason all the processes were normal. And $S_g{}^+$ is the contribution that is provided by the Bragg reflections abstracted from the umklapp interactions. The anomalous sign comes specifically from that part of the umklapp interactions which are the Bragg reflections.

---

† See Bailyn (1960), Appendix H for more details of these effects.

It should be kept in mind that in (3.3) the phonon–phonon and phonon-impurity interactions have been neglected. When these are taken into account, the relation in (3.3 *a*) is in particular no longer valid, and in general the α's become smaller. One may expect that although the onset (as T rises) of phonon-drag may well be represented by the approximation (3.1), it is quite possible that the dwindling away of the effect may require a more detailed knowledge of the α. This is in fact our explanation of the poor results for caesium above 11°K (see § 7).

§ 4. An Approximate Expression for the S_g^+'s

We shall leave S_g^- as in (3.3 *a*) and assume that the standard calculations or measurements of specific heat will determine it for our purposes. S_g^+ has to be calculated separately however. We do not pretend to any great accuracy in this calculation, but the result should give some indication of the correct temperature dependence. First we write (3.3 *b*) as

$$S_g^+ = -\frac{\Delta}{N|e|}\,\frac{1}{2\pi^3}\sum_j \mathbf{K}\cdot\int \alpha(j\mathbf{q};\,\mathbf{q}+\mathbf{K})[\nabla_q\hbar\omega]\frac{\partial N_0}{\partial T}\,d^3q. \tag{4.1}$$

The basic approximation to be made is that for each polarization j the α can be removed at some 'effective value' α_j to be incorporated subsequently in an experimentally determined adjustable parameter. Thus we allow

$$S_g^+ \simeq \sum_j A_j'\,dI_j/dT, \tag{4.2}$$

$$I_j = (1/\kappa)\mathbf{K}\cdot\int d^3q\,[\nabla_q\hbar\omega]N_0, \tag{4.3}$$

$$A_j' = \frac{\Delta}{Ne}\,\frac{\kappa}{2\pi^3}\,\alpha_j. \tag{4.4}$$

If we use the identity

$$[\nabla_q\hbar\omega]\frac{\partial N_0}{\partial T} = -\frac{\hbar\omega}{T}\,\nabla_q N_0, \tag{4.5}$$

then we can form a differential equation for I_j by integrating by parts

$$\left.\begin{aligned}\frac{dI_j}{dT} &= -\frac{\mathbf{K}}{\kappa}\cdot\int d^3q\,\frac{\hbar\omega}{T}\,\nabla_q N_0\\ &= I_s + I_j/T,\end{aligned}\right\} \tag{4.6}$$

where

$$I_s(T) = -\frac{1}{\kappa T}\mathbf{K}\cdot\int d^3q\,\nabla_q(\hbar\omega N_0) = -\frac{1}{\kappa T}\mathbf{K}\cdot\int \hat{n}\hbar\omega N_0\,dS_q. \tag{4.7}$$

Here $\hat{n}$ is an outward drawn normal to the surface involved. The total surface would actually be that over the region in which the α's are substantial in magnitude. Part of this surface will always coincide with S′ of fig. 1, and in fact the contribution from this part will be tremendously greater (because of the smaller q's) than from anywhere else on the surface. We then as our second approximation remove the integrand in (4.7) at an 'effective value' on S′ represented by a kind of Debye temperature Φ_j:

$$I_s(T) \cong S_j \left\langle \frac{\hbar\omega}{\kappa T} N_0 \right\rangle_{S'}, \qquad (4.8)$$

$$\left\langle \frac{\hbar\omega}{\kappa T} N_0 \right\rangle_{S'} \cong \frac{\Phi_j}{T} [\exp(\Phi_j/T)-1]^{-1}, \qquad (4.9)$$

$$S_j = -\kappa . \int_{S'} \hat{n} dS_q > 0. \qquad (4.10)$$

These Debye type temperatures Φ_j denote an average over a surface containing electrons with the *minimum* wave vector that can enter UK processes, in contrast to the usual Debye temperatures in which the maximum wave vector is sought. The 'effective surface' integral S_j is to be lumped with α_j and treated as an adjustable parameter.

No matter how we evaluate $I_s(T)$, eqn. (4.6) can be solved for I in terms of I_s:

$$I_j = T\left[\int^{T} \frac{1}{y} I_s(y) dy + C\right]. \qquad (4.11)$$

The term in the constant C is the solution of the homogeneous part of (4.6) C must be zero, as can be seen by evaluating (4.4) in the limit of extremely low T:

$$\lim_{T\to 0} I_j = -T\mathbf{K} . \int dS_q \hat{n} \exp[-\hbar\omega/\kappa T]. \qquad (4.12)$$

But this corresponds to the first term of the bracket of (4.11). For it is decreasing exponentially, and there is no other way to make (4.11) equal (4.12) than by assigning $C=0$. We then get with (4.8):

$$\begin{aligned} \frac{dI_j}{dT} &= I_s + \int^{I} \frac{1}{y} I_s(y) dy \\ &= S_j \left[\frac{z}{e^z-1} + \int_z \frac{dx}{e^x-1}\right] \ldots z = \Phi_j/T. \end{aligned} \qquad (4.13)$$

Let us now write the integral S_j of (4.10) as a fraction γ_j times the integral taken over the surface S' of fig. 1:

$$S_j = \gamma_j S_{\max}, \qquad (4.14)$$

$$S_{\max} = -\int_{S'} K . \hat{n}\, ds_q = 2{\cdot}824\pi k_0^3. \qquad (4.15)$$

Then if we define the function

$$\begin{aligned} F(z) &= \frac{\Delta}{N} \frac{\kappa}{e} \frac{1}{2\pi^3} S_{\max} \left[\frac{z}{e^z-1} + \int_z \frac{dx}{e^x-1}\right] \\ &= 367{\cdot}3 \left[\frac{z}{e^z-1} + \begin{cases} -\ln z + \dfrac{z}{2} - \dfrac{B_1}{2!}\dfrac{z^2}{2} + \ldots z < 2\pi \\ \displaystyle\sum_{m=1}^{\infty} m^{-1} \exp(-mz) \ldots z > 1 \end{cases}\right] \frac{\mu V}{{}^\circ\mathrm{K}}, \end{aligned} \qquad (4.16)$$

we shall have from (4.2), (4.13), (4.14), and (4.16):

$$S_g^+ \doteq \sum \alpha_j \gamma_j F\left(\frac{\Phi_j}{T}\right). \qquad (4.17)$$

We have the result in the form of an 'effective α_j' times an 'effective surface ratio γ_j', times a function F of temperature. The combination

$$A_j \equiv \alpha_j \gamma_j \qquad \text{(4.18)}$$

is treated as a constant adjusted to fit experiment, and the function $F(z)$ is shown in fig. 2.

This completes the derivation. It is not meant to be anything but a crude attempt at getting an expression which should represent in a fair way the temperature dependence of the phonon drag term S_g^+. The approximations (4.2), and (4.9) that went into this derivation were both of the same type, namely, it was assumed that quantities could be removed from under the integral sign at 'effective' values.

Fig. 2

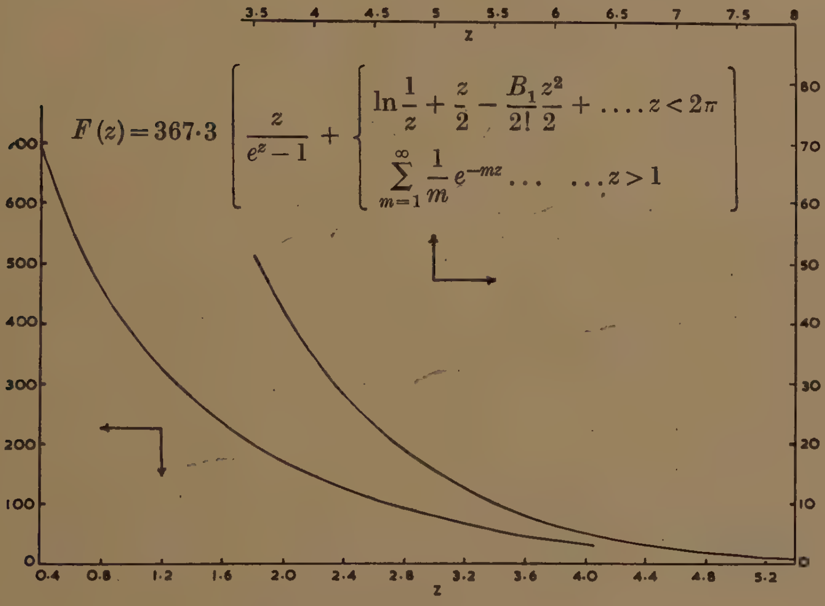

The function $F(z)$ of eqn. (4.16).

To improve on the approximations we have made would require a detailed spectrum calculation for each metal at each temperature and a detailed knowledge of α as a function of q and K, a project beyond the scope of this paper. However, in the next section we begin a discussion of a less ambitious but similarly directed programme which is a 'baby spectrum' calculation incorporating only a small number of points on S′ and evaluated for only two sets of temperature and elastic constant parameters. From this we hope to get a glimpse of how qualitatively the contributions from the various polarizations j and the various modes $\mathbf{q}$ compare.

§ 5. The Calculation of Table 1

We here begin an analysis of the contributions to S_g^+. The analysis is made by selecting a number of q's on the surface S′ of fig. 1 and computing numerically for the three polarizations the factors

$$R_j = 10T\frac{\partial N(j)}{\partial T}\left(\frac{q}{k_0}\right)^2 \quad \text{and} \quad \alpha_j \quad . \quad . \quad . \quad . \quad . \quad (5.1)$$

and their product. The product here may be related either to the integrand of (4.1) or to the integrand of (4.11) (or of (4.13)). In the former case, we would need $\nabla_q\omega$ to complete the integrand, but we shall suppose that this linear factor will not upset any qualitative conclusions that are drawn from the exponential dN/dT and the α's. In the latter case, we notice that for sufficiently large z (i.e. low T),

$$R_j = 10\frac{z(q/k_0)^2}{(e^z-1)(1-e^{-z})} \cong 10\left(\frac{q}{k_0}\right)^2 zN_0. \quad . \quad . \quad . \quad (5.2)$$

This is precisely the integrand in (4.11) (or in (4.13)), see (4.7).

The points chosen were on the intersection of S′ and the six planes

$$\begin{aligned} &q_x=0, \quad q_y=q_z,\\ &q_z=0, \quad q_x=q_z,\\ &q_x=q_y, \quad q_x-q_y+q_z=0. \end{aligned} \quad . \quad . \quad . \quad . \quad . \quad . \quad (5.3)$$

The results of the calculation are given in table 1. In addition to the qualitative conclusions about the relative importance of the various phonons, the numbers in table 1 enable us to make bounds for reasonable average values to be used for the Φ_j's. In this section we discuss the calculation that leads to table 1, and in the next section we discuss the conclusions and estimate the Φ_j. The first problem is the calculation of α.

From (2.2) we notice that the number of terms in the denominator of α will change from phonon to phonon depending on the number of UK processes in which a phonon can participate. If the number of types of interactions with electrons that a phonon can enter into is n, where $n=1+m$, m being the number of UK processes, and the 1 referring to the normal process, then we call this an 'n-process phonon'. The very smallest q's then are '1-process phonons'. In table 1 the various entries are labelled by this parameter n. We originally thought to make a calculation for each 'n-process region' in the q-sphere, each region containing only 'n-process phonons'. But the actual differences in values for the α's when they were calculated were not that great to warrant such a computation.

If the numerator and denominator of (2.2) are divided by the numerator, we get

$$\alpha(j\mathbf{q};\ \mathbf{q}+\mathbf{K}_1) = \left[1+\sum_{\mathbf{K}_2\neq\mathbf{K}_1}^{\{\mathbf{q}j\}}\beta(\mathbf{q}\mathbf{K}_1;\ \mathbf{K}_2)\right]^{-1} \dots \frac{B_0}{B} \ll 1, \qquad (5.4)$$

where, using eqn. (65) of Bailyn (1958) for the B's,

$$\beta(\mathbf{q}\mathbf{K}_1;\ \mathbf{K}_2) = \left\{\frac{\cos[\hat{\xi}(j\mathbf{q}),\ \mathbf{q}+\mathbf{K}_2]}{\cos[\hat{\xi}(j\mathbf{q}),\ \mathbf{q}+\mathbf{K}_1]}\right\}^2 \left|\frac{\mathbf{q}+\mathbf{K}_1}{\mathbf{q}+\mathbf{K}_2}\right| \left(\frac{I(\mathbf{q}+\mathbf{K}_2)}{I(\mathbf{q}+\mathbf{K}_1)}\right)^2. \qquad (5.5)$$

Here I is the interaction matrix element of the electrons (eqn. (5) of Bailyn (1958)):

$$I(\mathbf{q}+\mathbf{K})=N\int_{\text{crystal}} \psi_{\mathbf{k}'}{}^{*}\nabla v\psi_{\mathbf{k}}d^3r,$$
$$\mathbf{k}'-\mathbf{k}=q+K, \quad \ldots\ldots\ldots \quad (5.6)$$

where $\psi_{\mathbf{k}}$ is the wave function for the $\mathbf{k}$ electron, and $v(r)$ is the potential from an ion at $r=0$ plus the shielding electron cloud around it. $\hat{\xi}(j\mathbf{q})$ is the unit vector in the direction of vibration of the $\mathbf{q}j$ phonon. Since we are concerned mainly with the surface S′ of fig. 1, the I ratios in (5.5) will usually be either (a) between two UK processes with $|\mathbf{q}+\mathbf{K}_1|=2k_0$ and $|\mathbf{q}+\mathbf{K}_2|\simeq 2k_0$, or ($b$) between one UK process and one normal process with $|\mathbf{q}+\mathbf{K}_1|=2k_0$ and $|\mathbf{q}+\mathbf{K}_2|=q=0{\cdot}2k_0\ldots.0{\cdot}5k_0$. In case ($a$) the I^2 ratio is about 1, and in case (b) the ratio is between about 1·0 (for Na) and about 0·5 (for Cs). The latter numbers are taken from the unpublished work of Bailyn (1956), but the effect on our results of using the Bardeen (1937) values for them would be approximately the same†. None of the qualitative results that arise from table 1 are sensitive to particular values chosen for parameters. Recent corrections taking into account exchange and correlation effects (to be published†) also do not alter the order of magnitudes of these ratios, nor consequently the final conclusions. The longitudinal mode contribution was the most sensitive to the I ratios, and that mode for more than one reason has such a small effect that in the end we neglected it altogether (see § 6 below).

The velocities $v(j\mathbf{q})$ and directions of vibration $\hat{\xi}(j\mathbf{q})$ were calculated using the elastic limit spectrum in the Appendix. The $\hat{\xi}$ in that spectrum are functions only of the 'isotropy parameter' s of the elastic constants c_{ij}:

$$s=\frac{c_{11}-c_{44}}{c_{12}+c_{44}}, \quad \ldots\ldots\ldots \quad (5.7)$$

whereas the velocities depend on some additional elastic constant parameters. The elastic constants we used were calculated by the Fuchs method. The numbers cited by Huntington (1958) have since been improved using low-temperature compressibility data from the experiments of Swenson. (More details and data are discussed in a paper to be published†.) At the lowest temperatures (say 4°K), the values of s_0 are about 0·05, 0·15, 0·20, 0·23 and 0·27 for Li, Na, K, Rb, and Cs, respectively. s_0 is a small difference between large quantities, and very sensitive to the compressibilities, so these numbers are to be treated with caution. (By contrast $s_0=0{\cdot}7$ for gold, see Neighbors and Alers 1958). We made two complete calculations, one with $s_0=0{\cdot}1$ and the I^2 ratio in (5.5) equal to 1·0, the other with $s_0=0{\cdot}3$ and I^2 ratio equal to 0·5, only the latter given in table 1. These numbers were chosen as likely extreme situations. The $s_0=0{\cdot}3$ calculation would correspond roughly to Cs, whereas the $s_0=0{\cdot}1$ calculation we regard as very loosely corresponding to the sodium end

---

† *Added in proof.*—This work has since been published, see Bailyn (1960).

Table 1. First Half

Table 1. The ‘baby spectrum’ calculation for $s=0{\cdot}3$. n is the number of processes the phonon can engage in with electrons. $D_j=(\rho V_j^2/c_{44})^{1/2}$. The α’s are the relative probabilities introduced in § 2. The α'’s are the ‘absolute probabilities’ discussed in § 8. R is given by (5.1)

$q_z=0$	q_x	n	q/k_0	D_{I}	D_{II}	D_{L}	α_{I}	$\alpha_{\mathrm{I}'}$	α_{II}	$\alpha_{\mathrm{II}'}$	α_{L}	$\alpha_{\mathrm{L}'}$	$(\alpha R)_{\mathrm{I}}$	$(\alpha R)_{\mathrm{II}}$	$(\alpha R)_{\mathrm{L}}$
	0·0	5	0·30	1·00	1·00	1·33	0·50	(0·60)	0·00	(0·00)	0·10	(0·40)	0·22	0·00	0·02
	0·02	3	0·31	1·00	0·88	1·41	1·00	(0·60)	0·20	(0·10)	0·07	(0·30)	0·44	0·11	0·01
	0·4	3	0·34	1·00	0·64	1·54	1·00	(0·60)	0·48	(0·19)	0·05	(0·21)	0·44	0·47	0·01
	0·6	3	0·41	1·00	0·39	1·62	1·00	(0·60)	0·90	(0·26)	0·04	(0·14)	0·37	1·84	0·00
	0·71	5	0·49	1·00	0·32	1·63	0·25	(0·60)	0·25	(0·30)	0·03	(0·09)	0·09	0·79	0·00
	0·8	3	0·77	1·00	0·39	1·62	1·00	(0·60)	0·97	(0·37)	0·01	(0·03)	0·01	0·01	0·00
$q_x-q_yq_z=0$	q_x														
	0·0	2	0·20	1·00	0·32	1·63	0·00	(0·00)	0·00	(0·00)	0·17	(1·00)	0·00	0·00	0·03
	0·1	2	0·20	0·98	0·35	1·64	0·73	(0·02)	0·08	(0·00)	0·16	(0·98)	0·28	0·11	0·03
	0·2	2	0·21	0·94	0·43	1·64	0·78	(0·09)	0·03	(0·00)	0·16	(0·90)	0·33	0·03	0·03
	0·4	2	0·23	0·84	0·57	1·65	0·88	(0·21)	0·11	(0·02)	0·16	(0·77)	0·47	0·10	0·02
	0·6	3	0·31	0·95	0·41	1·64	0·76	(0·41)	0·52	(0·29)	0·07	(0·30)	0·36	0·87	0·01
	0·71	5	0·49	1·00	0·32	1·63	0·25	(0·60)	0·25	(0·30)	0·03	(0·09)	0·09	0·79	0·00
$q_x=q_y$	q_z														
	0·0	5	0·49	1·00	0·32	1·63	0·25	(0·60)	0·25	(0·30)	0·03	(0·09)	0·09	0·79	0·00
	0·1	4	0·40	0·99	0·34	1·64	0·45	(0·64)	0·50	(0·30)	0·02	(0·06)	0·19	1·29	0·01
	0·2	4	0·34	0·94	0·36	1·66	0·33	(0·67)	0·50	(0·30)	0·01	(0·03)	0·16	1·05	0·01
	0·4	4	0·28	0·79	0·50	1·70	0·19	(0·70)	0·50	(0·30)	0·00	(0·00)	0·15	0·71	0·00
	0·58	4	0·25	0·63	0·63	1·72	0·67	(0·40)	0·00	(0·00)	0·10	(0·60)	0·55	0·00	0·01
	0·6	3	0·25	0·62	0·65	1·72	0·13	(0·68)	0·50	(0·30)	0·00	(0·02)	0·11	0·39	0·00

Table 1. Second Half

$q_x=0$	q_z	n	q/k_0	D_{I}	D_{II}	D_{L}	α_{I}	$\alpha_{\mathrm{I}'}$	α_{II}	$\alpha_{\mathrm{II}'}$	α_{L}	$\alpha_{\mathrm{L}'}$	$(\alpha R)_{\mathrm{I}}$	$(\alpha R)_{\mathrm{II}}$	$(\alpha R)_{\mathrm{L}}$
	0·0	5													
	0·2	2	0·24	1·00	0·88	1·41	0·00	(0·00)	0·23	(0·09)	0·11	(0·91)	0·00	0·07	0·02
	0·4	2	0·22	1·00	0·64	1·54	0·00	(0·00)	0·03	(0·02)	0·10	(0·98)	0·00	0·02	0·02
	0·6	2	0·21	1·00	0·39	1·62	0·00	(0·00)	0·02	(0·00)	0·11	(1·00)	0·00	0·02	0·02
	0·71	2	0·20	1·00	0·32	1·63	0·00	(0·00)	0·00	(0·00)	0·17	(1·00)	0·00	0·00	0·03
$q_y=q_z$	q_x														
	0·0	2													
	0·1	2	0·20	0·98	0·34	1·64	0·63	(0·03)	0·00	(0·00)	0·16	(1·00)	0·30	0·00	0·03
	0·2	2	0·20	0·94	0·37	1·66	0·72	(0·09)	0·00	(0·00)	0·16	(0·99)	0·30	0·00	0·03
	0·35	2	0·21	0·83	0·46	1·69	0·85	(0·21)	0·00	(0·00)	0·18	(0·99)	0·43	0·00	0 03
	0·50	2	0·23	0·70	0·58	1·72	0·90	(0·40)	0·00	(0·00)	0·19	(0·99)	0·62	0·00	0·03
	0·58	4													
$q_x=q_z$	q_y														
	0·58	4													
	0·6	3	0·25	0·63	0·63	1·72	0·50	(0·30)	0·02	(0·03)	0·18	(0·67)	0·41	0·02	0·02
	0·7	3	0·24	0·75	0·54	1·71	0·50	(0·30)	0·50	(0·11)	0·11	(0·58)	0·32	0·48	0·02
	0·85	3	0·23	0·87	0·60	1·63	0·50	(0·30)	0·17	(0·02)	0·12	(0·68)	0·26	0·14	0 02
	0·95	3	0·25	0·95	0·79	1·49	0·50	(0·30)	0·00	(0·00)	0·14	(0·70)	0·23	0·00	0·03
	1·00	5													

of the alkalis, even though the s_0 of sodium is considerably higher. The point is that qualitatively these two calculations give the same result, and we concluded that this result will be valid for the actual metals. There is this quantitative difference, however, that the α's which are relatively large in the $s_0=0{\cdot}1$ calculation become relatively smaller in the $s_0=0{\cdot}3$ calculation. A rise in the matrix element I^2 ratio makes the α's smaller.

Finally we wish to point out an important distinction between the directions 011 and 110 in table 1. When (4.1) is reached, the sum over $\mathbf{K}$ in (3.3 *b*) has been reduced to just a term in one $\mathbf{K}$. This $\mathbf{K}$ we chose for the purpose of computing table 1 to be the vector whose tail is at the reciprocal lattice point 011 and whose tip is at 000. The $\mathbf{q}$-vector then starts at 000 and proceeds to some point on S′. The surface S′ is thus centred about $-\mathbf{K}$; hence we shall refer to it from now on as S′ (011). Now once this direction is chosen for $\mathbf{K}$, one should be careful to note that the 011 direction is the one and only direction of a phonon q on S′ (011) that corresponds to an interaction in which an electron $\mathbf{k}$ flips from a direction (011) of closest approach of the Fermi surface to the Brillouin Zone boundary to the opposite direction (011). There are other directions in a cubic crystal which are equivalent to the 011 direction (such as for example the 110 direction), but *relative to the surface* S′(011), these directions are obviously no longer equivalent. We mention this here since we shall find that on S′(011), the 110 direction is quite important, whereas the 011 direction is not. But the 110 phonons here do *not* correspond to interactions in which an electron in the direction of closest approach to the Brillouin Zone boundary flips to the opposite direction.

§ 6. DISCUSSION OF TABLE 1

Our first conclusion from table 1 is that the longitudinal mode contributes far less than either of the transverse modes, *both* because the longitudinal α's are small and because the longitudinal velocities v_{L} are large. We shall in fact neglect the longitudinal mode. It is interesting to note that the closer q gets to the 011 direction, the larger the contribution gets in this mode. The 011 direction corresponds as mentioned above to electrons in the direction of closest approach to the Brillouin Zone flipping to the opposite direction. If the longitudinal were the only mode contributing, the distance of closest approach would thus be as crucial a matter as hypothesized by Ziman (1959). S_g is the very small difference between the large numbers S_g^- and S_g^+, and it is possible that the small longitudinal contribution could still be significant. But it is so much smaller than the others, even for its relatively important directions that we can not see how we can pretend to an accuracy that would include it.

Our second conclusion is that in the transverse modes, the most important phonons are not the ones with the smallest wave vector q (i.e. not the 011 phonons). We can therefore not rely on the change in q magnitude to give the correct relative importance of the different *directions* in the shaded volume in fig. 1. (But we should expect to be able to rely on the change in

q to give the correct relative importance of phonons in a given direction, as q magnitude gets larger in that direction.) The transverse I mode (the one with the larger velocity) has appreciable contributions apparently from a considerable part of S′. We find that in a very rough way, an upper limit on q/k_0 (on S′) is about 0·50 which makes the γ_{I} of (4.14) approximately 0·15.

On the other hand, a much more restricted region of S′ seems to be important for the transverse II mode. This region contains the 110 direction significantly, and we estimate in a very rough way that it includes q/k_0's from about 0·35 to about 0·50. Such a region provides $\gamma_{\mathrm{II}}=0{\cdot}09$ approximately. However, the very erratic nature of the contributions from this mode seem to indicate that the contributions may not be sustained as the azimuthal angle covers its radians (about the polar axis which is **K**). It would not be unreasonable to expect that possibly only a fraction of $\gamma_{\mathrm{II}}=0{\cdot}09$ would be in fact contributing. Our attempts at fitting experiment place the adjustable parameter $\gamma_j\alpha_j$ at round 0·03 for this mode (varying slightly from metal to metal). The smallness of this number could be interpreted either as a result of small γ_{II}'s or small α_{II}'s. It appears to us much more consistent with table 1 to believe that the smallness arises from the small participating region rather than from the smallness of α in that region.

The transverse II mode contains phonons (near the 110 direction) which *individually* contribute to $S_g{}^+$ more than any other phonons from any mode. It strikes us as quite surprising that the q's of these phonons turn out to be as large as $0{\cdot}49k_0$, that is, well above twice the minimum wave vector magnitude $(0{\cdot}2k_0)$ that a phonon participating in an UK process can have.

The preceding discussion and computation was based on a spherical Fermi surface. If we contemplate a bulging of the Fermi surface toward the Brillouin Zone boundary at the direction of closest approach, then in fig. 1, this would correspond to the shaded volume bulging toward $q=0$. Such a bulging is most important for the 011 phonons (on S′ (011)), i.e. for the directions in which q is the smallest. Accompanying every bulge, there will also be an indentation somewhere on the Fermi surface, since the volume in k-space occupied by the electron distribution is the same no matter what the details of shape are. Eventually therefore, there will be a 'negative bulge effect' for electrons which flip in an UK process from one 'negative bulge' to the opposite direction. Such processes will usually require rather large q's. For the phonons which are important in the transverse modes and especially in the transverse II mode, we estimate that the 'positive' bulge effect is diminished from what one would expect if the most important phonons were in the 011 direction. We do not however anticipate that the 'negative-bulge' effect would have arrived for these phonons, as their q's are still small despite the fact that they are of the order of twice the minimum q's. In our crude result (4.13) the effect of a bulge could be taken into account by altering the values for the effective Φ_j's. Thus the Fermi surface distortion effect will be indistinguishable from just a different Debye temperature Φ_j[†] or a difference in spectrum characteristics. This seems to us a rather general result, and we regard as premature the hope of using phonon drag effects to indicate the degree of distortion of the Fermi surface. In our computations, as we went from Na to Cs, we have not postulated any unusual decreases in the Φ_j that would correspond to the progressive increase in distortion of the Fermi surface. (Small errors in Φ arising from say an inaccurate c_{44} or spectrum average errors or Fermi surface distortion can be indirectly and partially corrected by adjusting $\alpha\gamma$ (see below).)

§ 7. Numerical Computation

We have emphasized above that the calculations here are very crude, and the computed quantity very sensitive to parameter values; and we regard our attempt at fitting experiment as showing little more than that to within the crudeness of the computations, it is possible to get qualitatively correct curves over some of the temperature range. Ziman (1959) was the first to show that, despite the difficulties, numerical computations of at least some significance could be made.

The parameters Φ_j are decided upon in a 'consistent way' for the four metals Na, K, Rb, and Cs. They are defined symbolically from the Appendix by

$$\langle z_j \rangle \equiv \frac{\Phi_j}{T} = \frac{\theta}{T}\left\langle \frac{q}{k_0}\left(\frac{\rho V_j^{\,2}}{c_{44}}\right)^{1/2} \right\rangle_{\text{average}},$$
$$\theta = \frac{\hbar k_0}{\kappa}\left(\frac{c_{44}}{\rho}\right)^{1/2}, \quad . \quad . \quad . \quad . \quad . \quad . \quad . \quad . \quad . \quad (7.1)$$

the symbolic aspect being the nature of the average (i.e. it is a *function* of z that is actually averaged in (4.9)). ρ here is the density and κ the Boltzmann's constant. From our two calculations at $s = 0{\cdot}1$ and $s = 0{\cdot}3$ it appears that the product

$$\frac{q}{k_0}\left(\frac{\rho V_j^{\,2}}{c_{44}}\right)^{1/2} = \frac{\Phi_j(\mathbf{q})}{\theta}$$

does not vary much from metal to metal (i.e. as s_0 varies) for each direction $\hat{\mathbf{q}}$. Thus our 'consistent way' mentioned above is to allow, for each polarization, Φ_j/θ to take on for each j the same average value for all the metals. We have found that $\Phi_{\text{II}}/\theta = 0{\cdot}25$ and $\Phi_{\text{I}}/\theta = 0{\cdot}35$ enables us to get fair results. This would correspond for example to an average q/k_0 of about 0·4 for both polarizations and an average $(\rho V_j^{\,2}/c_{44})^{1/2}$ of about 0·90 for the transverse I vibrations and of about 0·62 for the transverse II vibrations. These numbers do not seem unreasonable in view of table 1. The θ's are calculated using computed elastic constants (see table II and Huntington 1958[‡]). In metals with higher θ the average in (7.1) at a given T will emphasize smaller $\Phi(\mathbf{q})$'s. Thus we expect that use of the same average Φ_j in all the metals (for each j) would in fact be giving a value which is too low for Cs as compared with Na. Such an effect would tend to offset the Fermi surface distortion effect. In any case it would seem to be small, and we have not attempted to take it into account.

[†] This point was also noted by Ziman (private communication).

[‡] See also Bailyn (1960).

The results of the computations are given in fig. 3, and some of the data in table 2. The first problem in comparing theory with experiment is to estimate the specific heat, which is required for S_g^-. Recently there have been measurements of this quantity for Li Na and K by Roberts (1957) in the temperature range 2–20°K. We notice that the Debye temperature computed by Roberts for K goes through a sizeable minimum at about $T = T_{\min} \simeq 6$°K. We interpret this result as an indication of the fact that as T decreases, the transverse II mode, with its lower velocities, tends to become more important. As T drops still further, the Debye temperature begins to rise. This is usually explained by supposing that for very small q, the density of states varies more swiftly than q^2 (which the Debye theory gives). Our crude reduction of a spectrum to two Φ_j's would enable us to provide the first effect, namely the lowering of the Debye temperature in the specific heat as T decreases, but it would be incapable of providing the second effect, the rise in the Debye temperature as T goes still lower. Thus the temperature range in which with our approximations to the spectrum we have at least a hope of getting a fit with experiment is the range above the minimum position. We shall attempt to fit, therefore, only this range for each metal. In the case of sodium, on the other hand, the specific heat experiments give a fairly constant Debye temperature. The explanation for this does not seem to have been determined†. Various theoretical curves for Bauer and Bhatia and Horton have been quoted in a review article by Parkinson (1958),

Table 2. Data used in the computations. The first seven rows give the values of the Debye temperatures of the specific heat

	Na	K	Rb	Cs
Θ(4°K)		84·4	54	41·5
Θ(6°K)		82·6	54	42·0
Θ(8°K)		84·5	55	42·5
Θ(10°K)	(155)	87·5	56	43·0
Θ(12°K)	150	89·5	57	43·5
Θ(16°K)	156	94·0	58	44·0
Θ(20°K)	163	96·0	58	44·0
$\alpha_{\mathrm{I}}\gamma_{\mathrm{I}}$	0·07	0·11	0·12	0·12
$\alpha_{\mathrm{II}}\gamma_{\mathrm{II}}$	0·035	0·029	0·028	0·030
Φ_{I}	60	34	20	15
Φ_{II}	43	24	15	11
θ°K	172	96	58	44

---

† See however footnote 24 of Bailyn (1958).

and all of them give a minimum in the Debye temperature more or less like what one finds experimentally for potassium, but not for sodium. Since the theory is unable to predict the specific heat of sodium, it seems unreasonable to suppose that it can predict the even more delicate quantity, the thermoelectric power. We can try however to use a consistently theoretical calculation, even though the specific heat part does not yield the observed specific heat behaviour. Thus we are led to use

Fig. 3

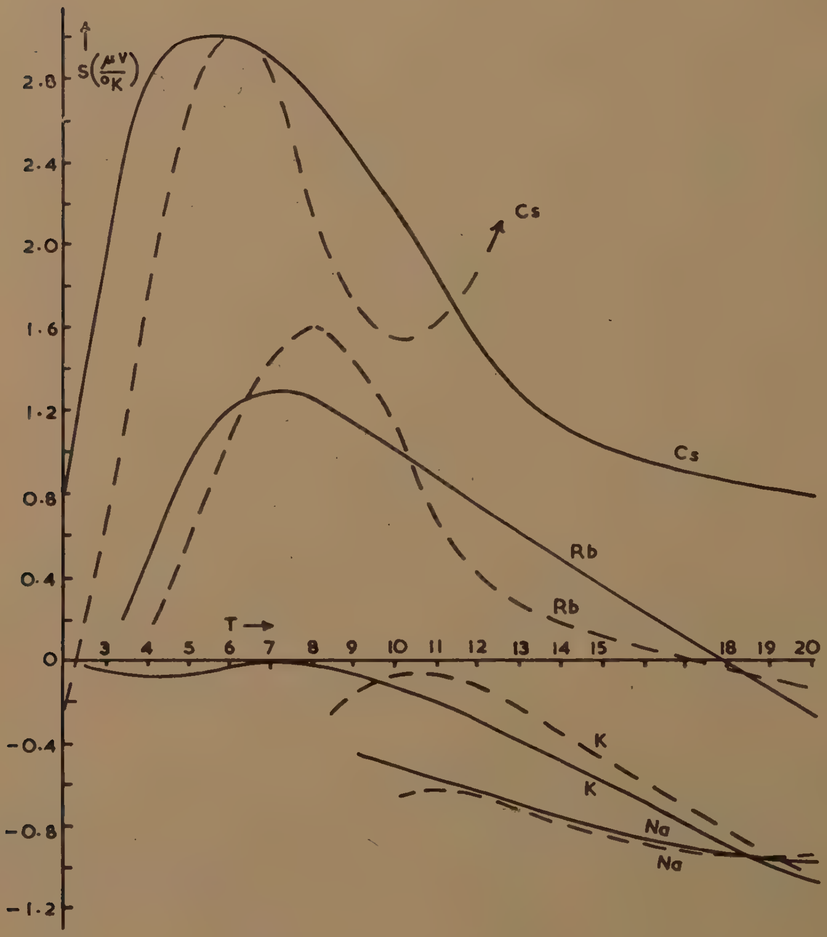

The thermoelectric power of the alkali metals. The dashed lines are the theoretical results, the full lines are the experimental. The wild high temperature caesium result is interpreted as caused by neglect of the phonon–phonon interactions; and the low temperature limitations on Na and K result from use of a spectrum which does not have a density of state function more accurate than the Debye approximation $\sim q^2$ for small q. The discussion is in § 7.

one of the theoretical curves cited by Parkinson for computing S_g^-. We have in fact used Bauer's curve D shown in fig. 12 of Parkinson's article. The curve has a minimum at about 11°K, so we have calculated results only for T greater than this. We can get some agreement as shown in fig. 3, but we do not dare to call it significant. The behaviour of sodium is surely not 'ideal'. This might be due in part to the martensitic transformation it undergoes at low temperatures.

For rubidium and caesium, there do not seem to be specific heat measurements over the necessary temperature range at all, so we manufactured specific heats by analogy with the observed potassium one. We anticipate that the specific heat Debye temperature will show a minimum in Rb and Cs just as in K, and that it will occur at a temperature which is proportional to the corresponding temperature in K, the constant of proportionality being $\theta_{\mathrm{Cs}}/\theta_{\mathrm{K}}$. We also shall regard the size of the minimum as being proportional to the size in K, with the same constant of proportionality. In this way we have constructed the specific heats for Rb and Cs that are given in table 2. We do not believe that more elaborate theoretical computations would be especially significant without more experimental data. It should be emphasized that we should also expect a similar behaviour in sodium, and in fact our specific heat taken from Bauer's work does show something of this sort of behaviour. (Bauer's minimum occurs at $T \simeq 11$°K and $(\theta_{\mathrm{Na}}/\theta_{\mathrm{K}})T_{\min \mathrm{K}} \simeq 11$°K). If we are consistent we must regard sodium as behaving anomalously, and that in fact is our view, as mentioned above.

The results of our calculation of S_g for the other metals are as follows. In potassium, the observed thermoelectric power hovers about an extremely small value as T approaches zero. We are able to match the observed values down to about 9°K. Below this our curve becomes considerably too large negatively. We attribute this, to the failure of our spectrum below the Debye Θ minimum in the specific heat. For potassium this should start in at around 7°K, (the minimum is reached at ~ 6°K). The remaining disagreement reflects the poorness of our approximations and perhaps the phonon–phonon interactions which may, even though small, have an important effect, since the resultant S_g is such a small difference between large numbers.

The rubidium and caesium curves are fairly successful. In the latter, however, above about 11°K, the calculated curve gets out of control. We attribute this to the decisive onset of phonon–phonon interactions. When these become large, the α's become temperature dependent, and another calculation entirely must be contemplated. The first place we would expect this drastic change in S_g would be in the higher temperatures for caesium, since caesium has the lowest θ. We therefore tentatively ascribe to this effect the wildness in the calculated curve for caesium above about 11°K.

It was partially the fear that this type of difficulty would interfere with all the calculations that caused us to be skeptical at first that any significant calculations could be made. Ziman (1959) was the first to show that calculations could be made by neglecting the phonon–phonon processes entirely. However, we suggest that they are entering finally in a decisive fashion here in the higher temperature range for caesium.

The small changes in the $\alpha\gamma$ parameter in going from K to Cs are quite essential in getting a fit with experiment. Those changes reflect the changes in going from metal to metal, and also indirectly the changes in Φ that are not taken into account by our 'systematic' method of determining Φ, such as possible erroneous c_{44} values, distortion of the Fermi surface, and spectrum details, all of which influence the same parameters Φ. There is experimentally an increasingly positive character of S_g as we go from Na to Cs that we have tried to match. Unfortunately we cannot trace the individual effects, and show how they would produce this result: all that we are able to do is provide a form for the result in terms of adjustable parameters. Qualitatively we can suggest the following possible origins of the increase in positive character in going from Na to Cs.

(A) The spectrum shape (the $\Phi(\mathbf{q})$'s) changes in a way that indicates increasing $S_g{}^+$ as s_0 increases; and we have found a general tendency for s_0 to increase as we go down the alkalis. What is important is the possibly different effect on $S_g{}^-$ from on $S_g{}^+$ caused by a change in the spectrum shape. Our results indicate that the temperature variation in the average Debye temperature of the specific heat ($\Theta(T)$) gives a large effect, and a difference in the behaviour of $\Theta(T)$ from the behaviour of an effective average $\Phi(T)$ (representing our two Φ's) owing to a change in the spectrum shape might well yield significant changes in the resultant S_g. It is clear that to pursue this point would require enormous calculations (note that simply a change in θ (eqn. (7.1)) would have a similar effect on $S_g{}^-$ as on $S_g{}^+$).

(B1) Under this heading and the next we shall be appealing to calculations which at the time of writing are unpublished but which should appear in the near future†. These calculations consist in an improvement of the matrix element, and a detailed calculation of the electrical and thermal conductivities using a phonon spectrum on the Born–von Karman model containing up to next-nearest neighbour interactions. The results of the matrix element calculation indicate that the I^2 ratio (in the discussion after eqn. (5.6)) decreases considerably as we go from Na to Cs. This results not only from the shielded ion perturbation but also and quite significantly from the exchange and correlation correction, which we have calculated numerically for the first time. Unfortunately the latter was done only for the three cases $r_s/a_h = 3$, 4 and 5, but we find that the increase over the 1937 Bardeen value of the I^2 ratio is 1·54, 0·91 and 0·65 for these three cases respectively. We assume that this tendency will continue for $r_s/a_h = 6$. What this means is that there is a significant relative increase of the (UK/non-UK) ratio as we go from Na to Cs, an increase that is completely absent from the original Bardeen calculation.

---

† *Added in proof.*—Now published: Bailyn (1960).

In addition there is a similar increase for the shielded-ion part itself. This could have a considerable effect, but as above, the calculation that would trace it through would have to be tremendous.

(B2) The results of our calculations of the electrical and thermal conductivities indicate that the highly anisotropic spectrum that we have calculated is fairly good for caesium but gets increasingly worse as we go from Cs to Na. This conclusion is based on the fact that our results as the temperature decreases are fairly good for Cs but get progressively worse for Rb, K and Na, the poorness being a too-large value of the calculated resistivity. These large values are the consequence of the few very small velocity phonons. The conclusion then is that these velocities in the case of sodium are in fact not so small. If in fact the high anisotropy as we have calculated it should be damped down as we go from Cs to Na, this means that the relative importance of the UK to non-UK effects should get similarly progressively damped and in a way not contemplated by the Born–von Karman spectrum including interactions up to next-nearest neighbours. Our spectrum analysis as done above would then be justified for caesium, but less so for sodium. This would also mean that considerable work lies ahead in getting a better spectrum for sodium. Our result here ties in with our considerations on the specific heat in sodium. Our feeling is that this aspect of the spectrum problem is the main source of the really great increase in the positive character of the caesium result (relative to rubidium, potassium and sodium).

(C) The progressive distortion of the Fermi surface would also seem to yield an increasingly positive S_g as we go from Na to Cs. In our rough expression (4.17) it would have the effect of lowering the Φ values, or in an indirect way raising the α s, since a lowering of Φ over a small temperature range can be imitated by raising of the $\alpha\gamma$ parameter. Ziman has interpreted the entire change in the positive character in going from Na to Cs as a consequence of this effect. Our point of view is that the many effects mentioned above very likely play even more important roles, and that it is hard if not impossible to distinguish one from another, since they may all be regarded as changing effective Φ values or effective $\alpha\gamma$ values. It is only by a very detailed calculation that one could eliminate the possibility of, or establish upper bounds to, the alterations caused by these effects. We therefore regard Ziman's conclusions with caution if only for his omitting such a detailed calculation. There are however more important criticisms we have of his method, which we shall discuss in the next section.

§ 8. COMPARISON WITH THE WORK OF ZIMAN

Since Ziman (1959) has put forth a calculation some time ago concerning the same quantity as discussed in this paper, it seems appropriate to compare his procedure with ours. We mentioned in the Introduction that we had objections to his method, and in this section we shall outline what they are. They may be separated into the three statements: (i) his variational principle is essentially weaker than ours (Bailyn (1958)†) and leads to what we consider an erroneous and rather complicated although perhaps approximate expression for the phonon–drag component to the thermoelectric power (i.e. eqn. (2) of Ziman (1959) compared to our eqn. (2.8)); (ii) his variational principle does not give any indication of the relationship between the hypotheses for the non-equilibrium part of the phonon distribution and the non-equilibrium part of the electron distribution, with the result that Ziman chose ansätze (eqn. (5) of Ziman 1959) which were inconsistent with the Boltzmann equations and which do not reflect the relative probabilities α which we have emphasized are characteristic of phonon-drag effects, and should appear in these distributions (see below); and (iii) in using a very simple spectrum for the phonons, he makes a computational error of qualitative significance, for he was led to suppose that the effect of the distortion of the Fermi surface was rather clear cut, and could be taken into account in a simple way, whereas in actual fact, the effect of the distortion of the Fermi surface should be considered in its effect on the *transverse* modes (the longitudinal one not being important) which are highly anisotropic (with the most important phonons not the ones with minimum q) and do not lend themselves to the simple calculation Ziman proposed. We shall comment further on the first two points.

(i) Ziman's variational principle was enunciated in 1956. His method was to add the 'entropy production' term from the phonon Boltzmann equation to that of the electron Boltzmann equation in a certain manner. When this was done he found that the resultant expression obeyed the conditions for the applicability of the Variational Principle with respect to variations either in the phonon distribution or the electron distribution. Our method was to assume the existence of a time of relaxation for the phonon–phonon collision term, solve the phonon Boltzmann equation for the non-equilibrium component of the phonon distribution in terms of the non-equilibrium electron distribution and then substitute that solution into the electron Boltzmann equation, which thereupon lent itself to a variation principle. In this way, there was only one unknown (the electron distribution). The convergence of the series (for the electrical resistivity) was the same as in the original work of Kohler. It is not clear to us what can be said about the convergence in Ziman's treatment. It is, nevertheless, curious that we have come out with expressions for S_g that are quite different. To be able to compare the methods in greater detail, we seek what connection our approach might have with an entropy of some sort. The connection can be obtained by following the interpretation of eqn. (14) of BI that is given at the end of § 3 of that paper. We rewrite this generalized Boltzmann equation symbolically as

$$\left(\frac{\partial f}{\partial t}\right)_{\text{field}}+\frac{\partial f}{\partial N}\left(\frac{\partial N}{\partial t}\right)_{\text{field}}=-\left(\frac{\partial f}{\partial t}\right)_{\text{coll}}-\frac{\partial f}{\partial N}\left(\frac{\partial N}{\partial t}\right)_{\text{elec. coll}}. \qquad (8.1)$$

---

† This article will be referred to as BI from hereon.

Here N represents the phonon distribution. The first term on the left is the alteration of the electron distribution $f(\mathbf{k})$ resulting from the direct action of the fields on it. The second term on the left (which in BI is denoted by U) is the alteration resulting from the indirect action of the fields on the electrons, through the phonons. (i.e. The fields will produce a non-equilibrium component in the phonon distribution which in turn passes some of this on to the electrons. This is the customary notion of 'phonon drag'.) Thus the two terms on the left provide the *total effect of the external fields* on the electrons which we indicate symbolically as

$$\left(\frac{df}{dt}\right)_{\text{field}} = \left(\frac{\partial f}{\partial t}\right)_{\text{field}} + \frac{\partial f}{\partial N}\left(\frac{\partial N}{\partial t}\right)_{\text{field}}. \quad . \quad . \quad . \quad (8.2)$$

The first terms on the right of (8.1) (which in BI is denoted by L_1) gives the change in the electron distribution arising from the collisions with the equilibrium part of the phonon distribution. The second term on the right (which in BI is denoted by L_2) gives the change in the electron distribution arising from collisions with that part of the non-equilibrium component of the phonon distribution that was produced by interaction with the electrons. Thus the two terms of the right provide the total change in the electron distribution arising from collisions with the phonons, when the indirect effect of the fields is subtracted off, which we represent symbolically by

$$\left(\frac{\partial f}{\partial t}\right)_{\text{coll}} = \left(\frac{df}{dt}\right)_{\text{coll}} + \frac{\partial f}{\partial N}\left(\frac{\partial N}{\partial t}\right)_{\text{elec. coll}}. \quad . \quad . \quad . \quad . \quad (8.3)$$

Thus our generalized Boltzmann eqn. (8.1) for the electrons is of the same form as the ordinary equation, and one can go about constructing entropy production in the usual way, and end up with precisely our variational principle. Thus, whereas Ziman constructs what he calls the total entropy production of the system, we construct what is a kind of *partial* entropy production, referring to the electrons. An entropy production for the electrons alone could be constructed as a product of affinities and fluxes in the way Ziman (1956) proposed, but the temperature affinity $X_k(\text{temp})$ (analogous to the electric field affinity in eqn. (25) of Ziman's paper) would have to reflect the left-hand side of (8.1):

$$X_k(\text{temp}) = -\frac{1}{T}\frac{dT}{dx}\left[-\frac{\hbar}{m}(E-\rho)k_x\frac{\partial f_0}{\partial E} - \sum_{qK}\frac{\partial N_0}{\partial \hbar\omega}\hbar\omega(jq)\frac{\partial \omega(jq)}{\partial q_x}\alpha(jq;\,q+K)\right].$$

(To get this result, one needs to evaluate the U of eqn. (14) of BI.) To complete the analogy with the formulation of Ziman, one needs to show that the operator on the right-hand side of (8.1) satisfies the correct symmetry conditions. That, however, was the burden of BI and has been shown.

It should be emphasized that we regard as the real justification of our results the statistical mechanical argument of BI. The thermodynamic garb is produced here solely to compare with Ziman's work.

There is the question however: *ought* there to be maximizing of the entropy of the electron system alone? We believe the answer to this is yes, for the reason that the electron–phonon interaction still results by assumption in a first-order deviation of the electrons from equilibrium, and one may therefore legitimately lump the non-equilibrium phonons in with the reservoir, and apply fluctuation theory to the description of the electron system in the environment of this complex reservoir. It then becomes a problem what to use for affinities, however, and the usefulness of this as a general principle disappears. On the other hand, if one follows the Ziman-type approach, one can define entropy production as Ziman in (1956) using the above affinity. Just what the relation between the Ziman-type entropy and the usual notion of entropy is has not been made altogether clear (see the comment of Prigogine at the end of the paper by Ziman (1956)). Perhaps the safest way is to regard Ziman's as simply a maximizing function. What we have shown in BI is that a stronger maximizing function exists the solutions from which cast doubts on the significance of Ziman's expressions. Thus, we have a much more restricted class of variations possible than does Ziman. The exact solutions of the Boltzmann equations will maximize both entropy productions, but our view is that if what is desired is a method for obtaining approximate solutions to the Boltzmann equations, then our method with a more restricted range of variations will yield a solution which converges more swiftly than the method with the larger range of variations. We are not sure that there might not exist some other quantity with an even more restricted range which would yield a better convergence still, but the fact that in the present paper we were able to derive our expression from a rather simple 'mechanical' model leads us to believe that there is, in fact, not. We thus regard the Ziman expression as a term whose significance is not obvious and which at best would be equivalent to ours.

The original restriction on our method, namely, that phonon–phonon interactions could be written in terms of a relaxation time, has been removed by Tsuji (1959), who showed that a generalization can be made whenever a certain inverse collision operator exists.

(ii) To get the best results from Ziman's method, one would expect to consult the Boltzmann equations to obtain the trial phonon distribution once the electron trial distribution is decided on. In a variational technique, one can avoid doing this and hope for the best, but when a relationship does exist, one would expect the *best* results from using it. Ziman chose the electron trial non-equilibrium distribution as a constant times **k**. It then follows immediately from the phonon Boltzmann equation (see eqns. (12), (13) and (69) of Bailyn 1958) that the corresponding trial phonon non-equilibrium distribution is obtained from $N = N_0 - (\partial N_0/\partial \hbar\omega)G$ where

$$G = \frac{\tau_c \hbar\omega \nabla_q \omega}{\sum_K B(j\mathbf{q};\ \mathbf{q}+\mathbf{K})} \frac{1}{T} \frac{dT}{dx} - \text{const.}\left[\sum_{\mathbf{K}}^{|j\mathbf{q}|} (\mathbf{q}+\mathbf{K})\alpha(j\mathbf{q};\ \mathbf{q}+\mathbf{K}) \right], \tag{8.4}$$

provided the phonon–phonon interactions are neglected. Here α is defined as in this paper and τ_c is a constant given by eqn. (70) of BI.

What Ziman uses for G instead is a constant times $\mathbf{q}$, which may be interpreted as an approximation to the first term of (8.4) (which arose from the drift term of eqn. (12) of BI). Such an approximation would not necessarily be a calamity, but in the phonon-drag effect, we have a resultant S_g which is a small difference between a large positive UK contribution and a large negative non-UK contribution. Now what Ziman neglects in (8.4) in particular are all the 'UK components' in the phonon distribution. We therefore do not see how a computation based on these trial distribution functions can be significant†.

It is a strange result however, that in our theory the terms in the square bracket of (8.4) affect only quantities (the d_{ij}'s of BI) which cancel out in our expression for S_g (see eqn. (86) of BI). Thus on our theory, the only part of (8.4) that finds itself in S_g is the term Ziman uses. Thus Ziman's guess for G is in a sense consistent with our theory but not with his own!

Finally, even if one accepts Ziman's expression, and accepts his neglect of the square bracket in (8.4), there is the denominator in (8.4) to be considered. In every interaction there will be an interaction matrix element which is proportional to

$$\alpha'_j(\mathbf{q})I(\mathbf{q}+\mathbf{K})^2/|\mathbf{q}+\mathbf{K}|, \qquad . \; . \; . \; . \; . \; . \; . \quad (8.5)$$

where

$$\alpha'_j(q)=\left[\hat{\xi}_j(\mathbf{q})\cdot\frac{\mathbf{q}+\mathbf{K}}{|\mathbf{q}+\mathbf{K}|}\right]^2. \qquad . \; . \; . \; . \; . \; . \quad (8.6)$$

Thus in the integrals, there will always be the first term of (8.4) times (8.5) from which it can be seen that a factor $\alpha(j\mathbf{q}\,;\;\mathbf{q}+\mathbf{K})$ will always emerge. If one neglects to consider this, then in effect one is replacing α by α'. (The factors I and $|\mathbf{q}+\mathbf{K}|$ in (8.5) will be constant over the important region, i.e. over the surface S′ of fig. 1, on which $|\mathbf{q}+\mathbf{K}|=2k_0$.) To see the consequence of this, we have placed beside each column of α's in table 1, a corresponding column of α''s. We notice that the α''s emphasize the small q's of the longitudinal mode quite considerably. Thus for still a third reason, we are doubtful of the significance of Ziman's treatment.

§ 9. SUMMARY

In this paper we have applied the theory of Bailyn (1958) to the case of the thermoelectric power of the alkali metals in the temperature range 2–20°K. A simple derivation of the basic equation was shown to be possible. It turns out that quantities that we have called 'relative probabilities' enter importantly in the drag effects. In order to see their characteristics, they were computed for several points by means of a simple spectrum using values for parameters that should reflect at least roughly the situation in the alkali metals, and neglecting the effect of phonon–phonon collisions. The conclusion drawn was that the longitudinal vibrations contributed so small an amount relative to the transverse vibrations that they were negligible. The remaining transverse vibrations betrayed the surprising characteristic of having the most important phonons not the ones with minimum q in the UK process, even in the low-temperature range considered. Treating the relative probability as a constant removable from under the integral sign (a *very* crude approximation), we were able to compute rather simple expressions for the phonon-drag of the thermoelectric power. From these expressions, numerical results were computed which indicate that the experiments are at least not inconsistent with the theory in its present state of crudeness. Our main attempt here has been to establish the basic equations, and to analyse qualitatively the nature of the contributions to the effect. At the end, we have stated our objections to a previous calculation of Ziman which also calculated the phonon-drag effect in the thermoelectric power of the alkali metals.

---

† We are of course relying here on the equations of Ziman (1959) in which (the total) G appears (our G is proportional to Ziman's Φ_g). It is *possible* that the sum in (8.4) is negligible, but that would have to be shown.

Acknowledgments

I wish to thank Dr. D. K. C. MacDonald for his stimulation and encouragement on this problem. Without it, this investigation would never have been undertaken or brought to the present point. I should also like to thank the Low-Temperature and Solid State Group of the National Research Council of Canada for harbouring me for some time during which this work was started.

APPENDIX

Solutions for the Phonon Equations of Motion in the Elastic Limit

The starting point is the determinantal equation given by deLaunay (1956), eqn. (10.9) page 266:

$$\begin{vmatrix} [(c_{11}-c_{44})q_x^2+c_{44}-\rho v^2] & (c_{12}+c_{44})q_xq_y & (c_{12}+c_{44})q_xq_z \\ (c_{12}+c_{44})q_xq_y & [(c_{11}-c_{44})q_y^2+c_{44}-\rho v^2] & (c_{12}+c_{44})q_yq_z \\ (c_{12}+c_{44})q_xq_z & (c_{12}+c_{44})q_zq_y & (c_{11}-c_{44})q_z^2+c_{44}-\rho v^2 \end{vmatrix}=0, \quad \ldots \quad \text{(A 1)}$$

where we have let deLaunay's frequency ν be qv, and where $q_xq_yq_z$ are the direction cosines (not the components). If we make the ansätz

$$\rho v^2=c_{44}+(c_{12}+c_{44})\lambda \quad \ldots\ldots\ldots \quad \text{(A 2)}$$

then (A 1) becomes with the definition (5.7)

$$\begin{vmatrix} sq_x^2-\lambda & q_xq_y & q_xq_z \\ q_xq_y & sq_y^2-\lambda & q_yq_z \\ q_xq_z & q_yq_z & sq_z^2-\lambda \end{vmatrix}=0. \quad \ldots \quad \text{(A 3)}$$

This equation determines the direction cosines of vibration, which therefrom depend only on the direction cosines $q_x q_y q_z$ of propagation and on s_0. It was solved numerically. One could attempt a calculation using the solution of a Born–von Karman model, but we have not done it for the phonon-drag problem.

We now wish to prove (3.5) for this spectrum:

$$q \,.\, \nabla_q \omega = qv. \tag{A 4}$$

Using (A 2), we get for our spectrum

$$\mathbf{q} \,.\, \nabla_q \omega = \mathbf{q} \,.\, \nabla(qv) = qv + q\frac{c_{12}+c_{44}}{2v\rho}[\mathbf{q} \,.\, \nabla\lambda]. \tag{A 5}$$

To get $\mathbf{q} \,.\, \nabla\lambda$ we appeal to the following version of (A 3):

$$\lambda^3 - s\lambda^2 - (1-s^2)I_2\lambda - (1-s)^2(2+s)I_3 = 0, \tag{A 6}$$

$$I_2 = q_x^2 q_y^2 + q_y^2 q_z^2 + q_z^2 q_x^2, \tag{A 7}$$

$$I_3 = q_x^2 q_y^2 q_z^2. \tag{A 8}$$

Then using the fact that $\mathbf{q} \,.\, \nabla I_2 = \mathbf{q} \,.\, \nabla I_3 = 0$, because

$$\mathbf{q} \,.\, \nabla q_i = 0. \tag{A 9}$$

(remember that the q_i are the direction cosines), we easily obtain from (A 6)

$$\mathbf{q} \,.\, \nabla\lambda = 0. \tag{A 10}$$

Hence (A 5) reduces to (A 4).

REFERENCES

BAILYN, M., 1956, Thesis, Harvard University. Available on Microfilm only; 1958, *Phys. Rev.*, **112,** 1587; 1960, *Phys. Rev.*, **1,** 1960.

BARDEEN, J., 1937, *Phys. Rev.*, **52,** 677.

DE LAUNAY, J., 1956, *Solid State Physics*, **2,** Ed. Seitz and Turnbull (New York: Academic Press Inc.).

HANNA, I. I., and SONDHEIMER, E. H., 1957, *Proc. roy. Soc.*, **239,** 247.

HUNTINGTON, H. B., 1958, *Solid State Physics*, **7,** Ed. Seitz and Turnbull (New York: Academic Press Inc.).

MACDONALD, D. K. C., 1954, *Physica*, **20,** 996.

MACDONALD, D. K. C., PEARSON, W. B., and TEMPLETON, I. M., 1958, *Proc. roy. Soc.* A, **248,** 107.

MOTT, N. F., and JONES, H., 1936, *The Theory of the Properties of Metals and Alloys* (Oxford: Clarendon Press).

NEIGHBORS, J. R., and ALERS, G. A., 1958, *Phys. Rev.*, **111,** 707.

PARKINSON, D. H., 1958, *Reports on Progress in Physics*, **21,** 226.

ROBERTS, L. M., 1957, *Proc. phys. Soc. Lond.*, **70,** 744.

TSUJI, M., 1959, *J. Phys. Soc. Japan*, **14,** 618.

ZIMAN, J. M., 1956, *Canad. J. Phys.*, **34,** 1256; 1959, *Phil. Mag.*, **39,** 371.

ERRATA

Palaeomagnetism of the British Carboniferous System, by C. W. F. Everitt and J. C. Belshé, 1960, *Phil. Mag.*, **5**, 675.

In the last column of the table on page 677 the ages of some of the rock formations are in error. The corrected figures are as follows.

Formation		Age (millions of years)
Staffordshire		240
South Wales		230–280
English Midlands	Sills	230
	Lava	270
Derbyshire	Sill	250 ?
	Lavas	270
Scotland (Kinghorn)	Lavas	280
	Sill	270 ?

[*The Editors do not hold themselves responsible for the views expressed by their correspondents.*]

Fig. 3

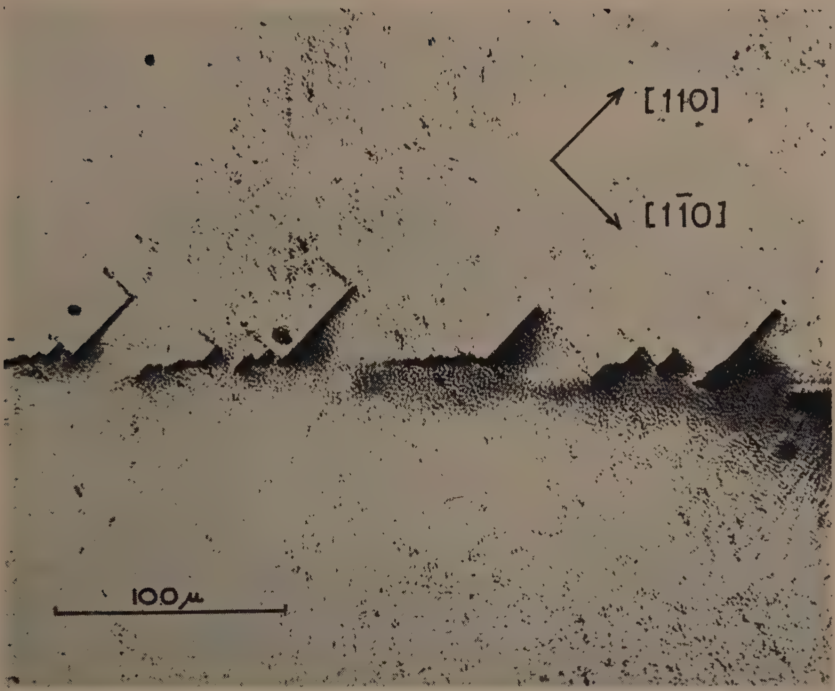
[110]
$[1\bar{1}0]$
100μ

Stroh-type cracks in lithium fluoride.

Fig. 4

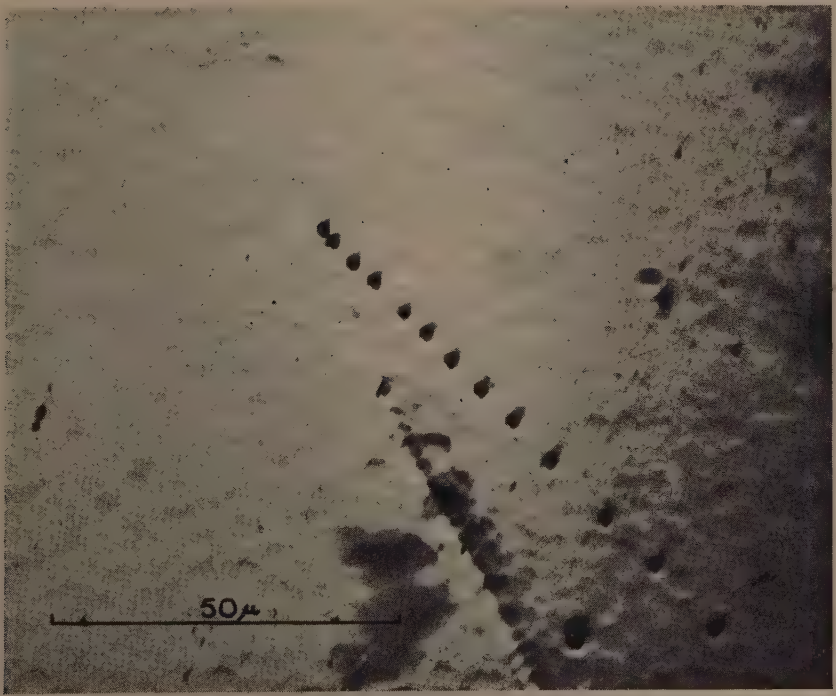

A pile up of edge-dislocations at a sub-boundary.

Fig. 5

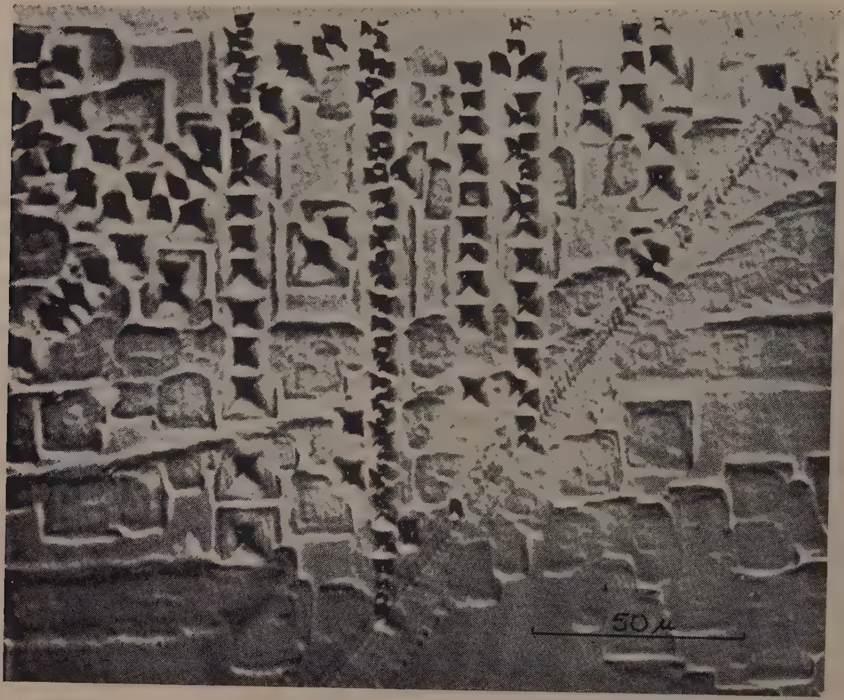

A pile up of screw-dislocations at a sub-boundary.

Fig. 6

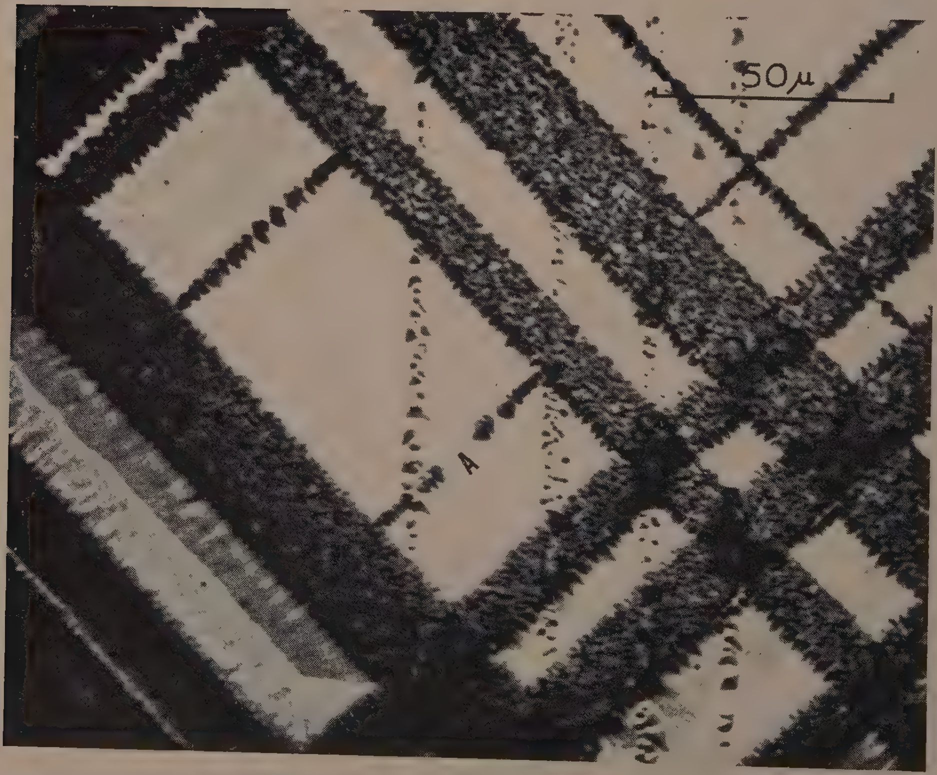

Broad-bands of edge dislocations acting as barrier to edge dislocations on intersecting system. Pile up of dislocations apparently from half-loop source at A.

Fig. 7

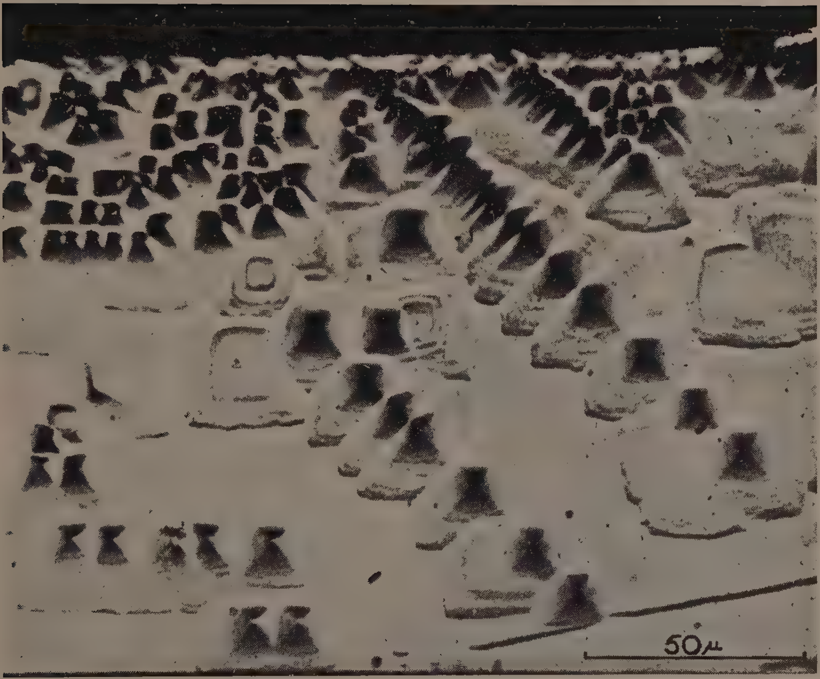

A pile up of edge dislocations beneath a surface coating.

Fig. 2

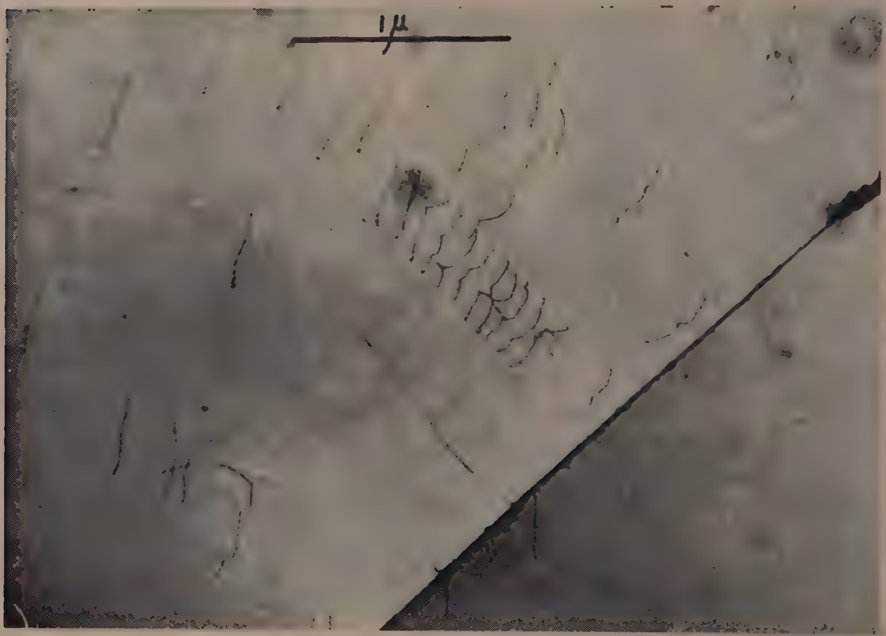

Screw dislocations on 45° planes. The diagonal line across the bottom right-hand corner is a cleavage crack.

Fig. 3

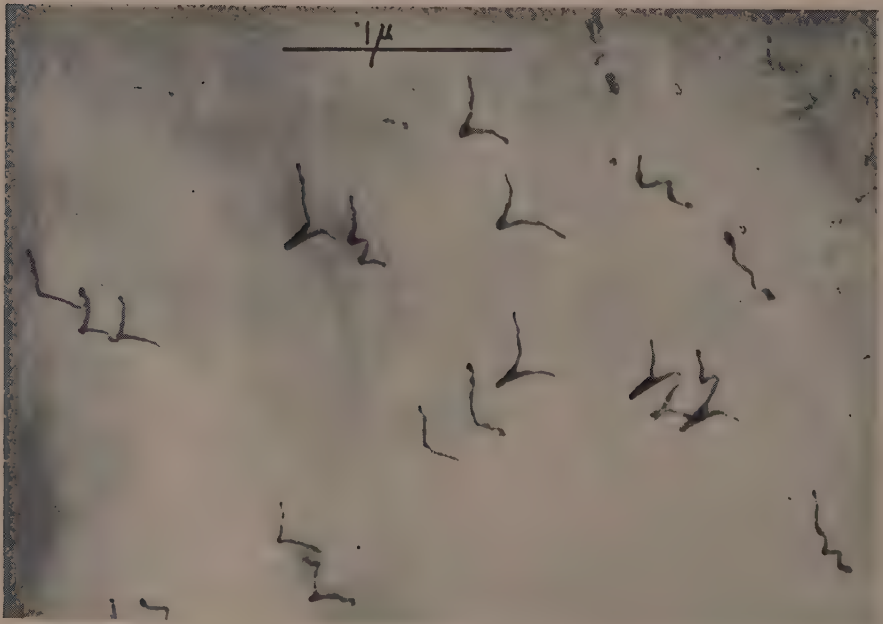

Dislocations on 45° planes after local heating in the electron beam.

Fig. 4

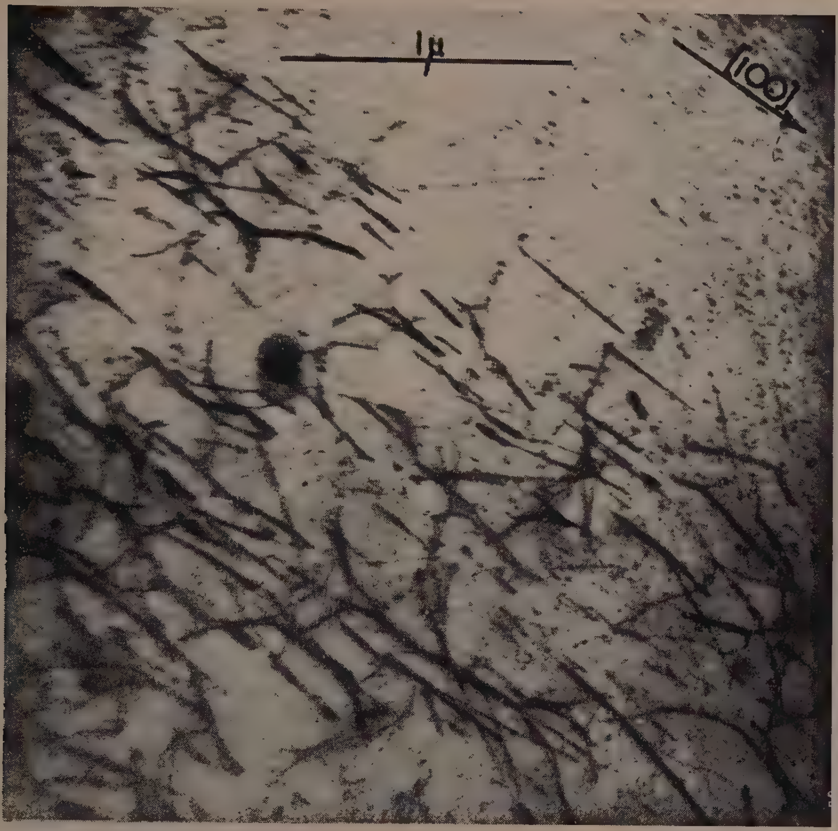

45° slip band showing plus–minus pairs.

Fig. 5

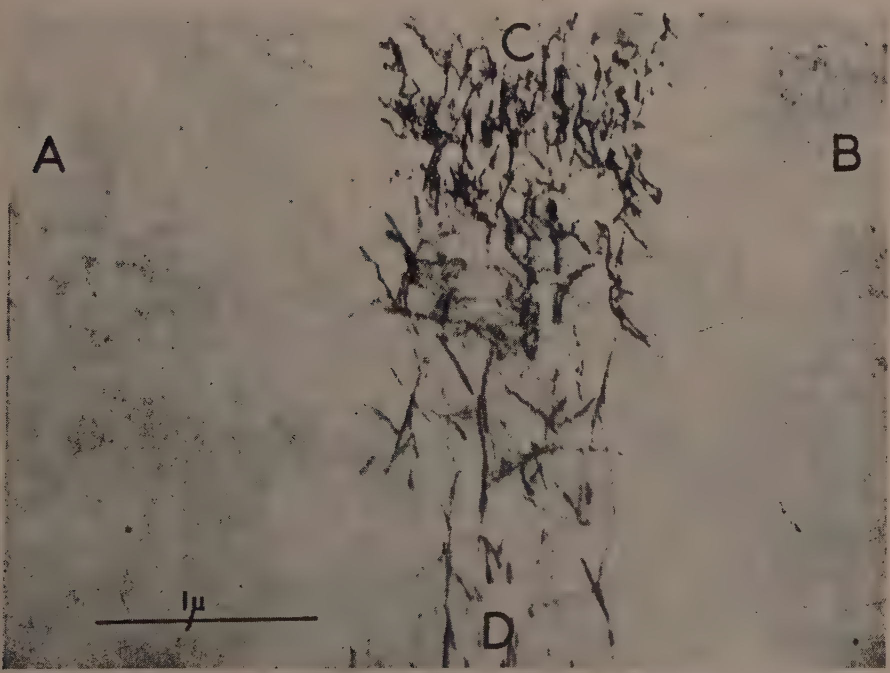

Two intersecting 45° slip bands. The band AB is almost out of contrast, though the tangle at the intersection of slip bands AB and CD is clearly visible.

Fig. 6

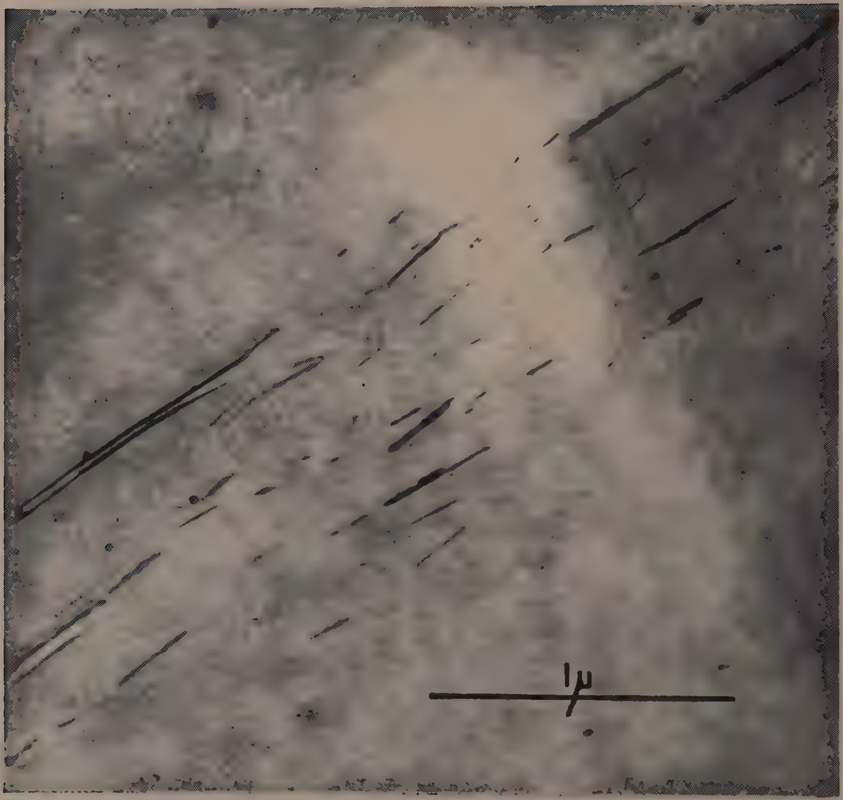

90° slip band.

Fig. 9

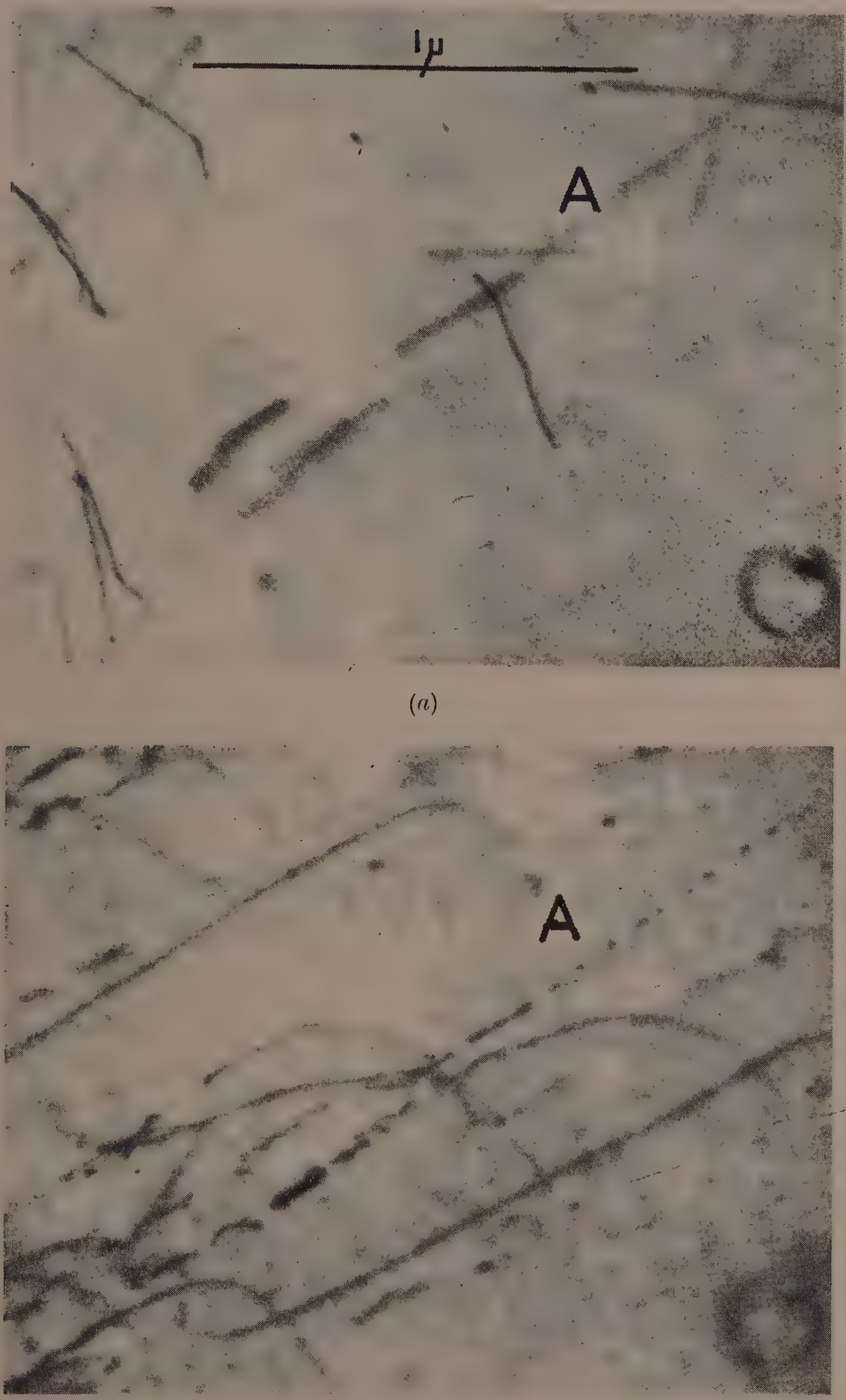

(*b*)

(*a*) Area containing plus–minus pairs before heating. (*b*) (Same area as *a*) after heating. The pair at A has broken up into loops.

Fig. 10

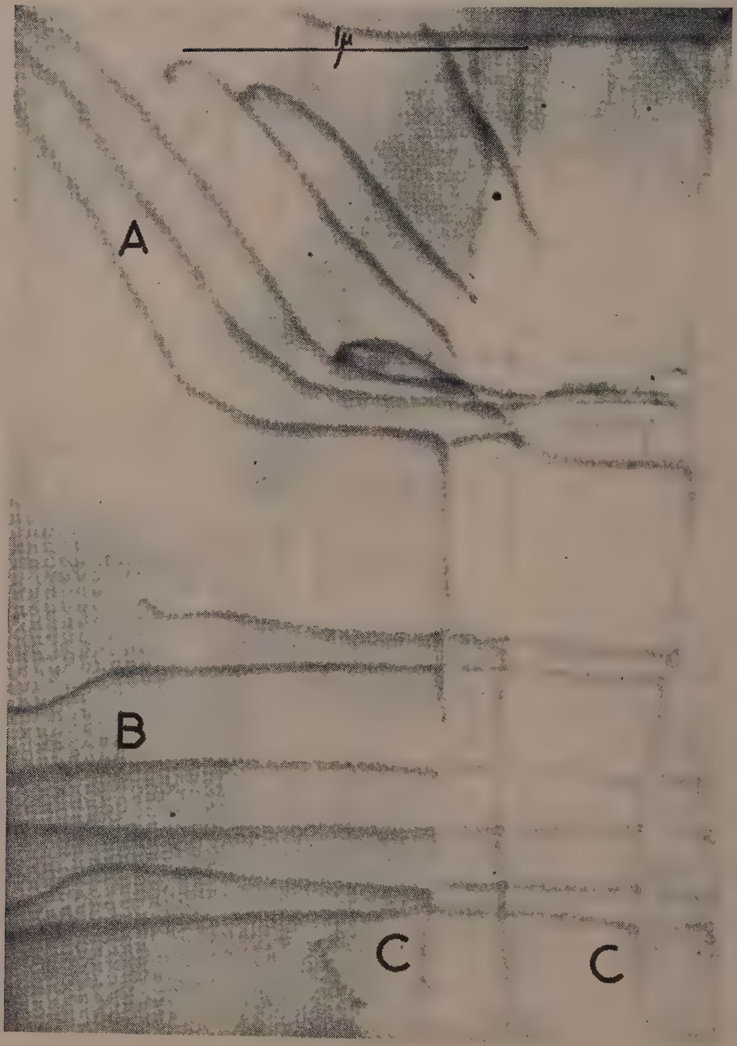

Dislocation interactions in MgO.

Fig. 11

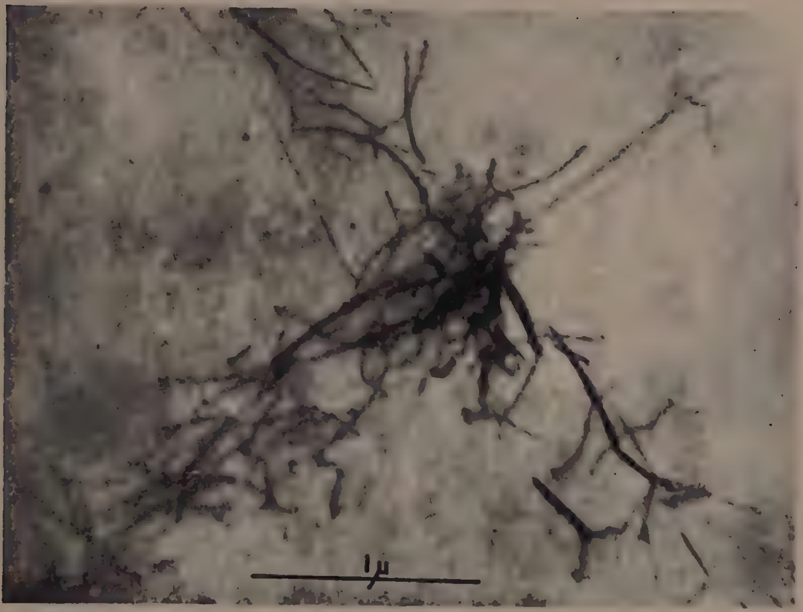

Intersection of two 45° slip bands.

Fig. 12

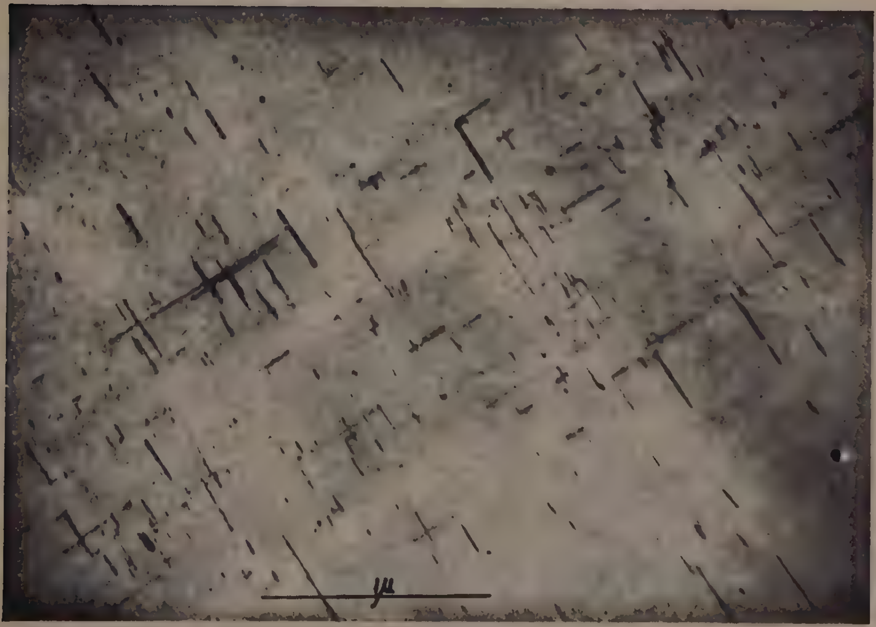

Intersection of two 90° slip bands.

Fig. 2

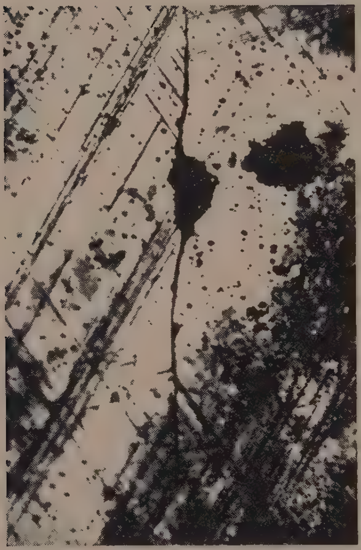

Short surface crack terminated by slip at tips. Slip lines revealed by selective tarnishing. ×700.

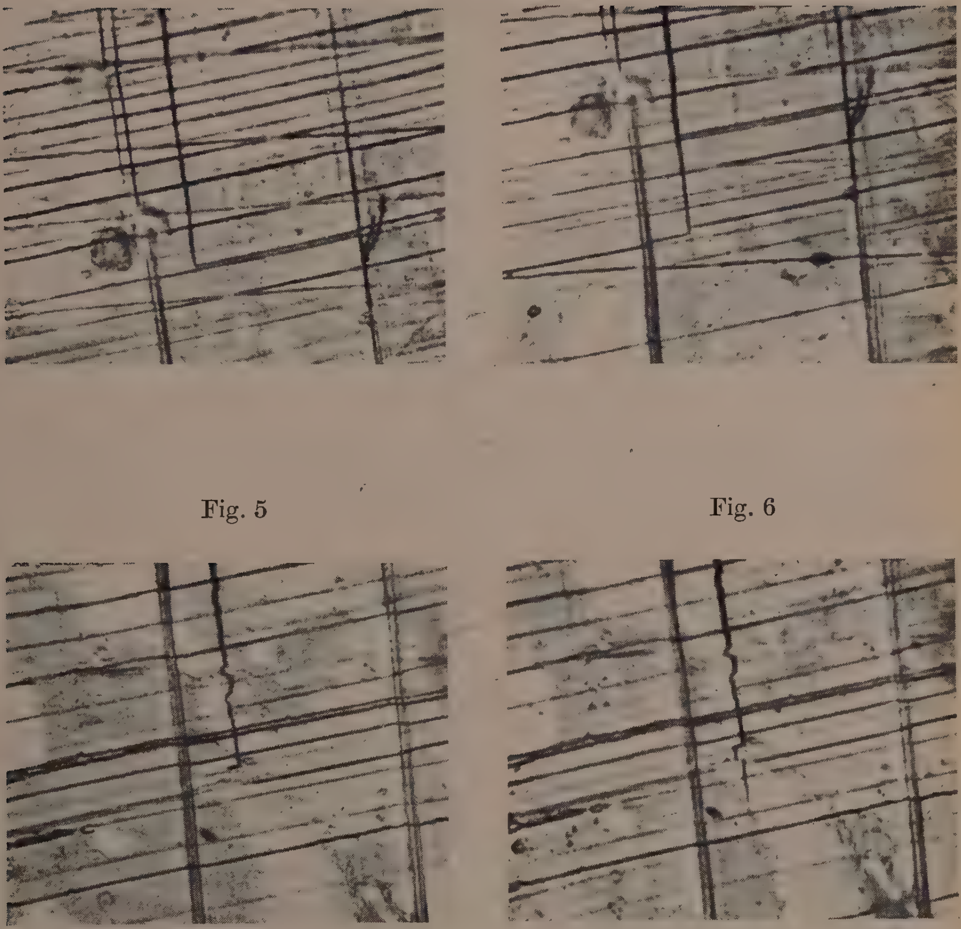

Fig. 3

Fig. 4

Fig. 5

Fig. 6

Figs. 3–6

Successive stages in the propagation of a stress-corrosion crack. ×1400.

Fig. 8

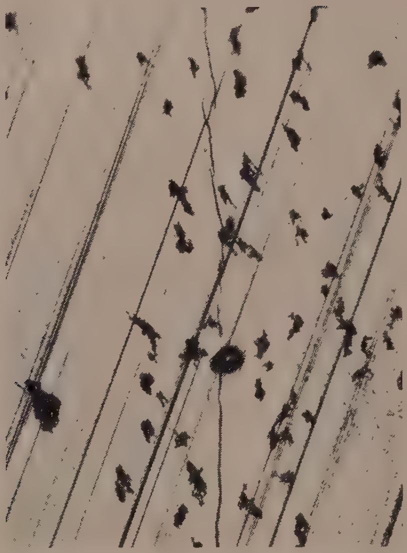

Crack pattern when operating slip plane is inclined to crack direction. ×450.

Fig. 9

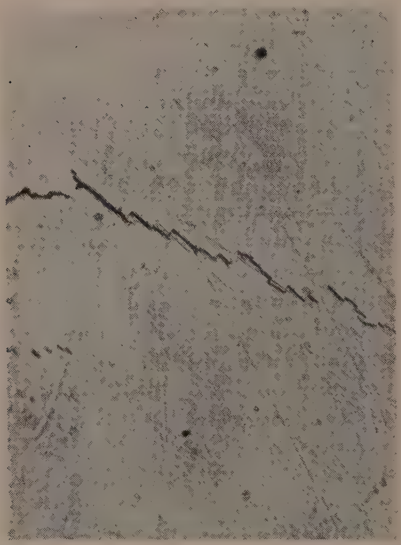

Transverse section through stress-corrosion cracks. ×500.

Fig. 10

Formation of microcracks on the surface of a single grain at the interaction of slip bands. ×450.

Fig. 11

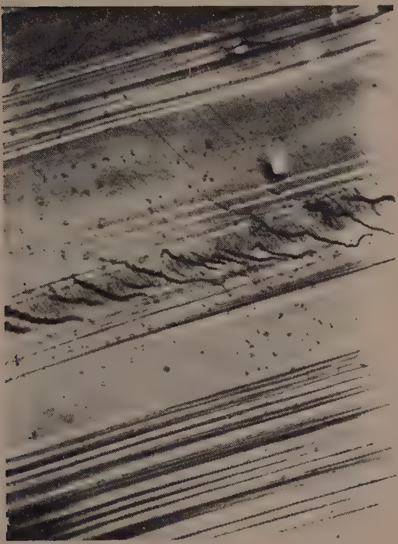

Cracks formed inside heavy slip bands. ×450.

Fig. 12

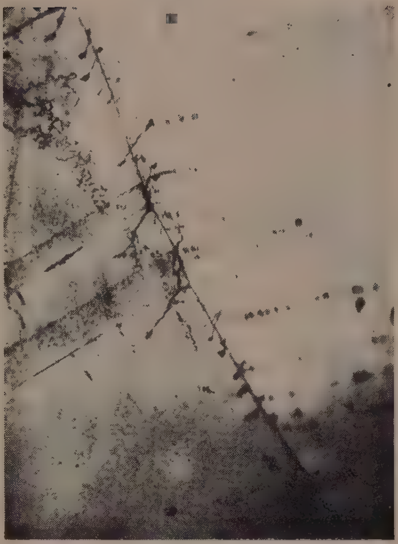

Formation of microcracks at grain boundary. ×450.

Fig. 13

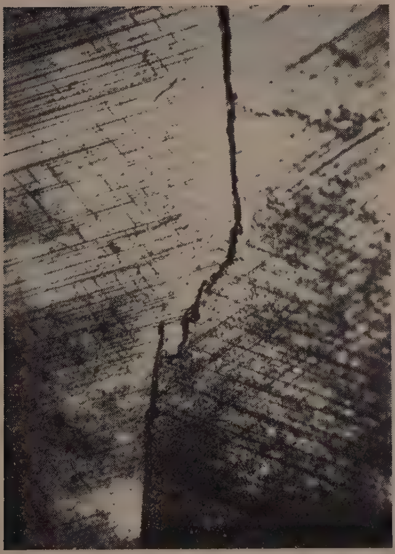

Fig. 14

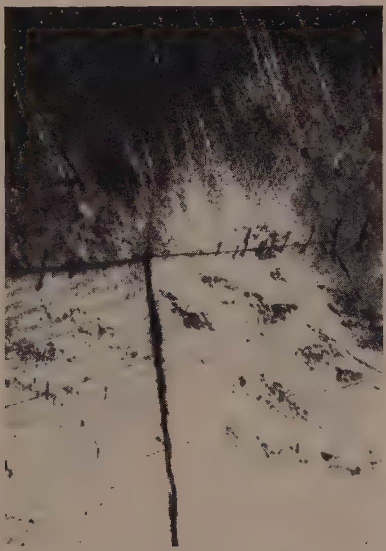

Figs. 13–14

Examples of extension of microcracks to produce grain boundary parting (principal tensile stress horizontal). ×450.

Fig. 15

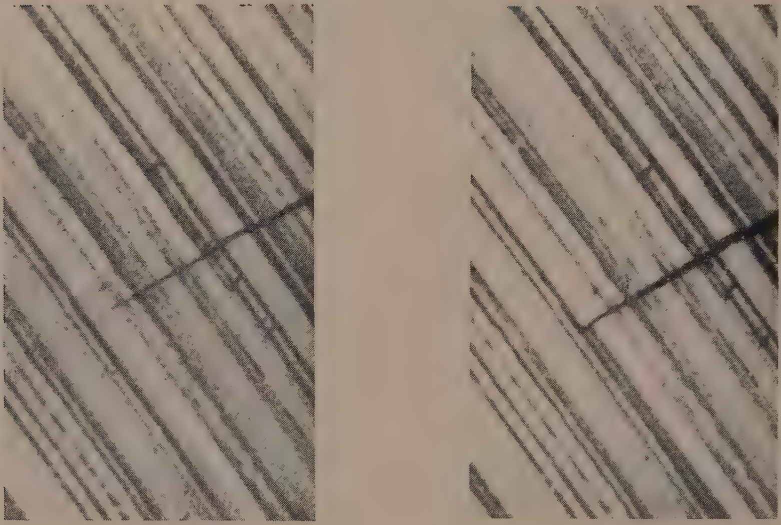
(*a*) (*b*)

Showing the plastic yielding around the tip of a newly halted crack on increasing the applied load. ×2000.

Fig. 16

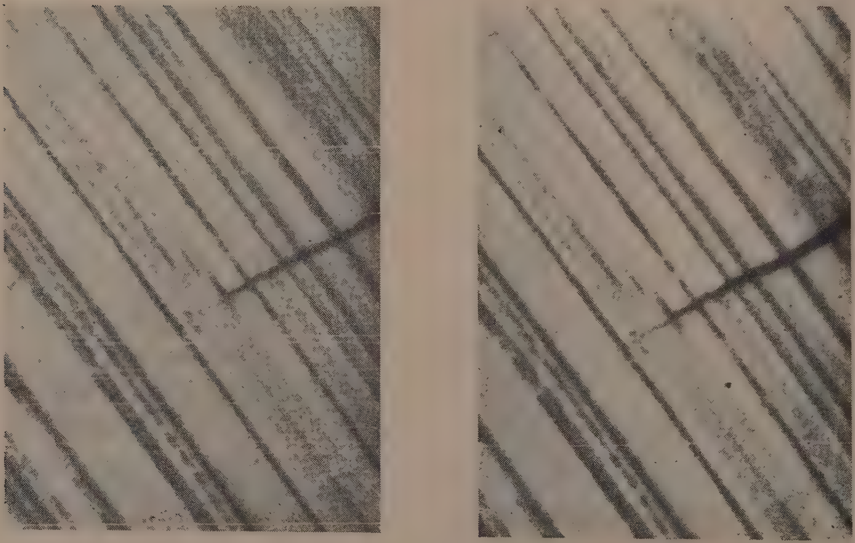
(*a*) (*b*)

Further cracking beyond the tip of an aged crack after increasing the applied load. ×2000.

The Fermi Surface in White Tin†

By A. V. GOLD
Royal Society Mond Laboratory, University of Cambridge, and Division of Pure Physics, National Research Council, Ottawa, Canada‡

and M. G. PRIESTLEY
Royal Society Mond Laboratory, University of Cambridge

[Received July 25, 1960]

ABSTRACT

The orientation dependence of the de Haas–van Alphen periods in tin single crystals has been studied in high pulsed magnetic fields. As many as seven periods have been found at some orientations, indicating that the Fermi surface is much more complicated than the 3-ellipsoid model suggested by Fawcett. The general degree of complexity of the results is much the same as that predicted by the free-electron model, but serious discrepancies are found when a detailed comparison is made. Effective mass values have been determined at the principal orientations from the temperature dependence of the amplitudes; these are compared with the results of cyclotron resonance experiments and with the free-electron orbit masses.

§ 1. INTRODUCTION

THE period, P, of the de Haas–van Alphen oscillations in a metal single crystal at low temperatures is related to the extreme (maximum or minimum) area of cross section, $\mathscr{A}_0$, of the Fermi surface normal to the magnetic field by the Onsager–Lifshitz and Kosevich relation:

$$P = 2\pi e/c\hbar\mathscr{A}_0. \qquad (1)$$

($\mathscr{A}_0$ in **k**-space), and from the temperature dependence of the oscillation amplitudes one can obtain the corresponding cyclotron (orbit) effective mass, m^*, which is defined by:

$$m^* = (\hbar^2/2\pi)(\partial\mathscr{A}/\partial E)_0. \qquad (2)$$

In principle a study of the variation of P and m^* with orientation is sufficient to determine the shape of the Fermi surface and the Fermi velocity at all points on the surface, and for a discussion of the present theoretical and experimental situation, the reader is referred to the review articles by Shoenberg (1957, 1960).

The orientation-dependence of the de Haas–van Alphen effect in metallic tin has been studied at magnetic fields up to 15 kG principally by Shoenberg

---

† Communicated by the Authors.

‡ N.R.C. Postdoctorate Fellow. Now at Physics Department, Iowa State University, Ames, Iowa, U.S.A.

(1952) and Berlincourt (1952), whose findings were, for the most part, consistent with a Fermi surface consisting of two small ellipsoids oriented along the tetragonal axis and capable of accounting for a total of about 10^{-2} carrier per atom at most. Subsequent preliminary studies using impulsive fields of up to 100 kG (Shoenberg 1953) revealed a rich variety of short-period de Haas–van Alphen oscillations associated with the major portions of the Fermi surface. A detailed orientation-dependence study of the periods in lead using the impulsive-field technique has been successful in determining the Fermi surface in this metal (Gold 1958; hereinafter referred to as (I)) and in this paper we describe such a study of metallic tin.

The high-field de Haas–van Alphen results turn out to be very complicated and are, in fact, of the same order of complexity as predicted by the simple free-electron model. We shall make use of this simple model, which proved helpful in the interpretation of the lead results, in an attempt to relate the observed results to the Brillouin zone scheme. However, we shall conclude that further information, in particular from de Haas–van Alphen studies at still higher fields and from ultrasonic attenuation, cyclotron resonance and magneto-resistance experiments, is necessary before all of the geometrical features of the Fermi surface can be established with reasonable certainty. We have also determined the effective masses corresponding to principal orientations; these are compared with the results of cyclotron resonance experiments and with the orbit masses predicted by the free-electron model.

§ 2. Experimental Results

The experimental method is the same as that described in (I) and in the review article by Shoenberg (1957), so that no further details will be given here. Since the high-field results are so complex, with up to seven periodic terms superimposed on one another at some orientations, it was essential to use the resonance method in order to sort out the various terms; the presence of a background of the other terms nevertheless resulted in a greater uncertainty of period measurement than was the case for the simpler lead results (I). The measurements were carried out on single crystal wires of length 8 mm and diameter 0·55 mm; these were prepared from Johnson Matthey spectroscopically pure tin and grown with a principal crystallographic axis along the wire. As was explained in (I), the absolute orientation of the crystal axes relative to the magnetic field was obtained finally from the symmetry of the period-orientation results. The period measurements were carried out at 1·2°K and using field pulses rising up to 80 kG in about 11 ms. A few measurements were also made along [001] and [110] in a field of 150 kG; this became possible (using a specially designed field coil) only after the bulk of the measurements had been completed. The higher field greatly increased the observed amplitudes but revealed no new very short periods.

Fig. 1

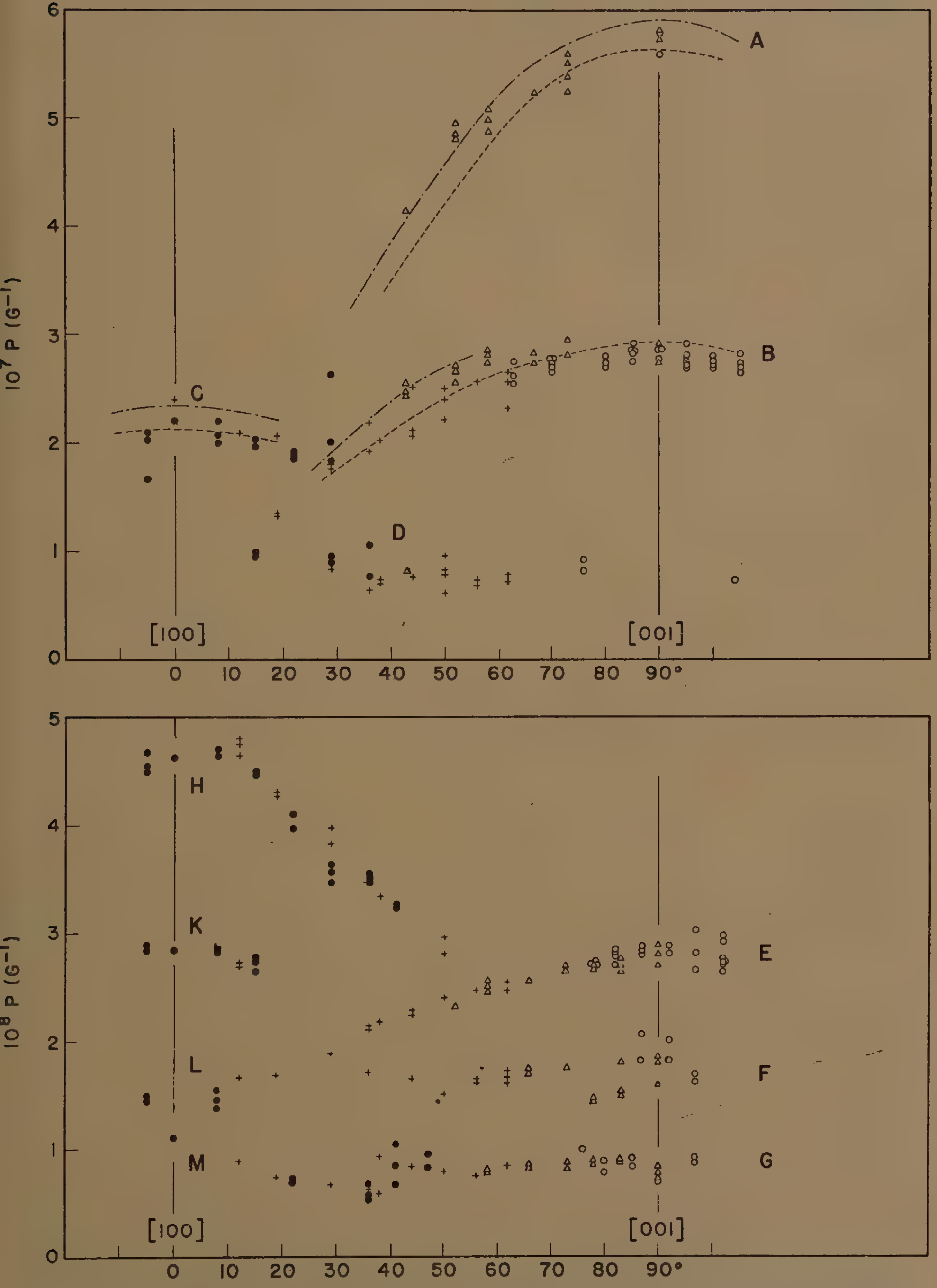

Variation of period with orientation of magnetic field in a (100) plane. Upper half: long-period oscillations; lower half: short-period oscillations. ○, △, specimens with [001] axis along wire; ●, specimen with [100] axis along wire; +, specimen with axis midway between [100] and [001] along wire. —·—·, Shoenberg (1952); – – –, Berlincourt (1952).

Fig. 2

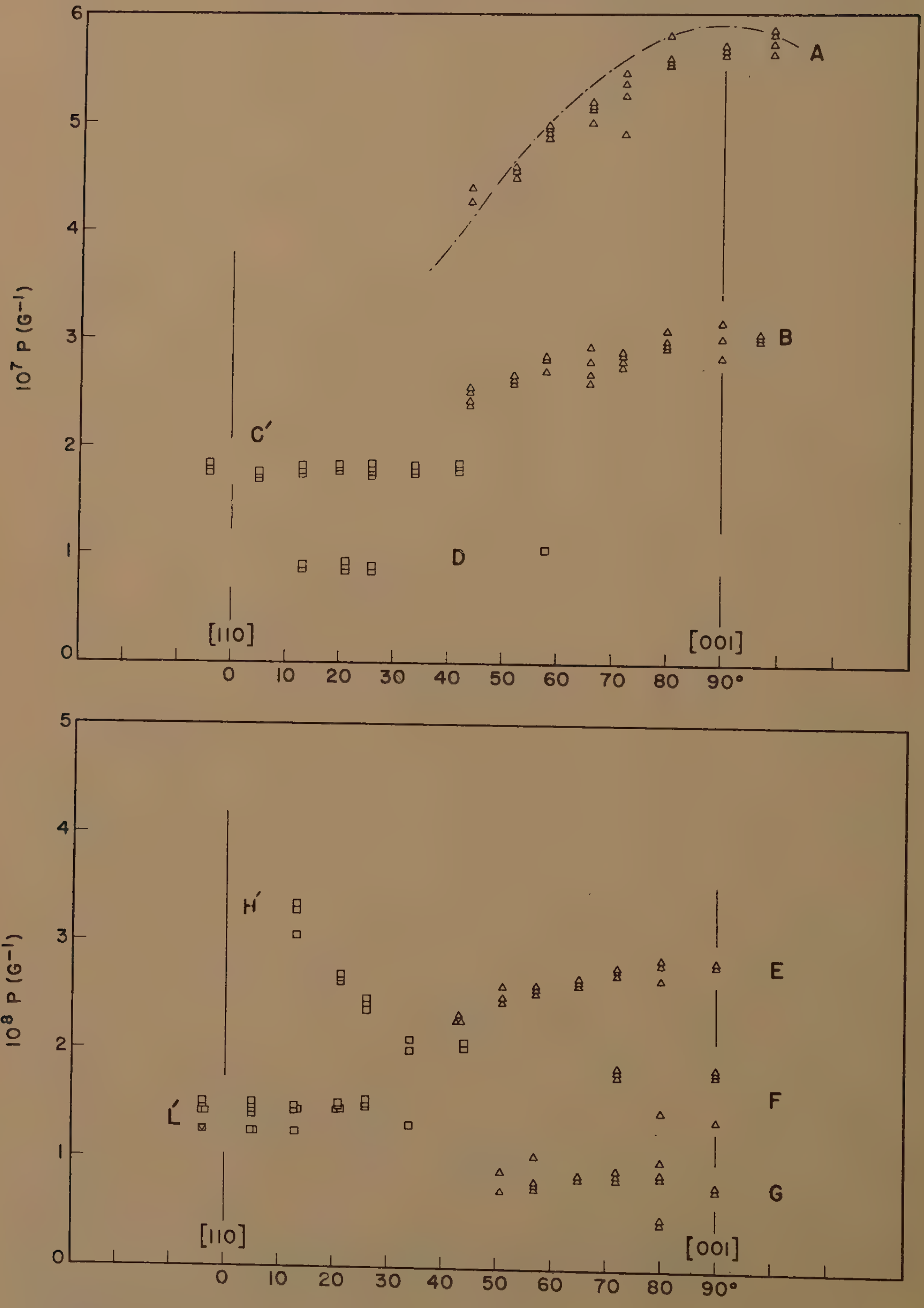

Variation of period with orientation of magnetic field in a (110) plane. Upper half: long-period oscillations; lower half: short-period oscillations. △, specimen with [001] axis along wire; □, specimen with [110] axis along wire. —•—•, Shoenberg (1952).

Figures 1, 2 and 3 show the variation of the periods with orientation of magnetic field in the (100), (110) and (001) planes, respectively. The results fall, broadly speaking, into two groups: long-period oscillations with $P \sim 10^{-7}\,\mathrm{G}^{-1}$ (upper diagrams) and short-period oscillations with $P \sim 10^{-8}\,\mathrm{G}^{-1}$ (lower diagrams). Also shown in the figures are smooth curves drawn through the long-period data obtained earlier by Shoenberg

Fig. 3

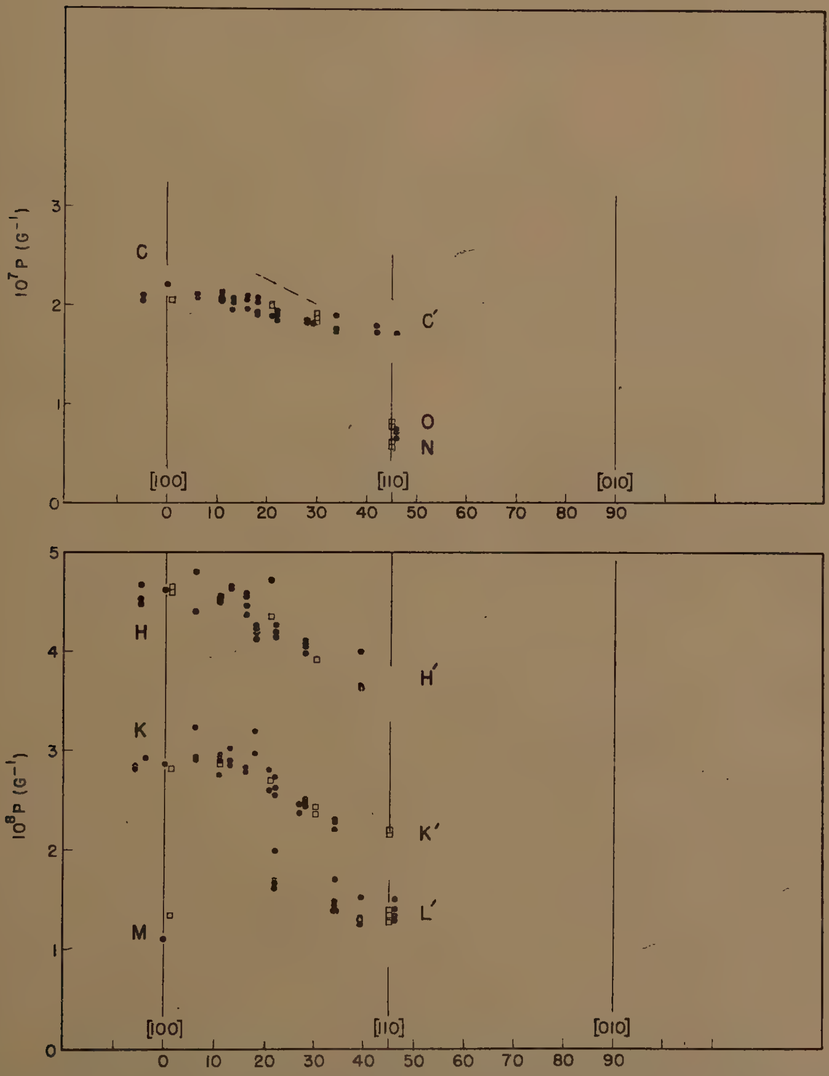

Variation of period with orientations of magnetic field in the (001) plane. Upper half: long-period oscillations; lower half: short-period oscillations. ●, specimen with [100] axis along wire; □, specimen with [110] axis along wire. —·—·, Shoenberg (1952).

Table 1

Observed periods and effective masses					m^*/m_0 from other experiments
Orientation	Oscillations	$P(\mathrm{G}^{-1})$	m^*/m_0	Possible free-electron-like interpretation. Zone, orbit	
[001]	A	5.70×10^{-7}	0·09	3δ	
			0·10 (B, S)		
	B	$2{\cdot}85 \times 10^{-7}$	0·15	5μ	
	E	$2{\cdot}80 \times 10^{-8}$	0·51	$4\,(b)\tau$	
	F	$1{\cdot}8 \times 10^{-8}$	0·64	5σ	0·78, 0·60, 0·54, 0·47 (KH)
	G	$0{\cdot}88 \times 10^{-8}$	0·70	$4\,(a)\,\zeta$	
[100]	C	$2{\cdot}10 \times 10^{-7}$	0·26	3γ	
			0·22 (B)		
	H	$4{\cdot}70 \times 10^{-8}$	0·45	$4\,(b)\xi(?)$	
	K	$2{\cdot}86 \times 10^{-8}$	0·50	$5\chi(?)$	
	L	$1{\cdot}45 \times 10^{-8}$		(?)	0·88, 0·27, 0·26 (KH)
	M	$1{\cdot}1 \times 10^{-8}$	1·27	$4\,(a)\eta$	
[110]	C′	$1{\cdot}6 \times 10^{-7}$	0·34	$3\gamma(?)$	
	L′	$1{\cdot}35 \times 10^{-8}$	0·75	(?)	
	K′	$2{\cdot}16 \times 10^{-8}$	1·16	(?)	
	N	$5{\cdot}7_7 \times 10^{-8}$		$4\,(a)\epsilon'$	
	O	$7{\cdot}8_5 \times 10^{-8}$		3ϵ	
Between [001] and [100] or [110]	D	$\doteqdot 0{\cdot}8$ to $0{\cdot}9 \times 10^{-7}$		(?)	

Notes: m_0 is the free-electron mass and the values of m^*/m_0 are reliable to about 10%. There was some indication of oscillations of period $0{\cdot}4 \times 10^{-8}\ \mathrm{G}^{-1}$ at orientations roughly midway beween [100] and [110]; however this feature was not reproducible and can probably be ascribed to noise effects. B, Berlincourt (1952); KH, Khaikin (1959); S, Shoenberg (1952). It is not certain which of the diad axes [100] or [110] Khaikin refers to.

(1952) and Berlincourt (1952) using the couple method at fields up to 15 kG, and it is satisfactory that the corresponding high-field results agree with the earlier low-field data. In table 1 we give values of the period and of the associated orbit effective mass at the principal orientations [001], [100] and [110].

Fig. 4

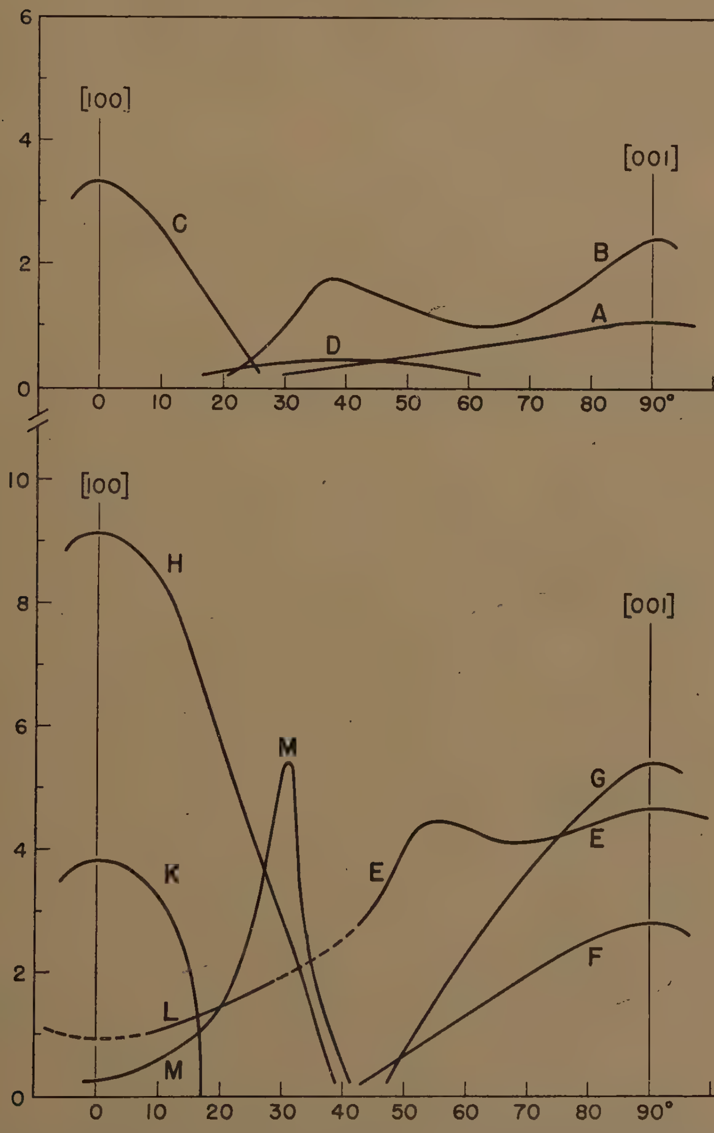

Variation of amplitudes with orientation of magnetic field in a (100) plane at 1·2°K (schematic). Upper half: long-period oscillations; lower half: short-period oscillations. The two drawings are on the same scale and the maximum amplitude corresponds to $|dI/dH| \sim 10^{-2}$.

Because of the considerable scatter of the experimental points and the rapid orientation dependence of amplitude (see fig. 4), it is not possible to decide unambiguously how to join up the experimental points into curves, without appeal to some theoretical model. For instance it is not clear whether the curve L in fig. 1 is a separate branch existing over only a limited angular range or whether it is an extension of E or of F, and there are clearly many similar ambiguities. For lead (I) certain features of the Fermi surface could be inferred by straightforward inspection of the data and the surfaces were then fitted into the Brillouin zone scheme using the free-electron model as a guide; however, we now find that for tin some theoretical model is necessary to suggest the very nature of the surfaces themselves.

§ 3. THE FREE-ELECTRON MODEL

The simple free-electron model has been remarkably successful in accounting for the geometrical features of the Fermi surfaces in the polyvalent metals lead (I) and aluminium (Heine 1957, Harrison 1959, 1960) and it now appears to have a good theoretical foundation (Harrison 1960, Cohen and Heine 1960). We now appeal to this model for help in understanding the complex period variations in figs. 1, 2 and 3.

The primitive Brillouin zone for the white-tin lattice is shown in fig. 5†. Since the primitive zone always accommodates two electrons per smallest unit cell of the real lattice and since for tin the smallest unit cell contains two atoms, it follows that the zone can accommodate one electron per atom. Assuming tin to have four valence electrons per atom, these can be accommodated within a sphere in **k**-space of volume $8(2\pi/a)^3(a/c)$ cm^{-3} and hence radius $1{\cdot}518\ (2\pi/a)$ cm^{-1}, where $a=5{\cdot}82$ Å and $c=3{\cdot}18$ Å are the lattice constants. This sphere completely encloses the primitive (first) zone so that the Fermi surface must lie entirely in higher zones in the extended zone scheme. In order to make comparison with experiment it is necessary to re-map the various portions of the surface in the higher zones into the primitive zone by translations of reciprocal lattice vectors. The extended zone scheme for the tin structure is extremely complicated and the very tedious remapping procedure was in part carried out for us by Petersen (private communication). Recently Harrison (1959) has described a much simpler procedure by which sections through the Fermi surface in the reduced zone scheme can be obtained directly and we have used Harrison's method to construct the surfaces shown in fig. 5, from sections in the central (100), (110) and (001) planes. The surfaces have been drawn more or less to scale, except that sharp corners have been rounded off, both because such a rounding is to be expected on account of band gaps, and in order to make the diagram clearer.

---

† The zone has been incorrectly described by Mott and Jones (1936); for a further discussion see Chambers (1956) and Barron and Fischer (1959). Space-group considerations of the tin structure have been given by Mase (1959).

Fig. 5.

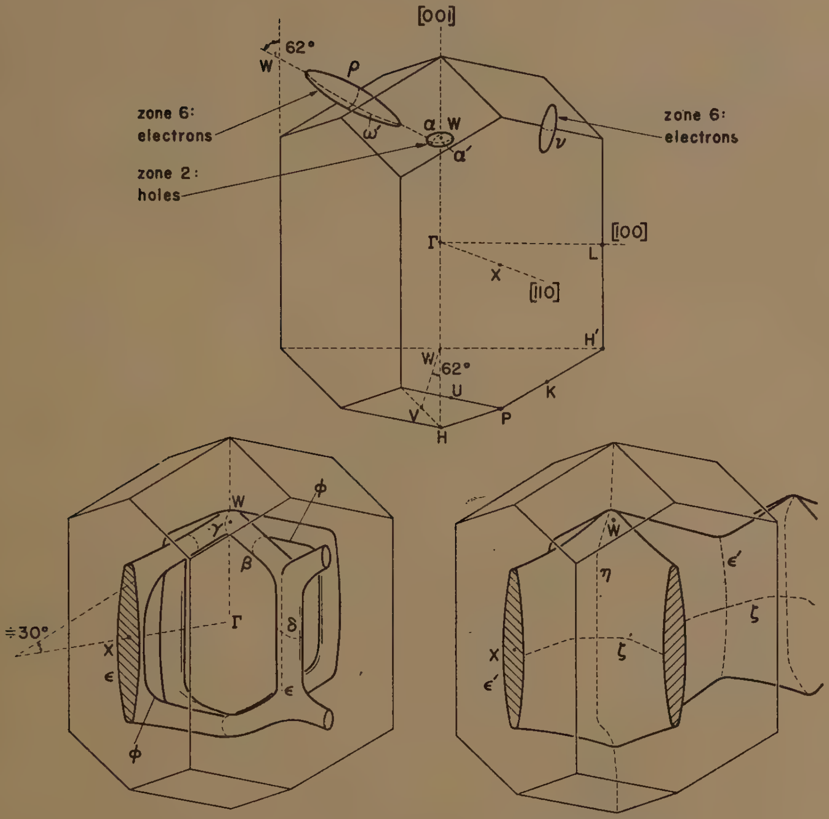
[001]
62°
W
ρ
zone 6:
electrons
ω′
α W
α′
ν
zone 6:
electrons
zone 2:
holes
Γ
[100]
L
X
[110]
H′
W
62°
U
K
V
P
H
W
φ
γ
β
Γ
δ
30°
X
ε
ε
φ
W
η
ε′
ζ
X
ε′
ζ

zone 3: holes

zone 4: (a) holes

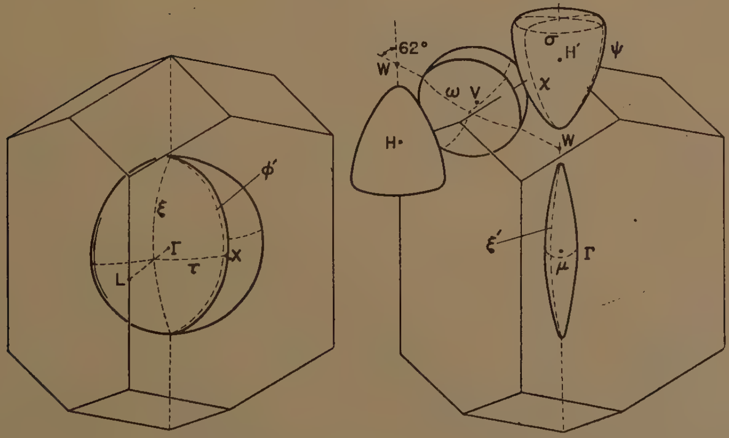
φ′
ξ
Γ
L
τ
X
62°
W
σ
H′
ψ
ω V
X
W
H
ξ′
Γ
μ

zone 4: (b) electrons

zone 5: electrons

The free-electron Fermi surface in the reduced-zone scheme. The principal dimensions of the zone are:

$$\Gamma\,\mathrm{L}=\frac{2\pi}{a},\quad \Gamma\,\mathrm{X}=\frac{1}{2}\left(\frac{2\pi}{a}\right),\quad \Gamma\,\mathrm{W}=\mathrm{LH}=\frac{1}{2}\left(\frac{a}{c}-\frac{c}{a}\right)\left(\frac{2\pi}{a}\right),\quad \mathrm{WH}=\left(\frac{c}{a}\right)\left(\frac{2\pi}{a}\right),$$

where $a=5{\cdot}82$ Å and $c=3{\cdot}18$ Å.

The predictions of the free-electron model are then as follows. The first zone is entirely filled and the second and third ones nearly so, except for two small pockets of holes centred on the points W in the second zone and a multiply-connected surface containing holes in the third zone. In the fourth zone the Fermi surface is one of two sheets and consists of a singly-connected surface 4 (*b*) formed by the intersection of two 'pancakes' containing electrons; this surface is surrounded by a region of unoccupied states which is in turn bounded by the multiply-connected surface 4 (*a*). In fig. 6 we show the central (001) section through the fourth zone, from which the relationship of the two surfaces to one another should become clear. The surfaces in the fifth zone all contain electrons and consist of a long ellipsoid along the tetragonal axis, 'pear-shaped' surfaces centred on the zone corners H (two surfaces per zone) and surfaces similar to that in zone 4 (*b*), but tilted and centred on the points V (four surfaces per zone). Finally we have in the sixth zone small ellipsoidal surfaces centred on the points V and still smaller ellipsoids centred on the points K, and inclined as shown; both sets of ellipsoids contain electrons.

Fig. 6

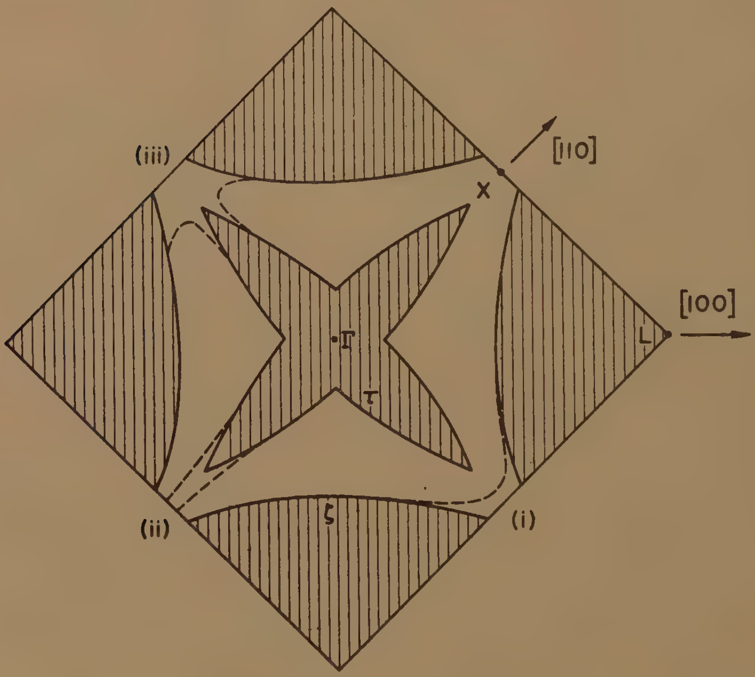

The central (001) section through the fourth zone showing the relation of the surfaces in zones 4 (*a*) and 4 (*b*) (fig. 5) to one another. The shaded regions are occupied.

We have indicated with broken curves in fig. 5 the principal orbits of maximum or minimum area of cross-section which would be expected to give rise to a de Haas–van Alphen effect. These orbits are labelled with small Greek letters and the associated de Haas–van Alphen periods from eqn. (1) are given in table 2. As Harrison (1960) has pointed out, his method of constructing the Fermi surface in the reduced-zone scheme also enables one to find the free-electron orbit masses (eqn. (2)) in a straightforward manner, and these masses are also given in table 2.

Table 2. The free electron model

Orientation	Zone, orbit	P(G^{-1})	m^*/m_0
[001]	2α	6×10^{-7}†	0·05†
	3δ	$4{\cdot}5\times10^{-7}$	0·061
	5μ	$1{\cdot}8\times10^{-7}$	0·089
	$4\ (b)\tau$	$2{\cdot}6\times10^{-8}$	0·40
	5σ	$1{\cdot}0\times10^{-8}$†	0·3†
	$4\ (a)\zeta$	$0{\cdot}87\times10^{-8}$	0·38
[100]	$2\alpha'$	$6{\cdot}6\times10^{-7}$	0·055
	3γ	$5{\cdot}5\times10^{-7}$	0·083
	5ω	$8{\cdot}0\times10^{-8}$	0·50
	$6\omega'$		
	$4\ (b)\xi$	$3{\cdot}8\times10^{-8}$	0·32
	$5\xi'$		
	5χ	$1{\cdot}8\times10^{-8}$	0·28
	$4\ (a)\eta$	$0{\cdot}75\times10^{-8}$	0·42
[110]	3ϵ	6×10^{-8}†	0·2†
	$4\ (a)\epsilon'$		
	$5\xi'$	$5{\cdot}2\times10^{-8}$	0·23
	5ψ	$1{\cdot}4\times10^{-8}$	0·34
	3ϕ	$0{\cdot}94\times10^{-8}$	1·00
	$4\ (b)\phi'$		
28° from [100] in (100) plane	6ρ	6×10^{-7}†	
≑30° from [110] in (110) plane	3β	6×10^{-7}†	

† Estimated values.

§ 4. COMPARISON WITH EXPERIMENT

Before carrying out a detailed comparison with experiment we note that the number of periods to be expected on the basis of the free-electron model is about nine when the magnetic field is along the [001] direction, and considerably more at other orientations. In practice the *maximum* number found at any orientation is about seven (figs. 1, 2 and 3), suggesting either that the actual Fermi surface may not be quite as complex as the literal free-electron model would predict or that some periods are being missed because of low amplitude. One can get some idea about which of the free-electron periods might be absent from considerations of the x-ray structure factor, which vanishes across the vertical {110} planes of the zone but not across the inclined {101} planes (Mott and Jones 1936, p. 164). This leads us to suggest that the (001) section through Γ of the actual Fermi surface might not be too different from that in the free-electron model, but small portions of the surface near the upper and lower ends of the zone might be considerably affected by the presence of energy gaps. In particular, the zones one to five are degenerate at the zone corner H in the free-electron model, but in going from H in the first zone to the corresponding point in the fifth zone we must cross four planes of the type {101} with non-vanishing structure factor; this means that we might expect the 'pear-shaped' surfaces centred on H to be reduced in size. Such considerations lead us to suggest that the small pockets of holes at W in the second zone may be filled, and that the two sets of ellipsoidal surfaces in the sixth zone together with the thin 'intersecting pancake' surfaces in the fifth zone may all be absent. Our simplifying proposals find some justification in the fact that we have found no experimental evidence for the particular period anisotropies expected for these surfaces; thus, for example, we should expect one of the larger ellipsoids in the sixth zone to exhibit a period *maximum* when the field is inclined at 28° to [100] in the (100) plane (i.e. field along the axis of an ellipsoid), but as can be seen from fig. 1 this does not happen. Again, the proposed simplifications result in a considerable reduction in the total surface area and so are, broadly speaking, in keeping with Chambers' (1952) findings that the total surface area is only 0·43 times the free electron value. In what follows we shall therefore compare the results of figs. 1, 2 and 3 with the surfaces in only the four lower diagrams of fig. 5, but excluding the thin 'intersecting pancake' surfaces in the fifth zone.

It is convenient to begin by considering first of all the long-period oscillations (upper halves of figs. 1, 2 and 3) which arise from the smaller portions of the Fermi surface. The period variations in both (100) and (110) planes of the groups A and B can be accounted for by surfaces of revolution parallel to the [001] axis; the angular variation of group A is approximately as the cosine of the angle measured from the [001] axis, thus suggesting a more or less cylindrical surface with its axis along [001], while that of group B is less rapid than the cosine suggesting a convex surface. According to the free-electron model we could therefore associate the A and B oscillations with the orbits δ and μ respectively and we see from tables 1 and 2 that the observed periods are in fact reasonably close to the free-electron values. We do not expect to be able to follow the A and B oscillations all the way to the [100] and [110] orientations since the orbits δ are then no longer defined while the orbit ξ' of the fifth-zone ellipsoid is not particularly favourable for a de Haas–van Alphen effect. These considerations suggest then that the C oscillations, which are strongest at [100], are not connected with the groups A and B and we tentatively ascribe them to the orbits γ of the third-zone surface. However the C oscillations extend all the way to [110] (C′ in fig. 3) and this is only possible if the slanting arms of the multiply-connected surface are not present (i.e. 'pinched off' near W). This proposal is supported by the fact that fig. 2 reveals no oscillations which can reasonably be ascribed to the β-orbits round these arms; the existence of β-orbits would require a period which had a *maximum* value at about 30° from [110] in a (110) plane (fig. 2). Finally, the very weak oscillations D are too vague to suggest anything definite.

We now turn to the short-period oscillations (lower halves of figs. 1, 2 and 3) which are related to much larger portions of the Fermi surface. The magnitudes of the three periods E, F and G observed at [001] agree reasonably well with the three short periods τ, σ, ζ, respectively, predicted by the free-electron model. The G oscillations are fairly isotropic away from [001] and this might be accounted for by the fact that the free-electron orbit η in zone 4 (a) is actually concave where it crosses the orbit ζ, so that the area of the orbit ζ would not be expected to vary much when the field is tilted some 30° to 40° from [001].

The short periods found near [100] and [110] have not, however, found a plausible interpretation in terms of the free-electron model. Thus the M oscillations, which probably have a maximum period at [100], might be associated with the orbits η in zone 4 (a), but their amplitude variation (fig. 4) finds no plausible explanation. Again the H and H′ branches might be associated with the orbits ξ in zone 4 (b), but they do not appear to join smoothly with the E branch as would be required by this interpretation. The results of fig. 1 and fig. 4 in fact strongly suggest that it is the L oscillations which join smoothly to E (i.e. that it is L which must be associated with ξ) but the period *minimum* L at [100] does not fit in with the model. It can be seen that the free-electron model predicts three short periods near [100] corresponding to the orbits ξ, χ and η, while actually four, viz. H, K, L and M, are observed. Finally we should expect strong oscillations corresponding to the orbits ϵ' of zone 4 (a) with a period *maximum* at [110], but no such maximum is observed; the weak oscillations N, observed only at [110], have about the right period, but this may be fortuitous. The further weak period O also found only at [110] might be due to the orbit ϵ in zone 3.

It is natural to enquire if slight modifications of the free-electron model might not help to eliminate the major discrepancies pointed out above. It turns out that only small changes are required to produce quite marked changes in the connectivity of the Fermi surface in the fourth zone. For instance the modification (i) of fig. 6 is rather attractive since it would remove the need for explaining the apparent lack of oscillations from the orbit ϵ', which would require a period maximum at [110]; although the orbit ζ is then round a region of unoccupied states rather than occupied states, the area enclosed by the orbit remains practically unaltered by this modification. On the other hand, modification (ii) would make the orbit τ larger than the orbit ζ, requiring a still shorter period at [001] and *two* period maxima at [110], while (iii) would join orbits τ and ζ into one much smaller orbit which cannot now account for the two shortest periods at [001]. None of these modifications can, however, account for the presence of the *four* periods H, K, L and M, near [100] nor for the cylinder or hyperboloid of revolution about [100] which is required to explain the oscillations H, H′. In fact the only way in which such a cylinder or hyperboloid might fit into the framework of the free-electron scheme is by supposing the surfaces shown at the top of the fifth zone (fig. 5) to be reduced in size and yet to be so merged together as to form a multiply-connected surface of tubes whose axes lie along [100] axes through V. These [100] tubes could then give rise to the oscillations H while the oscillations F might conceivably be associated with a hole orbit around four tubes. This would also require an additional short period at [110]; the period L′ is of the right order of magnitude but it should be a maximum rather than a minimum at [110].

We conclude that the general degree of complexity of the experimental results is much the same as that of the free-electron model and that some of the details, notably the observed periods near [001], agree reasonably well with it. The serious discrepancies at other orientations, however, suggest considerable departures from the free-electron scheme, but it is hardly worth while speculating further about conceivable departures until more accurate and detailed data are available or until a better theoretical model is proposed with which the data can be compared. A ‘tight-binding’ calculation might be of help in suggesting surfaces to account for the short-period results in particular, and such a calculation is at present being carried out by Dr. M. Miasek.

§ 5. DISCUSSION OF OTHER RELEVANT EXPERIMENTS

A certain amount of information about the Fermi surface in tin is available from other types of experiment and this will now be briefly reviewed.

The anomalous skin effect was studied by Fawcett (1955) (see also Chambers 1956) and though it is now clear that the 3-ellipsoid model he used to interpret his results is far too simple, the interpretation of the present results is far from definite enough to allow detailed comparison with Fawcett’s data. It is however worth mentioning that the free-electron surface of fig. 5 is quite capable of reproducing the salient features of the anisotropy in the surface conductivity. Thus the large radii of curvature of the orbits ζ and η in zone 4 (a), especially in the region where they cross, would result in a high surface conductivity when either the [001] or one of the [100] axes lies in the surface of the sample, which is just what Fawcett finds. It is impossible at this stage to deduce a value of the total surface area for comparison with Chambers’ (1952) result of

0·43 times the free-electron value†, and the same holds for a comparison with the electronic specific heat.

The most detailed study so far of cyclotron resonance in tin is that of Khaikin (1959) and, as can be seen from table 1, Khaikin's masses at [001] are in fair agreement with the de Haas–van Alphen ones. However, the agreement is poorer at [100], but it is not clear if [100] is the diad axis to which Khaikin refers. The high value of $m^* = 8{\cdot}5 m_0$ found by Khaikin at an intermediate orientation is indicative of a large closed orbit extending through several cells of the reciprocal lattice and the free-electron model would suggest that this is most likely to be associated with the multiply-connected surface of zone 4 (*a*). Assuming a free-electron-like interpretation of the present results, the de Haas–van Alphen effective masses are in as reasonable agreement with the free-electron ones as one might expect (tables 1 and 2), bearing in mind the discrepancies observed in other metals (Harrison 1960). Cyclotron resonance experiments using circularly polarized radiation would be most helpful in deciding which of the surfaces contain electrons and which holes.

The magneto-resistance results of Alekseevski and Gaidukov (1959) suggest that the Fermi surface of tin has open directions along [100] and [110] but this conclusion is based on only preliminary results. Further evidence on open orbits comes from ultrasonic attenuation experiments. Olsen and Morse (1959) find open orbits but no details are given. Mackintosh (private communication) also finds evidence for open directions along [100] and [110]. The suggestion of open orbits along [100] is not inconsistent with the de Haas–van Alphen data (see pp. 1101, 1102) but we have found no period maxima at [100]; however, further comparison is premature until more detailed results are available.

ACKNOWLEDGMENTS

We are indebted to Dr. D. Shoenberg, F.R.S., for his keen interest in this work and for his continued encouragement and advice. We are also grateful to Dr. R. F. Petersen for giving us sketches of parts of the Fermi surface in the reduced-zone scheme, to Dr. G. Fischer and Dr. V. Heine for helpful discussions and to Mr. H. L. Davies for help with the experiments.

Note added in proof.—We wish to point out that the free-electron surface of fig. 5 has been constructed assuming that electrons are Bragg-reflected at all proper Brillouin-zone planes whether or not the structure factor is zero; a vanishing structure factor does not necessarily imply an energy gap which is identically zero over the whole plane (see refs. at foot of p. 1096 Crystal symmetry requires the energy gap on the {110} zone faces, which have vanishing structure factor, to be zero *only* along the lines XL and XP

---

† Dr. Fawcett has informed us that his figure of 0·39 is low on account of a calibration error.

(Mase 1959; we are grateful to Dr. J. M. Keller for pointing this out to us). It appears that the only important alteration in the free-electron model brought about by this requirement is that an electron initially moving round orbit ζ in zone 4 (a) will continue round half the orbit δ in zone 3 after contacting the line XL of the (110) face, and so on. This results in a 'four-cornered rosette' orbit normal to [001] whose maximum linear extension (along [110]) is somewhat larger than that of the zone but whose area is practically the same as the original orbit ζ. However such a 'freak' orbit would have vanishingly small statistical weight and we have found no convincing experimental evidence for it.

REFERENCES

ALEKSEEVSKI, N. E., and GAIDUKOV, YU., P., 1959, *J. exp. theor. Phys., U.S.S.R.*, **37,** 672.

BARRON, T. H. K., and FISCHER, G., 1959, *Phil. Mag.*, **4,** 826.

BERLINCOURT, T. G., 1952, *Phys. Rev.*, **88,** 242.

CHAMBERS, R. G., 1952, *Proc. roy. Soc.* A, **215,** 481; 1956, *Canad. J. Phys.*, **34,** 1395.

COHEN, M. H., and HEINE, V., 1960 (to be published).

FAWCETT, E., 1955, *Proc. roy. Soc.* A, **232,** 519.

GOLD, A. V., 1958, *Phil. Trans.* A, **251,** 85.

HARRISON, W. A., 1959, *Phys. Rev.*, **116,** 555; 1960, *Ibid.*, **118,** 1190.

HEINE, V., 1957, *Proc. roy. Soc.* A, **240,** 340.

KHAIKIN, M. S., 1959, *J. exp. theor. Phys., U.S.S.R.*, **37,** 1473.

MASE, S., 1959, *J. phys. Soc., Japan*, **14,** 1538.

MOTT, N. F., and JONES, H., 1936, *Theory of Metals and Alloys* (Oxford: Clarendon Press).

OLSEN, T., and MORSE, R. W., 1959, *Bull. Amer. phys. Soc.* II, **4,** 167.

SHOENBERG, D., 1952, *Phil. Trans.* A, **245,** 1; 1953, *Physica*, **19,** 791; 1957, *Progress in Low Temperature Physics*, Vol. II, ed. C. J. Gorter (Amsterdam: North Holland Publ. Co.); 1960, *Proc. Intl. Conf. on Fermi Surfaces in Metals* (New York: Wiley).

The Determination of the Flux of Cosmic Ray Protons with Nuclear Emulsions†

By C. J. WADDINGTON
H. H. Wills Physical Laboratory, University of Bristol

[Received June 1, 1960]

ABSTRACT

The flux of protons in the primary cosmic radiation has been determined in a stack of nuclear emulsions exposed during 1954 over northern Italy. This determination, which depended on the observation of the nuclear interactions produced by the protons, gave a flux at the top of the atmosphere of 500 ± 70 protons/m^2 ster sec, a value in good agreement with that expected from counter measurements. A simple model of the variation of the proton flux with depth in the atmosphere has been derived which appears to be in reasonable agreement with the experimental data.

§ 1. INTRODUCTION

NUCLEAR photographic emulsions have been extensively used to investigate the heavier components of the primary cosmic radiation, but have not provided much information on the primary protons‡. Present data on these particles come entirely from measurements made with electronic counters. In particular, the Čerenkov-scintillator array of McDonald (1956) (see also McDonald and Webber (1959)) is almost entirely responsible for our present knowledge of the fluxes of these particles, since only this equipment appears able to discriminate adequately against the large background of upward moving albedo particles. Even this equipment, however, is unable to eliminate the re-entrant albedo, since these particles, which are predominantly electrons (McDonald and Webber 1959), have the same direction of flight as do those of primary origin. An alternative method of measuring these fluxes, and one which preferably discriminates against the re-entrant albedo, is thus very desirable. Such a method is provided by determining the flux from the nuclear interactions produced in nuclear emulsions.

§ 2. METHOD

When emulsions are used to investigate the heavier particles of the primary radiation it is usual to detect these nuclei by searching a given area for their tracks and from the frequency determining the flux. Such a procedure is hardly practical in the case of the primary protons due to the extremely tenuous nature of the tracks left by fast singly-charged particles as they traverse the emulsion. Furthermore, even if by very careful scanning it were possible to detect *all* the tracks of particles producing minimum ionization which crossed a given area in the emulsions, it would be extremely difficult to distinguish the tracks left by protons from those left by other energetic but secondary singly-charged particles. Nor, in general, would it be possible to obtain any indication of the direction of motion of these particles.

---

† Communicated by the Author.

‡ In what follows no distinction will be made between protons and the other isotopes of hydrogen that may be present in the primary cosmic radiation.

The nuclei of the primary radiation may, alternatively, be detected by observing the nuclear interactions, or 'stars', that they produce while passing through the emulsions. Until recently the determination of absolute fluxes from the frequency of these stars was also impracticable, due to the extreme difficulty of locating *all* the interactions that are produced in any given volume. However, now that systematic observations with beams of artificially accelerated protons are available, these detection inefficiencies can be calculated and allowed for.

The additional requirement that the observed particles should produce a nuclear interaction has the great advantage that it serves to remove all those weakly interacting secondary particles, i.e. μ-mesons and electrons, from the sample being considered, and thus greatly reduces the problem of how to take account of the albedo particles. The short lifetime of π-mesons means that the majority of those produced at any distance from the emulsions will have decayed to weakly interacting particles before they arrive. Thus only locally produced mesonic secondary particles are detected, and if the volume searched for stars is chosen to be near the top of the emulsion stack, then these will be predominantly upward moving, and can usually be eliminated from a study of the characteristics of the stars. The only serious contamination by secondary particles would appear to be that due to knock-on protons and to protons produced by the break-up of heavy nuclei above the emulsions. It appears to be possible to make a reasonable estimate of the abundance of these particles, and thus to calculate the flux at the top of the atmosphere.

§ 3. EXPERIMENTAL DETAILS

While no emulsion stacks which had been exposed at the same time as a Čerenkov-scintillor array were available in this laboratory, there was one which had a closely similar α-particle flux to that measured by counters. This stack was exposed on September 14, 1954 over northern Italy, and has previously been used to measure the α-particle flux and energy spectrum (Fowler and Waddington 1956), and the flux and charge spectrum of the heavier nuclei (Waddington 1957 a, Hillier and Rajopadhye 1958). This stack consists of 80, 6 in. × 8 in. 600 μ G5 emulsions, and was exposed for 5·75 hours at an altitude of about 106 000 ft. The flight curve has been published previously, e.g. the E stack (Rajopadhye and Waddington 1958).

A volume, all of which was less than 1 cm from the top of this stack, was scanned for stars which satisfied the following conditions.

(i) The star lay within the inner 80% of the emulsion thickness, since stars near an emulsion face are difficult to analyse.

(ii) Each star had to have three or more black or grey tracks ($N_h \geqslant 3$), one of which had a potential range more than 60 microns. This requirement on length removes those stars due to radioactive decays in the emulsion.

Each of the stars found was carefully examined under high magnification by one or two observers for the presence of minimum tracks produced by fast primary or secondary particles. In those cases where such a track was found to lie within 60° of the vertical the star was, with a few exceptions discussed later, denoted as one produced by an energetic downward moving particle. The flux of these particles, $J(X)$, which are assumed to be all protons, that is, neglecting any downward meson component, is then given by

$$J(X) = \frac{\lambda \, dN}{V \, . \, \Omega \, . \, t} \text{ particles/m}^2 \text{ ster sec} \quad . \; . \; . \; . \quad (1)$$

where λ is the interaction mean free path of protons in emulsion, measured in metres, dN is the number of stars produced by these protons, V is the scanned volume in cubic metres, Ω is the solid angle over which particles are accepted and t the duration of the exposure in seconds. This equation is derived assuming that the maximum distance a particle may traverse in the volume is much less than λ.

The value of dN obtained directly from scanning must be corrected for several forms of detection inefficiency.

3.1. *Detection Efficiency of Stars*

No attempt has been made to detect those stars with $N_h \leqslant 2$, since it is well known that area-scanning cannot hope to detect such stars efficiently. Instead a correction has been made by using the experimental data available on the interactions produced in nuclear emulsions by artificially accelerated protons. Winzeler *et al.* (1960) have published a N_h distribution for those stars found by 'along the track scanning' of 6·2 Bev protons. This distribution has been used to correct that found in this experiment. Figure 1 shows these distributions normalized for those stars with $N_h \geqslant 5$, since it appears that there has also been some loss of stars with $N_h = 3$ and 4 in this experiment. The correction factor derived for the loss of stars with $N_h < 5$ is $1{\cdot}56 \pm 0{\cdot}13$.

The validity of this procedure depends on the assumption that the N_h distribution is nearly independent of energy, which appears to be generally true for energies above 1 or 2 Bev. Furthermore, since the geomagnetic cut-off energy in this experiment was approximately 3·6 Bev for the protons, the median energy of these particles was about 5·7 Bev. Thus the majority of the primary protons had energies which are not too different from those of the artificially accelerated protons with which they are being compared.

Fig. 1

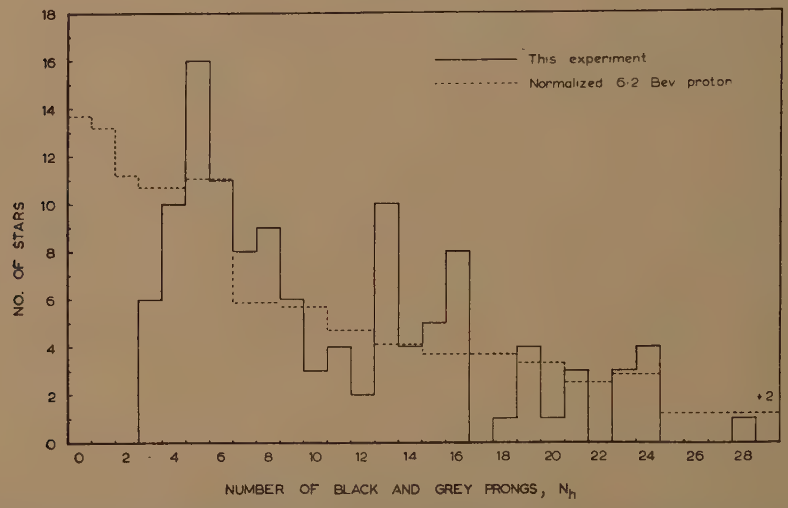

The N_h distribution observed in this experiment and that observed by Winzeler *et al.* (1960) on 6·2 Bev protons. These distributions are normalized for those stars with $N_h \geq 5$.

Fig. 2

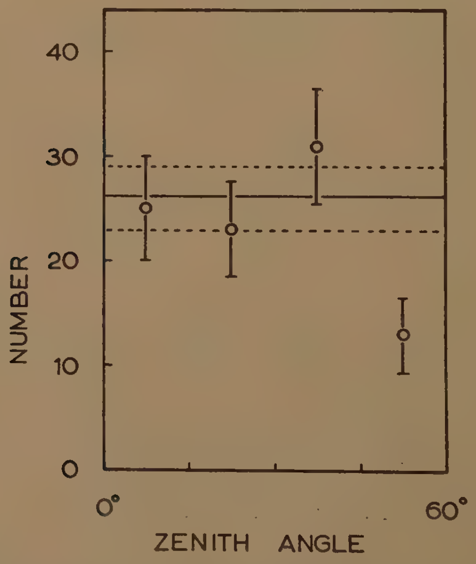

The zenith angle distributions of those tracks which could definitely be assumed to be due to primary particles. The data has been divided into four equal frequency intervals. The mean of the first three, together with its standard deviations are shown by the horizontal lines.

3.2. *Detection Efficiency for Primary Particles*

The tracks left by fast singly-charged particles are the most tenuous observable in nuclear emulsions and the most careful inspection is necessary to detect all such tracks associated with each star. Approximately one-third of all the stars were examined by two observers, and the good agreement between them suggests that both had very high efficiencies. However, such a comparison assumes that all tracks have an equal intrinsic probability of detection, and this may not be true. An alternative indication of the detection efficiency was supplied by studying the observed angular distribution of those particles which were assumed to be primary particles. It is reasonable to assume that the detection efficiency might be related to the zenith angle of the track, i.e. a particle dipping steeply in the emulsion might be more difficult to detect than one lying in the plane of the emulsion. The distribution of the space angles observed in this experiment is shown in fig. 2. It can be seen that if it is assumed that the incident particles are isotropically distributed there is a definite indication that particles with large space angles have been missed. To a first approximation these particles should be isotropically distributed and so a correction must be made for those missed. In this experiment, from a sample of 92 primary particles an additional 13·3 ± 4·7 were assumed to have been missed.

3.3. *Identification of Primary Particles*

When a star has more than one minimum track associated with it, it is not always clear which was produced by the primary particle. Thus it is necessary to consider each star in detail in an attempt to determine which track has the greatest probability of being due to the primary.

In an interaction of an energetic nucleon with an emulsion nucleus, the fast secondary particles are strongly collimated in the forward direction. As a result, in any particular star, the primary track may be taken as that which results in the least sum of the angles that the other minimum tracks make with the direction of motion of the assumed primary. In the majority of stars with three or more associated minimum tracks this condition is sufficient to determine the primary with a high degree of probability. However, in some cases no one track is clearly defined as being due to the primary.

For this reason those stars having a minimum track within the solid angle of acceptance, Ω, have been separated into seven groups. Sketch drawings of typical members of each group are shown in fig. 3.

(*a*) Stars with just one minimum track. Since any albedo of energetic neutral particles can be neglected, this minimum track has a high probability of being that due to the primary. In a sample of 100 stars, 18% were of this type.

(*b*) Stars with two minimum tracks, one of which is in the lower hemisphere. While either track could have been produced by the incident particle, there appears to be a much greater probability that the one in the upper hemisphere should be that due to the primary (see later). Frequency 19%.

(*c*) Stars with more than two minimum tracks, in which the only one in the upper hemisphere is clearly that due to the primary. Frequency 37%.

(*d*) As (*c*), but with two or more tracks in the upper hemisphere, only one of which is clearly due to the primary. Frequency 8%.

(*e*) As (*d*) but with no clear indication as to which track is due to the primary. These stars were given a weight depending on the number of tracks in the upper hemisphere within and outside Ω. Frequency 8%.

(*f*) Stars with more than two minimum tracks, in which one in the lower hemisphere is clearly produced by the primary. Frequency 5%.

(*g*) Stars with two or more minimum tracks, all in the upper hemisphere. These were given a weight as for (*e*). Frequency 5%.

Fig. 3

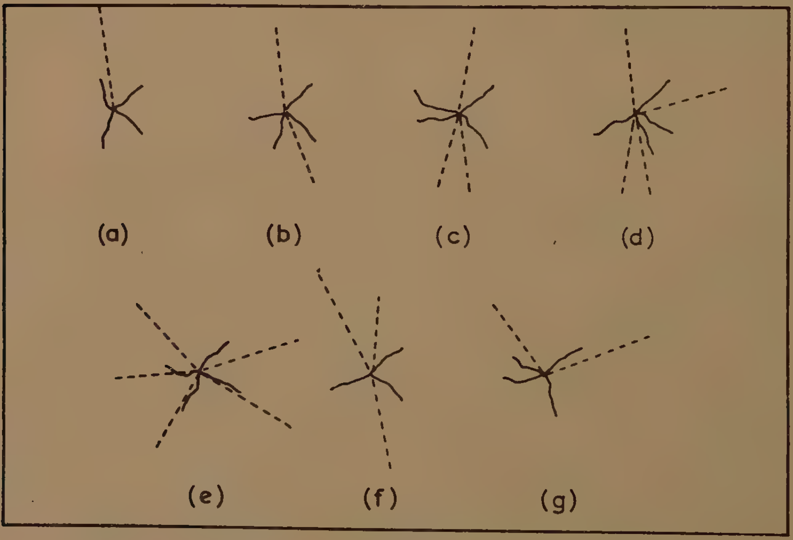

Sketch drawings of typical stars. Each star has $N_h = 4$.

Comparing groups (*c*) and (*d*) with group (*f*), it appears that only about 10% of the stars in groups (*b*) should have been produced by upward moving secondary particles. On a small sample of this sort, this is a negligible fraction. It could, of course, be further reduced by exposing a smaller stack of emulsions, so as to reduce the amount of local matter available to generate these particles.

§ 4. EXPERIMENTAL RESULTS

In scanning a volume of 1·47 cm^3, 101 stars were found which had primaries in the solid angle of acceptance and $N_h \geqslant 5$. To these were added 14·6 ± 5·1 stars to allow for the inefficiency of detecting primaries at large angles. The resulting 115·6 stars were multiplied by 1·56 ± 0·13, the correction factor for those stars with $N_h \leqslant 4$. Then, using eqn. (1), with $\lambda = 38{\cdot}2 \pm 1{\cdot}5$ cm, the value quoted by Winzeler *et al.* (1960), $\Omega = \pi$ steradians, and $t = 2{\cdot}07 \times 10^4$ sec, the time spent at ceiling altitude, $J(X) = 720 \pm 105$ protons/m^2 ster sec, where $J(X)$ was the flux of primary protons in the emulsion, and $X = 10$ g/cm^2 of residual matter.

§ 5. GROWTH CURVE OF PROTONS IN THE ATMOSPHERE

In order to extrapolate the flux value observed in the emulsions to the top of the atmosphere it is necessary to establish a growth curve for these particles. Furthermore, since in this experiment the emulsions were not re-orientated after they reached ceiling altitude it is essential to make a correction for those particles which entered while the emulsions were ascending and descending. For this purpose the growth curves must be known to appreciable depths in the atmosphere. It may be noticed that it is unnecessary to make a correction for those protons entering at sea level, since these will be closely collimated to the vertical, and it is unlikely that the stack would have been correctly orientated for them.

There appears to be little or no experimental evidence regarding the flux of energetic protons as a function of atmospheric depth, and it is therefore necessary to construct a growth curve from a theoretical model. The simple, and somewhat artificial one chosen here assumes that in a typical interaction of an energetic proton with an air nucleus the proton is generally not absorbed but merely degraded in energy. The energetic products of such an interaction consist mainly of π-mesons, which on the average take about one-third of the incoming energy (Zhdanov *et al.* 1960) and occasional knock-on protons. Thus the proton multiplicity, n, is greater than unity for a number of successive interactions. Eventually the protons are either absorbed, or their energies are reduced below that necessary to produce tracks of minimum ionization.

With these assumptions, if $J_p(x,\theta)$ is the flux of primary protons and protons produced by primary protons at a vertical depth x and zenith angle θ, and if J_0 is the flux of primary protons at the top of the atmosphere, then

$$J_p(x,0) = J_0 \exp(-x/\lambda_p)\left[1 + \frac{n_1 x}{\lambda_p} + \frac{n_1 n_2 x^2}{2\,!\,\lambda_p{}^2} + \dots\right] = J_0 f_1(x) \qquad (2)$$

where λ_p is the interaction mean free path of protons in air, taken to be 100 g/cm^2, and n_1, n_2, ... are the multiplicities in the first, second, ... interactions.

In this experiment, where particles were accepted at zenith angles of up to 60°, the flux at any depth x is given by

$$\int J_p(x,\theta)\,d\omega = 2\pi x \int_x^{2x} \frac{J_p(y,0)}{y^2}\,dy$$

where $y = x/\cos\theta$ (Rossi 1952)

$$= 2\pi x \int_x^{2x} \frac{J_0 f_1(y)}{y^2}\,dy = \pi J_{pp}$$

which may be solved graphically.

Fig. 4

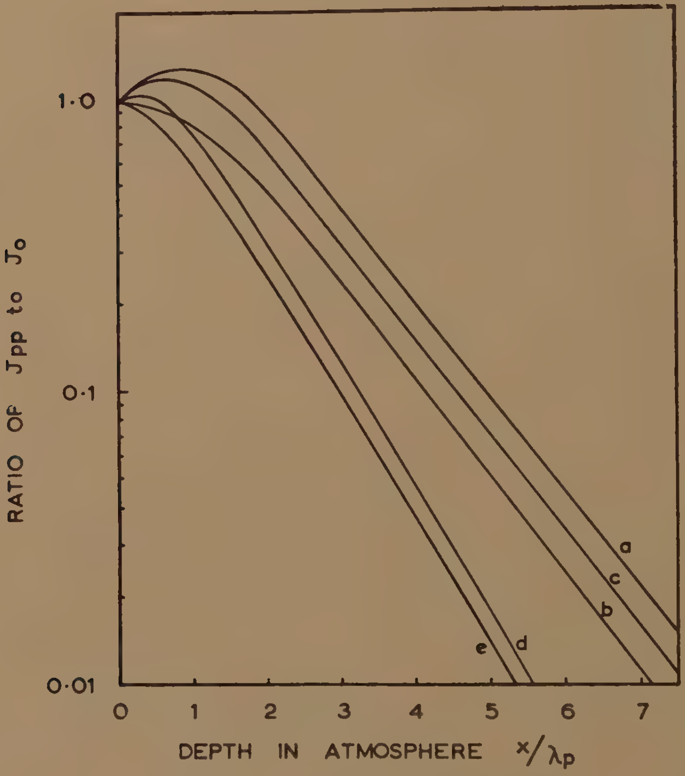

The variation of the ratio $J_{pp}\, J_0$ with x.

A plot of the ratio J_{pp}/J_0 against x is shown in fig. 4 for various cases. (a), (b) and (c) assume a three-stage process, i.e. use the first three terms of eqn. (2), with $n_1 = n_2 = 1{\cdot}5$; $n_1 = n_2 = 1{\cdot}0$ and $n_1 = 1{\cdot}5$, $n_2 = 1{\cdot}0$, respectively. (d) and (e) assume a two-stage process, with $n_1 = 1{\cdot}5$ and $n_1 = 1{\cdot}0$ respectively.

It has been assumed that a three-stage process is more appropriate for protons above a cut-off energy of about 3·6 Bev, whereas a two-stage process applies for protons of lower energy. The only experimental justification for this appears to be the approximately correct prediction of the sea-level proton flux mentioned later. A more refined model would have to take account of the range of energies of the primary protons. The values of n are somewhat more justifiable, since 1·5 and 1·0 represent reasonable limits and the combination of these two values in assumption (c) appears to represent the best model for this experiment.

Approximately 50% of the nucleons in the primary cosmic radiation do not enter the atmosphere as free protons, but bound in nuclei. The median energy of these bound nucleons is approximately half that of the free ones, due to the influence of the geomagnetic field. For this reason it has been assumed that the protons released from these nuclei are capable of producing one fewer interaction than are the free protons before they are removed. For simplicity these bound nuclei have been assumed to enter only in the form of α-particles, and the primary α-particle flux has been taken to be one-quarter of the primary proton flux.

Thus, corresponding to a two-stage process for free protons

$$J_\alpha(x,0)=2J_{\alpha 0}\frac{\lambda_p}{\lambda_p-\lambda_x}[\exp(-x/\lambda_p)-\exp(-x/\lambda_\alpha)]=J_{\alpha 0}f_2(x)$$

where λ_x is the interaction mean free path of α-particles in air, assumed to be half λ_p, and $J_{\alpha 0}$ is the assumed flux of α-particles at the top of the atmosphere.

So, as before

$$\pi J_{\alpha p}'=2\pi x\int_x^{2x}\frac{J_{\alpha 0}f_2(y)}{y^2}\,dy$$

where $J_{\alpha p}'$ is the flux of protons produced by α-particles in a two-stage process.

Similarly, in a three-stage process

$$J_\alpha(x,0)=2J_{\alpha 0}\frac{\lambda_p}{\lambda_p-\lambda_x}\left[\exp(-x/\lambda_\alpha)\left(\frac{n_1\lambda_x}{\lambda_p-\lambda_x}-1\right)\right.$$
$$\left.+\exp(-x/\lambda_p)\left(1+\frac{n_1x}{\lambda_p}-\frac{n_1\lambda_x}{\lambda_p-\lambda_\alpha}\right)\right]=J_{\alpha 0}f_3(x).$$

So, as before

$$\pi J_{\alpha p}''=2\pi x\int_x^{2x}\frac{J_{x0}f_3(y)}{y^2}\,dy.$$

Thus the total flux of protons, $J(x)$, at any depth x is given by

$$J(x)=J_{pp}+J_{\alpha p}.$$

Curves of the ratios J_{xp}/J_{x0} and $J(x)/J_0$ as a function of x are shown in figs. 5 and 6.

A *partial* test of the validity of this model is provided by comparing the flux predicted at sea level, i.e. $10\lambda_p$, with that measured experimentally. Mylroi and Wilson (1951) have measured a flux of 0·55 protons/m^2 ster sec at Manchester, England. This may be compared with the value of about 0·25 protons/m^2 ster sec predicted by models (d) and (e), which, because of the low cut-off energy over Manchester, should be the appropriate models. In view of the simplified nature of these models this agreement appears to be remarkably good.

Using the curves in fig. 6 it is possible to calculate the correction factor $f(t)$ for the ascent and descent of the balloon, as well as that for the overlying atmosphere during the level flight, $f(x)$. Values of $f(t)$ and $f(x)$ are shown in table 1, together with the resulting values of J_0, given by

$$J_0 = J(X) \,.\, f(t) \,.\, f(x),$$

where $J(X)$ is the flux measured in the emulsions (eqn. (1)).

Fig. 5

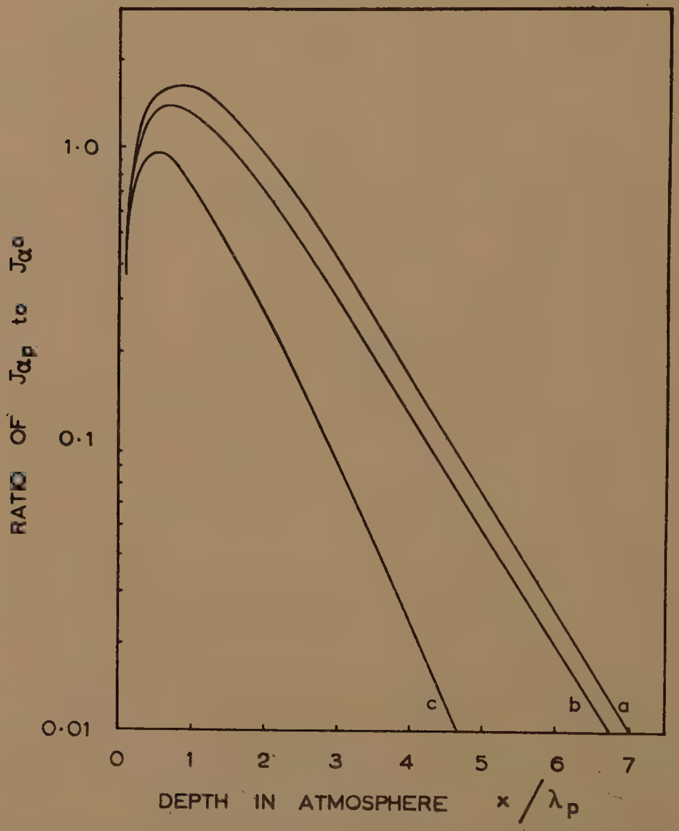

The variation of the ratio $J_{\alpha p}/J_{\alpha 0}$ with x. Curves a and b are for a three-stage process with $n_1 = 1{\cdot}5$ and $1{\cdot}0$ respectively, while curve c is for a two-stage process.

Thus, $J(X)$ when corrected to the top of the atmosphere becomes, under the most plausible assumptions, model (c).

$$J_0 = 500 \pm 70 \text{ protons/m}^2 \text{ ster sec}$$

where the quoted error does not include the uncertainties in the extrapolation to the top of the atmosphere.

This value of J_0 may be compared with that of

$$590 \pm 50 \text{ protons/m}^2 \text{ ster sec}^{\dagger}$$

Fig. 6

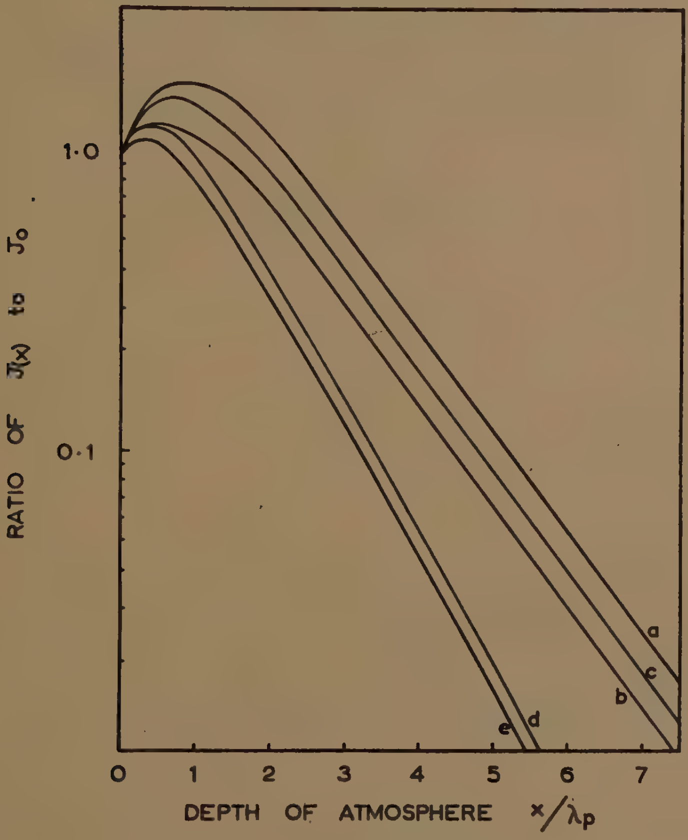

The variation of the ratio $J(x)/J_0$ with x.

Table 1. Correction Factors

Model	$f(t)$	$f(x)$	$f(t) \cdot f(x)$	J_0 (protons m^2 ster sec)
(*a*)	0·787	0·855	0·674	485 ± 70
(*b*)	0·829	0·910	0·753	540 ± 75
(*c*)	0·805	0·861	0·694	500 ± 70
(*d*)	0·850	0·905	0·769	555 ± 80
(*e*)	0·860	0·935	0·804	580 ± 85

---

† After correction for the re-entrant albedo of about 40 ± 10 particles/m^2 ster sec.

found by McDonald and Webber (1959) in a flight where the α-particles flux was almost precisely similar to that measured in this stack.

§ 6. CONCLUSIONS

The agreement between these two values of the proton flux appears reasonable, and suggests that there are no *serious* errors in either methods of determining these fluxes.

The fluxes of all the nucleonic components of the primary cosmic radiation have now been measured in the stack of emulsions used in this experiment. These flux values are shown in table 2.

Table 2. Fluxes of Nucleonic Components Measured in One Emulsion Stack

Component	Flux (particles m^2 ster sec)	Reference
Protons	500 ± 70	This work
α-particles	89 ± 8	Waddington (1957 b)
$3 \leqslant Z \leqslant 5$ nuclei	$2{\cdot}3 \pm 0{\cdot}4$	Waddington (1957 a)
$6 \leqslant Z \leqslant 9$ nuclei	$6{\cdot}1 \pm 0{\cdot}6$	,,
$Z \geqslant 10$ nuclei	$2{\cdot}5 \pm 0{\cdot}3$	,,

With this demonstration of the feasibility of measuring proton fluxes with nuclear emulsions it should now be possible to use available experimental material to investigate the behaviour of this component of the primary cosmic radiation in some detail. However, it must be noted that emulsion experiments are still not able to give any information on the individual energies of these protons. Also that the accuracy of this method is limited by the uncertainties of the correction for secondary protons. This can be reduced by using small stacks exposed at great altitudes which have been re-orientated after reaching ceiling altitude. Under these conditions, and with the better data from machine experiments that should soon be available, accuracies of better than ± 10% should be easily obtainable.

ACKNOWLEDGMENTS

The author is grateful to Professor C. F. Powell, F.R.S., for the facilities of his laboratory, and to Mrs. W M. Dyer for her valuable assistance with the scanning and examination of the stars.

REFERENCES

FOWLER, P. H., and WADDINGTON, C. J., 1956, *Phil. Mag.*, **1**, 637.
HILLIER, R. R., and RAJOPADHYE, V. Y., 1958, *Nuovo Cim.*, Suppl., **8**, 520.
MCDONALD, F. B., 1956, *Phys. Rev.*, **104**, 1723.

McDonald, F. B., and Webber, W. R., 1959, *Phys. Rev.*, **115**, 194.
Mylroi, M. G., and Wilson, J. G., 1951, *Proc. phys. Soc., Lond.* A, **64**, 404.
Rajopadhye, V. Y., and Waddington, C. J., 1958, *Phil. Mag.*, **3**, 25.
Rossi, B., 1952, *High Energy Particles* (Prentice-Hall Inc.), p. 440.
Waddington, C. J., 1957 a, *Phil. Mag.*, **2**, 1059; 1957 b, *Nuovo Cim.*, **6**, 748.
Winzeler, H., Klaiber, B., Koch, W., Nikolić, M., and Schneeberger, M., 1960, *Nuovo Cim.*, **17**, 8.
Zhdanov, G. B., Markov, P. K., Strel'tsov, V. N., Iret'yakov, M. I., Cheng P'U-Ying, and Shafranova, M. G., 1960, *J. exp. theor. Phys.* (*USSR*), **37**, 611 or *J.E.T.P.*, **10**, 433.

X-ray Evidence for Segregation of Solute to Stacking Faults in a Copper–Aluminium Alloy†

By R. W. Cahn and R. G. Davies
Department of Physical Metallurgy, The University, Birmingham 15, England

[Received May 27, 1960]

Abstract

A study was made of the intensity of scattering of monochromatic x-rays at small angles from a copper-base solid solution containing 15 at. % aluminium. The intensity of scattering from a rolled foil was found to increase after heating at 150–250°c, a temperature range in which the alloy hardens, and there is little or no recrystallization. This increase is attributed to segregation of aluminium to the ribbons of stacking fault between partial dislocations. Various confirmatory tests were performed to check the validity of this conclusion.

§ 1. Introduction

1.1. *Anneal Hardening*

The present experiment was designed as an adjunct to a study (Chinowsky and Cahn 1961) of the *anneal hardening* of α-aluminium bronze. The cold-worked alloy becomes harder if it is annealed below the recrystallization temperature ; α-brass and some other solid solutions behave similarly. Hasiguti (1955) proposed the term ‘ anneal hardening ’ to denote this phenomenon. Two alternative theories have been put forward to account for it :

(1) The alloy may possess short-range order which is partly destroyed by deformation, and re-established by annealing. *If* the locking is in part determined by short-range order, this process can account for anneal hardening.

(2) The dislocations formed during deformation may become locked by a segregation of solute atoms to the broad ribbons of stacking fault that separate the dissociated partial dislocations in an alloy of low stacking-fault energy. Such segregation has been postulated by Suzuki (1952). It can come about during an anneal following deformation, and cause the alloy to become harder.

It is known (Borie 1958, private communication, Houska and Averbach 1959, Davies and Cahn 1961) that α-Cu/Al is liable to extensive short-range order and that this decreases with increase of the annealing temperature. Yet a sample quenched from 600°c, and accordingly almost disordered, does not harden on tempering at 200°c (a treatment which re-establishes the order). For this, and other reasons, explanation (2) is more attractive, especially since α-brass and α-Cu/Al are known to have very low stacking-fault energies. More detailed discussion of the interpretation of anneal hardening will be found in a forthcoming paper by Chinowsky and Cahn.

---

† Communicated by the Authors.

1.2. *Small-angle X-ray Scattering due to Local Solute Segregation*

If ' Suzuki segregation ' does occur, it should be possible to detect it by means of small-angle scattering of x-rays. When a solid solution is freshly cold-worked, the new dislocations will be devoid of segregate. On subsequent annealing below the recrystallization temperature, solute will go to the stacking faults, which thus come to resemble GP zones in an age-hardened alloy. The local perturbations in the initially uniform electron density, resulting from a local concentration of solute, will in both cases give rise to an additional scattering of x-rays at small angles (Guinier and Fournet 1955). In the case of age-hardening alloys, such as Al/Ag and Al/Cu, this prediction has been amply confirmed (e.g. Walker and Guinier 1953). It was the purpose of the present experiment to look for this effect in an anneal-hardening alloy.

The following conditions must be met if such an experiment is to have any hope of success :

(1) The alloy must have solvent and solute of widely differing atomic numbers Z, since for a given dislocation density and a given degree of segregation, the intensity of small-angle scattering will be proportional to $(f_{\mathrm{solvent}}-f_{\mathrm{solute}})^2$, where the f's are atomic scattering factors. For small scattering angles, this $=(Z_{\mathrm{solvent}}-Z_{\mathrm{solute}})^2$.

(2) The alloy must have a high dislocation density so that there are enough scattering centres for the predicted effect to be detectable.

(3) The alloy must have a low specific stacking-fault energy, so that the ribbons of stacking fault between partial dislocations shall be wide; this again will enhance the scattered intensity.

A copper-base alloy containing 15 at. % aluminium, cold-rolled to 50% reduction or more, satisfies all these conditions and was chosen as experimental material. The low stacking-fault energy and consequently large total area of stacking-fault ribbon in filings of Cu/Al alloys was confirmed by Paterson's x-ray line shift method (Christian and Spreadborough 1957, Smallman and Westmacott 1957). Moreover, an analysis of the x-ray line broadening from Cu/Al filings, due to Guseva and Babareko (1959) yielded results closely similar to those obtained by Warren and Warekois (1955) in analysing line-widths from α-brass filings, and which they were able to interpret in terms of a faulted domain structure.

Since the present work was completed, Nakajima (1959) has published a note in which he claims to have detected an increment of small-angle x-ray scattering due to Suzuki segregation in a Cu/Ni alloy. It will be surprising if this claim can be substantiated, since the alloy used by Nakajima signally fails to satisfy condition (1), above.

1.3. *Double Bragg Reflection Mechanism*

A complication arises from the small-angle x-ray scattering which is observed directly after deformation, and which is predominantly due to repeated Bragg reflections from pairs of subgrains in the deformed structure (Beeman and Webb 1959, Neynaber *et al.* 1959, Fricke and Gerold 1958, 1959, Atkinson 1958). However, by careful comparative measurements of scattered intensity before and after heat treatment, this effect can be allowed for, and this has been done in the present experiments.

§ 2. EXPERIMENTAL METHODS

The small-angle scattering apparatus used is shown diagrammatically in fig. 1. A beam of copper Kα radiation, monochromated by an asymmetrically cut bent quartz crystal, passed through the alloy foil before being blocked by a beam stop at the focus. The alloy foil was set in a holder so arranged that the same area could be irradiated after the foil had been temporarily removed for heat treatment. The intensity of the beam was continuously monitored by a Geiger counter which measured the intensity of the (311) line diffracted by a very thin cold-rolled foil of aluminium, set in the beam behind the quartz crystal.

Fig. 1

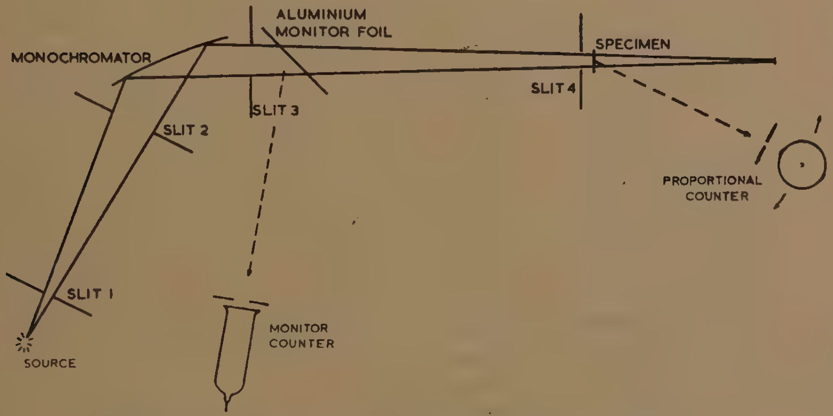

Schematic diagram of small-angle scattering apparatus.

The intensity scattered by alloy foil was measured by means of a proportional counter (20th Century Electronics Ltd.) set behind a slit on a rotating arm. Used in conjunction with a pulse amplifier and a pulse height analyser, this counter had a cosmic-ray background of only 4 counts/min. This rather elaborate counting equipment was essential since the scattered intensity was so small that a typical Geiger counter background of about 1 count/sec would have been of the same order as the 'signal'. Fluctuations of the beam intensity were allowed for by accumulating a fixed number of monitor counts, and counting the pulses arriving at the proportional counter during the corresponding period.

The high purity alloy used, containing 15 at. % aluminium, was rolled and carefully homogenized, reduced by further cold rolling to about 100 μ thickness, annealed and rolled down to 50 μ, and finally thinned uniformly to a thickness of about 15 μ by means of chemical polishing†.

§ 3. RESULTS

Figure 2 shows a scattering curve obtained from a cold-rolled alloy foil, using in front of the proportional counter a narrow slit that subtended 10′ of arc at the sample. The results in fig. 2 have been corrected for background count and for residual parasitic scattering, which was appreciable for scattering angles less than 1·8°. This curve is typical

Fig. 2

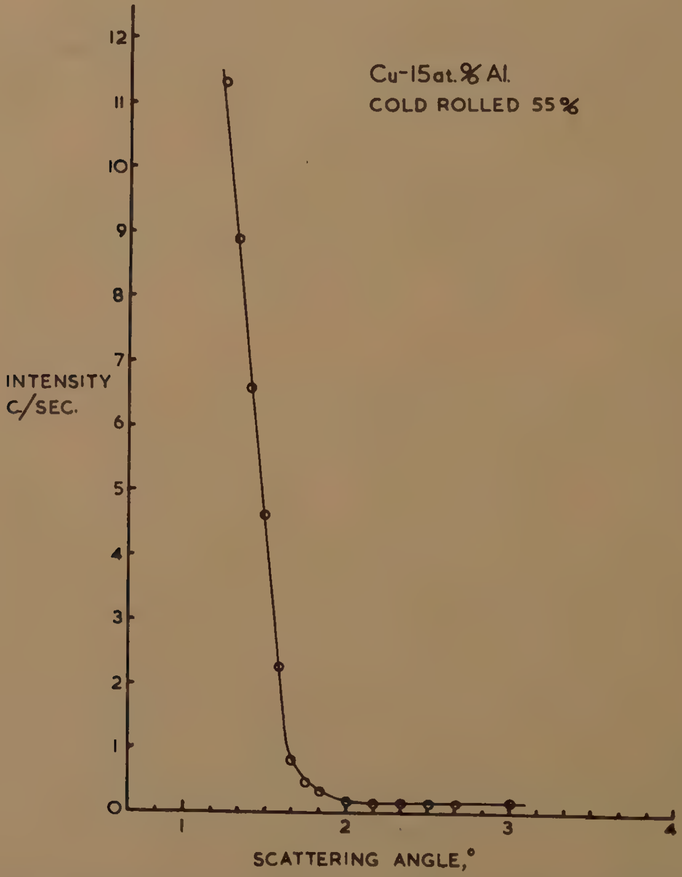

Small-angle scattering curve from an alloy foil rolled to 50% reduction. Correction for background count and parasitic scattering has been made.

---

† The polishing bath, used at 70°c, contained 50% glacial acetic acid, 30% conc. nitric acid, 10% conc. hydrochloric acid and 10% conc. orthophosphoric acid.

of those obtained for a rather weakly deformed metal (Neynaber *et al.* 1959, Webb and Beeman 1959).

The sample was then annealed progressively at 250°C and the scattered intensities at several angles between 1° and 1·7° were measured after each anneal. The intensities progressively increased, until after 13 hours' annealing all had increased by about 20%. This increase was statistically significant in spite of the fairly large probable error in counting.

Further experiments were now made using a larger slit at the counter, subtending 30′ of arc at the sample, and keeping to a fixed scattering angle of 2°, measured at the slit centre. In this way a higher statistical accuracy could be achieved. The intensities quoted hereafter are uncorrected for parasitic scattering (which was very weak at 2° scattering angle).

A foil was reduced 70% in thickness by rolling, cut in half and chemically thinned, and the intensity of x-ray scattering from each piece was measured. In each case this was about 470 counts during the period needed by the monitor to accumulate 30 000 counts. Most of this intensity was presumably due to double Bragg scattering. The pieces were then annealed in stages, one at 200°C and the other at 250°C, and the scattering from the same areas of the foils measured after each anneal. Figure 3 shows the results. The points denote the *increase* in the scattered intensity in terms of counts per 30 000 monitor counts ; the vertical line through each point represents the probable statistical error. The solid curves represent results for the isothermal hardening of a similar massive alloy sample†, plotted with a suitably normalized ordinate scale so that the hardness and intensity plots should concide as nearly as possible.

Figure 3 shows the following : (1) The intensity scattered from both samples increases significantly, the maximum increase from both samples being about 15%. (2) There is a very rapid initial rise in the scattering power ; an anneal of less than one minute at 200°C suffices to produce an 8% increase in intensity. (3) At 250°C, recrystallization begins after some hours for the degree of deformation used, and the scattered intensity then falls steeply. (4) The hardness increase at each stage is proportional to the increase of scattering power.

Attempts were made, using the point-focusing small-angle camera described by Atkinson (1958) (kindly loaned by Dr. P. B. Hirsch) to record the small-angle scattering photographically so as to study its distribution in azimuth, but these attempts failed because of the low intensity available.

§ 4. DISCUSSION

The results shown in fig. 3 might in principle be associated with any of the following changes in the specimen during anneal hardening :

(1) The re-establishment of short-range order.

(2) Growth of subgrains in the alloy and subsequent modification of the intensity of double Bragg reflection.

(3) Suzuki segregation of solute to the stacking faults.

---

† Results due to Mr. S. Chinowsky.

Alternative (1) is improbable since increase of order will diminish the weak Laue monotonic scattering (Warren and Averbach 1953) and should thus actually lead to a slight decrease of small angle scattering. As a check, a piece of the alloy foil was annealed at 600°c and quenched, which recrystallized and disordered it, and the scattered intensity at 2° was measured. The foil was then annealed 17 hours at 150°c, which suffices to produce substantial short-range order (Davies and Cahn 1961). The scattering intensity after this treatment had not changed, within the statistical counting error of ±3%. Alternative (1) is thus ruled out.

Fig. 3

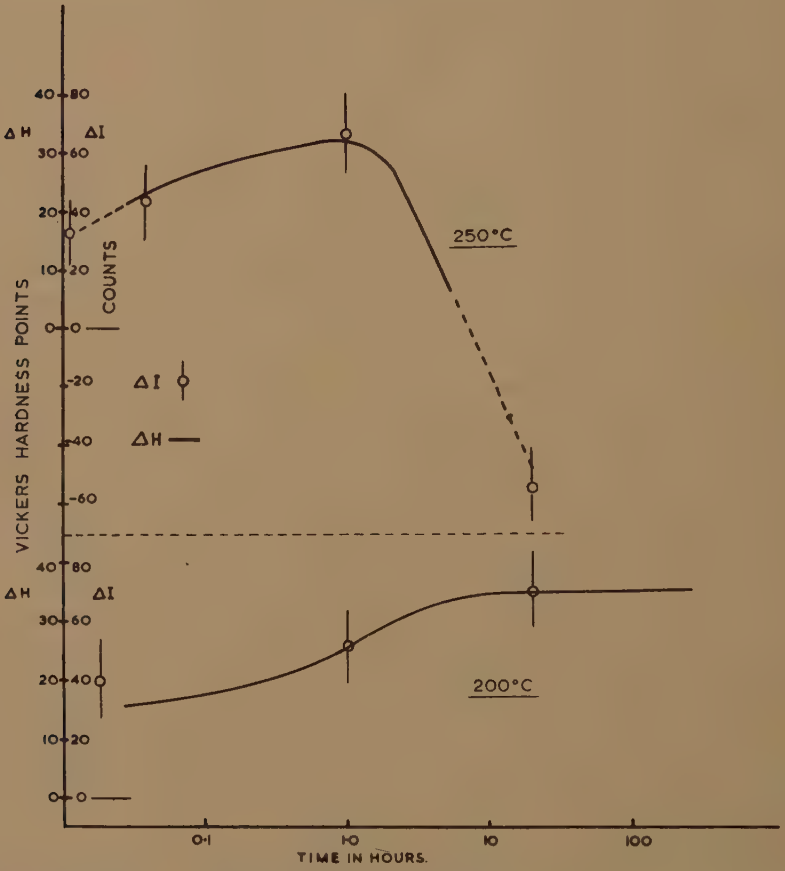

Isothermal kinetics, at 200 and 250°c, of the *change* in scattered x-ray intensity at 2°, and of the Vickers pyramid hardness.
X-ray results: Cu/15 at. % Al alloy, rolled 70%. Ordinate shows *increase* in counts per 30 000 monitor counts, above initial value of 470 counts.
Hardness results: Cu/14 at. % Al alloy, rolled 75%. Ordinate shows *increase* in Vickers hardness number.

Alternative (2) can also be excluded fairly definitively. The theory of double Bragg reflection (Webb and Beeman 1959) shows that the total scattered flux due to the double reflection mechanism is proportional to the inverse square of the mean subgrain diameter ; subgrain growth should thus lead to a rapid *reduction* of intensity scattered at small angles. This has indeed been confirmed by Reizman (1959), who studied the change, on annealing, of small-angle scattering from rolled copper foil. The resultant subgrain growth led to a *steady* decrease of the small-angle scattering ; there was no sign of a transient increase. We carried out an experiment to confirm this. Copper and alloy foils, rolled to approximately the same reduction, were each annealed 17 hours at 150°c, which is enough to harden the alloy considerably but not to cause any recrystallization in either the alloy or the copper. The x-ray scattering at 2° from the unannealed alloy was 927 ± 20 counts per 63 000 monitor counts, and it was 1076 ± 20 counts after heat treatment—an increase of 16%. The corresponding counts for the copper were 791 and 784 respectively ; the difference is not significant. A further anneal of 20 hours at 250°c caused substantial recrystallization of the copper and the count *fell* to 625. There is no reason why the double Bragg reflection process should be differently affected by heat treatment in the case of the alloy than in the case of copper.

There is therefore no cause, theoretical or experimental, to suppose that subgrain growth might in itself cause an increase of the small-angle scattering from the alloy.

§ 5. CONCLUSION

Having eliminated the alternatives, we are left with the conclusion that the increased small-angle scattering from the cold worked alloy, resulting from heat treatment at 150–250°c, is due to a segregation of solute to the stacking faults.

The present results are merely indicative; more detailed exploration is desirable of the isothermal kinetics of the change of the scattered intensity, of its dependence on the degree of deformation, on the state of polarization of the scattered x-rays, etc., but the low x-ray intensity available from our equipment precluded such a systematic study. In particular, experiments with rolled single crystals could show whether the distribution in azimuth of the scattered intensity was consistent with the presence of lamellar segregates parallel to the octahedral slip planes.

ACKNOWLEDGMENTS

We are indebted to Professor G. V. Raynor for his encouragement and providing laboratory facilities, to the D.S.I.R. for a grant to one of us (R.G.D.), and to Dr. P. B. Hirsch for a useful discussion and the loan of apparatus.

REFERENCES

ATKINSON, H. H., 1958, *Phil. Mag.*, **3,** 476.
CHINOWSKY, S., and CAHN, R. W., 1961, *J. Inst. Metals* (to be published).
CHRISTIAN, J. W., and SPREADBOROUGH, J., 1957, *Proc. phys. Soc. Lond.* B, **70,** 1151.
DAVIES, R. G., and CAHN, R. W., 1961, *Phil. Mag.* (to be published).
FRICKE, H., and GEROLD, V., 1958, *Naturwissenschaften*, **45,** 287; 1959, *J. appl. Phys.*, **30,** 661.
GUINIER, A., and FOURNET, G., 1955, *Small Angle Scattering of X-rays* (New York: Wiley).
GUSEVA, L. N., and BABAREKO, A. A., 1959, *Soviet Physics Doklady*, **4,** 129.
HASIGUTI, R. R., 1955, *J. Jap. Inst. Metals*, **19,** 103.
HOUSKA, C. R., and AVERBACH, B. L., 1959, *J. appl. Phys.*, **31,** 1525.
NAKAJIMA, K., 1959, *J. phys. Soc. Japan*, **4,** 1825.
NEYNABER, R. H., BRAMMER, W. G., and BEEMAN, W. W., 1959, *J. appl. Phys.*, **30,** 656.
REIZMAN, F., 1959, Ph.D. Thesis, University of Wisconsin (*Dissertation Abstracts* 1959, **20,** 1049).
SMALLMAN, R. E., and WESTMACOTT, K. H., 1957, *Phil. Mag.*, **2,** 669.
SUZUKI, H., 1952, *Sci. Rep. Res. Insts Tôhoku Univ.*, A, **4,** 455.
WALKER, C. B., and GUINIER, A., 1953, *Acta Met.*, **1,** 568.
WARREN, B. E., and AVERBACH, B. L., 1953, *Modern Research Techniques in Physical Metallurgy* (Cleveland: Amer. Soc. for Metals), 95.
WARREN, B. E., and WAREKOIS, E. R., 1955, *Acta Met.*, **3,** 473.
WEBB, M. B., and BEEMAN, W. W., 1959, *Acta Met.*, **7,** 203.

A Magnetic Study of Precipitation in a Gold–Cobalt Alloy†

By P. Gaunt
Department of Physics, University of Sheffield, Sheffield, 10

[Received May 26, 1960]

Abstract

The precipitation kinetics of a gold 1·5%, by weight, cobalt alloy have been followed by measuring the saturation magnetization of the precipitated cobalt and the results are compared with current theories. Marked differences were found between the ageing curves of air and water-quenched specimens. The remanent magnetization, coercive force and field to reduce remanence to zero of aged specimens have been measured and the results are discussed in terms of the single magnetic domain model. The magnetic properties are compared with those of the gold nickel system and the conclusion is reached that the dominant contribution to the anisotropy in the gold cobalt system is due to particle shape. In an appendix the remanence curve and coercivity for a random array of single domain ferromagnetic particles having a linear distribution of anisotropies have been calculated and shown to predict the main features of the observed results.

§ 1. Introduction

The magnetic properties of fine ferromagnetic precipitates in non-ferromagnetic matrices have been studied extensively in recent years and interpreted in terms of single domain theory. Much attention has been paid to the copper–cobalt system (Bate *et al.* 1955, Becker 1958, Mitui 1958), where the cobalt-rich precipitate is thought to form as the face-centred cubic allotrope (Rodbell 1958). Unfortunately the analogous system, copper–nickel, shows complete miscibility of the two constituents so that no comparison between the behaviour of the two face-centred cubic ferromagnetic metals in a copper matrix is possible. However, the gold–nickel and gold–cobalt systems both show limited solid solubility. The lattice parameters of the face-centred cubic forms of cobalt and nickel are very similar (3·545 kX and 3·517 kX), thus leading to similar disregistries between precipitate and gold matrix (lattice parameter 4·704 kX), of about 12%. The spontaneous magnetizations of cobalt and nickel do, however, differ considerably (164 and 58 e.m.u. per g), and any difference in magnetic properties between the two systems will be in large measure due to this. In particular, the theory of Stoner and Wohlfarth (1948) predicts that if the coercivity of an array of small single domain particles is due to shape anisotropy then it will be proportional to the spontaneous magnetization of the material. On the other hand, contributions due to crystalline and magnetostriction anisotropy will be inversely proportional to the spontaneous magnetization. A comparison of the two systems, with different spontaneous magnetizations but similar metallographic properties, should therefore indicate the dominant contribution to the observed anisotropy. The gold–nickel system has been investigated by Lothian *et al.* (1958), and results on the gold–cobalt system are presented in the present paper.

---

† Communicated by Professor W. Sucksmith.

According to the phase diagram of Raub and Walter (1950) it is possible to retain 1·5%, by weight, of cobalt in solid solution in gold at 960°C, and then to form a ferromagnetic precipitate, containing about 99% of cobalt, by ageing at a lower temperature. The allotropic transition from the face-centred cubic to the hexagonal close-packed form takes place at a temperature less than 500°C in cobalt–gold alloys containing 99% cobalt (Köster and Horn 1952). If, therefore, ageing is carried out at 500°C or above, the equilibrium precipitate will have a face-centred cubic structure.

§ 2. PREPARATION OF SPECIMENS

A gold–cobalt alloy containing 1·52%, by weight, of cobalt was made by melting the constituents together in an argon arc furnace on a water-cooled copper hearth. The alloy was then cast into a rod, about 0·4 cm in diameter and 5 cm long, by melting *in vacuo* in an evacuated silica tube using an induction furnace. This rod was homogenized, *in vacuo*, for 36 hours at 960°C before disc-shaped specimens about 0·1 cm thick were cut from the rod.

The specimens were annealed for 5 min at 960°C in evacuated silica capsules, and quenched to room temperature before ageing at 565°C. Some specimens were water-quenched, by withdrawing the silica capsules rapidly from the furnace and breaking them under cold water; others were quenched more slowly by allowing them to cool in air without breaking the tube.

§ 3. MEASUREMENTS OF SATURATION MAGNETIZATION

Magnetization at fields greater than 4000 oe was measured using a Sucksmith ring balance (Sucksmith 1929 and 1939).

The magnetization of a quenched unaged specimen was proportional to field at room temperature but showed a tendency towards saturation at liquid nitrogen temperature. Quenched specimens showed no remanent magnetization or coercive force.

After ageing for 3 min the magnetization curve did not extrapolate through the origin, there was a remanent magnetization, and a coercive force of 900 oe was required to reduce the magnetization to zero.

In order to determine the saturation moment of the ferromagnetic precipitate a correction was made for the paramagnetism of the matrix solid solution by subtracting the small magnetization of the quenched specimen from that of the aged ferromagnetic specimen at each measuring field. The saturation magnetization was then determined from a linear extrapolation against the reciprocal of the measuring field.

The increase in saturation magnetization with ageing time for water- and air-quenched alloys is shown in fig. 1. The maximum value of the saturation moment was 1·72 ± 0·02 e.m.u./g which compares with the 1·8 ± 0·1 e.m.u./g predicted for this alloy from the data of Raub and Walter (1950).

Fig. 1

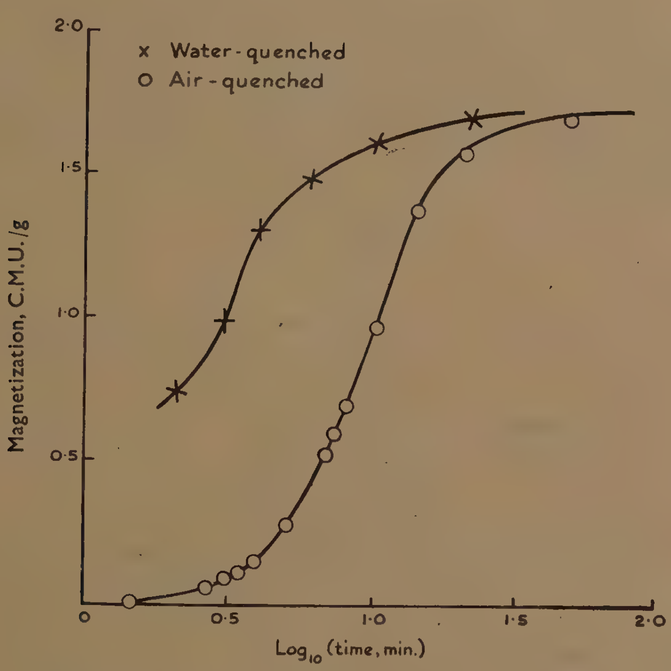

Variation of saturation magnetization with ageing time.

The initial rate of precipitation in water-quenched specimens was much greater than in air-quenched specimens. This is almost certainly due to there being a greater number of nucleation sites in the water-quenched alloys where the faster quench will retain the vacancies produced at the annealing temperature of 960°c.

§ 4. Remanent Magnetization

The remanent magnetization after the application of a field of 17 000 oe was measured using a torsion balance as described by Bate *et al.* (1955). The ratio of the remanent magnetization to the saturation magnetization was determined for 29 specimens including both air- and water-quenched specimens. There was no significant change in this ratio with ageing times from 1·5 to 50 min, the mean value of the ratio being 0·52, the standard deviation among the specimens being 0·05. The ratio of remanent to saturation magnetization is expected to be $\frac{1}{2}$ for a random array of single domain precipitate particles having predominantly uniaxial anisotropy (Wolhfarth 1955).

Complete remanence curves were plotted for a few specimens using the torsion balance. After ageing the specimen possesses zero magnetization, the individual particle moments lying along easy directions of magnetization. On applying and removing a small field, H, the magnetization of particles of low anisotropy is reversed and the specimen is left with a remanent magnetization $I_r(H)$. Further increase of H increases $I_r(H)$ until a saturation remanence, $I_r(\infty)$, is reached where all the particles have a component of magnetization parallel to the direction of the applied field. If a reverse field is now applied the remanent magnetization, $I_d(H)$, decreases to zero at H_r and to saturation remanence in the reverse direction at still higher fields.

Fig. 2

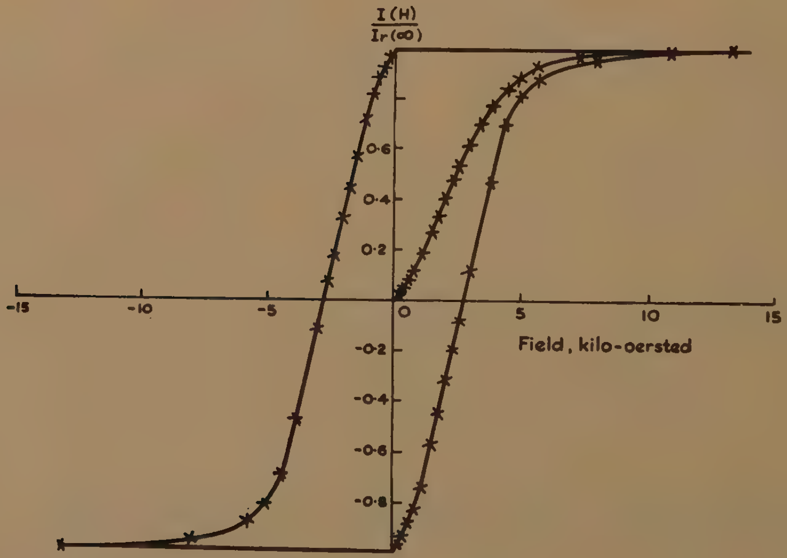

Remanence curve for a water-quenched specimen aged for 7 min.

A complete remanence curve for a water-quenched specimen, aged for 7 min, is shown in fig. 2. A field of more than 10 000 oe was required to produce saturation remanence indicating that the specimen must have contained particles with intrinsic coercivities as high as 10 000 oe.

('Intrinsic coercivity' of a particle is used to indicate the coercivity the particle would exhibit if the direction of lowest magnetic anisotropy

Fig. 3

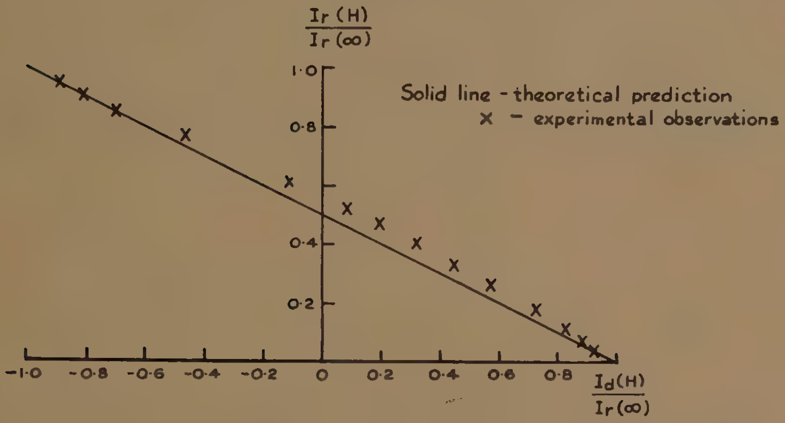

Relationship between initial remanence, $I_r(H)$, and demagnetizing remanence, $I_d(H)$.

Fig. 4

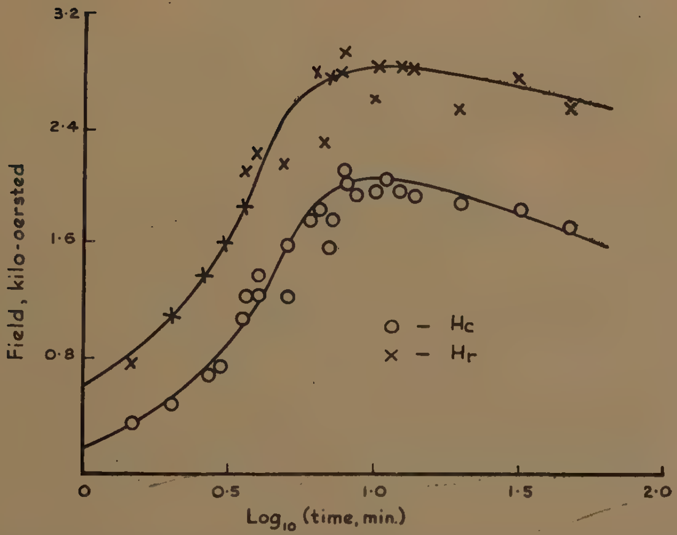

Variation of coercivity and remanence coercivity with ageing time for air-quenched specimens.

energy were parallel to the field.) It was of interest to compare these results with an expression of Wohlfarth (1958) which gives:

$$I_d(H) = I_r(\infty) - 2I_r(H).$$

This formula is easily proved for any array of non-interacting single domain particles of uniaxial anisotropy. In fig. 3, $I_d(H)$ is plotted against $I_r(H)$ showing a marked deviation from the ideal. The deviation may be due to the fact that the particles are not strictly uniaxial but possess mixed uniaxial and cubic anisotropies.

Fig. 5

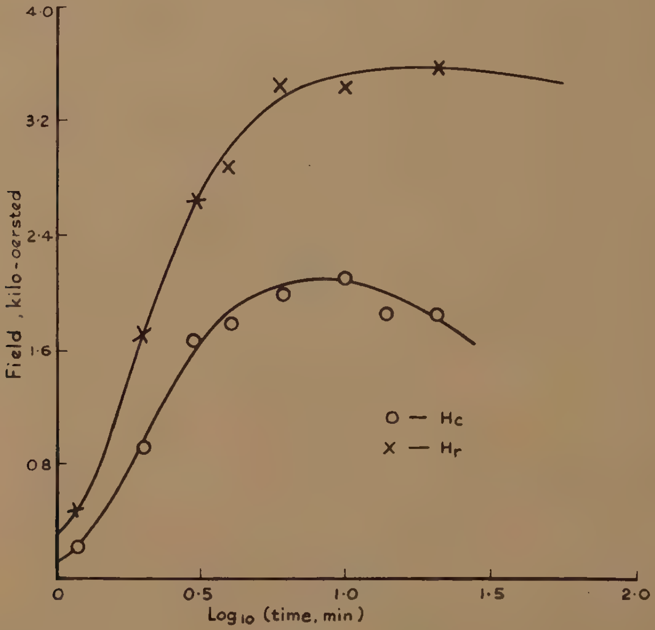

Variation of coercivity and remanence coercivity with ageing time for water-quenched specimens.

§ 5. COERCIVE FORCE AND FIELD TO REDUCE REMANENCE TO ZERO

Coercive forces greater than 900 oe were measured using the Sucksmith ring balance; forces less than 900 oe were determined with the torsion balance. The field to reduce remanence to zero, H_r, was also determined with the aid of the torsion balance. The variation of the two fields with ageing time in air-quenched specimens is shown in fig. 4. The maximum coercive force of 2050 ± 50 oe was attained after about 10 min ageing; the maximum H_r of 2800 oe being reached after about the same time. The ratio of the two fields was thus about 1·36 after 10 min ageing. For a random array of uniaxial single domain particles of uniform anisotropy this ratio should be 1·09 (Wohlfarth 1958); a ratio of 1·36 indicating a range of particle anisotropy of about the same order as observed by Lothian *et al.* (1958) in Au–Ni alloys. The change of the fields with time is consistent with the growth of single domain particles whose shape anisotropy increases as their size increases. The fall in the fields after the optimum ageing time is reached is then due to the onset of multi-domain behaviour when the particles reach a critical size. Water-quenched specimens behave similarly, as shown in fig. 5, reaching a maximum H_c of 2050 oe after about 10 min ageing but attaining a higher value of H_r at 3500 oe. The ratio H_r/H_c is thus about 1·7, indicating a greater range of particle anisotropy than is found in air-quenched specimens.

The coercivity of the aged specimens was increased by *c.* 600 oe on cooling to liquid nitrogen temperature. A graph of H_c against temperature for a water-quenched specimen aged for 10 min is shown in fig. 6.

Fig. 6

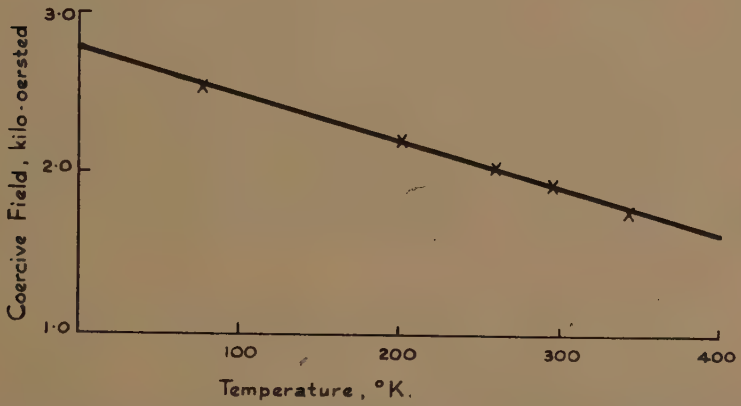

Variation of coercivity with temperature for a water-quenched specimen aged for 10 min.

§ 6. EFFECT OF STRAIN

A preliminary experiment indicated that the aged alloys behaved in a similar way to Au–Ni alloys (Lothian *et al.* 1958); that is, the coercivity is greatest perpendicular to the axis in a drawing experiment and parallel to the axis in a compression experiment. Thus the coercivity of an air-quenched Au–Co specimen increased from 1880 oe to 2200 oe parallel to the axis and decreased to 1510 oe perpendicular to the axis after a compressive strain of 6%. This contrasts with the observations of Livingston and Becker (1958) in a Cu–Co alloy where they observed enhanced coercivity parallel to a tension axis, and the increase in anisotropy energy produced by the strain was consistent, up to 20% strain, with homogeneous deformation of matrix and precipitate. The contrast in behaviour may be due to the high disregistry of 12% between precipitate and matrix in the Au–Ni and Au–Co systems compared with the 1·7% disregistry in the Cu–Co system: if the disregistry is small the particles will remain coherent with the matrix and dislocations will pass easily through the particles thus making shape deformation of the particles possible. If disregistry is large the particles quickly lose their coherence and the passage of dislocations is impeded by the particles.

§ 7. X-RAY MEASUREMENTS

Debye–Scherrer photographs of quenched and aged needle specimens were taken using copper radiation. No extra lines due to the precipitate phase were detected. The quenched specimens gave sharp reflections at all Bragg angles, and the lattice parameter of the solid solution was 4·0535 kX. Ageing an air-quenched specimen for 2·75 min caused the high-angle reflections to blur toward the low Bragg angle side of the photograph; this blurring becoming more pronounced with further ageing. After 18 min, precipitation was almost complete, and after 2500 min ageing the high angle lines were again sharp, the matrix having a lattice parameter of 4·0658 kX. The water-quenched specimens behaved similarly. The films show that as precipitate particles begin to form the matrix far from the particles is left unchanged in composition and a cobalt-depleted region surrounds the particle. This suggests that almost as soon as precipitation begins the full lattice disregistry of 12% must be accommodated at the matrix particle interface. As ageing proceeds the concentration gradient in the matrix becomes smaller until the cobalt concentration reaches its equilibrium value and the high angle diffraction lines become sharp.

§ 8. DISCUSSION

8.1. *Saturation Magnetization*

The saturation magnetization of the specimen is a direct measure of the amount of precipitate and it was of interest to compare the kinetics of the precipitation process with a formula of Zener (1949) which gives the fraction precipitated as:

$$\alpha = 1 - \exp\left[-\left(\frac{t}{\tau}\right)^m\right]$$

where τ and m are constants and t is the ageing time. Thus if $\log\log(\sigma_\infty/\sigma_\infty - \sigma_t)$ is plotted against $\log t$, where σ_∞ is the saturation magnetization after complete ageing and σ_t is the saturation magnetization after time t, it should give a straight line of slope m. In fig. 7 this function is plotted for both air- and water-quenched specimens. The graphs show that the increase of saturation magnetization with time (in minutes), can be well represented up to 60% precipitation, in air-quenched specimens by:

$$\sigma_t = 1{\cdot}72[1 - \exp - (t/7{\cdot}50)^{2{\cdot}46}]$$

and in water-quenched specimens by

$$\sigma_t = 1{\cdot}72[1 - \exp - (t/1{\cdot}66)^{1{\cdot}23}].$$

Ham (1958) has treated the problem of precipitation from a supersaturated solid solution in a rigorous way and has shown that a formula of the type derived by Zener should be a good approximation for the first 50% of the precipitation process. He has further shown that the exponent m will be 1·5 for any shape of particle in a diffusion-limited process, where surface and strain-energy effects are negligible, and in which the inter-particle separation is about ten times the particle diameter. The eccentricity of the particles in such a process will remain constant after a short initial transient. For situations where a surface reaction is dominant m tends to 3, while for diffusion-limited growth where the initial particle volume is greater than one-tenth the final volume, m will be between 1·0 and 1·5.

Fig. 7

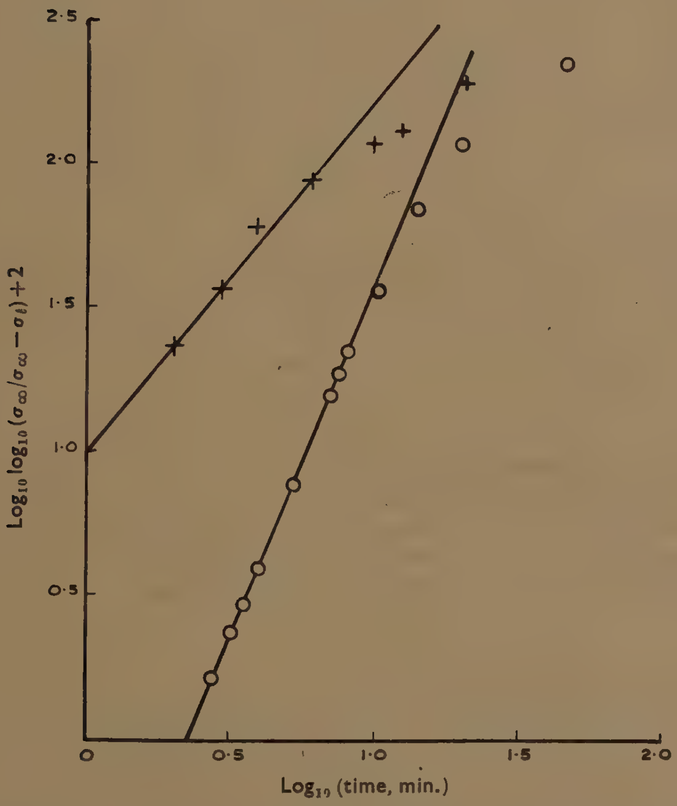

Logarithmic plot of saturation magnetization against ageing time.

For the air-quenched specimens $m > 1·5$, indicating that precipitation cannot be purely diffusion-limited and surface and strain-energy effects are probably important. In the water-quenched specimens $m < 1·5$ so that the nature of the nuclei formed by rapid quenching must be such that the coherency strains are more easily accommodated and large particles are formed in the initial transient process.

8.2. *Coercivity and Field to reduce Remanence to Zero*

The two fields H_c and H_r reached their maximum values after about 10 min ageing in both air- and water-quenched specimens. The optimum value of H_r was, however, significantly higher in water-quenched specimens although H_c was approximately the same for air- and water-quenched specimens. The larger value of H_r/H_c in water-quenched specimens indicates that they contain a wider range of particle anisotropies than the air-quenched specimens. This must be associated with the fact that as the optimum ageing time is reached in water-quenched specimens the supersaturation is small, precipitation being about 93% complete, but in air-quenched specimens it is larger since precipitation is only 55% complete. According to Nabarro (1940) a low supersaturation favours increasing eccentricity of the growing particle. Thus the shape anisotropy and hence the intrinsic coercivity of particles growing from a solution of low supersaturation will reach higher limiting values before the size of the particles allows domain walls to form. The range of anisotropies will therefore be wider in water-quenched specimens since particles of high anisotropy are favoured.

A graph of H_c against temperature, for a water-quenched alloy aged for 10 min is shown in fig. 6. The variation of H_c is linear over the range 77°K–380°K. Stacey (1959 a) has derived a formula relating the magnetic energy of a single domain particle to its volume v, and the coercivity of a random array H_c:

$$E = vH_cI_0 + kT\ln C\tau$$

where I_0 is the spontaneous magnetization per cm^3 of the particle, k is Boltzmann's constant, T is the absolute temperature, τ is the time taken to measure H_c, and C is a frequency factor whose maximum value at room temperature is given as $6 \times 10^{12}\,\mathrm{sec}^{-1}$ by Stacey (1959 b). Thus assuming I_0 is independent of T over the range considered:

$$\frac{dE}{dT} = vI_0\frac{dH_c}{dT} + k\ln C\tau + k/T\,.$$

(The factor k/T arises because $C \propto T$, Stacey 1949 b.) If now the magnetic energy is due to shape anisotropy alone then dE/dT is zero and the variation in coercivity arises only from temperature dependent fluctuations of the particle magnetization. Hence

$$v = -\frac{k(\ln C\tau + 1/T)}{I_0\,dH_c/dT}\,.$$

From the graph $dH_c/dT = -2{\cdot}87$ oe/c deg and taking τ as 1 sec (this is not critical), gives $v = 1{\cdot}010 \times 10^{-18}\,\mathrm{cm}^3$ and hence a particle radius of order 62 Å. This calculation gives an average size for the particles contributing to the observed coercivity. If the direction of low shape anisotropy is associated with a direction of low crystalline anisotropy energy, the contribution to dH_c/dT due to cubic crystalline anisotropy will be $-0{\cdot}66$ (Bean *et al.* 1959).

Thus

$$\frac{dE}{dT} = -0{\cdot}66 v I_0;$$

therefore

$$v = -\frac{k(\ln C\tau + 1/T)}{I_0(dH_c/dT + 0{\cdot}66)},$$

leading to a slightly larger value for v as $1{\cdot}311 \times 10^{-18}\,\mathrm{cm}^3$ and radius 68 Å.

The air-quenched specimens show approximately the same slope so that the particle radii are not appreciably different in air- and water-quenched specimens aged for 10 min. The value obtained above for the particle radius agrees with that found by Becker (1957) for the onset of ferromagnetic properties in copper–cobalt alloys.

8.3. *Remanent Magnetization*

The remanent magnetization of annealed specimens after the application of a field of 17 000 oe was half the saturation magnetization. This suggests that the precipitate particles have predominantly uniaxial magnetic anisotropy (Wohlfarth 1955). In fig. 2 the remanent magnetization was plotted against the applied field for a water-quenched specimen whose mean coercivity was 1570 oe and field to reduce remanence to zero was 2700 oe. The saturation remanence was not reached until a field greater than 10 000 oe was applied, showing that particles having intrinsic coercivities of this order were present. In the appendix a remanence curve for a simple linear distribution of anisotropies is calculated and compared with the experimental curve and using the linear distribution giving the best fit with the experimental remanence curve a value of H_c was calculated as 1440 oe.

The saturation remanence for an air-quenched specimen, for which H_r was 2500 oe and H_c 1850 oe, was reached at about 7000 oe, thus showing that a narrower range of anisotropies was present in these specimens.

The intrinsic coercive force of a prolate spheroid is given by $(N_b - N_a)I_0$ where N_b is the demagnetizing factor along the short axis and N_a along the long axis (Stoner and Wohlfarth 1948). The maximum value, for an infinitely long spheroid is thus given by $2\pi I_0$. For cobalt this value is 8962 oe but a spheroid of axial ratio 10 reaches 98% of this maximum value. A maximum contribution to the particle coercivity of $2K/I_0$ is possible due to crystalline anisotropy. If the precipitate is face-centred cubic this adds a maximum contribution of *c.* 1400 oe making a total of *c.* 10 400 oe. The observed maximum intrinsic coercivity can therefore be explained in terms of a cubic precipitate showing no magnetostriction effects. A magnetostriction contribution to the coercivity is possible if the precipitate experiences a uniaxial stress. This will only occur if the precipitate remains partially coherent with the matrix. In the gold–cobalt system the disregistry is about 12% so that the precipitate will begin to break away from the matrix when the particle diameter reaches 100/12 atom spacings since a dislocation can then be introduced to relieve the strain between the two lattices. Thus the precipitate will begin to break away from the matrix when its radius becomes greater than 30 Å, which is about half the lower limit of particle size to show ferromagnetic, rather than super-paramagnetic, behaviour (Becker 1957). The precipitate will therefore have started to break away after the optimum annealing time and there is not likely to be a large magnetostriction contribution to the magnetic anisotropy.

As shown in fig. 6, the remanence curve shows a marked deviation from the relation proposed by Wohlfarth (1958), relating the remanence $I_r(H)$ gained by the initial application of a field to an aged specimen and the remanence $I_d(H)$ remaining after the application of a demagnetizing field to a previously saturated specimen.

The relation will only be strictly obeyed for an array of perfectly uniaxial particles rather than the particles of mixed cubic and uniaxial anisotropy which are formed in practice. It is possible for particles in their initial state to have magnetization vectors not lying in the uniaxial direction but in one of the cubic easy directions.

The application and removal of a suitable field will turn these vectors into the easier uniaxial directions. On applying a demagnetizing field the cubic easy directions may no longer be available as remanence positions since there is no suitable field which will bring the magnetization vector close enough to the cubic axis for it to rest there on removal of the field ; the critical angle for reversal of the vector in the uniaxial direction being greater than the critical angle for return to the cubic direction. This means that the demagnetizing mode of the remanence curve will be harder than the initial magnetizing mode so that the remanence coercivity predicted from the initial magnetizing curve will be less than that found by demagnetization.

8.4. *Comparison with Au–Ni*

The maximum coercivity found by Lothian *et al.* (1958) in aged Au–Ni alloys was 325 oe. It was, however, observed that the coercivity increased if the alloy cross section was reduced by cold drawing. Thus Robinson (1957) found that after as little as 13% reduction the coercivity both parallel and perpendicular to the drawing axis increased to about 600 oe. The coercivity perpendicular to the axis was, however, greater than that parallel to the axis and further reduction increases this difference, the coercivity parallel to the axis decreasing. The initial rapid increase in coercivity can be explained if it is supposed that the elongated particles are in tension, thus giving a negative contribution to the coercivity. A small amount of cold work is then sufficient to relieve this tension as dislocations cross the particles. Orientation effects will, however, tend to make the coercivity parallel to the drawing axis less than that perpendicular to the axis.

The maximum coercivity observed in the Au–Co system was 2050 oe and in the compression experiment the coercivity parallel to the compression axis increased but perpendicular to the axis it decreased. An initial overall increase in coercivity, both parallel and perpendicular to the axis, was not therefore observed but the orientation effect was strong. Thus it appears that the magnetostriction contribution is much less than the shape anisotropy contribution in Au–Co. It is to be expected that the magnetostriction contribution will be smaller for cobalt than for nickel alloys since it is inversely proportional to the spontaneous magnetization.

The fact that the maximum observed coercivity in the cobalt alloys is bigger than in the nickel alloys suggests that the shape anisotropy term is dominant since this is proportional to the spontaneous magnetization. If it is further supposed that the particle shape is determined mainly by metallographic factors the constant of proportionality will be roughly the same for both systems because of the similarity of cobalt and nickel in structure and atomic size. With these assumptions it is possible to compare the two systems and estimate the magnetostriction contribution, to the anisotropy using the relation :

$$H_c = AI_s + \frac{B}{I_s} + \frac{C}{I_s}$$

where I_s is the spontaneous magnetization and A, B, and C are constants determining the shape, magnetostriction and magnetocrystalline contributions. Thus assuming A and B to be the same for both the nickel and cobalt systems and allowing 700 oe and 100 oe for the magnetocrystalline contributions in cobalt and nickel, gives :

$$1350 = 1400A + \frac{B}{1400} \text{ for cobalt,}$$

$$225 = 500A + \frac{B}{500} \text{ for nickel.}$$

This gives $A = 1{\cdot}04$ and $B = -1{\cdot}47 \times 10^5$.

The negative value of B is expected for nickel and cobalt in tension since the magnetostriction coefficient is negative for nickel in all directions and for cobalt in $\langle 111 \rangle$ directions. Using the formula of Stoner and Wohlfarth (1948) for the magnetostriction contribution from a random array of particles :

$$H_c = 0{\cdot}479 \frac{3\lambda b}{I_s}$$

where λ is the magnetostriction coefficient and b is the uniaxial tension, gives a value of about $3{\cdot}0 \times 10^{10}$ dynes/cm² for b.

This is small compared with the upper limit for b suggested by Stoner and Wohlfarth of about $2 \times 10''$ dynes/cm².

The value of A gives a mean value for the axial ratio of the elongated particles of approximately 1·6.

A suggested breakdown of the anisotropy contributions for the two systems is shown in the table :

	H_c	Shape	Crystalline	Magnetostriction
Co	2050	1455	700	-105
Ni	325	520	100	-295

Thus relaxation of tension, by slight cold working, in the Au–Ni alloys increases the coercivity to 620 oe which agrees with experiment. In the Au–Co alloy the increase in coercivity, due to relaxation of tension by cold work, is swamped by the changes due to the orientation of the much larger shape and crystalline anisotropy contributions.

ACKNOWLEDGMENTS

The author wishes to thank Professor W. Sucksmith for his help and encouragement in this work.

APPENDIX

REMANENT MAGNETIZATION AND COERCIVITY FOR A LINEAR DISTRIBUTION OF PARTICLE ANISOTROPY

Current theories based on the single magnetic domain hypothesis generally deal with arrays of particles of uniform anisotropy. In practice, and especially in heterogeneous alloys, a wide range of anisotropies is present and theories based on a single anisotropy must prove inadequate. The simplest distribution of anisotropies which can be considered, and whose parameters can be easily varied, is a linear distribution with an upper and lower cut-off value. Such an approximation is sufficiently good to indicate the main features of an array containing a range of anisotropies and in particular to show how the ratio H_r/H_c depends on this range.

For a linear distribution of particle anisotropy the volume of precipitate, dv, whose intrinsic coercive force lies between H_0 and (H_0+dH_0) is given by :

$$dv = A dH_0 \text{ for values of } H_0 \text{ between } H_1 \text{ and } H_2$$

where A is a constant and H_1 and H_2 are the lower and upper cut-off values of H_0. Such a distribution, with suitably chosen values of H_1 and H_2, gives quite a good approximation to the results obtained in the present work and shows how the ratio H_r/H_c varies with the range of anisotropies present.

Remanent Magnetization

The remanence $dI_r(H)$ for a random array of particles of intrinsic coercivity H_0 can be tabulated from the data of Stoner and Wohlfarth (1948) using the method of Wohlfarth (1955). This gives the remanence on first applying a field H to a completely random array and the field H_r is that which produces a remanence of half the maximum value.

Thus :

$$dI_r(H) = Af(H/H_0)dH_0 \; ;$$

therefore

$$\frac{dI_r(H)}{H} = Af(h)d\left(\frac{1}{h}\right)$$

where $h = H/H_0$; therefore

$$\frac{I_r(H)}{H} = A\int_{1/h=H_1/H}^{1/h=H_2/H} f(h)d(1/h). \qquad (1)$$

Fig. 8

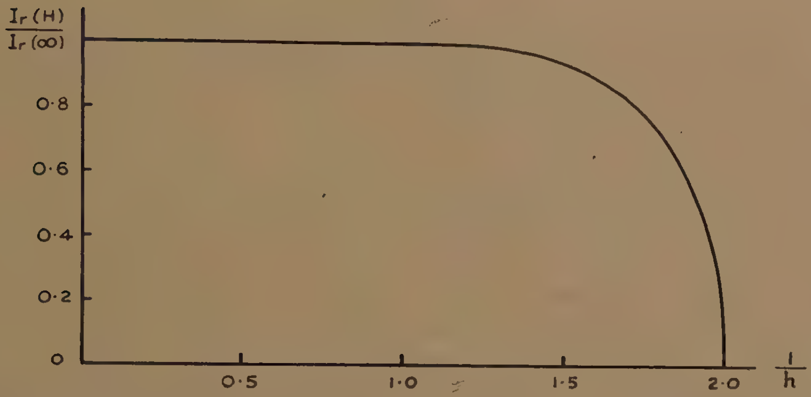

Variation of reduced initial remanence with reciprocal of reduced field for a random array of uniform anisotropy.

In fig. 8, $f(h)$ is plotted against $1/h$ and can be used to evaluate the integral of eqn. (1) for any particular value of H. When $H = H_2$ all the particles have turned toward the field direction and eqn. (1) becomes:

$$\frac{I_r(\infty)}{H_2} = A\int_{1/h=H_1/H}^{1/h=1} f(h)d(1/h) = A\,[1 - H_1/H_2].$$

Equation (1) can therefore be re-written as :

$$\frac{I_r(H)}{I_r(\infty)} = \frac{H}{H_2 - H_1}\int_{1/h=H_1/H}^{1/h=H_2/H} f(h)\,d(1/h) \qquad (2)$$

The field H_r is that for which $I_r(H)/I_r(\infty) = 0{\cdot}5$; therefore

$$0{\cdot}5 = \frac{H_r}{H_2 - H_1}\{1{\cdot}855 - (H_1/H_r)\} \text{ for } H_1/H_r \leqslant 1, (H_2/H_r) \geqslant 2.$$

Hence $H_r = 0{\cdot}269\ (H_2 + H_1)$ for $H_1/H_r \leqslant 1$, $H_2/H_r \geqslant 2$.

The values of H_r obtained experimentally from the initial and demagnetizing branches of the remanence curve were not the same ; the value from the demagnetizing branch being the greater. In fig. 9, therefore, the experimental value of $I_d(H)/I_r(\infty)$ from fig. 2 is compared with that for a linear array of anisotropies with $H_1=500$ and $H_2=9530$ using the relation of Wohlfarth (1958) :

Fig. 9

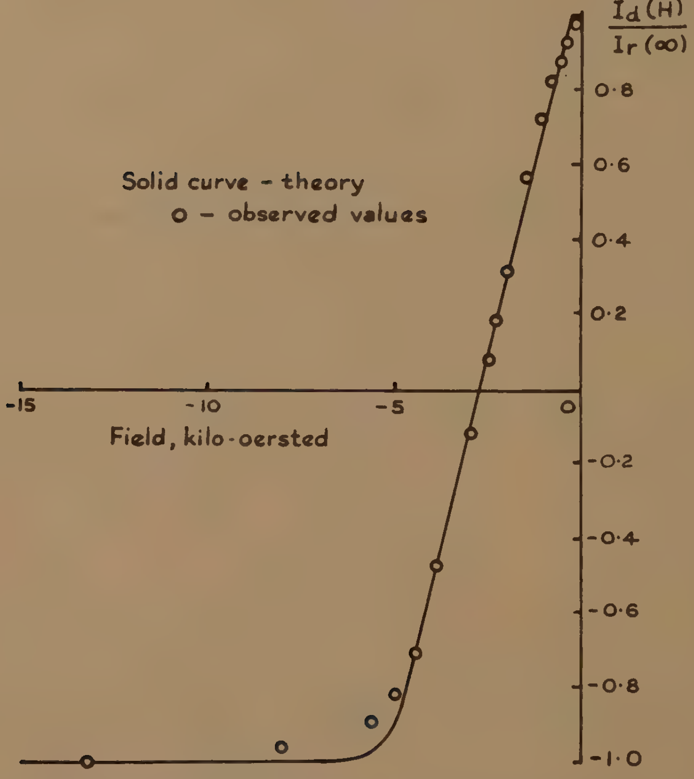

Comparison of demagnetizing remanence curve, for a linear anisotropy array, with observed values for a water-quenched specimen aged for 7 min.

$$I_d(H)=I_r(\infty)-2I_r(H)$$

to calculate $I_d(H)$. The theoretical curve has been chosen to fit at H_r and as closely as possible elsewhere. The uniform anisotropy distribution fits least well at the higher fields indicating that the true distribution contains fewer particles of anisotropy less than H_2 than is implied by the linear distribution.

Coercivity for a Linear Array

Stoner and Wohlfarth (1948) have tabulated the reduced magnetization curve for a random array of particles of intrinsic coercivity H_0. Thus by a similar argument to the above, for a linear anistropy distribution :

$$\frac{I(H)}{I(\infty)}=\frac{H}{H_2-H_1}\int_{1/h=H_1/H}^{1/h=H_2/H} g(h)\,d(1/h) \quad . \quad . \quad . \quad . \quad . \quad . \qquad (3)$$

where $I(H)$ is the intensity of magnetization for the demagnetizing branch of the curve. The reduced magnetization, $g(h)$, for a random array of particles of uniform anisotropy is plotted against $1/h$. the reciprocal of the reduced field, in fig. 10. The coercive field is a function of H_1 and H_2 and is that field for which the integrand of eqn. (3) is zero. It can be represented to an accuracy of better than 1% by :

Fig. 10

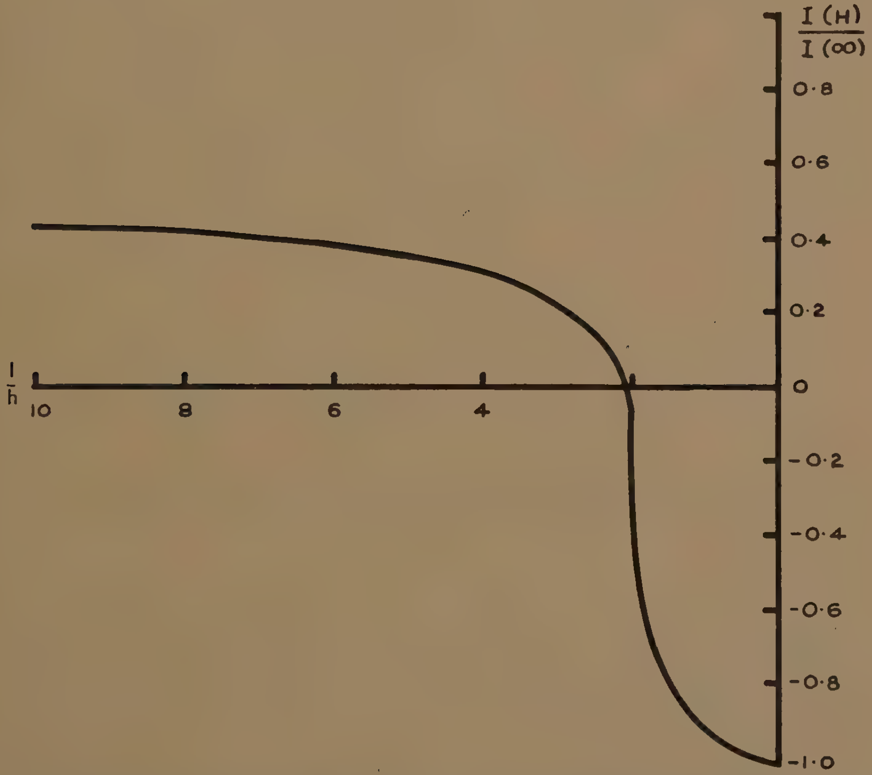

Variation of reduced magnetization, along demagnetizing branch, with reciprocal of reduced field for a random array of uniform anisotropy.

$$H_c=0{\cdot}133H_2\{1+2{\cdot}5(H_1/H_2)\}\ ;$$

further

$$H_r=0{\cdot}269\,H_2(1+H_1/H_2) \text{ for } H_1/H_2<1,\ H_2/H_r>2\ ;$$

therefore

$$H_r/H_c=2{\cdot}02\frac{1+H_1/H_2}{1+2{\cdot}5H_1/H_2}.$$

This formula is valid for values of H_r/H_c up to 0·37 when H_1/H_r becomes equal to one. For values of H_1/H_r greater than one H_r has to be calculated using fig. 8 to determine the appropriate integrand. In fig. 11 the ratio H_r/H_c is plotted against all possible values of H_1/H_2.

Fig. 11

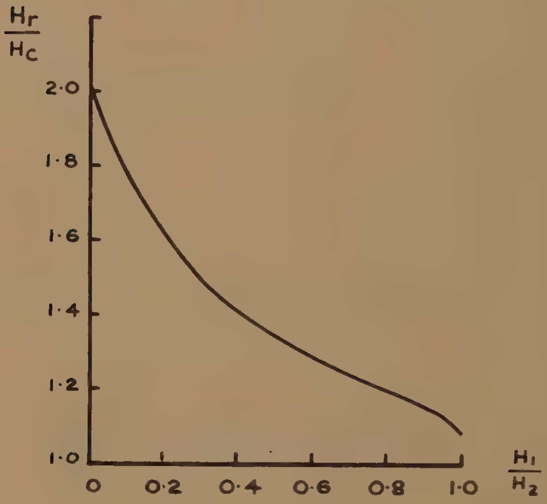

Variation of H_r/H_c with ratio of minimum to maximum anisotropy field in a linear anisotropy distribution.

For the water-quenched specimen considered above the observed values of H_r and H_c were 2700 and 1570 oe, so that H_r/H_c was 1·72. For the best fitted remanence curve the suggested value for H_1/H_2 of 0·0524 gives a value for H_r/H_c of 1·88 and for H_c of 1440 oe. Better agreement could doubtless be obtained by adopting a more realistic anisotropy distribution but the present approximation is sufficiently good to show the main features to be expected from an array of ferromagnetic particles having a range of anisotropies.

The calculations suggest that 2·02 will be the maximum possible value of H_r/H_c for such an array. Values of H_r/H_c greater than this could be produced in alloys containing a large proportion of super-paramagnetic material of zero coercivity. Thus almost all the values of H_r/H_c observed by Lothian *et al.* (1958), in Cu–Co alloys, were greater than 10 indicating a large super-paramagnetic contribution. However, in Au–Ni alloys and in the present work H_r/H_c was always less than 2, indicating that almost all the precipitate was in ferromagnetic form.

References

Bate, G., Schofield, D., and Sucksmith, W., 1955, *Phil. Mag.*, **46**, 621.

Bean, C. P., Livingston, J. D., and Rodbell, O. S., 1959, *J. Phys. Radium*, **20**, 298.

Becker, J. J., 1957, *Trans. Amer. Inst. min. (metall.) Engrs*, **209**, 59; 1958, *Ibid.*, **212**, 138.

Ham, F. S., 1958, *J. Phys. Chem. Solids*, **6**, 335.

Koster, W., and Horn, E., 1952, *Z. Met.*, **43**, 333.

Livingston, J. D., and Becker, J. J., 1958, *Trans. Amer. Inst. min. (metall.) Engrs*, **212**, 316.

Lothian, B. W., Robinson, A. C., and Sucksmith, W., 1958, *Phil. Mag.*, **3**, 999.

Mitui, T., 1958, *J. phys. Soc. Japan*, **13**, 549.

Raub, E., and Walter, P., 1950, *Z. Met.*, **41**, 234.

Robinson, A. C., 1958, Thesis, University of Sheffield.

Rodbell, D. S., 1958, *J. appl. Phys.*, **29**, 311.

Stacey, F. D., 1959 a, *Proc. phys. Soc. Lond.*, **73**, 517; 1959 b, *Ibid.*, **73**, 136.

Stoner, E. C., and Wohlfarth, E. P., 1948, *Phil. Trans.* A, **240**, 599.

Sucksmith, W., 1929, *Phil. Mag.*, **8**, 158; 1939, *Proc. roy Soc.* A, **170**, 551.

Wohlfarth, E. P., 1955, *Research*, **8**, S42; 1958, *J. appl. Phys.*, **29**, 595.

Zener, C., 1949, *J. appl. Phys.*, **20**, 950.

Movement of Point Defects During Fatigue of Aluminium Crystals†

By E. Roberts and R. W. K. Honeycombe
Department of Metallurgy, University of Sheffield

[Received May 27, 1960]

Abstract

The dynamic stress–strain behaviour of aluminium crystals fatigued in a push–pull machine at 13 cycles/second is outlined. Room temperature interruptions to tests carried out at −196°c, −78°c and 20°c resulted in a transitory hardening which is attributed to the movement of point defects to dislocations.

A study has been made of the behaviour of 99·99% aluminium single crystals fatigued in a push–pull machine at 13 cycles/second. The stress pulse was fed to the X-plates of an oscilloscope, while the strain was measured by a capacitance strain gauge connected to the Y-plates so that a dynamic hysteresis loop was obtained continuously during a fatigue test (fig. 1, Pl. 146). In this way the dynamic hardening of the crystals could be studied over a wide range of fatigue conditions.

In tests carried out at room temperature, the width of the hysteresis loop (dynamic plastic strain) obtained at a given alternating stress gradually decreased (fig. 1 (*a*), (*b*) and (*c*)) in the way observed for much lower frequencies by Thompson *et al.* (1955). The maximum hardening occurred within the first 5% of the fatigue life, and a steady state was reached after about 15–20% (fig. 1 (*c*)). However, in tests carried out at −78°c and −196°c, no cyclic hardening whatsoever was detected, the loop width remaining at a steady value for large numbers of cycles (> 200 000 cycles).

In these low temperature tests, it was found that intermediate resting at room temperature resulted in a hardening of the crystals when fatigue was resumed at −196°c or −78°c. Figure 2 (*a*) (Pl. 146) shows the hysteresis loop of a crystal 22B after 6500 cycles (± 1015 g/m^2 resolved shear stress) at −78°c; the crystal was then rested at room temperature for 60 min and the loop width on immediate re-testing is shown in fig. 2 (*b*). After a further 100 cycles (fig. 2 (*c*)) the loop width had reached a size comparable to that prior to the interruption. The hardening tended to be most pronounced in the initial stages of a test when the deformation was carried out at −196°c or −78°c (fig. 3), but a large effect was still obtained on resting a week after 4×10^4 cycles.

---

† Communicated by the Author.

In tests undertaken at room temperature, not only was the observed hardening greater (fig. 4 (*a*)) but the effect persisted longer as can be seen by comparing the behaviour of an identical crystal at −196°c (fig. 4 (*b*)).

Fig. 3

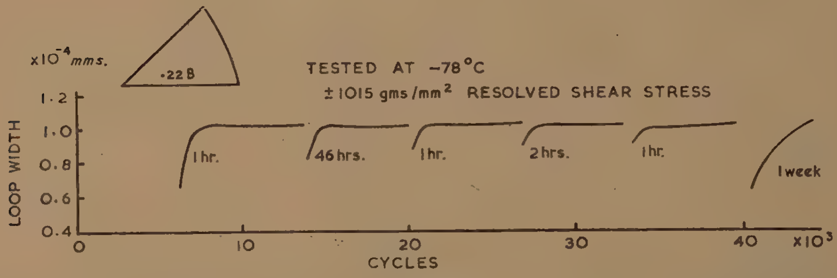

The effect of interruptions at room temperature on the loop width measured at −78°c.

Fig. 4

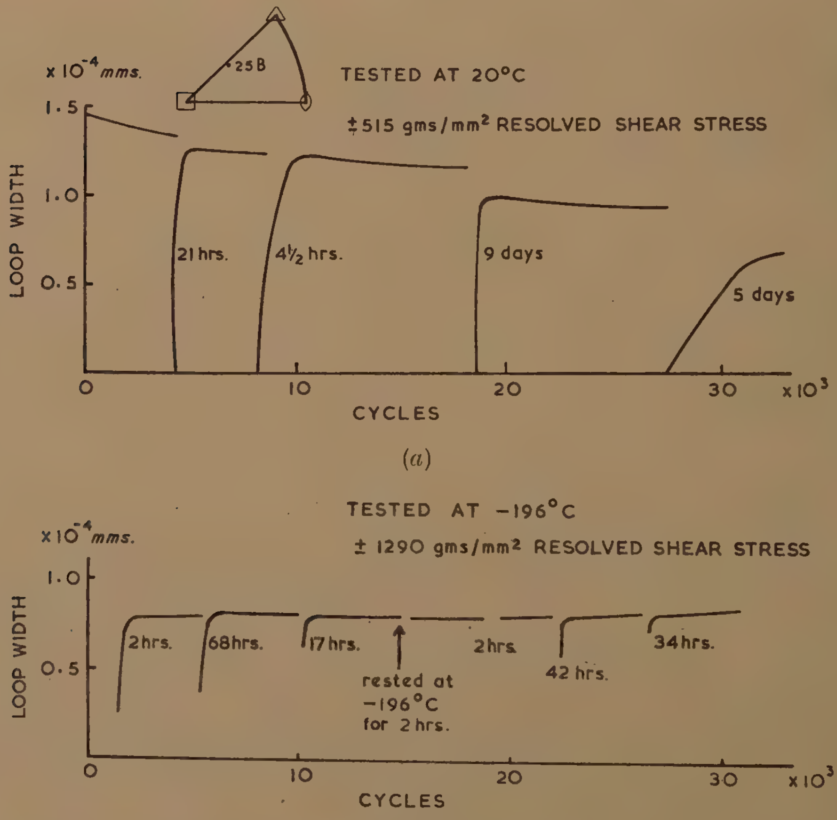

(*a*)

(*b*)

(*a*) The effect of room temperature interruptions on loop width measured at room temperature, (*b*) the effect of room temperature interruptions on the loop width measured at −196°c. (*a*) and (*b*) relate to tests carried out on identically oriented crystals.

The purity of the metal used is sufficiently high to exclude the possibility of impurity atom locking as a cause of the observed hardening, and to indicate instead point defects. Broom and Ham (1957, 1959) have suggested that point defects contribute to fatigue hardening by locking dislocations and moreover have shown yield phenomena when pure copper crystals previously fatigued at −196°c were deformed in tension in the range −196°c to 20°c. This view is supported by the electrical resistivity measurements of Rosenberg (1958) on copper fatigued at −253°c; the observed increase in resistivity is large with respect to that obtained as a result of uni-directional deformation and anneals out from −100°c upwards. The present experiments also indicate that point defects are formed during fatigue and migrate during resting at room temperature. It is thought that vacancy movement to dislocations will also explain the fatigue hardening observed in the present tests at room temperature.

The hardening obtained on resting is of a transitory nature for on further cycling the loop width (plastic strain) rapidly approached that which existed prior to resting. This appears to be in direct contrast to the results of tensile tests on fatigued crystals where a permanent upward displacement of the stress–strain curve was observed. The much bigger effect on the loop width observed at room temperature suggests that higher concentrations of point defects are generated than at lower temperatures, which would be in accord with the much heavier development of slip striae at room temperature (Hull 1958).

REFERENCES

BROOM, T., and HAM, R. K., 1957, *Proc. roy. Soc.* A, **242**, 166; 1959, *Ibid.*, **251**, 186.

HULL, D., 1958, *Phil. Mag.*, **3**, 513.

ROSENBERG, H. M., 1958, *Vacancies and other Point Defects in Metals and Alloys* (London : Institute of Metals), p. 206.

THOMPSON, N., COOGAN, C. K., and RIDER, J. G., 1955, *J. Inst. Met.*, **84**, 73.

The Variation with Time of the Flux and Energy Spectrum of Primary Cosmic Ray Alpha Particles†

By P. J. Duke
H. H. Wills Physics Laboratory, University of Bristol‡

[Received April 21, 1960]

Abstract

The total flux and energy spectrum of primary cosmic-ray alpha particles at the top of the atmosphere have been measured in emulsion stacks flown during September 1956 and June 1958. Values of 240 ± 26 and 130 ± 15 particles/m² steradian second respectively were obtained for the total flux. This reduction in the flux during June 1958 was caused by the partial removal of those alpha particles with energies between 100 and 2000 MEV/nucleon. These changes have been correlated with the 11-year cycle of solar activity.

§ 1. Introduction

It was pointed out by Forbush (1954) and others (e.g. Singer 1958), on the basis of observations made with neutron monitors at ground level, that periods of high solar activity, as measured by the Zurich sunspot number, were associated with a low cosmic-ray intensity. The corresponding variations in the flux and energy distribution of the primary radiation have been observed with nuclear plates flown to high altitudes and Freier *et al.* (1958) were able to show that the alpha particle flux in 1957 (measured over Minnesota) was reduced to about 50% of its value in 1954. Their results also indicated that this reduction was not caused by the application of an abrupt cut-off to the energy spectrum but that particles with energies as low as 200 MEV/nucleon were still able to reach the emulsions. The object of this present work has been to obtain further data on the energy spectrum and total flux of primary alpha particles using balloon-borne nuclear emulsions. The results have been obtained during September 1956 (Experiment 1) when the level of sunspot activity had risen considerably above the minimum of 1954 and in June 1958 (Experiment 2) near the maximum of the current solar cycle.

§ 2. Experimental Procedure

2.1. *September* 1956. *Experiment* 1

An emulsion stack consisting of 150 plates, each 40 cm × 30 cm × 600 μ in volume was flown to a mean height of 117 000 ft over Minnesota (North America) at a geomagnetic latitude of 55° N. for 6¼ hours. At this height the thickness of overlying air is equivalent to 6·5 g/cm². The observation and measurement of the alpha particles was divided into two parts, the first being the determination of the differential energy spectrum below 250 MeV/nucleon and the second the measurement of the total flux and the energy spectrum up to 1000 MeV/nucleon. For each section of the work a different sample of plates was searched using appropriate scanning criteria. In the first section only those tracks of density greater than 6 × minimum ionization were selected along a line 5 mm from the top edge of each plate. In the second section this density criterion was extended to 3 × minimum in order to include alpha particles of all possible energies. The alpha particles themselves were selected from all tracks recorded in the scanning by measuring the multiple coulomb scattering and grain density of each track. This method of identification was similar to that used by Fowler *et al.* (1958), except that in the present case the ionization was measured visually instead of using a densitometer. The scanning efficiency was checked in various ways. Some of the scanning was repeated by different observers and there was found to be no evidence for the omission of alpha particles. In addition, the number of alpha particles was found to be independent of the zenith angle (after correcting for atmospheric absorption) and the depth at which the track was found. It was assumed, therefore, that the scanning loss was negligible.

---

† Communicated by the Author.

‡ Now at the National Institute for Research in Nuclear Science, Harwell, Berkshire, England, and at present working at the Brookhaven National Laboratory, Upton, N.Y., U.S.A.

Fig. 1

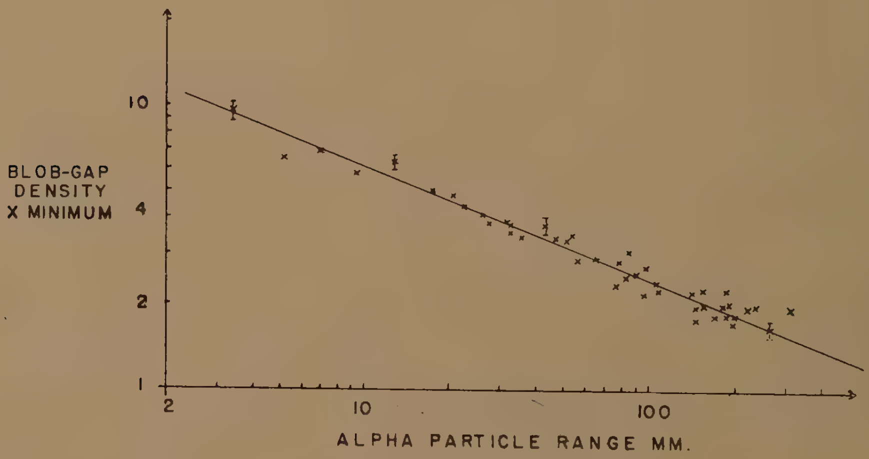

Blob-gap density–range relationship for alpha particles.

The methods used to obtain the alpha particle energies differed in parts 1 and 2 of experiment 1. In part 1 the measurement was based on a determination of either the grain density or the range of each track. Each alpha particle was followed through the emulsion stack until it either interacted, left the stack or came to rest. In the case of those particles which stopped, a measurement of the distance between the point of entry and the end point was sufficient to determine their energy. In those cases where the track did not end, the blob-gap density (Fowler and Perkins 1955) was measured either in the last few millimetres of available track or near to the point of entry. The blob-gap density was then related to the particle energy in the following way. A number of calibration plates were selected from those already scanned in part 1. These plates were searched for relativistic alpha particles which were used to give a value for the minimum blob-gap density in the plate concerned. All those alpha particles of known residual range which traversed the calibration plates were then blob-gap counted in those plates, to obtain a relationship between the blob-gap density, expressed as a multiple of the minimum density, and the residual range. The result of this procedure is shown in fig. 1. The full line shown in the figure was used to give the residual range of those alpha particles for which a direct range measurement could not be made. The energies which were obtained by this method were probably accurate to about ±10%.

In part 2, the alpha particle energies were obtained by a multiple coulomb scattering measurement, which was made over a length of track at least greater than 8 mm, using 500 μ cell sizes. The momentum and hence the energy of the particle was calculated using a value of the scattering constant obtained from the calculations of Fichtel and Friedlander (1958) and by eliminating the random noise between 500 μ and 1000 μ cell sizes, it being assumed that the contribution of the noise to the observations varied linearly with the cell size. This method gave a standard deviation of about ±15% in the energy region considered.

2.2. *June* 1958. *Experiment* 2

The dimensions of the stack in this second experiment were 20 cm × 12 cm × 600 μ and it was flown with the 20 cm edge uppermost over the same place as in Experiment 1 for $8\frac{1}{4}$ hours. The height was such that the mean thickness of air above the emulsions was 4 g/cm^2. The plates were scanned for all tracks greater than 3 × minimum, and the energies of the alpha particles were determined to an accuracy of 10–15% by multiple scattering measurements.

§ 3. RESULTS

The total fluxes were calculated using eqn. (1).

$$J = N\,\overline{\sec\theta}\,.\,\frac{1}{A}\,.\,\frac{1}{T}\,.\,\frac{1}{\Omega}\ \text{particles/m}^2\,\text{ster. sec.} \qquad (1)$$

J = Flux of alpha particles;

N = Number of particles;

A = Area of emulsion;

T = Time at maximum altitude;

Ω = Solid angle;

$\overline{\sec\theta}$ = Mean value of secant of zenith angle.

The values of N which were used in eqn. (1) were obtained from the numbers actually observed by correcting for the absorption of alpha particles and their production from the interactions of heavier nuclei in the emulsion and overlying atmosphere. These corrections were applied by inserting the fluxes of nuclei heavier than helium into the diffusion equations of Kaplon *et al.* (1954) and using the mean free paths and fragmentation probabilities of Rajopadhye and Waddington (1958). For the data of Experiment 1, values of 5, 15 and 5 particles/m^2 ster. sec were taken for the light, medium and heavy nuclei respectively, (cf. Dainton *et al.* (1952) and Kaplon *et al.* 1954), but for the results of Experiment 2 these values were reduced by 50%, it being assumed that the heavier components of the cosmic radiation decreased in the same proportion as the alpha particle flux (cf. Freier *et al.* 1959 a, b). The correction for those particles which arrived during the ascent of the emulsions was eliminated in Experiment 1 by launching the stack upside down and in Experiment 2 by launching it in an overturned position. The stacks were preset to rotate into the correct orientation when the maximum altitude was reached. Unfortunately, in Experiment 1, a short time was spent at altitude before rotation took place and a small correction was needed to allow for this.

Experiment number	Date	Number of alpha particles observed	Flux at top of atmosphere
1	September 18, 1956	200	240 ± 26 particles/m^2 ster. sec
2	June 14, 1958	167	130 ± 15 particles/m^2 ster. sec

The flux values which were obtained are shown in the table in which the errors shown are the standard deviations on the number of tracks observed, together with an allowance for the uncertainty in the thickness of the emulsion at the time of exposure. The number tabulated for Experiment 1 does not include the 75 particles with energies less than 250 MeV/nucleon which were obtained in part 1.

The differential energy spectra were obtained by extrapolating the observed energy of each alpha particle to the top of the atmosphere and then dividing the particles amongst suitable energy groups. The fluxes for each energy interval were found using eqn. (1) with the appropriate corrections. The resulting energy spectra are shown in fig. 2. There is good agreement between the two sets of low-energy results obtained in Experiment 1 even though the energies of the particles were found by different methods.

§ 4. Discussion

The results for the total flux of alpha particles obtained in the present experiment are compared in fig. 3 with other values obtained at a similar geomagnetic latitude but at different periods in the solar cycle (see Waddington (1960) for a list of references). The same figure also shows the variation with time of the Zurich sunspot number (Chernosky and Hagan 1958). It is clear that there is a strong anti-correlation between the alpha particle flux and the solar activity, as indicated by the sunspot number, so that periods of high solar activity are associated with a low flux of alpha particles. The most rapid change in the alpha particle flux coincides with the sharp rise to high sunspot number between 1955 and 1957.

Fig. 2

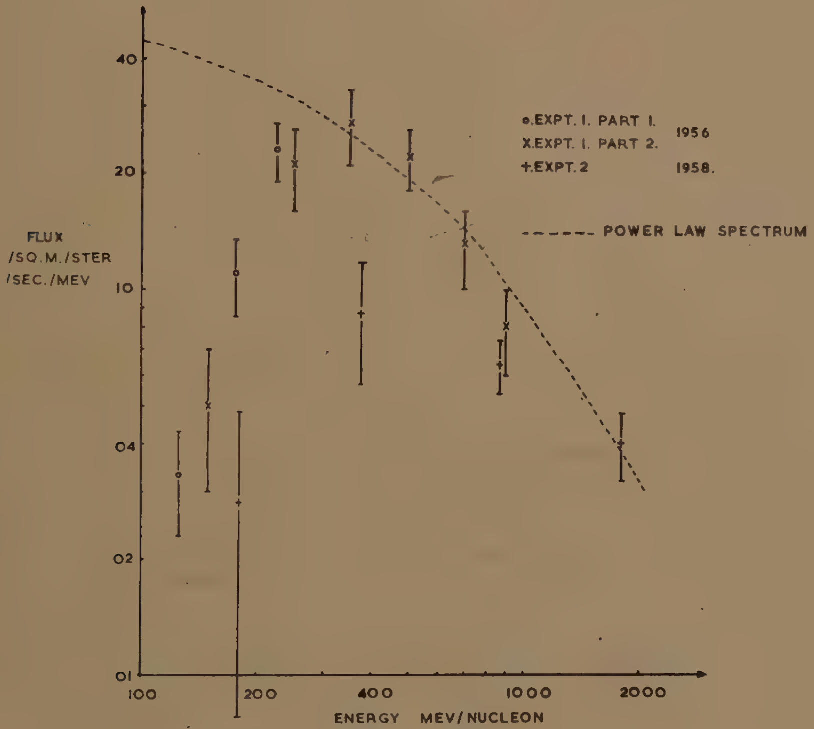

Differential energy spectrum.

The energy dependence of the variations can be seen from fig. 2. The spectrum obtained in September 1956 showed a pronounced peak in the region of 350 MeV/nucleon. At energies higher than that value the experimental points appeared to follow the power law given by eqn. (2) and shown by the hyphenated line in the figure:

$$\frac{dJ}{dE} = \frac{\text{Constant}}{(1+E)^{2\cdot5}}; \quad . \quad . \quad . \quad . \quad . \quad . \quad . \tag{2}$$

E = alpha particle energy in units of the particle rest energy. At energies below the peak there was a rapid decrease in intensity as the particle energy decreased to 100 Mev/nucleon. The alpha particle energy spectrum has been measured over a similar energy range in June 1954 at a geomagnetic latitude of 60 °N. and, over the same place as this experiment, in October 1950 (Fowler *et al.* (1957) and Fowler *et al.* 1958), and in August 1956 (McDonald 1958). The results of McDonald were obtained with a Čerenkov and a scintillation counter and are in good agreement both with the results of Fowler *et al.* in 1950 and with the present experiment. However, the spectrum obtained in 1954 differs from those just mentioned in that it rises to a higher value at the peak energy of 350 Mev/nucleon and

Fig. 3

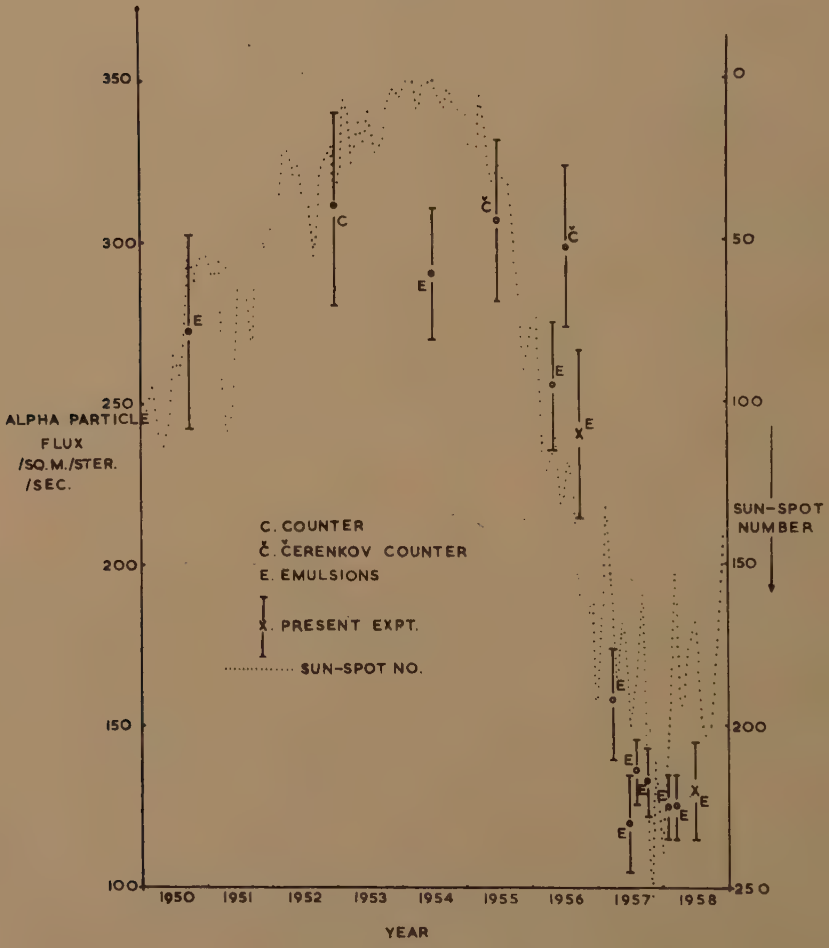

Variation of flux with time.

decreases less steeply between 350 and 150 Mev/nucleon. This may be related to the very low sunspot activity of 1954 compared with the increased activity in 1950 and 1956 on either side of the minimum. The spectrum of 1956 also showed that there was an appreciable number of alpha particles reaching the earth with energies approaching the limit of about 100 Mev/nucleon set by the air and packing materials above the emulsions. The fact that particles with energies as low as this were observed provided an upper limit to the cut-off energy over Minneapolis in 1956 which agrees with that observed by Fowler *et al.* (1957) in 1950 and which is somewhat lower than that given by the recent calculations of Quenby and Webber (1959).

The peak at 350 Mev/nucleon was still present in the 1958 results but it was much less prominent and the energy spectrum began to depart from the power law of eqn. (2) at a much higher energy, as can be seen in fig. 2. These results agree with those obtained in 1957 (Freier *et al.* 1959 b and Waddington 1960) and show that even during the years of maximum solar activity there are still an appreciable number of primary particles reaching the earth with energies as low as 200 Mev/nucleon as was observed by Freier *et al.* (1958). The height at which the emulsions were flown was sufficient to detect alpha particles of energy as low as about 80 Mev/nucleon but the number of particles observed with an energy of less than 200 Mev/nucleon was insufficient to determine the cut-off energy.

A number of attempts have been made to explain these variations but none are entirely satisfactory. Parker (1958 b) has attempted to explain the phenomena by invoking the solar wind hypothesis of Biermann (1951, 1952 and 1957). According to this theory, magnetic lines of force, emanating from the sun, are carried towards the outer regions of the solar system by a continual flow of ionized gas. It was predicted (Parker 1958 a) that this flow would become unstable in the region between the orbits of Mars and Jupiter and produce a shell of disordered magnetic field which would present a barrier to the incoming cosmic ray particles. Parker was able to show that for a given particle energy, the flux (J_0) in the vicinity of the earth would be related to that outside the barrier (J_∞) by eqn. 3.

$$J_0(E)=J_\infty(E)\exp\left\{-A\,.\left(\frac{Z}{M}\right)^2.\frac{E+1}{[E(E+2)]^{3/2}}\right\}. \qquad . \quad . \quad (3)$$

In this equation Z/M is the change to mass ratio of the particles concerned and A is a constant depending only on the magnetic and geomagnetic properties of the barrier. The results of calculations based on eqn. (3), and assuming that $J_\infty(E)$ was given by eqn. (2), are shown in fig. 4. The lower curve was obtained using a value of $A(Z/M)^2$ of 0·58 which is that required by the calculations of Parker. The upper curve uses a value for $A(Z/M^2)$ equal to 0·12. There is fair agreement between the theoretical predictions and the experimental results. Unfortunately the theory does not predict any variation in the energy spectrum above about 2 Bev/nucleon in contrast to the observations made using neutron monitors (Forbush 1954, 1958).

Fig. 4

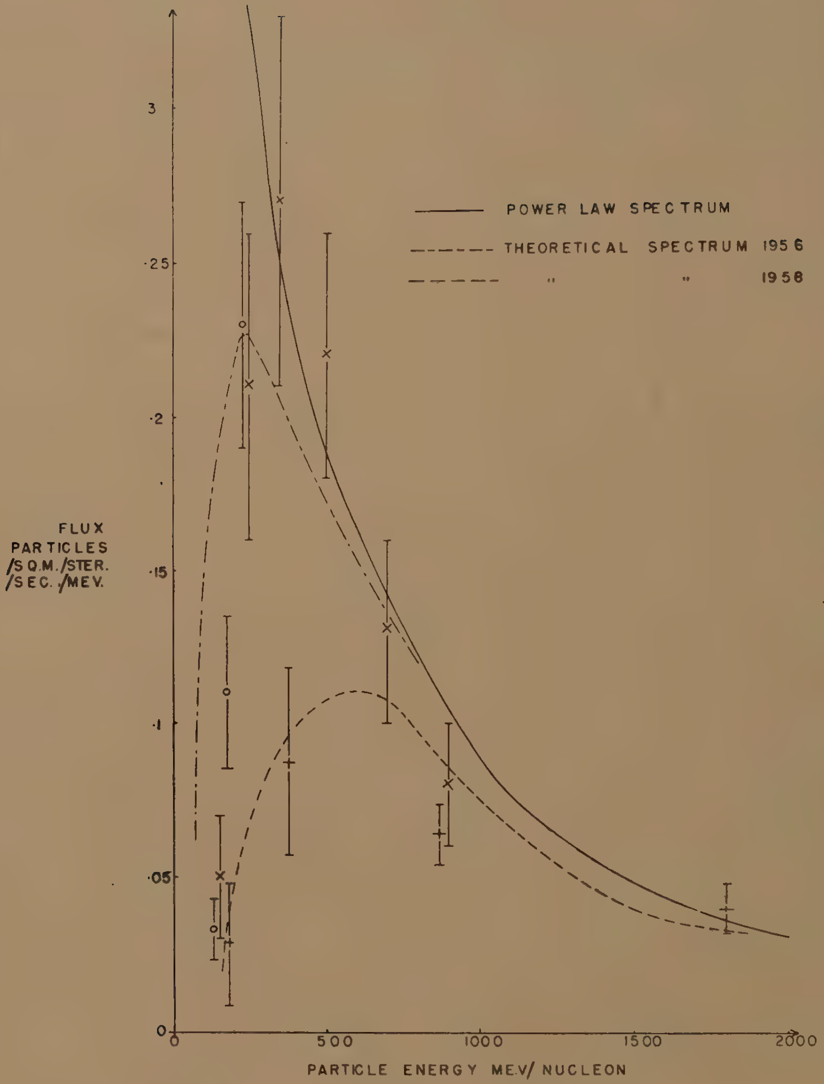

Comparison between theory and experiment.

§ 5. Conclusions

The total flux and the energy spectrum below about 2000 Mev/nucleon of primary cosmic ray alpha particles have been measured on two separate occasions. The results exhibit a strong anti-correlation between alpha particle intensity and solar activity and are in general agreement with the theory of Parker (1958 b). In spite of this, the theoretical understanding of the relationship between the cosmic-ray observations and the solar activity is still unsatisfactory.

ACKNOWLEDGMENTS

I am grateful to Professor C. F. Powell for his interest in this work and for his help and encouragement.

During the course of this experiment I have had many useful discussions with Dr. P. H. Fowler, Dr. C. J. Waddington, Dr. R. R. Hillier, and Mr. D. E. Evans.

I am indebted to the Misses B. Bolt, M. Brook, P. Curry, and P. Shore for their careful scanning of the plates and their assistance with some of the measurements.

This work was carried out during my period of tenure of a D.S.I.R. Research Fellowship.

REFERENCES

BIERMANN, L., 1951, *Z. Astrophys.*, **29,** 274; 1952, *Z. Naturforsch.* A, **7,** 127; 1957, *Observatory*, **77,** 109.
CHERNOSKY, E. J., and HAGAN, M. P., 1958, *J. geophys. Res.*, **63,** 775.
DAINTON, A. D., FOWLER, P. H., and KENT, D. W., 1952, *Phil. Mag.*, **43,** 729.
FICHTEL, C., and FRIEDLANDER, M. W., 1958, *Nuovo Cim.*, **10,** 1032.
FOWLER, P. H., FREIER, P. S., and NEY, E. P., 1958, *Nuovo Cim.* (Suppl.), **8,** 492.
FOWLER, P. H., and PERKINS, D. H., 1955, *Phil. Mag.*, **46,** 587.
FOWLER, P. H., WADDINGTON, C. J., FREIER, P. S., NAUGLE, J., and NEY, E. P., 1957, *Phil. Mag.*, **2,** 157.
FORBUSH, S. E., 1954, *J. geophys. Res.*, **59,** 525; 1958, *Ibid.*, **63,** 651.
FREIER, P. S., NEY, E. P., and FOWLER, P. H., 1958, *Nature, Lond.*, **181,** 1319.
FREIER, P. S., NEY, E. P., and WADDINGTON, C. J., 1959 a, *Phys. Rev.*, **113,** 921; 1959 b, *Ibid.*, **114,** 365.
KAPLON, M. F., NOON, J. H., and RACETTE, G. W., 1954, *Phys. Rev.*, **96,** 1408.
McDONALD, F. B., 1958, *Phys. Rev.*, **109,** 1367.
PARKER, E. N., 1958 a, *Phys. Rev.*, **109,** 1874; 1958 b, *Ibid.*, **110,** 1445.
QUENBY, J. J., and WEBBER, W. R., 1959, *Phil. Mag.*, **4,** 90.
RAJOPADHYE, V. Y., and WADDINGTON, C. J., 1958, *Phil. Mag.*, **3,** 19.
SINGER, S. F., 1958, *Progress in Elementary Particle and Cosmic Ray Physics*, **4,** 203 (Amsterdam: North-Holland Publishing Co.).
WADDINGTON, C. J., 1960, *Progress in Nuclear Physics*, **8** (London: Pergamon Press), to be published.

Soft X-ray Emission from Potassium Metal in the 40–1000 Å Range†

By R. S. Crisp‡
Department of Physics, University of Western Australia, Nedlands, W.A.

[Received June 1, 1960]

Abstract

The emission in the 40–1000 Å range, excited in a potassium target by electron bombardment, has been examined using the grazing incidence photon counting spectrometer described previously. A total of seven lines and bands are observed of which two are identified as the L and M valence spectra, three are identified as diagram lines, and two broad lines remain unidentified. An energy level scheme for solid potassium in emission has been constructed.

A note regarding the energy of the L_1 level in sodium, magnesium and aluminium is appended.

§ 1. Introduction

The M spectrum of solid potassium has been observed previously by Kingston (1951) and by Fisher *et al.* (1958) while Tyrén (1937) has observed the Ll, $L\eta$ doublet. Although the present research has been concerned principally with valence band spectra, in the case of potassium a number of atomic lines also fall in the relevant spectral range and their wavelengths may be measured. These lines can be identified by reference to the extrapolated energy values for the L and M levels, and hence exact values for these energy levels may be obtained.

§ 2. Instrumental

The spectrometer has been described in detail previously by Fisher *et al.* (1958). A number of modifications have been made subsequently and are discussed elsewhere by Crisp and Williams (1960). They include a cold baffle which nearly surrounds the target and which practically eliminated carbonaceous contamination (Crisp 1958, Ennos 1953, 1954), an improved photomultiplier detector, and replacement of the aluminium grating by a ruled glass grating which gave intense spectra down to 45 Å and enhanced reflectivity in high orders (Crisp 1960).

---

† Communicated by the Author.

‡ Now at National Research Council, Ottawa.

The targets were prepared by the evaporation of pure potassium, from a stainless-steel cup, on to a water-cooled copper target. The metal was loaded into the cup, freshly cut under the packing oil and wet with oil which was subsequently pumped off. In the preparation of an actual target, before depositing the specimen metal, the specimen chamber was 'gettered' by a massive evaporation of potassium and the copper target freshly cleaned by means of the scraper. Pressures of lower than 10^{-6} mm Hg were produced in this way and cleanliness of the specimen was ensured.

Wavelengths were calculated from the fiducial marker 'pips' on the chart records. The method of calculating the theoretical calibration curve has been indicated by Fisher *et al.* (1958) and Crisp (1960). A correction curve to this calibration was drawn using the emission edges of the L spectra of aluminium and magnesium, and the peak of the boron K spectrum in several orders. Skinner's (1940) wavelengths were taken as the 'true' wavelengths of these features and unknown wavelengths could then be determined absolutely with a probable error of ±0·5 Å. *Differences* in wavelength may be measured with an error of ±0·05 Å. The random errors incurred in making actual measurements on the charts may generally be reduced to a negligible figure by averaging a large number of records. The small systematic error introduced by the finite width of the analyser slit is automatically eliminated in the construction of the correction curve.

The slits were set at 40–45 μ and on the criterion of Fisher (1954) this corresponds to an optical resolution of 0·9 Å. The instrumental width referred to hereafter is merely this 0·9 Å converted to electron volts and will be somewhat smaller than the true 'line width' as used for example by Skinner (1940).

§ 3. EXPERIMENTAL RESULTS

The seven observed lines could be conveniently divided into three groups:

(i) The valence M spectrum (fig. 1†).

(ii) A number of diagram lines and the valence L spectrum (fig. 3).

(iii) Two unidentified broad lines designated X and Y for convenience (fig. 3).

The numerical data are set out in table 1, and the lines observed are illustrated in figs. 1 and 3 which are photographs of typical chart records. On each record the spectrum and order, target current and voltage, full scale counting rate and percentage error (Elmore and Sands 1949), optical resolution, target chamber vacuum and an approximate wavelength scale are indicated.

---

† Figures 1 and 3 are shown as plates.

Table 1. Emission lines from solid potassium
(Wavelengths for $M_{23}V$ are for the edge and extrapolated low energy limit)

Line	Peak (Å)	Peak energy (ev)	Half-width (ev)	Inst. width (ev)	Peak intensity counts/sec/mA at 4 kv
$M_{23}V$	$677{\cdot}9_2$ $\pm 0{\cdot}5$ 744 ± 1	$18{\cdot}28_7$ $\pm 0{\cdot}01$ $16{\cdot}66_3$ $\pm 0{\cdot}02$	$1{\cdot}62_4$ $\pm 0{\cdot}04$	0·025	500
L_3M_1 (Ll)	$47{\cdot}63_3$ $\pm 0{\cdot}15$	$260{\cdot}2_7$ $\pm 0{\cdot}8$	1·96 $\pm 0{\cdot}11$	1·4	2300
L_2M_1 ($L\eta$)	$47{\cdot}22_5$ $\pm 0{\cdot}15$	$262{\cdot}5_2$ $\pm 0{\cdot}8$	1·96 $\pm 0{\cdot}11$	1·4	1050
L_1L_3	$284{\cdot}6_9$ $\pm 0{\cdot}7$	$43{\cdot}54_8$ $\pm 0{\cdot}10$	$0{\cdot}7_5$ $\pm 0{\cdot}1$	0·14	30
$L_{23}V$	$41{\cdot}5_5$ $\pm 0{\cdot}4$	$298{\cdot}3_7$ $\pm 2{\cdot}7$	—	—	40
X	50·03 $\pm 0{\cdot}15$	$247{\cdot}8_0$ $\pm 0{\cdot}07$	$4{\cdot}99_6$ $\pm 0{\cdot}26$	1·25	850
Y	$103{\cdot}0_9$ $\pm 0{\cdot}6$	$120{\cdot}2_6$ $\pm 0{\cdot}7$	$2{\cdot}9_8$ $\pm 0{\cdot}3$	1·2	35

Additional information:

$E_{L\eta} - E_{Ll} = 2{\cdot}25 \pm 0{\cdot}3$ ev.
Edge width for $M_{23}V = 0{\cdot}19 \pm 0{\cdot}01$ ev.

§ 4. DISCUSSION

4.1. *The M Valence Spectrum*

The M band emitted when conduction (4s) electrons make transitions into ionized M_{23}(3p) levels is shown in fig. 1 and has been observed previously by Kingston (1951) and Fisher *et al.* (1958).

The b.c.c. alkali metal, potassium, has one valence electron per atom and is therefore expected to have a half-filled first Brillouin zone. In addition, since the first zone for an ideal b.c.c. lattice may contain 1·48 electrons per atom before the Fermi surface departs from a sphere, and since it has been calculated that for the real metal potassium the relative effective mass of the conduction electrons is 0·94 (Kittel 1956), it is anticipated that the conduction electrons in potassium will behave very much like free electrons. Hence the density of states function $N(E)$, is expected to vary parabolically with E as measured from the bottom of the band, to show a sharp cut-off at the Fermi surface and to show no evidence of zone overlap in the occupied states.

This behaviour is observed in the M emission curve of fig. 1 and in fig. 2 where the measured ordinates on the emission curve, which are recorded on a wavelength scale, are multiplied by the factor λ^3 and replotted on an energy scale to give the $f(E)N(E)$ curve (Tomboulian 1957). The broken curve in fig. 2 represents a parabolic (or $E^{1/2}$) extrapolation of the low energy portion of the curve in order to 'remove' the tail (Skinner 1940). The extrapolated bandwidth so obtained is $1{\cdot}62_4 \pm 0{\cdot}04$ ev which is smaller than the value $1{\cdot}9 \pm 0{\cdot}2$ ev given by Kingston (1951). The extrapolation shown in fig. 4 of Kingston's paper is hard to justify, and gives an excessive value for the bandwidth though the emission curve given is in close agreement with the present finding. Both these experimental values are less than the Sommerfeld 'free electron' width of 2·1 ev.

Fig. 2

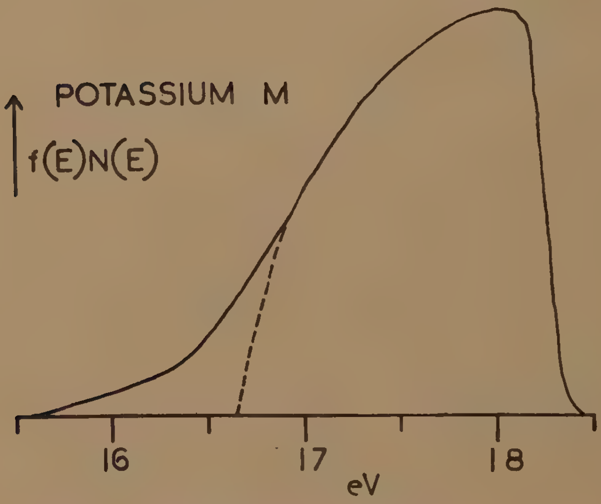

Plot of $f(E)N(E)$ vs. E deduced from the potassium M emission band.

The observed width of the emission edge is $0{\cdot}19 \pm 0{\cdot}01$ ev from 5% to 95% of the maximum intensity with the instrumental width 0·024 ev. It would appear, therefore, that about 0·17 ev of the edge width must be accounted for by temperature effects and by the width of the core level (M_2 or M_3) in emission.

There is no evidence of the edge doubling which is seen in the L spectra of the metals magnesium and aluminium, and which arises from the doublet nature of the 2p levels. The absence of edge doubling may result from either the M_2, M_3 separation being small (less than a few hundredths of an electron volt) or the M_2 band intensity being very low. Since an M_2, M_3 separation of at least some few tenths of an electron volt is expected by extrapolation from elements of higher atomic number, it must be concluded that the M_2 band intensity is very low ($<1\%$ of the M_3 band intensity). This conclusion is not entirely consistent with the results obtained by Skinner *et al.* (1954) for the M_2, M_3 separations and relative intensities for the iron transition series, but a similar near absence of the L_2 spectrum was observed in sodium by Skinner (1940).

The 0·17 ev breadth of the emission edge must then be explained partly by the width of the M_3 level and partly by temperature effects on the Fermi edge whose width from 5% to 95% of the maximum is equal to $6kT$. Since $6kT$ has values of 0·15 ev and 0·17 ev at temperatures of 20°c (cooling water temperature) and 56°c, it is seen that the maximum possible value of the M_3 width is 0·02 ev, or alternatively that the maximum possible temperature of the *emitting* atoms was 56°c. Either conclusion is quite consistent with the experimental conditions.

4.2. *The Diagram Lines and the L Valence Spectrum*

The various lines, other than the M valence band spectrum, are illustrated in fig. 3. The identifications are indicated and were made using the energy level values of Hill *et al.* (1952) and Fine and Hendee (1956) and the wavelengths of the Ll, Lη doublet given by Tyrén (1937). The peak wavelengths, widths, etc., are listed in table 1, as well as data for the two broad unidentified lines which for convenience are designated X and Y.

4.2.1. *The* 47 Å *doublet*

The doublet at 47 Å emitted when electrons make transitions from the M_1 (3s) level to the two L_{23} (3p) levels, was unresolved in first order but partially resolved in fourth order. Separation of the observed fourth-order spectrum into its two components was effected by assuming two nearly Gaussian profiles of equal widths with the intensity ratio of 2·2 : 1. Though this differs from the ideal ratio 2 : 1 it is consistent with the rapid fall of grating reflectivity in this region near cut-off. The absolute wavelength of either component is determined to 0·15 Å from fourth-order spectra, while the separation is measurable to within 0·05 Å from the same spectrum.

4.2.2. *The* 284 Å *line*, L_1L_3

Emission lines resulting from transitions within the L shell have been observed by Skinner (1940) and identified by Tomboulian and Cady (1941). The line identified as L_1L_3 in the present case is very weak (fig. 3), but it appeared on all records and its energy may be computed fairly accurately. Little can be said about the width except that it is less than 0·75 ev.

The line is identified as L_1L_3 rather than L_1L_2 or L_1L_{23} since the L_1L_3 intensity is expected to be at least twice as great as that of L_1L_2, and there is no sign of another line 15 Å distant as would be anticipated from the proposed L_2, L_3 separation of 2·25 ev.

The analogous line M_1M_3, expected at about 620 Å, was not observed.

Fig. 4

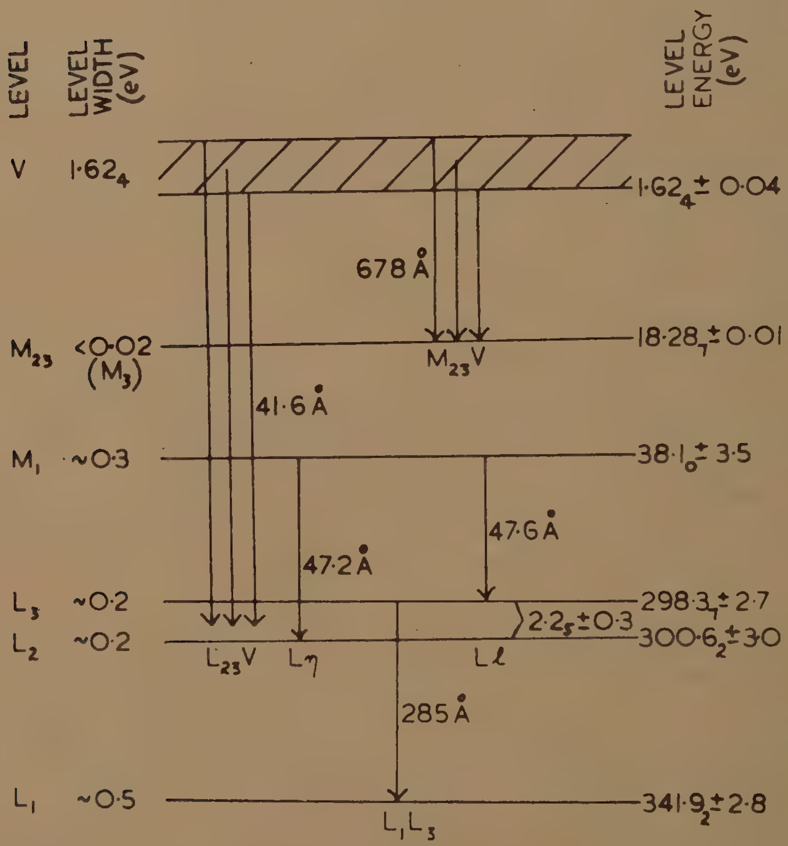
LEVEL
LEVEL WIDTH (eV)
LEVEL ENERGY (eV)
V
$1{\cdot}62_4$
$1{\cdot}62_4 \pm 0{\cdot}04$
678 Å
M_{23}
<0·02 (M_3)
$M_{23}V$
$18{\cdot}28_7 \pm 0{\cdot}01$
41·6 Å
M_1
~0·3
$38{\cdot}1_0 \pm 3{\cdot}5$
47·6 Å
47·2 Å
L_3
~0·2
L_2
~0·2
$298{\cdot}3_1 \pm 2{\cdot}7$
$2{\cdot}2_5 \pm 0{\cdot}3$
$300{\cdot}6_2 \pm 3{\cdot}0$
$L_{23}V$
$L\eta$
Ll
285 Å
L_1
~0·5
$341{\cdot}9_2 \pm 2{\cdot}8$
L_1L_3

Conventional energy level diagram for solid potassium constructed from observed emission wavelengths.

4.2.3. *The L_{23} valence spectrum*

A faint line at 41 Å is identified as the L_{23} valence spectrum (fig. 3). The intensity is very low on account of the proximity of the grating reflectivity cut-off but the line was seen on all records. The peak wavelength was computed by measuring the separation from the Ll, $L\eta$ doublet. This procedure gave a probable error of ±0·38 Å instead of ±0·7 Å if the peak wavelength had been obtained directly from the calibration table. Since the instrumental width in this region is 7·2 ev a value is not quoted for the band width. However, the 'line' will be several electron volts broad since the 1·62 ev spread of the valence electrons and the 2·25 ev separation of the L_2 and L_3 levels both contribute to its width.

4.3. *Unidentified Lines*

There remain two lines, X and Y, which will not fit in with the proposed energy level scheme of fig. 4. In addition, their widths are excessive and not compatible with the approximate level widths of fig. 4.

4.3.1. *The line X at* 248 *eV*

It is not feasible to ascribe the line X to emission from contamination of the target since its intensity was high, its intensity relative to Ll did not change with time and there was no trace of carbon K radiation or visible deterioration of the target after bombardment for half an hour or more. The line has also been observed by Jacob (1956, private communication). The line is not a satellite with an initial state of the type KL_2, KL_3, etc., since it is still observed at the same intensity relative to Ll when the target voltage is reduced to 2·5 kv. The ionization energy of the K level is about 3·6 kev. Furthermore there is no obvious parent line for a satellite with an initial state of the type L_1L_2, L_3L_2, etc.

If it is assumed that one of the states involved in the transition giving rise to the line X is L_2 or L_3, then the other must be a band of excitation (?) states, several electron volts wide and lying some 10 ev below the M_1 level. Such excitation states have been observed by Parratt (1959) for the *valence* levels of manganese.

4.3.2. *The line Y at* 120 *eV*

As with the line X, the line Y cannot be fitted to the proposed energy level scheme. However, its intensity is very low (~ 1/20 that of the line X) and it could conceivably have been emission from a contaminant though such a possibility seems remote. It is too broad to be the result of a transition between two sharp atomic levels though it may be an unresolved doublet. Once again it is hard to identify it as a satellite line for lack of a suitable parent potassium line.,

§ 5. THE ENERGY LEVEL DIAGRAM

The conventional energy level diagram for solid potassium, constructed entirely from the present data, is shown in fig. 4. The transitions observed are indicated, as well as the energies and widths computed from them for the valence, and the three L and three M levels. In constructing the diagram the peak of the $L_{23}V$ spectrum was assumed to be the peak of the L_3V component which is expected to be at least twice as intense as L_2V.

§ 6. L_1 LEVELS OF SODIUM, MAGNESIUM AND ALUMINIUM

The transition L_1L_3 in the metals sodium, magnesium and aluminium has been observed by Skinner (1940) and identified by Tomboulian and

Cady (1941). The value of the L_1 energy level relative to the highest occupied valence level may be calculated by summing the energy of the L_1L_3 transition, and the transition energy corresponding to the L_3 emission edge. Tomboulian and Cady (1941) have made this calculation using Skinner's (1940) data.

The L_1L_3 transition has been observed in the present case for these three metals. However, while the wavelengths for sodium (379·6 ± 1·0 Å) and magnesium (317·8 ± 0·5 Å) are in fair accord with previous results, that for aluminium (274·5 ± 0·5 Å) is not. A reason for the discrepancy is not forthcoming, though Skinner's (1940) wavelengths are quoted only as rough values in a footnote. The relevant data, and the calculation for the L_1 level energy, using Skinner's (1940) wavelengths for the L_3 emission edges, are given in table 2.

Table 2. Evaluation of the L_1 energy level in Na, Mg and Al

	Na	Mg	Al
λL_3 edge	405·45 ± 0·05	250·45 ± 0·05	170·56 ± 0·05
	(Wavelengths from Skinner 1940)		
E_{L_3} edge (ev)	30·577 ± 0·004	49·500 ± 0·010	72·67 ± 0·02
λL_1L_3	379·6 ± 1·0	317·8 ± 0·5	274·5 ± 0·5
	(Wavelengths from present investigation)		
	(375)	(317·4)	(290)
$E_{L_1L_3}$	32·66 ± 0·09 (33·06)	39·01 ± 0·06 (39·06)	45·16 ± 0·08 (42·67)
L_1 energy (ev)	63·24 ± 0·09 (63·64)	88·51 ± 0·07 (88·56)	117·85 ± 0·10 (115·34)

The values in parentheses, without errors, are from Skinner's (1940) wavelengths for the peak of the L_1L_3 lines.

ACKNOWLEDGMENTS

The author wishes to thank Dr. S. E. Williams, who supervised the work, for his help and suggestions, Professor A. G. McLellan of Christchurch for the loan of the glass grating, Dr. W. Baumgartner of Institut für technische Physik der E.T.H., Zurich, for co-operation in supplying the photomultiplier, and the Australian Atomic Energy Commission for a Postgraduate Research Studentship during the tenure of which the work was carried out. The continued interest of Professor C. J. B. Clews is gratefully acknowledged.

REFERENCES

CRISP, R. S., 1958, *Aust. J. Phys.*, **11,** 449; 1960, *Opt. Acta* (in the press).

CRISP, R. S., and WILLIAMS, S. E., 1960, *Phil. Mag.* (in the press).

ENNOS, A. E., 1953, *Brit. J. appl. Phys.*, **4,** 101; 1954, *Ibid.*, **5,** 27.

ELMORE, W. C., and SANDS, M., 1949, *Electronics* (McGraw-Hill), p. 250.

FINE, S., and HENDEE, C. F., 1956, *Norelco Reporter*, **3,** 113.

FISHER, P., 1954, *J. opt. Soc. Amer.*, **44,** 665.

FISHER, P., CRISP, R. S., and WILLIAMS, S. E., 1958, *Opt. Acta*, **5,** 31.

HILL, R. D., CHURCH, E. L., and MIHELICH, J. W., 1952, *Rev. sci. Instrum.*, **23,** 523.

KINGSTON, R. H., 1951, *Phys. Rev.*, **84,** 944.

KITTEL, C., 1956, *Introduction to Solid State Physics*, 2nd ed. (New York: John Wiley and Sons), p. 317.

PARRATT, L. G., 1959, *Rev. mod. Phys.*, **31,** 616.

POLLARD, J., 1953, *Rev. sci. Instrum.*, **24,** 996.,

SKINNER, H. W. B., 1940, *Phil. Trans.* A, **239,** 95.

SKINNER, H. W. B., BULLEN, T.G., and JOHNSTON, J. E., 1954, *Phil. Mag.*, **45,** 1070.

TOMBOULIAN, D. H., 1957, *Handb. Phys.*, **30** (Berlin: Springer), p. 246.

TOMBOULIAN, D. H., and CADY, W. M., 1941, *Phys. Rev.*, **59,** 422.

TYRÉN, F., 1937, *Ark. Mat. Astr. Fys.* A, **25,** 1.

The Influence of Solutes on Self-diffusion in Metals†

By A. B. Lidiard
Physics Department, The University, Reading, Berkshire

[Received June 20, 1960]

Abstract

A statistical theory of the effect of solutes on solvent self-diffusion in dilute alloys is given. It is based on the vacancy model used previously by Hoffman, Turnbull and Hart and includes a qualitative consideration of correlation effects. Two limiting cases are considered: (i) in which the vacancy jump frequencies are not greatly changed by the solute atoms (' weak perturbation ' limit), (ii) in which the vacancies attach themselves strongly to solute atoms and where the jump frequencies may be greatly different (' tight-binding ' limit). In both cases it is shown how experimental data on solute enhanced diffusion of solvent atoms combined with knowledge of solute tracer diffusion rates may be used to deduce ' correlation factors ' for solute diffusion. Analysis of existing data on dilute Ag alloys yields similar correlation factors whichever of the two limiting equations we use. The results are not consistent with the absence of isotope effects in Cd and In diffusion in Ag: this may indicate that the model is inadequate for the discussion of solute enhanced diffusion. Further experimental work, particularly on isotope effects, is called for.

§ 1. Introduction

A number of authors (Seitz 1950, Overhauser 1953, Hoffman *et al.* 1955, Hart *et al.* 1955, Hoffman 1958, Lazarus 1955, Lomer 1958, Reiss 1959) have treated the problem of the influence of small concentrations of solutes on metallic self-diffusion. These discussions have been based on a vacancy model of diffusion and have assumed the frequency of solute-vacancy exchange to be different from the rate of solvent-vacancy exchange in the pure solvent. The frequencies of solvent-vacancy exchange in the immediate vicinity of a solute atom also are assumed to be different from their values in the pure solvent. Longer range effects have sometimes been included (Overhauser 1953). In the present note we shall concern ourselves with the model which treats the effects of the solute atom on vacancy jump frequency as localized. This is the model which most authors have used, but their results are not always consistent. In particular, various results have been presented for the concentrations of vacancies in a dilute alloy. In the next section we present the statistical thermodynamic argument by which the correct results for the local model may be derived and in the following sections we consider the application to self-diffusion in a very dilute alloy. Then in § 3 we show how an analysis of the effects of solutes on solvent self-diffusion may be used to make inferences about *solute* diffusion. In particular we are able to derive values for the correlation factor for solute diffusion (LeClaire and Lidiard 1956, Manning 1959). Knowledge of these factors is necessary to theories of the elementary jump processes. The inferred values for a number of solutes in Ag are given in the table. Those for Cd and In are not consistent with the absence of isotope effects in the diffusion of these elements (Schoen 1958 a, b). This may indicate the inadequacy of the present model for the description of the effect of solutes on solvent self-diffusion; as the isotope effect experiments in principle yield more direct information about correlation factors their extension to other solutes would be valuable.

---

† Communicated by the Author.

§ 2. VACANCY CONCENTRATIONS IN A DILUTE ALLOY

We assume the alloy to be composed of N solvent atoms and N_i solute atoms randomly distributed. It will be supposed that the energy of formation of a vacancy at a site which is a nearest neighbour of a solute atom is different from the energy of formation at more distant sites, but we neglect any interaction between solute atoms and vacancies which are not nearest neighbours (this is in general agreement with the electronic theory of these interactions). We therefore specify the state of the system by giving the number of nearest-neighbour solute-vacancy pairs and the number, n_{v}, of 'free' vacancies. Let the former be $N_i p$, so that a fraction p of the impurity atoms are associated with vacancies.

If the Gibbs free energy of vacancy formation is g_{v} for a free vacancy and $(g_{\mathrm{v}}+\Delta g)$ for an associated vacancy, i.e. $-\Delta g$ is the energy of solute-vacancy association, the free energy of the crystal containing n_{v} free vacancies and $N_i p$ associated vacancies includes a term

$$n_{\mathrm{v}} g_{\mathrm{v}} + N_i p\,(g_{\mathrm{v}}+\Delta g). \qquad (2.1)$$

We must also calculate the configurational entropy associated with the various arrangements of defects all of energy (2.1), To do this we note first that the total number of lattice sites is

$$N_{\mathrm{s}} = N + N_i(1-p) + 2N_i p + n_{\mathrm{v}} = N + N_i + N_i p + n_{\mathrm{v}}. \qquad (2.2)$$

The number of ways of arranging the $N_i p$ solute-vacancy pairs among these N_{s} sites is

$$\frac{(z)^{N_i p}}{(N_i p)\,!} \prod_{s=0}^{(N_i p-1)} (N + N_i + N_i p + n_{\mathrm{v}} - 2s). \qquad (2.3)$$

Here z is the number of nearest neighbours, i.e., the number of distinct orientations of a solute-vacancy pair. Expression (2.3) neglects small hindrances to the rotation of one pair caused by the proximity of others; these are negligible at the low concentration limit of interest here. After we have arranged the solute-vacancy pairs in one of the above (2.3) configurations there remain $N + N_i - N_i p + n_{\mathrm{v}}$ sites. The n_{v} free vacancies, $N_i(1-p)$ free solute atoms and N solvent atoms are to be arranged on these sites subject to the condition that no vacancies and impurities be nearest neighbours of one another—since they would then constitute a solute-vacancy pair. First, the number of ways of putting the $N_i(1-p)$ free solute atoms onto the $N+N_i(1-p)+n_{\mathrm{V}}$ available sites is

$$\frac{(N+N_i(1-p)+n_{\mathrm{V}})\,!}{[N_i(1-p)]\,!\,(N+n_{\mathrm{V}}\,!)}\,. \qquad (2.4)$$

There then remain $N+N_i(1-p)+n_{\mathrm{V}}$ less $(z+1)N_i(1-p)$ sites on which to arrange the n_{V} vacancies. This can be done in

$$\frac{(N-zN_i(1-p)+n_{\mathrm{V}})\,!}{[N-zN_i(1-p)]\,!\,n_{\mathrm{V}}\,!} \qquad (2.5)$$

ways. The product of the expressions (2.3), (2.4) and (2.5) gives the total number of configurations of energy (2.1). Actually in these configurations we have included some, e.g. a solute atom in the vicinity of a solute-vacancy pair, to which strictly we should assign an energy different from (2.1), but these configurations are so few that no significant error is introduced into the calculation. From expressions (2.4)–(2.5) we can immediately write down the free energy of the crystal: relative to a crystal without vacancies it is

$$\begin{aligned} G = -\boldsymbol{k}T\ln\Biggl\{ & \frac{(z)^{N_ip}}{(N_ip)\,!}\prod_{s=0}^{(N_ip\quad 1)}(N+N_i+N_ip+n_{\mathrm{V}}-2s) \\ & \times\frac{(N+N_i(1-p)+n_{\mathrm{V}})\,!}{[N_i(1-p)]\,!\,(N+n_{\mathrm{V}})\,!} \\ & \times\frac{(N-zN_i(1-p)+n_{\mathrm{V}})\,!}{[N-zN_i(1-p)]\,!\,n_{\mathrm{V}}\,!}\Biggr\}+n_{\mathrm{V}}g_{\mathrm{V}}+N_ip(g_{\mathrm{V}}+\Delta g). \qquad (2.6) \end{aligned}$$

The average therodynamic values of n_{V} and p are obtained in the usual way by setting

$$\frac{\partial G}{\partial n}=0=\frac{\partial G}{\partial p}\,.$$

It is not difficult to show that these conditions lead to the following results, valid to first order in the concentration of solute atoms;

$$\frac{n_{\mathrm{V}}}{N_{\mathrm{S}}-N_ip-zN_i(1-p)}=\exp\left(-\frac{g_{\mathrm{V}}}{\boldsymbol{k}T}\right) \qquad (2.7)$$

and

$$N_ip=N_iz\exp\left(-\frac{g_{\mathrm{V}}+\Delta g}{\boldsymbol{k}T}\right). \qquad (2.8)$$

Hence the average number of free vacancies n_{V} is the same as in a pure solvent with only $N_{\mathrm{S}}-N_ip-zN_i(1-p)$ sites. The terms subtracted from the actual total number of sites N_{S} are the number of associated vacancy sites (N_ip) and the $zN_i(1-p)$ precluded sites around the unassociated impurities. The degree of association p, by (2.8), will in general be small compared to unity and (2.7) may then be re-expressed as

$$x_{\mathrm{V}}=(1-zc)\ \exp\left(-g_{\mathrm{V}}/\boldsymbol{k}T\right) \qquad (2.9)$$

where $x_V = n_V/N_s$ and $c = N_i/N_s$ are molar fractions of free vacancies and solute atoms. Equation (2.9) is the expression used by Lomer (1958): it has also been obtained by LeClaire (unpublished) who calculated the entropy term by writing down the number of ways that the N_ip pairs could be arranged on the $N_sz/2$ bonds of the lattice. In the following sections we shall use (2.7) as well as (2.8).

§ 3. APPLICATION TO SELF-DIFFUSION IN DILUTE ALLOYS OF FACE-CENTRED CUBIC STRUCTURE

The elementary random walk theory of diffusion in an isotropic lattice gives the following expression for the diffusion coefficient (see e.g. Chandrasekhar 1943),

$$D = \tfrac{1}{6}\,\Gamma s^2 \quad . \quad . \quad . \quad . \quad . \quad (3.1)$$

in which Γ is the average number of jumps made by a diffusing atom in unit time and s is the magnitude of the jump distance. A more complete analysis of vacancy diffusion includes a consideration of the effects of correlation between successive vacancy jumps† (Bardeen and Herring 1952). In the present connection we do not aim to include these rigorously; we proceed first on the assumption that (3.1) is valid and indicate possible ways in which correlation effects may enter. We confine ourselves to a face-centred cubic lattice and begin by calculating Γ.

In the present model of a dilute alloy there are several distinct vacancy jumps; these and their associated frequencies of occurance must be considered separately to arrive at a correct expression for Γ for the solvent atoms. We use the following notation taken from earlier papers on solute diffusion: an associated vacancy exchanges places with its solute atom w_2 times/sec, it exchanges places with a given one of the four sites which are nearest neighbours to both the vacancy and the solute w_1 times/sec and it jumps to a given one of the remaining seven of its nearest neighbour sites (i.e.dissociates) k_1 times/sec. The corresponding association frequency from a next nearest neighbour site of the solute to a nearest neighbour site is k_2. The frequency with which an unassociated vacancy jumps to another unassociated site is called w_0.

With this notation and the result (2.8) we can write down the number of solvent-vacancy exchanges/sec made by vacancies initially in positions nearest-neighbour to a solute atom;

$$12\,N_i \exp\left(-\frac{g_V+\Delta g}{kT}\right).\,(4w_1+7k_1). \quad . \quad . \quad . \quad . \quad . \quad (3.2)$$

We also want the number of association jumps which occur. Now, surrounding any solute atom there are 42 sites from which a nearest neighbour position can be reached in one jump; altogether there are 84 distinct jumps, each of frequency k_2. We want the number of impurity-vacancy pairs at these separations. Now the probability that any lattice site is occupied by a vacancy is n_V/N_s if no solute is in the surrounding nearest neighbour shell. Also the probability that any site is occupied by a solute atom is $N_i(1-p)/N_s$, if no vacancy is a nearest neighbour of that site. Hence the total number of solute-vacancy pairs at the separation from which an association jump can be made is

---

† This is the original paper on the topic; for a brief review of subsequent work see Lidiard (1958).

$$42\,N_i(1-p)\,n_V/N_s.$$

The total number of association jumps occurring per sec is likewise

$$84\,k_2\,N_i(1-p)\,n_V/N_s. \qquad \ldots\ldots \quad (3.3)$$

The remaining 420 jumps possible from these 42 sites around each solute atom are w_0 jumps and we shall assume that these occur with the same frequency as in the pure solvent. Their contribution is

$$420\,w_0 N_i(1-p) n_V/N_s. \qquad \ldots\ldots \quad (3.4)$$

So far we have accounted for $42N_i(1-p)n_V/N_s$ of the total of n_V free vacancies. The remainder,

$$n_V(1-42N_i(1-p)/N_s),$$

execute a total of

$$12w_0 n_V(1-42\,N_i(1-p)/N_s) \qquad \ldots\ldots \quad (3.5)$$

jumps per sec. We may note that inclusion of terms (3.4) and (3.5) is only possible for solute concentrations less than about 2%; otherwise overlapping of the spheres of influence of different solute atoms becomes important. The total number of solvent atom jumps per sec is given by the sum of terms (3.2)–(3.5) with n_V given by (2.7), and Γ, the average solvent atom jump frequency, is obtained by dividing this sum by the number of solvent atoms present. To the first order in c the result is

$$\Gamma = 12w_0 \exp(-g_V/\boldsymbol{k}T)\left[1-18c+c\exp(-\Delta g/\boldsymbol{k}T)\left(\frac{4w_1+14k_1}{w_0}\right)\right] \quad (3.6)$$

in which we have used the result that $k_2/k_1 = \exp(-\Delta g/\boldsymbol{k}T)$.

When now we wish to consider the diffusion coefficient of the solvent atoms it is necessary to include correlation effects. The simplest situation to handle is that where the solute atoms may be regarded as constituting a 'weak perturbation'; then none of the jump frequencies will be changed radically and correlation effects will be closely the same as in the pure solvent. Under these conditions we can go immediately from (3.6) to the equation

$$D_S(c) = D_S(0)\left[1-18c+c\exp(-\Delta g/\boldsymbol{k}T)\left(\frac{4w_1+14k_1}{w_0}\right)\right] \quad (3.7)$$

in which $D_S(c)$ is the diffusion coefficient of the solvent in an alloy containing a concentration c of solute.

Equation (3.7) may be a reasonable starting point. We have at present little knowledge of the relative magnitudes of w_1, w_2, k_0 and w_0, but a 'weak perturbation', assumption seems a better approximation than a model of tightly bound solute-vacancy pairs (§ 6), so far as one is able to judge directly from the relative diffusion rates of solutes and of the solvent. Other possibilities will be noted later.

Equation (3.7) may be written

$$D_s(c) = D_s(0)\,(1 + bc), \quad b = -18 + \frac{4(w_1 + 7k_1/2)}{w_0} \exp\left(-\frac{\Delta g}{kT}\right). \quad (3.8)$$

Now, this same model of the alloy yields the expressions

$$D_i = \frac{2s^2 w_2\,(w_1 + 7k_1/2)}{(w_1 + w_2 + 7k_1/2)} \exp\left(-\frac{g_{\mathrm{v}} + \Delta g}{kT}\right) \quad . \quad . \quad . \quad (3.9)$$

for the solute ('impurity') diffusion coefficient and

$$D_s(0) = 2s^2 w_0 (9/11) \exp\left(-\frac{g_{\mathrm{v}}}{kT}\right), \quad . \quad . \quad . \quad (3.10)$$

the 9/11 being an approximation to the correlation factor, f_0 (consistent with (3.9)) for solvent self-diffusion in the pure metal. The correlation factor for solute diffusion into pure solvent is the factor†

$$f_i \equiv (w_1 + 7k_1/2)/(w_1 + w_2 + 7k_1/2) \quad . \quad . \quad . \quad . \quad (3.11)$$

in (3.9) (LeClaire and Lidiard 1956); this is a quantity of interest to the electronic theory of solute diffusion since only if it is near to unity is the solute diffusion determined by w_2 alone, as often assumed. It is therefore interesting to note that eqns. (3.8), (3.9) and (3.10) allow us to write

$$f_i = 1 - \frac{4f_0}{(b + 18)} \left(\frac{D_i}{D_s(0)}\right). \quad . \quad . \quad . \quad . \quad . \quad (3.12)$$

We may note that this is consistent with the description of a weak perturbation, for as $D_i/D_s(0) \to 1$ and $b \to 0$, then $f_i \to f_0 = 9/11$, as it must do. The expression for b corresponding to (3.12) is

$$b = -18 + \frac{36}{11(1 - f_i)} \left(\frac{D_i}{D_s(0)}\right). \quad . \quad . \quad . \quad . \quad (3.13)$$

A qualitative consideration of correlation effects in other than the 'weak perturbation' limit indicates that (3.12) changes mainly in that the 18 is reduced. For a number of solutes b is several times 18 and the results are not greatly affected.

§ 4. EXPERIMENTAL RESULTS FOR Ag ALLOYS

Experimental results for a number of Ag alloys are available. $D_s(c)$ is often well represented by an exponential dependence $\exp(bc)$ rather than by the linear form (3.7); however, we are only interested in the limit of $c < 2\%$ and it is reasonable to assume that b in the exponential form has the same significance as here. Results for f_i calculated from (3.12) for 1000°K are given in the table, column $W.P.$ The use of Manning's expression in place of (3.11) and the consistent assumption $k_2 = w_0$ decreases the values of f_i in the table only very slightly.

---

† A more accurate expression for f_i is available in the special case when $k_2 = w_0$ (Manning 1959).

Values of b and $D_i/D_s(0)$ for various solutes in Ag at 1000°K (as interpolated from experimental results) and the values of the solute atom correlation factor f_i as deduced in weak perturbation and tight-binding approximations

Solute	b	$D_i/D_s(0)$	f_i, $W.P$	f_i, $T.B$
Pd	$-8{\cdot}2^a$	$0{\cdot}123^b$	0·96	—
Cu	$10{\cdot}2^c$	$1{\cdot}25^d$	0·86	—
Cd	$6{\cdot}9^e$	$3{\cdot}67^c$	0·52	0·46
In	$12{\cdot}7^c$	$5{\cdot}35^c$	0·43	0·48
Tl	$36{\cdot}4^f$	$8{\cdot}39^f$	0·50	0·72
Ge	$32{\cdot}7^c$	$9{\cdot}51^f$	0·39	0·61
Pb	$86{\cdot}0^c$	$11{\cdot}1^c$	0·65	0·89
Sb	$51{\cdot}7^g$	$7{\cdot}65^h$	0·64	0·86

Sources of experimental data in this table :

(a) N. H. Nachtrieb, quoted by H. Reiss in *Phys. Rev.*, **113**, 1445 (1959).
(b) N. H. Nachtrieb, J. Petit and J. Wehrenberg, *J. chem. Phys.*, **26**, 106 (1957).
(c) R. E. Hoffman, D. Turnbull and E. W. Hart, *Acta Met.*, **3**, 417 (1958).
(d) A. Sawatsky and F. E. Jaumot ; quoted by R. E. Hoffman, *Acta Met.*, **6**, 95 (1958).
(e) A. H. Schoen, Ph.D. Thesis, University of Illinois (1958).
(f) R. E. Hoffman, *Acta Met.*, **6**, 95 (1958).
(g) E. Sonder, *Phys. Rev.*, **100**, 1662 (1955).
(h) E. Sonder, L. M. Slifkin and C. T. Tomizuka, *Phys. Rev.*, **93**, 970 (1954).

For the calculation of $D_i/D_s(0)$ we have used

$$D_s(0) = 0{\cdot}442 \exp\left(-\frac{44{\cdot}27 \text{ k cals}}{kT}\right) \text{cm}^2/\text{sec}$$

as given by Schoen's analysis of the data of Slifkin, Sonder and Tomizuka.

§ 5. DISCUSSION OF RESULTS IN § 4

The correlation factor for solute diffusion in pure solvent, f_i, must by its definition lie between 0 and 1. It is encouraging that the values in the table all do lie within this range. It is encouraging also that the value for Cu in Ag, which we might expect to be a closely ideal system, is close to the value for Ag self-diffusion (i.e. 0·82 in the present approximation). There are indications that this is true also for Au in Ag (Slifkin, unpublished data). It is also worth drawing attention to the fact that none of the f_i values is small, and, although this is not a sensitive test of our 'weak perturbation' assumption, it is nevertheless consistent with it.

On the other hand, it must be pointed out that there exists the quite independent, and apparently direct, evidence of the isotope effect experiments for the diffusion of Cd and In in Ag which shows that the correlation factors for these solutes are small, i.e. that their diffusion is controlled by $(w_1+7k_1/2)$ and not by w_2 (Schoen 1958 a, Tharmalingam and Lidiard 1959). If these results are confirmed and extended to other elements we must infer from the table that a considerable part of b, i.e. of the enhancement of self-diffusion, is due to longer range effects than we have considered. Thus, while it appears from Schoen's work that the Overhauser type of theory cannot account for all the enhanced Ag diffusion caused by Cd and In solutes (Schoen 1958 b) it may account for part of it and so give lower f_i values than we have obtained here.

§ 6. COMPARISON WITH WORK OF HOFFMAN, TURNBULL AND HART AND WITH 'TIGHT-BINDING' MODEL

These authors (HTH) made the first quantitative application of the model described in this note to the problem of the enhancement of metallic self-diffusion by solutes. Not surprisingly, their result is similar in general form (see Hart *et al.* 1957). One obvious difference, though, is the occurrence of the number of nearest neighbours, 12, in place of the 18 in our eqn. (3.13). Thus their equation in our notation and for the f.c.c. lattice reads

$$b=-12+8\alpha_1\left(\frac{D_i}{D_S(0)}\right), \qquad (6.1)$$

in which α_1 is their quantity, "the number of effective solvent diffusion jumps per solvent atom while in the first co-ordination shell of the solute". The 12 in eqn. (6.1) arises in the HTH treatment through the use of eqn. (2.9) and the assumption that this gives the fraction of time that a given solvent atom diffuses with diffusion coefficient $D_S(0)$. The two treatments come closest to formal similarity if we take $k_2=w_0$, i.e. the assumption of very short range of interaction which is sometimes made. Terms (3.3) and (3.4) may then be taken together and the constant term in b then becomes -11 instead of -18 as in (3.8) and (3.13). The remaining difference of 1 is due to an apparent neglect by HTH of the fact, included in (3.6), that the molar fraction of solvent is $1-c$ and not 1. Actually such a comparison is rather forced since the HTH treatment, although it can be said to include the association jumps (if $k_2=w_0$), does not explicitly include the dissociation jumps (k_1). In fact if $k_2=w_0$ then $k_1\exp(-\Delta g/\boldsymbol{k}T)$ also equals w_0 and in place of (3.8) it would be consistent to write

$$b=-4+\frac{4w_1}{w_0}\exp\left(-\frac{\Delta g}{\boldsymbol{k}T}\right). \qquad (6.2)$$

The real point of alternatives such as these must however lie in the correlation effects. The correlations between subsequent jumps of a solvent atom and a prior jump are unlikely to be very different from those in the pure lattice if the prior jump is either a k_2 or a k_1 jump, particularly if $k_2=w_0$†. On the other hand, if the prior jump is a w_1-jump then the correlation effects may be different from those in the pure lattice especially when $w_2 \ll w_1$. If we introduce a different correlation factor for the w_1-jumps we must replace (6.2) by

---

† Dr. J. R. Manning in a private communication reports that this is confirmed by calculation.

$$b = -4 + \frac{4w_1 f_1}{w_0 f_0} \exp\left(-\frac{\Delta g}{kT}\right), \quad (k_2 = w_0) \quad . \quad . \quad . \quad (6.3)$$

in which f_0 is the correlation factor for the pure solvent metal ($= 0 \cdot 78$ accurately); the second correlation factor $f_1 \equiv f_1(w_2/w_1)$ is for an initial jump w_1 and has been calculated by Compaan and Haven (1956) and, more approximately, by Reiss (1959). Equation (6.3) and the corresponding expression

$$b = -4 + \frac{4f_1}{(1-f_i)}\left(\frac{D_i}{D_s(0)}\right), \quad . \quad . \quad . \quad . \quad . \quad (6.4)$$

with

$$f_i = w_1/(w_1 + w_2), \quad . \quad . \quad . \quad . \quad . \quad . \quad . \quad (6.5)$$

may be regarded as reasonable approximations to the 'tight-binding' limit, i.e., the opposite limit to (3.8) and (3.13). Owing to present limited knowledge of the function $f_1(w_2/w_1)$ solutions of (6.4) and (6.5) must be obtained by graphical interpolation between the values given by Compaan and Havan (1956). This yields the f_1 values given in the table under the coulmn headed T.B. (the second decimal figure is uncertain). For Cd and In the figures are little altered from those obtained in the weak perturbation limit; for the elements Tl–Sb they are increased by about 0·2. These changes come primarily from the incorporation into the equations of f_1, the values of which are several times less than the 9/11 assumed in the weak perturbation treatment. This means that in order to give the same observed effects it is necessary to have larger ratios of w_1/w_2 than are obtained if we use eqn. (3.8) (cf. the product $w_1 f_1$ which occurs in (6.3)). This in turn leads to larger values for f_i.

In a recent private communication to the author Dr. J. R. Manning reports a more extended discussion of the model with $k_2 = w_0$. He does not neglect k_1 in comparison with w_1 and w_2 as we have done. In addition he uses a more accurate expression for f_i (Manning 1959) and develops expressions for f_1 as function of w_1/k_1 and w_2/k_1. Experimental data on b and $D_i/D_s(0)$ is then used to infer w_1/k_1 and w_2/k_1 and hence f_i. The inferred values of w_1/k_1 and w_2/k_1 are large compared to unity and the f_i values agree well with those in the table, column T.B. These results may mean that more reliance should be placed on the T.B. values. However the inference of separate values for w_1/k_1 and w_2/k_1 is only possible on account of the assumption that $k_2 = w_0$; the sensitivity of the analysis to this assumption is not known.

§ 7. CONCLUSION

The table shows that the inferred correlation factors are not highly sensitive to the alternative mathematical assumptions which we have made about relative jump frequencies entering into this problem. In particular the values for Cd and In seem to be firm. These values are however in conflict with the much lower values demanded by Schoen's isotope effect experiments. The inference may be that the present model is too simplified to deal with the problem of solute enhanced diffusion and that effects of longer range must be included. However, we emphasise that the analysis presented here is perfectly consistent considered on its own, and that any such inference rests entirely on the isotope effect results for Cd and In in Ag. It would clearly be of interest to have these measurements extended to other solutes.

ACKNOWLEDGMENTS

The author is greatly indebted to Dr. J. R. Manning for stimulating correspondence and to Mr. A. D. LeClaire for his comments on the manuscript.

REFERENCES

BARDEEN, J., and HERRING, C., 1952, *Imperfections in Nearly Perfect Crystals* (New York : Wiley), p. 261.
CHANDRASEKHAR, S., 1943, *Rev. mod. Phys.*, **15,** 1.
COMPAAN, K., and HAVEN, Y., 1956, *Trans. Faraday Soc.*, **52,** 786.
HART, E. W., HOFFMAN, R. E., and TURNBULL, D., 1957, *Acta Met.*, **5,** 74.
HOFFMAN, R. E., 1958, *Acta Met.*, **6,** 95.
HOFFMAN, R. E., TURNBULL, D., and HART, E. W., 1955, *Acta Met.*, **3,** 417.
LAZARUS, D., 1955, *Impurities and Imperfections* (Cleveland : American Society of Metals), p. 107.
LECLAIRE, A. D., and LIDIARD, A. B., 1956, *Phil. Mag.*, **1,** 518.
LIDIARD, A. B., 1958, *Nuovo Cim.*, Suppl., **7,** 620.
LOMER, W. M., 1958, *Symposium on Vacancies and other Point Defects in Metals and Alloys* (London : Institute of Metals), p. 79.
MANNING, J. R., 1959, *Phys. Rev.*, **116,** 819.
OVERHAUSER, A. W., 1953, *Phys. Rev.*, **90,** 313.
REISS, H., 1959, *Phys. Rev.*, **113,** 1445.
SCHOEN, A. H., 1958 a, *Phys. Rev. Letters*, **1,** 138 ; 1958 b, Ph.D. Thesis, University of Illinois.
SEITZ, F., 1950, *Acta Cryst.*, **3,** 355.

Optical Model Analysis of Nuclear Scattering†

By B. Buck‡, R. N. Maddison and P. E. Hodgson
Clarendon Laboratory, Oxford

[Received June 15, 1960]

Abstract

The mathematical methods used in a calculation of nuclear interactions by the optical model are described, and the most efficient way of programming the calculation for an electronic computer investigated.

§ 1. General Formulation

When a nucleon or group of nucleons interacts with a nucleus, the behaviour of the system is determined by all the possible interactions between the nucleons present. This is very difficult to handle mathematically, so the optical model replaces all these separate interactions by a two-body interaction between the incident particle and the target nucleus of the form (Bjorklund and Fernbach 1958)

$$V(r)=V_c(r)+Uf(r)+iWg(r)+(U_s+iW_s)h(r)\,\boldsymbol{l}\,.\,\boldsymbol{\sigma} \qquad . \quad . \quad (1)$$

where r is the separation of the two particles, and U, W, U_s and W_s are the real and imaginary parts of the central and spin-dependent potentials respectively. V_c is the Coulomb potential, $f(r)$, $g(r)$ and $h(r)$ are functions giving the radial variations of the potentials (cf. § 4). This is equivalent to replacing the target nucleus by a potential well having both refracting and absorbing parts. The refracting potential U elastically scatters the incident particles, and the absorbing potential W takes account of all the inelastic processes, including inelastic scattering and absorption. The spin-dependent term given above is appropriate for the scattering of spin $\frac{1}{2}$ particles by spin 0 nuclei; for the scattering of particles of zero spin there is of course no spin-dependent term, while for the scattering of particles of higher spins more complex forms are required. In all optical model calculations it is usual to take the spin of the target nucleus to be zero.

To calculate the observable cross sections for two particles interacting through the above potential, Schrodinger's equation is applied to the whole system

$$\frac{h^2}{2\mu}\nabla^2\Psi+(E-V)\Psi=0 \qquad . \quad . \quad . \quad . \quad . \quad (2)$$

where E is the centre-of-mass energy.

---

† Communicated by the Authors.
‡ Now at Oak Ridge National Laboratory, Tennessee, U.S.A.

If the total wave function Ψ is expanded in spherical harmonies

$$\Psi=\sum_{jlm}\frac{U_{jl}(r)}{r}\sum_{\mu}C_{m\lambda\mu}{}^{jls}Y_l{}^{\lambda}(\theta,\phi)\chi_s{}^{\mu} \quad . \quad . \quad . \quad . \quad . \quad . \quad . \quad (3)$$

we obtain a series of equations for each radial wave function. The spin of the incident particle can couple in two ways to the orbital angular momentum l to give the total angular momentum $j=l\pm\frac{1}{2}$, and the eigenvalues of $\boldsymbol{l}.\boldsymbol{\sigma}$ corresponding to these two spin orientations are l and $-(l+1)$. The corresponding radial wave functions $U_l{}^+(r)$ and $U_l{}^-(r)$ satisfy the equations

$$\frac{d^2U_l{}^+(\rho)}{d\rho^2}+\left[1-\frac{V_c}{E}-\frac{Uf(\rho)+iWg(\rho)}{E}\right.$$
$$\left.-\frac{l(U_s+iW_s)h(\rho)}{E}-\frac{l(l+1)}{\rho^2}\right]U_l{}^+(\rho)=0, \quad . \quad . \quad . \quad (4a)$$

$$\frac{d^2U_l{}^-(\rho)}{d\rho^2}+\left[1-\frac{V_c}{E}-\frac{Uf(\rho)+iWg(\rho)}{E}\right.$$
$$\left.+\frac{(l+1)(U_s+iW_s)h(\rho)}{E}-\frac{l(l+1)}{\rho^2}\right]U_l{}^-(\rho)=0 \quad . \quad . \quad . \quad (4b)$$

where $\rho=kr$, k being the wave number $k=\sqrt{(2\mu E)}/\hbar$ where μ is the reduced mass of the incident particle, $\mu=A_I/(A_I+A_T)$, A_I and A_T being the masses of the incident and target particles in a.m.u. These radial wave functions are zero at the origin and beyond the nuclear field tend asymptotically to the forms

$$U_l{}^{\pm}(\rho)=F_l(\rho)+iG_l(\rho)+S_l{}^{\pm}[F_l(\rho)-iG_l(\rho)] \quad . \quad . \quad . \quad . \quad (5)$$

where the $S_l{}^{\pm}=\exp(2i\delta_l)$ are the (complex) elements of the scattering matrix, and $F_l(\rho)$ and $G_l(\rho)$ are regular and irregular solutions of the eqn. (4) without the nuclear terms. These functions are taken to have the asymptotic forms

$$F_l(\rho)\xrightarrow[\rho\to\infty]{}\sin\left[\rho-\gamma\ln 2\rho-\tfrac{1}{2}l\pi+\sigma_l\right], \quad . \quad . \quad . \quad . \quad (5a)$$

$$G_l(\rho)\xrightarrow[\rho\to\infty]{}\cos\left[\rho-\gamma\ln 2\rho-\tfrac{1}{2}l\pi+\sigma_l\right]. \quad . \quad . \quad . \quad . \quad (5b)$$

The non spin-flip and spin-flip scattering amplitudes are then

$$A(\theta)=f_c(\theta)+\frac{1}{2ik}\sum_{l=0}^{\infty}\{(l+1)S_l{}^{+}+lS_l{}^{-}-(2l+1)\}\exp(2i\sigma_l)P_l(\cos\theta) \quad (6a)$$

$$B(\theta)=\frac{1}{2ik}\sum_{l=0}^{\infty}\{S_l{}^{+}-S_l{}^{-}\}\exp(2i\sigma_l)P_l{}^{1}(\cos\theta) \quad . \quad . \quad . \quad . \quad . \quad . \quad (6b)$$

where $f_c(\theta)$ is the Coulomb scattering amplitude

$$f_c(\theta)=-\frac{\gamma}{2k}\operatorname{cosec}^2\frac{\theta}{2}\exp\left[2i\sigma_0-2i\gamma\ln\sin\theta/2\right] \quad . \quad . \quad . \quad (7)$$

where

$$\gamma=\frac{\mu Z_IZ_Te^2}{k\hbar^2},$$

Z_I and Z_T being the charges of the incident and target nuclei, and σ_l is the Coulomb phase shift for the lth partial wave.

The observable quantities may be expressed in terms of the scattering amplitudes. The differential cross section for elastic scattering is given by

$$\sigma(\theta)=|A|^2+|B|^2 \qquad . \quad . \quad . \quad . \quad . \quad . \quad . \quad . \quad (8)$$

and the polarization by

$$P(\theta)=\frac{2\,\mathrm{Im}\,AB^*}{|A|^2+|B|^2}\boldsymbol{n} \quad . \quad . \quad . \quad . \quad . \quad . \quad . \quad . \quad (9)$$

where $\boldsymbol{n}=\boldsymbol{k}_i\times\boldsymbol{k}\,/|\boldsymbol{k}_i\times\boldsymbol{k}_f|$.

The total absorption cross section is given by

$$\sigma_A=\frac{\pi}{k^2}\sum_{l=0}^{\infty}\{(l+1)(1-|S_l^+|^2)+l(1-|S_l^-|^2)\}. \quad . \quad . \quad . \quad (10)$$

If the incident particles are uncharged, V_c, $f_c(\theta)$ and σ_l are all zero, and the total elastic cross section is finite

$$\sigma_E=\frac{\pi}{k^2}\sum_{l=0}^{\infty}\{(l+1)|1-S_l^+|^2+l|1-S_l^-|^2\}. \quad . \quad . \quad . \quad . \quad (11)$$

The total cross section is

$$\sigma_T=\frac{2\pi}{k^2}\sum_{l=0}^{\infty}\{(l+1)(1+\mathrm{Re}\,S_l^+)+l(1-\mathrm{Re}\,S_l^-)\}. \quad . \quad . \quad . \quad (12)$$

In practice, partial waves with l greater than some value $l_{\max}$ do not contribute significantly to these summations and so they may be neglected.

§ 2. Method of Solution

The essential part of the calculation is the numerical integration of the radial wave eqns. (4) from the origin out to a distance ρ_M where the nuclear field is negligible. The wave function obtained by this integration of the internal equation must join smoothly to the external solution (5). Thus, if f_l is the logarithmic derivative of the internal wave function at ρ_M,

$$f_l^{\pm}=\left(\frac{F_l'(\rho)+iG_l'(\rho)+S_l^{\pm}[F_l'(\rho)-iG_l'(\rho)]}{F_l(\rho)+iG_l(\rho)+S_l^{\pm}[F_l(\rho)-iG_l(\rho)]}\right)_{\rho=\rho_M}. \quad . \quad . \quad (13)$$

Since $f_l^{\pm}$ is determined from the internal integration, and the F's and G's may be calculated as described below, this determines the $S_l^{\pm}$, and hence the observable quantities by the relations (6)–(12).

The internal integration was initially coded for the Runge–Kutta–Gill method, since this is available as a subroutine on the computer used. Advantage can, however, be taken of the absence of first derivatives in (4) to use the Fox–Goodwin method 7, and this is up to ten times faster. In the Runge–Kutta method the value of the function and its derivative is required at one point beyond the origin and in the Fox–Goodwin method the values of the function at two points beyond the origin are required before the numerical integration can begin. If these points are taken close to the origin a series solution of (4) may be obtained for small ρ, and very few terms suffice to give accurate starting values of the wave function and its derivative.

In the external region, the wave eqn. (4) reduces to

$$\frac{d^2U_l}{d\rho^2}+\left[1-\frac{2\gamma}{\rho}-\frac{l(l+1)}{\rho^2}\right]U_l=0. \quad . \quad . \quad . \quad . \quad . \quad (14)$$

For $\gamma \neq 0$ its solutions are the regular and irregular Coulomb wave functions $F_l(\rho)$ and $G_l(\rho)$. The F_l may be readily calculated by several methods among which the asymptotic series expansion, the Shepansky–Butler series and Miller's method (Stegun and Abramowitz 1955) were investigated. Miller's method was chosen for its simplicity and speed. This method sets $F_{l+1}(\rho)=0$, $\alpha F_l(\rho)=\epsilon$, where l is an integer $> l_{\max}$ ($l=60$ was used here), α is a constant to be determined, and ϵ a very small number. Using the recurrence relation

$$\frac{[\gamma^2+(l+1)^2]^{1/2}}{l+1} F_{l+1}(\rho) + \frac{[\gamma^2+l^2]^{1/2}}{l} F_{l-1}(\rho) = (2l+1)\left[\frac{\gamma}{l(l+1)} + \frac{1}{\rho}\right] F_l(\rho) \quad . \quad . \quad . \quad (15)$$

all the $\alpha F_l(\rho)$'s down to $\alpha F_0(\rho)$ may be calculated. The constant α was found from the Wronskian

$$F_0'(\rho)G_0(\rho) - F_0(\rho)G_0'(\rho) = 1 \quad . \quad . \quad . \quad . \quad . \quad (16)$$

where $F_0'(\rho)$ was found from the recurrence relation

$$\left[\frac{\gamma}{l+1} + \frac{l+1}{\rho}\right] F_l(\rho) - F_l'(\rho) = \frac{[\gamma^2+(l+1)^2]^{1/2}}{l+1} F_{l+1}(\rho) \qquad (17)$$

and $G_0(\rho)$ and $G_0'(\rho)$ were calculated as described below.

The irregular functions were evaluated using the expression (Froeberg 1955)

$$\left.\begin{aligned} G_0(\rho) &= s\cos(-\gamma\ln 2\rho+\rho+\sigma_0) - t\sin(-\gamma\ln 2\rho+\rho+\sigma_0), \\ G_0'(\rho) &= S\cos(-\gamma\ln 2\rho+\rho+\sigma_0) - T\sin(-\gamma\ln 2\rho+\rho+\sigma_0), \end{aligned}\right\} \quad . \quad (18)$$

where

$$s=\sum_{n=0}^{25} s_n, \quad t=\sum_{n=0}^{25} t_n; \quad S=\sum_{n=0}^{25} S_n, \quad T=\sum_{n=0}^{25} T_n.$$

The number of terms in these sums was found by experience to be adequate, and the individual terms were calculated from the recurrence relations

$$\left.\begin{aligned} s_{n+1} &= \frac{(2n+1)\gamma}{2\rho(n+1)} s_n - \frac{\gamma^2-n(n+1)}{2\rho(n+1)} t_n; \\ t_{n+1} &= \frac{(2n+1)\gamma}{2\rho(n+1)} t_n + \frac{\gamma^2-n(n+1)}{2\rho(n+1)} s_n. \\ S_{n+1} &= \frac{(2n+1)\gamma}{2\rho(n+1)} S_n - \frac{\gamma^2-n(n+1)}{2\rho(n+1)} T_n - \frac{s_{n+1}}{\rho}; \\ T_{n+1} &= \frac{(2n+1)\gamma}{2\rho(n+1)} T_n + \frac{\gamma^2-n(n+1)}{2\rho(n+1)} S_n - \frac{t_{n+1}}{\rho}. \end{aligned}\right\} \quad . \quad . \quad (19)$$

and the initial values

$$s_0=1, \quad s_1=\frac{\gamma}{2\rho}; \quad S_0=0, \quad S_1=\frac{\gamma^3-\gamma^2}{2\rho^2}-\frac{\gamma^2}{2\rho};$$

$$t_0=0, \quad t_1=\frac{\gamma^2}{2\rho}; \quad T_0=1-\frac{\gamma}{\rho}, \quad T_1=-\frac{\gamma^2}{\rho^2}+\frac{\gamma}{2\rho}.$$

The summations satisfy the relation

$$sT - St = 1. \qquad (20)$$

The convergence of these series improves as ρ increases, and to obtain accurate results a value of ρ substantially greater than ρ_M must be used. To ensure accuracy, ρ was first set to a suitable starting value, and the series summed. If the relation (20) was satisfied to one part in 10^4, the values were accepted; if not, ρ was increased until it was.

The values of $G_0(\rho_M)$ and $G_0'(\rho_M)$ were obtained from these $G_0(\rho)$, $G_0'(\rho)$, where $\rho > \rho_M$, by integrating the eqn. (14) inwards numerically. The $G_l(\rho_M)$ and $G_l'(\rho_M)$ were then found from (17) and (15).

The relations (15) and (17) are satisfied by both the F's and the G's. They may only be used downwards in l for the F's and upwards in l for the G's, when $l > \rho$; otherwise instabilities develop and all accuracy is lost (cf. Hartree 1952). Likewise, eqn. (14) may only be integrated outwards for the F's and inwards for the G's in the unstable regions.

The Coulomb phase shifts $\sigma_l(\gamma)$ were calculated from the asymptotic series expansion for large l ($l = 50$ was used)

$$\sigma_l(\gamma) = \alpha(l + \tfrac{1}{2}) + \gamma[\ln \beta - 1]$$
$$+ \frac{1}{\beta}\left[-\frac{\sin\alpha}{12} + \frac{\sin 3\alpha}{360\beta^2} - \frac{\sin 5\alpha}{1260\beta^4} + \frac{\sin 7\alpha}{1680\beta^6} - \frac{\sin 9\alpha}{1188\beta^8} + \dots\right] \qquad (21)$$

where

$$\alpha = \tan^{-1}[\gamma/(l+1)], \quad \beta = [\gamma^2 + (l+1)^2]^{1/2}$$

and the recurrence relation

$$\sigma_l(\gamma) = \sigma_{l+1}(\gamma) - \tan^{-1}[\gamma/(l+1)]. \qquad (22)$$

If $\gamma = 0$, the solutions of (14) are spherical Bessel and Neumann functions

$$F_l(\rho) = \rho j_l(\rho), \quad G_l(\rho) = -\rho n_l(\rho). \qquad (23)$$

The F's were calculated by Miller's method and the G's, using (19), with the initial values

$$j_0(\rho) = \frac{\sin\rho}{\rho}, \qquad j_1(\rho) = \frac{\sin\rho}{\rho^2} - \frac{\cos\rho}{\rho};$$
$$n_0(\rho) = -\frac{\cos\rho}{\rho}, \qquad n_1(\rho) = -\frac{\cos\rho}{\rho^2} - \frac{\cos\rho}{\rho}.$$

The F's and G's and their derivatives were required to satisfy the Wronskian

$$F_l'(\rho)G_l(\rho) - F_l(\rho)G_l'(\rho) = 1 \qquad (24)$$

for all l to two parts in 10^5.

§ 3. CHOICE OF PARAMETERS

Four parameters determine the numerical part of the calculation: (*a*) the matching radius ρ_M, (*b*) the number of steps in the Coulomb integration N_c, (*c*) the number of steps in the nuclear integration N_n, and (*d*) the number of partial waves ($l_{\max} + 1$). Within certain limits, the larger these numbers are the more accurate the final result, but the longer the time of computation. It is therefore necessary to choose them to minimize the time consistent with the desired accuracy of the final results.

Since the Coulomb integration is done only once, N_c can be chosen generously without substantially affecting the total time. This leaves ρ_M, N_n and l_{max} to be studied in detail. In general, such parameters can either be chosen once and for all, or calculated for each run by some empirical formula, or fixed automatically to satisfy some pre-determined accuracy criterion. The latter procedure is inherently the most satisfactory, but is only convenient for l_{max} in the present work. The nuclear integrations were performed for increasing l-values, until $1-|ReS_l|$ for the last partial wave became less than some small number ϵ. Such an automatic procedure would be possible to fix ρ_M and N_n also, but it is not efficient as the nuclear integrations would have to be done again and again for increasing ρ_M and N_n until some pre-set condition was satisfied. It is easier to use an empirical formula for them.

The best choice of ρ_M and N_n was investigated by calculating the scattering of 14 Mev neutrons by aluminium for a range of values, and recording the accuracy with which sample cross-sections and polarizations were determined. For this investigation, l_{max} was chosen considerably larger than usual. Some typical results are shown in tables 1–3. Since most of the computation time is taken up by the numerical integration, and this is proportional to $N_n l_{max}$, it is apparent from the table that, adequate accuracy for most purposes can be obtained by choosing $C=7$ where

$$\rho_M=\rho_R+C\alpha \qquad \text{. . . . . (25)}$$

where ρ_R and α are the nuclear radius and diffuseness in ρ units, $\rho_R=kR$, $\alpha=ka$.

The best value of ρ_M chosen in this way is very insensitive to E and A, so the above relation was written into the programme. The best values of N_n depend on E and A and it was found adequate to have ten steps per unit of ρ.

It would be possible to use varying step lengths for the numerical integration, the shorter steps where the wave function changes rapidly and the longer steps elsewhere. This would reduce the calculation time, but as the improvement is marginal it has not been done. A value of $\epsilon=0{\cdot}0001$ was found to give accuracies at least as good as the best in tables 1–3.

Combinations of the physical constants occur in three places in the calculation:

the Coulomb constant

$$\gamma=\frac{\mu Z_I Z_T e^2}{k\hbar^2}=0{\cdot}157454 Z_I Z_T (A_I/E_{lab})^{1/2} \qquad \text{. . . . (26)}$$

where E_{lab} is in Mev.

the wave number

$$k=0{\cdot}218728\,(\mu E_{CM})^{1/2} \qquad \text{. . . . . (27)}$$

and the coefficient of the spin–orbit term (see § 4).

$$\left(\frac{\hbar}{2Mc}\right)^2 = 0{\cdot}011057 \times 10^{-26}\,\text{cm}^2 \qquad . \; . \; . \; . \; . \quad (28)$$

Table 1. Percentage error in calculation of total cross section for 14 MeV neutrons on aluminium for various C and N_n

C	Number of integration steps N_n			
	15	20	25	30
6	0·05	0·03	0·03	0·03
7	0·06	0·02	0·02	0·02
8	0·07	0·02	0·011	0·008
9	0·11	0·02	0·008	0·003

Table 2. As table 1 for differential cross section at 0°

C	Number of integration steps N_n			
	15	20	25	30
6	0·66	0·47	0·44	0·43
7	0·60	0·25	0·19	0·18
8	0·84	0·18	0·09	0·08
9	1·35	0·20	0·07	0·04

Table 3. As table 1 for polarization at 120°

C	Number of integration steps N_n			
	15	20	25	30
6	−3·80	−0·76	−0·20	−0·03
7	−6·01	−0·82	+0·03	+0·27
8	−10·5	−3·09	−0·39	−0·04
9	−17·9	−4·20	−0·83	−0·32

The programme was arranged to read the parameters of each calculation from a separate data tape. The parameters were A_T, A_I, Z_T, Z_I, the masses (in a.m.u.) and charges of the target and incident particles respectively, the energy E of the incident particle in the laboratory system in MeV, the central and spin–orbit potentials (in MeV) and the parameters of their form factors (in 10^{-13} cm), the Coulomb radius r_c, and the angular range required in the output. A second data tape provides the experimental data with which the calculation is to be compared.

The output consists of all the input numbers, the range of the nuclear integrations, k, γ, the $S_l^{\pm}$, the $\sigma_A{}^l$ and σ_A (also $\sigma_E{}^l$, σ_E, σ_T for $Z_I=0$) $d\sigma/d\Omega$ and **P** for the angular range specified, and Δ_σ and Δ_P for each point of the experimental distribution, and their totals.

The time in seconds for a calculation on the Ferranti Mercury computer is approximately

$$T \approx 0{\cdot}5\, E_{\text{lab}} R^2 + 20 \quad . \quad . \quad . \quad . \quad . \quad . \quad . \quad (29)$$

where R is the nuclear radius in fermis. This is halved if there is no spin–orbit potential.

§ 4. Radial Variation of the Coulomb and Nuclear Potentials

The Coulomb potential was taken to be that due to a charged sphere of radius $R_c = r_c A^{1/3}$

$$\begin{aligned} V_c &= \frac{Z_I Z_T e^2}{2R_c}(3 - r^2/R_c{}^2) \quad \text{for} \quad r < R_c \\ &= \frac{Z_I Z_T e^2}{r} \qquad\qquad\qquad \text{for} \quad r > R_c. \quad . \quad . \quad . \quad (30) \end{aligned}$$

It would be more accurate to use the potential due to a charged sphere with a diffuseness corresponding to that of the nuclear potential. This would substantially increase the computation time, without significantly affecting the results. The interaction is insensitive to the radial form of the potential and the form (30) is adequate for all practical purposes. This is shown by the comparison in tables 4 and 6 between two calculations with identical parameters except for r_c.

The nuclear potentials can be represented by a number of form factors all having a rapid fall-off beyond the nuclear surface. Those used in the present programme were the Saxon–Woods form

$$f(r) = \frac{1}{1 + \exp\left(\dfrac{r-R}{a}\right)} \quad . \quad . \quad . \quad . \quad . \quad . \quad . \quad (31)$$

where $R = r_0 A^{1/3}$ is the nuclear radius and a the diffuseness of the nuclear surface, and the Gaussian form

$$g(r) = \exp\left[-\left(\frac{r-R}{a}\right)^2\right]. \quad . \quad . \quad . \quad . \quad . \quad . \quad (32)$$

The form factor for spin–orbit potential, by analogy with the Thomas term in atoms, was taken to be

$$h(r) = -\left(\frac{\hbar}{2Mc}\right)^2 . \frac{1}{r} . \frac{df(r)}{dr} . \quad . \quad . \quad . \quad . \quad . \quad . \quad (33)$$

The factor $(\hbar/2Mc)^2$, the square of half the Compton wavelength of the proton, is introduced simply to keep $h(r)$ dimensionless. Some authors use $(\hbar/m_\pi c)^2$, where m_π is the pion mass. The corresponding potentials must then be divided by $(2M/m_\pi)^2 = 180{\cdot}59$. The negative sign is introduced to keep $h(r)$ positive.

The programme was arranged to use the Saxon–Woods form for U, either the Saxon–Woods or the Gaussian for W, and the form given by (33) for the spin-orbit potentials.

The choice of a definite ρ_M for matching the internal and the external wave function is equivalent to cutting off the potential at that radius. The problem is then solved exactly for the cut-off potential. Since little is known about the nuclear field at such distances from the nucleus, nothing is lost by this procedure.

Table 4. Effect of altering Coulomb field. Calculation with same parameters as table 6 but with $r_c = 1{\cdot}4$ F (F $\equiv 10^{-13}$ cm)

θ_{CM}	$d\sigma/d\Omega$	P
20	2·818, 3	−0·0584
40	1·827, 2	0·0490
60	2·067, 1	0·2404
80	1·597, 1	−0·0965
120	3·442, 0	−0·7532
160	2·257, 0	0·6367
σ_R	1055·8 mB	

§ 5. PROGRAMME CHECKS

With a calculation of this complexity it is essential to check that no analytical or programming errors have been made. In the present case there are no simple limiting cases that could be used, and the whole calculation would take a prohibitively long time to check on a desk computer. The best check is to compare the results of some trial calculations with that of similar runs with exactly the same initial parameters using another programme written independently for another computer. Through the courtesy of Professor M. A. Melkanoff such runs have been made, and the results are given in tables 5 and 6. The agreement is generally satisfactory, and the remaining small discrepancies may be accounted for by slightly different choices of the numerical parameters in the programmes, and to the accumulation of small rounding errors. The agreement is sufficiently good for comparison with experimental data.

§ 6. COMPARISON WITH EXPERIMENTAL DATA

It is frequently necessary to compare the calculated angular distributions and polarizations with experimental data, and it is convenient to incorporate facilities for doing this into the programme. The experimental data forms part of the input, and when the rest of the calculation is complete, the values of

$$\Delta_\sigma = \sum \left[\frac{\left(\frac{d\sigma(\theta)}{d\Omega}\right)_T - \left(\frac{d\sigma(\theta)}{d\Omega}\right)_E}{\delta\left(\frac{d\sigma(\theta)}{d\Omega}\right)_E} \right]^2 \quad \text{and} \quad \Delta_P = \sum \left(\frac{P_T(\theta) - P_E(\theta)}{\delta P_E(\theta)} \right)^2 \qquad (34)$$

where the suffix E denotes experimental data, are calculated for each experimental point and included in the output.

Table 5. Comparison of present programme with that of Melkanoff for 17 MeV protons on gold, with $U = -48$ MeV, $W = -8$ MeV, $r_0 = 1{\cdot}3$ F, $r_C = 1{\cdot}3$ F, $a = 0{\cdot}5$ F, $A_1 = 1$, $A_T = 197$. Both form factors are Saxon–Woods, and there is no spin–orbit potential. All cross sections are in millibarns per steradian, and are written in floating point form

θ_{CM}	$d\sigma/d\Omega$ (Melkanoff)	$d\sigma/d\Omega$ (present work)
20	3·202, 4	3·203, 4
40	1·549, 3	1·549, 3
60	2·951, 2	2·951, 2
80	6·728, 1	7·624, 1
120	1·460, 1	1·458, 1
160	7·825, 0	7·807, 1
σ_R	984·7 mB	985·2 mB

Table 6. Comparison of present programme with that of Melkanoff for 17 MeV, protons on copper, with $U = -46$ MeV, $W = -9$ MeV, $U_S = -1444$ MeV, $W_S = 361$ MeV, $r_0 = 1{\cdot}33$ F, $r_C = 1{\cdot}33$ F, $a = 0{\cdot}48$ F, $A_1 = 1$, $A_T = 64$. (In all these check calculations Melkanoff's values of the constants in eqns. (26) and (27) were used. These are 0·158051 and 0·219438 respectively)

θ	$d\sigma/d\Omega$ (Melkanoff)	$d\sigma/d\Omega$ (present work)	P (Melkanoff)	P (present work)
20	2·807, 3	2·809, 3	−0·0590	−0·0578
40	1·819, 2	1·822, 2	0·0425	0·0426
60	2·140, 1	2·136, 1	0·2614	0·2623
80	1·563, 1	1·567, 1	−0·1213	−0·1168
120	3·396, 0	3·389, 0	−0·7876	−0·7811
160	2·310, 0	2·310, 0	0·6727	0·6646
σ_R	1054·7 mB	1055·0 mB		

Experimental differential cross sections are often subject to a larger absolute than relative error. If the incident particle is charged, and the cross-sections are available to small angles, it is then desirable to normalize the experimental cross-sections to the theoretical in this region. A facility to do this for a specified number of experimental points was incorporated in the programme.

ACKNOWLEDGMENTS

We would like to thank Professor D. H. Wilkinson, F.R.S., for suggesting and guiding this work, Professors F. Bjorklund, A. E. Glassgold and M. A. Melkanoff who have communicated details of their own optical model work, the Director of the Oxford University Computing Laboratory for the use of the computer, Miss N. Reynolds, Miss S. Tilley and the staff of the Computing Laboratory for their assistance, and the D.S.I.R. for its support.

Note added in proof.—Professor M. A. Melkanoff has now published (University of California Press, 1960) a detailed account of his own calculations, with full derivations of the equations used in the above paper.

REFERENCES

Bjorklund, F., and Fernbach, S., 1958, *Phys. Rev.*, **109,** 1295.
Fox, L., and Goodwin, E. T., 1949, *Proc. Camb. phil. Soc.*, **45,** 373.
Froeberg, C. E., 1955, *Rev. mod. Phys.*, **27,** 399.
Hartree, D. R., 1952, *Numerical Analysis* (Oxford: University Press), p. 246.
Hildebrand, F. B., 1956, *Introduction to Numerical Analysis* (McGraw-Hill), p. 233.
Shepansky, J. R., and Butler, S. T., 1956, *Nucl. Phys.*, **1,** 313.
Stegun, I., and Abramowitz, M., 1955, *Phys. Rev.*, **98,** 1851.

CORRESPONDENCE

Giant Spin Density Fluctuations

By J. C. Phillips†
Royal Society Mond Laboratory, Cambridge

[Received August 17, 1960]

Recently Overhauser (1960) has presented a one-dimensional model of interacting fermions which has the remarkable property that it exhibits in the Hartree–Fock approximation spin density fluctuations in the presence of an arbitrarily weak repulsive interaction. He has also argued that the qualitative features of his results can be obtained in two and three dimensions, and has thereby called into serious question the modern electron theory of metals.

Overhauser's spin-fluctuation state is based on energy gaps generated by exchange. The situation in one dimension is especially favourable for two reasons:

1. Very little additional kinetic energy is required to generate the spin fluctuations. In the weak coupling limit (Overhauser's $n \to \infty$) the additional longitudinal kinetic energy vanishes exponentially.

2. The exchange interaction is coherent in one dimension, since only one propagation vector **q** is used. In general the additional exchange energy ΔJ (we use Overhauser's notation) contains a factor $\delta_{qq'}$. If the electrons are divided into m equivalent groups with different **q**'s, ΔJ is multiplied by $1/m$. This has the effect of replacing n everywhere by mn.

To see how these factors nullify Overhauser's results in three dimensions, we consider the most favourable case, the cubic fluctuations sketched in Overhauser's fig. 2. In contrast to the one-dimensional case the perturbed states here necessarily have an additional 'transverse' kinetic energy ΔU arising from the non-spherical occupied region. Again choosing the most favourable case, $n=1$, we find

$$\begin{aligned} W &\simeq 2NE_{\mathrm{F}}(1-\coth 2mn), \\ &\simeq -4NE_{\mathrm{F}}\exp(-12) = -0{\cdot}024NE_{\mathrm{F}} \qquad (1) \end{aligned}$$

$$\Delta U \simeq 0{\cdot}024NE_{\mathrm{F}}, \qquad (2)$$

so that in this case the non-magnetic, ferromagnetic and spin-fluctuation states all have nearly the same energy. If $n<1$, however, the ferromagnetic state will be lowest (since its exchange energy is not reduced by the factor m^{-1}) while if $n > 1$ the non-magnetic state will be lowest. In normal metals

---

† National Science Foundation Post-doctoral Fellow.

$$n \simeq 4E_F / \langle v \rangle \simeq 10 \quad \ldots \ldots \quad (3)$$

with $\langle v \rangle = N\gamma/L \simeq 2\,\mathrm{ev}$, $E_F \simeq 5\,\mathrm{ev}$. Thus in normal metals W is negligible compared with ΔU.

Overhauser has suggested that ΔU can be reduced by increasing m. While it is not convenient to analyse all possible combinations of spin-fluctuation states, it can be seen from (1) that increasing m reduces W exponentially, while ΔU is decreased only like m^{-2}. Thus it appears that unless n is very near 1 either the non-magnetic or ferromagnetic Hartree–Fock states will have lower energy than Overhauser's spin-fluctuation states. This conclusion is apparently valid for fairly general short-range repulsive interactions (including screened Coulomb interactions).

Recently Kohn and Nettel (1960) have arrived at conclusions similar to ours in the weak interaction limit ($n \gg 1$), by very general arguments which apply explicitly to the Hartree state. While our arguments are more particular, they show directly why exchange generates spin density fluctuations in the Hartree–Fock states for one but not for two or three dimensions.

ACKNOWLEDGMENT

I am grateful to Dr. L. M. Falicov for assistance with certain calculations.

REFERENCES

KOHN W., and NETTEL, S. J., 1960, *Phys. Rev. Letters*, **5**, 8.
OVERHAUSER, A. W., 1960, *Phys. Rev. Letters*, **4**, 462.

The Etching of Sub-structures in Beryllium

By J. Sawkill and J. E. Meredith
Tube Investments Research Laboratories, Hinxton Hall, Cambridge

[Received July 27, 1960]

In the course of some work on the electropolishing of beryllium, using the commercial 'Disa Electropol' apparatus and electrolytes, it was found that beryllium was being etched in addition to being electropolished. With commercially pure cast beryllium both grain boundaries and sub-boundaries were delineated, and in addition there were etch figures in the grains. It was subsequently found that the commercial A2 electrolyte, containing, according to Jacquet (1956), perchloric acid, ethyl alcohol, and butyl cellosolve, could be used simply as an etchant on surfaces previously electropolished or mechanically polished. However, a fresh solution did not etch the boundaries. Only after electropolishing beryllium with it for a few hours did the solution work as an etchant. It was also discovered that the etchant did not pit the surface, but rather, it produced a deposit at the boundaries. For example, the boundaries could be 'moved' by brushing the surface, and observations in phase contrast illumination showed the boundaries to be standing proud of the general surface.

An attempt was made to analyse the deposit by evaporating a carbon film on to an etched surface, stripping it, and examining the film, with the deposit attached, by electron diffraction in an electron microscope. The deposit could easily be recognized in the microscope, but it did not give a crystalline diffraction pattern. Recently, however, etched surfaces have been examined in an electron probe x-ray microanalyser and the deposit has been shown to be copper.

The action of the etchant is thus to decorate the boundaries and other sites with copper, and it is presumed that the fresh solution did not etch because it did not contain copper ions, whereas the electropolishing of beryllium allowed the copper, present as an impurity in the metal, to go into solution. The next step was to add a few crystals of copper sulphate to the fresh A2 solution, and this then etched perfectly well. Finally, it has been shown that the A2 solution is not necessary as an ingredient. The best etchant found so far is an aqueous solution of copper sulphate, with the copper content at a few hundred parts per million. It is also possible to deposit silver at the boundaries using a silver nitrate solution, and gold using a gold chloride solution, although in the latter case the chloride ions cause excessive pitting of the surface.

Figures 1 and 2† show respectively the microanalyser electron image and x-ray image taken in copper radiation from a surface etched in copper sulphate solution. Figure 2 shows conclusively the copper at the three grain boundaries and additionally at sites within the grains. It was possible to prove that the radiation came from the deposit and not, for example, from the grain boundaries themselves.

Examples of the use of the copper sulphate etchant are given in figs. 3 and 4. Figure 3 is an optical micrograph of cast beryllium showing sub-boundaries and grain boundaries. Figure 4 shows the complex polygonized structure produced by deforming hot extruded beryllium at room temperature and annealing for 24 hours at 850°c. In both cases the misorientations across the sub-structures were such that they could not be detected by polarized light methods. Some recent experiments on the heat treatment of beryllium indicate that impurities in the metal may play a part in the etching reaction.

ACKNOWLEDGMENTS

We thank Mr. A. E. Parsons for assistance with the metallography and Miss M. Nevard for carrying out the x-ray microanalysis. Part of this work was supported by a contract from the U.K.A.E.A. This note is published by permission of the Chairman of Tube Investments Ltd.

REFERENCE

JACQUET, P. A., 1956, *Met. Rev.*, **1**, 214.

---

† All figures are shown as plates.

Stress Concentrations at Crystal Surfaces and the Embrittlement of Sodium Chloride

By D. M. Marsh
Tube Investments Research Laboratory, Hinxton Hall, Saffron Walden, Essex

[Received July 4, 1960]

The brittleness of ionic crystals has attracted considerable attention recently and the purpose of this letter is to suggest an explanation of this effect in terms of stress concentrations at surface steps and other irregularities. The author has been studying the stress concentrations which may exist at the root of such surface steps using frozen-stress photoelastic techniques on large models. The experimental results show that a step, as in fig. 1, exhibits a stress concentration factor at its root given by

$$\text{shear s.c.} = \text{tensile s.c.} = 1 + 0{\cdot}7\sqrt{(l/r)}.$$

This type of relation has been verified over large range of values of l/r and for two different riser angles. The point of note is that the stress concentration is found to be almost equal to that at a Griffith crack of comparable dimensions, and so may be very severe.

Fig. 1

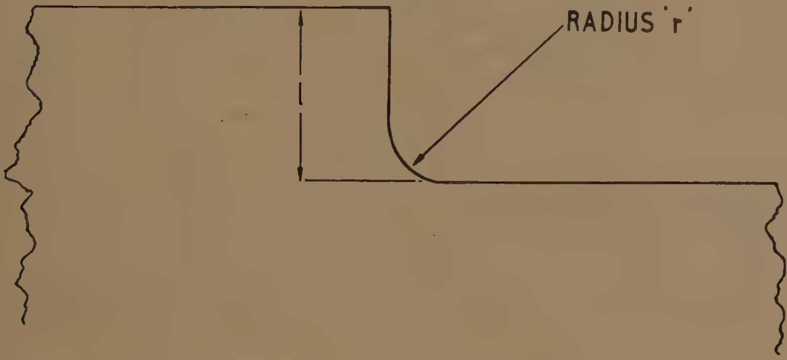

It is suggested that such stress concentrations embrittle ionic crystals by two alternative mechanisms:

(1) In a ductile crystal, failure is initiated at an internal defect which is only effective as a crack source after severe work-hardening and deformation of the whole crystal, as only then will it sustain a fatal stress concentration (Stokes *et al.* 1959 a). However, a surface stress concentration provides an alternative crack source which is available from the beginning of stressing and so may cause almost immediate failure.

(2) The surface stress concentration raises the stress locally so that a small length of crystal deforms and fractures before there is much overall strain. This embrittlement is assisted by the flow-induced fracture mechanism (Stokes *et al.* 1959 a) specific to ionic crystals, which limits the permissible *local* flow before fracture.

The experimental evidence for the first mechanism is provided by the fracture faces of many brittle specimens on which the surface defect responsible for failure can be clearly seen at the source of fracture. This experimental evidence was suggested by some interesting results of Stokes *et al.* (1959 b). They showed that NaCl single crystal bars could be made reliably and permanently ductile by washing, if every trace of solution was subsequently removed from the surface. However, their as-cleaved specimens were often brittle, and ductile specimens could be made brittle by two treatments :—

(1) If a drop of solution was allowed to dry on the surface to form a ‘ stain ’.

(2) If carborundum was sprinkled onto the specimens.

They further showed that while fracture of the ductile bars was initiated internally, the failure of brittle specimens started at the surface. However, the present author has found that not only is failure initiated at the surface in such specimens, but also that a surface step or notch could be found at the source of the fracture. For example, fig. 2 (*a*) (Pl. 151) shows that fracture started from a step on the surface of a ‘ stained ’ specimen and fig. 2 (*b*) shows initiation at a cleavage step which intersects the fracture face. The effect of cleavage steps may be further demonstrated by deliberately cleaving specimens slightly skew to the $\{100\}$ faces to give gross steps. Such specimens are invariably brittle. Fracture faces of carborundum-treated specimens show that failure starts from the roots of sharp notches which have been chipped out of the specimen surfaces. In contrast fig 2 (*c*) shows the internal initiation of fracture in a washed specimen.

In general a complete range of surface-initiated fractures may be found from those in which fracture is almost completely brittle as in fig. 2 (*b*) to those in which the surface stress concentration is small and considerable flow has occurred before failure. In the latter instances it is presumed that the small surface stress concentrations have been assisted by the long-range stress concentrations, created by plastic flow, which cause the characteristic ‘ chequerboard ’ patterns observed in polarized light.

Experimental evidence for the second embrittling mechanism (i.e. localization of strain) is provided by an experiment in which small semi-circular notches were washed out of NaCl bars before annealing. These were found to be brittle in four-point bending despite being given the standard washing treatment (Stokes *et al.* 1959 b) after the anneal. Micrographs in polarized light showed intense deformation at the notch only, while the fracture at the notch showed the characteristic ductile failure as in fig. 2 (*c*). Thus premature failure was by localization of slip rather than by limitation of slip.

One advantage of the present theory is that it provides a common mechanism for all of the above specimens and no evidence was found in NaCl for the special embrittling mechanism suggested by Stokes *et al.* (1959 b) to account for the brittleness of their stained specimens. However, microcracks such as they found in ‘ as-cleaved ’ MgO, certainly assist embrittlement when present.

It is important to ensure that the proposed mechanisms are not equally applicable to metals as these do not exhibit this embrittlement. It is also important to ask why the surface steps and notches do not render themselves harmless by flow as do stress concentrations in metals. Two obvious reasons are :

(1) The surface stress concentrations can be more easily and quickly relieved in metals owing to the higher mobility of dislocations and the larger number of slip systems available.

(2) In ionic crystals relief of the stress concentration by flow merely promotes failure by the second mechanism—a mechanism which is much more effective in ionic crystals due to the internal defect mentioned above.

In summary, it has been suggested that the embrittlement of NaCl is often due to the presence of surface steps and notches which act as stress raisers and cause premature failure by two distinct mechanisms. A fuller and more rigorous treatment of these ideas will appear elsewhere.

ACKNOWLEDGMENTS

My thanks are due to Mr. J. E. Gordon and other colleagues for their interest and helpful criticism of the manuscript. The letter is published by permission of the Chairman of Tube Investments Limited.

REFERENCES

STOKES, R. J., JOHNSTON, T. L., and LI, C. H., 1959 a, *Phil. Mag.*, **4**, 920; 1959 b, Sixth Tech. Rep. ONR Project No. 2456 (00) NR 032–451 (to be published in *Trans. Amer. Inst. min.* (*metall.*) *Engrs*).

REVIEWS OF BOOKS

Elements of the Kinetic Theory of Gases. By E. A. Guggenheim. (Pergamon Press, 1960.) [Pp. xii+92.] Price 17*s*. 6*d*.

The physicist or physical chemist whose knowledge of the kinetic theory of gases stops at about the level of the formula $\eta = \frac{1}{3}nm\bar{c}l$ is often daunted by the mathematical complexity which accompanies more exact treatments of transport phenomena. Professor Guggenheim does not eschew mathematics —that is not his purpose—but by taking as his standard example the hard sphere model of a gaseous molecule he is able to explain the physical basis of the sophisticated theory with a minimum of computational involvement. Moreover, he shows that even this crude model can be made to give fairly close agreement with experiment when it is worked out correctly. The moral of this analysis, that this sort of data does not give any exact indication of the form of intermolecular forces, he drives home by a similar careful discussion of the second virial coefficient in terms of the scarcely less crude square well potential. In a final chapter he employs data for solid as well as gaseous argon to synthesize an interaction potential for this particular atom. Here, as in the rest of the book, the clarity of the presentation gives great pleasure ; one can recommend the book with enthusiasm to anyone who wishes to take his understanding of kinetic theory beyond the scope of a normal undergraduate course.

A. B. P.

An Introduction to Thermonuclear Research. Albert Simon. (Pergamon Press, 1959.) [Pp. ix+182.] 35*s*.

The full title of this book, which is *An Introduction to Thermonuclear Research.— A series of lectures given in* 1955, gives a very good indication both of its scope and limitations. Although an enormous number of papers on controlled thermonuclear research have appeared since the removal of security restrictions in 1958, there have been very few attempts to provide books which assemble the material in an orderly fashion for the benefit of the non-specialist reader. Dr. Simon's book sets out to explain to such a reader what is being attempted, but does not attempt to explain what progress has been made in recent years. For no attempt has been made to refer to material published since 1956, and the reader who is looking for an up-to-date account of the subject will be disappointed. But the book does provide an excellent introductory account of the more important proposals for making thermonuclear reactors. It is clearly written, and the author explains the subject by means of simplified qualitative arguments, avoiding long and complicated mathematics.

The early chapters deal with the potentialities of fusion reactors, the basic conditions which have to be met in such reactors, and the motion of charged particles in magnetic fields. In the next four chapters, the author explains the fundamentals of the Stellarator, of mirror machines and of pinch devices. Finally there is a chapter on stability and another on the diffusion of plasma across magnetic fields. The emphasis throughout is on the principles involved, and very little is said about experimental apparatus or results.

T. F. J.

BOOK NOTICES

Progress in Elementary Particle and Cosmic Ray Physics. Vol. V. Edited by J. G. Wilson and S. A. Wouthuysen. (North Holland Publishing Company.) [Pp. 461.] £4 5*s*. 0*d*.

A Collection of Mathematical Problems. By S. M. Ulam. (New York: Interscience Publishers.) [Pp. 150.] $5.00.

Penetration of Charged Particles in Matter. Proceedings of an Informal Conference, Gatlinburg, Tennessee, September 15–18, 1958. Edited by E. A. Uehling. Nuclear Science Series Report No. 29. (Washington, D.C.: National Academy of Sciences, National Research Council, 1960.) $2.00.

A Physics Anthology. Edited by N. Clarke. (London: Chapman & Hall.) [Pp. 323.] £1 15*s*. 0*d*.

Physical Methods in Chemical Analysis. Vol. 1. Second revised edition. Edited by Walter G. Berl. (New York and London: Academic Press.) [Pp. 686.] $19.00.

Experimental Physics for Colleges. Revised edition. By Walter A. Schneider and Lloyd B. Ham. (New York: The Macmillan Company.) [Pp. 442.] £1 14*s*. 6*d*.

Chemical Instrumentation. A Systematic Approach to Instrumental Analysis. By Howard A. Strobel. (Reading, Massachusetts and London: Addison-Wesley Publishing Company.) [Pp. 653.] £3 14*s*. 0*d*.

University Physics. By F. C. Champion. (Glasgow: Blackie & Son Ltd.) [Pp. 786.] 30*s*.

Electromagnetic Wave Propagation. International Conference sponsored by the Postal and Telecommunications Group of the Brussels Universal Exhibition. Edited by M. Désirant and J. L. Michiels. (London and New York: Academic Press.) [Pp. 730.] $22.00.

ERRATA

On Dislocations Formed by the Collapse of Vacancy Discs, by C. ELBAUM, 1960, *Phil. Mag.*, 5, 669.

Page 670, line 12: increases *should read* decreases.

Page 671, eqn. (5): the equation should read as follows:

$$T_c = \frac{1 - A\dfrac{(\mu\mathbf{b}^3)_{T_0}}{U_f}\,1 + 300(\beta + 3\alpha)}{\dfrac{1}{T_M} + A\dfrac{(\mu\mathbf{b}^3)_{T_0}}{U_f}(\beta + 3\alpha)} \quad . \quad . \quad . \quad . \quad . \quad (5)$$

[*The Editors do not hold themselves responsible for the views expressed by their correspondents.*]

Fig. 1

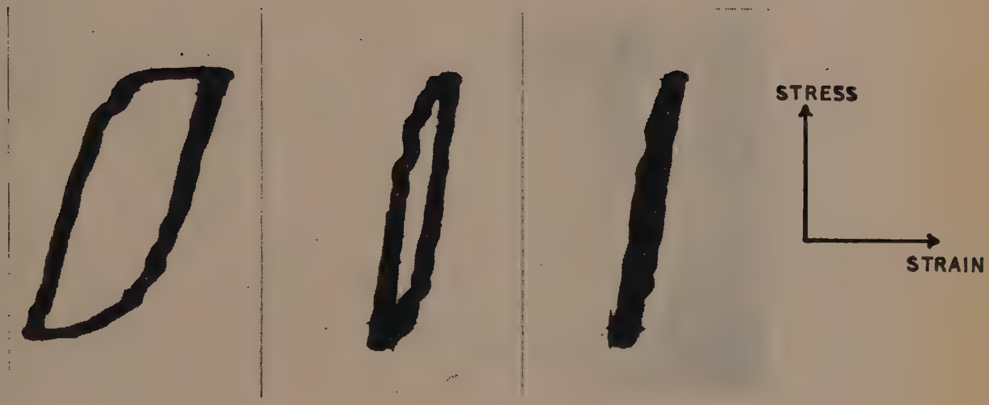

(*a*) (*b*) (*c*)

Hysteresis loops from an aluminium crystal fatigued at ± 700 g/mm^2 resolved shear stress at room temperature. (*a*) 400 cycles (0·6% life), (*b*) 2800 cycles (4% life), (*c*) 40 300 cycles (57% life).

Fig. 2

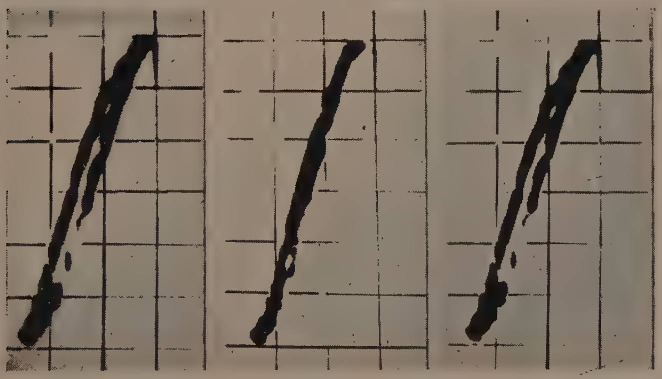

(*a*) (*b*) (*c*)

Hysteresis loops from a crystal fatigued at ± 1015 g/mm^2 resolved shear stress at −78°c. (*a*) 6500 cycles, (*b*) 6500 cycles, rested at room temperature then re-tested, (*c*) 6600 cycles.

Fig. 1

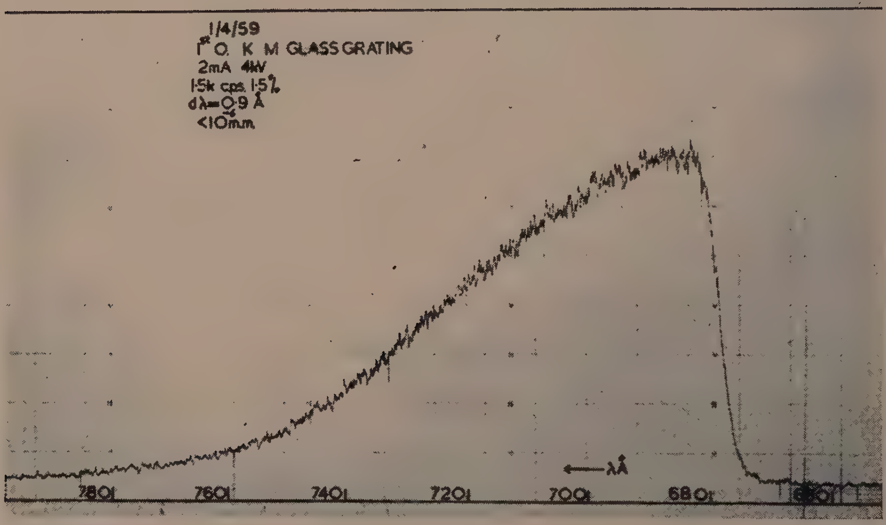

The M emission band of solid potassium.

Fig. 3

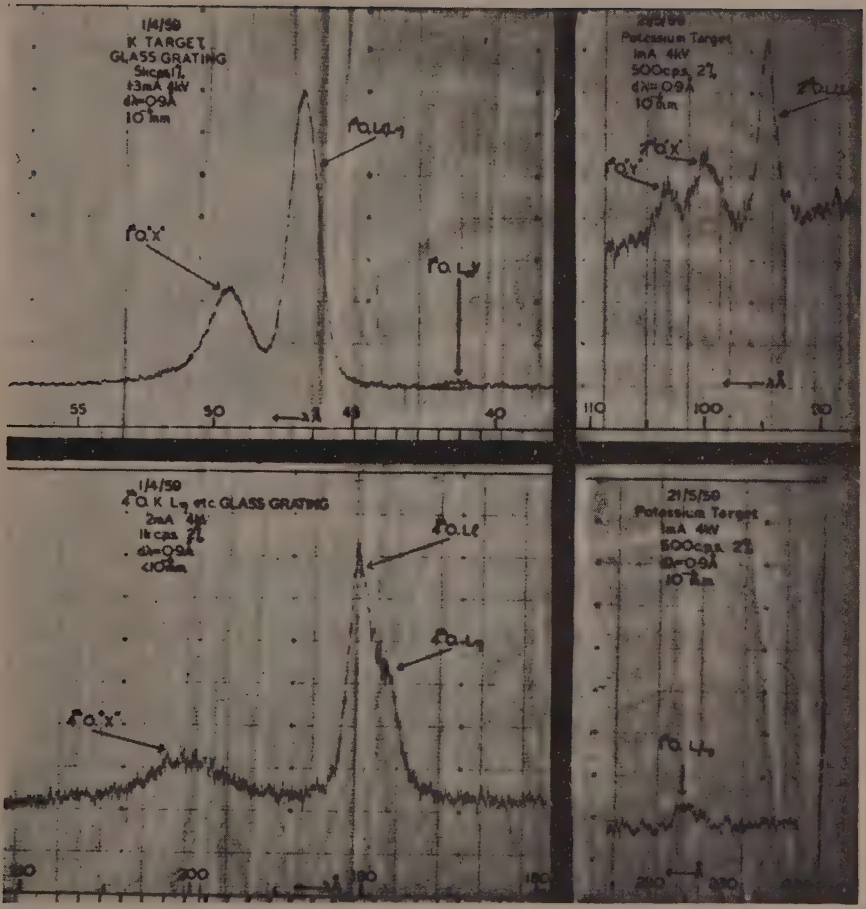

Emission lines from solid potassium in the 40–1000 Å range.

Upper left: 1st O.L_{23}V, 1st O.Ll, Lη, 1st O.X.
Upper right: 2nd O.Ll, Lη, 2nd O.X, 1st O.Y.
Lower left: 4th O.Lη, 4th O.Ll, 4th O.X.
Lower right: 1st O.L_1L_3.

Fig. 1

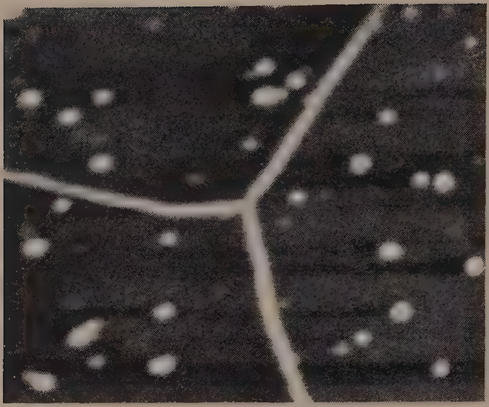

Microanalyser electron image of junction of grain boundaries.
Etched in copper sulphate solution. ×1450.

Fig. 2

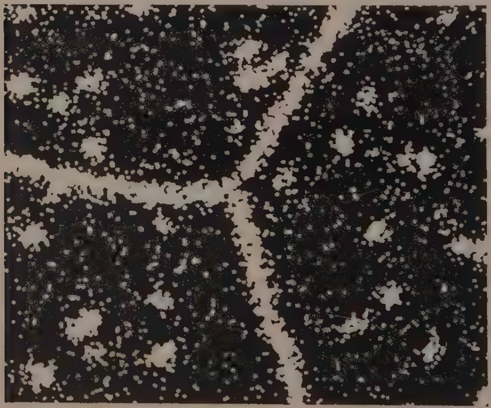

Same field as fig. 1, x-ray image taken in copper Kα radiation. ×1450.

Fig. 3

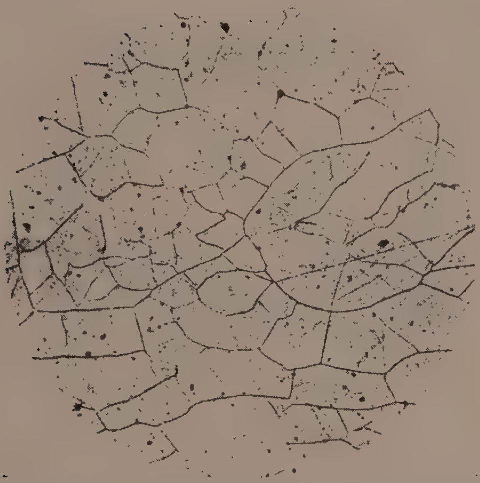

Optical micrograph of cast beryllium showing grain and sub-boundaries. Etched in copper sulphate solution. ×55.

Fig. 4

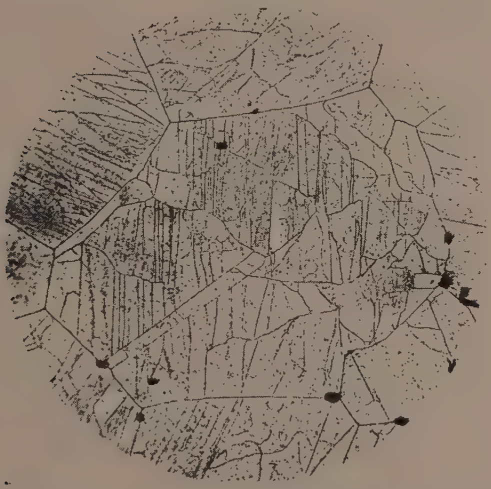

Complex polygonized structure in deformed and annealed beryllium. Etched in copper sulphate solution. ×110.

Fig. 2

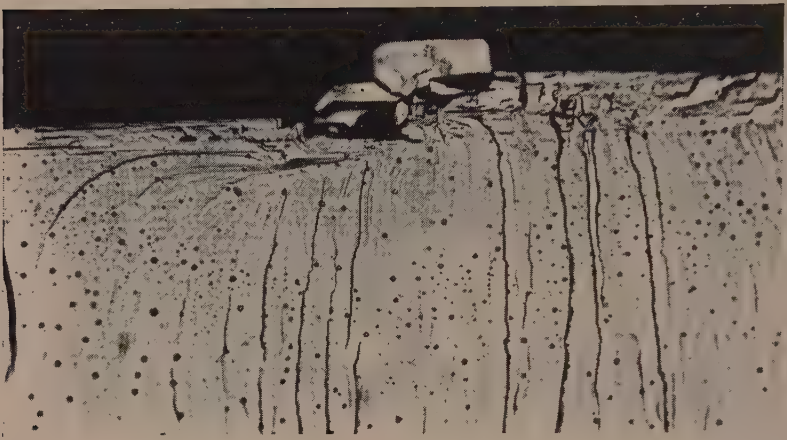

(*a*) ‘ Stained ’ specimen (× 570).

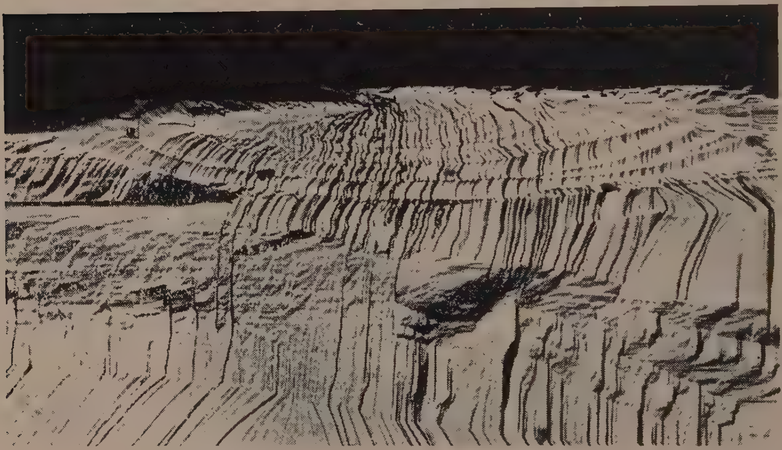

(*b*) As-cleaved specimen (× 100).

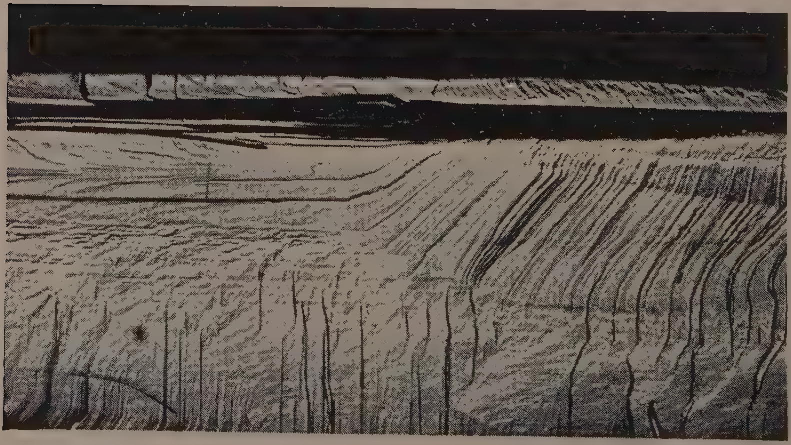

(*c*) Standard washed specimen (× 100).

Fracture faces of NaCl.

The Soft X-ray Spectra of Lithium, Magnesium and Aluminium and their Alloys†

By R. S. Crisp‡ and S. E. Williams
Department of Physics, University of Western Australia

[Received June 30, 1960]

Abstract

The Li K and Mg L_{23} spectra have been observed from a range of Li–Mg alloys, evidence for electron transfer from Mg being obtained. More distinct changes have been observed for the same spectra when Li was evaporated onto solid Mg and Mg onto solid Li. Changes in the Li K and Al L_{23} were observed when Li was evaporated onto Al and in the Al L_{23} when Al was evaporated onto Mg. No changes greater than 5×10^{-2} ev were observed in edge wavelengths or edge widths although marked depopulation of higher energy states occurred in Mg and Al. It is inferred that changes in the screening of K and L levels compensate almost exactly for the effects of electron transfer. The results of Catterall and Trotter (1959) were confirmed in that the Mg band contracted and the Li band extended on the low-energy side. Li deposited on Al shows a K spectrum without any metal edge, suggesting that the first zone is filled and that there is no overlap with the second zone.

§ 1. Introduction

The effect of alloying on the valence band energy levels of metals of low atomic number has been the subject of a number of investigations. Earlier work seeking possible changes in the soft x-ray spectra was hampered by the difficulties of photographic photometry in this region which makes accurate measurements of intensities almost impossible to obtain. The attendant need to dissipate large amounts of power in the alloy target and the inability of the photographic method to detect the short-term effects of target contamination are added handicaps. As a consequence few definite and confirmed effects resulting from alloying have been recorded.

Photoelectric detection based on photon-counting enables the reproduction and measurement of intensities to 1 or 2% in this region. The power dissipated in the target is reduced to about one-hundredth of that needed for photography, and changes of intensity with time resulting from target contamination can be observed and therefore often avoided.

The first changes caused by alloying in the Li–Mg system observed by photoelectric means were reported by Catterall and Trotter (1959). Evidence was obtained pointing to electron transfer from the constituent of higher to the constituent of lower valency while the spectrum of each constituent retained a recognizable though somewhat modified identity.

---

† Communicated by the Authors.
‡ Now at National Research Council, Ottawa.

The observations reported below, though based initially on the same alloy system, recorded the most marked changes in metallic combinations not normally regarded as involving alloying since they consisted of evaporated layers of one constituent on a solid, cooled base of the other. Since the changes can be most effectively interpreted in terms of electron transfer, alloying, even though it be very restricted in the dimension of depth, is assumed to occur.

§ 2. EXPERIMENTAL

The emission spectra were obtained with the photon-counting spectrometer previously described (Fisher *et al.* 1958). In the initial experiments on Li–Mg alloys, target currents up to 11 mA and voltages of 4 kv were used. The pressure in the specimen chamber was about 10^{-5} mm and carbonaceous contamination of the target surface by decomposed residual vapours was serious. With this type of contamination intensities decrease linearly with time (Crisp 1958 a). Subsequently the vacuum in the specimen chamber was improved to $1\text{–}2 \times 10^{-6}$ mm and the target was almost completely surrounded by a copper baffle cooled to −115°c by external conduction (Pollard 1953) to a rod immersed in liquid air. The cooling could be maintained indefinitely and the target was kept under vacuum for one or two days before making observations. So long as the baffle was cooled below −100°c carbonaceous contamination was reduced to a negligible amount. A glass window allowed observation of the interior of the specimen chamber.

The target current was stabilized to 0·5% (Crisp 1958 b), enabling relative intensities to be reproduced to within 1 or 2%. The variable speed drive was replaced by a gearbox with fixed speeds so that spectra could be accurately reproduced to a chosen wavelength scale. The use of more sensitive photomultipliers† allowed the reduction of target currents to about 1 mA. The aluminium grating used in previous work was replaced by a glass grating of similar constants. The resolution, calculated according to the criterion of Fisher (1954), was maintained at 0·9 Å.

A four-sided target with faces of Cu, Al, Mg and Be was used so that spectra for the relevant elements either from the solid or from evaporated layers on Cu could be recorded without breaking the vacuum. Solid Li specimens were accommodated in a different target. The tungsten carbide scraper was used to clean target surfaces when required. The target area covered by the electron beam is about 10 × 5 mm.

All spectra reproduced have been traversed from the high-energy side so that the recorder trace (i.e. the time axis) runs from right to left. The chart speed was always one inch per minute. If contamination is occurring the low-energy side will be reduced in intensity and the maximum may be shifted slightly towards higher energies. All wavelengths in a given spectrum appear to show similar rates of contamination with the exception of the Li 'line' at 253 Å which grows approximately as $[1-\exp(-xt)]$. The appearance of this 'line' and the closely associated fluroescence of the Li target will be discussed elsewhere, but it should be recorded that after it was discovered that a massive evaporation of Li has the effect of suppressing the appearance of the 'line' this precaution was always taken before recording a Li spectrum.

---

† Made by the Institut für technische Physik der E.T.H. (Abteilung für Industrielle Forschung).

Our Li K spectrum has been published elsewhere (Crisp and Williams 1960). The Mg L_{23} and Al L_{23} spectra seen by our instrument are shown in figs. 2 and 5† respectively. Although the resolution is insufficient to record the full height of the Al 'spike', the small kink at about 181 Å is always seen and constitutes a real feature of the spectrum not previously recorded. Its position corresponds to the minimum in Matyas' theoretical N(E) curve (Tomboulian 1957) which marks the lowest energy for states in the second Brillouin zone.

Edge wavelengths, taken at half maximum intensity of the edge were checked by reference to the fiducial marks made on the recorder trace at every revolution of the lead screw. Variations less than 0·2 Å (equivalent to about 0·05 ev) are considered to be within the limits of experimental error. Edge widths, taken between the points of 5% and 95% maximum intensity can be measured to the same accuracy.

§ 3. LITHIUM–MAGNESIUM ALLOYS

Solid specimens of alloys of Mg–Li containing 15, 40 and 70 at. % Li were examined. The alloys were received as metal bars contained in a clear, but unidentified packing oil. Specimens were milled to shape using the packing oil as cutting fluid. They were pressed into a frame which was soldered to the target holder with Woods' metal. Heating of the specimens was in this way kept to a minimum. Any oxidation of the target surface was subsequently removed in vacuum by the scraper. Thermal contact of the specimens with the water-cooled target holder was poor.

At target currents up to 11 mA and a pressure 8×10^{-6} mm a rapid time variation of intensity was observed for both Mg and Li. The form of the variation is shown in fig. 1. As the Li intensity increased a strong blue fluorescence appeared over the bombarded area. The time variation suggested that under the action of the beam Li atoms were migrating to the surface. Although spectra can be recorded at a time when the variation of intensity is slow, it is doubtful whether the surface layer examined has the same composition as the original alloy.

Subsequently, in the improved vacuum and with improved sensitivity, the intensity variation was examined for target currents between 0·7 and 4 mA. The intensity was then found to decay exponentially for both constituents with a half-intensity period about one minute for the 30/70 and 60/40 alloys and somewhat larger for the 85/15 alloy. This is approximately the same as the half-period for growth of the Li 'line'.

---

† Figures 2–5 are shown as plates.

Figure 2 shows recorded spectra† for the three alloys together with the spectrum of pure Mg. Contamination in these cases is slower but in the 30/70 alloy the Mg has disappeared in less than 9 min and has been replaced by the Li 'line'.

In general the changes in the Mg spectra agree with the results of Catterall and Trotter (1959). There is a distinct diminution of the Mg 'spike', indicating a depopulation of the higher electron states. This diminution becomes more marked as the fraction of Li increases, though its exact extent is masked by the overlap of the Li 'line'. The edge wavelength does not change appreciably and there is no convincing evidence that the edge is broadened. The low-energy maximum appears to shift from 261 Å in pure Mg to about 257 Å in the alloys, but this may again be caused by the Li 'line'. Because of low intensities and the effects of contamination it was not possible to obtain information about the shape of the Li K spectrum.

Fig. 1

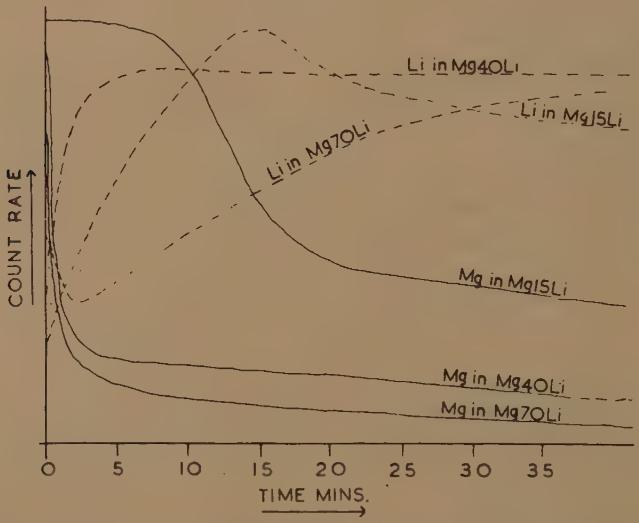

Time variation of intensity (counts per second) for Li K and Mg L_{23} spectra in various Li–Mg alloys. Target current 11 mA voltage 4 kv. Pressure 10^{-5} mm.

§ 4. Evaporated Layers

Since it appeared, from the intensity changes obtained with high target powers, that Li atoms were migrating toward the surface and possibly producing a lithium-rich layer on the surface, it was decided to look at the Mg spectrum when a lithium-rich layer was deliberately produced by evaporating Li onto a solid Mg target. The result was surprising. The Mg spectrum was modified to a much greater extent than in the alloy spectra. Subsequently, Mg was evaporated onto Li, producing further big changes in the Mg spectrum. The effect of evaporating Li, Na and K onto Be, Mg and Al was examined. Combinations for which alloying does not normally occur showed no spectrum changes. The only appreciable changes involved combinations of Li, Mg and Al which are discussed below.

---

† Date, target, full-scale count rate, percentage error at half-full scale (Elmore and Sands 1949) target current and voltage, optical resolution and pressure are recorded on each spectrum reproduced.

Examples of recorded spectra illustrating the effect of evaporating Li onto Mg and Al, Mg onto Li and Al onto Mg are shown in figs. 3, 4, and 5. Contamination was appreciable only in the case of Mg on Li where it has the effect of reducing intensities on the low energy side of the spectrum.

The changes in the spectra are so marked that it is assumed they are due to alloying, either instantaneously by diffusion following release of latent heat by the condensing element, or very rapidly under the action of the bombarding electrons, even though the underlying constituent is held at the temperature of the cooling water. In the interval of less than a minute between ceasing evaporation and recording the maximum of the Mg peak the changes have been completed. Alloying in thin films has been discussed by Weaver and Hill (1959) who record that Michel (1956) observed immediate alloying following successive evaporation of Ag–Zn and Ag–Sn. Michel's suggestion that alloy formation is observable for metal pairs whose diffusion constants at room temperature are larger than 10^{-20} cm^2/sec is not consistent with the observation of changes in the L_{23} spectrum of Al deposited on Mg, the only pair for which diffusion constants are available. Fujiki (1959) has observed instantaneous alloying following successive depositions of metal vapours on a Formvar film, but in this case the latent heat released is sufficient to raise the temperature of the film. However, Fujiki showed that alloy formation was promoted by small grain size and large area of the substrate surface. Target surfaces subjected to repeated scraping would meet these requirements. The Li–Mg, Li–Al and Al–Mg systems have not been studied by electron diffraction.

Film thicknesses could not be quantitatively controlled, although a degree of control was obtained by running the furnace at minimum power for evaporation and switching off at different intervals after a visible film first appeared. In this way 'thin' and 'thick' films could be deposited. As the emission spectrum is produced in a surface layer of the order of 10^4 Å thick (Skinner 1940), it is assumed that for appreciable emission to be observed the film thickness could be at least of the order of 10^3 Å.

The spectra of each element are discussed separately below to facilitate comparison of the modifications with the spectrum of the pure metal.

§ 5. MAGNESIUM

The L_{23} spectrum of pure Mg seen by our instrument is shown in fig. 2. In fig. 3 are shown the spectra of Mg when overlain by Li and when evaporated onto solid Li. In fig. 6 various Mg spectra have been superimposed with the intensity at the low-energy maximum adjusted to a constant value, the remainder of the spectrum being normalized accordingly.

Three spectra of pure Mg were averaged; three of Mg under Li, four of Mg over Li and four of Mg in Mg_2Sn. The wavelength of the high-energy edge has in each case been calculated by comparison with the edge of pure Mg obtained with the grating in the same adjustment. The averaged curves are taken from spectra in which evaporation has been continued until no further changes occur in the shape of the Mg spectrum. A light evaporation reduces the Mg spike slightly making the spectrum resemble that from an Mg–Li alloy.

Fig. 6

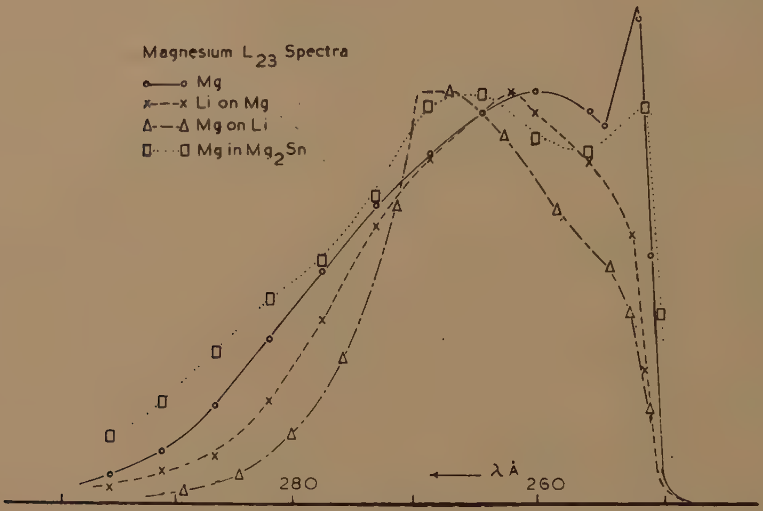

Smoothed averages of three spectra of pure Mg, three of Mg under Li, four of Mg deposited on Li and four of Mg in powdered Mg_2Sn. Intensities normalized to make the low-energy maxima equal.

From fig. 6 it is concluded that the edge wavelength is constant within the experimental uncertainty (5×10^{-2} ev), and that the width of the edge between the 5% and 95% maximum intensity points is similarly constant. Although the change in position of the low energy maximum from 260 Å for pure Mg to about 262 Å for Mg under Li is not established with certainty, the change to a flatter maximum with a mean at 267 Å for Mg on Li is real. This change represents a decrease of more than one electron volt in the energy of the states making contact with the boundary of the first Brillouin zone. Together with this shift in the maximum, the ratio of maximum intensity at the edge to maximum intensity in the band is 68% (probable error 1·5% from 17 spectra) for Li on Mg and 51% (probable error 3% from four spectra) for Mg on Li. The two spectra are quite distinct. On the low-energy side the Mg bandwidth is decreased in Mg under Li relative to pure Mg by about 0·5 ev. A similar decrease is found by comparing averaged spectra taken with the aluminium grating. This is in agreement with the results of Catterall and Trotter for Mg–Li alloys.

Although the Mg on Li shows a more marked decrease, this is largely if not wholly due to contamination. Assuming the contamination produced an exponential decrease in intensity (since it was associated with the appearance of fluorescence and the Li 'line') a rough correction of the intensities in the tail shows no definite decrease in the band width.

Li can dissolve in Mg to about 18 at. % and since the Mg remains in its h.c.p. state the Mg spectrum should not be much changed in shape. This is found to be so for Li on Mg. Mg can dissolve in Li to about 70 at. % Mg but the structure is b.c.c. and the Mg spectrum should be modified appropriately. The distinct difference between the Mg spectra noted above suggests that the Mg deposited on Li dissolves in the Li.

Between the maximum at 262 Å and the kink at 255 Å the intensities for pure Mg are higher than for Mg under Li. This difference, together with the possible shift of the maximum may result from a dilution of the spectrum of Mg containing dissolved Li by a small contribution from the spectrum of Mg dissolved in Li. In the case of Mg on Li the situation is reversed and the spectrum of Mg on Li may be diluted though the distinctive shape of the maximum is not lost.

Figure 6 also includes an averaged Mg spectrum from the intermetallic compound Mg_2Sn in powder form. Counting rates were low and the background was high in the four spectra averaged and only the general trend of the curve is significant, the position of the low energy maximum and the breadth of the band near the tail being to some extent dependent on the choice of background intensity. Since Mg_2Sn has a fluorite structure it was to be expected that the Mg L_{23} spectrum from this compound would be modified. However, it closely resembles the spectrum of pure Mg, the edge wavelength and edge width being unchanged. There is some indication of an increased band-width on the low-energy side. The result does not support Farineau's (1937) observation of similar K spectra for the constituents of the Al–Mg intermetallics, Al_2Mg_3 and Al_3Mg_2.

When Al is evaporated onto Mg no changes are observed in the Mg spectrum although as will be seen from fig. 5 the Al L_{23} is changed. Since a normal Mg L_{23} spectrum will be produced from the solid Mg target, this will be observed as well as that from the Mg in contact with the Al.

§ 6. ALUMINIUM

Figure 4 shows three recordings of the Al L_{23} spectrum for increasing thicknesses of Li deposited on solid Al. Figure 5 shows the normal Al spectrum seen by our instrument in which the resolution is insufficient to show the full extent of the high energy spike. There is also shown in fig. 5 the spectrum of Al evaporated onto Mg. Figure 7 shows the result of averaging three spectra of Al, four spectra of Al with a superimposed 'thick' layer of Li and two spectra of Al deposited on Mg.

The point chosen on the Al spectrum at which to normalize the intensities has been taken at about 189 Å. This is well below the maximum intensity of states in the first zone and was chosen on the assumption that the population of states in the first zone of Al would not be affected by alloying because the second zone is half-filled. This assumption is not borne out when the results are analysed.

The trend of absorption by Li is also indicated in fig. 7 following Skinner and Johnson (1937), with an arbitrary zero corresponding to the absorption at the low-energy side of the K edge. Li absorption should be roughly constant to the high-energy side of the normalizing wavelength. On the low-energy side there are two increases to a maximum at 196 Å which qualitatively correspond to the two regions in which the intensity of the modified spectrum of Al falls below that of pure Al. However, no quantitative match has been achieved and it appears that the N(E) curve of Al is modified in this region. The spectrum of Al on Mg shows distinct divergencies from that of pure Al in the same region and since these latter cannot be attributed to absorption they constitute further evidence for changes in the N(E) curve for the first zone.

Fig. 7

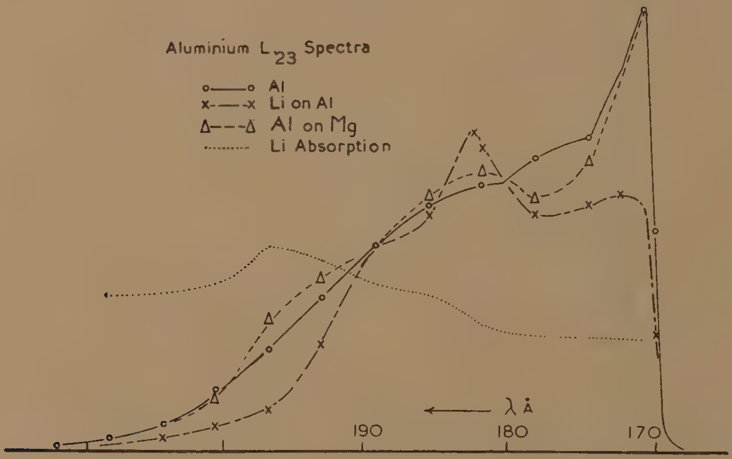

Smoothed averages of three L_{23} spectra of pure Al, four spectra of Al with a superimposed ‘ thick ’ layer of Li and two spectra of Al deposited on Mg. Intensities have been normalized to the same value at 189 Å. Kinks in the pure Al spectrum at 173 Å and 181 Å are reproducible. Li absorption in this region is also shown with an arbitrary zero and scale.

The prominent maximum at 183 Å may have been enhanced by the choice of normalizing wavelength and by Li absorption. Its position corresponds to the maximum density of states in the first Brillouin zone of pure Al. To the high-energy side the shape of the spectrum resembles Matyas' (Tomboulian 1957) theoretical N(E) curve with excision of states of higher energies. If, for the ‘ thick ’ layer of Li, it is assumed that no further change in the Al spectrum will result from increasing the thickness of Li, then by analogy with the case of Li on Mg, no dilution by the spectrum of normal Al from the underlying solid target should be present. Therefore the modified Al spectrum is the result of a combination of (i) structure changes which produce a different N(E) distribution, (ii) depopulation of higher energy states of the first and second zones resulting from electron transfer, and (iii) Li absorption whose undetermined extent makes estimates of the decrease in band width at the low energy side very hazardous.

For Al on Mg a normal Al spectrum produced in the unalloyed outer region of the Al film will dilute that from modified Al. The Al spike has not disappeared as with the thick Li layer and there is no absorption. However, structure changes in the alloyed Al could produce changes in the N(E) curve at lower energies. The choice of 189 Å as the normalizing wavelength then loses its significance.

The edge wavelength and edge width are apparently not changed and no edge shift to 171·8 Å reported by Gale and Trotter (1956) for Mg–Al alloys is present. Nothing can be said about the band width. There is no resemblance in the Al on Mg spectrum to the alloy spectra of Gale and Trotter.

§ 7. Lithium

The K spectrum of Li shows a distinct high energy edge extending to about 75% of the intensity at the maximum (Crisp and Williams 1960). On the low-energy side the shape and width of the band can be seriously affected by development of the Li 'line' whose maximum comes at 253 Å (Fisher *et al.* 1958). After the discovery that the development of the line and the associated fluorescence could be stopped by massive evaporation of Li as a 'getter' this was always done before recording Li spectra. The Li spectra of figs. 3 and 4 and the smoothed curves of fig. 8 are therefore not affected by the Li line.

Figure 8 shows the result of averaging four spectra of pure Li, four spectra of Li on Mg and four spectra of Li on Al. These have been normalized to the same intensity at the maximum and for the first two the edge is taken to extend to 75% of the maximum. Only two spectra of Li under Mg were recorded, neither suitable for analysis, and all that can be said is that for Li under Mg no differences from normal Li have been established.

Figure 3 shows that when Li is deposited on Mg there is a relative increase in intensities on the low-energy side of the spectrum. This accords with the observations of Catterall and Trotter for Li–Mg alloys. There is no observable change in edge wavelength, edge width or energy of the maximum. The latter energy is determined by the contact of the anisotropic Fermi surface with the first zone boundary and that this should be unchanged suggests that emission from the overlying b.c.c. Li is observed as well as that from the Li presumably dissolved in the h.c.p. Mg. Catterall and Trotter obtained a similar result for an alloy containing 20·9% atomic Li which presumably is mainly a solution of Li in Mg.

Figures 4 and 8 show that when Li is deposited on Al the Li spectrum is changed very radically. The high-energy edge has disappeared, the maximum has shifted and the band width has increased. The 'edge width' to 75% maximum intensity is now about 1·2 ev, comparable with the 'edge width' shown by non-conductors (Skinner 1940). The maximum has shifted about 0·5 ev to lower energies. The band width, including the tail, is about 8 ev compared with 4·2 ev for pure Li, for which the extrapolated band width is 3·0 ± 0·1 ev (Crisp and Williams 1960). If this spectrum comes from Li atoms at the interface combined with Al as LiAl, the first Brillouin zone of Li could be practically full. A spectrum such as that seen would be expected if the zone was full and an energy gap existed between first and second zones. Any zone overlap would prevent the disappearance of the edge.

Fig. 8

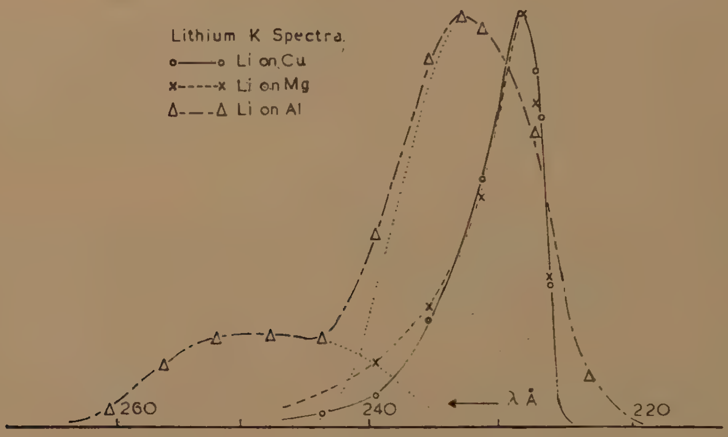

Smoothed averages of four K spectra of pure Li, four spectra of Li on Mg and four spectra of Li on Al. Intensities normalized to make the maxima equal. Dotted curves show a hypothetical separation of the Li on Al into two components, assuming the low-energy bulge is symmetrical about the maximum at 247 Å.

It should be emphasized that the low-energy bulge has nothing to do with the Li 'line'. Its maximum is at 247 Å compared with 253 Å for the 'line'. No fluorescence, which always accompanies the line, was visible on the target when these spectra were obtained. Figure 8 shows a tentative separation of the Li spectrum into two components assuming that the low-energy bulge is symmetrical about its maximum. The low energy component might result from the appearance of excitation states (Parratt 1959) of Li in LiAl. The width of the high energy component is about 5 ev.

§ 8. Discussion

The spectrum changes noted in Li–Mg alloys are seen to a much greater extent with evaporated layers. This is taken as evidence for instantaneous alloying at the interface. Observations made by Catterall and Trotter (1959) on Li–Mg alloys are supported by our results for both alloys and evaporated films. There is no change greater than 5×10^{-2} ev in edge wavelengths, or edge widths. The band width for the constituent of higher valency is lessened, the change showing up on the low-energy side. The band width of the constituent of lower valency is increased, the increase showing on the low-energy side. The exception is the case of Li deposited on Al in which the band shape is radically changed.

Since the Mg L_{23} under Li shows a complete loss of the spike, which is the result of second zone overlap, it is assumed that the depopulation of energy states due to electron transfer has progressed at least as far as the energy at the base of the spike, emptying the second zone entirely and the first zone also to some extent. However, the absence of any measurable change in energy of the edge shows that this emptying of the upper levels has been offset very effectively by changes in the screening of the L levels. The screening compensation is so much more exact than for the case of copper–zinc alloys discussed by Varley (1956), that a close connection between the extent of electron transfer, leading to changes in the population of energy states and the changes in screening of the inner levels, is indicated.

Since the edge has, in effect, moved up, the tail follows, and the energy range over which depopulation has occurred should be estimated from the narrowing of the band at the tail. It will be seen from fig. 6 that this energy range is approximately equal to that from the edge to the foot of the spike. If the structure remains the same the low-energy maximum should shift to higher energies by the same amount. This is not observed. As pointed out above, it is possible that the spectrum of h.c.p. Mg containing dissolved Li is diluted by the spectrum of Mg dissolved in b.c.c. Li for which the maximum is shifted to lower energies by the structure change. The required shift of low-energy maximum is seen in fig. 3 of Catterall and Trotter (1959) but the maximum for their pure Mg occurs at 264 Å compared with 260 ± 1 Å in our fig. 6.

The above considerations cannot apply to the intermetallic Mg_2Sn because it has a fluorite structure and the N(E) curve should be different. However, the increased band width, if real, is seen on the low-energy side as in Li, the edge energy being unchanged.

As regards Li on Mg, there is agreement with the observations of Catterall and Trotter that the intensities increase in the tail while the maximum does not change energy. If shielding is reponsible for there being no change in edge energy, increased population of high-energy states should move the maximum to lower energies and decrease the height of the edge. This has not been observed, either by Catterall and Trotter, for an alloy containing 20·9% atomic Li or by ourselves for Li on Mg. Whilst in our case the Li spectrum from the unalloyed part of the Li film would dilute that from the modified Li, the lack of any change at all in the maximum makes this an inadequate explanation.

The case of Li deposited on Al involves the most drastic change recorded in a soft x-ray spectrum. The energy at half-intensity of the modified Li spectrum is very nearly equal to the edge energy in pure Li, and the shift in maximum is approximately the same as the low-energy increase in band width. This accords with the arguments stated above. However, the shape of the maximum has changed considerably although the structure change from Li to LiAl is slight. If the tails and the maxima of the two spectra are brought into coincidence the pure Li edge approximately bisects the modified Li band. This supports the inference that the complete loss of high energy edge indicates a completely filled first zone with an energy gap above it.

The case of Al is more difficult to interpret. If, as assumed above the evaporation of Li was carried so far that no dilution by the normal Al L_{23} spectrum from the underlying solid is present, the observed Al spectrum results from the three effects previously listed. A structure change from f.c.c. Al to b.c.c. LiAl would produce a modification of the N(E) curve for Al, but its true extent is disguised by Li absorption.

Until the spectrum from bulk LiAl can be observed it is futile to analyse the modified Al spectrum. Dilution from pure Al may be reponsible for the greater prominence of the high energy spike in the Al overlying Mg. However, if this is so the modified Al spectrum must possess a more prominent maximum at 182 Å and the modification of the low-energy region would be more severe than appears in fig. 7.

ACKNOWLEDGMENTS

We are indebted to the Armour Research Foundation, Chicago, for the provision of the Li–Mg alloys; to Professor A. G. McLellan of Christchurch, New Zealand, for the loan of a glass grating, and to Dr. W. Baumgartner of E.T.H., Zurich, for assistance in providing specially modified photomultipliers. R.S.C. thanks the Australian Atomic Energy Commission for a Fellowship during the tenure of which this work was done. The continued interest and encouragement of Professor C. J. B. Clews is greatly appreciated.

REFERENCES

CATTERALL, J. A., and TROTTER, J., 1959, *Phil. Mag.*, **4,** 1164.

CRISP, R. S., 1958 a, *Aust. J. Phys.*, **11,** 449; 1958 b, *J. sci. Instrum.*, **35,** 470.

CRISP, R. S., and WILLIAMS, S. E., 1960, *Phil. Mag.*, **5,** 525.

ELMORE, W. C., and SANDS, M., 1949, *Electronics* (New York : McGraw-Hill), p. 250.

FARINEAU, J., 1937, *C. R. Acad.*, **205,** 365.

FISHER, P., 1954, *J. opt. Soc. Amer.*, **44,** 665.

FISHER, P., CRISP, R. S., and WILLIAMS, S. E., 1958, *Opt. Acta*, **5,** 31.

FUJIKI, J., 1959, *J. phys. Soc., Japan*, **14,** 913.

GALE, B., and TROTTER, J., 1956, *Phil. Mag.*, **1,** 759.

MICHEL, P., 1956, Thesis, University of Strasbourg (quoted by Weaver and Hill).

PARRATT, L. G., 1959, *Rev. mod. Phys.*, **31,** 616.

POLLARD, J., 1953, *Rev. sci. Instrum.*, **24,** 996.

SKINNER, H. W. B., 1940, *Phil. Trans*, **239,** 95.

SKINNER, H. W. B., and JOHNSON, J. E., 1937, *Proc. roy. Soc.* A, **161,** 420.

TOMBOULIAN, D. H., 1957, *Handb. Phys.*, **30,** 281 (Berlin : Springer).

VARLEY, J., 1956, *Nature, Lond.*, **178,** 939.

WEAVER, C., and HILL, R. M., 1959, *Advanc. Phys.*, **8,** 375.

Pitting of Aluminium at Grain Boundaries after Ageing†

By G. A. Bassett‡ and C. Edeleanu
Tube Investments Research Laboratories, Hinxton Hall, Essex

[Received June 16, 1960]

Abstract

Thin foils of 99·999% aluminium prepared by electropolishing have been found to develop surface pits along the grain boundaries during ageing at room temperature. It is suggested that the pits are formed by a vacancy mechanism, and that they are associated with the initiation of etch attack along the grain boundaries of aged pure aluminium.

§ 1. Introduction

The localization of etching attack of pure aluminium has been widely associated with the emergence of dislocations (see for example Amelinckx 1953, Lacombe 1947, Lacombe and Beaugard 1948) or with the segregation of impurities to the dislocation lines (Wyon and Crussard 1951, Forty and Frank 1955). In the case of the etching of slip lines on strained aluminium, Bassett and Edeleanu (1960) have advanced an alternative suggestion, that it is the rupture of the natural oxide film and its subsequent failure to repair perfectly, which plays an important part in the initiation of etch attack.

Braun, *et al.* (1958) have found that periods of room temperature ageing are necessary after the preparation of the specimen surface, before grain boundary etching is observed. They have suggested this behaviour is due to diffusion of impurities along the grain boundaries and into the oxide film.

A consideration of the likely residual impurities in high purity aluminium, and the thermodynamics of the replacement of aluminium in the oxide film with these impurities, makes this view difficult to accept. The work described now suggests a possible alternative explanation of grain boundary attack after ageing treatments.

§ 2. Experimental

Specimens of polycrystalline aluminium of 99·999% purity were prepared as foils thin enough for transmission electron microscopy,

---

† Communicated by the Authors.

‡ Present address: Physics Department, University of Bristol.

by electropolishing in a bath of one part perchloric acid to five parts ethyl alcohol. The initial foil was 0·001 in. thick and had a highly polished surface finish. Prior to electropolishing foils were heated to 600°C followed by air cooling. Electron microscope examination was carried out using a Siemens Elmiskop I operated at 80 or 100 kv, specimens being mounted in the stereo holder so that dislocations in the foils could be brought into satisfactory contrast.

After thinning, foils were aged, mounted on grids ready for examination in the microscope, in a vacuum desiccator for periods up to four months. Some foils were given an accelerated ageing treatment by maintaining at a temperature of 100°C in an air oven for 24 hours. For comparison with the thin film observations anodic film replicas of the foil surfaces have also been made.

§ 3. RESULTS AND INTERPRETATION

Some typical grain boundaries in a foil aged at room temperature for four months after thinning are shown in fig. 1 (*a*) and (*b*)†, and at a higher magnification in fig. 2. These micrographs reveal the formation of small surface pits along the grain boundaries. This pit formation is quite general, all grain boundaries appearing pitted. The higher magnification micrograph shows one example in which the pits are bounded by well-formed crystallographic faces. For comparison specimens before ageing have been examined and found to have grain boundaries which are completely free of pits of this type.

Accelerating the ageing process by holding a thin foil at 100°C for 12–24 hours it has been possible to photograph in the electron microscope the same grain boundary both before and after ageing. Figures 3 and 4 show such a pair of micrographs in which the appearance of pits at the grain boundary at A and B is clearly seen. A piece of dirt on the left-hand side of the picture forms a convenient point of reference.

The size of pits which have been observed lies between 100 Å and 1000 Å; some tendency for the pits to be larger but fewer in specimens aged at room temperature has been noticed compared with those in which the ageing was accelerated. Figure 5 gives some information of the depth of the pits where an array can be seen at both foil surfaces on an inclined grain boundary. The depth of these pits is about one-fifth of the foil thickness, judged from the interception of the extinction contours in the grain boundary. This figure makes quite evident that the pits are confined to the foil surfaces.

The relative shallowness of the pits has made their detection on oxide replicas uncertain. Although some oxide replicas have shown evidence of the pitting along the boundaries this has not always been seen. Carbon replicas have been tried but in general have failed to detect the pits. An explanation could be that the pits have formed under the natural oxide film and a carbon replica would then not reveal the pits unless the film was completely collapsed.

---

† All figures are shown as plates.

The electron micrograph, fig. 6, is typical of an aged thin foil which has been very lightly etched in $HCl/HNO_3/HF$. The disposition of the holes made in the foil by this treatment strongly suggests that etching started at the grain boundary pits produced on ageing. This type of etching behaviour was confined to aged specimens and was not observed on freshly prepared ones.

§ 4. DISCUSSION

Thin film electron microscope observations have shown that after ageing surface pits form along the grain boundaries in aluminium. Such behaviour can best be interpreted as a migration and aggregation of vacancies at the surface of metal and beneath the natural oxide film. The formation of surface pits on aluminium has previously been reported by Doherty and Davies (1959). In their experiments the pits visible under an optical microscope formed after a small, but critical, drop of temperature, after holding the aluminium specimen at a high temperature. Doherty and Davies interpret their results in terms of the aggregation of the excess vacancies produced by the temperature drop. It is interesting to note that they observe that pits form only in the grains and that near grain boundaries no pits are found; the boundaries acting as very effective sinks for vacancies.

In the present experiments any possible concentration of thermal vacancies quenched in from the heat treatment is too small to account for the pits. It is probable in any case that many quenched-in vacancies are annealed out during electropolishing when a thin foil may reach quite high temperatures. The present pits presumably must also result from segregation of vacancies but it would seem more reasonable that in this case the vacancies migrate across the specimen surface or grain boundary and that metal atoms move away from the region of the pit. The driving force is presumably the large surface energy associated with the T-like junction made by the grain boundary and outer surface and is the same as in thermal etching. The final stable condition in that case would be a trench rather than pits as now found but parametric or crystallographic factors may favour the formation of pits. It is not possible from the present work to say whether the effect is associated with a grain boundary diffusion of vacancies and metal or whether the outer surface is involved, but it seems likely in either case that the film above the voids will be disturbed and it is suggested that this will then favour local etching.

ACKNOWLEDGMENTS

We thank Professor F. C. Frank and several laboratory colleagues for helpful comments and discussion, and the Chairman of Tube Investments Ltd. for permission to publish the paper.

REFERENCES

AMELINCKX, S., 1953, *Phil. Mag.*, **44,** 1048.
BASSETT, G. A., and EDELEANU, C., 1960, *Phil. Mag.*, **5,** 707.
BRAUN, I., FRANK, E. C., and MEYRICK, G., 1958, *Phil. Mag.*, **35,** 1312.
DOHERTY, P. E., and DAVIES, R. S., 1959, *Acta. Met.*, **7,** 118.
FORTY, A. J., and FRANK, F. C., 1955, *J. phys. Soc., Japan*, **10,** 656.
LACOMBE, P., 1947, *Strength of Solids*, Report of Bristol Conference (London: Physical Society).
LACOMBE, P., and BEAUGARD, L., 1948, *J. Inst. Met.*, **78,** 7.
WYON, G., and CRUSSARD, C., 1951, *Rev. Métall.*, **48,** 121.

Etch Pits and Dislocations in Ice Crystals†

By G. W. BRYANT and B. J. MASON
Imperial College, London

[Received June 23, 1960]

ABSTRACT

Etching of ice crystals grown from both the vapour and the melt has revealed etch pits in concentrations of up to $10^6/\text{cm}^2$ which apparently mark the sites of emergent dislocations. Silvered Formvar replicas show the etch pits on the basal surface to be hexagonal pyramids on which spiral or closed terraces of steps are often visible. These features are interpreted in terms of the etching of helical dislocations. The etch pits tend to group themselves along low-angle grain boundaries and slip lines. When the crystal is mechanically stressed, etch channels appear on the basal plane along the $\langle 11\bar{2}0 \rangle$ directions which suggests that these are the preferred glide directions.

Double rows of small etch pits radiating from impurity specks and local centres of high stress probably mark the sites of dislocation loops intersecting the surface. Pyramidal hillocks appearing in concentrations of $10^5/\text{cm}^2$ on the basal faces of crystals grown from the vapour may be growth features and not the result of etching.

§ 1. INTRODUCTION

THERMAL or chemical etching acts by the preferential evaporation or dissolution of the surface at imperfections where molecules are surrounded by fewer nearest neighbours than usual and so are less strongly bound. The shape of an etch pit will depend upon the geometrical arrangement of the molecules in the particular crystal face and upon the relative rates of dissolution in directions parallel and perpendicular to the surface. The geometry of the etch pits may therefore allow the crystal face and the directions of crystallographic axes to be identified.

But much more important, it has recently been demonstrated, by several workers, that etch pits mark the locations of emergent dislocations. This has been most convincingly demonstrated by Jones and Mitchell (1957) who were able to decorate and make visible dislocations in silver-halide crystals by the preferential deposition there of metallic silver, and show that the terminations of dislocations in the crystal surface coincided with the positions of etch pits. Further evidence of this close association was provided by Johnston *et al.* (1957) who were able to match the etch pits appearing on opposite sides of an etched thin slice of a silicon crystal, the inference being that the members of a matched pair were joined by a dislocation line passing through the crystal normal to the surfaces. Furthermore, Johnston and Gilman (1959), during successive stressing and etching of lithium fluoride crystals, observed that successive rows of etch pits formed in the manner expected if they originated on dislocations which moved progressively under the applied stresses.

---

† Communicated by the Authors.

The rather extensive studies of etched crystals, mainly germanium and silicon, have revealed that:

(i) Although it is by no means certain that all emergent dislocations are revealed by the appearance of etch pits (dislocations of large Burgers vector will obviously be favoured), observations of the pits provide useful information on the density and distribution of dislocations.

(ii) Although screw and edge dislocations produce etch pits of similar shape, those associated with screw dislocations are generally smaller, more shallow, and less symmetrical than those associated with dislocations of strong edge character.

(iii) Having revealed the existence of helical dislocations by the decoration of fluorite crystals, Amelinckx, Bontinck and Dekeyser (1957) have suggested that etching of such dislocations may explain the occasional appearance of spiral pits on germanium and silicon.

(iv) Etch pits tend to group themsleves along slip lines and low-angle grain boundaries. The presence of etch pits not only reveals these features but a detailed study of the distribution, density, asymmetry and depth of the pits enables one to deduce the angle between grain boundaries and the directions of slip for both edge and screw dislocations.

Because a study of etch-pit formation appeared to offer a simple and powerful method of studying the dislocation structure of crystals, we decided to exploit it in our studies of ice crystals where dislocations have not been revealed by the appearance of spiral terraces of growth steps nor by attempts to decorate them.

The appearance of etch pits on the surfaces of ice crystals was first reported by Truby (1955). Hexagonal pyramidal features of base diameter $\frac{1}{2}$–20 μ and depth $\frac{1}{4}$–$\frac{1}{2}$ μ were observed and sometimes exhibited a stepped-layer structure concentric with the c axis. Higuchi (1958) and Muguruma and Higuchi (1959) discovered that etch pits could be produced on the surfaces of ice and snow crystals by etching with a Formvar solution. Hexagonal pits appeared on the basal surface of a snow crystal in concentrations of up to $10^5/\text{cm}^2$. After prolonged etching the bottom surfaces of the pits revealed the layer-type structure noted by Truby, the height of individual steps varying between 3 and 16 μ. These Japanese authors have used the etch pits to determine the size distribution of, and orientation of the crystal axes in, individual grains of polycrystalline ice.

The object of the present investigation was to make a more detailed study of etch pits on ice crystals and to relate them to the dislocation structure.

§ 2. ETCHING TECHNIQUE

Surfaces of ice crystals, grown from both the vapour and the melt, were etched with a 1% solution of polyvinyl formal (Formvar) in ethylene dichloride. A small quantity of the solution was poured onto the ice surface and the solvent allowed to evaporate and leave a thin, transparent, plastic film on the surface which could be peeled off and examined as a replica. Etching occurred because traces of water in the ethylene dichloride froze to produce filamentary ice crystals which subsequently evaporated to leave small holes in the Formvar film. Etching, by evaporation, then proceeded beneath these holes to produce wide, shallow pits on the ice surface. Smaller, pyramidal etch pits subsequently appeared inside these large pits as shown in fig. 1†. Subsequent applications of the Formvar solution gave rise, in similar manner, to further large pits which merged with earlier ones so that, eventually, the whole surface became etched. The etch pits could be studied at any stage by peeling off the plastic film with a piece of transparent adhesive tape, fixing it face upwards on a microscope slide and viewing it under the microscope in transmitted light. To obtain better contrast and resolution a thin layer of silver was evaporated onto the replica which, when viewed in reflected light with magnifications of × 400, revealed the detailed structure of the etch pits as shown in figs. 4 and 6.

§ 3. ETCH PITS ON ICE CRYSTALS GROWN FROM THE MELT

A rectangular metal channel was filled with distilled water and cooled slowly below 0°C in a cold room to produce a block of ice whose flat surfaces contained ice crystals of various orientations which could be identified by the shapes of the large etch pits. The ice block was placed in a refrigerator held at -20°C, its surface polished with fine emery paper followed by a silk cloth and plastic replicas of its surface taken at intervals of 24 hours.

The first replica showed only the fine scratches produced during polishing but the second replica, taken 24 hours later, showed a flat surface covered by wide, shallow etch pits about $100\,\mu$ across with a surface density of about $10^3/\text{cm}^2$. Etch pits appeared on all the exposed crystal faces, their shapes revealing the crystalline symmetry and the orientation of the face. Figure 2 shows shallow hexagonal pits on the basal surface, each about $100\,\mu$ in diameter, viewed in transmitted light.

The replica in fig. 1 shows many small pyramidal etch pits (seen inverted), 5 to $10\,\mu$ in diameter, formed inside a large, shallow pit on a basal surface. The smaller pits, appearing in concentrations of up to $10^5/\text{cm}^2$, were hexagonal in cross section with their sides usually parallel, but occasionally perpendicular, to the sides of the large pit. The heights of the pyramids were roughly equal to the diameters of their bases. Under vertical illumination the sides of the smaller pits appeared smooth but, when illuminated at a slight angle to the vertical, they appeared to be built up of several concentric steps each a few tenths of a micron in height. On many of the larger pyramids ($d > 10\,\mu$), these were accompanied by one, and sometimes two, large concentric steps of height up to 1 μ. A few per cent of these pits exhibited hexagonal spirals of similar step height—see fig. 3.

---

† All figures are shown as plates.

On some of the later replicas from completely etched surfaces, areas of basal surfaces were crossed by lines of hexagonal pyramidal pits forming etched channels. A silvered replica showing an (inverted) line of pyramidal pits is shown in fig. 4. These were formed at a grain boundary, the average-spacing of the pits divided into the intermolecular distance giving 30″ for the angle of misorientation.

Ice crystals were also grown from the melt by slowly cooling a wide shallow dish of water in such a manner that freezing started at the surface to produce large, flat, single crystals. These were removed with tweezers, frozen to a microscope slide, and examined by transmitted light under a microscope in a cold room held at −8°c. Etching of the surface with successive applications of Formvar solution was carried out as before but now evaporation proceeded much more rapidly and the etch pits on the basal surface, both large and small, tended to be circular rather than hexagonal. However, concentric rings about 1 μ in height and occasional spirals with one or two turns were still observed although smaller steps were now not visible.

In an attempt to study the effect of the inclusion of small, insoluble, foreign particles in the ice, the shallow dish of water was allowed to collect dust for a few days. Ice crystals were then formed on the surface as before and silvered replicas of their basal surfaces, taken at 30 min intervals, now revealed many patterns similar to those shown in fig. 5. Radiating from a small pyramidal etch pit are six double etch channels which, having obtained a length of about 10 μ, broaden to about double their original width and finally terminate in either another pyramidal etch pit or in the side of the large, shallow pit which contains them all. Broadening of the channel is sometimes accompanied by a change in direction of about 30°.

§ 4. SURFACE STRUCTURE OF CRYSTALS GROWN FROM THE VAPOUR

Single ice crystals were grown from the vapour, under carefully controlled conditions of temperature and supersaturation, in the diffusion cloud chamber described by Hallett and Mason (1958). The crystals were grown on a fine nylon fibre hanging vertically down the centre of the chamber; the crystal habit varied along the length of the fibre from hexagonal plates→needles→prismatic columns→plates→dendrites→plates →prisms as the temperature varied from 0°c to −50°c. Hexagonal plates of up to 5 mm diameter, needles up to 2 cm long × 2 mm wide, and dendrites 3 cm × 1 cm were grown in this way and transferred to the cold room for etching and surface examination by the techniques described above.

Replicas of previously unetched basal faces of plate-like crystals revealed, instead of etch pits, raised hexagonal pyramids, usually less than 10 μ in diameter. Under high magnification these exhibited concentric rings and spirals similar to those observed in etch pits. These hillocks, shown in fig. 6, were eroded by subsequent etching. They were accompanied by numerous smaller, circular imperfections too shallow to be definitely identified as either hills or depressions. Their surface density is about $10^5/\text{cm}^2$.

Replicas of previously unetched prism faces showed a high density, about $10^6/\text{cm}^2$, of features which were rectangular, aligned parallel to the *c* axis, and had four sloping walls—see fig. 7. Again they were so shallow that it was difficult to determine whether they were hills or depressions.

Etching with Formvar solution produced hexagonal etch pits on the basal surfaces of plate-like ice crystals in concentrations of order $10^4/\text{cm}^2$, the edges of the pits being parallel to the crystallographic $\langle 11\bar{2}0 \rangle$ directions—see fig. 8. Pits formed on the prism $(10\bar{1}0)$ faces of ice needles were rectangular in cross-section and mostly flat at the bottom as shown in fig. 9. Star-shaped etch channels were seen only very rarely in crystals grown from the vapour in virtually dust-free conditions; one such is shown in fig. 10. The channels run parallel to the $\langle 11\bar{2}0 \rangle$ axes of the crystal and are marked all along their length by very small pits less than 1 μ in diameter.

In an attempt to correlate the positions of etch pits arising on opposite sides of a plate crystal, about 100 μ thick, the crystal was suspended from a glass fibre and coated on both sides with Formvar solution. The plastic film was then removed by folding transparent adhesive tape round the crystal, peeling it off, and straightening the tape to obtain replicas of both faces side by side. Although both basal faces showed approximately the same density of etch pits, it was not possible to match their positions. This suggests that, if the pits were formed by the etching of dislocations, the latter followed rather devious paths in traversing the 100 μ thickness of crystal.

§ 5. The Movement of Dislocations under Mechanical Stress

Replicas of the surfaces of thin sheets of ice, 1–2 mm in thickness, produced by the freezing of water in a refrigerator, revealed large concentrations ($\sim 10^5/\text{cm}^2$) of etch channels oriented along the $\langle 11\bar{2}0 \rangle$ directions as shown in fig. 11. The specimens were subjected, at -20°c, to quite strong vibrations from the compressor of the refrigerator; when similar specimens were mounted on foam rubber, so that the vibrations were greatly damped, the number of etch channels was greatly reduced. We believe that the channels, which were tapered along their length, resulted from the movement of edge dislocations under mechanical stresses induced by the vibrations. During a period of 20 min the etch pit advanced about 15 μ during which time the specimen was subjected to about 30 000 vibrations.

The average movement per vibration was therefore about 5 Å, or about one inter-molecular spacing along the ⟨11$\bar{2}$0⟩ direction!

Similar sheets of ice were subjected, again at −20°c, to local stresses by dropping lead shot onto the surface from heights of a few inches. The replicas now revealed rosettes of the type shown in fig. 12 and noted earlier by Gilman and Johnston (1957) on the surfaces of lithium fluoride crystals. Arrays of etch channels, presumably associated with similar arrays of dislocations, radiated from large etch pits along the ⟨11$\bar{2}$0⟩ directions which again appear to be preferred glide directions.

§ 6. Discussion

The fact that the surface densities of the smaller etch pits on ice lie in the range 10^5 to $10^6/\text{cm}^2$ and are comparable to the observed densities of dislocations in other materials, suggests that they probably arose by the etching of emergent dislocations. A close association between dislocations and etch pits is also suggested by the latter tending to group preferentially along grain boundaries and slip lines.

The inverted pyramidal shape of the pits on the basal plane may be interpreted in terms of a dislocation being etched at similar rates in directions normal and parallel to the surface, the dislocation following a line drawn from the apex of the pyramid to the centre of the base. Anisotropic lateral etching on the prism faces is revealed by the rectangular shape of the pits.

In the present work it was usually not possible to determine whether the pits were generated about edge or screw dislocations but etching patterns sometimes appeared which indicated the presence of helical dislocations. These were first discovered by Bontinck and Amelinckx (1957), their formation being explained by Amelinckx, Bontinck, Dekeyser and Seitz (1957) who suggested that the condensation of vacancies on to a dislocation possessing a strong screw component could cause it to climb into a helix. Etching of such a dislocation, which may be regarded as an unwinding of the screw component, would then produce a pit in the form of a helical cone. Amelinckx, Bontinck and Dekeyser (1957) further demonstrate that bunching of the unwinding monolayers, caused by the rotation of the centre of etching along the helix, could form visible spiral steps whose spacing would be equal to the pitch of the helix and, in consequence, bear no direct relation to the Burgers vector of the underlying dislocation. This mechanism may well explain the appearance of the spiral steps in fig. 3, the height of which were of order 1 μ, and therefore comparable to the pitch of helical dislocations observed directly in other crystals.

It is also known that two parallel helices of opposite sign may combine to produce a row of closed loops and should this emerge from the etched surface at a slight angle to the vertical, it could give rise to etch pits consisting of a series of closed terraces as shown in fig. 6.

The double rows of symmetrical etch pits seen in fig. 10 may have originated on helical dislocations with axes parallel to the surface. In this and similar cases they may have been initiated by a dust particle in much the same way as Jones and Mitchell (1958) were able to generate helical dislocations and rows of prismatic loops by pressing small glass spheres into crystals of silver chloride.

Our attempts to reveal the three-dimensional structure of dislocations in ice, by adding to the water small quantities of silver nitrate in the hope that the silver ions might migrate preferentially to the dislocations line during the freezing process, have been unsuccessful.

The pyramidal hillocks, which appeared in concentrations of between 10^3 and $10^5/\text{cm}^2$ on the basal surfaces of crystals grown from the vapour in very clean conditions, were not observed on crystals grown from the melt. Although they may have been formed by etching during the preparation of the first replica, the fact that they were eroded and finally removed by subsequent etching leads us to think that they may have been formed by growth rather than by dissolution at preferred sites on the crystal surface. This point is not easy to check but is being investigated further.

The fact that dislocations spreading out from localized regions of high stress and etch pits moving under applied stresses show a very strong tendency to follow the $\langle 11\bar{2}0 \rangle$ directions suggests that these are preferred glide directions.

REFERENCES

AMELINCKX, S., BONTINCK, W., and DEKEYSER, W., 1957, *Phil. Mag.*, **2,** 1264.
AMELINCKX, S., BONTINCK, W., DEKEYSER, W., and SEITZ, F., 1957, *Phil. Mag.*, **2,** 355.
BONTINCK, W., and AMELINCKX, S., 1957, *Phil. Mag.*, **2,** 94.
GILMAN, J. J., and JOHNSTON, W. G., 1957, *Dislocations and Mechanical Properties of Crystals* (New York : Wiley), p. 116.
HALLETT, J., and MASON, B. J., 1958, *Proc. roy. Soc.* A, **247,** 440.
HIGUCHI, K., 1958, *Chamonix Symposium Int. Ass. Sci. Hydrol. Pub.*, No. 47, p. 249.
JOHNSTON, W. G., and GILMAN, J. J., 1959, *J. appl. Phys.*, **30,** 129.
JOHNSTON, W. G., LI, C. H., and KNUDSEN, C. I., 1957, *J. appl. Phys.*, **28,** 746.
JONES, D. A., and MITCHELL, J. W., 1957, *Phil. Mag.*, **2,** 1047; 1958, *Ibid.*, **3,** 1.
MUGURUMA, J., and HIGUCHI, K., 1959, *J. met. Soc., Japan*, **37,** 71.
TRUBY, F. R., 1955, *J. appl. Phys.*, **26,** 1416.

Measurement of the Debye–Waller Temperature Factor for Silver and α-iron†

By C. W. Haworth
Department of Metallurgy, Sheffield University; formerly Department of Metallurgy, Oxford University

[Received June 23, 1960]

Abstract

Measurements have been made of the variations with temperature of the intensities of x-ray diffraction lines from silver and iron. For silver the measurements were in the range 286–1100°K, and the Debye–Waller temperature factor corresponded to a characteristic temperature of 197°K at 286°K. For iron the measurements covered the range 286–1190°K, and corresponded to $\Theta = 389$°K, although there was a large scatter in the results due to crystal changes brought about by annealing. The intensity measurements showed no discontinuity at the Curie temperature, nor was there any anomaly in the spacing of the (110) planes.

§ 1. Introduction

The variations with temperature of the integrated intensity and peak height of x-ray diffraction lines 331, 551/333 and 422 for a silver powder specimen and 220 for an iron specimen, were measured at high temperatures. For silver an explicit volume dependence of the characteristic temperature was adequate to give the observed temperature dependence in terms of the Debye–Waller theory, the value $\Theta = 197$°K being obtained at room temperature. This result does not agree with the work of Andriessen whose results give $\Theta = 239$°K when recalculated to allow for lattice expansion, nor with the work of Boskovits *et al.* (1958) who obtained a large deviation from the theoretical intensity variation above 700°K. The present work does agree approximately with that of Spreadborough and Christian (1959 b).

The results for iron showed a much larger scatter than silver, associated with crystal changes brought about by prolonged annealing. No anomaly was observed at the Curie temperature, either in the intensity variations or in the spacing of the 110 planes.

§ 2. Theory

For the Debye–Waller theory, the temperature dependence of the intensity of an x-ray reflection is given by the factor $\exp(-2M)$ (following James 1954, 5.67), where

$$M = \frac{6h^2T}{mk\Theta_M{}^2}\frac{\sin^2\theta}{\lambda^2}\cdot\left\{\phi(x)+\frac{x}{4}\right\}. \qquad (1)$$

---

† Communicated by the Author.

The characteristic temperature Θ_M has been regarded as a constant in the above expression: amongst other things this is equivalent to assuming that the volume of the crystal remains constant as the temperature changes. Paskin (1957) has given a thermo-dynamical derivation of the variation of Θ_M (regarded as a temperature dependent parameter $\Theta(T)$) with volume, the relation for an isotropic crystal which obeys Gruneisen's expansion equation being written

$$\frac{\Theta(T)}{\Theta(T_0)}=\left(\frac{a_{T_0}}{a_T}\right)^{3\gamma} \quad . \quad . \quad . \quad . \quad . \quad . \quad . \quad . \quad . \quad . \quad (2)$$

where a_T is the lattice parameter at temperature T°K. The Gruneisen constant γ (following Hume-Rothery 1945) is calculated from the equation

$$\gamma=\frac{V\beta}{C_V k}$$

V being the atomic volume, C_V the atomic specific heat at constant value, β the volume coefficient of expansion and k the compressibility. The values used for the constant γ are 2·40 for silver and 1·6 for iron.

Substituting for $\Theta_M{}^2$ in eqn. (1) we have

$$M=\frac{6h^2T}{mk\,\Theta_{T_0}{}^2}\,\frac{\sin^2\theta}{\lambda^2}\,\Phi\{x\}T' \quad . \quad . \quad . \quad . \quad . \quad . \quad . \quad (3)$$

where $T'=T(a_T/a_{T_0})^{6\gamma}$ the 'adjusted' temperature allowing for the effect of lattice expansion, and

$$\Phi\{x\}=\{\phi(x)+x/4\}$$

is approximately unity and is tabulated by James (1954).

Neglecting the small effect due to change of Bragg angle θ with temperature, the intensity ρ_T of a given reflection at temperature T can be compared with the intensity at a temperature T_0, the relation being

$$\ln\left(\frac{\rho_T}{\rho_{T_0}}\right)=-\frac{12h^2}{mk\,\Theta_{T_0}{}^2}\,\frac{\sin^2\theta}{\lambda^2}\,\Phi\{x_0\}\left[\frac{\Phi\{x\}}{\Phi\{x_0\}}\,T'-T_0{}'\right]. \quad . \quad . \quad (4)$$

Thus a linear relation is expected between the parameter

$$Y=\frac{\lambda^2}{\sin^2\theta}\ln\left(\frac{\rho_T}{\rho_{T_0}}\right)$$

and the variable $T''=(\Phi\{x\}/\Phi\{x_0\}T'$. A very approximate value of Θ_{T_0} is satisfactory for calculating values of $\Phi\{x\}$, since this function is nearly unity for all values of x corresponding to temperatures above Φ_{T_0}. Any departure from a linear relation can be attributed to an additional dependence of Θ_M on temperature, above that related to the coefficient of expansion. From the slope of a linear relation a value of Θ_{T_0} can be obtained.

§ 3. Experimental Measurements and Results

3.1. *Silver*

Filings were prepared from pure (99·99%) silver, carefully cleaned and that portion which passed through a 350 mesh sieve prepared into a flat diffractometer specimen, held in a molybdenum trough.

This was mounted in a furnace built onto a Norelco diffractometer, described by Spreadborough and Christian (1959 a), and the specimen was annealed at 1020°K for ten hours *in vacuo*. It was found that subsequent annealing treatments at temperatures up to 870°K did not alter the room temperature line profiles of the 331, 422 or 511/333 reflections obtained using CuKα or MoKα radiation.

The integrated intensity for a given reflection obtained for a specimen temperature T_0 could then be compared with that obtained for a higher temperature T, using a planimeter to measure the total area under the $\alpha_1\alpha_2$ profile, above the background level in the immediate neighbourhood of the reflection. From these measurements values of Y corresponding to different temperatures could be obtained.

The background intensity in the neighbourhood of the line was observed to increase with increasing temperature of the specimen, but the variation of intensity with angle in the 'wings' of the Bragg peak was small. However, no attempt was made to obtain an absolute value for the Bragg scattering, but the variation with temperature of the intensity, measured over a small fixed angular range, was found.

The error due to including temperature diffuse scattering in the measurement of the integrated intensity has been discussed by Chipman and Paskin (1959), who showed that the error introduced by including all the wings of the lines (a procedure described by Renninger (1952)) would lead to a larger value of the characteristic temperature than the true one. However, if the temperature diffuse scattering over the small angular range measured is calculated, then the error in characteristic temperature caused by including all the temperature diffuse scattering in the measurements is less than 1% for any of the Bragg reflections used. For the experiments where the peak heights were compared, the error could be larger. The correct adjustment of the apparatus and the validity of background level was checked by observing the 2 : 1 intensity ratio of the $\alpha_1\alpha_2$ doublet lines.

Values of Y could also be calculated from variation in peak heights with temperature. The comparison between measurements based on integrated intensity values and on peak heights was made because:

(*a*) The theoretical calculations refer to the integrated values.

(*b*) Peak height measurements can be made more accurately than a complete profile, because small fluctuations in temperature (~ ±2°C) during the profile measurements cause change of Bragg angle which result in serious errors. Provided surface effects in the specimen did not produce asymmetry in an x-ray line, then instrumental effects are unlikely to introduce errors when comparing peak heights instead of integrated intensities. However, it was found that changes in crystalline arrangement introduced by annealing treatments produced greater changes in peak heights than in integrated intensities, and great care was necessary in making use of the peak height data. After repeated annealing at 1220°K the measurements were successfully extended up to 1100°K.

The graph of Y against the adjusted temperature T'' is shown in fig. 1, and is seen to be linear up to a specimen temperature of 1100°K, the highest temperature reached. The slope of the linear relation corresponds to a characteristic temperature of 197°K ± 6 at 286°K, whilst the usually accepted specific heat value is 210°K (James 1954). Other X-ray values for the characteristic temperature of silver, taken from the literature, but re-calculated using the method of analysis used in this paper, are:

Andriessen (1935)	$\Theta_M = 239$°K ± 5,
Boskovits *et al.* (1958)	$\Theta_M = 188$°K ± 12,

using only data for temperatures above 290°K, and

Spreadborough and Christian (1959 b)	$\Theta_M = 191$°K ± 8.

Fig. 1

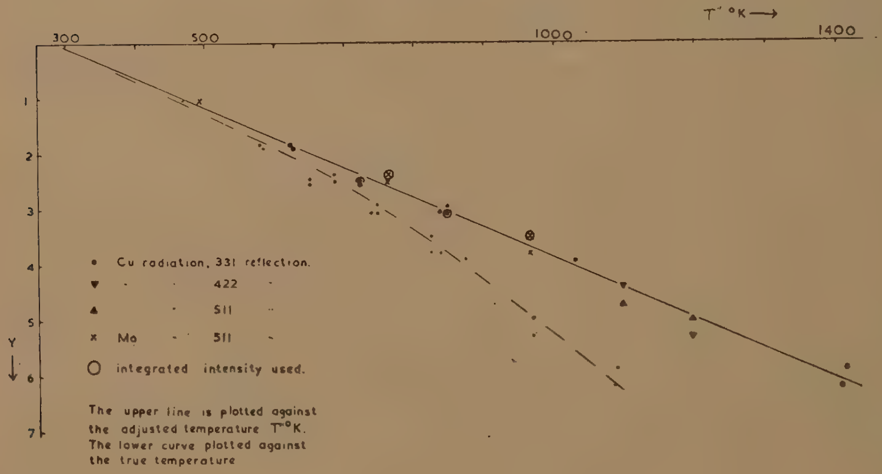

Of these results that of Andriessen gives a nearly linear relation up to 880°K, but the characteristic temperature obtained is much higher than expected. The work of Boskovits *et al.* gives an approximately linear relation from 290°K to 680°K, the slope of the relation agreeing with the present work to within the experimental error. Above 680°K, however, measurements at 780°K showed a more rapid diminution of X-ray intensity than expected, but such a derivation from linearity is not supported by the present work.

The method of correcting for the background used in the present work would tend to give too high a value for Θ_M. The value of the characteristic temperature used in X-ray measurements is expected to be larger than that used in the Debye specific heat theory, owing to different methods of averaging the velocities of longitudinal and transverse elastic waves in the crystal: in the case of silver we expect the X-ray characteristic temperature to be 4% greater than that used in specific heat measurements, from the work of Zener and Bilinsky (1936). The observed characteristic temperature pertaining to the X-ray temperature factor is, however, lower than the specific heat value.

3.2. *Iron*

Two iron specimens were prepared and used: one from Johnson Matthey iron sponge having an analysis 0·0053% Ni, 0·0003% Mn, 0·063% insoluble, and the other by filing B.I.S.R.A. H-iron under cold paraffin. In both cases the powders were carefully cleaned and then passed through a 350 mesh sieve before preparing into a specimen by pressing into a pure iron trough. The second specimen was vacuum-annealed for four hours at 1400°C before placing in the X-ray camera.

Using filtered iron radiation, the 220 reflection at approximately 145° 2θ, was measured. The integrated intensities at different temperatures were compared, the measurements being taken from the trace on an automatic recorder chart, corrected for counter dead-time losses. The results showed a larger scatter than in the case of silver, and a large number of chart recordings were used.

Fig. 2

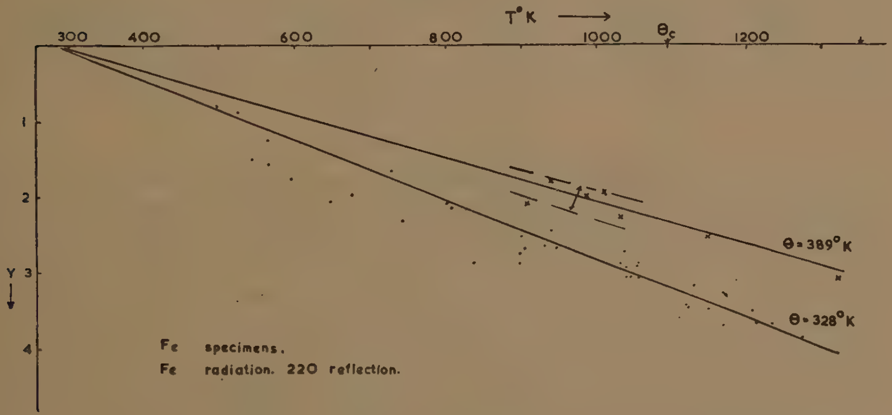

A graph of parameter Y against 'adjusted' temperature T'' was plotted, as in the case of silver, the adjustments to the temperature scale being made using the lattice parameter values of Basinski *et al.* (1955) $\gamma = 1{\cdot}60$ and $\Theta = 430$°K. The value of the characteristic temperature obtained from this graph would depend only to the second order upon the Θ value used in making the temperature adjustment.

The scatter of the results, as presented on this graph is seen to be much larger than in the case of silver, but does show that there is no marked anomaly in the temperature factor at the Curie temperature. This large scatter could have been due to statistical changes in the distribution of reflecting particles, but there was also a time-dependent, partly reversible effect, superimposed on the random variations. This is shown by the measurements represented by crosses on the graph, which were made immediately after heating to a higher temperature, whilst the other points correspond to measurements made after an annealing period of one hour or longer. This effect may be due to extinction variations brought about by polygonization or other changes in the iron crystals.

Fitting a straight line passing through $T_0 = 286$°K to these results, and using the same analysis as for silver gives a Θ_M value for the points repre sented by crosses of 389°K ± 17, and for the other points $\Theta_M = 328$°K ± 20. The largest characteristic temperature which can be fitted to any measurement is 403°K, whilst the accepted specific heat value for α-iron is 430°K. It would seem likely that the discrepancy may be associated with changes in extinction brought about by annealing. As in the case of silver, inclusion of temperature diffuse scattering in the measurements would lead to too high a value of Θ_M; although the error due to including all the diffuse scattering, calculated following Chipman and Paskin (but for a b.c.c. lattice) over the range measured of 1·6° 2θ, would lead to an error in Θ_M of less than 0·3%.

The variation in Bragg angle of the α_1 and α_2 peaks with temperature gave a measure of the thermal expansion of the 110 direction in the iron crystal, with a sensitivity of ±0·0002 kx in d value. No anomaly in thermal expansion was observed at the Curie temperature, in agreement with the work of Basinki *et al.* (1955), who used an extrapolation technique such that their lattice parameter results were effectively based upon a study of the 310 direction.

ACKNOWLEDGMENT

This work was carried out while the author held a research grant in the Department of Metallurgy, The University of Oxford. The author would like to thank Professor W. Hume-Rothery for his advice and encouragement.

REFERENCES

ANDRIESSEN, R., 1935, *Physica*, **2**, 417.

BASINSKI, Z. S., HUME-ROTHERY, W., and SUTTON, A. L., 1955, *Proc. roy. Soc.* A, **229**, 459.

BOSKOVITS, J., ROILOS, M., THEODOSSIOU, A., and ALEXOPOULOS, K., 1958, *Acta Cryst.*, **11**, 845.

CHIPMAN, D. R., and PASKIN, A., 1959, *J. appl. Phys.*, **30**, 1992.

HUME-ROTHERY, W., 1945, *Proc. phys. Soc. Lond.* A, **57**, 209.

JAMES, R. W., 1954, *Optical Principles of X-ray Diffraction* (London : Bell).

PASKIN, A., 1957, *Acta Cryst.*, **10**, 667.

RENNINGER, M., 1952, *Acta Cryst.*, **5**, 711.

SPREADBOROUGH, J., and CHRISTIAN, J. W., 1959 a, *J. sci. Instrum.*, **36**, 116; 1959 b, *Proc. phys. Soc. Lond.*, **74**, 609.

ZENER, C., and BILINSKY, S., 1936, *Phys. Rev.*, **50**, 101.

The Effect of Lattice Distortion Around Point Defects on the Scattering of Long Wavelength Neutrons†

By D. G. Martin
Metallurgy Division, Atomic Energy Research Establishment, Harwell, Berks

[Received May 13, 1960]

Abstract

In a crystalline element the scattering of long wavelength neutrons by a point defect and an atom are known to be identical. However, when lattice distortion around the point defect is also considered, this is no longer true; in particular the scattering of a point defect is now anisotropic and varies with wavelength. An expression for the cross section of a defect in a relaxed lattice has been derived and applied to f.c.c. and b.c.c. lattices, and in greater detail to copper and molybdenum where the magnitude of the relaxation around defects is known. It has been found that the scattering cross section is appreciably altered by the relaxation of the surrounding atoms, and in particular from those that are nearest neighbours to the defect. A neglect of this relaxation in the interpretation of a neutron scattering experiment could lead to an error of an order of magnitude in an estimate of the number of defects. Also a study of the variation in cross section with wavelength or scattering angle, which is analogous to an x-ray small angle scattering experiment, is incapable of determining uniquely the size of defect agglomerates in solids. However, under favourable circumstances, such experiments could become a useful technique for estimating the lattice distortion around defects.

§ 1. Introduction

Many experiments on solids irradiated by energetic particles have aimed at estimating the numbers and states of agglomeration of the resulting point defects. However, a unique description from experiments observing changes in physical properties has proved very difficult; probably the most unequivocal have been observations under the electron microscope, but unfortunately they are limited to agglomerates larger than about 15 Å.

The scattering of long wavelength neutrons, for which Bragg reflections are absent, is a particularly attractive tool for studying smaller agglomerates and elementary point defects in crystalline solids, because the scattering cross section per point defect is the experimentally known bound atom coherent scattering cross section. Experimentally the main difficulty in the past has been the low flux of long wavelength neutrons available from a reactor; this technique is likely to be exploited more, however, as cooled moderators (Butterworth *et al.* 1957) inside high flux reactors become available as neutron sources.

Initial experiments by Antal *et al.* (1955) were on neutron irradiated graphite. Their estimate of the defect concentration was in good agreement with theoretical predictions. They pointed out, however, that it may be in error for three reasons: (*a*) irradiation may alter the inelastic scattering cross section of the solid, (*b*) defects may be aggregated in pairs or larger defects, (*c*) there may be relaxation of atoms in the neighbourhood of the defect. Changes in the inelastic scattering cross section have been considered negligible because of the small change in Debye temperature after irradiation. Antal and Goland (1958) have discussed the effect of defect pairs on the wavelength dependence of the transmission cross section; they were able to determine the separation of defect pairs in neutron irradiated α–Al_2O_3, although the complexity of the material was an additional difficulty in the interpretation.

---

† Communicated by the Author.

We propose to discuss here the third possible source of error, namely the effect of lattice relaxation about the defect on the scattering cross section. Unfortunately the magnitude of this relaxation is uncertain in those materials that have been studied experimentally. However, it is, known approximately in certain metals, and for two of these, copper and molybdenum, the cross sections are calculated in this paper to illustrate the general principles.

§ 2. THEORY

Let us consider a perfect lattice of N atoms per unit volume to which ν atoms have been introduced randomly on interstitial sites, causing relaxation of μ atoms around each interstitial. We note here that the ensuing treatment is identical for ν vacancies.

The scattering amplitude per unit solid angle for unit incident flux

$$=b\left\{\sum_{p=1}^{N}\exp\left(-i\boldsymbol{\varkappa}\cdot\boldsymbol{\rho}_p\right)+\sum_{q=1}^{\nu}\sum_{r=0}^{\mu}\exp\left[-i\boldsymbol{\varkappa}\cdot(\boldsymbol{\xi}_q+\boldsymbol{\psi}_r)\right]-\sum_{q=1}^{\nu}\sum_{s=1}^{\mu}\exp\left[-i\boldsymbol{\varkappa}\cdot(\boldsymbol{\xi}_q+\boldsymbol{\varphi}_s)\right]\right\} \quad . \quad . \quad . \quad . \quad (1)$$

$$\equiv b[A+B-C] \quad . \quad . \quad . \quad . \quad . \quad . \quad . \quad . \quad (1a)$$

where b is the bound atom scattering amplitude per unit solid angle for unit incident flux, $\boldsymbol{\varkappa}$ is the scattering vector, magnitude $(4\pi\sin\theta)/\lambda$ (2θ=scattering angle, λ=neutron wavelength), $\boldsymbol{\rho}_p$ and $\boldsymbol{\xi}_q$ are vector distances from the origin of atoms in lattice and interstitial sites respectively, $\boldsymbol{\psi}_r$ is the vector distance of a relaxed atom from its neighbouring interstitial and $\boldsymbol{\varphi}_s$ is the corresponding distance of a lattice site vacated due to relaxation. The sum over p is for the perfect, unrelaxed lattice; that over r includes a term with $\boldsymbol{\psi}=0$, which corresponds to the contribution made by the interstitials to the scattering amplitude.

The scattering intensity is

$$b^2[AA^*+A(B^*-C^*)+A^*(B-C)+BB^*+CC^*-BC^*-CB^*]. \quad (2)$$

Beyond the Bragg cut off wavelength

$$AA^*\sim 1,$$

$$A(B^*-C^*)+A^*(B-C)\sim \nu^{1/2},$$

and turn out to be negligible compared with the other terms, which may be expressed thus:

$$b^2 \sum_{q,q'=1}^{\nu} \exp[-i\boldsymbol{\kappa}.(\boldsymbol{\xi}_q-\boldsymbol{\xi}_{q'})]\left\{ \sum_{r,r'=0}^{\mu} \exp[-i\boldsymbol{\kappa}.(\boldsymbol{\psi}_r-\boldsymbol{\psi}_{r'})] + \sum_{s,s'=1}^{\mu} \exp[-i\boldsymbol{\kappa}.(\boldsymbol{\varphi}_s-\boldsymbol{\varphi}_{s'})] - \sum_{r=0,s=1}^{\mu} \exp[-i\boldsymbol{\kappa}.(\boldsymbol{\psi}_r-\boldsymbol{\varphi}_s)] - \sum_{r=0,s=1}^{\mu} \exp[-i\boldsymbol{\kappa}.(\boldsymbol{\varphi}_s-\boldsymbol{\psi}_r)]\right\} . \quad . \quad . \quad . \quad (3)$$

The sum outside the brackets is of ν^2 vectors of random phase, apart from the restriction that $\boldsymbol{\xi}_q$, $\boldsymbol{\xi}_{q'}$ must lie on interstitial sites; it may be shown to equal $[\nu(N-\nu)]/N$. Hence in most practical cases, when ν is less than a few per cent of N, the sum equals ν to a good approximation, which is the value for a perfectly random array of ν interstitials.

The four series in brackets, which consist of three sums of the general type $\cos[\boldsymbol{\kappa}.(\mathbf{x}-\mathbf{y})]$, are correct for a single crystal, when the orientation of the relaxed zone about each interstitial is identical. For polycrystalline material we must average over all orientations of $(\mathbf{x}-\mathbf{y})$, resulting in a series of terms of the type

$$\frac{\sin[|\boldsymbol{\kappa}|\,.\,|\mathbf{x}-\mathbf{y}|]}{|\boldsymbol{\kappa}|\,.\,|\mathbf{x}-\mathbf{y}|}.$$

Hence the scattering intensity per unit incident flux, per unit solid angle, which is the differential scattering cross section is

$$\sigma_d = b^2\nu\left[\sum_{r,r'=0}^{\mu} \frac{\sin\left(\dfrac{4\pi\sin\theta}{\lambda}|\boldsymbol{\psi}_r-\boldsymbol{\psi}_{r'}|\right)}{\dfrac{4\pi\sin\theta}{\lambda}|\boldsymbol{\psi}_r-\boldsymbol{\psi}_{r'}|} + \sum_{s,s'=1}^{\mu} \frac{\sin\left(\dfrac{4\pi\sin\theta}{\lambda}|\boldsymbol{\varphi}_s-\boldsymbol{\varphi}_{s'}|\right)}{\dfrac{4\pi\sin\theta}{\lambda}|\boldsymbol{\varphi}_s-\boldsymbol{\varphi}_{s'}|} - 2\sum_{r=0,s=1}^{\mu} \frac{\sin\left(\dfrac{4\pi\sin\theta}{\lambda}|\boldsymbol{\psi}_r-\boldsymbol{\varphi}_s|\right)}{\dfrac{4\pi\sin\theta}{\lambda}|\boldsymbol{\psi}_r-\boldsymbol{\varphi}_s|}\right] . \quad . \quad . \quad (4)$$

The moduli represent distances within the relaxed region of the crystal surrounding one interstitial, and the three sums correspond to all distances between atoms, lattice sites, and an atom and lattice site respectively.

Integrating each term of (4) over 4π of solid angle we obtain the total cross section, which is obtained from a transmission experiment:

$$\sigma_t = 4\pi b^2\nu\left[\sum_{r,r'=0}^{\mu} \frac{\sin^2\left(\dfrac{2\pi}{\lambda}|\boldsymbol{\psi}_r-\boldsymbol{\psi}_{r'}|\right)}{\left(\dfrac{2\pi}{\lambda}|\boldsymbol{\psi}_r-\boldsymbol{\psi}_{r'}|\right)^2} + \sum_{s,s'=1}^{\mu} \frac{\sin^2\left(\dfrac{2\pi}{\lambda}|\boldsymbol{\varphi}_s-\boldsymbol{\varphi}_{s'}|\right)}{\left(\dfrac{2\pi}{\lambda}|\boldsymbol{\varphi}_s-\boldsymbol{\varphi}_{s'}|\right)^2} - 2\sum_{r=0,s=1}^{\mu} \frac{\sin^2\left(\dfrac{2\pi}{\lambda}|\boldsymbol{\psi}_r-\boldsymbol{\varphi}_s|\right)}{\left(\dfrac{2\pi}{\lambda}|\boldsymbol{\psi}_r-\boldsymbol{\varphi}_s|\right)^2}\right] . \quad . \quad (5)$$

The sums are identical to those in (4).

These summations are similar to those in the diffraction theory of polyatomic molecules (e.g. James 1948), where terms corresponding to all interatomic distances in the molecule are included; in comparison the sums here include vacant lattice sites, and some terms are negative.

Finally we observe that in a lattice containing two sorts of defects, both with relaxed neighbouring atoms, for example interstitials and vacancies, the total scattering is simply the sum of two series such as (4) or (5) to a good approximation, provided that the defect concentration is not greater than a few per cent.

§ 3. APPLICATION TO FACE-CENTRED AND BODY-CENTRED CUBIC METALS

We present here values of the total and differential scattering cross sections for a point defect in a f.c.c. and a b.c.c. metal considering relaxation of nearest neighbours only, the variable parameters being the relaxation ϵ, the wavelength and the scattering angle.

Figure 1 depicts the total cross section of an interstitial in copper as a function of neutron wavelength. Three values of ϵ, the distance that the six nearest neighbours have moved outwards from their lattice sites, are shown; in all cases ϵ is expressed in units of half the lattice spacing, a. For copper Huntington (1953) and Tewordt (1958) find values of ϵ ranging from 0·210 to 0·257. Cross sections are expressed as fractions of the very long wavelength value $4\pi b^2$; this is also the value σ_t that would be observed if the lattice was not relaxed. Values of a/λ on the abscissa enable these results to be applied directly to other f.c.c. lattices.

Figure 2 shows the variation in total cross section with ϵ for three values of a/λ.

The solid lines in fig. 3 depict the differential scattering cross section of an interstitial in copper as a function of angle. They are for a neutron wavelength of 7·6 Å, which corresponds to $a/\lambda = 0{\cdot}475$.

Figures 4–6 are the corresponding curves for a vacancy in copper, where the twelve nearest neighbours are relaxed inwards. Tewordt (1958) has found $\epsilon = 0{\cdot}019\sqrt{2}$ and $0{\cdot}023\sqrt{2}$, using two different potentials.

Figures 7–9 are the corresponding curves for a vacancy in a b.c.c. material with the eight nearest neighbours relaxed and λ and θ values that are applicable to molybdenum. The values of ϵ may be compared with that of $0{\cdot}0505\sqrt{3}$ calculated by Girifalco and Streetman (1958).

§ 4. DISCUSSION

The results of figs. 1–9 show how marked is the influence of reasonably expected values of relaxation on the scattering cross section. A neglect of it in metals could lead to an experimental estimate in the numbers of defects that was in error by a large factor.

It is pertinent to ask how much in error these results are compared with physical reality, when other neighbouring atoms are relaxed as well. Let us consider the 6(1, 0, 0) and 24(2, 1, 0) neighbours about an interstitial in copper relaxed to new positions $(1+\alpha,\ 0,\ 0)$, $(2+\omega,\ 1+\eta,\ 0)$, where coordinates, centred about the interstitial, are in units of $a/2$. Tewordt (1958) has shown that these are the two kinds of atoms most relaxed. Transmission and differential cross sections have been calculated for certain values of λ and θ, for $\alpha=0{\cdot}25$, $\omega=0{\cdot}050$, $\eta=0{\cdot}055$, which are

Fig. 1

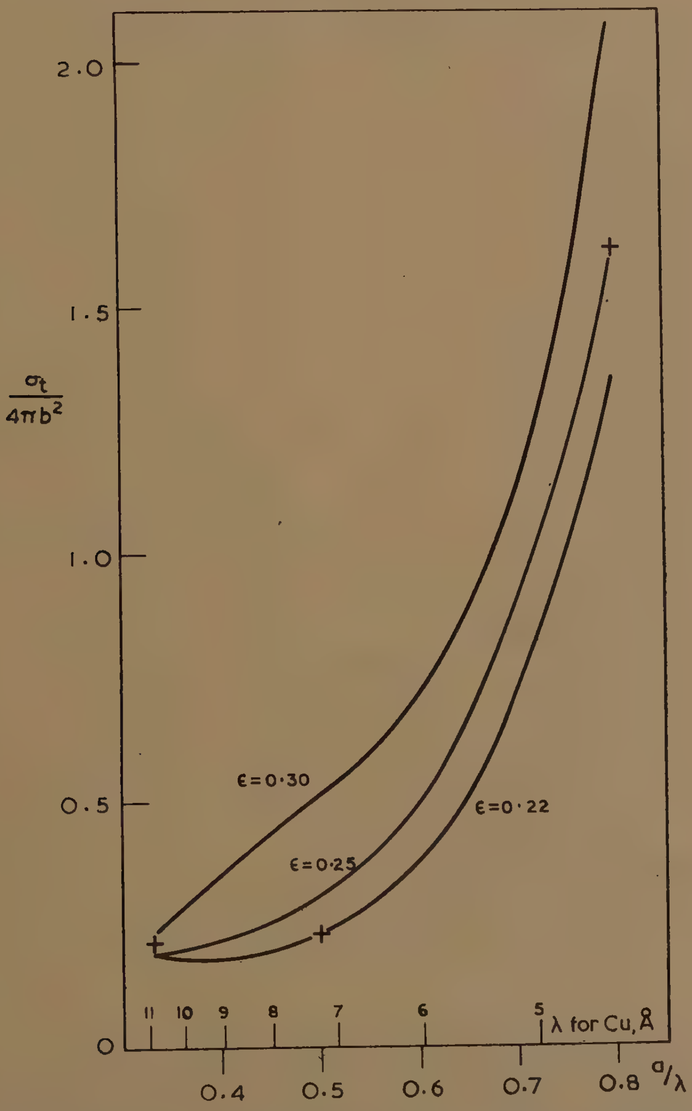

The total cross section σ_t of an interstitial in a f.c.c. lattice plotted as a function of wavelength. σ_t is divided by $4\pi b^2$, which is the total cross section of an interstitial in an unrelaxed lattice. The curves are results of calculations when only nearest neighbours are allowed to relax. The points make allowance for the relaxation of other neighbouring atoms as well, when $\epsilon=0{\cdot}25$. Values of these relaxations which are valid for copper were used.

values lying between those calculated by Tewordt using two different potentials. The results are presented as points on figs. 1 and 3, and may be compared with the curves for $\epsilon = 0{\cdot}25$, when relaxation of (2, 1, 0) atoms is neglected.

Fig. 2

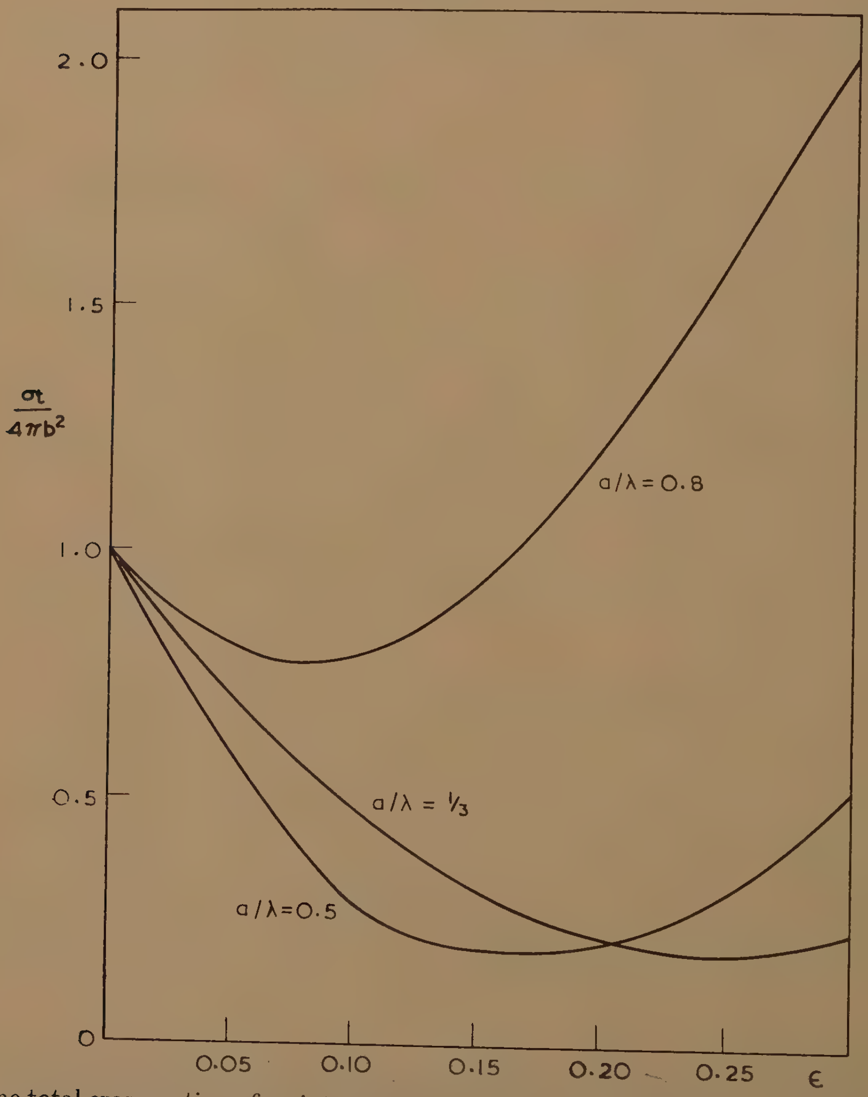

The total cross section of an interstitial in a f.c.c. lattice plotted as a function of the relaxation. The calculations make allowance for the relaxation of nearest neighbours only. For copper $\epsilon \sim 0{\cdot}25$.

Tewordt has also calculated the relaxation of next-nearest neighbours around a vacancy in copper. The nearest and next nearest neighbours, coordinates (1, 1, 0) and (2, 0, 0) are relaxed to $(1-\beta,\ 1-\beta,\ 0)$ and

$(2-\zeta, 0, 0)$ respectively, where $\beta=0{\cdot}020$ and $\zeta=0{\cdot}002$. The results are shown on figs. 4 and 6 and are to be compared with $\epsilon=0{\cdot}02\sqrt{2}$, when relaxation of $(2, 0, 0)$ atoms is neglected.

For a vacancy in molybdenum the coordinates of the relaxed nearest and next-nearest neighbours are $(1-\gamma, 1-\gamma, 1-\gamma)$ and $(2-\chi, 0, 0)$

Fig. 3

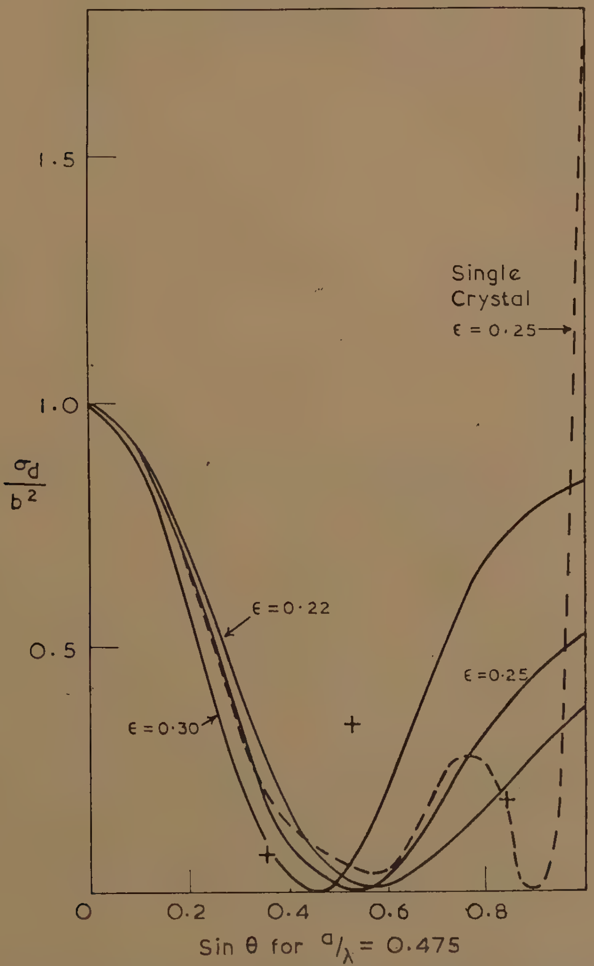

The differential cross section σ_d of an interstitial in copper, plotted as a function of angle. σ_d is divided by b^2, which is the differential cross section of an interstitial in the unrelaxed lattice. The neutron wavelength is 7·6 Å. Solid lines are results of calculations when only nearest neighbours are allowed to relax. The points make allowance for the relaxation of other neighbouring atoms as well, with $\epsilon=0{\cdot}25$. The broken line is for an interstitial in a copper single crystal for neutrons incident in the [100] direction and scattered in the (001) plane. Relaxation of nearest neighbours only is considered.

respectively, where $\gamma = 0{\cdot}0505$ and $\chi = 0{\cdot}0224$, using the results of Girifalco and Streetman (1958). The results may be compared with the nearest neighbour approximation for $\epsilon = 0{\cdot}05\sqrt{3}$.

These results indicate that the cross section is only slightly in error by neglecting the relaxation of next nearest neighbours. Only certain parts of the curves for an interstitial in copper, when the relaxation is very large, are measurably affected.

Fig. 4

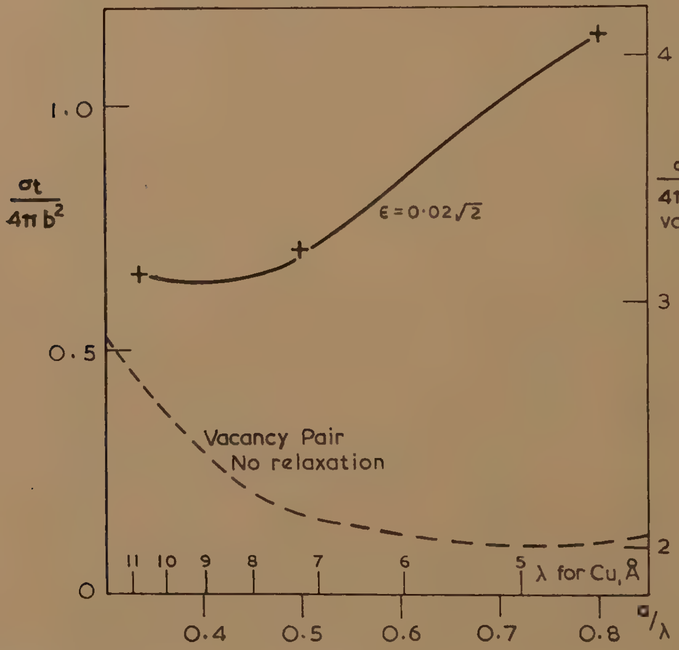

The total cross section σ_t of a vacancy in a f.c.c. lattice plotted as a function of wavelength. The solid line is the result of calculations when only nearest neighbours are allowed to relax. The points make allowance for the relaxation of next-nearest neighbours also, using values which are valid for copper. For comparison the broken line shows the total cross section of a vacancy pair in a f.c.c. lattice, assuming there is no relaxation of the surrounding lattice.

We do not expect the relaxation of atoms a large distance from the point defect to influence these scattering cross sections. This is because in the elastic continuum approximation the density of an infinite medium at any point remains unchanged when a point defect is introduced into it, so that the scattering intensity is zero, as in the perfect lattice.

All the results presented so far have been for randomly oriented polycrystalline solids. To evaluate the differential scattering cross section for a single crystal we must sum terms of the general type

Fig. 5

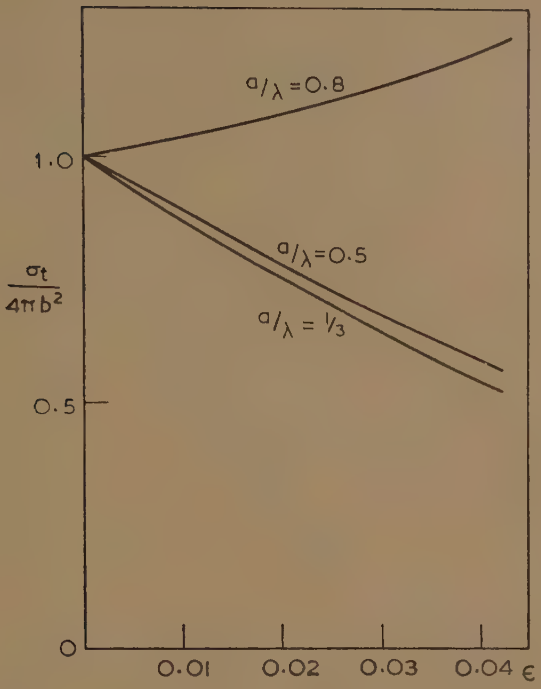

The total cross section of a vacancy in a f.c.c. lattice plotted as a function of the relaxation. The calculations make allowance for the relaxation of the nearest neighbours only. For copper $\epsilon \sim 0{\cdot}028$.

Fig. 6

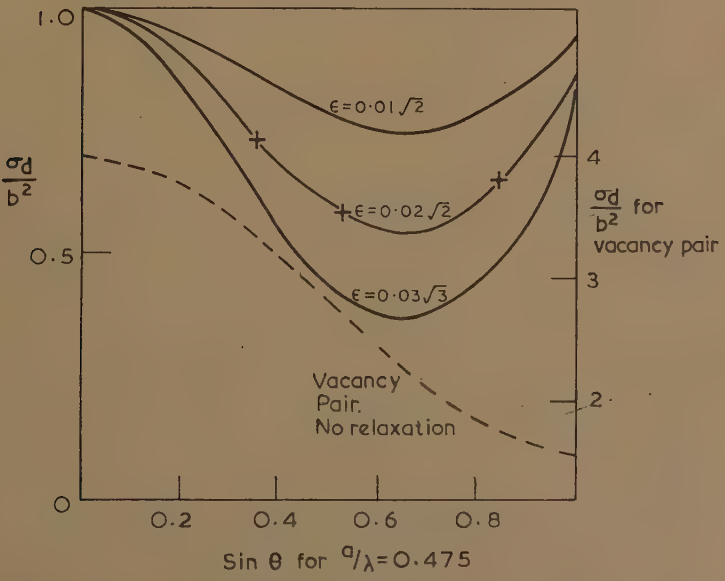

The differential cross section σ_d of a vacancy in copper, plotted as a function of angle. The neutron wavelength is 7·6 Å. Solid lines are results of calculations when only nearest neighbours are allowed to relax. The points make allowance for the relaxation of the next-nearest neighbours as well, with $\epsilon = 0{\cdot}02\sqrt{2}$. For comparison the broken line shows the differential cross section of a vacancy pair in copper, assuming there is no relaxation of the surrounding lattice.

$\cos[\boldsymbol{\kappa}\,.\,(\mathbf{x}-\mathbf{y})]$. The dashed curve in fig. 3 illustrates the differential cross section of an interstitial in a copper single crystal for $\epsilon=0{\cdot}25$. The beam is incident along the [100] axis and is scattered in the (001) plane. It is seen that for small phase differences, when θ is small, the scattering is the same as polycrystalline material; only at larger values of θ do the curves diverge.

Fig. 7

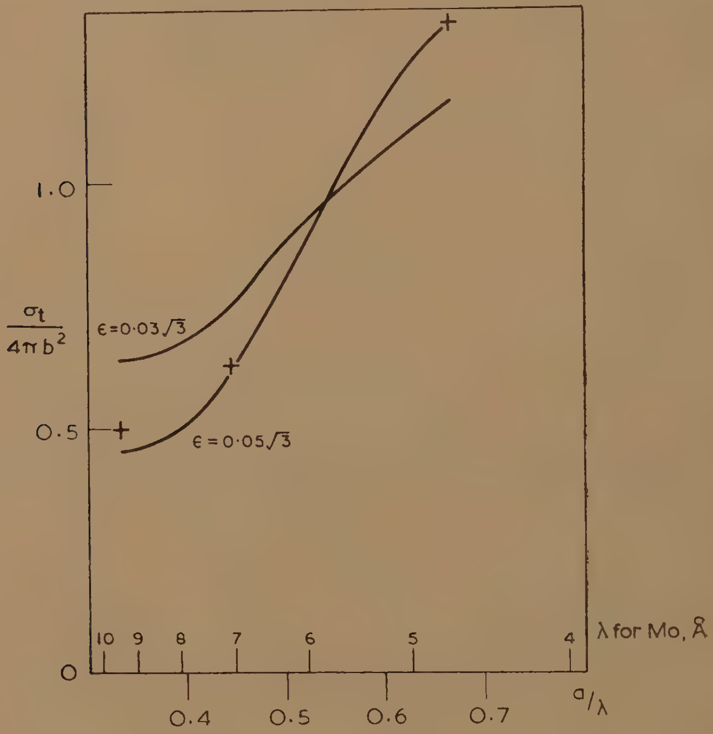

The total cross section σ_t of a vacancy in a b.c.c. lattice, plotted as a function of wavelength. The curves are results of calculations when only nearest neighbours are allowed to relax. The points make allowance for the relaxation of other neighbouring atoms, when $\epsilon=0{\cdot}05\sqrt{3}$. Values of these relaxations which are valid for molybdenum were used.

It was pointed out above that the cross section of agglomerated defects will depend on wavelength and angle. The scattering from a defect pair (neglecting relaxation) in copper is shown as a function of λ and θ in figs. 4 and 6 respectively, for comparison with relaxation effects. Apart from low scattering angles the curves are quite different, so that in principle the two effects are experimentally separable (but see next paragraph).

The results of this paper show that lattice relaxation and the state of agglomeration of defects influence the scattering cross section to a comparable extent. This is a serious disadvantage when neutron

Fig. 8

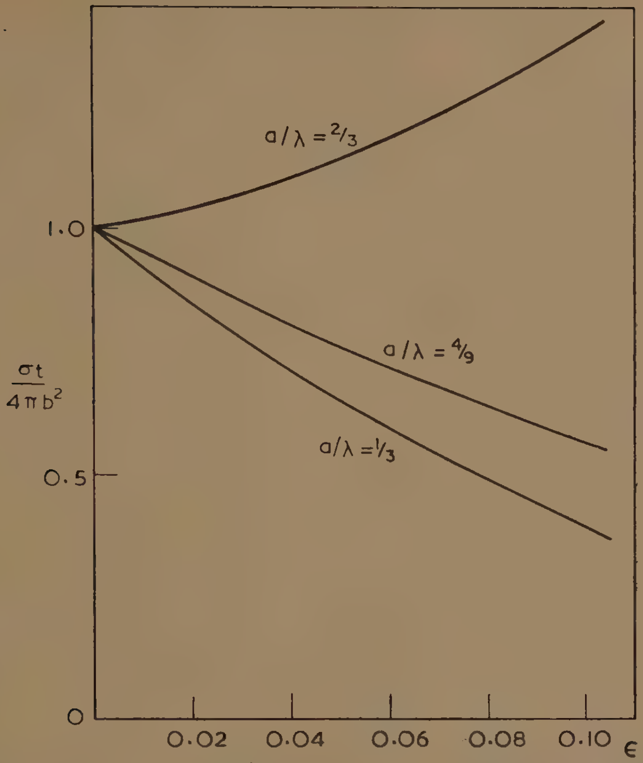

The total cross section of a vacancy in a b.c.c. lattice plotted as a function of the relaxation. The calculations make allowance for the relaxation of nearest neighbours only. For molybdenum $\epsilon \sim 0{\cdot}087$.

Fig. 9

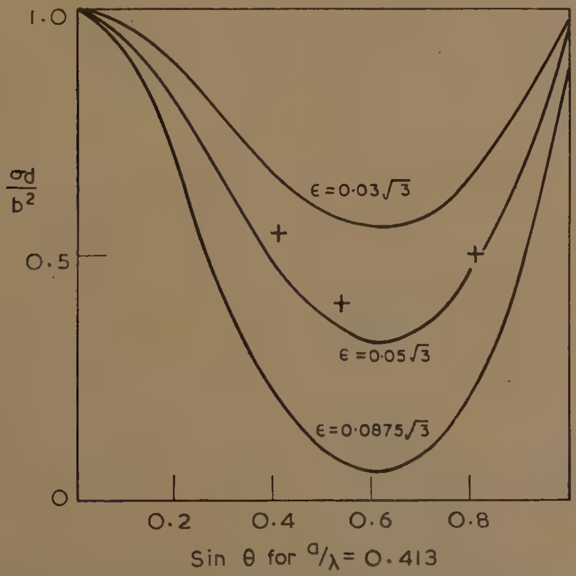

The differential cross section σ_d of a vacancy in molybdenum plotted as a function of angle. The neutron wavelength is 7·6 Å. Solid lines are results of calculations when only nearest neighbours are allowed to relax. The points make allowance for the relaxation of the next-nearest neighbours as well, with $\epsilon = 0{\cdot}05\sqrt{3}$.

scattering experiments are used to study the nature of defects produced after irradiation damage because these two effects cannot be distinguished, since only for certain elementary defects in a limited number of materials is the relaxation known. To illustrate this, fig. 4 depicts the scattering of a vacancy pair, without relaxation, the value of which is unknown. It may be that with relaxation included the curve would become a straight line independent of wavelength, like a defect with no relaxation, or alternatively have the shape like the other curve in fig. 4 which is for a single vacancy with relaxation, so that results would be ambiguous. Perhaps in certain particular cases, for example in materials possessing a more open structure, when relaxation should be less pronounced, or with single crystals, where the cross section fluctuates more rapidly with wavelength and scattering angle there may be less ambiguity.

However, if the size of defect agglomerates is known in a particular solid, measurements of the neutron scattering cross section will yield information about the relaxation of the surrounding lattice. One such example is a very dilute solid solution, when the solute atoms are effectively point singularities randomly dispersed in the solvent lattice; in particular, if this lattice possesses cubic symmetry, the relaxation of nearest neighbours around each solute atom may be determined directly from such an experiment.

REFERENCES

ANTAL, J. J., and GOLAND, A. N., 1958, *Phys. Rev.*, **112,** 103.
ANTAL, J. J., WEISS, R. J., and DIERNES, G. J., 1955, *Phys. Rev.*, **99,** 1081.
BUTTERWORTH, I., EGELSTAFF, P. A., LONDON, H., and WEBB, F. J., 1957, *Phil. Mag.*, **2,** 917.
GIRIFALCO, L. A., and STREETMAN, J. R., 1958, *J. Phys. Chem. Solids*, **4,** 182.
HUNTINGTON, H. B., 1953, *Phys. Rev.*, **91,** 1092.
JAMES, R. W., 1948, *The Optical Principles of the Diffraction of X-rays* (London: Bell), p. 482.
TEWORDT, L., 1958, *Phys. Rev.*, **109,** 61.

The Nature of Radiation-induced Point Defect Clusters†

By R. S. Barnes and D. J. Mazey
Atomic Energy Research Establishment, Harwell, Didcot, Berks

[Received June 21, 1960]

Abstract

The electron microscope has been used to examine point defect clusters produced in copper and aluminium foils bombarded with $1{\cdot}4 \times 10^{17}$ alpha-particles cm^{-2}. The foils were bombarded as a stack and, in copper, both those through which the alpha-particles had passed and that in which they came to rest appeared similar, containing dislocation loops ($r \sim 200$ Å) and a background of more numerous and smaller dots ($r \sim 20$ Å). The behaviour at grain boundaries suggested that these two types of cluster were due to different point defects. Whereas the dislocation loops normally annealed out at about 350°c, in the foil in which the alpha-particles came to rest (containing $\sim 10^{15}$ atoms of helium cm^{-2}) they grew to form a dislocation tangle, and eventually small helium bubbles ($r \sim 40$ Å) appeared in the same number as the original small dots. These results indicate that the dislocation loops are due to the clustering of *interstitial atoms* and the small dots are clusters formed from *vacancies*. It is also inferred that the helium atoms are in interstitial positions during the bombardment, and form bubbles by nucleating upon the clusters.

§ 1. Introduction

The much smaller energy needed to form a vacancy ensures that the point defect clusters observed in quenched metals are due to precipitation of the excess concentration of vacancies and not interstitial atoms. However, during atomic bombardment vacancies and interstitial atoms must be produced in nearly equal numbers, because they are produced by a collision process, and the effects observed may be due to either type of defect. Bombardment with alpha-particles introduces both point defect clusters and helium atoms, the latter on subsequent heating capture large numbers of vacancies (Barnes *et al.* 1958) and enable the nature of the point defect clusters to be determined.

Thin films of copper extracted from a solid block which had been bombarded with alpha-particles have been examined and helium bubbles observed within them (Barnes 1960). However, the extraction of thin films from a solid block is tedious and wasteful of material. The results described here were obtained by placing stacks of thin sheets of metal in the external beam of a cyclotron accelerating alpha-particles. These were then thinned by normal electrolytic methods until they could be viewed in transmission in the electron microscope. Sheets from various depths beneath the bombarded surface were studied and the effects produced by the passage of the alpha-particles (in the sheets near the surface) compared with those produced where the helium atoms were deposited (in the sheet corresponding to the end of the range of the alpha-particles).

---

† Communicated by the Authors.

Johnson Matthey spectroscopically standardized copper or aluminium was used and the sheets were initially either 0·002 in. or 0·001 in. thick and were vacuum annealed for 2 hours at 650°C before bombardment; during bombardment their temperature did not exceed 250°C. As the range of the 38 MeV alpha-particles from the cylotron was 0·009 in. in copper, about five 0·002 in. or nine 0·001 in. sheets were affected during each bombardment.

However, normally only one of the sheets contained the helium. This was located by observing the helium bubbles after heating a little of a sheet to about 800°C for 2 hours. Figure 1† shows the cross section of a 0·001 in. foil (after electrolytic polishing) containing unresolved helium bubbles near the grain boundaries (Barnes *et al.* 1958). Suitable masking enabled other pieces from this same sheet to be thinned (after the appropriate annealing treatment) leaving the centre of the helium layer within it.

§ 2. RESULTS

The photographs in figs. 2 and 3 were taken from foils, containing no helium, through which $1{\cdot}4 \times 10^{17}$ alpha-particles cm^{-2} ($32\,\mu$ amp hours) had passed. The appearance of the electron micrographs taken from various distances along the alpha-particle tracks showed little variation, each containing a number of relatively large dislocation loops ($r \sim 200$ Å) and a background of much smaller dark dots ($r \sim 20$ Å) (fig. 2). Figures 3 (*a*), (*b*) and (*c*) are successive photographs of a similar foil taken while it was at about 350°C in the 'hot-stage' of the electron microscope. At this temperature the loops disappeared in less than 30 min. Sheets were also annealed in a vacuum furnace at various temperatures. After a 2-hour anneal at 300°C there was little change in the appearance of the films, after the same time at 325°C slight annealing had occurred and after 4 hours at 350°C complete annealing of the loops had occurred.

The thin films in which the helium atoms had come to rest contained both large loops and small dots, which were not significantly different in size from the above (table), but the dots appeared to be localized around the loops (fig. 4). The annealing behaviour was however markedly different and the series of photomicrographs of foils annealed in a vacuum furnace shows this (fig. 5). Instead of the dislocation loops disappearing after 2 hours at 350°C (fig. 5 *a*) they enlarged and after 2 hours at 450°C (fig. 5 *b*) had become a tangle of dislocations. After this anneal there were small bubbles near the grain boundaries (fig. 5 *b*). After 2 hours at 550°C small bubbles pervaded the grains and on further heating for 2 hours at 750°C they became larger (fig. 5 *c* and *d*). At this temperature larger bubbles occurred along the grain boundaries (fig. 5 *e*) consistent with previous observation (Barnes 1960).

---

† All figures are shown as plates.

Aluminium foils through which the alpha-particles had passed contained no observable damage effects, but the foil with helium in, contained a dislocation tangle, and upon heating small helium bubbles appeared.

		Radius (r) cm	Number cm^{-2} (n)	Number of atom spaces cm^{-2} in	
				Loops $(4\pi/\sqrt{3})(r/a)^2n$	Spheres $(16\pi/3)(r/a)^3n$
Figure 2 (*a*)	Point defects only	$2\cdot2\times10^{-6}$	$4\cdot2\times10^{9}$	$1\cdot1\times10^{14}$	—
Figure 2 (*b*)	Point defects only	$2\cdot2\times10^{-6}$	$6\cdot4\times10^{9}$	$1\cdot7\times10^{14}$	—
Figure 4	He and point defects	$1\cdot6\times10^{-6}$	$1\cdot4\times10^{10}$	$2\cdot0\times10^{14}$	—
Figure 2 (*a*)	Point defects only	$2\cdot5\times10^{-7}$	$9\cdot0\times10^{10}$	$3\cdot6\times10^{13}$	$5\cdot0\times10^{14}$
Figure 4	He and point defects	$1\cdot9\times10^{-7}$	$1\cdot2\times10^{11}$	$2\cdot4\times10^{13}$	$3\cdot0\times10^{14}$
Figure 5 (*d*)	He bubbles	$4\cdot0\times10^{-7}$	$1\cdot4\times10^{11}$	—	$3\cdot2\times10^{15}$

The size and number per unit area of the dislocation loops (the first three rows), the dots (the next two rows) and the bubbles (last row) observed in the thin films. The foil thicknesses were approximately 1000 Å.

§ 3. DISCUSSION

Dislocation loops form in many metals during quenching (Hirsch *et al.* 1958) their number and size depending upon the quenching conditions. These loops which are produced by the precipitation of the highly super-saturated vacancies during the quench, do not normally contain stacking faults and are of dislocations with Burgers vectors $a/2$ [110]. The appearance of the copper sheets through which alpha-particles have passed (fig. 2) resembles that of a quenched foil. Closed loops can be identified but their shapes are less regular than those in quenched metals and in addition there is a very fine background of dots uniformly distributed throughout the foil. The annealing behaviour is similar to that of a quenched metal (Silcox and Whelan 1960) the loops disappearing after several hours at 350°c. The behaviour of the sheets containing the helium upon annealing is notably different and it is this which indicates the nature of the clusters†.

3.1. *Nature of Large Loops*

The larger dislocation loops ($r \sim 200$ Å) which formed in the copper disappeared at about 350°c but at this temperature began to grow when helium was present. As the helium atoms are known to be very effective in capturing vacancies (Barnes *et al.* 1958, Barnes 1960) they will extract vacancies from any nearby dislocation by climb, if the temperature is sufficient for vacancy formation and migration. In copper this temperature is about 350°c. Dislocation loops formed by the clustering of *vacancies* would contract in such a situation. Thus the growth of the large loops at this temperature suggests that they are formed by the clustering of *interstitial atoms.* The anneal also makes the loops more regular which would happen during climb. Their further growth to form a tangle of dislocation lines at 450°c is consistent with this.

The total area of these large loops can be used to estimate the number of agglomerated interstitial atoms. The values given in the table, assuming that the loops lie on $\{111\}$ planes, suggest that there are about $1{\cdot}6 \times 10^{14}$ interstitial atoms cm^{-2} both in those thin films containing helium and those not.

The annealing of the loops in regions containing no helium was such that the loops became smaller and disappeared after 2 hours at 350°c. Presumably the vacancies which were present in equal numbers to the interstitial atoms, annihilated these loops.

Near grain boundaries (fig. 2*b*) there is a zone ($\sim 8 \times 10^{-5}$ cm wide) which contains none of the larger loops. Presumably the interstitial atoms have been captured by the boundary instead of forming loops, suggesting that they can normally migrate distances of this magnitude during the bombardment.

3.2. *Nature of the Dots*

The background of small dots, seen in fig. 2 (*b*), continues right up to the grain boundary, with no depleted zone, suggesting that they have formed from point defects which can diffuse only $\gtrsim 500$ Å during the bombardment. They must be very different from those producing the large loops and are probably formed from the vacancies which must be present in nearly equal numbers.

It is very difficult to estimate the number of point defects clustered in these small dots which do not appear to be dislocation loops; their size is uncertain and may be determined by a strain field, also their number may be underestimated because many are too small to be resolved. An estimate (table) suggests that if they are dislocation loops there are only about one fifth as many vacancies in them as there are interstitial atoms agglomerated in the larger loops. However, if the same values are used, but it is assumed that they are spherical voids, the number of vacancies agglomerated in them (table) more nearly equals the number of interstitial atoms, as should be the case. Certainly very small vacancy clusters would have a lower energy if arranged as a sphere rather than as a plate (Kuhlman-Wilsdorf and Wilsdorf 1960)[†].

---

† A difference in annealing of hardness between regions through which alpha-particles had passed and the region in which they were deposited had been noticed previously (Ghosh *et al.* 1960).

The behaviour of the aluminium foils was similar to that of copper, but presumably in the former the vacancies and interstitial atoms had annihilated during the bombardment except where helium was present, where the appearance of the dislocation tangle and the formation of bubbles was almost the same as in the copper.

3.3. *Helium Bubble Nuclei*

After annealing at 450°C small gas bubbles can be seen as white dots near the grain boundaries on the photomicrographs (fig. 5*b*). Eventually after an anneal of 1 hour at 750°C these bubbles can be seen throughout the film if it is so oriented in the microscope that the dislocation lines do not give a contrast which obscures the bubbles (fig. 5*d*). These spots are 40 Å in radius and have the characteristics of gas bubbles; they are spherical, i.e. they appear round with light centres becoming darker at their edges, with no diffraction contrast. The bubbles appear in rows and lie upon the dislocation lines (Barnes 1959–1960). This can be demonstrated by re-orientating the foil to give contrast effects at the dislocations.

The number of helium bubbles observed once there are sufficient vacancies available is $\sim 10^{11}\,\mathrm{cm}^{-2}$ almost the same as the number of small dots (table). It seems possible that these dots are the nuclei upon which the helium bubbles form.

The number of helium atoms (m) contained in the films can be calculated from the photomicrographs of the bubbles, using the formula (Barnes 1959),

$$(2\gamma/r)\,\tfrac{4}{3}\pi r^3 n = mkT$$

where γ is the surface energy (about $10^3\,\mathrm{ergs\,cm}^{-2}$), r is the bubble radius (40 Å), n is their number in unit area of the film ($1{\cdot}4 \times 10^{11}\,\mathrm{cm}^{-2}$), k is Boltzmann's constant, and T the absolute temperature (1023°K), therefore $m = 1{\cdot}4 \times 10^{15}\,\mathrm{cm}^{-2}$ (i.e. an atomic concentration of approximately $1{\cdot}7 \times 10^{-3}$ in the copper). One concludes that there are approximately nine helium atoms for each interstitial atom in the loops and for each vacancy in the black dots. The small number of interstitial atoms observed in all these films (table) implies that most of the helium atoms were interstitial during the bombardment, because if each helium atom was substitutional $1{\cdot}4\times10^{15}$ vacancies cm^{-2} must be provided and $1{\cdot}4\times10^{15}$ interstitial atoms cm^{-2} would be left ; only 1/10th this number was observed.

[†] Recent observation of foils annealed for 1 hour at 400°C show that in some grains the remaining dots become triangular. This implies that the clusters are tetrahedra of stacking fault (Silcox and Hirsch 1959) both because of their shape and their stability above the self-diffusion temperature.

The clusters would capture helium atoms during irradiation and gas bubbles would form upon them. However, presumably because of the shortage of vacancies these bubbles do not grow and thus cannot accommodate further helium atoms. It can be estimated from the gas laws that only a fraction of the helium atoms reside in the vacancy clusters, during bombardment. Subsequent heating permits the acquisition of vacancies from the interstitial atom agglomerates, which grow. The number of vacancies these loops (radius ~ 200 Å) produce during their climb to form the tangle of dislocations (equivalent to a radius of about 1000 Å) is such that approximately two vacancies are provided per helium atom. This would be sufficient to enable each helium atom to become substitutional. The process ceases either because the helium bubbles eventually lock the dislocations and prevent their further climb, or because the dislocations become locked by mutual interaction. Whichever the reason, the structure remains stable until vacancies are provided from the grain boundaries (fig. 5 *e*) and then the helium atoms produce observable bubbles as described previously (Barnes 1960). The dislocation tangle also enlarges with further heating and continues to enlarge as the bubbles grow larger and reduce in number.

§ 4. Conclusions

Copper bombarded with $1{\cdot}4\times10^{17}$ alpha-particles cm^{-2} at about 200°c contains both dislocation loops $r\sim200$ Å formed by the clustering of interstitial atoms, and much smaller and more numerous dots ($r\sim20$ Å) which are probably clusters formed from the less mobile vacancies. On annealing at about 350°c the clusters annihilate one another by the generation and diffusion of single vacancies so that the material reverts much to its original state. However, when the material contains large numbers of helium atoms these stabilize the vacancy clusters, and at about 350°c they are able to grow by taking vacancies from the dislocation loops which, because they are formed from interstitial atoms grow, eventually becoming a tangle. The steady acquisition of vacancies by the small bubbles enables them to accommodate more helium atoms until eventually they can be clearly resolved in the electron microscope.

Thus it appears that the vacancies produced by irradiation provide some space for the helium atoms to form bubbles. However, more vacancies are supplied from the dislocation loops which climb, but the total number is limited as suggested previously (Barnes 1960) so that the size of the bubbles which form is too small to be detected using the normal optical microscope until large numbers of vacancies have been supplied from the grain boundaries.

ACKNOWLEDGMENTS

We are grateful to Mr. W. Hardy and his team at Birmingham University for conducting the cyclotron bombardments, and Mr. C. K. Jackson for his assistance with the electron microscopy, and in particular with the 'hot-stage' experiment.

REFERENCES

BARNES, R. S., 1959, *Nuclear Metallurgy*, **6,** 21; 1959–1960, *J. Inst. Met.*, **88,** 13; 1960, *Phil. Mag.*, **5,** 635.
BARNES, R. S., REDDING, G. B., and COTTRELL, A. H., 1958, *Phil. Mag.*, **3,** 97.
GHOSH, T. K., BEAVERS, J., and BARNES, R. S., 1960, *J. Inst. Met.* (in the press).
HIRSCH, P. B., SILCOX, J., SMALLMAN, R. E., and WESTMACOTT, K. H., 1958, *Phil. Mag.*, **3,** 897.
KUHLMANN-WILDORF, D., and WILSDORF, H. G. F., 1960, *J. appl. Phys.*, **31,** 516.
SILCOX, J., and HIRSCH, P. B., 1959, *Phil. Mag.*, **4,** 72.
SILCOX, J., and WHELAN, M. J., 1960, *Phil. Mag.*, **5,** 1.

The Growth of Prismatic Dislocation Loops during Annealing[†]

By C. A. JOHNSON[‡]
Materials Research Laboratory, University of California,
Berkeley, California

[Received June 20, 1960]

ABSTRACT

Recent observations of the growth of quenched-in dislocation loops during annealing are discussed. A mechanism for the coalescence of loops is proposed. The mechanism depends on short-circuit diffusion around the periphery of prismatic dislocation loops. This mechanism is contrasted with the theory of loop coalescence by vacancy diffusion through the matrix. It is shown that the experimental observations are in better accord with the short-circuit diffusion theory.

Interpretation of the experimental observations on the basis of the short-circuit mechanism leads to a value for the activation energy for diffusion along a dislocation line. For aluminium this value is calculated to be 0·7 ev.

§ 1. INTRODUCTION

IN recent electron-micrographic experiments on the annealing of quenched aluminium, Silcox and Whelan (1960) and Vandervoort and Washburn (1960) have observed that the density of dislocation loops present in the as-quenched material decreased markedly upon annealing. In the experiments of Silcox and Whelan, annealing was carried out in two distinct ways: annealing of the foil *in situ* within the microscope so that the details could be observed as annealing proceeded, and annealing of the bulk material before thinning, in which case the progress of annealing could not be followed continuously.

It was found that the annealing of loops in foil became noticeable at a temperature of 170°C and proceeded by the shrinking of all loops, and that there was no tendency for any of the loops to grow at the expense of the others. Silcox and Whelan have accounted for these observations by proposing that vacancies are evaporated from the periphery of each loop and that these vacancies then diffuse to the surface of the foil. Since the free surfaces of the foil provide a nearby sink for vacancies, this process can occur rapidly at moderate temperatures.

In specimens prepared from material annealed in bulk, however, they found that the decrease in loop density was accompanied by the growth of some loops. This agrees with the observations of Vandervoort and Washburn, who found that considerable loop growth occurred in samples prepared from bulk material which had been annealed for ten minutes at 150°C. In samples which had been annealed for ten minutes at 125°C little loop growth was observed, but after ten minutes at 200°C annealing of the loops seemed to be essentially complete, with only a very few large loops remaining.

[†] Communicated by the Author.

[‡] Graduate Physicist, Materials Research Laboratory, University of California, Berkeley 4, California.

That the growth of the loops must involve vacancy diffusion follows from the generally accepted view that the loops have originated by the collapse of vacancy precipitates. Accordingly, Silcox and Whelan have interpreted their observations on material annealed in bulk form in terms of the evaporation of vacancies from the periphery of a small loop, and the subsequent diffusion of these vacancies through the matrix to precipitate on a larger loop. The purpose of this paper is threefold: to propose a mechanism by which loop growth can occur without employing diffusion through the matrix between two loops, to contrast this process with the vacancy diffusion process proposed by Silcox and Whelan, and to interpret the experimental results in terms of both processes.

The diffusion of vacancies through the matrix (bulk self-diffusion) is not the only means by which loops could coalesce. It is proposed that an effective mechanism for the coalescence of loops involves a diffusion short-circuit process. This is illustrated in fig. 1, in which atoms diffuse rapidly along the periphery of the loop. The rate at which diffusion can take place along this short-circuiting path is determined by the activation energy for diffusion along a dislocation line. The activation energy for diffusion along dislocation lines has been determined for various metals (Hoffman and Turnbull 1951, Hendrickson and Machlin 1954, Turnbull and Hoffman 1954); the values obtained range between one-half and two-thirds of the activation energy for bulk diffusion. The activation energy for diffusion along dislocation lines in aluminium has not been measured, but it would be expected that it is appreciably lower than the activation energy for bulk self-diffusion.

The elastic interaction between two nearby loops provides a driving force tending to create a net flow of diffusing atoms from the closest to the more distant edges of both loops†. As shown in fig. 2, this short-circuit diffusion around the periphery of the loops caused the two loops to move together. For convenience this process will be called 'self-climb'. However, self-climb alone can only account for the coalescence of coplanar loops. Loops can, in principle, also move by prismatic glide along a cylindrical surface inclined to the plane of the loop and containing the Burgers vector of the loop. The combination of self-climb and prismatic glide would therefore permit the motion of loops in any direction. The limitations on prismatic glide of loops have been discussed by Kuhlmann-Wilsdorf (1958), and will also be discussed below.

---

† The elastic interactions providing this driving force will be smaller in the foil due to the fact that a thin film of material can relieve these stresses by buckling. A comprehensive treatment of the limitations on dislocation interactions imposed by the thinness of foils used in electron microscopy is to be published separately.

Examination of the micrographs published by Vandervoort and Washburn (1960) shows that, in specimens prepared from material annealed at 150°c, the loop density is considerably smaller than the loop density in as-quenched material and, moreover, that the loops which remain after annealing are often considerably larger than those found, on the average, in the as-quenched material. In particular, a number of pairs of loops are observed. The distance between the members of such a pair is commonly smaller than the diameter of either loop. This effect is particularly evident in fig. 7 of Vandervoort and Washburn's paper. From these observations the following conclusions have been drawn.

Fig. 1

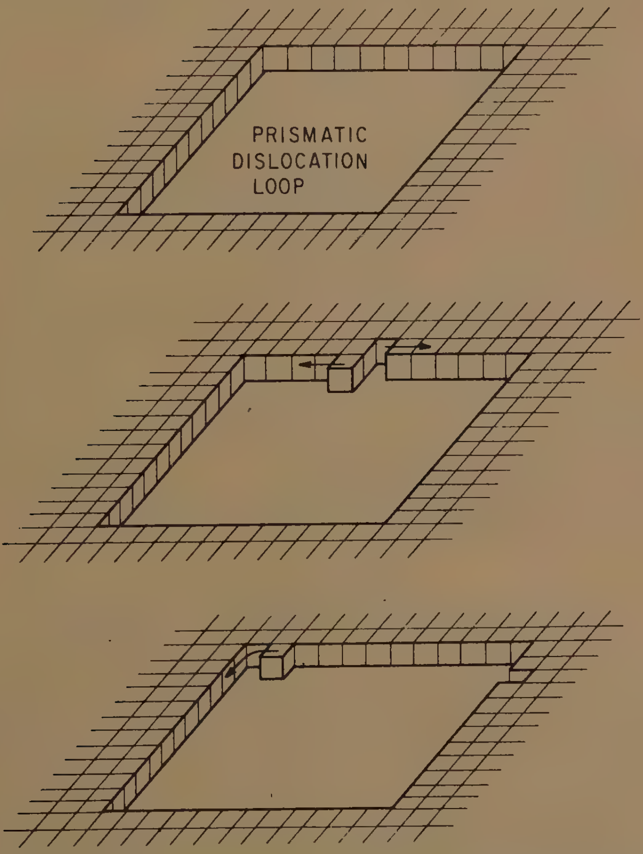

Formation and migration of defects involved in self-climb.

1. The coalescence of loops does not seem to be due to vacancy diffusion through the matrix. It is extremely difficult, for example, to understand how loops which are separated by distances such as those observed in the as-quenched material could have coalesced by diffusion through the matrix while some loops which are very near one another remained intact.

2. The self-climb mechanism can satisfactorily explain these observations. If this process controls the behaviour of loops during annealing, loops remain substantially intact until they finally merge, and this is consistent with the microscopic evidence.

Fig. 2

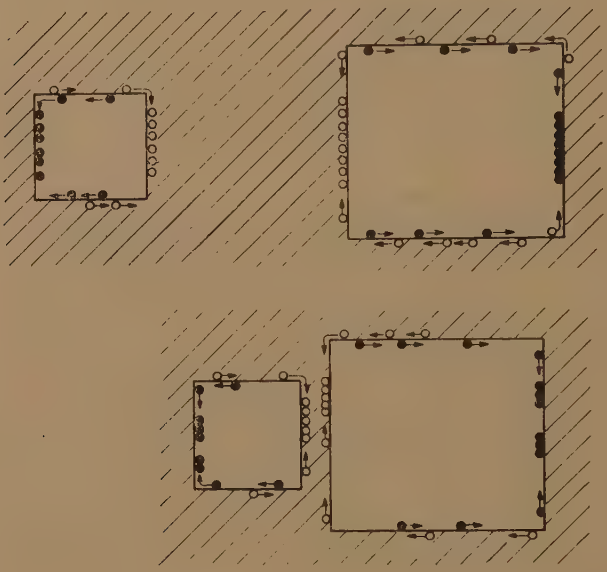

Successive stages in the coalescence of two coplanar loops by self-climb. The filled circles represent diffusing atoms and the open circles diffusing vacancies.

However, another point must be considered, namely, whether the closely coupled pairs observed were just about to coalesce, or whether there are cogent reasons why they could not merge completely.

It is possible for a vacancy plate on the (111) plane in a face-centred cubic metal to collapse in two different ways, depending on whether or not the atom planes above and below the plane of the plate are sheared along a direction lying in the plane of the plate as they come together. If no shear takes place, then Burgers vector of the resultant dislocation loop will be $(a/3)$ [111] and the loop will contain a stacking fault since the stacking sequence normal to the plane of the loop is ABCACABC.... No stacking faults were observed in the specimens examined by Vandervoort and

Washburn or by Silcox and Whelan. If, on the other hand, the atom planes above and below the plane of the vacancy plate are displaced with respect to one another as they come together by one of the shears $(a/6)[11\bar{2}]$, $(a/6)[\bar{2}11]$, $(a/6)[1\bar{2}1]$, then the stacking sequence will be the normal ABCABCA... so that the loop will not contain a fault, and the slip vector of the resulting loop will be $(a/2)[110]$, $(a/2)[011]$, or $(a/2)[101]$.

These slip vectors are translation vectors of the face-centred cubic lattice so that a dislocation loop having any of these three slip vectors can glide on a cylindrical surface inclined to the plane of the loop and containing (as the generators of the cylinder) the slip vector of the loop. However, in general not all parts of such a loop will be able to slip easily on this cylindrical surface since the surface will not be entirely composed of close-packed $\{111\}$ planes. Such a situation is shown in fig. 4 (a), in which the $[1\bar{1}0]$ segments of the loops can only slip on (001), while the segments oriented along $[\bar{1}01]$ and $[0\bar{1}1]$ slip readily on the close-packed $\{111\}$ planes. Since hexagonal loops corresponding to the configuration of fig. 4 (a) have often been found in foils, it is of interest to examine the possibility of slip on (001). Boas and Schmid (1931) have observed that macroscopic slip can occur on $\{100\}$ planes in aluminium at temperatures above 400°C. It is possible that the attractive force between the neighbouring $[1\bar{1}0]$ segments might be high enough to cause them to combine by slip on (001) even at temperatures as low as 150°C.

Fig. 3

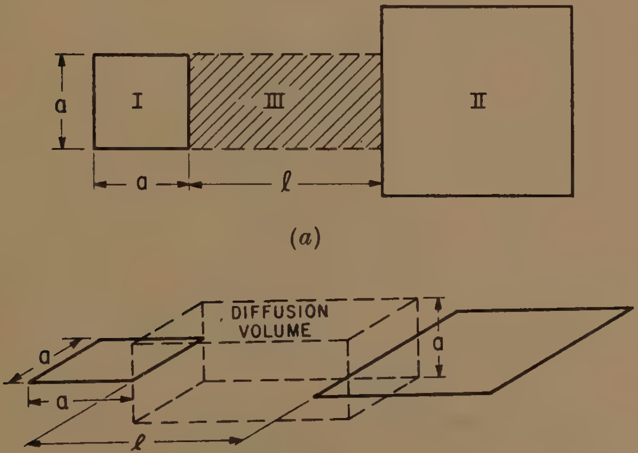

(*a*)

(*b*)

Geometries for calculating rates of loop coalescence.

(*a*) Geometry for coalescence of coplanar loops by self-climb. The areas I and II are the interiors of the loops.

(*b*) Geometry for coalescence of loops by bulk diffusion.

For the geometry of fig. 4 (*a*), where both loops have the same Burgers vector, the stress between the neighbouring $[1\bar{1}0]$ segments of the loops is

$$\sigma = \frac{\mu |b|}{2\pi(1-\nu)} \left(\frac{1}{\sqrt{2d}} \right)$$

where μ is the shear modulus, ν is Poisson's ratio, $|b|$ is the magnitude of the slip vector, and d is the distance between the respective (111) planes on which the loops lie. To estimate the magnitude of this stress it is necessary to make some estimate of the value of d. Bearing in mind that the foils used by Vandervoort and Washburn and Silcox and Whelan were of the order of 1000 Å thick it seems reasonable to choose $d \sim 200$ Å. Then $\sigma \sim 5 \times 10^8$ dynes/cm²; this is roughly one hundred times as great as the macroscopic shear stress at which glide begins on {111} in aluminium. Since Boas and Schmid (1931) found {100} slip at 400°c under conditions for which the shear stress on planes of the {100} type was only slightly larger than the shear stress acting on planes of the {111} type, the possibility of inducing {100} slip at 150°c by a stress one hundred times higher than that required for {111} slip cannot be discounted.

Fig. 4

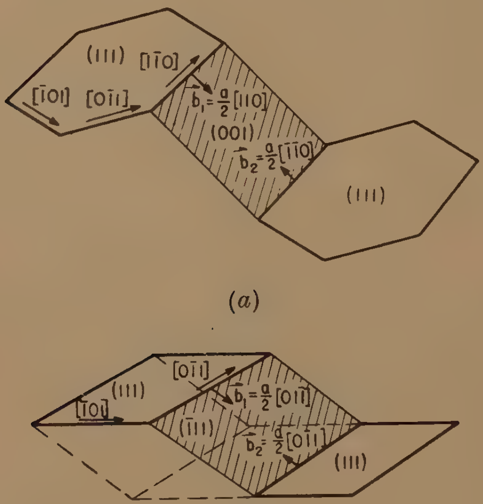
(111)
$[1\bar{1}0]$
$[\bar{1}01]$
$[0\bar{1}1]$
$\vec{b}_1 = \frac{a}{2}[110]$
(001)
$\vec{b}_2 = \frac{a}{2}[\bar{1}\bar{1}0]$
(111)
$[0\bar{1}1]$
(111)
$\vec{b}_1 = \frac{a}{2}[01\bar{1}]$
$[\bar{1}01]$
$(\bar{1}11)$
$\vec{b}_2 = \frac{a}{2}[0\bar{1}1]$
(111)

(*a*)

(*b*)

Coalescence of loops on parallel (111) planes by prismatic glide.
(*a*) Combination of non-coplanar hexagonal loops.
(*b*) Combination of loops capable of easy prismatic glide.

Prismatic glide of hexagonal dislocation loops has been observed by Hirsch *et al.* (1958). The observations were made on thin foils of quenched aluminium at temperatures lower than 100°c and provide strong experimental evidence for glide on {100} planes at ordinary temperatures.

As shown in fig. 4 (*b*), it is possible to construct a loop all parts of which are oriented for easy slip on close-packed planes. Non-coplanar loops of this type can readily coalesce by self-climb followed by prismatic glide on $\{111\}$ planes.

Fig. 5

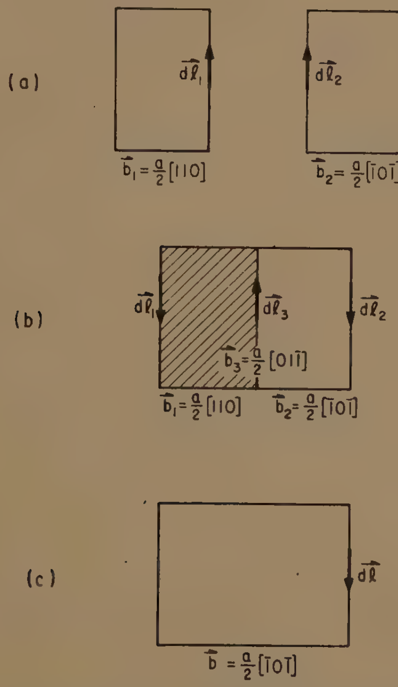
(a)
$\vec{d\ell}_1$
$\vec{d\ell}_2$
$\vec{b}_1 = \frac{a}{2}[110]$
$\vec{b}_2 = \frac{a}{2}[\bar{1}0\bar{1}]$
(b)
$\vec{d\ell}_1$
$\vec{d\ell}_3$
$\vec{d\ell}_2$
$\vec{b}_3 = \frac{a}{2}[01\bar{1}]$
$\vec{b}_1 = \frac{a}{2}[110]$
$\vec{b}_2 = \frac{a}{2}[\bar{1}0\bar{1}]$
(c)
$\vec{d\ell}$
$\vec{b} = \frac{a}{2}[\bar{1}0\bar{1}]$

Successive stages in the coalescence of coplanar loops on (111) with different Burgers vectors. The dislocation segment formed at the intersection of the loops sweeps over the shaded area in (*b*).

Coplanar loops having different slip vectors combine as shown in fig. 5. A segment of total dislocation is formed by the reaction

$$(a/2)[110]+(a/2)[\bar{1}0\bar{1}] \rightarrow (a/2)[01\bar{1}]$$

where the loops join. The glide plane of this segment is the plane of the loops themselves. The segment sweeps over the interior of one or the other of the two loops and combines with the dislocation bounding this loop according to the reaction

$$(a/2)[01\bar{1}]+(a/2)[\bar{1}\bar{1}0] \rightarrow (a/2)[\bar{1}0\bar{1}],$$

so that the slip vector of the resulting large loop is the slip vector of the 'unswept' small loop.

§ 2. KINETICS OF LOOP COMBINATION

In the following section the kinetics of loop coalescence by bulk diffusion and by self-climb will be examined and compared. Rates of coalescence for loops having the size and separation typical of as-quenched aluminium will be estimated, and the observations of Vandervoort and Washburn (1960) will be used to derive an approximate value of the activation energy for diffusion along a dislocation line in aluminium.

Figure 1 shows that the creation of an atom capable of diffusing rapidly in the core of the dislocation loop is accompanied by the creation of a vacancy on the periphery of the loop. Coalescence of neighbouring loops by self-climb requires the diffusion of atoms along the loop cores to the farther edges of the loops and the diffusion of vacancies along the loops to the closer edges; thus, the loops approach one another by the transport of material around each loop from the closer to the farther edge. Although a diffusing atom is effectively constrained to remain in the core of a loop by its strong repulsive interaction with the atoms surrounding the core, a vacancy can diffuse away from the periphery of the loop into the matrix. It is this possibility of evaporation of vacancies from a loop which leads to the coalescence of loops by bulk self-diffusion.

There are, however, two factors which argue against the evaporation of vacancies from the periphery of the loop. The first is that a vacancy created on the periphery of a dislocation loop must acquire an additional increment of energy to escape from the stress field of the loop. The second is that the rate of migration of a vacancy along the periphery of a dislocation loop should be much more rapid than the rate of migration away from the loop. In the absence of experimental values for the energy binding a vacancy to the compression side of a dislocation, and the activation energy for migration along a dislocation line, it is not possible to calculate the probability that a vacancy will escape from the periphery of a dislocation loop before it can diffuse along the loop and add to an incomplete row of vacancies. However, since the energy barrier a vacancy must surmount in diffusing away from the loop is an appreciable fraction of the difference between the activation energies for bulk diffusion and diffusion along a dislocation line, the probability of evaporation from the loop is small at temperatures below about 150°C.

The rate of transport of material from a source to a sink by means of diffusion is determined by the rate at which an individual carrier moves from source to sink and the number of carriers in the region in which diffusion is taking place. If it is assumed that the number of vacancies in the diffusion region is fixed (e.g. by requiring that thermodynamic equilibrium be maintained) then the number of vacancies diffusing from source to sink in time τ is

$$n=N(\tau/t) \qquad . \quad . \quad . \quad . \quad . \quad . \quad . \quad . \quad (1)$$

where N is the number of vacancies in the diffusion region and t is the average time required for a vacancy to diffuse from source to sink.

In calculating the rate of coalescence of two neighbouring loops by either the bulk self-diffusion process or the self-climb process, it will be assumed that the initial concentration of vacancies is the concentration present in thermodynamic equilibrium at the annealing temperature, and that this concentration is maintained as the loops coalesce.

If

$U_{\mathrm{f}}=$ the formation energy of a vacancy in perfect crystal,

$U_{\mathrm{m}}=$ the activation energy for migration of a vacancy in perfect crystal,

$U_{\mathrm{f}}'=$ the formation energy of a vacancy-atom defect pair capable of diffusing along a dislocation line,

$U_{\mathrm{m}}'=$ the activation energy for migration along a dislocation line,

then $U=U_{\mathrm{f}}+U_{\mathrm{m}}$ is the activation energy for bulk self-diffusion and $U'=U_{\mathrm{f}}'+U_{\mathrm{m}}'$ is the activation energy for self-diffusion along a dislocation line.

The time required for the coalescence of the two loops shown in fig. 3 will be calculated for the bulk diffusion process and for self-climb. For convenience one of the loops has been assumed to be much larger than the other, with the smaller loop having side a and the separation of the loops being l.

§ 3. Bulk Diffusion

On the basis of the bulk diffusion process it is to be expected that the smaller loop will shrink by evaporation of the $(a/a_0)^2$ vacancies from which it was formed, a_0 being the lattice constant of the crystal. These vacancies diffuse to the larger loop, causing to it grow. Referring to fig. 3, the distance these vacancies must diffuse is approximately l. Assuming a random walk, the average time taken for a vacancy to diffuse from the smaller to the larger loop is therefore

$$t\simeq\frac{l^2}{a_0{}^2\nu_0}\exp\left\{\frac{U_{\mathrm{m}}}{kT}\right\} \quad . \quad . \quad . \quad . \quad . \quad . \quad . \quad (2)$$

where ν_0 is the vibrational frequency of the lattice. The volume in which diffusion is taking place is assumed to be approximately a^2l, so that the number of vacancies in the diffusion region is

$$N\simeq\frac{a^2l}{a_0{}^3}\exp\left\{-\frac{U_{\mathrm{f}}}{kT}\right\} \quad . \quad . \quad . \quad . \quad . \quad . \quad . \quad . \quad (3)$$

Substituting t from eqn. (2) and N from eqn. (3) in eqn. (1) yields, for the time τ required for the loops to coalesce,

$$\tau=\frac{N}{nt}\simeq\frac{l}{a_0\nu_0}\exp\left\{\frac{U_{\mathrm{f}}+U_{\mathrm{m}}}{kT}\right\}=\frac{l}{a_0\nu_0}\exp\left\{\frac{U}{kT}\right\} \quad . \quad . \quad . \quad . \quad (4)$$

§ 4. SELF-CLIMB

If the loops of fig. 3 coalesce by self-climb then both will move; however, due to the longer diffusion path around the larger of the two loops and the greater amount of material which must be transported around it, this loop will move much more slowly than the small one. Motion of the larger loop will therefore be neglected.

The diffusion path around the periphery of the small loop is approximately $2a$ in length. Assuming random walk and the same value ν_0 for the atomic vibration frequency, the average time required for the transport of an atom from the near to the far side of the loop is

$$t' \simeq \frac{4a^2}{4\nu_0 a^2} \exp\left\{\frac{U_m'}{kT}\right\}. \qquad (5)$$

In order for the loops to coalesce, all the material in region III of fig. 3 must be transported around the loop so that if the quantities important in the self-climb process are denoted by affixing primes to the corresponding symbols in eqn. (1), then $n' \simeq al/a_0^2$. The number of atom-vacancy pairs present on the loop in thermodynamic equilibrium is

$$N' \simeq \frac{4a}{a_0} \exp\left\{-\frac{U_f'}{kT}\right\} \qquad (6)$$

so that from (1), (5) and (6), the time required for the loops to coalesce is

$$\tau' = \frac{n't'}{N'} \simeq \frac{a^2 l}{a_0^3 \nu_0} \exp\left\{\frac{U_f' + U_m'}{kT}\right\} = \frac{a^2 l}{a_0^3 \nu_0} \exp\left\{\frac{U'}{kT}\right\}. \qquad (7)$$

§ 5. COMPARISON WITH EXPERIMENTAL RESULTS

In the as-quenched material studied by Vandervoort and Washburn, the dislocation loops found were about 200–500 Å in size, and were separated by distances ranging from 1000 Å to 5000 Å. Bradshaw and Pearson (1957) have found $U = 1{\cdot}20$ ev for aluminium; the value of U' is not known. A reasonable estimate for the atomic vibration frequency is $\nu_0 \simeq 10^{13}$/sec.

Using the values $a = 300$ Å, $l = 3000$ Å, $\nu_0 \simeq 10^{13}$/sec, $U = 1{\cdot}20$ ev, $a_0 = 2{\cdot}86$ Å, and various values of U', the times τ and τ' have been calculated according to eqns. (4) and (7) for the temperature range of interest. These values are listed in the table.

Since Vandervoort and Washburn found considerable loop growth following ten minute (6×10^2 sec) anneals at 150°C, inspection of the times listed in the table shows that:

1. Bulk diffusion cannot account for the loop growth observed.

2. Self-climb occurring with an activation energy of about 0·7 ev does account for the observations.

3. Since the time τ' is much more sensitive to the value of U' than it is to the geometrical factors in eqn. (7), the uncertainty in the value of U' thus determined is relatively small.

4. This value of U' is consistent with the lowering of the activation energy for short-circuit diffusion processes that has been observed in other metals.

Approximate time required for combination of dislocation loops of diameter 300 Å, separated by 3000 Å

Temperature (°C)	Time required for combination of loops			
	Bulk diffusion ($U=1{\cdot}20$ ev)	Self-climb		
		$U'=0{\cdot}6$ ev	0·7 ev	0·8 ev
	Seconds			
100	$1{\cdot}6\times10^6$	125	2900	$6{\cdot}5\times10^4$
125	$1{\cdot}6\times10^5$	40	740	$1{\cdot}4\times10^4$
150	$2{\cdot}0\times10^4$	14	220	3400
175	3200	5·6	75	1000
200	620	2·5	29	340

§ 6. CONCLUSIONS

1. The coalescence of quenched-in dislocation loops in aluminium takes place by short-circuit diffusion around the periphery of each loop.

2. The activation energy for this short-circuit diffusion process is about 0·7 ev. (The measured value for the activation energy for diffusion through the aluminium lattice is 1·20 ev.)

ACKNOWLEDGMENTS

The author wishes to express his appreciation to the Office of Naval Research for financial support, and to Professor E. R. Parker and Dr. L. Himmel for invaluable assistance in the presentation of the material. He would also like to thank Drs. G. Thomas, R. de Wit and J. Nadeau for many very helpful discussions.

REFERENCES

BOAS, W., and SCHMID, E., 1931, *Z. Phys.*, **71,** 703.
BRADSHAW, F. J., and PEARSON, S., 1957, *Phil. Mag.*, **2,** 570.
HENDRICKSON, A., and MACHLIN, E. S., 1954, *Trans. Amer. Inst. min. (metall.) Engrs*, **156,** 82.
HIRSCH, P. B., SILCOX, J., SMALLMAN, R. E., and WESTMACOTT, K. H., 1958, *Phil. Mag.*, **3,** 897.
HOFFMAN, R. E., and TURNBULL, D., 1951, *J. appl. Phys.*, **22,** 634.
KUHLMANN-WILSDORF, D., 1958, *Phil. Mag.*, **3,** 125.
SILCOX, J., and WHELAN, M. J., 1960, *Phil. Mag.*, **5,** 1.
TURNBULL, D., and HOFFMAN, R. E., 1954, *Acta Met.*, **2,** 419.
VANDERVOORT, R., and WASHBURN, J., 1960, *Phil. Mag.*, **5,** 24.

The Magnetic Susceptibility of Vanadium–Chromium Solid Solutions†

By B. G. Childs, W. E. Gardner and J. Penfold
Atomic Energy Research Establishment, Harwell, Berks

[Received July 7, 1960]

Abstract

The magnetic susceptibilities of a number of solid solutions of chromium in vanadium have been measured at 20°, 77° and 293°K. The susceptibility at 20°K decreases with concentration from a value of 300×10^{-6} e.m.u./g atom for pure vanadium to 159×10^{-6} e.m.u./g atom for pure chromium. Fine structure is observed in several regions of the susceptibility–composition curve. The temperature dependence of the susceptibility of all the alloys investigated was small.

An interpretation of the susceptibility behaviour is given in terms of the collective electron model.

§ 1. Introduction

Magnetic susceptibility measurements can increase our understanding of the electronic band structure of metals and alloys. This applies especially to non-ferromagnetic transition metals—from which we have chosen vanadium—since a large part of their susceptibility is determined by the density of states of the conduction electrons at the Fermi level.

The most important property of vanadium, however, which led to its selection for the present investigation is its ability to dissolve appreciable amounts of the majority of the transition elements in its own period. The concentration ranges (in atomic per cent) over which these elements form stable primary solutions with vanadium are (Rostoker 1958): titanium 0–70, chromium 0–100, manganese 0–50, iron 0–30, cobalt 0–8, nickel 0–8 and copper 0–7. A comparison of the results for such vanadium alloys should, in principle, distinguish the effects of atomic concentration and electron transfer on the Fermi level and the shape of the conduction band.

In this paper we report the results of magnetic susceptibility measurements for solid solutions of chromium in vanadium. Subsequently we will compare these results with those for the other alloy systems.

§ 2. Preparation of the Specimens

The vanadium and chromium used for the alloys were obtained from a number of sources, purer materials being used during the course of the work as they became available. No systematic dependence of susceptibility upon the purities of these source materials was found for vanadium

---

† Communicated by the Authors.

or the vanadium-rich alloys containing up to about 30 at. % chromium. This was not the case, however, for chromium and so the chromium-rich alloys, which were all prepared towards the end of the investigation, were made using only the purest materials.

The suppliers of the vanadium were Johnson, Matthey and Company (J.M.), the Battelle Memorial Institute (B.M.I.) and the U.S. Bureau of Mines (U.S.B.M.). The methods of preparation and the purities (non-metallic elements being included in the analyses), were:

J.M.:	calcium reduction of vanadium pentoxide (99·63 weight %),
U.S.B.M.:	electrolytic refinement of vanadium metal (99·85 weight %),
B.M.I.:	Van Arkel process from vanadium iodide (99·92 weight %).

Detailed analyses have been given in an earlier paper (Childs *et al.* 1959 referred to henceforth as I).

The chromium was provided by Johnson, Matthey and Company (99·65 weight %) and the Fulmer Research Institute (99·99 weight %). The latter material (F.R.I.) had been hydrogen-reduced to lower its oxygen content to 0·0032 weight %.

Alloy buttons of about 3 g weight were prepared by melting together appropriate amounts of vanadium and chromium in an argon-arc furnace. The buttons, which were supported on a water-cooled copper hearth, were inverted and remelted a number of times so as to ensure adequate mixing of the two components. Contamination by oxygen or nitrogen during these melting operations was minimized by frequent gettering of the argon atmosphere with molten zirconium. A leak test on the apparatus was made before melting was begun.

After melting, the buttons were annealed, both to reduce small-scale concentration fluctuations caused by segregation on solidification of chromium-rich material, and to promote the formation of a random solid solution. Each button, supported on a plate of purified thoria, was sealed in an argon-filled silica tube and heated by high-frequency induction for one hour at 1600°C. A leak test and argon gettering operation was performed before the annealing.

The density and hardness (§ 3) of the button were then measured, after which susceptibility specimens approximately $8 \times 1{\cdot}5 \times 1{\cdot}5$ mm in size were cut from its centre using a clean Carborundum slitting wheel. A stream of coolant liquid (a water–oil emulsion) prevented excessive heating and oxidation of the specimens during this process. The specimens were finally degreased in alcohol, cleaned in dilute hydrochloric acid and washed in distilled water.

§ 3. EXAMINATION OF THE ALLOYS

Before a specimen was accepted for susceptibility measurement it was carefully examined in order to determine whether its composition, homogeneity and purity were satisfactory. This involved the following procedure.

3.1. *Composition*

The composition of each alloy button was determined from the initial weights of its constituents after correcting for the loss in weight which occurred on melting. The loss in weight, which was usually small, was assumed to be due almost entirely to chromium evaporation since the vapour pressure of chromium below 2000°c is more than one thousand times that of vanadium.

These composition values were confirmed for certain selected specimens by direct chemical analysis.

Fig. 1

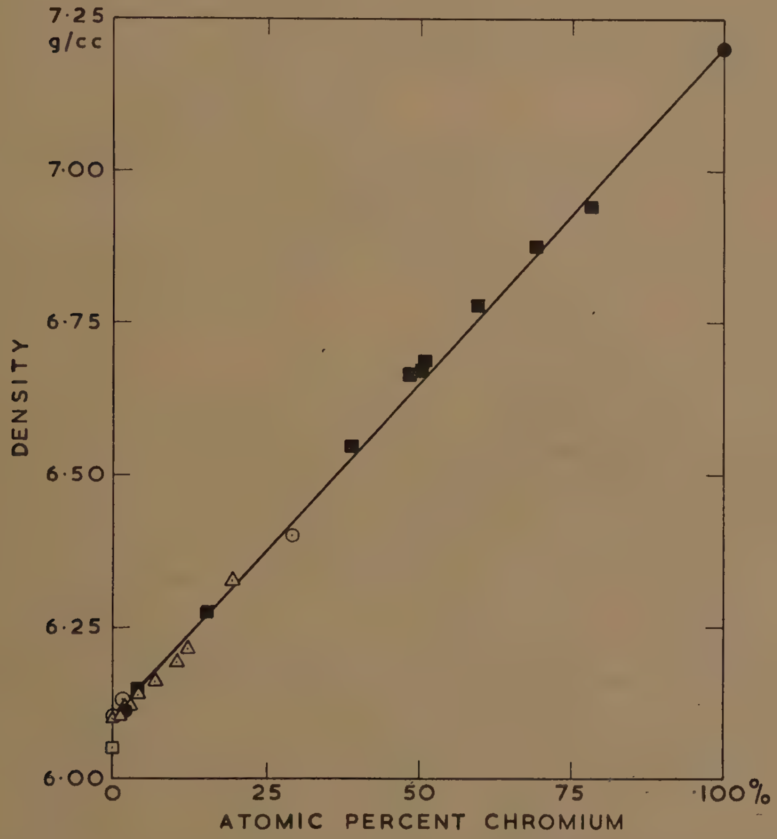

Variation in density with composition for the vanadium–chromium system.

- △ alloys of J.M. vanadium and J.M. chromium;
- ○ alloys of B.M.I. vanadium and J.M. chromium;
- ● alloys of B.M.I. vanadium and F.R.I. chromium;
- ■ alloys of U.S.B.M. vanadium and F.R.I. chromium.

The final composition values are estimated to be correct to within either ±0·5 at. % chromium or ±2% of the quoted chromium content, whichever is the lesser.

3.2. *Density*

The density of each annealed button was measured at room temperature using the standard water displacement method. The variation in density with composition for the vanadium–chromium solutions is shown in fig. 1. Within the accuracy of measurement the density values for all the specimens fall on a common curve.

The density values served as a further check on composition. They were also used (§ 6.3) in estimating the effects on the susceptibility values of changes in the interatomic spacing.

Fig. 2

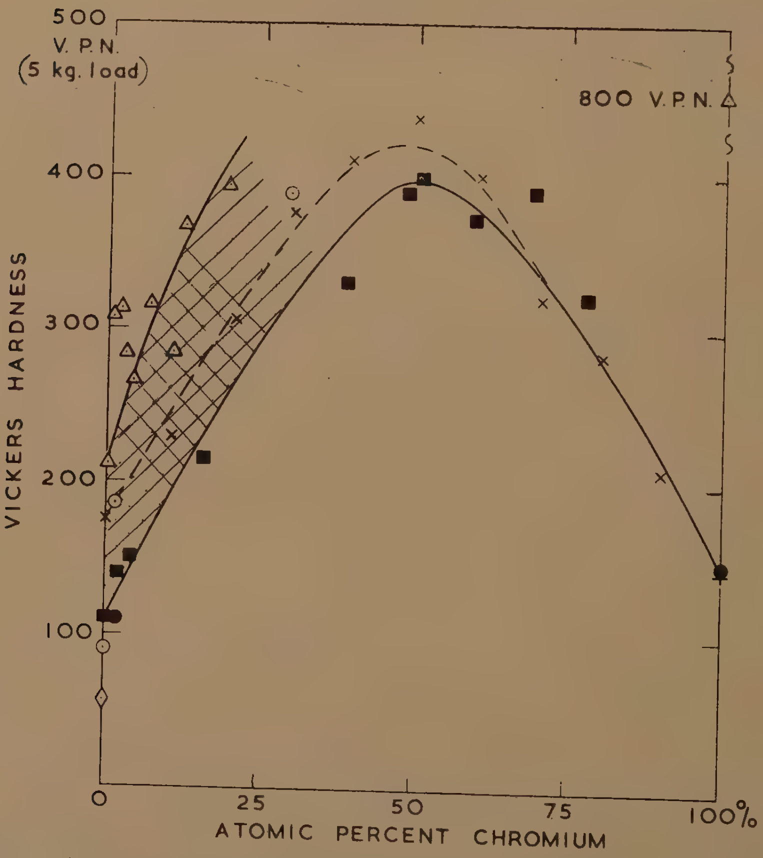

Hardness of the vanadium–chromium alloys as a function of composition.

△	alloys of J.M. vanadium and J.M. chromium;
○	alloys of B.M.I. vanadium and J.M. chromium;
●	alloys of B.M.I. vanadium and F.R.I. chromium;
■	alloys of U.S.B.M. vanadium and F.R.I. chromium.
◇	S.E.R.L., Baldock, vanadium.
×	Aeronautical Research Laboratories, Melbourne, chromium.
×– – –×	Carlson and Eustice (1959).

3.3. *Hardness*

After measuring its density the button was cut in half and the cut surface of one piece polished. The Vickers hardness of this piece was then measured at a number of points across the surface.

Any large-scale variation in concentration across the specimen (which was never found) would have produced a corresponding variation in hardness, whereas excessive contamination throughout the specimen (for example by oxygen) could be detected by the resulting high average hardness.

Figure 2 shows the hardness of a number of specimens as a function of their chromium concentration. Also plotted in this figure are hardnesses for vanadium, reported in I, and some additional values obtained from the results of Carlson and Eustice (1959). Their published results have been converted from Rockwell A to Vickers hardness values by Dr. O. N. Carlson (private communication).

The hardness of alloys prepared from the purest material—B.M.I. or U.S.B.M. vanadium and F.R.I. chromium—increased from about 90 VPN for pure vanadium to 400 VPN for 50% chromium. It then fell to 150 VPN for pure chromium. The hardness values of the alloys prepared from the less pure materials occupied a band approximately 150 VPN wide above the base curve.

3.4. *Microstructure*

The polished and etched surfaces of the buttons were examined at high magnification (×500) for traces of foreign material dispersed as a precipitate or in other form. Most of the specimens, in fact, contained such a dispersion usually as a fine filamentary network within the grains with, in some cases, isolated particles distributed at intervals along the grain boundaries. Typical micrographs (×250) of the alloys are reproduced in fig. 3 (Pl. 165).

The precipitate is presumably associated with the impurities initially present in the alloy constituents since its volume was generally much less for alloys made from the purest materials. Experiments with aged specimens (see § 5) showed, at least for the vanadium-rich alloys, that the susceptibility was not significantly altered unless the precipitate occupied more than one volume percent of the specimen. Such specimens were therefore rejected.

§ 4. SUSCEPTIBILITY MEASUREMENT

The method used to measure the susceptibility of the specimens has been described previously (Childs and Penfold 1957). The measurements were made using a Sucksmith ring balance to an estimated accuracy of ±1% relative to the susceptibility of tantalum ($0{\cdot}849 \times 10^{-6}$ e.mu./g) as standard. The apparatus was frequently re-calibrated during the course of the work. The measurements were made at three temperatures, 20°, 77° and 293°K.

§ 5. RESULTS

The mass susceptibility values are given in full in the table. This table includes some results for a pure vanadium sample (S.E.R.L.) which were not reported in I. This specimen was produced by the Van Arkel process and further refined by zone-melting at S.E.R.L. Baldock. The exceptionally low hardness of the specimen (57 VPN) indicated that its purity was greater than that of any other vanadium sample investigated.

The mass susceptibilities of vanadium–chromium solid solutions

Chromium concentration	Source		$\chi_m \times 10^6$ e.m.u./g at		
at. %	Vanadium	Chromium	20°K	77°K	293°K
0	J.M.	—	5·94	5·96	5·83
0	U.S.B.M.	—	5·83	5·86	5·77
0	B.M.I.	—	5·89	5·88	5·81
0	S.E.R.L.	—	5·92	5·95	5·86
1·00	J.M.	J.M.	5·87	5·83	5·63
1·57	B.M.I.	J.M.	5·64	5·67	5·55
1·91	B.M.I.	F.R.I.	5·59	5·62	5·51
1·96	J.M.	J.M.	5·64	5·63	5·57
1·96	U.S.B.M.	F.R.I.	5·46	5·50	5·37
2·84	J.M.	J.M.	5·64	5·64	5·57
3·90	U.S.B.M.	F.R.I.	5·82	5·72	5·64
4·00	J.M.	J.M.	5·74	5·68	5·75
6·9	J.M.	J.M.	5·62	5·63	5·54
10·5	J.M.	J.M.	5·65	5·63	5·57
12·2	J.M.	J.M.	5·30	5·30	5·27
15·3	U.S.B.M.	F.R.I.	5·27	5·28	5·26
19·2	J.M.	J.M.	5·49	5·45	5·43
29·1	B.M.I.	J.M.	5·05	5·04	5·02
38·5	U.S.B.M.	F.R.I.	4·84	4·79	4·79
48·8	U.S.B.M.	F.R.I.	4·88	4·90	4·76
50·0	U.S.B.M.	F.R.I.	4·79	4·81	4·73
50·5	U.S.B.M.	F.R.I.	4·91	4·89	4·76
59·5	U.S.B.M.	F.R.I.	4·04	4·04	4·04
69·2	U.S.B.M.	F.R.I.	3·51	3·51	3·58
77·8	U.S.B.M.	F.R.I.	3·27	3·17	3·23
100·0	—	J.M.	3·38	3·47	3·40
100·0	—	F.R.I.	3·01	2·99	3·19
100·0	—	A.R.L.	2·99	2·98	3·17

The estimated absolute accuracy of χ_m is $\pm 0{\cdot}10 \times 10^{-6}$ e.m.u./g.

The atomic susceptibilities at 20°K are shown as a function of the chromium concentration in fig. 4. Also included in this figure are some results obtained by Lingelbach (1958) at 100°K for alloys of high chromium concentration.

The suceptibility at 20°K decreases with concentration in an oscillatory manner up to 50 at. % of chromium and then falls sharply. Thus there are small minima at 2 and 15 at. %, with maxima at 6 and 20 at. % chromium. In addition there is a broad minimum at 32 at. % and a relatively broad maximum at 50 at. % chromium.

Fig. 4

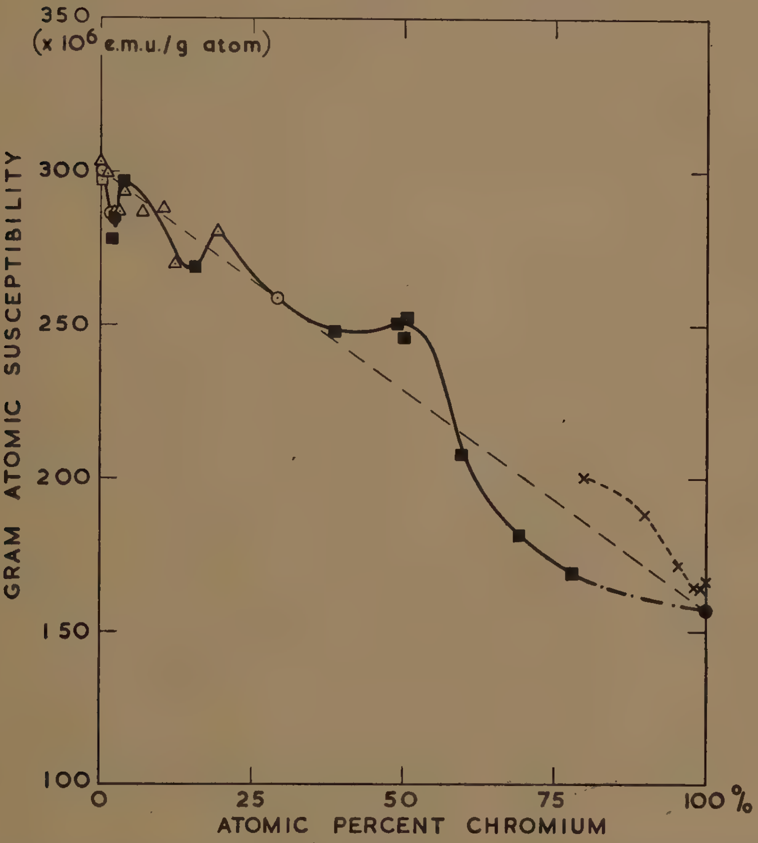

Atomic susceptibility at 20°K for the vanadium-chromium system as a function of composition.

△ alloys of J.M. vanadium and J.M. chromium;
⊙ alloys of B.M.I. vanadium and J.M. chromium;
● alloys of B.M.I. vanadium and F.R.I. chromium;
■ alloys of U.S.B.M. vanadium and F.R.I. chromium.
× Lingelbach (1958) 100°K.

In order to confirm this fine structure several alloys were investigated having compositions of about 2 at. % chromium and 50 at. % chromium. Four separate specimens having a nominal 2 at. % were prepared from various combinations of the vanadium and chromium source materials to determine whether this minimum was a genuine alloy effect unconnected with the presence of small amounts of impurities. The hardnesses of these specimens ranged from 110–314 VPN yet, as shown in the figure, their susceptibility values are grouped closely together and show no systematic dependence on hardness or on the purity of the source material. This satisfactory agreement suggested that it was not unreasonable to continue the curve through all our observed points and so obtain the rest of the fine structure.

The relatively broad maximum at 50 at. % chromium may be associated with the development of long-range order in this alloy. To test this possibility two specimens were prepared from buttons which were quenched rapidly from 1900°c to room temperature—the normal 1600°c annealing stage, followed by a relatively slow cooling of the alloy, being omitted. The susceptibility of these quenched specimens was the same, within experimental error, as that of the annealed and slowly cooled specimen. Thus ordering, if it occurs, must reach equilibrium in a period of less than a few seconds.

Some further evidence on this point was provided by a neutron diffraction study of the annealed specimen. No significant superlattice line (100) associated with the ordered state was detected. From an estimate of the errors of measurement it was concluded that the amount of long-range order present must be less than 10%. This result is expected since the proximity of vanadium and chromium in the electrochemical series and their similar atomic sizes do not energetically favour ordering.

Since the major emphasis in this work was on the behaviour of vanadium as a solvent metal no attempt was made to investigate the susceptibility variation for concentrations above 78 at. % chromium. However Lingelbach's (1958) results, some recent resistivity data (§ 6) and electronic specific heat measurements of Wei, Cheng and Beck (private communication) show that further fine structure in this region of the susceptibility curve may be expected.

The variation in susceptibility (table) between 20° and 293°K for all the alloys was very small and not appreciably dependent on concentration. On the average the susceptibility decreased by 1% over this temperature range. The absence of any strong temperature dependence for the 78 at. % chromium alloy is noteworthy since, for an 80 at. % chromium specimen, Lingelbach found the susceptibility to drop from 227×10^{-6} e.m.u./g atom at 66°K to 180×10^{-6} e.m.u./g atom at 293°K—a 20% variation. In view of the lack, in our results, of any systematic trend in the temperature coefficient of susceptibility between 0 and 78% chromium, it seems likely that this particular specimen of Lingelbach's was impure.

As mentioned earlier, the susceptibility of the J.M. chromium differed appreciably from that of the F.R.I. material, the values at 293°K being 177 and 166×10^{-6} e.m.u./g atom respectively. A third chromium sample, obtained from the Aeronautical Research Laboratories, Melbourne, which also contained only 0·003 weight % oxygen, had a susceptibility (165×10^{-6} e.m.u./g atom at 293°K) close to that of the F.R.I. sample. The higher value for the J.M. specimen is presumably due to the 0·37 weight % of impurity—mostly oxygen—contained in it.

In the case of vanadium and of the alloys with up to 30 at. % chromium, excessive contamination by oxygen and nitrogen (introduced either deliberately or by accidental mishandling during preparation) caused the susceptibility to decrease. This behaviour, which is opposite to that shown by chromium, has been mentioned in I for a sample of pure vanadium. This specimen decreased in susceptibility from 296 to 244×10^{-6} e.m.u./g atom on solution of 7 weight % of oxygen.

No significant difference was found between the susceptibility values for specimens prepared from the different source materials and having hardness values between the two curves shown in fig. 2. Samples with hardnesses much above the upper curve gave anomalously low susceptibility values and were rejected.

Some specimens which had, after the initial measurements, been allowed to stand at room temperature for more than one year showed an ageing effect whereby the susceptibility decreased with time. One such specimen—the 10·5 at. % chromium sample—decreased in susceptibility from 284 to 273×10^{-6} e.m.u./g atom at 293°K after 28 months. Removal, by etching, of a surface layer $1{\cdot}4 \times 10^{-3}$ cm thick did not affect the susceptibility of the specimen, thus indicating that the ageing process is a volume rather than a surface effect. This was confirmed by cutting a new specimen from the middle of one of the halves of the original alloy button. This new specimen had, within experimental error, the same diminished susceptibility.

This effect is presumably connected with impurity precipitation since, while the 10·5 at. % alloy originally appeared on metallographic examination perfectly free from inclusions—the grain boundaries being sharp and fine—re-examination after ageing revealed the presence of a substantial quantity of precipitate distributed preferentially along the grain boundaries but also throughout the grains.

§ 6. DISCUSSION

Before attempting to explain the variation with composition of the alloy susceptibilities, it is necessary to consider which of many conceivable magnetic processes contribute appreciably to the susceptibilities of the pure component metals.

6.1. *Vanadium Metal*

For vanadium the major contribution to the susceptibility most probably comes from the spin paramagnetism of the outer electrons (five per atom). If any of these electrons were in localized atomic-like orbitals then, from Hund's rule, their spins would necessarily be parallel. In consequence each atom would show a permanent magnetic moment, However, the results of neutron diffraction measurements made at 20°K by Shull and Wilkinson (1953) show that, within the limits of experimental error (0·1 Bohr magneton), there are no such moments, aligned or unaligned, on the vanadium atoms. All the outer electrons must therefore be in non-localized states in the conduction band of the metal where they will give rise to a Pauli-type paramagnetism.

Conduction electrons, if mutally non-interacting, contribute a term to the susceptibility per gram atom (Pauli 1927) given by

$$\chi_p = 2\beta^2 N n(E_0)$$

where N is Avogadro's number and β the Bohr magneton. $n(E_0)$, the density of states for one direction of spin per unit energy range per atom at the Fermi surface, may also be expressed by the relation (Mott and Jones 1936)

$$n(E_0) = \frac{3\gamma}{2\pi^2 k^2 N}$$

where k is Boltzmann's constant and γ is the temperature coefficient of the electronic specific heat per gram atom. Substituting for γ the value $8{\cdot}8 \times 10^{-3}$ J/g atom deg^2 obtained by Corak *et al.* (1954), we find that for vanadium $n(E_0) = 1{\cdot}86$ states/ev atom. The Pauli susceptibility for vanadium is thus 122×10^{-6} e.m.u./g atom. The observed value (χ_0) at 20°K, corrected (see later) for diamagnetic terms is 308×10^{-6} e.m.u./g atom.

Such a large difference between χ_0 and χ_p is not peculiar to vanadium but is observed in all transition metals. It has been attributed (e.g. Mott 1935) to a spin-interaction of a ferromagnetic nature between the conduction electrons. This 'exchange interaction' tends to increase the unbalance produced by the field in the number of parallel and anti-parallel electron spins and hence to increase the induced moment.

If we write (Stoner 1936)

$$\frac{1}{\chi_0} = \frac{1}{\chi_p} - K$$

then K, which is proportional to the exchange interaction, has a value for vanadium of 5000 g atom/e.m.u.

There are two small diamagnetic susceptibility contributions to be considered. The first of these, which is associated with the orbital motion of the tightly bound electrons on the vanadium ions, has a value (Van Vleck 1932) of $7{\cdot}7 \times 10^{-6}$ e.m.u./g atom, i.e. 2·5% of the susceptibility at room temperature. The second term arises from the curvature imposed by the magnetic field on the paths of the conduction electrons. This term cannot be calculated exactly but is probably negligibly small as the following rough argument shows.

The value for γ appropriate to a free electron gas containing five electrons per atom is $0{\cdot}94 \times 10^{-3}$ J/g atom deg^2 (Mott and Jones 1936). Vanadium metal, as mentioned however, has a γ of $8{\cdot}8 \times 10^{-3}$ J/g atom deg^2 so that the effective thermal mass, m_t, of the electrons at the Fermi surface is about nine times the normal electronic mass, m. We shall take m_t equal to m_a, the effective mass of the electrons accelerated by the magnetic field (Cohen 1958). Then, since the conduction electron diamagnetism (Landau 1930) is associated with the electronic orbits in momentum space it is inversely proportional to m_a^2 and not m^2. Thus, instead of being one-third of the paramagnetic susceptibility, as is the case for free electrons, this diamagnetic component for vanadium is only 0·4% of the paramagnetism.

6.2. *Chromium Metal*

Chromium is much more complex than vanadium in its magnetic behaviour. Shull and Wilkinson (1953) and later Corliss *et al.* (1959) found the metal to be antiferromagnetic with a mean moment per atom of $0{\cdot}4 \pm 0{\cdot}05\beta$. The magnetic susceptibility of an oxygen and nitgrogen-free polycrystalline specimen was measured over the temperature range 66° to 805°K by Lingelbach (1958). His graph shows a marked kink at a temperature (310°K) significantly close to the Néel temperature (T_N) of 308°K observed by Corliss *et al.* for a single crystal.

However, these results disagree with the value of T_N observed by Shull and Wilkinson, namely 475°K, on a polycrystalline specimen. This suggests that T_N may well depend on either the preparation or the impurity content of the sample. However it is difficult to reconcile this result with the fact that several of the properties of chromium show an anomaly only at about 310°K (Sully 1954). In particular, the heat capacity of a polycrystalline sample shows a lambda-type anomaly at 311·5°K (Beaumont *et al.* 1960). We shall therefore assume in our subsequent discussion of chromium that T_N is 310°K.

In contrast with the usual behaviour of antiferromagnetic materials the susceptibility above T_N does not decrease according to a Curie–Weiss law. Instead a progressive increase occurs, the value changing from 166×10^{-6} e.m.u./g atom at 310°K to 177×10^{-6} e.m.u./g atom at 800°K.

The electronic specific heat measurements made by Estermann *et al.* (1952) show that γ for pure chromium is $1{\cdot}54 \times 10^{-3}$ J/g atom deg². The density of states at the Fermi level calculated from this value is 0·33 states/ev atom—considerably less than that for vanadium. Wei *et al.* (1959) have found that γ increases rapidly as manganese and iron are dissolved in chromium. It seems likely therefore that the Fermi level for this metal falls just above a minimum in the density of states curve. This suggestion is well-supported by the measurements of soft x-ray absorption in thin films of chromium by Agarwal and Givens (1957).

The Pauli susceptibility of chromium at 0°K calculated from the above density of states value is 21×10^{-6} e.m.u./g atom. If we assume that the mean moment of each chromium atom above the Néel point is $0{\cdot}4\beta$ and the Curie–Weiss θ, like T_N, is 310°K, then the corresponding Curie–Weiss susceptibility at the Néel point is 194×10^{-6} e.m.u./g atom.

The sum of the Curie–Weiss and Pauli terms at 310°K (215×10^{-6} e.m.u./g atom) does not agree with the measured susceptibility value (173×10^{-6} e.m.u./g atom), corrected for the ion core diamagnetism ($6{\cdot}6 \times 10^{-6}$ e.m.u./g atom—Van Vleck 1932). This is not particularly significant since a slight increase in the value of θ could produce agreement. However, no change in θ or the mean moment per atom can account for an increase in the susceptibility of chromium above the Néel temperature. Thus according to the above figures the susceptibility should *decrease* by 87×10^{-6} e.m.u./g atom between 310° and 800°K instead of increasing by 11×10^{-6} e.m.u./g atom as observed.

It thus seems possible that, above the Néel temperature, there are no spins in chromium obeying a simple Curie–Weiss law and that a collective electron model, such as the one developed by Lidiard (1954), is more appropriate.

Assuming this to be the case, and extrapolating to 0°K the susceptibility values observed for temperatures above T_N, then the corrected value of the susceptibility (χ_0) in the absence of antiferromagnetism is 170×10^{-6} e.m.u./g atom. Taking χ_p as 21×10^{-6} e.m.u./g atom the value obtained for K is 42 000 g atom/e.m.u. The exchange interaction parameter is thus about eight times as large for chromium as for vanadium.

The calculated K values for 12 other transition metals for which the appropriate experimental data are available are less than 20 000 g atom/e.m.u., except for tungsten (24 000) and molybdenum (37 000). The fact that the interaction parameter is large for these other two group VI metals, lends support to the idea that it should also be large for chromium.

As we have implied the two diamagnetic contributions to the susceptibility of chromium are, as for vanadium, both small. Thus the effective thermal mass of the electrons at the Fermi surface in chromium, calculated in a similar way to that described for vanadium, is about 1·6 times the electronic mass. The Landau diamagnetic component is therefore about 13% of the Pauli paramagnetism and less than 2% of the observed paramagnetism at room temperature. The core diamagnetism is about 4% of this observed figure.

6.3. *Vanadium–Chromium Solid Solutions*

The fall in susceptibility with composition for the alloys up to 80 at. % chromium is most simply explained in terms of a collective electron model. Thus the fact that the susceptibilities of all the alloys, like that of vanadium, are only weakly temperature dependent is evidence that no free permanent moments appear on either the vanadium or the chromium atoms. This is supported by some resistivity measurements (De Vries 1959) which show that the Néel temperature of chromium is very dependent on small alloying additions. De Vries found, for example, that the addition of 1 at. % of vanadium decreases T_N by 85°K, which suggests that there should be no moments present on the chromium atoms in an 80 at. % chromium alloy.

If the structure of the vanadium conduction band is assumed to remain essentially unchanged on adding chromium, then the major effect of alloying will be to produce an increase in the Fermi energy as electrons from the chromium atoms enter the common band. The Fermi level for vanadium comes at a point where the density of states is high but decreasing (Kriessman and Callen 1954) while, as mentioned, that of chromium probably occurs just above a minimum in the band. Thus, on alloying, the Pauli paramagnetism should initially decrease and then, finally, increase slightly.

On the basis of this model the observed susceptibility curve would represent the density of states curve as modified by the exchange interaction effect. The exchange parameter also will vary with composition. A possible relationship involving K is suggested by its behaviour, mentioned previously, for a number of transition metals. K for these metals is roughly inversely proportional to χ_p. If this were also true for these alloys then the observed susceptibility–concentration curve would be a direct representation of the density of states curve. All the observed oscillations would then be reflections of fine structure in this curve.

Such oscillations would not produce a temperature variation in susceptibility greater than that observed between 20 and 300°K. In this temperature range the edge of the Fermi distribution is sufficiently smeared out so that only an average of the sharp oscillation at 2 at. %, for instance, will be observed. However, by assuming that K is temperature independent a simple calculation shows that below 20°K the susceptibility of the 2 at. % alloy may further decrease by about 3%.

A small correction to the above model is necessary to allow for the increase in width of the band which must occur as a result of the decrease in interatomic spacing on alloying (§ 3.2). For example, if the lattice parameter of vanadium were reduced from 3·03 Å to 2·88 Å (the value for chromium) then the Pauli susceptibility, assuming a parabolic density of states curve, would decrease by 10%. The effect accounts for about one tenth of the observed susceptibility decrease between vanadium and chromium.

A confirmation of some of these ideas must await measurements of the electronic specific heat of all these alloys. It is gratifying that the results obtained at a few concentrations for the vanadium–chromium system by Wei, Cheng and Beck (private communication) qualitatively support our conclusions.

ACKNOWLEDGMENTS

We wish to thank Mr. A. D. Le Claire, Dr. W. M. Lomer, Dr. W. Marshall and Dr. P. C. L. Pfeil for helpful discussions. We are also indebted to Mr. C. E. Austing for chemical analysis and members of the Alloys Section of the Metallurgy Division, Harwell for assistance in the preparation and examination of the specimens. Dr. D. H. Baker of the U.S. Bureau of Mines and Dr. A. Wexler of the Westinghouse Research Laboratories kindly supplied us with some of the vanadium used. Mr. A. Calverley kindly supplied us with the zone-refined vanadium specimen. Finally we should like to thank Professor P. A. Beck for communicating his results prior to publication.

REFERENCES

AGARWAL, B. K., and GIVENS, M. P., 1957, *Phys. Rev.*, **107,** 62.

BEAUMONT, R. H., CHIHARA, H., and MORRISON, J. A., 1960, *Phil. Mag.*, **5,** 188.

CARLSON, O. N., and EUSTICE, A. L., 1959, U.S.A.E.C. Report IS-47.

CHILDS, B. G., GARDNER, W. E., and PENFOLD, J., 1959, *Phil. Mag.*, **4,** 1126.

CHILDS, B. G., and PENFOLD, J., 1957, *Phil. Mag.*, **2,** 389.

COHEN, M. H., 1958, *Phil. Mag.*, **31,** 762.

CORAK, W. S., GOODMAN, B. B., SATTERTHWAITE, C. B., and WEXLER, A., 1954, *Phys. Rev.*, **96,** 1442.

CORLISS, L. M., HASTINGS, J. M., and WEISS, R. J., 1959, *Phys. Rev. Letters*, **3,** 211.

DE VRIES, G., 1959, *J. Phys. Radium*, **20,** 438.

ESTERMANN, I., FRIEDBERG, S. A., and GOLDMAN, J. E., 1952, *Phys. Rev.*, **87,** 582.

KRIESSMAN, C. J., and CALLEN, H. B., 1954, *Phys. Rev.*, **94,** 837.

LANDAU, L., 1930, *Z. Phys.*, **64,** 629.

LIDIARD, A. B., 1954, *Proc. roy. Soc.* A, **224,** 161.

LINGELBACH, R., 1958, *Z. phys. Chem.* (Neue Folge), **14,** 1.

MOTT, N. F., 1935, *Proc. phys. Soc. Lond.*, **47,** 571.

MOTT, N. F., and JONES, H., 1936, *The Theory of the Properties of Metals and Alloys* (Oxford: University Press).

PAULI, W., 1927, *Z. Phys.*, **41,** 81.

ROSTOKER, W., 1958, *The Metallurgy of Vanadium* (London: Chapman and Hall).

SHULL, C. G., and WILKINSON, M. K., 1953, *Rev. mod. Phys.*, **25,** 100.

STONER, E. C., 1936, *Proc. roy. Soc.* A, **154,** 656.

SULLY, A. H., 1954, *Chromium* (London: Butterworths Scientific Publications), Chap. 3.

VAN VLECK, J. H., 1932, *Electric and Magnetic Susceptibilities* (Oxford: University Press).

WEI, C. T., CHENG, C. H., and BECK, P. A., 1959, *Phys. Rev. Letters*, **2,** 95.

The Hyperfine Structure of ^{209}Bi†

By R. S. Title‡ and K. F. Smith
Cavendish Laboratory, Cambridge

[Received August 19, 1960]

Abstract

The hyperfine structure (H.F.S.) of the $J=3/2$ ground state of ^{209}Bi has been found by the atomic beam magnetic resonance method. Two of the three H.F.S. intervals were measured directly, giving

$$(W_{50}-W_{60})/h=2884{\cdot}7\pm0{\cdot}2\ \mathrm{Mc/s}$$

and $(W_{40}-W_{50})/h=2171{\cdot}5\pm0{\cdot}1$ Mc/s. These results are consistent with a magnetic dipole interaction constant A of $-446{\cdot}97\pm0{\cdot}04$ Mc/s and an electric quadruple interaction constant B of $-303{\cdot}3\pm0{\cdot}3$ Mc/s. The latter yields an uncorrected nuclear electric quadrupole moment of $-0{\cdot}34$ barns, and the field dependence of $\Delta F=0$ transitions gives $-1{\cdot}6433\pm0{\cdot}0002$ for the ground state g_J value. The results are discussed in terms of the intermediate coupling theory of Breit and Wills (1933).

§ 1. Introduction

Goudsmith and Back (1927) studied the H.F.S. of the ^{209}Bi ground state by optical means and showed that the ground state has a total width of about 0·08 cm^{-1}, or 2400 Mc/s, but they were unable to resolve the structure. Later Mrozowski (1942) resolved the largest of the three H.F.S. intervals and estimated a total width of about 6750 Mc/s; he also showed that the H.F.S. is inverted, i.e. the energy level with the smallest value of F has the largest energy and A is negative (see fig. 1). We have measured two of these intervals directly and the results are consistent with a total width of $6641{\cdot}2\pm0{\cdot}7$ Mc/s. Rochester (1960) has confirmed that the sign of A is negative by the method described in the following paper on ^{121}Sb.

The principles of the method, which was first applied to atoms by Kellog *et al.* (1939), are given in detail in the book by Ramsey (1956). The atomic beam passes in turn through an inhomogeneous deflecting field H_a, a homogeneous field H_c and a second inhomogeneous deflecting field H_b before falling on the detector (fig. 2). A weak oscillating magnetic field H_ν superimposed on the steady field H_c induces transitions between certain states W_1 and W_2 with greatest probability when $h\nu=|W_1-W_2|$. The deflecting fields are arranged so that only atoms which undergo suitable transitions in the C field, the 'flopped' atoms, are refocused on the detector, the others being deflected away from the axis. An increase in detected beam then indicates the resonance condition and thus allows measurement of the energy interval.

---

† Communicated by the Authors.
‡ Now at I.B.M. Poughkeepsie, New York, U.S.A.

§ 2. ENERGY LEVELS

The energy levels expected for ^{209}Bi ($J=3/2$, $I=9/2$) in a steady magnetic field H_c are shown schematically in fig. 1, which applies when the H.F.S. is inverted. The general way in which the energy of any level $W(F, m_F)$ varies with H_c and depends on the constants I, J, F, m_F, g_J, A and B can be calculated by methods described by Ramsey (1956). Perturbation theory, for example, yields the following expressions for frequencies associated with the $\Delta F=0$ transitions marked by arrows in fig. 1:

$$\nu_\alpha=\frac{1}{4}x+\frac{3}{4}y-\frac{27}{176\nu_1}x^2+\frac{15}{352\nu_1}x^3, \quad \ldots \ldots \quad (1)$$

$$\nu_\beta=\frac{3}{20}x+\frac{51}{60}y+\left[\frac{21}{176\nu_1}-\frac{224}{822\nu_2}\right]x^2 - \left[\frac{3}{1760\nu_1}-\frac{112}{1375\nu_2}\right]x^3 \quad \ldots \ldots \quad (2)$$

Fig. 1

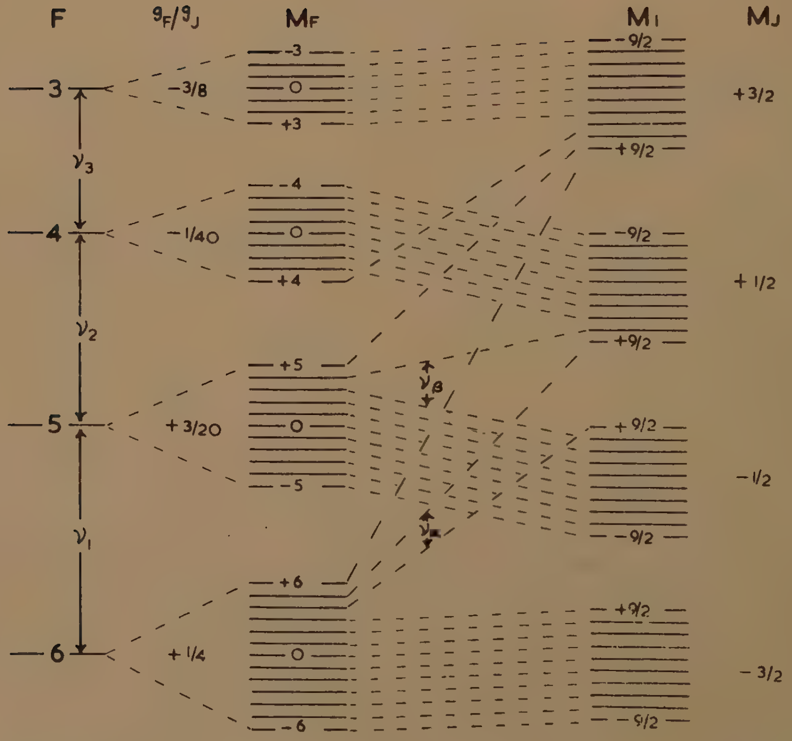
F
g_F/g_J
M_F
M_I
M_J
3
4
5
6
ν_3
ν_2
ν_1
−3/8
−1/40
+3/20
+1/4
−3
0
+3
−4
0
+4
+5
0
−5
+6
0
−6
−9/2
+9/2
−9/2
+9/2
+9/2
−9/2
+9/2
−9/2
+3/2
+1/2
−1/2
−3/2
ν_β
ν_α

The hyperfine structure of ^{209}Bi in weak and strong fields (schematic).

where $x = g_J \mu_0 H_c / h$ and $y = g_I \mu_0 H_c / h$. The interaction constants A and B are related to the zero field intervals by

$$\left.\begin{aligned} \nu_1 &= 6A + 2B/3, \\ \nu_2 &= 5A - 5B/23, \\ \nu_3 &= 4A - 2B/3, \end{aligned}\right\} \text{Mc/s.} \qquad (3)$$

Fig. 2

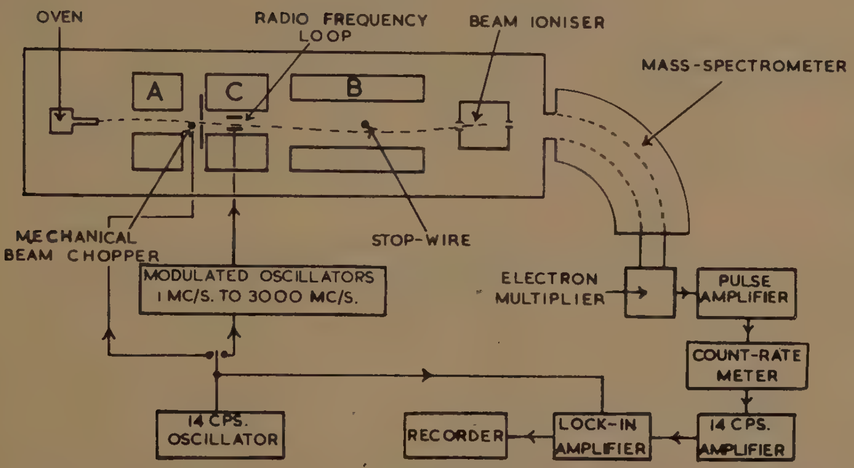
OVEN
RADIO FREQUENCY LOOP
BEAM IONISER
MASS-SPECTROMETER
A
C
B
MECHANICAL BEAM CHOPPER
STOP-WIRE
MODULATED OSCILLATORS 1 MC/S. TO 3000 MC/S.
ELECTRON MULTIPLIER
PULSE AMPLIFIER
COUNT-RATE METER
14 CPS. OSCILLATOR
RECORDER
LOCK-IN AMPLIFIER
14 CPS. AMPLIFIER

Schematic arrangement of the atomic beam magnetic resonance apparatus.

§ 3. APPARATUS

The apparatus used by Bellamy and Smith (1953) for radioactive alkalis was modified so that an atomic bismuth beam could be produced and detected. The 'flop-in' magnet system was arranged to refocus on the detector only those atoms in which the oscillating field caused transitions such that the sign of m_J was changed and the selection rules for magnetic dipole transitions $\Delta F = 0$, $\Delta m_F = \pm 1$ or $\Delta F = \pm 1$, $\Delta m_F = 0$ or ± 1 were satisfied. The transitions marked in fig. 1 are suitable and these were studied in some detail.

The atomic bismuth beam was produced in the oven shown in fig. 3, which is similar to that used by Leu and Fraser (1928). Electron bombardment of the molybdenum snout by a current of 100 mA at 1400 v produced a snout temperature of 200°K, sufficient to cause almost complete dissociation of the molecules coming from the oven cavity, which remained at a temperature nearer 1000°K. A 0·004 in. wide oven slit was machined in the end of the snout.

The beam was detected with an electron bombardment detector (Wessel and Lew 1953). Positive ions produced by an electron current of 4 mA were analysed and counted by the mass-spectrometer and electron-multiplier used earlier by Bellamy and Smith (1953). The count-rate increase on resonance was only about 3% because of a large ionizer background so it was advantageous to amplitude modulate the beam or the radio-frequency field and use a phase-sensitive detector. Total beam intensities normally used were estimated to be about 10^{10} atoms per second at the detector.

The homogeneous field H_c was calibrated as required by observing resonances with a potassium beam from a separate resistance heated oven mounted beside the bismuth oven, and this beam was detected by surface ionization. Data published by Kusch and Taub (1949) were used to calculate the magnitude of H_c for a given ^{39}K resonance frequency.

Fig. 3

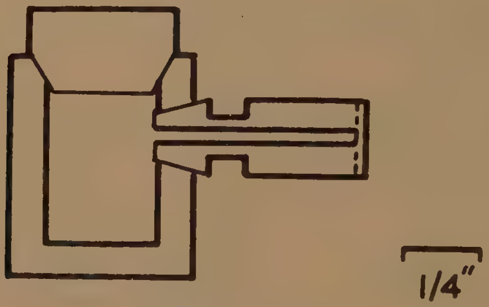

The bismuth oven.

The oscillating field was produced by a simple slotted hairpin in the *C* magnet gap. It could be positioned to stimulate σ transitions ($\Delta m_F = 0$, H_ν parallel to H_c) or π transitions ($\Delta m_F = \pm 1$, H_ν perpendicular to H_c) as required. Typical resonances were about 0·15 Mc/s wide and they were not broadened significantly by *C* field inhomogeneity. The σ resonances were double peaked, as one expects with this type of loop (Woodgate and Hellwarth 1956). Normal heterodyne methods were used to set the oscillator frequencies to about 2 parts in 10^6.

§ 4. RESULTS

The $\Delta F = 0$ transitions ν_α and ν_β indicated in fig. 1 were observed at each of the magnetic fields shown in the table. Insertion of these frequencies and fields into eqns. (1) and (2) then gave the values of ν_1 and ν_2 shown in the table, where it is seen that their accuracy increased rapidly with the magnitude of H_c. The nuclear magnetic resonance value of $+4·0797$ NM obtained by Protor and Yu (1950) was used for μ_I.

Having determined the H.F.S. intervals to about ± 20 Mc/s it was then possible to look for $\Delta F = \pm 1$ transitions and so determine the intervals with greater accuracy. Microwave triode oscillators were used to provide r.f. power in the frequency range required. Fifteen π transitions and nine σ transitions satisfy both the selection rules and the refocusing conditions in the apparatus, and all of these were observed in a field of 3·5 gauss.

Only the four transitions shown in fig. 1 were studied in detail, however, and the H.F.S. intervals and interaction constants which resulted after allowing for the field dependence were

$$\nu_1 = 2884{\cdot}7 \pm 0{\cdot}2\ \mathrm{Mc/s},$$
$$\nu_2 = 2171{\cdot}5 \pm 0{\cdot}1\ \mathrm{Mc/s}.$$

The interaction constants A and B with these intervals are

$$A = -446{\cdot}97 \pm 0{\cdot}04\ \mathrm{Mc/s},$$
$$B = -304{\cdot}25 \pm 0{\cdot}83\ \mathrm{Mc/s}.$$

Substitution of these intervals and the $\Delta F = 0$ frequencies ν_α and ν_β into eqns. (1) and (2) gives $1{\cdot}6433 \pm 0{\cdot}0002$ as an accurate value for g_J. The same result was obtained from both eqns. (1) and (2), thus showing that third-order perturbation theory yields a sufficiently accurate expression for the energy levels in this case. No direct measurement of ν_3 was carried out.

The observed frequencies ν_α and ν_β for the $\Delta F = 0$ transitions in different fields H_c, and the energy intervals ν_1 and ν_2 calculated using eqns. (1) and (2)

(^{39}K) (Mc/s)	H_c (gauss)	Observed frequencies		Calculated intervals	
		α (Mc/s)	β (Mc/s)	1 (Mc/s)	2 (Mc/s)
20·00	25·385	14·77 (5)	—	2909 (1100)	—
30·00	36·192	21·18 (5)	13·05 (3)	2800 (425)	2446 (170)
40·00	46·069	—	16·83 (2)	—	2198 (48)
60·00	63·665	37·76 (2)	23·78 (1)	2864 (51)	2191 (16)
120·00	105·768	64·00 (2)	41·64 (1)	2914 (20)	2184 (9)

§ 5. HYPERFINE STRUCTURE IN INTERMEDIATE COUPLING

Atomic bismuth has three electrons missing from the nearest closed shell and the five states of lowest energy belong to the p^3 configuration, for which the terms allowed by the Pauli principle are $^2P_{3/2}$, $^2P_{1/2}$, $^2D_{5/2}$, $^2D_{3/2}$ and $^4S_{3/2}$ in pure LS coupling. The coupling is intermediate between LS and jj for $J = 3/2$ states as indicated in fig. 4, so we represent the wavefunctions of these three states as linear combinations of the form

$$\psi(J=3/2) = c_1u_1 + c_2u_2 + c_3u_3 = d_1v_1 + d_2v_2 + d_3v_3 \quad . \quad . \quad . \quad (4)$$

where the v_k are the wavefunctions associated with the states $k = 1$, 2 and 3 in pure LS coupling and the u_k are the corresponding wave functions for pure jj coupling. The magnitudes of the c_k and the d_k depend on relative strengths for the Coulomb-repulsion and spin–orbit terms in the Hamiltonian, and there is a different set for each of the $J = 3/2$ states.

The wavefunctions for the $J=1/2$ and $J=5/3$ states are independent of coupling. The state of coupling is described by a parameter β, which can be determined by comparing the observed fine-structure with the theory, and the coefficients in eqn. (4) depend only on the energy W_k for each state k, and β. Formulae for the calculation of the c's are given by Breit and Wills (1933), Inglis and Johnson (1931) deal with the d's, and the general theory of intermediate coupling is discussed by Condon and Shortley (1931).

For the ground state of bismuth, one finds that $X=3111{\cdot}7\ \mathrm{cm}^{-1}$, $\beta=3{\cdot}10$, $c_1=-0{\cdot}188$, $c_2=+0{\cdot}345$, $c_3=+0{\cdot}918$, $d_1=-0{\cdot}354$, $d_2=-0{\cdot}515$ and $d_3=+0{\cdot}779$. The extent to which which the parameters β and X

Fig. 4

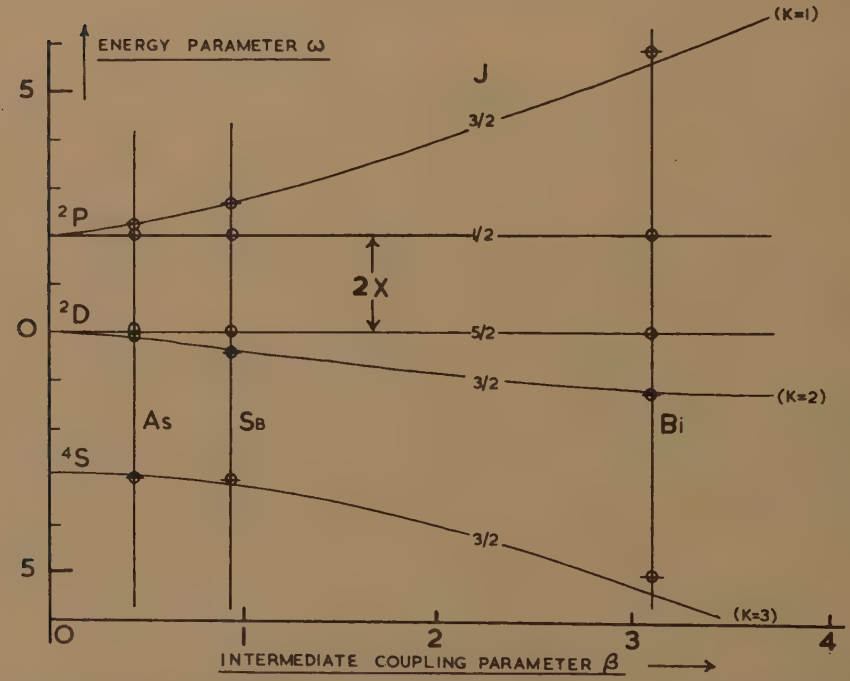

Atomic fine structure due to three p electrons in a state of intermediate coupling. The parameter β, defined by

$$\beta^2=\frac{4w_k(w_k+3)(w_k-2)}{9(w_k+3/5)},$$

is a measure of the coupling, the value being 0 for pure LS coupling and ∞ for pure jj coupling. The ordinate $w=2\,\dfrac{w_k-w_5}{w_4-w_5}$, a convenient function of energy, is plotted for the range $\beta=0$ to 4. The points represent optical results plotted at the value of the abscissa which affords the best fit to the theory. The states $J=1/2$ and $5/2$ have g_J, A and B values which are independent of β, although they may be perturbed by configuration interactions.

describe the energy levels is shown in fig. 4; the deviations may be due to the admixture of other configurations.

5.1. *Calculation of* g_J

The operator $g_J=(g_L L_Z+g_S S_Z)$ is diagonal in an LS$JM$ representation and the values of $\langle \mathrm{LS}J|g_J|\mathrm{LS}J\rangle$ are well known, so it is convenient to use the LS wavefunctions u_k for the calculation of g_J. First order theory gives

$$\left.\begin{aligned} g_J&=d_1^2\langle u_1|g_J|u_1\rangle+d_2^2\langle u_2|g_J|u_2\rangle+d_3^2\langle u_3|g_J|u_3\rangle,\\ g_J(J=3/2)&=d_1^2 g_J(^2\mathrm{P}_{3/2})+d_2^2 g_J(^2\mathrm{D}_{3/2})+d_3^2 g_J(^4\mathrm{S}_{3/2}).\end{aligned}\right\} \quad . \quad . \quad (5)$$

Substituting $g_J(^2\mathrm{D}_{3/2})=-0{\cdot}799$, $g_J(^2\mathrm{P}_{3/2})=-1{\cdot}334$, $g_J(^4\mathrm{S}_{3/2})=2{\cdot}002$ and the d values already listed into (5) gives $g_J=1{\cdot}651$ for the bismuth ground state, in reasonable agreement with the experimental result $-1{\cdot}6533(2)$.

5.2. *Calculation of A*

In order to calculate the expectation value of any operator $V=\sum V(\mathbf{r}_j)$, $\mathbf{r}_j$ being the position vector of the jth electron, one can use the jj wavefunctions v_k reduced to the form of sums and products of the single-electron wavefunctions (l,j,m), since the matrix elements $\langle l;j,m|V|l',j',m'\rangle$ can be calculated using the Dirac equation. Combining results for the p^3 configuration with (4) gives the magnitude of $\langle V\rangle$ for the state $J=3/2$, $M=3/2$ in terms of the single-electron matrix elements.

$$\begin{aligned}\langle V\rangle_{\frac{3}{2}\frac{3}{2}}=\langle \tfrac{3}{2}\tfrac{3}{2}|V|\tfrac{3}{2}\tfrac{3}{2}\rangle&+(c_1^2+\tfrac{4}{5}c_2^2)\langle \tfrac{3}{2}\tfrac{1}{2}|V|\tfrac{3}{2}\tfrac{1}{2}\rangle+(c_1^2+\tfrac{1}{5}c_2^2)\langle \tfrac{3}{2}-\tfrac{1}{2}|V|\tfrac{3}{2}-\tfrac{1}{2}\rangle\\ &+(\tfrac{1}{5}c_2^2+c_3^2)\langle \tfrac{1}{2}\tfrac{1}{2}|V|\tfrac{1}{2}\tfrac{1}{2}\rangle+(2/\sqrt{5})c_2(c_3-2c_1)\\ &\times(\tfrac{3}{2}-\tfrac{1}{2}|V|\tfrac{1}{2}-\tfrac{1}{2}\rangle+(2/\sqrt{5})\,c_2(2c_3-c_1)\langle \tfrac{3}{2}\tfrac{1}{2}|V|\tfrac{1}{2}\tfrac{1}{2}\rangle\\ &+(\tfrac{4}{5}c_2^2+c_3^2)\langle \tfrac{1}{2}-\tfrac{1}{2}|V|\tfrac{1}{2}-\tfrac{1}{2}\rangle. \quad . \quad . \quad . \quad . \quad . \quad . \quad (6)\end{aligned}$$

The single-electron matrix elements of $hA=\sum_j(\mu_I\,.\,\mathbf{H}_j)$, where $\mathbf{H}_j$ is the magnetic field at the nucleus due to the jth electron, have been calculated by Breit and Wills (1931), who show that

$$\left.\begin{aligned} ha'&=+2\mu_0^2 g_I\langle r^{-3}\rangle_{\mathrm{av}}\tfrac{8}{15}F_r'(lZ_i)=h\tfrac{3}{2}\langle \tfrac{3}{2}\tfrac{3}{2}|A|\tfrac{3}{2}\tfrac{3}{2}\rangle,\\ ha''&=+2\mu_0^2 g_I\langle r^{-3}\rangle_{\mathrm{av}}\tfrac{8}{3}F_r''(lZ_i)=h\tfrac{1}{2}\langle \tfrac{1}{2}\tfrac{1}{2}|A|\tfrac{1}{2}\tfrac{1}{2}\rangle,\\ ha'''&=-2\mu_0^2 g_I\langle r^{-3}\rangle_{\mathrm{av}}\tfrac{1}{6}G_r(lZ_i)\;=h\sqrt{2}\langle \tfrac{3}{2}\tfrac{1}{2}|A|\tfrac{1}{2}\tfrac{1}{2}\rangle,\\ A(J=\tfrac{3}{2})&=(c_1^2+\tfrac{6}{5}c_2^2+c_3^2)a'-\tfrac{1}{5}c_2^2a''-4\sqrt{\tfrac{2}{5}}c_2(c_1-c_3)a''',\\ A(J=\tfrac{5}{2})&=0{\cdot}8a'+0{\cdot}2a'',\\ A(J=\tfrac{1}{2})&=a'',\end{aligned}\right\} \quad . \quad (7)$$

where $F_r'(lZ_i)$, $F_r''(lZ_i)$ and $G_r(lZ_i)$ are relativistic factors of the order unity which are tabulated conveniently by Kopfermann (1958), page 445.

One way of estimating $\langle r^{-3}\rangle_{\mathrm{av}}$ is to make use of the expression

$$\tilde{a}=\beta X=2\mu_0^2 Z_i\langle r^{-3}\rangle_{\mathrm{av}}H(lZ_i) \quad . \quad . \quad . \quad . \quad (8)$$

where $\tilde{a}$ is the fine-structure interaction constant, which depends on the energy separation between two states independent of coupling, and the coupling parameter β (fig. 4). The effective atomic number Z_i is approximately equal to $Z-4$ for p electrons. Taking $X=3111{\cdot}7$ cm^{-1}, $\beta=3{\cdot}10$, the constants c already listed and the nuclear magnetic resonance value for g_I we get $+456$ Mc/s for $A(J=\frac{3}{2})$. This is opposite in sign to the experimental result $-446{\cdot}97\pm0{\cdot}04$ Mc/s. The eqns. (7) also predict a value wrong by a factor of five for the ratio a''/a', which can be deduced from the optical measurements of $A(J=\frac{5}{2})$ and $A(J=\frac{1}{2})$ made by Zeeman *et al.* (1930).

Breit and Wills (1933) suggested that such discrepancies might be due to interactions with other electronic configurations. Similar inconsistencies in the ratios of parameters have been found in the case of the 4s^{2}4p configuration of gallium (Koster 1952) and the 5p configuration of rubidium (Phillips 1956) and these have been explained in terms of s electron excitation. Koster (1952) showed that to a first-order approximation the fine structure is not affected by the admixture of excited s states, though it may have a significant effect on the H.F.S., so it may still be possible to use eqn. (6) to estimate $A(J=\frac{3}{2})$ if the a's are treated as parameters to be found by experiment. If a' and a'' are deduced from the optical H.F.S. measurement of $A(J=\frac{1}{2})$ and $A(J=\frac{5}{2})$, thus making first-order correcting for the configuration effects, and a''' is estimated from a'', the more accurately known parameter, $A(J=\frac{3}{2})$ comes to -413 ± 90 Mc/s, where the error reflects the uncertainty in the optical measurements. This result is in reasonable agreement with the experimental value. Further evidence for such configuration interactions in similar atoms is given in the following paper on the antimony isotopes.

5.3. *Nuclear Quadrupole Moment*

In order to calculate Q from the measured quadrupole interaction constant B it is necessary to estimate q_J, which is defined by

$$q_J=\langle-\textstyle\sum r_j^{-3}(3\cos^2\theta-1)\rangle_{JJ}$$

and then use $hB=e^2q_JQ$. Schuler and Schmidt (1936) calculated the single-electron matrix elements of q_J and substituted them into (6) to get

$$q_J(J=\tfrac{3}{2})=-\tfrac{2}{5}\langle r^{-3}\rangle_{\rm av}[R_r'(lZ_i)(c_1^2-c_3^2)+\sqrt{\tfrac{8}{5}}S_r(lZ_i)c_2(c_1+c_3)]. \quad (9)$$

The relativity correction factors $R(lZ_i)$ and $S(lZ_i)$ are listed in Kopfermann (1958, p. 448) and the c's have already been given. Koster (1952) showed that the admixture of some excited s state does not affect the fine structure, and likewise, it should not contribute to the quadrupole interaction, so eqn. (9) may give a reasonable value for q when $\langle r^{-3}\rangle_{\rm av}$ is estimated from fine-structure data and eqn. (8). When this is done one finds $Q=-0{\cdot}34b$. After making a Sternheimer (1952) correction, the result is increased slightly to $-0{\cdot}35b$. The error in Q due to the uncertainty in B is $\pm0{\cdot}001b$, but a much larger error is expected in Q because of the effects of other configuration interactions on the estimation of q_J and the uncertainty in the Sternheimer correction.

ACKNOWLEDGMENTS

The authors wish to thank Mr. P. C. B. Fernando for the construction of the high-frequency oscillator in these experiments and Mr. G. K. Rochester for the measurement of the sign of A.

Dr. R. S. Title wishes to acknowledge the scholarships awarded by the Royal Commission for the Exhibition of 1851 and by the National Research Council of Canada.

REFERENCES

BELLAMY, E. H., and SMITH, K., 1953, *Phil. Mag.*, **44,** 33.
BREIT, G., and WILLS, L., 1933, *Phys. Rev.*, **44,** 470.
CONDON, E. U., and SHORTLEY, G. H., 1951, *The Theory of Atomic Spectra* (Cambridge: University Press), p. 276.
GOUDSMIT, S., and BACK, E., 1927, *Z. Phys.*, **43,** 321.
INGLIS, D. R., and JOHNSON, M. H., 1931, *Phys. Rev.*, **38,** 1642.
KELLOG, J. M. B., RABI, I. I., RAMSEY, N. F., and ZACHARIAS, J. R., 1939, *Phys. Rev.*, **56,** 728.
KOPFERMANN, H., 1958, *Nuclear Moments.* English Edition (New York: Academic Press Inc.).
KOSTER, G. F., 1952, *Phys. Rev.*, **86,** 148.
KUSCH, P., and TAUB, H., 1949, *Phys. Rev.*, **75,** 1477.
LEU, A., and FRASER, R. G. J., 1928, *Z. Phys.*, **49,** 498.
MROZOWSKI, S., 1942, *Phys. Rev.*, **62,** 526.
PHILLIPS, M., 1956, *Phys. Rev.*, **103,** 322.
PROCTOR, W. G., and YU, F. C., 1950, *Phys. Rev.*, **78,** 471.
RAMSEY, N. F., 1956, *Molecular Beams* (Oxford: University Press).
SCHULER, H., and SCHMIDT, T., 1936, *Z. Phys.*, **99,** 717.
STERNHEIMER, R., 1952, *Phys. Rev.*, **86,** 316.
WESSEL, G., and LEW, H., 1953, *Phys. Rev.*, **92,** 641.
WOODGATE, G. K., and HELLWARTH, R. W., 1956, *Proc. phys. Soc. Lond.* A, **69,** 588.
ZEEMAN, P., BACK, E., and GOUDSMIT, S., 1930, *Z. Phys.*, **66,** 1.

The Hyperfine Structure of ^{121}Sb and ^{123}Sb†

By P. C. B. Fernando‡, G. K. Rochester, I. J. Spalding§
and K. F. Smith
Cavendish Laboratory, Cambridge

[Received August 19, 1960]

Abstract

The hyperfine structure of the $J=3/2$ ground state of ^{121}Sb and ^{123}Sb has been studied by the atomic beam magnetic resonance method, and the results are consistent with the following values for the interaction constants:

$$g_J=-1{\cdot}9705\pm0{\cdot}0002, \qquad A_{121}=-(299{\cdot}034\pm0{\cdot}004)\text{ Mc/s},$$
$$A_{123}=-(162{\cdot}451\pm0{\cdot}003)\text{ Mc/s}, \quad B_{121}=-(3{\cdot}68\pm0{\cdot}02)\text{ Mc/s},$$
and
$$B_{123}=-(4{\cdot}67\pm0{\cdot}03)\text{ Mc/s}.$$

To the accuracy of the measurements there was no evidence for an octupole interaction.

From the B values one obtains $Q_{121}=-(0{\cdot}20\pm0{\cdot}03)\times10^{-24}$ cm^2 and $Q_{123}=-(0{\cdot}26\pm0{\cdot}04)\times10^{-24}$ cm^2, and comparison of A_{121}/A_{123} with the ratio of g_{121}/g_{123} already published gives $-0{\cdot}318\pm0{\cdot}003\%$ for the hyperfine structure anomaly. Intermediate coupling theory accounts satisfactorily for g_J, but an admixture of excited s states is necessary to explain the observed magnetic interaction and anomaly.

§ 1. Introduction

Lowenthal (1929) investigated the optical Zeeman effect of the Sb I fine structure and showed that Russell–Saunders coupling of the valence electrons was not complete. He assigned an experimental value to the ground state g_J. Crawford and Bateson (1934) studied the optical H.F.S. of Sb IV and assigned nuclear spin (I) and nuclear magnetic moment (μ_I) values to the stable ^{121}Sb and ^{123}Sb isotopes. Loomis and Strandberg (1951) used the microwave resonance method to obtain an accurate value for the ratio of the quadrupole moments of these two isotopes and so stimulated further experiments on the optical hyperfine structure of Sb II by Sprague and Tomboulian (1953). Murakawa (1955) using separated isotopes, and Gordy (1955), obtained results for the ratio of the quadrupole moments somewhat different from those of Sprague. No direct optical observation of the atomic ground state H.F.S. has yet been made.

Dehmelt and Krüger (1951), and Wang (1955), measured the ratio Q_{121}/Q_{123} to about 1 in 6000 using pure nuclear quadrupole resonance techniques, and the ratio μ_{121}/μ_{123} has been measured accurately in nuclear resonance experiments by Cohen *et al.* (1950), Collins (1950) and Proctor and Yu (1950). Eisinger and Feher (1958) have recently re-measured μ_{121}/μ_{123} and used the Electron Nuclear Double Resonance (ENDOR) technique to measure the ratio A_{121}/A_{123} for the simpler $s_{1/2}$-like electronic configuration of Sb in silicon.

---

† Communicated by the Authors.
‡ Now at Physics Department, University of Columbo, Columbo, Ceylon.
§ Now at A.E.R.E. Harwell, Didcot, Berks.

We have used an atomic beam magnetic resonance apparatus to investigate the H.F.S. of the ground states of ^{121}Sb and ^{123}Sb. The field-dependent $\Delta F=0$ transitions and all the $\Delta F=1$ transitions were observed with both isotopes and from the results we deduce values of g_J, Q_{121} and Q_{123}, and also the H.F.S. anomaly, which is defined by $_{121}\Delta_{123}=(a_{121}/a_{123})(g_{123}/g_{121})-1$.

§ 2. APPARATUS

The apparatus for this experiment was the same as that used in the study of ^{209}Bi by Title and Smith (1960) (see preceding paper, which will be referred to as I).

Antimony dissociates at a higher temperature than bismuth so the oven snout was lengthened and made of tungsten instead of molybdenum. With this modification a convenient beam intensity was obtained when the end of the snout was hot enough to bring about a high degree of dissociation. Residual molecules were intercepted with a stop wire, and the signal-to-noise ratio was further improved by modulating the beam at 14 c.p.s. instead of 25 c.p.s. The output from the phase-sensitive detector was fed into a pen recorder which traced the resonance as the oscillator was scanned through the resonant frequency.

§ 3. PROCEDURE

The energy level diagrams for ^{121}Sb ($J=3/2$, $I=5/2$) and ^{123}Sb ($J=3/2$, $I=7/2$) are shown in fig. 1. The levels are inverted because A is negative. The interaction constants are related to the zero field intervals as follows:

^{121}Sb	^{123}Sb
$\nu_1=4A+4B/5+32C/5$	$\nu_1=5A+5B/7+40C/7$
$\nu_2=3A-9B/20-84C/5$	$\nu_2=4A-2B/7-88C/7$
$\nu_3=2A-4B/5+96C/5$	$\nu_3=3A-5B/7+88C/7$

where C is a possible magnetic octupole interaction constant.

ν_α and ν_β are the only two $\Delta F=0$ transitions which satisfy the refocusing conditions of the machine. They were followed up to fields of 100 gauss, and the magnitudes of the constants g_J, A and B deduced therefrom were used to calculate the approximate frequencies of the $\Delta F=1$ transitions. These were then measured directly to give more accurate values for A and B.

Since $m_F = 0$ levels are field independent to the first order, it is desirable to observe $\Delta F = 1$ transitions involving these levels because small fluctuations in magnetic field during the experiment are less important, the field correction to the final result is smaller, and small field inhomogeneities in the C magnet do not deform the line shape. All the refocused $\Delta F = 1$ transitions were scanned at C fields of about 1 gauss, and ν_2, the only field independent resonance which satisfied the refocusing conditions, was measured accurately. A double resonance technique introduced by Davis *et al.* (1949) was used to observe the field independent transitions ν_1 and ν_3. Two triode cavity oscillators were coupled to the same r.f. loop, the first was set on one of the two maxima associated with the ν_2 σ-transition (Woodgate and Hellwarth 1956), while the second was scanned through the frequencies expected for ν_1 and ν_3. The refocused beam intensity was reduced on resonance because of transitions to the upper or lower level and the double-humped ν_1 and ν_3 resonances traced by the recorder thus appeared inverted. Careful adjustment of both power levels was essential. The procedure was then repeated with the first oscillator set on the other maximum of the ν_2 resonance, but no shifts of frequency were found. From the three zero-field H.F.S. intervals measured in this way we deduced A and B and showed that C is zero within the accuracy of the measurements. The results are given in table 1.

Fig. 1

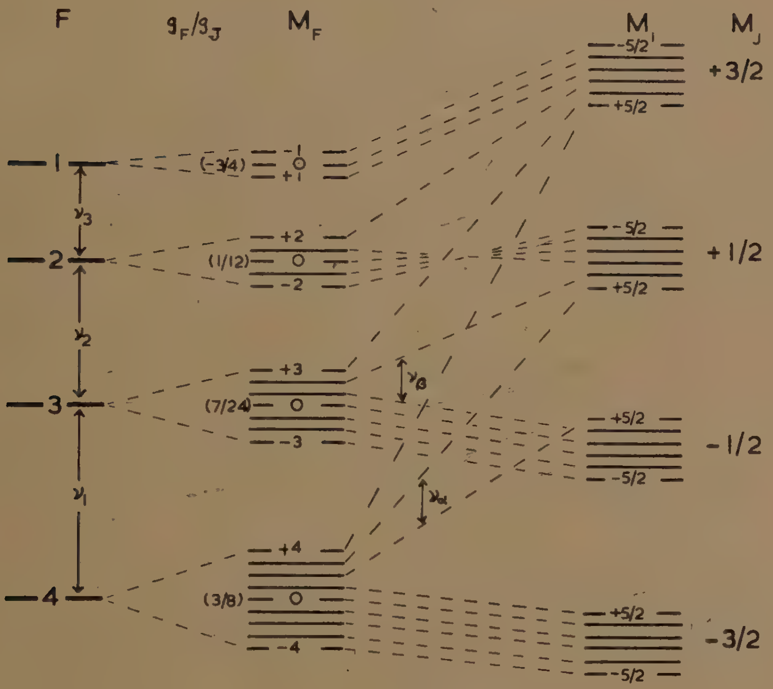

The sign of A_{121} was determined by a method used previously by King and Jaccarino (1954). Atoms with one sign of m_J, say $m_J = +\frac{1}{2}$, were removed by a stop wire in the A magnet and the low frequency $\Delta F = 0$ transition ν_β was used to refocus the $m_J = -\frac{1}{2}$ atoms on to the detector. A second frequency ν_F (fig. 2) was then applied to a separate r.f. loop some two inches nearer the detector, and the refocused beam decreased in intensity, showing that A is negative; had A been positive there would have been no change in intensity. A similar effect was obtained when the frequencies ν_β and ν_F were used in the reverse order and the atoms with $m_J = -\frac{1}{2}$ were suppressed instead of those with $m_J = +\frac{1}{2}$.

Table 1. Zero field intervals and interaction constants for ^{121}Sb and ^{123}Sb

^{121}Sb (Mc/s)	^{123}Sb (Mc/s)
$\nu_3 = 595{\cdot}12 \pm 0{\cdot}01$	$\nu_3 = 484{\cdot}02 \pm 0{\cdot}01$
$\nu_2 = 819{\cdot}45 \pm 0{\cdot}01$	$\nu_2 = 648{\cdot}46 \pm 0{\cdot}01$
$\nu_1 = 1199{\cdot}08 \pm 0{\cdot}01$	$\nu_1 = 815{\cdot}60 \pm 0{\cdot}01$
$A = -299{\cdot}034 \pm 0{\cdot}004$	$A = -162{\cdot}451 \pm 0{\cdot}003$
$B = -3{\cdot}68 \pm 0{\cdot}02$	$B = -4{\cdot}67 \pm 0{\cdot}03$
$g_J = -1{\cdot}9705 \pm 0{\cdot}0002$	

Fig. 2

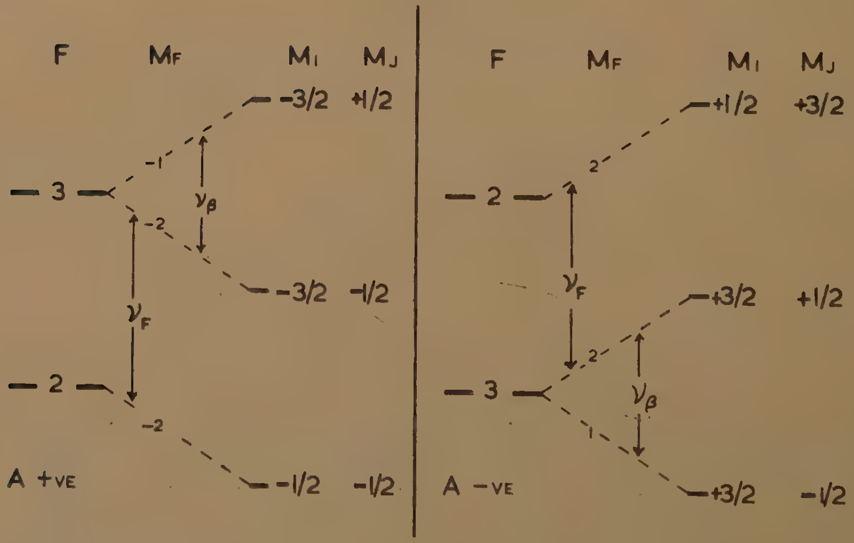

An accurate value of g_J can usually be obtained by substituting the H.F.S. intervals in the perturbation theory equations for the $\Delta F = 0$ transitions. However, the g_J's deduced from ν_α and ν_β differed by more than the probable error when perturbation theory up to the third order was used, so the secular equation was solved numerically using a digital computer. The values of g_J deduced from each transition were then identical over a wide range of C fields.

§ 4. DISCUSSION OF RESULTS

4.1. *Fine Structure and g_J*

Atomic antimony has two 5s electrons and three 5p electrons outside a closed sub-shell and the coupling of the p electrons is intermediate between LS and jj. The ground state wave function can be written in the form of eqn. (4) of I with

$$c_1=0\cdot361\pm0\cdot002,\quad c_2=-0\cdot689\pm0\cdot004,\quad c_3=-0\cdot628\pm0\cdot006,$$
$$d_1=-0\cdot188\pm0\cdot005,\quad d_2=+0\cdot057\pm0\cdot004,\quad d_3=0\cdot980\pm0\cdot002,$$
$$a=3270\cdot5\ \mathrm{cm}^{-1},\qquad \beta=0\cdot93\pm0\cdot02.$$

This value of β, which is slightly different from that obtained by Inglis and Johnson (1931) using the same theory, was estimated by making a simplified least squares fit of the theory to the fine structure measured optically by Lowenthal (1929). The error in β gives an indication of the closeness of the fit of the intermediate-coupling theory to the fine structure and the quoted errors in the c's and the d's are those which arise only from the uncertainty in β. It will be noted that the state is almost entirely LS coupled, being 98% $^4\mathrm{S}_{3/2}$.

The theoretical estimate, neglecting relativistic effects, of

$$g_J=-1\cdot971\pm0\cdot004$$

is obtained by substituting the above values of d_i in eqn. (5) of I. This is in good agreement with the experimental $g_J=1\cdot9705\pm0\cdot0002$.

4.2. *Comparison of A with Theory*

The intermediate-coupling theory fits the five fine-structure levels with only two parameters β and $\tilde{a}$, and the experimental agreement is quite good, so one might expect this theory to account for the observed hyperfine structure in a satisfactory manner. However, the calculation of A_{121} using this theory (eqn. (7)) gives $A_{121}=-15\pm5$ Mc/s, where the error is due to the uncertainty in β. For this calculation we used the g_I measured by Eisinger and Feher (1958), and the values $\tilde{a}=3041\cdot6\ \mathrm{cm}^{-1}$ and $\langle r^{-3}\rangle_{\mathrm{av}}=70\cdot8\ \text{Å}^{-3}$, which were obtained by substituting $\beta=0\cdot93$ and $X=3270\cdot4\ \mathrm{cm}^{-1}$ in (8). The experimental value of A_{121} is $-299\cdot032$ Mc/s. It is possible that the discrepancy is due to configuration interactions which do not alter either g_J or the form of the fine structure. In addition, the ratio a'/a'' deduced from (7) should be 0·17 for a pure p^3 configuration, whereas optical measurements of $A(\mathrm{P}_{1/2})$ and $A(\mathrm{D}_{5/2})$ by Badami (1932) yield 0·22. If we try to allow for the effect of any admixed configurations by treating the optical results $a' = 1068 \pm 350$ Mc/s and $a'' = 4740 + 140$ Mc/s as experimental parameters in the intermediate-coupling theory, a method which gave a reasonable fit in the case of Bi, we obtain

$$A(J = 5/2) = +274 \pm 400 \text{ Mc/s}.$$

The error here is associated with the optical measurements and the corresponding error due to the uncertainty in β is only 7 Mc/s. No conclusion about the validity of this procedure can be drawn because of the large error in the predicted value of $A(J = 3/2)$.

4.3. *Hyperfine Structure Anomaly*

The ratio g_{121}/g_{123} has been measured by Eisinger and Feher (1958) and this may be combined with our measurement of A_{121}/A_{123} to give $(-0{\cdot}317 \pm 0{\cdot}003)\%$ for the H.F.S. anomaly ${}_{121}\Delta_{123}$. Eisinger and Feher have also measured ${}_{121}\Delta_{123}$ for an atomic configuration which is essentially a pure s state and they obtained $(-0{\cdot}352 \pm 0{\cdot}005)\%$, which is only slightly larger than that measured for the intermediately-coupled p^3 configuration. They have considered several nuclear models and conclude that the model which gives the best result for μ_{121}, Q_{121} and Δ(s) is the configuration mixing model, for which $\Delta(s) = -0{\cdot}365\%$.

The Breit Rosenthal contribution to Δ is $\sim 10^{-2}\%$ for the atomic s state and is much smaller for p states. We have estimated the Bohr–Weisskopf anomaly for the configuration mixing model, using (6), and conclude that $\Delta(p^3)$ is probably smaller than $-0{\cdot}08\%$ if off-diagonal terms are neglected. The anomaly we have measured is typically that expected for an s state, and a small s state admixture could also account for the magnitude of A.

4.4. *Configuration Interactions*

The only configurations which can be mixed with the antimony ground state to produce a large hyperfine anomaly and almost no change of g_J are those in which s electrons are excited to higher s states. Koster (1952) and Phillips (1956) accounted for inconsistent values of a'/a'' in Ga and Rb, similar to those which we now find in Sb, by means of outer s electron excitation. Abragam (1955), Heine (1957), Sternheimer (1957), Cohen *et al.* (1959) and Blinder (1960) considered the exchange interactions between the aligned valence electrons and s electrons in different shells, and showed that different spin-up and spin-down electron densities at the nucleus are associated with each of the s shells. The contact term in the expression for A is then a sum of several terms, each with a sign and magnitude dependent on the overlap of the s and valency electron wave functions, and the resultant A is sensitive to the s wave functions used. No detailed calculation of this sort has been carried out for antimony.

The breakdown of LS coupling contributes only -15 Mc/s out of the total observed value of -299 Mc/s to A_{121}. If we assume then that most of the magnetic interaction is due to s electron excitation, any s state admixture which satisfactorily accounts for A gives automatically an

H.F.S. anomaly of the right sign and magnitude, irrespective of the detailed form of the calculations. In addition, excitation of s electrons to higher s states does not alter g_J, since the contribution from these electrons remains zero.

Table 2. Values for Q_{121}, Q_{123} and Q_{121}/Q_{123} reported in the literature

Method	Q_{121} $\times 10^{-24}$ cm^2	Q_{123} $\times 10^{-24}$ cm^2	Q_{121}/Q_{123}
Dehmelt and Krüger (1951) nuclear quadrupole resonance	—	—	0·7843 ± 0·0001
Loomis and Strandberg (1951), microwave spectrum of Sb H_2D	−0·35 to −0·50	−0·45 to −0·62	0·791
Sprague and Tomboulian (1953), optical H.F.S.	−1·2	−1·6	—
Murakawa (1955), optical H.F.S.	−0·52 ± 0·1	−0·67 ± 0·1	0·73 ± 0·06
Wang (1955), nuclear quadrupole resonance in crystals	—	—	0·7844 ± 0·0001
Gordy (1955), microwave absorption	−0·8	−1·0	0·784 ± 0·002
As reported in this paper	−0·20 ± 0·03	−0·26 ± 0·04	0·784 ± 0·008

4.5. *Quadrupole Moments*

Sternheimer (1957) has published a general discussion of the effects of core excitation with particular reference to the calculation of quadrupole moments. He has shown that the corrections can be quite large even when fine or hyperfine structure data are used to calculate $\langle r^{-3}\rangle_{\mathrm{av}}$, and that they are sensitive to the wave functions used for the core and valence electrons. If the excitation of s electrons to higher s states is the predominant effect, however, both the quadrupole interaction and the fine structure remain almost unchanged and we can use eqn. (9) of I to estimate Q. Quadrupole moments calculated in this way are compared with results obtained by other methods in table 2. The errors assigned to our Q values are those associated with the uncertainty in β, and no Sternheimer corrections have been made. Although there is some considerable disagreement about the magnitudes of the quadrupole moments, the signs are all negative and our value for Q_{121}/Q_{123} agrees with the quadrupole resonance results.

ACKNOWLEDGMENTS

The authors wish to thank Dr. Heine and Professor Bleaney for useful discussions about electron configuration interactions. They would also like to thank Dr. Oxley for devising a programme for the calculation of g_J, and the Director of the Mathematical Laboratory for the use of the electronc computer Edsac II.

REFERENCES

ABRAGAM, A., HOROWITZ, J., and PRYCE, M. H. L., 1955, *Proc. roy. Soc.* A, **230,** 169.
BADAMI, J. S., 1932, *Z. Phys.*, **79,** 230.
BLINDER, S. M., 1960, *Bull. Amer. phys. Soc.*, **5,** 14.
COHEN, M. H., GOODINGS, D. A., and HEINE, V., 1959, *Proc. phys. Soc. Lond.*, **73,** 811.
COHEN, V. W., KNIGHT, W. D., WENTINK, T., and KOSKI, 1950, *Phys. Rev.*, **79,** 191.
COLLINS, T. L., 1950, *Phys. Rev.*, **79,** 226.
CRAWFORD, M. F., and BATESON, S., 1934, *Canad. J. Res.* A, **10,** 693.
DAVIS, L., FELD, B., ZABEL, C., and ZACHARIAS, J., 1949, *Phys. Rev.*, **76,** 1082.
DEHMELT, H. G., and KRÜGER, H., 1951, *Z. Phys.*, **130,** 385.
EISINGER, J., and FEHER, G., 1958, *Phys. Rev.*, **109,** 1172.
GORDY, W., 1955, *Phys. Rev.*, **97,** 680.
GOUDSMIT, S., 1933, *Phys. Rev.*, **43,** 636.
HEINE, V., 1957, *Phys. Rev.*, **107,** 1002.
KING, J. G., and JACCARINO, V., 1954, *Phys. Rev.*, **94,** 1610.
KOSTER, G. F., 1952, *Phys. Rev.*, **86,** 148.
LOOMIS, G. C., and STRANDBERG, M. W. P., 1951, *Phys. Rev.*, **81,** 798.
LOWENTHAL, H., 1929, *Z. Phys.*, **57,** 828.
MURAKAWA, K., 1955, *Phys. Rev.*, **100,** 1371.
PHILLIPS, M., 1956, *Phys. Rev.*, **103,** 322.
PROCTOR, W. G., and YU, F. C., 1950, *Phys. Rev.*, **81,** 20.
SCHWARTZ, C., 1955, *Phys. Rev.*, **99,** 1035.
SPRAGUE, G. and TOMBOULIAN, D. H., 1953, *Phys. Rev.*, **92,** 105.
STERNHEIMER, R. M., 1957, *Phys. Rev.*, **105,** 168.
TITLE, R. S., and SMITH, K. F., 1960, *Phil. Mag.*, **5,** 1281.
WANG, C., 1955, *Phys. Rev.*, **99,** 566.
WOODGATE, G. K., and HELLWARTH, R. W., 1956, *Proc. phys. Soc. Lond.* A, **69,** 588.

CORRESPONDENCE

On the Scattering of Phonons by Spins at Low Temperatures
Experimental

By H. M. Rosenberg and B. Sujak†
The Clarendon Laboratory, Oxford

[Received August 29, 1960]

This paper reports some preliminary experiments which show how the heat conductivity of a dielectric crystal may be profoundly influenced by the presence of a small number of paramagnetic ions. Measurements of the thermal conductivity between 2 and 20°K have been made on crystals of Analar grade zinc sulphate, $ZnSO_4 . 7H_2O$ (maximum impurity 0·006%) and also on zinc sulphate crystals which contained 0·25, 1 and 5·6 at. % of $FeSO_4 . 7H_2O$. These measurements were compared with those on crystals of zinc sulphate which contained 5·7 at. % of a non-paramagnetic impurity, $MgSO_4 . 7H_2O$. All the crystals were 2 to 3 cm long and had a square cross section with a side of 3 to 4 mm. The measurements were made in a manner similar to that described by Rosenberg (1955).

Some of the results are shown in the figure (*a*). The curves for the pure material are on the whole of the usual type which one expects for the thermal conductivity of a dielectric crystal (see Berman 1953, Klemens 1956, or Ziman 1960, for general reviews). The rapid rise in conductivity on the high temperature side of the maximum is due to the decrease in the effectiveness of the scattering of the phonons by impurities or isotopes, and the decrease in conductivity at temperatures below the maximum is caused by the scattering of the phonons by the boundaries of the specimen or of small crystallites. It is unfortunate that it is not easy to grow very perfect crystals from a saturated aqueous solution and there is considerable scatter (from 25 to 50%) in the data from different crystals of the same composition.

The main interest lies in the measurements taken above the conductivity maximum. The extra thermal resistance in the specimens containing Fe^{2+} is shown in the figure (*b*). It will be noted that the addition of 5·6% Fe^{2+} decreases the conductivity and completely changes the temperature dependence from $T^{-1\cdot5}$ to about $T^{-0\cdot5}$. This change cannot be ascribed merely to an impurity scattering effect, because as the figure (*a*) shows, the conductivity of a specimen containing 5·7% Mg is very much closer to that of the pure material. This can be emphasized still further when we note that the thermal resistance due to impurity scattering is proportional to the *square* of the mass difference between the impurity and the other atoms (see Ziman 1960). Since the mass difference between Mg and Zn is about 41, whereas between Fe and Zn it is only 9·5, the effect of the Mg impurity should be very much greater than the Fe impurity instead of being much less.

---

† On leave from Zaklad Niskich Temperatur Instytutu Fizyki Polskiej, Akademii Nauk, Wrocław, Poland.

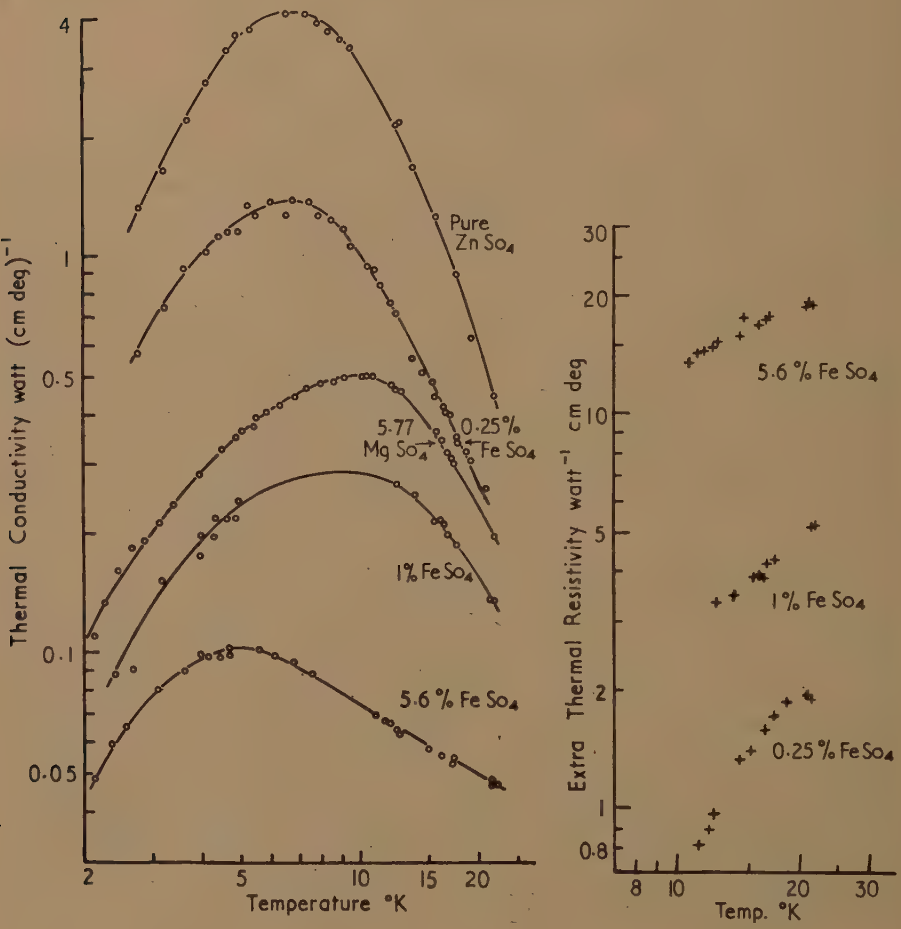

(*a*) (*b*)

(*a*) The thermal conductivity of pure hydrated zinc sulphate crystals and of zinc sulphate with 0·25, 1 and 5·6 at. % $FeSO_4 . 7H_2O$, and 5·7 at. % $MgSO_4 . 7H_2O$. (*b*) The extra thermal resistance in the zinc sulphate crystals which have additions of Fe^{2+}.

DISCUSSION

We suggest that the large decrease in conductivity which is observed for the specimens containing 5·6% Fe^{2+} is due to Raman type interactions between the phonons and the low-lying spin levels of the ferrous ion. By this we mean that a phonon interacts with a spin, flips it to another level and another phonon is emitted. Since, for the Fe^{2+} ion, the spin–lattice relaxation time is thought to be very short (see, for example, Tinkham 1956), the probability for this mechanism will be high. The theory of these processes has been given by Orbach (1960) and is presented in the following letter. He has also calculated the scattering due to direct processes, i.e. those in which a phonon of just the right energy is absorbed so that a spin may be flipped without the need for the emission of another phonon to maintain the energy balance, but he finds that the probability of such processes is much lower in the temperature region of our experiments than are the Raman processes.

Unfortunately a detailed calculation of the effect is not possible because the splitting of the lowest levels of the Fe^{2+} ion is not known. Some specific heat measurements have been made on the 5·6% Fe^{2+} crystal, however, and these have an anomaly with a peak at about 1·8°K, which can be ascribed to a splitting of 4·3 ± 0·2 degrees. If such a splitting is assumed, then Orbach's calculations yield an additional thermal resistivity of about the order of magnitude which we observe and with a temperature dependence which seems to vary with concentration as in fig. 1 (*b*) (see figure in following letter).

It is clear that more experiments must be made using other types of crystal (preferably without water of crystallization, because these are usually much more perfect). It is just possible that the difference in the curves which we observed are due to the fact that some specimens are not very perfect. It is known that some hexahydrate can co-exist with the heptahydrate and that there are in fact two crystallographic forms for the heptahydrate (Giauque *et al.* 1950). It does not seem likely, however, that the large change observed for the specimens containing 5·6% Fe^{2+} can be due entirely to defective crystals. Other types of spin–phonon interaction in heat conduction experiments have in fact been observed in ferrites (Friedberg and Douthett, 1958) and antiferromagnetics (Slack and Newman 1958) and these give further grounds for confidence in our results.

ACKNOWLEDGMENTS

We should like to thank Dr. R. Orbach for the very valuable discussions which led to the interpretation of the results and we are very grateful to Dr. P. D. F. Shaw for analysing the specimens and to Dr. C. A. Bailey for making the specific heat measurements.

REFERENCES

BERMAN, R., 1953, *Advanc. Phys.*, **2,** 103.
FRIEDBERG, S. A., and DOUTHETT, D., 1958, *Physica*, **24,** S 176.
GIAUQUE, W. F., BARIEAU, R. E., and KUNZLER, J. E., 1950, *J. Amer. chem. Soc.*, **72,** 5685.
KLEMENS, P. G., 1956, *Handb. der Phys.*, **14,** 198.
ORBACH, R., 1960, *Phil. Mag.*, **5,** 1303.
ROSENBERG, H. M., 1955, *Phil. Trans.* A, **247,** 441.
SLACK, G. L., and NEWMAN, R., 1958, *Phys. Rev. Letters*, **1,** 359.
TINKHAM, M., 1956, *Proc. roy. Soc.* A, **236,** 535.
ZIMAN, J. M., 1960, *Electrons and Phonons* (Oxford: Clarendon Press).

On the Scattering of Phonons by Spins at Low Temperatures
Theoretical

By R. Orbach
University of California, Department of Physics, Berkeley, California
and
Clarendon Laboratory, Oxford

The previous paper (Rosenberg and Sujak 1960) has described the observed effects of paramagnetic impurities on the thermal conductivity of a dielectric salt: $FeSO_4 . 7H_2O$ in $ZnSO_4 . 7H_2O$. It is the purpose of this letter to briefly analyse their results in terms of a theoretical model.

In the usual treatment of spin–lattice relaxation in paramagnetic salts (Van Vleck 1940) there are two important relaxation processes which are considered. The first, the so-called 'direct' process, involves the emission or absorption of a single phonon of the energy corresponding to the splitting $k\Delta$ (whether due to Zeeman or crystalline field effects) between the spin states of the ion. For Zeeman splittings the phonon energy is small in moderate fields, $\sim 0{\cdot}1\,^\circ\mathrm{K}$ for a $g=2$ and a field of 1000 gauss. There is, however, a second relaxation process, the so-called 'Raman' process, wherein a phonon is inelastically scattered by the spin and it is the *difference* between the initial and final state phonon energies which is equal to the splitting of the spin states $k\Delta$. The latter process involves all phonons, but primarily those at energy $\sim kT$ because they are most abundant. If $kT \gg$ the splitting, then the Raman process is usually dominant in spin–lattice relaxation.

We now reverse the tables and ask how the thermal resistance of a dielectric salt will be affected by paramagnetic impurities. That is, we must calculate the scattering cross section for phonons in the presence of spin–phonon interactions. We can then find the expected thermal resistance.

It is evident that if the splittings of the spin states $\Delta \ll T$, the direct process will lead to a negligible thermal resistance as the great bulk of phonons which carry the heat will have energy $\sim kT$ and could not be scattered by processes which are limited to phonons of the splitting energy. Thus, thermal resistance due to direct processes will be important for small splittings only at very low temperatures, on the order of $\leqslant \Delta$. However, as Raman process scattering affects all phonons, it can be expected to be the dominant mechanism for providing a significant thermal resistance at higher temperatures.

To gain a semi-quantitative estimate of the effects of Raman processes, we construct a phenomenological Hamiltonian $\mathscr{H}$ coupling the spin system to the lattice (Orbach 1960),

$$\mathscr{H}' = \Gamma \textstyle\sum_{l,j,m} [S_l^z S_l^j + S_l^j S_l^z]\, \epsilon_{zm}{}^{(1)} \epsilon_{mj}{}^{(2)}, \qquad . \quad . \quad . \quad . \quad (1)$$

where Γ is a phenomenological coupling constant, S_l^i is the ith component of the spin at the lth lattice site measured in units of $\hbar$, we sum over all spin sites l, and $\epsilon_{ij}^{(\alpha)}$ is i, jth component of strain for the phonon (α). We restrict j to equal either x or y in order that $\mathscr{H}'$ can 'flip' a spin. Equation (1) is then an expression for a Hamiltonian which annihilates or creates phonon (1), flips a spin, and creates or annihilates phonon (2). It applies to spin states which are not Kramer's degenerate in that it predicts a seventh power temperature dependence for the relaxation time.

If we consider Fe^{2+} in $ZnSO_4 . 7H_2O$, the Fe^{2+} will be in a predominantly tetragonal crystalline field with a slight orthorhombic distortion. Together with the spin–orbit coupling, this results in the removal of all orbital and spin degeneracy as the number of electrons is even. Normally, with only a tetragonal field, one would expect a doublet lowest, but the presence of the small orthorhombic term will slightly split the doublet levels. The specific heat measurements of Bailey (unpublished) show that under these considerations, the splitting of the lowest levels (presumably here the doublet levels) is $\Delta \approx 4{\cdot}3$ °K. Such a level scheme implies that eqn. (1) has the proper form.

We compute the spin–lattice relaxation time T_1 from eqn. (1) by standard means (Orbach, *loc. cit.*)

$$1/T_1 \cong 90S^4\Gamma^2/(\pi^3\rho^2v^{10}) \times (kT/\hbar)^7. \qquad . \quad . \quad . \quad . \quad (2)$$

Here, ρ is the density, v the phonon velocity (assumed the same for all modes for simplicity), and S the spin value. Likewise, one can easily compute the relaxation time for phonons via the interaction Hamiltonian (1) (Orbach, *loc. cit.*),

$$1/\tau = S^4\Gamma^2N_v/(12\pi\rho^2v^7) \times \{\omega^2[\omega^2+(k\Delta/\hbar)^2]\} \qquad . \quad . \quad . \quad (3)$$

where there are N_v spin impurities per unit volume, Δ is the splitting between the spin states in °K and ω is the phonon frequency. From a comparison of (3) and (2), it is clear that a short spin–lattice relaxation time T_1 implies a short phonon mean free path $= v\tau$.

If we compute the thermal resistance due to eqn. (3) by the usual methods (Klemens 1958) neglecting questions of thermal equilibrium within the phonon spectrum, we find a thermal resistance W given by,

$$1/W = 4v^6k\rho^2/(\pi S^4\Gamma^2N_v) \times (\hbar/kT)^2$$

$$\times \int \omega^2\, d\omega \exp(\hbar\omega/kT)/\{[\omega^2+(k\Delta/\hbar)^2][\exp(\hbar\omega/kT)-1]^2\}. \qquad (4)$$

For $\Delta \ll T$, this reduces to,

$$1/W \approx 4\rho^2kv^6/(\pi S^4\Gamma^2N_v) \times (\hbar/k\Delta). \qquad . \quad . \quad . \quad . \quad (5)$$

From paramagnetic resonance line broadening due to spin–lattice interactions for Fe^{2+} in ZnF_2, Tinkham (1956) found that $T_1 \sim 5\times10^{-9}$ sec at

$T = 20°\text{K}$. We correct for the difference in sound velocities between ZnF_2 and $ZnSO_4 . 7H_2O$ and, though the crystalline field effects are quite different, for an order of magnitude estimate we assume the spin–lattice coupling constant Γ stays roughly the same. Then, from (3), we estimate Γ^2, using $\rho = 2\,\text{g/cm}^3$, $v = 2{\cdot}1 \times 10^5\,\text{cm/sec}$, and an 'effective' spin $S = \frac{1}{2}$. We find $\Gamma^2 \sim 10^{-20}\,\text{ergs}^2$. Using this value, the thermal resistance W from eqn. (5) with, say, $5{\cdot}6\%\,Fe^{2+}$ in $ZnSO_4 . 7H_2O$ [i.e. $N_v = 2{\cdot}93 \times 10^{20}$ spins $\text{cm}^{-3}] \approx 30\,\text{watts}^{-1}\,\text{cm deg}$, in very good order of magnitude agreement with the mean experimental value (see figure). According to eqn. (5), W should be temperature independent and directly proportional to the splitting Δ and the concentration N_v.

In fact, for $5{\cdot}6\%\,Fe^{2+}$ in $ZnSO_4 . 7H_2O$, Rosenberg and Sujak find a thermal resistance which is temperature dependent (see figure). Further, the resistance does not appear to be directly proportional to concentration and the temperature dependence seems to vary with concentration. Both these apparent discrepancies can be removed by noting that our calculation of W may have been too naive. If we let $\Delta \to 0$, then eqn. (3) will have the same frequency dependence as one would find from impurity scattering, and the thermal resistance as given by eqn. (5) would vanish due to the heat flux of those phonons whose energy is $\ll kT$ not being significantly attenuated. In fact, as Δ is significantly less than T in the experiments of Rosenberg and Sujak, it would appear that just such a spurious effect might be entering here. Two apparently equivalent treatments have been given (Callaway 1959, Berman *et al.* 1959) to remedy such a situation. Both consider that the usually neglected momentum conserving (N) processes tend to bring the low frequency phonons back into equilibrium with the higher frequency phonons (of energy $\geqslant kT$) whose heat flux is much more effectively impeded by the non-momentum conserving processes (in their case, impurity scattering). We follow the treatment of Callaway because of its simplicity. We assume that a phonon of frequency ω has a lifetime τ_N due to N-processes given by

$$1/\tau_N = A\omega(kT/\hbar)^4 \quad . \; . \; . \; . \; . \; . \; . \; . \qquad (6)$$

where A is a constant. This is the usual expression for transverse phonons. Longitudinal phonons would obey a law like $1/\tau_N \approx A\omega^3(kT/\hbar)^2$ for an orthorhombic crystal, but, as we are interested in those phonons for which $\omega < kT/\hbar$, the N-process transverse phonon relaxation time (6) is much shorter than the N-process longitudinal phonon relaxation time. We make the rather reasonable assumption that the longitudinal phonons are in equilibrium with the transverse phonons and hence consider (6) as the overall effective N-process relaxation time. Our expression for the thermal resistance W is then, using the formalism due to Callaway,

$$1/W = 4v^6k\rho^2/(\pi S^4\Gamma^2N_v) \times (\hbar/kT)^2$$

$$\times \int \omega^3\,d\omega \exp(\hbar\omega/kT)/\{[\omega^3 + (k\Delta/\hbar)^2\omega + \alpha(T/\Delta)(kT/\Delta)^3]\,[\exp(\hbar\omega/kT) - 1]^2\} \quad . \; . \; . \qquad (7)$$

where α is a dimensionless constant giving the relative strength of the momentum conserving processes to the non-momentum conserving Raman processes. Explicitly,

$$\alpha = A(k\Delta/\hbar) \times 12\pi\rho^2 v^7/(S^4\Gamma^2 N_v). \quad . \quad . \quad . \quad . \quad . \quad . \quad (8)$$

Using the approximate theory due to Orbach (*loc. cit.*), we find that $A \sim 10^{-54}\,\mathrm{sec}^4$ utilizing the appropriate elastic properties of $ZnSO_4 . 7H_2O$.

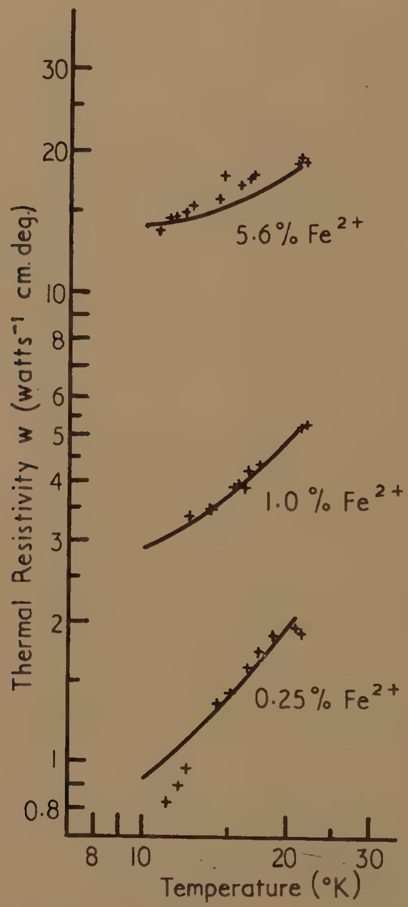

The calculated thermal resistance W due to substitutions of 0·25, 1·0 and 5·6 at. % ferrous sulphate in zinc sulphate given by eqn. (7), plotted against temperature. The crosses are the experimental points of Rosenberg and Sujak (previous paper) for the corresponding salts.

We evaluate the expresion for α for this value of A and for the values of ρ, v, Δ and Γ^2 given above. Respectively for 5·6%, 1% and 0·25% Fe^{2+} in $ZnSO_4 . 7H_2O$, $\alpha = 0{\cdot}001$, 0·0056 and 0·022. Inserting these values in eqn. (7) and evaluating the integral, we find the expected thermal resistance due to spin–phonon interactions in this salt. If we divide our order of magnitude results by a factor of ~ 2 in order to fit the experimental magnitude of W for 5·6% $FeSO_4$ at 10°K we find the theoretical curves of W against temperature T shown in the figure. These are to be compared with the experimental results of Rosenberg and Sujak given in the preceding paper which are also shown in the figure for convenience. Without any further adjustments the temperature dependence of W as predicted by eqn. (7) seems to fit the experimental data rather well for the substitution of 5·6% Fe^{2+}. The predicted change in temperature dependence with concentration and the relative magnitude of the thermal resistance also seem to be in excellent agreement with the experimental results for 1·0 and 0·25% Fe^{2+} over the measured temperature range.

This agreement would seem to justify our interpretation of the experimental results. In particular, the choice of the phenomenological spin–phonon coupling Hamiltonian (eqn. (1)) to give the corresponding phonon relaxation time (eqn. (3)), and the use of the N-processes to restore thermal equilibrium amongst the phonon modes would both appear to be consistent with the experimental results. Further investigations are planned in other better behaved substances (see preceding paper). It is hoped that the values of Γ and A can then be pinned down more closely and more accurate experimental results can be obtained.

ACKNOWLEDGMENTS

In acknowledgment, the author wishes to thank Professor C. Kittel for the original suggestion of this investigation and Dr. J. M. Ziman for valuable discussions. Appreciation is also due to Drs. W. M. Lomer and R. J. Elliott for their comments on the manuscript, and Mr. M. J. D. Powell who carried out the numerical integrations of eqn. (7).

REFERENCES

BERMAN, R., NETTLEY, P. T., SHEARD, F. W., SPENCER, A. N., STEVENSON, R. W. H., and ZIMAN, J. M., 1959, *Proc. roy. Soc.* A, **253**, 403.
CALLAWAY, J., 1959, *Phys. Rev.*, **113**, 1046.
KLEMENS, P. G., 1958, *Solid State Physics*, Vol. 7 (New York: Academic Press).
ORBACH, R., 1960, Ph.D. Thesis, University of California (unpublished).
ROSENBERG, H. M., and SUJAK, B., 1960, *Phil. Mag.*, **5**, 1299.
TINKHAM, M., 1956, *Proc. roy. Soc.* A, **236**, 535.
VAN VLECK, J. H., 1940, *Phys. Rev.*, **57**, 426.

The Spin of ^{124}Sb and the Spin and Moments of ^{122}Sb

By P. C. B. FERNANDO†, G. K. ROCHESTER and K. F. SMITH
Cavendish Laboratory, Cambridge

[Received August 19, 1960]

THE spin of ^{124}Sb and the spin and hyperfine structure of ^{122}Sb have been measured by the atomic beam magnetic resonance method. We find $I_{124}=3$, which verifies Steffen's (1960) β decay scheme for ^{124}Sb, and $I_{122}=2$, in agreement with Pipkin's (1958) independent measurement made by the paramagnetic resonance technique. The $\Delta F=1$ transitions $5/2,\ -1/2 \leftrightarrow 3/2,\ 1/2$ and $7/2,\ -3/2 \leftrightarrow 5/2,\ -3/2$ were among those observed in ^{122}Sb, and from these it was deduced that

$$A_{122}=+212{\cdot}01 \pm 0{\cdot}06 \text{ Mc/s} \quad \text{and} \quad B_{122}=+8{\cdot}7 \pm 0{\cdot}5 \text{ Mc/s}.$$

The assignment of the positive sign to A_{122} was made on the basis of the determination of the sign of μ_{121} by Eisinger and Feher (1958), that of μ_{122} by Pipkin (1958), and that of A_{121} by Rochester (1960). The ratio A_{122}/A_{121} is consistent with the ratio g_{122}/g_{121} derived from Pipkin's measurements, but we cannot deduce a value for the hyperfine structure anomaly because the error of $\pm 1\%$ in this g ratio is much greater than a typical s state anomaly (Fernando 1960). The uncorrected quadrupole moment deduced from B_{122} is $Q_{122}=(+0{\cdot}47 \pm 0{\cdot}03) \times 10^{-24}$ cm^2.

REFERENCES

EISINGER, J., and FEHER, G., 1958, *Phys. Rev.*, **109,** 1172.
FERNANDO, P. C. B., ROCHESTER, G. K., SPALDING, I. J., and SMITH, K. F., 1960, *Phil. Mag.*, **5,** 1291.
PIPKIN, F. M., 1958, *Phys. Rev.*, **112,** 935.
STEFFEN, R. M., 1960, *Phys. Rev. Letters*, **4,** 290.

---

† Now at University of Columbo, Columbo, Ceylon.

Activation of Single Phonon Infra-red Lattice Absorption in Neutron Irradiated Diamond

By S. D. Smith and J. R. Hardy†
J. J. Thomson Physical Laboratory, University of Reading

[Received October 13, 1960]

Lax and Burstein (1955) have proved that the symmetry of the perfect diamond structure forbids single phonon absorption of radiation. They have also shown that such absorption may be allowed when imperfections are present, since these can provide a local coupling between the fundamental lattice frequencies and the radiation field. They have ascribed the specimen dependent infra-red absorption, shown by natural type I diamonds, to a coupling of this kind. Such an absorption spectrum is shown in the figure (*a*) and one can see that the continuous absorption commences near the maximum lattice frequency which is known from Raman scattering measurements.

We have succeeded in activating a corresponding band in the absorption spectrum of a type II a diamond by fast neutron irradiation. Absorption spectra taken before and after a fast neutron dose of $3 \times 10^{17}/\text{cm}^2$ in a hollow uranium slug of the Harwell BEPO pile are shown in the figure (*b*). That taken prior to irradiation shows the negligible absorption characteristic of type II a crystals. After the irradiation the spectrum shows strong continuous absorption, commencing sharply at the Raman energy and extending to lower frequencies, which can only be explained satisfactorily as single phonon lattice absorption. This effect has not been observed previously, although a number of workers (see Kaiser and Bond 1959 for references) have examined specimens known to contain appreciable numbers of radiation produced defects. Moreover it seems that it is relatively easy to activate this absorption in diamond, compared with silicon, for which Fan and Ramdas (1959) have reported a dose of 10^{19} fast neutrons/cm^2 to be necessary to produce a similar effect. This conclusion is confirmed by the fact that a control specimen of silicon irradiated with the diamond showed no measurable single phonon absorption afterwards.

Kaiser and Bond (1959) have shown that the strengths of the 0·159, 0·148 and 0·139 ev peaks in the type I spectrum are directly proportional to nitrogen content. They have suggested that these peaks are due to absorption by molecular stretching vibrations of the C–N unit. If one compares the two spectra in the figure it is evident that the only marked difference, within the regions of continuous absorption, is in the vicinity of the two strong peaks (X) of the type I spectrum. We see that the 0·148 and 0·139 ev peaks are present in both spectra, although the position of the second peak is slightly influenced by the strength of the first. They are not dependent on the presence of nitrogen and therefore cannot arise from vibrations of C–N units. Their presence and that of the 0·125 ev peak in spectra activated by two very different coupling mechanisms implies that all three arise from maxima in the density of plane wave normal modes of the host lattice, since this is the only common

---

† A.E.I. Research Fellow.

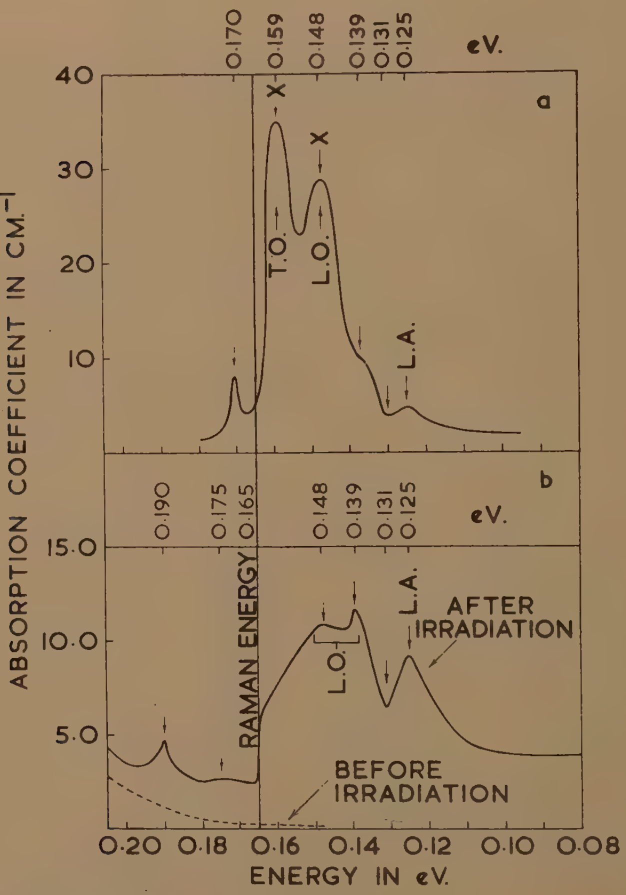

Absorption coefficient versus energy for:

(*a*) A type I diamond.

(*b*) A type II a diamond before and after a dose of 3×10^{17} fast neutrons/cm^2.

The various maxima are assigned to those in the density of normal modes thus : T.O. denotes that arising from the maximum density of transverse optical modes, L.O., that due to maximum density of longitudinal optical modes, and L.A. that associated with the maximum density of longitudinal acoustic modes.

factor involved. However, the 0·159 ev peak is apparently characteristic of the nitrogen impurity. Even so, one cannot regard it as arising from a local C–N vibration since the frequencies involved lie within the band of allowed lattice frequencies and energy absorbed near nitrogen impurities must propagate throughout the crystal, and this is exactly the process envisaged by Lax and Burstein (1955). Either this peak is due to exceptionally strong coupling to relatively few modes, or it corresponds to a sharp maximum in the density of normal modes of the whole lattice. We believe that the second explanation is correct, since one expects the transverse optical (T.O.) modes to show very little dispersion and to produce such a maximum. One way to explain the absence of this peak from the damage induced absorption spectrum is to assume that the coupling involved falls off rapidly close to the Raman frequency. The figure also shows isolated peaks lying above the maximum frequency for which lattice waves can propagate. However, Montroll and Potts (1955) have shown theoretically that vibrational modes localized about lattice imperfections would, if present, occur in this region. The dipole moment associated with such modes could cause the observed absorption. The peaks present in the spectrum of the irradiated diamond have evidently been produced directly by the bombardment and are presumably associated with specific defects (e.g. vacancies and interstitials). This appears to be the first time that such an effect has been observed in any material.

The continuous absorption produced by damage appears to be too strong to be associated solely with isolated point defects. A lower limit to the number required is given by assuming that they provide a coupling as efficient as that due to nitrogen atoms in type I crystals†. If one then considers the 0·148 ev peak, common to both spectra, one finds at least 10^{20} defects/cm^3 to be necessary to produce the observed intensity. This is at least an order of magnitude greater than the number one infers from the dose. Hence we suggest that most of the damage induced activation arises from regions of local disorder which probably involve more than 10^{20} atoms/cm^3.

Since we have associated the absorption peaks with maxima in the density of normal modes we have classified them in the figure according to the branches of the spectrum believed to be responsible (e.g. the 0·148 ev peak is believed to arise from the maximum density of longitudinal optical (L.O.) modes). The 0·139 ev peak is also associated with the L.O. branch. It could correspond to the maximum density of longitudinal acoustic (L.A.) modes, but this implies that the 0·125 ev peak is due to transverse acoustic (T.A.) modes. Since Phillips (1959) has concluded that the T.A. mode energy at the centre of a (111) zone face is 0·063 ev it seems unlikely that there will be a large number of such modes at twice this energy. Consequently if our assignment is correct, the 0·131 ev absorption minimum is associated with a similar feature in the density of L modes.

---

† R. J. Elliott (Clarendon Laboratory Dept., Ref. 23/60) has shown that, however the nitrogen in type I's is present, its extra electron is probably equally shared with the host lattice. The strength of the resultant dipole will then account for that of the 0·159 ev peak. It seems unlikely that irradiation produced point defects provide any more efficient coupling mechanism.

Our suggestion that practically no coupling to the transverse optical (T.O.) modes results from damage appears to be in marked contrast with the silicon results of Fan and Ramdas (1959) since their strong 20·5 micron band would seem, from the inelastic neutron scattering data of Brockhouse (1959), to arise from strong coupling to T.O. modes. We hope to clarify this by studying the activated absorption as a function of dose and annealing time.

We may conclude that activation of absorption in the ‘ one phonon ’ region by damage, strongly supports the theory that it is due to defect induced coupling to the fundamental lattice modes. Furthermore the common features of this and type I absorption indicate that the latter has a similar origin. Differences in detailed shape should thus be explicable in terms of the actual coupling mechanisms involved.

ACKNOWLEDGMENTS

We should like to thank Dr. E. W. J. Mitchell and Dr. C. D. Clark of this laboratory for valuable discussions during the course of this work, Mr. W. H. Wynd of A.E.R.E., Harwell, for irradiating the specimen, and one of us (S. D. S.) wishes to thank the C.E.G.B. for financial support.

REFERENCES

BROCKHOUSE, B. N., 1959, *Phys. Rev. Letters*, **2**, 256.
FAN, H. Y., and RAMDAS, A. K., 1959, *J. appl. Phys.*, **30**, 1127.
KAISER, W., and BOND, W. L., 1959, *Phys. Rev.*, **115**, 857.
LAX, M., and BURSTEIN, E., 1955, *Phys. Rev.*, **97**, 39.
MONTROLL, E. W., and POTTS, R. B., 1955, *Phys. Rev.*, **100**, 525.
PHILLIPS, J. C., 1959, *Phys. Rev.*, **111**, 147.

REVIEWS OF BOOKS

Figures of Equilibrium of Celestial Bodies. By Zdenek Kopal. (University of Wisconsin Press, 1960.) [Pp. 135.] $3.

Investigations into the shapes, gravitational fields, moments of inertia, oscillations, etc. of approximately spherical masses like the planets have led to important work by Clairaut, Laplace, Stokes and many other experts. This branch of applied mathematics has come into prominence recently on account of the use of gravity surveying and satellite orbits in the study of the shape of the Earth.

In the first of the three principal sections of his book, Professor Kopal presents a treatment of the problem on classical lines, based on the idea of a general disturbing potential, and using expansions in harmonic functions. In particular, the disturbing potential is taken as one representing the rotation of the body, or as one corresponding with equilibrium-tidal influences of an external mass.

Professor Kopal then extends the treatment to the second order of the distortions. In the third principal section, he considers ‘ interaction phenomena ’ connected with the essential non-linearity of the equations for the rotating body under tidal forces : at this stage, needless to say, the formulae become extremely complicated.

Much of the advanced work set out in the book is the result of the investigations of Professor Kopal himself.

There is also a short section dealing with dynamical considerations under the title ‘ non-radial oscillations ’.

Formulae connected with the external potential of the Earth are of course fundamental in the geodetic applications of artificial satellites, but the book contains no treatment of satellite orbits, and the second part of the title referring to ‘ motion of artificial satellites ’ may therefore be a little misleading.

J. E. J.

[*The Editors do not hold themselves responsible for the views expressed by their correspondents.*]

Fig. 2

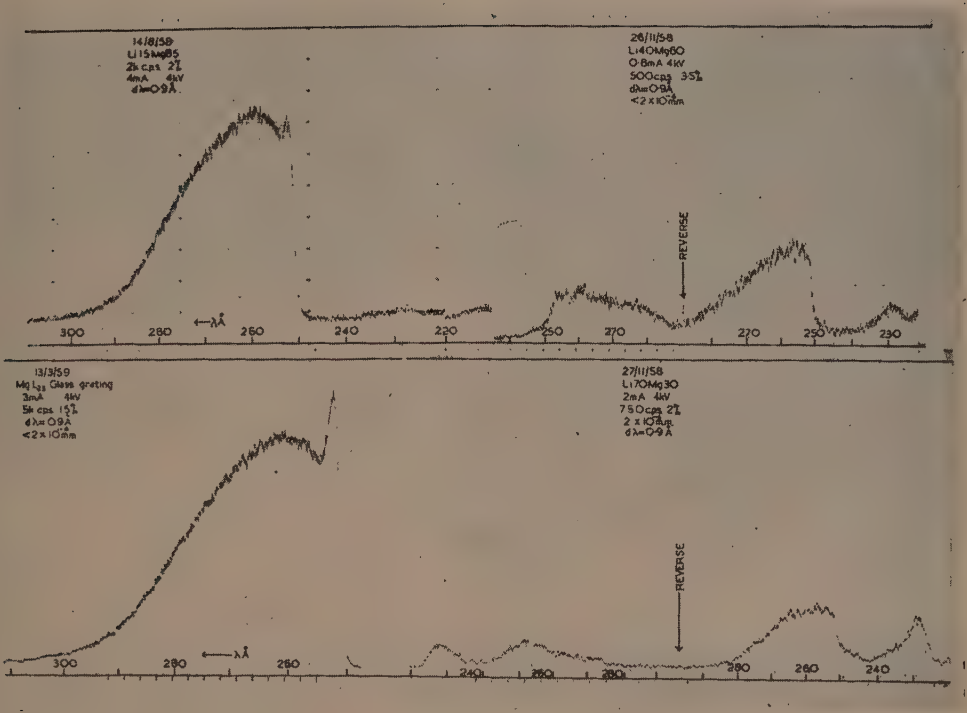

L_{23} spectra of pure Mg and Mg in Li15Mg85, Li40 Mg60 and Li70Mg30 alloys. Li K spectra for Li40Mg60 and Li70Mg30 alloys, in which cases the lead screw drive was reversed and the spectra retraversed to show the effect of contamination. In the Li70Mg30 alloy the Mg L_{23} has been replaced by the Li ‘ line ’ after reversal.

Fig. 3

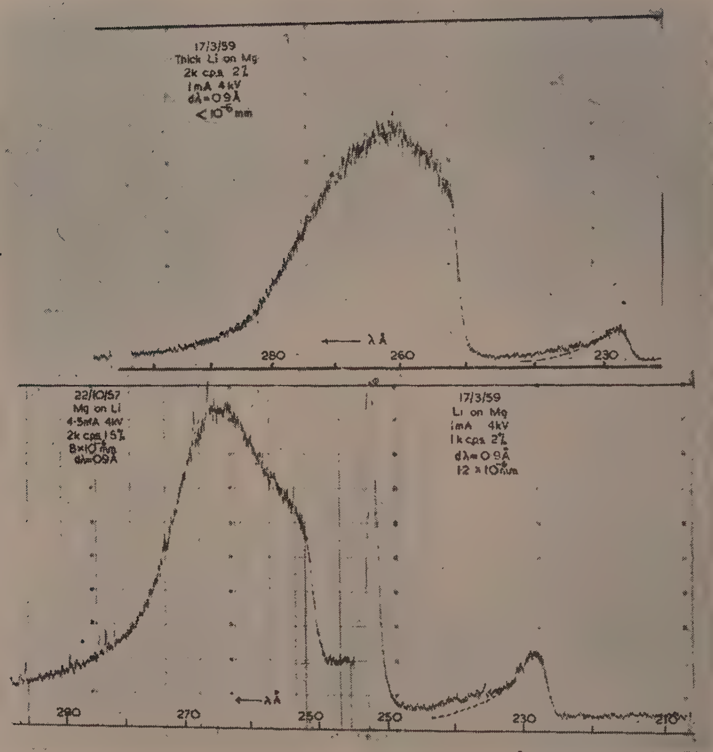

Mg L_{23} spectra for Li deposited on Mg and Mg deposited on Li. Two Li K spectra for Li on Mg. Profile of the normal Li K spectrum is shown by the broken lines.

Fig. 4

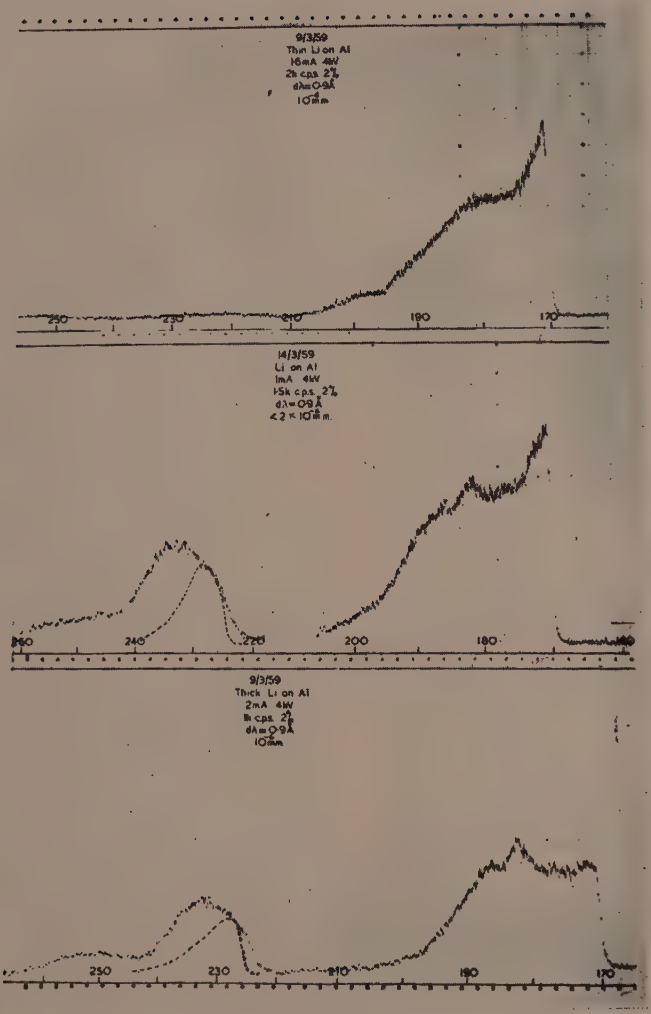

Al L_{23} spectra for ‘ thin ’, ‘ medium ’ and ‘ thick ’ coats of Li on Al and Li K spectra for ‘ medium ’ and ‘ thick ’ coats. Profile of the normal Li K spectrum is shown by broken lines.

Fig. 5

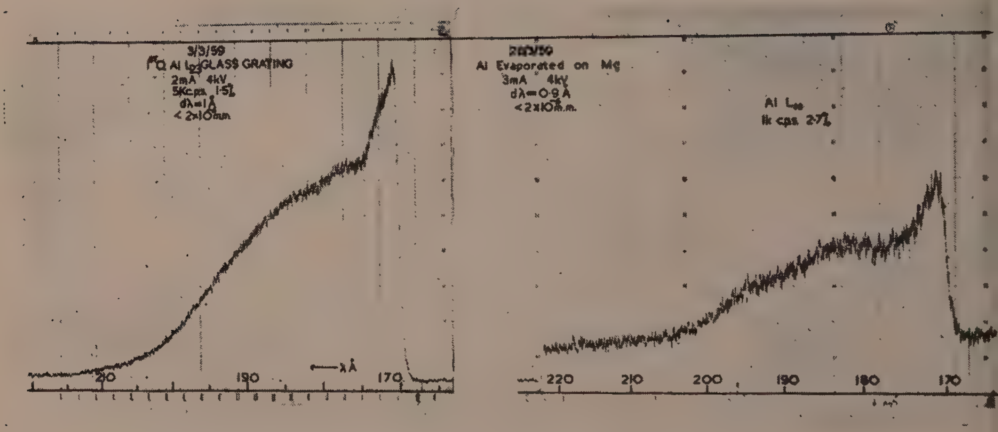

Al L_{23} spectra from pure Al and Al deposited on Mg. (*dλ* for the pure Al should be 0·9 Å not 1 Å.)

Fig. 1

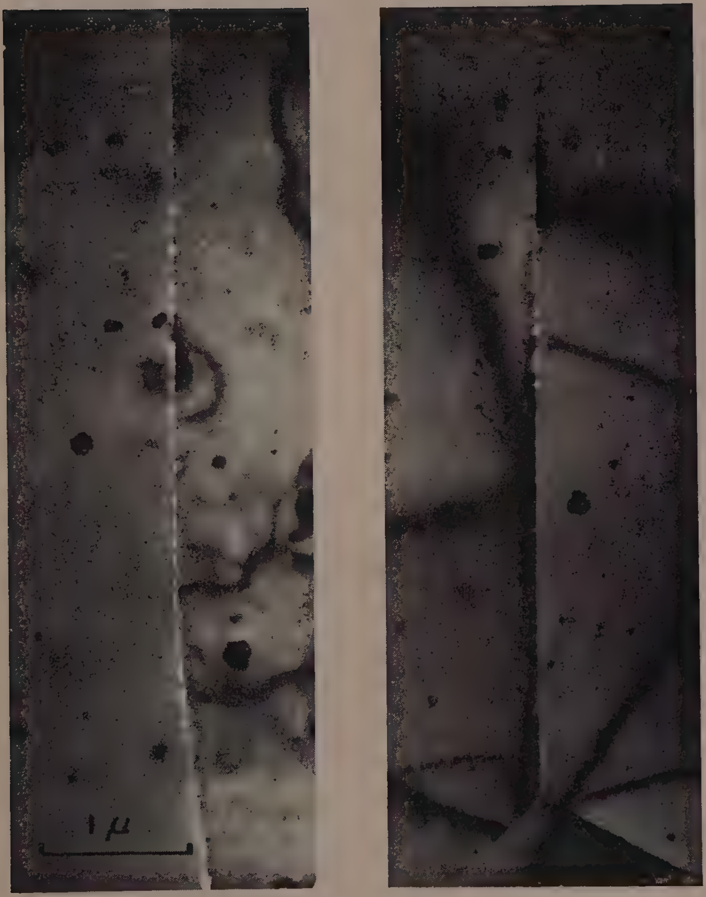

(a) (b)

Surface pits at the grain boundaries of a thin aluminium foil. ×20 000.

Fig. 2

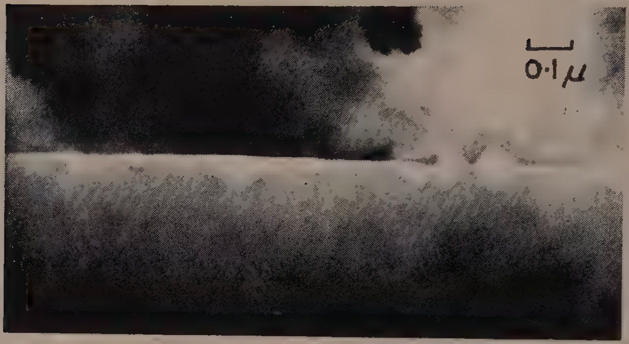

Surface pits at the grain boundaries of a thin aluminium foil. × 60 000.

Fig. 3

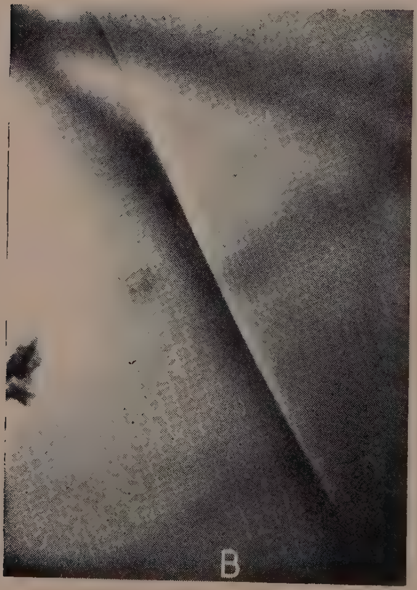

Grain boundary of aluminium foil before ageing. × 40 000.

Fig. 4

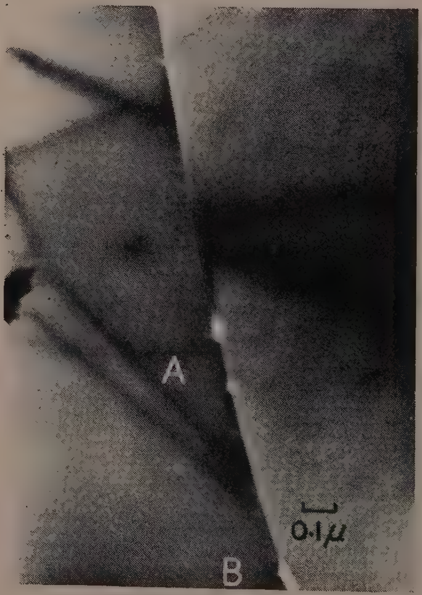

The boundary of fig. 3 after ageing. × 40 000.

Fig. 5

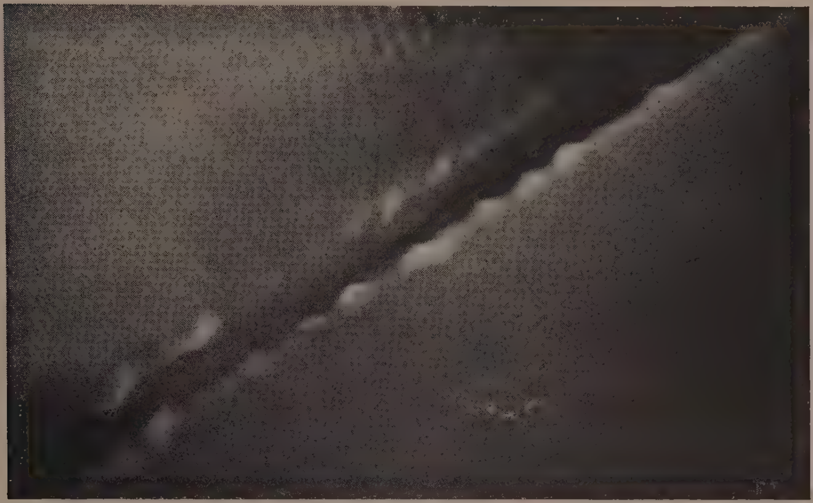

Pits at both surfaces of a thin aluminium foil. ×80 000.

Fig. 6

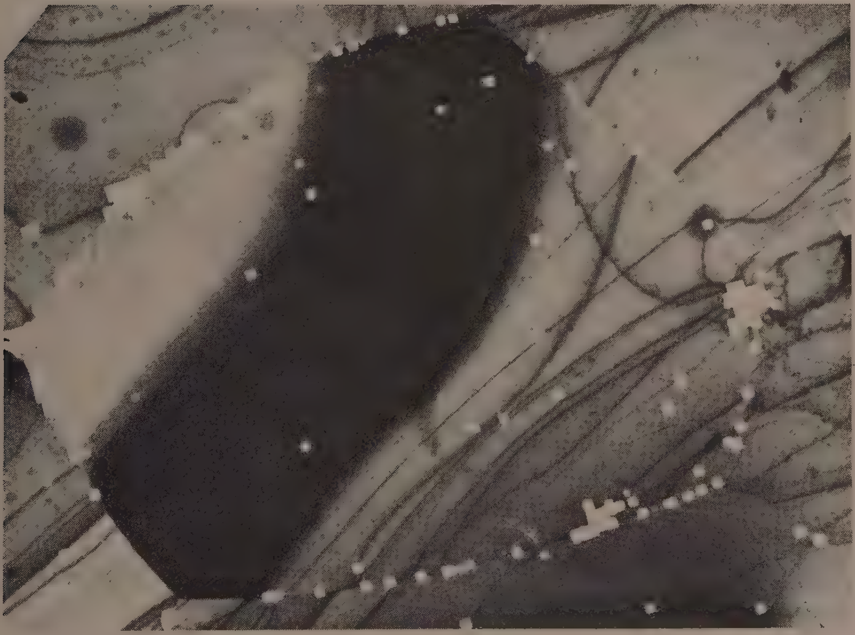

Etch pits in a thin aged aluminium foil. ×4000.

Fig. 1

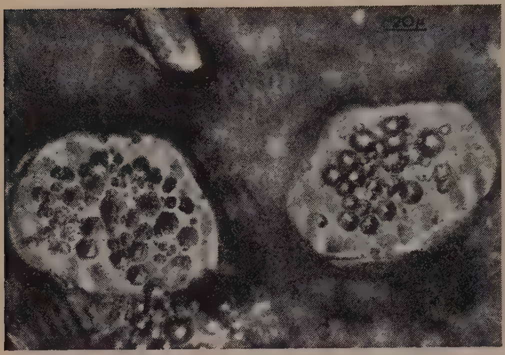

Large etch pits containing smaller hexagonal pits on the basal surface of ice grown from the melt. (Replica.)

Fig. 2

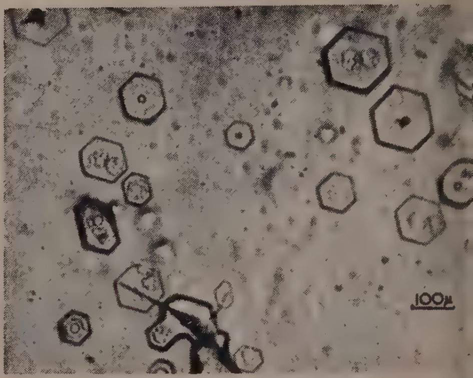

Hexagonal etch pits on the basal face ice.

Fig. 3

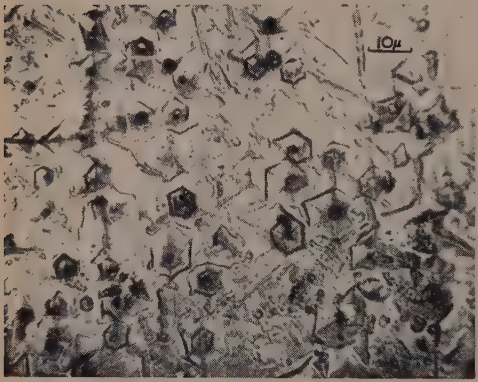

Replica of basal plane showing spiral steps on etch pits. (Replica.)

Fig. 4

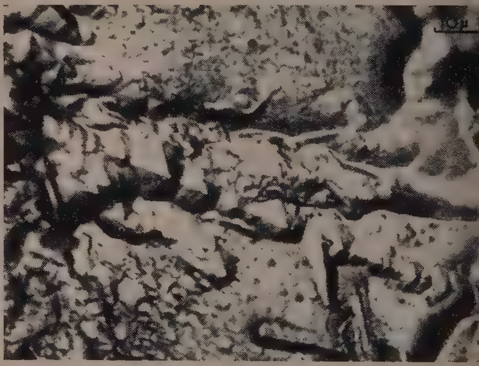

A line of pyramidal etch pits along low-angle grain boundary. (Replica.)

Fig. 5

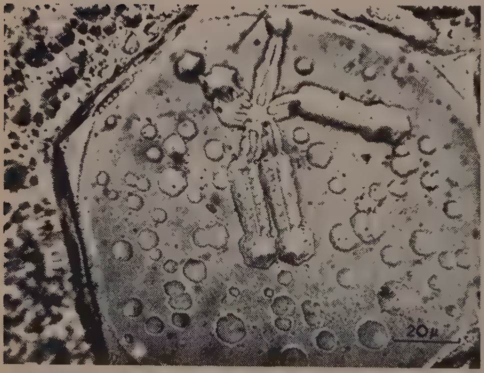

Etch channels on basal surface initiated by an included dust particle and terminating in etch pits. (Replica.)

Fig. 6

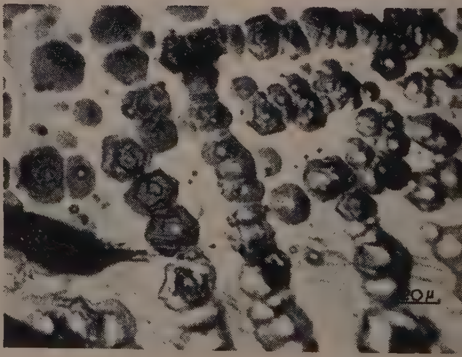

Pyramidal hillocks showing concentr and spiral steps on the basal face an ice crystal grown from the vapou (Replica.)

Fig. 7

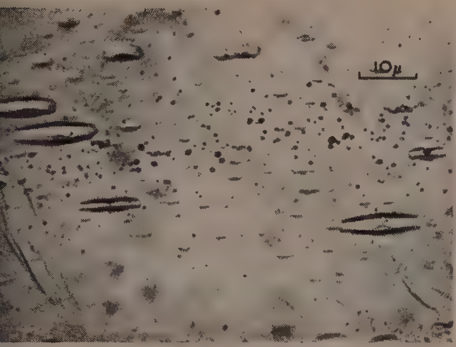

Elongated etch pits on the prism face of an ice crystal grown from the vapour. (Replica.)

Fig. 8

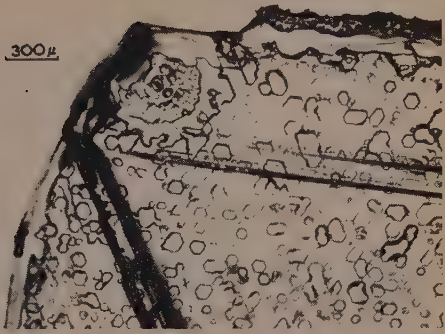

A high concentration of hexagonal etch pits on the basal surface of a plate-like crystal grown from the vapour.

Fig. 9

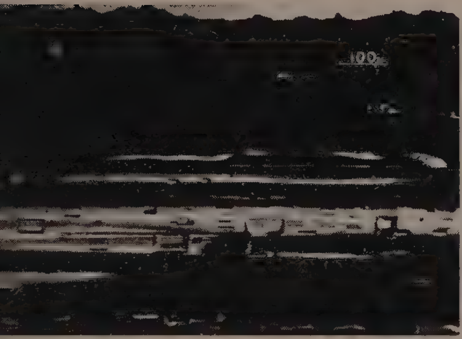

Rectangular etch pits on the prism faces of an ice needle.

Fig. 10

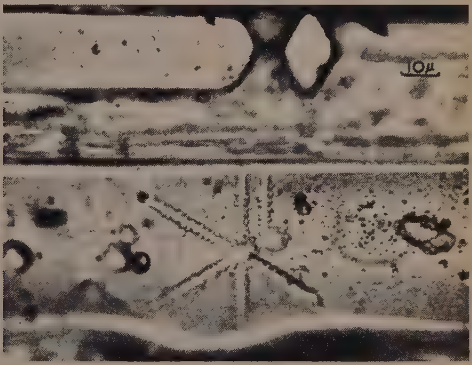

Etch channels radiating from an impurity speck in a plate-like crystal grown from the vapour. Each channel consists of a double row of small etch pits which probably represent the intersection of dislocation loops with the surface. (Replica.)

Fig. 11

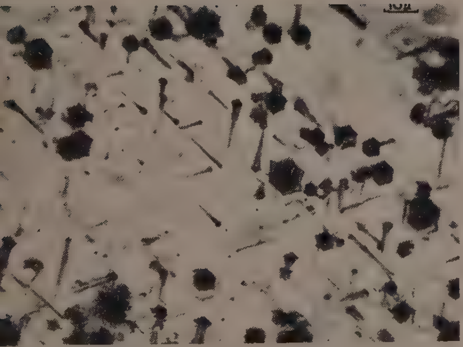

Etch channels oriented along the ⟨11$\bar{2}$0⟩ directions on the basal plane produced by the movement of dislocations under mechanical vibration at −20°c (Replica.)

Fig. 12

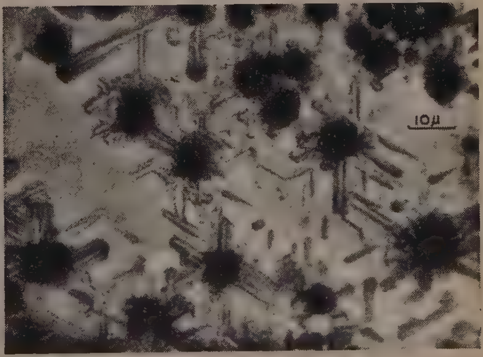

'Rosettes' produced by dropping lead shot on a basal surface of ice at −20°c. (Replica.)

Fig. 1

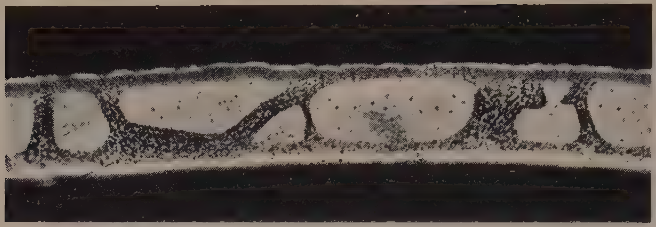

Cross section of a 0·001 in. copper foil after an anneal of 2 hours at 800°c to show the formation of helium bubbles near the grain boundaries. ×550.

Fig. 2

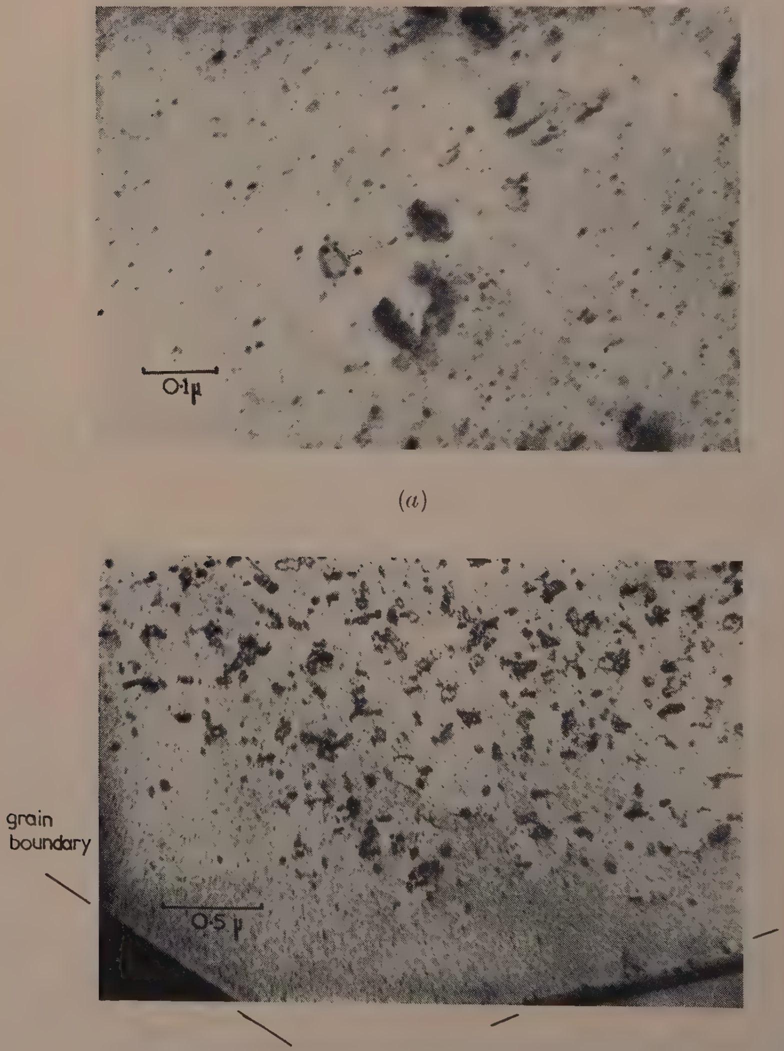

(*a*)

(*b*)

Two films of copper (*a*) and (*b*) through which $1{\cdot}4\times10^{17}$ alpha-particles cm^{-2} (32 µ amp hr.) have passed.

Fig. 3

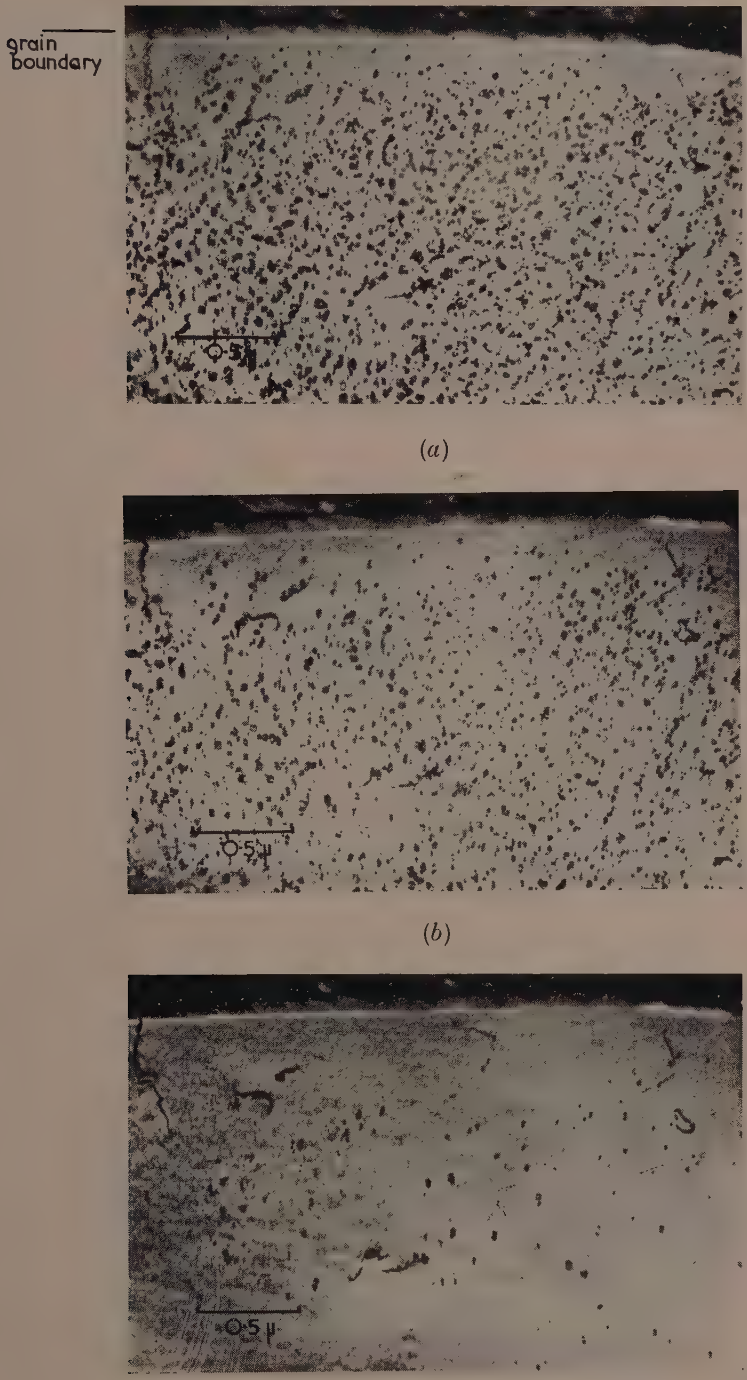
grain boundary
0·5 μ
0·5 μ
0·5 μ

(*a*)

(*b*)

(*c*)

Three successive photographs (*a*) $t=0$; (*b*) $t=15$ min ; (*c*) $t \simeq 20$ min showing annealing of damage in a copper film while at about 350°c on the 'hot-stage' of the electron microscope.

Fig. 4

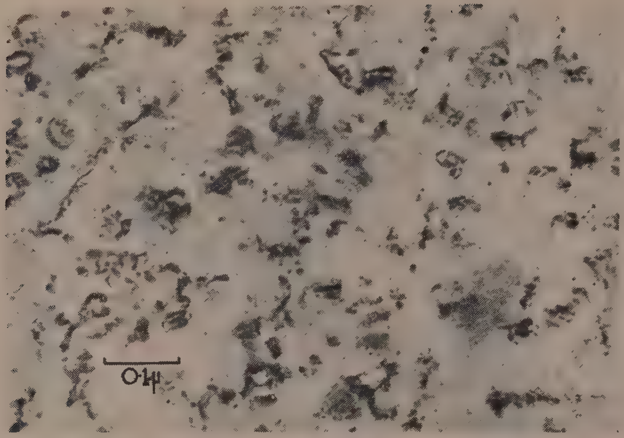

A thin film of copper containing helium atoms after bombardment with 1·4 × 10^{17} alpha-particles cm^{-2}.

Fig. 5

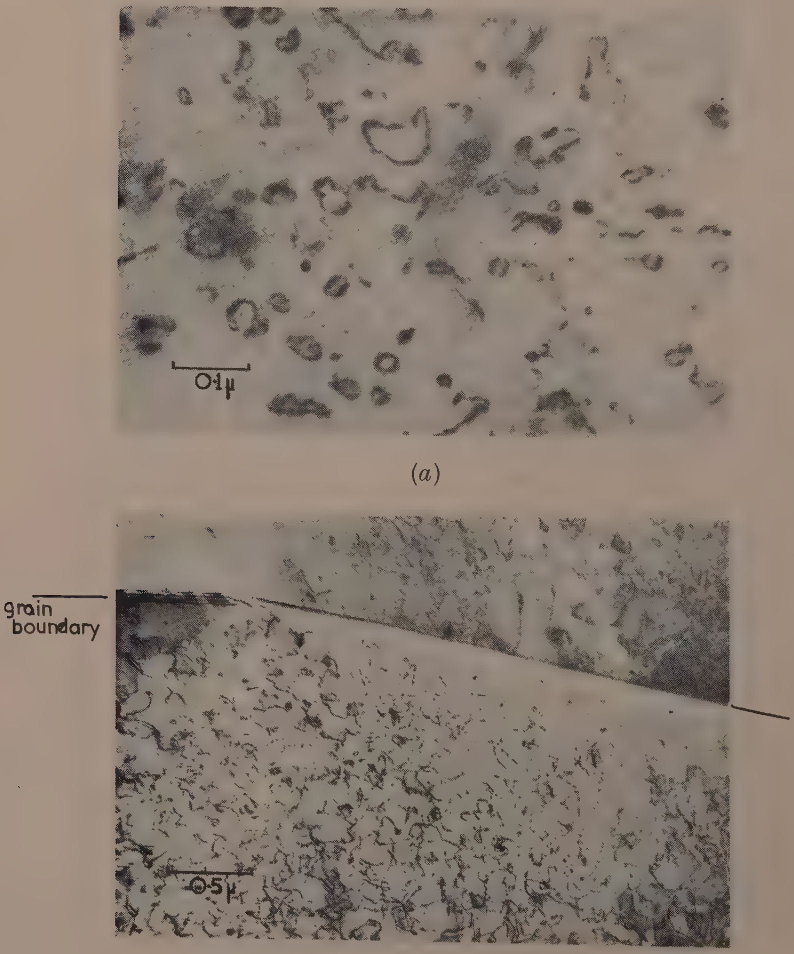
0·1μ
grain boundary
0·5μ

(*a*)

(*b*)

Fig. 5 (*continued*)

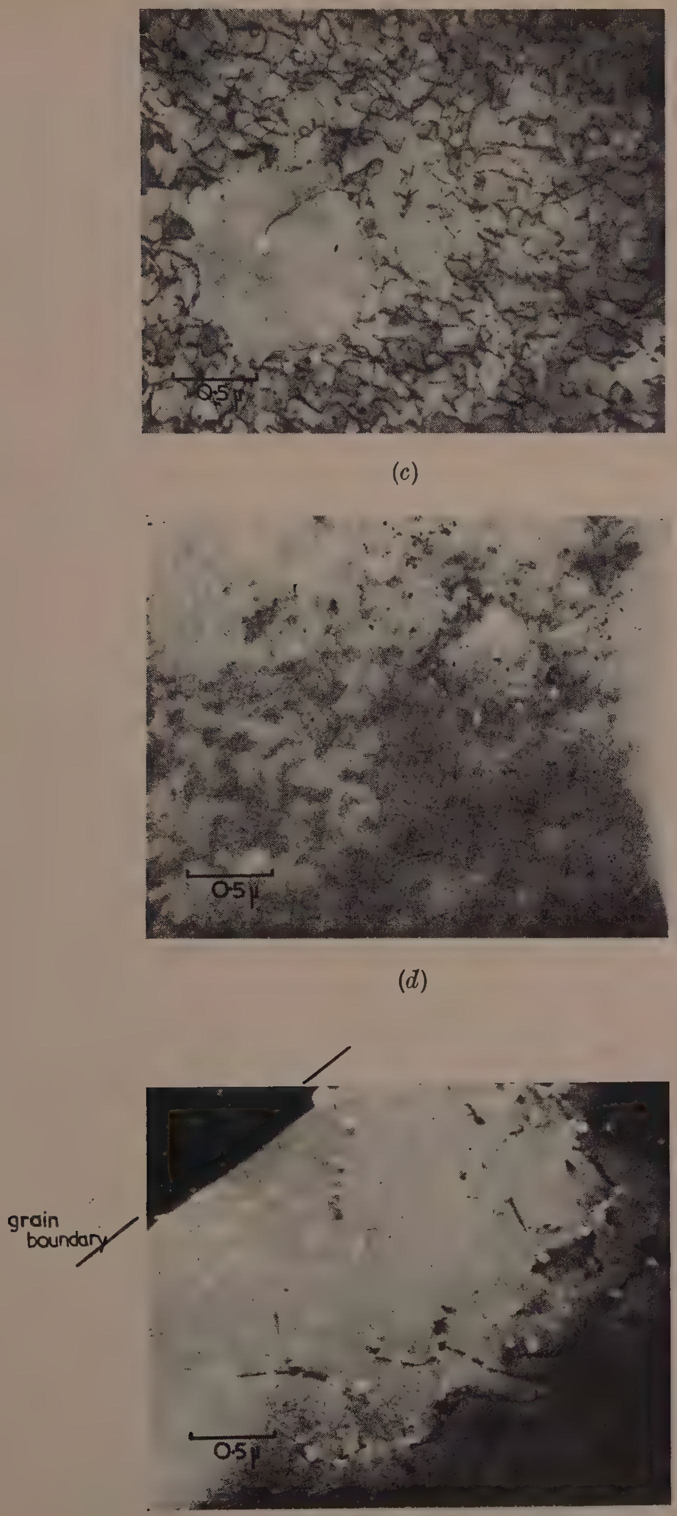

(*c*)

(*d*)

(*e*)

Copper films similar to that in fig. 4 but after (*a*) a 2-hour anneal at 3 *in vacuo*, (*b*) 2 hours at 450°c, (*c*) 1 hour at 750°c, (*d*) as for (*c*) with the dislocations out of contrast, (*e*) 2 hours at 750°c, near a g boundary (7×10^{16} alpha-particles cm^{-2}).

Fig. 3

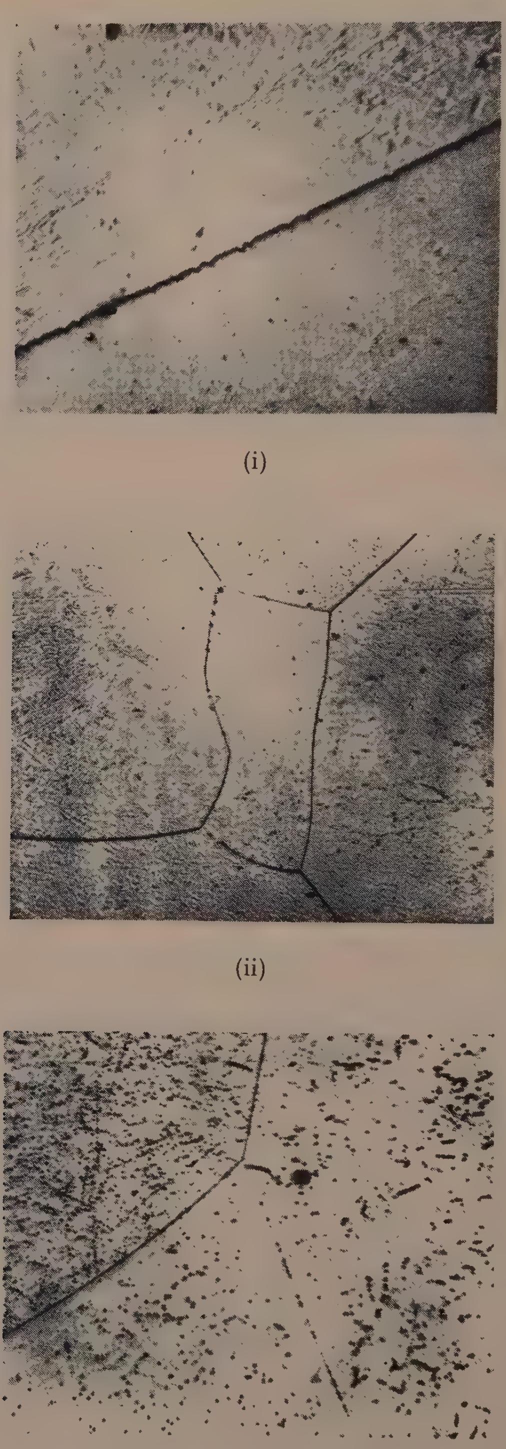

(i)

(ii)

(iii)

Typical micrographs of the alloys (× 250).
(i) 1·91 at. % chromium (F.R.I./B.M.I.);
(ii) 12·1 at. % chromium (J.M./J.M.);
(iii) 38·5 at. % chromium (F.R.I./U.S.B.M.).

SUBJECT INDEX

PAGE

Adsorbed gas films, study by electron diffraction 222

Aluminium:
- copper alloys, effect of quenching 200
- copper alloys, segregation of solute 1119
- dislocations in quenched 1, 24
- electropolishing, retention of vacancies 101
- etching of strained 709
- kinetics of ordering Fe_3Al 343
- pitting after ageing 1217
- point defects, movement during fatigue 1147
- point defects induced 1247
- unloading effects: also aluminium–zinc 947

Anisotropy of inertia mass 409

Argon, refractive indices, liquid and solid 355

Beryllium, etching of substructures 1195

Beryllium, internal friction peaks 325

Binary alloys, eutectic composition and immiscibility 383

Binary alloys, residual resistance 753

Brass, alpha-, creep 649

Brass, alpha-, stress corrosion cracking 1029

Brass, beta, nuclear magnetic resonance 899

Bubble chamber, liquid hydrogen 146, 154

Book notices 200, 648, 980, 1202

Book reviews 104, 194, 302, 421, 647, 763, 871, 975, 1201, 1315

Cadmium crystals, growth from vapour 473

Chromium, heat capacity anomaly 188

Copper:
- aluminium, segregation of solute 1119
- dilute alloys, internally oxidized 298
- point defects induced 1247
- silicon, internal oxidation, damping, capacity 140
- strain broadening, magnetic resonance lines 843
- thermoelectric power, pure 765

Cosmic rays:
- abundance of heavy nuclei 311
- extensive air showers 305
- flux of protons 1105
- intensity, interplanetary field 601
- muon decay, γ internal conversion 297
- primary alpha, flux and spectrum 1151
- solar daily variation 585

Cracks in magnesium oxide 407, 697

Creep, micro, in zinc whiskers 417

Creep in f.c. metals and α-brasses 649

Cyclotron resonance in lead 1001

de Haas–van Alphen effect 105, 115

Diamagnetic shielding of nuclei in metals 529

Diamond, single phonon infra-red lattice absorption 1311

Diamonds, semiconducting, infra-red absorption 127

Diffusion in metals 803, 1171

PAGE

Dislocations:
  aluminium, quenched substructure 24
  and etch pits in ice 1221
  angular 161
  bismuth and antimony tellurides 729
  charged, lithium fluoride 815
  formation by vacancy collapse 43, 669, 1203
  locking in α-iron 30
  magnesium oxide 192
  prismatic loops 1, 921, 1255
  quarter, talc 533
  silver, cold worked 485
  silver bromide, Burgers vector $a\langle 100\rangle$ 799
  silver bromide, loops 445
  zinc, climb of loops 873

Electrical resistance, iron aluminium 451
Electrical resistance, residual binary, alloys 753
Electrical resistivity, stacking faults 251
Electrical resistivity, quenched-in recovery, gold 687
Electron absorption, metal foils 967
Electron diffraction, absorbed gas films 222
Electron Fermi energy and work function 64

Fermi surface in white tin 1089
Ferromagnetism in palladium–iron alloys 335
Fracture, ductile, shear component 759

Gold, cobalt precipitation, magnetic study 1127
Gold, diffusion of platinum, atomic 803
Gold, quench hardening 939
Gold, quenched-in resistivity recovery 687
Graphite, radiation damage 621

Hall effect, liquid and solid mercury 100

Indium arsenide, thermal conductivity 84, 887
Internal friction, sodium chloride 425
Interstitial atoms in f.c.c. metals 853
Ionospheric drifts statistical theory 553
Iron:
  alpha, Debye–Waller factor 1229
  alpha, dislocation locking 30
  aluminium, electrical resistance 451
  kinetics of ordering Fe_3Al 343
  nickel films, microtwinning 373
  palladium, ferromagnetism 335
Irradiation:
  alpha, induced point defects 1247
  electron, damage in graphite 1049
  electron, hardening of lithium fluoride 237
  electron and neutron, optical absorption, sapphire . . . 1013
  neutron, damage in graphite 621
  neutron, damage and recovery in tungsten 278
  neutron, embrittlement of molybdenum 413
Ising model, magnetic properties 909
Isotopic spin selection rules 359, 365

PAGE
Krypton, solid, density and expansivity 186

Lead, cyclotron resonance 1001
Lead, density of states 70
Lead iodide crystals, decomposition 787
Lithium and Li–Mg alloys, nuclear magnetic resonance 467
Lithium, metallic, K emission 525
Lithium fluoride, charged dislocations 815
Lithium fluoride, hardening by irradiation 237
Lithium fluoride, mechanical properties 981

Magnesium oxide, cracks 407, 697
Magnesium oxide, deformed 991
Magnesium oxide, dislocations 192
Magnetic properties of the Ising model 909
Magnetic recording tapes, anhysteretic remanence 717
Magnetic study, gold–cobalt 1127
Magnetic susceptibility, vanadium–chromium 1267
Magnetoresistance, copper, silver and gold 111, 304
Mercury, Hall effect 100
Molybdenum, embrittlement by irradiation 413

Neutron scattering, effect of lattice distortion 1235
Nickel, annealing of deformed 499
Nickel, iron films, epitaxial, microtwinning 373
Nuclear interactions, 5·7 BEV protons 537
Nuclear magnetic resonance, β brass, Li and Li–Mg 467, 899
Nuclear magnetic resonance lines, strain broadening, copper 843
Nuclear scattering, optical model 1181
Nuclei :
  diamagnetic shielding in metals 529
  hyperfine structure, ^{209}Bi, ^{121}Sb, ^{123}Sb 1281, 1291
  isotopic spin selection rules 359, 365
  spin, ^{124}Sb and ^{122}Sb 1309

Optical constants, liquid silver 272
Optical transitions in alloys, selection rules 757

Permalloy, films, cross-tie walls 625
Photographic processes in crystals 723
Platinum, atomic diffusion in gold 803
Platinum, point defects 201
Polymers, fine structure of films 78
Precipitates, growth from solid solutions 176

Quench hardening, gold 939

Rock magnetism, carboniferous system 675, 1087
Rock magnetism, statistical methods 523
Rubber, fine structure of films 78

PAGE

- Scattering of phonons by spin 1299, 1303
- Silver:
  - cold worked, annealing 833
  - Debye–Waller factor 1229
  - evaporated, defects 571
  - Liquid, optical constants 272
- Silver bromide, dislocations 445, 799
- Silver chloride, photographic processes 723
- Silver chloride, reverse bending 441
- Sodium chloride, embrittlement, stress concentrations 1197
- Sodium chloride, internal function 425
- Sodium chloride, lattice vibrations 859
- Spectra, absorption, details in crystals 691
- Spectra, x-ray emission, metals and alloys 525, 1161, 1205
- Spin density fluctuations, giant 1193
- Stacking faults, electrical resistivity 251
- Stored energy, calculation, deformed isotropic material 519
- Stored energy, cold worked silver 485
- Stored energy, deformed nickel 499
- Stress corrosion cracking in alloys 1029

- Thermal conductivity, germanium, silicon and indium arsenide 84
- Thermal conductivity, impure indium arsenide 887
- Thermoelectricity, below 1°K 867
- Thermoelectric power, alkali metals, phonon component 1059
- Thermoelectric power, pure copper 765
- Thin films, thermal aspects of growth 1041
- Tin, white, Fermi surface 1089
- Tungsten, elastic and thermal properties 927
- Tungsten, neutron irradiated 278

- Vacancies in metals, generation 635

- Yield and flow stress in b.c.c. metals 745

- Zinc, pyramidal glide and dislocation loops 873
- Zinc, whiskers, microcreep 417
- Zirconium, elastic and thermal properties 927

INDEX OF AUTHORS (WITH TITLES)

PAGE

Alston, Margaret H., Cundy, D. C., Evans, W. H., Newport, R. W., and Williams, P. R.: A 10 in. diameter liquid hydrogen bubble chamber. 146
Amelinckx, S., and Delavignette, P.: Direct evidence for the presence of quarter-dislocations in talc monocrystals 533
Amelinckx, S., with Delavignette, P.: Dislocation nets in bismuth and antimony tellurides 729
Anderson, E., with Hume-Rothery, W.: Eutectic compositions and liquid immiscibility in certain binary alloys. 383
Ashby, M. F., and Smith, G. C.: Direct electron microscopy of thin foils of internally oxidized dilute copper alloys 298
Aubrey, J. E.: Cyclotron resonance in lead 1001

Bailey, J. E., and Hirsch, P. B.: The dislocation distribution, flow stress, and stored energy in cold-worked polycrystalline silver. 485
Bailey, J. E.: Electron microscope observations on the annealing processes occurring in cold-worked silver 833
Bailyn, M.: The phonon drag component of the thermoelectric power of the alkali metals at low temperatures 1059
Barnes, R. S.: The generation of vacancies in metals 635
Barnes, R. S., and Mazey, D. J.: The nature of radiation-induced point defect clusters 1247
Bartlett, J. T., and Mitchell, J. W.: The generation of dislocation loops at the surfaces of crystals of silver bromide. 445
Bartlett, J. T., and Mitchell, J. W.: Dislocations with Burgers vectors of $a\langle 100\rangle$ in crystals of silver bromide 799
Bassett, G. A., and Edeleanu, C.: Etching of strained aluminium 709
Bassett, G. A., and Edeleanu, C.: Pitting of aluminium at grain boundaries after ageing 1217
Beaumont, R. H., Chihara, H., and Morrison, J. A.: An anomaly in the heat capacity of chromium at 38·5°c 188
Belshé, J. C., with Everitt, C. W. F.: Palaeomagnetism of the British carboniferous system 675, 1087
Blount, E. I., with Cohen, M. H.: The g-factor and de Haas–van Alphen effect of electrons in bismuth 115
Bollmann, W.: Electron-microscopic observations on radiation damage in graphite 621
Bradley, E. F., and Porter, N. A.: Observations on extensive air showers. VIII: The distribution in declination and curvature of the shower front 305
Bryant, G. W., and Mason, B. J.: Etch pits and dislocations in ice crystals 1221
Buck, B., Maddison, R. N., and Hodgson, P. E.: Optical model analysis of nuclear scattering 1181
Bullough, R., and Newman, R. C.: The spacing of prismatic dislocation loops 921
Burbank, R. D., and Heidenreich, R. D.: Microtwinning in epitaxial nickel–iron films 373
Burke, J.: The kinetics of the growth of precipitates from solid solutions. 176
Burley, D. M.: Some magnetic properties of the Ising model 909

PAGE

Cahn, R. W., and Davies, R. G.: X-ray evidence for segregation of solute to stacking faults in a copper–aluminium alloy 1119
Cahn, R. W., with Feder, R.: Kinetics of ordering in Fe$_3$Al . . . 343
Cahn, R. W., and Feder, R.: The electrical resistance of iron–aluminium alloys and its dependence on crystallographic order . . . 451
Chihara, H., with Beaumont, R. H., and Morrison, J. A.: An anomaly in the heat capacity of chromium at 38·5°c 188
Childs, B. G., Gardner, W. E., and Penfold, J.: The magnetic susceptibility of vanadium–chromium solid solutions 1267
Ciccarello, I. S., Palma-Vittorelli, M. B., and Palma, M. U.: An electron spin resonance investigation of photographic processes in crystals of AgCl containing traces of CuCl 723
Clark, C. D., Kemmey, P., and Mitchell, E. W. J.: The infra-red absorption of hot semiconducting diamonds 127
Clarke, F. J. P., and Sambell, R. A. J.: Micro-cracks and their relation to flow and fracture in single crystals of magnesium oxide . . 697
Codd, I., and Petch, N. J.: Dislocation-locking by carbon, nitrogen and boron in α-iron 30
Cohen, M. H., and Blount, E. I.: The *g*-factor and de Haas–van Alphen effect of electrons in bismuth 115
Copley, G. J., with Feltham, P.: Creep in face-centred metals and solid solutions with reference to α-brasses 649
Conrad, H.: Effect of temperature on yield and flow stress of b.c.c. metals 745
Crangle, J.: Ferromagnetism in Pd-rich palladium–iron alloys . . 335
Crisp, R. S.: Soft x-ray emission from potassium metal in the 40–1000 Å range 1161
Crisp R. S., and Williams. S. E.: The K emission spectrum of metallic lithium 525
Crisp, R. S., and Williams, S. E.: The soft x-ray spectra of lithium. magnesium and aluminium and their alloys. 1205
Cundy, D. C., with Alston, Margaret H., Evans, W. H., Newport, R. W., and Williams, P. R.: A 10 in. diameter liquid hydrogen bubble chamber 146
Cundy, D. C., Evans, W. H., Hadley, D. W., Mason, P., Newport, R. W., Smith, J. R., and Williams, P. R.: Systematic track distortion in a 10 in. diameter liquid hydrogen bubble chamber 154
Cusack, N. E., with Kendall, P. W.: Hall effect in liquid and solid mercury 100

Das, T. P., and Sondheimer, E. H.: Diamagnetic shielding of nuclei in metals 529
Davies, R. G., with Cahn, R. W.: X-ray evidence for segregation of solute to stacking faults in a copper–aluminium alloy . . . 1119
Delavignette, P., with Amelinckx, S.: Direct evidence for the presence of quarter-dislocations in talc monocrystals 533
Delavignette, P., and Amelinckx, S.: Dislocation nets in bismuth and antimony tellurides 729
Dickson, E. W.: The observation of sharp internal friction peaks in beryllium 325
Dougherty, J. P.: A statistical theory of ionospheric drifts . . . 553
Drever, R. W. P.: Upper limit to anisotropy of inertial mass from nuclear resonance 409
Duke, P. J.: The variation with time of the flux and energy spectrum of primary cosmic ray alpha particles 1151

PAGE
Edeleanu, C., with Bassett, G. A.: Etching of strained aluminium . 709
Edeleanu, C., with Bassett, G. A.: Pitting of aluminium at grain boundaries after ageing 1217
Edeleanu, C., and Forty, A. J.: Some observations on the stress-corrosion cracking of α-brass and similar alloys 1029
Elbaum, C.: On dislocations formed by the collapse of vacancy discs 669, 1203
Elliot, H.: Cosmic-ray intensity variations and the interplanetary magnetic field 601
Englman, R.: Localized modes in crystals and sharp details of the optical absorption spectra 691
Evans, W. H., with Alston, Margaret H., Cundy, D. C., Newport, R. W., and Williams, P. R.: A 10 in. diameter liquid hydrogen bubble chamber 146
Evans, W., with Cundy, D. C., Hadley, D. W., Mason, P., Newport, R. W., Smith, J. R., and Williams, P. R.: Systematic track distortion in a 10 in. diameter liquid hydrogen bubble chamber . 154
Everitt, C. W. F., and Belshé, J. C.: Palaeomagnetism of the British carboniferous system 675, 1087

Faulkner, E. A.: Calculation of stored energy from broadening of x-ray diffraction lines 519
Faulkner, E. A.: Strain-broadening of nuclear magnetic resonance lines in copper 843
Feder, R., and Cahn, R. W.: Kinetics of ordering in Fe_3Al . . . 343
Feder, R., with Cahn, R. W.: The electrical resistance of iron–aluminium alloys and its dependence on crystallographic order . . . 451
Feltham, P., and Copley, G. J.: Creep in face-centred metals and solid solutions with special reference to α-brasses 649
Fernando, P. C. B., Rochester, G. K., and Smith, K. F.: The spin of ^{124}Sb and the spin and moments of ^{122}Sb 1309
Fernando, P. C. B., Rochester, G. K., Spalding, I. J., and Smith, K. F.: The hyperfine structure of ^{121}Sb and ^{123}Sb 1291
Figgins, B. F., and Smith, B. L.: Density and expansivity of solid krypton 186
Fine, M. E., with Freise, E. J., and Kelly, A.: The effect of electropolishing on the retention of vacancies during quenching in Al and Al alloys 101
Forty, A. J.: Observations of the decomposition of crystals of lead iodide in the electron microscope. 787
Forty, A. J., with Edeleanu, C.: Some observations on the stress-corrosion cracking of α-brass and similar alloys 1029
Freise, E. J., Fine, M. E., and Kelly, A.: The effect of electropolishing on the retention of vacancies during quenching in Al and Al alloys . 101

Gafner, G.: Thermal aspects of the growth of thin films by vacuum sublimation 1041
Gardner, W. E., with Childs, B. G., and Penfold, J.: The magnetic susceptibility of vanadium–chromium solid solutions . . . 1267
Gaunt, P.: A magnetic study of precipitation in a gold–cobalt alloy . 1127
Germer, L. H., Scheibner, E. J., and Hartman, C. D.: Study of adsorbed gas films by electron diffraction 222
Goggin, P. R., with Reynolds, W. N.: The annealing of electron irradiation damage in graphite 1049
Gibbons, T. B., and O'Hara, S.: The effect of internal oxidation on the damping capacity of copper–silicon alloys 140

PAGE

Gold, A. V.: The density of states in lead 70
Gold, A. V., MacDonald, D. K. C., Pearson, W. B., and Templeton, I. M.: The thermoelectric power of pure copper . . 765
Gold, A. V., and Priestley, M. G.: The Fermi surface in white tin . 1089
Groves, G. W., with Washburn, J., Kelly, A., and Williamson, G. K.: Electron microscope observations of deformed magnesium oxide . 991

Hadley, D. W., with Cundy, D. C., Evans, W. H., Mason, P., Newport, R. W., Smith, J. R., and Williams, P. R.: Systematic track distortion in a 10 in. diameter liquid hydrogen bubble chamber . 154
Hardy, J. R., and Karo, A. M.: Lattice vibrations of sodium chloride: Experimental and theoretical heat capacity data 859
Hardy, S. D., with Smith, S. D.: Activation of single phonon infra-red lattice absorption in neutron irradiated diamond 1311
Hartman, C. D., with Germer, L. H., and Scheibner, E. J.: Study of adsorbed gas films by electron diffraction 222
Hashimoto, H., Howie, A., and Whelan, M. J.: Anomalous electron absorption effects in metal foils 967
Haworth, C. W.: Measurement of the Debye–Waller temperature factor for silver and α-iron 1229
Heidenreich, R. D., with Burbank, R. D.: Microtwinning in epitaxial nickel–iron films 373
Hirsch, P. B., with Bailey, J. E.: The dislocation distribution, flow stress, and stored energy in cold-worked polycrystalline silver . 485
Hodgson, J. N.: Infra-red measurements of the optical constants of liquid silver 272
Hodgson, P. E., with Buck, B., and Maddison, R. N.: Optical model analysis of nuclear scattering 1181
Honeycomb, R. W. K., with Roberts, E.: Movement of point defects during fatigue of aluminium crystals 1147
Howie, A.: The electrical resistivity of stacking faults 251
Howie, A., with Hashimoto, H., and Whelan, M. J.: Anomalous electron absorption effects in metal foils 967
Hughes, D. G.: Nuclear magnetic resonance in lithium and dilute lithium–magnesium alloys 467
Hume-Rothery, W., and Anderson, E.: Eutectic compositions and liquid immiscibility in certain binary alloys 383

Johnson, A. A.: The embrittlement of molybdenum by neutron irradiation 413
Johnson, C. A.: The growth of prismatic dislocation loops during annealing 1255
Johnston, W. G.: An observation of crack formation in MgO . . 407
Jones, G. O., and Smith, B. L.: The refractive indices of liquid and solid argon 355

Kane, J. V., Pixley, R. E., and Wilkinson, D. H.: Isotopic spin selection rules. XIV: Transitions between mirror states in ^{13}C and ^{13}N . . 365
Kane, J. V., with Pixley, R. E., and Wilkinson, D. H.: Isotopic spin selection rules. XIII: The 6·92 Mev state of ^{16}O revisited . . 359
Karo, A. M., with Hardy, J. R.: Lattice vibrations of sodium chloride: Experimental and theoretical heat capacity data 859
Kauffman, J. W., with Meshii, M.: Recovery of quenched-in resistivity at high temperatures in gold 687
Kauffman, J. W., with Meshii, M.: The mechanism of quench-hardening and its recovery in gold 939

PAGE

Kelly, A., with Freise, E. J., and Fine, M. E.: The effect of electropolishing on the retention of vacancies during quenching in Al and Al alloys 101
Kelly, A., with Washburn, J., and Williamson, G. K.: Direct observation of dislocations in magnesium oxide 192
Kelly, A., with Washburn, J., Groves, G. W., and Williamson, G. K.: Electron microscope observations of deformed magnesium oxide . 991
Kemmey, P., with Clark, C. D., and Mitchell, E. W. J.: The infra-red absorption of hot semiconducting diamonds 127
Kendall, P. W., and Cusack, N. E.: Hall effect in liquid and solid mercury 100
Kronmüller, H., with Seeger, A., and Schiller, P.: Observation of interstitial atoms in f.c.c. metals 853

Le Claire, A. D., with Mortlock, A. J., and Rowe, A. H.: The atomic diffusion of platinum in gold 803
Lidiard, A. B.: The influence of solutes on self-diffusion in metals . 1171
Lovegrove, E., with Michell, D.: Investigation of the annealing of nickel deformed by compression by x-ray and stored energy measurements 499

MacDonald, D. K. C., Pearson, W. B., and Templeton, I. M.: Measurements of thermoelectricity below 1°K—IV 867
MacDonald, D. K. C., with Gold, A. V., Pearson, W. B., and Templeton, I. M.: The thermoelectric power of pure copper 765
Maddison, R. N., with Buck, B., and Hodgson, P. E.: Optical model analysis of nuclear scattering 1181
Makin, M. J., with Whapham, A. D.: The hardening of lithium fluoride by electron irradiation 237
Marsh, D. M.: Stress concentrations at crystal surfaces and the embrittlement of sodium chloride 1197
Martin, D. G.: The effect of lattice distortion around point defects on the scattering of long wavelength neutrons 1235
Mason, B. J., with Bryant, G. W.: Etch pits and dislocations in ice crystals 1221
Mason, P., with Cundy, D. C., Evans, W. H., Hadley, D. W., Newport, R. W., Smith, J. R., and Williams, P. R.: Systematic track distortion in a 10 in. diameter liquid hydrogen bubble chamber. . 154
Mayes, Valerie: A possible example of the muon radiative decay with internal conversion of the γ-ray 297
Mazey, D. J., with Barnes, R. S.: The nature of radiation-induced point defect clusters 1247
Meredith, J. E., with Sawkill, J.: The etching of sub-structures in beryllium 1195
Meshii, M., and Kauffman, J. W.: Recovery of quenched-in resistivity at high temperatures in gold 687
Meshii, M., and Kauffman, J. W.: The mechanism of quench-hardening and its recovery in gold 939
Michell, D., and Lovegrove, E.: Investigation of the annealing of nickel deformed by compression by x-ray and stored energy measurements 499
Mitchell, E. W. J., with Clark, C. D., and Kemmey, P.: The infra-red absorption of hot semiconducting diamonds. 127
Mitchell, E. W. J., Rigden, J. D., and Townsend, P. D.: The anisotropy of optical absorption induced in sapphire by neutron and electron irradiation 1013
Mitchell, J. W., with Bartlett, J. T.: The generation of dislocation loops at the surfaces of crystals of silver bromide. 445

PAGE

Mitchell, J. W., with Bartlett, J. T.: Dislocations with Burgers vectors of $a\langle 100\rangle$ in crystals of silver bromide 799
Morrison, J. A., with Beaumont, R. H., and Chihara, H.: An anomaly in the heat capacity of chromium at 38·5°c 188
Mortlock, A. J., Rowe, A. H., and Le Claire, A. D.: The atomic diffusion of platinum in gold 803
Myers, A.: Some elastic and thermal properties of zirconium and tungsten 927

Newman, R. C., with Bullough, R.: The spacing of prismatic dislocation loops 921
Newport, R. W., with Alston, Margaret H., Cundy, D. C., Evans, W. H., and Williams, P. R.: A 10 in. diameter liquid hydrogen bubble chamber 146
Newport, R. W., with Cundy, D. C., Evans, W. H., Hadley, D. W., Mason, P., Smith, J. R., and Williams, P. R.: Systematic track distortion in a 10 in. diameter liquid hydrogen bubble chamber . . . 154

O'Hara, S., with Gibbons, T. B.: The effect of internal oxidation on the damping capacity of copper–silicon alloys 140
Orbach, R.: On the scattering of phonons by spins at low temperatures: Theoretical 1303

Palma, M. U., with Ciccarello, I. S., and Palma-Vittorelli, M. B.: An electron spin resonance investigation of photographic processes in crystals of AgCl containing traces of CuCl 723
Palma-Vittorelli, M. B., with Ciccarello, I. S., and Palma, M. U.: An electron spin resonance investigation of photographic processes in crystals of AgCl containing traces of CuCl 723
Pearson, W. B., with Gold, A. V., MacDonald, D. K. C., and Templeton, I. M.: The thermoelectric power of pure copper 765
Pearson, W. B., with MacDonald, D. K. C., and Templeton, I. M.: Measurements of thermoelectricity below 1°K—IV 867
Penfold, J., with Childs, B. G., and Gardner, W. E.: The magnetic susceptibility of vanadium–chromium solid solutions . . . 1267
Petch, N. J., with Codd, I.: Dislocation-locking by carbon, nitrogen and boron in α-iron 30
Phillips, J. C.: Giant spin density fluctuations 1193
Phillips, V. A.: Direct observation of defects in evaporated silver . . 571
Piercy, G. R.: Point defects in platinum 201
Pixley, R. E., with Kane, J. V., and Wilkinson, D. H.: Isotopic spin selection rules. XIV: Transitions between mirror states in ^{13}C and ^{13}N 365
Pixley, R. E., Kane, J. V., and Wilkinson, D. H.: Isotopic spin selection rules. XIII: The 6·92 Mev state of ^{16}O revisited . . . 359
Porter, N. A., with Bradley, E. F.: Observations on extensive air showers. VIII: The distribution in declination and curvature of the shower front 305
Price, P. B.: On microcreep in zinc whiskers 417
Price, P. B.: On the growth of cadmium crystals from the vapour . 473
Price, P. B.: Pyramidal glide and the formation and climb of dislocation loops in nearly perfect zinc crystals 873
Priestley, M. G.: Magneto resistance of copper, silver and gold . 111, 304
Priestley, M. G., with Gold, A. V.: The Fermi surface in white tin . 1089

PAGE

Prutton, M.: Cross-tie walls in thin permalloy films . . . 625
Puttick, K. E.: The shear component of ductile fracture . . . 759

Quenby, J. J., and Thambyahpillai, T.: Atmospheric temperature effects on the solar daily variation of cosmic ray intensity . . . 585

Rajopadhye, V. Y.: Nuclear interactions of 5·7 BeV protons in photographic emulsions 537
Reynolds, W. N., and Goggin, P. R.: The annealing of electron irradiation damage in graphite 1049
Rigden, J. D., with Mitchell, E. W. J., and Townsend, P. D.: The anisotropy of optical absorption induced in sapphire by neutron and electron irradiation 1013
Roberts, E., and Honeycomb, R. W. K.: Movement of point defects during fatigue of aluminium crystals 1147
Rochester, G. K., with Fernando, P. C. B., Spalding, I. J., and Smith, K. F.: The hyperfine structure of ^{121}Sb and ^{123}Sb . . . 1291
Rochester, G. K., with Fernando, P. C. B., and Smith, K. F.: The spin of ^{124}Sb and the spin and moments of ^{122}Sb 1309
Rosenberg, H. M., and Sujak, B.: On the scattering of phonons by spins at low temperatures: Experimental 1299
Rowe, A. H., with Mortlock, A. J., and Le Claire, A. D.: The atomic diffusion of platinum in gold 803
Runcorn, S. K.: Statistical methods in rock magnetism . . . 523

Sambell, R. A. J., with Clarke, F. J. P.: Microcracks and their relation to flow and fracture in single crystals of magnesium oxide . . 697
Sawkill, J., and Meredith, J. E.: The etching of sub-structures in beryllium 1195
Scheibner, E. J., with Germer, L. H., and Hartman, C. D.: Study of adsorbed gas films by electron diffraction 222
Schiller, P., with Seeger, A., and Kronmüller, H.: Observation of interstitial atoms in f.c.c. metals 853
Schoeck, G., and Tiller, W. A.: On dislocation formation by vacancy condensation 43
Seal, M.: The fine structure of films of rubber and other polymers . 78
Seeger, A., Schiller, P., and Kronmüller, H.: Observation of interstitial atoms in f.c.c. metals 853
Sheard, F. W.: The thermal conductivity of impure InAs at high temperatures 887
Shoenberg, D.: The de Haas–van Alphen effect in copper, silver and gold 105
Silcox, J., and Whelan, M. J.: Direct observations of the annealing of prismatic dislocation loops and of climb of dislocations in quenched aluminium 1
Smith, J. R., with Cundy, D. C., Evans, W. H., Hadley, D. W., Mason, P., Newport, R. W., and Williams, P. R.: Systematic track distortion in a 10 in. diameter liquid hydrogen bubble chamber. . 154
Smith, B. L., with Figgins, B. F.: Density and expansivity of solid krypton 186
Smith, G. C., with Ashby, M. F.: Direct electron microscopy of internally oxidized dilute copper alloys 298
Smith, B. L., with Jones, G. O.: The refractive indices of liquid and solid argon 355
Smith, K. F., with Title, R. S.: The hyperfine structure of ^{209}Bi . . 1281

PAGE

Smith, K. F., with Fernando, P. C. B., Rochester, G. K., and Spalding, I. J.: The hyperfine structure of ^{121}Sb and ^{123}Sb 1291
Smith, K. F., with Fernando, P. C. B., and Rochester, G. K.: The spin of ^{124}Sb and the spin and moments of ^{122}Sb. 1309
Smith, S. D., and Hardy, J. R.: Activation of single phonon infra-red lattice absorption in neutron irradiated diamond 1311
Sondheimer, E. H., with Das, T. P.: Diamagnetic shielding of nuclei in metals 529
Spalding, I. J., with Fernando, P. C. B., Rochester, G. K., and Smith, K. F.: The hyperfine structure of ^{121}Sb and ^{123}Sb . . . 1291
Sprackling, M. T.: Reverse bending of crystals of silver chloride . . 441
Sproull, R. L.: Charged dislocations in lithium fluoride . . . 815
Stuckes, Audrey, A.: The thermal conductivity of germanium silicon and indium arsenide from 40°c to 425°c 84
Sujak, B., with Rosenberg, H. M.: On the scattering of phonons by spins at low temperatures: Experimental 1299

Templeton, I. M., with Gold A. V., MacDonald, D. K. C., and Pearson, W. B.: The thermoelectric power of pure copper. 765
Templeton, I. M., with MacDonald, D. K. C., and Pearson, W. B.: Measurements of thermoelectricity below 1°K—IV 867
Thambyahpillai, T., with Quenby, J. J.: Atmospheric temperature effects on the solar daily variation of cosmic ray intensity . . 585
Thomas, A. T.: Unloading effects in aluminium and aluminium–zinc single crystals 947
Thompson, M. W.: The damage and recovery of neutron irradiated tungsten 278
Tiller, W. A., with Schoeck, G.: On dislocation formation by vacancy condensation 43
Title, R. S., and Smith, K. F.: The hyperfine structure of ^{209}Bi . . 1281
Townsend, P. D., with Mitchell, E. W. J., and Rigden, J. D.: The anisotropy of optical absorption induced in sapphire by neutron and electron irradiation 1013

Vandervoort, R., and Washburn, J.: On the stability of the dislocation substructure in quenched aluminium 24
Varley, J. H. O.: An approximate correlation between the electron Fermi energy and work function of a metal. 64
Verboven, E.: On the residual resistance of binary alloys . . . 753

Waddington, C. J.: The relative abundances of the heavy nuclei in the primary cosmic radiation 311
Waddington, C. J.: The determination of the flux of cosmic ray protons with nuclear emulsions 1105
Washburn, J., Kelly, A., and Williamson, G. K.: Direct observation of dislocations in magnesium oxide 192
Washburn, J., Groves, G. W., Kelly, A., and Williamson, G. K.: Electron microscope observations of deformed magnesium oxide. . . 991
Washburn, J., with Vandervoort, R.: On the stability of the dislocation substructure in quenched aluminium 24
West, G. W.: Nuclear magnetic resonance in β brass 899
Westwood, A. R. C.: The effects of surface condition on the mechanical properties of lithium fluoride crystals 981
Whapham, A. D., and Makin, M. J.: The hardening of lithium fluoride by electron irradiation 237

PAGE

Whelan, M. J., with Hashimoto, H., and Howie, A.: Anomalous electron absorption effects in metal foils 967

Whelan, M. J., with Silcox, J.: Direct observations of the annealing of prismatic dislocation loops and of climb of dislocations in quenched aluminium 1

Whitworth, R. W.: Some effects of vibration on the internal friction of sodium chloride 425

Wilkinson, D. H., with Kane, J. V., and Pixley, R. E.: Isotopic spin selection rules. XIV: Transitions between mirror states in ^{13}C and ^{13}N 365

Wilkinson, D. H., with Pixley, R. E., and Kane, J. V.: Isotopic spin selection rules. XIII: The 6·92 Mev state of ^{16}O revisited . . 359

Williams, P. R., with Alston, Margaret H., Cundy, D. C., Evans, W. H., and Newport, R. W.: A 10 in. diameter liquid hydrogen bubble chamber 146

Williams, S. E., with Crisp, R. S.: The K emission spectrum of metallic lithium 525

Williams, S. E., with Crisp, R. S.: The soft x-ray spectra of lithium, magnesium and aluminium and their alloys. 1205

Williams, P. R., with Cundy, D. C., Evans, W. H., Hadley, D. W., Mason, P.. Newport, R. W., and Smith, J. R.: Systematic track distortion in a 10 in. diameter liquid hydrogen bubble chamber . 154

Williamson, G. K., with Washburn, J., Groves, G. W., and Kelly, A.: Electron microscope observations of deformed magnesium oxide . 991

Williamson, G. K., with Washburn, J., and Kelly, A.: Direct observation of dislocations in magnesium oxide 192

Wohlfarth, E. P.: The anhysteretic remanence of magnetic recording tapes 717

Yoffe, Elizabeth H.: The angular dislocation 161

Ziman, J. M.: A note on the selection rules for optical transitions in alloys 757

END OF THE FIFTH VOLUME

Printed by Taylor & Francis Ltd
Red Lion Court, Fleet Street, London, E.C.4